(昭和30年6月23日 第三種郵便物認可 J. Phys. Soc. Japan, Vol. 16, No. 7 昭和36年7月5日発行 毎月1回5日発行)

16 | Jl.-Dec. 1961

JOURNAL
OF THE
PHYSICAL SOCIETY
OF JAPAN

PT2

Volume 16 **Number 7**

July 1961

Published by the
PHYSICAL SOCIETY OF JAPAN

Journal of the Physical Society of Japan

Published monthly by the Physical Society of Japan and devoted to original papers in physics and related fields which materially contribute to the progress of physics

BOARD OF EDITORS (1960–1961)

M. Toda (Chief Editor), S. Asaka, M. Hatoyama, H. Horie, I. Imai, T. Inui, E. Ishiguro, K. Ishiguro, T. Kato, K. Kinosita, K. Kohra, H. Kumagai, G. Kuwabara, S. Miyahara, T. Nagamiya, Y. Nogami, S. Ogawa, T. Okada, S. Ono, K. Senda, T. Suzuki, H. Takeyama, H. Takahasi, Y. Tomono, S. Tomotika, R. Uyeda.

SUGGESTIONS TO OVERSEAS CONTRIBUTORS

Manuscript should be addressed to the Office of the Physical Society of Japan, Room No. 342, Physics Building, Faculty of Science, University of Tokyo, Bunkyo-ku, Tokyo.

Each manuscript should be prepared as concisely as possible. Its organization should conform to the following: title author's name, name and address of the author's institution, synopsis of about 100 words, body of the paper, list of references, tables and figures. The textual material should be typewritten, double-spaced on white bond paper of letter size. The original copy is required. Literature reference should be numbered consecutively. Figures and photographs will be printed in any of the following sizes (at the choice of the author): 3 cm, 6 cm, 12 cm in breadth, less than 18 cm in height. The original should be 2.5 to 3 times as large as the size in print. The drawing should be a very neatly prepared original with lettering, in Indian ink. Self-explanatory titles to figures and photographs are essential.

Short Note Section is provided for brief reports which need prompt publication. The manuscript of a Short Note should follow the same style and form as that required for a full paper with the exception that it needs no synopsis. The available space for a Short Note is one page of the Journal (about 800 words).

Galley proof only will be sent to the author. Proof should be carefully corrected and returned as soon as possible to the Office of the Society. For prompt publication, proof of the Short Note will sometimes be read by the Editor in place of the author.

Reprints may be ordered in lots of 50. The author or the author's institution is requested to pay charges according to the following formulae:

\$ $(2.00+0.10p^2+(3.00+0.01x')p+3A)$ for full paper, \$ $(4.50+0.01x')$ for Short Note. Here p stands for the number of printed pages of the paper, $x'=x-50$ where x is the number of copies required ($x \geqq 50$), and A stands for the number of sheets of art paper if any.

SUBSCRIPTION

Subscription orders as well as related inquiries should be addressed to the Office of the Society or to one of the following agents:

Maruzen Co. Ltd.: P. O. Box 605, Central, Tokyo
Nauka Ltd.: 2-chome, Jinbocho, Kanda, Tokyo
Charles E. Tuttle Co.: 15 Edogawa-cho, Bunkyo-ku, Tokyo
Charles E. Tuttle Co.: Rutland, Vermont, U.S.A.
Parkins Oriental Books: 5011, York Blvd., Los Angeles 42, Calif., U.S.A.

Subscription rate (for non-members, postage covered)

Annual..................\$ 15.00 Single issue ....\$ 1.50

Back numbers (postage covered)

	Yearly	Single copies, each
Vol. 1 (1946)	\$ 1.00	
Vol. 2 (1947) -6(1951)	\$ 5.00	\$ 1.00
Vol. 7 (1952) -9(1954)	\$ 6.00	\$ 1.20
Vol. 10 (1955)-12(1957)	\$ 8.00	\$ 1.00
Vol. 13 (1958)-15(1960)	\$12.00	\$ 1.20

—投稿規定は 1959 年発行の会員名簿に掲載してあります—

JOURNAL OF THE PHYSICAL SOCIETY OF JAPAN, Vol. 16, No. 7, JULY, 1961

Plane Polarization of 8.5 MeV Bremsstrahlung

By Katsufusa SHODA

Department of Physics, Tohoku University,
Sendai, Japan

(Received February 28, 1961)

The polarization of bremsstrahlung produced by 8.5 MeV electrons incident on thin Al, Ag, Au and U targets in a betatron was studied with D_2O-loaded nuclear emulsions. The Polarization was measured at the characteristic emission angle $\Theta = mc^2/E_0$ by observing the azimuthal angular distribution of photoprotons from deuterons.

The results show different energy dependence of polarization for different elements. For low Z targets the polarization is positive and large in the lower energy part of bremsstrahlung spectrum, in qualitative agreement with the theoretical calculations. For high Z targets the polarization is negative in the higher energy range and positive in the lower energy range. This reversal of the sign of polarization occurs at much lower energies than those expected from the theory.

§1. Introduction

Photons emitted in the bremsstrahlung process have been known to exhibit polarization.

The linear polarization of bremsstrahlung, P, is defined by

$$P = \frac{d\sigma_\perp - d\sigma_{/\!/}}{d\sigma_\perp + d\sigma_{/\!/}}$$

where $d\sigma_\perp$ and $d\sigma_{/\!/}$ are the differential cross sections for the production of bremsstrahlung photons polarized along the directions perpendicular and parallel respectively, to the emission plane given by the directions of the photon and the incident electron. These differential cross sections are functions of the electron energy E_0, the photon energy k, the angle θ between the photon and the incident electron and the atomic number Z of the target.

The polarization in non-relativistic bremsstrahlung was first studied theoretically by Sommerfeld$^{1)}$ and was later estimated numerically by Kirkpatrick and Wiedmann$^{2)}$. It has also been observed in a few experiments$^{3)}$. The observed results, however, are not always consistent with each other, although the most recent one of Kulenkampff et al.$^{3)}$ is in agreement with Sommerfeld's theory$^{1)}$.

The study of the relativistic case has been developed recently. A theoretical treatment for the relativistic case was first given by May and Wick$^{4)}$, using the method of virtual quanta$^{5)}$. Subsequently May$^{6)}$ investigated the polarization of bremsstrahlung due to electrons of $E_0 \gg 137Z^{-1/3}mc^2$ more carefully using the Born approximation for the electron wave functions and he summed over the directions of emergent electrons. According to his calculation the maximum polarization occurs at the characteristic angle, $\Theta = mc^2/E_0$, where m is the electron rest mass. His results are valid for complete screening and are applicable to $E_0 \gtrsim 16$ MeV for a target of very large Z. Olsen and Maximon$^{7)}$ treated the extreme relativistic case including both the Coulomb and screening corrections exactly. The final results, however, do not differ very much from May's ones. Gluckstern, Hull and Breit$^{8)}$ also calculated the differential cross sections by the Born approximation procedure. Gluckstern and Hull$^{9)}$ summed over the direction of the emergent electrons. The limit of validity of their Born approximation is the usual ones in the treatment of the bremsstrahlung process$^{10)}$. The low energy limits of validity are given by

$$(Ze^2/k) \ll 1\,, \quad \text{and} \quad (E_0 - mc^2)/mc^2 \gg (Z/137)^2\,.$$

Their calculations were carried out without screening corrections. They however estimated the effect of screening, and concluded that the results obtained without screening were approximately correct as long as $E_0 \ll 137Z^{-1/3}mc^2$ and $k \gtrsim mc^2$.

The effect of screening was treated more accurately by Fronsdal and Überall$^{11)}$ who used the Born approximation and an exponential atomic form factor to account for screening. Their results do not differ appreciably from Gluckstern and Hull's ones in the inter-

5/11 63/2 owen

mediate electron energy region.

The first experiment in relativistic energy range was performed by Phillips[12]. He used a betatron to produce 20 MeV bremsstrahlung from a 5 mil W target and detected the polarization by observing directions of photoprotons from deuterons. The results for photons from 6 to 15 MeV were in qualitative agreement with the theory. Tzara[13] also performed the experiment using 22 MeV bremsstrahlung from a 0.8 mil target and reported a very high polarization, i.e. $d\sigma_{\perp}/d\sigma_{\parallel}=3.5\pm0.5$. Muirhead and Mather[14] examined 11.5 MeV bremsstrahlung from a 5 mil Pt target. Their results did not show so large polarizations as the theory predicted. Dudley, Inman and Kenney[15] examined the polarization of 24 MeV bremsstrahlung from a 1 mil Al target using a linear accelerator. They obtained the following values of polarization for photons from 4 to 8 MeV; 24.2±18.1%, 33±15% and 12.3±10.2% at $\theta=\Theta$, 1.6Θ and 2.5Θ respectively.

Jamnik and Axel[16] examined the polarization of 15.1 MeV gamma rays from 25 MeV bremsstrahlung produced with the aid of a special betatron doughnut. They observed at $\theta=\Theta$ asymmetric azimuthal angular distributions of elastically scattered gamma rays from the 15.1 MeV level of C^{12} which had been interpreted as $M1$ transition. For an Al target the observed polarization was $d\sigma_{\perp}/d\sigma_{\parallel}=1.53\pm0.05$ and was in good agreement with the theoretical prediction. For a Pt target, $d\sigma_{\perp}/d\sigma_{\parallel}=1.28\pm0.04$, which was about 10% lower than the theoretical calculation neglecting screening. But according to them the screening and Coulomb corrections are expected to bring the theory into agreement with the experiment.

For 1.0 MeV bremsstrahlung from very thin targets (0.43 mg/cm² Au foil and 1.0 mg/cm² Al foil), Motz[17] observed photon energy dependence of polarization using Compton effect as a polarimeter and found such reversal of the sign of polarization as was predicted theoretically by Gluckstern-Hull[9]. The observed polarization, however, was slightly smaller than that of the theory. For Al the discrepancy is small, but for Au it is large and the energy dependence of polarization is similar to that for lower energy electrons. Motz and Placious[18] also examined the angular dependence of the polarization for 0.5 MeV bremsstrahlung near the high frequency limit and confirmed Gluckstern-Hull's equation[9]. They extended these experiments for several electron energies from 0.05 to 1.0 MeV[19], using thin Be, Al, and Au targets. The agreement with Gluckstern-Hull's estimation is fairly good.

The present author[20] examined the polarization of 8.5 MeV bremsstrahlung from a 80 μ Pt target in a synchrotron. The polarization was found to be negative and larger for higher energy gamma rays. The energy at which the polarization was estimated to be zero was 4.7±2 MeV.

It has been well established from these studies that bremsstrahlung produced by about 20 MeV electrons and also electrons of lower energy than 1 MeV is linearly polarized, and that the observed polarization is qualitatively in good agreement with the theory. But some difference in the energy dependences of polarization observed with Al and Au targets at 1 MeV suggests that the atomic number dependence of polarization may be somewhat different from the existing theory for low energy bremsstrahlung.

In the present work, the photon energy dependences of polarization for 8.5 MeV bremsstrahlung produced in thin Al, Ag, Au and U targets have been studied at the characteristic angle using D_2O-loaded plates. Since the effects of multiple scattering of electrons in targets might be serious, the experiments were performed with care at this point. Multiple scattering and other effects which affect the polarization seriously were monitored by observing the bremsstrahlung angular distribution which was sensitive to such effects. Finally the energy at which the reversal of the sign of polarization occurs, one of the important parameters in the polarization of bremsstrahlung, has been discussed.

§ 2. Experimental Procedure

a) *Preliminary experiments*

The polarization is known to be strongly dependent on the photon emission angle. Therefore it is important to keep both the oscillation amplitude and the cross section of incident electron beam small and also to reduce recirculation of the beam and multiple scattering in the target.

The experimental arrangement is shown in Fig. 1. To intercept electrons scattered in the target a beam stopper (Pt 1.5 mm thick) was placed near the gun which was 15 mm apart from the stable orbit. The target position was so decided as to give a high intensity yield of bremsstrahlung. Jamnik and Axel[16] investigated the relation between the multiple scattering in the target and the position of the beam stopper. No such investigation was performed in the present experiment. Thus the position in our case may not be the best to prevent multiple scattering, but this position was necessary to have a resonable intensity. Examples of the dependence of beam intensities on the target position and the expander current are demonstrated in Fig. 2 and Fig. 3 for 25 MeV excitation, because at this energy the intensity is the strongest. The bremsstrahlung intensity from the beam stopper increases suddenly at a certain value of the expander current, suggesting that circulating electrons become strongly divergent in the orbit expansion. The expander current was chosen as small as allowable in the present experiment.

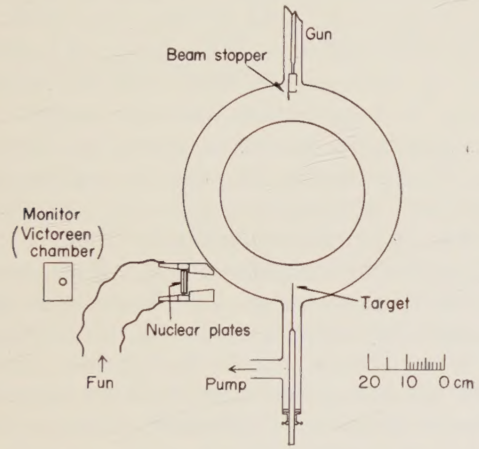

Fig. 1. Experimental arrangement.

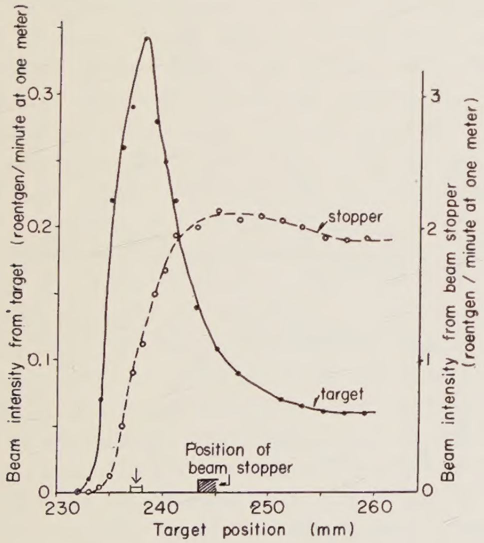

Fig. 2. Dependence of the beam intensity on target position.
Electron energy: 25 MeV. Radius of the betatron orbit: 232 mm. Position of the beam stopper: $r=243$ mm. Target: 1 mm×2 mm Al 10 μ thick. Full line: bremsstrahlung intensity from the target. Broaken line: bremsstrahlung intensity from the beam stopper. The arrow shows the final target position.

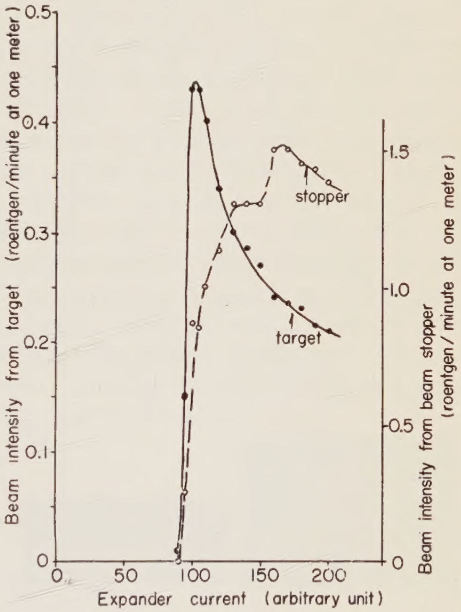

Fig. 3. Dependence of the beam intensity on expander current.
Electron energy: 25 MeV. Radius of the betatron orbit: 232 mm. Position of the target: $r=238$ mm. Position of the beam stopper: $r=245$ mm. Target: 1 mm×2 mm Al 10 μ thick. Full line: bremsstrahlung intensity from the target. Broaken line: bremsstrahlung intensity from the beam stopper.

The cross section and the oscillation amplitude of the electron beam were measured by autoradiography of induced activity on a 20 μ copper target at 25 MeV. The horizontal component of the amplitude of electron oscillation and the dimension of the beam cross section were estimated from the width and the length of strongly active area along the target edge in Fig. 4 (a) and the amplitude of oscillation was found to be smaller than 0.3 mm and the dimension of beam cross section was about 4 mm in diameter at 25 MeV. The result of another experiment using the target of different shape has shown that the horizontal and vertical components of the amplitude of electron oscillation are nearly equal. No such experiment was performed at 8.5 MeV. However the amplitude of electron oscillation at 8.5 MeV would not be expected to be very different from those at 25 MeV, because the amplitude of electron oscillation is in inverse proportion to the square root of electron momentum which is about twice as large in 8.5 MeV as in 25 MeV of electron energy. The amplitude of electron oscillation causing ambiguity of the order of $\Theta/10$ in the beam direction is estimated to be about 1.5 mm at 8.5 MeV. The beam oscillation therefore would not affect the present experimental results very much. However, to keep the ambiguity in the beam direction below the order of $\Theta/10$ the cross section of the beam must be smaller than 3 mm in diameter. Hence we have used a target of about 1.5 mm × 1 mm. Figs. 4 (b) and (c) are the autoradiograph and its photometry curve taken with the induced activity in a thin target which has the same thickness (3 μ) and dimension and was held in the same conditions as in the polarization experiments. The region of activity is somewhat broader than that of Cu target, which shows some undesirable effect such as multi-revolution of scattered electrons (one type of multiple scattering).

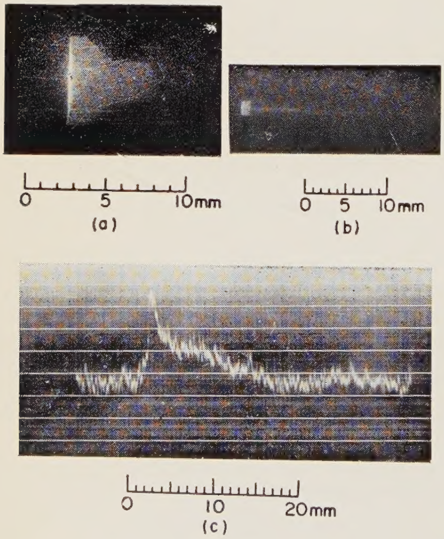

Fig. 4. Autoradiographs of induced activity on a 20 μ Cu target placed at $r=235$ mm (a), and on a 3 μ Ag target kept in the same conditions as in the polarization experiments (b), and its photometry curve (c).

To reduce multiple scattering of electrons in the targets supposed to have the largest effect on the observation of polarization, very thin targets were used as shown in Table I. They were supported by supporters of 0.3 mm wide cut out from the same foils as targets except U target which was supported by an Al supporter of 10 μ thick and 0.3 mm wide. The doughnut was supported in such a way that the vibration of target did not occur even at the maximum excitation.

The effect of multiple scattering was estimated by examining the bremsstrahlung angular distributions with Fuji Type 80 X-ray films calibrated for the dose-density curve. Since the subtraction of background radiation from the doughnut is not easily done exactly, certain systematic errors may be included in

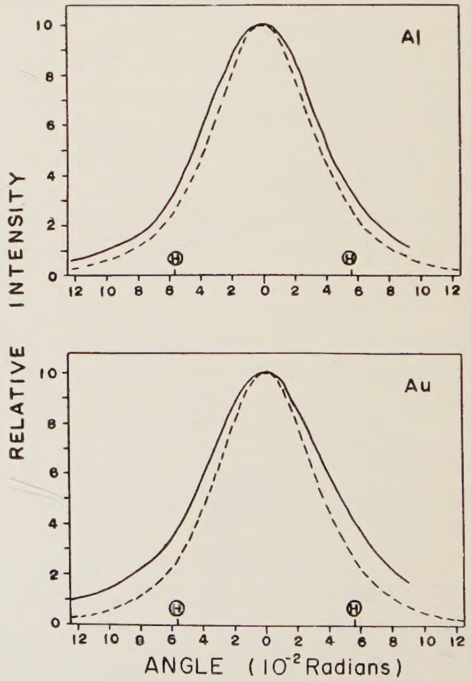

Fig. 5. Examples of bremsstrahlung angular distributions in the same arrangement as in the observation of polarization.
Full lines: experimental results.
Broaken lines: theoretical curves.

the results of angular distributions. Fig. 5 shows the examples of experimental results on the angular distribution of 8.5 MeV bremsstrahlung in the polarization experiment. Theoretical curves in the figure were calculated by the simple formula

$$F(\theta)=1/[1+(E_0\theta/mc^2)^2]^2 ,$$

which has been known to be in good agreement with the experiments on very thin targets[21]. It may be concluded that the deviations of experimental curves from theoretical ones are not so large, if the experimental error is taken into account.

b) *Measurement of polarization*

The polarization of bremsstrahlung was examined with Ilford C2, 200 μ nuclear plates soaked to be saturated with D_2O. The plates were mounted on a thin watertight bakelite holder containing excess D_2O and exposed to the beam at 28 cm from the target in a lead chamber which shielded them from gamma rays coming from the doughnut and other parts of the betatron. In front of the chamber a lead-stacked collimator having a conical aperture was placed to limit the exposed area to 5 cm in diameter. A lead plate of 1 mm thick was interposed to reduce the fogging of nuclear plates due to attenuating soft gamma rays. The plate holder was cooled by air blowing. With this precaution the fading of the tracks was not serious. The plates were developed by an amidol developer, pH. of which was adjusted to be 5.2 with HCl in order to minimize fogging.

Scanning was performed along a circular ring of 1.6 cm in mean radius and 2 mm in width, which corresponded $\theta=\Theta(1\pm1/16)$. The center of the bremsstrahlung beam was determined by photometry of the plates and also by the X-ray film examination of 25 MeV bremsstrahlung which produced a smaller spot than 8.5 MeV beam. The error in the determination of center was estimated to be nearly equal to or smaller than 2 mm. Tiyoda binoculare microscopes were used for the scanning at a multiplication of 60×1.5×10.

The length of proton tracks was determined by measuring the projected length of the tracks on the plane of the emulsion and the depth of the tracks corrected for the schrinkage factors which were determined by measuring the thickness of emulsion after soaking with a micrometer. For the range-energy relations of D_2O soaked emulsion, the table calculated by Krohn and Schrader[22] was used. The emission angle ϕ of proton tracks was determined by calculating the angle between the projected direction of the tracks in the

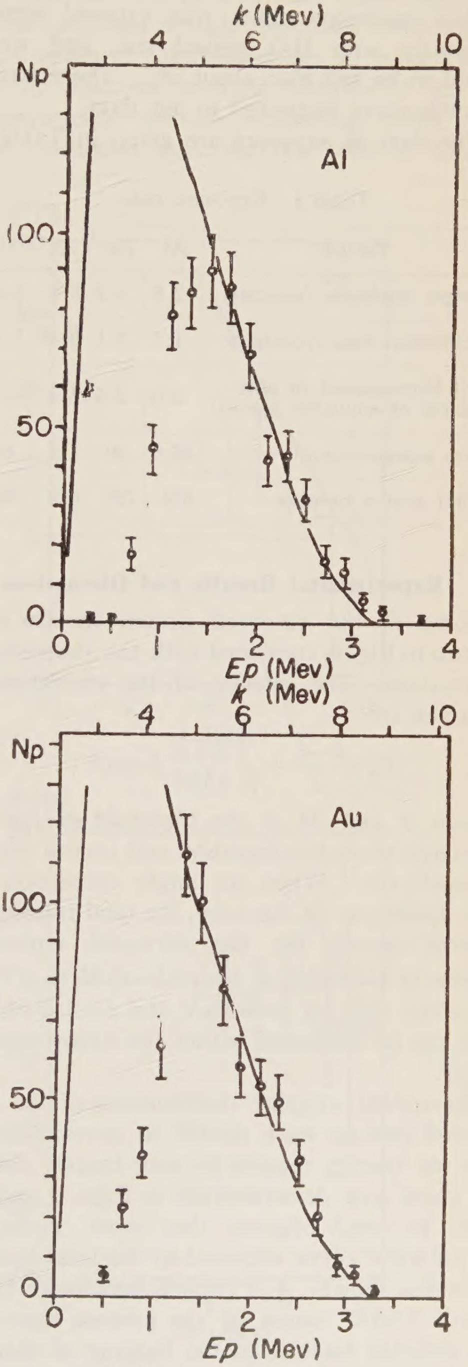

Fig. 6. Examples of photoproton spectra obtained with polarized bremsstrahlung.

plane of emulsion and the radial direction of scanning point. Only the tracks running within the glancing angle of ±45° from emulsion plane were observed. The yields of photoprotons from the elements in the emulsion except deuteron and neutron recoil protons were determined by examining H_2O soaked emulsions which was exposed simultaneously with D_2O soaked one, and were found to be less than about 5%. These backgrounds were neglected in our data.

The data of exposure are given in Table I.

Table I. Exposure data.

Target	Al	Ag	Au	U
Target thickness (mg/cm²)	2.5	3.2	5.6	8.5
Irradiation dose (roentgen)	1.7	1.1	0.46	1.74
D_2O impregnated in unit volume of emulsion (g/cm³)	2.0	2.6	2.3	2.0
Area scanned (mm²)	85.6	90	113	69
Total proton number	624	726	644	962

§ 3. Experimental Results and Discussions

Some of the observed proton spectra are shown in Fig. 6, combined with the theoretical estimation. The energy of the photoproton is given by

$$E_p=\frac{k-\mathcal{E}}{2}+\sqrt{\frac{k-\mathcal{E}}{4Mc^2}}\,k\cos\theta$$

where $\mathcal{E}$ and M is the threshold energy of deuteron photodisintegration and proton mass, respectively. When an angle correction is not applied as in our case, the total fractional energy spread for the surveyed emission angles of 45°～135° is $\frac{1}{2}(k/\sqrt{(k-\mathcal{E})Mc^2})$. This is about 7% for $k=5$ MeV and $\mathcal{E}=2.23$ MeV, and can be neglected within the experimental error.

Azimuthal angular distributions of the observed protons were plotted in several gamma ray energy regions for each target. Some of them are demonstrated in Figs. 7 and 8, and in each figure the most probable $A+B\sin^2\theta$ curve obtained by the least square fit is also shown. For gamma rays lower than about 5 MeV, some of the protons may not be detected because of the fogging of plates, but this does not seriously affect the results of angular distributions.

Photodisintegration of deuteron is known to be induced by strong $E1$ and weak $M1$ transitions except near the threshold. The ratio

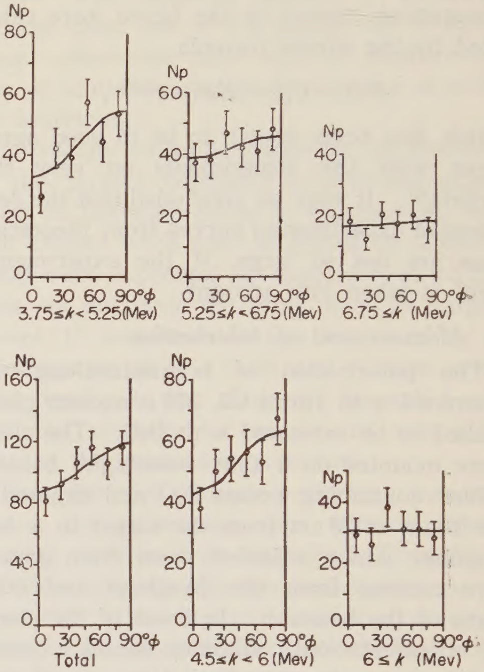

Fig. 7. Azimuthal angular distributions of photoprotons obtained with polarized bremsstrahlung from an Al target.

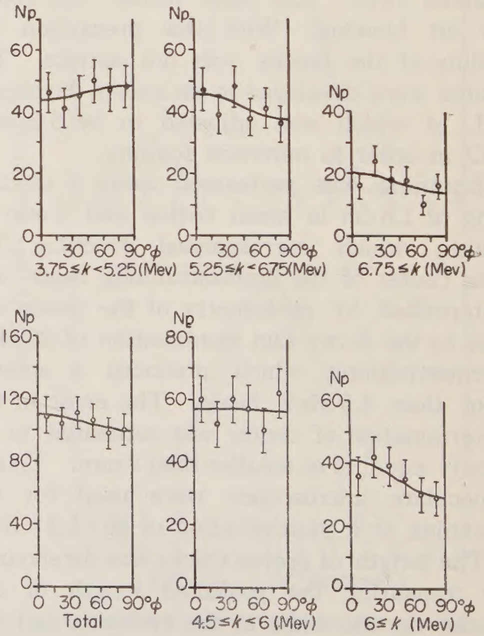

Fig. 8. Azimuthal angular distributions of photoprotons obtained with polarized bremsstrahlung from an Au target.

of $M1$ transition to $E1$ is about 5% for 6 MeV gamma rays and can be neglected in the higher energies. In $E1$ transition, protons are mainly emitted in the direction of the electric vector of gamma rays, and in $M1$ transition in the direction of the magnetic vector. The polarization degrees of bremsstrahlung therefore are immediately determined from the curves given in azimuthal angular distributions.

Fig. 9 shows the energy dependence of polarization thus evaluated. The $M1$ transition was neglected in the calculation. This neglect will not change the results beyond the present experimental error. Errors given in the figure are only statistical ones. Theoretical curves obtained by Gluckstern-Hull's equations[9] with approximate screening corrections are also given in the same figure.

As has been already described above, absolute values of polarization are strongly affected by electron multiple scattering. In our experiments multiple scattering effect was not examined quantitatively and no correc-

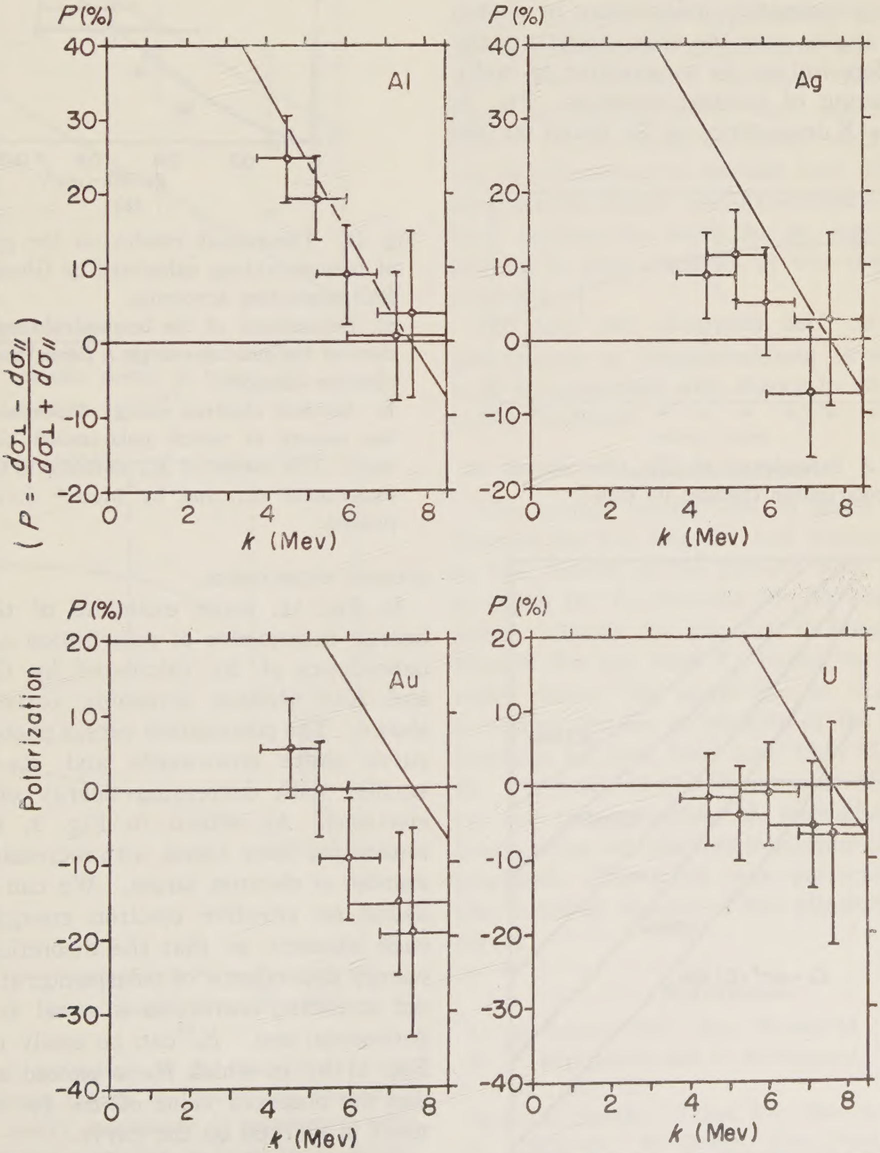

Fig. 9. Dependence of the bremsstrahlung polarization on photon energy for an electron kinetic energy of 8.5 MeV and for a characteristic photon emission angle. The solid lines are theoretical curves calcnlated by Gluckstern and Hull with approximate corrections for screening.

tions were applied for it. The experimental data therefore will deviate in the absolute values of polarization, but the qualitative aspects of energy dependence of polarization will not be changed seriously by the effect of multiple scattering. The energy dependence of polarization deviates fairly strongly from theoretical curves. The deviation is larger for higher Z targets and the data on Au is in agreement with that of earlier data on Pt[20].

According to Gluckstern and Hull[9], the energies E_R at which polarization changes its sign are approximately independent of photon emission angles near the characteristic angle. E_R therefore will not be so sensitive to multiple scattering of incident electrons. Fig. 10 shows the Z dependence of E_R found in the present experiment.

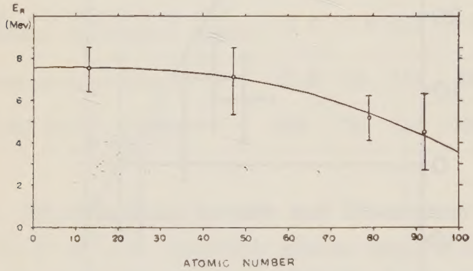

Fig. 10. Z dependence of E_R, the energy at which polarization changes its sign.

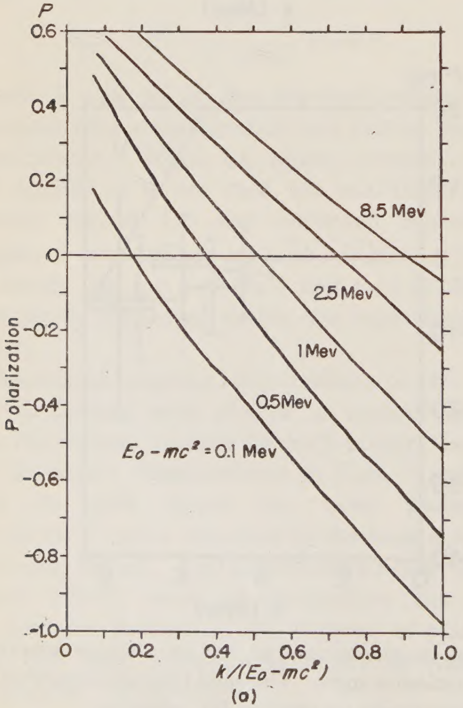

(a)

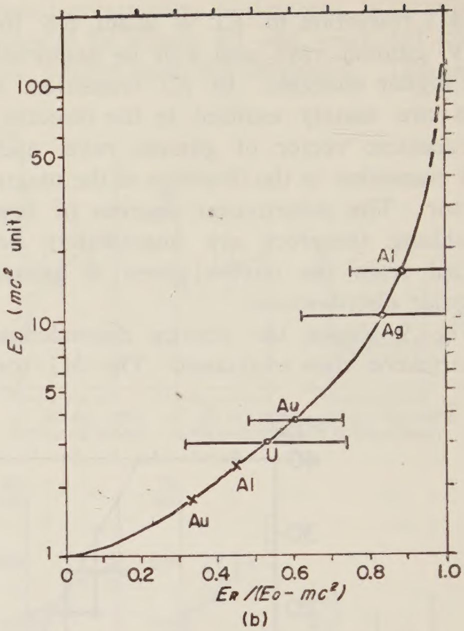

(b)

Fig. 11. Theoretical results on the polarization of bremsstrahlung calculated by Gluckstern and Hull neglecting screening.

a) Dependence of the bremsstrahlung polarization on the photon energy k for several incident electron energies.

b) Incident electron energy dependence of E_R, the energy at which polarization changes its sign. The values of E_R obtained in the present experiment (○) and by Motz[17] (×) are also plotted.

In Fig. 11, some examples of the photon energy dependence of polarization and the E_0 dependence of E_R calculated by Gluckstern and Hull without screening correction are shown. The polarization versus photon energy curve shifts downwards and E_R becomes smaller with decreasing energy of primary electrons. As shown in Fig. 9, the same tendencies were found with increasing atomic number of electron target. We can therefore define an effective electron energy E_0' for each element so that the theoretical photon energy dependence of polarization at E_0' without screening correction is equal to the experimental one. E_0' can be easily read from Fig. 11 (b), in which E_R is plotted against E_0 and the observed value of E_R for each element is marked on the curve.

In Fig. 12 the Z dependence of E_0' thus determined is shown in two types of plotting. The lines were drawn in the figure so as to fit the experimental values assuming that E_0' approached 8.5 MeV with decreasing Z. Motz's data[17)] for 1 MeV electrons are also plotted by the same method. In Fig. 12 (a) both Motz's and the present data can be expressed by a common empirical formula $E_0'-mc^2 \propto \exp(-0.023Z)$. According to Fig. 12 (b) Motz's data seem to correspond to the lower Z region than 47 in the present data. For larger Z than 47, our curve can be crudely expressed by a formula $E_0'-mc^2 \propto Z^{-2}$, although there may be no definite theoretical meanings in these empirical relations.

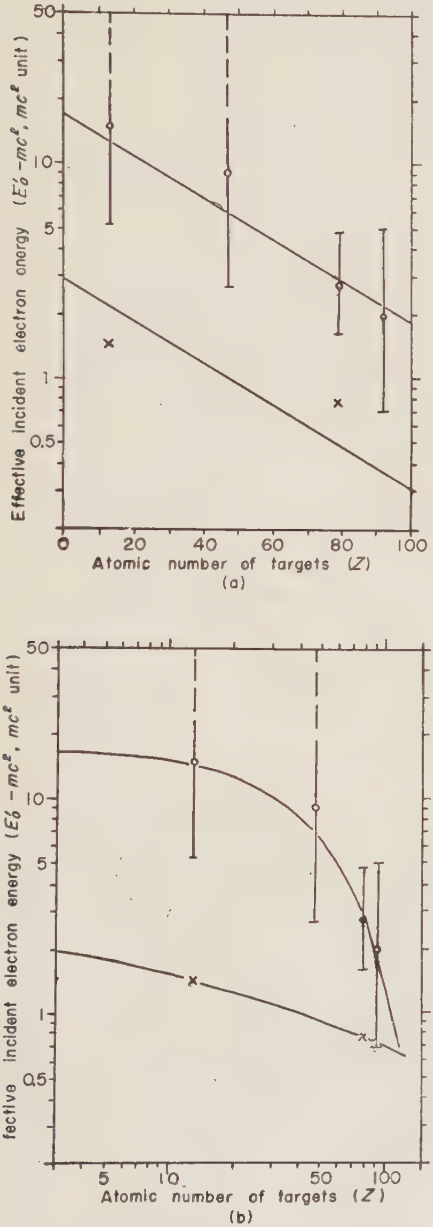

Fig. 12. Z dependence of E_0', the effective incident electron energy for which the theoretical photon energy dependence of polarization without screening correction is equal to the experimental one. ○: The present writer's; ×: Motz's.

Sommerfeld[1)], Kirkpatrick and Wiedmann[2)] showed that in the non-relativistic case the polarization is constant for equal values of V/Z^2, where V is an electron voltage. If one assumes $E_0'-mc^2 \propto V/Z^2$, this is just the relation found in the present experiment for large Z targets as far as Z dependence is concerned. This coincidence may be accidental, because our experiments are not in the non-relativistic region and we can not apply non-relativistic formula. However the same tendencies were also suggested by Motz[17)] in his study on 1 MeV electrons. It will be interesting to disclose such differences between the theory and experiment, but further discussions seem to be inappropriate because of poor statistics in the present experiment.

For thin low Z-targets such as Al, the polarization of bremsstrahlung is considered to be in agreement with theory in all electron energy regions.

Acknowledgement

The author would like to thank Prof. M. Kimura for his interest and encouragement in the course of the present work, and also to thank Dr. K. Okamoto for his kind discussions. Thanks are also due to Miss N. Endo, Miss N. Ito and Miss R. Onuma for scanning many plates. He would like to thank Prof. S. Ogawa and his co-workers of the Research Institute for Iron Steel and Other Metals, and Dr. Y. Amako of the Department of Chemistry, for the operation of microphotometers. Cooperation of the betatron crew is also appreciated. The work was performed under the financial support of the Ministry of Education.

References

1) A. Sommerfeld: Ann. Physik **11** (1931) 257.
2) P. Kirkpatrick and L. Wiedmann: Phys. Rev. **67** (1945) 321.
3) C. G. Barkla: Trans. Roy. Soc. (London) **204** (1905) 467. W. Duane: Proc. Natl. Acad. Sci. **15** (1929) 805. H. Kulenkampff: Physik. Z. **30** (1929) 513. B. Dasannacharya: Phys. Rev.

35 (1930) 129; also **36** (1930) 1675. P. Kirkpatrick, Phys. Rev. **38** (1931) 1938. D. S. Piston: Phys. Rev. **49** (1936) 275. Kulenkampff, Leisegang and Scheer: Z. Physik **137** (1954) 435.

4) G. C. Wick: Phys. Rev. **81** (1951) 467. M. M. May and G. C. Wick: Phys. Rev. **81** (1951) 628.

5) C. F. von Weizsäcker: Z. Physik **88** (1934) 612. E. J. Williams: Kgl. Danske Widenskab. Selskab, Mat.-fys. Medd. **13** (1935) No. 4.

6) M. M. May: Phys. Rev. **84** (1951) 265.

7) H. Olsen and L. C. Maximon: Phys. Rev. **114** (1959) 887.

8) R. L. Gluckstern, M. H. Hull, Jr. and G. Breit: Science **114** (1951) 480. R. L. Gluckstern, M. H. Hull, Jr. and G. Breit: Phys. Rev. **90** (1953) 1026.

9) R. L. Gluckstern and M. H. Hull, Jr.: Phys. Rev. **90** (1953) 1030.

10) W. Heitler: *The Quantum Theory of Radiation* (Oxford University Press, London, 1954), third edition, p. 242. H. A. Bethe and W. Heitler: Proc. Roy. Soc. (London) **A**, **146** (1934) 83.

11) C. Fronsdal and H. Überall: Phys. Rev. **111** (1958) 580.

12) K. Phillips: Phil. Mag. **44** (1953) 169.

13) C. Tzara: Compt. rend. **239** (1954) 44.

14) E. G. Muirhead and K. B. Mather: Australian J. Phys. **7** (1954) 527.

15) J. M. Dudley, F. W. Inman and R. W. Kenney: Phys. Rev. **102** (1956) 925. *Conference on Photonuclear Reactions, N. B. S.* April 30, 1958.

16) D. Jamnik and P. Axel: Phys. Rev. **117** (1960) 194.

17) J. W. Motz: Phys. Rev. **104** (1956) 557.

18) J. W. Motz and R. C. Placious: Phys. Rev. **112** (1958) 1039.

19) J. W. Motz and R. C. Placious: Nuovo Cim. **15** (1960) 571.

20) K. Shoda: unpublished data (1958).

21) L. H. Lanzl and A. O. Hanson: Phys. Rev. **83** (1951) 959.

22) V. E. Krohn, Jr. and E. F. Shrader: Phys. Rev. **86** (1952) 391.

JOURNAL OF THE PHYSICAL SOCIETY OF JAPAN, Vol. 16, No. 7, JULY, 1961

Decay of Rh^{102} and Levels in Ru^{102}

By Kazuo HISATAKE

Tokyo Institute of Technology, Meguro-ku, Tokyo

(Received March 3, 1961)

The decay of Rh^{102} has been investigated using scintillation spectrometers and a magnetic beta-ray spectrometer. The negatron spectrum have the end-point energy of 1.15 Mev and the positron spectrum consists of two groups of end-point energies of 1.30 Mev and 0.82 Mev. All of beta-spectra involved appear to have approximately "the allowed shape of the Fermi plot". 12 gamma transitions were assigned to Ru^{102} from the internal conversion spectrum and the single and coincidence gamma-ray spectra. Gamma-gamma angular correlations have also been measured. The results are consistent with the following level scheme for Ru^{102}: 0.476(2+), 1.106(2+), 1.53(3+), 1.85(?), 1.87(1+, 2+, or 3+), 2.06(?), and 2.23(3−) Mev. The transition between the first and second 2+ state was found to consist primary of E2 transition. The branching ratio obtained for the cascade to crossover transition from the second 2+ level is (4.2±0.8).

§1. Introduction

Energy Levels of even-even nuclei of medium weight are very interesting for the study of nuclear structure. Nuclear spectra in the region far from closed shells have well been explained by the collective nuclear model of Bohr and Mottelson1),2). On the other hand, nuclear spectra of even-even nuclei near closed shells have been less described by the present nuclear models. Scharff-Goldhaber and Weneser[3] pointed out some regularities of the first and second excited states of even-even nuclei in this region and succeeded in explaining some of the character of these nuclei by the use of the Bohr-Mottelson collective theory. Since then, several nuclear models for the even-even nuclei in this region (so-called the vibrational region) have been presented and succeeded in explaining only some of characters of the nuclear spectra. The present status between theory and experiment for even-even nuclei in the vibrational region have been summarized by Horie[4] and Stelson[5].

In the present paper the energy levels of Ru^{102}, which is just in the vibrational region, have been studied observing beta-rays and gamma-rays from the decay of Rh^{102}. Rh^{102} was first discovered by O. Minakawa[6] in 1941, by bombarding Rh^{103} with fast neutrons. He observed that Rh^{102} had both positrons and negatrons using a G-M counter with magnetic field. The half-life of Rh^{102} was determined to be 210±6 days. Since then, several people[7-16] including the author have studied the decay of Rh^{102}. The tentative decay scheme of Rh^{102} was given by the author and Kurbatov[16]. In the mean time Coulomb excitation has been giving valuable informations on the low-lying states of the even-even nuclei including Ru^{102} [17,18]. In this situation it is felt that the extensive study of energy levels of Ru^{102} is necessary.

There was a good opportunity to bombard Ru for many hours by protons of the 63″ cycltron at the Institute for Nuclear Study, University of Tokyo, and to get relatively strong Rh^{102} activity. The development of chemistry for the separation of Rh from Ru made possible to have a good beta source. In this paper the extensive study of the decay of Rh^{102} is reported.* After all the experimental work was done, McGowan and Stelson[19] reported their preliminary work on the decay of Rh^{102}. Their result is in fairly good agreement with the present work.

§ 2. Source Preparation

The Rh^{102} used in the present work was prepared by a (p, n) reaction on natural ruthenium and 97% enriched ruthenium 102 powder. The energy of protons was about 13 Mev. Total bombarded protons were 800 μA hours for natural Ru and 2000 μA hours for enriched Ru^{102}. About three months after each bombardment radioactive rhodium was chemically separated. The procedure of the chemical separation is as follows**: After 10 mg of iron as ferric chloride was added as the collector, bombarded ruthenium target was fused with potassium hydroxide and potassium nitrate at about 500°C for 30 min. in a gold crucible. The residue was collected with centrifugation and fused with potassium pylosulfate. Rhodium was coprecipitated with ferric hydroxide. The precipitate was dissolved in hydrochloric acid, and ferric chloride was removed with ether extraction.

The half-life of the bombarded material was followed by a G. M. counter for two years and was found to be (206±3) days. Thus almost all of the bombarded material was found to be Rh^{102}.

§ 3. Total Beta-Spectra

a) *The beta-source and the beta-ray spectrometer*

The beta-source was mounted on 1 mg/cm^2 mylar film by a drop method. The estimated source thickness was about 1 mg/cm^2. The beta spectrometer used was INS III magnetic spectrometer, which is a sector type double focusing beta spectrometer of $\rho=18$ cm. Analyzed beta-particles were detected with a G.M. counter, the window of which was approximately 1.5 mg/cm^2. The beta spectrometer was operated with momentum resolution 0.9% and was calibrated with the conversion lines of I^{131}, Hg^{203}, Cs^{137} and Co^{60}. The reproducibility of the calibration was within 0.5%. (The deviation was caused by the hysteresis of iron material of the spectrometer) The overall performance of the spectrometer was tested with P^{32} and Rb^{86}. The beta spectrum of P^{32} mounted on 1 mg/cm^2 mylar film showed a straight line down to 300 kev, and the beta spectrum of Rb^{86} exhibited " the unique first forbidden type ", as was expected.

b) *The positron spectrum*

Fig. 1 shows the Kurie plot of the positron spectrum of Rh^{102}. It can be seen that the spectrum is complex. The upper energy group (called β_2^+) slightly shows a deviation from the allowed shape but cannot be assigned to be the unique first forbidden type; the experimental shape factor of this positron group is shown in Fig. 2 together with the theoretical shape factor of the unique first forbidden type (a_1). It is concluded from Fig. 2 that the positron spectrum of Rh^{102} cannot be the unique first forbidden type but nearly the allowed shape. The Kurie plot of the second positron group (called β_1^+) approximately shows a straight line as low as 300 kev. The deviation from a straight line below 300 kev is believed to be due to scattering of beta particles mainly in the source and its backing.

---

* Preliminary reports of this present work were given by the author in the 1959 Spring Meeting and in the 1960 Spring Meeting of the Physical Society of Japan.

** The chemical procedure will be described in detail elsewhere by H. Shimojima.

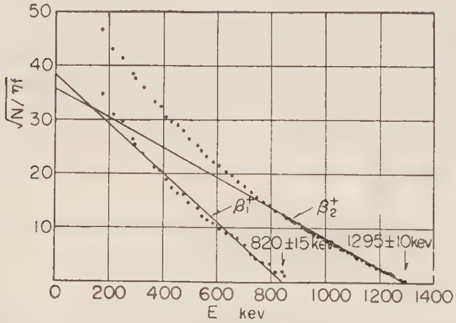

Fig. 1. The Kurie plot of the spectrum of Rh^{102}. The spectrum was taken 110 days after activation.

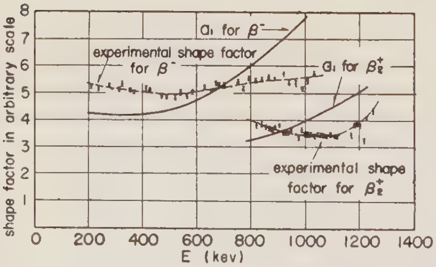

Fig. 2. Experimental shape factors of the positron and negatron spectra. The theoretical shape factors of the unique first borbidden type, a_1, are also shown in the figure by solid curves.

c) *The negatron spectrum*

The Kurie plot of the negatron spectrum of Rh^{102} is shown in Fig. 3. The points of of internal conversion peaks are omitted in the Kurie plot analysis. The Kurie plot of the negatron spectrum approximately shows a straight line down to 250 kev although a slight deviation appears between 600 and 400 kev. The shape factor of the negatron spectrum is shown in Fig. 2. From Fig. 2 it can be seen that the shape factor of negatrons is different from that of the unique first forbidden type (a_1) but nearly that of the allowed type although the shape factors of positrons and negatrons are are a little different. The end-point energies and relative intensities of the two positron groups and the negatron group (callen β^-) are tabulated in Table I. The results are almost in agreement with the previous results[9,10,13] although the 400 kev positron group reported by Marquez[13] was not observed.

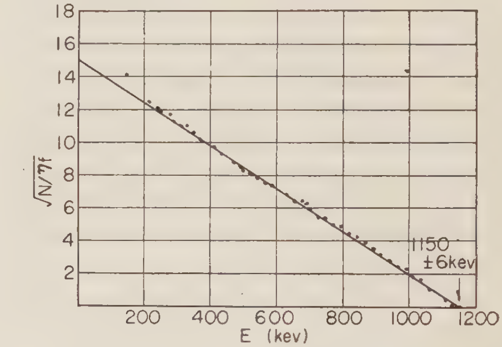

Fig. 3. The Kurie plot of the negatoron spectrum of Rh^{102}, leaving out the conversion electrons. The spectrum was taken 115 days after activation.

Table I. The end-point energy and intensity of each positron and negatron group of Rh^{102}.

Group	End-point energy (kev)	Intensity ($\beta^-=100$)
β_1^+	820±15	21.2±0.5
β_2+	1295±10	54.6+1.0
β^-	1150± 6	100 ±1.5

d) *The internal conversion spectrum*

The internal conversion spectrum of Rh^{102} was studied from 40 kev to 1150 kev carefully. The spectrum is shown Fig. 4. The energy values of the peaks are indicated by arrows in the figure. The three conversion groups below 310 kev and the 533 kev K peak with the 553 kev L peak are attributed to Rh^{101}, as was reported previously[14,17,20]. It is considered that Rh^{101} was produced by the Ru^{102} (p, $2n$) Rh^{101} reaction. The energies and relative intensities of the conversion peaks are

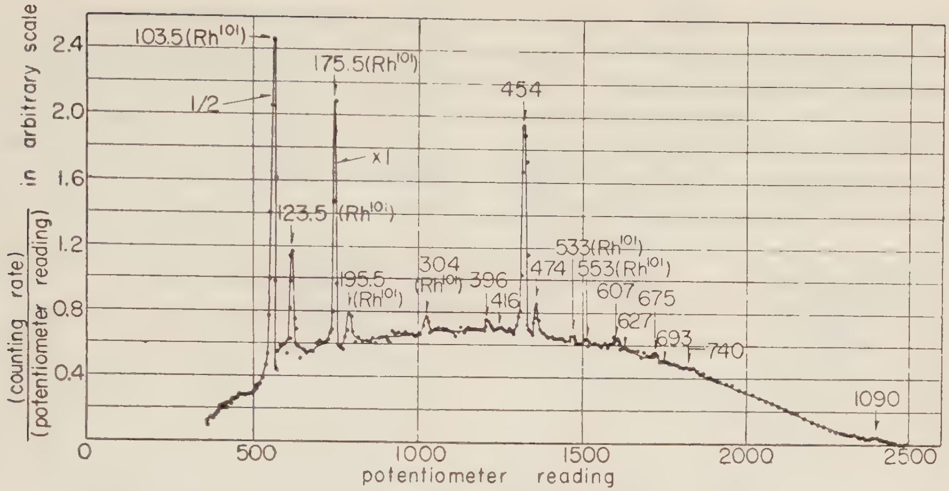

Fig. 4. The internal conversion spectrum of Rh^{102}. Several conversion lines of Rh^{101} also appear in the spectrum. Energies of peaks (kev) are indicated by arrows. The spectrum was taken 120 days after activation.

Table II. Internal conversion spectrum of Rh^{102}.

Energy of conversion electrons (kev)	Origin of conversion electrons	Energy of transition energy (kev)	Intensity of conversion electrons ($\beta^- = 100$)	$\frac{K}{L+M}$	K conversion coefficient	Multiporarity
396 ± 3	K	418 ± 3	0.077 ± 0.019	4.5 ± 2.1		
416 ± 4	L		0.017 ± 0.04			
454 ± 2	K	476 ± 2	1.80 ± 0.06	7.2 ± 0.8	5.2×10^{-3}*	$E2$
474 ± 3	L		0.25 ± 0.02			
607 ± 4	K	629 ± 4	0.13 ± 0.01	6.8 ± 1.9	$(2.9 \pm 0.3) \times 10^{-3}$	$E2$
627 ± 5	L		0.019 ± 0.004			
675 ± 5	K	697 ± 5	0.060 ± 0.004	2.4 ± 1.3	$(2.1 \pm 0.4) \times 10^{-3}$	$E2$, $M1$
693 ± 7	L		0.025 ± 0.110			
740 ± 10	K	762 ± 10	0.033 ± 0.010		$(1.5 \pm 0.7) \times 10^{-3}$	$M1$, $E2$
1090 ± 15	K	1112 ± 15	0.0015 ± 0.0006			

* The theoretical K conversion coefficient of Rose is used for the 0.476 Mev transition, which is probably $E2$ transition.

tabulated in Table II together with the $K/L+M$ ratios. Since the 476 kev transition is already known to be $E2$ transition[17,18] which is also consistent with the present $K/L+M$ ratio, the internal conversion coefficients of transitions can be obtained from the combination of the relative intensities of internal conversion electrons with the gamma-ray intensities, which is described in the next section. The K conversion coefficients thus obtained are tabulated in the sixth column of Table II. In the last column of Table II multipole assignments from the K conversion coefficients are given. The K conversion coefficients of the 0.418 and 1.11 Mev transitions are not given because the respective gamma rays were not resolved by the scintillation spectrometer.

§ 4. The Gamma-Ray Spectra of Rh^{102}

The gamma-ray spectra of Rh^{102} were observed with a scintillation spectrometer with $2'' \times 2''$ and $1\frac{1}{2}'' \times 1\frac{1}{2}''$ NaI(Tl) crystals mounted on 6292 DuMont and 6342A RCA photomultiplier tubes. The data were taken with a ten-channel pulse-height analyzer. For the study of the coincidence spectra a conventional fast-slow coincidence circuit with a resolving time 2τ of 0.36μsec was used.

The spectra were taken mainly about 400

days after the bombardments. The single spectrum below 1.4 Mev is shown in Fig. 5. The energies of the observed peaks are indicated in the figure. The peaks of 0.125, 0.190 and 0.315 Mev were already assigned to be Rh^{101} gamma-rays. The 0.48 Mev peak are composed by the 0.476, 0.42 and 0.511 (annihilation radiation) Mev gamma rays; the 0.42 Mev transition was resolved only in the internal conversion spectrum, as is shown in Fig. 4. The small bumps at 0.69 and 0.76 Mev are revealed to be true peaks by coincidence measurements. The broad peaks at ~1 Mev are resolved into three peaks of

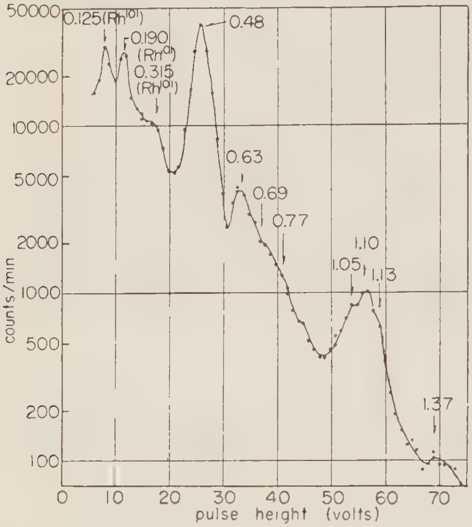

Fig. 5. The gamma ray spectrum of Rh^{102} below 1.4 Mev. Energies of peaks (Mev) are indicated by arrows.

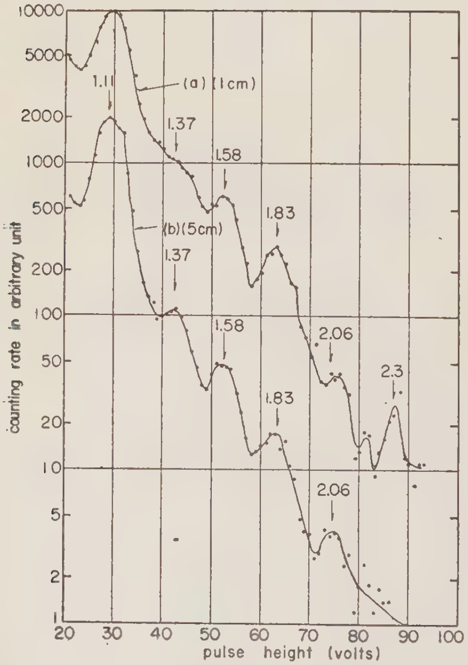

Fig. 6(a) and 6(b). The gamma ray spectrum of Rh^{102} above 1 Mev. Source-to detector distances are 1 cm (a) and 5 cm (b).

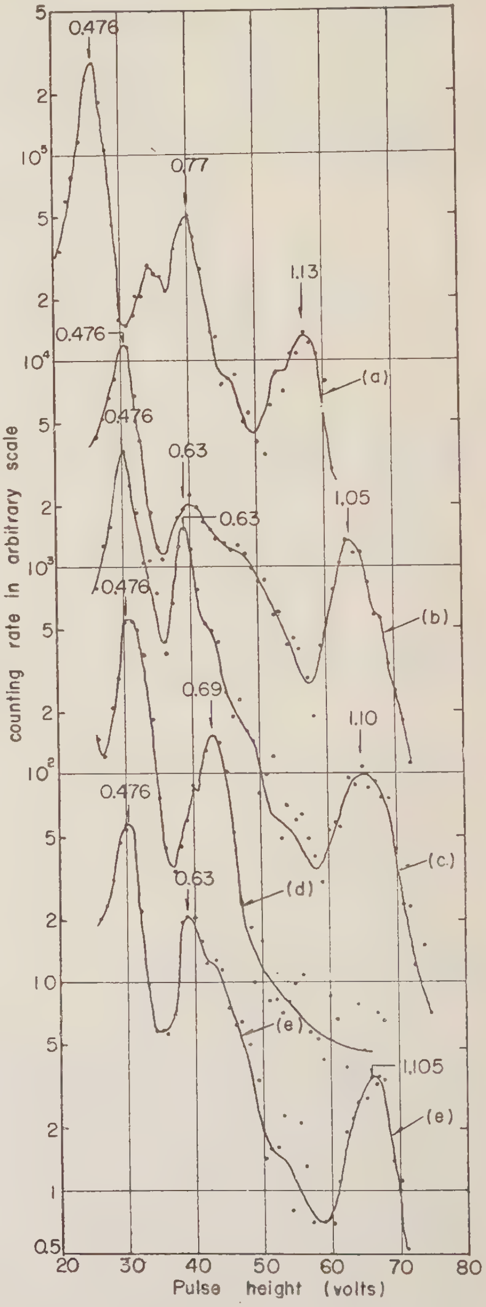

Fig. 7(a)-7(e). The gamma ray spectra of Rh^{102} in coincidence with the (a) 0.63, (b) 0.69, (c), 0.77, (d) 1.05 and (e) 1.13 Mev gamma rays. The energy scale of (a) is different from the others.

Table III. Rh^{102} gamma-ray energies and relative intensities. The data from the internal conversion spectrum are also included. The intensities from the conversion spectrum are obtained from multipole assignments which are indicated in parentheses. The intensities of the beta groups are also listed for comparison. The concluded intensity values summarized from several methods are shown in the last column.

E_r (Mev)	Relative intensity										Concluded intensity
	K internal conversion	Single spectra		Spectra in coincidence with gamma rays of energies (Mev)							
		5 cm	1 cm	0.476	0.511	0.63	0.69	0.76	1.05	1.13	
0.418	3.7(M1)			yes							4
0.476	100(E2)	100			yes	13	8.0	4.0	12	5	100
0.511	45			yes	50						45
0.629	13.2	14		13			1.0	6.4		4.1	13
0.697	7.5(E2) 9.3(M1)	12		8.3		0.5			6.4		8.2
0.762	5.0(E2) 6.3(M1)					6.4					6.3
1.05		26	26	14.4			6.4				11
1.106								1.3		1.2	4.2
1.13	7.2(E2)					4.1					5.0
1.37		0.9	0.4	0.5							0.9
1.58		0.5	0.7	0.2							0.5
1.83		0.3	0.9								0.3
2.06		0.2	0.2								0.2
beta group E_{max} (Mev)											
β^- 1.15											29.6
β_1^+ 0.82											6.3
β_2^+ 1.295											16.2

1.05, 1.106 and 1.13 Mev in the coincidence spectra.

The gamma-rays above 1.2 Mev were found to be very weak. The summing peaks could be found in this region. The summing peak efficiencies for various distances were calibrated with the 1.17 and 1.33 Mev gamma rays of Co^{60}. The single gamma-ray spectra above 1 Mev are showo in Figs. 6a and 6b observed with source-to-detector distances of 1 cm and 5 cm, respectively. It is found from the figures that peaks at 1.37, 1.57 and 2.06 Mev are true peaks and the peak at 2.3 Mev is a summing peak; the peak at 1.83 Mev perhaps consists of both kinds.

The intensities of the gamma-rays were determined by measuring the area under the full-energy peak and by correcting for the full-energy peak efficiencies and for Compton continua of high energy gamma-rays. The intensities, which are normalized to a value of 100 for the intensity of the 0.476 Mev gamma-ray, are listed in Table III, together with coincidence and magnetic spectrometer data.

The gamma-ray spectra in coincidence with the 0.476, 0.63, 0.69, 0.76, 1.05, 1.13 and 0.511 (annihilation radiation) Mev gamma rays were investigated. Figs. 7 (a–e) show the spectra show the spectra in coincidence with the 0.63, 0.69, 0.77, 1.05 and 1.13 Mev gamma rays. In Fig. 7a, there appears a predominant peak at 0.77 Mev, which is only a small bump in the single spectrum (Fig. 5). The 1.05 Mev gamma-ray is resolved in Fig. 7b. In Fig. 7d, there is a predominent peak at 0.69 Mev, which exhibits a bump in Fig. 5. The 1.106 gamma-ray, which is found to be a cross-over gamma-ray between the second excited and the ground state of Rh^{102}, can be seen in Figs. 7c and 7e. The intensities in the coincidence spectra corrected for the detector efficiencies, for Compton continua and for gamma-ray summing in the crystal, are tabulated in Table III. The intensity of the annihilation radiation in coincidence with the other annihilation quantum, 50, was obtained by using the annihilation radiation of Na^{22}. In the last column in Table III is shown the concluded intensity values of the gamma rays. The errors of those intensities might be about 10 to 20%. These results are consistent with the decay scheme of Rh^{102} which is shown Fig. 8 and will also be discussed in § 6.

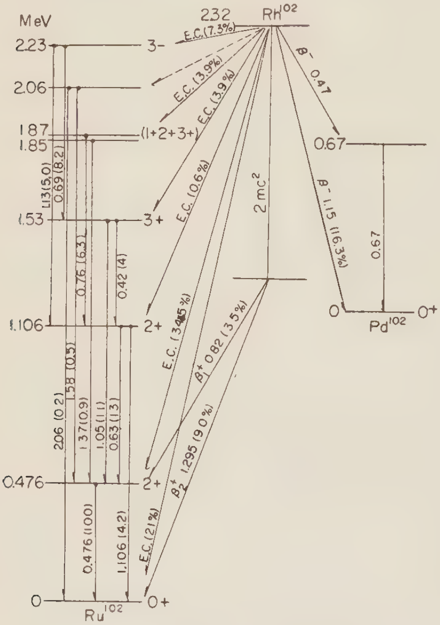

Fig. 8. Decay scheme of Rh^{102} and energy level diagrams of Ru^{102} and Pd^{102}. Energies are given in Mev and intensities are included in parentheses.

§ 5. Gamma-Gamma Angular Correlations in Rh^{102}

For gamma-gamma angular correlation measurements the source was 10 cm from the face of the 2″×2″ NaI crystal and 7.5 cm from the face of the $1\frac{1}{2}''\times1\frac{1}{2}''$ crystal. Data were taken every 22.5° between 90° and 180°. A least-square fit of the data was made to $W(\theta)=1+A_2P_2(\cos\theta)+A_4P_4(\cos\theta)$ following Rose's method[21]. The results were then corrected for the finite angular resolution of the detectors[21,22] and for the Compton continua from the higher gamma rays.

a) *The angular correlation for the 0.63–0.476 Mev cascade*

To obtain the angular correlation for the 0.63–0.476 Mev cascade, a single channel pulse-height analyzer of one detector ($1\frac{1}{2}''\times1\frac{1}{2}''$ NaI) was set with a wide channel width so that almost all the peak area of 0.476 Mev could be detected since no coincidences were observed between the annihilation radiation and the 0.63 Mev gamma ray; the effect from the 0.42–0.63 Mev cascade was estimated to be negligibly small. The other detector (2″×2″ NaI) was connected to a ten-channel pulse-height analyzer to avoid the 0.69 and 0.511 Mev coincidence peaks. The observed coincidences were corrected for the Compton continua from the 1.1 Mev gamma ray group which was in coincidence with the 0.476 Mev gamma ray. The observed correlation function corrected also for the finite angular resolution of the detectors was found to be

$$W_{0\ 0.63-0.476}(\theta)=1+(0{,}049\pm0.012)P_2(\cos\theta)$$
$$+(0.274\pm0.018)P_4(\cos\theta)\ .$$

Since the 0.476 Mev peak detected by the single channel pulse-height analyzer as a gate for coindidences contains the Compton continua of the 0.77 and 1.13 Mev gamma rays which are in coincidence with the 0.63 Mev gamma ray, the above correlation function should be corrected for the 0.63–0.76 and 0.63–1.13 Mev cascades. The observed correlation function of the 0.63–0.76 and 0.63–1.13 Mev cascades were found to be

$$W_{0.76-0.63}(\theta)=1+(0.009\pm0.020)P_2(\cos\theta)$$
$$+(0.022\pm0.028)P_4(\cos\theta)$$

and

$$W_{1.13-0.63}(\theta)=1+(-0.292\pm0.032)P_2(\cos\theta)$$
$$+(-0.0235\pm0.049)P_4(\cos\theta)\ ,$$

respectively. The ratios of the counting rates of these cascades to the counting rate of the 0.476–0.63 Mev cascade are found to be 0.082 for the 0.63–0.76 Mev cascade and 0.040 for the 0.63–1.13 Mev cascade. Thus the final correlation function for the 0.476–0.63 Mev cascade was determined to be

$$W_{0.63-0.476}(\theta)=1+(0.064\pm0.014)P_2(\cos\theta)$$
$$(0.312\pm0.032)P_4(\cos\theta)$$

The experimental correlation function is consistent with the theoretical correlation function for the spin sequence 2 $(D+Q)$ 2 (Q) with $\delta=5.5^{+0.7}_{-0.5}$, where δ is defined as the ratio of the reduced matrix element of quadrupole transition to dipole transition. The determination of δ-values is illustrated in

Fig. 9, where A_2 and A_4 in the correlation functions are taken as the abscissa and the ordinate, respectively, and δ-values are the parameters of the respective ellipses; in Fig. 9 the ellipses of the (3–2–0), (2–2–0) and (1–2–0) correlation functions are shown.

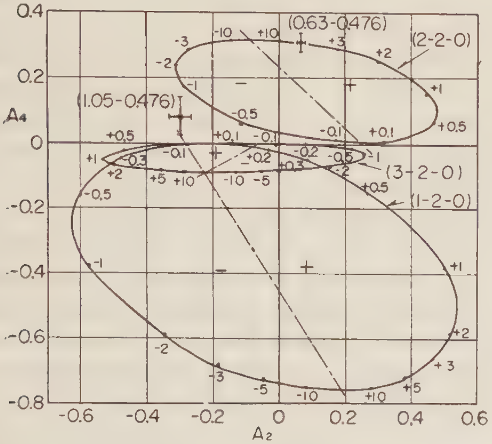

Fig. 9. Coefficients of angular correlation functions for (3-2-0), (2-2-0) and (1-2-0) cascades. δ is taken as a parameter of each ellipse.

b) *The angular correlation for the 1.05–0.476 Mev cascade*

The angular correlation for the 1.05–0.476 Mev cascade was observed similarly. Since the 1.13 Mev gamma ray is also in coincidence with the 0.476 Mev gamma ray, care was taken to select only the 1.05 Mev gamma ray. For this purpose the coincidence spectra in coincidence with the 0.476 Mev gamma ray between 1.0 and 1.2 Mev were carefully taken with the ten pulse-height analyzer at the five angles in which the angular correlation was observed. It was also observed that the coincidence counts for 180° were abnormally high in comparison with the coincidence counts for the other four angles. By changing the source-to-detector distance it was found that the sum coincidence peak between the 0.476 and 0.511 Mev gamma rays was in coincidence with the other annihilation quantum emitting to the opposite direction. For this reason the coincidence counts for 180° were omitted from the data. The observed correlation function for the 1.05–0.476 Mev cascade which was corrected for the finite angular resolution of the detectors was

$$W_{0\,1.05-0.476}(\theta)=1+(-0.252\pm0.028)P_2(\cos\theta)+(0.066\pm0.049)P_4(\cos\theta)\,.$$

This correlation function should be corrected for that of the 0.69–1.05 Mev cascade, which was found to be

$$W_{0.69-1.05}(\theta)=1+(0.122\pm0.038)P_2(\cos\theta)+(-0.222\pm0.061)P_4(\cos\theta)\,,$$

experimentally; the finite angular resolution was corrected for. The ratio of the coincidence counts of the 0.69–1.05 Mev cascade to those of the 0.476–1.05 Mev cascade is observed to be 0.11. The final correlation function was determined to be

$$W_{1.05-0.476}(\theta)=1+(-0.298\pm0.034)P_2+(0.093\pm0.055)P_4(\cos\theta)\,.$$

The unique spin assignment for the 1.53 Mev level of Ru^{102} is difficult only from this correlation function, as is seen in Fig. 9; 3, 1 and 2 are equally probable. 0 and 4 are excluded. However, the data of the relative intensities of the gamma rays give the spin of 3 uniquelly, as will be discussed in the following section. If the spin of the 1.53 Mev level is 3, the δ-value for the 1.05 Mev transition is determined to be 0.3±0.1 from Fig. 9. The reason for the large error in the correlation function for the 0.476–1.05 Mev cascade is probably due to the poor resolution of the 1.05 Mev peak from the 1.13 Mev peak.

c) *The angular correlations for the 0.76–0.63 and the 1.13–0.63 Mev cascades*

The angular correlations for the 0.76–0.63 and the 1.13–0.63 Mev cascades were also studied. The observed correlation functions, which are corrected for the finite angular resolution of the detectors, are described in § 5 (a); the errors mentioned above are only statistical ones. From these correlation functions the spins of the 1.87 and 2.23 Mev levels of Ru^{102} can be obtained since the δ value of the 0.63 Mev transition is already determined. These correlation functions, however, involve other errors than statistical ones because of the poor energy resolution of the detectors. Therefore the unique assignment of those levels is rather difficult. The spin assignment of the 1.87 Mev level is 1, 2 or 3; 0 and 4 are excluded. On the other hand the assignment of the 2.23 Mev level is rather uniquely determined to be 3 even if the error involved are large. The δ-value of the 1.13 Mev transition cannot be determined because of the large experimental error.

§ 6. Discussion

The log ft values of the decay of Rh^{102} to the states of Ru^{102} and Pd^{102} are discussed. In order to obtain the ft value of the transition to the ground states of Ru^{102}, the ratio of orbital electron capture to positron emission is necessary. Since the positron spectrum associated with this transition (β_2^+) exhibits the allowed shape approximately, the capture to positron ratio is considered to be approximately that of the allowed transition[23]. The capture to positron ratio of the allowed transition is found to be 2.3 for the transition to the ground state of Ru^{102} using the Feeberg's chart[24]. In the same way the capture to positron ratio of the transition to the first excited state of Ru^{102} is obtained to be 10. This value is in good agreement with the experimental value of (11±2), which was determined from the relative intensities of the gamma-rays and the total beta-rays. The branching ratio of the transition to each state was obtained from the decay scheme shown in Fig. 8. The values of the branching ratios and the log ft values tabulated in Table IV.

Table IV. Branching ratio and log ft values of Rh^{102} decay.

Terminating level (Mev)		Branching ratio (%)	Log ft
0	Ru^{102}	30	8.6
0.476		38	8.1
1.106		0.6	9.7
1.53		3.9	8.6
1.87		3.9	8.1
2.23		7.3	5.5
0	Pd^{102}	16.3	9.6

All the log ft values obtained are between 8 and 9, except for the transition terminating to the 2.23 Mev state of Ru^{102}. Those transitions are considered to be the first forbidden transitions. Since the parities of the ground states of Ru^{102} and Pd^{102} are positive, the parities of those terminating levels are positive. The log ft of 9.8 for the transition to the second 2+level is compared with the log ft of 8.1 for the transition to the first 2+level. The forbiddeness of the beta transition to the higher 2+state was indicated by M. Sakai[25]. The transition terminating to the 2.23 Mev level of Ru^{102} is considered to be the allowed transition since the log ft value is 5.5.

The spin and parity of the first excited state of Ru^{102}, 2+, was confirmed by the $K/L+M$ ratio of the internal conversion spectrum and the angular correlation function. This state was also studied with Coulomb excitation by Temmer and Hydenberg[17] and by Stelson and McGowan[18]. The half-life of this state was estimeted to be about 2×10^{-11} sec by Coulomb excitation. This half-life value is shorter by 50 than that for a single-particle transition. The collective nature of this state is evident.

The spin of the second level of Ru^{102} was determined to be 2+ by the correlation function for the 0.63–0.476 Mev cascade; the positive parity was already determined by the ft value. The $E2$–$M1$ mixing ratio of the transition between the 1.105 and the 0.476 Mev states was determined to be $\delta=5.5^{+0.7}_{-0.5}$. This value of δ can be compared with those for Ru^{100} and Pd^{106}; δ for Ru^{100} [26] was reported to be $-3.1^{+1.6}_{-2.2}$ and δ for Pd^{106} was to be +30[27]. The $E2$–$M1$ mixing ratios of the transitions between the second 2+ and the first 2+ levels for several even nuclei have been discussed by M. Sakai[28] and S. S. Malik et al.[29] The branching ratio of the cascade to the crossover gamma rays from the second 2+ level is found to be about 5 from the intensity ratio of the 0.63 Mev gamma ray to the 1.106 Mev gamma ray in coincidence with the 0.76 Mev gamma ray and is to be about 3.4 from the same ratio in coincidence with the 1.13 Mev gamma ray; the angular correlation effects have been corrected for. The average of the two values would be 4.2±0.8 if the same level is considered. The difference between these value, however, is just outside of the experimental error and may suggest the doublet of of the 1.106 Mev level which was anticipated by the vibrational model of Sharff-Goldhaber and Weneser[3]. The doublet of this state has also been suggested by McGowan and Stelson[19]. McGowan and Stelson[19] give the value of 1.5±0.3 for the ratio. The ratio $B(E2, 2'\rightarrow2)/B(E2, 2'\rightarrow0)$, which is the ratio of the reduced $E2$ transition probability between the second and the first 2+ level to that between the second 2+ level and the ground state is determined to be (65±15). The theoretical value of this ratio calculated by the formula of Davydov and Filippov[30] is 30. The $E2$ transitions from the second 2+ levels of even-even nuclei was summarized by Van Patter[31]. The second 2+ state of Ru^{102} was also studied with Coulomb excitation by Stelson and McGowan[32].

The spin of the third excited state of Ru^{102} can be determined by the angular correlation function for the 1.05–0.476 Mev cascade and by the intensity ratios of the gamma rays originating from this state. The correlation function suggest 3, 1 or 2 for the spin of this state. The relative intensity of the transition between the 1.53 Mev and the ground state of Ru^{102} was found to be <0.1; the gamma ray of 1.57 Mev is probably different from the 1.55 Mev transition. On the other hand, the relative intensities of the transitions from the 1.53 Mev state to the 1.106 Mev state (2+) and to the 0.476 Mev state (2+) are found to be 4 and 11, respectively. Therefore, the spin assignment of 1 and 2 is excluded for the 1.53 Mev state. Thus the spin assignment of the 1.53 Mev state is concluded to be 3. This spin assignment is in agreement with that of McGowan and Stelson[19]. It is noted that Davydov and Filippov[30] suggest the first 3+ level at 1.58 Mev.

The 1.85 Mev state of Ru^{102} is found by the coincidences between the 0.476 and the 1.37 Mev gamma rays. This state is probably different from the 1.87 Mev state, which is given by the 0.76–0.63–0.476 Mev cascade transition. A weak transition of about (1.83 ± 0.04) Mev was also found in the single gamma ray spectrum, as is shown in Fig. 6b. It is not certain whether the transition may be associated with the 1.85 Mev state or with the 1.87 Mev state. The spin assignment of the 1.87 Mev state is 1, 2 or 3 from the correlation function for the 0.76–0.63 Mev cascade. It is noted that McGowan and Stelson[19] assigned 0+ for the 1.84 Mev level of Ru^{102}.

The 2.06 Mev gamma ray, which was found in the single gamma ray spectrum (Fig. 6b) indicates the 2.06 Mev level of Ru^{102}. It is noted that a faint peak at about 1.6 Mev was found in the gamma ray spectrum in coincidence with the 0.476 Mev. It also confirms the existence of the 2.04 Mev state. McGowan and Stelson[19] also reported the existence of the 2.04 Mev level. Their spin assignment for this state is 2.

No transition which might be associated with Pd^{102} was found either in the single and coincidence gamma ray spectra or in the internal conversion spectrum although the systematics of the first excited states of even-even nuclei expects the first 2+ state of Pd^{102} between 0.65 and 0.7 Mev[33]. Recently beta-gamma coincidences in Rh^{102} have been studied by the author[34]. The preliminary result suggests new transition of 0.67 Mev in coincidence with that beta group, the end-point energy of which is about 0.47 Mev. Since the end-point energy of the main negatron group is 1.15 Mev and the annihilation radiation is in coincidence with no other than the other than the 0.476 Mev gamma ray, the new gamma ray is probably the transition between the first excited and the ground state of Pd^{102}. The gamma ray of 0.68 Mev was also found in the decay of Ag^{102} by Y. Hashimoto et al. University of Tokyo[35].

The spin and parity of the ground state of Rh^{102} is discussed. Since the ground states of Ru^{102} and Pd^{102} are 0+ and the first excited state of Ru^{102} is 2+, the spin and the parity of the ground state of Rh^{102} is considered to be 1− or 2− from the selection rule of the first forbidden beta transition. If the spin and the parity of Rh^{102} were 2−, both the high energy component of the positron spectrum (β_2^+) and the negatron spectrum would show the unique first forbidden spetrum shape. The fact that the experimental spectra approximately show the allowed shape makes the assignment of 1− favourable. The assignment of 1−, however, is against the Nordheims strong rule[36,37] and the spin assignment of the 2.23 Mev level of Ru^{102}. The log ft value of 5.5 is given for the transition terminating the 2.23 Mev level of Ru^{102}, which is already assigned to be 3−. It is inconsistent with the assignment of 1− for Rh^{102} from the selection rule of the allowed beta decay; 2− is more favourable from this point. No consistent assignment for Rh^{102} is not given so far. This may be indication of the existence of a very low energy isomer in Rh^{102}, which is inferred by McGowan and Stelson[19].

Added in Proof

After submitting this paper, the author received a preprint of work by F. K. McGowan and P. H. Stelson (submitted to Phys. Rev.)

Their results are in general agreement with the present one except for one point, although they did not measure any beta-spectra. The only different point is the angular correlation function of the 0.63–0.476 Mev cascade. It is found that the experimental point at 180° of the author is 7% higher than the least square fit for the coincidences of the five angles; the statistical error at 180° is ±1.4%. The coincidences at 180° is considered to be too high probably due to some indirect effect of the annihilation radiation. If one omits the experimental point at 180°, the new least square fit corrected for the finite angular resolution would be

$$W_{0.63-0.476}(\theta)=1+(0.016\pm0.013)P_2(\cos\theta)+(0.158\pm0.021)P_4(\cos\theta)\ .$$

The final correlation function would be

$$W_{0.63-0.476}(\theta)=1+(0.031\pm0.16)P_2(\cos\theta)+(0.179\pm0.025)P_4(\cos\theta)\ ,$$

which is almost in agreement with that of McGowan and Stelson. Thus the consistent δ-value for the 0.630 Mev transition cannot be obtained unless one assumes a 2+ and 4+ doublet at 1.106 Mev, as was done by McGowan and Stelson. On the other hand, no doublet of the 0.630 Mev transition was found in the internal conversion spectrum within the resolution of the spectrometer, say, 1%. Further study will be necessary for this transition.

Acknowledgment

The author wishes to express his sincere thanks to Dr. J. D. Kurbatov for his suggesting this research; Mr. H. Shimojima and Mr. H. Nagao for their chemical separation; Mr. N. Ono, Mr. M. Koike, Mr. Y. Tokita and Mr. H. Arai for their assistance in taking and analyzing experimental data. The author is also thankful to the cycltron crew and the beta group of the institute for Nuclear Study, University of Tokyo, for their kind cooperation.

References

1) A.Bohr and B. R. Mottelson: Mat. Fys. Medd. Dan. Vid. Selsk. **27** (1953) No. 16.
2) K. Alder, A. Bohr, T. Huvs, B. Mottelson and A. Winther: Revs. Mod. Phys. **28** (1956) 432.
3) G. Scharff-Goldhaber and J. Weneser: Phys. Rev. **98** (1955) 212.
4) H. Horie: JAERI **4016** (in Japanese), Japan Atomic Energy Research Institute, (1960) pp. 2.
5) P. H. Stelson: Proceedings of the International Conference on Nuclear Structure, Kingston, Canada, (1960) pp. 787.
6) O. Minakawa: Phys. Rev. **60** (1941) 689.
7) N. Hole: Arkiv, Mat. Astron, Fysik **32A**, (1945) No. 3.
8) W. H. Sullivan, N. R. Sleight and E. M. Gladrow, NNES-PPR **9** (1951) 356.
9) L. Marquez: Phys. Rev. **95** (1954) 67.
10) D. B. Kochendorfer and D. J. Farmer: Phys. Rev. **96** (1954) 855A.
11) P. Avignon: Comptes Rendue Acad. Sci. **240–2** (1955) 176.
12) M. Bes and H. Bosch: Comptes Rendus Acad. Sci. **240–3** (1955) 294.
13) D. J. Farmer: Phys. Rev. **99**, (1955) 659A.
14) J. D. Kurbatov, K. Hisatake and J. T. Jones: Bull. Am. Phys. Soc. **1** (1956) 134.
15) N. Goldberg: Bull. Am. Phys. Soc. **2** (1957) 230.
16) K. Hisatake and J. D. Kurbatov: Bull. Am. Phys. Soc. **3** (1958) 315.
17) G. M. Temmer and N. P. Heydenburg: Phys. Rev. **104** (1956) 967.
18) P. H. Stelson and F. K. McGowan: Phys. Rev. **110** (1958) 489.
19) F. K. McGowan and P. H. Stelson: Bull. Am. Phys. Soc. **5** (1960) 448.
20) B. L. Sharma and M. L. Pool: Bull. Am. Phys. Soc. **4** (1959) 151.
21) M. E. Rose: Phys. Rev. **91** (1953) 610.
22) E. L. Church and J. J. Kraushaar: Phys. Rev. **88** (1952) 419.
23) H. Brysk and M. E. Rose: ORNL **1830**, Oak Ridge National Laboratory (1955).
24) E. Feenberg and G. Trigg: Revs. Mod. Phys. **22** (1950) 399.
25) M. Sakai: Rep. Inst. Nucl. Study, University of Tokyo, INSJ-6 July (1959).
26) M. Koike, N. Ono, K. Takahashi and K. Hisatake: The Autumn Meeting of the Physical Society of Japan, 1960.
27) R. L. Robinson and F. K. McGowan: Phys. Rev. **119** (1960) 1692.
28) M. Sakai: Rep. Inst. Nucl. Study: University of Tokyo INSJ-6 Feb (1958).
29) S. S. Malik, V. R. Potnis and C. E. Mandeville: Nuclear Phys. **11** (1959) 691.
30) A. S. Davydov and G. F. Filippov: Nuclear Phys. **8** (1958) 237.
31) D. M. Van Patter: Nuclear Phys. **14** (1959/60) 42.
32) P. H. Stelson and F. K. McGowan: Phys. Rev. **121** (1961) 209.
33) M. Nozawa and T. Yamazaki: JAERI **4016**

(in Japanese), Japan Atomic Energy Research Institute, (1960) pp. 44.
34) K. Hisataka: to be published.
35) Y. Hashimoto: Private Communication (1961).
36) L. W. Nordheim: Revs. Mod. Phys. **23** (1951) 322.
37) M. H. Brennan and A. M. Brenstein: Phys. Rev. **120** (1960) 927.

JOURNAL OF THE PHYSICAL SOCIETY OF JAPAN Vol. 16, No. 7, JULY, 1961

Ferromagnetic Crystalline Anisotropy of $MeFe_2O_4$-Fe_3O_4 Ferrite Solid Solutions

By Nahonori MIYATA

Department of Physics, Yokohama National University, Yokohama

(Received October 20, 1960)

The ferrite crystals of ternary system $(Mn_xFe_yNi_z)Fe_2O_4$, where $x+y+z=1$, were grown by the Bridgman method in the air. According to the X-ray analysis, they have the spinel structure, except in the region near $NiFe_2O_4$, and their lattice constants depend linearly on the concentration: $a=(8.518-0.125y-0.176z)\pm0.005$ A. The ferromagnetic crystalline anisotropy was measured by the torque method in the temperature range between 90°K and 300°K. In normal specimens K_1 decreases with decreasing temperature. $NiFe_2O_4-Fe_3O_4$ system shows an anomalous temperature dependence for a wide range of concentration: K_1 increases and changes its sign from negative to positive at low temperature. This will be due to the short range order of Fe^{2+} and Fe^{3+} at the octahedral site of the spinel lattice. If such an anomaly is subtracted, K_1 of the ternary system becomes maximum at a certain Fe_3O_4 concentration. This can be attributable to the special contribution of Fe^{2+}-ion.

The crystals of $(Zn_{1-y}Fe_y)Fe_2O_4$ binary system were also investigated. They have the spinel structure with the lattice constant of $a=(8.445-0.052y)\pm0.005$ A. The relation of the anisotropy constant to y also indicates the contribution of Fe^{2+} mentioned above.

§1. Introduction

The interesting characteristics of the dependence of the ferromagnetic crystalline anisotropy of the $MnFe_2O_4$-Fe_3O_4 system on the composition were reported previously by the author and his colaborator[1] and by Penoyer and Shafer.[2] Our knowledge seemed to be insufficient for understanding the mechanism of these phenomena. The study has been extended to the $MnFe_2O_4$-Fe_3O_4-$NiFe_2O_4$ ternary system and $ZnFe_2O_4$-Fe_3O_4 binary one. Ni and Zn were chosen for the third and fourth elements on account of the expectation of their stability of the ionic state (Ni^{2+} and Zn^{2+}) and that of the preference for the lattice site (B- and A-site, respectively) in the spinel type structure. On account of the lack of the phase diagram of these ferrite solid solutions, the method of preparation of the crystals was first investigated. After that, the ferromagnetic crystalline anisotropy of the crystals was measured by the torque method in the temperature range between 90°K and 300°K. Interesting features were observed and discussed from the view point of the theory developed recently.

§2. Crystal Growth and Chemical Analysis

Single crystals were grown by the same method as reported in the previous paper.[1] Fe_2O_3, $MnCO_3$, NiO, ZnO and MgO were used for the raw materials. The ferrite powder, made by the usual ceramic technique, was melted and crystallized by the Bridgman method in the Pt-crucible in the air atmosphere with the speed of 2.8 cm/hr (0.8°C/min). After the cooling at the rates of about 2°C/min (1600~1300°C), 5°C/min (1300~1000°C) and 10°C/min (1000~600°C), the crystal was taken out from the furnace.

Main metallic elements were chemically analysed for all specimen used in the experiment. Larger segregation was observed in $ZnFe_2O_4$-Fe_3O_4 system than in $MnFe_2O_4$-Fe_3O_4-$NiFe_2O_4$ ternary one, as shown in Table I. The analysis could not determine the excess or deficiency of oxygen compared with the stoichiometric composition more accurately than ±5% of the oxygen content. But the measurement of the electric conductivity,[3] which was considered to indicate the number of Fe^{2+}-ions, suggested the realization of the nearly stoichiometry of the oxygen content.

Table I. Examples of chemical analysis. It indicates segregation of crystals.

(a) $MnFe_2O_4$-Fe_3O_4-$NiFe_2O_4$ system

Approximate expression	Element	Position	
		Top	Bottom
$Ni_{0.2}Fe_{2.8}O_4$	Ni Fe	0.21 2.79	0.18 2.82
$Ni_{0.5}Fe_{2.5}O_4$	Ni Fe	0.52 2.48	0.50 2.50
$Mn_{0.4}Fe_{2.6}O_4$	Mn Fe	0.38 2.62	0.37 2.63
$Mn_{0.4}Ni_{0.2}Fe_{2.4}O_4$	Mn Ni Fe	0.41 0.19 2.40	0.42 0.19 2.39

(b) $ZnFe_2O_4$-Fe_3O_4 system

Approximate expression	Element	Position	
		Top	Bottom
$Zn_{0.15}Fe_{2.85}O_4$	Zn Fe	0.12 2.88	0.16 2.84
$Zn_{0.25}Fe_{2.75}O_4$	Zn Fe	0.24 2.76	0.30 2.70
$Zn_{0.45}Fe_{2.55}O_4$	Zn Fe	0.45 2.55	0.48 2.52
$Zn_{0.6}Fe_{2.4}O_4$	Zn Fe	0.56 2.44	0.61 2.39
$Zn_{0.85}Fe_{2.15}O_4$	Zn Fe	0.81 2.19	0.86 2.14

Co-impurity in the specimen was 0.01% or less. Specimens used in the experiment were cut from the bottom of the crystals, because the top was crystallographically less perfect and might be oxidized during the cooling after the crystal growth. The compositions of $(Mn_xFe_yNi_z)Fe_2O_4$ ternary ferrite specimens are shown in Fig. 1 and those of $(Zn_{1-y}Fe_y)Fe_2O_4$ binary system are $y=0.84$, 0.70, 0.52 and 0.39. $(Mg_{1-y}Fe_y)Fe_2O_4$ system was tried, too. But it succeeded only in the case of $y=0.87$, on account of the relatively high melting point of Mg-rich specimens.

§ 3. Crystallographic Investigation

(1) $(Mn_xFe_yNi_z)Fe_2O_4$

The crystal structure and the lattice con-

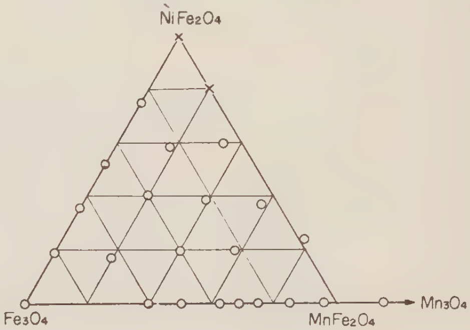

Fig. 1. Composition of specimens of $MnFe_2O_4$-Fe_3O_4-$NiFe_2O_4$ ternary ferrite solid solution. ○: single spinel phase, ×: two phase.

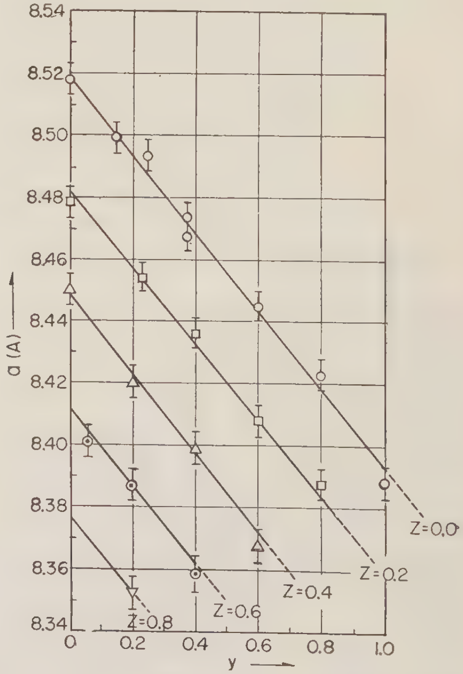

Fig. 2(a). Lattice constants of $(Mn_xFe_yNi_z)Fe_2O_4$ solid solution. (the lattice constant of NaCl, 5.640 A, is chosen as the standard). Lines show $a=(8.518-0.125y-0.176z)$A, in which z is taken as a parameter.

stant were investigated at room temperature by X-ray analysis. Except in the region near Ni-ferrite (shown as × in Fig. 1), where the spinel phase exists together with another phase, all specimens (○ in Fig. 1) have the spinel structure and their lattice constants depend linearly on the composition: the lattice constant of a specimen, the composition of which is expressed as $(Mn_xFe_yNi_z)Fe_2O_4$, where $x+y+z=1$, is approximately shown as

$$a=(8.518-0.125y-0.176z)\pm0.005\text{ A.} \quad (1)$$

Here the lattice constant of NaCl, 5.640A, is chosen as the standard.[4] The comparison between experimental results and the equation (1) is shown in Fig. 2(a).

(2) *$(Zn_{1-y}Fe_y)Fe_2O_4$*

All specimens investigated have also the spinel type structure and their lattice constants are $a=(8.445-0.052y)\pm0.005$A (Fig. 2(b)).

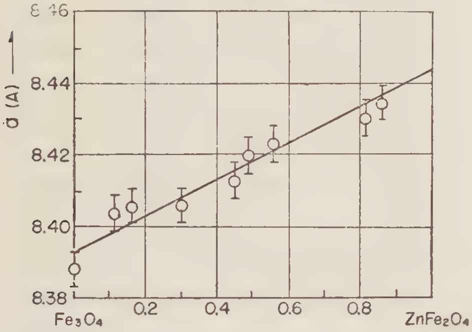

Fig. 2(b). Lattice constants of $ZnFe_2O_4$-Fe_3O_4 system.

§ 4. Experiments on the Ferromagnetic Crystalline Anisotropy

(1) *Method*

Usually the ferromagnetic crystalline anisotropy energy with cubic symmetry is expressed as $E=K_1(\alpha_1^2\alpha_2^2+\alpha_2^2\alpha_3^2+\alpha_3^2\alpha_1^2)+K_2\alpha_1^2\alpha_2^2\alpha_3^2$, where $(\alpha_1, \alpha_2, \alpha_3)$ is the direction cosine of the magnetization. The constants, K_1 and K_2, were measured in the temperature range between 90°K and 300°K by observing the torque exerted on the spherical specimen (about 1 mm in diameter) set in the uniform magnetic field. Specimens were set by the X-ray method so as to rotate about [110]- or [100]-axis within the accuracy of ±1°. The magnetic field was 3500～10500 Oe.

At room temperature the observed torque curve agreed to the curve calculated with K_1-term only, except in the case of small K_1. K_2-term had to be taken into account to explain the torque curve of some specimens at low temperatures.

(2) *Results*

(a) *$(Mn_xFe_yNi_z)Fe_2O_4$*

The dependency of K_1 on the temperature of each specimen and on the concentration of three binary systems, $MnFe_2O_4$-Fe_3O_4,

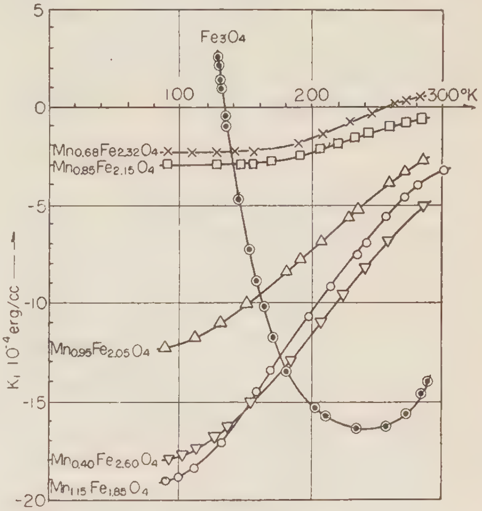

Fig. 3(a). Temperature dependency of K_1 of $MnFe_2O_4$-Fe_3O_4 system.

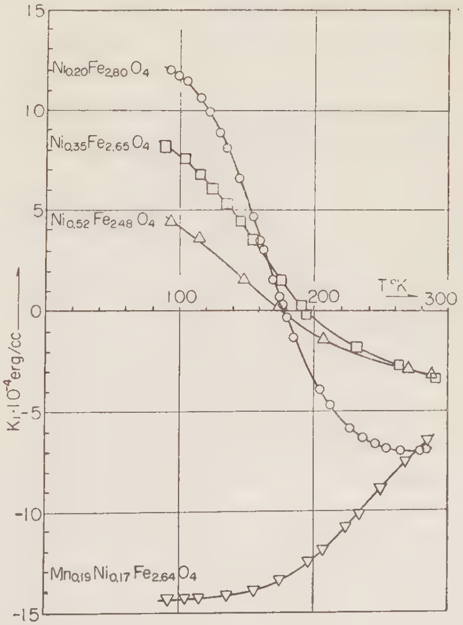

Fig. 3(b). Temperature dependency of K_1 of $NiFe_2O_4$-Fe_3O_4 system, and effect of small Mn addition (▽).

$NiFe_2O_4$-Fe_3O_4 and $MnFe_2O_4$-$NiFe_2O_4$, are shown in Fig. 3(a), (b), (c) and Fig. 4(a), (b), (c). K_1 at 290°K and K_1 and K_2 at 90°K are tabulated in Table II.

In most specimens, except $NiFe_2O_4$-Fe_3O_4 system, K_1 decreases with decreasing temperature. The special character of $NiFe_2O_4$-Fe_3O_4 system, in which K_1 increases with decreasing temperature and goes from negative to positive, will be discussed in § 5. The addition of $MnFe_2O_4$ makes this phenomenon disappear as seen in Fig. 3(b). The application of magnetic field during cooling of the specimens shows no effect on this anomaly.

Penoyer and Shafer's data²⁾ on $MnFe_2O_4$-Fe_3O_4 system accord with ours. It is noticed that K_1 of $Mn_{0.68}Fe_{2.32}O_4$ is positive at room temperature and becomes negative at low temperature. The systematic study on other

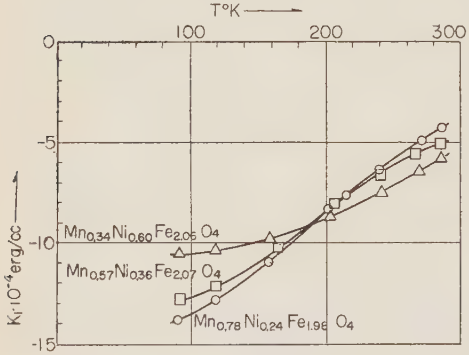

Fig. 3(c). Temperature dependency of K_1 of $MnFe_2O_4$-$NiFe_2O_4$ system.

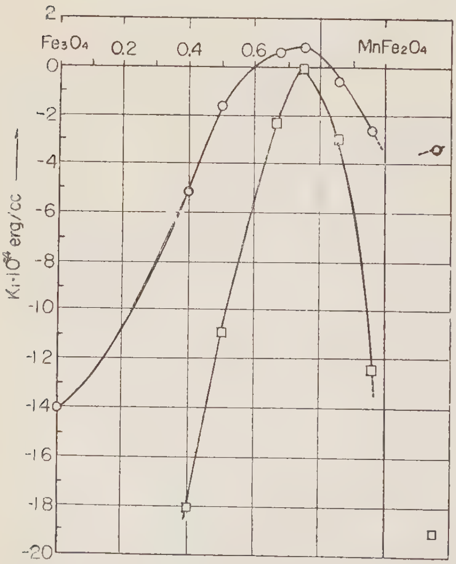

Fig. 4(a). Concentration dependency of K_1 of $MnFe_2O_4$-Fe_3O_4 system. ○: 290°K, □: 90°K.

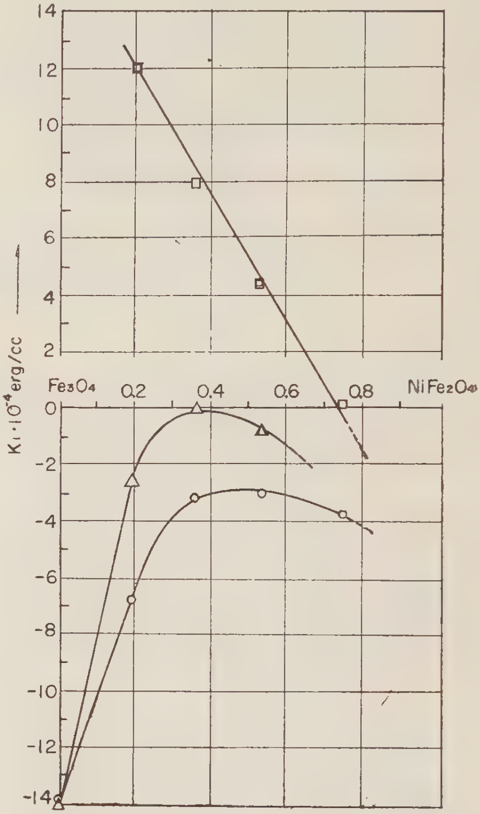

Fig. 4(b). Concentration dependency of K_1 of $NiFe_2O_4$-Fe_3O_4 system. ○: 290°K, △: 190°K, □: 90°K.

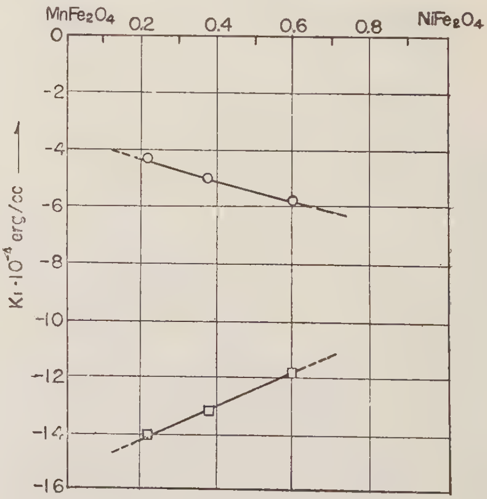

Fig. 4(c). Concentration dependency of K_1 of $MnFe_2O_4$-$NiFe_2O_4$ system. ○: 290°K, □: 90°K.

ferrite solid solutions has not been presented. Bozorth *et al*[5] reported on $Ni_{0.8}Fe_{2.2}O_4$ that the anisotropy measured by the torque method was nearly the same at room temperature and at 77°K. This is consistent with the character of $NiFe_2O_4$-Fe_3O_4 system mentioned here.

The observed concentration dependency of the anisotropy will be discussed in § 5.

Table II. K_1 and K_2 of $(Mn_xFe_yNi_z)Fe_2O_4$ at 290°K and 90°K.

Composition of specimen			At 290°K	At 90°K	
Mn x	Fe $2+y$	Ni z	$K_1\cdot10^{-4}$ erg/cc	$K_1\cdot10^{-4}$ erg/cc	$K_2\cdot10^{-4}$ erg/cc
0.00	3.00	0.00	−14.		
0.40	2.60	0.00	− 5.0	−18.	
0.50	2.50	0.00	− 1.6	−10.7	
0.68	2.32	0.00	+ 0.6	− 2.3	
0.75	2.25	0.00	+ 0.9	0.	−9.
0.85	2.15	0.00	− 0.5	− 2.9	
0.95	2.05	0.00	− 2.5	−12.3	−2.
1.15	1.85	0.00	− 3.3	−19.0	
0.00	2.80	0.20	− 6.7	+12.3	− 9.
0.00	2.65	0.35	− 3.3	+ 7.9	−10.
0.00	2.48	0.52	− 3.2	+ 4.4	−12.
0.00	2.25	0.75	− 3.8	+ 0.5	−19.
0.78	1.98	0.24	− 4.1	−13.5	−10.
0.57	2.07	0.36	− 5.0	−12.7	− 9.
0.34	2.06	0.60	− 5.7	−10.4	
0.19	2.64	0.17	− 5.9	−14.3	0.
0.40	2.40	0.20	− 3.9	−12.0	−6.
0.57	2.23	0.20	− 2.8	− 9.5	−8.
0.20	2.40	0.40	− 4.5	− 6.2	−8.
0.38	2.23	0.39	− 4.4	−10.5	−3.
0.17	2.25	0.58	− 4.7	− 6.6	−9.

Table III. K_1 of $(Zn_{1-y}Fe_y)Fe_2O_4$ at 290°K and 90°K.

Composition of specimen		$K_1\cdot10^{-4}$ erg/cc at 290°K	$K_1\cdot10^{-4}$ erg/cc at 90°K
Zn $1-y$	Fe $2+y$		
0.16	2.84	−9.0	−15.9
0.30	2.70	−5.0	−21.3
0.48	2.52	−1.2	−15.3
0.61	2.39	−0.7	− 9.2

(b) $(Zn_{1-y}Fe_y)Fe_2O_4$

The temperature and concentration dependency of K_1 of $(Zn_{1-y}Fe_y)Fe_2O_4$ system are given in Fig. 5 and 6, respectively. Except the case of $y=0.84$, where the increase of

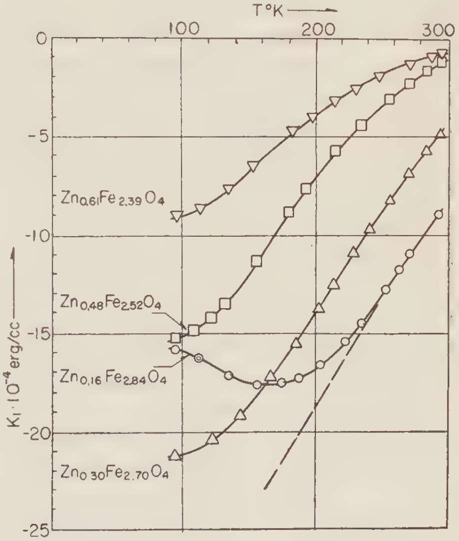

Fig. 5. Temperature dependency of K_1 of $ZnFe_2O_4$-Fe_3O_4 system.

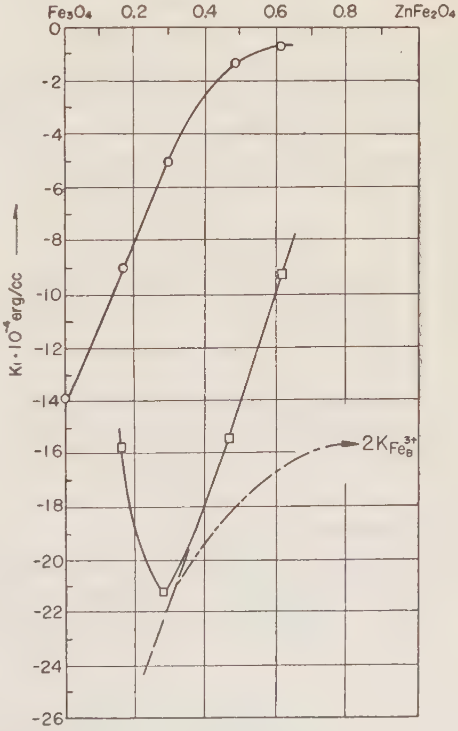

Fig. 6. Concentration dependency of K_1 of $ZnFe_2O_4$-Fe_3O_4 system. ○: 290°K, □: 90°K.

K_1 at low temperatures may be attributed to the short range order of Fe^{2+} and Fe^{3+} (§ 5), all specimens show the normal temperature dependency. If the effect of short range order is neglected (shown as the dashed curve in the figures), $|K_1|$ at a fixed temperature decreases with the decrease of Fe_3O_4 concentration. The cause of this tendency is naturally understood as a result of the breaking of the simple Néel model with increasing of $ZnFe_2O_4$ concentration. $ZnFe_2O_4$ is not ferromagnetic, so that it has no ferromagnetic anisotropy.

(c) *$Mg_{0.13}Fe_{2.87}O_4$*

The temperature dependency of K_1 of $Mg_{0.13}Fe_{2.87}O_4$ is shown in Fig. 7. This specimen is taken out from the furnace at about 1400°C and cooled rapidly in the air. As is shown, K_1 increases and becomes positive at low temperatures. Folen and Rado[6] reported that K_1 *vs.* temperature curve of $Mg_{0.5}Fe_{2.5}O_4$ showed a minimum at 180°K. From these results we conclude that $MgFe_2O_4$-Fe_3O_4 system shows a similar (but smaller) dependence of $K_1(T)$ on the concentration compared with $NiFe_2O_4$-Fe_3O_4 system.

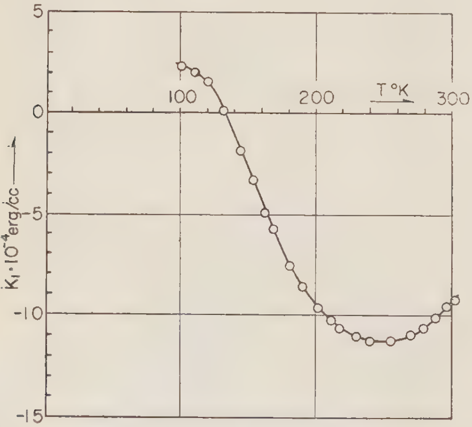

Fig. 7. Temperature dependency of K_1 of $Mg_{0.13}Fe_{2.87}O_4$.

§ 5. Discussions on Anisotropy

It is well known that the one-ion model has been proved successful in the theory of the ferromagnetic crystalline anisotropy of ferrites.[7]

(1) First, *the temperature dependency of K_1 of $NiFe_2O_4$-Fe_3O_4 system* is explained. It is shown by the chemical analysis that the phenemenon is not due to the Co-impurity and can be regarded as the real nature of this system. Ni^{2+}-ions at A-site can contribute to the large positive K_1 like Co^{2+}-ions at B-site, but the magnetization at 0°K is contrary to such a kind of ion distribution.

The abrupt change of the anisotropy of Fe_3O_4, observed at the temperature region just above the transition (about 120°K), is attributed to the electronic short range order of Fe^{2+} and Fe^{3+} on the B-site of the spinel lattice[8]. This character is known to remain as well when the small amount of other ferrite is added to magnetite. $Zn_{0.16}Fe_{2.84}O_4$ in Fig. 5 is an example. The characteristic temperature dependency of K_1 of $NiFe_2O_4$-Fe_3O_4 may also have the same origin. It is reasonably understood from this view point that this character is more remarkable in Fe_3O_4 side than $NiFe_2O_4$ side in this system. Similar character of $MgFe_2O_4$-Fe_3O_4 system, which is stated in § 4(2)(c), can be attributed to the same origin. In order to explain the experimental results (the effect of addition of $MnFe_2O_4$, Fig. 3(b)) completely, it is necessary to assume further that Mn-ion suppresses the growth of the short range order.

In the case of $ZnFe_2O_4$-Fe_3O_4 there are only Fe^{2+} and Fe^{3+} on B-site, since Zn^{2+}-ion is believed to occupy A-site. The ionic distribution of magnetite side of $MnFe_2O_4$-Fe_3O_4 system is, probably, similar to this case. On the contrary, in the case of $NiFe_2O_4$-Fe_3O_4 or $MgFe_2O_4$-Fe_3O_4, there are foreign ions, Ni^{2+} or Mg^{2+}, on B-site. The abnormal character of $K_1(T)$ mentioned here is smallest in $ZnFe_2O_4$-Fe_3O_4 or $MnFe_2O_4$-Fe_3O_4 systems. That is, the short range order of Fe^{2+} and Fe^{3+} is favourable in the circumstances of the presence of foreign ions, Ni^{2+} or Mg^{2+}, on B-site compared with that of Zn^{2+} or Mn^{2+} on A-site. This tendency is consistent with the experimental result obtained by Epstein,[9] in which he reported that the change of the electric conduction during the low temperature transition of magnetite become obscure more rapidly by the addition of $ZnFe_2O_4$ or $MnFe_2O_4$ than by $NiFe_2O_4$ or $CoFe_2O_4$.

(2) *General concentration dependency of the anisotropy of $MeFe_2O_4$-Fe_3O_4 system*

(a) If we substruct from the observed anisotropy the large positive contribution of electronic short range order at low temperature described in (1), the qualitative relation of K_1 *vs.* composition of $NiFe_2O_4$-Fe_3O_4 system may be represented by that at room temperature in Fig. 4(b). It is remarked that the Curie temperature is nearly the same for this system. In such a situation $NiFe_2O_4$-Fe_3O_4 system has qualitatively a common feature as $MnFe_2O_4$-Fe_3O_4 system, which is also the feature of the ternary system $(Mn_xFe_yNi_z)$-Fe_2O_4: with the increase of Fe_3O_4 concentration, K_1 first increases and after passing a maximum it tends to decrease.

(b) In the case of $(Zn_{1-y}Fe_y)Fe_2O_4$, although the break of the simple Néel model should be taken into account, it is well known from the measurement of the magnetization that this model is still correct in the range of $y \gtrsim 0.7$. If the simple Néel model is imagined to hold over the whole range, the anisotropy of *ferromagnetic* $ZnFe_2O_4$ will be $2K_{\mathrm{Fe}^{3+}_{\mathrm{B}}}$, twice of the contribution to the anisotropy of Fe^{3+} on the B-site, compared with the anisotropy of $NiFe_2O_4$, which is given by $K_{\mathrm{Fe}^{3+}_{\mathrm{A}}}+K_{\mathrm{Fe}^{3+}_{\mathrm{B}}}$ (it is concluded theoretically that the contribution of Ni^{2+} on the anisotropy is very small[7]). According to Folen and Rado[6], $K_{\mathrm{Fe}^{3+}_{\mathrm{A}}}>0$ and $K_{\mathrm{Fe}^{3+}_{\mathrm{B}}}<0$. As K_1 of $NiFe_2O_4$ at 90°K is about -9×10^4 erg/cc, the anisotropy of *ferromagnetic* $ZnFe_2O_4$ is estimated as follows:

$$\begin{aligned} K_{\mathrm{ZnFe_2O_4}} &= 2K_{\mathrm{Fe}^{3+}_{\mathrm{B}}} < 2(K_{\mathrm{Fe}^{3+}_{\mathrm{A}}}+K_{\mathrm{Fe}^{3+}_{\mathrm{B}}}) \\ &= 2K_{\mathrm{NiFe_2O_4}} = -18\times10^4 \ \mathrm{erg/cc}. \end{aligned}$$

The chained curve in Fig. 6 indicates the qualitative dependence of the anisotropy on the concentration at 90°K on the assumption of *ferromagnetic* $ZnFe_2O_4$ mentioned above. It shows a maximum like the case of (a).

(c) According to the simplest assumption that each cation at a given lattice site has the specified anisotropy independent of the presence of the other kind of cation and the substitution of metallic ions are made monotonously on each site, it is expected that K_1 depends linearly on the composition. However, contrary to such an expectation, non-linear dependence of K_1 on the concentration of Fe_3O_4 is a general character of the anisotropy of $MeFe_2O_4$-Fe_3O_4 solid solutions as mentioned above. It is suggested[10] that it can be ascribed to a special character of Fe^{2+}-ion in a crystalline field, giving rise to either positive anisotropy or negative one.

(3) *$MnFe_2O_4$-$NiFe_2O_4$ system*

$MnFe_2O_4$ has 80% normal spinel structure as shown by the neutron diffraction experiment. But, for $MnFe_2O_4$-$NiFe_2O_4$ system, there is no data on the ionic distribution. We can see in Fig. 4(c) that the concentration dependency of the anisotropy is monotonic, in contrast to that of ferrite system containing Fe^{2+} ions.

§6. Conclusions

By the analysis of the experimental results on the ferromagnetic crystalline anisotropy of $(MeFe_2O_4)_{1-y}-(Fe_3O_4)_y$ ferrite solid solutions, where Me=Mn, Ni, Mn-Ni, Zn or Mg, two problems are pointed out:

(1) In most cases, the anisotropy constant decreases (increase of the absolute value of negative anisotropy) with decrease of temperature. But, for Fe_3O_4-rich specimens it increases after passing a minimum and this tendency is remarkable in the case of Me=Ni, less remarkable in Me=Mg and least in Me =Mn, Mn-Ni or Zn. This increase of the anisotropy at low temperature is mainly attributed to the electronic short range order of Fe^{2+} and Fe^{3+} on the B-site of the spinel lattice.

(2) If the increase of K_1 at low temperatures mentioned in (1) is substructed, the concentration dependency of the anisotropy shows a maximum and is attributed to the special character of the contribution of Fe^{2+}-ion to the anisotropy.

Acknowledgment

The author wishes to express his hearty thanks to Prof. Z. Funatogawa for his encouragement throughout this work. He is indebted to Mr. T. Karasawa and other members of Tokyo Denki Kagaku Kogyo Co. and Dr. K. Inoue of Nippon Discharge Machining Laboratories, Inc.. Thanks are also due to Dr. M. Tachiki of Osaka University and to Mr. Y. Gondo and Mr. S. Usami in our laboratory for their valuable discussions. This work is partly supported by the Scientific Research Expenditure of the Ministry of Education.

References

1) Z. Funatogawa, N. Miyata and S. Usami: J. Phys. Soc. Japan **14** (1959) 1583.

2) R. F. Penoyer and M. W. Shafer: J. Appl. Phys. **30** Suppl. (1959) 315S.
3) N. Miyata: J. Phys. Soc. Japan **16** (1961) 206.
4) National Bureau of Standard Circular 539 **2** (1953) 41.
5) R. M. Bozorth *et al*: Phys. Rev. **99** (1955) 1898.
6) V. J. Folen and G. T. Rado: J. Appl. Phys. **29** (1958) 438.
7) K. Yoshida and M. Tachiki: Progr. Theor. Phys. **17** (1957) 331.
8) S. Chikazumi: unpublished.
9) P. A. Miles *et al*: Rev. Mod. Phys. **29** (1957) 294.
10) M. Tachiki: private communication.

JOURNAL OF THE PHYSICAL SOCIETY OF JAPAN, Vol. 16, No. 7, JULY, 1961

Polarization Waves in Solids

By Tatsumi KUROSAWA*

The Institute for Solid State Physics,
University of Tokyo, Tokyo, Japan

(Received January 30, 1961)

A general theory of the polarization waves in crystals is developed in connection with the optical and the dielectric properties of the crystals. The result includes, in more general form, the relations by Szigeti and Fröhlich about the lattice vibrations in ionic crystals and the theory by Heller and Marcus for the exciton. The theory is applied to the analysis of the infra-red data of $BaTiO_3$-type crystals.

§ 1. Introduction

Polarization waves in solids are concerned with a wide range of phenomena in solid state physics. The transverse modes of the polarization waves interact with light and determine the optical properties of the solids. The longitudinal modes interact with the electric field caused by charged particles are interchange the energy with them. The polarization waves are also responsible for the dielectric properties of the solids. Thus, it is expected that there may be relations between these phenomena, for they come from the same origin, the polarization waves. In fact, several authors, for instance, Szigeti[1], Fröhlich[2),3)] and Mott[4], derived several important relations between them.

In this paper, the polarization waves in solids are treated from the above-mentioned standpoint. Several phenomenological relations unknown previously are derived, and some known facts are interpreted from a viewpoint different from that used hitherto.

In § 2, a general theory of the lattice waves in ionic crystals is developed; the results include the relations derived by Szigeti and Fröhlich, in more general form. In § 3, the theory of § 2 is applied to alkali halide and $BaTiO_3$-type crystals. In the latter cases, the result from the simple ionic model is found to be in large disagreement with the experiment, and a tentative interpretation based upon the ionic model is done in Appendix. In § 4, several problems with respect to the electronic polarization waves are treated similarly as in § 2; for instance, the well-known theory of the exciton by Heller and Marcus is re-interpreted from a different viewpoint.

§ 2. Theory of Lattice Waves in Ionic Crystals

A theory of the lattice vibrations in simple ionic crystals has been developed by Szigeti[1]. We shall extend the theory to more complicated crystals, e.g. perovskite type crystals.

Let the number of atoms (ions) in a unit cell be n, and we enumerate them $1, 2, \cdots, n$. In the first place, we take up a needle-like sample of the crystal. Let us imagine that the ions displace in the direction of the needle. Let the displacements of the ions $1, 2, \cdots, n$ be $x_1, x_2, \cdots, x_n$ respectively. The polarization is induced as the result. If the displacements are small the induced polarization must be represented by a linear function of them[†];

---

* Present address: Faculty of Engineering, Chuo University, 1-1 Koishikawa-cho, Bunkyo-ku, Tokyo.

$$P=N\sum_i e_i^* x_i , \tag{2-1}$$

where N is the number of the unit cells in unit volume. Of course

$$\sum_i e_i^*=0 . \tag{2-2}$$

Generally speaking, e_i^*'s are tensor and the direction of the polarization does not necessarily agree with that of the displacement. However, such a generalization is rather trivial and useless. Hence we assume that e_i^*'s are scalar and the direction of the polarization agrees with that of the needle. Thus, there is no electric field in the crystal.

In the next place, let us consider the case that there exists an electric field E in the crystal. If the ions are held undisplaced at their original positions, the polarization is given by

$$P_0=\frac{1}{4\pi}(\kappa_0-1)E , \tag{2-3}$$

where κ_0 is the high frequency dielectric constant. If the ions displace[††], the polarization is given by

$$P=\frac{1}{4\pi}(\kappa_0-1)E+N\sum_i e_i^* x_i , \tag{2-4}$$

because there is no cross term. This equation does not depend on the shape of the sample; the effect of the shape is represented by the depolarization field and included in E. The first term is purely electronic and the second term is due to the displacements of the ions.

The static dielectric constant κ is determined as follows: We write the energy increment per unit volume due to the displacements $x_1, x_2, \cdots, x_n$ $(E=0)$ as

$$\frac{1}{2}N\sum_{i,j} S_{ij}x_i x_j .$$

When the electric field E exists, the interaction energy between the electric field and the polarization should be added;

$$-(P-P_0)E=-EN\sum_i e_i^* x_i .$$

The equilibrium displacement x_i^0 under the electric field is determined by the condition of minimum energy. Thus x_i^0's are given by

$$\sum_j S_{ij}x_j^0=e_i^*E \qquad i=1, 2, \cdots, n . \tag{2-5}$$

Furthermore, if the electric field oscillates with a frequency ω

$$\sum_j S_{ij}x_j^0(\omega)-M_i\omega^2 x_i^0(\omega)=e_i^*E , \tag{2-6}$$

where M_i is the mass of the i-th ion. $\kappa(\omega)$ is given by

$$\kappa(\omega)=\kappa_0+(1/E)\cdot 4\pi N\sum_i e_i^* x_i^0(\omega) . \tag{2-7}$$

Next, we consider the polar mode lattice waves with sufficiently long wavelength; long compared with the lattice constant but short compared with the size of the sample. In this case, the following relations are well-known[2)]: for the transverse waves[†††]

$$E=0 , \tag{2-8}$$

and for the longitudinal waves

$$E=-4\pi P , \tag{2-9}$$

where P is the polarization due to the wave. Therefore, writing the displacement of the i-th ion as $x_i \exp(i\Omega_t t)$, we have the equation determining the frequency of the transverse waves;

$$\sum_j S_{ij}x_j-M_i\Omega_t^2 x_i=0 , \tag{2-10}$$

and of the longitudinal waves;

$$\sum_j S_{ij}x_j-M_i\Omega_l^2 x_i=-4\pi e_i^* P , \tag{2-11}$$

where

$$P=N\sum_i e_i^* x_i+\frac{1}{4\pi}(\kappa_0-1)(-4\pi P) ,$$

or

$$P=\frac{N}{\kappa_0}\sum_i e_i^* x_i . \tag{2-12}$$

Therefore, Eq. (2-11) is rewritten as

$$\sum_j S_{ij}x_j+\frac{4\pi N}{\kappa_0}e_i^*\sum_j e_j^* x_j-M_i\Omega_l^2 x_i=0 . \tag{2-13}$$

[†] The state of the polarization due to the displacement may be very complicated; the polarization due to the displacement of the i-th ion comes from not only the i-th ion but also the induced polarization on the other ions. If the displacements are small, however, the general form of the polarization is given by Eq. (2-1).

[††] We regard the displacements as variable irrespective of the electric field.

[†††] Here we restrict ourselves to such a case that the long polarization waves can be divided into the longitudinal and the transverse waves.

because the electric field $-4\pi P$ acts as a restoring force, the frequency of the longitudinal waves is generally higher than that of the transverse ones and the difference is proportional to e^{*2}.

We write the eigenfrequencies of Eq. (2-10) as $\Omega_{t1}, \Omega_{t2}, \cdots, \Omega_{tn-1}$ (we ignore another eigenfrequency $\Omega_t=0$ which corresponds to the acoustical mode) and the eigenvector belonging to $\Omega_{t\nu}$ as $x_{1\nu}, \cdots, x_{n\nu}$. The ortho-normal condition is

$$\sum_i M_i x_{i\nu} x_{i\nu'} = A\delta_{\nu\nu'} , \tag{2.14}$$

where A is a constant.

The n-dimensional vector $(x_1{}^0(\omega), \cdots, x_n{}^0(\omega))$ in Eq. (2-6) can be represented by a linear combination of the eigenvectors $(x_{1\nu}, \cdots, x_{n\nu})$'s;

$$x_i{}^0(\omega) = \sum_\nu a_\nu(\omega) x_{i\nu} \qquad \text{for all} \quad i .$$

Inserting this into Eq. (2-6), multiplying $x_{i\nu}$ and summing over i, we find that

$$a_\nu(\omega) = \frac{E}{A(\Omega_{t\nu}{}^2-\omega^2)} \sum_i e_i{}^* x_{i\nu} .$$

By remembering Eq. (2-7), we have the following dispersion relation:

$$\kappa(\omega) = \kappa_0 + 4\pi N \sum_\nu \frac{(\sum_i e_i{}^* x_{i\nu})^2}{\sum_i M_i x_{i\nu}{}^2} \cdot \frac{1}{\Omega_{t\nu}{}^2-\omega^2} . \tag{2-15}$$

If there are only two ions in a unit cell as alkali halide crystals, this is simplified as follows:

$$\kappa(\omega) = \kappa_0 + \frac{4\pi N e^{*2}}{\mu(\Omega_t{}^2-\omega^2)} , \tag{2-16}$$

where μ is the reduced mass of the two ions.

By substituting the expression

$$x_i = \sum_\nu b_\nu x_{i\nu} ,$$

for x_i of Eq. (2-13), we obtain

$$b_\nu = -\frac{4\pi N}{A(\Omega_{t\nu}{}^2-\Omega_l{}^2)\kappa_0} \sum_j e_j{}^* x_j \sum_i e_{i'}{}^* x_{i'\nu} .$$

By multiplying $e_i{}^* x_{i\nu}$ and summing over i and ν, we have the equation giving Ω_l;

$$\frac{4\pi N}{\kappa_0} \sum_\nu \frac{(\sum_i e_i{}^* x_{i\nu})^2}{\sum_i M_i x_{i\nu}{}^2} \cdot \frac{1}{\Omega_{t\nu}{}^2-\Omega_l{}^2} = -1 . \tag{2-17}$$

Comparing (2-17) with (2-15), we see that

$$\kappa(\Omega_l) = 0 . \tag{2-18}$$

This relation can be derived directly from Eq. (2-9) which states that $D=0$[3]. In general, Eq. (2-17) has $n-1$ roots. We write them as $\Omega_{l1}, \cdots, \Omega_{ln-1}$. It is easily found from Eq. (2-17) that

$$\Omega_{t1} \leq \Omega_{l1} \leq \Omega_{t2} \leq \cdots \leq \Omega_{tn-1} \leq \Omega_{ln-1} . \tag{2-19}$$

The equality happens when Ω_t's degenerate.

Let us note that $\kappa(\omega)$ has the following properties: (1) $\kappa(\omega)$ has the poles at $\Omega_{t1}, \cdots, \Omega_{tn-1}$. (2) $\kappa(\omega)$ has the zeros at $\Omega_{l1}, \cdots, \Omega_{ln-1}$. (3) $\kappa(\omega)$ tends to κ_0 for large ω. Therefore, if we take the summation of (2-15) over ν in the following form:

$$\kappa(\omega) = \frac{\sum_{k=0}^{n-1} c_k \omega^{2k}}{\Pi_\nu(\Omega_{t\nu}{}^2-\omega^2)} , \tag{2-20}$$

this must be factorized as follows:

$$\kappa(\omega) = \kappa_0 \prod_\nu \left(\frac{\Omega_{l\nu}{}^2-\omega^2}{\Omega_{t\nu}{}^2-\omega^2}\right) . \tag{2-21}$$

Especially, if we put $\omega=0$,

$$\frac{\kappa}{\kappa_0} = \prod_\nu \frac{\Omega_{l\nu}{}^2}{\Omega_{t\nu}{}^2} . \tag{2-22}$$

This is a generalization of the well-known similar relation in the diatomic case[1].

By comparing the coefficients of ω^{2n-4} of (2-20) and (2-21), we find a relation;

$$4\pi N \frac{\sum_\nu(\sum_i e_i{}^* x_{i\nu})^2}{A} = \kappa_0 \sum_\nu (\Omega_{l\nu}{}^2-\Omega_{t\nu}{}^2) . \tag{2-23}$$

On the other hand, the vector $(e_1{}^*, \cdots, e_n{}^*)$ can be expanded by the vectors $(M_1 x_{1\nu}, \cdots, M_n x_{n\nu})$'s;

$$e_i{}^* = \frac{1}{A} \sum_\nu (\sum_j e_j{}^* x_{j\nu}) M_i x_{i\nu} .$$

By multiplying this by $e_i{}^*/M_i$ and summing over i, we have

$$\sum_\nu (\sum_i e_i{}^* x_{i\nu})^2 = A \cdot \sum_i \frac{e_i{}^{*2}}{M_i} .$$

Thus, Eq. (2-23) becomes

$$4\pi N \sum_i \frac{e_i{}^{*2}}{M_i} = \kappa_0 \sum_\nu (\Omega_{l\nu}{}^2-\Omega_{t\nu}{}^2) . \tag{2-24}$$

Here, we shall comment on the relation between the present $e_i{}^*$ and the effective charge $e_s{}^*$ introduced by Szigeti[1]. We may define his effective charge by writing the polarization in a spherical sample of a diatomic crystal as $Ne_s{}^*x$ when the positive and the negative ions displace homogeneously with the relative displacement x. According to the present viewpoint, the polarization of the spherical sample is given by

$$P = \frac{1}{4\pi}(\kappa_0-1)\left(-\frac{4\pi}{3}P\right) + N\sum e_i{}^* x_i ,$$

from Eq. (2-4), because the depolarization field in the spherical sample is $(-4\pi P/3)$. Or,

$$P=\frac{3}{\kappa_0+2}N\sum e_i^* x_i\,. \tag{2-25}$$

In the diatomic case, writing $x_1-x_2=x$ and $e_1^*=-e_2^*=e^*$, we have

$$e_s^*=\frac{3}{\kappa_0+2}e^*\,, \tag{2-26}$$

and in general

$$e_{si}^*=\frac{3}{\kappa_0+2}e_i^*\,. \tag{2-27}$$

Combining Eqs. (2-16) and (2-26), we get the relation derived by Szigeti;

$$\kappa=\kappa_0+\left(\frac{\kappa_0+2}{3}\right)^2\cdot\frac{4\pi N e_s^{*2}}{\mu\Omega_t^2}\,. \tag{2-28}$$

Similarly, if we write the polarization due to the longitudinal wave as

$$P=N\sum_i e_{li}^* x_i\,,$$

we obtain

$$e_{li}^*=\frac{e_i^*}{\kappa_0}\,. \tag{2-29}$$

This agrees with the effective charge introduced by Callen[5] in the diatomic case.

In some cases, e_s^* is appropriate to discuss the microscopic properties of the polarization. On the other hand, the present e_i^*, which corresponds to the effective charge of the transverse wave, is more directly related to the optical and the dielectric properties of the crystal as seen from Eq. (2-15).

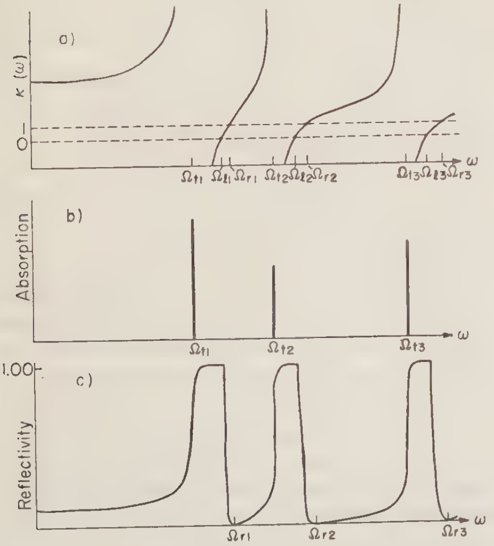

Fig. 1. General features of the dielectric constant, the optical absorption and the reflectivity of crystals.

According to Eq. (2-15), the general features of $\kappa(\omega)$ are schematically as Fig. 1a and the optical properties become as Fig. 1b and 1c; the absorption intensity has peaks at Ω_t's and the peak height is proportional to $(\sum e_i^* x_i)^2/\sum M_i x_i^2$, the crystal shows the metallic reflection when $\kappa(\omega)<0$ and the reflectivity is zero at Ω_r where $\kappa(\Omega_r)=1$.

§ 3. Application of the Theory

Alkali halide and other simple ionic crystals

For these crystals, the analysis by Szigeti[1] and Fröhlich[2] has been known, and we have little to be added to them. We tabulated the values of e^* and e_s^* in Table I for reference. As Szigeti has pointed out, e_s^*/e should be an integer if the simple ionic model were a good approximation†. We have shown that the deviation of e_s^*/e from an integer may be interpreted as brought by the short range

Table I. The values of the effective charge.

	e^*	e_s^*		e^*	e_s^*
LiF	1.12	0.86	RbCl	1.17	0.84
NaF	1.16	0.93	RbBr	1.17	0.81
NaCl	1.06	0.75	CsCl	1.32	0.86
NaBr	1.08	0.70	CsBr	1.29	0.81
NaI	1.16	0.71	AgCl	1.58	0.79
KCl	1.09	0.79	TlCl	2.60	1.10
KBr	1.10	0.76	CuCl	2.04	1.10
KI	1.08	0.69	MgO	2.90	1.76

Table II. Comparisons between the calculated κ from (3-1) and the observed κ.

	λ_t (μ)	λ_r	κ_0	κ	
				cal.	obs.
NaCl	61.1	31	2.25	5.86	5.62
TlCl	117	~45	5.10	28.7	31.9
ZnS	33	24	5.07	8.69	8.3
CdTe	69	58	8.53	11.7	~11

---

† Through the present paper, we mean by the term "simple ionic model" that the binding is perfectly ionic and the interaction between the polarizations can be expressed only by the Lorentz correction, and by "ionic model" we take into account the short range interaction energies between the polarizations especially the cross terms like $B_{ij}x_i p_j$, where p_j is the electronic polarization of the j-th ion.

interaction energy due to the interionic overlapping which causes cross terms between the ionic displacement and the electronic polarization, at least in the case of the alkali halide crystals[6].

In order to verify the theory of § 2, we compare in Table II the dielectric constant κ obtained experimentally and that calculated from the following relation:

$$\kappa-1=(\kappa_0-1)\frac{\Omega_r^2}{\Omega_t^2}\,,$$

and from the observed values of κ_0, Ω_t and Ω_r,[7]† where the above relation is a special case of the more general relation;

$$\kappa(\omega)-1=(\kappa_0-1)\prod_\nu \frac{\Omega_{r\nu}^2-\omega^2}{\Omega_{t\nu}^2-\omega^2}\,, \qquad (3\text{-}1)$$

this can be derived similarly as Eq. (2-21).

$BaTiO_3$ and the related crystals

We take up these crystals, because of the comparatively satisfactory experimental data about them as well as their peculiar dielectric properties.

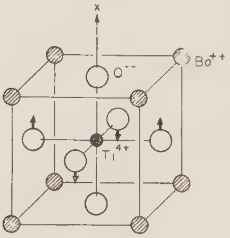

Fig. 2. The crystal structure of $BaTiO_3$ crystal.

These crystals have five ions in a unit cell and have fifteen independent modes of the lattice waves; three acoustical and twelve optical. However, three optical modes illustrated in Fig. 2 (two oxygen ions oscillate to the opposite direction with the same amount) have no dipole moment and are optically inactive. Thus, there remain three longitudinal modes and 3×2 transverse modes for sufficiently long waves. Last[8] has observed two absorption peaks (Ω_t) and two reflection minima†† (Ω_r) for $BaTiO_3$, $SrTiO_3$ and $PbTiO_3$ crystals. Furthermore, we can guess that the one more Ω_t may be nearly zero from their quite large κ. The one more Ω_r has not been observed. We tabulated them in Table III. If Ω_{r1} were observed, we could determine $(\sum_i e_i^*x_i)^2/\sum_i M_ix_i^2$'s of three modes using Eq. (2-15)†††. Furthermore, if a quite precise measurement using the isotopes were performed, it would be possible to determine the e_i^* of each ion separately. Although it is also possible to estimate the $(\sum e_i^*x_i)^2/\sum M_ix_i^2$ from the absorption intensity, practically the reliable determination is difficult.

Table III. (cm⁻¹).

	$SrTiO_3$	$BaTiO_3$	$PbTiO_3$
Ω_{t1}	~0	~0	~0
Ω_{r1}	?	?	?
Ω_{t2}	395	400	405
Ω_{r2}	490	475	455
Ω_{t3}	610	545	590
Ω_{r3}	890	800	(800)

Table IV. The values of $4\pi N\sum_i e_i^{*2}/M_i$ (10^6 cm⁻²).

	From the infra-red data	From the simple ionic model
$SrTiO_3$	2.26~2.96	17.4
$BaTiO_3$	1.95~2.71	10.6
$PbTiO_3$	2.02~3.00	12.3

Nevertheless, we can derive an inequality about the effective charges. In the same way as the derivation of Eq. (2-24), we have

$$4\pi N\sum_i \frac{e_i^{*2}}{M_i}=(\kappa_0-1)\sum_\nu(\Omega_{r\nu}^2-\Omega_{t\nu}^2)\,. \qquad (3\text{-}2)$$

On the other hand, clearly

$$\Omega_{t2}>\Omega_{r1}>\Omega_{t1}\simeq 0\,.$$

Thus we have the upper and lower limits of the $\sum e_i^{*2}/M_i$ (Table IV).

---

† We have used Ω_r, because it can be more easily determined than Ω_l from usually available experimental data.

†† The reflection is not perfectly zero because of the absorption tail at Ω_r.

††† In the case of $BaTiO_3$ crystal, it may help the understanding to imagine the following process: When the $BaTiO_3$ crystal is compressed the curie point T_c is lowered because of the increased interionic repulsive forces. If the compression is continued, the T_c will be lowered down to 0°K and the crystal will lose its ferroelectricity. We may expect, however, that rather a small contraction of the lattice constant (about 2~3%) and rather a small increase of the repulsive force is sufficient to remove the ferroelectricity on the one side and causes no appreciable change of the other properties; Ω_t, Ω_l, Ω_r and e_i^* on the other side.

For comparison, we calculate the $\sum e_i^{*2}/M_i$ assuming the simple ionic model, where e_i^*'s can be calculated by the following process:

$$e_i^* = Z_i e + \sum_j \varepsilon_{ji} \tag{3-3}$$

and

$$p_i = \sum_j \varepsilon_{ij} x_j \,, \tag{3-4}$$

where Z_i, x_i, p_i are the valency (e.g. $Z_{\mathrm{Ti}} = +4$), the displacement and the electronic polarization of the i-ion respectively. p_i is given by

$$p_i = \alpha_i F_i \tag{3-5}$$

and

$$F_i = N\{\sum_j L_{ij} p_j + \sum_j L_{ij} Z_j e(x_j - x_i)\}\,, \tag{3-6}$$

where α_i and F_i are the polarizability and the local field. The coefficients L_{ij}'s are given by many authors[9], for instance when $i = \mathrm{Ti}^{4+}$ and $j = \mathrm{O}_{\iota}^{--}$, $L_{ij} = 4\pi \times 2.727$. We calculated $\sum e_i^{*2}/M_i$'s (Table IV), by substituting for α_i the following values: 0.2 (Ti^{4+}), 1.6 (Sr^{++}), 2.5 (Ba^{++}), 3.1 (Pb^{++}) and 2.2×10^{-24} cm^3 (O^{--}).[†] The values of $\sum e_i^{*2}/M_i$ from the infra-red data are only 1/5~1/4 times of those from the simple ionic model, although the above polarizabilities are consistent with κ_0. On the other hand, in the case of alkali halide crystals, if we assume the simple ionic model as above and take the polarizabilities as consistent with κ_0, e^* is given by

$$e^* = \left(\frac{\kappa_0 + 2}{3}\right) e\,.$$

Thus the ratio of the infra-red value to the simple ionic model value of $\sum e_i^{*2}/M_i$ is $(e_s^*/e)^2$, that is about 0.5~0.9. In this case, we have interpreted the difference by the effect of the short range interaction energy between the ionic displacement and the electronic polarization of ions; the displacement works to induce the electronic polarization with the opposite direction through the overlapping between ions. However, the ratios 1/5~1/4 seem too small to be interpreted by the same effect.

The experiments about the spontaneous polarization of $\mathrm{BaTiO_3}$ are also consistent with the present analysis about the effective charge. The spontaneous polarization is given by

$$P_s = N \sum_i e_i^* x_i^s \,, \tag{3-7}$$

where x_i^s is the spontaneous displacement of the i-th ion and has been determined from the experiments of the neutron[11] or the x-ray diffraction[12]. Although e_i^* of each ion is not known, we have an inequality;

$$P_s^2 = (N \sum_i e_i^* x_i^s)^2 \leq N^2 \sum_i \frac{e_i^{*2}}{M_i} \sum_i M_i x_i^{s2} \,. \tag{3-8}$$

By substituting for x_i^s's the values from the neutron diffraction experiment, we have

$$P_s < 31 \text{ microcoulomb/cm}^2 \,.$$

The x_i^s's from the x-ray diffraction give nearly the same result. The direct experimental value of P_s by Merz[13] is 26 microcoulomb/cm^2. The spontaneous displacement x_i^s can be regarded as brought by the instabilized transverse vibration mode with the lowest frequency Ω_{t1} and as again stabilized by unharmonicity. Therefore, if the $(\sum e_i^* x_i)^2/\sum M_i x_i^2$ of the Ω_{t1} mode were known, the P_s could be estimated more precisely;

$$P_s^2 = N^2 \left[\frac{(\sum_i e_i^* x_i)^2}{\sum_i M_i x_i^2} \right]_{\Omega_{t1}\,\text{mode}} \times \sum M_i x_i^{s2} \,. \tag{3-9}$$

Nevertheless, the inequality (3-8) is consistent with the experiment.

There may be two possible standpoints in interpreting the difference between calculated (simple ionic model) values and the observed (infra-red) values of the effective charge; one attributes the disagreement to the homopolar-binding, and another interprets it within the range of the ionic model. Although it is not within the scope of the present analysis to discuss this problem, a trial upon the latter standpoint is done in Appendix.

It may be allowable to interpret a ferroelectric crystal as a crystal of which the polar mode lattice wave of $\vec{k}=0$ is unstable (in the first approximation) and an antiferroelectric crystal as a crystal of which a lattice wave of $\vec{k} \neq 0$ (e.g. at the zone boundary) is unstable, in the case of the ionic crystals. Generally speaking, the $\vec{k}$-dependence of the frequency of the polar mode lattice wave is rather small and has complicated properties, therefore the theoretical prediction whether a crystal is ferroelectric or antiferroelectric is a delicate problem.

[†] The values for Ti^{4+}, Sr^{++} and Ba^{++} are taken from the paper of Tessman, Kahn and Shockley[10], that of O^{--} ion is adjusted to give the optical dielectric constant κ_0 of $\mathrm{BaTiO_3}$ and $\mathrm{SrTiO_3}$ and that of Pb^{++} ion is taken to be consistent with κ_0 of $\mathrm{PbTiO_3}$.

§4. The Electronic Polarization Waves

It is possible to apply the viewpoints in §2 to the case of the electronic polarization waves in some degree.

Notes on the theory of Heller and Marcus

Let us suppose an atom (or an ion or a molecule) under an oscillating electric field F with a frequency ω. The induced dipole moment is

$$m=\alpha(\omega)F\,, \tag{4-1}$$

where let the polarizability $\alpha(\omega)$ be scalar and given by

$$\alpha(\omega)=\frac{e^2}{m_e}\sum_i\frac{f_i}{\omega_i^2-\omega^2}\,. \tag{4-2}$$

The oscillator strength f_i satisfies the sum rule;

$$\sum_i f_i=n\,, \tag{4-3}$$

where n is the number of the electrons belonging to the atom.

In the next place, let us suppose a crystal consisting of these atoms and the polarization waves propagating in it. The electronic polarization of the i-th atom is given by

$$\vec{m}_i=\vec{m}_0\cdot\exp(i\vec{k}\vec{R}_i-i\omega_k t)\,. \tag{4-4}$$

The relations (2-8) and (2-9) for sufficiently long waves are valid also in this case. If we neglect the overlapping between the atoms, the interaction between the polarizations is only the dipole-dipole one. This interaction can easily be taken into account merely by considering the local field acting on each atom due to the dipole moments on the other atoms. For instance, in the case of the polarization waves of $k=0$ in a cubic crystal, the local field F is given by

$$F=E+\frac{4\pi}{3}P\,. \tag{4-5}$$

Therefore, by combining the Eqs. (2-8), (4-1), (4-2) and (4-5), we find that the frequency Ω_t of the transverse wave in this case must satisfy the following relation:

$$\frac{4\pi}{3}N\alpha(\Omega_t)=\frac{\omega_p^2}{3}\sum_i\frac{f_i}{\omega_i^2-\Omega_t^2}=1\,, \tag{4-6}$$

where

$$\omega_p^2=\frac{4\pi Ne^2}{m_e}\,. \tag{4-7}$$

Similarly, the frequency of the longitudinal wave is given by

$$-\frac{2\omega_p^2}{3}\sum_i\frac{f_i}{\omega_i^2-\Omega_l^2}=1\,. \tag{4-8}$$

On the other hand, under the same assumptions the dielectric constant $\kappa(\omega)$ is given by

$$\kappa(\omega)=1+\frac{4\pi N\alpha(\omega)}{1-(4\pi/3)N\alpha(\omega)}\,. \tag{4-9}$$

Comparing Eqs. (4-6) and (4-8) with (4-9), we can ascertain that Ω_t's and Ω_l's correspond to the poles and the zeros of $\kappa(\omega)$ respectively, as in §2.

Eqs. (4-6) and (4-8) can be transformed as follows: e.g. in the case of $i=1$

$$\Omega_{t1}^2-\omega_1^2=-\frac{f_1\omega_p^2}{3}\cdot\frac{\kappa^{(1)}(\Omega_{t1})+2}{3} \tag{4-10}$$

and

$$\Omega_{l1}^2-\omega_1^2=\frac{2f_1\omega_p^2}{3}\cdot\frac{3\kappa^{(1)}(\Omega_{l1})}{\kappa^{(1)}(\Omega_{l1})+2}\,, \tag{4-11}$$

where $\kappa^{(1)}(\omega)$ is given by

$$\kappa^{(1)}(\omega)=1+\frac{4\pi N\alpha^{(1)}(\omega)}{1-(4\pi/3)N\alpha^{(1)}(\omega)} \tag{4-12}$$

and

$$\alpha^{(1)}(\omega)=\frac{e^2}{m_e}\sum_{i\neq1}\frac{f_i}{\omega_i^2-\omega^2}\,,$$

that is, $\kappa^{(1)}(\omega)$ is the dielectric constant due to the oscillators other than the ω_1-oscillator. Eqs. (4-10) and (4-11) represent the shift of the atomic levels due to the dipole interaction in the crystal.

If we put $\kappa^{(1)}(\omega)=1$ (i.e. neglect the effect of the other levels) and take only the first order term of f_1, (4-10) and (4-11) can be simplified as

$$\Omega_{t1}=\omega_1-\frac{f_1\omega_p^2}{6\omega_1}$$

and

$$\Omega_{l1}=\omega_1+\frac{f_1\omega_p^2}{3\omega_1}\,. \tag{4-13}$$

These results agree with the energy of the exciton of $k=0$ by Heller and Marcus[14].

If there are many excited states, however, each mode of the polarization waves should be represented by a mixture of various atomic excitations; the dipole moment due to an atomic excitation induces that corresponding to the other atomic excitations. The latter is superposed on the former and the resultant dipole moment is $\{\kappa^{(1)}(\Omega_t)+2\}/3$ times the original one in the case of the transverse waves. The local field, that is the variation in the restoring force, is proportional to the dipole moment, thus we have the factor $\{\kappa^{(1)}(\Omega_t)+2\}/3$ of Eq. (4-10).

The frequency of the polarization wave with an arbitrary $\vec{k}$ is to be easily found, if we perform the dipole sum as Lyddane and Herzfeld[15)] have done and calculate the local field at an atom.

If we express the dielectric constant $\kappa(\omega)$ as

$$\kappa(\omega)=1+\frac{4\pi Ne^2}{m_e}\sum_i \frac{F_i}{\Omega_{ti}^2-\omega^2}, \qquad (4\text{-}14)$$

F_i corresponds to the oscillator strength of the i-th excitation mode *in the crystal*; it is proportional to the optical absorption intensity and (4-14) has the same form as the expression of $\kappa(\omega)$ neglecting the local field correction;

$$\kappa(\omega)=1+4\pi N\alpha(\omega)=1+\frac{4\pi Ne^2}{m_e}\sum_i \frac{f_i}{\omega_i^2-\omega^2}.$$

Comparing (4-9) and (4-14), we have a relation after simple manipulations;

$$F_1=f_1\left\{\frac{\kappa^{(1)}(\Omega_{t1})+2}{3}\right\}^2 \Big/ \left\{1+\frac{f_1\omega_p^2}{9}\left[\frac{d\kappa^{(1)}(\omega)}{d(\omega^2)}\right]_{\omega=\Omega_{t1}}\right\} \simeq f_1\left\{\frac{\kappa^{(1)}(\Omega_{t1})+2}{3}\right\}^2. \qquad (4\text{-}15)$$

This represents the change of the absorption intensity in the crystal. The change is caused by the mixing of the other atomic excitation modes. The relation with a similar property has been derived by Dexter[16)]. Furthermore, the following relations are readily found:

$$\sum_i F_i=\sum f_i=n, \qquad (4\text{-}16)$$

this is natural,

$$\kappa(\omega)=\prod_i\left(\frac{\omega^2-\Omega_{li}^2}{\omega^2-\Omega_{ti}^2}\right) \qquad (4\text{-}17)$$

and

$$\frac{1}{2}\sum_i(\Omega_{li}^2-\omega_i^2)=\sum_i(\omega_i^2-\Omega_{ti}^2)=\frac{n}{3}\omega_p^2. \qquad (4\text{-}18)$$

In the above discussions, we adopted a semi-classical approach. However, so far as the interaction between the atoms is the dipole-dipole one and the response of the atom to the electric field is given by (4-1) and (4-2), the above discussions would hold even if the motion of the system were governed by any mechanics; the relations (4-10), (4-11) and (4-15) are to be equivalent to the results calculated quantum mechanically up to the higher order terms of the interaction. The response (4-1), however, holds only for sufficiently weak electric fields except the case of the harmonic oscillator. On the other hand, an atomic transition causes finite electric fields on the neighbouring atoms, namely, the electric field due to the electronic polarization wave fluctuates up to finite values even if it is sufficiently small on an average, such a situation differs from the classical polarization waves. Thus the deviations from the above relations are expected in quantum mechanics. It is not difficult to verify that the above relations agree with the quantum mechanical results up to the terms of f_i's and f_if_j's $(i\neq j)$ in the power series expansions with respect to f_i's. It is supposed, however, that both do not agree for higher order terms in general.†

On the other hand, the level scheme given by Eqs. (4-10) and (4-15) is equivalent to the expression of $\kappa(\omega)$ given by (4-9), therefore the deviation from the so-called Lorentz correction is expected in quantum mechanics from the order of f^3 even if the interaction is only the dipole-dipole one.††

---

† Although it is difficult to investigate quantum mechanically the higher order terms than f^2 in general, we can verify this supposition for special cases, for instance; (1) Two atom system. (2) A crystal composed of the atoms with three atomic levels; s (ground state), p and d levels. In this case, the exact polarization waves should include d-component as well as s- and p-components at the same time differing from the classical polarization waves. (3) In the case of the extremely strong interaction, Ω_{t1} becomes zero or imaginary (see Eq. (4-10)), but such a behaviour cannot be expected in general.

†† The same conclusion has been independently obtained by T. Izuyama (private communication).

The above discussions are more suitably applied to molecular crystals rather than to ionic crystals. In most molecular crystals, however, the crystal structure is complicated and the local field is not simply given by (4-5). In order to apply the above theory to these crystals, it is necessary to perform the complicated dipole sum. It is rather trivial, however, to generalize the theory to these cases unless the practical problems are treated.

Similarly as above, the dipole moment due to the excitation of an impurity atom in a crystal induces the dipole moments of the surrounding atoms, therefore the absorption spectra of the impurity atom change from those of the free atom; the shift of the frequency and the change of the intensity are caused[16].

General electronic polarization waves

The properties of the more general electronic polarization waves have been discussed by many authors[3),4),17)], therefore we briefly summarize them from the present standpoint.

The frequency of the longitudinal polarization wave of $k=0$ satisfies again the relation;

$$\kappa(\Omega_l)=0\ . \tag{4-19}$$

So that, if $\kappa(\omega)$ is represented by the expression like (4-14),

$$\Omega_{l1}{}^2-\Omega_{t1}{}^2=\left(\frac{4\pi Ne^2F_1}{m_e}\right)\Big/\left\{1+\frac{4\pi Ne^2}{m_e}\sum_{i\neq 1}\frac{F_i}{\Omega_{ti}{}^2-\Omega_{l1}{}^2}\right\}=\frac{4\pi Ne^2F_1}{m_e\kappa^{(1)}(\Omega_{l1})}\ . \tag{4-20}$$

Particularly, in the case of $\Omega_{t1}=0$, that is in metals, Ω_{l1} becomes the plasma frequency of the electron system shielded by the dielectric constant $\kappa^{(1)}(\Omega_{l1})$.

In general, however, crystals have continuous absorption spectra, hence the roots of Eq. (4-19) are complex. In this case, it is appropriate to investigate the relation between the response of the system to the electric field $E(t)$ and that to the electric displacement $D(t)$. The electric current in a crystal induced by microscopically homogeneous $E(t)$ and $D(t)$ is generally given by

$$\begin{aligned} J(t)&=\int_{-\infty}^{\infty}\Phi(t-t')E(t')\,dt' \\ &=\int_{-\infty}^{\infty}\Psi(t-t')D(t')\,dt'\ . \end{aligned} \tag{4-21}$$

Clearly, the response functions $\Phi(t)$ and $\Psi(t)$ have the following properties: (1) $\Phi(t)=\Psi(t)=0$, for $t<0$. (2) $\Phi(t)$ and $\Psi(t)$ are real. (3) $\Phi(0)=Nne^2/m_e$, where Nn is the total number of the electrons per unit volume, $\Phi(0)$ is the current which is induced instantly by the electric field of $\delta(t)$ type. By noting that

$$D(t)=E(t)+4\pi\int_{-\infty}^{t}J(t')\,dt'\ , \tag{4-22}$$

we have

$$\Psi(t)=\Phi(t)-4\pi\int_0^t dt'\Phi(t-t')\int_0^{t'}dt''\Psi(t'')\ . \tag{4-23}$$

If we write

$$\Phi(t)=\frac{1}{2\pi}\int_{-\infty}^{\infty}\sigma(\omega)\,e^{i\omega t}\,d\omega$$

and

$$\Psi(t)=\frac{1}{2\pi}\int_{-\infty}^{\infty}s(\omega)\,e^{i\omega t}\,d\omega\ , \tag{4-24}$$

(where $\sigma(\omega)=\sigma^*(-\omega)$ and $s(\omega)=s^*(-\omega)$ because of the reality of $\Phi(t)$ and $\Psi(t)$), we have from Eq. (4-23)

$$s(\omega)=\frac{\sigma(\omega)}{1-4\pi i\sigma(\omega)/\omega}\ . \tag{4-25}$$

From the definitions of $\sigma(\omega)$ and $s(\omega)$, it is clear that their physical meaning is that the current due to the oscillating E and D with the frequency ω is given by

$$J=\sigma(\omega)E=s(\omega)D\ . \tag{4-26}$$

Moreover, because

$$1-\frac{4\pi i\sigma(\omega)}{\omega}=\kappa(\omega)\ , \tag{4-27}$$

the relation (4-25) is equivalent to

$$s(\omega)=\frac{\sigma(\omega)}{\kappa(\omega)}\ . \tag{4-28}$$

This is rather trivial.

On the other hand, if we put $t=0$ in Eq. (4-23), we have

$$\Psi(0)=\Phi(0)=\frac{Nne^2}{m_e}\ . \tag{4-29}$$

By comparing this with (4-24), we have the sum rules;

$$\int_0^{\infty}\sigma_r(\omega)\,d\omega=\int_0^{\infty}s_r(\omega)\,d\omega=\frac{\pi Nne^2}{m_e}\ , \tag{4-30}$$

where σ_r and s_r are the real parts of σ and s respectively. Furthermore, from Eq. (4-25)

$$s(\omega)-\sigma(\omega)=4\pi i\,\frac{\sigma(\omega)s(\omega)}{\omega}\,,$$

therefore

$$\begin{aligned}0&=\int_{-\infty}^{\infty}\frac{\sigma(\omega)s(\omega)}{\omega}\,d\omega\propto\int_{-\infty}^{\infty}\omega\,\frac{(\kappa-1)^2}{\kappa}\,d\omega\\&=\int_0^{\infty}\omega\left(\kappa-\kappa^*+\frac{1}{\kappa}-\frac{1}{\kappa^*}\right)d\omega\\&\propto\int_0^{\infty}\left\{\sigma_r(\omega)-\frac{\sigma_r(\omega)}{|\kappa(\omega)|^2}\right\}d\omega\end{aligned}$$

or

$$\int_0^{\infty}\sigma_r(\omega)\,d\omega=\int_0^{\infty}\frac{\sigma_r(\omega)}{|\kappa(\omega)|^2}\,d\omega=\frac{\pi Nne^2}{m_e}\,. \tag{4-31}$$

On the other hand, the rate of the energy loss per unit volume of the crystal, if $E=E_0\cos\omega t$ and $D=D_0\cos\omega t$, is given by

$$\text{Loss}=\frac{1}{2}\sigma_r(\omega)E_0^2=\frac{\sigma_r(\omega)}{2|\kappa(\omega)|^2}D_0^2\,. \tag{4-32}$$

Thus the relations (4-30) and (4-31) are the sum rules concerning the electric current and the energy loss due to E and D respectively. The conductivity $\sigma_r(\omega)$ determines the intensity of the optical absorption and the $\sigma_r(\omega)/|\kappa(\omega)|^2$ does the energy loss[†] of a high energy charged particles[3)], for the charged particle acts as a source of D rather than of E.

The oscillator strength of the exciton in alkali halide crystals

As stated in § 3, we can determine $(\sum e_i^* x_i)^2/\sum M_i x_i^2$'s which correspond to the oscillator strength in the electronic case, from Ω_t (absorption peak) and Ω_r (reflection minimum) instead of the absorption intensity. The similar method is applicable to the electronic case, if the absorption peak is isolated. For instance, in the case of the so-called exciton absorption in alkali halide crystals, $\kappa(\omega)$ is given by

$$\kappa(\omega)=\frac{4\pi Ne^2}{m_e}\frac{f}{\Omega_t^2-\omega^2}+\kappa'(\omega)\,,$$

near the exciton peak, where f is the oscillator strength of the exciton level and N is the number of unit cells per cm³, $\kappa'(\omega)$ is the dielectric constant coming from the other levels. The reflection minimum arises when $\kappa(\Omega_r)=1$. We estimate $\kappa'(\omega)$ from the reflectivity of the region over $(\hbar\Omega_t-0.2\,\text{ev})\sim(\hbar\Omega_t-0.5\,\text{ev})$, since it may be approximately regarded as a constant within the narrow frequency range from $(\hbar\Omega_t-0.5\,\text{ev})$ to $\hbar\Omega_r$. The results are summarized in Table V. The oscillator strength of the exciton level is rather small, if we remember that there are at least six electrons participating in the exciton level in a unit cell. The contribution to κ_0 from the exciton level is about 0.1. This method may be useful to estimate the oscillator strength when the quantitative data of the absorption intensity are not available, although it is not new in principle.

Table V. The oscillator strength of the exciton.

	κ'	$\hbar\Omega_t$	$\hbar(\Omega_r-\Omega_t)$	f
NaI	3.7	5.6 ev	0.12 ev	0.19
KI	4.1	5.8	0.12	0.27
RbI	3.7	5.7	0.15	0.33

The author wishes to express his gratitude to Prof. J. Yamashita for his helpful discussions.

Appendix. The Effective Charge of BaTiO$_3$ Crystal

As stated in § 3, the ratio;

$$\frac{(\text{the experimental value of }\sum_i e_i^{*2}/M_i\text{ from the infra-red data})}{(\text{the calculated value of }\sum_i e_i^{*2}/M_i\text{ from the simple ionic model})} \tag{A-1}$$

is 1/5~1/4 in BaTiO$_3$ and the related crystals. We investigate here whether such a great difference may be interpreted by the ionic model or not. In the case of alkali halide crystals, the ratio (A-1) is 0.5~0.9, and we can interpret[6)] the difference by assuming the short range interaction energy between the polarization due to the ionic displacement and the electronic polarization, although we cannot explain it by the simple ionic model only.

[†] Of course, the weight with respect to the final states of the particle must be multiplied to this.

In the case of $BaTiO_3$ and the related crystals, we attempt to bring the ratio (A-1) from $1/5 \sim 1/4$ to 0.5 within the range of the simple ionic model and expect that the remaining difference may be interpreted by the similar mechanism as in alkali halide crystals.

The large calculated values of $\sum e_i^{*2}/M_i$ come mainly from the large polarizability of the oxygen ions. However, the polarizabilities assumed in § 3 are not well-founded, although they are consistent with the experimental κ_0. Therefore we regard them as the adjustable parameters and examine whether the above ratio can be brought to the expected value ($\simeq 0.5$) or not with the reasonable values of them.

It is a way to this purpose to decrease the polarizability of the O^{--} ions and increase that of the divalent metal ion. The polarizability of Ti^{4+} ion is too small to influence the result. It is necessary, however, to compensate the decrease of the polarizability of three O^{--} ions with the increase of that of only one metal ion to hold the κ_0 unchanged, so that unreasonably large polarizability of the metal ion is necessary to bring the ratio (A-1) to the expected range. For instance, if we put the polarizability of Sr^{++} ion as 3.4 A^3 instead of 1.6 A^3 in § 3 the above ratio for $SrTiO_3$ becomes 0.5. This value of the polarizability is inconsistent with κ_0 of SrO crystal, in which the *total* polarizability is to be 3.5 A^3.

Another way is to assume the anisotropic polarizability of the O^{--} ions. It is well-known that the polarizability of O^{--} ion fluctuates from compound to compound and generally increases with the volume per O^{--} ion[10]. In the $BaTiO_3$ type crystals, the ionic configuration is close-packed in the Ti–O direction and loose-packed in the Ba–O direction (Table VI), so that, it is probable that the polarizability of the O^{--} ion is small in the Ti–O direction and large in the Ba–O direction. Since the most important contribution to the calculated values of $\sum e_i^{*2}/M_i$ comes from the electronic polarization of the so-called O_a ion, the above assumption is favorable to our purpose. For instance, in the case of $BaTiO_3$ crystal, the following polarizabilities bring the above ratio to 0.5 and are also consistent with κ_0: O^{--} ion (Ti–O direction) 1.7 A^3, (Ba–O direction) 2.5 A^3, Ba^{++} ion 2.5 A^3 and Ti^{4+} ion 0.2 A^3 (the last two values are equal to those in § 3). The circumstances are nearly the same in the other titanates. The polarizability of O^{--} ion varies considerably from compound to compound, e.g. 1.6 A^3 in MgO and 3.0 A^3 in BaO crystals, so that the anisotropy as above is possible. Of course, the above discussions only suggest a possibility of the ionic model and do not deny the possibility of the homopolar binding.

Table VI.

	I	II	(I–II)	III	IV
$CaTiO_3$	2.70	0.99	1.71	1.23	2.40
$SrTiO_3$	2.76	1.13	1.63	1.27	2.57
$BaTiO_3$	2.83	1.35	1.48	1.32	2.76

I. O^{--}–Me^{++} distance; II. Ionic radius of Me^{++} ion; III. (Ti^{4+}–O^{--} distance)–(Ionic radius of the Ti^{4+} ion); IV. O^{--}–Me^{++} distance in MeO crystal (10^{-8} cm).

References

1) B. Szigeti: Trans. Faraday Soc. **45** (1949) 155; Proc. Roy. Soc. (London) **A, 204** (1950) 51.
2) H. Fröhlich: *Theory of Dielectrics* (Clarendon Press, 1949) § 18.
3) H. Fröhlich and H. Pelzer: Proc. Phys. Soc. **A, 68** (1955) 525.
4) N. F. Mott: Proceedings of the 10th Solvay Congress, Brussels, 1954.
5) H. Callen: Phys. Rev. **76** (1949) 1394.
6) J. Yamashita and T. Kurosawa: J. Phys. Soc. Japan **10** (1955) 610.
7) M. Czerny: Z. Phys. **65** (1930) 600. H. Yoshinaga: Phys. Rev. **100** (1955) 753. A. Mitsuishi et al.: The 15th annual meeting of the Physical Society of Japan (1960).
8) J. T. Last: Phys. Rev. **105** (1957) 1740.
9) See for instance, J. C. Slater: Phys. Rev. **78** (1950) 748.
10) J. R. Tessman, A. H. Kahn and W. Shockley: Phys. Rev. **92** (1953) 890.
11) B. C. Frazer, H. R. Danner and R. Pepinsky: Phys. Rev. **100** (1955) 745.
12) W. Känzig: Helv. Phys. Acta **24** (1951) 175.
13) W. J. Merz: Phys. Rev. **91** (1953) 513.
14) W. R. Heller and A. Marcus: Phys. Rev. **84** (1951) 809.
15) Lyddane and Herzfeld: Phys. Rev. **54** (1938) 846.
16) D. L. Dexter: Phys. Rev. **101** (1956) 48.
17) See for instance, D. Pines: Rev. Mod. Phys. **28** (1956) 184.
18) E. A. Taft and H. R. Philipp: J. Phys. Chem. Solids **3** (1957) 1.

JOURNAL OF THE PHYSICA SOCIETY OF JAPAN Vol. 16, No. 7, July, 1961

Cleavage Fracture in Single Crystals of Silicon Iron

By Ryūkichi HONDA

National Research Institute for Metals
2-300, *Nakameguro, Meguro-ku, Tokyo*

(Received February 1, 1961)

Sheet specimens of single crystal of 2.9% silicon iron with {110} surface have been extended in the ⟨100⟩, ⟨110⟩ and ⟨111⟩ directions respectively at −196°C, until they have fractured. The twins and slip lines have been observed in the course of extension as well as after the fracture. The following two mechanisms by which slip or twinning causes the cleavage have been confirmed. In ⟨100⟩ extension, a twin stopped intersecting with another twin along the ⟨110⟩ direction causes a cleavage on the {100} plane parallel to the intersection line. In ⟨110⟩ extension, two {110} slip systems intersecting along the ⟨100⟩ direction cause a cleavage on either of two {100} planes parallel to the intersecting line. Cleavage in ⟨111⟩ extension seems to be understood by extended applications of the latter mechanism.

§1. Introduction

Generally, the cleavage stress actually observed in materials is less than that estimated for ideal crystals by two orders of magnitude or so.[1),2)] This discrepancy is the central problem on which emphasis has been laid so far in the theory of brittle facture in metals and other crystals at low temperature, because the cleavage fracture is the most characteristic feature of the brittleness. Microscopic defects such as inclusions or pre-existing microcracks are not sufficient to explain this discrepancy except in special cases. Grain boundaries might be responsible for it in some cases. But there must be other causes of cleavage fracture, because single crystals are more brittle and have more tendency to cleavage under the stress in certain directions than polycrystals.

To overcome this difficulty, many possible mechanisms of cleavage fracture have been discussed. Twins and cleavages occur frequently in the similar conditions, that is, at low temperature,[2)–4)] at high strain rate[2),3)] and so on. Also, prestrain often decreases both tendencies towards twinning and cleavage.[2),3),5),6)] But the role of the twin as the cause of cleavage fracture remained ambiguous until recent days. Hull[7)] reported recently fine observations about the twins and cracks in single crystals of silicon ions. He showed that almost all cleavage cracks observed after the facture at −196°C were located at the intersecting points of certain twin pairs. Perhaps these cracks were actually initiated by the intersecting twins. But the mechanism by which the intersecting twins cause a cleavage fracture was not clear, together with the answer to the question whether other important causes of the cleavage facture do exist or not.

According to many reports so far published, cleavage fracture is preceded by plastic deformation, especially in certain cases by slip.[8)] Several authors have discussed and calculated the large concentrated stress produced by a pile-up group of dislocations which are forced to stay by a strong obstacle.[9),10)] This large stress field has often been considered in relation to the cleavage crack. In line with this, Stroh[1),11)] elaborated a theory of cleavage fracture. As the strong barrier in b. c. c. metals, Cottrell[12)] has suggested a sessile dislocation which can be formed by coalescence of a pair of two suitable dislocations. Following his suggestion, a calculation was made recently about the magnitude of the stress produced by a double dislocation pile-up on two intersecting slip planes.[13)] Theoretically, these discussions and calculations support the great possibility of cleavage initiation by the mechanism of pile-up dislocations. The observations of the regular row of pile-up dislocations itself were reported by several workers. Especially Smith[14] reported recently an observation of this row on one {110} plane in α-iron. But the direct experimental evidence that the cleavage fracture is caused by pile-up group or groups of dislocations was very meager as yet.

There have also been proposed other mechanisms of cleavage fracture, including Allen's consideration[15] by which no yielding is necessary for the initiation of cleavage. The present purpose is to reply to the following questions, concerning the cleavage in b.c.c. metals.

1) Does the twin actually cause the cleavage fracture? In what case and by what mechanism?
2) Does the slip actually cause the cleavage fracture? In what case and by wheat mechanism?
3) Does any other mechanism remain to be considered?

§ 2. Experimental Procedure

Single crystals of silicon iron have been extended in the [001], [110] and [111] directions respectively in liquid nitrogen (−196°C) by a hard tensile machine, until they have fractured. Twins and slip lines which have appeared on the two surfaces and two sides of the specimens have been observed mainly by optical microscope. These observations have been made at the room temperature at the several points in the course of extension as well as after the fracture, by interrupting the extension and removing the specimens from the tensile machine. The cleavage faces also have been examined.

Single crystal sheets used were prepared by strain-annealing method from polycrystalline sheets and kindly supplied by Dr. Taoka and his group in our institute. The initial polycrystalline sheets contained 2.9 wt. % Si and 0.017 wt. % C but these elements are though to have slightly diminished during the recrystallization in the atmosphere of dry hydrogen. The surfaces of these single crystal sheets coincide with the {110} plane, which will be designated as (1$\bar{1}$0) in this work, with the deviation less than 5 degrees according to the result of X-ray analysis.

From these sheets, three kinds of specimens were cut by the use of wheel cutter. The longitudinal direction, that is, tensile axes of them coincide with the [001], [110] and [111] directions respectively with the deviation less than 5 degrees. They were shaped with fine file by hand. Their surfaces and sides were made flat and strain-free by electropolishing following the method of Jacque. The size and shape of these specimens are shown in Fig. 1. The width of the narrowest region of each specimen was not the same for all specimens. But the effect of this divergence was trivial.

The rate of extension was about 3×10^{-4}/sec. Nine specimens of each kind were examined. The time elapsed during the microscopic examination in the course of extension was about 20 minutes to 1 hour in each observation at room temperature.

§ 3. Results

3.1 Case of [001] extension.

A typical stress-strain curve observed in the case of extension in [001] direction is shown in Fig. 2. The characteristic feature of this curve is straightness interrupted by several abrupt load drops. Accompanying the abrupt load drop, a click was usually heard. Fracture took place always suddenly and total plastic elongation up to the fracture was 1 to 2 percent.

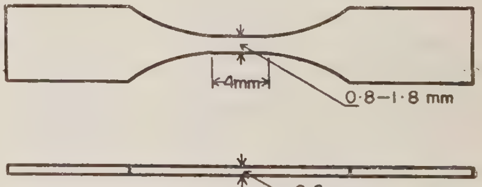

Fig. 1. Size and shape of specimens.

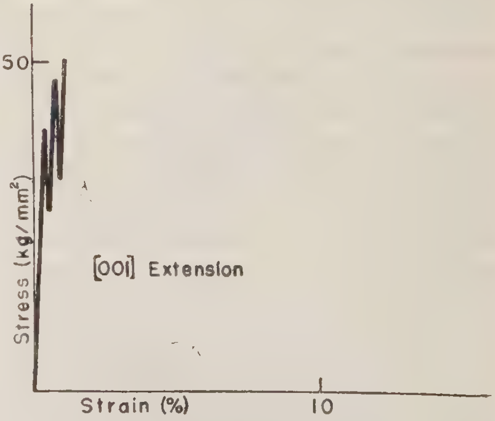

Fig. 2. Stress-strain curve in [001] extension.

In the case [001] extension, after any one abrupt load drop during the extension, a number of traces of twins have been observed as shown in Fig. 3(a) and (b). These traces are thin regions with finite width, the boundaries of which are straight in major part. Sometimes zig-zag markings are observed along the boundaries of them. Their orientations examined geometrically are parallel to the traces of the {112} planes. These features accord with the characteristic ones reported about the deformation twins in α-iron and other b.c.c. metals. With each

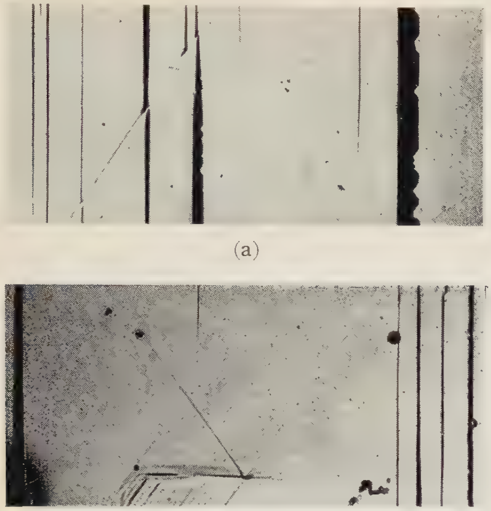
(a)

(b)

←[001] Tensile Axis→

Fig. 3. Twins seen on [001] specimen. ×200.
(a) Surface. (b) Side.

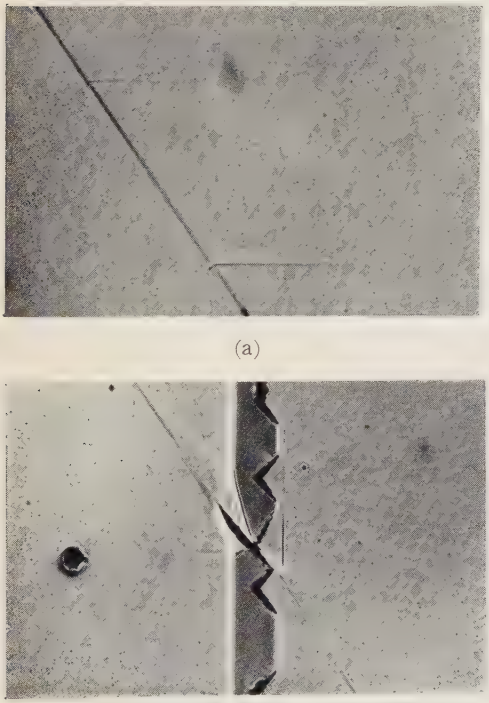
(a)

(b)

←[001]→ Tensile Axis→

Fig. 6. Twin intersections seen on surface of [001] specimen. ×500.
(a) ⟨110⟩ type. Localized slip lines are also seen.
(b) ⟨012⟩ type.

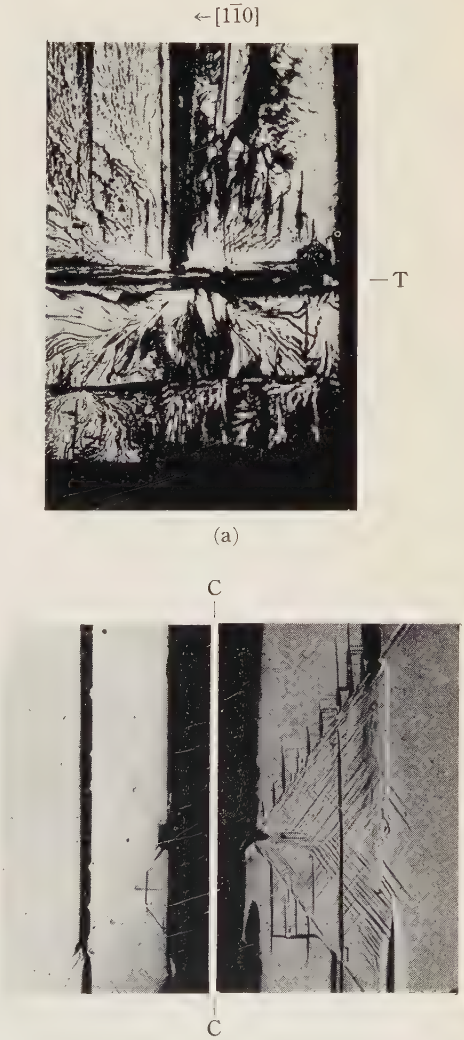

(a)

←(001] Tensile Axis→

(b)

Fig. 7. (a) Cleavage face in [001] specimen.
T--*T*: twin intersection shown in (b). ×200.
(b) Twin intersection of ⟨110⟩ type on cleavage face seen on surface of [001] specimen.
C--*C*: cleavage face shown in (a). ×200.
Specimen is the same in (a) and (b).

abrupt load drop, these twins were found to increase in their number and width. The deformation twins observed are classified by their orientations into four groups. Each group corresponds to one of the four {112} planes, on which resolved shear stress along ⟨111⟩ direction is maximum among all twelve {112} planes as shown in Appendix. These four planes are (112), $(\bar{1}12)$, $(11\bar{2})$ and $(1\bar{1}2)$ planes, and their traces on the surface and the side of [001] specimens are shown in Fig. 4 (a) and (b) to be compared with Fig. 3 (a) and (b).

The intersections of these four groups of twins are classified geometrically into two types. The intersecting line of twins on the (112) and $(11\bar{2})$ planes is parallel to the $[1\bar{1}0]$ direction and that of twins on the $(\bar{1}12)$ and $(1\bar{1}2)$ planes to the [110] direction, as exemplified in Fig. 5. The intersections of

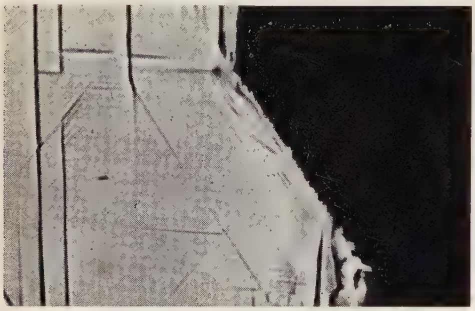
←[001] Tensile Axis→

Fig. 8. Deflection of cleavage face along twin-matrix interface seen on surface of [001] specimen.
C--*C*: cleavage face. ×500.

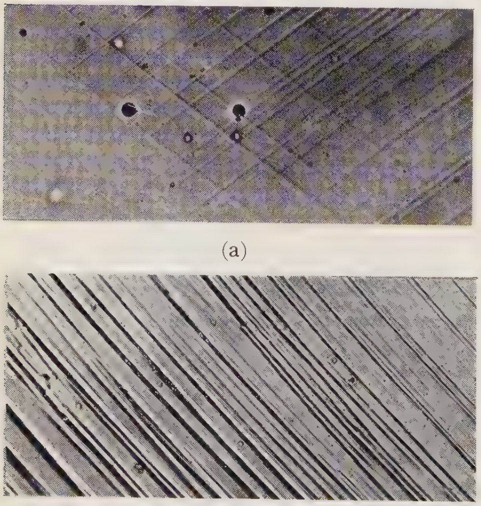
(a)

(b)

←[110] Tensile Axis→

Fig. 10. Slip lines on [110] specimen. ×200.
(a) Surface. (b) Side.

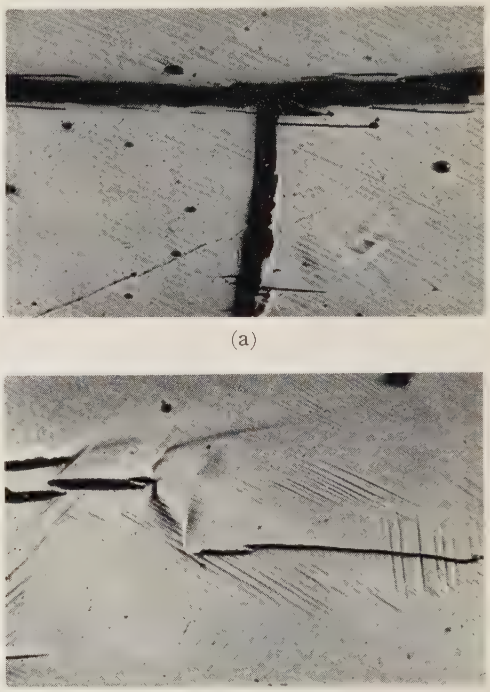
(a)

(b)

←[110] Tensile Axis→

Fig. 13. (a) and (b). Longitudinal cleavage cracks seen on surfaces of [110] specimens. Transversal cleavage has also occurred in one side of longitudinal crack shown in (a). (a) ×100. (b) ×500.

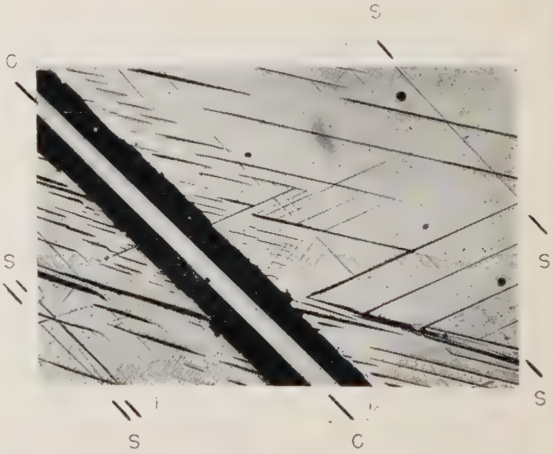

Fig. 14. Slip lines (*S*--*S*) and transversal cleavage face (*C*--*C*) parallel on side of [110] specimen. Twins and localized slip lines appeared after the fracture are also seen ×200.

these twin pairs may be shortly called ⟨110⟩ type. Other four pairs among four groups intersect along ⟨012⟩ lines. The intersections of these pairs may by called ⟨012⟩ type.

The microscopic observations show a characteristic difference between these two types of intersections. In a intersection of ⟨110⟩ type, one of two twins is usually stopped at the intersecting point, as seen in Fig. 6(a). Sometimes two twins which form the

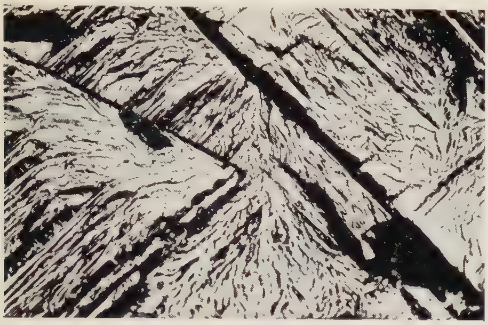

[001]→

Fig. 15. Transversal cleavage face in [110] specimen. ×200.

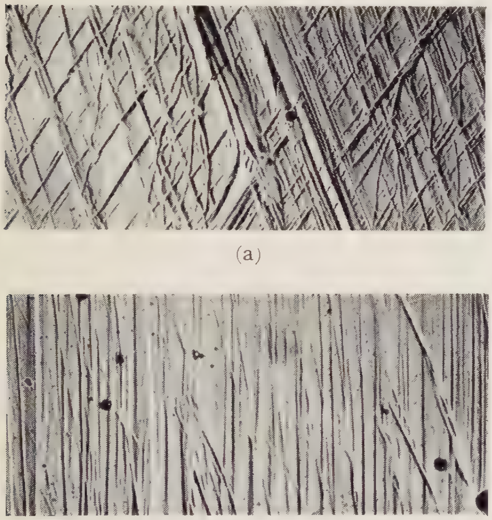

(a)

(b)

←[111] Tensile Axis→

Fig. 17. Slip lines on [111] specimen. ×200.
(a) Surface. (b) Side.

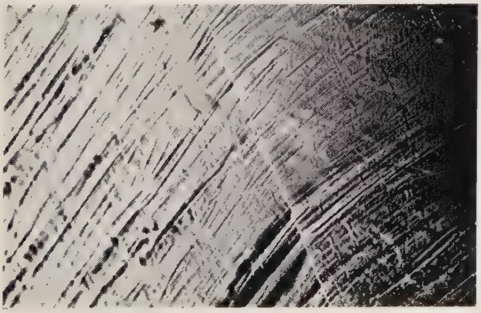

←[111] Tensile Axis→

Fig. 19. Bend plane of kink in [111] specimen seen on surface. ×200.

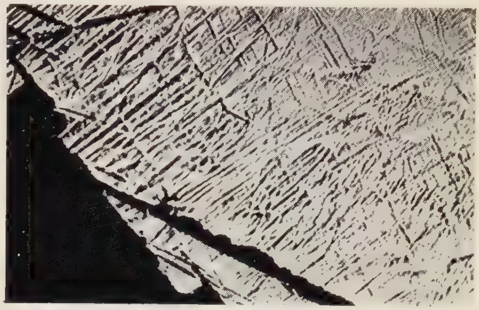

←[111] Tensile Axis→

Fig. 20. Complicated slip lines and cleavage face seen on surface in the neck of [111] specimen. Twins are also seen. ×200.

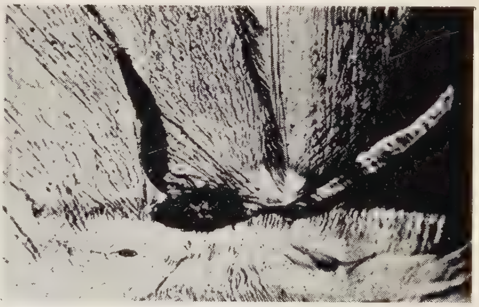

Fig. 21. Cleavage face which might be on {110} plane in [111] specimen. ×200.

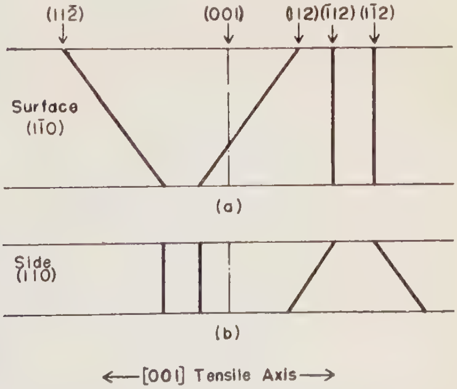

Fig. 4. Traces of operative twinning planes and cleavage plane on [001] specimen.
(a) Surface.
(b) Side. ——: twinning plane, —·—: cleavage plane.

⟨110⟩ intersection on the cleavage face seem as if they had run through each other. But the one half of either twin is thought to have been formed after the cleavage had been initiated. Indeed, this situation has been shown in some observations. On the other hand, in more than one third of observed intersections of ⟨012⟩ type, two intersecting twins have run through each other as shown in Fig. 6(b).

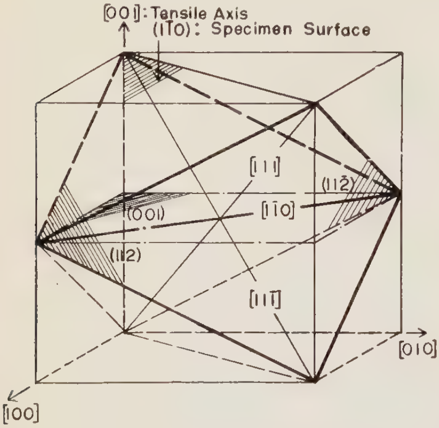

Fig. 5. Twin intersection of ⟨110⟩ type in [001] extension. ——: twinning plane, ——·——: intersecting line, ——·——: cleavage plane.

At the neighboring regions of the intersections of ⟨110⟩ type, short traces considered to be slip lines have been often observed, as seen in Fig. 6(a). They run from the intersecting points along the trace of {110} plane which involes the intersecting line of two twins. Their length is about 0.01–0.1 mm and they fade away at one end. Sometimes other localized slip lines have also been observed around twins and cleavage faces.

The specimens extended in [001] direction have always fractured by cleavage on (001) plane. The cleavage face, as shown in Fig. 7(a), is a plane face with many steps along twins. Also many fine patterns sometimes called river patterns[16] are observed on them. As an important fact, it could be pointed out that always one and only one intersection of two twins of ⟨110⟩ type is observed on the cleavage face as shown in Fig. 7(b). Not all the twin intersections of ⟨110⟩ type have caused cleavage fractures but many intersections of ⟨110⟩ type have been observed already in the course of extension. In a few specimens, the only one ⟨110⟩ intersection detected on cleavage face coincides with one of ⟨110⟩ intersections observed in advance in the course of extension. Sometimes cleavage face deflects from (001) plane and runs for a short distance along twin-matrix interface, as seen in Fig. 8.

3.2 Case of [110] extension.

A typical stress-strain curve is shown in Fig. 9. Several abrupt load drops usually accompanying audible click are observed also in each [110] extension. But here, more or less continuous flow occurs in the later stage of extension and after the elongation from a few to about ten percent the specimens have suddenly fractured by cleavage.

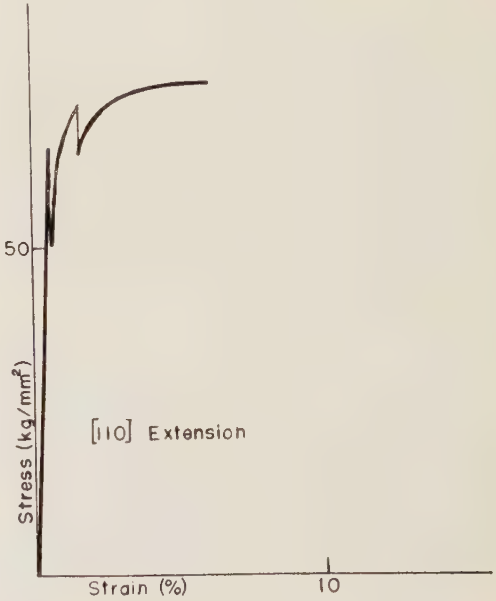

Fig. 9. Stress-strain curve in [110] extension.

The observation in the course of extension shows a distinct difference from the case of [001] extension. That is, no twins have been detected in advance to the occurrence of fracture, although many lines have appeared and increased with abrupt load drops, see Fig. 10(a) and (b). These lines are surely slip lines, for they are parallel to the traces of four {110} planes which have maximum resolved shear stress in the [111] or the [111̄] direction on them among all {110} slip systems, as shown in Appendix.

Traces of these planes on the surface and side of the specimen are shown in Fig. 11(a) and (b), to be compared with Fig. 10(a) and (b). The slip lines on the surface have appeared perhaps due to the small deviation of that face from the exact (1$\bar{1}$0) plane, in spite of the fact that the slip directions must be parallel to this plane. Slip lines appeared after the first abrupt load drop or after the first and second were parallel to one {110} plane. Until the fracture occurred, slip lines appeared usually on two {110} planes in each specimen. In two specimens, many cross slips were observed on the sides.

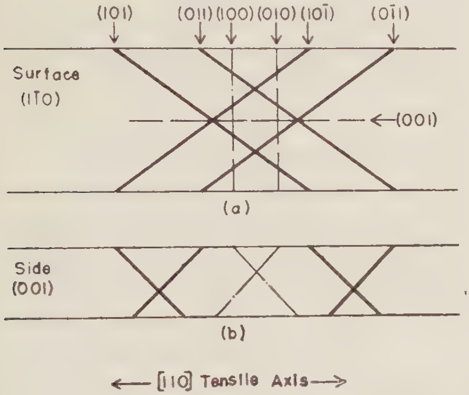

Fig. 11. Traces of operative slip planes and cleavage planes on [110] specimen.
(a) Surface.
(b) Side. ——: slip plane, ——·——: cleavage plane.

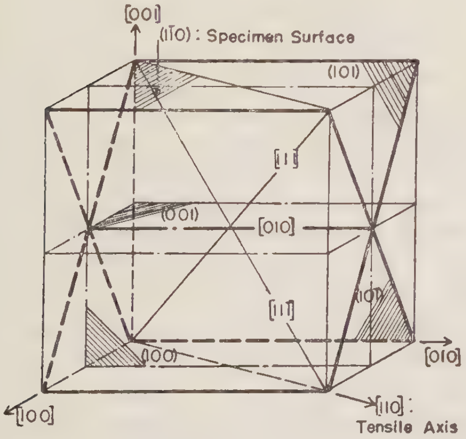

Fig. 12. Slip intersection of ⟨100⟩ type in [110] extension. ——: slip plane, ——·——: intersecting line, ---·——: cleavage plane.

Geometrically intersections among these four slip systems are classified into two types. The pair of (101) [11$\bar{1}$] and (10$\bar{1}$) [111] and that of (011) [11$\bar{1}$] and (0$\bar{1}$1) [111] intersect along the ⟨100⟩ lines, as exemplified in Fig. 12. The other four pairs intersect along the ⟨111⟩ directions. It has been found that the fracture has occurred only after the intersections of ⟨100⟩ type. The fracture took place not always immediately after the first ⟨100⟩ intersections but usually after the succeeding elongation of several percent. In seven specimens, the slip lines remained parallel on the side until the fracture, though the intersections of slip lines were observed on the surface, as shown in Fig. 10. That is, in each of these specimens, only either one of two kinds of ⟨100⟩ intersections has occurred until the fracture.

A remarkable fact is the appearance of large or small longitudinal cracks on (001) plane parallel to the tensile axis. In four specimens, these cracks of length more than 1 mm have been detected in each specimen as shown in Fig. 13(a) and (b).

The specimen fractured finally by transversal cleavage on (100) or (010) plane. It has been also found that the transversal cleavage planes correspond to the kinds of intersections of ⟨100⟩ type in the following way. When the intersecting line between the two slip planes is [010], the transversal cleavage plane is (100) and when the intersecting line is [100], the transversal cleavage plane is (010). As illustrated in Fig. 12, the traces on the (001) plane of transversal cleavage plane and of intersecting slip planes must be all parallel if the above correspondence is actually correct. In each specimen in which the observed ⟨100⟩ intersections were confined to only one kind, this correspondence has been distinctly verified by the observation of the sides which is the (001) plane, as seen in Fig. 14.

After the fracture, some twins have been observed around the cleavage face but no definite configuration was detected which suggests the function of these twins in the initiation of the cleavage. These twins are thought to have taken place as sequential products at the instant of the cleavage fracture. Localized slip lines which are also thought to be the sequential products have been detected occasionally after the fracture. The longitudinal and transversal cleavage faces have also a number of steps along twins and river patterns between them. Transversal cleavage face is shown in Fig. 15.

3.3 Case of [111] extension.

A typical stress-strain curve is shown in Fig. 16. The characteristic feature is a round load drop with which a sharp neck is formed. The ductility was fairly large. Several little abrupt load drops have been observed in many specimens. The click was heard with the abrupt load drop but not with the round one. The fracture took place after the round load drop with or without succeeding elongation of several percent and still pretty suddenly.

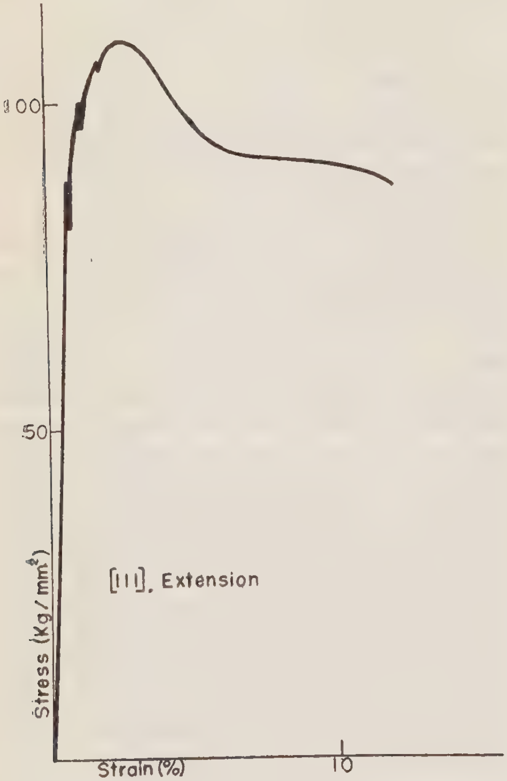

Fig. 16. Stress-strain curve in [111] extension.

Many slip lines have appeared with the abrupt load drops and during the continuous flow. But no twins have been detected in advance to the fracture. Geometrically there exist six {110} slip systems on three {110} planes which have maximum resolved shear stress, as listed in Appendix. The slip lines observed in the early stage of extension or outside the neck almost lie on these three {110} planes and many cross slips are observed, as shown in Fig. 17(a), (b) and Fig. 18(a), (b). In severe neck, on the other hand, slip lines which might be on {112} or {123} planes have been observed, together with closely distributed slip lines on the above {110} planes. But, there the slip lines are so complicated that unquestionable identification of slip systems was rather difficult. Also, a configuration or configurations which have the appearance of kinks have been formed in or around the neck. A bend plane appeared in the kinks is shown in Fig. 19.

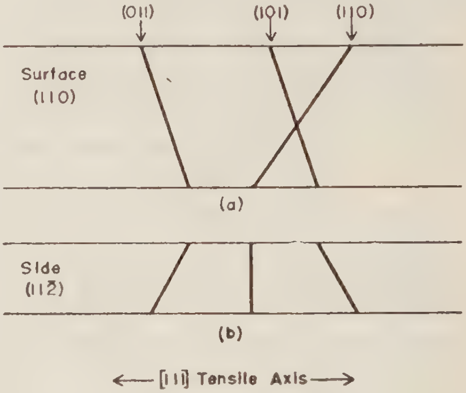

Fig. 18. Traces of operative slip planes on [111] specimen.
(a) Surface. (b) Side.

The fracture occurred through the neck but is still due to the cleavage as seen in Fig. 20. In almost every specimen, not only one but two or three cleavage faces, usually intersecting perpendicularly, have been observed. Nearly all of the observed cleavage faces are thought to be on the {100} planes from their orientation and their structures are more or less similar to those of cleavage faces appeared in [001] and [110] extension. But two of them are pretty deviated from any one of the {100} planes and might be on the {110} planes. These two have somewhat different surface structures and are curved in their boundary regions as shown in Fig. 21. The indices of these planes were difficult to decide exactly due to the heavy deformation even with X-ray analysis. A number of twins have been observed only after the fracture but they do not seem to have played the significant role for the initiation of cleavage.

§ 4. Discussions

4.1 Case of [001] extension.

In the case of [001] extension, twins will be mainly discussed because slip is not observed except that located in special zones. Prior to the analysis of cleavage fracture, the difference between two types, ⟨110⟩ and ⟨012⟩, of twin intersections will be made clear. We have already recognized that in the ⟨110⟩ intersections, one twin is stopped by the other and in ⟨012⟩ intersections, many two twins run through each other, as shown in Fig. 6. Consideration of a characteristic property of twinning leads us naturally to the understanding of this situation. Twinning can operate in one direction but not in the opposite direction. This property will be easily understood from the configuration of atom displacement in twinning. Fig. 22 shows twinning on the (112) and (11$\bar{2}$) planes seen on the (1$\bar{1}$0) plane in b.c.c. crystals. The twinning can occur in the directions pointed by arrows. The shear stress components in these possible twinning directions is positive when the external tension is in the [001] direction or negative when the tension is in the [110] direction. Thus, it is reasonable that the twins on the (112) or (11$\bar{2}$) planes have been observed only in the [001] extension but not in the [110] extension.

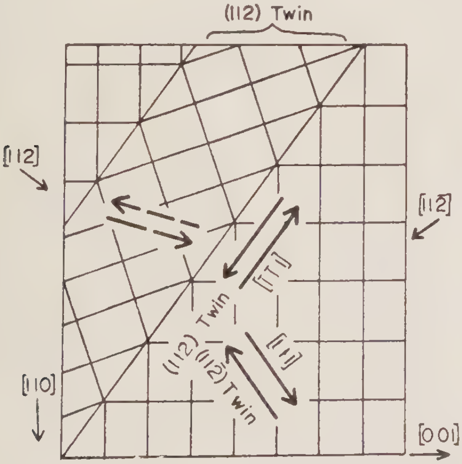

Fig. 22. Possible twinning directions on (1$\bar{1}$0) plane are shown by solid arrows in original lattice and by dotted arrows in (112) twin region.

Returning to the case of [001] extension, let us consider an example of ⟨110⟩ twin intersections in which a (11$\bar{2}$) twin grows and meets with a (112) twin, as shown in Fig. 23. In this case, (11$\bar{2}$) twin cannot penetrate into the (112) twin region by twinning, because the orientation of the new {112} plane within the (112) twin region is deviated from that of the original (11$\bar{2}$) plane and moreover the component of shear stress in the possible twinning direction on that {112} plane is negative, as shown by dotted arrows in Fig. 22. On the other hand, in the ⟨012⟩ twin intersection, there is a {112} plane in either twin, on which the other twin can penetrate into the former twin, though some difficulty should be accompanied by the penetration because of a deflection of the twinning plane.

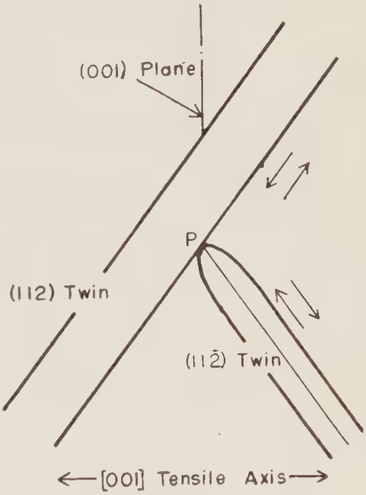

Fig. 23. ⟨110⟩ type twin intersection seen on (1$\bar{1}$0) plane.

Thus, the difference of two types of twin intersections can be understood. Beside the intersections on cleavage faces mentioned in 3.1, there have been observed a few exceptional examples of ⟨110⟩ intersections, in which two twins seem to have run through each other. In these intersections, perhaps the stopped twin has produced a new twin just at the opposite side of stopping twin. But this process is naturally rare, because a twin will be hardly generated in a region without suitable defects.

Now, the mechanism by which the ⟨110⟩ twin intersection causes a cleavage fracture is argued as follows. In Fig. 23 a twinned region is supposed to be stopped at the top *P* by another twin. Then, the outer part of that stopped twin will be pushed to the obstacle and cause a large stress around the top. By comparing the work done by the external stress with the work done by the concentrated shear stress at the top in the process of virtual advance of the top P by twinning, the concentrated shear stress τ_c is estimated as

$$\tau_c = n\tau , \qquad (1)$$

where n is the number of twinning layers in that twin, and τ is the external shear stress. In the stable configuration, this shear stress must be compensated by the elastic stress in the obstacle region and this compensation stress will appear as tensile and compressive stress on the upper and lower side of the twinning plane through P respectively. The direction of them is considered to be nearly parallel to the twinning direction and their magnitude will be of the order of τ_c or $n\tau$. These situations are very analogous to the case of pile-up dislocations.

This concentrated stress will cause a cleavage if it is sufficiently large. When the external tension is σ, the thickness of the stopped twin is d and the normal component of the concentrated tensile stress on the (001) plane is S,

$$\tau = 0.472\sigma \text{ (Appendix)} , \qquad (2)$$

$$n = \sqrt{6}\, d/a , \qquad (3)$$

and

$$S = n\tau/\sqrt{3} = 0.668\sigma d/a , \qquad (4)$$

where a is the lattice constant. For the observed order of $\sigma = 50\,\text{kg/mm}^2$ and $d = 0.5\,\mu$, S is estimated to be $6\times10^4\,\text{kg/mm}^2$. This roughly estimated value is considered to be enough to cause a cleavage fracture. Since the concentrated stress is produced along the intersecting line, cleavage can occur only on a plane parallel to that line. Here the (001) plane satisfies this condition, as understood from Fig. 5.

The localized short slip lines observed at the intersecting points of ⟨110⟩ type give an evidence of localized stress concentration. In the ⟨012⟩ type of intersection, large stress concentration is not produced, because each twin, owing to the possibility of mutual penetration, does not act as a strong barrier to the other and hence no cleavage occurs. The observed one-to-one correspondence between the (001) cleavage and the ⟨110⟩ twin intersection shows conclusively that the cleavage fracture in [001] extension has always been caused by the mechanism of the twin intersection of ⟨110⟩ type mentioned above.

4.2 Case of [110] extension.

Here, the slip is observed to be the main mode of deformation. On the (112) and (11$\bar{2}$) planes, resolved shear stress is fairly large but it is negative to the twinning direction, as shown in Fig. 22. Actually, twins have not been observed on these planes. After the fracture a number of twins on other {112} planes have been observed, but they do not seem to have played significant role in the initiation of cleavage fracture. Therefore, only the function of slip will be discussed in the following analysis.

Cottrell[12)] has suggested that in b.c.c. metals certain two {110} dislocations, for example, (101)$a/2[\bar{1}\bar{1}1]$ and (10$\bar{1}$)$a/2[111]$ can coalesce to form one dislocation, Burger's vector of which is $a[001]$ and the energy of which is lower than the sum of energies of two dislocations to be coalesced. This coalescence occurs along the [010] direction in which the two slip planes intersect. The succesive dislocations which follow the already coalesced dislocations on both slip planes pile up before or run into the coalesced dislocation, because it is sessile. The (001) plane which involves the intersecting line receives a large normal tension under this circumstance. In this way Cottrell has explained the cleavage fracture in b.c.c. metals.

The observed slip systems in the case of [110] extension are predominantly confined on the {110} planes in accordance with other report concerning the slip systems of silicon iron.[4)] Moreover, the intersections of two slip systems of ⟨100⟩ type mentioned in 3.2 are essentially equivalent to those proposed by Cottrell. The direction of slip in the case of [001] extension considered by him is opposite to that in the case of [110] extension now under consideration. But this difference can be thought as trivial, for the same dislocations can cause an opposite shear moving to the opposite directions. Of course, a slip shear in one direction itself can be caused by either of two kinds of dislocations with opposite signs moving to the opposite directions. Hence the combination of Burger's vectors of dislocations running towards the intersecting line is not necessarily suitable for the coalescence. But this situation exists both in Cottrell's case and in the present case. Anyway, about half of the pairs of intersecting slip systems are expected to be caused by dislocation groups suitable for the coalescence.

The cleavage fracture in [110] extension has always taken place after the occurrence of the slip intersections of ⟨100⟩ type. This behavior is in accord with the first requirement of Cottrell's mechanism.

It is easily checked up that by the Cottrell's mechanism, the cleavage must take place on the (001) plane, even in the case of [110] extension, no matter which kind of intersections of ⟨100⟩ type is responsible. Actually, cleavages on the (001) plane have frequently been observed as large or small longitudinal cracks, as shown in Fig. 13.

In the above argument, the numbers of pile-up dislocations were implicity assumed as nearly equal in both slip planes. If the number is extremely small on one plane compared with that on the other, the concentrated tensile stress is directed nearly parallel to ⟨111⟩ direction, and the two {100} planes parallel to the intersecting line receive equally a large normal tension. One of these two is again the (001) plane on which the observed longitudinal cracks exist. The other is the (100) or (010) plane, if the intersecting line is [010] or [100] respectively. The transversal cleavage planes actually observed are found to be in full agreement with this consideration.

Thus, the mechanism of pile-up dislocations before a coalesced one is entirely conformable to every feature observed. Hence, the cleavage fracture in [110] extension is concluded to have occurred always by this mechanism.

4.3 Case of [111] extension

Here, the six {110} slip systems operative in the early stage of extension intersect along ⟨111⟩ lines, if they are not on the same plane and many cross slips have been observed as expected naturally. Then, the formation of sessile dislocation and the pile-up of many dislocations are probable, if any, only along the ⟨111⟩ direction. The large ductility observed in this case seems natural because the ⟨111⟩ lines are not parallel to any {100} plane. For, the observed cleavage planes are predominantly the {100} planes in b. c. c. metals and other crystallographic planes seem to have higher surface energy considering the elastic anisotropy and shapes of etching pits.

The mechanism of cleavage fracture itself is not clear in this case, though the slip seems to play the important role here again. As one possible mechanism, it is proposed that cleavages are caused by the intersections of {112} or {123} slip systems as well as of {110} slip systems. All the slip dislocations in b.c.c. metals have the Burger's vectors of $a/2\langle 111\rangle$ and any pair of these vectors sums to $a\langle 100\rangle$ or $a\langle 110\rangle$ according to their relative sign. Thus, when two slip planes intersect, the formation of coalesced and sessile dislocation is always probable excluding the case of cross slip. Hence, if the intersecting line of two slip systems is on one {100} plane, pile-up group or groups of dislocations may cause a cleavage on this plane. In fact, it seems that several pairs of slip systems observed in the neck of [111] specimens might be those in which two slip system intersect on the {100} plane. These pairs might be the cause of cleavage fracture on the {100} planes in [111] extension, because the cleavage fracture has taken place through the neck. On the other hand, {110} slip systems intersecting along the ⟨111⟩ direction might cause occasionally a cleavage on a plane parallel to this intersecting line also by the mechanism of pile-up dislocations. The cleavage which seems to have occurred on the {110} plane might be caused by this mechanism. The {110} cleavage planes are also reported in tantalum[17)] and niobium[18)].

Finally, it will be suggested that the present mechanisms of cleavage fracture do not conflict with the ductile-brittle transition. Twins are not formed and hence do not cause a cleavage in higher temperature. The concentrated stress caused by intersecting slip systems may also be easily released by the occurrence of other slips at higher temperature. In the case of twin intersections, this release has been observed as localized slip lines. Dissociation of coalesced dislocation might also occur frequently in the higher temperature. There might be some intermediate temperature region in which the formation of twins is not possible but intersecting slips can still cause a cleavage fracture under the tension in the [001] direction.

These two mechanisms of cleavage fracture mentioned above, one by intersecting twins and the other by intersecting slips, stand obviously in close parallelism in their essential points. At first, the plastic flow is blocked by the intersection in both mechanisms, although the mechanisms of blockage are different in them, and a large concentrated stress is consequently produced along the intersecting line. Secondly, the interesting line lies on the {100} plane which has the weakest resistance against the cleavage among all other crystallographic planes. Thirdly, the concentrated stress acts as a large normal tension on this weak plane and causes a cleavage fracture.

The cleavage behavior in the silicon iron will be considered to have common feature to some extent with that of other b. c. c. metals, because the behavior of twinning or slip is pretty similar in other b.c.c. metals.

§ 5. Conclusions

In the cleavage fracture of single crystals of silicon iron extended at −196°C, two mechanisms of cleavage fracture have been experimentally confirmed. One is a mechanism by which a definite type of twin intersections causes a cleavage fracture on the {100} plane. The other is that by which a definite type of the {110} slip intersections causes a cleavage fracture on the {100} planes.

The cleavage fracture of specimens extended in the ⟨100⟩ direction is always explained by the former mechanism and that of specimens extended in the ⟨110⟩ direction is always explained by the latter mechanism. The cleavage fracture of specimens extended in the ⟨111⟩ direction may be explained by extended applications of the latter mechanism.

These two mechanisms, one by twins and the other by slips, are similar in their essential points.

Acknowledgement

The author wishes to express his hearty thanks to Dr. U. Hashimoto, Director of National Research Institute for Metals, and Prof. S. Kaya, President of the University of Tokyo, for their continual encouragement throughout this work. He is grateful to Dr. T. Kawada and Dr. T. Taoka for their cordial guidance in this work. Also his thanks are due to Dr. Taoka and his group for the kind supply of single crystal sheets of silicon iron.

Appendix

Ratios of resolved shear stress in {110} and {112} deformation systems in b. c. c. structure to external tension in three important directions.

Deformation systems	Directions of external tension	[001]	[110]	[111]
{110} systems (slip)	$(011)[11\bar{1}]$	0.408	0.408	0.272
	$(011)[1\bar{1}1]$	0.408	0	0.272
	$(10\bar{1})[1\bar{1}1]$	0.408	0	0
	$(10\bar{1})[111]$	0.408	0.408	0
	$(0\bar{1}1)[111]$	0.408	0.408	0
	$(0\bar{1}1)[\bar{1}11]$	0.408	0	0
	$(101)[\bar{1}11]$	0.408	0	0.272
	$(101)[11\bar{1}]$	0.408	0.408	0.272
	$(\bar{1}10)[11\bar{1}]$	0	0	0
	$(\bar{1}10)[111]$	0	0	0
	$(110)[1\bar{1}1]$	0	0	0.272
	$(110)[\bar{1}11]$	0	0	0.272
	$(112)[11\bar{1}]$	0.472	0.472	0.314
	$(2\bar{1}1)[11\bar{1}]$	0.236	0.236	0.157
	$(\bar{1}21)[11\bar{1}]$	0.236	0.236	0.157

{112} systems (twinning and slip)	$(\bar{1}12)[1\bar{1}1]$	0.472	0	0.157
	$(121)[1\bar{1}1]$	0.236	0	0.314
	$(21\bar{1})[1\bar{1}1]$	0.236	0	0.157
	$(11\bar{2})[111]$	0.472	0.472	0
	$(\bar{2}11)[111]$	0.236	0.236	0
	$(1\bar{2}1)[111]$	0.236	0.236	0
	$(1\bar{1}2)[\bar{1}11]$	0.472	0	0.157
	$(12\bar{1})[\bar{1}11]$	0.236	0	0.157
	$(211)[\bar{1}11]$	0.236	0	0.314

References

1) A. N. Stroh: Advances in Physics **6** (1957) 418.
2) N. J. Petch: Progress in Metal Physics Vol. **5** ed. by B. Chalmers et al. (Pergamon Press, London, 1954) art. 1, 1.
3) E. O. Hall: Twinning and Diffusionless Transformation in Metals (Butterworths Scientific Publications, London, 1954) 66p.
4) C. S. Barrett, G. Ansel and R. F. Mehl: Trans. Amer. Soc. Metals **25** (1937) 702.
5) A. T. Churchman and A. H. Cottrell: Nature (London) **167** (1951) 943.
6) W. D. Biggs and P. L. Pratt: Acta Met. **6** (1958) 694.
7) D. Hull: Acta Met. **8** (1960) 11.
8) G. T. Hahn, B. L. Averbach, W. S. Owen and M. Cohen: Fracture ed. by B. L. Averbach et al. (Proceedings of an International Conference in Swampscott, M. I. T. and John Wiley and Sons, 1959) art. 5, 91.
9) J. D. E. Eshelby, F. C. Frank and F. R. N. Nabarro: Phil. Mag. **42** (1951) 351.
10) J. S. Koehler: Phys. Rev. **85** (1952) 480.
11) A. N. Stroh: Proc. Roy. Soc. **223** A (1954) 404, ibid. **232** A (1955) 548.
12) A. H. Cottrell: Trans. AIME **212** (1958) 192.
13) Y. T. Chou, F. Garofalo and R. W. Whitmore: Acta Met. **8** (1960) 480.
14) E. Smith: Acta Met. **6** (1960) 403.
15) N. P. Allen: J. Iron Steel Inst. (London) **191** (1959) 1. Fracture (see ref. 8) art. 7, 123.
16) J. M. Berry: Trans. Amer. Soc. Metals **51** (1959) 556.
17) C. S. Barrett and R. Bakish: Trans. AIME **212** (1958) 122.
18) A. T. Churchman: J. Inst. Metals **88** (1960) 221.

JOURNAL OF THE PHYSICAL SOCIETY OF JAPAN Vol. 16, No. 7, JULY, 1961

Some Remarks on the Phenomenological Theory of Ferroelectricity

By Shozo SAWADA and Ikushi YOSHIDA*

Tokyo Institute of Technology, Tokyo

(Received February 16, 1961)

The free energy of a ferroelectric was expanded as an even power-series of polarization in the customary phenomenological theory. For the case of the transition of the second order, the condition was examined under which the well-known relation holds that the temperature-gradients of reciprocal susceptibility immediately below and above the transition point stand in the ratio $-2:1$, and it was shown that this relation is valid regardless of the number of terms taken in the expansion and the temperature-dependence of their coefficients. When the transition is of the first order, on the contrary, this ratio was found to be very sensitive to them, though a simple ratio $-8:1$ is obtained by postulating the temperature-independent coefficients of fourth- and sixth-powers and neglecting terms of higher powers. A similar result was also obtained concerning the antiferroelectricity.

§1. Introduction

To explain the ferroelectricity of $BaTiO_3$ Devonshire[1] expanded the free energy A in an even power-series of polarization P and postulated a linear temperature-dependence on the coefficient of the term of second power only, and succeeded in deriving several important thermodynamical relations and in accounting for the occurrence of phase transitions. A fair success was also due to him in a theoretical reasoning of the temperature-dependencies of quantities such as spontaneous polarization or susceptibility. Merz[2] was able to explain why a single crystal of $BaTiO_3$ describes a double hysteresis-loop just above the transition from the tetragonal ferroelectric- to the cubic paraelectric-phase on the groucd of Devonshire's phenomenological theory. Kittel[3], on the other hand, suggested a possibility of antiferroelectricity applying a similar phenomenological theory to a crystal composed of two sub-lattices, and indeed soon afterwards Shirane *et al*[4] found that $PbZrO_3$ is antiferroelectric. Cross[5] extended the theory to that of a three-dimensional case.

A closer fit of results derived from the phenomenological theory to experimental facts will necessarily require much more terms of expansion and much more coefficients which are temperature-dependent. In fact, a series of works have been made along this line of development. In the phenomenological theory of $BaTiO_3$, Kholodenko[6] and Drougard *et al*[7] postulated a temperature dependence on the coefficient of fourth power also, and moreover added other terms of sixth power not taken into account by Devonshire. A temperature dependence on the coefficient of sixth power was postulated by Kawabe[8]. Terms of eighth- and tenth-powers were added by the same author for a better explanation of the lowest phase-transition of $BaTiO_3$.

Here we examined generally the effect of increasing the number of terms of expansion and allowing complex temperature dependencies for the coefficients on the temperature depencence of susceptibility, in the phenomenological theory of a uniaxial ferroelectric. The susceptibility is a more directly and more precisely measurable quantity than others such as spontaneous polarization (determined by the observation of hysteresis loop or by the measurement of pyrocurrent) or a bias effect of phase transition. This was the main reason why we adopted the susceptibility as a quantity to judge the propriety of theory. Discussions on the other quantities will similarly be made.

§2. General Formulation

The free energy per unit volume of a ferroelectric is expanded as follows;

---

* Now at the Central Research Institute, Fuji Iron and Steel Co., Ltd.

$$A(P,T)=A_0(T)+2\sum_{n=1}^{\infty}h_n(T)P^{2n}\,, \tag{1}$$

where P is the electric polarization and T is the absolute temperature. The external field E and hence the susceptibility η are obtained by successive differentiation of Eq. (1) with respect to P, as

$$E=\left(\frac{\partial A}{\partial P}\right)_T=4P\sum_{n=1}^{\infty}nh_n(T)P^{2(n-1)}\,, \tag{2}$$

$$\frac{1}{\eta}=\left(\frac{\partial E}{\partial P}\right)_T=4\sum_{n=1}^{\infty}nh_n(T)P^{2(n-1)}+8P^2\sum_{n=2}^{\infty}n(n-1)h_n(T)P^{2(n-2)}\,. \tag{3}$$

The spontaneous polarization P_s is obtained as a root of the equation

$$\sum_{n=1}^{\infty}nh_n(T)P_s^{2(n-1)}=0\,, \tag{4}$$

which comes from Eq. (2) for $E=0$. As $A_F=A_P$ is required at $T=T_c$,

$$\sum_{n=1}^{\infty}h_n(T)P_s^{2n}=0 \qquad (T=T_c) \tag{5}$$

is readily obtained from Eq. (1). Combined with Eq. (4), Eq. (3) gives the paraelectric and ferroelectric susceptibilities as

$$\frac{1}{\eta_P}=4h_1(T)\,, \tag{6}$$

$$\frac{1}{\eta_F}=8P_s^2\sum_{n=2}^{\infty}n(n-1)h_n(T)P_s^{2(n-2)}\,. \tag{7}$$

Here the "ratio of temperature gradients of reciprocal susceptibility" p is defined by

$$p=\frac{d}{dT}\left(\frac{1}{\eta_F}\right)\Big]_{T=T_c-0}\Big/\frac{d}{dT}\left(\frac{1}{\eta_P}\right)\Big]_{T=T_c+0}\,. \tag{8}$$

Eqs. (6) and (7) give

$$p=\frac{2}{\{dh_1(T)/dT\}}\left\{P_s^2\sum_{n=2}^{\infty}n(n-1)\frac{dh_n(T)}{dT}P_s^{2(n-2)}+\sum_{n=2}^{\infty}n(n-1)^2h_n(T)P_s^{2(n-2)}\frac{dP_s^2}{dT}\right\}\Big]_{T=T_c-0}\,, \tag{9}$$

or by Eq. (4) p is further rewritten as

$$p=\frac{2}{\{dh_1(T)/dT\}}\left\{P_s^2\sum_{n=2}^{\infty}n(n-1)\frac{dh_n(T)}{dT}P_s^{2(n-2)}\right.$$
$$\left.-\frac{\left(\sum_{n=1}^{\infty}n\frac{dh_n(T)}{dT}P_s^{2(n-1)}\right)\left(\sum_{n=2}^{\infty}n(n-1)^2h_n(T)P_s^{2(n-2)}\right)}{\sum_{n=2}^{\infty}n(n-1)h_n(T)P_s^{2(n-2)}}\right\}\Bigg]_{T=T_c-0}\,. \tag{10}$$

Values of p of several substances known as ferroelectrics are listed in Table I. It is noticed that there are three groups, i.e., the first group with p of about -10, the second group with p of about -2 and the third group with p considerably smaller than -2 in the absolute values.

§ 3. The Second-Order Transition

As is well-known, the phase transition is of the second order under the conditions

$$h_1(T)=h_1^0(T-T_0) \qquad (h_1^0>0)\,, \tag{11a}$$

$$h_2=\text{const.}>0\,, \tag{11b}$$

and

$$h_n=0 \qquad (n\geq 3)\,, \tag{11c}$$

and the following equations are readily obtained, giving the two linear relations of $1/\eta$ *vs* T as shown in Fig. 1:

$$1/\eta_P=4h_1\,, \tag{12}$$

$$1/\eta_F=-8h_1\,. \tag{13}$$

The ratio of their gradients is always $-2:1$.

Now, the conditions (11a)~(11c) are too severe and following two conditions will be sufficient for the transition to be of the second order;

Table I. p-values of some ferroelectrics.

Substance	p	Reference
$BaTiO_3$	-10	9)
$NaNO_2$	-9.6	10)
$KNbO_3$	-7	11)
$CaB_3O_4(OH)_3\cdot H_2O$	-3.4	12)
NH_4HSO_4	-2.9	13)
$(CH_2NH_2COOH)_3\cdot H_2SO_4$	-2.7	14)
$RbHSO_4$	-2.7	15)
$(NH_3CH_3)Al(SO_4)_2\cdot 12H_2O$	-2.5	16)
$NaKC_4H_4O_6\cdot 4H_2O$	-2.3	17)
$LiNH_4C_4H_4O_6\cdot H_2O$	-2.3	18)
$(CH_2NH_2COOH)_3\cdot H_2BeF_4$	-2.11	14)
KH_2PO_4	-1.8	19)
$(NH_2CH_2COOH)_2\cdot HNO_3$	-1.4	20)
KD_2PO_4	-0.415	21)
$NH_2CH_2COOH\cdot AgNO_3$	-0.377	22)

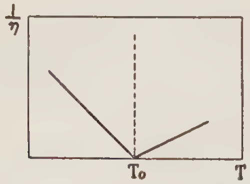

Fig. 1. Schematic variation of reciprocal susceptibility *vs* temperature for the second-order transition under the conditions (11).

(i) $h_1(T)$ has a positive temperature dependence and vanishes at a temperature T_0; and

(ii) $h_2(T_0)>0$ ($h_2(T)$ may have any temperature dependence).

We now take into account every terms of Eq. (1) and give arbitrary temperature dependencies to every coefficients under the single condition that the transition be of the second order.

Since the transition is of the second order we have $P_s^2(T_c)=0$ at $T=T_c=T_0$, and hence from Eq. (10) it is readily seen that

$$p=-2\,. \tag{14}$$

It has been well-known that Eq. (14) holds under the severe conditions (11a)~(11c), but now it should be stressed-on that Eq. (14) is really a universal relation valid very generally with a sole restriction that the transition is of the second order, no matter how many number of terms of expansion may be taken into account or whatever temperature dependence may be postulated for each coefficient.

As is seen from Eq. (6) $1/\eta_P$ is independent of the coefficients higher than $h_1(T)$, and hence $1/\eta_P$ *vs* T is always a straight line as far as the linear temperature dependence (11a) is postulated for $h_1(T)$. $1/\eta_F$ *vs* T will generally deviate from a straight line, but, if the expansion is stopped at the fourth-power term, Eq. (13) will hold even when the coefficient of the fourth-power term is temperature-dependent, as is seen by introducing Eq. (4) into Eq. (7), and hence $1/\eta^F$ *vs* T gives a straight line as far as Eq. (11a) is valid.

§ 4. The First-Order Transition

It is well-known that the transition is of the first order under postulations

$$h_1(T)=h_1^0(T-T_0) \qquad (h_1^0>0)\,, \tag{15a}$$

$$h_2=\text{const.}<0\,, \tag{15b}$$

$$h_3=\text{const.}>0\,, \tag{15c}$$

and

$$h_n=0 \qquad (n\geq 4)\,, \tag{15d}$$

and that then the jump of the susceptibility at the transition follows the rule

$$\eta_F\Big]_{T=T_c-0}\Big/\ \eta_P\Big]_{T=T_c+0}=1/4\,. \tag{16}$$

$1/\eta_F$ is now no longer a linear function of T even in this simplified case. Eq. (7) can be rewritten by use of Eq. (4) as

$$1/\eta_F=-16h_1(T)+\frac{16}{3}\frac{h_2^2}{h_3}\left(1+\sqrt{1-\frac{h_3}{h_2^2}3h_1(T)}\right) \tag{17}$$

and its temperature coefficient is given by

$$d(1/\eta_F)/dT=-32\frac{dh_1(T)}{dT}\left(\frac{1}{2}+\frac{1}{4}\frac{1}{\sqrt{1-\frac{h_3}{h_2^2}3h_1(T)}}\right). \tag{18}$$

From Eq. (18) it is readily seen that the value $\{d(1/\eta_F)/dT\}/\{dh_1(T)/dT\}$ decreases with decreasing temperature, the lower limit of which being given by an inequality

$$\frac{d(1/\eta_F)/dT}{dh_1(T)/dT} < -16\,. \tag{19}$$

As Eqs. (4) and (5) give

$$4h_1(T_c) = h_2^2/h_3 \tag{20}$$

at $T=T_c$, Eq. (18) readily gives

$$d(1/\eta_F)/dT\Big]_{T=T_c-0} = -32 dh_1(T)/dT\Big]_{T=T_c-0}$$

and, needless to say, Eq. (12) holds also for the first-order transition. Hence we have a remarkable result

$$p = -8 \tag{21}$$

which is valid independently of h_2 and h_3. The relation $1/\eta$ *vs* T is schematically shown in Fig. 2.

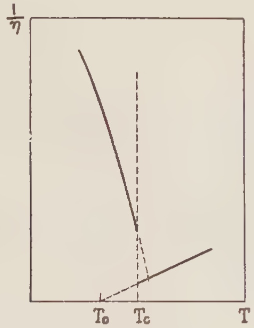

Fig. 2. Schematic variation of reciprocal susceptibility *vs* temperature for the first-order transition under the conditions (15).

Eq. (21) does not generally hold if the conditions (15) are loosened when the transition is of the first order. If temperature dependencies are postulated on h_2 and h_3, as an example of loosening the conditions (15b) and (15c), Eq. (10) gives

$$\left. p = -8\left\{1 - \frac{3}{4}\frac{dh_2(T)/dT}{dh_1(T)/dT}\frac{h_2(T)}{h_3(T)} + \frac{3}{8}\frac{dh_3(T)/dT}{dh_1(T)/dT}\left(\frac{h_2(T)}{h_3(T)}\right)^2\right\}\right]_{T=T_c}. \tag{22}$$

In another example in which a positive temperature-independent coefficient h_4 is introduced, while h_2 and h_3 are still assumed temperature-independent, we have

$$p = -10 + \frac{2}{\sqrt{1-3h_2h_4/h_3^2}}\,. \tag{23}$$

It can generally be said that p is rather sensitive to the form of the expansion of free energy when the transition is of the first order.

§ 5. Special Transitions

According as $h_2(T_c) \gtrless 0$, the transition becomes of the second order or of the first order, respectively. In this section, the intermediate case, i.e., $h_2(T_c)=0$ will be discussed.

(i) The second-order transition:

$$h_2(T_0) = 0\,, \tag{24a}$$

$$h_3(T_0) > 0\,, \tag{24b}$$

$$\text{no restriction on } h_n(T_0) \quad (n \geq 4)\,. \tag{24c}$$

Eq. (10) reduces to

$$p = -2\left.\frac{\sum_{n=2}^{\infty} n(n-1)^2 h_n(T) P_s^{2(n-2)}}{\sum_{n=2}^{\infty} n(n-1) h_n(T) P_s^{2(n-2)}}\right]_{T=T_c-0}, \tag{25}$$

for $P_s^2(T_c)=0$ when the transition is of the second order. Under the conditions (24), this equation results in

$$p = -4\,. \tag{26}$$

Under the more general conditions

$$h_n(T_0) = 0 \qquad (n = 1, 2, \cdots, N-1)\,, \tag{27a}$$

$$h_N(T_0) > 0\,, \tag{27b}$$

$$\text{no restriction on } h_n(T_0) \quad (n \geq N+1)\,, \tag{27c}$$

we have the generalized rule

$$p = -2(N-1)\,. \tag{28}$$

(ii) The first-order transition:

$$h_2 = 0\,, \tag{29a}$$

$$h_3 = \text{const.} < 0\,, \tag{29b}$$

$$h_4 = \text{const.} > 0\,, \tag{29c}$$

$$h_n = 0 \qquad (n \geq 5)\,. \tag{29d}$$

Although $P_s^2(T_0) \neq 0$ for the first-order transition, the fact that $dh_n/dT=0$ $(n \neq 1)$ makes Eq. (25) hold for this case, too. As Eqs. (4) and (5) give

$$P_s^2 = -\frac{2h_3}{3h_4} \qquad (T = T_c - 0)\,, \tag{30}$$

p can be readily calculated as

$$p = -12\,. \tag{31}$$

Under the more general conditions

$$h_n = 0 \qquad (n \neq N, n \neq M, M > N), \tag{32a}$$

$$h_N = \text{const.} < 0\,, \tag{32b}$$

$$h_M = \text{const.} > 0\,, \tag{32c}$$

Eqs. (4) and (5) give

$$P_s^{2(M-N)}(T_c) = -\frac{(N-1)h_N}{(M-1)h_M}, \tag{33}$$

and hence p is calculated as

$$p = -2(N+M-1). \tag{34}$$

It seems rather unlikely that the term next to the second-power one is not the fourth but the higher one in the expansion of the free energy, but there seems to be no reason for excluding such a postulation as a conventional expression for a *steep* potential in a phenomenological discussion. It is noteworthy that the absolute value of p is always increased in such a steep potential, compared to a usual one of non-vanishing fourth-power term, for both first- and second-order transitions.

§ 6. Antiferroelectricity

Kittel[3] phenomenologically treated the antiferroelectricity considering polarizations P_1 and P_2 of two equivalent sublattices. A discussion parallel to the preceding sections is possible for this case, being almost unaltered. The free energy per unit volume of an antiferroelectric is now expanded as

$$A(P_1, P_2, T) = A_0(T) + f(P_1^2 + P_2^2) + gP_1P_2 + \sum_{n=2}^{\infty} h_n(P_1^{2n} + P_2^{2n}). \tag{35}$$

When $g > 0$ a solution $P_1 = -P_2$ gives a lower free energy than the solution $P_1 = P_2$, causing an antiferroelectricity.

According as $h_2(T_c) \gtrless 0$, the transition is of the second or the first order respectively, provided that $2f - g$ has a positive temperature dependence. The magnitude of g is an index of the dominance of antiferroelectricity over ferroelectricity, and if it has a temperature dependence no simple relation is obtained for p.* For a discussion of antiferroelectricity, g is now postulated as temperature-independent, and then it can be shown again that the rule $p = -2$ holds for the second-order transition even when any number of terms are taken into account in the expansion and any temperature dependence is postulated for every coefficients. For the first-order transition, on the contrary, an expression of p is complex in general, but Eq. (21) holds under the conditions (15), whereas Eq. (16) does not.

§ 7. Discussions

It has been found that p is always equal to -2 when the transition is of the second order except in the very special cases discussed in § 5. This is indeed supported by the fact that values of p of the second group in Table I are near -2. It can be concluded, therefore, that the value of p is very insensitive to the functional form of free energy for the second-order transition. This result suggests that little will be gained by elaborating the functional form of free energy in a phenomenological discussion of a ferroelectric with the second-order transition.

In the case of the first-order transition, on the other hand, the situation is quite different and p is very sensitive to the functional form of free energy, and it takes the ideal value -8 only when the severe conditions (15) are imposed. Values of p of the first group in Table I are, nevertheless, rather close to -8. In the present stage it is uncertain whether this fact shows the validity of the severe conditions (15) or it is merely an "accidental" result of canceling of the deviations from Eq. (15) in several coefficients. Whichsoever the true explanation may be, it seems difficult to seek the physical meaning of each term of such an expansion because of at least two facts; i.e., that the value of p is affected very sensitively by the functional form of expansion, and that each term of the expansion has the same order of magnitude showing no tendency of convergence. The circumstance that many terms are needed to reasonably explain the various relations at the phase transition seems to show an evidence of a limit of phenomenological theory in this direction of progress.

It is interesting to note that p of the second group in Table I have a general tendency of deviating from -2, the theoretical value, towards larger side in the absolute value. Hoshino *et al*[14] insisted that the absolute value of p of $(CH_2NH_2COOH)_3 \cdot H_2SO_4$ is larger than 2 because of the domain clamping which reduces the dielectric constant in the ferroelectric phase, and a similar deviation in the case of $CaB_3O_4(OH)_3 \cdot H_2O$ was attributed by Wieder[12] to a thermodynamical fact that the adiabatic dielectric constant is smaller than the isothermal one in the ferroelectric phase. A variety of reasons causing the deviation

---

* In this case, p is defined by

$$p = d(1/\eta_{AF})/dT \Big]_{T=T_c-0} \Big/ d(1/\eta_P)/dT \Big]_{T=T_c+0}.$$

of p from -2 may be considered. The values of p of the third group in Table I are less than 2 in the absolute value. These values do not seem to have a simple explanation.

References

1) A. F. Devonshire: Phil. Mag. [7] **40** (1949) 1040; *ibid.* **42** (1951) 1065.
2) W. J. Merz: Phys. Rev. **91** (1953) 513.
3) C. Kittel: Phys. Rev. **82** (1951) 729.
4) G. Shirane, E. Sawaguchi and Y. Takagi: J. Phys. Soc. Japan **6** (1951) 208.
5) L. E. Cross: Phil. Mag. [8] **1** (1956) 76.
6) L. P. Kholodenko: Sov. Phys. JETP **4** (1957) 847.
7) M. E. Drougard, R. Landauer and D. R. Young: Phys. Rev. **98** (1955) 1010.
8) K. Kawabe: J. Phys. Soc. Japan **14** (1959) 1755.
9) W. J. Merz: Phys. Rev. **76** (1949) 1221.
10) S. Sawada et al: to be published.
11) G. Shirane, H. Danner, A. Pavlovic and R. Pepinsky: Phys. Rev. **93** (1954) 672.
12) H. H. Wieder: J. Appl. Phys. **30** (1959) 1010.
13) R. Pepinsky, K. Vedam, S. Hoshino and Y. Okaya: Phys. Rev. **111** (1958) 1508.
14) S. Hoshino, T. Mitsui, F. Jona and R. Pepinsky: Phys. Rev. **107** (1957) 1255.
15) R. Pepinsky and K. Vedam: Phys. Rev. **117** (1960) 1502.
16) R. Pepinsky, F. Jona and G. Shirane: Phys. Rev. **102** (1956) 1181.
17) J. Hablützel: Helv. Phys. Acta **12** (1939) 489.
18) W. J. Merz: Phys. Rev. **82** (1951) 562.
19) H. M. Barkla and D. M. Finlayson: Phil. Mag. [7] **44** (1953) 109.
20) R. Pepinsky, K. Vedam, S. Hoshino and Y. Okaya: Phys. Rev. **111** (1958) 430.
21) W. Bantle: Helv. Phys. Acta **15** (1942) 373.
22) R. Pepinsky, Y. Okaya, D. P. Eastman and T. Mitsui: Phys. Rev. **107** (1957) 1538.

JOURNAL OF THE PHYSICAL SOCIETY OF JAPAN Vol. 16, No. 7, JULY, 1961

Fermi Momentum for Free Electron Metals Perturbed by Localized Imperfections

By Akira SUGIYAMA

Nagoya Technical College, Nagoya

(Received June 4, 1960)

The Fermi momentum k_m and the interior density ρ_i are calculated for free electron metals perturbed by localized imperfections, and the Thomas-Fermi relation $\rho_i = k_m^3/3\pi^2$ is verified up to the higher order. Then it is shown that the Friedel theorem can be based on the above relation. When the Fermi momentum k_m is expressed in terms of the phase shift η of the free electron wave function, the charge neutrality condition in the interior leads to the Friedel sum rule for the case of the plane surface as well as of the point imperfection.

§1. Introduction

As for the heap up charge of free electrons around a localized imperfection in metals, Friedel[1-3] suggested a theorem, which plays an important role in the theory of imperfections[4-8].

In treating the heap up charge he did not discuss directly the complicated behaviour of the electron density around the imperfection, but took account of the effect of the imperfection on the almost uniform density in the region far from the imperfection where the perturbation potential due to the imperfection vanishes but the effect is integrated to give the phase shift of the electron wave function.

It is important in his treatment that the uniform density in the interior should be discussed up to higher orders. But he based his theorem on the Weyl-Laue theorem[9], which is not valid up to the higher order that he required. And therefore his verifications are not considered to be rigorous. Plaskett[10] investigated the validity of the Friedel theorem for the one-dimensional metal, but he made use of a somewhat ambiguous averaging process.

The main purpose of the present paper is to verify the Friedel theorem based upon the Thomas-Fermi relation between the interior density ρ_i and the Fermi momentum*) k_m for the perturbed electron gas, because the Thomas-Fermi relation in the interior, not the Weyl-Laue theorem, can be proved to be valid up to the required higher order. Some of the relations of which use were made beforehand in the previous paper[11] (hereafter referred to as I) are verified in this paper.

§ 2. Model and Formulation of the Problem

The notations and the model in the present paper are the same as those in I; we regard the metal as the system composed of the jelly of positive charge having the volume V_0 and the uniform density ρ_0 and of the assembly of N_0 $(=\rho_0 V_0)$ free electrons. For the free electron gas in a potential box bounded by the infinite wall the ordinary Weyl-Laue theorem is true; the number $N(k)$ of the electronic states of momentum smaller than k is given as $k^3V/3\pi^2$, where V is the volume of the box, independently of its concrete shape.

Now we consider the effect of a localized imperfection on the distribution of the free electrons. It can be studied, without so great loss of generality, by investigating the influence of some appropriate surface potential barrier; for example, even the potential due to an atomic vacancy can be regarded as the one due to a cavity surface.

In this case, as was pointed out in I, we make use of the more precise expression for the Weyl-Laue theorem $N(k)\simeq k^3V/3\pi^2-k^2S/8\pi$, where S is the area of the boundary surface. From this expression it appears that we can straightforwardly conclude the relation

$$N(k_m)=\rho_i V-Q_0 S\ , \tag{2.1}$$

where the interior density $\rho_i=k_m{}^3/3\pi^2$ and the charge expelled from unit area of the infinite wall $Q_0=k_m{}^2/8\pi$; the validity of the relation (2.1), however, is not self-evident, but is required to be verified.

When the infinite wall is replaced by a more realistic potential barrier, the situation is more complicated, where we have no clear-cut definition of the volume and of the Fermi momentum. The volume is clearly defined only in the case of a step potential barrier. The potential barrier gives rise to a phase shift in the electron wave, and results in deforming the quantized points in the $\boldsymbol{k}$-space. The exact Fermi momentum k_m must be calculated for this deformed lattice.

Accordingly we must consider the following points:

(1) Order of the validity of the Thomas-Fermi relation in the interior for the electron gas bounded by the infinite wall.

(2) The relation between the Fermi distribution in the case of the infinite wall and that in the case of any other potential barrier.

(3) The validity of the Thomas-Fermi relation for the electron gas bounded by any surface potential barrier.

(4) The explicit expressions both for the Fermi momentum and for the interior density in terms of the phase shift.

(5) The rigorous verification of the Friedel theorem and his sum rule.

For simplicity we shall discuss mainly the the system bounded by the plane surface, say the plate metal with the finite width L_0 in the x-direction and infinite in the other two directions.

We start with the case of the infinite wall potential $V^{(1)}(x)$ which is infinite on the edge planes $x=0$ and L_0. Imposing the usual cyclic boundary condition of the period L_1 in the y and the z directions, we get the wave function $\psi^{(1)}(\boldsymbol{k},\ \boldsymbol{r})$, for the free electron, which is obtained by replacing L in Eq. (2.17) of I by L_0, as $\chi^{(1)}(k_x,\ x)\ =\sqrt{2/L_0}\sin(k_x x)$ etc.

Then we consider the case of the surface potential barrier $V^{(*)}(\boldsymbol{r})=V^{(*)}(x)$, which has the symmetry with respect to the midpoint $x_c=L_0/2$ and vanishes in the sufficient interior of the system and exceeds the Fermi energy $k_m{}^2/2$ outside the system. The wave function is expressed as

$$\psi^{(*)}(\boldsymbol{k},\ \boldsymbol{r})=\{1+\delta(k_x)\}\cdot\chi^{(*)}(k_x,\ x)\cdot(1/L_1)\cdot\exp i(k_y y+k_z z)\ , \tag{2.2}$$

---

*) Atomic units are used.

where

$$\delta(k_x) = -\frac{1}{L_0}\frac{\partial}{\partial k_x}\eta(k_x)\ , \tag{2.3}$$

and $\eta(k_x)$ is the phase shift. In terms of $\eta(k_x)$, $\chi^{(*)}$ is expressed as $\sqrt{2/L_0}\cdot\sin\{k_x x+\eta(k_x)\}$ in the interior of the metal. The relation (2.3) is deduced in the appendix.

§ 3. The Thomas-Fermi Relation in the Case of the Infinite Wall

In the case of the infinite wall the wave vector is quantized to be $\boldsymbol{k}^{(1)}(\boldsymbol{n})$; $k_x^{(1)}=(\pi/L_0)\cdot n_x$, $n_x=+1,\ +2,\ \cdots$, $k_y^{(1)}=(2\pi/L_1)n_y$, $n_y=0,\ \pm1,\ \pm2,\ \cdots$, etc. The Fermi momentum $k_m^{(1)}$ is determined by the equation

$$N^{(1)}(k_m^{(1)}) = N_0(=k_F^3 L_0 L_1^2/3\pi^2)\ , \tag{3.1}$$

where $N^{(1)}(k)$ represents the number of states of momentum smaller than k in this case and $k_F=(3\pi^2\rho_0)^{1/3}$, defined by the positive charge density ρ_0 or by the total number N_0 of free electrons, is the Fermi momentum for the uniform electron gas. Since $N^{(1)}(k_m)$ has been obtained as Eq. (2.19) in I, we have

$$k_m^{(1)} = k_F + \frac{\pi}{4L_0} = k_F\left(1+\frac{\pi}{4L_0 k_F}\right). \tag{3.2}$$

The density of the electron gas $\rho^{(1)}(\boldsymbol{r})$ is obtained by replacing L in Eq. (2.21) of I by L_0. And we get the interior density

$$\rho_i^{(1)} = \frac{k_F^3}{3\pi^2}+\frac{k_F^2}{4\pi L_0} = \rho_0+\frac{k_F^2}{4\pi L_0}\ ,$$

and then

$$= k_m^{(1)3}/3\pi^2\ . \tag{3.3}$$

Thus the Thomas-Fermi relation is verified up to the first order in $1/L_0 k_F$ $(=S/V\cdot k_F)$, and therefore the validity of the relation (2.1) is verified.

§ 4. The Thomas-Fermi Relation in the Case of Any Surface Potential Barrier

Now we consider the case of any potential barrier $V^{*}(x)$. The wave vector is expressed as the lattice point $\boldsymbol{k}^{(*)}(\boldsymbol{n})$ deformed from $\boldsymbol{k}^{(1)}(\boldsymbol{n})$;

$$\boldsymbol{k}^{(*)}(\boldsymbol{n}) = \boldsymbol{k}^{(1)}(\boldsymbol{n})+\Delta\boldsymbol{k}\ ,$$

where

$$(\Delta\boldsymbol{k})_x = -\frac{2}{L_0}\eta(k_x^{(*)}) \simeq -\frac{2}{L_0}\eta(k_x^{(1)})\ , \qquad (\Delta\boldsymbol{k})_y=(\Delta\boldsymbol{k})_z=0\ . \tag{4.1}$$

Further we assume that the potential does not trap any electrons; and then

$$\eta(0)=0\ . \tag{4.2}$$

4.1 Fermi momentum

In the approximation of the first order in $1/L_0 k_F$, we obtain

$$\begin{aligned} N^{(*)}(k) &= \frac{L_1^2}{2\pi}\sum_{n_x=1}^{n_1}\{k^2-k_x^{(*)2}(n_x)\} \\ &= \frac{k^3}{3\pi^2}L_0 L_1^2-\frac{k^2}{4\pi}L_1^2+\frac{2L_1^2}{\pi^2}\int_0^k \eta(k_x)\cdot k_x\,dk_x\ , \end{aligned} \tag{4.3}$$

where n_1 is given by $k_x^{(*)}(n_1)=k$. Similarly to $k_m^{(1)}$, we can determine the Fermi momentum

$k_m^{(*)}$ from $N^{(*)}(k_m^{(*)})=N_0$ as

$$k_m^{(*)}=k_m^{(1)}(1+\mathcal{E}) ,$$

where

$$\mathcal{E}\fallingdotseq-\frac{2}{L_0k_F^3}\cdot\int_0^{k_F}\eta(k_x)\cdot k_x\,dk_x ,$$

or

$$k_m^{(*)}=k_F+\frac{2}{L_0}\left\{\frac{\pi}{8}-\frac{1}{k_F^2}\int_0^{k_F}\eta(k_x)\cdot k_x\,dk_x\right\} . \tag{4.4}$$

Then we investigate the relation between the Fermi distributions in the cases of $V^{(1)}(x)$ and of $V^{(*)}(x)$, and examine the correctness of the usual assumption that the Fermi distribution in the $\boldsymbol{n}$-space is preserved when we replace $V^{(1)}$ by $V^{(*)}$.

A lattice point $\boldsymbol{n}$ corresponds to $\boldsymbol{k}^{(1)}(\boldsymbol{n})$ and to $\boldsymbol{k}^{(*)}(\boldsymbol{n})$, respectively in the case of $V^{(1)}$ and $V^{(*)}$. If the Fermi distribution in the $\boldsymbol{n}$-space be preserved, the one-to-one correspondence can hold between the lattice points in the $\boldsymbol{k}$-space in the Fermi distribution for $V^{(1)}$ and those for $V^{(*)}$. But this is not true, since the Fermi distribution is spherical in the $\boldsymbol{k}$-space in both cases. In fact, the Fermi top in the $\boldsymbol{n}$-space is not preserved; it is $n_1^{(1)}=L_0k_m^{(1)}/\pi$ in the n_x-direction and $n_2^{(1)}=L_1k_m^{(1)}/2\pi$ in the n_y and n_z-directions in the case of $V^{(1)}$, but $n_1^{(*)}=n_1^{(1)}[1+\mathcal{E}+\{2\eta(k_F)/L_0k_F\}]$ and $n_2^{(*)}=n_2^{(1)}(1+\mathcal{E})$ in the case of $V^{(*)}$.

To the approximation of the first order in $1/L_0k_F$, however, the one-to-one correspondence holds, and then the Fermi distribution in the $\boldsymbol{n}$-space is preserved. It can be verified as follows.

If we assume the validity of the one-to-one correspondence, the Fermi surface in the $\boldsymbol{k}$-space for $V^{(*)}$ is obtained from the Fermi sphere for $V^{(1)}$ by the correspondence of $\boldsymbol{k}^{(1)}(\boldsymbol{n})$ to $\boldsymbol{k}^{(*)}(\boldsymbol{n})$. Therefore the perturbation energy ΔE_p is obtained conventionally by summing the energy change $\boldsymbol{k}^{(1)}\Delta\boldsymbol{k}$ over the preserved Fermi distribution in the $\boldsymbol{n}$-space;

$$\Delta E_p=\frac{L_0}{\pi}\cdot\int_0^{k_F}k_x\cdot(\Delta\boldsymbol{k})_x\cdot\frac{L_1^2}{2\pi}(k_F^2-k_x^2)\cdot dk_x=-\frac{L_1^2}{\pi^2}\int_0^{k_F}\eta(k_x)\cdot k_x(k_F^2-k_x^2)\cdot dk_x . \tag{4.5}$$

On the other hand, we can obtain ΔE_p more exactly as the difference between the ground state energy $E^{(1)}$ in the case of $V^{(1)}$ and that $E^{(*)}$ in the case of $V^{(*)}$, which are calculated from the expressions for $N^{(1)}(k)$ and $N^{(*)}(k)$ as

$$\left.\begin{aligned}
E^{(1)}&=\int_0^{k_m^{(1)}}\frac{1}{2}k^2\frac{\partial N^{(1)}}{\partial k}dk=\frac{k_F^5}{10\pi^2}L_0L_1^2+\frac{k_F^4}{16\pi}L_1^2 ,\\
E^{(*)}&=\int_0^{k_m^{(*)}}\frac{1}{2}k^2\frac{\partial N^{(*)}}{\partial k}dk=\frac{k_F^5}{10\pi^2}L_0L_1^2\\
&\qquad+2L_1^2\left\{\frac{k_F^4}{32\pi}-\frac{1}{2\pi^2}\int_0^{k_F}\eta(k_x)\cdot k_x(k_F^2-k_x^2)\cdot dk_x\right\} ,
\end{aligned}\right\} \tag{4.6}$$

where we use Eqs. (3.2) and (4.4) respectively. The difference $E^{(*)}-E^{(1)}$ agrees with the conventionally calculated ΔE_p. Thus the assumption has been proved to be valid, and then we can regard the deformed sphere as an approximate Fermi distribution in the case of $V^{(*)}$.

Although it seems rather artificial to consider such deformed Fermi sphere, it is convenient to calculate ΔE_p and advantageous in the point; (i) we can replace the summation by an approximate integral over the preserved Fermi distribution in the $\boldsymbol{n}$-space, (ii) we can apply to the case of the point imperfection.

Then we shall give the definition of the average Fermi momentum over the deformed Fermi sphere. We start with a simple deformation, a uniform expansion, of the lattices caused by the addition of Z electrons or by the contraction of the potential box in the x-direction by $2b$. Such perturbation causes the Fermi sphere to expand uniformly by Δk_m and the interior density to increase by $\Delta\rho_i$. These changes are connected by the relation

$$\Delta\rho_i = \frac{k_m^{(1)2}}{\pi^2}\Delta k_m \simeq \frac{k_F^2}{\pi^2}\Delta k_m\,, \tag{4.7}$$

where

$$\Delta\rho_i = Z/L_0L_1^2\,, \quad \text{and} \quad 2b\rho_i/L_0\,,$$

respectively in the case of the addition and of the contraction. In order to generalize Eq. (4.7) to more complicated deformations, we rewrite $\Delta\rho_i$ as

$$\Delta\rho_i = \frac{1}{2\pi^3}\cdot\Delta k_m\iint d\omega = \frac{1}{2\pi^3}\cdot\iint(\Delta\boldsymbol{k}_m)_n d\omega\,,$$

where $d\omega$ is the surface element on the Fermi (hemi-) sphere and $(\Delta\boldsymbol{k}_m)_n$ is the component of the displacement normal to the Fermi surface, the integral being carried out over the Fermi surface. Then it is reasonable to define the average displacement $\langle\Delta k_m\rangle$ and consequently the average Fermi momentum $\langle k_m^{(*)}\rangle$ as

$$\langle\Delta k_m\rangle = \frac{\iint(\Delta\boldsymbol{k}_m)_n\,d\omega}{\iint d\omega} = \frac{1}{2\pi k_F^2}\iint(\Delta\boldsymbol{k}_m)_n d\omega \tag{4.8}$$

and

$$\langle k_m^{(*)}\rangle = k_m^{(1)} + \langle\Delta k_m\rangle\,, \tag{4.9}$$

in a general case where $(\Delta\boldsymbol{k}_m)_n$ may depend on the directions. The validity of the definition is proved as follows: Since $(\Delta\boldsymbol{k}_m)_n = -(2/L_0)\cdot\eta(k_x)\cdot k_x/k_F$ and the surface element between k_x and k_x+dk_x is $2\pi k_F dk_x$, we have

$$\langle\Delta k_m\rangle = -\frac{2}{L_0k_F^2}\int_0^{k_F}\eta(k_x)k_x dk_x\,.$$

This gives the same expression for $\langle k_m^{(*)}\rangle$ as $k_m^{(*)}$ given by Eq. (4.4). Thus the validity has been verified.

The relation (4.7) is also valid for $\langle\Delta k_m\rangle$ as well as for Δk_m. In terms of $\rho_i^{(*)} = \rho_i^{(1)} + \Delta\rho_i$, it is rewritten as $\rho_i^{(*)} = \langle k_m^{(*)}\rangle^3/3\pi^2$, which will be verified in the next section.

4.2 Interior density

The free electron density $\rho^{(*)}(\boldsymbol{r})$ in the case of $V^{(*)}$, defined as

$$\rho^{(*)}(\boldsymbol{r}) = \rho^{(*)}(x) = \frac{1}{2\pi}\sum_{n_x=1}^{n_1^{(*)}}\{1+\delta(k_x^{(*)}(n_x))\}^2|\chi^{(*)}(k_x^{(*)}(n_x),\ x)|^2\{k_m^{(*)2} - k_x^{(*)2}(n_x)\}\,,$$

cannot be expressed in a simpler form. But the asymptotic behaviour $\rho_i^{(*)}$ in the interior can be reduced to a simple expression in terms of the phase shift up to the first order in $1/L_0k_F$ as follows.

Making use of the approximation

$$\{1+\delta(k_x^{(*)})\}^2\cdot|\chi^{(*)}|^2 \simeq |\chi^{(1)}|^2 + (|\chi^{(*)}|^2 - |\chi^{(1)}|^2) + 2\delta(k_x^{(*)})\cdot|\chi^{(*)}|^2\,,$$

we divide the summation into three parts. The first part including $|\chi^{(1)}|^2$,

$$\frac{1}{\pi L_0}\sum\{k_m^{(*)2} - k_x^{(1)2}(n_x) + \frac{4}{L_0}k_x^{(1)}(n_x)\cdot\eta(k_x^{(1)})\}\cdot\sin^2\{k_x^{(1)}(n_x)\cdot x\}$$

is reduced in the interior to

$$\frac{k_m^{(*)3}}{3\pi^2} + \frac{2}{\pi^2L_0}\cdot\int_0^{k_F}\eta(k_x)\cdot k_x dk_x - \frac{2}{\pi L_0^2}\cdot\sum\eta(k_x^{(1)})\cdot k_x^{(1)}(n_x)\cdot\cos(2k_x^{(1)}x)\,,$$

and the second and the third parts are approximated by

$$\frac{1}{\pi L_0}\cdot\sum\left(k_m^{(1)2}-k_x^{(1)2}\right)\cdot\sin\left\{\eta(k_x^{(1)})\cdot\left(1-\frac{2x}{L_0}\right)\right\}\cdot\sin\left\{2k_x^{(1)}x+\eta(k_x^{(1)})\cdot\left(1-\frac{2x}{L_0}\right)\right\},$$

and

$$\frac{1}{\pi^2}\int_0^{k_F}\delta(k_x)\cdot(k_F^2-k_x^2)\cdot dk_x-\frac{1}{\pi L_0}\sum\delta(k_x^{(1)})\cdot(k_m^{(1)2}-k_x^{(1)2})\cdot\cos\left\{2k_x^{(1)}x+2\eta(k_x^{(1)})\left(1-\frac{2x}{L_0}\right)\right\}.$$

Then we investigate $\lim_{x\to\infty}\rho^{(*)}(x)$, where x/L_0 is kept to be a constant C. In these three parts, we meet terms of the type

$$S(N)=\sum_{n=1}^{N}f\left(\frac{n}{N}\right)\cdot\sin\left\{2\pi Cn+g\left(\frac{n}{N}\right)\right\}$$

with smooth functions $f(x)$ and $g(x)$. This sum has the properties

$$\left.\begin{aligned}&\lim_{N\to\infty}S(N)/N=0\,,\\ \text{and, when } f(0)=f(1)=0\,,\quad&\\ &\lim_{N\to\infty}S(N)=0\,.\end{aligned}\right\}\tag{4.10}$$

Making use of Eqs. (2.3), (4.2) and (4.10), we obtain

$$\rho_i^{(*)}=\lim_{x\to\infty}\rho^{(*)}(x)=k_m^{(*)3}/3\pi^2\,,\tag{4.11}$$

or, from Eq. (4.4), rewrite this as

$$\rho_i^{(*)}=\rho_i^{(1)}-\frac{2}{\pi^2L_0}\int_0^{k_F}\eta(k_x)\cdot k_xdk_x=\rho_0+\frac{2}{\pi^2L_0}\left\{\frac{\pi}{8}k_F^2-\int_0^{k_F}\eta(k_x)\cdot k_xdk_x\right\}.\tag{4.12}$$

Thus the Thomas-Fermi relation has been verified in the interior up to the first order in $1/L_0k_F$.

§ 5. Rigorous Verification of the Friedel Theorem

So far we have considered the effect of the perturbation potential of a given form upon the electron density and the Fermi distribution. However, a localized imperfection is specified not by a perturbation potential but by an arrangement of the positive ions, or by an approximate distribution of the positive jelly. And the perturbation potential due to the imperfection ought to be determined by taking account not only of change in the positive jelly but also of the screening effect of the electron gas self-consistently.

Friedel investigated the condition under which the perturbation on the free electron should be localized around the imperfection, and could formulate the condition as the Friedel theorem, which can be stated as follows:

(i) *Localization.* Far from the imperfection, the density of the free electron gas tends to a (almost) constant value $\rho_i=k_m^3/3\pi^2$.

(ii) *Preservation of the Fermi momentum.* The coulomb field due to a localized imperfection should be completely screened by the perturbed electron gas. The charge of the electron gas, therefore, should be neutralized in the region far from the imperfection by the charge of the positive jelly; $\rho_i=\rho_0$, or $k_m=k_F$. The latter is called the Friedel theorem in a strict sense.

(iii) *Sum rule.* For a (isotropic) point imperfection in a spherical metal of large radius R, the heap up charge Q of the electrons around the imperfection is expressed as

$$Q=\frac{2}{\pi}\cdot\sum_{l=0}^{\infty}(2l+1)\cdot\eta_l(k_F)\,,\tag{5.1}$$

where η_l is the phase shift of the electrons in the l-state.

This theorem has been explained by Friedel in various ways[1-3]. But he did not consider so carefully to which order the equations $\rho_i=k_m^3/3\pi^2$ and $k_m=k_F$ are valid. In order to deduce the sum rule he developed two different methods.

(a) He expressed[2] the contribution $(\varDelta Q)_l$ of the l-electrons to Q as

$$(\varDelta Q)_l=\frac{1}{R}\frac{\partial}{\partial k}\eta_l(k)\,. \tag{5.2}$$

Summing this over all electrons, he derived Eq. (5.1). Although Eq. (5.2) has a wide applicability, his deduction was not rigorous, since he did not relate $\partial\eta_l/\partial k$ with the change in the normalization factor.

(b) As another proof, he showed[1] that Eq. (5.1) can be obtained by summing $(2R/\pi)\cdot(\eta_l(k_F)/R)\cdot(2l+1)$ over all l-states, where $\eta_l(k_F)/R$ is the displacement of the Fermi momentum for the l-electrons and $2R/\pi$ is the state density in regard to k for $l\ll Rk$. In this method, however, the ordinary Weyl-Laue theorem is implicitly assumed to be valid up to the higher order.

We shall now attempt a more rigorous verification of the Friedel theorem. From the preceding discussion about the plane surface it follows that the relation $\rho_i=k_m^3/3\pi^2$ is valid up to the first order in $S/V\cdot k_F$. This will be generalized to any localized imperfections. And the long-range nature of the coulomb force also requires the validity of $k_m=k_F$ at least up to the first order*) in $S/V\cdot k_F$. The preceding discussion also shows that it is possible to replace the Fermi momemtum in (i) and (ii) by the average Fermi momentum. For detailed treatment of (iii) we classify the imperfections into two types.

5.1 Plane surface potential

Now we assume that the Friedel formula (5.2) is applicable also to the surface potential barrier. Then the contribution $\varDelta Q$ of the electron of momentum $\boldsymbol{k}$ to the heap up charge Q per unit area of the surface will be expressed as

$$\varDelta Q=\frac{1}{L_0}\frac{\partial}{\partial k_x}\eta(k_x)\,, \tag{5.3}$$

and then

$$Q=\varSigma\varDelta Q=\frac{1}{2\pi^2}\int_0^{k_F}\frac{\partial\eta}{\partial k_x}\cdot(k_F{}^2-k_x{}^2)dk_x=\frac{1}{\pi^2}\int_0^{k_F}\eta(k_x)k_xdk_x\,,$$

where we use Eq. (4.2).

Since the infinite wall expels $Q_0=k_F{}^2/8\pi$ per unit area, the total heap up charge is $Q-Q_0$. The charge neutrality condition in the interior requires $Q=Q_0$, and is expressed as

$$\int_0^{k_F}\eta(k_x)\cdot k_xdk_x=\pi k_F{}^2/8\,. \tag{5.4}$$

This is correct, because this is derived by substituting $\rho_i{}^{(*)}=\rho_0$ in Eq. (4.12) and also by inserting $k_m{}^{(*)}=k_F$ in Eq. (4.4). Accordingly the formula (5.3) has been verified.

5.2 Point imperfection

The verification of the Friedel theorem proceeds similarly to the case of the plane surface barrier, except that the sums of trigonometrical functions in the latter case are replaced by those of Bessel functions. The summation involves more complicated calculations. And then we shall investigate only the outline of the verification.

We start with a free electron metal bounded by a spherical infinite wall of radius R. The radial part of the wave function is given by $N_l(k)\cdot J_{(l+1/2)}(k\cdot r)$, where N_l is the normalization factor and J_ν is the Bessel function of ν-th order. Then we introduce an isotropic imperfection at the center of the metal. The radial part of the wave function in the region far from the center and the outer boundary becomes

---

*) More exactly, $\lim\limits_{L_0\to\infty}(\rho_i-\rho_0)\cdot L_0{}^{3/2}=0$ for the plane surface and $\lim\limits_{R\to\infty}(\rho_i-\rho_0)\cdot R^{5/2}=0$ for the point imperfection.

$$N_l(k)\left\{1-\frac{1}{R}\cdot\frac{\partial}{\partial k}\eta_l(k)\right\}\{J_{(l+1/2)}(k\cdot r)-(-)^{l+1}\cdot\tan\eta_l\cdot J_{-(l+1/2)}(k\cdot r)\},$$

just as in the case of the plane surface barrier.

The imperfection changes the Fermi momentum of the l-electrons by $(\varDelta k_m)_l$. Since the state density of the l-electrons with regard to k is $(2R/\pi)\cdot\sin\tau(k)$, where $\cos\tau(k)=(2l+1)/2Rk$, the average Fermi momentum should be defined as

$$\langle k_m\rangle=k_F+\langle\varDelta k_m\rangle,$$

where

$$\langle\varDelta k_m\rangle=\frac{\Sigma(2l+1)\sin\tau(k_F)\cdot(\varDelta k_m)_l}{\Sigma(2l+1)\sin\tau(k_F)}=\frac{3}{2}\frac{1}{(R\cdot k_F)^2}\sum_{l=0}^{Rk_F}(2l+1)\{\sin\tau(k_F)\}\cdot(\varDelta k_m)_l\,. \tag{5.5}$$

The displacement $(\varDelta k_m)_l$ for an isotropic imperfection is expressed in terms of the phase shift $\eta_l(k)$ as $(\varDelta k_m)_l=-\eta_l(k_m)/R\simeq-\eta_l(k_F)/R$. The linear dimension D of the imperfection is assumed to be far smaller than R. This, together with the properties $\eta_l\simeq 0$ for $l\gg Dk_F$, permits the approximation

$$\sum_{l=0}^{Rk_F}(2l+1)\cdot\eta_l(k_F)\sin\tau(k_F)\simeq\sum_{l=0}^{Dk_F}(2l+1)\cdot\eta_l(k_F)\simeq\sum_{l=0}^{\infty}(2l+1)\cdot\eta_l(k_F)\,,$$

and then

$$\langle\varDelta k_m\rangle=-\frac{3}{2R^3k_F^2}\sum_{l=0}^{\infty}(2l+1)\cdot\eta_l(k_F)\,. \tag{5.6}$$

Just as in the case of the plane surface potential barrier, we assume the validity both of the Thomas-Fermi relation in the region far from the center and the boundary and of the relation (5.6). Then we can get $\varDelta\rho_i=k_F^2\langle\varDelta k_m\rangle/\pi^2$ again. Since the decrease in the interior density should be attributed to the heap up of electrons around the localized imperfection at the center, we get the heap up of electrons as

$$Q=-V\cdot\varDelta\rho_i=-\frac{4}{3\pi}\cdot R^3k_F^2\langle\varDelta k_m\rangle=\frac{2}{\pi}\sum_{l=0}^{\infty}(2l+1)\cdot\eta_l(k_F)\,, \tag{5.7}$$

verifying the Friedel sum rule.

When an impurity atom with $(1+Z)$ valency is introduced in monovalent metals, the Friedel theorem requires that $\langle\varDelta k_m\rangle=0$. This is rewritten as the usual Friedel sum rule

$$Z=\frac{2}{\pi}\sum_{l=0}^{\infty}(2l+1)\cdot\eta_l(k_F)\,, \tag{5.8}$$

because the displacement $\langle\varDelta k_m\rangle$ is composed of two terms; the first $\langle\varDelta k_m\rangle_1$, caused by the increase of Z free electrons, is

$$\langle\varDelta k_m\rangle_1=\frac{\pi^2}{k_F^2}\frac{Z}{V}=\frac{3}{2R^3k_F^2}\cdot\frac{\pi}{2}\cdot Z\,,$$

and the second $\langle\varDelta k_m\rangle_2$, caused by the screened potential due to Z valency impurity ion, is given by Eq. (5.6). Equation $\langle\varDelta k_m\rangle_1+\langle\varDelta k_m\rangle_2=0$ leads to Eq. (5.8), and therefore the Friedel sum rule in the form (5.8) is proved to be an expression of the Friedel theorem in terms of the phase shift.

§ 6. Conclusion

The definite answers to five problems in § 2 have been given for the case where the localized imperfection is a plane surface. The effect of the surface potential barrier is integrated into the phase shift of the free electron wave in the interior. The phase shift affects both the Fermi momentum and the interior density. Eliminating the phase shift from the expressions for the Fermi momentum and for the interior density, we can find the familiar Thomas-Fermi relation between them.

The Friedel theorem can be based on the higher order validity of the Thomas-Fermi relation. The Friedel theorem and his sum rule are proved to be the results from the charge neutrality in the interior in terms of the Fermi momentum and of the phase shift, respectively.

The Friedel sum rule given by Eq. (5,4) for a plane surface, together with the expression (4.6) for the ground state energy, has played an important role in I. Strictly speaking, the present verification is restricted to the case of the plane surface. Therefore it is desirable that treatments[12] based on the orthodox perturbation theory should be carried out in the case of general imperfections.

Acknowledgement

The author expresses his thanks to Prof. Tomiyuki Toya, Prof. Huzio Nakano , Prof. Ryogo Kubo and Dr. Satoru Miyake for their advices and discussions, and also to Prof. Minoru Tunekawa for his assistance in mathematical analysis. This work has been supported in part by the Scientific Research Fund of Ministry of Education.

Appendix. Deduction of Eq. (2.3)

From the symmetry of $\chi^{(*)}$ with respect to $x_c=L_0/2$, it follows that

$$\{1+\delta(k_x)\}^2\int_{-\infty}^{L_0/2}|\chi^{(*)}(k_x,\ x)|^2dx=\frac{1}{2}\,. \tag{A.1}$$

Since the perturbation is localized around the surface, we have $|\delta|\ll 1$ and then

$$\delta(k_x)\simeq\frac{1}{2}-\int_{-\infty}^{L_0/2}|\chi^{(*)}(k_x,\ x)|^2dx\,. \tag{A.2}$$

The integration can be carried out, in the way similar to Friedel's. The wave equation for $\chi^{(*)}$ is

$$\frac{1}{2}\frac{\partial^2}{\partial x^2}\chi^{(*)}(k_x,x)+\{E(\boldsymbol{k})-V^{(*)}(x)\}\cdot\chi^{(*)}(k_x,\ x)=0\,, \tag{A.3}$$

where

$$E(\boldsymbol{k})=|\boldsymbol{k}|^2/2\,.$$

Provided L_0 is so large that the eigen values are distributed almost continuously, we differentiate Eq. (A.3) with regard to k_x;

$$\frac{1}{2}\frac{\partial^3\chi^{(*)}}{\partial k_x\partial x^2}+\{E(\boldsymbol{k})-V^{(*)}(x)\}\frac{\partial\chi^{(*)}}{\partial k_x}+k_x\chi^{(*)}=0\,. \tag{A.4}$$

By subtracting $\chi^{(*)}$ times (A.4) from $\partial\chi^{(*)}/\partial k_x$ times (A.3) we get

$$\frac{1}{2}\frac{\partial}{\partial x}\left\{\frac{\partial\chi^{(*)}}{\partial x}\frac{\partial\chi^{(*)}}{\partial k_x}-\frac{\partial^2\chi^{(*)}}{\partial x\partial k_x}\chi^{(*)}\right\}=k_x\cdot\chi^{(*)2}\,. \tag{A.5}$$

Integrating Eq. (A.5) with regard to x, we have

$$k_x\int_{-\infty}^{L_0/2}|\chi^{(*)}|^2dx=k_x\left\{\frac{1}{2}+\frac{1}{L_0}\frac{\partial}{\partial k_x}\cdot\eta(k_x)\right\}, \tag{A.6}$$

where we use the behaviour of $\chi^{(*)}$ for $x\to-\infty$ and $x=L_0/2$. Then, from Eq. (A.2) it follows that

$$\delta(k_x)=-\frac{1}{L_0}\frac{\partial}{\partial k_x}\eta(k_x)\,. \tag{A.7}$$

Finally we treat a more general case where the surface barrier depends not only on x but also on $\boldsymbol{k}$. Now the potential has non-vanishing values in the interior. We obtain the phase shift $\eta(\boldsymbol{k})$ and energy eigen values $E(\boldsymbol{k})$ as somewhat complicated functions of $\boldsymbol{k}$. The previous results, however, are only little modified. We get

$$\delta(\boldsymbol{k})=-\frac{1}{L_0}\frac{\partial}{\partial k_x}\eta(\boldsymbol{k})\,,\qquad\text{and}\qquad(\Delta\boldsymbol{k})_x=-\frac{2}{L_0}\cdot\eta(\boldsymbol{k})\,,\qquad(\Delta\boldsymbol{k})_y=(\Delta\boldsymbol{k})_z=0\,,$$

as the generalization of Eqs. (2.3) and (4.1). The definitions (4.8) for $\langle\Delta k_m\rangle$ and (4.9) for $\langle k_m^{(*)}\rangle$ are still valid. For the charge neutrality condition (5.4), we obtain

$$\frac{1}{2\pi}\iiint\frac{\partial\eta}{\partial k_x}dk_xdk_ydk_z=\frac{\pi}{8}k_F^2\,,$$

where the integral is carried out over all occupied states, or, by making use of the Gauß theorem for the surface integral, we get

$$\frac{1}{2\pi k_F^2}\iint_{\text{Fermi surface}}(\Delta k_m)_n d\omega+\frac{\pi}{4L_0}=0$$

for the condition $\langle k_m^{(*)}\rangle=k_F$.

References

1) J. Friedel: Phil. Mag. **43** (1952) 153; Advances in Phys. **3** (1954) 446; Ann. Physique **9** (1954) 158.
2) J. Friedel: Phil. Mag. **43** (1952) 153, particularly in appendix (i).
3) J. Friedel: Phil. Mag. **43** (1952) 1115.
4) M. F. Abelès: Compt. rend. **237** (1953) 796.
5) F. G. Fumi: Phil. Mag. **46** (1955) 1007.
6) F. J. Blatt: Phys. Rev. **108** (1957) 285.
7) A. Seeger et al.: Z. Phys. **144** (1956) 637; **145** (1956) 161; **146** (1956) 217, 242.
8) K. Yosida: Phys. Rev. **106** (1957) 893.
9) M. v. Laue: Ann. Physik. **44** (1914) 1197.
10) J. S. Plaskett: Proc. Phys. Soc. London **66 A** (1953) 178.
11) A. Sugiyama: J. Phys. Soc. Japan **15** (1960) 965.
12) R. Kubo and S. Miyake: Unpublished, read at the 13th Ann. Meeting of Phys. Soc. Japan (1958).

JOURNAL OF THE PHYSICAL SOCIETY OF JAPAN, Vol. 16, No. 7, JULY, 1961

Antiferromagnetic Resonance in $CoCl_26H_2O$

By Muneyuki DATE
Department of Physics, Faculty of Science, Osaka University, Osaka

(Received March 8, 1961)

Antiferromagnetic resonance experiment was performed on a single crystal of $CoCl_26H_2O$ in the frequency range of 9.5 to 47 kMc/sec at liquid helium temperature. The result can be understood by the theory of antiferromagnetic resonance developed by Nagamiya and Yosida and also by Ubbink et al., except for certain systematic deviations from the theory. These deviations can be removed by introducing a large anisotropic exchange interaction of the symmetric tensor form in place of the ordinary small anisotropy energy. Thus, the effective fields acting on sublattice magnetizations, M^+ and M^-, are assumed to be of the form

$$H_E{}^{\pm}=-AM^{\mp}-\Gamma M^{\pm}-A'M^{\mp}-\Gamma'M^{\pm}\ ,$$

where A and Γ are the isotropic molecular field constants and A' and Γ' are newly introduced anisotropic molecular field tensors. It was found that the symmetry axes of A' and Γ' coincide with those of the g-tensor and their components are given by

$$A_x'=0.25\text{ A}\ ,\qquad A_y'=0.20\text{ A}\ ,\qquad A_z'=-0.45\text{ A}\ ,$$
$$\Gamma_x'=0.19\text{ A}\ ,\qquad \Gamma_y'=0.18\text{ A}\ ,\qquad \Gamma_z'=-0.37\text{ A}\ ,$$

where x, y and z correspond to the c-, b- and a'-axes, respectively. Line width measurements were also performed in the para- and antiferromagnetic regions and a rapid narrowing was observed at low temperatures.

§1. Introduction

Since theoretical studies[1] of antiferromagnetic resonance and observations[2] of such a resonance in $CuCl_22H_2O$ were made, attempts to find similar resonances in other antiferromagnetic substances have been made by several researchers. Unlike the case of para- or ferromagnetic resonance, however, the possibility to observe antiferromagnetic resonance under ordinary resonance conditions is confined to a relatively few number of antiferromagnetic substances for the reason that the required frequency or magnetic field is too high in most of antiferromagnetic substances. Let us consider the simplest case of uniaxial anisotropy energy. The resonance frequency ω in this case is given by

$$\frac{\omega}{\gamma}=\sqrt{2H_AH_E}\pm H\ ,\qquad H_E\gg H_A,\ H\ ,$$

where γ is the gyromagnetic ratio, H_A the anisotropy field, H_E the exchange field and H is the external magnetic field applied along the easy axis. H_A may range between 10^3 and 10^5 Oe, and for antiferromagnetics with Néel temperature of $\sim10^2$°K, H_E may be $\sim10^6$ Oe. Therefore, a high frequency or a strong external magnetic field will be required to satisfy the resonance condition. Substances in which antiferromagnetic resonance was observed up to the present time are $CuCl_22H_2O$ by the Leiden group[2], $CuBr_22H_2O$ by the present author[3], MnF_2 by Johnson and Nethercot[4] and Foner[5], Cr_2O_3 by Dayhoff[6] and Foner[7], $CuCl_22D_2O$ by the present author[8], FeF_2 by Tinkham and Ohlman[9], and NiO by Kondoh[10]. The latter two observations were made with far-infrared technique, and Foner used high pulse magnetic fields.

So far as the author is aware of, no experiment has been reported on the antiferromagnetic resonance in cobaltous compounds. In the antiferromagnetic resonance in compounds containg Co^{++} ions, the contribution of the orbital angular momentum should play a role. Usually, the effect of orbital angular momentum can be expressed in terms of the effective g-tensor. However, in the phenomenon of antiferromagnetic resonance, this g-tensor can be reduced further to an isotropic tensor by introducing a modified external field, as was discussed by Ubbink[2] and Nagamiya[1] in the case of $CuCl_22H_2O$. In $CoCl_26H_2O$, however, the deviation of the g-

value from the free spin value is so large and the exchange interaction so small that it is interesting to check whether such a reduction alone is sufficient or not. It is also interesting to investigate the resonance line width, because the presence of the orbital angular momentum will give rise to a short spin-lattice relaxation time and a large anisotropic exchange interaction, both of which will broaden the resonance line, especially in the paramagnetic resonance.

Among the cobaltous compounds, $\mathrm{CoCl_2 6H_2O}$ is one of the most stable hydrated salts and can be easily obtained from the saturated aqueous solution. The antiferromagnetic behavior of the salt was first discovered by Haseda and Kanda[11] from the measurement of the powder susceptibility. The x-ray analysis of the crystal structure[12], the specific heat measurement[13] and the single crystal susceptibility[14],[15] were reported recently. It has become clear that this salt is antiferromagnetic below 2.29°K, and this has been also confirmed by a proton resonance experiment[16].

As was reported in a previous short note[17], the present author observed the antiferromagnetic resonance in $\mathrm{CoCl_2 6H_2O}$. In the present paper, detailed results and discussion of the experiment will be given.

§ 2. Crystal Structure and Spin Orientation

The X-ray analysis of $\mathrm{CoCl_2 6H_2O}$ was performed by Mizuno, Ukei and Sugawara[12]. The crystal structure is monoclinic ($\beta=122°19'$) and the lattice constants were determined to be $a=10.34$ Å, $b=7.06$ Å and $c=6.67$ Å. The space group is C_{2h}^3-C2/m and the unit cell contains two $\mathrm{Co^{++}}$ ions which form a base-centered structure. Two $\mathrm{Cl^-}$ ions and four water molecules are octahedrally coordinated to each $\mathrm{Co^{++}}$ ion so as to form a $\mathrm{CoCl_2 4H_2O}$ group. The crystal has a layer structure parallel to (001) and shows a perfect cleavage along this plane. A simplified model of the arrangement is shown in Fig. 1 (a) and (b). As is seen in Fig. 1 (a), there are two equivalent slightly distorted octahedrons in a unit cell, whose principal axes are perfectly parallel, so that the magnetic analysis of this crystal can easily be compared with that of $\mathrm{CuCl_2 2H_2O}$. The angular relation between the octahedrons and the unit cell is shown in Fig. 1 (c), in which we introduced two new axes a' and a'' for convenience.

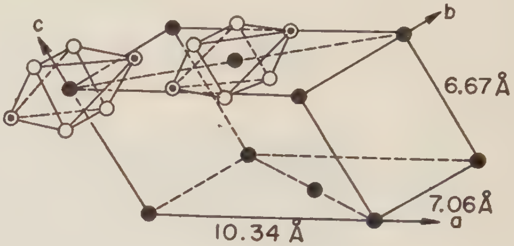

(a) Schematic view of the unit cell. Two free water molecules are not drawn. There are two octahedrons in a unit cell having equivalent crystallographic orientations.

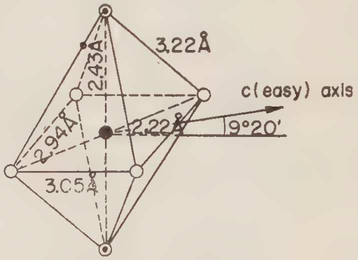

(b) A unit octahedron.

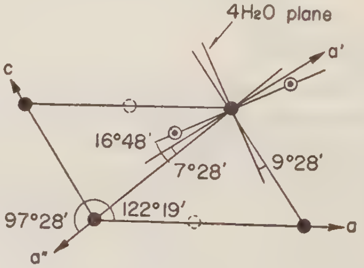

(c) Angular relations between the axes in ac-plane.

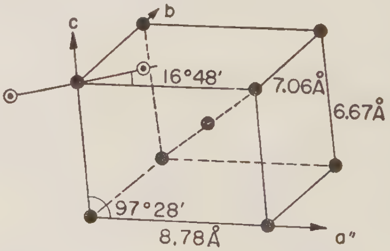

(d) Modified unit cell showing a slightly deformed body centered structure.

● ---- $\mathrm{Co^{++}}$ ion
⊙ ---- $\mathrm{Cl^-}$ ion
○ --- $\mathrm{H_2O}$ molecule

Fig. 1. Crystal structure of $\mathrm{CoCl_2 \cdot 6H_2O}$.

The a'-axis was defined to be perpendicular to both the b- and c-axes; the new rectangular coordinate axes, a', b and c are convenient to analyse experimental data as will be shown in the following sections. On the other hand, the a''-axis is profitable for some calculations such as those of dipolar width and dipolar sum, because the unit cell can be regarded as a slightly deformed body-centered structure. The schematic view of the unit cell is shown in Fig. 1 (d).

The spin orientation at low temperature was determined to be parallel to the c-axis from the susceptibility, proton resonance and antiferromagnetic resonance experiments. It is interesting to note that the spin direction does not coincide with any of the principal axes of the unit octahedron as in $CuCl_22H_2O$. Moreover, it should be mentioned that the spin direction in $NiCl_26H_2O$[18], which is isomorphous to $CoCl_26H_2O$, is not along the c-axis but it is along the b-axis.

Unfortunately, no neutron diffraction experiment is reported so that we do not know the super-structure of spins. As is shown in Fig. 1 (b), there are slight differences among the H_2O–H_2O distances in the unit octahedron, which may produce an orthorhombic crystalline electric field upon the Co^{++} ion. However, the g-values determined by susceptibility measurement show tetragonal symmetry so that small orthorhombicity may not be important. Accordingly, we shall hereafter not care about this orthorhombicity. Throughout the present paper, we do not use the unit octahedron coordinate system, which is inclined by about 9°20′ to the cba,-coordinate system. One of the reasons for this is the fact that the magnetic easy axis is the c-axis which is not in the 4–H_2O plane, as is shown in Fig. 1 (b). The other reason concerns with our experimental accuracy: the paramagnetic resonance line width is so broad that it is not possible to discriminate which of the coordinate systems coincides with the principal axes of the g-tensor. In other words, we encounter no practical contradiction when we use the cba'-coordinate system.

§ 3. Experimental Method

(1) Preparation of the specimen

The specimens used in this experiment were grown from the saturated aqueous solution of pure cobaltous chloride at room temperature. Dark red single crystals having well developed (100) faces were obtained, which show a perfect cleavage along the (100) plane. To prevent deliquescence, single crystals were preserved in pure clock oil. The volume of the single crystals used in the experiment was 1∼10 mm³, varying with the frequency used, i.e. 47∼9.5 kMc/sec.

(2) Microwave equipments and cryostats

Microwave oscillator tubes used for the experiment are klystrons 2K25, 2K33, 35V10 and 50V10 which can be used in the range of 10, 24, 34 and 50 kMc/sec, respectively. Usual experimental apparatus and techniques were used to observe the paramagnetic and antiferromagnetic resonance absorption in $CoCl_26H_2O$.

The cut view of the cryostats are shown in Fig. 2 (a) and (b). Microwave transmission method was used for 34 and 47 kMc/sec, and wave guide and coaxial cable reflection method were respectively adopted for the 24 and 10 kMc/sec regions. German silver wave guide with a wall thickness of 0.3 mm was useful to prevent fast evaporation of liquid helium. Specimens were always immersed in the liquid helium bath in order to secure the precise temperature of the specimens. The microwave loss and frequency shift of the resonant cavity due to the filling up of liquid helium are practically negligible. A cylindrical doubly tuned resonant cavity was used for the resonance in the 10 and 24 kMc/sec regions. This cavity was originally designed for a three level maser in the 10 GC region[19] and the cut view of it is shown in Fig. 2 (b). Cu–Ni alloy was used for all the metal parts of the coaxial cable and RG–55U polyethylene pipe was utilized as a dielectric spacer. Under these conditions, one liter liquid helium can be maintained for more than ten hours, during which experiments in the 10 and 24 kMc/sec regions could be carried out.

Microwave power levels are of the order of milliwatts, and no saturation effect of the antiferromagnetic resonance was yet observed at this power level.

§ 4. Paramagnetic Resonance

The paramagnetic resonance measurement was performed above T_N using microwaves

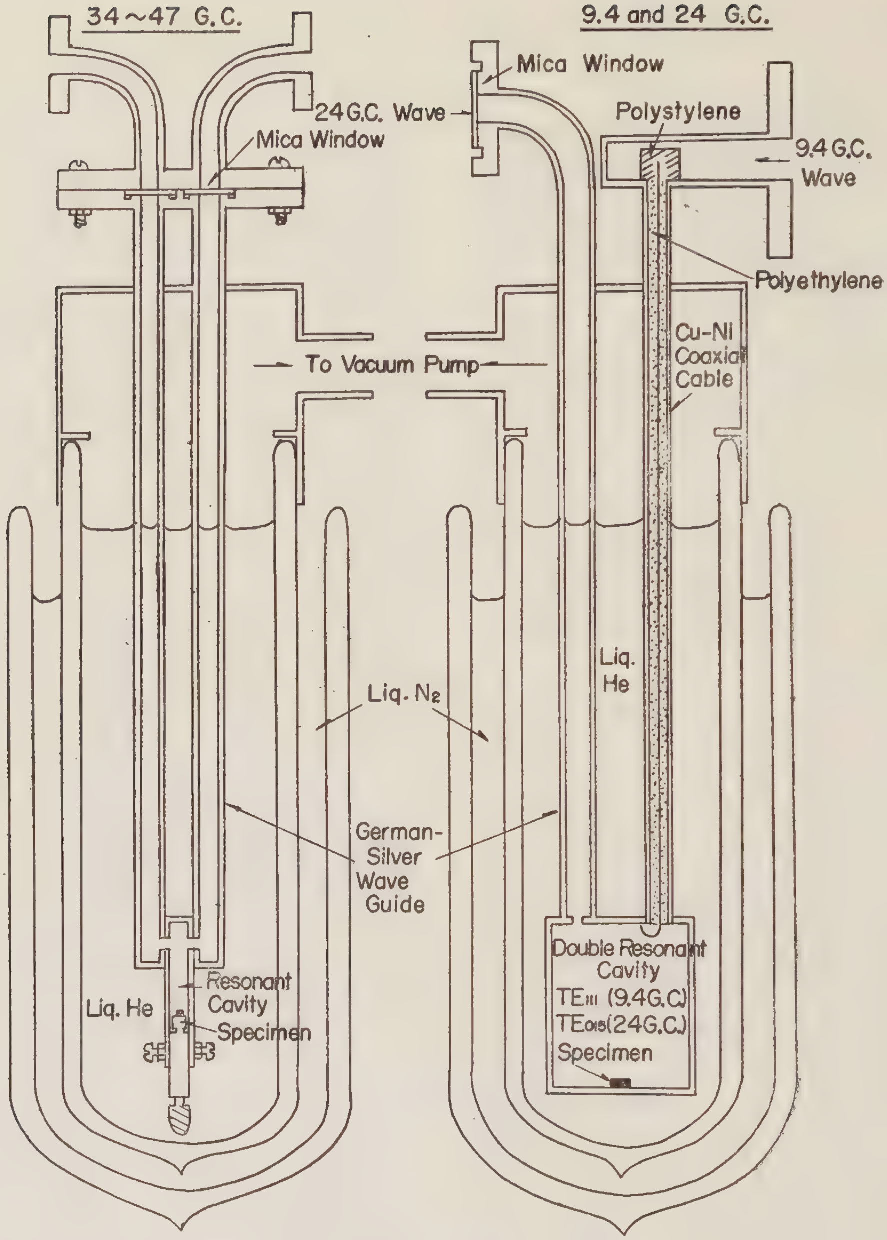

Fig. 2. Cut view of the cryostats.

of the 10, 24 and 34 kMc/sec regions. However, no resonance was observed at 10 and 24 kMc/sec. It was seen only in the 34 kMc/sec region. Even in this range, there was no resonance absorption above the liquid helium temperature and a very broad resonance line was observed at 4.2° as is shown in Fig. 3.

It is well known that the line width of paramagnetic resonance under usual condi-

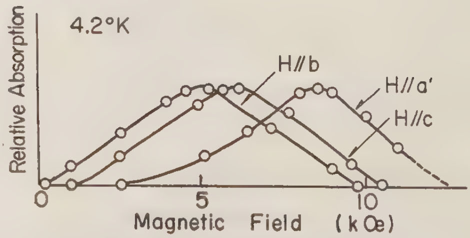

Fig. 3. Paramagnetic resonance curves of $CoCl_2 \cdot 6H_2O$ at 35.55 kMc/sec.

tions is determined by dipolar interaction and exchange effect. Usually the former causes a broadening and the latter produces a narrowing effect if the exchange interaction is isotropic. The calculated dipolar width of $CoCl_26H_2O$ along the principal axes using the theory of Van Vleck[20] are

$$\left.\begin{aligned}\Delta H_{a'}&=\ 620\text{ gauss}\,,\\ \Delta H_b&=2000\text{ gauss}\,,\\ \Delta H_c&=2200\text{ gauss}\,,\end{aligned}\right\}$$

where $\Delta H_{a'}$, ΔH_b and ΔH_c represent the full half width along the crystallographic axes.

From the above calculation, it is clear that the experimental line width can not be explained by the usual dipolar and exchange effects.

As is seen in Fig. 3, the widths are $\Delta H_{a'}\sim 4500$, $\Delta H_b\sim 5000$ and $\Delta H_c\sim 5000$ gauss respectively, whereas only $100\sim 200$ gauss can be expected on the basis of the calculated dipolar width and the exchange narrowing effect[21].

Two origins of these extremely broad paramagnetic resonance lines may be considered. One of them is a short spin-lattice relaxation time of Co^{++} ion and the other is the broadening due to an anisotropic exchange interaction. It is well known that the spin-lattice relaxation time T_1 of Co^{++} ion in paramagnetic state is very short and frequently resonance cannot be observed because of the violation of the relation: $T_1<$ Larmor precession time, under usual experimental conditions. If we assume that the line width is due to the spin-lattice relaxation time only, T_1 will be estimated to be about 4×10^{-12} sec at 4.2°K. However, anisotropic exchange interaction may also make a large contribution to the resonance line width. Because of lack of the precise treatment of the line width due to an anisotropic exchange interaction, no quantitative analysis can be performed, but we shall see in following sections that there exists a considerably large anisotropic exchange interaction among the cobaltous ions so that the extreme broadening of the resonance line can entirely due to this anisotropic exchange interaction.

The g-values are as given in Fig. 4. The principal g-values obtained in our experiment are $g_{a'}=2.9$, $g_b=5.0$ and $g_c=4.0$. It is interesting to compare our data with the results of the susceptibility measurements by Haseda[14] and by Flippen and Friedberg[15]. Haseda obtained $g_{a'}=2.7$, $g_b=4.9$ and $g_c=4.9$ in accord with Flippen and Friedberg. Their data are referred to in Fig. 4 with a dotted line.

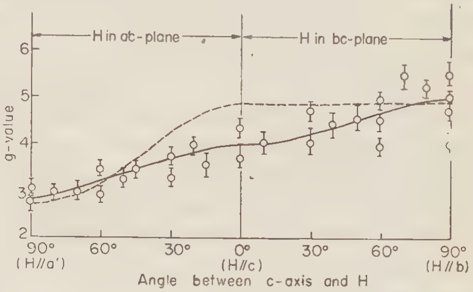

Fig. 4. Angular dependence of g-value in the range of $34\sim 37$ kMc/sec at 4.2°K. Dotted line shows the result obtained from susceptibility data.

Is must be noted that a considerable difference is present in g_c. This discrepancy could be explained as follows. From the result of our experiment, existance of a considerable amount of antiferromagnetic short range order at 4.2°K might be concluded, and this is consistent with the result of the specific heat measurement performed by Robinson and Friedberg[13]. As will be shown in the following section, there is an antiferromagnetic field higher than the paramagnetic resonance field along the c-axis below the Néel temperature, and to this the paramagnetic resonance field appears to join as temperature is decreased and passed through the Néel point. Therefore, it is possible that the observed paramagnetic resonance field is shifted to the higher side; this may probably be due to the existance of short range order. Accordingly, the resonance g-value may be considered as apparent; so we shall use the g-value obtained from the susceptibility data in analysing the results of our antiferromagnetic resonance experiment.

Now let us consider briefly the ground state of Co^{++} ion in $CoCl_26H_2O$. As is well known, the ground state of Co^{++} ion is ^4F, which splits into an orbital singlet and two orbital triplets in a crystalline field of cubic symmetry. As early as 1951, Abragam and Pryce[22] calculated the set of levels arising from ^4F for the case of trigonal and tetragonal symmetries including the effect of spin-orbit coupling. Recently, optical absorption spectra of $CoCl_26H_2O$ and $CoBr_26H_2O$ were investigated by Pappalardo[23] and the results were analysed by Koide[24] who included the higher multiplet levels neglected by Abragam and Pryce. However, no data of the crystal structure of $CoCl_26H_2O$ were available at that time so that they assumed the crystalline electric field to be cubic. Accordingly their results cannot be applied to the analysis of the present paramagnetic resonance experiment. Considering the effect of higher multiplet levels to be small, comparison between the theoretical and experimental g-value was made, and the result is shown in Fig. 5. The agreement is satisfactory.

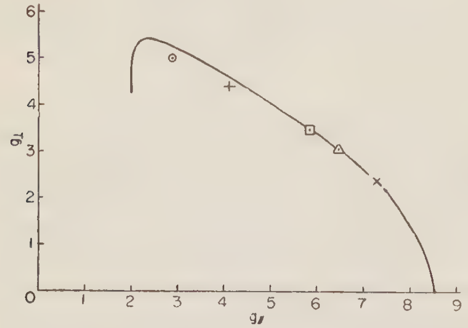

⦿ $CoCl_2 \cdot 6H_2O$
⊡ $CoSiF_6 \cdot 6H_2O$
△ $Co(NH_4)_2 \cdot (SO_4)_2 \cdot 6H_2O$
× $Co_3Bi_2(NO_3)_{12} \cdot 24H_2O$ magnetic complex I
+ 〃 〃 II

Except for $CoCl_2 \cdot 6H_2O$, data come from Bowers and Owen: Rep. on Prog. in Phys. **18** (1955) 304.

Fig. 5. g-value of the Co^{++} ion under the tetragonal field. Theoretical curve is after Abragam and Pryce (ref. 22).

§ 5. Antiferromagnetic Resonance

As was described in the preceding section, very broad paramagnetic resonance was observed in the 34 kMc/sec region at 4.2°K. Below 4.2°K, the resonance line becomes more broad and weak, being accompanied with a slight shift toward the antiferromagnetic resonance field observed below T_N. These effects could be due to increasing short range order with decreasing temperature. Pure antiferromagnetic resonance was observed below 2.0°K and the results are shown in Figs. 6~14. Satisfactory data of the temperature dependence could not be obtained because the Néel temperature is so low and moreover the line width was very large at intermediate temperatures. Except for this point, a satisfactory amount of experimental data was obtained. In Figs. 6 and 7, the temperature and angular dependences in the bc-

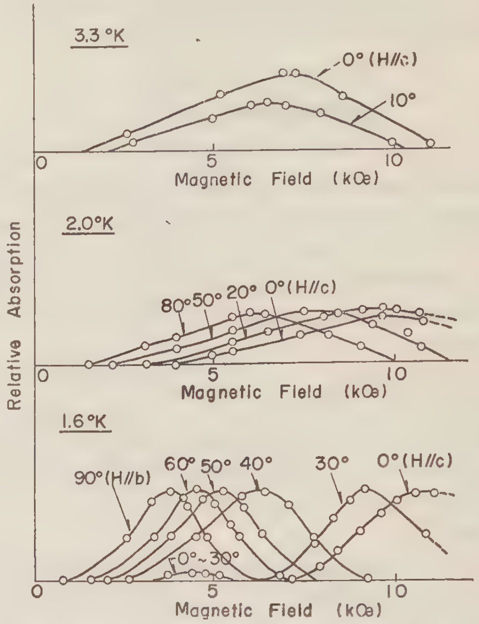

Fig. 6. Temperature and angular dependence of resonance lines in bc-plane at 34.820 kMc/sec.

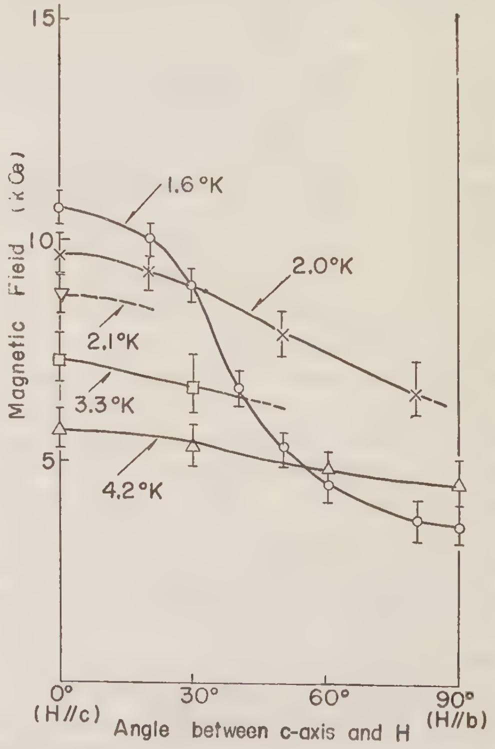

Fig. 7. Temperature and angular dependence of resonance points in bc-plane at 34.820 kMc/sec.

plane at 34 kMc/sec region are shown. With decreasing temperature, the resonance line becomes sharp and its angular dependence increases. Similar behavior of resonance line was reported in the case of $CuCl_22H_2O$. On the other hand, weak and angular independent resonance line was observed near the *c*-axis, along which the spins align at low temperatures. The resonance curves are shown in Figs. 8 and 9. This resonance cannot be seen below 35 kMc/sec and the origin of this weak absorption is not clear. Above 1.7°K, this

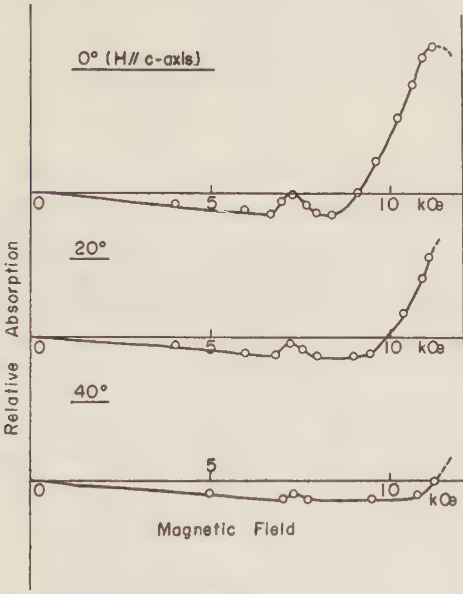

Fig. 8.

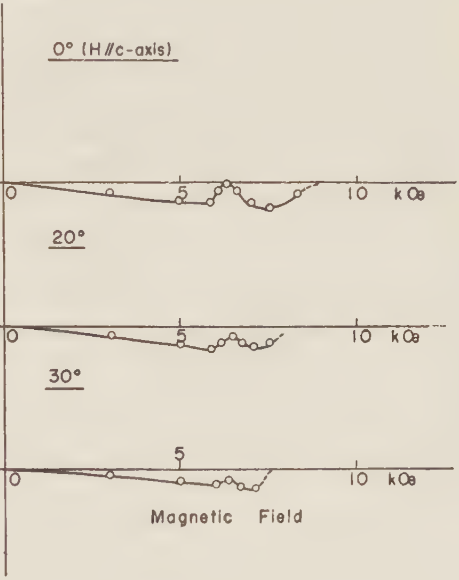

Fig. 9.

Fig. 8. Low field resonance in the *a*′*c*-plane at 35.550 kMc/sec (1.°5).
Fig. 9. Low field resonance in the *bc*-plane at 35.550 kMc/sec (1.5°K).

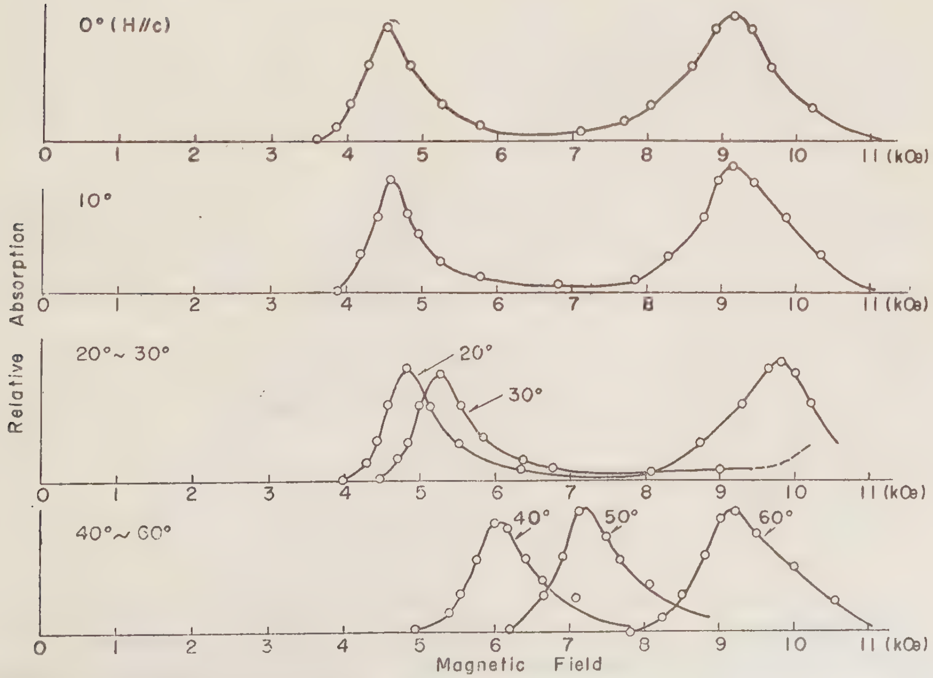

Fig. 10. Antiferromagnetic resonance lines of $CoCl_2 \cdot 6H_2O$ in *a*′*c*-plane at 23.580 kMc/sec (1.47°K)

curious resonance vanishes. The experimental results of the 24 kMc/sec region are summarized in Figs. 10∼12. In this frequency range, the results are similar to those in $CuCl_2 2H_2O$. It must be noticed that a dip of the resonance diagram of $CuCl_2 2H_2O$ in the *ab*-plane is not seen in $CoCl_2 6H_2O$ in the corresponding *cb*-plane. This fact was confirmed with 9 *k*Mc/sec, the result being shown in Figs. 13 and 14. The frequency dependences at the lowest temperature are illustrated in Fig. 15. From this figure, it is seen that the present results are analogous to those for $CuCl_2 2H_2O$, though qualitatively. However, our experimental results cannot be explained

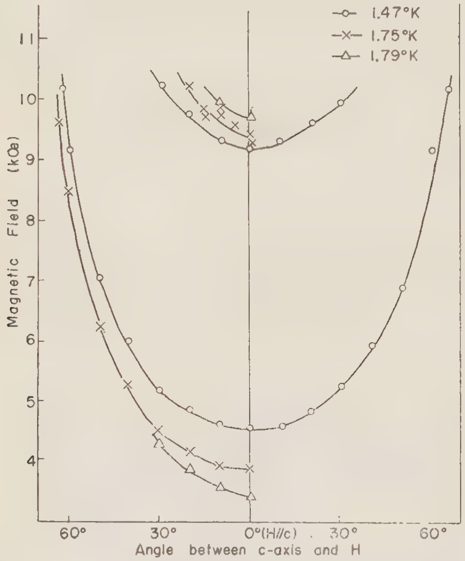

Fig. 11. Angular and temperature dependence of resonance points in *a'c*-plane at 23.58 kMc/sec.

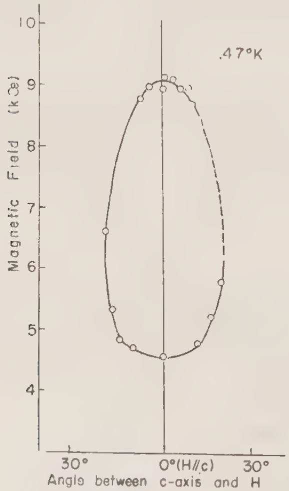

Fig. 12. Angular dependence of resonance points in *bc*-plane at 22.5 kMc/sec.

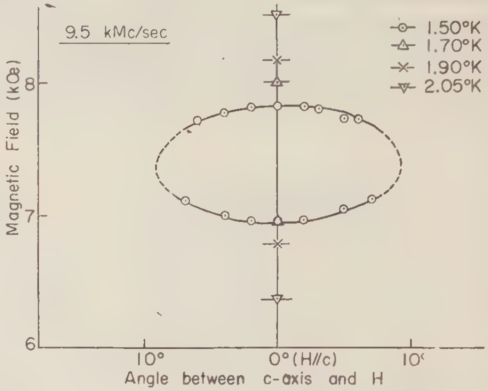

Fig. 13. Angular and temperature dependences of the resonance points in *bc*-plane.

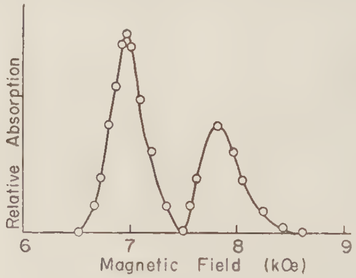

Fig. 14. Antiferromagnetic resonance lines at 9.5 kMc/sec and *H*//*c*-axis (1.5°K).

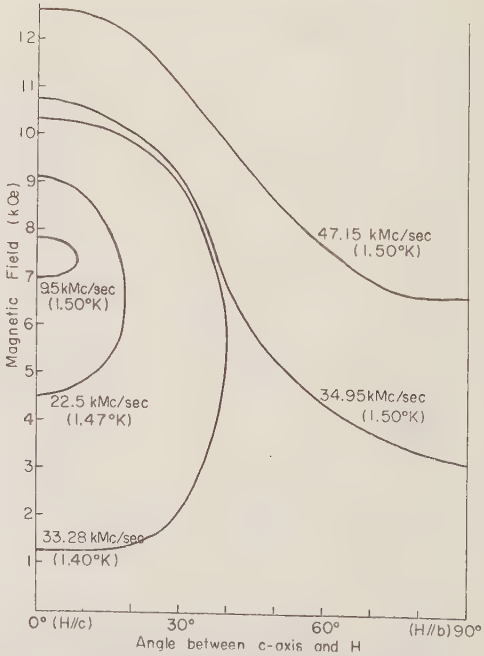

Fig. 15. Angular and frequency dependence of resonance point in *bc* plane.

by the theory of antiferromagnetic resonance of orthorhombic anisotropy developed by Nagamiya, Yosida and Ubbink by a mere adjustment of the parameters contained in the theory: a systematic deviation was observed between the theory and the experiment as was described in a previous short report[17]. A detailed analysis of the present results by improved theory including a large anisotropic exchange interaction will be discussed in the following section.

§ 6. Analysis of the Experimental Result

As was described in the preceding section, the qualitative aspect of antiferromagnetic resonance in $CoCl_26H_2O$ is analogous to that in $CuCl_22H_2O$. So we performed at first the analysis of the experimental results following Nagamiya and Yosida's treatment of $CuCl_2$-$2H_2O$.

First of all, the reduction of the g-tensor to a scalar g-factor must be considered. This can be easily done by introducing a modified magnetic field defined by the following relation:

$$H=(g/2)H_{\mathrm{exp}} \qquad (1)$$

where H and H_{exp} are the reduced field and experimental field, respectively. In $CoCl_2$-$6H_2O$, $H_{a'}=1.5H_{a'\mathrm{exp}}$, $H_b=2.5H_{b\,\mathrm{exp}}$ and $H_c=2.5H_{c\,\mathrm{exp}}$, using the g-values from the paramagnetic susceptibility data. Hereafter we shall use the fictitious field H in place of the real experimental field H_{exp}. Using Eq. (1), the experimental results can be adjusted so as to be compared directly with the Nagamiya-Yosida theory. The result is shown in Fig. 16. The open circles show the experimental results and the dotted line represent the results of the calculation. We assumed the temperature parameter α to be 0.83 using the susceptibility data. It will be seen that there is a considerable discrepancy between theory and experiment. Generally speaking, the experimental resonance field shifts to the higher field side with respect to the calculated one in both the c- and b-directions. Moreover, the critical field resonance to be observed at finite temperature could not be detected.

At the origin of these discrepancies, we considered several correction factors, such as the magnetization effect, demagnetization effect, higher order anisotropy energy and anisotropic exchange interaction[25]. Among these effects, however, it was found that only anisotropic exchange interaction of symmetric tensor form can explain the discrepancy. Let

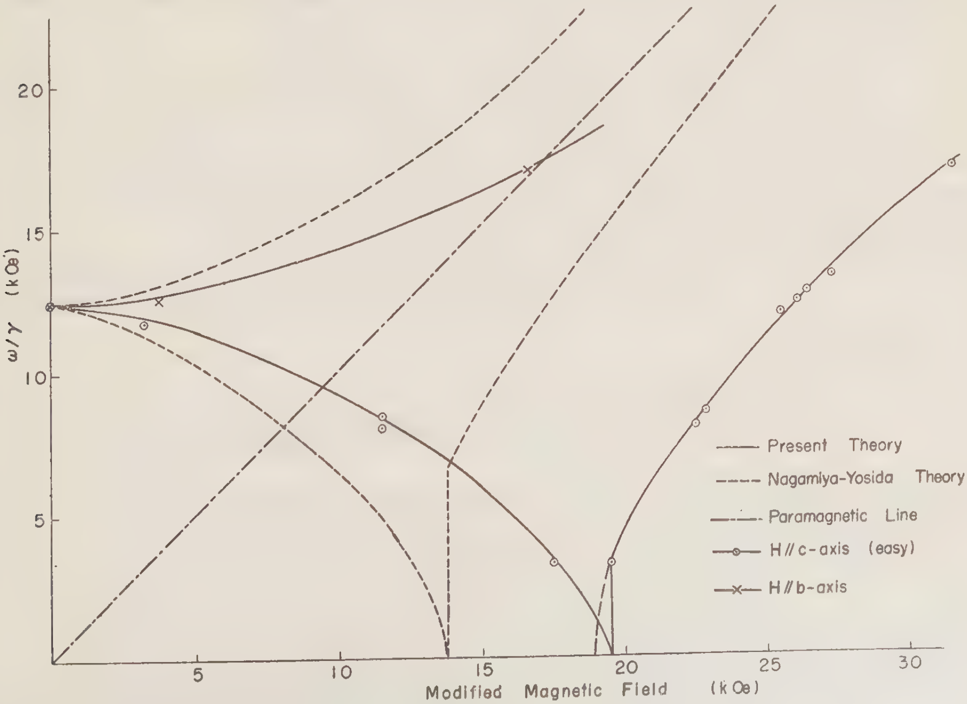

Fig. 16. Frequency-field diagram of the resonance points (1.5°K)

us consider the equation of antiferromagnetic oscillation including an anisotropic exchange interaction of symmetric tensor form. For convenience, we use Nagamiya's notation except for the anisotropic exchange interaction. The equation of motion of the two sublattice magnetizations are

$$\frac{1}{\gamma}\frac{d}{dt}M^{\pm}=M^{\pm}\times(H+H_E^{\pm})\,, \tag{2}$$

where γ is the gyromagnetic ratio, $M^{\pm}$ is the magnetization of the $+$ and $-$ sublattices, H and H_E represent the external magnetic field and the exchange field, respectively. Following Nagamiya and Yosida's procedure, we define

$$M=M^{+}+M^{-}\,,\qquad M'=M^{+}-M^{-}\,. \tag{3}$$

Now an anisotropic exchange interaction will be introduced in the following way. The exchange energy is defined by

$$E_{ex}=AM^{+}M^{-}+\frac{1}{2}\Gamma(M^{+2}+M^{-2})+M^{+}A'M^{-}+\frac{1}{2}(M^{+}\Gamma'M^{+}+M^{-}\Gamma'M^{-})\,. \tag{4}$$

The first and second terms represent the isotropic exchange interactions which are present in the Nagamiya-Yosida theory, where A and Γ are scalars. The third and 4th terms are the anisotropic part of the exchange energy having the tensor form given by

$$A'=\begin{pmatrix} A_x' & 0 & 0 \\ 0 & A_y' & 0 \\ 0 & 0 & A_z' \end{pmatrix},\qquad \Gamma'=\begin{pmatrix} \Gamma_x' & 0 & 0 \\ 0 & \Gamma_y' & 0 \\ 0 & 0 & \Gamma_z' \end{pmatrix}, \tag{5}$$

where the diagonal sum of both tensors is assumed to be zero, namely,

$$A_x'+A_y'+A_z'=0\,,\qquad \Gamma_x'+\Gamma_y'+\Gamma_z'=0\,. \tag{6}$$

It may be noted that the anisotropy energy used in the Nagamiya-Yosida theory is equivalent to the fourth term in Eq. (4), but that the third term expressed by $M^{+}A'M^{-}$ is newly introduced in the present treatment. Moreover, since we are dealing with the case of an effective spin of 1/2, any one ion type anisotropy energy does not appear.

With the use of (3), we rewrite Eq. (2) in terms of M and M'. Then adding and substructing the two equations (2), we obtain the following equations:

$$\frac{1}{\gamma}\frac{d}{dt}M=M\times H+\frac{1}{2}M\times(H_E^{+}+H_E^{-})+\frac{1}{2}M'\times(H_E^{+}-H_E^{-})\,, \tag{7}$$

$$\frac{1}{\gamma}\frac{d}{dt}M'=M'\times H+\frac{1}{2}M\times(H_E^{+}-H_E^{-})+\frac{1}{2}M'\times(H_E^{+}+H_E^{-})\,. \tag{8}$$

The exchange field H_E is now obtained from the relation

$$\delta E_{ex}=-H_E^{+}\delta M^{+}-H_E^{-}\delta M^{-}\,, \tag{9}$$

the result being

$$\begin{aligned} H_E^{\pm}&=-AM^{\mp}-\Gamma M^{\pm}-A'M^{\mp}-\Gamma'M^{\pm}\\ &=-\frac{1}{2}\{A(M\mp M')+\Gamma(M\pm M')+A'(M\mp M')+\Gamma'(M\pm M')\}\,. \end{aligned} \tag{10}$$

Using Eq. (10), the components of Eqs. (7) and (8) can be written as follows:

$$\left.\begin{aligned} \frac{1}{\gamma}\frac{d}{dt}M_x&=H_zM_y-H_yM_z+\frac{1}{2}(P_y-P_z)M_yM_z+\frac{1}{2}(Q_z-Q_y)M_y'M_z'\\ \frac{1}{\gamma}\frac{d}{dt}M_y&=H_xM_z-H_zM_x+\frac{1}{2}(P_z-P_x)M_zM_x+\frac{1}{2}(Q_x-Q_z)M_z'M_x'\\ \frac{1}{\gamma}\frac{d}{dt}M_z&=H_yM_x-H_xM_y+\frac{1}{2}(P_x-P_y)M_xM_y+\frac{1}{2}(Q_y-Q_x)M_x'M_y' \end{aligned}\right\} \tag{11}$$

$$\left.\begin{aligned}
\frac{1}{\gamma}\frac{d}{dt}M_x'&=H_zM_y'-H_yM_z'+\left\{A+\frac{1}{2}(P_y+Q_z)\right\}M_yM_z'-\left\{A+\frac{1}{2}(P_z+Q_y)\right\}M_zM_y'\\
\frac{1}{\gamma}\frac{d}{dt}M_y'&=H_xM_z'-H_zM_x'+\left\{A+\frac{1}{2}(P_z+Q_x)\right\}M_zM_x'-\left\{A+\frac{1}{2}(P_x+Q_z)\right\}M_xM_z'\\
\frac{1}{\gamma}\frac{d}{dt}M_z'&=H_yM_x'-H_xM_y'+\left\{A+\frac{1}{2}(P_x+Q_y)\right\}M_xM_y'-\left\{A+\frac{1}{2}(P_y+Q_x)\right\}M_yM_y'
\end{aligned}\right\}\tag{12}$$

where new parameters P and Q are used which are defined by

$$P=A'+\Gamma', \qquad Q=A'-\Gamma'. \tag{13}$$

Of course P and Q are tensors whose diagonal sum is equal to zero. To obtain the resonance conditions of the system represented by the equation of motion (11) and (12), we assume that the deviation of M and M' from their equilibrium values is small and retain in the equations only the first order terms. As long as the external field is small compared with the exchange field, these equation of small oscillation derived from Eqs. (11) and (12) can be simplified, and the results in several important cases are as follows.

(1) The applied field is parallel to the x-axis (c-axis).

In this case we have to distinguish between three cases, that is, $H<H_c$, $H=H_c$ and $H>H$, where H_c is the critical field at which the direction of M' turns in the xy-plane.

(a) $H<H_c$. The vectors M and M' both point to the x-direction so that (11) and (12) can be written as the variational form:

$$\left.\begin{aligned}
&\frac{1}{\gamma}\frac{d}{dt}\delta M_x=0\\
&\frac{1}{\gamma}\frac{d}{dt}\delta M_y=H\delta M_z+\frac{1}{2}(P_z-P_x)M_x\delta M_z+(Q_x-Q_z)M_0\delta M_z'\\
&\frac{1}{\gamma}\frac{d}{dt}\delta M_z=-H\delta M_y+\frac{1}{2}(P_x-P_y)M_x\delta M_y+(Q_y-Q_x)M_0\delta M_y'
\end{aligned}\right\}\tag{14}$$

$$\left.\begin{aligned}
&\frac{1}{\gamma}\frac{d}{dt}\delta M_x'=0\\
&\frac{1}{\gamma}\frac{d}{dt}\delta M_y'=H\delta M_z'+2\left\{A+\frac{1}{2}(P_z+Q_x)\right\}M_0\delta M_z-\left\{A+\frac{1}{2}(P_x+Q_z)\right\}M_x\delta M_z'\\
&\frac{1}{\gamma}\frac{d}{dt}\delta M_z'=-H\delta M_y'+\left\{A+\frac{1}{2}(P_x+Q_y)\right\}M_x\delta M_y'-2\left\{A+\frac{1}{2}(P_y+Q_x)\right\}M_0\delta M_y
\end{aligned}\right\}\tag{15}$$

where the external magnetic field H_x is written as H. Taking δM_y, δM_z, $\delta M_y'$ and $\delta M_z'$ proportional to $\exp(i\omega t)$, we obtain the determinantal equation

$$\begin{vmatrix}
\frac{-i\omega}{\gamma} & H\left\{1+\frac{1}{2}(P_z-P_x)\chi_{\parallel}\right\} & 0 & (Q_x-Q_z)M_0\\
-H\left\{1-\frac{1}{2}(P_y-P_x)\chi_{\parallel}\right\} & \frac{-i\omega}{\gamma} & (Q_y-Q_x)M_0 & 0\\
0 & 2\left\{A+\frac{1}{2}(P_z+Q_x)\right\}M_0 & \frac{-i\omega}{\gamma} & H\left[1-\left\{A+\frac{1}{2}(P_x-Q_z)\right\}\chi_{\parallel}\right]\\
-2\left\{A+\frac{1}{2}(P_y+Q_x)\right\}M_0 & 0 & -H\left[1-\left\{A+\frac{1}{2}(P_x+Q_y)\right\}\chi_{\parallel}\right] & \frac{-i\omega}{\gamma}
\end{vmatrix}=0 \tag{16}$$

Reducing the determinant, we obtain a complicated expression for the resonance condition, which, however, can be simplified when $\omega/\gamma=0$ or $H=0$ as follows:

$$\frac{\omega}{\gamma}=0:\quad H^2\left\{1-\frac{1}{2}(P_y-P_x)\chi_\parallel\right\}\left[1-\left\{A+\frac{1}{2}(P_x+Q_z)\right\}\chi_\parallel\right]$$
$$+2(Q_y-Q_x)\left\{A+\frac{1}{2}(P_y+Q_x)\right\}M_0^2=0\,, \tag{17}$$

$$H=0:\quad \left(\frac{\omega}{\gamma}\right)^2=2(Q_x-Q_y)\left\{A+\frac{1}{2}(P_z+Q_x)\right\}M_0^2\,. \tag{18}$$

(b) $H>H_c$. In this case M is parallel to the x-axis but M' is perpendicular to it and points to the y-axis (b-axis). The equations are

$$\left.\begin{aligned}\frac{1}{\gamma}\frac{d}{dt}\delta M_x&=(Q_z-Q_y)M_0\delta M_z'\\ \frac{1}{\gamma}\frac{d}{dt}\delta M_y&=H\delta M_z+\frac{1}{2}(P_z-P_x)M_x\delta M_z\\ \frac{1}{\gamma}\frac{d}{dt}\delta M_z&=-H\delta M_y+\frac{1}{2}(P_x-P_y)M_x\delta M_y+(Q_y-Q_x)M_0\delta M_x'\end{aligned}\right\} \tag{19}$$

$$\left.\begin{aligned}\frac{1}{\gamma}\frac{d}{dt}\delta M_x'&=-2\left\{A+\frac{1}{2}(P_z+Q_y)\right\}M_0\delta M_z\\ \frac{1}{\gamma}\frac{d}{dt}\delta M_y'&=H\delta M_z'-\left\{A+\frac{1}{2}(P_x+Q_z)\right\}M_x\delta M_z'\\ \frac{1}{\gamma}\frac{d}{dt}\delta M_z'&=-H\delta M_y'+\left\{A+\frac{1}{2}(P_x+Q_y)\right\}M_x\delta M_y'+2\left\{A+\frac{1}{2}(P_x+Q_y)\right\}M_0\delta M_x\end{aligned}\right\} \tag{20}$$

Solving these equations, we can obtain the resonance conditions as

$$\left(\frac{\omega}{\gamma}\right)^2=H^2\left\{1+\frac{1}{2}(P_z-P_x)\chi_\perp\right\}\left\{1+\frac{1}{2}(P_y-P_x)\chi_\perp\right\}-2(Q_x-Q_y)\left\{A+\frac{1}{2}(P_z+Q_y)\right\}M_0^2 \tag{21}$$

$$\left(\frac{\omega}{\gamma}\right)^2=2(Q_y-Q_z)\left\{A+\frac{1}{2}(P_x+Q_y)\right\}M_0^2-H^2\left\{1-\left[A+\frac{1}{2}(P_x+Q_y)\right]\chi_\perp\right\}$$
$$\times\left\{1-\left[A+\frac{1}{2}(P_x+Q_z)\right]\chi_\perp\right\} \tag{22}$$

(2) The applied field is parallel to the y-axis.

In this case the resonance equation can be solved in the same way as in the case (1) (b), and the result is

$$\left(\frac{\omega}{\gamma}\right)^2=H^2\left\{1+\frac{1}{2}(P_x-P_y)\chi_\parallel\right\}\left\{1+\frac{1}{2}(P_z-P_y)\chi_\perp\right\}+2(Q_x-Q_y)\left\{A+\frac{1}{2}(P_z+Q_x)\right\}M_0^2 \tag{23}$$

Now let us consider the experimental result shown in Fig. 16. The most precise experimental point is the resonance frequency at $H=0$. This frequency was determined to be

$$\nu=34{,}630\pm50\ \text{Mc/sec}\,. \tag{24}$$

So the resonance constants should be so adjusted that a good accord with the experimental result is obtained at $H=0$.

Then the anisotropic exchange tensors P and Q are determined in the following way. Using the experimental results, $(\omega/\gamma)^2$ of Eqs. (21) and (23) can be expressed respectively as

$$(\omega/\gamma)^2=0.45H^2-161\,, \tag{21'}$$
$$(\omega/\gamma)^2=0.50H^2-153\,. \tag{23'}$$

Comparing Eqs. (21) with (21′) and (23) with (23′), the following relations are obtained:

$$\{1+\tfrac{1}{2}(P_z-P_x)\chi_\perp\}\{1+\tfrac{1}{2}(P_y-P_x)\chi_\perp\}=0.45 \tag{25}$$
$$\{1+\tfrac{1}{2}(P_x-P_y)\chi_\perp\}\{1+\tfrac{1}{2}(P_z-P_y)\chi_\perp\}=0.50 \tag{26}$$

Strictly speaking, the susceptibilities in Eqs. (25) and (26) are not the same because $\chi_\perp$ in

(25) means the perpendicular susceptibility along the c-axis when $H>H_c$ while $\chi_\perp$ in (26) is that along the *b*-axis; if there is a large anisotropy in the *bc*-plane, they cannot be equal to each other. Namely $\chi_{\perp H /\!/ x\text{-axis}}=1/(A+\frac{1}{2}P_x)$ and $\chi_{\perp H /\!/ y\text{-axis}}=1/(A+\frac{1}{2}P_y)$ as can be calculated from the torque balance equation. However, as will be seen from Eqs. (25) and (26) P_x/P_y is nearly equal to one so that $(P_x-P_y)/A$ may be negligible in Eqs. (25) and (26). Thus, solving these equations, we get the components of the *P*-tensor as

$$\left.\begin{aligned} P_x&=(0.44\pm0.04)A\,, \\ P_y&=(0.38\pm0.04)A\,, \\ P_z&=-(0.82\pm0.04)A\,. \end{aligned}\right\} \qquad (27)$$

To determine the *Q*-tensor, we compare Eqs. (23) and (23′) and obtain the following relation:

$$2(Q_x-Q_y)\{A+\tfrac{1}{2}(P_z+Q_x)\}M_0{}^2=153\,. \qquad (28)$$

Further, we have the following ratio by comparing Eq. (16) with the corresponding experimental result:

$$(Q_x-Q_z)/(Q_x-Q_y)=3.5\,. \qquad (29)$$

Together with the relation $Q_x+Q_y+Q_z=0$, the components of the *Q*-tensor can be calculated, if we could determine *A* and M_0 in Eq. (28). *A* can be determined from susceptibility data obtained by Haseda and Friedberg et al., namely, $\chi_{\perp b}=1/(A+\frac{1}{2}P_y)=9\times10^{-4}$ /gram. M_0 can be calculated from the definition, $M_0=\frac{1}{2}Ng\mu_B\langle S\rangle$, where $\langle S\rangle$ is the thermal average of the spin. At absolute zero, M_0 can be calculated using the observed *g*-value, and at 1.5°K, i.e. the temperature of our measurements, it can be determined with reference to the proton resonance measurements performed by Sugawara. This M_0 is the magnitude of sublattice magnetizations in an external field small compared with H_c, in which case they lie along the easy axis. M_0 in Eq. (23) correspond to this M_0, whereas M_0 in Eqs. (21) and (22) is the magnitude of sublattice magnetizations when they are along the *y*-axis. These two quantities may be assumed to be equal to each other for the same reason as that mentioned in the argument concerning $\chi_{\perp H /\!/ x\text{-axis}}$ and $\chi_{\perp H /\!/ y\text{-axis}}$. Thus the Q-tenson is determined to be

$$\left.\begin{aligned} Q_x&=(0.055\pm0.002)A\,, \\ Q_y&=(0.018\pm0\text{-}002)A\,, \\ Q_z&=-(0.073\pm0.002)A\,. \end{aligned}\right\} \qquad (30)$$

It is interesting to note that the ratio P/Q is of the order of 10 which means $A'/\Gamma'\sim1$. Using Eqs. (27) and (30), A' and Γ' are calculated as

$$\left.\begin{aligned} &A_x'=0.25A\,, \quad A_y'=0.20A\,, \quad A_z'=-0.45A\,, \\ &\Gamma_x'=0.19A\,, \quad \Gamma_y'=0.18A\,, \quad \Gamma_z'=-0.37A\,. \end{aligned}\right\} \qquad (31)$$

The results calculated with these values represented by full lines in Fig. 16, which are in satisfactory agreement with the experimental points.

§ 7. Discussion of the Resonance Conditions

In the preceding section we showed that a revised resonance formula can satisfactorily explain our experimental results with the use of anisotropic exchange constants A' and Γ'. These tensors have the same symmetry with that of the *g*-tensor. Accordingly such anisotropic exchange interaction may come mainly from the isotropic exchange interactions, which become anisotropic in the effective spin hamiltonian which is obtained when the true spin is replaced by the effective spin of $\frac{1}{2}$. In $CuCl_22H_2O$, in which the anisotropy of the *g*-tensor is not so large as in $CoCl_26H_2O$, these anisotropic parts of exchange interactions are small compared with the isotropic parts, so that the old theory was satisfactorily applicable. However, there may be other causes which may produce the anisotropic exchange interaction. The magnetic dipole interaction may make a contribution to some extent. This interaction can be represented by a tensor form. Thus, A' and Γ' determined by the present study include this effect. Though we cannot evaluate its contribution quantitatively, since we do not know the spin arrangement in antiferromagnetic state, it may be relatively small and will not account for the main experimental results. The dipolar interaction was also incapable of accounting for the width of the paramagnetic resonance, as was discussed in a previous section.

As other correction factors the 4-th order anisotropy energy and demagnetization effect may be considered. The former can be introduced in the following form:

$$E=L_1\alpha^4+L_2\beta^4+L_3\gamma^4+L_4\alpha^2\beta^2 \qquad (32)$$

where L_1, L_2,, $\cdots$, L_4 are constants and α, β, γ represent the direction cosines of the spins along the x, y and z-axes, respectively. Using this energy, we can obtain the resonance formula including 4-th order anisotropy constants. However, it was found that this energy is unimportant and is whithin experimental errors.

Next, let us consider the demagnetization effect. To take this into acconnt, external field H must be reduced to

$$H-(iN_xM_x+jN_yM_y+kN_zM_z)\ . \tag{33}$$

Substituting this in the equation of motion, we can see easily that the resonance formula can be obtained with the substitution of

$$\frac{1}{2}\begin{pmatrix} P_x & 0 & 0 \\ 0 & P_y & 0 \\ 0 & 0 & P_z \end{pmatrix} \quad \text{by} \quad \begin{pmatrix} \frac{P_x}{2}+N_x-\frac{4\pi}{3} & 0 & 0 \\ 0 & \frac{P_y}{2}+N_y-\frac{4\pi}{3} & 0 \\ 0 & 0 & \frac{P_z}{2}+N_z-\frac{4\pi}{3} \end{pmatrix}, \tag{34}$$

where $4\pi/3$ comes from the Lorentz field correction. In our experiments, however, this correction is also negligible, so that the obtained anisotropic exchange interaction coefficients can be regarded as the intrinsic parameters of the antiferromagnetic $CoCl_2$-$6H_2O$.

§ 8. Line Width

Line width measurements were performed in the paramagnetic state as well as in the antiferromagnetic state of $CoCl_26H_2O$. Two examples of the angular dependence are shown in Fig. 17. One of them is the result for in the bc-plane at 34.820 kMc/sec and the other is that for in the $a'c$-plane at 23.580 kMc/sec, and the high and low field branches corresponding to those of Fig. 11. Temperature dependences of the resonance line width at various frequencies are summalized in Fig. 18. As was described in Section 4, an anomalous broadening of the paramagnetic resonance line was observed at 4.2°K, which

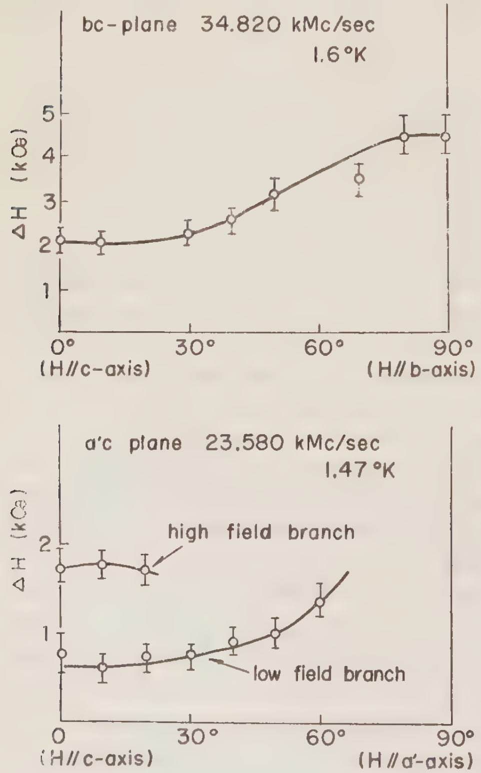

Fig. 17. Angular dependence of the line width.

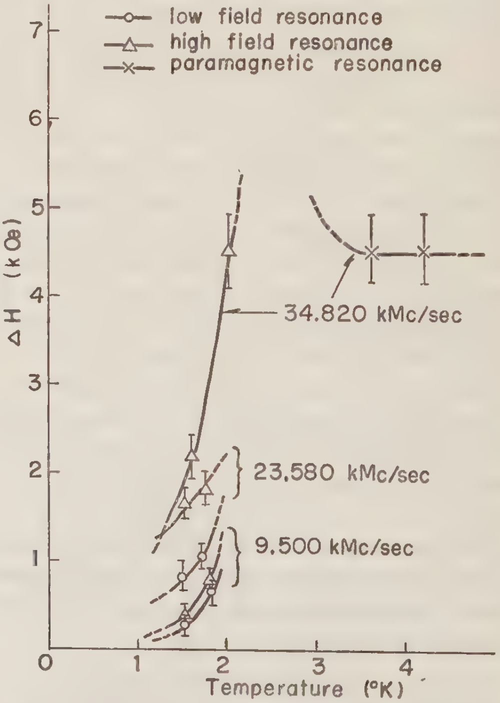

Fig. 18. Temperature dependence of the line width ($H//c$-axis).

may be due to the anisotropic exchange interaction among Co^{++} ions as was introduced in the foregoing section. Below the Néel temperature, however, a considerable narrowing effect was seen in all the crystalline directions as shown in Fig. 18. An interesting result was obtained in the measurement of the frequency dependence, namely, the fact that the line width increases with increasing resonance frequency. This fact cannot be explained by a simple theory of antiferromagnetic resonance line width discussed by Townes, Johnson and Nethercot[4]. Imperfections of the crystal, such as antiferromagnetic domain boundaries, dislocations, or the presence of chemical impurities, may not be responsible for the main origin of the line width, because the extrapolated value of the width to 0°K is estimated to be zero in almost all cases.

In must be added that there was no trace of side peaks which were frequently observed in $CuCl_22H_2O$, $CuBr_22H_2O$ and MnF_2.

Acknowledgement

The present work was initiated at the low temperature division, Institute for Iron, Steel and Other Metals, Tohoku University, and was completed in the low temperature laboratory of Osaka University. The author wishes to express his thanks to Prof. Fukuroi at Tohoku University for offering the facility of making this low temperature experiment and to Prof. Itoh, Prof. Nagamiya and Dr. Kanamori for valuable discussions and suggestions on the present problem.

References

1) General theory of antiferromagnetic resonance was developed by T. Nagamiya (1951), C. Kittel (1951) and F. Keffer and C. Kittel (1952) Theory of antiferromagnetic resonance in $CuCl_22H_2O$ was discussed by T. Nagamiya (1954) and (1956), K. Yosida (1952) and J. Ubbink (1953). T. Nagamiya: Prog. Theor. Phys. **6** (1951) 342, **11** (1954) 309 and **15** (1956) 306. C. Kittel: Phys. Rev. **82** (1951) 565. F. Keffer and C. Kittel: Phys. Rev. **85** (1952) 329. K. Yosida: Prog. Theor. Phys. **7** (1952) 25 and **7** (1952) 425. J. Ubbink: Physica **19** 623.

2) The most complete accounts of the experimental results are contained in the thesis of J. Ubbink (1953) and that of H. J. Gerritsen (1955). These accounts are duplicated in a series of papers starting with that of Poulis, van den Handel, Ubbink and Gorter: Phys. Rev. **82** (1952) 552. The paper by Gerritsen and Garber: Physica **22** (1956) 418 gives later references. See also T. Nagamiya, K. Yosida and R. Kubo: Advances in Physics, **4** (1955) 1.

3) M. Date: Phys. Rev. **104** (1956) 623.

4) F. M. Johnson and A. H. Nethercot, Jr.: Phys. Rev. **104** (1956) 847; **114** (1959) 705.

5) S. Foner: Phys. Rev. **104** (1957) 683.

6) E. S. Dayhoff: Phys. Rev. **107** (1957) 84.

7) S. Foner: J. Phys. Rad. **20** (1959) 336.

8) M. Date: J. Phys. Soc. Japan **12** (1957) 1168.

9) R. C. Ohlman: thesis, Univ. of California, June (1960).

10) H. Kondoh: J. Phys. Soc. Japan **15** (1960).

11) T. Haseda and E. Kanda: J. Phys. Soc. Japan **12** (1957) 1051.

12) J. Mizuno, K. Ukei and T. Sugawara: J. Phys. Soc. Japan **14** (1959) 383.

13) W. K. Robinson and S. A. Friedberg: Phys. Rev. **117** (1960) 402.

14) T. Haseda: J. Phys. Soc. Japan **15** (1960) 483.

15) R. B. Flippen and S. A. Friedberg: J. Applied Phys. **31** (1960) 338.

16) T. Sugawara: J. Phys. Soc. Japan **14** (1959) 1248.

17) M. Date: J. Phys. Soc. Japan **14** (1959) 1244.

18) T. Haseda, H. Kobayashi and M. Date: J. Phys. Soc. Japan **14** (1959) 1724.

19) T. Fukuroi, E. Uchida, M. Date, F. Inaba and O. Nanjo: presented at the annual meetings of the Phys. Soc. Japan, April (1960).

20) J. H. Van Vleck: Phys. Rev. **74** (1948) 1168.

21) P. W. Anderson and P. R. Weiss: Rev. Mod. Phys. **25** (1953) 269.

22) A. Abragam and M. H. L. Pryce: Proc. Roy. Soc. **A, 206** (1951) 173.

23) R. Pappalardo: Phil. Mag. **4** (1959) 219.

24) S. Koide: Phil. Mag. **4** (1959) 243.

25) T. Moriya: Phys. Rev. Letters **4** (1960) 228.

JOURNAL OF THE PHYSICAL SOCIETY OF JAPAN Vol. 16, No. 7, JULY, 1961

Thermal Properties of $NaNO_2$

By Shoichiro NOMURA

Physics Department, Tokyo Institute of Technology
Oh-okayama, Meguro, Tokyo

(Received April 1, 1961)

Specific heat and thermal expansion coefficients of $NaNO_2$ crystal were measured from room temperature to 210°C. A conduction-type calorimeter was adopted for the measurement of the specific heat and a differential-type dilatometer for the measurement of the thermal dilatation. A λ-type anomaly in specific heat was observed near the transition temperature, the transition heat being calculated as *ca* 285 cal/mol. The crystal expands in the *a* and *b* direction, while it contracts in the *c* direction with increasing the temperature, and further the transition is accompanied by abrupt changes in the cell dimensions. Our results on thermal dilatation were compared with the ones obtained from the x-ray data. Ferroelectricity in $NaNO_2$ was discussed in connection with our results on thermal properties.

§ 1. Introduction

Ferroelectricity in $NaNO_2$ has first been revealed by the measurements of the dielectric properties[1] and further ascertained by the observations of the domain structure[2]*. The ferroelectric axis of $NaNO_2$ crystal lies in the *b* direction of the orthorhombic structure, the space group of which is C_{2v}^{20} (I_{m2m})[4,5,6]. (The crystallographic *a*, *b*, and *c* axes adopted by Ziegler[4] will be used throughout the present paper.) The crystal undergoes a phase transition at the Curie temperature near 160°C, from the state of lower symmetry to the state of higher symmetry. The space group of higher symmetry is D_{2h}^{25} (I_{mmm})[7,8,9], which corresponds to the paraelectric phase. The unit cell has two molecular units, both above and below the Curie point.

Before the ferroelectricity in $NaNO_2$ has been found, several investigations were made concerning this phase transformation. Jaffray[10] studied the transition by means of differential thermal analysis and found out an abrupt anomaly in specific heat at 160~162°C. Analysing the x-ray data, Strijk and MacGillavry[7,8] reported that $NaNO_2$, which is orthorhombic hemihedral at ordinary temperature, shows an abrupt change in the temperature coefficients of the all dimensions at about 158°C and the original strong piezoelectric effect disappears above this temperature. He pointed out further that the change is probably caused by the occurrence of two symmetrical sets of atomic positions in an average structure.

Since the occurrence of ferroelectricity in $NaNO_2$ became clear, it has been necessary to measure the various properties in detail near the transition temperature, for developing a thorough discussion about the ferroelectricity in $NaNO_2$. For this purpose, we have measured the thermal properties of $NaNO_2$: specific heat and thermal dilatation, in the temperature range from ordinary temperature to 210°C and tried to make their characters clear. (The specific heat is the one at constant pressure.) In this paper, these experimental results are described and some discussions on the ferroelectricity in $NaNO_2$ are presented.

§ 2. Experimentals

a) *Specific heat*

The adopted method was of the conduction-type, in which the thermo-electromotive force of the differential thermo-couple was recorded when the temperature of the furnance was varied in a definite manner. But the detailed descriptions on the apparatus and the measuring method are omitted here, since they have been described in the other paper[11,12].

Before the beginning of the measurement, a powder sample of $NaNO_2$ of 16 grs was dried at about 100°C during 12 hrs. in the container of the calorimeter. The measurement was done under the pressure of 10^{-2} mm Hg, and the rate of heating of the sample was kept nearly constant about 1°C/min, by a controll of the furnace input voltage. The calibration curve of the calorimeter was taken by using both Al_2O_3 and SiO_2 powders and nearly same curves were obtained in the two cases.

---

* Recently, Dr. Shibuya have carried out x-ray studies of the phase transition in $NaNO_2$, using the Bragg reflections, and the critical scatterings[3].

b) *Thermal dilatation*

The magnitude of the linear thermal expansion coefficients of $NaNO_2$ crystal being of the order of 10^{-4}°C^{-1}, the measurement of the thermal dilatation was easily done by using an usual dilatometer of differential type, in which an optical lever combined with a fine roller was adopted, a fused silica rod being used for comparison. The diameter r of the roller and the distance D between the mirror and the scale were 0.24 cm and 148.2 cm respectively, so the dilatation of the sample, enlarged $2D/r=1235$ times, was observed on the scale. The calibration of the dilatometer was done by using a copper rod. The rate of the temperature increase of the sample in the measurement was 1°C/min in avarage, but in the vicinity of the transition temperature, it was slowed down less than 0.1°C/min.

Samples of rod shape were cut out from the crystals prepared by the fusion method, of which description was given in our previous paper[2]. The lengths of the a, b, and c crystal rods were 0.848 cm, 0.997 cm, and 1.040 cm respectively.

§ 3. Results and Discussions

a) *Specific heat*

The specific heat of $NaNO_2$ in the temperature range from 50°C to 220°C is shown in Fig. 1. A large anomaly of λ-type is observed near the transition temperature. The anomaly appears from near 110°C, in the temperature region far below the transition temperature and reaches to a peak at 161°C. It is noticiable that the anomaly remains in the paraelectric region upto about 170°C, though its magnitude decreases rapidly with increasing the temperature. The transition heat was estimated as 285 cal/mol, the magnitude of which depends upon to some extent the situation of the curve of the normal specific heat shown by a dashed line in the figure, and the transition entropy was calculated as 0.7 cal/°C mol.

Our result on specific heat coincides with Jaffray's work[10], that the transition is not accompanied by a latent heat, but an abrupt anomaly in specific heat. This seems to be favorable to the view that the transition is of the second kind. At the present step, however, we had better refrain from judging the kind of the transition in $NaNO_2$, because a detection of a small amount of latent heat is beyond the ability of our calorimater.

b) *Thermal dilatation*

The temperature dependences of the thermal dilatation in each direction of the crystal

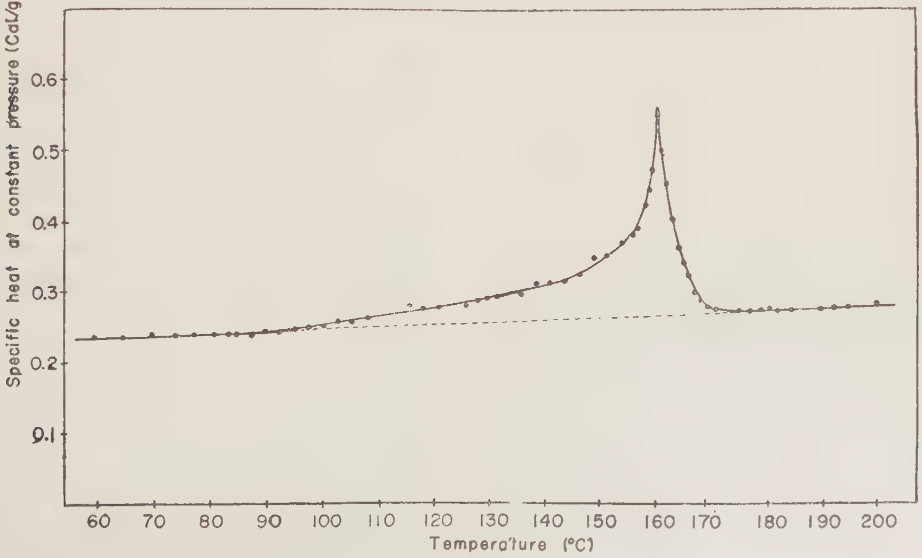

Fig. 1. The specific heat of $NaNO_2$.

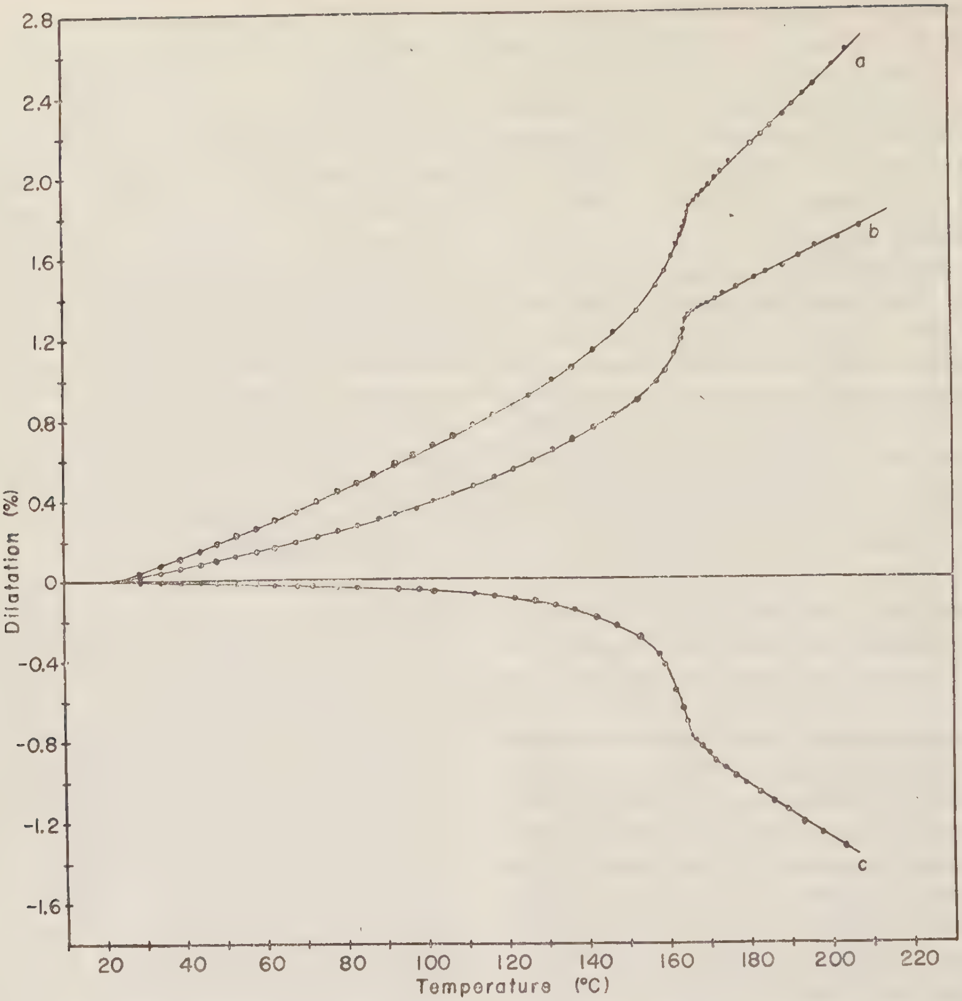

Fig. 2. The thermal dilatation of $NaNO_2$ crystal. The relative change of the length, taken as zero at 20°C, is expressed in each direction of the crystal axes.

axes of the orthorhombic structure are illustrated in Fig. 2, where the changes in length of the crystal rods are plotted in percents, the lengths at 20°C being taken as the original ones in all directions. It is quite obvious that the crystal expands in the *a* and *b* direction, while it contracts in the *c* direction with increasing the temperature. The linear thermal expansion coefficients obtained from the curves of the dilatation are shown in Fig. 3. Sharp peaks are observed in all directions at 164°C and anomalies can be observed also far below the transition temperature, as in the case of the specific heat. The coefficient of the *a* direction is larger than that of the *b* direction, though the peak value at the transition is superior in the later. Above 168°C, the coefficients take nearly constant values, excepting for in the *c* direction, in which a minor anomaly is noticed near 170°C*.

To show how the cell dimensions vary at the transition temperature, the dilatation curve in the *b* direction in the vicinity of the transition temperature is enlarged in Fig. 4. Judging from this curve, we may say that the transition is not accompanied by a discontinuous change in the cell dimensions but rather a continuous one, though its variation is steep, and if some amounts of the discontinuity occurred at the transition temperature, it should be smaller than $4\times10^{-2}\%$

---

* Dr. Hoshino and Shibuya have reported that the minor anomaly of this kind was observed not only in the *c* direction but also in the *a* and *b* direction by his x-ray analysis. (J. Phys. Soc. Japan **16** (1961) 1254.)

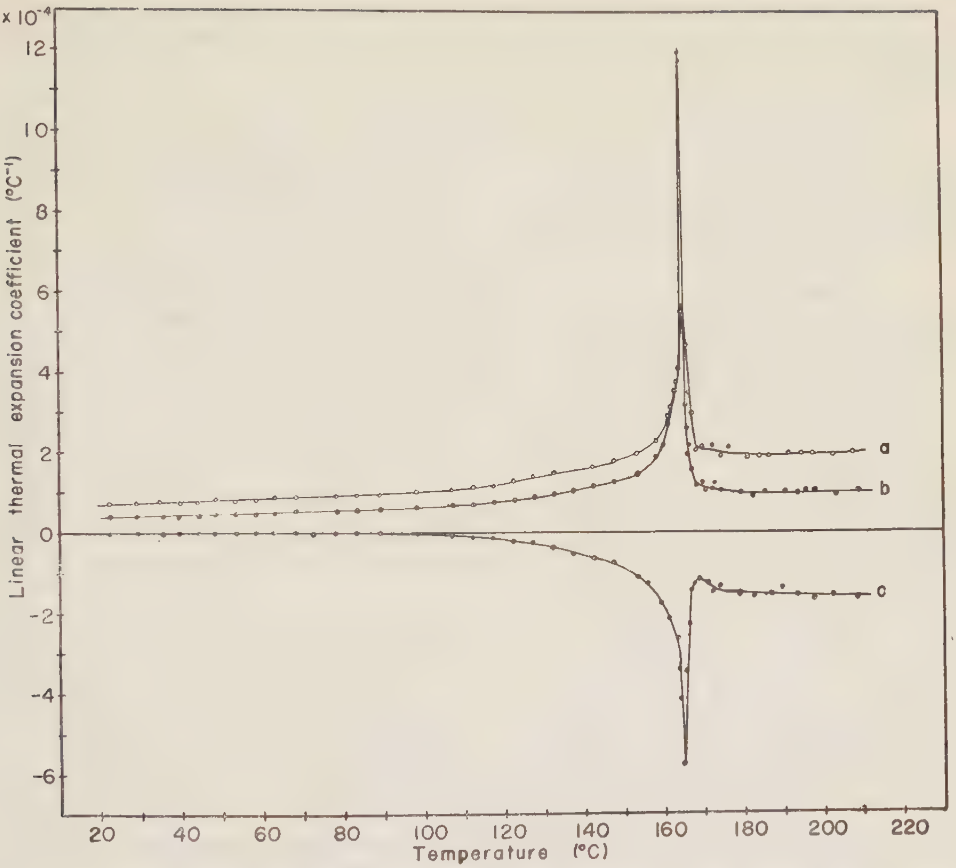

Fig. 3. The linear thermal expansion coefficients in the directions of the crystal axes of NaNO$_2$.

in its magnitude in the b direction.

Our results on the thermal dilatation show the same characteristic as the ones obtained from the x-ray data$^{7),8)}$, but quantitatively some discrepancies exist between them. The situations are illustrated in Table I, where the percentages of the changes in the cell dimensions caused by rising the temperature of the crystal from room temperature to 205°C, are given in both cases. The values obtained by the dilatometric method are smaller than the ones by the x-ray method in all directions. It may be natural that they should show some differences in their magnitude, because one of them is due to the macroscopic measurement, while the other is the microscopic one. The existence of the domain boundaries and some kinds of crystal imperfections may be considered to be the causes for the discrepancies. As the discrepancy is remarkable in the a direction, it may be related with the fact that the domain boundaries lie parallel to the bc plane$^{2)}$. In high temperature, moreover, a plastic flow might be slightly induced by a mechanical stress owing to the metal springs, holding the sample in the dilatometer. This flow effect seems to be supported by our recent experiments on the deformation of the crystal with a two dimensional stress*.

Table I. The comparion of the magnitudes of the dilatation. The values of the cell dimensions are quoted from "Crystal Structures Vol. Ⅲ (1951) (by R. W. Wyckoff)".

	cell dimension (Å)		dilatation (%)	
	26°C	205°C	x-ray	dilatometer
a	3.570	3.69	3.3	2.6
b	5.578	5.68	1.8	1.7
c	5.390	5.33	−1.1	−1.3

c) *Relations with the ferroelectricity*

The spontaneous polarization P_s of a ferroelectric crystal intimately relates with the

---

* S. Nomula: unpublished.

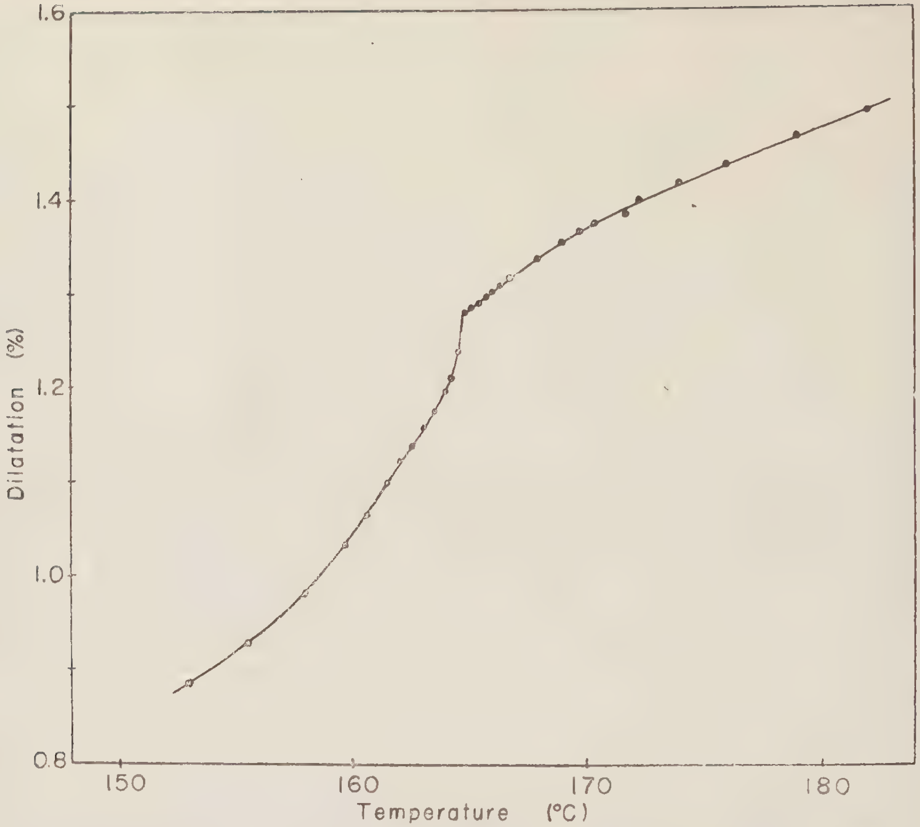

Fig. 4. The dilatation curve in the b direction in the vicinity of the transition temperature.

transition heat Q from the ferroelectric state to the para electric state. We have the well-known formula[13].

$$Q \simeq 2\pi \cdot \frac{T_0}{C} \cdot P_s^2 , \qquad (1)$$

which holds experimentaly to a good approximation in many kinds of ferroelectrics, where T_0 is the transition temperature and C is the Curie-Weiss constant. Putting the numerical values on T_0, C, and P_s as follows,

$$T_0 = 437°\text{K}$$
$$C = 5000°\text{K}$$
$$P_s = 8.6\mu\text{C/cm}^2*$$

we obtain the value of Q as 279 cal/mol. The agreement with experiment is satisfactory when the experimental difficulties are considered that are encountered in the measurement of the transition heat and the spontaneous polarization.

Ferroelectricty in $NaNO_2$ is probably due to the alignment of NO_2^- radicals along the b direction, and the disordering of their sense is realized above the Curie temperature. The order of the alignment of NO_2^- radicals ought to be estimated from the magnitude of the transition heat and also the transition entropy.

Since a strict calculation of the transition entropy of $NaNO_2$ seems to be complicated, we give here a rough estimation on it. Supposing that a NO_2^- radical has two equilibrium positions in its surrounding, being of opposite sense along the b direction and the transformation is accompanied by the order-disorder arrangement of NO_2^- radicals between them. If the parameter of the long range order is denoted by s, the entropy of the system S will be represented by a simple calculation, neglecting the effect due to the short range interaction, as follows,

$$S = -kN\left\{\frac{1+s}{2}\ln\left(\frac{1+s}{2}\right) + \frac{1-s}{2}\ln\left(\frac{1-s}{2}\right)\right\}, \qquad (2)$$

where N is the total number of the radicals and k is the Boltzman's canstant[14]. In the case of $s=0$, which corresponds to the completely disordered state, S becomes 1.38 cal/°C·mol. Subtracting the transition entropy of 0.7 cal/°C·mol from it, we get 0.68 cal/°C·mol, which may be considered as the value of S at ordinary temperature. Therefore the parameter s at ordinary temperature is calculated as 0.78 from Eq. (2). Thus *ca* 89% of NO_2^- radicals are expected to arrange in one sense and the others in the opposite. Perhaps this may be true, though the numerical value of s might differ somewhat from our estimation. Considering the effects of Na^+ ions, which give a restriction for the disordering behaviors of NO_2^- radicals, we ought to give a smaller value than 1.38 cal/°C·mol as the entropy of the system in the disordered state. Then the ordering parameter s at ordinary temperature will more approach to 1 than the value estimated above.

---

* This is the value at room temperature obtained from the pyroelectric measurement.

It seems to be sure that the anomalies in the specific heat and dilatation observed above the transition temperature, including the minor anomaly in the dilatation, should be due to the short range interactions between the constituent ions. From the consideration on the interatomic distances of the constituents and the behavior of the domain boundary in the crystal$^{2)}$, we may imagine that the disordering arrangement of NO_2^- radicals is easily realized in the direction perpendicular to the b axis, keeping their alignments along the b direction, and even in the paraelectric phase the alignment is held in short range. The recent x-ray study by Tanizaki$^{15)}$ is considered to show an evidence of the remaining of the short range order above the Curie temperature. These problems will be discussed further in our subsequent paper.

Acknowledgement

The author expresses his sincere gratitude to Prof. Sawada for many helpful discussions.

References

1) S. Sawada, S. Nomura, S. Fujii and I. Yoshida: Phys. Rev. Letters **1** (1958) 320.
2) S. Nomura, Y. Asao and S. Sawada: J. Phys. Soc. Japan. **16** (1961) 917.
3) I. Shibuya: J. Phys. Soc. Japan **16** (1961) 490.
4) G. E. Ziegler: Phys. Rev. **38** (1931) 1040.
5) G. B. Carpenter: Acta. Cryst. **5** (1952) 132.
6) M. R. Truter: Acta. Cryst. **7** (1954) 73.
7) B. Strijk and C. H. MacGillavry: Rec. trav. chim. **62** (1943) 705.
8) B. Strijk and C. H. MacGillavry: Rec. trav. chim. **65** (1946) 127.
9) B. C. Frazer, R. Ueda and M. I. Kay: Paper 15-24 5th International Congress of Crystallography, at Cambridge, England, Aug. 1960.
10) J. Jaffray: J. recherches centr. natl. recherche sci. (Paris) (1947) 153.
11) S. Sawada: Rep. Inst. Sci. Tech. Univ. Tokyo **10** (1956) 107.
12) S. Nomura, T. Kawakubo and T. Yanagi: J. Phys. Soc. Japan. **16** (1961) 706.
13) W. Känzig: Solid State Physics **4** (1957).
14) T. Nagamiya: Proc. Phys.-Math. Soc. Japan **24** (1942) 137.
15) S. Tanizaki: J. Phys. Soc. Japan **16** (1961) 579.

JOURNAL OF THE PHYSICAL SOCIETY OF JAPAN Vol. 16, No. 7, JULY, 1961

Notes on the Lustre of Moiré Patterns

By Jien NISHIWAKI

Department of Physics, Faculty of Science, Tokyo Metropolitan University
Setagaya, Tokyo, Japan

(Received March 4, 1961)

Moiré patterns produced by passing diffuse light from uniformly illuminated background through two net or gauze screens of suitable mesh size, set face-parallel, one behind the other with a space in between, are tinged with some lustre which is more or less vitreous or slightly metallic. A number of results obtained by visual observation and photographing show that this is a typical case in which the so-called false stereoscopic effect gives rise to the impression of gloss.

§ 1. Introduction

There are a number of cases in which one perceives lustre on a surface that is not specularly reflective[1]. One of the most well-known is the case of binocular lustre shown by Dove[1] and Kiesow[1]. For example, when two figures of the type shown in Fig. 1 are stereoscopically brought together, lustre appears on the sectors which are not lustrous when viewed separately. It should be noted that, of the corresponding two sectors which are to be brought together, one is white and the other is black.

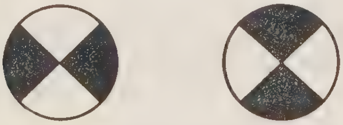

Fig. 1. A pair of drawings for stereoscope to demonstrate binocular lustre.

It is also known that, even in ordinary binocular vision, a similar, but false, stereoscopic effect may often give rise to the impression of gloss when the two eyes do not receive the same images[1]. The following sections give some of the evidence showing that the case of Moiré patterns is a typical one of such cases which has not been so far wellknown.

§ 2. Appearance of Moiré Patterns

Moiré patterns produced by passing diffuse light from uniformly illuminated background—for instance, a sheet of white mat paper of ample size—through two pieces of net or gauze, set face-parallel, one behind the other with a space in between, are tinged with some lustre. It is rather difficult to describe it precisely in words: roughly speaking, it is vitreous in general appearance, slightly metallic in some cases, varies with the conditions of illumination and other factors.

Fig. 2 shows photographs of Moiré Patterns obtained on five specimens prepared with wire gauze of mesh 50 and wire diameter of 0.15 mm. For the spacing, d, between the front and back gauze screens, 0, 5, 10, 15 and 20 mm were used. The effective diameter for all was 6 cm. The specimens were so constructed that all the patterns gave roughly equall perception with respect to their shapes or distributions. By hand, it was difficult to obtain the same pattern from all the specimens, because of inhomogeneities in mesh.

In actual observation, the specimens were set against a large ground glass window pane illuminated from behind by daylight at about 3000 lux. The specimen on the extreme left ($d=0$) had the lowest lustre while that on the extreme right ($d=20$) the highest when viewed from 4 to 5 meters. The lustre decreased with the increasing distance between the observer and specimens, thus, as the observer backed away step by step from the specimens, the lustre of the second ($d=5$) and the rest specimens became in turn equal to the first. The distances at which the lustre of the last four specimens became equal to that of the first were estimated by two observers B and C. Plots of mean values of the estimation repeated six times for every specimen are shown in Fig. 3, the disagreement between the two being attributable to personal error.

On the other hand, the pattern shifted on the plane of the gauze and changed its shape when the position of the eye was changed sidewards. Hence the pattern that appeared to the right eye would not have been identical to that appeared to the left eye. From this and from a more remarkable fact that the

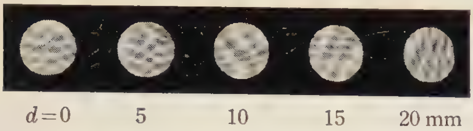

Fig. 2. Patterns obtained on five specimens constructed with ♯50 wire gauze: d is the spacing between front and back gauze screens.

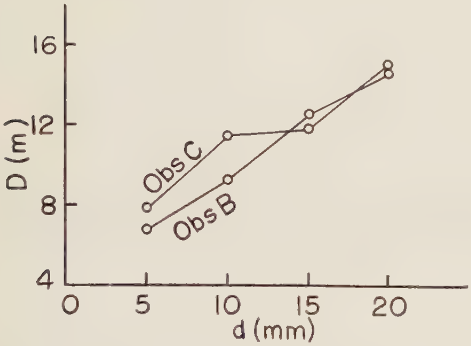

Fig. 3. Distance D between the observer and specimens at which the lustre of the last four specimens became equal to that of the first ($d=0$).

lustre on the pattern almost disappeared from all the specimens when viewed with one eye even from the distance 4 meters with which the above experiment started, it was presumed that the perceived lustre in this case was attributed to the false stereoscopic effect mentioned in the preceding section. As is readily expected, the difference between the patterns appearing to the right and left eyes will increase with the spacing between the two gauze screens and decrease with the distance between the observer and specimen under such viewing conditions as used in obtaining the results shown in Fig. 3. Hence, those obtained results themselves justify the above presumption. Another evidence will follow next.

§ 3. Best Conditions for the Lustre

By taking the false stereoscopic effect into account, one can easily calculate the best conditions for obtaining the lustre. In Fig. 4, E_r and E_l represent the observer's eyes, the interspacing of which is denoted by Δ. The distance between the observer and the front screen is denoted by D and the spacing between the front and back screens by d. Under actual conditions of observation D is large compared to d. When the observer fixes his eyes to a point, P, on the plane of the front screen the following conditions are required. For his right eye E_r wires of the back screen come between those of the front screen obstructing the light from background,

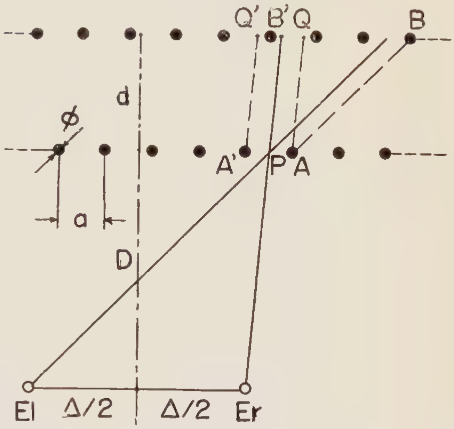

Fig. 4. Schematic illustration of the best conditions for obtaining the lustre.

hence this part appears dark. But, for his left eye E_l, the former are shadowed by the latter, hence this appears bright. The relative positions of the wires A, A' and B', and of A and B settle these particular conditions which are easily found to be expressed by

$$BQ+\phi<BB'<BQ+QQ'-\phi\ ,$$

where ϕ is the diameter of the wire. BQ is given by $\Delta d/D$. Putting $QQ'=AA'=a$ and $BB'=na$, we obtain

$$\frac{\Delta}{D}d+<na<\frac{\Delta}{D}d+a-\phi\ ,$$

or

$$\frac{\Delta}{na-\phi}d<D<\frac{\Delta}{(n-1)a+\phi}d\ , \qquad (1)$$

where a is the spacing of wires and n an positive integer. In the case of $n=1$, Eq. (1) is reduced to

$$\frac{\Delta}{a-\phi}d<D<\frac{\Delta}{\phi}d\ . \qquad (2)$$

To compare the result of this simple calculation with what is to be obtained by visual observation, a pair of wire screens of $\phi=0.84$ mm and $a=2.5$ mm were used. For the specimens used in the preceding section, such comparison was difficult owing to the slow change of the lustre with the distance D. Substituting the above values into Eq. (2) and assuming $\varDelta$ to be 70 mm, we obtain $42d<D<83d$. In Fig. 5, the upper and lower lines represent the cases of $D=83d$ and $D=42d$. The lustre will be most apparent in the region between the two lines.

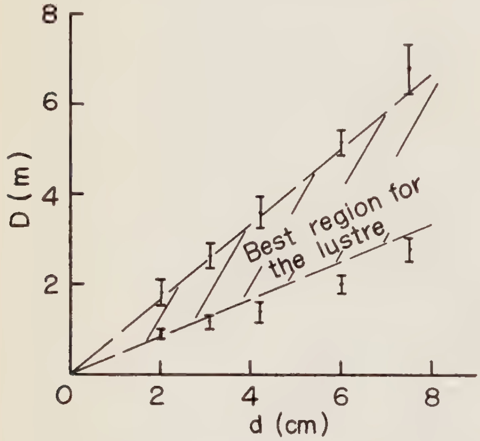

Fig. 5. Calculated range for good lustre and visual estimates of margins of the range.

In visual observation, margins of the range between which the lustre was most apparent were determined for each of five given spacings $d=2.0$, 3.1, 4.2, 6.0 and 7.5 cm. The mean and standard deviation of estimates—repeated twelve times for every margin—given by three observers are also plotted in Fig. 5. The correlation of the observed values with the calculated ones is satisfactorily well.

These results were obtained for the specimen prepared in the following way. Of the two wire net screens that were used, the first one was set parallel to and close to a ground glass window pane illuminated from behind by daylight at about 3000 lux, and the second screen was leant against the first. The second screen was masked with a sheet of black paper which had equally spaced four rows of horizontal slit, 20 cm long and 1.6 cm wide, through which the observations were made. By varying the slope of the second screen, and also shifting the mask over the screen, the observer could use the spacing between the screens along the centre lines of the slits as desired. The margins were estimated by the observer fixing his eyes at the centre of the slit under observation and, step by step, approaching to or backing away from the slit.

Fig. 6 shows as an example a stereo-photograph of a pattern taken at the distance of 175 cm from the slit with the spacing of 4.2 cm between the front and back screens. As regards the distance D and the spacing d, this setting falls almost on the lower border line of calculated range given in Fig. 5 for effective lustre to appear. The right and left halves of the photograph are what come into view to the observer's right and left eyes respectively, and the bright and dark portions on the right half are almost reversed on the left half; this is why the pattern appears to have lustre when viewed with both eyes.

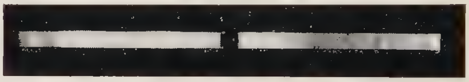

Fig. 6. Stereo-photograph of a pattern taken at 175 cm from the slit, the spacing between screens being 4.2 cm.

For the ranges of clearly perceived lustre given by Eq. (1) (the case of $n>1$), observation was to be made very close to the present specimen which was not practicable because the wires of the screens were seen quite distinctly.

§ 4. Conclusion

Every day, numbers of examples of the lustre due to the false stereoscopic effect are around us. The effect occurs when the two eyes receive different images with respect to the same part on a surface. Once one is aware of it, he can frequently see the examples, in general, on the high glossy surfaces which are lustrous too when viewed with one eye. In the case of Moiré patterns as produced in this work, lustre appears only when viewed with both eyes and was found to be due purely to the false stereoscopic effect.

The author expresses his sincere thanks to Professor E. Fukushima for his suggestion and intimate advice.

Reference

1) V. G. W. Harrison: Definition and Measurement of Gloss, 1945, PATRA.

JOURNAL OF THE PHYSICAL SOCIETY OF JAPAN Vol. 16, No. 7, JULY, 1961

Effect of Incoherent Waves on the Electron Microscopic Images of Crystals

By Yoshihiro KAMIYA and Ryozi UYEDA

Physical Institute, Nagoya University, Nagoya, Japan

(Received, April 7, 1961)

The electron micrographs of crystalline specimens are taken by placing the aperture of the objective lens at various positions. Extinction contours, equal-thickness fringes and dislocation images are observed under a condition that none of the coherent waves—the transmitted and diffracted waves—enters the aperture. This implies that the above contrast effects are formed by incoherent waves which are neglected in current theories of diffraction contrast.

§ 1. Introduction

In the electron microscopic images of crystals, various kinds of contrast are observed: extinction contours, equal-thickness fringes[1], dislocation images[2] etc. These contrast effects are closely related to the Bragg reflection and can be interpreted by diffraction theories[3]. It is generally believed that the most reliable interpretation is given by the dynamical theory taking into account the effect of absorption[4]. However, the incoherent waves are perfectly neglected in the current theories of contrast.

In the present experiment, electron micrographs of crystalline specimens were taken by placing the aperture of the objective lens at various positions. One of the remarkable results is that equal-thickness fringes are observed on dark field images even under the condition that no diffracted beam enters the aperture. The aim of the present paper is to point out the effect of incoherent waves on the formation of contrast.

§ 2. Experiments

The electron microscope used in the present experiment was Hitachi HU-10. The accelerating voltage was 75 kV. The diameter of the objective aperture was about 10 μ, namely 1.3×10^{-3} rad. in scattering angle. Specimens used were molybdenite films and magnesium oxide crystallites.

Electron micrographs were taken by placing the aperture of the objective lens at the following (Figs 2 and 4).

(a) Bright field: The transmitted beam enters the objective aperture.

(b) Usual dark field: The transmitted beam does not enter the objective aperture while one diffracted beam does.

(c) Special dark field: None of the transmitted and diffracted beams enters the objective aperture. Only the background scattering does. In (b) and (c), adjectives *usual* and *special* are used because (b) is adopted usually in routine experiments and (c) is adopted specially in the present experiment.

It should be noted here that as shown in Fig. 7 c the incident spot and the strong diffraction spots are not sharp on diffraction patterns. Examining carefully, however, it is found that the diffuse background due to incoherent waves is considerably strong around each sharp spot due to the coherent wave—the transmitted or diffracted wave. In the above classification, the transmitted and diffracted beams mean only the sharp beams corresponding to coherent waves.

§ 3. Results

(i) *Extinction contours*

Fig. 1 reproduces the images of molybdenite film taken by placing the objective aperture at various positions: Figs. 1 a, b, c and d correspond, respectively, to aperture positions a, b, c and d indicated in Fig. 2. The molybdenite film was placed directly on a specimen grid without any supporting film. Thus the part of field which is free of the film is perfectly dark in dark field images (Figs. 1 b, c and d). Although extinction contours which appear on bright field and usual dark field images are well-known, those on special dark field images have not yet been studied. Comparing Figs. 1 a with c, the following conclusion may be obltained: The contrast of

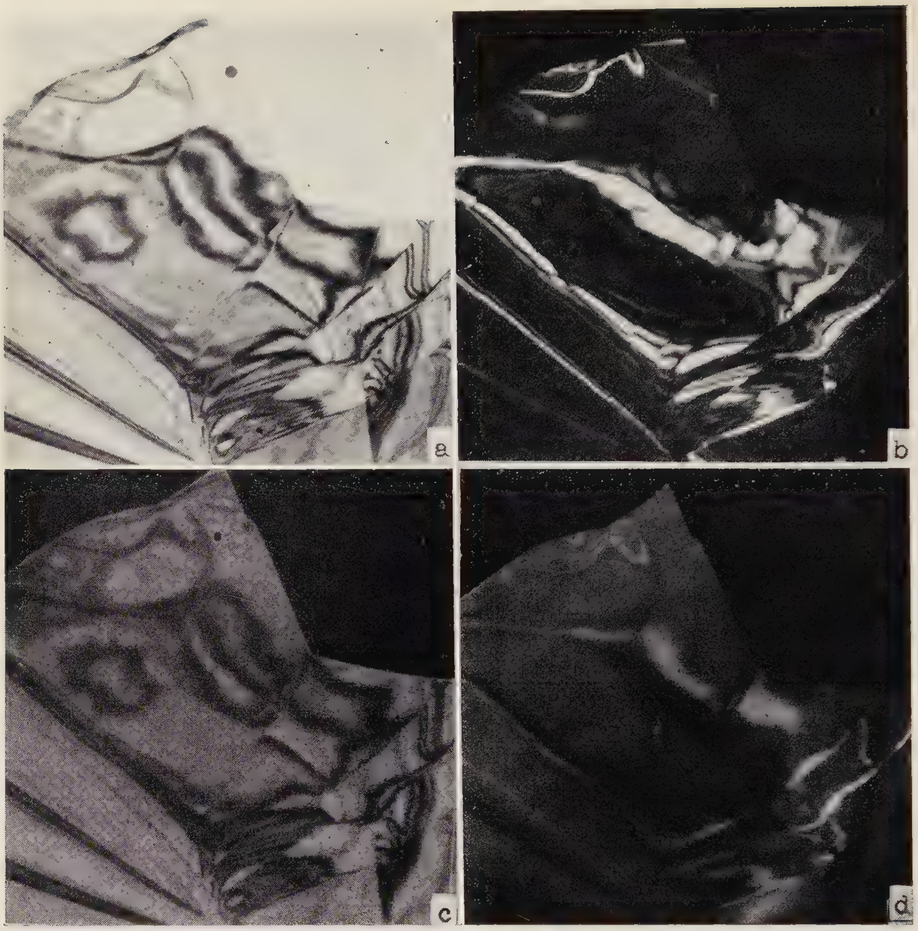

Fig. 1. Extinction contours of a molybdenite film. ×9,000.
a) Bright field. b) Usual dark field. c) Special dark field at a small angle.
d) Special dark field at a large angle. (Aperture positions indicated in Fig. 2).

special dark field image is similar to that of bright field image, provided that the former is taken by placing the objective aperture close to the incident spot. A similar conclusion is obtained when the objective aperture is placed close to a Bragg spot: the special dark field image is similar to the usual dark field image corresponding to the Bragg spot (Fig. 1 d).

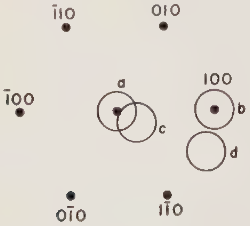

Fig. 2. Indicating size and positions of the objective aperture for Fig. 1. Positions a, b, c, and d correspond respectivety to Figs. 1 a, b, c, and d.

(ii) *Equal-thickness fringes*

Fig. 3 reproduces images of magnesium oxide crystallites. The aperture position corresponding to each micrograph is shown in Fig. 4. Again, nothing new is observed in the equal-thickness fringes on bright field and

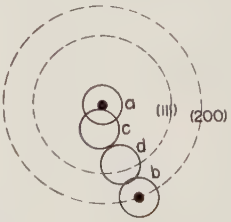

Fig. 4. Indicating size and positions of objective aperture for Fig. 3. Positions a, b, c, and d correspond respectively to Figs. 3 a, b, and d.

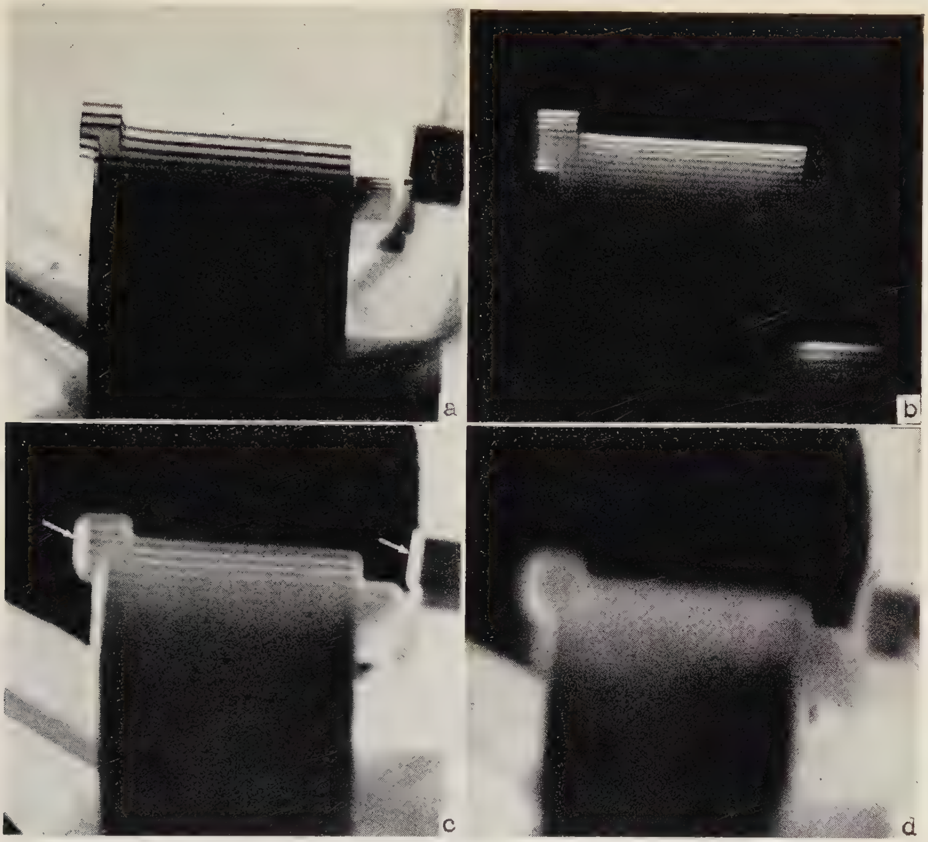

Fig. 3. Equal-thickness fringes of magnesium oxide crystallites. ×90,000.
a) Bright field. b) Usual dark field. c) Special dark field at a small angle.
d) Special dark field at a large angle. (Aperture positions indicated in Fig. 4)*.

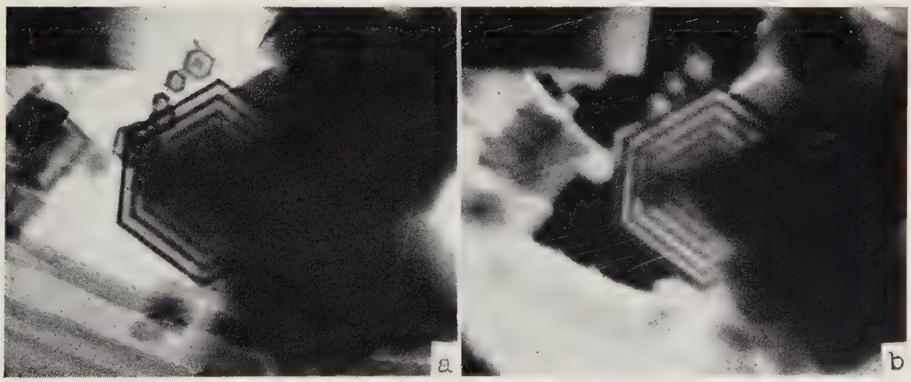

Fig. 5. Equal-thickness fringes of magnesium oxide. ×90,000.
a) Bright field. b) Special dark field at a small angle.

usual dark field images** but those on special dark field images are interesting. By comparing Figs. 3 a and c, the same conclusion as that described in the previous subsection on extinction contours is obtained. The contrast of fringes on a special dark field image becomes quickly low when the objective aperture is shifted to large scattering angles. No fringe is observed in Fig. 3 d which is taken at a large angle. Fig. 5 reproduces another example showing equal-thickness fringes on a bright field image and those of a special dark field image.

---

* Faces indicated by arrows are remarkably bright. This may be caused by the specular reflection of the incident wave[10].

** The difference of spacings observed in Figs. 3 a and b is due to the change of crystal orientation.

In this case one might suspect that the equal-thickness fringes in Fig. 3 c and Fig. 5 b might have been produced by coherent waves which are deviated slightly due to double refraction effects[5]. As illustrated in Fig. 6, the coherent wave penetrating a crystal produces two pairs of spots P and P' and Q and Q'. It is possible that one of the pairs, say P and P', passes through the objective

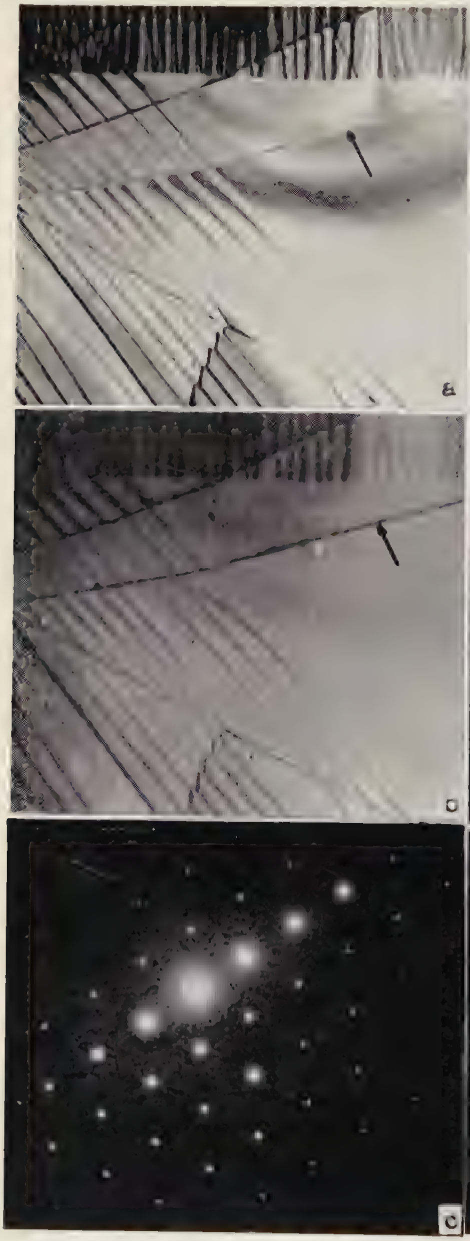

Fig. 7

Fig. 8.

Fig. 7. Images of dislocations in a thin molybdenite film. ×120,000.
a) Bright field. b) Special dark field at a small angle. c) Diffraction pattern.

Fig. 8. Images of dislocations in a thick molybdenite film. ×3,600.
a) Bright field. b) Special dark field at a small angle. c) Diffraction pattern.

aperture even when the central spot 0 is stopped. In such a case, the image of the face CD is expected to appear much brighter than the face AB. Since no such effect is observed in Fig. 5 b, the suspicion is cleared.

(iii) *Images of dislocations*

Figs. 7 and 8 reproduce the images of dislocations in molybdenite films⁶⁾. In each figure, (a) is a bright field image and (b) is a special dark field image. The latter are taken by placing the objective aperture close to the incident spot. Figs. 7 and 8 are from a thin specimen (~200Å) and a thick specimen (>1,000Å), respectively. The approximate thickness was inferred from diffraction patterns (Figs. 7 c and 8 c). Comparing (a) and (b) of both figures, the same conclusion as described in the previous subsection is obtained also for dislocation images. In thick specimens, a bright field image is only a little sharper than the corresponding special dark field image. In thin specimens, the difference in sharpness is a little more conspicuous compared with thick specimens. Sometimes, details of contrast are different as indicated by arrows in Figs. 7 a and b. In Fig. 7 b the upper side of the indicated dislocation line is always dark while the lower side is slightly light. On the other hand, in Fig. 7 a the corresponding line has a complicated structure.

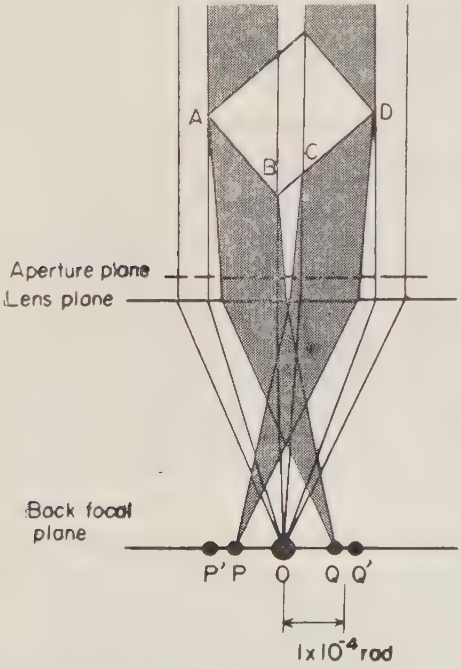

Fig. 6. Illustration of refraction effect.

§ 4. Discussion

In cases of the bright field and the usual dark field, coherent waves enter the objective aperture. Since incoherent waves also enter the objective aperture with coherent waves, a bright field image or a usual dark field image is a superposition of a partial image formed by coherent waves and that by incoherent waves. This fact has been pointed out by one of the present authors (R.U.) and the different natures of partial images have been explained in the previous paper⁷⁾. Therefore, the explanation is not repeated here.

The intensities of partial images in a bright field image can be estimated from the ratio of exposure times for the bright field and special dark field images. The ratio is small when the crystal is thin. For example, it is 1:15 in Fig. 7. This implies that in Fig. 7 a the part due to coherent waves is much stronger than that due to incoherent waves. On the other hand, the ratio is comparable with unity when the crystal is thick. For example, it is 1:2 in Fig. 8. Taking into account that the intensity of incoherent waves decreases rapidly with the scattering angle, ratio 1:2 implies that in Fig. 8 a the part due to incoherent waves prevails over that due to coherent waves.

It is concluded in Sec. 3 that the contrast of special dark field images is similar to that of bright field images, provided that the former is taken by placing the objective aperture close to the incident spot. This is possible only when the contrast of the transmitted wave and that of the accompanying incoherent waves vary in a similar manner. For example, if the contrast of the transmitted wave oscillates according to Pendellösung, that of the accompanying incoherent waves must have a similar oscillation. To understand such a behavior of incoherent waves, the dynamical theory must be generalized to include incoherent waves. Although such a theory is most difficult, the theory of Kikuchi pattern by Kainuma⁸⁾ may be the first step to the generalization.

Recently, the behaviors of stacking fault, extinction contour and dislocation images in the case of thick crystals were explained by a dynamical theory, taking into account the effect of absorption4),9). However, the agreement may be fortuitous because the theory neglects the part due to incoherent waves. In the case of thick crystals, the neglected part prevails over the calculated part, according to the present result. If correct figures of the absorption coefficient were available and they were adopted in the calculation, the result would explain only the part due to coherent waves. Agreement between the theory and experiment is possible so far as the contrast due to the coherent waves and that due to accompanying incoherent waves are similar. It is not known to what extent the similarity holds. The difference of contrast observed in Figs. 7a and b may be an example where the similarity breaks.

We thank Professor N. Kato and Professor Y. Kainuma for their helpful discussions.

References

1) S. Leisegang: *Handbuch der Physik* Vol. 33 (Springer, Berlin 1956) p. 397.
2) P. B. Hirsch, R. W. Horne and M. J. Whelan: Phil. Mag. **1** (1956) 677.
3) P. B. Hirsch, A. Howie and M. J. Whelan: Phil. Trans. Roy. Soc. London **252** (1960) 499.
4) H. Hashimoto, A. Howie and M. J. Whelan: Phil. Mag. **5** (1960) 967.
5) H. Raether: *Handbuch der Physik* Vol. 7 (Springer, Berlin 1957) p. 443.
6) Y. Kamiya, K. Ando, M. Nonoyama and R. Uyeda: J. Phys. Soc. Japan **15** (1960) 2025.
7) R. Uyeda: J. Phys. Soc. Japan **10** (1955) 256.
8) Y. Kainuma: Acta Cryst. **8** (1955) 247.
9) A. Howie and M. J. Whelan: Read before the Fifth International Congress and Symposia, Cambridge, 1960.
10) S. Miyake, K. Kohra and M. Takagi: Acta Cryst. **7** (1954) 393.

Journal of the Physical Society of Japan, Vol. 16, No. 7, July, 1961

Flow Birefringence of Polymer Solutions

By Ryuzo Koyama

Electrical Communication Laboratory, Musashino, Tokyo

(Received January 27, 1961)

By making use of a gaussian chain model for a polymer molecule, a theoretical calculation on the flow birefringence of polymer solution is carried out, in which the optical internal field in the polymer molecule in solvent is taken into account.

The obtained expression for the intrinsic birefringence contains a quadratic form of the refractive index of solvent, and this can account for several experimental results. The expression for the intrinsic extinction angle also has a certain optical factor, and thus it predicts that the extinction angle depends on the refractive index of the solvent.

Assuming that there is no hydrodynamic interaction between molecular segments, we carried out some numerical calculations to the optical factors. The result can well reproduce the recent experimental values of the polystyrene molecules, and of the polymethylmethacrylate molecules.

§ 1. Introduction

The recent studies on polymer solution show that the observed value of the flow birefringence of polymer solution depends on the refractive index of solvent, and this fact is explained by introducing the effect of the optical internal field in polymer solution into the theoretical considerations. This problem was first discussed by Sadron, Peterlin and Stuart, and Cerf1) by means of models such as a rigid ellipsoid and a deformable elastic sphere. Lately Tsvetkov2) and Copic3) also treated it with more detailed models. Thus, these theories can well explain the observed reslt through the form anisotropy of polymer molecule and the optical internal field.

We can consider a similar problem in the case of the extinction angle of the birefringence, though such an effect has not been observed in experiments. The expressions for the extinction angle which have been obtained heretofore do not contain any optical parameters, and hence the extinction angle has been considered to be determined from the purely mechanical condition of that polymer solution as in the case, for example, of the viscosity of the solution. However, the recent detailed theoretical treatment by Copic[3] which is based on a dumbbell model throws doubt upon the above statement. According to his calculations, in case of the rigid polymer molecule with infinite internal viscosity the expression of the intrinsic orientation number* has a certain optical factor which depends on the optical constants of the polymer solution, whereas in case of the soft polymer molecule with negligible internal viscosity such an optical factor again does not appear in his expression.

In the following discussion the calculations are based on a gaussian chain model recently used by several authors[4],[5] in which the method of determining the molecular configuration is more direct than those of the earlier works, and the optical factors for both birefringence and extinction angle are examined.

§ 2. Average Polarizability of a Polymer Molecule and Flow Birefringence of the Polymer Solution

In the following calculation, the solute polymer molecule is assumed to be a gaussian chain formed by a large number of the identical segments in linear connection. The connecting point of the segments is represented by a bead and is subjected to the viscous resistance from the solvent. The polymer molecule is also supposed to have an internal viscosity accompanied by its internal deformation, which can be treated by the method given by Cerf[5] on this model.

It is assumed that the segment has no permanent dipole, but may have an induced dipole in the presence of an applied electric field. The segment is supposed to be axially symmetric about the axis joining its two ends, and its dielectric property is represented by two components of polarizability, one of which is parallel to the axis, and the other is perpendicular to this axis. Also, the polymer molecule is assumed to be sufficiently small compared with the wave length of the light, so that the phase of incident ray is put to be the same everywhere in a polymer molecule at any time, and the method of quasi-static treatment can be applied.

When the electric field is applied to a polymer molecule, it induces an electric dipole in each segment, and this dipole produces the secondary electric field in the same molecule. In such a case the total electric field E_i acting on a segment i can be written in a form of superposition as follows

$$E_i=E+\sum_{k(\neq i)} T_{ik}p_k\,, \tag{1}$$

where the term $T_{ik}p_k$ represents the induced field from the dipole p_k on the segment k. The summation over k is taken over all the segments other than i of the same molecule, because in our case the polymer solution is so diluted that the interactions between different molecules can be neglected by virtue of their very large distances. The interaction tensor T_{ik} is a function of the relative coordinates r_{ik} of two segments i and k, and is given in the diadic notation by

$$T_{ik}=n_0^{-2}r_{ik}^{-3}(3r_{ik}r_{ik}/r_{ik}^2-1)\,, \tag{2}$$

where n_0 represents the index of refraction of the solvent.

On the other hand the electric polarizability tensor α_i of a segment i is given by the relation:

$$p_i=\alpha_i E_i\,, \tag{3}$$

and also for the given external electric field E we can define the total electric polarizability tensor A of a whole polymer molecule by the following relation,

$$\sum_i p_i=AE\,. \tag{4}$$

Therefore, from these relations the average polarizability of a polymer molecule $\langle A\rangle$ can

---

* The intrinsic orientation number $[\omega]$ is defined as

$$[\omega]=\lim_{\substack{G\to 0\\ c\to 0}}(\pi/4-\chi)/G\eta_0$$

and this is different from the intrinsic extinction angle defined by Eq. (31) by the factor η_0.

be written in the following form:

$$\langle A\rangle=\langle A_1\rangle+\langle A_2\rangle\,, \tag{5}$$

$$\langle A_1\rangle=\sum_i\langle\alpha_i\rangle\,, \tag{5$'$}$$

$$E\langle A_2\rangle=\sum_i\sum_{k(\neq i)}\langle\alpha_i T_{ik}p_k\rangle\,. \tag{5$''$}$$

The notation $\langle\ \rangle$ means the average over all the possible internal configurations of a polymer molecule for the given external condition of the solution. In order to calculate such an average value we can employ the distribution function of polymer molecule if it is known, or in some cases we may use the differential equation satisfied by the distribution function.

At the present discussion we are treating a polymer molecule which is immersed in a solvent, and E_i ($i=1, 2, \cdots, N$) should be the internal electric field acting on the segment i in the solvent. For this purpose we shall substitute for α_i of Eqs. (5), (5′) and (5′′) the effective polarizability α_i' given by

$$\alpha_i'=\alpha_i-P_0\,, \tag{6}$$

where P_0 corresponds to the polarizability of a mass of solvent which is excluded by one segment in the solution. In the subsequent calculation we shall assume that every segment has an equal spherical form in solution, and the velocity gradient does not affect the molecular construction of solvent, so that P_0 is a constant scalar quantity. In this way the effect of the internal field in the solvent can be taken into account in our theoretical calculations.

We can use for α_i the expression of the polarizability tensor obtained by Kuhn and Grün[6] for the statistical chain segment. By using their result the component of polarizability α_i' parallel to the axis of the segment, γ_1, and that perpendicular to the same axis, γ_2, are written respectively as

$$\begin{aligned}\gamma_1&=P-P_0+2Ql^2\,,\\ \gamma_2&=P-P_0-Ql^2\,,\end{aligned} \tag{7}$$

where P and Q are constants depending upon the constitution of the segment, and l denotes the end-to-end length of the segment. From the above expressions the polarizability α_i' can be written in tensor form as follows;

$$\alpha_i'=3Q\cdot\begin{pmatrix} x_{ii-1}^2+\beta & x_{ii-1}y_{ii-1} & x_{ii-1}z_{ii-1}\\ y_{ii-1}x_{ii-1} & y_{ii-1}^2+\beta & y_{ii-1}z_{ii-1}\\ z_{ii-1}x_{ii-1} & z_{ii-1}y_{ii-1} & z_{ii-1}^2+\beta \end{pmatrix}, \tag{8}$$

$$\begin{aligned} x_{ii-1}&=x_i-x_{i-1}\,,\\ y_{ii-1}&=y_i-y_{i-1}\,,\\ z_{ii-1}&=z_i-z_{i-1}\,,\\ \beta&=(P-P_0-Ql^2)/3Q\,, \end{aligned}$$

where $r_i(x_i, y_i, z_i)$ represents the cartesian coordinates of the i-th linking point of segment in the polymer chain.

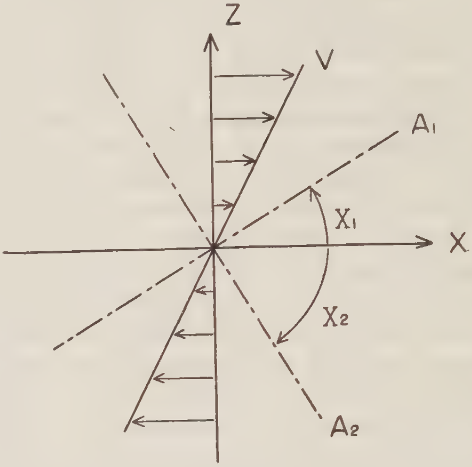

Fig. 1. Physical conditions and cartesian coordinate axes.

For simplicity, we assume a laminar flow in the polymer solution, and we choose the directions of the cartesian coordinate axes so that the macroscopic flow of the solution $v(v_x, v_y, v_z)$ can be represented by the following expressions:

$$\begin{aligned} v_x&=G\cdot z\,,\\ v_y&=0\,,\\ v_z&=0\,, \end{aligned} \tag{9}$$

where G denotes the magnitude of the velocity gradient.

In order to discuss the flow birefringence by an incident light propagating in the y-direction under this condition we have to know only two expressions for the matrix elements $\langle A_{xx}-A_{zz}\rangle$ and $\langle A_{xz}\rangle$ of the polarizability tensor of Eq. (5). The corresponding expressions for the first term $\langle A_1\rangle$ in Eq. (5) can be obtained by using Eq. (8), and they can be reduced into the following forms, as have been already done by Zimm[4] and by Cerf[5],

$$\langle A_{1xx}-A_{1zz}\rangle=(3/2)\cdot QD\delta^{-3}\cdot\sum_{p=1}^{N}\lambda_p{}^{-2}g_p\cdot G\,, \tag{10}$$

$$\langle A_{1xz}\rangle=(3/2)\cdot QD\delta^{-2}\cdot\sum_{p=1}^{N}\lambda_p{}^{-1}\cdot G\,, \tag{11}$$

where the constants D and δ are represented by the frictional constant ζ of a bead in the solvent, the absolute temperature T, the Boltzmann's constant k and by the mean square length of a segment at equilibrium state l_0^2, as follows,

$$\begin{aligned} D&=kT\cdot\zeta^{-1}\,, \\ \delta&=3kT\cdot l_0^{-2}\zeta^{-1}\,, \end{aligned} \tag{12}$$

N is the total number of segments in the molecule, λ_p is given by the relation:

$$\lambda_p=\nu_p\mu_p\,, \tag{13}$$

where μ_p and ν_p are the p-th eigenvalues of two matrices $\mathbf{A}$ and $\mathbf{H}$ respectively, whose elements are defined as follows,

$$\mathbf{A}=\begin{pmatrix} 1 & -1 & 0 & 0 & \cdots & \cdots & 0 \\ -1 & 2 & -1 & 0 & & & \cdot \\ 0 & -1 & 2 & -1 & & & \vdots \\ 0 & 0 & -1 & 2 & & & \vdots \\ \vdots & & & & \ddots & & 0 \\ \vdots & & & & -1 & 2 & -1 \\ 0 & \cdots & \cdots & \cdots & 0 & -1 & 1 \end{pmatrix}, \tag{14}$$

$$\begin{aligned} &H_{ii}=1\,, \\ &H_{ij}=(6\pi^3)^{-1/2}\zeta\eta_0^{-1}l_0^{-1}\cdot|i-j|^{-1/2}\,,\quad i\neq j\,, \\ &\qquad\qquad (i,\,j=0,1,2,\cdots,N)\,, \end{aligned} \tag{15}$$

in which η_0 represents the viscosity of the solvent. In a special case where the hydrodynamic interaction between the beads in polymer molecule is neglected, the matrix $\mathbf{H}$ is a unit matrix, so that

$$\begin{aligned} &\nu_p=1\,, \\ &\lambda_p=\mu_p\,,\qquad (p=1,2,\cdots,N)\,, \end{aligned} \tag{16}$$

Further, g_p in Eq. (10) is given by

$$g_p=1+\rho_p\nu_p \tag{17}$$

for the polymer molecule having very small internal viscosity, or

$$g_p=2+\lambda_p\cdot\sum_q\lambda_q^{-1} \tag{18}$$

for the polymer molecule having infinite internal viscosity. ρ_p in Eq. (17) is given by the element of the internal viscosity matrix, φ_p, which is referred to the p-th normal coordinates of the molecule, as follows, (cf. reference 5),

$$\rho_p=\zeta^{-1}\varphi_p\,. \tag{19}$$

Next, we proceed to the calculation of the second term $\langle A_2\rangle$ in Eq. (5). We substitute the interaction tensor T_{ik} by its average value $\langle T_{ik}\rangle$, as is often done in case of the hydrodynamic interaction tensor in viscosity theories[4),5)], and thus we have an approximate expression:

$$\langle A_2\rangle=\sum_i\sum_{k(\neq i)}\langle\alpha_i'\langle T_{ik}\rangle p_k\rangle/E\,. \tag{20}$$

Thus by using Eq. (3), this can be developed as

$$\langle A_2\rangle=\sum_i\sum_{k(\neq i)}\langle\alpha_i'\langle T_{ik}\rangle\alpha_k'\rangle+\sum_i\sum_{k(\neq i)}\sum_{l(\neq k)}\langle\alpha_i'\langle T_{ik}\rangle\alpha_k'\langle T_{kl}\rangle\alpha_l'\rangle+\cdots\,. \tag{21}$$

For small velocity gradient G we assume a following approximate pair distribution function $f_{ik}(r)$ of two beads i and k,

$$\begin{aligned} &f_{ik}(r)=f_{ik}^{(0)}(r)[1+G\cdot\delta_{ik}xz+G^2\cdot(\vartheta_{ik}^2a_{ik}^2+\alpha_{ik}^2x^2+\beta_{ik}^2y^2+\gamma_{ik}^2z^2)]\,, \\ &f_{ik}^{(0)}(r)=\left(\frac{1}{2\pi a_{ik}^2}\right)^{3/2}\cdot\exp\left\{-\frac{r^2}{2a_{ik}^2}\right\}\,, \end{aligned} \tag{22}$$

where the constants a_{ik}, δ_{ik}, ϑ_{ik}, α_{ik}, β_{ik} and γ_{ik} are determined by the relations:

$$\begin{aligned} \langle(x_k-x_i)^2\rangle&=\int f_{ik}(r)x^2\,dr\,, \\ \langle(y_k-y_i)^2\rangle&=\int f_{ik}(r)y^2\,dr\,, \\ \langle(z_k-z_i)^2\rangle&=\int f_{ik}(r)z^2\,dr\,, \\ \langle(x_k-x_i)(z_k-z_i)\rangle&=\int f_{ik}(r)xz\,dr\,. \end{aligned} \tag{23}$$

Applying the above distribution function to Eq. (21) we arrive at the following results:

$$\langle A_{2xx}-A_{2zz}\rangle=(9/5)(3/2\pi)^{1/2}\cdot(P-P_0)^2 n_0^{-2} l_0^{-5} D\delta^{-3}\cdot\sum_{p=1}^{N} f_p \mu_p^{-1}\lambda_p^{-2} g_p\cdot G \tag{24}$$

$$\langle A_{2xz}\rangle=(9/5)(3/2\pi)^{1/2}\cdot(P-P_0)^2 n_0^{-2} l_0^{-5} D\delta^{-2}\cdot\sum_{p=1}^{N} f_p \mu_p^{-1}\lambda_p^{-1}\cdot G \tag{25}$$

where f_p is given by

$$f_p=\sum_{i}\sum_{k(\neq i)}(Q_{kp}-Q_{ip})^2\cdot|k-i|^{-5/2}\ , \tag{26}$$

and Q_{ip} represents the element of a matrix **Q** which transforms the normal coordinates $\rho(u, v, w)$ into the cartesian coordinates $r(x, y, z)$ of the molecule in the following manner

$$\begin{aligned} x_i&=\sum_{p=0}^{N} Q_{ip}u_p\ ,\\ y_i&=\sum_{p=0}^{N} Q_{ip}v_p\ ,\\ z_i&=\sum_{p=0}^{N} Q_{ip}w_p\ . \end{aligned} \tag{27}$$

In the above calculation the terms of higher power of velocity gradient G are neglected.

In the experimental study of the flow birefringence one observes usually the magnitude of birefringence and the direction of the optical axes. As is shown in Fig. 1, under the condition of Eq. (9) the polymer solution has ordinarily two optical axes in the xz-plane, one of which A_1 lies in the first and the third quadrants, and the other A_2 lies in the second and the fourth quadrants. We denote the principal refractive indices of the polymer solution in the directions of the axes A_1 and A_2 as n_1 and n_2 respectively, also denote the acute angle between the A_1 axis and x axis as χ_1. Then we define the magnitude of birefringence $\varDelta n$ and the extinction angle χ by the following relations,

$$\begin{aligned} \varDelta n&=n_1-n_2\ ,\\ \chi&=\chi_1\ . \end{aligned} \tag{28}$$

For the comparison with the experimental results, we also define two quantities, the intrinsic birefringence $[\varDelta n]$ and the intrinsic extinction angle $\tan\alpha$ as follows,

$$\begin{aligned} [\varDelta n]&=\lim_{\substack{c\to 0\\ G\to 0}}(\varDelta n/Gc)\ ,\\ \tan\alpha&=\lim_{\substack{c\to 0\\ G\to 0}}(\pi/4-\chi)/G\ , \end{aligned} \tag{29}$$

where c denotes the weight concentration of the polymer in the solution. The value of $\tan\alpha$ represents the initial gradient of the curve $-\chi_1$ vs. G at the infinitely dilute solution.

On the other hand, the quantities $[\varDelta n]$ and $\tan\alpha$ are represented, in terms of the polarizability tensor $\langle A\rangle$, as follows,

$$[\varDelta n]=4/9\cdot\pi N_a M^{-1}(n_0^2+2)^2 n_0^{-1}\cdot\lim_{G\to 0}\langle A_{xz}\rangle/G \tag{30-1}$$

$$\tan\alpha=1/4\cdot\lim_{G\to 0}\langle A_{xx}-A_{zz}\rangle/\langle A_{xz}\rangle G\ , \tag{30-2}$$

where N_a is the Avogadro's number, and M is the molecular weight of the polymer. Now, we put:

$$\lim_{G\to 0}\frac{\langle A_{2xx}-A_{2zz}\rangle}{\langle A_{1xx}-A_{1zz}\rangle}=a_0\Theta\ , \tag{31}$$

$$\lim_{G\to 0}\frac{\langle A_{2xz}\rangle}{\langle A_{1xz}\rangle}=b_0\Theta\ , \tag{32}$$

$$\Theta=32\cdot5^{-1}\cdot3^{1/2}\cdot\pi^{-2}(P-P_0)^2N^{1/2}Q^{-1}(n_0{}^2+2)n_0{}^{-2}l_0{}^{-5}\,, \tag{33}$$

where it is assumed that the limiting values are finite and definite. Then $[\varDelta n]$ and $\tan\alpha$ are rewritten as

$$[\varDelta n]=[\varDelta n]_0(1+b_0\Theta)\,, \tag{34}$$

$$\tan\alpha=\tan\alpha_0\cdot\frac{1+a_0\Theta}{1+b_0\Theta}\,, \tag{35}$$

where $[\varDelta n]_0$ and $\tan\alpha_0$ represent the respective quantities when the optical interaction between segments is neglected. a_0 and b_0 are numerical constants, and by introducing the results of Eqs. (10), (11), (24) and (25) into Eqs. (31) and (32), they can be written as follows,

$$a_0=8^{-1}(\pi/2)^{3/2}N^{1/2}\cdot\sum_{p=1}^{N}f_p\mu_p{}^{-1}\lambda_p{}^{-2}g_p\bigg/\sum_{p=1}^{N}\lambda_p{}^{-2}g_p\,, \tag{36}$$

$$b_0=8^{-1}(\pi/2)^{3/2}N^{1/2}\cdot\sum_{p=0}^{N}f_p\mu_p{}^{-1}\lambda_p{}^{-1}\bigg/\sum_{p=0}^{N}\lambda_p{}^{-1}\,. \tag{37}$$

Kuhn and Grün[6] obtained the following formulas for a random chain segment constitued of ν monomer units

$$\begin{aligned}P&=(\alpha_1+2\alpha_2)/3\,,\\ Q&=(\alpha_1-\alpha_2)/5\nu a^2\,,\end{aligned} \tag{38}$$

where a represents the effective bond length of a monomer unit, and α_1 and α_2 denote the components of polarizability of the monomer unit, which are parallel and perpendicular to the monomer bond respectively.

Also, from the Clausius-Mrssotti's equation we can derive a relation:

$$\begin{aligned}(P-P_0)^2n_0{}^{-2}&=\left(\frac{9}{2\pi N_s}\right)^2\frac{n_p{}^2}{(n_p{}^2+2)^4}\left(\frac{\varDelta n_0}{n_0}\right)^2,\\ \varDelta n_0&=n_0-n_p\,,\end{aligned} \tag{39}$$

where n_p is the refractive index of the pure polymer, and N_s is the number density of segment in this polymer.

Substituting Eqs. (38) and (39) into Eq. (33), we can obtain another expression of Θ as follows,

$$\Theta=2\cdot3^{1/2}\left(\frac{18}{\pi^2}\right)^2\cdot\frac{n_p{}^2(n^2+2)}{(n_p{}^2+2)^4(\alpha_1-\alpha_2)}\cdot\left(\frac{\varDelta n_0}{n_0}\right)^2\cdot\left(\frac{N_m}{N_0}\right)^2\langle L^2\rangle^{-3/2}\,, \tag{40}$$

where $N_m=N\nu$ is the total number of monomer unit in one polymer molecule, $N_0=\nu N_s$ is the number density of solvent molecule in the pure solvent, and

$$\langle L^2\rangle=Nl_0{}^2 \tag{41}$$

is the mean square length of a polymer molecule in the solution.

§ 3. Calculation for Free Draining Molecule

As is seen in the previous theories[4),5)] it is possible to perform some analytical calculations, when the hydrodynamic interaction between the beads is neglected.

In this case the matrix element Q_{ip}, and λ_p and μ_p can be calculated as follows:

$$Q_{ip}=\left(\frac{2}{N+1}\right)^{1/2}\cdot\cos\left(\frac{i+1/2}{N+1}\cdot p\pi\right), \tag{42}$$

$$\mu_p=\lambda_p=4\cdot\sin\left(\frac{1/2}{N+1}\cdot p\pi\right). \tag{43}$$

Inserting these into Eq. (17), and transforming the summation over suffices i and k into the double integral, we can obtain the formulas:

$$f_p=16(2\pi)^{1/2}(N+1)^{-3/2}\cdot\sigma_p\,, \tag{44}$$

$$\sigma_p=p^{1/2}\int_0^{(\pi/2)p}\sin^2y\,dy\int_0^y\sin^2x/x^5\cdot dx\,. \tag{45}$$

The values of the integrals σ_p were evaluated by numerical calculations from $p=1$ to $p=20$. Employing these results in Eq. (44), and substituting Eqs. (43), (44), into Eqs. (36) and (37), we calculated the constants a_0 and b_0. The results are:

$$\begin{aligned} &a_0=1.53 \quad \text{for} \quad \rho_1=0\,, && a_0/b_0=1.20=6/5\,,\\ &a_0=1.51 \quad \text{for} \quad \rho_1=1/4\,, && a_0/b_0=1.18\,,\\ &a_0=1.39 \quad \text{for} \quad \rho_1=\infty\,, && a_0/b_0=1.09=13/12\,,\\ &b_0=1.28\,. \end{aligned} \tag{46}$$

Now referring to Eqs. (34) and (35), we have the formulas on the flow birefringence in the free draining polymer molecule.

The expression of Θ, i.e. Eq. (40), has a factor $(n_0-n_p)^2$, so that our result for $[\Delta n]$ predicts that when the refractive indices of solvents used in an experiment are sufficiently close to that of the polymer, the observed values of flow birefringence depend upon the refractive index of solvent in a form of parabolic relation. This is in agreement with several experimental results. For the comparison with experimental results we adopted the recent experimental data of Tsvetkov[2], and Tsvetkov and Petrova[7] of polystyrene and polymethylmethacrylate in several solvents.

In Fig. 2 and Fig. 3 the experimental data[2] for polystyrene of molecular weight $M_1=0.57\times10^6$ and $M_2=1.29\times10^6$ are plotted against the refractive indices of solvents. The curves 1 and 1′ show the calculated values of $[\Delta n]$, where the values of the parameters are respectively chosen as follows:

$$\begin{aligned} &[\Delta n]_0=-2.90\,,\\ &b_0\Theta/(n_0-n_p)^2=-46.55\,,\\ &n_p=1.6 \qquad \text{for curve 1}\,, \end{aligned} \tag{47-1}$$

and

$$\begin{aligned} &[\Delta n]_0=-4.50\,,\\ &b_0\Theta/(n_0-n_p)^2=-55.56\,,\\ &n_p=1.6 \qquad \text{for curve 1}'\,, \end{aligned} \tag{47-1′}$$

Thus our calculation are found to reproduce the experimental values quite well.

The figures also show the theoretical values of $\tan\alpha/\tan\alpha_0$ by the curves 2, 3, 2′ and 3′ which are respectively calculated from the same values of the parameters. The curves 2 and 2′ represent the case of zero internal viscosity, in which the value $a_0/b_0=1.20$ is used in the calculation. The curves 3 and 3′

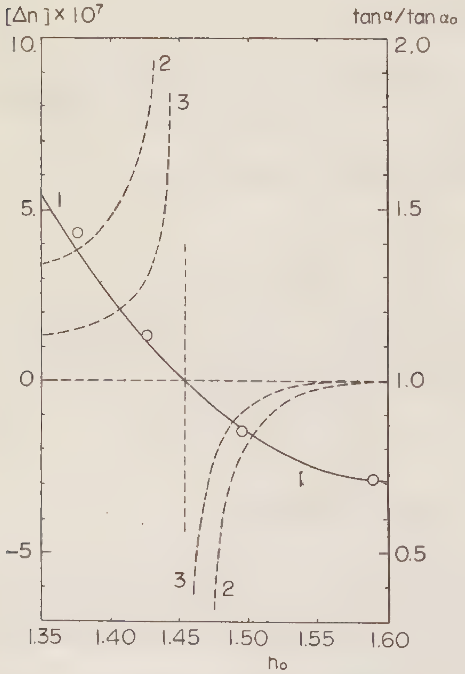

Fig. 2. Comparison of calculation with experimental values for polystyrene molecules ($M=0.57\times10^6$).

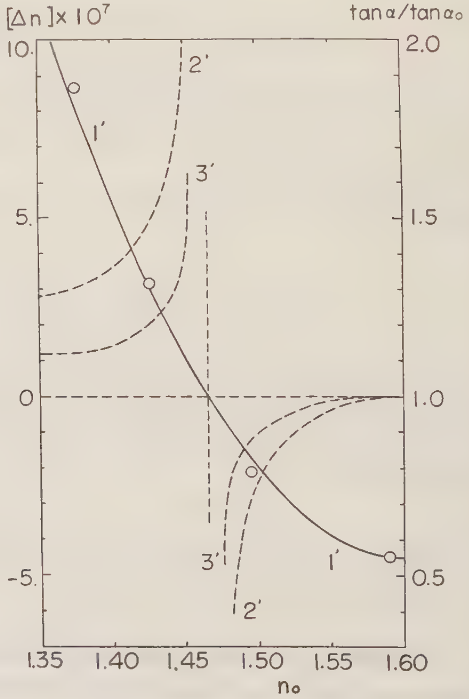

Fig. 3. Comparison of calculation with experimental values for polystyrene molecules ($M=1.29\times10^6$).

represent the case of infinite internal viscosity, in which the value $a_0/b_0=1.09$ is used.

As for the dependence of the extinction angle upon the refractive index of solvent the experimental result is not yet reported.

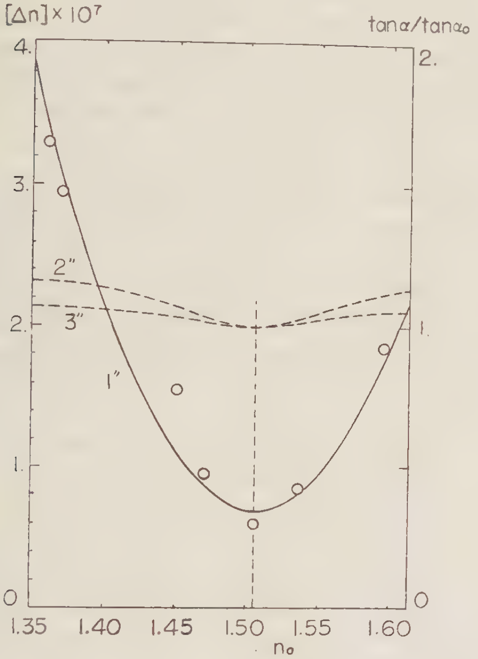

Fig. 4. Comparison of calculation with experimental values for polymethylmethacrylate molecules.

In Fig. 4 the experimental values[7] of birefringence for the polymethylmethacrylate molecules of the molecular weight $M=4.5\times 10^5$ are plotted against the refractive indices of the solvents. The curve 1'' shows the calculated value of $[\Delta n]$, where the values of the parameters are chosen as follows:

$$[\Delta n]_0=7.0\times10^{-8}\ ,\quad b_0\Theta/(n_0-n_p)^2=186\ ,\quad n_p=1.505\ . \tag{47-1''}$$

The curves 2'' and 3'' show the theoretical values of $\tan\alpha/\tan\alpha_0$ calculated from the same values of parameters. The curve 2'' corresponds to the case of zero internal viscosity in which $a_0/b_0=1.20$; and the curve 3'' to the case of infinite internal viscosity in which $a_0/b_0=1.09$.

§ 4. Summary and Discussions

Our result shows that the observed values of the birefringence and of the extinction angle depend on the refractive index of the solvent, and the numerical calculation for $[\Delta n]$ can well reproduce the experimental values of the polystyrene molecules and of the polymethylmethacrylate molecules.

Our theory is a generalization of that of Cerf[5] who neglected the optical interaction between the molecular segments. When this interaction is neglected in our calculation, the expressions of $[\Delta n]$ and of $\tan\alpha$ must therefore coincide with those of Cerf for small internal viscosity as well as for infinite internal viscosity. Indeed, in the case of negligible optical interaction we obtain

$$[\Delta n]_0=\frac{4}{45}\pi\frac{(n_0{}^2+2)}{n_0}(\alpha_1-\alpha_2)\frac{\eta_0[\eta]}{kT}\ , \tag{48}$$

and

$$\tan\alpha_0=C_1\cdot\frac{M\eta_0[\eta]}{RT}+C_2\cdot\frac{\mathscr{F}\langle L^2\rangle}{kT} \tag{49-1}$$

for small internal viscosity, and

$$\tan\alpha_0=C_1{}'\cdot\frac{M\eta_0[\eta]}{RT} \tag{49-2}$$

for infinite internal viscosity, where $\mathscr{F}=\varphi_1 N$ gives the magnitude of internal viscosity, and constants C_1, C_2 and $C_1{}'$ depend on the hydrodynamic interaction between molecular segments. When the hydrodynamic interaction is small, they take the values:

$$C_1=0.2\ ,\quad C_2=0.0062\ ,\quad C_1{}'=0.9\ , \tag{50-1}$$

and when the hydrodynamic interaction is large they take the values:

$$C_1=0.1\ ,\quad C_2=0.0045\ ,\quad C_1{}'=0.705\ , \tag{50-2}$$

Introduction of Eqs. (48), (49-1) and (49-2) into Eqs. (34) and (35) yields

$$[\Delta n]=\frac{4}{45}\pi\cdot\frac{(n_0{}^2+2)^2}{n_0}\cdot\frac{\eta_0[\eta]}{kT}(\Theta_i+b_0\Theta_f)\ , \tag{51}$$

$$\tan\alpha=\left(C_1\cdot\frac{M\eta_0[\eta]}{RT}+C_2\cdot\frac{\mathscr{F}\langle L^2\rangle}{kT}\right)\cdot\frac{\Theta_i+a_0\Theta_f}{\Theta_i+b_0\Theta_f} \tag{52-1}$$

(for small internal viscosity) and

$$\tan\alpha=C_1{}'\cdot\frac{M\eta_0[\eta]}{RT}\cdot\frac{\Theta_i+a_0\Theta_f}{\Theta_i+b_0\Theta_f} \tag{52-2}$$

(for infinite internal viscosity), where Θ_i and Θ_f are defined by

$$\begin{aligned}\Theta_i&=\alpha_1-\alpha_2\ ,\\ \Theta_f&=(\alpha_1-\alpha_2)\Theta\\ &=2.3^{1/2}\left(\frac{18}{\pi}\right)^2\cdot\frac{n_p{}^2(n^2+2)}{(n_p{}^2+2)^4}\cdot\left(\frac{\Delta n_0}{n_0}\right)^2\\ &\quad\cdot\left(\frac{N_m}{N_0}\right)^2\cdot\langle L^2\rangle^{-3/2}\ ,\end{aligned}\tag{54}$$

In the above expressions the optical factor Θ_f takes always the positive value, and it contains a factor $(\Delta n_0)^2=(n_0-n_p)^2$, therefore in the neighbourhood of $n_0=n_p$ the curve $[\Delta n]$ vs. n_0 is approximately expressed by a parabola which is concave upwards and has a minimum point at $n_0=n_p$, as is seen in Figs. 2 and 3. On the other hand the factor Θ_i can take either the positive or the negative value according as $\alpha_1>\alpha_2$ or $\alpha_1<\alpha_2$. From these properties the results can be classified into several cases in which the curve $[\Delta n]$ vs. n_0 and the curve $\tan\alpha$ vs. n_0 have different figures (Figs. 5, 6 and 7).

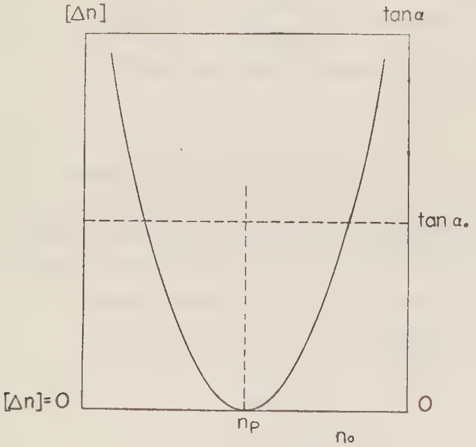

Fig. 6. Curves of $[\Delta n]$ vs. n_0, and of $\tan\alpha$ vs n_0 for $\alpha_1=\alpha_2$.

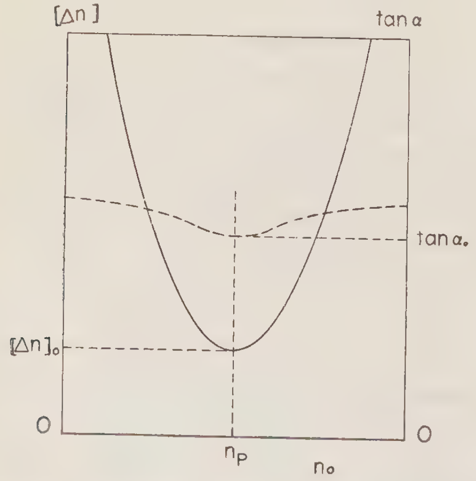

Fig. 5. Curves of $[\Delta n]$ vs. n_0, and of $\tan\alpha$ vs. n_0 for $\alpha_1>\alpha_2$

(i) $\alpha_1>\alpha_2$, $\Theta_i>0$ (Fig. 5)

In this case both $[\Delta n]$ and $\tan\alpha$ take always the positive value. The curve $[\Delta n]$ vs. n_0 and that $\tan\alpha$ vs. n_0 have their minimum points at $n_0=n_p$. The curves are shown in Fig. 5, and this case corresponds to that of Fig. 4.

(ii) $\alpha_1=\alpha_2$, $\Theta_i=0$ (Fig. 6)

In this special case $[\Delta n]$ also takes the positive value except at the minimum point where it becomes to zero. The optical factor in the expression of $\tan\alpha$ vanishes, so that $\tan\alpha$ does not depend on the refractive index of solvent. The curves are shown in Fig. 6.

(iii) $\alpha_1<\alpha_2$, $\Theta_i<0$ (Fig. 7)

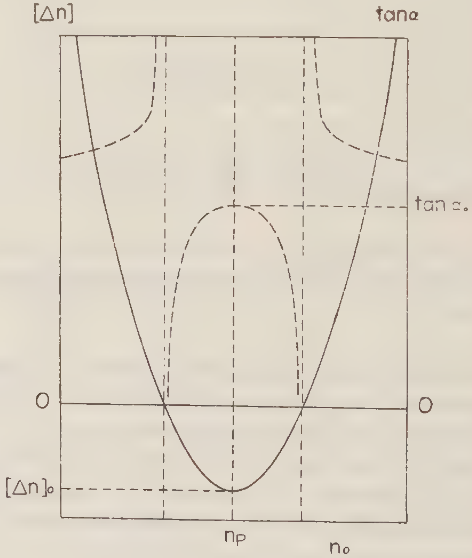

Fig. 7. Curves of $[\Delta n]$ vs. n_0, and of $\tan\alpha$ vs. n_0 for $\alpha_1<\alpha_2$.

In this case $[\Delta n]$ takes negative value when $|\Delta n_0|=|n_0-n_p|$ is small, but it takes the positive value when $|\Delta n_0|$ is large. The behavior of $\tan\alpha$ is quite different from that of the other two cases. The curve $\tan\alpha$ vs. n_0 has a maximum point at $n_0=n_p$, where $[\Delta n]$ takes a minimum value. At the special point at which $[\Delta n]$ vanishes, that is, where the equation:

$$\Theta_i+b_0\Theta_f=0 \tag{55}$$

is satisfied, the curve $\tan\alpha$ vs. n_0 is discontinuous. The pattern of these curves are shown in Fig. 7, and this case corresponds to that of Fig. 2 and Fig. 3.

As we can see in Eqs. (51), (52-1) and (52-2), the optical factors of $[\Delta n]$ and $\tan\alpha$ consist of two factors Θ_i and Θ_f. The former Θ_i represents simply the intrinsic optical anisotropy of a monomer unit of the polymer $\alpha_1-\alpha_2$, and so this is independent of the optical interaction. The latter Θ_f comes from the optical interaction between molecular segments in the solvent, and it depends on the refractive index of solvent. So our result shows that when the optical interaction between segments does not exist, or when it is negligible, the observed values of $[\Delta n]$ and of $\tan\alpha$ do not depend on the refractive index of the solvent. Also it is shown that when the observed values of $[\Delta n]$ and $\tan\alpha$ do not depend on the refractive index of solvent, then the effect of the optical interaction is negligible in such a system.

However we can see that in a certain case, as is shown in Fig. 6 of the case (ii), where the optical anisotropy of the monomer unit is very small, or when $|\alpha_1-\alpha_2|$ has very small value, the value of $\tan\alpha$ becomes almost independent of the refractive index of the solvent, even though the optical interaction between segments is very large.

It is generally recognized that when the absolute value of the ratio of the two optical factors $\Theta=\Theta_f/\Theta_i$ is sufficiently smaller than unity, the effect of the optical interaction on the observed results is negligible as compared with that of the intrinsic optical anisotropy. So, when we choose an appropriate small number, ε, we can determine a domain of the refractive index of solvent, in which the effect of optical interaction is negligible, by a following definition:

$$-\varepsilon<\Theta<\varepsilon\,, \qquad 0<\varepsilon\ll 1\,. \tag{56}$$

Then from Eq. (40) the magnitude δn_0 for this domain:

$$n_p-\delta n_0<n_0<n_p+\delta n_0$$

can be expressed by the following equation:

$$\begin{aligned}\delta n_0&=\sqrt{\varepsilon/|\Theta_0|}\,,\\ \Theta_0&=\Theta/(\Delta n_0)^2\,.\end{aligned} \tag{57}$$

According to this definition the magnitude δn_0 is proportional to $\sqrt{|\alpha_1-\alpha_2|}$, therefore this domain is enlarged as the optical anisotropy of monomer unit becomes large. Also the magnitude of δn_0 is independent of the sign of $\alpha_1-\alpha_2$.

The results in Eqs. (51), (52-1) and (52-2) can be compared with those of the theory of Copic[3] (C-theory), which is based on the dumbbell model. The expressions of C-theory are given by

$$[\Delta n]=\frac{4}{27}\pi\cdot\frac{(n_0{}^2+2)^2}{n_0}\cdot\frac{\eta_0[\eta]}{RT}\cdot(\theta_i+\theta_f)\,, \tag{58}$$

and

$$\tan\alpha=\frac{1}{2}\cdot\frac{\eta_0[\eta]}{RT} \tag{59-1}$$

for negligible internal viscosity, and

$$\tan\alpha=\frac{7}{6}\cdot\frac{\eta_0[\eta]}{RT}\cdot\frac{\vartheta_i+6/7\cdot\theta_f}{\vartheta_i+\vartheta_f} \tag{59-2}$$

for infinite internal viscosity, where ϑ_i and θ_f are parameters depending upon the optical constants of the polymer solution, which are given by

$$\vartheta_i=\frac{3}{5}(\alpha_1-\alpha_2)\,, \tag{60}$$

$$\vartheta_f=\frac{16}{15}\cdot\left(\frac{3}{2\pi}\right)^{1/2}\left(\frac{9M}{4\pi\rho N}\right)^2\langle L^2\rangle^{-3/2}\cdot\frac{n_0{}^2(n_p{}^2-n_0{}^2)^2}{(n_p{}^2+2n_0{}^2)^2}\,. \tag{61}$$

As we can see in the above results, both theories give the similar form of equation for $[\Delta n]$ and $\tan\alpha$, except $\tan\alpha$ for negligible internal viscosity, where the expression of C-theory has no optical parameter. Our result shows that the observed value of $\tan\alpha$ depends on the refractive index of solvant because of an optical factor $\Theta_i+a_0\Theta_f/\Theta_i+b_0\Theta_f$ as in case of $[\Delta n]$. So when $[\Delta n]$ vanishes at a certain value of the refractive index of solvent, which is given by the equation:

$$\Theta_i+b_0\Theta_f=0 \tag{55}$$

the value of $\tan\alpha$ is discontinuous at this point, as is seen in Figs. 2 and 3.

In case of the polymer molecule with infinite internal viscosity our numerical calculation gives a value $a_0/b_0=13/12$, and this value should correspond to the value 6/7 in C-theory, which is the coefficient of ϑ_f in Eq. (59-2). Probably such a difference of the values comes from the differences in the theoretical models and in the mathematical approximations used in the two theories.

The constants a_0 and b_0 are at first defined by Eqs. (31) and (32) in terms of the elements of polarizability tensor, $\langle A_1\rangle$ and $\langle A_2\rangle$ only. But our calculations of such quantities were performed through some mathematical approximations, such as $T_{ik}=\langle T_{ik}\rangle$ as is done in Eq. (20). One can still imagine that another more rigourous theory would give a relation:

$$a_0=b_0 \quad \text{or} \quad a_0/b_0=1\,, \tag{62}$$

and as the result the optical factor of tan α in Eq. (52) or (35) will disappear, and such a calculation will predict non-dependence of tan α upon the refractive index of the solvent.

The equation: $a_0=b_0$, that is $a_0/b_0=1$ requires the relation:

$$\lim_{G\to 0}\frac{\langle A_{2xx}-A_{2zz}\rangle}{\langle A_{1xx}-A_{1zz}\rangle}=\lim_{G\to 0}\frac{\langle A_{2xz}\rangle}{\langle A_{1xz}\rangle}\,. \tag{63}$$

The experimental varification of this relation will be considerably difficult, because the calculation shows that the birefringence $[\Delta n]$ vanishes at the critical point where tan α is discontinuous, so the absolute value of Δn becomes very small in the neighbourhood of this point.

Finally it is to be noted that there is another difference of the results of tan α between C-theory and our theory. As we can see in the above result, the calculated values of the constant a_0/b_0 are larger than unity for both small and infinite internal viscosities of the molecules. But on the other hand C-theory gives values not larger than unity, i.e., unity and 6/7 for small and infinite internal viscosities respectively. This result yields a remarkable difference between the patterns of the curves: tan α vs. n_0 in two theories. That is, if the value of a_0/b_0 is smaller than unity as in the case of C-theory, the curve comes just into the position of its reflected image on the other side of the straight line:

$$\tan\alpha=constant=\tan\alpha_0$$

which is parallel to the abscissa, and so in the neighbourhood of the critical point tan α takes the different sign. Such a difference of the two theories might originate in the theoretical models and in the mathematical approximations used in them.

The author is very grateful to Professor Ch. Sardon and to Professor R. Cerf of the "Centre de Recherches sur les Macromolécules", who gave him facilities and invaluable suggestions for this work during his stay in Strasbourg.

References

1) Ch. Sadron: J. Physique Radium **8** (1957) 481. A. Peterlin and H. A. Stuart: Z. f. Physik, **112** (1939) 1, and "Doppelbrechung, insbesondere künstliche Doppelbrechung", Hand- und Jahrbuch der Chemischen Physik. Volum **8**, R. Cerf. J. Chim. Physique **48** (1951) 59.
2) V. Tsvetkov: J. Polymer Sci. **23** (1957) 151.
3) M. Copic: J. Chem. Phys. **26** (1957) 1382 and J. Polymer Sci. **20** (1956) 593.
4) P. E. Rouse, Jr.: J. Chem. Phys. **21** (1953) 1272.
B. H. Zimm: J. Chem. Phys. **24** (1956) 269, etc..
5) R. Cerf: J. Physique Radium **19** (1958) 122, and "La dynamique des solutions de macromolécules dans un champ de vitesses", Fortschritte der Hochpolymeren-Forschung/Advances in Polymer Science. 1. Band, 3. Heft p. 382. Springer-Verlag (1959). R. Koyama and R. Cerf: J. Physique Radium **21** (1960) 503.
6) W. Kuhn and F. Grün: Kolloid Z. **101** (1942) 248.
7) V. N. Tsvetkov and A. Petrova: J. Phys. Chem. (U.S.S.R.) **23** (1949) 368.

JOURNAL OF THE PHYSICAL SOCIETY OF JAPAN, Vol. 16, No. 7, JULY, 1961

An Expression for Orientation in Cellulose Fibres

By V. D. GUPTA*

Textile Research Institute, Princeton, New Jersey, U. S. A.

(Received January 31, 1961)

Hermans' orientation factor can be evaluated only when the diatropic and paratropic interferences arise from planes which form an orthogonal set. This is only approximately satisfied in case of both Cellulose I and Cellulose II. In the present communication an exact expression has been derived which can be evaluated from x-ray measurements, angle between face normals of paratropic interferences and the optical constants.

The problem of crystallite orientation in natural and synthetic fibres has been solved by many workers[1-4]. It has been studied both from x-ray and optical methods. The x-ray method is more useful because optical methods furnish informations merely as to the average orientation of the entire fibrous substance whereas the x-ray method gives orientation of only the crystallite components. Hermans and others[5] have worked out an expression for a quantitative evaluation of the crystallite orientation in cellulose. This is, however, applicable only when the diatropic and paratropic interferences arise from an orthogonal set of planes and it is only approximately satisfied in case of both Cellulose I and Cellulose II. In the present paper an exact expression has been derived.

Section I

In Fig. 1a let one of the axes of the polarisation ellipsoid coincide with the crystallographic b axis which represents the direction along the cellulose chains and σ_1, σ_0, σ_3 the three polarisabilities. Further let b denote the normal to the diatropic planes $0k0$ and a_0, a_3 those to h_10l_1 and h_20l_2 respectively. The pricipal axis σ_1 of the polarisation ellipsoid coincides with b and σ_0, σ_3 lie in the plane a_0a_3. If δ is the angle $\widehat{\sigma_0a_0}$, θ_1 is $\widehat{bf}$, ψ_0 is $\widehat{\sigma_0f}$ and ψ_3 is $\widehat{\sigma_3f}$, the polarisability in the direction of the fibre axis resulting from unit electric field in the direction of the fibre axis is

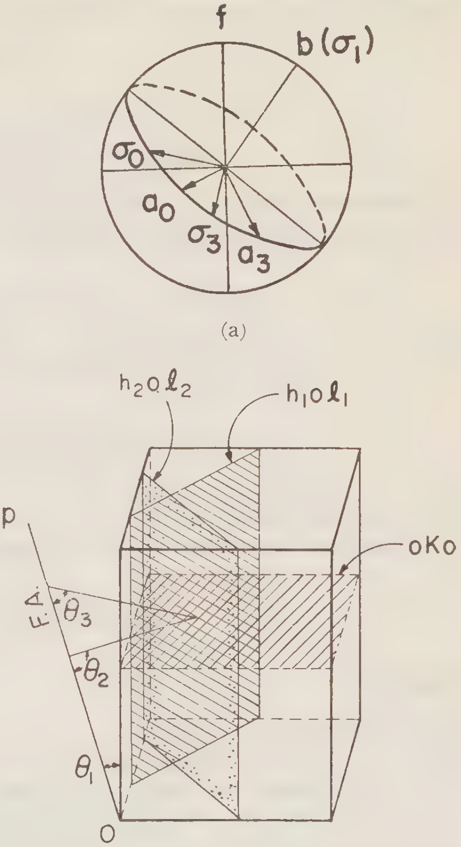

(a)

(b)

Fig. 1.

$$\sigma_{\|}=\sigma_1\cos^2\theta_1+\sigma_0\cos^2\psi_0+\sigma_3\cos^2\psi_3\,, \tag{1}$$

and averaging over all positions of the crystal

$$\sigma_{\|}=\sigma_1\overline{\cos^2\theta_1}+\sigma_0\overline{\cos^2\psi_0}+\sigma_3\overline{\cos^2\psi_3}\,.$$

---

* On leave from the Physics Department, University of Allahabad, India.

It is obvious that

$$\cos\psi_0 = \operatorname{cosec}\alpha\{\sin(\alpha+\delta)\sin\theta_2 - \sin\delta\sin\theta_3\}$$
$$\cos\psi_3 = \operatorname{cosec}\alpha\{-\cos(\alpha+\delta)\sin\theta_2 + \cos\delta\sin\theta_3\}\ ,$$

where α is the anngle $\widehat{a_0 a_3}$.

Also

$$\overline{\cos^2\theta_1} = 1 - \operatorname{cosec}^2\alpha(\overline{\sin^2\theta_2} + \overline{\sin^2\theta_3})\ ,$$

(see Section II) where θ_2, θ_3 are the angles which the normals to the two paratropic planes make with the fibre axis and are measured from the equator in the x-ray photograph when this relation is satisfied. Making these substitutions in I we have,

$$\sigma_{\parallel} = \sigma_1 - \operatorname{cosec}^2\alpha[\sigma_1 - \sigma_0\sin^2(\alpha+\delta) - \sigma_3\cos^2(\alpha+\delta)]\,\overline{\sin^2\theta_2}$$
$$-\operatorname{cosec}^2\alpha[\sigma_1 - \sigma_0\sin^2\delta - \sigma_3\cos^2\delta]\,\overline{\sin^2\theta_3}\ ,$$

remembering that $\overline{\sin\theta_2\sin\theta_3} = 0$.

Polarisability perpendicular to the fibre

$$\sigma_{\perp} = \tfrac{1}{2}(\sigma_1 + \sigma_0 + \sigma_3 - \sigma_{\parallel})\ ,$$
$$\sigma_{\perp} = \tfrac{1}{2}[\sigma_0 + \sigma_3 + \operatorname{cosec}^2\alpha\{\sigma_1 - \sigma_0\sin^2(\alpha+\delta) - \sigma_3\cos^2(\alpha+\delta)\}\overline{\sin^2\theta_2}$$
$$+\operatorname{cosec}^2\alpha(\sigma_1 - \sigma_0\sin^2\delta - \sigma_3\cos^2\delta)\,\overline{\sin^2\theta_3}]\ .$$

The orientation factor f is defined as the ratio between the actual double refraction of the crystalline material and that at complete orientation. Hence

$$f = \frac{\sigma_{\parallel} - \sigma_{\perp}}{(\sigma_{\parallel} - \sigma_{\perp})_c}\ ,$$
$$f = 1 - \frac{3}{2}\left[\frac{\operatorname{cosec}^2\alpha\{\sigma_1 - \sigma_0\sin^2(\alpha+\delta) - \sigma_3\cos^2(\alpha+\delta)\}}{\sigma_1 - \frac{1}{2}(\sigma_0 + \sigma_3)}\right]\overline{\sin^2\theta_2}$$
$$-\frac{3}{2}\left[\frac{\operatorname{cosec}^2\alpha(\sigma_1 - \sigma_0\sin^2\delta - \sigma_3\cos^2\delta)}{\sigma_1 - \frac{1}{2}(\sigma_0 + \sigma_3)}\right]\overline{\sin^2\theta_3}\ ,$$

which is the general equation.

If we assume $\sigma_0 = \sigma_3$ as is true for most of the cellulose fibres,

$$f = 1 - \frac{3}{2}\operatorname{cosec}^2\alpha\,(\overline{\sin^2\theta_2} + \overline{\sin^2\theta_3})\ .$$

Section II

Relation between θ_1, θ_2 and θ_3:

Let the normals to three planes $0k0$, $h_1 0 l_1$ and $h_2 0 l_2$ represent the three axes fixed in space and $0P$ the direction of the fibre axis. The angles θ_1, θ_2 and θ_3 are then as shown in the figure. If l be a vector along the fibre axis and a_1, a_2 and a_3 its components, we can write,

$$l = a_1 i + a_2 j + a_3 k\ ,$$

where i, j, k, l are unit vectors. Or

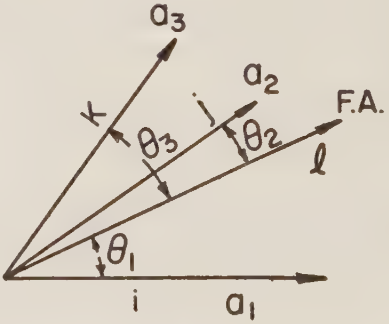

Fig. 2.

$$l.l = a_1^2 + a_2^2 + a_3^2 + 2a_1a_2 i.j + 2a_2a_3 j.k + 2a_1a_3 i.k = 1\ . \qquad \text{(a)}$$

Again we have,

$$\cos\theta_1=a_1+a_2 i.j+a_3 i.k\ ,$$
$$\cos\theta_2=a_1 j.i+a_2+a_3 j.k\ ,$$
$$\cos\theta_3=a_1 k.i+a_2 k.j+a_3\ .$$

Solving these equations for a_1, a_2 and a_3 we get

$$a_1=\begin{vmatrix}\cos\theta_1 & i.j & i.k\\ \cos\theta_2 & 1 & j.k\\ \cos\theta_3 & k.j & 1\end{vmatrix}\div\begin{vmatrix}1 & i.j & i.k\\ j.i & 1 & j.k\\ k.i & k.j & 1\end{vmatrix},$$

and two similar determinants for a_2, a_2 and a_3.

In a monoclinic system $0k0$ is orthogonal to $h_1 0 l_1$ and $h_2 0 l_2$ and therefore,

$$i.j=0\ ,$$
$$i.k=0\ ,$$
$$j.k=\cos\alpha\ \text{(say)}\ .$$

On simplification of these determinants we have

$$a_1=\cos\theta_1\ ,$$
$$a_2=(\cos\theta_2-\cos\alpha\cos\theta_3)/\sin^2\alpha\ ,$$
$$a_3=(\cos\theta_3-\cos\alpha\cos\theta_2)/\sin^2\alpha\ .$$

Substituting these values in (a) we get,

$$\sin^2\theta_1=\operatorname{cosec}^2\alpha(\cos^2\theta_2+\cos^2\theta_3)-2\operatorname{cosec}\alpha\cot\alpha\cos\theta_2\cos\theta_3\ .$$

If, however, the angles θ_2 and θ_3 are measured from the equator and an average value of the angles is taken,

$$\overline{\sin^2\theta_1}=\operatorname{cosec}^2\alpha(\overline{\sin^2\theta_2}+\overline{\sin^2\theta_3})\ ,$$

The values of $\overline{\sin^2\theta_2}$ and $\overline{\sin^2\theta_3}$ can be evaluated from the x-ray photographs in the usual manner. The author has also derived a general expression for the angle between face normals in a crystallographic system⁶⁾. This is given by,

$$\cos^{-1}\frac{T(x,y)}{\sqrt{T(x,x)T(y,y)}}\ .$$

Where $T(x, y)$ is

$$\frac{\sin^2\alpha}{x_1y_1}+\frac{\sin^2\beta}{x_2y_2}+\frac{\sin^2\gamma}{x_3y_3}+(\cos\gamma\cos\beta-\cos\alpha)\left(\frac{1}{x_3y_2}+\frac{1}{x_2y_3}\right)$$
$$+(\cos\gamma\cos\alpha-\cos\beta)\left(\frac{1}{x_3y_1}+\frac{1}{x_1y_3}\right)+(\cos\alpha\cos\beta-\cos\gamma)\left(\frac{1}{x_1y_2}+\frac{1}{x_2y_1}\right),$$

where x_1, x_2, x_3 and y_1, y_2, y_3 are the intercepts along three axes and α, β, γ are the axial angles. For a monoclinic system (to which cellulose belongs) the angle between the paratropic planes in terms of Miller indices and axial lengths is given by:

$$\cos^{-1}\frac{h_1h_2\dfrac{bc}{a}+l_1l_2\dfrac{ab}{c}-b\cos\beta\,(l_1h_2+h_1l_2)}{\sqrt{\left(\dfrac{h_1^2}{a^2}+\dfrac{l_1^2}{c^2}-\dfrac{2l_1h_1}{ac}\cos\beta\right)\left(\dfrac{h_2^2}{a^2}+\dfrac{l_2^2}{c_2}-\dfrac{2h_2l_2}{ac}\cos\beta\right)}}\ .$$

Here a is the monoclinic angle. Thus the orientation factor can be completely evaluated.

An experimental determination of this is being carried out and will be shortly reported elsewhere.

References

1) W. A. Sisson and G. L. Clark: Ind. Eng. Chem., Anal. Ed. **5** (1933) 296.
2) E. E. Berkley: Textile Research Journal **9** (1939) 335.
3) R. Hoseman: Z. Physik. Chem. **179A** (1937) 356.
4) R. S. Stein: J. Polymer Sci. **31** (1958) 327.
5) J. J. Hermans and P. H. Hermans et al.: Rec. trav. Chim. **65** (1946) 427.
6) V. D. Gupta: Under Publication Zeits fur Krist.

JOURNAL OF THE PHYSICAL SOCIETY OF JAPAN, Vol. 16, No. 7, JULY, 1961

The Confinement of Plasma by the Heliotron Magnetic Field

By Kōji Uo

Electrical Engineering Institute, Faculty of Engineering,
Kyōto University, Kyōto

(Received February 1, 1961)

A magnetic field named the Heliotron field is produced by the electric current in a series of pair coils wound around the discharge tube with regular intervals. The electric current in each coil of the pair differs both in intensity and direction. The lines of force in this field undulate near the tube axis without cutting the wall, while these near the tube wall cross the wall. Thus the high temperature plasma can be produced by ohmic heating in the central region of this field being prevented from touching the wall. This field is found to satisfy the necessary condition for the equilibrium. The interchange instability of the plasma confined in this field is discussed. A general expression is given for the magnetic field, and it is shown that the Heliotron B magnetic field, the cylindrical cusp field, the helical winding field of the Stellarater and the Picket-Fence field are derived as special cases of this general formula.

§1. Introduction

There are two different types in the confinement of high temperature plasma by a magnetic field. The magnetic pressure is comparable with the plasma pressure in one type, and in the other the magnetic pressure is much larger than the plasma pressure. For example, the pinch type machine belongs to the first type and the mirror type machine and the Stellarator to the second.

Recently two machines of the second type have been constructed successively in Kyoto University and named the Heliotron A and the Heliotron B[1]. The Heliotron* magnetic field uses series of pair colis which are wound around the discharge tube of toroidal shape with regular intervals. In general, the electric current in each coil of a pair is different in both intensity and direction. The magnetic field produced by these currents are composed of two different regions. In the region near the tube axis the magnetic lines of force undulate along the axis without cutting the wall, whereas those near the tube wall cross the boundary making short arcs inside the wall. Therefore, the high-temperature plasma can be produced by ohmic heating only in the central region of the magnetic field, since particles near the wall cannot be accelerated sufficiently by the applied axial electric field.

Thus it may be said that the machine has the effect of preventing the hot plasma from directly touching the wall, and it does not need such an apparatus as the aperture limiter which was used in the Stellarater in order to limit the radius of the plasma column.

---

* The basic plan of the Heliotron field was first presented at the meeting of Thermonuclear Conference of Japan (May 5, 1958), and was published in Kakuyūgō Kenkyū, **1**, (1958) 20.

The Heliotron A of toroidal shape was constructed first. Its discharge tube was made of Zircon ceramic with the torus radius of 30 cm, the inner radius of the tube of 8 cm, and the thickness of the tube wall of 1 cm. It had six apertures for observation. Unfortunately the Heliotron A was damaged presumably due to the residual stress in the ceramic and the mechanical stress caused by the field coils which were wound around the torus tube.

Next, the Heliotron B has been constructed. Its discharge tube has the shape of the race-track, and is made of strainless steel. Its curved part has nearly same size as the Heliotron A, and the length of its straight part is 50 cm, the inner radius of the tube 8.4 cm, and the wall thickness 0.2 cm. It has nine apertures for observation. The field intensity is about 20,000 gausses. Now, various experiments are being carried on with the Heliotron B.

In this paper, we describe first the configuration of the Heliotron magnetic field and discuss the condition for the confinement of high temperature plasma in this field. Secondly, it will be shown that this field satisfies the necessary condition for the equilibrium within the framework of the magnetohydrodynamic approximation. Lastly, we will discuss the interchange instability of plasma in this field.

§ 2. General Configuration of the Heliotron Magnetic Field

Let us consider a magnetic field produced by the electric current in the coils, which are wound, as shown in Fig. 2.1, around a torus tube with regular intervals. The outline of the magnetic field in a cylindrical section involving the tube axis is shown graphically in Fig. 2.2.

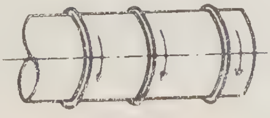

Fig. 2.1.

It is assumed that the charged particles in slightly ionized gas in the tube move along the lines of force being accelerated by an electric field, and that the plasma is so dilute and the magnetic field is so strong that the magnetic pressure p_{mag} is much larger than the plasma pressure p_{gas}. In this case charged particles inside the curve AB of Fig. 2.2 are accelerated over a long distance and obtain high energy. On the other hand, particles outside AB run along the lines of force which are interupted by the tube wall and therefore they cannot obtain high energy. Thus it may be expected that we can generate the discharge only in the region inside the curve because the electric conductivity along the direction becomes so poor near the wall that the high temperature plasma in

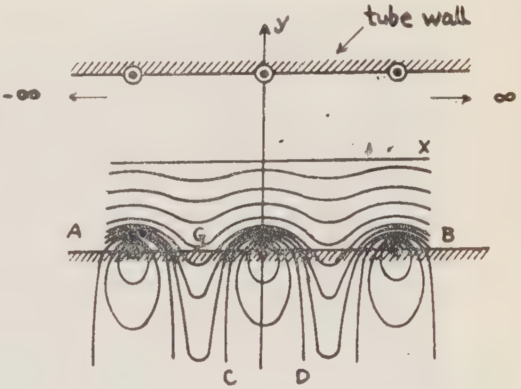

Fig. 2.2. The lines of force inside the curve AB undulate along the axis without cutting the wall whereas those outside the curve AB cross the wall and those outside CD are the leakage flux.

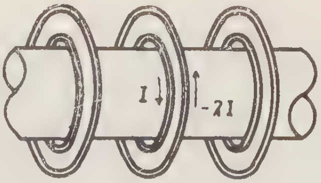

Fig. 2.3.

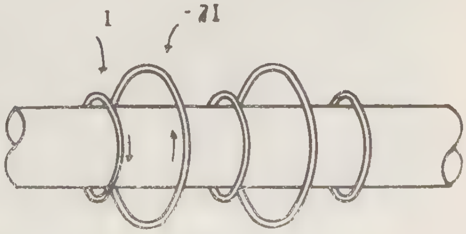

Fig. 2.4.

inner region is prevented to reach the wall except at the point G (see Fig. 2.2.)

This field appears to be effective for protecting the wall against the hot plasma and for decreasing the influx of impurity from the wall. At point G however, the high temperature plasma touches the wall. In order save this defect double rows of coils as shown in Figs. 2.3 and 2.4 are introduced. The direction of electric current in outer coils is opposite to inner one. The magnetic lines of force in these fields are roughly skeched in Fig. 2.5 and 2.6.

In these fields the magnetic lines of force inside AMB do not touch the wall, whereas all lines outside AMB cross the wall leaving short arcs inside the wall. The lines of force near the axis are completely separated from those near the wall, and therefore the high temperature plasma confined by the lines of force inside AMB do not touch the wall at all. Therefore, these fields are evidently more advantageous for confining hot plasma than the field shown in Fig. 2.2.

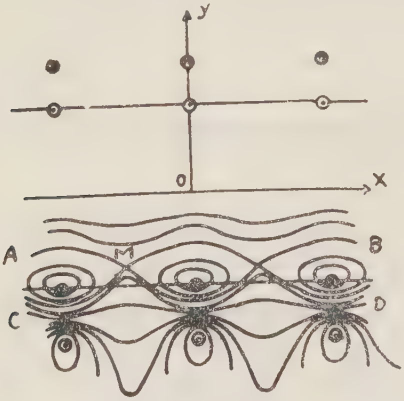

Fig. 2.5.

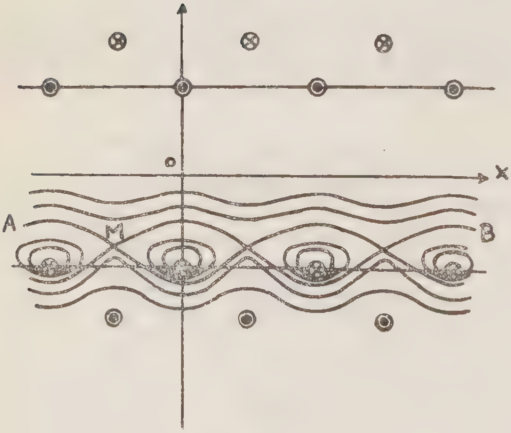

Fig. 2.6.

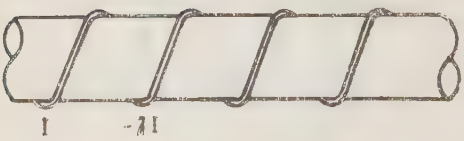

Fig. 2.7.

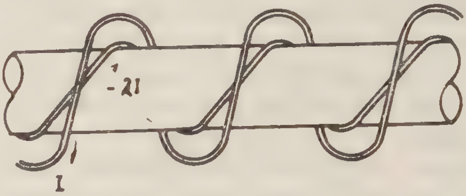

Fig. 2.8.

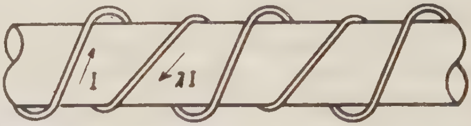

Fig. 2.9.

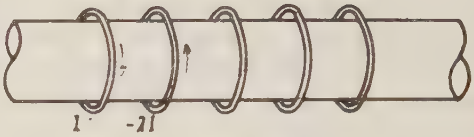

Fig. 2.10.

The rows of coils in Fig. 2.4 may be modified as shown in Fig. 2.7, or coils may be wound helically around the tube as shown in Figs. 2.8~2.10. In the latter case the lines of force also become helical, and this field may be called the Heliotgon H field.

The magnetic fields generated by these double rows of coils are named the Heliotron magnetic field. Let us denote the ratio of electric currents in two coils of a pair by λ. If we put $\lambda=1$ in the windings of Figs. 2.7 and 2.10, they reduce to the Picket Fence field and to the field produced by the helical windings of the Stellarator respectively.

It is one of the merits of the Heliotron field that we can bore apertures for observation without introducing correction coils, which are usually necessary for eliminating the field distortion caused by the irregularity of the coils near the apertures.

The patterns of the magnetic fields produced by the windings are observed experimentally by the iron sand method, and their pictures are shown in Figs. 2.11, 2.12 and 2.13.

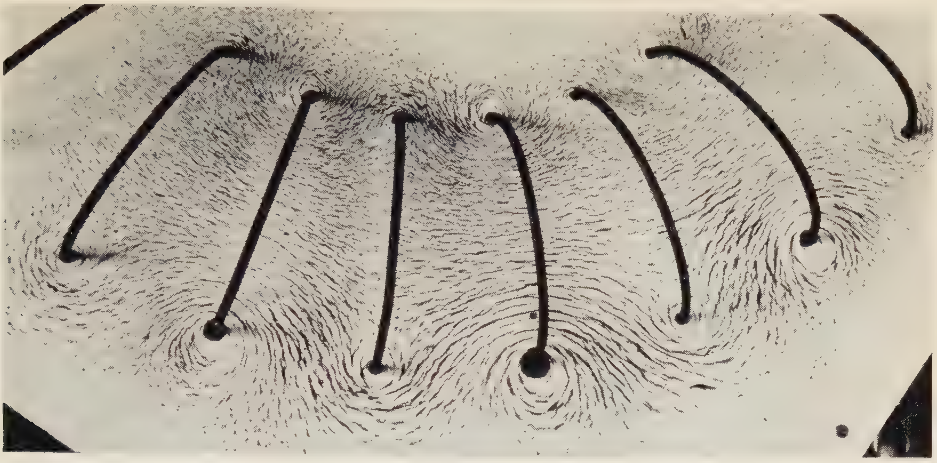

The Heliotron B Magnetic Field, $\lambda=0.33$
Fig. 2.11.

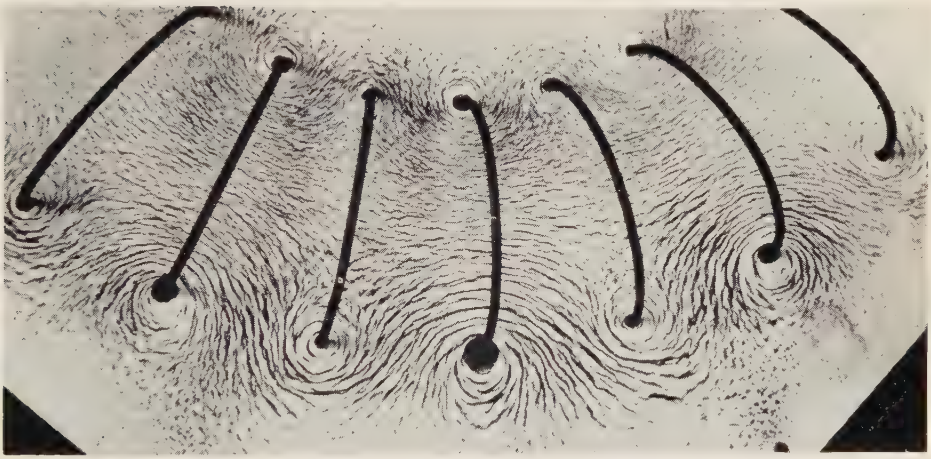

The Heliotron B Magnetic Field, $\lambda=0.5$
Fig. 2.12.

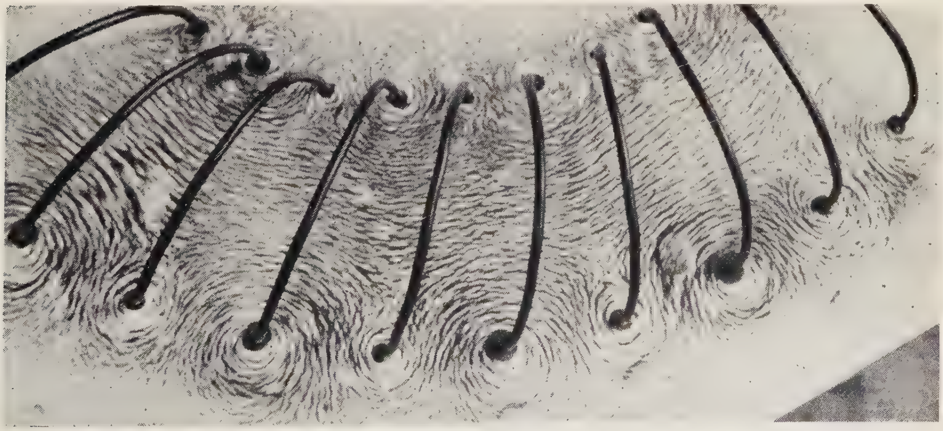

The Heliotron H Magnetic Field, $\lambda=0.5$
Fig. 2.13.

§ 3. Basic Equations of the Cylindrical Magnetic Field

If we assume that a cylindrical magnetic field is generated by the coils wound around a cylindrical tube and no current exists inside of it, we have

$$\mathrm{rot}\,\boldsymbol{B}=0\ . \tag{3.1}$$

Then the magnetic flux density $\boldsymbol{B}$ is given by

$$\boldsymbol{B}=\mathrm{grad}\,\phi\ , \tag{3.2}$$

where ϕ is a scalar function. From Eqs. (3.1) and (3.2) we have

$$\nabla^2\phi=0\ , \tag{3.3}$$

and if we solve this Laplace equation we obtain $\boldsymbol{B}$ from Eq. (3.2). Equation (3.3) may be expressed in the cylindrical coordinates (ρ, θ, z) as

$$\frac{\partial^2\phi}{\partial\rho^2}+\frac{1}{\rho}\frac{\partial\phi}{\partial\rho}+\frac{1}{\rho^2}\frac{\partial^2\phi}{\partial\theta^2}+\frac{\partial^2\phi}{\partial z^2}=0\ . \tag{3.4}$$

Let us assume ϕ in the following form:

$$\phi=F(\rho)G(\theta)S(z)\ , \tag{3.5}$$

where $S(z)$ and $G(\theta)$ are periodic functions of z and θ respectively. Substituting (3.5) into Eq. (3.4) and solving the resultant ordinary differential equations we have the following solution (see Appendix II):

$$\begin{aligned}\phi&=e_1\log\rho+e_2\theta+e_3z\\&+\sum_{\nu=1}^{\infty}\sum_{n=0}^{\infty}\{c_\nu\cos(\nu\kappa z)+d_\nu\sin(\nu\kappa z)\}(P_n\cos n\theta+Q_n\sin n\theta)\\&\times\{A_nI_n(\nu\kappa\rho)+B_nK_n(\nu\kappa\rho)\}\end{aligned} \tag{3.6}$$

where $e_1\log\rho$, $e_2\theta$ and e_3z are particular solutions of Eq. (3.4), and κ, c_ν, d_ν, P_n, Q_n, A_n and B_n are numerical constants. If we impose the bundary conditions

$$\begin{aligned}|\boldsymbol{B}|&\neq\infty &&\text{for}\quad \rho=0\\ B_\rho&=0 &&\text{for}\quad n\theta+\nu\kappa z=m\pi\ , \qquad m=0,1,2,\cdots\end{aligned} \tag{3.7}$$

to (3.6), ϕ becomes

$$\phi=e_3z+\sum_{\nu=1}^{\infty}\sum_{n=0}^{\infty}A_{n\nu}I_n(\nu\kappa\rho)\sin(n\theta+\nu\kappa z)\ . \tag{3.8}$$

Substituting (3.8) into Eq. (3.2) we have

$$B_\rho=\kappa\sum_{\nu=1}^{\infty}\sum_{n=0}^{\infty}\nu A_{n\nu}I_n'(\nu\kappa\rho)\sin(n\theta+\nu\kappa z)\ , \tag{3.9}$$

$$B_\theta=\frac{1}{\rho}\sum_{\nu=1}^{\infty}\sum_{n=0}^{\infty}nA_{n\nu}I_n(\nu\kappa\rho)\cos(n\theta+\nu\kappa z)\ , \tag{3.10}$$

$$B_z=e+\kappa\sum_{\nu=1}^{\infty}\sum_{n=0}^{\infty}\nu A_{n\nu}I_n(\nu\kappa\rho)\cos(n\theta+\nu\kappa z)\ , \tag{3.11}$$

and the magnetic lines of force are obtained by solving the following differential equation:

$$\frac{d\rho}{B_\rho}=\frac{\rho d\theta}{B_\theta}=\frac{dz}{B_z}\ , \tag{3.12}$$

§ 4. Equations for the Heliotron B Magnetic Field

Putting

$$n=0\,, \tag{4.1}$$

in (3.9)~(3.11), we have the expression for the axisymmetrical magnetic field of the Heliotron B type as follows:

$$\left.\begin{aligned} B_\rho&=\kappa\sum_{\nu=1}^{\infty}\nu A_{0\nu}I_1(\nu\kappa\rho)\sin(\nu\kappa z)\,,\\ B_\theta&=0\,,\\ B_z&=e_3+\kappa\sum_{\nu=1}^{\infty}\nu A_{0\nu}I_0(\nu\kappa\rho)\cos(\nu\kappa z)\,, \end{aligned}\right\} \tag{4.2}$$

The magnetic field given by (4.2) approximately expresses the situation in the region inside the curve AMB of Fig. 2.5. Putting, as a simplest case,

$$\nu=1 \tag{4.3}$$

in (4.2), we have

$$\left.\begin{aligned} B_\rho&=\kappa A_{01}I_1(\kappa\rho)\sin\kappa z\,,\\ B_z&=e_3+\kappa A_{01}I_0(\kappa\rho)\cos\kappa z\,. \end{aligned}\right\} \tag{4.4}$$

Expression (4.4) can also be derived from the vector potential given by Lüst and Schlüter²⁾.

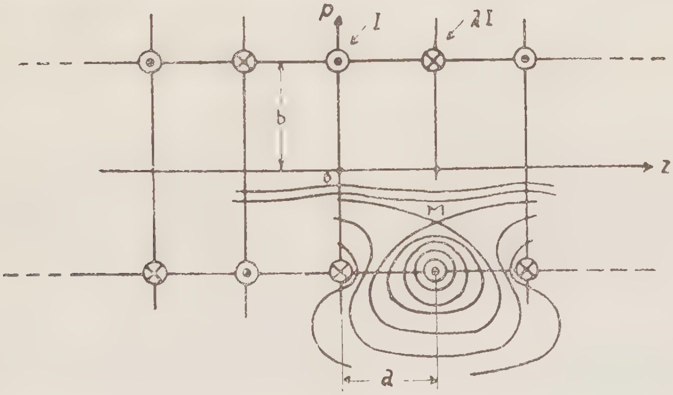

Fig. 4.1.

Now we take (4.4) as an approximate expression of the Heliotron B magnetic field. First we have to determine the integration constants κ, e_3, A_{01}. The assumption that the field is periodic in the z direction gives (see Fig. 4.1)

$$\kappa=\pi/a\,. \tag{4.5}$$

Putting

$$\alpha=(\pi/a)z\,,\qquad \beta=(\pi/a)\rho\,, \tag{4.6}$$

(4.4) becomes

$$\left.\begin{aligned} B_\rho&=\kappa A_{01}I_1(\beta)\sin\alpha\,,\\ B_z&=e_3+\kappa A_{01}I_0(\beta)\cos\alpha\,. \end{aligned}\right\} \tag{4.7}$$

In order to determine constants A_{01} and e_3, we have to calculate the intensity of the magnetic field along the axis of the colis as shown in Fig. 4.1. Coils have the radius b in common and their centres are located on the z axis with equal interval a. The electric currents in these coils are I and $-\lambda I$ alternately.

The magnetic flux density along the axis due to a single coil placed at the origin is

$$B_{0z}=(\mu_0 b^2 I/2)(b^2+z^2)^{3/2}\ .$$

Therefore the flux density along the axis due to all coils is given by

$$B_{0z}=\frac{\mu_0 b^2 I}{2}\sum_{\nu=-\infty}^{\infty}[\{b^2+(z-2\nu a)^2\}^{-3/2}-\lambda\{b^2+(z-\overline{2\nu+1}\,a)^2\}^{-3/2}]\ . \tag{4.8}$$

Let the flux density at the origin (0, 0) and the point (0, a), B_{00} and B_{0z} respectively, they are given by

$$\left.\begin{aligned} B_{00}&=\{\mu_0 b^2 I/(2a^3)\}(S_1-\lambda S_2)\ ,\\ B_{0}&=\{\mu_0 b^2 I/(2a^3)\}(S_2-\lambda S_1)\ , \end{aligned}\right\} \tag{4.9}$$

where

$$\left.\begin{aligned} S_1&=\frac{a^3}{b^3}\left\{1+\frac{b^3}{4a^3}\frac{1}{\sqrt{(1+b^2/4a^2)^3}}+\frac{b^3}{a^3}\left(0.0505-0.0035\frac{b^2}{a^2}+\cdots\right)\right\}\ ,\\ S_2&=\frac{2}{\sqrt{(1+b^2/a^2)^3}}+\left(0.1036-0.0107\frac{b^2}{a^2}+\cdots\right)\ . \end{aligned}\right\} \tag{4.10}$$

B_{00} and B_{0a} are determined by (4.9) and (4.10) if the aspect ratio of the coils a/b and the current ratio λ are given. From (4.7) we have

$$e_3=\frac{1}{2}(B_{00}+B_{0a})=\frac{\mu_0 b^2 I}{4a^3}(S_1+S_2)(1-\lambda)\ , \tag{4.11}$$

$$B_e=\kappa A_{01}=\frac{1}{2}(B_{00}-B_{0a})=\frac{\mu_0 b^2 I}{4a^3}(S_1-S_2)(1+\lambda)\ . \tag{4.12}$$

Denoting the coordinates of the equilibrium point M by $[\rho_e, (2n+1)a]$ in the (ρ, z) coordinate or $[\beta_e, (2n+1)\pi]$ in the (β, α) coordinate, we have, from (4.7),

$$e_0=I_0(\beta_e)=\frac{e_3}{\kappa A_{01}}=\frac{1-\lambda}{1+\lambda}\frac{S_1+S_2}{S_1-S_2}\ . \tag{4.13}$$

The position of the equilibrium point is also dependent upon a/b and λ. Substituting (4.12) and (4.13) into (4.7) we have

$$\left.\begin{aligned} B_\rho&=B_e I_1(\beta)\sin\alpha\ ,\\ B_z&=B_e\{I_0(\beta_e)+I_0(\beta)\cos\alpha\}\ . \end{aligned}\right\} \tag{4.14}$$

Again substituting (4.14) into Eq. (3.12), we obtain

$$\frac{d\rho}{dz}=\frac{d\beta}{d\alpha}=\frac{I_1(\beta)\sin\alpha}{I_0(\beta_e)+I_0(\beta)\cos\alpha}\ . \tag{4.15}$$

Integrating (4.15), we obtain the following equation for the line of force:

$$\cos\alpha=\frac{I_0(\beta_e)}{2I_1(\beta)}\beta\left(\frac{\beta_0^2}{\beta^2}-1\right)\ , \tag{4.16}$$

where β_0 is the parameter which designates the line of force. For the lines of force inside the equilibrium point M, β_0 of a line of force equal to the value of β on the lines of force at $\alpha=\pi/2$. The field represented by (4.14) and (4.16) is shown graphically in Fig. 4.2. But the solution given by (4.16) does not represent the true situation near the coil. In order to obtain better approximation we must compute the line of force using the complete expression (4.2). If λ tends to S_2/S_1 it may be seen from (4.13) that β_e becomes 0, that is, the equilibrium points come to the axis as shown in Fig. 4.3. Further increasing the value of λ we find that there appear two equilibrium points on the axis in one period (see Fig. 4.4). Finally for $\lambda=1$ the equilibrium points coinside with the points $[0, (n+1/2)\pi]$ on the axis (Fig. 4.5), and the magnetic field becomes the Picket Fence field. Figs. 4.3∼4.5 have been drawn using (A.4).

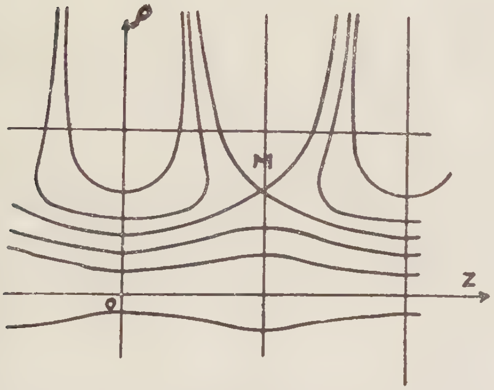

Fig. 4.2.

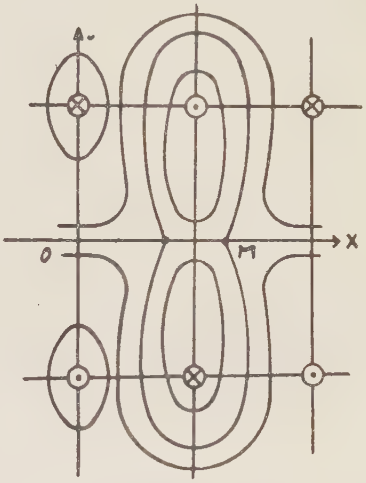

Fig. 4.4.

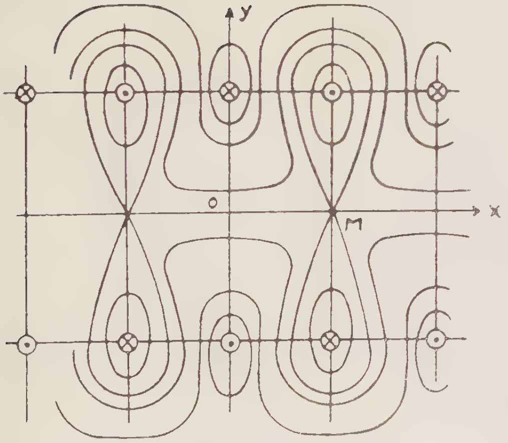

Fig. 4.3.

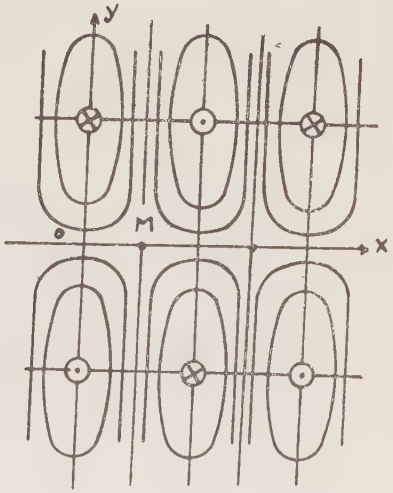

Fig. 4.5.

§ 5. Cylindrical Cusp Field

The magnetic fields given by (3.9)∼(3.11) include the cylindrical cusp fields as a special case. If we put, in (3.9)∼(3.11),

$$\left.\begin{array}{l}\nu=1\,,\\ \kappa z\to 0\,,\end{array}\right\} \qquad (5.1)$$

and expand the modified Bessel functions, we have the following expression:

$$\left.\begin{aligned} B_\rho &= \sum_{n=1}^{\infty} \frac{\kappa^n A_{n1}}{2^n(n-1)!}\rho^{n-1}\sin n\theta\,, \\ B_\theta &= \sum_{n=1}^{\infty} \frac{\kappa^n A_{n1}}{2^n(n-1)!}\rho^{n-1}\cos n\theta\,, \\ B_z &= e_3 + \sum_{n=1}^{\infty} \kappa\rho \frac{\kappa^n A_{n1}}{2^n(n-1)!}\rho^{n-1}\cos n\theta\,. \end{aligned}\right\} \tag{5.2}$$

The limit $\kappa z \to 0$ means that the period of the field in the z direction tends to infinite and in this case $\kappa\rho \to 0$. We have to ignore the term $n=0$, since this gives $B_\theta = B_\rho = 0$. For simplicity, let us take the term $n=m$ alone:

$$\left.\begin{aligned} B_\rho &= c_m \rho^{m-1}\sin m\theta\,, \\ B_\theta &= c_m \rho^{m-1}\cos m\theta\,, \\ B_z &= e_3\,, \end{aligned}\right\} \tag{5.3}$$

where

$$c_m = \kappa^m A_{m1}/\{2^m(m-1)!\}\,. \tag{5.4}$$

In (5.3) we neglected the second term of B_z as $\kappa\rho$ is assumed to be small. From (3.12) it will be seen that the projection of the line of force (5.3) to a plane perpendicular to the tube axis is represented by

$$\rho^m = \rho_0{}^m \left| \frac{1}{\cos m\theta} \right|, \tag{5.5}$$

where ρ_0 is the value of ρ at $\theta=0$.

Fig. 5.1 shows the magnetic fields in the neighbourhood of the tube axis, which are given by putting $m=1$, $m=2$ and $m=3$ in (5.3) and (5.5). The magnetic fields given by (5.3) are made by superposing a constant magnetic field in the z direction upon the field which is produced by the linear currents put on the tube wall parallel to the tube axis. The flux density of the fields takes the minimum value e_3 on the axis.

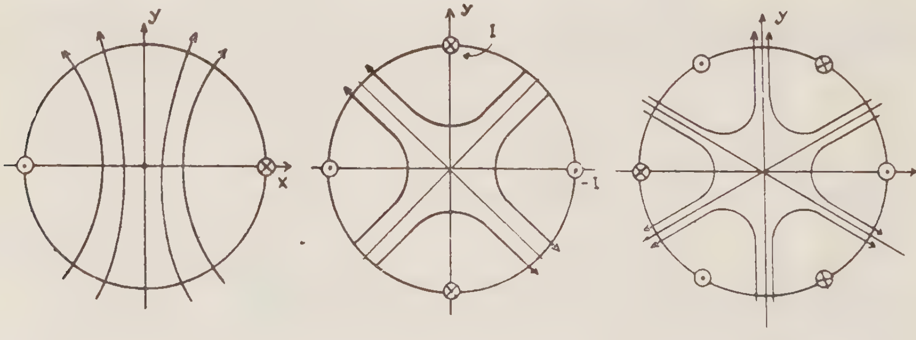

$m=1$
(a)

$m=2$
(b)

$m=3$
(c)

Fig. 5.1.

Further it may be noted that the intensity of the magnetic field decreases towards the axis and thus this part of the field appears to be a sort of magnetic bottle. However Fig. 5.1 shows that the lines of force of the field cross the tube wall, and therefore the dilute plasma, in which particles move along the lines of force, cannot be confined within this bottle. Only exceptional case $e_3=0$ may be the one in which case the dense plasma can be confined in this bottle.

§ 6. The Heliotron H Magnetic Field (Helical Heliotron)

For $n \neq 0$, (3.9)~(3.11) give the magnetic field produced by making the coils of the Heliotron

B (Fig. 2.4) helically around the tube as shown in Fig. 6.1. This field gives a transitional type from the Heliotron B field to the cylindrical cusp field, and it may be hoped to have the merits of both types of the field. Putting $\nu=1$ and $n=m$ in (3.9)~(3.11), we have

$$\left.\begin{aligned} B_\rho&=\kappa A_{m1} I_m'(\beta)\sin u\,,\\ B_\theta&=\kappa A_{m1}\frac{m}{\beta}\,I_m(\beta)\cos u\,,\\ B_z&=e_3+\kappa A_{m1} I_m(\beta)\cos u\,,\end{aligned}\right\}\tag{6.1}$$

where

$$u=n\theta+\alpha\,.\tag{6.2}$$

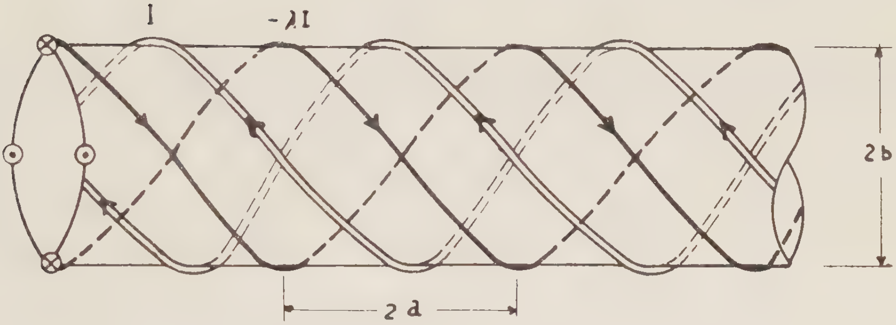

Fig. 6.1.

Assuming that

$$\left.\begin{aligned} &B_z=0 \quad \text{for}\quad \beta=\beta_e \text{ and } u=\pi,\\ &B_z=B_0 \quad \text{for}\quad u=\pi/2,\end{aligned}\right\}\tag{6.3}$$

we have

$$e_3=B_0\,,\qquad \kappa A_{m1}=B_0/\{I_m(\beta_e)\}\,.\tag{6.4}$$

Substituting (6.4) into (6.1) we obtain

$$\left.\begin{aligned} B_\rho&=B_0\{I_m'(\beta)/I_m(\beta_e)\}\sin u\,,\\ B_\theta&=(m/\beta)\{I_m(\beta)/I_m(\beta_e)\}\cos u\,,\\ B_z&=B_0\left\{1+\frac{I_m(\beta)}{I_m(\beta_e)}\cos u\right\}.\end{aligned}\right\}\tag{6.5}$$

The field given by (6.5) is produced by m pairs helical winding. From (3.12) we have

$$\frac{d\beta}{du}=\frac{\beta B_\rho}{mB_\theta+\beta B_z}\,.\tag{6.6}$$

Substituting (6.5) into (6.6) we obtain

$$\left\{\beta+\left(\frac{m^2}{\beta}+\beta\right)\frac{I_m(\beta)}{I_m(\beta_e)}\cos u\right\}d\beta-\beta\,\frac{I_m'(\beta)}{I_m(\beta)}\sin u du=0\,.\tag{6.7}$$

Equation (6.7) becomes a total differential equation by multiplying an integrating factor, and its solution is given by

$$\frac{\beta^2}{2}+\beta\frac{I_m'(\beta)}{I_m(\beta_e)}\cos u=c'\,,\tag{6.8}$$

where c' is a constant. If we assume that, along the line of force,

$$\beta=\beta_0 \qquad \text{for} \quad u=\pi/2\,, \tag{6.9}$$

we obtain the expression for the magnetic line of force

$$\cos u=\frac{I_m(\beta_e)}{2I_m'(\beta)}\beta\left(\frac{\beta_0{}^2}{\beta^2}-1\right). \tag{6.10}$$

From (6.10) we can see that β is a function of $\cos u$ alone. This means that the lines of force inside the point $[\beta=\beta_e,\ u=\pi]$ undulate in the band

$$\beta_{\min}\leq\beta\leq\beta_{\max}\,. \tag{6.11}$$

Therefore, if we take the field which satisfies the condition

$$\beta_e<(\pi/a)\times(\text{inner tube radius})\,, \tag{6.12}$$

the lines of force inside the equilibrium point do not cross the tube wall. An exact expression for the field produced by m pairs helical winding is given by

$$\left.\begin{aligned} B_\rho&=\kappa\sum_{s=1}^{\infty}c_nI_n'(\beta)\sin u_n\,,\\ B_\theta&=\frac{\kappa}{\beta}\sum_{s=1}^{\infty}nc_nI_n(\beta)\cos u_n\,,\\ B_z&=e_3+\kappa\sum_{s=1}^{\infty}c_nI_n(\beta)\cos u_n\,,\end{aligned}\right\} \tag{6.13}$$

where

$$n=ms\,, \qquad u_n=ms\theta+\alpha\,. \tag{6.14}$$

If we put $m=0$ in (6.10) it reduces to (4.16).

§ 7. Equilibrium of the Plasma in the Heriotron Field

Under the magnetohydrodynamical approximation the equilibrium condition of the plasma is given by

$$\nabla p=\boldsymbol{j}\times\boldsymbol{B}\,, \tag{7.1}$$

where the gravitational force is neglected. Equation (7.1) shows that the isobaric surfaces

$$p=\text{const}\,, \tag{7.2}$$

are weaved by the lines of current and magnetic lines of force. We define a function U by the integral along the line of force

$$U=-\int\frac{dl}{B}\,, \tag{7.3}$$

where integration is carried out over one period of the line of force. We see that the isobaric surfaces coinside with the surfaces of constant U. However, assuming ϕ to be constant we have the relation

$$-U=\int\frac{dl}{B}=\frac{1}{\phi}\int dSdl=\frac{1}{\phi}V\,, \tag{7.4}$$

where dS is the sectional area of the infinitesimal flux tube and V is its volume involved in one period. Thus $-U$ is found to be proportional to the volume of the flux tube, and we can conclude that the isobaric surfaces coincide with the magnetic surfaces weaved by the lines of force along which the volume of the flux tube is constant[3].

Besides, in order to make the magnetic surfaces coinside with the equilibrium surfaces so as to confine the plasma, it is required that the isobaric surfaces be toroidal and, for practical use, be inside the toroidal discharge tube and not cross the tube wall. For example, in the case of the field produced by coils wound uniformly around a circular toroidal tube such as Zeta, the magnetic flux density B is inversely proportional to R, the distance of the line of force from the toroidal center. Then the constant U surfaces are given by

$$R=\text{const.} \tag{7.5}$$

The surfaces are coaxial cylinders with the axis which coinside with the toroidal axis, and they are not toroidal. Therefore, these surfaces cannot be the equilibrium surfaces. Physically, in this case, the plasma current flows in the direction of the troidal axis and produces the charge separation which destroys the plasma confinement.

On the other hand, in the case of the undulated field, U takes different values at different distances from the tube axis. When the tube is a straight cylinder, the constant U surfaces become coaxial cylinders whose axis coincides with the tube axis. In the case of the troidal undulated field, the surfaces become toroidal and their axes are different from the tube axis as shown in Fig. 7.1(a). In this case, the cross-sectional area of the constant U surfaces, which do not cross the troidal tube wall, becomes very small unless one makes the the troidal radius sufficiently large compared with the tube radius or the amplitude of the undulation of the line of force sufficiently large.

The Heliotron B field, has the equilibrium points distributed periodically inside the wall. Since the flux density B becomes 0 at these points we can make U as large as we wish in the vicinity of the points. In Fig. 7.1(b), the thick solid line represent the boundary of the cross section of the magnetic surface weaved by the constant U lines of force passing through the equilibrium points. In the Heliotron B field therefore, all the constant U surfaces are located inside the solid line and make toroidal surfaces. Since it is easy to have the equilibrium points inside the tube wall, it may be said that the Heliotron field essentially satisfies the necessary condition for the equilibrium.

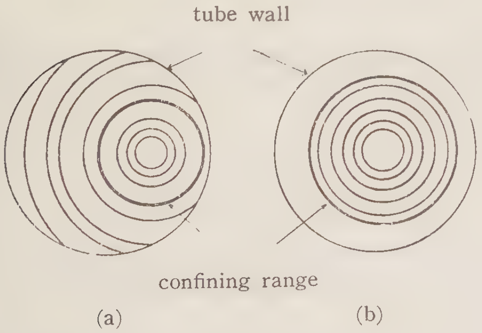

Fig. 7.1.

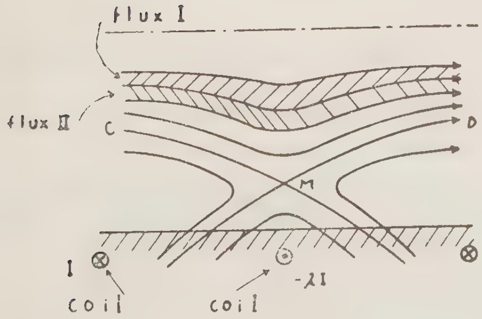

Fig. 8.1.

§ 8. Interchange Instability of the Plasma in the Heliotron B Field

Let us consider the interchange instability[4)] of the plasma confined in the Heliotron B field shown in Fig. 8.1 from the particle-dynamical point of view. In Fig. 8.1 M is an equilibrium point of the magnetic field. The change in plasma energy $\varDelta E_p$, which is caused by the interchange of the plasma contained in flux tube I with that in II of equal magnetic flux, is given by

$$\varDelta E_p = -\delta N_0 \delta w_0 , \tag{8.1}$$

with

$$\delta N_0 = N_{02} - N_{01} , \tag{8.2}$$

$$\delta w_0 = \iint \delta w(\mu, w) f(\mu, w)\, d\mu dw , \tag{8.3}$$

where N_{01} and N_{02} are number of particles contained in flux tube I and II respectively, $\delta w(\mu, w)$ is the change in energy of a single particle which has magnetic moment μ and total energy w, and $f(\mu, w)$ is the distribution function. The condition for stability is expressed by $\varDelta E_p > 0$. If $\delta w_0 > 0$ the plasma is stable for interchange instability from the orbit theory[4)], and we discuss the case $\delta w_0 < 0$. In this case plasma cannot be stable except for the case $\delta N_0 > 0$. Now,

$$N_0 = n_0 V = n_0 k_0 \int \frac{dl}{B} , \tag{8.4}$$

where n_0 denotes the average density of the plasma in the flux tube of volume V, and k_0 is a positive constant. The condition $\delta N_0 > 0$ is reduced to

$$\delta \int \frac{dl}{B} \Big/ \int \frac{dl}{B} > -\delta n_0 / n_0 . \tag{8.5}$$

The average density n_0 must be zero on the line of force CMD which forms the plasma boundary, and $\delta \int \frac{dl}{B}$ is positive inside CMD in the Heliotron B field. In order to examine the condition (8.5), we expand (4.14) and (4.16) putting

$$\left.\begin{aligned}\alpha&=\pi+\xi\,, && (\xi/\pi)^2\ll 1,\\ \beta&=\beta_e-\eta\,, && (\eta/\beta_e)^2\ll 1,\end{aligned}\right\} \tag{8.6}$$

and we have

$$B_z=a_0(e_0+e_1\sqrt{\xi^2+u^2}+e_2\xi^2)\,, \tag{8.7}$$

where a_0 is a constant and e_0, e_1, e_2 and u are functions of β_0. We put

$$Q=\int\frac{dl}{B}=k\int_0^{\pi}\frac{d\alpha}{B_z}=Q_0+Q_1\,, \tag{8.8}$$

where

$$Q_0=k\int_0^{\tau}\frac{d\xi}{B_z}\,,\qquad Q_1=k\int_0^{\pi-\tau}\frac{d\alpha}{B_z}\,, \tag{8.9}$$

and τ is a small positive constant which satisfies $(\tau/\pi)^2\ll 0$. In the vicinity of CMD we find that Q_0 is very large and Q_1 a constant value Q_{10}. Denote the value of β_0 on the line CMD by β_{0e}, then if β_0 approaches to β_{0e} we find that (see Appendix III)

$$Q\approx Q_c+\log\frac{1}{\sqrt{\beta_{0e}^2-\beta_0^2}}\,,\qquad Q_c=\text{const} \tag{8.10}$$

and that the condition (8.5) is reduced to

$$\frac{1}{n_0}\frac{\partial n_0}{\partial\beta_0}>-\frac{\beta_0}{\beta_{0e}^2-\beta_0^2}\Big/\left\{Q_c+\log\frac{1}{\sqrt{\beta_{0e}^2-\beta_0^2}}\right\}. \tag{8.11}$$

If n_0 is expressed by

$$n_0=n_{01}=k_0\Big/\left\{Q_c+\log\frac{1}{\sqrt{\beta_{0e}^2-\beta_0^2}}\right\}^m,\qquad k_0>0 \tag{8.12}$$

The stability condition becomes

$$1>m>0\,. \tag{8.13}$$

If the average density distribution satisfies the condition (8.11) the plasma is stable for interchange instability. But if the effect of diffusion gives finite gradient of n_0 in the vicinity of CMD, the stability condition will not be satisfied and the interchange instability will occur. When the plasma temperature becomes sufficiently high the effect of diffusion becomes weaker, and we may expect that the rate of growth of instability is also very small. These questions must be clarified through the future experiments by the Heliotron B.

The author wishes to acknowledge to Professor S. Hayashi for his continual encouragement and to Professor C. Hayashi for his helpful advices. He is also grateful to Professor T. Kihara, Mr. Y. Terashima and Mr. S. Hamada for their valuable discussions.

Appendix I

In order to investigate the qualitative feature of the axisynmmetric Heliotron field, first we approximate a part of the torus tube by a straight tube and then replace the magnetic field in the straight tube produced by the series of coil pairs (see Fig. 2.1) by the field produced by infinite rows of straight currents (see Fig. A.1). The vector potential of the magnetic field produced by these currents is given by

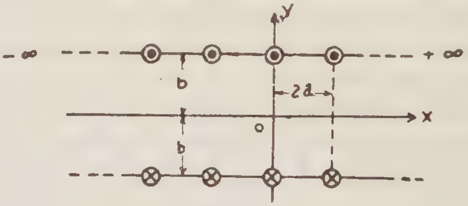

Fig. A.1.

$$\left.\begin{aligned}A_{x0}&=A_{y0}=0\,,\\ A_{z0}&=\frac{\mu_0 I}{4\pi}\sum_{\nu=-\infty}^{\infty}\log\frac{(x+2\nu a)^2+(y+b)^2}{(x+2\nu a)^2+(y-b)^2}\\ &=\frac{\mu_0 I}{4\pi}\log\frac{\cosh(\pi/a)(y+b)-\cos(\pi/a)x}{\cosh(\pi/a)(y-b)-\cos(\pi/a)x}.\end{aligned}\right\} \tag{A.1}$$

The equation of line of force is expressed by

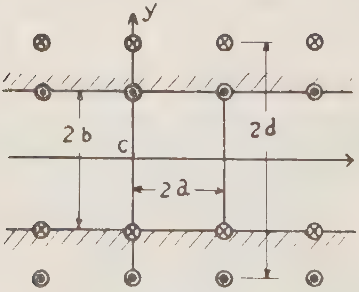

Fig. A.2.

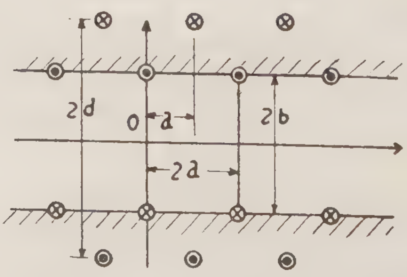

Fig. A.3.

$$\cos\frac{\pi}{a}=\cosh\frac{\pi}{a}b\cosh\frac{\pi}{a}y-\coth\zeta\sinh\frac{\pi}{a}b\sinh\frac{\pi}{a}y\,, \tag{A.2}$$

where ζ is a parameter which designates the line of force. Using Eq. (A.2) we can draw Fig. 2.2 as the qualitative skech of the magnetic field made by the double coil series as shown in Fig. 2.1. In similar way we can calculate the vector potential of the double current rows as shown in Figs. A.2 and A.3 respectively:

$$A_x=A_y=0\,,\quad A_z=\frac{\mu_0 I}{4\pi}\log\frac{\{\cosh(\pi/a)(y+b)-\cos(\pi/a)x\}\{\cosh(\pi/a)(y-d)-\cos(\pi/a)x\}^{\lambda}}{\{\cosh(\pi/a)(y-b)-\cos(\pi/a)x\}\{\cosh(\pi/a)(y+d)-\cos(\pi/a)x\}^{\lambda}}\,, \tag{A.3}$$

$$A_x=A_y=0\,,\quad A_z=\frac{\mu_0 I}{4\pi}\log\frac{\{\cosh(\pi/a)(y+b)-\cos(\pi/a)x\}\{\cosh(\pi/a)(y-d)+\cos(\pi/a)x\}^{\lambda}}{\{\cosh(\pi/a)(y-b)-\cos(\pi/a)x\}\{\cosh(\pi/a)(y+d)+\cos(\pi/a)x\}^{\lambda}}\,, \tag{A.4}$$

These magnetic fields are shown graphically in Figs. 2.5 and 2.6.

Appendix II

Since $S(z)$ in (3.5) is a periodic function of z, we have

$$S(z)=\sum_{\nu=1}^{\infty}S_\nu=\sum_{\nu=1}^{\infty}\{c_\nu\cos(\nu\kappa z)+d_\nu\sin(\nu\kappa z)\}\,, \tag{A.5}$$

where κ, c_ν, d_ν are constants. Substituting (3.5) and (A.5) into (3.4) we have

$$\sum_{\nu=1}^{\infty}\left\{G\cdot S_\nu\left(\frac{\partial^2 F}{\partial\rho^2}+\frac{1}{\rho}\frac{\partial F}{\partial\rho}-\nu^2\kappa^2 F\right)+\frac{F\cdot S_\nu}{\rho^2}\frac{\partial^2 G}{\partial\theta^2}\right\}=0\,. \tag{A.6}$$

Since the above equation must be satisfied for arbitrary values of z, we have the following relation

$$\frac{\rho^2}{F}\left(\frac{\partial^2 F}{\partial\rho^2}+\frac{1}{\rho}\frac{\partial F}{\partial\rho^2}-\nu\kappa^2 F\right)=-\frac{1}{G}\frac{\partial^2 G}{\partial\theta^2}\,, \tag{A.7}$$

The left-hand side of the above equation is a function of ρ alone and the right-hand side θ alone, and therefore both sides must be a constant, n^2 say. Thus we obtain the following two equations:

$$\frac{\partial^2 F}{\partial\rho^2}+\frac{1}{\rho}\frac{\partial F}{\partial\rho}-\left(\frac{n^2}{\rho^2}+\nu^2\kappa^2\right)F=0\,, \tag{A.8}$$

$$\frac{\partial^2 G}{\partial\theta^2}+n^2 G=0\,. \tag{A.9}$$

In n is a positive integer, the general solution of Eq. (A.8) is expressed by

$$F(\rho)=\sum_{n=0}^{\infty}\{A_n I_n(\nu\kappa\rho)+B_n K_n(\nu\kappa\rho)\}\,, \tag{A.10}$$

and that of Eq. (A.9) is given by

$$G(\theta)=\sum_{n=0}^{\infty}(P_n\cos n\theta+Q_n\sin n\theta)\,. \tag{A.11}$$

Substituting (A.5), (A.10) and (A.11) into (3.5) and adding simple particular solutions of Eq. (3.4), we obtain the solution (3.6).

Appendix III

Substituting (8.6) into (4.14) and expanding it we obtain

$$B_2=a_0\left(a_1\eta-a_2\eta^2+\frac{1}{2}\xi^2+\cdots\right) \tag{A.12}$$

where

$$\left.\begin{array}{l} a_0=B_eI_0(\beta_e)\ , \qquad a_1=I_1(\beta_e)/I_0(\beta_e)\ , \\ a_2=(1/2)(1-a_1/\beta_e)\ . \end{array}\right\} \tag{A.13}$$

As the same way, from Eq. (4.16) we have

$$\frac{\xi^2}{u^2}-\frac{(\eta-p)^2}{v^2}=-1\ , \tag{A.14}$$

where

$$\left.\begin{array}{l} p=g_1\zeta/(1-g_2\zeta)\ , \\ u^2=2g_0\zeta\left\{1+\dfrac{g_1{}^2}{2g_0(1-g_2\zeta)}\zeta+\dfrac{g_1{}^2}{2(1-g_2\zeta)}\zeta^2\right\}, \\ v^2=u^2/\{(1-g_2\zeta)(1+g_0\zeta)\}\ , \end{array}\right\} \tag{A.15}$$

$$\left.\begin{array}{l} g_0=1/(2a_1\beta_e)\ , \\ g_1=1\Big/\left\{(2a_1{}^2\beta_e)\left(1+\dfrac{1}{2a_1\beta_e}\zeta\right)\right\}, \\ g_2=\left(1-\dfrac{a_1}{2\beta_e}\right)\Big/\left\{a_1{}^3\beta_e\left(1+\dfrac{1}{2a_1\beta_e}\zeta\right)\right\}, \end{array}\right\} \tag{A.16}$$

and

$$\zeta=\beta_{0e}^2-\beta_0{}^2\ . \tag{A.17}$$

β_{0e} is the value of β_0 of the line of force passing through the equilibrium point. Eliminating η in (A.12) by using (A.14), we have (8.7), and where

$$\left.\begin{array}{l} e_0=p(a_1-a_2p)-a_2v^2\ , \\ e_1=(v/u)(a_1-2a_2p)\ , \\ e_2=(1/2)-a_2v^2/u^2\ . \end{array}\right\} \tag{A.18}$$

Putting in (8.9)

$$x=\sqrt{\xi^2+u^2}\ , \qquad u_0=\sqrt{u^2+\tau^2}\ , \tag{A.19}$$

reduces to

$$Q_0=\frac{2}{a_0e_2\kappa}\int_0^{u_0}\frac{dx}{x^2+(e_1/e_2)x+(e_0/e_2-u^2)}\,\frac{1}{\sqrt{x^2-u^2}}dx\ . \tag{A.20}$$

Q_0 is expressed by

$$\left.\begin{array}{l} Q_0=\dfrac{2}{a_0e_2\kappa}\,\dfrac{1}{x_1-x_2}\,(Q_{01}-Q_{02})\ , \\ Q_{01}=\dfrac{x_1}{\sqrt{u^2-x_1{}^2}}\left\{\dfrac{\pi}{2}+\tan^{-1}\dfrac{x_1u_0-u^2}{\sqrt{(u^2-x_1{}^2)\tau^2}}\right\}, \\ Q_{02}=\dfrac{x_2}{\sqrt{x_2{}^2-u^2}}\log\left[\dfrac{(u-x_2)\{(x_2u_0-u^2)-\sqrt{(x_2{}^2-u^2)(u_0{}^2-u^2)}}{(u_0-x_2)(x_2-u)u}\right], \end{array}\right\} \tag{A.21}$$

where x_1 and x_2 are the roots of the following equation:

$$x^2+(e_1/e_2)x+(e_0/e_2-u^2)=0\ . \tag{A.22}$$

When ζ becomes very small, Q_0 is approximately expressed by (8.10).

References

1) Uo, K.: Kakuyūgō Kenkyū, **1** (1958) 12, **2** (1959) 247, **3** (1959) 679.
2) Lüst, R. and Schlüter, A.: Z. Naturforschg. **12** a (1957) 850.
3) Kadmtsev, B. B.: Plasma Physics and the Problem of Controled Thermonuclear Reactions IV (1957) 17.
4) Rosenbluth, M. N. and Longmire, C. L.: Annals of Physics, **1** (1957) 120.

JOURNAL OF THE PHYSICAL SOCIETY OF JAPAN, Vol. 16, No. 7, JULY, 1961

Microwave Study of Non-ionizing Shock Waves

By Susumu TAKEDA
Nagoya University, Nagoya, Japan
and Michel Roux
University of Illinois, Urbana, Illinois, U.S.A.

(Received February 16, 1961)

The interaction of microwave with gaseous plasmas is used to study weak shock waves in low pressure gases. In order to study by this method shock waves of low Mach number, which are incapable of ionizing the gaseous medium in which they propagate, this medium is weakly preionized.

In a tube of 5 mm in diameter, condenser discharges are fired for the production of shock waves up to 200 joules, in a pressure range of 4–13 mm Hg in Neon and Argon and with Mach number up to 5, and it is found that the measured electron density increase across the discontinuity is in the ratio of the gas density ratio. The electron temperature, deduced from the measured electron-ion collision frequency, is, as expected, lower than the gas temperature estimated from the Mach number.

§ 1. Introduction

It is now known that shock waves may be produced, particularly in gases at relatively low pressure, by strong electrical condenser discharges. Fowler[1] first found that a shock wave was produced in T-shaped gas tube, in which a pulse discharge was fired between internal electrodes. More recently, measurements have been performed on shock waves and many papers reported results on optically and spectroscopically studied shock waves. Trials[2], [3] by microwave techniques have also been reported to measure parameter associated with shocks. Schultz[3] noticed that it would be possible but difficult to determine by microwave techniques both the electron density and collision frequency in a plasma produced by an ionizing shock wave. On the other hand, since generally a microwave signal, is highly attenuated[4], when it propagates through plasmas produced in low pressure gas, in which the plasma frequency associated with the electron density reaches a critical value corresponding to the microwave frequency, the propagation method with such microwaves is restricted in its application.

The impedance of a small plasma volume can be measured at higher densities, provided a condition[5] is satisfied. If the method reported here satisfies this condition, the range of measurements can be extended to electron densities higher than the critical value. In this experiment the transient impedance of a small plasma post is measured by modification[6] of the standard microwave method. Since this impedance is related to the electron density and the collision frequencies, time resolved photographs of microwave standing wave amplitudes can yield both the electron density and collision frequency in a transient non-recurrent plasma. By using these techniques, shock waves produced by electrical discharges have been investigated.

The method requires a minimum detectable electron density. When strong shocks are studied, this is provided by the ionizing shock waves themselves. However in order to study weak, that is non-ionizing shocks, a plasma with the appropriate electron density has to be provided by auxiliary pre-ionization, as used by der Agobian[2].

§ 2. Experimental apparatus and procedures

The apparatus consists of a shock tube and a microwave circuit. The shock tube of 40 cm. in length and 0.5 cm. in diameter is placed across two waveguides as shown in Fig. 1, in which X-band low level microwave is propagated. These waveguides may be placed at any desirable distance from one another; they are connected through a directional coupler to the same microwave source. In order to increase the resolution, at least one of these waveguides is tapered to a flat section, as seen in the upper left corner of Fig. 1. The first waveguide is terminated with a movable short. The probe detectors 1 and 2 are located in this waveguide, as seen in the figure in each side of the shock tube. The fraction of the microwave energy taken from the first waveguide through a directional coupler, propagates in the second waveguide, and is detected there by the probe detector 3.

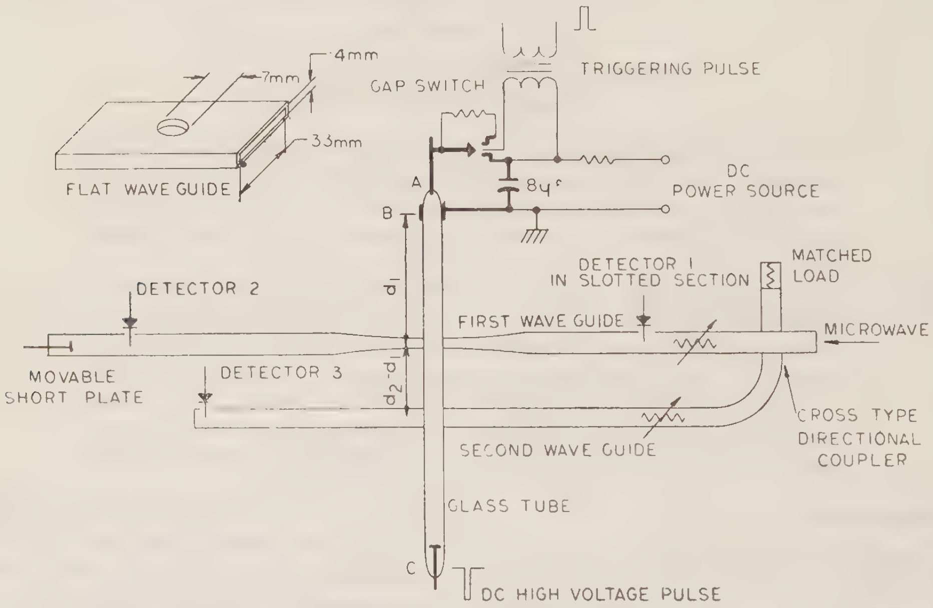

Fig. 1. Diagram of the experimental apparatus.

The shock waves are produced in the tube, filled with a gas at the desired pressure, by discharging between electrodes A and B an $8\,\mu$F condenser charged up to 7 KV. The ringing frequency of this circuit is 130 KC. The maximum stored energy and the discharge current are respectively 200 joules and 10^4 A. In order to reduce the ignition delay time, the condenser discharge path is very weakly ionized by a small DC current passing between the electrodes A and B through a high resistance shunting the gap switch. In order to provide the plasma in which the shock wave will propagate, a pulsed DC discharge pre-ionizes the gas between electrodes B and C. The shock wave is initiated in the course of the decay of this pre-ionization and timed in such a way as to reach the wave guide section at some easily detectable values of the electron density n and collision frequency ν in the decaying plasma. Probes 1 and 2 detect the time varying standing wave that is established in the first waveguide by the movable short, modulated by the decaying plasma and further altered by the passage of the shock wave in the waveguide. Their signals are displayed on a dual trace oscilloscope. From the time varying amplitude of each of these signals, the momentaneous impedance of the plasma post can be determined, which in turn yields the plasma parameters n and ν in the absence as well as in the presence of the shock wave.

The signals from detectors 3 and 1 or 2 yield the time interval for the shock wave to propagate from the first to the second waveguide and hence its local velocity. Since the discharge is non-recurrent, the displayed traces on the oscilloscope are recorded photographically for analysis. Concurrently with the microwave observation, a photomultiplier is used for the detection of any discontinuity in the visible light intensity which is produced by propagating shock waves in the plasma afterglow.

An evacuating system evacuates the tube down to pressure of 10^{-7} mm Hg. However an appreciable amount of impurities of metal vapor comes out of the electrodes during each condenser discharge. The effect of these impurities can be observed either directly by the change in color of the plasma column or by the shortened decay of the repeated disintegrating plasma. Running the recurrent pulsed discharge in the tube for a short time, however, it is observed that the plasma decay and the color soon recover to its original condition. Apparently most of the metallic impurities from the electrodes are thought to deposite on the electrodes and glass surfaces. Since it is inconvenient to replace the gas in the tube after each condenser discharge, several such discharges were shot in the same gas after the recovery of the above mentioned original conditions. The situation is improved by the use of activated charcoal maintained at low temperature in a side tube close to the electrodes A and B.

§ 3. Principles of the Measurements

The method is capable of yielding the velocity of shock waves in plasmas and the variation of background plasma parameters, n and ν as a result of shock wave propagation. The velocity of the propagating shock wave decreases as it proceeds along the tube. Hence one can speak about an average velocity over a length of propagation path and of a local or instantaneous velocity, if the path is short with respect to the total path. When the distance d covered by the shock wave in time t takes the form $d=t^{\beta}$, the local velocity $v_t=\beta\,(d/t)=\beta\times(\text{mean velocity})=\beta\bar{v}$. When the time for a wave to reach the distances d_1 and d_2 respectively are measured to be t_1 and t_2, β is determined from

$$\beta=\frac{\log d_2/d_1}{\log t_2/t_1}, \tag{1}$$

and $\bar{v}$ is proportional to $d^{(\beta-1)/\beta}$.

For the reason mentioned above, the initial conditions of the discharge can not be reproduced exactly. These are isolated (one shot transients repeated at a few seconds intervals. Hence the usual microwave techniques applicable to study the phenomena occurring regularly at high repetition rate are here inapplicable. In particular, the standard techniques to find the plasma impedance from the shift of the minimum position and the ratio of a standing wave produced in the waveguide by a recurrent plasma cannot be used here. Thus the modified method to measure the transient plasma impedance under the conditions of these experiments has been used.

The principle of the method is the two probe observation of an existing wave pattern modified by the changing parameters of a gaseous plasma post located in a certain position in the waveguide. To analyze the change in the standing wave pattern, these two probes, 1 and 2, are positioned on each side of the plasma post. The one in the input side of the post is placed at a minimum position of the standing wave pattern in the absence of the plasma. The other is placed preferably at a maximum of the standing wave pattern. The introduction of a plasma and change of its parameters shift the standing wave pattern. From the change in the signal amplitudes of probes 1 and 2, displaced simultaneously on the oscilloscope, the impedance of the plasma post is obtained. This impedance then yields the plasma parameters n and ν. The method, contrary to the other microwave propagation methods, is not strictly limited in measuring electron densities up to that value which corresponds to the plasma frequency, provided that the electron density along the tube axis is uniform. Although it is not strictly the case, in these experiments, in view of the small height of the plasma involved in the flat waveguide (4 mm.) this assumption appears to be approximately justified.

At this point, attention should be drawn to the following. The amplitude of the signal without plasma, at the minimum of the standing wave is 0.005 of the amplitude at the maximum of the standing wave. The existence of the detectable signal at the standing wave minimum is due to various losses in the microwave circuit. A large fraction of this loss is due to the energy leaking from the waveguide through the hole, accomodating the glass tube. The total microwave energy loss in the presence of the plasma obviously includes the energy radiated through the hole-increases and is a function of the plasma parameters n and ν. In view of the lack of precise knowledge of this enhanced radiated energy loss, which occurs for some large values of the electron density the method at present time is restricted in its application for values of the electron density smaller than this value. This fact also limits the range in which the electron collision frequency can be determined.

§ 4. Compressing and Heating Processes by Shock Waves

The ratio of the pressure p_2 and gas density ρ_2 behind the shock front to p_1 and ρ_1 in the undisturbed region before the shock front are known from the thermodynamical theory,[7]

$$p_2/p_1=\frac{2\gamma M^2-(\gamma-1)}{\gamma+1},$$

$$\rho_2/\rho_1=\frac{M^2(\gamma+1)}{M^2(\gamma-1)+2}. \qquad (2)$$

where M is the Mach number, or the ratio of the propagation velocity of the shock wave to the sound velocity in the undisturbed medium, and γ is the ratio of the specific heats. From the relation between gas temperature, pressure and density $T\sim p/\rho$, the ratio T_2/T_1 of the gas temperature behind and before the shock wave is written as

$$T_2/T_1=\left\{1+\frac{M^2(\gamma-1)}{2}\right\}\left\{\frac{4\gamma M^2-2(\gamma-1)}{M^2(\gamma+1)^2}\right\} \qquad (3)$$

The undisturbed region referred to above in this experiment is the decaying gaseous plasma. In view of its low degree of ionization and low ion temperature the medium is unaltered for sound wave propagation. Hence the above relation apply. When the medium which is the mixture of three gases, the electron, ion and neutral gases, is compressed by a propagating weak (non-ionizing) shock discontinuity, it may be assumed that any constituents of this mixture are compressed in the same ratio, that is $n_2/n_1\sim\rho_2/\rho_1$, where n_1 and n_2 refer to the electron density in the undisturbed plasma and behind the shock front respectively.*

This is so, if during the short time compression, the electron and ion losses are negligible. The theoretical value of the rare gas density and temperature ratio n_2/n_1 and T_2/T_1, where $\gamma=1.67$, are plotted as functions of the Mach No. M in Figs. 5 and 7.

It is well known that in electrical discharges in gases, the electron temperature T_e, is generally higher than the ion temperature T_i, which is nearly equal or somewhat higher than the gas temperature T_g. However, in an already weakly ionized gas, the passage of a weak shock wave heats the neutral atom and the ion gases more efficiently than the electrons. As a result,

$$T_e\leq T_g \text{ or } T_i \qquad (4)$$

The time rate of the electron temperature increase in this case is described by the following equation,

$$\frac{dT_e}{dt}=\frac{1}{\tau_{ei}}(T_i-T_e)+\frac{1}{\tau_{en}}(T_g-T_e)+K\nabla^2T_e \qquad (5)$$

The symbols τ_{ei} and τ_{en} represent respectively the characteristic times for equipartition of the temperature between ions and electrons and atoms and electrons, K is a coefficient due to thermal conduction. Then Eq. (5) and the relation $n_2/n_1\sim\rho_2/\rho_1$ show that when the plasma is heated by the shock wave, the electron density immediately follows the gas density increase, while the electron temperature reaches its maximum value with some delay.

§ 5. Experimental Results

At first the shock propagation velocity was measured by using the probes 2 and 3. The lower trace in Fig. 2 shows the signal from the first waveguide. There are two noticeable discontinuities in each trace: the first one, pointed by (a), is due to the shock wave, the second one (b) is thought to correspond to the plasma expanding from the condenser discharge region. Without pre-ionization, (a) disappears, because the relatively weak shock wave does not produce enough electrons to be detected by the microwave method described here. The discontinuity (b) in the microwave signals, resulting from the interaction of the wave with the electrons in the expanding plasma, which appear clealy even without any pre-ionization, decays rapidly over the distance from its origin; and so does its velocity.

---

* Strictly speaking, the ion gas density is first increased by the propagating shock in view of the large collision cross section for momentum transfer of the heavy particles involved, and then, as a consequence of the resulting space charge in the plasma, the increasing electron density follows in a time interval (during a few plasma oscillations), which is short with respect to the shock propagation time scale.

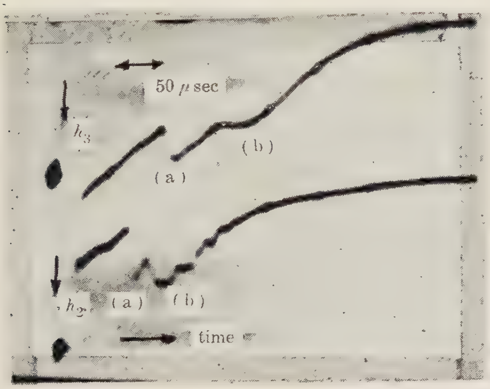

Fig. 2. Microwave signal amplitudes h_2 and h_3 versus time from the first and second waveguids, 50 μ sec/division, Ne, $p=5.8$ mm Hg, 5 K.V. 8 μF.

For the arrival time t_1 and t_2 of the peak (a) at the first and the second wave guide and for distances $d_1=23.5$ cm and $d_2=29.5$ cm, a value of the exponent β in Eq. (1) was found to be 0.47 ± 0.02 in Neon gas. The pressure and the condenser voltage ranged respectively between 4–13 mm Hg and 3–7 KV. The local shock velocity (Mach No.) at the level of the waveguide then can be easily calculated from the measured mean velocity (d_1/t_1) and β.

The plasma background for weak shock wave propagation studies by microwaves is also useful in another way. Indeed the decaying plasma gives rise to an afterglow which can be observed by means of a photomultiplier at any position along the tube, and in particular in the waveguide. In the course of the shock propagation in the plasma, the afterglow must also be altered. Hence optical observations on the afterglow, correlated with microwave measurements, provides an additional mean of investigation in these studies, as illustrated in Fig. 3. However, when the condenser discharge giving rise to the shock wave is produced between electrodes A and B in Fig. 1, a small discharge current is also flowing simultaneously between electrodes B and C. This stray current enhances the pre-ionization. The associated afterglow is shown in Fig. 3 (trace (II)). For very intense condenser discharge, the intensity of this visible enhanced afterglow may be such that the discontinuity in this light intensity, produced by the propagating weak shock wave illustrated by (a) in Fig. 3 is difficult to observe.

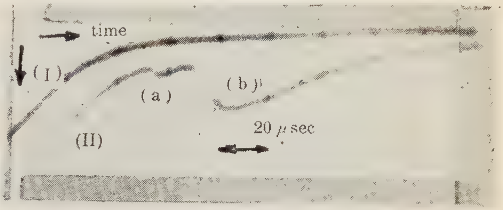

Fig. 3. Light signals versus time. (I): with pre-ionization; (II): with condenser discharge and pre-ionization. 20 μ sec/division, Ne, $p=4.5$ mm Hg, 5 K.V. 8 μF. Light intensity in arbitrary units.

The visible afterglow is generally attributed to recombination of electrons and positive ions in decaying plasmas. The discontinuity in the visible light of this afterglow, at any one time and space position in the shock tube, may provably be attributed to the alteration of the recombination procedure by the weak shock discontinuity. It is known that the light intensity of recombination, which is proportional to the number densities of the recombining charge and the recombination coefficient is dependent upon the relative velocities (temperatures) of these charges. Hence a sudden variation either in the densities of the recombining charges and or in their temperature should bring about a change in the visible light intensity. However, the effects on the light intensity of the change in densities are opposite to those of the change in temperatures, because the recombination coefficient decreases with increasing temperatures. As a result of these compensating effects, the discontinuity in the visible afterglow, due to shock waves, may be small. The enhanced visible intensity in the afterglow, indicated by (b) in Fig. 3, is again thought to be related to the expanding plasma following the shock discontinuity. The light signals (a) and (b) in this figure, obtained from the first waveguide, correspond to the microwave signals (a) and (b) in Fig. 2, observed in this same wave guide.

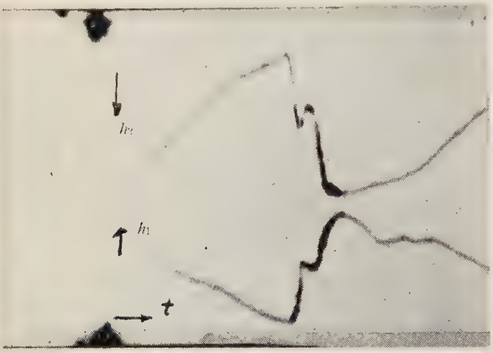

(A): Ne, p=4.1 mm Hg, 4.3 K.V. 8 μF

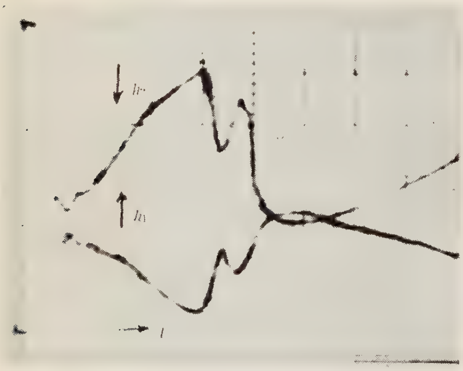

(B): Ne, p=7.6 mm Hg, 4.5 K.V. 8 μF.

Fig. 4. Microwave Signal amplitudes h_1 and h_2 versus time in the shock wave experiments, 20 μ sec/division, 8 μF

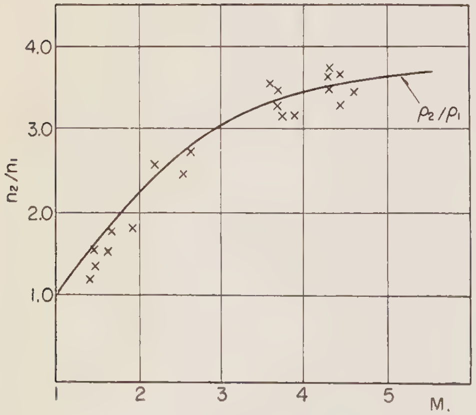

Fig. 5. Comparison between the gas density ratio ρ_2/ρ_1 calculated from the Mach no., and the measured electron density ratio n_2/n_1. Ne, p= 4~13 mm Hg.

Next, the electron density n_2 and n_1 across the shock front was calculated from the photographically recorded traces of the two microwave signals detected by the two probes 1 and 2. Figs. 4 (A) and (B) show examples of two signal h_1 and h_2. The ratio of the electron densities n_2/n_1 is calculated and plotted versus Mach No. in Fig. 5 (crosses). For comparision, the theoretically predicted ratio of gas density ρ_2/ρ_1 as a function of Mach No. is also shown in the figure (solid line). It is apparent that the variation of the ratio of electron densities across the shock discontinuity as a function of shock velocity follows quite closely that of the gas densities. It appears therefore reasonable to assume that the electron density increase, due to weak shock wave propagating in such plasmas, is a consequence of the compression of the weakly ionized gas. The possible discrepancy in the range of small Mach No. (1~2) is likely due to the duration of the compression, which is then comparable to (or longer than) the characteristic time for recombination and/or diffusion losses of electrons. In the plasma considered, since the electron-atom collision frequence ν_{en} for momentum transfer is negligibly smaller than the electron-ion collision frequency ν_{ei} in the temperature range involved, the electron temperature is obtained from the electron temperature dependence, $\nu_{ei}/n \sim T_e^{-3/2}$.

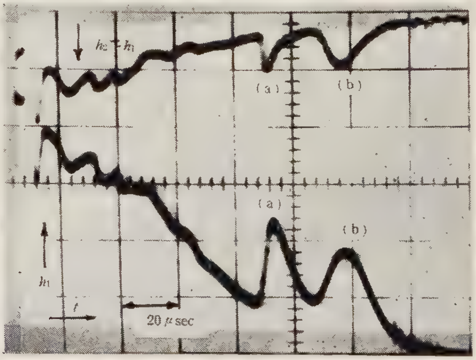

Fig. 6. (A) Microwave signal amplitudes h_1 and h_2-h_1 versus time. 20 μ sec/division, Argon, p=12.4 mm Hg, 5 K.V. 8 μF.

From the recorded typical microwave probe signals, illustrated in Fig. 6 (A), the variation of the electron density and the electron temperature of the plasma, in the presence of a propagating shock wave, is computed and plotted in Fig. 6(B). Another example of such electron density and electron temperature variation, due to weak shock waves propagated in plasmas under different conditions, is seen in Fig. 6 (C). It is seen on these figures that the electron temperature does not reach its maximum at the same time as the electron density does. As discussed above, since the energy transfer from the propagating shock wave is very efficient only to the ions, the electron gas should be heated by the warm gas of the ions. This process, however, proceeds with a rather long time constant τ_{ei}; hence a delay in the temperature rise of the electron gas. This delay is obviously shorter for shocks of higher Mach No. These observations appear to justify our assumption in Eq. (5). Although no delay is expected in the electron density rise due to compression, there is some observed. The observed rate of electron density increase may depend upon the shape of the shock discontinuity and the length of the shock tube comprised in the waveguide, which in these experiments was 4 mm. Fig. 7 compares the theoretical neutral gas temperature behind the shock front (upper line), calculated from the measured Mach No. by Eq. (3), to the measured corresponding electron temperature, where both temperatures are normalized to 300°K.

The shock velocity (Mach No.) increases with decreasing gas pressure at constant condenser

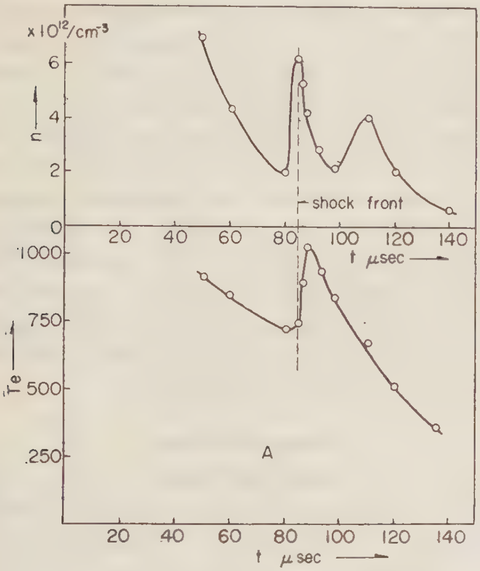

Fig. 6. (B) Changes in the electron density and the electron temperature versus time, computed from Fig. 6 (A).

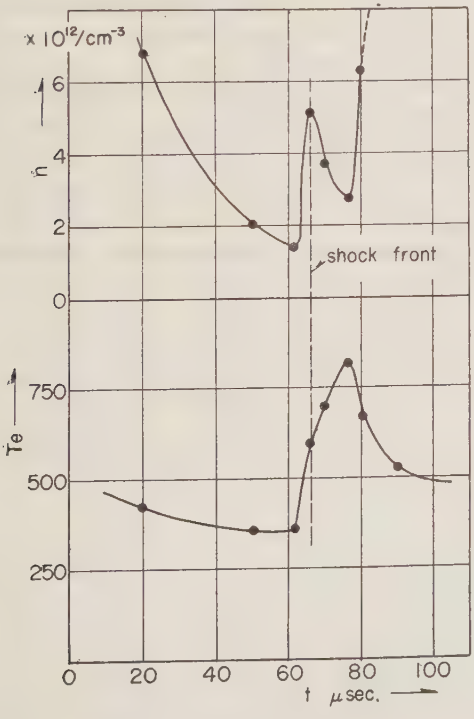

Fig. 6. (C) Same as Fig. 6 (B), but for $p=7.6$ mm Hg, 4.5 K.V. 8 μF.

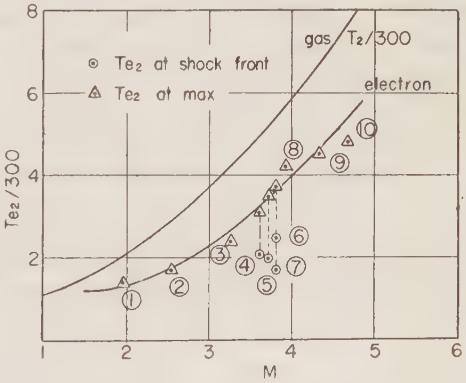

Fig. 7. Comparison of the neutral gas temperature, calculated from the Mach. no., to the electron temperature behind the shock, where both temperatures are normalized to 300°K.

	Gas	p	kV
①	Ne	11.6	3.5
②	〃	8.0	3.8
③	〃	12.0	4.4
④	〃	4.1	4.15
⑤	〃	7.6	4.5
⑥	A	12.4	5.0
⑦	Ne	4.1	4.3
⑧	〃	8.3	4.95
⑨	〃	4.1	4.5
⑩	A	9.1	4.75

voltage and at constant gas pressure but increasing condenser voltage. It is observed that in addition to an enhanced shock velocity, in particular at lower gas pressures, the time separation of the discontinuities (a) and (b) (Fig. 6 (A)) of the probe detected microwave signals is shortened. This indicates an increased velocity of the expanding initially highly ionized gas.

§ 6. Summary and Conclusion

The method described above, which is based on the known interaction of low level microwaves with free electrons in weakly ionized low pressure gases at relatively low temperatures, proved to be a convenient one for the study on non-ionizing shock waves. The main shock characteristics, which are accessible to direct determination, are the instaneous and average velocities of shock discontinuities which are propagated in low pressure and low temperature (~300°K) weakly ionized gases. Associated with the change in shock propagation velocities, the exchange between the propagating shock discontinuities and the ionized gaseous medium is studied in some detail through the intermediary of the electron gas. Indeed, as known from previous plasma studies, the electron gas of the plasma interacts strongly with both the charged (and the neutral) heavy particles of the background plasma, with which the propagating shock wave exchange energy with great efficiency.

In addition to the electro-magnetic behavior, the optical properties of the background plasma are also put to contribution in these studies. Since these latter properties are also essentially dependent upon the energy state (or temperature) of the electron gas in the plasma, any change of the energy state of the electrons brought about-in particular, by the propagating shock waves-provides us with independent but complementary means of observation and information, which are directly correlated with the microwave measurements.

While the microwave measurements described in this paper are relative to **X**-band (-9000 MC) frequencies, the method is not limited to this frequency band; higher or lower microwave frequencies could be used in principle. The best appropriate microwave frequencies for these studies can generally be determined by geometrical considerations. Similarly the background gases to be used for weak shock wave propagation studies, their pressure and degree of ionization, are not limited to the cases reported here.

Acknowledgment

The authors deeply appreciate Prof. L. Goldstein who directed the whole work and greatly helped them to prepare the manuscript.

References

1) R. G. Fowler: Rhys. Rev. **82** (1951) 879.
2) M. Roger der Agobian: C. R. **248** (1959) 1308.
3) D. L. Schultz: Proc. of 4th International Conference on Ionization Phenomena in Gases, II, 1118. Uppsala (1959)
4) For example, L. Goldstein: Advance in Elect. Physics **7** (1955) 399-503.
5) S. J. Buchsbaum and S. C. Brown: Phys. Rev. **106** (1957) 196.
6) S. Takeda: J. of Phys. Soc. Japan **16** (1961) 1267.
7) A. Kantrowitz et al.: J. Appl. Physics **23** (1952) 1390.

JOURNAL OF THE PHYSICAL SOCIETY OF JAPAN, Vol. 16, No. 7, JULY, 1961

Scattering of Microwaves from a Cylindrical Plasma in the Born Approximation. II.

By Yukio MIDZUNO

Department of Physics, Faculty of Science, University of Tokyo

(Received March 29, 1961)

The scattering of a microwave, which is fed by an oscillating electric dipole, is treated in the Born approximation. When the source is a dipole $p_0 e^{j\omega t}\boldsymbol{e}_z$, where $\boldsymbol{e}_z$ is a unit vector in the z direction, the scattered field from a collisionless cylindrical plasma is given by

$$\boldsymbol{E}_s(\boldsymbol{r}, t)=p_0\sqrt{\frac{\pi}{2}}e^{(3/4)\pi j}\frac{k^4}{\sqrt{kl\rho(l+\rho)}}e^{j(\omega t-kl-k\rho)}\int_0^\infty \eta(\rho')J_0\left(2k\rho'\sin\frac{\theta}{2}\right)\rho' d\rho' \boldsymbol{e}_z\,,$$

where $(l, \pi, 0)$ and $(\rho, \theta, 0)$ are the cylindrical coordinates of the source and the observing point, respectively, $\eta(\rho')$ is $\omega_p{}^2/\omega^2$ with the plasma frequency ω_p and here only the term lowest in $1/kl$ and $1/k\rho$ is retained. Formulas are also derived to the next order in $1/kl$ and $1/k\rho$, when the plasma has collision loss and the dipole source has the axis in any one of the three independent directions. Remarks and discussions are given on the nature and the accuracy of the formulas. Finally the cases, where the observing point does not lie on the plane $z=0$, are treated in the lowest order in $1/kl$ and $1/k\rho$.

§1. Introduction

In a previous paper[1)], the scattering of a plane microwave from a cylindrical plasma was discussed in the Born approximation[1)], hereafter the paper is refered as Paper I. But, being radiated from an electromagnetic horn in real experiments[2)], the incident wave has rather a spherical character. Since there is an essential difference between a plane wave and a spherical wave, it would be desirable to treat also the scattering of an incident wave of the latter type.

In paper I, two methods were given for deriving the scattering formula for a plane incident wave in the Born approximation. One of them consists of deriving a wave equation for a medium with an effective dielectric constant, separating it into equations for the incident wave of E-type and for that of H-type, and solving them by means of the Fourier transforms. But unless the incident wave is uniform along the axis of the cylindrical plasma, the separation into equations of E-type and H-type cannot be effected and this method cannot be applied. In the other method, the scattered field is obtained by summing all radiations from electrons in the plasma, which are forced to oscillate by the electric field of the incident wave. This method can be applied to spherical waves, too, and has an advantage of elucidating the mechanism of the scattering.

Our method has a resemblance to that in the theory of the Rayleigh scattering[3)], which was developed for the purpose of discussing the scattering of light by the sky. It is also akin to the method which is used to deal with the scattering of microwaves by a small conducting object. The latter consists of the evaluation of the current density in the object induced by the incident wave and the summation of the radiation from the current distribution. But it seems that no one has yet derived a compact formula of the scattered wave from an object with a finite dimension in this method.

In this paper, we treat the scattering of an electric dipole radiation by a cylindrical plasma. In section 2, an outline of our method of calculation is given. Section 3 deals with the scattered field at a point on such a plane, which contains the source point and is perpendicular to the axis of the cylinder. Subsection 3.1 treats the case where the source is an oscillating electric dipole with a moment parallel to the axis of the cylinder, demonstrating our method in some detail. Subsections 3.2 and 3.3 treat the cases where the axes of the dipole sources are perpendicular to the axis of the cylinder and each other. Section 4 gives some remarks concerning our formulas. In section 5 the accuracy of our formulas is discussed. Section 6 deals with the scattered field when the observing point is arbitrary except that it lies at a great distance from the cylinder. Subsections 6.1 and 6.2 are devoted to the derivation of the formulas for the sources treated in the first part.

§ 2. Method of Calculation

We take a coordinate system such that the z-axis coincides with the axis of the cylindrical plasma and the source of the incident wave lies at a point S on the negative x-axis. We assume that the distance l between S and the origin is very large compared with the radius ρ_0 of the cylinder. We shall use also the cylindrical coordinate system (ρ, θ, z) with the same z-axis in which the line $\theta=0$ coincides with the x-axis. (Fig. 1)

When the source at S is an oscillating electric dipole $\boldsymbol{p}_0(t)$, the electric field produced by it at another point Q, whose coordinates are $\boldsymbol{r}'(x', y', z')$ or (ρ', θ', z'), is given by[4)]

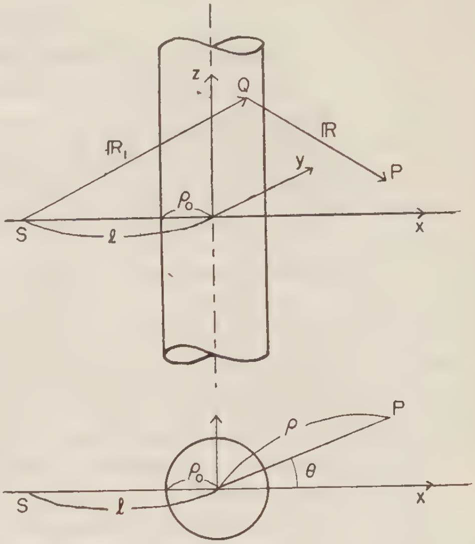

Fig. 1.

$$\boldsymbol{E}_0(\boldsymbol{r}', t)=\boldsymbol{E}_0^{(1)}(\boldsymbol{r}', t)+\boldsymbol{E}_0^{(2)}(\boldsymbol{r}', t)+\boldsymbol{E}_0^{(3)}(\boldsymbol{r}', t)\,, \tag{2.1}$$

with

$$\boldsymbol{E}_0^{(1)}(\boldsymbol{r}', t)=-\frac{\ddot{\boldsymbol{p}}_0}{c^2R_1}+\frac{\boldsymbol{R}_1(\ddot{\boldsymbol{p}}_0\cdot\boldsymbol{R}_1)}{c^2R_1^3}\,, \tag{2.2}$$

$$\boldsymbol{E}_0^{(2)}(\boldsymbol{r}', t)=-\frac{\dot{\boldsymbol{p}}_0}{cR_1^2}+\frac{3\boldsymbol{R}_1(\dot{\boldsymbol{p}}_0\cdot\boldsymbol{R}_1)}{cR_1^4}\,, \tag{2.3}$$

$$\boldsymbol{E}_0^{(3)}(\boldsymbol{r}', t)=-\frac{\boldsymbol{p}_0}{R_1^3}+\frac{3\boldsymbol{R}_1(\boldsymbol{p}_0\cdot\boldsymbol{R}_1)}{R_1^5}\,, \tag{2.4}$$

where $\boldsymbol{R}_1$ is the vector from S to Q, $R_1\equiv|\boldsymbol{R}_1|$, c is the light speed and

$$\boldsymbol{p}_0\equiv\boldsymbol{p}_0\left(t-\frac{R_1}{c}\right), \quad \dot{\boldsymbol{p}}_0\equiv\frac{\partial}{\partial t}\boldsymbol{p}_0\left(t-\frac{R_1}{c}\right), \quad \ddot{\boldsymbol{p}}_0\equiv\frac{\partial^2}{\partial t^2}\boldsymbol{p}_0\left(t-\frac{R_1}{c}\right). \tag{2.5}$$

Let us consider the motion of an electron under the influence of the electric field of the incident wave. We neglect the thermal motion of the electron and let the electron oscillate about the point Q. We consider the case where there is a uniform static external magnetic field $\boldsymbol{B}_0$ parallel to the z-axis and no external electric field exists. Further we assume that the amplitude of the oscillation of the electron is much smaller than the wave length of the incident wave. Then the equation of motion for the electron with the coordinate denoted by $\tilde{\boldsymbol{r}}$ is given by

$$m\frac{d^2\tilde{\boldsymbol{r}}}{dt^2}=-e\boldsymbol{E}_0(\boldsymbol{r}', t)-\frac{e}{c}\frac{d\tilde{\boldsymbol{r}}}{dt}\times\boldsymbol{B}_0-m\nu\frac{d\tilde{\boldsymbol{r}}}{dt}\,, \tag{2.6}$$

where m, $-e$, and ν is the mass, charge and the collision frequency of an electron respectively. If $\boldsymbol{p}_0(t)$ is proportional to $e^{j\omega t}$, $\boldsymbol{E}_0(\boldsymbol{r}', t)$ has the same property. Then, on assuming that $\tilde{\boldsymbol{r}}-\boldsymbol{r}'$ is also proportional to $e^{j\omega t}$, the equation (2.6) is easily solved and the dipole moment $\boldsymbol{p}(t)$ due to this electron is obtained as

$$\boldsymbol{p}(t)=-\frac{e^2}{m\omega^2}\begin{pmatrix} L & jM & 0 \\ -jM & L & 0 \\ 0 & 0 & N \end{pmatrix}\cdot \boldsymbol{E}_0(\boldsymbol{r}', t)\,, \tag{2.7}$$

where

$$L=\frac{1-j\beta}{(1-j\beta)^2-\gamma^2}\,,\qquad M=\frac{\gamma}{(1-j\beta)^2-\gamma^2}\,,\qquad N=\frac{1}{1-j\beta}\,, \tag{2.8}$$

with $\beta=\nu/\omega$, $\gamma=\omega_c/\omega$ and ω_c is the electron cyclotron frequency, $\omega_c=e|\boldsymbol{B}_0|/mc$.

When $\boldsymbol{p}(t)$ is obtained, the scattered electric field at a point P due to this electron is given by an expression similar to (2.1):

$$(\boldsymbol{E}_s(\boldsymbol{r}, t))_{\mathrm{Q}}=(\boldsymbol{E}_s^{(1)}(\boldsymbol{r}, t))_{\mathrm{Q}}+(\boldsymbol{E}_s^{(2)}(\boldsymbol{r}, t))_{\mathrm{Q}}+(\boldsymbol{E}_s^{(3)}(\boldsymbol{r}, t))_{\mathrm{Q}}\,, \tag{2.9}$$

where

$$(\boldsymbol{E}_s^{(1)}(\boldsymbol{r}, t))_{\mathrm{Q}}=-\frac{\ddot{\boldsymbol{p}}}{c^2R}+\frac{\boldsymbol{R}(\ddot{\boldsymbol{p}}\cdot\boldsymbol{R})}{c^2R^3}\,, \tag{2.10}$$

$$(\boldsymbol{E}_s^{(2)}(\boldsymbol{r}, t))_{\mathrm{Q}}=-\frac{\dot{\boldsymbol{p}}}{cR^2}+\frac{3\boldsymbol{R}(\dot{\boldsymbol{p}}\cdot\boldsymbol{R})}{cR^4}\,, \tag{2.11}$$

$$(\boldsymbol{E}_s^{(3)}(\boldsymbol{r}, t))_{\mathrm{Q}}=-\frac{\boldsymbol{p}}{R^3}+\frac{3\boldsymbol{R}(\boldsymbol{p}\cdot\boldsymbol{R})}{R^5}\,. \tag{2.12}$$

Here we have denoted by $\boldsymbol{R}$ the vector from Q to P, whose coordinates are $\boldsymbol{r}(x, y, z)$ or (ρ, θ, z), $R=|\boldsymbol{R}|$ and $\boldsymbol{p}$, $\dot{\boldsymbol{p}}$, $\ddot{\boldsymbol{p}}$ are given by expressions similar to (2.5):

$$\boldsymbol{p}\equiv\boldsymbol{p}\left(t-\frac{R}{c}\right),\qquad \dot{\boldsymbol{p}}\equiv\frac{\partial}{\partial t}\boldsymbol{p}\left(t-\frac{R}{c}\right),\qquad \ddot{\boldsymbol{p}}\equiv\frac{\partial^2}{\partial t^2}\boldsymbol{p}\left(t-\frac{R}{c}\right). \tag{2.13}$$

The total scattered field observed at P is evaluated by summing the contributions of all electrons in the plasma.

$$\begin{aligned}\boldsymbol{E}_s(\boldsymbol{r}, t)&=\int n(\boldsymbol{r}')(\boldsymbol{E}_s(\boldsymbol{r}, t))_{\mathrm{Q}}d\boldsymbol{r}' \\ &=\frac{m\omega^2}{4\pi e^2}\iiint \eta(\rho')(\boldsymbol{E}_s(\boldsymbol{r}, t))_{\mathrm{Q}}dz'd\theta'\rho'd\rho'\,,\end{aligned} \tag{2.14}$$

where $n(\boldsymbol{r}')$ is the number density of electrons, which is assumed to be independent of z' and θ', $\eta(\rho')=\omega_p^2/\omega^2$ with the plasma frequency ω_p $(=(4\pi e^2 n(\rho')/m)^{1/2})$ and the integration should be carried out over the entire space.

The integral is very complicated in general. But since our object is to get the formulas only for very large kl and $k\rho$, where $k=\omega/c$ is the wave number of the incident wave, we need only the asymptotic expressions of these integrals for such cases. This enables us to perform the integration with respect to z' and θ' analytically, and we get the final result in the form of an expansion with respect to $1/kl$, $1/k\rho$ and $1/k(l+\rho)$.

When $kl\gg 1$, it is clear from their expressions that $\boldsymbol{E}_0^{(2)}(\boldsymbol{r}', t)$ is smaller than $\boldsymbol{E}_0^{(1)}(\boldsymbol{r}', t)$ by one order in $1/kl$, and that $\boldsymbol{E}_0^{(3)}(\boldsymbol{r}', t)$ is in turn smaller than $\boldsymbol{E}_0^{(2)}(\boldsymbol{r}', t)$ by one order. Similarly when $k\rho$ is very large, $(\boldsymbol{E}_s^{(2)}(\boldsymbol{r}, t))_{\mathrm{Q}}$ and $(\boldsymbol{E}_s^{(3)}(\boldsymbol{r}, t))_{\mathrm{Q}}$ are smaller than $(\boldsymbol{E}_s^{(1)}(\boldsymbol{r}, t))_{\mathrm{Q}}$ by one and two orders with respect to $1/k\rho$, respectively. Therefore, if we wish to have the dominant term of the scattered field, we need only to retain $\boldsymbol{E}_0^{(1)}(\boldsymbol{r}', t)$ in (2.1), $(\boldsymbol{E}_s^{(1)}(\boldsymbol{r}, t))_{\mathrm{Q}}$ in (2.10) and the leading term of the asymptotic expansion of the integral with respect to z'. If we wish to get the terms of next order, we need to consider each case separately where the terms of next order are taken in only one of three steps of the procedure mensioned above, and to add up their contributions, and so on. This procedure shows us very clearly the origin of each term in the final result.

§ 3. The Scattered Field at a Point with $z=0$.

In this section we derive formulas for the scattered field at a point with $z=0$. Since this case would be most important for real experiments, we derive the leading terms and the terms of next order in $1/kl$ and $1/k\rho$.

3.1. *An electric dipole source with a moment parallel to the z-axis.*

Let us first put an electric dipole of the following type at S.

$$\boldsymbol{p}_0(t)=p_0e^{j\omega t}\boldsymbol{e}_z\ , \tag{3.1}$$

where p_0 is a constant and $\boldsymbol{e}_z$ is the unit vector in the z-direction. The field of the incident wave at Q is given by (2.1). The dominant term $\boldsymbol{E}_0^{(1)}(\boldsymbol{r}',t)$ is written explicitly as

$$\boldsymbol{E}_0^{(1)}(\boldsymbol{r}',t)=k^2p_0\exp\left[j(\omega t-kR_1)\right]\frac{1}{R_1^3}\left[-(l+x')z'\boldsymbol{e}_x-y'z'\boldsymbol{e}_y+\xi_1^2\boldsymbol{e}_z\right]\ , \tag{3.2}$$

where

$$\left.\begin{aligned}&R_1^2=(l+x')^2+y'^2+z'^2\equiv\xi_1^2+z'^2\ ,\\&\xi_1^2=l^2+2l\rho'\cos\theta+\rho'^2\ ,\end{aligned}\right\} \tag{3.3}$$

and $\boldsymbol{e}_x$ and $\boldsymbol{e}_y$ are the unit vectors in x and y directions respectively. Here again we can handle the contributions from the x, y and z components of $\boldsymbol{E}_0^{(1)}(\boldsymbol{r}',t)$ separately. It will be shown later that the dominant term of the scattered field comes from the z-component of $\boldsymbol{E}_0^{(1)}(\boldsymbol{r}',t)$, which we denote by $E_{0z}(\boldsymbol{r}',t)$. $E_{0x}(\boldsymbol{r}',t)$, the x-component of $\boldsymbol{E}_0^{(1)}(\boldsymbol{r}',t)$, gives a contribution smaller than $E_{0z}^{(1)}(\boldsymbol{r}',t)$ by one order in $1/kl$, and $E_{0y}^{(1)}(\boldsymbol{r}',t)$ gives that smaller than $E_{0z}^{(1)}(\boldsymbol{r},t)$ by two order. Therefore, we need to consider only $E_{0z}^{(1)}(\boldsymbol{r}',t)$ and $E_{0x}^{(1)}(\boldsymbol{r}',t)$ of the three components of $\boldsymbol{E}_0^{(1)}(\boldsymbol{r}',t)$ for our purpose. Similarly $\boldsymbol{E}_0^{(2)}(\boldsymbol{r}',t)$ is given by

$$\boldsymbol{E}_0^{(2)}(\boldsymbol{r},t)=-jkp_0\exp\left[j(\omega t-kR_1)\right]\frac{1}{R_1^4}\left[-3(l+x')z'\boldsymbol{e}_x-3y'z'\boldsymbol{e}_y+(R_1^2-3z'^2)\boldsymbol{e}_z\right]\ , \tag{3.4}$$

of which we need to retain $E_{0z}^{(2)}(\boldsymbol{r},t)$ only.

(a) *The dominant term*

At first we derive the dominant term. Inserting the expression for $E_{0z}^{(1)}(\boldsymbol{r},t)$ into (2.7), we get

$$\boldsymbol{p}(t)=-\frac{e^2}{m\omega^2}k^2p_0N\exp\left[j(\omega t-kR_1)\right]\frac{\xi_1^2}{R_1^3}\boldsymbol{e}_z\ , \tag{3.5}$$

Then (2.10) gives

$$(\boldsymbol{E}(\boldsymbol{r},t))_{\mathrm{Q}}=-\frac{e^2}{m\omega^2}k^4p_0N\exp\left[j(\omega t-kR_1-kR)\right]\frac{\xi_1^2}{R_1^3R^3}\{\xi^2\boldsymbol{e}_z+(x-x')z'\boldsymbol{e}_x+(y-y')z'\boldsymbol{e}_y\}\ , \tag{3.6}$$

where

$$\left.\begin{aligned}&R^2=(x-x')^2+(y-y')^2+z'^2\equiv\xi^2+z'^2\ ,\\&\xi^2=\rho^2-2\rho\rho'\cos(\theta-\theta')+\rho'^2\ .\end{aligned}\right\} \tag{3.7}$$

The total scattered field at P is given by (2.14). The x and y components vanish in the course of the integration with respect to z', and we have

$$\boldsymbol{E}_s(\boldsymbol{r},t)=-\frac{1}{4\pi}k^4p_0e^{j\omega t}\int_0^\infty N\eta(\rho')\rho'd\rho'\int_0^{2\pi}d\theta'\xi_1^2\xi^2\int_{-\infty}^{\infty}\frac{1}{R_1^3R^3}\exp\left[-jk(R_1+R)\right]dz'\boldsymbol{e}_z\ . \tag{3.8}$$

Here we need the asymptotic expression of this integral for large kl and $k\rho$. From (3.3) and (3.7) this means that we need the asymptotic expansion for the case where $k\xi_1\gg1$ and $k\xi\gg1$. This expansion is accomplished in Appendix A with the result,

$$\int_{-\infty}^{\infty} \frac{1}{R_1{}^3 R^3} \exp\left[-jk(R_1+R)\right] dz'$$
$$= \frac{\sqrt{2\pi}}{\xi_1{}^2\xi^2\sqrt{k\xi_1\xi(\xi_1+\xi)}} \exp\left[-jk(\xi_1+\xi)-\frac{\pi}{4}j\right]\left\{1-\frac{1}{8}j\left[15\frac{1}{k(\xi_1+\xi)}-9\frac{1}{k\xi_1}-9\frac{1}{k\xi}\right]\right.$$
$$\left. +O\left(\frac{1}{(k\xi_1)^2}, \frac{1}{k^2\xi_1\xi}, \frac{1}{(k\xi)^2}\right)\right\}. \tag{3.9}$$

When we demand the dominant term, only the leading term of (3.9) is needed and ξ_1 and ξ can be replaced by l and ρ, respectively, except in the argument of the exponential function, where these should be replaced by the first and second terms in their expansions:

$$\left.\begin{aligned} \xi_1 &= l+\rho'\cos\theta'+\frac{1}{2}\frac{\rho'^2}{l}\sin^2\theta'+\cdots, \\ \xi &= \rho-\rho'\cos(\theta'-\theta)+\frac{1}{2}\frac{\rho'^2}{\rho}\sin^2(\theta'-\theta)+\cdots. \end{aligned}\right\} \tag{3.10}$$

Inserting these expressions into (3.8), we get the dominant term as follows.

$$\boldsymbol{E}_{s0}(\boldsymbol{r}, t) = \frac{1}{2\sqrt{2\pi}} e^{(3/4)\pi j} k^4 p_0 \frac{1}{\sqrt{kl\rho(l+\rho)}} e^{j(\omega t-kl-k\rho)}$$
$$\times \int_0^{\infty} N\eta(\rho')\rho' d\rho' \int_0^{2\pi} \exp\left[2jk\rho'\sin\frac{\theta}{2}\sin\left(\theta'-\frac{\theta}{2}\right)\right] d\theta' \boldsymbol{e}_z$$
$$= p_0\sqrt{\frac{\pi}{2}} e^{(3/4)\pi j} \frac{k^4}{\sqrt{kl\rho(l+\rho)}} e^{j(\omega t-kl-k\rho)} \int_0^{\infty} N\eta(\rho') J_0\left(2k\rho'\sin\frac{\theta}{2}\right)\rho' d\rho' \boldsymbol{e}_z. \tag{3.11}$$

Here $J_n(x)$ is the Bessel function of nth order, and we have used the formula

$$\int_0^{2\pi} e^{ja\cos\theta}\cos n\theta d\theta = 2\pi j^n J_n(a), \tag{3.12}$$

(b) *Terms of the next order*

The terms of the next order consist of the following contributions:

1) the next order terms of equation (3.8),
2) the terms which come from $E_{0z}^{(1)}(\boldsymbol{r}', t)$ and $(\boldsymbol{E}_s{}^{(1)}(\boldsymbol{r}, t))_Q$,
3) the terms which come from $E_{0z}^{(1)}(\boldsymbol{r}', t)$ and $(\boldsymbol{E}_s{}^{(2)}(\boldsymbol{r}, t))_Q$,
4) the terms which come from $E_{0z}^{(2)}(\boldsymbol{r}', t)$ and $(\boldsymbol{E}_s{}^{(1)}(\boldsymbol{r}, t))_Q$.

In the latter three contributions, only the leading terms need to be retained.

When we insert (3.9) and (3.10) into (3.8), expand it, retain only the terms of next order in $1/kl$ and $1/k\rho$ and perform the integration with respect to θ', we get

$$\boldsymbol{E}_{s0}(\boldsymbol{r}, t)+\boldsymbol{E}_{s1}^{(1)}(\boldsymbol{r}, t) = \frac{1}{2\sqrt{2\pi}} e^{(3/4)\pi j} k^4 p_0 \frac{1}{\sqrt{kl\rho(l+\rho)}} e^{j(\omega t-kl-k\rho)}$$
$$\times \int_0^{\infty} N\eta(\rho')\rho' d\rho' \int_0^{2\pi} \exp\left[2jk\rho'\sin\frac{\theta}{2}\sin\left(\theta'-\frac{\theta}{2}\right)\right] d\theta'$$
$$\times\left\{1+\frac{1}{kl}\left[-\frac{k\rho'}{2}\cos\theta'-\frac{j(k\rho')^2}{2}\sin^2\theta'+\frac{9}{8}j\right]\right.$$
$$+\frac{1}{k\rho}\left[\frac{k\rho'}{2}\cos(\theta'-\theta)-\frac{j(k\rho')^2}{2}\sin^2(\theta'-\theta)+\frac{9}{8}j\right]$$
$$\left.+\frac{1}{k(l+\rho)}\left[k\rho'\sin\frac{\theta}{2}\sin\left(\theta'-\frac{\theta}{2}\right)-\frac{15}{8}j\right]\right\}\boldsymbol{e}_z$$

$$
\begin{aligned}
&= p_0\sqrt{\frac{\pi}{2}}\,e^{(3/4)\pi j}\frac{1}{\sqrt{kl\rho(l+\rho)}}e^{j(\omega t-kl-k\rho)}\int_0^\infty N\eta(\rho')\rho'd\rho'\Big\{J_0\Big(2k\rho'\sin\frac{\theta}{2}\Big)\\
&\quad+\frac{1}{8}j\Big(\frac{1}{kl}+\frac{1}{k\rho}\Big)\Big[(9-2k^2\rho'^2\cos\theta)J_0\Big(2k\rho'\sin\frac{\theta}{2}\Big)+2k^2\rho'^2J_2\Big(2k\rho'\sin\frac{\theta}{2}\Big)\Big]\\
&\quad+\frac{1}{8}j\frac{1}{k(l+\rho)}\Big[-15J_0\Big(2k\rho'\sin\frac{\theta}{2}\Big)+8k\rho'\sin\frac{\theta}{2}J_1\Big(2k\rho'\sin\frac{\theta}{2}\Big)\Big]\Big\}\boldsymbol{e}_z\,, \qquad (3.13)
\end{aligned}
$$

where we have used (3.12). The first term of this expression is the dominant term derived in the last sub-section and the other terms are the contributions of the first type mensioned above.

In dealing with the contribution of the second type, we can replace $l+x'$ by l in $E_{0x}^{(1)}(\boldsymbol{r}, t)$:

$$
E_{0x}^{(1)}(\boldsymbol{r}', t)=-k^2p_0\exp[j(\omega t-kR_1)]\frac{lz'}{R_1{}^3}. \qquad (3.14)
$$

Then from (2.7) and (2.10) we get

$$
\boldsymbol{p}(t)=\frac{e^2}{m\omega^2}k^2p_0\exp[j(\omega t-kR_1)]\frac{lz'}{R_1{}^3}(L\boldsymbol{e}_x-jM\boldsymbol{e}_y)\,, \qquad (3.15)
$$

$$
\begin{aligned}
(\boldsymbol{E}_s{}^{(1)}(\boldsymbol{r}, t))_Q=&\frac{e^2}{m\omega^2}k^4p_0\exp[j(\omega t-kR_1-kR)]\frac{lz'}{R_1{}^3R^3}\{z'(Lx-jMy)\boldsymbol{e}_z+[L(R^2-x^2)+jMxy]\boldsymbol{e}_x\\
&-[jM(R^2-y^2)+Lxy]\boldsymbol{e}_y\}\,, \qquad (3.16)
\end{aligned}
$$

where we have used the fact that when only the leading terms are desired, we can replace $x-x'$ and $y-y'$ by x and y, respectively. The x and y components vanish in the course of the integration with respect to z'. Here we need the asymptotic expression of the following integral, which is easily obtained from the formula in Appendix A.

$$
\begin{aligned}
&\int_{-\infty}^{\infty}\frac{z'^2}{R_1{}^3R^3}\exp[-jk(R_1+R)]dz'\\
&=\int_{-\infty}^{\infty}\frac{R^2-\xi^2}{R_1{}^3R^3}\exp[-jk(R_1+R)]dz'\\
&=\frac{\sqrt{2\pi}}{\xi_1\xi\sqrt{k\xi_1\xi(\xi_1+\xi)}}\frac{1}{k(\xi_1+\xi)}\exp\Big[-jk(\xi_1+\xi)-\frac{3}{4}\pi j\Big], \qquad (3.17)
\end{aligned}
$$

Thus we have the following contribution.

$$
\begin{aligned}
\boldsymbol{E}_{s1}^{(2)}(\boldsymbol{r}, t)=&p_0\sqrt{\frac{\pi}{2}}\,e^{(3/4)\pi j}\frac{k^4}{\sqrt{kl\rho(l+\rho)}}e^{j(\omega t-kl-k\rho)}\\
&\times\frac{1}{k(l+\rho)}j\int_0^\infty(L\cos\theta-jM\sin\theta)\eta(\rho')J_0\Big(2k\rho'\sin\frac{\theta}{2}\Big)\rho'd\rho'\boldsymbol{e}_z\,. \qquad (3.18)
\end{aligned}
$$

Similarly the contributions of the third and the fourth type are obtained as follows.

$$
\boldsymbol{E}_{s1}^{(3)}(\boldsymbol{r}, t)=-p_0\sqrt{\frac{\pi}{2}}\,e^{(3/4)\pi j}\frac{k^4}{\sqrt{kl\rho(l+\rho)}}e^{j(\omega t-kl-k\rho)}\frac{1}{k\rho}j\int_0^\infty N\eta(\rho')J_0\Big(2k\rho'\sin\frac{\theta}{2}\Big)\rho'd\rho'\boldsymbol{e}_z\,. \qquad (3.19)
$$

$$
\boldsymbol{E}_{s1}^{(4)}(\boldsymbol{r}, t)=-p_0\sqrt{\frac{\pi}{2}}\,e^{(3/4)\pi j}\frac{k^4}{\sqrt{kl\rho(l+\rho)}}e^{j(\omega t-nl-k\rho)}\frac{1}{kl}j\int_0^\infty N\eta(\rho')J_0\Big(2k\rho'\sin\frac{\theta}{2}\Big)\rho'd\rho'\boldsymbol{e}_z\,. \qquad (3.20)
$$

(c) *The total result*

The scattered field at P due to the cylindrical plasma is the sum of expressions (3.13), (3.18), (3.19) and (3.20).

$$
\begin{aligned}
\boldsymbol{E}_s(\boldsymbol{r},t)=p_0\sqrt{\frac{\theta}{2}}\,e^{(3/4)\pi j}\frac{k^4}{\sqrt{kl\rho(l+\rho)}}e^{j(\omega t-kl-k\rho)}&\left\{\int_0^\infty N\eta(\rho')J_0\left(2k\rho'\sin\frac{\theta}{2}\right)\rho'd\rho'\right.\\
&+\frac{1}{8}j\left(\frac{1}{kl}+\frac{1}{k\rho}\right)\int_0^\infty N\eta(\rho')\left[(1-2k^2\rho'^2\cos\theta)J_0\left(2k\rho'\sin\frac{\theta}{2}\right)\right.\\
&\left.+2k^2\rho'^2J_2\left(2k\rho'\sin\frac{\theta}{2}\right)\right]\rho'd\rho'\\
&+\frac{1}{8}j\frac{1}{k(l+\rho)}\int_0^\infty\left[(8(L\cos\theta-jM\sin\theta)-15N)\eta(\rho')J_0\left(2k\rho'\sin\frac{\theta}{2}\right)\right.\\
&\left.\left.+8N\eta(\rho')k\rho'\sin\frac{\theta}{2}J_1\left(2k\rho'\sin\frac{\theta}{2}\right)\right]\rho'd\rho'+\cdots\right\}\boldsymbol{e}_z\,.
\end{aligned}
\tag{3.21}
$$

This expression is symmetric in l and ρ, as expected from the symmetry of our problem.

3.2. *The dipole source parallel to the y-axis*

Next, we consider an electric dipole source with a moment parallel to the y-axis.

$$
\boldsymbol{p}_0(t)=p_0'e^{j\omega t}\boldsymbol{e}_y\,. \tag{3.22}
$$

Then the electric field of the incident wave is given by

$$
\boldsymbol{E}_0(\boldsymbol{r}',t)=\boldsymbol{E}_0^{(1)}(\boldsymbol{r}',t)+\boldsymbol{E}_0^{(2)}(\boldsymbol{r}',t)+\boldsymbol{E}_0^{(3)}(\boldsymbol{r}',t)\,, \tag{3.23}
$$

with

$$
\left.
\begin{aligned}
\boldsymbol{E}_0^{(1)}(\boldsymbol{r}',t)&=k^2p_0'\exp[j(\omega t-kR_1)]\frac{1}{R_1^3}[-(l+x')y'\boldsymbol{e}_x+(R_1^2-y'^2)\boldsymbol{e}_y-z'y'\boldsymbol{e}_z]\,,\\
\boldsymbol{E}_0^{(2)}(\boldsymbol{r}',t)&=-jkp_0'\exp[j(\omega t-kR_1)]\frac{1}{R_1^4}[-3(l+x')y'\boldsymbol{e}_x+(R_1^2-3y'^2)\boldsymbol{e}_y-3z'y'\boldsymbol{e}_z]\,.
\end{aligned}
\right\}
\tag{3.24}
$$

$\boldsymbol{E}_0^{(3)}(\boldsymbol{r},t)$ is smaller than $\boldsymbol{E}_0^{(2)}(\boldsymbol{r}',t)$ by one order in $1/kl$ and is negligible. Here the dominant contribution comes from $E_{0x}^{(1)}(\boldsymbol{r}',t)$. In the following the calculation proceeds much the same way as that in the last section with a little more tedious labor. Here we give only the final result.

$$
\begin{aligned}
\boldsymbol{E}_s(\boldsymbol{r}',t)=p_0'\sqrt{\frac{\pi}{2}}\,e^{(3/4)\pi j}\frac{k^4}{\sqrt{kl\rho(l+\rho)}}e^{j(\omega t\ \ kl-k\rho)}&\left\{\int_0^\infty(L\cos\theta-jM\sin\theta)\eta(\rho')J_0\left(2k\rho'\sin\frac{\theta}{2}\right)\rho'd\rho'\boldsymbol{e}_\theta\right.\\
+\int_0^\infty\eta(\rho')\rho'd\rho'&\left\{\left(\frac{1}{k(l+\rho)}+\frac{1}{k\rho}\right)jJ_0\left(2k\rho'\sin\frac{\theta}{2}\right)(L\sin\theta+jM\cos\theta)\right.\\
&\left.+\frac{1}{k\rho}jk\rho'\cos\frac{\theta}{2}J_1\left(2k\rho'\sin\frac{\theta}{2}\right)(L\cos\theta-jM\sin\theta)\right\}\boldsymbol{e}_\rho\\
+\int_0^\infty\eta(\rho')\rho'd\rho'&\left\{\frac{1}{8}\left(\frac{1}{kl}+\frac{1}{k\rho}\right)j\left[(L\cos\theta-jM\sin\theta)\left(-7J_0\left(2k\rho'\sin\frac{\theta}{2}\right)\right.\right.\right.\\
&\left.+2k^2\rho'^2\left(-\cos\theta\,J_2\left(2k\rho'\sin\frac{\theta}{2}\right)+J_2\left(2k\rho'\sin\frac{\theta}{2}\right)\right)\right)\\
&\left.+(L\sin\theta+jM\cos\theta)8k\rho'\cos\frac{\theta}{2}J_1\left(2k\rho'\sin\frac{\theta}{2}\right)\right]\\
+\frac{1}{8}\frac{1}{k(l+\rho)}j(L\cos\theta-jM\sin\theta)&\left.\left.\left(J_0\left(2k\rho'\sin\frac{\theta}{2}\right)+8k\rho'\sin\frac{\theta}{2}J_1\left(2k\rho'\sin\frac{\theta}{2}\right)\right)\right\}\boldsymbol{e}_\theta+\cdots\right\}\,,
\end{aligned}
\tag{3.25}
$$

where $\boldsymbol{e}_\rho$ and $\boldsymbol{e}_\theta$ are the unit vectors of the directions of ρ and θ respectively.

3.3. *The dipole source parallel to the x-axis*

When an electric dipole parallel to the x-axis is placed at S, the leading term of the scattered field corresponds to the terms of the next order terms for the dipole source parallel to other axis. Thus we need only the lowest terms in $1/kl$ and $1/k\rho$, and the analysis is very simple compared with other two cases. Here again we give the final result only.

$$\boldsymbol{p}_0(t)=p^{0\prime\prime}e^{j\omega t}\boldsymbol{e}_x\,, \tag{3.26}$$

$$\begin{aligned}\boldsymbol{E}_s(\boldsymbol{r},t)=p_0''\sqrt{\frac{\pi}{2}}\,e^{(3/4)\pi j}\frac{k^4}{\sqrt{kl\rho(l+\rho)}}e^{j(\omega t-kl-k\rho)}\int_0^\infty \eta(\rho')J_0\left(2k\rho'\sin\frac{\theta}{2}\right)\rho'd\rho'\\ \times\frac{1}{k(l+\rho)}\,j\left\{N\boldsymbol{e}_\rho+\frac{\rho}{l}(L\sin\theta+jM\cos\theta)\boldsymbol{e}_\theta\right\}+\cdots\,.\end{aligned} \tag{3.27}$$

§4. Remarks

In this section we give some remarks concerning our formulas. The dominant terms of the electric fields of the incident waves at the origin are

$$\boldsymbol{E}_0(0,t)=E_{0z}(0,t)\boldsymbol{e}_z\,,$$

where

$$E_{0z}(0,t)=k^2p_0\frac{1}{l}\exp\left[j(\omega t-kl)\right]\,, \tag{4.1}$$

for the dipole source parallel to the z-axis and

$$\boldsymbol{E}_0(0,t)=E_{0y}(0,t)\boldsymbol{e}_y\,,$$

where

$$E_{0y}(0,t)=k^2p_0'\frac{1}{l}\exp\left[j(\omega t-kl)\right]\,, \tag{4.2}$$

for the dipole parallel to the y-axis. Thus the dominant terms of the scattered field at P are given by

$$\boldsymbol{E}_{s0}(\boldsymbol{r},t)=\sqrt{\frac{\pi}{2}}\,e^{(3/4)\pi j}\frac{1}{\sqrt{1+(\rho/l)}}E_{0z}(0,0)\frac{1}{\sqrt{k\rho}}e^{j(\omega t-k\rho)}\int_0^\infty k^2N\eta(\rho')J_0\left(2k\rho'\sin\frac{\theta}{2}\right)\rho'd\rho'\boldsymbol{e}_z\,, \tag{4.3}$$

for the dipole source parallel to the z-axis and

$$\begin{aligned}\boldsymbol{E}_{s0}(\boldsymbol{r},t)=\sqrt{\frac{\pi}{2}}e^{(3/4)\pi j}\frac{1}{\sqrt{1+(\rho/l)}}E_{0y}(0,0)\\ \times\frac{1}{\sqrt{k\rho}}e^{j(\omega t-k\rho)}\int_0^\infty k^2(L\cos\theta-jM\sin\theta)\eta(\rho')\,J_0\left(2k\rho'\sin\frac{\theta}{2}\right)\rho'd\rho'\boldsymbol{e}_\theta\,,\end{aligned} \tag{4.4}$$

for the dipole parallel to the y-axis, respectively. These expressions show us that, when $l\gg\rho$, these scattered fields tend to those for the plane incident waves of the respective type, which were derived in Paper I. On the other hand, if $\rho\gg l$, these scattered fields are proportional to $(k\rho)^{-1}\exp\left[j(\omega t-k\rho)\right]$, which is the characteristic factor of the spherical wave, as should be.

Since the expression (4.3) for the dominant term depends only on the field intensity at the origin, it seems to be valid for more general types of sources than a dipole. In fact we shall show in Appendix C that it is valid independently of the details of the angular distribution of the incident wave, provided that its intensity at the origin is given by (4.1) and some weak conditions are satisfied. Similarly the expression (4.4) is also valid for any incident wave under similar conditions as above. Thus they may be applied to real experiments, too, where horns are used as the source of the incident wave.

In Paper I, it was shown that for some special types of the density distributions of the plasma, the integration in the scattering formulas can be performed analytically. For the distributions mensioned there, the integrations of our formulas are also performed analytically. For example, let us take the density distribution of J_0 type[5];

$$\eta(\rho)=\begin{cases}\eta_0J_0(\zeta_1\rho/\rho_0) & \text{for}\quad \rho<\rho_0\\ 0 & \text{for}\quad \rho>\rho_0\,,\end{cases} \tag{4.5}$$

where η_0 is a constant and ζ_1 $(=2.4048\cdots)$ is the least zero point of $J_0(x)$. Then we have

$$\int_0^1 zJ_0(\alpha z)J_0(\xi_1 z)dz=\frac{\zeta_1}{\zeta_1^2-\alpha^2}J_0(\alpha)J_1(\zeta_1)\,, \tag{4.6}$$

and, on differentiating this by α once and twice, we get

$$\int_0^1 z^2J_1(\alpha z)J_0(\zeta_1 z)dz=-\frac{\zeta_1 J_1(\zeta_1)}{(\zeta_1^2-\alpha^2)^2}[2\alpha J_0(\alpha)-(\zeta_1^2-\alpha^2)J_1(\alpha)]\,, \tag{4.7}$$

$$\int_0^1 z^3J_2(\alpha z)\,J_0(\zeta_1 z)dz=\frac{\zeta_1 J_1(\zeta_1)}{(\zeta_1^2-\alpha^2)^3}[8\alpha^2J_0(\alpha)-4\alpha(\zeta_1^2-\alpha^2)J_1(\alpha)+(\zeta_1^2-\alpha^2)^2J_2(\alpha)]\,. \tag{4.8}$$

Using these expressions, we get, e.g., from (3.21) the following expressions for the dipole source parallel to the z-axis.

$$\begin{aligned}\boldsymbol{E}_s(\boldsymbol{r},t)=p_0\sqrt{\frac{\pi}{2}}e^{(3/4)\pi j}\frac{k^2}{\sqrt{kl\rho(l+\rho)}}e^{j(\omega t-kl-k\rho)}\frac{\zeta_1J_1(\zeta_1)}{\zeta_1^2-\alpha^2}(k\rho_0)^2\eta_0\Big\{NJ_0(\alpha)+\frac{1}{8}j\left(\frac{1}{kl}+\frac{1}{k\rho}\right)N\\ \times\left[\left(1-2(k\rho_0)^2\left(1-\frac{4}{\zeta_1^2-\alpha^2}\right)\left(\cos\theta+\frac{2\alpha^2}{\zeta_1^2-\alpha^2}(1+\cos\theta)\right)\right)J_0(\alpha)\right.\\ \left.+2(k\rho_0)^2\left(1-\frac{2\alpha^2}{\zeta_1^2-\alpha^2}(1+\cos\theta)\right)J_2(\alpha)\right]\\ +\frac{1}{8}j\frac{1}{k(l+\rho)}\left[\left(8(L\cos\theta-jM\sin\theta)-N\left(15+\frac{8\alpha^2}{\zeta_1^2-\alpha^2}\right)\right)J_0(\alpha)\right.\\ \left.+4\alpha NJ_1(\alpha)\right]+\cdots\Big\}\boldsymbol{e}_z\,,\end{aligned} \tag{4.9}$$

where $\alpha=2k\rho_0\sin(\theta/2)$.

§ 5. Accuracy of the Dominant Terms

Our formulas are asymptotic expressions valid for very large kl and $k\rho$. Since these are quantities of order of several tens in real experiments, dominant terms seem to give a sufficiently accurate field. But here it should be noted that the coefficients of the correction terms are functions of $k\rho_0$ as seen, e.g., from (4.9). Since these coefficients have terms of higher powers of $k\rho_0$ than the dominant term, there would be some fear that the correction terms may overcome the dominant terms when $k\rho_0$ is large compared with 1 in the real experiments, where kl and $k\rho$ are not sufficiently large. This means merely that when $k\rho_0$ is large, the incident wave cannot be regarded as the far field of the source unless the distance to the source is very large and the scattered field cannot be regarded as the far field from the scatterer unless the observing point lies at very remote place. In other words, the condition for the far field depends not only on the distances to the source and the observing point compared with the wave length and the dimension of the scatterer, but also on the ratio of the latter two.

It would be, therefore, desirable that the comparison of our formulas with real experiments is carried out for such a large kl and $k\rho$ that the correction terms have only small effect on the scattered field. An estimation for the advisable value of kl and $k\rho$ is obtained when we compare terms of the next order with the dominant term for the special case of $\theta=0$. For example, we take the case given by the expression (4.9), and put it in the following form.

$$\begin{aligned}\boldsymbol{E}_s(\boldsymbol{r},t)=p_0\sqrt{\frac{\pi}{2}}e^{(3/4)\pi j}\frac{k^2}{\sqrt{kl\rho(l+\rho)}}e^{j(\omega t-kl-k\rho)}\,\eta_0(k\rho_0)^2\frac{J_1(\zeta_1)}{\zeta_1}\\ \times\left\{F_0(\theta)+\frac{1}{2}\left(\frac{1}{kl}+\frac{1}{k\rho}\right)jF_1^{(1)}(\theta)+\frac{2}{k(l+\rho)}jF_1^{(2)}(\theta)+\cdots\right\}\boldsymbol{e}_z\,.\end{aligned} \tag{5.1}$$

When the plasma is collisionless and there is no external magnetic field, $L=N=1$, $M=0$ and the expression for $\theta=0$ reduces to

$$\left.\begin{aligned} &F_0(0)=1\,, \\ &F_1^{(1)}(0)=\frac{1}{4}\left(1-2\left(1-\frac{4}{\zeta_1^2}\right)(kp_0)^2\right), \\ &\qquad=0.25-0.15417(k\rho_0)^2\,, \\ &F_1^{(2)}(0)=-\frac{7}{16}=-0.4375\,. \end{aligned}\right\} \tag{5.2}$$

Table I.

$k\rho_0$	$F_1^{(1)}(0)$
2	−0.37
4	−2.22
6	−5.30
8	−9.62
10	−15.17

Table 1 gives the values of $F_1^{(1)}(0)$ as a function of $k\rho_0$; kl and $k\rho$ should be at least ten fold larger than the absolute value of $F_1^{(1)}(0)$ given in this table. When the radius of the discharge tube is equal to the wave length, $k\rho_0\approx6$. The table tells us that then we should choose l and ρ larger than 9 times of the wave length, which is of reasonable scale in practical experiments, too. But even when we choose kl and $k\rho$ as such, we must be careful when $F_0(\theta)$ tends to zero if we wish to use the dominant term only.

§ 6. The Scattered Field at an Arbitrary Point

In this section we derive the scattered field at an arbitrary point. The observing point is located at $P(\rho, \theta, z)$ with $k\rho\gg1$ and arbitrary θ and z. Because of the complexity of the calculation, we give here only the dominant terms of the scattered field. In this case we need only to retain the lowest terms with respect to $1/kl$ and $1/k\rho$ at every step of the calculation. This simplifies our analysis considerably.

6.1. *The dipole source parallel to the z-axis*

Let us put the dipole source given by (3.1) at S. Then the field of the incident wave at Q is given by (3.2). It should be noted here that, contrary to the previous case, $E_{0x}^{(1)}(\boldsymbol{r}', t)$ gives a term of the same order as that given by $E_{0z}^{(1)}(\boldsymbol{r}', t)$. $E_{0y}^{(1)}(\boldsymbol{r}', t)$ gives a higher order term than other two and can be neglected here, too. At first we consider the contribution from $E_{0z}^{(1)}(\boldsymbol{r}', t)$.

$$E_{0z}^{(1)}(\boldsymbol{r}', t)=k^2p_0\exp[j(\omega t-kR_1)]\frac{\xi_1^2}{R_1^3}\,, \tag{6.1}$$

where R_1 and ξ_1 are the same as that defined by (3.3). Using (2.7) and (2.10) we find the contribution of the electron located at Q as follows.

$$(\boldsymbol{E}^{(1)}(\boldsymbol{r}, t))_Q=-\frac{e^2}{m\omega^2}k^4p_0N\exp[j(\omega t-kR_1-kR)]\frac{\xi_1^2}{R_1^3R^3}\{\xi^2\boldsymbol{e}_z-(x-x')(z-z')\boldsymbol{e}_x-(y-y')(z-z')\boldsymbol{e}_y\}\,, \tag{6.2}$$

where

$$R^2=|\boldsymbol{R}|^2=\xi^2+(z-z')^2\,, \tag{6.3}$$

with ξ defined by (3.7). In summing the contributions from all electrons in the cylindrical plasma, we need the asymptotic expression of the following integral for large kl and $k\rho$:

$$I_{m,n}=\int_{-\infty}^{\infty}\frac{1}{R_1^mR^n}\exp[-jk(R_1+R)]dz'\,. \tag{6.4}$$

This is accomplished in Appendix B and the result is

$$I_{m,n}=\sqrt{2\pi}\,e^{-(\pi/4)j}\frac{(\xi_1+\xi)^{m+n-2}\exp[-jk\sqrt{(\xi_1+\xi)^2+z^2}]}{\xi_1^{m-1}\xi^{n-1}\sqrt{k\xi_1\xi}\,[(\xi_1+\xi)^2+z^2]^{(1/2)(m+n)-(3/4)}}\,. \tag{6.5}$$

On the other hand, in the course of the derivation of (6.5), we find that the following rule can be used in the evaluation of the integral, when we want to get the dominant terms only.

For example, let us take an integral of the following form;

$$\int_{-\infty}^{\infty}\frac{\xi_1^2}{R_1^3R^3}(x-x')(z-z')\exp[-jk(R_1+R)]dz'\,. \tag{6.6}$$

Then we regard the integrand as the product of $(R_1R)^{-3}\exp[-jk(R_1+R)]$ and $\xi_1^2(x-x')(z-z')$. The former factor gives the contribution given by (6.5). In other factors, we replace

$$\left.\begin{array}{lll} z' & \text{by} & lz/(l+\rho)\,, \\ z-z' & \text{by} & \rho z/(l+\rho)\,, \\ x-x' & \text{by} & \rho\cos\theta\,, \\ y-y' & \text{by} & \rho\sin\theta\,. \end{array}\right\} \tag{6.7}$$

Finally we make the product of these factors and get the dominant term of the asymptotic expansion of the integral. When it is convenient, some R^2 can be also regarded as an extra factor in the integrand and is replaced by $\rho^2[1+z^2/(l+\rho)^2]$. In this way the integral (6.6) can be evaluated to be

$$\begin{aligned}&\sqrt{2\pi}e^{-(\pi/4)j}\frac{(l+\rho)^4\exp[-jk\sqrt{(\xi_1+\xi)^2+z^2}]}{l^2\rho^2\sqrt{kl\rho}\,[(l+\rho)^2+z^2]^{9/4}}\times l^2\rho\cos\theta\frac{\rho z}{l+\rho}\\ &=\sqrt{2\pi}e^{-(\pi/4)j}\frac{(l+\rho)^3z\cos\theta}{\sqrt{kl\rho}\,[(l+\rho)^2+z^2]^{9/4}}\exp[-jk\sqrt{(\xi_1+\xi)^2+z^2}]\,.\end{aligned} \tag{6.8}$$

At the final step of our calculation, we have to perform the integration with respect to θ'. Inserting the expansion of the argument of the exponential function

$$\sqrt{(\xi_1+\xi)^2+z^2}=\sqrt{(l+\rho)^2+z^2}+\frac{l+\rho}{\sqrt{(l+\rho)^2+z^2}}\rho'(\cos\theta'-\cos(\theta'-\theta))+\cdots\,, \tag{6.9}$$

into the integrand and retaining the terms of lowest order only, we have

$$\int_0^{2\pi}[-jk\sqrt{(\xi_1+\xi)^2+z^2}]d\theta'=\exp[-jk\sqrt{(l+\rho)^2+z^2}]\cdot 2\pi J_0\left(\frac{l+\rho}{\sqrt{(l+\rho)^2+z^2}}2k\rho'\sin\frac{\theta}{2}\right). \tag{6.10}$$

In this way the contribution to the scattered field from the z-component of the incident wave is found to be

$$\begin{aligned}&-\frac{1}{4\pi}k^4p_0\int_0^{\infty}N\eta(\rho')\rho'd\rho'\int_0^{2\pi}d\theta'\int_{-\infty}^{\infty}dz'\exp[j(\omega t-kR_1-kR)]\\ &\quad\times\frac{\xi_1^2}{R_1^3R^3}\{\xi^2e_z-(x-x')(z-z')e_x-(y-y')(z-z')e_y\}\\ &=p_0\sqrt{\frac{\pi}{2}}\,e^{(3/4)\pi j}\frac{k^4(l+\rho)^4}{\sqrt{kl\rho}\,[(l+\rho)^2+z^2]^{9/4}}\exp[j(\omega t-k\sqrt{(l+\rho)^2+z^2})]\\ &\quad\times\int_0^{\infty}N\eta(\rho')J_0\left(\frac{l+\rho}{\sqrt{(l+\rho)^2+z^2}}2k\rho'\sin\frac{\theta}{2}\right)\rho'd\rho'\left[e_z-\frac{z}{l+\rho}e_\rho\right].\end{aligned} \tag{6.11}$$

Similarly the contribution from the x component of the incident wave are evaluated. Thus adding these two contributions, we get the total scattered field:

$$\boldsymbol{E}_s(\boldsymbol{r}, t) = p_0\sqrt{\frac{\pi}{2}}e^{(3/4)\pi j}\frac{k^4(l+\rho)^4}{\sqrt{kl\rho}\,[(l+\rho)^2+z^2]^{9/4}}\exp\left[j(\omega t - k\sqrt{(l+\rho)^2+z^2})\right]$$
$$\times\int_0^\infty \eta(\rho')J_0\left(\frac{l+\rho}{\sqrt{(l+\rho)^2+z^2}}2k\rho'\sin\frac{\theta}{2}\right)\rho' d\rho'\left\{\left[N+\frac{z^2}{(l+\rho)^2}(L\cos\theta - jM\sin\theta)\right]\boldsymbol{e}_z\right.$$
$$-\frac{z}{l+\rho}\left[N+\frac{z^2}{(l+\rho)^2}(L\cos\theta - jM\cos\theta)\right]\boldsymbol{e}_\rho$$
$$\left.+\frac{z}{l+\rho}\left(1+\frac{z^2}{(l+\rho)^2}\right)(L\sin\theta + jM\cos\theta)\,\boldsymbol{e}_\theta\right\}. \tag{6.12}$$

6.2. *The dipole source parallel to the y or x-axis*

When the dipole cource has a moment parallel to the y or x-axis, the calculation is similar as that in the previous subsection. In this subsection we give only the result.

When a dipole source

$$\boldsymbol{p}_0(t) = p_0' e^{j\omega t}\boldsymbol{e}_y\,, \tag{6.13}$$

is located at S, the scattered field at P is given by

$$\boldsymbol{E}_s(\boldsymbol{r}, t) = p_0'\sqrt{\frac{\pi}{2}}e^{(3/4)\pi j}\frac{k^4(l+\rho)^2}{\sqrt{kl\rho}\,[(l+\rho)^2+z^2]^{5/4}}\exp\left[j(\omega t - k\sqrt{(l+\rho)^2+z^2})\right]$$
$$\times\int_0^\infty \eta(\rho')J_0\left(\frac{l+\rho}{\sqrt{(l+\rho)^2+z^2}}2k\rho'\sin\frac{\theta}{2}\right)\rho' d\rho'\left\{\left(1+\frac{z^2}{(l+\rho)^2}\right)(L\cos\theta - jM\sin\theta)\boldsymbol{e}_\theta\right.$$
$$\left.+\frac{z^2}{(l+\rho)^2}(L\sin\theta + jM\cos\theta)\boldsymbol{e}_\rho - \frac{z}{l+\rho}(L\sin\theta + jM\cos\theta)\,\boldsymbol{e}_z\right\}. \tag{6.14}$$

When a dipole source is of the following form

$$\boldsymbol{p}_0(t) = p_0'' e^{j\omega t}\boldsymbol{e}_x\,, \tag{6.15}$$

we have

$$\boldsymbol{E}_s(\boldsymbol{r}, t) = p_0''\sqrt{\frac{\pi}{2}}e^{(3/4)\pi j}\frac{k^4(l+\rho)^3 z}{\sqrt{kl\rho}\,[(l+\rho)^2+z^2]^{9/4}}\exp\left[j(\omega t - k\sqrt{(l+\rho)^2+z^2})\right]$$
$$\times\int_0^\infty \eta(\rho')J_0\left(\frac{l+\rho}{\sqrt{(l+\rho)^2+z^2}}2k\rho'\sin\frac{\theta}{2}\right)\rho' d\rho'\left\{\frac{z}{l+\rho}\left[N+\frac{z^2}{(l+\rho)^2}(L\cos\theta - jM\sin\theta)\right]\boldsymbol{e}_\rho\right.$$
$$\left.-\frac{z}{l+\rho}\left(1+\frac{z^2}{(l+\rho)^2}\right)(L\sin\theta + jM\cos\theta)\,\boldsymbol{e}_\theta - \left[N+\frac{z^2}{(l+\rho)^2}(L\cos\theta - jM\sin\theta)\right]\boldsymbol{e}_z\right\}. \tag{6.16}$$

§ 7. Conclusion

So far we have derived the scattered field from a cylindricol plasma in the Born approximation, when an incident wave is radiated from a point source of an oscillating electric field. Generally speaking, our formulas are useful when $k\rho_0$ is not large, and the comparison with experiments should be carried out under the condition that the dominant terms have sufficient accuracy. When $k\rho_0$ is very large, the conventional method[2] of regarding the plasma as a plane slab may be a good approximation. It is hoped anyhow that our formulas would be of help for analysis of experiments of the scattering of microwaves from a cylindrical plasma.

The author wishes to express his sincere thanks to Professor T. Kihara for his continual guidance and his kindness in reading the original manuscript.

Appendix A. Derivation of Equation (3.9)

Here we handle a little more general integral of the following type.

$$
\begin{aligned}
I_{m\ n}&=\int_{-\infty}^{\infty}\frac{1}{R_1{}^m R^n}\exp\left[-jk(R_1+R)\right]dz'\\
&=2\int_0^{\infty}\frac{1}{(z'^2+\xi_1{}^2)^{m/2}(z'^2+\xi^2)^{n/2}}\exp\{-jk[(z'^2+\xi_1{}^2)^{1/2}+(z'^2+\xi^2)^{1/2}]\}dz' \,. \qquad (A.1)
\end{aligned}
$$

Introducing a new variable u by

$$u=k[(z'^2+\xi_1{}^2)^{1/2}+(z'^2+\xi^2)^{1/2}]-(\lambda_1+\lambda)\,, \qquad (A.2)$$

where $\lambda_1\equiv k\xi_1$ and $\lambda\equiv k\xi$, we get

$$
\begin{aligned}
I_{m,n}=2^{m+n}k^{m+n-1}\exp\left[-j(\lambda_1+\lambda)\right]\int_0^{\infty}&\frac{(u+\lambda_1+\lambda)^{m+n-2}[(u+\lambda_1+\lambda)^4-(\lambda_1{}^2-\lambda^2)^2]e^{-ju}}{[(u+\lambda_1+\lambda)^2+\lambda_1{}^2-\lambda^2]^m[(u+\lambda_1+\lambda)^2-\lambda_1{}^2+\lambda^2]^n}\\
\times&\frac{du}{[(u+\lambda_1+\lambda)^4-2(u+\lambda_1+\lambda)^2(\lambda_1{}^2+\lambda^2)+(\lambda_1{}^2-\lambda^2)^2]^{1/2}}\,. \qquad (A.3)
\end{aligned}
$$

We assume that $\lambda_1+\lambda\equiv A$ is very large and introduce g_1, g and x by

$$\lambda_1=g_1A\,, \qquad \lambda=gA \qquad \text{and} \qquad u=Ax\,. \qquad (A.4)$$

Then we have

$$I_{m,n}=\left(\frac{k}{A}\right)^{m+n-1}e^{-jA}\frac{\sqrt{2}}{g_1{}^{m-(1/2)}g^{n-(1/2)}}\int_0^{\infty}s(x)e^{-jAx}dx\,, \qquad (A.5)$$

where $s(x)$ is independent of A and has the following asymptotic properties:

$$
s(x)\longrightarrow\begin{cases}\dfrac{1}{\sqrt{x}}\left\{1+\left(m+n-\dfrac{9}{4}-\left(m-\dfrac{3}{4}\right)\dfrac{1}{g_1}-\left(n-\dfrac{3}{4}\right)\dfrac{1}{g}\right)x+\mathrm{O}(x^2)\right\} & \text{as} \quad x\to 0\,,\\[2ex] 2^{m+n-(1/2)}\,g_1{}^{m-(1/2)}\,g^{n-(1/2)}\dfrac{1}{x^{m+n}}\left(1+\mathrm{O}\left(\dfrac{1}{x}\right)\right) & \text{as} \quad x\to\infty\,.\end{cases} \qquad (A.6)
$$

We divide the integral (A.5) into two parts. The first part is obtained as follows.

$$\int_0^{\infty}\frac{1}{\sqrt{x}}e^{-jAx}dx=\frac{1}{\sqrt{A}}\int_0^{\infty}\frac{e^{-ju}}{\sqrt{u}}du=\sqrt{\frac{\pi}{A}}e^{-(\pi/4)j}\,. \qquad (A.7)$$

The second part is evaluated by the integration by parts:

$$
\begin{aligned}
&\int_0^{\infty}\left[s(x)-\frac{1}{\sqrt{x}}\right]e^{-jAx}dx\\
&=\frac{1}{jA}\int_0^{\infty}\frac{\partial}{\partial x}\left[s(x)-\frac{1}{\sqrt{x}}\right]e^{-jAx}dx\\
&=\frac{1}{2jA}\left(m+n-\frac{9}{4}-\left(m-\frac{3}{4}\right)\frac{1}{g_1}-\left(n-\frac{3}{4}\right)\frac{1}{g}\right)\int_0^{\infty}\frac{e^{-jAx}}{\sqrt{x}}dx\left(1+\mathrm{O}\left(\frac{1}{A}\right)\right)\\
&=\frac{1}{2jA}\sqrt{\frac{\pi}{A}}e^{-(\pi/4)j}\left(m+n-\frac{9}{4}-\left(m-\frac{3}{4}\right)\frac{1}{g_1}-\left(n-\frac{3}{4}\right)\frac{1}{g}\right)\left(1+\mathrm{O}\left(\frac{1}{A}\right)\right)\,. \qquad (A.8)
\end{aligned}
$$

Substituting these into (A.5), we have the desired result,

$$
\begin{aligned}
I_{m,n}=&\frac{\sqrt{2\pi}}{\xi_1{}^{m-1}\xi^{n-1}\sqrt{k\xi_1\xi(\xi_1+\xi)}}\exp\left[-jk(\xi_1+\xi)-\frac{\pi}{4}j\right]\\
&\times\left\{1-\frac{1}{2}j\left[\left(m+n-\frac{9}{4}\right)\frac{1}{k(\xi_1+\xi)}-\left(m-\frac{3}{4}\right)\frac{1}{k\xi_1}-\left(n-\frac{3}{4}\right)\frac{1}{k\xi}\right]+\cdots\right\}\,. \qquad (A.9)
\end{aligned}
$$

Appendix B. Derivation of Equation (6.5)

$$I_{m,n} \equiv \int_{-\infty}^{\infty} \frac{1}{(\xi_1^2+z'^2)^{m/2}(\xi^2+(z-z')^2)^{n/2}} \exp\{-jk[(\xi_1^2+z'^2)^{1/2}+(\xi^2+(z-z')^2)^{1/2}]\} dz' . \tag{B.1}$$

Let us introduce a new variable v by

$$v=(\xi_1^2+z'^2)^{1/2}+(\xi^2+(z'-z)^2)^{1/2} . \tag{B.2}$$

(B.2) is a quadratic equation for z' and can be easily solved.

$$z'=\frac{1}{2(v^2-z^2)}\{z(v^2+\xi_1^2-\xi^2-z^2)\pm v\sqrt{(v^2-\xi_1^2-\xi^2-z^2)^2-4\xi_1^2\xi^2}\} , \tag{B.3}$$

The v takes its minimum value $[(\xi_1+\xi)^2+z^2]^{1/2}$ at $z'=z\xi_1/(\xi_1+\xi)$ and at this point two roots (B.3) for z' coincide each other. Thus we divide the integral (B.1) into two parts

$$I_{m,n}=\int_{z\xi_1/(\xi_1+\xi)}^{\infty} dz' + \int_{-\infty}^{z\xi_1/(\xi_1+\xi)} dz' . \tag{B.4}$$

When we deal with the first term, we take in the expression (B.3) the upper sign, and for the second integral we take the lower sign.

Further we introduce a variable u as in the previous section.

$$u=kv-\sqrt{(\lambda_1+\lambda)^2+\lambda_2^2} , \tag{B.5}$$

where λ_1 and λ were defined in the previous section and $\lambda_2 \equiv kz$. Then the analysis proceeds as before. We get an integral of the form:

$$\int_0^{\infty} s(u)e^{-ju}du . \tag{B.6}$$

If we want the dominant terms, we need only to retain the leading term of the expansion of $s(u)$ for small u. The factor $1/\sqrt{u}$ is provided by dz'/du, and we get the final results,

$$I_{m,n}=\sqrt{2\pi}\, e^{-(\pi/4)j} k^{m+n-1} \frac{(\lambda_1+\lambda)^{m+n-2}\exp[-j\sqrt{(\lambda_1+\lambda)^2+\lambda_2^2}]}{\lambda_1^{m-1}\lambda^{n-1}\sqrt{\lambda_1\lambda}\,[(\lambda_1+\lambda)^2+\lambda_2^2]^{(1/2)(m+n)-3/4}} . \tag{B.7}$$

In the course of the derivation mentioned above, we find that, if there is some extra factor in the integrand, it can be replaced by the leading term of the expansion in u of itself. Thus it is allowed to use the rule of the replacement given by (6.7) used in section 6.

Appendix C. The generality of the Dominant Terms

The formulas for the dominant terms given by expressions (4.3) and (4.4) are valid for more general spherical waves than that radiated by an oscillating electric dipole, provided the fields of the incident waves at the origin are $E_{0z}(0, t)$ and $E_{0y}(0, t)$ respectively. This is shown in the following.

Let us put, for example, an electromagnetic horn at S toward the origin of our coordinate system. The electric field of the incident wave at the origin is assumed to be of z direction. Then the dominant contribution to the scattered field at a point P with $z=0$ comes from the z component of the incident wave, which would be of the following form in the cylindrical plasma.

$$E_{0z}(r, t)=E_{0z}^{(0)}\frac{1}{R_1}\exp[j(\omega t-kR_1)]\tilde{F}\left(\frac{x'}{l}, \frac{y'}{l}, \frac{z'}{l}\right) , \tag{C.1}$$

where $\tilde{F}(x'/l, y'/l, z'/l)$ is a slowly varying function of the arguments and finite for all points in the cylinder and $\tilde{F}(0, 0, 0)=1$. Since the radius of the cylinder ρ_0 is much smaller than

l, we can replace $\tilde{F}(x'/l, y'/l, z'l)$ by $\tilde{F}(0, 0, z'/l) \equiv F(z')$ provided we wish to get the dominant term only. Thus we have

$$E_{0z}(r', t) = E_{0z}^{(0)} \frac{1}{R_1} \exp\left[j(\omega t - kR_1)\right] F(z') , \tag{C.2}$$

and the integral corresponding to (3.9) is

$$\int_{-\infty}^{\infty} \frac{1}{R_1 R^3} F(z') \exp\left[-jk(R_1 + R)\right] dz' . \tag{C.3}$$

When we introduce new variables used in Appendix A, we find that in the extra factor of the integrand such as $F(z')$, we need only the leading term in the power expansion with respect to z'. Thus the asymptotic expression of (C.3) depends only on $F(0)=1$ and not on the details of the angular distributions. The same is true for (4.4) and this proves our statement at the beginning of this appendix.

References

1) Y. Midzuno: J. Phys. Soc. Japan **16** (1961) 971.
2) S. Glasstone and R. H. Lovberg: *Controlled Thermonuclear Reactions* (D. van Nostrand Co. Inc., Princeton, 1960) 170 p.
3) J. C. Slater and N. H. Frank: *Electromagnetism* (McGraw-Hill Book Co. Inc., N. Y., 1947) 159 p.
4) J. A. Stratton: *Electromagnetic Theory* (McGgraw-Hill Book Co. Inc., N. Y., 1947) 434 p.
5) M. J. Druyvesteyn and F. M. Penning: Revs. Modern Phys. **12** (1940) 87.

Journal of the Physical Society of Japan Vol. 16, No. 7, July, 1961

Temperature Dependences of the Fundamental Absorption Tail of KCl and the Absorption due to Bromines in KCl

By Koichi KOBAYASHI
Institute for Solid State Physics, University of Tokyo, Tokyo
and Tetsuhiko TOMIKI
Department of Physics, Tohoku University, Sendai

(Received March 7, 1961)

Optical absorptions of the fundamental absorption tail of specially purified KCl and those due to bromines in KCl were measured between room temperature and 196°C. The latters were estimated from the differences between the fundamental absorption tails of pure KCl and KCl with bromine of which concentration was 1.3×10^{-4} in mole fractian. Measured absorption coefficients were corrected by considering the errors due to the finite band width of the spectrometer. The fundamental absorption tail of KCl was found to be represented by the Urbach rule with $\sigma = 0.80 \pm 0.02$ and $h\nu_0 = 7.76 \pm 0.10$ ev. The long wavelength side of the bromine absorption was able to be described by the same rule where $\sigma = 0.51 \pm 0.03$ and $h\nu_0 = 7.35 \pm 0.15$ ev.

§1. Introduction

The absorption coefficients of some ionic crystals at their fundamental absorption tails have been known to change in an exponential manner as a function of photon energy and of temperature. This is known as the Urbach rule and was first found by Urbach[1] in silver bromide. For alkali halides, Martienssen[2] has made the measurement of the absorption tail on pure KBr, and Haupt[3] on pure KI, and they have found that these tails can be described fairly well by the Urbach rule over a very wide range of temperature and absorption coefficient. The tails of these crystals are believed to be due to exciton absorptions so that their results have given important informations to an exciton picture in alkali halides.

The purpose of this study is of twofold. The following is the first one. No work relating to the Urbach rule has been made on the fundamental absorption tail of KCl, the most typical substance among potassium halides. As has been reported in our previous paper[4)], we have succeeded to prepare pure KCl with clean fundamental absorption tail by an elimination of impurity bromines which are present in fairly large amount in crystals commonly used. Therefore, it would be worthwhile to investigate the fundamental absorption tail of this *pure* KCl.

Secondly, studies on the absorption tails which have been made so far are on pure alkali halides and the observed exciton absorptions are due to halide ions which are surrounded by halide ions of the same kind and alkaline ions. If one replaces the environment around halide ion, of which optical excitation we are interested in, with other halides but the same alkalines and compares its absorption to that of pure one, one might be able to obtain some other informations on excitons in alkali halides through an effect of a local change of a lattice constant and an electronic configuration.

We have found the absorption band due to bromine in KCl at the tail of the fundamental absorption of the host crystal[4)]. The concentration of bromine in this case was as low as 10^{-4} in mole fraction and the bromines were beleived to be distributed randomly throughout the crystal, so that the interaction between bromine ions was considered to be almost negligble. Therefore, if one uses this crystal, one might be able to investigate the exciton absorption due to bromine in an isolated state in KCl lattice. This situation would be almost an ideal one for the present purpose.

In the present study, we have measured absorption coefficients of the long wavelength tail of the fundamental absorptions of *pure* KCl and KCl containing bromine of 1.3×10^{-4} in mole fraction at several different temperatures. The fundamental absorption tail of KCl has been obtained from the measurement on the former crystal. The absorption due to bromine has been estimated from the results of both crystals. It has been found that both the fundamental absorption tail of *pure* KCl and the long wavelength side of the absorption due to bromine in KCl can be described fairly well by the Urbach rule.

§ 2. Measurements and Results

The specially purified KCl crystal used in this study as a *pure* one was KCl-aK-1[4)] which contained bromines of 9×10^{-6} in mole fraction and divalent metallic ion impurities of 1×15^{15} per cc. KCl-bK-1[4)] was the KCl crystal, which we were interested in measuring its bromine absorption, contained bromines of 1.3×10^{-4} in mole fraction and divalent metallic ion impurities of 4×10^{15} per cc. Hydroxyl ions of the concentration of 2×10^{15} per cc[4)] were found in both crystals.

Optical transmissions at the absorption tails of both crystals were measured with a vacuum ultraviolet spectrometer at 26, 56, 100, 147, and 196°C. The temperature was held constant within ±1°C throughout a run. In determining absorption coefficients from transmission measurements, it is necessary to take into account the light losses due to scattering at the surface and in the volume of the crystal, as well as the specular reflection losses at the surface. However, as have been shown in our previous paper[4)], the scatter correction is found to be negligible in these crystals and the absorption coefficient can be estimated fairly well from the observed transmittance and the reflectivity calculated from the refractive index. The refrative indices at room temperature used in this study were those given by Gyulai[5)] and by Hartman *et al*[6)], the latter of which were normalized to the former at 185 mμ.

The values of refractive index of KCl at higher temperatures were not available. Thus the room temperature dispersion curve was shifted to the longer wavelength side by an amount corresponding to the wavelength difference between the positions of the absorption tails at room temperature and higher temperature so as to estimate the high temperature dispersion curves. In order to justify this method, absorption coefficients were estimated from the observed transmittances of crystals with different thicknesses and the assumed dispersion curves at different temperatures. All of them were found to be zero within our experimental error at 240 mμ where no absorption have been found in these crystals[4]. This would indicate that the above procedures are suitable to the estimation of refractive indices at higher temperatures, and the absorption coefficients at 56, 100, 147, and 196°C were calculated by using the assumed curves.

It has been pointed out by Moser and Urbach[7] that an appreciable error might be introduced into a determination of an absoption coefficient, K, as a result of using a finite band width in a measurement of a transmission where an absorption coefficient changes markedly with a wavelength, λ. Their analysis shows that if a band width is finite and an absorption coefficient is represented by $K = K_1 \exp(-b\lambda)$, where K_1 and b are constants, an absorption coefficient calculated from a measured transmittance of a crystal with certain thickness must be different from that of a crystal with other thickness, and only an observed absorption coefficient which satisfy the condition, $Kd=1$, is a *true* absorption coefficient of a crystal with a thickness, d.

Figs. 1 and 2 are examples of the present measurements of the absorption coefficients at the tails of KCl-aK-1 and KCl-bK-1 at 56°C and 147°C. They were calculated from the measured transmittances of the crystals with different thicknesses of which magnitudes are indicated at the upper right hand of the figures. One may readily see that the observed absorption coefficients are always higher for the crystal with smaller d. This is the tendency which can be derived from the analysis by Moser and Urbach[7]. Double circles in both figures are the points where Kd is unity. These points are well represented by straight lines in log K *versus* photon energy plots as indicated as dashed lines.

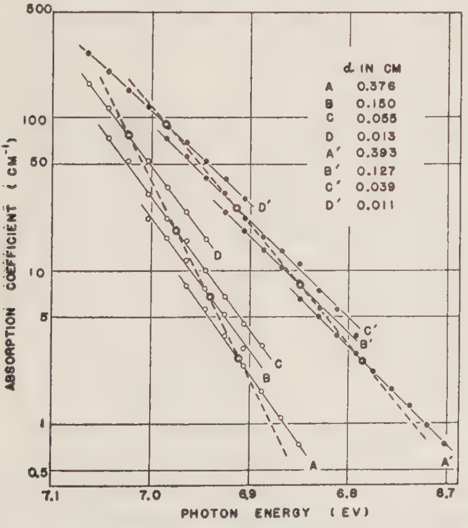

Fig. 1. Absorption spectra at the fundamental absorption tails of *pure* KCl (KCl-aK-1) and KCl containing bromines (KCl-bK-1) at 56°C. The open circles are the absorption coefficients calculated from the observed transmittances of KCl-aK-1 with different thicknesses and the filled ones are those of KCl-bK-1. The dashed lines are those which connect the points where $Kd=1$ (double circles).

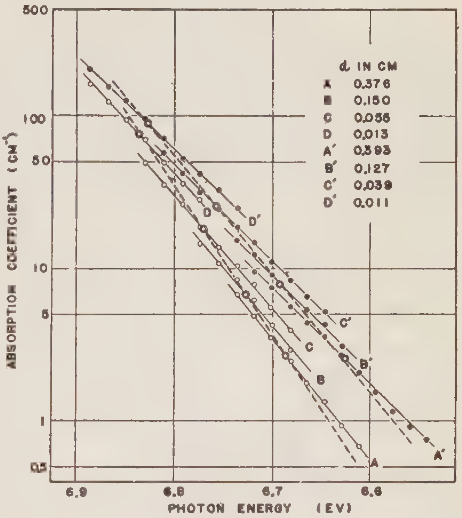

Fig. 2. Absorption spectra at the fundamental absorption tails of *pure* KCl (KCl-aK-1) and KCl containing bromines (KCl-bK-1) at 147°C. The open circles are the absorption coefficients calculated from the observed transmittances of KCl-aK-1 with different thicknesses and the filled ones are those of KCl-bK-1. The dashed lines are those which connect the points where $Kd=1$ (double circles).

This exponential behavior of the absorption coefficient to the photon energy may indicate that the analysis by Moser and Urbach is applicable to the present observed values since the exponential behavior may hold to photon energy as well as to wavelength if the range of wavelength is small. Therefore, the points at $Kd=1$ are the absorption coefficients free from errors due to the finite band width, and the dashed lines may be the *true* absorption tails of both crystals.

Measurements on crystals with different thicknesses at other temperatures have indicated also the same features as described above. Fig. 3 shows the absorption tails of *pure* KCl (KCl-aK-1) at five different temperatures. The open circles are the points which satisfy the condition, $Kd=1$, in observed absorption curves of crystals with different thickcesses. The lines which connect these points are linear in $\log K$ *versus* photon energy diagram and their slopes are decreased as the temperature is increased. Fig. 4 shows the photon energies corresponding to constant absorption coefficient in the curves in Fig. 3 as a function of temperature. The dashed lines are the extrapolations of the lines which connect the points with constant K. They are found to cross one another at zero degree Kelvin.

From Figs. 3 and 4, it might be found that the fundamental absorption tail of KCl can be represented by the Urbach rule,

$$K=K_0 \exp\left[-\frac{\sigma(h\nu_0-h\nu)}{kT}\right], \qquad (1)$$

where K_0 and σ are constants, $h\nu$ the photon energy at K and T, and $h\nu_0$ the extrapolated photon energy at zero degree Kelvin. Taking into account the errors due to the measure-

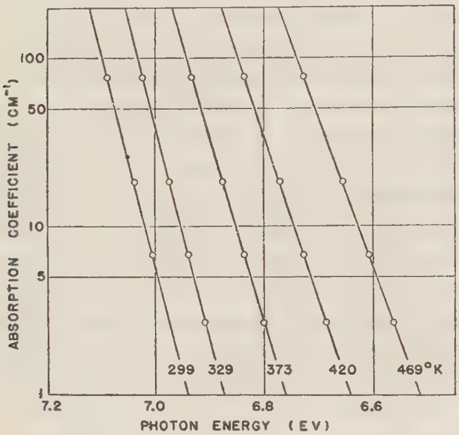

Fig. 3. Fundamental absorption tails of *pure* KCl at seveval different temperatures. The open circles are the points which satisfy the condition, $Kd=1$. in observed absorption curves of crystals with different thicknesses. Temperatures are indicated in this figure in an absolute scale.

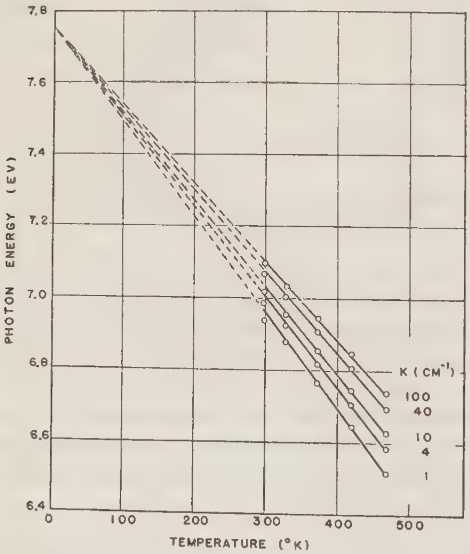

Fig. 4. Photon energies corresponding to a constant absorption coefficient in the curves in Fig. 3 as a function of temperature. They are represented by full lines for constant K of which magnitudes are indicated at the right hand side of this figure. The dashed lines are their linear extrapolations.

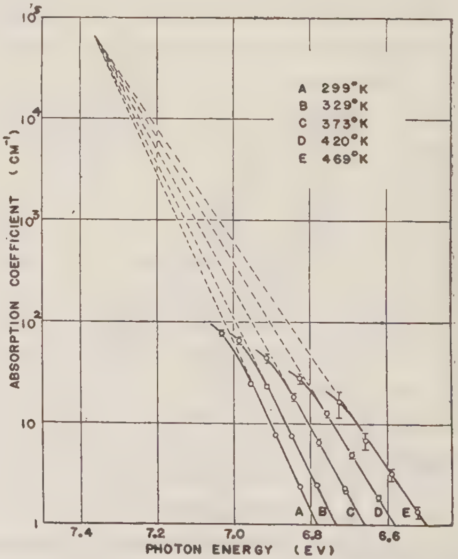

Fig. 5. Absorption Spectra at the long wavelength side of the absorption band due to bromine in KCl at different temperatures which are indicated in this figure in an absolute scale. The full lines are those which connect the observed absorption coefficents and the dashed ones are those extrapolated linearly to high absorption coefficient.

ments, it was found that $h\nu_0$ is 7.76±0.10 ev and σ is 0.80±0.02.

The absorptions due to bromine in KCl-bK-1 were estimated at five different temperatures by subtracting the *true* absorption curves of KCl-aK-1 from those of KCl-bK-1. The results are shown in Fig. 5. One may note that these absorptions are due to bromines with their concentrations of 1.2×10^{-4} in mole fraction since the concentration of bromine in KCl-aK-1 is 9×10^{-6} and in KCl-bK-1 is 1.3×10^{-4}. In the low absorption coefficient region, absorption curves are linear in log K *versus* photon energy plots and their slopes are decreased as the temperature is increased. The dashed lines are their linear extrapolations to high K value where they are found to cross one another at one point. The highest points among the observed ones are found to deviate from the linear relationship since they are the points which are close to the maxima of the absorption bands[4].

Fig. 6 shows the photon energies where K is constant in the absorption curves of bromine for different temperatures. The open circles in this figure are the values obtained from the observed curves and the filled ones are from the linearly extrapolated lines in Fig. 5. The dashed lines in Fig. 6 are the extrapolations of the lines which connect the points with constant K. They are found to cross one another at zero degree Kelvin.

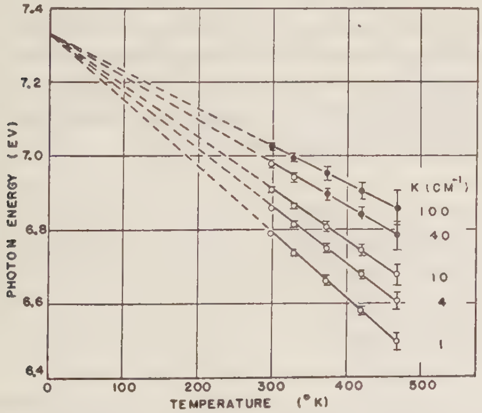

Fig. 6. Photon energies corresponding to a constant absorption coefficient in the absorption curves of bromine in KCl as a function of temperature. The open circles are taken from the observed curves in Fig. 5 and the filled ones are from the linearly extrapolated lines as indicated as dashed lines in Fig. 5. They are represented by full lines for constant K of which magnitudes are indicated at the right hand side of this figure. The dashed lines are their linear extrapolations.

From Figs. 5 and 6, it might be found that the absorption due to bromine in KCl can be described fairly well by the Urbach rule with $h\nu_0=7.35\pm0.15$ ev and $\sigma=0.51\pm0.03$ in equation (1). The absorptions shown in Figs. 5 and 6 are of bromines of 1.2×10^{-4} in mole fraction and thus the magnitude of K_0 was estimated as being in the range between 3×10^9 and 2×10^8 cm^{-1} with such a condition that all chlorine ions in KCl are supposed to be replaced by bromine ions without introducting both the change in lattice constant and the interaction between bromine ions. If the lattice constant of KBr is used in the above estimation, K_0 may be smaller by about ten percent.

§ 3. Discussion

In the present study, σ of the fundamental absorption tail of pure KCl has been obtained as 0.80±0.02. σ of KBr has been given by Martienssen[2] as 0.79 and of KI by Haupt[3] as 0.82. Their magnitudes are almost the same in spite of their different lattice constants and halogens. The fundamental absorption tails of these crystals are believed to be due to exciton excitations of halogens. According to Toyozawa[8], σ may be represented by $C/|E_2|$ where C is an appropriate elastic constant and E_2 a constant to a quadratic term of deformation in the expression of electronic energy change as a function of deformation. Therefore, the differences of the lattice constant and the kind of halogen seem to be rather insensitive to the determination of the magnitude of $C/|E_2|$ of the exciton excitation of pure potassium halides.

It has been known that KCl and KBr make a good solid solution. The concentration of bromine in KCl-bK-1 is as small as 1.3×10^{-4}. Therefore, the bromines may be distributed randomly and the interaction between bromines through the host matrix may be negligible in this crystal. Thus the absorptions due to the presence of bromine in KCl investigated in this study may be due to the isolated bromine ions which simply occupy the chlorine lattice sites.

An exact nature of this absorption due to bromine in KCl is hardly to be known. However, the position of the maximum of this absorption band can be estimated roughly by the assumption that the absorption is due to bromines themselves. The electron affinity of chlorine is 87.1 Kcal and of bromine is 81.2 Kcal⁹⁾, and the maximum of the first absorption peak of the exciton doublet of KCl is at somewhere around 7.52 ev at room temperature¹⁰⁾. Then the bromine absorption in KCl is expected to have its maximum at around 7.26 ev at room temperature which is not far different from 7.12 ev⁴⁾, the observed position of the maximum. The maximum absorption coefficient of the bromine absorption in KCl after being normalized to such a condition that all chlorine ions in KCl are replaced by bromine ions, can be estimated as about $1\times 10^6\,\mathrm{cm}^{-1}$ from the maximum height of the bromine absorption in KCl-bK-1⁴⁾. This magnitude is of a comparable order to the maximum hight of the exciton absorption in KBr²⁾. Therefore, it would be rather unlikely that this absorption is due to optical excitations of twelve chlorines at the second nearest neighbour sites around the bromine, but is very likely to be due to the bromines themselves.

It has been shown that the bromine absorption in KCl can be described by the Urbach rule. However, the magnitude of σ of the bromine absorption in KCl is 0.51 ± 0.03 which is far smaller than 0.79 of bromine in KBr²⁾ and 0.80 ± 0.02 of chlorine in KCl. The small magnitude of σ of the bromine absorption in KCl might be understood by different C and /or different E_2 from those of pure potassium halides as a result of strong distortion around the bromine ions. It may be desirable to study further on the absorption bands of halogens in mixed crystals of other combinations, such as I in KCl and in KBr, to investigate an effect of distortion on an exciton excitation through a magnitude of σ.

Acknowledgement

We wish to thank Professor M. Ueta for his allowing us to use his vacuum ultraviolet spectrometer. One of us (K. K.) is also indebted to Professors T. Inui and Y. Toyozawa for helpful discussions. A part of this work was supported by the Research Grant from the Ministry of Education.

References

1) F. Urbach: Phys. Rev. **92** (1953) 1324.
2) W. Martienssen: J. Phys. Chem. Solids **2** (1957) 257.
3) U. Haupt: Z. Phys. **157** (1959) 232.
4) K. Kobayashi and T. Tomiki: J. Phys. Soc. Japan **15** (1960) 1982.
5) Z. Gyulai: Z. Phys. **46** (1927) 80.
6) P. L. Hartman, J. R. Nelson and J. G. Siegfried: Phys. Rev. **105** (1957) 123.
7) F. Moser and F. Urbach: Phys. Rev. **102** (1956) 1519. See also reference 3).
8) Y. Toyozawa: Prog. Theor. Phys. **12** (1959) 111, Supplement.
9) N. F. Mott and R. W. Gurney: *Electronic Processes in Ionic Crystals* (Oxford at the Clarendon Press, 1946) 8p.
11) J. E. Eby, K. J. Teegarden and D. B. Dutton: Phys. Rev. **116** (1959) 1099.

JOURNAL OF THE PHYSICAL SOCIETY OF JAPAN, Vol. 16, No. 7, JULY, 1961

On the Commencement of the Hartmann Flow of Conducting Fluid

By Akira OGAWA
Institute of Polytechnics, Osaka City University
Yoshio SONE
Faculty of Engineering, Kyoto University

(Received February 16, 1961)

The effect of the transverse magnetic field on the commencement of the two dimensional Poiseuille flow of conducting fluid between two parallel walls is discussed. Owing to the invariance of the flow characteristics in the direction parallel to the walls, the fundamental equations reduce to linear equations and can be solved exactly. Several limiting cases are surveyed on the basis of the solution obtained. Detailed numerical calculation is also made for a special case in which the values of the Reynolds number, the magnetic Reynolds number and the pressure number are all equal to unity.

§ 1. Introduction

In the present paper we study the commencement of the so-called Hartmann flow of a conducting fluid. Suppose that the fluid is at rest between two infinitely large and parallel flat plates of perfect conductor and that the uniform magnetic field is applied normal to the plate for $t<0$. From the time $t=0$ on, uniform pressure gradient $\partial p/\partial x$ which is constant in later time is applied along the walls. Then, the fluid will begin to move under the influence of the viscous, the inertia and the Lorentz forces. The velocity profile and the magnetic field will approach asymptotically those of Hartmann flow.

For this flow, it can be expected that the fluid velocity as well as the magnetic field do not change in the direction parallel to the plates. The fundamental equations governing the fields then reduce to linear equations which can be solved by the method of Fourier expansion.

On examination of the solution it turns out that the flow and magnetic field converge with time to those in Hartmann flow monotonically or in damped vibration in general. The latter case (vibration) could not be found in ordinary viscous flow. When the conductivity of the fluid is infinite, there can be no steady flow but an ultimate state of equilibrium or of undamped oscillation according as the viscosity is finite or zero.

§ 2. Fundamental Equations

The fundamental equations of magneto-hydrodynamics (in rationalized M. K. S. units) are:

$$\mathrm{div}\,\hat{B}=0 \tag{1}$$

$$\mathrm{rot}\,\hat{H}=\hat{j} \tag{2}$$

$$\mathrm{rot}\,\hat{E}=-\frac{\partial\hat{B}}{\partial\hat{t}} \tag{3}$$

$$\hat{j}=\sigma(\hat{E}+\hat{v}\times\hat{B}) \tag{4}$$

$$\frac{D}{D\hat{t}}\hat{v}=-\frac{1}{\rho}\,\mathrm{grad}\,\hat{p}+\nu\Delta\hat{v}+\frac{1}{\rho}(\hat{j}\times\hat{B}) \tag{5}$$

$$\mathrm{div}\,\hat{v}=0 \tag{6}$$

where $\hat{E}$ is the electric field, $\hat{H}$ the magnetic field, $\hat{B}$ the magnetic induction, $\hat{j}$ the current density, σ the electrical conductivity, $\hat{v}$ the fluid velocity, $\hat{p}$ the pressure, ρ the density, ν the kinematic viscosity and $\hat{t}$ the time. The fluid is assumed to be homogeneous and isotropic so that $\hat{B}=\mu\hat{H}$ where μ is the mag-

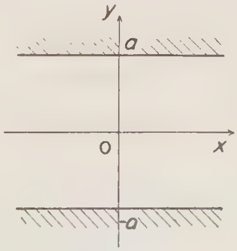

Fig. 1. Coordinate system.

netic permeability.

We choose the Cartesian coordinate system $(\hat{x}, \hat{y}, \hat{z})$ in such a way that the walls are normal to the $\hat{y}$-axis and situated at $\hat{y}=\pm a$ and that the pressure gradient is in the direction of $\hat{x}$-axis (Fig. 1).

It may by assumed in the present problem that

$$\hat{\boldsymbol{v}}=(\hat{u}, 0, 0)\,, \qquad \hat{\boldsymbol{B}}=(\hat{B}_x, \hat{B}_y, 0) \qquad (7)^*$$

and that $\hat{u}$, $\hat{B}_x$ and $\hat{B}_y$ are all independent of $\hat{x}$. Then $\hat{\boldsymbol{v}}$ satisfies the equation (6) evidently. With the assumption (7) the equation (1) to (5) are simplified as follows: From (1)

$$\frac{\partial \hat{B}_y}{\partial \hat{y}}=0$$

that is, $\hat{B}_y$ is a function of $\hat{t}$ only. Then, if we eliminate $\hat{\boldsymbol{j}}$ and $\hat{\boldsymbol{E}}$ from (2), (3) and (4), we obtain

$$\frac{1}{\mu\sigma}\frac{\partial^2 \hat{B}_x}{\partial \hat{y}^2}+\hat{B}_y\frac{\partial \hat{u}}{\partial \hat{y}}=\frac{\partial \hat{B}_x}{\partial \hat{t}} \qquad (8)$$

and

$$0=\frac{d\hat{B}_y}{d\hat{t}} \quad \text{or} \quad \hat{B}_y=\text{const.}=B_0 \qquad (9)$$

Later, B_0 will be equated to the applied magnetic induction. Using (9), Eq. (8) becomes:

$$\frac{1}{\mu\sigma}\frac{\partial^2 \hat{B}_x}{\partial \hat{y}^2}+B_0\frac{\partial \hat{u}}{\partial \hat{y}}=\frac{\partial \hat{B}_x}{\partial \hat{t}} \qquad (8')$$

Further, elimination of $\hat{\boldsymbol{j}}$ from (2) and (5) yields

$$\frac{\partial \hat{u}}{\partial \hat{t}}=-\frac{1}{\rho}\frac{\partial \hat{p}}{\partial \hat{x}}+\nu\frac{\partial^2 \hat{u}}{\partial \hat{y}^2}+\frac{B_0}{\rho\mu}\frac{\partial \hat{B}_x}{\partial \hat{y}} \qquad (10)$$

$$0=\frac{1}{\rho}\frac{\partial \hat{p}}{\partial \hat{y}}+\frac{\hat{B}_x}{\rho\mu}\frac{\partial \hat{B}_x}{\partial \hat{y}} \qquad (11)$$

Here $\partial\hat{p}/\partial\hat{x}$ is applied pressure gradient which is assumed to be constant and will be denoted by $-A$.

Boundary and initial conditions are as follows:

$$\left.\begin{array}{ll} \text{on } \hat{y}=a, & \hat{u}=0 \quad \text{(no slip condition)} \\ & \dfrac{\partial \hat{B}_x}{\partial \hat{y}}=0 \quad \left(\begin{array}{l}\text{walls are assumed to}\\ \text{be perfect conductor}\end{array}\right) \\ \text{on } \hat{y}=0, & \dfrac{\partial \hat{u}}{\partial \hat{y}}=0 \quad \text{(symmetry)} \\ & \hat{B}_x=0 \quad \text{(symmetry)} \end{array}\right\} \qquad (12)$$

$$\text{at} \quad \hat{t}=0, \quad \hat{u}=0, \quad \hat{B}_x=0, \quad \hat{B}_y=B_0 \qquad (13)$$

Hereafter we use for the sake of convenience the non-dimensional quantities

$$u=\hat{u}/\sqrt{Aa/\rho}\,, \quad B_x=\hat{B}_x/B_0\,, \quad y=\hat{y}/a\,,$$
$$p=\hat{p}/Aa \quad \text{and} \quad t=\hat{t}/\sqrt{\rho a/A}\,.$$

With these transformations the fundamental equations become

$$\frac{\partial B_x}{\partial t}=\frac{1}{R_m}\frac{\partial^2 B_x}{\partial y^2}+\frac{\partial u}{\partial y} \qquad (8'')$$

$$\frac{\partial u}{\partial t}=1+\frac{1}{R}\frac{\partial^2 u}{\partial y^2}+s^2\frac{\partial B_x}{\partial y} \qquad (10')$$

$$0=\frac{\partial p}{\partial y}+s^2 B_x\frac{\partial B_x}{\partial y} \qquad (11')$$

where $R=\sqrt{Aa/\rho}\cdot(a/\nu)$ is the Reynolds number, $R_m=\sigma\mu a\sqrt{Aa/\rho}$ the magnetic Reynolds number and $s^2=B_0{}^2/\mu Aa$ the pressure number. Also the boundary and initial conditions are written as

$$\left.\begin{array}{lll} \text{on} & y=1\,, & u=0 \\ & & \dfrac{\partial B_x}{\partial y}=0 \\ \text{on} & y=0\,, & \dfrac{\partial u}{\partial y}=0 \\ & & B_x=0 \end{array}\right\} \qquad (12')$$

$$\text{at} \quad t=0\,, \quad u=0\,, \quad B_x=0 \qquad (13')$$

§ 3. Solution

We seek the solution by dividing it into steady and unsteady parts, that is

$$\left.\begin{array}{l} B_x=B^0(y)+B(y, t) \\ u\;\;=u^0(y)+U(y, t) \end{array}\right\} \qquad (14)$$

where B^0, u^0 are the steady parts and B, U the unsteady parts. Each satisfies the following equations and boundary conditions:

$$\left.\begin{array}{l} 0=\dfrac{1}{R_m}\dfrac{d^2B^0}{dy^2}+\dfrac{du^0}{dy} \\ 0=1+\dfrac{1}{R}\dfrac{d^2u^0}{dy^2}+s^2\dfrac{dB^0}{dy} \end{array}\right\} \qquad (15)$$

$$\left.\begin{array}{lll} y=1; & u^0=0\,, & \dfrac{dB^0}{dy}=0 \\ y=0; & \dfrac{du^0}{dy}=0\,, & B^0=0 \end{array}\right\} \qquad (16)$$

$$\left.\begin{array}{l} \dfrac{\partial B}{\partial t}=\dfrac{1}{R_m}\dfrac{\partial^2 B}{\partial y^2}+\dfrac{\partial U}{\partial y} \\ \dfrac{\partial U}{\partial t}=\dfrac{1}{R}\dfrac{\partial^2 U}{\partial y^2}+s^2\dfrac{\partial B}{\partial y} \end{array}\right\} \qquad (17)$$

---

* The quantities in the parentheses represent the $\hat{x}$, $\hat{y}$, $\hat{z}$ components respectively.

$$\left.\begin{aligned} y=1;\quad & U=0\,,\quad \frac{\partial B}{\partial y}=0 \\ y=0;\quad & \frac{\partial U}{\partial y}=0\,,\quad B=0 \end{aligned}\right\} \tag{18}$$

$$t=0;\quad U=-u^0\,,\quad B=-B^0 \tag{19}$$

Steady solution.

Eq. (15) for the steady motion may be integrated once by using (16), i. e.

$$\left.\begin{aligned} 0&=\frac{1}{R_m}\frac{dB^0}{dy}+u^0 \\ 0&=y+\frac{1}{R}\frac{du^0}{dy}+s^2B^0 \end{aligned}\right\} \tag{15′}$$

The solution of these equations can be found in closed forms*. For later convenience, however, we shall obtain here the solution in a form of Fourier series. That is, we assume

$$\left.\begin{aligned} u^0&=\sum_{n=1}^{\infty} M_n\cos\alpha_n y \\ B^0&=\sum_{n=1}^{\infty} N_n\sin\alpha_n y \end{aligned}\right\} \tag{20}$$

$$\alpha_n=(2n-1)\pi/2$$

On substitution of (20) into (15′), we obtain M_n and N_n in the forms:

$$\left.\begin{aligned} M_n&=\frac{(-1)^{n-1}\times 2R}{\alpha_n(\alpha_n^2+H^2)} \\ N_n&=\frac{(-1)^n\times 2RR_m}{\alpha_n^2(\alpha_n^2+H^2)} \end{aligned}\right\} \tag{21}$$

where $H=(RR_ms^2)^{1/2}$ is the Hartmann number.

Unsteady solution.

For solving Eq. (17) we assume the following expansions:

$$\left.\begin{aligned} U&=\sum_{n=1}^{\infty} f_n(t)\cos\alpha_n y \\ B&=\sum_{n=1}^{\infty} g_n(t)\sin\alpha_n y \end{aligned}\right\} \tag{22}$$

Substitution of (22) into (17) yields the equations for $f_n(t)$ and $g_n(t)$:

$$\left.\begin{aligned} \alpha_nf_n+\left(g_n'+\frac{\alpha_n}{R_m}g_n\right)&=0 \\ \left(f_n'+\frac{\alpha_n^2}{R}f_n\right)-s^2\alpha_ng_n&=0 \end{aligned}\right\} \tag{23}$$

where the prime denotes differentiation with respect to t. Also, from (19) and (20) the initial conditions for $f_n(t)$, $g_n(t)$ are found to be

$$\left.\begin{aligned} f_n(0)&=-M_n \\ g_n(0)&=-N_n \end{aligned}\right\}\ (n=1,2,\cdots) \tag{24}$$

The general solutions of (23) may be given by

$$\left.\begin{aligned} f_n&=F_n^{(1)}\exp(\lambda_n^{(1)}t)+F_n^{(2)}\exp(\lambda_n^{(2)}t) \\ g_n&=G_n^{(1)}\exp(\lambda_n^{(1)}t)+G_n^{(2)}\exp(\lambda_n^{(2)}t) \end{aligned}\right\} \tag{25}$$

$$(\lambda_n^{(1)}\neq\lambda_n^{(2)})$$

where

$$\begin{aligned} \lambda_n^{(1),(2)}&=\frac{\alpha_n^2}{2}\left\{-\left(\frac{1}{R}+\frac{1}{R_m}\right)\pm\sqrt{\left(\frac{1}{R}-\frac{1}{R_m}\right)^2-\frac{4s^2}{\alpha_n^2}}\right\} \\ &=\frac{\alpha_n^2}{2RR_m}\left\{-(R+R_m)\pm\sqrt{(R_m-R)^2-\frac{4H^2}{\alpha_n^2}}\right\} \end{aligned}$$

$$G_n^{(1),(2)}=\kappa_n^{(1),(2)}F_n^{(1),(2)}$$

$$\kappa_n^{(1),(2)}=\frac{RR_m(\lambda_n^{(1),(2)}+(\alpha_n^2/R))}{H^2\alpha_n}$$

Two arbitrary constants $F_n^{(1)}$ and $F_n^{(2)}$ can be determined by the initial conditions (24), that is

$$\left.\begin{aligned} F_n^{(1)}&=\frac{N_n-\kappa_n^{(2)}M_n}{\kappa_n^{(2)}-\kappa_n^{(1)}} \\ F_n^{(2)}&=\frac{\kappa_n^{(1)}M_n-N_n}{\kappa_n^{(2)}-\kappa_n^{(1)}} \end{aligned}\right\} \tag{26}$$

If $\lambda_n^{(1)}$ is a complex root, $F_n^{(1)}$ and $F_n^{(2)}$ are complex conjugate of each other, and then putting $\lambda_n^{(1)}=-\beta_n+i\gamma_n$, $F_n^{(1)}=\sigma_n+i\omega_n$, we may obtain the expression for f_n, g_n in real variables β_n, γ_n, σ_n, ω_n. That is

$$f_n=2\exp(-\beta_nt)\{\sigma_n\cos\gamma_nt-\omega_n\sin\gamma_nt\} \tag{27}$$

and similar expression for g_n may be easily obtained by only replacing σ_n and ω_n by the real and imaginary parts of $G_n^{(1)}$ respectively.

If $\lambda_n^{(1)}=\lambda_n^{(2)}\equiv\lambda_n$, above expressions for f_n, g_n become invalid. For this case, the solutions may be written as

$$\left.\begin{aligned} f_n&=(F_n^{(1)}t+F_n^{(2)})\exp(\lambda_nt) \\ g_n&=(G_n^{(1)}t+G_n^{(2)})\exp(\lambda_nt) \end{aligned}\right\} \tag{28}$$

where

$$F_n^{(1)}=\frac{\alpha_n^2}{2}\left(\frac{1}{R_m}-\frac{1}{R}\right)F_n^{(2)}+s^2\alpha_nG_n^{(2)}$$

$$G_n^{(1)}=-\alpha_nF_n^{(2)}+\frac{\alpha_n^2}{2}\left(\frac{1}{R}-\frac{1}{R_m}\right)G_n^{(2)}$$

$$s^2=\frac{\alpha_n^2}{4}\left(\frac{1}{R}-\frac{1}{R_m}\right)^2$$

---

* $u^0=\dfrac{R}{H^2}\left(1-\dfrac{\cosh Hy}{\cosh H}\right)$,

$B^0=-\dfrac{RR_m}{H^2}\left(y-\dfrac{\sinh Hy}{H\cosh H}\right)$.

Two arbitrary constants $F_n^{(2)}$, $G_n^{(2)}$ are determined by the initial conditions (24) as follows:

$$\left.\begin{aligned} F_n^{(2)} &= -M_n \\ G_n^{(2)} &= -N_n \end{aligned}\right\} \tag{29}$$

§ 4. Special Cases

We shall here examine some limiting cases of the preceding solution as for the parameters R, R_m and s^2.

i) $R \to \infty$

In the limit $t \to \infty$, fluid velocity becomes constant and uniform.

ii) $R_m \to \infty$

All the fluid motion dies out for $t \to \infty$ and a new equilibrium condition is attained monotonically or in damped oscillation according to the value of λ_n.

iii) $R_m \to \infty$ and $R \to \infty$

For this case we may find an analogy with vibrating string under uniform gravity. That is, the displacement of the fluid particles or of the line of magnetic induction corresponds to that of the string, A/ρ to gravitational acceleration g and $B_0^2/\rho\mu$ to the tension of the string divided by the linear density.

iv) $R_m \to 0$

This is the case of purely viscous flow. The flow approaches the so-called plane Poiseuille flow monotonically.

v) $R_m \to 0$ and $s^2 R_m$=finite

Applied magnetic field does not change and remains uniform, but the flow is affected by the magnetic field and approaches a modified Poiseuille flow monotonically.

§ 5. Numerical Calculations

Numerical calculations of the velocity distribution and of the displacement of line of magnetic induction have been carried out for the case $R = R_m = s^2 = 1$. The results are given in Fig. 2.

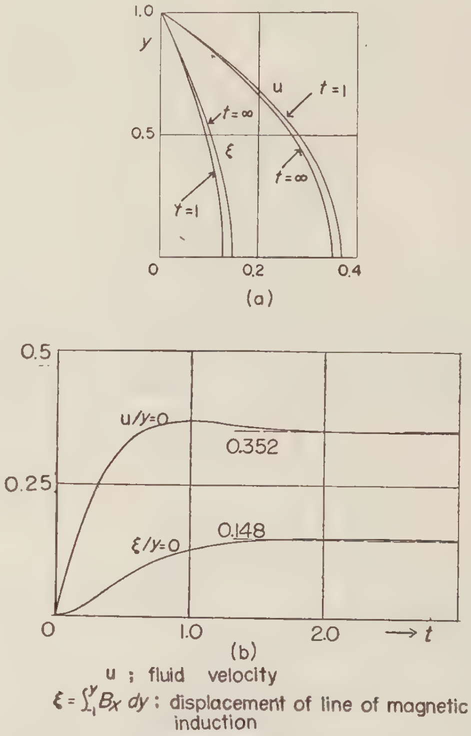

Fig. 2. Fluid velocity and displacement of line of magnetic induction.

Acknowledgement

The authors wish to express their cordial thanks to Prof. K. Tamada and Prof. Y. Shibaoka for their interest and encouragement throughout this work.

JOURNAL OF THE PHYSICAL SOCIETY OF JAPAN, Vol. 16, No. 7, JULY, 1961

The Hall Effect in the Viscous Flow of Ionized Gas between Parallel Plates under Transverse Magnetic Field

By Hiroshi SATO

Aeronautical Research Institute, University of Tokyo, Tokyo

(Received March 2, 1961)

The electrical conductivity of an ionized gas is anisotropic in the presence of magnetic field (Hall effect). The conductivity is expressed by a tensor in the same form for both fully and partially ionized gases. By the use of modified Ohm's law and conventional magnetohydrodynamical equations the incompressible viscous flow between parallel plates under the transverse magnetic field is analyzed and an exact solution is obtained when the magnetic Reynolds number is small. The numerical results reveal a remarkable effect of anisotropy of conductivity. The acceleration and deceleration of viscous ionized gas under combined electric and magnetic fields are also calculated.

§ 1. Introduction

The effect of transverse magnetic field on the flow of electrically-conducting fluid in a two-dimensional channel has been treated theoretically by Hartmann[1]. He has obtained an exact solution of magnetohydrodynamical equations of viscous incompressible fluid. The theoretical results showed a fair agreement with experimental results obtained by Hartmann and Lazarus[2]. It is obvious that nothing is to be added to Hartmann's result as far as the fluid remains ohmic and of isotropic conductivity. These two conditions hold for the liquid metal, but they do not hold for an ionized gas in many cases. The mechanism of conduction in ionized gases is different from that in metallic substances. The electric current in ionized gas is usually carried by electrons which undergo successive collisions with other charged or neutral particles. Exactly speaking, the ionized gas is not an ohmic conductor. The current is not proportional to the applied potential except when the electric field is very weak. The conventional magnetohydrodynamical treatment is no more valid under the strong electric field. In the second place, the conductivity of ionized gas is affected by the magnetic field. Due to the gyration and drift of charged particles the conductivity parallel to the electric field is reduced and the current is induced in the direction normal to both electric and magnetic fields. This phenomenon has been known as the "Hall effect". The effect can be taken into account within the range of magnetohydrodynamical approximation. An example of Hall effect was shown by Tani in the viscous flow in a square channel[3]. In the following treatment the proportionality of current and applied electric field is assumed and the conductivity is expressed by a tensor instead of a scalar. A conventional magnetohydrodynamical calculation is carried out for the viscous incompressible flow between two parallel plates under the transverse electric and magnetic fields.

The author expresses his thanks to Professor Itiro Tani for may valuable suggestions. Acknowledgement is extended to Mrs. M. Nakai who has carried out the numerical calculations.

§ 2. Considerations on the Anisotropy of Conductivity

Equations of motion and current for the steady flow of neutral fully-ionized gas are under proper assumptions expressed as[4)]

$$\boldsymbol{j}\times\boldsymbol{B}-\nabla p+\rho\nu\Delta\boldsymbol{v}=0 \qquad (1)$$

$$\boldsymbol{E}+\boldsymbol{v}\times\boldsymbol{B}+\boldsymbol{E}_e-\frac{c}{en}\boldsymbol{j}\times\boldsymbol{B}-\frac{\boldsymbol{j}}{\sigma_0}=0 \qquad (2)$$

in which vectors, $\boldsymbol{j}$, $\boldsymbol{B}$ and $\boldsymbol{E}$ are the current density, the magnetic flux density and the electric field, respectively. Also p is the pressure, ρ the density, ν the kinematic viscosity, $-e/c$ the electron charge in e. m. u. and n is the number density of ions which is equal to that of electrons. $\boldsymbol{E}_e$ denotes the equivalent electric field due to the gradient of electron pressure p_e, namely, $\boldsymbol{E}_e=(c/en)\nabla p_e$.

The conductivity σ_0 is defined as a coefficient of proportionality between the current density and the collision term in the equation of motion of charged particles as is shown in reference 4. From equation (2) the current density is expressed as

$$\left.\begin{aligned} \boldsymbol{j}_\perp &= \sigma_1(\boldsymbol{E}+\boldsymbol{v}\times\boldsymbol{B}+\boldsymbol{E}_e)_\perp \\ &\quad -\sigma_2(\boldsymbol{E}+\boldsymbol{v}\times\boldsymbol{B}+\boldsymbol{E}_e)_\perp\times\frac{\boldsymbol{B}}{B} \\ \boldsymbol{j}_{/\!/} &= \sigma_0(\boldsymbol{E}+\boldsymbol{E}_e)_{/\!/} \end{aligned}\right\} \tag{3}$$

in which B is the magnitude of $\boldsymbol{B}$, subscripts $\perp$ and $/\!/$ denote component vectors normal and parallel to $\boldsymbol{B}$, respectively and

$$\sigma_1=\frac{\sigma_0}{1+\sigma_0^2(cB/en)^2}, \qquad \sigma_2=\frac{\sigma_0^2(cB/en)}{1+\sigma_0^2(cB/en)^2}$$

The conductivity σ_0 is defined in the absence of magnetic field and σ_1 and σ_2 are the modified conductivities parallel and normal to the direction of electric field, respectively, when the magnetic field is present. Using the mean collision time between ion and electron τ, the conductivity is expressed as

$$\sigma_0=\frac{ne^2\tau}{c^2m_e}$$

where m_e is the mass of electron. Substituting this in the expressions for σ_1 and σ_2, and using the gyration frequency of electron ω_e $(=eB/cm_e)$, we obtain

$$\sigma_1=\frac{\sigma_0}{1+\omega_e^2\tau^2}$$

$$\sigma_2=\frac{\sigma_0\omega_e\tau}{1+\omega_e^2\tau^2}$$

In the case of partially-ionized gas a similar simplified treatment gives the equation of current as[5]

$$\boldsymbol{E}+\boldsymbol{v}\times\boldsymbol{B}+\boldsymbol{E}_e-\frac{c}{en}\boldsymbol{j}\times\boldsymbol{B}$$

$$-B\left(\kappa+\kappa_e+\frac{f^2}{\kappa_i}\right)\boldsymbol{j}-\frac{f^2}{B\kappa_i}\boldsymbol{E}_e\times\boldsymbol{B}=0 \tag{4}$$

in which f is the ratio of number density of neutral particles to the total number density, and

$$\kappa_i=\frac{1}{2\omega_i\tau_i}, \qquad \kappa_e=\frac{1}{\omega_e\tau_e}, \qquad \kappa=\frac{1}{\omega_e\tau}$$

ω_i is the gyration frequency of ions and τ_e, τ_i and τ are the mean collision time between electron and neutral particle, ion and neutral particle and electron and ion, respectively.

The above equation is reduced to

$$\begin{aligned} \boldsymbol{j}_\perp &= \frac{1}{B^2\{1+(\kappa+\kappa_e+f^2/\kappa_i)^2\}}\frac{en}{c} \\ &\quad \times\left[\left(\kappa+\kappa_e+\frac{f^2}{\kappa_i}\right)(\boldsymbol{E}+\boldsymbol{v}\times\boldsymbol{B}+\boldsymbol{E}_e)_\perp B\right. \\ &\quad -(\boldsymbol{E}+\boldsymbol{v}\times\boldsymbol{B}+\boldsymbol{E}_e)_\perp\times\boldsymbol{B} \\ &\quad \left.-\frac{f^2}{\kappa_i}\left\{(\boldsymbol{E}_{e\perp}\times\boldsymbol{B})\left(\kappa+\kappa_e+\frac{f^2}{\kappa_i}\right)+B\boldsymbol{E}_{e\perp}\right\}\right] \end{aligned} \tag{5}$$

In the absence of magnetic field this becomes

$$\boldsymbol{j}_\perp=\frac{e^2n}{c^2m_e}\cdot\frac{1}{1/\tau+1/\tau_e}(\boldsymbol{E}+\boldsymbol{E}_e)_\perp$$

The conductivity σ_0 might be defined as

$$\sigma_0=\frac{e^2n}{c^2m_e}\Big/(1/\tau+1/\tau_e)$$

The magnitude of $f^2/\kappa_i=2f^2\omega_i\tau_i$ is estimated as follows. For the partially-ionized gas f^2 is of the order of unity. Since the gyration frequency of ions ω_i is equal to $\omega_e m_e/m_i$, $\omega_i\tau_i$ is very small compared with unity unless the magnetic field is extremely strong and the gas is very tenuous. Therefore, f^2/κ_i is in many cases very small in comparison with unity. Then, by neglecting small quantities the equation (5) is simplified as

$$\begin{aligned} \boldsymbol{j}_\perp &= \sigma_1(\boldsymbol{E}+\boldsymbol{v}\times\boldsymbol{B}+\boldsymbol{E}_e)_\perp \\ &\quad -\sigma_2(\boldsymbol{E}+\boldsymbol{v}\times\boldsymbol{B}+\boldsymbol{E}_e)_\perp\times\frac{\boldsymbol{B}}{B} \end{aligned} \tag{6}$$

in which

$$\sigma_1=\frac{\sigma_0}{1+\omega_e^2\{1/(1/\tau+1/\tau_e)\}^2}$$

$$\sigma_2=\frac{\sigma_0\omega_e\{1/(1/\tau+1/\tau_e)\}}{1+\omega_e^2\{1/(1/\tau+1/\tau_e)\}^2}$$

The above expression for $\boldsymbol{j}$ agrees with that of fully ionized gas when τ_e approaches infinity. The generalized forms for σ_1 and σ_2 are

$$\left.\begin{aligned} \sigma_1 &= \frac{\sigma_0}{1+\alpha^2} \\ \sigma_2 &= \frac{\sigma_0\alpha}{1+\alpha^2} \end{aligned}\right\} \tag{7}$$

When the tensor notation is used for the conductivity as $\boldsymbol{\sigma}=(\sigma_{ij})$, the current density is expressed by

$$\boldsymbol{j}=\boldsymbol{\sigma}(\boldsymbol{E}+\boldsymbol{v}+\boldsymbol{B}+\boldsymbol{E}_e)$$

Taking the direction of magnetic field as the y-axis the conductivity tensor becomes

$$\boldsymbol{\sigma}=\begin{pmatrix} \sigma_1 & 0 & \sigma_2 \\ 0 & \sigma_0 & 0 \\ -\sigma_2 & 0 & \sigma_1 \end{pmatrix} \tag{8}$$

§ 3. Fundamental Equations for the Flow between Parallel Plates

The viscous flow of ionized gas between two parallel plates is considered. Fig. 1 shows the co-ordinate system. The x-axis is taken in the direction of hydrodynamic pressure gradient in the plane parallel to the channel walls—not in the direction of flow. A parallel, uniform magnetic field B_0 is applied in the y-direction. The height of channel is denoted by $2h$ and the width is assumed to be very large compared with $2h$.

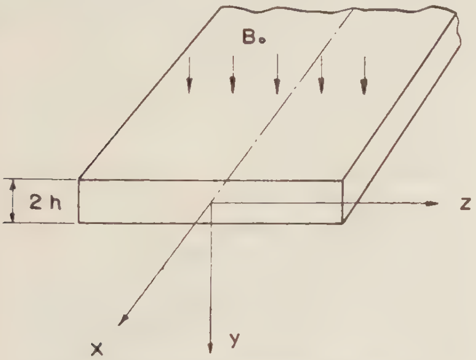

Fig. 1. The co-ordinate system.

Following assumptions are made.

1. The density of gas is everywhere constant.
2. The ionization is in equilibrium which is not affected by the applied electric and magnetic fields.
3. The effect of space charge is neglected.
4. The flow is fully developed and stationary, that is $\partial/\partial x=0$, $\partial/\partial t=0$ except $\partial p/\partial x \neq 0$
5. The magnetic Reynolds number R_m is small, namely, the induced magnetic field is small compared with the applied field. Therefore, components in the conductivity tensor are expressed in terms of B_0.
6. The flow is "two-dimensional", namely, $\partial/\partial z=0$.

The fundamental equations to be solved are equations (1) and (2) together with continuity relations

$$\operatorname{div} \boldsymbol{v}=0\,, \qquad \operatorname{div} \boldsymbol{j}=0$$

Boundary conditions are $\boldsymbol{v}=0$ at $y=\pm h$.

The fundamental equations are simplified by above-mentioned assumptions and boundary conditions as

$$-\frac{\partial p}{\partial x}\left[1-s\left(1-\frac{\sigma_1}{\sigma_0}\right)\right]+\rho\nu\frac{d^2u}{dy^2}$$
$$+B_0[-\sigma_1(E_z+uB_0)+\sigma_2(E_x-wB_0)]=0$$

$$s\frac{\partial p}{\partial x}\frac{\sigma_2}{\sigma_0}+\rho\nu\frac{d^2w}{dy^2}$$
$$+B_0[\sigma_1(E_x-wB_0)+\sigma_2(E_z+uB_0)]=0$$

in which $s=p_e/p$ is the ratio of the electron pressure to the total pressure. The value of s is 1/2 for neutral fully-ionized plasma and approximately zero for weakly-ionized gas. u, w and E_x, E_z are x- and z-components of velocity and electric field, respectively. The conductivity is expressed by the equation (8).

In order to make above two equations non-dimensional, the characteristic length h and velocity $u_p=-(\partial p/\partial x)(h^2/\nu\rho)$ are introduced. For the simple Poiseuille flow, the mean velocity over the cross-section is 1/3 in u_p unit. Using the same notations u, w for u/u_p and w/u_p and y for y/h, we obtain non-dimensional equations:

$$k_1+\frac{d^2u}{dy^2}-\frac{\sigma_1}{\sigma_0}H_a{}^2(m_z+u)+\frac{\sigma_2}{\sigma_0}H_a{}^2(m_x-w)=0 \tag{9}$$

$$k_2+\frac{d^2w}{dy^2}+\frac{\sigma_1}{\sigma_0}H_a{}^2(m_x-w)+\frac{\sigma_2}{\sigma_0}H_a{}^2(m_z+u)=0 \tag{10}$$

in which

$$k_1=1-s\left(1-\frac{\sigma_1}{\sigma_0}\right), \qquad k_2=-s\frac{\sigma_2}{\sigma_0}$$
$$m_x=\frac{E_x}{B_0u_p}, \qquad m_z=\frac{E_z}{B_0u_p}$$

and the Hartmann number H_a is defined as

$$H_a{}^2=B_0{}^2h^2\sigma_0/\nu\rho$$

When w is eliminated from equations (9) and (10), a fourth order linear differential equation is obtained for u. Considering boundary conditions, the solution is in a form

$$u=A_1\cosh py\cos qy+A_2\sinh py\sin qy+C_1$$

in which

$$p=\frac{H_a}{\sqrt{2}}\left(\frac{\sqrt{\sigma_1{}^2+\sigma_2{}^2}+\sigma_1}{\sigma_0}\right)^{1/2}$$
$$q=\frac{H_a}{\sqrt{2}}\left(\frac{\sqrt{\sigma_1{}^2+\sigma_2{}^2}-\sigma_1}{\sigma_0}\right)^{1/2}$$
$$C_1=-m_z+\frac{\sigma_0(k_1\sigma_1-k_2\sigma_2)}{H_a{}^2(\sigma_1{}^2+\sigma_2{}^2)}$$

The solution for w is

$$w=A_2\cosh py\cos qy-A_1\sinh py\sin qy+C_2$$

with

$$C_2=m_x+\frac{\sigma_0(k_1\sigma_2+k_2\sigma_1)}{H_a{}^2(\sigma_1{}^2+\sigma_2{}^2)}$$

Coefficients A_1 and A_2 are determined from boundary conditions as

$$A_1=\frac{-C_1\cosh p\cos q+C_2\sinh p\sin q}{\sinh^2 p+\cos^2 q}$$

$$A_2=\frac{-C_1\sinh p\sin q+C_2\cosh p\cos q}{\sinh^2 p+\cos^2 q}$$

The non-dimensional electric field m_x and m_z are to be determined by boundary conditions at large x and z.

The mean velocity over the cross-section is given by

$$\bar{u}=\int_0^1 u dy\,, \qquad \bar{w}=\int_0^1 w dy$$

In the solution obtained above w has non-zero values varying in the y-direction. Therefore, side walls at large z must have a shape which is adapted to the flow direction there. This is not a realistic configuration. The present solution is considered to be useful at the central part of a very wide channel and for the flow between two concentric cylinders which have a very large radius compared with the gap of both cylinders.

Another solution is obtained under the condition, $w=0$ instead of $\partial/\partial z=0$. If $\partial^2 u/\partial z^2$ is neglected compared with $\partial^2 u/\partial y^2$, the solution for u is the same as that obtained by Hartmann except the reduction of Hartmann number due to the reduction of conductivity by the magnetic field. The hydrodynamic pressure gradient $\partial p/\partial z$ appears for balancing the magnetic pressure. This solution was first suggested by Yoichi Mimura[6]. There is no reason to reject the flow pattern of this kind. However, it is obvious that the assumption $\partial/\partial z=0$ is more general than $w=0$ everywhere.

§ 4. Calculated Results

Numerical results on the effect of transverse magnetic field are presented here for two cases, one for insulated side walls and the other, for short-circuited conducting side walls.

When the side walls—walls at large distance in z-direction—are made of the non-conducting material, the induced electric current does not go out of the channel but circulates in the fluid. Therefore, an additional condition for the current is

$$\int_0^1 j_z dy=0$$

If the insulation at large x is also assumed, another relation is obtained as

$$\int_0^1 j_x dy=0$$

These conditions of insulation at large distance are physically realized for instance, when the flow of ionized gas is surrounded by the cold non-conducting gas.

Constants in the solution are determined by these two conditions. Solutions for u, w, j_x and j_z are all independent of the partial pressure of electron gas s.

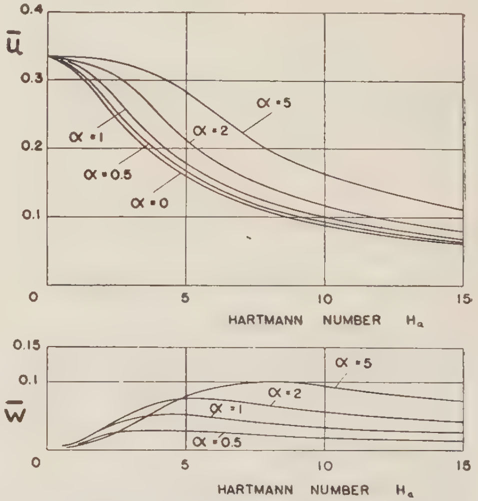

Fig. 2. Mean velocity. Insulated walls. $\bar{u}$ and $\bar{w}$ are non-dimensionalized by u_p. $H_a=B_0h\sqrt{\sigma_0/\nu\rho}$

Numerical results are shown in Fig. 2 in which $\bar{u}$ and $\bar{w}$ are plotted against Hartmann number H_a based on the conductivity in the absence of magnetic field. The effect of magnetic field on the volume flow at a given pressure gradient becomes less remarkable as α is increased. This fact is easily understood by considering the more reduction of conductivity in the direction of induced electric field for larger α. The reduction of conductivity corresponds to the decrease of Hartmann number. The magnitude of $\bar{w}$ becomes large as α is increased but $\bar{w}$ never exceeds $\bar{u}$ for the same values of α and H_a.

Fig. 3 shows the velocity distribution u and w. Since velocity components are non-dimensionalized by u_p, the velocity on the centre-line for Poiseuille flow ($H_a=0$) is 0.5. As α

is increased, the deviation from the pure Hartmann flow becomes remarkable. The velocity gradient at the wall ($y=\pm 1$) remains unchanged for u and is kept to be zero for w for all values of α and H_a. This fact is of some physical interest. The shear flow having a zero velocity gradient at the wall is known as being very unstable—in other words, there is a great possibility of transition to turbulent flow. Even if the distribution of u is stable for external disturbances, the whole layer may become turbulent when the distribution of w is the unstable one. A similar situation has been pointed out on the three-dimensional boundary layer along a swept-back wing. Thus, it is expected that the Hall effect in ionized gas destabilizes the laminar flow.

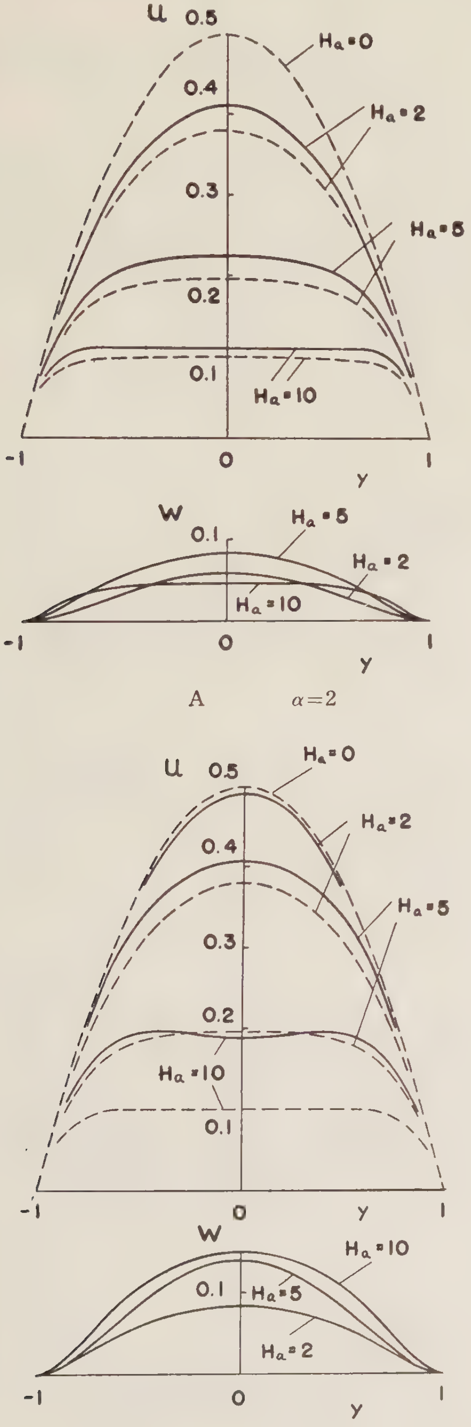

A $\alpha=2$

B $\alpha=5$

Fig. 3. Velocity distribution. Insulated walls. Broken line: Hartmann's calculation.

When the side walls are made of conducting material and short-circuited by an external conductor, the induced electric current flows out of the channel. In this case no electric potential exists between side walls. If we assume the zero electric field also in x-direction, we have

$$m_x=0\ , \qquad m_z=0$$

These conditions are realized, for instance, for the flow between two concentric cylinders under the radial magnetic field with the pressure gradient parallel to the axis of cylinder.

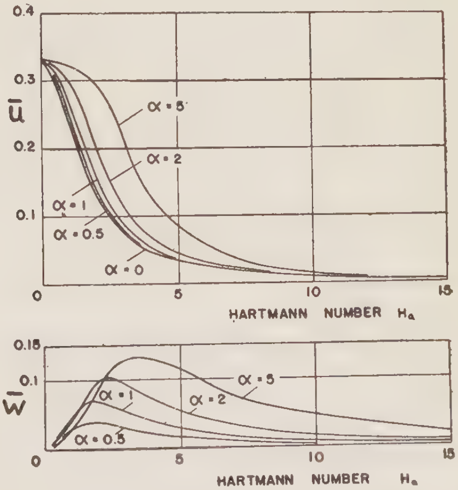

Fig. 4. Mean velocity. Conducting walls. $s=0$ $\bar{u}$ and w are non-dimensionalized by u_p.

Using above relations, $\bar{u}$ and $\bar{w}$ are calculated by the same procedure as the case of insulated walls. For conducting walls, the velocity distribution depends on s. Fig. 4 shows numerical results on $\bar{u}$ and $\bar{w}$ for $s=0$; —weakly-ionized gas. The effect of deceleration due to the magnetic field is more remarkable than the case of insulated walls, although the general trend of curves is the same. Results for $s=1/2$—fully-ionized neutral plasma are shown in Fig. 5. The more reduction of mass flow is obvious for both $\bar{u}$ and $\bar{w}$. In this case the limiting value of $\bar{u}$ at $H_a=0$ is not equal for various values of α.

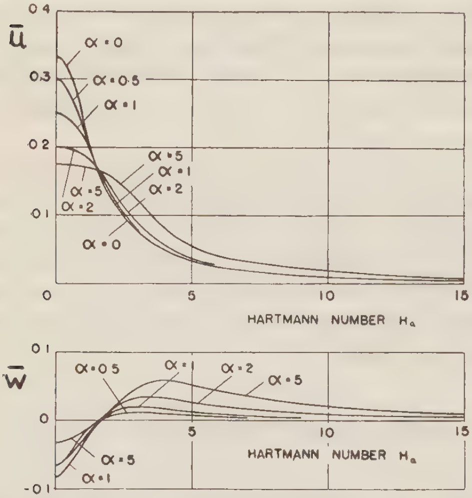

Fig. 5. Mean velocity. Conducting walls. $s=1/2$

The lateral component $\bar{w}$ starts from non-zero negative value and becomes positive at a certain Hartmann number. These situations are made clear by considering the effect of electron pressure in the case of vanishing magnetic field. The electric field induced by the pressure gradient of electron gas is expressed by $\boldsymbol{E}_e=(c/en)\nabla p_e$ and the current density vector $\boldsymbol{j}_e$ has components as

$$\boldsymbol{j}_e:\ \left(\frac{s}{B_0}\frac{\partial p}{\partial x}\frac{\sigma_2}{\sigma_0},\quad 0\,,\quad -\frac{s}{B_0}\frac{\partial p}{\partial x}\left(1-\frac{\sigma_1}{\sigma_0}\right)\right)$$

hence the electromagnetic body force is

$$\boldsymbol{j}_e\times\boldsymbol{B}_0:\ \left(s\left(1-\frac{\sigma_1}{\sigma_0}\right)\frac{\partial p}{\partial x},\quad 0\,,\quad s\frac{\sigma_2}{\sigma_0}\frac{\partial p}{\partial x}\right)$$

Since $\partial p/\partial x$ is negative, both components are negative and moreover they are independent of field strength as far as σ_1/σ_0 and σ_2/σ_0 remain constant. This means that the electromagnetic body force is present in the limiting case of vanishing magnetic field. Thus $\bar{u}$ at $H_a=0$ is reduced as α is increased and $\bar{w}$ at $H_a=0$ has a negative value. On the other hand, when $\boldsymbol{B}_0$ is exactly equal to zero, $\sigma_1=\sigma_0$ and $\sigma_2=0$, hence the electromagnetic body force is zero.

In the case of conducting side walls the velocity gradient at the wall is dependent on α and H_a for both u and w. The gradient for w is not zero in contrast with the case of insulated walls.

§ 5. Considerations on Power Generation and Acceleration by Crossed Electric and Magnetic Fields

As shown above the transverse magnetic field decelerates the flow of ionized gas.

On the other hand, the electric power can be taken out when the side walls are made of conducting material. The total current in the z-direction is expressed by

$$J_z=\int_{-h}^{h} j_z dy=\sigma_0 u_p B_0\frac{2h}{1+\alpha^2}\left(\bar{u}+\alpha\bar{w}+\frac{s\alpha^2}{H_a{}^2}\right)$$

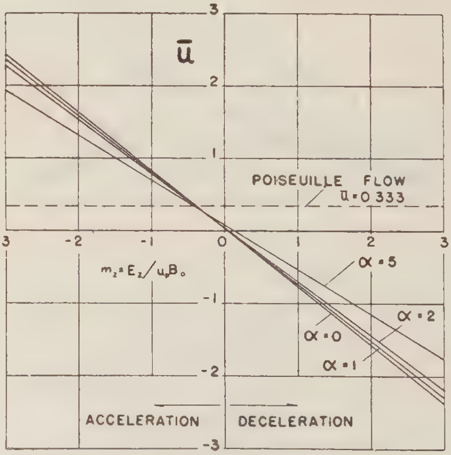

A $H_a=2$

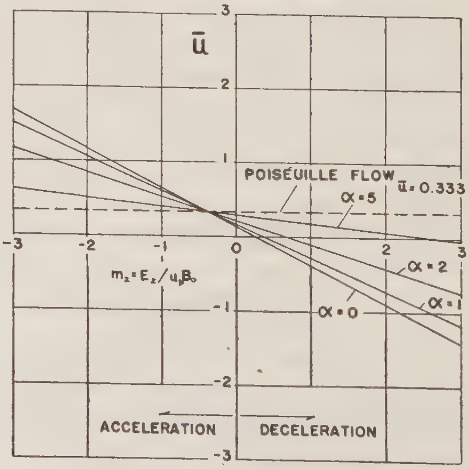

B $H_a=5$

Fig. 6. Acceleration and deceleration due to combined electric and magnetic fields.

It is obvious that the Hall effect reduces the current output. When an external electric field is applied normal to the pressure gradient and magnetic field, the flow is either accelerated or decelerated depending on the direction of the field. Some examples of mean velocity $\bar{u}$ in the presence of transverse electric field are shown in Fig. 6 in which E_x is assumed to be zero and s is set to be zero. The flow rate can be several times that of simple Poiseuille flow or can be made zero with a proper choice of strength of electric field.

Here arises a serious question. Even if the magnetic Reynolds number is small when the external electric field is not applied, does the same assumption hold for the large value of m_z? The answer for this is following.

The magnitude of applied electric field is roughly m_z times the field induced by the flow. Therefore, the current, the magnetic field induced by the current and the magnetic Reynolds number in the presence of applied electric field are m_z times those in the absence of external field. Unless m_z is too large, the magnetic Reynolds number is still small and the present procedure of calculation is valid.

The voltage which makes $\bar{u}=0$ may be termed "choking voltage". It decreases as Hartmann number is increased. At the choke condition, there is no net flow in x-direction but this does not necessarily mean that the flow speed is zero everywhere. In general, there exist the flow in z-direction and a local flow in x-direction. When $\alpha=0$, u and w are everywhere zero at choking condition. For non-zero value of α, the fluid near the center of channel moves against the hydrodynamic pressure gradient whereas the fluid near the wall flows along the pressure gradient. A complete choking——$u=0$ everywhere——is realized at the infinite Hartmann number, for instance, for the inviscid flow.

§ 6. Concluding Remarks

The electrical conductivity of ionized gas under the magnetic field is expressed by a tensor. The investigation based on a simple model of ionized gas has ascertained the validity of tensor expression for both fully ionized and partially ionized gases. An incompressible, viscous channel flow has been analyzed by introducing the tensor conductivity under the condition of small magnetic Reynolds number. An exact solution has been obtained for the velocity as well as the electric current in cases of insulated and conducting side walls. The numerical results reveal the decrease of retarding effect of the transverse magnetic field for larger rate of anisotropy of conductivity. The magnitude of velocity component normal to the hydrodynamic pressure gradient and the magnetic field becomes remarkable as the anisotropy of conductivity increases. A possible role of the lateral velocity component in the transition to the turbulent flow has been pointed out.

The acceleration of flow by combined electric and magnetic fields is analyzed and numerical results are given.

References

1) J. Hartmann: Kgl. Danske Vidensk. Selsk. Mat-Fys. 15 (1937) No. 6.
2) J. Hartmann and F. Lazarus: Kgl. Danske Vidensk. Selsk. Mat-Fys. 15 (1937) No. 7.
3) I. Tani: to be published in J. Aerospace Sciences.
4) L. Spitzer: *Physics of Fully Ionized Gases* p. 18 (Interscience Publ. 1956).
5) T. G. Cowling: *Magnetohydrodynamics* p. 100 (Interscience Publ. 1957).
6) Y. Mimura: Private Communication.

JOURNAL OF THE PHYSICAL SOCIETY OF JAPAN Vol. 16, No. 7, JULY, 1961

Hydromagnetic Oseen Flow past an Elliptic Cylinder in a Uniform Magnetic Field

By Tosio MIYAGI

Junior College of Engineering, University of Osaka Prefecture,
Neyagawa, Osaka

(Received March 22, 1961)

This paper deals with the flow of a viscous, incompressible and electrically conducting fluid past an inclined elliptic cylinder in a parallel magnetic field, making use of a perturbation method similar to Oseen approximation. Approximate formulae for the forces experienced by the cylinder are obtained only to the lowest order of the Reynolds number and the magnetic Reynolds number. The drag and lift coefficients are then expressed as functions of five non-dimensional parameters, i.e., the Reynolds number, the magnetic Reynolds number, the pressure number, the thickness-ratio and the angle of incidence of the cylinder. Numerical calculations for the drag and lift coefficients as well as their ratio are carried out for various values of these five parameters. It may be noted in the numerical results that the angle of incidence of the cylinder at which the lift coefficient has a maximum value increases with the increase of the pressure number S when $S<1$, and the reverse is the case when $S>1$.

§ 1. Introduction

In the present paper is discussed the flow of a viscous, incompressible and electrically conducting fluid past an inclined elliptic cylinder in a magnetic field, which is uniform and parallel to the uniform main stream at infinity. The similar problem in ordinary hydrodynamics has been discussed by Imai[1] and Hasimoto[2] on the basis of Oseen's linearized equations of motion. In the present problem, however, the fluid is electrically conductive and flows in a magnetic field, so that the effect of interaction between the motion of the fluid and the magnetic field should be taken into account. Hence, we must solve simultaneously the hydrodynamic equations and the magnetic equations, viz. the modified Navier-Stokes equation and the Maxwell equations combined with the equation of continuity and the equation called Ohm's law, respectively.

Recently, the problem of the hydromagnetic flow past a fixed body in a parallel magnetic field has been treated by Yosinobu[3] by the use of a perturbation method similar to Oseen approximation in ordinary hydrodynamics. It is shown in his paper that the electric field must vanish throughout the whole field in the case of two-dimensional flow and that both the modified Navier-Stokes equation and the magnetic equation may be linearized by neglecting square and higher order terms of the perturbed velocity $\boldsymbol{u}$ and the perturbed magnetic field $\boldsymbol{h}$, which are assumed to be small compared with the uniform velocity U_0 and the uniform magnetic field H_0 at infinity, respectively. Hence, for the present problem, we can start from his linearized fundamental equations expressed in non-dimensional forms.

The approximate expressions for the drag and lift coefficients, C_D and C_L, are obtained only to the lowest order term with respect to the Reynolds and the magnetic Reynolds numbers. They are expressed as functions of five non-dimensional parameters, viz. the pressure number S, the thickness-ratio t and the angle of incidence of the cylinder α, in addition to the Reynolds number R and the magnetic Reynolds number R_m.

Numerical calculations for C_D, C_L and their ratio C_L/C_D are carried out for various values of the parameters R, R_m, S, t and α. The angle of incidence α_L at which C_L has a maximum value as well as the angle of incidence α_R at which C_L/C_D has a maximum value are numerically computed only for a flat plate. Some remarkable effects of the presence of the magnetic field are found in the numerical results and may be summed up as follows:

(1) C_D, C_L and C_L/C_D decrease with the increase of S when $S<1$ and the reverse is the case when $S>1$. (2) α_L increases slightly towards 45° with the increase of S when $S<1$ and the reverse is the case when $S>1$, and α_R, too, behaves in like manner.

§ 2. Fundamental Equations

Let us consider the two-dimensional steady flow of viscous, incompressible and electrically conducting fluid past an inclined elliptic cylinder in a magnetic field, which is uniform and parallel to the uniform main stream at infinity. We take the rectangular coordinates (x', y') in the plane of fluid motion in such a way that the origin coincides with the centre of the cylinder and the x'-axis is parallel to the uniform main stream at infinity. As the fundamental equations for the present problem, we here adopt a system of linearized equations which has been proposed by Yosinobu[3]. For the field outside the cylinder they can be written in the following non-dimensional forms:

$$R\frac{\partial u}{\partial x}=-\frac{\partial p}{\partial x}+\Delta u\,, \tag{1}$$

$$R\frac{\partial v}{\partial x}=-\frac{\partial p}{\partial y}+\Delta v+M^2(g-v)\,, \tag{2}$$

$$\frac{\partial g}{\partial x}-\frac{\partial f}{\partial y}=R_m(-v+g)\,, \tag{3}$$

$$\frac{\partial u}{\partial x}+\frac{\partial v}{\partial y}=0\,, \tag{4}$$

$$\frac{\partial f}{\partial x}+\frac{\partial g}{\partial y}=0\,, \tag{5}$$

where (x, y) are the non-dimensional rectangular coordinates referring to a characteristic length of the cylinder, L_0, (u, v) and (f, g) the x- and y-components of the perturbed velocity $\boldsymbol{u}/U_0$ and the perturbed magnetic field $\boldsymbol{h}/H_0$ respectively, p the non-dimensional pressure, and Δ stands for $\partial^2/\partial x^2+\partial^2/\partial y^2$. The system contains three independent non-dimensional parameters, the Reynolds number $R=L_0U_0/\nu$, the magnetic Reynolds number $R_m=\mu\sigma_e L_0U_0$, the Hartmann number $M=(\sigma_e/\rho\nu)^{1/2}L_0\mu H_0=(SRR_m)^{1/2}$, where ρ, ν, σ_e and μ are the density, the coeffieient of kinematic viscosity, the electric conductivity and the magnetic permeability of the fluid, respectively, and $S=\mu H_0^2/\rho U_0^2$ is the pressure number.

On the other hand, the governing equations for the magnetic field inside the cylinder can be written in the following non-dimensional forms, since no electric current exists there:

$$\frac{\partial g^*}{\partial x}-\frac{\partial f^*}{\partial y}=0\,, \tag{6}$$

$$\frac{\partial f^*}{\partial x}+\frac{\partial g^*}{\partial y}=0\,, \tag{7}$$

where (f^*, g^*) are the x- and y-components of the perturbed magnetic field inside the cylinder $\boldsymbol{h}^*/H_0$. Here and hereafter the asterisk (*) is added for the quantities inside the cylinder. The boundary conditions at the surface of the cylinder are the non-slip condition for the fluid velocity and the continuity of the lines of magnetic induction, and those at infinity are the uniformity of the flow and the magnetic fields. Thus we have

$$\left.\begin{array}{l} 1+u=0\,,\quad v=0\,, \\ \mu H_\perp=\mu^* H_\perp^*\,, \\ H_{/\!/}=H_{/\!/}^*\,, \end{array}\right\}\ \text{at the surface of the cylinder,} \tag{8}$$

$$u=v=f=g=0 \qquad \text{at infinity,} \tag{9}$$

where μ^* is the magnetic permeability of the cylinder, and the subscripts $\perp$ and $/\!/$ denote the normal and tangential components of the magnetic field at the surface of the cylinder, respectively.

Now, we introduce the stream function ψ and the magnetic stream functions χ and χ^*, sucy that

$$u=\frac{\partial\psi}{\partial y}\,,\qquad v=-\frac{\partial\psi}{\partial x}\,, \tag{10}$$

$$f=\frac{\partial\chi}{\partial y}\,,\qquad g=-\frac{\partial\chi}{\partial x}\,, \tag{11}$$

$$f^*=\frac{\partial\chi^*}{\partial y}\,,\qquad g^*=-\frac{\partial\chi^*}{\partial x}\,, \tag{12}$$

which satisfy identically Eqs. (4), (5) and (7), respectively. Substituting (10), (11) and (12) into Eqs. (1), (2), (3) and (6) and carrying out some calculations, we arrive at the following three partial differential equations for ψ, χ and χ^*:

$$\Delta\left[\Delta-2k_1\frac{\partial}{\partial x}\right]\left[\Delta-2k_2\frac{\partial}{\partial x}\right]\psi=0\,, \tag{13}$$

$$\Delta\left[\Delta-2k_1\frac{\partial}{\partial x}\right]\left[\Delta-2k_2\frac{\partial}{\partial x}\right]\chi=0\,, \tag{14}$$

$$\Delta\chi^*=0\,, \tag{15}$$

where

$$\left.\begin{array}{l} k_1=\frac{1}{4}[R+R_m+\{(R-R_m)^2+4M^2\}^{1/2}]\,, \\ k_2=\frac{1}{4}[R+R_m-\{(R-R_m)^2+4M^2\}^{1/2}]\,. \end{array}\right\} \tag{16}$$

Here, ψ and χ can be expressed by the sum of the solutions of the following three differential equations:

$$\left.\begin{aligned}&\left(\Delta-2k_1\frac{\partial}{\partial x}\right)(\psi_1,\ \chi_1)=0\ ,\\ &\left(\Delta-2k_2\frac{\partial}{\partial x}\right)(\psi_2,\ \chi_2)=0\ ,\\ &\Delta(\psi_3,\ \chi_3)=0\ .\end{aligned}\right\}\tag{17}$$

Since the flow field and the magnetic field are both uniform at infinity, ψ and χ can now be written down in the forms:

$$\left.\begin{aligned}\psi&=y+\psi_1+\psi_2+\psi_3\ ,\\ \chi&=y+\chi_1+\chi_2+\chi_3\ .\end{aligned}\right\}\tag{18}$$

Integrating Eq. (3) once with respect to x by making use of (17), we can readily find the following relations between ψ and χ:

$$\left.\begin{aligned}\psi_1&=\left(1-\frac{2k_1}{R_m}\right)\chi_1\ ,\\ \psi_2&=\left(1-\frac{2k_2}{R_m}\right)\chi_2\ ,\\ \psi_3&=\chi_3\ .\end{aligned}\right\}\tag{19}$$

Thus, we have obtained the set of linear differential equations (15) and (17) to be solved with the boundary conditions (8) and (9).

§ 3. Solution for an Inclined Elliptic Cylinder

Now, we introduce the elliptic coordinates $(\xi,\ \eta)$ related with $(x,\ y)$ by the equation:

$$x+iy=ce^{-i\alpha}\cosh(\xi+i\eta)\ ,\tag{20}$$

where α is the angle between the uniform flow and the major axis of the ellipse. Then, the surface of the elliptic cylinder is given by $\xi=\xi_0$. Taking the major diameter of the ellipse as the characteristic length L_0, the non-dimensional constant c in (20) is expressed as:

$$\left.\begin{aligned}&c=\frac{\sigma}{1+\sigma^2}\ ,\\ &\text{where}\\ &\sigma=e^{-\xi_0}\ .\end{aligned}\right\}\tag{21}$$

The thickness-ratio of the ellipse is then defined as:

$$t=\frac{1-\sigma^2}{1+\sigma^2}\ .\tag{22}$$

The fundamental equations in (17) are then transformed into

$$\left.\begin{aligned}&\left[\frac{\partial^2}{\partial\xi^2}+\frac{\partial^2}{\partial\eta^2}-k_1^2c^2(\cosh^2\xi-\cos^2\eta)\right](e^{-k_1x}\psi_1)=0\ ,\\ &\left[\frac{\partial^2}{\partial\xi^2}+\frac{\partial^2}{\partial\eta^2}-k_2^2c^2(\cosh^2\xi-\cos^2\eta)\right](e^{-k_2x}\psi_2)=0\ ,\\ &\left[\frac{\partial^2}{\partial\xi^2}+\frac{\partial^2}{\partial\eta^2}\right]\psi_3=0\ ,\end{aligned}\right\}\tag{23}$$

respectively. The general solutions satisfying Eqs. (23) and the boundary conditions (9) at infinity are

$$\left.\begin{aligned}\psi_1&=\sum_{n=0}^{\infty}[a_n^{(1)}F_n^{(1)}(\xi,\ \eta)+b_n^{(1)}G_n^{(1)}(\xi,\ \eta)]\ ,\\ \psi_2&=\sum_{n=0}^{\infty}[a_n^{(2)}F_n^{(2)}(\xi,\ \eta)+b_n^{(2)}G_n^{(2)}(\xi,\ \eta)]\ ,\\ \psi_3&=A_0\xi+B_0\eta+\sum_{n=1}^{\infty}\frac{e^{-n(\xi-\xi_0)}}{n}(A_n\cos n\eta+B_n\sin n\eta)\ ,\end{aligned}\right\}\tag{24}$$

where

$$\left.\begin{aligned}F_n^{(j)}(\xi,\ \eta)&=e^{k_jx}\mathrm{FEK}_n^{(j)}(\xi)\mathrm{ce}_n^{(j)}(\eta)\ ,\qquad (j=1,\ 2)\\ G_n^{(j)}(\xi,\ \eta)&=\int_{\eta_0}^{\eta}\left(\frac{\partial}{\partial\xi}-2k_j\frac{\partial x}{\partial\xi}\right)F_n^{(j)}(\xi,\ \eta)d\eta\\ &\quad-\int_{\xi}^{\infty}\left\{\frac{\partial}{\partial\eta_0}-2k_j\frac{\partial x(\xi,\ \eta_0)}{\partial\eta_0}\right\}F_n^{(j)}(\xi,\ \eta_0)d\xi\ ,\end{aligned}\right\}\tag{25}$$

and $a_n^{(j)}$'s, $b_n^{(j)}$'s, A_n's and B_n's are constants to be determined by the boundary conditions

(8). $\mathrm{ce}_n^{(j)}(\eta)$'s are fundamental solutions, periodic in η with period 2π, of the Methieu equation:

$$\left[\frac{d^2}{d\eta^2}+(\lambda_n^{(j)}+k_j^2c^2\cos^2\eta)\right]\mathrm{ce}_n^{(j)}(\eta)=0\,, \tag{26}$$

where $\lambda_n^{(j)}$ is a constant of separation and takes a characteristic value for $\mathrm{ce}_n(\eta)$. They can be expressed in Fourier series as[4]:

$$\left.\begin{aligned}\mathrm{ce}_{2m}^{(j)}(\eta)&=(-1)^m\sum_{p=0}^{\infty}a_{2p}^{(2m)}\cos 2p\eta\,,\\ \mathrm{ce}_{2m+1}^{(j)}(\eta)&=(-1)^m\sum_{p=0}^{\infty}a_{2p+1}^{(2m+1)}\cos(2p+1)\eta\,,\end{aligned}\right\} \tag{27}$$

where $a_{2p}^{(2m)}$'s and $a_{2p+1}^{(2m+1)}$'s are constants depending on $\lambda_n^{(j)}$ and $k_j^2c^2$. On the other hand, $\mathrm{FEK}_n^{(j)}(\xi)$'s are fundamental solutions of the associated Mathieu equation for the characteristic values of $\lambda_n^{(j)}$ in (26):

$$\left[\frac{d^2}{d\xi^2}-(\lambda_n^{(j)}+k_j^2c^2\cosh^2\xi)\right]\mathrm{FEK}_n^{(j)}(\xi)=0\,, \tag{28}$$

and tend to zero as ξ tends to infinity. They can be expressed in series of products of the modified Bessel functions[4]:

$$\left.\begin{aligned}\mathrm{FEK}_{2m}^{(j)}(\xi)&=\frac{1}{A_0^{(2m)}}\sum_{p=0}^{\infty}A_{2p}^{(2m)}I_p(v_1^{(j)})K_p(v_2^{(j)})\\ \mathrm{FEK}_{2m+1}^{(j)}(\xi)&=\frac{1}{B_1^{(2m+1)}}\sum_{p=0}^{\infty}B_{2p+1}^{(2m+1)}[I_p(v_1^{(j)})K_{p+1}(v_2^{(j)})-I_{p+1}(v_1^{(j)})K_p(v_2^{(j)})]\,,\end{aligned}\right\} \tag{29}$$

where

$$\left.\begin{aligned}&v_1^{(1)}=\tfrac{1}{2}k_1ce^{-\xi}\,, && v_2^{(1)}=\tfrac{1}{2}k_1ce^{\xi}\,,\\ &v_1^{(2)}=\tfrac{1}{2}|k_2|ce^{-\xi}\,, && v_2^{(2)}=\tfrac{1}{2}|k_2|ce^{\xi}\,,\\ &A_{2p}^{(2m)}=(-1)^{m+p}a_{2p}^{(2m)}\,, && B_{2p+1}^{(2m+1)}=(-1)^{m+p}a_{2p+1}^{(2m+1)}\,.\end{aligned}\right\} \tag{30}$$

The fundamental equation (15) for the magnetic stream function χ^* inside the cylinder is also transformed into $(\partial^2/\partial\xi^2+\partial^2/\partial\eta^2)\chi^*=0$. The general solution of this equation which is regular at $\xi=0$ is given in the form:

$$\chi^*=A_0^*+\sum_{n=1}^{\infty}\frac{c}{n}(A_n^*\cos n\eta+B_n^*\sin n\eta)\cosh n\xi\,, \tag{31}$$

where A_n^*'s and B_n^*'s are constants to be determined by the boundary conditions. Applying the boundary conditions (8) to the general solutions (24) and (31), we have

$$\left.\begin{aligned}&\left(\frac{\partial\psi}{\partial\xi}\right)_{\xi=\xi_0}=A_0+c(\cos\alpha\sin\eta\cosh\xi_0-\sin\alpha\cos\eta\sinh\xi_0)\\ &\qquad-\sum_{n=1}^{\infty}(A_n\cos n\eta+B_n\sin n\eta)+\sum_{n=0}^{\infty}\sum_{j=1}^{2}\left[\frac{\partial}{\partial\xi}\{a_n^{(j)}F_n^{(j)}+b_n^{(j)}G_n^{(j)}\}\right]_{\xi=\xi_0}=0\,,\\ &\left(\frac{\partial\psi}{\partial\eta}\right)_{\xi=\xi_0}=B_0+c(\cos\alpha\cos\eta\sinh\xi_0+\sin\alpha\sin\eta\cosh\xi_0)\\ &\qquad-\sum_{n=1}^{\infty}(A_n\sin n\eta-B_n\cos n\eta)+\sum_{n=0}^{\infty}\sum_{j=1}^{2}\left[\frac{\partial}{\partial\eta}\{a_n^{(j)}F_n^{(j)}+b_n^{(j)}G_n^{(j)}\}\right]_{\xi=\xi_0}=0\,,\\ &\left(\frac{\partial\chi}{\partial\xi}-\frac{\partial\chi^*}{\partial\xi}\right)_{\xi=\xi_0}=A_0+c(\cos\alpha\sin\eta\cosh\xi_0-\sin\alpha\cos\eta\sinh\xi_0)\\ &\qquad-\sum_{n=1}^{\infty}(A_n\cos n\eta+B_n\sin n\eta)+\sum_{n=0}^{\infty}\sum_{j=1}^{2}\left(1-\frac{2k_j}{R_m}\right)^{-1}\left[\frac{\partial}{\partial\xi}\{a_n^{(j)}F_n^{(j)}+b_n^{(j)}G_n^{(j)}\}\right]_{\xi=\xi_0}\\ &\qquad-\sum_{n=1}^{\infty}c(A_n^*\cos n\eta+B_n^*\sin n\eta)\sinh n\xi_0=0\,,\end{aligned}\right\} \tag{32}$$

$$\left.\begin{aligned}&\left(\frac{\partial\chi}{\partial\eta}-\frac{\mu^*}{\mu}\frac{\partial\chi^*}{\partial\eta}\right)_{\xi=\xi_0}=B_0+c(\cos\alpha\cos\eta\sinh\xi_0+\sin\alpha\sin\eta\cosh\xi_0)\\&\quad-\sum_{n=1}^{\infty}(A_n\sin n\eta-B_n\cos n\eta)+\sum_{n=0}^{\infty}\sum_{j=1}^{2}\left(1-\frac{2k_j}{R_m}\right)^{-1}\left[\frac{\partial}{\partial\eta}\{a_n{}^{(j)}F_n{}^{(j)}+b_n{}^{(j)}G_n{}^{(j)}\}\right]_{\xi=\xi_0}\\&\quad+\frac{\mu^*}{\mu}\sum_{n=1}^{\infty}c(A_n{}^*\sin n\eta-B_n{}^*\cos n\eta)\cosh n\xi_0=0\,.\end{aligned}\right|$$

Expanding the terms $[\partial F_n{}^{(j)}/\partial\xi]_{\xi=\xi_0}$ etc. in Fourier series:

$$\left.\begin{aligned}\left(\frac{\partial F_n{}^{(j)}}{\partial\xi}\right)_{\xi=\xi_0}&=A^{(j)}_{n0}+\sum_{m=1}^{\infty}(A^{(j)}_{nm}\cos m\eta+C^{(j)}_{nm}\sin m\eta)\,,\\\left(\frac{\partial G_n{}^{(j)}}{\partial\xi}\right)_{\xi=\xi_0}&=B^{(j)}_{n0}+\sum_{m=1}^{\infty}(B^{(j)}_{nm}\cos m\eta+D^{(j)}_{nm}\sin m\eta)\,,\\\left(\frac{\partial F_n{}^{(j)}}{\partial\eta}\right)_{\xi=\xi_0}&=E^{(j)}_{n0}+\sum_{m=1}^{\infty}(E^{(j)}_{nm}\cos m\eta+G^{(j)}_{nm}\sin m\eta)\,,\\\left(\frac{\partial G_n{}^{(j)}}{\partial\eta}\right)_{\xi=\xi_0}&=F^{(j)}_{n0}+\sum_{m=1}^{\infty}(F^{(j)}_{nm}\cos m\eta+H^{(j)}_{nm}\sin m\eta)\,,\end{aligned}\right\}\tag{33}$$

and equating to zero the coefficients of $\cos m\eta$ and $\sin m\eta$ in (32), we have

$$\left.\begin{aligned}&A_0+\sum_{n=0}^{\infty}\sum_{j=1}^{2}(a^{(j)}_nA^{(j)}_{n0}+b^{(j)}_nB^{(j)}_{n0})=0\,,\\&-A_m+\sum_{n=0}^{\infty}\sum_{j=1}^{2}(a^{(j)}_nA^{(j)}_{nm}+b^{(j)}_nB^{(j)}_{nm})=\frac{1-\sigma^2}{2(1+\sigma^2)}\sin\alpha\cdot\delta_{1m}\,,\\&-B_m+\sum_{n=0}^{\infty}\sum_{j=1}^{2}(a^{(j)}_nC^{(j)}_{nm}+b^{(j)}_nD^{(j)}_{nm})=-\frac{1}{2}\cos\alpha\cdot\delta_{1m}\,,\\&B_0+\sum_{n=0}^{\infty}\sum_{j=1}^{2}(a^{(j)}_nE^{(j)}_{n0}+b^{(j)}_nF^{(j)}_{n0})=0\,,\\&B_m+\sum_{n=0}^{\infty}\sum_{j=1}^{2}(a^{(j)}_nE^{(j)}_{nm}+b^{(j)}_nF^{(j)}_{nm})=-\frac{1-\sigma^2}{2(1+\sigma^2)}\cos\alpha\cdot\delta_{1m}\,,\\&-A_m+\sum_{n=0}^{\infty}\sum_{j=1}^{2}(a^{(j)}_nG^{(j)}_{nm}+b^{(j)}_nH^{(j)}_{nm})=-\frac{1}{2}\sin\alpha\cdot\delta_{1m}\,,\\&A_0+\sum_{n=0}^{\infty}\sum_{j=1}^{2}\left(1-\frac{2k_j}{R_m}\right)^{-1}(a^{(j)}_nA^{(j)}_{n0}+b^{(j)}_nB^{(j)}_{n0})=0\,,\\&-A_m+\sum_{n=0}^{\infty}\sum_{j=1}^{2}\left(1-\frac{2k_j}{R_m}\right)^{-1}(a^{(j)}_nA^{(j)}_{nm}+b^{(j)}_nB^{(j)}_{nm})-A_m{}^*c\sinh m\xi_0=\frac{1-\sigma^2}{2(1+\sigma^2)}\sin\alpha\cdot\delta_{1m}\,,\\&-B_m+\sum_{n=0}^{\infty}\sum_{j=1}^{2}\left(1-\frac{2k_j}{R_m}\right)^{-1}(a^{(j)}_nC^{(j)}_{nm}+b^{(j)}_nD^{(j)}_{nm})-B_m{}^*c\sinh m\xi_0=-\frac{1}{2}\cos\alpha\cdot\delta_{1m}\,,\\&B_0+\sum_{n=0}^{\infty}\sum_{j=1}^{2}\left(1-\frac{2k_j}{R_m}\right)^{-1}(a^{(j)}_nE^{(j)}_{n0}+b^{(j)}_nF^{(j)}_{n0})=0\,,\\&B_m+\sum_{n=0}^{\infty}\sum_{j=1}^{2}\left(1-\frac{2k_j}{R_m}\right)^{-1}(a^{(j)}_nE^{(j)}_{nm}+b^{(j)}_nF^{(j)}_{nm})-B_m{}^*\frac{\mu^*}{\mu}c\cosh m\xi_0=-\frac{1-\sigma^2}{2(1+\sigma^2)}\cos\alpha\cdot\delta_{1m}\,,\\&-A_m+\sum_{n=0}^{\infty}\sum_{j=1}^{2}\left(1-\frac{2k_j}{R_m}\right)^{-1}(a^{(j)}_nG^{(j)}_{nm}+b^{(j)}_nH^{(j)}_{nm})+A_m{}^*\frac{\mu^*}{\mu}c\cosh m\xi_0=-\frac{1}{2}\sin\alpha\cdot\delta_{1m}\,,\end{aligned}\right\}\tag{34}$$

where δ_{1m} equals 1 for $m=1$ and zero for $m\neq1$. Eliminating A_m's, B_m's, $A_m{}^*$'s and $B_m{}^*$'s in the above equations, we arrive at

$$\left.\begin{aligned}
&\sum_{n=0}^{\infty}\sum_{j=1}^{2}\left[a_n^{(j)}(A_{nm}^{(j)}-G_{nm}^{(j)})+b_n^{(j)}(B_{nm}^{(j)}-H_{nm}^{(j)})\right]=\frac{\sin\alpha}{1+\sigma^2}\delta_{1m}\,,\\
&\sum_{n=0}^{\infty}\sum_{j=1}^{2}\left[a_n^{(j)}(C_{nm}^{(j)}+E_{nm}^{(j)})+b_n^{(j)}(D_{nm}^{(j)}+F_{nm}^{(j)})\right]=-\frac{\cos\alpha}{1+\sigma^2}\delta_{1m}\,,\\
&\sum_{n=0}^{\infty}\sum_{j=1}^{2}\Bigg[a_n^{(j)}\left\{\left(1-\frac{2k_j}{R_m}\right)^{-1}-1\right\}\left(\frac{\mu^*}{\mu}\cosh m\xi_0A_{nm}^{(j)}+\sinh m\xi_0G_{nm}^{(j)}\right)\\
&\qquad+b_n^{(j)}\left\{\left(1-\frac{2k_j}{R_m}\right)^{-1}-1\right\}\left(\frac{\mu^*}{\mu}\cosh m\xi_0B_{nm}^{(j)}+\sinh m\xi_0H_{nm}^{(j)}\right)\Bigg]=0\,,\\
&\sum_{n=0}^{\infty}\sum_{j=1}^{2}\Bigg[a_n^{(j)}\left\{\left(1-\frac{2k_j}{R_m}\right)^{-1}-1\right\}\left(\frac{\mu^*}{\mu}\cosh m\xi_0C_{nm}^{(j)}-\sinh m\xi_0E_{nm}^{(j)}\right)\\
&\qquad+b_n^{(j)}\left\{\left(1-\frac{2k_j}{R_m}\right)^{-1}-1\right\}\left(\frac{\mu^*}{\mu}\cosh m\xi_0D_{nm}^{(j)}-\sinh m\xi_0F_{nm}^{(j)}\right)\Bigg]=0\,.
\end{aligned}\right\}\qquad(35)$$

We shall now seek for $a_n^{(j)}$'s and $b_n^{(j)}$'s for small values of k_1 and k_2. Using the relations

$$\left.\begin{aligned}
&\frac{\partial F_n}{\partial\xi}=e^{kx}\left[\mathrm{FEK}_n'(\xi)+k\frac{\partial x}{\partial\xi}\mathrm{FEK}_n(\xi)\right]\mathrm{ce}_n(\eta)\,,\\
&\frac{\partial G_n}{\partial\xi}=e^{kx}\,\mathrm{FEK}_n(\xi)\left[k\frac{\partial x}{\partial\eta}\mathrm{ce}_n(\eta)-\mathrm{ce}_n'(\eta)\right],\quad\text{etc.}\,,
\end{aligned}\right\}\qquad(36)$$

it is found that the Fourier coefficients $A_{nm}^{(j)}$'s, $B_{nm}^{(j)}$'s etc. are of the order of k^{m-2n} for $m>n$, of k^{2-m} or k^{-m} for $m=n\neq0$ and of k^{-m} for $m<n$, and especially when $m=n=0$, $A_{00}^{(j)}=F_{00}^{(j)}=O(k^0)$, $B_{00}^{(j)}=O(k^4)$ and $E_{00}^{(j)}=0$. On the other hand, if the orders of $a_n^{(j)}$'s and $b_n^{(j)}$'s are all assumed to be k^{2n-1}, it is sufficient, so far as we are concerned with the first approximation, to take only the following terms of the Fourier coefficients:

$$\left.\begin{aligned}
&A_{00}^{(j)}=-1+O(k_j^2)\,,\qquad B_{00}^{(j)}=O(k_j^4)\,,\\
&E_{00}^{(j)}=0\,,\qquad F_{00}^{(j)}=-1+O(k_j^2)\,,\\
&A_{01}^{(j)}=\frac{k_j\cos\alpha}{2(1+\sigma^2)}[\{\Omega_j(1-\sigma^2)-(1+\sigma^2)\}+O(k_j^2)]\,,\\
&B_{01}^{(j)}=\frac{k_j\sin\alpha}{2(1+\sigma^2)}(1-\sigma^2)[\Omega_j+O(k_j^2)]\,,\\
&C_{01}^{(j)}=\frac{k_j\sin\alpha}{2(1+\sigma^2)}[\{\Omega_j(1+\sigma^2)-(1-\sigma^2)\}+O(k_j^2)]\,,\\
&D_{01}^{(j)}=-\frac{k_j\cos\alpha}{2}[\Omega_j+O(k_j^2)]\,,\\
&E_{01}^{(j)}=\frac{k_j\sin\alpha}{2(1+\sigma^2)}(1-\sigma^2)[\Omega_j+O(k_j^2)]\,,\\
&F_{01}^{(j)}=-\frac{k_j\cos\alpha}{2(1+\sigma^2)}[\{\Omega_j(1-\sigma^2)+(1+\sigma^2)\}+O(k_j^2)]\,,\\
&G_{01}^{(j)}=-\frac{k_j\cos\alpha}{2}[\Omega_j+O(k_j^2)]\,,\\
&H_{01}^{(j)}=-\frac{k_j\sin\alpha}{2(1+\sigma^2)}[\{\Omega_j(1+\sigma^2)+(1-\sigma^2)\}+O(k_j^2)]\,,
\end{aligned}\right\}\qquad(37)$$

where

$$\Omega_1=-\left[\gamma+\ln\left\{\frac{k_1}{4(1+\sigma^2)}\right\}\right],\qquad\Omega_2=-\left[\gamma+\ln\left\{\frac{|k_2|}{4(1+\sigma^2)}\right\}\right]$$

and $\gamma=0.57721\cdots$ is Euler's constant.

Thus, we can determine $a_n^{(j)}$'s and $b_n^{(j)}$'s as functions of R, R_m, S, σ and α to the lowest order of k_1 and k_2, and on inserting the constants thus determined into (34), the values of the constants A_0 and B_0 can easily be obtained. Thus,

$$\left.\begin{aligned} A_0 &= \frac{-R_m\sigma^2(k_1-k_2)^2\sin 2\alpha}{k_1k_2[\{2(k_1\Omega_1-k_2\Omega_2)-R_m(\Omega_1-\Omega_2)\}^2-(k_1-k_2)^2(1+\sigma^4+2\sigma^2\cos 2\alpha)]}\,, \\ B_0 &= \frac{-R_m(k_1-k_2)[\{2(k_1\Omega_1-k_2\Omega_2)-R_m(\Omega_1-\Omega_2)\}-(k_1-k_2)(1+\sigma^2\cos 2\alpha)]}{k_1k_2[\{2(k_1\Omega_1-k_2\Omega_2)-R_m(\Omega_1-\Omega_2)\}^2-(k_1-k_2)^2(1+\sigma^4+2\sigma^2\cos 2\alpha)]}\,, \end{aligned}\right\} \tag{38}$$

which, to the first approximation, are independent of the ratio of the magnetic permeabilities μ^*/μ.

§ 4. Drag and Lift Coefficients

Next, we shall proceed to the calculation of the forces experienced by the elliptic cylinder. In the two-dimensional problem, they have been discussed in general by Yosinobu[3] and have been written in the forms:

$$D=-\frac{8\pi}{R_m}\rho\nu U_0k_1k_2B_0\,, \qquad L=-\frac{8\pi}{R_m}\rho\nu U_0k_1k_2A_0\,. \tag{39}$$

Thus, in the present problem, using the values of A_0 and B_0 as given by (38), they are given by

$$\left.\begin{aligned} D &= 8\pi\rho\nu U_0\frac{(k_1-k_2)[\{2(k_1\Omega_1-k_2\Omega_2)-R_m(\Omega_1-\Omega_2)\}-(k_1-k_2)(1+\sigma^2\cos 2\alpha)]}{\{2(k_1\Omega_1-k_2\Omega_2)-R_m(\Omega_1-\Omega_2)\}^2-(k_1-k_2)^2(1+\sigma^4+2\sigma^2\cos 2\alpha)}\,, \\ L &= 8\pi\rho\nu U_0\frac{\sigma^2(k_1-k_2)^2\sin 2\alpha}{\{2(k_1\Omega_1-k_2\Omega_2)-R_m(\Omega_1-\Omega_2)\}^2-(k_1-k_2)^2(1+\sigma^4+2\sigma^2\cos 2\alpha)}\,, \end{aligned}\right\} \tag{40}$$

and the drag and lift coefficients, defined as $C_D=D/(\frac{1}{2}\rho U_0^2L_0)$ and $C_L=L/(\frac{1}{2}\rho U_0^2L_0)$, become

$$\left.\begin{aligned} C_D &= \frac{16\pi}{R}\frac{(k_1-k_2)[\{2(k_1\Omega_1-k_2\Omega_2)-R_m(\Omega_1-\Omega_2)\}-(k_1-k_2)(1+\sigma^2\cos 2\alpha)]}{\{2(k_1\Omega_1-k_2\Omega_2)-R_m(\Omega_1-\Omega_2)\}^2-(k_1-k_2)^2(1+\sigma^4+2\sigma^2\cos 2\alpha)}\,, \\ C_L &= \frac{16\pi}{R}\frac{\sigma^2(k_1-k_2)^2\sin 2\alpha}{\{2(k_1\Omega_1-k_2\Omega_2)-R_m(\Omega_1-\Omega_2)\}^2-(k_1-k_2)^2(1+\sigma^4+2\sigma^2\cos 2\alpha)}\,, \end{aligned}\right\} \tag{41}$$

For the particular values of the parameters, the above formulae degenerate into various known results which have been obtained previously by several authors.

(I) *Case of $R_m=0$*

Since the electric conductivity of the fluid is supposed to be zero when $R_m=0$, there exists no current in the field, so that the flow field can be described just as in ordinary hydrodynamics. Putting $R_m=0$ in (16), we have $k_1=R/2$ and $k_2=0$, and the formulae (41) are reduced to

$$\left.\begin{aligned} C_D &= \frac{16\pi}{R}\frac{2\Omega_1-(1+\sigma^2\cos 2\alpha)}{4\Omega_1^2-(1+\sigma^4+2\sigma^2\cos 2\alpha)}\,, \\ C_L &= \frac{16\pi}{R}\frac{\sigma^2\sin 2\alpha}{4\Omega_1^2-(1+\sigma^4+2\sigma^2\cos 2\alpha)}\,, \end{aligned}\right\} \tag{42}$$

where $\Omega_1=-[\gamma+\ln\{R/8(1+\sigma^2)\}]$. It will readily be seen that, to the first approximation, these results are in accordance with those obtained previously by Imai[1] and Hasimoto[2].

(II) *Case of $S=0$*

When $S=0$, in other words, when the magnetic field vanishes, the flow field can also be described by ordinary hydrodynamics. Putting $S=0$ in (16), we have $k_1=R/2$ and $k_2=R_m/2$, and the formulae (41) degenerate into (42) again.

(III) *Case of $\sigma=0$*

When the thickness-ratio t is equal to unity, i.e., when $\sigma=0$, the elliptic cylinder is reduced to a circular cylinder. Putting $\sigma=0$ in (40), we have

$$\left.\begin{aligned} D &= \frac{16\pi\rho\nu U_0(k_1-k_2)}{(R_m-2k_2)(1+2\Omega_2)-(R_m-2k_1)(1+2\Omega_1)} \\ L &= 0\,, \end{aligned}\right\} \tag{43}$$

where $\Omega_j=-[\gamma+\ln(|k_j|/4)]$. These formulae coincide with those given by Yosinobu[3].

(IV) *Case of $R=R_m=0$ with finite M*

When the velocity of the fluid is very small but the magnetic field is very strong so that the Hartmann number $M=(RR_mS)^{1/2}$ remains finite, the field may be dealt with by the so-called hydromagnetic Stokes approximation. Putting $R=R_m=0$, but retaining M to be finite in (16), we have $k_1=M/2$ and $k_2=-M/2$, and the formulae (40) are reduced to

$$\left.\begin{aligned} D&=8\pi\rho\nu U_0\frac{2\Omega-(1+\sigma^2\cos 2\alpha)}{4\Omega^2-(1+\sigma^4+2\sigma^2\cos 2\alpha)}\,,\\ L&=8\pi\rho\nu U_0\frac{\sigma^2\sin 2\alpha}{4\Omega^2-(1+\sigma^4+2\sigma^2\cos 2\alpha)}\,,\end{aligned}\right\}\qquad(44)$$

Table I-1. Values of C_D for $R=0.1$, $R_m=0.1$ and $t=0$.

S	0°	9°	18°	27°	36°	45°	54°	63°	72°	81°	90°
0	45.71	45.97	46.73	47.89	49.34	50.92	52.48	53.86	54.95	55.64	55.88
0.001	45.71	45.97	46.72	47.89	49.34	50.92	52.47	53.86	54.94	55.63	55.87
0.01	45.67	45.93	46.69	47.85	49.29	50.87	52.43	53.81	54.89	55.58	55.81
0.1	45.28	45.53	46.27	47.41	48.83	50.38	51.90	53.26	54.32	55.00	55.23
0.3	44.28	44.52	45.22	46.30	47.65	49.12	50.57	51.86	52.88	53.52	55.74
0.5	43.00	43.23	43.88	44.90	46.16	47.54	48.90	50.11	51.06	51.67	51.88
0.8	39.88	40.07	40.62	41.47	42.54	43.70	44.86	45.89	46.70	47.22	47.40
1.0	0	0	0	0	0	0	0	0	0	0	0
1.2	39.88	40.07	40.62	41.47	42.54	43.70	44.86	45.89	46.70	47.22	47.40
1.5	43.00	43.23	43.88	44.90	46.16	47.54	48.90	50.11	51.06	51.67	51.88
2.0	45.71	45.97	46.73	47.89	49.34	50.92	52.48	53.87	54.95	55.64	55.88
3.0	48.79	49.09	49.97	51.33	53.01	54.84	56.64	58.23	59.48	60.27	60.54
5.0	52.31	52.67	53.71	55.31	57.28	59.43	61.53	63.38	64.83	65.74	66.06
10	57.13	57.58	58.87	60.85	63.29	65.91	68.47	70.72	72.46	73.56	73.94
30	65.89	66.55	68.42	71.25	74.71	78.39	81.92	84.97	87.33	88.80	89.31

Table I-2. Values of C_D for $R=0.1$, $R_m=0.1$ and $t=0.1$.

S	0°	9°	18°	27°	36°	45°	54°	63°	72°	81°	90°
0	47.32	47.54	48.17	49.15	50.38	51.72	53.04	54.22	55.14	55.73	55.93
0.001	47.31	47.53	48.17	49.15	50.37	51.71	53.03	54.21	55.13	55.72	55.92
0.01	47.27	47.49	48.12	49.10	50.32	51.66	52.98	54.16	55.08	55.67	55.87
0.1	46.85	47.07	47.69	48.65	49.84	51.15	52.45	53.60	54.51	55.08	55.28
0.3	45.78	45.98	46.57	47.48	48.62	49.87	51.10	52.20	53.06	53.61	53.79
0.5	44.42	44.61	45.16	46.01	47.08	48.24	49.39	50.42	51.23	51.75	51.93
0.8	41.15	41.25	41.71	42.43	43.33	44.31	45.29	46.16	46.85	47.29	47.44
1.0	0	0	0	0	0	0	0	0	0	0	0
1.2	41.09	41.25	41.71	42.43	43.33	44.31	45.29	46.16	46.85	47.29	47.44
1.5	44.42	44.61	45.16	46.01	47.07	48.24	49.39	50.42	51.23	51.75	51.93
2.0	47.32	47.52	48.17	49.15	50.38	51.71	53.04	54.22	55.14	55.73	55.93
3.0	50.62	50.87	51.62	52.76	54.18	55.74	57.27	58.63	59.69	60.37	60.60
5.0	54.42	54.72	55.60	56.95	58.63	60.45	62.24	63.83	65.07	65.86	66.13
10	59.66	60.03	61.13	62.81	64.88	67.12	69.32	71.25	72.75	73.71	74.03
30	69.27	69.82	71.41	73.83	76.79	79.95	83.00	85.66	87.71	89.01	89.44

Table I-3. Values of C_D for $R=0.1$, $R_m=0.1$ and $t=0.5$.

S	0°	9°	18°	27°	36°	45°	54°	63°	72°	81°	90°
0	52.81	52.91	53.20	53.64	54.20	54.82	55.43	55.98	56.41	56.69	56.79
0.001	52.80	52.90	53.19	53.64	54.20	54.81	55.42	55.97	56.41	56.68	56.78
0.01	52.75	52.85	53.14	53.58	54.14	54.76	55.37	55.92	56.35	56.63	56.72
0.1	52.23	52.33	52.61	53.04	53.59	54.19	54.79	55.33	55.75	56.02	56.12
0.3	50.90	50.99	51.26	51.67	52.19	52.76	53.33	53.84	54.24	54.50	54.59
0.5	49.22	49.31	49.56	49.94	50.43	50.96	51.49	51.96	52.34	52.58	52.66
0.8	45.17	45.24	45.45	45.77	46.17	46.62	47.07	47.46	47.78	47.98	48.05
1.0	0	0	0	0	0	0	0	0	0	0	0
1.2	45.17	45.24	45.45	45.77	46.17	46.62	47.07	47.46	47.78	47.98	48.05
1.5	49.22	49.31	49.56	49.94	50.43	50.96	51.49	51.96	52.34	52.58	52.66
2.0	52.81	52.91	53.20	53.64	54.20	54.82	55.43	55.98	56.41	56.69	56.79
3.0	56.96	57.07	57.41	57.93	58.59	59.31	60.03	60.57	61.18	61.50	61.61
5.0	61.81	61.95	62.35	62.98	63.76	64.61	65.46	66.22	66.82	67.20	67.33
10	68.66	68.84	69.34	70.12	71.10	72.17	73.22	74.16	74.91	75.38	75.54
30	81.72	81.97	82.72	83.87	85.29	86.83	88.35	89.70	90.75	91.42	91.65

where $\Omega=-[\gamma+\ln\{M/8(1+\sigma^2)\}]$. It can easily be confirmed that in the special case of $\sigma=1$, these formulae are in agreement with those obtained by Hasimoto[5] for a flat plate, who discussed a more general case in which the direction of the magnetic field is arbitrary. In the other special case of $\sigma=0$, the formula for the drag is immediately reduced to

$$D=\frac{8\pi\rho\nu U_0}{2\Omega+1}\,, \tag{45}$$

where $\Omega=-[\gamma+\ln(M/8)]$, which agrees with that for a circular cylinder as given by Yosinobu and Kakutani[6].

§ 5. Numerical Results

Detailed numerical calculations for the drag and lift coefficients have been carried out for various values of the parameters, using the formulae (41). In order to avoid confusion, however, we shall give here mainly the results for the case of $R=R_m=0.1$ for four different elliptic cylinders: $t=0$ (flat plate), 0.1, 0.5 and 1 (circular cylinder).

Table I-4. Values of C_D for $t=1.0$.

S	$R=1.0$ $R_m=1.0$	$R=1.0$ $R_m=0.1$	$R=0.1$ $R_m=1.0$	$R=0.1$ $R_m=0.1$
0	12.55	12.55	58.38	58.38
0.001	12.55	12.55	58.37	58.38
0.01	12.52	12.54	58.27	58.31
0.1	12.23	12.44	57.22	57.68
0.3	11.53	12.19	54.61	56.06
0.5	10.70	11.90	51.42	54.03
0.8	8.95	11.24	44.24	49.19
1.0	0	0	0	0
1.2	9.07	10.83	44.91	49.19
1.5	10.70	11.11	53.05	54.03
2.0	12.55	11.34	61.45	58.38
3.0	15.32	11.69	72.56	63.49
5.0	19.20	12.33	87.19	69.59
10	27.81	13.74	110.17	78.39
30	—	18.08	162.17	95.89

Table I gives the values of the drag coefficient C_D and they are plotted in Figs. 1~4. In Figs. 1, 2 and 3 the values of C_D are plotted against the pressure number S, the angle of incidence α being 0°, 45 and 90° respectively. In Fig. 4 is shown the dependency of C_D upon the angle of incidence α in the case of a flat plate. Table II and Figs. 5~6 give the value of the lift coefficient C_L for the three elliptic cylinders, C_L being evidently zero in the case of a circular cylinder. Table III and Fig. 7 give the values of the ratio C_L/C_D for the three elliptic cylinders. Fig. 5 gives the dependency of C_L upon S at the angle of incidence $\alpha=45°$ and Figs. 6~7 show the variations of C_L and C_L/C_D with the angle of incidence α,

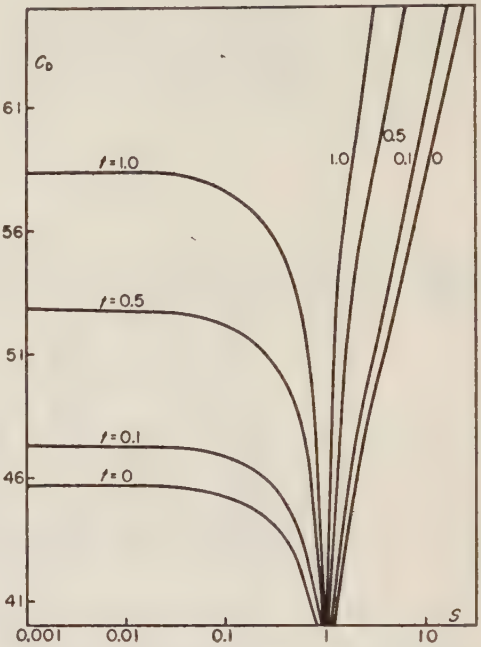

Fig. 1. Drag coefficient C_D plotted against the pressure number S, for $R=R_m=0.1$ and the angle of incidence $\alpha=0°$.

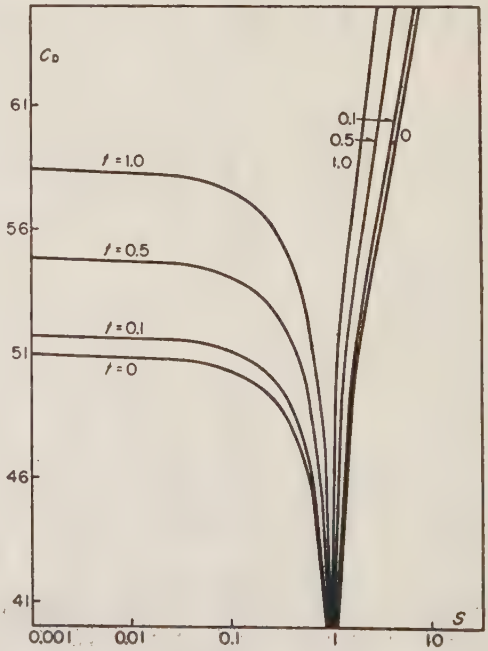

Fig. 2. Drag coefficient C_D plotted against S, for $R=R_m=0.1$ and $\alpha=45°$.

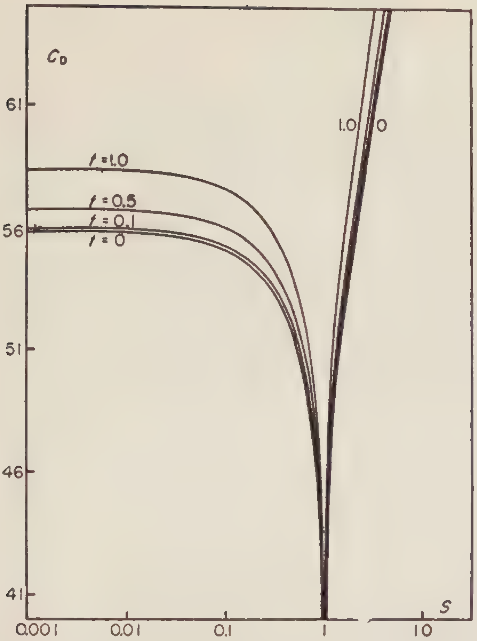

Fig. 3. Drag coefficient C_D plotted against S, for $R=R_m=0.1$ and $\alpha=90°$.

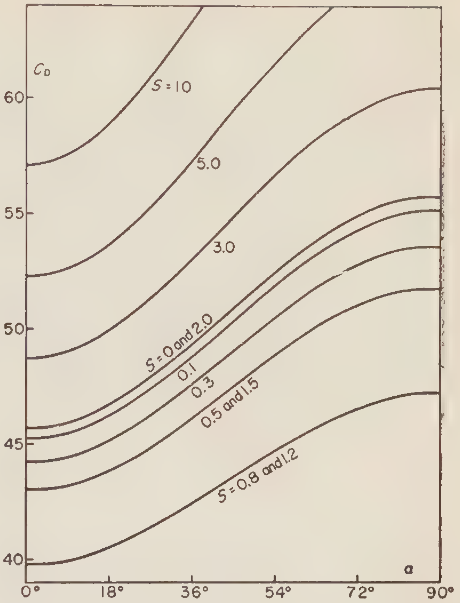

Fig. 4. Drag coefficient C_D plotted against the angle of incidence α, for $R=R_m=0.1$ in the case of flat plate ($t=0$).

Table II-1. Values of C_L for $R=0.1$, $R_m=0.1$ and $t=0$.

S	0°	9°	18°	27°	36°	45°	54°	63°	72°	81°	90°
0	0	2.017	3.822	5.230	6.105	6.369	6.010	5.077	3.668	1.922	0
0.001	0	2.016	3.822	5.230	6.105	6.369	6.010	5.077	3.668	1.922	0
0.01	0	2.012	3.821	5.229	6.103	6.367	6.008	5.076	3.667	1.919	0
0.1	0	1.968	3.730	5.105	5.960	6.218	5.869	4.959	3.583	1.887	0
0.3	0	1.859	3.524	4.824	5.634	5.881	5.553	4.693	3.393	1.778	0
0.5	0	1.726	3.273	4.484	5.238	5.471	5.169	4.370	3.160	1.656	0
0.8	0	1.431	2.714	3.721	4.352	4.550	4.303	3.642	2.636	1.382	0
1.0	0	0	0	0	0	0	0	0.	0	0	0
1.2	0	1.431	2.714	3.721	4.352	4.550	4.303	3.642	2.636	1.382	0
1.5	0	1.726	3.273	4.483	5.238	5.471	5.169	4.370	3.160	1.656	0
2.0	0	2.017	3.822	5.230	6.105	6.369	6.010	5.077	3.668	1.922	0
3.0	0	2.388	4.523	6.184	7.209	7.510	7.077	5.971	4.310	2.256	0
5.0	0	2.876	5.442	7.430	8.647	8.991	8.458	7.124	5.136	2.687	0
10	0	3.671	6.935	9.448	10.964	11.367	10.662	8.958	6.446	3.368	0
30	0	5.592	10.529	14.266	16.449	16.935	15.777	13.179	9.440	4.918	0

Table II-2. Values of C_L for $R=0.1$, $R_m=0.1$ and $t=0.1$.

S	0°	9°	18°	27°	36°	45°	54°	63°	72°	81°	90°
0	0	1.710	3.243	4.442	5.190	5.421	5.122	4.331	3.132	1.641	0
0.001	0	1.710	3.242	4.441	5.189	5.420	5.120	4.330	3.131	1.641	0
0.01	0	1.706	3.235	4.432	5.178	5.408	5.110	4.321	3.125	1.638	0
0.1	0	1.668	3.164	4.334	5.065	5.291	4·999	4.228	3.058	1.603	0
0.3	0	1.575	2.986	4.092	4.784	4.999	4.725	3.998	2.892	1.516	0
0.5	0	1.461	2.771	3.799	4.443	4.645	4.392	3.717	2.690	1.410	0
0.8	0	1.208	2.292	3.144	3.680	3.851	3.645	3.088	2.236	1.173	0
1.0	0	0	0	0	0	0	0	0	0	0	0
1.2	0	1.208	2.292	3.144	3.680	3.851	3.645	3.088	2.236	1.173	0
1.5	0	1.461	2.771	3.788	4.443	4.645	4.392	3.717	2.690	1.410	0
2.0	0	1.710	3.243	4.442	5.190	5.421	5.122	4.331	3.132	1.642	0
3.0	0	2.031	3.848	5.267	6.147	6.412	6.051	5.111	3.693	1.935	0
5.0	0	2.453	4.644	6.348	7.399	7.706	7.260	6.124	4.420	2.314	0
10	0	3.143	5.944	8.109	9.428	9.793	9.203	7.746	5.581	2.918	0
30	0	4.824	9.096	12.350	14.277	14.739	13.769	11.527	8.272	4.314	0

Table II-3. Values of C_L for $R=0.1$, $R_m=0.1$ and $t=0.5$.

S	0°	9°	18°	27°	36°	45°	54°	63°	72°	81°	90°
0	0	0.794	1.507	2.070	2.426	2.543	2.411	2.045	1.483	0.778	0
0.001	0	0.793	1.507	2.069	2.426	2.543	2.411	2.045	1.482	0.778	0
0.01	0	0.792	1.503	2.065	2.420	2.537	2.405	2.040	1.479	0.777	0
0.1	0	0.773	1.468	2.016	2.364	2.478	2.349	1.993	1.445	0.759	0
0.3	0	0.727	1.381	1.897	2.224	2.332	2.212	1.876	1.361	0.714	0
0.5	0	0.672	1.276	1.753	2.056	2.156	2.045	1.736	1.259	0.661	0
0.8	0	0.550	1.045	1.436	1.684	1.767	1.677	1.424	1.033	0.542	0
1.0	0	0	0	0	0	0	0	0	0	0	0
1.2	0	0.550	1.045	1.436	1.684	1.767	1.677	1.424	1.033	0.542	0
1.5	0	0.672	1.276	1.753	2.056	2.156	2.045	1.736	1.259	0.661	0
2.0	0	0.794	1.507	2.070	2.426	2.543	2.411	2.045	1.483	0.778	0
3.0	0	0.952	1.808	2.482	2.907	3.046	2.886	2.446	1.773	0.930	0
5.0	0	1.164	2.210	3.031	3.549	3.714	3.516	2.979	2.157	1.132	0
10	0	1.518	2.880	3.947	4.614	4.823	4.560	3.854	2.792	1.464	0
30	0	2.412	4.568	6.245	7.278	7.582	7.144	6.027	4.350	2.278	0

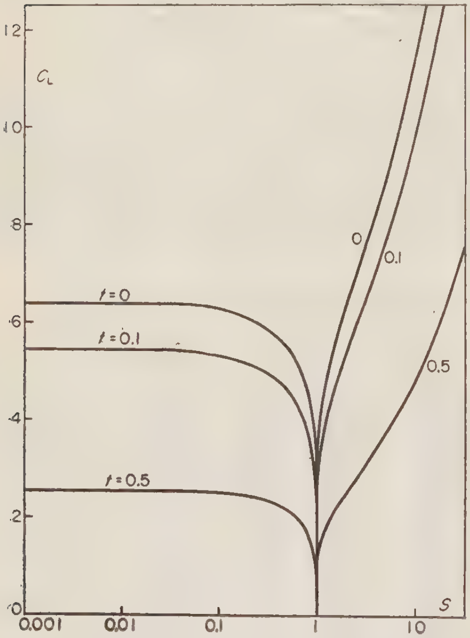

Fig. 5. Lift coefficient C_L plotted against the pressure number S, for $R=R_m=0.1$ and the angle of incidence $\alpha=45°$.

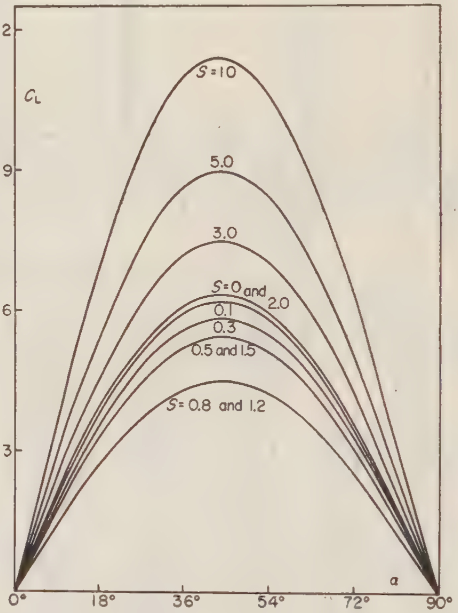

Fig. 6. Lift coefficient C_L plotted against the angle of incidence α, for $R=R_m=0.1$ in the case of flat plate ($t=0$).

Table III-1. Values of C_L/C_D for $R=0.1$, $R_m=0.1$ and $t=0$.

S	0°	9°	18°	27°	36°	45°	54°	63°	72°	81°	90°
0	0	0.0439	0.0818	0.1092	0.1237	0.1251	0.1145	0.0943	0.0668	0.0345	0
0.001	0	0.0439	0.0818	0.1092	0.1237	0.1250	0.1145	0.0942	0.0667	0.0345	0
0.01	0	0.0438	0.0817	0.1091	0.1236	0.1249	0.1144	0.0941	0.0667	0.0345	0
0.1	0	0.0432	0.0806	0.1077	0.1221	0.1234	0.1131	0.0931	0.0660	0.0341	0
0.3	0	0.0418	0.0779	0.1042	0.1182	0.1177	0.1098	0.0905	0.0642	0.0332	0
0.5	0	0.0399	0.0746	0.0999	0.1135	0.1151	0.1057	0.0872	0.0619	0.0321	0
0.8	0	0.0357	0.0668	0.0897	0.1023	0.1041	0.0959	0.0794	0.0564	0.0293	0
1.0	0	0	0	0	0	0	0	0	0	0	0
1.2	0	0.0357	0.0668	0.0897	0.1023	0.1041	0.0959	0.0794	0.0564	0.0293	0
1.5	0	0.0399	0.0746	0.0999	0.1135	0.1151	0.1057	0.0872	0.0619	0.0321	0
2.0	0	0.0439	0.0818	0.1092	0.1237	0.1251	0.1145	0.0943	0.0668	0.0345	0
3.0	0	0.0487	0.0905	0.1205	0.1360	0.1369	0.1249	0.1025	0.0725	0.0374	0
5.0	0	0.0546	0.1013	0.1343	0.1509	0.1513	0.1375	0.1124	0.0792	0.0409	0
10	0	0.0637	0.1178	0.1553	0.1733	0.1725	0.1557	0.1267	0.0890	0.0458	0
30	0	0.0840	0.1539	0.2002	0.2202	0.2160	0.1926	0.1551	0.1081	0.0551	0

Table III-2. Values of C_L/C_D for $R=0.1$, $R_m=0.1$ and $t=0.1$.

S	0°	9°	18°	27°	36°	45°	54°	63°	72°	81°	90°
0	0	0.0360	0.0673	0.0904	0.1030	0.1048	0.0966	0.0799	0.0568	0.0295	0
0.001	0	0.0360	0.0673	0.0904	0.1030	0.1048	0.0966	0.0799	0.0568	0.0295	0
0.01	0	0.0359	0.0672	0.0902	0.1029	0.1047	0.0964	0.0798	0.0567	0.0294	0
0.1	0	0.0354	0.0663	0.0891	0.1016	0.1034	0.0953	0.0789	0.0561	0.0291	0
0.3	0	0.0342	0.0641	0.0862	0.0984	0.1002	0.0925	0.0766	0.0545	0.0283	0
0.5	0	0.0327	0.0614	0.0826	0.0944	0.0963	0.0889	0.0737	0.0525	0.0273	0
0.8	0	0.0293	0.0550	0.0741	0.0849	0.0869	0.0805	0.0669	0.0477	0.0248	0
1.0	0	0	0	0	0	0	0	0	0	0	0
1.2	0	0.0293	0.0549	0.0741	0.0849	0.0869	0.0805	0.0669	0.0477	0.0248	0
1.5	0	0.0327	0.0614	0.0826	0.0944	0.0963	0.0889	0.0737	0.0525	0.0273	0
2.0	0	0.0360	0.0673	0.0904	0.1030	0.1048	0.0966	0.0799	0.0568	0.0295	0
3.0	0	0.0399	0.0746	0.0998	0.1134	0.1150	0.1057	0.0872	0.0619	0.0320	0
5.0	0	0.0448	0.0835	0.1115	0.1262	0.1275	0.1166	0.0959	0.0679	0.0351	0
10	0	0.0523	0.0972	0.1291	0.1453	0.1459	0.1328	0.1087	0.0767	0.0396	0
30	0	0.0691	0.1274	0.1673	0.1859	0.1844	0.1654	0.1346	0.0943	0.0485	0

Table III-3. Values of C_L/C_D for $R=0.1$, $R_m=0.1$ and $t=0.5$.

S	0°	9°	18°	27°	36°	45°	54°	63°	72°	81°	90°
0	0	0.0150	0.0283	0.0386	0.0448	0.0464	0.0435	0.0365	0.0263	0.0137	0
0.001	0	0.0150	0.0283	0.0386	0.0448	0.0464	0.0435	0.0365	0.0263	0.0137	0
0.01	0	0.0150	0.0283	0.0385	0.0447	0.0463	0.0434	0.0365	0.0263	0.0137	0
0.1	0	0.0148	0.0279	0.0380	0.0441	0.0457	0.0429	0.0360	0.0259	0.0135	0
0.3	0	0.0143	0.0269	0.0367	0.0426	0.0442	0.0415	0.0349	0.0251	0.0131	0
0.5	0	0.0136	0.0258	0.0351	0.0408	0.0423	0.0397	0.0334	0.0241	0.0126	0
0.8	0	0.0122	0.0230	0.0314	0.0365	0.0379	0.0356	0.0300	0.0216	0.0113	0
1.0	0	0	0	0	0	0	0	0	0	0	0
1.2	0	0.0122	0.0230	0.0314	0.0365	0.0379	0.0356	0.0300	0.0216	0.0113	0
1.5	0	0.0136	0.0258	0.0351	0.0408	0.0423	0.0397	0.0334	0.0241	0.0126	0
2.0	0	0.0150	0.0283	0.0386	0.0448	0.0464	0.0435	0.0365	0.0263	0.0137	0
3.0	0	0.0167	0.0315	0.0428	0.0496	0.0514	0.0481	0.0403	0.0290	0.0151	0
5.0	0	0.0188	0.0354	0.0481	0.0557	0.0575	0.0537	0.0450	0.0323	0.0168	0
10	0	0.0221	0.0415	0.0563	0.0649	0.0668	0.0623	0.0520	0.0373	0.0194	0
30	0	0.0294	0.0522	0.0745	0.0853	0.0873	0.0809	0.0672	0.0479	0.0249	0

Table IV. Values of α_L for $t=0$ (degree).

S	$R=1.0$ $R_m=1.0$	$R=1.0$ $R_m=0.1$	$R=0.1$ $R_m=1.0$	$R=0.1$ $R_m=0.1$
0	41.70	41.70	44.27	44.27
0.001	41.71	41.71	44.27	44.27
0.01	41.72	41.71	44.28	44.28
0.1	41.85	41.73	44.30	44.29
0.3	42.22	41.87	44.37	44.33
0.5	42.59	42.02	44.45	44.38
0.8	43.33	42.34	44.59	44.48
1.0	—	—	—	—
1.2	43.32	42.53	44.57	44.48
1.5	42.59	42.40	44.40	44.38
2.0	41.71	42.30	44.20	44.27
3.0	40.07	42.12	43.89	44.20
5.0	36.73	41.80	43.40	43.97
10	22.32	41.00	42.45	43.70
30	—	37.79	39.32	42.91

respectively, in the case of a flat plate.

From these tables and figures, it will be seen that the drag and lift coefficients decrease with the increase of the pressure number S when $S<1$, and the reverse is the case when $S>1$. Furthermore, it will be seen that the drag coefficient increases monotonically with the increase of either of the thickness-ratio

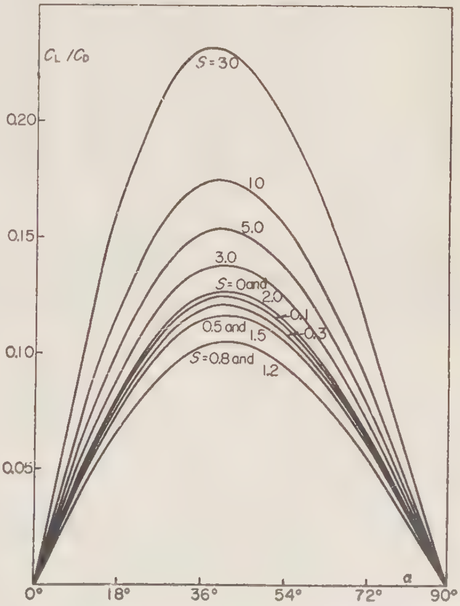

Fig. 7. Values of C_L/C_D plotted against the angle of incidence α, for $R=R_m=0.1$ in the case of flat plate ($t=0$).

or the angle of incidence of the cylinder and that the variation of the drag coefficient is very small. Whereas, the dependency of the lift coefficient on either of the thickness-ratio or the angle of incidence is remarkable.

On the other hand, the angle of incidence α_L at which the maximum lift occurs is, by (41), obtained from the equation:

$$\cos 2\alpha_L = \frac{2\sigma^2(k_1-k_2)^2}{\{\Omega_2(R_m-2k_2)-\Omega_1(R_m-2k_1)\}^2-(k_1-k_2)^2(1+\sigma^4)} . \tag{46}$$

In like manner, the angle of incidence α_R at which C_L/C_D has a maximum value is given by

$$\cos 2\alpha_R = \frac{\sigma^2(k_1-k_2)}{\{\Omega_2(R_m-2k_2)-\Omega_1(R_m-2k_1)\}-(k_1-k_2)} . \tag{47}$$

The values of α_L and α_R have also been calculated only in the case of a flat plate, and the results are shown in Tables IV~V. α_L increases towards 45° with the increase of S when $S<1$, and decreases with the increase of S when $S>1$, as is shown in Figs. 6 and 7. α_R shows a similar tendency to α_L.

Table V. Values of α_R for $t=0$ (degree)

S	$R=1.0$ $R_m=1.0$	$R=1.0$ $R_m=0.1$	$R=0.1$ $R_m=1.0$	$R=0.1$ $R_m=0.1$
0	36.42	36.42	41.40	41.40
0.001	36.43	36.42	41.41	41.41
0.01	36.45	36.43	41.41	41.41
0.1	36.69	36.51	41.48	41.46
0.3	37.29	36.73	41.67	41.57
0.5	37.92	36.96	41.86	41.69
0.8	39.26	37.49	42.33	42.02
1.0	—	—	—	—
1.2	39.23	37.81	42.29	42.02
1.5	37.92	37.59	41.76	41.69
2.0	36.42	37.41	41.20	41.40
3.0	34.12	37.13	40.44	41.06
5.0	30.04	36.61	39.40	40.65
10	16.54	35.41	37.66	40.03
30	—	31.25	33.14	38.47

As we can see from the formulae (41), $S=1$ is a singular point. This singularity is wholly due to the breakdown of the present perturbation method of solution at $S=1$, as has been discussed for a circular cylinder by Yosinobu³⁾ and for a finite flat plate by Greenspan and Carrier⁷⁾.

Acknowledgements

The writer wishes to express his cordial thanks to Professor S. Tomotika for his continual guidance and encouragement throughout this work, and especially for his kind inspection of the manuscript. The writer's thanks are also due to Dr. H. Yosinobu for his kind advice and helpful discussions.

References

1) I. Imai: Proc. Roy. Soc. **A**, **224** (1954) 141.
2) H. Hasimoto: J. Phys. Soc. Japan **8** (1953) 653.
3) H. Yosinobu: J. Phys. Soc. Japan **15** (1960) 175.
4) N. W. McLachlan: '*Theory and Application of Mathieu Functions*' (Oxford Univ. Press, 1947) 248.
5) H. Hasimoto: to be published.
6) H. Yosinobu and T. Kakutani: J. Phys. Soc. Japan **14** (1959) 1433.
7) H. P. Greenspan and G. F. Carrier: J. Fluid Mech. **6** (1959) 77.

JOURNAL OF THE PHYSICAL SOCIETY OF JAPAN, Vol. 16, No. 7, JULY, 1961

Molar Sound Velocity in Inorganic Melts and Solutions

By S. V. SUBRAHMANYAM AND J. BHIMASENACHAR
Physics Department, S. V. University, Tirupati, India

(Received March 27, 1961)

From an examination of the available ultrasonic and density data, in the case of eleven inorganic melts, the relation between the molar volume (M/ρ) and sound velocity, V, is found to be $MV^{2/3}/\rho=S$ where S is a constant independent of temperature. The molar sound velocity S is found to be an additive property. The contributions of different ions to the molar sound velocity of a liquid have been evaluated.

The variation, of $V^{2/3}/\rho$ with percentage weight of the solute in aqueous solutions for a number of univalent electrolytes, is found to be linear. The linear plots are extrapolated to get the value of $V^{2/3}/\rho$ for 100 percent of the solute. These values are multiplied by the respective values of the molecular weights of the solutes to give the molar sound velocity for the substance-Such extrapolated values have been found to correspond to the molar sound velocity of the substance in the liquid phase.

§ 1. Introduction

Higgs and Litovitz[1] showed that the ratio of the temperature coefficient of sound velocity (dv/dt) to the temperature coefficient of density ($d\rho/dt$) to be a constant and equal to 1.5 for a series of inorganic melts rather than 3 as in the case of organic liquids. This relationship can be written down as

$$1/V\ dV/dt=3/2\ d\rho/dt$$

where V is the sound velocity and ρ is the density. Integration and multiplication by molecular weight (M) leads to $MV^{2/3}/\rho=S$, where S is a constant independent of temperature.

The present investigation has been taken up to verify the above relation and examine whether the molar sound velocity is an additive function of the individual ions. The molten salts that have been chosen for the purpose constitute a set of inorganic liquids in which the intermolecular bonding is ionic in character. An attempt has also been made to correlate the molar sound velocity in the pure liquid with that in the aqueous solution of the substance.

§ 2. Result and Discussion

A) Molar sound velocity in molten salts

Values of S, the molar sound velocity, at different temperatures have been evaluated for eleven melts and are given in Table 1. The sound velocity data used in these calculations are taken from the work of Higgs and Litovitz[1] on lithium nitrate and Bockris and Richards[2] for the rest of the substances. The density data for the nitrates are taken from the International critical Tables[3] and for the rest of the substances from the work of Yaffe and Artsdalen[4]. In all cases, the molar sound velocity is found to be independent of temperature.

We now propose to examine whether the molar sound velocity is an additive function of the individual ions. It can be taken to be an additive function of ions, if a relation of the following type is satisfied:

$$S_{\mathrm{LiNO_3}}=S_{\mathrm{LiCl}}+S_{\mathrm{NaNO_3}}-S_{\mathrm{NaCl}}$$

Use of the average values of S's for these substances leads to $5.63=4.55+6.62-5.46$ ($=5.71$) — a clear demonstration of the additive nature of the constants. Similar tests in other cases also reveal the additive nature of molar sound velocity. It can therefore be assumed that the positive and negative ions make contributions S^+ and S^- to the total molar sound velocity S.

The contributions of different anions and cations are obtained by the following process. Assuming an arbitrary value for the nitrate ion, the contributions of Na^+, K^+ and Li^+ are calculated by subtracting this assumed value for NO_3^- from the corresponding values of S for $NaNO_3$, KNO_3 and $LINO_3$. Using these values for Na^+, K^+ and Li^+, the contributions of Cl^-, Br^- and I^- are evaluated from the S values of the corresponding halides. The

Table I, Molar Sound Velocity in melts.

T°C	S 10^4 CGS	T°C	S 10^4 CGS	T°C	S 10^4 CGS	T°C	S 10^4 CGS
$LiNO_3$		LiCl		LiBr		NaI	
260	5.64	780	4.54	600	4.43	700	5.99
320	5.61	830	4.54	700	4.42	800	6.00
380	5.59	880	4.55	800	4.4s	900	6.02
$NaNO_3$		930	4.55	900	4.40	KI	
310	6.66	980	4.55	1000	4.39	700	7.31
336	6.65	NaCl		NaBr		800	7.31
362	6.63	810	5.46	800	5.31	900	7.31
388	6.62	850	5.46	850	5.31		
414	6.60	900	5.46	900	5.32		
KNO_3		950	5.46	950	5.33		
330	7.89	1000	5.45	KBr			
380	7.87	KCl		750	6.62		
430	7.83	780	6.65	800	6.63		
480	7.80	830	6.65	850	6.64		
530	7.75	880	6.65	900	6.64		
		930	6.66	950	6.64		
		980	6.66	1000	6.64		

Table II. Contributions of different ions to the molar sound velocity of inorganic liquids (in 10^4 CGS units)

Substance	S_{ex}	S_{Melt}	S^+	S^-	Average value of S^+ or S^-
$LiNO_3$	—	5.68	2.41	3.22	3.22 (NO_3^-)
$NaNO_3$	6.97	6.62	3.40	3.22	
KNO_3	7.78	7.90	4.68	3.22	
LiCl	—	4.55	2.41	2.14	2.09 (Cl^-)
NaCl	5.85	5.46	3.40	2.06	
KCl	0.71	6.66	4.68	1.98	
LiBr	—	4.42	2.41	2.00	1.96 (Br^-)
NaBr	5.25	5.32	3.40	1.92	
KBr	6.07	6.64	4.68	1.96	
NaI	5.70	6.00	3.40	2.60	2.62 (I^-)
KI	6.32	7.31	4.68	2.63	
CsCl	—	6.62	4.52	2.10	4.67 (Cs^+)
CsBr	—	6.7	4.82	1.97	

assumed value for NO_3^- is continuously adjusted until consistent values for Cl^-, Br^- and I^- are obtained. A value of 3.22 for the nitrate ion is found to give most consistent results, and the values of the contributions of different ions, arrived at on this basis, are given in Table II. The calculations are extended to the case of CsCl and CsBr leading to an average S^+ value of 4.67 for Cs.

All the substances studied in this investigation are univalent electrolytes and it will be interesting to see whether these simple relations hold good in polyvalent electrolytes also. Experimental work on these lines is in progress.

B) Molar Sound Velocity in Solutions

Investigations regarding the variation of sound velocity with concentration of a solute in one or more solvents often lead to interesting data characteristic of the solute. It is known[5] that in many organic solute-solvent systems, the plots of velocity *Vs* percentage weight are linear. In such cases the velocity for 100 percent of the solute can be evaluated by extrapolation of the graph. It has been found by the authors[6] that the extrapolated value is independent of the solvent and corresponds to the velocity in the liquid phase of the substance (near the melting point).

In the case of aqueous solutions of electrolytes, the plots of velocity *Vs* percentage weight are very often non-linear. Even in cases where it is linear, the extrapolated value is found to be very much larger than the velocity in the melt. This discrepancy is possibly due to the large difference between the temperatures at which these substances exist as liquids and the temperature at which the extrapolated value is obtained. This difficulty can be overcome by examining a property like molar sound velocity which does not vary with temperature.

It has been shown in section A that in the case of inorganic substances the molar sound velocity is given by $MV^{2/3}/\rho$. An evaluation of this constant cannot be made for an ionic solution since the significance of M becomes hazy. As an alternative the variation of $V^{2/3}/\rho$ with percentage weight of the solute is studied in the case of a number of aqueous solutions of electrolytes, using the existing data[7,8]. It is found that the plots are linear in all cases.

The linear plots are extrapolated to get the value of $V^{2/3}/\rho$ for 100 percent of the solute. These values are multiplied by the respective values of the molecular weights of the solutes to give the molar sound velocity for the substance. Such extrapolated values are shown in column 2 of Table II. The agreement between the extrapolated and experimental S values is good. This result indicates the possibility of evaluating the sound velocity in the melt from a knowledge of the variation of sound velocity and density in aqueous solutions of the substance.

The authors take this opportunity to thank the authorities of Sri Venkateswara University for all the facilities given to them.

References

1) Higgs and T. A. Litovitz: J. Acoust. Soc. Am. **32** (1960) 1108.
2) S. o'M. Bockris and N. E. Richards: Proc. Roy. Soc. (London) A **241** (1957) 44.
3) International Critical Tables: Vol. 3, p. 22.
4) I. S. Yaffe and E. R. Van Artsdalen: J. Phys. Chem. **59** (1955) 118.
5) W. Schaffs: Z. Physik. **105** (1937) 658.
6) S. V. Subrahmanyam and J. Bhimasenachar: J. Acoust. Soc. Am. **32** (1960) 703.
7) W. Prosorow: Journ. f. Physikal. Chemie (USSR), **14** (1940) 384.
8) S. V. Subrahmanyam and J. Bhimasenachar: J. Acoust. Soc. Am. **32** (1960) 835.

JOURNAL OF THE PHYSICAL SOCIETY OF JAPAN, Vol. 16, No. 7, JULY, 1961

Experimental Studies on Sonoluminescence and Ultrasonic Cavitation

By Katsuo NEGISHI

Kobayasi Institute of Physical Research, Kokubunji, Tokyo

(Received April 10, 1961)

Using a miniature spherical hydrophone made of barium titanate, the individual cavity collapse was detected as a sharp impulse (0.5 μs width) slightly after the pressure maximum of sound cycle. When may cavities collapsed simultaneously, sinusoidal sound-pressure waveform was turned into saw-tooth form. By comparing the flash of sonoluminescence with the instantaneous change of scattered light from cavitating bubbles in dark-fiield illumination, the sonoluminescence from water has been decided to occur during the final stages of the bubble collapse. The sonoluminescence from aqueous solutions of various sodium salts, organic solvents and luminol has been also examined. The luminescence of luminol has been applied to develop a new method for the visualization of ultrasonic fields.

§ 1. Introduction

It was first observed in the early 1930's by Frenzel and Schultes[1] and independently by Zimakov[2] that a weak emission of light occurred in liquids subjected to ultrasonic waves. The term 'sonoluminescence' was introduced by the formers after the method of excitation, as against electroluminescence, photoluminescence, etc. Following this discovery, many investigations on the nature and the origin of this phenomenon were carried out mainly by chemists, early observations being made mostly with dark-adapted eyes. It was revealed that the sonoluminescence is closely connected to the chemical action of ultrasonic waves and it occurs in liquids only when they are cavitated in sound fields.

In 1937, Chambers[3] studied 36 pure liquids in acoustic field of 9 kc/s and found 14 of them to luminesce. He showed that the brightness of luminescence increases as the temperature decreases, and as the product of the d pole moment and viscocity of the liquid increases. Harvey[4] distinguished sonic chemiluminescence from sonoluminescence. He considered that the sonic chemiluminescence occurs as a result of chemical reaction caused by ultrasonically activated oxygen, as shown in alkaline solution of luminol, while the sonoluminescence is not due to activated oxygen. It is, however, difficut to distinguish seriously between the two in some cases, as is to be seen later.

In recent years, quantitative measurements of weak luminescence have become rather easy by use of a high sensitive photomultiplier tube. Quantitative measurements of sonoluminescence were made by Griffing and Sette[5],[6] and by Prudhomme[7],[8] in relation to the chemical effect produced by ultrasonic cavitation and especially on the influence of the dissolved gases. They observed that the intensity of luminescence from sonically irradiated water increased with chemical yields (H_2O_2, etc.) and was enhanced by dissolving heavy rare gases like krypton and xenon. Interesting results on the spectrum of sonoluminescence were obtained by Günther *et al*[9],[10] and Srinivasan[11], who observed that the spectral distribution was a continuum resembling that of a blackbody radiating at 6,000°–10,000°K. Jarman[12] has studied the temperature dependence of luminescence from 15 pure liquids and found that the intensity of luminescence was more properly correlated with (surface tension)^2/(vapour pressure) than Chambers' correlation

There are several hypotheses on the origin of sonoluminescence, which is also connected closely to the mechanism of the chemical action of ultrasonic waves[37],[38]:

a) The electrical microdischarge theory, proposed by Frenkel[13], postulates that thin lens-shaped cavities are abruptly produced in the liquid by negative pressures due to the sound waves and electric charges of different signs appear on both walls of the cavities respectively as a result of the statistical fluctuation of charge distribution in the liquid. The electric field grows as the cavity grows into a spherical shape and then discharge takes place in spherical cavities.

b) The mechano-chemical theory, proposed by Weyl and Marboe[14),15)], assumes that light is emitted by photochemical recombination of free ions which are produced when molecules are mechanically dissociated at nascent surfaces of the growing cavities.

c) The thermo-chemical theory, described by Griffiing and Sette[6)], also attributes the emission of light to the photochemical recombination of free ions, although this theory supposes the production of ions as due to thermal dissociation in collapsing bubble.

d) The hot spot theory, originated by Noltingk and Neppiras[16),17)], proposes that sonoluminescence is merely the blackbody radiation from the gas within cavitation bubbles, which is incandesced by adiabatic compression when the bubbles collapse.

e) The triboluminescence theory, described by Chambers[3)], presumes that, when the quasi-crystalline structure of the liquid is fractured by cavitation, triboluminescence occurs as is often observed in breakdown of certain crystals.

f) The balloelectric theory, proposed by Harvey[4)], assumes the appearance of electric charges on the surface of bubbles in analogy to Lenard potentials observed on liquid drops in gases. It is stated that the potential rises as the cavity collapses because of the decrease in capacity.

There is no sufficient knowledge to decide which of the above theories on sonoluminescence is really valid. Of these theories, the discharge theory has been accepted by fairy many investigators until recent years without direct experimental evidence. Other probable theories are the hot spot theory (d) and the thermo-chemical theory (c), while the others are almost ignored at present. If one of these theories is valid, it should be expected that sonoluminescence occurs as a discrete flash of light at a definite phase of the sound cycle: *e.g.* in the discharge theory it should occur during the process of bubble growth, and in the hot spot theory at the phase of bubble collapse. In this respect, some experimental investigations have been made recently, and in fact it has been found that sonoluminescence consists of discrete flashes of light, but there are some disagreements as regards the phase relation. Wagner[18)] and Jarman[12)] have decided the phase of flash of the luminescence from water or aqueous solutions of some inorganic salts with respect to the sound-pressure cycles measured by hydrophones, and obtained results which are in favour of the discharge theory, while Gunther *et al*[19),20)] attained to an opposed result supporting the hot spot theory. Meyer and Kuttruff[21)], using high-speed photographic technique, showed that the flashes from ethylene glycol occurred during the final stage of bubble collapse, yet its phase with respect to the sound cycle (2.5 kc/s) was uncertain.

There are, moreover, many aspects of sonoluminescence and its relation to cavitation and chemical action, which are not clarified as yet. The present paper aims to clarify these points. Some applications of the sonoluminescence in visualizing the cavitation field are also presented.

§ 2. Pressure Waveform of Ultrasonic Waves Accompanying Cavitation

Prior to the observation of sonoluminescence, the phase of bubble collapse with respect to the pressure cycle of sound in aerated water was determined with the help of a miniature barium titanate hydrophone illustrated in Fig. 1. Powder of barium titanate plastered to a spherical platinum core 1.5 mm in diameter was sintered at about 1,400°C, so that the final diameter became 2 mm. This element was fixed to a porcelain tube 2 mm in diameter with molten glass and whole of the outer surface was coated with fired-on

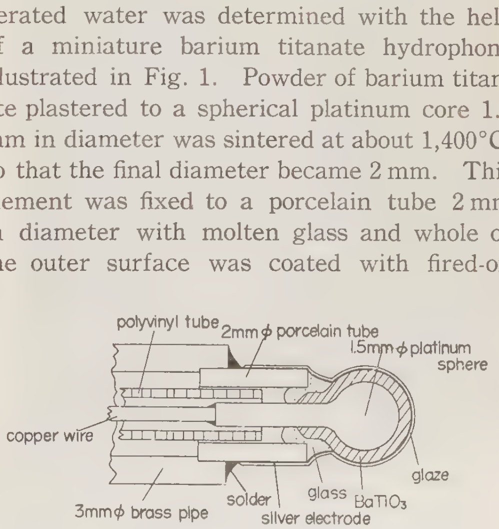

Fig. 1. Miniature barium titanate hydrophone.

silver electrode and furthermore with glaze for the mechanical protection of the silver surface. The porcelain tube was soldered to a brass tube 3 mm in diameter which served for the outer conductor. The accomplished element was polarized by DC voltage of about 500 V. This hydrophone had a electric capacitance of about 250 pF and a pressure sensitivity of about −140 dB, though not accurately calibrated.

A 24 kc/s window-type nickel transducer (radiating surface $4\times4.5\,\mathrm{cm}^2$) was used to radiate pulsed ultrasonic waves in an anechoic tank. On the back surface of the transducer, a simple accelerometer-type vibration pickup made of lead zirconate titanate was attached in order to observe the velocity waveform of the transducer after integrating the pickup singal.

Typical pressure waveforms of 0.3 ms pulses obtained at a point 1 cm in front of the center of the transducer surface are given in Fig. 2. The velocity amplitude of the transducer was about 10 cm/s. Because of the very short pulse width and the low pulse recurrence (one pulse per second), only a few cavitations were produced, so that individual shock waves caused by the collapses of cavities were observed as sharp positive impulses of about 0.5μs width. As the hydrophone used has a poor response in the frequency range above 1 Mc/s, the peak pressure of the shock waves indicated in the figures may be considerablly lower than the true value, and their width also may be broadened. The bubble collapse always occurs slightly after the pressure maximum, as is shown in the theoretical result of Noltingk and Neppiras[16].

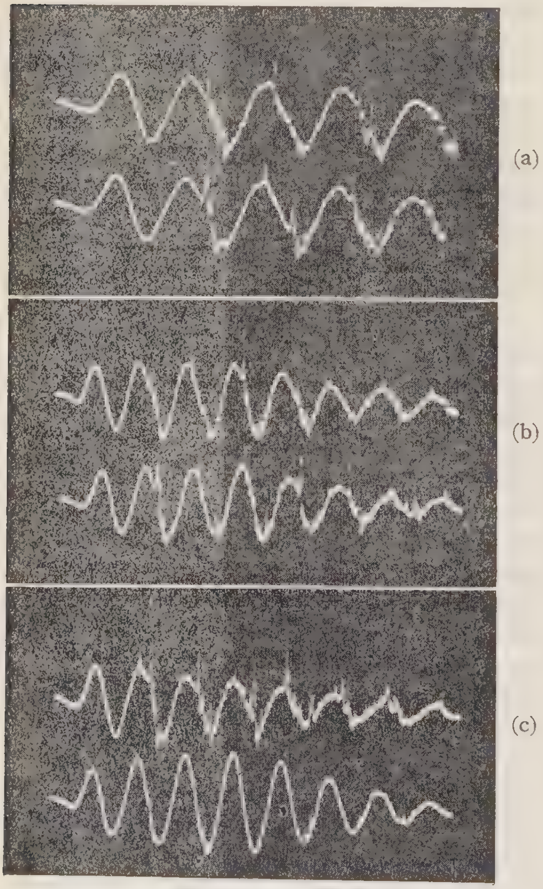

Fig. 2. Sound-pressure waveforms of 24 kc/s pulsed ultrasonic waves of 0.3 ms width in aerated water, showing shock waves caused by cavitation.

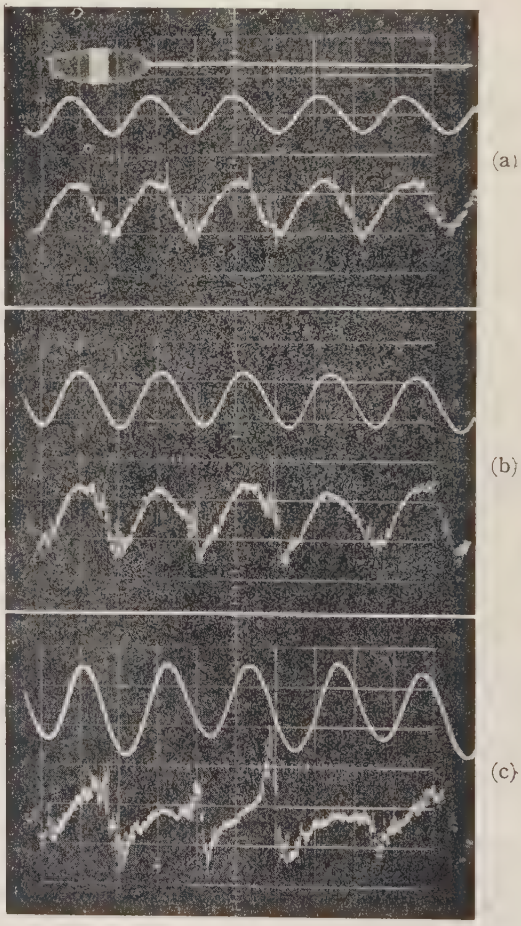

Fig. 3. Stationary parts of pressure waveforms (lower trace) and velocity waveforms (upper trace) of the transducer emitting 1.5 ms pulse, velocity amplitude being 11 cm/s in (a), 19 cm/s in (b) and 30 cm/s in (c).

The lower trace of Fig. 2 (c) is a pressure waveform obtained when cavitation is occasionally suppressed under the same condition as the upper trace. Comparing the two waveforms, it is clearly shown that the amplitude of the fundamental sound-pressure wave is attenuated by cavitation.

For longer ultrasonic pulses, say 1.5 ms width, many cavitations were simultaneously produced owing to the increasing number of cavitation nuclei created by the preceding cavitations, and consequently the pressure waveform was no longer sinusoidal, but was turned into saw-tooth form with large positive peaks. Some pressure waveforms of the stationary part of 1.5 ms pulse at a point adjacent to the transducer are shown in Fig. 3. The velocity waveform of the transducer are also shown in the same figure (upper trace), the velocity amplitude being 11 cm/s in (a), 19 cm/s in (b) and 30 cm/s in (c), respectively. It is to be concluded that the pressure peaks in comparatively long pulses or continuous waves correspond to the phase of the maxima of the bubble collapse because the pressure peak is nothing but the accumulated result of the shock waves produced by the collapsing bubbles. The generation of the subharmonic component is clearly to be seen in Fig. 3 (c). It is noticeable that the subharmonic component appears not only in the sound-pressure but also in the velocity waveform in Fig. 3 (c).

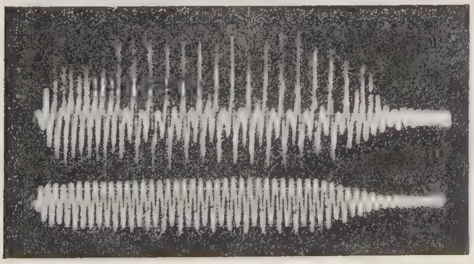

Fig. 4. Pressure waveform of 1.5 ms pulse at a point adjacent to the transducer (upper) and 5 cm in front of it (lower).

Total length oscillograms of 1.5 ms pulse are given in Fig. 4, the upper trace being the pressure waveform at a point adjacent to the transducer and the lower one at 5 cm in front of it. It requires several cycles of sound accompanying cavitation before the subharmonic component begins to appear, as is shown in Fig. 4. Subharmonics in the pressure waveform is thought to be due to the nonlinear oscillation of bubbles whose resonance frequencies are lower than the exciting frequency. As these larger bubbles are produced possibly by the accumulation of smaller ones, it may be understood that subharmonics occur after some periods of sound accompanied by cavitation. Subharmonics in pressure waves also may have a reaction on the velocity waveform of the transducer. As the cavitation region is localized near the center of the transducer surface when such short ultranic pulse is emitted, the saw-tooth waveform fades out rapidly as the distance increases from the radiating surface, and the waveform at a distance becomes similar to the velocity waveform of the transducer, as shown in the lower trace of Fig. 4.

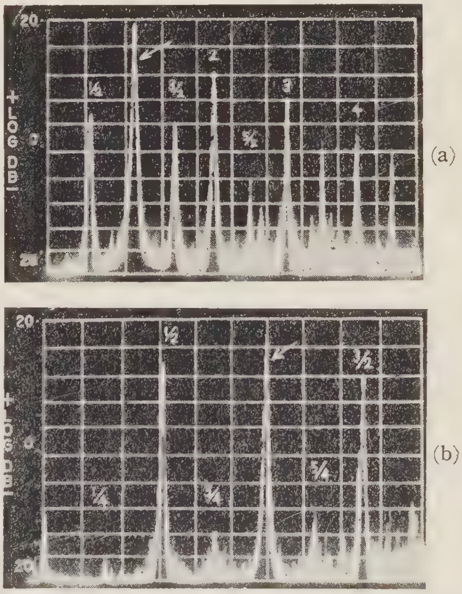

Fig. 5. Cavitation noise spectra of 24 kc/s continuous ultrasonic waves. Inscribed numbers show the spectral orders.

Cavitation noise spectra of 24 kc/s continuous ultrasonic waves are shown in Fig. 5. The fundamental frequency is indicated by the arrow and the spectral orders are also inscribed in the figure, the vertical scale being in dB. Higher harmonics and subharmonics of $n/2$ series and $n/4$ series (n=integers) are remarkable and no $n/3$ component is found. Also a continuous background noise is observed. This is presumably produced by the collapsing bubbles and especially many oscillating bubbles of various sizes in the ultrasonic field. On the other hand, at higher fundamental frequencies, *e.g.* at 500 kc/s, subharmonics of $n/2$ series and $n/3$ series were found, sometimes accompanying $n/6$ series, whereas no $n/4$ series was observed.

§ 3. Phase Relation Between Sonoluminescence and Cavitating Bubbles in Water

The phase relation between sonoluminescence and cavitating bubbles in water has been determined with respect to the sound-pressure cycles[24]. The experimental arrangement is shown in Fig. 6. A ferrite transducer resonating at 28 kc/s (radiating surface $4\times4\,cm^2$) was employed to radiate ultrasonic waves in a glass tank ($23\times45\times23\,cm^3$) filled with tap water. Experiments were also done by employing water purified by passing through ion-exchange resin, but the result was quite similar as in the case of the tap water. A full-sized image of the cavitation region before the transducer stub was projected on a screen with a small opening (2 mm in diameter) by a lens, and light from a small region at 1 cm in front of the stub center was fed to a photomultiplier tube through this opening. The photomultiplier tube used was a Du Mont type 6292 (sensitive for 300 to 600 mμ), which was connected to a regulated high voltage supply of 1,2000 V. The output voltage across a 5,000 ohm resistor connected to the anode collector of the tube was displayed after 60 dB amplification on a cathod ray oscilloscope triggered by the input voltage of the transducer. A light source was used for dark-field illumination of the cavitating bubbles from which light was scattered corresponding to the instantaneous change of bubble volume. In complete darkness, sonoluminescence was observed on the oscilloscope screen as discrete flashes once every sound cycle. When the dark-field illumination was switched on, a curve representing the instantaneous bubble volume was obtained on the oscilloscope under a reduced amplification, instead. The intensity of the scattered light from cavitating bubbles was by far the stronger than the luminescence, so that the curve of the bubble volume was not affected by the luminescence. The time constant of the apparatus was of the order of 10^{-7} sec, and the individual luminescence pulses were observed as sharp impulses of this decay time. Although both luminescence and bubble volume could not be observed at the same time, the phase relation between the two phenomena was clearly determined by this procedure, since the triggering condition of the oscilloscope was common.

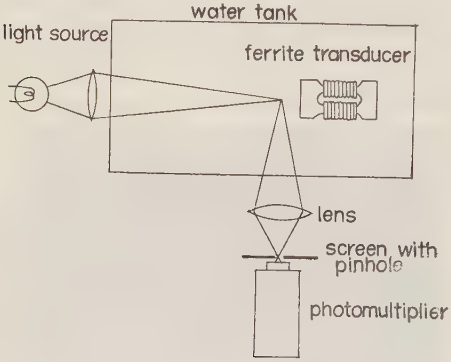

Fig. 6. Experimental arrangement

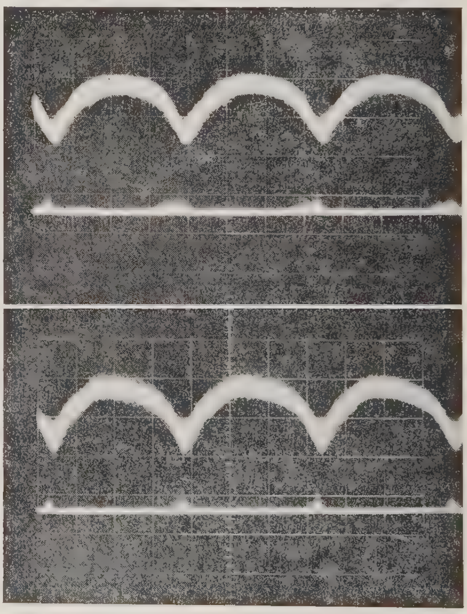

Fig. 7. Volume change of cavitating bubbles (upper trace) and sonoluminescence (lower trace) in fresh tap water (a) and in water of appreciably reduced air content (b).

Fig. 7 (a) is a double exposured oscillogram of the bubble volume and the sonoluminescence in fresh tap water (extremely supersaturated with air) showing hundreds of overlapping sweeps. The luminescence pulse begins to appear at about 1/5 period before the phase of minimum bubble volume, and goes to its maximum intensity at the minimum bubble volume, *i.e.* at the instant of complete collapse of the bubble; thereafter it rapidly fades out. In water of appreciably reduced air content, the luminescence pulses begin to appear at about 1/10 period before the bubble collapse as shown in Fig. 7 (b).

The sound-pressure waveform and change in bubble volume were observed simultaneously and are shown in Fig. 8. At the minimum of bubble volume, a remarkable positive peak was produced by superposed shock waves as mentioned in the previous section. A slight difference between the bubble volume curve of Fig. 7 and Fig. 8 is due to the fact that the output of the photomutiplier was AC-coupled to the oscilloscope in the case of Fig. 7 and DC-coupled in Fig. 8.

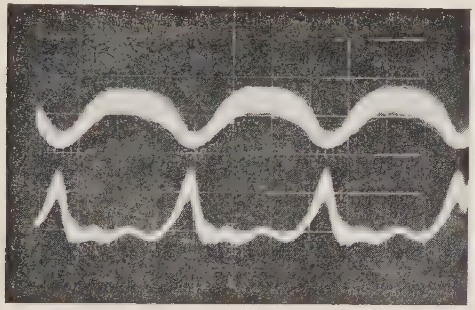

Fig. 8. Curve of bubble volume (upper) and sound-pressure waveform (lower).

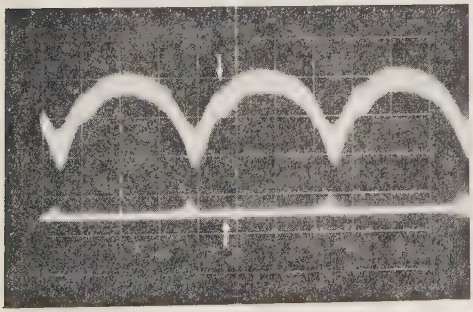

Fig. 9. Volume change of cavitating bubbles with small dips and sonoluminescence with secondary flashes (indicated by arrows).

Often, a secondary luminescence flash occurred shortly after the main flash at an appreciably high transducer input. In phase with the secondary flash, a secondary pressure peak appeared in the sound-pressure waveform, and furthermore, a small dip appeared in the curve of the bubble volume, showing that some of the bubbles rebounded and then collapsed again shortly after their first collapse, emitting a secondary flash. This is noticeable in Fig. 9.

When the transducer input was increased until subharmonic components appeared in the pressure waveform, cavitation was irregularly blown away from the stub and sonoluminescence was inhibited rather than enhanced.

§ 4. Sonoluminescence of Some Aqueous Solutions

It is known that the sonoluminescence from water is enhanced by the addition of some inorganic salts, carbon disulfide or carbon tetrachloride, whereas it is inhibited by the addition of a volatile liquid such as ether or alcohol. An examination of the effects of some additives on the sonoluminescence from water was made with the apparatus shown in Fig. 10. This arrangement fulfilled the requirement that the photomultiplier had to receive a sufficient luminous flux from a small amount of liquid. In this apparatus, the liquid needed was only 20 cc. The output current of the photomultiplier was measured by a vacuum-tube microammeter.

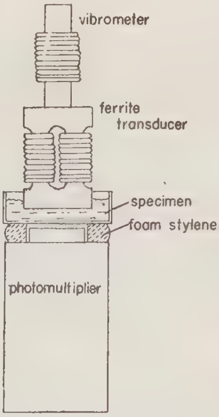

Fig. 10. Experimental apparatus.

The ferrite transducer was the same one as used in the previous experiment, but a vibrometer transducer of the same type as the main one but of smaller thickness was attached to indicate the velocity amplitude of the stub by the open-circuit voltage. The two transducers were so glued that the axes of the magnetic flux of the driving and the pickup cores at the glued surface were perpendicular to each other, thus the magnetic coupling between the two coils was negligible in practice. The vibrometer sensitivity was 1.9 V/cm/s, the calibration being made by an optical interference technique. It is to be remembered that sound-pressure amplitude of 1 atm. in water corresponds to particle velocity of 6.75 cm/s. Although the stub velocity is not directly connected to the intensity of sound in the liquid of small quantity as in this case, the stub velocity is nevertheless proportional to the pressure amplitude of sound.

As the intensity of luminescence gradually decreased with increasing temperature caused by the continuous irradiation of ultrasonic waves, the luminous flux was read as fast as possible, so that the temperature rise was below 5°C during the observation. By this procedure, readings were obtained with rather good reproducibility. Water used in this experiment was purified by passing through the ion-exchange resin.

Experimental results on the effect of the addition of various sodium salts are shown in Fig. 11 at various sound intensities. The enhancing effect of sodium chloride was not so remarkable as reported by Jarman[22] who observed that 2 N solution of sodium chloride luminesced about seven times brighter than tap water just above the cavitation threshold. This is possibly due to the difference of experimental conditions. The luminescence begins as the sound intensity attains the cavitation threshold, and the light intensity increases with increasing sound intensity. But the readings of the luminous flux are rather unstable near the cavitation threshold. 2 N solution of sodium carbonate gave brighter luminescence than the others, while the addition of sodium hydrogen carbonate considerably inhibited the sonoluminescence of water.

Effects of the addition of various organic solvents and bromine have been also examined and the results are given in Fig. 12. Most of these additives were hardly miscible with water, so that 20 cc of water was saturated by the addition of a few drops of them. Enhancing effects of carbon disulfide, bromine and methyl iodide were striking and those of carbon tetrachloride and trichloroethylene

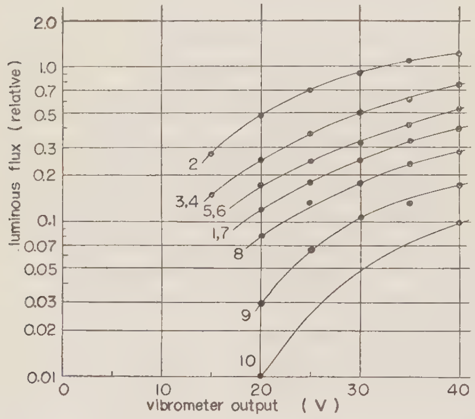

Fig. 11. Intensity of sonoluminescence from aqueous solution of various sodium salts in dependence on the vibrometer output.

1.	tap water	
2.	$2n$	Na_2CO_3
3.	$2n$	NaCl
4.	$2n$	$Na_2S_2O_3$
5.	$2n$	$NaNO_3$
6.	$2n$	$NaSO_3$
7.	$2n$	$NaNO_2$
8.	$1n$	Na_2SO_3
9.	$0.5n$	$NaHCO_3$
10.	$1n$	$NaHCO_3$

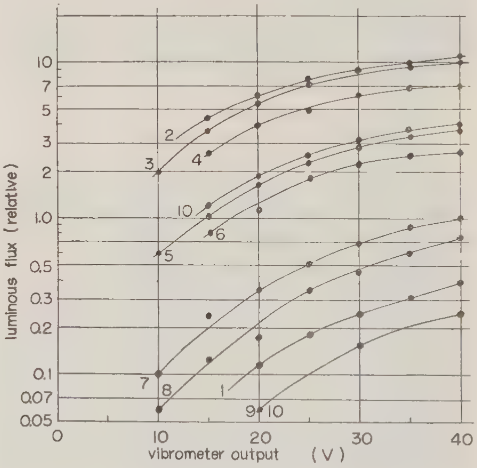

Fig. 12. Sonoluminescence from aqueous solutions of various organic liquids and bromine.

1.	tap water
2.	CS_2
3.	Br
4.	CH_3I
5.	CCl_4
6.	C_2HCl_3
7.	C_6H_5Br
8.	$C_6H_5NH_2$
9.	C_6H_6
10.	50% glycerine
11.	5% ethylene glycol

Table I. Sonoluminescence from aqueous solutions of organic solvents and their physical properties.

	Intensity of luminescence	Density	Boiling point	Vapour pressure (20°C)	Solubility to water (20°C)	Specific heat ratio of vapour
	(relative)	g/cc	°C	mm Hg	wt %	
CS_2	11	1.27	46.25	298	0.217	1.63
Br_2	10	3.14	58.7	173	3.41	1.32
CH_3I	7	2.29	45	331	1.40	1.28
CCl_4	3.5	1.57	76.7	91	0.08	1.13
C_2HCl_3	2.7	1.47	87	60	0.1	—
C_6H_5Br	1.0	1.50	155.9	5.67 (30°C)	0.045 (30°C)	—
$C_6H_5NH_2$	0.75	1.02	184.3	2.4 (50°C)	3.49	—
(H_2O)	0.40	1.00	100.0	17.54	—	1.33
C_6H_6	0.25	0.88	80.5	74.7	0.072	1.4

were also noticed. Bromobenzene and aniline were not so effective. It is interesting to find that substances showing the large enhancing effect have some common features, *e.g.* relatively large density, low boiling point and small solubility to water (cf. Table I). Furthermore, they give no or only very faint luminescence when subjected to ultrasonic waves in pure liquid state (*i.e.* without water). On the other hand, ethylene glycol and glycerine produce bright luminescence when subjected to ultrasonic waves, whereas the addition of small quantities of them to water does not strongly affect the sonoluminescence from water. 50% glycerine (in volume), however, luminesced with considerable brightness.

In spite of the wide variety of the intensity of sonoluminescence from these solutions, it was found that all of them luminesced at the phase of minimum bubble volume as in the case of pure water.

§ 5. Sonic Chemiluminescence of Luminol

Luminol (3-aninophthalhydrazide) in alkaline solution gives a brilliant bluish luminescence, when it is oxidized in various ways and particularly with hydrogen peroxide in the presence of activators like hemin. It is not surprising, then, to find that this solution luminesces with comparatively intense brightness, visible without dark-adaptation, when it is cavitated by ultrasonic waves. The behaviour of luminol solution when saturated with various gases has been examined in ultrasonic fields by Harvey[4] who concluded that most of light from this solution has the chemiluminescent origin. There are some other confirmations supporting his conclusion.

Results measured with the apparatus of Fig. 10 showed that luminol in neutral solution gave the same faint luminescence as observed in pure water, but the addition of sodium carbonate in this solution enhanced the lumin-

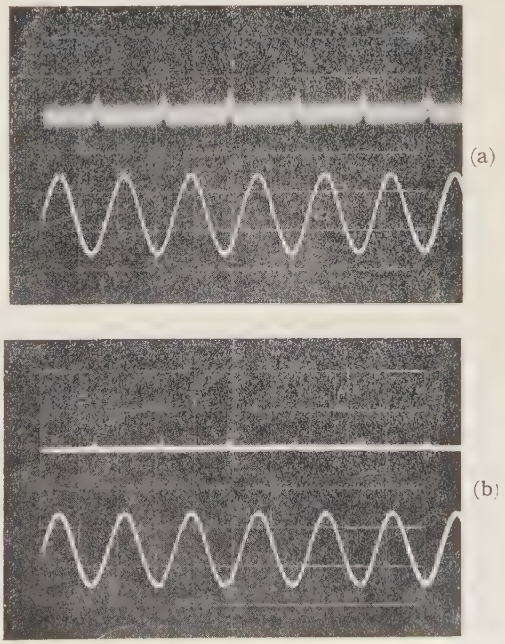

Fig. 13. Luminescence of luminol solution (a) and pure water (b) in upper trace and vibrometer output in lower trace.

escence by as much as 1,000 times. This corresponds to the fact that luminol is chemiluminescent in alkaline solution only.

The oscillographic studies on the luminescence of luminol solution also confirmed the chemiluminescent origin of the emitted light. Fig. 13 (a) shows a waveform of luminescence of luminol in the upper trace and an output voltage in the lower trace, and Fig. 13 (b) shows those of water. Just as in the case of pure water, discrete luminescence flashes occurred in luminol solution at the phase of minimum bubble volume and were somewhat higher than those of water, and in addition a continuous luminescence appeared. At higher ultrasonic intensities, this discrete flash disappeared and the continuous luminescence became predominant.

The luminescence of luminol solution arised as soon as cavitation was built up by starting the ultrasonic oscillator. When the oscillator was switched off, discrete flashes, of course, disappeared immediately after the cavitation was ceased, but a continuous afterglow remained with a decay time of about 1/20 sec. The result of simultaneous observation of the luminescence of luminol solution and the output voltage of the vibrometer is shown in Fig. 14.

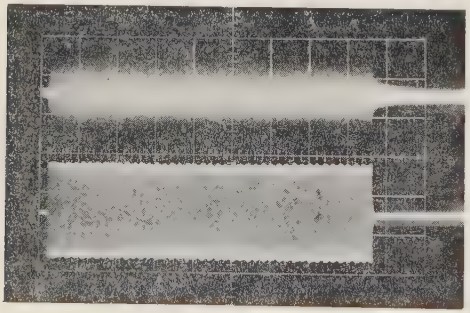

Fig. 14. Luminescence of luminol solution and vibrometer output. Sweep speed = 50 ms/div.

All of these experimental results show that most of light from luminol solution originates from the chemiluminescence of luminol caused by cavitation products, excluding discrete flashes occuring at the phase of the bubble collapse. The discrete flashes are to be attributed to the same origin as in water and aqueous solutions of salts. Presumably the flashes are mostly attributed to the presence of sodium carbonate in the solution. The brightness of luminol solution in ultrasonic fields was not improved by the addition of hemin, showing that the luminescence of luminol solution was chiefly due to the free radicals (OH and others) rather than hydrogen peroxide formed by the ultrasonic cavitation.

The intensity of luminescence from luminol solution somewhat varied with the concentration of sodium carbonate and luminol. Fig. 15 shows the luminous flux from the solution of luminol (concentration 100 mg/1) for various sodium carbonate contents, and Fig. 16 shows the luminous flux *vs.* luminol content curve for 0.1 N sodium carbonate solution. For dilute solutions of luminol (concentration below 0.1 mg/1), the intensity of luminescence decreased rapidly with the sound irradiation time. This is possibly due to the consumption of luminol. In Fig. 16, this concentration range is represented in a broken line.

The relation between ultrasonic intensity and luminous flux from luminol solution re-

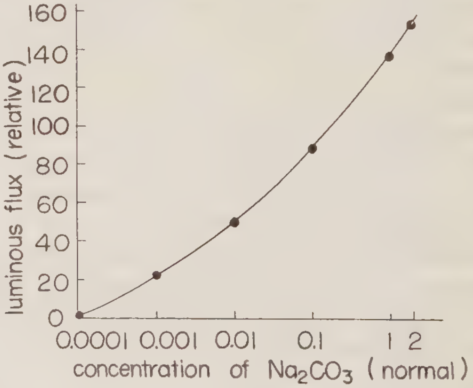

Fig. 15. Luminescence intensity *vs.* sodium carbonate concentration for luminol solution of 100 mg/l in concentration. (Vibrometer output = 40 V)

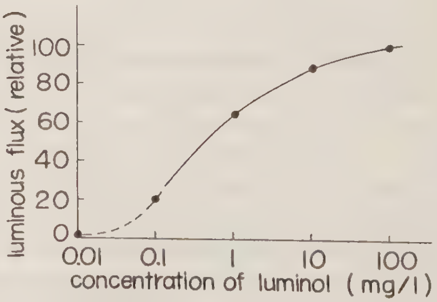

Fig. 16. Luminescence intensity *vs.* luminol content for 0.1 N sodium carbonate solution. (Vibrometer output = 40 V)

sembles that of Fig. 12 except the difference in absolute level, when it is measured with the apparatus of Fig. 10. In the different types of ultrasonic fields, however, different relations are observed as described below.

The ultrasonic intensity *vs.* luminous flux characteristics was studied for a ultrasonic frequency of 470 kc/s with the apparatus shown in Fig. 17. A glass tube 2.8 cm in diameter with a thin polyethylene membrane as the bottom was set so that the focus of a concave transducer was placed in the tube about 1 cm above the bottom. The ultrasonic field in the tube was rather uniform except near the bottom. The concave barium titanate transducer, 8 cm in diameter and 10 cm in focal length, was used by reason of its suitability in suppressing the cavitation in the coupling medium: cavitation causes the waste of ultrasonic power propagating in the medium. By the same reason, degassed water was used as the coupling medium. The luminous flux was measured in relation to the input voltage of the transducer employing a photomultiplier tube placed closely to the glass tube.

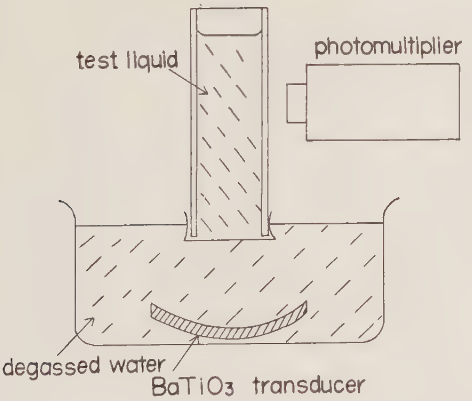

Fig. 17. Arrangement for observation of luminescence at 470 kc/s.

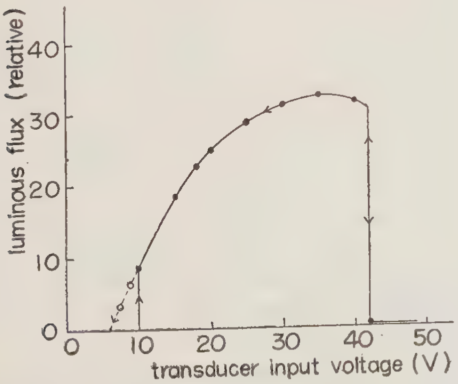

Fig. 18. Relation between ultrasonic intensity and luminescence from luminol solution at 470 kc/s.

The experimental result is shown in Fig. 18. When the input voltage attained to 10 V, the luminescence appeared abruptly, and thereafter its intensity increased with the input voltage up to 30 V. Beyond this, the luminous flux showed a tendency to saturate, but when the input voltage exceeded 42 V, the luminescence suddenly disappeared; no detectable luminescence (or only very faint luminescence) remained above 42 V. If the input voltage of the transducer was decreased from 50 V, the luminous flux varied just as in the case of increasing voltages, but the luminescence remained down to 7 V. This corresponds to the fact that cavitation once occurred has a tendency to be maintained at lower sound intensities than the threshold. The ultrasonic intensity in the glass tube at the input voltage of 42 V was estimated as 2 W/cm² from the measurement of the radiation pressure.

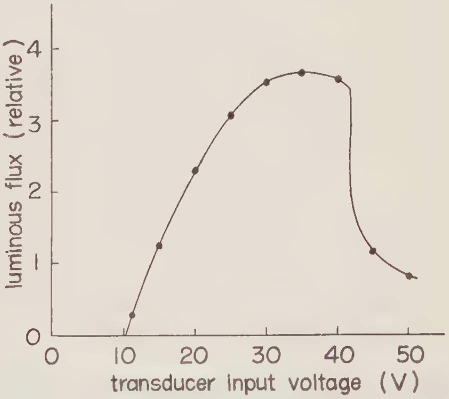

Fig. 19. Relation between ultrasonic intensity and luminescence from aqueous solution of carbon disulfide at 470 kc/s.

The abrupt decrease of luminous flux at high ultrasonic intensities was observed not only in the luminol solution, but also in every sonoluminescent liquids. As an example, the experimental result on the aqueous solution of carbon disulfide is shown in Fig. 19.

It is known that the optimum sound intensity exists for the chemical action of ultrasonic waves, *e.g.* the production of nitrous acid in aerated water, the liberation of iodine from the aqueous solution of sodium iodide, the reduction of potassium permanganate, etc.[25][26]. Although the complete explanation of these phenomena is not yet given, it seems that these phenomena are directly connected with the nature of cavitation. The maximum of chemical yield is observed in experimental arrangements which are essentially the same as Fig. 17. On the other hand, it is reported that in stationary wave system, both chemical yields and luminescence do not decrease at higher ultrasonic intensities, but only saturate[27]. Further discussions will be made in the later section.

§ 6. Discussions on the origin of sonoluminescence

Although no conclusive evidence supporting one of the above-mentioned theories on the origin of sonoluminescence has been discovered as yet, there are many respects in which some of the theories are inadequate. The electrical microdischarge theory proposed by Frenkel[13] now appears to be inadmissible because of the phase relation of sonoluminescence (cf. Table II): according to his account, the discharge should take place through the low-pressure gas in the expanding cavities, whereas sonoluminescence proved to occur during the final stages of the cavity collapse. Furthermore, his assumption of lens-shaped cavity formation has no experimental evidence, and if realized, it may be only in completely degassed water, whereas sonoluminescence occurs only in engassed liquids. The discharge theory cannot be supported also by the fact that no line or band spectra of the dissolved gases have been observed in the spectra of sonoluminescence. The triboluminescence theory and the mechano-chemical theory also seem to be implausible because of the phase relation of sonoluminescence (cf. Table II) and of the assumptions involved in these theories. The balloelectric theory, though consistent as regards the phase relation, also seems implausible. While it is known that the balloelectric charge is highly dependent on the conductivity of the liquids, the sonoluminescence is rather unaltered or enhanced in electrolytic salt solutions as above stated (cf. § 4).

Table II. Moment of flash of sonoluminescence as expected from various theories on its origin

Moment of flash / Theory	Cavity growth	Cavity collapse
(a) microdischarge	○	
(b) mechano-chemical	○	
(c) thermo-chemical		○
(d) hot shot		○
(e) triboluminescence	○	
(f) balloelectric		○

Now it appears to be credible that sonoluminescence is basically thermal in origin. Noltingk and Neppiras[16,17] showed theoretically that a cavity collapses so fast that the gas within it is adiabatically compressed and its temperature increases up to 10,000°K. Such a fast collapse of cavity is accompanied with a shock wave in the liquid phase, as detected by a hydrophone as shown in Fig. 2. These shock waves have also been observed by Bohn[23] and Günther *et al.*[20] The continuous spectra of sonoluminescence observed by Srinivasan[11] and Günther *et al.*[9][10] resemble that of a blackbody radiating between 6,000°K and 11,000°K. (Also the line spectra were observed together with the continuum in aqueous solutions of inorganic salts[10][39]; *e.g.* Na-D-line is observed in NaCl-solution). This is, of course, not a conclusive evidence of the hot spot theory: as indicated by Jarman[22], the spectra of certain chemiluminescence, particularly bioluminescence, also resemble that of the blackbody radiation. However, it seems that no fact directly contradicts to the hypothesis of the thermal origin of sonoluminescence. The phase relation of sonoluminescence decided conclusively by the present work is a strong support of this hypothesis: sonoluminescence does occur during the final stages of the cavity collapse. Probably, a cavity expands and collapses emitting a single flash of light, and a cavity, which expands to a larger size, collapses at a later phase of the pressure cycle accompanying a higher temperature rise and thus a brighter luminescent flash. Therefore, Fig. 7 suggests that cavities successively collapse in order of their expanded sizes emitting flashers of increasing intensity, till finally, the cavities of larger sizes cannot collapse, causing the disappearance of luminescence.

The sonoluminescence from water is quenched if the cavity contains too much water vapour. For the pressure inside the cavity to increase, the molecules of gas and vapour have to strike the collapsing cavity wall and then to rebound. When the molecules of water vapour strike the wall of the liquid water, a large portion of them might be adsorbed on the wall, causing a smaller increase of the pressure and then the quenching of sonoluminescence. The absorption of energy by the dissociation of water molecules also causes the reduction of temperature within the collapsing cavities. The appreciable increase of sonoluminescence from water by the addition of some inorganic salts is possibly due to the vapour-pressure lowering. The quenching effect of sodium hydrogen carbonate is thought to be due to the liberation of carbon dioxide which is known to be a substance quenching the sonoluminescence of water.

Liquids which are highly volatile and immiscible with water, like carbon disulfide, have small affinities with water. Therefore, in the aqueous solution of such a liquid, the pressure inside the collapsing cavities could increase without the adsorption of vapour molecules. Furthermore, the blackbody radiation from the incandesced gas and vapour within the cavities might be enhanced by the presence of solid carbon liberated from the vapour molecules. The analogy between sonoluminescence and luminescence in a shock tube has been indicated by Jarman[22)], and Fairbain and Gaydon[35)] has noticed dusty carbon liberated from carbon disulfide or carbon tetrachloride in the shock tube after shock waves had propagated several times in it. Noltingk and Neppiras[16)] also showed that the temperature inside the collapsing cavity increases in propotion to $(\gamma-1)$, where γ is the ratio of the specific heats. However, γ-values of such vapours shown in Table I are not higher than that of air ($\gamma=1.40$) or water ($\gamma=1.33$) except carbon disulfide. This may suggest that sonoluminescence is not simply a blackbody radiation but also some ionic processes (or dissociation of neutral molecules) as observed in high current density arcs[36)] are to be taken into consideration. In the visible region, high current density arcs through rare gases show high luminous efficiencies particularly in krypton and xenon. This is also true both in sonoluminescence and luminescence in shock tubes.

There is another possible explanation for the enhancing effect of organic impurities: colloidal particles of these hydrophobic organic liquids suspending in water may act as cavitation nuclei causing the occurrence of cavitation to increase.

In summarizing, it is concluded that sonoluminescence is basically thermal in origin: the high temperature occurs in the cavitation bubbles as a result of the adiabatic compression of bubbles when they collapse. The hot spot theory is plausible, though also the thermochemical mechanism is not excluded. Further investigations are desirable to clarify the more detailed mechanism of sonoluminescence and sonic chemiluminescence: accurate observations of spectral lines and bands, particularly in the ultraviolet part will be of some use.

§ 7. Application of luminol to visualization of ultrasonic fields

Many methods of the visualization of ultrasonic fields are known such as optical, chemical, mechanical and electrical methods[28)]. The optical method utilizing the diffraction of light by ultrasonic waves is often used because the image formation is well analysed theoretically and beautiful photographs are obtainable[29)]. Some limitations, however, exist in this method: the applicable frequencies are ordinarily above 0.5 Mc/s and only the images viewed along the direction parallel to the wave fronts are obtained, and furthermore, a special optical apparatus is required. The chemical method, using sonosensitive compounds, are applicable to visualize the intensity distribution on arbitrary section of ultrasonic fields. Reported sonosensitive compounds are thermo-

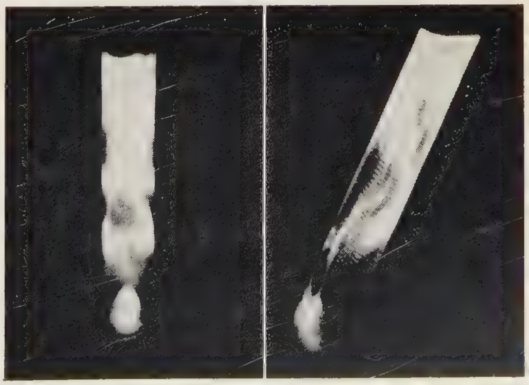

Fig. 20. 30 cc test irradiated by 500 kc/s ultrasonic waves.

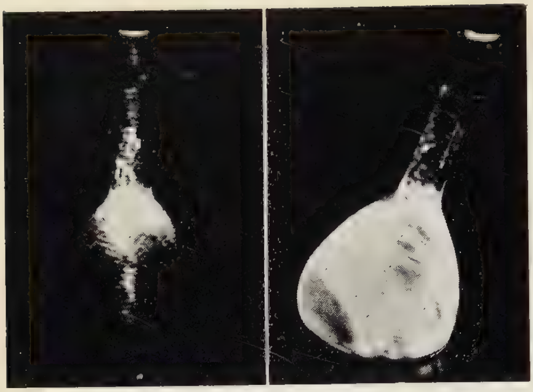

Fig. 21. 100 cc flat-bottomed flask irradiated by 500 kc/s ultrasonic waves.

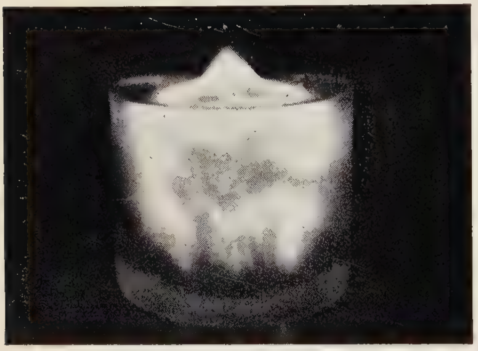

Fig. 22. Ultrasonic fountain in 1 liter beaker.

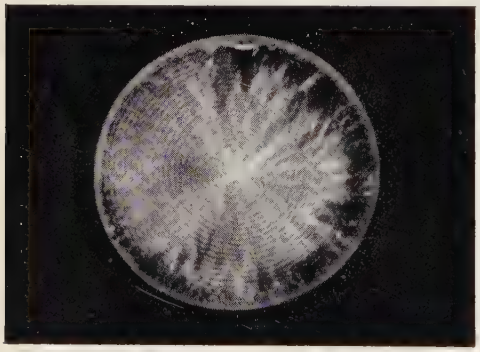

Fig. 23. Stationary wave pattern of a 400 kc/s cylindrical barium titanate transducer.

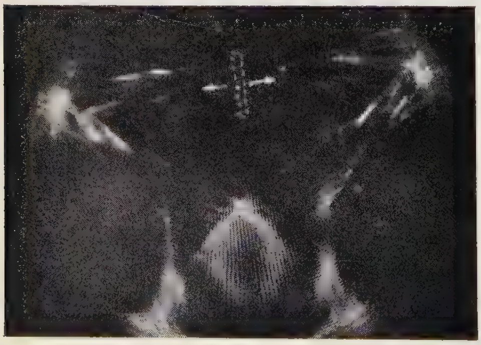

Fig. 24. Interference pattern of 500 kc/s ultrasonic waves in circular tank

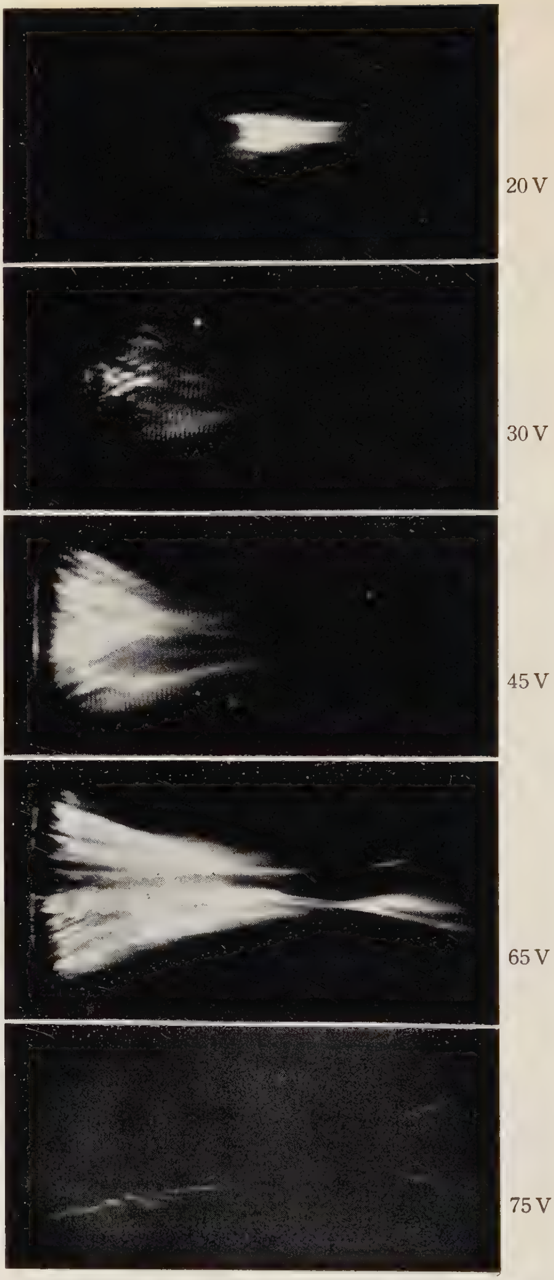

Fig. 25. Ultrasonic fields of a concave barium titanate transducer (470 kc/s, 8 cm diameter, 10 cm focal length) at various input voltages.

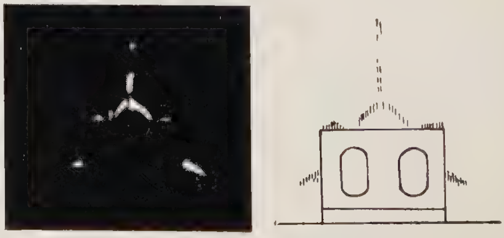

Fig. 26. Ultrasonic cavitation field (left) of a 50 kc/s ferrite transducer (right).

sensitive coloured compounds like mercury silver iodide (Ernst and Hoffmann[30]), thermosensitive phosphors (Schreiber *et al.*[31]), Pétermann[32]), Ernst *et al.*[30]), photographic paper in dilute developer (Torikai and Negishi[33]), starch plate in iodine solution (Bennett[34]), etc. In these methods, however, there exist some disadvantages related to the insertion of sonosensitive screens or plates in ultrasonic fields. In mechanical[40]) and electrical methods[41]), particular image converters are required for the visualization of ultrasonic fields.

A new chemical method of the visualization of ultrasonic fields has been developed here as an application of the sonic chemiluminescence of luminol. In this method—the luminol method, it is possible to observe the three-dimensional structure of the ultrasonic field without giving any disturbance to it. The luminescence from luminol solution is considered to be an instantaneous measure of the oxidation action of ultrasonic waves, so that the observed luminous structure shows, exactly speaking, not the intensity distribution of the ultrasonic fields, but rather the instantaneous distribution of ultrasonic oxidation. Further advantages of this method are that no special optical or other apparatus is required, and that the application of this method is not limited by the shape of the liquid container. The luminol method is thought to be an only adequate method whereby internal fields of vessels like flask can be visualized.

Some disadvantages, however, exist in this method: the luminescence from luminol in ultrasonic fields is so weak that the observation must be made in a dark room, and this method becomes useless for ultrasonic fields in which no cavitation occurs. Then, the applicable ultrasonic frequencies are limited practically up to 5 Mc/s.

There is no critical concentration of luminol or sodium carbonate; for example, 0.2 g of luminol and 5 g of sodium carbonate in 1,000 cc water is of use. If a barium titanate transducer is immersed directly in this solution without electric insulation, it is short-circuited by the electric conduction of the solution, and then its electro-acoustic efficiency is much decreased. Even in such a case, if the frequency of the transducer is higher than 400 kc/s, this method is applicable by reducing the concentration of sodium carbonate until considerable ultrasonic power can be radiated from the transducer. When a lower frequency barium titanate transducer is used, it must be electrically insulated because its impedance becomes higher than the leakage resistance of the solution. Practically, it is desirable to maintain the temperature of luminol solution below 25°C, as the luminescence from luminol decreases with increasing temperature.

Many photographs of ultrasonic fields were taken in a dark room, using a camera with F:2.4 lens and Fuji SSS films (ASA 200). The appropriate exposure time was two minutes or so. Some examples of ultrasonographs taken by the luminol method are shown in Fig. 20 to Fig. 26.

Fig. 20 shows 30 cc test tubes irradiated from the bottom by 500 kc/s ultrasonic waves. The ultrasonic field in the tube never becomes uniform.

Fig. 21 shows a flat-bottomed flask (100 cc) irradiated by 500 kc/s ultrasonic waves. When the ultrasonic waves are irradiated perpendicularly to the bottom, only a small part of the incident ultrasonic power penetrates through it (left photograph). At an appropriate incident angle, however, the bottom becomes more transparent and a larger amount of the ultrasonic power penetrates into the flask (right photograph). At higher ultrasonic intensities, the luminescence from the flask disappears. In experiments on the ultrasonic treatments of liquids, careful attentions must be paid to such phenomena. Some disagreements reported in experimental results of ultrasonic treatment are thought to originate at least partly from these phenomena.

Fig. 22 shows a ultrasonic fountain induced by a 500 kc/s barium titanate transducer (5 cm in diameter) placed on the bottom of 1 liter beaker.

Fig. 23 shows an internal field of a 400 kc/s cylindrical barium titanate transducer (9 cm in inner diameter, 2.6 cm in height). Beautiful concentric circles of stationary wave pattern are noticed.

Fig. 24 shows a interference pattern of 500 kc/s ultrasonic waves in a circular glass tank (24 cm in diameter). The ultrasonic waves, radiated from both faces of the transducer as indicated by arrows, are reflected by the tank wall and then interfere with each other.

Fig. 25 shows ultrasonic fields of a concave barium titanate transducer (470 kc/s, 8 cm in diameter, 10 cm in focal length) at various input voltages. At 20 V, only the focal region luminesces. As the input voltoges are increased, the luminous region spreads towards the transducer, and at 65 V, the whole region of the converging sound beam between the transducer and the focus luminesces but no luminescence is found at the focal region. At 75 V, all luminescence suddenly disappears except at the fringe of the sound field. This shows that the oxidation by ultrasonic waves is suppressed when the ultrasonic intensity is too high. In spite of the difference in sound intensities at various points in the sound field, the luminescence disappears simultaneously not only in the case of the concave transducer (Fig. 25), but also in experiments in the flask and the test tube. This suggests that cavitation occurs somewhat co-operatively at least in high frequency ultrasonic waves.

Fig. 26 shows a cavitation field of 50 kc/s ferrite transducer. The cavitation field in this case looks entirely different as compared with those at high frequencies, the luminous region being mainly restricted on the radiating surface of the transducer and on the axis of the sound beam.

§ 8. Summary

Shock waves caused by the ultrasonic cavitation were detected in water by a miniature spherical hydrophone made of barium titanate. When a few cavitations were produced, the bubble collapse occurred slightly after the pressure maximum of the sound-pressure cycle as shown theoretically by Noltingk and Neppiras. When many cavitations were simultaneously produced, large positive peaks of saw-tooth form appeared in the pressure waveform owing to the superposition of many shock waves. By observing the scattered light from the cavitating bubbles in dark-field illumination, these large peaks were confirmed to occur at the phase of minimum bubble volume.

In this very phase, *i.e.* at the instant of complete collapse of the bubbles, the sonoluminescence from water did occur as discrete flashes of light. The sonoluminescence from aqueous solutions of some sodium salts and some organic liquids were also studied. The addition of heavy, volatile and immiscible organic liquids as carbon disulfide or methyl iodide enhanced the sonoluminescence from water. The luminescence from the alkaline solution of luminol in ultrasonic fields was found to consist of discrete flashes and superposed continuous light. The latter disappeared with a decay time of about 1/20 sec when the ultrasonic waves were turned off. The intensities of both the sonoluminescence from water (or aqueous solutions) and the sonic chemiluminescence of luminol showed peculiar dependence on ultrasonic intensity. The luminescence increased with increasing sound intensity at first, but decreased (or nearly vanished) rather suddenly at a high sound intensity.

The discussion on the origin of sonoluminescence were made and it is concluded that sonoluminescence is basically thermal in origin: the high temperature occurs in the cavitation bubbles as a result of the adiabatic compression of bubbles when they collapse.

As an application of luminescence from luminol solution, a new method for the visualization of ultrasonic fields was developed. This method has the advantage of applicability to the three-dimensional case without giving any disturbance to the fields. Moreover, the application of this method is not limited by the shape of the liquid container.

Acknowledgement

The author wishes to express his sincere thanks to Dr. O. Nomoto for the kind guidance and useful discussions. He is also grateful to Dr. M. Marutake for the encouragement during the course of this study.

References

1) H. Frenzel and H. Schultes: Z. Phys. Chem. **B 27** (1934) 421.
2) P. V. Zimakov: Compt. Rend. Acad. Sci. USSR. **3** (1934) 450.
3) L. A. Chambers: J. Chem. Phys. **5** (1937) 290.
4) E. N. Harvey: J. Amer. Chem. Soc. **61** (1939) 2392.
5) V. Griffing and D. Sette: Phys. Rev. **87** (1952) 234.
6) V. Griffing and D. Sette: J. Chem. Phys. **23** (1955) 503.
7) R. O. Prudhomme et R. H. Busso: Compt. Rend. **235** (1952) 1486.
8) R. O. Prudhomme et T. Guilmart: J. chim. phys. **54** (1957) 336.

9) P. Günther, Z. U. Grisar und E. Heim: Z. Electrochem. **61** (1957) 188.
10) P. Günther, E. Heim und H. V. Borgstedt: Z. Electrochem. **63** (1959) 43.
11) D. Srinivasan and L. V. Holroyd: Phys. Rev. **99** (1955) 633.
12) P. Jarman: Proc. Phys. Soc. (London) **73** (1959) 628.
13) J. Frenkel: Acta Physicochim. URSS. **12** (1940) 317.
14) W. A. Weyl and E. C. Marboe: Research **2** (1949) 19.
15) W. A. Weyl: J. Colloid Sci. **6** (1951) 389.
16) B. E. Noltingk and E. A. Neppiras: Proc. Phys. Soc. **B**, **63** (1950) 674.
17) E. A. Neppiras and B. E. Noltingk: Ibid. **B**, **64** (1951) 1032.
18) W. U. Wagner: Z. angew. Phys. **10** (1958) 445.
19) P. Günther, E. Heim, A. Schmitt und W. Zeil: Z. Naturforsch. **12** (1957) 521.
20) P. Günther, E. Heim und G. Eichkorn: Z. angew. Phys. **11** (1959) 274.
21) E. Meyer und H. Kuttruff: Z. angew. Phys. **11** (1959) 325.
22) P. Jarman: J. Acous. Soc. Amer. **32** (1960) 1459.
23) L. Bohn: Acustica **7** (1957) 201.
24) K. Negishi: Acustica **10** (1960) 124.
25) N. Sata and K. Nakasima: Bull. Chem. Soc. Japan **18** (1943) 220.
26) O. Nomoto and S. Okui: J. Phys. Soc. Japan **3** (1948) 47.
27) O. Lindström: J. Acous. Soc. Amer. **27** (1955) 654.
28) cf. L. Bergmann: *Der Ultraschall; S. Hirzel Verlag, Stuttgart* (1954) P. 248.
29) Y. Torikai and K. Negishi: J. Phys. Soc. Japan **8** (1953) 119.
30) P. J. Ernst and C. W. Hoffmann: J. Acous. Soc. Amer. **24** (1952) 207.
31) H. Schreiber und W. Degner: Ann. Phys. **7** (1950) 275.
32) L. Pétermann: Helv. Phys. Acta. **24** (1951) 596.
33) Y. Torikai and K. Negishi: J. Phys. Soc. Japan **10** (1955) 1110.
34) G. S. Bennett: J. Acous. Soc. Amer. **29** (1957) 145.
35) A. R. Fairbairn and A. G. Gaydon: Proc. Roy. Soc. **A 239** (1957) 464.
36) Y. Tanaka, A. S. Jursa and F. J. LeBlanc: J. Opt. Soc. Amer. **48** (1958) 304.
37) I. E. El'piner: Akust. Zh. **5** (1959) 133. Soviet Physics-Acoustics **5** (1959) 135.
38) I. E. El'piner: Akust. Zh. **6** (1960) 3. Soviet Physics-Acoustics **6** (1960) 1.
39) E. Heim: Z. angew. Phys. **12** (1960) 423.
40) *e.g.* R. Pohlman: Z. Phys. **113** (1939) 697.
41) *e.g.* W. Freitag und H. J. Martin: Acustica **8** (1958) 197.

JOURNAL OF THE PHYSICAL SOCIETY OF JAPAN Vol. 16, No. 7, JULY, 1961

Experimental Evidence for Frank's Theorem on Dislocations by X-ray Diffraction Micrography

By Mitsuru YOSHIMASTU

Rigaku Denki Co. Ltd., Hajima, Akijima, Tokyo

(Received March 3, 1961)

In X-ray diffraction micrographs of a silicon single crystal, some nodes where three dislocation lines meet were observed. The Burgers vectors of these dislocations were determined, except of their sense, from the change in intensity contrast with different reflecting lattice planes. Frank's theorem, corresponding to Kirchhoff's law for electric current, was experimentally confirmed.

§1. Introduction

It is well known as Frank's theorem[1], corresponding to Kirchhoff's law of electric current, that the sum of the Burgers vectors of dislocations meeting at a node must vanish if each dislocation is considered to go into the node. However, so far as the author knows, it seems that this theorem have not been experimentally confirmed till quite recently. Fujita et al have confirmed the theorem for the graphite crystal by using the moirè pattern of electron micrographs[2].

Although many dislocation lines were almost always observed in the X-ray diffraction micrographs of silicon single crystals obtained by Lang's method, any node has not been observed where several dislocation lines meet. The specimens used previously were cut parallel or vertical to the growth axis and were thin. The probability for a node to be found in the interior of the specimen is considered to be small. It is expected that the chance observing the node is increased if a specimen plate is cut parallel to a plane in which dislocations exist. It is considered that such a situation is realized in the {111} planes oblique to the growth axis. In the X-ray diffraction micrographs of such a specimen, we have observed some points at each of which three dislocation lines meet. From the change in intensity contrast with different reflecting lattice planes, we determined the Burgers vectors of these dislocations and tried to confirm Frank's theorem.

§ 2. Experimental

A specimen of thin plate was prepared from a twinned silicon crystal. The specimen was polished with the carborundum of ♯1600 and etched with the CP-4 solution. The thickness of specimen was 0.65 mm.. The orientation of specimen is shown with a pole figure in Fig. 1.

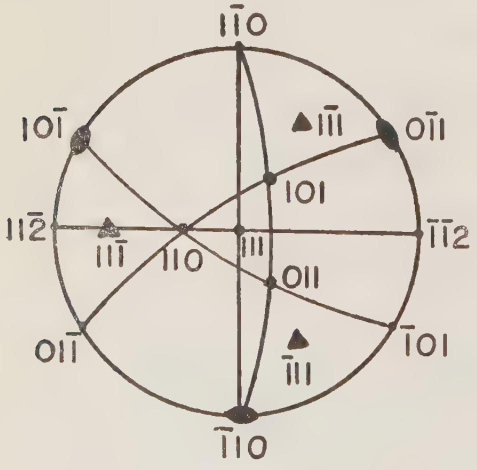

Fig. 1. The pole figure of the specimen. X-ray diffraction photographs are obtained by diffraction from the lattice planes of poles marked by ▲ and ●. The three round great circles show the trace of planes which belong to the pole $[\bar{1}\bar{1}1]$, $[\bar{1}11]$ and $[11\bar{1}]$.

Experimental arrangement is essentially the same as that of Lang[3] except technical details, the schematic diagram being shown in Fig. 2. A fine focus X-ray source of apparent size $40\mu\times30\mu$ is used. The distance from the specimen to the source is about 200 mm., the one from the specimen to the plate, 15～20 mm.. To take a photograph from a wide area of the crystal, the crystal and the plate are moved right and left at the same time by a combination of a gear and a synchronous motor. Deflection of the crystal orientation during translation is within 2 second angular range. The X-ray tube with Ag target was operated with 50 kilo constant voltage and 1 mA.

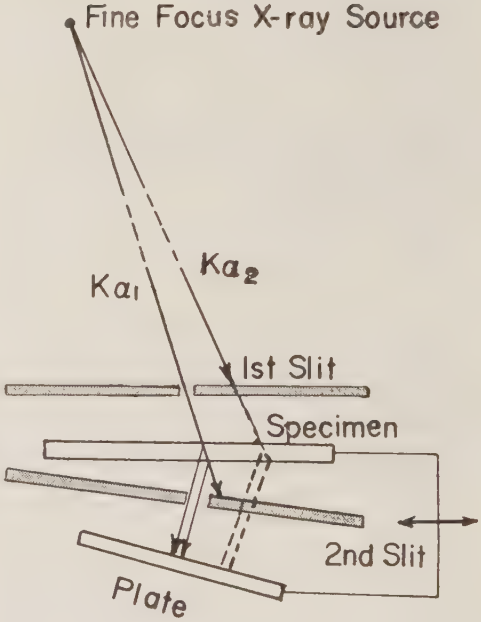

ig. 2. Schematic diagram of experimental arrangement. The pathes of $K\alpha_1$ and $K\alpha_2$ radiations which are emitted from a point source and diffracted from a lattice plane in the crystal are drawn. The difference in the direction of $K\alpha_1$ and $K\alpha_2$ is exaggerated.

In order to obtain diffraction images with a high resolution, X-rays which contribute to the images must be limited to the $K\alpha_1$ radiation. This can be made possible by using a collimating system with a small angular spread $\Delta\theta < \dfrac{\Delta\lambda}{2d\cos\theta}$, where $\Delta\lambda = \lambda_{k\alpha_2} - \lambda_{k\alpha_1}$, d, lattice spacing and θ, the Bragg angle. In this case, a fine adjustment of the crystal is necessary for realizing the Bragg reflection. Practically, the difficulty of the fine adjustment was avoided in the following way. The slit was at first widely opened. In this case, however, the $K\alpha_2$ as well as $K\alpha_1$ radiations are diffracted from a same lattice plane but at different regions in the crystal, the former resulting in the poor resolution. Next, the width of the first slit was made narrower to cut off the $K\alpha_2$ radiation contributing to the diffraction image.

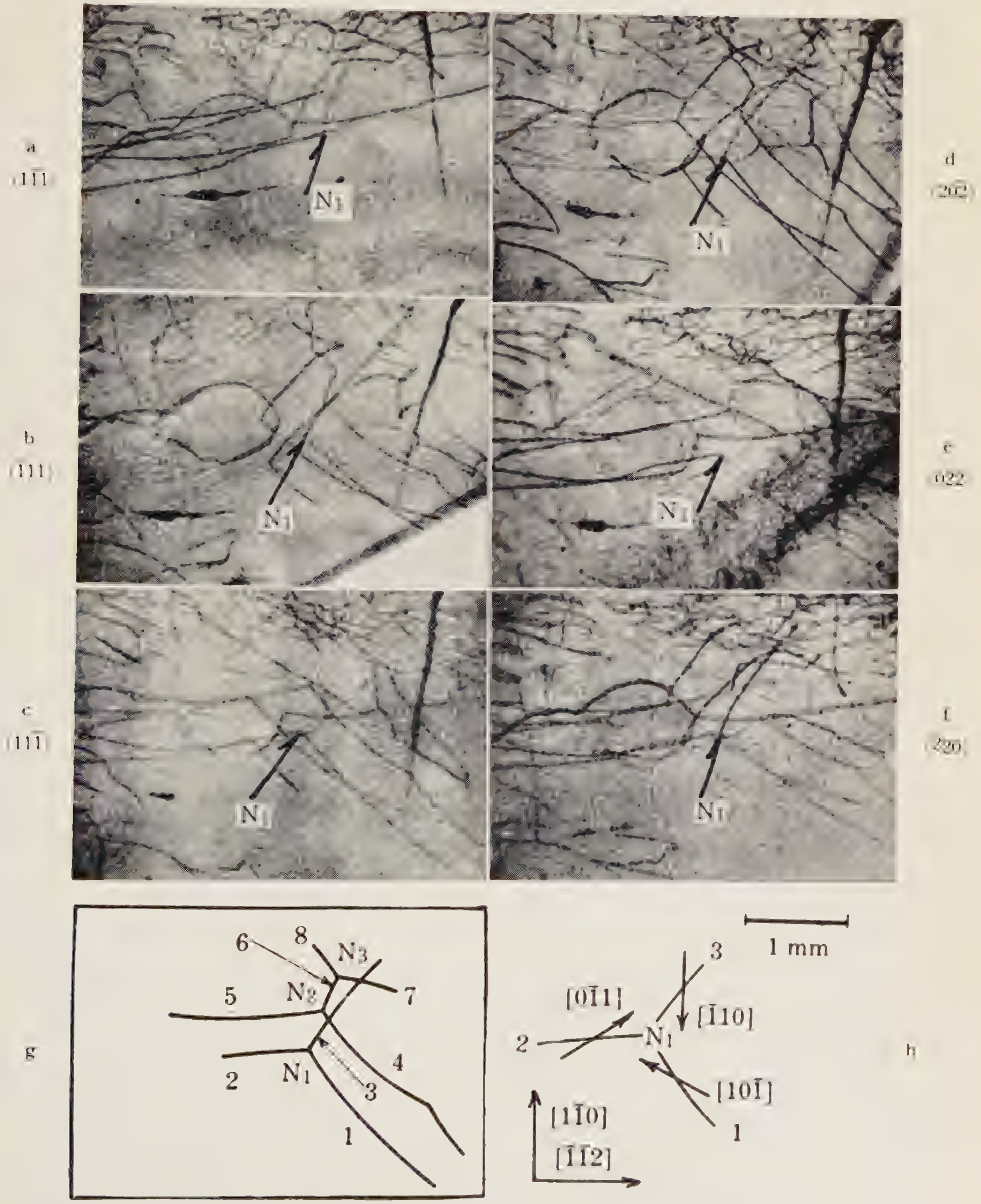

Fig. 3. X-ray diffraction micrographs taken with various reflecting planes. (g) is a schematic drawing of dislocation lines meeting at nodes, being sketched from (d). (h) shows the Burgers vectors of dislocation lines meeting at a node N_1.

§ 3. Results and discussions

X-ray diffraction photographs from the same region of specimen were obtained for various reflecting lattice planes, as shown in Fig. 3. In them some nodes at which three dislocation lines meet are observed. Three sets are shown schematically in Fig. 3 (g).

The Burgers vectors of dislocation lines meeting a node were determined on the basis of following two facts. (i) The intensity contrast due to dislocation lines is considered to be maximum when the Burgers vector is parallel to the normal of reflecting lattice plane; we would call this the maximum condition. (ii) The intensity contrast vanishes when the Burgers vector is vertical to the normal of reflecting lattice plane (the zero condition), although the dependency with the intermediate angle between the Burgers vector and the normal might not be monotonous. The direction of Burgers vector in silicon crystals is usually considered to be parallel to one of ⟨110⟩ directions. Therefore, a dislocation with a certain Burgers vector should represent the highest contrast for one of {220} reflections, for example the (220) reflection, and no intensity contrast should occur for reflection from planes parallel to the [110] direction.

It is practically convenient to examine at first the zero condition for {111} reflections. There are three directions of ⟨110⟩ parallel to one of {111} planes. When a dislocation image is found to vanish for one of {111} planes, for instance, (111), the Burgers vector must be one of three ⟨110⟩ directions parallel to (111). If another one of {111} reflections, for instance, the $(11\bar{1})$ reflection do not reveal the dislocation image, the Burgers vector is determined to be parallel to the intersecting line of the above two planes, the $[1\bar{1}0]$ direction. On the contrary, if the $(11\bar{1})$ reflection reveals the dislocation image, the possibility of the $[1\bar{1}0]$ direction is denied. However, it is not always possible to examine the zero condition for all {111} reflections. In this case, ambiguity is left among a few directions. This ambiguity is removed by examining the maximum condition mentioned above for some appropriate planes of {110}.

Let us notice dislocation lines meeting a node N_1 shown in Fig. 3 (g) and first determine the Burgers vector of the dislocation 1. The dislocation image disappears for the $(1\bar{1}1)$ reflection, Fig. 3 (a), among experimentally observable {111} reflections. This means that the Burgers vector must exist in the $(1\bar{1}1)$ plane according to the zero condition. From the pole figure of the specimen, Fig. 1, it is known that three $[10\bar{1}]$, [110] and [011] directions are parallel to the $(1\bar{1}1)$ plane. On the other hand, the diffraction photographs obtained from the $(\bar{1}11)$ plane and the $(11\bar{1})$ plane clearly show the dislocation image of 1, as seen in Fig. 3 (b) and Fig. 3 (c) respectively. The $(\bar{1}11)$ plane is parallel to [110], and the $(11\bar{1})$ plane is parallel to [011]. Thus, the possibility of the [110] or the [011] directions have been denied, and the $[10\bar{1}]$ direction is left as only one possibility for the Burgers vector. This could not be experimentally comfirmed by the reflection from the (111) plane containing the $[10\bar{1}]$ direction. However, it can be confirmed by the maximnm condition. Fig. 3 (d), (e) and (f) show the experimentally observable {220} diffraction photographs. The $(20\bar{2})$ diffraction photograph obtained from the $(10\bar{1})$ plane vertical to the $[10\bar{1}]$ direction, Fig. 3 (d), shows the highest intensity contrast for the dislocation 1 among them. Accordingly, the Burgers vector of the dislocation 1 is concluded to be parallel to the $[10\bar{1}]$ direction.

In the same way, the Burgers vector of the dislocation 2 and 3 are determined to be parallel to the $[0\bar{1}1]$ and the $[\bar{1}10]$ directions respectively. These three directions are on the same plane (111).

It is to be noticed here that the sense of the Burgers vector cannot be determined from the intensity contrast in the X-ray diffraction micrography. The sense of the Burgers vector of each dislocation has two possibilities. If the sense is taken in such a way as shown in Fig. 3 (h), the sum of the Burgers vectors of above three dislocations vanishes. This fact is no more than Frank's theorem. At least, under a suitable condition mentioned above, Frank's theorem can be experimentally confirmed by a X-ray diffraction micrography only assuming the sense of the Burgers vector.

By the similar procedures, the Burgers vectors of other dislocation lines 4, 5, 6, 7, and 8 in Fig. 3(g) are concluded to be parallel to the directions $[10\bar{1}]$, $[0\bar{1}1]$, $[\bar{1}10]$, $[0\bar{1}1]$, and $[10\bar{1}]$ respectively. Of course, it is apparent that the Burgers vectors of these dislocations satisfy Frank's theorem at each node N_2 and N_3 when the sense of these Burgers vectors is appropriately chosen as in the previous case.

Acknowledgements

The author would like to express his sincere thanks to Dr. Y. Shimura, President of Rigaku Denki Co. for his kind encouragements, and to Professor K. Kohra for his suggestions of this problem and advices, and to Professor T. Suzuki for his discussions. His thanks are also due to K. Sakayama for his skillful technical assistances.

References

1) F. C. Frank: Phil. Mag. **42** (1951) 809.
2) E. Fujita and K. Izui: J. Phys. Soc. Japan **16** (1961) 214.
3) A. R. Lang: Acta Cryst. **12** (1959) 249; J. Appl. Phys. **30** (1959) 1748.

Errata

A New Method to Determine Hydration Energy of Ion

By Yoshio ISHIDA

J. Phys. Soc. Japan **15** (1960) 1707

P. 1707	left column	line 28	···	$\phi_{\beta 0}$ is nearly equal to $\phi_{\beta 0}$
	should be read		···	$\phi_{\varepsilon 0}$ is nearly equal to $\phi_{\beta 0}$
	right column	Eq. (4)		$\sqrt{R^2+\rho^2+2R\rho\cos\theta}$
	should be read			$\sqrt{R^2+\rho^2-2R\rho\cos\theta}$

Short Notes

This section is intended to secure prompt publication of important discoveries in physics. The reports should not exceed 800 words in length. A figure of size 7 cm×7 cm will be counted as 150 words.

J. PHYS. SOC. JAPAN **16** (1961) 1470

Antiferromagnetism of MnHg

By Yasuaki NAKAGAWA and Tomiei HORI

Department of Physics and Chemistry,
Gakushuin University, Mejiro
Tokyo

(Received February 27, 1961)

The existence of an intermetallic compound of Mn and Hg with an equiatomic composition, MnHg, has been confirmed by Lihl[1] and de Wet[2], as having the simple B2 (CsCl) type of structure. The latter author has also measured the magnetic susceptibility at 90, 195° and 295°K, and suggested that it is probably antiferromagnetic at low temperatures. Since the atomic arrangements in MnHg are similar to those in MnAu[3] and MnPd[4], the detailed studies on the antiferromagnetism may be interesting in view of the theory of magnetism of metals.

In the present note, the experimental investigations are reported on the magnetic susceptibility, the electrical resistivity, and the crystal structure in the temperature range from 90 to 360°K. The specimens used were prepared as follows: pure Hg and the powders of electrolytic Mn were mixed at the desired proportion, sealed in an evacuated quartz tube, heated to 400°C, and then held at this temperature for 35 hours. It was confirmed by the X-ray diffraction patterns that the products consisted of only MnHg.

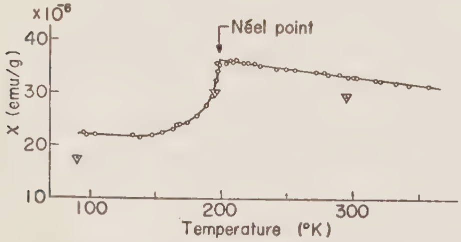

Fig. 1. Magnetic susceptibility, χ, of MnHg. (▽: de Wet[2])

The magnetic susceptibility was measured by Faraday's method. It is independent of magnetic fields up to 12 koe, and the temperature dependence is shown in Fig. 1, in which the values obtained by de Wet[2] are also plotted. The Néel point may be 198°K at which the susceptibility has a maximum value. Above the Néel temperature, however, the susceptibility cannot be satisfactorily expressed by the Curie-Weiss law, i.e. the effective Bohr magneton number derived from the experimental curve is unreasonably large.

The electrical resistivity was determined by means of the measurements of the torque exerted on the small specimen by a 50 cps rotating magnetic field. The apparatus is similar to that reported by Braunbeck.[5] The absolute values of the resistivity were obtained by comparing with the torque exerted on a standard specimen of copper, though the results were not so accurate. The temperature dependence of the resistivity exhibits an anomaly at the Néel point, as shown in Fig. 2.

It was proved by the X-ray diffraction method* that MnHg was not transformed from cubic to tetragonal structure at low temperatures, in contrast to MnAu and MnPd. The lattice constants determined from the (110) lines are also shown in Fig. 2.

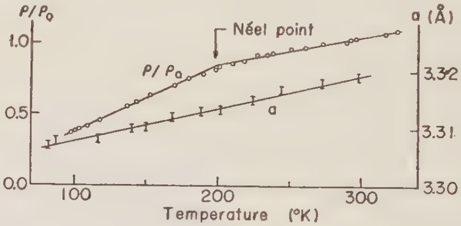

Fig. 2. Electrical resistivity, ρ, and lattice constant, a, of MnHg. Resistivity at 0°C, ρ_0, is about $5\times10^{-5}\,\Omega$ cm. Crystal structure is of the CsCl type.

It may be concluded from the above experiments that MnHg is antiferromagnetic at the temperatures below 198°K.

References

1) F. Lihl: Monatsh. Chem. **86** (1955) 196.
2) J. F. de Wet: Angew. Chem. **67** (1955) 208.
3) G. E. Bacon and R. Street: Proc. Phys. Soc. **72** (1958) 470.
4) E. Raub and W. Mahler: Z. Metallkunde **45** (1954) 430.
5) W. Braunbeck: Z. Phys. **73** (1932) 312.

---

* The authors are indebted to Prof. K. Yasukochi and Mr. K. Kanematsu of Nihon University for a low-temperature X-ray diffractometer used in this investigation.

J. Phys. Soc. Japan **16** (1961) 1471

On the Faraday Effect in Many-Valley Semiconductors

By Louis Gold

Radiation Laboratory and the Department of Nuclear Engineering University Michigan, Ann Arbor

(Received April 10, 1961)

In developing the complete classical electrodynamics for free carriers in many-valley semiconductors, a new relation for the Faraday rotation has been deduced which reveals the imprecise nature of earlier formulae. Since there is active research continuing in such materials as n-germanium1), it appears appropriate to make immediately available a basic relation which properly describes the phenomenon.

The general formula, including collisional damping, will be left for a fuller description. In the infrared region where collisions may be ignored in the usual manner, the index of refraction μ may be written in the form

$$\mu^2=1-\frac{2x^2}{[\ ]_3\mp\sqrt{[\ ]_3{}^2-4([\ ]_1[\ ]_2-[\ ]_4)}} \tag{1}$$

where the abbreviations denote

$$[\ ]_i=a_{ii}+\frac{a_{i3}{}^2}{x^2-a_{33}} \qquad \text{for } i=1,\,2$$

$$[\ ]_3=a_{11}+a_{22}+\frac{a_{13}{}^2+a_{23}{}^2}{x^2-a_{33}}$$

$$[\ ]_4=\frac{w_c{}^2}{\omega^2}+\left(a_{12}+\frac{a_{13}a_{23}}{x^2-a_{33}}\right)^2 \tag{2}$$

and

$$x^2=\frac{3N_0q^2/m_2}{\omega^2}\,, \qquad \omega_c=\frac{3qB}{m_2}$$

The basic physical quantities that enter are: ω the impressed frequency, N_0 the carrier density in each valley, q the electronic charge and m_2 the transverse mass.

The a_{jk} relate to the transformed mass tensor in the frame of reference where the magnetic field $\vec{B}$ is along the z-axis which also corresponds to the direction of wave propagation. The components in the cubic reference frame

$$\overleftrightarrow{m}_{\text{cubic}}=\frac{1}{3}m_2(a_{jk}) \tag{3}$$

where

$$a_{11}=a_{22}=a_{33}=K+2$$
$$a_{jk}=a_{kj}=S_i(K-1)\,,$$
$$i\neq j\neq k\neq i\,, \qquad K=m_1/m_2 \tag{3a}$$

transform via

$$a_{jk}=\frac{\partial x_j}{\partial x_{j'}}\cdot\frac{\partial x_k}{\partial x_{k'}}a_{j'k'} \tag{4}$$

Specification of the separate contributions to the rotation for the four sets of energy surfaces derives from selection of the S_i having values ±1 as described elsewhere2). If the chemical potential changes at high magnetic field producing a redistribution of electrons, then each valley must be accordingly weighted (allowance also being made for N_0 changes in x2).)

It may be seen that the familiar Appleton-Hartree relation obtains from (1) if the scalar mass limit is imposed. Thus in the usual way, the choice of sign specifies either the ordinary or extraordinary circularly polarized component of the wave. Prior relations, such as that of Stephen and Lidiard3), bear little resemblance to (1) and do not reduce to the Appleton-Hartree formula for an isotropic mass medium.

Finally, a resonance behavior may be expected in the Faraday rotation since for the extraordinaay component large changes occur when

$$\omega^2=\frac{1}{2}\,\omega_p{}^2\,\frac{A_1\pm\sqrt{A_1{}^2+(\omega_c{}^2/\omega_p{}^2)A_2}}{A_2}\,,$$

$$\omega_p{}^2=\frac{3N_0q^2}{m^2} \tag{5}$$

wherein

$$A_1=a_{12}{}^2-a_{11}a_{22}-\frac{\omega_c{}^2}{\omega_p{}^2}a_{33}$$

$$A_2=a_{11}a_{23}{}^2+a_{22}a_{13}{}^2+a_{33}a_{12}{}^2-(a_{11}a_{22}a_{33}+2a_{12}a_{13}a_{23}) \tag{5a}$$

Precisely these critical frequencies (resonances) were derived earlier4) in an effort to comprehend how magnetoplasma effects may influence cyclotron resonance determinations; it was pointed out then that new peaks would appear in the intermediate region where $\omega_c/\omega_p \sim 1$, the regime $\omega_p \ll \omega_c \sim \omega_p$, however, corresponding to "pure" cyclotron resonance.

References

1) B. Hartmann and B. Kleman: Ark. f. Fisik **18** (1960) 75.

2) L. Gold and L. M. Roth: Phys. Rev. **103** (1956) 61.

3) M. J. Stephen and A. B. Lidiard: J. Phys. Chem. Solids **9** (1959) 43.

4) L. Gold: Bull. APS **2** (1957) 314.

J. PHYS. SOC. JAPAN **16** (1961) 1472

Passage Effect in the Electron Spin Resonance of Fe-Doped Silicon

By Takeo IGO
Electrical Communication Laboratory
Musashino-shi, Tokyo

(Received May 15, 1961)

Recently Weger[1] investigated the effect of passage upon the ESR signal of an inhomogeneously broadend line. He studied shape and amplitude of the signal under various passage conditions theoretically and checked the theoretical predictions experimentally.

It is reported here that a passage effect was observed in the ESR of Fe-doped silicon[2],[3] and the relaxation time, T_1, was estimated from the passage conditions.

In Fig. 1 is shown the dispersion signal in-phase with respect to the modulation obtained at pumped helium temperature (~2°K) with a p-type sample of silicon into which Fe was diffused at 1100°C for about an hour. The signal is obtained by superimposing a modulation field at a frequency of 70 cps on the static magnetic field and then detecting the real part of the rf susceptibility which varies at this frequency using a phase sensitive detector.

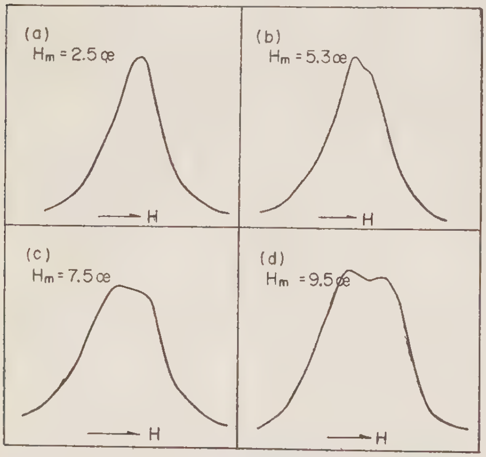

Fig. 1. In-phase dispersion signal in Fe-doped silicon as a function of magnetic field for several values of H_m. The static magnetic field is parallel to [$\bar{1}$01] direction. $T \approx 2$°K.

It is clear from Fig. 1 that the signal in-phase with respect to the modulation behaves unusually when the modulating field intensity, H_m, increases. When H_m is small, it has a typical line shape for an adiabatic rapid passage line, with a g-value of 2.07 independent of the crystal orientation and a half-width of about 10 oersteds. When H_m is increased, the line shape changes as shown in the figures (b), (c) and (d). At intermediate H_m-values, the top of the line is flattened, and then the saddle appears at large H_m-values. The in-quadrature signal, however, showed no such an unusual behavior. These behaviors of signals, according to Weger,[1] can be expected for an inhomogeneously broadend line with T_1-short compared with, or of the same order as, the modulation period. When H_m is small, all the spin packets covered by H_m are traversed (adiabatically) rapidly and an "absorption-type" signal is observed. As H_m is large enough, however, the adiabatic condition is violated over a portion of the modulation cycle. Then a "dispersion-derivative-type" signal arises from the non-adiabatically traversed spin packets. Since this "dispersion-derivative-type" signal is in-phase with respect to the modulation, it does not mix in the in-quadrature signal, but it mixes in the in-phase signal, yielding the observed results.

Occurence of such a passage effect depends on the ratio $H_1/\omega_m H_m T_1$. If we increase the rf field intensity, H_1, the unusual behavior should occur at at a larger value of H_m. This was verified experimentally. This and the fact that the DPPH marker signal was quite normal exclude the possibility that our observation is due to an instrumental effect. (Because the phase-setting was discrete, the phase was not exactly set to in-phase or in-quadrature position. The positions was determined by maximizing or minimizing the marker signal.)

The conditions under which the above passage effect occurs are (assuming $T_2 = T_1$):

$$(H_1/\omega_m H_m) < T_1 , \qquad \omega_m T_1 \ll 1 ,$$

$$\gamma H_1 T_1 \gg 1 , \qquad \gamma H_1^2 \gtrless (dH/dt) .$$

We can estimate T_1 from these conditions. In our estimation T_1 is of the order of 10^{-4} sec. T_1 is also determined directly from the saturation measurement. Preliminary saturation measurements gave a value of the same order as the above as T_1.

It is a pleasure to thank Mr. T. Asakawa for preparing the samples. I wish to express my thanks to Dr. T. Shindo and Dr. E. Yamaka for their interest in this work.

References

1) M. Weger: B.S.T.J. **39** (1960) 1013.
2) G. W. Ludwig, H. H. Woodbury, and R. O. Carlson: Phys. Rev. Letters **1** (1958) 295; H. H. Woodbury and G. W. Ludwig: Phys. Rev. **117** (1960) 102.
3) G. Feher: Phys. Rev. **114** (1959) 1219.

J. PHYS. SOC. JAPAN **16** (1961) 1473

Logarithmic Growth of the Cesium Antimonide Films on Antimony

By Kiyoshi MIYAKE

*Electrical Communication Laboratory, Nippon Telegraph and Telephone Public Corporation, Tokyo, Japan**

(Received January 23, 1961)

The reaction of cesium vapor with antimony film is a kind of reaction in which an electro-positive gas, namely, cesium vapor makes contact with antimony film which behaves as an electro-negative metal, followed by the formation of cesium antimonide. The compound has a very high resistivity, and has been suggested to be CsSb.[1),2)] The present note deals with experimental determination of the growth rate of this compound film.

Antimony was evaporated in a cylindrical glass envelope on to a square glass plate. A U-shaped trap for cesium vapor and a tube containing metallic cesium were connected to the one end of the glass envelope. The evaporation was carried out at room temperature in a vacuum better than 3×10^{-8} mm Hg, the rate being 0.01-0.002 mg per cm^2 per min.[3)] The film thickness ranged from 250 to 1100 A. Such films are known to be crystallized.[4)] The original resistance of the film was calculated from the dimensions (4×10 mm) and the electrical resistivity in bulk. The resistance between two leads attached on the opposite edges of the glass plate was measured prior to the reaction.

The resistivity of CsSb grown on the surface of antimony is about 10^7 times that of antimony in bulk.[1),2)] Hence it may be assumed that the resistance of the film is, at least in the early stage of the reaction, equal to that of the unaffected antimony film. If the compound layer is homogeneous, the thickness of the layer should be proportional to that of the antimony layer consumed by the reaction. We assume, for the time, that these are identical, although an increase in thickness of the film during the formation of cesium antimonide has been reported.[5)] Thus, the thickness of the growing layer can be determined from the measurement of electrical resistance.

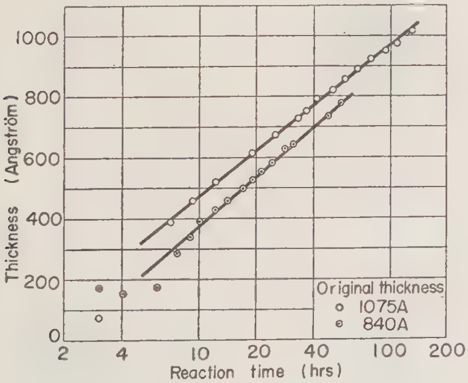

Fig. 1. Thickness of the CsSb layer grown on antimony films *vs.* the reaction time.

The measurement was carried out at room temperature in complete darkness and under conditions in which the rate of supply of the cesium vapor was higher than the formation rate of the compound. Fig. 1 shows the thickness of the compound layer grown on antimony film *vs.* the logarithm of time. As is seen in the figure, the relation between the thickness x, in A, and time t, in hours, is given by

$$x=k\log(t/c+1)\,, \tag{1}$$

where, k and c are constants. Usually, there is an induction period for the reaction, which is slightly longer than c. For one specimen and for $t\gg c$, the relation between x and t is well represented by Eq. (1). However, the values of k and c differ for different samples. The former ranged between 310 and 520 A, and the latter between 1.1 and 3.2 hrs. For thin films ($x<300$ A) and for the induction period the observed points are scattered.

Eq. (1) no longer holds when the thickness of the unaffected antimony layer is reduced to less than about 50 A, and a comparatively long time is required for the whole layer to be changed into the compound. Therefore, the formation process of the compound in this stage is considered to be different from that in the early stage. The variations in k and c for different samples may be due to the difference in microscopic surface conditions and in crystalline structure of the films.[6)]

References

1) H. Miyazawa, *et al.*: J. Phys. Soc. Japan **7** (1952) 647.
2) K. Miyake: J. Appl. Phys. **31** (1960) 76.
3) R. B. Jones and A. M. Glover: 1946, U. S. 2, 401,735, June 11.
4) A. Götzberger: Z. Phys. **142** (1955) 182.
5) K. Jack and M. Wachtel: Proc. Roy. Soc. A **239** (1957) 46.
6) A. Frimer: Doklady Akad. Nauk. SSSR **63** (1948) 255.

---

* Present address. Musashi Works, Hitachi Ltd., 1450 Kodaira-machi, Tokyo, Japan.

J. PHYS. SOC. JAPAN **16** (1961) 1474

Electron Distribution in $KMnF_3$, $KFeF_3$, $KCoF_3$ and $KNiF_3$

By Atsushi OKAZAKI and Yasutaka SUEMUNE
Department of Physics, Faculty of Science, Kyusyu University, Fukuoka, Japan

(Received March 4, 1961)

The structures of $KMnF_3$, $KFeF_3$, $KCoF_3$ and $KNiF_3$ are of the cubic perovskite type at room temperature[1], while that of $KCuF_3$ shows the Jahn-Teller distortion.[2] The electron distributions in the former four compounds are determined by an X-ray analysis. The experimental and analytical details are similar to those in the case of $KCuF_3$ [2]. For these compounds the [001] projections of the electron distribution obtained by the F_0 synthesis are shown in Fig. 1, where F_0 means the observed structure factor. In all the cases the electron distributions around F^- ions are elongated in the direction perpendicular to the 3*d* metal-fluorine-3*d* metal bonds. This elongation may be attributed either to anisotropic temperature effects or to the fact that the centre of F^- ion occupies such positions as being distributed with uniform probability along a circle. The analysis is now being undertaken.

References

1) A. Okazaki and Y. Suemune: J. Phys. Soc. Japan **16** (1961) 671.
2) A. Okazaki and Y. Suemune: Ibid. **16** (1961) 176.

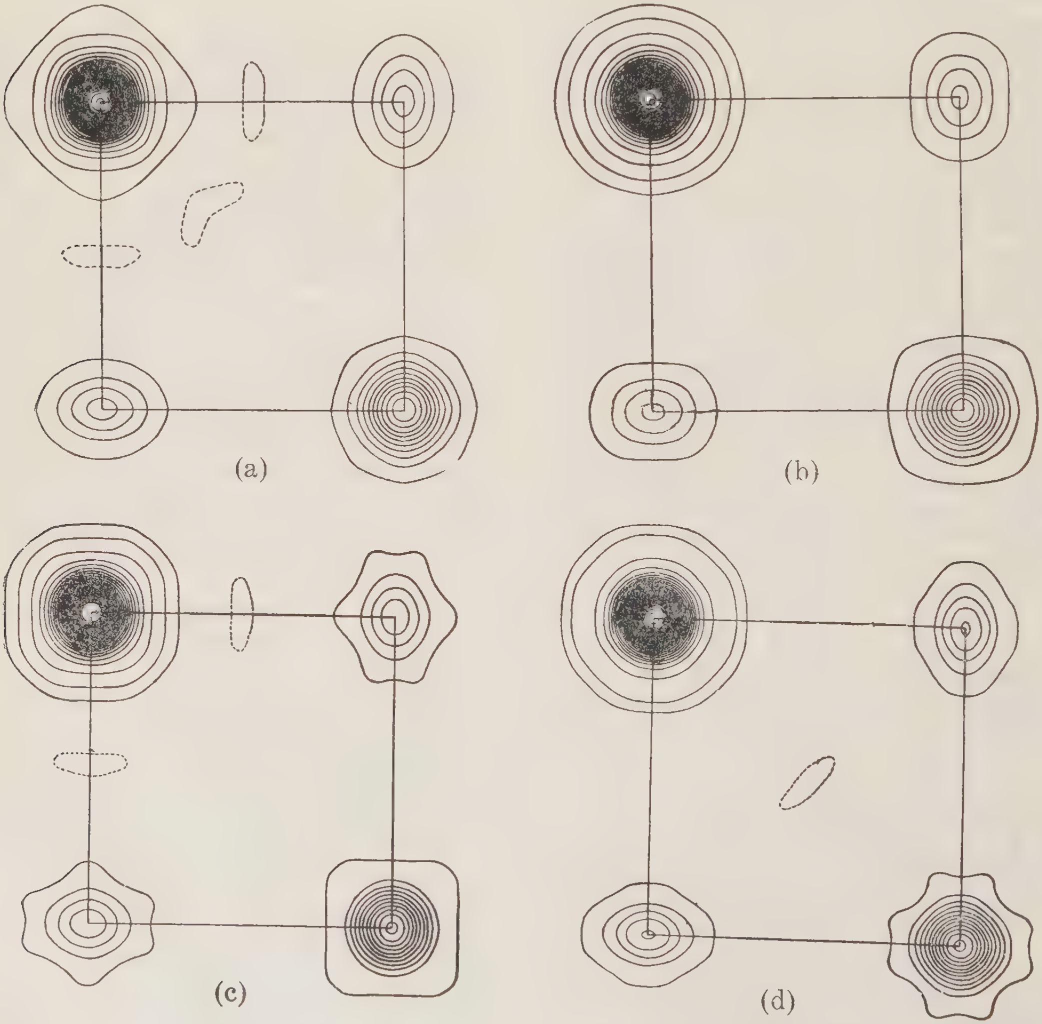

Fig. 1. Electron-density projections along [001] at room temperature, (a): $KMnF_3$, (b): $KFeF_3$, (c): $KCoF_3$ and (d): $KNiF_3$, with contours at intervals of 5 e. Å^{-2}. Dotted lines indicate 0 e. Å^{-2}. One fourth of the unit cell is shown for each compound.

J. PHYS. SOC. JAPAN **16** (1961) 1475

A Note on the Magnetoresistance of PbTe at High Magnetic Fields

By Eizaburo YAMADA and Kisaburo SHOGENJI
Hitachi Central Research Laboratory,
Kokubunji, Tokyo

(Received March 27, 1961)

At high magnetic fields the magnetoresistance of crystals is known to show an oscillatory behavior as a function of H. This phenomenon is due to the quantization of the electron orbits, and the degeneracy of the electrons is necessary for its appearance. PbTe crystal is favorable for investigation of this phenomenon, since its electrons have a large mobility and are degenerate at low temperatures. Recently an experiment has been carried out by Kanai *et al.*[1]. We comment here theoretically on this phenomenon.

When a high magnetic field ($\omega_c\tau \gg 1$), whose direction is chosen as z-axis, is applied to a crystal and the electrons of the crystal are degenerate, the conductivity tensor due to an energy ellipsoid with anisotropic effective mass is expressed as[2]

$$\sigma=\left|\begin{array}{ccc} \frac{\alpha_{xx}}{\alpha_1}\frac{Se^2}{m\omega_0{}^2\tau} & -\frac{ne^2}{m\omega_0}+\frac{\alpha_{xy}}{\alpha_1}\frac{Se^2}{m\omega_0{}^2\tau} & \frac{\alpha_2}{\alpha_1}\frac{ne^2}{m\omega_0}+\frac{\alpha_{xz}}{\alpha_1}\frac{Se^2}{m\omega_0{}^2\tau} \\ \frac{ne^2}{m\omega_0}+\frac{\alpha_{xy}}{\alpha_1}\frac{Se^2}{m\omega_0{}^2\tau} & \frac{\alpha_{yy}}{\alpha_1}\frac{Se^2}{m\omega_0{}^2\tau} & -\frac{\alpha_3}{\alpha_1}\frac{ne^2}{m\omega_0}+\frac{\alpha_{yz}}{\alpha_1}\frac{Se^2}{m\omega_0{}^2\tau} \\ -\frac{\alpha_2}{\alpha_1}\frac{ne^2}{m\omega_0}+\frac{\alpha_{xz}}{\alpha_1}\frac{Se^2}{m\omega_0{}^2\tau} & \frac{\alpha_3}{\alpha_1}\frac{ne^2}{m\omega_0}+\frac{\alpha_{yz}}{\alpha_1}\frac{Se^2}{m\omega_0{}^2\tau} & \frac{\det\alpha}{\alpha_1}\frac{Se^2\tau}{m} \end{array}\right|, \qquad (1)$$

$$\omega_0=\frac{eH}{mc}, \qquad \omega_c{}^2=\alpha_1\omega_0{}^2, \qquad \alpha_1=\alpha_{xx}\alpha_{yy}-\alpha_{xy}{}^2 \qquad \text{etc.},$$

where α_{ij}'s are dimensionless constants which represent relative inclination of H to the principal axes of the ellipsoid. S and τ are the density of states and the relaxation time respectively. Both are functions of the Fermi level ζ and show a periodic variation with $1/H$.

PbTe has a cubic symmetry and its electronic band structure is expressed by <111> 8 or 4 valley model.[3),4)] When H is applied in the [100], [111] or [110] direction of PbTe, non-vanishing elements of conductivity tensor of the crystal are: σ_{xx}, σ_{yy}, σ_{zz} and the anti-symmetric part $\sigma_{xy}=-\sigma_{yx}$. These are obtained by summing up the elements of Eq. (1) for all the valleys. The elements of the resistivity tensor become as

$$\left.\begin{array}{ll} \rho_{xx}=\sigma_{xx}/(\sigma_{xx}\sigma_{yy}+\sigma_{xy}{}^2)\,, & \rho_{zz}=1/\sigma_{zz}\,, \\ \rho_{xy}=\sigma_{xy}/(\sigma_{xx}\sigma_{yy}+\sigma_{xy}{}^2)\simeq 1/\sigma_{xy}\,. & \end{array}\right\} \qquad (2)$$

From Eqs. (1) and (2) ρ_{xx} is known to be proportional to $S\tau^{-1}$, ρ_{zz} to $(S\tau)^{-1}$, whereas ρ_{xy} independent of S and τ. Thus ρ_{xx} and ρ_{zz} show an oscillation, but ρ_{xy} does not.

In spite of the above discussion, the Hall coefficient of Bi shows an oscillation[5)]. The reason, we think, is as follows. In Bi $p \simeq n$, so the leading term of σ_{xy} becomes small, and the oscillation is due to higher order terms of H^{-1} which are neglected in the above.

The period of oscillation is determined by the cyclotron mass $m_c=\alpha_1{}^{-1/2}m$, which is a function of the relative direction of H with respect to the ellipsoid. The variation of ρ_{xx} and ρ_{zz} is generally superposition of the oscillations having different periods, each of which has its origin in one of the valleys. The periods of PbTe are shown in Table for several directions of H.

Table. The periods of oscillation due to each valley. $\Delta(1/H)$ in $e\hbar/m_\perp c\zeta$. $r=m_\perp/m_{/\!/}$.

Valley \ Direction of H	[001]	[111]	[110]
[111], $[\bar{1}\bar{1}\bar{1}]$	$\sqrt{\frac{r}{3}(1+2r)}$	1	$\sqrt{\frac{r}{3}(2+r)}$
$[\bar{1}11]$, $[1\bar{1}\bar{1}]$	$\sqrt{\frac{r}{3}(1+2r)}$	$\sqrt{\frac{r}{9}(1+8r)}$	r
$[\bar{1}\bar{1}1]$, $[11\bar{1}]$	$\sqrt{\frac{r}{3}(1+2r)}$	$\sqrt{\frac{r}{9}(1+8r)}$	$\sqrt{\frac{r}{3}(2+r)}$
$[1\bar{1}1]$, $[\bar{1}1\bar{1}]$	$\sqrt{\frac{r}{3}(1+2r)}$	$\sqrt{\frac{r}{9}(1+8r)}$	r

More general and detailed discussion will be published in the near future[2)].

References

1) Y. Kanai, R. Nii and N. Watanabe: J. Phys. Soc. Japan **15** (1960) 1717.
2) E. Yamada and K. Shogenji: to be published.
3) K. Shogenji and S. Uchiyama: J. Phys. Soc. Japan **12** (1957) 1477; **14** (1959) 1360.
4) R. S. Allgaier: Phys. Rev. **112** (1958) 828; **119** (1960) 554.
5) A. H. Kahn and H. P. R. Frederikse: *Solid State Physics* vol. **9**, ed. by F. Seitz and D. Turnbull (Academic Press, 1959) p. 257.

Note added in proof: Recently, Kuglin et al. (Phys. Rev. Letters **6** (1961) 177.) have found two of the periods listed above.

J. Phys. Soc. Japan **16** (1961) 1476

Optical Constants of LiF in the Extreme Ultraviolet

By Riso Kato

Department of Physics, Faculty of Science, Kyoto University

(Received April 26, 1961)

Reflection and absorption spectra of LiF single crystal were reported in a previous work[1]. Detailed analyses and discussions could not be made, however, because the previous data contained fairly large errors. Data were refined by improving the reflectometer and by careful treatment of specimen surface. Fig. 1 shows the reflection and absorption spectra refined in the present work.

LiF becomes transparent below 11.8 ev and the reflection from the back surface of specimen contributes to the reflectivity in the region. Consequently the observed reflection spectrum shows the minimum and maximum near the tail of fundamental absorption as seen in Fig. 1. The previous data were disturbed by the hydrolysis of crystal surface, because LiF was found to be easily hydrolysed slightly above room temperature in air to give a broad absorption ranging from 12 to 8 ev. The values of relectivity in the transparent region were corrected by the theory of multiple reflection and the phase associated with the reflection characteristic was computed by using Kramers-Kronig relation to get the optical constants from the reflectivity. Corrected values of reflectivity fitted very well with those calculated from known refractive indices in the near ultraviolet. Reflectivities in the region above 13.2 ev contain rather large errors as shown in Fig. 1 and were adjusted so as to give zero absorption in the transparent region in the course of phase computation. The full line in Fig. 1 shows the reflection spectrum, corrected in the above way, used for phase computation.

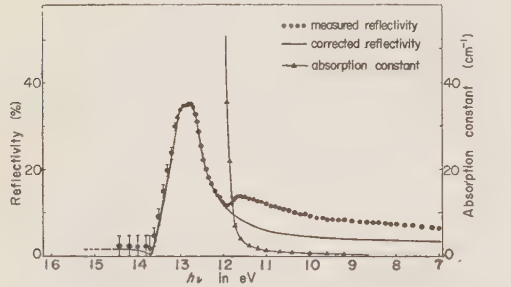

Fig. 1. Reflection and absorption spectra of LiF single crystal measured at room temperature.

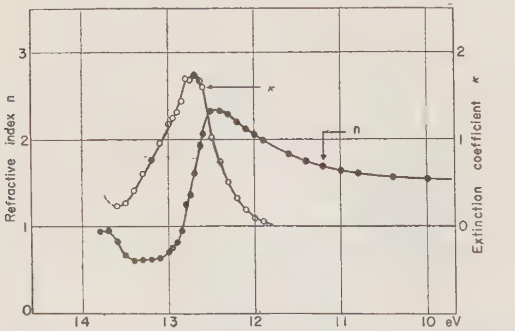

Fig. 2. Refractive index and extinction coefficicnt of LiF *versus* photon energy.

Variations of the refractive index and extinction coefficient *versus* photon energy calculated from the phase and reflectivity are plotted in Fig. 2. The absolute value of absorption constant ($K=4\pi\kappa/\lambda$) and the peak position of the first exciton band at room temperature were obtained as follows: $K_{\max}=2.2\times10^6\ \mathrm{cm}^{-1}$ and $h\nu=12.7\pm0.1$ ev.

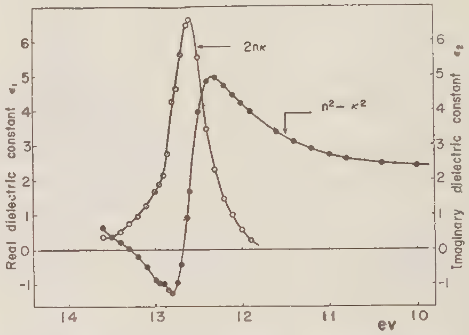

Fig. 3. Real and imaginary parts of dielectric constant of LiF *versus* photon energy.

Real and imaginary parts of dielectric constant ($\varepsilon_1=n^2-\kappa^2$, $\varepsilon_2=2n\kappa$) are plotted in Fig. 3 and the oscillator strength of the present band is obtained from the following formula

$$2n\kappa=\sum_i \frac{\omega_p^2 f_i \omega\beta_i}{(\omega_i^2-\omega^2)^2+\beta_i^2\omega^2},$$

assuming that only $i=0$ term is effective in the region. Constants in the formula $\hbar\omega_0=12.6\pm0.1$ ev, $\hbar\beta_0=0.42\pm0.02$ ev are obtained from Fig. 3 and $\omega_p^2=4\pi Ne^2/m$. The obtained value is 0.069 ± 0.005/electron or 0.42 ± 0.03/ion, which is in good agreement with the theoretical value on NaCl calculated by Dexter[2] on the basis of excitation model.

Details of the experiment and analyses as well as the effect of hydrolysis will be reported in a near future.

References

1) R. Kato *et al.*: J. Phys. Soc. Japan **15** (1960) 2105.
2) D. L. Dexter: Phys. Rev. **108** (1957) 707.

J. PHYS. SOC. JAPAN **16** (1961) 1477~1478

Temporary Bleaching of Color Centers in KCl Crystal

By Masamitsu HIRAI, Mikihiko IKEZAWA
and Masayasu UETA

*Department of Physics, Faculty of Science,
Tohoku University, Sendai.*

(Received May 4, 1961)

Alkali halide crystals colored additively or by X-ray irradiation exhibit several electron captured centers called *F*, *M*, *R* and *N*. Among these centers only *F* has been clarified by Pick[1] to have the property to trap one more electron and convert to *F′* center at low temperature. Concerning other complex centers, there may be possibilities of electron trappings to form *M′*, *N′* etc. on the analogy of *F*→*F′*. However, there are no detailed experiments showing such facts so far we know. It will be due to the thermal unstability of the trapped electrons. The short life trapping states of electron will be observed by the temporary absorption changes of complex centers under the simultaneous illumination of F-light which produces free electrons. Ingenious techniques of temporary bleaching were first adopted by Lambe and Compton[2] and successively by Compton and Klick[3] in NaCl.

A KCl crystal additively colored and containing *F* centers with a concentration of 2.7×10^{16}/cc was cleaved to a piece of $6\times7\times10\,\text{mm}^3$. The crystal was illuminated by F-light at room temperature so as to produce *M*, *N* and *R* centers as shown in Fig. 1 curve (a). The crystal was cooled down to 90°K and was illuminated by a intense dc incandescent lamp filtered to produce *F* band light. The absorption change of the crystal in the region between 400 mμ and 1100 mμ was measured with a chopped light of 8 cps to avoid the error due to the scattered illuminating F-light. Absorption measurements were performed along the direction perpendicular to the illuminating F-light. Curve (b) in Fig. 1 shows the temporary change of the transmission of the crystal thus measured. The ordinate indicates the increase of transmission expressed by arbitrary unit.

As seen from the figure, with the decrease of *F* band, *M* and *N* bands also decrease. The transmission-decrease in the whole region between 500 mμ and 750 mμ is considered to be due to the formation of *F′* band.

Curves (F), (M) and (N) in Fig. 2 show the rates of transmission-increases with time in *F*, *M* and *N* bands, respectively. In the case of *F* band, transmission increases gradually after the start of F-light illumination and it decreases a bit after the illumination is turned off. However, if the crystal is illuminated with red light covering *F′* absorption band region, the transmission of *F* band returns to the initial value. In cases of *M* and *N* bands, after the F-light is turned off, transmissions return to the value before the illumination. Moreover, in the case of *M* band, the decay of the transmission is slower than that in *N* band.

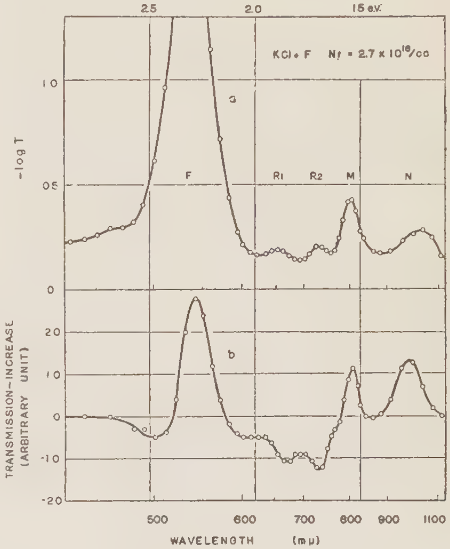

Fig. 1. a: The absorption curve of the crystal containing *F*, *M*, *R* and *N* centers at 90°K.
b: The temporary increases of the transmission of the crystal illuminated with *F*-light at 90°K.

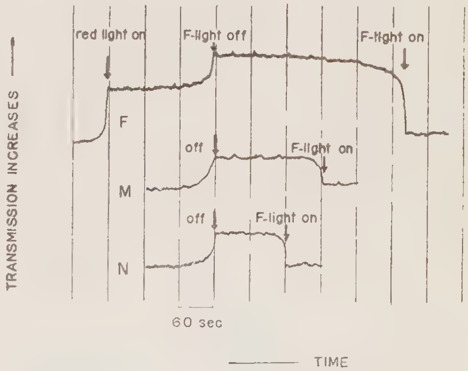

Fig. 2. The transmission changes with time in *F*, *M* and *N* bands.

These facts may show that electrons released from *F* centers are trapped temporarily by *M* and *N* centers forming *M′* and *N′*-type centers and cause decreases of *M* and *N* bands. The *M′* and *N′*-type centers are quite unstable at 90°K and *N′* center is more unstable than *M′*.

The detailed studies of color centers by the temporary bleaching have beeing carried out in KCl crystals in various stages of center formation.

References

1) H. Pick: Ann. d. Physik **31** (1938) 365.
2) J. Lambe and W. D. Compton: Phys. Rev. **106** (1957) 694.
3) W. D. Compton and C. C. Klick: Phys. Rev. **112** (1958) 1620.

J. Phys. Soc. Japan **16** (1961) 1478

Magnetic Annealing Effect in Cobalt

Takashi SAMBONGI and Tadayasu MITUI

Department of Physics, Faculty of Science,
Hokkaido University

(Received May 1, 1961)

Recently, Takahashi and Kōno1) observed that a ferromagnetic anisotropy is induced in Co when annealed in magnetic field. In this effect the allotropic transformation of Co at 417°C2) seems to play an important rôle. The present study was made for the purpose of making clear the origin of this anisotropy induced by magnetic annealing.

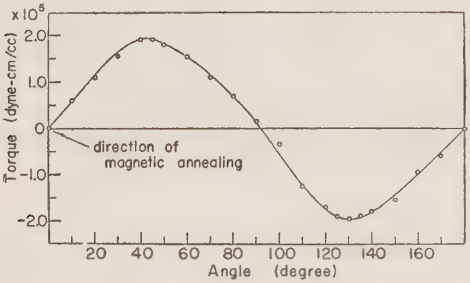

Fig. 1. Torque curve measured at room temperature.

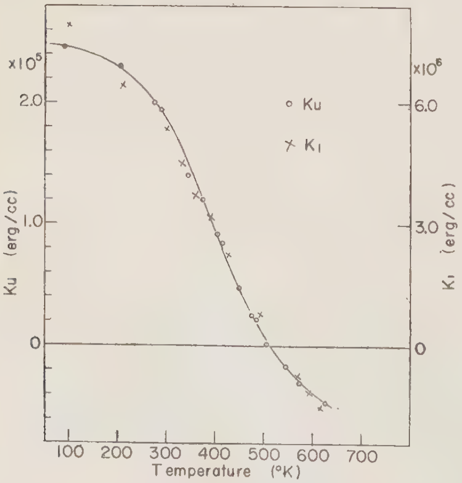

Fig. 2. Temperature dependence of the induced anisotropy, compared with the crystal anisotropy energy measured by Sucksmith and Thompson.

Several polycrystalline specimens were prepared from Co metal of ca. 99.3% purity. After melted in vacuo and annealed at 1000°C, they were machined into disc shape of ca. 15 mm in diameter and ca. 1 mm in thickness. The specimens were annealed at 600°C for 2 hours, and then cooled with cooling rate about 5°/min, in an applied magnetic field of about 8 KOe from above the transformation temperature. Torque curves were measured in effective magnetic field of about 10 KOe by an air-bearing torque magnetometer at room temperature.

An example of them is shown in Fig. 1, which shows a uniaxial anisotropy with the direction of easy magnetization perpendicular to that of magnetic field applied on cooling.

The temperature dependence of the induced anisotropy energy K_u was measured over the temperature range from 90°K to 700°K, compared with the crystal anisotropy energy K_1 measured by Sucksmith and Thompson3) as shown in Fig. 2.

From this result one can deduce the origin of the induced anisotropy. As well known, on the transformation of Co, one of the 4 sets of the {111} plane of f. c. c. phase is conserved parallel to the (00·1) plane of h. c. p. phase, so there are possibilities that one f. c. c. grain is transformed into at most 4 h. c. p. grains of different orientation. When applied magnetic field, each grain will transform preferentially so that the f. c. c. (111) plane of the least angle to the direction of magnetic field should be parallel to the h. c. p. (00·1) plane. So the orientation of h. c. p. grains is no longer completely random and a uniaxial anisotropy is observed with the direction of easy magnetization perpendicular to that of magnetic annealing when measured below 250°C.

In this mechanism the magnetic field may play some rôle only in the process of developing the stacking faults, nuclei of h. c. p. phase4), which lie in the f. c. c. (111) plane with the least angle to the direction of magnetic field.

We propose that contribution of crystal anisotropy energy to the mechanism of this effect may be more important than that of magnetoelastic energy in the dynamics of the allotropic transformation of Co.

The detail will soon be published in this journal.

References

1) M. Takahashi and T. Kōno: J. Phys. Soc. Japan **15** (1960) 936.
2) T. B. Hess and C. S. Barrett: Trans. A. I. M. E. **194** (1952) 645.
3) W. Sucksmith and J. E. Thompson: Proc. Roy. Soc. **A, 225** (1954) 362.
4) A. Seeger: Z. Metallkde. **44** (1953) 247, **47** (1956) 653.

J. Phys. Soc. Japan **16** (1961) 1479

Mössbauer Effect of the Intermetallic Compound UFe_2

By Shigehiro Komura, Nobuhiko Kunitomi,
Poh-Kun Tseng, Naomoto Shikazono
and Hidekuni Takekoshi
*Jepan Atomic Energy Research Institute,
Tokai-mura, Ibaraki-ken*

(Received May 23, 1961)

In the previous note[1] the intermetallic compound UFe_2 has been found to be ferromagnetic with Curie temperature at 195°K. The magnetic moment associated with this ferromagnetism has also been determined to be 1.13 Bohr magnetons per molecule of UFe_2, magnetic moment contributions of each constituent atoms, uranium and iron, are still left to be clarified.

In our present investigation the hyperfine field at the position of Fe^{57} nuclei in UFe_2 has been measured by means of Mössbauer effect. The transmission through the powdered UFe_2 sample of 14.4 kev gamma-ray emitted from Co^{57} incorporated in silicon has been observed at liquid nitrogen temperature as a function of the velocity of gamma-ray source. The UFe_2 sample used for the present experiment is the same one as that prepared in the magnetic measurement[1].

The absorption lines for UFe_2, stainless steel and metallic iron at room temperature as well as that for UFe_2 at liquid nitrogen temperature have been measured for comparison as shown in Fig. 1. The spread of six absorption lines observed for metallic iron at room temperature which are shown schematically in the Fig. 1c) corresponds to the hyperfine field of 330 koe[2] and are taken to be the standard of hyperfine field. One of six absorption lines for metallic iron illustrated in the Fig. 1c) gives the linewidth of the both natural and instrumental origin which is independent of the hyperfine field.

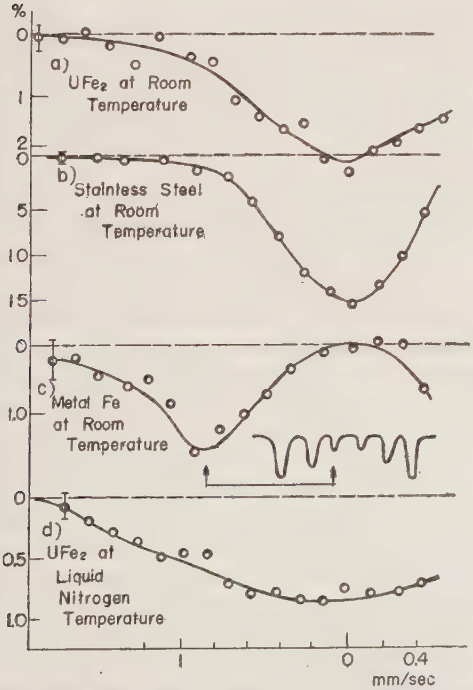

Fig. 1. Absorption spectra obtained with Fe^{57} in UFe_2 and with some other samples as references.

The estimated value for the hyperfine field at the position of Fe^{57} nuclei in UFe_2 at room temperature has been determined from the observed linewidth of Fig. 1a) to be 20 ± 8 keo which is slightly larger than that for stainless steel at room temperature shown in Fig. 1b). The value for the hyperfine field at the position of Fe^{57} nuclei in UFe_2 at liquid nitrogen temperature has also been found from Fig. 1d) to be 65 ± 8 koe which may be compared consistently with the value for the magnetic moment of 1.13 Bohr magnetons per molecule of UFe_2.

The absorption pattern for UFe_2 at liquid nitro-temperature does not resolve into six lines but spreads broadly. Contrary to the expectation from the fact that the intensity of the two outer-most absorption lines is three times larger than that of two central lines in usual Mössbauer experiment of Fe^{57}, the both ends of the pattern decrease gradually with the velocity of the gamma-ray source. This indicates that the hyperfine field of Fe^{57} in UFe_2 may take the fluctuating values below 65 koe. The reason for this is still uncertain because of the possible oxidation of the UFe_2 sample during Mössbauer experiment and the insufficient resolution of the measurement.

The investigation of neutron diffraction for UFe_2 which are now being carried out in our laboratory may clarify the magnetic moment of each constituent atoms in UFe_2 and the origin of the fluctuating hyperfine field further.

The present authors are indebted to Mr. Y. Hamaguchi for his valuable discussions.

References

1) S. Komura, N. Kunitomi, Y. Hamaguchi and M. Sakamoto: preceding note J. Phys. Soc. Japan, **16** (1961) 1486.
2) G. K. Wertheim: Phys. Rev. Letters, **4** (1960) 403.

J. Phys. Soc. Japan **16** (1961) 1480~1481

On Radiations from Plasma in a Static Magnetic Field

By Kenji Mitani and Hiroshi Kubo
Yoshida College, Kyoto University

(Received March 3, 1961)

Gross[1] and Bernstein gave a dispersion relation for plasma oscillation in a static magnetic field. Kato[3] observed the above oscillations in a weak magnetic field. Here it is reported that the radiation which seems to be associated with their theory have been found. Measurements were carried out, by use of a 3 cm microwave radiometer[4], on extraordinary waves radiated from the plasma perpendicularly to the applied magnetic field.

Fig. 1 shows the resonance curves obtained. In each curve, a minor peak appears on each side of the main peak, which, for various reasons, can be considered to be the cyclotron radiation, and will be called C-type peak. Of minor peaks, one on the left-hand side of the mine peak will be called P_1-type peak and the other P_2-type peak. The magnetic field intensity of P_1-type peak is weaker than that of C-type, while the magnetic field intensity of P_2-type is stronger than that of C-type.

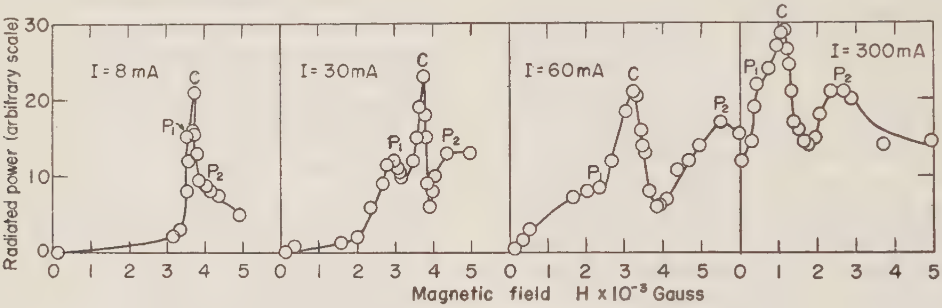

Fig. 1. Resonance curves for various discharge currents.

In Fig. 2, the square of the normalised magnetic strength giving the maximum intensity γ^2 is plotted against the normalised number density of electron η, where γ is defined as the ratio of the cyclotron frequency ω_c to the microwave frequency ω, and η the ratio of the square of the plasma frequency $\omega_p{}^2=4\pi e^2N/m$ to ω^2, in which e, m and N are the charge, mass and number density of electron. N's are the values measured by the probe method in the absence of magnetic field, and then reduced to the case in the presence of magnetic field. In this figure, the crosses (×) show the experimental values for C-type, the solid circles (●) for P_1-type and the open circles (○) for P_2-type; and the solid curve C is obtained from the theoretical relation $\gamma^2=1-\eta$ for cyclotron resonance, where the collision is neglected because its effect is not significant.

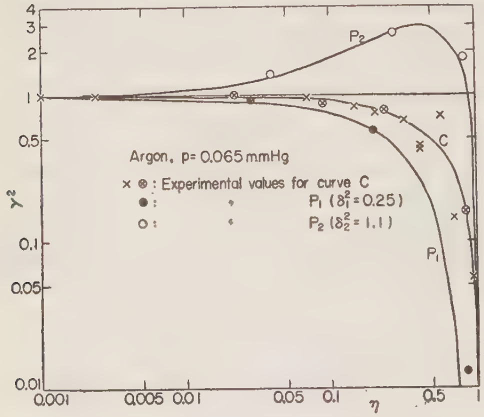

Fig. 2. Dispersion relations for C-, P_1- and P_2-type radiation. The points ●, ○ and ⊗ correspond respectively to the experimental peak values P_1's, P_2's and C's in Fig. 1.

Now the P-type radiation (the radiation at P-type peak) will be compared with the theoretical results by Gross, who gave a dispersion relation for plasma oscillation in a static magnetic field:

$$1-\eta=\tfrac{1}{2}(\gamma^2+\delta^2)\pm\tfrac{1}{2}[(\gamma^2-\delta^2)^2+4\eta\gamma^2]^{1/2}\ ,$$

where δ is ck/ω, in which c is the light velocity and k the wave number in plasma; δ is also expressed by λ/λ_p, in which λ and λ_p are wavelengths in free space and in plasma. Furthermore in the above equation, the positive sign is adapted for $\delta^2<1$ and the negative for $1<\delta^2$. The solid curves P_1 and P_2 were calculated from the above equation for $\delta^2=0.25$ and $\delta^2=1.1$ respectively. These curves agree well with the experimental results. From these values of δ^2, the wavelength of P_1-type and P_2-type peaks are calculated to be about 6 cm and 3 cm in plasma, these values being harmonic in the ratio of 2:1.

Furthermore, it is found in our experiment that, when the P-type radiations exist, the power of cyclotron radiation were several decibels above the level of black body radiation.

In conclusion, it seems most reasonable to relate the P-type radiation with Gross's expression. The authors greatefully acknowledge their indebtedness to Professor S. Kojima at University of Education for his encouragement and helpful discussion. The authors' thanks are also due to Professor I. Takahashi at Kyoto University for his kind suggestion and discussion.

References

1) E. P. Gross: Phys. Rev. **82** (1951) 232.
2) I. B. Bernstein: Phys. Rev. **109** (1958) 10.
3) K. Kato: J. Phys. Soc. Japan **15** (1960) 1093.
4) K. Mitani, H. Kubo and A. Nishino: Nuclear Fusion Research **3** (1960) (In Japan).

J. PHYS. SOC. JAPAN **16** (1961) 1481~1482

Magnetic Annealing of Cobalt

By C. D. GRAHAM, JR.

General Electric Research Laboratory
Schenectady, New York

(Received March 8, 1961)

Takahashi and Kōno have reported very large negative values of the uniaxial magnetic annealing anisotropy K_u in cobalt, and have suggested that this anisotropy is associated with the cubic-to-hexagonal phase change which occurs near 400°C.[1] This note presents a more detailed mechanism for the magnetic annealing, and describes an experiment which confirms the proposed mechanism.

Face-centered-cubic cobalt transforms martensitically to hexagonal cobalt in such a way that the [0001] direction of a hexagonal grain is parallel to a <111> direction of its parent cubic grain.[2] Since there are four <111> directions in a cubic grain, there are four possible orientations for a hexagonal grain within each cubic grain; normally, all four orientations should occur with equal probability. However, in the presence of a saturating magnetic field there will be an energy difference of (K_1+K_2) between hexagonal grains with [0001] axes parallel and perpendicular to the applied field. Here K_1 and K_2 are the first and second crystal anisotropy constants of hexagonal cobalt, at the transformation temperature. At 400°C, according to the data of Sucksmith and Thompson,[3] this energy difference amounts to about 1.6×10^6 erg/cm³, and acts to favor hexagonal grains with [0001] axes perpendicular to the applied field $[(K_1+K_2)<0]$. Thus the presence of a strong field during the transformation should tend to produce a fiber texture in a polycrystalline cobalt sample, with [0001] directions approximately perpendicular to the field applied during cooling. This fiber texture is froxen into the material at all lower temperatures and causes the observed uniaxial anisotropy.

Just below the transformation temperature, the induced uniaxial anisotropy K_u will be positive; that is, the easy direction will be parallel to the field applied during cooling. At about 300°C, the crystal anisotropy (K_1+K_2) goes through zero and becomes positive for lower temperatures; the induced anisotropy K_u must also go through zero at this temperature, since the induced anisotropy results only from the presence of a crystallographic texture in the material. Below 300°C, K_u must therefore be negative, meaning that the easy axis is perpendicular to the field applied during cooling. For all temperatures below the transformation, the temperature dependence of K_u should be the same as that of the crystal anisotropy (K_1+K_2), except that K_u will be negative when (K_1+K_2) is positive, and vice versa.

To test this hypothesis, an untextured polycrystalline cobalt disk, 12.5 mm in diameter by 0.125 mm thick, was cooled in a hydrogen atmosphere from about 900°C to room temperature with a field of 3000 Oe applied along a diameter. A torque curve measured at 10,000 Oe after this treatment showed the presence of a uniaxial induced anisotropy with $K_u=-200{,}000$ erg/cm³, which is about three times larger than the value given by Takahashi and Kōno. This uniaxial anisotropy was then determined as a function of temperature from room temperature up to 325°C, by immersing the sample in a heated silicone oil bath while measuring the torque curves. The results are shown in Fig. 1, along with the values of (K_1+K_2) taken from Sucksmith and Thompson. Both curves go through zero just below 300°C and both are nearly linear with temperature, thus confirming the prediction of the model. The curve of K_u vs. temperature was retraced exactly on returning to room temperature, indicating that no permanent structural changes

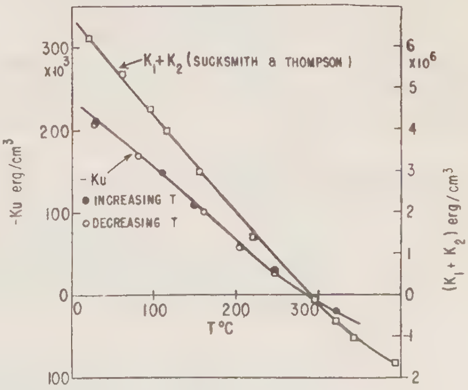

Fig. 1. Induced anisotropy K_u and magnetocrystalline anisotropy (K_1+K_2) vs. temperature.

had occurred on heating.

The measured anisontropy of 200,000 erg/cm^3 at room temperature is about 6% of the value predicted by this model if an initially untextured cubic material is transformed completely to hexagonal cobalt with the maximum possible fiber texture. The predicted torque curves for the induced anisotropy are not exactly of the form $-K_u \sin 2\theta$, largely because of the influence of the K_2 term; the measured torque curves appear to be quite accurately $\sin 2\theta$ in form. The difference is presumably due to smearing out of the ideal texture assumed in the calculation.

I am grateful to J. D. Livingston and J. M. Lommel for helpful discussions of the problem.

References

1) M. Takahashi and T. Kōno: J. Phys. Soc. Japan **15** (1960) 936.
2) E. O. Hall: *Twinning and Diffusionless Transformations in Metals* (Butterworths Scientific Publications, London, 1954) pp. 152 ff.
3) W. Sucksmith and J. E. Thompson: Proc. Roy. Soc. (London) **A, 225** (1954) 362.

J. Phys. Soc. Japan **16** (1961) 1482

Drift Mobility of Photo-Injected Electrons in Hexane-Silicone Mixture

By Pyon-un CHONG and Yoshio INUISHI

College of Engineering, Osaka University, Osaka, Japan

(Received May 9, 1961)

As was reported previously[1) 2)], drift mobility μ of photo-injected electrons in n-Hexane and in Benzene has following characteristics.

(1) They do not show any field dependency upto 0.5 MV/cm being 1×10^{-3} cm^2/sec. V for Hexane and 0.45×10^{-3} cm^2/sec. V for Benzene at 20°C.

These magnitude are much smaller than the value for perfect free electrons in inert liquids[3)].

(2) With decreasing viscosity due to increasing temperature, drift mobility μ increases following a kind of Stokes type law

$$\mu = \mathrm{k}\cdot\eta^{-n} \qquad (1)$$

n is 2 for n-Hexane and 1.5 for Benzene.

From these experimental facts the migration of either attached negative ions or polaron-like electrons following injection of electrons from cathode was speculated to be the mechanism of the conduction in pure liquid.

To clarify these points further, several experiments[4)] have been continued by us with the same apparatus which was described in our previous papers.[1) 2)]

In this paper the mobility of photo-injected electrons in n-Hexane-Silicone oil mixture will be mentioned. The Silicone oil used has mean molecular weight 1200 and viscosity 6×10^{-2} poise at 20°C.

By mixing n-Hexane and the Silicone at various proportion, it has been possible to vary the viscosity of the mixture for a wide range. Fig. 1 shows the dependence of the drift mobility of photo-injected carrier on the viscosity of the mixture. Although mobility decreases with increasing viscosity, it is not possible to cover all range by simple Stokes law (1) with constant n.

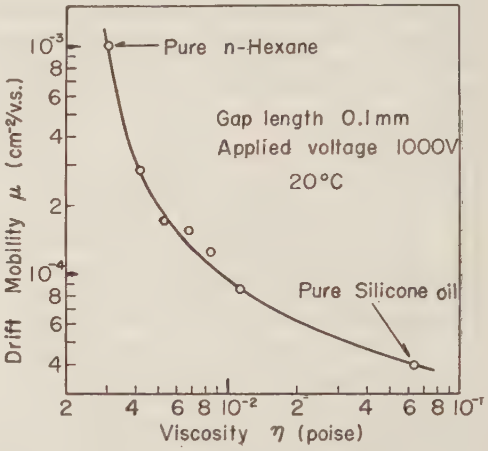

Fig. 1. The relation between μ and η in n-Hexane Silicone oil mixture.

For larger Silicone content n is almost equal to 1 and Stokes type law (1) seems to be valid. These situations may be possibly due to larger electron attachment cross section in Silicone and negative ion migration produced by attachment. On the contrary, the mobility in pure Hexane seems to be abnormally higher than the value obtained from extrapolation of the mixture value. Measurement in n-Hexane vapour shows little attachment. Accordingly we may speculate the migration of polaron in pure Hexane. Initial steep decrease of the mobility with increasing Silicone might be related to the attachment due to Silicone or impurities in Silicone.

References

1) P. CHONG and Y. INUISHI: Tech. Rep. Osaka Univ. **10** (1960) 545.
2) P. CHONG, T. SUGIMOTO and Y. INUISHI: J. Phys. Soc. Japan, **15** (1960) 1137.
3) M. S. MALKING and H. L. SHULTZ: Phys. Rev. **83** (1951) 1051.
4) P. CHONG: Thesis, Osaka University (unpublished)

J. PHYS. SOC. JAPAN **16** (1961) 1483

Magnetic Domain Observation of $BaFe_{12}O_{19}$ by Faraday Effect

By Hiroshi KOJIMA and Kimiyoshi GOTO

The Research Institute for Scientific Measurements, Tohoku University, Sendai, Japan

(Received March 14, 1961)

Magnetic domain of $BaFe_{12}O_{19}$ after magnetizing at various field was observed by Faraday effect. Small single crystals have been prepared by the similar method as Brixner1). That is, 1.67 g Fe_2O_3 with 55 g $BaCl_2$ in an alumina crucible was heated at 1250°C for 4 hr in O_2 stream and cooled at the rate of 5°C/hr to room temperature, then the mixture was washed with hot HCl solution. After magnetic separation black magnetic crystals about 2–3 mm in diameter were obtained and their X-ray powder pattern was in agreement with ASTM File Card 7-276. From these crystals, thin platelets 1–10μ in thickness were selected under microscope and fixed on an ordinary coverglass of 0.15 mm thick with Cemedine.

Domain structure on c-plane was observed by a polarising microscope. The colour of transparent platelets for tungsten lamp were dark red to yellowish orange according to their thickness, so that the contrast of the domain can be increased with red or orange filter. After applying various fields domain structure was observed at elevated temperature up to 250°C without magnetic field. Fig. 1 shows the domain structures of the platelets, 6.0μ thick and the following results were obtained from these investigations:

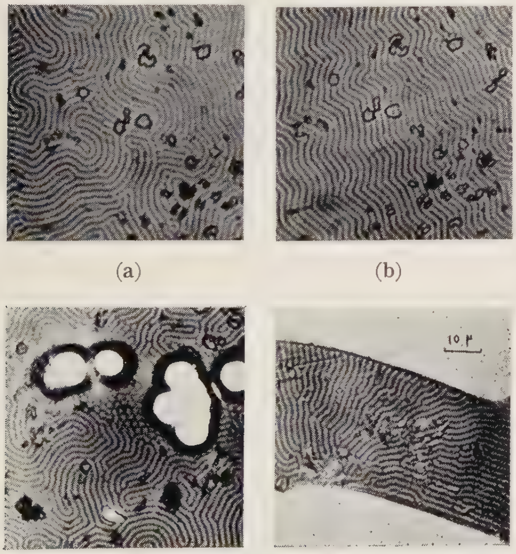

(a) (b)

(c) (d)

Fig. 1. Domain patterns of $BaFe_{12}O_{19}$.
(a) demagnetized state,
(b) after applying 8190 Oe parallel to c-axis,
(c) ‘trapped’ cylindrical domain near holes,
(d) nucleation center after applying 5760 Oe.
Magnification is same for all photographs.

(1) Labyrinth pattern was observed for demagnetized crystal, ((a)).

(2) Comparatively parallel domain was observed after magnetized at high field ((b)), and the critical field from which, opening of the hysteresis loop occurs, was about 6000 Oe and rather high comparing with the results of Kooy and Enz2). After decreasing the field from the region between 2440 Oe and 5760 Oe, the specimen may take the mentioned both kinds of patterns at random case by case.

(3) Cylindrical domain, which is stable only at higher field as reported by Kooy, was often ‘trapped’ near crystal imperfection, i.e. hole, edge or sometimes even in the middle of plane surface, ((c)).

(4) Parallel domain usually spreads from a nucleation center but some crystals have no center at all. These domains were essentially straight but slightly waved and the period became larger when the applyed field was increased.

(5) Saturation field became naturally much higher, if the field was applyed perpendicular to c-axis. In this case, after magnetizing just below saturation, ‘crushed’ labyrinth along the direction of applyed field was observed, which shows that the domain wall parallel to the field is more stable than the perpendicular one.

(6) Domain could hardly observed at 250°C due to the decrease of contrast but increase of domain width could be clearly followed up to about 200°C.

(7) Calculated thickness3) of the platelets from the domain width was reasonable comparing with the value measured by microscope but the increasing rate of domain width during heating was fairly larger than the theoretically expected one.

Details will be published in the near future.

References

1) L. H. Brixner: J. Am. Chem. Soc. **81** (1959) 3841.
2) C. Kooy and U. Enz: Philips Res. Rep. **15** (1960) 7.
3) C. Kittel: Rev. Mod. Phys. **21** (1949) 541.

J. PHYS. SOC. JAPAN **16** (1961) 1484

The Growth of Zinc Sulphide Single Crystals from Flux

By Yo MITA

Research Laboratory, Nippon Electric Company, Kawasaki, Japan

(Received April 24, 1961)

As zinc sulphide is a material that evaporates at the temperature far below the melting point, normal solidifying crystallization technique fails. The single crystals of it are generally obtained by evaporation or vapour-reaction method. The growth from solutions has not been reported so far except hydrothermal synthesis[1] because of the difficulty in obtaining fluxes or solvents that are suitable for this purpose. On the other hand it is well known in the case of phosphor firing that the addition of a few percent of flux, such as alkali halides, promotes the crystallization of phosphor particles. However, the size of the obtained crystals is extremely small and rarely exceeds ten microns.

Attempts have been made to grow single crystals of zinc sulphide with considerable size, using sodium chloride as solvent flux. The schematic figure of the furnace used in the experiments is illustrated in Fig. 1. The growing apparatus is composed of double quarts tubes, the inner of which contains about 100 grams of sodium chloride as flux and ten grams of luminescent pure zinc sulphide powder as starting materials. The outer tube is at first sealed and evacuated at 200°C for a few hours for dehumidification. Then it is warmed up to about 1070°C in the atmosphere of dried nitrogen, where it is held at least ten hours. The system is subsequently cooled at the rate of 10~20 deg/hr above the transition point at 1040°C and then cooled with much faster rate. The crystals are grown as the result of spontaneous nucleation and subsequent growth in the flux or on the surface of the ZnS powder. Most crystals are needle-like with maximum size about 10 mm in length and 0.2 mm in diameter. However, if the system has been warmed up above 1100°C, no needle-like crystals can be obtained, owing presumably to the abrupt change in crystal habit.

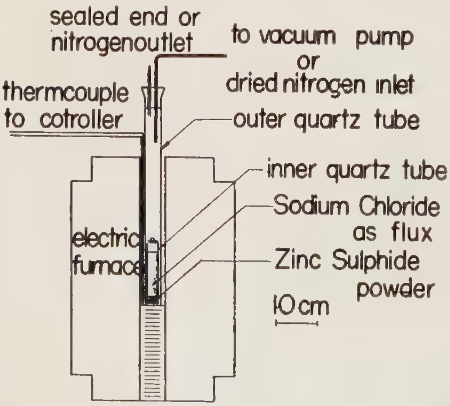

Fig. 1. Cross section of the furnace and growing devices.

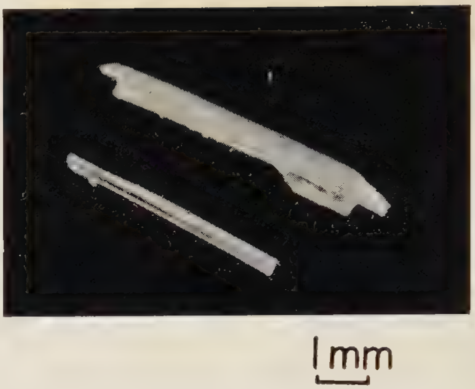

Photo. 1. Single crystals of zinc sulphide.

The X-ray and polarising microscope examinations indicate that the structure of these crystals is mainly wurtzite type, and that their long axis coincides with crystallographic *c*-axis. Mixed structure is found, however, in the crystals that have been slowly cooled beyond the transition point.

Spectroscopic analysis shows the presence of sodium of the amount from 0.05% to 0.5%. It also detects the traces of Fe, Cu, and Si which are supposed to have come from flux.

The crystals show very weak luminescence of yellow-green when irradiated with 3650Å UV light. The emission colour, however, changes to blue-white with increasing exciting light intensity. The phosphorescence is always yellow-green in both cases.

The yellow-green emission seems presumably due to accidental impurities. Another emission of blue-white, may be attributed to host crystals activated with chlorine.

The author would express his sincere gratitude to Dr. Osamu Harashima, who has guided and encouraged him, and to Mr. Ichizo Uchida for his continuous support and valuable discussions.

References

1) A. Kremheller et al.: J. Electrochem. Soc. **107** (1960) 12.
2) F. A. Kröger: J. O. S. A. **39** (1949) 670.

J. PHYS. SOC. JAPAN **16** (1961) 1485

Effect of Neutron Irradiation on Carrier Lifetime in Si

By Kenji MATSUURA and Yoshio INUISHI
Faculty of Engineering, Osaka University

(Received May, 9, 1961)

The effect of neutron irradiation on the carrier lifetime τ in silicon and its annealing process were observed.

Single crystal specimens of N-type Si were irradiated with thermal neutrons in No. 16 hole of Japan Research Reactor No. 1. After a dose of 1.1×10^{15} nvt, the decay in photo-conductivity at room temperature with X_e light pulse (1 μS) excitation was observed by microwave absorption method.[1) 2)] As shown in Fig. 1, the decay curve shows fast recombination decay component (τ_r) and slow thermal release component (τ_t) without D. C. bias light shining, but the longer decay time component disappeared under strong external bias light illumination. Accordingly shallow trapping centers (which were not found before irradiation) must have been introduced in Si by neutron irradiation. These shallow trap formation was not found in case of γ-irradiation. By measuring temperature dependence of slow decay time constant τ_t, energy levels of these shallow traps were found to locate at 0.17 ev above the valence band (or below the conduction band) for 40 Ω cm, Sb-doped pulled Si, whereas 0.11 ev in 20 Ω cm floating zoned N-type Si.

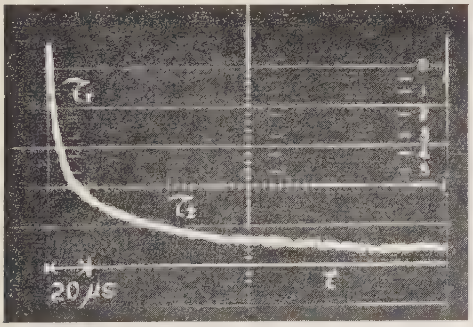

Fig. 1.

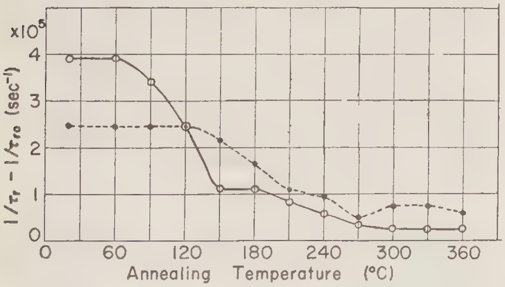

Floating zoned N type Si: Solid line —○—
(τ_{r0}=21 μS. resistivity before irrad.=20 Ω·cm)
Pulled N type Si (Sb doped): Dotted line ---●---
(τ_{r0}=40 μS. resistivity before irrad.=40 Ω·cm)

Fig. 2. Isochronal annealing of two different kind N type Si, following 1.1×10^{15} nvt neutron irradiation. Annealing time of these crystals is ten minutes at each temperature. (τ_{r0} is the recombination lifetime before neutron irradiation.)

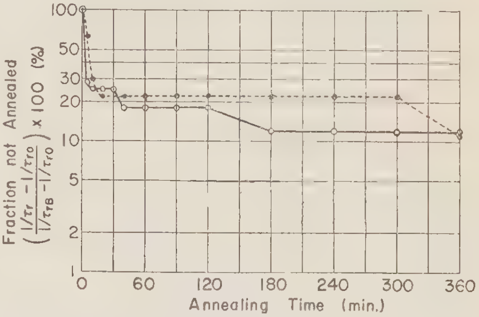

Annealing Temperature=250°C
Floating zoned N type Si: Solid line —○—
(τ_{r0}=15 μS, resistivity before irrad=20 Ω·cm)
Pulled N type Si: Dotted line ---●---
(τ_{r0}=14 μS, resistivity before irrad=40 Ω·cm)

Fig. 3. Isothermal annealing curves of a pulled N-type Si and a floating zoned N-type Si following 1.1×10^{15} nvt neutron irradiation. (τ_{r0} and τ_{rB} are the recombination lifetimes before and jus tafter neutron irradiation, respectively)

The isochronal and isothermal annealing curves of recombination lifetime τ_r are shown in Fig. 2 and Fig. 3 respectively. The annealing curves seem to consist of 2 steps as shown in Fig. 2 and Fig. 3. The activation energy for pulled Si seems to be a little larger than that for floating-zoned Si, and the lifetime is more deeply damaged in the latter than in the former at the same nvt. The abnormal peak in annealing curve which was found in pulled Si in the case of γ-irradiation[2)], was not found in this case.

The relation between lifetime damage and A-center formation is being investigated.

References

1) A. P. RAMSA, H. JACOBS and F. A. BRAND: Appl. Phys. **30** (1959) 1054.
2) K. MATSUURA and Y· INUISHI: J. Phys. Soc. Japan. **16** (1961) 339.

J. PHYS. SOC. JAPAN **16** (1961) 1486

Ferromagnetism of the Intermetallic Compound UFe_2

By Shigehiro KOMURA, Nobuhiko KUNITOMI,
Yoshikazu HAMAGUCHI and Masanobu SAKAMOTO
Japan Atomic Energy Research Institute,
Tokai-mura, Ibaraki-ken

(Received May 23, 1961)

The intermetallic compound UFe_2 has been known to be ferromagnetic[1], but no detailed observation of the magnetic properties of UFe_2 has been reported. In this study the magnetic properties of UFe_2 has been investigated for the temperature range from 300°K down to 100°K and it has been found that UFe_2 really shows an evidence of ferromagnetism with Curie temperature at 195°K.

The materials used for the sample were 99.9% metallic uranium and 99.9% electrolytic iron. The quantities of materials according to the formula UFe_2 were melted together in vacuum with an induction furnace in a crucible of sintered alumina. The materials were held at 1300°C for an hour, then cast into a graphite vessel and cooled down naturally to room temperature. The sample has been proved to be stoichiometric within 1% by chemical analysis and no extra lines other than UFe_2 have been observed in X-ray diffraction patterns.

The temperature variation of magnetization of UFe_2 under various magnetic fields up to 6.5 koe has been measured over the temperature range from 225°K to 104°K and replotted isothermally as a function of field as given in Fig. 1. By extrapolating the plots to zero field at each temperature by means of the least square method using the formula

$$J(H, T)=J(O, T)+aH-b/H^2\ ,$$

the temperature dependence of the spontaneous magnetization of UFe_2 has been obtained as shown in Fig. 2. The Curie temperature of 195°K and the spontaneous magnetization at absolute zero of 18.0 emu/g and hence the effective Bohr magneton number of 1.13 per molecule of UFe_2 have been determined from Fig. 2.

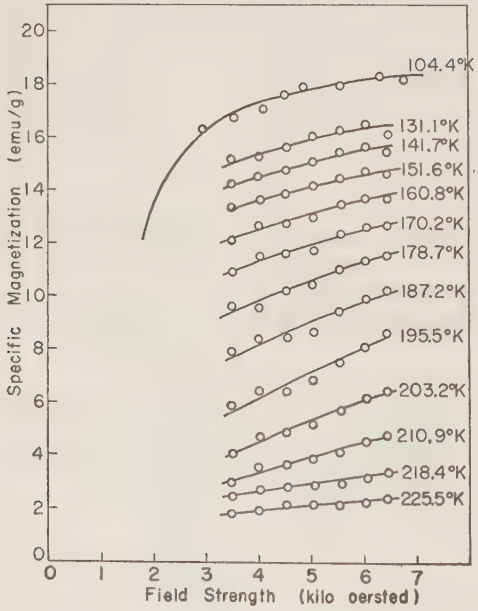

Fig. 1. Magnetization curves of UFe_2 at various temperatures.

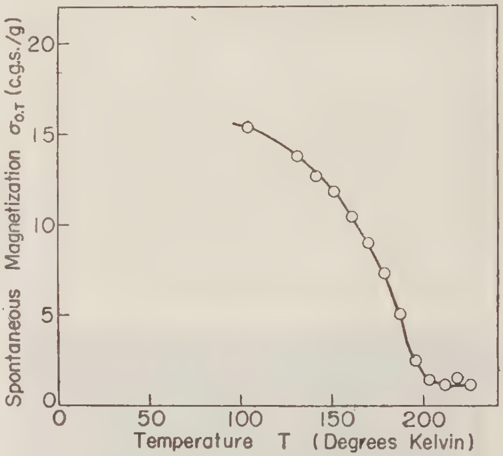

Fig. 2. Spontaneous magnetization vs. temperature curve of UFe_2.

It is interesting to compare the present result with that for the antiferromagnetic UMn_2[2] which shows lambda type anomaly of susceptibility at 260°K with a small parasitic ferromagnetism below 230°K. As UMn_2 and UFe_2 are isostructural, the study of the ternary alloys of these three elements may reveal some interesting information concerning the electronic structure and are now in progress in our laboratory.

The authors express their thanks to Mr. H. Watanabe for the sample preparation and to Mr. H. Motohashi for-X-ray analysis.

References

1) P. Gordon: Thesis, Department of Metallurgy, Massachusetts Institute of Technology, 1949 (unpublished)
2) S. T. Lin and A. R. Kaufmann: Phys. Rev., **108** (1957) 1171.

J. PHYS. SOC. JAPAN **16** (1961) 1487~1488

Oscillations in a Plasma in a Weak Magnetic Field

By Shoji KOJIMA, Eiichi KAWASAKI* and Kiyoe KATO

Tokyo University of Education, Otsuka, Tokyo

(Received April 8, 1961)

One of the authors (K. K.) reported the plasma type oscillations in a bounded plasma in a weak external magnetic field[1]. Here similar experiments are performed at somewhat different conditions, and standing waves between electrodes are observed. These happen when either the discharge tube has the cathode of a good electron emission or the pressure of the tube is sufficiently low.

The discharge tubes were filled with mercury vapour. When the pressure of the tube was about 10^{-4} mm Hg, the oscillations were detected by a super-regenerative detector adjusted to the frequency of 714 Mc. A result is reproduced as a function of discharge current I_p and of magnetic field strength H in Fig. 1. The intensities of oscillations I_n which were measured simultaneously on a oscilloscope are also shown in the same figure. It is found from these results that the oscillations have large dependence on the discharge current, but small on the magnetic field except for quenching at $f_d = n \cdot f_c$, where f_d is the frequency of the detector and f_c the electron cyclotron frequency. Such oscillations were investigated in detail in the region from 250 gauss to 450 gauss when the pressure was 8×10^{-4} mm Hg and it was observed that they have the fine structure as shown in Fig. 2. Then, the existence of the standing waves between electrodes was verified and numbers of half-waves were measured by a movable probe. The obtained number is indicated at the corresponding oscillation in the same figure. The fine structure seems to be originated from change o the number.

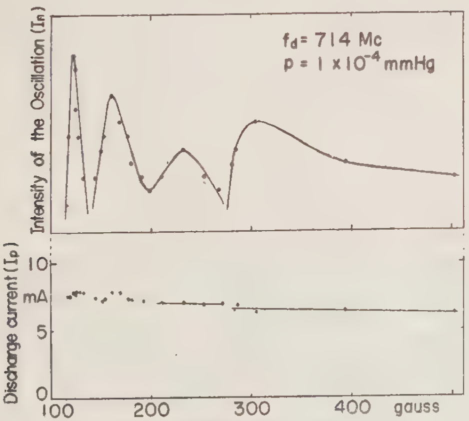

Fig. 1. Plots of discharge current *vs.* external magnetic field strength for the oscillations of constant frequency, and change of intensity of of the oscillation.

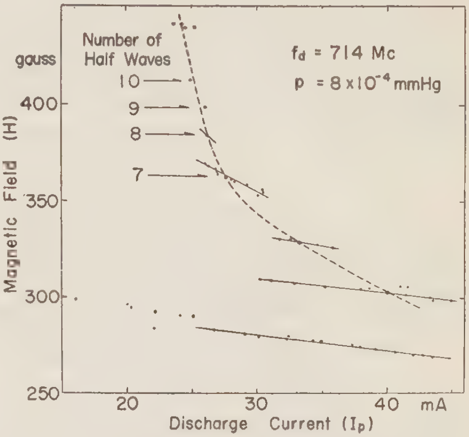

Fig. 2. Plots showing relation of magnetic field strength and discharge currents which generate the oscillations of 714 Mc.

In the previous experiments, only the weak electron beam could be obtained because of the higher pressure and of the poor electron emission of the cathode, and by it the local oscillation was excited mainly. Such local oscillations were observed without external magnetic field by Merrill and Webb[2], Kojima et al.[3] and Mahaffey[4]. In the previous paper, it was reported that the local oscillation propagates predominantly in a direction perpendicular to the magnetic field, which was applied parallel to the discharge current. Now that the pressure is low and the tubes have cathodes of a excellent electron emission characteristic in the present experiment, the strong electron beam can be obtained. This strong electron beam excites the plasma oscillation along its path. This phenomenon was verified with a external electron beam by Boyd et al.[5] and Kharchenko et al.[6]. The standing waves between electrodes are formed by the beam when the plasma frequency is adequate against the distance between electrodes. Such standing waves will grow up to the perfect ones of Looney-Brown type[7] in the suitable uniform plasma. Hence they propagate in a direction parallel to the magnetic field and are almost indepent of its strength.

References

1) K. Kato: J. Phys. Soc. Japan **15** (1960) 1093.
2) H. J. Merrill and H. Webb: Phys. Rev. **55** (1939) 1191.

---

* Nihon University, Kandasurugadai, Tokyo.

3) S. Kojima, K. Kato and S. Hagiwara: J. Phys. Soc. Japan **12** (1957) 1276. S. Kojima, K. Kato, S. Hagiwara and R. Matsuzaki: J. Phys. Soc. Japan **14** (1959) 821.
4) D. W. Mahaffey: J. Electronics and Control **6** (1959) 193.
5) G. D. Boyd, L. M. Field and R. W. Gould: Phys. Rev. **109** (1958) 1393.
6) I. F. Kharchenko, Ya. B. Fainberg, R. M. Nikolaev, E. A. Kornilov, E. A. Lutsenko and N. S. Pedenko: Sov. Phys. JETP **11** (1960) 493.
7) D. H. Looney and S. C. Brown: Phys. Rev. **93** (1954) 965.

J. PHYS. SOC. JAPAN **16** (1960) 1488~1489

ESR Spectra of Irradiated Polyvinylalcohol and Its Related Compounds

By Seiji OGAWA*

Japanese Association for Radiation Research on Polymers, Tokyo

(Received April 18, 1961)

ESR Spectrum of γ-irradiated polyvinylalcohol (PVA) is of a superposition of two types of patterns which are easily separated at suitable conditions. One of them is a triplet pattern spaced by 35 gauss and the other is a diffuse singlet which has longer life at room temperature but more rapidly decays near the second order transition temperature than the former.

As in the cases of other various organic solids, the reasonable interpretation of those spectra has not been well established. The obscurity in the interpretation of ESR spectra of organic free radicals trapped in solid state may partially be caused by the fact that the two protons of β-methylene group bonded to the central carbon atom where the unpaired electron is localized do not always contribute equally to the hyperfine structure of ESR spectrum[1].

Characteristic ESR spectrum of irradiated cyclohexanediol-1, 4 is triple triplet (Fig. 1-a). As the interpretation of the spectrum the following considerations may be reasonable: In the free readical

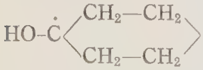

$\mathrm{HO}\text{-}\dot{\mathrm{C}}\langle{}^{\mathrm{CH_2-CH_2}}_{\mathrm{CH_2-CH_2}}\rangle\mathrm{CHOH}$

the two axially bonded protons of the two β-CH_2 groups contribute to the hyperfine structure with splitting 37 gauss and the two equatorially bonded protons with 11 gauss. These splittings are reasonable values, satisfying

$$\Delta H=40\cos^2\theta\,,\qquad \theta_e-\theta_a=120^\circ\,.$$

Here θ denotes the rotation angle between the C–H bond and a p-orbit of the unpaired electron around the C–C bond.[1)-3)]

In the case of messo-pentanediol-2, 4, which resembles to PVA in chemical structure, a double quartet spectrum (Fig. 1-b) is obtained at room temperature and the spectrum changes to the one as shown in Fig. 2-c when cooled to or below 110° K. This change is reversible. This indicates that the rotation of the CH_3 group bonded to the central carbon atom of the free radical is not free enough at low temperature. The chemical structure of the corresponding free radical may be considered as

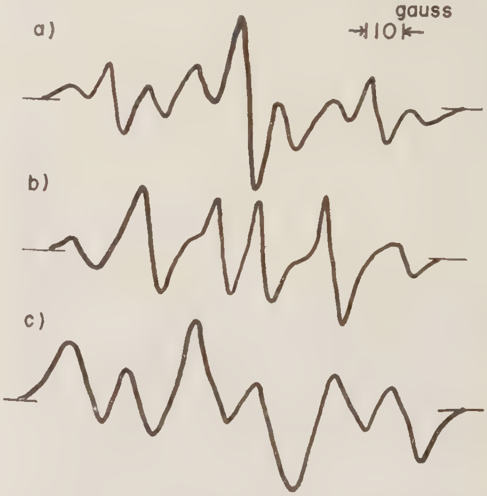

Fig. 1. ESR spectra of irradiated alcohols.
a) Cyclohexanediol-1, 4. Splitings, 37±2 gauss and 11±2 gauss. Line width, 6 gauss.
b) Pentanediol-2, 4 at 300°K. Splittings, 32±2 and 21±2 gauss. Line width, 6 gauss.
c) Pentanediol-2, 4 at 77°K. Splittings, 35±2 and 16±2 gauss. Line width, 12 gauss.

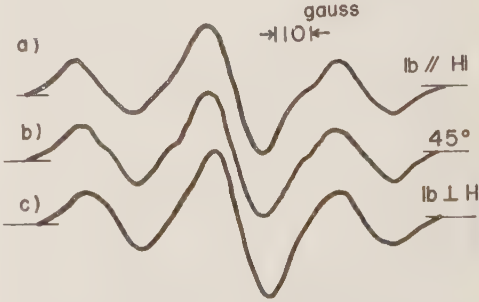

Fig. 2. ESR spectra of irradiated PVA fibre (draw ratio 10).
a) b-axis parallel to magnetic field **H**.
b) b-axis rotated by 45° to **H**.
c) b-axis normal to **H**.
Splitting, 35±3 gauss. Line width, 15 gauss.

---

* On leave from Dai Nippon Spinning Company, Ltd.

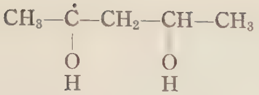

$$\mathrm{CH_3{-}\underset{\underset{H}{O}}{\dot{C}}{-}CH_2{-}\underset{\underset{H}{O}}{CH}{-}CH_3}$$

One proton of the CH_2 group is to lie on the nodal plane of the p-orbit of the unpaired electron and the free radical could take such a steric configuration if the original hydrogen bonds in the crystal reserved almost completely.

In the case of PVA the triplet pattern may be interpreted similarly as pentanediol-2, 4. The free radical which corresponds to the triplet pattern is known to be trapped almost in crystalline parts of irradiated PVA and the triplet pattern of orientated PVA fibre, thermally elongated by the ratio of drawing, 10, does not display the orientation dependence which is expected for α-H. The splitting of 35 gauss is also too large for α-H. (Fig. 2-a, b, c) So it seems reasonable to consider that the free radical does not contain α-H and the structure is $\mathrm{\sim CH_2{-}\underset{OH}{\dot{C}}{-}CH_2\sim}$. It can be said safely that the identification of free radicals in solid state is difficult for a system without some regularity in the steric configuration of β-H.

The author would like to express his thanks to Dr. E. Nagai for his offering pentanediol-2, 4.

References

1) H. M. McConnell: J. Chem. Phys. **32** (1960) 1535.
2) A. D. McLachlan: Molec. Phys. **1** (1958) 233.
3) P. G. Lykos: J. Chem. Phys. **32** (1960) 625.

J. PHYS. SOC. JAPAN **16** (1961) 1489

Emission Spectra of Potassium Bromide-Thallium Phosphors

By Tokumichi TAMAI and Eiichi MATSUI

Department of Physics, Faculty of Science, Kyoto University

(Received April 26, 1961)

Emission spectra of potassium bromide-thallium phosphors have been studied at liquid nitrogen, dry ice plus alcohol, and room temperatures. Single crystals were the same ones whose absorption spectra have been reported[1]. Monochromatic excitation was provided by a quartz prism spectrometer with a high pressure xenon are lamp; the intensity of emission was measured at right angles to the crystal by an RCA 1P28 photomultiplier after dispersion of the emission in a Beckman type monochromator. Spectral sensitivity of the photomultiplier was taken from the data in the RCA tube handbook.

Emission spectra of the potassium bromide-thallium phosphors have been reported by several authors[2]. The present authors have obtained results slightly different from previous investigators at A and C bands and also found the emission excited at B band. Fig. 1 shows emission spectra at three different temperatures. Emission curves excited at A, B and C bands were the same. The emission curve at room temperature shows a single broad flat-topped peak centered at 350 mμ. The curve at liquid nitrogen temperature consists of two well-resolved bands at 317 mμ and 365 mμ. Both bands show approximately Gaussian shape. Further discussion with detailed measurements will be reported in a near future.

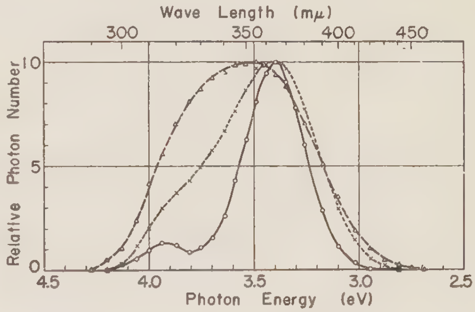

Fig. 1. Emission spectra of potassium bromide-thallium phosphor.
Measurements; ○: at liquid nitrogen temperature, ×: at dry ice plus alcohol temperature, △: at room temperature.

The authors would like to exprees their gratitude to Prof. Y. Uchida for his kind guidance and continual interest in the work.

References

1) T. Tamai: J. Phys. Soc. Japan **15** (1960) 2116.
2) W. von Meyeren: Z. Phys. **61** (1930) 321; P. Pringsheim: Rev. Mod. Phys. **14** (1942) 132; H. Lautz and H. Muuss: Z. Phys. **155** (1959) 531; P. D. Johnson and F. E. Williams: Phys. Rev. **117** (1960) 964.

J. PHYS. SOC. JAPAN **16** (1961) 1490

Tetragonal Distortion in Copper Manganite-Chromite System

By Syôhei MIYAHARA, Kiyoshi MURAMORI
and Naoki TOKUDA

Department of Physics, Faculty of Science, Hokkaido University, Sappro, Japan

(Received May 11, 1961)

According to Dunitz and Orgel[1] cupric and manganese ions in spinel crystals give rise to crystal distortions of a type of $c/a<1$ and $c/a>1$ for occupations of tetrahedral and octahedral sites respectively. $CuCr_2O_4$ in which cupric ions are placed in tetrahedral sites, has been confirmed experimentally to be a tetragonal structure with $c/a<1$[2]. In $CuMn_2O_4$ where cupric and manganese ions are placed in tetrahedral and octahedral sites respectively, directions of distortions by both ions in tetrahedral and octahedral sites are opposite and therefore these distortions will be partly compensated. In order to investigate the crystal structure in such a situation as in $CuMn_2O_4$, copper manganite-chromite system have been studied.

Specimens are prepared from powders of CuO, Cr_2O_3 and Mn_3O_4 which are made by calcining each salts. The mixtures are fired for three days in air at 800°C. Both specimens cooled slowly from 800°C to room temperature at the rate of 15°C/h and quenched in water have been measured with a X-ray diffractometer.

Lattice parameters of the system at the room temperature are shown Fig. 1. The system has a cubic structure in the range $0\leqq a\leqq 1.0$ and a tetragonal structure with $c/a<1$ in the range $1.0<a\leqq 2.0$ where a cubic structure coexists except $a=2.0$. In the cubic region lattice parameters of specimens depend on a heat treatment and the degree of the dependence decrease with the increasing of the chromium concentration. Therefore it will be caused by manganese ions distorted oppositely to cupric ions. In the two phase region, increasing the chromium composition the intensity of the tetragonal phase decreases continuously and disappears at a $a=2.0$. On the other hand the intensity of the cubic phase decreases continuously with the decreasing of the chromium concentration and disappears at $a=1.0$.

As is shown in Fig. 1 increasing chromium concentration the lattice parameter of the cubic structure in the two phase region deviates gradually from cube root of the unit cell volume of the tetragonal structure.

As is shown in Fig. 2, the tetragonality is gradually decreased by the substitution of the manganese ions for the chromium ions, it will be however seen that the tetragonality remains even near the specimen where the tetragonality phase disappears.

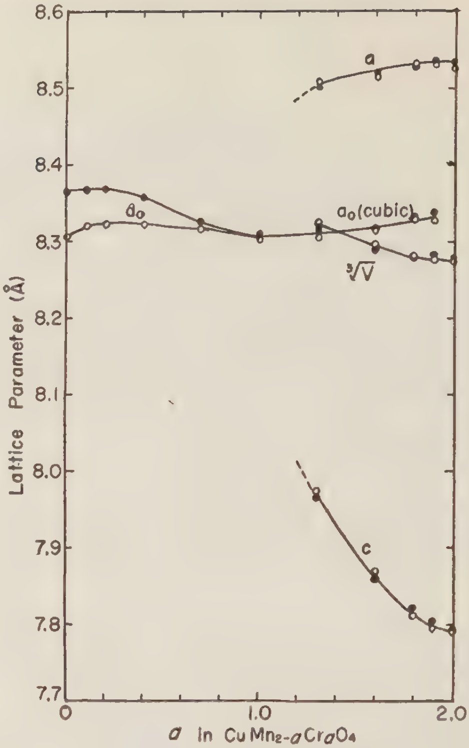

Fig. 1. The lattice parameter versus chromium concentration a.
○: specimen cooled slowly.
●: specimen quenched in water.

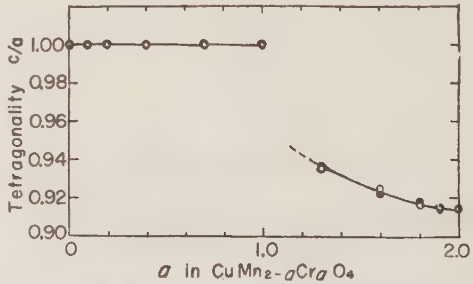

Fig. 2. The tetragonality versus chromium concentration a.
○: specimen cooled slowly.
●: specimen quenched in water.

It is noticed that in the cubic rigion the lattice parameter and the diffraction line width of the specimen depend on a heat treatment of the specimen, while in the two phase region, they do not depend on it and even of the intensities of the both structures do not.

References

1) J. D. Dunitz and L. E. Orgel: J. Phys. Chem. Solids **3** (1957) 20.
2) S. Miyahara and H. Ohnishi: J. Phys. Soc. Japan **12** (1956) 1296.

BACK NUMBER

SUPPLEMENT
of the
Progress of Theoretical Physics

1960 (No. 13—No. 16, $1.00 (¥ 300) per copy) .... **$4.00** (¥ **1,200**)

No. 13. General Theory and Numerical Tables of Clebsch-Gordan Coefficients .... T. Shimpuku
Spinor Field and Its Transformations .... Z. Tokuoka

No. 14. Properties of *d*-Electrons in Complex Salts. I–III .... M. Kotani, Y. Tanabe & S. Sugano

No. 15. Formal Theory of Green Functions .... T. Kato, T. Kobayashi & M. Namiki
Some Aspects of Many-Body Problem .... N. Fukuda & Y. Wada

No. 16. A Study on the Structure of the Extensive Air Shower .... S. Fukui, H. Hasegawa, T. Matano, I. Miura, M. Oda, K. Suga, G. Tanahasi & Y. Tanaka
Heavy Primary Cosmic Radiations—*Prince Albert Project*— .... H. Aizu, Y. Fujimoto, S. Hasegawa, M. Koshiba, I. Mito, J. Nishimura & K. Yokoi
Rapid Thermonuclear Reactions in Supernova Explosion .... S. Hayakawa, C. Hayashi & M. Nishida

---

1961 (No. 17—No. 20, $1.00 (¥ 300) per copy) .... **$4.00** (¥ **1,200**)

No. 17. (Introduction by Syoten Oka)
Theoretical Study on the Effective Magnetic Moments of Some Hemeproteins .... M. Kotani
Physical Chemistry of Muscle Protein "Actin" .... F. Oosawa, S. Asakura & T. Ooi
The Role of "Relaxing Factor" in Contraction-Relaxation Cycle of Muscle .... S. Ebashi
Interactions of Plasma Proteins and Polymeric Materials .... H. Noguchi
Aggregation of Polyelectrolytes in Solutions .... N. Imai
Roles of the Hydrogen Bond System in Biologically Important Molecules .... R. Itoh
Ein quantenchemischer Einblick für Biosynthese .... K. Ohki
Approach to the Determination of Nucleotide Sequence in Nucleic Acids .... F. Egami
Infrared Spectra and Secondary Structure of Deoxyribonucleic Acid .... M. Tsuboi
Ribonucleic Acid and Protein Synthesis .... M. Takanami & S. Osawa
DNA-mediated Transformation in Bacteria .... H. Saito
A Biophysical Consideration of Radiation Mutagenesis .... S. Kondo
Feedback Mechanism of Chemical System from the Viewpoint of Information Technology .... M. Sugita

No. 18. Parametric Integral Formulas and Analytic Properties in Perturbation Theory .... N. Nakanishi
Wightman Functions, Retarded Functions and Their Analytic Continuations .... H. Araki

No. 19. Structure of Elementary Particles (to be published during 1961).

No. 20. Origin of Cosmic Rays; Stellar Evolution (to be published during 1961).

PROGRESS OF THEORETICAL PHYSICS

CONTENTS

Progress of Theoretical Physics Vol. 24, No. 4, October 1960

Energy Spectrum and Scattering Problem in Quantized Field Theory .... Shūkō AZUMA..689
Flow over a Wavy Wall in Magneto-Gas-Dynamics. Part I—*Equilibrium Flow*— .... O. P. BHUTANI..721
On the Principle of Invariance in a Semi-Infinite Inhomogeneous Atmosphere .... Sueo UENO..734
Local Properties in Non-Equilibrium Systems .... J. M. BLATT..741
Nuclear Potential in Many-Body Problems .... J. OSADA and M. TAKEDA..755
Internal Quantum States of Hyperspherical (Nakano) Relativistic Rotators .... D. BOHM, P. HILLION and J. P. VIGIER..761
On the Nucleon-Nucleon Scattering Phase Shifts and the High Energy Nucleons Elastically Scattered from Light Nuclei .... Yoshiyuki SAKAMOTO..783
Photodisintegration of the Deuteron in Medium Energy Range and the Pion Theoretical Nuclear Forces .... J. IWADARE and M. MATSUMOTO..797
A Quantitative Investigation on the "Compositeness" of a Particle .... G. KONISHI and K. YAMAMOTO..817
Propagation of Shock Waves in Inhomogeneous Gases. III—*Spherical Shock Waves*— .... Yôrô ÔNO..825
Symmetrical Properties of Two-Dimensional Ising Lattices .... I. SYOZI and S. NAYA..829
P-Wave Pion-Pion Interaction .... Yoneji MIYAMOTO..840
The Meissner Effect in the Quasi-Chemical Equilibrium Theory of Superconductivity .... J. M. BLATT..851
Elastic Ether Theory of Elementary Particles. I—*Classical Theory*— .... Hideo FUKUTOME..877
Collective Excitation of Electrons in Degenerate Bands. II—*Collective Excitations in a Metallic p-Band*— .... Takeo IZUYAMA..899
Letters to the Editor:
  Remarks on the Viscous Dissipation in Relativistic Hydrodynamics .... M. HAMAGUCHI..908
  A Note on Exciton Multiplicities .... R. S. KNOX..909
  On Mass Formula and New Image of Elementary Particles .. A. OHMAE..910
  On the New Constant and the Strangeness .... A. OHMAE..913
  Birkhoff's Theorem for Electromagnetic Fields in General Relativity .... A. DAS..915
  Moving Effect of Nucleon to Meson Field .... T. SASAKAWA..917
  0^- Second Excited State of ^{32}S .... T. WAKATSUKI, Y. HIRAO, E. OKADA and I. MIURA..918
  Distribution of Particles in a Low Density Fermion System with Attractive Interactions .... Y. WADA..920

Price $ 1.25 per copy
$ 15.00 per year (postage inclusive)
Annual dues for foreign members (individual subscribers)
$ 12.00 (postage inclusive)
" for foreign members of the Physical Society of Japan
$ 10.00 (postage inclusive)

Application for membership, subscriptions and orders for back numbers should be sent, directly or through book-dealers, to

The Publication Office
in
Yukawa Hall, Kyoto University, Kyoto, Japan

. . . .

JOURNAL OF THE PHYSICAL SOCIETY OF JAPAN, Vol. 16, No. 8, AUGUST, 1961

The Second Excited State of Sn^{120}

By Mitsuhiro KAWAMURA, Atsushi AOKI
Department of Physics, Kyoto Prefectural University, Kyoto
and Hidetsugu IKEGAMI
Institute for Nuclear Study, University of Tokyo, Tokyo

(Received April 26, 1961)

The directional correlation and the polarization-direction correlation of the 1.03 Mev–1.17 Mev gamma-gamma cascade in Sn^{120} have been measured. It is found that the spin and the parity of the second excited state of Sn^{120} is 4 and even, respectively.

§1. Introduction

McGinnis[1)] proposed the decay scheme of Sb^{120m} having a half-life of 5.8-day, on the basis of the measurements of the spectrum of gamma ray and that of conversion electron. One of the present authors[2)] (H. I.) revised recently the decay scheme of Sb^{120m}, as shown in Fig. 1.

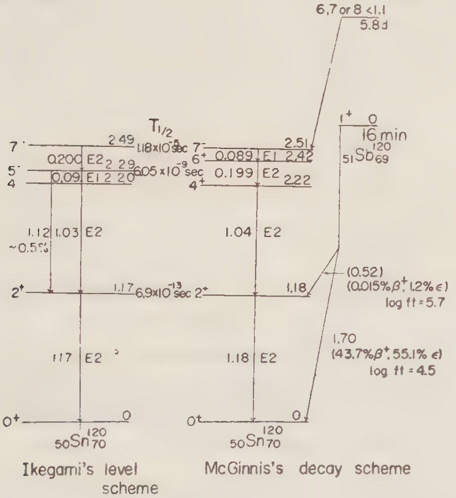

Fig. 1. Revised level scheme of Sn^{120} by Ikegami confirmed partly by present work. Decay scheme of Sb^{120m} proposed by McGinnis is also shown.

For the medium weight even-even nuclei to which Sn^{120} belongs, several nuclear models[3)–5)] are used to explain the level spacings, the spins and the parities of the excited states as well as the transition probabilities. The second excited state of Sn^{120} is rather considered as the vibrational state than as the rotational state from the ratio of the energy of the second excited state to that of the first excited state. According to the quadrupole vibrational model of the even-even nuclei with spherical equilibrium shape, this level is expected as the degenerated two-phonon state having the level assignment of either 4^+, 2^+ or 0^+. Moreover, in the case of the spin value 2 of the second excited state, the transition to the first excited state from the second excited state, is characterized by the predominant E2 transition in Scharff-Goldhaber and Weneser's free vibrational model[3)], while by the predominant M1 transition in Shapiro's prediction[6)]. Therefore, in order to resolve the ambiguity of the level assignment and the character of the gamma ray, it is very interesting that the directional correlation and the polarization-direction correlation measurements of the 1.03 Mev–1.17 Mev gamma-gamma cascade in Sn^{120} are performed.

§2. Source preparation and Gamma Ray Spectra

1) *Source preparation*

The 5.8-day Sb^{120m} was prepared by the irradiation of natural tin metal containing a fractional chemical impurity of about 1.7×10^{-5} with an internal beam of 12–14 Mev proton in a 64 inch cyclotron at the Institute for Nuclear Study, University of Tokyo, leading to the reaction Sn(p, n)Sb. Irradiated tin was dissolved in aqua regia, then converted into 8N hydrochloric acid solution and extracted with isopropyl-ether repeatedly. The organic layer was washed with 3N hydrochloric acid and the solvent was evaporated off in the presence of 3N hydrochloric acid containing a small amount of hydro-oxylamine hydrochloride. This residual acid solution was used as the source for the measurement of gamma ray spectrum and the directional correlation experiment. In the measurement of the polarization-direction correlation experiment, the source was electro-deposited onto the thin copper foil and made into a small ball and stuffed in a vinylchloride container whose wall thickness was about 1 mm and its volume 1 mm$\phi \times$2 mm.

2) Gamma ray spectra

The single gamma ray spectra were measured with a 20-channel pulse-height analyzer, as shown by curve A in Fig. 2.

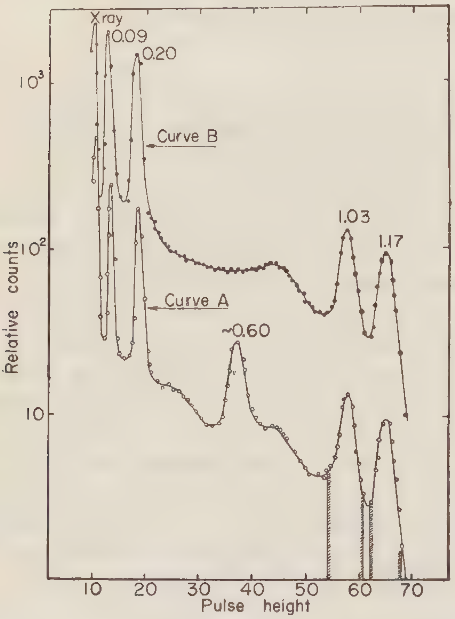

Fig. 2. Gamma ray spectra of Sb^{120m}. Curves A and B give the spectra obtained from natural and enriched tin, respectively. The shaded portions represent the windows of the pulse-height analyzers in the measurement of the directional correlation.

The peaks corresponding to the 0.09, 0.20, 1.03 and 1.17 Mev decay with a half-life of about 6-day, but the peak appearing at about 0.6 Mev decays with a half-life of about 3-day. The latter peak was considered reasonably as the composed peak of the cascade gamma rays[7)] of Te^{122} following the decay of Sb^{122} arising from the reaction $Sn^{122}(p, n)Sb^{122}$. In Fig. 2, curve B was obtained from 98% enriched Sn^{120} whose chemical form was SnO_2. The peak corresponding to about 0.6 Mev disappears completely.

§ 3. Directional Correlation Measurement

The source material was prepared in the form of $SbCl_3$ in HCl solution and filled in a 5 mm in diameter and 5 mm long Lucite case whose wall-thickness was 2.0 mm. The attenuation of the correlation coefficient due to the quadrupole interaction in the intermediate state in the liquid form is considered to be negligibly small, as the mean life of the first excited state of Sn^{120} is very short which is measured as 1.0×10^{-12} sec from the Coulomb excitation experiment[8)]. A gamma ray goniometer at the Institute for Nuclear Study was used. The Dumont 6292 and RCA 6342 photomultiplier tubes mounted with NaI(Tl) crystals of $1^3/_4$ in. $\phi \times 2$ in. were used as detectors. The distance between the source and the front face of each crystal was 7 cm. The coincidence circuit was operated at a resolving time $2\tau = 4 \times 10^{-7}$ sec and the windows of the pulse-height analyzers were set on the shaded portions in Fig. 2. The measurement was carried out at direction angles of 90°, 112.5°, 135°, 157.5° and 180°. The accidental coincidence counts amounted to 1–7% of total conicidence counts. The experimental result and the most fitted curve are shown in Fig. 3.

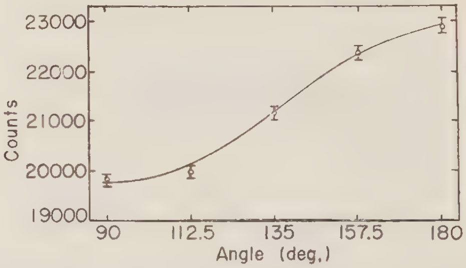

Fig. 3. Directional correlation of the 1.03 Mev–1.17 Mev gamma-gamma cascade. The solid curved represents the least-squares fit of the experimental data.

The measured coefficients take the following values:

$$A_2' = +0.0984 \pm 0.0013 ,$$
$$A_4' = +0.0094 \pm 0.0005 .$$

In order to obtain the true coefficients, the attenuation factors due to the angular resolution were measured by the use of Lawson and Frauenfelder's method[9)]. The gamma rays from Co^{60} coming through the collimator, were detected so as to count only the photopeaks. The measured angular resolution curves are shown in Fig. 4.

The attenuation factor Q_λ is expressed as follows, using the angular resolution curve $f(\theta)$:

$$Q_\lambda=(J_\lambda/J_0)^2\ ,$$

where $J_\lambda=\int f(\theta)P_\lambda(\cos\theta)|\sin\theta|d\theta$. The attenuation factors obtained experimentally are

$$Q_2=0.926\ ,$$
$$Q_4=0.773\ .$$

Using these values, the corrected coefficients A_λ are determined as follows:

$$A_2=+0.106\pm0.002\ ,$$
$$A_4=+0.012\pm0.001\ .$$

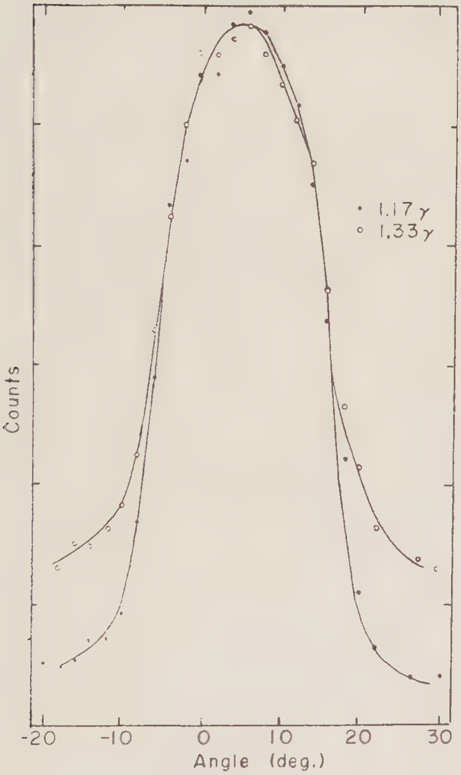

Fig. 4. Angular resolution curves measured at a distance of 7 cm for the 1.33 Mev and 1.17 Mev gamma ray from Co^{60} source.

§ 4. Polarization-Direction Correlation Measurement

The gamma ray polarimeter reported previously[10)] was used for the measurement of the polarization-direction correlation of the 1.03 Mev–1.17 Mev gamma-gamma cascade. Its photograph is shown in Fig. 5.

In this apparatus, the crystals for the direction and the side counters were both NaI(Tl) of $1^1/_2$ in. in diameter and 1 in. thick, and the scattering phosphor was a plastic scintillator of 4 cm in diameter and 4.5 cm long which was composed of polystyrene, *p* terphenyl (1%), POPOP (0.03%) and zincstearate (0.03%). The distance between the source and the front face of the crystal for the direction counter and that of the scattering phosphor were both 5 cm. The crystal for the side counter was placed at such a position that the distance between the front face of its crystal and the center axis of the scattering phosphor was 5 cm and the mean scattering angle at which the scattering events were detected was about 80°. The asymmetry ratio of the gamma ray polarimeter in the arrangement mentioned above was estimated as $R=2.12$ for 1 Mev gamma ray[11)]. The electronic circuit was the same one used in the measurement[10)] of Cd^{114}. To eliminate the false coincidence count, the pulse-height analyzers in the side counter channel and the scattering phosphor channel were adjusted to stop out the pulses corresponding to the energy less than 320 Kev and 250 Kev, respectively. The pulse-height analyzer in the direction counter channel was adjusted so as to count only the gamma ray higher than 430 Kev. By these adjustment of the electronic circuit, the contribution from the

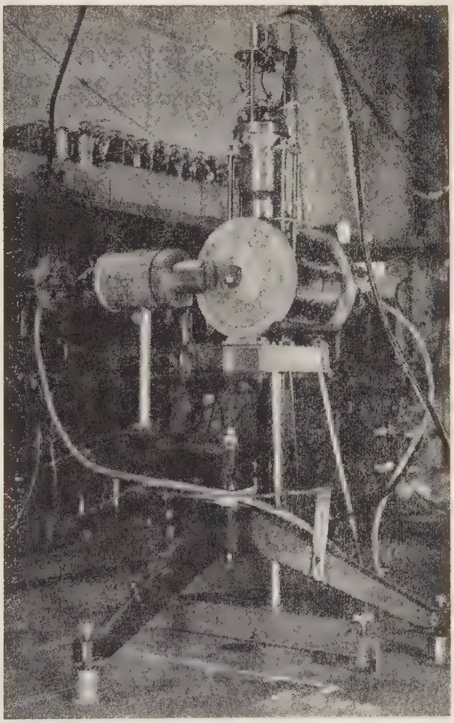

Fig. 5. Photograph of the gamma ray polarimeter.

gamma-gamma cascade[1),2)] containing either 0.09 Mev or 0.20 Mev gamma ray was removed completely.

Nevertheless, as the source was made from natural tin, the contribution from the 0.69 Mev –0.56 Mev gamma-gamma cascade in Te^{122} might be contained. But it was ascertained that its contribution was less than 1% of that from the 1.03 Mev–1.17 Mev gamma-gamma cascade on the seventh day after bombardment, so that the analysis of data was not affected at all by this contribution. Under the above-mentioned experimental condition, the measurement was carried out at a direction angle of 90° and the polarization of either 1.03 Mev or 1.17 Mev gamma ray was detected. The measured asymmetry are shown in Table I with the one in the case of Ti^{46} gamma-gamma cascade in which the gamma ray energy is almost the same as the present ones.

Table I. Measured asymmetry in the measurement of the polarization-direction correlation.

Nucleus	Cascade	$N_{\parallel}/N_{\perp}$ (90°)
Sn^{120}	1.03 Mev–1.17 Mev	0.92±0.03
Ti^{46}	0.89 Mev–1.12 Mev	0.92±0.02

§ 5. Result and Discussion

The measured directional correlation pattern agrees well with the one expected for the decay sequence of 2(D+Q)2(Q)0 ($\delta=-0.18$) as well as 4(Q)2(Q)0, so that we cannot accept the alternative.

The averaged polarization-direction correlation function[12)] can be expressed as follows:

for 4(E2)2(E2)0

$$\langle W(\theta,\varphi)\rangle_{AV}=1+0.1020P_2(\cos\theta)+0.0091P_4(\cos\theta)+[-0.0510P_2^2(\cos\theta)+0.0008P_4^2(\cos\theta)]\cos 2\varphi$$

and for 2(M1+E2)2(E2)0, where $\delta=-0.18$

$$\langle W(\theta,\varphi)\rangle_{AV}=1+0.1121P_2(\cos\theta)+0.0102P_4(\cos\theta)+[-0.1025P_2^2(\cos\theta)+0.0009P_4^2(\cos\theta)]\cos 2\varphi$$

and the p-value[13)] which is defined as the ratio of $\langle W(90°,90°)\rangle_{AV}$ to $\langle W(90°,0°)\rangle_{AV}$, takes the following values:

for 4(E2)2(E2)0 $p=1.40$,
and for 2(M1+E2)2(E2)0,
where $\delta=-0.18$ $p=1.99$.

Therefore, it is possible to exclude sharply the alternative, by means of the polarization-direction measurement. The asymmetry obtained in the polarization-direction correlation measurement agrees very well with the measured one for the gamma-gamma cascade in Ti^{46} which has the well-established decay sequence of 4(E2)2(E2)0 and its gamma ray energies are almost the same as that in Sn^{120} detected in the present experiment. As the asymmetry is expected to be 0.81 for the decay sequence of 2(M1+E2)2(E2)0 ($\delta=-0.18$), this decay sequence should not be accepted. Consequently, it is concluded that the spin and the parity of the second excited state is 4 and even, respectively and the transition from the second excited state to the first excited one is pure electric quadrupole transition.

This result is consistent with that obtained from the internal conversion measurement of 1.03 Mev gamma ray by several authors[1)].

Since the degeneracy of the second excited state is a consequence of the harmonic oscillator approximation in the surface vibrational model, it is expected that the degeneracy will be removed by higher order term in the nuclear energy[14)]. The level assignment of 16 min Sb^{120} is considered[1)] as 1^+, on the basis of the information of the transition to the ground and the first excited states of Sn^{120}, so that the transition from the 1^+ level of Sb^{120} to the second 2^+ level of Sn^{120}, if it exist, could be detected. In order to realize this possibility, 16 min Sb^{120} was produced by the bombardment of 98% enriched Sn^{120} by 7–8 Mev proton or the irradiation of natural Sb by the fast neutron which is emmitted in the bombardment of 24 Mev deuteron on graphite target, and the gamma ray spectra were measured carefully.

However, the evidence of the existence of second 2^+ level was not obtained.

From these experimental results, the 2.20 Mev level may by regarded as a two quasi-particle excitation level $(h_{11/2})^2$ in Kisslinger and Sorensen's model[15)] on the single closed shell nuclei.

However, as the absence of the second 2^+

level may be caused by the strong degeneracy of the triplet, the possibility of a two phonon vibrational level still remains.

Acknowledgement

The authors wish to express their hearty gratitude to Prof. T. Hayashi of Kyoto Prefectural University for his valuable discussions and to Dr. K. Saito of Institute for Nuclear Study of University of Tokyo for his co-operation in chemical separations.

They are also indebted to the cyclotron crew of the Institute for Nuclear Study for the operation of the machine.

References

1) C. L. McGinnis: Phys. Rev. **109** (1958) 888; H. Ikegami: Phys. Rev. **120** (1960) 2185; B. Skytte Jensen, O. B. Nielsen and O. Skilbreid: Nucl. Phys. **19** (1960) 654.
2) H. Ikegami and T. Udagawa: INSJ Report **31**, to be published in Phys. Rev.
3) G. Scharff-Goldhaber and J. Weneser: Phys. Rev. **98** (1955) 212.
4) L. Wilets and M. Jeans: Phys. Rev. **102** (1956) 788.
5) A. S. Davidov and G. F. Fillipov: Nucl. Phys. **8** (1958) 237; **10** (1959) 654; A. S. Davidov and V. S. Rostovsky: Nucl. Phys. **12** (1959) 58.
6) I. S. Shapiro: Sov. Phys. JETP **3** no. 5 (1956) 779.
7) D. Strominger, J. M. Hollander and G. T. Seaborg: Rev. Mod. Phys. **30** (1958) 698.
8) P. H. Stelson and F. K. McGowan: Bull. Am. Phys. Soc. **2** (1957) 69.
9) J. S. Lawson, Jr. and H. Frauenfelder: Phys. Rev. **91** (1953) 649.
10) M. Kawamura: J. Phys. Soc. Japan **15** (1960) 3.
11) M. Kawamura, A. Aoki and T. Hayashi: Soc. Rep. Kyoto Pref. Univ. **3** (1959) A5.
12) L. C. Biedenharn and M. E. Rose: Rev. Mod. Phys. **25** (1953) 729.
13) F. Metzger and M. Deutsch: Phys. Rev. **78** (1950) 551.
14) K. Alder, A. Bohr, T. Huus, B. Mottelson and A. Winther: Rev. Mod. Phys. **28** (1956) 432.
15) L. S. Kisslinger and R. A. Sorensen: K. Danske Vidensk. Selsk. Mat. Fys. Medd. **32** (1960) no. 9.

JOURNAL OF THE PHYSICAL SOCIETY OF JAPAN, Vol. 16, No. 8, AUGUST 1961

Nuclear Ground-State Energies

By Masami YAMADA

Science and Engineering Research Laboratory, Waseda University
Kikui-cho, Shinjuku-ku, Tokyo

and Zyun-itiro MATUMOTO

Nuclear Physics Division, Japan Atomic Energy Research Institute
Tokai-mura, Ibaraki-ken

(Received May 4, 1961)

The proton and neutron separation energies and the β-decay energies are estimated for most of the nuclei that have been dis- covered or will be discovered in near future. In this estimation four semi-empirical rules for the proton and neutron separation energies are used in addition to the available experimental data. These rules are also used to eliminate the wrong data and to correct the wrong interpretations of the experimental results. The "best" values thus obtained are tabulated. Explanations are given for some of the data which are eliminated or need large adjustments.

§1. Introduction

It is needless to say that the nuclear (ground-state) binding energies, or equivalently the nuclear masses, are very important quantities for nuclear physics. A great many data have been acquired till now, and a quick view of them may be obtained in the recent papers of Everling et al.[1] In spite of these efforts, however, the overall situation is still not satisfactory. If one looks into the data, one will be confused by many irregularities that are theoretically inexplicable. Most of these irregularities seem to be false ones being due to incorrect or insufficient experiments.

The elimination of such false data has been facilitated by the use of mass formulas and nuclear systematics, in particular the β-decay energy systematics[2,3]. These have been also useful to estimate the binding energies for which no or only poor experimental data are available.

In this paper we advance this kind of study. By making use of a systematics which is explained in the next section, we try to eliminate the false data and estimate the " best " values as accurately as possible.

§ 2. Systematics for the Proton and Neutron Separation Energies

There are many kinds of systematics concerned with the nuclear binding energies. The systematics we use in this paper is that for the separation energies of the last protons or neutrons. We denote the proton and neutron separation energies of the nucleus with Z protons and N neutrons as $S_p(Z, N)$ and $S_n(Z, N)$ respectively. Our systematics consists of the following four rules.

1. $S_p(Z, \text{even-}N)$ for a fixed Z value increases smoothly (almost linearly) with N.
2. $S_n(\text{even-}Z, N)$ for a fixed N value increases smoothly (almost linearly) with Z.
3. $S_p(\text{odd-}Z, \text{odd-}N)$ is larger, and $S_p(\text{even-}Z, \text{odd-}N)$ is smaller than the values inferred from the smooth curves of the rule 1. Similarly, $S_n(\text{odd-}Z, \text{odd-}N)$ is larger, and $S_n(\text{odd-}Z, \text{even-}N)$ is smaller than the values inferred from the smooth curves of the rule 2.
4. $S_p(Z, N+1)$ is not much smaller than $S_p(Z, N)$, and $S_n(Z+1, N)$ is not much smaller than $S_n(Z, N)$.

Although the legitimacy of the above rules should be tested by the experimental data, we shall give some theoretical bases for them in the following.

The non-smoothness of the nuclear properties as functions of Z and N seems to be caused mainly by the Pauli exclusion principle. For example, there should be no magic number if there were no exclusion principle. If one plots $S_p(Z, N)$ as a function of Z, big discontinuities occur at the proton magic numbers. The β-decay energy systematics[2,3] has the same kind of discontinuities. These discontinuities are inconvenient to estimate the unmeasured quantities and also to examine the reliabilities of the experimental data. On the other hand, if one plots $S_p(Z, N)$ for a fixed Z value as a function of N as is used in the rule 1, the last proton which is our central object is always the same Z-th proton. Therefore, we can expect that the effect of the exclusion principle is mostly avoided in this kind of plots and a smooth function is obtained. The same argument holds for the rule 2.

Sometimes, however, the addition of neutrons or protons causes so marked change to the nuclear properties that the above-mentioned smoothness is broken. We have found three cases in which the rules 1 and 2 do not hold well. First, a discontinuity occurs when the point, $Z=N$, is passed through. This discontinuity is probably due to the symmetry energy between the protons and the neutrons which includes a part proportional to $|N-Z|$[4]. Second, discontinuities may occur for the plots of the rule 1 when N passes through a magic number, and for the plots of the rule 2 when Z passes through a magic number. This kind of discontinuity is much smaller than the discontinuity of $S_p(Z, N)$ as a function of Z which occurs when Z passes through a magic number. Third, discontinuities may occur when the nuclei change their shapes markedly. A typical example is that for the neutron numbers changing from 88 to 90.

When the spin-parities of the low-lying states of the odd-mass nuclei are known, we can modify the rules 1 and 2 slightly. To do so, we deal with the proton and neutron separation energies from (or to) the lowest states with particular spin-parities instead of those from (or to) the ground states. For example, we consider the energies which are necessary for removing the last protons from the lowest $5/2^+$ states of the Sb isotopes. The modified rule 1 is that these energies increase smoothly with N. We can also deal with the energies which are necessary for removing the last protons from the lowest $7/2^+$ states of the Sb isotopes. They increase smoothly with N, too. These modified rules are expected to hold somewhat better than the original ones.

In the above arguments the reason why N must be even for the rule 1 and Z must be even for the rule 2 is not stated. It will be easily seen that no odd-odd nucleus is concerned with the rules 1 and 2. Suppose a proton is added to the nucleus with even-Z protons and odd-N neutrons. If there were no directional coupling between the added proton and the original nucleus, the binding energy of the added proton would take a value which is close to that obtained from the interpolation of the plots of the rule 1, and the ground state of the final odd-odd nucleus would be a degenerate state with several spin values. Actually, however, there is some directional coupling, and the degenerate state splits into single-spin states. Among these states, our object is the ground state which has the largest binding energy. The binding energy of this ground state will be larger than that of the above-mentioned degenerate state; and accordingly, the proton separation energy of the odd-odd nucleus will be larger than that obtained from the interpolation of the plots of the rule 1. The rest of the rule 3 is explained in the same way. This rule was first discovered by Way[5], and de-Shalit[6] gave an explanation from the standpoint of the shell model.

We can refine the rule 3 in the following way. We arrange the nuclei and the proton and neutron separation energies as Fig. 1.

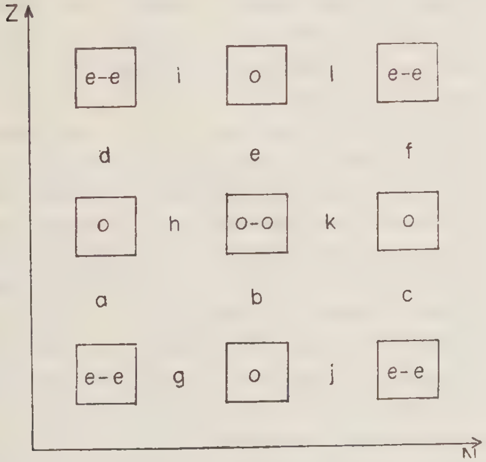

Fig. 1. Arrangement of nuclei. "e-e", "o-o" and "o" mean the even-even, odd-odd, and odd-mass nuclei respectively. The letters between the nuclei stand for the proton and neutron separation energies.

The refined rule 3 is

$$(2b-a-c)-(2e-d-f)$$
$$=(2h-g-i)-(2k-j-l)>0.$$

It follows from this inequality that the distance between the mass surfaces of the odd-odd and odd-mass nuclei is smaller than that between the odd-mass and even-even ones. There is no definite exception to the refined rule 3, while there are a few exceptions to the original rule 3.

The rule 4 is almost purely empirical. However, the following reasoning, though the possibility of its justification in near future is doubtful, may be helpful to understand it. $S_p(Z, N+1)$ may be divided into $S_p(Z, N)$ and the interaction energy between the Z-th proton and the $N+1$-th neutron. Probably, there are both attractive and repulsive parts in the interaction between a proton and a neutron. In forming the ground state of the $(Z, N+1)$ nucleus the Z-th proton and the $N+1$-th neutron take such configurations that the attractive part is in the most use and the repulsive part in the least use. Thus, the net interaction between the Z-th proton and the $N+1$-th neutron is attractive (at least, not strongly repulsive); and consequently, $S_p(Z, N+1) \gtrsim S_p(Z, N)$.

Actually, there are cases in which $S_p(Z, N)$'s are slightly larger than $S_p(Z, N+1)$'s. The rule 4 is stated in a somewhat vague way taking account of this situation.

§ 3. Estimation and Tabulation of S_p, S_n, Q_β

As is mentioned in § 1, our systematics explained in § 2 is not clearly seen when the raw data are plotted with preliminarily estimated S_p and S_n values. We use every kind of data concerned with the ground-state binding energies. They include the reaction Q-values, the α- and β-decay Q-values, and the mass values. Next, we adjust the data within the errors so as to fit the systematics. The errors of the mass-spectroscopic data are taken to be three times those given in the literatures. For the other kinds of data the errors in the literatures are adopted in this stage. For the data without errors the authors' judgments are used. At the same time we improve the estimations of the S_p and S_n values. It should be noted that these adjustments and improvements are not very simple since many quantities are mutually correlated. For example, $a+h=b+g$

in Fig. 1. Although this procedure greatly improves the fit of the systematics, there still remain some deviations. Looking into the data which cause these deviations we usually find doubtful points in the experiments or in the interpretations of the experimental results. Then, we either eliminate these data or give different interpretations to them. After re-improving the estimations of the S_p and S_n values we get the final results. *The important thing to be mentioned is that a good fit of the data to our systematics is attained without adjusting the well-established experimental data.*

To collect the experimental data we mainly use the compilations of the nuclear data[7,…,12]. Most of the data which appeared after these compilations had published are also included, but some of them may have escaped from the authors' attention. Some of the new data which do not differ from the old ones significantly are neglected, since the inclusion of them does not seem to be so urgent as it necessitates tremendous labor. Most of the references of the new data can be found in the blue "Recent References" sheets of Nuclear Data Sheets[7]. Therefore, the references of the new data are given only when they are not found in the above sheets[13,…,54]. For many nuclei with mass numbers $A \leq 70$, the binding energies are very precisely known. For these nuclei the values in Reference 1 are used with very few changes. As is seen from the argument in § 2 our systematics is not very effective to estimate the binding energies of the relatively few nuclei with $Z > N$. In such cases we use the systematics of the Coulomb energy differences between the mirror nuclei.

The "best" values of the proton and neutron separation energies and the β-decay Q-values (Q^- for β^--decay and Q_ε for electron capture decay), which are the results of the above final adjustments, are tabulated in Table I. The value which is obtained directly from experiment is marked the asterisk, *. Some kinds of averages of the experimental data also belong to this class. For $A \leq 70$ the results of the least squares method[1] are classified here. The value which is obtained from the experimental value after adjustment within the error is marked the dagger, †. The experimental data with much poorer accuracies than those of the adopted values (calculated or estimated values) are excluded from the above two classes even though they coincide. The mark, ♯, is attached to the value which is obtained from the experimental value after adjustment beyond the error. The value without any mark and without parentheses is calculated from the experimental data, either adjusted or unadjusted. The value in parentheses is the estimated value. Even though a value may be calculated from the experimental data, it is put in parentheses if some of the experimental data need so much adjustments as to nullify the original data.

The above marks are not sufficient to indicate all the locations and adjustments of the experimental data. The locations of the experimental Q-values of the α-decays and some of the reactions are not seen in Table I. For the mass-spectroscopic measurements such doublet values that are connected *only* with S_p, S_n, or Q_β are marked, but all others are not. For example, the existence of the mass difference measurement of $\mathrm{Gd}^{155}-\mathrm{Gd}^{154}$ is indicated by the mark on $S_n(\mathrm{Gd}^{155})$, but no mark is attached to $S_p(\mathrm{Ba}^{134})$ though the masses of ${}_{56}\mathrm{Ba}^{134}$ and ${}_{55}\mathrm{Cs}^{133}$ themselves have been measured. It seems better to indicate the existence of the mass measurement and the adjustment of its value in the table of masses which may be published elsewhere. Of course, the data which have no corresponding marks are also used to get the "calculated" values in Table I. For some of these data which need large adjustments discussions are given in § 4 in the same way as the data with marks.

We do not go deep into the estimation of the uncertainties of the values in Table I because it is complicated too much. We simply divide the whole values into five classes according to their uncertainties. These classes are shown in Table II, in which the "uncertainty" should be taken as the maximum of possible errors. The values in the first class have sufficient precisions for our systematics and for most other purposes. Since it is not our aim to discuss the accuracy of a few keV, the values are given only to two places of decimals in MeV units. If one wants more accuracy, one should consult References 1, 7, etc. The estimated values and the values adjusted beyond the errors cannot be precise

Table I. The "best" values of the proton separation energies (S_p), the neutron separation energies (S_n), the β^--decay Q-values (Q^-), and the electron capture Q-values (Q_ε). The values are in MeV units. For notation see Table II.

Nucleus	S_p	S_n	Q^- or Q_ε
n	—	—	β^- 0.78*
n^2	—	(~−0.5)	β^- (~3.5)
n^3	—	$(\sim -4._0)$	β^- $(\sim 13._8)$
n^4	—	$(\sim -2._0)$	β^- $(\sim 13._8)$
H^1	—	—	—
H^2	2.23*	2.23*	—
H^3	(~9.0)	6.26*	β^- 0.02*
H^4	$(\sim 11._0)$	$(\sim -2._0)$	β^- $(\sim 22._6)$
H^5	$(\sim 12._5)$	$(\sim -0._6)$	β^- $(\sim 22._2)$
He^2	(~−1.4)	—	ε (~2.8)
He^3	5.49*	(~9.1)	—
He^4	19.81*	20.58	—
He^5	$(\sim 20._9)$	−0.96*	—
He^6	$(\sim 23._8)$	1.92	β^- 3.51*
He^7		$(\sim -1._2)$	β^- $(\sim 12._0)$
He^8		$(\sim 1._8)$	β^- $(\sim 12._2)$
Li^3	$(\sim -5._2)$	—	ε $(\sim 13._5)$
Li^4	$(\sim -3._0)$	$(\sim 11._3)$	ε $(\sim 22._8)$
Li^5	−1.97*	$(\sim 21._6)$	ε 0.2_3
Li^6	4.65*	5.66	—
Li^7	9.98*	7.25*	—
Li^8	$(\sim 13._2)$	2.03*	β^- 16.00
Li^9	$(\sim 14._0)$	$\sim 2._6$	β^- $\sim 15._1$†
Be^4	$(\sim -3._4)$	—	ε $(\sim 13._9)$
Be^5	$(\sim -2._0)$	$(\sim 12._7)$	ε $(\sim 22._8)$
Be^6	0.4_6	$(\sim 24._0)$	ε 4.4_2*
Be^7	5.61	10.8_1	ε 0.86*
Be^8	17.25	18.90	—
Be^9	16.88	1.67	—
Be^{10}	$\sim 21._1$	6.81*	β^- 0.56*
Be^{11}		0.5_3	β^- 11.4_8*
Be^{12}		$(\sim 3._9)$	β^- $(\sim 11._0)$
B^7	$(\sim -3._4)$		ε $(\sim 13._4)$
B^8	0.13	$(\sim 14._3)$	ε 17.98
B^9	−0.19	18.58	ε 1.07*
B^{10}	6.59*	8.44*	—
B^{11}	11.23	11.46*	—
B^{12}	14.0_7	3.37*	β^- 13.37
B^{13}	$(\sim 15._1)$	4.8_8	β^- 13.4_3
C^8	$(\sim -0._6)$		ε $(\sim 14._1)$
C^9	$(\sim 0._0)$	$(\sim 14._9)$	ε $(\sim 17._8)$
C^{10}	4.0_3	$(\sim 22._6)$	ε 3.6_2*
C^{11}	8.69	13.1_0	ε 1.98*
C^{12}	15.96	18.72	—
C^{13}	17.53	4.95*	—

Table I. (Continued)

Nucleus	S_p	S_n	Q^- or Q_ε
C^{14}	20.8_3	8.18*	β^- 0.16*
C^{15}		1.22*	β^- 9.77
C^{16}		4.25	β^- 8.02
C^{17}		$(\sim 1._1)$	β^- $(\sim 12._8)$
C^{18}		$(\sim 4._0)$	β^- $(\sim 11._6)$
N^{11}	(~−2.4)		ε (~14.7)
N^{12}	0.3_4	(~15.8)	ε 17.6_0*
N^{13}	1.94	20.3_3	ε 2.22*
N^{14}	7.55*	10.55	—
N^{15}	10.21	10.83*	—
N^{16}	11.49	2.50*	β^- 10.41
N^{17}	13.1_1	5.87	β^- 8.68
N^{18}	$(\sim 14._9)$	$(\sim 2._8)$	β^- $(\sim 13._9)$
N^{19}	$(\sim 16._1)$	$(\sim 5._3)$	β^- $(\sim 12._6)$
O^{12}	$(\sim 0._4)$		ε $(\sim 14._6)$
O^{13}	(~1.5)	$(\sim 16._9)$	ε (~18.0)
O^{14}	4.62	(~23.4)	ε 5.15*
O^{15}	7.29	13.22	ε 2.76*
O^{16}	12.13	15.67	—
O^{17}	13.77	4.14*	—
O^{18}	15.94*	8.05*	—
O^{19}	$(\sim 17._1)$	3.96*	β^- 4.82*
O^{20}	$(\sim 19._4)$	7.61	β^- 3.80
O^{21}		(~2.9)	β^- (~9.0)
O^{22}		(~6.4)	β^- $(\sim 7._5)$
F^{15}	(~−2.4)		ε (~14.8)
F^{16}	−0.75	(~14.8)	ε 15.63
F^{17}	0.60*	17.01	ε 2.76*
F^{18}	5.60	9.14	ε 1.67*
F^{19}	7.99	10.44*	—
F^{20}	10.63	6.60*	β^- 7.03*
F^{21}	11.1_0	8.08	β^- 5.70
F^{22}	$(\sim 13._1)$	$(\sim 4._9)$	β^- $(\sim 11._2)$
F^{23}	(~13.6)	$(\sim 6._9)$	β^- (~9.5)
Ne^{16}	$(\sim 0._2)$		ε $(\sim 13._8)$
Ne^{17}	(~1.5)	$(\sim 16._1)$	ε (~14.7)
Ne^{18}	4.1_4	(~19.6)	ε 4.2_2*
Ne^{19}	6.41	11.4_1	ε 3.25*
Ne^{20}	12.84	16.87	—
Ne^{21}	13.00	6.76*	—
Ne^{22}	15.29	10.37*	—
Ne^{23}	$(\sim 15._6)$	5.19	β^- 4.38
Ne^{24}	(~17.6)	8.8_9	β^- 2.4_5*
Ne^{25}		(~4.3)	β^- (~7.2)
Ne^{26}		(~6.4)	β^- (~6.9)
Na^{19}	(~−0.7)		ε (~11.3)
Na^{20}	(~2.1)	(~14.2)	ε ~14.0‡
Na^{21}	2.45	(~17.2)	ε 3.52*
Na^{22}	6.74	11.05	ε 2.84*

Table I. (Continued)

Nucleus	S_p	S_n	Q^- or Q_ε	
Na^{23}	8.79	12.41		—
Na^{24}	10.56	6.96*	β^-	5.52*
Na^{25}	10.7_1	9.0_5	β^-	3.8_0*
Na^{26}	(~ 12.5)	$\sim 6.0_9$	β^-	$\sim 8.8_0$†
Na^{27}	(~ 12.9)	(~ 6.7)	β^-	(~ 8.5)
Mg^{20}	(~ 2.5)		ε	(~ 10.9)
Mg^{21}	(~ 3.1)	(~ 14.7)	ε	(~ 13.4)
Mg^{22}	5.1_8	(~ 19.4)	ε	5.0_9
Mg^{23}	7.5_7	13.4_4	ε	4.0_6*
Mg^{24}	11.69	16.5_3		—
Mg^{25}	12.06	7.33*		—
Mg^{26}	14.1_1	11.10*		—
Mg^{27}	$\sim 14.4_6$	6.44*	β^-	2.62*
Mg^{28}	(~ 16.2)	8.50	β^-	1.84*
Mg^{29}		(~ 4.5)	β^-	(~ 6.7)
Mg^{30}		(~ 7.3)	β^-	$(\sim 5._4)$
Al^{23}	(~ 0.2)		ε	(~ 12.5)
Al^{24}	$\sim 1.7_3$	(~ 15.0)	ε	$\sim 14.0_2$*
Al^{25}	2.2_9	$\sim 17.0_9$	ε	4.2_6*
Al^{26}	6.30	11.3_4	ε	4.01*
Al^{27}	8.27	13.07		—
Al^{28}	9.56	7.72*	β^-	4.64*
Al^{29}	10.4_1	9.3_6	β^-	3.7_6*
Al^{30}	$(\sim 11._9)$	$(\sim 6._0)$	β^-	$(\sim 8._4)$
Al^{31}	(~ 12.5)	$(\sim 7._9)$	β^-	(~ 7.1)
Si^{24}	(~ 3.4)		ε	(~ 10.8)
Si^{25}	(~ 3.9)	(~ 15.5)	ε	(~ 12.4)
Si^{26}	5.5_6	(~ 18.7)	ε	5.0_0
Si^{27}	7.4_7	13.2_5	ε	4.8_2*
Si^{28}	11.58	17.1_8		—
Si^{29}	12.33	8.48*		—
Si^{30}	13.5_9	10.61*		—
Si^{31}	$(\sim 14._2)$	6.59*	β^-	1.48*
Si^{32}	(~ 15.6)	9.3_1	β^-	0.1_0*
Si^{33}		(~ 5.0)	β^-	(~ 5.2)
Si^{34}		(~ 7.8)	β^-	(~ 4.0)
Si^{35}		(~ 2.5)	β^-	(~ 9.8)
Si^{36}		(~ 6.1)	β^-	$(\sim 7._6)$
P^{27}	(~ 0.7)		ε	(~ 11.8)
P^{28}	$\sim 2.2_8$	(~ 14.9)	ε	$\sim 14.1_2$†
P^{29}	2.74	$\sim 17.6_4$	ε	4.96*
P^{30}	5.58*	11.33	ε	4.25*
P^{31}	7.29	12.32		—
P^{32}	8.63	7.94*	β^-	1.71*
P^{33}	9.4_2	10.10	β^-	0.25*
P^{34}	(~ 11.0)	6.5_7	β^-	5.1_0*
P^{35}	(~ 11.5)	(~ 8.3)	β^-	(~ 3.8)
P^{36}	$(\sim 12._9)$	(~ 3.9)	β^-	$(\sim 9._8)$
P^{37}	$(\sim 13._3)$	(~ 6.5)	β^-	$(\sim 7._7)$

Table I. (Continued)

Nucleus	S_p	S_n	Q^- or Q_ε	
S^{28}	(~ 2.4)		ε	(~ 11.7)
S^{29}	(~ 3.0)	(~ 15.4)	ε	(~ 13.9)
S^{30}	4.5_5	(~ 19.2)	ε	6.0_0*
S^{31}	6.1_0	12.8_8	ε	5.4_4*
S^{32}	8.86	15.0_8		—
S^{33}	9.57	8.64*		—
S^{34}	10.89	11.42		—
S^{35}	11.3_0	6.98	β^-	0.17*
S^{36}	(~ 12.9)	9.88		—
S^{37}	$(\sim 13._4)$	4.3_8	β^-	4.8_0*
S^{38}	$(\sim 14._8)$	7.9_1	β^-	3.0_0*
S^{39}		(~ 4.2)	β^-	(~ 6.8)
S^{40}		(~ 7.8)	β^-	$(\sim 4._9)$
Cl^{31}	(~ 0.1)		ε	(~ 12.0)
Cl^{32}	$\sim 1.5_8$	(~ 14.4)	ε	$\sim 12.7_2$†
Cl^{33}	2.29*	$\sim 15.7_9$	ε	5.57
Cl^{34}	5.2_2	11.5_8	ε	5.4_2*
Cl^{35}	6.37	12.5_7		—
Cl^{36}	7.96	8.58*	β^- ε	0.71* 1.14
Cl^{37}	8.40	10.32		—
Cl^{38}	10.1_3	6.11*	β^-	4.92*
Cl^{39}	10.2_9	8.07	β^-	3.43*
Cl^{40}	(~ 11.9)	~ 5.8	β^-	~ 7.5*
Cl^{41}	(~ 12.0)	(~ 7.9)	β^-	(~ 5.7)
A^{32}	(~ 2.5)		ε	(~ 11.1)
A^{33}	(~ 3.3)	(~ 15.2)	ε	(~ 11.7)
A^{34}	$(\sim 4.7_0)$	(~ 17.2)	ε	$(\sim 6.1_0)$
A^{35}	5.8_1	$(\sim 12.6_9)$	ε	5.9_8*
A^{36}	8.51	15.2_7		—
A^{37}	8.72	8.79*	ε	0.82*
A^{38}	10.24	11.84		—
A^{39}	10.72	6.58	β^-	0.56*
A^{40}	12.52	9.88		—
A^{41}	~ 12.8	6.09*	β^-	2.49*
A^{42}	(~ 14.4)	$(\sim 9.5_1)$	β^-	$(\sim 0.5_0)$
A^{43}		(~ 5.7)	β^-	(~ 4.5)
A^{44}		(~ 8.9)	β^-	$(\sim 2.5_0)$
A^{45}		(~ 5.6)	β^-	(~ 6.2)
A^{46}		(~ 8.5)	β^-	$(\sim 4._6)$
A^{47}		(~ 3.7)	β^-	$(\sim 9._8)$
A^{48}		$(\sim 5._9)$	β^-	$(\sim 8._8)$
K^{35}	(~ 0.1)		ε	(~ 11.8)
K^{36}	(~ 1.7)	(~ 14.3)	ε	(~ 12.8)
K^{37}	1.8_9	(~ 15.5)	ε	6.1_2*
K^{38}	5.13	12.0_3	ε	5.93
K^{39}	6.37	13.08		—
K^{40}	7.58	7.80*	β^- ε	1.32* 1.51*

Table I. (Continued)

Nucleus	S_p	S_n	Q^- or Q_ε
K^{41}	7.80	10.10	—
K^{42}	9.22	7.52*	β^- 3.53*
K^{43}	$(\sim 9.3_7)$	9.64	β^- 1.82*
K^{44}	(~ 10.6)	6.8_8	β^- 6.0_8*
K^{45}	$(\sim 11.0_1)$	$(\sim 9.2_9)$	β^- $(\sim 4.2_0)$
K^{46}	$(\sim 12._3)$	(~ 6.9)	β^- (~ 7.7)
K^{47}	$(\sim 12._7)$	(~ 8.8)	β^- $(\sim 6._1)$
K^{48}	$(\sim 13._9)$	(~ 5.0)	β^- $(\sim 11._2)$
K^{49}	$(\sim 14._1)$	$(\sim 6._1)$	β^- $(\sim 10._3)$
Ca^{36}	(~ 2.6)		ε (~ 10.9)
Ca^{37}	(~ 3.0)	(~ 14.7)	ε (~ 11.7)
Ca^{38}	(~ 4.6)	(~ 17.0)	ε (~ 6.7)
Ca^{39}	5.6_9	(~ 13.2)	ε 6.6_1*
Ca^{40}	8.34	15.7_3	—
Ca^{41}	8.90	8.36*	ε 0.41
Ca^{42}	10.28	11.47	—
Ca^{43}	10.68	7.93*	—
Ca^{44}	12.17	11.14*	—
Ca^{45}	12.7_1	7.42*	β^- 0.25*
Ca^{46}	$(\sim 13.8_2)$	10.40	—
Ca^{47}	$(\sim 14._2)$	7.30	β^- 1.97*
Ca^{48}	$(\sim 15._4)$	10.0_0	β^- 0.2_0*
Ca^{49}	$(\sim 15._6)$	5.1_6	β^- 5.1_0*
Ca^{50}	$(\sim 16._7)$	(~ 7.2)	β^- (~ 4.2)
Ca^{51}		$(\sim 3._2)$	β^- $(\sim 8._3)$
Ca^{52}		$(\sim 5._7)$	β^- $(\sim 7._0)$
Sc^{39}	(~ -1.0)		ε (~ 13.4)
Sc^{40}	~ 1.0	(~ 15.2)	ε ~ 13.9*
Sc^{41}	0.9_4*	~ 15.6	ε 6.6_4
Sc^{42}	~ 4.8	~ 12.2	ε ~ 5.9*
Sc^{43}	4.93	~ 11.6	ε 2.22*
Sc^{44}	6.71	9.71	ε 3.65*
Sc^{45}	6.89	11.32	—
Sc^{46}	8.24	8.77*	β^- 2.37*
			ε 1.38
Sc^{47}	8.49	10.65	β^- 0.61*
Sc^{48}	9.41	8.23	β^- 3.99*
Sc^{49}	9.4_8	10.0_7	β^- 2.0_7*
Sc^{50}	$(\sim 10.6_3)$	$\sim 6.3_1$	β^- $\sim 6.7_0$†
Sc^{51}	(~ 10.7)	(~ 7.3)	β^- (~ 5.8)
Sc^{52}	$(\sim 11._9)$	$(\sim 4._4)$	β^- $(\sim 9._7)$
Sc^{53}	$(\sim 12._1)$	$(\sim 5._9)$	β^- $(\sim 8._4)$
Ti^{40}	(~ 1.9)		ε (~ 12.5)
Ti^{41}	(~ 1.5)	(~ 14.8)	ε (~ 13.3)
Ti^{42}	(~ 3.7)	(~ 17.8)	ε (~ 7.7)
Ti^{43}	(~ 3.9)	(~ 12.3)	ε (~ 7.0)
Ti^{44}	(8.7_7)	(~ 16.5)	ε (0.1_6)
Ti^{45}	8.48	(9.4_2)	ε 2.06*
Ti^{46}	10.35	13.19	—

Table I. (Continued)

Nucleus	S_p	S_n	Q^- or Q_ε
Ti^{47}	10.47	8.89	—
Ti^{48}	11.44	11.62*	—
Ti^{49}	11.35	8.15*	—
Ti^{50}	12.2_3	10.94	—
Ti^{51}	$\sim 12.2_8$	6.36	β^- 2.46*
Ti^{52}	(~ 13.3)	$(\sim 8.2_7)$	β^- $(\sim 1.5_0)$
Ti^{53}	$(\sim 13._5)$	$(\sim 4.5_8)$	β^- $(\sim 5.7_5)$
Ti^{54}	$(\sim 14._7)$	$(\sim 7.0_7)$	β^- (~ 4.3)
Ti^{55}		$(\sim 3._7)$	β^- $(\sim 8._1)$
Ti^{56}		$(\sim 5._8)$	β^- $(\sim 7._1)$
V^{45}	(~ 1.4)		ε (~ 7.2)
V^{46}	5.3_8	(~ 13.4)	ε 7.0_3*
V^{47}	5.19	13.0_0	ε 2.91*
V^{48}	6.82	10.52	ε 4.02*
V^{49}	6.75	11.55	ε 0.61*
V^{50}	7.94	9.34	β^- 1.04
			ε 2.21
V^{51}	8.04	11.04	—
V^{52}	8.99	7.30*	β^- 3.99
V^{53}	$(\sim 9.5_5)$	$(\sim 8.8_3)$	β^- $(\sim 3.1_0)$
V^{54}	(~ 10.6)	(~ 5.7)	β^- (~ 7.1)
V^{55}	(~ 11.0)	(~ 7.4)	β^- (~ 5.8)
V^{56}	$(\sim 12._1)$	$(\sim 4._8)$	β^- $(\sim 9._4)$
V^{57}	$(\sim 12._5)$	$(\sim 6._2)$	β^- $(\sim 8._5)$
Cr^{46}	(~ 4.8)		ε (~ 7.8)
Cr^{47}	(~ 4.6)	(~ 13.2)	ε (~ 7.6)
Cr^{48}	(8.3_4)	(~ 16.7)	ε (1.4_0)
Cr^{49}	8.21	(10.3_9)	ε 2.56*
Cr^{50}	9.59	12.93	—
Cr^{51}	9.50	9.25	ε 0.75*
Cr^{52}	10.52	12.05	—
Cr^{53}	11.15	7.94	—
Cr^{54}	$(\sim 12.0_4)$	9.72	—
Cr^{55}	(~ 12.4)	6.0_1	β^- 2.8_3*
Cr^{56}	(~ 13.5)	$\sim 8.4_9$	β^- 1.6_1*
Cr^{57}	$(\sim 13._8)$	$(\sim 5.2_2)$	β^- $(\sim 5.3_0)$
Cr^{58}	$(\sim 15._0)$	$(\sim 7.3_0)$	β^- $(\sim 4.2_5)$
Cr^{59}		(~ 4.2)	β^- (~ 7.7)
Cr^{60}		(~ 6.6)	β^- (~ 6.4)
Mn^{49}	(~ 1.9)		ε (~ 7.7)
Mn^{50}	4.5_7	(~ 13.1)	ε 7.5_8*
Mn^{51}	5.2_9	13.6_5	ε 3.1_8*
Mn^{52}	6.56	10.5_3	ε 4.70*
Mn^{53}	6.56	12.05	ε 0.60*
Mn^{54}	7.56	8.94	β^- 0.69
			ε 1.38*
Mn^{55}	8.06	10.22	—
Mn^{56}	9.3_1	7.27*	β^- 3.71*
Mn^{57}	$\sim 9.7_3$	$\sim 8.9_1$	β^- $\sim 2.4_5$†

Table I. (Continued)

Nucleus	S_p	S_n	Q^- or Q_ε	
Mn^{58}	$(\sim 10.7_7)$	$(\sim 6.2_5)$	β^-	$(\sim 6.2_5)$
Mn^{59}	$(\sim 11.1_6)$	$(\sim 7.6_9)$	β^-	$(\sim 5.1_5)$
Mn^{60}	(~ 12.2)	(~ 5.3)	β^-	(~ 8.6)
Mn^{61}	(~ 12.6)	(~ 6.9)	β^-	(~ 7.3)
Fe^{50}	(~ 4.0)		ε	(~ 8.3)
Fe^{51}	(~ 4.8)	(~ 13.9)	ε	(~ 8.1)
Fe^{52}	7.3_6	(~ 16.2)	ε	2.38*
Fe^{53}	7.2_7	10.4_4	ε	3.9_9*
Fe^{54}	8.85	13.6_2		—
Fe^{55}	9.21	9.30*	ε	0.23*
Fe^{56}	10.20	11.21		—
Fe^{57}	10.57	7.64*		—
Fe^{58}	$\sim 11.7_2$	10.05*		—
Fe^{59}	$(\sim 12.0_6)$	6.59*	β^-	1.56*
Fe^{60}	$(\sim 13.1_3)$	(8.7_6)	β^-	(0.3_0)
Fe^{61}	(~ 13.4)	$(\sim 5.5_5)$	β^-	$\sim 4.1_0$†
Fe^{62}	(~ 14.5)	$(\sim 7.9_6)$	β^-	$(\sim 2.8_0)$
Fe^{63}		$(\sim 4.7_6)$	β^-	$(\sim 6.4_0)$
Fe^{64}		$(\sim 7.4_6)$	β^-	(~ 4.8)
Co^{53}	(~ 1.5)		ε	(~ 8.2)
Co^{54}	4.5_5	(~ 13.5)	ε	8.2_9*
Co^{55}	5.06	14.1_3	ε	3.46*
Co^{56}	5.85	10.0_9	ε	4.58*
Co^{57}	6.02	11.39	ε	0.84*
Co^{58}	6.95	8.57	β^-	0.38
			ε	2.31*
Co^{59}	7.37	10.46		—
Co^{60}	8.28	7.50*	β^-	2.82*
Co^{61}	(8.8_7)	9.3_5	β^-	1.29*
Co^{62}	$\sim 9.9_8$	6.6_6	β^-	5.22*
Co^{63}	$(\sim 10.3_8)$	$\sim 8.3_6$	β^-	$\sim 3.7_0$†
Co^{64}	(~ 11.5)	(~ 5.9)	β^-	(~ 7.5)
Co^{65}	$(\sim 11.8_5)$	(~ 7.8)	β^-	$(\sim 5.8_0)$
Ni^{54}	(~ 4.3)		ε	(~ 8.4)
Ni^{55}	(~ 4.7)	(~ 13.9)	ε	(~ 8.6)
Ni^{56}	$(\sim 7.1_9)$	(~ 16.6)	ε	$(\sim 2.1_2)$
Ni^{57}	7.36	$(\sim 10.2_6)$	ε	3.24*
Ni^{58}	8.17	12.19		—
Ni^{59}	8.60	9.00*	ε	1.08*
Ni^{60}	9.53	11.39		—
Ni^{61}	9.86	7.82*		—
Ni^{62}	11.1_0	10.59		—
Ni^{63}	11.28	6.84*	β^-	0.07*
Ni^{64}	$\sim 12.5_8$	9.66		—
Ni^{65}	(~ 12.8)	6.1_3	β^-	2.1_0*
Ni^{66}	$(\sim 13.9_8)$	8.9_6	β^-	0.20*
Ni^{67}		$(\sim 5.3_0)$	β^-	$(\sim 4.0_0)$
Ni^{68}		$(\sim 7.8_7)$	β^-	(~ 2.4)
Ni^{69}		(~ 4.6)	β^-	(~ 6.0)

Table I. (Continued)

Nucleus	S_p	S_n	Q^- or Q_ε	
Ni^{70}		(~ 7.6)	β^-	(~ 3.9)
Cu^{57}	(~ 0.7)		ε	(~ 8.8)
Cu^{58}	2.9_4	(~ 12.5)	ε	8.47*
Cu^{59}	3.42*	12.6_7	ε	4.80
Cu^{60}	4.46	10.0_3	ε	6.15*
Cu^{61}	4.81	11.74	ε	2.23*
Cu^{62}	5.8_8*	8.8_9	ε	3.93*
Cu^{63}	6.13	10.84		—
Cu^{64}	7.20	7.92*	β^-	0.57*
			ε	1.68*
Cu^{65}	7.45*	9.91		—
Cu^{66}	8.3_7	7.06*	β^-	2.63*
Cu^{67}	8.5_2	9.10	β^-	0.57*
Cu^{68}	(~ 9.5)	(~ 6.3)	β^-	(~ 4.5)
Cu^{69}	$(\sim 9.7_8)$	(~ 8.2)	β^-	$(\sim 2.7_5)$
Cu^{70}	(~ 10.7)	(~ 5.5)	β^-	(~ 6.5)
Cu^{71}	(~ 11.0)	(~ 7.9)	β^-	(~ 4.3)
Zn^{58}	(~ 2.2)		ε	(~ 9.5)
Zn^{59}	(~ 2.7)	(~ 13.0)	ε	(~ 9.2)
Zn^{60}	$(\sim 5.0_5)$	(~ 15.0)	ε	$(\sim 4.2_0)$
Zn^{61}	$\sim 5.4_5$	$(\sim 10.4_4)$	ε	$\sim 5.5_0$†
Zn^{62}	6.4_2	$\sim 12.7_0$	ε	1.69*
Zn^{63}	6.69	9.16	ε	3.37*
Zn^{64}	7.71	11.85		—
Zn^{65}	7.78	7.99	ε	1.35*
Zn^{66}	8.91	11.04		—
Zn^{67}	8.89	7.05		—
Zn^{68}	9.99	10.20*		—
Zn^{69}	(~ 10.1)	6.4_1	β^-	0.90*
Zn^{70}	$(\sim 11.2_6)$	9.2_9		—
Zn^{71}	(~ 11.4)	$\sim 5.6_9$	β^-	2.9_0*
Zn^{72}	(~ 12.5)	$(\sim 8.9_9)$	β^-	$\sim 0.5_0$‡
Zn^{73}		$(\sim 5.4_0)$	β^-	$(\sim 4.4_0)$
Zn^{74}		$(\sim 8.4_0)$	β^-	$(\sim 2.1_0)$
Zn^{75}		$(\sim 4.9_1)$	β^-	$(\sim 6.0_0)$
Zn^{76}		$(\sim 7.6_9)$	β^-	(~ 4.1)
Ga^{63}	$(\sim 2.6_8)$		ε	$(\sim 5.7_0)$
Ga^{64}	4.0_0	$(\sim 10.4_8)$	ε	7.07*
Ga^{65}	3.95	11.8_0	ε	3.26*
Ga^{66}	5.0_9	9.1_3	ε	5.17*
Ga^{67}	5.27	11.2_2	ε	1.00*
Ga^{68}	6.50	8.28	ε	2.92*
Ga^{69}	6.5_3	10.2_3		—
Ga^{70}	7.8_5	7.7_3*	β^-	1.65*
			ε	0.65*
Ga^{71}	7.8_1	9.2_4*		—
Ga^{72}	$(\sim 8.7_1)$	$(\sim 6.5_9)$	β^-	4.00*
Ga^{73}	$(\sim 9.0_2)$	$(\sim 9.3_0)$	β^-	1.55*
Ga^{74}	$(\sim 9.7_2)$	$\sim 6.1_0$	β^-	5.6_0*

Table I. (Continued)

Nucleus	S_p	S_n	Q^- or Q_ε	
Ga^{75}	$(\sim 10.1_3)$	$\sim 8.8_1$	β^-	3.3_0*
Ga^{76}	(~ 11.0)	(~ 5.8)	β^-	(~ 7.1)
Ga^{77}	$(\sim 11.1_8)$	(~ 7.9)	β^-	$(\sim 5.1_0)$
Ge^{64}	$(\sim 4.7_0)$		ε	$(\sim 5.0_0)$
Ge^{65}	$(\sim 4.6_2)$	$(\sim 10.4_0)$	ε	$(\sim 6.4_0)$
Ge^{66}	$(\sim 5.9_5)$	$(\sim 13.1_3)$	ε	$\sim 2.4_0$‡
Ge^{67}	6.0_4	$(\sim 9.2_2)$	ε	4.4_0*
Ge^{68}	$(\sim 7.3_0)$	$(\sim 12.4_8)$	ε	$(\sim 0.2_0)$
Ge^{69}	7.2_2	$(\sim 8.2_0)$	ε	2.23*
Ge^{70}	8.6_0	11.6_1		—
Ge^{71}	8.2_2	7.3_6	ε	0.23*
Ge^{72}	$(\sim 9.8_1)$	$(\sim 10.8_3)$		—
Ge^{73}	$(\sim 10.0_7)$	$\sim 6.8_5$‡		—
Ge^{74}	10.9_2	10.1_5		—
Ge^{75}	11.3_3	6.5_1	β^-	1.19*
Ge^{76}	$\sim 12.1_1$	$\sim 9.5_9$		—
Ge^{77}	(~ 12.2)	$\sim 5.8_6$	β^-	2.75*
Ge^{78}	$(\sim 13.1_3)$	$(\sim 8.8_1)$	β^-	$(\sim 0.9_0)$
Ge^{79}		$(\sim 5.7_0)$	β^-	$(\sim 4.0_0)$
Ge^{80}		$(\sim 8.3_3)$	β^-	$(\sim 2.1_0)$
Ge^{81}		$(\sim 4.8_4)$	β^-	$(\sim 5.9_5)$
Ge^{82}		$(\sim 7.2_9)$	β^-	(~ 4.4)
As^{69}	$(\sim 3.4_2)$		ε	$\sim 4.0_0$†
As^{70}	4.2_8	$\sim 9.0_6$	ε	6.5_5*
As^{71}	4.5_7	11.9_0	ε	2.01*
As^{72}	$(\sim 5.6_8)$	$(\sim 8.4_7)$	ε	4.36*
As^{73}	$(\sim 5.7_0)$	$(\sim 10.8_4)$	ε	0.3_7*
As^{74}	6.8_2	$\sim 7.9_7$	β^-	1.36*
			ε	2.55*
As^{75}	6.9_2	10.2_5†		—
As^{76}	7.7_1	7.3_0*	β^-	2.97*
			ε	$\sim 1.1_0$
As^{77}	$\sim 7.8_3$	9.71	β^-	0.68*
As^{78}	$\sim 8.9_3$	$\sim 6.9_6$	β^-	$\sim 4.2_0$*
As^{79}	$(\sim 8.9_2)$	$\sim 8.8_0$	β^-	2.3_0*
As^{80}	$(\sim 9.6_4)$	$\sim 6.4_3$	β^-	$\sim 5.8_0$†
As^{81}	$(\sim 10.0_1)$	$(\sim 8.6_9)$	β^-	3.8_0*
As^{82}	(~ 10.9)	(~ 5.7)	β^-	(~ 7.4)
As^{83}	$(\sim 11.3_4)$	(~ 7.7)	β^-	$(\sim 5.6_5)$
Se^{70}	$(\sim 6.1_8)$		ε	$(\sim 2.1_0)$
Se^{71}	$\sim 6.4_2$	$(\sim 9.3_0)$	ε	$\sim 4.7_0$†
Se^{72}	$(\sim 7.3_9)$	$(\sim 12.8_7)$	ε	$(\sim 0.3_0)$
Se^{73}	$(\sim 7.3_1)$	$(\sim 8.3_9)$	ε	2.75*
Se^{74}	$\sim 8.5_5$	$\sim 12.0_8$		—
Se^{75}	8.6_0	8.0_2	ε	0.87*
Se^{76}	9.4_9	11.1_4		—
Se^{77}	9.61	7.42*		—
Se^{78}	10.38	10.48*		—
Se^{79}	$\sim 10.3_2$	$\sim 6.9_0$	β^-	0.16*

Table I. (Continued)

Nucleus	S_p	S_n	Q^- or Q_ε	
Se^{80}	11.3_4	9.93		—
Se^{81}	$\sim 11.7_1$	6.6_9	β^-	1.5_5*
Se^{82}	$\sim 12.3_6$	9.3_4*		—
Se^{83}	(~ 12.6)	$\sim 5.9_7$	β^-	3.4_0*
Se^{84}	$(\sim 13.4_4)$	$(\sim 8.5_7)$	β^-	$(\sim 1.6_5)$
Se^{85}		$(\sim 4.4_9)$	β^-	$(\sim 6.2_2)$
Se^{86}		(~ 6.1)	β^-	(~ 5.5)
Br^{73}	$(\sim 3.1_6)$		ε	$(\sim 4.4_5)$
Br^{74}	(~ 4.1)	(~ 9.3)	ε	(~ 7.2)
Br^{75}	4.2_3	(~ 12.2)	ε	3.0_1*
Br^{76}	5.5_6	9.3_5	ε	4.8_0†
Br^{77}	5.27	10.8_6	ε	1.36*
Br^{78}	6.13	8.28	β^-	$\sim 0.7_5$
			ε	3.57*
Br^{79}	$\sim 6.2_8$	$\sim 10.6_3$‡		—
Br^{80}	7.26	7.88*	β^-	2.00*
			ε	1.89*
Br^{81}	7.4_6	10.1_3*		—
Br^{82}	8.3_6	7.5_9	β^-	3.09*
			ε	0.2_0
Br^{83}	8.5_9	9.5_7	β^-	1.00*
Br^{84}	$\sim 9.4_4$	6.8_2	β^-	4.6_8*
Br^{85}	$(\sim 9.9_3)$	$\sim 9.0_6$	β^-	$\sim 2.8_0$*
Br^{86}	(~ 10.8)	(~ 5.4)	β^-	(~ 7.3)
Br^{87}	(~ 10.9)	(~ 6.2)	β^-	$\sim 6.6_0$‡
Kr^{74}	$(\sim 6.1_5)$		ε	(~ 2.4)
Kr^{75}	(~ 6.3)	$(\sim 9.5_1)$	ε	$(\sim 5.1_0)$
Kr^{76}	$(\sim 7.2_7)$	$(\sim 13.1_5)$	ε	$(\sim 1.3_0)$
Kr^{77}	$\sim 7.0_7$	$(\sim 9.1_6)$	ε	3.0_0†
Kr^{78}	$\sim 8.2_4$	$\sim 12.0_3$		—
Kr^{79}	$\sim 8.2_3$	8.2_6†	ε	1.62*
Kr^{80}	9.10	11.50		—
Kr^{81}	(9.1_5)	(7.9_3)	ε	(0.2_0)
Kr^{82}	9.9_0	$(\sim 10.8_8)$		—
Kr^{83}	9.7_9	7.4_8		—
Kr^{84}	10.7_2	10.5_0*		—
Kr^{85}	11.0_8	7.1_8	β^-	0.67*
Kr^{86}	$\sim 11.9_0$	9.8_8		—
Kr^{87}	(~ 12.0)	5.5_3*	β^-	$\sim 3.8_0$†
Kr^{88}	$(\sim 12.8_6)$	$\sim 7.0_4$	β^-	3.0_0†
Kr^{89}		$(\sim 4.8_1)$	β^-	$(\sim 5.4_0)$
Kr^{90}		$(\sim 6.4_8)$	β^-	$(\sim 4.4_1)$
Rb^{77}	$(\sim 2.8_7)$		ε	$(\sim 5.5_0)$
Rb^{78}	(~ 3.7)	(~ 10.0)	ε	(~ 7.5)
Rb^{79}	$(\sim 3.8_8)$	(~ 12.2)	ε	$(\sim 3.6_0)$
Rb^{80}	$\sim 5.1_2$	$(\sim 9.5_0)$	ε	$\sim 5.6_0$†
Rb^{81}	(4.9_1)	$(\sim 11.2_9)$	ε	2.24*
Rb^{82}	$(\sim 5.9_3)$	$(\sim 8.9_5)$	ε	4.17*
Rb^{83}	(5.9_5)	$(\sim 10.9_0)$	ε	(0.7_5)

Table I. (Continued)

Nucleus	S_p	S_n	Q^- or Q_ε	
Rb^{84}	7.0_7	(8.6_0)	β^-	0.91*
			ε	2.65*
Rb^{85}	7.0_7	10.5_0†		—
Rb^{86}	8.5_1	8.6_2	β^-	1.78*
			ε	$\sim 0.5_9$
Rb^{87}	$\sim 8.5_5$	9.9_2*	β^-	0.27*
Rb^{88}	$\sim 9.2_6$	6.2_4*	β^-	5.1_7*
Rb^{89}	$(\sim 9.4_3)$	$(\sim 7.2_1)$	β^-	$\sim 4.3_0$‡
Rb^{90}	$(\sim 10.1_1)$	$(\sim 5.4_9)$	β^-	6.5_9*
Rb^{91}	$(\sim 10.3_4)$	$(\sim 6.7_1)$	β^-	$(\sim 5.6_5)$
Sr^{78}	$(\sim 5.9_4)$		ε	(~ 3.3)
Sr^{79}	(~ 6.1)	$(\sim 10.1_6)$	ε	$(\sim 5.3_0)$
Sr^{80}	$(\sim 6.9_2)$	$(\sim 13.0_0)$	ε	$(\sim 1.8_0)$
Sr^{81}	$(\sim 6.6_1)$	$(\sim 9.1_9)$	ε	$(\sim 3.9_0)$
Sr^{82}	$(\sim 7.7_7)$	$(\sim 12.4_5)$	ε	$(\sim 0.4_0)$
Sr^{83}	$(\sim 7.7_2)$	$(\sim 8.9_0)$	ε	$(\sim 2.4_0)$
Sr^{84}	(8.7_2)	$(\sim 11.9_1)$		—
Sr^{85}	8.6_1	8.4_8	ε	1.11*
Sr^{86}	9.6_1	11.5_1		—
Sr^{87}	9.4_1	8.4_2*		—
Sr^{88}	10.63	11.14*		—
Sr^{89}	10.7_3	6.3_4‡	β^-	1.46*
Sr^{90}	$(\sim 11.3_0)$	7.78	β^-	0.54*
Sr^{91}	11.5_8	5.7_7	β^-	2.67*
Sr^{92}	$(\sim 12.2_2)$	7.3_5	β^-	1.9_2*
Sr^{93}		$(\sim 5.5_2)$	β^-	$(\sim 3.8_0)$
Sr^{94}		$(\sim 6.9_5)$	β^-	$(\sim 3.0_0)$
Sr^{95}		$(\sim 4.7_7)$	β^-	$(\sim 5.4_5)$
Sr^{96}		$(\sim 6.4_3)$	β^-	(~ 4.5)
Y^{83}	$(\sim 3.6_2)$		ε	$(\sim 4.5_0)$
Y^{84}	(~ 4.4)	(~ 9.7)	ε	(~ 6.7)
Y^{85}	$(\sim 4.6_8)$	(~ 12.2)	ε	$(\sim 3.0_2)$
Y^{86}	$\sim 5.3_4$	$(\sim 9.1_5)$	ε	5.3_8*
Y^{87}	$\sim 5.7_2$	$\sim 11.8_8$	ε	$\sim 1.9_2$†
Y^{88}	6.7_3	$\sim 9.4_3$	ε	3.6_3*
Y^{89}	7.0_2	11.4_3*		—
Y^{90}	7.53	6.85*	β^-	2.24*
Y^{91}	7.6_6	7.9_1	β^-	1.54*
Y^{92}	8.4_9	6.6_0	β^-	3.6_0*
Y^{93}	8.5_4	7.4_0	β^-	2.8_9*
Y^{94}	$(\sim 9.1_7)$	$\sim 6.1_5$	β^-	5.0_0*
Y^{95}	$(\sim 9.4_4)$	$(\sim 7.2_2)$	β^-	$(\sim 4.2_0)$
Y^{96}	(~ 10.1)	(~ 5.5)	β^-	(~ 6.6)
Y^{97}	$(\sim 10.2_8)$	(~ 6.6)	β^-	$(\sim 5.6_7)$
Zr^{84}	$(\sim 6.3_8)$		ε	(~ 2.5)
Zr^{85}	(~ 6.5)	$(\sim 9.8_6)$	ε	$(\sim 4.8_4)$
Zr^{86}	$(\sim 7.2_2)$	$(\sim 12.8_5)$	ε	$(\sim 1.1_4)$
Zr^{87}	$\sim 7.5_8$	$(\sim 9.5_0)$	ε	3.5_2†
Zr^{88}	$(\sim 7.9_5)$	$(\sim 12.2_5)$	ε	$(\sim 0.7_0)$

Table I. (Continued)

Nucleus	S_p	S_n	Q^- or Q_ε	
Zr^{89}	7.8_0	$(\sim 9.2_9)$	ε	2.84*
Zr^{90}	8.31	11.94		—
Zr^{91}	8.6_7	7.2_1*		—
Zr^{92}	9.4_2	8.66*		—
Zr^{93}	9.5_1	6.6_9*	β^-	0.06*
Zr^{94}	$\sim 10.3_7$	$\sim 8.2_6$		—
Zr^{95}	10.6_4	6.4_2*	β^-	1.12*
Zr^{96}	$(\sim 11.3_0)$	$(\sim 7.8_8)$	β^-	$(\sim 0.2_0)$
Zr^{97}	(~ 11.4)	$(\sim 5.6_3)$	β^-	2.6_9†
Zr^{98}	$(\sim 12.1_8)$	$(\sim 7.2_9)$	β^-	$(\sim 1.5_0)$
Zr^{99}		$(\sim 4.8_0)$	β^-	$(\sim 4.3_0)$
Zr^{100}		$(\sim 6.9_0)$	β^-	(~ 2.8)
Nb^{87}	$(\sim 3.6_2)$		ε	$(\sim 5.1_0)$
Nb^{88}	(~ 4.2)	(~ 10.1)	ε	(~ 7.3)
Nb^{89}	$(\sim 4.5_0)$	(~ 12.6)	ε	4.0_0†
Nb^{90}	5.0_4	9.8_3	ε	6.11*
Nb^{91}	(5.2_3)	(12.1_2)	ε	(1.2_0)
Nb^{92}	5.7_7	7.7_5	β^-	0.4_1
			ε	2.1_1
Nb^{93}	5.9_7	8.8_6*		—
Nb^{94}	6.48	7.20*	β^-	2.0_7*
			ε	$\sim 1.0_0$
Nb^{95}	6.7_6	$\sim 8.5_4$	β^-	0.93*
Nb^{96}	7.3_0	6.9_6	β^-	3.13*
Nb^{97}	$(\sim 7.5_4)$	$\sim 8.1_2$	β^-	1.93*
Nb^{98}	$\sim 8.0_1$	$\sim 6.1_0$	β^-	4.8_0†
Nb^{99}	$(\sim 8.3_2)$	$(\sim 7.6_0)$	β^-	$(\sim 3.3_1)$
Nb^{100}	(~ 8.9)	(~ 5.4)	β^-	(~ 6.2)
Nb^{101}	$(\sim 9.1_7)$	(~ 7.1)	β^-	$(\sim 4.6_0)$
Mo^{88}	$(\sim 5.6_1)$		ε	(~ 3.7)
Mo^{89}	(~ 6.0)	$(\sim 10.4_4)$	ε	$(\sim 5.8_1)$
Mo^{90}	$\sim 6.5_0$	$(\sim 13.1_0)$	ε	2.5_4*
Mo^{91}	(6.9_0)	$(\sim 10.2_2)$	ε	4.44*
Mo^{92}	7.3_8	12.6_0*		—
Mo^{93}	7.5_9	7.9_6*	ε	0.4_9*
Mo^{94}	8.4_9	9.7_6		—
Mo^{95}	$\sim 8.6_9$	$\sim 7.4_0$		—
Mo^{96}	9.31	9.16*		—
Mo^{97}	$\sim 9.2_7$	$\sim 6.9_2$*		—
Mo^{98}	$\sim 10.1_2$	$\sim 8.9_7$‡		—
Mo^{99}	$(\sim 10.1_3)$	$(\sim 6.1_1)$	β^-	1.37*
Mo^{100}	$(\sim 10.8_3)$	$\sim 8.3_0$†		—
Mo^{101}	(~ 11.0)	$(\sim 5.5_4)$	β^-	2.8_2*
Mo^{102}	$(\sim 11.6_6)$	$(\sim 7.8_4)$	β^-	$(\sim 1.2_0)$
Mo^{103}		$(\sim 5.1_9)$	β^-	$(\sim 3.9_5)$
Mo^{104}		$(\sim 7.4_4)$	β^-	$(\sim 2.2_5)$
Tc^{91}	$(\sim 3.1_4)$		ε	$(\sim 6.3_0)$
Tc^{92}	(~ 3.8)	(~ 10.9)	ε	(~ 8.0)
Tc^{93}	4.0_2	(~ 12.8)	ε	3.16*

Table I. (Continued)

Nucleus	S_p	S_n	Q^- or Q_ε	
Tc^{94}	4.6_8	8.6_2	ε	4.30*
Tc^{95}	$\sim 4.9_6$	$\sim 10.0_4$	ε	1.66*
Tc^{96}	$\sim 5.6_6$	$\sim 8.1_0$	β^-	$(\sim 0.3_2)$
			ε	$\sim 2.7_2$†
Tc^{97}	$(\sim 5.9_8)$	$(\sim 9.4_8)$	ε	$(\sim 0.1_6)$
Tc^{98}	$(\sim 6.6_9)$	$(\sim 7.6_3)$	β^-	1.7_0*
			ε	$(\sim 1.5_0)$
Tc^{99}	$(\sim 6.7_0)$	$(\sim 8.9_8)$	β^-	0.29*
Tc^{100}	$(\sim 7.1_9)$	$(\sim 6.6_0)$	β^-	3.3_7*
			ε	$(\sim 0.3_3)$
Tc^{101}	$(\sim 7.5_8)$	$\sim 8.6_9$	β^-	1.6_3*
Tc^{102}	$(\sim 8.2_6)$	$(\sim 6.2_2)$	β^-	$\sim 4.4_0$†
Tc^{103}	$(\sim 8.3_6)$	$(\sim 7.9_4)$	β^-	$(\sim 2.7_5)$
Tc^{104}	$(\sim 8.9_1)$	$(\sim 5.7_4)$	β^-	$(\sim 5.6_5)$
Tc^{105}	$(\sim 9.1_4)$	$(\sim 7.6_7)$	β^-	$(\sim 3.8_6)$
Ru^{92}	$(\sim 5.7_2)$		ε	(~ 4.4)
Ru^{93}	(~ 6.0)	$(\sim 11.1_5)$	ε	$(\sim 6.0_5)$
Ru^{94}	$(\sim 6.6_4)$	$(\sim 13.4_7)$	ε	$(\sim 1.2_0)$
Ru^{95}	$(\sim 6.9_1)$	$(\sim 8.8_9)$	ε	$(\sim 2.3_5)$
Ru^{96}	$(\sim 7.6_4)$	$(\sim 10.7_7)$		—
Ru^{97}	$(\sim 7.8_6)$	$(\sim 8.3_2)$	ε	$(\sim 0.8_4)$
Ru^{98}	$(\sim 8.5_5)$	$(\sim 10.1_7)$		—
Ru^{99}	$(\sim 8.4_9)$	$(\sim 7.5_7)$		—
Ru^{100}	(9.1_9)	(9.6_8)		—
Ru^{101}	$\sim 9.5_4$	6.9_5†		—
Ru^{102}	(9.8_4)	(8.9_9)		—
Ru^{103}	$\sim 9.9_1$	6.29*	β^-	0.75*
Ru^{104}	$(\sim 10.6_1)$	(8.6_4)		—
Ru^{105}	$(\sim 10.7_5)$	(5.8_8)	β^-	1.9_0*
Ru^{106}	$(\sim 11.3_7)$	(8.2_9)	β^-	0.04*
Ru^{107}		(5.5_7)	β^-	(3.0_0)
Ru^{108}		$(\sim 7.8_7)$	β^-	$(\sim 1.1_8)$
Ru^{109}		$(\sim 5.1_1)$	β^-	$(\sim 4.2_0)$
Ru^{110}		$(\sim 7.5_2)$	β^-	$(\sim 2.4_0)$
Rh^{95}	$(\sim 2.9_6)$		ε	$(\sim 5.1_5)$
Rh^{96}	(~ 3.6)	(~ 9.6)	ε	(~ 6.3)
Rh^{97}	$(\sim 3.8_4)$	(~ 11.0)	ε	$(\sim 3.7_0)$
Rh^{98}	$(\sim 4.7_9)$	$(\sim 9.2_7)$	ε	$\sim 4.6_0$†
Rh^{99}	$(\sim 4.6_9)$	$(\sim 10.0_7)$	ε	2.1_0*
Rh^{100}	(5.2_6)	$(\sim 8.1_4)$	ε	3.64*
Rh^{101}	(5.5_1)	(9.9_3)	ε	(0.6_6)
Rh^{102}	(5.9_3)	(7.3_7)	β^-	1.11*
			ε	2.28*
Rh^{103}	6.26	9.32*		—
Rh^{104}	6.7_6	6.7_9*	β^-	2.44*
			ε	(1.1_0)
Rh^{105}	(7.0_0)	8.8_8	β^-	0.56*
Rh^{106}	(7.5_5)	(6.4_3)	β^-	3.53*
Rh^{107}	7.7_8	8.5_3	β^-	1.5_0*

Table I. (Continued)

Nucleus	S_p	S_n	Q^- or Q_ε	
Rh^{108}	$(\sim 8.2_7)$	$\sim 6.0_5$	β^-	$\sim 4.5_0$†
Rh^{109}	$(\sim 8.5_3)$	$(\sim 8.1_3)$	β^-	$(\sim 2.5_8)$
Rh^{110}	$(\sim 9.1_4)$	$(\sim 5.7_2)$	β^-	$(\sim 5.6_0)$
Rh^{111}	$(\sim 9.3_4)$	$(\sim 7.7_2)$	β^-	$(\sim 3.6_6)$
Pd^{96}	$(\sim 5.3_4)$		ε	(~ 3.5)
Pd^{97}	(~ 5.5)	$(\sim 9.7_2)$	ε	$(\sim 4.7_0)$
Pd^{98}	$(\sim 6.1_9)$	$(\sim 11.6_7)$	ε	$(\sim 2.3_0)$
Pd^{99}	$(\sim 6.0_9)$	$(\sim 9.1_7)$	ε	$\sim 3.2_0$‡
Pd^{100}	$(\sim 7.0_8)$	$(\sim 11.0_6)$	ε	(0.2_8)
Pd^{101}	$(\sim 7.3_4)$	$(\sim 8.4_0)$	ε	1.8_1†
Pd^{102}	(7.7_0)	$(\sim 10.2_9)$		—
Pd^{103}	7.9_8	7.6_5	ε	0.5_6*
Pd^{104}	8.4_5	9.7_9		—
Pd^{105}	8.6_6	7.0_0*		—
Pd^{106}	(9.1_8)	(9.4_0)		—
Pd^{107}	9.2_5	6.5_0	β^-	0.04*
Pd^{108}	9.7_7	9.0_5		—
Pd^{109}	$\sim 9.9_3$	6.2_1	β^-	1.11*
Pd^{110}	$(\sim 10.5_4)$	(8.7_4)		—
Pd^{111}	$(\sim 10.6_0)$	(5.7_8)	β^-	2.2_4†
Pd^{112}	$(\sim 11.2_3)$	8.3_5	β^-	0.30*
Pd^{113}		$(\sim 5.3_2)$	β^-	$(\sim 3.5_0)$
Pd^{114}		$(\sim 8.0_5)$	β^-	$(\sim 1.5_0)$
Pd^{115}		$(\sim 4.9_5)$	β^-	$(\sim 4.6_0)$
Pd^{116}		$(\sim 7.5_5)$	β^-	$(\sim 2.7_0)$
Ag^{101}	$(\sim 3.3_5)$		ε	$(\sim 4.2_7)$
Ag^{102}	$(\sim 4.0_0)$	$(\sim 9.0_5)$	ε	$(\sim 5.5_1)$
Ag^{103}	$\sim 4.1_7$	$(\sim 10.4_6)$	ε	$\sim 2.7_0$†
Ag^{104}	4.7_4	$\sim 8.2_2$	ε	4.27*
Ag^{105}	(5.0_2)	(10.0_7)	ε	(1.2_0)
Ag^{106}	(5.6_5)	(7.6_3)	β^-	(0.3_0)
			ε	2.97*
Ag^{107}	5.7_5	9.5_0†		—
Ag^{108}	6.45	7.20*	β^-	1.6_7†
			ε	1.8_2*
Ag^{109}	6.5_4	9.1_4*		—
Ag^{110}	7.14	6.81*	β^-	2.87*
			ε	(0.8_2)
Ag^{111}	(7.2_4)	(8.8_4)	β^-	1.05*
Ag^{112}	7.8_7	6.4_1	β^-	4.04*
Ag^{113}	8.0_4	8.5_2	β^-	2.00*
Ag^{114}	$(\sim 8.7_6)$	$\sim 6.0_5$	β^-	$\sim 5.0_0$†
Ag^{115}	(8.7_7)	$\sim 8.0_5$	β^-	$\sim 3.1_0$*
Ag^{116}	$(\sim 9.4_7)$	$(\sim 5.6_5)$	β^-	$(\sim 6.2_0)$
Ag^{117}	$(\sim 9.5_9)$	$(\sim 7.6_7)$	β^-	$(\sim 4.3_0)$
Cd^{102}	$(\sim 5.5_0)$		ε	$(\sim 2.7_7)$
Cd^{103}	$(\sim 5.7_2)$	$(\sim 9.2_7)$	ε	$(\sim 3.9_6)$
Cd^{104}	$(\sim 6.3_1)$	$(\sim 11.0_5)$	ε	$(\sim 1.1_3)$
Cd^{105}	$(\sim 6.5_5)$	$(\sim 8.4_6)$	ε	$\sim 2.7_4$‡

Table I. (Continued)

Nucleus	S_p	S_n	Q^- or Q_ε	
Cd^{106}	(7.1_5)	$(\sim 10.6_7)$		—
Cd^{107}	7.2_8	(7.7_6)	ε	1.44*
Cd^{108}	8.0_9	10.3_1		—
Cd^{109}	8.2_0	7.3_1	ε	0.16*
Cd^{110}	8.90	9.84		—
Cd^{111}	(9.1_1)	(7.0_2)		—
Cd^{112}	9.6_7	9.4_0		—
Cd^{113}	9.7_4	$6.4_8^{\dagger}$	β^-	0.31*
Cd^{114}	10.2_6	9.05*		—
Cd^{115}	$\sim 10.3_7$	6.1_5	β^-	1.45*
Cd^{116}	(11.0_7)	(8.7_5)		—
Cd^{117}	$(\sim 11.1_9)$	$(\sim 5.7_7)$	β^-	$(\sim 2.5_5)$
Cd^{118}	$(\sim 11.8_4)$	$(\sim 8.3_2)$	β^-	$(\sim 0.7_0)$
Cd^{119}		$(\sim 5.4_4)$	β^-	$(\sim 3.7_0)$
Cd^{120}		$(\sim 8.0_0)$	β^-	$(\sim 1.8_0)$
Cd^{121}		$(\sim 5.2_5)$	β^-	$(\sim 4.6_5)$
Cd^{122}		$(\sim 7.7_1)$	β^-	$(\sim 2.8_0)$
Cd^{123}		$(\sim 5.0_2)$	β^-	$(\sim 5.6_2)$
Cd^{124}		$(\sim 7.4_3)$	β^-	$(\sim 3.8_0)$
In^{105}	$(\sim 2.8_8)$		ε	$(\sim 4.8_0)$
In^{106}	$(\sim 3.5_4)$	$(\sim 9.1_2)$	ε	$(\sim 6.3_5)$
In^{107}	$(\sim 3.6_8)$	$(\sim 10.8_1)$	ε	$\sim 3.3_0^{\dagger}$
In^{108}	$\sim 4.4_2$	$\sim 8.5_0$	ε	5.1_1*
In^{109}	4.5_1	10.4_0	ε	2.02*
In^{110}	5.1_0	7.9_0	ε	3.9_6*
In^{111}	(5.3_2)	(10.0_6)	ε	(0.9_2)
In^{112}	6.0_1	(7.7_1)	β^-	0.66*
			ε	2.61*
In^{113}	6.0_1	9.4_0		—
In^{114}	6.8_4	7.3_2	β^-	1.98*
			ε	1.4_2*
In^{115}	6.8_2	9.0_2*	β^-	0.50*
In^{116}	7.4_7	$6.8_0^{\dagger}$	β^-	3.2_9*
			ε	(0.5_0)
In^{117}	(7.5_4)	8.8_2	β^-	1.47*
In^{118}	$(\sim 8.2_4)$	$\sim 6.4_7$	β^-	$\sim 4.4_0^{\dagger}$
In^{119}	$(\sim 8.3_6)$	$\sim 8.4_4$	β^-	$2.5_0^{\dagger}$
In^{120}	$(\sim 9.0_2)$	$(\sim 6.1_0)$	β^-	$(\sim 5.5_0)$
In^{121}	$(\sim 9.1_2)$	$(\sim 8.1_0)$	β^-	$(\sim 3.6_0)$
In^{122}	$(\sim 9.7_3)$	$(\sim 5.8_6)$	β^-	$(\sim 6.5_0)$
In^{123}	$(\sim 9.8_6)$	$(\sim 7.8_4)$	β^-	$(\sim 4.5_8)$
In^{124}	$(\sim 10.4_5)$	$(\sim 5.6_1)$	β^-	$(\sim 7.4_2)$
In^{125}	$(\sim 10.5_4)$	$(\sim 7.5_2)$	β^-	$(\sim 5.6_0)$
Sn^{106}	$(\sim 4.9_9)$		ε	$(\sim 3.3_5)$
Sn^{107}	$(\sim 5.1_3)$	$(\sim 9.2_6)$	ε	$(\sim 4.9_0)$
Sn^{108}	$(\sim 5.8_6)$	$(\sim 11.5_4)$	ε	$(\sim 1.8_6)$
Sn^{109}	$(\sim 5.8_2)$	$(\sim 8.4_6)$	ε	$(\sim 3.8_0)$
Sn^{110}	$(\sim 6.7_2)$	$(\sim 11.3_0)$	ε	$(\sim 0.4_0)$
Sn^{111}	$(\sim 6.7_6)$	$(\sim 7.9_4)$	ε	2.5_2*

Table I. (Continued)

Nucleus	S_p	S_n	Q^- or Q_ε	
Sn^{112}	(7.5_9)	$(\sim 10.8_9)$		—
Sn^{113}	$\sim 7.6_2$	$\sim 7.7_4$	ε	$\sim 1.0_0^{\dagger}$
Sn^{114}	8.5_2	$\sim 10.3_0$		—
Sn^{115}	8.7_4	7.5_4		—
Sn^{116}	9.3_1	$9.5_9^{\dagger}$		—
Sn^{117}	9.5_1	$7.0_0^{\dagger}$		—
Sn^{118}	10.0_9	$9.4_0^{\dagger}$		—
Sn^{119}	$\sim 10.1_6$	6.5_4*		—
Sn^{120}	10.8_2	$9.1_0^{\ddagger}$		—
Sn^{121}	$(\sim 10.9_2)$	6.2_0*	β^-	0.38*
Sn^{122}	$(\sim 11.5_8)$	$8.7_6^{\ddagger}$		—
Sn^{123}	$(\sim 11.6_4)$	$5.9_2^{\ddagger}$	β^-	1.42*
Sn^{124}	$(\sim 12.2_5)$	$8.4_5^{\dagger}$		—
Sn^{125}	$(\sim 12.3_4)$	$5.7_0^{\dagger}$	β^-	2.34*
Sn^{126}	$(\sim 12.9_2)$	$(\sim 8.1_0)$	β^-	$(\sim 0.4_5)$
Sn^{127}		$(\sim 5.4_8)$	β^-	$(\sim 3.2_2)$
Sn^{128}		$(\sim 7.8_1)$	β^-	$(\sim 1.4_5)$
Sn^{129}		$(\sim 5.3_0)$	β^-	$(\sim 4.1_0)$
Sn^{130}		$(\sim 7.4_7)$	β^-	$(\sim 2.4_0)$
Sb^{111}	$(\sim 2.1_3)$		ε	$(\sim 5.0_3)$
Sb^{112}	$(\sim 2.8_5)$	$(\sim 8.6_6)$	ε	$(\sim 7.2_6)$
Sb^{113}	$(\sim 2.9_5)$	$(\sim 10.9_9)$	ε	$(\sim 4.0_1)$
Sb^{114}	$(\sim 3.5_9)$	$(\sim 8.3_8)$	ε	$(\sim 5.9_3)$
Sb^{115}	3.7_3	$(\sim 10.4_4)$	ε	3.03*
Sb^{116}	$\sim 4.3_0$	$\sim 8.1_1$	ε	4.5_1*
Sb^{117}	$\sim 4.4_0$	$\sim 9.6_9$	ε	1.8_2*
Sb^{118}	$\sim 4.9_2$	$\sim 7.5_2$	ε	3.7_0*
Sb^{119}	5.1_8	$\sim 9.6_6$	ε	0.58*
Sb^{120}	5.6_0	6.9_6	β^-	(1.0_0)
			ε	2.72*
Sb^{121}	5.8_0	9.3_0*		—
Sb^{122}	6.3_9	6.7_9*	β^-	1.97*
			ε	1.59*
Sb^{123}	6.5_6	$8.9_3^{\dagger}$		—
Sb^{124}	6.9_9	6.3_5	β^-	2.92*
			ε	0.6_8
Sb^{125}	7.2_6	8.7_2	β^-	0.76*
Sb^{126}	$(\sim 7.7_7)$	$(\sim 6.2_1)$	β^-	$(\sim 3.6_0)$
Sb^{127}	$(\sim 7.9_2)$	$(\sim 8.2_5)$	β^-	$1.6_7^{\dagger}$
Sb^{128}	$(\sim 8.4_8)$	$(\sim 6.0_4)$	β^-	$(\sim 4.3_0)$
Sb^{129}	$(\sim 8.6_2)$	$(\sim 7.9_5)$	β^-	$(\sim 2.5_0)$
Sb^{130}	$(\sim 9.0_9)$	$(\sim 5.7_7)$	β^-	$(\sim 5.2_0)$
Sb^{131}	$(\sim 9.2_8)$	$(\sim 7.6_6)$	β^-	$(\sim 3.4_7)$
Te^{112}	$(\sim 3.8_6)$		ε	$(\sim 4.0_2)$
Te^{113}	$(\sim 4.0_1)$	$(\sim 8.8_1)$	ε	$(\sim 6.2_0)$
Te^{114}	$(\sim 4.7_0)$	$(\sim 11.6_8)$	ε	$(\sim 2.9_0)$
Te^{115}	$(\sim 4.8_6)$	$(\sim 8.5_4)$	ε	$(\sim 4.8_0)$
Te^{116}	$(\sim 5.5_1)$	$(\sim 11.0_9)$	ε	$(\sim 1.8_2)$
Te^{117}	$\sim 5.4_1$	$(\sim 8.0_1)$	ε	3.5_0*

Table I. (Continued)

Nucleus	S_p	S_n	Q^- or Q_ε	
Te^{118}	$(\sim 6.3_4)$	$(\sim 10.6_2)$	ε	$(\sim 0.4_0)$
Te^{119}	$\sim 6.5_9$	$(\sim 7.7_7)$	ε	2.2_9†
Te^{120}	(7.1_8)	$(\sim 10.2_5)$		—
Te^{121}	(7.5_2)	(7.3_0)	ε	(1.0_0)
Te^{122}	7.9_8	(9.7_6)		—
Te^{123}	(8.0_5)	(6.8_6)	ε	(0.1_0)
Te^{124}	8.4_9	(9.3_7)		—
Te^{125}	8.7_0	6.5_6*		—
Te^{126}	9.0_3	9.0_5*		—
Te^{127}	$(\sim 9.1_4)$	6.3_2	β_-	0.69*
Te^{128}	$(\sim 9.5_6)$	(8.6_7)		—
Te^{129}	$(\sim 9.6_7)$	(6.1_5)	β^-	1.48*
Te^{130}	$(\sim 10.1_9)$	(8.4_7)		—
Te^{131}	$(\sim 10.3_5)$	(5.9_3)	β^-	2.28*
Te^{132}	$(\sim 10.8_0)$	8.1_1	β^-	0.50*
Te^{133}		$(\sim 5.8_0)$	β^-	$(\sim 3.0_4)$
Te^{134}		$(\sim 7.5_0)$	β^-	$(\sim 1.7_8)$
Te^{135}		$(\sim 3.4_3)$	β^-	$(\sim 6.0_8)$
Te^{136}		$(\sim 5.1_5)$	β^-	$(\sim 4.8_0)$
I^{119}	$(\sim 3.4_8)$		ε	$(\sim 3.5_1)$
I^{120}	$(\sim 4.0_7)$	$(\sim 8.3_6)$	ε	$(\sim 5.4_0)$
I^{121}	(4.1_6)	$(\sim 10.3_4)$	ε	2.3_6*
I^{122}	(4.8_4)	(7.9_8)	ε	4.14*
I^{123}	(4.9_1)	(9.8_3)	ε	(1.1_7)
I^{124}	(5.3_7)	(7.3_2)	β^-	0.3_2
			ε	3.22*
I^{125}	5.6_3	9.6_3	ε	0.1_5*
I^{126}	6.1_4	7.0_7	β^-	1.25*
			ε	2.13*
I^{127}	6.2_3	9.1_4*		—
I^{128}	6.6_9	6.7_8#	β^-	2.12*
			ε	(1.2_0)
I^{129}	(6.8_5)	8.8_3	β^-	0.19*
I^{130}	7.2_1	6.5_1	β^-	2.95*
			ε	(0.4_8)
I^{131}	(7.4_3)	8.6_9	β^-	0.97*
I^{132}	7.8_3	6.3_3	β^-	3.57*
I^{133}	8.0_6	8.3_4	β^-	1.7_6*
I^{134}	$(\sim 8.5_0)$	$\sim 6.2_4$	β^-	4.1_5*
I^{135}	$(\sim 8.7_3)$	$\sim 7.7_3$	β^-	2.8_0†
I^{136}	$(\sim 9.1_7)$	$\sim 3.8_7$	β^-	7.0_0*
I^{137}	$(\sim 9.3_1)$	$(\sim 5.2_9)$	β^-	$(\sim 5.7_5)$
Xe^{120}	$(\sim 5.3_8)$		ε	$(\sim 2.2_0)$
Xe^{121}	$(\sim 5.5_1)$	$(\sim 8.4_9)$	ε	$(\sim 4.0_5)$
Xe^{122}	$(\sim 6.1_7)$	$(\sim 11.0_0)$	ε	$(\sim 1.0_3)$
Xe^{123}	(6.1_9)	$(\sim 8.0_0)$	ε	2.8_6*
Xe^{124}	(6.8_6)	(10.5_0)		—
Xe^{125}	(7.0_9)	(7.5_5)	ε	(1.7_6)
Xe^{126}	7.5_4	(10.0_8)		—

Table I. (Continued)

Nucleus	S_p	S_n	Q^- or Q_ε	
Xe^{127}	(7.6_6)	(7.1_9)	ε	(0.7_0)
Xe^{128}	8.1_2	(9.6_0)		—
Xe^{129}	8.2_4	6.9_0		—
Xe^{130}	8.6_8	9.2_7		—
Xe^{131}	8.8_8	6.7_1		—
Xe^{132}	9.1_2	8.9_3*		—
Xe^{133}	9.3_2	6.5_3	β^-	0.43*
Xe^{134}	9.6_1	8.6_3		—
Xe^{135}	$\sim 9.7_5$	6.3_8	β^-	1.16*
Xe^{136}	$\sim 10.0_9$	8.0_7		—
Xe^{137}	$(\sim 10.2_6)$	(4.0_4)	β^-	(4.2_2)
Xe^{138}	$(\sim 10.7_7)$	(5.8_0)	β^-	(2.9_0)
Xe^{139}		$(\sim 3.8_1)$	β^-	$(\sim 5.0_0)$
Xe^{140}		$(\sim 5.6_3)$	β^-	$(\sim 3.7_6)$
Cs^{123}	$(\sim 3.0_4)$		ε	$(\sim 4.1_8)$
Cs^{124}	$(\sim 3.5_4)$	$(\sim 8.5_0)$	ε	$(\sim 6.1_8)$
Cs^{125}	(3.7_0)	$(\sim 10.6_6)$	ε	3.0_7*
Cs^{126}	$(\sim 4.2_4)$	$(\sim 8.0_9)$	ε	$\sim 5.0_6$†
Cs^{127}	(4.3_2)	$(\sim 10.1_6)$	ε	2.09*
Cs^{128}	$(\sim 4.8_2)$	$(\sim 7.6_9)$	ε	4.0_0*
Cs^{129}	(4.9_9)	$(\sim 9.7_7)$	ε	(1.1_3)
Cs^{130}	5.5_0	(7.4_1)	β^-	0.4_4*
			ε	2.9_9*
Cs^{131}	5.5_7	9.3_4	ε	0.36*
Cs^{132}	6.0_9	7.2_3	β^-	(1.2_1)
			ε	2.0_6
Cs^{133}	6.1_8†	9.0_2*		—
Cs^{134}	6.5_5	6.9_0†	β^-	2.05*
			ε	1.3_0
Cs^{135}	6.7_6	8.8_4	β^-	0.21*
Cs^{136}	(7.2_7)	(6.8_9)	β^-	(2.5_0)
			ε	(0.0_2)
Cs^{137}	7.4_8	(8.2_8)	β^-	1.18*
Cs^{138}	(7.9_2)	(4.4_8)	β^-	5.2_9#
Cs^{139}	$(\sim 8.0_3)$	$(\sim 5.9_1)$	β^-	$\sim 4.1_0$†
Cs^{140}	$(\sim 8.6_1)$	$(\sim 4.3_9)$	β^-	$(\sim 6.2_0)$
Cs^{141}	$(\sim 8.7_0)$	$(\sim 5.7_2)$	β^-	$(\sim 5.0_0)$
Ba^{124}	$(\sim 5.1_2)$		ε	$(\sim 2.6_0)$
Ba^{125}	$(\sim 5.2_5)$	$(\sim 8.6_3)$	ε	$(\sim 4.6_3)$
Ba^{126}	$(\sim 5.8_1)$	$(\sim 11.2_2)$	ε	$(\sim 1.5_0)$
Ba^{127}	$(\sim 5.8_7)$	$(\sim 8.1_5)$	ε	$(\sim 3.5_1)$
Ba^{128}	$(\sim 6.4_1)$	$(\sim 10.7_0)$	ε	$(\sim 0.5_0)$
Ba^{129}	$(\sim 6.5_4)$	$(\sim 7.8_2)$	ε	2.4_5*
Ba^{130}	(7.0_7)	$(\sim 10.3_0)$		—
Ba^{131}	(7.1_4)	(7.4_8)	ε	(1.4_2)
Ba^{132}	(7.6_6)	(9.8_6)		—
Ba^{133}	7.7_5	(7.3_2)	ε	0.4_9*
Ba^{134}	8.1_7	9.4_4		—
Ba^{135}	8.2_7	7.0_0†		—

Table I. (Continued)

Nucleus	S_p	S_n	Q^- or Q_ε	
Ba^{136}	8.6_1	9.1_8†		—
Ba^{137}	(8.6_7)	6.9_5*		—
Ba^{138}	8.9_9	8.6_0*		—
Ba^{139}	(9.2_3)	4.7_2*	β^-	2.38*
Ba^{140}	$\sim 9.8_1$	6.4_9	β^-	1.05*
Ba^{141}	$(\sim 9.9_4)$	(4.5_2)	β^-	(3.3_4)
Ba^{142}	$(\sim 10.5_0)$	(6.2_8)	β^-	$(\sim 2.1_3)$
Ba^{143}		$(\sim 4.0_7)$	β^-	$(\sim 4.4_5)$
Ba^{144}		$(\sim 6.1_8)$	β^-	$(\sim 2.7_9)$
La^{129}	$(\sim 3.0_5)$		ε	$(\sim 3.9_9)$
La^{130}	$(\sim 3.5_5)$	$(\sim 8.3_2)$	ε	$(\sim 5.9_7)$
La^{131}	(3.7_4)	$(\sim 10.4_9)$	ε	2.9_6*
La^{132}	$(\sim 4.2_8)$	$(\sim 8.0_2)$	ε	4.8_0*
La^{133}	(4.3_3)	$(\sim 9.9_1)$	ε	(2.2_1)
La^{134}	$\sim 4.9_6$	$(\sim 7.9_5)$	ε	$\sim 3.7_0$*
La^{135}	(4.9_7)	$(\sim 9.4_5)$	ε	(1.2_5)
La^{136}	$\sim 5.6_0$	$(\sim 7.6_3)$	β^-	$\sim 0.2_5$
			ε	$\sim 2.8_0$*
La^{137}	(5.6_4)	$(\sim 9.2_2)$	ε	(0.5_3)
La^{138}	6.1_3	(7.4_4)	β^-	1.01*
			ε	1.6_9
La^{139}	6.3_2	8.7_9*		—
La^{140}	6.7_6	5.1_6†	β^-	3.80*
La^{141}	7.0_8	6.8_1	β^-	2.43*
La^{142}	$(\sim 7.6_3)$	$\sim 5.0_7$	β^-	$\sim 4.5_0$*
La^{143}	$(\sim 7.7_4)$	$(\sim 6.3_9)$	β^-	$(\sim 3.2_5)$
La^{144}	$(\sim 8.1_9)$	$(\sim 4.5_2)$	β^-	$(\sim 5.6_5)$
La^{145}	$(\sim 8.3_4)$	$(\sim 6.3_3)$	β^-	$(\sim 3.9_9)$
Ce^{130}	$(\sim 5.1_7)$		ε	$(\sim 2.3_7)$
Ce^{131}	$(\sim 5.3_1)$	$(\sim 8.4_6)$	ε	$(\sim 4.4_0)$
Ce^{132}	$(\sim 5.8_4)$	$(\sim 11.0_2)$	ε	$(\sim 1.4_0)$
Ce^{133}	$(\sim 5.8_8)$	$(\sim 8.0_6)$	ε	$(\sim 3.2_5)$
Ce^{134}	$(\sim 6.4_7)$	$(\sim 10.5_0)$	ε	$(\sim 0.7_0)$
Ce^{135}	$(\sim 6.4_7)$	$(\sim 7.9_5)$	ε	$(\sim 2.2_0)$
Ce^{136}	$(\sim 7.1_0)$	$(\sim 10.0_8)$		—
Ce^{137}	$(\sim 7.0_9)$	(7.6_2)	ε	(1.3_5)
Ce^{138}	(7.6_7)	(9.8_0)		—
Ce^{139}	7.7_4	7.5_1	ε	0.27*
Ce^{140}	8.1_8	9.2_3†		—
Ce^{141}	8.4_6	5.4_4†	β^-	0.58*
Ce^{142}	8.7_9	7.1_4†		—
Ce^{143}	$\sim 8.8_6$	5.1_4†	β^-	1.45*
Ce^{144}	$(\sim 9.3_9)$	6.9_2	β^-	0.32*
Ce^{145}	$(\sim 9.5_4)$	$(\sim 4.6_7)$	β^-	$\sim 2.6_0$‡
Ce^{146}	$(\sim 10.0_0)$	$(\sim 6.7_9)$	β^-	1.0_0*
Ce^{147}		$(\sim 4.4_7)$	β^-	$(\sim 3.4_5)$
Ce^{148}		$(\sim 6.6_6)$	β^-	$(\sim 1.8_0)$
Ce^{149}		$(\sim 4.4_5)$	β^-	$(\sim 4.2_0)$
Ce^{150}		$(\sim 6.5_4)$	β^-	$(\sim 2.6_5)$

Table I. (Continued)

Nucleus	S_p	S_n	Q^- or Q_ε	
Pr^{135}	$(\sim 3.4_4)$		ε	$(\sim 3.7_3)$
Pr^{136}	$(\sim 3.9_7)$	$(\sim 8.4_8)$	ε	$(\sim 5.3_3)$
Pr^{137}	$(\sim 4.0_9)$	$(\sim 10.2_0)$	ε	2.7_5†
Pr^{138}	$(\sim 4.5_7)$	$(\sim 8.1_0)$	ε	$(\sim 4.4_5)$
Pr^{139}	4.7_3	$(\sim 9.9_6)$	ε	2.0_0*
Pr^{140}	5.1_1	7.8_9	ε	3.3_4†
Pr^{141}	5.2_4	9.3_6*		—
Pr^{142}	5.6_6	5.8_6†	β^-	2.15*
			ε	0.7_0
Pr^{143}	5.8_1	7.2_9	β^-	0.93*
Pr^{144}	6.4_6	5.7_9	β^-	2.99*
Pr^{145}	6.4_9	6.9_5	β^-	1.80*
Pr^{146}	$(\sim 7.0_1)$	$\sim 5.1_9$	β^-	4.2_0*
Pr^{147}	$(\sim 7.1_4)$	$(\sim 6.9_2)$	β^-	$(\sim 2.5_4)$
Pr^{148}	$(\sim 7.6_8)$	$(\sim 5.0_1)$	β^-	$(\sim 4.8_9)$
Pr^{149}	$(\sim 7.8_7)$	$(\sim 6.8_5)$	β^-	$(\sim 3.1_4)$
Pr^{150}	$(\sim 8.4_1)$	$(\sim 4.9_9)$	β^-	$(\sim 5.4_9)$
Pr^{151}	$(\sim 8.6_5)$	$(\sim 6.7_8)$	β^-	$(\sim 3.8_0)$
Nd^{136}	$(\sim 5.4_0)$		ε	$(\sim 2.3_0)$
Nd^{137}	$(\sim 5.4_7)$	$(\sim 8.5_5)$	ε	$(\sim 3.9_5)$
Nd^{138}	$(\sim 6.0_2)$	$(\sim 10.7_5)$	ε	$(\sim 1.3_0)$
Nd^{139}	$(\sim 6.1_8)$	$(\sim 8.2_6)$	ε	$(\sim 3.0_0)$
Nd^{140}	(6.6_4)	$(\sim 10.4_2)$	ε	(0.4_7)
Nd^{141}	6.7_8	(8.0_3)	ε	1.80*
Nd^{142}	7.2_3	9.8_1		—
Nd^{143}	7.4_4	6.0_7†		—
Nd^{144}	8.0_0	7.8_5†		—
Nd^{145}	7.9_7	5.7_6†		—
Nd^{146}	8.6_1	7.5_9†		—
Nd^{147}	$\sim 8.6_8$	5.2_6	β^-	0.90*
Nd^{148}	$(\sim 9.1_2)$	7.3_6		—
Nd^{149}	$(\sim 9.2_1)$	5.1_0	β^-	1.6_4†
Nd^{150}	$(\sim 9.7_0)$	7.3_4	β^-	$(\sim 0.0_2)$
Nd^{151}	$(\sim 9.8_0)$	$\sim 5.0_9$	β^-	2.4_0*
Nd^{152}	$(\sim 10.2_9)$	$(\sim 7.2_7)$	β^-	$(\sim 0.8_5)$
Nd^{153}		$(\sim 5.0_2)$	β^-	$(\sim 3.3_6)$
Nd^{154}		$(\sim 6.4_5)$	β^-	$(\sim 2.5_0)$
Pm^{139}	$(\sim 3.0_3)$		ε	$(\sim 4.4_5)$
Pm^{140}	$(\sim 3.5_4)$	$(\sim 8.7_7)$	ε	$(\sim 6.1_0)$
Pm^{141}	$(\sim 3.6_8)$	$(\sim 10.5_6)$	ε	3.5_7†
Pm^{142}	4.2_3	$\sim 8.5_8$	ε	4.8_0*
Pm^{143}	$(\sim 4.2_9)$	$(\sim 9.8_7)$	ε	$(\sim 1.0_0)$
Pm^{144}	$(\sim 4.7_7)$	$(\sim 6.5_5)$	β^-	$(\sim 0.5_0)$
			ε	$(\sim 2.3_0)$
Pm^{145}	4.8_4	$(\sim 7.9_2)$	ε	0.14*
Pm^{146}	5.3_0	6.2_2	β^-	1.53*
			ε	1.5_1
Pm^{147}	5.3_8	7.6_7	β^-	0.22*
Pm^{148}	6.0_2	5.9_0	β^-	2.46*

Table I. (Continued)

Nucleus	S_p	S_n	Q^- or Q_ε	
			ε	0.5_6
Pm^{149}	5.9_6	7.3_0	β^-	1.06^*
Pm^{150}	$(\sim 6.5_8)$	$(\sim 5{\cdot}7_2)$	β^-	$\sim 3.3_4^{\ddagger}$
Pm^{151}	$\sim 6.7_0$	$(\sim 7.4_7)$	β^-	$\sim 1.6_0^{\dagger}$
Pm^{152}	$(\sim 7.3_4)$	$(\sim 5.7_2)$	β^-	$(\sim 3.9_5)$
Pm^{153}	$(\sim 7.6_0)$	$(\sim 7.5_3)$	β^-	$(\sim 2.2_0)$
Pm^{154}	$(\sim 8.1_7)$	$(\sim 5.5_9)$	β^-	$(\sim 4.6_1)$
Pm^{155}	$(\sim 8.4_1)$	$(\sim 6.6_9)$	β^-	$(\sim 3.6_0)$
Sm^{140}	$(\sim 4.9_4)$		ε	$(\sim 3.0_5)$
Sm^{141}	$(\sim 5.0_8)$	$(\sim 8.9_1)$	ε	$(\sim 4.7_0)$
Sm^{142}	$\sim 5.6_0$	$(\sim 11.0_8)$	ε	$\sim 2.2_0^{\dagger}$
Sm^{143}	$(\sim 5.6_9)$	$(\sim 8.6_7)$	ε	$\sim 3.4_0^{\dagger}$
Sm^{144}	$(\sim 6.2_7)$	$(\sim 10.4_5)$		—
Sm^{145}	$(\sim 6.5_0)$	6.7_8	ε	0.6_4^*
Sm^{146}	6.9_7	8.3_9		—
Sm^{147}	7.1_1	6.3_7		—
Sm^{148}	7.5_8	8.1_4^*		—
Sm^{149}	7.5_8	$5.9_0^{\dagger}$		—
Sm^{150}	8.28	8.00^*		—
Sm^{151}	$(\sim 8.2_8)$	5.7_3	β^-	0.08^*
Sm^{152}	$\sim 8.8_9$	8.0_8		—
Sm^{153}	$(\sim 8.9_5)$	5.7_8	β^-	0.81^*
Sm^{154}	$(\sim 9.4_2)$	(8.0_0)		—
Sm^{155}	$(\sim 9.5_1)$	(5.6_8)	β^-	1.75^*
Sm^{156}	$(\sim 9.9_9)$	7.1_7	β^-	$0.8_6^{\dagger}$
Sm^{157}		$(\sim 5.3_0)$	β^-	$(\sim 2.9_5)$
Sm^{158}		$(\sim 6.8_7)$	β^-	$(\sim 1.8_5)$
Sm^{159}		$(\sim 4.8_2)$	β^-	$(\sim 4.1_5)$
Sm^{160}		$(\sim 6.3_4)$	β^-	$(\sim 3.1_5)$
Eu^{143}	$(\sim 2.6_4)$		ε	$(\sim 5.2_5)$
Eu^{144}	$(\sim 3.1_2)$	$(\sim 9.1_5)$	ε	$(\sim 6.5_5)$
Eu^{145}	$(\sim 3.3_0)$	$(\sim 10.6_3)$	ε	$(\sim 2.7_0)$
Eu^{146}	$\sim 3.7_3$	$(\sim 7.2_1)$	ε	$\sim 3.8_8^*$
Eu^{147}	$(\sim 3.8_8)$	$(\sim 8.5_4)$	ε	$(\sim 1.7_1)$
Eu^{148}	$(\sim 4.2_7)$	$(\sim 6.7_6)$	β^-	$(\sim 0.0_0)$
			ε	$(\sim 3.0_9)$
Eu^{149}	(4.4_0)	$(\sim 8.2_7)$	ε	(0.7_2)
Eu^{150}	4.8_8	(6.3_8)	β^-	$1.0_2^{\dagger}$
			ε	2.3_4
Eu^{151}	5.0_2	$8.1_4^{\dagger}$		—
Eu^{152}	5.4_3	6.1_4	β^-	1.81^*
			ε	1.86^*
Eu^{153}	5.8_1	$8.4_5^{\ddagger}$		—
Eu^{154}	(6.5_2)	(6.4_9)	β^-	1.97^*
			ε	(0.7_0)
Eu^{155}	(6.6_5)	8.1_3	β^-	0.25^*
Eu^{156}	7.2_5	6.2_8	β^-	2.5_9^*
Eu^{157}	7.4_7	7.3_9	β^-	$1.5_6^{\dagger}$
Eu^{158}	$(\sim 7.9_4)$	$(\sim 5.7_7)$	β^-	$(\sim 3.7_0)$

Table I. (Continued)

Nucleus	S_p	S_n	Q^- or Q_ε	
Eu^{159}	$(\sim 8.1_9)$	$(\sim 7.1_2)$	β^-	$(\sim 2.5_0)$
Eu^{160}	$(\sim 8.7_1)$	$(\sim 5.3_4)$	β^-	$(\sim 4.7_0)$
Eu^{161}	$(\sim 8.9_1)$	$(\sim 6.5_4)$	β^-	$(\sim 3.7_0)$
Gd^{144}	$(\sim 4.6_7)$		ε	$(\sim 3.7_0)$
Gd^{145}	$(\sim 4.8_0)$	$(\sim 9.2_8)$	ε	$\sim 5.0_5^{\dagger}$
Gd^{146}	$(\sim 5.3_1)$	$(\sim 11.1_4)$	ε	$(\sim 1.1_2)$
Gd^{147}	$(\sim 5.5_1)$	$(\sim 7.4_1)$	ε	$(\sim 2.2_5)$
Gd^{148}	$(\sim 5.9_8)$	$(\sim 9.0_1)$	ε	$(\sim 0.0_0)$
Gd^{149}	$(\sim 6.1_9)$	6.9_7	ε	$(\sim 1.3_0)$
Gd^{150}	(6.6_2)	8.7_0		—
Gd^{151}	(6.7_3)	(6.4_9)	ε	(0.6_3)
Gd^{152}	7.1_7	(8.5_8)		—
Gd^{153}	7.4_0	6.3_7	ε	0.2_7^*
Gd^{154}	(7.6_8)	(8.7_3)		—
Gd^{155}	7.6_0	6.4_1^*		—
Gd^{156}	8.0_9	$8.6_2^{\dagger}$		—
Gd^{157}	8.1_7	6.3_6^*		—
Gd^{158}	8.6_9	$7.9_1^{\dagger}$		—
Gd^{159}	$(\sim 8.8_4)$	(5.9_2)	β^-	0.94^*
Gd^{160}	$(\sim 9.2_6)$	(7.5_4)		—
Gd^{161}	$(\sim 9.4_6)$	(5.5_4)	β^-	2.0_2^*
Gd^{162}	$(\sim 9.9_7)$	(7.0_5)	β^-	$(\sim 1.0_0)$
Gd^{163}		$(\sim 4.9_6)$	β^-	$(\sim 3.3_2)$
Gd^{164}		$(\sim 6.4_2)$	β^-	$(\sim 2.3_5)$
Tb^{149}	$(\sim 2.5_0)$		ε	$(\sim 3.6_9)$
Tb^{150}	$(\sim 2.9_6)$	$(\sim 7.4_3)$	ε	$(\sim 4.9_6)$
Tb^{151}	$(\sim 3.1_2)$	$(\sim 8.8_6)$	ε	$(\sim 2.5_9)$
Tb^{152}	$(\sim 3.7_0)$	$(\sim 7.0_7)$	ε	$(\sim 4.1_0)$
Tb^{153}	$(\sim 3.9_3)$	$(\sim 8.8_1)$	ε	$(\sim 1.6_6)$
Tb^{154}	$(\sim 4.3_5)$	$(\sim 6.7_9)$	β^-	$(\sim 0.2_9)$
			ε	$(\sim 3.6_0)$
Tb^{155}	(4.6_9)	$(\sim 9.0_7)$	ε	(0.9_4)
Tb^{156}	$(\sim 5.1_8)$	$(\sim 6.9_0)$	β^-	$(\sim 0.5_0)$
			ε	$(\sim 2.6_6)$
Tb^{157}	(5.3_5)	$(\sim 8.7_9)$	ε	(0.2_3)
Tb^{158}	(5.8_5)	(6.8_6)	β^-	(0.8_8)
			ε	(1.2_8)
Tb^{159}	(6.0_8)	8.1_4^*		—
Tb^{160}	(6.5_6)	(6.4_0)	β^-	1.83^*
			ε	(0.2_0)
Tb^{161}	(6.7_8)	7.7_6	β^-	0.54^*
Tb^{162}	$(\sim 7.2_7)$	$(\sim 6.0_3)$	β^-	$(\sim 2.7_0)$
Tb^{163}	(7.5_0)	$(\sim 7.2_8)$	β^-	(1.6_0)
Tb^{164}	$(\sim 7.9_9)$	$(\sim 5.4_5)$	β^-	$(\sim 3.8_7)$
Tb^{165}	$(\sim 8.1_4)$	$(\sim 6.5_7)$	β^-	$(\sim 2.9_0)$
Dy^{150}	$(\sim 5.0_5)$		ε	$(\sim 1.6_0)$
Dy^{151}	$(\sim 5.1_9)$	$(\sim 7.5_7)$	ε	$(\sim 2.8_9)$
Dy^{152}	$(\sim 5.7_5)$	$(\sim 9.4_2)$	ε	$(\sim 0.5_4)$
Dy^{153}	$(\sim 5.8_4)$	7.1_6	ε	$(\sim 2.1_9)$

Table I. (Continued)

Nucleus	S_p	S_n	Q^- or Q_ε	
Dy^{154}	$(\sim 6.3_0)$	9.2_7		—
Dy^{155}	$(\sim 6.4_2)$	(6.9_1)	ε	1.8_7*
Dy^{156}	(6.6_2)	(9.2_7)		—
Dy^{157}	$(\sim 6.6_3)$	(6.9_1)	ε	(1.3_8)
Dy^{158}	(6.9_6)	(9.1_2)		—
Dy^{159}	(6.9_8)	(6.8_8)	ε	0.38*
Dy^{160}	(7.4_5)	(8.6_1)		—
Dy^{161}	7.5_2	6.4_7†		—
Dy^{162}	7.9_5	8.1_9†		—
Dy^{163}	$(\sim 8.1_0)$	6.1_8†		—
Dy^{164}	(8.5_4)	7.7_2†		—
Dy^{165}	$(\sim 8.6_9)$	(5.6_0)	β^-	1.28*
Dy^{166}	$(\sim 9.1_4)$	(7.0_3)	β^-	0.49*
Dy^{167}		$(\sim 5.2_3)$	β^-	$(\sim 2.4_5)$
Dy^{168}		$(\sim 6.7_1)$	β^-	$(\sim 1.5_0)$
Dy^{169}		$(\sim 4.8_2)$	β^-	$(\sim 3.5_5)$
Dy^{170}		$(\sim 6.1_6)$	β^-	$(\sim 2.7_5)$
Ho^{155}	$(\sim 2.5_8)$		ε	$(\sim 3.5_5)$
Ho^{156}	$(\sim 3.0_9)$	$(\sim 7.4_2)$	ε	$(\sim 5.4_0)$
Ho^{157}	$(\sim 3.2_8)$	$(\sim 9.4_6)$	ε	$(\sim 2.8_5)$
Ho^{158}	$(\sim 3.7_9)$	$(\sim 7.4_2)$	ε	$(\sim 4.5_5)$
Ho^{159}	$(\sim 4.0_0)$	$(\sim 9.3_3)$	ε	$(\sim 2.1_0)$
Ho^{160}	$(\sim 4.5_4)$	$(\sim 7.4_2)$	ε	3.2_9*
Ho^{161}	(4.7_1)	$(\sim 8.7_8)$	ε	(0.9_8)
Ho^{162}	$(\sim 5.1_1)$	$(\sim 6.8_7)$	β^-	$(\sim 0.1_0)$
			ε	$(\sim 2.3_0)$
Ho^{163}	(5.3_9)	$(\sim 8.4_7)$	ε	(0.0_1)
Ho^{164}	(5.7_2)	(6.5_1)	β^-	0.9_9*
			ε	(1.2_2)
Ho^{165}	(6.1_0)	8.1_0*		—
Ho^{166}	(6.7_3)	(6.2_4)	β^-	1.85*
Ho^{167}	6.9_0	7.2_0	β^-	1.0_0*
Ho^{168}	$(\sim 7.4_3)$	$(\sim 5.7_6)$	β^-	$(\sim 3.0_0)$
Ho^{169}	$(\sim 7.5_9)$	$(\sim 6.8_7)$	β^-	$(\sim 2.0_5)$
Ho^{170}	$(\sim 8.1_2)$	$(\sim 5.3_6)$	β^-	$(\sim 4.0_5)$
Ho^{171}	$(\sim 8.3_5)$	$(\sim 6.3_8)$	β^-	$(\sim 3.2_5)$
Er^{156}	$(\sim 4.8_4)$		ε	$(\sim 1.8_0)$
Er^{157}	$(\sim 4.9_3)$	$(\sim 7.5_1)$	ε	$(\sim 3.7_5)$
Er^{158}	$(\sim 5.2_9)$	$(\sim 9.8_2)$	ε	$(\sim 1.3_5)$
Er^{159}	$(\sim 5.3_5)$	$(\sim 7.4_8)$	ε	$(\sim 3.2_0)$
Er^{160}	$(\sim 5.7_3)$	$(\sim 9.7_1)$	ε	$(\sim 0.9_1)$
Er^{161}	$(\sim 5.7_5)$	$(\sim 7.4_4)$	ε	$(\sim 2.2_5)$
Er^{162}	(6.1_9)	$(\sim 9.2_2)$		—
Er^{163}	$(\sim 6.3_8)$	(7.0_6)	ε	$(\sim 1.3_1)$
Er^{164}	(6.7_2)	(8.8_1)		—
Er^{165}	(6.9_7)	(6.7_6)	ε	(0.3_5)
Er^{166}	(7.3_0)	(8.4_3)		—
Er^{167}	7.4_1	6.3_5†		—
Er^{168}	7.9_8	7.7_6*		—

Table I. (Continued)

Nucleus	S_p	S_n	Q^- or Q_ε	
Er^{169}	$(\sim 8.1_4)$	(5.9_2)	β^-	0.34*
Er^{170}	$(\sim 8.6_2)$	(7.3_6)		—
Er^{171}	$(\sim 8.8_5)$	(5.5_8)	β^-	1.48*
Er^{172}	$(\sim 9.3_5)$	(6.8_8)	β^-	$(\sim 0.8_0)$
Er^{173}		$(\sim 5.0_8)$	β^-	$(\sim 2.6_7)$
Er^{174}		$(\sim 6.3_6)$	β^-	$(\sim 2.0_0)$
Er^{175}		$(\sim 4.7_4)$	β^-	$(\sim 3.7_1)$
Er^{176}		$(\sim 6.0_7)$	β^-	$(\sim 2.9_6)$
Tm^{161}	$(\sim 2.6_6)$		ε	$(\sim 4.0_0)$
Tm^{162}	$(\sim 3.1_9)$	$(\sim 7.9_7)$	ε	$(\sim 5.2_5)$
Tm^{163}	$(\sim 3.4_3)$	$(\sim 9.4_6)$	ε	$(\sim 2.8_5)$
Tm^{164}	$(\sim 4.0_9)$	$(\sim 7.7_2)$	ε	3.9_4*
Tm^{165}	$(\sim 4.0_8)$	$(\sim 8.8_0)$	ε	$(\sim 1.9_0)$
Tm^{166}	$(\sim 4.4_6)$	$(\sim 7.1_4)$	ε	$\sim 3.1_9$‡
Tm^{167}	(4.8_2)	$(\sim 8.7_9)$	ε	(0.7_5)
Tm^{168}	(5.1_8)	(6.7_1)	β^-	(0.1_5)
			ε	(1.8_0)
Tm^{169}	(5.4_8)	8.0_6*		—
Tm^{170}	(6.0_7)	(6.5_2)	β^-	0.97*
			ε	(0.5_0)
Tm^{171}	(6.2_8)	7.5_6	β^-	0.10*
Tm^{172}	$(\sim 6.9_0)$	$(\sim 6.2_0)$	β^-	$(\sim 2.0_2)$
Tm^{173}	(6.9_7)	$(\sim 6.9_5)$	β^-	(1.3_8)
Tm^{174}	$(\sim 7.5_8)$	$(\sim 5.6_9)$	β^-	$(\sim 3.2_0)$
Tm^{175}	$(\sim 7.6_7)$	$(\sim 6.4_5)$	β^-	$(\sim 2.5_0)$
Tm^{176}	$(\sim 8.2_5)$	$(\sim 5.3_2)$	β^-	$(\sim 4.2_0)$
Tm^{177}	$(\sim 8.3_5)$	$(\sim 6.1_7)$	β^-	$(\sim 3.5_1)$
Yb^{162}	$(\sim 4.4_9)$		ε	$(\sim 2.7_0)$
Yb^{163}	$(\sim 4.5_8)$	$(\sim 8.0_6)$	ε	$(\sim 4.1_0)$
Yb^{164}	$(\sim 5.0_2)$	$(\sim 9.9_0)$	ε	$(\sim 1.9_2)$
Yb^{165}	$(\sim 4.9_2)$	$(\sim 7.6_2)$	ε	$(\sim 3.1_0)$
Yb^{166}	$(\sim 5.5_0)$	$(\sim 9.3_8)$	ε	$(\sim 0.8_6)$
Yb^{167}	$(\sim 5.7_6)$	$(\sim 7.4_0)$	ε	$(\sim 2.2_5)$
Yb^{168}	(6.0_8)	$(\sim 9.1_1)$		—
Yb^{169}	(6.3_8)	(7.0_1)	ε	(0.9_0)
Yb^{170}	(6.7_0)	(8.3_8)		—
Yb^{171}	6.8_7	6.6_9†		—
Yb^{172}	7.4_4	8.1_2†		—
Yb^{173}	$(\sim 7.5_5)$	6.3_1†		—
Yb^{174}	(8.1_1)	7.5_1†		—
Yb^{175}	$(\sim 8.1_7)$	(5.7_5)	β^-	0.47*
Yb^{176}	$(\sim 8.7_4)$	7.0_2		—
Yb^{177}	$(\sim 8.9_0)$	5.4_8	β^-	1.3_8*
Yb^{178}	$(\sim 9.4_8)$	(6.7_5)	β^-	$(\sim 0.6_0)$
Yb^{179}		$(\sim 4.8_8)$	β^-	$(\sim 2.6_0)$
Yb^{180}		$(\sim 6.0_4)$	β^-	$(\sim 2.0_0)$
Lu^{167}	$(\sim 2.8_2)$		ε	$(\sim 3.8_0)$
Lu^{168}	$(\sim 3.3_8)$	$(\sim 7.9_6)$	ε	$(\sim 4.9_5)$
Lu^{169}	$(\sim 3.5_8)$	$(\sim 9.2_6)$	ε	$(\sim 2.7_0)$

Table I. (Continued)

Nucleus	S_p	S_n	Q^- or Q_ε	
Lu^{170}	$(\sim 4.0_{5})$	$(\sim 7.5_{3})$	ε	3.5_{5}*
Lu^{171}	$(\sim 4.1_{9})$	$(\sim 8.5_{2})$	ε	$(\sim 1.7_{2})$
Lu^{172}	$(\sim 4.6_{5})$	$(\sim 7.1_{5})$	ε	$(\sim 2.6_{9})$
Lu^{173}	(4.8_{3})	$(\sim 8.3_{0})$	ε	(0.7_{0})
Lu^{174}	(5.1_{3})	(6.6_{1})	β^-	(0.2_{4})
			ε	(1.6_{0})
Lu^{175}	(5.4_{3})	7.8_{1}*		—
Lu^{176}	6.0_{9}	$6.4_{1}\dagger$	β^-	1.02*
			ε	0.1_{4}
Lu^{177}	6.0_{7}	7.0_{0}	β^-	0.50*
Lu^{178}	$(\sim 6.5_{7})$	$(\sim 5.9_{8})$	β^-	$(\sim 2.2_{0})$
Lu^{179}	(6.7_{0})	$(\sim 6.8_{8})$	β^-	(1.5_{0})
Lu^{180}	$(\sim 7.2_{6})$	$(\sim 5.4_{4})$	β^-	$(\sim 3.4_{8})$
Lu^{181}	$(\sim 7.4_{4})$	$(\sim 6.2_{2})$	β^-	$(\sim 2.8_{8})$
Hf^{168}	$(\sim 4.2_{2})$		ε	$(\sim 2.9_{6})$
Hf^{169}	$(\sim 4.3_{2})$	$(\sim 8.0_{6})$	ε	$(\sim 4.1_{6})$
Hf^{170}	$(\sim 4.8_{4})$	$(\sim 9.7_{8})$	ε	$(\sim 1.9_{1})$
Hf^{171}	$(\sim 4.9_{8})$	$(\sim 7.6_{7})$	ε	$(\sim 2.7_{6})$
Hf^{172}	$(\sim 5.4_{6})$	$(\sim 9.0_{0})$	ε	$(\sim 0.9_{1})$
Hf^{173}	$(\sim 5.6_{1})$	(7.3_{0})	ε	(1.9_{1})
Hf^{174}	(6.0_{7})	(8.7_{6})		—
Hf^{175}	(6.3_{7})	(6.9_{1})	ε	(0.6_{6})
Hf^{176}	6.6_{5}	(8.0_{9})		—
Hf^{177}	6.7_{1}	$6.4_{7}\dagger$		—
Hf^{178}	7.3_{9}	$7.6_{8}\dagger$		—
Hf^{179}	$(\sim 7.6_{0})$	$6.1_{8}\dagger$		—
Hf^{180}	(8.1_{4})	$7.4_{2}\dagger$		—
Hf^{181}	$(\sim 8.3_{2})$	5.6_{2}	β^-	1.02*
Hf^{182}	$(\sim 8.8_{5})$	(6.7_{5})	β^-	(0.3_{3})
Hf^{183}		$(\sim 5.0_{1})$	β^-	$(\sim 2.3_{0})$
Hf^{184}		$(\sim 6.6_{5})$	β^-	$(\sim 1.1_{9})$
Hf^{185}		$(\sim 4.6_{7})$	β^-	$(\sim 3.3_{5})$
Hf^{186}		$(\sim 6.3_{0})$	β^-	$(\sim 2.3_{0})$
Ta^{173}	$(\sim 3.1_{7})$		ε	$(\sim 3.3_{5})$
Ta^{174}	$(\sim 3.7_{3})$	$(\sim 7.8_{6})$	ε	$(\sim 4.2_{5})$
Ta^{175}	$(\sim 3.8_{3})$	$(\sim 8.8_{6})$	ε	$(\sim 2.3_{0})$
Ta^{176}	$(\sim 4.4_{0})$	$(\sim 7.4_{8})$	ε	$(\sim 2.9_{1})$
Ta^{177}	$\sim 4.5_{4}$	$(\sim 8.2_{3})$	ε	1.1_{5}*
Ta^{178}	$(\sim 5.0_{0})$	$(\sim 6.9_{3})$	ε	$(\sim 1.9_{0})$
Ta^{179}	5.3_{1}	$(\sim 7.9_{9})$	ε	0.0_{9}*
Ta^{180}	5.6_{4}	6.5_{1}	β^-	0.6_{4}
			ε	1.0_{0}
Ta^{181}	5.8_{6}	7.6_{4}*		—
Ta^{182}	6.3_{0}	6.0_{6}*	β^-	1.8_{0}#
Ta^{183}	(6.5_{2})	6.9_{8}	β^-	1.07*
Ta^{184}	$(\sim 7.0_{6})$	$(\sim 5.5_{4})$	β^-	$\sim 3.0_{4}$#
Ta^{185}	$(\sim 7.2_{4})$	$(\sim 6.8_{3})$	β^-	1.9_{0}*
Ta^{186}	$(\sim 7.8_{2})$	$(\sim 5.2_{5})$	β^-	$(\sim 4.0_{4})$
Ta^{187}	$(\sim 7.8_{8})$	$(\sim 6.3_{6})$	β^-	$(\sim 2.9_{3})$

Table I. (Continued)

Nucleus	S_p	S_n	Q^- or Q_ε	
W^{174}	$(\sim 4.3_{1})$		ε	$(\sim 2.7_{7})$
W^{175}	$(\sim 4.4_{1})$	$(\sim 7.9_{6})$	ε	$(\sim 3.6_{7})$
W^{176}	$(\sim 4.9_{3})$	$(\sim 9.3_{8})$	ε	$(\sim 1.7_{7})$
W^{177}	$(\sim 5.0_{8})$	$(\sim 7.6_{3})$	ε	$(\sim 2.3_{7})$
W^{178}	$(\sim 5.6_{0})$	$(\sim 8.7_{5})$	ε	$(\sim 0.5_{5})$
W^{179}	$(\sim 5.9_{1})$	(7.2_{4})	ε	(1.3_{0})
W^{180}	6.3_{7}	(8.4_{5})		—
W^{181}	6.6_{8}	6.8_{2}	ε	0.1_{8}*
W^{182}	7.0_{8}	8.0_{4}		—
W^{183}	7.2_{6}	6.2_{4}*		—
W^{184}	7.8_{0}	$7.5_{1}\dagger$		—
W^{185}	$(\sim 7.9_{5})$	(5.6_{9})	β^-	0.43*
W^{186}	(8.5_{1})	(7.3_{9})		—
W^{187}	$(\sim 8.5_{1})$	5.2_{5}*	β^-	1.31*
W^{188}	$(\sim 9.2_{2})$	(7.0_{7})	β^-	(0.2_{0})
W^{189}		$(\sim 5.0_{1})$	β^-	$(\sim 2.1_{9})$
W^{190}		$(\sim 6.7_{4})$	β^-	$(\sim 0.9_{5})$
W^{191}		$(\sim 4.9_{3})$	β^-	$(\sim 2.9_{9})$
W^{192}		$(\sim 6.4_{4})$	β^-	$(\sim 2.0_{0})$
Re^{179}	$(\sim 3.2_{0})$		ε	$(\sim 3.2_{6})$
Re^{180}	$(\sim 3.7_{8})$	$(\sim 7.8_{2})$	ε	$(\sim 3.8_{9})$
Re^{181}	$(\sim 3.9_{9})$	$(\sim 8.6_{6})$	ε	$(\sim 2.0_{5})$
Re^{182}	$(\sim 4.4_{4})$	$(\sim 7.2_{7})$	ε	$(\sim 2.8_{2})$
Re^{183}	(4.7_{1})	$(\sim 8.3_{1})$	ε	(0.7_{5})
Re^{184}	$(\sim 5.1_{2})$	$(\sim 6.6_{5})$	β^-	$(\sim 0.0_{0})$
			ε	$(\sim 1.6_{1})$
Re^{185}	(5.3_{4})	$(\sim 7.7_{3})$		—
Re^{186}	(5.9_{1})	(6.2_{6})	β^-	1.07*
			ε	0.7_{0}
Re^{187}	5.7_{8}	$7.2_{6}\dagger$	β^-	<0.01*
Re^{188}	6.4_{8}	5.9_{5}	β^-	2.12*
Re^{189}	(6.4_{2})	(7.0_{0})	β^-	(1.0_{0})
Re^{190}	$(\sim 6.9_{1})$	$(\sim 5.5_{0})$	β^-	$(\sim 3.2_{5})$
Re^{191}	$(\sim 7.1_{4})$	$(\sim 6.9_{7})$	β^-	$(\sim 1.9_{5})$
Re^{192}	$(\sim 7.6_{6})$	$(\sim 5.4_{5})$	β^-	$(\sim 4.0_{4})$
Re^{193}	$(\sim 7.8_{2})$	$(\sim 6.6_{0})$	β^-	$(\sim 3.0_{0})$
Os^{180}	$(\sim 4.4_{2})$		ε	$(\sim 2.6_{2})$
Os^{181}	$(\sim 4.5_{7})$	$(\sim 7.9_{7})$	ε	$(\sim 3.3_{1})$
Os^{182}	$(\sim 5.1_{3})$	$(\sim 9.2_{2})$	ε	$(\sim 1.3_{6})$
Os^{183}	$(\sim 5.3_{6})$	$(\sim 7.5_{0})$	ε	$(\sim 2.1_{7})$
Os^{184}	(5.8_{7})	$(\sim 8.8_{2})$	ε	$(\sim 0.0_{0})$
Os^{185}	$(\sim 5.9_{7})$	(6.7_{5})	ε	0.9_{8}*
Os^{186}	(6.5_{5})	(8.3_{1})		—
Os^{187}	6.4_{9}	$6.2_{0}\dagger$		—
Os^{188}	7.2_{8}	8.0_{6}*		—
Os^{189}	7.2_{2}	$5.8_{9}\dagger$		—
Os^{190}	(7.9_{7})	$7.7_{5}\dagger$		—
Os^{191}	$(\sim 8.1_{4})$	(5.6_{7})	β^-	0.31*
Os^{192}	$(\sim 8.7_{1})$	(7.5_{4})		—

Table I. (Continued)

Nucleus	S_p	S_n	Q^- or Q_ε	
Os^{193}	$(\sim 8.8_2)$	(5.5_6)	β^-	1.14*
Os^{194}	$(\sim 9.4_0)$	(7.1_8)	β^-	(0.0_5)
Os^{195}		$(\sim 5.1_3)$	β^-	$(\sim 2.3_0)$
Os^{196}		$(\sim 6.8_2)$	β^-	$(\sim 1.1_5)$
Os^{197}		$(\sim 4.9_4)$	β^-	$(\sim 3.2_5)$
Os^{198}		$(\sim 6.3_9)$	β^-	$(\sim 2.3_5)$
Ir^{183}	$(\sim 2.7_5)$		ε	$(\sim 3.9_7)$
Ir^{184}	$(\sim 3.1_9)$	$(\sim 7.9_4)$	ε	$(\sim 4.8_5)$
Ir^{185}	$(\sim 3.3_8)$	$(\sim 9.0_1)$	ε	$(\sim 2.5_9)$
Ir^{186}	$(\sim 3.7_2)$	$(\sim 7.0_9)$	ε	$\sim 3.8_1$*
Ir^{187}	$(\sim 4.0_1)$	$(\sim 8.6_0)$	ε	$(\sim 1.4_1)$
Ir^{188}	4.6_5	$(\sim 6.8_4)$	ε	2.6_3*
Ir^{189}	(4.6_2)	(8.0_3)	ε	(0.4_9)
Ir^{190}	(5.0_2)	(6.2_9)	β^-	(0.7_0)
			ε	(1.9_5)
Ir^{191}	(5.2_0)	(7.9_3)		—
Ir^{192}	5.6_6	6.1_3	β^-	1.45*
			ε	$1.1_0^{\ddagger}$
Ir^{193}	(5.9_1)	7.7_9*		—
Ir^{194}	6.4_5	6.1_0	β^-	2.24*
Ir^{195}	(6.6_5)	7.3_8	β^-	$1.0_5^{\dagger}$
Ir^{196}	$(\sim 7.1_9)$	$(\sim 5.6_7)$	β^-	$(\sim 3.3_0)$
Ir^{197}	$(\sim 7.4_1)$	$(\sim 7.0_4)$	β^-	$2.0_5^{\dagger}$
Ir^{198}	$(\sim 7.9_6)$	$(\sim 5.4_9)$	β^-	$\sim 4.1_0^{\dagger}$
Ir^{199}	$(\sim 8.1_1)$	$(\sim 6.5_4)$	β^-	$(\sim 3.1_5)$
Pt^{184}	$(\sim 4.1_5)$		ε	$(\sim 3.0_1)$
Pt^{185}	$(\sim 4.3_4)$	$(\sim 8.1_3)$	ε	$(\sim 3.8_9)$
Pt^{186}	$(\sim 4.8_5)$	$(\sim 9.5_2)$	ε	$(\sim 1.4_6)$
Pt^{187}	$(\sim 5.2_0)$	$(\sim 7.4_4)$	ε	$(\sim 2.6_2)$
Pt^{188}	$(\sim 5.5_4)$	$(\sim 8.9_4)$	ε	0.5_2*
Pt^{189}	(5.5_1)	(6.8_1)	ε	(1.7_4)
Pt^{190}	(6.2_1)	(8.7_3)		—
Pt^{191}	(6.3_4)	(6.4_2)	ε	(0.8_1)
Pt^{192}	6.8_0	(8.3_9)		—
Pt^{193}	6.9_6	6.2_9	ε	0.0_5
Pt^{194}	7.5_5	$8.3_8^{\dagger}$		—
Pt^{195}	7.6_5	6.2_0*		—
Pt^{196}	8.1_9	7.92*		—
Pt^{197}	$(\sim 8.3_1)$	5.7_9	β^-	0.7_5*
Pt^{198}	$(\sim 8.8_1)$	(7.5_4)		—
Pt^{199}	$(\sim 8.9_1)$	$(\sim 5.5_9)$	β^-	1.7_0*
Pt^{200}	$(\sim 9.4_7)$	$(\sim 7.1_0)$	β^-	$(\sim 0.9_0)$
Pt^{201}		$(\sim 5.2_4)$	β^-	$(\sim 2.7_0)$
Pt^{202}		$(\sim 6.7_6)$	β^-	$(\sim 1.8_0)$
Pt^{203}		$(\sim 4.7_7)$	β^-	$(\sim 3.9_0)$
Pt^{204}		$(\sim 6.3_2)$	β^-	$(\sim 3.0_0)$
Au^{189}	$(\sim 3.1_1)$		ε	$(\sim 2.9_2)$
Au^{190}	$(\sim 3.7_0)$	$(\sim 7.4_0)$	ε	$(\sim 4.2_5)$
Au^{191}	$(\sim 3.7_7)$	$(\sim 8.8_0)$	ε	$(\sim 1.8_7)$

Table I. (Continued)

Nucleus	S_p	S_n	Q^- or Q_ε	
Au^{192}	(4.3_7)	$(\sim 7.0_2)$	ε	3.2_4*
Au^{193}	(4.4_1)	(8.4_3)	ε	(1.1_0)
Au^{194}	5.0_3	(6.9_1)	ε	2.57*
Au^{195}	5.1_5	8.5_0	ε	0.2_7*
Au^{196}	5.6_1	6.6_6	β^-	0.70*
			ε	$1.5_3^{\ddagger}$
Au^{197}	5.7_6	$8.0_7^{\dagger}$		—
Au^{198}	6.4_6	6.4_9*	β^-	1.37*
			ε	(0.3_0)
Au^{199}	(6.5_1)	7.5_9	β^-	0.46*
Au^{200}	$\sim 7.2_2$	6.3_0	β^-	2.2_0*
Au^{201}	$(\sim 7.1_6)$	7.0_4	β^-	$1.4_0^{\dagger}$
Au^{202}	$(\sim 7.7_8)$	$(\sim 5.8_6)$	β^-	$(\sim 3.3_0)$
Au^{203}	$(\sim 7.8_9)$	$(\sim 6.8_7)$	β^-	$(\sim 2.4_0)$
Au^{204}	$(\sim 8.5_4)$	$(\sim 5.4_2)$	β^-	$(\sim 4.5_0)$
Au^{205}	$(\sim 8.5_7)$	$(\sim 6.3_5)$	β^-	$(\sim 3.8_0)$
Hg^{190}	$(\sim 4.5_0)$		ε	$(\sim 2.1_2)$
Hg^{191}	$(\sim 4.6_1)$	$(\sim 7.5_1)$	ε	$(\sim 3.4_1)$
Hg^{192}	$(\sim 5.2_6)$	$(\sim 9.4_5)$	ε	$(\sim 0.9_8)$
Hg^{193}	$(\sim 5.3_1)$	$(\sim 7.0_7)$	ε	2.3_4*
Hg^{194}	(5.9_3)	$(\sim 9.0_5)$	ε	(0.2_0)
Hg^{195}	(5.9_9)	(6.9_7)	ε	(1.7_3)
Hg^{196}	6.5_8	(9.0_9)		—
Hg^{197}	(6.6_9)	(6.7_7)	ε	(0.6_0)
Hg^{198}	7.0_8	(8.4_7)		—
Hg^{199}	7.2_7	6.6_8*		—
Hg^{200}	7.72	8.04*		—
Hg^{201}	7.6_6	6.24		—
Hg^{202}	8.3_8	7.76		—
Hg^{203}	$(\sim 8.4_9)$	5.9_7	β^-	0.49*
Hg^{204}	$(\sim 9.1_4)$	7.5_2		—
Hg^{205}	$(\sim 9.3_7)$	$\sim 5.6_5$	β^-	$\sim 1.5_0^{\dagger}$
Hg^{206}	$(\sim 9.9_0)$	$(\sim 6.8_8)$	β^-	(1.2_0)
Hg^{207}		$(\sim 3.6_2)$	β^-	$(\sim 4.3_8)$
Hg^{208}		$(\sim 4.8_5)$	β^-	$(\sim 3.3_6)$
Hg^{209}		$(\sim 3.3_9)$	β^-	$(\sim 4.8_8)$
Hg^{210}		$(\sim 4.7_4)$	β^-	$(\sim 3.8_6)$
Tl^{195}	$(\sim 3.0_2)$		ε	$(\sim 3.1_7)$
Tl^{196}	$(\sim 3.6_4)$	$(\sim 7.5_9)$	ε	$(\sim 4.6_7)$
Tl^{197}	$(\sim 3.6_9)$	$(\sim 9.1_4)$	ε	$(\sim 2.3_0)$
Tl^{198}	(4.3_3)	$(\sim 7.4_2)$	ε	3.3_5*
Tl^{199}	(4.4_0)	(8.5_3)	ε	(1.5_0)
Tl^{200}	4.81	(7.0_9)	ε	2.45*
Tl^{201}	4.9_9	8.2_2	ε	$0.4_7^{\dagger}$
Tl^{202}	(5.5_6)	(6.8_1)	ε	$1.4_2^{\ddagger}$
Tl^{203}	5.6_7	(7.8_7)		—
Tl^{204}	6.3_4	$6.6_4^{\ddagger}$	β^-	0.77*
			ε	0.39*
Tl^{205}	6.3_7	7.5_4*		—

Table I. (Continued)

Nucleus	S_p	S_n	Q^- or Q_ε	
Tl^{206}	$\sim 7.3_0$	6.5_8	β^-	1.51*
Tl^{207}	(7.2_2)	6.8_1	β^-	1.4_4*
Tl^{208}	$(\sim 7.4_3)$	3.8_3	β^-	4.99*
Tl^{209}	$(\sim 7.4_9)$	4.9_1	β^-	4.0_1
Tl^{210}	$(\sim 7.8_2)$	3.7_2	β^-	5.4_8
Tl^{211}	$(\sim 7.8_6)$	(4.7_8)	β^-	(4.4_8)
Pb^{196}	$(\sim 4.2_1)$		ε	$(\sim 2.6_0)$
Pb^{197}	$(\sim 4.4_1)$	$(\sim 7.7_9)$	ε	$(\sim 3.9_5)$
Pb^{198}	$(\sim 4.8_2)$	$(\sim 9.5_6)$	ε	$(\sim 1.8_1)$
Pb^{199}	$(\sim 4.8_9)$	$(\sim 7.4_8)$	ε	$(\sim 2.8_6)$
Pb^{200}	(5.4_1)	$(\sim 9.0_5)$	ε	(0.9_0)
Pb^{201}	(5.5_4)	(7.2_2)	ε	(1.9_0)
Pb^{202}	(5.9_8)	(8.6_6)	ε	0.05*
Pb^{203}	(6.1_6)	(6.9_9)	ε	0.9_3*
Pb^{204}	6.6_2	8.3_4		—
Pb^{205}	6.7_1	6.7_3	ε	0.05*
Pb^{206}	7.3_1	8.1_4*		—
Pb^{207}	7.46	6.74*		—
Pb^{208}	8.0_4	7.38*		—
Pb^{209}	8.14	3.93*	β^-	0.64*
Pb^{210}	8.4_2	5.1_9	β^-	0.06*
Pb^{211}	8.4_8	3.7_8	β^-	1.3_9*
Pb^{212}	(8.8_8)	5.1_8	β^-	0.58*
Pb^{213}		(3.6_7)	β^-	(2.0_6)
Pb^{214}		(5.1_1)	β^-	1.0_3*
Pb^{215}		$(\sim 3.3_4)$	β^-	$(\sim 2.9_1)$
Pb^{216}		$(\sim 5.0_4)$	β^-	$(\sim 1.7_0)$
Bi^{199}	$(\sim 1.9_5)$		ε	$(\sim 4.7_5)$
Bi^{200}	$(\sim 2.3_7)$	$(\sim 7.9_0)$	ε	$(\sim 5.9_0)$
Bi^{201}	$(\sim 2.5_1)$	$(\sim 9.1_9)$	ε	$(\sim 3.9_3)$
Bi^{202}	$(\sim 2.8_5)$	$(\sim 7.5_6)$	ε	$(\sim 5.0_3)$
Bi^{203}	(2.9_7)	$(\sim 8.7_8)$	ε	3.2_4†
Bi^{204}	(3.2_5)	(7.2_7)	ε	(4.3_0)
Bi^{205}	3.2_9	(8.3_8)	ε	2.6_5*
Bi^{206}	(3.6_1)	(7.0_4)	ε	(3.7_5)
Bi^{207}	3.5_7	(8.1_1)	ε	2.3_8
Bi^{208}	3.7_6	6.9_2	ε	2.8_4
Bi^{209}	3.79	7.4_1*		—
Bi^{210}	4.4_7	4.6_1*	β^-	1.16*
Bi^{211}	4.3_9	5.1_1	β^-	0.6_0
Bi^{212}	4.9_8	4.3_7	β^-	2.25*
Bi^{213}	4.9_5	5.1_5	β^-	1.4_5‡
Bi^{214}	(5.3_6)	4.0_8	β^-	3.26*
Bi^{215}	5.4_7	5.2_2	β^-	2.1_5
Bi^{216}	$(\sim 5.9_6)$	$(\sim 3.8_3)$	β^-	$(\sim 4.1_0)$
Bi^{217}	$(\sim 6.0_3)$	$(\sim 5.1_1)$	β^-	$(\sim 2.9_0)$
Po^{200}	$(\sim 3.1_1)$		ε	$(\sim 4.0_1)$
Po^{201}	$(\sim 3.1_0)$	$(\sim 7.8_9)$	ε	$(\sim 5.3_1)$
Po^{202}	$(\sim 3.5_7)$	$(\sim 9.6_6)$	ε	$(\sim 3.2_1)$

Table I. (Continued)

Nucleus	S_p	S_n	Q^- or Q_ε	
Po^{203}	$(\sim 3.5_9)$	$(\sim 7.5_8)$	ε	$(\sim 4.4_1)$
Po^{204}	(3.9_7)	$(\sim 9.1_6)$	ε	(2.5_2)
Po^{205}	(4.0_7)	(7.3_8)	ε	(3.5_2)
Po^{206}	(4.3_5)	(8.6_5)	ε	(1.9_1)
Po^{207}	(4.4_2)	(7.1_1)	ε	2.9_1*
Po^{208}	4.6_4	8.3_3	ε	1.5_0
Po^{209}	4.7_1	6.9_9	ε	1.9_2
Po^{210}	4.9_8	7.6_8		—
Po^{211}	4.93	4.55		—
Po^{212}	5.8_5	6.02		—
Po^{213}	5.8_2	4.3_5		—
Po^{214}	6.5_6	5.8_9		—
Po^{215}	6.5_9	4.1_1	β^-	0.7_4
Po^{216}	7.1_5	5.7_8		—
Po^{217}	$(\sim 7.2_3)$	(3.9_1)	β^-	(1.5_2)
Po^{218}	$(\sim 7.7_8)$	(5.6_6)	β^-	0.3_9
Po^{219}		$(\sim 3.8_1)$	β^-	$(\sim 2.1_6)$
Po^{220}		$(\sim 5.3_8)$	β^-	$(\sim 1.1_0)$
Po^{221}		$(\sim 3.7_3)$	β^-	$(\sim 2.8_5)$
Po^{222}		$(\sim 5.2_5)$	β^-	$(\sim 1.7_5)$
At^{205}	$(\sim 1.9_6)$		ε	$(\sim 4.6_4)$
At^{206}	$(\sim 2.2_9)$	$(\sim 7.7_1)$	ε	$(\sim 5.5_8)$
At^{207}	(2.4_3)	$(\sim 8.7_9)$	ε	3.9_0
At^{208}	(2.6_9)	(7.3_7)	ε	(4.8_5)
At^{209}	2.7_5	(8.3_9)	ε	3.4_5
At^{210}	(2.9_3)	(7.1_6)	ε	(3.9_7)
At^{211}	3.0_0	(7.7_6)	ε	0.7_7
At^{212}	(3.5_0)	(5.0_5)	ε	(1.7_4)
At^{213}	3.5_4	(6.0_6)	ε	0.0_3
At^{214}	4.0_5	4.8_6	β^-	(1.0_0)
			ε	1.0_6
At^{215}	4.0_7	5.9_1	β^-	0.0_5
At^{216}	4.5_4	4.5_8	β^-	2.0_3
			ε	0.4_6
At^{217}	4.6_5	5.8_9	β^-	0.7_6
At^{218}	(5.2_7)	4.5_3	β^-	2.7_5
At^{219}	5.1_9	5.5_8	β^-	1.6_0
At^{220}	$(\sim 5.7_0)$	$(\sim 4.3_2)$	β^-	$(\sim 3.6_0)$
At^{221}	(5.8_0)	$(\sim 5.4_8)$	β^-	(2.5_0)
At^{222}	$(\sim 6.2_2)$	$(\sim 4.1_5)$	β^-	$(\sim 4.3_5)$
At^{223}	$(\sim 6.3_5)$	$(\sim 5.3_8)$	β^-	$(\sim 3.2_5)$
Rn^{206}	$(\sim 3.2_3)$		ε	$(\sim 3.7_0)$
Rn^{207}	$(\sim 3.2_2)$	$(\sim 7.7_0)$	ε	$(\sim 4.7_9)$
Rn^{208}	(3.5_7)	$(\sim 9.1_4)$	ε	(3.0_2)
Rn^{209}	(3.6_9)	(7.4_9)	ε	(3.9_2)
Rn^{210}	(3.9_5)	(8.6_5)	ε	(2.4_3)
Rn^{211}	(4.0_9)	(7.3_0)	ε	2.8_9
Rn^{212}	4.2_4	7.9_1	ε	(0.0_3)
Rn^{213}	(4.4_3)	(5.2_4)	ε	(0.8_5)

Table I. (Continued)

Nucleus	S_p	S_n	Q^- or Q_ε	
Rn^{214}	(5.0_8)	(6.7_1)		—
Rn^{215}	5.1_8	(4.9_6)		—
Rn^{216}	5.8_4	6.5_7		—
Rn^{217}	5.8_7	4.6_2		—
Rn^{218}	6.5_0	6.5_2		—
Rn^{219}	6.4_0	4.4_3	β^-	0.2_4
Rn^{220}	7.1_4	6.3_2		—
Rn^{221}	$(\sim 7.2_0)$	(4.3_8)	β^-	(1.0_0)
Rn^{222}	(7.7_2)	(6.0_0)		—
Rn^{223}	$(\sim 7.8_5)$	(4.2_8)	β^-	(1.7_6)
Rn^{224}	$(\sim 8.2_9)$	(5.8_2)	β^-	$(\sim 0.7_0)$
Rn^{225}		$(\sim 3.9_8)$	β^-	$(\sim 2.6_5)$
Rn^{226}		$(\sim 5.7_2)$	β^-	$(\sim 1.3_0)$
Rn^{227}		$(\sim 3.9_0)$	β^-	$(\sim 3.2_5)$
Rn^{228}		$(\sim 5.3_6)$	β^-	$(\sim 2.2_5)$
Fr^{212}	(2.1_1)		ε	(5.0_1)
Fr^{213}	$(\sim 2.2_1)$	(8.0_0)	ε	$(\sim 2.2_5)$
Fr^{214}	$(\sim 2.6_8)$	$(\sim 5.7_1)$	ε	$(\sim 3.2_5)$
Fr^{215}	(2.7_1)	$(\sim 6.7_4)$	ε	(1.4_7)
Fr^{216}	$(\sim 3.1_6)$	$(\sim 5.4_1)$	ε	$(\sim 2.6_3)$
Fr^{217}	3.2_4	$(\sim 6.6_5)$	ε	0.6_0
Fr^{218}	3.9_4	5.3_2	β^-	(0.5_0)
			ε	1.8_0
Fr^{219}	3.8_9	6.4_7		—
Fr^{220}	4.6_7	5.2_1	β^-	1.2_7
			ε	0.8_7
Fr^{221}	4.6_0	6.2_5	β^-	0.2_0
Fr^{222}	(5.2_0)	(4.9_8)	β^-	(2.0_8)
			ε	(0.0_2)
Fr^{223}	5.2_6	(6.0_6)	β^-	1.1_5
Fr^{224}	$(\sim 5.7_4)$	$(\sim 4.7_6)$	β^-	$(\sim 2.9_0)$
Fr^{225}	(5.8_5)	$(\sim 5.9_3)$	β^-	(1.8_5)
Fr^{226}	$(\sim 6.2_4)$	$(\sim 4.3_7)$	β^-	$(\sim 3.9_0)$
Fr^{227}	$(\sim 6.3_7)$	$(\sim 5.8_5)$	β^-	$(\sim 2.6_0)$
Fr^{228}	$(\sim 6.8_3)$	$(\sim 4.3_6)$	β^-	$(\sim 4.5_5)$
Fr^{229}	$(\sim 6.9_6)$	$(\sim 5.4_9)$	β^-	$(\sim 3.5_5)$
Ra^{213}	$(\sim 3.2_0)$		ε	$(\sim 4.0_3)$
Ra^{214}	$(\sim 3.3_8)$	$(\sim 8.1_9)$	ε	$(\sim 1.5_5)$
Ra^{215}	$(\sim 3.5_6)$	$(\sim 5.8_9)$	ε	$(\sim 2.4_0)$
Ra^{216}	(4.2_3)	$(\sim 7.4_1)$	ε	$(\sim 0.4_0)$
Ra^{217}	$(\sim 4.4_3)$	(5.6_1)	ε	(1.4_4)
Ra^{218}	(5.0_4)	(7.2_6)		—
Ra^{219}	5.0_3	(5.3_1)	ε	0.6_6
Ra^{220}	5.7_1	7.1_5		—
Ra^{221}	5.6_7	5.1_8		—
Ra^{222}	6.2_8	6.8_6		—
Ra^{223}	(6.4_3)	5.1_3		—
Ra^{224}	6.8_8	6.5_1		—
Ra^{225}	$(\sim 7.0_0)$	4.8_8	β^-	0.36*

Table I. (Continued)

Nucleus	S_p	S_n	Q^- or Q_ε	
Ra^{226}	(7.4_9)	6.4_2		—
Ra^{227}	$(\sim 7.6_7)$	4.5_5	β^-	1.3_1*
Ra^{228}	$(\sim 8.1_3)$	6.3_1	β^-	0.05*
Ra^{229}	$(\sim 8.2_6)$	$(\sim 4.4_9)$	β^-	$(\sim 1.9_5)$
Ra^{230}	$(\sim 8.6_2)$	$(\sim 5.8_5)$	β^-	$(\sim 1.0_0)$
Ra^{231}		$(\sim 4.3_0)$	β^-	$(\sim 2.7_0)$
Ra^{232}		$(\sim 5.6_3)$	β^-	$(\sim 1.7_5)$
Ac^{217}	$(\sim 1.9_3)$		ε	$(\sim 2.9_0)$
Ac^{218}	$(\sim 2.3_8)$	$(\sim 6.0_6)$	ε	$(\sim 4.1_0)$
Ac^{219}	$(\sim 2.4_8)$	$(\sim 7.3_6)$	ε	$(\sim 2.0_5)$
Ac^{220}	$(\sim 3.0_2)$	$(\sim 5.8_5)$	ε	$(\sim 3.3_5)$
Ac^{221}	3.0_7	$(\sim 7.2_0)$	ε	1.3_3
Ac^{222}	3.8_6	5.9_7	ε	2.2_2
Ac^{223}	3.8_0	6.8_0	ε	0.5_5
Ac^{224}	4.3_6	5.6_9	β^-	0.2_9
			ε	1.3_7
Ac^{225}	4.4_6	6.6_1		—
Ac^{226}	4.9_5	5.3_7	β^-	1.1_7*
			ε	0.6_9
Ac^{227}	5.0_8	6.5_5	β^-	0.05*
Ac^{228}	5.5_8	5.0_5	β^-	2.1_3†
Ac^{229}	(5.6_6)	(6.3_9)	β^-	(1.0_0)
Ac^{230}	$(\sim 6.0_7)$	$(\sim 4.9_0)$	β^-	$(\sim 2.9_0)$
Ac^{231}	$(\sim 6.2_2)$	$(\sim 6.0_0)$	β^-	2.0_0†
Ac^{232}	$(\sim 6.6_0)$	$(\sim 4.6_8)$	β^-	$(\sim 3.7_5)$
Ac^{233}	$(\sim 6.7_5)$	$(\sim 5.7_8)$	β^-	$(\sim 2.8_0)$
Th^{218}	$(\sim 3.1_8)$		ε	$(\sim 2.1_0)$
Th^{219}	$(\sim 3.3_3)$	$(\sim 6.2_1)$	ε	$(\sim 3.2_5)$
Th^{220}	$(\sim 3.8_2)$	$(\sim 7.8_5)$	ε	$(\sim 1.2_5)$
Th^{221}	$(\sim 3.9_2)$	$(\sim 5.9_5)$	ε	$(\sim 2.5_0)$
Th^{222}	(4.4_9)	$(\sim 7.7_7)$	ε	(0.7_0)
Th^{223}	4.4_3	(5.9_1)	ε	1.5_9
Th^{224}	5.2_1	7.5_8		—
Th^{225}	5.2_6	5.7_5	ε	0.5_7
Th^{226}	5.7_6	7.1_1		—
Th^{227}	5.8_2	5.4_3		—
Th^{228}	6.4_0	7.1_3		—
Th^{229}	6.6_1	5.2_6		—
Th^{230}	(7.0_2)	6.8_0		—
Th^{231}	$(\sim 7.2_2)$	5.1_0	β^-	0.38*
Th^{232}	7.6_5	6.4_3		—
Th^{233}	$(\sim 7.8_0)$	4.8_3	β^-	1.2_3*
Th^{234}	$(\sim 8.1_5)$	6.1_3	β^-	0.2_2
Th^{235}		$(\sim 4.6_3)$	β^-	$(\sim 1.8_0)$
Th^{236}		$(\sim 5.6_9)$	β^-	$(\sim 1.1_0)$
Th^{237}		$(\sim 4.3_7)$	β^-	$(\sim 2.5_0)$
Th^{238}		$(\sim 5.5_2)$	β^-	$(\sim 1.7_0)$
Pa^{223}	$(\sim 2.3_3)$		ε	$(\sim 2.8_0)$
Pa^{224}	$(\sim 2.9_0)$	$(\sim 6.4_8)$	ε	$(\sim 3.9_0)$

Table I. (Continued)

Nucleus	S_p	S_n	Q^- or Q_ε	
Pa^{225}	(2.9_7)	$(\sim 7.6_5)$	ε	(2.0_0)
Pa^{226}	3.6_2	(6.4_0)	ε	2.7_1
Pa^{227}	3.6_6	7.1_5	ε	0.9_9
Pa^{228}	4.2_5	6.0_2	ε	2.1_0
Pa^{229}	4.2_1	7.0_9	ε	0.2_7
Pa^{230}	4.8_5	5.9_0	β^-	0.41*
			ε	1.1_7
Pa^{231}	4.7_0	6.6_5		—
Pa^{232}	5.2_7	5.6_7	β^-	1.24*
			ε	0.3_8
Pa^{233}	5.2_8	6.4_4	β^-	0.57*
Pa^{234}	5.5_7	5.1_2	β^-	$2.3_0^{\ddagger}$
Pa^{235}	5.6_5	6.2_1	β^-	1.4_0*
Pa^{236}	$(\sim 6.0_1)$	$(\sim 4.9_9)$	β^-	$(\sim 2.9_0)$
Pa^{237}	$(\sim 6.0_9)$	$(\sim 5.7_7)$	β^-	2.3_0*
Pa^{238}	$(\sim 6.4_4)$	$(\sim 4.7_2)$	β^-	$(\sim 3.6_8)$
Pa^{239}	$(\sim 6.5_5)$	$(\sim 5.6_3)$	β^-	$(\sim 2.9_0)$
U^{224}	$(\sim 3.7_0)$		ε	$(\sim 2.0_0)$
U^{225}	$(\sim 3.7_7)$	$(\sim 6.5_5)$	ε	$(\sim 3.1_0)$
U^{226}	(4.3_2)	$(\sim 8.2_0)$	ε	(1.3_0)
U^{227}	4.3_6	(6.4_4)	ε	2.0_1
U^{228}	4.9_9	7.7_8	ε	0.2_5
U^{229}	4.9_8	6.0_1	ε	1.3_3
U^{230}	5.5_3	7.6_4		—
U^{231}	5.5_1	5.8_8	ε	0.3_6
U^{232}	6.1_8	7.2_7		—
U^{233}	6.2_3	5.7_7		—
U^{234}	6.6_4	6.8_5		—
U^{235}	6.8_8	5.3_1		—
U^{236}	7.1_1	6.4_9		—
U^{237}	$(\sim 7.2_9)$	5.1_7	β^-	0.52*
U^{238}	7.6_2	6.1_0		—
U^{239}	$(\sim 7.7_5)$	4.8_5	β^-	1.28*
U^{240}	(8.0_7)	5.9_5	β^-	0.49*
U^{241}		$(\sim 4.6_1)$	β^-	$(\sim 1.8_6)$
U^{242}		$(\sim 5.4_9)$	β^-	$(\sim 1.3_2)$
U^{243}		$(\sim 4.2_8)$	β^-	$(\sim 2.6_0)$
U^{244}		$(\sim 5.3_3)$	β^-	$(\sim 1.9_0)$
Np^{229}	$(\sim 2.7_3)$		ε	$(\sim 2.5_0)$
Np^{230}	$(\sim 3.2_1)$	$(\sim 6.4_9)$	ε	$(\sim 3.6_5)$
Np^{231}	3.2_7	$(\sim 7.7_0)$	ε	1.8_3
Np^{232}	$(\sim 3.7_9)$	$(\sim 6.4_0)$	ε	$(\sim 2.7_0)$
Np^{233}	3.8_9	$(\sim 7.3_7)$	ε	1.1_0
Np^{234}	4.2_5	6.1_3	ε	1.8_2*
Np^{235}	4.3_6	6.9_6	ε	0.17
Np^{236}	4.7_7	5.7_2	β^-	0.52*
			ε	0.9_4
Np^{237}	4.9_1	6.6_3		—
Np^{238}	5.2_8	5.4_9	β^-	1.29*
			ε	0.0_9
Np^{239}	5.3_5	6.2_2	β^-	0.73*
Np^{240}	5.6_6	5.1_6	β^-	2.05*
Np^{241}	5.6_9	5.9_8	β^-	1.3_6*
Np^{242}	$(\sim 6.0_3)$	$(\sim 4.9_5)$	β^-	$(\sim 2.6_6)$
Np^{243}	$(\sim 6.1_0)$	$(\sim 5.5_6)$	β^-	$(\sim 2.2_0)$
Np^{244}	$(\sim 6.4_5)$	$(\sim 4.6_3)$	β^-	$(\sim 3.5_0)$
Np^{245}	$(\sim 6.5_0)$	$(\sim 5.3_8)$	β^-	$(\sim 2.9_0)$
Pu^{230}	$(\sim 3.8_6)$		ε	$(\sim 1.8_5)$
Pu^{231}	$(\sim 4.0_3)$	$(\sim 6.6_6)$	ε	$(\sim 2.8_9)$
Pu^{232}	4.4_8	$(\sim 8.1_5)$	ε	$(\sim 1.1_4)$
Pu^{233}	$(\sim 4.5_8)$	6.5_0	ε	2.0_1
Pu^{234}	4.9_6	7.7_5	ε	0.3_9
Pu^{235}	5.0_6	6.2_3	ε	1.1_2
Pu^{236}	5.4_6	7.3_6		—
Pu^{237}	5.6_2	5.8_8	ε	0.2_3
Pu^{238}	6.0_0	7.0_1		—
Pu^{239}	6.1_7	5.6_6		—
Pu^{240}	6.4_3	6.4_8		—
Pu^{241}	6.5_6	5.2_9	β^-	0.02*
Pu^{242}	6.8_3	6.2_5		—
Pu^{243}	$(\sim 6.9_8)$	5.1_0	β^-	0.5_8*
Pu^{244}	$(\sim 7.3_5)$	(5.9_3)	β^-	(0.0_0)
Pu^{245}	$(\sim 7.5_0)$	$(\sim 4.7_8)$	β^-	$(\sim 1.3_0)$
Pu^{246}	$(\sim 7.8_8)$	$(\sim 5.7_6)$	β^-	$\sim 0.4_3^{\dagger}$
Pu^{247}		$(\sim 4.3_2)$	β^-	$(\sim 2.1_0)$
Pu^{248}		$(\sim 5.3_1)$	β^-	$(\sim 1.4_0)$
Am^{235}	$(\sim 3.0_5)$		ε	$(\sim 2.4_0)$
Am^{236}	$(\sim 3.5_3)$	$(\sim 6.7_1)$	ε	$(\sim 3.0_5)$
Am^{237}	3.6_4	$(\sim 7.4_7)$	ε	1.4_6
Am^{238}	$(\sim 3.9_8)$	$(\sim 6.2_2)$	ε	$(\sim 2.2_5)$
Am^{239}	4.0_6	$(\sim 7.0_9)$	ε	0.8_2
Am^{240}	(4.3_0)	(5.9_0)	ε	(1.4_0)
Am^{241}	4.5_3	(6.7_1)		—
Am^{242}	4.7_2	5.4_8	β^-	0.7_2*
			ε	0.7_5
Am^{243}	4.9_0	6.4_3	β^-	0.0_0
Am^{244}	5.1_5	5.3_5	β^-	$1.4_0^{\dagger}$
			ε	(0.0_0)
Am^{245}	(5.3_0)	6.0_8	β^-	0.88*
Am^{246}	$(\sim 5.4_1)$	$\sim 4.8_9$	β^-	$\sim 2.4_0^{\dagger}$
Am^{247}	$(\sim 5.6_4)$	$(\sim 5.9_9)$	β^-	$(\sim 1.6_0)$
Am^{248}	$(\sim 5.9_3)$	$(\sim 4.6_1)$	β^-	$(\sim 3.1_5)$
Am^{249}	$(\sim 6.0_3)$	$(\sim 5.4_1)$	β^-	$(\sim 2.4_5)$
Cm^{236}	$(\sim 3.9_8)$		ε	$(\sim 1.9_5)$
Cm^{237}	$(\sim 4.0_9)$	$(\sim 6.8_2)$	ε	$(\sim 2.6_0)$
Cm^{238}	4.4_4	$(\sim 7.8_2)$	ε	$(\sim 1.0_0)$
Cm^{239}	$(\sim 4.5_8)$	(6.3_6)	ε	(1.7_3)
Cm^{240}	4.9_7	(7.4_8)	ε	(0.1_5)

Table I. (Continued)

Nucleus	S_p	S_n	Q^- or Q_ε	
Cm^{241}	(5.1_3)	6.0_6	ε	0.8_0
Cm^{242}	5.4_2	7.0_0		—
Cm^{243}	5.6_5	5.7_1	ε	0.0_0
Cm^{244}	5.9_7	6.7_5		—
Cm^{245}	6.1_8	5.5_6		—
Cm^{246}	6.5_1	6.4_1		—
Cm^{247}	$(\sim 6.8_1)$	(5.1_9)	β^-	(0.0_7)
Cm^{248}	$(\sim 6.9_8)$	(6.1_6)		—
Cm^{249}	$(\sim 7.0_8)$	$(\sim 4.7_1)$	β^-	$0.9_6{}^\dagger$
Cm^{250}	$(\sim 7.4_1)$	$(\sim 5.7_4)$	β^-	$(\sim 0.1_8)$
Bk^{241}	$(\sim 2.9_8)$		ε	$(\sim 2.3_0)$
Bk^{242}	$(\sim 3.3_2)$	$(\sim 6.4_0)$	ε	$(\sim 2.9_0)$
Bk^{243}	3.4_4	$(\sim 7.1_2)$	ε	1.4_9
Bk^{244}	(3.7_5)	(6.0_2)	ε	(2.2_2)
Bk^{245}	3.9_4	(6.9_4)	ε	0.8_4
Bk^{246}	(4.2_6)	(5.8_8)	ε	(1.3_7)
Bk^{247}	4.4_8	(6.6_3)		—
Bk^{248}	(4.9_1)	5.6_2	β^-	$0.6_5{}^*$
			ε	(0.4_7)
Bk^{249}	(4.8_9)	6.1_4	β^-	0.13^*
Bk^{250}	5.1_4	4.9_6	β^-	$1.7_6{}^*$
Bk^{251}	$(\sim 5.2_9)$	$(\sim 5.8_9)$	β^-	$(\sim 0.9_8)$
Cf^{242}	$(\sim 4.0_6)$		ε	$(\sim 1.5_6)$
Cf^{243}	$(\sim 4.1_5)$	$(\sim 6.4_9)$	ε	$(\sim 2.1_9)$
Cf^{244}	4.5_1	$(\sim 7.4_8)$	ε	(0.7_3)
Cf^{245}	(4.6_1)	6.1_2	ε	1.5_5
Cf^{246}	5.0_4	7.3_7	ε	(0.0_6)
Cf^{247}	(5.1_8)	(6.0_2)	ε	(0.6_7)
Cf^{248}	5.4_9	(6.9_4)		—
Cf^{249}	5.4_9	5.6_2		—
Cf^{250}	5.9_4	6.5_9		—
Cf^{251}	$(\sim 6.0_9)$	$(\sim 5.1_1)$		—
Cf^{252}	$(\sim 6.3_5)$	$(\sim 6.1_5)$		—
Cf^{253}		$(\sim 4.8_7)$	β^-	0.27^*
E^{246}	$(\sim 3.0_8)$		ε	$(\sim 3.5_1)$
E^{247}	$(\sim 2.9_4)$	$(\sim 7.2_3)$	ε	$(\sim 2.3_0)$
E^{248}	$(\sim 3.3_2)$	$(\sim 6.4_0)$	ε	$(\sim 2.8_4)$
E^{249}	3.4_3	$(\sim 7.0_5)$	ε	1.4_1
E^{250}	$(\sim 3.8_4)$	$(\sim 6.0_3)$	ε	$(\sim 1.9_7)$
E^{251}	4.0_2	$(\sim 6.7_7)$	ε	$(\sim 0.3_1)$
E^{252}	$(\sim 4.3_6)$	$\sim 5.4_5$	β^-	$\sim 0.2_4$
			ε	$(\sim 1.0_1)$
E^{253}	(4.3_6)	6.1_5		—
E^{254}	4.6_7	5.1_8	β^-	0.9_6
Fm^{248}	$(\sim 3.8_2)$		ε	$(\sim 1.8_0)$
Fm^{249}	$(\sim 3.9_7)$	$(\sim 6.5_5)$	ε	$(\sim 2.3_0)$
Fm^{250}	4.3_6	$(\sim 7.4_4)$	ε	$(\sim 0.8_9)$
Fm^{251}	$(\sim 4.5_0)$	(6.1_7)	ε	$(\sim 1.4_9)$
Fm^{252}	4.9_1	(7.1_8)		—

Table I. (Continued)

Nucleus	S_p	S_n	Q^- or Q_ε	
Fm^{253}	$(\sim 4.9_3)$	$(\sim 5.4_7)$	ε	$(\sim 0.4_4)$
Fm^{254}	5.3_6	$(\sim 6.5_8)$		—
Fm^{255}	$(\sim 5.4_2)$	$(\sim 5.2_4)$		

Table II. Notation in Table I. For details see the text.

Example	*Comment*
$1.2_3{}^*$	The asterisk, *, means a measured, unadjusted value.
$1.2_3{}^\dagger$	The dagger, †, means a value which is obtained from the experimental value after adjustment within the error.
$1.2_3{}^\sharp$	The mark, ♯, means a value which is obtained from the experimental value after adjustment beyond the error.
1.2_3	A value without any mark is a calculated value.
(1.2_3)	A value in parentheses is an estimated value.

Example	*Uncertainty*	
1.23^*, $1.23^\dagger$, 1.23	$0<$	≤ 0.04
$1.2_3{}^*$, $1.2_3{}^\dagger$, $1.2_3{}^\sharp$, 1.2_3, (1.2_3)	$0.04<$	≤ 0.25
$\sim 1.2_3{}^*$, $\sim 1.2_3{}^\dagger$, $\sim 1.2_3{}^\sharp$, $\sim 1.2_3$, $(\sim 1.2_3)$	$0.25<$	≤ 0.50
$\sim 1.2^*$, $\sim 1.2^\dagger$, $\sim 1.2^\sharp$, ~ 1.2, (~ 1.2)	$0.50<$	≤ 1.0
$\sim 1._2{}^*$, $\sim 1._2{}^\dagger$, $\sim 1._2{}^\sharp$, $\sim 1._2$, $(\sim 1._2)$	$1.0<$	

enough to belong to this class. The uncertainties of the estimated values are estimated fairly conservatively. The probability that the estimated range does not include the real value is perhaps a few percent at most. Such uncertainties of the well-estimated values are about 0.2 MeV, and these values belong to the second class.

By the authors' judgment some data are assigned larger errors than those given in the literatures, and are classified into the lower grades. Typical ones are the mass-spectroscopic data, for which three times the errors in the literatures are assigned.

The values in Table I are also shown in graphical form in Figs. 2 to 5 in order to see how our systematics holds. Furthermore, Fig. 6 in which some of the S_p(odd-Z, N)'s calculated from Reference 1 are plotted will show how the plots look without any adjustment.

§ 4. Discussions of Particular Data

In this section we discuss the data which need large adjustments or re-interpretations. The data which cause some deviations from our systematics are also discussed even though they are not adjusted appreciably.

Discussions are given in the order of increasing atomic numbers. The mass-spectroscopic data are discussed in the last.

Na^{20}, Q_ε. The value, 15.3 MeV, obtained from the Ne^{20}(p, n) threshold[55] is too large. The systematics of the Coulomb energy differences suggests $Q_\varepsilon \sim 14.0$ MeV, and this value is also supported by the rule 3. The observed threshold may be due to the excited states of Na^{20}.

Co^{57}, Q_ε. There are two experimental values, 0.57 ± 0.03 MeV obtained from the measurement of the internal bremsstrahlung[56], and 0.837 ± 0.003 MeV obtained from the Fe^{57}(p, n) threshold[20]. The rule 3 is consistent only with the latter value. The observation of a higher energy γ-ray[57] also supports the latter value.

Zn^{72}, Q^-. The reported weak $\sim$1.6 MeV β^--ray[58] is certainly not due to this nucleus.

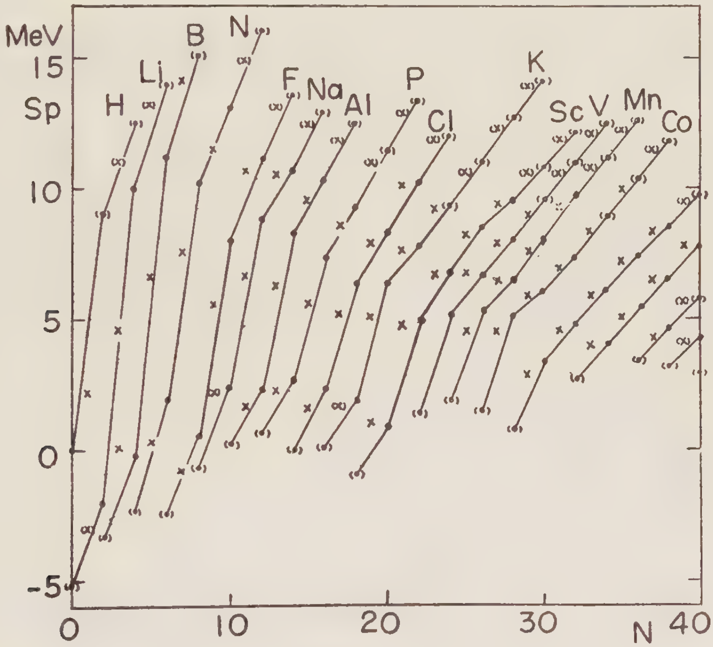

Fig. 2(a).

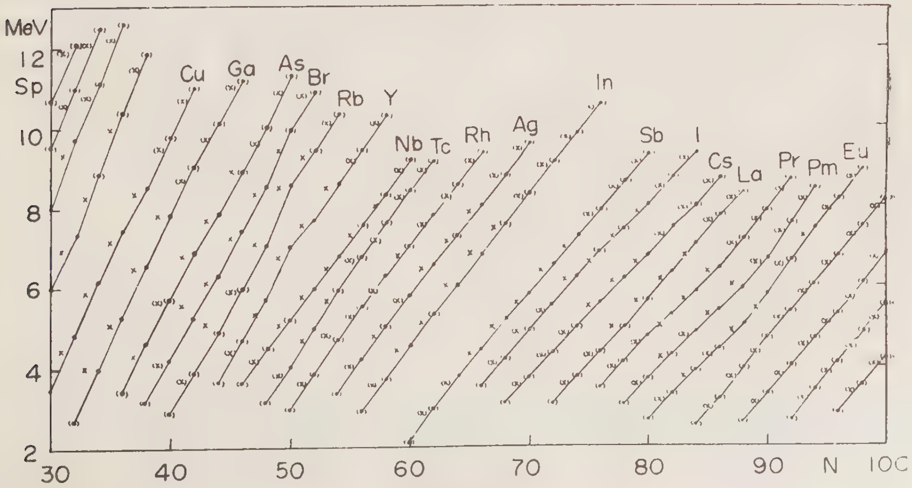

Fig. 2(b).

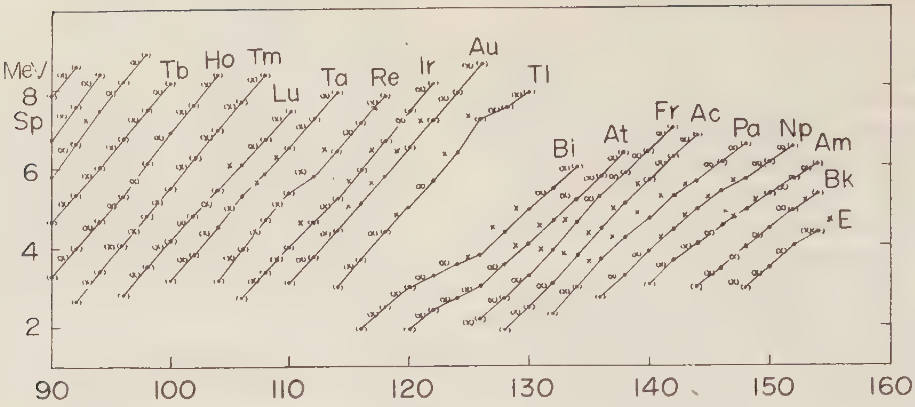

Fig. 2(c).

Fig. 2. The "best" values of S_p(odd-Z, N)'s. The dots are S_p(odd-Z, even-N)'s, and the crosses are S_p(odd-Z, odd-N)'s. The marks with parentheses represent the estimated values, and the marks without parentheses represent the measured (unadjusted or adjusted) or calculated values.

The estimated value is only $\sim 0.5_0$ MeV.

Ge^{66}, Q_ε. Our systematics predicts a considerably smaller value for $Q_\varepsilon(Ge^{66})$ than the β-decay energy systematics[2)]. Ricci et al.[59)] fitted their experimental results to a decay scheme with $Q_\varepsilon = 2.95 \pm 0.15$ MeV in accordance with the β-decay energy systematics. However, it is more likely that the weak 2.0 MeV β^+ does not exist in the decay of Ge^{66} and the strong 1.3 MeV β^+ proceeds to the low-lying states of Ga^{66}. This problem is also related to $Q_\varepsilon(Ge^{68})$. The β-decay energy systematics predicts $\sim 0.7_0$ MeV for $Q_\varepsilon(Ge^{68})$, while our system-

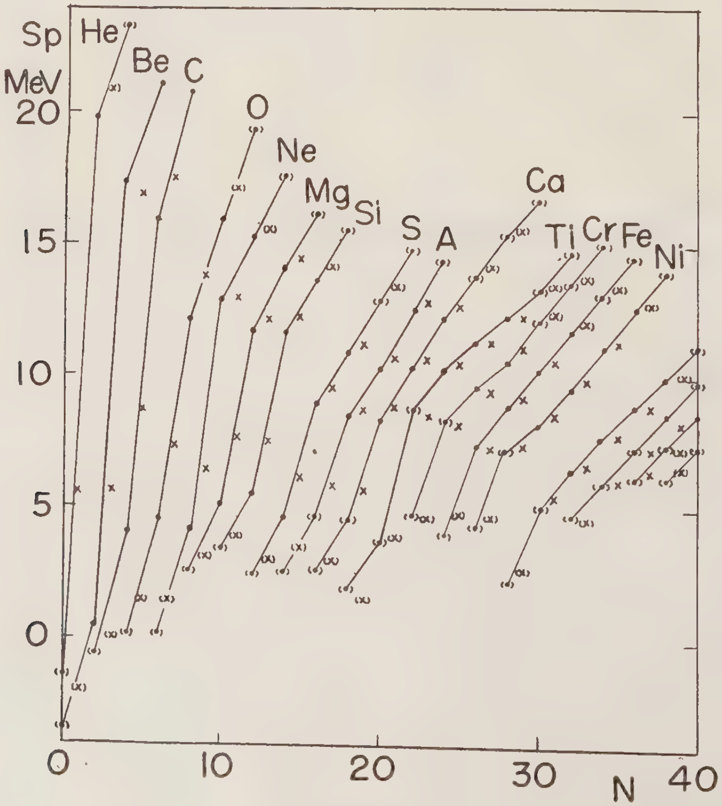

Fig. 3(a).

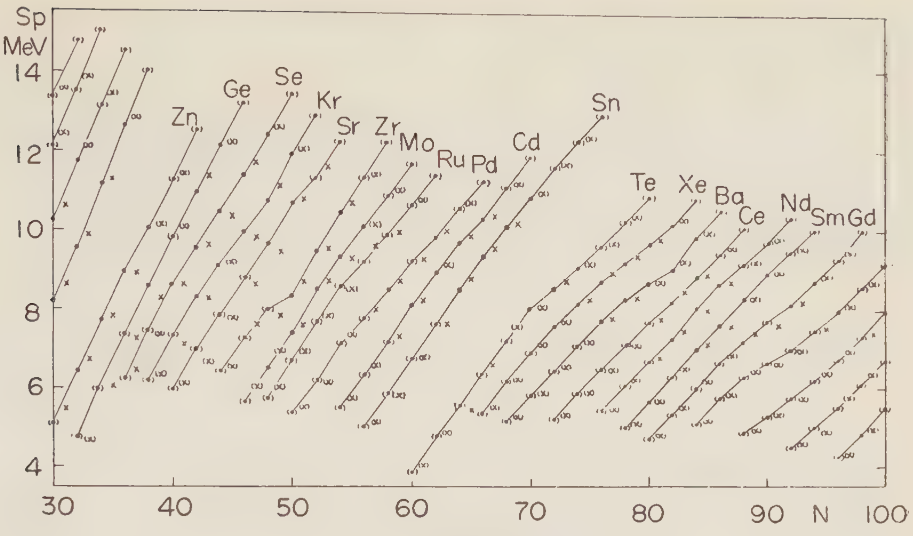

Fig. 3(b)

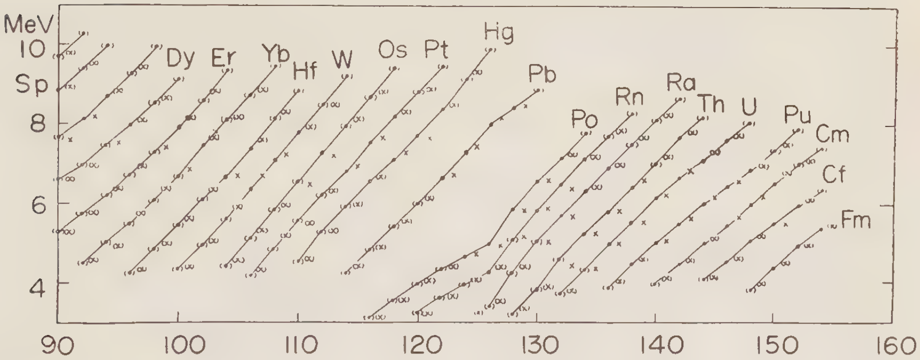

Fig. 3(c).

Fig. 3. The "best" values of S_p(even-Z, N)'s. The dots are S_p(even-Z, even-N)'s, and the crosses are S_p(even-Z, odd-N)'s. See also the caption of Fig. 2.

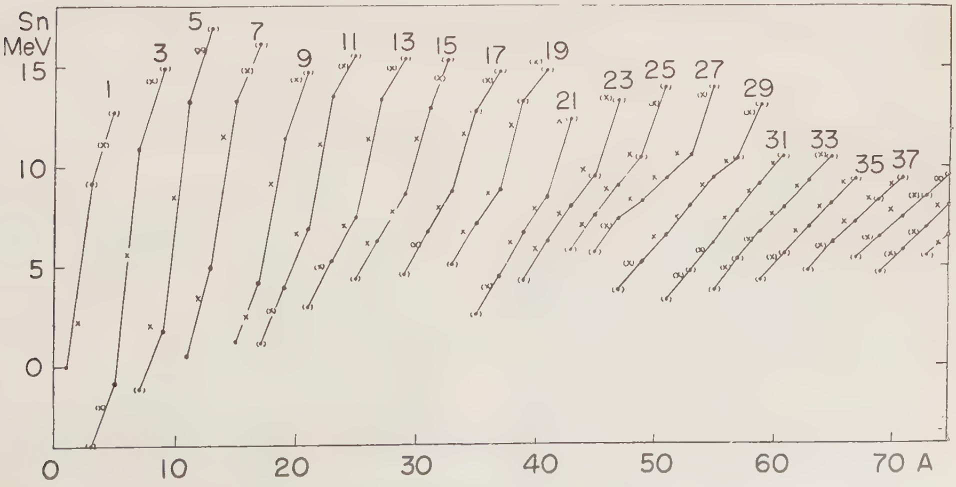

Fig. 4(a).

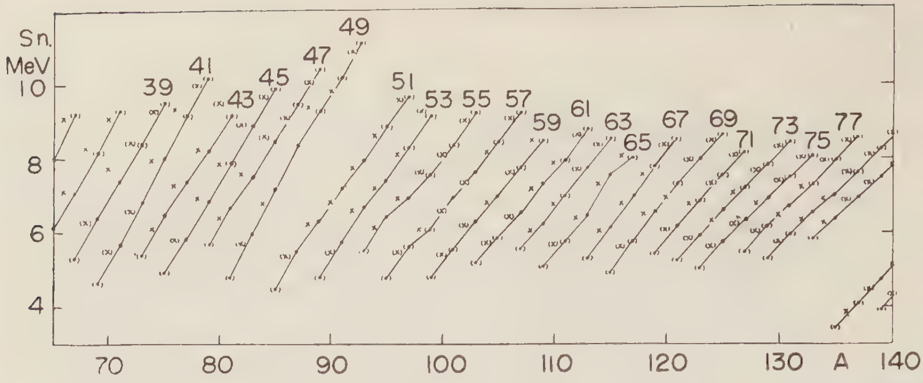

Fig. 4(b).

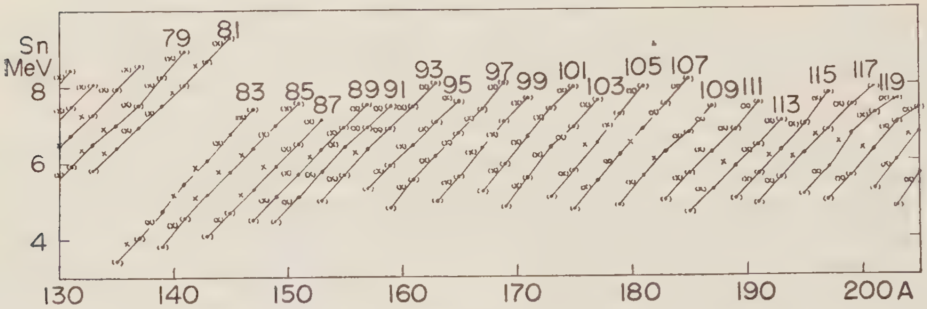

Fig. 4(c).

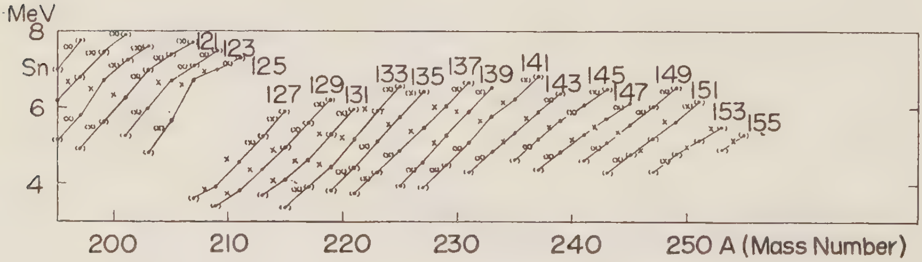

Fig. 4(d).

Fig. 4. The "best" values of $S_n(Z, \text{odd-}N)$'s. The dots are $S_n(\text{even-}Z, \text{odd-}N)$'s, and the crosses are $S_n(\text{odd-}Z, \text{odd-}N)$'s. The numbers attached to the lines are N's. See also the caption of Fig. 2.

atics predicts $\sim 0.2_0$ MeV. The latter value is more plausible since no γ-ray has been observed in the decay of Ge^{68} in spite of the expected lowlying 0^+ state of Ga^{68}.

Br^{79}, S_n. The value obtained from the recent $Br(\gamma, n)$ threshold measurement[60] is too small. This threshold may be due to the excited states of Br^{80}. The mass-spectroscopic data favor this interpretation.

Br^{87}, Q^-. 8.0 MeV obtained by the absorption method[61] is too large for this Q-value. We adopt $\sim 6.6_0$ MeV. It should be noted that this nucleus is a delayed-neutron emitter and its Q^--value cannot be much smaller than 6.5 MeV.

Kr^{74}, Q_ε. The assignment[62] of the 3.1±0.1 MeV β^+ activity to Kr^{74} does not seem to be correct. The estimated value for Q_ε is only ~2.4 MeV. (~1.4 MeV for the maximum β^+ energy).

Rb^{89}, Q^-. The decay scheme is so complicated that a simple measurement of the β-rays with a scintillation spectrometer will not be sufficient. Thus, it will not be unreasonable to amend the original value, 3.92±0.05 MeV[63], to $\sim 4.3_0$ MeV.

Sr^{89}, S_n. The adopted value has been calculated from Q_ε(Y^{88}), S_n(Y^{89}), and Q^-(Sr^{89}). It is appreciably smaller than that obtained from the measurements7) of the Sr(d, p) Q-value. The observed Q-value may, at least partly, be due to the isotopes other than Sr^{88}. The Sr^{88}(d, p) reaction has the smallest Q-value among the Sr(d, p) reactions.

Y^{88}, Q_ε. 3.63±0.01 MeV obtained from the Sr^{88}(p, n) threshold23) is adopted rather than 3.44±0.02 MeV obtained from the β^+ energy7). The former is definitely in better fit to our systematics.

Mo^{98}, S_n. The reported value, 8.29±0.10 MeV, from the Mo^{97}(d, p) reaction64) is too small. The estimated value is ~8.8$_0$ MeV. Therefore, we tentatively assume that the reported value is that for the first excited state of

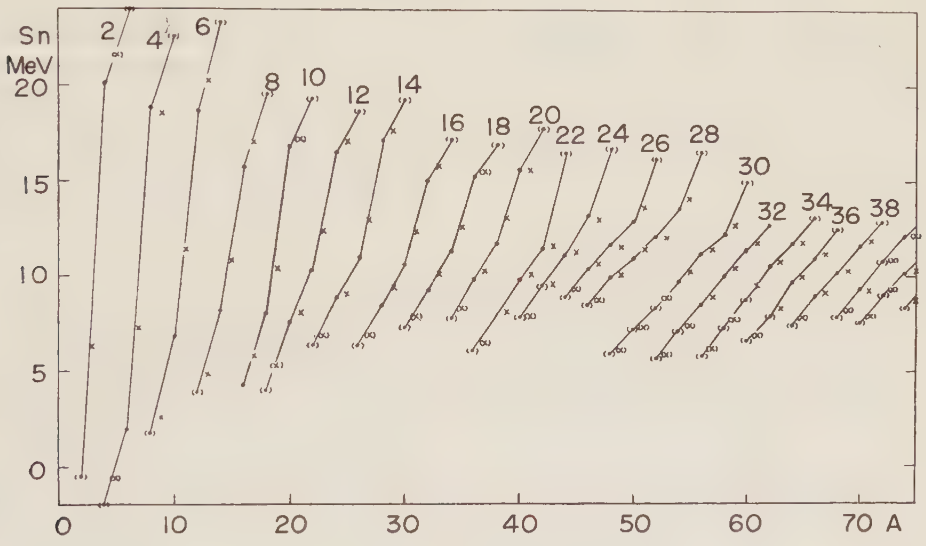

Fig. 5(a).

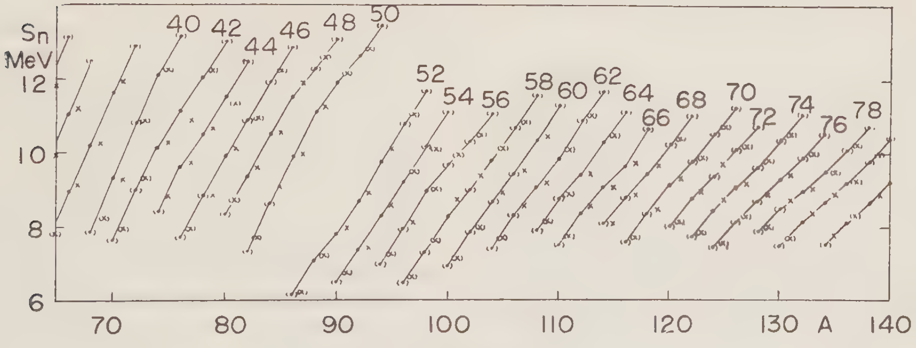

Fig. 5(b).

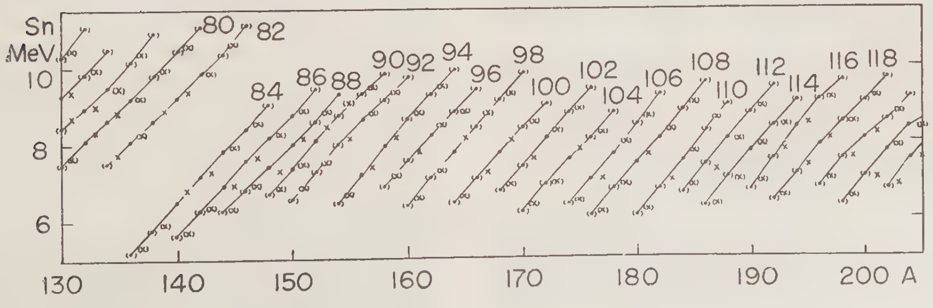

Fig. 5(c).

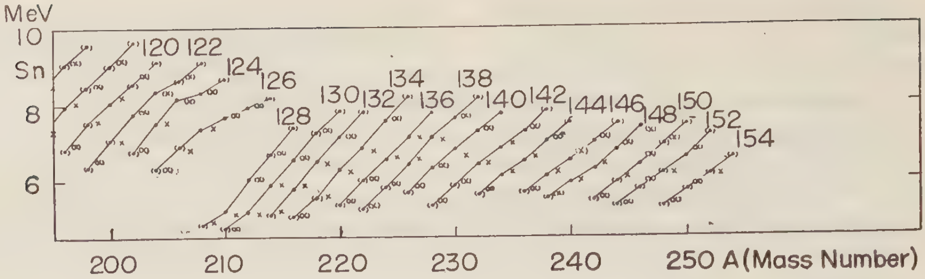

Fig. 5(d).

Fig. 5. The "best" values of $S_n(Z, \text{even-}N)$'s. The dots are $S_n(\text{even-}Z, \text{even-}N)$'s, and the crosses are $S_n(\text{odd-}Z, \text{even-}N)$'s. The numbers attached to the lines are N's. See also the caption of Fig. 2.

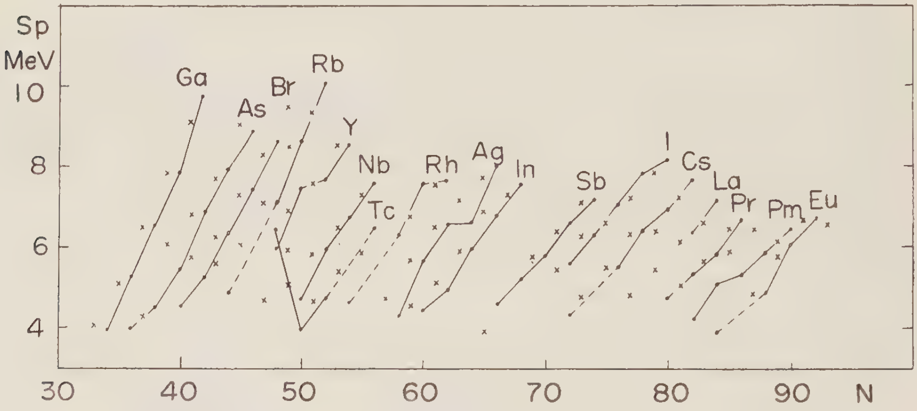

Fig. 6. Unadjusted $S_p(\text{odd-}Z, N)$'s which have been calculated from Reference 1. See also the caption of Fig. 2.

Mo^{98} with the excitation energy of 0.78 MeV, and adopt the smallest value within the error limit. With this value there still remains a fairly large violation of the rules 1 and 2 around Mo^{98}. This violation may be true since the first excited state of Mo^{98} has an anomalously large excitation energy. However, it is also possible that the real value of $S_n(Mo^{98})$ is about 8.8 MeV and the rules 1 and 2 hold better. The increase of $Q^-(Zr^{97})$ and the decrease of $Q^-(Nb^{94})$ would also be helpful to reduce the violation of the rules 1 and 2.

Pd^{99}, Q_ε. Our systematics suggests $Q_\varepsilon \sim 3.2_0$ MeV. Although this value is not very accurate, it is unlikely that the 2.0 MeV β^+ is in coincidence with the 0.67 MeV γ as is stated in Reference 65.

Pd^{101}, Q_ε. A somewhat larger value than the reported value[65], 1.76±0.05 MeV, is preferable. It is likely that a $7/2^+$ level lies slightly above the $9/2^+$ isomer of Rh^{101} and the low-energy γ-ray ($\lesssim 0.05$ MeV) between these states escaped the detection. From the modified rule 2, $5/2^+$ is preferred to $7/2^+$ for the ground state of Pd^{101}.

Pd^{111}, Q^-. The S_n values for the $N=65$ and 66 nuclei do not fit well to the rule 2, either modified or unmodified. Part of this deviation is probably real being due to the large binding energy of the $s_{1/2}$ neutron in the magic nucleus, Sn^{115}. The other part of the deviation may be reduced if $Q^-(Pd^{111})$ is larger than adopted.

Cd^{105}, Q_ε. The value in Nuclear Data Sheets[7] is too large. We tentatively assume that the 1.69 MeV $\beta^{+66)}$ proceeds to the 0.026 MeV level of Ag^{105} instead of the 0.37 MeV level, but the resulting Q_ε still seems to be somewhat too large.

Sn^{113}, Q_ε. There are two contradictory results, 1.3±0.3 MeV obtained from the internal bremsstrahlung[26] and 0.684±0.005 MeV obtained from the $\varepsilon_{LM}/\varepsilon_K$ ratio[67]. Since these experiments are difficult, both data do not seem to be reliable. We adopt ~1.0_0 MeV, but this estimation is not very accurate because of the proton magic number. More experiment is desirable.

$Sn^{120,122,123}$, S_n's. The S_n values of the tin isotopes measured by Cohen and Price[27] seem to be systematically too large. If their S_n values are reduced by 0.1 MeV, they become fit to our " best " values within the errors of ~0.1 MeV.

Te^{118}, $Q_{\varepsilon\varepsilon}$. 4.3 MeV is adopted in Nuclear Data Sheets[7]. However, a somewhat smaller value is preferable. We adopt 4.1 MeV, which is consistent with the new measurements of Q_ε(3.5^m Sb^{118}) as 2.7 MeV by Sorokin et al.[29] and Kocher et al.[30] but not with the old ones[7].

Te^{119}, Q_ε. We adopt the decay scheme of Zaitseva et al.[29] and Nuclear Data Sheets[7]. The decay scheme of Kocher et al.[30] includes several unreasonable points and is in disagreement with our systematics.

I^{128}, S_n. The measured Q-value of the $I^{127}(d, p)$ reaction[64] is too small for the ground-state Q-value. It is probably due to the transition to the excited states of I^{128}.

Cs^{138}, Q^-. It was already pointed out in Nuclear Data Sheets[7] that the reported Q^- is too small. The only way to fit to our systematics is to assume that the 3.40 MeV β^- proceeds to the 1.89 MeV level of Ba^{138} rather than to the 1.43 MeV level.

Ce^{142}, Q_α. There is a report[68] of α-decay with a Q-value of 1.5_4 MeV. The Q-value calculated from the adopted values in Table I is only 1.2_2 MeV. It is unlikely that Ce^{142} decays at an observable rate. Therefore, we neglect the above report. This conclusion is supported by Reference 36.

Nd^{144}, Q_α. The measured value is 1.89 ± 0.02 MeV[36], and we adopt 1.9_1 MeV. This value may be still somewhat too small. The Q_α's of Hf^{174} and Pt^{190} by the same authors[36] also seem to be a little too small. However, the situation is not so clear that we can adjust them beyond the errors.

Pm^{150}, Q^-. We re-interpret the 3.00 MeV β^- as going to the 0.34 MeV level of Sm^{150} rather than to the 0.78 MeV level[7].

Eu^{147}, Q_ε. The reported value[69], 1.29 ± 0.02 MeV, is wrong. We can set a lower bound of this quantity as 1.4 MeV from $Q_\alpha(Eu^{147})$, $Q_\alpha(Sm^{147})$, and the lower bound of $Q_\varepsilon(Pm^{147})$.

Eu^{153}, S_n. The reported (γ, n) threshold value[70] seems to be too large. The excited states of Eu^{150} and Eu^{152} are probably responsible for it. In this deformed-nucleus region several (γ, n) threshold values[70] seem to be somewhat too large. Some of them may be due to the excited-state thresholds.

Gd^{153}, Q_ε. The latest value[38] is in better agreement with our systematics than the older ones[7].

Tb^{154}, Q_ε. $Q_\varepsilon \geq 3.82 \pm 0.05$ MeV[71] of 18^h Tb^{154} is too large for the ground-state Q-value. Therefore, we assume this state to be an excited state. 8^h Tb^{154} may be the ground state.

Dy^{154}, Q_α. The long-lived activity with $Q_\alpha =$ 3.0 MeV[72] is much more likely to be due to the ground state of Dy^{154} than the activity with $Q_\alpha = 3.44 \pm 0.05$ MeV[73]. The pairing energies of the 65-th and 66-th protons in Dy^{150} and Dy^{152} are very large. The assignments of the α-activities of Dy should be checked once more.

Tm^{166}, Q_ε. The highest-energy β^+-decay proceeds to the 0.08 MeV level of Er^{166} rather than to the 0.26 MeV level[74]. The recent measurement[75] of the spin of Tm^{166} as 2 supports this interpretation.

Ta^{182}, Q^-. For the Q-value of $Ta^{181}(\gamma, n)$ 8.1^h Ta^{180} we accept the result of Welsh and Donahue[40] (-7.60 ± 0.08 MeV) rather than that of Geller et al.[70] (-7.852 ± 0.026 MeV), and adopt -7.6_8 MeV. Then, $S_p(W^{182})$ which is calculated from $S_n(Ta^{182})$ and $Q^-(Ta^{182})$[7] seems to be too small. Therefore, we assume that the 0.514 MeV β^- of Ta^{182} proceeds to the 1.290 MeV level of W^{182} instead of the 1.222 MeV level. This interpretation is plausible from a consideration of the β and γ intensities.

Ta^{184}, Q^-. 2.67 ± 0.07 MeV adopted in Nuclear Data Sheets[7] seems to be too small. The experiment is not complete enough to make one stick to this value. We adopt ~3.0_4 MeV.

Ir^{192}, Q_ε. Antonova et al.[76] reported $Q_\varepsilon =$ 1.95 ± 0.01 MeV based on the observation of a low-energy β^+ group ($E_{max} = 0.24 \pm 0.01$ MeV). However, we neglect it because the estimated Q_ε is only 1.1_0 MeV.

Pt^{197}, Q^-. Although we do not change the value of Potnis et al.[77], a smaller value is preferable. It should be checked whether the 0.67 MeV β^- is really in coincidence with the 0.077 MeV γ.

Au^{196}, Q_ε. We adopt 1.5_8 MeV in agreement with the mass-spectroscopic data, while Gupta[78] reported $Q_\varepsilon=0.91\pm0.05$ MeV from the $\varepsilon_L/\varepsilon_K$ ratio. This experiment of $\varepsilon_L/\varepsilon_K$ seems to be too difficult to get a reliable result.

Tl^{202}, Q_ε. 1.11 ± 0.02 MeV obtained from the $\varepsilon_L/\varepsilon_K$ ratio[79] is too small. Our estimated value is 1.4_2 MeV.

Tl^{204}, S_n. 6.54 ± 0.03 MeV obtained from the $Tl(n,\gamma)$ reaction[80] seems to be somewhat too small. The transitions to the excited states of Tl^{204} and Tl^{206} are probably responsible for it.

$Bi^{198,199,201,203}$, Q_α's. The α-activities assigned to these nuclei[8] have too large Q-values. We neglect these data. The assignments should be investigated once more.

Bi^{213}, Q^-. The measured total energy release of the $A=4n+1$ natural decay chain seems to be somewhat too small. The new measurements of the α-energies by Vorob'ev et al.[45] relieved this difficulty a little. We adopt $Q^-(Bi^{213})=1.4_5$ MeV instead of 1.39 ± 0.02 MeV[10,81], and obtain a good fit to our systematics.

Ra^{221}, Q_α. 6.83 ± 0.03 MeV obtained with the ionization chamber[82] seems to be too small. We adopt 7.0_1 MeV. Probably most of the α-decays proceed to the excited states of Rn^{117} as is seen in the α-decays of Ra^{223} and Cf^{249}.

Pa^{234}, Q^-. Although the situation around this nucleus is not very clear, the older value, 2.305 MeV[83], is slightly preferred to the recent value, 2.404 ± 0.003 MeV[84], for $Q^-(1.17^m\, Pa^{234})$. We adopt 2.3_2 MeV for this quantity and 2.3_0 MeV for $Q^-(6.7^h\, Pa^{234})$ as the ground-state Q-value. The latter value is not in good agreement with the reported value, 2.383 ± 0.009 MeV[85]. The complicated decay schemes of $1.17^m\, Pa^{234}$ and $6.7^h\, Pa^{234}$ in References 84 and 85 do not seem to be established well.

Am^{246}, Q^-. The adopted values around this nucleus violate the rule 3 slightly. The easiest way to avoid it is to assume that $25^m\, Am^{246}$ is an excited state, but other ways are possible. Since the situation is not clear, we tentatively assume $25^m\, Am^{246}$ to be the ground state.

$Fm^{251,253}$, Q_α's. The measured α-energies[86] are too small for the ground-state transitions. Probably the main α's proceed to the excited states as is seen in the Cf^{249} decay.

Mass data[7,11,12,54]. Our systematics is not directly related to the mass values themselves but to the mass differences between adjacent nuclei. We can say that the difference between the observed masses of Te^{130} and Xe^{130} is in error. However, it is not easy to decide which mass is in error. We can calculate the masses by adding the adopted S_p's and S_n's. Most of the mass values thus obtained should be assigned enormous errors because many S_p's and S_n's are added. However, it is interesting to see how the "best" mass values fit the measured ones. In the calculation of the "best" masses we have to designate the route of the addition of S_p's and S_n's on the Z-N plane since the rounding-offs in the adopted S_p's and S_n's may cause some differences for different routes. We choose a route near the β-stable line and calculate the masses. The resulting "best" masses may be published elsewhere. The agreement between the "best" masses and the measured values for the nuclei with $A\geq70$ is as follows. (We discuss only the nuclei whose masses were measured in comparison with the nuclei with $A<70$. When more than one experimental mass value are available for a nucleus we use the precisest value.) For 111 nuclei the differences between the "best" masses and the experimental values are less than three times the experimental errors (the errors given in the literatures). The differences are three to five times the experimental errors for 28 nuclei. (Ge^{70}, As^{75}, $Kr^{80,83}$, Rb^{85}, $Pd^{102,104,106}$, Cd^{106}, In^{115}, Te^{120}, Xe^{128}, Cs^{133}, Ba^{134}, Ce^{142}, Nd^{150}, $Gd^{156,160}$, Yb^{170}, Lu^{175}, $Hf^{176,179,180}$, W^{180}, Os^{192}, Pt^{195}, Hg^{200}, U^{235}). The differences are more than five times the experimental errors for 17 nuclei. (Ge^{72}, Nb^{93}, $Pd^{108,110}$, $Te^{126,128,130}$, Xe^{130}, Sm^{147}, Ta^{181}, W^{186}, Re^{187}, $Hg^{196,198,199}$, Pb^{208}, U^{238}). The largest difference is that of Nb^{93}, and is 12 times the experimental error. It is well known that the real errors of the mass-spectroscopic data are three or more times those given in the literatures. Therefore, the above agreements seem to be reasonable.

§ 5. General Discussion

In this paper we have tried to adjust the experimental data so as to fit to our systematics. It remains to be seen whether we have over-adjusted or under-adjusted the data.

As was already mentioned in § 2 the fit of our systematics is not very good in some nuclear regions. We shall get informations on the nuclear structure, especially on the relation between the proton and neutron configurations, by investigating the reason for these anomalies. We do not go deep into this problem in this paper. We also omit the discussion of the pairing energies etc.

As the basic data for estimating unkown separation energies all the experimental data do not have an equal weight. Near the β-stable line on the Z-N plane we have relatively many experimental data, and the weight of each datum is small. In these regions we can detect the wrong data rather easily. On the other hand, the data are few in the regions far from the β-stable line, and the weight of each datum is large. Unfortunately, the detection of the errors in these regions is rather difficult. Therefore, there is a danger that many estimated values in these regions are in error because of a rather small number of wrong experimental data. We hope that the Q-values in these regions will be measured with great care.

The tabulation in this paper is necessarily of tentative nature. We expect that it will be revised in case of necessity.

The authors are greatly indebted to Mr. T. Yamauchi for the preparation and the continual revision of the manuscript of the bulky table.

References

1) F. Everling, L. A. König, J. H. E. Mattauch and A. H. Wapstra: Nuclear Phys. **15** (1960) 342; **18** (1960) 529.
2) K. Way and M. Wood: Phys. Rev. **94** (1954) 119.
3) H. E. Suess and J. H. D. Jensen: Arkiv Fysik **3** (1951) 577. H. E. Suess: Phys. Rev. **81** (1951) 1071.
4) J. M. Blatt and V. F. Weisskopf: *Theoretical Nuclear Physics* (J. Wiley & Sons, Inc., New York, 1952) p. 241.
5) K. Way: *Nuclear Masses and Their Determinations*, edited by H. Hintenberger (Pergamon Press, London, 1956); Amsterdam Conference, July, 1956.
6) A. de-Shalit: Phys. Rev. **105** (1957) 1528.
7) *Nuclear Data Sheets*, compiled by Nuclear Data Group (National Academy of Sciences-National Research Council, Washington, D. C., U.S.A.).
8) D. Strominger, J. M. Hollander and G. T. Seaborg: Rev. Mod. Phys. **30** (1958) 585.
9) B. S. Dzhelepov and L. K. Peker: *Decay Schemes of Radioactive Nuclei* (Academy of Sciences of the USSR Press, Moscow, Leningrad, 1958).
10) W. Kunz and J. Schintlmeister: *Tabellen der Atomkerne*, Teil I, Band 1, 2 (Akademie-Verlag, Berlin, 1958, 1959).
11) *Nuclear Data Tables* (Nuclear Data Project, National Academy of Sciences-National Research Council, Washington, D. C., U.S.A.).
12) Rev. Mod. Phys. **26** (1954) No. 4; **29** (1957) No. 4.
13) S. Hinds, R. Middleton, A. E. Litherland and D. J. Pullen: Phys. Rev. Letters **6** (1961) 113. (C^{16})
14) N. Jarmie and M. G. Silbert: Phys. Rev. **120** (1960) 914. (N^{17}, O^{20})
15) E. L. Robinson, B. T. Lucas and O. E. Johnson: Phys. Rev. **122** (1961) 202. (Na^{26})
16) F. Ajzenberg-Selove, L. Cranberg and F. S. Dietrich: Bull. Am. Phys. Soc. **5** (1960) 493. (Mg^{22})
17) F. Ajzenberg-Selove and K. L. Dunning: Phys. Rev. **119** (1960) 1681. (Si^{26})
18) E. L. Robinson, J. I. Rhode and O. E. Johnson: Phys. Rev. **122** (1961) 879. (S^{30})
19) R. G. Johnson, L. F. Chase and W. L. Imhof: Bull. Am. Phys. Soc. **5** (1960) 406. (S^{30})
20) C. H. Johnson and A. Galonsky: Bull. Am. Phys. Soc. **5** (1960) 443. (Co^{57}, Q_ε)
21) T. H. Jacobi, H. A. Howe and J. R. Richardson: Phys. Rev. **117** (1960) 1086. (Ga^{64})
22) C. Ythier and R. van Lieshout: J. phys. radium **21** (1960) 470. (Se^{81}, Q^-)
23) J. W. Nelson, H. S. Adams, R. H. Davis, J. D. Fox, N. P. Heydenburg, H. S. Plendl, R. K. Sheline and G. M. Temmer: Bull. Am. Phys. Soc. **5** (1960) 424. (Y^{88}, Q_ε)
24) H. Nutley and J. B. Gerhart: Phys. Rev. **120** (1960) 1815. (Ag^{104})
25) Y. Yoshizawa: Private communication, April, 1961. (In^{108})
26) W. E. Phillips and J. I. Hopkins: Phys. Rev. **119** (1960) 1315. (Sn^{113}, Q_ε)
27) B. L. Cohen and R. E. Price: Phys. Rev. **121** (1961) 1441. ($Sn^{116,\cdots,125}$, S_n)
28) B. S. Jensen, O. B. Nielsen and O. Skilbreid: Nuclear Phys. **19** (1960) 654. (Sb^{116})

29) N. G. Zaitseva, M. Ya. Kuznetsova, I. Yu. Levenberg, V. N. Pokrovskii and V. A. Khalkin: Izv. Akad. Nauk SSSR Ser. Fiz. **24** (1960) 1083. A. A. Sorokin, A. Bedesku, M. V. Klimentovskaya, L. N. Kryukova, K. P. Mitrofanov, V. V. Murav'eva, V. N. Rybakov, G. Chandra and V. S. Shpinel': Izv. Akad. Nauk SSSR Ser. Fiz. **24** (1960) 1484. (Sb^{118}, Te^{118,119})

30) C. W. Kocher, A. C. G. Mitchell, C. B. Creager and T. D. Nainan: Phys. Rev. **120** (1960) 1348. (Sb^{118}, Te^{118,119})

31) E. Eichler, J. W. Chase, N. R. Johnson and G. D. O'Kelley: Bull. Am. Phys. Soc. **5** (1960) 448. (I^{133})

32) N. R. Johnson, E. Eichler, G. D. O'Kelley, J. W. Chase and J. T. Wasson: Bull. Am. Phys. Soc. **5** (1960) 448. (I^{134})

33) E. Arbman and I. B. Häller: Nuclear Phys. **22** (1961) 341. (Ba^{129})

34) E. I. Biryukov, O. I. Grigor'ev, B. S. Kuznetsov and N. S. Shimanskaya: Izv. Akad. Nauk SSSR Ser. Fiz. **24** (1960) 1135. (Pr^{140}, Q_ε)

35) V. R. Burmistrov and V. P. Radchenko: Zh. Eks. Toer. Fiz. **39** (1960) 584. (Nd^{144}, S_n)

36) R. D. Macfarlane and T. P. Kohman: Phys. Rev. **121** (1961) 1758. (Nd^{144}, Gd^{152}, Hf^{174}, Pt^{190}, Q_α's)

37) E. G. Funk, Jr., J. W. Mihelich and C. F. Schwedtfeger: Phys. Rev. **120** (1960) 1781. (Pm^{146}, Q^-; Eu^{146}, Q_ε)

38) H. Leutz: Z. Phys. **159** (1960) 462. (Gd^{153}, Q_ε)

39) A. Abdurazakov, K. Gromov. B. Dalkhsuren, B. Dzhelepov, I. Levenberg, A. Murin, Yu. Norseyev, V. Pokrovsky, V. Chumin and I. Yutlandov: Nuclear Phys. **21** (1960) 164. A. A. Abdurazakov, K. Ya. Gromov, B. S. Dzhelepov, Yu. V. Norseyev, G. Ya. Umarov and V. G. Chumin: Izv. Akad. Nauk SSSR Ser. Fiz. **24** (1960) 278. (Tm^{164})

40) R. E. Welsh and D. J. Donahue: Phys. Rev. **121** (1961) 880. (Ta^{181})

41) G. Scharff-Goldhaber, D. E. Alburger and M. McKeown: quoted by W. R. Kane, G. T. Emery, G. Scharff-Goldhaber and M. McKeown, Phys. Rev. **119** (1960) 1953. (Ir^{186,188})

42) S. Homma, T. Kuroyanagi and H. Morinaga: J. Phys. Soc. Japan **16** (1961) 841. (Ir^{195,197})

43) V. A. Kravtsov: Izv. Akad. Nauk SSSR Ser. Fiz. **25** (1961) 130. (Pt^{194}, S_n)

44) M. Sakai, M. Nozawa, K. Sugiyama, H. Ikegami and T. Yamazaki: Fukuoka Meeting of Phys. Soc. Japan, October, 1960. (Tl^{198})

45) A. A. Vorob'ev, A. P. Komar and V. A. Korolev: Zh. Eks. Teor. Fiz. **39** (1960) 70. (Po^{213}, At^{217}, Q_α's)

46) G. Goetze: Z. Phys. **158** (1960) 347. (Ra^{228}, Q^-)

47) K. Takahashi and H. Morinaga: Nuclear Phys. **21** (1960) 133. (Ac^{231})

48) K. Takahashi and H. Morinaga: Nuclear Phys. **15** (1960) 664. (Pa^{237})

49) M. E. Bunker, B. J. Dropesky, J. D. Knight, J. W. Starner and B. Warren: Phys. Rev. **116** (1959) 143. R. M. Lessler and M. C. Michel: Phys. Rev. **118** (1960) 263. (U^{240}, Np^{240})

50) J. E. Gindler and D. W. Engelkemeir: Phys. Rev. **119** (1960) 1645. (Np^{235}, Q_α)

51) R. Vandenbosch: Phys. Rev. **113** (1959) 259. (Np^{241}, Q^-)

52) F. Asaro, I. Perlman, J. O. Rasmussen and S. G. Thompson: Phys. Rev. **120** (1960) 934. (Am^{242})

53) S. E. Vandenbosch, H. Diamond, R. K. Sjoblom and P. R. Fields: Phys. Rev. **115** (1959) 115. (Bk^{249,250}, Q^-'s)

54) V. B. Bhanot, W. H. Johnson, Jr. and A. O. Nier: Phys. Rev. **120** (1960) 235. R. A. Demirkhanov, T. I. Gutkin and V. V. Dorokhov: Dokl. Akad. Nauk SSSR **124** (1959) 301; Sov. Phys. Doklady **4** (1959) 105. R. A. Demirkhanov, T. I. Gutkin and V. V. Dorokhov: Izv. Akad. Nauk SSSR Ser. Fiz. **25** (1961) 124. (Masses)

55) L. W. Alvarez: Phys. Rev. **80** (1950) 519.

56) R. C. Jung and M. L. Pool: Bull. Am. Phys. Soc. **1** (1956) 172.

57) J. M. Cork, M. K. Brice and L. C. Schmid: Phys. Rev. **99** (1955) 703. J. M. Ferguson: Nuclear Phys. **10** (1959) 405.

58) J. M. Siegel and L. E. Glendenin: National Nuclear Energy Series **9** (1950) 549.

59) R. A. Ricci, R. K. Girgis and R. van Lieshout: Nuclear Phys. **21** (1960) 177.

60) K. N. Geller, E. G. Muirhead and J. Halpern: quoted in Reference 7, NRC 59-2-51.

61) A. F. Stehney and N. Sugarman: Phys. Rev. **89** (1953) 194.

62) J. H. Gray, III, H. L. Hamester and A. A. Caretto, Jr.: Phys. Rev. **120** (1960) 977.

63) G. D. O'Kelley, N. H. Lazar and E. Eichler: Phys. Rev. **102** (1956) 223.

64) N. S. Wall: Phys. Rev. **96** (1954) 664.

65) S. Katcoff and H. Abrash: Phys. Rev. **103** (1956) 966.

66) F. A. Johnson: Can J. Phys. **31** (1953) 1136.

67) K. S. Bhatki, R. K. Gupta, S. Jha and B. K. Madan: Nuovo Cimento **6** (1957) 1461.

68) W. Riezler and G. Kauw: Z. Naturforsch. **12a** (1957) 665.

69) C. F. Schwerdtfeger, J. W. Mihelich and B. Harmatz: Bull. Am. Phys. Soc. **4** (1959) 426.

70) K. N. Geller, J. Halpern and E. G. Muirhead: Phys. Rev. **118** (1960) 1302.

71) N. M. Anton'eva, A. A. Bashilov, B. S. Dzhe-

lepov and B. K. Preobrazhenskii: Dokl. Akad. Nauk SSSR **119** (1958) 241; Sov. Phys. Doklady **3** (1958) 289.
72) R. D. Macfarlane: quoted by K. S. Toth and J. O. Rasmussen, Nuclear Phys. **16** (1960) 474.
73) K. S. Toth and J. O. Rasmussen: Phys. Rev. **109** (1958) 121.
74) R. G. Wilson and M. L. Pool: Phys. Rev. **119** (1960) 262.
75) J. C. Walker and D. L. Harris: Phys. Rev. **121** (1961) 224.
76) S. F. Antonova, S. S. Vasilenko, M. G. Kaganskii and D. L. Kaminskii: Zh. Eks. Teor. Fiz. **38** (1960) 379; Sov. Phys. JETP **11** (1960) 276.
77) V. R. Potnis, C. E. Mandeville and J. S. Burlew: Phys. Rev. **101** (1956) 753.
78) R. K. Gupta: Proc. Phys. Soc. (London) **71** (1958) 330.
79) R. K. Gupta: Arkiv Fysik **17** (1960) 337.
80) G. A. Bartholomew and B. B. Kinsey: Can. J. Phys. **31** (1953) 1025.
81) F. Wagner. Jr., M. S. Freedman, D. W. Engelkemeier and L. B. Magnusson: Phys. Rev. **88** (1952) 171.
82) W. W. Meinke, A. Ghiorso and G. T. Seaborg: Phys. Rev. **81** (1951) 782.
83) P. H. Stoker, M. Heerschap and Ong Ping Hok: Physica **19** (1953) 433, 1034.
84) H. Schneider, P. W. de Lange and J. W. L. de Villiers: Nuovo Cimento **14** (1959) 11.
85) P. W. de Lange, H. Schneider and J. W. L. de Villiers: Nuovo Cimento **14** (1959) 681.
86) S. Amiel: Phys. Rev. **105** (1957) 1412. S. Amiel, A. Chetham-Strode, Jr., G. R. Choppin, A. Ghiorso, B. G. Harvey, L. W. Holm and S. G. Thompson: Phys. Rev. **106** (1957) 553.

JOURNAL OF THE PHYSICAL SOCIETY OF JAPAN Vol. 16, No. 8, AUGUST, 1961

The $N^{14}(d, \alpha)C^{12}$ Ground-State Reaction in the Energy Range of Deuteron from 1.5 to 3.0 MeV

By Toshiyuki ISHIMATSU
Department of Physics, Kyusyu University, Hukuoka, Japan

(Received March 14, 1961)

The angular distribution for the $N^{14}(d, \alpha)C^{12}$ ground-state reaction was obtained at seven deuteron energies between 1.5 and 3.0 MeV, and the excitation function for this reaction at the laboratory angle of 30° was determined in the same energy range of deuteron. The angular distribution varies remarkably with deuteron energy, suggesting that the reaction proceeds mainly via compound nucleus formation. The energy dependence of the 30°-differential cross section and the total cross section indicate the presence of overlapping resonances at the excitation energy of about 22.6 MeV in the compound nucleus, O^{16}.

§1. Introduction

Many investigations have shown that nuclear reactions induced by particles having energies of 10 to 50 MeV, in which the final nuclei are left in low-lying states, procceed mainly via direct interaction processes. In particular, (d, p) and (d, n) reactions on light nuclei proceed via a stripping process even at deuteron energies below 10 MeV, and in some cases angular distributions for these reactions show patterns characteristic of the stripping process down to deuteron energies of about 1 MeV. So it is interesting to investigate a (d, α) reaction at low deuteron energies and to compare the results, particularly the energy dependence of the total cross section, with those of the (d, p) and (d, n) reactions on the same nuclide in the same energy range of deuteron, in order to understand the reaction mechanisms of these reactions at low energies.

Recently, the $N^{14}(d, p)N^{15}$ and $N^{14}(d, n)O^{15}$ reactions leading to the ground states of the final nuclei have been studied in this laboratory in the energy range of deuteron from 1.5 to 3 MeV[1),2)]. Either of the angular distributions of these proton and neutron groups has a forward peak characteristic of the stripping process in the whole energy range studied, and also has a remarkable backward peak whose intensity relative to the forward peak shows considerable and rather irregular variation with deuteron energy. Moreover, the angular distributions for the two reactions are similar to each other at the same deuteron energy, and the energy dependences of the total cross sections are quite similar to each other, particularly either of them shows a definite peak at the deuteron energy of about 2.75 MeV. In view of these situations, it was attempted to study the $N^{14}(d, \alpha)C^{12}$ ground-state reaction in the energy range of deuteron from 1.5 to 3 MeV. This reaction has such a high Q-value of 13.57 MeV that it is comparatively easy to study it with a conventional scintillation spectrometer even at such low bombarding energies. It seems interesting to see whether the energy dependence of the angular distribution for the $N^{14}(d, \alpha)C^{12}$ ground-state reaction has some correspondence to that for the $N^{14}(d, p)N^{15}$ ground-state or $N^{14}(d, n)O^{15}$ ground-state reaction, and whether the excitation function of the former reaction has a maximum at about 2.75 MeV of deuteron energy where either of the latter two reactions has a definite maximum.

So far, the $N^{14}(d, \alpha)C^{12}$ reactions has been studied by several authors. Booth et al.[3)] measured the differential cross sections for the two most energetic alpha-particle groups at three energies of deuteron below 1 MeV. They carried out an analysis of the angular distributions in terms of Legendre polynomials and found that the terms of higher order polynomials than $P_3(\cos\theta)$ have no appreciable contribution, and inferred that a direct interaction mechanism does not play any important role in the reaction. Gibson and Thomas[4)] measured the angular distribution of the ground-state alpha particles at the deuteron energy of 8 MeV, and found a complex angular distribution. It shows a pattern characterized by strong forward and backward peakings and maxima occurring at approximately symmetrical angular positions about 90°, i.e., at about 40°, 90° and 140°. Hu[5)] studied the angular distributions of the ground- and first-excited state alpha particles at three deuteron energies about 11 MeV, and obtained the results which can be explained fairly well on the basis of a direct interaction mechanism, so called pick-up process. At the deuteron energy of 21 MeV, Fischer and Fischer[6)] studied the same alpha-particle groups as studied by Hu and found the angular distributions not inconsistent with the pick-up process. It is suggested from the above informations that the direct process plays a substantial role in the $N^{14}(d, \alpha)C^{12}$ ground-state reaction at deuteron energies above 11 MeV, and the decrease of deuteron energy from 11 to 8 MeV produces a remarkable change of the angular distribution for this reaction, indicating the decrease of the contribution of the direct process.

§ 2. Experimental Methods

This experiment was carried out with the electrostatic generator at Kyusyu University. The deuteron beam, analyzed with a 45° deflecting magnet, passed through two slits which were 26 cm distant from each other and entered into a scattering chamber, and fell on a nitrogen target mounted at the center of the chamber. The first slit, 80 cm distant from the exsit of the beam-analyzing magnet, consisted of two electrically insulated tantalum plates and served to pick up error signals for the stabilizer of accelerating voltage. Its width could be changed by moving the plates with a screw system drived at the outside of the beam conducting tube, and in this work was set to be 1 mm. The second slit, 30 cm distant from the target, was made of a silver plate pierced with a circular opening of 4 mm in diameter. The scattering chamber of 23 cm in diameter had windows on its side wall at intervals of 15°, starting on one side at 7.5° to the beam direction and at 15° on the other side. Each window consisted of a circular opening of 3 mm in diameter covered with a nickel foil of 0.05 mil in thickness.

The nitrogen target was melamine, $(C_3H_6N_6)$, deposited by vacuum evaporation on a silver foil of 2 mg/cm² in thickness. The thickness of the melamine layer was measured to be 0.39 mg/cm² by weighing the backing foil with a chemical balance before and after the evaporation of melamine onto it. This value of thickness corresponds to an energy loss of about 80 keV for 2.0-MeV deuteron.

Charged particles produced by the deuteron bombardment of the target came out of the scattering chamber through the side windows and entered into a detector mounted close to one of the windows. Two types of detectors were used to detect the alpha particles from the $N^{14}(d, \alpha)C^{12}$ ground-state reaction which we call α_0 hereafter. The first one was a conventional scintillation counter which had been used in this laboratory to study (d, p) reactions on some light nuclei, and consisted of a CsI(Tl) crystal of the dimension of $(1.5\,\text{cm})^2 \times 1$ mm and a DuMont 6291 photomultiplier. When the detector was mounted on the scattering chamber, the distance between the crystal and the nickel foil of the window was about 1 cm. Output pulses from the photomultiplier were amplified and analyzed by a 20-channel pulse-height analyzer. In the pulse-height spectra obtained at angles less than about 105°, the α_0 peak was completely separated from the other peaks of charged particles, as shown in Fig. 3, therefore, the detector of the first type could be used. At backward angles larger than about 120°, the α_0 peak overlapped on the peaks of low energy protons, and the detector of the second type, shown in Fig. 1, had to be used to discriminate alpha particles from protons. This detector was a counter telescope, consisting of a proportional counter that measured specific energy losses of passing particles, and a scintillation counter that determined the energies of incoming particles. The diameter of the cylindrical cathode of the proportional counter was 2.5 cm and the center wire was a steel wire of 0.03 mm in diameter. The particles passed through the proportional counter in parallel with the central wire and entered into a scintillation crystal. The sensitive length of the proportional counter was 2 cm. The entrance for the particles is a circular opening of 6 mm in diameter covered with 0.05-mil nickel foil. The counter was filled with argon mixed with 3 per cent of carbon dioxide at a pressure of 15 cm Hg. The scintillation counter was a CsI(Tl) crystal of 1 mm in thickness mounted on a DuMont 6291 photomultiplier. The sensitive area of the crystal was defined by a circular opening of 10 mm in diameter, 36 mm apart from the entrance. Outputs from the proportional and scintillation counters were fed to a coincidence circuit of resolving time of 1 microsecond after passing severally through an amplifier and a pulse-height discriminator. A 20-channel pulse-height analyzer, gated by the outputs from the coincidence circuit due to the alpha particles, determined the pulse-height spectrum of the alpha particles. Fig. 2 shows a block diagram of the electronic circuits. The bias level of the discriminator following the proportional counter was set as follows. At a forward angle, a pulse-height spectrum was taken in the above mentioned way and was compared to that taken by keeping the gate of the 20-channel analyzer open regardless of the coincidence pulses. Since in the latter spectrum the α_0 peak was separated completely from the other peaks, the areas of the α_0 peaks in the two spectra could be compared with each other after normalized to a fixed number of monitor counts. The bias level was fixed to a value not so high that the area of the α_0 peak in the former spectrum was smaller than that in the latter, and not so low that pulses due to low energy protons remained in the former spectrum. Fig. 3 shows pulse-height spectra taken with the counter telescope at the laboratory angle of 45° and at the deuteron energy of 2.23 MeV, one of which is a coincidence-gated spectrum and the other is a open gate spectrum. A scintillation counter similar to the detector of the first type was mounted on the 22.5° window and was used

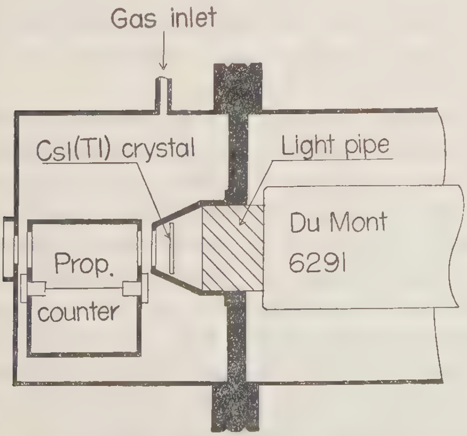

Fig. 1. The schematic diagram of the counter telescope for alpha-particle detection.

as a monitor counter. Of the pulses from the monitor, only the pulses corresponding to the protons from the $N^{14}(d, p)N^{15}$ ground-state reaction were selected by means of a pulse-height discriminator and were registered.

When the counter telescope was used for alpha-particle detection, it was cared that the multiple scattering of alpha particles in the counter gas, the nickel foils on the side window of the scattering chamber and the entrance of the telescope, and the air between these two foils, might cause some losses of alpha particles and distort the alpha-particle angular distributions. So that, the angular distributions of the α_0 group were determined with the counter telescope in the angular range from 15° to 120° at the deuteron energies of 1.94 and 2.47 MeV, and were compared to those obtained with the first type detector at the same deuteron energies. At either energy, the two angular distributions agreed within statistical uncertainties, when they were normalized to each other. It is seen from this fact that, when the counter telescope was used, the multiple scattering would not have any serious effect at least on the shape of the alpha-particle angular distribution, because the sensitive area of the scintillation crystal of the first type detector subtended a sufficiently large solid angle to the side window of the scattering chamber, and therefore, the losses of alpha particles attributed to the multiple scattering may be considered to be negligible when the measurements were done with the first type detector.

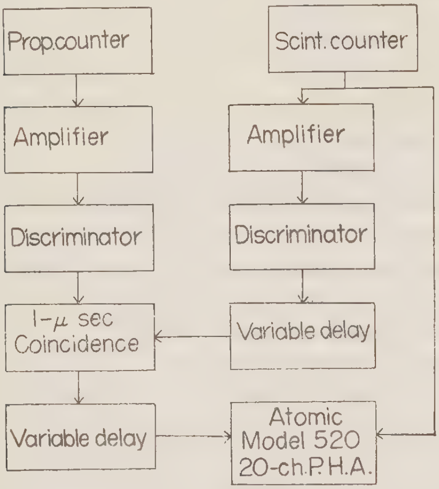

Fig. 2. The block diagram of the electronic circuits for the counter telescope.

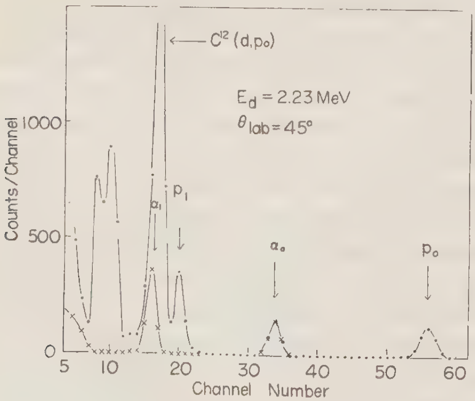

Fig. 3. Pulse-height spectra taken with the counter telescope at the laboratory angle of 45° and at the deuteron energy of 2.23 MeV. The curve connecting crosses is the coincidence-gated spectrum and the curve connecting dots is the open gate spectrum.

The deuteron beam was stopped in a Faraday cup of 3 cm in diameter and 5 cm in depth, and the integrated beam current was determined with a current integrator similar to that designed by Higinbotham and Rankowitz[7]. The secondary electrons emitted from the cup were suppressed by the magnetic field produced by two pieces of Ferite attached to the cup. When the excitation function was measured, the cup was positioned as close to the target as possible in order to avoid the effect of the deuteron scattering in the backing material of the target, since at small angles this effect was expected to be considerable for the deuterons of energies below 3 MeV. The distance between the forward edge of the cup and the center of the target was chosen to be 5 cm, as the excitation function was measured at the laboratory angle of 30°.

The total counts of the α_0 group obtained at different counter angles and a certain deuteron energy were normalized to a fixed number of the monitor counts to get the angular distribution in the laboratory system. The forward angular distribution determined with the first type detector and the backward distribution determined with the second type detector were normalized to each other at two or three angles where the measurements were done with both of the detectors. The excitation function at the laboratory angle of 30° was obtained by normalizing the total counts of the α_0 group obtained at the fixed counter angle of 30° and at different deuteron energies to a certain value of the integrated beam current.

§ 3. Results and Discussions

Figs. 4, 5 and 6 show the angular distributions of the α_0 group at the deuteron energies of 1.48, 1.73, 1.94, 2.23, 2.49, 2.74 and 3.02 MeV. These energy values refer to the mean deuteron energies in the melamine target. Uncertainties of the experimental values shown in these figures are only statistical. Fig. 7 shows the excitation function of the $N^{14}(d, \alpha)C^{12}$ ground-state reaction at the laboratory angle of 30°, and the energy dependence of the total cross section for the same reaction derived from integration of the α_0-group angular distributions shown in Figs. 4, 5 and 6 over the whole solid angle. Each experimental point in the 30°-excitation function given in Fig. 7 represents an average of the values obtained in several runs and the two points at the deuteron energies of 1.94 and 2.49 MeV were both determined as the average of five experimental values, from the distribution of which the standard deviations of the two points are both estimated to be 2%.

The scales on the ordinates of these figures were determined on the basis of the absolute differential cross sections at the laboratory angle of 30°, which were obtained in the 30°-excitation function measurement from the data of the counts of the α_0 group, the target thickness, the integrated beam current and the geometry of the experimental arrangement. The inaccuracy in the scale of the absolute differential cross section is estimated to be ±15%, which is mainly attributed to the uncertainty of the target thickness. Kawai[1)] determined the absolute differential cross section of the $N^{14}(d, p)N^{15}$ reaction in the energy range of deuteron from 1 to 3 MeV, by determining the intensity ratio of the two proton groups, that is, the ground-state proton group from the $N^{14}(d, p)N^{15}$ reaction and the proton group from the $D(d, p)T$ reaction, emitted simultaneously from the deuteron bombardment of a mixture of nitrogen and deuterium gases, and by using the known differential cross section of the $D(d, p)T$ reaction. Accordingly, it was tried to determine the differential cross section of the $N^{14}(d, \alpha)C^{12}$ ground-state reaction, at several deuteron energies, by determining the intensity ratio of the two particle groups, the α_0 group, and the ground-state proton group from the $N^{14}(d, p)N^{15}$ reaction, emitted at the laboratory angle of 30° simultaneously from the deuteron bombardment of the melamine target, and using the differential cross section of the $N^{14}(d, p)N^{15}$ ground-state reaction obtained by Kawai. The values of the 30°-differential cross section obtained by the above mentioned method agree within 5% with those given in Figs. 4 to 7 at every deuteron energies where the measurements where the measurements were done. This excellent agreement is probably fortuitous in view of the experimental accuracies, it is, however,

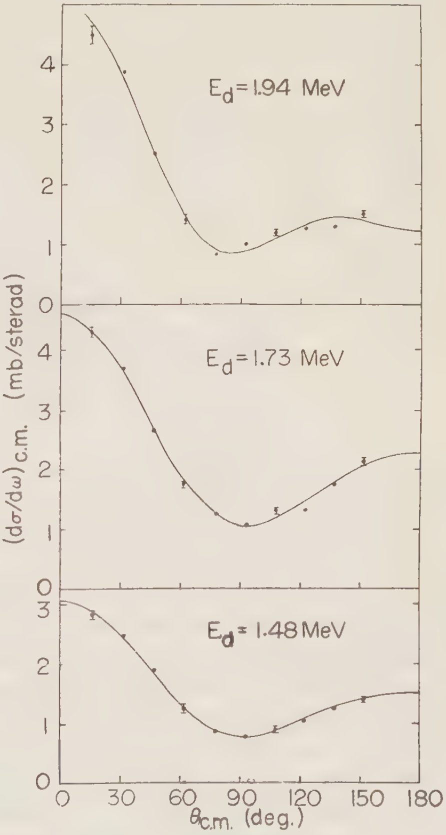

Fig. 4. Angular distributions for the $N^{14}(d, \alpha)C^{12}$ ground-state reaction at the deuteron energies of 1.48, 1.73 and 1.94 MeV. The solid curves represent the series of Legendre polynomials, $\sum_l a_l P_l(\cos\theta)$, where the coefficients a_l were determined by the least square fits of the experimental angular distributions to the series and are given in Table I.

thought to be some evidence of reliability of our methods of target preparation, target-thickness determination and beam-current integration, because, in Kawai's method of cross-section determination, it is unnecessary to know the absolute values of the target thickness and the integrated beam current.

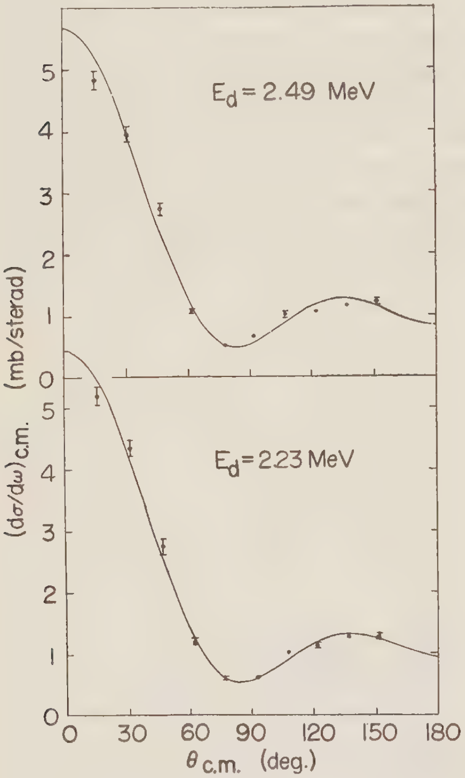

Fig. 5. Angular distributions for the $N^{14}(d, \alpha)C^{12}$ ground-state reaction at the deuteron energies of 2.23 and 2.49 MeV. The solid curves have the same meaning as in Fig. 4.

The angular distribution of the α_0 group changes considerably with deuteron energy and at energies above 2.7 MeV a large second maximum appears at about 120°, and at 3.0 MeV the forward peak, observed at the lower energies, disappears suddenly and an alternative peak appears at about 30°. This behavior of the anfular distribution may be understood qualitatively by assuming that the reaction proceeds mainly via compound nucleus formation and a few excited states in the compound nucleus are involved in the reaction. The asymmetry of the angular distribution about 90° suggests the interference effects between the compound states of opposite parities. The reaction concerned forms the compound nucleus, O^{16}, at an excitation energy as high as 22 to 23 MeV, but there exist some evidences suggesting that O^{16} has a relatively small level density even at such a high excitation energy. For instance, Penfold and Spicer[8] have reported the presence of four levels in O^{16} in the range of excitation energy from 22 to 23 MeV by studying the breaks in the yield curve of the $O^{16}(\gamma, n)O^{15}$ reaction. The present 30°-excitation function for the $N^{14}(d, \alpha_0)C^{12}$ reaction also shows a resonance-like structure which may be indicative of the excited states in O^{16} as discussed later. The energy dependence of the total cross section, obtained by integration of the angular distributions at different energies over the whole solid angle, is similar to that of the 30°-differential cross section, though the similarity is not so definite because of the large intervals between the adjacent experimental points.

Table I. Coefficients, a_l, obtained by the least square fits of the α_0-angular distributions at different deuteron energies to the series of Legendre polynomials, $W(1+a_1P_1+a_2P_2+\cdots)$.

E_d(MeV)	a_1	a_2	a_3	a_4
1.48	0.39	0.77	0.21	—
1.73	0.45	0.86	0.19	—
1.94	0.65	0.95	0.55	—
2.23	0.83	1.27	0.81	—
2.47	0.83	1.27	0.87	—
2.74	0.60	0.65	0.50	−0.62
3.02	0.55	−0.25	−0.20	−1.01

The least square fits of the experimental angular distributions to the series of Legendre polynomials, $\Sigma_l a_l P_l(\cos\theta)$, were carried out. The coefficients a_l obtained in the analysis are given in Table I and the resulting curves are shown by the solid curves in Figs. 4, 5 and 6. The angular distributions at deuteron energies up to 2.47 MeV can be represented approximately in terms of the Legendre polynomials up to $P_3(\cos\theta)$. At 2.74 and 3.02 MeV, large $P_4(\cos\theta)$ terms are required to get the only approximate fits of the experimental results. At 3.02 MeV, the resulting curve has negative values at angles larger than about 160° indicating that the large higher order terms are also required to get the approximate fit of the actual angular distribution over the whole angular range. In general, the fits obtained here are not so good except for the 1.48-MeV angular distribution, but it will be insignificant to obtain further fits with the higher order Legendre polynomials in view of the experimental uncertainties. It is well known that the complexity of the angular distribution in angle of the outgoing particles is not higher than $(\cos\theta)^{2L}$ when a nuclear reaction proceeds via compound nucleus formation and only a restricted range of orbital angular momenta $l \leqq L$ are effective in producing the reaction. But, if the resonance level of the compound nucleus has a total angular momentum J, which is less than the maximum orbital angular momentum L, the complexity is not higher than $(\cos\theta)^{2J}$. In order to get some informations about the angular momenta involved in the reaction concerned, we calculated the relative penetrabilities of the partial waves of incident deuteron into N^{14} nucleus at two deuteron energies of 1.5 and 2.5 MeV, using the data given by Bloch et al.[9] and the value of nuclear radius of 4.8×10^{-13} cm. The results are given in Table II. Energies of the outgoing alpha particles are too high above the potential barrier to impose any restriction to the angular distribution because of the orbital angular momentum. It will be seen that the complexities of the experimental angular distributions at deuteron energies up to about 2.7 MeV are substantially restricted by the maximum effective orbital angular momentum of incident deuteron, L, rather than the maximum of the total angular momenta of the compound states effective in producing the reaction, $J_{\max}$, since these angular distributions are approximately represented in terms of the Legendre polynomials up to $P_4(\cos\theta)$ and L is taken to be equal to 2 at deuteron energies below 2.5 MeV as seen in Table II.

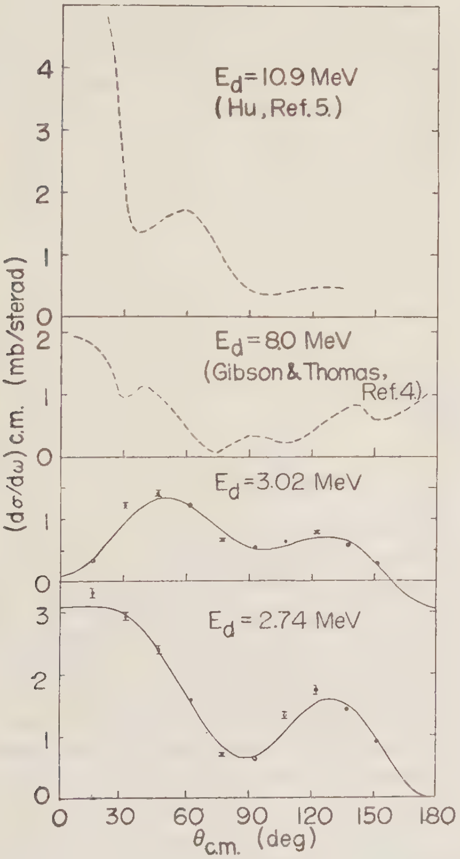

Fig. 6. Angular distributions for the $N^{14}(d, \alpha)C^{12}$ ground-state reaction at the deuteron energies of 2.74 and 3.02 MeV. The solid curves have the same meaning as in Fig. 4. Angular distributions for the same reaction at 8.0 and 10.9 MeV, obtained by Gibson and Thomas[4] and Hu[5] respectively, are also shown for the sake of comparison.

Table II. Calculated relative penetrabilities of the partial waves of deuteron into N^{14} nucleus. The value of nuclear radius of 4.8×10^{-13} cm was used in the calculations.

E_d(MeV)	l			
	0	1	2	3
1.5	1	0.47	0.09	8×10^{-3}
2.5	1	0.64	0.21	0.03

In other words, $2\leqq J_{\max}\leqq 4$ in this energy range of deuteron, because the maximum channel spin of the incident channel is equal to 2. The poorer fit of the angular distribution at 2.74 MeV in terms of $P_l(\cos\theta)$ up to $l=4$ is probably indicative of a small contribution of the incident f wave. The requirement of the terms of higher order Legendre polynomials than $P_4(\cos\theta)$ at 3.02 MeV, however, will not be able to be understood merely by the increased contribution of the f wave or an onset of any reaction mechanism other than the compound nucleus formation. Alternatively, the abrupt change of the angular distribution in the energy range from 2.5 to 3.0 MeV are thought to be due to the level structure of the compound nucleus, O^{16}. In view of the small total cross section at 3.02 MeV, it seems reasonable that at this energy, the contribution of the compound states, which can be excited by the incident wave with orbital angular momentum $l \leq 2$, largely decreases and the contribution of the f wave or some other direct process becomes comparatively important. In that case, the broad peak that is observed in the excitation functions shown in Fig. 7 may be attributed to the overlapping resonances due to the compound states in O^{16}, each of which has a total angular momentum $J \leq 4$. Moreover, parities of these states must be even, if their total angular momenta are even, and must be odd if their total angular momenta are odd, because the total angular momenta and parities of alpha particle and the C^{12} ground state are both zero and even.

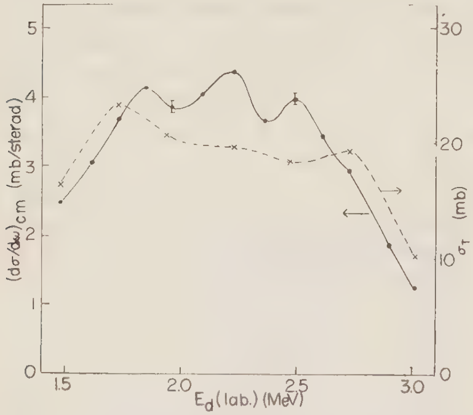

Fig. 7. The excitation function for the $N^{14}(d, \alpha)C^{12}$ ground-state reaction at the laboratory angle of 30° and the energy dependence of the total cross section for the same reaction derived from integration of the angular distributions shown in Figs. 4, 5 and 6. The former is shown by a curve connecting dots, and the latter by a curve connecting crosses.

Some informations about the compound states contributing to the broad peak are obtained, when the 30°-excitation function for the $N^{14}(d, \alpha_0)C^{12}$ reaction obtained in the present experiment is compared with the 0°-excitation function for the $N^{14}(d,n_0)O^{15}$ reaction determined by Weil and Jones[10]. They have determined the absolute cross section for this reaction at 0° to the incident beam in the bombarding energy range from 0.6 to 5.3 MeV. The excitation function shows a strong resonance-like structure, and broad peaks are observed at the deuteron energies of about 1.5, 2.7 and 4.2 MeV. Superposing on the strong gross structure, weaker anomalies are also found at 1.81, 2.18, 2.41 and 2.67 MeV in the energy range of deuteron from 1.7 to 3.0 MeV. On the other hand, in the 30°-excitation function for the $N^{14}(d, \alpha_0)C^{12}$ reaction, peaks are observed at the deuteron energies of about 1.85, 2.2 and 2.5 MeV and perphaps at about 2.7 MeV, in spite of rather poor energy resolution of the measurement. These two excitation functions are shown in Fig. 8. The positions of the anomalies in both excitation functions are coincident very well, suggesting that these anomalies correspond to the excited states in O^{16}. In the excitation function for the $N^{14}(d, n_0)O^{15}$ reaction, anomalies are also present at 1.15, 1.52, 1.62, 2.85 and 3.16 MeV in the energy range of deuteron below 3.5 MeV.

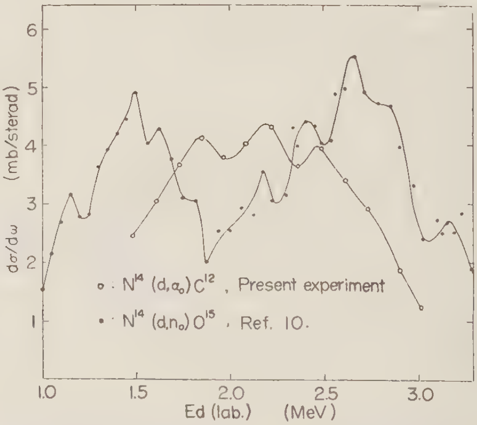

Fig. 8. Excitation functions for the $N^{14}(d, \alpha)C^{12}$ ground-state and $N^{14}(d, n)O^{15}$ ground-state reactions at the laboratory angles of 30° and 0° to the incident beam direction, respectively. The latter is taken from reference 10. The scale of differential cross section refers to c.m. system for the former, and to laboratory system for the latter.

Morita[11] has measured the excitation function for the $N^{14}(d, n_0)O^{15}$ reaction in the energy range of deuteron from 1.0 to 2.2 MeV at the laboratory angles of 0°, 90° and 165° to the beam direction. His result at 0° agrees well with the result obtained by Weil and Jones, showing a broad peak at about 1.5 MeV and weak anomalies at about 1.2, 1.5, 1.6 and

1.8 MeV. The 90°-excitation function is rather flat and shows a similar trend in gross structure to the 0°-excitation function, and a weak anomaly is also seen at about 1.2 MeV. while, the 165°-excitation function shows a prominent broad peak at about 1.9 MeV and a weak anomaly at about 1.8 MeV. It appears that there are some other anomalies in the 90°- and 165°-excitation functions though they are not so definite because of comparatively low energy resolution. Energy level diagrams for O^{16} in the region of excitation from 20 to 24 MeV showing the results of the three experiments are shown in Fig. 9.

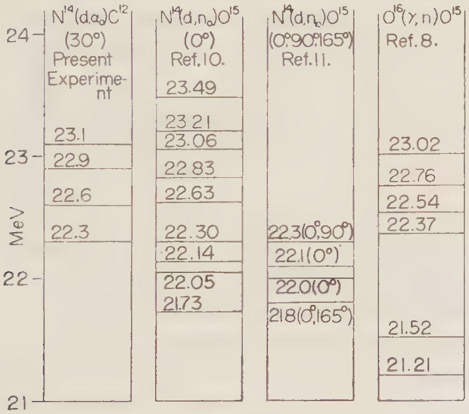

Fig. 9. Energy level diagrams for O^{16} in the range of excitation energy from 20 to 24 MeV showing the results of several experiments.

It is interesting to note that the broad peaks, seen in the excitation function at a certain angle of observation for the $N^{14}(d,n_0)O^{15}$ reaction, do not necessarily correspond to the excited states in O^{16} but to variation of the angular distribution with bombarding energy, and that superposing on them, there are relatively narrow resonances which correspond to the excited states in O^{16}. This resonance-like variation of the angular distribution cannot be explained on the basis of the simple stripping theory, while there exists no positive evidence that the variation is an interference effect due to the level structure of O^{16}. To get further informations about this point, it is desired to study the $N^{14}(d, \alpha)C^{12}$ and $N^{14}(d, p)N^{15}$ reactions at higher energy resolution in the region of bombarding energy concerned.

In Fig. 9, an energy level diagram for O^{16} showing the results obtained by Penfold and Spicer[8] is also shown. It is seen in this figure that the four levels in the range of excitation energy from 22 to 23 MeV observed for the $O^{16}(\gamma, n)O^{15}$ reaction agree in position with those observed for the other two reactions. Penfold and Spicer conclude from an analysis of the widths and integrated cross sections that the four levels observed for the $O^{16}(\gamma, n)O^{15}$ reaction are reached by electric dipole absorption by comparison with Wilkinson's equation[12]. Therefore, these four states should be $T=1$ states, if isotopic spin is a good quantum number. While, isotopic spins of the ground state of N^{14} and deuteron are both equal to zero, so that $N^{14}+d$ can only form $T=0$ states in O^{16}. Accordingly, the agreement in position between the states in O^{16} excited in the three reactions suggests that isotopic spin is not a very good quantum number in this region of excitation as is stated by Wilkinson[13]. The agreement, however, may be accidental in view of the facts that the scale of the excitation energy given in reference 8 can be in error by as much as 300 keV at 23 MeV, and the measurement was not done in the range of excitation energy from 21.5 to 22.1 MeV in reference 8. In any case, it appears that there is no decisive reason that excludes the correlation between the broad resonances in the region of excitation energy from 22 to 23 MeV in O^{16} observed for the $N^{14}(d, \alpha)C^{12}$ ground-state reaction in this work and for the $O^{16}(\gamma,p)$[14,15], $O^{16}(\gamma, n)$[16], $O^{16}(\gamma, 4\alpha)$[17,18] and $N^{15}(p, \gamma)$[19] reactions.

Acknowledgements

We are indebted to the members of the nuclear laboratory of Kyusyu University for their supports throughout this work. We also express our cordial thanks to Prof. S. Morita for his discussions and constant encouragement and to Prof. T. Eguchi for his discussions.

References

1) N. Kawai: J. Phys. Soc. Japan **16** (1961) 157.
2) S. Morita, N. Kawai, Y. Goto, T. Maki and M. Mukae: J. Phys. Soc. Japan **15** (1960) 2170.
3) D. L. Booth, F. U. Price, D. Roaf and G. L. Salmon: Proc. Phys. Soc. London **A**, **71** (1958) 325.

4) W. M. Gibson and E. E. Thomas: Proc. Roy. Soc. **A**, **210** (1951) 543.
5) C. Hu: J. Phys. Soc. Japan **15** (1960) 1741.
6) G. E. Fischer and V. K. Fischer: Phys. Rev. **114** (1959) 533.
7) W. A. Higinbotham and S. Rankowitz: Rev. Sci. Instr. **22** (1951) 688.
8) B. M. Penfold and A. S. Spicer: Phys. Rev. **100** (1955) 1377.
9) I. Bloch, M. H. Hull, Jr., A. A. Broyles, W. G. Bouricius, B. E. Freeman and G. Breit: Rev. Mod. Phys. **23** (1951) 147.
10) J. L. Weil and K. W. Jones: Phys. Rev. **112** (1958) 1975.
11) S. Morita: J. Phys. Soc. Japan **13** (1958) 126.
12) D. H. Wilkinson: Phil. Mag. **44** (1953) 450, 1019.
13) D. H. Wilkinson: Phil. Mag. **1** (1956) 379.
14) L. Cohen, A. K. Mann, B. J. Patton, K. Reibel, W. E. Stephens and E. J. Winhold: Phys. Rev. **104** (1956) 108.
15) C. Milone, S. Milone-Tamburino, R. Rinzivillo, A. Rubbino and C. Tribuno: Nuovo Cimento **7** (1958) 729.
16) C. Milone: Phys. Rev. Letters **3** (1959) 43.
17) P. Stoll: Helv. Phys. Acta **27** (1954) 395.
18) W. K. Dawson and D. Livesey: Can. J. Phys. **34** (1956) 241.
19) S. G. Cohen, P. S. Fischer and E. K. Warburton: Phys. Rev. Letters **3** (1959) 433.

JOURNAL OF THE PHYSICAL SOCIETY OF JAPAN, Vol. 16, No. 8, AUGUST, 1961

Level Structure of Nd^{144}

By Kazusuke SUGIYAMA, Akira FURUSAWA, Shogo HAYASHIBE
and Motoharu KIMURA

Department of Physics, Faculty of Science, Tohoku University, Sendai

(Received May 1, 1961)

The energies and spins of lower excited levels in Nd^{144} have been established by studies of the beta decay of $Ce^{144}-Pr^{144}$ and the electron capture decay of Pm^{144}. The experiments include the energy and relative intensity measurements, and directional correlation measurements of gamma rays by several NaI (Tl) scintillation counters. The level of Nd^{144} is populated at the 695 keV and 2190 keV from decay of Pr^{144}, and the 695 keV, 1310 keV, and 1780 keV from the decay of Pm^{144}. The levels at the 1220 keV and the 1560 keV which have been found by the neutron capture gamma ray measurements could not be found in both decay in the limit of about one percent.

§ 1. Introduction

The levels of ${}_{60}Nd_{84}{}^{144}$ have been studied by a number of investigators[1] from $Ce^{144}-Pr^{144}-Nd^{144}$ negatron chain decay, and the decay scheme has also been proposed. Moreover, the directional correlation of 1490 keV−695 keV cascade has been measured also by a few investigators[2], and these results were consistent with a 1–2–0 spin sequence though there were some disagreement on the correlation coefficients.

On the other hand S. Ofer[3] has studied an electron capture decay of Pm^{144}, and reported three gamma rays, 695, 610 and 475 keV, and measured directional correlations of these radiations. He proposed 2^+ for 695 keV level, 4^+ for 1310 keV level and 6^+ for 1780 keV level.

Recently, the analyses of gamma rays following neutron capture in Nd^{143} were made by a few investigators[4),5)]. Although many levels in Nd^{144} were reported, there were serious discrepancies against each other. (see Fig. 6).

The purpose of the present work is to clarify the previous results of the level structure of Nd^{144} by means of a coincidence spectrum works and directional correlation measurements of gamma rays not only on the negatron decay of Pr^{144} but also on the electron capture decay of Pm^{144}, and furthermore, to search the 1220 keV 2^+ level[4] and the 1560 keV (2 or 3^+) level[5] found in the de-excitation of neutron capture of Nd^{143}.

§ 2. Experimental procedures

a) Source preparations

Ce^{144} was obtained from the Oak Ridge National Laboratory in the form of $CeCl_3$ in HCl solution. Pm^{144} was produced by the bombardment of Nd_2O_3 with 14 MeV protons in the 160 cm cyclotron of the Institute for Nuclear Study, University of Tokyo. After the bombardment, the activity was separated chemically by an ion-exchange column, and the source was made in the form of the $PmCl_3$ in HCl solution. It was necessary to cool down for a long time since there were severel radioactive isotopes owing to the use of natural Neodymium.

b) Coincidence studies

Gamma-gamma coincidence measurements were examined with a 3 in. dia. × 3 in. long, and a 2 in. dia. × 2 in. long NaI (T1) scintillation counters in combination with a 256 channel pulse height analyser. A diode fast-slow coincidence circuit was used, and it was operated at a resolving time (2τ) of 2×10^{-7} sec.

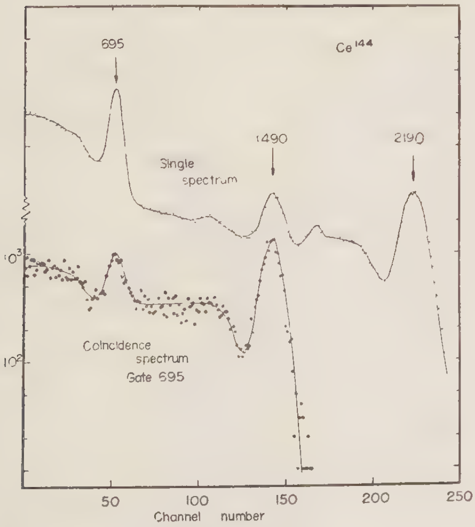

Fig. 1. Scintillation pulse height spectra in Ce^{144} using a 3 in. × 3 in. NaI (T1) with 35 mm dia. 50 mm long lead slit.

——•—— ; single spectrum

——●——; coincidence spectrum with the 695 keV photo-peak

In the decay of Pr^{144}, an observed gamma-gamma coincidence spectrum is shown in Fig. 1 with a single gamma ray spectrum.

The coincidence spectra in the decay of Pm^{144} are shown in Fig. 2 also with a single spectrum.

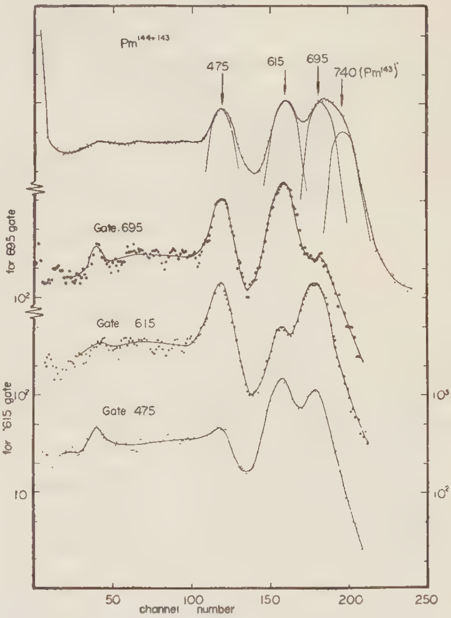

Fig. 2. Scintillation pulse height spectra in Pm^{144} using a 3 in. × 3 in. NaI (T1) with 35 mm long lead slit.

• —— ; single spectrum

● — ; coincidence spectrum with the 695 keV photo-peak

• ; coincidence spectrum with the 615 keV photo-peak

• —— ; coincidence spectrum with the 475 keV photo-peak

c) Directional correlation measurements

The directional correlation measurements were carried out using two 1½ in. long NaI (T1) crystals and RAC 6810A photomultipliers. The potomultipliers were operated at high voltage (1500∼1900 volts) and were fed to the diode fast-slow coincidence circuit which was operated at $2\tau=9\times10^{-9}$ sec. The goniometer is driven automatically, and a camera method to record the data on scalers can be used and in addition a rotating source method was also employed to correct excentricity and inhomogenity in source material. These electronic circuit block diagram and a goniometer are shown in Figs. 3 and 4 respectively.

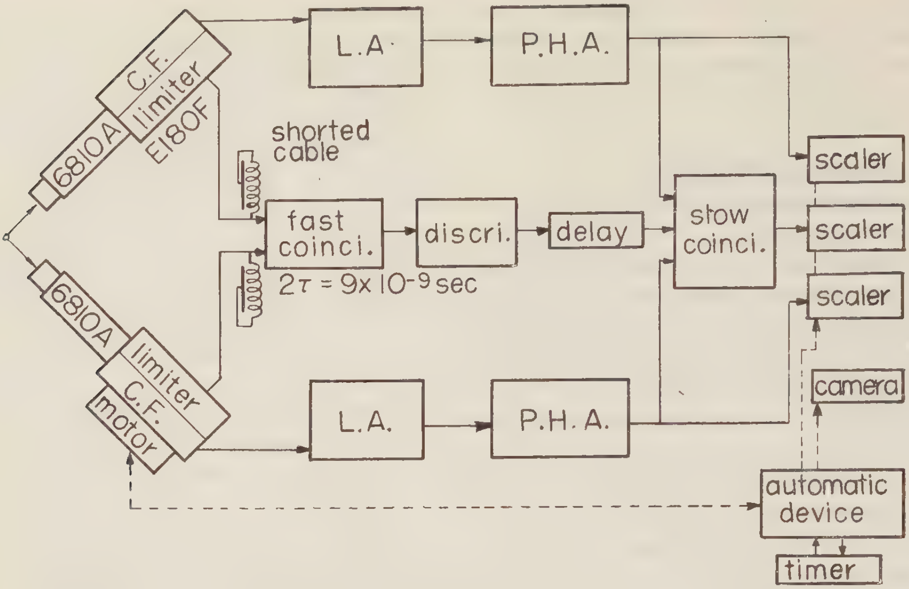

Fig. 3. Block diagram of the gamma-gamma directional correlation arrangement. High voltage power supply for photomultipliers was omitted in this figure.

The measured correlation coefficients were corrected for a finite angle resolution. A method of this correction was employed as follows; finite angle resolutions were measured by using colimated gamma rays through a 3 mm dia. 50 mm long and 10 mm dia. 50 mm long aperture. We used Cs^{137} (661 keV), Co^{60} (1.17 and 1.33 MeV) and annihilation gamma ray from Na^{22} as gamma ray sources. The correction factor $J\nu/J_0$ was calculated using a formula given by Lawson and Frauenfelder[6].

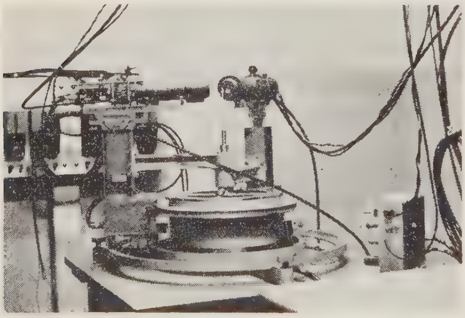

Fig. 4. The anglar correlation apparatus.

Table I. Energy and relative intensity of gamma radiations in Pr^{144} and Pm^{144}.

	Gamma rays (keV)	Relative intensity
Decay of Pr^{144}	695 1490 2190	100 30 60
Decay of Pm^{144}	695 615 475	100 100 46

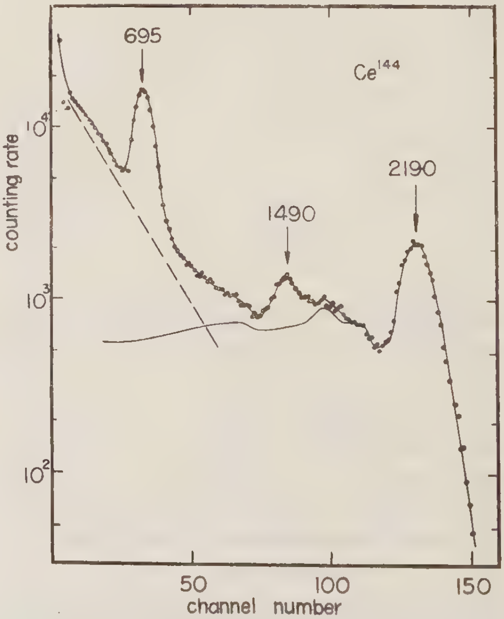

Fig. 5. Scintillation pulse height spectrum in Ce^{144} using a 5 in.×4 in. well type NaI (T1) crystal for summing measurement. The source was contained in a 10 mm dia. plastic cylindrical holder covered by a 0.5 mm thick lead plate.

§ 3. **Results**

a) Gamma rays belonging to Nd^{144} are tabulated in Table I.

These results are not inconsistent with earlier investigations. The 520 keV gamma ray corresponding transition from the 1220 keV 2^+ level to the 695 keV first excited level, and the 970 keV gamma ray corresponding transition from the 2190 keV level to the 1220 keV are not detectable within the limits of one percent. We have tried to find the 1220 keV level reported by Burmistrov et al.[4] using a summing method by a 5 in. dia. and 4 in. long well type NaI (T1) crystal. It was concluded that the 1220 keV level did not exist. It was also concluded by using similar procedures that the 1560 keV did not exist in both decays of Pr^{144} and Pm^{144} in the limit of a few percent.

b) Directional correlation coefficients corrected for the finite angle resolution for each measurement are tabulated in Table II.

Table II. A_2 and A_4 obtained in directional correlation measurements in Pr^{144} and Pm^{144}.

$W(\theta)=1+A_2\cdot P_2(\cos\theta)+A_4\cdot P_4(\cos\theta)$

		A_2	A_4
In Pr^{144}	695 γ−1490 γ	-0.27 ± 0.02	0.04 ± 0.03
In Pm^{144}	695 γ−615 γ	0.115 ± 0.009	-0.025 ± 0.014
	695 γ−475 γ	0.070 ± 0.020	0.054 ± 0.043
	615 γ−475 γ	0.072 ± 0.004	0.021 ± 0.007
Theoretical values	1 (D) 2 (Q) 0	−0.25	0
	4 (Q) 2 (Q) 0	0.102	0.009
	6 (Q) 4 (Q) 2		
	*6 (Q) 4 (−) 2 (Q) 0		

* Intermediate radiation unobserved.

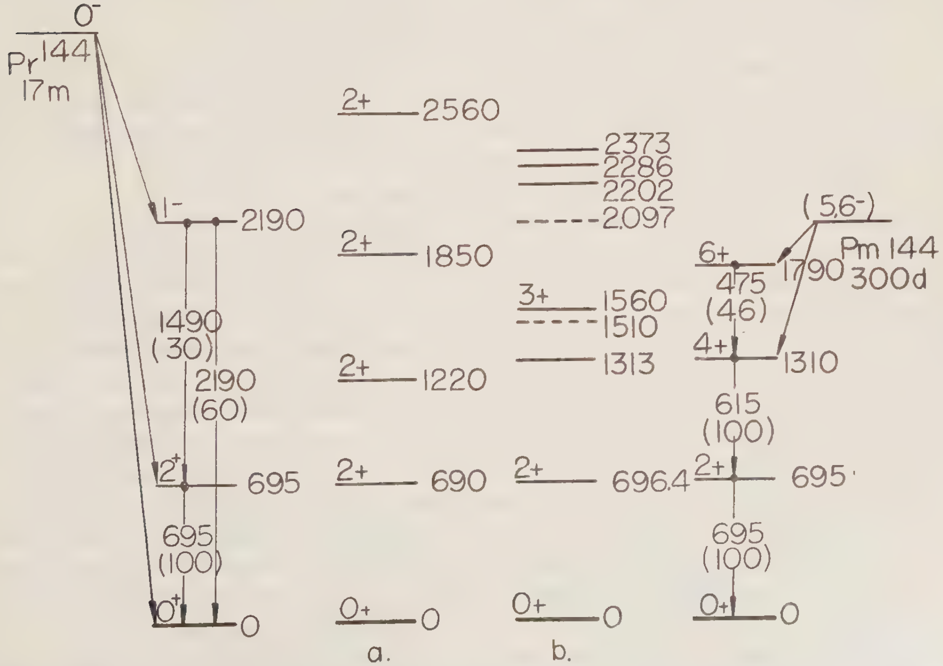

Fig. 6. Energy levels of Nd^{144}. The results of Burmistrov (a) and of Campion et al. (b) obtained by neutron capture gamma ray analysis are also shown.

On the basis of above results, the level scheme of Nd^{144} is given in Fig. 6.

§ 4. Discussion

Many attempts have been made to explain the level structure of even-even nuclei. The Bohr-Mottelson model[7] gives a fairly successful explanation in neutron regions, $90 \leqslant N \leqslant 114$ and $136 \leqslant N$.

However, in the region of so-called intermediate nuclei this model fails to explain many experimental results. Nd^{144} is also this case. $E_4/E_2 = 1.88$ and $E_6/E_2 = 2.56$ for Nd^{144} can not be interpreted even if an interaction of rotation and vibration is taken into account, where E_I is the energy of the first spin I level.

For the even-even nuclei in the region $50 < N < 90$, it has been usual to describe the energy levels as the vibrational excitation. The energy spectrum thus obtained has a uniform spacing

$$\hbar\omega_2 = \hbar\left(\frac{C_2}{B_2}\right)^{1/2}$$

(for quadrupole vibration)

and a level of the energy

$$E^{(n)} = (n + 5/2) \cdot \hbar\omega_2$$

may be characterized as containing n phonons each of which carries a spin 2^+. The first excited level is one phonon excited state, and the two phonon excited states are multiply degenerate, the spin of which are 0^+, 2^+, 4^+, and the three phonon excited states are also multiply degenerate, 0^+, 2^+, 4^+, 6^+. It seems plausible to explain the energy spectrum of Nd^{144} by means of this vibrational model. The 0^+ and the second 2^+ levels are not found in the present experiment, probably because the higher levels have higher spins and will not decay to these levels of low spins, in the decay of Pm^{144}.

If a 0^+ or 2^+ level exists near the 1310 keV 4^+ level, log f_0t to this level in $Pr^{144} \rightarrow Nd^{144}$ beta decay is 4.65 and the beta ray branching ratio is 0.5∼0.1%. Then the 610 keV gamma ray from this level to the first 2^+ level would be observed at 30∼7% of the 695 keV gamma ray. Furthermore the 880 keV gamma ray from the 2190 keV to this level also would be observed at ∼4%. Both gamma rays were not observed. There is no further quantitative prediction from the vibrational model.

From the other point of view, B. J. Raz[8] has proposed a model which took into account an interaction between the nuclear core and two outer particles. He assumed the configuration of two particles was $(7/2)^2$ with $I = 0$, 2, 4 and 6, and the two body interaction which gave a suitable level scheme for Ca^{48} was found to be of reasonable strength.

We apply his method to the present case. According to his theory the two body interaction is given by

$$H_{12} = 3D[3 - \boldsymbol{\sigma} \cdot \boldsymbol{\sigma}_2] \cdot \hbar\omega \cdot \exp(-r^2/r_0^2).$$

This calculation included energy spectra relative to the first 2^+ level changing two parameters D and x which is a nuclear deformation

$$x = k(5/16\pi j \hbar\omega C)^{1/2}$$

If we choose the case of $D = 0.20$ and $x = 0.4$, we find

$$E_4/E_2 = 2.0, \quad E_6/E_2 = 2.5, \quad E'_2/E_2 = 3.3,$$

where E'_2 is the energy of the second 2^+ level. From $E_2 = 695$ keV and above ratios,

$$E_4 = 1390 \text{ keV}, \quad E_6 = 1740 \text{ keV}, \quad E'_2 = 2300 \text{ keV},$$

these values are rather in agreement with the present experimental values, except for the second 2^+ level which is undetectable because of its high energy. A small nuclear deformation $x = 0.4$ is plausible for a near closed shell nucleus ${}_{60}Nd_{84}{}^{144}$.

The levels of odd spin and odd parity are found for many even-even nuclei, and they are interpreted as an octupole vibrational level, and the 2190 keV 1^- level might belong to this kind of level.

Recently A. S. Davydov et al[9]. have developed the axially asymmetric rotor model, in which a nucleus is classified by a parameter γ, which determines the deviation of the shape of the nucleus from axial symmetry through an energy ratio of the second 2^+ level to the first 2^+ level. Many observed energy spectra of even-even neclei, the region of which is much wider than the Bohr-Mottelson model could explain, could be rather satisfactorily explained by assuming various values of γ. Although the values of γ varies between 0 and $\pi/3$, the predicted value of E_4/E_2 is larger than 2.6 over all ranges of γ.

A new development[10] of this model has shown the energy ratio of 1.9 of the first 4^+ level to the first 2^+ level corresponding to

$\gamma=30^\circ$ and $\mu=1.0$, where μ is the non-adiabaticity parameter. Then, the energy ratio of the second 2^+ level to the first 2^+ level is 1.8, and if we take the experimental value of the first 2^+ state of Nd^{144}, the second 2^+ is 1200 keV. Similarly it is concluded that the first 3^+ level is the 1900 keV. This is excluded by the results of Campion et al5). Futhermore, there is a discrepancy on 6^+ level. According to the new Davydov model10), the first 6^+ level of the nucleus having $\gamma=30^\circ$ is 1960 keV, although our experimental result indicates a 6^+ level at 1780 keV.

Acknowledgements

We wish to express our appreciations to Drs. N. Suzuki, S. Oki for the chemical separation of the source material and to Drs. H. Ikegami, E. Takekoshi, K. Nakai, J. Matsumoto for the generous cooperation and the helpful discussions. We are also grateful to the Cyclotron crew and the Beta Group of Institute of Nuclear Study, University of Tokyo, for their help on the Bombardment. This work was supported by the Scientific research grant of the Ministry of Education.

References

1) D. E. Alburger, J. J. Kraushaar: Phys. Rev. **87** (1952) 448.
F. T. Porter, C. S. Cook: Phys. Rev. **87** (1952) 464.
W. S. Emmerich, W. J. Auth, J. D. Kurbatov: Phys. Rev. **94** (1954) 110.
J. M. Cork, M. K. Brice, L. C. Schmid: Phys. Rev. **96** (1954) 1295
R. L. Hicok, W. A. Mckinley, S. C. Fulty: Phys. Rev. **109** (1958) 113.
F. T. Porter, P. P. Day: Phys. Rev. **114** (1959) 1286.

2) D. E. Albueger, J. J. Kraushaar: ibid. Steffen; Phys. Rev. **95** (1954), 614.
R. L. Graham, J. S. Geiger, T. A. Eastwood: Can. J. Phys. **36** (1958) 1084.

3) S. Ofer: Phys. Rev. **113** (1959) 895.
K. S. Toth, O. B. Nielsen: Phys. Rev. **115** (1959) 1004.
E. G. Funk, Jr., J. W. Mihelich, C. F. Schwerdtfeger: Phys. Rev. **120** (1960) 1781.

4) V. R. Burmistrov, V. P. Radchenko; Zh. Eks. Teor. Fiz. **39** (1960) 584.

5) P. J. Campion, J. W. Knowles, G. A. Bartholomew: Bull. Am. Phys. Soc. **4** (1959) 247.
P. H. Stelson, *Kingston Conference on Nuclear Structure* (1960) p. 787.
J. E. Draper, R. L. Hickok: Nucl. Phys. **19** (1960) 436.

6) J. S. Lawson, Jr., H. Frauenfelder: Phys. Rev. **91** (1953) 649.

7) A. Bohr and B. Mottelson: K. Danske Vidensk, Mat. Fys. Medd. **27**, No. 16 (1953).

8) B. J. Raz: Phys. Rev. **114** (1959) 1116.

9) A. S. Davydov and G. F. Fillipov: Nucl. Phys. **8** (1959) 237.

10) A. S. Davydov and A. A. Chaban: Nucl. Phys. **20** (1960) 499.

JOURNAL OF THE PHYSICAL SOCIETY OF JAPAN, Vol. 16, No. 8, AUGUST, 1961

Magnetic Susceptibilities of Cr and Cr-Fe Alloy

By Masao SHIMIZU*

Department of Physics, Faculty of Science,
Tokyo Metropolitan University, Tokyo

and Takeshi TAKAHASHI

Physics Institute, Yamanashi University, Kofu

(Received March 1, 1961)

The magnetic susceptibilities of Cr and Cr-Fe are investigated by the use of the band picture for 3d electrons. The temperature increase of the magnetic susceptibility of Cr is attributed to a minimum of the electron state density. For the shape of the band of Cr two models are adopted, and the calculated susceptibilities are compared with the observed ones. According to this comparison the shape of the band of Cr is discussed, and the result on its shape is compared with that calculated from the specific heat measurement at low temperatures by Cheng et al.

§ 1. Introduction

In the previous paper[1] (we refer this as (I) hereafter) we analyzed the susceptibilities of Cr and Cr-Fe alloy by making use of the band picture and obtained reasonable results. One of the difficulties of our previous calculation is the fact that the calculated susceptibilities at lower temperatures are rather large and are not necessarily in agreement with the observed ones. Since the band shape of our model shown in Fig. 1 of (I) (we refer this as model (1) hereafter) would be rather different from that of the real band in the neighbourhood of the "minimum" of the electron state density, so we could not avoid the disagreement between the calculated values of susceptibilities and their observed values at lower temperatures.

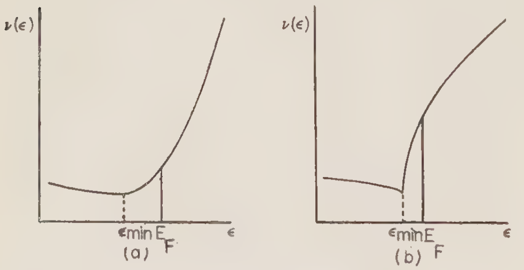

Fig. 1. Electronic state density; (a): model (2), (b): model (3).

Recently, however, McGuire has reported that the susceptibility of Cr increases with decreasing temperature at very low temperatures ($\chi_g=3.9-4.0\times10^{-6}$ e.m.u. g^{-1} at 4.2°K)[2], but details are not reported yet. At any rate, as our model (1) is not so satisfactory, in this paper we attempt to calculate susceptibilities for different models and to find what sort of model for the electron state density of Cr would be the best.

As we described in (I), if the Fermi level at 0°K is near a "real minimum" of the state density the temperature coefficient of the susceptibility is positive at lower temperatures. So we adopt the following band with a real minimum in the state density, $\nu(\mathcal{E})$, (we refer this as model (2)).

$$\nu(\mathcal{E})=\begin{cases} b+a_1(\mathcal{E}_m-\mathcal{E})^2\,, & \text{for } \mathcal{E}<\mathcal{E}_m\,; \\ b+a_2(\mathcal{E}-\mathcal{E}_m)^2\,, & \text{for } \mathcal{E}_m<\mathcal{E}\,, \end{cases} \qquad (1)$$

where $\mathcal{E}_m$ is the energy at which $\nu(\mathcal{E})$ is minimum. This is shown in Fig. 1 (a).

Moreover, calculations are carried out for the model shown in Fig. 1 (b) (we refer this as model (3)). The state density of this model is given by

$$\nu(\mathcal{E})=\begin{cases} b'+a_1'(\mathcal{E}_m-\mathcal{E})^{1/2}\,, & \text{for } \mathcal{E}<\mathcal{E}_m\,; \\ b'+a_2'(\mathcal{E}-\mathcal{E}_m)^{1/2}\,, & \text{for } \mathcal{E}_m<\mathcal{E}\,. \end{cases} \qquad (2)$$

§ 2. Calculations of Paramagnetic Susceptibilities for Models (2) and (3)

From a similar calculation to that in (I), we obtain for model (2)

---

* Now at the Department of Applied Physics, Faculty of Engineering, Nagoya University, Nagoya.

$$\eta+[pF_2(\eta)-F_2(-\eta)]\left(\frac{T}{T^*}\right)^2=\left\{\begin{array}{ll}(1+\frac{1}{3}pr^2)r(T^*/T)\,, & \text{for}\quad r>0\,;\\ (1+\frac{1}{3}r^2)r(T^*/T)\,, & \text{for}\quad r<0\,,\end{array}\right\} \tag{3}$$

and

$$\frac{\chi}{2b\mu_B{}^2}=1+2[pF_1(\eta)+F_1(-\eta)]\left(\frac{T}{T^*}\right)^2. \tag{4}$$

From these equations the Fermi energy, $\mathcal{E}_F$, and the susceptibility, χ, are determined as functions of temperature, respectively. Here, $p=a_2/a_1$, $kT^*=(b/a_1)^{1/2}$, $r=\mathcal{E}_0/kT^*=\mathcal{E}_0(a_1/b)^{1/2}$, $\mathcal{E}_0=(\mathcal{E}_F)_{T=0}$, $\eta=\mathcal{E}_F/kT$, $F_n(\eta)=\int_0^\infty\frac{x^n dx}{e^{x-\eta}+1}$, $n=0, 1, 2$, and μ_B is the Bohr magneton. $\mathcal{E}_F$ is measured from $\mathcal{E}_m$ to the right. Now, let the susceptibilities of a transition metal and its dilute alloy with another metal be χ and $\chi+\Delta\chi$, respectively, we obtain

$$\frac{\mu_B{}^2}{kT^*}\frac{\Delta N}{\Delta\chi}=\frac{\frac{1}{2}+[pF_1(\eta)+F_1(-\eta)](T/T^*)^2}{pF_0(\eta)-F_0(-\eta)}\frac{T^*}{T}\,, \tag{5}$$

where ΔN is the increase of the number of d electrons.

The results of our calculations for the temperature variations of the susceptibility at several values of r when $p=10$ are shown in Fig. 2. We make use of the numerical values of $F_2(\eta)$ and $F_1(\eta)$ which have been given by Rhodes[3]. As we have described in § 1, if $\mathcal{E}_0$ is at the real minimum of the state density χ will increase with temperature monotonously. In fact, as we can see in Fig. 2, for $r\leq 1/\sqrt{p}$ susceptibilities increase with increasing temperature continually. It can also be seen that the increases of the susceptibilities for model (2) at higher temperatures are more rapid than those for model (1). This fact is due to the following reason. As the state density in model (2) is proportional to $\mathcal{E}^2$, the number of electrons which contribute to the susceptibility will increase with increasing temperature rather rapidly. So, as we can see in Eq. (4), susceptibilities for model (2) increase, being proportional to T^2, at higher temperatures. On the other hand susceptibilities for model (1) vary as $T^{1/2}$ at higher temperatures.

For model (3) equations which correspond to Eqs. (3), (4) and (5) for model (2) become

$$\eta+[p'F_{1/2}(\eta)-F_{1/2}(-\eta)]\left(\frac{T}{T'^*}\right)^{1/2}=\left\{\begin{array}{ll}(1+\frac{2}{3}p'r'^{1/2})r'(T'^*/T)\,, & \text{for}\quad r'>0\,:\\ (1+\frac{2}{3}|r'|^{1/2})r'(T'^*/T)\,, & \text{for}\quad r'<0\,,\end{array}\right\} \tag{6}$$

$$\frac{\chi}{2b'\mu_B{}^2}=1+[p'F_{1/2}{}'(\eta)+F_{1/2}{}'(-\eta)]\left(\frac{T}{T'^*}\right)^{1/2}, \tag{7}$$

and

$$\frac{\mu_B{}^2}{kT'^*}\frac{\Delta N}{\Delta\chi}=\frac{1+[p'F_{1/2}{}'(\eta)+F_{1/2}{}'(-\eta)](T/T'^*)^{1/2}}{p'F_{1/2}{}''(\eta)-F_{1/2}{}''(-\eta)}\left(\frac{T}{T'^*}\right)^{1/2}, \tag{8}$$

where $p'=a_2'/a_1'$, $kT'^*=(b'/a_1')^2$, $r'=\mathcal{E}_0/kT'^*=\mathcal{E}_0(a_1'/b')^2$,

$$F_{1/2}(\eta)=\int_0^\infty\frac{x^{1/2}dx}{e^{x-\eta}+1}\,,\qquad F_{1/2}{}'(\eta)=\frac{dF_{1/2}(\eta)}{d\eta}\quad\text{and}\quad F_{1/2}{}''(\eta)=\frac{d^2F_{1/2}(\eta)}{d\eta^2}.$$

The results of the calculations for model (3) are not so different from those for model (1) (Fig. 3(a) in (I)).

Neglecting the difference between densities of pure Cr and dilute alloy of Fe in Cr, and that between the atomic weights of Cr and Fe, we obtain $\Delta N=1.16\times10^{22}qx$ per gram, then

$$\frac{1}{\Delta\chi}=139\frac{T^*}{qx}\frac{\frac{1}{2}+[pF_1(\eta)+F_1(-\eta)](T/T^*)^2}{pF_0(\eta)-F_0(-\eta)}\left(\frac{T}{T^*}\right)^{-1},\qquad\text{for model (2)}\,, \tag{5'}$$

$$\frac{1}{\Delta\chi}=139\frac{T'^*}{qx}\frac{1+[p'F_{1/2}{}'(\eta)+F_{1/2}{}'(-\eta)](T/T'^*)^{1/2}}{p'F_{1/2}{}''(\eta)-F_{1/2}{}''(-\eta)}\left(\frac{T}{T'^*}\right)^{1/2},\qquad\text{for model (3)}\,, \tag{8'}$$

where x is the fraction of Fe atoms and q the increase of d electrons per Fe atom. Both equations give the relation, $1/\Delta\chi \propto T$, at $T \to \infty$.

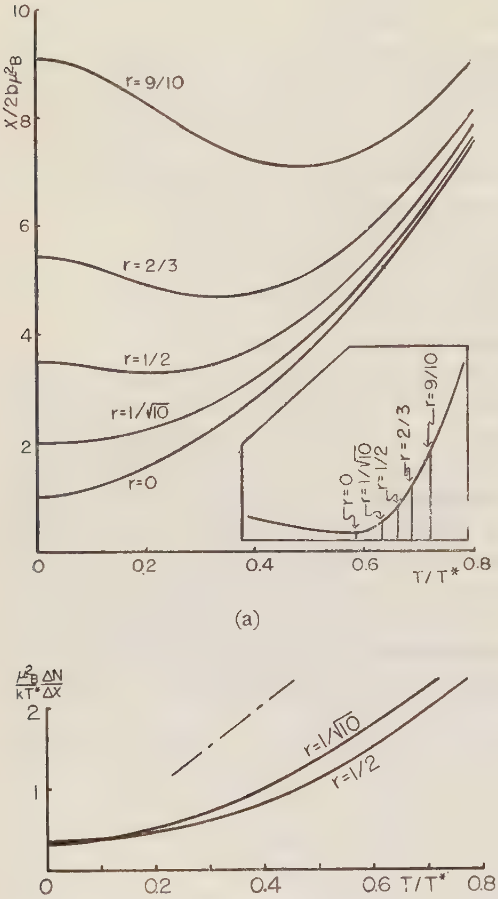

(a)

(b)

Fig. 2. (a) Calculated temperature-variations of susceptibilities in the case of model (2) for $p=10$. (b) Calculated temperature-variations of $\Delta\chi$ in the case of model (2) for $p=10$. $-\cdot-$ is the asymptote for $T\to\infty$.

§ 3. Comparison with Experimental Results and Discussion

In Fig. 3 (a) the observed values of susceptibilities for Cr are compared with the calculated values for model (2) in the case where $p=10$, $r=1/\sqrt{10}$, $T^*=8{,}000$°K and $p=10$, $r=1/2$, $T^*=4{,}000$°K. In Fig. 3 (b) the observed values of $\Delta\chi$ for the alloy of 1.05% Fe in Cr are compared with the calculated values of $\Delta\chi$ for the same parameters with those mentioned above. The values of a, in Fig. 3 (a) are determined so as to get the best agreement between the calculated values and the observed ones for susceptibilities at the highest temperature, and the values of q are determined so as to get the best agreement in the intermediate region of temperature. When r is larger or smaller than the values given above, the agreement between the calculated values of χ and the observed ones becomes unsatisfactory. Anyhow, if the suitable values are taken for parameters the calculated values for model (2) can be fitted with the observed ones for χ. However, by using the same values of parameters with those for χ, satisfactory agreement cannot be obtained between the observed values and the calculated ones of $\Delta\chi$ for model (2). The calculation has been performed for $p=30$, but the result is not so different from that shown in Fig. 3.

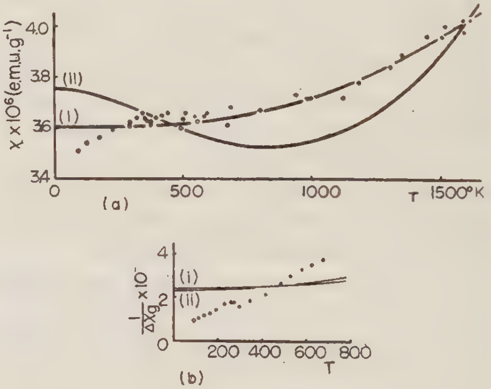

Fig. 3. (a) Comparison between calculated susceptibilities for model (2) and experimental ones for Cr. (b) Comparison between calculated susceptibilities for model (2) and experimental ones for an alloy, 1.05% Fe in Cr. (i) Calculated for $p=10$, $r=1/\sqrt{10}$, $T^*=8{,}000$°K, $a_1k^2=1.64\times10^{26}$ erg^{-1}g^{-1}deg^{-2}, $b=1.050\times10^{34}$ erg^{-1}g^{-1} and $q=14.0$. (ii) Calculated for $p=10$, $r=\frac{1}{2}$, $T^*=4{,}000$°K, $a_1k^2=3.81\times10^{26}$ erg^{-1}g^{-1}deg^{-2}, $b=0.609\times10^{34}$ erg^{-1}g^{-1} and $q=8.0$

• : Experimental results by McGuire and Kriessman[4].

○ : Experimental results by Newmann and Stevens[5].

In Fig. 4 the comparison between the results of the observation and the calculation for model (3) in the cases where $p=10$, $r=1/100$, $T^*=30{,}000$°K and $p=10$, $r=1$, $T^*=350$°K is shown. The results of these cases are similar to those for model (1) (Fig. 6 and 7 in (I)). This resemblance would not be strange because the shapes of the bands that we make use of are similar to each other for both models.

In the first place it has been expected that the calculation would agree with observation when model (2) is adopted, because $\nu(\mathcal{E})$ has a real minimum. Really, at lower temperatures it is possible to obtain a rather good agreement for χ, but for $\Delta\chi$ it is quite impossible. This fact is due to the rapid temperature increase of the calculated values of χ in the higher temperature regions. Namely, we must use the calculated curves of χ in Fig. 2 (a) in the region where T/T^* is rather small in order to get a satisfactory agreement between calculations and observations, but for such small values of T/T^* the calculated curves of $1/\Delta\chi$ in Fig. 2 (b) are not yet straight, and those curves cannot agree with the experimental curve which is proportional to T approximately.

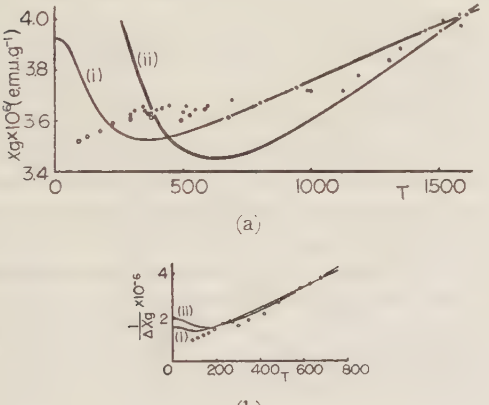

(a)

(b)

Fig. 4. (a) Comparison between calculated susceptibilities for model (3) and experimental ones for Cr. (b) Comparison between calculated susceptibilities for model (3) and experimental ones for an alloy, 1.05% Fe in Cr. (i) Calculated for $p=10$, $r=1/100$, $T^*=30{,}000$°K, $a_1k^{1/2} = 0.0660 \times 10^{34}$ erg^{-1}g^{-1}deg$^{-1/2}$, $b' = 1.14 \times 10^{34}$ erg^{-1}g^{-1} and $q=10.0$. (ii) Calculated for $p=10$, $r=1$, $T^*=350$°K, $a_1k^{1/2} = 0.0151 \times 10^{34}$ erg^{-1}g^{-1} deg$^{-1/2}$, $b'=0.282\times10^{34}$ erg^{-1}g^{-1} and $q=5.2$.
• and ∘ are the same with those in Fig. 3.

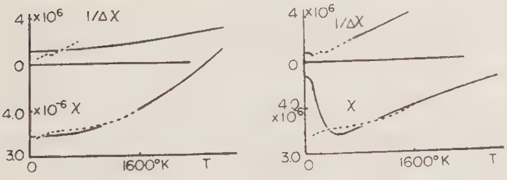

(a) (b)

Fig. 5. Schematic representation of comparison between theoretical results and experimental ones, (a) for model (2) and (b) for model (3).

On the other hand for models (1) and (3) the calculated values of χ do not increase so rapid as for model (2). Therefore, we can use the χ *vs.* T/T^* curves in the region where T/T^* is rather large, and then $1/\Delta\chi$ *vs.* T/T^* curves become linear for such values of T/T^*. In Fig. 5 this circumstance is illustrated schematically.

As we have seen, in order to fit the calculated values with the observed ones the temperature dependences of χ at rather high temperature are important, and these dependences are determined by the shapes of the band which we adopt. The highest temperature of the observation is nearly 1,600°K. The calculated values of χ in the neighbourhood of this temperature will be determined by the shape of the band within the region of $\mathcal{E}/k\sim10^3$°K around $\mathcal{E}_0$. From the analyses mentioned above it can be seen that model (3) for the electron state density of Cr is a better approximation than model (2) and that if $\nu(\mathcal{E})$ is more convexed to the axis of energy than that in model (3) it will be more suitable. Moreover, since the real band must be closed it seems to be reasonable to consider that model (3) where the state density is concave downwards is better than model (2) where it is concave upwards.

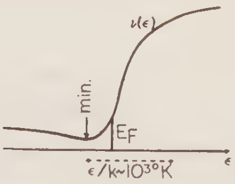

Fig. 6. Schematic representation of the energy band of Cr.

Therefore the conclusion in (I) is supplemented as follows. The state density of the band of Cr is convexed as $\mathcal{E}^{1/2}$ or more within the region of $\mathcal{E}/k\sim10^3$°K around the Fermi level at 0°K in the neighbourhood of a minimum of the state density. Therefore the schematic shape of the band for Cr will be something like the $\nu(\mathcal{E})$ in Fig. 6.

Recently Cheng et al⁽⁶⁾. have calculated the state densities of transition metals and their alloys from the data of the low temperature specific heat. Their results are shown by the curve denoted by C. W. B. in Fig. 7. In the derivation of this curve γ values are not diminished by 1.7×10^{-4} cal mole^{-1} deg^{-2} (the γ value for Cu), for s band would contribute to the susceptibility. Cheng et al. used $\gamma=\frac{1}{3}\pi^2k^2N(E)$ for Cr-Fe, but we calculate $N(E)$ for Cr-Fe so as to fit the saturation values of the magnetic moment with observed ones[7]. So their calculation (Fig. 15 in reference 6) is a little different from ours. In Fig. 7, the state densities calculated for models (2) and (3) by using the values of parameters obtained in Figs. 3 and 4 are shown, too. It will be seen that model (3) is more consistent with the measurements of specific heat than model (2), and that the curve shown in Fig. 6 resembles to the curve obtained by Cheng et al.

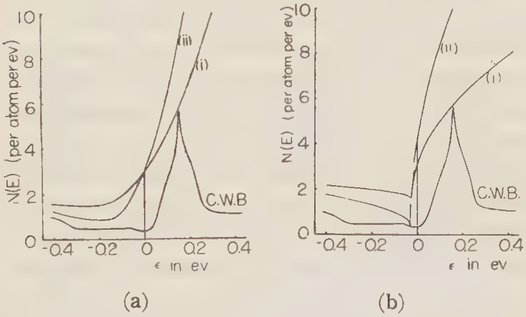

Fig. 7. The numbers of the electronic states per atom per ev: $N(E)$. (a): model (2), (b): model (3), (i) and (ii) are the same with those shown in Figs. 3 and 4. The result by Cheng et al. is shown by the curve denoted by C. W. B. The origin of ε is set at the Fermi energy at 0°K.

Finally, it is pointed out that the fact that the hyperfine effective field of Fe^{57} is not observed from the measurement of the Mössbauer effect of Fe^{57} in Cr-Fe alloy[8] is consistent with the band picture of this alloy, because the definite magnetic moment will not exist on an iron atom in the band picture.

References

1) M. Shimizu and T. Takahashi: J. Phys. Soc. Japan **15** (1960) 2236.
2) T. R. McGuire: Bull. Am. Phys. Soc. **5** (1960) 456.
3) P. Rhodes: Proc. Roy. Soc. **204**, **A** (1950) 396.
4) T. R. McGuire and C. J. Kriessman: Phys. Rev. **85** (1952) 452.
5) M. M. Newmann and K. W. H. Stevens: Proc. Phys. Soc. London **74** (1959) 290.
6) C. H. Cheng, C. T. Wei and P. A. Beck: Phys. Rev. **120** (1960) 426.
7) R. M. Bozorth: Ferromagnetism (D. Van Nostrand Company, N. Y. 1951).
8) K. Ono: private communication.

JOURNAL OF THE PHYSICAL SOCIETY OF JAPAN, Vol. 16, No. 8, AUGUST, 1961

Interaction Effects in Potassium Ferricyanide

By Taiichiro OHTSUKA*

The Research Institute for Iron, Steel and Other Metals. Tohoku University, Sendai.

(Received April 4, 1961)

The character and magnitude of the exchange interaction between the ferric ions in $K_3Fe(CN)_6$ have been investigated by, (1) observation of the paramagnetic resonance spectrum of coupled Fe-Fe pairs in semi-dilute crystals and, (2) adiabatic demagnetization of concentrated crystals. The results show that the exchange between magnetically similar ions contains an appreciable anisotropic part of the order of 0.07 cm^{-1}. No lines corresponding to dissimilar ion pairs were found. From the two types of experiments, it is concluded that the isotropic part of exchange between similar ions, J_s, is about 0.25 cm^{-1} and that the exchange between dissimilar ions is very small.

§1. Introduction

The knowledge of the interaction between magnetic centers is useful in understanding the magnetic properties of the bulk material. Through extensive measurements on $[IrCl_6]$ complexes, it has been shown by the Oxford group that the paramagnetic resonance technique lends a powerful tool in obtaing imformation of this type. The method consists of analysing the features of the resonance lines due to isolated exchange coupled ion pairs existing in crystals diluted by isomorphous non-magnetic ions. In particular, when an anisotropic interaction is present the lines will show a splitting depending on the degree of anisotropy. The anisotropy may be either due to anisotropic exchange[1)] or dipolar interaction[2)].

The possible existence of a relatively large anisotropic exchange in $K_3Fe(CN)_6$ was first noted by Bleaney and Ingram[3)] in their interpretation of the abnormally large line width observed in paramagnetic resonance of concentrated salts. Its existence was confirmed by McKim and Wolf[4)] who observed a large anisotropy of the Weiss constant. They showed, however, that the line width could only be explained when the number of nearest neighbours n is taken to be two whereas the crystal structure suggests $n=6$ of which four are dissimilar and two are similar ions. The Weiss constant, on the other hand, reflects only an average of the existing interactions and it is necessary to discriminate between different species before correlation with some of the bulk properties can be made.

The principal aim of the present work was to investigate the finer details of the interaction by the resonance method.

Adiabatic demagnetization experiments were undertaken in order to obtain knowledge on the possible magnetic transition caused by the interactions. An attempt was then made to correlate the results of the two types of experiments with each other and with the values of the Weiss constant. The analysis has led us to the conclusion that the total exchange interaction between dissimilar ions is very small and that the interaction between similar ion contains a large anisotropic part which amounts to 25% of the isotropic exchange.

§2. Crystal Structure

There has been some controversy as to the structure of the isomorphous series $K_3M^{+3}(CN)_6$ (M=Fe, Co, Mn, Cr) since the first study made by Gottfried and Nagelschmidt[5)]. The foregoing authors reported a monoclinic, pseudo-orthorhombic (C_{2h}^5) structure with $Z=4$ (number of molecules per unit cell) for $K_3Fe(CN)_6$. Barkhatov and Zhdanov[6)] pointed out that the choice of a pseudo-orthorhombic unit cell is incorrect and that the true unit cell is monoclinic with $Z=2$ and $\beta\sim107$. More recent work conducted by Kohn and Townes[7)] has revealed the coexistence of four types of unit cells (polytypism). Of the four, two, namely a monoclinic $1M$ (C_{2h}^5) and orthorhombic $2Or$ (D_{2h}^{14}) cell, were found to predominate.

---

* Now at The Institute for Solid State Physics, University of Tokyo, Tokyo.

Table I.

	$K_3Co(CN)_6$[7]		$K_3Fe(CN)_6$	
	20*r*	1*M*	Monoclinic[6]	Orthorhombic[8]
a	13.31±.04 Å	7.00±.02	7.04	13.5
b	10.37±.02	10.38±.01	10.44	10.5
c	8.35±.01	8.37±.02	8.4	8.5
β		107°19±3′	107°20′	
Z	4	2	2	4
Space Group	D_{2h}^{14}	C_{2h}^{5}	C_{2h}^{5}	D_{2h}^{14}

They found that the orthorhombic cell could be generated by alternate stacking of the monoclinic cell along [100]. No polytypism in $K_3Fe(CN)_6$ has been reported but Kohn et al. note the possibility as an orthorhombic (D_{2h}^{14}) cell has been found by Okaya and Pepinsky[8]. Representative cell dimensions are listed in Table I. We have used the values for the monoclinic cell in calculating the dipolar interaction. The difference between the Co and Fe salts is seen to be small.

The atomic positions for the monoclinic cell is shown in Fig. 1. Each Co (or Fe) ion is surrounded by six CN groups in an approximately octahedral configuration. The axes of the octahedron and the Co-CN, C-N distances have been determined by Barkhatov et al. and more recently by Curry and Runciman[9] who studied $K_3Co(CN)_6$ by neutron diffraction methods. Fig. 2 shows the arrangement of atoms in a projection on a plane normal to the *c*-axis together with the Co-C, C-N distances derived by Curry et al. The arrangement is expected to be similar for the ferric salt.

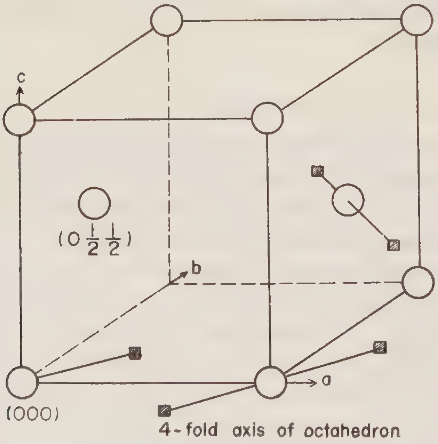

2 Co in (000); $(0\frac{1}{2}\frac{1}{2})$
2 K_1 in $(00\frac{1}{2})$; $(0\frac{1}{2}0)$
2 K_2 in $\pm(xyz, x, \frac{1}{2}-y, \frac{1}{2}+z)$
with $x=\frac{1}{2}$, $y=\frac{1}{4}$, $z=\frac{1}{8}$
Open circles indicate Co ions

Fig. 1. The unit cell for $K_3Co(CN)_6$.

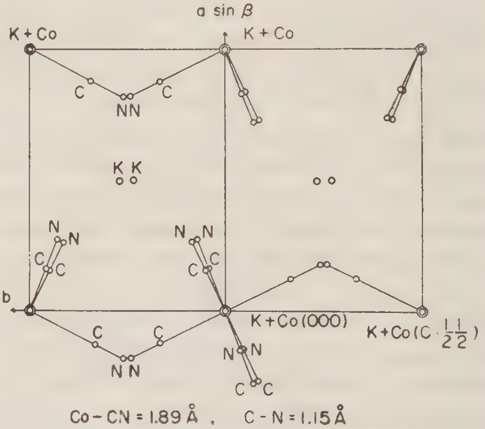

Fig. 2. Arrangement of atoms for $K_3Co(CN)_6$ in a projection on a plane normal to the *c*-axis.

§ 3. Properties of the Fe^{3+} ion in $K_3Fe(CN)_6$

It is well known that the ground configuration of the Fe^{3+} ion in the $[Fe(CN)_6]^{-3}$ complex is $(d\varepsilon)^5$ with $S=1/2$, in contrast with $(d\varepsilon)^3(d\gamma)^2$, $S=5/2$ observed in ionic salts. This has been attributed to strong covalency and/or to a cubic crystalline field strong enough to destroy the Russel-Saunders coupling. The ground level in a cubic field is thus six-fold degenerate, an orbital triplet with two-fold spin degeneracy. Spin-orbit coupling splits this into a quadruplet and a spin doublet, the doublet lying lowest. Fields of lower symmetry also give similar contributions. In particular they split the excited quadruplet into two doublets. The energy levels have been studied by Howard[10], Kotani[11] and Kamimura[12]. The conclusion relevant to our study is that the ground doublet lies some several hundred cm^{-1} below the excited doublets and hence will be the only level populated at low temperatures. Stevens[13], in his theory of $[XY_6]$ type complexes, gave a general derivation of the energy eigenvalues for octahedral symmetry and, in particular, showed that the ground doublet can be expressed conveniently by a suitable linear combination of d orbitals. This expression has been extended to the case of rhombic symmetry by Bleaney and O'Brien[14].

The expression they give is as follows:

$$\left.\begin{aligned} |+\rangle &= [\sin\gamma|a'\rangle\alpha+\cos\gamma|b_+'\rangle] \\ &\qquad\times\cos\theta+\sin\theta|b_-'\rangle\beta \\ |-\rangle &= -[\sin\gamma|a'\rangle\beta-\cos\gamma|b_-'\rangle\alpha] \\ &\qquad\times\cos\theta+\sin\theta|b_+'\rangle\alpha \end{aligned}\right\} \qquad (1)$$

Here $|a\rangle\sim|xy\rangle$ and $|b_\pm\rangle\sim\mp i/\sqrt{2}\{|xz\rangle\pm i|yz\rangle\}$ where $|xy\rangle$, $|yz\rangle$, $xz\rangle$ denote the angular part of the $d\varepsilon$ wave functions. α and β are the spin wave function. Due to the presence of orbital degeneracy under octahedral symmetry and the action of the spin-orbit interaction, these states contain both orientations of the real spin. The states denoted by $|+\rangle$ and $|-\rangle$ correspond to a doublet which can be expressd by an "effective spin" $s=1/2$. We shall use small and capital letters for the effective and real spins, respectively. Operating with in these states with the magnetic moment operator $(\boldsymbol{L}+2\boldsymbol{S})$ yields the g-factors in terms of the effective spin. The g-factors observed in diluted salts by Baker et al.[15] are: $g_x=2.35$, $g_y=2.10$, $g_z=0.91_5$. Two magnetically similar but differently oriented ions are observed. The symmetry of each ion is orthorhombic. The z-axis coincides with the c-axis for both ions and the x, y axes lie in the ab plane. This implies that the octahedron shown in Fig. 2 is rotated by 45° about the tetragonal axis for the ferric ion. The x-axes for the two ions make angles of ±30°, respectively, with the a-axis. The two ions are thus identical along the a, b and c-axes.

Bleaney et al.[14] found that the observed g-factors could not be fitted by the parameters γ and θ alone and that it was necessary to introduce an additional parameter k and replace $\boldsymbol{L}$ by $k\boldsymbol{L}$. The values for the parameters which give the experimental g-factors are; $\cot\gamma=1.00_6$, $\tan\theta=-0.028$, $k=0.87_5$. The factor k was introduced by Stevens[13] in order to account for the departure of the magnetic electrons from a pure d-state due to charge transfer between the p-electrons of the ligands. The magnitude of k indicates the presence of large covalency between the Fe ion and the CN group. This together with the fact that the CN molecular orbitals of adjacent octahedrons may overlap to a certain degree (Fig. 2) suggests the possibility of superexchange interaction existing between neighbouring Fe^{3+} ions. The relative position of the octahedrons implies that this interaction will be different for similar and dissimilar neighbours. The effect of incomplete quenching of the orbital angular moment on superexchange will be discussed briefly in § 6.

§ 4. Paramagnetic Resonance

1) The Spin Hamiltonian. It has been shown by Baker and Bleaney[16] that the features of the paramagnetic resonance spectrum of two identical ions coupled by anisotropic exchange can be expressed by,

$$\mathscr{H}=g\beta\boldsymbol{H}\cdot(\boldsymbol{s}+\boldsymbol{s}')+\boldsymbol{s}\cdot\boldsymbol{K}\boldsymbol{s} \qquad (2)$$

Here $K_{ij}=J+J_{ij}$ where J and J_{ij} $(i, j=x, y, z)$ denote the isotropic and anisotropic parts of the exchange, respectively. In our case $\boldsymbol{s}$ is the effective spin with $s=1/2$. Eq. (2) can then be written in terms of the total spin $\boldsymbol{T}=\boldsymbol{s}+\boldsymbol{s}'$ as follows,

$$\begin{aligned}\mathscr{H}&=g\beta\boldsymbol{H}\cdot\boldsymbol{T}+\frac{1}{2}J\left[T(T+1)-\frac{3}{2}\right]\\ &\quad+\frac{1}{2}J_{xx}T_x^2+\frac{1}{2}J_{yy}T_y^2+\frac{1}{2}J_{zz}T_z^2\end{aligned} \qquad (3)$$

where $T=0$ or 1. The energy levels for H parallel to z are given by;

$$\left.\begin{aligned} &T=1 \text{ (triplet)}\\ &\left.\begin{matrix}E_2\\E_1\end{matrix}\right\}=\frac{1}{4}J+\frac{1}{4}J_z\\ &\qquad\pm\left[(g_z\beta H)^2+\frac{1}{4}\left\{\frac{1}{2}(J_x-J_y)\right\}^2\right]^{1/2}\\ &E_3=\frac{1}{4}J-\frac{1}{2}J_z\\ &T=0 \text{ (singlet)}\\ &E_4=-\frac{3}{4}J \end{aligned}\right\} \qquad (4)$$

It is seen that the triplet which is seperated from the singlet by J is split by the anisotropic component. The allowed transitions

($T_z=\pm1$) take place between E_1, E_2 ($T_z=\pm1$) and E_3 ($T_z=0$) of the triplet. The use of the isolated ion g-factor for the coupled pair will be discussed in connection with the experimental results.

2) Experimental Procedure. The spin-lattice relaxation time of Fe^{3+} in $K_3Fe(CN)_6$ is very short and resonance can only be observed at low temperatures[3]. Measurements were all made at liquid helium temperatures using a wavelength of 3.2 cm. Description of the apparatus has been given elsewhere[17].

Single crystals of the concentrated salt and salts diluted by $K_3Co(CN)_6$ with various concentrations of Fe^{3+} ranging from about 1% to 10% were grown from a saturated aqueous solution. Crystals which were clear and showed no macroscopic twinning were used. Measurements on concentrated salts gave line widths similar in magnitude ($\sim 0.1\ cm^{-1}$) to those obtained by Bleaney et al.[3] at liquid hydrogen temperatures thus confirming their conclusion that the width is not due to spin-lattice relaxation. A brief description of the results on semi-dilute crystal has already been given[18]. We shall present here the details of the results and the method of analysis.

3) Features of the spectrum. An example of the spectrum along the a and b-axes for a -5% and -10% Fe^{3+} sample is given in Fig. 3. The spectrum for the c-axis is shifted to much higher fields. It is seen that besides the line of strong intensity corresponding to the isolated ion, several satellites appear. The magnitude and the axis of the g-factor for the isolated ion is in good agreement with the results obtained by Baker et al. for more dilute salts. The line width for all the lines is about 40G for the spectrum in the ab-plane and 160G for the c-axis. The large line width for the c-axis has made the resolution and determination of the positions of the lines relatively poor for this direction.

The intensity of the satellite lines was about one tenth of the isolated ion line. This is just about what one would expect from coupled pairs if one assumes that the Fe^{3+} ions are randomly situated. However this does not mean that the satellites are all due to pairs. The problem is thus to pick out those lines due to coupled pairs and then to see which of the two possible types of pairs (similar and dissimilar ion pairs) they arise from. Because of the smallness of the isotropic part, the temperature dependence of the intensity could not be used in the assignment of the lines. This fact also prevented determination of the isotropic part by the resonance method. Actually no change was observed be-

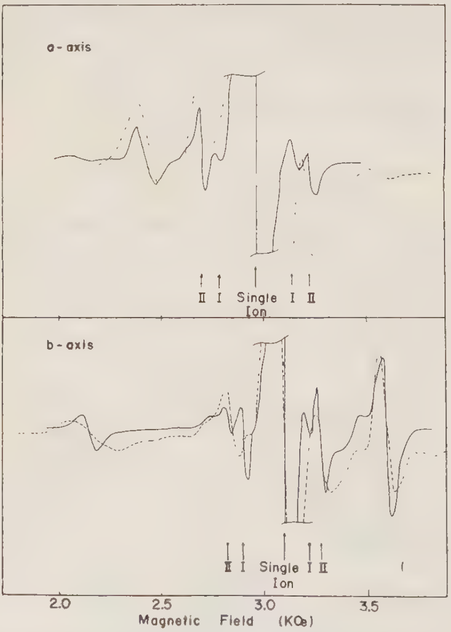

Fig. 3. Spectrum with the magnetic field parallel to the a and b-axes, —— 5% Fe - - - - - 10% Fe The intensities have not been normalized.

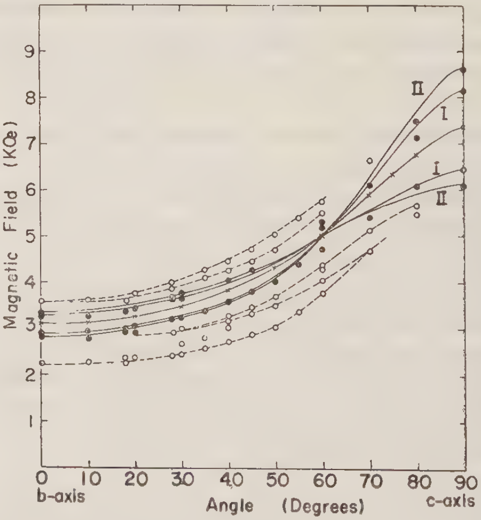

Fig. 4. Angular variation in the bc-plane. Dotted lines have been drawn through experimental points. Solid line for —×— is the single ion line. Solid line for I and II calculated with $|D_I| = 0.041\ cm^{-1}$, $|E_I| = 0.016$; $|D_{II}| = 0.054$, $|E_{II}| = 0.016$.

tween 4.2 and 1.6°K. The criterion we used was to note that the pair lines should be displaced symmetrically about the isolated ion line and that they must have an angular dependence of the dipolar type as can be seen from Eq. 3. It was observed that only the sets of lines marked I and II in Fig. 4 conformed to the properties of a coupled pair. For more concentrated salts I and II could not be distinguished.

The origin of the lines outside of sets I and II is not clear at present. They do not appear to arise from coupled pairs. They also do not seem conform to the anisotropy demanded by Eq. 1. However as they appear reproducibly from salt to salt, we shall briefly summarize their general feature. The lowest field line for the *a*-axis splits into three components when rotated in the *ab*-plane. They merge together again at the *b*-axis at a much lower field with reduced intensity. The anisotropy in the *ab*-plane is just the opposite of that of the isolated ion line except for the for the third component. The intensity of the highest field line is reduced when rotated from the *b*-axis and is barely observable for the *a*-axis. Thus the intensities of the lowest and highest field lines are interchanged in going over from the *a* to the *b*-axis. The weighted mean of all the lines gives $g_a \simeq 2.3$, $g_b \simeq 2.2$. This is in accord with the measurements of the concentrated salt. However Baker et al. have observed that g_b differs appreciably when the direction of the *rf*-field, h_{rf}, is changed from $h_{rf}//c$-axis to $h_{rf} \perp c$. For the former case, $g_b=2.21$ and for the latter, $g_b=2.39$. In connection with this anomalous behaviour, it is interesting to note that the intensity of the lowest field line is observed to be reduced when $h_{rf}//c$ (Fig. 4 shows the spectrum with $h_{rf} \perp c$). No change was observed for the high field line. This would correspond to a shift to low *g*-values in the concentrated salt. The lowest field line may also account for the anomalous behaviour of the susceptibility χ, namely the interchange of the rhombic anisotropy from $\chi_a > \chi_b$ to $\chi_b > \chi_c$ when the sample is cooled below 100°K if it is assumed that the line is associated with a low temperature pase. The occurence of such a phase is inferred from the reported anomaly of χ_a and χ_c[19] and the specific heat[20] at 130°K. The nature and origin of such a phase is, however, difficult to understand. Further studies of the anomalous lines are necessary before definite conclusions can be made.

4) Analysis of sets I and II. From observation of the angular variation of the splittings, the axes for both sets I and II were determined to lie along the crystal *a*, *b* and *c*-axes. The symmetry is rhombic and the principal axis *z* is along the *c*-axis as can be seen from the behavior in the *bc*-plane (Fig. 5). The dipolar type of angular variation is noted. The angular variation in the *ab*-plane is complicated because the two ions in the unit cell are now magnetically different. However the sets I and II can be followed and their variation indicates that both sets arise from a coupled pair of similar ions. From the splitting along the crystal axes, the anisotropic exchange parameters may be deduced using Eq. 4. The values obtained are listed in Table II. The solid line in Fig. 5 was calculated from the formula for the variation of the splitting Δ in a plane which includes the principal axis, namely:

$$\Delta = D(3p^2 \cos^2 \theta - 1) - 3E(q^2 \sin^2 \theta) \qquad (5)$$

Here $|D| = 3/4|J_c'|$, $3|E| = 3/4|J_a' - J_b'|$, $p = g_c/g$, $q = g_b/g$ g is the component of the *g*-tensor in the direction of the field making an angle θ with the *c*-axis. Higherorder terms have

Table II.

Set	i (axis)	a	b	c
I	J_i'*	$-0.028\,\mathrm{cm}^{-1}$	-0.020	$+0.055$
	d-d	$+0.010$	-0.004	0.000
	J_i***	-0.038	-0.016	$+0.055$
II	J_i'	-0.037	-0.029	$+0.072$
	d-d	$+0.010$	-0.004	0.000
	J_i	-0.047	-0.025	$+0.072$
Average of J_i for I and II		-0.043	-0.021	$+0.064$
J_i from Weiss const.**** with $n=2$		-0.044	-0.024	$+0.067$

* J' denotes the observed splitting.

** Dipolar interaction for similar ion pairs with fields along respective axes.

*** Anisotropic exchange interaction. Correction and sign assignments given by methods persented in text.

**** Due to McKim and Wolf(4).

been neglected.

The apparent splitting includes contributions from the dipolar interaction which amounts to about 20% of the observed values and thus cannot be neglected. The contribution depends on the angle between the line connecting the ions and the direction of the applied field and the magnetic moment induced in that direction. The former serves to distinguish between the two possible types of ion pairs and the latter, because of the anisotropic g-factor, to determine the sign of J_c. The interdependence of the sign of J_i and the dipolar interaction is depicted fn Fig. 5.

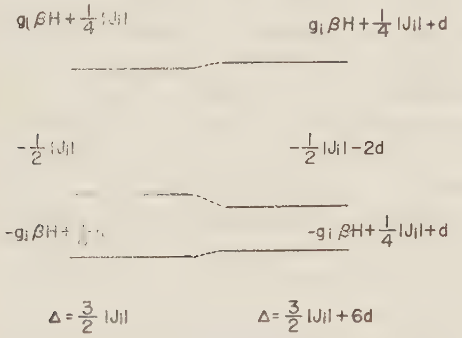
$g_i\beta H+\frac{1}{4}|J_i|$
$g_i\beta H+\frac{1}{4}|J_i|+d$
$-\frac{1}{2}|J_i|$
$-\frac{1}{2}|J_i|-2d$
$-g_i\beta H+$
$-g_i\beta H+\frac{1}{4}|J_i|+d$
$\Delta=\frac{3}{2}|J_i|$
$\Delta=\frac{3}{2}|J_i|+6d$

Fig. 5. Effect of dipolar interaction. Δ=splitting $d=-\frac{1}{2}g_i^2\beta^2\frac{(1-3\cos^2\theta)}{r^3}$

It is seen that for $J_i>0$ a positive dipolar interaction will increase the splitting due to anisotropic exchange whereas for $J_i<0$, the splitting will be reduced. Because of the difference in the magnetic moment induced for different axes, the condition that the sum of the anisotropic component $J_a+J_b+J_c=0$ will be unbalanced. This is evidenced in the fact that the apparent splittings cannot be made to add to zero. The dipolar interaction was calculated using the observed g-factors, cell dimensions and the atomic positions. The contribution for similar ion pairs are listed in Table II. As the sign of J_i is not determined experimentally, both signs were assumed. It turned out that for $J_{a,b}<0$, $J_a+J_b=J_c$ was fulfilled well after correction (Table 2). For $J_{a,b}>0$ a 10% difference arises between J_a+J_b and J_c. When dissimilar ion pairs are assumed, a 10% difference arises regardless of the sign of $J_{a,b}$. As this is outside the experiment error, it is concluded that I and II are due to similar ion pairs, in accord with the variation in the ab-plane, and that $J_c>0$.

It is not obvious whether one should use the cell dimensions for the ferric or the cobaltic salt in calculating the dipolar interaction. The difference however is small and amounts to only a few percent in the correted values. In this connection, it is noted that lines of I and II are not located exactly symmetrically about the isolated ion line. The asymmetry is small amounting to only about 0.8%. It is, however, systematic in that the asymmetry for the a- and b-axes are opposite. (The c-axis could not be determined with certainty.) As Judd[21] has shown that the difference in the g-factor of a pair and a single ion depends on the non-orthogonality of overlapping orbitals and is negligible, this implies that the rhombic axes for the Fe pairs are rotated by a few degrees in the ab-plane relative to those of the isolated ion. Correction to the absolute value of g is, however, within experimental error and the use of the single ion values is justified.

The existence of two sets of values for similar ion pairs was unexpected. This may be due to the fact that the interaction constants for the two predominant polytypes observed in the cobalt salt is different. Definite evidence of the effect of polytypism on resonance as has been established for the case of Cr^{3+} [7] is, however, lacking for Fe^{3+} * and further studies are necessary to clarify this situation. It is interesting to note that the average of the two sets agrees very well with the values derived from the Weiss constant in both magnitude and sign when the number of nearest neighbours n is taken to be two (Table 2). Although an agreement to this extent may only be accidental because of the possible difference between the interactions existing in concentrated and dilute salts, it gives evidence in favour of the conclusions reached because if one or both of the sets were due to dissimilar ion pairs where $n=4$, the discrepancy would be much too large. The fact that lines attributable to dissimilar ion pairs were not observed may be due to either the smallness of the exchange or the

---

* *Note added in proof.* We have recently made experiments on a sample where resonance which can be associated with ions in a monoclinic cell was clearly observed. The z-axis was found to be inclined 4° from the c-axis.

exchange being isotropic. The results of the magnetic specific heat by McKim et al. infer that the former is most probably the case. The problem of isotropic exchange will be discussed in connection with the results of the adiabatic demagnetization experiments.

§ 5. Adiabatic Demagnetization

The spin Hamiltonian (Eq. 2) yields the following expression for the Weiss constant Θ.

$$-\Theta_i = \frac{s(s+1)}{3k} \sum_i \sum_j n_j K_{ii}^{(j)}\,, \qquad i=x, y, z \qquad (5)$$

Here n_j denotes the number of nearest neighbours of type j. A total of the isotropic exchange may by derived by noting that the anisotropic part must add to zero and that $n=2$ and 4 for similar and dissimilar ion neighbours, respectively. The values observed by McKim et al. yield $2J_d + J_s = 0.28_7\ \text{cm}^{-1}$ where J_d and J_s denote the isotropic exchange constant for dissimilar and similar pairs, respectively. J_d and J_s cannot be distinguished unless an independent relation between the two quantities is obtained. It was with the hope that the possible magnetic transition temperature might provide this relation, although approximate, that demagnetization experiments were undertaken. It turned out, however, that the actual situation is complicated and only a rough estimate could be made. The other purpose was to probe into the nature of the transition created by exchange with a known large anisotropic part.

1) Experimental procedure. Undiluted $K_3Fe(CN)_6$ single crystals of the size necessary for demagnetization experiments (~2 gr) were difficult to grow free of macroscopic twinning. Therefore the samples used were twinned to some degree although clear crystals showing least twinning were chosen. As twinning occurs on the a-plane and the magnetic axes coincide with the crystal axes, no essential change in magnetic properties is expected unless the spin deviates from the crystal axes when ordered. Of the six samples used, one showed a high transition temperature. Outside of this effect no appreciable difference in the properties measured was observed.

Three different types of measurements were carried out; the determination of the 1) entropy-susceptibility, 2) susceptibility-temperature and 3) entropy-temperature relations. The description of the adiabatic cell is given in Fig. 6. For the first type of measurement, a sample (~1.5 gr) ground to an ellipsoidal shape was placed on a pedestal made out of thin walled glass (Fig. 7a). For the second and third measurements, a glass support described in Fig. 7b was used. A flat surface of about 2-3 cm² was ground on the sample with fine emery paper and attached to both sides of a copper plate 0.15 mm thick using

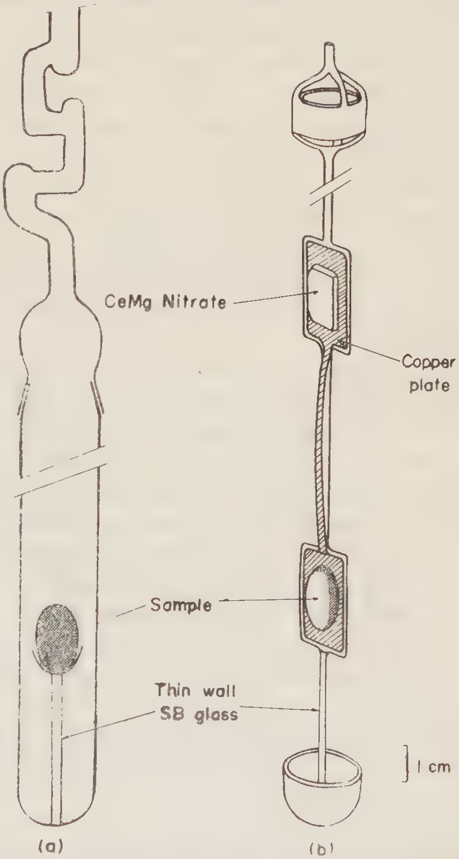

Fig. 6. Adiabatic cell (a) and sample-thermometer support (b).

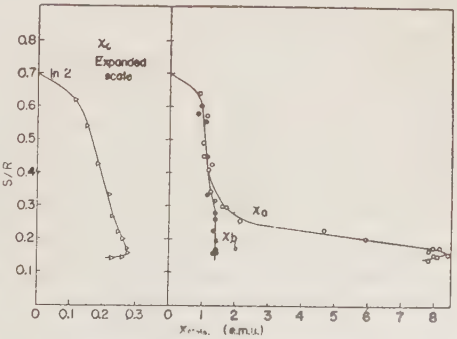

Fig. 7. Entropy versus susceptibility. The scale for χ_c has been expanded.

a n-propyl alcohol-glycerol mixture as a binder. The sample was then bounded tightly by cotton thread. The system was connected to a similar plate 9 cm above via a copper strip. To this a single crystal of cerium magnesium nitrate was bounded by similar means. This was used as the thermometer for temperature determinations. Preliminary measurements using a ferric alum sample proved this type of arrangement to give sufficiently good heat transfer rates at temperatures about ~0.1°K. At the lowest temperature reached in the actual experiment (~0.2°K), the cerium salt and sample came into thermal equilibrium in about one to two minutes. The extraneous heat input into the sample was about 50–80 ergs/min. Separate measurements made with varying vacuum conditions, degree of radiation shielding, types of support and cell indicate that most of this is due to mechanical vibration.

The susceptibility was measured using a mutual inductance Hartsohn bridge circuit. A. C. of 160 cps was used for measurements (1). For (2) and (3), D. C. was used and null detection made by a ballistic galvanometer. Isothermal magnetization was carried out at 1.1°K. A 40 KW electromagnet provided a field of up to 24 KOe in a 63 mm gap. The sample was always magnetized along the a or b-axis. The cerium salt was oriented so that the hexagonal axis, where g is very small, was parallel to the applied field. This was to prevent the possible magnetization of the cerium salt in a fringing field. The dewar and vacuum system is conventional and will not be described.*

The result for the entropy-susceptibility measurement is shown in Fig. 7. The features to be noted are the sharp rise in the susceptibility along the a-axis, χ_a, and the fact that about 85% of the total spin entropy is lost before the susceptibility indicates an anomaly. Thus a peak in the susceptibility was only barely observable after demagnetizing from the highest field. This was unfortunate because it barred detailed measurements to be made below the anomaly. Fig. 8 shows an example of the field dependence of χ_a for two entropy values corresponding, respectively, to a point just below the anomaly and a point at which χ_a starts to rise rapidly. For the higher entropy value the behaviour is paramagnetic whepeas for the lower value, a relatively small field (~10 Oe) produces a sharp decrease down to just about the value one would expect from the Curie-Weiss curve. The inference of the sharp rise and field dependence of χ_a is that a small ferromagnetic component is present along the a-axis.

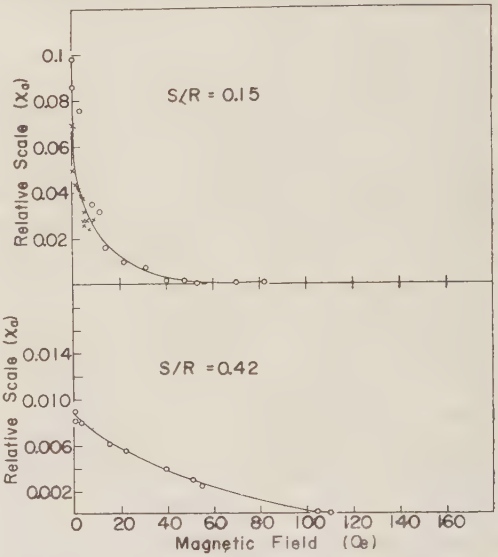

Fig. 8. Field dependence of adiabatic susceptibility along the a-axis.

The susceptibility-temperature relation was determined by alternately measuring the sample and cerium salt susceptibilities during warm up after demagnetizing from various fields. As the heat transfer rate exceeded that of the extraneous heat leak for the lower temperatures, thermal equilibrium was assured. However for temperatures above ~0.5°K, an increased warming up rate caused departures from equilibrium which was reflected in a scatter of the data for the higher temperature region. Reproducibility was good for the lower temperatures. The increased warming up rate is probably due to gaseous conduction of the residual gas as prolonged pumping of the cell reduced the rate appreciably. The high temperature region is, however, not of particular interest because the results around ~0.4°K fall on an extension of the Curie-Weiss curve within experimental error which we estimate to be ~10%. Thus further efforts such as the use of guard salts were not made.

Six different samples were measured. Except for one sample which reproducibly showed deviation towards higher temperatures, the results for different samples agreed with each other within 15%. The results for χ_a near the region of maximum susceptibility showed an appreciable scatter, however, due partly to the fact that the susceptibility changes very rapidly in a narrow temperature range. However the temperature for the anomaly did not not differ. A representative curve is shown in Fig. 9. An annoying fact is that a definite maximum in the susceptibility was not observed in contrast to the entropy-susceptibility measurements. The reason for this is not clear but may be due to the presence of the thermometer salt. The shape of the sample was also not quite spherical. The other features, i. e. the sharp rise in χ_a, a broad flat region for χ_b were, however, common for both types of experiments. It is seen that the anomaly takes place near 0.2°K.

---

* The major portion of the demagnetization apparatus was constructed by Mr. A. Ōtsubo.

The entropy-temperature relation was obtained by measuring the temperature after demagnetizing from different magnetic fields. Measurements were taken for about 3 to 4 minutes after thermal equilibrium had been attained. No change in the susceptibility of the cerium salt was noted during this interval. Due to reasons mentioned previously, the cell was pumped for about 1.5 hrs before demagnetization in determining temperatures above ~0.5°K. The results are shown in Fig. 10.

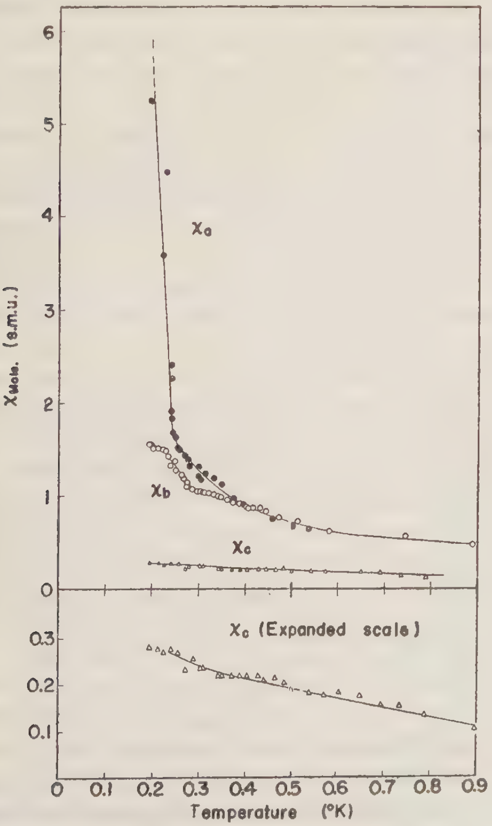

Fig. 9. Susceptibility versus Temperature.

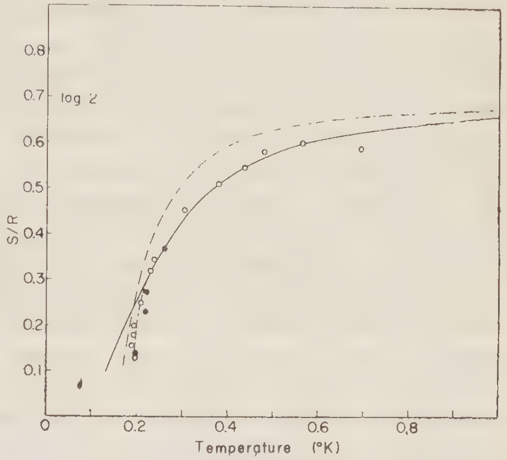

Fig. 10. Entropy versus Temperature. —o— Sampl #4; —•— Sample #6
Solid line: Linear Ising chain with $J_d=0$, $K_c=0.35\ \text{cm}^{-1}$
Broken line: Molecular field approximation with $J_d=0$, $J_s=0.29\ \text{cm}^{-1}$, $J_i=$Table 2.

It is seen that a rapid reduction of entropy takes place at about the same temperature of the magnetic anomaly. This temperature reproduced within 5% for a single sample and showed about a 20% scatter for five different samples. The error in the absolute value of temperature is estimated to be about 20%. Averaging the values obtained for different samples, we locate the "transition" temperature at 0.2±0.04°K. The nature of this "transition" will be discussed below.

2) Discussion of the results. If the interactions J_s and J_d differ from each other, it is expected that initial ordering of the spins will progress through the larger of the two. Now it has been observed by McKim et al.[3] that the magnetic specific heat can only be fitted with the Weiss constant when the number of nearest neighbours is taken to be two. This, together with the fact that resonance attributable to dissimilar ions was unobserved, gives evidence that J_d is small. On the other hand, the magnitude of aniso-

tropic exchange infers that $J_s \gtrsim 0.1\,\mathrm{cm}^{-1}$. Thus it is reasonable to assume that ordering will first take place within mutually independent linear chains of similar ions along the *a*-axis. The fact that the bulk of the total entropy is lost before an anomaly is observed supplies further evidence for this to be the case as it is well known that a linear chain can possess only short range order at finite temperatures. The sign of the Weiss constant and the anisotropic part of the exchange indicate that the spins will be aligned antiparallel to each other along the *c*-axis perpendicular to the chain. A second order transition, if any, will be created by the interchain interaction, namely J_a. Unfortunately there are no reliable theories which express the behaviour near the transition point for such a complicated situation. Onsager[22] has treated a similar case for the two dimensional anisotropic Ising net but extension to three dimensions has not been made. Our assumption demands, however, that the bulk of the entropy curve reflects the properties of a linear chain. Thus we have neglected J_a and have calculated the entropy of an Ising chain in order to see to what extent our assumption holds. The Ising approximation should give a good description as $J_c > J_a$, J_b and $J_s \sim 0.1\,\mathrm{cm}^{-1}$. The entropy is readily derived from the expression of the free energy[23] and is,

$$S = R\{\ln(2\cosh L) - L\tanh L\}$$

where $L = J/kT$. This has been calculated taking $J = J_s + J_c$. The value of $2J_a + J_s$ previously determined gives $J_s = 0.29\,\mathrm{cm}^{-1}$ for $J_a = 0$. For J_c, the average value (Table 2) was used. The results are shown as a solid line in Fig. 10. As the spins are not quite free at the temperature at which the entropy is determined (1.1°K), the experimental points have been corrected neglecting the cross term between the Zeeman and interaction energies. The reduction from the free spin value amounts to 3% at 1.1°K. There is some ambiguity in this correction because different values of J_s and J_a and different approximations lead to different corrections. However as the temperature is high, extreme cases differ by only ~1% and is within experimental error.

It is seen that the Ising chain expresses the observed values well down to $S/R \simeq 0.25$. For comparison, a curve calculated by the molecular field approximation using the same J_s but including J_a and J_b is also shown. The deviation is appreciable at higher entropy values which is expected as the molecular field approximation does not account for short range order. Although it may not be permissible to apply two dimensional calculations to our case, Onsager's rectangular net results indicate a deviation from the linear chain specific heat curve slightly below its maximum for a ratio of intra to interchain exchange as small as 10^{-2}. The specific heat maximum of our Ising chain corresponds to 0.22°K. Thus the deviation of the experimental points from the Ising curve at low entropy values is most probably caused by a small but finite J_a. Its magnitude, together with the location of a possible Néel temperature, however, cannot be estimated with certainty. The presence of a Néel temperature T_N is indicated in the magnetic measurements which also show that T_N cannot be too far below 0.2°K. The best we can say at present is that,

$$J_s \cong 0.25\,\mathrm{cm}^{-1}, \qquad J_a \sim 0.01\,\mathrm{cm}^{-1}$$

The presence of two sets of constants for the anisotropic part may introduce some complication but we believe that this will not alter the estimated value of J_s very much.

As for the susceptibility, the relatively broad region of χ_b may be due to short range order. Not much can be said about χ_c because of the relatively poor accuracy due to its smallness. However it follows the Curie-Weiss curve down to $\sim T_N$. The anomalous behavior of χ_a is possibly connected with the presence of a small ferromagnetic moment along the *a*-axis indicated in the field dependence measurements. The fact that the anomaly is restricted to the *a*-axis can be understood if it is assumed that the ferromagnetic component is due to spins aligned not quite antiparallel to each other in a direction resulting in an incomplete compensation of the magnetic moment along the *a*-axis. Moriya[24] has shown that a sharp increase in the susceptibility near T_N along the direction of the uncompensated moment may be expected. Just how this uncompensation, if any, can occur for our case is not clear. It is noted, however, that polytypism may give rise to this effect if it is assumed that the principal axis of anisotropic exchange deviates from the *c*-axis in the *ac*-plane which can be expected for the monoclinic structure. The resonance results, however, indicate that the deviation must be smaller than the error determined by the residual line width. The spins of dissimilar ions will now align not quite parallel (or antiparallel) to each other in the ordered state due to the strong action of the crystalline field. It can be seen that this spin structure will give rise to an uncompensated moment along the a-axis at the boundaries of the polytypes. A larger moment is expected when the dissimilar spins align (almost) antiparallel because then the boundaries parallel to the a-plane (the twinning plane) contribute. Although the resonance results indicate at least two types of unit cells, further studies are necessary before any conclusions can be made and the discussed model remains only a possibility. The sharp rise, however, would be difficult to understand if the crystal structure is homogeneous.

§ 6. Discussions

Although the isotropic part cannot be determined precisely, it is seen that the exchange interaction between similar ions contains an appreciable anisotropic part. Judd[21] has shown in a general way using group theoretical methods how a wave function of the form Eq. 1 may lead to anisotropic exchange. Some of the consequences of his theory may be seen by observing the form of the product determinantal states for two ions constructed from Eq. 1, namely,

$$\Phi(++) = \frac{1}{\sqrt{2}}\{|+\rangle_1(1)|+\rangle_2(2)-|+\rangle_1(2)|+\rangle_2(1)\} \tag{7}$$

and similar expressions for $\Phi(+-)$, $\Phi(-+)$ and $\Phi(--)$. Here the subscript refers to the ion and the bracketed number, the electron. The explicit expression will not be given but it can readily be seen that various types of exchange integrals corresponding to different combination of orbitals will occur when operated on by an interaction operator. Not all of these integrals participate in the interaction and some physical reasoning is necessary in order to pick out the predominant ones pertaining to the actual arrangement of the ions. Actually the interaction takes place via the CN groups. Thus the orbitals used in the product states should be understood as hybridized orbitals containing $p\pi$ orbitals of the cyanide group with the same symmetry properties as $|a\rangle$ or $|b_{\pm}\rangle$. The arrangement of the orbitals for a similar ion pair is illustrated in Fig. 11. As the magnetic z-axis of the ferric ion coincides with the c-axis, the octahedron observed in the cobatic salt (Fig. 2) has been rotated 45° about the tetragonal axis. The p orbital drawn in Fig. 12 has the same symmetry properties as $|a\rangle$. The relative positions indicate that this orbital will have the largest overlap. Thus the predominant exchange integral will be of the combination,

$$\mathscr{J}=\langle a_1(1)a_2(2)|\mathscr{H}_{\text{exch.}}|a_1(2)a_2(1)\rangle$$

Correspondence with the effective spin exchange constant determined by experiment can be made by operating with the real spin operator $\mathscr{J}\boldsymbol{S}_i\boldsymbol{S}_j$ on the product states (Eq. 7).

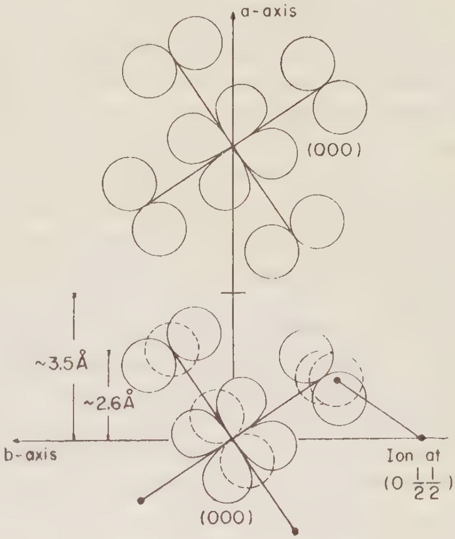

Fig. 11. Arrangement of the orbitals in the ab-plane. The p-orbitals shown have the same symmetry as $|a\rangle$. The octahedron of Fig. 2 has been rotated by 45° about the 4-fold axis. The dashed circle is the p-orbitals which combine with $|\pm b\rangle$.

Neglecting other combinations of orbitals, it can be seen that $1/4\mathscr{J}=J_s$. In other words, the predominant exchange integral pertaining to real spins gives rise to only isotropic exchange in the effective spin formalism. The factor 1/4 arises from the value of the coefficient $\sin^2\gamma=1/2$ as determined by Bleaney and O'Brien. The anisotropic part arises from a combination of the integrals of the from $\langle a_1(1)b_2(2)|\mathscr{H}_{\text{exch.}}|a_1(2)b_2(1)\rangle$ and $\langle a_1(1)b_2(2)|\mathscr{H}_{\text{exch.}}|b_1(2)a_2(1)\rangle$

They cannot be determined uniquely from experiment and the most we can say is that they are of the order of 0.01 cm^{-1}. Integrals involving only $|b_\pm\rangle$ type orbitals are expected to give negligible contribution. The magnitude of the predominant exchange between the p-orbitals of the CN group can also be estimated using the form of hybridized orbital given by Stevens[13)], namely,

$$|a\rangle = N(|a'\rangle + \lambda|a''\rangle)$$

where $|a'\rangle$ refers to the d-orbital and $|a''\rangle$ the p-orbital with the same symmetry. N is the normalizing constant. $N\lambda$ can be determined from the relation $k=1-2\lambda^2N^2$. Inserting the value of k determined by Bleaney et al., we get $N^2\lambda^2=0.0625$. Thus,

$$\langle a_1''(1)a_2''(2)|\mathscr{H}_{\text{exch.}}|a_1''(2)a_2(1)''\rangle \sim 100\ \text{cm}^{-1}.$$

The poor symmetry (Fig. 11) does not allow us to go further and relate this with the properties of the cyanogen molecule as has been done by Griffths et al.[1)] for the chlorine molecule.

As for the dissimilar ion pair, the predominant interaction is expected to take place via $|b_\pm\rangle$ orbitals in contrast to the similar ion case as can be inferred from Figs. 2 and 11. The distance between the CN groups is somewhat (~10%) larger. Although a larger distance suggests a smaller interaction, it cannot be said that this leads, by comparing with the similar ion value, to the order of magnitude estimated from experiment because the arrangement of the orbitals is slightly different for the two cases.

Acknowledgement

I would like to thank Prof. E. Kanda for his encouragement throughout the course of this work. Discussions on some of the technical aspects of the demagnetization experiments with Dr. T. Haseda and Mr. A. Ohtsubo have been invaluable. Mr. T. Sato kindly prepared the single crystals. I also wish to thank Drs. T. Sugano, T. Murao and J. Kanamori for stimulating discussions.

References

1) J. H. E. Griffths, J. Owen, G. Park and M. F. Partridge: Proc. Roy. Soc. **A**, **250** (1959) 84.
2) B. A. Coles, J. W. Orton and J. Owen: Phys. Rev. Lett. **4** (1960) 116.
3) B. Bleaney and D. J. E. Ingram: Proc. Phys. Soc. London **A**, **65** (1952) 953.
4) F. R. McKim and W. P. Wolf: Proc. Phys. Soc. London **B**, **69** (1956) 1231.
5) C. Gottfried and J. G. Nagelschmidt: Z. Krist. **73** (1930) 357.
6) V. Barkhatov and H. Zhdanov: Acta. Physiochim. URSS **16** (1942) 43.
7) J. A. Kohn and W. D. Townes: Acta. Cryst. (To be published.) rf. also J. O. Artman, J. C. Murphy, J. A. Kohn and W. D. Townes: Phys. Rev. Lett. **4** (1960) 607. I would like to thank Dr. Artman for informing me of the work of Kohn and Townes.
8) Y. Okaya and R. Pepinsky: (1956) Abstract of paper presented at meeting of Amer. Crystallographic Assoc., French Lick, Indiana.
9) N. A. Curry and W. A. Runciman: Acta Cryst. **12** (1959) 674.
10) J. B. Howard: J. Chem. Phys. **3** (1958) 813.
11) M. Kotani: J. Phys. Soc. Japan **4** (1949) 293.
12) H. Kamimura: J. Phys. Soc. Japan **11** (1956) 1171.
13) K. W. H. Stevens: Proc. Roy. Soc. **A**, **219** (1953) 542.
14) B. Bleaney and M. C. M. O'Brien: Proc. Phys. Soc. London **B**, **69** (1956) 1216.
15) J. M. Baker, B. Bleaney and K. D. Bowers: Proc. Phys. Soc. London **B**, **69** (1956) 1205.
16) J. B. Baker and B. Bleaney: *Proc. of the International Conf. on Low Temperatures* (Paris 1955). rf. also (1)
17) T. Ohtsuka, H. Abe and E. Kanda: Sci. Rept. RITU, Tohoku Univ. **9** (1957) 476.
18) T. Ohtsuka; J. Phys. Soc. Japan **15** (1960) 939.
19) G. Shoffa, O. Ristan and K. Ruckpaul: Sov. Phys. JETP **35** (8) (1959) 445. rf. also (14).
20) C. C. Stephenson and J. C. Morrow: J. Amer. Chem. Soc. **78** (1956) 275.
21) B. R. Judd: Proc. Roy. Soc. **A**, **250** (1959) 110.
22) L. Onsager: Phys. Rev. **65** (1944) 117.
23) G. H. Wannier: Rev. Mod. Phys. **17** (1945) 50.
24) T. Moriya: Phys. Rev. **117** (1960) 635.

JOURNAL OF THE PHYSICAL SOCIETY OF JAPAN, Vol. 16, No. 8, AUGUST, 1961

Theory of Seebeck Effect in Plastically Deformed Semiconductors

By Tokio OHTA

Department of Physics, Defense Academy, Yokosuka

(Received April 28, 1961)

The effects of the reduction of free electron density due to the dislocation-acceptors and the scattering due to the space charge around the dislocation on the thermoelectric power of *n*-type materials are theoretically investigated in the temperature covering from impurity- to transition-range and compared with the experimental data for near intrinsic *n*-Ge in only the transition range of temperature. In the intrinsic range of temperature the scattering effect due to the lattice deformation around the dislocation is discussed and compared also with the experimental data.

§ 1. Introduction

Recently many studies[1] have been actively done about the effects of edge dislocation in semiconductors on the electrical conductivity, the Hall effect, and the recombination rate. The experimental data are explained by the assumption[2] that edge dislocations in *n*-type materials act as rows of closely spaced acceptor centers and a dislocation accepts electrons to become a line of negative charge surrounded by the cylindrical layer of positive space charge.

On the other hand it is well known that thermoelectric power informs directly the value of Fermi energy in the crystal and when the crystal is composed of *p*- and *n*-type materials, the contributions to the thermoelectric power from each materials are obtained by rather simple analysis. According to this account the study of thermoelectric power in the deformed semiconductors is believed to be very useful in confirming the dislocation-acceptor model, whether or not the space charge cylinder is of *p*-type, and the scattering mechanism due to the dislocation for both electrons and holes.

Pearson[3] performed preliminary measurements for the effect along the discussion similar to Ohta[4] a few years ago but no conclusive results were obtained. This seems to be attributed to the low resistivity of the used sample. Yamashita and Ohta[5] have measured the effect in near intrinsic *n*-Ge as well as in *p*-Ge in the transition range of temperature. In this paper not only the general theory of the effect in the different temperature ranges is studied but also the foundation of the conversion of near intrinsic *n*-type materials to *p*-type by the cold-worked deformation is discussed comparing with the experimental data.

§ 2. Thermoelectric Power and Fermi Energy

According to the usual method of Boltzmann transport equation, the general expression for thermoelectric power of crystals is written as

$$Q=-(1/(eT))[J_2/J_1-(1/J_1)\times\{B_1(e)/m_e^2\cdot\zeta+B_1(h)m_h^2\cdot(\varDelta+\zeta)\}]\,, \tag{2.1}$$

where $-\zeta$ is the Fermi energy, m_e and m_h are the effective masses of electron and hole respectively, $\varDelta$ is the gap energy between the bottom of *c*-band and the top of *v*-band, e is the magnitude of electron charge, and T is absolute temperature. The notations which denote integrations are

$$\left.\begin{matrix}J_1\\J_2\end{matrix}\right\}=\frac{B_{1,2}(e)}{m_e^2}\pm\frac{B_{1,2}(h)}{m_h^2}\,, \tag{2.2}$$

$$B_j(e)=\int_0^\infty \eta^j l_e(\partial f_e/\partial\eta)\,d\eta\,, \tag{2.3}$$

$$B_j(h)=\int_0^\infty \eta'^j l_h(\partial f_h/\partial\eta')\,d\eta'\,, \tag{2.4}$$

where η and η' $(=\eta+\varDelta)$ are the energies, l_e and l_h are the mean free paths, f_e and f_h are the unperturbed distribution functions of electrons and holes respectively.

Let us give a brief review of the charged dislocation model in order to obtain the Fermi energy in Eq. (2.1). The energy diagram around a charged dislocation is shown in Fig. 1, where δ' and δ_d show the dislocation-acceptor level and chemical donor level respectively.

The positive space charge in the cylindrical volume is $\pi R^2(N_D-N_A)$, where R is the radius of cylinder, N_D and N_A are the chemical donor and acceptor densities. The density of accepted electrons at a dislocation is $f_D(T)/S$, where S is the inter dangling bonds spacing and $f_D(T)$ is a fraction of dislocation-acceptors that are full at T°K, *i.e.*, as many as $N_{\mathrm{disl}}f_D(T)/S$ $(=n_d)$ electrons are accepted at N_{disl} dislocations. As there is no electron in the cylinder the free electron density in the crystal with the dislocation density N_{disl} is reduced to $(1-\mathcal{E})n_e$, where $\mathcal{E}=\pi R^2 N_{\mathrm{disl}}$ and n_e is the value in the absence of dislocations.

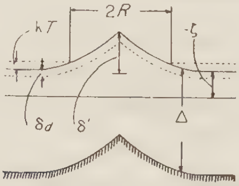

Fig. 1. Space charge potential around a charged dislocation.

The electrical neutrality of the crystal needs

$$(1-\mathcal{E})n_e=n_h+N_b-(n_i+n_d)\ , \tag{2.5}$$

where n_h is the free hole density and is not influenced at low temperature, while it increases by the contribution excited from the dislocation-acceptors in the transition range of temperature, N_b and n_i are the densities of chemical donors which reserve electrons at 0°K and the electrons at impurity levels respectively. Assuming Boltzmann distribution for free carriers and Fermi distribution for the electrons at the impurities[6] and dislocation-acceptors, *i.e.*,

$$f_D(T)=f_D(0)/[1+\exp\{-(\delta'+\zeta)/(kT)\}]\ , \tag{2.6}$$

we obtain the explicit formula for Fermi energy from Eq. (2.5).

In the impurity range of temperature where $\delta'\gg\delta_d>kT$, the Fermi energy is given by

$$\begin{aligned}\zeta=kT\ln\,[&(N_b'-N_D)/(2A_e)\\ &+\{((N_b'-N_D)/(2A_e))^2\\ &+N_D\exp\,(-\delta_d/(kT))/A_e\}^{1/2}]\ ,\end{aligned} \tag{2.7}$$

and in the transition range of temperature where $\Delta>\delta'>kT\gg\delta_d$, it is given by

$$\begin{aligned}\zeta=kT\ln\,[&N_b''/(2A_e)\\ &+\{(N_b''/(2A_e))^2+A_h\exp\,(-\Delta/(kT))/A_e\\ &+N_{\mathrm{disl}}f_D(0)\exp\,(-\delta'/(kT))/(A_eS)\}^{1/2}]\ .\end{aligned} \tag{2.8}$$

In Eqs. (2.7) and (2.8) we put

$$\left.\begin{matrix}A_e\\ A_h\end{matrix}\right\}=\left.\begin{matrix}(1-\mathcal{E})\\ 1\end{matrix}\right\}\cdot\frac{2(2\pi m_{e,h}kT)^{3/2}}{h^3}\ , \tag{2.9}$$

$$\left.\begin{aligned}N_b'\ &=N_b\ -N_{\mathrm{disl}}f_D(0)/S\ ,\\ N_b''&=N_b'-N_{\mathrm{disl}}f_D(0)/S\ .\end{aligned}\right\} \tag{2.10}$$

§ 3. Scattering Effects in Different Temperature Ranges

Assuming the random distribution of the sectional centers of the cylinders of which directions along the length are parallel to each other, we study the scattering effects of the electrons moving on the vertical plane to the dislocation line.

In the impurity range of temperature the electron mean free path due to phonon-scattering is comparable to the cylinder radius, so that the additivity of the reciprocal mean paths is held in so far as inter cylindrical spacing is larger than the mean free path. Then we have

$$l_e^{-1}=l_L^{-1}+l_i^{-1}+l_c^{-1}\ , \tag{3.1}$$

where l_L, l_i, and l_c are the mean free paths due to phonon-, impurity-, and cylinder-scattering respectively. The l_c is given by $l_c=(3/8)/(RN_{\mathrm{disl}})$.

Putting Eq. (3.1) into Eqs. (2.1) and (2.3), we obtain

$$\begin{aligned}Q=(k/e)[&\zeta/(kT)\\ &-\{(2-x^2+x^3\varphi(x))/(1-x^2\psi(x))\}]\end{aligned} \tag{3.2}$$

with

$$\left.\begin{aligned}\varphi(x)&=C_{\mathrm{i}}(x)\sin x-S_{\mathrm{i}}(x)\cos x+\tfrac{1}{2}\pi\cos x\ ,\\ \psi(x)&=-C_{\mathrm{i}}(x)\cos x-S_{\mathrm{i}}(x)\sin x+\tfrac{1}{2}\pi\sin x\ ,\end{aligned}\right\} \tag{3.3}$$

where

$$\begin{aligned}x=[&(1/(2\kappa^2))N_D(1-\mathcal{E})\pi e^4\\ &\times\ln\{1+(3\kappa kT/(e^2(N_D(1-\mathcal{E}))^{3/4}))^2\}]^{1/2}\\ &/\{(kT)(l_L^{-1}+l_c^{-1})\}\ ,\end{aligned} \tag{3.4}$$

κ being the dielectric constant, is the ratio of electron mobility by impurity-scattering to that by both the cylinder- and phonon-scattering, and the expression for l_i given by Conwell and Weisskopf[7] is used. It is noticed that the density of ionized impurity-scatterers is reduced to $N_D(1-\mathcal{E})$. Eq. (2.7) is used in the Fermi term in Eq. (3.2).

As is well known the phonon drag effect is overwhelming in this temperature range and it is necessary to study the interaction effect between the dislocation and the effect.

Phonon drag effect is in general sensitive to the electron density in the valleys, while the lattice deformation around the dislocation would change the density in the different valleys and an anisotropy is expected in the thermoelectric power, but in the impurity range of temperature the cylinder covers almost all of the lattice deformation region so that negligible effects appear. At just below the room temperature there must be an appreciable effect. Drabble[8] has also pointed out the effect. In p-type materials the effect is very complicated and is not studied in this paper.

In the transition range of temperature the effect of charged dislocation on the thermoelectric power is studied on the basis of the following three points of view: (1). The radius of the cylinder decreases but the electron mean free path due to phonon-scattering becomes far less than the radius (a typical ratio is of order 10^{-3}), so that the conducting electron follows curved path that wind around the cylinders. Such distorsion of the electron stream line reduces effectively the apparent mobility μ_e^*, which is related with the free mobility μ_e by $\mu_e^*=g(\mathcal{E})\mu_e$ where $g(\mathcal{E})$ is a factor exhibiting the winding effect[2]. The hole mobility μ_h^* is, however, subject to slight effect and the approximation $\mu_h^*=\mu_h$ is held. (2). There is no electron in the cylinder but intrinsic holes and excited holes from the dislocation-acceptors can exist. Then the cylinder becomes effective p-type materials having no electron even at high temperature. (3). In near intrinsic n-type materials, it is possible that the majority carrier is converted in the presence of high density of the dislocation-acceptors.

The combined thermoelectric power (Q) of the mother material (Q_0) and the cylinder (Q_c) is given by

$$Q=\{(1-\mathcal{E})(1+K)Q_0+\mathcal{E}Q_c\}/\{1+(1-\mathcal{E})K\}\,, \tag{3.5}$$

with

$$Q_0=(k/e)\{-2(K-1)/(K+1)+\zeta/(kT)+\varDelta/(kT(K+1))\}\,, \tag{3.6}$$

$$Q_c=(k/e)\{2+(\varDelta+\zeta)/(kT)\}\,, \tag{3.7}$$

where K is the ratio of electron to hole conductivity and is given by

$$K=(1-\mathcal{E})\,g(\mathcal{E})\mu_e n_e/(\mu_h n_h)\,. \tag{3.8}$$

Eq. (2.8) is used in the Fermi term in Eqs. (3.6) and (3.7).

In the intrinsic range of temperature or in p-type materials the dislocations put off the space charge and the lattice deformation around it scatters carriers. With use of the expression of the mobility given by Dexter and Seitz[9], the effect is adequately taken into account in the expression of the thermoelectric power. It is given by

$$Q=-(k/e)\{(\mu_e/\mu_h-1)/(\mu_e/\mu_h+1)\}[\varDelta/(2kT)+(2-3\sqrt{\pi}\,\alpha/4+\alpha^2-\cdots)/(1-\sqrt{\pi}\,\alpha/2+\alpha^2-\cdots)] \tag{3.9}$$

with

$$\alpha=\frac{3\pi}{32}\cdot\frac{E^2\lambda^2 l_L N_{\text{disl}}}{\hbar(kT)^{3/2}}\cdot\left(\frac{m^*}{2}\right)^{1/2}\cdot\left(\frac{1-2\nu}{1-\nu}\right)^2, \tag{3.10}$$

where the scattering-effect due to the ionized impurity is neglected because the effect is less than that due to the naked dislocation in the intrinsic range of temperature unless the density is very high. Evaluating α for electrons in Ge, so that the coupling constant $E=10$ eV, the magnitude of Burger's vector $\lambda=4$ Å, Poisson ratio $\nu=0.4$, the mean free path due to phonon-scattering $l_L=50$ Å, $m^*=0.6$ m, and $T=400$°K, we find $\alpha=0.1$ for $N_{\text{disl}}=1.6\times10^7\ \text{cm}^{-2}$.

§ 4. Comparison with Experiments and Discussions

Comparing with the experimental data for n-Ge given by Yamashita and Ohta[5], we discuss the present theory. The measured values for n-Ge whose room temperature resistivity is 46 $\Omega\cdot$cm are shown in the transition range of temperature in Fig. 2. The marks ×, ○, and ▲ are referred to the sample as grown, the first sample as bent, and the second sample as bent respectively. The first and the second have the radii of curvature of 1.8 cm and 8.0 cm respectively, the both are annealed after bending in order to remove the annealable point defects which are introduced during the bending. Curve A is plotted with use of Eqs. (3.6) and (2.8) putting $f_D=0$ and the assumed values, $\varDelta=(0.785-4.5\times10^{-4}T)$ eV, $m_e=0.6\,m$, $m_h=0.3\,m$. Curve B is so plotted as it is most fit to the experimental values putting the values $\delta'=0.2$ eV, $S=3.5$ Å, $N_{\text{disl}}=1.6\times10^7\ \text{cm}^{-2}$, $R=10^{-4}$ cm, and $\mathcal{E}=0.5$ into

Eqs. (3.5)~(3.8) and (2.8), then it becomes that $f_D(0)\approx 0.2$, while the value due to Read[2] is about 0.1, and $K\approx 0.2$ at about 300°K. The K-value may be interpreted as follows: The dislocation-acceptor density is 4.7×10^{14} cm^{-3}, while the chemical donor density is 3.6×10^{13} cm^{-3} and hole density increases by the excitation from the acceptors so that the ratio of electron to hole density becomes about 1/2 because the electron density is reduced to below 1×10^{13} cm^{-3} by the trapping at the acceptors. Then the value $g(\mathcal{E})\approx 0.4$ at $\mathcal{E}=0.5$ is obtained by Eq. (3.8). The temperature dependencies of $\mu_{e,h}$ are calculated after Morin and Maita[10].

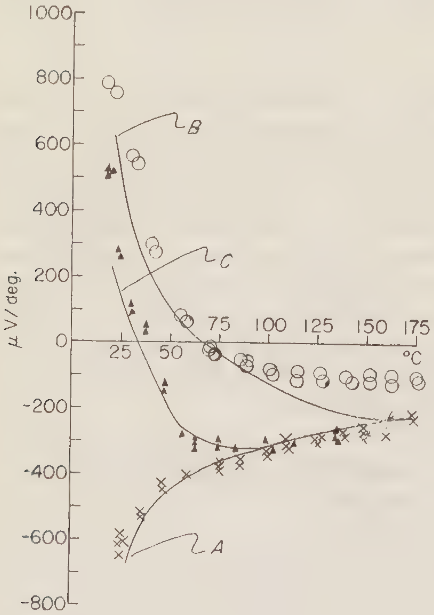

Fig. 2. Experimental data and the theoretical curves for T. E. P. of the deformed 46 Ω·cm n-Ge.

The discrepancy between curve B and the experimental values at above 100°C is attributed to the scattering effect by the naked dislocations. With use of Eq. (3.9) and the proper values of the parameters, the discrepancy will disappear. It is noticed that the effect is appreciable only in the temperature range where thermoelectric power is nearly independent of temperature (the curve is nearly parallel to T-axis) and decreases as temperature exceeds over the range. The effect is also observed in p-Ge[5]. Curve C is plotted in the similar way to curve B assuming $\mathcal{E}=0.1$. In this case both the combination- and the winding-effects are small, while the reduction of electrons and the increase of holes play the essential role. The effect from the naked dislocations is also very small.

The prominent differences of the n-p conversions between by the deformation and by the thermal one are: (1). In the former case the sign of thermoelectric power changes at higher temperature than in the latter case. (2). In the former case the absolute value of thermoelectric power becomes fairly small.

More detailed discussions about the experimental values of various samples will be described in the forthcoming paper[5].

Acknowledgement

The author would like to express his cordial thanks to Prof. Y. Uemura (Tokyo Univ.) for his very useful suggestions and valuable discussions. Thanks are also due to Prof. K. Tomita (Univ. of Kyoto) for his detailed discussions, to Dr. T. Yamashita (Defense Academy) for his valuable discussions about the analysis of the experimental data, and to Dr. J. R. Drabble (Res. Lab. of G.E. Corps.) for his helpful comments about the effect of the strain.

References

1) G. L. Pearson, W. T. Read and F. J. Morin: Phys. Rev. **93** (1954) 666. R. A. Logan, G. L. Pearson and D. A. Kleiman: J. Appl. Phys. **30** (1959) 885. W. Bardsley: *Progress in Semiconductors* **4** (Heywood, London) 1960, pp. 157. This reference contains references to other relevant works.
2) W. T. Read: Phil. Mag. **45** (1954) 775, 1119; **46** (1955) 197.
3) G. L. Peason: Private communication.
4) T. Ohta: J. Phys. Soc. Japan **15** (1960) 197.
5) T. Yamashita and T. Ohta: This issue. The outline was read at the Spring Meeting of the Phys. Soc. of Japan at Osaka Univ., Apr., 1961.
6) See for example, W. Shockley: *Electrons and Holes in Semiconductors* (Nostrand, New York) 1950.
7) E. Conwell and V. F. Weisskopf: Phys. Rev. **69** (1946) 258.
8) J. R. Drabble: Private communication.
9) D. L. Dexter and F. Seitz: Phys. Rev. **86** (1952) 964.
10) F. J. Morin and J. P. Maita: Phys. Rev. **94** (1954) 42.

JOURNAL OF THE PHYSICAL SOCIETY OF JAPAN Vol. 16, No. 8, AUGUST, 1961

Measurement of Seebeck Effect in Plastically Bent Germanium

By Tadayoshi YAMASHITA and Tokio OHTA

Department of Physics, Defense Academy, Yokosuka

(Received May 4, 1961)

The changes of the thermoelectric powers and the electrical resistivities of several kinds of n-Ge and p-Ge due to plastic bending are measured in the temperature covering the transition- and intrinsic-ranges and analyzed by the theory. The value of the dislocation-acceptor level is estimated to be about 0.2 eV. The n-Ge sample near intrinsic is converted to p-type by the bending, while n-Ge with low resistivity and p-type samples show the slight effect. The difference of n-p conversion due to the deformation from the thermal conversion is discussed.

§ 1. Introduction

The study of thermoelectric power in n-type semiconductors under plastic deformation is very useful to confirm the charged dislocation model[1)]. In the transition range of temperature it provides reliable information of the following three effects: (1). *Scattering-effect.* The carriers are scattered by the space charge cylinder around a dislocation whose radius is far larger than their mean free path, while they are scattered by the lattice deformation when it has no charge. (2). *Combination-effect.* The observable thermoelectric power is the combined one of the n-type mother material with the p-type cylinder. (3) *Conversion-effect of the majority carrier.* In the n-type materials near intrinsic, the type of majority carrier is converted by introducing the high density of the dislocation-acceptors. Ohta[1)] has formulated all these effects and given Eq. (1.1) for the measurable thermoelectric power Q:

$$Q=\{(1-\varepsilon)(1+K)Q_0+\varepsilon Q_c\}/\{1+(1-\varepsilon)K\}\,, \tag{1.1}$$

with

$$Q_0=(k/e)\{-2(K-1)/K+1)$$
$$+\zeta/(kT)+\Delta/(kT(K+1))\}\,, \tag{1.2}$$

$$Q_c=(k/e\{2+(\Delta+\zeta)/(kT)\}\,, \tag{1.3}$$

$$K=(1-\varepsilon)g(\varepsilon)\mu_e n_e/(\mu_h n_h)\,, \tag{1.4}$$

where Q_0 and Q_c are the thermoelectric powers of the mother material and the cylinder respectively, ε is the ratio of the volume of all cylinders to that of the bulk crystal, $-\zeta$ is the Fermi energy, e is the magnitude of electron charge, Δ is the gap energy between c- and v-band, and $g(\varepsilon)$ exhibits the scattering-effect of electron due to the space charge cylinder. The reduction of free electron density and the increase of hole density are expressed in Eq. (1.4), where n_e, μ_e and μ_h are the free electron density, the electron and hole mobilities in the absence of dislocations respectively. n_h is the free hole density in the presence of dislocations.

In the present paper the thermoelectric powers and the resistivities of several kinds of Ge are measured and analyzed from the transition to the intrinsic range of temperature.

The values of the dislocation-acceptor level is estimated by the measured values of the conductivities. The value of K is discussed. The scattering-effects due to the naked dislocation for n-Ge and p-Ge are also studied in the intrinsic range of temperature.

§ 2. Samples and Measurements

Three kinds of antimony-doped (T, E, and O in our sign) and one kind of indium-doped (Y in our sign) germanium-single crystals were cut in wafers of the size of 25×6×3 mm^3. The crystal axes were so chosen that the parallel array of pure edge dislocations are introduced, the inter dangling bonds spacing being about 3.5Å, by bending round the [$\bar{1}\bar{1}$2] -axis as shown in Fig. 1.

On the surface of the wafer two caves with diameter of about 1.5 mm were grounded

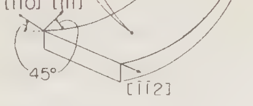

Fig. 1. Bent Ge-wafer and the crystal axes.

whose distance was about 1.0 cm. After polishing with 1200-mesh emery powder the wafers were etched in CP4 soaking in concentrated HNO_3, rinsing in deionized water, soaking in aqueous KCN solution, and again rinsing in deionized water. When the wafer was bent, the edges were put on graphite electrodes and heated to 600~650°C by passing a current through it in the atmosphere of argon gas and bent by pressing it with use of a graphite block having two knife edges. Two thermocouples composed of No. 36 chromel-alumel wires were attached to each cave with use of platinum foil to give good electrical and thermal contact.

The sample was placed inside an apparatus with a graphite contact on one end and another graphite contact with a heater at the other end and inserted holizontally in an electric furnance. The temperature difference between the caves was kept to 1.0°C during the measurement. Both the Seebeck voltages and the resistivities before and after bending were measured at the temperature range between 25°C and 300°C by means of a K-type potentiometer with the attentions pointed out by Middleton and Scanlon[2].

In order to study the effect of annealable point defects introduced during the bending the values as bent and annealed after bending were measured. In the Table I the kinds of samples, the radii of curvature, and the annealing data are listed.

Table I.

Samples	as grown		as bent	annealed	
	room temp. resistivity	impurity density	radius of curvature	annealed hours and temp.	
TNO. 2	0.23 Ω. cm	7.1×10^{15}/c.c	1.2 cm	20 h,	500°C
ENO. 2	46	3.6×10^{13}	1.8	18	650
ENO. 3	〃	〃	8.0	18	500
ONO. 6	25	6.6×10^{13}	1.5	18	500
ONO. 7	〃	〃	3.7	18	500
YNO. 1	18	2.0×10^{14}	1.3	3	973

Table II.

	TNO. 2	ENO. 2	ENO. 3	ONO. 6	ONO. 7	YNO. 1
R cm	7.1×10^{-6}	1.1×10^{-4}	1.1×10^{-4}	7.4×10^{-5}	7.4×10^{-5}	——
N_{disl}/cm^2	2.1×10^{7}	1.6×10^{7}	3.2×10^{6}	1.7×10^{7}	6.5×10^{6}	2.1×10^{7}
ε	3×10^{-3}	0.5	0.1	0.3	0.1	——
n_{da}/c.c.	6.2×10^{14}	4.7×10^{14}	9.4×10^{13}	4.7×10^{14}	1.9×10^{14}	——

§ 3. Results and Analyses

The values of radius R of the space charge cylinder, the dislocation density N_{disl}, the ratio ε of all the cylinders to mother bulk volume, and the dislocation-acceptor density n_{da} are estimated, assuming that the inter dangling bonds spacing S is 3.5Å and the fraction of dislocation-acceptor density that are full f_D is 4.5×10^{-2} at 300°K, and listed in the Table II.

The resistivity for TNO. 2 at about 300°K increases about ten times as large as the as grown by the deformation, while the change of thermoelectric power is very small.

The measured values of resistivities for E-kind samples are shown in Fig. 2. For ENO. 2 bent heavily the resistivity is reduced appreciably at high temperature and it becomes p-type, while for ENO. 3 bent slightly the resistivity is reduced a little and it also becomes p-type. The n-p conversion corresponds to the effect described in § 1. Curve C in Fig. 2 shows that the annealable point defects introduced during the bending act as effective acceptor-centers because the material shows stronger p-type, the situation is in accordance with the fact hitherto known[3].

The measured values and the analytical curves for E-kind samples are plotted in Fig. 3. The curves are drawn with use of the following semi-empirical method. Estimating n_e, μ_e and μ_h after Morin and Maita[4], the Fermi-term in Eqs. (1.2) and (1.3) are given by

$$(\Delta+\zeta)/(kT)=11.78+\ln(1+K)-\ln\sigma-0.83\ln T\,, \qquad (3.1)^{*}$$

where σ $(\Omega\cdot\mathrm{cm})^{-1}$ is measured conductivity and Δ is assumed to be $\Delta=(0.785-4.5\times10^{-4}\cdot T)$ eV. Curve A in Fig. 3 is plotted after Eqs. (1.2), (3.1) and Fig. 1. Curve B in Fig. 3 is plotted after Eqs. (1.1)~(1.4), into which ε-value shown in the Table II is substituted, and Eq. (3.1). In this case there is no fits unless the value $K\approx0.2$ at about 300°K is given. Using ζ given by Eq. (3.1) with $K=0.2$, we evaluate the carrier density and obtain $n_h/n_e\approx2$. This shows that $g(\varepsilon)\approx0.4$ at $\varepsilon=0.5$.

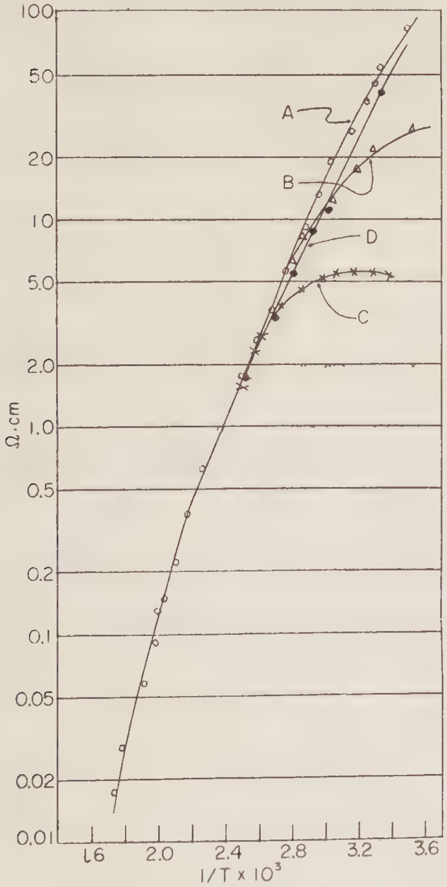

Fig. 2. Temperature dependency of resistivity for E-kind samples. Curve A is referred to the as grown, curve B; to ENO. 2 annealed after bending, curve C; to ENO. 3 as bent, and curve D; to ENO. 3 annealed after bending.

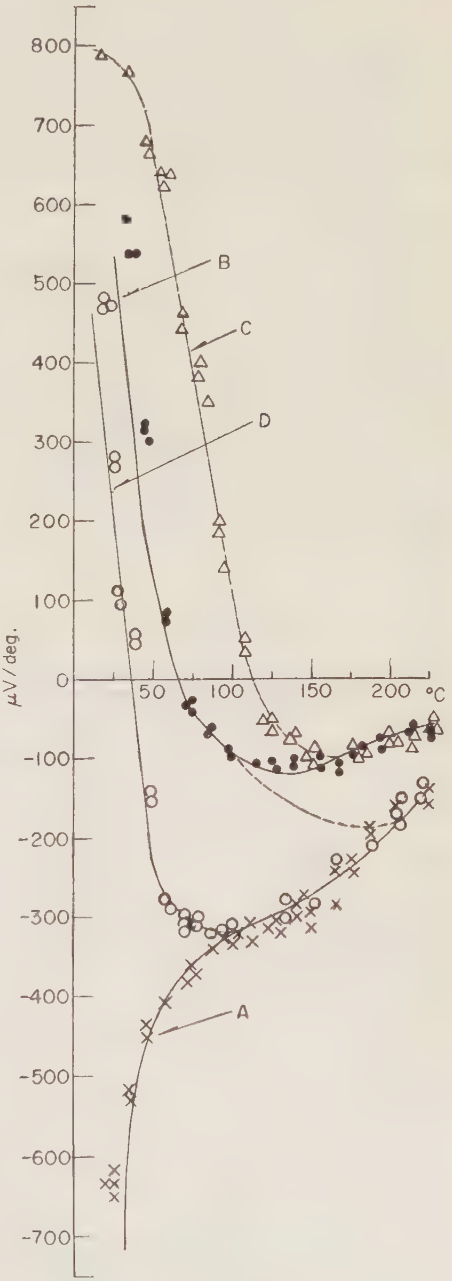

Fig. 3. Thermoelectric powers for E-kind samples. Curve A is referred to the as grown, curve B; to ENO. 2 annealed after bending, curve C; to ENO. 3 as bent, and curve D; to ENO. 3 annealed after bending.

The scattering-effect due to the naked

---

[*] Effective masses $m_e=0.6m$ and $m_h=0.3m$ are assumed.

dislocations is observed at above 100°C and the curve B above 100°C in Fig. 3 is drawn after Eq. (1.2) where the factor 2 is replaced by $(2-\alpha)/(1-\xi)$ with $\xi\approx 0$, $\varepsilon=0$, and $0.5<\alpha<1$, the dotted curve ramified is for the case neglected the effect.

Comparing the experimental value of ζ given by Eq. (3.1) with theoretical equation[1], we obtain the value of about 0.2 eV for the dislocation-acceptor level. Almost the same value is also obtained in the case of ONO. 6.

Curve C in Fig. 3 empirically drawn for ENO. 3 shows that the annealable defects act

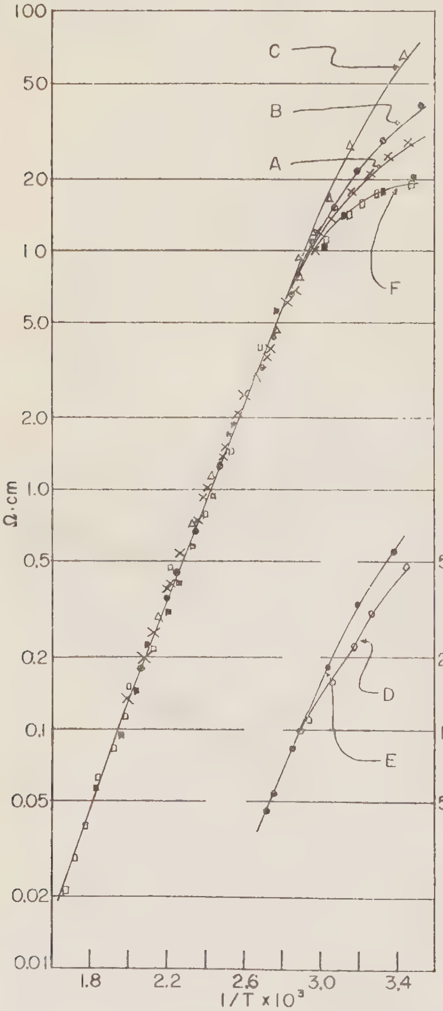

Fig. 4. Temperature dependency of resistivities for O- and Y-kind samples. Curve A is referred to O-kind as grown, curve B; to ONO. 6 as bent, curve C; to ONO. 6 annealed after bending, curve D; to ONO. 7 as bent, curve E; to ONO. 7 annealed after bending, curve F; to Y-kind as grown and as bent.

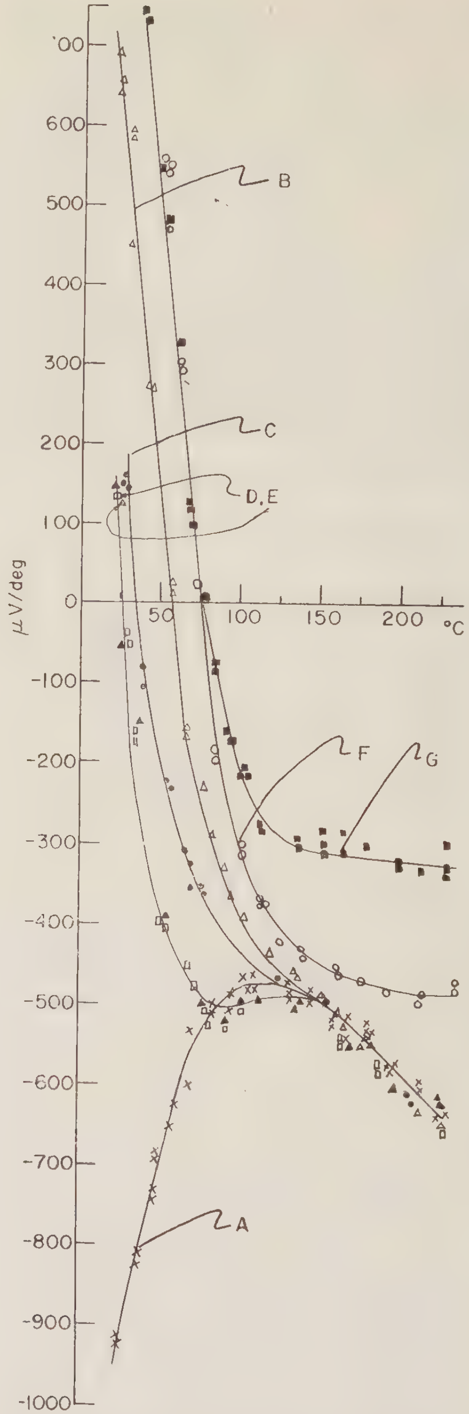

Fig. 5. Thermoelectric powers for O- and Y-kind samples. Curve A is referred to O-kind as grown, curve B; to ONO. 6 as bent, curve C; to ONO. 6 annealed after bending, curve D; to ONO. 7 as bent, curve E; to ONO. 7 annealed after bending, curve F; to Y-kind as grown, and curve G; to Y-kind as bent.

as effective acceptors whose density is so high that an appreciable scattering-effect is observed.

Curve D in Fig. 3 is plotted after the similar manner to that of the curve B in Fig. 3. In this case both the combination- and scattering-effects are small, while the reduction of free electrons and the increase of holes play essential role.

The measured values of resistivities for O- and Y-kind samples are shown in Fig. 4. The effects of charged dislocations are to increase the resistivities in contrast with E-kind case. The change of the values as well as the temperature dependency are explained with use of Read's theory as in the cases hitherto known[5]. Y-kind sample is of *p*-type and the scattering-effect due to the naked dislocations on the resistivity is too small to be observed as is seen from curve F in Fig. 4. The effect on the thermoelectric power is, however, appreciable generally in the temperature range where the thermoelectric power is nearly independent of temperature. The curve G in Fig. 5 is an example case.

All the curves in Fig. 5 are drawn empirically. The explanations for the behaviors of the curves are essentially the same as for E-kind samples. But the following points should be noticed. As shown in curve C in Fig. 5 the charged dislocations reduce the absolute value of thermoelectric power fairly. This informs that the majority carrier in O-kind materials at room temperature is not always converted to hole if we consider the combination-effect with $\varepsilon=0.3$. Such an explanation is supported by curve E in Fig. 5 where the values are shifted more to negative sign side because of the small combination-effect ($\varepsilon=0.1$).

It is, however, incomprehensive that the scattering-effect due to the naked dislocations on the thermoelectric power for ONO. 6 is unexpectedly small in the intrinsic range of temperature although it contains very high density of the dislocations.

Illustrating ENO. 3 as an example case, we show that it is impossible to explain the effect of the deformation on the thermoelectric power by only the effect of the point defects. If the curve C in Fig. 3 is due to the holes ionized from the acceptors whose level depth is $\Delta-(0.1\sim0.05)$ eV[3] the acceptor density must be about $10^{20}\sim10^{18}\,\mathrm{cm}^{-3}$, which is unreasonably high. If the curve D in Fig. 3 is due to the holes ionized from the acceptors surviving the annealing the acceptor density must be about $10^{18}\sim5\times10^{15}\,\mathrm{cm}^{-3}$. The values are enough to cause an appreciable scattering-effect at intrinsic range of temperature, which is not observed in the curve. Therefore we may conclude that the curve is almost perfectly due to charged dislocations.

References

1) T. Ohta: J. Phys. Soc. Japan **15** (1960) 197. The full report is in this issue.
2) A. E. Middleton and W. W. Scanlon: Phys. Rev. **92** (1953) 219.
3) For example, A. G. Tweet: Phys. Rev. **99** (1955) 1245. J. N. Hobster and P. Breidt: J. Appl. Phys. **28** (1957) 1214.
4) F. J. Morin and J. P. Maita: Phys. Rev. **94** (1954) 42.
5) For example, R. A. Logan, G. L. Pearson, and D. A. Kleiman: J. Appl. Phys. **30** (1959) 885.

Journal of the Physical Society of Japan, Vol. 16, No. 8, August, 1961

On the Interference Phenomena of Compton Scattering from Diamond

By Yasuharu Yoneda

Department of Applied Physics Faculty of Engineering
Kyushu University Fukuoka

(Received February 4, 1961)

An explanation is given on the divergent beam pattern due to Compton scattering. The pattern is not caused by a point source of X-rays outside of crystal but by interference of X-rays produced uniformly in a small crystal. It is shown experimentaly that the interference lines can appear even for a pretty small crystal if a micro-beam is used.

§1. Introduction

Grenville Wells[1] obtained divergent-beam patterns from diamond and other crystals with a parallel X-ray beam, and ascribed the origin of such interference patterns to either Compton scattering or scattering due to imperfections, or both. Norman[2] confirmed by using a filter technique that the origin of divergent radiation is due to Compton scattering. He observed: (i) The interference lines appear from imperfect crystals, but not from perfect crystals; (ii) There seems to exist a certain minimum in the size of diamond crystals to give rise to the lines, since the interference lines are observed for a crystal of 2×0.5 mm with the incident X-rays of 1 mm cross-section, but not for a crystal of 0.5×0.5 mm, though both of the crystals are obtained from a same large crystal; (iii) The interference lines have fine structures.

From (i) he concluded it as probable that the Compton interference is caused not only by the primary extinction effect but also by the secondary extinction effect, as Lonsdale[3] suggested for the usual divergent beam patterns obtained with the X-ray point source lying outside the crystal. He considered that crystals must be large enough so that the secondary extinction effect is appreciable to give rise to the interference lines. According to him, the relative position of the light and dark lines in the fine structure are always complementary to that of the Kossel pattern which appears by the dynamical effect in a perfect crystal. This fact supports the explanation of the interference lines by the secondary extinction effect. As to the fine structure of the lines, he compared it with the pair of reflection and deficiency lines in the usual divergent beam pattern given by a X-ray point source outside the crystal, as shown in Fig. 1, and considered that the separation of the two lines become very small if the distance between the source and the crystal and the crystal thickness are reduced.

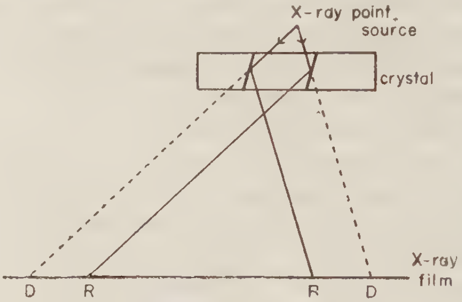

Fig. 1. The explanation of appearance of reflection and deficiency lines by a point X-ray source outside the crystal.

In the present study the interference lines were observed for several specimens of diamond with the parallel beam of X-rays of various sizes, and a conclusion somewhat different from that by Norman[2] was obtained with regard to the condition of the appearance of the interference lines. In order to explain this and the fine structure, we have considered the process of the appearance of the interference lines in more detail, taking into account the fact that the source of the divergent beam due to Compton scattering is not a point source, but distributed over the whole region irradiated with the impinging X-ray beam.

§2. Experiment

The Cu radiation from a rotating anode X-ray source of variable focal-size was used.[4]

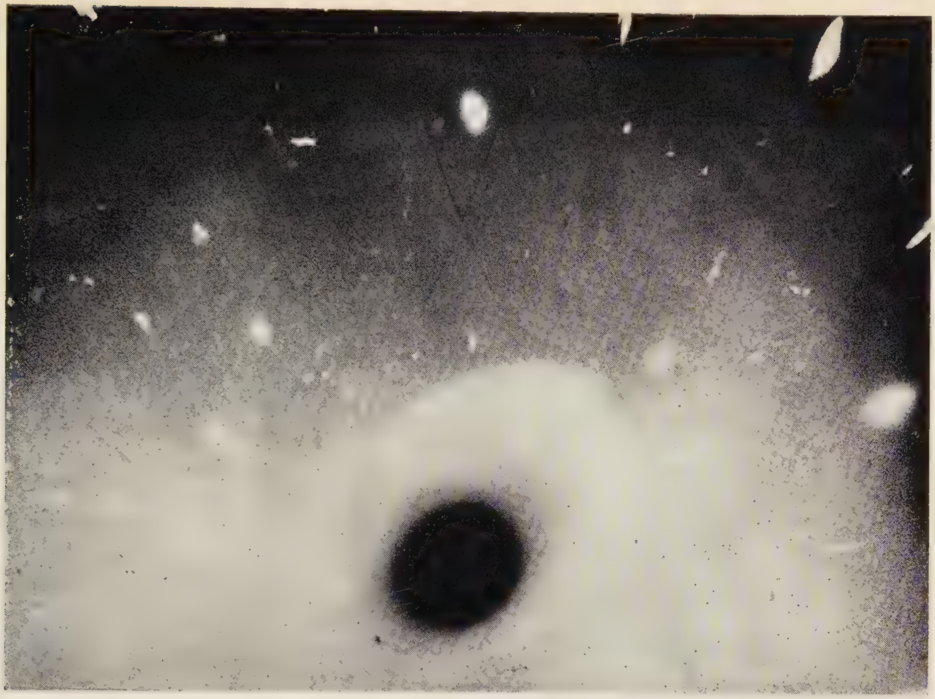

Fig. 2. Divergent beam pattern; Impinging beam in [110] direction, $[1\bar{1}0]$ vertical. No filter Cu radiation 40 KVP, 40 mA, apparent focus 0.2×0.5 mm, exposure time 40 hrs. the diameter of impinging X-ray beam 0.1 mm, distance from specimen to flat film is 30 mm, positive figure. ×2.5.

The source can be operated for a long time without trouble with the focus 0.2×0.5 mm, and with 50 mA at 40 kV.

Several brownish diamond crystals from Borneo, about 3—0.2 mm in size were used. The interference lines with the fine structures were observed as reported by Norman.[2] An example is shown in Fig. 2, where four interference lines corresponding to the reflection {111} with fine structures composed of light and dark lines are observed besides the Laue spots.

This photograph was obtained from a crystal of 0.2×0.4 mm with the impinging X-ray beam of the diameter 0.1 mm. It is to be noted that no interference line was observed from the same specimen with the impinging X-ray beam of the diameter 0.3 mm. The size of the crystal used in the present experiment is smaller than the one used by Norman,[2] which was 0.5×0.5 mm in size. This fact suggests that the minimum size for the appearance of the interference lines, if it exists, seems to be still smaller than he suggested, and that the cross section of the impinging beam is a factor more important than the crystal size for small crystals.

§ 3. Consideration on the appearance of the interference lines

The angular width of Bragg reflection due to the spectral line breadth of X-rays is given by

$$d\theta=\frac{d\lambda}{\lambda}\tan\theta \tag{1}$$

where θ is the Bragg angle of the reflecting planes and λ wave length.

If $\Delta\lambda$ is the line breadth of Compton shift line due to the initial random velocities of electrons bound in atoms, $d\theta$ is given by

$$d\theta=\frac{\Delta\lambda}{\lambda}\tan\theta \tag{2}$$

According to Du Mond and Kirkpatrick[5] and Du Mond,[6] $d\theta$ is estimated to be about 0.51° for the reflection (111) planes with Cu $K\alpha$.

In order to explain the structure of the light and dark lines, it is assumed that the source of the divergent beams are distributed in a small crystal whose absorption is almost negligible, and that the divergent beams are reflected by the lattice planes in the same crystal. Let us first consider the case where the breadth of Compton shift line is neglected, and assume, for simplicity, that the crystal has a rectangular section $\boldsymbol{ABCD}$ in Fig. 3 (a), and AB makes 45° angle with the lattice plane $\boldsymbol{L}(hkl)$, and that the Bragg angle for $\boldsymbol{L}$ is 45°. Incident X-rays $\boldsymbol{i}$ which have been emitted in the crystal, form 90° angle with reflected X-rays $\boldsymbol{r}$. It is not necessary in this case to consider X-rays coming from outside. The reflected X-rays leaving the crystal through the point $\boldsymbol{P}$ should have been reflected at some point on $\boldsymbol{PQ}$, and their incident X-rays should have been emitted at some point within the area $\boldsymbol{ABPQ}$. The variation of intensity of reflected X-rays along $\boldsymbol{AD}$, therefore, is given approximately by the line $\boldsymbol{a}$. The intensification toward the side $\boldsymbol{D}$ may be said as a pile-up effect. On the other hand, a part of X-rays traveling in the direction of $\boldsymbol{r}$ are reflected on the lattice plane $(\bar{h}\bar{k}\bar{l})$. This negative intensity is constant along $\boldsymbol{AD}$ and shown by the line $\boldsymbol{b}$. The line $\boldsymbol{c}$ is the sum of the intensities $\boldsymbol{a}$ and $\boldsymbol{b}$. This explains the appearance of the light and dark line.

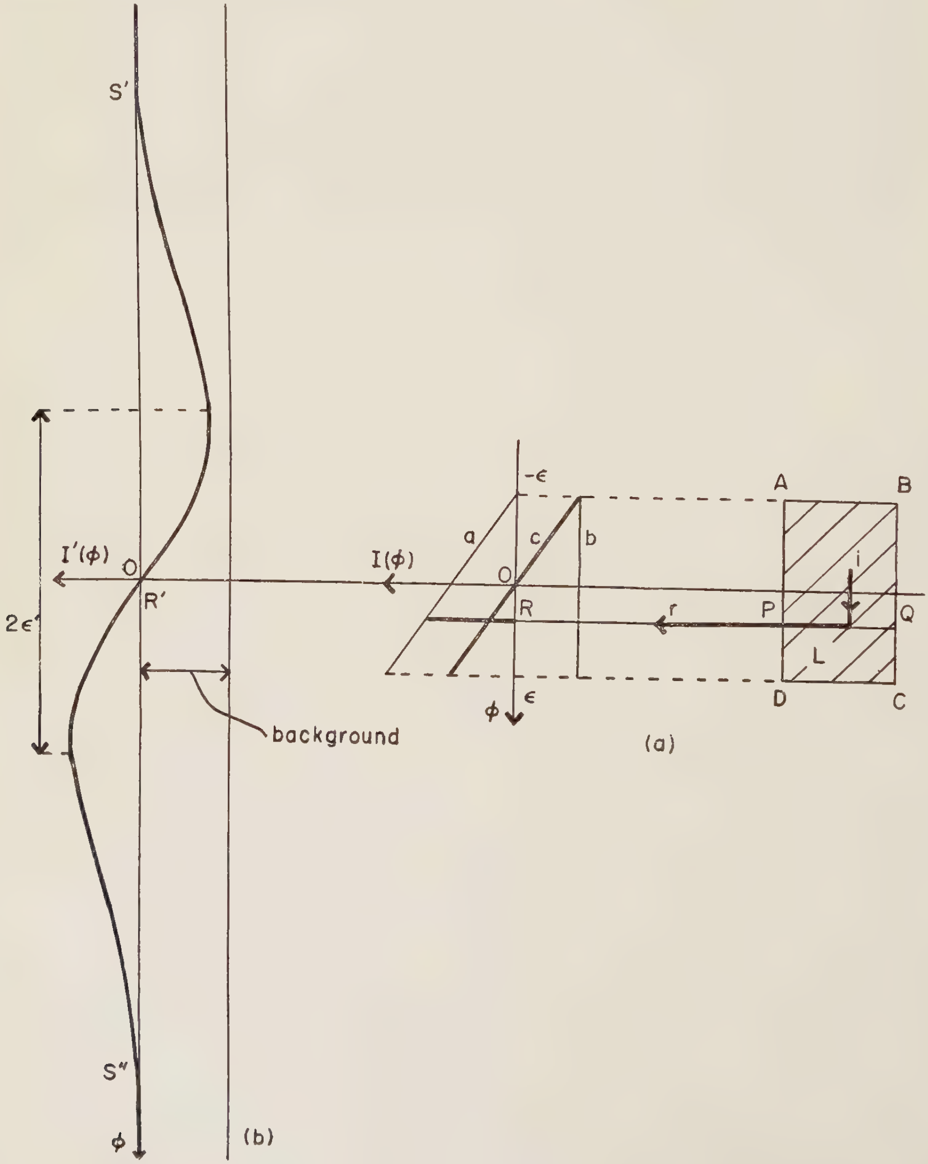

Fig. 3. The interpretation of the fine structure of a interference line due to Compton scattering.

Let us consider next the breadth of Compton shift line. Corresponding to the simple case considered above, the intensity of the light and dark lines is assumed to be as follows:

$$\left.\begin{aligned} I(\phi)&=-m\phi \qquad \text{for} \quad |\phi|\leq\mathcal{E} \\ I(\phi)&=0 \qquad\quad\ \text{for} \quad |\phi|>\mathcal{E} \end{aligned}\right\} \tag{3}$$

where ϕ is the angle measured from the centre of the reflection of X-rays, m a constant and $\pm\mathcal{E}$ the angle of both the ends of the light and dark lines. If the breadth of Compton shift line can be expressed by $1/\sqrt{2\pi}\sigma \exp(-\phi^2/2\sigma^2)$, where the value σ is determined by the wave length and the angle of deviation from the impinging X-ray beam, the intensity of X-rays will be expressed by the convolution of these two functions as follows:

$$I'(\phi)=\int_{\phi-\varepsilon}^{\phi+\varepsilon}\frac{1}{\sqrt{2\pi}\sigma}\exp(-u^2/2\sigma^2)\{-m(\phi-u)\}du$$

$$=-\frac{m\phi}{\sqrt{2\pi}\sigma}\left\{\int_0^{\phi+\varepsilon}\exp(-u^2/2\sigma^2)du\right.$$

$$\left.-\int_0^{\phi-\varepsilon}\exp(-u^2/2\sigma^2)du\right\} \tag{4}$$

$$+\frac{m}{\sqrt{2\pi}\sigma}[\exp\{-(\phi-\mathcal{E})^2/2\sigma^2\}$$

$$-\exp\{-(\phi+\mathcal{E})^2/2\sigma^2\}]\,. \tag{5}$$

The numerical calculations of (5) is shown in Fig. 3 (b), where the half-value width of $1/\sqrt{2\pi}\sigma \exp(-\phi^2/2\sigma^2)$ is taken to be $4\mathcal{E}$. The distance between the minimum and maximum of the intensity is larger than that in Fig. 3 (a), but the centre remains at the same position where the intensity gradient is the largest in both cases. The light and dark lines in Fig. 2 shows slow intensity variation in their both sides. This variation is clearly seen also in the microphotometer traces of Norman,[2)] as is shown in Fig. 4. In the photograph, however, the breadth of the part near R' where the intensity gradient is large, or the maximum and minimum interval ($2\mathcal{E}'$ of Fig. 3 (b)) are apt to be taken for the breadth of the light and dark lines, due to the strong background. For this reason, they sometimes look sharper than the actual width ($S'S''$ of Fig. 3 (b)), as seen in Fig. 2.

The X-rays emitted in ***i*** and ***r*** directions in Fig. 3 (a) have different wave length in accordance with Compton's formula when their angles to the direction of impinging X-rays from outside are different. The lines ***a*** and ***b*** of Fig. 3 (a) should, then, shift slightly corresponding to the difference in the angles of Bragg reflection, but this effect makes no great contribution to the appearance of the light and dark lines. Fig. 2 corresponds to a case with no such difference in wave length.

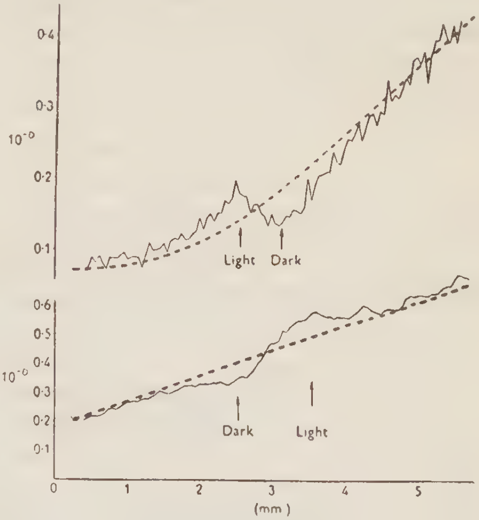

Fig. 4. Microphotometer traces of the interference lines by N. Norman.[2)] Ordinate scale 10^{-D}, where D is film density. Dotted lines are written by the author, as the correspondency to Fig. 3 (b).

The external form of crystal is generally complicated and the relation between incident X-rays and reflected X-rays in a crystal is not so simple as shown in Fig. 2. However an explanation quite similar to the above is possible for a crystal having a cross section of parallelogram formed by the lines paralleled in ***i*** and ***r*** directions. In more general cases, it may be possible to calculate the intensity theoretically by the convolution using more variables. In general, a kind of pile-up effect will always take place, and the breadth of the interference line will be in the order of the linear dimension of the crystal in the direction ***AD*** in Fig. 3 (a). For the crystal used in the observation of Fig. 2, the magnitude of projection corresponding to $2\mathcal{E}$ of Fig. 3 (a) is 0.24 mm, and on the film this corresponds approximately to 0.26°. Since the half width of Compton shift line is about 0.51° as mentioned before, we have $2\mathcal{E}'\approx 0.5°$, and the observed value of $2\mathcal{E}'$ 0.4−1° is in the range of agreement with the calculation.

The author wishes to express his sincere thanks to Prof. T. Futagami for his obtaining necessary diamonds and continued encouragement. The author's thanks are also due to Dr. N. Norman of Central Institute for Industrial Research, Norway for his invaluable comment and advice. Also the author is indebted very much to Prof. K. Kohra of Tokyo University for his kind discussion.

References

1) H. J. Grenville-Wells: Nature **168** (1951) 219.
2) N. Norman: Acta Cryst. **11** (1958) 1.
3) K. Lonsdale: Phil. Trans. A. **240** (1947) 219.
4) Y. Yoneda, K. Kohra, T. Futagami, and M. Koga: Tech. Reports Kyushu Uni. (in Japanese) **27** (1954) 87.
5) J. W. M. Du Mond and H. A. Kirkpatrick: Phys. Rev. **37** (1931) 136.
6) J. W. M. Du Mond: Rev. Mod. Phys. **5** (1933) 1.

JOURNAL OF THE PHYSICAL SOCIETY OF JAPAN Vol. 16, No. 8, AUGUST, 1961

The Crystal Structure of Nickel Chloride Hexahydrate, $NiCl_2 \cdot 6H_2O$*

By Joji MIZUNO

Takarazuka Radiation Laboratory, Division of Sumitomo Atomic Energy Industries, Ltd. Takarazuka Japan

(Received March 30, 1961)

The crystal structure of $NiCl_2 \cdot 6H_2O$ has been determined by the X-ray single crystal method. The unit cell is monoclinic with $a=10.23$ Å, $b=7.05$ Å, $c=6.57$ Å and $\beta=122°10'$. The space group is C_{2h}^3-C2/m and the unit cell contains two formula units. The atomic arrangement is quite the same as that of $CoCl_2 \cdot 6H_2O$ and thus the structure model adopted for this salt has again been confirmed to be correct, as compared with the model proposed by Stroganov *et al.*.

§ 1. Introduction

Previously, the author determined the crystal structure of cobalt chloride hexahydrade, $CoCl_2 \cdot 6H_2O$[1], by the X-ray single crystal method. This crystal structure is as follows: (1) two chlorine atoms and four water molecules are octahedrally coordinated to cobalt atom to form the group $[CoCl_2 \cdot 4H_2O]$, (2) the other two water molecules of the formula unit are located between the groups $[CoCl_2 \cdot 4H_2O]$ arranged in the direction of the b axis and they form the O···H–O type hydrogen bonds with the neighbouring water molecules of the groups $[CoCl_2 \cdot 4H_2O]$, and thus these groups are joined with one another through these hydrogen bonds in parallel with the b axis, and (3) the structure is composed of atomic layers parallel to (001). This structure model was entirely different from that proposed by Stroganov *et al*. and was proved to be reasonable by the following studies on $CoCl_2 \cdot 6H_2O$ at low temperatures: studies on the paramagnetic susceptibilities by Haseda and Kanda[2] and by Haseda[3], on the proton magnetic resonance by Sugawara[4] and on the specific heat by Robinson and Friedberg[5].

Haseda and Date[6] measured the paramagnetic susceptibilities of $NiCl_2 \cdot 6H_2O$ in powdered samples at low temperatures and found the different magnetic behavior from that of powdered samples of $CoCl_2 \cdot 6H_2O$, though the two salts were supposed to be isomorphous. Therefore, it was required to examine whether these two paramagnetic salts were certainly isomorphous or not. The present work was thus undertaken. In the previous paper[1], it was reported that according to the preliminary study, $NiCl_2 \cdot 6H_2O$ seemed to resemble $CoCl_2 \cdot 6H_2O$ in its atomic arrangement. By the present detailed structure analysis, it was proved that the former salt is quite isomorphous with the latter.

---

* This work was done at the Research Institute for Iron, Steel and Other Metals, Tohoku Univ., Sendai, Japan.

From the result of the preliminary study described above, Haseda, Kobayashi and Date[7)] considered that the anomalous magnetic behavior of a powdered sample of $NiCl_2 \cdot 6H_2O$ below about 10°K was also caused by the antiferromagnetic transition, as was the case for $CoCl_2 \cdot 6H_2O$. They measured the paramagnetic susceptibility on a single crystal of $NiCl_2 \cdot 6H_2O$ and confirmed that this salt is antiferromagnetic below about 6°K.

Thus, the structure model concluded for $CoCl_2 \cdot 6H_2O$ was again confirmed to be correct for $NiCl_2 \cdot 6H_2O$ by both the structural and magnetic studies. This increases very much the reliability for the proposed structure model.

§ 2. Crystallographic Data from the Literature on $NiCl_2 \cdot 6H_2O$

In "*Chemische Kristallographie*, I Teil" (Groth, 1906)[8)], the following data are given for monoclinic prismatic $NiCl_2 \cdot 6H_2O$: the axial ratios $a : b : c$ are 1.4678 : 1 : 0.9426, β being 122°30′. The (001)-cleavage is perfect. It is green or grass-green in colour. The density is given as 1.921 gr/cm³.

§ 3. Experimental

The light green single crystals of $NiCl_2 \cdot 6H_2O$ were grown from saturated aqueous solution. They were the same in the habit as described by Groth and accordingly they could be regarded as monoclinic prismatic. The two fragments along the a and the b axes which were about $0.4 \times 0.45 \times 2.5\ \mathrm{mm}^2$ and $0.25 \times 0.3 \times 2.5\ \mathrm{mm}^3$ in dimension, respectively, were cut out of these single crystals, sealed into grass capillary tubes in contact with chronometer oil and used for X-ray study. Under these conditions, they remained stable during the experiment.

Rotation photographs about the a and the b axes and oscillation photographs about the b axis were taken with Ni-filtered Cu$K\alpha$ and Zr-filtered Mo$K\alpha$ radiations. Multiple-film equi-inclination Weissenberg photographs of zero- and the first-layer were taken about the a and the b axes using Zr-filtered Mo$K\alpha$ radiation.

The unit cell parameters measured from these X-ray diffraction photographs are as follows:

$$a = 10.23\ \text{Å},\ b = 7.05\ \text{Å},\ c = 6.57\ \text{Å},\ \beta = 122°10'$$

$$a : b : c = 1.45 : 1 : 0.932$$

From these parameters and the density value, 1.92 gr/cm³, the number of the formula units in the unit cell was calculated to be 1.96, which meant the existence of two formula units per unit cell. From the crystal form and the observed extinctions, (hkl) with $k+k$=odd, $(h0l)$ with h=odd and $(0k0)$ with k=odd, the most probable space group was assumed as $C_{2h}^3 - C2/m$.

The relative intensities of reflections were estimated visually by comparison with the time-exposure calibrated strips. Some intensities, which were very faint and hardly visualized, were estimated as one-third or one-fifth of the lowest intensities of the strips. All of them were corrected for Lorentz and polarization factors in the usual way.

The linear absorption coefficient was calculated to be $30.4\ \mathrm{cm}^{-1}$ for Mo$K\alpha$ radiation. Using this coefficient, the rough absorption correction was made by assuming cylindrical shape of the sample.

§ 4. Determination of the Structure

The unit cell parameters, the values, $\sin\theta/\lambda$, and the relative intensities of reflections on photographs were quite similar to those of $CoCl_2 \cdot 6H_2O$ and thus the same structure model as that of this salt was primarily assumed for the present salt.

At first, based on the assumed model, the atomic parameters could approximately be determined by the trial-and-error method, using the $F(h0l)$'s obtained from oscillation photographs taken about the b axis with Zr-filtered Mo$K\alpha$ radiation. They are listed in Table I. The reliability factor, $R = \Sigma||F_o| - |F_c||/\Sigma|F_o|$, was 0.155. Referring to the data of $CoCl_2 \cdot 6H_2O$, the value of B, the coefficient in the exponent of the isotropic temperature factor $\exp[-B \cdot \sin^2\theta/\lambda^2]$, was assumed to be 1.5 Å² for Ni^{2+} and 3.0 Å² for Cl^- and O^{2-}, respectively.

As the next step, the atomic parameters were refined, using the $F(h0l)$'s and $F(0kl)$'s obtained from Weissenberg photographs. Fourier projections and the difference Fourier projections on (010) and the plane normal to

Table I. Atomic parameters.

Atom	x		y		z	
	From oscillation photo.	From Weissenberg photo.	From oscillation photo.	From Weissenberg photo.	From oscillation photo.	From Weissenberg photo.
Ni	0	0	0	0	0	0
Cl	0.275	0.271	0	0	0.173	0.167
O_I	0.0288	0.0312		0.208	0.255	0.251
O_{II}	0.283	0.288	0	0	0.692	0.702

O_I: $4H_2O$ coordinated to Ni^{2+} ion. O_{II}: $2H_2O$ far from Ni^{2+} ion.

Table II. Comparison between F_c and $|F_0|$ for the $(h0l)$ and $(0kl)$ reflections ($NiCl_2 \cdot 6H_2O$).

h	0	l	$\lvert F_0 \rvert$	F_c
2	0	0	5.0	4.4
4	0	0	25.2	24.1
6	0	0	2.3	2.8
8	0	0	6.2	5.6
10	0	0	1.6	2.2
12	0	0	0.7	0.8
14	0	0	0.5	1.1
0	0	1	17.4	16.8
2	0	1	2.8	1.5
4	0	1	4.2	4.2
6	0	1	2.0	1.5
8	0	1	0.6	0.9
10	0	1	1.9	2.1
12	0	1	0.5	0.3
$\bar{2}$	0	1	11.9	12.3
$\bar{4}$	0	1	20.9	19.9
$\bar{6}$	0	1	7.5	7.6
$\bar{8}$	0	1	12.0	10.8
$\overline{10}$	0	1	1.5	2.0
$\overline{12}$	0	1	5.1	4.2
$\overline{14}$	0	1	0.8	0.8
0	0	2	12.2	−11.7
2	0	2	10.5	10.0
4	0	2	3.7	4.4
6	0	2	7.9	7.7
8	0	2	0.7	0.1
10	0	2	4.1	3.2
12	0	2	0.5	0.9
$\bar{2}$	0	2	5.1	4.6
$\bar{4}$	0	2	1.5	1.8
$\bar{6}$	0	2	2.4	1.0
$\bar{8}$	0	2	9.0	8.9
$\overline{10}$	0	2	0.6	0.8
$\overline{12}$	0	2	6.8	5.5
$\overline{14}$	0	2	0.8	0.8
$\overline{16}$	0	2	2.7	1.8
0	0	3	2.5	2.3
2	0	3	12.2	12.5
4	0	3	2.2	2.3
6	0	3	6.5	7.0
8	0	3	1.3	1.8
10	0	3	2.0	2.4
$\bar{2}$	0	3	9.8	9.6
$\bar{4}$	0	3	0.4	− 1.3
$\bar{6}$	0	3	4.4	3.3
$\bar{8}$	0	3	0.5	−0.6
$\overline{10}$	0	3	2.3	2.9
$\overline{12}$	0	3	1.5	1.2
$\overline{14}$	0	3	0.9	1.4
$\overline{16}$	0	3	1.3	1.2
0	0	4	7.7	7.5
2	0	4	6.2	7.0
4	0	4	4.9	5.4
6	0	4	0.9	2.2
8	0	4	2.6	2.4
10	0	4	1.0	0.2
$\bar{2}$	0	4	16.1	16.5
$\bar{4}$	0	4	3.2	3.0
$\bar{6}$	0	4	16.6	15.8
$\bar{8}$	0	4	1.5	− 1.7
$\overline{10}$	0	4	8.1	7.3
$\overline{12}$	0	4	1.3	− 0.7
$\overline{14}$	0	4	2.7	2.2
$\overline{16}$	0	4	0.8	0.4
0	0	5	4.6	4.8
2	0	5	1.2	1.2
4	0	5	2.6	3.3
6	0	5	0.9	− 0.3
8	0	5	1.0	1.5
$\bar{2}$	0	5	5.7	6.2
$\bar{4}$	0	5	6.5	6.6
$\bar{6}$	0	5	10.0	9.9
$\bar{8}$	0	5	5.0	5.2
$\overline{10}$	0	5	7.9	6.9
$\overline{12}$	0	5	1.2	2.1
$\overline{14}$	0	5	4.5	3.1
$\overline{16}$	0	5	0.8	0.6
0	0	6	4.1	4.7
2	0	6	0.7	− 0.5
4	0	6	1.8	2.2
6	0	6	1.1	0.6
$\bar{2}$	0	6	1.8	− 2.7
$\bar{4}$	0	6	6.3	7.1
$\bar{6}$	0	6	0.6	− 0.7
$\bar{8}$	0	6	7.1	6.3
$\overline{10}$	0	6	2.0	2.5
$\overline{12}$	0	6	4.1	3.2
$\overline{14}$	0	6	3.1	3.0
$\overline{16}$	0	6	0.9	1.1
0	0	7	3.2	3.5
2	0	7	0.7	1.3
4	0	7	1.2	1.9
$\bar{2}$	0	7	0.5	0.1
$\bar{4}$	0	7	3.6	4.6
$\bar{6}$	0	7	0.6	− 1.0
$\bar{8}$	0	7	3.7	3.8
$\overline{10}$	0	7	0.7	− 0.2
$\overline{12}$	0	7	2.8	2.6
$\overline{14}$	0	7	0.6	0.7
$\overline{16}$	0	7	1.5	1.4
0	0	8	1.1	1.4
2	0	8	1.8	2.3
$\bar{2}$	0	8	3.1	3.8
$\bar{4}$	0	8	1.7	2.6
$\bar{6}$	0	8	2.3	2.9
$\bar{8}$	0	8	2.6	3.3
$\overline{10}$	0	8	0.7	0.1
$\overline{12}$	0	8	2.6	2.8
$\overline{14}$	0	8	0.6	− 0.3
$\overline{16}$	0	8	2.0	1.5
0	0	9	0.5	0.3
$\bar{2}$	0	9	1.5	2.6
$\bar{4}$	0	9	0.7	1.3
$\bar{6}$	0	9	3.0	3.3
$\bar{8}$	0	9	1.6	2.2
$\overline{10}$	0	9	2.0	2.4
$\overline{12}$	0	9	1.8	2.2
$\overline{14}$	0	9	1.0	1.1
$\overline{16}$	0	9	1.1	1.2
$\bar{2}$	0	10	0.7	0.2
$\bar{4}$	0	10	0.7	0.2
$\bar{6}$	0	10	1.5	1.9
$\bar{8}$	0	10	0.9	0.3
$\overline{10}$	0	10	2.3	2.6
$\overline{12}$	0	10	1.1	0.6
$\overline{14}$	0	10	2.0	2.0
$\bar{8}$	0	11	0.5	0.1
$\overline{10}$	0	11	0.7	1.2

$$R=\frac{\Sigma|\,|F_0|-|F_c|\,|}{\Sigma|F_0|}=0.133$$

Table II. (Continued)

0	k	l	$\|F_0\|$	F_c
0	2	0	19.0	18.3
0	4	0	20.7	20.5
0	6	0	10.2	10.0
0	8	0	4.4	4.9
0	10	0	4.2	3.4
0	0	1	17.3	16.8
0	2	1	14.1	13.6
0	4	1	9.4	9.0
0	6	1	5.6	5.8
0	8	1	3.4	3.4
0	10	1	1.4	1.8
0	0	2	11.7	−11.8
0	2	2	7.6	7.1
0	4	2	1.5	− 1.9
0	6	2	0.6	0.7
0	8	2	1.5	1.2
0	10	2	0.7	0
0	0	3	2.4	2.0
0	2	3	2.1	1.5
0	4	3	1.0	0.9
0	6	3	0.8	0.6
0	8	3	0.6	0.4
0	10	3	0.7	0.4
0	0	4	8.1	7.3
0	2	4	0.6	− 0.4
0	4	4	2.9	3.3
0	6	4	1.6	1.4
0	8	4	1.0	0.6
0	0	5	4.5	4.5
0	2	5	3.9	4.4
0	4	5	3.2	3.5
0	6	5	2.3	2.5
0	8	5	1.4	1.6
0	0	6	3.8	4.4
0	2	6	6.4	6.8
0	4	6	3.0	3.7
0	6	6	2.5	3.1
0	8	6	2.1	1.9
0	0	7	2.6	3.2
0	2	7	2.1	3.1
0	4	7	1.5	2.5
0	6	7	1.6	1.8
0	0	8	1.2	1.1
0	2	8	0.5	0.9
0	4	8	0.9	0.7

$$R = \frac{\Sigma|\,|F_0| - |F_c|\,|}{\Sigma|F_0|} = 0.088$$

the *a* axis were synthesized. After these procedures, the atomic parameters were finally determined as shown in the column "Weiss. photo." in Table I. These parameters are almost the same as those of $CoCl_2 \cdot 6H_2O$, except for *z* parameter for Cl^-. The value of *B* for Ni^{2+} was improved to be 2.0 Å^2 for $F(h0l)$'s and 2.4 Å^2 for $F(0kl)$'s, respectively. The reliability factors were 0.133 and 0.088 for all $(h0l)$ and $(0kl)$ structure amplitudes, for which the maximum observed values of $\sin\theta/\lambda$ were 0.8417 and 0.7804, respectively. The numbers of $(h0l)$ and $(0kl)$ reflections were 128 and 45, respectively. A comparison between observed and calculated structure factors is given in Table II. The Fourier projections finally synthesized are shown in Fig. 1 (a) and (b). The calculations of the final Fourier syntheses were carried out with PC–1 Parametron Computer of Tokyo University.

The schematic representation and the arrangement of atoms projected on (010) plane are shown in Fig. 2 and Fig. 3, respectively. As seen from these figures, $NiCl_2 \cdot 6H_2O$ is quite isomorphous with $CoCl_2 \cdot 6H_2O$. That is, two Cl^- ions and four water molecules are octahedrally coordinated to Ni^{2+} ion to form the group $[NiCl_2 \cdot 4H_2O]$ and these groups are joined with one another in parallel with the

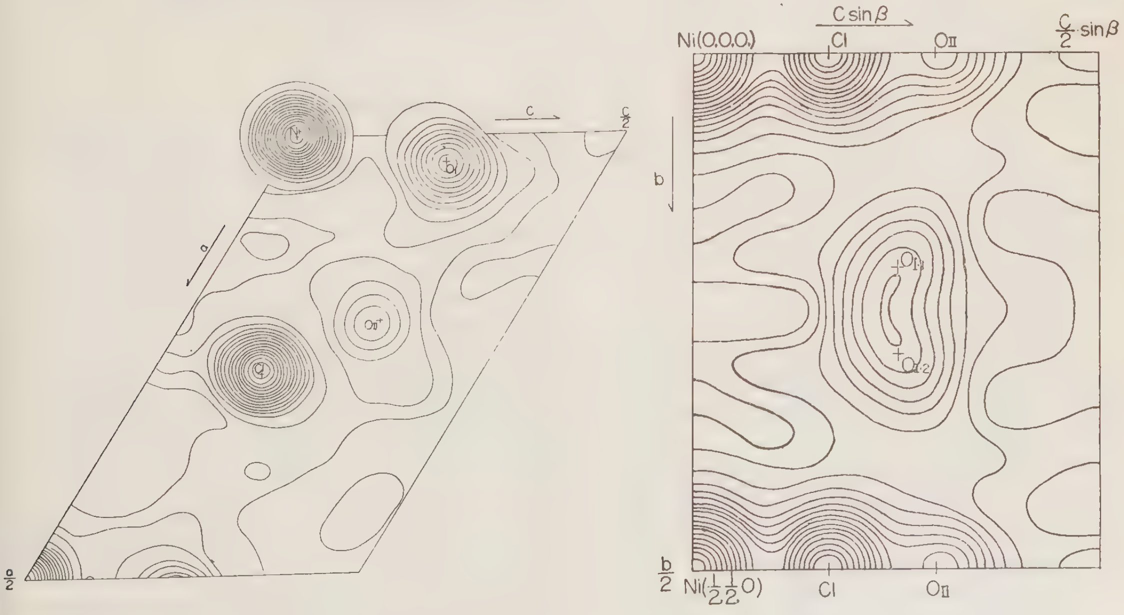

(a) (b)

Fig. 1. The final Fourier projections of electron density on (010), (a) and on a plane normal to the *a* axis, (b). Contours are drawn at intervals of 2*e* Å^{-2}. Co atom is contoured at intervals of 4*e* Å^{-2}. Crosses show the finalc atomi positions.

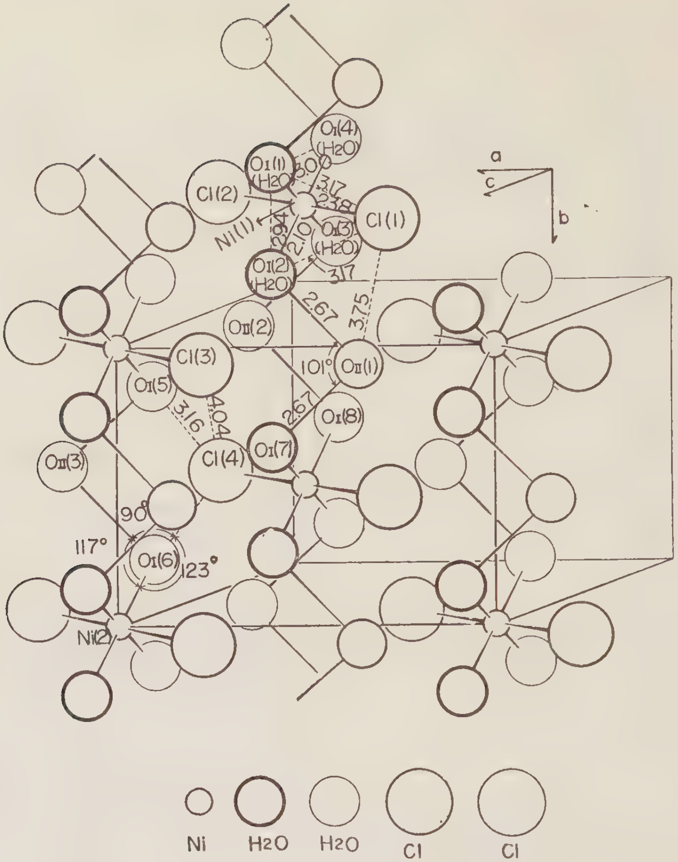

Fig. 2. The schematic representation of the crystal structure of $NiCl_2 \cdot 6H_2O$.

Tabl III. Interatomic distances (in Å) and interbond angles.

$NiCl_2 \cdot 6H_2O$		$CoCl_2 \cdot 6H_2O$	$NiCl_2 \cdot 6H_2O$		$CoCl_2 \cdot 6H_2O$
Refer to Fig. 2			Refer to Fig. 3		
Ni(1)-O_I(1, 2, 3, 4)	2.10	2.12	O_I(1)-O_I(2)	3.65	3.69
Ni(1)-Cl(1, 2)	2.38	2.43	O_I(1)-O_{II}(1)	3.11	3.14
Ni(1)-O_{II}(1)	4.05	4.07	O_I(2)-O_{II}(1)	3.75	3.77
O_I(1)-O_I(4)	3.00	3.05	Cl(1)-O_{II}(1)	3.43	3.48
O_I(1)-O_I(2)	2.94	2.94	Cl(2)-O_{II}(1)	3.16	3.20
Cl(1)-O_I(1)	3.17	3.22	O_{II}(1)-O_{II}(2)	4.22	4.26
O_I(2)-O_{II}(1) O_I(7)-O_{II}(1)	2.67	2.69	Ni(1)-O_{II}(2)	4.05	4.07
O_I(5)-Cl(4) O_I(6)-Cl(4)	3.16	3.17			
Cl(3)-Cl(4)	4.04	4.07			
Cl(1)-O_{II}(1)	3.75	3.77			
∠O_I(2)-O_{II}(1)-O_I(7)	101°	100°			
∠O_{II}(3)-O_I(6)-Ni(2)	117°	115°			
∠Cl(4)-O_I(6)-Ni(2)	123°	124°			
∠O_{II}(3)-O_I(6)-Cl(4)	90°	90°			

b axis by O···H–O type hydrogen bonds between O_I and O_{II}. The structure is also composed of atomic layers parallel to (001). Thus, the perfect cleavage parallel to (001) can reasonably be explained. In Table III, interatomic distances and interbond angles are given and for reference, data of $CoCl_2\cdot 6H_2O$ are added. As shown in Table III, interatomic distances are generally shorter than the corresponding ones of $CoCl_2\cdot 6H_2O$.

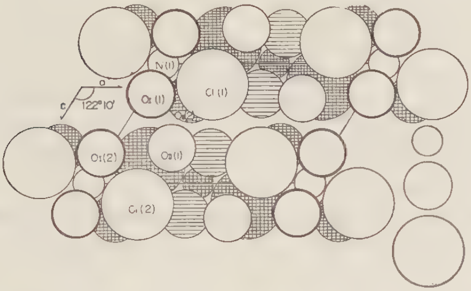

Fig. 3. The arrangement of atoms projected on (010).

§ 5. Discussion

In the structure analysis of $CoCl_2\cdot 6H_2O$, the most probable space group, $C^3_{2h}-C2/m$, was adopted, based on the Laue photograph taken with the radiation perpendicular to (100), the crystal form and the observed extinctions. The structure analysis was carried out and the decidedly reliable structure was found without any inconsistency. Thus, the space group, $C^3_{2h}-C2/m$, was correct for $CoCl_2\cdot 6H_2O$.

In the present study, the structure model was assumed for $NiCl_2\cdot 6H_2O$, based on the assumed space group and referring to the data of $CoCl_2\cdot 6H_2O$ and the analysis was carried out, using (*h*0*l*) and (0*kl*) data alone. Therefore, it must deliberately be examined whether the assumed structure model is correct or not, from the same reason as decribed in the previous paper[1]. Using sixty-one *F*(*h*1*l*)'s obtained from Weissenberg photographs in the present work, observed and calculated structure factors were compared with respect to the four kinds of the atomic arrangement, (I), (II), (III) and (IV) which were discussed on the structure determination on $CoCl_2\cdot 6H_2O$. In the arrangement (I), the reliability factor, *R* was 0.137. In the arrangement (II), *R* was 0.238 and the arrangements (III) and (IV) proved to be out of question. Thus, the structure model (I) and the space group, $C^3_{2h}-C2/m$, adopted for $CoCl_2\cdot 6H_2O$ was confirmed to be correct for $NiCl_2\cdot 6H_2O$, too. This result makes assurance for the present structure model doubly sure. A comparison between $|F_0|$ and F_c for the (*h*1*l*) reflections are given in Table IV.

Table IV. A Comparison between $|F_0|$ and F_c for the (*h*1*l*) reflections.

h	*k*	*l*	$\lvert F_0\rvert$	F_c
3	1	0	16.3	18.8
7	1	0	12.4	10.3
11	1	0	5.1	4.0
1	1	1	5.6	4.2
1	1	2	1.9	−2.5
1	1	3	6.1	5.4
1	1	4	13.0	12.0
1	1	5	6.0	6.8
1	1	$\bar{2}$	17.8	21.3
1	1	$\bar{3}$	9.8	9.9
1	1	$\bar{4}$	0	−0.3
1	1	$\bar{5}$	0	0.8
1	1	$\bar{6}$	2.6	3.3
1	1	$\bar{7}$	2.9	3.9
1	1	$\bar{8}$	2.2	3.2
3	1	1	12.1	11.6
3	1	2	9.7	8.8
3	1	3	5.2	5.2
3	1	$\bar{1}$	9.4	7.3
3	1	$\bar{2}$	8.7	−9.0
3	1	$\bar{3}$	4.1	3.6
3	1	$\bar{4}$	14.8	14.2
3	1	$\bar{5}$	9.3	9.5
3	1	$\bar{6}$	2.8	4.2
5	1	1	0	0.2
5	1	2	2.6	3.3
5	1	3	5.0	5.3
5	1	4	5.4	5.5
5	1	$\bar{1}$	12.2	11.9
5	1	$\bar{2}$	19.7	18.3
5	1	$\bar{3}$	10.0	8.5
5	1	$\bar{4}$	2.6	2.7
5	1	$\bar{5}$	2.0	2.2
5	1	$\bar{6}$	0.8	1.4
5	1	$\bar{7}$	2.5	3.3
5	1	$\bar{8}$	4.5	5.0
5	1	$\bar{9}$	2.2	3.0
7	1	1	7.1	6.9
7	1	2	2.1	2.7
7	1	$\bar{1}$	6.4	4.8
7	1	$\bar{2}$	1.4	−1.7
7	1	$\bar{3}$	0	1.7
7	1	$\bar{4}$	8.0	6.7
7	1	$\bar{5}$	9.2	8.2
7	1	$\bar{6}$	7.6	7.3
7	1	$\bar{7}$	2.0	3.0
9	1	1	0.	0.1
9	1	2	2.7	3.0
9	1	3	2.7	3.0
9	1	$\bar{1}$	4.5	4.7
9	1	$\bar{2}$	10.2	7.8
9	1	$\bar{3}$	7.4	6.6
9	1	$\bar{4}$	4.6	4.9
9	1	$\bar{5}$	2.2	2.5
9	1	$\bar{6}$	0	−0.2
9	1	$\bar{7}$	1.3	1.9
9	1	$\bar{8}$	4.5	4.4
9	1	$\bar{9}$	2.6	3.3
11	1	$\bar{5}$	5.2	4.6
11	1	$\bar{6}$	7.3	6.1
11	1	$\bar{7}$	2.8	3.0

$$R=\frac{\Sigma|\,|F_0|-|F_c|\,|}{\Sigma|F_0|}=0.137$$

The coefficient of the temperature factor, *B*, for Ni^{2+} ion, was differently assumed for *F*(*h*0*l*)'s and *F*(0*kl*)'s, which gave the highest reliability factor. A more precise experiment must be done, however, to examine whether this result is related or not to the fact that the four water molecules coordinated to Ni^{2+} ion are not strictly arranged in a square, but in a rectangle with two side lengths, 3.00 Å and 2.94 Å.

The interatomic distances are compared between $CoCl_2$, $CoCl_2\cdot 2H_2O$, $CoCl_2\cdot 6H_2O$ and $NiCl_2\cdot 6H_2O$ as follows:

	$CoCl_2$[9]	$CoCl_2 \cdot 2H_2O$[10]	$CoCl_2 \cdot 6H_2O$	$NiCl_2 \cdot 6H_2O$
Co(or Ni)–Cl	2.51	2.53, 2.54	2.43	2.38
Co(or Ni)–O		1.93	2.12	2.10
Cl–O		3.18, 3.19	3.22	3.17

The author wishes to express his sincere thanks to Professor S. Ogawa of the Research Institute for Iron, Steel and Other Metals, Tohoku Univ. for his continued encouragement throughout the present work. His hearty thanks are also due to Professor T. Sugawara of the Institute for Solid State Physics, Tokyo Univ. and Dr. T. Haseda, Mr. T. Ukei and Mr. T. Sato of the Research Institute for Iron, Steel and Other Metals, Tohoku Univ. for their valuable discussions and the preparation of the good single crystals. He is also indebted to Dr. Y. Takeuchi and the members of Professor R. Sadanaga's Laboratory, Tokyo Univ. for their aids in calculations using PC-1 Parametron Computer.

References

1) J. Mizuno: J. Phys. Soc. Japan **15** (1960) 1412.
2) T. Haseda and E. Kanda: J. Phys. Soc. Japan **12** (1957) 1051.
3) T. Haseda: J. Phys. Soc. Japan **15** (1960) 483.
4) T. Sugawara: J. Phys. Soc. Japan **14** (1959) 1248.
5) W. K. Robinson and S. A. Friedberg: Phys. Rev. **117** (1960) 402.
6) T. Haseda and M. Date: J. Phys. Soc. Japan **13** (1958) 175.
7) T. Haseda, H. Kobayashi and M. Date: J. Phys. Soc. Japan **14** (1959) 1724.
8) P. Groth: *Chemische Kristallographie*, **I** Teil (Wilhelm Engelmann, Leipzig, 1906) 248.
9) H. Grime and J. A. Santos: Zeit. Krist. **88** (1934) 136.
10) B. K. Vainstein: Doklady Akad. Nauk SSSR. **68** (1949) 301.

JOURNAL OF THE PHYSICAL SOCIETY OF JAPAN Vol. 16, No. 8, AUGUST, 1961

The Dynamic Bulk and Shear Viscosity of High Polymers, 1.

By Ryusuke KONO

Department of Applied Physics, Defence Academy,

(Received March 6, 1961)

The result of the transverse and longitudinal wave measurement on two groups of high polymers were presented as a function of temperature at frequency of 2.5 Mc. One group contains those polymers with no or slight steric hindrances, i. e. polyvinylchloride, vulcanized rubber and polytrifluoromonochloroethylene. The other includes the materials with strong steric hindrances i. e. polyethyl methacrylate, poly-n-butyl methacrylate and poly-i-butyl methacrylate.

The relaxation of shear deformation can be explained by the widely distributed relaxation times irrespective of the coupling between the molecules and the steric hindrance of side chain groups on the main chain. On the other hand, the relaxation of volume deformation depends on the intermolecular force and the steric hindrance. In poly-i-butyl methacrylate, the relaxation associated with volume deformation may be explained by the single relaxation theory.

§ 1. Introduction

In recent years an energy-dissipating process associated with volume deformation for high polymers has been studied by several workers. The information on this subject is rather contradictory for the primary dispersion region of high polymers. Marvin et al[1]. have found that the imaginary part of bulk modulus is of comparable order of magnitude with that of shear modulus, whereas Nolle and Sieck[2], Cunningham and Ivey[3] have claimed that the imaginary part of bulk modulus is much smaller than that of shear modulus. Recently Wada et al[4]. have arrived at a reliable conclusion that the imaginary part of bulk modulus in styrene-butadiene rabber was of the same order of magnitude as that of shear modulus, so that the prediction by Cunningham and Ivey might not be true in GR-S which is a sort of styrene-butadiene rubber.

The activation energies associated with volume and shear deformation have been found to be almost the same in polyisobutyrene. The curve of the imaginary part of bulk modulus against frequency or temperature is sharper than that of shear modulus in polyisobutyrene and butyl rubber. This means that distribution of the relaxation time associated with volume deformation is narrower than that with shear deformation. In case of polystyrene, on the other hand, it was reported in the previous paper[5] that the activation energy associated with volume deformation was somewhat larger than that associated with shear deformation, so that the molecular mechanism involved in the two types of deformation may be different. In polyisobutyrene there is, from stereochemical reasons, little steric hindrance of side chain groups on the main chain, while in polystyrene and polymethyl methacrylate there should be some steric hindrance of side chain groups. One might then expect some effect of the side chain on the volume and the shear deformation mechanisms.

It is the purpose of this work to present the results of the transverse and longitudinal wave measurements on high polymers as functions of temperature.

As usual, the propagation of longitudinal and transverse waves in a viscoelastic medium is described, if steady-state sinusoidal time dependence of stress and strain is achieved, by emloying the complex bulk modulus $K^* = K_1 + iK_2 = K_1 + i\omega\zeta$ and the complex shear modulus $G^* = G_1 + iG_2 = G_1 + i\omega\eta$, where ζ is the dynamic bulk viscosity, η the dynamic shear viscosity and ω the radian frequency. If the longitudinal-wave modulus is written as $M^* = M_1 + iM_2 = K^* + 4G^*/3$, the relations among the velocity, the attenuation and the modulus at a given radian frequency ω can be described as follows.

$$G_1 = \frac{\rho v_t^2 (1 - (\alpha_t^2 v_t^2/\omega^2))}{(1 + (\alpha_t^2 v_t^2/\omega^2))^2} \qquad (1)$$

$$G_2 = \frac{\rho v_t^2 (2\alpha_t v_t/\omega)}{(1 + (\alpha_t^2 v_t^2/\omega^2))^2} \qquad (2)$$

$$M_1 = K_1 + 4G_1/3 = \frac{\rho v_l^2 (1 - (\alpha_l^2 v_l^2/\omega^2))}{(1 + (\alpha_l^2 v_l^2/\omega^2))^2} \qquad (3)$$

$$M_2 = K_2 + 4G_2/3 = \frac{\rho v_l^2 (2\alpha_l v_l/\omega)}{(1 + (\alpha_l^2 v_l^2/\omega^2))^2} \qquad (4)$$

where v_l represents the velocity of longitudinal waves, v_t the velocity of transverse, α_l the attenuation of longitudinal waves, α_t the attenuation of transverses waves, and ρ the density. The values of G_1, G_2, K_1 and K_2 are calculable using the measurable values of ρ, v_l, v_t, α_l and α_t.

There is, however, a basic experimental difficulty in obtaining the data of K_2. The value of K_2 is derived from a comparison of the velocity and attenuation of shear waves and longitudinal waves. Since the attenuation of shear waves in polymers is generally very large, the observed values of velocity and attenuation are likely to include appreciable errors. When the value of G_2 is of the comparable size with M_2, probable error in the calculated values of K_2 for vulcanized rubber presented in this work amounts to 40 percent, K_2 being obtained as a combined result of shear and longitudinal wave measurements. When the values of G_2 is much smaller than M_2, as in the case of polystyrene and polymethyl methacrylate, probable error in K_2 is less than 10 percent. In this case the accuracy in K_2 and G_2 is sufficient to permit a more detailed evaluation as to the relations between the shear and volume deformation mechanisms.

The experimental apparatus here employed for the longitudinal and transverse wave measurement is the same as that reported in the previous paper[5]. Silicone oil and ethyl alcohol were used as transmission medium above and below the room temperature, respectively. The rate of heating was kept at about 15 deg/hr.

§ 2. Samples

Experiments were made on vulcanized rubber with 5 percent sulphur, polyvinylchloride (PVC), polytrifluoromonochloroethylene (Kel-F), polyethyl methacrylate (PEMA), poly-n-butyl methacrylate (PnBMA), poly-i-butyl methacrylate (PiBMA). The sample thickness of vulcanized rubber ranged from 0.03 to 0.5 cm. The composition of vulcanized rubber was 100 gr. Hevea smoked sheet and 5 gr. sulphur. The samples were cured for 120 minutes at 150°C±1°C. PEMA, PnBMA and PiBMA were prepared by block polymerization from carefully purified monomers. Original stocks were plates of 0.5 cm in thickness. The PVC and the Kel-F were supplied by Nagahama Plastic Company and Du Pond Chemical Company, respectively. Original stocks of each samples except vulcanized rubbers were annealed at 100°C for one hour and cut out from a common plate in order to reduce variation between samples. These samples were 0.05 to 0.5 cm in thickness.

§ 3. Results

In Figs. 1～6, K_1, K_2, G_1, and G_2 are plotted against temperature for vulcanized rubber, Kel-F, PVC, PEMA, PnBMA and PiBMA, respectively, calculated from the smoothed experimental results according to the relations (1), (2), (3) and (4). It was impossible to make any measurements for the shear wave in the region shown by the dotted line because of the high attenuation. The direct determination of the values of K_1 and K_2 in dotted line was impossible, but they can be determined since the longitudinal waves were measured throughout the temperature range covered, and since the values of G_1 and G_2 were very small in comparison with that of M_1 and M_2. In these figures it is obviously seen from the experimental results that an energy-dissipating process associated with volume deformation is found in all these polymers. The curves of K_2 and G_2 versus temperature all exhibit peaks in the temperature region studied. For vulcanized rubber, PVC and Kel-F the temperature at the peak of K_2 is almost the same as that of G_2, while for

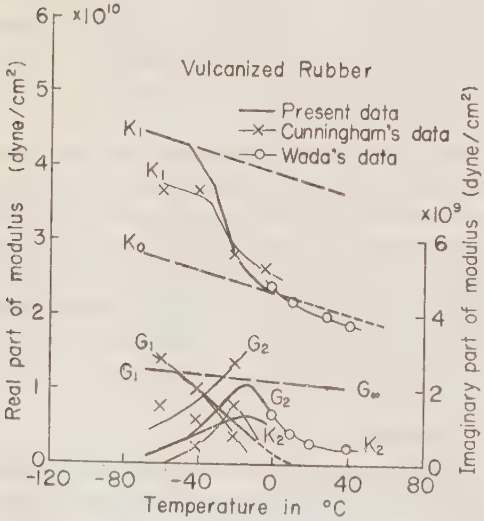

Fig. 1. Real and imaginary part of the shear and bulk modulus versus temperature for vulcanized rubber.

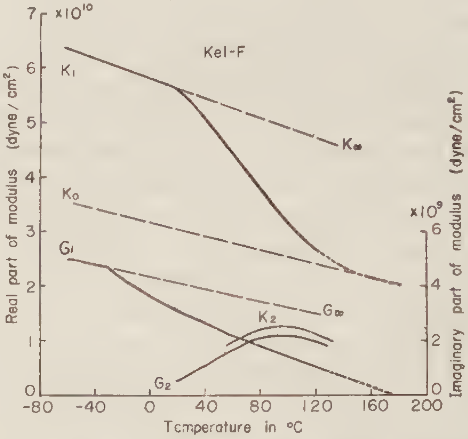

Fig. 2. Real and imaginary part of the shear and bulk modulus versus temperature for polytrifluoromonochloroethylene.

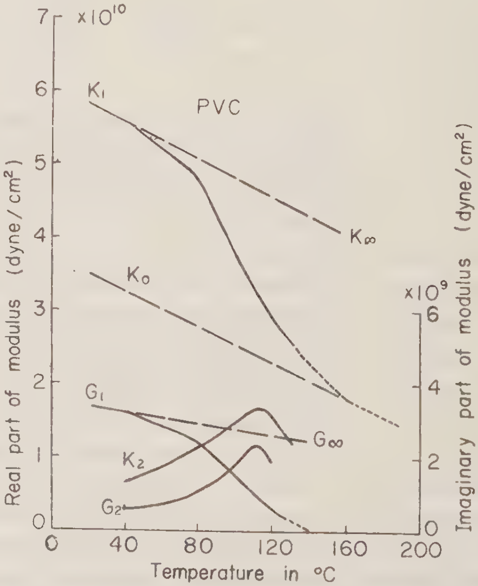

Fig. 3. Real and imaginary part of the shear and bulk modulus versus temperature for polyvinylchloride.

PEMA, PnBMA and PiBMA, the former is somewhat higher than the latter as shown in Fig. 4, 5 and 6.

The results of vulcanized rubber are shown in Fig. 1 together with Cunningham's[3] and Wada's[4] data. Above 0°C, the values of K_1 in the present work and Wada's work are in statisfactory agreement, with each other, whereas our K_2 is somewhat smaller than Wada's value. The values of G_2 of the present work is smaller than Cunningham's data and is rather comparable with their K_2. It may be safely said that the prediction of $K_2 \ll G_2$ might not be the cese, as already mentioned by Wada for GR-S.

It is obviously found from these experimental results that the temperature dependence of the molecular mechanism associated with volume deformation in vulcanized rubbers, PVC and Kel-F is very similar to that with the shear deformation, as is the case with styrene-butadiene rubber,[4] butyl rubber[3] and polyisobutyrene.[1]

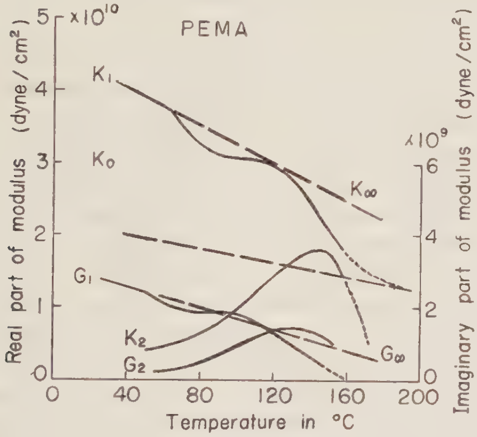

Fig. 4. Real and imaginary part of the shear and bulk modulus versus temperature for polyethyl methacrylate.

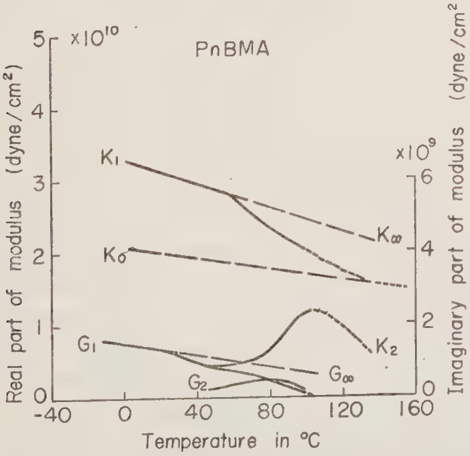

Fig. 5. Real and imaginary part of the shear and bulk moduls versus temperature for poly-n-butyl methacrylate.

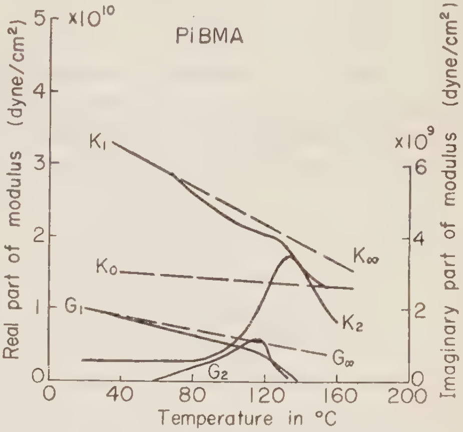

Fig. 6. Real and imaginary part of the shear and bulk modulus versus temperature for poly-i butyl methacrylate.

From the viewpoint of the chemical structure of these polymers, a coupling between the dipoles, crystallization or vulcanization contributes significantly to the cohesion, for substances where no or slight steric hindrance exists. As reported in the previous paper for polystyrene, the temperature at the maximum value of K_2 is higher than that of G_2 and the activation energy associated with volume deformation is larger than that of shear deformation. The molecular mechanisms involved in the two types of deformation are different. In these polymers they are subjected to steric hindrance by side chain groups on the main chain. It is expected that the difference between the volume and the shear deformation mechainisms might be related to steric hindrance, and so the methacrylate series were investigated.

Density, $T(K_{2m})$ and $T(G_{2m})$ versus numbers of side chain C-atoms in methacrylate series are shown in Fig. 7, where $T(K_{2m})$ and $T(G_{2m})$ represent the temperatures at the maximum value of K_2 and G_2, respectively. The dashed portions of the curves indicate the data for the case of isobutyl group. Density decreases with increasing number of side chain C-atoms. The values of K_1 and G_1, $T(K_{2m})$ and $T(G_{2m})$ decrease with increasing length of side chain except PiBMA. One get $T(K_{2m}) \fallingdotseq T(G_{2m})$ in Fig. 7, extraporating to zero side chain C-atom, where no or slight steric hindrance exists. $T(K_{2m})$ is less dependent on length of side chain than $T(G_{2m})$. The difference between $T(K_{2m})$ and $T(G_{2m})$ increases with increasing length of the side chain. Thus it is expected that the intramolecular degrees of freedom associated with volume deformation are more decreased by length of the side chain than those associated with shear deformation.

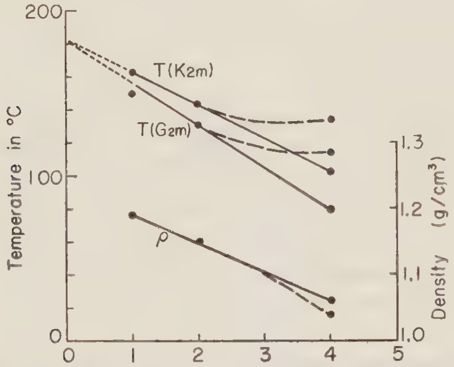

Fig. 7. Density, $T(K_{2m})$ and $T(G_{2m})$ versus numbers of side chain C- atoms for methacrylate series.

§ 4. Discussion

Eyring[6] has proposed a hole theory of liquids which has been very successful in explaining experimental data and has had great influence on theoretical considerations of the viscosity. The problem of shear viscosity is fundamentally the same for long-chain polymers as for simple liquids unless the cooperative movements between the molecules exist. Long chain molecules are flexible and can take up many different shapes and each segments in the long chain molecules have individual relaxation times, so that relaxation times for shear viscosity should be widely distributed. When a shearing stress is put on such a molecule, segments of the molecule connected by chemical-bonds are forced to move cooperatively. Thus they are transformed from one configuration to another configuration. A model in such a case is schematically shown in Fig. 8a, where ● represents a segment and ○ a hole. Through a number of successive segmental jumps the resultant movement of the molecule as a whole is accomplished. These segmental jumps caused by the application of a shearing stress produce a shear deformation. On the other hand when an external pressure is applied to these molecules as shown in Fig. 8b, only several segments of the molecule arround the hole will be locally displaced due to rearrangement of the segments. Hence, in the case of bulk viscosity, the difference between long chain polymers and simple liquids is expected to be much less than in the case of shear viscosity, as pointed out by Hirai and Eyring.[7] Therefore in the case of bulk viscosity, K_2 in dependence on frequency or temperature is expected to be explained by a single relaxation theory.

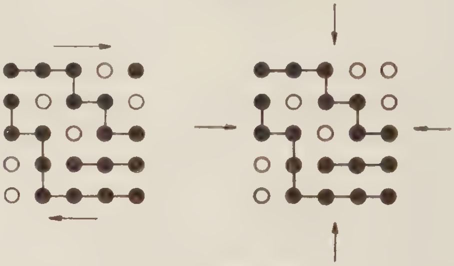

Fig. 8. A model for shear deformation (a) and volume deformation (b) in long-chain polymer.

When a distribution of relaxation times exists for the shear and bulk relaxation processes, the expressions for G_1, G_2, K_1 and K_2 are given as follows (cf. Litovitz[8]):

$$\frac{G_1}{G_\infty}=\int_0^\infty \frac{\omega^2\tau_s^2 g(\tau_s)d\tau_s}{1+\omega^2\tau_s^2}\equiv I(G_1) \qquad (5)$$

$$\frac{G_2}{G_\infty}=\int_0^\infty \frac{\omega\tau_s g(\tau_s)d\tau_s}{1+\omega^2\tau_s^2}\equiv I(G_2) \qquad (6)$$

$$\frac{K_1-K_0}{K_\infty-K_0}=\int_0^\infty \frac{\omega^2\tau_v^2 k(\tau_v)d\tau_v}{1+\omega^2\tau_v^2}\equiv I(K_1) \qquad (7)$$

$$\frac{K_2}{K_\infty-K_0}=\int_0^\infty \frac{\omega\tau_v k(\tau_v)d\tau_v}{1+\omega^2\tau_v^2}\equiv I(K_2) \qquad (8)$$

Here G_∞ is the shear modulus in the high frequency or in the glassy state, $G_\infty g(\tau_s)d\tau_s$ the contribution to the shear modulus by those molecules which have relaxation times in a range $d\tau_s$ near τ_s, K_∞ the bulk modulus in the high frequency or in the glassy state, K_0 static bulk modulus or bulk modulus in flow state, $(K_\infty-K_0)k(\tau_v)d\tau_v$ the contribution to the high frequency bulk modulus of those molecules having individual relaxation time in a range $d\tau_v$ near τ_v. $g(\tau_s)$ and $k(\tau_v)$ are the distribution functions of shear and volume deformation, respectively.

If one assumes a Gaussian distribution, one can show that for $\omega\tau'_s=\omega\tau'_v=1$,[9] i. e., at the maximum value of G_2 and K_2

$$I(G_1)=I(K_1)=\frac{1}{2} \qquad (9)$$

$$I(G_2)<\frac{1}{2},\ I(K_2)<\frac{1}{2} \qquad (10)$$

where τ_s' and τ_v' determine the position of the maximum of the distribution and represent the most probable relaxation times. The narrower the distribution of relaxation times, the larger becomes the maximum value of $I(G_2)$ and $I(K_2)$, approaching to the maximum value 1/2 of the single relaxation process.

The values of $I(G_1)$, $I(G_2)$, $I(K_1)$ and $I(K_2)$ in PVC, vulcanized rubber and Kel-F are plotted against temperatures in Fig. 9. In these polymers, it is to be seen that $T(K_{2m})\doteqdot T(G_{2m})$ and the maximum value of $I(K_2)$ and $I(G_2)$ are 0.15. The value of $I(K_1)$ and $I(G_1)$, $I(K_2)$ and $I(G_2)$ are almost the same throughout the temperature region studied. Thus it can be expected in the case of PVC that volume deformation mechanism becomes closely related to shear deformation mechanism. These circumstances may be explained as follows. When external pressure is applied as shown in Fig. 8b, the process of the rearrangement of molecules consists of combined elemental processes, each elementary process being very similar to that in shear viscosity. The combined process consists of movements of several segments arround a hole. The displacement of one segment to the hole has a great influence upon the motion of the neighbouring segments and the cooperative movement may take place due to a strong coupling of the molecules in PVC.

As shown in Fig. 9, the value of $T(K_{2m})$ is almost the same as that of $T(G_{2m})$ in Kel-F and vulcanized rubber. The relation (9) nearly holds true at the temperature of $T(K_{2m})$. This suggests that the activation energy in shear deformation is almost the same as that in volume deformation and $g(\tau_s)$ and $k(\tau_v)$ might be Gaussian distribution functions. On the other hand, temperature dependence of $I(K_2)$ is different from that of $I(G_2)$. The former is dependent more strongly on temperature than the latter. So relaxation times associated with volume deformotion may probably be distributed over narrower region than that

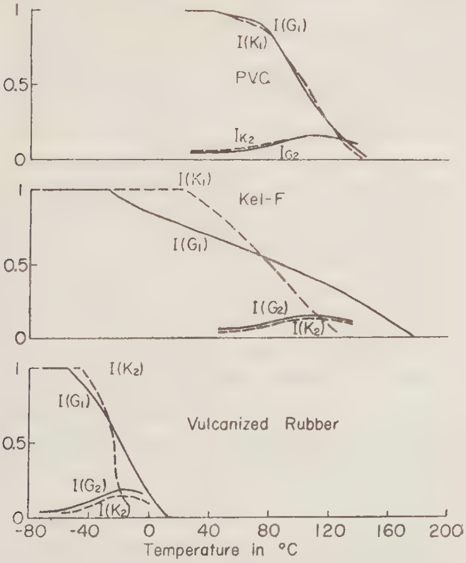

Fig. 9. The relaxational part of the bulk and the shear modulus versus temperature for polyvinylchloride, polytrifluoromonochloroethylene and vulcanized rubber

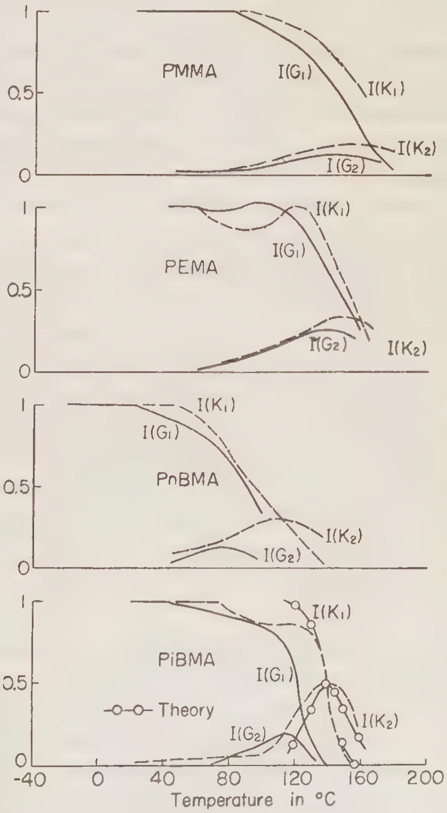

Fig. 10. The relaxational part of the bulk and the shear modulus versus temperature for methacrylate series

with shear deformation. Moreover the lower values of $T(K_{2m})$ and $T(G_{2m})$ in Kel-F and vulcanized rubber than in PVC, may be ascribed to the weaker coupling of the molecules in vulcanized rubber and Kel-F than in PVC. The weaker the coupling of the molecules, the more the volume deformation mechanism may be different from the shear deformation mechanism. This situation is much remarkable in the cases of polystyrene and methacrylate series where strong steric hindrances exist.

The value of $I(G_1)$, $I(G_2)$, $I(K_1)$ and $I(K_2)$ in methacrylate series are plotted against temperatures in Fig. 10. Although the maximum values of $I(G_2)$ in methacrylate series are almost the same, the maximum values of $I(K_2)$ increase towards the maximum value of 1/2 with increasing number of side chain C-atoms. The curve of $I(K_2)$ versus temperature in PiBMA approaches to the shape predicted by the single relaxation theory using the experimental value of activation energy 30 Kcal/mol.[10] This result probably means that no or slightly cooperative motion between the segments takes place in the case of volume deformation. Thus only several segments of the molecule arround a hole are displaced when external pressure is applied to those molecules of PiBMA as shown in Fig. 8b.

In these polymers studied, the relaxation of shear deformation is explained by the widely distributed relaxation times irrespective of the coupling of the molecules and the steric hindrance of side chain groups. On the other hand relaxation of volume deformation depends on the intermolecular force and the steric hindrance of side chain groups. The volume deformation becomes more different from the shear deformation with increasing length of side chain groups in methacrylate series.

§ 5. Conclusion

From the foregoing consideration, it seems reasonable to conclude as follows

1) The value of K_2 is of comparable size with G_2 and an energy dissipating process associated with volume deformation is found in all the polymers studied. It may be safely side that the prediction of $K_2 \ll G_2$ by Cunningham is not valid for vulcanized rubber.

2) The difference between $T(K_{2m})$ and $T(G_{2m})$ increases with increasing length of the side chain methacrylate series. Thus it is expected that intramolecular freedom associated with volume deformation is more restricted by the existence of the side chain than that associated with shear deformation.

3) The volume deformation mechanism is different from the shear deformation mechanism. The difference between the two types of deformation may be explained by the hole theory. In the case of shear deformation, the resultant movement of a molecule due to a large number of successive segmental jums to a hole is important. On the other hand, in the case of volume deformation, several segments of the molecules arround a hole are displaced, so that the hole plays an important role. In PiBMA the curve of relaxational part of bulk modulus versus temperature approaches to the shape predicted by the single relaxation theory.

Acknowledgements

I wish to express my sincere gratitude to Dr. N. Hirai of Okayama University, not only for the discussion of the problem, but also for his criticism and encouragement. Thanks are also due to Professor K. Shimo and Professor A. Soeya of Defence Academy for some valuable suggestions. The aid of Mr. I. Aoe at the Institute of Dainihon Gum in obtaining the sample of vulcanized rubber is gratefully acknowledged. Mr. Y. Yatabe at Nihon Kogaku Plastic Co. furnished the sample of methacrylate series, for which I thank him.

References

1) R. S. Marvin, R. Aldrich and H. S. Sack: J. Appl. Phys. **25** (1954) 1213
2) A. W. Nolle and P. W. Sieck: J. Appl. Phys. **23** (1952) 888
3) J. R. Cunningham and D. G. Ivey: J. Appl. Phys. **27** (1956) 967
4) Y. Wada, H. Hirose, H. Umebayashi and M. Otomo: J. Phys. Soc. Japan **15** (1960) 2324
5) R. Kono: J. Phys. Soc. Japan **15** (1960) 718
6) H. Eyring: J. Chem. Phys. **4** (1936) 283. W. Kauzman and H. Eyring: J. A. S. A. **62** (1940) 3113
7) N. Hirai and H. Eyring: J. Appl. Phys. **29** (1958) 810; J. Polymer Sci. **37** (1959) 51
8) R. Piccirelli and T. A. Litovitz: J. A. S. A. **29** (1957) 1009
9) W. A. Yager: Physics **7** (1936) 434
10) R. Kono: to be published.

Journal of the Physical Society of Japan Vol. 16, No. 8, August, 1961

Ionization Efficiency Curves for A^+, Kr^+, N_2^+, and CO^+ by Electron Impact

By Yozaburo Kaneko

Department of Physics, Faculty of Science, Tokyo Metropolitan University,
Setagaya, Tokyo

(Received April 10, 1961)

The shape of ionization efficiency curves (I. E. curves) obtained by essentially monoenergetic electron is studied by means of the threshold law. In the I. E. curves for N_2^+ and CO^+, some humps which are attributed to autoionization processes are found. These processes occur at 16.2 ± 0.1 eV for N_2^+ and at 15.6 ± 0.1 eV and 18.4 ± 0.1 eV for CO^+. Though the shape of I. E. curve for Kr^+ obtained in this work is similar to that of Fox et al and Frost et al, it is difficult to interpret this shape by autoionization process only. The I. E. curve for A^+ shows large tailing of 0.50 ± 0.05 eV which can not be explained by doublet of ground state of A^+. The ionization potentials determined for rare gases and some diatomic molecules agree well with spectroscopic values and the previous electron impact data.

§1. Introduction

In ionization process by electron impact, the curve representing the variation of ion current as function of energy of ionizing electron is called "Ionization Efficiency curve (I. E. curve)"[1]. A number of studies on the shape of the I. E. curve near threshold have been made recently. Theoretical investigations of the threshold law of I. E. curve were made by Wigner[2], Wannier[3], Geltman[4], and Morrison[5].

In an experimental investigation of the I. E. curve, it is very powerful to use monoenergetic electron beam. Fox, Hickam, Kjeldass, and Grove[6,7] developed an experimental technique, so-called R. P. D. method, in which ionization is made by essentially monoenergetic electron. From the experiments on I. E. curves of rare gases, Fox deduced the following rules; the probability of single ionization near the threshold is proportional to the excess electron energy, and the probabilities for various ionization processes can be superposed independently. The R. P. D. method has been used by several investigators and brought many successful results in the study of fine structure of I. E. curves.

On the other hand, Morrison[8] proposed a method to measure the first differential of I. E. curve directly. It is thought that the method has an advantage to separate different processes superposed, because a differentiation makes a break in I. E. curve prominent. By use of this method, autoionization process in the ionization of N_2 was detected by Dorman, Morrison and Nicholson[9]. This process was not observed by Fox et al[10], and Frost and McDowell[11] by the use of R. P. D. method. In fact, as most I. E. curves consist of more than two processes, they must be analyzed carefully.

In this report, the I. E. curves for A^+, Kr^+, N_2^+ and CO^+ obtained by R. P. D. method are analyzed by means of threshold law, and the results obtained are compared with that of the other workers.

§2. R. P. D. Method

The principle of R. P. D. method which was developed by Fox et al is described briefly in this section. By using R. P. D. method though a monoenergetic electron beam is not produced actually, substantially the same effect is obtained in ionization as by a monoenergetic electron beam.

There is an electrode in the path of electron beam. By applying a retarding potential to this electrode, a part of electrons which has smaller kinetic energy than this potential is prevented from passing through the electrode. Ionization is made by the other part of electrons which has passed through the electrode, being accelerated by the potential Va between tihs electrode and the ionization chamber.

Now, by varying the retarding potential by a small amount of ΔV_R, "difference ion current ΔI" is obtained in correspondence to this ΔV_R. The difference ion current ΔI should be essentially the same to the ion current which would be obtained by the electron beam having an energy of Va and an energy width of ΔV_R. Thus, the method is called "Retarding Potential Difference Method (R. P. D. method)".

Strictly speaking, Fox's method is a combination of R. P. D. method and the pulsing method which will be described in section 3. However, the term "R. P. D. method" is often used in the same meaning as Fox's method.

§ 3. Apparatus and Experimental Procedure

The mass spectrometer used in this experiment is of a 90° sector type, and the ion orbit radius is 11.5 cm. R. P. D. method is used for ion source of this mass spectrometer, so that ionization may essentially be effected by monoenergetic electron. Electrodes of the ion source, however, are somewhat different from Fox's ion source. Details of this apparatus were described elsewhere[12].

A schematic diagram of the ion source and the control circuit is shown in Fig. 1. There are three electrodes between filament and the ionization chamber. The slits in electrodes 1, 2 and 3 are 1 mm wide and 3 mm long, and the entrance slit of the ionization chamber 4 is 0.5 mm wide, 3 mm long, and 1 mm deep. In order to avoid immersion field, all of the slits are covered with tungsten nets which are 140 mesh/inch (56 mesh/cm). The electrodes are gold plated to prevent the contact potential. Retarding potential is applied to the electrode 3, and electron accelerating voltage is applied between this electrode and the ionization chamber. The value of ΔV_R, namely, energy width of ionizing electron, can be selected as any value, and is usually decided as 0.1 eV.

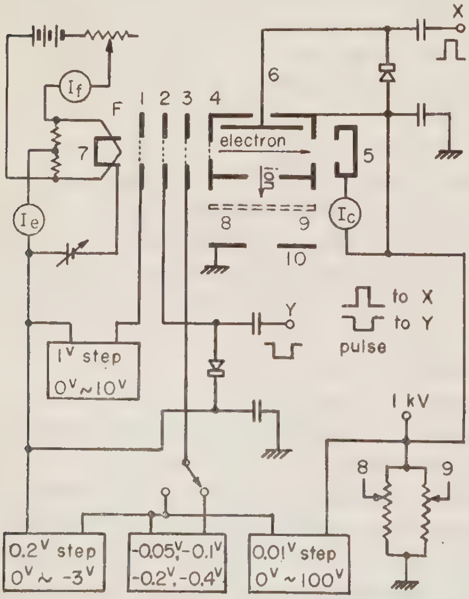

Fig. 1. A schematic diagram of the ion source and the control circuit.

In the previous study[12], characteristics of this ion surce were studied and an adequate operating condition was found. For example, when potentials of the electrodes 1, 2 and 3 measured from the filament are 2 V, 0 V and -0.8 V respectively, and ΔV_R is selected as 0.1 eV, difference ion current becomes 15% of total ion current. This efficiency is three times as good as that of the other workers[7], and increases signal to noise ratio relatively. There is an ion repeller electrode 6 in the ionization chamber. Generally, ion repelling voltage disturbs the energy distribution of electrons greatly. Two synchronized square wave pulses as shown in Fig. 1 are applied to the electrode 2 and the ion repeller electrode in order to make ionization in field free space. To determine the ionization potential, energy scale must be corrected, but the correction in this experiment is always less than 0.2 eV for fresh electrodes.

The combination of secondary electron multiplier and Barth's circuit electrometer with UX-54, or sometimes the electrometer solely, is used for ion current detector. The multiplier is an Inghram type and consists of fifteen dinodes of Ag-Mg (Mg 1.7%). The total gain is 5×10^5 for total voltage of 4.5 KV applied, and the noise level at no-signal is found to be 2×10^{-17} A. The galvanometer connected to the output of the electrometer has a zero point compensation circuit, so that difference ion current may be measured in full scale.

It is important to keep the "effective" number of ionizing electron constant when electron accelerating voltage is varied. As ions detected at the collector of mass spectrometer seems to be made at a very small part in the ionization chamber, electrons only which pass through this part could be "effective". It is very difficult to examine experimentally that the "effective" number of electron is kept constant. For example, to keep electron collector current constant not always means to keep "effective" number of electron constant. However, in the previous study, it was found that the "effective" number of electron seems to be almost constant in the energy range of 10 V between the accelerating voltage of 10 V and 100 V, though it is not accurate in larger range. For more precise study, it is necessary to measure simultaneously the I. E. curves of the sample gas and referring gas of which I. E. curve lies in the same energy range. In this experiment, the measurements were made for A and N_2, CO and Kr simultaneously. Pressure of the gases was controled as to obtain almost the same slope for each I. E. curve. All of the curves were measured more than ten runs. Though the ion source was dismantled to refresh the electrodes several times through the experiment, the typical shapes of I. E. curves which are described in section 4 did not change. The sample gases used in this experiment are purest in commercial grade, and are not refined specially.

§ 4. Experimental Results and Discussion

A^+

As the difference of ionization potential between A and N_2 is only about 0.2 eV, the shapes of I. E. curves particular to these two gases can be obtained without instrumental effects, by introducing the two gases into the mass spectrometer simultaneously. The curve is shown in Fig. 2.

Fox, Hickam, Kjeldaas and Grove⁶⁾ applied for the first time the R. P. D. method to A^+ and found that it is linear in the range of about 1.5 eV above threshould. Cloutier and Schiff¹³⁾, measuring I. E. curve for A^+ by means of the modified R. P. D. method, reported that it is quite linear in the range of about 2.5 eV above threshold and that the effect of doublet of the ground state of A^+ on the I. E. curve is too small to be detected. In this experiment, however, the I. E. curve for A^+ shows a large tailing below 17.2 eV though it is linear at higher energy. This is quite different from the results of Fox et al and Cloutier et al. In this experiment, the difference between initial onset of the curve and the crossing point of energy axis and extension of linear part is measured to be 0.50±0.05 eV*, and the difference between the initial onset and the position where the curve deviates from linear part is 1.6±0.1 eV*.

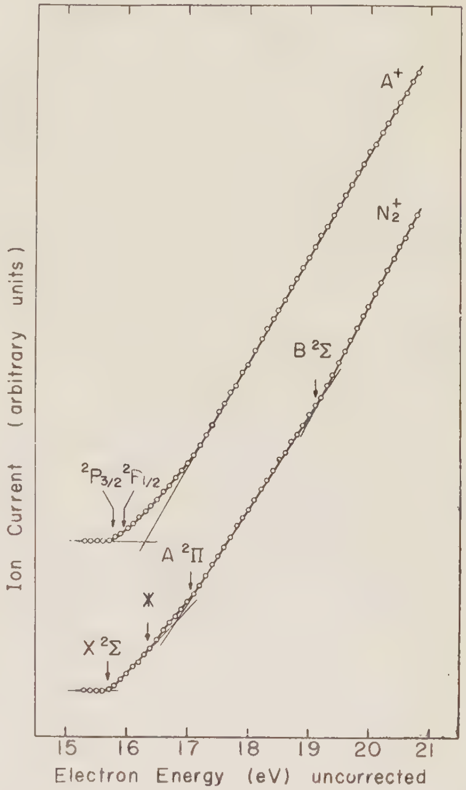

Fig. 2. I. E. curves for A^+ and N_2^+. Arrows indicate the positions where successive ionization processes occur.

The possible causes of this tailing of I. E. curve for A^+ could be instrumental and/or essential. There could be the following three factors in the instrumental effect on the I. E. curve:

1. thermal energy distribution of electron emitted from hot filament,
2. immersion field of ion accelerating voltage penetrating into ionization chamber, and
3. variation in number of effective ionizing electron.

The first factor of thermal energy distribution would not be larger than 0.05 eV, provided that the experiment is made by means of the R. P. D. method using $\Delta V_R=0.1$ eV. There is little possibility that the second factor, though emphasized by Cloutier[13], has an effect on this curve, because in addition to that the pulsing method is used in ion repeller voltage to make ionization in field free space, the ion focusing half plates 8 and 9 in Fig. 1 are at the same potential as the ionization chamber at the expense of focusing efficiency. Furthermore, both the facts that initial onset of the curve almost constantly appears at 15.7 eV nearly similar to the ionization potential for A^+ without correction of energy scale, and that a distinctly fine structure is found at N_2^+ curve, show electron energy spread is negligibly small. There is no way to examine the third factor experimentally. The N_2^+ curve measured simultaneously, however, does not show a tail as seen in the A^+ curve, and resembles those obtained by the other workers[10]. Granting that this I. E. curve for A^+ is caused by some experimental factor, if the curve was tried to be corrected linear by using a suitable normalizing function, the N_2^+ curve then would be a quite strange one. From these considerations, the shape of I. E. curve for A^+ seems not to be instrumental but substantial.

---

* These values are corrected by effect of 0.1 eV of electron energy spread.

Though ground state of A^+ is doublet of $^2P_{3/2}$ and $^2P_{1/2}$, this cannot be a cause of the tailing, because separation of this doublet is only 0.18 eV. Any excited state is not known for more than 13 V above the ground state. No conclusion, therefore, can be deduced on the tailing of I. E. curve for A^+. It should be remarked, however, that Stevenson and Hipple[14] found that A^+ has a longer tail by 0.3 eV than Ne^+ in their measurement using electron of wide energy spread, and that Mariner and Bleakney[15] pointed out that this difference cannot be explained by doublet of ground state of A^+.

N_2^+

Three distinct breaks are observed in the N_2^+ curve, and the curve between these breaks is nearly linear. These breaks are considered to correspond to ionization to $X\,^2\Sigma$, $A\,^2\Pi$ and $B\,^2\Sigma$ state of N_2^+, and their ionization potentials, as shown in Table I, agree well with the spectroscopic values and the electron impact values obtained by Frost and McDowell[11]. Though Frost reported a large break corresponding to $C\,^2\Sigma$ at 23.53 eV, the I. E. curve for N_2^+ increases almost linearly up to 25 eV as well as A^+ and does not show such a large break in this experiment. Relative ionization probabilities to each state calculated from gradient of each linear part differ remarkably from the value of Frost and McDowell, as shown in Table II.

Table I. Threshold values for ionization processes for N_2^+ (eV).

Energy states	This work	Previous electron impact values a	Photo-ionization values b	Spectro-scopic values c
$X\,^2\Sigma$	15.63±0.02	15.63	15.6	15.56
*	16.2 ±0.1	—	(16.2)	—
$A\,^2\Pi$	17.00±0.05	16.84	16.9	16.93, 16.69
$B\,^2\Sigma$	18.94±0.06	18.76	18.8	18.75
	—	—	20.7	—
$C\,^2\Sigma$	—	23.53	—	23.58

a: reference (11).
b: reference (18).
c: reference (20).

Table II. Relative ionization probabilities for N_2^+.

	This work	Fox et al[10]	Frost et al[11)a]
$I(A\,^2\Pi)/I(X\,^2\Sigma)$	0.5_0	0.2_0	~ 6
$I(B\,^2\Sigma)/I(X\,^2\Sigma)$	0.4_0	0.5_5	~ 4
$I(C\,^2\Sigma)/I(X\,^2\Sigma)$	—	—	~36

a: calculated by the author from Fig. 3. of reference (11).

The points measured deviate above from the linear curve at about 16.5 eV. This part is demonstrated with expanded scale in Fig. 3**b**. The length of vertical lines indicates the amount of mean deviation of the points measured. The hump of the curve is thought to correspond to the autoionization process pointed out by Dorman et al[9]. Autoionization is the ionization caused by radiationless transition to an ionic state from an excited state of molecule which lies above ionic state, for example:

$$N_2+e \longrightarrow N_2^*+e, \quad N_2^* \longrightarrow N_2^+ +e\ .$$

Morrison[5,9] suggested that the threshold law for excitation process should be a step function or proportional to square root of excess energy. Provided that probability of single ionization is linear to excess electron energy, and each process is superposed independently, the I. E. curve theoretically predicted should be as shown in Fig. 3**a**. The first ionization begins at the point O, the autoionization begins at P, and the second ionization begins at R in the theoretical curve. The solid line iodicates a step function law and the dotted line, a square root law. The curve **a** and **b** in Fig. 3 are in a very good correspondence. The results of the experiment fit the square root law better than the step function law, but a positive conclusion cannot be drawn from this owing to scattering of measured points. Fig. 3**c** is I. E. curve for N_2^+ obtained by Clarke[16] using a mass spectrometer which has an electron energy selector in the ion source. Fig, 3**d** is integration by the author of Dorman's first differential I. E. curve for N_2^+[9]. They resemble much in shape. It is no wonder that Dorman's curve has a large tailing, in proportion to a large energy spread of electron. What should be surprising is that a fine structure can be detected by the method of Dorman et al. even using electron of so large energy spread. A structure corresponding to this process is not found in the I. E. curves by Fox et al.[10], Frost et al.[11] and Cloutier et al[14].

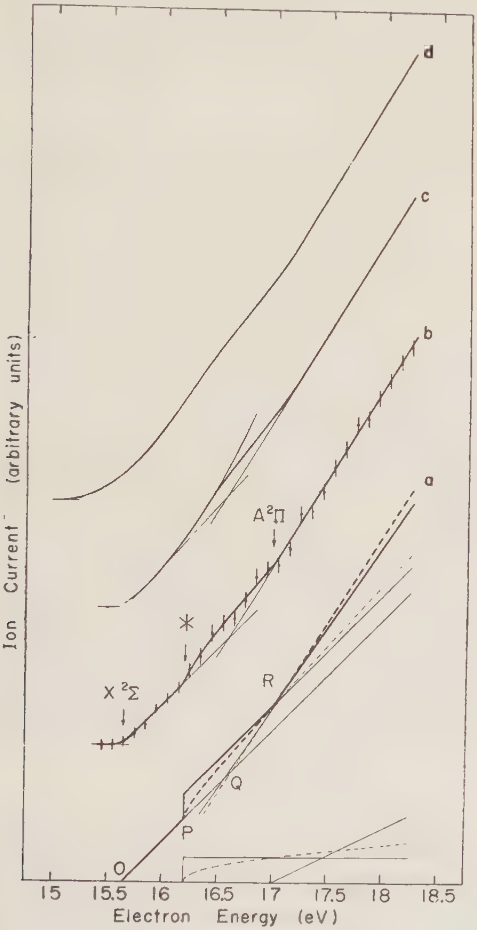

Fig. 3. Comparison between the theoritical and experimental I. E. curves for autoionization process in N_2^+. Curve **a** is theoretically predicted I. E. curve, the solid line indicates a step function law and the dotted line, a square root law. Curve **b** is experimental I. E. curve in the present work, and length of vertical lines indicate the amount of mean deviation of measured points. Curve **c** is experimental I. E. curve obtained by Clarke. Curve **d** is I. E. curve calculated from Dorman's first differential I. E. curve by integration.

As deduced from the above considerations, the second ionization potential should not be a crossing point, Q, of extensions of two linear parts but R in Fig. 3**a**. Each threshold value determined by referring to Fig. 3**a** is shown in Table 2. This seems to be more reasonable than Clarke's explanation that the shape of N_2^+ curve is due to excitation to vibrational states of N_2^+, and the second ionization potential is defined as a crossing point of the extensions of linear parts.

CO^+

CO^+ is similar to N_2^+ in electron configura-

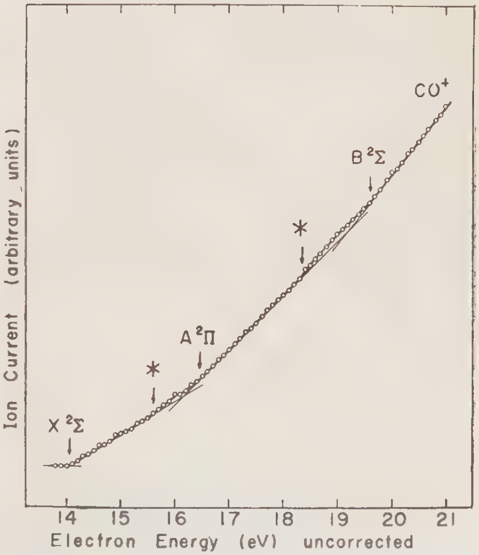

Fig. 4. I. E. curve for CO^+. Arrows indicate the positions where successive ionization processes occur.

tion. Fox, Hickam and Kjeldass[10] reported an autoionization process of CO at about 19 eV. The I. E. curve obtained is shown in Fig. 4. The I. E. curve for CO^+ may be divided into three linear parts as N_2^+. Deviation of the measured points from the linear curve can be observed also at about 16 eV in addition to about 19 eV. From the same analysis as used for N_2^+, it proved that autoionization processes occur at 15.5±0.1 eV and 18.5±0.1 eV. Each of the threshold values shown in Table III, agree satisfactorily with the spectroscopic value and Weissler's[18] value by photoionization.

Table III. Threshold values for ionization processes for CO^+ (eV).

Energy states	This work	Previous electron impact values a	Photo-ionization values b	Spectro-scopic values c
X $^2\Sigma$	14.11±0.03	14.1	13.9	14.01
*	15.6±0.1	—	15.5	—
A $^2\Pi$	16.5±0.1	16.5	16.6	16.53
*	18.4±0.1	—	18.4	—
B $^2\Sigma$	19.6±0.1	19.0	20.1	19.67

a: calculated by the author from reference (10) correcting X $^2\Sigma$ state to be 14.1 ev.
b: reference (18).
c: reference (17).

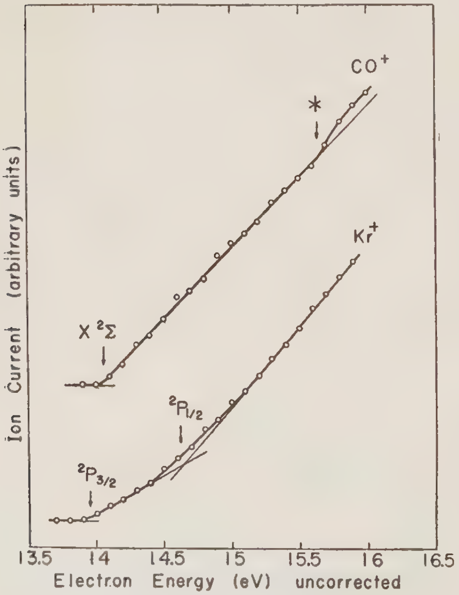

Fig. 5. I. E. curve for Kr^+. The curve for CO^+ is superposed for reference. Arrows indicate the positions where successive ionization processes occur.

Kr^+

The I. E. curve for Kr^+ is shown in Fig. 5, and the curve for CO^+ is superposed for reference. The ground state of Kr^+ is doublet of $^2P_{3/2}$ and $^2P_{1/2}$,and $^2P_{1/2}$ state lies 0.67 eV above $^2P_{3/2}$ state. The extensions of lower and upper linear part of Kr^+ curve cross at about 0.7 eV above the initial onset, so this crossing point seems to correspond to ionization to $^2P_{1/2}$ state. However, the I. E. curve for Kr^+ does not break but bends at about this crossing point. This shape of Kr^+ curve is the same as that of Fox et al[19]. and Frost et al[11].

Fox attributed this bending to autoionization. From the previous considerations, however, autoionization should produce such an I. E. curve as shown in Fig. 3**a**, and the second ionization potential most not be at Q but at R in Fig. 3**a**. Nevertheless, in this experiment the difference between the crossing point of extensions of two linear parts and the initial onset of the curve appears to be 0.7 eV, which almost corresponds to the enegy separation of doublet. So were the results of measurements by Fox et al. and Frost et al. The bending of I. E. curve for Kr^+, therefore, cannot be explained by autoionization process, unless it is assumed that excitation probability abruptly decreases with increase of electron energy. Though the autoionization process may be one of the possible causes, yet a consideration should be given on any other causes, such as the one that produced a bending in the I. E. curve for A^+.

§ 5. Conclusion

The R. P. D. method is powerful. In case of autoionization, however, deviation of the measured points from linear curve is certainly very small, so that I. E. curve should be analyzed carefully. It is not unreasonable that Dorman et al. remarked on a doubt on validity of the R. P. D. method. However, as proved by present experiment on N_2^+ and CO^+, it is not very difficult to detect autoionization process by a careful study of the I. E. curves obtained. In addition, because of a small electron energy spread in R. P. D. method, the critical energy values obtained have a high accuracy and are fully comparable with the spectroscopic value or data of photo ionization.

To explain the experiment on Kr^+, more knowledge on probability of the excitation process is required. The reason of the bending in I. E. curve for A^+ can not be explained. A^+ has been used frequently as a calibration ion of energy scale in the appearance potential study. However, it is proved by this experiment that initial onset method must be adopted when A^+ is used as calibration ion of energy scale and that a true value of appearance potential is obtained* in this way. Ionization potentials of rare gases and some diatomic molecules obtained in this experiment by means of R. P. D. method and the initial onset method using A^+ as calibration ion are shown in Table IV. These agree well with the spectroscopic values and the previous electron impact data.

Table IV. Ionization potentials of rare gases and diatomic molecules (eV).

Ions	This work	Previous electron impact values a	Spectroscopic values a
He^+	24.59 ± 0.03	24.46	24.580
Ne^+	21.52 ± 0.03	21.53	21.559
A^+	15.755	15.77	15.755
Kr^+	14.00 ± 0.03	14.0_0	13.966
H_2^+	15.50 ± 0.03	15.44	15.427
N_2^+	15.63 ± 0.02	15.60	15.557
CO^+	14.11 ± 0.03	14.1	14.009

a: reference (20)

Acknowledgement

The author would like to express cordial appreciation to Professor Kiyoshi Kido for his interest in this research. The author also feels grateful to Assistant Professor Ichiro Kanomata for his kind guidance and encouragement throughout the work, and to Mr. Takeo Oguri for his cooperation rendered to assemble the apparatus.

References

1) F. H. Field and J. L. Franklin: *Electron Impact Phenomena* (Academic Press, New York, 1957) 12p.
2) E. P. Wigner: Phys. Rev. **73** (1948) 1002.
3) G. H. Wannier: Phys. Rev. **100** (1955) 1180.
4) S. Geltman: Phys. Rev. **102** (1956) 171.
5) J. D. Morrison: J. Appl. Phys. **28** (1957) 1409.
6) R. E. Fox, W. M. Hickam, T. Kjeldaas, Jr., and D. J. Grove: Phys. Rev. **84** (1951) 859.
7) R. E. Fox, W. M. Hickam, D. J. Grove, and T. Kjeldaas, Jr.: Rev. Sci. Instr. **26** (1955) 1101.
8) J. D. Morrison: J. Chem. Phys. **21** (1953) 1767.
9) F. H. Dorman, J. D. Morrison, and A. J. C. Nicholson: J. Chem. Phys. **32** (1960) 378.
10) R. F. Fox and W. M. Hickam: J. Chem. Phys. **22** (1954) 2059.
11) D. C. Frost and C. A. McDowell: Proc. Roy. Soc. **A232** (1955) 227.
12) I. Kanomata, Y. Kaneko, and T. Oguri: J. Appl. Phys. Japan **30** (1961) 502.
13) G. G. Cloutier and H. I. Schiff: *Advance in Mass Spectrometry*, edited by J. D. Waldron (Pergamon Press, London, 1959) 473p.
14) D. P. S. Stevenson and J. A. Hipple: Phys. Rev. **62** (1942) 237.
15) T. Mariner and W. Bleakney: Phys. Rev. **72** (1947) 807.
16) E. M. Clarke: Can. J. Phys. **32** (1954) 764.
17) G. Herzberg: *Spectra of Diatomic Molecules* (D. Van Nostrand Co., New York 1950) Table 39.
18) G. L. Weissler, J. A. R. Samson, M. Ogawa and G. R. Cook: J. Opt. Soc. Am. **49** (1959) 338.
19) R. E. Fox, W. M. Hickam, and T. Kjeldaas, Jr.: J. Chem. Phys. **89** (1953) 555.
20) Appendix of reference (1).

---

* There are several methods to determine the appearance potential. The initial onset method is that the appearance potential is decided at the initial onset of the I. E. curve.

JOURNAL OF THE PHYSICAL SOCIETY OF JAPAN Vol. 16, No. 8, AUGUST, 1961

Three-Level Maser Action in Gas
I. Theory of Multiple Quantum Transition and Doppler Effect in Three-Level Gas Maser

By Tatsuo YAJIMA

Department of Physics, Faculty of Science, University of Tokyo, Tokyo

(Received March 4, 1961)

The multiple quantum process in the off-resonant condition of the three-level gas maser is discussed. The intensity of the emission produced by this process is calculated by a perturbation theory and also by a more general treatment which is the application of Javan's theory to the off-resonant case. Some graphical representations of the signal line under off-resonant pumping are given for the purpose of comparison with experiment.

The Doppler effect in three-level maser action is analyzed from both semiclassical and quantum mechanical points of view under the presence of collision relaxation. It was shown that in a saturation process between two levels, Doppler effect behaves as to contribute to both line-width and relaxation time for the transition, and that under strong pumping, Doppler effect in pumping transition has a marked influence on both intensity and shape of the signal line through the effect of multiple quantum transition.

§ 1. Introduction

The three-level masers have been extensively studied on paramagnetic solid state materials. It is to be noted, however, that any other system can possibly be used as a three-level maser if there are three energy levels between which two appropriate transitions are allowed. The possibility and usefulness of the three-level gas maser as a spectrometer as well as an amplifier has already been discussed[1)-6)], and its applications to radio-frequency and microwave spectroscopy have been demonstrated experimentally in certain molecules[3),5)]. The three-level maser action in gas system involves various effects which cannot be treated by a simple theory, and the full accounts of these are of importance for further development of gas maser.

The first of these is the quantum mechanical behavior of the three-level maser. It brings out various interesting phenomena which cannot be predicted from the semi-classical theory dealing with only the population change as has been developed by Bloembergen[7)]. It provides a new type of maser action which produces net induced emission without the requirement of " negative temperature " of the system. The quantum mechanical theories of the three-level maser have been worked out by several authors[2),8)-12)] using a density matrix or its equivalent representation. However, very few experiments concerned with these effects have been carried out probably because of the experimental difficulties.

The three-level gas maser is quite favorable for the study of the quantum mechanical effect, because this effect can be realized more easily in the gas maser than in the solid state maser for the following reason. The quantum mechanical effect in the three-level maser arises from the phase coherent interaction between molecules and radiation fields which produces such phenomena as resonant modulation effect in the emission line and multiple quantum transition* like Raman process. All such effects increase with increasing pumping power. The general condition for the marked appearance of the quantum mechanical effect can then be stated as that the pumping transition must occur appreciably within a time of phase coherence or transverse relaxation of the system. This is expressed in the form as

---

* The word of double or multiple quantum transition is used sometimes for particular cases where two or more photons of the *same* frequencies are simultaneously absorbed or emitted. Here, the word is used for more general cases where frequencies of photons are *not equal*.

$$\frac{\mu\mathcal{E}}{\hbar} \gtrsim \frac{1}{T_2} \sim \Delta\nu \tag{1}$$

where $\mathcal{E}$ is the electric or magnetic field strength of the pumping radiation, μ the electric or magnetic dipole matrix element involved in the transition, T_2 the transverse relaxation time, and $\Delta\nu$ the line-width. In the gas system for which $T_1 \approx T_2$, where T_1 is the longitudinal relaxation time, Eq. (1) is nearly equivalent to the condition for saturation of pumping transition, and the quantum mechanical effect appears with the saturation. On the other hand, in the paramagnetic materials met in most solid state masers for which $T_1 \gg T_2$, the effect appears at the pumping power level of far beyond the value necessary for saturation. The interaction energy between the radiation field and the dipole moment, $\mu\mathcal{E}$, is much higher in the gas maser than in the solid state maser, because the former involves electric dipole transitions, while the latter involves magnetic dipole transitions. In the same radiation field, the interaction energy for 1 Debye, the order of molecular electric dipole moment, is larger by about 100 times than that for 1 Bohr magneton, the order of electron spin magnetic moment. The line-width of gas molecules can be reduced to 100 kc or below by lowering the gas pressure, while minimum attainable line-width of electron spin resonance is of the order of 1 Mc. These facts mean that in the gas maser the condition (1) can be attained using the pumping power of about 10^{-6} times as large as the power required in the solid state maser, if the circuit conditions are the same for both cases.

The resonant modulation effect in a three-level maser is important when the radiation is nearly resonant. This has been discussed by various authours.[2),9),10),12)] The multiple quantum transition involved in the three-level maser action[2),11)] appears in a clear form when the three-level maser is operated in the off-resonant conditions. The off-resonant behavior has been treated by Yatsiv[11)] for particular condition of frequencies and general relaxation processes which can conveniently be applied to the case of magnetic resonance.

It this paper we shall discuss the theory of the off-resonant three-level gas maser in the form which is convenient for comparison with the experiment to be described in II. Also the influence of Doppler effect on the behavior of the three-level maser will be discussed because of its basic importance and the close relation with the off-resonant behavior mentioned above.

§ 2. Perturbation Treatment of Double Quantum Transition

Consider a three-level system of a gas molecule as shown in Fig. 1. The two transitions (1↔3) and (2↔3) are assumed to be allowed and their frequencies are designated as ν_{p0} and ν_{s0}, respectively. If the ratio ν_{p0}/ν_{s0} has an appropriate value and a large radiation power at the frequency ν_{p0} is applied to saturate the transition (1↔3), then the net induced emission at the frequency ν_{s0} will occur as a result of population inversion between the levels 2 and 3. This is the usual three-level maser action in a semiclassical explanation.

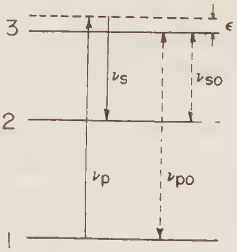

Fig. 1. Double quantum transition in a three-level system.

Quantum theory predicts, however, that even when the frequencies of the fields, ν_p and ν_s, are off-resonant beyond the line-width, the molecular transition can also occur accompanied by simultaneous absorption and emission of radiations, if the frequency condition

$$\nu_p - \nu_{p0} = \nu_s - \nu_{s0} = \mathcal{E} \tag{2}$$

is satisfied. This is the pure double quantum transition associated with the three-level maser. In this transition process, the molecule initially in the state 1 makes a transition to the state 2 with the simultaneous absorption of one photon of $h\nu_p$ and emission of one photon of $h\nu_s$, and the molecule initially

Table I.

State of total system	State of molecule	Number of photons, $h\nu_p$	Number of photons, $h\nu_s$	Total energy
Initial (I)	1	n_p	n_s	$W_I = W_0$
Intermediate (M)	3	n_p-1	n_s	$W_M = W_0 - h\varepsilon$
Final (F)	2	n_p-1	n_s+1	$W_F = W_0$

in the state 2 makes a transition to the state 1 by the reverse process. Then, net induced emission occurs at the frequency ν_s when the population of lower state 1 exceeds that of 2.

Let us calculate the intensity of this emission by a second order time-dependent perturbation theory using quantized field[13]. Although the same result can be derived from a more general equation given later, the perturbation treatment may be helpful in understanding the essential feature of the process. Similar kind of calculation will also be useful for the consideration of a more complicated case such as triple quantum transition.

consider a quantum mechanical system consisting of one molecule and two radiation fields of frequencies, ν_p and ν_s, which are assumed to satisfy Eq. (2). Two radiations are here called the pumping and the signal, respectively. Suppose the three states of the total system as described in Table I.

The perturbation Hamiltonian for electric dipole transition is written as

$$\begin{aligned} \mathscr{H} &= -\boldsymbol{\mu}\cdot(\boldsymbol{E}_s+\boldsymbol{E}_p)\,, \\ \boldsymbol{E}_s &= (q_s+q_s^*)\boldsymbol{u}_s\,, \\ \boldsymbol{E}_p &= (q_p+q_p^*)\boldsymbol{u}_p\,, \end{aligned} \tag{3}$$

where $\boldsymbol{E}_s$ and $\boldsymbol{E}_p$ are the electric fields, and $\boldsymbol{\mu}$ is the molecular electric dipole moment. The subscripts s and p indicate signal and pumping, respectively. Here q_s, q_s^*, q_p, q_p^* are the operators representing the amplitudes of the fields, whose non-zero matrix elements are $q_{n,n+1}=q^*_{n+1,n}=\sqrt{\hbar(n+1)/4\pi\nu}$. The vectors $\boldsymbol{u}_s$ and $\boldsymbol{u}_p$ represent space distribution of the fields. For simplicity of treatment they are assumed hereafter to be uniform and mutually parallel.

The probability that the system which exists in the state I at the time t_0 makes transition to the state F through the state M during a time $t-t_0$ is given by

$$p(t-t_0)=\left|\frac{(F|\mathscr{H}|M)(M|\mathscr{H}|I)}{W_M-W_0}\right|^2\frac{(t-t_0)^2}{\hbar^2}\,. \tag{4}$$

There are also other transition paths via other intermediate states, but these may be neglected because of their small transition probabilities relative to the one given above, when the frequency deviation ε is much smaller than transition frequencies of the molecule.

Using the relation $\langle \boldsymbol{E}^2\rangle = E^2/2 = \langle 2qq^*\rangle \boldsymbol{u}^2$, and considering the situation n_s, $n_p \gg 1$, Eq. (4) becomes

$$p(t-t_0)=\left(\frac{|\bar{\mu}_{31}|E_p}{2\hbar}\right)^2\left(\frac{|\bar{\mu}_{23}|E_s}{2\hbar}\right)^2\frac{(t-t_0)^2}{4\pi^2\varepsilon^2}\,, \tag{5}$$

where E_p and E_s are the peak electric fields, $\bar{\mu}_{23}$ and $\bar{\mu}_{31}$ the dipole matrix elements along the direction of fields for the transition $(2\leftrightarrow 3)$ and $(3\leftrightarrow 1)$, respectively. The reverse process where initial and final states are interchanged occurs with the same probability as far as the spontaneous emission can be neglected.

When the random collisions of molecules with the mean free time τ is assumed, the rate of net population change between states 1 and 2, whose equilibrium populations are n_1 and n_2, is given by

$$(n_2-n_1)\int_{-\infty}^{t}\frac{p(t-t_0)}{\tau^2}e^{-(t-t_0)/\tau}dt_0\,. \tag{6}$$

Then, the net absorption coefficient at the frequency ν_s becomes

$$\begin{aligned} \alpha_s &= \frac{2(n_2-n_1)h\nu_s w_s w_p}{P_s\tau\varphi^2}\,, \\ w_s &\equiv \left(\frac{|\bar{\mu}_{23}|E_s}{2h\Delta\nu}\right)^2, \quad w_p \equiv \left(\frac{|\bar{\mu}_{13}|E_p}{2h\Delta\nu}\right)^2 \\ \varphi &\equiv \frac{\varepsilon}{\Delta\nu}\,, \end{aligned} \tag{7}$$

where $\Delta\nu = 1/(2\pi\tau)$ is the half line-width and P_s is the incident radiation power at the frequency ν_s, and w_p is called a "pumping parameter" hereafter.

On the one hand, the absorption coefficient at the center of the transition (2↔3) without saturation and pumping radiation is given by

$$\alpha_{s0}=\frac{2(n_2-n_3)w_s h\nu_{s0}}{P_s\tau}\,. \qquad (8)$$

Taking the ratio of Eq. (7) and Eq. (8), one obtains

$$\frac{\alpha_s}{\alpha_{s0}}=-\left(\frac{n_1-n_2}{n_2-n_3}\right)\frac{w_p}{\varphi^2}\,\frac{\nu_s}{\nu_{s0}}\,. \qquad (9)$$

Considering the situation where $h\nu_s$, $h\nu_p \ll kT$ and $\nu_s \sim \nu_{s0}$, it becomes

$$\frac{\alpha_s}{\alpha_{s0}}=-\left(\frac{\nu_{p0}}{\nu_{s0}}-1\right)\frac{w_p}{\varphi^2}\,. \qquad (10)$$

Eq. (10) shows that α_s is always negative (representing the presence of emission) as long as $\nu_{p0}>\nu_{s0}$, and that $|\alpha_s|$ increases proportionally with the pumping power and rapidly decreases with the deviation of frequency from resonance.

The intensity of the emission, α_s, in an actual gas can be estimated easily from Eq. (10), since α_{s0} and $|\bar{\mu}_{13}|^2$ can be calculated at once by the usual method of microwave spectroscopy[14].

When w_p/φ^2 increases to a value of the order of 1, the saturation of double quantum transition occurs, and the approximation used here breaks.

§ 3. General Off-Resonant Behavior

In order to obtain the results for arbitrary strength and frequency of two radiation fields, the time-dependent schrödinger equation must be solved directly without using the perturbation theory. A general solution of this problem has been obtained by Javan[2)] for the gas system under strong collisions, and the resonant behavior was discussed. The off-resonant behavior of the three-level gas maser, which has not fully been discussed, is considered here together with the examination of the validity of perturbation treatment given in § 2.

Consider the three-level system as in Fig. 1, but the applied frequencies, ν_p and ν_s, are now assumed to be arbitrary. Then, the absorption coefficient α_s at the frequency ν_s for small signal power under the pumping radiation of the frequency ν_p and of arbitrary power level is given by the following formula according to the method of Javan,

$$\begin{aligned}\frac{\alpha_s}{\alpha_{s0}}=&\left\{(1+a)^2-(R-1)\frac{w_p}{\beta^2}\right\}\frac{1}{4\{1+(\beta-\delta)^2\}}+\left\{(1-a)^2-(R-1)\frac{w_p}{\beta^2}\right\}\frac{1}{4\{1+(\beta+\delta)^2\}}\\&-\left\{(1-a^2)+(R-1)\frac{w_p}{\beta^2}\right\}\frac{(\beta^2-\delta^2)(1+2\beta^2)-1}{(1+4\beta^2)\{1+(\beta-\delta)^2\}\{1+(\beta+\delta)^2\}}\\&\equiv f(\varphi_s,\varphi_p,w_p,R)\,, \qquad (11)\end{aligned}$$

where

$$\beta\equiv\left(\frac{1}{4}\varphi_p{}^2+w_p\right)^{1/2},\qquad \delta\equiv\frac{1}{2}\varphi_p-\varphi_s\,,\qquad a\equiv\frac{\varphi_p}{2\beta}\,,$$

$$w_p\equiv\left(\frac{|\bar{\mu}_{13}|E_p}{2h\Delta\nu}\right)^2=\frac{2\pi|\mu_{13}|^2P_0}{3ch^2(\Delta\nu)^2S}\,,\qquad |\bar{\mu}_{13}|^2=\frac{1}{3}|\mu_{13}|^2\,,$$

$$R\equiv\nu_{p0}/\nu_{s0}\,,$$

$$\varphi_s\equiv(\nu_s-\nu_{s0})/(\Delta\nu)\,,$$

$$\varphi_p\equiv(\nu_p-\nu_{p0})/(\Delta\nu)\,,\qquad \Delta\nu=1/(2\pi\tau)\,,$$

Here α_{s0} is the absorption coefficient at $\nu_s=\nu_{s0}$ without pumping, P_0 the pumping power for plane polarized wave, S the cross-sectional area of the power flow.

Eq. (11) is equivalent to Eq. (16) plus Eq. (19) in Ref. (2), but here the expression has been slightly modified for the convenience of studying off-resonant behavior and of numerical representations of the results. In Eq. (11), the approximations $\nu_s/\nu_{s0}\approx 1$ and $h\nu/kT\ll 1$ are also used as before.

When we have $\nu_p-\nu_s=\nu_{p0}-\nu_{s0}$ or $\varphi_p=\varphi_s\equiv\varphi$, Eq. (11) reduces to a relatively simple form as

$$\frac{\alpha_s}{\alpha_{s0}}=\frac{(1+w_p)(1+4w_p+\varphi^2)-Rw_p\{3(1+w_p)+\varphi^2\}}{(1+4w_p+\varphi^2)\{(1+w_p)^2+\varphi^2\}}\,. \qquad (12)$$

For $\varphi=0$, it reduces to

$$\frac{\alpha_s}{\alpha_{s0}}=\frac{1+w_p(4-3R)}{(1+4w_p)(1+w_p)}\ . \tag{13}$$

This is a relation for the resonant three-level gas maser. For $\varphi^2\gg1$, Eq. (12) approaches to the asymptotic formula

$$\frac{\alpha_s}{\alpha_{s0}}=\frac{1}{\varphi^2}-\frac{(R-1)w_p}{\varphi^2}\ . \tag{14}$$

The first term represent the tail of original absorption line arising from the first order or the single quantum transition between levels 2 and 3. The second term represents the emission due to the pure double quantum transition which is in full rgreement with the result of perturbation theory given by Eq. (10). Note that, when $w_p>1/(R-1)$, the double quantum transition dominates over the single quantum transition and the emission can be obtained.

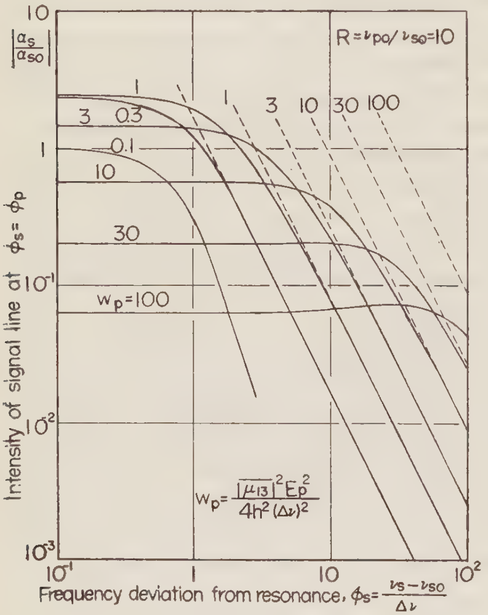

(a)

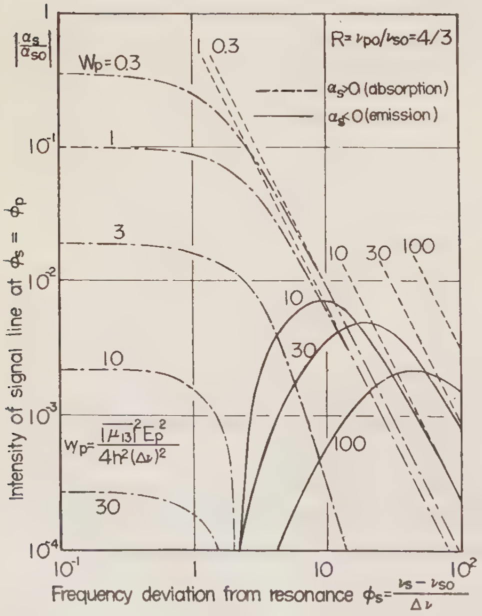

(b)

Fig. 2. Signal intensity in a double quantum transition, when $\nu_p-\nu_{p0}=\nu_s-\nu_{s0}$.
(a) $\nu_{p0}/\nu_{s0}=10$. (b) $\nu_{p0}/\nu_{s0}=4/3$.

Eq. (12) is plotted as a function of normalized frequency deviation, φ, in Fig. 2 (a), (b) in order to show a saturation behavior of the double quantum transition. The dotted lines represent the result of Eq. (14). It can be seen from Fig. 2 that the perturbation treatment is approximately valid in the region where $\varphi\gtrsim w_p$. Also, as shown in Fig. 2 (b), appreciable emission can occur at a sufficiently off-resonant region even in the case of $R\leq4/3$, where the emission does not occur for $\varphi=0$ at any pumping power level.

In addition to the saturation of intensity, the frequency shift of the double quantum transition from the relation $\varphi_s=\varphi_p$ occurs when w_p/φ^2 becomes fairly large. Therefore, in the region where saturation effect cannot be neglected, the peak intensity of emission is somewhat higher than that indicated in Fig. 2. It can be seen from Eq. (11) that in general two peaks of emission or absorption in a single line occurs approximately at

$$\varphi_s=\frac{1}{2}\varphi_p\pm\left(\frac{1}{4}\varphi_p^2+w_p\right)^{1/2}. \tag{15}$$

When the pumping frequency is far off-resonant ($\varphi_p^2\gg1$), one of the peaks approaches to the center of the original line, and the other peak goes to the emission line corresponding to $\varphi_p=\varphi_s$. For $w_p/\varphi_p^2\ll1$, Eq. (15) can be expanded in powers of w_p/φ_p^2, and the latter peak occurs at

$$\varphi_s=\varphi_p\left(1+\frac{w_p}{\varphi_p^2}+\cdots\right). \tag{16}$$

This represents the frequency shift of the double quantum transition in the first order approximation. It is noted that in this approximation the fractional frequency shift of the double quantum transition is proportional to its intensity. This can be explained in the following way. For appreciable occurrence of the higher order transition such as double quantum transition, considerable mixing of the two states by a strong pumping field is necessary. This causes a frequency modulation of wave functions which depends on the field intensity, and then results in the shift of transition frequency from that of the pure double quantum transition. Thus the intensity and the frequency shift of double quantum transition are unseparably related. Further, because the frequency shift of the double quantum transition at off-resonance can be considered to arise from the same origin as that of the resonant modulation effect which splits the emission line at resonance, the multiple quantum effect and the resonant modulation effect in the three-level masers are also closely related. That is, when one of the effects is large, the other effect is also large.

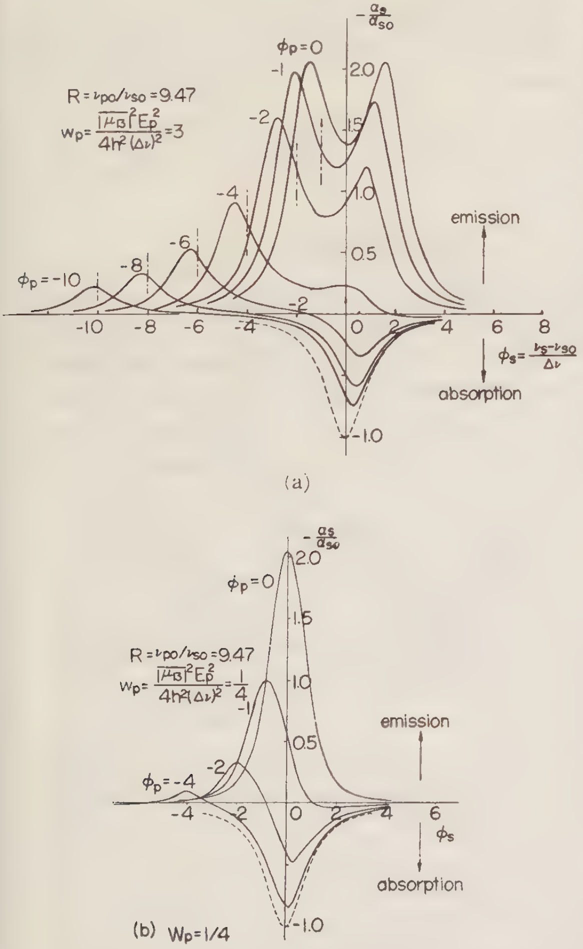

Fig. 3. Shape of signal line under off-resonant pumping. The dotted curve shows absorption line without pumping, and the vertical lines indicate the position of $\varphi_s=\varphi_p$.
(a) $w_p=3$. (b) $w_p=1/4$.

The whole behavior of the three-level gas maser from resonance to far off-resonance is clearly represented by plotting the shape of signal lines according to Eq. (11). This is shown in Fig. 3 (a), (b). For relatively strong pumping, the effects of resonant modulation, frequency shift of double quantum transition, and the double quantum emission line at far off-resonance are illustrated notably in Fig. 3 (a). On the other hand, for a weaker pumping, all the above effects scarcely appear as shown in Fig. 3 (b). The value of *R* in Fig. 3 is that of the three-level system used in the experiment to be described in II, and then these curves can be directly compared with experiment.

In actual molecules, each spectral line of the three-level system consists of several Stark or Zeeman components which coincide in frequency without external static field. Therefore, the above treatment is not exact but only describes an average characteristics, because individual components have different dipole matrix elements and hence show different behavior in a pumping process. Correct account of this effect will result in some deviations from the results given above. However, we shall not deal with the effect here since it complicates the problem very much.

§ 4. Doppler Effect

In general, the effective operation of a three-level gas maser is achieved at a low pressure, where Doppler broadening may no longer be neglected against pressure broadening. In this section we discuss the Doppler effect in a three-level gas maser where arbiary ratio of pressure broadening and Doppler broadening of a spectral line occurs. Before proceeding the calculation, we make following assumptions to simplify the problem.

(a) The molecular collision is hard, i.e., the radiation process is perfectly interrupted upon each collision, and immediately after collision the molecules redistribute their velocity as well as their internal energy according to the Boltzmann law.

(b) The presence of radiation fields does not affect the above distribution immediately after collision.

These assumptions may be a good approximation in treating the electric dipole transition of gas molecules at microwave frequencies. Under these assumptions, each radiation process between two successive collisions can be considered as an elementary process which is statistically independent. Then, Doppler effect in any radiation process can be calculated simply by averaging the process over the Maxwell-Boltzmann velocity distribution of molecules.

Consequently, when the Doppler effect is taken into account, a physical quantity, $nF(\nu)$, should be replaced by the form

$$n\int_{-\infty}^{\infty} F(\nu+\nu_d)\frac{q}{\sqrt{\pi}}\exp(-q^2\nu_d^2)d\nu_d\ , \tag{17}$$

where

$$q=\frac{c}{\nu}\left(\frac{m}{2kT}\right)^{1/2}=\frac{1}{(\Delta\nu)_d}\ .$$

Here n is the equiliblium population of a level, ν the applied frequency, and $(\Delta\nu)_d$ the Doppler width*.

(i) *Semiclassical Aspect*

Semiclassical approximation of the three-level maser action requires that the actions of two radiation fields, the signal and the pumping, can be considered separately. That is, the role of the pumping is only to change the populations of levels, and the signal responds to only the change of population regardless of the pumping mechanism. Further, in an ideal gas system the saturation of one transition does not affect the population of the other levels, because of the equal relaxation times between various levels. Then, the problem may be separated into two parts. The first is the saturation behavior of the pumping transition under Doppler effect, and the second is the one concerned with the signal. Since the latter is essentially the same problem as that in usual spectral lines, the former is considered first.

Suppose that a strong radiation of frequency ν is applied between two levels, 1 and 3, whose separation is ν_0 in frequency. Then the net population change, $\Delta n_3-\Delta n_1=2\Delta n_3$, is given by the theory of saturation effect as

$$2\Delta n_3=(n_1-n_3)\frac{4w_p}{1+4\pi^2(\nu-\nu_0)^2\tau^2+4w_p}\ , \tag{18}$$

$$w_p\equiv\left\{\frac{|\bar{\mu}_{13}|E_p}{2h(\Delta\nu)_p}\right\}^2\ , \qquad (\Delta\nu)_p=\frac{1}{2\pi\tau}\ ,$$

where n_1 and n_3 are the equilibrium population of levels, 1 and 3, $(\Delta\nu)_p$ the half-width due to pressure broadening. Under the presence of Doppler effect, the fractional change of population becomes by using the formula (17)

$$\frac{2\Delta n_3}{n_1-n_3}=\frac{4w_pq}{\sqrt{\pi}}\int_{-\infty}^{\infty}\frac{\exp(-q^2\nu_d^2)d\nu_d}{1+4\pi^2\{\nu_d+(\nu-\nu_0)\}^2\tau^2+4w_p}\ . \tag{19}$$

When $\nu=\nu_0$, it becomes after some change of variables

$$\frac{2\Delta n_3}{n_1-n_3}=\frac{4w_p}{1+4w_p}G(r\sqrt{1+4w_p})\ , \tag{20}$$

where

$$G(x)\equiv\frac{x}{\sqrt{\pi}}\int_{-\infty}^{\infty}\frac{1}{1+\xi^2}e^{-x^2\xi^2}d\xi\ ,^{**}$$

and

$$r\equiv\frac{q}{(2\pi\tau)}=\frac{(\Delta\nu)_p}{(\Delta\nu)_d}\ .$$

Eq. (20) gives general formula of fractional population change between two levels for arbitrary power level and Doppler broadening, and the result of numerical calculation is

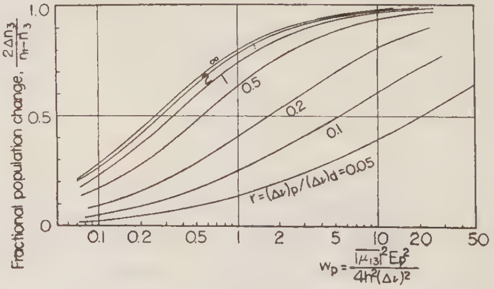

Fig. 4. Fractional population change in a saturation process between two levels under Doppler effect.

---

[*] The relation between $(\Delta\nu)_d$ and the usual half Doppler width $(\Delta\nu)_d^*$ is $(\Delta\nu)_d^*=\sqrt{\ln 2}(\Delta\nu)_d=0.832(\Delta\nu)_d$. Here $(\Delta\nu)$ is used as a Doppler width for convenience.

[**] The function $G(x)$ can be transformed in the form

$$G(x)=xe^{x^2}(\sqrt{\pi}-2\int_0^x e^{-t^2}dt)\ ,$$

whose asymptotic expressions are given by

$$G(x)\sim 1-\frac{1}{2}\frac{1}{x^2}+\frac{3}{4}\frac{1}{x^4}-\cdots \qquad \text{for} \quad x\gg 1$$

$$\sim x(\sqrt{\pi}-2x+\sqrt{\pi}x^2-\cdots) \qquad \text{for} \quad x\ll 1$$

given in Fig. 4.

By a similar approach, the absorption coefficient at the center of a line without saturation effect is given by

$$\alpha=\alpha_0 G(r)\ , \tag{21}$$

where α_0 is the value of α without Doppler effect. Then, a relation

$$G(r)=\frac{(\Delta\nu)_p}{(\Delta\nu)_T}\ , \tag{22}$$

can be obtained, where $(\Delta\nu)_T$ is the total line-width including both pressure-width and Doppler-width.

The Doppler effect at pumping frequency in the three-level gas maser is considered to affect the signal intensity through the population change. When $h\nu_{p0}\ll kT$, the general expression for the absorption coefficient at the center of the signal line including Doppler effects in both signal and pumping frequencies can then be given by

$$\alpha_s=\alpha_{s0}\left\{1-\frac{2w_p RG(r_p\sqrt{1+4w_p})}{1+4w_p}\right\}G(Rr_p)\ , \tag{23}$$

where

$$R\equiv\nu_{p0}/\nu_{s0}\ ,\qquad r_p=(\Delta\nu)_p/(\Delta\nu)_{dp}\ .$$

Here $(\Delta\nu)_{dp}$ is the Doppler-width for the pumping frequency, and α_{s0} the value of α_s without pumping and Doppler effect.

Now, returning to Eq. (20), we consider the physical meaning involved in it by examining some special situations.

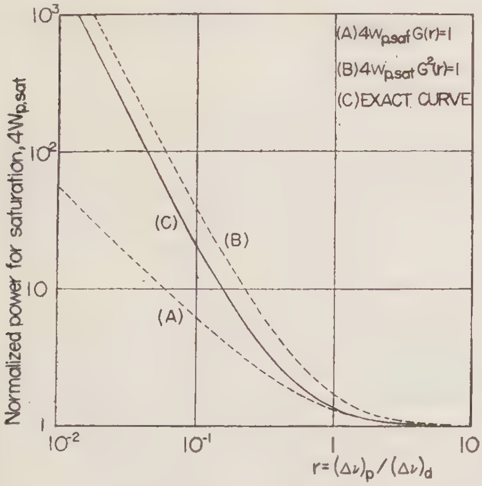

Fig. 5. Normalized power for saturation as a function of $r=(\Delta\nu)_p/(\Delta\nu)_d$. (A) and (B) are the approximate relations, and (C) is the exact curve.

(a) The case of saturation

We choose the value, $2\Delta n_3/(n_1-n_3)=1/2$, as a representative level of saturation, and will then plot a normalized power necessary for saturation, $4w_{p,\mathrm{sat}}$, as a function of $r=(\Delta\nu)_p/(\Delta\nu)_d$. The result is shown in Fig. 5 together with two approximate relations (A) and (B) designated below.

$$\text{(A)}\quad 4w_{p,\mathrm{sat}}G(r)=\frac{|\bar{\mu}_{13}|^2 E_p{}^2}{h^2(\Delta\nu)_p(\Delta\nu)_T}=1 \tag{24}$$

$$\text{(B)}\quad 4w_{p,\mathrm{sat}}G^2(r)=\frac{|\bar{\mu}_{13}|^2 E_p{}^2}{h^2(\Delta\nu)_T{}^2}=1\ . \tag{25}$$

According to a simple saturation theory[14], (A) means that Doppler effect contributes only to line-width, i.e., to transverse relaxation and not to longitudinal rexation, while (B) means that Doppler effect contributes equivalently both to transverse and longitudinal relaxation. At first sight, (A) seems to be a good approximation because Doppler effect is not an energy dissipating process. Fig. 5 indicates, however, that (B) is clearly a better approximation for $r\ll 1$ (Doppler broadening dominant) although (A) is better for $r\gg 1$ (pressure broadening dominant). This fact has already been pointed out by Shimoda[3], but it is proved here more explicitly. The asymptotic forms of the three curves for $r\ll 1$ become

$$\begin{aligned}
&\text{(A)}\quad 4w_{p,\mathrm{sat}}=\frac{1}{\sqrt{\pi}\,r}=0.564\frac{1}{r}\\
&\text{(B)}\quad 4w_{p,\mathrm{sat}}=\frac{1}{\pi r^2}=0.318\frac{1}{r^2}\\
&\text{(C)}\quad 4w_{p,\mathrm{sat}}=\frac{1}{r^2}\left\{G^{-1}\left(\frac{1}{2}\right)\right\}^2=0.187\frac{1}{r^2}\ ,
\end{aligned} \tag{26}$$

The discrepancies of the numerical factors between (B) and (C) varies to some extent depending on the selection of saturation level and the definition of total line-width, and therefore is not essential.

(b) Weak field case

Eq. (20) can be expanded in powers of w_p and by using Eq. (22) it becomes

$$\frac{2\Delta n_3}{n_1-n_3}=4w_pG(r)=4w_p\frac{(\Delta\nu)_p}{(\Delta\nu)_T} \tag{27}$$

This may be interpreted as that Doppler effect behaves in a manner described in the relation (A) at the early stage of saturation.

Semiclassical treatment of Doppler effect in three-level maser action is, of course, a rough approximation in cases of gases, but it will serve as a method of order estimation of the effect.

(ii) *Quantum Mechanical Aspect*

From the quantum mechanical point of view, the actions of signal and pumping radiations in a three-level maser cannot be treated separately, and they must be considered simultaneously.

Consider a three-level system as discussed in § 3. The absorption coefficient (being negative for emission) of the gas at the signal frequency ν_s under the presence of pumping radiation at the frequency ν_p has been given by Eq. (11),

$$\alpha_s=\alpha_{s0}f(\varphi_s,\ \varphi_p,\ w_p,\ R)\ , \tag{11'}$$

The expression of α_s including Doppler shifts of both the signal and the pumping frequencies can be derived in a similar manner as before in the form

$$\alpha_s=\alpha_{s0}\int_{-\infty}^{\infty}f\left(\frac{1}{R}x+\varphi_s,\ x+\varphi_p,\ w_p,\ R\right)\frac{r_p}{\sqrt{\pi}}\exp(-r_p^2x^2)dx\ , \tag{28}$$

where

$$r_p\equiv\frac{c}{\nu_p}\left(\frac{m}{2kT}\right)^{1/2}(\Delta\nu)_p=\frac{(\Delta\nu)_p}{(\Delta\nu)_{dp}}$$

Here $(\Delta\nu)_p$ is the pressure-width, $(\Delta\nu)_{dp}$ the Doppler-width for the pumping frequency. Since Eq. (28) is too complicated to be discussed generally, we shall consider some special cases to clarify the essential features of the effect when the quantum mechanical effects are important.

In the case when $R=\nu_{p0}/\nu_{s0}\gg1$, the Doppler effect at the signal frequency and the terms $(1+a)^2$, $(1-a)^2$, $(1-a^2)$ in the function f can be neglected. Further assume $\nu_p=\nu_{p0}$ (resonant pumping). Then, Eq. (28) becomes

$$\frac{\alpha_s}{\alpha_{s0}}=\int_{-\infty}^{\infty}f(\varphi_s,\ x,\ w_p,\ R)\frac{r_p}{\sqrt{\pi}}\exp(-r_p^2x^2)dx\ . \tag{29}$$

Eq. (29) means that in this case the total shape of the signal line can be given simply by superposing various line components for off-resonant pumping as has been shown in Fig. 3 with a weight factor of Boltzmann distribution. Then, it becomes clear that for large pumping power level Doppler effect at the pumping frequency affects not only the intensity of the signal line, but also have a large influence on the shape of the signal line, due to the double quantum transition which is considerably strong even in the far off-resonant conditions.

For strong pumping, $w_p\gg1$, the third term in the function f can be neglected and Eq. (29) reduces to the form

$$\begin{aligned}\frac{\alpha_s}{\alpha_{s0}}=-\frac{w_pr_p(R-1)}{\sqrt{\pi}\{(1+\varphi_s^2-w_p)^2+4w_p\varphi_s^2\}}\Bigg[&\frac{1}{\sqrt{w_p}}(1+\varphi_s^2-w_p)\int_{-\infty}^{\infty}\frac{1}{1+x^2}\exp(-4r_p^2w_px^2)dx\\&-2\varphi_s\int_{-\infty}^{\infty}\frac{x}{1+x^2}\exp\{-r_p^2N(x+\sigma)^2\}dx+(w_p+\varphi_s^2-1)\int_{-\infty}^{\infty}\frac{1}{1+x^2}\exp\{-r_p^2N(x+\sigma)^2\}dx\Bigg],\end{aligned} \tag{30}$$

where

$$N\equiv\left(1+\frac{w_p}{1+\varphi_s^2}\right)^2,\qquad \sigma\equiv\frac{\varphi_s(1+\varphi_s^2-w_p)}{(1+\varphi_s^2+w_p)}\ .$$

When $r_p\gg1$, it reduces to the equation for no Doppler effect

$$\frac{\alpha_s}{\alpha_{s0}}=-\frac{1}{4}(R-1)\left\{\frac{1}{1+(\sqrt{w_p}+\varphi_s)^2}+\frac{1}{1+(\sqrt{w_p}-\varphi_s)^2}\right\}\ . \tag{31}$$

When $r_p\ll1$, it approaches to the asymptotic formula

$$\frac{\alpha_s}{\alpha_{s0}}=-r_p\sqrt{\pi}(R-1)\frac{\sqrt{w_p}(1-w_p+\varphi_s^2)-w_p(1-w_p-\varphi_s^2)}{(1-w_p+\varphi_s^2)^2+4w_p\varphi_s^2}\ . \tag{32}$$

The solutions, (31) and (32), are compared in Fig. 6 (a), (b).

For $r_p \ll 1$, the doublet structure in the emission line disappears, and it becomes a broader single line having a normalized half-width of about $\Delta\varphi_s \sim \sqrt{w_p}$. This can be interpreted as that the Doppler broadening at the pumping frequency is converted partly into the signal line through the double quantum transitions and hence the broadening of the signal line occurs. This Doppler-broadened signal line will split into doublet again, if the pumping parameter w_p is increased to a larger value. This can be proved from Eq. (30) in a way that, when $w_p \to \infty$, the ratio, α_s/α_{s0} at $\varphi_s=0$, approaches to zero, while α_s/α_{s0} at $\varphi_s=\sqrt{w_p}$ approaches to a finite value of $-(R-1)G(2r_p)/4$

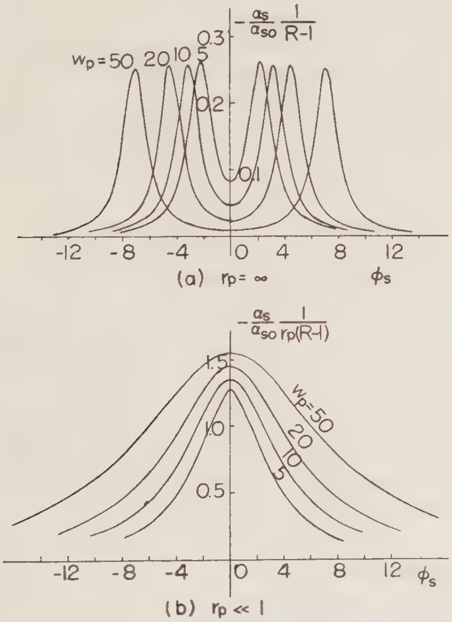

Fig. 6. Comparison of signal line-shape between two cases. (a) no Doppler effect ($r_p \to \infty$) and (b) large Doppler effect ($r_p \ll 1$). $r_p=(\Delta\nu)_p/(\Delta\nu)_{dp}$. $w_p=|\bar{\mu}_{13}|^2E_p^2/[4h^2(\Delta\nu)^2]$. $R=\nu_{p0}/\nu_{s0} \gg 1$.

where G is a function given in Eq. (20).

The Doppler effect is particularly important when the three-level gas masers are applied to the following cases (a) and (b) where Doppler broadening in pumping transition dominates over pressure broadening.

(b) Gas pressure is extremely low as in the case of high resolution radio-frequency spectroscopy of the signal transition[3].

(b) The pumping frequency lies in a shorter wavelength region as in the case of detecting the pumping transition in that frequency[4,5], or in the case of signal amplification by the use of such a pumping frequency.

§ 5. Concluding Remarks

In order to understand the basic characteristics of the three-level gas maser, two problems were theoretically discussed. The one is the multiple quantum process in the off-resonant conditions and the other is the Doppler effect which has a close relation with the former. In conclusion we shall discuss briefly some related problems concerned with the quantum mechanical behavior which have not been mentioned.

An important special case of the off-resonant three-level maser occurs when the separation of the levels 2 and 3 in Fig. 1 becomes so small that a condition, $\nu_{s0} \ll \mathcal{E} \ll \nu_{p0}$, holds. A number of energy level schemes applicable to such situation can be found in the rotational spectrum of slightly asymmetric molecules. This is essentially similar to the two-level Raman-type maser discussed by Javan[15], because the latter requires that at least one of the two levels is degenerate for the case of gas, and indeed it can be considered as a limiting case of the above situation. However, the equations for this case cannot be obtained simply by taking a limit of $\nu_{s0} \to 0$ in the present equations, because various approximations used here become invalid in such a limiting case.

When any energy level of a three-level system has a structure composed of closely spaced levels such as hyperfine levels or accidentally lying near-by levels, a complicated situation will occur. A strong pumping radiation will mix up many such quantum states, and then all these states will interact with the radiation simultaneously.

In the three-level system we can obtain the net induced emission only by a pumping source at the frequency higher than that of the signal, although the quantum mechanical effect widely extends the condition for the occurrence of induced emission. However, it can easily be shown that the net induced emission can be obtained by using lower frequency pumping for a wide range of conditions, if the triple quantum transition in a multi-level system is used. Although it may be hard to obtain a strong emission sufficient for practical use by this process, it will serve as a method of generation or amplification of shorter microwaves in some cases.

The complete understanding of the above problems requires another elaborate analyses starting from fundamental equations. Full discussion on these problems will then be postponed.

Acknowledgement

The author wishes to express his sincere thanks to Prof. K. Shimoda for his kind guidance and continued encouragement throughout this work. He also thanks Mr. H. Takuma for his interest and discussions on the present subject.

References

1) N. G. Bassov and A. M. Prokhorov: J.E.T.P. (USSR) **28** (1955) 249.
2) A. Javan: Phys. Rev. **107** (1957) 1579.
3) K. Shimoda: J. Phys. Soc. Japan **14** (1959) 954.
4) K. Shimoda: J. Phys. Soc. Japan **14** (1959) 966.
5) T. Yajima and K. Shimoda: J. Phys. Soc. Japan **15** (1960) 1668.
6) K. Shimoda: to be published in Nuovo Cimento.
7) N. Bloembergen: Phys. Rev. **104** (1956) 324.
8) P. W. Anderson: J. Appl. Phys. **28** (1957) 1049.
9) V. M. Kontorovich and A. M. Prokhorov: J.E.T.P. (USSR) **33** (1957) 1428.
10) A. M. Clogston: J. Phys. Chem. Solid **4** (1958) 271.
11) S. Yatsiv: Phys. Rev. **113** (1959) 1538.
12) P. N. Butcher: in "*Quantum Electronics*" ed. by C. H. Townes (Columbia Univ. Press 1960) p. 189.
13) See, W. Heitler: "*Quantum theory of Radiation*" (Oxford at the Clarendon Press 1954).
14) See, C. H. Townes and A. L. Schawlow: "*Microwave Spectroscopy*" (McGraw-Hill 1955).
15) A. Javan: Bull. Am. Phys. Soc. Ser II, **3** (1958) 213; J. Phys. Radium **19** (1958) 806; Private communication to Prof. K. Shimoda.

JOURNAL OF THE PHYSICAL SOCIETY OF JAPAN, Vol. 16, No. 8, AUGUST, 1961

Some Optical Properties of Lead Activated Potassium Halide Phosphors

By Yozo KAIFU

Institute of Pelytechnics, Osaka City University

(Received February 16, 1961)

Absorption, emission and excitation spectra of KCl:Pb and KBr:Pb have been measured at various temperatures. These observed spectra are similar to those of KCl:Tl, and the absorption bands seemed to be due to transitions in Pb^{++} ions which occupies the normal positive ion sites. The two principal excited states are $^1P_1$ and $^3P_1$ of Pb^{++} ion. 273 mμ absorption, 345 mμ emission in KCl:Pb and 302 mμ absorption, 365 mμ emission in KBr:Pb are attributed to $^3P_1-{}^1S_0$ transitions perturbed by surrounding host lattice ions. The excitation to $^1P_1$ state does not manifest any distinct emission which is different from the case of Tl activated phosphors. The near ultra-violet emission suffers violent thermal quenching at room temperature, and the activation energies of these non-radiative process are found to be 0.28 eV and 0.18 eV for KCl:Pb and KBr:Pb, respectively.

Several discussions using a single configuration coordinate model are given.

§1. Introduction

It may be considered that the studies of alkali halide phosphors provide several fundamental informations about the luminescence process, since these phosphors have relatively simple structure among the inorganic phosphor. Pohl and his collaborators[1),2)] studied the optical properties of various alkali halides activated by a small amount of heavy metal ions and found the characteristic absorption bands existing on the long wavelength side of the fundamental absorption band of the pure substance.

In most cases, the luminescence can be observed by the excitation of these characteristic bands. However, detailed investigations including emission process about these phosphors have not been carried out except for the thallium activated one. The absorption spectra of lead activated alkali halide phosphors have been investigated by several authors[2)], and the positions of the absorption peaks were summarized in the recent publication[3)]. The emission spectra of these phosphors, on the other hand, have received little attention[4),5)].

The theoretical approach to simple inorganic phosphors has been developed by von Hippel[6)] and Seitz[7)] by introducing a configuration coordinate model. These were applied to thallium activated potassium chloride quantum mechanically[8)], and also semiempirically[9)]. A general interpretation of these luminescence center has been given by these treatments, but several criticisms on these treatments were presented[10)], so further tests of these points are important.

The author made an attempt to investigate the absorption, emission and excitation spectra of lead activated potassium halides, and considered the properties of the luminescence centers in connection with the thallium activated alkali halides.

§2. Experimental Procedures

Single crystals of KCl:Pb were grown from melts of pure alkali halides and lead halides of reagents grade purity, using the Kyropoulos technique. Any special treatment on the exclusion of trace impurities in the pure reagents was not conducted*, and single crystals obtained from the same alkali halide reagents were used as standard substances for optical measurements, and the effects of trace impurities were considered by relative measurements with respect to the standard substance.

Concentrations of lead in the single crystals were analysed by the following chemical method. The lead in the crystals were converted to precipitation of lead chromate, and the quantities of lead ions in the precipitate were volume-metrically determined by means of iodometry. The lead concentrations in the crystal were about one tenth of the lead concentration of the melt, and there were some variation of the concentration affected by the position of same grown crystal.

---

* These metal impurities introduced in single crystals were estimated to be about 10^{-6} mole.

The crystals grown from the high concentration of lead halide, i.e. above 0.3 mole percent $PbCl_2$ melts, were transparent at above 300°C. Cooling to room temperature, however, they became opaque indicating that colloidal aggregates of lead ions were grown in the crystal. As these crystals did not show efficient luminescence, and were considered to have more complex structure of luminescence center than the crystals of low lead concentrations, optical measurements for these crystals of high lead concentrations were not carried out in the present study.

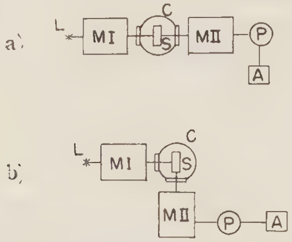

Fig. 2. Experimental arrangements for
a) measurements of absorption spectra.
b) measurements of emission spectra.

L: hydrogen lamp,
C: cryostat,
S: specimen,
P: 1P28 photo tube,
A: amplifier and detecting meter,
M-I, M-II: monochromators.

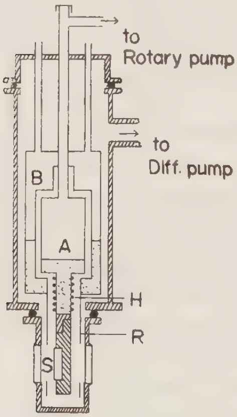

Fig. 1. Cryostat used for the optical measurements.

A: inner vessel,
B: outer vessel,
S: specimen,
H: electric heater,
R: radiation shield.

A cryostat was designed to hold a crystal sample at any temperature between about 70°K and 400°K for sufficiently long time for optical measurements (Fig. 1). It has double Dewar containers having radiation shield and a relatively large sample holder made of copper block. The temperature was measured with a copper-constantan thermocouple which was placed close to the sample. The experimental arrangements are shown in Fig. 2 a, b, and detailed explanations are given in the next section.

§ 3. Experimental Results

a) *Absorption spectra*

Absorption spectra of Pb-activated alkali halide single crystals were measured with an automatic recording spectrophotometer at room temperature. The measurements at various temperatures were performed with two monochromators and a cryostat arrangements shown in Fig. 2a. This reduces the error introduced by the fluorescence of the crystal to negligible amount. The absorption curves were measured referring to the non-activated single crystals adjusting the absorption coefficient of each crystals to zero at 400

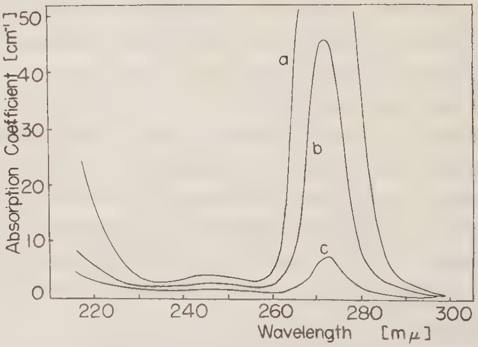

Fig. 3. Absorption spectra of KCl:Pb at room temperature. The concentrations of lead added to the melt are a: 0.1 mole %, b: 0.03 mole % c: 0.005 mole %.

mμ, where they were considered to be transparent.

The observed absorption spectra at room temperature are shown in Fig. 3 and Fig. 4 for various Pb-concentrations. The absorption at 273 mμ (hereafter will be called the A-band), found by previous investigators as a characteristics band of lead activator[2], is also evident in the present figure (Fig. 3). Another band had been found by earlier investigators at 196 mμ (B-band) for KCl:Pb. As our equipment is unreliable below about 220 mμ, we could not study the behavior of this band. But the rise of the absorption curves at the short wavelength region may correspond to this band. A small hump appears at 247 mμ in the KCl:Pb spectra. But as it seems to be independent with the concentration of lead in the crystal, this band may be due to some impurities such as thallium. Increasing the concentration of lead, the absorption coefficients of A-band increase namely proportionally to the lead content, and bands corresponding to paired centers did not appear in the present studies.

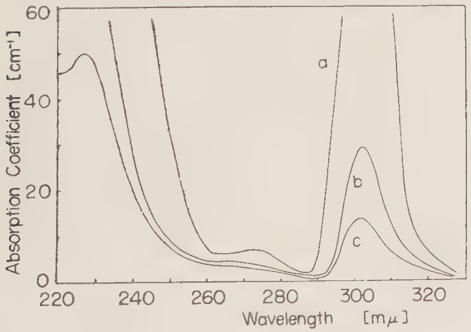

Fig. 4. Absorption spectra of KBr:Pb at room temperature. The concentrations of lead added to the melt are a: 0.1 mole %, b: 0.02 mole %, c: 0.005 mole % (absorption coef. ×2).

The oscillator strength of A-band is calculated with the Smakula's equation[11]:

$$Nf = 0.87 \times 10^{17} \frac{n}{(n^2+2)^2} \alpha_m \cdot W \,\mathrm{cm}^{-3} \qquad (1)$$

where f is the oscillator strength, n: the index of refraction, N: the concentration of the center per unit volume, α_m: the maximum absorption coefficient in reciprocal centimeter, and W: the half width of the band in eV. Using the observed absorption data and the concentration of lead in the crystal, this value is found as 0.075 and is nearly the same as that of 247 mμ band in KCl:Tl[15].

In KBr:Pb, strong two bands appear at about 302 mμ (A-band) and 227 mμ (B-band), and these also agree with the results of earlier measurements. In the present investigation, however, two new bands are observed at longer wavelength side of A-band and at about 272 mμ. As shown in Fig. 4, 302mμ band is asymmetrical, falling off in intensity more sharply at the shorter wavelength side than at the longer wavelength side. This indicates overlapping of another absorption band at the longer wavelength side. By the low temperature measurement, this point was justified, showing a small absorption band appears at 308 mμ at −190°C (Fig. 6).

The asymmetric shape of 302 mμ band is independent of the lead concentration, and found in the crystals even at very low lead content, then the center corresponding to this band may be considered as single Pb ion near a lattice defect rather than pairs of Pb ions. A similar result was found in the excitation spectra of NaCl:Pb showing that the asymmetrical 273 mμ band (may correspond to A-band of NaCl:Pb) was consisted of two excitation bands[4].

Another new observed band around 272 mμ

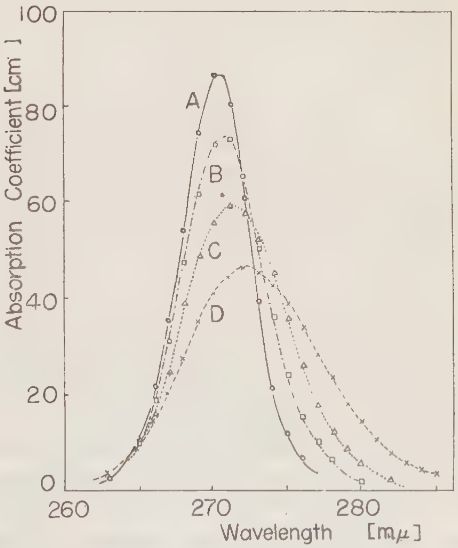

Fig. 5. Absorption Spectra of KCl:Pb at various temperatures. The concentrations of lead added to the Melt are 0.03 mole %.

A; −194°C, B; −155°C
C; −60°C, D; +80°C

is seen in Fig. 4 in a crystal at higher lead content, and is more sharply resolved by an excitation measurement disclosing this band consists of two band.

Burstein and his associates[12] showed that the absorption spectra of NaCl:Pb are very sensitive to its thermal history. In the present study, however, it is found that A-absorption bands of KCl:Pb and KBr:Pb are not almost altered by thermal treatments. In KBr:Pb, however, the absorption band at 272 mμ and the longer wavelength tail of B-band are fairly sensitive to its thermal treatment or a strain in the crystal. Comparing with the results of Burstein and his associates, it may be considered that the states of lead ion in potassium halide are more stable than that in sodium halide.

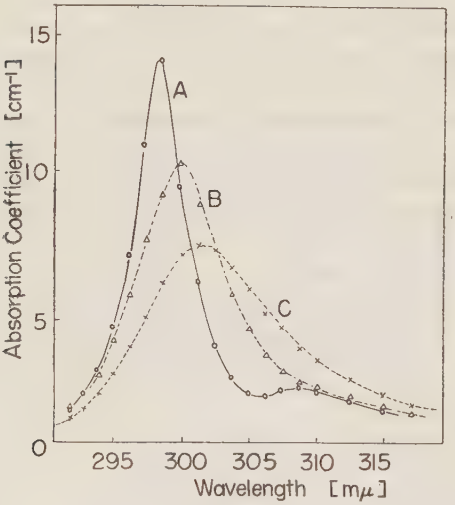

Fig. 6. Absorption spectra of KBr:Pb at various temperatures. The concentration of lead added to the melt is 0.005 mole %.
A: −190°C, B: −100°C, C: +25°C

The temperature variation of the absorption spectra was studied in detail on the A-band, and some of these results are shown in Fig. 5 and 6. In the KCl:Pb, the peak of the absorption band is shifted to the shorter wavelength side, and the band becomes sharper with lowering the temperature, but the integrated absorption area is nearly constant. These behaviors are similar to the F-center in alkali halide crystals. Similar results are obtained in the KBr:Pb, but in this case the band is asymmetric, as stated above, with lowering the temperature this band splits, and additional peak appears at longer wavelength side.

By configuration coordinate (C.C.) model, it is suggested that the absorption and emission band of luminescence center are Gaussian in shape as a first approximation. Hesketh and Schneider[13] discussed the absorption curve of F-center and derived an empirical expression of the absorption curve as follows:

$$\alpha=\alpha_0 \exp[-a(E-E_0)^b] \qquad (2)$$

where α_0 and a are constants, α: the coefficient of absorption, b: a constant which should be 2 for the curve to be Gaussian, E: the photon energy of the light at which α is measured, E_0: the photon energy of the peak of the absorption curve. Fig. 7 shows a plot of $(\ln \alpha_0/\alpha)^{1/2}$ as a function of E under the assumption that the absorption curve is Gaussian, wherein the constant a seems to be of different values in the right and left side of the absorption peak. The constant $|a|$ at higher energy side of E_0 is slightly larger than that of lower energy side at liquid nitrogen temperature. However, at higher temperature these difference is not detected*. In any case it is seen from Fig. 7 that A-

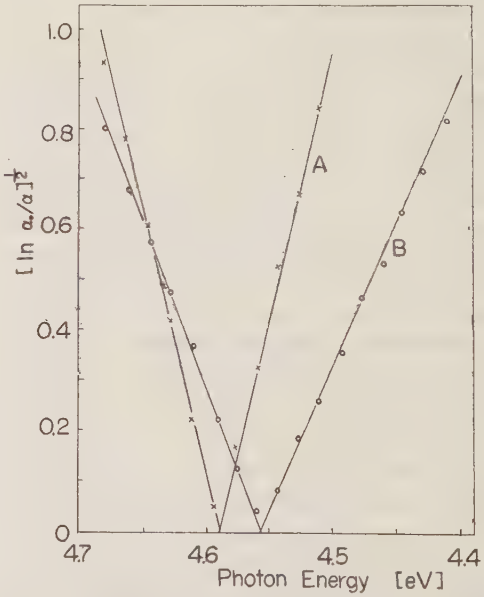

Fig. 7. Gaussian plots of the absorption bands for KCl:Pb (0.03 mole %)
A: −195°C, B: −60°C.

---

* Markham[14] attempted to synthesize more rigorous theory on the band shape and the half width of the absorption band.

absorption band of KCl:Pb is nearly Gaussian in shape above the liquid nitrogen temperature.

The variation of the bandwidth with temperature is shown in Fig. 8 for KCl:Pb, wherein the bandwidth at half maximum, normalized at 300°K, are plotted against $T^{1/2}$ in order to show the approach at high temperature to the $T^{1/2}$ dependence of the width of absorption curve. The C.C. model predicts that the width of absorption band at half maximum, W_a, is given by

$$W_a = A[\coth(h\nu_g/2kT)]^{1/2} \qquad (3)$$

where A is a constant, h: Planck's constant, k: Boltzman's constant, and T: the absolute temperature. In this expression ν_g is a vibrational frequency which influences the center in its ground state. From Fig. 8 it is clearly seen that experimental points best fit the solid curve when Eq. (3) is used by choosing $\nu_g = 3.6 \times 10^{12}$ sec^{-1}.

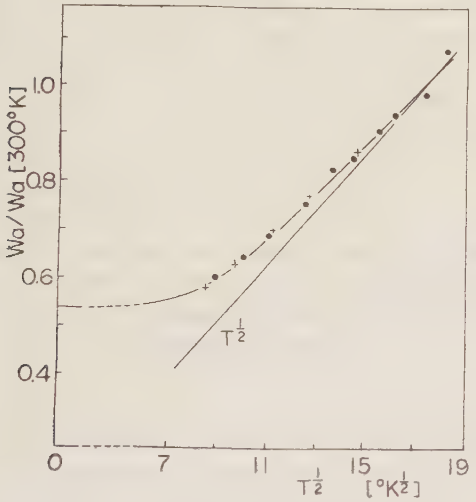

Fig. 8. The temperature variation of the absorption band width at half maximum for KCl:Pb.

● 0.03 mole % Pb
+ 0.005 mole % Pb

In KBr:Pb, these plots are not shown, since the absorption bands are not Gaussian in shape and have overlapping of other band at higher temperature.

b) *Emission spectra*

The apparatus used in this study consists of following arrangement. A monochromator with a hydrogen lamp was used for the irradiation of the sample. The fluorescence of the sample was observed with another monochromator and a 1P28 phtomultiplier in the direction normal to the exciting light (Fig. 2b). The latter monochromator, which has a band

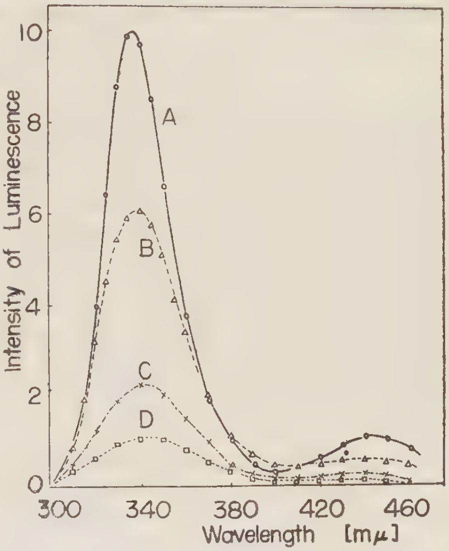

Fig. 9. Emission spectra of KCl:Pb at various temperatures. The concentration of lead added to the melt is 0.03 mole %.

A: −190°C, B: 0°C,
C: +50°C, D: +80°C.

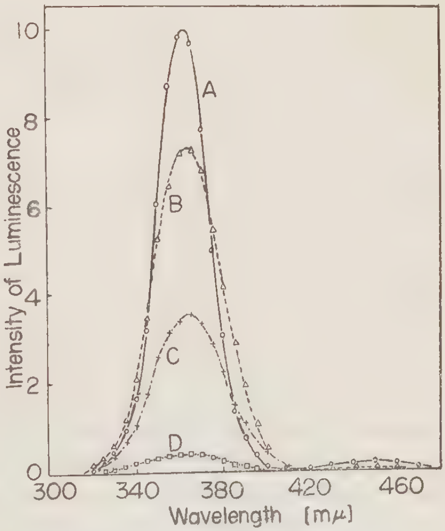

Fig. 10. Emission spectra of KBr:Pb at various temperature.
The concentration of lead added to the melt is 0.1 mole %.

A: −193°C B: −120°C
C: −95°C, D: −45°C.

pass of about 5 mμ at 350 mμ, is calibrated for spectral transmission and sensitivity of the phototube, in order to ascertain the real shape of the emission spectra.

The emission spectra were studied under the irradiation of light in the A-absorption band. Typical emission spectra are shown in Fig. 9 and 10 at various temperatures. The emission spectra consist of intense near ultra-violet band and weak visible band. As the visible band is very weak, special care in measurements are necessary for accurate determination of the peak position and the band shape. The peak of the near ultra-violet band lies at 345 mμ for KCl:Pb and 365 mμ for KBr:Pb at room temperature. These peaks shift toward the red in passing from chloride to bromide, in accordance to the general rule of alkali halide phosphors.

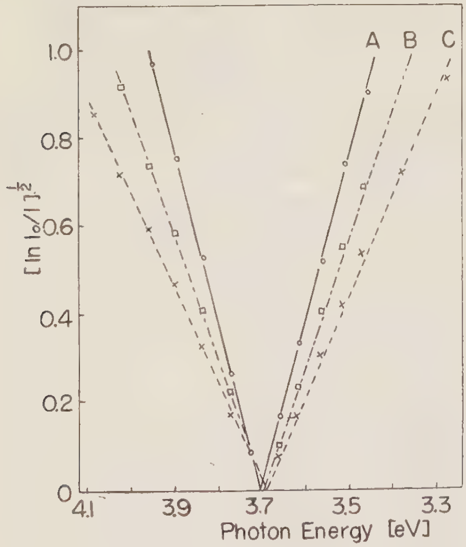

Fig. 11. Gaussian plots of the emission bands for KCl:Pb (0.03 mole % Pb).

A: 193°C, C: −95°C, C: 67°C.

By lowering the temperature, the peak of the emission band also shifts toward the short wavelength. The shape of the emission band is nearly Gaussian as shown by Fig. 11, in which $(\ln I_0/I)^{1/2}$ is plotted as a function of the emission photon energy. Here I_0 and I are the emission intensities at the peak of the band and photon energy E, respectively. These plots fairly well fit into equation similar to (2), showing that the observed near ultra-violet emission band is not a composite band but a single emission band.

Fig. 12 shows a relation between half maximum band width and the temperature. Points indicating the observed values also fit the solid and dotted curves, by assuming ν_e: $4.0\times10^{12}\,\mathrm{sec}^{-1}$. and $3.0\times10^{12}\,\mathrm{sec}^{-1}$. for KCl:Pb and KBr:Pb, respectively. Here ν_g of Eq. (3) is replaced by ν_e which corresponds to a vibrational frequency that influence the luminescence center in its excited state.

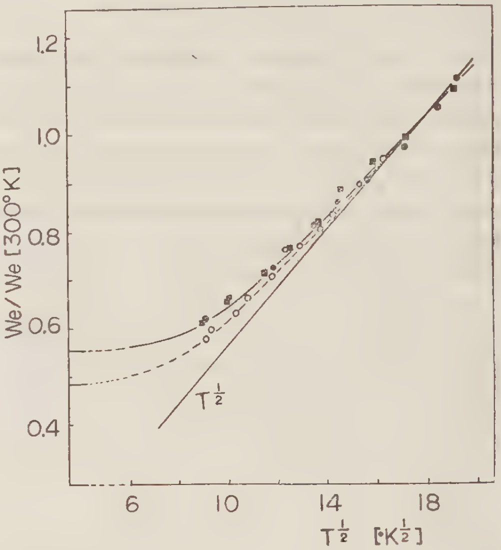

Fig. 12. The temperature variations of the emission band width at half maximum.

KCl:Pb —●— 0.03 mole % Pb
—■— 0.1 mole % Pb
KBr:Pb --○-- 0.02 mole % Pb

Extrapolating these curves, we get the values of half maximum band width at 0°K as 0.26 eV and 0.20 eV for KCl:Pb and KBr:Pb, respectively.

Fig. 9 and 10 also show that the fluorescence of lead activated potassium halides are greatly enhanced at low temperature. By detailed experimental investigation about the temperature variation of the emission intensity, it is justified that the probability of non-radiative transitions to the ground state is appreciably large even at room temperature. At liquid nitrogen temperature, however, it is found that the quantum yields of these emission are nearly unity by relative measurements with KCl:Tl phosphor, which is reported to have a quantum yield of unity for 305 mμ emission band.

Fig. 13 shows the results of these measurements. The probability for these nonradiative transitions may be expressed as

$$P_Q = s\exp(-E_Q/kT)\,, \tag{4}$$

where, E_Q and s are activation energy and frequency factor. It may be considered that the probability of a spontaneous emission, $1/\tau$, is temperature independent as a first approximation, then the luminescence efficiency, η, is given by

$$\eta = [1 + s\tau\exp(-E_Q/kT)]^{-1}\,. \tag{5}$$

In Fig. 13, the luminescence intensity normalized at lowest temperature values is plotted on a logarithmic scale as a function of $1/T$ °K. The quenching rates of the higher temperature portion correspond to the activation energies of 0.28 eV for KCl:Pb and 0.18 eV for KBr:Pb. Assuming τ as 10^{-7} sec., the frequency factor for this process is of the order of the vibrational frequency, i.e. 10^{12} sec^{-1} or greater.

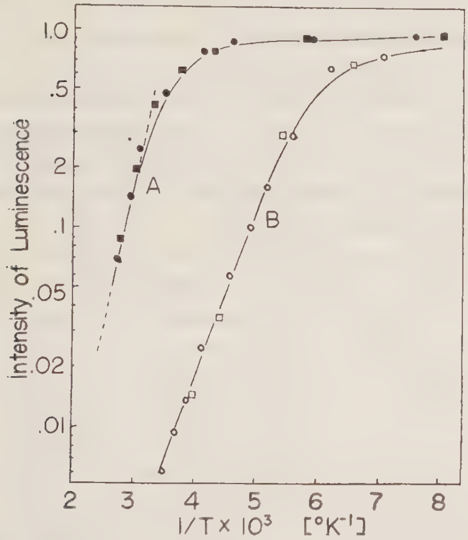

Fig. 13. Temperature variations of the emission intensities for KCl:Pb (A) and KBr:Pb (B).

The emission spectrum of high lead content of KCl:Pb is changed by aging of several weeks at room temperature, where by the near ultra-violet emission band becomes broad, and its maximum is shifted to the red by some ten mμ. By thermal treatment at about 400°C, however, the emission band turns into ordinary single Gaussian band such as in a crystal of low lead concentrations. In the preparation of a crystal, it is found that colloidal aggregates of lead ions are easily produced in alkali halide crystals containing high lead concentrations. These change of emission spectra may be considered due to aggregation of lead ions in the crystals.

c) *Excitation spectra*

The apparatus used in this study is as follow: a monochromator with a Beckmann hydrogen lamp is used to irradiate the sample. The fluorescence of the sample is observed with the 1P28 photomultiplier in the direction normal to the exciting light. A filter is inserted between the sample and the phototube to cut off the reflected exciting light and to transmit the main emitting light of the phosphor. The filter employed is Matsuda UV–D1 which transmits light waves between about 310 mμ and 400 mμ, covering the near ultra-violet emission spectra of KCl:Pb and KBr:Pb. The energy of the exciting light on the specimen is corrected by a 1P28 photomultipler covered with sodium salicylate.

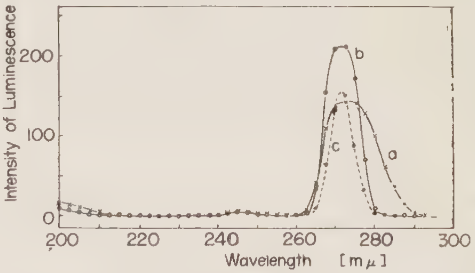

Fig. 14. Excitation spectra of KCl:Pb. The concentration of lead added to the melt are 0.1 mole % (solid line) and 0.005 mole % (dotted line).

a: +27°C, b, c: −193°C.

Typical excitation spectra of KCl:Pb and KBr:Pb are shown in Figs. 14 and 15. In KCl:Pb, the near ultra-violet emission band is favored by the excitation of A-absorption band. Especially with specimen of low lead concentration, the excitation band coincides very well with the absorption band at 273mμ with respect to band shape and temperature variation of the peak position. In the case of high lead content, the excitation peak is flat owing to the saturated absorption of the exciting light. Appearance of the near ultra-violet emission under the excitation of B-band was not ascertained, as our equipment could not give reliable results below 220 mμ. Comparing with the absorption spectra, however, it may be considered that B-band is not very effective in stimulation the near ultra-violet emission.

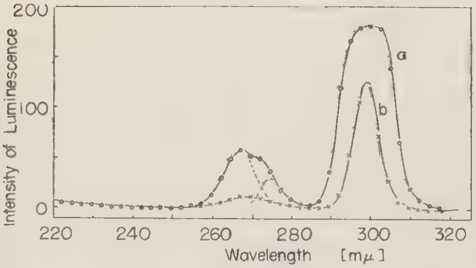

Fig. 15. Excitation spectra of KBr:Pb at −196°C. a: 0.1 mole %, b: 0.02 mole %.

In KBr:Pb, the near ultra-violet emission is also favored by the excitation of A-band, but is not favored by the excitation of B-band peaked at 227 mμ. The new absorption band around 272 mμ is also found in this excitation spectra. Excitation intensity of this band gradually increases with the same rate as A-band by lowering the temperature. Accordingly, these excitation and absorption bands are considered due to some composite lead centers. As in the absorption spectra, the intensity of this band is changed by the thermal history of the specimen. It may be clear by Fig. 15 that this band consists of two bands peaking at about 268 mμ and 275 mμ at liquid nitrogen temperature.

§ 4. Computation of Configuration Coordinate Curve

The continuous dielectric model is inadequate to describe the optical properties of the Pb-center, since the experimentally derived ground state frequency ν_g is fairly small compared with the longitudinal optical vibration frequency ν_0 of the host crystal ($\nu_0=6.3\times 10^{12}\,\mathrm{sec}^{-1}$ for KCl[9]). Therefore, the C.C. model will be applied to the Pb-center to compute the ground and excited state energy curves.

The evaluation of C.C. curves are carried out in accordance to the method described by Klick[16]. In these treatments, it is assumed that; (1) the predominant vibrational mode of the center is the breathing mode, so that a single coordinate may be used, (2) the energy curves are parabolic so that the center acts as a simple harmonic oscillator in both states, (3) the initial state of the center is treated by quantum mechanical method whereas the final state curve is treated classically, (4) the slope of the final state curve is taken to be a constant value over the range of transition coordinates.

The above mentioned single coordinate is taken as the distance from the center to the nearest neighboring halogen ion assuming that lead ions replace the potassium ions in the cubic lattice, being surrounded by six halogen ions.

To describe the C.C. curves, four constants are necessary. K_g and K_e are force constants for the ground and excited states, X_0 and E_0 are the displacement of the minimum of the excited state from the ground state minimum along the coordinate axis and energy axis, respectively. In addition, the mass of the oscillator system, M, is needed. Williams had shown that the effective mass of a Tl-center in KCl is the sum of the masses of the six nearest halogen ions multiplied by a factor of 1.2, considring the effect of other host lattice ions[17]. The specific assumption on the mass is not critical in most applications of these curves. Thus the mass of the oscillator will be assumed in the manners described above.

Using these constants, experimental data

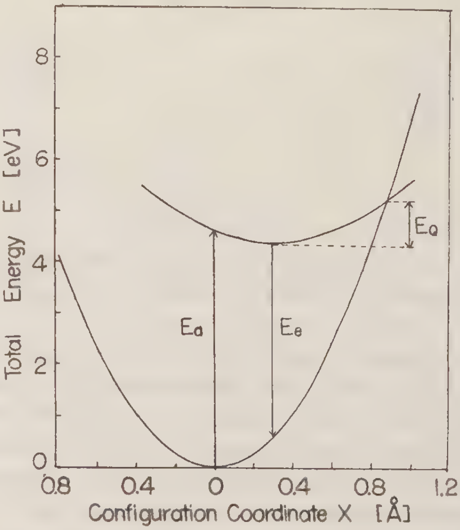

Fig. 16. Calculated configuration coordinate curves for the ground and lowest excited states of Pb-center in KCl.

may be expressed by the following equations: ν_g may be represented in terms of the forgoing constants as

$$\nu_g \fallingdotseq (2\pi)^{-1}(K_g/M)^{1/2}\ . \qquad (6)$$

Energies at the peaks of the absorption and emission bands are expressed as

$$E_a = E_0 + K_e X_0^2/2 \qquad (7)$$

$$E_e = E_0 - K_g X_0^2/2 \qquad (8)$$

in these expression, where the zero point energy (in the order of 0.01 eV) is neglected. The width of the absorption band at half maximum is given by

$$W_a \fallingdotseq 1.355\times10^{-13} K_e X_0(\nu_g/K_g)^{1/2} \qquad (9)$$

in ergs. at the low temperature limit.

Eqs. (6), (7), (8) and (9) were used to compute the C.C. curves for the Pb-center in KCl. The experimental values used are the following: $M=4.16\times10^{-22}$ gr., $\nu_g=3.6\times10^{12}$ sec^{-1}, $E_a=4.59$ eV, $E_e=3.71$ eV and $W_a=0.089$ eV. The resultant curves are illustrated in Fig. 16, and calculated constants are shown in Table I. The calculated values for KCl:Tl by Klick are also found in Table I[18].

Table I. The Calculated and Observed Constants of the Configuration Coordinate Curves.

	K_g ev/A^2	K_e eV/A^2	X_0 Å	E_0 eV	ν_{ec} $\times10^{12}$ sec^{-1}	ν_{eo} $\times10^{12}$ sec^{-1}	W_{ec} eV	W_{eo} eV
KCl:Pb	13.4	5.6	0.30	4.35	2.3	4.0	0.28	0.26
KCl:Tl[18]	16.8	6.4	0.36	5.05	2.5	5.6	0.26	0.32

With these constants and equations for the excited state similar to Eqs. (6) and (9), it becomes possible to predict the vibrational frequency at the excited state and the width of the emission band at the low temperature limit, assuming that the mass of the oscillator is identical for the system in its ground and excited states. These values are also shown as ν_{ec} and W_{ec} in Table I together with the corresponding observed values, ν_{eo} and W_{eo}.

From these values in Table I, it is clear that the force constant for the excited state is smaller than that of the ground state. This is also presumed from the difference of the band width between the emission and absorption spectra, and indicates that the excited state has more diffuse charge distributions than the ground state. This conclusion seems to be a character of the impurity center, in which the impurity is a positive ion in ionic crystals. The calculated value of the emission band width coincides farely well with the observed value, but some discrepancy is found in the excited frequency.

The height of the intersection of the ground and excited state curves above the minimum of the excited state curve corresponds to the activation energy, E_Q, of the non-radiative transition of the luminescence center. This value is found to be about 0.9 eV. In this calculation, it is assumed that the ground state curve is parabolic at even higer energy. It may be considered that the potential curve rises more rapidly than a parabola at these large amplitude of the oscillation owing to the repulsive force. Thus calculation gives somewhat larger value of the activation energy. Even if these effects are considered, it seems to be too large compared with the observed value, namely 0.28 eV.

§ 5. Discussion

It may be considered that the luminescence centers of these lead activated alkali halide phosphors are composed of Pb-ion surrounded by the negative ions of the host crystals. Hence the electronic configurations of the central ion may be described as $5d^{10}\ 6s^2$ for the ground state and $5d^{10}\ 6s6p$ for the excited state, similar to the case of Tl-activated one. KCl:Tl is the most widely studied phosphor both side in experiment and theory. Therefore Pb-phosphors are considered here in connection with Tl-phosphors.

The observed absorption spectra of Pb-phosphors are remarkably similar to those of Tl-phosphors. Two strong absorption bands (A- and B-band) may be considered as corresponding to the transitions for two excited states, $^1P_1$ and $^3P_1$, from the ground state, $^1S_0$, of Pb-ion perturbed by the surrounding host lattice ions. In KCl:Pb, the $^1P_1$ absorption band (B-band) occurs at 196 mμ whose energy is almost the same as that of KCl:Tl, but the $^3P_1$ absorption band (A-band) is shifted to the longer wavelength side than in KCl:Tl. Similar results are also found in KBr case, accordingly the separations between the $^1P_1$ and $^3P_1$ states are larger in Pb-phosphors than Tl-phosphors. These are expected from the fact that a larger spin-orbit interaction exists for the Pb-centers.

The near ultra-violet emission band may be regarded as the reverse process of A-absorption by the results of the excitation measurements, therefore these transitions are attributed to $^3P_1 \rightarrow {}^1S_0$, which appears at longer wavelength than Tl-phosphors. The photon energies at the peaks of the emission bands are found to be 3.71 eV and 3.14 eV for KCl:Pb and KBr:Pb, respectively. The Stockes' shifts of these $^1S_0 \rightarrow {}^3P_1$ transitions, however, have the same values within experimental error in both Pb- and Tl-phosphors but are changed by the different host lattices, namely, 0.87 eV for KCl and 0.76 eV for KBr. These Stockes' shifts are originated from the energy dissipation in the lattice after an optical transition. It is therefore not surprising that these values are more intimately related to the host lattice than the center ion, and the unique values for each host crystals may be accidental.

In the excitation spectra, the light in $^1P_1$-absorption band does not excite emission so intensely as the excitation of $^3P_1$ band. In Tl-phosphors, the excitation of $^1P_1$ band yields emission in both near ultra-violet and visible bands, which correspond to the transitions of $^3P_1 \rightarrow {}^1S_0$ and $^1P_1 \rightarrow {}^1S_0$, respectively[19).* If we consider the present results in connection with those of Tl-phosphors, the weak visible emission may be considered as corresponding to the transition of $^1P_1 \rightarrow {}^1S_0$. However, the visible emission here is too weak to carry out reliable excitation measurements. The light in $^1P_1$-absorption band does not stimulate the near ultra-violet emission. The situation is different in the case of Tl-phosphors. These indicate that the internal conversion between $^1P_1$ and $^3P_1$ states does not take place effectively in Pb-phosphrs. In either case, the reverse process of $^1S_0 \rightarrow {}^1P_1$ absorption is not observed as effective photoluminescence process. Hence the author considers that $^1P_1$ state is susceptible to non-radiative transition.

Similar phenomena are also found for $^3P_1$-state by the temperature variation of the near ultra-violet emission. As it is shown in Fig. 13, Pb-phosphors do not show so efficient a luminescence as Tl-phosphors above room temperature. At liquid nitrogen temperature, these efficiencies are increased up to that of Tl-phosphors which is considered to be nearly unity. The above phenomena indicate that the $^3P_1$-state also suffers non-radiative transition at room temperature. The activation energies of this process are found to be 0.28 eV for KCl:Pb and 0.18 eV for KBr:Pb, therefore the non-radiative process operate more effectively in KBr lattice than KCl lattice.

In the C.C. model, the activation energy E_Q corresponds to the height of the intersection of the ground $^1S_0$ and excited $^3P_1$ energy curves above the minimum of $^3P_1$ state. The smallness of E_Q may be expected as a result from the diffuseness of the excited state, thus $^3P_1$ states of Pb centers in both alkali halides interact more strongly with the states of the host lattice ions than Tl-centers.

On the other hand, a positive ion vacancy is introduced in the neighbourhood of Pb-ions owing to the charge compensation of the host lattice. If these positive ion vacancies occupy a neighboring site of the luminescence center as observed in NaCl:Mn[20), it may be presumed that these vacancies play an important part in the above non-radiative process.

Fredericks and Scott[21) have shown that Pb-centers in KCl at high temperature migrate as if they were negative ions such as $PbCl_6^{4-}$ by measurements of the ionic conductivity. Several questions are presented whether these complex ions exist in the crystals at lower temperature[3). However, it may be seen that Pb-ions in alkali halides are more intimately mixed with the negative ions of the host lattice than for the case of Tl-ions. The present results favor the view that these interactions are more strong in KBr than in KCl lattice.

The one dimentional C.C. model interpretes fairly well the observed results for the shape and the band width of the spectra in Pb-phosphors. The temperature variations of the band width are also well interpreted by this model. However, calculation on this model with observed absorption data does not bring reasonable results for the emission data. This model also does not elucidate the difference of the non-radiative process between Pb- and Tl-phosphors, since the calculated value of the activation energy in Pb-phosphor is greater than the Tl-phosphor, which is opposite direction to the experimental results.

---

* Recently, several question are presented against this old interpretation of the visible emission in KCl:Tl.

These indicates the possibility of the application of one dimentional C.C. model. Namely, this model describes the optical properties related to a single state fairly well, but it does not present satisfactory results for the process related to both the ground and excited states such as non-radiative transition. The author supposes that these limitation come from the simplified assumption adopted in this model where the breathing mode of vibration is always effective in both states. If another mode of vibration is broken out after optical transition, the values of the final state calculated by this model with the data of initial state will not give satisfactory results.

Recently, Karo, McComble and Murray[22] found that main contribution to the breadth of F-band come from modes in fairly small range of frequencies in which the empirical configuration frequency is included. Therefore, the present results obtained for the ground and excited frequencies, ν_{g0} and ν_{e0}, may be considered to have close resemblance to real frequencies.

To make more advanced treatments of Pb-center including non-radiative process, it may be necessary to use of a multidimensional C.C. treatment, developed and applied by Kamimura and Sugano[23] for KCl:Tl, considering the effects of the all excited level such as $^1P_1$, $^3P_2$, $^3P_1$ and $^3P_0$ states of Pb-ions.

§ 6. Summary

1) Absorption spectra of lead activated phosphors are nearly the same as the results of earlier investigations. Two intense bands (A- and B-bands) are considered as transitions of $^1S_0 \to {}^3P_1$ and $^1S_0 \to {}^1P_1$ in Pb^{++} ion perturbed by host lattice ions.

2) Emission band observed in near-ultraviolet region may be ascribed to $^3P_1 \to {}^1S_0$ transition.

3) The excitation of $^1P_1$ state does not result in any distinct emission different from the case of Tl-phosphors. This indicates that $^1P_1$-state of Pb-center is susceptible to non-radiative transition.

4) $^3P_1$-state also suffers non-radiative transition at room temperature. The activation energies of this process are found as 0.28 eV and 0.18 eV for KCl:Pb and KBr:Pb, respectively.

5) These results favor the view that Pb-ions in alkali halide are intimately mixed with the negative ions of the host lattice, but is not well interpreted by the use of a semiempirical C.C. treatment.

6) The temperature variations of the absorption and emission band width are fairly well interpreted by a simple C.C. model, and the C.C. frequencies of the luminescence center in KCl:Pb are found as 3.6×10^{-12} sec^{-1} and 4.0×10^{12} sec^{-1} for the ground and excited states, respectively.

7) C.C. curves for KCl:Pb are calculated by a semiempirical method. Some results expected from these curves are compared with the observed data; the agreement in emission band width and disagreements in the activation energy for non-radiative process and the effective vibrational frequency of the center at excited state are obtained.

Acknowledgements

The author would like to express his thanks to Prof. T. Okuda for his guidance during the course of this study, and also to Prof. M. Sawada and Prof. T. Nagamiya of Osaka University for their kind advice and comments on this manuscript. His thanks are also due to Mr. T. Miwa for his assistance in the process of chemical analysis of the specimen.

References

1) R. Hilsch and R. W. Pohl: Z. Phys. **48** (1928) 384, ibid **57** (1929) 145, ibid **59** (1930) 812.
2) R. Hilsch: Z. Phys. **44** (1927) 860, Proc. Phys. Soc. **49** (1937) 40, M. Forro: Z. Phys. **56** (1929) 543.
3) D. S. McClure: Solid State Physics, ed. by Seitz and Turnbull, Vol. 9 (1959) Academic press. inc.
4) J. H. Schulman, R. J. Ginter and C. C. Klick: J. Opt. Soc. Amer. **40** (1950) 854.
5) M. Kato: Sci. Rep. Phys. Chem. Res. Tokyo

41 (1943) 113.

6) A. von Hippel: Z. Phys. **101** (1936) 680.

7) F. Seitz: Trans. Farad. Soc. **35** (1939) 79.

8) F. E. Williams: J. Chem. Phys. **19** (1951) 457.

9) G. Russel and C. C. Klick: Phys. Rev. **101** (1956) 1473.

10) D. A. Patterson and C. C. Klick: Phys. Rev. **105** (1957) 401.

11) D. L. Dexter: Solid State Physics, ed. by F. Seitz and D. Turnbull, Vol. 6 (1958) Academic press, New York.

12) E. Burstein, J. J. Oberly, B. W. Henvis and J. W. Davisson: Phys. Rev. **81** (1951) 459.

13) R. V. Hesketh and E. E. Schneider: Phys. Rev. **95** (1954) 837.

14) J. J. Markham: Rev. Mod. Phys. **31** (1959) 956.

15) R. S. Knox and D. L. Dexter Phys. Rev. **104** (1956) 1245.

16) C. C. Klick: Phys. Rev. **85** (1952) 154. C.C. Klick and J. H. Schulman: Solid State Physics, ed, by F. Seitz and D. Turnbll, Vol. 5 (1957) Academic Press, New York.

17) F. E. Williams: J. Phys. Chem. **57** (1953) 780.

18) C. C. Klick: Phys. Rev. **85** (1952) 154.

19) P. D. Johnson and F. E. Williams: J. Chem. Phys. **20** (1952) 124.

20) G. D. Watkins and R. M. Walker: Bull. Amer. Phys. Soc. **1** (1956) 837. K. Morigaki, M. Fujimoto and J. Itoh: J. Phys. Soc. Japan **13** (1958) 1174.

21) W. J. Fredericks and A. B. Scott: J. Chem. Phys. **28** (1958) 249.

22) A. M. Karo, C. W. McCombie and A. M. Murray: Phys. Rev. **119** (1960) 504.

23) H. Kamimura and S. Sugano: J. Phys. Soc. Japan **14** (1959) 1612.

Journal of the Physical Society of Japan, Vol. 16, No. 8, August, 1961

Local Description of the Flow behind a Steady, Two-Dimensional, Curved Shock Wave*

By Zirō Hasimoto and Shigeki Morioka

Department of Mathematics and Physics, Faculty of Science and Engineering, Ritumeikan University, Kyoto

(Received February 16, 1961)

The local properties of the rotational flow field behind a steady, two-dimensional, curved shock wave which occurs in a supersonic uniform flow of a perfect gas are considered. The states of flow field in the vicinity of a point on a shock wave are described as a power series about this point under the assumption that the shape of the shock wave is regular. The hodograph transformation of such a field becomes singular at the points where Jacobian relating to the transformation vanishes. The fields in the vicinity of such singular points are discussed in detail.

§ 1. Introduction

We shall consider the flow behind a steady, two-dimensional, curved shock wave which occurs in a supersonic uniform flow of a perfect gas. We assume that the viscosity and thermal conductivity of the gas can be neglected. In general, however, the flow field behind the shock wave is rotational. When the shape of the shock wave is given as a regular curve, the flow field immediately behind the shock can be determined by the shock conditions. It is the purpose of the present paper to describe the local field behind a shock wave as the series expansion about the field value immediately behind the shock, and to transform such a local field to the hodograph plane. First, in Section 2, we give the expressions for the derivatives of the velocity components immediately behind the shock wave. These derivatives are necessary for the determination of the coefficients in the expansion formulas for the various quantities of flow as seen in the following sections. These derivatives enable us to determine the directions and curvatures of the lines of constant speed, deflection, pressure, and density immediately behind the shock wave (Section 3). The pressure distribution on a streamline behind a shock wave is formulated in Section 4. The formula thus obtained seems to be useful to find the pressure distribution over the surface of a curved airfoil in the neighbourhood of its leading edge when a shock wave is attached to the edge.

---

* The results in §§ 4, 5, 6 of this paper have been reported in part by one of the authors (Z.H.) (Ref. 1).

In the transformation of such local field onto the hodograph plane, we find that there occur certain cases when the Jacobian defined by Eq. (31) vanishes. This is the case, for example, when the shock spine coincides with the shock polar in the hodograph plane, or when the shock wave has an inflection point. The singularity at such points and the flow fields in the vicinity of those point are discussed in Sections 5 and 6.

§ 2. Derivatives of the Velocity Components Immediately behind a Shock Wave

We choose the origin of the coodinate system at a point of interest on a shock wave, and take the x_1-axis in the direction of the velocity vector immediately behind the shock wave and the x_2-axis perpendicularly to it (see Fig. 1). The shock conditions can be expressed as follows,

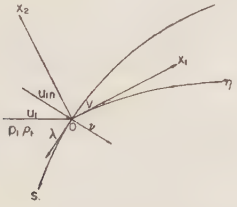

Fig. 1.

$$\left.\begin{aligned} u_\alpha &= u_{1\alpha} - \frac{2(\rho_1 u_{1n}{}^2 - \gamma p_1)\nu_\alpha}{(\gamma-1)\rho_1 u_{1n}} \qquad (\alpha=1,2) \\ p &= p_1 + \frac{2}{\gamma+1}(\rho_1 u_{1n}{}^2 - \gamma p_1) \\ \rho &= \rho_1 + \frac{2\rho_1(\rho_1 u_{1n}{}^2 - \gamma p_1)}{2\gamma p_1 + (\gamma+1)\rho_1 u_{1n}{}^2}\,, \end{aligned}\right\} \tag{1}$$

where u_α, p and ρ are the velocity components, the pressure, and the density immediately behind the shock wave; those with the subscript 1 denote the values in front of the shock wave; ν_α are the components of the normal unit vector to the shock line; $u_{1n} = u_{1\alpha}\nu_\alpha$; and γ is the ratio of the specific heats. Differentiating Eq. 1 with respect to the arc-length along the shock line, we obtain[2]

$$\left.\begin{aligned} u_{\alpha,\beta}\lambda_\beta &= A_\alpha \kappa \\ p_{,\beta}\lambda_\beta &= B\kappa \\ \rho_{,\beta}\lambda_\beta &= C\kappa\,, \end{aligned}\right\} \tag{2}$$

where λ_β denote the components of the tangential unit vector to the shock line, the subscript, β denote $\partial/\partial x_\beta$ and κ is the curvature of the shock line. The curvature of the shock line is assumed to be positive for the shock wave convex to the x_2-axis. In the above equations the summation convention is used and this convention will be used throughout this paper. A_α, B and C are given as

$$\left.\begin{aligned} A_1 &= -\lambda_1\lambda_2\left(\frac{4}{\gamma+1} + \frac{[\rho]^2}{\rho\rho_1}\right)v \\ A_2 &= \left\{\frac{4}{\gamma+1}\lambda_1{}^2 - \frac{[\rho]}{\rho}\left(\lambda_1{}^2 + \frac{\rho}{\rho_1}\lambda_2{}^2\right)\right\}v \\ B &= \frac{4}{\gamma+1}\lambda_1\lambda_2\rho v^2 \\ C &= 2\frac{\lambda_1}{\lambda_2}\left(\rho_1 - \frac{\gamma-1}{\gamma+1}\rho\right)\,, \end{aligned}\right\} \tag{3}$$

where $[\rho] = \rho - \rho_1$ and v is the speed of flow immediately behind the shock wave. On the other hand, the flow behind a shock is governed by the following equations

$$\left.\begin{aligned} &p_{,\alpha} + \rho u_\sigma u_{\alpha,\sigma} = 0 && \text{(Equation of motion)} \\ &\rho_{,\alpha} + \rho u_{\sigma,\sigma} = 0 && \text{(Equation of continuity)} \\ &\rho u_{\alpha,\beta} u_\alpha u_\beta - \gamma p u_{\sigma,\sigma} = 0 && \text{(Entropy is constant along each streamline)}\,. \end{aligned}\right\} \tag{4}$$

Solving Eqs. (2) and (4) simultaneously, the first derivatives $u_{\alpha,\beta}$ of the velocity components u_α immediately behind a shock wave are obtained in the form

$$u_{\alpha,\beta} = F_{\alpha\beta}\kappa\,, \tag{5}$$

where

$$\left.\begin{aligned} F_{11}&=\frac{1}{m^2\lambda_2^2-1}\left(\lambda_1\frac{B}{\rho v}+\lambda_2A_2\right)\\ F_{12}&=\frac{1}{\lambda_2}(A_1-\lambda_1F_{11})\\ F_{21}&=-\frac{1}{m^2\lambda_2^2-1}\left\{\lambda_1A_2+\lambda_2(m^2-1)\frac{B}{\rho v}\right\}\\ F_{22}&=(m^2-1)F_{11}\ , \end{aligned}\right\} \tag{6}$$

and m denotes the Mach number immediately behind a shock wave. Further differentiation of the first two of Eq. (2) with respect to the arc-length s along the shock line yields

$$\left.\begin{aligned} u_{\alpha,\beta\gamma}\lambda_\beta\lambda_\gamma&=-u_{\alpha,\beta}\lambda_{\beta,\gamma}\lambda_\gamma+\frac{dA_\alpha}{ds}\kappa+A_\alpha\frac{d\kappa}{ds}\\ p_{,\beta\gamma}\lambda_\beta\lambda_\gamma&=-p_{,\beta}\lambda_{\beta,\gamma}\lambda_\gamma+\frac{dB}{ds}\kappa+B\frac{d\kappa}{ds}\ , \end{aligned}\right\} \tag{7}$$

where

$$\left.\begin{aligned} \frac{dA_1}{ds}&=-\frac{4}{\gamma+1}\left(\lambda_1^2-\frac{\rho}{\rho_1}\lambda_2^2\right)v\kappa-\lambda_1\lambda_2\left(1-\frac{\rho_1}{\rho}\right)v\frac{C\kappa}{\rho}\\ \frac{dA_2}{ds}&=-\frac{4}{\gamma+1}\lambda_1\lambda_2\left(1+\frac{\rho}{\rho_1}\right)v\kappa-\left(\lambda_1^2\frac{\rho_1}{\rho}+\lambda_2^2\right)v\frac{C\kappa}{\rho}\\ \frac{dB}{ds}&=\frac{4}{\gamma+1}\left(\lambda_1^2-\frac{\rho^2}{\rho_1^2}\lambda_2^2\right)\rho_1v^2\kappa\ . \end{aligned}\right\} \tag{8}$$

Differentiating, on the other hand, the first and the third of Eq. (4) along the axes of the coordinate system, we get

$$\left.\begin{aligned} &\rho u_\sigma u_{\alpha,\sigma\gamma}+p_{,\alpha\gamma}=-(\rho_{,\gamma}u_\sigma u_{\alpha,\sigma}+\rho u_{\sigma,\gamma}u_{\alpha,\sigma})\\ &\rho u_\alpha u_\beta u_{\alpha,\beta\gamma}-\gamma p u_{\sigma,\sigma\gamma}=-(\rho_{,\gamma}u_{\alpha,\beta}u_\alpha u_\beta+\rho u_{\alpha,\beta}u_{\alpha,\gamma}u_\beta+\rho u_{\alpha,\beta}u_\alpha u_{\beta,\gamma}-\gamma p_{,\gamma}u_{\sigma,\sigma})\ . \end{aligned}\right\} \tag{9}$$

The respective terms on the right hand sides of Eqs. (7) and (9) can be determined by using the preceding results. Solving Eqs. (7) and (9) simultaneously, these second derivatives of the velocity components immediately behind the shock wave are obtained as follows:

$$u_{\alpha,\beta\gamma}=G_{\alpha\beta\gamma}\frac{d\kappa}{ds}+H_{\alpha\beta\gamma}\kappa^2\ , \tag{10}$$

where

$$\left.\begin{aligned} G_{111}&=-\frac{1}{(m^2\lambda_2^2-1)^2}\left\{2\lambda_1\lambda_2A_2+[\lambda_1^2+(m^2-1)\lambda_2^2]\frac{B}{\rho v}\right\}\\ G_{112}&=\frac{1}{(m^2\lambda_2^2-1)^2}\left\{[\lambda_1^2+(m^2-1)\lambda_2^2]A_2+2(m^2-1)\lambda_1\lambda_2\frac{B}{\rho v}\right\}\\ G_{122}&=\frac{1}{\lambda_2^2}\{-\lambda_1^2G_{111}-2\lambda_1\lambda_2G_{112}+A_1\}\\ G_{211}&=G_{112}\ ,\qquad G_{212}=(m^2-1)G_{111}\ ,\qquad G_{222}=(m^2-1)G_{112} \end{aligned}\right\} \tag{11}$$

$$\left.\begin{aligned} H_{111}&=\frac{1}{(m^2\lambda_2^2-1)^2}\{2(m^2-1)\lambda_1\lambda_2^3L_0-[3\lambda_1^2-(m^2-1)\lambda_2^2]\lambda_2^2L_1\\ &\qquad-2\lambda_1\lambda_2^3L_2+[\lambda_1^2+(m^2-1)\lambda_2^2]L_3-2\lambda_1\lambda_2L_4\}\\ H_{112}&=\frac{1}{(m^2\lambda_2^2-1)^2}\{[\lambda_1^2-3(m^2-1)\lambda_2^2]\lambda_1^2L_0+2\lambda_1^3\lambda_2L_1\\ &\qquad+[\lambda_1^2+(m^2-1)\lambda_2^2]\lambda_2^2L_2-2(m^2-1)\lambda_1\lambda_2L_3+[\lambda_1^2+(m^2-1)\lambda_2^2]L_4\}\\ H_{122}&=\frac{1}{\lambda_2^2}\{-\lambda_1^2H_{111}-2\lambda_1\lambda_2H_{112}+L_5\}\\ H_{211}&=H_{112}-L_0\ ,\qquad H_{212}=(m^2-1)H_{111}-L_1\ ,\qquad H_{222}=(m^2-1)H_{112}-L_2 \end{aligned}\right\} \tag{12}$$

$$\left.\begin{aligned}
L_0&=-\frac{m^2}{v}\left(\frac{\lambda_1}{\lambda_2}F_{11}+F_{12}\right)F_{11}-\frac{1}{\lambda_2}\frac{C}{\rho}F_{11}\\
L_1&=-\frac{m^2}{v}\{[(\gamma-1)m^2+2]F_{11}{}^2+(F_{12}+F_{21})F_{21}\}\\
L_2&=-\frac{m^2}{v}\left\{\frac{\lambda_1}{\lambda_2}m^2F_{11}+(m^2+1)F_{12}+[(\gamma+1)m^2-1]F_{21}\right\}F_{11}-\frac{1}{\lambda_2}\frac{C}{\rho}m^2F_{11}\\
L_3&=-\frac{1}{v}\{-\lambda_1{}^2F_{11}F_{22}+F_{12}F_{21}+\lambda_1\lambda_2m^2F_{11}F_{21}+\lambda_2{}^2F_{22}{}^2\}\\
&\quad-\lambda_2\frac{C}{\rho}F_{21}-\lambda_1F_{21}+\lambda_2F_{11}-\frac{1}{\rho v\kappa}\frac{dB}{ds}\\
L_4&=-\lambda_1F_{22}+\lambda_2F_{21}+\frac{1}{\kappa}\frac{dA_2}{ds}\\
L_5&=-\lambda_1F_{12}+\lambda_2F_{11}+\frac{1}{\kappa}\frac{dA_1}{ds}\ .
\end{aligned}\right\}\qquad(13)$$

§ 3. Directions and Curvatures of the Lines of Constant Speed, Deflection, Pressure, and Density Immediately behind a Shock Wave

Consider the line of constant speed passing through a point on a shock wave. Let l_1 denote the arc length measured from the shock wave along the line (see Fig. 2). Let ψ_1 denote the angle of inclination of this line (say l_1-line) refered to stream-lines. ψ_1 is measured positively counterclockwise. Then,

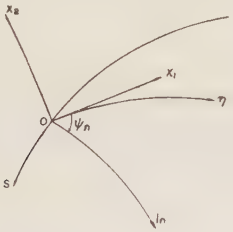

Fig. 2.

$$\frac{dw}{dl_1}=\frac{\partial w}{\partial x_1}\cos\psi_1+\frac{\partial w}{\partial x_2}\sin\psi_1=0$$

since the flow speed $w=\sqrt{u_\sigma u_\sigma}$ is constant along the l_1-line. Hence,

$$\tan\psi_1=-\frac{u_\sigma u_{\sigma,1}}{u_\sigma u_{\sigma,2}}\ . \qquad (14)$$

Evaluating Eq. (14) at the point immediately behind the shock wave, we get

$$\tan\psi_1=-\frac{u_{1,1}}{u_{1,2}} \qquad (15)$$

because of $u_1=v$ and $u_2=0$. Differentiating Eq. (14) along l_1-line and using Eq. (15), we get the expression for the curvature of the line of constant speed immediately behind the shock wave:

$$\frac{d\psi_1}{dl_1}=-\frac{\cos^3\psi_1}{u_{1,2}}\left\{u_{1,11}+2u_{1,12}\tan\psi_1+u_{1,22}\tan^2\psi_1+\frac{1}{v}(u_{2,1}+u_{2,2}\tan\psi_1)^2\right\}\ . \qquad (16)$$

As to the directions and curvatures of the lines of constant deflection, pressure, and density, we can obtain, by the same procedure as above, the following expressions:

$$\left.\begin{aligned}
\tan\psi_2&=-\frac{u_{2,1}}{u_{2,2}}\\
\frac{d\psi_2}{dl_2}&=-\frac{\cos^3\psi_2}{u_{2,2}}\{u_{2,11}+2u_{2,12}\tan\psi_2+u_{2,22}\tan^2\psi_2\}
\end{aligned}\right\}\qquad(17)$$

$$\left.\begin{aligned}
\tan\psi_3&=-\frac{u_{1,1}}{u_{2,1}}\\
\frac{d\psi_3}{dl_3}&=-\frac{\cos^3\psi_3}{u_{2,1}}\Big\{u_{1,11}+(u_{1,12}+u_{2,11})\tan\psi_3+u_{2,12}\tan^2\psi_3\\
&\qquad+\frac{1}{v}(u_{1,2}+u_{2,2}\tan\psi_3)(u_{2,1}+u_{2,2}\tan\psi_3)\Big\}
\end{aligned}\right\}\qquad(18)$$

$$\left.\begin{aligned} \tan\psi_4 &= -\frac{u_{1,1}}{u_{1,2}+\gamma(u_{2,1}-u_{1,2})} \\ \frac{d\psi_4}{dl_4} &= -\frac{\cos^3\psi_4}{\rho_{,2}}\{\rho_{,11}+2\rho_{,12}\tan\psi_4+\rho_{,22}\tan^2\psi_4\}\,, \end{aligned}\right\} \tag{19}$$

where

$$\frac{\rho_{,11}}{\rho_{,2}} = -\frac{u_{\sigma,\sigma1}}{u_{\sigma,\sigma}}\tan\psi_4 - \frac{1}{v}\{u_{2,1}-(u_{\sigma,\sigma}+u_{1,1})\tan\psi_4\}$$

$$\frac{\rho_{,12}}{\rho_{,2}} = -\frac{u_{\sigma,\sigma2}}{u_{\sigma,\sigma}}\tan\psi_4 - \frac{1}{v}\{u_{\sigma,\sigma}+u_{2,2}-u_{1,2}\tan\psi_4\}$$

$$\begin{aligned} \frac{\rho_{,22}}{\rho_{,2}} = &-\frac{\gamma(u_{2,12}-u_{1,22})+u_{1,22}}{u_{1,1}}\tan\psi_4 \\ &+\frac{1}{v}\left\{\frac{u_{\sigma,\sigma}}{\tan\psi_4}+(\gamma u_{\sigma,\sigma}-u_{2,2})\frac{u_{1,2}}{u_{1,1}}-\frac{u_{2,2}{}^2}{u_{1,1}}\tan\psi_4\right\}. \end{aligned}$$

Here, ψ_2, ψ_3, and ψ_4 denote respectively the inclinations of the lines of constant deflection, pressure, and density (say l_2-, l_3-, and l_4-line respectively) against the streamline (see Fig. 2). In general, the differential coefficient of a certain quantity Q along a certain l_n-line is given by

$$\frac{dQ}{dl_n} = Q_{,1}\cos\psi_n + Q_{,2}\sin\psi_n\,.$$

Hence, the differential ratio of any quantities Q and Q' along any l_n-line is given by

$$\left(\frac{\partial Q}{\partial Q'}\right)_{l_n} = \frac{Q_{,1}+Q_{,2}\tan\psi_n}{Q'_{,1}+Q'_{,2}\tan\psi_n}\,, \tag{20}$$

where $Q_{,\beta}$, $Q'_{,\beta}$ and $\tan\psi_n$ all can be expressed with $u_{\alpha,\beta}$.

§4. Pressure Distribution on a Streamline behind a Shock Wave

The pressure distribution on the streamline through the origin of the coordinate system can be expressed in the expansion form:

$$P = p + p'\eta + \frac{1}{2}p''\eta^2 + \cdots\,, \tag{21}$$

where η is the distance measured from the shock wave along the streamline; p is the pressure at the origin and has been given in Eq. (1); p' and p'' are the first and the second derivatives of the pressure with respect to η at the origin, and are deduced from Eqs. (4) and (9) as follows

$$\left.\begin{aligned} p' &= -\rho v u_{1,1} \\ p'' &= -\rho v u_{1,11} + \rho(u_{1,1}u_{1,2} - u_{1,2}u_{2,1} - u_{2,1}{}^2)\,. \end{aligned}\right\} \tag{22}$$

On the other hand, the curvature of the streamline and its variation along the streamline can be expressed at the origin as

$$\left.\begin{aligned} K &= \frac{u_{2,1}}{v} \\ \frac{dK}{d\eta} &= \frac{1}{v}u_{2,11} - \frac{2}{v^2}u_{2,1}u_{1,1} + \frac{1}{v^2}u_{2,1}u_{2,2}\,, \end{aligned}\right\} \tag{23}$$

where K is assumed to be positive when the streamline is concave toward the positive direction of the x_2-axis. Elimination of κ and $d\kappa/d\eta$ from Eqs. (22) and (23) (see Eqs. (5) and (10)) yields

$$\left.\begin{aligned} p' &= -\rho v^2 \frac{F_{11}}{F_{21}} K \\ p'' &= -\rho v^2 \left\{ \frac{G_{111}}{G_{211}} \frac{dK}{d\eta} + \left[\frac{G_{111}}{G_{211}} (-vH_{211} + 2F_{11}F_{21} - F_{21}F_{22}) \right.\right. \\ &\qquad \left.\left. + vH_{111} - F_{11}F_{22} + F_{12}F_{21} + F_{21}^2 \right] \frac{K^2}{F_{21}^2} \right\} . \end{aligned}\right\} \tag{24}$$

As an example of applying Eq. (24) to a practical problem, we shall obtain the pressure distribution near the leading edge along the surface of a circular-arc profile with an attached shock wave (see Fig. 3). For a circular-arc profile,

$$\frac{dK}{d\eta} = 0 \qquad \text{and} \qquad \eta = -\frac{1}{K}(\omega - \theta) ,$$

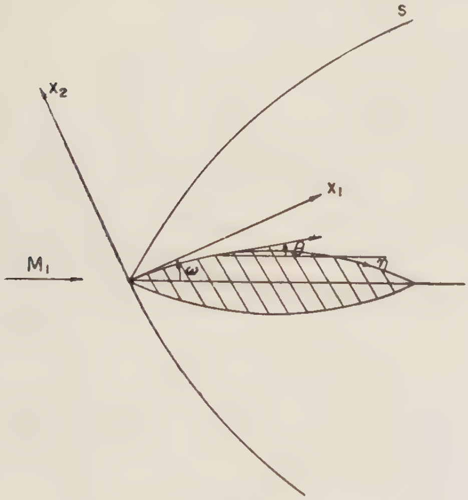

Fig. 3.

where θ denotes the angle which the tangent to the profile makes with the direction of the uniform flow in front of the shock wave and ω denotes the direction of x_1-axis refered to the uniform flow. In Fig. 4, the values $\frac{1}{K}\frac{p'}{p}$ and $\frac{1}{K^2}\frac{p''}{p}$ are shown against the Mach number M_1 associated with the uniform flow in front of the shock wave for $\omega = 10°$, 20°, and 30°. The pressure distribution in the neighbourhood of the leading edge of the circular-arc profile in the uniform stream of $M_1 = 3$ and 4, respectively, is shown in Fig. 5 for the case $\omega = 30°$. For comparison, Thomas' result is plotted in Fig. 5 too.[3] His method is, by considering pressure as a function of θ and entropy S, to derive the pressure over the surface of the profile from the pressure immediately behind the shock wave. He gives the following formula which is correct to the first order in the entropy change.

$$P = p + \left(\frac{\partial p}{\partial S}\right)_\theta \Delta S . \tag{25}$$

The coefficient $(\partial p/\partial S)_\theta$ can be obtained by taking $Q = p$, $Q' = S$, and $n = 2$ in Eq. (20) as

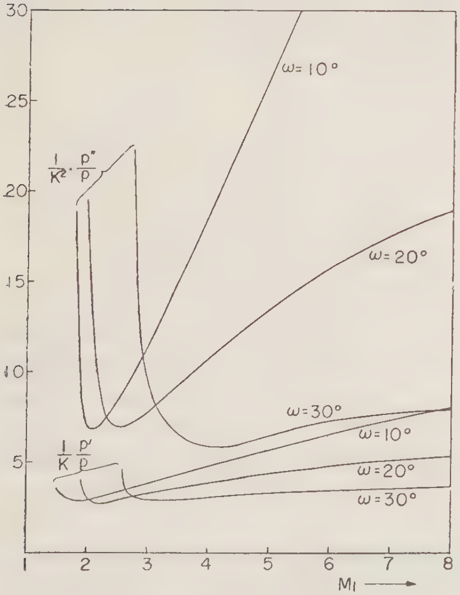

Fig. 4. Values $\frac{1}{K}\frac{p'}{p}$ and $\frac{1}{K^2}\frac{p''}{p}$ for the circular-arc profile at $\omega = 10°$, 20°, and 30°.

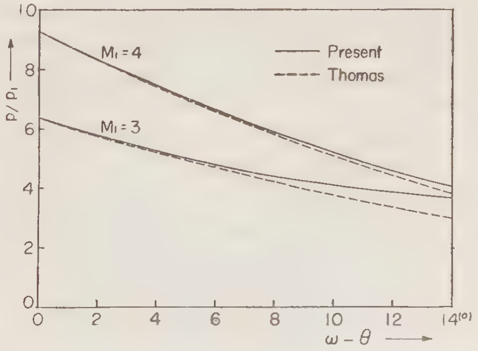

Fig. 5. Pressure distribution near the leading edge of the circular-arc profile (for $M_1 = 3$ and 4; $\omega = 30°$).

follows:

$$\left(\frac{\partial p}{\partial S}\right)_\theta=\frac{p}{R}\frac{u_{1,1}u_{2,2}-u_{2,1}{}^2}{u_{2,1}(u_{2,1}-u_{1,2})}. \tag{26}$$

And

$$\Delta S=\frac{R}{\gamma-1}\left\{\ln\frac{p}{p_1}\left(\frac{\rho_1}{\rho}\right)^\gamma-\ln\frac{p_0}{p_1}\left(\frac{\rho_1}{\rho_0}\right)^\gamma\right\}, \tag{27}$$

where p_0 and ρ_0 denote the values of p and ρ immediately behind the shock wave at the leading edge, and R is the gas constant.

§ 5. Flow in the Vicinity of the Point at which the Spine Coincides with the Shock Polar

The directions of the spine and shock polar in the hodograph plane are given, respectively, by

$$\frac{u_{2,1}}{u_{1,1}} \quad \text{and} \quad \frac{u_{2,\sigma}\lambda_\sigma}{u_{1,\sigma}\lambda_\sigma}. \tag{28}$$

Hence, the condition that these two coincide is

$$\frac{u_{2,1}}{u_{1,1}}-\frac{u_{2,\sigma}\lambda_\sigma}{u_{1,\sigma}\lambda_\sigma}=0. \tag{29}$$

Using Eqs. (2), (3), (5) and (6), the above condition can be transformed as

$$\begin{aligned}(M_1{}^2\sin^2\alpha_c-1)\{&4\gamma^2(\gamma-1)M_1{}^6\sin^6\alpha_c\\&-[2\gamma(\gamma^2-1)M_1{}^2-2(9\gamma^2-4\gamma-1)]M_1{}^4\sin^4\alpha_c\\&-[(\gamma+1)(\gamma^2+6\gamma-3)M_1{}^2\\&+2(\gamma^2-12\gamma-1)]M_1{}^2\sin^2\alpha_c\\&-[2(\gamma+1)(\gamma+3)M_1{}^2+4(\gamma-1)]\}=0,\end{aligned} \tag{30}$$

where α_c is the shock angle at the point where the directions of the spine and shock polar coincide in the hodograph plane. Fig. 6 shows the M_1-α_c curve. Since we assume the uniform flow ahead of the shock front in the present paper, the portion of the α_c-curve for $M_1<(2/\sqrt{3})$ must be left out of consideration, except for the case $M_1\sin\alpha_c-1=0$ when the shock wave degenerates into a Mach line. Thus, the directions of the spine and shock polar coincide at the point in the supersonic region for $(2/\sqrt{3})<M_1<\sqrt{(\gamma^2+4\gamma-5)/(\gamma+3)}$ ($=1.69$ for $\gamma=1.4$), whilst at the point in the subsonic region between the sonic point and the maximum deflection point for $M_1>\sqrt{(\gamma^2+4\gamma-5)/(\gamma+3)}$ (see Fig. 7).

By introducing a Jacobian J such that

$$J=\frac{\partial(u_1,u_2)}{\partial(x_1,x_2)}=u_{1,1}u_{2,2}-u_{2,1}u_{2,1}, \tag{31}$$

the condition (29) can be rewritten as

$$J=0.$$

This shows that the Jacobian defined as above vanishes at the point where the directions of the spine and shock polar coincide. Since $J_{,\alpha}$ does not vanish in general, this is the singular point of first order and there exists the singular line starting from this point[4].

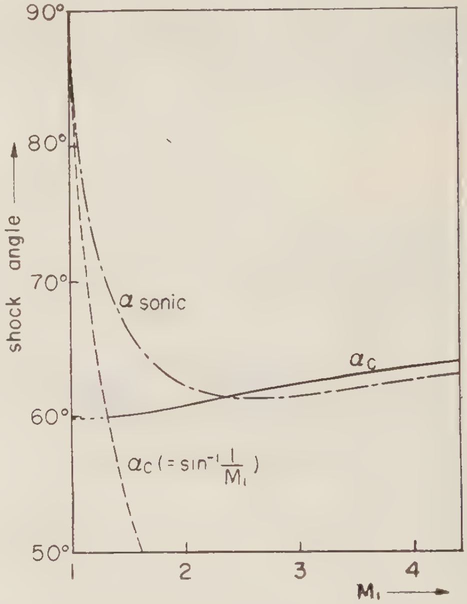

Fig. 6. Curves α_c versus M_1. α_c denotes the shock angle when the directions of the spine and shock polar coincide; α_{sonic} denotes the shock angle at which the velocity immediately behind the shock is sonic.

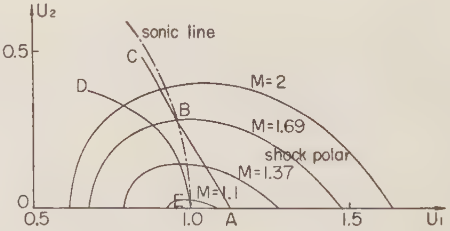

Fig. 7. Hodograph plane; curve ABC is the locus of the point where the spine coincides with the shock polar. In the right hand side of curve DE, there occurs multiplicity of the flow pattern for the inflected shock wave.

Let us assume the singular line to be expressed in the form

$$x_2=bx_1+\cdots. \tag{32}$$

Then, the coefficient b can be determined by inserting Eq. (32) into

$$J=\frac{\partial U_1}{\partial x_1}\frac{\partial U_2}{\partial x_2}-\frac{\partial U_1}{\partial x_2}\frac{\partial U_2}{\partial x_1}=0\,, \tag{33}$$

where

$$\frac{\partial U_\alpha}{\partial x_\beta}=u_{\alpha.\beta}+u_{\alpha,\beta\gamma}x_\gamma+\cdots\ .$$

The streamlines in the vicinity of the origin satisfy the equation

$$\frac{dx_2}{dx_1}=\frac{u_{2,\sigma}x_\sigma+\frac{1}{2}u_{2,\alpha\beta}x_\alpha x_\beta+\cdots}{v+u_{1,\sigma}x_\sigma+\frac{1}{2}u_{1,\alpha\beta}x_\alpha x_\beta+\cdots}\ . \tag{34}$$

We assume that the streamlines in the neighbourhood of the origin are expressed in the form

$$x_2=a_0+a_1x_1+\tfrac{1}{2}a_2x_1^2+\cdots\ . \tag{35}$$

Then the coefficients a_1 and a_2 can be expressed with a_0 by inserting Eq. (35) into Eq. (34) and by equating the terms of same order in x_1 on the both sides. The transformation from the physical plane to the hodograph plane is performed by

$$U_\alpha=u_\alpha+u_{\alpha,\beta}x_\beta+\tfrac{1}{2}u_{\alpha,\beta\gamma}x_\beta x_\gamma+\cdots\ . \tag{36}$$

In the special case where

$$M_1=\sqrt{(\gamma^2+4\gamma-5)/(\gamma+3)}\ ,$$

the spine coincides with the shock polar at the sonic point. In this case, the calculation is simplified since $u_{1,2}=u_{2,2}=u_{2,22}=0$ and hence $a_1=0$. Fig. 8-a shows the streamlines and the branch line in the physical plane for $\kappa=1$, $d\kappa/ds=0$. Fig. 8-b shows schematically the image of these in the hodograph plane.

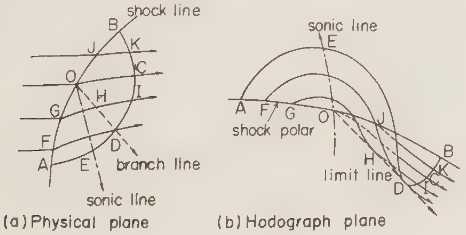

(a) Physical plane (b) Hodograph plane

Fig. 8. Flow pattern in the vicinity of the point at which shock spine coincides with shock polar ($M_1=1.69$, $\kappa=1$ and $d\kappa/ds=0$).

§6. Flow in the Vicinity of an Inflection Point

If a shock wave has an inflection point, as in the case of a detached shock wave which lies upstream in a wind tunnel at a low supersonic choked state[5)], $u_{\alpha,\beta}=0$ since $\kappa=0$ at that point. Hence, in such a case

$$J=J_{,\alpha}=0 \tag{37}$$

at this points. Thus, this is a singular point of the second order[4)], and is isolated only for

$$\begin{aligned}D\equiv&(u_{1,11}u_{2,22}-u_{1,22}u_{2,11})^2\\&-4(u_{1,12}u_{2,22}-u_{1,22}u_{2,12})\\&\times(u_{1,11}u_{2,12}-u_{1,12}u_{2,11})<0\ .\end{aligned} \tag{38}$$

When the shock angle at the inflection point is less than a certain value, the flow behind it has a multiplicity in the hodograph plane. Such a state occurs at the points in the subsonic region (see Fig. 7). The streamlines and the branch lines in the vicinity of an inflection point and their corresponding hodograph images can be obtained by the same way as in the preceding section. In Fig. 9, the directions of the branch lines, the shock line, and the streamline passing through the inflection point are shown as the functions of the shock angle α_i for $M_1=2$. In this case, the singular point is isolated for $\alpha_i>68.9°$, while there exist two branch lines for $\alpha_i<68.9°$. For $68.9°>\alpha_i>62.3°$, only the streamlines through the shock segment concave to the flow behind it traverse the two branch lines. Fig. 10 shows the streamlines and the

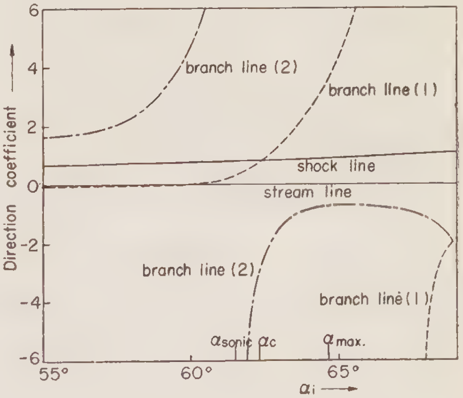

Fig. 9. Directions of the branch lines, the shock line, and the streamline passing through the inflection point for the case $M_1=2$.

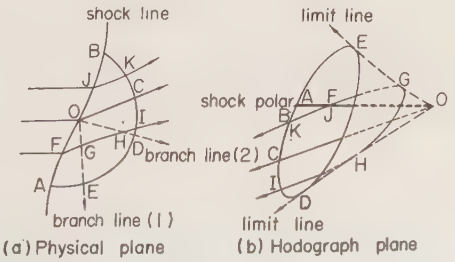

(a) Physical plane (b) Hodograph plane

Fig. 10. Flow pattern in the vicinity of the inflection point. ($M_1=2$; $\alpha_i=64.7°$)

branch lines for $\alpha_i=64.7°$ in the physical plane and the corresponding schematic pattern in the hodograph plane. The value $\alpha_i=64.7°$ is the shock angle at the maximum deflection point for case $M_1=2$. For $62.3°>\alpha_i>59.6°$ every streamline traverses one branch line. Here, $\alpha_i=59.6°$ corresponds to the case when one of the branch lines coincides with the streamline. Fig. 11 shows the streamlines and the branch lines in the physical plane and the corresponding schematic hodograph pattern for $\alpha_i=62°$. For $\alpha_i<59.6°$, the two branch lines are traversed only by the streamlines through the shock segment concave to the flow behind it.

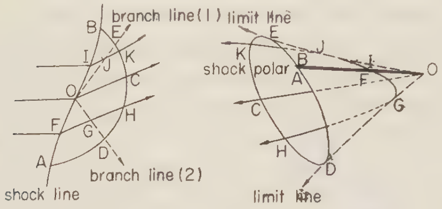

(a) Physical plane (b) Hodograph plane

Fig. 11. Flow pattern in the vicinity of the inflection point. ($M_1=2$; $\alpha_i=62°$)

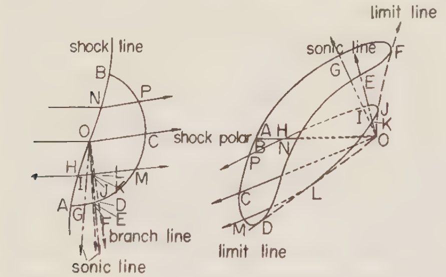

(a) Physical plane (b) Hodograph plane

Fig. 12. Flow pattern in the vicinity of the inflection point. ($M_1=1.3$; $\alpha_i=65°7'$ sonic point))

Let us consider the case when the inflection occurs at the sonic point. If the sonic lines starting from this point are assumed to be expressed in the form,

$$x_2=cx_1+\cdots\ , \tag{39}$$

c can be determined by inserting above expression into

$$\left.\begin{aligned} &U_\alpha U_\alpha=a_*^2\\ &U_1=a_*+\tfrac{1}{2}u_{1,\alpha\beta}x_\alpha x_\beta+\cdots\\ &U_2=\tfrac{1}{2}u_{2,\alpha\beta}x_\alpha x_\beta+\cdots\ , \end{aligned}\right\} \tag{40}$$

where a_* denotes the sonic speed. Thus, there exist the real values of c for

$$u_{1,12}{}^2-u_{1,11}u_{2,11}\geqq 0\ . \tag{41}$$

So that, it is possible that there exists a local supersonic region behind the inflection point. This is the case, in fact, when the Mach number is less than 1.37. Fig. 12 shows the streamlines, the branch lines, and the sonic lines in the physical plane for $M_1=1.3$ together with the corresponding schematic hodograph pattern.

References

1) Z. Hasimoto: Proceedings of the 9th International Congress of Applied Mechanics, (1956).
2) T. Y. Thomas: J. Math. Phys. **26** (1947) 62.
3) T. Y. Thomas: Proc. Nat. Acad. Sci. **15** (1950) 113.
4) J. W. Craggs: Proc. Cambr. Phil. Soc. **44** (1948) 360.
5) S. Morioka: J. Aero. Sci. **24** (1957) 831.

JOURNAL OF THE PHYSICAL SOCIETY OF JAPAN Vol. 16, No. 8, AUGUST, 1961

Two-Dimensional Supersonic Jet of a Conducting Inviscid Gas in the Presence of a Uniform Magnetic Field

By Shigeki MORIOKA

Department of Physics and Mathematics, Faculty of Science and Engineering, Ritumeikan University, Kyoto

(Received February 20, 1961)

The behaviour of the two-dimensional supersonic jet of an ideal gas with weak electric conductivity in the presence of a uniform magnetic field is considered on the basis of the linearized theory. In general, the boundary of the jet can be expressed by the formula which contains the terms yielding the monotonic change of the width of the jet and its deflection due to the inclination of the lines of force in addition to the term in the ordinary gasdynamics. The expressions for these terms are shown explicitly.

§1. Introduction

The problems of jet in the ordinary gasdynamics have been investigated in detail by S. I. Pai, D. C. Pack, and others[1,2]. On the other hand, the behaviour of the jet of a perfectly conducting gas in the presence of a magnetic field parallel to the stream can be obtained by making suitable substitution of the parameters in the known results of the linearized theory for the ordinary gasdynamic case[3]. In this paper, we consider the behaviour of the two-dimensional supersonic jet of an ideal gas with weak conductivity in the presence of a uniform magnetic field.

Let a jet issue as a uniform, supersonic stream of an ideal gas from a nozzle of a semi-width L, with velocity U_1, pressure p_1, density ρ_1, ratio of the specific heats γ_1, and electric conductivity σ into a conducting ideal gas with pressure p_2, density ρ_2, ratio of the specific heats γ_2. (The electric conductivity of the surrounding fluid may be arbitrary in Secs. 2 and 4 since we assume that $\boldsymbol{E}+\mu\boldsymbol{v}\times\boldsymbol{H}=0$. On the other hand, in Sec. 3 it must be so small that $\boldsymbol{j}=\sigma(\boldsymbol{E}+\mu\boldsymbol{v}\times\boldsymbol{H})$ is negligible for the value $\boldsymbol{E}+\mu\boldsymbol{v}\times\boldsymbol{H}$ assumed to be sufficiently small. Here, μ, $\boldsymbol{v}$, $\boldsymbol{H}$ and $\boldsymbol{E}$ denote permeability, velocity, magnetic- and electric-field intensity respectively.) The heat-conductivity and viscosity are neglected. We assume that the difference of the pressures p_1-p_2 is small compared with p_1 and that the interaction between the magnetic field and the conducting stream is sufficiently small. Therefore, the problem can be linearized. In the following, we consider three cases: (1) the surrounding fluid is at rest, a uniform magnetic field exists, and N, $Rm\ll 1$; (2) the surrounding fluid moves with a supersonic velocity $\boldsymbol{U}_2$ to the same direction as the jet, a uniform magnetic field $\boldsymbol{H}$ and a uniform electric field $\boldsymbol{E}=-\mu(\boldsymbol{U}_2\times\boldsymbol{H})$ exist, and N, $Rm\ll 1$; (3) the surrounding fluid is at rest, a strong magnetic field parallel to the jet exists, and $N\simeq 1$ though $Rm\ll 1$. Here, $N=RmS$; $Rm=\sigma\mu U_1L$ and $S=\mu H^2/\rho_1U_1^2$ are respectively the magnetic Reynolds number and the pressure number in the jet; and μ is assumed to be constant everywhere. These cases will be formulated as the boundary value problems and will be solved by using Laplace transformation in Sections 2, 3 and 4, respectively.

The fundamental relations necessary in the following are

$$\left.\begin{aligned}
&\operatorname{div}(\rho\boldsymbol{v})=0\,,\\
&\rho(\boldsymbol{v}\operatorname{grad})\boldsymbol{v}=-\operatorname{grad}p+\mu(\boldsymbol{j}\times\boldsymbol{H})\\
&\operatorname{div}\boldsymbol{H}=0\,,\\
&\operatorname{rot}\boldsymbol{H}=\boldsymbol{j}\,,\\
&\boldsymbol{j}=\sigma(\boldsymbol{E}+\mu\boldsymbol{v}\times\boldsymbol{H})\,,\\
&\rho(\boldsymbol{v}\operatorname{grad})p-\gamma p(\boldsymbol{v}\operatorname{grad})\rho=(\gamma-1)\rho(\boldsymbol{j}^2/\sigma)\,.
\end{aligned}\right\} \tag{1}$$

The electric field $\boldsymbol{E}$ is constant for two-dimensional motion and it is assumed to be zero in Cases 1 and 3 and to be $-\mu(\boldsymbol{U}_2\times\boldsymbol{H})$ in Case 2.

§2. Jet Issuing into a Fluid at Rest

In this section, we consider the two-dimensional supersonic jet of a conducting gas issuing into a fluid at rest in the presence of a uniform magnetic field. We choose the origin of the coordinate system at the middle of the exit, and we take the x-axis parallel to the direction of the velocity at the exit and the y-axis perpendiculary to it. The inclination of the magnetic field is assumed to be α with respect to the x-axis. Then, we can put as follows,

$$\left.\begin{aligned} &\boldsymbol{v}=U_1(1+u')\boldsymbol{e}_1+U_1v'\boldsymbol{e}_2\ ,\\ &\boldsymbol{H}=\lambda_1H(1+h_x')\boldsymbol{e}_1+\lambda_2H(1+h_y)\boldsymbol{e}_2\ ,\\ &\boldsymbol{E}=0\ ,\ p=p_1(1+p')\ ,\ \rho=\rho_1(1+\rho')\ ,\end{aligned}\right\} \qquad (2)$$

where $\boldsymbol{e}_1$ and $\boldsymbol{e}_2$ denote the fundamental unit vectors; $\lambda_1=\cos\alpha$; $\lambda_2=\sin\alpha$; and u', v', h_x', h_y', p' and ρ' are dimensionless small quantities. The space coordinates are made non-dimensional with L. Substituting Eq. (2) into Eq. (1) and neglecting higher order terms, we obtain

$$\left.\begin{aligned} &\frac{\partial v'}{\partial x}-\frac{\partial u'}{\partial y}=N\lambda_1\lambda_2\ ,\\ &-(M_1^2-1)\frac{\partial u'}{\partial x}+\frac{\partial v'}{\partial y}=\gamma_1M_1^2N\lambda_2^2\ ,\\ &\lambda_1\frac{\partial h_x'}{\partial x}+\lambda_2\frac{\partial h_y'}{\partial y}=0\ ,\\ &\lambda_2\frac{\partial h_y'}{\partial x}-\lambda_1\frac{\partial h_x'}{\partial y}=Rm\lambda_2\ ,\\ &p'=-\gamma_1M_1^2(u'+N\lambda_2^2x)\ ,\\ &\rho'=-M_1^2(u'+\gamma_1N\lambda_2^2x)\ ,\end{aligned}\right\} \qquad (3)$$

where $M_1=U_1/\sqrt{\gamma_1p_1/\rho_1}$ is the Mach number and N, Rm are assumed to be sufficiently small. We introduce the velocity potential defined by

$$u'=\frac{\partial\phi}{\partial x}\ ,\qquad v'=\frac{\partial\phi}{\partial y}+N\lambda_1\lambda_2x\ . \qquad (4)$$

Then, it satisfies the equation

$$-(M_1^2-1)\frac{\partial^2\phi}{\partial x^2}+\frac{\partial^2\phi}{\partial y^2}=\gamma_1M_1^2N\lambda_2^2\ . \qquad (5)$$

On the other hand, multiplying the element ds of a streamline by the modified momentum equation;

$$\frac{1}{2}\ \mathrm{grad}\ \boldsymbol{v}^2-\boldsymbol{v}\times\mathrm{rot}\ \boldsymbol{v}+\frac{1}{\rho}\mathrm{grad}\ p$$

$$-\frac{\mu}{\rho}(\boldsymbol{j}\times\boldsymbol{H})=0\ ,$$

and integrating it along a streamline under the approximation of Eq. 2, we get the relation

$$p=p_1-\rho_1U_1^2u'-\sigma\mu^2U_1H^2\lambda_2^2x\ .$$

Then, the condition that the pressure is constant on the boundary of the jet can be expressed as

$$\frac{\partial\phi}{\partial x}=\varepsilon-N\lambda_2^2x\quad \text{for}\quad x>0\ ,\quad |y|=1\ , \qquad (6)$$

where $\varepsilon=(p_1-p_2)/\rho_1U_1^2$. As the condition at the exit, we assume a uniform flow; that is,

$$\phi=\frac{\partial\phi}{\partial x}=0\qquad \text{for}\quad x=0\ ,\quad |y|<1\ . \qquad (7)$$

If we assume $\sigma\neq0$ for $x<0$ and $\lambda_1\lambda_2\neq0$, the flow is rotational upstream of the exit ($x<0$) as is seen from Eq. 3. Therefore, in order that this condition (7) is valid for the given shape of the nozzle in the presence of a uniform magnetic field and is consistent with the basic equations, we must assume that the flow of the jet has no conductivity upstream of the exit, i.e., for $x<0$, except for the case $\lambda_1\lambda_2=0$. This assumption means the abrupt rising of the temperature leading to the ionization of the gas at the exit. It, however, may be permissible as a model of practical jet exhausts. The Laplace transformation of Eqs. (5) and (6) leads to

$$\frac{\partial^2\overline{\phi}}{\partial y^2}-(M_1^2-1)s^2\overline{\phi}=\frac{\gamma_1M_1^2N\lambda_2^2}{s}\ , \qquad (8)$$

$$\overline{\phi}=\frac{\varepsilon}{s^2}-\frac{N\lambda_2^2}{s^3}\quad \text{for}\quad x<0\ ,\quad |y|=1\ , \qquad (9)$$

where $\overline{\phi}=\int_0^x e^{-sx}\phi(x,y)dx$ and Eq. (7) has been used. The solution of Eq. (8) which satisfies Eq. (9) can be found as

$$\overline{\phi}=\frac{(\varepsilon/s^2)+(\delta/s^3)}{e^{m_1s}+e^{-m_1s}}(e^{m_1sy}+e^{-m_1sy})-\frac{\gamma_1M_1^2N\lambda_2^2}{m_2^2s^3}\ , \qquad (10)$$

where

$$\delta=\frac{[(\gamma_1-1)M_1^2+1]N\lambda_2^2}{m_1^2}\quad \text{and}\quad m_1^2=M_1^2-1\ .$$

If we assume the boundary of the jet in the form $y=\pm1+F(x)_\pm$, then

$$F(x)_\pm=\int_0^x\left[\frac{\partial\phi}{\partial y}\right]_{y=\pm1}dx+\frac{1}{2}N\lambda_1\lambda_2x^2\ .$$

Hence, the Laplace transformation yields

$$\overline{F}(s)_\pm=\pm\left(\frac{m_1\varepsilon}{s^2}+\frac{m_1\delta}{s^3}\right)\tanh m_1s+N\lambda_1\lambda_2\frac{1}{s^3}\ .$$

By making the inverse transformation, the boundary of the jet can be found as

$$\begin{aligned} F(x)_\pm=&\pm m_1\varepsilon H(x,4m_1)\\ &\pm m_1\delta\int_0^x H(x,4m_1)dx+\frac{1}{2}N\lambda_1\lambda_2x^2\ , \end{aligned} \qquad (11)$$

where $H(x, 4m_1)=\begin{cases} x \ (0\leq x\leq 2m_1) \\ 4m_1-x \ (2m_1\leq x\leq 4m_1) \end{cases}$ is a triangular wave function. The first term is the same as that in the gasdynamic case; the second term, which has the integrated form of the function in the first term, expresses the monotonic spreading of the width of the jet; and the third term expresses the deflection of the whole jet due to the inclination of the lines of force.

§ 3. Jet Issuing into a Uniform Supersonic Stream

We consider, in this section, the two-dimensional supersonic jet of a conducting gas issuing into a uniform supersonic stream with a velocity U_2 parallel to the jet in the presence of a uniform magnetic field $\boldsymbol{H}$ and a uniform electric field $\boldsymbol{E}=-\mu(\boldsymbol{U}_2\times\boldsymbol{H})$. This corresponds to the case in which we observe the jet that issues with velocity U_1 relative to the moving nozzle with velocity U_2, in the coordinate system moving with the velocity U_2. Introducing the velocity potentials ϕ_1, ϕ_2 defined by

$$\left.\begin{aligned} u_1'&=\frac{\partial\phi_1}{\partial x}, & v_1'&=\frac{\partial\phi_1}{\partial y}+\eta N\lambda_1\lambda_2 x, \\ u_2'&=\frac{\partial\phi_2}{\partial x}, & v_2'&=\frac{\partial\phi_2}{\partial y}, \end{aligned}\right\} \qquad (12)$$

(where, suffices 1 and 2 refer respectively to the jet and to the surrounding fluid), by the procedure similar to that in the preceding section, we can obtain the following boundary value problem for the present case;

$$\left.\begin{aligned} &-(M_1^2-1)\frac{\partial^2\phi_1}{\partial x^2}+\frac{\partial^2\phi_1}{\partial y^2}=[(\gamma_1-1)\eta+1]\eta M_1^2 N\lambda_2^2 \quad \text{(for jet)}, \\ &-(M_2^2-1)\frac{\partial^2\phi_2}{\partial x^2}+\frac{\partial^2\phi_2}{\partial y^2}=0 \quad \text{(for surrounding stream)}, \end{aligned}\right\} \qquad (13)$$

$$\left.\begin{aligned} &\phi_1=\frac{\partial\phi_1}{\partial x}=0 \quad \text{for} \quad x=0, \quad |y|<1, \\ &\phi_2=\frac{\partial\phi_2}{\partial x}=0 \quad \text{for} \quad x=0, \quad |y|>1, \\ &\phi_2<\infty \qquad \text{at} \quad |y|\to\infty, \\ &\left.\begin{aligned} &\frac{\partial\phi_1}{\partial x}-\beta\frac{\partial\phi_2}{\partial x}=\varepsilon-\eta N\lambda_2^2 x \\ &\frac{\partial\phi_1}{\partial y}-\frac{\partial\phi_2}{\partial y}=-\eta N\lambda_1\lambda_2 x \end{aligned}\right\} \quad \text{for} \quad x>0, \quad |y|=1, \end{aligned}\right\} \qquad (14)$$

where $\eta=1-\dfrac{U_2}{U_1}$ and $\beta=\dfrac{\rho_2 U_2^2}{\rho_1 U_1^2}=\dfrac{\gamma_1 M_1^2}{\gamma_2 M_2^2}$. Here, for the condition at the exit of the nozzle, we must again make the same assumption as that in the preceding section; that is, it must be assumed that the flow of the jet has the conductivity only for $x>0$, except for the case $\lambda_1\lambda_2=0$. The Laplace transformations of Eqs. (13) and (14) yield

$$\left.\begin{aligned} &\frac{\partial^2\phi_1}{\partial y^2}-m_1^2 s^2\overline{\phi_1}=[(\gamma_1-1)\eta+1]\eta M_1^2 N\lambda_2^2/s, \\ &\frac{\partial\overline{\phi_2}}{\partial y^2}-m_2^2 s^2\overline{\phi_2}=0, \end{aligned}\right\} \qquad (15)$$

$$\left.\begin{aligned} &\overline{\phi_2}<\infty \quad \text{at} \quad |y|\to\infty, \\ &\left.\begin{aligned} &\overline{\phi_1}-\beta\overline{\phi_2}=\frac{\varepsilon}{s^2}-\frac{\eta N\lambda_2^2}{s^3} \\ &\frac{\partial\overline{\phi_1}}{\partial y}-\frac{\partial\overline{\phi_2}}{\partial y}=-\frac{\eta N\lambda_1\lambda_2}{s^2} \end{aligned}\right\} \quad \text{for} \quad x>0, \quad |y|=1. \end{aligned}\right\} \qquad (16)$$

The solution of Eq. (15) which satisfies the conditions of Eq. (16) is found as

$$\overline{\phi_1}=\frac{m\mathcal{E}}{m+\beta}\frac{1}{s^2}\frac{e^{m_1sy}+e^{-m_1sy}}{e^{m_1s}+\nu e^{-m_1s}}+\frac{m\delta'}{m+\beta}\frac{1}{s^3}\frac{e^{m_1sy}+e^{-m_1sy}}{e^{m_1s}+\nu e^{-m_1s}}-\frac{\beta\zeta}{m+\beta}\frac{1}{s^3}\frac{e^{m_1sy}-e^{-m_1sy}}{e^{m_1s}-\nu e^{-m_1s}}$$
$$-\frac{[(\gamma_1-1)\eta+1]\eta M_1{}^2N\lambda_2{}^2}{m_1{}^2s^3}, \tag{17}$$

where

$$\left.\begin{aligned}&m=\frac{m_2}{m_1}=\frac{\sqrt{M_2{}^2-1}}{\sqrt{M_1{}^2-1}}, \qquad \nu=\frac{m-\beta}{m+\beta},\\ &\delta'=[(\gamma_1-1)M_1{}^2\eta+1]\eta N\lambda_2{}^2/m_1{}^2,\\ &\zeta=\eta N\lambda_1\lambda_2/m_1{}^2.\end{aligned}\right\} \tag{18}$$

Hence

$$\overline{F}(s)_\pm=\frac{1}{s}\left[\frac{\partial\overline{\phi_1}}{\partial y}\right]_{y=\pm1}+\eta N\lambda_1\lambda_2\frac{1}{s^3}=\pm\frac{m_2\mathcal{E}}{m+\beta}\frac{1}{s^2}\frac{1-e^{-2m_1s}}{1+\nu e^{-2m_1s}}\pm\frac{m_2\delta'}{m+\beta}\frac{1}{s^3}\frac{1-e^{-2m_1s}}{1+\nu e^{-2m_1s}}$$
$$-\frac{m_1\beta\zeta}{m+\beta}\frac{1}{s^3}\frac{1+e^{-2m_1s}}{1+\nu e^{-2m_1s}}+\eta N\lambda_1\lambda_2\frac{1}{s^3}.$$

The inverse transformation yields the following expression for the boundary of the jet in the neighbourhood of the exit.

$$F(x)_\pm=\pm\frac{m_2\mathcal{E}}{m+\beta}\left\{x-(1+\nu)\sum_{n=1}^{\infty}(-\nu)^{n-1}(x-2n\cdot m_1)\cdot u(x-2n\cdot m_1)\right\}$$
$$\pm\frac{m_2\delta'}{m+\beta}\int_0^x\left\{x-(1+\nu)\sum_{n=1}^{\infty}(-\nu)^{n-1}(x-2n\cdot m_1)\cdot u(x-2n\cdot m_1)\right\}dx$$
$$-\frac{m_1\beta\zeta}{m+\beta}\int_0^x\left\{x+(1+\nu)\sum_{n=1}^{\infty}\nu^{n-1}(x-2n\cdot m_1)\cdot u(x-2n\cdot m_1)\right\}dx+\frac{1}{2}\eta N\lambda_1\lambda_2x^2, \tag{19}$$

where $u(x-x_0)=\begin{cases}0 & (x<x_0)\\ 1 & (x>x_0)\end{cases}$ is a unit step function. The first term is the same as that in the gasdynamic case; the second term, which has the integrated form of the function in the first term, expresses the monotonic spreading or contracting of the width of the jet due to the magnetic field according as $\delta'>0$ $\left(0<\frac{U_2}{U_1}<1 \text{ or } \frac{U_2}{U_1}>1+\frac{1}{(\gamma_1-1)M_1{}^2}\right)$ or $\delta'<0$ $\left(1<\frac{U_2}{U_1}<1+\frac{1}{(\gamma_1-1)M_1{}^2}\right)$; and the third and the fourth terms express as a whole the deflection of the jet due to the inclination of the lines of force. Here it should be noticed that the direction of the deflection changes at $U_2=U_1$. On the other hand, the stream line through the origin is expressed by

$$F(x)_{y=0}=-\frac{2m_1\beta\zeta}{m+\beta}\int_0^x\left\{\sum_{n=1}^{\infty}\nu^{n-1}[x-(2n-1)m_1]\cdot u[x-(2n-1)m_1]\right\}dx+\frac{1}{2}\eta N\lambda_1\lambda_2x^2. \tag{20}$$

§ 4. Jet of a Weakly Conducting Gas Issuing into the Fluid at Rest in the Presence of a Strong Magnetic Field Parallel to the *x*-Axis

In this case, we can put as follows,

$$\left.\begin{aligned}&\boldsymbol{v}=U_1(1+u')\boldsymbol{e}_1+U_1v'\boldsymbol{e}_2,\\ &\boldsymbol{H}=H(1+h_x')\boldsymbol{e}_1+Hh_y'\boldsymbol{e}_2,\\ &\boldsymbol{E}=0, \quad p=p_1(1+p'), \quad \rho=\rho_1(1+\rho').\end{aligned}\right\} \tag{21}$$

Then, Eq. (1) reduces to

$$\left.\begin{aligned}
&\frac{\partial u'}{\partial x}+\frac{\partial v'}{\partial y}+\frac{\partial \rho'}{\partial x}=0\,,\\
&\frac{\partial u'}{\partial x}=-\frac{1}{\gamma_1 M_1^2}\frac{\partial p'}{\partial x}\,,\\
&\frac{\partial v'}{\partial x}=-\frac{1}{\gamma_1 M_1^2}\frac{\partial p'}{\partial y}+N(h'-v')\,,\\
&\frac{\partial h_x'}{\partial x}+\frac{\partial h_y'}{\partial y}=0\,,\\
&\frac{\partial h_y'}{\partial x}-\frac{\partial h_x'}{\partial y}=Rm(h_y'-v')\,,\\
&\frac{\partial p'}{\partial x}-\gamma_1\frac{\partial \rho'}{\partial x}=0\,.
\end{aligned}\right\}\tag{22}$$

We assume that $N=RmS\simeq 1$ though $Rm\ll 1$ and we neglect the deviation of the magnetic field due to the interaction. Then, the stream function ψ defined by

$$u'=-\frac{1}{M_1^2-1}\frac{\partial\psi}{\partial y}\,,\qquad v'=-\frac{\partial\psi}{\partial x}\,,\tag{23}$$

satisfies the equation

$$\frac{\partial^2\psi}{\partial x^2}-(M_1^2-1)\frac{\partial^2\psi}{\partial y^2}+N\frac{\partial\psi}{\partial x}=0\,.\tag{24}$$

The boundary conditions for ψ are given as follows

$$\left.\begin{aligned}
&\psi=\frac{\partial\psi}{\partial x}=0 && \text{for } x=0,\ 1>y>0\,,\\
&\frac{\partial\psi}{\partial x}=0 && \text{for } x>0,\ y=0\,,\\
&\frac{\partial\psi}{\partial y}=-(M_1^2-1)\mathcal{E} && \text{for } x>0,\ y=1\,.
\end{aligned}\right\}\tag{25}$$

The Laplace transformations of Eqs. (24) and (25) yield

$$\frac{\partial^2\bar{\psi}}{\partial y^2}-m_1^2(s^2+Ns)\bar{\psi}=0\,,\tag{26}$$

$$\left.\begin{aligned}
&\psi=0 && \text{for}\quad y=0,\quad x>0\,,\\
&\frac{\partial\bar{\psi}}{\partial y}=-\frac{m_1^2\mathcal{E}}{s} && \text{for}\quad y=1,\quad x>0\,.
\end{aligned}\right\}\tag{27}$$

The solution of Eq. (26) which satisfies the condition (27) is

$$\bar{\psi}=-\frac{m_1\mathcal{E}\{\exp(m_1\sqrt{s^2+Ns}\,y)-\exp(-m_1\sqrt{s^2+Ns}\,y)\}}{s\sqrt{s^2+Ns}\,\{\exp(m_1\sqrt{s^2+Ns})+\exp(-m_1\sqrt{s^2+Ns})\}}\,.\tag{28}$$

The boundary of the jet is given by $F(x)=-[\psi]_{y=1}$ for this case. Then,

$$\bar{F}(s)=\frac{m_1\mathcal{E}}{s\sqrt{s^2+Ns}}\,\frac{1-\exp(-2m_1\sqrt{s^2+Ns})}{1+\exp(-2m_1\sqrt{s^2+Ns})}\,.\tag{29}$$

If we consider the region where N/s is sufficiently small and adopt the first two terms in the expansion with respect to it, we obtain

$$\bar{F}(s)=m_1\mathcal{E}\frac{1}{s^2}\,\frac{1-\nu' e^{-2m_1 s}}{1+\nu' e^{-2m_1 s}}-\frac{m_1 N\mathcal{E}}{2}\,\frac{1}{s^3}\,\frac{1-\nu' e^{-2m_1 s}}{1+\nu' e^{-2m_1 s}}\,,\tag{30}$$

where

$$\nu' = e^{-m_1 N} . \tag{31}$$

The boundary of the jet in the neighbourhood of the exit can be expressed as follows, by taking the inverse transformation,

$$F(x) = m_1 \varepsilon \left\{ x + 2 \sum_{n=1}^{\infty} (-\nu')^n (x - 2n \cdot m_1) \cdot u(x - 2n \cdot m_1) \right\} - \frac{1}{2} m_1 N \varepsilon \int_0^x \left\{ x + 2 \sum_{n=1}^{\infty} (-\nu')^n (x - 2n \cdot m_1) \cdot u(x - 2n \cdot m_1) \right\} dx . \tag{32}$$

This expression reduces to that in the gas-dynamic case as $N \to 0$. The interaction between the magnetic field and the conducting stream has an influence such as to reduce the deviation of the width of the jet from that at the exit as well as the amplitude, as should be expected.

The writer wishes to express his hearty thanks to Prof. Z. Hasimoto for valuable discussion and to Dr. T. Sakurai for kind inspection of the manuscript.

References

1) S. I. Pai: Fluid dynamics of jet (D. Van Nostrand, 1954) 46.
2) D. C. Pack: J. Aero. Sci. **23** (1956) 747.
3) S. Morioka: J. Phys. Soc. Japan **15** (1960) 1516.

JOURNAL OF THE PHYSICAL SOCIETY OF JAPAN, Vol. 16, No. 8, AUGUST, 1961

Steady Temperature in a Composite Elliptic Cylinder

By Václav VODIČKA
Plzeň, Czechoslovakia

(Received April 27, 1961)

Classical methods are used to determine the steady temperature distribution in a finite elliptic cylinder consisting of any number of plane-parallel layers. As illustration of the general procedure, the case of a homogeneous isotropic elliptic cylinder is treated in some detail.

§ 1. Description of the Problem

The cylindrical body

$$b^2x^2 + a^2y^2 - a^2b^2 \leq 0 , \qquad 0 \leq z \leq z_n$$

is made of n homogeneous and isotropic parts

$$b^2x^2 + a^2y^2 - a^2b^2 \leq 0 , \qquad z_{k-1} \leq z \leq z_k , \qquad 1 \leq k \leq n , \qquad z_0 = 0 ,$$

with the conductivities λ_k, respectively. The problem in question is that of finding the steady temperature field in the solid provided that its curved surface $b^2x^2 + a^2y^2 - a^2b^2 = 0$ has steadily the temperature zero, whereas the other surfaces $z = 0$, $z = z_n$ are kept at two temperatures given in functions $f(\xi, \eta)$, $g(\xi, \eta)$ of the elliptic coordinates ξ, η to be introduced later-see (2.1). In addition to this we shall consider such a tight contact between adjacent layers of the body that it is possible to calculate with a continuous variation of the temperature within the whole cylinder.

§ 2. Mathematical Statement

Introducing the coordinates ξ, η, z of the elliptic cylinder by

$$x=c\,\mathrm{ch}\,\xi\cos\eta\,,\qquad y=c\,\mathrm{sh}\,\xi\sin\eta\,,\qquad z=z\,,\qquad c=\sqrt{a^2-b^2}\,, \tag{2.1}$$

our problem reduces to determining the solution $u_k=u_k(\xi,\eta,z)$ of the familiar equations

$$\left.\begin{aligned}&\frac{1}{c^2(\mathrm{ch}^2\xi-\cos^2\eta)}\left(\frac{\partial^2 u_k}{\partial\xi^2}+\frac{\partial^2 u_k}{\partial\eta^2}\right)+\frac{\partial^2 u_k}{\partial z^2}=0\,,\\ &\qquad 0\leq\xi<\xi_0\,,\quad 0\leq\eta\leq 2\pi\,,\quad z_{k-1}<z<z_k\,,\quad 1\leq k\leq n\,,\quad \xi_0=\lg\frac{a+b}{c}\end{aligned}\right\} \tag{2.2}$$

$$u_1(\xi,\eta,0)=f(\xi,\eta)\,,\qquad u_n(\xi,\eta,z_n)=g(\xi,\eta)\,,\qquad 0\leq\xi<\xi_0\,,\quad 0\leq\eta\leq 2\pi \tag{2.3}$$

$$\left.\begin{aligned}&u_{k+1}(\xi,\eta,z_k)=u_k(\xi,\eta,z_k)\,,\qquad 0\leq\xi<\xi_0\,,\quad 0\leq\eta\leq 2\pi\\ &\frac{\partial u_{k+1}}{\partial z}=\Lambda_k\frac{\partial u_k}{\partial z}\,,\qquad \Lambda_k=\frac{\lambda_k}{\lambda_{k+1}}\,,\\ &\qquad 0\leq\xi<\xi_0\,,\quad 0\leq\eta\leq 2\pi\,,\quad z=z_k\,,\quad 1\leq k\leq n-1\end{aligned}\right\} \tag{2.4}$$

$$u_k(\xi_0,\eta,z)=0\,,\qquad 0\leq\eta\leq 2\pi\,,\quad z_{k-1}<z<z_k\,,\quad 1\leq k\leq n\,. \tag{2.5}$$

§ 3. Particular Integrals

Assuming the integrals of (2.2) in the form

$$v_k(\xi,\eta,z)=X(\xi)Y(\eta)Z_k(z)\,,\qquad 1\leq k\leq n \tag{3.1}$$

one finds with a free parameter ω on one hand

$$Z_k(z)=A_k\,\mathrm{ch}\,\omega(z-z_{k-1})+B_k\,\mathrm{sh}\,\omega(z-z_{k-1})\,,\qquad 1\leq k\leq n \tag{3.2}$$

and on the other

$$\frac{d^2X}{d\xi^2}-(\rho-2q\,\mathrm{ch}\,2\xi)X=0\,,\qquad \frac{d^2Y}{d\eta^2}+(\rho-2q\cos 2\eta)Y=0\,; \tag{3.3}$$

ρ is another free parameter and q depends upon ω through the relation

$$q=\frac{1}{4}c^2\omega^2 \tag{3.4}$$

Using Whittaker's notation and taking into account the obvious periodicity of the required temperature functions with regard to η, we have to consider only the particular integrals[1]

$$ce_m(\eta,q)\,,\quad m=0,1,2,\cdots,\qquad se_m(\eta,q)\,,\quad m=1,2,3,\cdots \tag{3.5}$$

of the second equation (3.3). It should be remarked that it belongs to every term $ce_m(\eta,q)$ of the first sequence (3.5) the well-known expression $\rho=\rho_m^{(1)}(q)$ of ρ in terms of the only free parameter q and similarly one has another known form $\rho=\rho_m^{(2)}(q)$ of ρ for every $se_m(\eta,q)$.

As for the first equation (3.3), its particular integrals are the modified functions $Ce_m(\xi,q)$, $Fe_m(\xi,q)$ for $\rho=\rho_m^{(1)}(q)$ and $Se_m(\xi,q)$, $Ge_m(\xi,q)$ for $\rho=\rho_m^{(2)}(q)$. Hence, taking $\rho=\rho_m^{(1)}(q)$, the above formulae (3.1), (3.2) yield two infinite sets

$$\left.\begin{aligned}&v_{km}(\xi,\eta,z)=Ce_m(\xi,q)ce_m(\eta,q)Z_k(z,q)\,,\\ &w_{km}(\xi,\eta,z)=Fe_m(\xi,q)ce_m(\eta,q)Z_k(z,q)\,,\\ &\qquad\qquad 1\leq k\leq n\,,\quad m=0,1,2,\cdots\end{aligned}\right\} \tag{3.6}$$

of particular solutions of the equations (2.2) and similarly we obtain

$$\left.\begin{aligned} V_{km}(\xi, \eta, z) &= Se_m(\xi, q)se_m(\eta, q)Z_k(z, q) , \\ W_{km}(\xi, \eta, z) &= Ge_m(\xi, q)se_m(\eta, q)Z_k(z, q) , \\ & 1 \leq k \leq n , \quad m=1, 2, 3, \cdots \end{aligned}\right\} \tag{3.7}$$

by putting $\rho=\rho_m^{(2)}(q)$ in the above Mathieu equations (3.3). Here

$$Z_k(z, q) = A_k \operatorname{ch} \omega(z-z_{k-1}) + B_k \operatorname{sh} \omega(z-z_{k-1}) , \qquad 1 \leq k \leq n \tag{3.8}$$

the constants A_k, B_k of integration depending in general upon the parameter q; the same holds by virtue of (3.4) also in the case of ω.

But considering the continuity of the required temperature and of the heat flux in the plane $\xi=0$ passing through the both foci of the base of our cylindrical body and using the elementary properties of Mathieu functions entering in (3.6) and (3.7), there remain only the sets $v_{km}(\xi, \eta, z)$, $V_{km}(\xi, \eta, z)$ of particular integrals suitable for dealing with our problem.

As for the only free parameter q, it is to be found according to the conditions (2.5), i.e. from the equations

$$\left.\begin{aligned} Ce_m(\xi_0, q) &= 0 , \qquad m=0, 1, 2, \cdots, \quad \text{if } \rho=\rho_m^{(1)}(q) \\ Se_m(\xi_0, q) &= 0 , \qquad m=1, 2, 3, \cdots, \quad \text{if } \rho=\rho_m^{(2)}(q) . \end{aligned}\right\} \tag{3.9}$$

There corresponds, to each value of m, an infinite set

$$q_{mr} , \qquad r=1, 2, 3, \cdots$$

of positive roots $q=q_{mr}$ of the equation $Ce_m(\xi_0, q)=0$ and another set

$$Q_{mr} , \qquad r=1, 2, 3, \cdots$$

of positive numbers, each satisfying the condition $Se_m(\xi_0, Q)=0$. These roots q_{mr}, Q_{mr} are known as the parametric zeros of belonging modified functions $Ce_m(\xi, q)$, $Se_m(\xi, q)$ at $\xi=\xi_0$.

In this way we find two doubly infinite systems

$$\left.\begin{aligned} & v_{kmr}(\xi, \eta, z) = Ce_m(\xi, q_{mr})ce_m(\eta, q_{mr})Z^{(1)}_{kmr}(z) , \\ & \quad Z^{(1)}_{kmr}(z) = A_{kmr} \operatorname{ch} \omega_{mr}(z-z_{k-1}) + B_{kmr} \operatorname{sh} \omega_{mr}(z-z_{k-1}) , \\ & \quad \omega_{mr} = \frac{2}{c}\sqrt{q_{mr}} , \qquad 1 \leq k \leq n , \quad m=0, 1, 2, \cdots, \quad r=1, 2, 3, \cdots \\ & V_{kmr}(\xi, \eta, z) = Se_m(\xi, Q_{mr})se_m(\eta, Q_{mr})Z^{(2)}_{kmr}(z) , \\ & \quad Z^{(2)}_{kmr}(z) = C_{kmr} \operatorname{ch} \Omega_{mr}(z-z_{k-1}) + D_{kmr} \operatorname{sh} \Omega_{mr}(z-z_{k-1}) , \\ & \quad \Omega_{mr} = \frac{2}{c}\sqrt{Q_{mr}} , \qquad 1 \leq k \leq n , \quad m=1, 2, 3, \cdots, \quad r=1, 2, 3, \cdots \end{aligned}\right\} \tag{3.10}$$

of particular solutions of the set of equations (2.2), each satisfying, besides, the boundary condition (2.5).

It is an easy matter to subject the coefficients $A_{kmr}, \cdots, D_{kmr}$ to such relations, that the above systems (3.10) satisfy also the conditions (2.4) at the surfaces of separation between neighbouring layers of the body. This will be so, if and only if

$$\begin{aligned} & A_{k+1,mr} = A_{kmr} \operatorname{ch} \omega_{mr} l_k + B_{kmr} \operatorname{sh} \omega_{mr} l_k , \\ & B_{k+1,mr} = \Lambda_k(A_{kmr} \operatorname{sh} \omega_{mr} l_k + B_{kmr} \operatorname{ch} \omega_{mr} l_k) , \\ & \quad l_k = z_k - z_{k-1} , \quad 1 \leq k \leq n-1 , \quad m=0, 1, 2, \cdots, \quad r=1, 2, 3, \cdots \end{aligned}$$

$$\begin{aligned} & C_{k+1,mr} = C_{kmr} \operatorname{ch} \Omega_{mr} l_k + D_{kmr} \operatorname{sh} \Omega_{mr} l_k , \\ & D_{k+1,mr} = \Lambda_k(C_{kmr} \operatorname{sh} \Omega_{mr} l_k + D_{kmr} \operatorname{ch} \Omega_{mr} l_k) , \\ & \quad l_k = z_k - z_{k-1} , \quad 1 \leq k \leq n-1 , \quad m=1, 2, 3, \cdots, \quad r=1, 2, 3, \cdots . \end{aligned}$$

Writing these equations in the matrix form[2)]

$$\left.\begin{aligned}
&K_{k+1,mr}=M_k(q_{mr})K_{kmr}\,, \qquad 1\leq k\leq n-1\,,\quad m\geq 0\,,\quad r\geq 1\,,\\
&\quad K_{kmr}=\left\|\begin{matrix}A_{kmr}\\ B_{kmr}\end{matrix}\right\|\,, \qquad 1\leq k\leq n\,,\\
&\quad M_k(q_{mr})=\left\|\begin{matrix}\operatorname{ch}\omega_{mr}l_k\,, & \operatorname{sh}\omega_{mr}l_k\\ \Lambda_k\operatorname{sh}\omega_{mr}l_k\,, & \Lambda_k\operatorname{ch}\omega_{mr}l_k\end{matrix}\right\|\,, \qquad 1\leq k\leq n-1\,,\quad m\geq 0\,,\quad r\geq 1
\end{aligned}\right\}\tag{3.11}$$

$$\left.\begin{aligned}
&L_{k+1,mr}=N_k(Q_{mr})L_{kmr}\,, \qquad 1\leq k\leq n-1\,,\quad m\geq 1\,,\quad r\geq 1\,,\\
&\quad L_{kmr}=\left\|\begin{matrix}C_{kmr}\\ D_{kmr}\end{matrix}\right\|\,, \qquad 1\leq k\leq n\,,\\
&\quad N_k(Q_{mr})=\left\|\begin{matrix}\operatorname{ch}\Omega_{mr}l_k\,, & \operatorname{sh}\Omega_{mr}l_k\,,\\ \Lambda_k\operatorname{sh}\Omega_{mr}l_k\,, & \Lambda_k\operatorname{ch}\Omega_{mr}l_k\end{matrix}\right\|\,, \qquad 1\leq k\leq n-1\,,\quad m\geq 1\,,\quad r\geq 1\,,
\end{aligned}\right\}\tag{3.12}$$

we readily obtain the expression

$$\left.\begin{aligned}
&K_{k+1,mr}=R_k(q_{mr})\left\|\begin{matrix}A_{1mr}\\ B_{1mr}\end{matrix}\right\|\,, \qquad 1\leq k\leq n-1\,,\quad m\geq 0\,,\quad r\geq 1\,,\\
&L_{k+1,mr}=S_k(Q_{mr})\left\|\begin{matrix}C_{1mr}\\ D_{1mr}\end{matrix}\right\|\,, \qquad 1\leq k\leq n-1\,,\quad m\geq 1\,,\quad r\geq 1\,,\\
&\qquad R_k(q_{mr})=M_k(q_{mr})M_{k-1}(q_{mr})\cdots M_1(q_{mr})\,,\\
&\qquad S_k(Q_{mr})=N_k(Q_{mr})N_{k-1}(Q_{mr})\cdots N_1(Q_{mr})
\end{aligned}\right\}\tag{3.13}$$

of all the unknown coefficients $A_{kmr},\cdots,D_{kmr}$ $(1\leq k\leq n)$ in terms of the undetermined $A_{1mr},\cdots,D_{1mr}$.

Writing

$$R_k(q_{mr})=\|\kappa_{kmr}^{(\alpha,\beta)}\|\,,\qquad S_k(Q_{mr})=\|\lambda_{kmr}^{(\alpha,\beta)}\|\,,\qquad \alpha,\beta=1,2$$

and using the relations (3.13), our expressions $Z_{kmr}^{(1)}(z)$ and $Z_{kmr}^{(2)}(z)$ from (3.10) become

$$\left.\begin{aligned}
&Z_{1mr}^{(1)}(z)=A_{1mr}\operatorname{ch}\omega_{mr}z+B_{1mr}\operatorname{sh}\omega_{mr}z\,,\\
&Z_{k+1,mr}^{(1)}(z)=A_{1mr}[\kappa_{kmr}^{(11)}\operatorname{ch}\omega_{mr}(z-z_k)+\kappa_{kmr}^{(21)}\operatorname{sh}\omega_{mr}(z-z_k)]\\
&\qquad +B_{1mr}[\kappa_{kmr}^{(12)}\operatorname{ch}\omega_{mr}(z-z_k)+\kappa_{kmr}^{(22)}\operatorname{sh}\omega_{mr}(z-z_k)]\,,\\
&\qquad\qquad 1\leq k\leq n-1\,,\quad m\geq 0\,,\quad r\geq 1\\
&Z_{1mr}^{(2)}(z)=C_{1mr}\operatorname{ch}\Omega_{mr}z+D_{1mr}\operatorname{sh}\Omega_{mr}z\,,\\
&Z_{k+1,mr}^{(2)}(z)=C_{1mr}[\lambda_{kmr}^{(11)}\operatorname{ch}\Omega_{mr}(z-z_k)+\lambda_{kmr}^{(21)}\operatorname{sh}\Omega_{mr}(z-z_k)]\\
&\qquad +D_{1mr}[\lambda_{kmr}^{(12)}\operatorname{ch}\Omega_{mr}(z-z_k)+\lambda_{kmr}^{(22)}\operatorname{sh}\Omega_{mr}(z-z_k)]\,,\\
&\qquad\qquad 1\leq k\leq n-1\,,\quad m\geq 1\,,\quad r\geq 1\,.
\end{aligned}\right\}\tag{3.14}$$

Recapitulating, we see that the relations (3.10) and (3.14) define two doubly infinite systems

$$v_{kmr}(\xi,\eta,z)\,,\quad V_{kmr}(\xi,\eta,z)\,,\qquad 1\leq k\leq n,\ r\geq 1,\ m\geq 0 \text{ for } v_{kmr} \text{ and } m\geq 1 \text{ for } V_{kmr}$$

of particular integrals, each group satisfying not only the equations (2.2), but also the additional conditions (2.4) and (2.5). Our problem reduces then to determining the coefficients $A_{1mr},\cdots,D_{1mr}$ entering in (3.14).

§ 4. Determination of $A_{1mr},\cdots,D_{1mr}$

Let $h(\xi,\eta)$ be a continuous single-valued function within the region $0\leq\xi<\xi_0$, $0\leq\eta\leq 2\pi$ and let $h(\xi_0,\eta)=0$ for $0\leq\eta\leq 2\pi$. Such a function can be represented by the well-known series

$$
\begin{aligned}
&h(\xi,\eta)=\sum_{m=0}^{\infty}\sum_{r=1}^{\infty}h_{mr}^{(c)}Ce_m(\xi,q_{mr})ce_m(\eta,q_{mr})+\sum_{m=1}^{\infty}\sum_{r=1}^{\infty}h_{mr}^{(s)}Se_m(\xi,Q_{mr})se_m(\eta,Q_{mr})\,,\\
&h_{mr}^{(c)}=\frac{\int_0^{\xi_0}\int_0^{2\pi}(\operatorname{ch}2\xi-\cos 2\eta)h(\xi,\eta)Ce_m(\xi,q_{mr})ce_m(\eta,q_{mr})d\xi d\eta}{\pi\int_0^{\xi_0}(\operatorname{ch}2\xi-\Theta_{mr})Ce_m^2(\xi,q_{mr})d\xi}\,,\\
&h_{mr}^{s}=\frac{\int_0^{\xi_0}\int_0^{2\pi}(\operatorname{ch}2\xi-\cos 2\eta)h(\xi,\eta)Se_m(\xi,Q_{mr})se_m(\eta,Q_{mr})d\xi d\eta}{\pi\int_0^{\xi_0}(\operatorname{ch}2\xi-\Psi_{mr})Se_m^2(\xi,Q_{mr})d\xi}\,,\\
&\begin{matrix}\Theta_{mr}\\ \Psi_{mr}\end{matrix}=\frac{1}{\pi}\int_0^{2\pi}\begin{matrix}ce_m^2(\eta,q_{mr})\\ se_m^2(\eta,Q_{mr})\end{matrix}\cos 2\eta d\eta\,,
\end{aligned}
\tag{4.1}
$$

this expansion being valid in the whole extent $0\leq\xi\leq\xi_0$, $0\leq\eta\leq 2\pi$.

Let us assume, that the given functions $f(\xi,\eta)$, $g(\xi,\eta)$ from (2.3) have the properties just imposed on $h(\xi,\eta)$ and let us assume the required solution $u_k(\xi,\eta,z)$ of our original problem (2.2)-(2.5) in the form

$$u_k(\xi,\eta,z)=\sum_{m=0}^{\infty}\sum_{r=1}^{\infty}v_{kmr}(\xi,\eta,z)+\sum_{m=1}^{\infty}\sum_{r=1}^{\infty}V_{kmr}(\xi,\eta,z)\,,\qquad 1\leq k\leq n\,,\tag{4.2}$$

the eigenfunctions $v_{kmr}(\xi,\eta,z)$, $V_{kmr}(\xi,\eta,z)$ being defined by the relations (3.10), (3.14).

Then the only pair of unsatisfied conditions (2.3) appears in the form of two requirements

$$f(\xi,\eta)=\sum_{m=0}^{\infty}\sum_{r=1}^{\infty}Z_{1mr}^{(1)}(0)Ce_m(\xi,q_{mr})ce_m(\eta,q_{mr})+\sum_{m=1}^{\infty}\sum_{r=1}^{\infty}Z_{1mr}^{(2)}(0)Se_m(\xi,Q_{mr})se_m(\eta,Q_{mr})\,,$$

$$g(\xi,\eta)=\sum_{m=0}^{\infty}\sum_{r=1}^{\infty}Z_{nmr}^{(1)}(z_n)Ce_m(\xi,q_{mr})ce_m(\eta,q_{mr})+\sum_{m=1}^{\infty}\sum_{r=1}^{\infty}Z_{nmr}^{(2)}(z_n)Se_m(\xi,Q_{mr})se_m(\eta,Q_{mr})\,,$$

$$0\leq\xi<\xi_0\,,\quad 0\leq\eta\leq 2\pi\,.$$

Equating this with (4.1) and using (3.14) gives the set of equations

$$
\left.
\begin{aligned}
&Z_{1mr}^{(1)}(0)=A_{1mr}=f_{mr}^{(c)}\,,\qquad Z_{1mr}^{(2)}(0)=C_{1mr}=f_{mr}^{(s)}\,,\\
&Z_{nmr}^{(1)}(z_n)=A_{1mr}(\kappa_{n-1,mr}^{(11)}\operatorname{ch}\omega_{mr}l_n+\kappa_{n-1,mr}^{(21)}\operatorname{sh}\omega_{mr}l_n)\\
&\qquad+B_{1mr}(\kappa_{n-1,mr}^{(12)}\operatorname{ch}\omega_{mr}l_n+\kappa_{n-1,mr}^{(22)}\operatorname{sh}\omega_{mr}l_n)=g_{mr}^{(c)}\,,\\
&Z_{nmr}^{(2)}(z_n)=C_{1mr}(\lambda_{n-1,mr}^{(11)}\operatorname{ch}\Omega_{mr}l_n+\lambda_{n-1,mr}^{(21)}\operatorname{sh}\Omega_{mr}l_n)\\
&\qquad+D_{1mr}(\lambda_{n-1,mr}^{(12)}\operatorname{ch}\Omega_{mr}l_n+\lambda_{n-1,mr}^{(22)}\operatorname{sh}\Omega_{mr}l_n)=g_{mr}^{(s)}
\end{aligned}
\right\}
\tag{4.3}
$$

for the undetermined values $A_{1mr},\cdots,D_{1mr}$. The Fourier coefficients $f_{mr}^{(c)},\cdots,g_{mr}^{(s)}$ entering in the system (4.3) are to be calculated according to (4.1).

§ 5. Recapitulation and Solution of the Original Problem

Solving the above equations (4.3) and substituting the resulting values $A_{1mr},\cdots,D_{1mr}$ into (3.14) gives us the expressions $Z_{kmr}^{(1)}(z)$, $Z_{kmr}^{(2)}(z)$ needed in (3.10). Nevertheless, detailed calculation does not lead to any simple formulae and so we shall break our considerations at the present stage. Instead of continuing the laborious calculations it will prove useful to give a brief summary of all the preceding results and to show, in what a way they enable us to obtain the solution of our original problem (2.2)-(2.5).

1. Using the given constants

$$a,\ b,\ 0=z_0<z_1<z_2<\cdots<z_n\,,\quad \lambda_1,\ \lambda_2,\ \cdots,\ \lambda_n\,,$$

we first calculate the auxiliary values

$$c=\sqrt{a^2-b^2}\,,\quad \xi_0=\lg\frac{a+b}{c}\,,\quad l_k=z_k-z_{k-1}\,,\quad 1\le k\le n\,,\qquad \Lambda_k=\frac{\lambda_k}{\lambda_{k+1}}\,,\quad 1\le k\le n-1\,. \tag{5.1}$$

2. Solving the equations (3.9) gives us the parametric zeros q_{mr}, Q_{mr} of the modified functions $Ce_m(\xi, q)$, $Se_m(\xi, q)$ at $\xi=\xi_0$.

3. Using the given functions $f(\xi, \eta)$, $g(\xi, \eta)$, we calculate their Fourier coefficients $f_{mr}^{(c)}$, $f_{mr}^{(s)}$, $g_{mr}^{(c)}$, $g_{mr}^{(s)}$ by means of (4.1).

4. Having used (3.10) to find the values ω_{mr}, Ω_{mr}, it is an easy matter to write down the matrices $M_k(q_{mr})$, $N_k(Q_{mr})$, as defined in (3.11) and (3.12).

5. The essence and the most difficult part of the problem lie in constructing the matrices $R_k(q_{mr})$, $S_k(Q_{mr})$, as given by the two last formulae (3.13).

6. Knowing the elements $\kappa_{kmr}^{(\alpha,\beta)}$, $\lambda_{kmr}^{(\alpha,\beta)}$, $\alpha, \beta=1, 2$ of $R_k(q_{mr})$ and $S_k(Q_{mr})$, we can proceed to establish the equations (4.3). Solving them gives the coefficients $A_{1mr}, \cdots, D_{1mr}$.

7. Using (3.14) yields the expressions $Z_{kmr}^{(1)}(z)$, $Z_{kmr}^{(2)}(z)$ and herewith we obtain by (3.10) the particular integrals $v_{kmr}(\xi, \eta, z)$, $V_{kmr}(\xi, \eta, z)$.

Having performed all the operations indicated in the preceding seven stages, we can write down the final solution of the original problem, according to the formula (4.2).

§ 6. A Homogeneous Cylinder

To illustrate our general deductions by at least one example, let us treat the case

$$\Lambda_1=\Lambda_2=\cdots=\Lambda_{n-1}=1$$

corresponding to a homogeneous isotropic cylinder.

A simple calculation gives

$$R_k(q_{mr})=\begin{Vmatrix}\operatorname{ch}\omega_{mr}z_k\,, & \operatorname{sh}\omega_{mr}z_k\\ \operatorname{sh}\omega_{mr}z_k\,, & \operatorname{ch}\omega_{mr}z_k\end{Vmatrix}\,,\qquad S_k(Q_{mr})=\begin{Vmatrix}\operatorname{ch}\Omega_{mr}z_k\,, & \operatorname{sh}\Omega_{mr}z_k\\ \operatorname{sh}\Omega_{mr}z_k\,, & \operatorname{ch}\Omega_{mr}z_k\end{Vmatrix}\,,\qquad 1\le k\le n-1\,,$$

and the equations (4.3) become

$$A_{1mr}=f_{mr}^{(c)}\,,\qquad C_{1mr}=f_{mr}^{(s)}\,,$$

$$A_{1mr}\operatorname{ch}\omega_{mr}z_n+B_{1mr}\operatorname{sh}\omega_{mr}z_n=g_{mr}^{(c)}\,,$$

$$C_{1mr}\operatorname{ch}\Omega_{mr}z_n+D_{1mr}\operatorname{sh}\Omega_{mr}z_n=g_{mr}^{(s)}\,.$$

Solving with respect to $A_{1mr}, \cdots, D_{1mr}$ and substituting into (3.14) leads to the common expressions

$$Z_{kmr}^{(1)}(z)=\frac{1}{\operatorname{sh}\omega_{mr}z_n}[f_{mr}^{(c)}\operatorname{sh}\omega_{mr}(z_n-z)+g_{mr}^{(c)}\operatorname{sh}\omega_{mr}z]\,,$$

$$Z_{kmr}^{(2)}(z)=\frac{1}{\operatorname{sh}\Omega_{mr}z_n}[f_{mr}^{(s)}\operatorname{sh}\Omega_{mr}(z_n-z)+g_{mr}^{(s)}\operatorname{sh}\Omega_{mr}z]$$

holding for all $1\le k\le n$.

Using (3.10) and (4.2) gives us the final solution in the form

$$\begin{aligned}u(\xi, \eta, z)=&\sum_{m=0}^{\infty}\sum_{r=1}^{\infty}\frac{Ce_m(\xi, q_{mr})ce_m(\eta, q_{mr})}{\operatorname{sh}\omega_{mr}z_n}[f_{mr}^{(c)}\operatorname{sh}\omega_{mr}(z_n-z)+g_{mr}^{(c)}\operatorname{sh}\omega_{mr}z]\\ &+\sum_{m=1}^{\infty}\sum_{r=1}^{\infty}\frac{Se_m(\xi, Q_{mr})se_m(\eta, Q_{mr})}{\operatorname{sh}\Omega_{mr}z_n}[f_{mr}^{(s)}\operatorname{sh}\Omega_{mr}(z_n-z)+g_{mr}^{(s)}\operatorname{sh}\Omega_{mr}z];\end{aligned} \tag{6.1}$$

the meaning of all the abbreviations is explained in § 5.

§7. Final Remarks

1. The above expansion (4.1) can be deduced under more general conditions than those cited at the beginning of § 4. Thus, it would be possible to moderate in some measure the requirements imposed upon the given functions $f(\xi, \eta)$, $g(\xi, \eta)$ entering in (2.3).

2. It may be reasoned that the solution of many problems like that treated above would be greatly simplified by building up a theory of Mathieu transforms. This can be done in quite an analogous manner to, for instance, the case of the familiar Hankel transforms. The outlines of such a theory and a number of applications to mathematical physics will be the object of separate papers.

References

1) N. W. McLachlan: Theory and Application of Mathieu Functions (Oxford, 1947).
2) V. Vodička: J. Phys. Soc. Japan **15** (1960) 1332.

JOURNAL OF THE PHYSICAL SOCIETY OF JAPAN Vol. 16, No. 8, AUGUST, 1961

Ultrasonic Dispersion in Acetone

C. Raghupathi RAO

Department of Physics, Nizam College, Hyderabad-Dn. India

(Received March 13, 1961)

The study of dispersion of acoustic velocity in acetone employing ultrasonic waves of very high frequencies up to 180 Mc/s has been made for the first time and no positive evidence of dispersion could be established. It is shown that the angular distribution of high frequency diffraction is less in acetone than that in water, as this depends only on the parameter $\pi L/\lambda^*$ where L corresponds to the length of the sound path traversed by the light beam and λ^* corresponds to the sound wavelength in the medium.

§ 1. Introduction

The study of dispersion in liquids has been carried out by many workers[1)-3)] but dispersion has not been positively established in many cases. Raghavendra Rao[4)] observed definite evidence of dispersion of acoustic velocity in liquids. He determined the hypersonic velocities in a number of organic liquids by a study of the fine structure of monochromatic radiations scattered by liquids. He reported a decrease of acoustic velocity by about 225 m/sec in acetone. Venkateswaran[5)] reported a decrease of acoustic velocity in acetone by about 20 m/sec at 28°C, while Fabelinskii[6)] observed no change. Rank, Shull and Axford[7)] observed an increase of 125 m/sec at −78°C. The accuracy of hypersonic measurements, however, is comparatively small. So, it is interesting and useful to perform the measurements by using ultrasonic waves of very high frequencies in liquids to detect or disprove dispersion positively.

§ 2. Method

Ultrasonic velocities have been measured using the usual Debye and Sears'[8)] optical diffraction method at low frequencies up to 80 Mc/s and the simultaneous excitation method[9)] at high frequencies upto 180 Mc/s. It is possible to excite the first order diffraction lines symmetrically on either side of zero order up to 80 Mc/s in the normal incidence position of the crystal holder but at higher frequencies, the crystal holder is to be tilted to the appropriate Bragg angle[10)] so that a single diffraction order makes its appearance. The fringe width of the high frequency diffraction order is computed by measuring its distance on a comparator from the low frequency diffraction lines.

§ 3. Results and Discussion

The ultrasonic velocities measured in this way are given in Table I for various frequencies from 28 to 180 Mc/s. The study of dispersion of acoustic velocity in acetone employing ultrasonic waves of very high frequencies up to 180 Mc/s is made for the first time and Table I clearly shows the absence of dispersion at these frequencies.

Table I.

λ=5893 A.U. Temperature=28°C.

Frequency in Mc/s v^*	Fringe width 'd' in cms	v^*/d	Velocity in metres/sec
28.19	0.4678	60.27	1184
48.73	0.8122	59.99	1179
73.08	1.2120	60.30	1184
149.80	2.4901	60.17	1182
180.25	2.9900	60.26	1184

§ 4. Angular Distribution of High Frequency Diffraction

The high frequency diffraction order generally persists in the field of view over an angle on either side of its Bragg position. This angular width over which the diffraction order appears is termed as "the angular distribution of high frequency diffraction". In order to find the variation of this distribution of diffraction with increasing frequencies in acetone, this investigation is undertaken.

The expression[11)] $I_{+1}=I_m\left\{\frac{\sin(\pi L/\lambda^*)\phi}{(\pi L/\lambda^*)\phi}\right\}^2$ is useful in this study. I_{+1} denotes the intensity of the first order, L represents the length of the ultrasonic path travelled by the light beam, λ^* corresponds to the sound wavelength in the medium and ϕ shows the angle of deviation of the sound wave-front from the Bragg position. It can be seen by differentiating the above expression that the angular distribution of high frequency diffraction depends only on the value of the parameter $\pi L/\lambda^*$. At higher frequencies this parameter increases, making the high frequency diffraction order appear over a very small angle. That is to say, for very high frequencies and large lengths of the sound field, the phenomenon of characteristic reflection of light gains importance.

With the help of the Photo-tube, the intensity of the first order of diffraction is measured and plotted against the tilt of the crystal holder. The theoretical curves and the experimental ones obtained by the Photo-

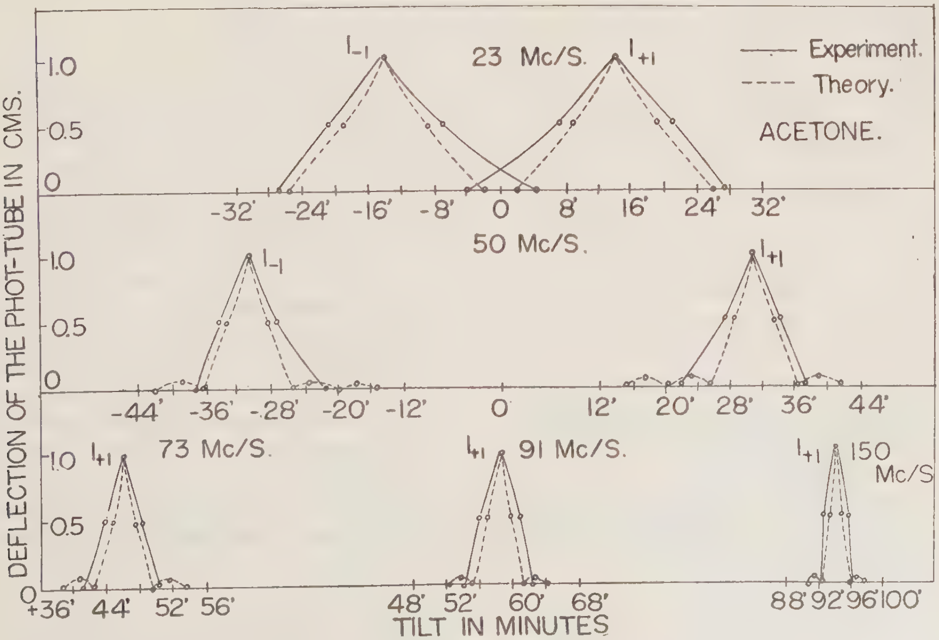

Fig. 1. Angular distribution of high frequency diffraction in acetone. Comparison between theory and experiment.

tube are shown in Fig. 1 to facilitate comparision. For all the frequencies employed in this study, the maximum intensity of the first order of diffraction is adjusted to be the same and the effect of tilt studied by the Photo-tube. It will be noticed, firstly, that the curves become narrower as one approaches higher frequencies, showing their dependence on the parameter $\pi L/\lambda^*$; secondly, that the theoretical curves are always bound within the experimental curves and thirdly, that the theoretical curves show a sharp fall in intensity while the fall in the experimental curves is very gradual. These deviations in intensity can, however, be explained as mainly due to the fact that the sound field is not the ideal plane wave with un-damped amplitude as assumed in the theory.

A comparision of the angular distribution of high frequency diffraction in water and acetone is very instructive. At 50 Mc/s both the diffraction orders on either side of the zero order persist through a large angle, though faintly, in water; while a single diffraction order appears over a small angle in respect of acetone. This behaviour of the diffraction pattern at this frequency in the two liquids is shown in Fig. 2. The angular distribution of high frequency diffraction is less in acetone than that in water[12] This is due to the small wave-length of sound in acetone, its ultrasonic velocity being smaller than that in water.

In conclusion, the author's thanks are due to Dr. S. Bhagavantam for his keen interest in this work.

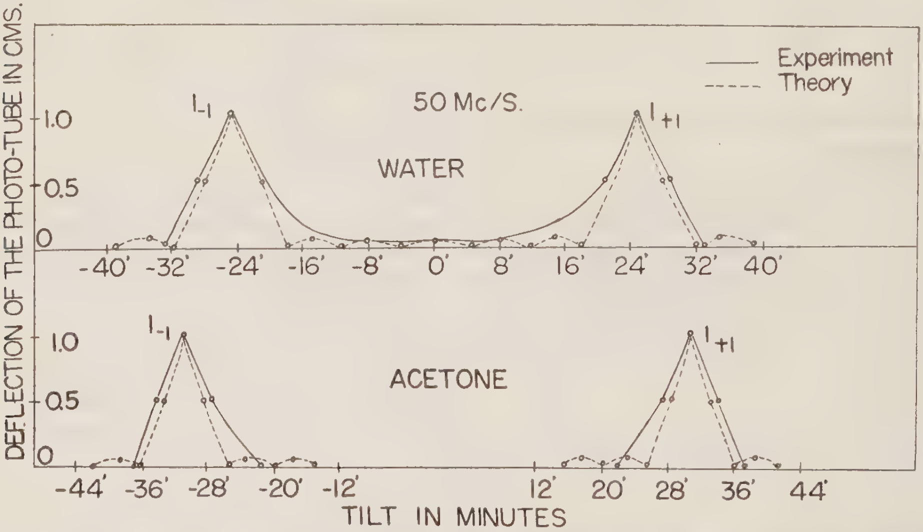

Fig. 2. Comparision of Angular distribution of high frequency diffraction in acetone and water.

References

1) R. Bär: Proc. Ind. Acad. Sci. **8**, **A** (1938) 289.
2) A. K. Dutta: Phys. Zeitschr **39** (1938) 186.
3) S. Parathasarathy: Curr. Sci. **6** (1937) 55.
4) B. V. Raghavendra Rao: Proc. Ind. Acad. Sci. **7**, **A** (1938) 163.
5) C. S. Venkateswaran: ibid. **15**, **A** (1942) 371.
6) C. S. Fabelinskii: Uspekhi Fiz. Nauk. **43** (1957) 355.
7) D. H. Rank, E. R. Shull and D. W. E. Axford: Nature **164** (1949) 67.
8) P. Debye and F. Sears: Proc. Nat. Acad. Sci. **18** (1932) 409.
9) S. Parathasarathy, A. Pande and M. Pancholy: J. Sci. Ind. Res. **3** (1945) 299.
10) S. Bhagavantam and B. R. Rao: Nature **161** (1948) 927.
11) E. David: Phys. Zeitschr **38** (1937) 587.
12) C. R. Rao: Proc. Ind. Acad. Sci. **42** (1955) 158.

Short Notes

This section is intended to secure prompt publication of important discoveries in physics. The reports should not exceed 800 words in length. A figure of size 7 cm×7 cm will be counted as 150 words.

J. Phys. Soc. Japan **16** (1961) 1639

Paramagnetic Resonance of Cobalt in Cadmium Chloride and Cadmium Bromide

By Kazuo Morigaki*

Department of Physics,
Osaka University, Osaka

(Received May 17, 1961)

Paramagnetic resonance of Co^{2+} ions present as substitutional impurities in single crystals of cadmium chloride and cadmium bromide has been observed below about 40°K using the frequency of 9300 Mc/sec.

The orbital ground state of Co^{2+} ion in the cubic crystalline field has a threefold degeneracy, which is split into a singlet and a doublet if the trigonal field acts on the ion in addition to the cubic field. Each Co^{2+} ion substituting cadmium ion is subjected to a crystalline field of approximately cubic symmetry with a trigonal component in the $CdCl_2$-type lattice. The observed spectra of Co^{2+} ions in cadmium chloride can be described by the following spin Hamiltonian,

$$\mathscr{H}=g_{/\!/}\beta H_zS_z'+g_{\perp}\beta(H_xS_x'+H_yS_y')$$
$$+AI_zS_z'+B(I_xS_x'+I_yS_y')$$

with effective electron spin $S'=1/2$, nuclear spin $I=7/2$, $g_{/\!/}=3.04\pm0.02$, $g_{\perp}=4.95\pm0.02$, $A=(36\pm6)\times10^{-4}\,\mathrm{cm}^{-1}$, $B=(169\pm9)\times10^{-4}\,\mathrm{cm}^{-1}$ at 4.2°K, and $g_{/\!/}=3.03\pm0.02$, $g_{\perp}=4.95\pm0.02$, $A=(36\pm6)\times10^{-4}\,\mathrm{cm}^{-1}$, $B=(167\pm9)\times10^{-4}\,\mathrm{cm}^{-1}$ at 1.4°K, where the z direction is chosen to coincide with the c axis of the crystal.** The above spin Hamiltonian indicates that the lowest level of Co^{2+} ions in the cadmium chloride crystal is an orbital singlet. The observed values of $g_{/\!/}$ and $g_{\perp}$ can be explained by the theory of Abragam and Pryce[1)].

The paramagnetic resonance spectrum of Co^{2+} ions in cadmium bromide at about 10°K can be fitted with the above spin Hamiltonian with the following values of the parameters; $g_{/\!/}=2.71\pm0.05$, $g_{\perp}=4.99\pm0.05$, $A=(32\pm8)\times10^{-4}\,\mathrm{cm}^{-1}$, $B=(175\pm10)\times10^{-4}\,\mathrm{cm}^{-1}$, $S'=1/2$, and $I=7/2$.

The resonance lines of Co^{2+} ions in cadmium chloride and cadmium bromide can be saturated at relatively small power (below half a milliwatt) of the microwave at liquid helium temperature. The measurement of saturation of the resonance lines of Co^{2+} ions in cadmium chloride was done at 4.2°K and 1.4°K in the case of the static magnetic field perpendicular to the c axis in which eight h.f.s. lines could be observed. The saturation behaviour is an inhomogeneous type at both temperatures and the products of T_1 and T_2 are given as follows: $T_1\cdot T_2=6.6\times10^{-12}\,\mathrm{sec}^2$ at 4.2°K and $T_1\cdot T_2=3.1\times10^{-11}\,\mathrm{sec}^2$ at 1.4°K.

As the measuring temperature is increased above 4.2°K, the resonance lines are broadened gradually and above about 40°K they become unobservable because of the too short spin—lattice relaxation time. The spin—lattice relaxation time at about 40°K estimated from the line width is 1.4×10^{-9} sec. The temperature dependence of the spin—lattice relaxation time is understood by the direct process in the interaction between phonons and spins in the temperature range from 1.4°K to 4.2°K and by the Raman process in the temperature range from 20°K to 40°K.

Besides the allowed transitions described above the forbidden transitions which correspond to a simultaneous flipping of electron and nuclear spins in the same and opposite directions are observed at 4.2°K in the case of cadmium chloride crystal when the oscillating magnetic field has a component parallel to the static magnetic field. In the static magnetic field perpendicular to the c-axis, each line of seven forbidden h.f.s. lines is located in the middle between every eight allowed h.f.s. lines. The relative intensities of the forbidden lines in themselves are in good agreement with those calculated from the formula of the transition probability given by Jeffries[2)] using the above parameters of the spin Hamiltonian, but the ratio of the intensity of the forbidden lines to that of the allowed lines is five times as large as that expected from the theory of Jeffries.

The full accounts of this report will be published in a near future. The author would like to thank Professor J. Itoh for his helpful discussions.

References

1) A. Abragam and M. H. L. Pryce: Proc. Roy. Soc. **A, 206** (1951) 173.
2) C. D. Jeffries: Phys. Rev. **117** (1960) 1056.
3) J. R. Orton: Rep. Prog. Phys. **22** (1959) 208.

---

* Present address: Sony Corporation Research Laboratory, Hodogaya, Yokohama.

** The above values of $g_{/\!/}$, $g_{\perp}$, A and B agree with those measured at 20°K by M. F. Partridge which are quoted in reference 3.

J. PHYS. SOC. JAPAN **16** (1961) 1640

Oscillator Strength of I⁻-Absorption Band in KCl Crystal

By Takehiko ISHII

Department of Physics, The Faculty of Science, Tohoku University

(Received June 5, 1961)

A KCl crystal containing a small amount of KI shows an absorption band due to the presence of I⁻ ions[1]. The absorption peak of this band appears at the wavelength of 188 mμ at room temperature. If the concentration of I⁻ ions in the crystal is known and the absorption curve is precisely measured, one can calculate the oscillator strength of this band using Smakula's formula. The oscillator strength of the I⁻-absorption band has been determined by this principle.

Five KCl single crystals containing different amounts of KI were grown from the melt in air by Kyropoulos method. The absorption spectrum of each crystal was measured at room temperature with a vacuum spectrophotometer constructed in our laboratory[2]. The resolving power of the spectrophotometer was set to give $\Delta\lambda \sim 0.5$ mμ in the present case. The absorption spectra are shown in Fig. 1. The absorption peak was located at 188.5 mμ and the half width of the band was 0.31 ev. The optical density at the band peak of specimen No. 5, in which the concentration of I⁻ ions is 1.17×10^{19} cm⁻³, is too large to be directly measured and was estimated from the band tail.

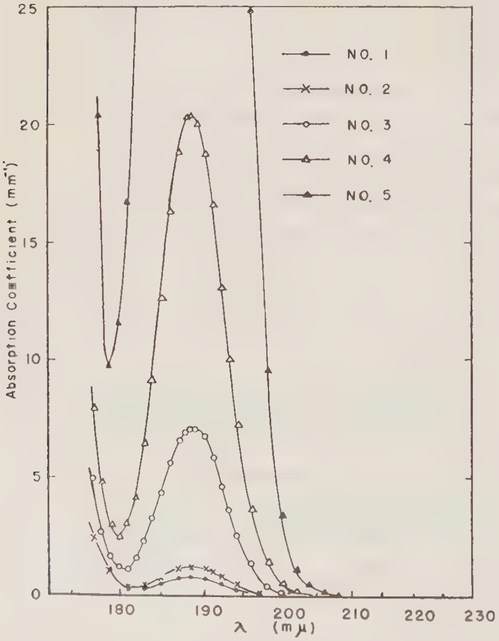

Fig. 1. Absorption spectra of KCl crystal containing various amounts of KI.

The concentrations of I⁻ ions in the crystals were determined by chemical anylysis. Potassium iodide in specimen was oxidized to give IO_3^- with potassium permanganate, and liberation of iodine from IO_3^- was made by adding KI. The concentration of freed iodine was determined by photocolorimetric iodimetry using starch. In KCl crystal Br⁻ ions are usually contained as an impurity. In the present chemical analysis, a procedure which is not affected by the presence of Br⁻ ions is employed. The result of this colorimetric analysis is tabulated in Table I.

Table I. Concentration of I⁻ ions and calculated oscillator strength.

Specimen	α_m (cm⁻¹)	n_0 (cm⁻³)	f
No. 1	7.77	7.25×10^{16}	0.29
No. 2	12.4	1.21×10^{17}	0.27
No. 3	70.7	5.90×10^{17}	0.32
No. 4	204	1.70×10^{18}	0.32
No. 5	1450	1.17×10^{19}	0.33

The height of the absorption maximum is not proportional to the concentration of KI added before melting, but seems to be proportional to that in the crystal. The oscillator strength is calculated with Smakula's formula

$$n_0 f = 1.31\times10^{17}\times\frac{n}{(n^2+2)^2}\alpha_m W\,,$$

where n_0 is the concentration of I⁻ ions in cm⁻³; n is the refractive index of the crystal at 188.5 mμ, α_m is the absorption coefficient in cm⁻¹ at 188.5 mμ and W is the half width of the band in ev. In the present case, the value of $n=1.796$ is adopted which is obtained with appropriate interpolation of the data measured by Martens and Gyulai[3]. The oscillator strength is given as $f=0.30\pm0.04$ by taking the mean of the values in the Table I.

The author expresses his cordial thanks to Mr. S. Tamura, the Institute for Solid State Physics, University of Tokyo, for his guidance in chemical analysis. He also appreciates Professors M. Ueta and K. Kobayashi for their kind interests and useful discussions throughout this work.

References

1) K. Nakamura et al.: J. Phys. Soc. Japan **16** (1961) 1262; H. Mahr: Bull. Amer. Phys. Soc. Series II **6** (1961) 114.
2) M. Ueta, M. Hirai and H. Watanabe: J. Phys. Soc. Japan **14** (1959) 253.
3) F. F. Martens: Ann. Physik **6** (1901) 603. Z. Gyulai: Z. Phys. **46** (1927) 80.

J. PHYS. SOC. JAPAN **16** (1961) 1641

Magnetic After Effects in Manganese Zinc Ferrites

By Tsuneo AKASHI and Takashi OKADA

Research Laboratory, Nippon Electric Company, Limited, Tokyo

(Received March 2, 1961)

Co-existence of the Richter Type after effect and the time decrease of initial permeability has been observed in many ferro- and ferri-magnetic materials such as iron-steel[1),2)], Mn-Zn ferrites[3),4)], Ni-Zn ferrites[5)] and Mn-ferrites[6)]. Snoek has proposed the theory[1),2)] that the two effects are caused by the impurity atoms in ferro magnetic materials. In ferrites, it has been assumed by many authors[3),5)] that the transition $Fe^{++} \rightleftarrows Fe^{+++}$ is responsible for the two effects.

In this short note, we report the influence of partial oxygen pressure of the atmosphere (PO_2) during sitering process (1200C° 4 hr) on the two effects, observed for several Mn-Zn ferrites whose composition are given in Table I.

Table I.

Sample No	Fe_2O_3 (mol %)	MnO (mol %)	ZnO (mol %)
1	48	33.2	18.8
2	49	32.6	18.5
3	51	32.3	17.7
4	53	30.1	16.9
5	55	28.7	16.3

Richter Type after effects observed in the samples having the same composition and being sintered in various atmospheres are shown in Fig. 1. The peak values of tan δ increased with the decreas of PO_2. The temperatures at which the peaks occured, were found to be dependent on the composition of the ferrite but not on PO_2. As is usually accepted, the Richter type after Effects, observed in the samples having excess Fe_2O_3 (before sintering) is caused by the transition of electrons between Fe^{++} and Fe^{+++}. Thus the present results indicate that Fe^{++} content in the Mn-Zn ferrite would be decreased with the increase of PO_2.

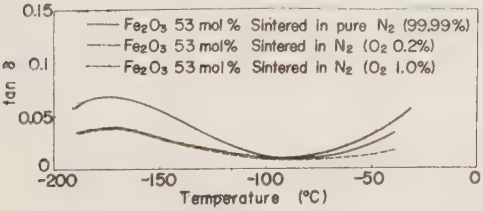

Fig. 1. Richter type after effects in Mn-Zn ferrites.

Time decrease of initial permeability obtained can be expressed by

$$\Delta\mu/\mu=(\alpha/\mu)\log(t/t_0) \qquad (1)$$

where $\Delta\mu$ is the decrease of initial permeability after $t=t_0$. The observed relations between α/μ and composition of the ferrites are shown in Fig. 2 as a function of PO_2. α/μ are sensitive to the compositions as well as PO_2. It is interesting to note that the assumptions that the transition of electrons between Fe^{++} and Fe^{+++} is also responsible for the time decrease of initial permeability may not be valid, because the increase of PO_2, i.e., decrease of Fe^{++}, gave rise to the increase of α/μ.

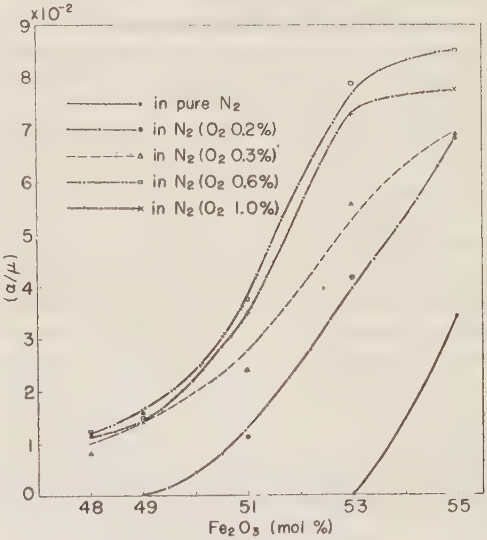

Fig. 2. The decrease of initial permeability in Mn-Zn ferrites after sintering.

The authors wish to express their sincere thanks to Dr. M. Kobayashi rnd Dr. Y. Ishikawa for their kind guidance.

References

1) J. L. Snoek: Physica **5** (1938) 663.
2) J. L. Snoek: Physica **6** (1939) 161.
3) J. L. Snoek: New Developments in Ferromagnetic Materials (Elsevier, Amsterdam, 1949).
4) Wiji and Heide: Rev. Mod. Phys. **25** (1953) 99.
5) A. Marais et T. Merceron: Comp. Rand. Acad. Sci. (1957) 2511.
6) W. A. Cropo: J. Appl. Phys. **31** (1960) 2675.

J. Phys. Soc. Japan **16** (1961) 1642~1643

Some Properties of Complex Oxides $AB_{0.5}B'_{0.5}O_3$ of Perovskite Type

By Shoichiro NOMURA and Tatsuyuki KAWAKUBO

Physics Department,
Tokyo Institute of Technology,
O-okayama, Meguro-ku, Tokyo

(Received May 9, 1961)

Recently it has been reported by Brixner[1] that several oxides of $AB_{0.5}B'_{0.5}O_3$ type (A=Ba, Sr: B=W, Mo: B'=Ni, Co) show the perovskite structure, cubic for the oxide of barium and tetragonal for the oxide of strontium. We have made x-ray measurements on the oxides in which Ba and Sr atoms are mixed at various ratio in the position of A, and also measurements of electric conductivity on Sr oxides.

The specimens were prepared by the method of two successive solid-state reactions at 1250~1350°C and 1 atom pressure of air. The crystal structure at room temperature was determined from the powder diffraction patterns, using CuK_α radiation, and it was ascertained that all of these oxides are of perovskite type and further that the dimensions of the unit cell a and c can be represented as $a=2a_0$, $c=2c_0$, where a_0 and c_0 are those of the unit cell of typical perovskite structure containing one molecule in it. This fact suggests us that the rock-salt type ordered arrangement of B and B' ions is realized in the crystal. The values of the cell dimensions are in good agreement with Brixner's data[1]. The ordered arrangement was not broken by quenching from temperature as high as 1250°C.

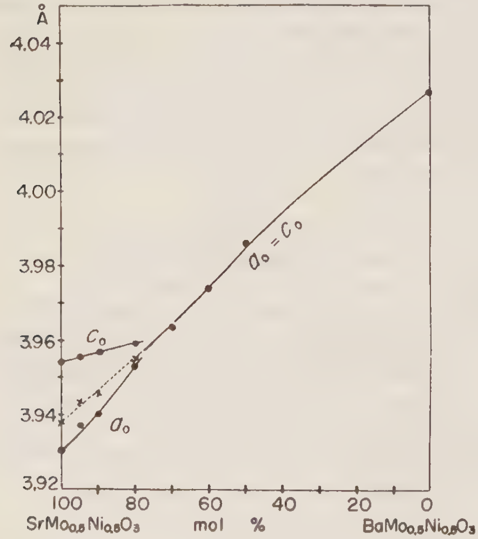

Fig. 1. Cell dimensions for the system of $BaMo_{0.5}Ni_{0.5}O_3$-$SrMo_{0.5}Ni_{0.5}O_3$. The crosses represent the values of $\sqrt[3]{a_0^2c_0}$.

By replacing some of Sr ions with Ba ions, the unit cell volume of the oxides of strontium increased and the tetragonality decreased with the increasing content of Ba ions until it became 1. As an example, the result for $BaMo_{0.5}Ni_{0.5}O_3-SrMo_{0.5}Ni_{0.5}O_3$ system is shown in Fig. 1, where the cell volume varies almost continuously with the content of Ba ions, passing through the transition from the tetragonal- to cubic-phase.

The electrical conductivities of these samples in the temperature range from r.t. to 300°C were measured by the two terminal method and an anomaly was found for each oxide of strontium. The results obtained are exhibited in Fig. 2. The

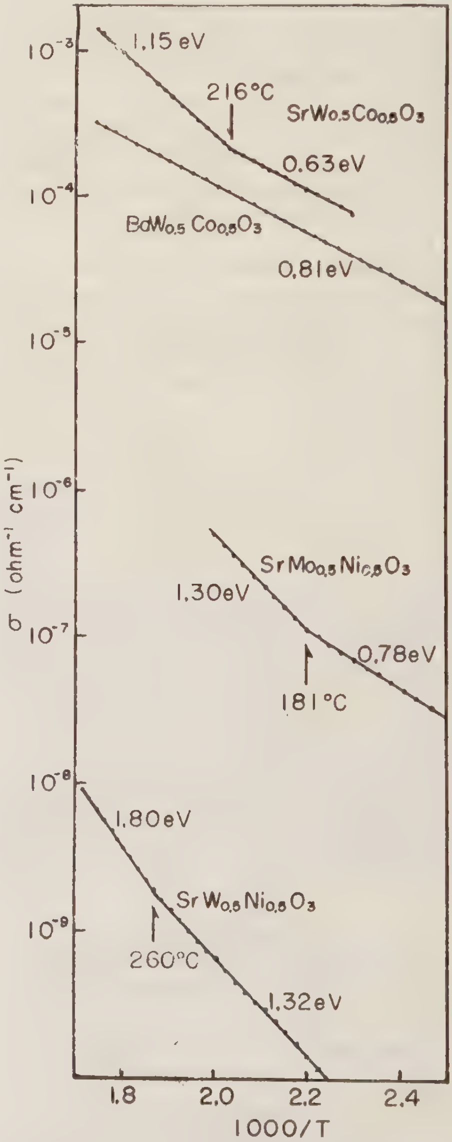

Fig. 2. Electrical conductivity *vs* temperature characteristics.

logarithmic law of conductivity holds for all samples. It is to be noted that for each oxide of strontium the activation energy abruptly changes its value at a certain temperature, while for oxide of barium it remains constant in the temperature range concerned. The anomaly observed in the electrical conductivity-temperature characteristics is considered to be due to the crystal deformation accompanied by the polymorphic transition from the tetragonal- to cubic-phase.

We may conclude from these measured results that the transformation from the tetragonal- to cubic-phase can be induced in the oxides of strontium by raising the temperature as well as by replacing Sr ions partly with Ba ions. The detailed investigations are now in progress.

The authors wish to express their thanks to Mr. H. Machino for his helps in the experimental procedures.

Reference

1) L. H. Brixner: J. Phys. Chem. **64** (1960) 165.

J. PHYS. SOC. JAPAN **16** (1960) 1643

Cross Modulation Line Profiles in Cyclotron Resonance Experiments

By Louis GOLD

Radiation Laboratory and Department of
Nuclear Engineering University of
Michigan, Ann Arbor, Michigan

(Received May 10, 1961)

Work is in progress to characterize the line profiles associated with d.c. cross modulation signals recorded in cyclotron resonance experiments with semiconductors. For a many-valley semiconductor, rather complicated algebraic expressions need to be elaborated for this purpose. It will thus be possible in the future to investigate scattering processes and related phenomena directly from cross modulation data.

The theory differs substantially from conventional treatment of cyclotron resonance, incorporating fully the dispersive behavior of the free carriers; the cross modulation effect is intimately connected with the role of the magnetoplasma. Hence delineation of the cross modulation response requires identification of the appropriate dispersion relation which is embodied in the following finding for the effective conductivity σ in the circumstance of zero bias voltage.

$$\sigma_{\text{eff}}=-i\omega\left\{\frac{-f_2\pm\sqrt{f_2^2-4f_1\left(a_{11}-\frac{\omega_p^2}{\omega^2}\right)\frac{\omega_p^4}{\omega^4}}}{2f_1}\right\}. \qquad (1)$$

For the collision-free limit, the functions $f_{1,2}$ take on the values

$$\left.\begin{aligned} f_1&=f(a_{jl})-\frac{\omega_p^2}{\omega^2}(a_{22}a_{33}-a_{23}^2)-\frac{\omega_c^2}{\omega^2}a_{33}\,,\\ f_2&=\frac{\omega_p^2}{\omega^2}(a_{12}^2-a_{11}a_{22})+(a_{22}+a_{33})\frac{\omega_p^4}{\omega^4}+\frac{\omega_c^2\omega_p^2}{\omega^4}\,,\end{aligned}\right\} \qquad (2)$$

where a_{jl} are the dimensionless components of the mass tensor $\overleftrightarrow{m}$ (whose longitudinal and transverse components are reprectively m_1 and m_2)

$$\overleftrightarrow{m}=\frac{m_2}{3}((a_{jl}))\,, \qquad (3)$$

as dictated by orientation of the electric vector and the d.c. magnetic field $\vec{H}$ relative to the crystal axes; the other quantities are:

$$\left.\begin{aligned} f(a_{jl})&=a_{11}a_{22}a_{33}+2a_{12}a_{13}a_{23}\\ &\quad-(a_{11}a_{23}^2+a_{22}a_{13}^2+a_{33}a_{12}^2)\,,\\ \omega_p^2&=\frac{3Nq^2}{m_2}\,,\qquad \omega_c=\frac{3qH}{m_2}\,,\end{aligned}\right\} \qquad (4)$$

where N is the electron density (charge q).

The foregoing supposes strict alignment of the external magnetic field normal to the direction of the electromagnetic wave. The cross modulation resonances in this circumstance, originating when $f_1=0$, are given by

$$\omega_{\text{res}}^2=\frac{\omega_p^2(a_{22}a_{33}-a_{23}^3)+\omega_c^2a_{33}}{f(a_{jl})}\,. \qquad (5)$$

It may be recognized that this corresponds to the coupled plasma and cyclotron oscillations in the scalar mass limit, $\omega^2=\omega_p^2+\omega_c^2$. In the limit where $\omega_p\ll\omega_c\sim\omega$, the usual cyclotron resonances arise[2].... a result which is independent of the orientation of the fluctuating fields and the wave front itself.

Now, unlike the ordinary cyclotron resonance situation where the number of lines depends only upon the direction of the externally applied magnetic field, additional lines may appear if the perturbing fields shift direction as can arise in a dispersive medium. The nature of these lines was described some time ago[3] and the present analysis has strengthened the suspicion that the origin of ghost-lines[4] may indeed be linked to coupling of plasma and cyclotron modes.

A more complete understanding of this phenomenon (strange sensitivity of the cross modulation spectra to various conditions such as changes in light intensity[4]) should emerge upon a detailed examination of the line shapes where expression (1) is properly modified to include the role of collisions and realignment of the wave normal.

References

1) L. Gold and L. M. Roth: Phys. Rev. **103**, (1956) 61; **107** (1957) 358.
2) L. Gold: J. Electronics **2** (1956) 131.
3) L. Gold: Bull. APS Series II, **2** (1957) 314; J. Electr. and Control **4** (1958) 409.
4) Zeiger, Rauch and Behrndt: Phys. Rev. Letters **1** (1958) 59; J. Phys. Chem Solids **8** (1959) 496.

J. PHYS. SOC. JAPAN **16** (1961) 1644

Temperature Distribution around the Rest or Moving Solid-Liquid Interface in a Rod

By Mikio YAMAMOTO

The Research Institute for Iron, Steel and Other Metals, Tôhoku University, Sendai

(Received March 20, 1961)

It has already been known that a high yield percentage in growing single crystals from the melt is obtained by the high purity of the material used, low velocity of crystallization, and high temperature gradient in the specimen[1]. It has also been found that the orientation distribution of single crystals grown at high rates from the melt shows a remarkable anisotropy[2]. The interpretation of these facts requires the clarification of the process of solidification and of the associated factors.

We have considered the temperature distribution around the solid-liquid interface as one of such factors and calculated it as a function of the temperature gradient in the furnace and of the moving velocity of the interface or the velocity of crystallization for the case of an infinitely long rod which is either at rest or moving at a constant velocity, R, in an infinitely long cylindrical vacuum furnace having a uniform temperature gradient, G_f (>0). It is assumed that the solid-liquid interface is planar and that the temperature distribution in the normal cross-section of the rod is uniform so that the heat convection does not occur in the liquid.

Let us denote the temperature of the furnace as T_f, the cross-sectional area of the rod as A, its circumference as S, its density as ρ, its specific heat as c, its thermal conductivity as k, its emissivity as σ, its temperature as T, its temperature gradient as G, its melting point as T_E, its latent heat of solidification as L, the positional coordinate along the rod axis as x, and the time as t. We indicate quantities associated with solid and with liquid, respectively, by putting the subscripts s and l. Taking $x=0$ at the interface separating the solid portion $(x<0)$ and the liquid one $(x>0)$ and denoting the moving velocity of the interface as R_i, we have, at the interface,

$$k_sA_sG_{so}-k_lA_lG_{lo}=\rho_sA_sL_iR\ , \tag{1}$$

which was already obtained by Goss[3], and, for the solid and liquid portions,

$$-R_i(\partial T/\partial\xi)_t=\alpha(\partial^2T/\partial\xi^2)_t+(S/A)\beta(T_f^4-T^4)\ , \tag{2}$$

where

$$\xi=x+R_it\ , \tag{3}$$

$$\alpha=k/\rho c \qquad \text{and} \qquad \beta=\sigma/\rho c\ .$$

From Eqs. (2) and (1), we get an equation

$$\begin{aligned}&(1/2)(T_o-T_{fo})[(\rho_lc_lA_l-\rho_sc_sA_s)R_i+k_lA_l\{(R_i^2/\alpha_l^2)-4(R_i/\alpha_l)G_f/(T_o-T_{fo})\\&\quad+4K_l(T_o+T_{fo})(T_o^2+T_{fo}^2)\}^{1/2}+k_sA_s\{(R_i^2/\alpha_s^2)-4(R_i/\alpha_s)G_f/(T_o-T_{fo})\\&\quad+4K_s(T_o+T_{fo})(T_o^2+T_{fo}^2)\}^{1/2}]=(k_lA_l-k_sA_s)G_f+\rho_sA_sLR_i\ ,\end{aligned} \tag{4}$$

where

$$K=(S/A)(\sigma/k)\ .$$

Eq. (4) yields, for small G_f and R_i,

$$T_{fo}=T_E-\{(BG_f+DR_i)/2T_E^{3/2}\}\ , \tag{5}$$

$$\left.\begin{aligned}G_{lo}&=G_f-K_l^{1/2}(BG_f+DR_i)\ ,\\G_{so}&=G_f+K_s^{1/2}(BG_f+DR_i)\ ,\end{aligned}\right\} \tag{6}$$

and

$$\left.\begin{aligned}T_l&=T_f+\{(BG_f+DR_i)/2T_E^{3/2}\}\exp[-(R_i/2\alpha_l)-2K_l^{1/2}T_E^{3/2}\{1-(3/8)(BG_f+DR_i)/T_E^{3/2}\}]x\ ,\\T_s&=T_f+\{(BG_f+DR_i)/2T_E^{3/2}\}\exp[-(R_i/2\alpha_s)+2K_s^{1/2}T_E^{3/2}\{1-(3/8)(BG_f+DR_i)/T_E^{3/2}\}]x\ ,\end{aligned}\right\} \tag{7}$$

where

$$B=(k_lA_l-k_sA_s)/\{(S_lA_lk_l\sigma_l)^{1/2}+(S_sA_sk_s\sigma_s)^{1/2}\}$$

and

$$D=\rho_sA_sL/\{(S_lA_lk_l\sigma_l)^{1/2}+(S_sA_sk_s\sigma_s)^{1/2}\}\ .$$

These equations indicate that, for the rest interface $(R_i=0)$, $T_E \gtrless T_{fo}$, $G_{lo} \gtrless G_f$, and $G_{so} \gtrless G_f$ according as $k_lA_l \gtrless k_sA_s$ as for usual metals or for bismuth[3], and that, for the moving interface during solidification $(R_i>0)$, as R_i increases, eventually T_E becomes larger than T_{fo}, G_{lo} becomes negative, and G_{so} becomes greater than G_f, even in the case $k_lA_l<k_sA_s$.

These results of calculation are found to accord well with the results of Goss and Weintroub's[3),4)] experiments with moving rod in a fixed furnace, which measured $\partial T/\partial t=R_iG$. The detail will be published elsewhere soon.

References

1) See e.g. U. Marius: Progr. Metal Physics **5** (1954) 279.
2) See e.g. M. Yamamoto and J. Watanabé: Sci. Rep. RITU **A**, **12** (1960) 486.
3) A. J. Goss: Proc. Phys. Soc. **B**, **66** (1953) 525.
4) A. J. Goss and S. Weintroub: Proc. Phys. Soc. **B**, **65** (1952) 561.

J. PHYS. SOC. JAPAN **16** (1961) 1645

Electron Spin Resonance in Neutron-Irradiated LiF

By Kazuo MORIGAKI*

Department of Physics,
Osaka University, Osaka

(Received June 1, 1961)

Electron spin resonance in neutron-irradiated LiF has been studied at 4.2°K and 1.4°K with various power levels of the microwave to examine whether the resonance line is due to more than one magnetic centers. Single crystals of LiF obtained from Harshaw were exposed at room temperature to thermal neutron with neutron doses of 2×10^{16} nvt and 1×10^{16} nvt. The partially resolved h.f.s. with $g=2.002\pm0.002$ were observed in these crystals. The spacings between neighboring h.f.s. lines are given for some orientations of the magnetic field as follows: 14.7 G for [111], 14.4 G for [001], 12.0 G for [110], and 6.8 G for the direction making the angle of 70° with the [001] axis in a (110) plane. It was found that the entire line shape which is Gaussian at the small rf field depends strongly on the intensity of the rf field. The line width (ΔH_{ms}) decreases and partially resolved structures become less emphasized with increase of the intensity of the rf field as shown in Fig. 1. On the other hand, the spacing between h.f.s. lines does not change with the intensity of the rf field and as to the line widths of resolved h.f.s. lines little change is observed over the power range of the microwave available in this experiment, but a slight increase is recognized at the maximum microwave power.

A sample with 2×10^{16} nvt irradiation was kept at 290°C for 15 minutes, followed by quenching to room temperature.** By this heat treatment the line shape was transformed into Lorentzian. In the magnetic field parallel to [111] partially resolved h.f.s. lines were observed with spacing of 14.9 G. The line width of the broad line is almost isotropic to be given as 77 G at the small rf field. The decrease in the line width and the ratio of h_2 to h_1 with increasing intensity of the rf field was observed in a manner similar to that in the case of the sample before heat treatment. The resonance line saturates in smaller rf field than that on the samples before heat treatment.

A possible explanation for the above experimental results is given as follows: Two distinct types of magnetic centers contribute to the resonance spectrum, one of which is responsible for the resolved h.f.s. and the other gives a broad line superposed on the resolved h.f.s.. A broad line of Lorentzian shape appears with increase of the intensity of the rf field owing to a difference of saturation behavior between both magnetic centers. The former is the F center distributed isolately over the crystal, and the latter may be the aggregate F centers which interact each other to narrow the resonance line owing to the exchange interaction among them, but are not so aggregate that they form a colloid. Transformation of the line shape associated with heat treatment indicates that isolated F centers diffuse to form aggregate states.

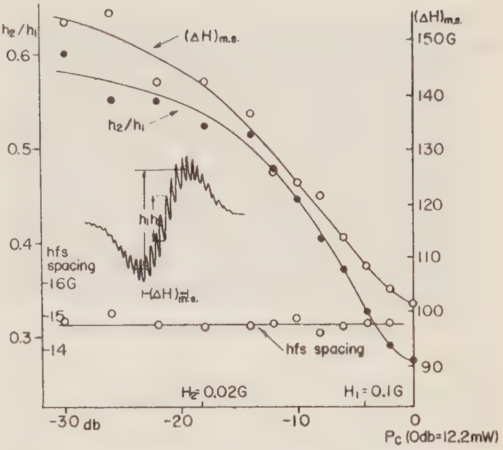

Fig. 1. Dependence of the ratio of h_2 to h_1, the line width, and the spacing of neighboring h.f.s. lines on the microwave power inside the cavity, P_c, in the magnetic field parallel to [111] at 1.4°K. The spectrum observed at 1.4°K and at P_c of -14 db ($H_1=0.033$ G) is also shown in the figure.

Recently Kim, Kaplan, and Bray[1] reported observations of the resonance lines similar to those described here, but their suggestion that the resolved h.f.s. is not due to the F center is inconsistent with our interpretation. On the other hand, our interpretation supports the conclusion of Holton, Blum, and Slichter[2],[3] that the resolved h.f.s. is due to the F center.

The full accounts of this report will be published in a near future. The author would like to thank Professor J. Itoh for helpful discussions and Mr. H. Betsuyaku of Japan Atomic Energy Research Institute for suppling the crystals receiving neutron irradiations.

References

1) Y. W. Kim, R. Kaplan and P. J. Bray: Phys. Rev. Letters **6** (1961) 4.
2) W. C. Holton, H. Blum and C. P. Slichter: Phys. Rev. Letters **5** (1960) 197.
3) H. Blum and W. C. Holton: Bull. Am. Phys. Soc. Ser. II **6** (1961) 112.

---

* Present address: Sony Corporation Research Laboratory, Hodogaya, Yokohama.

** A prolonged heat treatment at 250°C (for 10 hr) gave the new anisotropic spectrum which consisted of many lines.

J. PHYS. SOC. JAPAN **16** (1961) 1646

Linewidth of Cyclotron Resonance of Pure Germanium

By Hazimu KAWAMURA, Masakazu FUKAI,
Yoshikazu HAYASHI and Tamotsu HASHIMURA

Institute for Solid State Physics,
University of Tokyo

(Received June 23, 1961)

The width of the cyclotron resonance line increases with the increase of the microwave power absorbed by crystal as the result of the rise of electron temperature and the consequent increase of the collision frequency. The experiment was made on nearly intrinsic germanium with excess donor concentration of $7\times10^{12}/\mathrm{cm}^3$ at 1.6°K by making use of 6 mm microwave. The free carriers were generated by means of infrared light chopped at 75 cycle/sec. The microwave power was changed by a calibrated attenuator. The maximum power (0 db) falling on the sample cavity is in the order of 1 mW.

Fig. 1 is an example of the resonance pattern displayed on X-Y recorder. The four peaks correspond to the four valleys which have different cyclotron masses for given direction of magnetic field. If the linewidth is resulted only from the finite free time of the carriers, the line shape is Lorentzian and its half width $\Delta H/H$ is equal to $1/\omega\tau$, where ω is the microwave frequency and τ is mean free time of the carriers. From the resonance curves for different powers, we can see that the linewidth becomes broader with the increase of applied power. It may also be noted that $\omega\tau$ is larger for heavier mass valley. It is natural that the rate of power absorption is reciprocally proportional to the mass m^* in the direction of oscillating electric field. In Fig. 2 $1/\omega\tau$ is plotted as a function of P/m^* in log-log scale, where P is the relative power falling on the specimen. It is shown that $1/\omega\tau\propto(P/m^*)^{1/n}$ where n is 2.9 ± 0.3, except in the region of less than one microwatt, where $1/\omega\tau$ tends to a finite value corresponding to the state that electron and lattice are in equilibrium.

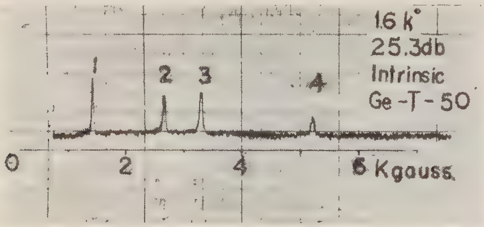

Fig. 1. The cyclotron resonance absorption of pure Ge at 1.6°K. $N_D=7\times10^{12}\,\mathrm{cm}^{-3}$. Microwave power is -25.3 db (~1 micro-watt).

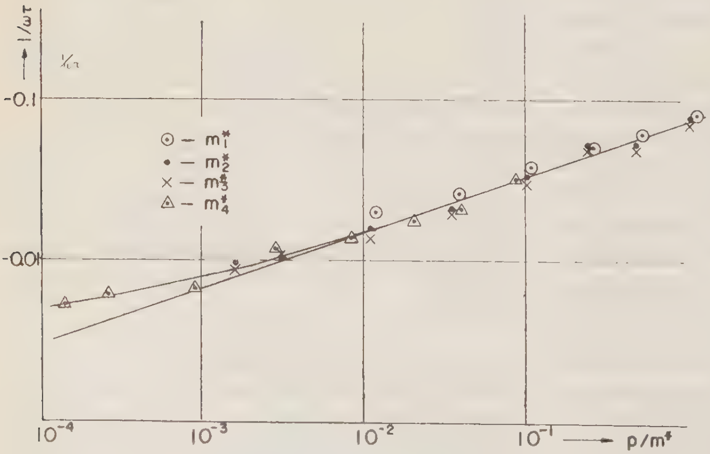

Fig. 2. Linewidth as the function of P/m^*, where P is the applied power and m^* is the effective mass along the direction of oscillating electric field.

If E is the microwave field in the specimen, the rate of power absorption is given by $(eE)^2\tau/m^*$. The rate of energy loss is given by $\langle\Delta\varepsilon\rangle/\tau$, where $\langle\Delta\varepsilon\rangle$ is the mean energy loss per collision. When the lattice temperature is much less than the electron temperature, electron can lose energy only by the spontaneous emission of phonon. The momentum of emitted phonon is roughly equal to the momentum of electron on the average. Hence we find that $\langle\Delta\varepsilon\rangle=\hbar\omega=\hbar c\sigma\simeq\hbar c\kappa$, where σ and k are the momentum of phonon and electron. In this situation $1/\tau$ is proportional to k^2 instead of k, since the factor $2n+1$ $(=2kT/\hbar\omega)$ in the expression of $1/\tau$ should be replaced by one for the case that only the spontaneous emission is effective, and ω is proportional to k. Thus $\langle\Delta\varepsilon\rangle$ becomes proportional to $1/\sqrt{\tau}$. Putting the rate of energy loss and gain are equal, we get the relation that $1/\tau$ is proportional to $(P/m^*)^{1/2.5}$, since P is proportional to E^2. Michel et al.[1] has recently observed the $P^{1/4}$ relation, but we cannot understand the discrepancy.

We should like to express our thanks to Prof. Toyozawa for his suggestive discussion.

Reference

1) R. E. Michel and B. Rosenblum: Bull. Am. Phys. Soc. Series II **6** (1961) 115.

J. Phys. Soc. Japan **16** (1961) 1647~1648

Etch Pits on X-Ray Damaged Rochelle Salt

By Kenkichi Okada

Department of Fine Measurements, Nagoya Institute of Technology, Nagoya, Japan

(Received June 2, 1961)

Recently Takahashi and Nakamura[1] published a theory of domains anchored to screw dislocations in ferroelectric crystals, and they pointed out that the dislocations play important roles in certain behaviors of ferroelectrics. Dislocation etch pits were found by Nakamura[2] and Ohi [3,4] on GASH crystals, and by Toyoda[5] on triglycine sulfate crystals. Furthermore, Nakamura and Ohi[6] made a thorough investigation on etch pits on c-plates of rochelle salt. Longer sides of the quadrangular pyramidal pits are in the a-direction. It was concluded that these etch pits correspond to emergence points of dislocation lines running parallel to the c-axis. In rochelle salt crystal there exist open-cored dislocations parallel to the c-axis which are called *sudarés* among Japanese researchers. Some of the etch pits correspond to the *sudarés*.

In the previous paper[7], a phenomenological theory of the ferroelectric properties of damaged rochelle salt was reported. A model was proposed, in which polar anisotropy centers introduced by irradiation interact with the other regions. In order to obtain more concrete image of the polar anisotropy centers in the model, effects of X-rays on the dislocation etch pit pattern and on the distribution of the *sudaré* were studied. An X-ray tube was running at 40 kV and 15 mA. At the ferroelectric temperature region, plates of rochelle salt were irradiated for about 3 hours and were etched by distilled water.

Damaged crystals revealed etch pits of hip roof shape of which ridges were along the a-direction. Fig. 1 illustrates an etch pattern of a natural c-face. The left two-thirds were exposed to the irradiation, while the right one-third was kept virgin under a lead plate protector. In the damaged region, pits which have been arranged in a linear array are extended in hip roof shape by the irradiation. This observation may lead us to the supposition that some serious changes in dislocations would be introduced by irradiation.

It was reported by a few investigators[8,9] that the *sudarés* are increased by X- and γ-radiations. Fig. 2 is a micro-photograph of *sudarés* induced by irradiation in an a-cut plate. *Sudarés* observed in a c-plate are given in Fig. 3. It must be noted that, before the irradiation they are very few and almost undetectable in these plates. Immediately after the irradiation, they are also very few and can hardly be seen. These photographs were obtained a day after irradiation. *Sudarés* which are seen as fine lines in a-plates and as bright spots in c-plates are arranged in a plane perpendicular to the b-axis.

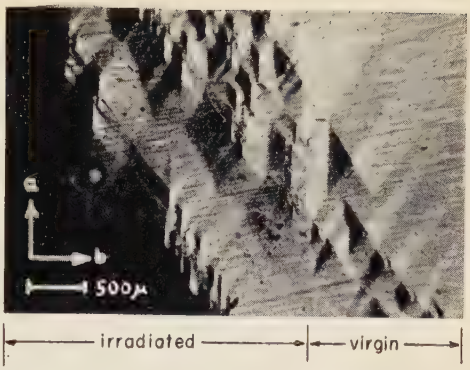

Fig. 1 Changes in etch pits on a natural c-face of rochelle salt crystal by irradiation. The left two-thirds are damaged, but the right one-third is kept virgin.

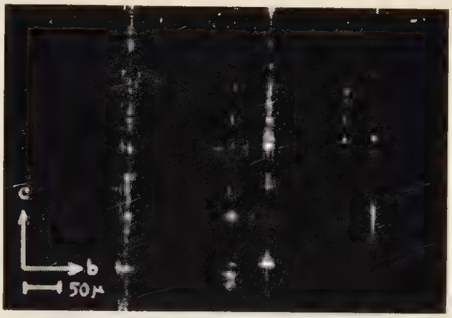

Fig. 2 Open-cored dislocations (sudaré) in a damaged a-cut plate of rochelle salt.

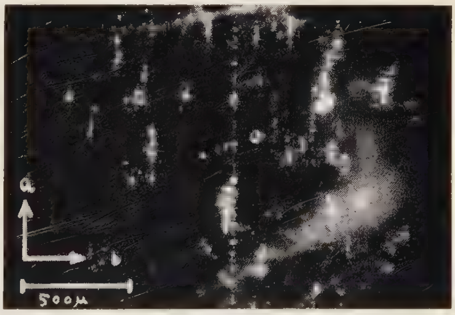

Fig. 3 *Sudarés* in a damaged c-cut plate of rochelle salt.

It was confirmed that these *sudarés* arranged in a plane correspond to the hip roof etch pit. It seems that irradiations induce *sudarés* along the other crystallographic directions than before and give rise to changes in etch patterns on the a- and b-faces also. These observations are now in progress, and will be published in the future.

References

1) H. Takahasi and T. Nakamura: J. Phys. Soc. Japan **15** (1960) 853.
2) T. Nakamura: J. Phys. Soc. Japan **14** (1959) 1022.
3) T. Nakamura and K. Ohi: J. Phys. Soc. Japan **15** (1960) 1348.
4) T. Nakamura and K. Ohi: Natural Science Rep. Ochanomizu Univ. **11** (1960) 161.
5) H. Toyoda: J. Phys. Soc. Japan **15** (1960) 1539.
6) T. Nakamura and K. Ohi: J. Phys. Soc. Japan **16** (1961) 209.
7) K. Okada: J. Phys. Soc. Japan **16** (1961) 414.
8) S. Miyake: Read before the Annual Meeting of Physico-Mathematical Society of Japan, May 1946.
9) Y. Ohta, K. Saheki and T. Nagamura: Read before the Conference on Dielectrics, Sept. 1960, Sapporo.

J. PHYS. SOC. JAPAN **16** (1961) 1648

Spin Echoes of Co^{59} in fcc Cobalt Metal

By Kiyoshi SUGIBUCHI, Motohiro MATSUURA and Tsuneo HASHI

Department of Physics, Kyoto University, Kyoto

(Received June 26, 1961)

The NMR of Co^{59} in ferromagnetic cobalt metal was first observed by Gossard and Portis.[1,2] The subsequent works[3,4,5] were carried out mostly by the steady-state method. The present note reports some of the experimental results obtained by the application of the pulse method. The apparatus was almost the same as that used previously for pulsed PQR experiments in bromine compounds,[6] but some modifications were made in pulsed oscillator so as to measure the shorter relaxation times.

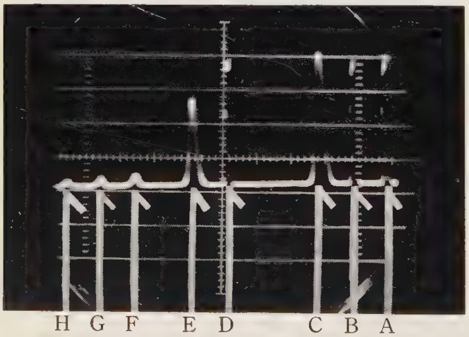

Fig. 1. Spin-echoes of Co^{59} in fcc cobalt metal.
A: first pulse E: second echo (stimulated echo)
B: second pulse F: third echo
C: first echo G: fourth echo
D: third pulse H: fifth echo
Sweep length is about 100 μ sec.

The pulse width used was 2 μ sec or less. The sample consisted of finely divided multidomain particles. The experiments were carried out in the temperature range from 77°K to 300°K.

The strong spin-echo signals were observed, as shown in Fig. 1. The observed values of spin-echo envelope decay time T_2 were almost independent of temperature and about 15 μ sec.

The spin-lattice relaxation time T_1 was measured by the following procedure. The spin system was first saturated by a train of strong rf pulses and then the recovery of longitudinal component of magnetization from saturation was measured from the amplitude of the spin-echo signal produced by application of a pair of pulse at a later time. The observed values of T_1 were 300 ± 30 μsec at 77°K and $85\pm10\mu$ sec at 300°K, and were nearly inversely proportional to the temperature. Both the value and the temperature dependence are different from those reported by Gossard and Portis.[2] The origin of the disagreement is not clear but partly may be due to the difference in the measuring techniques.

It was found that the time constant T_m of the stimulated echo decay curve was generally shorter than T_1 obtained by the above method and could be represented by the following formula:

$$1/T_m = 1/T_1 + k\tau^2$$

where τ is the time interval between the first and the second pulse. The above formula has the same form as that derived by Hahn.[7] This implies the existence of spin diffusion between spins at the different positions of the frequency spectrum, though Hahn's analysis is not directly applicable to the present case. The obtained values of k are about 4×10^{14} sec^{-3} and almost independent of the temperature. The order of magnitude of $k^{-1/3}$ is equal to that of T_2.

The authors would like to express their sincere thanks to Professor I. Takahashi for his continued interest and discussion. Thanks are also due to Dr. Y. Nakamura and Dr. T. Takada of the Department of Chemistry, Kyoto University, for their kind assistances in preparing the sample.

References

1) A. C. Gossard and A. M. Portis: Phys. Rev. Letters **3** (1959) 164.
2) A. M. Portis and A. C. Gossard: J. Appl. Phys. **31** (1960) 205S.
3) Y. Koi, A. Tsujimura and Y. Yukimoto: J. Phys. Soc. Japan **15** (1960) 1342.
4) Y. Koi, A. Tsujimura and T. Kushida: J. Phys. Soc. Japan 15 (1960) 2100.
5) R. Street, D. S. Rodbell and W. L. Roth: Phys. Rev. **121** (1961) 84.
6) T. Hashi: J. Phys. Soc. Japan **13** (1958) 911
7) E. L. Hahn: Phys. Rev. **80** (1950) 580.

J. Phys. Soc. Japan **16** (1961) 1649~1650

Group Velocity of Moving Striations in Hg-A Discharge

By Hiroshi Yoshimoto and
Yoshihiko Yamashita
Department of Physics, Okayama University

(Received June 3, 1961)

Wojaczek[1] first measured the velocity of the wave packet obtained by his perturbation method in argon discharge, and he deduced that the velocity corresponds to the group velocity of moving striations. His measurements, however, were concerned only with the current region in which the natural moving striations cannot appear. We have carried out the similar measurements in Hg-A discharge not only in the Wojaczek's current region but also in the current region in which the natural moving striations can appear (abbreviated as the current region I and II respectively), and could catch the feedback figures of perturbations on the screen of cathode ray oscilloscope. The discharge tube and other apparatus used have been described elsewhere[2]. In this experiment, pentodes were inserted in series with the discharge tube to modulate the current by the pulses applied to their control grids.

The perturbations of plasma are originated by the current pulses at the negative end of the positive column, and propagate towards the anode in the form of wavepacket shown in Fig. 1, while the each wave in a wavepacket propagates towards the cathode and this wave corresponds to the moving striation. The traveling velocity of the wavepacket is nearly equal to that of moving striation. Some examples of these velocities are columned in Table I. These features can be expected from the dispersion relation of moving striation obtained experimentally by one of us[3]. Thus, it is concluded that the moving striation is a backward wave. The occurrence of wavepacket by this pulse method indicates that the plasma of positive column has a resonance frequency for the moving striation.

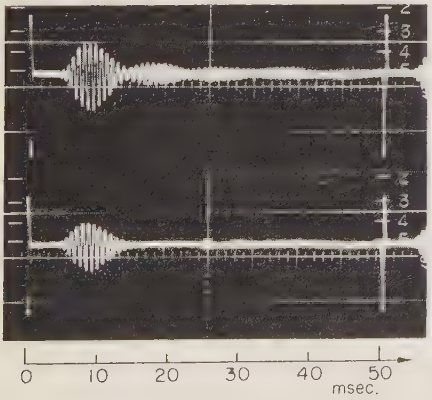

Fig. 1. Photographs of wavepacket at 5 cm from the anode. Current: 160 mA. Mag. Field: 80 gauss. Tube Diameter: 25 mm.

Table I.

Current (mA)	Velocity of wave-packet (m/s)	Velocity of moving striation (m/s)
140	48	49
150	47	50
160	47	51
170	49	54

Tube Diameter: 25 mm. Room Temp: 16°C.

Moving towards the anode, the wavepacket increases and decreases its amplitude in the current region II and I respectively. At the critical current the wavepacket travels without changing its amplitude. These circumstances are shown in Fig. 2.

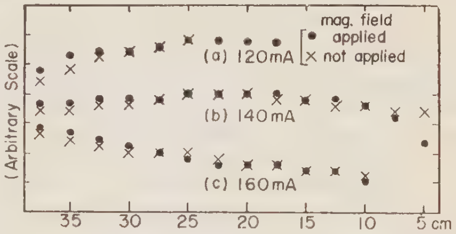

Fig. 2. The amplitude of wavepacket *versus* the distance from the anode. The curves (a) and (b) correspond to the current region II, and the curve (c) to the current region I.

In the curren region II, several sub-wavepackets are observed to follow the primary wavepacket as seen from Fig. 1 (a). The time intervals between the successive wavepacket are all the same in magnitude corresponding just to the transit-time in which the wavepacket travels from the negative end of the positive column to the anode. When a magnetic field is applied in front of the anode perpendicularly to the tube axis, these sub-wavepackets disappear as seen from Fig. 1 (b). While the propagation characteristics of wavepacket remains unchanged in the positive column excepting the domain of the magnetic field. For instance, this circumstance concerning the amplitude of wavepacket is given in Fig. 2. These results ascertain that the sub-wavepackets are the feedback figures of the primary wavepacket. This feedback occurs in such a way that the wavepacket, arriving at the anode, gives a disturbance to the current which induces a new perturbation of plasma at the negative end of positive column. The magnetic field makes the wavepacket damp away preventing its feedback.

References

1) K. Wojaczek: Ann. Physik [7] 2 (1958) 68.
2) H. Yoshimoto, M. Sato and Y. Nakao: J. Phys. Soc. Japan **13** (1958) 734.
3) H. Yoshimoto: Preprint for the Spring Meeting of the Physical Society of Japan (1959) (in Japanese).

J. PHYS. SOC. JAPAN **16** (1961) 1650~1651

The Colloidal Band in KCl Containing NaCl

By Shinichi NAKASHIMA

Matsushita Electronics Corporation
Takatsuki, Osaka

(Received June 5, 1961)

When additively colored alkali halides are exposed to a heat and light treatment a transformation of the *F*-band to a narrow band at a longer wavelength is observed. This Phenomenon is attributed to the transformation of *F*-centers into colloidal particles of the reduced metal. Using the Mie theory, Doyle[1)] and Scott[2)] calculated the wavelength for maximum absorption in the colloidal band. According to Doyle's calculation in the limit of very small particles, the position of the colloidal band in pure KCl is 8200 Å which is in agreement with the results of the observation[1)].

The present report describes the effect of sodium ions on the colloidal band in KCl. KCl crystals were grown from melts to which NaCl was added. The crystals were colored additively in potassium metal vapor. The density of *F*-centers in each crystal was about 10^{17} per cm³. When the additively colored crystals were heated and exposed to the light of a tungsten lamp, the *F*-baed vanished and a narrow band of increasing height appeared at a wavelength well below 8200 Å. Fig. 1 shows the absorption curves of the bands which grow by heating the additively colored KCl-NaCl mixed crystals at 200°C. For a larger doping amount of NaCl in KCl the absorption band grows at shorter wavelengths. In Fig. 2 the position of the absorption bands is plotted as a function of the NaCl concentration in KCl. The concentration of NaCl was analyzed spectrographically. The concentration of NaCl in the most pure KCl was less than 10^{15} per cm³.

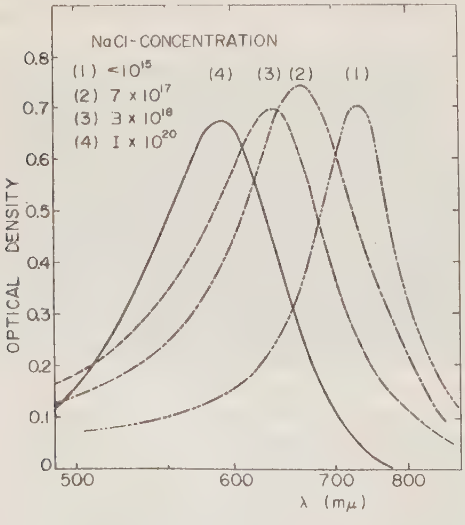

Fig. 1. The colloidal bands in KCl crystals containing various amount of NaCl.

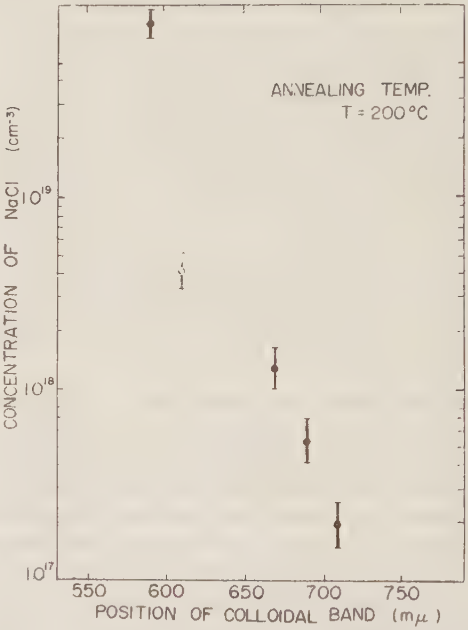

Fig. 2. The position of the colloidal bands in KCl-NaCl mixed crystals as a function of the NaCl concentration.

The position of the absorption band was hardly changed at the temperatures between 15°C and −196°C, but shifted to longer wavelengths with increasing temperature of annealing. Savostinova has pointed out that the position of the colloidal band shifts to longer wavelengths as the particle size increases. The absorption bands in KCl-NaCl mixed crystals appear, however, at shorter wavelength side of the colloidal band in pure KCl, so that the absorption bands can not be identified with the potassium colloidal bands. These absorption bands can not be attributed to a *R'*-band but to K-Na alloy colloids. Applying Doyle's calculations to K-Na alloy colloids, we can estimate the ratio of Na to K in the K-Na alloy colloids. It follows that for the colloidal particle having an absorption maximum at 5900 Å, atomic ratio of Na to K is 60 per cent and at 7100 Å, it is 10 per cent. Comparing the above results with the NaCl concentration of Fig. 2, it is clear that the ratio of Na to K in K-Na alloy colloids is much larger than the ratio of NaCl to KCl of the mixed crystals. This difference might be due to a nonuniform distribution of NaCl in the KCl crystal. In order to confirm the assignment, the colloidal band in KCl containing LiCl is being investigated.

The author wishes to thank Assistant Professor K. Fukuda for his helpful discussions and Professor Y. Uchida for his encouragement.

References

1) W. T. Doyle: Phys. Rev. **111** (1958) 1067.
2) A. B. Scott: J. Phys. Chem. **57** (1953) 757.
3) M. Savostinova: Z. Phys. **64** (1930) 262.

Errata

A Direct Determination of the Crystal Structure of Ethylenediammonium Sulphate

By Kiichi SAKURAI

J. Phys. Soc. Japan **16** (1961) 1205

p. 1209, Table IV. The F_c's for the following reflections should be given negative signs.

(400) (600) (130) (190) (220) (240) (260) (280) (2 10 0) (350) (370) (390) (4 10 0) (660) (680) (008) (00 12) (021) (025) (027) (028) (029) (02 11) (02 13) (02 15) (02 19) (02 20) (02 21) (041) (047) (04 11) (04 13) (04 17) (069) (06 13) (06 17) (06 17) (083) (084) (087) (089) (08 11) (08 15) (0 10 1) (0 10 5) (0 10 7) (0 10 9)

PROGRESS OF THEORETICAL PHYSICS

CONTENTS

Progress of Theoretical Physics — Vol. 24, No. 5, November 1960

On the Screening of Magnetic Interaction by Degenerate Free Electrons .... Noboru TAKIMOTO .. 923
Macroscopic Causality and Lower Limit for the Momentum Derivative of the Scattering Phase Shift .... Takesi OGIMOTO .. 949
Baryon Parity and Polarization Experiment .... Kiyoshi NAKAYAMA .. 953
On the Theory of Rearrangement Collisions .... Sigenobu SUNAKAWA .. 963
Some Considerations on the Low-Energy Pion-Nucleon Scattering .... Kin-ichi ISHIDA .. 980
Collective Representation of the Many-Particle System Interacting through Arbitrary Two-Body Potential .... Naomi SHOHNO .. 991
Isobar Model and the S-wave Pion-Nucleon Scattering .... Yasunori FUJII .. 1013
A Semiphenomenological Proton-Proton Potential .... Tetsuo HAMADA .. 1033
Scattering of Electrons by the Thermal Motion of Impurity Ions. II .... Shigeharu KOSHINO .. 1049
Impurity Induced Infrared Lattice Vibration Absorption .... R. F. WALLIS and A. A. MARADUDIN .. 1055
$M1$-Transition in V^{51} and Configuration Mixing .... Toshiya KOMODA .. 1078
On the Kinetic Equation for a High Temperature Plasma ... Yoshi H. Ichikawa .. 1083
On Radiative Corrections due to Soft Photons .... Toshiyuki MUROTA .. 1109
Applications of Mellin Transforms to Some Problems of Statistical Mechanics .... Giiti IWATA .. 1118

Letters to the Editor:

- On High Energy Charge Exchange Collision .... T. TAKEMIYA and Y. SAKAMOTO .. 1123
- A Note on Exchange Reaction .... T. SASAKAWA .. 1125
- Mass Differences of Charged and Neutral States of Elementary Particles .... I. M. Freeman .. 1128
- Effect of the Particle-Hole Pair Interactions in Nuclear Many-Body Problem .... M. YASUNO .. 1129
- Possible Methods for Detecting Intergalactic Hydrogen ... S. HAYAKAWA .. 1131
- Electric Polarizability of Nucleon .... T. SAWADA .. 1132

Progress of Theoretical Physics — Vol. 24, No. 6, December 1960

Space Time Description of Collision and Decay Processes .... Masakuni IDA .. 1135
On Some Peculiar Role of the Cosmological Constant in the General Theory of Relativity and in the Schrödinger Theory of Non-Symmetric Field .... H. NARIAI and Y. UENO .. 1149
On the Semi-Classical Treatments of the Meson-Nucleon Scattering .... Shin ISHIDA .. 1166
Theory of Finite Nuclei in Statistical Method with Correlation Correction. I .... Yasuo HARA .. 1179
Cluster Expansion Technique in the Many-Fermion Systems. I .... Ki-ichi NAKAMURA .. 1195
On the Possibility of the Existence of a New Meson ... C. ISO and T. KOBAYASHI .. 1215
On Hugenholtz-Pines' Theory about Ground State Energy of Interacting Bosons .... Setsuo MISAWA .. 1224
On the Structure of Extensive Air Showers. II .... Akira UEDA .. 1231
Pion-Nucleon Scattering and Pion-Pion Interaction .... Shin ISHIDA .. 1262

On the Validity of Multiple Dispersion Representations .....Noboru NAKANISHI..1275
Lattice Vibration and Random Walk Problems ....Ei TERAMOTO..1296
High Energy Elastic Scattering of Nucleon from Nuclei—*Analyses of Experimental Data*— ....T. TAKEMIYA, T. SASAKAWA and Y. SAKAMOTO..1307
On the Method of the Theory of Nuclear Forces ....M. TAKETANI and S. MACHIDA..1317
Two Nucleon Potential with Full Recoil. I—*General Formalism and One-Pion-Exchange Potential*— ....N. HOSHIZAKI and S. MACHIDA..1325
Time Dependent Problems of the Localized Lattice Vibration ....E. TERAMOTO and S. TAKENO..1349

Letters to the Editor:

On the Scattering of K^+ by Nucleon at Low Energies ....M. AZUMA and T. EBATA..1369
Electromagnetic Vertex for $\Sigma^0\to\Lambda^0+\gamma$ ....H. KATSUMORI..1371
The Analyticity Properties of the Bethe Salpeter Amplitude ....K. WATANABE..1373
Note on the $D(\gamma p)n$ Reaction at the γ-Ray Energy of 164 Mev ....M. MATSUMOTO..1376
Collision Broadening of the Landau Levels...T. OHTA and T. MIYAKAWA..1378
Application of ρ-Meson Theory to 5 Mev π^--p Data .....H. NAKAMURA..1380
Contents and Author Index to Vol. 24 .... i-x

Progress of Theoretical Physics Vol. 25, No. 1, January 1961

A Possible Symmetry in Sakata's Model for Bosons-Baryons System. III ....M. IKEDA, Y. MIYACHI, S. OGAWA, S. SAWADA and M. YONEZAWA.. 1
Electromagnetic Structure of the Nucleon...K. KAWARABAYASHI and S. MACHIDA.. 17
Nuclear Deformation and Nuclear Force. I ....Sinobu Nagata.. 35
Nuclear Deformation and Nuclear Force. II ....K. IKEDA, S. NAGATA and K. TAKADA.. 51
Nuclear Forces in the Momentum Space..............J. GOTO and S. MACHIDA.. 64
Single Pion Production Process in Pion-Nucleon Collision and the Sakata Model ....Shoji SAWADA.. 83
Energy Spectrum of Lattices with Defects. I—*General Theory*—..Shozo TAKENO..102
Symmetry in Sakata's Model and Weak Interactions. II...............................M. IKEDA, Y. MIYACHI and S. OGAWA..121

Letters to the Editor:

A calculation of the Electrical Conductivity ....N. MATSUDAIRA..153
Remarks on Eden's "Proof" of the Mandelstam Representation ....N. NAKANISHI..155
Note on the Pion Propagator in the Composite Theory........T. KANKI..156
On the Small-Angle Scattering of High-Energy Protons......S. OHNUMA..158
Electromagnetic Mass Shift of Σ Hyperons ....H. KATSUMORI..159

Progress of Theoretical Physics Vol. 25, No. 2, February 1961

A Theory of the Magneto-Optical Absorption ....Makoto OKAZAKI..163
Approximate Solution of the Bethe-Salpeter Equation for Two Fermions ....Masaaki KAWAGUCHI..178
On the Electromagnetic Mass Differences among the Sigma Hyperons..Yoshiko SUGIMOTO..189
On the $KK\pi\pi$ Interactions ....Keiji IGI..201
Note on the Integral Representation of Commutators.........Kunio YAMAMOTO..211
The Polarity of the Diatomic Molecule ....Kiyosi O-OHATA..215
Electromagnetic Structure of the Nucleon and the Composite Model for Pion ....Chiaki IHARA..229

Compound Nucleus Processes in the Reactions between Complex Nuclei...... .... Tetsuo KAMMURI..235
A Semi-phenomenological Neutron-Proton Potential.............Tetsuo HAMADA..247
On the Charge Exchange Collision in Nucleon-Deuteron ....Yoshiyuki SAKAMOTO..259
New Analyses of Anomalous Imaginary Part ....Jun OTOKOZAWA..277

Letters to the Editor:

Non-Adiabatic Effects on the Bound States of the μ-Mesonic Proton-Deuteron System.......................H. NARUMI and S. MATSUO..290
Excited State in Λ-π System and K^--p Collision ....S. MINAMI..292
The Effect of Pion-Pion Interaction to the Pion-Nucleon Small P-Wave Phase Shifts ....K. ISHIDA..294
Validity of the Integral Representations for the Vertex Part in Perturbation Theory ....N. NAKANISHI..296
Motion of a Charged Particle in a Static Magnetic Field with Axial Symmetry ....H. OBAYASHI..297
Very High Energy Nuclear Reactions and Alpha-Particle Model ....H. HASEGAWA and K. ITO..300
On the G_A/G_V Ratio in β-Decay. II...........................C. IHARA..301

Errata:

On Hugenholtz-Pine's Theory about Ground State Energy of Interacting Bosons (Vol. 25, p. 1225) ....S. MISAWA..303

Progress of Theoretical Physics Vol. 25, No. 3, March 1961

Unified Gravitational and Electromagnetic Waves ....P. C. VAIDYA..305
Quantum Statistics of Interacting Electron Gas in a Strong Magnetic Field .. .. H. ICHIMURA and S. TANAKA..315
Dynamical Theory of Ultrasonic Attenuation in Metals ......Noboru TAKIMOTO..327
The Non-leptonic Decays of Hyperons.................Z. MAKI and Y. OHNUKI..353
Integral Representation of Absorptive Part of Vertex Function .... Kunio YAMAMOTO..361
Soluble Examples in Field Theory with Fermi Interactions ....Yasusi ATAKA..369
Phase Shift and Identities in Quantized Field Theory ....Shûkô AZUMA..381
Dispersion Relations and High Energy Limits in Quantum Field Theory. II.. ....Seiya ARAMAKI..404
Effective Interaction in Nuclear Many Body Problem ....Masaru YASUNO..411
Pion Theory of Nuclear Forces and Low Energy P-Wave Phase Shifts .... S. OTSUKI, M. TAKETANI, R. TAMAGAKI and W. WATARI..427
The Theory of Superconductivity in the Tamm-Dancoff Approximation .... B. P. NIGAM..436
Pion-Pion Interaction and Nuclear Forces.......................Yasunoai FUJII..441
Transition Amplitudes in Perturbation Theory and Dyson's Integral Representation ....G. KONISI and K. YAMAMOTO..461
Variational Calculation of the Scattering Lengths in Electron-Hydrogen Scattering ....Y. HARA, T. OHMURA and T. YAMANOUCHI..467
On Energy Matrices for the Independent Particle Model .... H. HORIE and K. SASAKI..475
Photopion Production and $(\gamma, 3\pi)$ Interaction ....Masaaki KATO..493

Letters to the Editor:

A New Solution of the Clock Paradox...................E. KURONUMA..508
The Effect of Short-Range Order on Paramagnetic Resonance...Y. ŌSAKA..510
A Note on the Treatment of Bound State Problem.............S. SATO..512
Electric Polarizability of the Neutron ......A. KANAZAWA and S. TANI..514
Contents of Journal of Phys. Soc. of Japan, Vol. 16, No. 2 ....i–ii

Progress of Theoretical Physics Vol. 25, No. 4, April 1961

Theory of Polaron Mobility .... Yukio ŌSAKA..517
A New Approach to the Theory of Classical Fluids. III—*General Treatment of Classical Systems*— .... T. MORITA and K. HIROIKE..537
Geometrical Study of the Pair Distribution Function in the Many-Body Problem .... Masami YAMADA..579
Spin Waves in MnF_2 and the Inelastic Scattering of Neutrons .... O. NAGAI and A. YOSHIMORI..595
Characteristic Functional for Plasma Turbulence .... Keniti GOTO..603
Antisymmetric Treatment of Deuteron-Stripping Reaction —*Stripping and Heavy-Particle Stripping Reactions*— .... T. HONDA and H. UI..613
Deuteron Stripping and Heavy-Particle-Stripping Reactions .... T. HONDA and H. UI..635
$KK\pi\pi$-Interaction and Nucleon Core .... Shigeo MINAMI..646
On the Stability of the Hartree-Fock Solution in Many-Body Problem........ .... K. SAWADA and N. FUKUDA..653
Pion-Nucleon Interaction and Multiple-Production Experiment................ ....H. EZAWA, O. KAMEI, K. MORI, H. SHIMOIDA and T. YONEYAMA..667
Strange Neutrino and a Composite Model for Elementary Particle. I .... T. OUCHI and K. SENBA..684
A Remark on the Strangeness and Isotopic Spin for Leptons .... T. OKABAYASHI, S. NAKAMURA and Y. NISIYAMA..701

Letters to the Editor:

Low Density Fermion System with Strong Attractions .... Y. WADA..713
The Cerenkov Self-Excitation of the Electron .... T. ERBER..714
Nucleon-Nucleus Scattering and the Choice between Sets of Nucleon-Nucleon Phase Shifts .... A. M. SAPERSTEIN..716
Elastic Scattering of Fast Electrons by the Helium Atom and the Interelectronic Correlation .... M. INOKUTI..717
On the "Nagoya Model" of the Elementary Particles...N. St. KALITZIN..719
Double Dispersion Representation of Vertex Function ....K. YAMAMOTO..720
The Equivalence of Hamiltonians of Holstein-Primakoff and Dyson in Spin-Wave Theory in Ferromagnetism .... T. OGUCHI..721
On the Critical Scattering of Neutrons ...... H. MORI and K. KAWASAKI..723
Contents of Journal of Phys. Soc. of Japan, Vol. 16, No. 3 .... i-ii

Progress of Theoretical Physics Vol. 25, No. 5, May 1961

P-wave Resonance in Pion-Pion Scattering .... Miwae YAMAZAKI..727
Quantum Statistical Analogue of Ward's Identity .... K. WATANABE, O. KAMEI and H. EZAWA..735
On an Extension of the Mathematical Framework of the Quantum Theory .. .. H. WAKITA..743
Dispersion Relations for Kaon-Nucleon Scattering and $KK\pi\pi$ Interaction .... Keiji IGI..753
Low-Energy Limit Theorems and Dispersion Relations ..... Ken KAWARABAYASHI..780
The Effect of the Pion-Pion Interaction on the Pion-Nucleon Scattering .... Kin-ichi ISHIDA..797
Exact Treatment of the Bound State Problems in the Non-Relativistic Quantum Field Theory .... Nobumichi MUGIBAYASHI..803
A Shell Model Calculation for Scattering of Electrons by Be^9............... .... Y. R. WAGHMARE and S. P. PANDYA..822
On the Axial Vector Current Conservation .... Yasuhisa KATAYAMA..827

Letters to the Editor:

Comments on Fermi's Statistical Theory of High Energy Nuclear Events... K. B. FENTON..842

The Kinetic Equation for Plasmas and Its Solution ....T. MORITA..843
On the Kinetic Electrons in Metals at Low Temperatures....T. MORITA..845
Mass of a Neutral Vector Meson and p-p Scattering ....S. OHNUMA..847
Weak Interactions at High Energies ....
................K. FUJII, H. NAGAI, T. SAKUMA and T. TSUCHIDA..849
Magnetoresistance in Nondegenerate Semiconductors Considering Electron-Electron Scattering ....D. B. AGARWAL..851
Interaction between Alpha Particles ....
.....................I. SHIMODAYA, R. TAMAGAKI and H. TANAKA..853
Two-Nucleon Spin-Orbit Forces and the Doublet Splitting in Low Energy n-α Scattering ....Y. TAKAMURA and R. TAMAGAKI..855
Cosmological Implication of Physical Constants.....................
.................................S. HAYAKAWA and H. TANAKA..858
Invariance of Planck's Constant in Revised Relativity of J. Palacios
....A. H. KLOTZ..860
An Isobaric State K^* in K-π System and p-$\bar{p}\rightarrow K+\bar{K}+\pi+\pi$ Process
....S. MINAMI..861
K Meson-Nucleon Interaction at High Energy ....S. MINAMI..963
Quantum Theory of Spin Diffusion..........H. MORI and K. KAWASAKI..866
The τ^+-decay and the Boson Isobar with $I=2$ of the Sakata Model ..
.........................S. SAWADA, T. UEDA and M. YONEZAWA..868
A Note on Baryon-Baryon Interaction ....
.........G. BHAMATHI, S. INDMATHI, T. K. RADHA and R. THUNGA..870
Contents of Journal of Phys. Soc. of Japan, Vol. 16, No. 4 ....i–ii

---

Price	\$ 1.25 per copy
	\$ 15.00 per year (postage inclusive)

Annual dues for foreign members (individual subscribers)
\$ 12.00 (postage inclusive)
〃 for foreign members of the Physical Society of Japan
\$ 10.00 (postage inclusive)

Application for membership, subscriptions and orders for back numbers should be sent, directly or through book-dealers, to

The Publication Office
in
Yukawa Hall, Kyoto University, Kyoto, Japan

. . . .

ANNOUNCEMENT

REVISED Price List of Back Numbers (for subscribers abroad)

*Vols. 1–4	\$ 6.40 each
*Vols. 5 & 6	\$13.00 each (single copy: \$2.50)
*Vols. 7 and succeeding ones	\$ 8.00 each (single copy: \$1.50)

Back number prices are effective for volumes other than last four (4) volumes (the current volume inclusive).

Thus, volumes 1 through 16 will be regarded as back numbers while volume 20 is being published.

The revised prices will be effective on and after August 1, 1958.

. . . .

JOURNAL OF THE PHYSICAL SOCIETY OF JAPAN, Vol. 16, No. 9, SEPTEMBER, 1961

Nuclear Elastic Scattering of Photons near the Particle Threshold Energy (I)

By Tsutomu TŌHEI, Masumi SUGAWARA, Shigeki MORI
and Motoharu KIMURA

Department of Physics, Faculty of Science, Tohoku University, Sendai

(Received March 3, 1961)

The elastic scattering of photons near the particle threshold energy was studied for Al, Si, S, K, Ca, Ni, Cu, Cd, Sn, Pb and Bi. The bremsstrahlung x-rays from a 25 Mev betatron were used. The pulse of the primary x-rays was expanded up to about 30 μ sec to decrease the pile-up effect. The scattered photons were detected at the scattering angle of 120 degrees with the scintillation spectrometer using an $8''\phi\times8''$NaI(Tl) crystal and a 30 channel pulse height analyser gated by the expansion signal of the betatron orbit. The energy at which the cross section has a peak was compared with the particle threshold energy and the value of cross section was compared with that of particle emission.

§ 1. Introduction

The elastic scattering of photons in the energy region of the giant resonance was studied by Fuller and Hayward[1]. They reported two maxima in the elastic scattering cross section, i. e. one around the particle threshold and the other around the energy where the giant resonance of the photon absorption has maximum value. According to Bethe and Ashkin[2] it is illustrated qualitatively that the peaks around the particle thresholds appear, since the particle emissions which do not take place below the threshold suppress the photon emissions. The available information[3] on the radiation widths of excited levels at nearly several Mev above the ground state was also obtained from the neutron scattering and capture experiments. The studies[4] using the monochromatic 7 Mev γ-rays of the reaction $F^{19}(p, \alpha, \gamma)O^{16}$ revealed that the observed widths and spacings are approximately in agreement with the modified single particle calculation by Weisskopf and Blatt[5].

Recently Fujii[6] has shown theoretically that the nucleus of the core plus one nucleon can be excited owing to the absorption of γ-ray by the last nucleon. According to his theory this excited state should be observed in several Mev above the ground state.

The bremsstrahlung x-rays from the 25 Mev Tohoku betatron have been used to study the elastic scattering cross sections near the particle threshold energies. According to the present experimental result, the energies of the peak of the cross sections near the particle threshold are in agreement with the threshold energies of (γ, p) or (γ, n) in most elements, as were predicted qualitiatively by Bethe and Ashkin[2].

§ 2. Experimental Procedure

The procedure of the present experiment is essentially the same as Fuller and Hayward's[1]. The experimental arrangement is shown in Fig. 1.

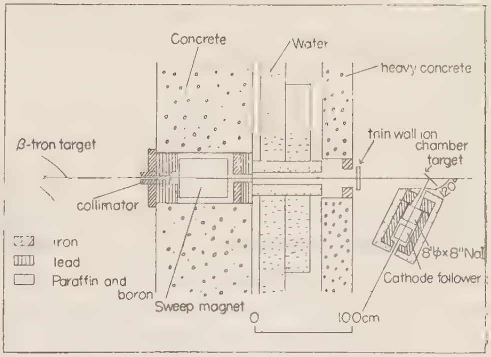

Fig. 1. Experimental arrangement.

The primary x-rays were collimated to 1¾ inches in diameter at the target by lead and iron collimators. The photon detector was an $8''\phi\times8''$ NaI(Tl) crystal with three Du Mont 6363 photomultiplier tubes and was located in a lead container which has 6 inches thick walls at both the betatron room and the collimator sides and has 4 inches thick walls in other sides. The container was surrounded with borax and paraffin.

The measurements were performed setting the detector at the two positions. In the first case the detector was placed at the scattering angle of 120 degrees and the spectra of photons scattered from the target in each betatron energy were measured. In the second case the spectra of bremsstrahlung itself at 0 degree without the target were measured. The tapered lead slit, 4 inches in diameter, was placed in front of the crystal and was filled with 1½ inches thick paraffin in order to remove electrons and low energy photons emitted from the target. On the other hand, a 2 inches diameter, 10 inches long lead slit was used as a collimator in the direct beam. In front of this collimator 12 inches long aluminum and 4 inches long lead absorbers were placed to reduce the intensity of x-rays from the betatron so that pile-up might be negligible. The x-rays were monitored by a thin wall ionization chamber connected to a vibrating reed electrometer. The block diagram of electronic devices is shown in Fig. 2.

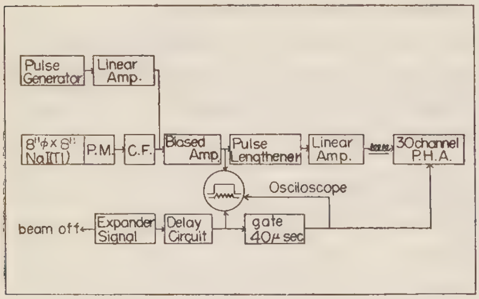

Fig. 2. Block diagram of electronic devices.

The pulses from the detector were amplified by a fast biased amplifier followed by a pulse lengthener and the lengthened pulses were analysed by a 30 channel pulse height analyser. The analyser was operated for the time interval of 40 μ sec in each operation cycle by a gating circuit so that only those pulses occurring in that interval around the primary x-ray pulses were counted. With this gating action the cosmic γ-ray background was reduced to the order of 0.3 counts per hour per one channel at the 7 Mev region. In order to estimate the contribution to the counts of the background γ-rays induced by neutrons in the primary x-ray beam, the test experiment was performed with a Ra-Be neutron source. Judging from the results of this experiment, this background was negligible. The pile-up effect was carefully decreased to the negligible magnitude by expanding the width of the primary x-rays to about 30 μ sec.

In Table I the target thickness is listed. The potassium sample was in the form of K_2CO_3 and the other samples were in metallic form.

Table I. The target thickness.

target	thickness (g/cm²)
Al	8.16
Si	2.20
S	10.16
K*	3.48
Ca	2.33
Ni	11.05
Cu	11.0
Cd	9.28
Sn	9.10
Pb	14.4
Bi	14.8

* K: the sample of K_2CO_3

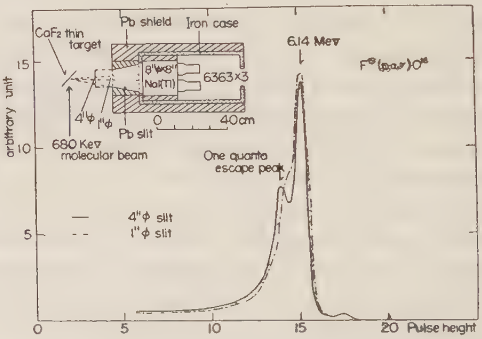

Fig. 3. The response curve of the 8″$\phi\times$8″ NaI(Tl) for the 6.14 Mev γ-rays from the reaction of $F^{19}(p, \alpha, \gamma)O^{16}$. The solid line is the result obtained with the same geometry as the case of scattering experiment, when the γ-rays were collimated to 4 inches in diameter in front of crystal. The dashed line is the results obtained with the tapered lead slit of 1″ diameter.

The measurements were made at the betatron energies from 5 Mev to 12 or 16 Mev with the interval of 1 Mev. In each betatron energy the bias of the fast biased amplifier was adjusted so that the pulses corresponding to the highest energy portion of bremsstrahlung were recorded in the given part of channels of the 30 channel pulse height analyser. The counts in the top ten channels of the spectra which correspond to photons in energy interval of 1 Mev from the top of the bremsstrahlung were summed up. C_s

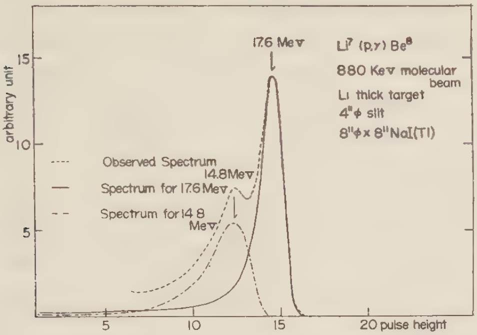

Fig. 4. The response curve of the $8''\phi\times 8''$ NaI(Tl) for 17.6 Mev γ-rays from the reaction of Li^7 (p, γ)Be^8. The dotted line is the measured spectrum. The solid line for the 17.6 Mev γ-rays was evaluated from the dotted line by extracting the contribution of the 14.8 Mev γ-rays. The intensity ratios $I_{17.6}/I_{14.8}$ was assumed to be 1.7[8]. These were measured with the same geometry as in the case of the scattering experiment.

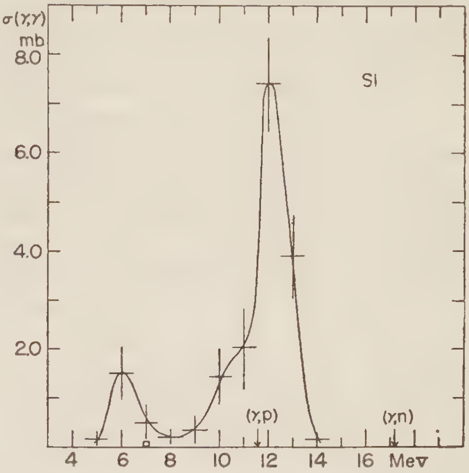

Fig. 5. The elastic scattering cross section of photons by Si. The arrows of (γ, p) or (γ, n) indicate the positions of the particle threshold energies of Si^{28}. □: data from the experiment of the monochromatic γ-rays[4].

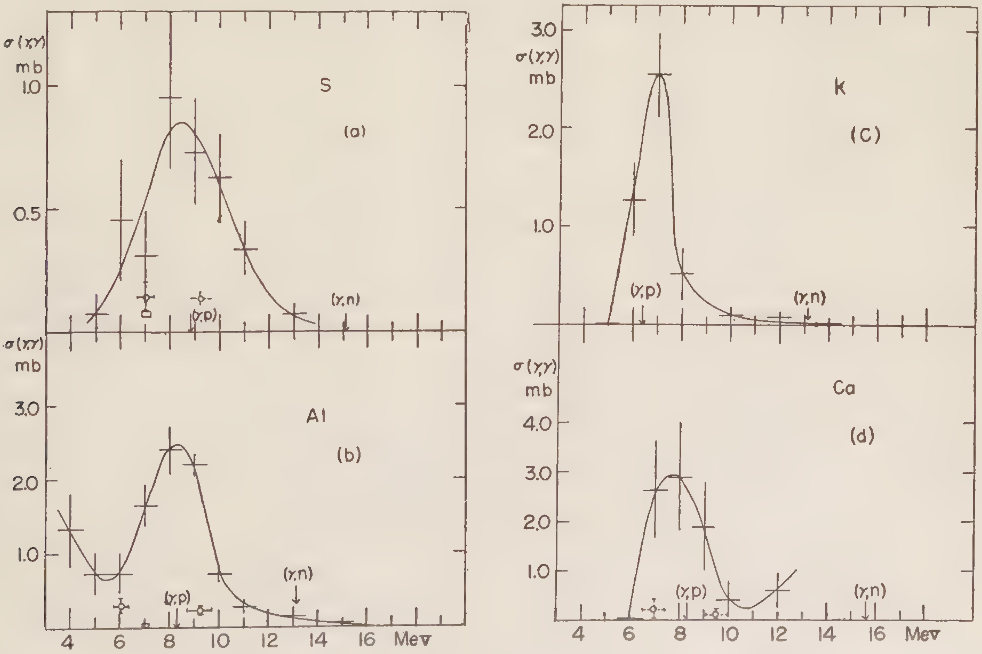

Fig. 6. The elastic scattering cross section of photons. ⊢○⊣: data from Fuller and Hayward[1].
□: data from the experiment used monochromatic γ-rays[4].
(a): $\sigma(\gamma, \gamma)$ by S. The arrows indicate the positions of the particle threshold energies of S^{32}.
(b): $\sigma(\gamma, \gamma)$ by Al. The arrows indicate the positions of the particle threshold energies of Al^{27}.
(c): $\sigma(\gamma, \gamma)$ by K. The arrows indicate the positions of the particle threshold energies of K^{39}.
(d): $\sigma(\gamma, \gamma)$ by Ca. The arrows indicate the positions of the particle threshold energies of Ca^{40}.

and C_d are the counts at the given scattering angle and the ones in the direct beam position, respectively. They were corrected for the electronic absorption using White's table[7].

The elastic cross sections are calculated from the ratios of C_s to C_d for each betatron energy. This method is appropriate, since the monitor response was not needed for the calculation of the cross sections. We do not give the detailed explanation of it, because Fuller and Hayward discussed it thoroughly in Ref. 1.

The response function of the NaI(Tl) crystal with the present geometry was measured with the 6.14 Mev and 17.6 Mev γ-rays obtained from the reactions $F^{19}(p, \alpha, \gamma)O^{16}$ and $Li^7(p, \gamma)Be^8$. In Figs. 3 and 4 the response curves for γ-rays of these reactions are shown.

In the calculation of the cross sections we assumed that the angular distributions of the scattered γ-rays are isotropic and that the angle subtended by the collimator at the target can be calculated numerically from the geometry.

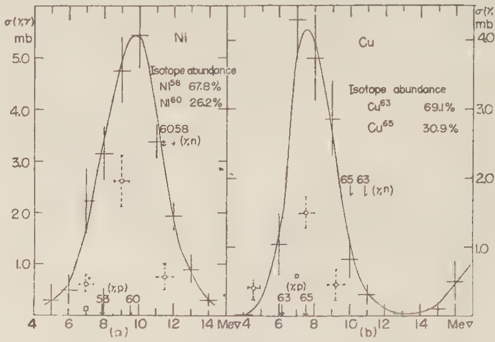

Fig. 7. The elastic scattering cross sections of photons. ⊢○⊣: data from Fuller and Hayward[1]. □: data from the experiment using the monochromatic γ-rays[4].

(a): $\sigma(\gamma, \gamma)$ by Ni. The arrows indicate the positions of the (γ, p) and (γ, n) threshold energies of Ni^{58} and Ni^{60}.

(b): $\sigma(\gamma, \gamma)$ by Cu. The arrows indicate the positions of (γ, p) and (γ, n) threshold energies of Cu^{63} and Cu^{65}.

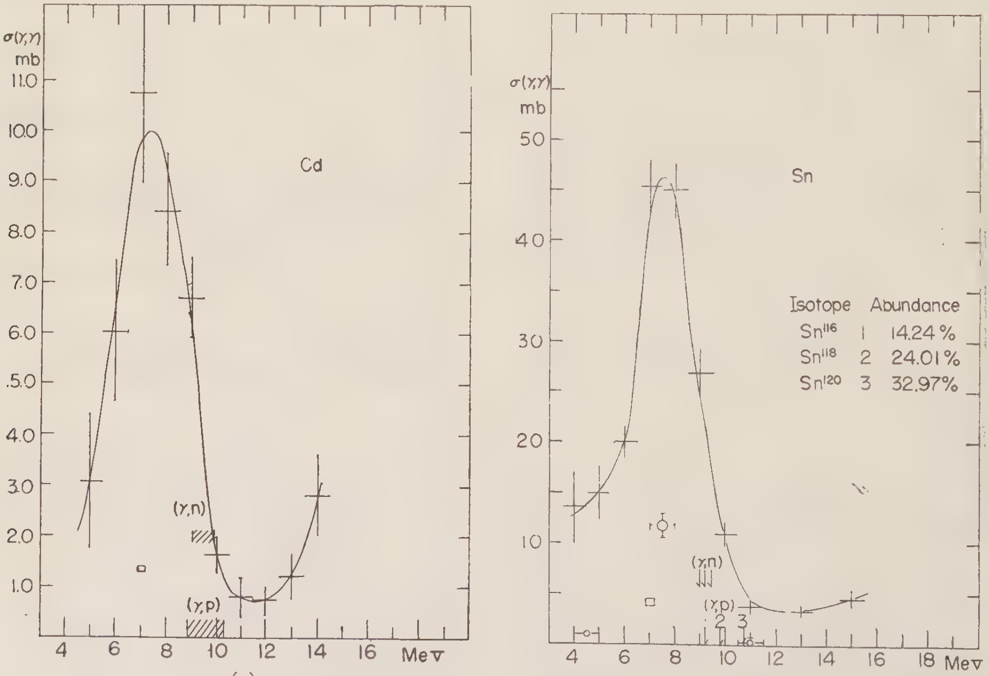

(a) (b)

Fig. 8. The elastic scattering cross sections of photons. ⊢○⊣: data from Fuller and Hayward[1]. □: data from monochromatic γ-rays[4].

(a): $\sigma(\gamma, \gamma)$ by Cd. The arrows indicate the positions of (γ, p) and (γ, n) threshold energies of many isotopes.

(b): $\sigma(\gamma, \gamma)$ by Sn. The arrows indicate the positions of (γ, p) and (γ, n) threshold energies of Sn^{116}, Sn^{118} and Sn^{120}. Numbers 1, 2 and 3 correspond to Sn^{116}, Sn^{118} and Sn^{120}.

§ 3. Results

Experimental results are plotted in Figs. 5–9. Here the vertical lines are the statistical errors and the energy spread indicated is the width due to the channels which are summed up as was stated before.

The shapes of the energy dependence of the cross sections are not inconsistent with those of Fuller and Hayward[1], but our absolute values of the cross sections are different in most elements. This discrepancy is not so serious, considering the difficulty of the experiments of this kind.

In comparison with the particle threshold energies, the peak positions of $\sigma(\gamma,\gamma)$ are in good agreement with the (γ,p) threshold energies for light nuclei such as Al, S, K, Ca and Ni, and with the (γ,n) threshold energies for heavy nuclei such as Pb. In the case of Cd and Sn, the peaks are slightly below the particle threshold.

In the case of Bi, however, the peak position is above the threshold. This fact is interesting, because the peak above the threshold can not appear by the process such as mentioned by Bethe and Ashkin. Therefore the peak of the cross section in Bi seems to occur by the process of the single particle excitation predicted by Fujii[6], since Bi^{209} is composed of a double magic core and one outer nucleon.

The case of Si is different from the others. Three somewhat sharp resonances were observed at 12.0 Mev, 10.4 Mev and 6.0 Mev, while the sharp resonance peaks were found at 11.4 Mev and 10.4 Mev by the other experiments[9],[10].

This fact suggests that the peaks below the particle thresholds in photon elastic scattering consist of the assembly of the sharp resonances, especially, in light elements. But it is not clear whether the resonance in other elements decomposes into many levels or not, if we restrict ourselves only to these results.

The energy dependence of the cross sections

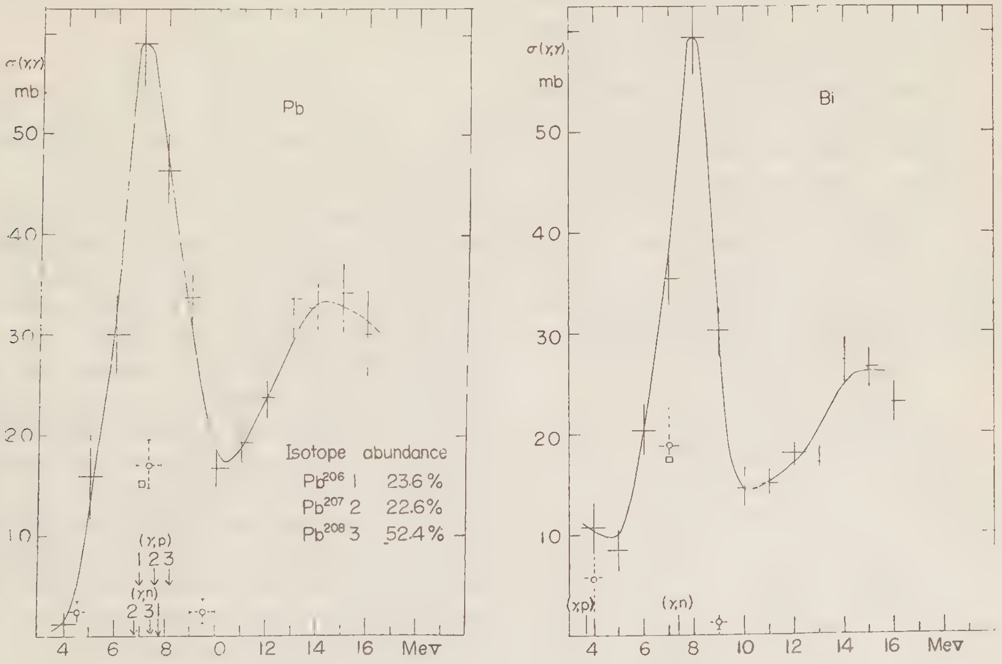

(a)

(b)

Fig. 9. The elastic scattering cross sections of photons. ├○┤: data from Fuller and Hayward[1].

□: data from monochromatic γ-rays[4].

(a): $\sigma(\gamma,\gamma)$ by Pb. The arrows indicate the positions of (γ,p) and (γ,n) threshold energies of isotopes. Numbers 1, 2 and 3 correspond to Pb^{206}, Pb^{207} and Pb^{208}.

(b): $\sigma(\gamma,\gamma)$ by Bi. The arrows indicate the positions of (γ,p) and (γ,n) threshold energies of Bi^{209}

Table II. The summary of the cross sections and the threshold energies.

Element	$E_{\max}$ (MeV)	$E_{th}(\gamma, p)$ (MeV)	$E_{th}(\gamma, n)$ (MeV)	$\frac{\sigma(\gamma,\gamma)}{\sigma_{Pb}(\gamma,\gamma)}$	$\frac{\sigma(\gamma,p)}{\sigma_{Pb}(\gamma,n)}$	$\frac{\sigma(\gamma,n)}{\sigma_{Pb}(\gamma,n)}$
Al	8.3	8.27	13.07	0.04	0.02	
S	8.5	8.8	15.07	0.02	0.06	
Si	12.0	11.59	17.18	0.12	0.05	
K	7.0	6.39	13.09	0.04	0.07	
Ca	8.0	8.34	15.73	0.05	0.07	
Ni58 60	9.8	7.91 9.53	11.93 11.39	0.09	0.15	
Cu63 65	7.5	6.12 7.46	10.83 9.92	0.07	0.11	
Cd	7.5	~9.5	~9.3	0.18		0.50
Sn	7.5	~9.8	~9.2	0.75		0.63
Pb	7.2	~7.5	~7.5	1.00		1.00
Bi	8.0	3.7	7.4	1.00		1.00

near the particle threshold is generally in agreement with the idea of the competition with the particle emission, if we disregard the elements such as Si, the exceptional element in the present experiment.

In Table II, the summary of these cross sections is shown. The first column shows the energies at which the cross sections have maxima. The second and the third columns show (γ, p) and (γ, n) threshold energies quoted from the nuclear data[11], respectively. The fourth column contains ratios of the peak values of the cross sections to that of Pb. In fifth and sixth columns of Table II, (γ, n) and (γ, p) cross sections normalized to (γ, n) cross section of Pb are listed.

For the determination of $\sigma(\gamma, p)/\sigma_{Pb}(\gamma, n)$ we assumed the following approximate equations;

$$\frac{\sigma(\gamma, p)}{\sigma_{Pb}(\gamma, n)} = \frac{\int \sigma(\gamma, p) dE}{\int \sigma_{Pb}(\gamma, n) dE}$$

and

$$\frac{\sigma(\gamma, n)}{\sigma_{Pb}(\gamma, n)} = \frac{\int \sigma(\gamma, n) dE}{\int \sigma_{Pb}(\gamma, n) dE} .$$

The values of $\int \sigma(\gamma, p) dE$ were calculated from the data summarized by Weinstock and Halpern[12]. As these data were given in the unit of protons per mole per roentgen, the integrated cross sections in the unit of Mev-mb were approximately calculated by assuming that the value of Cu in unit of Mev-mb is given by

$$\int \sigma(\gamma, p) dE = \int \sigma_{\text{total}} dE - \int \sigma(\gamma, n) dE .$$

We assumed $\int \sigma_{\text{total}} dE = 0.06 \frac{ZN}{A} (1+0.8x)$ and $x=0.4$, which was determined semi-empirically by

$$\int \sigma_{\text{total}} dE \simeq \int \sigma(\gamma, n) dE$$

for Pb. The values of $\int \sigma(\gamma, n) dE$ were quoted from Ref. 13.

As mentioned above, the peak positions of the cross sections in most elements are in agreement with the threshold energies of (γ, p) or (γ, n). This fact will support, as mentioned by Bethe and Ashkin, that the peaks around the particle thresholds in most of elements appear by the competition with the particle emission. From this point of view the cross section should be approximately proportional to that of (γ, p) or (γ, n), since the (γ, γ) cross section is only the lower part of the giant resonance. This proportionality seems to be roughly satisfied when we compare the fifth column with the last two columns excepting the case of Si.

Acknowledgment

The authors indepted to the Van de Graaff group in Tokyo University for their help in measuring the response curves of the 6.14 Mev and 17.6 Mev γ-rays from $F^{19}(p, \alpha, \gamma)O^{16}$ and $Li^7(p, \gamma)Be^8$ reactions. The authors also ex-

press sincere thanks to Dr. K. Okamoto, who is now at Tohoku University, for his helpful discussions.

References

1) E. G. Fuller and E. Hayward: Phys. Rev. **101** (1956) 692.
2) see E. Segre: *Experimental Nuclear Physics*, vol. 1, p. 346.
3) J. S. Levin and D. J. Hughes: Phys. Rev. **101** (1956) 1328.
4) K. Reibel and A. K. Mann: Phys. Rev. **118** (1960) 701.
5) J. M. Blatt and V. F. Weisskopf: *Theoretical Nuclear Physics*, p. Chap. XII.
6) S. Fujii: Progr. Theor. Phys. **21** (1959) 511.
7) K. Siegbarn: *Beta and Gamma ray spectroscopy.*
8) M. B. Stearns and B. D. McDaniel: Phys. Rev. **82** (1951) 450.
9) R. A. Tobin: Phys. Rev. **120** (1960) 175.
10) M. Sugawara: to be published.
11) *Nuclear data sheets, National Academy of Sciences*···N.R.C.
12) E. W. Weinstock and J. Halpern: Phys. Rev. **94** (1954) 1651.
13) R. Montalbetti, L. Katz and J. Goldenberg: Phys. Rev. **91** (1953) 659.

JOURNAL OF THE PHYSICAL SOCIETY OF JAPAN, Vol. 16, No. 9, SEPTEMBER, 1961

Some New Activities Produced by Fast Neutron Bombardments

By Kasuke TAKAHASHI*, Tokihiro KUROYANAGI,† Haruo YUTA††,
Kyûya KOTAJIMA*, Kunio NAGATANI**
and Haruhiko MORINAGA*

Department of Physics, Tôhoku University, Sendai, Japan

(Received April 18, 1961)

Several new nuclides were produced in the internal target of the INS cyclotron from the fast neutron bombardments of Ge, Mo, Gd, Er, Yb and Hf. Their radiation characteristics were determined with the aid of beta and gamma ray scintillation spectrometers. The new activities observed are as follows:

Nuclides	Half-lives	Beta rays	Gamma rays
Ga^{76}	32±3 sec	~6.0 MeV	0.57, 0.96, 1.12 MeV
Nb^{98}	51±5 min	3.5±0.1 MeV others	0.78 MeV many others
Nb^{100}	11.5±1.0 min	4.2±0.1 MeV others	0.53 MeV many others
Eu^{160}	~2.5 min	3.6±0.5 MeV	none
Ho^{168}	~3.5 min	~2.2 MeV	0.85 MeV
Ho^{170}	45±5 sec	~3.1 MeV	0.43 MeV
Tm^{174}	~5.0 min	2.5±0.1 MeV	none
Tm^{176}	1.5±0.3 min	4.2±0.1 MeV	none
Lu^{180}	2.5±0.5 min	3.3±0.1 MeV	none

The radiation characteristics were analysed in the light of the unified model and the conventional nuclear level systematics.

§ 1. Introduction

The study of short half-lived activities with rather high decay energy often yields useful information on nuclear properties. It is because of following reasons: 1) Because of its high decay energy, many excited states in the daughter nuclides are looked at. 2) It can add more to the nuclear systematics. We have been following this line of study by using the (γ, p) reaction and scintillation spectroscopy. We have found many new activities and thus many new nuclear states[1]. The paper which describes results of a part of such investigation carried on the rare earth region[2] will be published later.[2]

In this paper, we describe results of the study of neutron excess short-lived activities produced by the (n, p) reactions. The fast neutron bombardments and the activity measurements were carried out at the Institute for Nuclear Study of University of Tôkyo as one of the co-operation project of the Institute. The technique of measuring the activities and the method of analysis are very much similar to those of previous works.

§ 2. Experimental Procedures

The fast neutron beam was obtained by bombarding an internal graphite target with 20-MeV deuterons of the 160 cm variable energy cyclotron at the Institute for Nuclear Study of University of Tokyo. Samples to be activated by the fast neutrons were placed just behind the graphite target in the internal neutron target assembly in order to make the activation as effective as possible. A very schematic drawing is shown in Fig. 1. The intensity of the fast neutron beam was approximately $10^8\ n/\text{cm}^2\cdot\text{sec}$ at the bombarding position as estimated from the yield of the 9.5-min Mg^{27} produced by the $Al^{27}(n, p)$ reaction. Considerable amount of thermal neutron flux was also present which made the measurements complicated in some cases. After the bombardments the samples were pulled out from the bombarding position by a string. Usually it took only about half a minute before starting the counting after the bombardment in most of the cases. Because of rather short half-lives of the activities produced, no chemical treatment was performed except for the case of molybdenum.

---

* Now at Department of Physics, University of Tôkyo, Bunkyô-ku, Tokyo, Japan.

† Now at Japan Atomic Energy Research Institute, Tôkai-Mura, Ibaraki-ken, Japan.

†† Now at Department of Physics, University of Pennsylvania, Philadelphia, Pennsylvania, U.S.A.

** Now at Department of Physics, Yale University, New Haven, Connecticut, U.S.A.

The energy and half-life measurements of beta and gamma rays were performed with scintillation spectrometers with a 60 channel pulse height analyser of a differential discriminator type. For the measurement of half-lives, single channel analysers were also employed.

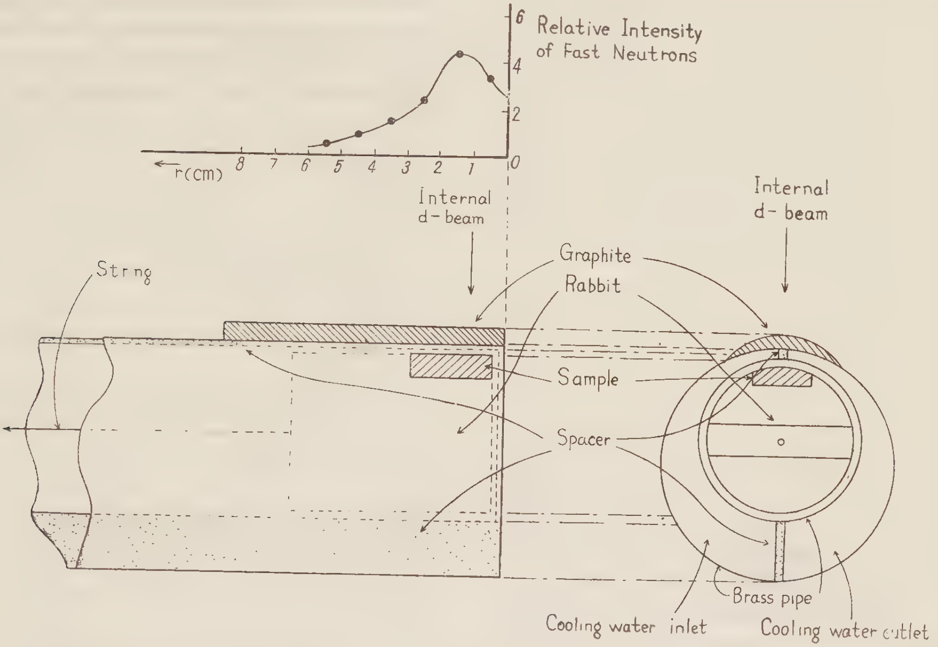

Fig. 1. Schematic picture of internal target system and distribution of fast neutron flux along the radial direction as measured by the $Al^{27}(n, p)Mg^{27}$ reaction.

The gamma rays were detected by NaI(Tl) crystals either 7.6 cmφ × 7.6 cm or 3.8 cmφ × 3.8 cm. Energy calibrations were made by the well known peaks of the gamma rays from In^{114}, Au^{198}, Cs^{137}, Zn^{65} and Na^{22} and the sum peak at 1.788 MeV of Na^{22}. Analysis of spectra was made with the comparison of the spectral shapes of gamma rays from these sources, obtained with the same geometry.

In the present work, since most of activities produced by the (n, p) reactions have rather high beta-decay energy, a large plastic scintillator of 5.1 cmφ × 5.1 cm was employed for the beta ray measurement in spite of its poorer resolution and its high sensitivities of gamma rays. Consequently many of the Kurie plots showed considerable non-linearity at the lower energy side of the curve (cf. Fig. 2). We

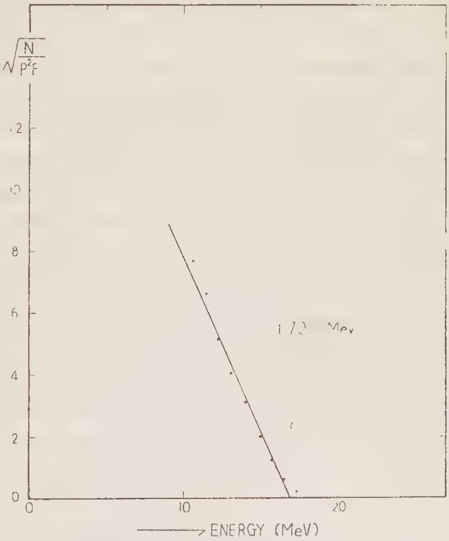

Fig. 2. Kurie plot of the beta ray spectrum of P^{32} obtained with the beta ray scintillation spectrometer.

could, thus, determine end-point energies for only one or two main branchings of the beta rays. For energy calibration, the beta rays from P^{32}, In^{114}, Cu^{66} and Ag^{112} were used. Fig. 3 shows a standard calibration curve for the beta ray scintillation spectrometer.

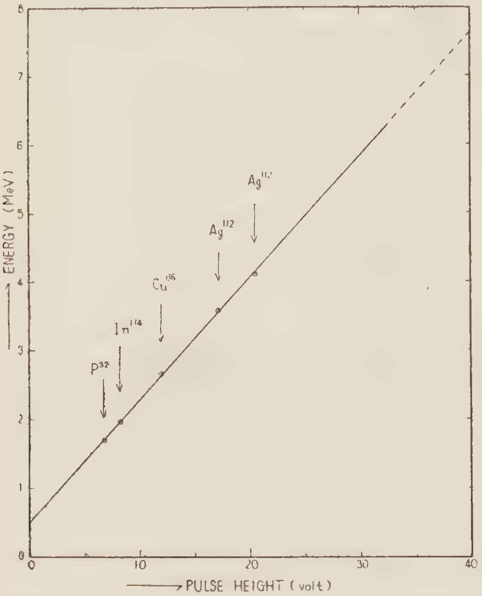

Fig. 3. Typical calibration curve for the beta ray scintillation spectrometer.

§ 3. Results and Discussions

Nine nuclides, Ga^{76}, Nb^{98}, Nb^{100}, Eu^{160}, Ho^{168}, Ho^{170}, Tm^{174}, Tm^{176} and Lu^{180} were studied from the (n, p) reactions of natural germanium, molybdenum, gadolynium, erbium ytterbium and hafnium. Some additional information about the decay characteristics were also obtained for, Tm^{173}, Lu^{178} and Lu^{179}. But in the present paper, no description was made for Tm^{173}, Lu^{178} and Lu^{179} because these are reported in the following paper rather in detail together with other newly found activities from the (γ, p) reactions[2]. Since Dy^{164} has very large thermal neutron capture cross section, bombardment of dysprosium was seriously disturbed by slow neutrons. Accordingly, no conclusive new information was obtained in the case of dysprosium.

1) Ga^{76}

Fig. 4 shows a decay curve of higher energy beta-ray components from Ga activities obtained from the neutron bombardment of germanium. An extremely pure metallic germanium sample was bombarded for about two minutes. Besides the well known high energy component from Ga^{74}($T_{1/2}$=8 min), a very short-lived activity of high energy is seen. The half-life was about 32 sec.

The end-point energy of the activity was determined to be about 6.0 MeV from the analysis of the Kurie plot (Fig. 5). The value is quite comparable to the decay energy of Ga^{76} to be produced by the (n, p) reaction on Ge^{76} (abundance=7.67%). Since no other product

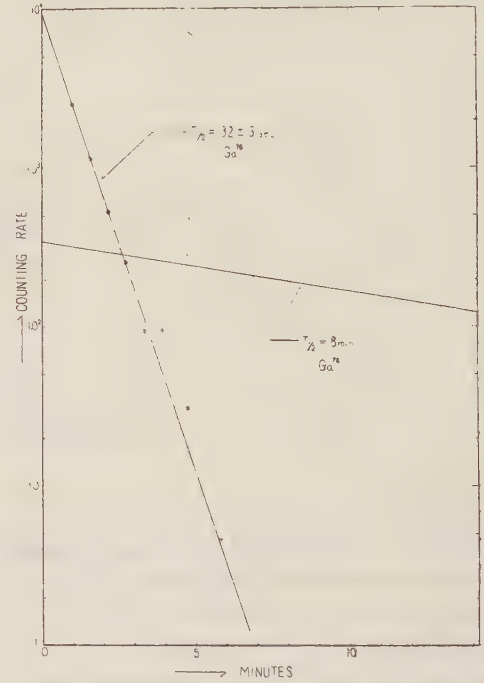

Fig. 4. Decay curve of the beta rays higher than 3.2 MeV from the metallic germanium sample bombarded with neutrons.

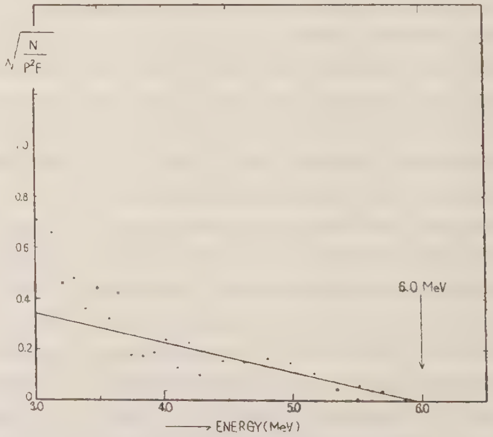

Fig. 5. Kurie plot of the beta rays from a neutron bombarded germanium sample.

of fast neutron reaction on Ge can give such a high energy electron radiation and the cross section to produce the activity is equal in order of magnitude to that of $Ge^{74}(n, p)Ga^{74}$ reaction, the activity is safely assigned to Ga^{76}. The spin-parity value of ${}_{31}Ga^{76}_{45}$ being most likely 2−, or any way not very high, the occurrance of the 6.0-MeV beta ray end-point is reasonable by a comparison with the expected value of the decay energy from the beta decay energy systematics ($E_\beta \sim 7.5$ MeV).

A short half-life of about 1 min or less was also observed in the decay superposed on the 0.58-MeV gamma ray from the 8-min Ga^{74}. Since Ge^{76} has the first excited state observed by the Coulomb excitation at 0.57 MeV³⁾, the short-lived component is assumed to belong to the Ga^{76} activity. This further supports the assignment of this short-lived activity to Ga^{76}.

In addition to the 0.57-MeV gamma ray, a few gamma rays of, 1.12 MeV and 0.96 MeV and some others were observed having a similar short half-life of one minute or less. Although the assignment to Ga^{76} was not completely certain because of the presence of strong disturbing gamma rays of nearly same energies in Ga^{74}. The gamma ray of 1.12 MeV, however, is considered to correspond to the gamma ray decaying from the second 2+ level of Ga^{76} to the ground state which has recently been observed by the Coulomb excitation⁴⁾.

2) Nb^{98} and Nb^{100}

About 10 minutes' bombardment was performed on molybdenum sample. In this case, the half-lives of the activities Nb^{98} and Nb^{100} had been found to be about 10 min or larger in the preliminary experiments. This made it possible to make chemical treatments separating the niobium activities produced by the (n, p) reactions from such disturbing molybdenum activities as Mo^{91}, Mo^{91m} and Mo^{101} which were produced by the reactions of $Mo(n, 2n)$ and $Mo(n, \gamma)$.

The procedures for chemical separation were as follows: after the bombardment of a powder sample of ammonium molybdate, the sample was dissolved into a hot water. In order to make solution acidic, small amount of dilute HCl solution was added. Here, the several millilitre of $FeCl_3$ solution was added. Fe^{+++} ion was used as a carrier of Nb ions. Then, the whole solution was gradually made basic with the addition of ammonia water just enough for making the precipitates of $Fe(OH)_3$.

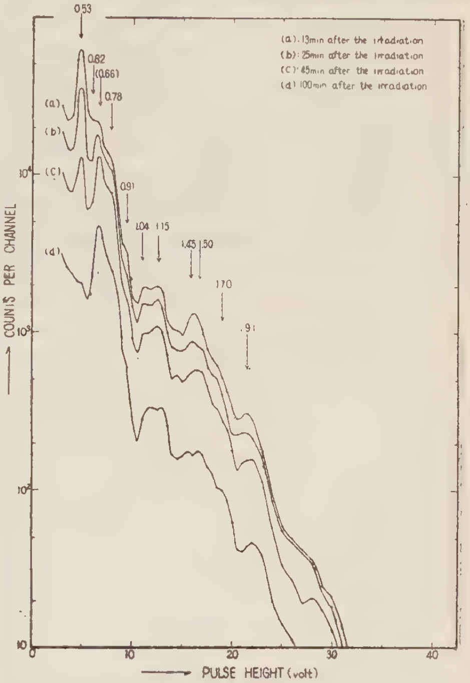

Fig. 6. Typical gamma ray spectra and the variations with time from the chemically separated niobium activities. Here the long-lived and background activities are already subtracted.

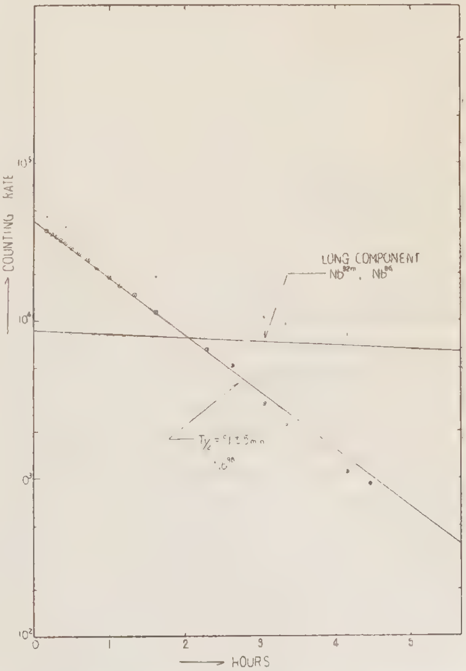

Fig. 7. Decay curve of the 0.78 MeV gamma ray from the niobium activities.

The precipitates with the co-precipitates of Nb activities were centrifuged and washed with dilute ammonium molybdate solution. After the filtration, the precipitates on the filter paper were dried up. It took about 8 or 9 min to carry out the whole chemical procedures.

Fig. 6 shows the gamma ray spectra and their decays obtained for the chemically separated Nb activities. We followed the decays of the gamma ray peaks and observed the two new activities having the half-lives of about 51 min and 11 min. Fig. 7 and Fig. 8 show decay curves obtained for the peaks at 0.78 MeV and 0.53 MeV. The former decays with the half-life of 51 minute and the latter decays with the half-life of 11 minutes. Quite the same results were obtained from the measurements with a single channel analyser. A summary of the results of the gamma ray measurements is given in Table I.

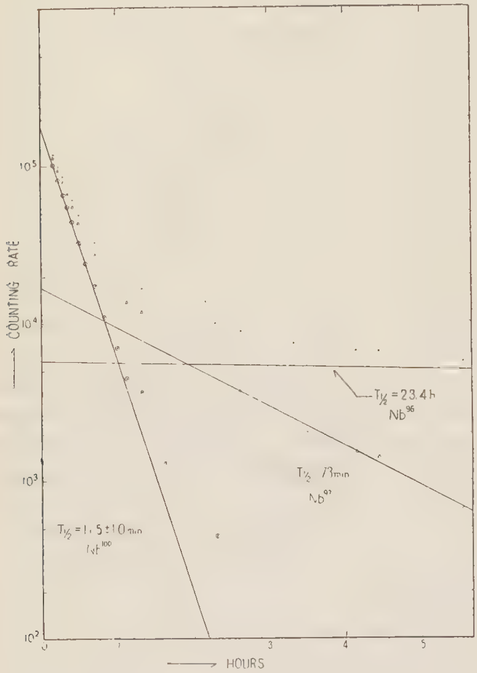

Fig. 8. Decay curve of the 0.53 MeV gamma ray from the niobium activities.

From the results of the Coulomb excitation experiments, the first excited states of Mo^{98} and Mo^{100} are found at 0.78 MeV and 0.53 MeV, respectively[3]. Therefore the 50-min and the 11-min lives are tentatively assigned to the isotopes Nb^{98} and Nb^{100}, respectively.

Table I. Gamma rays from Nb^{98} and Nb^{100}.

Nb^{98}		Nb^{100}	
Energy (MeV)	Relative Intensity	Energy (MeV)	Relative Intensity
0.78	100	0.53	100
0.90	30	0.62	60
1.04	25	1.04	10
1.17	30	1.15	10
1.40	15	1.47	5
1.50	20		
1.70	5		
1.91	5		

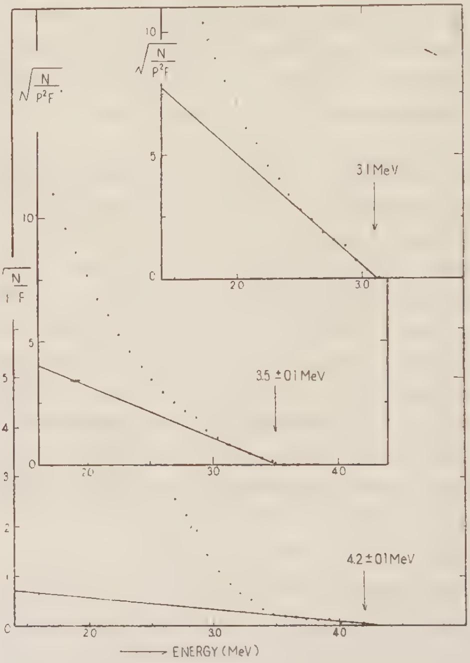

Fig. 9. Kurie plots of the beta rays from the chemically separated niobium activities about 10 min after the irradiation.

Similar decay characters were observed in the decays of the beta ray spectra. The Kurie plot analysis of the beta rays was performed for each spectrum obtained at various times after the termination of bombardment. Fig. 9 shows the Kurie plot for the beta spectrum measured at about 10 minutes after the bombardment, and Fig. 10 shows the spectrum obtained at about 120 minutes after the bombardment when the short component had almost completely decayed. From the analysis of these curves, end-point energies of the beta rays from two activities were determined and several branchings were also suspected to be present with the reference to the results of of a gamma ray measurement. The results are given in Table II. Values of the maximum energies of the beta rays from Nb^{98} and Nb^{100} are in good agreement with the expected values, about 4.2 MeV for Nb^{98} and approximately 4.9 MeV for Nb^{100}, estimated by the conventional beta decay energy systematics. This further supports the above assignments of the activities to Nb^{98} and Nb^{100}.

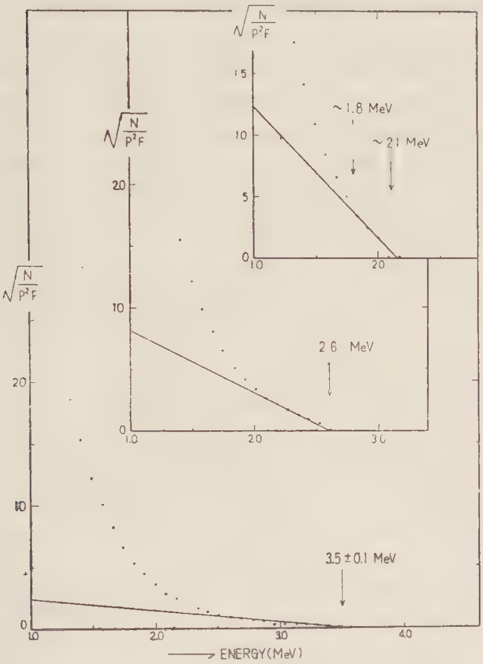

Fig. 10. Kurie plots of the beta rays from the chemically separated niobium activities about 120 min after the bombardment.

Table II. Summary of the beta rays from Nb^{98} and Nb^{100}.

Nb^{98}		Nb^{100}	
Energy (MeV)	Relative Intensity	Energy (MeV)	Relative Intensity
3.5 ± 0.1	intense	4.2 ± 0.1	$\lesssim 10$ (%)
2.6	most intense	3.5 ± 0.1	~45
~2.1		3.1	~45
~1.8		~2.1	~

Recently, Stelson and McGowan have reported the de-excitation gamma ray of 1.050 MeV from the second 2+ state of Mo^{100} as observed in their Coulomb excitation experiment of Mo^{100}.⁵⁾ The above-observed gamma ray of 1.04 MeV from Nb^{100} as shown in Table I, seems to correspond to this de-excitation gamma ray.

3) Eu^{160}

Among the activities produced from gadolynium bombarded with neutrons, only Eu^{160} is expected to have rather high energy beta ray. A decay of the beta rays higher than 2.0 MeV was followed with a single channel analyser. The bias energy of 2.0 MeV was so chosen that most of the activities produced from the (n, γ), the $(n, 2n)$ and the (n, α) reactions of gadolynium were excluded. A result of the measurement is shown in Fig. 11. After the subtraction of the 60-min component from Eu^{158}, an activity of about 2.5 min was observed.

The end-point energy of this short-lived beta ray was determined to be about 3.6 MeV from the Kurie plot analysis. (Fig. 12) The value of the end-point is quite similar to that expected from the beta decay energy systemactics for Eu^{160} (3.5 MeV). The yield of the 3.6-MeV component of about 2.5 min was of same order of magnitude expected for Eu^{160}.

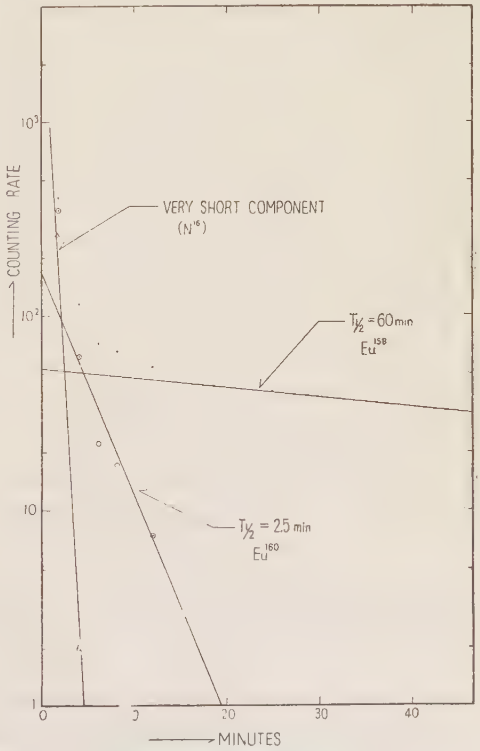

Fig. 11. Typical decay curve of electron radiations higher than 2.0 MeV from a neutron bombarded gadolynium oxide sample.

in comparison with that of the 2.7–MeV beta ray from the 60–min. Eu^{158}. Therefore, one may consider the 2.5–min activity can be assigned to Eu^{160}.

Gamma ray measurements showed no appreciable gamma ray with the 2.5–min life at an energy region higher than 100 keV. Because of the presence of strong gamma rays of about 4 min from Gd^{161} which was produced from the neutron capture, a weak gamma ray may have been missed. We can, however, conclude that most of the beta rays from Eu^{160} decay to the ground state of Gd^{160} or the neighbouring state. The net log *ft* value for the beta transition to lower states in Gd^{160} is, then, approximately 6.2. From the analysis of the Nilsson diagram[6),7)] and the coupling scheme[8)] of the deformed intrinsic states for odd-odd nuclei, the ground state of Eu^{160} is expected to have 1−. Accordingly a beta transition of the first forbidden type is expected. The log *ft* value obtained above, therefore, is plausible from this point of view. The value can be considered to give a further support for the assignment of the newly found activity of 2.5 min to Eu^{160}.

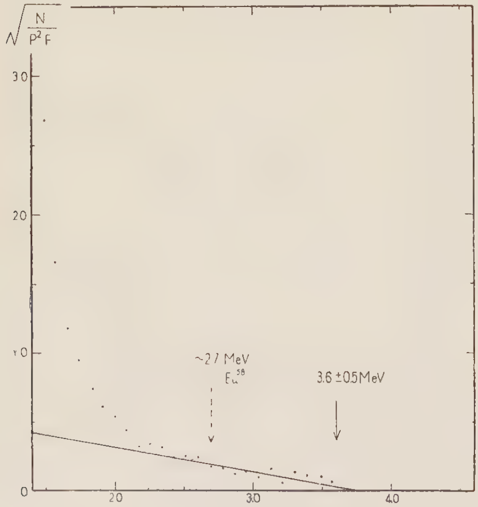

Fig. 12. Kurie plot of the beta rays from a neutron bombarded gadolynium oxide.

4) Ho^{168} and Ho^{170}

About 2-min bombardment was performed for a natural sample of erbium oxide. Activities of Ho^{168} and Ho^{170} were produced from the (n, p) reactions on Er^{168} and Er^{170}. Half-lives of the beta rays from a bombarded sample were measured with a single channel beta ray spectrometer. Fig. 13 shows a typical decay curve of the beta rays higher than 1.8 MeV. Since very small amount of chlorine was present in the sample of erbium, weak high energy beta rays from Cl^{34} and S^{37} which were produced from the $Cl^{35}(n, 2n)$ and the $Cl^{37}(n, p)$ reactions were observed. After the subtraction of the 32–min activity of Cl^{34}, two new activities of 3.5 min and of 45 sec were found. The half-life of the 3.5–min activity, however, has some ambiguities because of the presence of a weak beta ray from the 5.0–min S^{37}. From the Kurie plot analysis of the beta rays from the bombarded sample of erbium oxide, these two short-lived beta rays were proved to have end-points of 2.2 MeV and of 3.1 MeV, respectively. These results are given in Fig. 14.

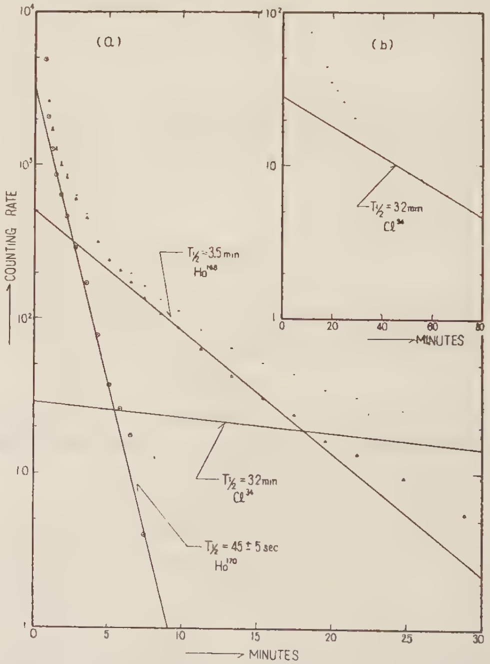

Fig. 13. Decay curves of the electron radiations higher in energy than 1.8 MeV from a neutron irradiated erbium oxide. Fig. (a) shows the early part of the curve and Fig. (b) gives the later part.

Among many activities produced from natural erbium by the neutron-induced reactions, conceivable nuclides which would have such short lives and high beta decay energies are only Ho^{168} and Ho^{170}, or Dy^{165} and Dy^{167} produced by the (n, α) reactions on Er^{168} and Er^{170}.

However, in the gamma ray measurement well known gamma rays from Dy^{165} which would be produced from the $Er^{168}(n, \alpha)$ reaction, were not observed clearly. Thus one may probably assign these two activities, the 2.2–MeV beta activity of 3.5 min to Ho^{168} and the 3.1–MeV of 45 sec to Ho^{170}, from the analyses of the conventional energy systematics (2.8 MeV for Ho^{168} and 3.7 MeV for Ho^{170}) and of the experimental yield ratios. The above assignments concerning Ho^{168} and Ho^{170} agree well with the results of the recent work reported by Willie and Fink[9].

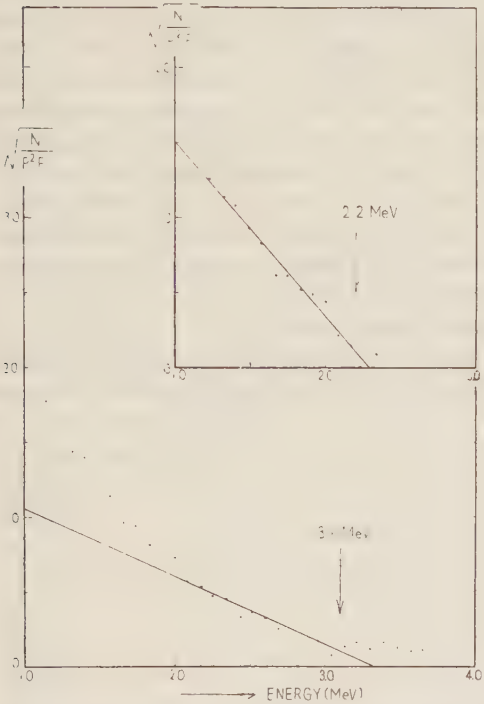

Fig. 14. Kurie plots of the short-lived beta rays from a neutron bombarded erbium oxide sample.

Some weak gamma rays were observed in the gamma ray measurement having half-lives of about 4 min and of 1 min or less. A peak near 0.85 MeV had the 4-min half-life and one at about 0.43 MeV was found to be of the 1-min life. This suggests us that some weak lower energy branchings of the beta rays may be included in the decay of both Ho^{168} and Ho^{170}. Because of a very low intensity of the 0.43–MeV gamma ray, however, most of the beta rays from Ho^{170} are considered to go to the ground state and its vicinity of Er^{170}. A rough estimation gives the log *ft* value of approximately 6. Since the ground state of Ho^{170} is expected to have 1+ from the coupling rule for deformed intrinsic states, an allowed transition is expected. Therefore, this log *ft* value is considered to be a reasonable value.

5) Tm^{174} and Tm^{176}

An oxide powder of natural ytterbium was bombarded for two minutes. Tm^{176} which may be produced from the $Yb^{176}(n, p)$ reaction, was expected to have a beta ray of approximately 4.0 MeV. So, a half-life measurement was performed for beta ray component higher than 3.3 MeV, at which energy any other product activities produced by neutron-induced reactions were excluded. A previously unknown activity of 1.5 min was observed. Similar value of half-life was found in a beta spectrum measurement. Accordingly one may tentatively assign this new isotope to Tm^{176}.

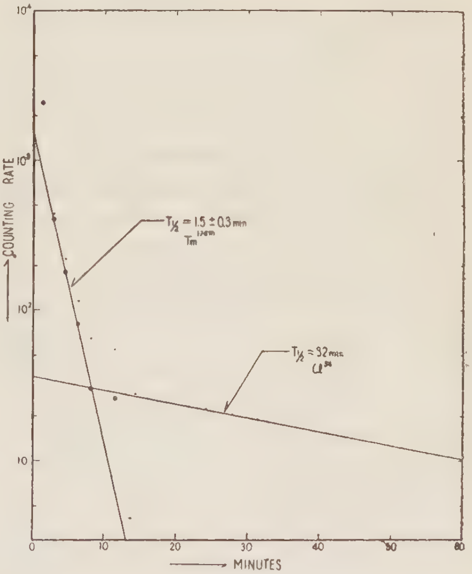

Fig. 15. Decay curve of the high energy electron radiations ($E_\beta \gtrsim 3.3$ MeV) from a neutron irradiated ytterbium oxide.

Fig. 15 shows one of the decay curves obtained. In Fig. 15, the 32–min component was considered to come from Cl^{34} as observed in the case of Ho activities.

A result of the Kurie plot analysis is given in Fig. 16. The value of the end-point was somewhat larger than that estimated from the beta decay energy systematics. Therefore, this new activity may be rather ascribed to an isomer of Tm^{176}. (The level systematics using Nilsson diagram and the coupling rule for the levels of odd-odd nuclei seems to support this assignment).

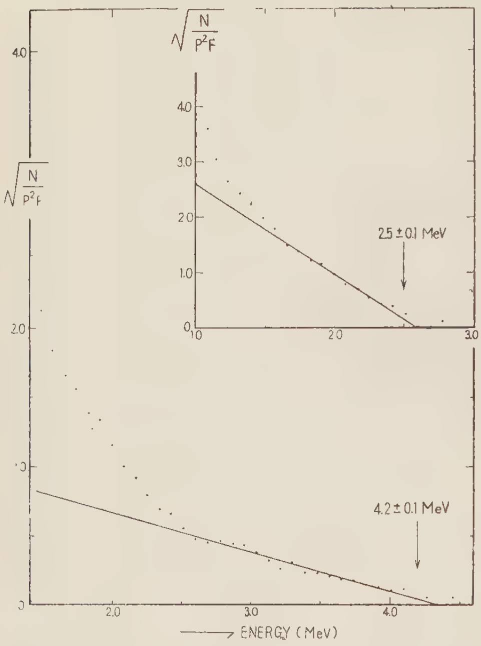

Fig. 16. Kurie plots of the short-lived beta rays from a neutron irradiated ytterbium oxide.

A lower energy beta ray component shown in Fig. 16 was found to decay with the half-life of about 5.0 min. Fig. 17 shows a decay curve of the lower energy component whose energies are ranging from 1.7 MeV to 2.4 MeV. The 1.5-min activity is due to the beta ray from Tm^{176m}. Therefore, one may expect the 5.0-min activity to be attributed to the previously unknown nuclide Tm^{174}. The same assignment has been proposed by Willie and Fink in their recent paper[9]. The end-point energy of 2.5 MeV is very close to the value estimated from the systematics for Tm^{174}.

No appreciable gamma ray decaying with a half-life of 1.5 min was observed in a gamma ray measurement, although some lower energy gamma rays than 0.15 MeV may be missed. From this fact, main component of the beta rays from the 1.5-min activity is considered to the ground state. If this activity is actually due to Tm^{176m}, it probably has zero spin and negative parity from the level systematics in this region, a first forbidden transition can be expected. Because of scarcity of the data, however, the assignment must be considered to be very tentative.

Though some weak gamma rays were found to decay with a half-life of about 5.0 min, no

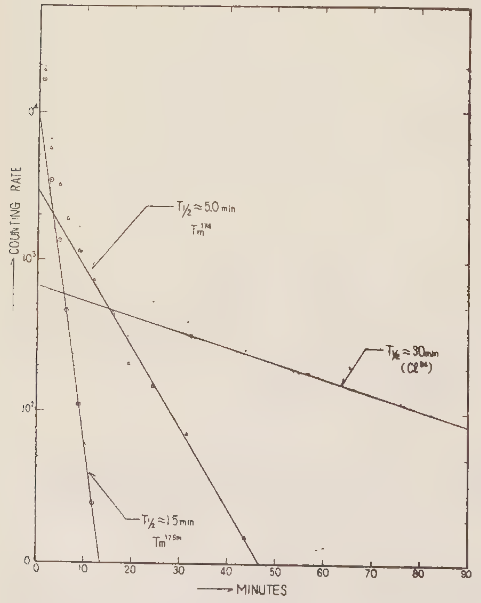

Fig. 17. Decay curve of the electron radiations whose energies are ranging from 1.7 MeV to 2.4 MeV, from a neutron bombarded ytterbium oxide.

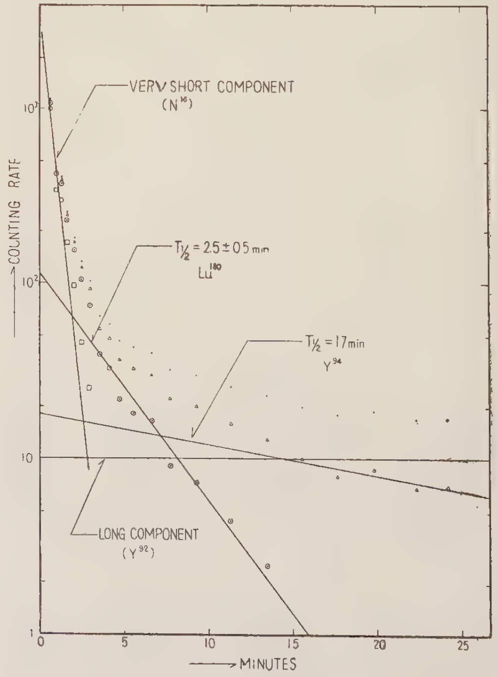

Fig. 18. Decay curve of the beta rays higher in energy than 3.0 MeV from a neutron irradiated metallic hafnium.

decisive information was obtained.

In addition, information about Tm^{172} and Tm^{173} obtained in the present work are in the good agreement with those observed in the experiment performed with activities produced from the (γ, p) reactions[2)].

6) Lu^{180}

A pure metallic hafnium was bombarded for two minutes. Since the beta dacay energy of Lu^{180} was estimated to be about 3.4 MeV from the beta ray energy systematics and the value of end-point for Lu^{178} has been known to be 2.2 MeV from the result of our previous experiment by the photoreactions of Hf, a decay of the beta rays higher than 3.0 MeV, in this case, was followed with a single channel beta ray spectrometer. A result of the measurement is shown in Fig. 18. Usually there are considerable amount of order of a percent of zirconium impurity even in a fairly pure sample of hafnium. In the present case the amount of zirconium impurity has been analysed to be 0.90 percent. So, the contributions from yttrium activities produced from the (n, p) reactions of zirconium impurity can be roughly estimated. In Fig. 18, the contributions of the high energy beta rays from Y^{92} and Y^{94} were subtracted in this way, after the long time measurement. As a result, an unknown activity of the 2.5–min life was found.

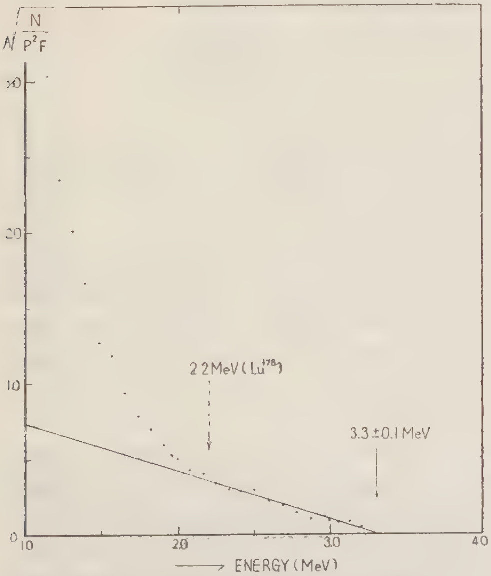

Fig. 19. Kurie plot of the 2.5-min beta ray from a neutron bombarded hafnium sample.

The end-point energy of this short-lived activity was determined to be 3.3±0.1 MeV from the Kurie plot analysis of the beta rays. Fig. 19 shows the result of the Kurie plot analysis after the subtraction of the 5.0–MeV beta ray from $Y^{94}(T_{1/2}=17$ min). The value of the energy indicated by a dashed arrow is considered to correspond to the end-point of Lu^{178} and agrees well with the value obtained for Lu^{178} produced from the $Hf^{179}(\gamma, p)$ reaction. Among the activities produced from the (n, p), (n, α) and other neutron-induced reactions of Zr and Hf, there is not any possible nuclide except Lu^{180} which has such a high energy beta ray and such a short life. Therefore, this unknown activity may be reasonably assigned to Lu^{180}.

In addition, informations concerning the decay characteristics of Lu^{178} and Lu^{179} obtained in the present work are found to be in good agreement with those from the (γ, p) reaction experiment[2)].

In gamma ray measurements, however, no conclusive information was obtained, because of the strong disturbing gamma rays from Hf^{179m} and Hf^{180m}. There is, however, an evidence that several peaks in the gamma ray spectrum included short components, which probably correspond to the four minutes activity obtained by Aten, Jr. and Funke-Klopper after the chemical separation of luthesium isotope[10)]. It seems that the activity we obtained and that found by Aten et al belongs to different isomers in analogy with the cases of Lu^{176} and Lu^{178}. Then, the 2.5–min activity with a high energy beta component represents the low spin state and the 4.5–min component with several gamma rays, which are probably in the cascade, is very much likely to correspond to the decay of the higher spin state.

Acknowledgement

The authors wish to express their sincere appreciation to the operation crew of the Institute for Nuclear Study for the operation of the cyclotron and for helpful assistances throughout the work. They are also indebted to the members of radio-chemistry, especially to Professor K. Saito for his invaluable suggestion to the chemical procedure separating niobium activity from molybdenum. The authors are grateful to the electronic technical staff and the members of the nuclear spectroscopy group of the Institute for their help and maintenance of the electronic equipments during the course of our experiment.

References

1) H. Morinaga, T. Kuroyanagi, H. Mitsui and K. Shoda: J. Phys. Soc. Japan **15** (1960) 213.
H. Yuta and H. Morinaga: Nuclear Phys. **16** (1960) 119.
K. Kotajima and H. Morinaga: Nuclear Phys. **16** (1960) 231.
K. Takahashi and H. Morinaga: Nuclear Phys. **21** (1960) 133.
2) T. Kuroyanagi, H. Yuta, K. Takahashi and H. Morinaga: to be published in J. Phys. Soc. Japan.
3) D. Strominger, J. M. Hollander and G. T. Seaborg: Table of Isotopes, Rev. Mod. Phys. **30** (1958) 585.
4) F. K. McGowan and P. H. Stelson: Bull. Am. Phys. Soc. **4** (1959) 232.
D. M. Van Patter: Nuclear Phys. **14** (1959) 42.
5) P. H. Stelson and F. K. McGowan: Phys. Rev. **121** (1961) 209.
6) S. G. Nilsson: Mat. Fys. Medd. Dan. Vid. Selsk. **29** No. 16 (1955).
7) B. R. Mottelson and S. G. Nilsson: Mat. Fys. Skr. Dan. Vid. Selsk. **1** No. 8 (1959).
8) C. J. Gallagher and S. A. Moszkowski: Phys. Rev. **111** (1958) 1282.
9) R. G. Willie and R. W. Fink: Phys. Rev. **118** (1960) 242.
10) A. H. W. Aten, Jr. and A. G. Funke-Klopper: Physica **26** (1960) 79.

Journal of the Physical Society of Japan, Vol. 16, No. 9, September, 1961

Weak Gamma Rays in the Decay of La^{140}

By Hidekuni TAKEKOSHI, Naomoto SHIKAZONO and Poh-Kun TSENG

Japan Atomic Energy Research Institute, Tokai-mura, Japan

(Received May 31, 1961)

Weak gamma rays of energy 0.63 MeV was found in the decay of La^{140} by means of a scintillation summing Compton spectrometer. This gamma rays are ascribed to the transition between the 2.53-MeV and 1.90-MeV states of Ce^{140}. The transition between this 1.90-MeV state and the 1.60-MeV state was not detected. The results of the present investigations on the conversion electrons and Gamma rays support the suggestion of Dželepow *et al* that the 1.90-MeV state is a O^{+} one.

§1. Introduction

Gamma rays in the decay of 40-hour La^{140} have been studied by a number of investigators[1], and the level scheme of Ce^{140} is fairly well established. In Fig. 1, a level scheme is duplicated from the *Nuclear Data Sheets*[1]. Cork *et al*[2] and Bashilov *et al*[3] observed that the spectrum of electrons had strong lines corresponding to a transition energy of 1.90 MeV. Dželepow *et al*[4] searched for gamma rays corresponding to the transition by means of a Compton-recoil spectrometer, and showed that, if such existed, the yield was less than 0.4×10^{-3} quantum per disintegration. They also reconfirmed the electron lines, and thus concluded the existence of a 0^{+} level of 1.902 MeV which decayed to the ground state of Ce^{140} by a $0^{+}\rightarrow0^{+}$ transition.

In the present paper, a search for gamma rays leading to or leaving this 1.902 MeV level was performed, data of which would form another support for the existence of this level.

§2. Experimental

A sample of spectroscopically-pure lanthanum oxide obtained from Johnson, Mathey & Co., Ltd. was irradiated in a Water-Boiler type reactor at JAERI. The gamma rays from this sample were analyzed by means of a NaI(Tl) summing Compton spectrometer[5]. The gamma rays from the source fall on a

1 inch×1 inch cylindrical crystal after being throughly collimated by a lead block with a hole 1.2 cm in diameter and 20 cm in length. Another crystal, 3 inches in diameter and 3 inches in length, is placed just beside the first crystal with it center axis lying on the plane of the front surface of the first one. The secondary photons, which are produced by Compton scattering in the first crystal, are caught by the second crystal, and the pulses from the two crystals in coincidence are summed to yield pulses corresponding to the full energy of the primary photons.

The spectra of the summed pulses are shown in Fig. 2, in which a, b, c, d and e indicate the spectrum taken with the second crystal pulse-height selector set at 0.14∼0.18, 0.18∼0.24, 0.24∼0.28, 0.28∼0.32 and 0.37∼0.47 MeV respectively. The gamma rays of energies of 0.33, 0.43, 0.485, 0.75, 0.815 and 0.92 MeV which are already reported[1)] are seen in the figure. Besides the peaks of these gamma ray, a small peak is seen at 0.63 MeV, which possibly be ascribed to the transition between the 2.53 and 1.90 MeV states. The order of the yield of this gamma rays is estimated to be 1×10^{-3} quantum per disintegration. Since the spin and parity of the ground state of La^{140} are 3^-, the beta transition to the 1.90 MeV state of Ce^{140} is forbidden. The 1.90 MeV state must be fed by the transitions from the upper levels which have spins 1 or 2. The 2.53 MeV gamma rays are relatively strong and the 2.53 MeV state is considered to be $2^{+1)}$. The 1.90 MeV state will, therefore, be fed by the transition from this state. The peak corresponding to the transition between the 1.90 MeV and 1.60 MeV state was not found. Since this peak might be obscured

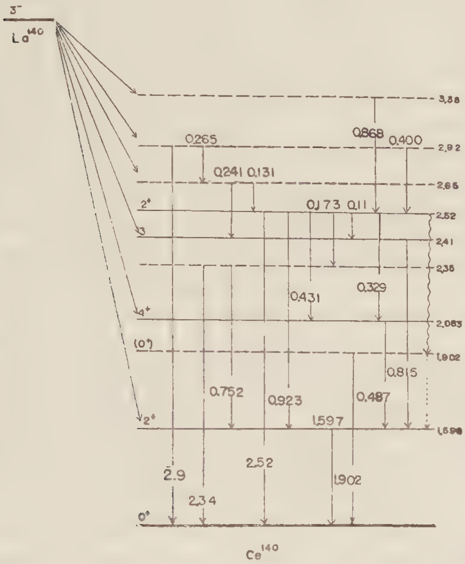

Fig. 1. Level scheme of Ce^{140} duplicated from the *Nuclear Data Sheets.*

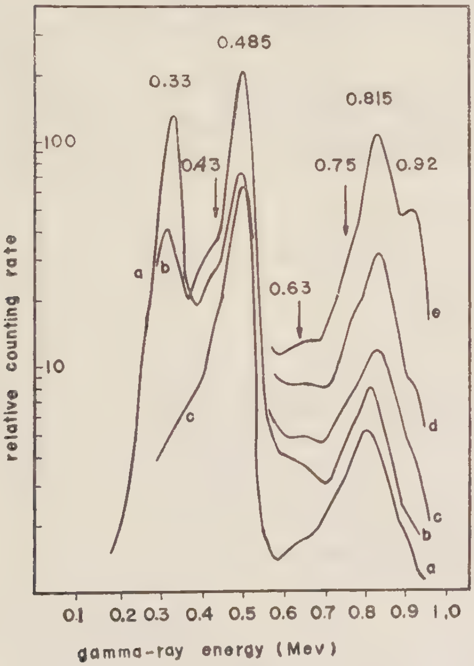

Fig. 2. Spectra of Ce^{140} gamma rays obtained with a scintillation summing Compton Spectrometer. a, b, c, d and e indicate the spectra taked with the second crystal pulse-height selector set at 0.14∼0.18, 0.18∼0.24, 0.24∼0.28, 0.28∼0.32 and 0.37∼0.47 MeV respectively.

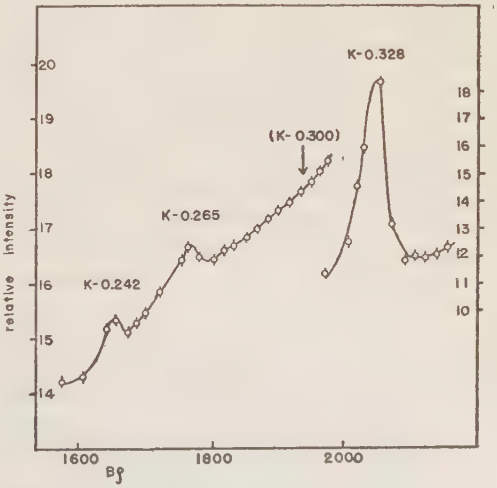

Fig. 3. Spectrum of conversion electrons of Ce^{140} (Bρ=1550∼2150).

by the intense 0.33 MeV gamma rays, the spectrum of conversion electrons was measured carefully by a magnetic spectrometer of 15 cm radius, the source being prepared from an equiliblium Ba^{140}-La^{140} mixture by the ion exchange method. The results are shown in Fig. 3. No bump is seen in the spectrum at the $B\rho$-value corresponding to 0.30 MeV gamma rays. The upper limit of the yield of this conversion electrons is estimated to be less than 8.7×10^{-5} per disintegration. If we assume that this 0.30 MeV transition is a pure E2 one, then the upper limit of the yield of this gamma rays will be 2×10^{-3} per disintegration (conversion coefficient $\alpha_k=4.6\times10^{-2}$)$^{6)}$.

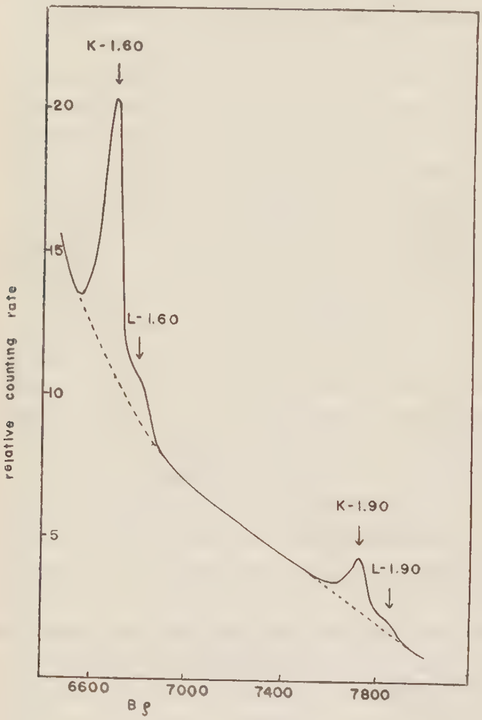

Fig. 4. Spectrum of conversion electrons of Ce^{140} ($B\rho=6400\sim8000$).

In Fig. 4, another part of the conversion-electron spectrum is shown. The existence of K- and L-lines of 1.90 MeV transition is obvious. The yield is about 20% of that of the 1.60 MeV conversion electrons. The K-conversion coefficient of 1.60 MeV gamma rays, which are emitted in almost every disintegration of La^{140}, is determined to be 6.3×10^{-4} from the ratio of the area of the conversion-electron peak to that of the beta ray spectrum. Then the yield of the K-conversion electrons of the 1.90 MeV transition turns out to be 1.0×10^{-4} per disintegration.

An estimation of the upper limit of the yield of 1.90 MeV gamma rays was made by use of a scintillation pair spectrometer. The results are shown in Fig. 5. The yield of 1.90 MeV gamma rays, if such exist, will be less than 1.2×10^{-3} quantum per disintegration. These results are in good agreement

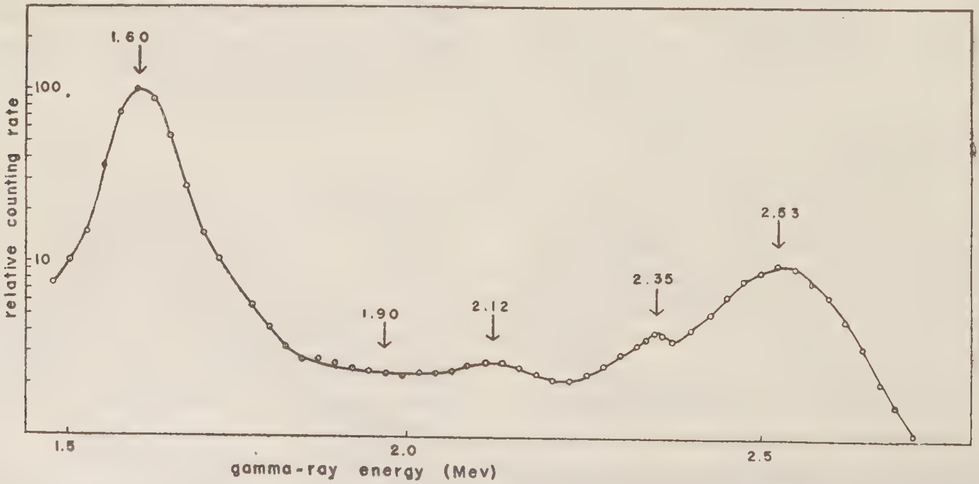

Fig. 5. Spectrum of Ce^{140} gamma rays obtained with a scintillation pair spectrometer. The peak at 2.12 MeV will be the satellite 1.60-MeV gamma rays which were counted by the following process; one of the annihilation quanta escaped the centre crystal and was captured by one of the side crystals and at the same moment a gamma quantum in cascade with this 1.60-MeV gamma quantum, passing through the lead shield, fell on the other side crystal.

with those of Dželepow *et al.*

High energy gamma rays of 2.35 and 2.53 MeV are seen in Fig. 5. By comparing their peak heights with that of 1.60 MeV gamma rays, the yield of 2.35 and 2.53 MeV gamma rays are estimated to be 4×10^{-3} and 2.5×10^{-2} quanta per disintegration respectively. Then the ratio of the yield of the 2.53 MeV gamma rays to that of 0.63 MeV gamma rays (1×10^{-3} quantum per disintegration) turns out to be about 20, a figure which is acceptable if the spin and parity of the 2.53 MeV state are assumed to be 1^{+}4), but out of theoretical expectation7) if otherwise (2^{+})1).

Acknowledgements

The authors wish to thank Teruo Momota for his interest and encouragement. They also wish to thank Haruo Natume for preparing the La^{140} source and Kazumi Ideno for his assistance.

References

1) *Nuclear Data Sheets*: Compiled by National Research Council, (USA National Acad. of Sciences Publishing Office, Washington, 1959).
2) J. Cork. J. Le Blanc, A. Stoddard, D. Martin, C. Branyan and W. Childs: Phys. Rev. **83** (1951) 856.
3) A. A. Bashilov, B. S. Dželepow, N. D. Novosiltseva and L. S. Chervinkya: Izvestiya Akad. Nauk SSSR, ser. fiz. **22** (1958) 179.
4) B. S. Dželepow, Yu. V. Kholnov and V. P. Prikhodtseva: Nuclear Physics, **9** (1958/59) 665.
5) H. Takekoshi: Rev. Sci. Instr. **12** (1960) 1280.
6) L. A. Sliv and I. M. Band: *Table of Internal Conversion Coefficients of Gamma Radiation, Part 1: K-shell*, (USSR Acad. of Sciences Publishing House, Moscow-Leningrad, 1956).
7) J. M. Blatt and V. F. Weisskopf: *Theoretical Nuclear Physics* (John Wiley & Sons, 1954) p. 623.

JOURNAL OF THE PHYSICAL SOCIETY OF JAPAN, Vol. 16, No. 9, SEPTEMBER, 1961

The Magnetic Investigation of Cu-Butyrate Monohydrate and Cu-Stearate.

By Takashi WATANABE

Department of Physics, Faculty of Science,
Tokyo Metropolitan University, Tokyo, Japan

(Received August 17, 1959)

The magnetic susceptibilities of Cu-n butyrate monohydrate, Cu-stearate and Cu-acetate monohydrate were measured in the temperature range from 90°K to the room temperature. The energy of exchange interaction J between the cupric ions Cu^{++} in the nearest neighbour sites were evaluated from the observed values and the relation $\chi_m=(0.125\,g^2/T)\cdot[1+(1/3)\exp(+J/kT)]^{-1}$. The magnitude of J-values thus obtained were $J_{\text{Cu-butyrate}}=430\pm150°\text{K}$, $J_{\text{Cu-stearate}}=485\pm15°\text{K}$ and $J_{\text{Cu-acetate}}=430\pm15°\text{K}$. And it seems that the g-value of Cu-stearate is somewhat larger than the value of Cu-acetate monohydrate.

§1. Introduction

The two cupric ions of Cu-acetate monohydrate are expected to be located at a very short distance in the crystalline state from the results of the measurements of magnetic susceptibility (Guha1); Perakis, Serres and Karantassis2) and Martin and Waterman3)) and paramagnetic resonance (Bleaney and Bowers4)).

Van Nickerk and Schoening (1953)5) have stated that the copper acetate monohydrate consists of a dimeric molecule such as $Cu_2\cdot(CH_3COO)_4\cdot2H_2O$ in which the distance between the two cupric ions is 2.64A. The experiment of paramagnetic resonance of Cu-butyrate monohydrate and Cu-propionate

1) Cu-*n* butyrate monohydrate $Cu(C_3H_7COO)_2 \cdot H_2O$

Table I.

T°K	$\chi_m \cdot 10^6$	$1/\chi_m \cdot 10^{-3}$	p^2_{exp}	T°K	$\chi_m \cdot 10^6$	$1/\chi_m \cdot 10^{-3}$	p^2_{exp}
289.6	851	1.17	1.83	205	793	1.26	1.20
273	846	1.18	1.71	186	741	1.35	1.01
260	840	1.19	1.62	160	654	1.53	0.76
245	836	1.20	1.52	130	526	1.93	0.48
228	833	1.27	1.41	85	372	2.69	0.21

2) Cu-stearate $Cu(C_{17}H_{35}COO)_2$

Table II.

T°K	$\chi_m \cdot 10^6$	$1/\chi_m \cdot 10^{-3}$	p^2_{exp}	T°K	$\chi_m \cdot 10^6$	$1/\chi_m \cdot 10^{-3}$	p^2_{exp}
296	898	1.02	1.98	177	638	1.57	0.82
245	867	1.15	1.58	165	623	1.61	0.74
233	846	1.18	1.47	156	519	1.93	0.57
220	798	1.25	1.30	131	444	2.25	0.40
209	738	1.36	1.13	98	386	2.59	0.26
189	722	1.39	1.00				

3) Cu-acetate monohydrate $Cu(CH_3COO)_2 \cdot H_2O$

Table III.

T°K	$\chi_m \cdot 10^6$	$1/\chi_m \cdot 10^{-3}$	p^2_{exp}	T°K	$\chi_m \cdot 10^6$	$1/\chi_m \cdot 10^{-3}$	p^2_{exp}
296	883	1.13	1.95	228	851	1.17	1.44
273	883	1.13	1.80	208	827	1.21	1.28
269	884	1.13	1.78	195	797	1.25	1.15
262	885	1.13	1.73	182	753	1.32	1.01
259	887	1.12	1.72	161	657	1.52	0.77
256	887	1.12	1.71	141	439	2.08	0.43
252	880	1.13	1.65	124	423	2.36	0.36
244	883	1.13	1.61	97	204	4.90	0.11
236	873	1.14	1.54	90	180	5.50	0.09

monohydrate was carried out by Abe et al[6], and the spectroscopic measurement of these salt was carried out by Tsuchida and Yamada[7]. These salts show the behavior similar to that of Cu-acetate monohydrate found in the above mentioned studies. The results in the present study for Cu-butyrate monohydrate and Cu-stearate also show the same character as that of Cu-acetate monohydrate.

The method of measurement and the apparatus used are those which have been constantly used in our laboratory and the detail was given in the other report of present author[8]. The merit of figure is $(1.000 \pm 0.015) \cdot 10^{-6}$ e.m.u./gram and the strength of magnetic field used is about 6000 Oe in the air gap of 3 cm. The cooling method is the indirect heat leak method[8] and the measuring temperature is controlled by liquid nitrogen or dry ice in alcohol.

Cu-*n* butyrate monohydrate, and Cu-acetate monohydrate were prepared by Kanto Chemical Co. These samples are carefully purified and recrystallized in water free alcohol by the present author. Cu-stearate was kindly supplied from Dr. S. Yamada.

§ 2. The Results of the Measurement

The results of the magnetic measurement are given in the following tables (Tables I, II and III) and in Fig. 1. In these tables, p^2_{exp} are the empirical value of the square magnetic moment of electron spin in the Bohr magneton unit evaluated by the relation

$$\chi_m = \frac{N\beta^2 p^2}{3kT} + N\alpha = \frac{0.125p^2}{T} + N\alpha \qquad (1)$$

where χ_m, β, N and k are values of the molar susceptibility, the Bohr magneton, the Avogadro number, and the Boltzmann factor.

The following values of molar susceptibility are used as the diamagnetic correction[9]

$(C_3H_7COO)_2^{--} = -108.0\cdot10^{-5}$,

$(C_{17}H_{35}COO)_2^{--} = -437.0\cdot10^{-6}$,

$(CH_3COO)_2^{--} = -62.8\cdot10^{-6}$,

$H_2O = -12.9\cdot10^{-6}$,

and the correction of temperature independent term of paramagnetic ion Cu^{++} ($N\alpha$) is $60\cdot10^{-6}$[4].

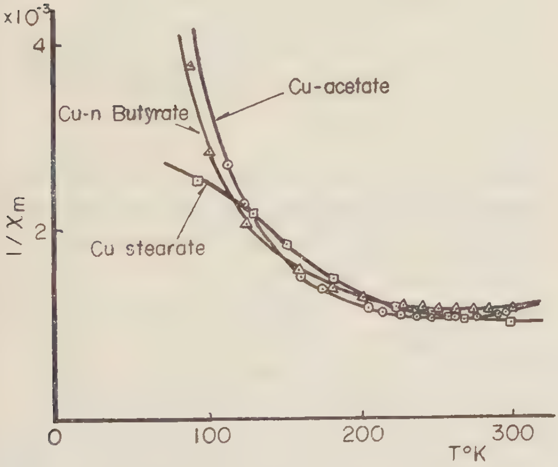

Fig. 1. Relation between the reciprocal magnetic susceptibilities per mole χ_m and T.

§ 3. Discussion

a) Calculation of the exchange interaction energy from the experimental results

The present result for Cu-acetate monohydrate at low temperature agrees well with the result given by Perakis et al[2], while the values of χ_m and p^2 in the Tables I, II and III are different from those given by Guha[1] at low temperature. The temperature at which the value of susceptibility shows a maximum value seems to shift to a higher temperature as the ligand proceeds from acetate to stearate. But the values of susceptibility of Cu-*n* butyrate monohydrate and Cu-stearate at about 100°K are larger than that of Cu-acetate monohydrate. It seems that these unexpected results arise from a paramagnetic impurity (it may be free cupric ion Cu^{++}). In the experiment of paramagnetic resonance of Cu-acetate monohydrate[4], the observed parallel and perpendicular g-values with respect to the principal axis agreed very closely with the values in other copper compounds such as the Tutton salts. It seems reasonable to assume that the individual copper ion is in the ^2D state as shown in Fig. 5. In the present case, it is assumed that Cu-*n* butyrate monohydrate and Cu-stearate are also in the same state as Cu-acetate monohydrate. Accordingly, it is considered that the magnetic character of these salts depends on the electronic splitting of singlet and triplet due to exchange interaction between two cupric ions in the nearest neighbour sites. A rough quantitative conclusion can be drawn from this assumption in the case of powdered samples.

The exchange interaction energy between two nearest copper ions is expressed as $-JS_1S_2$, where J is negative. The orbital ground level in ^2D state of Cu^{++} is singlet and the effect of anisotropic field may accordingly be neglected. Thus we get the Hamiltonian[10] as follows,

$$\begin{aligned}\mathscr{H} &= JS_1S_2 + g\beta SH \\ &= \left(\frac{1}{2}\right)\cdot JS(S+1) + g\beta MH + \text{constant.}\end{aligned}$$

where, $S = S_1 + S_2$. The partition function which corresponds to the above Hamiltonian is

$$Z = \sum \exp(-\mathscr{H}/kT) = 1 + \exp(-J/kT) \cdot \{3 + (g\beta H/kT)^2\} \qquad (2)$$

provided that $S = 1$ or 0, $M = \pm1$ or 0. The molar susceptibility χ_m are given as,

$$\chi_m = \frac{Ng^2\beta^2}{kT} \cdot \frac{\exp(-J/kT)}{1 + 3\exp(-J/kT)}$$

and adding the term of temperature independent paramagnetism of Cu^{++} ion ($N\alpha = 60\cdot10^{-6}$ e.m.u./mol) to the above relation

$$\chi_m = \frac{0.125\,g^2}{T} \cdot \frac{1}{1 + (1/3)\cdot\exp(J/kT)} + 60\cdot10^{-6}. \qquad (3)$$

The constant J of these salts can be estimated from the observed p^2 and the relation (3). The values of g^2, g and J determined in this

Table IV.

	g^2	g	J
Cu-acetate monohydrate	4.74 ± 0.2	2.18 ± 0.05	430±15°K
Cu-n butyrate monohydrate	4.45 ± 0.2	2.11 ± 0.05	430±15
Cu-stearate	5.40 ± 0.2	2.32 ± 0.05	485±15

way are shown in Table IV.

The calculated square magnetic moment p^2_{cal}, evaluated from the relations (1) and (3) by the use of the values in Table IV, are represented by solid curves in Figs. 2, 3 and 4 together with the observed values p^2_{exp} which are represented by broken curves. The curves show that the estimated values of J and g for acetate and butyrate are resonable but the values for stearate are not so reliable because p^2_{exp} deviates considerably from the curves of p^2_{cal} as shown in Fig. 4.

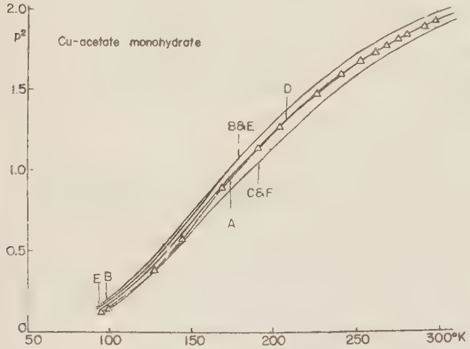

Fig. 2. Relation p^2 and T of Cu-acetate monohydrate.
A: —△—— is experimented curve, B~E are calculated curves. B: $g^2=4.74$, $J=415$°K, C: $g^2=4.74$, $J=445$°K, D: $g^2=4.74$, $J=430$°K, E: $g^2=4.94$, $J=430$°K, F: $g^2=4.54$, $J=430$°K.

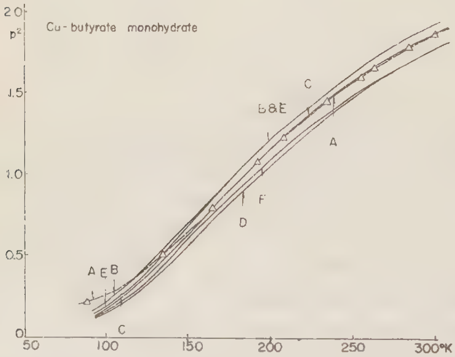

Fig. 3. Relation p^2 and T of Cu-n butyrate monohydrate.
A: ——△— is experimental curve, B~E are calculated curves. B: $g^2=4.45$, $J=415$°K, C: $g^2=4.45$, $J=430$°K, D: $g^2=4.45$, $J=445$°K, E: $g^2=4.65$, $J=430$°K, F: $g^2=4.25$, $J=430$°K.

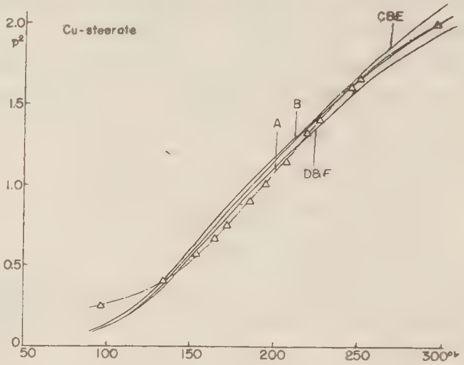

Fig. 4. Relation p^2 and T of Cu-stearate.
A: —△— is experimental curve, B~E are calculated curves. B: $g^2=5.40$, $J=485$°K, C: $g^2=5.40$, $J=470$°K, D: $g^2=540$, $J=500$°K, E: $g^2=5.60$, $J=485$°K, F: $g^2=520$, $J=485$

b) g-value

The g-value of Cu-butyrate monohydrate agrees roughly with the value of Cu-acetate monohydrate in the present magnetic measurement, as seen in Table IV. This result shows the fact that the copper ion of these salts is placed in a similar crystalline field. Such a consideration as above mentioned may be reasonable because these salts have the same coordinated ligand except in the number of carbon chain of normal alkyl group—C_3H_6-radicals and CH_3-radicals for Cu-n butyrate and Cu-acetate respectively. However the g-value of Cu-stearate differs considerably from the value of Cu-acetate monohydrate.

The g-values of Cu-n butyrate monohydrate and Cu-acetate monohydrate agree with the value in the other copper compounds such as the Tutton salt. Therefore it may reasonably be assumed that the individual copper ion in these two salts is subject to the similar type of crystalline field with the cubic and tetragonal symmetry. While Cu-stearate has not coordinating water molecule $-H_2O$ and the effect of low symmetry crystalline field may be different from the above two salts.

The orbital levels of the cupric ion Cu^{++} split into higher triplet and lower doublet in the cubic field and this doublet splits into two singlets (A and B) and the other triplet splits into a doublet (C and D) and a singlet (E) in the tetragonal field, as shown in Fig. 5. Each orbital level has an additional double degeneracy associated with the electron spin of 1/2.

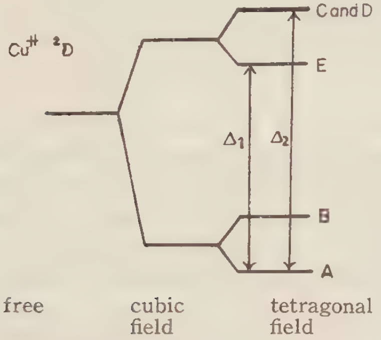

Fig. 5. Energy splitting ^2D level of Cu^{++} ion by crystalline field (not to scale).

If the energy of states (E) and (C, D) relative to the state (A) are denoted by Δ_1 and Δ_2 respectively, the g-values of the parallel and perpendicular components to z-axis of Cu-acetate monohydrate are given by Bleaney and Bowers[3] are following,

$$g_{\parallel}=2(1-4\lambda/\Delta_1)\,, \qquad (4)$$
$$g_{\perp}=2(1-\lambda/\Delta_2)\,.$$

If the spin-orbit coupling constant for free ion $\lambda=828\ \mathrm{cm}^{-1}$ [11] is used, the orbital splitting of Cu-acetate monohydrate can be obtained by them as $\Delta_1=20700\ \mathrm{cm}^{-1}$ and $\Delta_2=15000\ \mathrm{cm}^{-1}$, by use of the above results of paramagnetic resonance. Assuming the same crystalline field as in the Cu-acetate monohydrate and using $g=2.38$ given by the present authors, the numerical values of Δ_1 and Δ_2 evaluated from the relation (4) are about 15% smaller than the value of Cu-acetate monohydrate in the case of Cu-stearate.

c) Exchange interaction

If we consider that the distance between Cu^{++} ions is 2.64A, it seems that the exchange interaction energy of about 400°K can be hardly expected only from the direct coupling between Cu^{++} ions. The super-exchange interaction between two Cu^{++} ions through the nearest carboxyl radial should be also consideration for the interpretation of the exchange interaction energy of these salts.

In addition it should be noted that there is a marked difference in the exchange interaction energy between Cu-stearate and Cu-acetate monohydrate, that is

$$J_{\text{Cu-stearate}}-J_{\text{Cu-acetate}}\approx 55^\circ\mathrm{K}=38\ \mathrm{cm}^{-1}\,.$$

§ 4. Conclusion

1) Since the g-value of Cu-*n* butyrate monohydrate gives the same value as that of the Cu-acetate monohydrate, the symmetry properties and the magnitude of the crystalline field in these salts are similar to each other.

2) Since the Cu-stearate has no coordinated water molecule, the crystalline field and exchange energy in this salt seem to be different from those in the other two salts.

In conclusion, the present author wishes to express his sincere gratitude to Prof. K. Kido who encouraged him for the proceeding of the present study, also to Dr. S. Yamada of Faculty of Science, Osaka University who kindly supplied the sample of copper stearate and to Dr. P. H. Kim for his helpful discussion.

References

1) B. C. Guha, Proc. Roy. Soc. **A, 206** (1951) 353.
2) P. N. Perakis, M. A. Serres and T. Karantassis, Le Journal de Physique **17** (1956) 134.
3) R. L. Martin and H. Waterman, J. Chem. Soc. (1957) 2545.
4) B. Bleaney and K. Bowers, Proc. Roy. Soc. **A, 214** (1952) 451.
5) van Niekerk and L. Schoening, Acta Cryst. **6** (1953) 227.
6) H. Abe, The Symposium of Physical Soc. of Japan in Autumn (1956) and private communication.
7) R. Tsuchida and S. Yamada, Nature **176** (1955) 1171. R. Tsuchida and S. Yamada, ibid **181** (1958) 479.
S. Yamada, H. Nakamura and R. Tsuchida, Bull. Chemi. Soc. Japan **31** (1958) 303.
8) K. Kido and T. Watanabe, J. Phys. Japan **14** (1959) 1217.
9) K. Kido, Sci. Rep. Tohoku Univ. **21** (1932) 149.
10) J. Wücher, Physica **20** (1954) 361.
11) B. Bleaney and K. Stevence, Reports on Progress in Physics vol. XVI (1953) 145.

JOURNAL OF THE PHYSICAL SOCIETY OF JAPAN, Vol. 16, No. 9, SEPTEMBER, 1961

Velocity of Slowly Moving Dislocation

By Tomoyuki TAKEUCHI

National Research Institute for Metals, Nakameguro Meguro Tokyo

(Received December 10, 1960)

It is assumed that the observed dislocation velocity is the average velocity during the successive jumps, and that the jumping distances are large compared with the atomic spacing. The excitation probabilities for large jumps are calculated by the forces on dislocation, in which the thermal effects are introduced as the fluctuation of the local shear stress. The dislocation velocity in otherwise perfect crystals of relatively large Peierls stress are obtained as the functions of applied stress and temperature.

§1. Introduction

When a dislocation line moves, it is required to surmount the Peierls potential hills. Whether the dislocation goes over each hill with the thermal assistances, or it moves a large distance when the dislocation is once excited to go over a hill, is an essential problem in the considerations of the dislocation motion.

There are two experiments which reveal the motion of a dislocation line. The one is the direct observations of dislocation motion under the electron microscope, and the other is the observation of the dislocation motion under the applied stress by means of the etch pits. The former shows qualitatively the discontinuous motions having jumps and stays, and the latter[1] shows that a dislocation line moves by the successive jumps of about one micron of distance. If these facts are the normal properties of the dislocation in motion, it is suggested that the thermally excited dislocation line can move a large distance compared with the atomic spacing.

According to this standpoint, the average velocity v of a dislocation under the successive jumps can be expressed by the product of the jumping distance D and the jumping frequency ν:

$$v = D\nu\,. \tag{1}$$

When the stress and temperature dependence of the jumping distance is very small compared with that of the jumping frequency, the functional relations of dislocation velocity with the applied stress and the deformation temperature can be expressed approximately by those of jumping frequency.

For simplicity, the following considerations on the excitation probability are restricted to the case of a straight dislocation line in otherwise perfect crystals. Then the force which restrain the excitation of the dislocation motion is the Peierls stress. The jumping processes are treated as independent to each other, which is the meaning of the slowly moving dislocation. A distinct feature of the following considerations is the calculation of the excitation probability of dislocation by the use of the thermal forces, i.e. fluctuating local shear stress.

§2. Fluctuation of Local Shear Stress

The probability that a small region of the crystal has a component of the shear stress fluctuation $\Delta\sigma$ is

$$w = C\exp\left(-\frac{V(\Delta\sigma)^2}{2GkT}\right),$$

where G is the shear modulous and V is volume of the small region. In order to treat the fluctuation of the local shear stress around the dislocation line, V is expressed by the product of the effective cross-sectional area f (atoms) and the length l (atomic planes) of the dislocation:

$$V = v_0 f l\,,$$

where v_0 is the volume of atom or molecule. The probability that the dislocation segment is under the stress fluctuation $\Delta\sigma$ is

$$w(l,\Delta\sigma) = C\exp\left\{-\frac{\alpha}{T}l(\Delta\sigma)^2\right\}, \tag{2}$$

where

$$\alpha = v_0 f/2Gk\,. \tag{3}$$

In the consideration of the fluctuation, any fixed volume is usually considered. However, in the case of the dislocation in otherwise perfect crystals, there is no need to consider a fixed length of the dislocation line. Then it is assumed that some region of a dislocation line can be excited when a fluctuation satisfying specified conditions on l and $\Delta\sigma$ (see the following section) appears somewhere of the dislocation line. Under these conditions, factor C in (2) would be of the form

$$C=\phi(l)\left(\frac{\alpha l}{T}\right)^{1/2}, \tag{4}$$

where $\phi(l)$ arises from the freedom of the position of the fluctuation, and is considered to be $\phi(l)\propto l^0\sim l^{-2}$, which gives only a minor effect to the final results.

§ 3. The Conditions for the Excitation of Dislocation Line

At first, the apparent stress required to elongate the total length of the dislocation line is introduced. Suppose a length l of the dislocation has moved for m units distance of the Peierls potential, then the work done by the stress σ_l is

$$W=\sigma_l b(a_l)(cm)\ ,$$

where b is the magnitude of Burgers vector, a and c are the units of the atomic planes. By this motion, the total length of the dislocation line increases by $2m$ atomic planes, then the increase of the dislocation energy is $2mE$, where E is the energy per atomic plane. The necessary stress σ_l satisfying the condition $2mE=W$ is given by

$$\sigma_l=\beta/l\ , \tag{5}$$

where

$$\beta=2E/bac=2E/v_0\ . \tag{6}$$

In order to displace a length of the dislocation line from the initial position of the of the Peierls potential valley, the sum of the applied stress σ and the fluctuation stress $\Delta\sigma$ should be larger than the sum of the Peierls stress σ_0 and the stress required to increase the total length of the dislocation line β/l:

$$\Delta\sigma>\sigma_0-\sigma+\frac{\beta}{l}\ . \tag{7}$$

In order to displace a segment l of a dislocation line for large distance, the energy required to increase the line length should be provided by the applied stress alone, thus

$$l>\beta/\sigma\ . \tag{8}$$

When the both conditions (7) and (8) are satisfied, the excited segment of the dislocation line can be accelerated.

§ 4. Excitation Probability

When a fluctuation stress satisfying (7) appears on the dislocation line of the length satisfying (8), the motion of the dislocation line for large distance is started. Then the excitation probability of dislocation is

$$P(T,\sigma)=\int_{\beta/\sigma}^{\infty}dl\int_{\sigma_0-\sigma+\beta/l}^{\infty}C\exp\left\{-\frac{\alpha}{T}l(\Delta\sigma)^2\right\}d(\Delta\sigma)\ . \tag{9}$$

Integration with respect to $(\Delta\sigma)$ gives, when $f(l)\gg 1$,

$$P(T,\sigma)=\int_{\beta/\sigma}^{\infty}\frac{\phi(l)}{2}\ \frac{\exp\{-f(l)\}}{\{f(l)\}^{1/2}}dl\ , \tag{10}$$

where

$$f(l)=\frac{\alpha}{T}l\left(\sigma_0-\sigma+\frac{\beta}{l}\right)^2. \tag{11}$$

Integration with respect to l is rather complicated, and the following consideration gives the approximate integration. $f(l)$ can be rewritten as

$$f(l)=\frac{\alpha\beta}{T}(\sigma_0-\sigma)\left\{\left(\frac{\sigma_0-\sigma}{\beta}\cdot l\right)^{1/2}+\left(\frac{\sigma_0-\sigma}{\beta}\cdot l\right)^{1/2}\right\}^2,$$

then it is found that $f(l)$ is minimum at $l(\sigma_0-\sigma)/\beta=1$ and $\exp\{-f(l)\}$ is maximum at this point. When $\alpha\beta(\sigma_0-\sigma)/T\gg 1$, $\exp\{-f(l)\}$ has a sharp maximum. In this case, the probability density is predominant at the largest of $\exp\{-f(l)\}$ over the range of the integration. Inserting $l=\beta/\sigma$ when $\beta/\sigma>\beta/(\sigma_0-\sigma)$, and $l=\beta/(\sigma_0-\sigma)$ when $\beta/\sigma<\beta/(\sigma_0-\sigma)$ into the integrand of (10), the approximate functional relations of the excitation probabilities can be expressed by

$$P(T,\sigma)=B_1\exp\left(-\frac{\alpha\beta\sigma_0^2}{T\sigma}\right) \qquad \text{for} \quad \frac{\hat{\beta}}{\sigma}>\frac{\hat{\beta}}{\sigma_0-\sigma} \tag{12a}$$

$$=B_2\exp\left(-\frac{4\alpha\beta(\sigma_0-\sigma)}{T}\right) \qquad \text{for} \quad \frac{\hat{\beta}}{\sigma}<\frac{\hat{\beta}}{\sigma_0-\sigma}\,, \tag{12b}$$

where B_1 and B_2 are the functions of T and σ, which can be calculated, if necessary, by more accurate calculations.

§ 5. Dislocation Velocity

The excitation frequency ν of the dislocation line for large jumps is

$$\nu=\nu_0 P(T,\sigma)\,, \tag{13}$$

where ν_0 would be of the order of Debye frequency. From (1), (12), (3), (6) and (13), the dislocation velocity is obtained as

$$v=A_1\exp\left(-\frac{fE\,\sigma_0^2}{GkT\sigma}\right) \qquad \text{for} \quad \sigma<\sigma_0/2 \tag{14a}$$

$$=A_2\exp\left(-\frac{4fE(\sigma_0-\sigma)}{GkT}\right) \qquad \text{for} \quad \sigma_0/2<\sigma<\sigma_0\,, \tag{14b}$$

where

$$A_1=D\nu_0B_1 \qquad \text{and} \qquad A_2=D\nu_0B_2\,.$$

In order to compare (14) with the observed dislocation velocities, it is convenient to use the velocity-stress relations at constant temperature. When the relation (14a) is rewritten in the form

$$v\propto\sigma^n \tag{15}$$

in the small range of applied stress, the corresponding value to n is given by

$$n=\left(\frac{\partial\ln v}{\partial\ln\sigma}\right)_T=a_1+\frac{fE\sigma_0^2}{GkT\sigma}\,, \tag{16a}$$

in which the term a_1 arises from $\phi(l)$ in (4) and the integration processes, and is about 0.5~2.5. The similar calculation for (14b) gives

$$n=a_2+\frac{4fE\sigma}{GkT}\,, \tag{16b}$$

in which the term a_2 is of the order of one except at very low temperature. When n is very large compared with a_1 and a_2, the terms A_1 and A_2 can be set to be constant as an approximate functional form of the dislocation velocity. In this case, the stress and temperature relations at constant velocity are of the form

$$\sigma\propto\frac{1}{T} \qquad \text{for} \quad \sigma<\sigma_0/2 \tag{17a}$$

and

$$\sigma_0-\sigma\propto T \qquad \text{for} \quad \sigma_0/2<\sigma<\sigma_0\,. \tag{17b}$$

§ 6. Discussion

In the preceding calculations, three parameters are used: effective cross-sectional area of dislocation f, dislocation energy E, and Peierls stress σ_0. These parameters can be estimated from the observed values of n by the relation (16a).

From the observed dislocation velocities (10^{-2}~10^{-7} cm/sec) at 300°K, it had been shown that $n\approx 18$ ($\sigma\approx 0.25\,\text{kg/mm}^2$) for the softened crystals of lithium fluoride[1], and $n\approx 38$ ($\sigma\approx 12\,\text{kg/mm}^2$) for silicon-iron crystals[2]. Neglecting the term a_1 in (16a), and using the above observed values and $G=11.6\times 10^3\,\text{kg/mm}^2$ (Si–Fe) and $3.5\times10^3\,\text{kg/mm}^2$(LiF), one gets $fE\sigma_0^2=400\,\text{eV}\,(\text{kg/mm}^2)^2$ for LiF and $fE\sigma_0^2=1.35\times10^5\,\text{eV}\,(\text{kg/mm}^2)^2$ for Si–Fe. When the values $f=16$ atoms and $E=2$ eV per atomic plane are tentatively assumed, the Peierls stress becomes $\sim 3.5\,\text{kg/mm}^2$ for the lithium fluoride crystal and $\sim 60\,\text{kg/mm}^2$ for the silicon-iron crystal.

The condition ($n\gg 1$) used for the final results (14) and (17) is satisfied for the slowly moving dislocation in the crystals of relatively large Peierls stress under the moderate temperature range.

The important points of the present treatment are the excitation conditions (7) and

(8). Especially, (8) is the expression of the jumping motion of the dislocation line for many atomic spacings. The excitations of the dislocation line merely through (7) without satisfying (8) are considered to be not essential for the plastic deformation of the crystals, and are neglected in the calculation of the dislocation velocity. Such excitations would cause the motions of dislocation line similar to Brownian motion[3,4]. The theory of Lothe and Hirth[5] on the dislocation dynamics is essentially based on this motion.

It is the excitation condition (8) that distinguishes the present model from the current theories. In order to test the validity of the model, the assumption of the jumping distances large compared with the atomic spacing, which seems to be supported by the experimental evidences[1], should be explained by another theory.

Acknowledgements

The writer wishes to thank Dr. T. Kawada for interest in this problem. He is also indebted to Dr. H. Suzuki of Japan Atomic Energy Research Institute for kind discussions and for suggesting improvements in the presentation of this paper.

References

1) W. G. Johnston and J. J. Gilman: J. Appl. Phys. **30** (1959) 129.
2) D. F. Stein and J. R. Low: J. Appl. Phys. **31** (1960) 365.
3) H. Donth: Z. Phys. **149** (1957) 111.
4) J. Lothe: Z. Phys. **157** (1960) 457.
5) J. Lothe and J. P. Hirth: Phys. Rev. **115** (1959) 543.

Journal of the Physical Society of Japan, Vol. 16, No. 9, September, 1961

A Note on the Theory of Barium Titanate

By Hidetosi TAKAHASI

Department of Physics, University of Tokyo

(Received April 3, 1961)

A careful consideration on lattice vibrations in the ionic ferroelectric crystals such as $BaTiO_3$ reveals that a correct physical picture of the ferroelectric transition in these crystals may rather be regarded as an order-disorder transition of orientation of dipoles. A strong local order in the disordered phase is a characteristic feature. The model gives natural interpretation of the occurrance of three successive transitions in $BaTiO_3$, and predicts dielectric dispersion of relaxation type in the paraelectric phase.

§1. Introduction

Quite a number of papers have appeared dealing with the theory of the ferroelectricity of barium titanate since the discovery of the substance being ferroelectric. The first paper by Mason and Matthias[1] assumed each titanium ion to be situated in a multiple-well potential field, and tried to interpret the ferroelectric transition as an order-disorder transition of the distribution of the Ti atoms among these potential wells. A subsequent paper by Devonshire,[2] as well as one by Slater,[3] denied the possibility of a multiple-well potential in the paraelectric phase, and gave a theory based on a single-well potential. The transition to ferroelectric phase occurs, just as in Mason-Matthias's theory, as a result of Lorentz interaction among Ti ions, but the transition is not of the order-disorder type but a simple simultaneous spontaneous shift of the Ti ions parallel to one crystallographic axis. Since then, the latter theory got wide acceptance and Mason-Matthias's theory seems to have been completely discarded.

It is doubtless that Mason and Matthias's assumption of the existence *a priori* of a multiple-well potential for the Ti atom is entirely inadequate for the paraelectric barium titanate. Nevertheless, it is the purpose of the present note to point out that a closer investigation of the model of Devonshire and Slater leads to a physical picture which is strikingly akin to Mason-Matthias's model, and that the ferroelectric transition of barium titanate is also properly an order-disorder transition.

§ 2. Nature of the Thermal Motion

In the theory of Devonshire and Slater, the ferroelectric transition of barium titanate is explained as follows. Each Ti atom in the paraelectric (cubic) phase of $BaTiO_3$ is situated in a field of the surrounding atoms which is practically harmonic, that is, a linear restoring force acts on the Ti atom when it is displaced from the centre of the cell. In addition, there is a Lorentz (electrostatic) interaction among these Ti atoms, which is negative and is proportional to the square of the displacement when all the Ti atoms are displaced in the same direction and by the same amount. If the coefficient of restoring force is small enough so that interaction energy dominates, the simultaneous displacement of all Ti atoms lowers the total energy and a spontaneous displacement takes place, and the crystal becomes ferroelectric.

In order to explain the transition, that is, the appearance of spontaneous displacement within a specified temperature region, one has to assume some form of temperature dependence in either or both of these coefficients. There are at least two possible origins for such a temperature dependence: thermal expansion and the anharmonicity of the potential.

The effect of the thermal expansion on the one hand tends to favour the spontaneous displacement at higher temperature by decreasing the restoring force, but on the other hands tends to disfavour it by decreasing the Lorentz energy. The anharmonic term in the potential in general tends to increase the effective restoring force with temperature, since, with increasing amplitude of the thermal motion, the atom tends to spend more time in the vicinity of surrounding atoms, where the potential is 'harder', that is, has a greater second derivative. The usually negative temperature coefficient of the dielectric constant in the paraelectric region and the fact that ferroelectric phase lies *below* the transition point seems to show that the effect of anharmonicity is the most important.

In the above argument, the thermal motion of an atom was considered independently of the other atoms in the crystal, that is, we used the Einstein model.

In order to take a more detailed account of the effect of thermal motion, let us now try to use the Debye model. The motion of each atom is now considered as a superposition of a great many normal oscillation modes, which are regarded as being approximately independent of each other. The modes are grouped to several branches, which are either acoustical or optical, and only the acoustical branch contains modes of a wide range of frequency, including those of very low frequency. We are, however, interested in the motion of an atom relative to its neighbours, and since the low-frequency acoustical modes are those for which the relative positions of neighbouring atoms are little changed, we can neglect these low-frequency modes. Then we have only to consider the modes lying in a relatively narrow frequency region. This means that we may approximate all the modes by a single frequency, and the former consideration based on the Einstein model is justified.

However, in *potentially ferroelectric* crystals, that is, the paraelectric state of ferroelectric substances, the situation is somewhat different. In such crystals, the frequency of the long-wave optical modes also becomes very low, and the lowest frequency tends to zero as the temperature tends to the Curie point (assumed to be a second order transition). Since the amplitude of thermal oscillation is inversely proportional to the frequency, these slow oscillations will have very large amplitude, and it is probable that most part of the relative thermal motion of the atoms are the contribution of these slow oscillations.

§ 3. Role of Anharmonicity

So far we have neglected the anharmonicity of the interatomic forces. One of the effect of anharmonicity will be to cause the coupling between different normal modes.

However, an attempt to develop a consistent theory taking account of the anharmonicity faces an unexpected difficulty.

From what was said in the preceding section it follows that the temperature dependence of the frequency spectrum of the optical modes is actually an indirect effect of the coupling of modes due to the anharmonicity. Accordingly, a more rigorous approach would be to start by taking the normal mode spectrum at the absolute zero temperature, and to consider thereupon the effect of coupling between these modes. In ordinary substances, such a treatment may give a satisfactory theory, although it may lead to a rather elaborate formulation. In ferroelectric substances such as barium titanate, however, it would lead to a fundamental difficulty, since the frequency of certain long-wave modes become *imaginary*, corresponding to the fact that unpolarized state of $BaTiO_3$ is unstable at low temperature.

The origin of this difficulty will be traced to the fact that the amplitude of thermal motion in such substance is so large, and the Lorentz interaction of the atoms is so strong, that a conventional quasi-harmonic picture of the thermal motion becomes entirely invalid. It seems more probable that the displacement of most Ti atoms in $BaTiO_3$ is saturated, even in paraelectric state, and the effect of thermal motion would be to bring a Ti atom from one saturated position to the other, just as in KH_2PO_4 and other dipole-type ferroelectrics. In such a situation, the Debye approach as considered above seems quite inadequate. However, in the following sections we will try to make a qualitative picture of such potentially ferroelectric crystals, so as to become the basis of a more quantitative theory.

§ 4. Proposed Picture of the Barium Titanate above the Curie Point.

In accordance with the above considerations, the following picture will be proposed for the paraelectric phase of the barium titanate (Fig. 1).

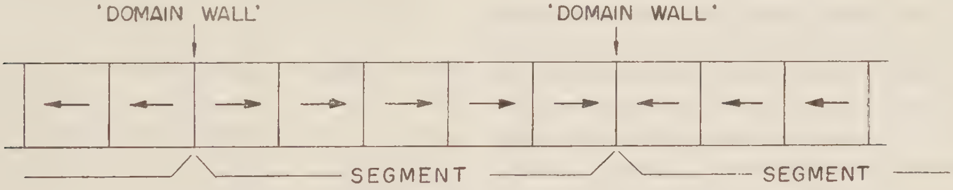

Fig. 1. One-dimensional picture of the paraelectric state. Arrows indicate displacement of Ti atoms.

Consider a row of unit cells extending in the direction of one of the crystal axes. Every Ti atom on this row is displaced from the centre of the cell to either direction along the row, producing dipole moments of either direction but of constant magnitude. The directions of these dipoles are not independent of each other, but the adjacent dipoles strongly tend to be parallel so that the whole row is split up into a number of *segments*, so that within each segment the dipoles are all parallel but the dipoles in the adjacent segments are directed oppositely. These segments are not fixed, but their boundaries or the 'domais walls' are always moving randomly back and forth, with eventual creation and annihilation of segments, or 'pairs' of the boundaries. If we fix our eyes on a single Ti atom, it is normally at rest in one of the extreme positions in the cell (making, of course, a small thermal vibration about this position), but eventually it jumps from one extreme position to the other and vice versa, as the 'domain wall' passes the cell in question.

The reader will at once notice the striking resemblance of this picture with Mason-Matthias model. In fact, the ferroelectric transition deduced from our model will be essentially an order-disorder transition of the orientation of dipoles of fixed magnitude. However, in spite of the apparent similarity, a fundamental difference must be noticed. Mason and Matthias assumed, *a priori*, that there exist several equilibrium positions for each individual Ti atom, and considered the order-disorder transition by interactions. That is, the permanent dipole they assumed existed entirely independently of the surrounding atoms and the interactions affected only the alignment of dipoles. In our picture, on the contrary, we assume that the dipoles or the displacement of Ti atoms are created just by the cooperative effect, namely, the Lorentz interaction of a great many atoms within the row, even in the paraelectric phase. In the transition to ferroelectric state, the length of the segment becomes infinite (that is, of macroscopic size), while a transverse ordering also appear. Thus we are dealing with an order-disorder transition with a high degree of local order in the disordered phase. It is to be noted that this high local ordering is the characteristic feature of our picture.

§ 5. Three-Dimensional Picture.

In the foregoing we have restricted ourselves in a somewhat unnatural way to discussion of the interaction of dipoles within a single row of cells, and also the possibility of displacement of atoms in other crystallographic axes has been neglected. Now the former restriction seems to be justified on the ground of the special feature of barium titanate that the Lorentz interaction energy between adjacent rows of dipoles is probably very weak compared to that between the cells within the same row.[4] In the following we will extend the model to include the dipole orientation in three dimensions.

Since the symmetry of barium titanate is cubic, there is no reason to exclude the possibility for the Ti atom to be displaced parallel to the other two crystallographic axes. It may be possible that the displacement of an atom in one direction (say z direction) prevents the displacement of the same atom in a direction orthogonal to it. Here, however, it will be assumed that the displacement of the same atom can occur along the three crystallographic axes simultaneously, and independently of each other. Thus we can imagine three orthogonally intersecting bundles of rows of cells, each being of the kind just described, running parallel to the three crystallographic axes respectively. Accordingly, each Ti atom is displaced in one of the eight crystallographic directions equivalent to (111) hence having the displacement vector ($\pm\delta$, $\pm\delta$, $\pm\delta$). Each one Ti atom defines three orthogonal segments of the rows of cells, and the displacement of that Ti atom is the vectorial sum of the displacements associated with each of these three segments. An example of the configuration of the displacements is given in Fig. 2 in a two-dimensional form for illustration.

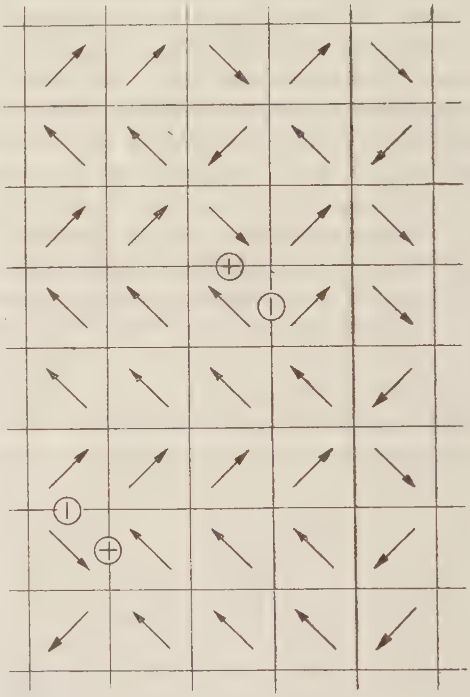

Fig. 2. Two-dimension illustration of dipole configuration. Note the flux closure.

In the simple one-dimensional picture, it was necessary to care for the free electric pole that is produced at every 'domain wall'. The present three-dimensional picture has the advantage that a free pole produced in one row of cells can be neutralized by a free pole of opposite polarity produced in another intersecting row, resulting in approximate flux closure. In Fig. 2 is an example of such a closure configuration. In this way, a rather complex pattern of flux-closed dipole configuration may be obtained. Since a great energy is required to create a free pole, it is probable that actual configurations mostly take the form with closed electric flux

§ 6. Consequences.

Our picture can give a natural explanation of the occurrance of three successive phase transitions: cubic→tetragonal→orthorhombic→trigonal, in $BaTiO_3$ upon cooling. At high temperatures, the configuration of dipoles is completely disordered although a strong local order exists. As the temperature is lowered, a point is reached where a complete order is set up in the z-component of the dipole moment, the x- and y-components being still disordered. The crystal becomes tetragonal. Setting up of the order in the z-component and the accompanying lattice distortion somewhat affects the parameters relating to the x- and y-components, but on still lowering the temperature, another transition takes place and the y-component of the dipole moment becomes also ordered. The x-component still remains disordered owing to the accompanying change of parameters. Now the crystal is orthorhombic.

At a still lower temperature, the last transition takes place and the x-component of the dipole moment becomes also ordered, and now the dipoles are completely ordered. This is the trigonal phase.

The above discussion may of course be too simple to be of general validity, but the fact that the form stable in lower temperature has always less randomness and hence less entropy than the form stable at higher temperature is very convincing.

One consequence of our picture that may be verified by experiment is the dielectric dispersion in the paraelectric region. The current model which assumes a temperature-dependent restoring force for the Ti atoms, gives a resonance type dispersion with a rather low resonance frequency, the resonance frequency varying proportionally to $T-T_c$ where T_c is the extrapolated Curie point. Our model would give, on the contrary, a relaxation type dispersion of some form. Existing data on the dispersion is not sufficient to decide which of the two models is correct. It may also be possible to test the correctness of our model by X-ray structure analysis. Since the existing result of the analysis did not take the disordered structure into account, it seems worthwhile to reexamine the existing data in the light of the new assumption.

§ 7. Conclusion

Starting from an accepted model of barium titanate and following purely logical steps, we have arrived at a physical picture which is unexpectedly similar to the long abandoned model due to Mason and Matthias. The argument has been throughout qualitative and the result has been formulated in a rather idealized form, and the author does not claim that the current model should be completely replaced by the present one. The real picture would be something midway between the two extremes. Anyway the aim of the present note is to suggest the possibility of a new viewpoint in the theory of barium titanate and to emphasize the importance of statistical approach to the ferroelectrics of $BaTiO_3$ type. A quantitative analysis of the model along this line remains still to be done.

The work was supported by the Grant for Scientific Researches from Education Ministry.

References

1) W. P. Mason and B. T. Matthias: Phys. Rev. **74** (1948) 1622.
2) A. F. Devonshire: Phil. Mag. (7) **40** (1944) 1040.
3) J. C. Slater: Phys. Rev. **78** (1950) 748.
4) W. Kinase and H. Takahasi: J. Phys. Soc. Japan **10** (1955) 942.

JOURNAL OF THE PHYSICAL SOCIETY OF JAPAN, Vol. 16, No. 9, SEPTEMBER, 1961

Internal Magnetic Field in Rare Earth Metals

By Jun KONDO

The Institute for Solid State Physics, University of Tokyo, Tokyo

(Received May 4, 1961)

The effective magnetic field at nuclei in rare earth metals has been calculated. The contribution from the orbital angular momentum of 4f-electrons was found to amount to several thousand kilo-oersteds.

We have calculated the effective magnetic field at nuclei in rare earth metals. This arises from four sources.

1. It comes from the magnetic moments of all rare each ions except the one whose nucleus we are considering. The intensity of this field amounts to 10∼20 koe.

2. The s-f interaction may polarize the spins of conduction electrons and this may result in an effective field at nuclei through the hyperfine interaction between conduction electrons and nuclei. Inferring from the magnitude of this interaction in 3d metals, this field may be several hundred kilo-oersteds.

3. The spins of inner shell electrons may be polarized by the spin moments of 4f electrons to some extent. This may also results in an effective field at nuclei. We can get a rough idea about the magnitude of this field from the observed values of hyperfine interactions in ESR experiments of the Gd^{+++} and Eu^{++} ions which have no orbital angular momenta. These are around 300 koe.

4. The orbital angular momenta of 4f electrons of the ion whose nucleus we are considering produce a large amount of magnetic field at the nucleus which amounts to several thousand kilo-oersteds. Thus in the following we shall confine ourselves to this source of magnetic field and calculate its magnitude, neglecting the first three sources. We shall note that the spin angular momenta also produce a magnetic field and we shall take account of this contribution in the following calculation. But we shall find that the magnitude of the field from spin angular momenta is about one tenth of that from orbital angular momenta.

The Hamiltonian for the nuclear hyperfine interaction has been given by A. Abragam and M. H. L. Pryce[1] as follows:

$$H=2g_n\mu_N\mu_B\sum_i\{(\boldsymbol{l}_i-\boldsymbol{s}_i)\cdot\boldsymbol{I}/r_i^3+3(\boldsymbol{r}_i\cdot\boldsymbol{s}_i)(\boldsymbol{r}_i\cdot\boldsymbol{I})/r_i^5\}+\{e^2Q/2I(2I-1)\}\sum_i\{I(I+1)/r_i^3-3(\boldsymbol{r}_i\cdot\boldsymbol{I})^2/r_i^5\}\,, \tag{1}$$

where μ_N and μ_B are the nuclear and Bohr magnetons, respectively, and g_nI is the magnetic moment (in units of nuclear magneton) of the nucleus. Q is the electric quadrupole moment of the nucleus. Except samarium and europium, we may consider only the lowest multiplet of the ion, which will be specified by L, S and J. Then the above Hamiltonian can be represented by

$$H=2g_n\mu_N\mu_B\zeta\langle r^{-3}\rangle(\boldsymbol{J}\cdot\boldsymbol{I})+\{3e^2Q/4I(2I-1)\}\beta\langle r^{-3}\rangle\sum_{i=1}^5 J_iI_i\,, \tag{2}$$

where

$$\zeta=2-g_J+\xi[L(L+1)(g_J-1)-3(2-g_J)\{J(J+1)-L(L+1)-S(S+1)\}/2]\,, \tag{3}$$

$$g_J=1+\{S(S+1)-L(L+1)+J(J+1)\}/J(J+1)\,, \tag{4}$$

$$\xi=(2l+1-4S)/S(2l-1)(2l+3)(2L-1)\qquad(l=3)\,, \tag{5}$$

$$\beta=\pm2S\xi\gamma\,, \tag{6}$$

$$\begin{aligned}\gamma=(2-g_J)^2&-(J+L+S+2)(J-L+S+1)(J+L-S+1)(-J+L+S)/4(J+1)^2(2J+1)(2J+3)\\&-(J+L+S+1)(J-L+S)(J+L-S)(-J+L+S+1)/4J^2(2J-1)(2J+1)\,.\end{aligned} \tag{7}$$

The sign of β depends on whether the shell is less than or more than half-filled. J_i are defined as follows;

$$J_1=\{3J_z^2-J(J+1)\}/\sqrt{3}\ .\qquad J_2=J_x^2-J_y^2\ ,\qquad J_3=J_yJ_z+J_zJ_y\ ,$$
$$J_4=J_zJ_x+J_xJ_z\ ,\qquad J_5=J_xJ_y+J_yJ_x\ , \tag{8}$$

I_i being defined by similar equations.

Equation (2) can be written as

$$H=A(\boldsymbol{J}\cdot\boldsymbol{I})+B\sum_{i=1}^{5}J_iI_i\ . \tag{9}$$

Table I.

	$g_nI\langle r^{-3}\rangle$ (n.m. Å^{-3})	$Q\langle r^{-3}\rangle$ (barn Å^{-3})	A (10^{-4}cm^{-1})	B (10^{-4}cm^{-1})	AJ/h (Mc/sec)	H_{eff} (koe)
Pr^{141}	$+145^a$		$+360$		4300	3600
Nd^{143}	$-\ 40^b$	$<\ 44^b$	$-\ 67$	<0.1	95	4200
Nd^{145}	$-\ 24.8^b$	$<\ 44^b$	$-\ 44$	<0.1	590	4200
Tb^{159}	103^c		180		3200	4200
Dy^{161}	27.4^d	83.7^d	26	0.22	590	7300
Dy^{163}	39.2^d	100^d	38	0.26	850	7300
Ho^{165}	263^e	56^e	270	0.05	6500	9000
Er^{167}	40^b	800^b	42	0.81	950	9000
Tm^{169}	$-\ 18.4^f$		-134		2400	7900
Yb^{171}	$+\ 42.0^g$		$+300$		3200	4200
Yb^{173}	$-\ 58.8^g$		$-\ 85$		890	4200

a: from ref. (2), *b*: from ref. (3), *c*: from ref. (4), *d*: from ref. (5), *e*: from ref. (6), *f*: from ref. (8) and (9), *g*: from ref. (7).

In order to obtain the magnitudes of A and B, we must know the values of $g_nI\langle r^{-3}\rangle$ and $Q\langle r^{-3}\rangle$. We may assume that the 4f wave functions in rare earth metals is not very different from those in paramagnetic salts, so that we may put the values of $g_nI\langle r^{-3}\rangle$ and $Q\langle r^{-3}\rangle$ found in ESR experiments of rare earth ions in these salts into the expressions of A and B. The values of $g_nI\langle r^{-3}\rangle$ and $Q\langle r^{-3}\rangle$ (in units of nuclear magneton × Å^{-3} and barn × Å^{-3}, respectively) from ESR experiments[2)-7)] are listed in the second and third columns of the Table I. In the case of thulium, there is no resonance data, but g_nI and $\langle r^{-3}\rangle$ have separately been obtained from optical data[8),9)]. Then, A and B are given in units of 10^{-4}cm^{-1} in the fourth and fifth columns of the table. The resonance frequency of NMR experiments at low temperatures is given by $\langle J_z\rangle A/h$, when B vanishes. The values of JA/h are listed in the sixth column of the table in units of Mc/sec. Using the published data for nuclear magnetic moments[8),10)] and assuming $\langle J_z\rangle=J$, we can obtain the magnitude of the internal magnetic field at the nucleus, which is listed in the last column of the table in units of koe. The direction of the field is parallel to that of the magnetic moment of the ion, because $\langle \boldsymbol{L}\rangle$ is parallel to $\langle \boldsymbol{J}\rangle$ and so the magnetic moment associated with $\boldsymbol{L}$ is parallel to the total magnetic moment of the ion.

The author thanks to Professor K. Yosida and Mr. H. Miwa for many suggestions and discussions.

References

1) A. Abragam and M. H. L. Pryce: Proc. Roy. Soc. **205** (1951) 135.
2) J. M. Baker and B. Bleaney: Proc. Phys. Soc. A, **68** (1955) 936.
3) R. J. Elliott and K. W. H. Stevens: Proc. Roy. Soc. **219** (1953) 387.
4) J. M. Baker and B. Bleaney: Proc. Roy. Soc. **245** (1958) 156.
5) J. G. Park: Proc. Roy. Soc. **245** (1958) 118.
6) J. M. Baker and B. Bleaney: Proc. Phys. Soc. A, **68** (1955) 1090.
7) A. H. Cooke and J. G. Park: Proc. Phys. Soc. A, **69** (1956) 282.
8) B. Bleaney: Proc. Phys. Soc. A, **68** (1955) 937.
9) K. H. Lindenberger: Z. Phys. **141** (1955) 476.
10) K. F. Smith: Prog. Nucl. Phys. **6** (1957) 52.

JOURNAL OF THE PHYSICAL SOCIETY OF JAPAN, Vol. 16, No. 9, SEPTEMBER, 1961

Quenched-in Vacancy in Solid Solution Alloys

By Yoshikazu HAMAGUCHI

Japan Atomic Energy Research Institute
Tokai-mura, Ibaraki-ken, Japan

(Received May 11, 1961)

From the difference in the electrical resistivity change induced by quenching between pure Au and Au-Pd solid solutions, the binding energy for a vacancy and a solute atom was determined. The rate of decrease of quenched-in additional resistivity with decreasing temperature in the alloy was more rapid than in the pure metal and the resistivity after quenching was smaller than that before quenching in high concentration alloys below a certain quenching temperature. It was concluded that the interaction of a Pd atom and a vacancy in Au-Pd alloys was attractive, which formed a contrast with the expectation of Lazarus theory, and an additional resistivity by the solute atom was conceled partly by the binding of the vacancy. In Ag-Pd alloys the same results would be expected.

§ 1. Introduction

Excess charge introduced by solute atoms interacts with free electrons in the solvent metal. This resultant effect is expressed by the screening potential around the solute atom.

According to the theory of Mott[1], the interaction energy between an impurity and a neighbouring monovalent ion at a distance r_0 is

$$\Delta E_e(r_0)=\frac{Ze^2}{r_0}\exp[-qr_0] \qquad (1)$$

Z being the valence difference and q the screening constant.

This interaction energy might be an important cause for the electrical resistivity due to a solute atom, the formation energy of imperfections and the activation energy or impurity diffusion.

Using the simplified model which has been adopted by Lazarus[2], in which the change in formation energy of a vacancy adjacent to the impurity is assumed to be given by $-\Delta E_e$, and the change in energy of motion is given by the change in the microscopic (110) shear modulus resulting from the perturbation ΔE_e, it is concluded that the activation energy Q for diffusion of the impurity is changed relative to the values for self-diffusion of the solvent in the same face-centered cubic lattice in the way

$$Q\,(\text{impurity})-Q\,(\text{solvent})=$$
$$-\Delta E_e(r_0)\left\{1-\frac{1}{4}(q^2r_0^2-5qr_0-5)\right\} \qquad (2)$$

Even by a more improved theory, no change in introduced in the essential relation between Q(impurity) − Q(solvent) and valence difference.

These theories are in fairly good agreement with the experiment for impurity diffusion in silver, but in poor agreement with those for that in copper, especially for negative valence impurity diffusions. One of the causes for this discrepancy is in the use of an oversimplified model to calculate the changes in formation energy and jump probability for a vacancy. Now it is desired to obtain the formation energy of a vacancy adjacent to the impurity by the other method and to compare it with the theoretical value.

For pure metals, such as Au[3),4)] Ag[5),6)] and Cu, the formation energies of a vacancy have been obtained by the measurements of the quenched-in resistivity increase, thermal expansion at high temperatures and so on. These results are consistent with the self-diffusion data. Applying these techniques to the alloys of noble metals and comparing the results with those for pure noble metals, it is expected that the formation energy of a vacancy influenced by the alloying element is obtained. First of all, the quenching method has been tried for its simplicity.

As the testing materials, silver alloys containing a element of positive excess valence for the solute should be best for comparing the results with the diffusion data, but to our regret, in these alloys the decrease in the electrical resistivity by the evaporation of solute atoms during the heating was much larger than the increase by the formation of excess vacancies, so that the accuracy of the measurements was very poor. For this reason Au-Pd alloys were selected as a specimens, regardless of the lack of impurity diffusion study for these combinations. Both alloys form the continuous series of solid solution, and there are no phases such as a long range ordered phase. Pd atom has the valence difference of -1 to both solvents.

§ 2. Experimental Procedure

The raw materials for the specimens were 99.95 % pure Au, 99.95 % pure Ag and 99.5% pure Pd. The concentration of Pd in both alloys were 1, 2, 3 and 4 weight per cent, and the form of the specimens were wires of 0.25 and 0.4 mm diameters, which were obtained from Tanaka Kikinzoku K. K. The concentrations of Pd were checked by the X-ray measurement of lattice parameters of those wires.

Two kinds of heating method were used, one of which was a current-heating method and the other was a furnace-heating method. The former was used for pure Au, Au 1 % and 2 % Pd alloys of two kinds, of wire, and the latter for Au-3 %, 4 % Pd alloys, pure Ag and Ag-Pd alloys of 0.4 mm diameter wire.

The instrument for the current-heating method was almost like that used by Bauerle and Koehler for pure Au[3)], but some improvements were made in heating and quenching in the atmospheres of A or He. The gauge length was about central 5 cm of about 18 cm length and the temperature was determined by measuring its resistance. The quenching rate was measured with an oscilloscope to be about 2.5×10^4 degrees per second for the 0.4 mm diameter pure Au specimen, and was the same as the rate of Bauerle and Koehler.

The furnace-heating method was very simple: a specimen, annealed in vacuum at about 850°C and slowly cooled, was suspeneded in the furnace, and then, after heating about 2~10 minutes at a certain temperature, was dropped into room temperature water. The cooling rate in this technique would be several times slower than that in the former technique. In addition, the specimen migh be streched during the setting on the instrument. Thus the results by this method would have less accuracy than that by the former. In the experiment of silver alloys, a virgin specimen was used in each quenching to avoid the accumulated contamination due to oxidation and others, but in gold alloys the same specimen was used through a series of quenchings.

§ 3. Results

Experimental results for Au and Au alloys are shown in Figs. 1 and 2, in which the specific resistivity increase and its logarithm are plotted respectively *versus* reciprocal of the quenching temperature.

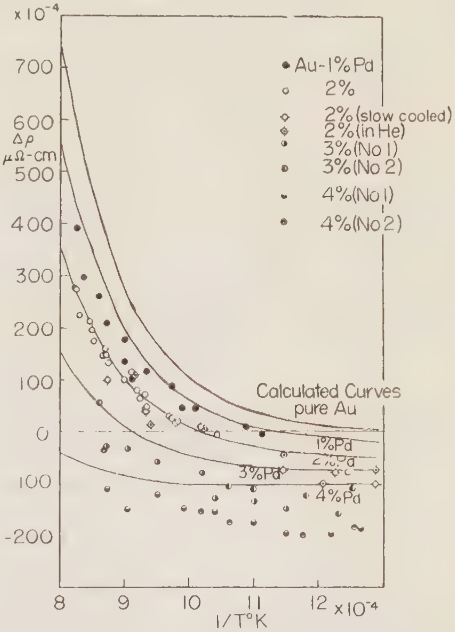

Fig. 1. The specific resistivity increase *versus* reciprocal of the quenching temperature in Au and Au-Pd alloys, and the calculated curves by Eq. (4).

In pure Au it was found that the resistivity increase on quenching could be described by the equation

$$\varDelta\rho = NA\exp(-E/kt) \qquad (3)$$

were $\varDelta\rho$ is the specific resistivity increase, NA is a constant, E is the energy required to form a defect, k is the Boltzmann constant and T is the quenching temperature. The results for the three different specimens fell almost on the same line in the semilogarithmic plot, and the formation energy is obtained as about 0.90 ev, which is a little smaller than that by Bauerle and Koehler[3)] and a little larger than that by Lazarev and Ovcharenko.[4] The value of NA is also obtained as about 1×10^{-4} Ω-cm. In the case of the alloy specimens, as would be expected, the experimental data deviated from the straight line in the semilogarithmic plot, and the deviation increased with increasing Pd content. In addition, it was very surprising that when the Pd content increased more than 1 %, the decrease in the resistivity due to quenching appeared below a certain temperature, the temperature becoming higher with increasing Pd content, as shown in Fig. 1. In 3 and 4 % alloys there were minima at about 500°C.

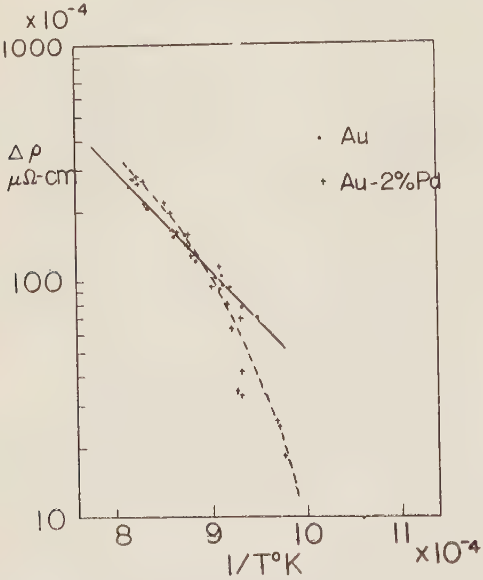

Fig. 2. A semilogarithmic plot of the specific resistivity increase *versus* reciprocal of the quenching temperature in Au and Au-2% Pd alloy.

Attempts were made to check some systematic errors, which might be important, on 2 % alloy. First of all, to rule out the possibility that for the insufficient preannealing the residual stress was annealed out during the quench-heating, specimen were annealed prior to the measurement about 4 hrs. at 850°C in vacuum, furnace cooled to room temperature, and then set carefully to the measuring instrument. In this case the decreases in resistivity were about the same amount (Fig. 1). By this check a possibility of formation of a short range ordered arrangement of solute atoms during the quench-heating may also be rule out. Another possible source of the resistivity decrease on quenching would be a evaporation of solute atoms during the quench-heating. This effect would not be very large as the melting temperature of Pd was high enough, but the results were calibrated by the measurements of the resistance of the slowly cooled state at the initial, middle and final points of one experimental series. Finally it was examined whether a change in the quenching atmosphere had an influence on the amount of resistivity quenched in. The quenching in He gas gave about the same resistivity as that quenched in A gas, so that the influence would be not so large (this is also shown in Fig. 1).

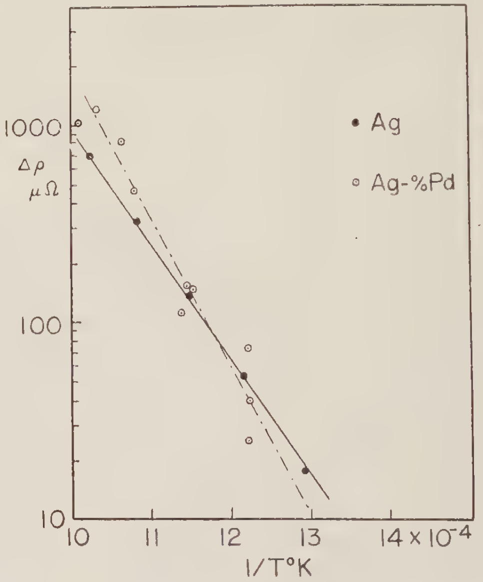

Fig. 3. A semilogarithmic plot of the resistivity increase *versus* reciprocal of the quenching temperature in Ag and Ag-Pd alloy. (the size of specimens are about 0.4 mm$\phi\times$200 mm)

The results for Ag and Ag-2 % Pd alloy are shown in Fig. 3, and the activation energy for Ag is about 1.1 ev, which is almost identical to the results of Doyama and Koehler.[5] The data on the alloy were not so well reproducible mainly due to the contamination. In spite of this the change of quenched-in resistivity with the content of the solute element would be of the same type with that in Au alloys. The change was obtained qualitatively by preliminary experiments of quenching in air.

§ 4. Discussion

As seen in the the experimental results, the formation energy of a vacancy in the pure metal could be obtained directly from the gradient of the straight line in Fig. 2, but in the alloys some further considerations were needed for the analysis of the results, for the data deviated from the straight line. The characteristic nature in the alloys was that the quenched-in resistivity decreased with increasing alloy content and became negative below a certain temperature.

In the pure metal all lattice sites are equivalent and it is sufficient to describe the quenching resistivity with only one activation energy. In the alloys, however, there are two kinds of lattice site, that is, one which is adjacent to the solute atom and is affected by an electrostatic potential of the solute atom, and the other which is not affected by the solute atom and in which the formation energy of a vacancy seems to be equal to that in the pure solvent metal.

The quenched-in resistivity increase may be expressed by the following equation,

$$\Delta\rho_{\text{alloy}} = NA[(1-12x)\exp\{-E/kT\} + (B/A)\cdot 12x\exp\{-(E+\Delta E)/kT\}] \quad (4)$$

where the difference of the formation energy of a vacancy in the free site from that in the adjacent site is described as ΔE, N is the total number of lattice sites in the unit volume, x is the atomic content of solute atoms and A and B are, respectively, the resistivity increase due to one vacancy in the free and the adjacent lattics sites.

In Eq. (4) some assumptions are made: first the region in which the formation energy of a vacancy is influenced by the solute atoms is restricted to the nearest neighbour site, second the solute atoms are dispersed perfectly at random, because the probability of a Pd atom pair may be negligible until the 4 % alloy, and third the quenched-in vacancy is retained in the specimen perfecly during the quenching, or the rate of escape of the vacancies is equal in both sites.

There are some questions in the first assumption. The calculation of screening potential of an solute atom in a dilute solution shows[7] that it is concentrated around the solute atom, so the influence on the next-nearest neighbour lattice site can be neglected, which may justify our assumption. But when the concentration of solute atoms becomes large the mutual interference between solute atoms may not be neglected, and the form of the screening potential should be deformed. When the deformation occurs, we cannot assert that the effect of the solute atom on the next-nearest neighbour site is negligibly small. However, for the simplification of our qualitative discussion the first assumption is adopted.

The values of B/A and ΔE are determined, independent to the values of A and E, in such a way that the calculated values of the temperatures at which $\Delta\rho_{\text{alloy}}$ is equal to zero have a best agreement with the measured values of those for four kinds of alloy. The values B/A and ΔE are -6.5×10^{-5} and -0.85 ev, respectively. Then, using those values the values NA and E in Eq. (4) are determined as 2.3×10^{-4} Ω-cm and 0.87 ev The calculated and the measured values of $\Delta\rho_{\text{alloy}}$ make a qualitatively good fit in the alloy, the calculated curves being shown in Fig. 1 as the full line. The calculated curve can also explain the fact that $\Delta\rho_{\text{alloy}}$ have a minimum in the 4 % alloy at about 500°C.

Because of the less accuracy, especially in high concentration alloys, the reliability about the numerical results are poor. But it should seem to be sure that ΔE had the large negative value and B had the small negative value.

The fact that ΔE has the negative value forms a striking contrast with that expected from the diffusion data. Moreover, the other important result is that the coefficient B has the negative value. This means that the increasing of resistivity with the solute atoms which have a negative valence in the monovalent metal can be canceled by the binding of the vacancy or other imperfections to the solute atom. In the case when the solute atoms have a positive valence difference, i. e. Zn, Ga and Ge in Cu, such cancel out effect due to the binding with a vacancy may be theoretically expected. But when the solute is a transition element, the effect can not be easily understood for the existence of defect 3d electrons. We have known from the calculations by Seeger and Bross[8] and Sugiyama [9] that the formation energy and the contribution to the electrical resistivity for the pair vacancy are smaller than two times of them for the single vacancy. So it may be possible to explain our results by the model that one vacancy in the pair is replaced by the negatively charged solute atom and in this pair the wave functions of electrons may deform to exhibit a scattering to the conduction electrons.

Similer experimental result showing the attractive interaction between a solute atom and a vacancy have been reported in a Al–Cu alloy be Kimura et al,[11] and the decreasing of the resistivity after quenching have also obtained in Cu–Al alloy.[12]

In our results the value of ΔE is unexpectedly large, so it is desired to obtain the density of vacancies by other methods, such as the thermal expansion method, and compare it with the results by the quenched-in resistivity method. Because there are two parameters to be determined, B and ΔE, in the latter.

About the silver alloys the exact experimental results on high concentration alloys could not be obtained, however, from the preliminary tests on 4 and 6% alloys it may be expected that the formation energy and the contribution of vacancies adjacent to solute atoms in the electrical resistivity are similar to those in Au–Pd alloys.

In order to make certainty of our conclusions that the origin of the quenched in resistivity change is the quenched-in vacancies of both kinds, one of which are in the free lattice sites and the other of which are in the adjacent lattice sites to the impurity ions, it is desired to make recovery experiments on these alloys. The recovery experiments on Au–2% Pd alloy at about 90°C has been insufficient to a quantitative discussion, but two qualitative results was obtaind. First, the rate of the recovery of the resistivity in the alloy was slower than in pure Au for the quenching from about 850°C. Second, the negative quenched-in resistivity that appeared in quenching from 650°C had to tendency to recover to the initial zero value.

There will be many causes to hinder the recovery of vacancies, i. e. increasing of the migration energy of the vacancy, decreasing of the number of sink sites, et al. The fact that the value of NA from the pure Au is smaller than that from the alloys can be explained by the assumption that more free vacancies are retained in alloys mainly because the escape of vacancies is obstructed by solute atoms. This fact also explains the first result. But the other explanation can be also possible, that is, decreasing of the resistivity by the disappearence of free vacancies is partly canceled with increasing of it by the disappearance of the trapped vacancies. To decide on a definite conclusion it is desired to determine the migration energies of free and trapped vacancies, but there will be may difficulties to determine those because many complex factors should be analysed. The second result will mean that the origin of negative resistivity may no be something like precipitation but may be imperfections, especially vacancies, and this will support our conclusions.

§5. Conclusions

It was found that the difference of the quenched-in resistivity increase between Au and Au-Pd alloys was remarkable, and it had a certain relation with the concentration of solute atom. The resistivity increase in alloys could be described qualitatively with two activation energies. The difference between two energies, ΔE, would mean the change in formation energy of a vacancy at the lattice site adjacent to the solute atom. The obtained value of ΔE in Au-Pd alloys was negative and unexpectedly large. Moreover, the increase of resistivity with the solute atoms must have canceled by the binding with a vacancy.

Unfortunately the measurement is much more difficult for alloys than for pure metals. For quantitative discussions it would be necessary to obtain more careful and accurate results. And it has been very much desired to obtain the value ΔE by other method for the comparison with the results by the resistivity method.

The author wish to express his hearty thanks to Dr. Y. Takagi for his interest and encouragement in this work, and Drs. N. Kunitomi and H. Suzuki for their encouragement and valuable discussions. His thanks is also to Miss S. Kimura for her continued assistance in this work.

References

1) N. F. Mott: Proc. Cambridge Phil. Soc. **32** (1936) 281.

2) D. Lazarus: Solid State Physics, **10** (1960) 71.
3) J. E. Bauerle and S. Koehler: Phys. Rev. **107** (1957) 1493.
4) B. J. Lazarev and O. N. Ovcharenko: Soviet Physics JETP **36** (1959) 42.
5) M. Doyama and J. S. Koehler: Phys. Rev. **119** (1960) 939.
6) R. O. Simmons and R. W. Balluffi: Phys. Rev. **119** (1960) 600.
7) H. Fujiwara: J. Phys. Soc. Japan **13** (1958) 250.
8) A. Seeger and H. Bross: J. Phys. Chem. Solids **6** (1958) 324; Z. Physik **145** (1959) 161.
9) A. Sugiyama: J. Phys. Soc. Japan **15** (1960) 965.
10) J. Friedel: Canad. J. Phys. **34** (1956) 1190.
11) H. Kimura, A. Kimura and R. R. Hashiguti: (private communication).
12) M. S. Wechsler and R. H. Kernoban: Acta Metall. **7** (1959) 599.

JOURNAL OF THE PHYSICAL SOCIETY OF JAPAN, Vol. 16, No. 9, SEPTEMBER, 1961

Some Experimental Studies on the Parasitic Ferromagnetism of $\alpha\mathrm{Fe_2O_3}$

By Akira TASAKI and Shūichi IIDA

Department of Physics, Faculty of Science, University of Tokyo

(Received June 3, 1961)

The temperature dependence of magnetization of polycrystalline hematite ($\alpha\mathrm{Fe_2O_3}$) which contains several per cent of foreign atoms (Al, Mn, Ga and Cr) was measured at various field strengths. The results were analyzed into so-called parasitic magnetic moment σ_0 and susceptibility term χ_g. It has been found that the parasitic nature of σ_0 is not influenced severely by the addition of foreign atoms but the transition temperature is lowered in general and the step transition in σ_0 *vs* temperature curve becomes gradual.

The residual magnetization was measured with an astatic magnetometer. It was found that the memory effect (in the ratio of the residual magnetization between before and after cooling treatment) is little affected by the addition of foreign atoms or by change in oxidation. The residual magnetization decreased by about 50% at the first cooling-heating cycle, but is maintained completely in following cycles.

§1. Introduction

Hematite ($\alpha\mathrm{Fe_2O_3}$) is an antiferromagnet, it is accompanied by a weak ferromagnetism, which is called "parasitic ferromagnetism", above the transition temperature (−15°C). It is known from studies by neutron diffraction[1] that the spins lie in the basal plane (111) above the transition temperature and below it the spin direction is parallel to the [111] direction. In order to explain the parasitic ferromagnetism, many studies have been made and several mechanisms have been proposed. These proposed mechanisms can be classified into two: the "homogeneous" theory and the "inhomogeneous" theory. According to the inhomogeneous theory, this parasitic ferromagnetism is thought to have its origin in the magnetic moment of some other phase ($r\mathrm{Fe_2O_2}$ etc.) or imperfectly compensated magnetic moments of the sublattices originating in irregularities of spin alignment around the impurity atoms or lattice imperfection[2,3]. On the other hand, the homogeneous theory ascribes this phenomenon to an intrinsic nature of the crystal structure. Dzyaloshinsky[4] has pointed out that the low symmetry of the atomic arrangement in this rhombohedral antiferromagnet should result in a spin canting when the spins lie in the basal plane and that this atomistic canting is the origin of the parasitic ferromagnetism. An semi-quantitative theory of this spin canting has been presented by Moriya[5]. According to this theory, there exists between spins of the magnetic ions the anisotropic interaction, in additions to the ordinary super-exchange interaction, that causes spin canting, as the crystal symmetry is so low and the orbital moment of the magnetic ions is not completely quenched. Although there are several unknown factors, the main feature of the parasitic ferromagnetism is explained by this homogeneous theory.

In a previous paper[6], we have reported our study of the influence of oxidation and reduction on this parasitic ferromagnetism; it was found that the origin of this weak ferromagnetism was not the same for the isotropic part and for the anisotropic part. The isotropic part (after Néel) remains below the transition temperature of −15°C, but the other part disappears completely at this point on cooling down. Since the isotropic part largely changed with the progress of oxidation or reduction and became almost zero by a proper heat treatment, we are led to believe that the origin of this part is due to the non-stoichiometry of αFe_2O_3. The anisotropic part, however, did not change by these treatments; therefore this part is certainly due to Dzyaloshinsky's mechanism, i.e., it should be explained by the homogeneous theory.

In the present work, we have studied the effect of the substitution of cations and the memory phenomenon. Regarding the substitution effect, Haigh[7] has already studied the influence of the addition of Ti and Al on the residual magnetization of αFe_2O_3.

§ 2. Experimental Procedures

Specimens

The weighed electrolytic iron* and another metal (Al, Mn, Ga or Cr) were dissolved separately in nitric acid. However, as Ga was not dissolved easily, a small amount of sulfuric acid was added in this case. The solutions were mixed with a desired proportion and the mixture was dried by infrared-ray lamp. Then the dried oxide was ground, densely packed into a platinum crucible, heated to 1000°C and kept for 3 hours in air. The specimens that contained manganese were kept at 800°C for 24 hours in air to eliminate the presence of Mn^{2+} ions. By these procedures, polycrystalline specimens containing 1, 2 and 4 at. % concentration of each added element were prepared.

Magnetic measurements

The magnetic measurements were made with a magnetic balance automatically controlled[8]. The magnetization of αFe_2O_3 is expressed by

$$\sigma=\sigma_0+\chi H\ , \qquad (1)$$

where σ_0 is the saturation magnetization of the so-called parasitic ferromagnetism and χ is the susceptibility. These two terms are functions of temperature. In order to separate these two terms at a given temperature, the magnetization was measured at three different field strengths, i.e. 4.80, 8.80 and 13.36 KOe. The temperature measurements were made with a copper-constantan thermocouple which was inserted into the powdered sample.

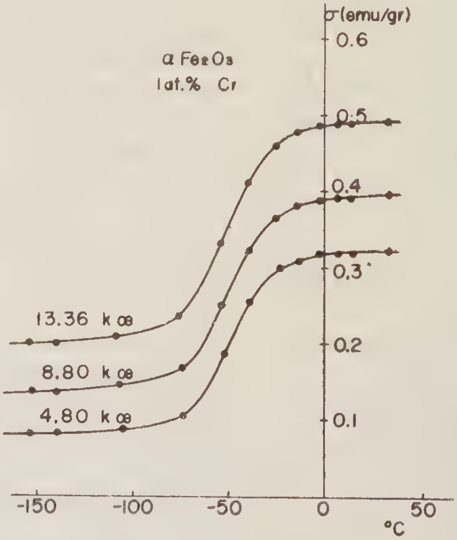

Fig. 1. Magnetization *vs* temperature curves of αFe_2O_3 added with 1% Cr, at three different field strengths.

Since the temperature was not maintained constant during the magnetization measurements at the three different field strengths, the separation of σ_0 and χ was made by using the curves that are shown in Fig. 1. Strictly speaking, the linear relation between field strength and magnetization does not hold exactly, especially above the transition temperature. In the present work, however, we have disregarded this effect.

---

* In the course of the present study we once prepared αFe_2O_3 from carbonyl iron of commercial grad and found that this αFe_2O_3 showed a high isotropic term (~0.4 emu/g). In natural crystals, we also found frequently the same character. But when we prepared αFe_2O_3 from spectroscopically pure iron (Johnson-Mathey Co.) or from electrolytic iron, there was no such term.

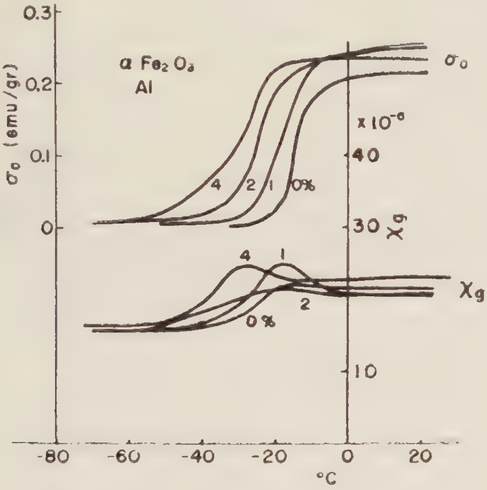

(a)

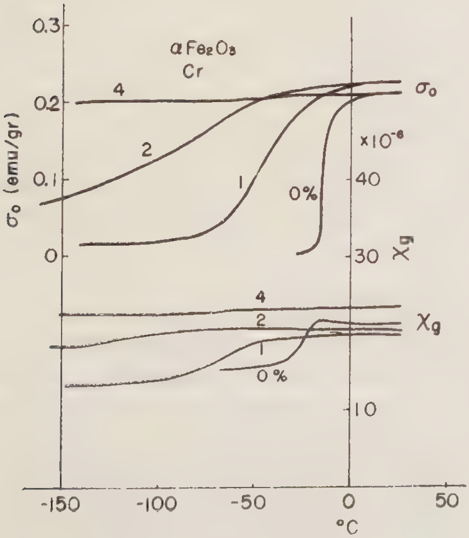

(b)

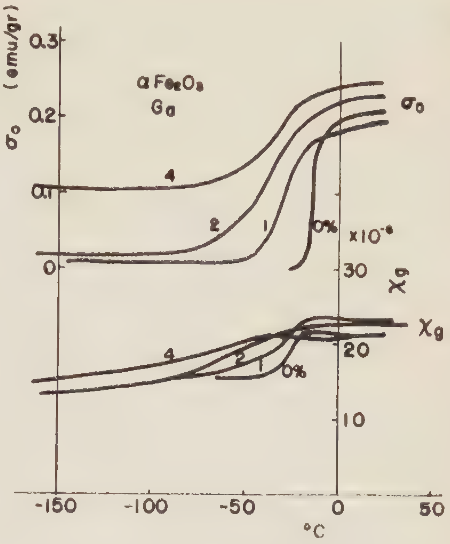

(c)

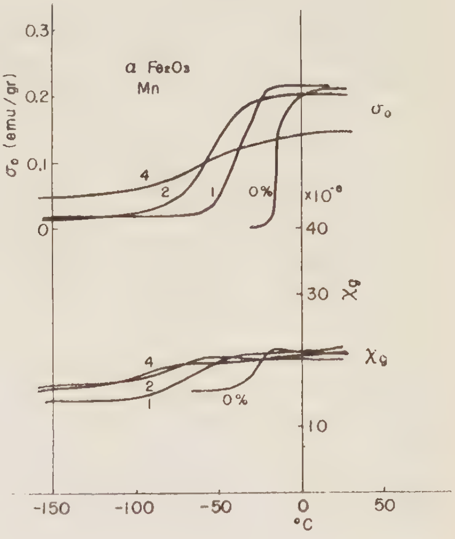

(d)

Fig. 2. Parasitic ferromagnetism σ_0 and susceptibility χ_g *vs* temperature curves of αFe_2O_3 that contain foreign atoms of 1, 2 and 4% with respect to iron atoms.

An astatic magnetometer, which was used to measure the residual magnetization, consists of two 5 mm length magnets suspended 15 cm apart in opposit directions and a fine phosphor-bronze wire suspending the two magnet system. The terrestrial magnetic field at the magnetometer was compensated by a pair of Helmholtz coils. Our experimental procedure was as follows: at first, a specimen was magnetized in a strong field (~30 KOe) at room temperature, and the residual magnetization of the specimen was measured. Then the specimen was cooled down through the transition temperature, and after the temperature recovered to room temperature, the magnetization was measured again.

§ 3. Experimental Results

Fig. 2 shows the experimental results. We notice that the transition temperature decreases in all cases, especially in the case of Cr.

Above the transition temperature, the values of σ_0 are almost the same, except for the case of 4% Mn, and below it they become almost zero. This means that the isotropic part of σ_0 is zero in almost all cases, except when Mn or Ga is added to 4%, in which case this isotropic part appears slightly. The susceptibility χ_g shows corresponding variation to that of σ_0, and in each case the transition temperature of χ_g is nearly equal to that of σ_0. In the case of Al, each χ_g *vs* T curve shows a maximum at the transition temperature.

The Néel temperature was measured with the same magnetic balance that was used for magnetization measurements. Fig. 3 shows the Néel temperature as a function of the concentration of foreign atoms. In all cases, the Néel temperature decreases by the addition of foreign atoms and, except in the case of Cr, decrement of the Néel temperature appears to be saturated by 1 or 2 at. % addition.

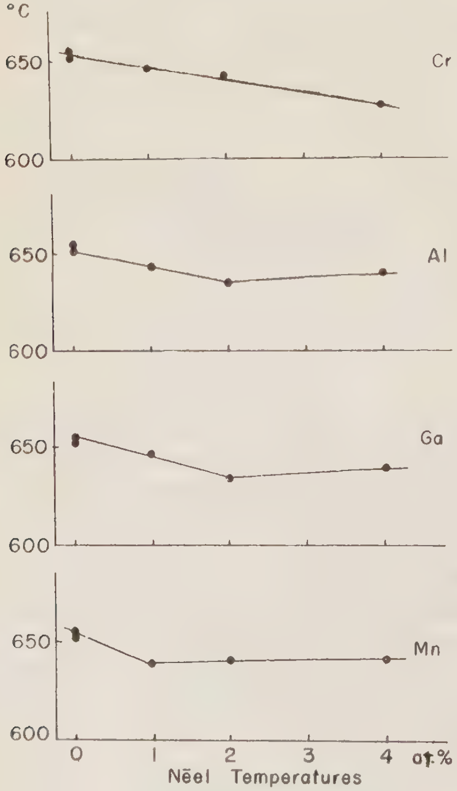

Fig. 3. Variation of Néel temperature of αFe_2O_3 when foreign atoms are added with several per cent with respect to iron atoms.

In Fig. 4, the ratio of the residual magnetization before and after the cooling treatment is shown. According to this result, memory of the residual magnetization does not depend on the addition of foreign atoms nor on oxidation. Fig. 5 shows the effect of repetition of cooling treatments. It is a very interesting fact that, except for the first cooling-heating cycle, the ratio of the residual magnetization of the nth cycle to the $(n+1)$th cycle is nearly 100 %.

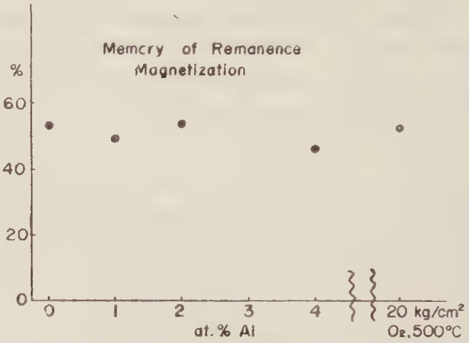

Fig. 4. Residual magnetization of αFe_2O_3 at room temperature after a cooling-heating cycle *vs* concentration of foreign atoms and oxidation.

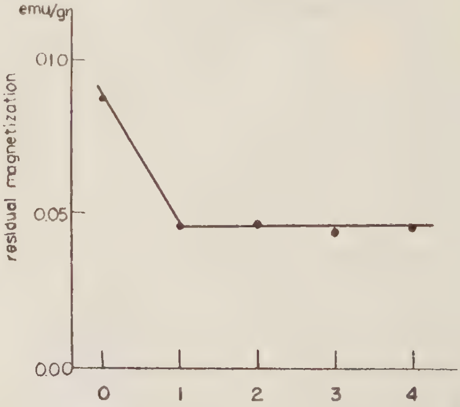

Fig. 5. Residual magnetization of polycrystalline αFe_2O_3 at room temperature after cooling-heating cycles.

§ 4. Discussion of the Results

By the present study it has become clear that, when a small amount of foreign atoms is added, the absolute value of σ_0 does not change appreciably, while the transition temperature of σ_0 decreases considerably. The former fact can be understood easily as a confirmation that the anisotropic parasitic ferromagnetism is not caused by impurity atoms.

However, it is not easy to understand the latter fact, if we assume that this change of easy axis from within the basal plane to along the c-axis is due to the difference in temperature variation of the two distinguished mechanisms for the anisotropy energy of this crystal. The competition between the one-ion type anisotropy energy of Fe^{3+} due to the crystalline field, and the magnetostatic dipole-dipole interaction between Fe^{3+} ions will lead to an increase of the transition temperature when a small amount of Fe^{3+} ions are substituted by foreign non-magnetic ions. It is a simple conclusion that the one-ion type anisotropy energy decreases linearly with the concentration of Fe^{3+} ions, whereas the dipole-dipole interaction energy decreases quadratically. If we denote the corresponding energy differences between the two spin orientations as $E_{\text{cryst}}(T, x)$ and $E_{\text{dip}}(T, x)$, then

$$|E_{\text{cryst}}(T, 0)|<|E_{\text{dip}}(T, 0)| \quad \text{when} \quad T>T_t \, , \qquad (2)$$

$$|E_{\text{cryst}}(T, 0)|=|E_{\text{dip}}(T, 0)| \quad \text{at} \quad T=T_t \, , \qquad (3)$$

and

$$|E_{\text{cryst}}(T, 0)|>|E_{\text{dip}}(T, 0)| \quad \text{when} \quad T<T_t \, . \qquad (4)$$

On the other hand, when $x \langle\langle 1$.

$$E_{\text{cryst}}(T, x)=E_{\text{cryst}}(T, 0)\ (1-x) \, , \qquad (5)$$

$$E_{\text{dip}}(T, x)=E_{\text{dip}}(T, 0)\ (1-x)^2$$
$$=E_{\text{dip}}(T,0)\ (1-2x+x^2) \, , \qquad (6)$$

so that for $T=T_t$, $x \ll 1$,

$$|E_{\text{cryst}}(T_t, x)|>|E_{\text{dip}}(T_t x,)| \, . \qquad (7)$$

In the case of Al, as shown in Fig. 2, each χ_a *vs* T curves shows a maximum at the transition temperature. Although there is some possibility that errors in the temperature measurement introduced a considerable effect on the analyzed curve in the transition temperature region, this maximum seems to be a little more pronounced than being due to such possible experimental errors. It is suggested that in this system presence of the field induced rotation of the spin axis of antiferromagnet might be the possible origin of this maximum. It is also possible for all cases that, in a certain narrow range of temperature at the transition, the easy axis of spin lies in a certain direction which is between the c-axis and c-plane[9].

It might be very probable that, in the case of Cr, the magnetic interactions of Cr would introduce a large effect on the decrease of the transition temperature. But, as shown in Fig. 3, no peculiarities are found in the decreasing behavior of the Néel temperature for Cr. In the case of Mn, the presence of Jahn-Teller effect of Mn^{3+} ion might be expected. But we cannot find any peculiarities in Fig. 2. Further, the isotropic part which appears in the case of 4 % Ga is not understood.

It is noted that, in all the cases, the addition of foreign atoms not only decreases the transition temperature, but also makes the transition gradual. Although, in general, it is thought that the existence of impurities make a sharp phase transition gradual, this is not expected *a priori*. We have made a short statistical calculation for this impurity effect. In the calculation we have assumed a distribution of small regions each of which is affected by the presence of impurity atoms and have a lower transition temperature. It is also assumed that the size of each region is a constant and the variation in population of impurity atoms in each region is statistical. Then, for the case of Cr, the calculation gives a value of 200 atoms (5 atomic distance) by which the three experimental curves with different impurity content are represented adequately. However, in other cases, this calculation can not reach a self-consistent result.

The memory phenomenon is another interesting feature of αFe_2O_3. It has been known for polycrystalline specimens that the residual magnetization, which has temporarily disappeared by cooling, recovers to 50% of the initial value after heating. It has also been ascertained that the direction of the magnetization is unchanged. In the present work, we have found that the memory amount does not depend on the presence of impurity atoms nor on the change of oxidization and that, when the cooling-heating cycles are repeated, the memory amount is always almost 100%[10], except for the first one cycle. The first fact indicate that the memory does not depend on the amount of impurity atoms nor on lattice imperfections. In other words, the origin of this memory phenomenon seems to be purely intrinsic rather than due to inhomogeneities. As this concept is consistent with the second fact, we are led to think that there is a tight correlation between the phases of the states above and below the transition temperature and that, when the spin changes its direction, there must be a reversible route of the transition by which the phase of the spin states is conserved. In a previous paper¹¹⁾, Siratori and the present authors have already offered a possible mechanism of this tight correlation based on the presence of a trigonal symmetry anisotropy energy of the crystal and assuming tentatively the presence of another uniaxial type anisotropy energy.

Quite recently, an interesting character of this memory phenomenon has been discovered by Akimoto et al¹²⁾. When the specimen was cooled odd times, the amount of memorized residual magnetization was larger (more than by 10%) than when it was cooled even times, except after the first one cycle. This effect was found to become eminent when the specimen is magnetized in a weak magnetic field. Such a tendency has been also recognized in our measurement, but we have not studied it in detail nor have we any good explanation for this effect.

It is hoped that more precise and fundamental measurements are performed on single crystals. It should be added that our measurements of torque performed on well-selected natural single crystals (which have almost zero isotropic part) have given the presence of a uniaxial anisotropy of ~40 dyne-cm/gr., as a primary anisotropy in the (111) plane. Although we have tried to make a synthetic single crystal large enough for the torque measurements, we have yet been unsuccessful*. The effect of Fe^{4+} is now being studied by using an oxygen pressure of 1000 Kg/cm². The results will be published shortly.

Acknowledgement

The authors wish to express their hearty thanks to Prof. T. Nagata and Dr. S. Akimoto of the Geophysical Department who kindly permitted us to use their astatic magnetometer and to refer to their unpublished results.

References

1) C. G. Shull, W. A. Strauser and E. O. Wollan: Phys. Rev. **83** (1951) 333.
2) L. Néel: Rev. Mod. Phys. **25** (1953) 58.
3) Y. Y. Li: Phys. Rev. **101** (1956) 1451.
4) I. Dzyaloshinsky: J. Phys. Chem. Solids **4** (1958) 241.
5) T. Moriya: Phys. Rev. **117** (1960) 635.
6) A. Tasaki, K. Siratori and S. Iida: J. Phys. Soc. Japan **15** (1960) 1535.
7) G. Haigh: Phil. Mag. **2** (1957) 505.
8) F. A. Mauer: Rev. Sci. Inst. **25** (1954) 598.
9) L. R. Bickford, JR.: Phys. Rev. **119** (1960) 1000.
10) S. T. Lin: J. Appl. Phys. Suppl. **32** (1961) 394S.
11) K. Siratori, A. Tasaki and S. Iida: J. Phys. Soc. Japan **15** (1960) 2357.
12) Private communication (to be published in Nature).

---

* Note added in proof: We have just succeeded in getting a sufficiently large synthetic single crystals of αFe_2O_3. The result of the measurement will be given lately.

Journal of the Physical Society of Japan Vol. 16, No. 9, September, 1961

Determination of the Extension of Linear Polymer Molecule in the Solution by the Light Scattering

By Yasuhiro Miyake

Department of Physics, Faculty of Science,
Hokkaido University, Sapporo, Japan

(Received March 6, 1961)

With use of Peterlin and Mizutani's light scattering function $P(\theta)$, a simple method has been developed to determine the mean square end-to-end distance $\langle r^2\rangle$. Following Peterlin and Mizutani, $\langle r^2\rangle$ is assumed to be proportional to N^γ, where N is the degree of polymerization and γ is a parameter. Obtained values of $\langle r^2\rangle$ are $(5.53)^2\times10^{-16}N^{1.15}$, $(42.51)^2\times10^{-16}N^{0.70}$, and $(6.39)^2\times10^{-16}N^{1.11}$ for polystyrene in toluene, in methylethylketone and in cyclohexane solutions, respectively. These results suggest that the excluded volume of chain elements and the interaction between the polymer and the solvent are important factors to determine the extension of polymer molecules in both good and poor solvents. Brief discussions on the polydispersity of the system are also given.

§ 1. Introduction

Recently, several theories have been developed on the high polymer solution taking into account of the excluded volume effect of the chain element and the interaction between the elements and the solvents[1]. These theories give expressions for the molecular extension of high polymer, which are somewhat different from that derived on the basis of the random flight theory. In order to examine the significance of this difference, experiments have been carried out to obtain informations of the molecular extension.

The light scattering measurement seems to be one of the most powerful tools to investigate the molecular extension or the mean square end-to-end distance $\langle r^2\rangle$. Debye and Zimm[2] first gave an expression for the light scattering function, $P(\theta)$, on the basis of the random flight theory and determined $\langle r^2\rangle$ experimentally. Peterlin[3] and Mizutani[4] (abbreviated as P–M below) independently proposed the same expression for $P(\theta)$ considering the recent development of the theories on the high polymer solution. Although expressions which are more accurate than that of P–M have been given by several authors[5],[6], it is very laborious to determine $\langle r^2\rangle$ using them, as seen in the work of Hyde et al[6]. Therefore, P–M expression will be used throughout in the present work. In the next section it will be shown that P–M expression of $P(\theta)$ is especially suitable for the present approximate method of calculation. In sections 3 and 4 experimental procedures and results will be given. In section 5, the condition will be given, under which our method gives as good results as others. The polydispersity will also be discussed.

§ 2. Method of Determining the Parameters

By changing some of the notations, P–M expression for the mean square end-to-end distance $\langle r^2\rangle$ and the scattering function $P(\theta)$ of a linear molecule can be rewritten as

$$\langle r^2\rangle = C_2 N^\gamma , \tag{1}$$

$$P(\theta)=2/N\int_0^N (1-Z/N)\exp(-uC_2Z^\gamma)\,dZ\ . \tag{2}$$

Here N is the degree of polymerization, γ and C_2 parameters, and $u=(8\pi^2/3\lambda^2)\sin^2\theta/2$, λ being the wave length of the light in the solvent, θ the angle between the primary and scattered beams. The relation between the intensity of the scattered light $I(\theta)$ and $P(\theta)$ is first given by Zimm[2]:

$$I(\theta)/C=KMP(\theta)\{1-2A_2MP(\theta)C\}\ , \tag{3}$$

where M is the molecular weight of the solute, A_2 the second virial coefficient, C the concentration and K the proportionality constant. As seen in Eq. (1), we can estimat $\langle r^2\rangle$ from γ and C_2. In the following it will be discussed how to determine γ and C_2 by the experimental observation of $P(\theta)$.

Expanding Eq. (2) and then integrating it, we obtain the following result

$$\begin{aligned} P(\theta)=1 & \\ &-(2uC_2N^{\gamma}/1!)\{1/(\gamma+1)-1/(\gamma+2)\} \\ &+(2u^2C_2{}^2N^{2\gamma}/2!)\{1/(2\gamma+1)-1/(2\gamma+2)\} \\ &-(2u^3C_2{}^3N^{3\gamma}/3!)\{1/(3\gamma+1)-1/(3\gamma+2)\} \\ &+(2u^4C_2{}^4N^{4\gamma}/4!)\{1/(4\gamma+1)-1/(4\gamma+2)\}-\cdots . \end{aligned} \tag{4}$$

As an approximation, those terms with higher power than u^2 are neglected and Eq. (4) is rewritten as

$$\begin{aligned} P(\theta)=1-\{2BC_2N^{\gamma}/(\gamma+1)(\gamma+2)\}U \\ +\{B^2C_2{}^2N^{2\gamma}/(2\gamma+1)(2\gamma+2)\}U^2 , \end{aligned} \tag{5}$$

where $B=8\pi^2/3\lambda^2$, $U=\sin^2\theta/2$. In Eq. (5), the second and third terms show the initial slope and the curvature of $P(\theta)$ plotted against U, respectively. Using these two quantities the the parameters are determined in the following manner. The initial slope K_1 is given by

$$K_1=2BC_2N^{\gamma}/(\gamma+1)(\gamma+2) . \tag{6}$$

Hence

$$C_2=K_1(\gamma+1)(\gamma+2)/2BN^{\gamma} . \tag{7}$$

With the aid of Eq. (7), Eq. (1) can be rewritten as

$$\langle r^2\rangle=C_2N^{\gamma}=K_1(\gamma+1)(\gamma+2)/2B . \tag{8}$$

Let us now consider a region where the curve begins to depart from the initial slope but is negligibly affected by the U^3 term. This curvature is determined by the coefficient of the third term in Eq. (5), which is expressed as

$$K_2=B^2C_2{}^2N^{2\gamma}/(2\gamma+1)(2\gamma+2) . \tag{9}$$

Eqs. (6) and (9) give the following equation for γ

$$\gamma^3+5\gamma^2+(8-16X)\gamma+4-8X=0 , \tag{10}$$

where

$$X=K_2/K_1{}^2 . \tag{11}$$

Eq. (10) has three roots for γ, of which the positive one has a physical significance. It is easy to prove Eq. (10) has a positive root only if

$$X>1/2 . \tag{12}$$

With the aid of obtained value of γ, we can calculate C_2 and $\langle r^2\rangle$ using Eqs. (7) and (8). Then Eq. (10) can be rewritten as

$$X=(\gamma+1)(\gamma+2)^2/8(2\gamma+1) , \tag{13}$$

which means that X does not depend on N. The algebraic equation for γ as given by Eq. (10) is quite simple. This comes from the present use of an approximate equation of P-M expression of $P(\theta)$.

§ 3. Apparatus and Experimental Procedure

The light scattering apparatus similar to Brice's photometer[7] has been constructed. Slit systems for incident and scattered light have been designed considering Hermans' factor[8]. A high pressure mercury lamp and a solution filter gave satisfactorily monochromatic light of wave length of 4358 A[9]. The sample solution in a cylindrical cell was held on a black copper plate which was kept at a constant temperature (±0.2°C) by circulating water. The accuracy in the measurement of the relative intensity of the scattered light in the angular range from 35° to 145° was checked using the θ dependence of the intensities of toluene and cyclohexane. Fig. 1 shows intensities of the scattered light from these liquids. The dissymmetry coefficients Z calculated from these data are 1.01 and 1.00, respectively. These results suggest reliability of our apparatus. Commercial polystyrene was fractionated twice by the precipitation method and divided into thirty fractions. Three fractions were chosen from these thirty and used as the solute. Toluene, methylethylketone (M.E.K.) and cyclohexane were used as the solvents, which were purified by the usual method[10]. Polystyrene solutions of various concentrations were made by diluting the mother solution, which was 0.5 g solute per 100 cc for each solvent and were stirred for about eight hours at 50°C. The diluted solutions were further stirred for about one hour at room temperature and then freed from dust by repeating filtration four and five times with the sintered glass filter of No. 4. For the system of polystyrene in

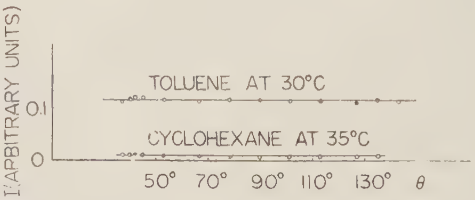

Fig. 1. Intensity of scattered light obtained for toluene and cyclohexane.

cyclohexane, the solution was stirred once again for about one hour at 35°C immediately before the measurement. The measurements of the scattered light were made at 30°C for toluene and M.E.K. solutions and at 35°C for cyclohexane solution. Toluene, M.E.K. and cyclohexane solvents are examples of good, poor and Θ solvents, respectively. Benzene was used as the scattering standard to reduce the measured relative intensity of the scattered light into the absolute intensity.

Table I. Reciprocal reduced intensities $C/I(\theta)$.
Polystyrene F. 1-2 at 30°C

in toluene

concentration	0.2%	0.05%
$\sin^2\theta/2$		
0.12	1.28	0.74
0.20	1.34	0.78
0.30	1.42	0.87
0.40	1.49	0.94
0.50	1.60	1.02
0.60	1.67	1.10
0.70	1.70	1.17

in M.E.K.

0.15%	0.09%	0.05%
$\sin^2\theta/2$		
1.47	1.22	
1.61	1.32	1.08
1.72	1.47	1.24
1.82	1.58	1.35
1.97	1.70	1.47
2.05	1.79	1.59

Polystyrene F. 7-1 in toluene at 30°C

concentration	0.2%	0.075%
$\sin^2\theta/2$		
0.12	1.64	1.14
0.20	1.62	1.03
0.30	1.70	1.19
0.40	1.72	1.25
0.50	1.75	1.28
0.60	1.78	1.31
0.70	1.78	1.35

Polystyrene F. 1-3 in cyclohexane at 35°C

concentration	0.3%	0.2%	0.1%
$\sin^2\theta/2$			
0.12	1.26	1.25	1.26
0.15	1.29		
0.20	1.32	1.32	1.28
0.30	1.41	1.40	1.41
0.40	1.50	1.52	1.50
0.50	1.60	1.59	1.58
0.60	1.70	1.69	1.70

§ 4. Results

Results of the present light scattering measurements of three fractions are given in Table I and an example of Zimm plot[11] is shown in Fig. 2, in which $P(\theta)$ vs. U and $1/P(\theta)$ vs. U relations were obtained from Zimm plot. The initial slope K_1 was determined by use of these curves. The absolute values of initial slopes of both curves should theoretically coincide. Here K_2 was determined by the plot of $P(\theta)-(1-K_1U)$ vs. U^2, of which the initial slope is K_2 itself. The values of γ and C_2 were obtained from Eqs. (7) and (10). The molecular weight M and thus the degree of polymerization N were determined from Zimm plot of Eq. (3). The values of the refractive index increment, $\partial n/\partial C$, which were necessary to determine K in Eq. (3), were taken from other articles[11]. Thus, the molecular extension in the solution was determined from Eq. (1). Results are given in Table II, in which the values calculated from Zimm's data[11] are also shown. For comparison, $\langle r^2\rangle_z$ and the square of characteristic length, b_2, which were obtained from Zimm's expression for $P(\theta)$[2] are also given. (Eq. (2) can be reduced to Zimm's $P(\theta)$ by putting $\gamma=1$ and $C_2=b_2$.)

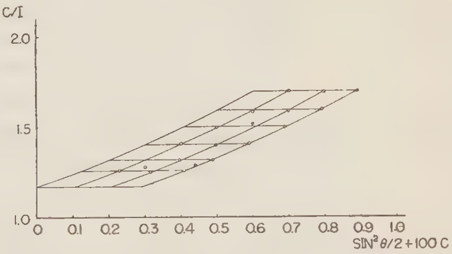

Fig. 2. Light scattering data for polystyrene F. 1-3 in cyclohexane at 35°C.

§ 5. Discussion

The coefficients K_1 and K_2 (cf. Eqs. (6) and (9)) have been determined using the slope

Table II. Summary of the obtained values.

Polystyrene system	$N\times10^3$	K_1	K_2	X	γ	$\langle r^2\rangle^{1/2}$ $\times10^{-8}$	$C_2^{1/2}$ $\times10^{-8}$	$\langle r^2\rangle_z^{1/2}$ $\times10^{-8}$	$b_2^{1/2}\times10^{-8}$
F. 1-2.-toluene at 30°C	25.7	1.433	1.656	0.807	1.147	1869.2	5.53	1761.0	10.99
F. 7-1.-toluene at 30°C	0.23	0.400	0.133	0.833	2.620	1553.6	0.06	930.6	19.32
RT-H-toluene* at 20°C	38.9	3.60	3.75	0.289				2791.0 2680.0**	14.15 10.7**
F. 1-2.-M.E.K. at 30°C	25.7	1.370	0.808	0.646	0.700	1510.0	42.51	1720.0	10.73
Ep-2-M.E.K.* at 67°C	7.32	0.347						866.7 828.0**	10.12 7.30**
F. 1-3.-cyclohexane at 35°C	13.0	0.640	0.325	0.793	1.111	1231.4	6.39	1177.0	10.03
RT-H-M.E.K.* (89%)-2-propanol (11%) at 20°C	38.9	1.670	1.896	0.680	0.805	1746.6	24.94	1901.0 1490.0**	9.64 5.95**

*: From Zimm's data[11].

**: The value cited from the Table in Zimm's article[11].

In the last two columns our values calculated from Zimm's $P(\theta)$[2] (see section (1)) are given. b_2, square of a characteristic length of chain, is equal to C_2 when $\gamma=1$.

and curvature of $P(\theta)$ in the vicinity of $\theta\approx0$. In general, the accuracy in measurement of the small angle scattering is poorer than that of the large angle scattering. We could, however, obtain very good linear relations both for $P(\theta)$ vs. U and $P(\theta)-(1-K_1U)$ vs. U^2 curves. The relative errors in both K_1 and K_2 seem to be of the order of $\sim5\%$. Also the present method has been checked by using Zimm's data and the values of $\langle r^2\rangle$ which are very close to those reported by Zimm has been obtained as shown in Table II.

The fundamental assumptions in the derivation of P-M's $P(\theta)$ are that the solution is non-branched, monodispersed system. These are the reason why we chose very well fractionated polystyrene, which was expected to have no branches[12],[13]. There appears, however, to be some effect due to small polydispersity such as will be discussed below. According to Flory's interpretation[14], the parameter γ expresses the long-range effect on $\langle r^2\rangle$ while C_2 is closely related to the short-range effect. The deviation of γ from unity is expected to be positive in good solvents, negative in poor solvents and zero in Θ solvent[4],[6]. On the other hand, C_2 is large if the solvent is poor and high polymer is stiff, while it is small if the solvent is good and high polymer is flexible.

Further discussions will be given on these parameters and $\langle r^2\rangle$ for our examples of good, poor and Θ solvents. Toluene was studied as an example of good solvent. As seen in Table II, the values of γ are larger than unity in both the F. 1-2 and F. 7-1 solutions as expected. The values, however, are not the same in both cases. This seems to come from the fact that γ depends on a molecular weight distribution as seen in Appendix. The values of γ and C_2 of F. 1-2 seem to be reasonable. The value of γ is in good agreement with that obtained from the well fractionated samples of polymethylmethacrylate in acetone solution by Cantow and Schulz[15] and the rather small value of C_2 suggests

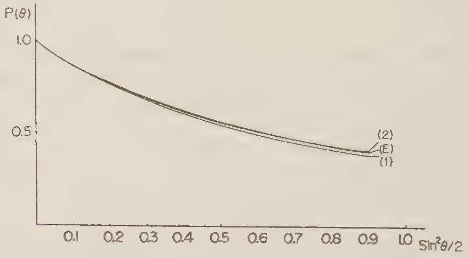

Fig. 3. Experimental values of light scattering intensity in comparison with calculated light scattering functions for polystyrene F. 1-2 in toluene at 30°C. (1): $\gamma=1$, (2): $\gamma=1.15$, (E): Experimental.

that the polymer is flexible. $\langle r^2\rangle^{1/2}$ is about 10% larger than $\langle r^2\rangle_z^{1/2}$ calculated from Zimm's $P(\theta)$. Fig. 3 shows experimentally determined $P(\theta)$ curve in comparison with P–M's $P(\theta)$ and Zimm's $P(\theta)$ calculated from with use of the parameters in Table II. P–M's $P(\theta)$ gives much better agreement with experimental $P(\theta)$ than Zimm's $P(\theta)$. In F. 7–1, γ is rather large and C_2 is too small. Probably these rather unreasonable values are caused by the fact that the solution was actually polydispersed and by the experimental errors in determining the molecular weight. In the calculation of γ of RT.H-toluene at 20°C, it was turned out that X does not satisfy the condition of Eq. (12) and no positive root for γ could be obtained from Eq. (10). Probably this result was caused by too large molecular size of the polymers. In such a case, higher order terms of $P(\theta)$ expansion which were neglected in Eq. (5) become significant even for small angle scattering. In the system of polystyrene in M.E.K. solution, which is an example of a little poor solvent[14], γ obtained by our measurement is slightly smaller than unity as shown in Table II. This fact seems to be in contradiction to Flory's theory[6),14] because our observation was done at the temperature much higher than Θ temperature. The value of C_2 of this system also seems to be too large. Zimm[11] reported $C/I(\theta)$ values for this system (Ep-2-M.E.K.). We have evaluated $P(\theta)$ from his data and Eq. (3) and plotted it against U. It was difficult to interpret the obtained curve by adjusting the parameters in $P(\theta)$ given by Eq. (5). Hence, no values of γ and C_2 are given in Table II. It should be mentioned here that Boyer et al[16] reported somewhat strange behavior of this system. Further investigation seems to be needed. For the system of polystyrene in cyclohexane solution, which is an example of the Θ solvent ($\Theta=$34.5°C), the obtained γ is larger than unity and C_2 seems to be slightly too small. These values suggest that the polymer molecule in this solution is fairly flexible, the fact which can be hardly expected from the usual behavior of the Θ solvent. For definite conclusion, however, effect of polydispersity on the experimental values of γ and C_2 should be studied in detail. In the last row of Table II, values of the parameters are given for RT-H-M.E.K. (89%)-2-propanol (11%), which is a very poor solvent as shown by Zimm[11]. These values have been calculated using Zimm's data[11] of $C/I(\theta)$. His measurements were carried out at a temperature well below the Θ temperature. As seen in Table II, $\gamma<1$ and $C_2\gtrsim b_2$, which are reasonable values for a poor solvent. In Table II, as described above, $\langle r^2\rangle^{1/2}$ was calculated on the basis of P-M expression of $P(\theta)$ where the excluded volume and molecular interactions were taken into account, while $\langle r^2\rangle_z^{1/2}$ was calculated using Zimm's $P(\theta)$ based on the random flight theory. The table shows $\langle r^2\rangle^{1/2}$ is generally different from $\langle r^2\rangle_z^{1/2}$ by about 10%. Other authors[5),6),15),17] also reported such values of this difference and the dependence of $\langle r^2\rangle$ on N similar to the present results. In conclusion it may be stated that the present method provides a simple way to determine $\langle r^2\rangle$ with better accuracy than that of Zimm. For a further improvement of this light scattering method, probably one has to consider the effect of polydispersity in more detail.

Appendix

It has been shown by Zimm[2),12] that for a polydisperse system characterized by its normalized weight distribution $f(N)$, $P(\theta)$ is given by the following expression:

$$P(\theta)=\int Nf(N)P_N(\theta)\,dN\Big/\int Nf(N)dN\,. \quad \text{(A.1)}$$

Substituting Eq. (5) into $P_N(\theta)$ of Eq. (A.1), assuming that C_2 and γ are independent of N and denoting the weight average value of any function $\varphi(N)$ by $\langle\varphi(N)\rangle$, we obtain the following equation.

$$P(\theta)=1-g_1(\langle N^{\gamma+1}\rangle/\langle N\rangle)U + g_2(\langle N^{2\gamma+1}\rangle/\langle N\rangle)U^2\,, \quad \text{(A.2)}$$

where

$$g_1=2BC_2/(\gamma+1)(\gamma+2)\,,$$
$$g_2=B^2C_2^2/(2\gamma+1)(2\gamma+2)\,,$$

which are independent of N. Using Eq. (A.2) and Liapounoff's inequality[12], X is given as

$$X=(g_2/g_1^2)\langle N\rangle\langle N^{2\gamma+1}\rangle/\langle N^{\gamma+1}\rangle^2\geqq(g_2/g_1^2)\,. \quad \text{(A.3)}$$

From Eq. (A.3), it can be seen that X depends on the polydispersity and has a greater value than that in the system of monodispersity. It can be proved from Eq. (10) that the larger X is, the greater the value of γ. In Eq. (A.3) X in appearance depends on N, but actually it depends only upon molecular weight distribution itself. It might be worth noting that in Eq. (10) the effect of the change in X on γ is emphasized by the coefficients 16 and 8, respectively.

Acknowledgements

The author is indebted to Prof. J. Furuichi for encouragement throughout the investigation and to Prof. H. Mizutani and the members of High Polymer Research Group in this laboratory for their useful discussions. The author is also indebted to Dr. N. Yamada, in Electrical Communication Laboratory, Musashino, Tokyo, for his advice on constructing the apparatus.

References

1) H. Tompa: *Polymer Solution* (Butterworth Sci. 1956).
2) P. Debye: J. Phys. and Coll. Chem. **51** (1947) 18. B. H. Zimm: J. Chem. Phys. **16** (1948) 1093.
3) A. Peterlin: J. Chem. Phys. **23** (1955) 2464.
4) H. Mizutani: J. Phys. Soc. Japan **11** (1956) 245.
5) S. Saito: Bull. Kobayashi Inst. Phys. Res. **3** (1953) 134. H. Yamakawa and M. Kurata: J. Phys. Soc. Japan **13** (1958) 78. A. Miyake: J. Phys. Soc. Japan **15** (1960) 875.
6) A. J. Hyde and F. T. Wall: J. Polymer Sci. **33** (1958) 129.
7) B. A. Brice, M. Halwer and R. Speiser: J. Opt. Soc. Amer. **40** (1950) 768.
8) J. J. Hermans and S. Levinson: J. Opt. Soc. Amer. **41** (1951) 460.
9) R. W. Wood: *Physical Optics* (The MacMillan Co. New York) p. 16.
10) A. Weissberger, E. S. Proskauer, T. A. Riddick and E. E. Toops: *Organic Solvents* (Interscience Pub. Ltd. London, 1955).
11) B. H. Zimm: J. Chem. Phys. **16** (1948) 1099. P. Outher, C. I. Carr and B. H. Zimm: J. Chem. Phys. **18** (1950) 830.
12) M. Goldstein: J. Chem. Phys. **21** (1953) 1255. H.Benoit: J. Polymer Sci. **11** (1953) 507. H. Benoit, A. M. Heltzer and P. Doty: J. Phys. Chem. **58** (1954) 635.
13) J. G. Bevington, G. M. Guzman and H. W. Melville: Proc. Roy. Soc. London S. A **221** (1954) 453.
14) P. J. Flory: *Principles of Polymer Chemistry* (Cornell University Press, 1953) p. 317, 423, 625.
15) H.J. Cantow and G.V. Schulz: Z. Phys. Chem. (N. F.) **1** (1954) 365; **2** (1954) 117.
16) R. F. Boyer and D. J. Streeter: J. Polymer Sci. **12** (1954) 124. R. F. Boyer and R. S. Spencer: J. Polymer Sci. **3** (1948) 97.
17) N. T. Notly and P. J. W. Debye: J. Polymer Sci. **17** (1955) 99; **24** (1957) 275.

JOURNAL OF THE PHYSICAL SOCIETY OF JAPAN, Vol. 16, No. 9, SEPTEMBER, 1961

Three-Level Maser Action in Gas
II. Experimental Study on Formic Acid

By Tatsuo YAJIMA

Department of Physics, Faculty of Science,
University of Tokyo, Tokyo

(Received March 4, 1961)

The quantum mechanical behavior of the three-level maser was experimentally studied by using the rotational spectrum of HCOOH molecule at microwave frequencies. By using the $2_{11} \leftarrow 1_{10}$ line at the frequency of 46581 Mc as the pumping, the induced emission of the $2_{11} \rightarrow 2_{12}$ line at the frequency of 4916 Mc was obtained. For a strong pumping, the splitting of emission line due to resonant modulation effect was observed. The line-shape of emission signal under off-resonant pumping was studied in detail. The emission spectrum due to simultaneous emission and absorption of two photons corresponding to the signal and the pumping was observed for the condition of far off-resonant pumping. The results were compared with the theory described in the previous paper, and was found to be in good agreement in many respects. Some discrepancies concerning emission intensity are also discussed. An application of the multiple quantum transition to a four-level system of HCOOH is described.

§ 1. Introduction

The principle of the three-level maser has usually been stated in terms of "negative temperature" which yields net induced emission as a result of population inversion between two levels. This is only a semiclassical explanation, and the quantum mechanical theories of three-level maser predicted various behavior which can not be explained by the semi-classical theory as has been described in the previous paper[1] (hereafter referred to as Part I). However, the observations of such effects have not yet been reported in the numerous experimental works of the solid state microwave masers. This is due to the facts that, under the circumstances of usual operation, the action of a solid state maser obeys semiclassical theory to a good approximation because of their relaxation properties, and that an enormous pumping power is required for the appearance of the quantum mechanical effects. On the other hand, the three-level gas maser can conveniently be used to study these effects by the reason as described in Part I. Therefore, an experiment of gas maser to realize and examine this new type of maser action was planned.

The quantum mechanical effects in the three-level maser are the characteristics of a molecular system which is subject to two or more coherent radiations, and the phenomena such as resonant modulation effect and multiple quantum transition are expected to appear in the emission spectrum. The resonant modulation effect has been studied in the microwave absorption spectrum of OCS molecule.[2] The multiple quantum transitions, which do not obey usual Bohr frequency condition, have also been widely observed in the various fields[3] such as atomic and molecular beam spectroscopies, paramagnetic resonance in gases and solids, nuclear magnetic resonance and recently in the rotational spectrum of gas molecule.[4] As to the net induced emission spectra, there have been few experimental results which involve such effects. The spectrum of induced emission as well as absorption by a double quantum transition in a two level system has been observed at radio frequencies in electron spin resonance of DPPH and other materials.[5] Recently, Elschner[6] reported the observation of the quantum mechanical behavior of the three-level maser using a free radical $(SO_3)_2NO^{--}$ in alkaline aqueous solution at signal frequencies of 13∼16 Mc. In the microwave frequencies, however, such a type of emission signal has not been obtained yet.

In the present paper we report the observation of the quantum mechanical behavior of the emission spectrum in the three-level maser using rotational spectrum of gas molecules at microwave frequencies. The results were compared with the calculated ones described in Part I.

§ 2. Molecular Energy levels suitable for Experiment

Many energy level systems which constitute three-level masers can be found in the rotational levels of molecules. However, there are some restrictions for the use in the experiment of the type intended here. Two conditions must be considered in choosing molecular energy levels. The first is that the available microwave power is sufficient to achieve strong enough pumping for the marked appearance of the quantum mechanical effects. This requires the pumping transition to have large transition probability and to be in a conventional frequency range. The condition can be expressed in the form which is equivalent to Eq. (1) of Part I.

$$w_p = \frac{2\pi\,|\,\mu_p\,|^2 P_0}{3ch^2(\Delta\nu)^2 S} \gtrsim 1 \;,$$

where P_0 is the pumping power for plane polarized wave, μ_p the dipole matrix element for the pumping transition, $\Delta\nu$ the half line-width, S the cross-sectional area of the wave-guide, and w_p is called the pumping parameter. The second condition is that the intensity of the signal line must be strong enough for observing the details of the line shape in both the presence and absence of pumping radiation. This requires that the absorption coefficient of the signal line must be of the order of 10^{-7} cm^{-1} or more, and the ratio of the pumping and the signal frequencies must be sufficiently high. Generally speaking, the heavier molecules are more suitable for the former condition because of their closely spaced energy levels, while the lighter molecules are more suitable for the latter condition because of their strong intensity of the spectrum. Further, asymmetric top molecules may be preferable because of their variety of energy levels and allowed transitions.

Considering these circumstances, the molecule of formic acid, HCOOH, was selected. HCOOH is a slightly asymmetric prolate rotor molecule, and has a large number of K-type doubling transitions, one of which can be used as the signal transition. These K-type doubling transitions are connected with each other by relatively strong R^a-type transitions, one of which can be used as the pumping transition. The three-level system used in the present experiment is shown in Fig. 1. The frequencies, the dipole matrix elements and other quantities of two transitions are listed in Table I. The pumping parameter, w_p, which is an important measure of the degree of pumping is shown in Fig. 2 as a function of the pumping power, P_0/S, and the half line-width, $\Delta\nu$. The microwave spectrum and the molecular structure of HCOOH have been studied by many workers[7], and the frequency of the pumping transition, $2_{11} \leftarrow 1_{10}$, has already been measured. The signal transition, $2_{11} \leftarrow 2_{12}$, was measured first in our experiment so far as the author is aware, and its frequency was found to agree within 0.2 Mc with the calculated value using rotational constants obtained by Trambarulo *et al*

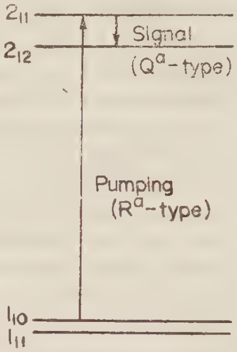

Fig. 1. A three-level system of HCOOH.

Table I. Two transitions in the three-level system of HCOOH.

	signal	pumping
transition	$2_{11} \rightarrow 2_{12}$	$2_{11} \leftarrow 1_{10}$
type	Q^a	R^a
frequency (Mc)	4916.35	46581.3
component of the dipole moment (Debye)	$\mu_a = 1.42$	$\mu_a = 1.42$
square of the dipole matrix element (Debye²)	0.34	1.00
absorption coefficient* (cm^{-1})	2.1×10^{-7}	3.1×10^{-5}
maximum emission coefficient (cm^{-1})	5.1×10^{-7}	

* Calculated under the assumption of $\Delta\nu = 15$ Mc /mmHg.

by using a rigid rotor approximation. There are also many b-type transitions in HCOOH which constitute three-level masers, but these were not used in our experiment, since the dipole moment along b-axis is very small in this molecule.

The other molecule which can be used for the present purpose is vinyl cyanide or acrylonitrile, CH_2CHCN, which has a large dipole moment of 3.89 Debye.[8] A preliminary observation of the spectrum showed that the lines were rather weaker and broader than expected probably due to the quadrupole hyperfine effects and low vibrational frequencies. Therefore, the three-level maser experiment has not yet been performed on this molecule.

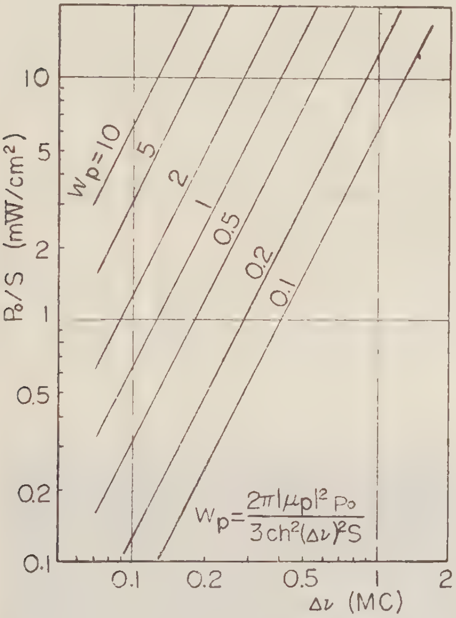

Fig. 2. Calculated pumping parameter, w_p, as a function of half line-width, $\Delta\nu$, and pumping power, P_0/S.

The emission coefficient, α_e, (negative absorption coefficient) is related to the effective Q value of the emission, Q_e, as

$$\frac{1}{Q_e}=\frac{\lambda\alpha_e}{2\pi},$$

where λ is the free space wavelength. If the gaseous materials are filled in a cavity whose loaded Q is Q_L, the self-sustained oscillation will occur, when $Q_L > -Q_e$. The realization of oscillation in the above three-level systems is hard, if not impossible in principle, because the required Q_L is nearly 10^6. Another levels or molecules should be considered for the purpose of oscillation or net amplification.

§ 3. Apparatus

The maser experiment on HCOOH molecule was performed by using a waveguide absorption cell which constitutes a travelling wave type maser. A block diagram of the whole experimental arrangement is shown in Fig. 3.

The absorption cell is made of 7000 Mc band waveguide of 3 meters in length, with the cross-section of 34.85 mm × 15.85 mm I.D. The signal frequency lies near the cut-off frequency of the fundamental TE_{10} mode. This results in an increase of the absorption coefficient of the signal line by a factor of about

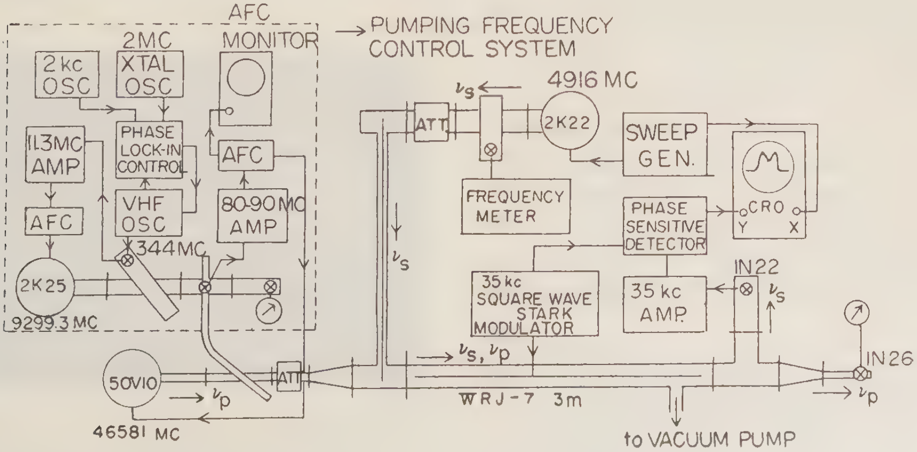

Fig. 3. Apparatus for the study of three-level maser action in HCOOH.

2 compared with the value in the free space, although the waveguide loss also increases to some extent. A usual Stark septum was inserted for Stark modulation with a particular precaution against the attenuation of millimeter-wave pumping field due to supporting insulator. For the more effective pumping, a coaxial absorption cell of much smaller cross-sectional area seemed to be preferable. Preliminary test of such a cell showed, however, excessive attenuation of the pumping field, and hence it was not used.

The weak signal power was supplied by a 2K22 klystron, and was introduced to the cell through a coaxial line feeder. The pumping power was supplied by a millimeter wave klystron 50V10 which yields maximum power of about 30 mW at the pumping frequency. In order to prevent the pumping power from entering the detector, the signal wave was separated from the pumping wave after passing through the cell by using a T-junction. The short millimeter-waves in an over-sized waveguide propagate nearly straight without detectable leakage in the side arm of a T-junction, while the long signal wave propagates into the side arm.

A square-wave Stark modulation at a frequency of 35 kc was employed to observe the signal line with good sensitivity. The undisplaced main line was used to observe three-level maser action. All the Stark components of the signal were pushed far away from the main line by a sufficiently strong Stark voltage of about 600 V to avoid a confusion, because after a phase sensitive detector the Stark component appears in the opposite sign to the main line and hence looks like an emission signal. The three-level maser action were observed and recorded on an oscilloscope screen by sweeping the signal frequency around its resonant value with fixed pumping frequency. A slow sweep of about 5 sec. period and corresponding large time constant at the output of the phase sensitive detector were used to attain a good signal-to-noise ratio.

The most difficult work in the present experiment was the high stabilization of the frequency of pumping klystron near the resonant value. An automatic frequency control system using heterodyne method and phase lock-in method was adopted and worked well with the stability of about $10^{-6} \sim 10^{-7}$. This part is indicated in an enclosure of dotted line in Fig. 3. Using a 2 Mc crystal oscillator as a standard, a 2K25 klystron is stabilized at the frequency of 9299 Mc by the same method as used in the frequency control system of the ammonia frequency standard.[9] A beat signal between 50V10 and the stabilized 2K25 is then amplified by a receiver tunable in a range 80∼90 Mc, and the output of a frequency discriminator is fed back to control 50V10 klystron. The fine control and the measurement of the pumping frequency were carried out by controlling the tuning frequency of the above receiver with the AFC on.

§ 4. Experimental Results and Comparison with the Theory

In order that the pumping effect is large, the gas pressure must be low so that the line-width is narrow enough. The line-width is limited, however, by the broadening due to the wall collision and the Doppler effect.

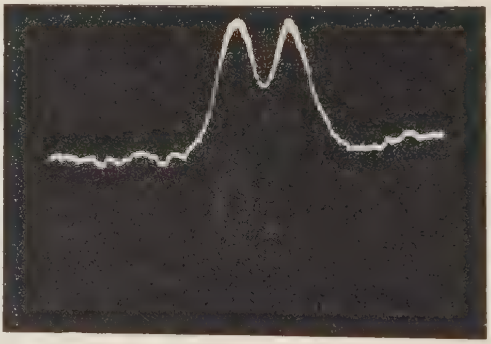

(a)

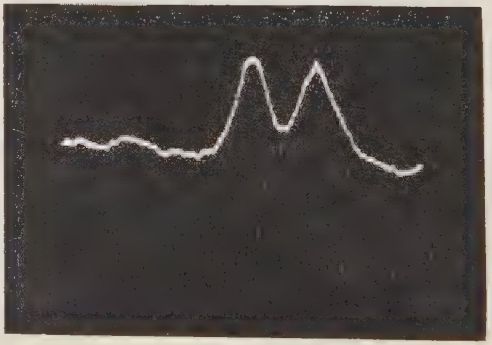

(b)

Fig. 4. Typical patterns of the emission doublet in the three-level gas maser. The gas pressure in (b) is lower than in (a).

The wall collision width is calculated as 4.4 kc for the cell used, and the Doppler widths for signal and pumping are 4.5 kc and 43 kc, respectively. When the half-width of actual signal line becomes below about 100 kc, the intensity was found to decrease more rapidly than expected probably due to increasing impurity, and therefore most experiments were carried out with the line-width of above 100 kc.

Now, the three-level maser action was observed when the gas pressure is reduced below about 10^{-2} mm Hg with a pumping power of 30 mW. When the pumping frequency is resonant, the intensity of the absorption signal decreases initially, then the emission line appears and finally the line splits into a doublet. Typical patterns of the emission doublets are shown in Fig. 4. This may be interpreted as the resonant modulation effect which is one of the quantum mechanical effects in the three-level maser. For sufficiently strong pumping, the separation of two peaks is theoretically given by

$$2(\varDelta\nu)_m=\frac{|\bar{\mu}_p|\,E_p}{h}$$

where E_p is the peak electric field of the pumping radiation, and $\bar{\mu}_p$ the electric dipole matrix element along the direction of electric field for the pumping transition. In general, the separation is slightly dependent on the absorption line-width due to the effect of the interference between two peaks. The separations were measured for several values of absorption line-width, $\varDelta\nu$, with a nearly constant pumping power, and was compared with the theory. The result is shown in Fig. 5. The theoretical curve was calculated from Eq. (11) of Part I, using the values $P_0=30$ mW, $S=5.53$ cm², $|\mu_p|^2=1.00$ (Debye)², and $R=9.47$. The error of the effective pumping power was estimated to be about 30% considering the

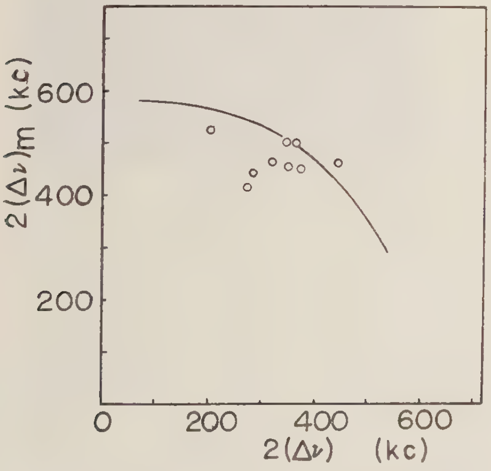

Fig. 5. Separation of two peaks in the emission doublet, $2(\varDelta\nu)_m$, as a function of absorption line width, $2(\varDelta\nu)$. The solid line is the calculated curve, and the open circles are the observed points.

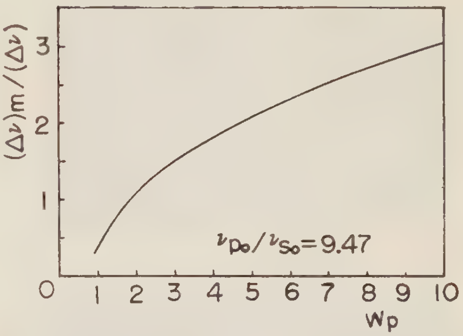

Fig. 6. Theoretical curve of $(\varDelta\nu)_m/(\varDelta\nu)$ versus pumping parameter, w_p.

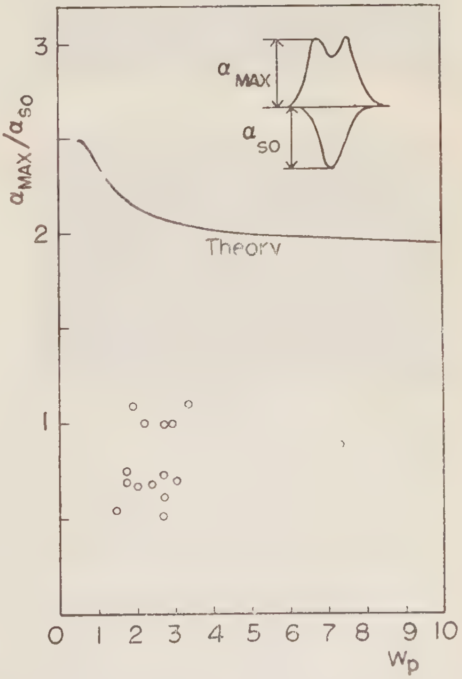

Fig. 7. Ratio of maximum emission and absorption intensities, $\alpha_{\max}/\alpha_{s0}$, as a function of pumping parameter, w_p. The solid line is the theoretical curve, and the open circles are the observed points.

effect of non-uniform field distribution and the accuracy of power measurement. In view of this, the agreement between observed and calculated values seems to be satisfactory. Then, the doublet separation may be used to determine the value of the pumping parameter, w_p, experimentally without detailed knowledge of the pumping power. A theoretical curve which determines the values of w_p from the observed values of $(\Delta\nu)_m/(\Delta\nu)$ is shown in Fig. 6. This curve and all other theoretical curves described below were derived numerically on the basis of Eq. (11) of Part I. The value of w_p was varied in the experiment mainly by the change of gas pressure. Fig. 7 shows observed and calculated values of the ratio of maximum emission and absorption intensities, $\alpha_{\max}/\alpha_{s0}$, as a function of w_p. It was found that the observed intensity of emission is about 1/2~1/3 times as large as the value expected from the theory. Fig. 8 shows observed and calculated values of the ratio of minimum and maximum emission intensities in a doublet structure of the emission line, $\alpha_{\min}/\alpha_{\max}$, as a function of w_p. The general tendency of the experimental results was found to agree with the theory, but it is noted that the observed values are slightly smaller than the calculated ones.

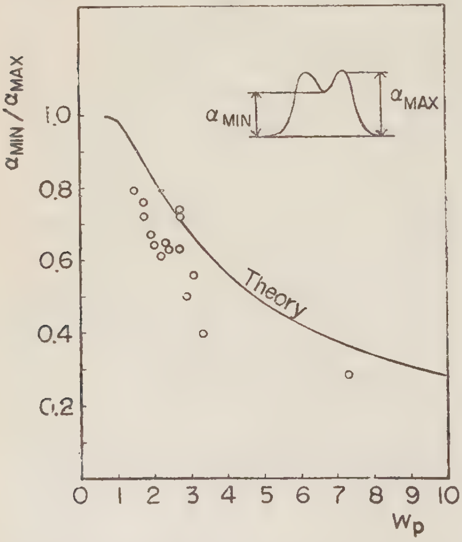

Fig. 8. Ratio of minimum and maximum intensities in a doublet structure of the emission line, $\alpha_{\min}/\alpha_{\max}$, as a function of pumping parameter, w_p. The solid line is the theoretical curve, and the open circles are the observed points.

The line-shapes of the signal are studied in detail when the pumping frequency is shifted from the resonant value. Typical oscilloscope traces of a series of results are shown in Fig. 9, where each photograph corresponds to the different pumping frequency with the same pumping power and gas pressure. It is shown in Fig. 9 that, when the pumping frequency is shifted gradually from resonance, the frequency at the peak of emission doublet shifts and the peak intensity decreases. Finally, one of the peaks becomes a weak emission line separated entirely from the original absorption line. This is the induced emission due to double quantum transition associated with the three-level maser. The whole behavior agrees at least qualitatively with the calculated line-shapes as given in Fig. 3 of Part I. A number of series of such experiments were made, and the change of frequency and relative intensity of the emission peak as a function of pumping frequency are then compared with the theory more quantitatively. The results are shown in Fig. 10 and Fig. 11. The theoretical curves were calculated by the help of the curves such as given in Fig. 3 of Part I. Fig. 10 reveals that the frequency shift of the emission peak agrees well with the theory within the experimental accuracy, and that, when the pumping frequency is shifted sufficiently from resonance, it actually approaches to the following relation,

$$\nu_s-\nu_{so}=\nu_p-\nu_{po}\,,$$

where ν_s and ν_p are the signal and pumping frequencies, and ν_{so} and ν_{p0} are their resonant values. The agreement of general tendency between theory and experiment in Fig. 11 may also be recognized, although the accuracy of the measurement of intensity is rather poor because of the circuit charactor. However, one finds a discrepancy that a distinct maximum occurs in the experimental curve while it is much smaller in the theory. The whole off-resonant behavior was also found to occur in the same way whether the pumping frequency is higher or lower than the resonant frequency, as expected from the theory.

§ 5. Discussion

It was shown by the experimental results described above that various quantum mechanical effects predicted from the theory can be realized in the three-level gas maser, and that

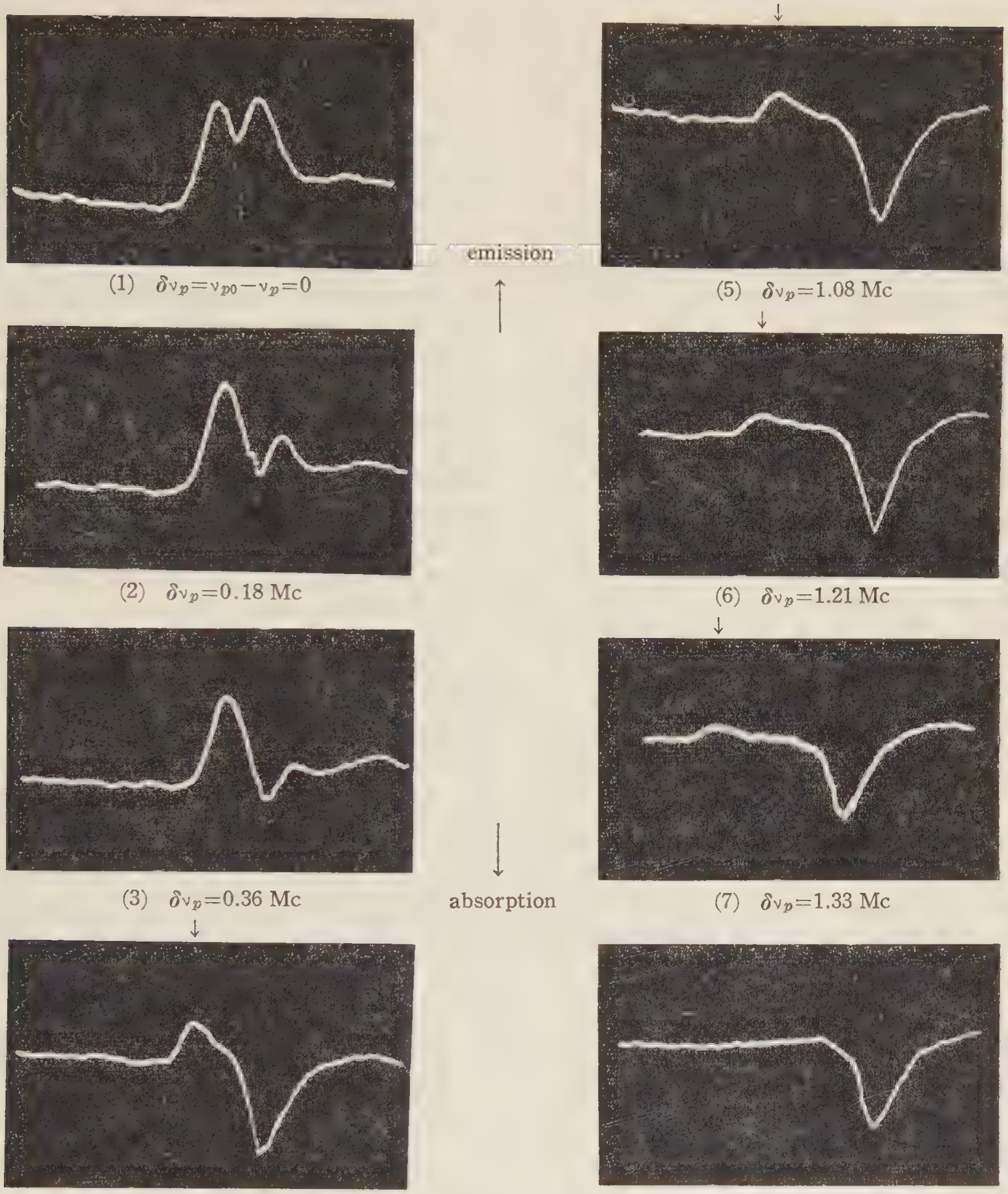

(1) $\delta\nu_p=\nu_{p0}-\nu_p=0$

(2) $\delta\nu_p=0.18$ Mc

(3) $\delta\nu_p=0.36$ Mc

(4) $\delta\nu_p=0.78$ Mc

(5) $\delta\nu_p=1.08$ Mc

(6) $\delta\nu_p=1.21$ Mc

(7) $\delta\nu_p=1.33$ Mc

(8) Original absorption line

Fig. 9. Signal lines of the three-level gas maser, when the pumping frequency is shifted from resonance. $\delta\nu_p$ is the deviation of pumping frequency from the resonant value. The vertical arrows in each figure indicate the emission lines due to double quantum transition separated from the original absorption line. The abscissa represents the signal frequency with the sweep range of about 3.5 Mc. The pumping power was kept at 30 mW.

the main characteristics agree with the theory well. There are, however, some discrepancies between theory and experiment which are summarized as follows.

(1) The observed intensity of the emission at resonance is about 1/2∼1/3 times as large as the value expected from the theory. (Fig. 7).

(2) The observed valley in the emission doublet is slightly deeper than that of the theory. (Fig. 8).

(3) A maximum occurs in the experimental curve of peak emission intensity versus pumping frequency. (Fig. 11).

Possible origins of these discrepancies will be discussed briefly in the following.

According to the theory described in Part I, the influence of the Doppler effect on the intensity and shape of the signal line may be neglected in the present case, since the Doppler-width for pumping frequency is 1/3~1/5 times as large as the total line-width.

A transient effect caused by a finite collision relaxation time will decrease the emission intensity, when the frequency of Stark modulation is not low enough. The amount of decrease by this effect is estimated as about 20% for the modulation frequency and gas pressures used.

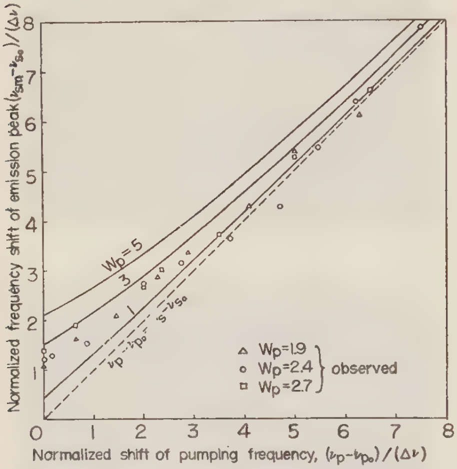

Fig. 10. Frequency shift of the emission peak as a function of pumping frequency. Solid lines are the theoretical results, and observed points are indicated by △, ○, □. The dotted line represents the relation, $\nu_s-\nu_{so}=\nu_p-\nu_{po}$.

$w_p=2\pi|\mu_p|^2P_0/[3ch^2(\Delta\nu)^2S]$

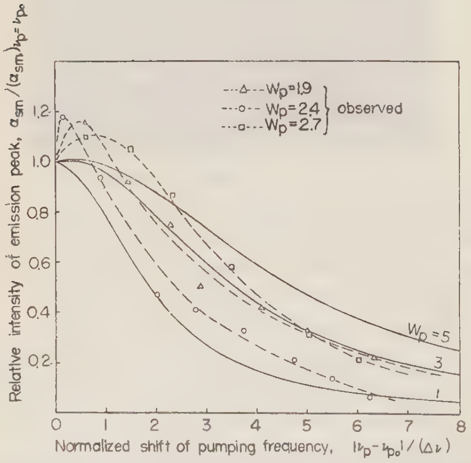

Fig. 11. Intensity of emission peak as a function of pumping frequency. Solid lines are the theoretical results, and dotted lines are the experimental results.

$w_p=2\pi|\mu_p|^2P_0/[3ch^2(\Delta\nu)^2S]$

The main part of the above discrepancies may be attributed to the effect of spatial inhomogeneity of the pumping radiation field. The inhomogeneity arises from the standing wave formation in both transverse and longitudinal directions of the waveguide and from the attenuation of pumping field along the cell. If a considerable region of weak field occurs by this effect, a residual absorption will overlap the emission spectrum. All the discrepancies indicated above may be explained by this mechanism at least qualitatively. However, correct estimation of the effect is difficult because a complicated field distribution is expected due to multimode transmission of the pumping wave in an over-sized waveguide absorption cell.

The degeneracy of each rotational level by a magnetic quantum number M will also contributes to the above discrepancies as has been pointed out in § 3 of Part I. This effect is somewhat analogous to the inhomogeneous field effect in the sense that different transition probabilities associated with different Stark or Zeeman components result in an "inhomogeneous" pumping action.

For complete account of the above effects,

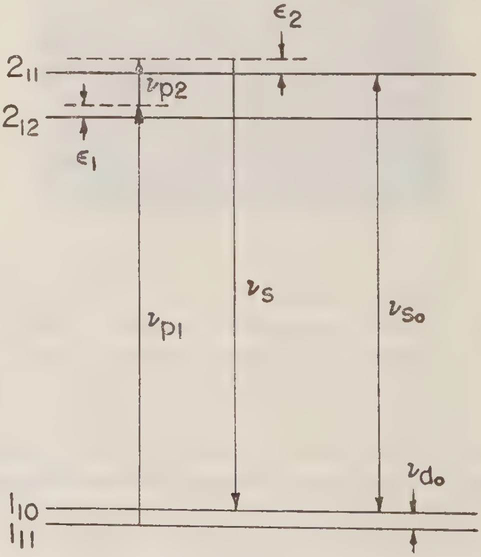

Fig. 12. A four-level system involving triple quantum transition. Induced emission at the frequency ν_s can be obtained by the two pumping radiations of the frequencies ν_{p1} and ν_{p2}.

more refined experiments and theoretical considerations will be necessary.

§ 6. Application to Four-level System

An interesting application of the multiple quantum transition to four-level system is possible as pointed out in Part I. The principle can be illustrated by the same level system of HCOOH as used in the present experiment. Consider a four-level system as shown in Fig. 12, where a new level of 1_{11} participates in the action. Suppose that a weak radiation of the frequency ν_s, and two strong radiations of the frequencies, ν_{p1} and ν_{p2}, are applied to the system. The frequencies, ν_s, ν_{p1}, ν_{p2}, are assumed to be slightly off-resonant from the transition frequencies of $2_{11} \leftrightarrow 1_{10}$, $2_{12} \leftrightarrow 1_{11}$, $2_{11} \leftrightarrow 2_{12}$, respectively, and to satisfy the relation

$$\nu_{p1}+\nu_{p2}-\nu_s=\nu_{do},$$

where ν_{do} is the transition frequency of $1_{11} \leftrightarrow 1_{10}$. The frequency deviations, ε_1 and ε_1, from resonance are assumed to be much smaller than transition frequencies of the molecule.

Then the net induced emission at the frequency ν_s can be obtained for a normal state of populations as a result of triple quantum transition, in which the absorption of two photons, $h\nu_{p1}$ and $h\nu_{p2}$, and the emission of one photon, $h\nu_s$, occur simultaneously. This is a type of maser using the pumping frequency lower than that of signal. The intensity of the emission thus obtained can be calculated by the similar method as used in § 2 of Part I as

$$\alpha_s=-\alpha_{so}\frac{\nu_{do}}{\nu_{so}}\left[\frac{|\bar{\mu}_{p1}|^2\,|\bar{\mu}_{p2}|^2\,E_{p1}{}^2E_{p2}{}^2}{16\,h^4\varepsilon_1{}^2(\varepsilon_1-\varepsilon_2)^2}\right],$$

where α_{so} is the absorption coefficient at the frequency ν_{so} without pumping, $\bar{\mu}_{p1}$ and $\bar{\mu}_{p2}$ the dipole matrix elements of the pumping transitions, E_{p1} and E_{p2} the peak electric field intensities of the pumping radiations. Assuming that the value of the quantity in the square bracket can be increased to the order of unity, and using the values $\alpha_{so}=3.1\times10^{-5}$ cm^{-1}, $\nu_{do}=1639$ Mc, $\nu_{so}=46581$ Mc, then $|\alpha_s|$ amounts to $10^{-6}\sim10^{-7}$ cm^{-1}. This is of detectable intensity, though it is not enough for net amplification or oscillation. More intensive emission from this type of maser will be attained by the use of another molecular levels.

§ 7. Conclusion

The multiple quantum transitions and other phenomena in the gas masers studied here are the typical aspects of the nonlinear properties in the interaction between radiations and a molecular system. They extend the functions of the maser for both spectroscopic and other purposes such as generation, amplification and detection of radiations. The success of the present experiment on an emission spectrum at microwave frequency will open a way of studying and applying these phenomena at higher frequencies in the various fields of quantum electronics. The extremely strong radiations which can be produced by the infrared and optical masers will be quite useful for the study of the above mentioned phenomena at these higher frequencies.

Acknowledgement

The author would like to express his hearty thanks to Prof. K. Shimoda for his kind guidance and continued encouragement in the course of this work. He is also indebted to Mr. H. Takuma for his helpful advice on the experimental technique and to Mr. K. Takagi for his assistance in the measurement.

References

1) T. Yajima: J. Phys. Soc. Japan **16** (1961) 1594.
2) S. H. Autler and C. H. Townes: Phys. Rev. **100** (1955) 703.
3) See, P. Kusch and V. W. Hughes: "Atomic and Molecular Beam Spectroscopy" Sec. 30, Handbuch der Physik, Band XXXVII/I (1959). See also, references in the paper, P.P. Sorokin, I. L. Gelles and W. V. Smith: Phys. Rev. **112** (1958) 802.
4) A. Battaglia, A. Gozzini and E. Polacco: Nouvo Cimento **14** (1959) 1076.
5) J. M. Winter: J. Phys. radium **19** (1958) 802. J. Burget, M. Odehnal, V. Petricek and J. Sacha: Czech. J. Phys. **10** (1960) 547. T. Hashi: J. Phys. Soc. Japan **16** (1961) 1243.
6) B. Elschner: Presented at the international school of physics at Varenna, Italy in Aug. 1960.
7) R. G. Lerner, B. P. Dailey and J. P. Friend: J. Chem. Phys. **26** (1957) 680. G. Erlandsson: J. Chem. Phys. **28** (1958) 71. R. Trambarulo, A. Clark and C. Hearns: J. Chem. Phys. **28**

(1958) 736. R. Keller and W. D. Gwinn: Private communication to Prof. Shimoda.
8) W. S. Wilcox, J. H. Goldstein and J. W. Simmons: J. Chem. Phys. **22** (1954) 516. C. C. Costain and B. P. Stoicheff: J. Chem. Phys. **30** (1959) 777.
9) K. Shimoda: J. Phys. Soc. Japan **9** (1954) 378; **13** (1958) 939.

JOURNAL OF THE PHYSICAL SOCIETY OF JAPAN, Vol. 16, No. 9, SEPTEMBER, 1961

Plasma Oscillations in External Fields

By Masao SUMI

Electrical Communication Laboratory,
Musashino-shi, Tokyo, Japan

(Received May 18, 1961)

Plasma oscillations are considered under uniformly applied electric and magnetic fields. When the external field is so weak that the particle runaway is not yet appreciable and the drift motion between electrons and ions is regarded as quasi-stationary compared with the oscillation frequency and particle gyrations, the usual Laplace transform method can be approximately employed. The dispersion relation thus obtained describes the excitation of ion waves. Behaviors of these waves are discussed, their temporal developments being taken into account.

§ 1. Introduction

Plasma oscillations have been studied extensively both in the absence of external fields and in the presence of a static magnetic field. In these cases a stationary state independent of time has been taken and a time-dependent fluctuation has been treated as a perturbation which grows up under suitable conditions.

When an electrostatic field is applied to the plasma, electrons and ions begin to flow in opposite directions, resulting the so-called current-carrying plasma. It is well known that the mutual motion between electron and ion gases causes electrostatic oscillations, or ion plasma waves. Many works have been carried out concerning ion wave instabilities brought about under a constant relative drift motion[1)–6)].

There have been a few papers in which the relative velocity between electrons and ions varying with time by an applied electric field is taken into consideration. Such cases were discussed by Fried et al.[7)] in special situations and by Kovrizhnykh[8)] in the strong field limit where collisions are neglected. A general treatment of this problem, however, would be very complicated, because runaway and oscillatory phenomena arise simultaneously and are related with each other. It would be, therefore, of significance to provide a simpler treatment of the same problem before the particle runaway is developed remarkably. In fact, as will be seen later, the drift between electrons and ions that changes gradually with time due to the electric field would be regarded as quasi-stationary and hence oscillations would take place adiabatically, provided following two conditions are fulfilled:

a) The externally applied electric field is so weak that the velocity increment gained by an electron during one cycle of excited oscillation is very small compared to the mean thermal speed of electrons

b) The period of excited oscillations is much shorter than the mean collision time between electrons and ions.

Then it will be shown that results obtained on plasma oscillations in the absence of electric field can be applied formally in the presence of an electric field. Ion waves excited will be discussed at every stage of increasing drift velocity. Thus it will be possible to trace the temporal change of ion plasma waves under an external electric field.

§ 2. Fundamental Equations

We consider a uniform plasma composed of electrons and ions of one kind, extending to infinity under external electric and magnetic fields.

We take the Boltzmann-Vlasov equations for distribution functions of velocity of electrons and ions

$$\frac{\partial f_e}{\partial t}+\boldsymbol{v}\frac{\partial f_e}{\partial \boldsymbol{x}}-\frac{e}{m}(\boldsymbol{E}+\boldsymbol{v}\times\boldsymbol{B})\frac{\partial f_e}{\partial \boldsymbol{v}}=\left.\frac{\delta f_e}{\delta t}\right|_{\mathrm{coll}}, \tag{2.1}$$

$$\frac{\partial f_i}{\partial t}+\boldsymbol{v}\frac{\partial f_i}{\partial \boldsymbol{x}}+\frac{Ze}{M}(\boldsymbol{E}+\boldsymbol{v}\times\boldsymbol{B})\frac{\partial f_i}{\partial \boldsymbol{v}}=\left.\frac{\delta f_i}{\delta t}\right|_{\mathrm{coll}}, \tag{2.2}$$

where suffixes e and i refer, respectively, to electrons with mass m, charge $-e$ and ions with mass M, charge Ze. The long-range interaction between particles is included in the fluctuating part of the electric field $\boldsymbol{E}$, and the short-range interaction arising from encounters closer than the Debye radius is represented by the collision terms on the right. In this paper we will mainly discuss plasma oscillations, so that the fluctuating magnetic field produced by the fluctuating convection current and displacement current is neglected. Hence the Maxwell equations are reduced to the Poisson equation

$$\frac{\partial \boldsymbol{E}}{\partial \boldsymbol{x}}=\frac{e}{\varepsilon_0}\int(Zf_i-f_e)d\boldsymbol{v}\,. \tag{2.3}$$

To solve these fundamental equations, the distribution functions and the electric field are Fourier-analysed in space as

$$f_j(\boldsymbol{v},\boldsymbol{x},t)=f_{j0}(\boldsymbol{v},t)+\int f_{jk}(\boldsymbol{v},t)e^{i\boldsymbol{k}\boldsymbol{x}}d\boldsymbol{k}\,,\qquad (j=e,\,i) \tag{2.4}$$

$$\boldsymbol{E}(\boldsymbol{x},t)=\boldsymbol{E}_0(t)+\int \boldsymbol{E}_k(t)e^{i\boldsymbol{k}\boldsymbol{x}}d\boldsymbol{k}\,, \tag{2.5}$$

where $\boldsymbol{E}_0(t)$ is the uniformly applied electric field.

The uniform parts of (2.1) and (2.2) are now given by

$$\frac{\partial f_{e0}}{\partial t}-\frac{e}{m}(\boldsymbol{E}_0+\boldsymbol{v}\times\boldsymbol{B}_0)\frac{\partial f_{e0}}{\partial \boldsymbol{v}}-\frac{e}{m}\int \boldsymbol{E}_k\frac{\partial f_{ek}}{\partial \boldsymbol{v}}d\boldsymbol{k}=\left.\frac{\delta f_{e0}}{\delta t}\right|_{\mathrm{coll}}, \tag{2.6}$$

$$\frac{\partial f_{i0}}{\partial t}+\frac{Ze}{M}(\boldsymbol{E}_0+\boldsymbol{v}\times\boldsymbol{B}_0)\frac{\partial f_{i0}}{\partial \boldsymbol{v}}+\frac{Ze}{M}\int \boldsymbol{E}_k\frac{\partial f_{ik}}{\partial \boldsymbol{v}}d\boldsymbol{k}=\left.\frac{\delta f_{ik}}{\delta t}\right|_{\mathrm{coll}}, \tag{2.7}$$

where the third terms on the left-hand side of both equations represent non-linear contributions which may be negligible in small amplitude oscillations. When the uniform electric field has a perpendicular component to the magnetic field and both fields are either static or varied slowly compared with plasma oscillations and particle gyrations, there occurs a flow of the plasma with a velocity $\boldsymbol{v}_D=(\boldsymbol{E}_0\times\boldsymbol{B}_0)/B_0^2$, which is perpendicular to both the electric and the magnetic fields. So far as the plasma oscillation is concerned, this drift merely causes the Doppler shift of oscillating frequency. We may therefore choose the electric field parallel to the magnetic field without loss of general feature of oscillations. (2.6) and (2.7) are thus simplified to the following equations:

$$\frac{\partial f_{e0}}{\partial t}-\frac{e}{m}E_0\frac{\partial f_{e0}}{\partial v_{/\!/}}+\omega_{ce}\frac{\partial f_{e0}}{\partial \varphi}=\left.\frac{\delta f_{e0}}{\delta t}\right|_{\mathrm{coll}},$$

$$\frac{\partial f_{i0}}{\partial t}+\frac{Ze}{M}E_0\frac{\partial f_{i0}}{\partial v_{/\!/}}-\omega_{ci}\frac{\partial f_{i0}}{\partial \varphi}=\left.\frac{\delta f_{i0}}{\delta t}\right|_{\mathrm{coll}},$$

where the velocity vector $\boldsymbol{v}$ is expressed by three components $(v_\perp\cos\varphi,\ v_\perp\sin\varphi,\ v_{/\!/})$, and $\omega_{ce}=eB_0/m$ and $\omega_{ci}=ZeB_0/M$ are the cyclotron frequencies of electrons and ions respectively. If we assume, furthermore, the cylindrical symmetry in velocity space, both $\partial f_{e0}/\partial\varphi$ and $\partial f_{i0}/\partial\varphi$ vanish. Then we get

$$\frac{\partial f_{e0}}{\partial t}-\frac{e}{m}E_0\frac{\partial f_{e0}}{\partial v_{/\!/}}=\left.\frac{\delta f_{e0}}{\delta t}\right|_{\mathrm{coll}}, \tag{2.8}$$

$$\frac{\partial f_{i0}}{\partial t}+\frac{Ze}{M}E_0\frac{\partial f_{i0}}{\partial v_{/\!/}}=\left.\frac{\delta f_{i0}}{\delta t}\right|_{\text{coll}}. \tag{2.9}$$

These equations describe the time variation of the uniform part of distribution functions under the uniformly applied electric field and are considered as basic equations for the so-called runaway phenomena.

In the extreme case of collisionless plasma, we obtain at once from (2.8) and (2.9)

$$f_{e0}=f_{e0}\left(v_\perp,\, v_{/\!/}+\frac{e}{m}\int^t E_0(t)dt\right),$$

$$f_{i0}=f_{i0}\left(v_\perp,\, v_{/\!/}-\frac{Ze}{M}\int^t E_0(t)dt\right).$$

If we have initially the Maxwellian distributions, we get displaced Maxwellian forms in which the mean velocity varies with time by the applied field; electrons and ions are accelerated in opposite directions, giving rise to an electric current in the plasma.

When collisions are introduced, electron-ion encounters randomize the directed motion imparted by the field, thus bringing about the Joule heating, electron-electron and ion-ion encounters, on the other hand, tend to make the respective velocity distribution of electrons and ions a Maxwellian form in a very short time because of much larger transfer of momentum between like particles. As is well known, however, in the case of strong field, all particles can be runaway and the Maxwellian form of particle distribution deforms appreciably almost in one electron-ion mean collision time[8]. In the case of weak field, a particle having a speed exceeding the mean random speeds of both electrons and ions must be runaway owing to the decreasing dynamical frictions for such a particle, and a particle slower than the mean random speed cannot enter the runaway state by the acceleration alone owing to the increasing dynamical friction with the particle speed, but can diffuse gradually into the runaway state by very close collisions and by the gradual decrease of the dynamical friction with the rise of electron temperature due to the Joule heating. Hence the distribution becomes non-Maxwellian in time even in the weak field.

For electrons we may employ the displaced Maxwellian distribution until νt becomes roughly $(E_c/E_0)^2$ when $(E_0/E_c)\lesssim 1$, where E_0 is assumed time-independent, ν the mean electron-ion collision frequency and E_c the critical field connected with ν as

$$\nu=\frac{eE_c}{mv_e}=\frac{\omega_e^4}{4\pi n_e v_e^3}\ln\Lambda\,,$$

where n_e=the electron number density, $\omega_e^2=n_e e^2/m\varepsilon_0$, $\Lambda=d/p$, d=the Debye length, and p=the minimum impact parameter.

For ions, we shall later neglect their drift velocity because of their large mass and we may therefore take the Maxwellian distribution. Then the displaced velocity $u(t)$ becomes the relative drift velocity between electron and ion gasses.

Neglecting the non-linear and collisional terms, we can describe the fluctuating parts of (2.1) and (2.2) as

$$\frac{\partial f_{ek}}{\partial t}+i\boldsymbol{k}\cdot\boldsymbol{v}f_{ek}-\frac{e}{m}(\boldsymbol{E}_0+\boldsymbol{v}\times\boldsymbol{B}_0)\frac{\partial f_{ek}}{\partial \boldsymbol{v}}-\frac{e}{m}\boldsymbol{E}_k\frac{\partial f_{e0}}{\partial \boldsymbol{v}}=0\,, \tag{2.10}$$

$$\frac{\partial f_{ik}}{\partial t}+i\boldsymbol{k}\cdot\boldsymbol{v}f_{ik}+\frac{Ze}{M}(\boldsymbol{E}_0+\boldsymbol{v}\times\boldsymbol{B}_0)\frac{\partial f_{ik}}{\partial \boldsymbol{v}}+\frac{Ze}{M}\boldsymbol{E}_k\frac{\partial f_{i0}}{\partial \boldsymbol{v}}=0\,. \tag{2.11}$$

When the electric field $\boldsymbol{E}_0$ is parallel to the magnetic field $\boldsymbol{B}_0$, (2.10) and (2.11) can be written as

$$\frac{\partial f_{ek}}{\partial t}+i\boldsymbol{k}\cdot\boldsymbol{v}f_{ek}-\frac{e}{m}E_0\frac{\partial f_{ek}}{\partial v_{/\!/}}+\omega_{ce}\frac{\partial f_{ek}}{\partial \varphi}-\frac{e}{m}\boldsymbol{E}_k\frac{\partial f_{e0}}{\partial \boldsymbol{v}}=0, \tag{2.12}$$

$$\frac{\partial f_{ik}}{\partial t}+i\boldsymbol{k}\cdot\boldsymbol{v}f_{ik}+\frac{Ze}{M}E_0\frac{\partial f_{ik}}{\partial v_{\parallel}}-\omega_{ci}\frac{\partial f_{ik}}{\partial\varphi}+\frac{Ze}{M}\boldsymbol{E}_k\frac{\partial f_{i0}}{\partial\boldsymbol{v}}=0\,. \tag{2.13}$$

For the electric field $\boldsymbol{E}_k$, we require the Poisson equation

$$i\boldsymbol{k}\cdot\boldsymbol{E}_k=\frac{e}{\varepsilon_0}\int(Zf_{ik}-f_{ek})d\boldsymbol{v}\,. \tag{2.14}$$

By use of three equations (2.12)-(2.14), oscillation phenomena will be discussed in the following section.

§ 3. Derivation of the Dispersion Relation

In the usual problem of plasma oscillations, the uniform distribution functions f_{e0} and f_{i0} are independent of time and we can solve the equations by the Laplace transform method. In the presence of an electric field, on the contrary, f_{e0} and f_{i0} become time-dependent and we cannot directly adopt a similar method as before. For a weak field, however, it is likely that f_{e0} and f_{i0} are so slowly varying functions of time as compared with oscillating frequencies that they may be regarded as quasi-stationary. Oscillations will take place adiabatically under the circumstance determined by f_{e0} and f_{i0} changing with time. Thus we may put

$$\frac{1}{f_{e0}}\frac{\partial f_{e0}}{\partial t}\ll\omega \quad\text{and}\quad \frac{1}{f_{i0}}\frac{\partial f_{i0}}{\partial t}\ll\omega\,, \tag{3.1}$$

where ω is the angular frequency of oscillation. If (3.1) holds, it would be reasonable to replace f_{e0} and f_{i0} by time-dependent functions in a dispersion relation, which is obtained by considering f_{e0} and f_{i0} as time-independent and by employing the usual Laplace transformation. The dispersion relation so obtained will describe characteristics of the oscillation in an approximate way.

Now we suppose that $f_{e0}(\boldsymbol{v}, t)$ and $f_{i0}(\boldsymbol{v}, t)$ satisfy the relation (3.1), these functions thus being regarded time-independent for the present in solving the equations (2.12)-(2.14). So far as the form of the dispersion relation is concerned, the Laplace transform method is equivalent to taking all the oscillating quantities with a time factor of $\exp(-i\omega t)$. Hence we get from (2.12)

$$\frac{\partial f_{ek}}{\partial\varphi}-\frac{eE_0}{m\omega_{ce}}\frac{\partial f_{ek}}{\partial v_{\parallel}}-\frac{i}{\omega_{ce}}(\omega-k_{\parallel}v_{\parallel}-k_{\perp}v_{\perp}\cos\varphi)f_{ek}=\frac{e}{m\omega_{ce}}\boldsymbol{E}_k\frac{\partial f_{e0}}{\partial\boldsymbol{v}}\,. \tag{3.2}$$

To get a solution as a power series in a parameter proportional to E_0, we write the zeroth approximation of f_{ek} as[9]

$$f_{ek}^{(0)}=\int_{-\infty}^{\varphi}G_e(\omega, \varphi, \varphi')\frac{e}{m\omega_{ce}}\boldsymbol{E}_k\frac{\partial f_{e0}}{\partial\boldsymbol{v}'}d\varphi'\,, \tag{3.3}$$

where $\boldsymbol{v}'=(v_{\perp}\cos\varphi', v_{\perp}\sin\varphi', v_{\parallel})$, $Im(\omega)>0$ and

$$G_e(\omega, \varphi, \varphi')=\exp\left[\frac{i}{\omega_{ce}}\{(\omega-k_{\parallel}v_{\parallel})(\varphi-\varphi')-k_{\perp}v_{\perp}(\sin\varphi-\sin\varphi')\}\right]. \tag{3.4}$$

By virtue of (3.3), the equation (3.2) becomes, to the first approximation of f_{ek},

$$\frac{\partial f_{ek}^{(1)}}{\partial\varphi}-\frac{i}{\omega_{ce}}(\omega-k_{\parallel}v_{\parallel}-k_{\perp}v_{\perp}\cos\varphi)f_{ek}^{(1)}=\frac{e}{m\omega_{ce}}\left(\boldsymbol{E}_k\frac{\partial f_{e0}}{\partial\boldsymbol{v}}+E_0\frac{\partial f_{ek}^{(0)}}{\partial v_{\parallel}}\right). \tag{3.5}$$

This gives

$$f_{ek}^{(1)}=-\frac{ie}{m\omega_{ce}}\int_{-\infty}^{\varphi}G_e(\omega, \varphi, \varphi')\left[\boldsymbol{k}\frac{\partial f_{e0}}{\partial\boldsymbol{v}'}+\frac{eE_0}{m}\frac{\partial}{\partial v_{\parallel}}\int_{-\infty}^{\varphi'}G_e(\omega, \varphi', \varphi'')\boldsymbol{k}\frac{\partial f_{e0}}{\partial\boldsymbol{v}''}\,d\varphi''\right]d\varphi'\psi_k\,, \tag{3.6}$$

where the electric field is expressed by the electric potential as $E_k=-ik\psi_k$ and $\boldsymbol{v}''=(v_\perp\cos\varphi'', v_\perp\sin\varphi', v_{/\!/})$.

Similarly, we obtain from (2.13) the ion component to the same approximation

$$f_{ik}^{(1)}=-\frac{iZe}{M\omega_{ci}}\int_{-\infty}^{\varphi}G_i(\omega,\varphi,\varphi')\left[\boldsymbol{k}\frac{\partial f_{i0}}{\partial\boldsymbol{v}'}-\frac{ZeE_0}{M}\frac{\partial}{\partial v_{/\!/}}\int_{-\infty}^{\varphi'}G_i(\omega,\varphi',\varphi'')\boldsymbol{k}\frac{\partial f_{i0}}{\partial\boldsymbol{v}''}\,d\varphi''\right]d\varphi'\psi_k\,, \tag{3.7}$$

where

$$G_i(\omega,\varphi,\varphi')=\exp\left[-\frac{i}{\omega_{ci}}\{(\omega-k_{/\!/}v_{/\!/})(\varphi-\varphi')-k_\perp v_\perp(\sin\varphi-\sin\varphi')\}\right]. \tag{3.8}$$

(3.6) and (3.7) are inserted into the Poisson equation (2.14), which yields the dispersion relation to this approximation

$$\begin{aligned}D(\boldsymbol{k},\omega)=k^2-i\Bigg[&\frac{e^2}{m\varepsilon_0\omega_{ce}}\int d\boldsymbol{v}\int_{-\infty}^{\varphi}G_e(\omega,\varphi,\varphi')\left\{\boldsymbol{k}\frac{\partial f_{e0}}{\partial\boldsymbol{v}'}+\frac{eE_0}{m\omega_{ce}}\frac{\partial}{\partial v_{/\!/}}\int_{-\infty}^{\varphi'}G_e(\omega,\varphi',\varphi'')\boldsymbol{k}\frac{\partial f_{e0}}{\partial\boldsymbol{v}''}\,d\varphi''\right\}d\varphi'\\&-\frac{(Ze)^2}{M\varepsilon_0\omega_{ci}}\int d\boldsymbol{v}\int_{-\infty}^{\varphi}G_i(\omega,\varphi,\varphi')\left\{\boldsymbol{k}\frac{\partial f_{i0}}{\partial\boldsymbol{v}'}+\frac{ZeE_0}{M\omega_{ci}}\frac{\partial}{\partial v_{/\!/}}\int_{-\infty}^{\varphi''}G_i(\omega,\varphi',\varphi'')\boldsymbol{k}\frac{\partial f_{i0}}{\partial\boldsymbol{v}''}\,d\varphi''\right\}d\varphi'\Bigg]=0\,.\end{aligned} \tag{3.9}$$

The Laplace transform method leads the identical relation with (3.9). One should note that this relation is valid only for $Im(\omega)>0$. After making use of some formulas of integrals and recurrence formulas of the Bessel functions, we can rewrite (3.9) in the form valid over the whole region of complex ω plane. Then we get

$$\begin{aligned}1+2\pi\sum_{l=-\infty}^{\infty}\Bigg[&\frac{1}{n_e}\left(\frac{\omega_e}{k}\right)^2\int_{C_{el}}\frac{dv_{/\!/}}{\omega-k_{/\!/}v_{/\!/}-l\omega_{ce}}\left\{1-\frac{ieE_0k_{/\!/}}{m(\omega-k_{/\!/}v_{/\!/}-l\omega_{ce})^2}\right\}\\&\qquad\times\int_0^\infty\left(k_{/\!/}\frac{\partial f_{e0}}{\partial v_{/\!/}}+\frac{l\omega_{ce}}{v_\perp}\frac{\partial f_{e0}}{\partial v_\perp}\right)J_l^2\left(\frac{k_\perp v_\perp}{\omega_{ce}}\right)v_\perp dv_\perp\\&+\frac{1}{n_i}\left(\frac{\omega_i}{k}\right)^2\int_{C_{il}}\frac{dv_{/\!/}}{\omega-k_{/\!/}v_{/\!/}+l\omega_{ci}}\left\{1+\frac{iZeE_0k_{/\!/}}{M(\omega-k_{/\!/}v_{/\!/}+l\omega_{ci})^2}\right\}\\&\qquad\times\int_0^\infty\left(k_{/\!/}\frac{\partial f_{i0}}{\partial v_{/\!/}}-\frac{l\omega_{ci}}{v_\perp}\frac{\partial f_{i0}}{\partial v_\perp}\right)J_l^2\left(\frac{k_\perp v_\perp}{\omega_{ci}}\right)v_\perp dv_\perp\Bigg]=0\,.\end{aligned} \tag{3.10}$$

Here n_i=the ion number density, $\omega_i=n_i(Ze)^2/M\varepsilon_0$; the contour C_{el} and C_{il} are chosen so as to go from negative infinity to positive infinity on the real axis, passing the lower side of all singularities of the integrand on the complex $v_{/\!/}$ plane. Instability of the oscillation will arise, in particular, when (3.10) has a solution for $I_m(\omega)>0$.

When the distribution functions are separable with respect to variables, they can be written as

$$f_{e0}(\boldsymbol{v})=n_eg_{e\perp}(v_\perp)g_{e/\!/}(v_{/\!/});\ \ f_{i0}(\boldsymbol{v})=n_ig_{i\perp}(v_\perp)g_{i/\!/}(v_{/\!/})\,. \tag{3.11}$$

Then (3.10) becomes

$$\begin{aligned}1+2\pi\sum_{l=-\infty}^{\infty}\Bigg[&\left(\frac{\omega_e}{k}\right)^2\int_{C_{el}}\frac{dv_{/\!/}}{\omega-k_{/\!/}v_{/\!/}-l\omega_{ce}}\left\{1-\frac{ieE_0k_{/\!/}}{m(\omega-k_{/\!/}v_{/\!/}-l\omega_{ce})^2}\right\}\\&\qquad\times\left\{k_{/\!/}\frac{dg_{e/\!/}}{dv_{/\!/}}\int_0^\infty g_{e\perp}J_l^2\left(\frac{k_\perp v_\perp}{\omega_{ce}}\right)v_\perp dv_\perp+l\omega_{ce}g_{e/\!/}\int_0^\infty\frac{dg_{e\perp}}{dv_\perp}J_l^2\left(\frac{k_{/\!/}v_{/\!/}}{\omega_{ce}}\right)dv_\perp\right\}\\&+\left(\frac{\omega_i}{k}\right)^2\int_{C_{il}}\frac{dv_{/\!/}}{\omega-k_{/\!/}v_{/\!/}+l\omega_{ci}}\left\{1+\frac{iZeE_0k_{/\!/}}{M(\omega-k_{/\!/}v_{/\!/}+l\omega_{ci})^2}\right\}\\&\qquad\times\left\{k_{/\!/}\frac{dg_{i/\!/}}{dv_{/\!/}}\int^\infty g_{i\perp}J_l^2\left(\frac{k_\perp v_\perp}{\omega_{ci}}\right)v_\perp dv_\perp-l\omega_{ci}g_{i/\!/}\int_0^\infty\frac{dg_{i\perp}}{dv_\perp}J_l^2\left(\frac{k_\perp v_\perp}{\omega_{ci}}\right)dv_\perp\right\}\Bigg]=0\,.\end{aligned} \tag{3.12}$$

The dispersion relation (3.10) or (3.12) has been derived under the assumption that the distribution functions are stationary. If the distribution functions change with time in accordance with the condition (3.1), the dispersion relation we are looking for is given by simply considering f_{e0} and f_{i0} as time-varying. Then the relation between the complex frequency and the wave vector obtained from the dispersion relation becomes also slowly varying with time.

We shall next specify the distribution functions to investigate the more realistic case. As was discussed in the last section, it may be allowed to take the distribution functions as Maxwellian before the particle runaway becomes remarkable. Hence in (3.12) we put

$$g_{e\perp}(v_\perp)=\frac{1}{\pi v_e^2}\exp\left[-\left(\frac{v_\perp}{v_e}\right)^2\right], \qquad g_{e\parallel}(v_\parallel, t)=\frac{1}{\sqrt{\pi}\, v_e}\exp\left[-\left\{\frac{v_\parallel-u(t)}{v_e}\right\}^2\right], \tag{3.13}$$

$$g_{i\perp}(v_\perp)=\frac{1}{\pi v_i^2}\exp\left[-\left(\frac{v_\perp}{v_i}\right)^2\right], \qquad g_{i\parallel}(v_\parallel)=\frac{1}{\sqrt{\pi}\, v_i}\exp\left[-\left(\frac{v_\parallel}{v_i}\right)^2\right], \tag{3.14}$$

where $u(t)$ denotes the relative drift speed between electron and ion gases, $v_e=(2\kappa T_e/m)^{1/2}$ and $v_i=(2\kappa T_i/M)^{1/2}$, T_e and T_i, temperatures of electrons and ions respectively, being also functions of time because of Joule heating. If the electrons flow in the positive direction, or $u(t)>0$, the electric field must be in the negative direction and therefore $E_0=-|E_0|$. (3.12) becomes

$$\begin{aligned}1+2\sum_{l=-\infty}^{\infty}\Bigg[&\left(\frac{\omega_e}{kv_e}\right)^2\exp\left\{-\frac{1}{2}\left(\frac{k_\perp v_e}{\omega_{ce}}\right)^2\right\} I_{|l|}\left(\frac{k_\perp{}^2 v_e{}^2}{2\omega_{ce}{}^2}\right)\\ &\times\left\{1+i\left(\sqrt{\pi}\,\Omega_{e0}\exp(-\Omega_{el}{}^2)[1+\Phi(i\Omega_{el})]+\frac{2e|E_0|}{mk_\parallel v_e{}^2}[1+Q_{el}(k_\parallel, \omega)]\right)\right\}\\ &+\left(\frac{\omega_i}{kv_i}\right)^2\exp\left\{-\frac{1}{2}\left(\frac{k_\perp v_i}{\omega_{ci}}\right)^2\right\} I_{|l|}\left(\frac{k_\perp{}^2 v_i{}^2}{2\omega_{ci}{}^2}\right)\\ &\times\{1+i\sqrt{\pi}\,\Omega_{i0}\exp(-\Omega_{il}{}^2)[1+\Phi(i\Omega_{il})]\}\Bigg]=0\,,\end{aligned} \tag{3.15}$$

where

$$\left.\begin{aligned}Q_{el}(k_\parallel, \omega)=&-\Omega_{e0}\Omega_{el}+i\frac{\sqrt{\pi}}{2}\left\{\Omega_{el}(3-2\Omega_{el}{}^2)+\frac{l\omega_{ce}}{k_\parallel v_e}(1-2\Omega_{el})\right\}\\ &\times\exp(-\Omega_{el}{}^2)[1+\Phi(i\Omega_{el})]\,,\\ \Omega_{el}=&\frac{(\omega-k_\parallel v_\parallel-l\omega_{ce})}{k_\parallel v_e}\,,\\ \Omega_{il}=&\frac{(\omega+l\omega_{ci})}{k_\parallel v_i}\,,\\ \Phi(x)=&\frac{2}{\sqrt{\pi}}\int_0^x e^{-t^2}dt\,.\end{aligned}\right\} \tag{3.16}$$

§4. Ion Plasma Oscillation

In this section we discuss in detail the plasma oscillation which is excited by the mutual drifting motion between electron and ion gases and is characterized by the dispersion relation (3.15).

Let us consider the case in which the dispersion relation (3.15) is reduced to a simpler form. One of such cases is realized by assuming

$$\left.\begin{aligned}&\text{a)}\ \ |\omega-k_\parallel u|/k_\parallel v_e\ll 1\,, \qquad &&\text{b)}\ \ |\omega|/k_\parallel v_i\gg 1\,,\\ &\text{c)}\ \ k_\perp v_e/\omega_{ce}\ll 1\,, &&\text{d)}\ \ k_\perp v_i/\omega_{ci}\ll 1\,.\end{aligned}\right\} \tag{4.1}$$

The assumptions (4.1) imply that a) the phase velocity of the wave parallel to the magnetic field is much slower than the electron thermal velocity v_e as seen by drifting electrons, while b) it is faster than the ion thermal velocity; c) and d) represent that the wave-length of the wave component perpendicular to the magnetic field is much greater than the gyration radius of electrons and ions, since $k_\perp$ is inversely proportional to the wavelength and v_e/ω_{ce} or v_i/ω_{ci} is the gyration radius of electrons or ions respectively.

In this approximation (3.15) becomes

$$1+2\left(\frac{\omega_e}{kv_e}\right)^2\left(1+i\sqrt{\pi}\frac{\omega-k_{\parallel}u}{k_{\parallel}v_e}+\frac{ie|E_0|}{2mk_{\parallel}v_e^2}\right)-\left(\frac{\omega_i}{kv_i}\right)^2\left\{\left(\frac{k_{\parallel}v_i}{\omega}\right)^2-\frac{1}{2}\left(\frac{k_\perp v_i}{\omega_{ci}}\right)^2\right\}=0\,.$$

From this we find

$$\left(\frac{\omega}{\omega_i}\right)^2=(k_{\parallel}\lambda_e)^2\left[1+(k\lambda_e)^2+\frac{ZT_e}{2T_i}(k_\perp R_i)^2-i\sqrt{\pi}\left\{\frac{u}{v_e}-\frac{\omega}{k_{\parallel}v_e}\left(1+\frac{e|E_0|}{2\sqrt{\pi}\,m\omega v_e}\right)\right\}\right]^{-1}, \tag{4.2}$$

where $\lambda_e=v_e/\sqrt{2}\,\omega_e$ and $R_i=v_i/\sqrt{2}\,\omega_{ci}$. If the electric field E_0 is so weak that the velocity increment of an electron during one cycle of oscillation is much smaller than the thermal velocity of electrons, we can put

$$\left|\frac{eE_0}{mv_e\omega}\right|\ll 1. \tag{4.3}$$

This has a relation with (3.1), which will be examined in the last section. When (4.3) is satisfied, the last term in the last bracket of the denominator of (4.2) can be neglected. Taking into account of the first inequality a) in (4.1), we get from (4.2)

$$\frac{\omega}{\omega_i}=\frac{\pm k_{\parallel}\lambda_e}{[1+(k\lambda_e)^2+(ZT_e/2T_i)(k_\perp R_i)^2]^{1/2}}\left[1+\frac{i\sqrt{\pi}}{2}\frac{\{(u/v_e)-(\omega/k_{\parallel}v_e)\}}{\{(1+(k\lambda_e)^2+(ZT_e/2T_i)(k_\perp R_i)^2\}}\right]. \tag{4.4}$$

Thus writing $\omega=\omega_0+i\gamma$ and neglecting higher order terms, we have

$$\frac{\omega_0}{\omega_i}=\frac{k_{\parallel}\lambda_e}{[1+(k\lambda_e)^2+(ZT_e/2T_i)(k_\perp R_i)^2]^{1/2}}\,, \tag{4.5}$$

$$\frac{\gamma}{\omega_i}=\frac{\sqrt{\pi}\,k_{\parallel}\lambda_e}{2[1+(k\lambda_e)^2+(ZT_e/2T_i)(k_\perp R_i)^2]^{3/2}}\left[\frac{u}{v_e}-\frac{(m/2M)^{1/2}}{\{1+(k\lambda_e)^2+(ZT_e/2T_i)(k_\perp R_i)^2\}}\right], \tag{4.6}$$

where only the positive root is retained by the physical reasoning that the wave velocity must be positive for $u(t)>0$. This is formally the same results as that obtained by Bernstein et al[4], except that the electron drift velocity and the temperatures of electrons and ions are supposed time-varying in our case.

It should be noted that (4.4) must be consistent with b) in (4.1). Hence we obtain from (4.4)

$$\left|\frac{\omega}{k_{\parallel}v_i}\right|\approx\frac{(T_e/2T_i)^{1/2}}{[1+(k\lambda_e)^2+(ZT_e/2T_i)(k_\perp R_i)^2]^{1/2}}\gg 1\,. \tag{4.7}$$

It is clear from this that

$$(T_e/T_i)^{1/2}\gg 1 \tag{4.8}$$

is necessary for such approximations. When the ion temperature is finite to the extent that (4.8) holds, the inequality (4.7) becomes invalid for too large value of $k\lambda_e$; in fact the accurate calculation shows that the system becomes stable for $k\lambda_e$ greater than some critical value[2),3)]. On the other hand, in the limit of zero temperature of ions (4.7) is valid for all values of $k\lambda_e$, exhibiting the existence of excited oscillations for any wave number.

When the wave vector is not parallel to the magnetic field and makes the angle θ with it, we can put $k_{\parallel}=k\cos\theta$ and $k_\perp=k\sin\theta$. We see from (4.5) and (4.6) that the wave do not propagate in the direction perpendicular to the magnetic field and that the frequency and the growth rate are nearly proportional to $\cos\theta$.

We consider for the present an extreme

case in which $T_e/T_i \to \infty$ and $k_\perp \to 0$, that is, the ion temperature is negligible compared to the electron temperature and the wave propagates in the direction of magnetic field. Then the frequency of the oscillation becomes

$$\omega_0 \approx \begin{cases} kv_e(m/2M)^{1/2} & \text{for} \quad k\lambda_e \ll 1\,, \\ \omega_i & \text{for} \quad k\lambda_e \gg 1\,. \end{cases} \tag{4.9}$$

This means that the excited wave is the so-called ion waves. The instability condition is that the growth rate γ becomes positive, namely from (4.6)

$$\frac{u}{v_e} > \frac{(m/2M)^{1/2}}{[1+(k\lambda_e)^2]^{1/2}}\,. \tag{4.10}$$

If u is smaller than $v_e(m/2M)^{1/2}$, the wave corresponding to $k\lambda_e > [(v_e/u)(m/2M)^{1/2}-1]$ becomes unstable and the wave in the range $0 < k\lambda_e < [(v_e/u)(m/2M)^{1/2}-1]$ is stable. If u becomes greater than $v_e(m/2M)^{1/2}$, then the waves for all k are unstable. The maximum growth rate lies $k\lambda_e \approx \sqrt{2}\,y$ for $y \equiv (v_e/u)(m/2M)^{1/2} \gtrsim 1$ and near $k\lambda_e \approx 1/\sqrt{2}$ for $y \ll 1$. Since we find $|\omega|/kv_e \lesssim (m/2M)^{1/2} \ll 1$ from (4.4), the condition a) in (4.1) is fulfilled when u/v_e is much smaller than unity. Features of oscillation in this range are shown in Fig. 1.

When u/v_e becomes comparable with unity, a) in (4.1) must be replaced by

$$|\omega - ku|/kv_e \lesssim 1\,. \tag{4.1}$$

Keeping other conditions b), c) and d) in (4.1) unaltered, we find, instead of (4.2), in the limit of $k_\perp \to 0$ or $k_{/\!/} \to k$,

$$\left(\frac{\omega}{\omega_i}\right)^2 = \frac{(k\lambda_e)^2}{(k\lambda_e)^2 + G(z)}\,, \tag{4.12}$$

where $G(z) = 1 + i\sqrt{\pi}\,ze^{-z^2}[1+\Phi(iz)]$, $z = (\omega - ku)/kv_e$. When $|z| \sim 1$ as seen in (4.11), we get $|G(z)| \sim 1$. From (4.12) we have also in this case,

$$\left|\frac{\omega}{kv_e}\right| \lesssim \left(\frac{m}{2M}\right)^{1/2}, \tag{4.13}$$

for any $k\lambda_e$. Hence (4.11) gives

$$1 \gtrsim (u/v_e) \gg |\omega|/kv_e\,. \tag{4.14}$$

Therefore we may take approximately the variable z as real or $z = -(u/v_e)$, which gives easily the real and imaginary parts of $G(z)$ as

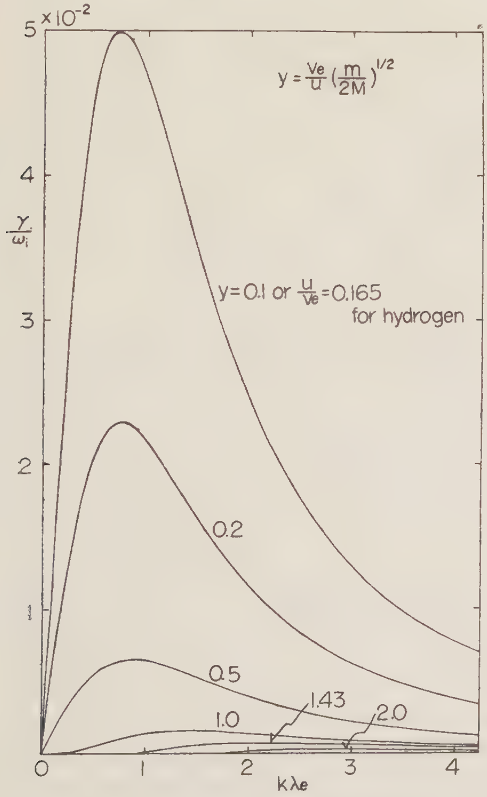

Fig. 1. The growth rate of ion wave propagating in the direction of magnetic field versus the wave number when $u/v_e \ll 1$.

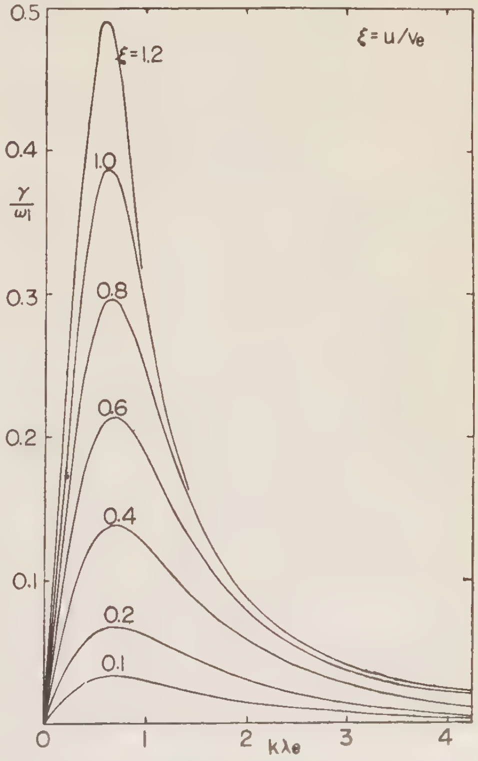

Fig. 2. The growth rate of ion wave propagating in the direction of magnetic field versus the wave number when $1 \gtrsim u/v_e$.

$$ReG(z)=1-2\xi w(\xi)\ ,$$
$$ImG(z)=-\sqrt{\pi}\,\xi e^{-\xi^2}\ ,$$

where $\xi\equiv u/v_e$, $w(\xi)=-i(\sqrt{\pi}/2)e^{-\xi^2}\Phi(i\xi)=e^{-\xi^2}\int_0^\xi e^{t^2}dt$ and its numerical table is available[11]. In terms of variables

$$a\equiv(k\lambda_e)^2+1-2\xi w(\xi)\ ,$$
$$b\equiv-\sqrt{\pi}\,\xi e^{-\xi^2}\ ,$$

we find from (4.12)

$$\frac{\omega_0}{\omega_i}=k\lambda_e\left(\frac{\sqrt{a^2+b^2}+a}{a^2+b^2}\right)^{1/2}, \qquad (4.15)$$

$$\frac{\gamma}{\omega_i}=k\lambda_e\left(\frac{\sqrt{a^2+b^2}-a}{a^2+b^2}\right)^{1/2}. \qquad (4.16)$$

When $b^2/a^2\ll1$, these are reduced to $\omega_0/\omega_i=k\lambda_e/(2a)^{1/2}$ and $\gamma/\omega_i=k\lambda_e/(2a)^{3/2}$ which coincide with (4.5) and (4.6) respectively. Figs. 2 and 3 are obtained for $1\gtrsim\xi\gg(m/M)^{1/2}$ by use of (4.15) and (4.16).

For $\xi>1$, the error caused by presuming z as real becomes remarkable with increasing ξ.

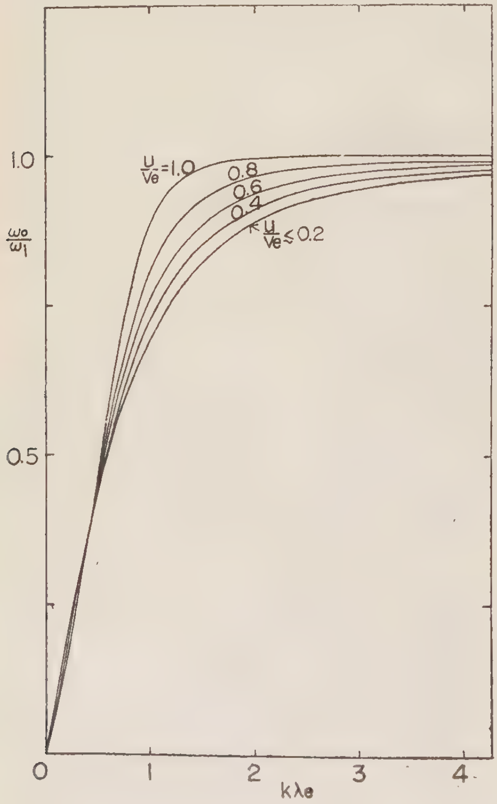

Fig. 3. The frequency of ion wave propagating in the direction of magnetic field versus the wave number when $1\geqq u/v_e$.

In the extreme case of $\xi\gg1$, we have $|z|\gg1$ and again a simple form of dispersion relation for a wave propagating parallel to the magnetic field

$$1=\left(\frac{\omega_e}{\omega-ku}\right)^2+\left(\frac{\omega_i}{\omega}\right)^2. \qquad (4.17)$$

This type of waves has been discussed in many papers. It is, however, quite analogous to the excitation of electron plasma waves by an injected electron beam. The system represented by (4.17) correspond to the system consisting of a medium plasma with a very low density n_p and a beam with a very high density n_b such that the ratio n_b/n_p is equal $(\omega_e/\omega_i)^2=M/Zm$. The detailed features of excited waves in such a system have been investigated by the present author[12]. But we are not interested in such details here, since runaway electrons deform the Maxwellian distribution in the region of large drift velocities. Then the electron distribution would have second maximum and hence electron plasma waves would be excited, the frequency of which is the order of magnitude of ω_e.

As shown above, in the limit of $T_e/T_i\rightarrow\infty$, even an infinitecimal drift velocity excites a wave with $k\rightarrow\infty$. When T_i becomes finite, the drift velocity must exceed some minimum value for instability, which increases with the ion temperature. In the case of $T_e/T_i\gtrsim1$, this minimum drift speed is about the mean thermal speed of electrons, $u\approx v_e$[2)-4)].

§ 5. Excitation of Ion Waves

Now we shall investigate behaviors of ion waves excited by an applied electric field. It was shown in the previous section that characteristics of ion waves are varied with the drift velocity. As the drift velocity increases with time, we find that the growth rate of ion wave rises gradually in time. The waves thus excited would have characteristics corresponding to $k\lambda_e\approx1/\sqrt{2}$ after some appreciable time, since the growth rate exhibits a maximum almost at that point. We know from Fig. 3 that the frequency of the wave is not sensitive to the drift velocity and is slightly below the ion-plasma frequency at $k\lambda_e\approx1/\sqrt{2}$. According to Dreicer[9], the drift velocity has been plotted against νt, the time normalized by the mean collision time. To make a rough estimation for $(E_0/E_c)^2\ll1$, the drift velocity u/v_e may be approximated as linearly proportional to νt. In addition, we see in Fig. 2 that the growth rate γ/ω_i at $k\lambda_e \approx 1/\sqrt{2}$ is nearly proportional to the drift velocity u/v_e. Thus we can assume γ/ω_i proportional to νt. For a given wave number k, we have the component of electric field

$$E_k(t) = E_k(0) \exp\left[\int^t \{\gamma_k(t) + i\omega_{0k}(t)\} dt\right] \quad (5.1)$$

where γ_k and ω_{0k} are obtained in Figs. 1–3. By the assumption just mentioned,

$$\gamma_k(t)/\omega_i \approx A(k)\nu t \, .$$

Hence

$$\int_0^t \gamma_k(t) dt = A(k)\frac{\omega_i}{\nu}\int_0^{\nu t} \nu t\, d(\nu t) = \frac{A(k)\omega_i}{2\nu}(vt)^2 \, .$$

The electric field is written as

$$E(z,\,t) = \int E_k(0) \exp\left[\frac{\omega_i}{2\nu}(\nu t)^2 A(k) + i(kz - \omega_{0k}t)\right] dk, \quad (5.2)$$

where a slight change of ω_{0k} with time is neglected. Since $A(k)$ has its maximum at $k\lambda_e \approx 1/\sqrt{2}$, the saddle point method yields the result for a large value of νt,

$$E(z,\,t) \approx E_k(0)\left[\frac{4\pi\nu}{-\omega_i A''(k_m)}\right]^{1/2} \frac{1}{\nu t} \times \exp\left[\frac{\omega_i}{2\nu} A(k_m)(\nu t)^2\right] \exp[i(k_m z - \omega_{0k_m} t)] \, , \quad (5.3)$$

where k_m is the value of k which is close to $1/\sqrt{2}\lambda_e$ and corresponds to the maximum of γ and where $A''(k) = d^2A(k)/dk^2$. Thus for a sufficiently large νt, $E(z, t)$ is grown up to an exceedingly high level, in which the linear theory employed here breaks down. We have to go back to the fundamental equations, taking into account of the non-linear terms. If the growth of oscillation would be permissible up to very large amplitude, it would have an important effect on the consequences of runaway phenomena.

Finally let us examine the condition hitherto employed for the approximate treatment of the present paper. The conditions are

(i) $\dfrac{1}{f_{e0}}\dfrac{\partial f_{e0}}{\partial t} \ll \omega$, (3.1)

(ii) $\left|\dfrac{eE_0}{mv_e\omega}\right| \ll 1$, (4.3)

(iii) $\nu \ll |\omega|$.

The last one is necessary for collisional terms in (2.11) and (2.12) to be negligible and also necessary for oscillations to sustain over many cycles. (i) is a necessary condition for quasi-stationary approximation, while it will turn out that (ii) gives a sufficient condition in a wide range of electron velocity.

In the limit of neglecting collisions, we obtain f_{e0}, for which the Maxwellian form

$$f_{e0} = \frac{n_e}{\sqrt{\pi}\, v_e} \exp\left[-\left\{\frac{v - u(t)}{v_e}\right\}^2\right],$$

is assumed initially, where $u(t) = e|E_0|t/m$ and E_0 is constant. Hence

$$\frac{1}{f_{e0}}\frac{\partial f_{e0}}{\partial t} = -\frac{2\{v - u(t)\}}{v_e}\frac{e|E_0|}{mv_e} \, .$$

As we are considering the case of $u(t) \lesssim v_e$, the condition (i) is satisfied if (ii) holds except for the velocity range of $v \gg v_e$. The particle number belonging to the range of $v \gg v_e$ is so small that their effect would be resonably discarded.

Owing to the effect of collisions, the temporal change of $u(t)$ becomes slower than that in the absence of collisions. Thus we may take (ii) as a still more sufficient condition. The condition (iii) is independent of (i) and (ii), but it is related with the parameter E_0/E_c representing the strength of applied electric field. In fact (ii) is written as

$$\left|\frac{\nu E_0}{\omega E_c}\right| \frac{eE_c}{mv_e\nu} \ll 1 \, .$$

By the definition of E_c, (2.10), it becomes

$$\left|\frac{\nu E_0}{\omega E_c}\right| \ll 1 \, .$$

Since $\nu/|\omega| \ll 1$, the condition (ii) is consistent with (iii) at least for $|E_0|E_c \lesssim 1$. If $\nu/|\omega|$ is extremely small compared to unity, a consistent case exists even for $|E_0|/E_c \gg 1$.

Strong oscillations observed in the Stellarator[13] may probably be instabilities of this type. Kovrizhnykh remarked[8] that instabilities he discussed correspond to the short-life time in the Stellarator. However it should be noted that the electric field applied in the Stellarator was not so strong as to allow the treatment by Kovrizhnykh, but it was so weak as to satisfy the criterion presented in this investigation.

Acknowledgment

The author is indebted to Professor T. Kihara for valuable comments on this work.

References

1) G. Ia. Miakishev and A. A. Luchina: Sov. Phys. J.E.T.P. **1** (1955) 21.
2) O. Buneman: Phys. Rev. **115** (1959) 503.
3) O. Penrose: Phys. Fluids **3** (1960) 258.
4) E. A. Jackson: ibid. **3** (1960) 786.
5) Ira B. Bernstein and R. M. Kulsrud: ibid. **3** (1960) 937.
6) B. D. Fried and R. W. Gould: ibid. **4** (1961) 139.
7) B. D. Fried, M. Gell-Mann, J. D. Jackson and H. M. Wyld: J. Nuclear Energy, Pt. C, **1** (1960) 190.
8) L. M. Kovrizhnykh: Sov. Phys. TP. **5** (1961) 1122.
9) H. Dreicer: Phys. Rev. **115** (1959) 238; ibid. **117** (1960) 329.
10) Ira B. Bernstein: Phys. Rev. **109** (1959) 10.
11) K. A. Karpov: Tablitsi funktsii $w(z)=e^{-z^2}\int_0^z e^{x^2}dx$ v Kompleksnoi oblasti (Abad. Nauk S.S.S.R., Moskow, 1954).
12) M. Sumi: J. Phys. Soc. Japan **13** (1958) 1476.

JOURNAL OF THE PHYSICAL SOCIETY OF JAPAN, Vol. 16, No. 9, SEPTEMBER, 1961

Characteristics of an Ammonia Beam Maser

By Koichi SHIMODA

Department of Physics, Faculty of Science, University of Tokyo, Tokyo

(Received May 29, 1961)

Design, construction and operating characteristics of an ammonia beam-type maser are described with particular emphasis on the $J=3$, $K=2$ line. The maser with an eight-pole focuser of 40 cm lengh starts oscillation on the 3, 2 line at a focuser voltage of 5.6 kV when the maximum available source flux of about 1.2×10^{18} molecules per second is used.

Threshold conditions of oscillation as functions of the focuser voltage, lengths of the focuser and of the cavity are calculated by the theory on the Maxwell velocity distribution.

The observed frequency-change with the cavity tuning and with the focuser voltage is compared with theory in some detail. The effect of traveling wave component in the cavity and the pulling due to cavity tuning are calculated. It is shown that the frequency shift with the focuser voltage becomes very small, when the beam flux is reduced.

§1. Introduction

Ammonia molecules which are effused from a beam source travel through a inhomogeneous field in the focuser. The focusing field selects only the molecules in the upper inversion state so that they can emit microwave energy in the cavity which is resonant at an inversion frequency of ammonia. Since the first maser¹⁾ was constructed at Columbia University, the ammonia beam maser has been studied extensively in several laboratories.

A theory on the uni-velocity assumption can explain some of the fundamental characteristics of the beam-type maser²⁾, but the distribution of molecular velocities must be taken into account in order to interpret its detailed performance. A theory of the beam-type maser on the Maxwell distribution of molecular velocities at the entrance of the focuser has been developed by using realistic assumptions³⁾,⁴⁾.

The ammonia beam maser is a very stable oscillator at a frequency near 24 Gc. A frequency stability of 1×10^{-10} or better for a period of several hours has been obtained with a carefully constructed cavity resonator and with its temperature control⁵⁾,⁶⁾. However, when the $J=3$, $K=3$ line of $N^{14}H_3$ is used, the determination of the line center is found to be uncertain⁷⁾,⁸⁾,⁹⁾ by more than ±200 cps or $\pm1\times10^{-8}$. From a theoretical investigation on the assumption of the Maxwell velocity distribution, the complicated frequency shift of the 3,3 line maser was explained as the effect of unresolved hyperfine structure due to the electric quadrupole moment of N^{14} nucleus[3].

It was suggested to use the 3,2 line, because the quadrupole hyperfine structure vanishes as $eqQ\{1-3K^2/J(J+1)\}=0$, only when $J=3$ and $K=2$[3]. The maser on the 3,2 line was first constructed by Bonanomi et. al. and showed better stability[10]. Another possibility to improve the accuracy in determining the line center is to use ammonia of concentrated $N^{15}H_3$.

The aim of the present series of papers is to describe fairly complete characteristics of ammonia beam masers. In particular, studies on the 3,2 line will be described in some detail. The previous works (2), (3) and (7) will hereafter be written as SWT, I and II, respectively.

§ 2. Description of Apparatus

The construction of the apparatus is similar to that reported in II, except for a few improvements. The vacuum chamber is a vertical tube of 9 cm diameter which is directly connected to a 4-inch oil diffusion pump. Vertical and horizontal cross-sections of the maser are shown in Fig. 1 and in Fig. 2.

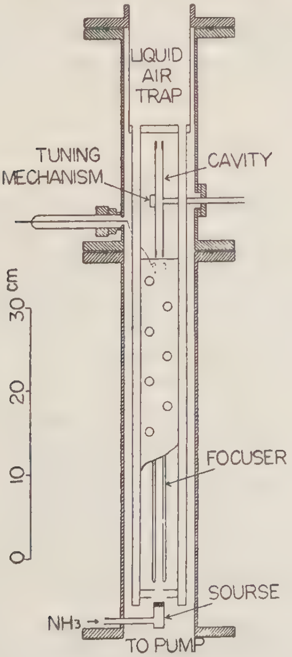

Fig. 1. Vertical cross-section of the maser

The eight-pole focuser is made of steel rods of 3 mm diameter and 40 cm length, the diameter of the focusing field being 10 mm. Neither special polishing nor cleaning of the electrode was carried out. When the high voltage is applied in push-pull to the alternate electrodes, the breakdown voltage is over 25 kV, but it is about 20 kV, when either four electrodes are grounded. Thus the maser was normally operated at a focuser voltage below 18 kV.

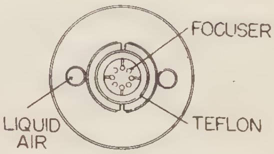

Fig. 2. Horizontal cross-section of the maser (focuser).

In order to trap the scattered molecules the focuser is surrounded by a copper cylinder of 1 mm thickness which is cooled by two straight tubes of 10 mm outer diameter which are filled with liquid nitrogen. The two tubes are connected to the bottom plate of a liquid nitrogen reservoir.

The nozzle of the beam source is constructed from a bunch of holes of 1 mm diameter. The insertion of cold diaphragms between the source and the focuser is quite effective in decreasing the scattered molecules around the focuser and in increasing the effective beam intensity. With a single diaphragm which was used for the 3,3 line maser, the maximum available source flux was about 5×10^{17} molecules per second without considerably increasing the collisions of molecules in the beam. When two diaphragms of 1 mm thickness with a separation of 10 mm as shown in Fig. 1 are used, the maximum source flux is about $1.1\sim1.2\times10^{18}$ molecules per second.

The cylindrical cavity resonator of TM_{010} mode has been exclusively used since it gives the best performance. The cavity is 12 cm in length and nearly 10 mm in diameter. The inlet and outlet holes for the beam are 8 mm in diameter and 10 mm in length. A coupling hole to the waveguide is about 2.1 mm in diameter through the cavity wall of 0.5 mm thickness.

The cylinder is slotted lengthwise to allow a rapid tuning by thermal expansion of the wolfram wire of $0.2\sim0.25$ mm diameter. The cross-section of the cavity to show the method of thermal tuning is illustrated in Fig. 3. The length of the wolfram wire was so chosen that the thermal expansion of the copper cylinder due to a change of the ambient temperature can be compensated by the small expansion of wolfram. The wolfram wire is heated by an 800 cps feedback bridge oscillator which stabilizes the temperature of the wolfram wire, since its resistance increases with temperature. A schematic diagram is shown in Fig. 4.

The measured value of the loaded Q of the cavity was between 7000 and 9000 depending on the size of the coupling hole. The maser starts oscillation on the 3,2 line with a minimum focuser voltage of 5.6 kV at the maximum source flux of about 1.2×10^{18} molecules per second. The cavity can be tuned in the frequency range of over 10 Mc. An example of the pulling of the frequency of the maser with the heating current through the wolfram wire is shown in Fig. 5.

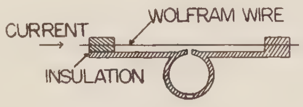

Fig. 3. Thermal tuning of the cavity.

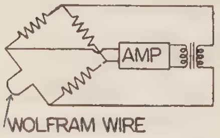

Fig. 4. Bridge oscillator for thermal tuning.

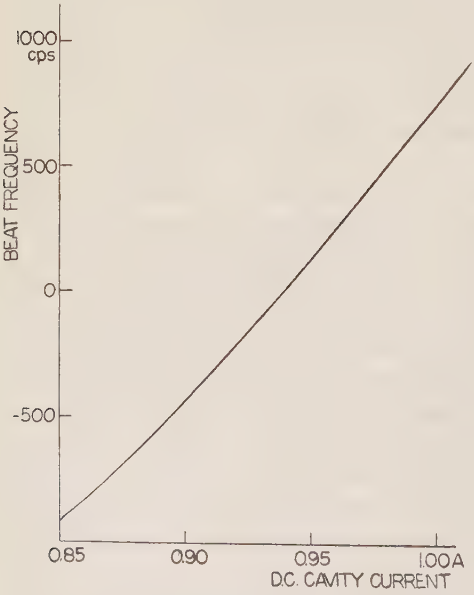

Fig. 5. Variation of the maser frequency with the heater current.

If the source pressure is increased beyond the optimum value of about 2 mmHg, the threshold focuser voltage rises because of the increase of collisions of molecules in the beam. The tank pressure was measured by an ionization gauge connected to the vacuum chamber through a tube. Therefore, the indicated pressure by the gauge must be smaller than the actual gas pressure in the chamber which is still smaller than the pressure around the beam in the focuser.

§ 3. Beam Source

Several quantities which describe the intensity of the beam are defined and their relations are discussed in the following.

The number of molecules which flow out of the source in a unit time into a small solid angle $d\Omega$ is written as $S(\Omega)d\Omega$. The directivity of the source is expressed by the angular dependence of $S(\Omega)$, which usually takes a maximum value $S(0)$ along the axis of the focuser.

The total source flux is therefore given by $S=\int S(\Omega)d\Omega$. This is equal to the number of molecules which must be supplied to the source in a unit time. When the molecule is effused from the source surface which is perpendicular to the axis, it will take any direction with the same probability so that

$$S=\int S(0)\cos\theta d\Omega$$

$$=\int_0^{\pi/2} 2\pi S(0)\cos\theta\sin\theta d\theta=\pi S(0)\,. \qquad (1)$$

If the diaphragm is placed between the nozzle and the focuser, the source that is the starting point of the molecular trajectory should be taken in the hole on the diaphragm. The source flux $S(\Omega)$ will therefore be considered as a number of molecules coming out through a hole on the diaphragm in a unit time irrespective of their rotational states.

On the assumption that the velocities of molecules in the hole on the diaphragm is given by the Maxwell-Boltzmann distribution*, the density of molecules in a particular rotational state designated by J and K is

---

* It is not correct nor necessary to assume that the Maxwell distribution holds for molecules with velocities at a large angle from the axis.

$$N(J, K)=\frac{\sqrt{\pi}\,S}{\alpha A_s}f(J, K)=\frac{\pi^{3/2}S(0)}{\alpha A_s}f(J, K)\,, \tag{2}$$

where $f(J, K)$ is the fraction of molecules in the upper or lower level of the inversion doublet, A_s the source area and α the most probable velocity. The $N(J, K)$ may be called the density of molecules in the source. The values of $f(J, K)$ for ammonia at a room temperature are $f(3,3)=3.24\%$ and $f(3, 2)=1.47\%$.

§ 4. Focusing or State-Separation

Molecules in the upper inversion state are deflected towards the axis by the electrostatic field in the focuser, while those in the lower state are deflected away. Thus the focuser acts as a state-separator. The flux of state-separated beam which enters the cavity has been calculated in I. Since the state-separation is not complete for molecules having large velocities, the difference of the beam flux of the upper state molecules and that of lower state molecules must be considered. Calculation of the excess flux of molecules in the upper state has been carried out[3] by using a simple and practical criterion for the velocity selection as given by (2.9) in I.

As was discussed in I, slower molecules have larger probability of making transitions while they stay in the cavity, and the effective beam intensity, n_{eff}, may be defined by

$$n_{\text{eff}}=\frac{n}{\langle v\rangle^2}\alpha^2\,, \tag{3}$$

where n is the state-separated beam flux, and $\langle v\rangle$ the effective average velocity.

According to Eqs. (2.14) and (2.15 *a* or *b*) in I, the effective beam intensity can be calculated in a reasonable approximation as

$$n_{\text{eff}}=\frac{NR^2}{\sqrt{\pi}\,L^2}A_l\alpha[1.5772-\exp(-a^2)-(1+a^2)$$
$$\times\mathrm{Ei}(-a^2)+\ln a^2+a^2\,\mathrm{Ei}(-b^2)]\,, \tag{4}$$

where A_l is the area of inlet hole of the cavity, L the length, R the radius of the cavity. Two parameters are

$$a=\frac{L}{R}\frac{v_c}{\alpha} \quad\text{and}\quad b=\frac{2}{\pi}\frac{l}{R'}\frac{v_c}{\alpha}\,,$$

where v_c is the critical radial velocity, l the length and R' the radius of the focuser. Equation (4) may be rewritten from (2) in the form

$$n_{\text{eff}}=\frac{A_l}{A_s}\frac{R^2}{L^2}Sf(J, K)\,y(a, b)\,, \tag{5}$$

$$y(a, b)=1.5772-\exp(-a^2)-(1+a^2)\,\mathrm{Ei}(-a^2)+\ln a^2+a^2\,\mathrm{Ei}(-b^2)\,. \tag{6}$$

The threshold value of the effective beam intensity to start oscillation in the cavity which has a quality factor Q has been given by Eq. (3.6) in I.

$$n_{\text{th}}=\frac{n_0}{\langle v_0\rangle^2}\alpha^2=\frac{h\alpha^2A}{4\pi^2\bar{\mu}^2QL} \tag{7}$$

This equation is essentially the same as Eq. (30) in SWT. Then a variable θ which is defined by

$$\theta=\sqrt{(\omega-\omega_0)^2+x^2}\,\frac{L}{2\langle v\rangle} \tag{8}$$

is related to the effective beam intensity in the form given by Eq. (3.8) in I as

$$\frac{n_{\text{eff}}}{n_{\text{th}}}=\frac{\theta^2}{\sin^2\theta}\,. \tag{9}$$

Now the theory is compared with experimental results. The observed amplitude of oscillation on the 3,2 line is shown in Fig. 6 as a function of the focuser voltage. The result in Fig. 6 was obtained when the cavity is tuned to the frequency of the line so that $\omega-\omega_0\ll x$. If the molecular velocity is constant, the value of θ must be proportional to the observed amplitude which is the relative magnitude of the rf field in the cavity. The theoretical saturation curve given by Eq. (31) in SWT or Eq. (9) does not fit the experimental results, if a change in the effective

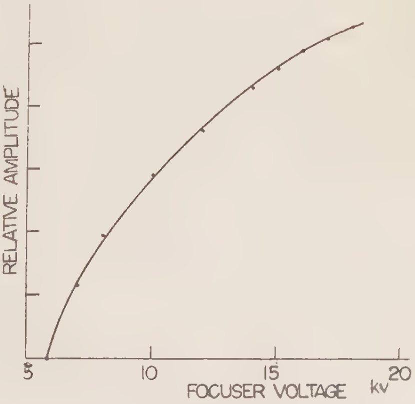

Fig. 6. Amplitude of oscillation on the 3, 2 line plotted against the eight-pole focuser voltage.

average velocity with the focuser voltage is not taken into account. The value of θ for $\omega-\omega_0 \ll x$ is

$$\theta=\frac{xL}{2\langle v\rangle}=\frac{\bar{\mu}L}{2\hbar\langle v\rangle}E\,. \qquad (10)$$

The effective average velocity was given by Eq. (2.24) in I in a fairly good approximation as

$$\langle v\rangle=\frac{\pi L+2l}{2\pi R}v_c\,,$$

where $R=R'$ is assumed. Calculated values of v_c from a weighted average of M^2 are shown in Fig. 7 for the $J=3$, $K=2$ state in an eight-pole focuser.

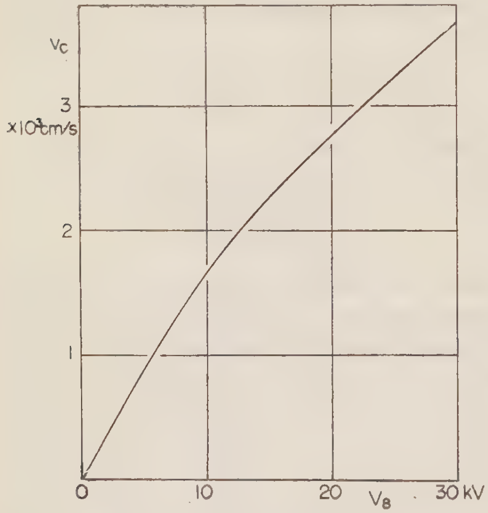

Fig. 7. Critical radial velocity of ammonia for $J=3$, $K=2$, $<M^2>=7$ in an eight-pole focuser with $R=0.5$ cm.

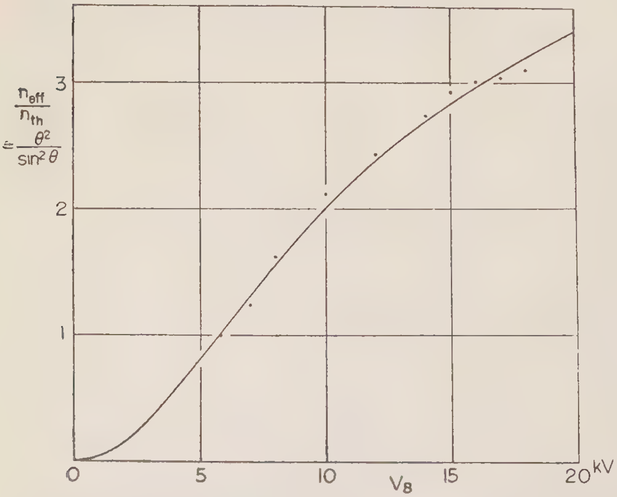

Fig. 8. Theoretical values of n_{eff}/n_{th} and experimental values of $\theta^2/\sin^2\theta$.

By assuming a proportionality factor between the observed amplitude and x, values of $\theta^2/\sin^2\theta$ can be computed. They are shown in Fig. 8 together with a theoretical curve of $n_{\text{eff}}/n_{\text{th}}$ calculated from Eqs. (5) and (7). Theoretical values were calculated for a threshold focuser voltage of 5.8 kV.

The threshold value of the effective beam intensity for the 3,2 line is calculated from Eq. (7) when $Q=8000$, $L=12$ cm and $\alpha=5.3\times10^4$ cm/s to be

$$n_{\text{th}}=n_0\frac{\alpha^2}{\langle v_0\rangle^2}\simeq1.65\times10^{13}\text{ molecules/sec.}$$

Then the source flux which fits the experimental results in Fig. 7 or Fig. 8 is calculated as $S=1.1\times10^{18}$ molecules per second in consistent with the observed flow rate which was only crudely measured.

§ 5. Design Considerations

In order to get oscillation on a weak line the maser must be carefully designed. Since the velocity distribution theory has been found to be good as described in the former section and in II, design considerations according to this theory are given below.

There have been some discussions about the choice of the number of poles of the focuser. The maximum electric fiield on the electrode and the transparency that is the relative area of the gap between electrodes have been discussed. However, it must be remarked that the scattering of molecules is the most important factor in obtaining a strong beam intensity.

When the Stark energy is proportional to the square of the electric field, the focusing force in a quadrupole focuser is proportional to the radial distance r of the molecule. Therefore, molecules which leave the source at a point other than that on the axis are not well focused.

The force in a $2n$-pole focuser is expressed by

$$F\propto r^{2n-3}\,.$$

Hence the focusing force in an eight-pole forcuser is proportional to r^5 and it is very small (less than 8%) in the region where $r<0.6R$. Then, the focuser can accept broader beam from the source and the distribution of upper-state molecules in the focused beam is broader than in the quadrupole focuser for which the molecules are more concentrated on the axis. For the same total beam flux, therefore, the maximum density of molecules is smaller in the eight-pole focuser and also the gas pressure at the entrance of the focuser is more reduced.

Because a focuser of too large number of poles produces essentially no electric field in the region near the axis, the molecules in the lower state cannot be removed from the beam. The effective beam flux is reduced by the presence of lower state molecules and by the increase of scattering by collisions between molecules.

The best number of poles depends on the focuser voltage and the Stark behavior of the molecule, but the eight-pole focuser is considered to be near the optimum in most cases. The six- or ten-pole focuser would be as good.

It is true that the focusing criterion of velocities given in I as

$$v_r < v_c \qquad \text{and} \qquad v_z < \frac{2}{\pi}\frac{l}{R'}v_c$$

must be somewhat modified for a $2n$-pole focuser with $2n \neq 4$. As far as the limiting trajectory is concerned, one might suppose that the factor $2/\pi$ should be replaced by unity, when $2n$ is large. However, a more plausible estimate for the average molecules becomes rather close to $2/\pi$, when the distributions of the starting points and of the directions of the molecular velocities are considered. Therefore, expressions obtained in II and in § 4 may be used for multipole focusers as well.

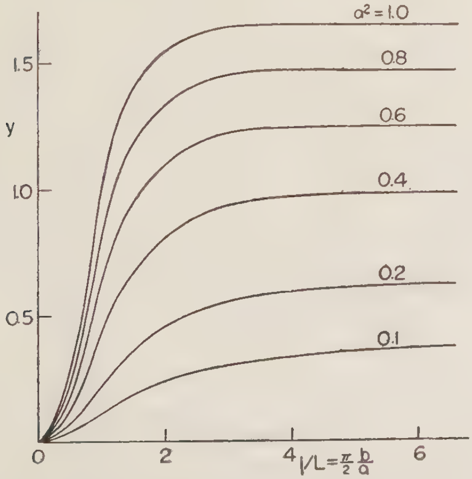

Fig. 9. Effective beam intensity vs. length of the focuser.

The theory allows an evaluation of the change in the effective beam intensity with the length of the focuser, l. Calculated values of $y(a, b)$ which is proportional to the effective beam intensity as given by Eq. (5) are shown in Fig. 9.

Although Eq. (6) was obtained on the assumption of $a<b$, the result may be extrapolated to $l=L$. Besides, another simple estimate is employed to draw curves in the range between $l=0$ and L. It can be concluded from these curves that the focuser length of 2 to 4 times as long as the length of the cavity is usually sufficient. It is noted that the saturation with the length of the focuser is slower at the lower focuser voltage.

Now the performance of the maser against the length of the cavity L is considered. Although the threshold beam intensity decreases with the increase of the cavity length, a very long cavity is not useful, because the velocities of molecules in the beam are not parallel but divergent. The threshold source flux against the cavity length L is calculated from Eqs. (5) and (7) in the form

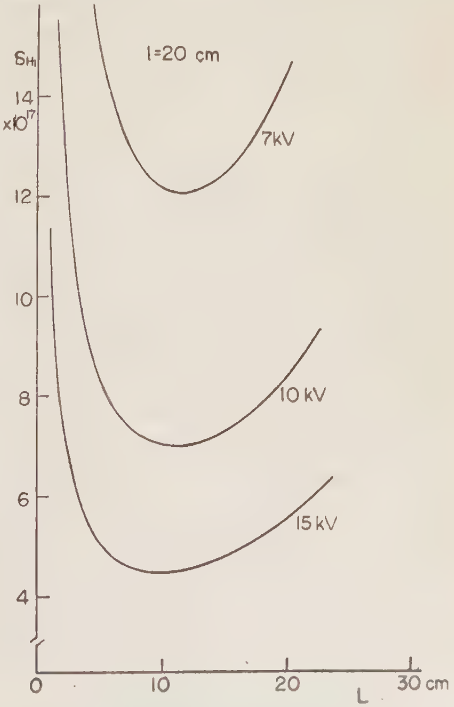

Fig. 10. Threshold source flux for the 3, 2 line vs. cavity length when l=20 cm.

$$S_{\mathrm{th}}=\frac{g}{fR^2}\frac{L}{y}\,, \tag{11}$$

where $A_i=A_s$ is assumed and

$$g=\frac{h\alpha^2A}{4\pi^2\bar{\mu}^2Q}$$

is a constant, if a small change in Q of the cavity with its length is neglected. Some examples for the 3,2 line of ammonia are illustrated in Figs. 10, 11, and 12. They are culculated for $Q=8000$, $\alpha=5.3\times10^4$ cm/s, $R=0.5$ cm, and $l=20$, 30, 40 cm respectively.

These curves show very clearly the optimum length of the cavity. The higher the focuser voltage the larger the beam divergence, hence the cavity length must be smaller. The above calculation has neglected collisions of molecules which become more frequent in a long cavity. Therefore, the optimum cavity length in an actual case would be somewhat shorter than that can be found from these curves.

In conclusion, it may be noted that the experimental apparatus described in § 1 ($l=40$ cm and $L=12$ cm) is very near the optimum design.

Finally, the evaluation for the 3,3 line is mentioned. Because the Stark shift is determined by the value of $\mu KME/J(J+1)$, three curves corresponding to focuser voltages of $V_8=7$, 10, and 15 kV for the 3,2 line must have the same form for the 3,3 line at voltages 2/3 times the above values, those are 4.7, 6.7 and 10 kV respectively. The ordinate must be multiplied by a factor

$$\frac{f(3{,}2)}{f(3{,}3)}\cdot\frac{g(3{,}3)}{g(3{,}2)}=0.112\,,$$

when the quality factor of the cavities are equal.

The threshold flux as a function of the eight-pole focuser voltage is shown in Fig. 13 for the 3,3 line. The observed threshold voltage of $V_8=2.4$ kV reported in II with an estimated source flux of 5×10^{17} molecules per second is in good agreement with theory.

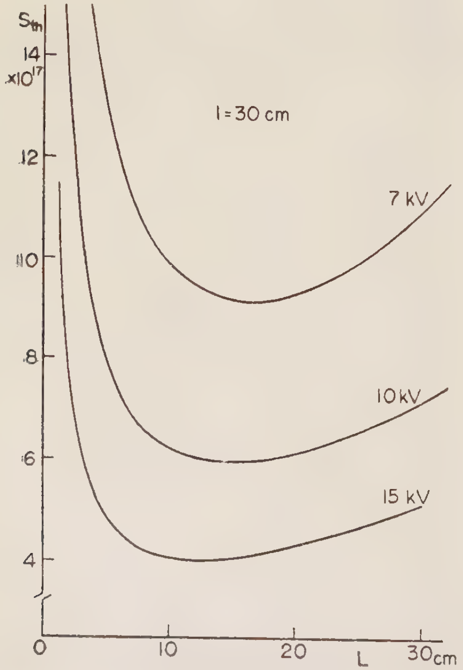

Fig. 11. Threshold source flux for $l=30$ cm.

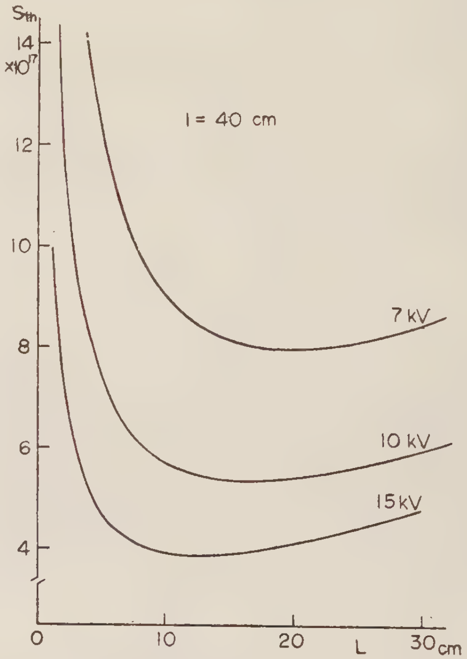

Fig. 12. Threshold source flux for $l=40$ cm.

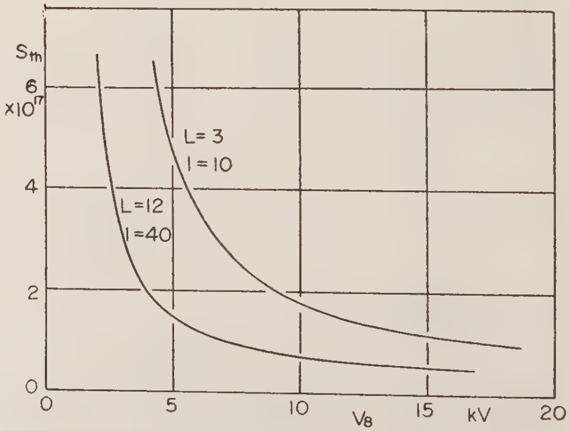

Fig. 13. Threshold condition for the 3, 3 line.

Another example obtained by a small maser of $l=10$ cm and $L=3.2$ cm gave the minimum threshold voltage of 4.85 kV[11], which is also consistent with the theoretical evaluation.

§ 6. Frequency Shifts

The frequency shift of the 3,2 line maser was measured by beating with another similar maser. Comparison of its frequency with the frequency standards will be reported shortly.

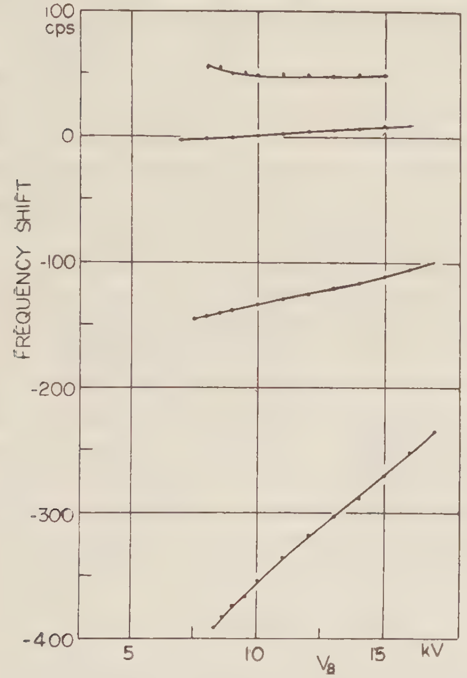

Fig. 14. Frequency shift vs. forcuser voltage, $S\doteqdot 9\times10^{17}\,\mathrm{s}^{-1}$.

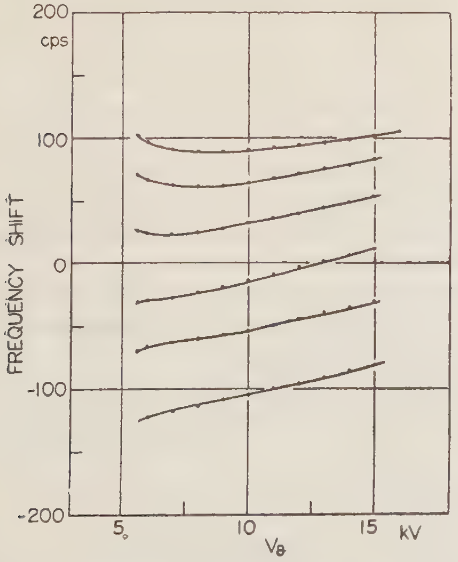

Fig. 15. Frequency shift vs. focuser voltage, $S=1.2\times10^{18}\,\mathrm{s}^{-1}$.

Typical results of the frequency shift with the focuser voltage and with the cavity tuning are shown in Fig. 14 and Fig. 15, where each curve corresponds to a different cavity tuning. Fig. 15 was obtained with the maximum source flux of about 1.2×10^{18} molecules per second and Fig. 14 was for a somewhat reduced source flux.

Comparison of these curves with Fig. 11 in II shows that the 3,2 line allows a more accurate setting of the line center. However, the presence of frequency shift due to the traveling wave component in the cavity make it difficult to find the line center within an accuracy of better than $\pm1\times10^{-9}$ from such results. A theoretical explanation will be given in § 7.

Some additional causes of the frequency shift of the maser were observed. The one is the frequency shift caused by the Stark effect due to the stray electrostatic field of the focuser. It is true that the fringing field of the focuser does not intrude inside the cavity, but an appreciable amount of the rf field is protruding out of the inlet hole of the cavity, where the electrostatic field produced by the focuser is not negligible. Thus molecules which emit rf energies near the inlet hole of the cavity tend to shift the frequency of oscillation.

This type of Stark shift is estimated to be much smaller than the traveling wave effect, but it was experimentally measured by using a dummy focuser which was placed at a distance 3 mm from the cavity. The observed increase of frequency with the dummy focuser voltage is shown in Fig. 16. This shift is proportional to the square of the focuser voltage as expected.

Since the operating focuser is actually about

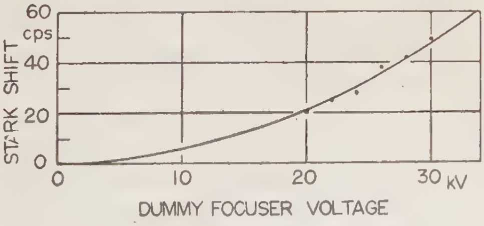

Fig. 16. Stark shift of the maser oscillation due to the fringing field.

9 mm away from the cavity, the Stark shift at a focuser voltage of 15 kV is estimated as +2 cps. This Stark shift can be made smaller, if the potentials of the alternate electrodes of the focuser are $+V/2$ and $-V/2$. Insertion of a shielding diaphragm between the cavity and the focuser would considerably reduce this effect.

The other type of the observed frequency shift is the effect of the background pressure. The change in the oscillating frequency caused by the leakage of air into the vacuum tank was measured in the pressure range between 3×10^{-7} mm Hg and 1×10^{-5} mm Hg on the reading of an ionization gauge.

The observed frequency shift was found to be approximately proportional to the tank pressure and to the amount of frequency pulling f_m-f_0, where f_m is the oscillating frequency and f_0 the line center. An empirical equation for the frequency change Δf_p caused by a pressure increase of p mm Hg was obtained in the form

$$\Delta f_p=2\times10^4(f_m-f_0)p \tag{12}$$

in cycles per second.

This type of frequency shift can be explained by the increase of the cavity pulling due to the decrease of the amplitude of oscillation through the reduction of the beam intensity by scattering of molecules. Eq. (12) is not accurate, since the observed tank pressure may be in error, and because it could not be kept constant while the frequency was measured under a deteriorated vacuum. Besides, frequency changes of less than a few cycles per second corresponding to small amounts of pulling were not measured.

Another type of frequency shift is a small change in frequency due to the collision between ammonia molecules, and it will be discussed in a paper which will appear shortly.

§7. Calculation of Traveling Wave Effect

The presence of traveling wave component corresponding to a small net power flow in the cavity produces a frequency shift due to its Doppler effect. A basic analysis of this type of frequency shift has been given by SWT. Even when the output waveguide is coupled to the cavity at the middle of its length, the power emitted by molecules flows against the direction of the beam when the rf amplitude is small, whereas it flows in the forward direction when the amplitude is large so that most of the molecules deliver their energy in the former part of the cavity. Therefore, the frequency shift due to the traveling wave effect is negative for the case of little saturation, and positive for high saturation.

Now the variation of traveling wave component with saturation is calculated. A crude calculation reported before[12] is reformed as follows. The rf power lost by the cavity wall is distributed along the length of the cavity depending on the distribution of the rf field. The output power is of course lost from the cavity through the coupling hole. The average position of the power dissipation is written as Z, a distance measured from the inlet hole of the cavity. Hence for a cavity of symmetrical mode with output waveguide at the middle of its length Z is equal to $L/2$.

The power delivered by molecules at a distance z from the inlet hole flows in the average to the forward or backward direction according as the sign of $Z-z$. Besides, the magnitude of power flow is proportional to $Z-z$. Therefore, the total power flow in the cavity is given by

$$P_t=K\int_0^L(Z-z)\sin\frac{2\theta z}{L}\,dz\ , \tag{13}$$

because the power emitted by molecules between z and $z+dz$ is proportional to

$$\sin\frac{2\theta x}{L}\,dz\ ,$$

in the TM_{010} cavity[2]. The stored energy is

$$W=K\frac{QL}{\omega_0}\int_0^L\sin\frac{2\theta z}{L}\,dz\ , \tag{14}$$

where K is the same constant as in Eq. (13) and the resonant frequency of the cavity $\omega_0/2\pi$ is taken equal to the transition frequency of the molecule.

Then the amount of the traveling wave component expressed by Q_t is calculated from Eqs. (13) and (14) as

$$\frac{1}{Q_t}=\frac{P_t}{\omega_0 W}=\frac{1}{Q}\left\{\frac{Z-L}{L}+\frac{2\theta-\sin2\theta}{2\theta(1-\cos2\theta)}\right\}. \tag{15}$$

Equation (15) may be rewritten as

$$\frac{Q}{Q_t}=\frac{1}{f_2(\theta)}-d\ , \tag{16}$$

where

$$d=\frac{L-Z}{L}$$

and

$$f_2(\theta)=\frac{2\theta(1-\cos 2\theta)}{2\theta-\sin 2\theta}$$

which is the function illustrated in Fig. 2 in SWT.

The frequency of oscillation ω' shifted by the traveling wave effect is calculated by Eq. (55) in SWT which can be written as

$$\frac{\omega'-\omega_0}{\omega_0}=\frac{4\pi^2 vL}{Q_t\lambda^2\omega_0}\left[1-\frac{1}{4}f_2(\theta)\right] \tag{17}$$

Substitution of Eq. (16) gives

$$\frac{\omega'-\omega_0}{\omega_0}=\frac{\pi}{2Q}\frac{v}{c}\frac{L}{\lambda}\left[4-f_2(\theta)\right]\left[\frac{1}{f_2(\theta)}-d\right] \tag{18}$$

Variations of the frequency shift due to the traveling wave effect with the values of θ and d are illustrated in Fig. 17.

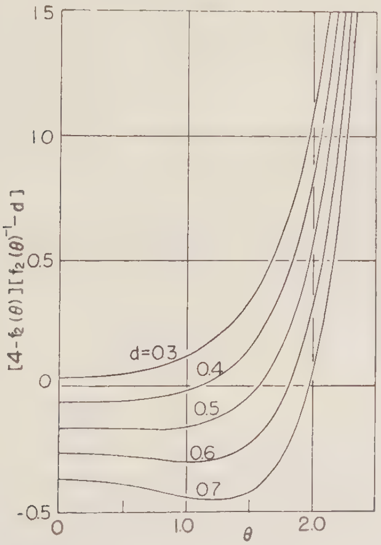

Fig. 17. Graphical representation of $[4-f_2(\theta)]\times[f_2(\theta)^{-1}-d]$.

The observed frequency of a maser on the 3,2 line or on the line of $N^{15}H_3$ includes both the traveling wave effect and the cavity pulling. The frequency pulling by the cavity was theoretically obtained by SWT after a slight modification as

$$\frac{\omega-\omega'}{\omega_0}=\frac{Q}{\pi}\frac{v}{c}\frac{\lambda}{L}f_2(\theta)\cdot\frac{\omega_c-\omega_0}{\omega_0}, \tag{19}$$

where ω is the frequency of the maser, ω_c the resonant frequency of the cavity.

From Eqs. (18) and (19) the theoretical frequency shift due to the cavity pulling together with the traveling wave effect can easily be computed. Numerical results for the values

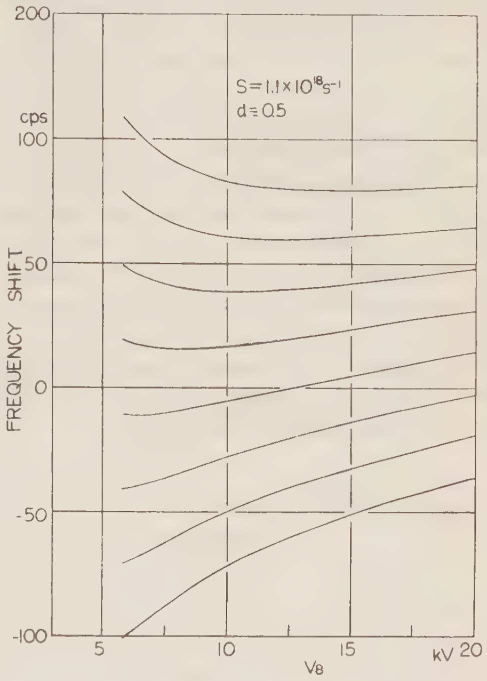

Fig. 18. Theoretical frequency shift vs. focuser voltage for d=0.5, $S=1.1\times10^{18}\,s^{-1}$, $Q=8000$, $L=12$ cm.

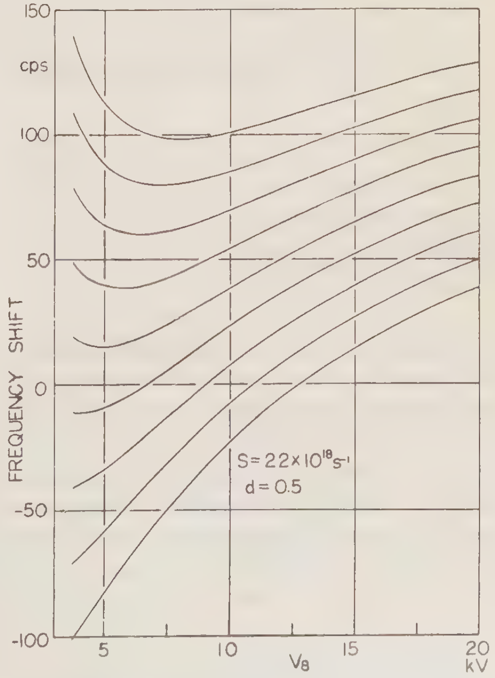

Fig. 19. Theoretical frequency shift vs. focuser voltage, $S=2.2\times10^{18}\,s^{-1}$.

of $\nu_0=22.834$ Mc, $Q=8000$, $L=12$ cm, $v=6\times10^4$ cm/s, and $d=0.5$ are shown. Fig. 18 shows the frequency shift with the focuser voltage for a source flux of $S=1.1\times10^{18}$ molecules per second corresponding to the threshold voltage of 5.8 kV. This may be compared with the experimental result of Fig. 15 which shows a little larger increase in frequency with the focuser voltage.

It is found that the character of the frequency shift strongly depends on the beam intensity. The frequency shift corresponding to the increased source flux of $S=2.2\times10^{18}$ molecules per second is larger as shown in Fig. 19. Hence it seems reasonable to conclude that the experimental characteristics of Fig. 15 for the threshold voltage of 5.6 kV is quite consistent with this theory.

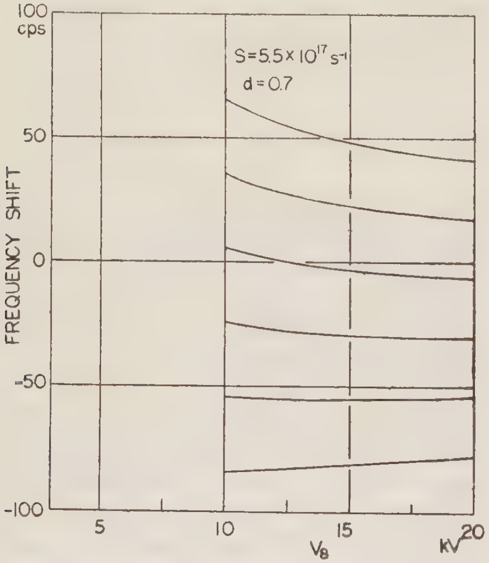

Fig. 20. Theoretical frequency shift vs. focuser voltage, $S=5.5\times10^{17}$ s^{-1}.

A reduction of beam intensity by a factor of two results in the threshold voltage of 10 kV. The frequency shift calculated for $S=5.5\times10^{17}$ molecules per second is shown in Fig. 20. It is rather surprising to see that the change of frequency becomes extremely small in this case. A middle curve in Fig. 20 shows that the frequency changes by less than ±0.3 cps in the range of focuser voltage between 11 and 19 kV.

Compared with Fig. 15, Fig. 14 shows smaller voltage dependence of the frequency. This can be considered as an exprimental evidence of the theoretical result. However, it cannot be concluded that the stability as shown by Fig. 20 is exactly realizable, since the theory did not take the velocity distribution in calculating the traveling wave effect. Also there are causes of frequency shift which were not included in the result of Fig. 20.

Concerning the stability of the absolute frequency, it may be remarked that even when the waveguide is coupled to the cavity at the middle of its length, the effective value of Z is not equal to $L/2$ because of some possible inhomogeneity of the rf field. For example, if the rf field is weaker in the part of the cavity near the focuser, the effective value of Z is smaller than $L/2$ and d is larger than 0.5. The frequency characteritic for a large value of $d=0.7$ is shown in Fig. 21, where the apparent line center is about 50 cps lower.

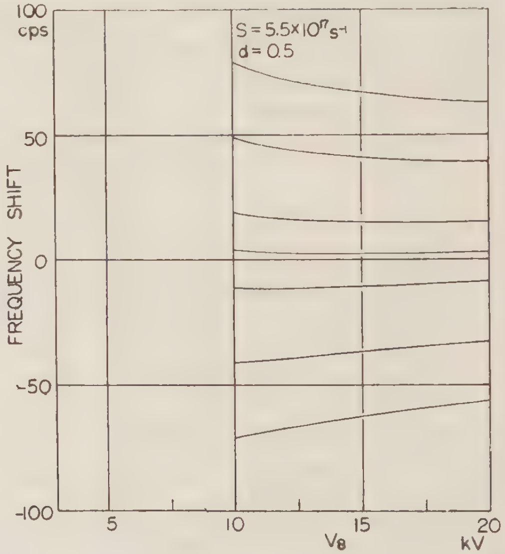

Fig. 21. Theoretical frequency shift vs. focuser voltage for $d=0.7$, $S=5.5\times10^{17}$ s^{-1}.

Determination of the line center by the magnetic perturbation method will be discussed in the paper which follows next. Experimental results on the stability, resettability and reproducibility of the 3,2 line maser will also be discussed.

Acknowledgment

The author wishes to express his appreciation to Mr. Noboru Kohno who assisted in the construction and operation of the apparatus.

References

1) J. P. Gordon, H. J. Zeiger and C. H. Townes: Phys. Rev. **99** (1955) 1264.
2) K. Shimoda, T. C. Wang and C. H. Townes: Phys. Rev. **102** (1956) 1308.
3) K. Shimoda: J. Phys. Soc. Japan **12** (1957) 1006.
4) H. G. Venkates and M. W. P. Strandberg: J. Appl. Phys. **31** (1960) 396.
5) R. C. Mockler and J. A. Barnes: NBS Report 6078 (1959).
6) A. M. J. Mitchell, K. G. Roots and G. Phillips: Electronic Tech. April 1960, P 136.
7) K. Shimoda: J. Phys. Soc. Japan **13** (1958) 939.
8) J. C. Helmer: J. Appl. Phys. **28** (1957) 212. F. S. Barnes: Proc. I. R. E. **47** (1959) 2085.
9) J. Bonanomi, J. De Prins, J. Herrmann et P. Kartschoff: Helv. Phys. Acta **30** (1957) 492.
10) J. Bonanomi et al.: Helv. Phys. Acta **31** (1958) 286.
11) K. Shimoda: Report on Atomic Frequency Standard **1** (1958) 17, (in Japanese).
12) K. Shimoda: Proceeding of Conference on Quantum Electronics **1** (1960) 25.

JOURNAL OF THE PHYSICAL SOCIETY OF JAPAN, Vol. 16, No. 9, SEPTEMBER, 1961

Optical Study of Aniline Hydrobromide Single Crystal

By Tsuruji IWAI

Faculty of Science, Osaka University

(Received April 20, 1961)

A domain structure previously concluded by an X-ray study of aniline hydrobromide was directly confirmed by optical means. The domain walls were found to move easily by a shearing force. The temperature dependence of the extinction angle was obtained. The thermal transition of transparency was measured, and interpreted on the basis of the domain structure. The refractive indices were also measured. Although the double refraction was found to be fairly large, any anisotropy of optical absorption was not detected within the limit of experimental error.

§ 1. Introduction

According to an X-ray investigation reported by Taguchi,[1] aniline hydrobromide is orthorhombic above 27.5°C, and is monoclinic below this temperature. His conclusion is that below the transition temperature crystals which appear to be single crystals in the macroscopic observation consist, in fact, of domains having two different orientations, the *b*- and *c*-axes in common. On passing upward the transition temperature, the domains disappear and the crystals transform into orthorhombic single crystals.

The axial angle β was found to vary reversibly with temperature, in the range from the transition temperature down to about -60°C. Finally he concluded on the basis of the crystal structure below and above the transition temperature[2] that this phase transition is of the type of order-disorder associated with the hydrogen atom bound to the nitrogen atom. This point of view has recently been confirmed by a specific heat measurement.[3] A dielectric measurement seems to support this point of view.[4]

The method of the "Thermal Transition of Transparency" developed by Horie *et al.*[5)-7)] has been proved to be very useful to elucidate the temperature variation of a domain structure. In the following, a study on the domain structure of aniline hydrobromide by means of the method of the thermal transition of transparency, together with other optical properties of the same material will be given.

§ 2. Optical Observation of Domain Structure

A microscopic observation of thin specimens was carried out, in order to confirm the existence of the domain structure reported by Taguchi.[1]

1) *Domain Structure and Temperature Dependence of Extinction Angle*

Crystals of aniline hydrobromide used in this investigation were prepared by slow evaporation from a methyl alcohol solution. They show apparently the orthorhombic symmetry, predominant faces being {100} and {001}. These crystals did show any domain structure, even when viewed at right angles to the *a*- or *c*-faces under the polarizing microscope. This does not contradict to the conclusion given by the X-ray investigation, because if the domain walls are all parallel to the *bc*-plane, the extinction positions for all of the domains coincide with each other, as far as the *a*- or *c*-faces are concerned. However, a plate which was cut parallel to the *b*-plane and carefully polished did actually exhibit a polydomain structure at room temperature, and it was found that the domain walls were all parallel to the *bc*-plane. This is in good agreement with the conclusion given by the X-ray study. The domain structure is caused by the monoclinicity of the crystal and is similar to that of the monoclinic tungsten oxide, WO$_3$.[8,9] The extinction positions differ from each other for adjacent domains as shown in Photo. 1. Therefore, by measuring the angle between these two extinction positions at different temperatures, the temperature dependence of the inclination of the optic elasticity axis to the *c*-axis, φ, can be obtained. The results are shown in Fig. 1.

The variation of φ with temperature is gradual over a wide range of temperature, and it is quite similar to that of the axial angle β. Any temperature hysteresis was not observed. On heating the crystal, the domain structure disappears above 27.5°C, because each of the optic elasticity axes in any one of domains coincides with either *a*- or *c*-axis in the orthorhombic phase.

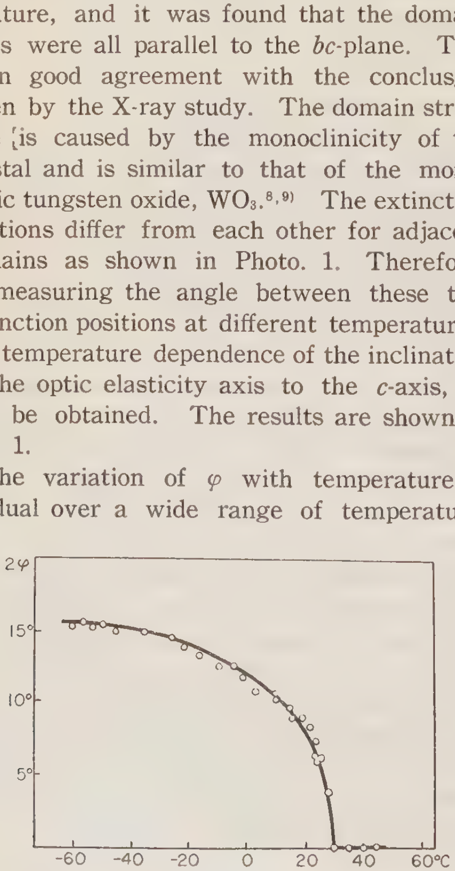

Fig. 1. Angle of twice φ *versus* temperature.
φ: the angle between the optic elasticity axis and *c*-axis.

2) *Effect of Mechanical Force on Domain Structure*

Crystals of aniline hydrobromide are composed of many domains at room temperature. As a result, the *c*-face has a zigzag structure due to the monoclinic angle. If a stress is applied in such a direction that the zigzag structure is smoothed out, the domain walls are expected to move as was reported for the case of WO$_3$.[8] In fact, the domain walls were found to move quite easily, even when a weak shearing stress was applied.

Photo. 2(a) shows the domain structure of a *b*-cut crystal placed between crossed Nicols. The planes of polarization are shown with crosses in Photos. 2, (a) to (f). The domains which look dark will be called type I and the other type II. When a shearing stress X_z is applied, the domains of type II begin to grow at the expense of those of type I, and as a result the zigzag structure becomes smooth to some extent, as shown in Photo. 2(b). On the contrary, if a stress is applied to the opposite direction, just the reverse process can be observed. A successive change in domain widths due to increasing shear is shown in Photos. 2, (c) to (d). If the shearing becomes sufficiently large, the crystal finally assumes nearly a single domain structure, as shown in Photo. 2(d). When such a crystal having a nearly single domain structure is heated above 27.5°C and then cooled down through this temperature, it shows a polydomain structure again, which is almost similar to the original one, as shown in Photo. 2(e). Some one of domains becomes a wedge-shaped one in the course of vanishment under the influence of a shearing stress. An example is shown by the arrow in Photo. 2(f).

§ 3. Temperature Dependence of Refractive Index

To measure the refractive index of a tiny crystal such as barium titanate,[10] Chaulnes' method has hitherto been used. This method, however, gives only a mean value of the refractive indices. Sawada and Danielson[11] have modified this method to determine the principal indices of refraction, by using plane-polarized light. This method was applied to *a*- and *c*-crystals of aniline hydrobromide about 300μ in thickness. A tungsten lamp was used a light source, because an ordinary monochromatic light source was insufficient in intensity for this purpose. Especially, the multi-domain structure of the monoclinic phase makes the measurement extremely difficult. However, as mentioned above, the domain walls can easily be removed away by a shearing stress. The measurement was carried out by use of a wide single domain region obtained in this way. The results are shown in Fig. 2, where the three principal indices of refraction are denoted by n_x, n_y and n_z, respectively.

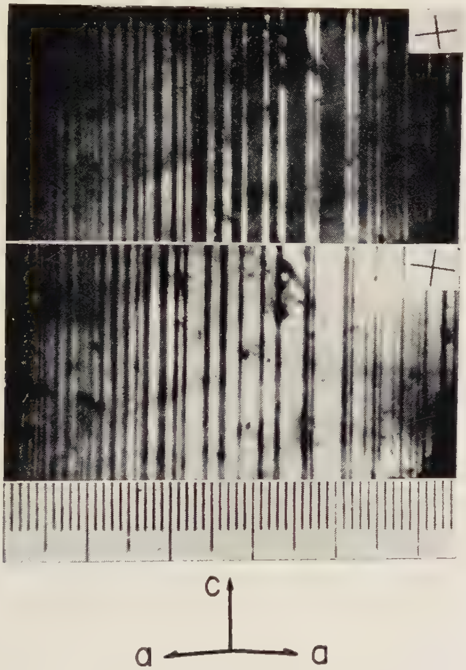

Photo. 1. Alternating extinction, accompany with different extinction positions (10^{-2} mm/div.).

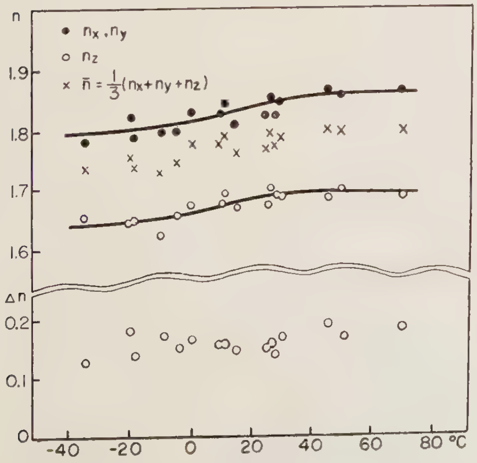

Fig. 2. Refractive indices *versus* temperature.

Any measurable difference between n_x and n_y is not detected and the birefringence $\Delta n=n_x-n_z$ remains unchanged, within the limit of experimental error over a wide temperature range from 70° to about -40°C, and besides the following relation holds throughout for the two phases: $n_x \approx n_y > n_z$. Thus, aniline hydrobromide is optically negative, in agreement with the description of Groth.[12] The temperature dependence of the refractive indices is quite small. However, the observed values decrease slightly, as the temperature is lowered. A qualitative reason for this tendency might be as follows. On cooling the crystal, the structural change occurs at 27.5°C. As the result, the local field which is acting on constituents of the crystal and effective to the refractive indices also changes.

§4. Optical Absorption

In order to see if there is any anisotropy of absorption, measurements were made by means of a microscopic spectrograph.[13] The apparatus is a combination of a microscope and a spectrograph, all of the optical elements being made of quartz. An iron arc was used

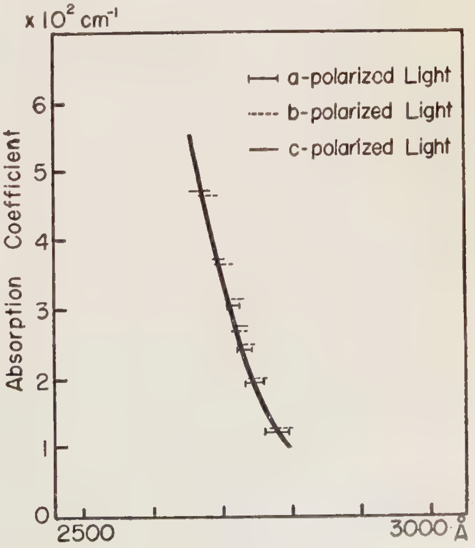

Fig. 3. Optical absorption.

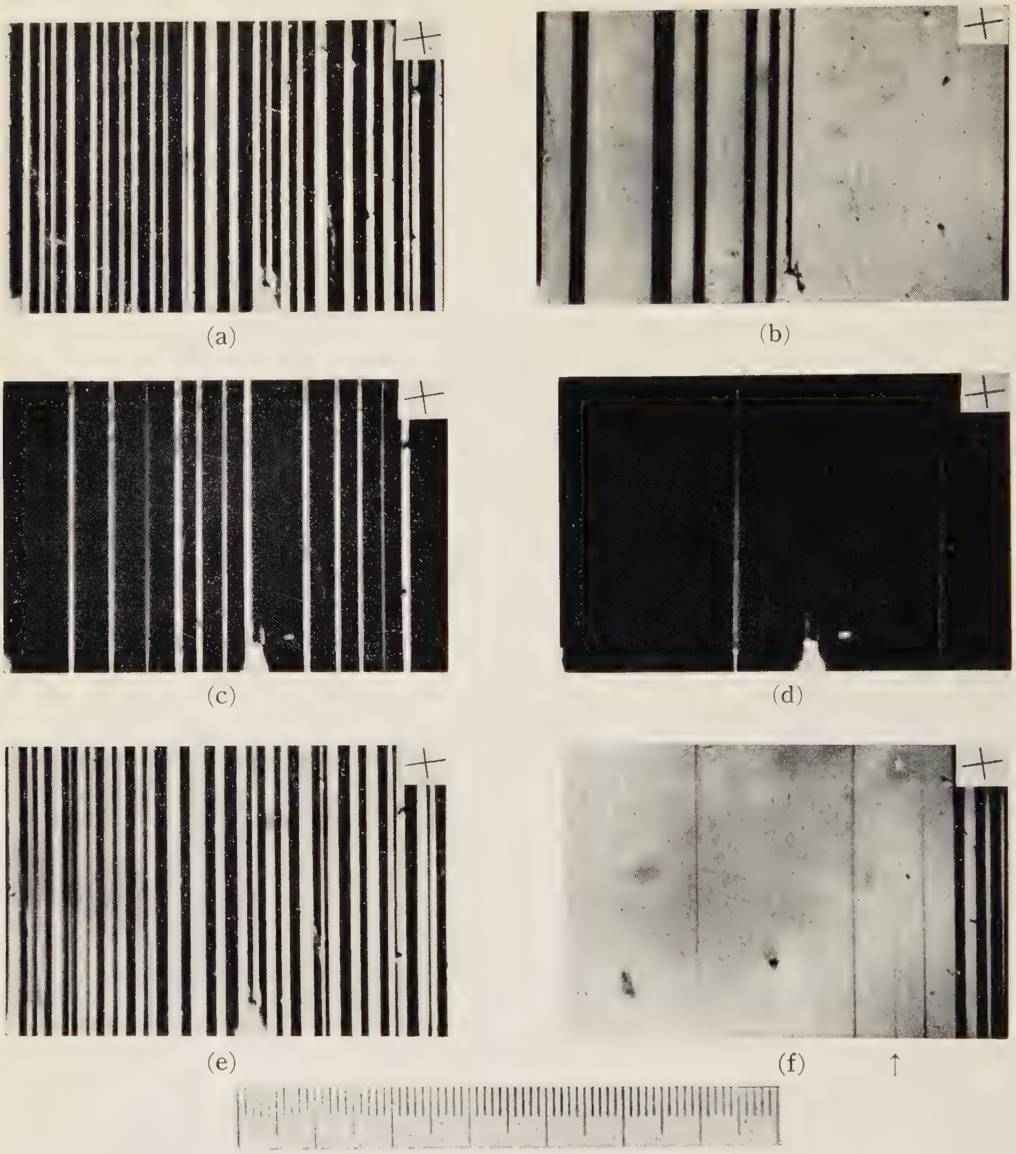
(a) (b) (c) (d) (e) (f) ↑

Photo. 2. Shearing stress effect on the domain structure (10^{-2} mm/div.).

as a light source. The *a*- and *c*-crystals about 300μ in thickness were used as specimens. The absorption spectrum for plane-polarized light was taken at 30°C. The result obtained is shown in Fig. 3, where the light polarized in the direction parallel to each of the *a*-, *b*- and *c*-axes is called *a*-, *b*- and *c*-polarized light. (The direction of polarization is given by the direction of electric vector.) The absorption curve is rather steep and the threshold lies at about 2750Å. Any distinct defference among the absorption edges for the three different polarized lights was not detected within the limit of experimental error.

In a crystal whose symmetry is lower than cubic, the crystalline field splits otherwise a degenerate electronic state into its components. This effect causes the crystal to give rise an anisotropy of absorption, as has been found in several transparent crystals.[14] In addition to this effect, another type of anisotropy arising from level splitting due to intermolecular resonance has also been reported to take place in some molecular crystals.[15] From these points of view, it may be concluded that splitting of the electronic states in aniline hydrobromide is too small to give rise to any anisotropy in its optical absorption.*

§ 5. Thermal Transition of Transparency

The thermal transition of transparency (T.T.T., for brevity) for aniline hydrobromide was observed with the aid of an experimental arrangement which has already been described in detail.[5] Natural light from a tungsten lamp was projected perpendicularly onto a virgin crystal, and its enlarged image was focussed by a microscope on a diaphragm just in front of a multiplier photo-tube, the photo-current of which was magnified by a D.C. amplifier. The temperature of the specimen was controlled by an electric heater and liquid air in a modified Dewar flask.

A virgin *c*-crystal about 300μ in thickness was used as a specimen. As has been mentioned in §2, the virgin crystal does not show any domain structure visible under a polarizing microscope. The T.T.T. obtained is shown in Fig. 4, where open circles represent the experimental plotting. On cooling the crystal down through the transition temperature, its transparency decreases at first rapidly and then tends asymptotically to a certain limit below −60°C. The temperature hysteresis loop associated with the phase transition as seen in $BaTiO_3$[5-7] was not observed.

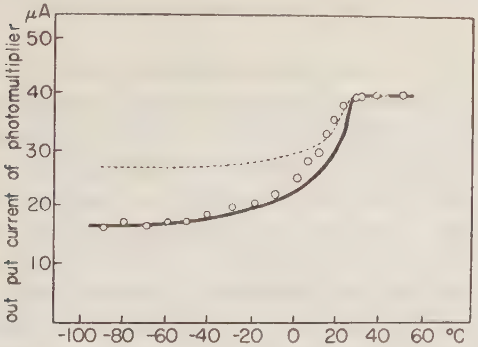

Fig. 4. Thermal transition of transparency.
- - - -: calculated value by flat boundary surface assumption.
——: calculated value by zigzag boundary surface assumption.

This T.T.T. curve is quite similar to the temperature dependence of the axial angle β.

§ 6. Interpretation of T.T.T.

The T.T.T. of barium titanate has interpreted by Horie *et al.*[5,6] on the basis of the domain structure and of crystal optics. A similar consideration is now applied to the case of aniline hydrobromide.

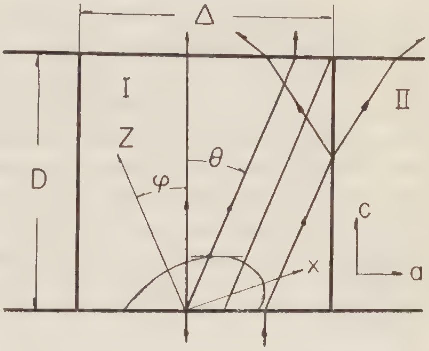

Fig. 5. Optical paths in the monoclinic phase (case of flat boundary surface).

When natural light falls perpendicularly onto a *c*-crystal, the light is decomposed into two extraordinary waves. The intersections of these wave surfaces with the *b*-plane are a circle and an ellipse. If the *c*-face is assumed to be flat, only the wave with elliptic section is deflected sideways owing to reflection and refraction at a domain boundary, as explained in Fig. 5. If the intensity of light transmitted through the crystal is called I in the orthorhombic phase, and $I-\delta I$ in the monoclinic phase, a consideration similar to that given in the case of $BaTiO_3$ leads to the following equations:

$$\delta I \approx \frac{1}{2}\cdot\frac{D|\tan\theta|}{\overline{\varDelta}} I \qquad (1)$$

and

$$\tan\theta \approx \left\{\left(\frac{n_x}{n_z}\right)^2 - 1\right\}\varphi, \qquad (2)$$

where D is the thickness of the crystal, $\overline{\varDelta}$ is the mean domain width and θ is the angle of refraction as shown in Fig. 5; and it is assumed that $\varphi \ll 1$. From the measurement of the refractive indices, n_x/n_z was found to vary only slightly with temperature. Therefore, the change in transparency, δI, is expected to depend linearly on φ. The values of n_x/n_z and φ were determined experimentally, and the values of D and $\bar{\Delta}$ were obtained by microscopic observation as follows: $D=290\mu$; $\bar{\Delta}=7.7\mu$. On substituting these values into the above equations, the curve of T.T.T. is calculated, which is shown by the dashed curve Fig. 4. However, a remarkable difference between the observed and calculated values is noticed especially at lower temperatures.

---

* In some substances such as CdS, $BaTiO_3$ and WO_3, splitting of the electronic level due to the crystalline field is estimated by several authors[14] at 0.02~0.07 ev. Splitting due to intermolecular resonance observed in some crystals of aromatic molecules is also of the order of 0.01 ev.[15] In the present experiment, the experimental error is of the order of magnitude of 0.03 ev.

Eq. (1) is derived under the assumption that the crystal surface is perfectly flat. Actually, that is not the case owing to twinning. According to the X-ray study,[1] β varies gradually with temperature and becomes 91°22′ at −110°C and the c-faces in adjacent domains make an angle of 2°44′ with each other. In such a case, the wave with circular section may also be deflected. As a result, Eqs. (1) and (2) will be modified as follows (see Appendix):

$$\delta I \approx \frac{1}{2}\cdot\frac{D(|\tan\theta_1|+|\tan\theta_2|)}{\bar{\Delta}} I, \qquad (1')$$

$$\tan\theta_1 \approx \left\{\left(\frac{n_z}{n_x}\right)^2-1\right\}\varphi + \left(\frac{n_z}{n_x}\right)^2\left(1-\frac{1}{n_x}\right)\left(\beta-\frac{\pi}{2}\right) \qquad (2')$$

and

$$\tan\theta_2 \approx \left(1-\frac{1}{n_y}\right)\left(\beta-\frac{\pi}{2}\right), \qquad (2'')$$

where the terms dependent on $\Delta\beta=\beta-\pi/2$ show the correction due to non-flatness of the c-face. The angle $\Delta\beta$ varies in a manner similar to φ with temperature, as mentioned in §2. By use of the above equations, the theoretical curve for the T.T.T. is refined as shown by the solid curve in Fig. 4. The corrected curve is in good agreement with the experimental result.

Consequently, the T.T.T. of aniline hydrobromide can be understood on the basis of the domain structure and of crystal optics. The T.T.T. method can be applied to virgin crystals without any treatment, such as cutting or polishing which is necessary to make a direct observation of the domain structure. The T.T.T. method, therefore, is proved to be a useful means to investigate the phase transition of aniline hydrobromide.

§ 7. Conclusions

(1) A microscopic observation confirms the domain structure which has been concluded by the X-ray study. The domain structure is due to the monoclinicity as seen in WO_3, and disappears in the orthorhombic phase. The domain walls are all parallel to the bc-plane. These results obtained by microscopic observation support the conclusion given by the X-ray investigation. In addition, it is observed that the domain walls move easily under the influence of a weak shearing stress.

(2) The inclination of the optic elasticity axis to the c-axis in the b-plane, φ, varies reversibly with temperature. The variation of φ is continuous and gradual over a wide temperature range, and is similar to that of the axial angle β given by the X-ray study.

(3) The transparency also varies gradually and reversibly with temperature, and its variation is similar to that of the axial angle β. Such a behavior can clearly be understood on the basis of the domain structure and of crystal optics. Accordingly, aniline hydrobromide seems to be another typical example which proves the T.T.T. method as a useful means of optical study of phase transition.

(4) The refractive indices vary slightly with temperature. The crystal of aniline hydrobromide is optically negative in both the high and low temperature modifications.

Acknowledgments

This work has been carried out under the guidance of Professor T. Horie, to whom the author wishes to express his sincere gratitude. The author wishes to express his sincere gratitude to Professor T. Watanabe for his valuable suggestions and kind advice. The author also wishes to express his sincere thanks to the late Dr. I. Taguchi for useful discussions and facilities for the preparations of specimens. He is much indebted to Dr. K. Kawabe of Kobe University and Dr. H. Akao for their useful discussions and criticisms.

Appendix

Correction for Non-Flatness of c-Face

1) *Elliptic section:* The incident and the refracted wave fronts are denoted by OA and A′P, respectively in Fig. 6. If assumed AA′=1, the coordinates (x_1, z_1) of the point A′ are given by

$$x_1 = -\frac{\cos(\varphi+\Delta\beta)}{\sin\Delta\beta}, \quad z_1 = \frac{\sin(\varphi+\Delta\beta)}{\sin\Delta\beta}. \tag{3}$$

If the coordinates of P are denoted by (X, Z), the following equation are obtained at once:

$$n_z^2X^2 + n_x^2Z^2 = 1, \quad n_z^2Xx_1 + n_x^2Zz_1 = 1\,. \tag{4}$$

Let θ_1 be the angle between the direction of the refracted ray and the z-axis. Then

$$\tan(\varphi+\theta_1) = \frac{X}{Z}\,. \tag{5}$$

From these five equations we have

$$\tan\theta_1 = \left\{\left(\frac{n_x}{n_z}\right)^2 - 1\right\}\varphi + \left(\frac{n_z}{n_x}\right)^2\left(1 - \frac{1}{n_x}\right)\Delta\beta + \mathrm{O}(\alpha^3)\,, \tag{6}$$

where $\mathrm{O}(\alpha^3)$ means the term of higher powers than the third in φ and $\Delta\beta$.

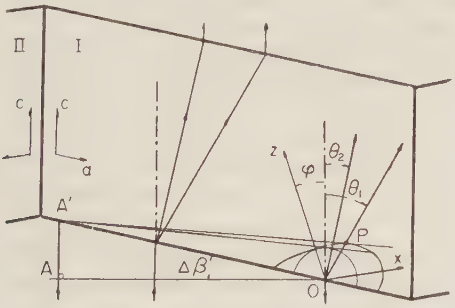

Fig. 6. Optical paths in the monoclinic phase (case of zig-zag boundary surface).

2) *Circular section:* If the angle between the direction of the refracted ray and the z-axis is called θ_2, a calculation similar to that mentioned just above leads to the following equation:

$$\tan\theta_2 = \left(1 - \frac{1}{n_y}\right)\Delta\beta + \mathrm{O}(\alpha^3). \tag{7}$$

The apparatus is insensitive to the beams deflected from the direction of incidence to the side by angles larger than 1°30′. According to a calculation similar to the case of barium titanate based upon crystal optics, the wave with elliptic section which encountered a domain boundary does not fall upon the detector at least below 25°C. As for the case of circular section, such a condition is satisfied at least below 20°C. Hence the relation (1′) holds at least below 20°C.

References

1) I. Taguchi: Thesis, Osaka Univ. (1958).
2) I. Nitta, T. Watanabe and I. Taguchi: to be published.
3) H. Suga: Thesis, Osaka Univ. (1958).
4) K. Kawabe: The autumn meeting of the Physical Society of Japan, September 27, 1960.
5) T. Horie, K. Kawabe and T. Iwai: Ann. Rep. Sci. works, Fac. Sci. Osaka Univ. **4** (1956) 45.
6) T. Horie, K. Kawabe, M. Tachiki and S. Sawada: J. Phys. Soc. Japan **10** (1955) 541.
7) K. Kawabe: J. Phys. Soc. Japan **14** (1959) 1755.
8) S. Tanisaki: J. Phys. Soc. Japan **13** (1958) 363.
9) S. Sawada and G. C. Danielson: Phys. Rev. **113** (1959) 1005.
10) G. Busch, H. Flury and W. Merz: Helv. Phys. Acta **21** (1948) 212.
11) S. Sawada and G. C. Danielson: Phys. Rev. **113** (1959) 1008.
12) P. Groth: "Chemische Kristallographie" **4** (1917) pp. 170.
13) M. Kobayashi and R. Tsuchida: J. Chem. Soc. Japan **60** (1939) 769. (in Japanese)
14) G. Dresselhaus: Phys. Rev. **105** (1957) 135.
J. L. Birman: Phys. Rev. **114** (1959) 1490.
R. C. Casella and R. P. Keller: Phys. Rev. **116** (1959) 1469.
T. Iwai: J. Phys. Soc. Japan **15** (1960) 1596.
15) H. Winston: J. Chem. Phys. **19** (1951) 156.
D. S. McClue and O. Schnepp: J. Chem. Phys. **23** (1955) 1575.

JOURNAL OF THE PHYSICAL SOCIETY OF JAPAN, Vol. 16, No. 9, SEPTEMBER, 1961

On the *R* Centers in Lithium Fluoride

By Akizo OKUDA

Department of Mathematics and Physics, Ritsumeikan University, Kyoto

(Received June 2, 1961)

In colored LiF crystals, two bands at 320 and 378 mμ have been investigated and assigned as R_1 and R_2 bands by the correspondences to R bands in other alkali halides. Intensity ratio of the R_1 band to the R_2 band is almost constant irrespective of irradiation conditions of β- or γ-rays as well as of photochemical treatments. Both the bands are bleached by irradiation with either R_1 or R_2 light, where the former has a higher efficiency for the bleaching. The results support the interpretation that R_1 and R_2 bands are due to transitions in the same center. Emission spectra by excitation with R_1 and R_2 lights are distinct: the latter has a peak at 495 mμ and the former at 730 mμ or above.

By polarized R lights, dichroism is induced in the R_1, R_2 and M bands and also polarization of the emissions is observed. Then symmetries of the models which have been proposed as complexes of F centers are examined by the experimental results and it is considered that F_3-model lying in [111] plane is the most adequate for R center. In addition to characteristic M-center luminescence, which has a peak at 710 mμ and value of 0.6 for P[011], an emission band at 525 mμ is observed by M-light excitation but P-factor for this emission is less than that of the M-center luminescence.

§ 1. Introduction

In the alkali halides, it is well known that M-, R_1-, and R_2-absorption bands, which appear on long-wavelength side of F band, are due to transitions in the electron-trapped centers. Among them M band has extensively been studied by many authors and the model of M center has fairly definitely been explained.

However, two essentially different interpretations have been put for R bands. In 1946, Seitz[1] first proposed that the R_1 and R_2 bands arise from the F_2^+ and F_2 centers, respectively, consisting of one and of two electrons trapped at a pair of adjacent negative-ion vacancies. But afterwards, Herman, Wallis, and Wallis[2] observed constant intensity-ratio of R_1 and R_2 bands and considered that both R bands arise from transitions in the same center. Furthermore, from the theoretical calculations based upon Seitz's model, they concluded that F_2 center is responsible for both R bands. Van Doorn[3] proposed single F_3-model lying in the [111] plane from anisotropic behavior of R-band emissions in KCl and NaCl crystals. Recently, Pick[4] proposed a new idea for the F-center associations and suggested three distinct transition moments for R centers on the basis of the F_3-model.

On the other hand, Lambe and Compton[5] observed temporary bleaching effects of R bands in NaCl crystals under strong auxiliary lights and interpreted R_1- and R_2-absorption bands as the transitions in distinct centers. Subsequently, Compton and Klick[6] studied more extensively the temporary bleaching and concluded that R, M, and N centers are located near each other but one cannot decide from the temporary bleaching experiments whether both R_1 and R_2 bands are transitions in two distinct centers or two transitions in the same center.

In the previous paper, the author and others[7] have shown that R_1 and R_2 bands in LiF crystals are due to two transitions in the same center, the symmetry axis of which lies along the body diagonal of the crystal. In the present paper, the detailed results will be reported on correlations between R_1 and R_2 bands under various conditions in Part I, and on anisotropic behaviors of the absorption and luminescence of R bands in Part II. Hitherto the assignment for R_1 and R_2 bands in LiF crystal has not been confirmed[8] and no information concerning the luminescence of *R* centers has been reported. Therefore, the results will also be reported with these respects in Part I.

Usually *R* bands are produced by optical bleaching of *F* band in additively colored crystals or by prolonged irradiation with ionizing radiation. In the case of LiF crystals, however, the additive coloring could not be realized by ordinary procedure, so that in the course of the present work only ionizing radiations were employed for the coloration of the crystals.

§ 2. Experimental Procedure

LiF materials were purified and prepared from LiCl and NH_4HF_2 and single crystals of LiF were produced by Kyropoulos' method from the melts in a vacuum-type furnance whose inner atmosphere was circulated with dried nitrogen gas of low pressure[9]. Samples of about 0.3~1 mm in thickness were cleaved from the crystals. Most samples in this work were colored by exposure to 1-Mev electrons from a Van de Graaff accelerator. In this case, the exposure times and intensities of the flux were varied to obtain appropriate concentration of color centers, where the temperature of the samples was kept at −70°C or at room temperature before the exposure but it was raised under exposure. Some samples were colored by exposure to γ-rays from Co^{60} at room temperature.

The optical absorption for the colored samples was measured with a modified Shimadzu Model QR or Beckman Model DU spectrophotometer. For the purpose of bleaching colored samples, a xenon-arc lamp of 500 watts or a high pressure mercury lamp with quartz envelope was used through a quartz prism monochromator (aperture, $F=2.5$) or suitable filters.

Emission and excitation spectra were obtained by the arrangements shown in Fig. 1. In this figure M I is the Shimadzu Model QR monochromator and M II is the quartz prism monochromator which is used for excitation in the emission-spectrum measurement and for filtration of the luminescence in the excitation-spectrum measurement. An RCA 1P28 photomultiplier or a Toshiba 7305 photomultiplier with a D.C. amplifier was used depending upon the spectral location investigated, and in some cases a Toshiba PT-25-V1 phototube was employed as a check. As the light source for the excitation of luminescence, the xenon-arc lamp or a tangsten lamp was employed, and the emission and excitation spectra were corrected by a thermopile.

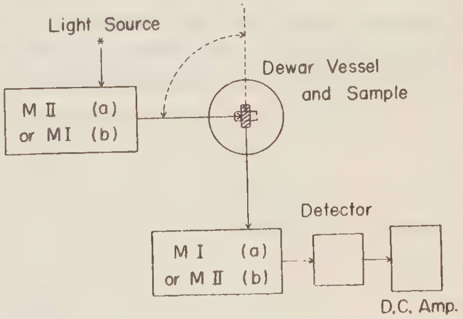

Fig. 1. Experimental arrangements used for studying the luminescence. (a) For measurement of emission spectra. (b) For measurement of excitation spectra. M: monochromator.

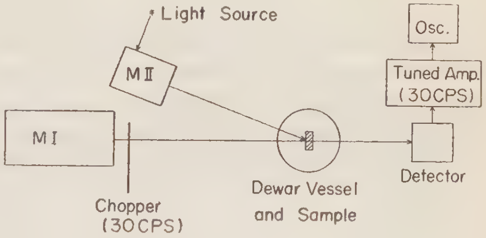

Fig. 2. Experimental arrangement used for studying the effect of temporary bleaching. M: monochromator.

Temporary bleaching effect was studied with the arrangement shown in Fig. 2. The experimental technique used in this measurement was similar to that used by Lambe and Compton except the direction of auxiliary light. The change in transmission of sample induced by irradiation with intense auxiliary light was measured at a given wavelength. The light for the transmission measurement was chopped at 30 cps and the detector was also tuned for this frequency, where the xenon-arc lamp was used as the auxiliary light source.

In order to investigate the anisotropy of color centers, dichroism induced by irradiation with polarized light was measured with a Foucault- or Nicol-prism polarizer. Further, polarization of luminescence was measured with the arrangements shown in Fig. 3. (a) is that for R_1- and R_2-band emissions, where two suitable filters are inserted in the optical path; and (b) is that for *M*-band emission, where the spectral distribution of the degree of polarization is measured through the monochromator (M I). In these cases the Foucault- or Nicol-prism, or a polaroid was employed as the polarizer depending upon the spectral location of exciting lights, and a polaroid was used as the analyzer.

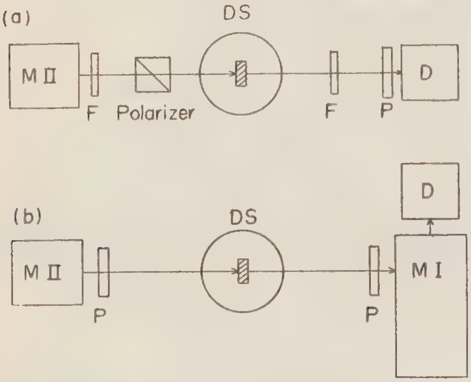

Fig. 3. Experimental arrangements used for the measurements of the polarization of luminescence. (a) For *R*-band emissions. (b) For *M*-band emission. M: monochromator, F: filter, P: polaroid, DS: dewar vessel and sample, D: detector.

In low temperature measurements, the samples were kept at liquid air temperature by using a Dewar vessel with three windows of quartz plate.

I. Absorption and Luminescence

§ 3. Experimental Results

3.1 *Absorption*

After prolonged or intense exposure to Van de Graaff electrons or γ-rays, LiF crystals showed two absorption bands at about 320mμ and at 378 mμ in the region between *F* band at 248 mμ and *M* band at 447 mμ at room temperature. Although the assignment for *R* bands in LiF crystals has not been confirmed, we tentatively assume that the two bands correspond to R_1 and R_2 bands, respectively, according to Penneman and Powers[10]. It will be shown in the next paragraph that this assignment is correct. In addition to these *R* bands, another weak and broad band with peak at 350 mμ appeared immediately after the ionizing radiations, but this band was so unstable that it was bleached out, scarcely affecting R_1- and R_2-band intensities, by brief exposure to ultraviolet light or by preserving at room temperature for a few days[11].

The relative intensities of *F*, *R* and *M* bands after electron bombardment or γ-ray

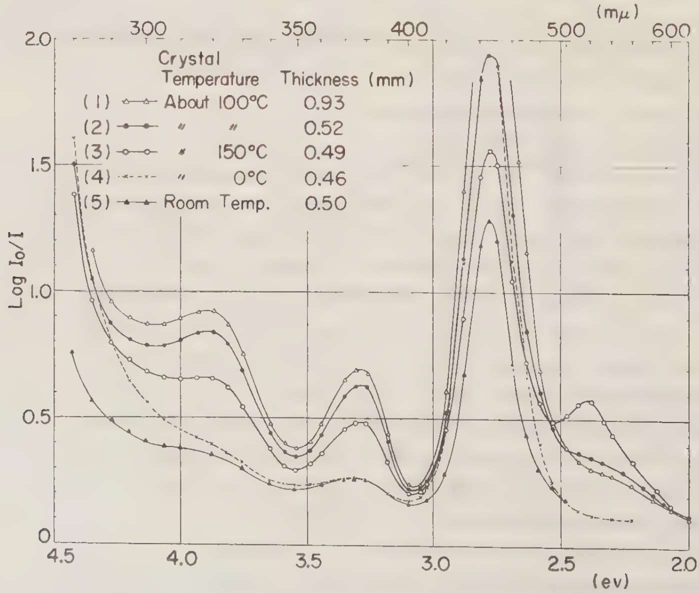

Fig. 4. Absorption spectra of several LiF crystals exposed to Van de Graaff electrons, (1)—(4), or γ-rays, (5). The measurements were made at room temperature.

irradiation differed depending upon the irradiation conditions, for instance, irradiation time or crystal temperature. In the case of electron bombardment, R bands prominently appeared at crystal temperature of about 100°C and only weakly at the temperature lower than 0°C or higher than 200°C, with about 10^8 rad exposure. In these cases it was noticed that the intensity ratios of R_1 and R_2 bands (R_1/R_2) are essentially constant irrespective of irradiation conditions, that is, of concentrations of other centers. Fig. 4 gives the absorption curves in several colored samples. The ratios in some crystals are not certain, because of overlapping of the R_1 band and F-band tail and rise of the background in this region.

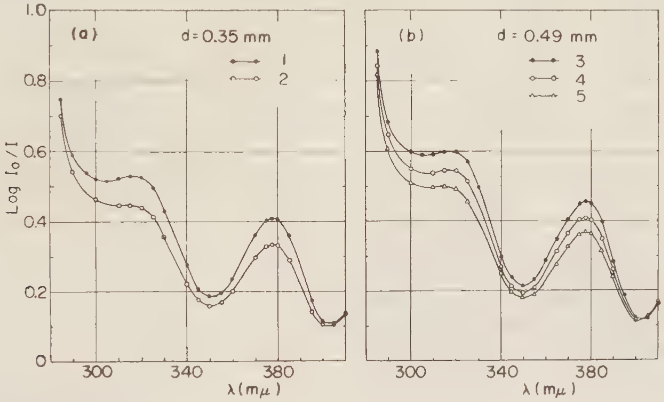

Fig. 5. Optical bleaching of R-bands in LiF crystals by irradiation (a) with R_1-light and (b) with R_2-light, at room temperature. (1) Absorption before irradiation in a crystal. (2) After irradiation with 330 mμ light. (3) Absorption before irradiation in another crystal. (4) After irradiation with 385 mμ light, and (5) further with 365 mμ light. Measurements were made at room temperature.

When a colored sample exhibiting R bands was exposed to R_1 light (330 mμ, band pass ~10 mμ) at room temperature, both R_1- and R_2-band intensities were decreased together and M-band intensity was enhanced. The same effect was observed when a sample was exposed to R_2 light (365 mμ or 385 mμ, band pass~20 mμ). These results are given in Fig. 5 and it is found that the ratios of decrements in R band intensities, $-\Delta R_1/(-\Delta R_2)$, are essentially constant as shown in Fig. 6, about 1.2. When a sample was exposed to R_1 light at 100°C and absorption was measured at room temperature, the above ratio was almost unaltered. By the successive irradiation with R_1 light at room temperature, R bands were gradually decreased maintaining the above relation, and in final stage at which the R bands were almost bleached, the ratio was still nearly uncharged and the peaks of the bands did not seem to shift in the course of bleaching. The typical absorption spectra observed at liquid air temperature will be shown just later (Fig. 9). It was observed in the above bleaching experiments that both R bands are more effectively reduced by R_1 light than by R_2 light. The relative efficiency of the bleaching for absorbed quanta is shown in Table I, making use of the results in Fig. 5, where R-light intensities are corrected by a thermopile.

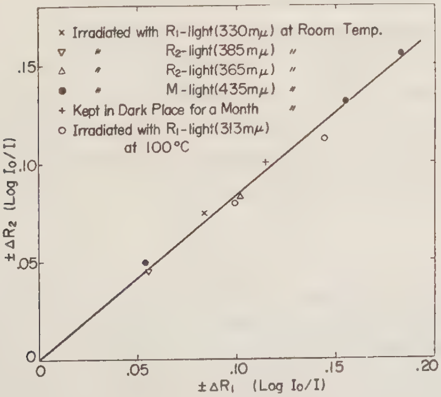

Fig. 6. Relation between the increment or decrement of R_1- and R_2-band peaks in several LiF crystals after various treatments, measured at room temperature.

Table I. Relative efficiency of the bleaching of R bands for absorbed quanta, at room temperature.

Irradiating light	Efficiency
330 mμ	1.0
365 mμ	1.8×10^{-2}
385 mμ	7.4×10^{-3}

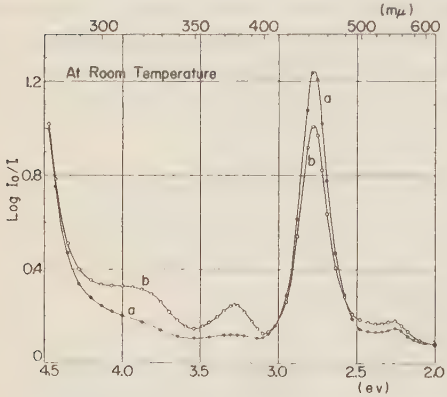

Fig. 7. Developing of R bands by irradiation with M light. (a) Absorption after irradiation with R light. (b) Absorption after subsequent irradiation with M light (435 mμ line of mercury arc), at room temperature.

Two observations were done after the R-bands bleaching with R_1 light. First, when a sample was irradiated by intense M light (435 mμ line of mercury arc) at room temperature, M-band intensity was reduced and R-band intensities were again increased as shown in Fig. 7*. Second, when a sample was kept in dark place at room temperature for a few months, the same effect was observed. In these cases the ratio of increments in R-band intensities, $\Delta R_1/(\Delta R_2)$, was again equal to that obtained in the bleaching experiments as shown in Fig. 6. The M band developed with R_1-light irradiation was more easily bleached by M-light irradiation than ordinary M band in the crystals which had not been irradiated by R light beforehand.

A colored sample exhibiting R bands was thermally pulse-annealed as follows: the sample was placed for two minutes at a high temperature and cooled quickly to room temperature at which absorption was measured. Starting from room temperature, the annealing temperature was raised by 20°C in successive processes. Then, the R_1 and R_2 bands began to bleach at the same temperature of about 200°C, as shown in Fig. 8. But in this case the ratio of decrements was uncertain because of the rise of background on the R_1-band region**.

After electron bombardment, absorption

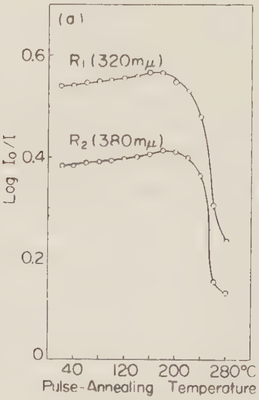

Fig. 8(a).

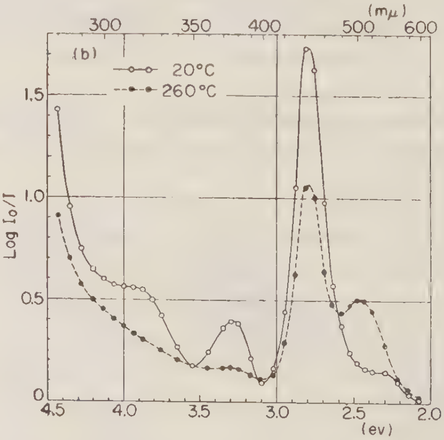

Fig. 8(b).

Fig. 8. Thermal stability of R bands in a LiF crystal. (a) Absorption intensities after pulse-annealing, measured at room temperature. (b) Absorption spectra for the initial and the later stages of the annealing, measured at room temperature.

---

* When colored crystals were irradiated simultaneously by the lights in R and M bands (for instance, carbon or mercury arc with suitable filter), a weak band with peak at about 375 mμ and a fairly strong band with peak at 550 mμ, which might correspond to N band, were developed on short-wavelength side of R band and long-wavelength side of M band, respectively.

** This may be attributed to a colloidal band with peak at 270 mμ[8].

spectra of samples showed fine structure in the R_2-band region at liquid air temperature as reported by Delbecq and Pringsheim[8]. A typical absorption spectrum is given in Fig. 9 curve (a). The appearance and regular spacing of the peaks of about 240 cm^{-1} are in accordance with those already reported. When the absorption spectrum at liquid air temperature is compared with that at room temperature given in Fig. 9 curve (a′), the peak of R_2 band does not shift in contrast with the peak of R_1 band which shifts to short-wavelength side at low temperature. When the sample was irradiated by R_1 light at room temperature like the above procedure and the absorption was measured at liquid air temperature, the fine-structure intensity was decreased in company with the decrease in the R_1- and R_2-band intensities as shown in Fig. 9 curves (b), (c) and (d). It seems that also one proportionality is maintained for the R_1, R_2 and the fine-structure intensities in each stage. Again, when the sample was irradiated by M light at room temperature and the absorption was measured at liquid air temperature, then the fine structure also appeared in company with the R_1 and R_2 bands.

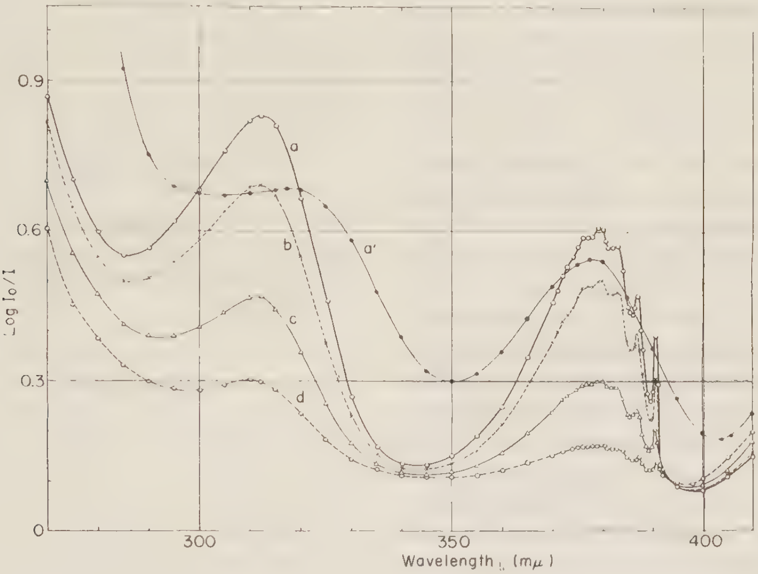

Fig. 9. Variation of the R bands and the fine structure by irradiation with R_1 light (320 mμ) at room temperature. (a) and (a′) Initial state measured at liquid air and room temperature, respectively. (b) After irradiation for 3 minutes, measured at liquid air temperature. (c) and (d) After irradiation for 13 and 53 minutes, respectively, measured at liquid air temperature.

No bleaching of R bands was observed by the irradiation with R light at liquid air temperature. On the other hand, temporary bleaching effects of crystals were observed by auxiliary R_2-light at liquid air temperature, and not by auxiliary R_1-light, which is probably due to weak intensity of R_1 light. A typical result is shown in Fig. 10. It is seen that the magnitudes of bleaching for R_1 and R_2 bands are nearly equal and also some changes in absorption are induced in other spectral region. The temporary bleaching

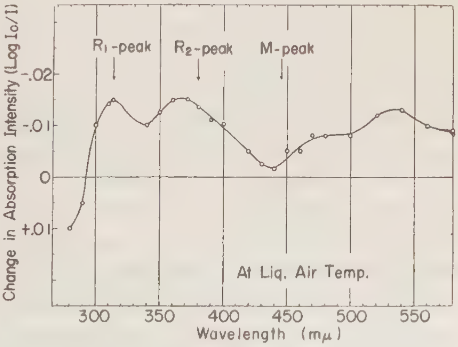

Fig. 10. Temporary change in absorption induced by irradiation with light in the R_2 band.

was not observed at room temperature.

3.2 *Luminescence*

When LiF crystals showing R bands were excited with light in R_1 or R_2 band at liquid air and room temperatures, luminescence was observed. The emission spectra observed at liquid air temperature are shown in Fig. 11. Curve (a) is that excited with R_1 light and has a peak at 730 mμ or above; curve (b) is that excited with R_2 light and has two peaks, the one at 495 mμ and the other at 710∼730 mμ, whose intensity is lower than that of the former, and by spectrographic examinations no fine structure was observed in the R_1- and R_2-band emissions. Since the red emission excited with the R_1 or R_2 light is comparatively weak and the sensitivity of the photomultiplier used in this work is depressed at longer-wavelength region than 700 mμ, locations of the emission peaks observed in this region are uncertain to some extent.

Luminescence excited with the M light was measured since the LiF crystals exhibiting the R-band luminescence showed fairly intense M-band absorptions and also intense emissions by excitation with M light. The spectrum has two peaks at 525 mμ and at 710 mμ, as shown in Fig. 11 curve (c) and the intensity ratio of the former to the latter differed in different samples.

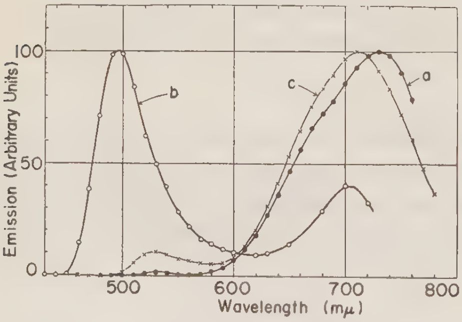

Fig. 11. Emission spectra of a LiF crystal. (a): excitation with R_1 light (315 mμ); (b): with R_2 light (380 mμ); (c): with M light (450 mμ). Measurements were made at liquid air temperature.

No significant difference was observed between the emission spectrum at liquid air temperature and that at room temperature in a crystal, but at room temperature the red emission excited by R_2 light increased partly because of the overlapping of R_2- and M-absorption bands and the resolution of two emission bands excited by M light was lowered. In general, emission excited by M, R_1 or R_2 light was quenched in the crystals containing very high concentration of centers both at room and low temperatures.

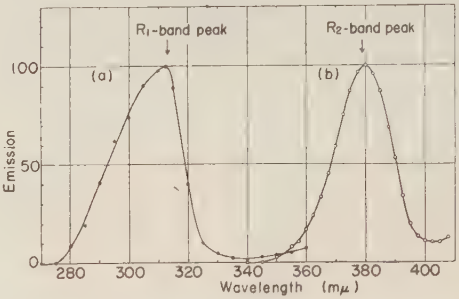

Fig. 12. Excitation spectra for R_1- and R_2-band emissions at liquid air temperature. (a) For R_1-band emission (650 mμ). (b) For R_2-band emission (495 mμ).

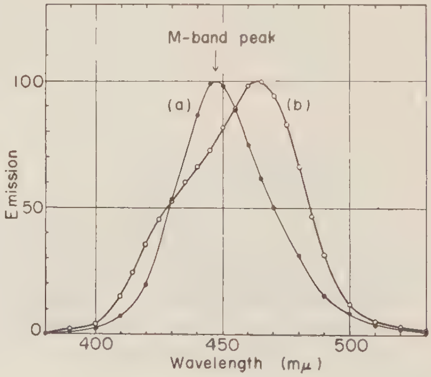

Fig. 13. Excitation spectra for M-band emission at liquid air temperature. (a) For 650 mμ emission. (b) For 525 mμ emission.

Excitation spectra for the luminescence were measured at liquid air temperature. In Fig. 12, (a) gives excitatian spectrum of R_1-absorption region for 650 mμ emission (band pass∼40 mμ) which is the peak of the R_1 emission with the detector used*. It is seen that the peak of the spectrum almost coincides with that of R_1-absorption but the long-wavelength tail is weakened in contrast with the absorption. (b) gives that of R_2-absorption region for 495 mμ emission (band pass∼25 mμ). It is seen that the peak and half width coincide with those of R_2-absorption band, but the fine structure, which is observed in absorption spectrum, is not detected. The excitation spectra of *M*-band region for 650 mμ emission (band pass$\sim$40 mμ) and for 525 mμ emission (band pass$\sim$30 mμ) are shown in Fig. 13. In the former the peak and half width almost coincide with those of *M*-absorption band, but in the latter the peak shifts to long-wavelength side of *M*-absorption peak and a small hump is also observed on short-wavelength side.

---

* Photomultiplier 7305.

As described in the foregoing section, *M* band is enhanced by irradiation with R_1 light and as mentioned above, the emission spectrum excited by *M* light has two peaks. So it is desirable to observe the change in the luminescence after the enhancement of *M* band. The result is shown in Fig. 14. It was found that after the enhancement of *M* band, the intensity of the 710 mμ emission band was increased while that of the 525 mμ emission band was almost unchanged.

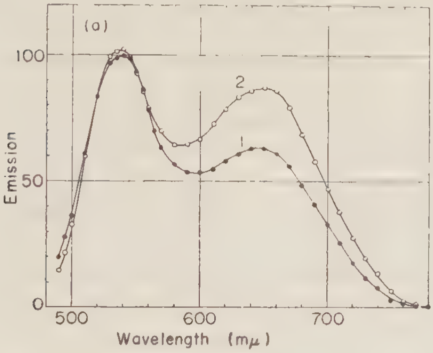

Fig. 14(a).

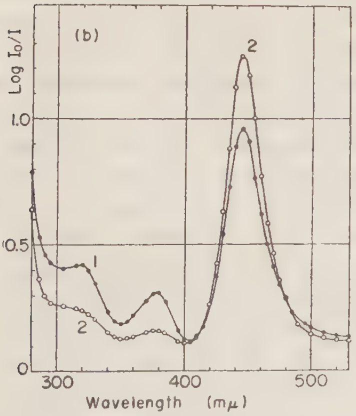

Fig. 14(b).

Fig. 14. Variation of *M*-band emission and of *M*-absorption band. (a) Emission spectra excited with *M* light (450 mμ). (b) Absorption spectra. In both figures, (1): initial state; (2): after irradiation with R_1-light at room temperature. Measurements were made at room temperature. In the emission spectra, the ordinate represents direct signal of the detector.

On the emission excited by *M* light in LiF crystals, its peak has been reported as 650 mμ by Molner[12] and as 705 mμ by Klick[13] using densitometer trace of film. Now, in the present work two emission bands were observed by excitation with *M* light and the 525 mμ emission band was comparable to the 710 mμ emission band only in such crystals that intensities of *M*-absorption band were very weak. This fact and the results of excitation spectra lead to the consideration that the 710 mμ emission band is responsible for *M*-center luminescence. This consideration will also be justified by the degree of polarization for the luminescence in Part II.

In the crystals used for measurements of *R*-band emissions, no strong absorption other than *M* and *R* bands was observed in the region of longer wavelength than 300 mμ. Therefore, on R_1-excitation, the emission with peak at 730 mμ or above may be due to R_1-luminescence—transition from R_1-excited state to ground state—but it might also contain some component of the *M*-center luminescence, since the R_1-band emission coincides on short-wavelength side with the 710 mμ emission band observed by *M*-excitation. Then, on R_2-excitation, the emission with peak at 495 mμ may be due to R_2-luminescence and the red emission to R_1-luminescence or to *M*-center luminescence.

§ 4. Discussions

4.1 *Assignments for R_1 and R_2 bands*

First, Penneman and Powers proposed the classification of absorption bands in colored LiF crystals and they designated the absorption bands at 313 mμ and 380 mμ as R_1 and R_2 bands, respectively. Afterwards, Delbecq and Pringsheim[8] suggested that these assignments were suspicious because of the peculiarity of these bands. That is, the so-called R_2 band (380 mμ band) is accompanied by the fine structure and these bands are unstable with ultraviolet light. These phenomena are not the case for *R* bands in other alkali halides[12].

In the present paper we have tentatively assumed that the absorption bands at 320 mμ

and at 378 mμ are R_1 and R_2 bands, respectively. Now the experimental results in § 3 indicate that the properties of these bands agree, in many respects, with those which have been reported for R bands in other alkali halides: a) The bands at 320 and 378 mμ lie between F and M bands, and no other absorption band is appreciable in this region except for these bands which are fairly stable under various conditions. b) The bands appear in later stages of coloration by ionizing radiation, that is, the centers, which are responsible for these bands, are produced after the production of F and M centers[1]. c) The intensity ratio of these bands seems to be essentially constant under various conditions. This phenomenon corresponds to that observed in KCl and other crystals[2),14)]. d) In the experiment of pulse annealing the bands are more unstable than F or M band. It has also been reported that R bands in additively colored KCl crystals are more unstable than F and M bands[15]. The results of the present work, however, seem to combine in some extent with the effect of bleaching of V-type centers, since some bleachings of M and F bands are observed simultaneously with that of R bands. e) After irradiation with light in the so-called R_1 band polarized along [011] direction, both bands show dichroism in directions along [011] and [0$\bar{1}$1] in the same sense, which was previously reported and will be considered again in detail in Part II. This effect has also been observed in KCl crystals[16]. Further, these bands are developed together by irradiation with the light in F band, as pointed out by Delbecq and Pringsheim[17].

The R bands in LiF crystals are unstable with R light at room temperature, contrary to those in other alkali halides. However, R bands in NaCl are temporary unstable under irradiation with R light at low temperature like those in LiF. Hence the difference in optical stability of R bands at room temperature may result from secondary effects in these crystals. Therefore, although some peculiarity still remains in the fine structure which is observed at low temperature in the R_2-band region, it may be considered that the structure is characteristic to R centers in LiF crystals.

4.2 *Correlation between R_1 and R_2 bands*

Delbecq and Pringsheim reported that the bands at 320 mμ and 380 mμ appear together after irradiation with a short-wavelength ultraviolet ($\lambda < 253.7$ mμ) and decrease with subsequent irradiation of X-rays and disappear together after irradiation with a long-wavelength ultraviolet ($\lambda = 300 \sim 400$ mμ) or after heating to 100~200°C. In the foregoing section, these bands have just been assigned as R_1 and R_2 bands, so that a very intimate relation seems to exist between R_1 and R_2 bands.

As described in § 3, it has been found that both R bands are bleached together with a constant ratio of decrements in their intensities, $-\Delta R_1/(-\Delta R_2)$, by irradiation with light in either of R_1 or R_2 band at room temperature; and especially by the R_1 light irradiation, this relation is unaffected until the greater parts of R_1 and R_2 bands are bleached. These results certainly indicate that R_2 and R_1 bands are due to transitions from the ground state to a first excited state and to a second excited state, respectively, supporting rather the suggestion by Herman *et al.* than the consideration by Lambe and Compton that two distinct R_1 and R_2 centers are intimately connected in the crystal.

Other results supporting this consideration are summarized as follows: R_1 and R_2 bands are produced with a nearly constant ratio of their intensities (R_1/R_2), irrespective of processes of the formation (exposure to γ-rays or electron bombardment, or M-light irradiation after bleaching of R centers) and of concentrations of other centers (F, M or presumably N centers). Further, in thermal treatment, both R bands begin to bleach together at the same temperature. In R bands bleaching with R lights at room temperature, the efficiency of bleaching is higher for the light in the band of higher-energy side, as shown in Table I. In this connection, it is of interest to note that in KCl crystals, Cole and Friauf[18] have reported a higher quantum efficiency of photoelectron for R_1 band than for R_2 band.

It has been found that different emission bands are observed in the LiF crystal by the excitations with R_1 and R_2 lights as decribed in § 3, while the same emission has been reported by R_1- and R_2-light excitations in KCl or NaCl crystal5),19). This fact may indicate that the correlation between the configuration coordinate curves of energy for R_1 and R_2 states in LiF crystal somewhat differs from that in KCl or NaCl crystal. Being compared with the spectral locations of M-band emissions, R_1-emission in LiF crystal might correspond to the R-emissions reported in KCl or NaCl crystal.

The absorption of R bands is complicated at low temperature. The fine structure in the region of R_2 band rises and falls together with R bands, following the destruction and formation of R centers by R_1- or M-light irradiation as described in § 3, or by F-light irradiation8). While, the structure has not been detected in the excitation spectrum of R_2-band region in the present study. Thus it is difficult to decide whether the structure is associated with the R_2 band itself or not. If the structure is not associated with the R_2 band, it may correspond to some vibrational levels in any other electronic transition than R_2 transition and it may be possible, though not yet confirmed, that the structure appears in a region outside of R_2 band in other alkali halides. On the other hand, if the structure is associated with the R_2 band, it may be expected that no structure is observed in other alkali halides with the slight difference of configuration coordinate curves described above. In this case, the configuration coordinate curves of excited R_1 and R_2 states may cross one another and only the R_2 state which does not interact with R_1 state may have clearly-resolved levels of vibration as in the case of LiF. In fact, the structure in LiF is quite obscure in high-energy side, as shown in Fig. 9.

4.3 *Correlation with other centers*

In the results of temporary bleaching, any change of absorption other than those of R bands might be contained in the R-bands region. In general, however, the magnitudes of bleaching for R_1 and R_2 bands are nearly equal in accordance with the foregoing discussion that both bands are due to transitions in the same center. Nevertheless fairly strong correlations seem to exist between the R centers and other centers, as suggested by Compton and Klick6). It is observed that intensity on higher-energy side than the R_1 band is enhanced under the irradiation with R_2 light and the same effect has also been observed in NaCl crystals. This effect is probably attributed to the production of F centers by the action of R_2 light.

M-center luminescence might be contained in the emission with R_1-light excitation, as described in § 3.2. If this is the case, the experimental result that the excitation spectrum is weak in intensity on long-wavelength side compared with R_1-absorption band might be interpreted as follows: M-center luminescence may more participate on the high-energy side of R_1 band, because M centers, in general, seem to have a high efficiency for the luminescence. However, such a hypotheticalconsi deration will need finer experiments, in which the R_1 and M luminescence could be observed separately.

After the bleaching of R bands by R_1-light irradiation at room temperature, the intensity of M band is increased and at the same time the intensity of M-band emission with peak at 710 mμ is also enhanced. It is considered, therefore, that M centers are produced with destruction of R centers in the course of the bleaching. The results and discussions concerning M band will be summarized in Part II.

II. Anisotropy of *R* Center

§ 5. Experimental Results

5.1 *Preferential bleaching*

When LiF crystals showing R bands were irradiated with the R_1 light polarized along [011] direction at room temperature, the absorption intensities of both R_1 and R_2 bands polarized along [011] were more reduced than those polarized along $[0\bar{1}1]$, as previously reported7). The decrement ratios in intensity for both directions, $-\Delta R_i[0\bar{1}1]/(-\Delta R_i/011])$, are approximately equal for R_1 and R_2 bands and estimated to be about 1/2～1/3 in early stage of the bleaching. As the irradiation with polarized R_1 light was prolonged, the absorption intensities for both directions and also the amounts of dichroism continued to reduce, as shown in Fig. 15. After dichroism was induced for both R bands in a crystal by the irradiation with [011]-polarized R_1 light, the crystal was kept in dark place for about thirty days at room temperature. Then, it was found that the absorptions in both directions were increased by the same amount in optical density, in either case of R_1 and R_2 band, as shown in Fig. 16. This fact may indicate that apparent re-orientation does not take place in the ground state of R center at room temperature. It has already been reported that when KCl crystals are irradiated with [011]-polarized R lights, weak dichroism appears in the same sense by nearly the same amount, for both R bands[16]. Being compared with the dichroism in KCl crystals, the above results of LiF crystals also give a support for the assignment of R bands in LiF crystal, as described in § 4.1.

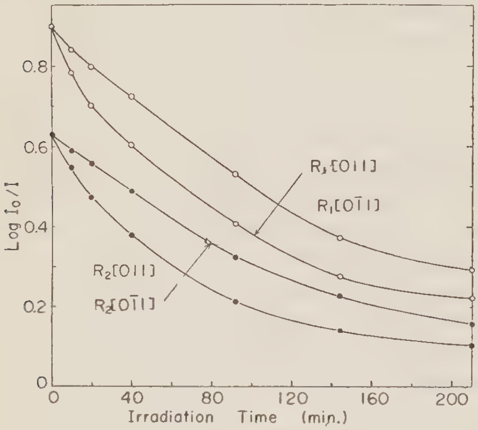

Fig. 15. Preferential bleaching of R_1 and R_2 bands in a LiF crystal by irradiation with the R_1 light polarized along [011] at room temperature.

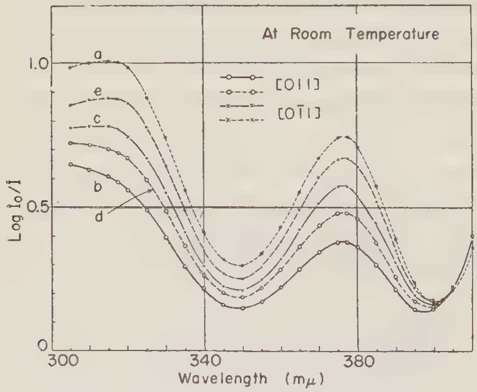

Fig. 16. Stability of the dichroism in R bands. Dotted curve, (a): initial state. Solid curves, (b) and (c): after irradiation with R_1 light polarized along [011] direction at room temperature. Dashed curves, (d) and (e): after the crystal being kept in dark place for a month at room temperature.

When LiF crystals showing R bands were irradiated with R_1 light polarized along [001] direction at room temperature, absorption intensities along [001] and [010] directions were reduced in both R bands, but no dichroism was observed in them.

After irradiation with [011]-polarized R_1 light, dichroism in [011] and [01̄1] directions also appeared in the region of M band but the sign was reverse to that of the R-band dichroism as shown by solid curves in Fig. 17. Then, the crystal was subsequently irradiated by unpolarized M light and as shown by dotted curves in Fig. 17, the dichroism of M-band region almost disappeared, while the R-band intensities along both directions increased scarcely altering the magnitudes of dichroism.

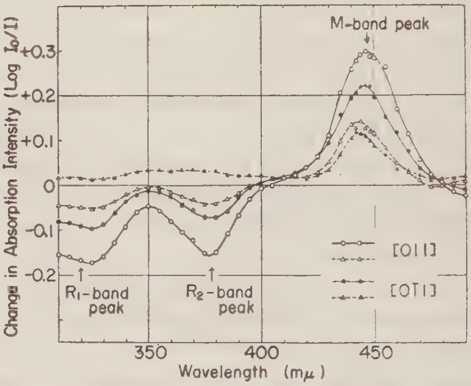

Fig. 17. Changes in absorption intensity on the region of M and R bands polarized along [011] and [01̄1], respectively. Solid curves: after irradiation with R_1 light polarized along [011]. Dotted curves: then after irradiation with unpolarized M light (450 mμ). The original M-band intensity was 1.18. The measurements and bleachings were made at room temperature.

5.2 *Polarization of luminescence*

The polarization of the luminescence of R and M bands were studied in several samples. Exciting light incident upon [100] face of the crystal was polarized first in the [011] direction and then in the [001] direction with the polarizer. Then the emission intensities $I_{\parallel}$ and $I_{\perp}$ were measured with the analyzer parallel and perpendicular to the polarizer, respectively. The degree of polarization expressed as P-factor is given by

$$P[ijk]=\frac{I_{\parallel}-I_{\perp}}{I_{\parallel}+I_{\perp}},$$

Table II. The *P*-factor of the luminescence in LiF crystals excited by polarized *R* lights, at liquid air temperature.

Exciting light	*P*[011]	*P*[001]
R_1 band	0.34～0.39	0.23～0.29
R_2 band	0.15～0.22	0.02～0.08

where [*ijk*] represents the direction of polarization for the exciting light. Results for the R_1- and R_2-band emission, which were obtained at liquid air temperature, are shown in Table II. The values vary in different samples as indicated, presumably due to the concentration of centers contained in each sample. In the above measurements of *P*-factor, it must be noted that R_1-band emission might contain *M*-center luminescence as described in § 3.2 and R_2-band emission might exclusively consist of R_2-luminescence*. Therefore, only *P*-factors of R_2-band emission are significant in the above results. These values are nearly the same as those reported in KCl and NaCl crystals$^{3),5)}$ and are quite small compared with the values which will be expected from the directions of optical dipole moments lying in the face diagonals of the crystal.

As for the *M*-band emission, spectral distribution of the *P*-factor was measured at room temperature. The result is shown in Fig. 18. It is seen that the values of *P*[011] are approximately 0.6 on long-wavelength side and gradually diminish on short-wavelength side.

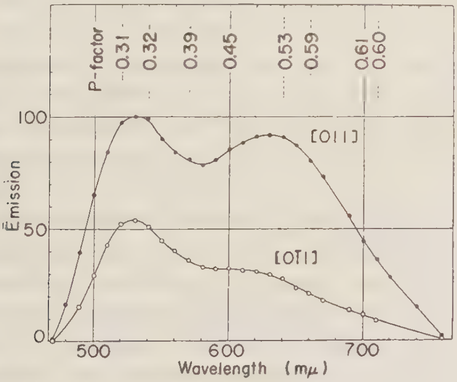

Fig. 18. Anisotropic spectra of *M*-band emission. Crystal was irradiated by *M* light (450 mμ) polarized along [011] direction at room temperature. The ordinate represents direct signal of the detector.

§ 6. Discussions and Conclusion

6.1 *Anisotropy of R center*

In Part I it has been shown that R_1 and R_2 bands in alkali halides arise from transitions in the same center. In this section, the optical dipole moments associated with the *R* absorptions will be considered in connection with the results obtained in the last paragraph and compared with the expected dipole moments of the models which have been proposed as *F*-center coagulations.

It is well known that if symmetry of a color center in an alkali halide is lower than cubic, the absorption shows some dichroism after preferential bleaching with polarized light and also the emission expected by polarized light shows some polarization. The changes introduced in absorption intensities can be calculated as shown by Compton and Klick$^{20)}$, provided that any re-orientation of the center does not take place in the course of the bleaching. Similarly, the *P*-factor of luminescence can be also calculated. These expected values are listed in Table III in the case of an optical dipole oriented along ⟨001⟩, ⟨011⟩, or ⟨111⟩.

As described in § 5, both *R* bands show dichroism in the same sense after bleaching by [011]-polarized R_1 light and no dichroism by [001]-polarized R_1 light. By comparing with Table III, it might be suggested that optical dipole associated with R_1 band is oriented along ⟨111⟩. However, the observed decrement ratios of 1/2～1/3 in the directions of face diagonal, $-\Delta R_1[0\bar{1}1]/(-\Delta R_1[011])$, are larger than the expected value. The expected value will be increased if re-orientation of the center takes place in the ground state, and lowered if it takes place in the excited state. From the experimental fact described in § 5, it may be considered that apparent re-orientation does not take place in the ground state, in the course of the bleaching with polarized R_1 light at room temperature. The above considerations may be also applicable to the dipole oriented along ⟨011⟩ direction. Besides, observed values of *P*[011] and *P*[001] for R_2 luminescence (Table II) are also dif-

---

* The photomultiplier 1P28 was used in this measurement and signal of the red emission with R_2 excitation was negligibly small compared with that of the R_2-luminescence.

Table III Anisotropy of absorption and luminescence expected from simple optical dipoles.

Direction of optical dipole moment	Irradiated with [011]-polarized light		Irradiated with [001]-polarized light	
	Initial ratio of decrements of absorption along $[0\bar{1}1]$ and $[011]$ $-\Delta[0\bar{1}1]/(-\Delta[011])$	$P[011]$	Initial ratio of decrements of absorption along $[010]$ and $[001]$ $-\Delta[010]/(-\Delta[001])$	$P[001]$
⟨001⟩	1/1	0	0	1.0
⟨011⟩	1/5	0.66	1/2	0.33
⟨111⟩	0	1.0	1/1	0

ferent from the values in Table III for the dipole oriented along ⟨111⟩ or ⟨011⟩ direction. Therefore, the experimental results may be inconsistent with the R_2-model proposed by Seitz or F_2-model, which consists of a pair of adjacent negative ion vacancies with two trapped electrons. In this model, at least one of the R bands is considered to associate with simple optical dipole oriented along ⟨011⟩. In fact, Herman *et al.* have suggested, from the theoretical consideration on hydrogen-molecular model of F_2 center, that R_1 and R_2 bands may correspond to ${}^1\Sigma_g{}^+ - {}^1\Pi_u$ and ${}^1\Sigma_g{}^+ - {}^1\Sigma_u{}^+$ transitions, respectively; the doubly degenerate ${}^1\Pi_u$ state may be splitted in the crystalline field, and the optical dipole moment of the transition ${}^1\Sigma_g{}^+ - {}^1\Sigma_u{}^+$ is oriented along the axis of the molecule—the face diagonal of the crystal—and those of the transition ${}^1\Sigma_g{}^+ - {}^1\Pi_u$ are perpendicular to the face diagonal. Therefore, it cannot be explained by the dipoles in this model that R_1 and R_2 bands show the dichroism in the same sense. Even if we assume that R_1 and R_2 bands correspond to two transitions whose upper states arise from a splitting of the degenerate ${}^1\Pi_u$ state, it may be also difficult to explain the experimental results. R_1-model proposed by Seitz or $F_2{}^+$-model, which consists of a pair of adjacent negative ion vacancies with a trapped electron, may be similarly situated as F_2-model.

These difficulties may arise from the models composed of two vacancies. Then, we consider centers composed of three vacancies. First, the center consisting of a pair of negative ion vacancies and an adjacent positive ion vacancy with a trapped electron—M-center model by Seitz[1] or Knox[21]—will be discarded from a consideration similar to the above discussion. For example, optical dipoles associated with A_1-B_1 and A_1-B_2 transitions in C_{2v} symmetry are oriented along ⟨011⟩ and ⟨001⟩ directions, respectively. Next, a center will be discussed which consists of three F centers lying in a [111] plane and has its symmetry axis along ⟨111⟩ direction. Such a model has been suggested for R center by van Doorn[3] and Pick[4].

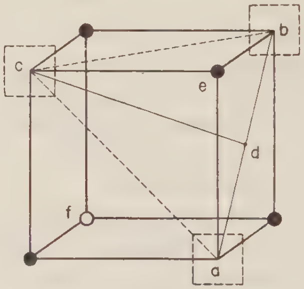

Fig. 19. F_3-model of R-center.

Fig. 19 gives the configuration of vacancies in this model, where a, b, and c mean negative ion vacancies, and the configuration has eight possible vacancy-orientations in the crystal (see, Fig. 20 in Appendix). The potential for a trapped electron in this configuration has the symmetry of C_{3v} and two types of transition may be considered; an optical dipole of one transition is oriented along the ⟨111⟩ symmetry axis of the center and that of the other transition, whose upper state is doubly degenerate, is in the [111] plane perpendicülur to the symmetry axis. Then it is assumed that the degeneracy of the upper state is removed by a distortion of the ionic arrangement with which the arrangement perhaps forms a isosceles triangle in the [111] plane and R_1 and R_2 bands correspond to transitions from the ground state to the two splitted states. The origin of the distortion

Table IV. Anisotropy of absorption and luminescence expected from the F_3-model.

	Irradiated with R_1 or R_2 light polarized along [011]		Irradiated with R_1 or R_2 light polarized along [001]	
	Initial ratio of decrements of absorption along $[0\bar{1}1]$ and [011] $-\Delta R_i[0\bar{1}1]/(-\Delta R_i[011])$	$P[011]$	Initial ratio of decrements of absorption along [010] and [001] $-\Delta R_i[010]/(-\Delta R_i[001])$	$P[001]$
R_1 band	1/1.66 (1/2~1/3)	0.25	1/1 (1/1)	0
R_2 band	1/1.66 (1/2~1/3)	0.25 (0.15~0.22)	1/1 (1/1)	0 (0.02~0.08)

Values observed in this work are indicated in parentheses.

might be attributed to a localized distribution of electron in the center. In such a situation, three ionic arrangements are producible for a vacancy orientation and the optical dipoles associated with the R_1 and R_2 bands may be approximately parallel to the face diagonal and perpendicular to it in the degenerate plane, for instance along *ab* and *cd* in Fig. 19, respectively, or *vice versa*, and potential barrier may be inconsiderable between two ionic arrangements in a vacancy orientation, in contrast with that of a vacancy re-orientation. Hence it is assumed that exchanges among three ionic arrangements (ionic re-orientation) frequently occur around the ⟨111⟩ symmetry axis in a vacancy orientation and, on the contrary, the vacancy re-orientations are scarcely realized, during the bleaching process at room temperature. Then the preferential bleaching by polarized light in such a model can be calculated by the procedure shown in Appendix. The results are listed in Table IV, indicating that the expected values in the [011] and [001] directions for both R bands are in good accordance with the experimental results. Further, provided that random ionic re-orientations occur in the excited states, P-factors of R_2 luminescence also agree with the experimental results as shown in Table IV.

It should be noted that the same anisotropy as described above will be expected if the F_3-model is associated with a positive ion vacancy, *e*, or a pair of positive and negative ion vacancies, *e* and *f*, in Fig. 19. Pick has considered perturbation of an F center within the F_3-model having C_{3v} symmetry and suggested that optical dipoles associated with R_1 and R_2 bands are parallel to the face diagonal of crystal and perpendicular to it in the [111] plane, respectively, and that the dipole associated with R_F band, which overlaps to F band, is parallel to the symmetry axis of ⟨111⟩. In the present treatments of R-center anisotropy, besides R_1 and R_2 bands, another band is also expected to appear and optical dipole associated with it may be approximately oriented along the ⟨111⟩ axis. Further, the same dichroism in both R dands will be induced by irradiation with [011]-polarized light in its band as also expected by Pick.

By making use of the F_3-model discussed above, the fine structure in R_2 band might be interpreted as follows: in the center there is a molecular-like bond inducing the distortion of C_{3v} symmetry and the bond is fairly isolated from lattice vibrations of the host crystal while it associates with a local vibration corresponding to the observed fine structure.

6.2 *Correlation with other centers*

As described in Part I, the M centers produced by R_1 light irradiation seem to be converted into R centers by M-light irradiation more easily than the M centers which have existed before R_1-light irradiation. This fact may suggest that an R center is decomposed by R_1-light irradiation into two nearly located components—an M center and some lattice defect, for instance an F center—and these components easily combine with each other by M-light irradiation and form an R center. In connection with the results of anisotropy of R center, the interaction of R center with other centers should be taken into consideration. As described in § 5, dichroism induced in the M band by [011]-polarized R_1 light almost disappears after subsequent irradiation with unpolarized M light and at the same time R bands recover scarcely altering the differences of intensities in [011] and [0$\bar{1}$1]. Hence, it is unlikely that the R-band dichroism induced by polarized R_1 light results from M centers located in the neighborhood and that also V-type centers are significant in the anisotropies of the R and M centers. Contrary to M and V-type centers, F centers might be important since high concentrations of F centers are contained in the crystals investigated. By reflecting upon the cubic symmetry of F centers, however, it may be considered that anisotropy of R centers could not be changed essentially by them. Further the dichroism in M band may be attributed to the M centers which are directly produced from R centers by polarized R_1-light irradiation and the M centers may be re-oriented in the process of recombination described above.

The interactions between R centers and other centers, however, may exist more or less, as reported in the temporary-bleaching experiment and the dichroism in KCl crystals[22], and these interactions might make the magnitude of dichroism and the value of P-factor diverge to some extent.

In addition to the 710 mμ emission band, the 525 mμ emission band is observed by excitation with M light and the excitation spectrum for this emission somewhat differs from the M-absorption spectrum. Further, the value of P[011] for this emission band is small compared with the value of 0.6 for the 710 mμ emission band*. These results support the conclusion that the 710 mμ emission band corresponds to M-center luminescence as described in §3. It is not possible to assign the origin of the 525 mμ emission but it is certain that M center possessing ⟨011⟩ symmetry does not act directly as an emitter for this emission.

6.3 *Conclusion*

It has been concluded in Part I that R_2 and R_1 bands are due to transitions from a ground state to a first excited state and to a second excited state, respectively, in the same center. Under the above conclusion, the experimental results of the dichroism and the polarization of luminescence have been examined by the models proposed so far on complexes of F centers. Then, as far as the symmetry of the center is concerned, F_3-model lying on [111] plane is more adequate for R center than F_2- or F_2^+-model, or M-center models proposed by Seitz and Knox. From the consideration of optical dipole moments in the F_3-model, however, it may be reasonable to accept the deviation of C_{3v} symmetry and the occurrence of ionic reorientation in the course of the bleaching or in the excitation.

Although the interaction between R centers and other centers might be fairly strong, it may be considered that experimental results concerning the dichroism of absorption and the polarization of luminescence are essentially due to anisotropy of R center itself.

Acknowledgements

The author wishes to express his cordial thanks to Prof. Y. Uchida and Dr. K. Fukuda of Kyoto University for their valuable discussions and encouragements throughout this work. His thanks are also due to Dr. E. Mukoyama of Toyo Rayon Co. and Mr. Y. Nakayama of Kyoto University for the facilities afforded in β-ray and γ-ray irradiations and to Mr. K. Asai for his assistance in the latter part of this work.

This work was partly supported by a grant from the Ministry of Education.

Appendix

On the F_3-model described in §6.1, the eight possible vacancy-orientations are separated into such two groups, A and B in Fig. 20, that each orientation in the group A or B has the same directional dependence of the optical dipoles upon the polarization of light.

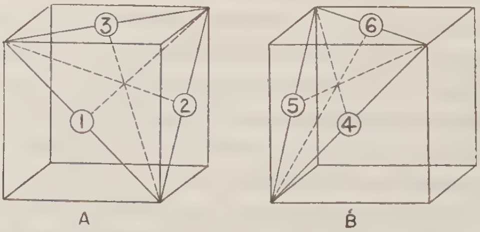

Fig. 20. Directions of optical dipoles associated with R_1 and R_2 bands in the F_3-model.

---

* The value of P[011] for the M-center luminescence has already been reported to be 0.6 by Lambe, Compton[5], and Feofilov[23].

Therefore it is sufficient to consider six ionic-arrangements in Fig. 20: 1, 2, and 3 in A; and 4, 5, and 6 in B, where dotted line in each arrangement means the symmetry axis of isosceles triangle in the distorted C_{3v}. First, we consider the case where optical dipole associated with R_1 absorption is oriented along the face diagonal of the crystal and that associated with R_2 absorption is perpendicular to it.

The R centers are oriented with equal concentration, n_0, in each ionic-arrangement in the group A and B before irradiation with polarized light. After irradiation with the [011]-polarized R_1 light, each n_0 may change into n_i, where subscript i means i-ionic arrangement in Fig. 20. If any vacancy re-orientation is not induced during the irradiation with R_1 light, the changing rate of n_i may be expressed as follows:

$$\frac{dn_1}{dt}=-n_1\beta+\frac{1}{\tau}(n_j-n_1)\,,\qquad \frac{dn_j}{dt}=-n_j\frac{\beta}{4}+\frac{1}{2\tau}(n_1-n_j)\,,$$

$$\frac{dn_4}{dt}=\frac{1}{\tau}(n_k-n_4)\,,\qquad \frac{dn_k}{dt}=-n_k\frac{\beta}{4}+\frac{1}{2\tau}(n_4-n_k)\,,$$

$$j=2,\ 3;\ k=5,\ 6$$

where $1/\tau$ is a frequency of the ionic re-orientation and β is a bleaching constant. If τ is very small, the concentrations are approximately given by

$$n_1=n_0\exp(-\beta t/2)=n_j\,,\qquad n_4=n_0\exp(-\beta t/6)=n_k\,.$$

Then, the absorption intensities of R_1 band in the [011] and [0$\bar{1}$1] directions are given as follows:

$$\kappa_1[011]=\frac{3}{2}\alpha_1 n_0\exp(-\beta t/2)+\frac{1}{2}\alpha_1 n_0\exp(-\beta t/6)\,,$$

$$\kappa_1[0\bar{1}1]=\frac{1}{2}\alpha_1 n_0\exp(-\beta t/2)+\frac{3}{2}\alpha_1 n_0\exp(-\beta t/6)\,,$$

where α_1 is a constant. By considering the angle between the direction of polarization and the direction of R_2 optical dipole, the absorption intensities of R_2 band are also calculated in both directions:

$$\kappa_2[011]=\frac{3}{2}\alpha_2 n_0\exp(-\beta t/2)+\frac{1}{2}\alpha_2 n_0\exp(-\beta t/6)\,,$$

$$\kappa_2[0\bar{1}1]=\frac{1}{2}\alpha_2 n_0\exp(-\beta t/2)+\frac{3}{2}\alpha_2 n_0\exp(-\beta t/6)\,,$$

where again α_2 is a constant. Then initial bleaching ratio in both directions can be estimated for R_1 and R_2 bands:

$$\frac{\Delta\kappa_1[0\bar{1}1]}{\Delta\kappa_1[011]}=\frac{\Delta\kappa_2[0\bar{1}1]}{\Delta\kappa_2[011]}=\frac{3}{5}\,.$$

This means the same sense dichroism for R_1 and R_2 bands.

In a similar way, after irradiation with [001]-polarized R_1 light, the absorption intensities of R_1 and R_2 bands in the [001] and [010] directions are given under the same assumptions as described above:

$$\kappa_1[001]=\kappa_1[010]=2\alpha_1 n_0\exp(-\beta t/3)\,,$$

$$\kappa_2[001]=\kappa_2[010]=2\alpha_2 n_0\exp(-\beta t/3)\,.$$

In this case, therefore, no dichroism is observable. If we exchange the direction of optical dipole of R_1 absorption for that of R_2 absorption, the same results as described above will be obtained.

References

1) F. Seitz: Rev. Mod. Phys. **18** (1946) 384; ibid. **26** (1954) 7.
2) R. Herman, M. C. Wallis and R. F. Wallis: Phys. Rev. **103** (1956) 87.
3) C. Z. van Doorn: Philips Res. Rep. **12** (1957) 309.
4) H. Pick: Z. Phys. **159** (1960) 69.
5) J. Lambe and W. D. Compton: Phys. Rev. **106** (1957) 684.
6) W. D. Compton and C. C. Klick: Phys. Rev. **112** (1958) 1620.
7) K. Fukuda, A. Okuda and Y. Uchida: J. Phys. Soc. Japan **15** (1960) 538.
8) C. J. Delbecq and P. Pringsheim: J. Chem. Phys. **21** (1953) 794. P. Pringsheim: Z. Phys. **136** (1954) 573. H. Yagi: J. Phys. Soc. Japan **11** (1956) 430.
9) K. Fukuda, A. Okuda and Y. Uchida: J. Appl. Phys. Japan **27** (1958) 535.
10) R. A. Penneman, and J. A. Powers: Ref. 8.
11) K. Fukuda and A. Okuda: Bull. Chem. Res. Kyoto Univ. **37** (1959) 321.
12) J. P. Molnar: Thesis Massachusetts Inst. Tech. (1948).
13) C. C. Klick: Phys. Rev. **79** (1950) 894.
14) D. H. Goode and P. A. Schroeder: Phys. Rev. **115** (1959) 1426.
15) G. R. Cole, and R. J. Friauf: Phys. Rev. **105** (1957) 1464. M. Ueta and M. Hirai: J. Phys. Soc. Japan **14** (1959) 546. T. Tomiki: J. Phys. Soc. Japan **15** (1960) 488.
16) G. Kuwabara, and A. Misu: J. Phys. Soc. Japan **13** (1958) 1066.
17) St. Petroff: Z. Phys. **127** (1950) 443. Ref. 12.
18) G. R. Cole and R. J. Friauf: Phys. Rev. **107** (1957) 387.
19) C. Z. van Doorn and Y. Haven: Philips Res. Rep. **11** (1956) 479.
20) W. D. Compton and C. C. Klick: Phys. Rev. **110** (1958) 349.
21) R. S. Knox: Phys. Rev. (L) **2** (1959) 87.
22) H. Kanzaki: Phys. Rev. **110** (1958) 1063. T. Ishii, T. Tomiki, and M. Ueta: J. Phys. Soc. Japan **14** (1959) 1415.
23) P. P. Feofilov: Doklady Akad. Nauk **92** (1953) 743.

JOURNAL OF THE PHYSICAL SOCIETY OF JAPAN, Vol. 16, No. 9, SEPTEMBER, 1961

Impulsive Motion of a Circular Cylinder in a Viscous Fluid at Small Reynolds Numbers

By Sinzi KUWABARA

Aeronautical Research Institute, University of Tokyo

(Received June 2, 1961)

The drag of a circular cylinder set in uniform motion impulsively from rest in a viscous fluid is calculated. On the assumption of small Reynolds numbers, Oseen's equations for unsteady motion are employed. The two limiting cases corresponding to the initial and final periods, respectively, are investigated.

§1. Introduction and Summary

Studies on steady slow motion of one or many bodies in a viscous fluid have been made by many authors, but there have been few works concerning the unsteady slow motion. Oseen has investigated the impulsive motion of a sphere on the basis of the Stokes approximation[1]. The impulsive motion of a circular cylinder has been studied by Blasius[2] and Goldstein and Rosenhead[3]. Their investigations have been based on the boundary-layer equations, hence their results are valid only for the large Reynolds numbers. In the present paper, we shall study the motion of a circular cylinder started impulsively from rest with a constant velocity in a viscous fluid.

Since we shall assume the Reynolds number to be small, it may be reasonable to make use of Oseen's equations for the unsteady motion. Also, use will be made of the Laplace transformation. Since it is difficult to solve this problem completely, we shall only treat the two limiting cases corresponding to the final and initial periods, respectively. For the final period, it is found that the drag of the circular cylinder approaches gradually the value for the steady case as the time from start increases. For the initial period, on the other hand, the drag decreases rapidly from infinity, i.e., inversely proportionally to the square root of time.

Numerical calculations have been carried out for the Reynolds numbers 0.08, 0.4 and 1, respectively. The two asymptotic solutions corresponding to the initial and the final periods, respectively, seem to continue each other fairly well.

§ 2. Basic Equations

We consider the motion of a circular cylinder which starts impulsively from rest with a constant velocity U in a viscous fluid. We assume that the Reynolds number $R=2aU/\nu$ is small compared with unity, where a is the radius of the circular cylinder and ν is the kinematic viscosity, so that we may conveniently use the Oseen approximation. Oseen's equations and the equation of continuity can be written in non-dimensional forms as follows:

$$\frac{\partial u}{\partial t}+\frac{\partial u}{\partial x}=-\frac{\partial p}{\partial x}+\frac{1}{2k}\Delta u\,, \tag{2.1}$$

$$\frac{\partial v}{\partial t}+\frac{\partial v}{\partial x}=-\frac{\partial p}{\partial y}+\frac{1}{2k}\Delta v \tag{2.2}$$

and

$$\frac{\partial u}{\partial x}+\frac{\partial v}{\partial y}=0\,, \tag{2.3}$$

where (x, y) are the cartesian coordinates, t is the time, (u, v) the velocity components, p the pressure and $2k=aU/\nu=R/2$. Here the units of length, time, velocity, and pressure have been taken as a, a/U, U and ρU^2, respectively, where ρ is the density of the fluid.

From (2.1) and (2.2), we have

$$2k\left(\frac{\partial \omega}{\partial t}+\frac{\partial \omega}{\partial x}\right)=\Delta\omega\,, \tag{2.4}$$

where ω is the non-dimensional vorticity defined as

$$\omega=\frac{\partial v}{\partial x}-\frac{\partial u}{\partial y}\,. \tag{2.5}$$

Introducing the complex variables

$$z=x+iy\,, \qquad \bar{z}=x-iy\,, \tag{2.6}$$

and

$$W=u-iv\,, \tag{2.7}$$

we have

$$\frac{\partial W}{\partial \bar{z}}=-\frac{1}{2}i\omega \tag{2.8}$$

from (2.3) and (2.5).

Let us define the Laplace transform of $f(x, y, t)$ as

$$f^*(x, y, p)=\int_0^\infty f(x, y, t)e^{-pt}\,dt\,, \tag{2.9a}$$

$$f(x, y, t)=\frac{1}{2\pi i}\int_{c-i\infty}^{c+i\infty} f^*(x, y, p)e^{pt}\,dp\,, \qquad \mathscr{R}e\, c>0\,. \tag{2.9b}$$

Then, we can transform (2.4) and (2.8) as follows:

$$2k\left(p\omega^*+\frac{\partial \omega^*}{\partial x}\right)=\Delta\omega^*\,, \tag{2.10}$$

$$\frac{\partial W^*}{\partial \bar{z}}=-\frac{1}{2}i\omega^*\,. \tag{2.11}$$

The general solution of (2.10) which vanishes at infinity is easily obtained as follows:

$$\omega^*=\tfrac{1}{2}e^{kx}\sum_{n=0}^{\infty}(C_n e^{ni\theta}+\bar{C}_n e^{-ni\theta})K_n(\kappa r)\,, \tag{2.12}$$

where (r, θ) are the polar coordinates, C_n the complex coefficients, K_n the modified Bessel functions of the first kind and $\kappa=\sqrt{k^2+2kp}$. In a manner similar to Imai's method of solving Oseen's equations[4], the general solution of (2.11) with (2.12) can be obtained as

$$W^*=-\frac{i}{4}\sum_{n=0}^{\infty}(C_n W_n+C_n W_{-n})\,, \tag{2.13}$$

where

$$\frac{\partial W_n}{\partial \bar{z}}=e^{kx}K_n(\kappa r)\,e^{ni\theta}\,. \tag{2.14}$$

Integrating (2.14), we have

$$W_n=\frac{k}{\kappa}\,W_{n-1}-\frac{2}{\kappa}e^{kx}K_{n-1}(\kappa r)\,e^{(n-1)i\theta}\,. \tag{2.15}$$

Replacing n by $-n+1$, we have

$$W_{-n}=\frac{\kappa}{k}\,W_{1-n}+\frac{2}{k}e^{kx}K_n(\kappa r)\,e^{-ni\theta}\,. \tag{2.16}$$

Repeated application of the recurrence formulae (2.15) and (2.16) gives respectively

$$W_n=\left(\frac{k}{\kappa}\right)^n W_0-\frac{2}{\kappa}e^{kx}\sum_{m=0}^{\infty}\left(\frac{k}{\kappa}\right)^{n-1-m}K_m(\kappa r)\,e^{mi\theta}\,, \tag{2.17}$$

$$W_{-n}=\left(\frac{\kappa}{k}\right)^n W_0+\frac{2}{k}e^{kx}\sum_{m=1}^{n}\left(\frac{\kappa}{k}\right)^{n-m}K_m(\kappa r)\,e^{-mi\theta}\,. \tag{2.18}$$

Inserting these into (2.13), we obtain

$$\begin{aligned}W^*=&-\frac{i}{4}\,W_0\sum_{n=0}^{\infty}\left\{\left(\frac{k}{\kappa}\right)^n C_n+\left(\frac{\kappa}{k}\right)^n\bar{C}_n\right\}\\&+\frac{i}{2k}e^{kx}\left[A_1K_0(\kappa r)+\sum_{m=1}^{\infty}(A_{m+1}\,e^{mi\theta}-\bar{B}_m\,e^{-mi\theta})K_m(\kappa r)\right]+\frac{df^*}{dz}\,.\end{aligned} \tag{2.19}$$

where

$$W_0=\frac{2}{\kappa^2 z}\exp\left(\tfrac{1}{2}kz\right)\int^{\kappa r}\exp\left(kt^2/2\kappa^2 z\right)K_0(t)t\,dt\,, \tag{2.20}$$

$$A_n=\sum_{m=n}^{\infty}\left(\frac{k}{\kappa}\right)^{m-n-1}C_m\,,\qquad B_n=\sum_{m=n}^{\infty}\left(\frac{\kappa}{k}\right)^{m-n}C_m\,, \tag{2.21}$$

and $f^*(z)$ is an arbitrary analytic function of z.

In view of the fact that W_0 is a many-valued function of (r,θ), and that the complex velocity W should be one-valued, we must have

$$\sum_{n\ 0}^{\infty}\left\{\left(\frac{k}{\kappa}\right)^n C_n+\left(\frac{\kappa}{k}\right)^n\bar{C}_n\right\}=0\,. \tag{2.22}$$

Thus, we finally obtain

$$W^*=\frac{i}{2k}\left[A_1K_0(\kappa r)+\sum_{n=1}^{\infty}(A_{n+1}\,e^{ni\theta}-\bar{B}_n\,e^{-ni\theta})\,K_n(\kappa r)\right]+\frac{df^*}{dz}\,, \tag{2.23}$$

where f^* should be expressed as

$$f^*(z)=\frac{1}{p}z+\frac{m^*+i\Gamma^*}{2\pi}\ln z+\frac{a^*}{z}+\cdots\,. \tag{2.24}$$

For the initial period, we assume that $p\gg 1$ and so $\kappa\gg 1$. From (2.21) we can see that B_n is a series in the ascending powers of the large factor κ/k, so that (2.23) is useless for the initial period.

Repeated application of the recurrence formula (2.15) only gives

$$W^*=\frac{i}{2\kappa}e^{kx}\left\{A_0'K_0(\kappa r)+\sum_{n=1}^{\infty}(A_n'e^{ni\theta}+B_n'e^{-ni\theta})K_n(\kappa r)\right\}+\frac{df^*}{dz}\,, \tag{2.25}$$

where

$$A_n' = \sum_{m=n+1}^{\infty} \left(\frac{k}{\kappa}\right)^{m-n-1} C_m\,, \qquad n=0,\,1,\,2,\,\cdots \tag{2.26a}$$

and

$$B_n' = \sum_{m=0}^{n-1} \left(\frac{k}{\kappa}\right)^{n-1-m} \bar{C}_m + \sum_{m=0}^{\infty} \left(\frac{k}{\kappa}\right)^{m+n-1} C_m\,, \qquad n=1,\,2,\,\cdots\,. \tag{2.26b}$$

This is useful for the initial period.

To the Stokes approximation of the unsteady motion, we have the vorticity equation and its general solution in transformed forms as

$$2kp\omega^* = \varDelta\omega^*\,, \tag{2.27}$$

$$\omega^* = \frac{1}{2} \sum_{n=0}^{\infty} (C_n e^{ni\theta} - \bar{C}_n e^{-ni\theta}) K_n(\kappa r)\,, \tag{2.28}$$

where C_n are the arbitrary constants and $\kappa=\sqrt{2kp}$. In a manner similar to the preceding procedure, we obtain

$$W^* = \frac{i}{2\kappa} \left\{ A_0'' K_0(\kappa r) + \sum_{n=1}^{\infty} (A_n'' e^{ni\theta} + B_n'' e^{-ni\theta}) K_n(\kappa r) \right\} + \frac{df^*}{dz}\,, \tag{2.29}$$

$$A_n'' = C_{n+1}\,, \quad n=0,\,1,\,2,\,\cdots\,; \qquad B_1'' = C_0 + \bar{C}_0\,; \qquad B_n'' = \bar{C}_{n-1}\,, \quad n\ -2,\,3,\,\cdots\,. \tag{2.30}$$

It will be seen that on puttin $k\to 0$ and $kp=$finite, (2.25) and (2.26) reduce to (2.29) and (2.30) as should be expected.

The condition of no-slip on the surface of the profile can be written as

$$W^* = 0 \qquad \text{on the profile.} \tag{2.31}$$

The forces experienced by the cylinder are calculated by integrating the stresses on the surface of the cylinder. It is easily obtained from Imai's formula[5]:

$$C_D - iC_L = -\frac{4}{R} \oint_C \frac{\partial\omega}{\partial\bar{z}} \bar{z}\, d\bar{z} = -\frac{8i}{R} \oint_C \frac{\partial^2 W}{\partial\bar{z}^2} \bar{z}\, d\bar{z}\,, \tag{2.32a}$$

or its transformed form

$$C_D^* - iC_L^* = -\frac{4}{R} \oint \frac{\partial\omega^*}{\partial\bar{z}} \bar{z}\, d\bar{z}\,, \tag{2.32b}$$

where $C_D = X/(\frac{1}{2}\rho U^2\cdot 2a)$ and $C_L = Y/(\frac{1}{2}\rho U^2\cdot 2a)$ are the drag and lift coefficients, and $(X,\,Y)$ are the force components, and integration being taken along the profile C. This formula has originally been derived for the case of steady motion but it can easily be shown that the formula is valid for the unsteady case as well, provided the profile is chosen as the path of integration.

§ 3. The Final Period

For the final period, we can put $p \ll 1$ and hence $\kappa \fallingdotseq k \ll 1$, so that

$$C_n = O(k^n) \tag{3.1}$$

in view of the form of ω^* as given by (2.12). Then, we take the transformed velocity and vorticity as

$$W^* = \frac{i}{2k} e^{kx} \left\{ \frac{k}{\kappa} C_1 K_0(\kappa r) - \bar{C}_1 K_1(\kappa r) e^{\ i\theta} \right\} + \frac{1}{p} + \frac{m^*}{2\pi} \frac{1}{z} + \cdots\,, \tag{3.2}$$

$$\omega^*=\frac{1}{2}e^{kx}(C_1e^{i\theta}+\bar{C}_1e^{-i\theta})K_1(\kappa r) \tag{3.3}$$

retaining only the terms of order of κ^2. C_1 and m^* can be determined so as to satisfy the boundary condition (2.31). Thus, we have

$$C_1=2i\kappa\Big/\left\{p\left(K_0+\frac{1}{2}\kappa K_1\right)\right\}, \tag{3.4}$$

$$\frac{m^*}{2\pi}=\kappa K_1\Big/\left\{kp\left(K_0+\frac{1}{2}\kappa K_1\right)\right\}, \tag{3.5}$$

where we have put $K_0=K_0(\kappa)$ and $K_1=K_1(\kappa)$ for brevity.

Substituting from (3.4) into (3.13), we have

$$\omega^*=-\frac{2\kappa e^{kx}K_1(\kappa r)}{p(K_0+\frac{1}{2}\kappa K_1)}\sin\theta\,. \tag{3.6}$$

Expanding the Bessel functions K_0 and K_1, and retaining only the first dominant terms, we have

$$\omega^*=-\frac{2e^{kx}\sin\theta}{pr(-\ln\frac{1}{2}\kappa-\gamma+\frac{1}{2})}, \tag{3.7}$$

which gives, by the inverse Laplace transformation,

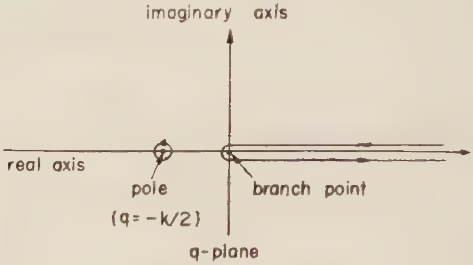

Fig. 1. The contour of integration used for (3.8).

$$\omega=-\frac{2e^{kx}\sin\theta}{2\pi i\cdot r}\exp(-kt/2)\int_C\frac{i\pi e^{-qt}\,dq}{(q+k/2)\{-\frac{1}{2}\ln 2kq+\ln 2-\gamma+\frac{1}{2})^2+\pi^2/4\}}, \tag{3.8}$$

where $q=-p+k/2$, $\gamma=0.57721\ldots$ is Euler's constant and the contour of integration is as shown in Fig. 1.

Substitution from (3.8) into (3.32a) gives

$$C_D=C_D^{(0)}+\frac{16}{R}\exp(-R^2\tau/16)\int_0^\infty\frac{e^{-s}\,ds}{(s+R^2\tau/16)\{(-\ln s+\beta)^2+\pi^2\}} \tag{3.9}$$

$$=C_D^{(0)}+\frac{16}{R}\exp(-R^2\tau/16)\int_0^1\frac{d\eta}{(-\ln\eta+R^2\tau/16)\{(-\ln(-\ln\eta)+\beta)^2+\pi^2\}}, \tag{3.10}$$

where

$$C_D^{(0)}=8\pi/\{R(S+\tfrac{1}{2})\}, \tag{3.11}$$

$\tau=2t/R$ and $\beta=\ln\tau+\ln 4-2\gamma+1$. $C_D^{(0)}$ is the drag coefficient for the steady motion.

§ 4. The Initial Period

For the initial period, we put $p\gg1$ and so $\kappa\gg1$. Also we assume that C_n in (2.12) are all of the same order of magnitude. Then remembering (2.25) and (2.24), we write the transformed velocity as

$$\begin{aligned}W^*=&\frac{i}{2\kappa}e^{kx}[C_1K_0(\kappa r)+C_2K_1(\kappa r)e^{i\theta}+C_3K_2(\kappa r)e^{2i\theta}+\cdots\\&+(C_0+\bar{C}_0)K_1(\kappa r)e^{-i\theta}+\bar{C}_1K_2(\kappa r)e^{-2i\theta}+\cdots]\\&+\frac{1}{p}+\frac{m^*}{2\pi}\frac{1}{z}+\frac{a^*}{z^2}+\cdots,\end{aligned} \tag{4.1}$$

where only the lowest order terms in k/κ are retained. Introducing (4.1) into the boundary condition (2.31), we have

$$C_0+\bar{C}_0=\frac{m^*ki}{\pi}\,; \qquad C_1=2i\kappa/(pK_0)\,; \qquad C_n=0\,, \quad n\geq 2\,. \tag{4.2}$$

Since ω^* should be an odd function of θ for the case of a circular cylinder, we have from (2.12)

$$C_0+\bar{C}_0=0 \tag{4.3}$$

so that

$$m^*=0\,. \tag{4.4}$$

Substituting from (4.2) and (4.4) into (2.12), we have

$$\omega^*=-\frac{\kappa}{q-k/2}\,e^{kx}\frac{K_1(\kappa r)}{K_0(\kappa)}\sin\theta\,, \tag{4.5}$$

where we have put $q=p+k/2$ so that $\kappa=\sqrt{2kq}$. Using the asymptotic expansions of Bessel functions, we obtain

$$\begin{aligned}\omega^*=&-\sqrt{\frac{2kq}{r}}\,\frac{\exp\,[kx-\sqrt{2kq}\,(r-1)]}{q-k/2}\\ &\times\left\{1+\frac{3}{8}\frac{1}{\sqrt{2kq}\cdot r}-\frac{5}{128}\frac{1}{2kq\cdot r^2}+\frac{105}{1024}\frac{1}{(2kq)^{3/2}r^3}+\cdots\right\}\\ &\times\left\{1-\frac{1}{8}\frac{1}{\sqrt{2kq}}+\frac{9}{128}\frac{1}{2kq}-\frac{75}{1024}\frac{1}{(2kq)^{3/2}}+\cdots\right\}^{-1}\sin\theta\,.\end{aligned} \tag{4.6}$$

Application of (2.32b) and its inverse transformation fails owing to the divergence of the integral appearing in the inverse transformation. To avoid this difficulty, we take as the contour of integration C in (2.32b) a circle of radius r (>1). Thus we have

$$\begin{aligned}\oint\frac{\partial\omega^*}{\partial\bar{z}}\,\bar{z}\,d\bar{z}&=-\frac{2\pi kqr}{q-k/2}\,\frac{K_2(\kappa r)}{K_0(\kappa)}\\ &=-\frac{2\pi kqr^2}{q-k/2}\left\{1+\frac{15}{8}\frac{1}{\sqrt{2kqr}}+\frac{105}{128}\frac{1}{2kq\cdot r^2}-\frac{315}{1024}\frac{1}{(2kq)^{3/2}\cdot r^3}+\cdots\right\}\\ &\quad\times\left\{1-\frac{1}{8}\frac{1}{\sqrt{2kq}}+\frac{9}{128}\frac{1}{2kq}-\frac{75}{1024}\frac{1}{(2kq)^{3/2}}+\cdots\right\}^{-1}.\end{aligned} \tag{4.7}$$

For the calculation of ω and $\oint\frac{\partial\omega}{\partial\bar{z}}\,\bar{z}\,d\bar{z}$ by inverse Laplace transformation, we have adopted a method of successive approximation, that is, retaining the first term of the asymptotic expansion of each of K_0, K_1 and K_2 for the zero-th approximation, the first two terms of the expansion for the first approximation and so on.

i) The zero-th approximation. We put

$$\omega^*=-\sqrt{\frac{2k}{q}}\,\exp\,[kx-\sqrt{2kq}\,(r-1)]\sin\theta\,, \tag{4.8}$$

$$\oint\frac{\partial\omega^*}{\partial\bar{z}}\,\bar{z}\,d\bar{z}=-2\pi kr^{3/2}\exp\,[kx-\sqrt{2kq}\,(r-1)]\,, \tag{4.9}$$

for the zero-th approximation as mentioned above. We can carry out easily the inverse transformation and have

$$\omega=-\frac{2}{\sqrt{\pi\tau r}}\exp\left(-\frac{1}{4\tau}(r-1)^2\right)\sin\theta\,, \tag{4.10}$$

$$\oint\frac{\partial\omega}{\partial\bar{z}}\,\bar{z}\,d\bar{z}=-\frac{\sqrt{\pi}}{2}\,r^{3/2}(r-1)\tau^{-3/2}\exp\left(-\frac{1}{4}(r-1)^2/\tau\right) \tag{4.11}$$

where $\tau=t/2k$ and we have omitted the factor $\exp(-kx-k^2\tau)$ as well as in the higher approximations, because we restrict our consideration to the region near the cylinder and the initial period. This omission makes our approximation equivalent to the Stokes type. The same result would be obtained from (2.29) and (2.30).

Substitution from (4.11) to (2.32a) gives

$$C_D=0\,. \tag{4.13}$$

ii) The first approximation. In this approximation, we put

$$\omega^*=-2\sqrt{\frac{2k}{qr}}\exp\left[-\sqrt{2kq}\,(r-1)\right]\frac{\sqrt{q}+3/(8\sqrt{2k}\cdot r)}{\sqrt{q}-1/(8\sqrt{2k})}\sin\theta\,, \tag{4.14}$$

$$\oint\frac{\partial\omega^*}{\partial\bar{z}}\,\bar{z}\,d\bar{z}=-2\pi kr^{3/2}\exp\left[-\sqrt{2kq}\,(r-1)\right]\frac{\sqrt{q}+15/(8\sqrt{2k}\cdot r)}{\sqrt{q}-1/(8\sqrt{2k})}\,. \tag{4.15}$$

Then, we have

$$\begin{aligned}\omega=-\frac{2}{\sqrt{r}}\Bigg[&\frac{1}{\sqrt{\pi\tau}}\exp\left(-\frac{1}{4\tau}(r-1)^2\right)+\frac{1}{8}\left(1+\frac{3}{r}\right)\exp\left(-\frac{1}{8}(r-1)+\tau^2/64\right)\\&\times\mathrm{Erfc}\left(\frac{r-1}{2\sqrt{\tau}}-\frac{1}{8}\sqrt{\tau}\right)\Bigg]\sin\theta\,,\end{aligned} \tag{4.16}$$

$$\begin{aligned}\oint\frac{\partial\omega}{\partial\bar{z}}\,\bar{z}\,d\bar{z}=-\pi r^{3/2}\Bigg[&\frac{1}{2\sqrt{\pi}}(r-1)\tau^{-3/2}\exp\left(-\frac{1}{4}(r-1)^2/\tau\right)\\&+\frac{1}{8}\left(1+\frac{15}{r}\right)\left\{\frac{1}{\sqrt{\pi\tau}}\exp\left(-\frac{1}{4}(r-1)^2/\tau\right)+\frac{1}{8}\exp\left(-\frac{1}{8}(r-1)+\tau/64\right)\right.\\&\left.\times\mathrm{Erfc}\left(\frac{1}{2}(r-1)\Big/\sqrt{\tau}-\frac{1}{8}\sqrt{\tau}\right)\right\}\Bigg]\,,\end{aligned} \tag{4.17}$$

where

$$\mathrm{Erfc}\,x=\frac{2}{\sqrt{\pi}}\int_x^\infty\exp(-t^2)\,dt\,.$$

Substitution from (4.17) into (2.32a) gives

$$C_D=\frac{8\pi}{R}\left\{\frac{1}{\sqrt{\pi\tau}}+\cdots\right\}. \tag{4.18}$$

iii) The second approximation gives

$$\begin{aligned}\omega=-\frac{2}{\sqrt{r}}\Bigg[&\frac{1}{\sqrt{\pi\tau}}\exp\left(-\frac{1}{4\tau}(r-1)^2\right)+D\exp\left(-\xi(r-1)+\xi^2\tau\right)\mathrm{Erfc}\left(\frac{r-1}{2\sqrt{\tau}}-\xi\sqrt{\tau}\right)\\&+\bar{D}\exp\left(-\bar{\xi}(r-1)+\bar{\xi}^2\tau\right)\mathrm{Erfc}\left(\frac{r-1}{2\sqrt{\tau}}-\bar{\xi}\sqrt{\tau}\right)\Bigg]\sin\theta\,,\end{aligned} \tag{4.19}$$

where

$$D=-\frac{8i}{\sqrt{17}}\left\{\frac{\xi}{8}\left(1+\frac{3}{r}\right)-\frac{3}{128}\left(3+\frac{5}{r^2}\right)\right\} \tag{4.20}$$

and

$$\xi=\frac{1}{16}(1+i\sqrt{17})\,,\qquad \bar{\xi}=\frac{1}{16}(1-i\sqrt{17})\,. \tag{4.21}$$

We have

$$C_D=\frac{8\pi}{R}\left\{\frac{1}{\sqrt{\pi\tau}}+\frac{1}{2}+\cdots\right\}. \tag{4.22}$$

iv) The third approximation gives

$$\omega=\omega_0+\omega_1+\omega_2+\omega_3\ , \tag{4.23}$$

where

$$\omega_0=-\frac{2}{\sqrt{\pi\tau r}}\exp\left(-\frac{1}{4\tau}(r-1)^2\right)\sin\theta\ , \tag{4.24}$$

$$\omega_i=\frac{2}{\sqrt{r}}\,\frac{D_1\xi_i^2-D_2\xi_i+D_3}{(\xi_k-\xi_i)(\xi_i-\xi_j)}\exp\left[-\xi_i(r-1)+\xi_i^2\tau\right]\mathrm{Erfc}\left(\frac{r-1}{2\sqrt{\tau}}-\xi_i\sqrt{\tau}\right)\sin\theta\ , \tag{4.25}$$

(i, j, k) being even permutation of $(1, 2, 3)$, with

$$D_1=\frac{1}{8}\left(1+\frac{3}{r}\right),\qquad D_2=\frac{3}{128}\left(3+\frac{5}{r^2}\right),\qquad D_3=\frac{5}{1024}\left(5+\frac{7}{r^3}\right) \tag{4.26}$$

and

$$\xi_1=0.401830\ ,\qquad \xi_2=-0.138415+i0.402980\ ,\qquad \bar{\xi}_3=\xi_2\ , \tag{4.27}$$

which are the roots of the cubic equation

$$\xi^3-\frac{1}{8}\xi^2+\frac{9}{128}\xi-\frac{75}{1024}=0\ . \tag{4.28}$$

Also we have

$$C_D=\frac{8\pi}{R}\left[\frac{1}{\sqrt{\pi\tau}}+\frac{1}{2}-\frac{1}{4}\sqrt{\frac{\tau}{\pi}}+\cdots\right]. \tag{4.29}$$

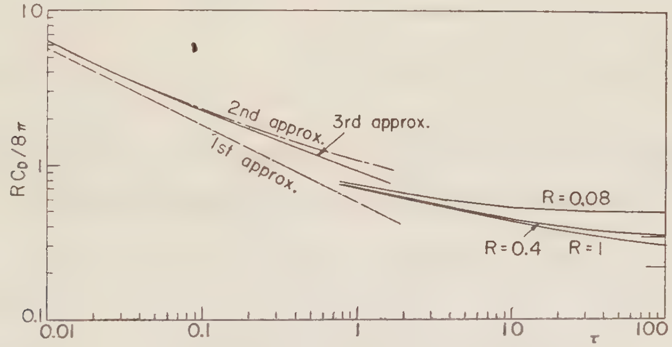

Fig. 2. $RC_D/8\pi$ vs. τ. The horizontal lines drawn on the right edge show the asymptotic values, which correspond to the steady case.

Table I. Calculated values of $RC_D/8\pi$ for various values of τ.

1) Final period solution (3.10)

R \ τ	1	2	5	10	20	50	100	∞
0.08	0.6970	0.5993	0.4948	0.4323	0.3823	0.3305	0.2997	0.2209
0.4	0.7037	0.6077	0.5061	0.4482	0.4047	0.3665	0.3508	0.3426
1	0.7435	0.6542	0.5689	0.5290	0.5080	——	——	0.4994

2) Initial period solution (4.29)

Approx. \ τ	0.01	0.02	0.05	0.1	0.2	0.5	1
1st	5.642	3.989	2.523	1.784	1.262	0.7979	0.5642
2nd	6.142	4.489	3.023	2.284	1.762	1.298	1.064
3rd	6.128	4.469	2.992	2.240	1.693	1.198	0.9231

Being equivalent to Stokes' approximation, the values of $RC_D/8\pi$ are independent of R.

§ 5. Numerical Discussions

Numerical calculations have been carried out for $R=0.08$, 0.4 and 1. Fig. 2 and Table I show the numerical values of $RC_D/8\pi$ for various values of τ. The asymptotic solution corresponding to $\tau\to\infty$ has been obtained by the numerical integration of (3.10).

The asymptotic functional form of $RC_D/8\pi$ corresponding to $\tau\to 0$ is not dependent on R but only on τ as in natural in the Stokes approximation. From (4.13) we find that the zero-th approximation does not contribute to the drag coefficient. The asymptotic solutions for $\tau\to 0$ and $\tau\to\infty$ seem to continue to each other fairly well in the intermediate region of τ.

Acknowledgement

The author wishes to express his sincere thanks to Professor Isao Imai for his continual guidance and encouragement throughout this study. He is also indebted to Professor Hidenori Hasimoto and Professor Yorisaburo Takaisi for their invaluable discussions. This work was supported by the grant-in-aid for the fundamental scientific research of the Ministry of Education.

References

1) C. W. Oseen: *Hydrodynamik*, 132–134.
2) H. Blasius: Zeitschr. f. Math. u. Phys. **56** (1908) 20.
3) S. Goldstein and L. Rosenhead: Proc. Cambr. Phil. Soc. **32** (1936) 392.
4) I. Imai: Proc. Roy. Soc. **A**, **224** (1954) 141.
5) I. Imai: Proc. Roy. Soc. **A**, **208** (1951) 487.
6) A. Erdélyi: *Tables of Integral Transforms* vol. I (McGraw-Hill Book Co., Inc., 1954).

JOURNAL OF THE PHYSICAL SOCIETY OF JAPAN, Vol. 16, No. 9, SEPTEMBER, 1961

Study of Temperature Variation of Ultrasonic Velocity and Adiabatic Compressibility in Some Liquids—Part I

By P.R.K.L. PADMINI and B. RAMACHANDRA RAO
Ultrasonic Laboratories, Physics Department, Andhra University, Waltair, INDIA

(Received May 27, 1961)

Temperature variation of ultrasonic velocity and density is studied in some organic liquids, low melting point organic solids in melt state, and corrosive inorganic liquids. It is found that in all the cases the ultrasonic velocity decreased linearly with increase of temperature. The temperature independence of Rao's molar sound velocity was studied for the first time in corrosive inorganic liquids and is established. The new relations put forward by Kishimoto and Nomoto for temperature coefficients of velocity, density and adiabatic compressibility in terms of boiling point are examined and confirmed. The relation put forward by Lagemann $M^{1/2}$. $\Delta V/\Delta T$ was also examined.

§ 1. Introduction

Considerable work has already been done on the study of temperature variation of ultrasonic velocity in liquid state by Freyer, Hubbard and Andrews[1], Lagemann, McMillan and Woolf[2], Bär[3], Bhagavantam and Joga Rao[4], Suryaprakasam[5], Willard[6], Iyengar[7], Sette[8] and others. These investigators found that ultrasonic velocity decreased linearly with increase of temperature in all the liquids except water. From a systematic study of the temperature coefficient of ultrasonic velocity in liquids, Lagemann[9] and his collaborators concluded that the successive substitution of a heavier atom in a molecule leads to successively smaller temperature coefficients. They have also obtained the following empirical relation connecting the molecular weight and the temperature gradient of the ultrasonic velocity,

$$\frac{\varDelta V}{\varDelta T}M^{1/2}=39.09\ . \tag{1}$$

They have also noticed that this relation does not hold good for highly associated liquid like water, acetonitrile etc.

From a systematic study of the temperature variation of ultrasonic velocity and density, M.R. Rao[10] observed that the ratio of temperature coefficient of velecity to density is nearly constant and is approximately equal to 3. From this he deduced the relation

$$M/\rho(V)^{1/3}=R\ , \tag{2}$$

where R is a constant independent of temperature which is known as Rao's constant, V is ultrasonic velocity and M/ρ is molar volume. Following Rao's equation, Wada[11] has deduced the following relation connecting adiabatic compressibility and density

$$\frac{1}{\beta_s}\frac{d\beta_s}{dt}=7\alpha \tag{3}$$

where β_s is adiabatic compressibility and "α" is the coefficient of expansion.

Nomoto and Kishimoto[12] deduced Rao's relation theoretically using Lennard-Jones and Devonshires[13] liquid model improved by Wentorf-Buchler, Hirschfelder and Curtiss[14] by taking into consideration the effect of the second and third layer molecules. Kishimoto and Nomoto[15] recently deduced from the above equation the following relation, at temperatures corresponding to $0.9\,T_b$ where T_b is the boiling point

$$\frac{1}{\beta_T}\frac{d\beta_T}{dt}=6.5\alpha \tag{4}$$

where β_T is isothermal compressibility and using the data available for about 28 organic liquids these authors have plotted the value of $1/\beta_s\cdot d\beta_s/dT$ versus "α" and found that there is good degree of linearity and obtained a value of 6.85 for this ratio which is in good agreement with equation (4).

Following the same lines of theoretical study Kishimoto and Nomoto[16] have shown in a comparison paper that the temperature coefficient of isothermal compressibility, ultrasonic velocity and density at temperatures corresponding to $T=0.9\,T_b$, are inversely proportional to the boiling point. However they found that the coefficients experimentally found are not in agreement with the predictions of the theory. In the present investigation the authors have investigated the temperature effect on ultrasonic velocity in several new liquids including some corrosive liquids with a view to check up Rao's relation, Lagemann's empirical formula and theoretical equations deduced by Kishimoto and Nomoto.

§ 2. Experimental Technique

The ultrasonic velocities at various temperatures are determined by the fixed path interferometer developed by B.R. Rao and K.S. Rao[17] for the study of temperature variation in liquids using a crystal oscillator. For highly corrosive liquids which attack the metal of the ultrasonic cell, an all glass—cell has been used. This glass cell is made of a wide pyrex glass tube whose ends are closed by two thin flat glass sheets which are fused all around the edges maintaining the plane parallelism. A side tube serves as the inlet as well as the out-let for the liquids under study. The thermometer is introduced through the inlet after introducing the liquid. This cell has the advantage that it can be used for any corrosive liquid or liquids giving dangerous fumes. Available data for the temperature variation of density for some of liquids studied is taken from International Critical Tables (I.C.T.). The densities at various temperature are determined for the remaining liquids for which the data is not available in I.C.T.. The liquids used are either B.D.H. or E. Merck quality and are distilled before use. As it is difficult to handle the corrosive liquids they are not distilled.

§ 3. Results and Discussion

The velocity—temperature graphs for various liquids studied are given in Figs. 1 to 5.

The parameters, $\varDelta V/\varDelta T$, $1/V\cdot dV/dT$, $1/\rho\cdot d\rho/dT$, $1/\beta_s\cdot d\beta_s/dT$ are calculated and presented in the Table I.

As expected the velocity in all the liquids studied decreased linearly with increase of temperature, a feature which is characteristic of all the liquids except water.

From a study of the data available for a large number of homologous series of organic liquids it may be easily noticed that the value of $\Delta V/\Delta T$ generally decreases with increase of molecular weight, a feature which is implicit in Lagemann's relation (1). Lagemann has pointed out that the successive substitution of a heavier atom in a molecule results in a decrease of the temperature coefficient $\Delta V/\Delta T$. Examining the data presented in table I in the light of this rule the large value of 6.02 for $\Delta V/\Delta T$ in the case of iso-propylamine may be explained as due

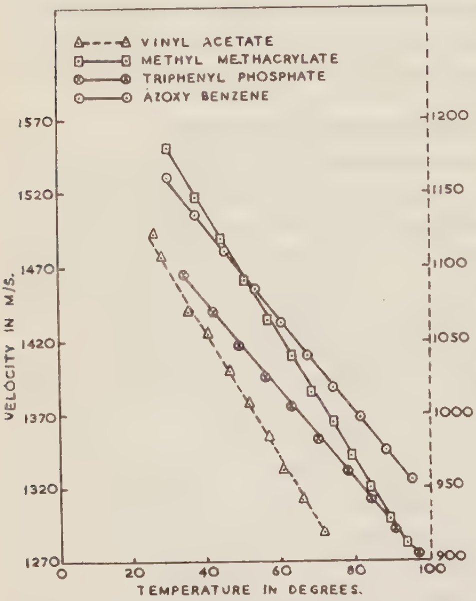

Fig. 1. Variation of ultrasonic velocity with temperature in liquids vinyl acetate, methylmethacrylate, triphenyl Phosphate and azoxybenzene.

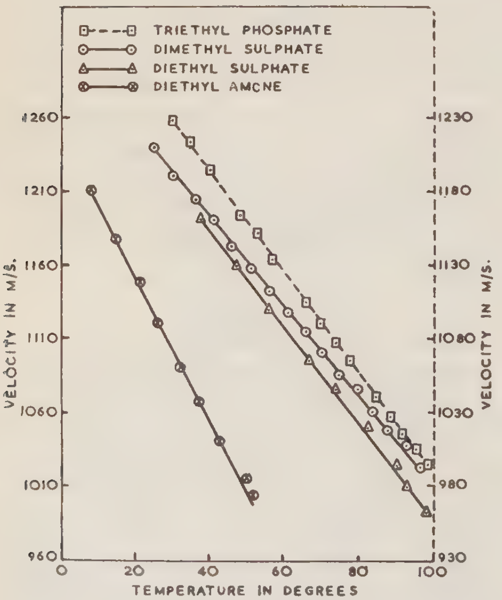

Fig. 2. Variation of ultrasonic velocity with temperature in triethylphosphate, Dimethyl sulphate. Diethylsulphate and Diethylamine.

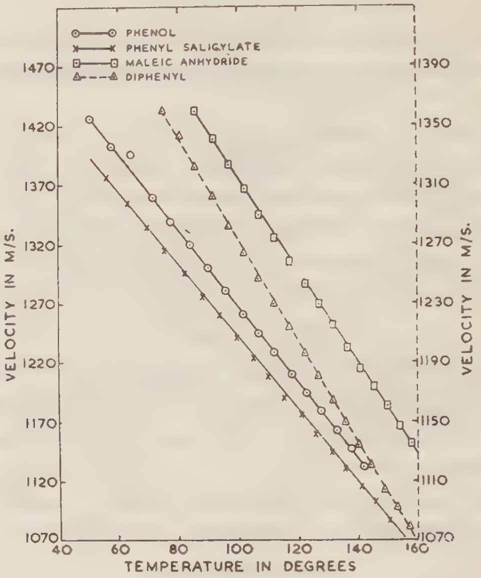

Fig. 3. Variation of ultrasonic velocity with temperature in Phenol, Phenyl Salicylate, Maleic Anhydride, and Diphenyl.

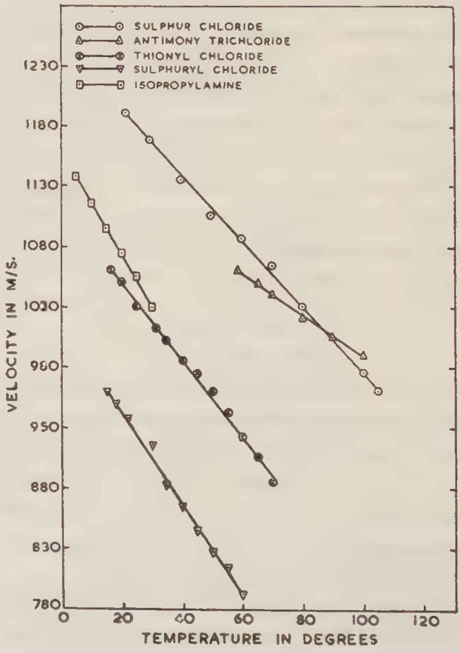

Fig. 4. Variation of ultrasonic velocity with temperature in sulphur chloirde, Antimony Trichloride, Thionyl chloride sulphuryl chloride and Isopropylamine.

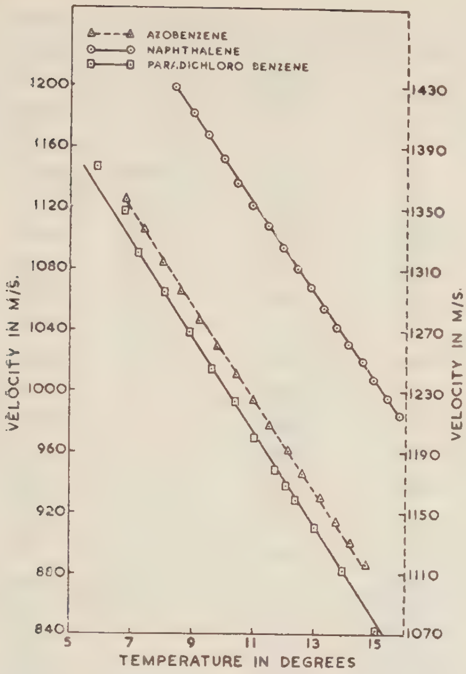

Fig. 5. Variation of ultrasonic velocity with temperature in Azobenzene, Naphthaline and Paradichlorobenzene.

to its lower molecular weight compared to diethylamine. Similar feature is noticed in the pairs of liquids ethyl and triphenyl phosphates, sulphur chloride and thionyl chloride and in the series of monomers. However the case of pairs of liquids like dimethyl diethyl sulphate, sulphur chloride and sulphuryl chloride, and azo and azoxybenzene, the results are not in accordance with the above rule in that the values of $\Delta V/\Delta T$ increased with increase of molecular weight. Although there are several exceptions to this rule, examining the data as a whole it will be seen that there is a general qualitative agreement. As for instance antimony trichloide which has a fairly high molecular weight has a low value of $\Delta V/\Delta T$, namely 2.0 whereas isopropylamine which has the lowest molecular weight among all the chemicals studied here has the highest value of 6.02 for $\Delta V/\Delta T$, the other values being intermediate. The values of $M^{1/2}\ \Delta V/\Delta T$ presented in the table I for all the liquids reveal that some liquids show large deviations from Lagemann's empirical value of 39.0.

Table I.

S_1 No.	Compound	Mol. weight	dV/dT	$M^{1/2}$ (dV/dT)	R (Experimental)	$\frac{(1/V)(dV/dT)}{(1/\rho)(d\rho/dT)}$	$\frac{(1/\beta_s)(d\beta_s/dT)}{(1/\rho)(d\rho/dT)}$
1	Diethylamine	73.11	4.390	37.54	1083.0	3.05	7.04
2	Isopropyl amine	59.11	6.020	46.50	897.0	—	—
3	Dimethyl sulphate	126.10	3.033	34.05	1025.0	2.74	6.47
4	Diethyl sulphate	154.10	3.089	38.35	1393.0	3.00	6.90
5	Sulphur chloride	135.04	2.778	32.28	853.5	2.73	6.72
6	Thionyl chloride	119.00	3.180	34.68	738.1	2.48	6.35
7	Sulphuryl chloride	135.00	3.800	44.15	793.0	3.54	8.08
8	Ethyl phosphate	182.20	4.150	56.02	1835.0	2.97	6.93
9	Triphenyl phosphate	326.20	3.853	69.58	3016.0	3.61	8.31
10	Azobenzene	182.20	2.993	40.40	1935.0	2.91	6.76
11	Azoxybenzene	198.30	3.095	43.59	1955.0	3.01	6.56
12	Vinyl acetate	86.08	4.347	39.79	958.8	3.51	7.95
13	Methyl methacrylate	101.00	4.159	41.60	1126.0	4.57	10.42
14	Ethyl methacrylate	114.10	4.028	45.96	1319.0	3.11	6.55
15	Naphthalene	128.20	2.894	32.70	1387.0	3.24	7.68
16	Diphenyl	154.20	3.533	43.87	1731.0	3.11	7.17
17	Phenyl salicylate	214.20	3.074	44.99	2035.0	3.68	8.87
18	Phenol	94.11	3.351	25.81	1014.0	2.96	7.39
19	p-Dichlorobenzene	147.01	3.219	39.02	1235.0	3.16	7.32
20	Maleic anhydride	98.06	4.100	40.60	815.0	—	—
21	Antimony trichloried	228.22	2.000	30.21	857.8	2.85	6.61

Table II.

S_1 No.	Compound	Boiling point T_b °K	$\frac{1}{V}\frac{dV}{dT}$ $\times 10^3$	$\frac{1}{\rho}\frac{d\rho}{dT}$ $\times 10^3$	$\frac{1}{\beta_s}\frac{d\beta_s}{dT}$ $\times 10^3$	$\frac{T_b}{\rho}\frac{d\rho}{dT}$	$\frac{1}{T_b}\times 10^3$
1	Diethylamine	329.0	4.11	1.12	9.50	0.37	3.04
2	Dimethyl sulphate	461.8	2.70	0.99	6.39	0.46	2.17
3	Diethyl sulphate	481.0	2.92	0.98	6.79	0.47	2.07
4	Sulphur chloride	408.6	2.58	0.95	6.35	0.39	2.45
5	Thionyl chloride	355.0	2.98	1.20	7.63	0.43	2.82
6	Sulphuryl chloride	342.0	4.16	1.17	9.48	0.33	2.92
7	Ethyl phosphate	489.0	3.05	1.01	6.99	0.50	2.04
8	Triphenyl phosphate	518.0	2.26	0.62	5.19	0.32	1.93
9	Azobenzene	570.4	2.46	0.85	5.73	0.48	1.75
10	Azoxybenzene	—	2.32	0.77	5.05	—	—
11	Vinyl acetate	355.0	4.39	1.25	9.94	0.43	2.90
12	Methyl methacrylate	373.0	4.28	0.94	9.77	0.35	2.68
13	Ethyl methacrylate	390.0	4.19	1.35	8.82	0.53	2.56
14	Naphthalene	490.0	2.51	0.77	5.94	0.38	2.04
15	Diphenyl	527.9	2.75	0.89	6.36	0.47	1.89
16	Phenyl salicylate	446.0	2.46	0.67	5.93	0.30	2.24
17	Phenol	455.0	2.63	0.89	6.58	0.41	2.20
18	p-Dichlorobenzene	446.0	2.12	0.99	7.23	0.44	2.24
19	Antimony tpichloride	496.0	1.75	0.62	4.07	0.31	2.02

For instance the value is higher than the Lagemann's constant by 40% in the case of triphenyl phosphate. The deviation is as much as 30% in the case of ethyl phosphate. The values obtained are very low in the case of phenol and antimony chloride, the deviations being 56% and 30% respectively. For liquids isopropylamine, sulphur chloride, sulphuryl chloride, ethyl methacrylate the deviation lies between 10 to 20%. The remaining liquids show quite a good agreement with Lagemann's formula.

From an examination of the molar sound velocity values at different temperatures for each substance, it was noticed that there was a remarkable degree of constancy over the range of temperature investigated, the maximum variation being generally not above 1% for most of the liquids. An examination of the data for ratio of temperature coefficient of velocity and density presented in Table II shows that this ratio is fairly constant giving an average value of about 3.1 which is in agreement with the value of 3 assumed by Rao for obtaining the relation (3). In a similar manner if we examine the ratio of the temperature coefficient of adiabatic compressibility and density, the ratio is found to vary between 6.3 and 8.8 the average value being about 7.2. This value is in reasonable agreement with the value of 6.85 obtained by Nomoto for the same ratio from a study of the data of large number of organic liquids. The remarkable degree of constancy of Rao's constant in the case of liquids like sulphur chloride, thionyl chloride, sulphuryl chloride and antimony trichloride, shows that Rao's relation is valid even for inorganic liquids. Further investigations in several other inorganic liquids are

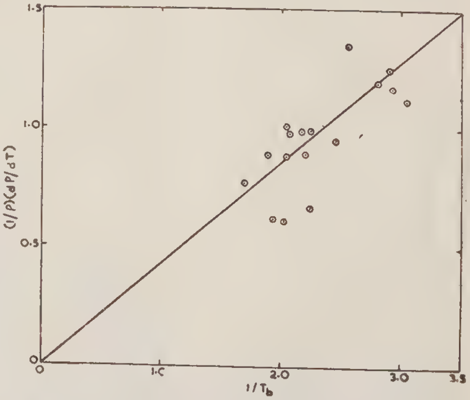

Fig. 6. Relation between $1/\rho\cdot d\rho/dT$ and boiling point.

necessary to confirm this result. In the case of substances like naphthalene, azobenzene, phenol etc. which are solids at room temperature, it is evident that Rao's relation holds good in the melt state over a fairly wide range of temperature.

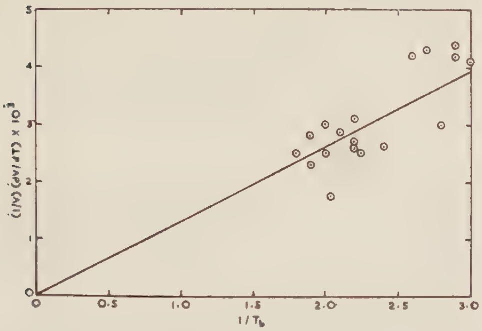

Fig. 7. Relation between $1/V\cdot dV/dT$ and boiling point.

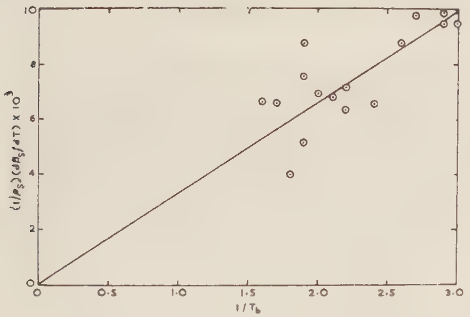

Fig. 8. Relation between $\frac{1}{\beta}\frac{d\beta}{dT}$ and boiling point.

In order to examine the relations put forward by Kishimoto and Nomoto between temperature coefficient of velocity, density, adiabatic compressibility and the boiling point, the values $1/V\cdot dV/dT$, $1/\rho\cdot d\rho/dT$ and $1/\beta_s\cdot d\beta_s/dT$, are calculated for all the new liquids studied and the results are presented in the Table II along with the boiling point T_b and its reciprocal. Thhe values thus obtained are plotted in Figs. 6, 7 and 8. For the three plots presented in these figures it may be seen that most of the points fall roughly on a line passing through the origin indicating that both the temperature coefficients of velocity, density and compressibility are nearly linear functions of reciprocal of the boiling points. From these experimental graphs the following relations are obtained.

$$\frac{1}{\rho}\frac{d\rho}{dT}=-\frac{0.41}{T_b}$$

$$\frac{1}{\beta_s}\frac{d\beta_s}{dT}=\frac{3.3}{T_b}$$

$$\frac{1}{V}\frac{dV}{dT}=-\frac{1.32}{T_b}.$$

Comparing these equations with those obtained by Kishimoto and Nomoto from a study of a large number of organic liquids for which data is available in literature it may be seen that there is fairly good agreement. The gradient of the compressibility graph which is 3.3 is higher than the value of 2.8 obtained by Kishimoto and Nomoto. Similarly the gradient of velocity boiling point graphs is about 1.32 and this is little higher than the value of 1.2 obtained by these authors. The gradient of the $\alpha-1/T_b$ graph was given as 0.41 by Kishimoto and Nomoto and this value is in excellent agreement with the average value of $T_b\cdot\alpha$ product obtained here. Thus it may be seen that the linear variation relationships given by Kishimoto and Nomoto are confirmed by the present investigation for the new liquids studied and it is evident that these relations have a wide applicability.

Acknowledgement

The authors are indebted to Council of Scientific and Industrial Research, New Delhi for the financial aid of this project.

References

1) E. B. Freyer, J. C. Hubbard and D. W. Andrews: J. Ameri. Chem. Soc. **51** (1929) 759–770.
2) R. T. Lagemann, D. R. McMillan, Jr. and E. Woolf: J. Chem. Phys. **17** (1949) 369–373.
3) R. Bär: Proc. Ind. Acad. Sci. **8–A** (1938) 289.
4) S. Bhagavantam and C. V. Joga Rao: Proc. Ind. Acad. Sci. **9–A** (1939) 312.
5) V. Suryaprakasame: Proc. Ind. Acad. Sci. **12–A** (1940) 341.
6) G. W. Willard: J. Acous. Soc. Amer. **19** (1947) 235–41.
7) K. S. Iyengar: Proc. Ind. Acad. Sci. **33–A** 127–29 (1951).
8) D. Sette: Z. Natur-for-Shung, 5a, (1950) 170–71.
9) R. T. Lagemann, D. R. McMillan and W. E. Woolf,: J. Chem. Phys. **17** (1949) 369.
10) M. R. Rao: Ind. J. Phys. **14** (1940) 109.
11) Y. Wada: J. Phys. Soc. Japan **4** (1949) 280.
12) O. Nomoto and T. Kishimoto: J. Phys. Soc. Japan **9** (1954) 59–77.

13) J. E. Lennard Jones and A. F. Devonshire: Proc. Roy. Soc. **163 A** (1937) 53.

14) R. H. Wentorf, Jr., R. J. Buchler, J. O. Hirschfelder and C. F. Curtiss: J. Chem. Phys. **18** (1950) 1484.

15) T. Kishimoto and O. Nomoto: J. Phys. Soc. Japan **9** (1954) 67-72.

16) T. Kishimoto and O. Nomoto: J. Phys. Soc. Japan **9** (1954) 73-77.

Errata

Cleavage Fracture in Single Crystals of Silicon Iron

By Ryūkichi HONDA

J. Phys. Soc. Japan **16** (1961) 1309

Page	Column	Line	Wrong	Corrected
1309	left	2 from the bottom	ions	iron
1310	left	19	wheat	what
1310	left	10 from the bottom	though	thought
1313	right	4	a	an
1315	left	8	on	parallel to
1315	right	19	been detected	been observed and several shorter cracks have been detected
1317	left	20	is	are

Short Notes

This section is intended to secure prompt publication of important discoveries in physics. The reports should not exceed 800 words in length. A figure of size 7 cm×7 cm will be counted as 150 words.

J. PHYS. SOC. JAPAN **16** (1961) 1777

Scintillation from the Solid Xenon

By Sigeo TAKEMOTO, Takeo HASEGAWA
and Saburo HOMMA
*Department of Physics, Tohoku University,
Sendai, Japan*

(Received July 5, 1961)

Xenon was investigated by Sayres and Wu[1] as a gas scintillation counter. According to their experiment, the scintillation pulse height produced by Po^{210} alpha particles was very low in comparison with CsI(Tl); but when the photomultiplier was used with a wave length shifter, quaterphenyl, the pulse height increased by a factor of 106/6. Therefore the large part of the scintillation spectrum of xenon gas produced by alpha particles might be beyond the short wave length limit of the photomultiplier.

In the present experiment, the xenon gas was frozen by a liquid air and the scintillation pulse from the solid xenon due to Po^{210} alpha particles were measured with an electronic system consisted of DuMont 6291 photomultiplier, cathode follower and Iwasaki 30 MC synchroscope (vertical rise time 1.2×10^{-8} sec).

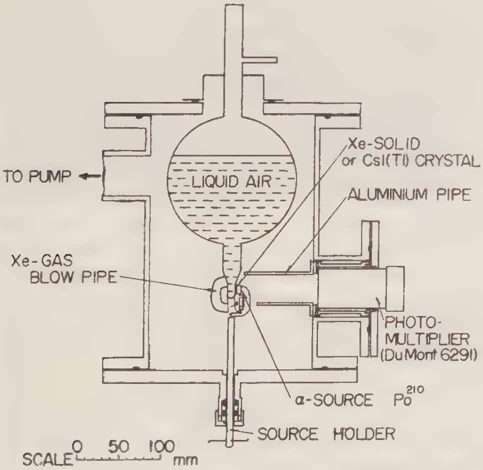

Fig. 1. The experimental apparatus for the measurement of the scintillation light from the solid xenon.

Fig. 1 shows the experimental apparatus. About 20 cc xenon gas was blown upon the flat surface of a stainless vessel in which liquid air was contained. The gas was frozen instantaneously on the stainless surface. The thickness of the frozen xenon was about 10 mg/cm², which was enough to stop the 5.3 MeV alpha particles. The scintillation light from the solid xenon entered into the photomultiplier through an aluminium pipe. A typical example of the scintillation pulses from the solid xenon is shown in Fig. 2 in comparison with CsI(Tl) (10 mmϕ ×1 mm, at room temperature). The pulse height of the solid xenon was about 1/3 times as high as that of CsI(Tl). The fluctuation of the alpha pulse height in the solid xenon scintillator might be chiefly due to the poor transparency and the inhomogeneity of the frozen material. In order to make the pulse height increase, a wave length shifter, sodium salicylate, was placed on the photomultiplier, but no remarkable improvement in the pulse height was observed. Therefore the scintillation spectrum of the solid xenon might be considered to be in the sensitive part of the photomultiplier.

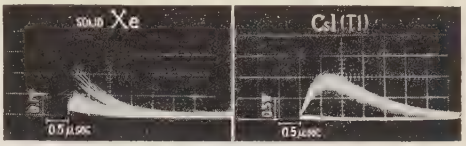

Fig. 2. A typical example of the output pulse from the cathode follower (measured with Iwasaki 30 MC synchroscope).

The decay time was also studied using the above synchroscope and was obtained to be less than 6×10^{-8} sec for the solid xenon.

From the present experiment the possibility of xenon as the liquid scintillator might be suggested.

Reference

1) A. Sayres and C. S. Wu: Rev. Sci. Inst. **28** (1957) 758.

J. Phys. Soc. Japan **16** (1961) 1778

Proton Magnetic Resonance and the Polymorphism of Triglycerides

By Haruo Nakajima
Department of Physics, Faculty of Science, Hokkaido University, Sapporo, Japan

(Received June 5, 1961)

The crystalline modifications of the saturated triglycerides have been studied by thermal, x-ray, and infra-red techniques.[1),2)] In order to investigate the molecular motion in the different crystalline forms and the mechanism of double melting, measurements of the temperature dependence of the proton magnetic resonance absorption spectrum were carried out on two of the triglycerides, tristearin $(C_{17}H_{35}COO)_3C_3H_5$ and tripalmitin $(C_{15}H_{31}COO)_3C_3H_5$, in their β- and α-form. The stable β-forms of both triglycerides were prepared by crystallizing the samples from toluene; the less stable α-forms, by quenching the molten samples in water-ice mixture.

The second moments of the resonance absorption spectrum of tristearin in both crystalline forms are plotted against temperature in Fig. 1. Their experimental error is about ±5% at room temperature and is about ±10% far below it. The similar behavior and similar numerical value are seen in the temperature dependence of the second moment of tripalmitin. The center peaks of the resonance absorption derivative, which are prominent above room temperature and are out of scale at higher temperatures, seem to be of a liquid-like nature. The second moments of the absorption derivative except the center peaks are determined above 40°C. They may be called as the second moments of the solid part. The glycerole residue is likely to play an important part in the center peaks.

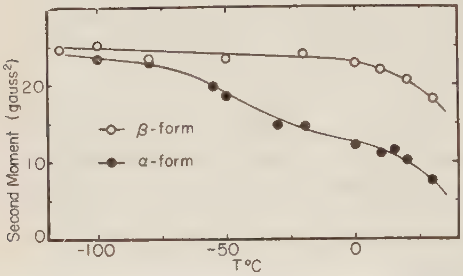

Fig. 1. Second moment versus temperature curves for β- and α-form of tristearin.

At the temperatures below about −80°C, the second moments of both crystalline forms are fairly close to the rigid structure value for a single chain of the acid-radical in the molecule. The difference in the intermolecular contribution to the second moment between both forms may be very slight at these temperatures, if they have the different crystalline structures. On the other hand, hindered rotation or oscillation of the molecule about its chain axis in the crystal may explain the decrease in the second moment of the α-form above −50 °C.[3)] This is parallel to the result of the x-ray and infra-red measurements[4)] that the α-form has hexagonal packing rather than a vitreous form[1)] at room temperature.

At the lower melting point of each triglyceride, 54°C for tristearin and 44°C for tripalmitin, a transition of the crystalline structure from the α- to the β-form is seen in the resonance absorption spectra of the solid part of the α-form. Fig. 2 represents this transition (a) in the second moment of the solid part of tristearin and (b) in the line shape of tripalmitin. The increase in the second moment with increasing temperature was reported in the case of liquid crystal.[5)] No change in the line shape of the α-form has been noticed beyond the experimental error for several weeks at room temperature.

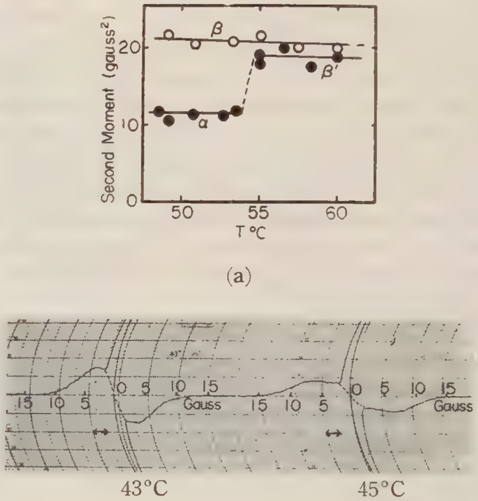

(a)

(b)

Fig. 2. Transition from the α- to the β-form.
(a) Second moment versus temperature curves of the solid part of tristearin.
(b) Proton resonance derivatives of tripalmitin at 43° and 45°C.

References

1) C. E. Clarkson and T. Malkin: J. Chem. Soc. (1934) 666.
2) D. Chapman: J. Chem. Soc. (1956) 2522.
3) E. R. Andrew: J. Chem. Phys. **18** (1950) 607.
4) E. S. Lutton: J. Amer. Chem. Soc. **67** (1954) 524.
5) R. Köhler: Ann. Physik **6** (1960) 241.

J. PHYS. SOC. JAPAN **16** (1961) 1779

Observation of the Tracks of Fission Fragments in Molybdenite

By Kazuhiko IZUI and F. Eiichi FUJITA*
Japan Atomic Energy Research Institute
Tokai-mura, Ibaragi-ken, Japan

(Received May 8, 1961)

Recently electron microscopy of fission fragment-irradiated materials such as mica1), evaporated film of uranium oxide2) and graphite3) has revealed the presence of the tracks of fission fragments exhibiting the thermal spike effects4) of them.

Present note reports some remarkable features of the tracks of the fission fragments in molybdenite crystal observed with an electron microscope, which would make possible to give a detailed analysis of the thermal spike region.

The thin film of molybdenite was superposed on the evaporated film of uranium and exposed to the thermal neutrons in JRR-1 reactor to the total doses of the order of $10^{16} n/\mathrm{cm}^2$ together with the uranium film and then observed with Hitachi electron microscope of HU-10 type after detaching the uranium film.

The tracks of fission fragments were observed as shown in photo. 1 where many of them appear as straight lines about 100Å wide and some of them as linear arrays of spots. The contrasts of the tracks are reversed to that of the matrix crystal in some parts of the regions where the extinction contour bands appear, which indicate that they are the diffraction contrasts caused by the variations in the Bragg conditions in the crystal. These narrow regions along the tracks seem to be small recrystallized regions produced by thermal spike effects of the fission fragments passing through the crystal, as pointed out in the case of graphite3).

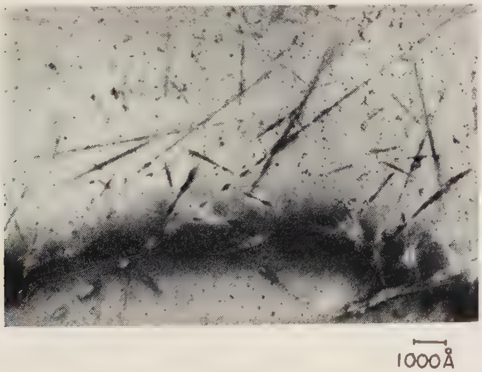

Photo. 1.

In some case the appearences of the tracks are modified by varying the diffraction condition in the crystal as shown in photo. 2(a) and 2(b) which are the photographs taken from the same area in the slightly different inclination of the specimen to the electron beam. In photo. 2(a) the track consists of a linear array of shots, while in photo. 2(b) it contains not only spots but light narrow lines about 50Å wide penetrating the centers of each spots.

It may be concluded from these facts that the structure of the thermal spike region is of the form which is illustrated in Fig. 1, where dotted lines indicate the spreading of the strain field around the spike region. The origin of such structure may be attributed to the un-uniformity in solidification of the molton material in the spike region which had initially uniform cylindrical shape.

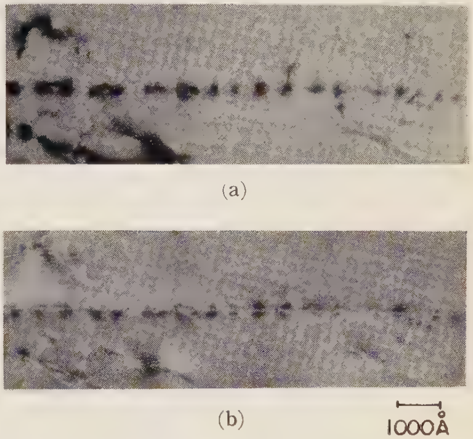

(a)

(b)

Photo. 2.

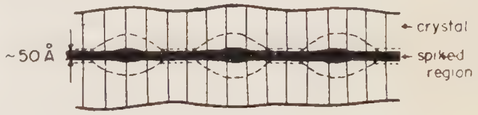

Fig. 1.

The authors wish to express their hearty thanks to Prof. R. Uyeda of Nagoya University for his suggestion to do this experiment and for his offering molybdenite sample.

References

1) E. C. H. Silk and R. S Barnes: Phil. Mag., **4** (1959) 970
2) T. S. Noggle and J. O. Stiegler: J. Appl. Phys., **31** (1960) 2199.
3) K. Izui and F. E. Fujita: J. Phys. Soc. Japan, **16** (1961) 1032.
4) F. Seitz and J. S. Koehler: *Solid State Physics*, **2** (1956) 305.

---

* Present address: Brookhaven National Laboratory, Upton, L.I., N.Y., U.S.A.

J. PHYS. SOC. JAPAN **16** (1961) 1780~1781

On the Extraordinary X-ray Diffraction Intensities of Quenched TiC Powder

By Shiro FUJISHIRO

Department of Chemistry, Faculty of Science, Kyoto University, Kyoto, Japan

(Received June 19, 1961)

Titanium carbide, that has a high melting point and a great hardness, appears to be an intermetallic compound with a strong directional bonding between Ti and C[1]. The heat of formation of TiC, that is a measure of the bond strength, is about 30-40 Kcal[2],[3] at room temperature, much greater that that of ordered alloys. This fact suggests a highly ordered arrangement of Ti and C in the crystal. A rough calculation based on the quasi-chemical method[4], however, showed that the number of Ti-C bond decreases gradually with temperature, particularly above 2500°K.

The original purpose of the present experiment was, therefore, to detect the exchange of Ti and C in their sites due to thermal vibration on X-ray data. Quenched specimens of TiC have been investigated in the present experiment but no such effect was found. On the contrary, extraordinary diffraction patterns were obtained, that would not be explained only by frozen vacancies or atoms in the wrong lattice sites. Powdered titanium carbide prepared from titanium sponge was employed as the specimen. Lattice parameter was 4.321±0.001 Å. The specimen in a graphite basket was suspended from the top of a quartz furnace tube by means of a thin tungsten wire. In the bottom of the tube liquid argon was stored, which was cooled by liquid nitrogen from outside to minimize the evaporation of liquid argon. Purified argon gas was flashed and passed always through the system during a run. This procedure prevents TiC from oxidation or nitriding. High temperatures up to 2500°C were attained by means of an induction unit. After the specimen was maintained at a desired temperature for a sufficient time, the top of tungsten wire was unhooked so that the specimen fell into the pool of liquid argon. In order to determine the structure of the quenched specimen, this was immediately tested by means of a Geiger-flex X-ray diffractometer. In Fig. 1 the chart at the top shows the diffraction pattern for an ordinary TiC powder. The middle chart was obtained from TiC which had been quenched from 2500°C, in which the diffraction intensities of (111), (220) and (222) were remarkably increased. Neither line broadening nor significant change in lattice parameter occurred as a consequence of quenching. By annealing this specimen at 500°C for an hour in vacuum, the chart at the bottom was obtained. This would indicate a stage of recovery, whereas no such sign occurred when the identical specimen was aged at room temperature for a week. Repeated experiments gave the same results although the degree of increase of the intensities depended on the quenching rate, the temperature at which and the time for which the specimen was maintained.

Gilman[5] reported that in NaCl type crystals the glide {110}<110> or {100}<110> occurs, depending on the polarizability of a crystal and the temperature It seems that the anisotropic contraction due to quenching may cause this sort of slips, but if it were so, the line broadening and the shift of scattering angles must be observed[6].

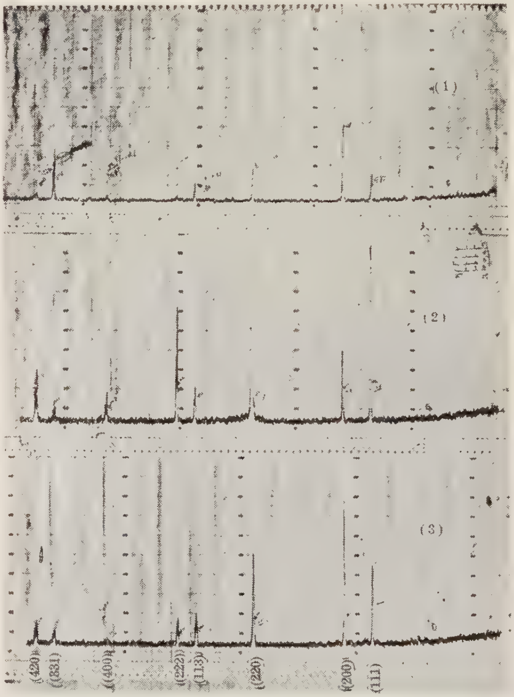

Fig. 1. X-ray analysis for TiC powder by CuKα.

A tentative calculation showed that the slip {100}<100> with a vector of half of the unit cell and with an appropriate periodicity results not in line broadening but in an increase of intensity at (111) as being expressed by $\alpha(F_{Ti}+F_C)^2$. In an ordinary crystal this is given by $\alpha(F_{Ti}-F_C)^2$. Here α is a constant, F_{Ti} and F_C are the atomic structure factors of Ti and C, respectively.

As no decisive conclusion, however, can be drawn from the above results, further investigation will be done to elucidate this phenomenon. The author wishes to express his appreciation to professors S. Kachi and R. Maddin for stimulating discussions.

References

1) R. E. Rundle: Acta Cryst., **1** (1948) 180.
2) G. L. Humphrey: J. A. C. S. **73** (1951) 2261.

3) S. Fujishiro and N. A. Gokcen: J. Phys. Chem., **65** (1961) 161.
4) B. L. Averbach, P. A. Flinn and M. Cohen: Acta Metallurgica, **2** (1954) 92.
5) J. J. Gilman: *ibid.* **7** (1959) 608.
6) C. N. J. Wagner: *ibid.* **5** (1957) 427.

J. Phys. Soc. Japan **16** (1961) 1781

The Flow of a Viscous Fluid past a Porous Flat Plate

By Mitutosi Kawaguti

Railway Technical Research Institute, Tokyo

(Received July 28, 1961)

It is of theoretical as well as practical interest to study the flow past a bluff body which has numerous gaps, such as railway bridges, snow break forests, etc. As a first step to this study, we have investigated the flow of a viscous fluid past a porous flat plate through which the fluid may pass with the velocity proportional to the pressure difference between the both sides of the plate. First, assuming that the Reynolds number of the flow is sufficiently small, we have obtained the Oseen approximate solution for the flow past a (non-porous) flat plate which is put perpendicularly to the flow, and have calculated the pressure difference between the upstream and the downstream sides of the plate. Next, we have studied the correction due to the flow through the plate.

The Oseen solution for the flow past a two-dimensional ordinary flat plate may be easily obtained with Imai's method[1]. Thus, the complex velocity at the point P (whose complex coordinate is z) can be given as

$$W=-\frac{1}{2}\frac{U}{S}\left\{\left(Z-\frac{1}{Z}\right)-\left(\frac{1}{Z}-\overline{Z}\right)\right\}\frac{Z}{Z^2+1}$$
$$+\frac{1}{2}\frac{U}{S}\ln Z\overline{Z}+O(k)\,, \tag{1}$$

where the breadth of the plate is assumed as 4, and

$$z=Z-Z^{-1}\,,\qquad S=\ln(2/k)-0.57721\cdots\,,$$
$$k=U/2\nu\,,$$

U and ν being the undisturbed velocity and the kinematic viscosity, respectively.

The pressure distribution over the surface of the plate is given as

$$p=\pm\rho\nu(U/S)(1-y^2/4)^{-1/2}+\text{const.}+O(k^2)\,,\quad (z\equiv x+iy)\,,$$
$$(+\text{: upstream side},\ -\text{: downstream side}). \tag{2}$$

Then the flow velocity through the flat plate U_t is assumed as

$$U_t=K\Delta p/\rho U=(2\nu K/S)G(y)\,, \tag{3}$$

where

$$G(y)=(1-y^2/4)^{-1/2}$$

and K is a proportional constant which may be determined theoretically or experimentally.

Now we shall approixmate the function $G(y)$ by

$$F(y)=A+B\int_{-2}^{+2}\frac{Y}{Y-y}\,dY\,. \tag{4}$$

The first and the second terms in (4) correspond to a uniform flow and the flow due to a linear distribution of vortices over the surface of flat plate respectively. A and B may be determined from appropriate conditions on $F(y)$. (For example, $A=1.564$, $B=-0.141$, if we adopt the condition that $F(y)$ and $G(y)$ coincide with each other at the points $y=0$, $y=\pm1$. It has been found that some other conceivable conditions give the values A and B much the same order of magnitude as above.)

Next, we consider the correction to the drag of the flat plate due to the presence of gaps. It is easily shown that the second term in $F(y)$ does not contribute to the drag. The contribution of the first term in $F(y)$ to the drag may be obtained, by superposing on the uniform flow U the flow that is at rest at infinity and has the velocity $u_0U=2\nu KA/S$ on the flat plate. But, such a flow may be obtained by superposition of the uniform flow of velocity $-u_0U$ past a fixed non-porous flat plate and a uniform flow u_0U.

Finally the drag of the porous flat plate has been obtained as

$$C_D=\frac{D}{\frac{1}{2}\rho U^2L}=\frac{8\pi}{RS}(1-u_0)+O(R)+O(K)$$
$$=\frac{8\pi}{RS}\left(1-\frac{8KA}{RS}\right)+O(R)+O(K), \tag{5}$$

where $R=UL/\nu$ is the Reynolds number, L being the breadth of the plate.

Reference

1) I. Imai: Proc. Roy. Soc. **A**, **224** (1954) 141.

J. Phys. Soc. Japan **16** (1961) 1782

Observations on the Etch Patterns in Deformed KCl Crystals

By Masayoshi Sakamoto

Department of Physics,
Tokyo College of Science,
Shinjuku-ku, Tokyo, Japan

(Received June 2, 1961)

Recently Gilman and Johnston[1] proposed a mechanism of dislocation multiplication in alkali-halide crystals, which includes a double cross-glide mechanism similar to that formerly proposed by Koehler[2] and Orowan[3]. According to this mechanism, a length of a gliding screw dislocation moves by cross-glide onto a nearby plane parallel to the original glide plane and a multiplication results from prismatic loops or trails formed by jogs on moving screw dislocations. These screw dislocations must have many cusps, because of dragging force exerted by the trails. Therefore, it is especially of interest, with regard to this mechanism, to observe etch patterns of deformed KCl crystals. The present report describes the results of observations on etch patterns on surfaces, nearly parallel to {110} plane or glide plane, of mechanically deformed KCl crystal.

Specimens were subjected to a light compression or bending, and single slip bands were produced. A cut was made with wet nylon string, in the portion where density of slips is low, along a plane parallel to the glide plane as AB in Fig. 1. The surface obtained by cutting was scraped carefully about $100\sim200\mu$ in depth by chemically polishing method, followed by etching with the technique used in the previous work[4]. Many photographs of the etch patterns were taken on crystals obtained by these procedures. Each of these surfaces seems to be in tilt by a small angle against the {110} plane, taking into account the method of cutting and scraping.

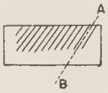

Fig. 1. Cutting of the specimen.

A typical example of the photographs is shown in Fig. 2. It may be recognized as a remarkable feature that there are several paired etch pits among many normal ones and that both trails of these paired etch pits are closing together in the [100] direction or, conversely, sometimes opening out probably in the [0$\bar{1}$1] direction oppositely, both in cusp shape, as shown in Fig. 3(a) and (a′). Some examples of the cusp-like pits are shown by arrows in the photograph.

On the other hand, mechanically deformed specimens were kept at $500\sim600$°C for several hours. It was observed on these specimens that some change in the form of paired etch pits has taken place. Fig. 3(b) shows their shape which is surrounded by straight lines instead of smooth curves on the specimen before the treatment.

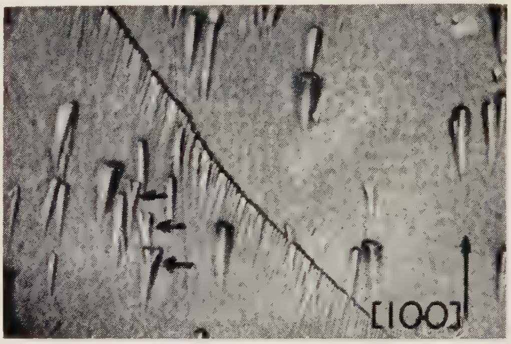

Fig. 2. Paired etch pits.

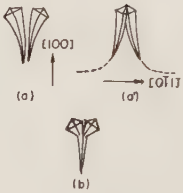

Fig. 3. Sketches of paired pits.

The two features described above are observed only on the surfaces near the {110} plane of deformed crystals. Therefore, these paired etch pits may be interpreted to be the cusps attached to the screw dislocations. The shape change of paired etch pits by the heat treatment may be conceived to result from the tension of dislocation and the interaction between oppositely signed dislocations. It must be noted that in the present work patterns of stepped trails were also observed, providing another evidence to the mechanism above.

References

1) J. J. Gilman and W. G. Johnston: J. Appl. Phys. **31** (1960) 632; **31** (1960) 687.
2) J. S. Koehler: Phys. Rev. **86** (1952) 52.
3) E. Orowan: *Dislocations in Metals*, (AIME, New York, 1954), p. 103.
4) M. Sakamoto and S. Kobayashi: J. Phys. Soc. Japan **13** (1958) 800; **13** (1958) 1231.

J. Phys. Soc. Japan **16** (1961) 1783

Preparation of Gallium Phosphide Crystals and Their Etch Pattern

By Sigeru Iizima and Makoto Kikuchi
Electrotechnical Laboratory,
Tokyo, Japan

(Received July 13, 1961)

Crystals of gallium phosphide are made from the elements in an inactive atmosphere. As shown in Fig. 1, the quartz boats containing elemental gallium and phosphorus respectively are placed in a quartz tube which is closed at one end. This tube is placed in a large outer quartz tube, and heated in the flow of argon gas, so that the temperatures at the quartz boat containing gallium metal and the other containing phosphorus are controlled at 1200°C and 150–400°C, respectively. Heating and controlling of the temperatures are achieved by using Pt wire wound furnace and the potentiometer type controller. After heating for 20 hours, the furnace is switched off and cooled down to room temperature.

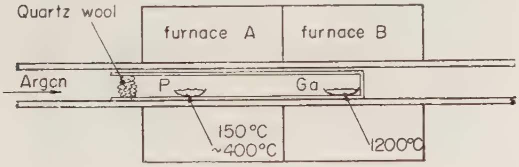

Fig. 1. Diagram of apparatus used for preparing gallium phosphide.

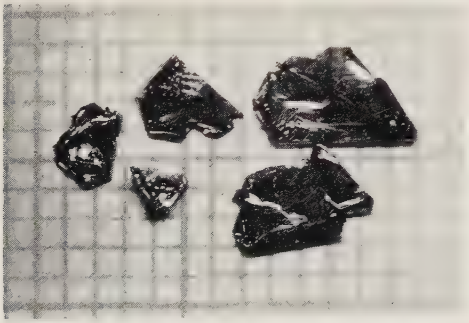

Fig. 2. Plate-shaped crystals of gallium phosphide. Scale: 1 mm a division.

Plate-shaped crystals about 0.3 mm thick are found in the gallium metal, and by treating in hot dilute HCl excess gallium can be removed (Fig. 2). On the inner wall of the inner quartz tube, there grow very thin and flexible ribbon-shaped crystals (Fig. 3).

Crystal of gallium phosphide has the structure of zinc blende type, and the flat faces of the plate-shaped crystals are {111} faces. When etched in a mixture of 1 part HNO_3 and HF for 15 minutes, on one face of the plate-shaped crystal appears a characteristic etch pattern which resembles that of germanium (111) face etched by superoxol (Fig. 4(a)). On the opposite face, no characteristic pattern can be found (Fig. 4(b)). White and Roth[1] have reported the observation of polarity of gallium arsenide crystals. Probably, a similar consideration may be admitted that the face with the characteristic pattern is correlated with White and Roth's case 2 in which the gallium atoms are on the outside of the double layer.

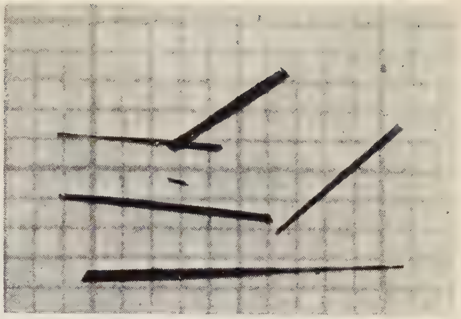

Fig. 3. Ribbon-shaped crystals of gallium phosphide. Scale: 1 mm a division.

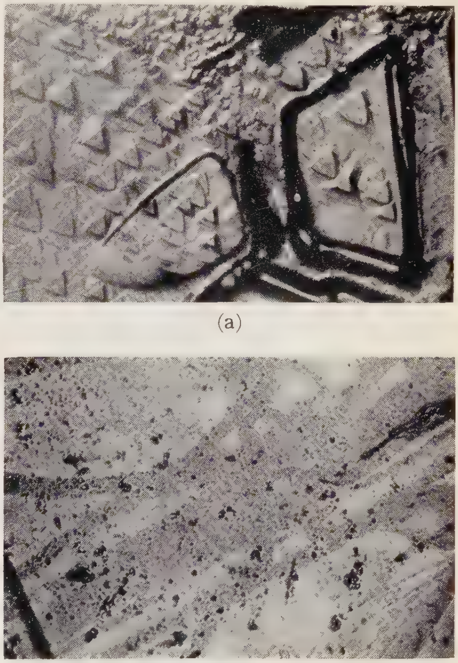

(a)

(b)

Fig. 4. (a) Characteristic etch pattern on one face. (b) The opposite face. Diagonal of the figures is about 1.5 mm.

Reference

1) J. G. White and W. C. Roth: J. A. P. **30** (1959) 946.

J. Phys. Soc. Japan **16** (1961) 1784~1785

Electroluminescence in Gallium Phosphide Single Crystals

By Sigeru Iizima and Makoto Kikuchi
Electrotechnical Laboratory,
Tokyo, Japan

(Received July 13, 1961)

Point contact V-I characteristics and electroluminescent properties of gallium phosphide crystals synthesized in argon atmosphere at elevated temperature[1] are observed. Resistivities of our crystals, which are not doped with any impurities purposely, range from 0.1 to 1 ohm-cm and the conductivity is *n*-type.

On making the large-area contact to the plate-shaped crystal with silver paint on the one side and making metal point contact on the other, good rectification effects are observed. A typical V-I characteristic is shown in Fig. 1. As is shown in the figure, breakdown voltage of our samples is about 5-10 volts. When the breakdown occurs, orange-yellow light emission is observed, as is shown in Fig. 2. It looks likely that the light emission prevails over the whole crystal, but it is probably due to the internal reflection of the light emitted at the point contact. The fact that light is emitted only when the breakdown occurs in our crystal is seen from the photograph of Fig. 3. Upper trace in the figure shows the change of the light intensity received by photomultiplier tube 7306, and lower trace shows the change of the current which flows through the contact, when ac voltage of 400 cps is applied. The absence of electroluminescence at the forward bias is probably due to the presence of the deathnium levels caused by considerable amount of impurities unintentionally introduced in our crystals.

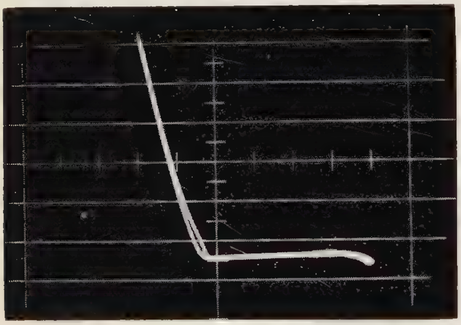

Fig. 1. Point contact V-I characteristic in our typical *n*-type crystal. Abscissa: voltage, 2 volts per division; ordinate: current, 250 μA per division.

Fig. 4 shows the trace of current *vs* light intensity characteristic. From the figure, it appears that

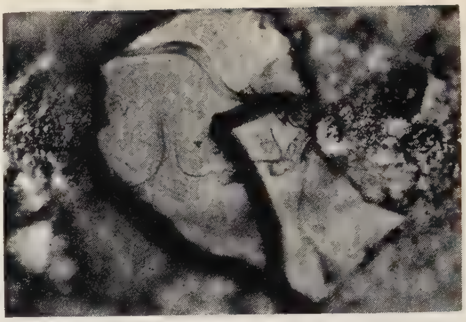

(a)

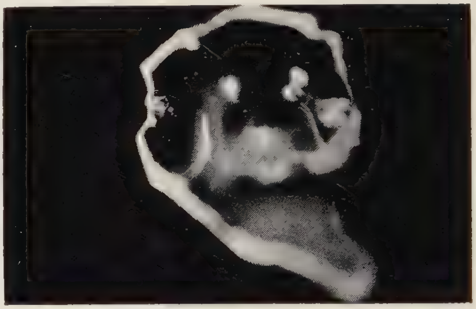

(b)

Fig. 2. Photograph of GaP crystal with point contact, (a) by external illumination; (b) by electroluminescence.

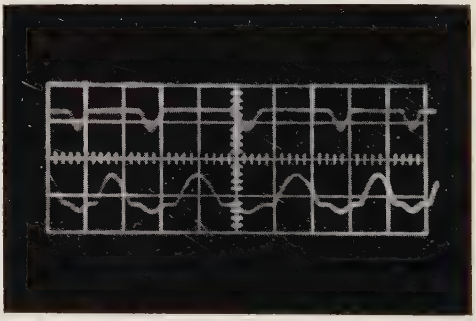

Fig. 3. Upper trace: light intensity; lower trace: current, 10 mA per division.

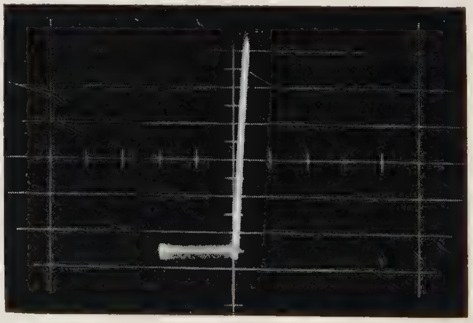

Fig. 4. Current *vs* light intensity characteristic. Abscissa: current, 2 mA per division; ordinate: light intensity, arbitrary scale.

light intensity is proportional to the backward breakdown current. This suggests that the bimolecular radiative recombination is the dominant effect when the light is emitted at the breakdown region.

Reference

1) S. Iizima and M. Kikuchi: *Preparation of Gallium Phosphide Crystals and Their Etch Pattern.* Preceding paper, in this journal.

J. PHYS. SOC. JAPAN **16** (1961) 1785~1786

Crystal Distortion of FeO on Cooling past its Néel Temperature

By Yoshiko SUZUKI and Eiichi ASADA

Government Chemical Industrial Research Institute, Tokyo

(Received May 31, 1961)

It is well known that FeO becomes antiferromagnetic on cooling past the Néel temperature and the crystal lattice exhibits a small rhombohedral distortion from its original simple NaCl-type structure[1].

The magnitude of the distortion is affected by the content of excess oxygen over FeO and this can be varied over a relatively wide rang; B.T.M. Willis and H. P. Rooksby[2] has reported that the distortion diminishes with decreasing iron concentration, that is, with increasing departure from stoichiometric FeO.

In the present, in order to investigate the crystallographic transition point and the dependence of the distortion of FeO on the temperature, X-ray diffraction measurement was made continuously over a range from room temperature to 83°K. Rate of increasing and decreasing temperature were both 2°C/min.. Ferrous oxalate was precipitated from solution of ferrous chloride which was prepared from electrolytic iron. Precipitate was decomposed by heating at 800°C in vaccuo, thus sample **I** was obtained. Because this product gave lines of free iron as well as ferrous oxide on the X-ray powder pattern, it was again heated at 1000°C for several hrs.. This was called sample **II**, and it gave no line of free iron and showed an increased lattice parameter by 0.003 Å.

Observed diffraction line was (220) in cubic index which splitted into (211) and $(10\bar{1})$ in rhombohedral indices. In sample **II**, the line was gradually broadened on initial stage of cooling below the room temperature and became splited into two lines from which rhombohedral lattice constants a and α were calculated. The split grew larger as the temperature approached to 83°K.

Fig. 1 show the half-value breadth of the line and the rhombohedral angle α versus temperature relations.

In sample **I**, the line (220) was broadened similarly as in sample **II**, but remained unsplit even at liquid-nitrogen temperature. The starting temperatures of line brodening which coincide with each other in sample **I**, and **II**, are in good accord with transition temperature determined by means of the measurements of specific heat[3] or of dilatometry[4], but not of magnetic susceptibility[5] as shown in Table I.

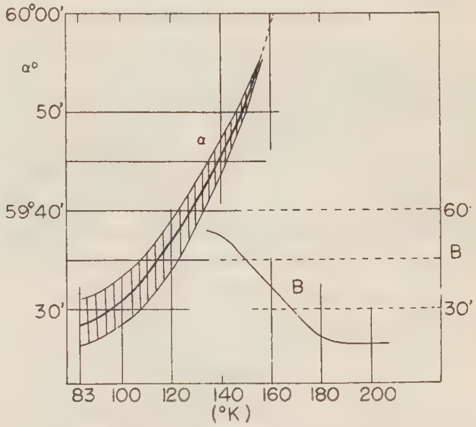

Fig. 1. Half-value breadth B of (220) and rhombohedral angle α versus temperature.

Table I.

Specific heat[3]	183-184°K
Dilatometry[4]	186°K
Magnetic susceptibility[5]	198°K
X-ray photografic[6]	203°K
X-ray diffractometer	180-185°K

R. Collongues[7] suggested that FeO with minimum iron content may distort to tetragonal symmetry. But in our present experiment, all X-ray patterns of sample **I** were in good agreement with those of the initial stage of sample **II**.

Further, with purpose to increase iron content and to make change in the Néel temperature, about 5 mole % of Fe powder (sample **III**) and Mn, Cr, Co, Cu, Zn powder etc. were mixed into sample **I**, sintered in vaccuo at 1000°C for several hrs. and quenched in water. Fig. 2 shows the differences of the distance of (111) and that of (100) for these samples.

So it is obvious that metalic ingredients, such as Mn, Cr, Co, etc. lower the crystallographic transition point as well as the magnitude of distortion at 83°K, whereas excess oxygen over FeO affects only the magnitude of distortion.

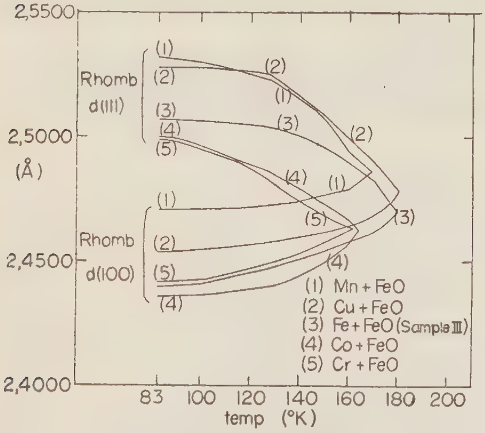

Fig. 2. Magnitude of Split of (111) Cub. → (111) Rhom. and (100) Rhom.

References

1) W. L. Roth: Phys. Rev. **110** (1958) 1333.
2) B. T. M. Willis and H. P. Rooksby: Acta Cryst. **6** (1953) 827.
3) Russell and Millar: J. Amer. Chem. Soc. **51** (1929) 215.
4) M. M. Foëx: Compt. rend. **227** (1948) 193.
5) M. M. Henri Bizette: Compt. rend. **207** (1938) 450.
6) N. C. Tombs and H. P. Rooksby: Nature **165** (1950) 442.
7) R. Collongues: Acta. Cryst. **7** (1954) 213.

J. Phys. Soc. Japan **16** (1961) 1786~1787

Note on Fe^{3+} ions in Spinel Structure

By Yoshikazu Sugiura

Sony Corporation Research Laboratory
Hodogaya, Yokokama

(Received June 3, 1961)

It was reported in the author's previous paper[1)] that the line widths of paramagnetic resonance absorption of Fe^{3+} ions in $MgAl_2O_4$ and $ZnAl_2O_4$ increased with the increasing concentration of ions, but decreased down when the concentration was further increased beyond a certain value. These phenomena were explained as the result of line broadening by dipolar interaction and narrowing by exchange interaction. It has been found, however, that if we assume that Fe^{3+} ions are randomly distributed and take the exchange interaction into consideration in the calculation of second and fourth moments based on the method of Kittel and Abrahams[2)], the maximum of line width is not expected for all concentration range.

We will give here another explanation based on the change in distribution of Fe^{3+} ions in A and B sites with their concentrations.

In the following calculation it is assumed that exchange interaction is isotropic and the terms linear in exchange interactions is neglected to their square terms. To compare with the results of experiments with polycrystalline samples the second and fourth moment are averaged over all angles. The second moments are calculated in spinel structure as follows,

$$\text{on A site:}\quad h^2\langle\Delta\nu^2\rangle=\tfrac{1}{3}S(S+1)\{0.655x^2+1.133xy)f\,\frac{g^4\beta^4}{(a/4)^6}\,,$$

$$\text{on B site:}\quad h^2\langle\Delta\nu^2\rangle=\tfrac{1}{3}S(S+1)\{1.514y^2+1.133xy\}f\,\frac{g^4\beta^4}{(a/4)^6}\,,$$

where f is the concentration of magnetic ions, and x and y are the rates of magnetic ions occupying A ane B sites, respectively. $(x+y=1)$. a is the lattice constant and β is the Bohr magneton.

When f is low, only the linear terms of f contribute to the fourth moment. Assuming that the line shape is Lorentzian with cut-off frequency[2)], the line widths are obtained from the second and fourth moments. In Fig. 1 the dotted lines show the total width between maximum slopes in the absorption curve for $x=1$ or $y=1$ neglecting A_{aa} and A_{bb}, the exchange interactions between the magnetic ions occupying the sites indicated by suffixes. The full lines show $\Delta H_{\max,\,\text{slope}}$ obtained by subtracting the width due to the crystalline field from the experimental value. In low f region Fe^{3+} ions are assumed to occupy A sites in $MgAl_2O_4$ and B sites in $ZnAl_2O_4$, consistent with the assumption used in calculating the crystalline fields on A and B sites. It is estimated from the difference between the calculated and experimental curves that $A_{aa}/g\beta=0.7\times10^3$ Oe for $MgAl_2O_4$ and $A^{bb}/g\beta=1.1\times$

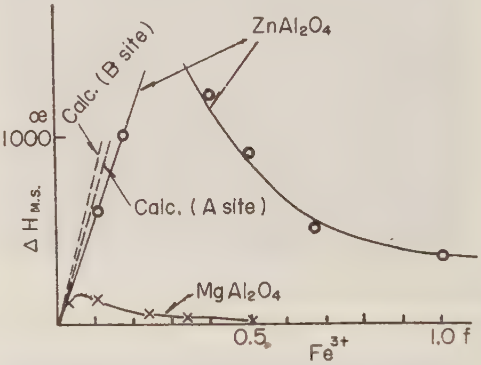

Fig. 1.

10^3 Oe for $ZnAl_2O_4$. These values are slightly smaller than the one estimated from Curie point.

In high f region, the calculated line widths increase proportional to $f^{1/2}$ and no maximum appears. So the following assumptions are proposed to explain the experimental results. In $ZnAl_2O_4$, Fe^{3+} ions occupy only B sites for low f, but the number of ions occupying A sites increase with f and the line widths decrease through the narrowing effect of large exchange interaction A_{ab} between the magnetic ions in A and B sites. In $MgAl_2O_4$ the variation of distribution has a reverse tendency.

Considering only the large exchange interaction A_{ab}, f^2 term in the fourth moment is as follows,

on A sites: $h^4\langle\Delta\nu^4\rangle=K\{43.62x^2y+59.80xy^2\}$,

on B sites: $h^4\langle\Delta\nu^4\rangle=K\{76.42xy^2+34.90x^2y\}$,

$$K=\tfrac{1}{3}\{S(S+1)^2\}f^2\frac{g^4\beta^4}{(a/4)^6}A^2_{ab}\ .$$

The distributions of Fe^{3+} ions in A and B sites estimated to fit the calculated line widths to the experimental ones with $A_{ab}/g\beta=3\times10^5$ are shown in Fig. 2. Even in limiting case $ZnFe_2O_4$, almost all Fe^{3+} ions occupy B sites and this tendency is not contradictory to the so-called normal spinel structure of $ZnFe_2O_4$. In Mg(Al, Fe)O_4, 15% of Fe^{3+} ions occupy B sites and the variation of distribution with the concentration seems to show the transition to the so-called inverse spinel structure of $MgFe_2O_4$.

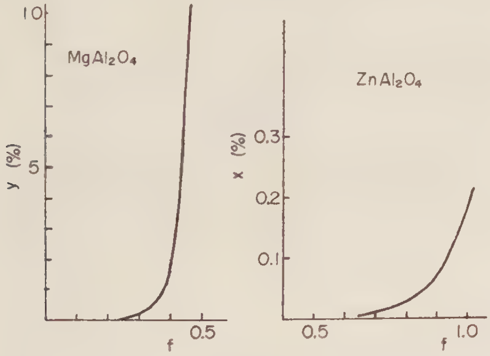

Fig. 2.

The authors wish to express their sincere thanks to Profs. R. Uyeda and K. Yoshida and Dr. H. Yoshioka for their helpful discussions.

References

1) Y. Sugiura: J. Phys. Soc. Japan **15** (1960) 1217.
2) C. Kittel and E. Abrahams: Phys. Rev. **90** (1953) 238.

J. Phys. Soc. Japan **16** (1961) 1787~1788

Surface Field Effect and Noise in Ge Grain Boundary

By Yoshio Inuishi, Ken Kotani* and Ichiro Tsurumi*

College of Engineering, Osaka University, Osaka
**Kobe Kogyo Co., Kobe*

(Received June 5, 1961)

Effects of surface field on the current across the grain boundary in n type Ge, and accompanying noise were studied. 9.6° grain boundary was formed in an n type Ge crystal (5.8 Ω cm) with [100] common axis and sealed into vacuum glass tube with a field effect electrode of conducting glass, attached on the surface through a mica separater. (See Fig. 1) The current I across boundary *vs.* applied voltage V is shown in Fig. 1 taking field effect voltage V_F as parameter. I–V curve seems to follow the hyperbolic tangent relation derived by Mueller[1] and show saturation followed by soft breakthrough. The saturation current at room temperature increases remarkably by negative field voltage ($V_F<0$) application which produces p type inversion layer on the both n type Ge surfaces and a kind a channel for hole current across boundary. Positive field voltage, which should form n type layer bridging grain boundary, did not produce remarkable effect except at very high value of V_F.

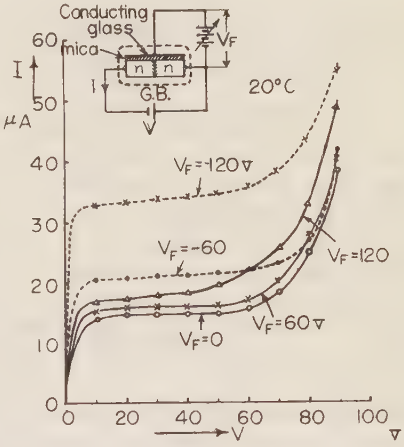

Fig. 1. Current *vs.* voltage across Ge grain boundary at various surface field.

Fig. 2 shows the current I and mean square short circuit noise current $\langle\Delta i^2\rangle$ at 1 KC as functions of surface field voltage V_F at room temperature. One can see that the increase in surface channel current (hole) is accompanied by the increase in $1/f$ noise just as the case of PN junction[2]. Photocurrent response around boundary was obtained by shinning fine beam of chopped light through conducting glass electrode at various field voltage V_F as shown in Fig. 3, which evidently shows the growth of p type channel for $V_F<0$.

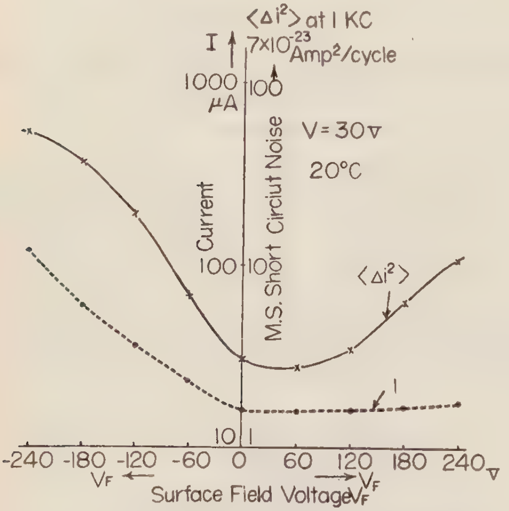

Fig. 2. Current and noise *vs.* surface field voltage.

Without field voltage ($V_F=0$), the I-V curve seems to be little affected by the surface component showing minimum saturation current. (Fig. 2) Noise spectrum, however, shows small $1/f$ component beside larger G-R component at lower frequency. This fact might suggest inherent $1/f$ noise and barrier height fluctuation at the grain boundary.

At lower temperature (−40°C), positive surface field voltage produces remarkable increase in saturation current and noise, on the contrary to the case of room temperature. The mechanism of this phenomena is not clear, but the importance of electron current across boundary in lower temperature[1] seems to be the case. Thanks go to Mr. Shibaike who has carried this experiment.

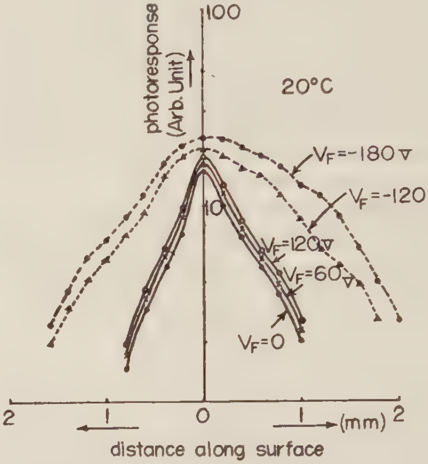

Fig. 3. Local photoresponce around grain boundary at various surface field.

References

1) R. K. Mueller: J. A. P. **32** (1961) 635.

2) K. Komatsubara, Y. Inuishi, H. Edagawa and T. Shibaike: J. Phys. Soc. Japan **15** (1960) 1713.

J. PHYS. SOC. JAPAN **16** (1961) 1789

Semiconducting Properties of $SnSe_2$ and $GeSe_2$*

By Sizuo ASANABE

Fundamental Research Laboratory, Nippon Electric Co. Ltd., Kawasaki-shi, Japan

(Received June 23, 1961)

In connection with the semiconducting properties of SnSe[1),2)] and GeSe[3)], the compounds $SnSe_2$ and $GeSe_2$ were prepared, by melting the stoichiometric amounts of their component materials (Sn, J. M. 4-nines; Ge, about 8-nines; Se, 5-nines) in evacuated quartz tubes. The present note reports some semiconducting properties observed on these compounds.

(i) $SnSe_2$: In Fig. 1 are shown the electrical resistivitiy ρ and Hall coefficient R (negative), measured in the temperature range from 100°K to 800°K using an ordinary d.c. method. The curves A were obtained on the specimen quenched from 430°C and the curves B on the same specimen by repeating the measurements. Both the resistivity and Hall coefficient fall abruptly at about 700°K, being characteristic of ordinary semiconductors. This indicates the onset of intrinsic conduction and therefore, from the resistivity curve in this temperature range the energy gap can be estimated to be about 1.0 eV. The Hall mobility corresponding to the curves A and B in Fig. 1 is in good agreement above 250°K but at lower temperatures it decreases slightly as the measurement is repeated. The temperature dependence of the Hall mobility can be interpreted on the assumption of both acoustical and optical mode scatterings:

$$1/\mu=4.0\times10^{-6}T^{3/2}+8.3\times10^{-2}\{\exp(720/T-1\}^{-1},$$

choosing Debye temperature so that the curve may fit the experimental points. The irreversible changes in ρ and R in Fig. 1 may be ascribed to the similar change in carrier concentrations as observed previously in SnSe[2),4)] and GeSe[3)].

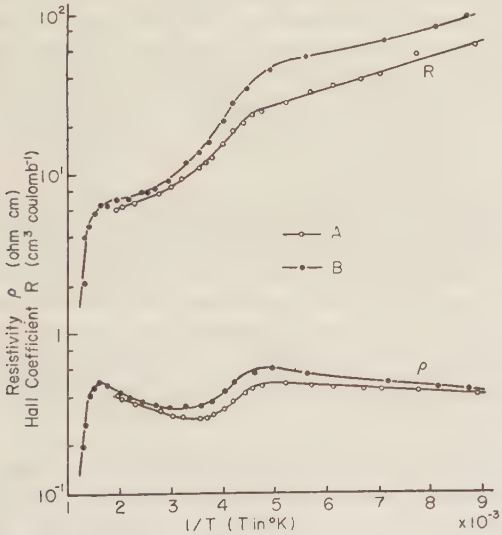

Fig. 1. Resistivity and Hall coefficient, inverse absolute temperature curves for a $SnSe_2$ crystal.

(ii) $GeSe_2$: $GeSe_2$ is a yellow crystal with strong cleavage. The resistivity, being too high to be measured at room temperature, can be measured at high temperatures as shown in Fig. 2. From the slope of the curves obtained on two specimens the energy gap is estimated to be nearly 2.3 eV. On the other hand, the optical absorption of the film evaporated on a quartz plate was measured by using combination of a medium size quartz spectrograph and a "Speckker" diaphragm photometer. The absorption edge at room temperature was found at 5300Å, corresponding to 2.35 eV which was in good agreement with the thermal data.

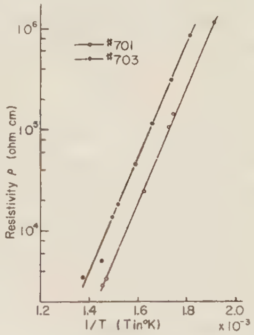

Fig. 2. Resistivity, inverse absolute temperature curves for $GeSe_2$ crystals.

The author should express his sincere thanks to the late Prof. Dr. A. Okazaki for his kind guidance and encouragement and to the members of his laboratory for their interests in the present investigation.

References

1) Y. Matsukura, T. Yamamoto and A. Okazaki: Mem. Fac. Sci. Kyusyu Univ. Ser. **B**, **1** (1953) 98.
2) S. Asanabe: J. Phys. Soc. Japan **14** (1959) 281.
3) S. Asanabe and A. Okazaki: J. Phys. Soc. Japan **15** (1960) 989.
4) J. Umeda: J. Phys. Soc. Japan **16** (1961) 124.

---

* This work was performed at Kyusyu University.

J. PHYS. SOC. JAPAN **16** (1961) 1790

Temperature Dependence of Nuclear Resonance Absorption Line Width in Dy^{161}.

By Poh-Kun TSENG, Naomoto SHIKAZONO,
Hidekuni TAKEKOSHI and Tokio SHOJI

Department of Nuclear Physics, Japan Atomic Energy Research Institute

(Received May 10, 1961)

Ofer et al[1] investigated the spectrum of the recoilles resonance absorption of the 25.7-kev gamma rays in the decay of Tb^{161} using a Dy_2O_3 absorber and Tb^{161} emitter embedded in Gd_2O_3, and found that the spectrum had a triangular shape with a width about an order of 100 times as large as the natural width. They gave an interpretation that both the emission and absorption line would have approximately rectangular shapes produced by the hyper-fine splitting due to the internal paramagnetic field.

We have measured the spectrum varying the temperature of the Dy_2O_3 absorber. The method is the same as the previous one[2]. Tb^{161} was separated from a neutron-irradiated Gd_2O_3 sample by the ion exchange method.

The experiment were done keeping the absorber at the following temperature:

1) liquid nitrogen temperature,
2) room temperature,
3) 100°C,
4) 200°C,

while the source was kept at room temperature.

The absorption spectra are shown in Fig. 1. The width of the spectrum decreases to about one half as the temperature of the absorber rises from the liquid-nitrogen temperature to 200°C, while the depth of the spectrum changes only slightly. The width of the absorption line is shown in Fig. 2 as a function of the temperature of the absorber. The widths of the absorption line in Fig. 2 were obtained by subtracting the widths of the emission line from those of the observed spectra, because the width of the observed spectra are considered to be the sum of those of the emission and absorption line.

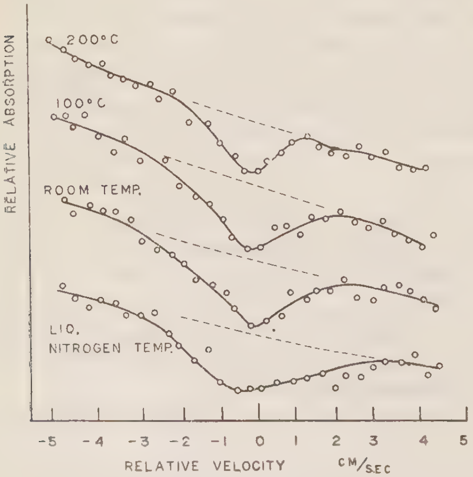

Fig. 1. The temperature dependence of the absorption spectrum as a function of relative velocity between source and absorber.

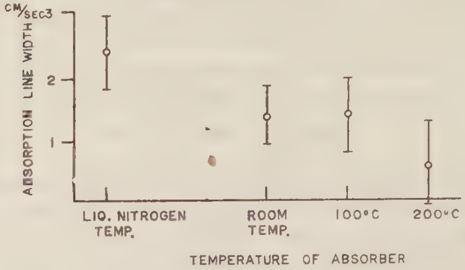

Fig. 2. The absorption line width as a function absorber temperature.

Measurements at the room temperature were made so carefully that hyper-fine structure, if any, might be revealed, but none was observed within the resolution of our experiment, which was less than the natural width of the gamma ray. The reason for the absence of the hyper-fine structure is considered to be that the emission and absorption lines are continuous by nature due to the paramagnetic relaxation.

The fact that the width of the absorption spectrum becomes smaller at higher temperature, while the depth of the spectrum decreases only slightly, will be useful for the measurement of the hyper-fine structure. If Tb^{161} nuclei were embedded in some kind of ferromagnetic material in which internal field at the nuclei would be of the order of 10^6 oe, then, the Zeeman splitting of emission lines would be larger than the width of the absorption line at 200°C which is about one tenth of the width at the room temperature. Under this condition we would be able to observe sixteen lines[3] in the absorption spectrum. The above method would also be applicable to the observation of the hyper-fine structure in other rare-earth nuclei.

We would like to thank T. Momota for his encouragement and H. Amano, H. Nakamura and N. Masaki for preparing the Tb^{161} source.

References

1) S. Ofer, P. Aviv, R. Bouminger A. Marinov and G. Cohen: Phys. Rev. **120** (1960) 406.
2) P. Tseng, N. Shikazono and H. Takekoshi: Genshikakukenkyu (in Japanese), **5** (1960) 89.
3) Ground state of the Dy^{161} is $5/2^+$ and the 25.7 kev state is $5/2^-$. Transition between these states is electric dipole.

J. PHYS. SOC. JAPAN **16** (1961) 1791

Cubic Contribution to EPR of Mn^{++} in $MgCl_2$

By Hiroaki MATSUMOTO, Kuniya FUKUDA
Masumi TAKESHIMA and
Yoichi UCHIDA
Department of Physics, Faculty of Science, Kyoto University

(Received June 28, 1961)

Our recent studies on EPR of $MgCl_2$-Mn have revealed that the spin Hamitonian has cubic symmetry term and the values of its parameters given in the previous report[1] need some corrections.

The EPR spectrum of Mn^{++} in $MgCl_2$ single crystal (1.13 mole % of Mn) is shown in Fig. 1 for the static magnetic field parallel to the crystal *c*-axis. These spectral lines are analysed with the spin Hamiltonian:

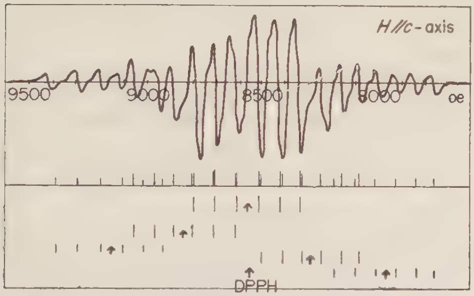

Fig. 1. EPR spectrum of $MgCl_2$-Mn.

$$\mathcal{H}=g\beta \boldsymbol{HS}+\boldsymbol{D}S_z^2+(\boldsymbol{a}/6)(S_\xi^4+S_\eta^4+S_\zeta^4)+\boldsymbol{ASI}\,,$$

where

$$g=2.000\pm0.001\,,\ \boldsymbol{D}=(-135\pm5)\times10^{-4}\,\mathrm{cm}^{-1}\,,\ \boldsymbol{a}=(11\pm5)\times10^{-4}\,\mathrm{cm}^{-1}\ \text{and}\ \boldsymbol{A}=(-82\pm4)\times10^{-4}\,\mathrm{cm}^{-1}\,.$$

The calculated line sites shown in the lower part of Fig. 1 are in good agreement with the observed spectrum.

The optical absorption spectra of $MnCl_2$ single crystals, in which the ligand field on Mn^{++} is the same as that in $MgCl_2$, were analysed by Pappalardo and Stout *et al*[2] and the values of cubic crystalline field parameter *Dq* were obtained as 750 cm^{-1} (Pappalardo) and 830 cm^{-1} (Stout). From these values the parameter $\boldsymbol{a}$ can be evaluated by Watanabe's theory[3] or Powell *et al*'s relation[4], as shown in the following table. The agreement of these values with that derived from the analysis of our spectrum is not so bad. The covalency effect between Mn^{++} and Cl^- as indicated by Pappalardo and Stout (the covalency parameter $\varepsilon=0.03$ or 0.13), if included in the theory, would give better agreement between the experimental value of $\boldsymbol{a}$ and the calculated one. *Dq* can be calculated from the spatial distribution of Cl^- ions and that of 3*d* electrons in Mn^{++} ion[3]. The appropriate value of *Dq* (800 cm^{-1}) can be obtained by using Slater type wave function[5] when screening constant of a 3*d* electron is put to be 0.6 instead of 0.35 for free ion.

The axial field parameter of Mn^{++} is calculated from the above Slater type wave function and electrostatic potential of neighbouring ions as follows[3]:

$$\Delta=13.7\times10^3\,\mathrm{cm}^{-1}\,.$$

From this Δ value and the experimental value of $\boldsymbol{D}$, M′ of Watanabe's theory[3] is evaluated to be 0.35 cm^{-1}.

$MgCl_2$ with 4.93 mole % of manganese showed a broad EPR line as shown in Fig. 2. This broad line cannot be explained by dipole broadening of *hf* lines in Fig. 1 with the assumption of uniform distribution of Mn^{++} ions in $MgCl_2$. This may suggest that manganese ions are not uniformly distributed in annealed $MgCl_2$ single crystals with higher concentration.

Table I. Calculated values of $\boldsymbol{a}$ from optical data of *Dq*.

Dq	$\boldsymbol{a}$ ($10^{-4}\,cm^{-1}$)	
	Watanabe	Powell *et al*
Pappalardo	4	6.3
Stout	6	8.3

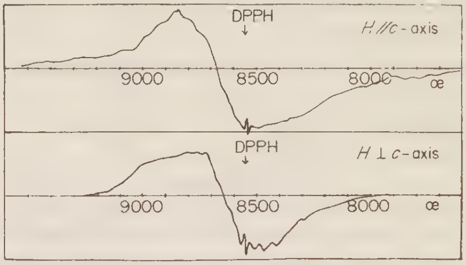

Fig. 2. Broad EPR line of $MgCl_2$-Mn (4.93 mole % of Mn).

The authors are indebted to the Research Laboratory of Matsushita Electronic Corporation for chemical analysis of manganese in $MgCl_2$.

References

1) K. Fukuda, H. Matsumoto, T. Takagi and Y. Uchida: J. Phys. Soc. Japan **16** (1961) 1256.
2) R. Pappalardo: J. Chem. Phys. **31** (1959) 1050; **33** (1960) 613. J· W. Stout: J. Chem Phys. **31** (1959) 709; **33** (1960) 303.
3) H. Watanabe: Progr. Theor. Phys. **18** (1957) 405; Phys. Rev. Letters **4** (1960) 410.
4) M. J. D. Powell, J. R. Gabriel and D. F. Johnson: Phys. Rev. Letters **5** (1960) 145.
5) J. C. Slater: Phys. Rev. **36** (1930) 57.

J. Phys. Soc. Japan **16** (1961) 1792~1793

An Evidence for the Existence of a Diffusion Layer in the Melting Process of Semiconductors

By Shoji TAUCHI

Central Research Laboratory, Hitachi, Ltd., Kokubunji, Tokyo

(Received July 6, 1961)

Formerly Burton *et al*[1] introduced the concept of the diffusion layer for the growth of the crystals in order to interprete the dependency of the segregation coefficient on the growth conditions. We found, in the course of the molten diffused process of Ge and Si[2], that a diffusion layer also exists in the melting process of a crystal. In this process, after a small portion of the collector crystal is melted slowly and uniformly until it reaches the state in which both melting and growing phenomena completely stop; while maintaining this state for a required period the base and emitter impurities diffuse from the melt into the crystal thus forming a very thin and uniform base layer.

If we assume that the density of impurities in the melt directly under the crystal is equal to that corresponding to the initial doping to the melt, calculated conditions for the formation of base layer are not statisfied experimentally. In order to account for this discrepancy we propose the following model. In the process of melting the crystal a thin layer is formed in the melt which contains neither the base nor the emitter impurities directly under the crystal. The base and emitter impurities diffuse across this layer and then into the crystal. Denoting the *effective width* of the diffusion layer as δ, the net impurity distribution in the base region is given as follows:

$$N_b(x)=N_{b0}\,\mathrm{erfc}\left(\frac{\delta}{2\sqrt{D_M t_m}}+\frac{x}{2\sqrt{D_b t_m}}\right)-N_{e0}\,\mathrm{erfc}\left(\frac{\delta}{2\sqrt{D_M t_m}}+\frac{x}{2\sqrt{D_e t_m}}\right)-N_{c0} \qquad (1)$$

where N_{b0} and N_{e0} respectively denote the density of the base and emitter impurities at the crystal surface in contact with the melt, D_b and D_e the diffusivity of the base and emitter impurities in the crystal, t_m the diffusion time, N_{c0} the collector impurity concentration and D_M the diffusivity of the emitter and base impurities in the melt, assumed to be the same value ($5\times10^{-5}\,\mathrm{cm^2/sec}$) for simplicity.

From equation (1) the relation between the limiting value for N_{b0} (which is defined as N_{b0}^*) and δ becomes

$$\left(\frac{D_b}{D_e}-1\right)\left(\frac{x_m}{2\sqrt{D_b t_m}}\right)^2+\frac{\delta}{\sqrt{D_b t_m}}\left(\sqrt{\frac{D_b}{D_e}}-1\right)\times\left(\frac{x_m}{2\sqrt{D_b t_m}}\right)-\ln\left(\frac{N_{e0}}{N_{b0}}\sqrt{\frac{D_b}{D_e}}\right)=0 \qquad (2)$$

$$N_b(x_m)=0$$

where x_m denotes the distance from the crystal surface to the maximum point of the base impurity concentration. By successive experiments we have determined the limiting value of N_{b0}^* enough to produce a base layer. From this and using the equation (2), we can find the value of $\delta/2\sqrt{D_M t_m}$. This value and the density of impurities as well as N_{b0}^* are given in the Table I. The last column gives the value of δ.

Table I. The width of the diffusion layer.

Material	N_{c0} ($\mathrm{cm^{-3}}$)	N_{e0} ($\mathrm{cm^{-3}}$)	N_{b0} ($\mathrm{cm^{-3}}$)	t_m (sec)	$\frac{\delta}{2\sqrt{D_M t_m}}$	δ (mm)
Si	1.6×10^{16}	2.4×10^{18}	8×10^{16}	15	0.3	0.16
Ge	1.4×10^{16}	8×10^{17}	3.5×10^{16}	15	0.4	0.22

Another evidence for the existence of the diffusion layer is the comparison between the experimental value of the base width[2),3)] and its expected value. For Si *npn* junction if the presence of the diffusion layer is not taken into account the expected values are fairly larger than the observed ones. If it is assumed that $\delta/2\sqrt{D_M t_m}=0.2$, the agreement is quite good as can be seen in the Fig. 1.

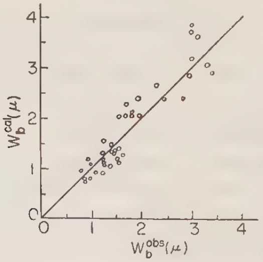

Fig. 1. Comparison of the calculated and observed values of the base width in silicon *npn* junction.

The details will be published in the near future in this Journal.

Appreciation for kind advice and encouragement it given to Mr. M. Tomono, Mr. H. Ueda and Mr. H. Kodera.

References

1) J. A. Burton, R. C. Prim and W. P. Slichter: J. Chem. Phys. **21** (1953) 1957, 1991.

2) S. Tauchi; Solid State Electronics: **2** No. 4 (1961) 216.
3) C. S. Fuller and J. H. Ditzensberger: J. Appl. Phys. **27** (1956) 544.

J. PHYS. SOC. JAPAN **16** (1961) 1793~1794

The Dynamic Bulk and Shear Viscosities of Polyvinylchloride

By Ryusuke KONO
Department of Applied Physics, Defence Academy, Yokosuka

(Received July 4, 1961)

In recent years an energy-dissipating process associated with volume deformation for various rubbers has been studied by several workers[1]. Following previous work[2] by the author on polystrene and polymethyl methacrylate, the dynamic bulk and shear viscosities of polyvinylchloride were measured in frequencies of 1, 2.25 and 5 Mc/s at temperatures encompassing the transition from glassy to flow state.

Experimental apparatus for the longitudinal and transverse wave measurement was the same as that reported in the previous paper[2].

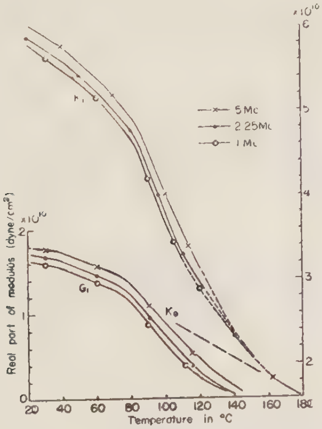

Fig. 1. Real part of the shear and bulk moduli versus temperature.

The real part of the shear modulus G_1 and bulk modulus K_1, the imaginary part of the shear modulus G_2 and longitudinal wave modulus M_2 $(=K_2+4G_2/3)$ are plotted against temperature in Figs. 1 and 2, respectively. The glass transition temperature is 78°C by the measurement of linear thermal expansion. An increase in G_1 and K_1 with increasing frequency is noted even in the glassy region, showing much more remarkable dispersion in the transition region. It was impossible to make any measurements for the shear wave in the region shown by the dotted line because of the high attenuation. The direct determination of the values of K_1 in flow state was impossible, but it can be determined since the values of G_1 in this state were very small in comparison with that of the real part of longitudinal wave modulus M_1 $(=K_1+4G_1/3)$. The dashed line in Fig. 1 represents the bulk modulus in flow state K_0. An extended frequency plot based on the reduced variable technique of Ferry and others[3] (after making a small correction by multiplying the modulus at absolute temperature T by a factor T_0/T) is carried out. The shifted curves of G_1, K_{1p} $(=K_1-K_0)$, G_2 and M_2 for polyvinylchloride at a reference temperature of $T_0=125$°C are shown in Fig. 3. The peak in G_2 occurs almost at the same reduced frequency as that in K_2. The shifting factor a_T versus temperature for shear modulus and bulk modulus are

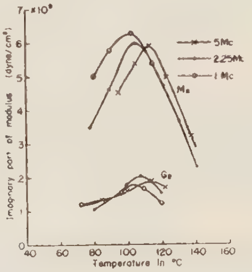

Fig. 2. Imaginary part of the shear and longitudinal wave moduli versus temperature.

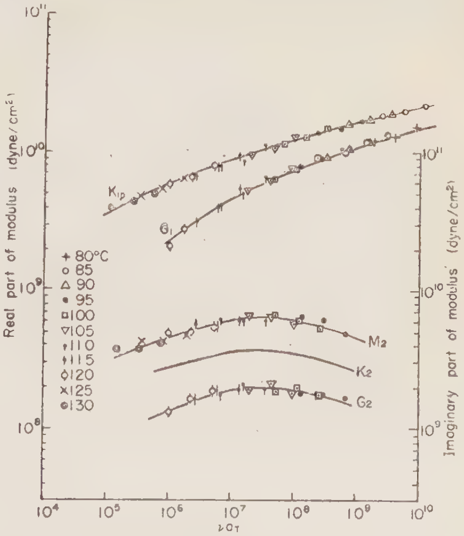

Fig. 3. Real and imaginary parts of the reduced shear and bulk moduli reduced to 125°C.

shown in Fig. 4. Williams-Landel-Ferry's[4] equation fits the experimental data obtained in the temperature range 105°C to 135°C when T_s is chosen as 125°C. If logarithms of the factor a_T for G_1 and K_{1p} are plotted against $1/T$, the plots fall on a single straight line. Thus the apparent activation energy for volume deformations is nearly equal to that for shear deformations. The value of activation energy is 59 Kcal/mol.

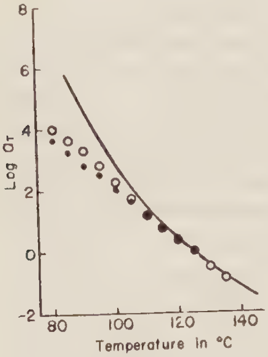

Fig. 4. Shifting factor a_T versus temperature for shear modulus (closed circles) and bulk modulus (open circles) reduced to 125°C. Solid line represents Williams-Landel-Ferry's equation (T_s= 125°C).

It is concluded at once from these results that temperature and frequency dependence, the activation energy, relaxation times for bulk modulus are quite similar to those for shear modulus. Thus the molecular mechanism in the volume and shear deformations should be the same for polyvinylchloride.

References

1) A. W. Nolle and P. W. Sieck: J. Appl. Phys. **23** (1952) 888. R. S. Marvin, R. Aldlich and H. S. Sack: ibid. **25** (1954) 1213. J. R. Cunningham and D. G. Ivey: ibid. **27** (1956) 967. Y. Wada, H. Hirose, H. Umebayashi and M. Otomo: J. Phys. Soc. Japan **15** (1960) 2324.
2) R. Kono: J. Phys. Soc. Japan **15** (1960) 718.
3) See, for example, J. D. Ferry: J. Amer. Chem. Soc. **72** (1950) 3746.
4) M. L. Williams, R. F. Landel and J. D. Ferry: J. Amer. Chem. Soc. **77** (1955) 3701.

J. PHYS. SOC. JAPAN **16** (1961) 1794~1795

Reflection of a Weak Shock Wave in a Perfectly Conducting Gas

By Shigeki MORIOKA

Department of Physics,
Faculty of Science and Engineering,
Ritumeikan University, Kyoto

(Received May 29, 1961)

In this note, discussion is made on the "regular" reflection[1] of a weak plane shock wave propagating in a homogeneous, perfectly conducting gas from a solid wall, in the presence of a uniform magnetic field parallel to the wall. Let us take the system of reference in which the shocks are at rest. Let α be the shock angle, θ the deflection of flow, M the Mach number, A the Alfvén number and p the pressure, and let suffixes 1, 2, 3 denote the various quantities pertaining to the regions bounded by the wall and the shocks as shown in Fig. 1. Then, $x_\nu = \tan(\alpha_\nu - \theta_\nu)/\tan\alpha_\nu$ satisfies the equation

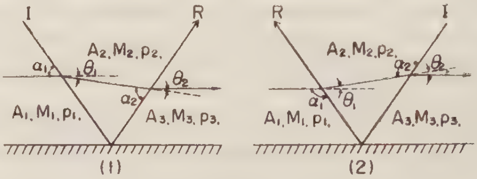

Fig. 1. Regular reflection of plane shock wave. (1) for A_1, $M_1>1$, (2) for A_1, $M_1<1$ and $M_1^2+A_1^2+1>0$.

$$\begin{aligned}&(\gamma+1)(A_\nu^2-1)^2M_\nu^2x_\nu^3\\&+(A_\nu^2-1)\{(\gamma+1)M_\nu^2-2A_\nu^2-(\gamma-1)A_\nu^2M_\nu^2\\&\qquad-(\gamma M_\nu^2+2A_\nu^2)\cot^2\alpha_\nu\}x_\nu^2\\&-\{(2-\gamma)A_\nu^2+(\gamma-1)\}M_\nu^2\cot^2\alpha_\nu x_\nu-M_\nu^2\cot^2\alpha_\nu=0\\&\qquad\qquad(\nu=1,2)\,. \qquad (1)\end{aligned}$$

Assuming that the incident shock is weak and hence so is the reflected shock, we can put

$$\cot^2\alpha_\nu=\lambda_\nu^2(1-\varepsilon_\nu)\,,\quad x_\nu=1-\delta_\nu\,,\quad |\varepsilon_\nu|,\ |\delta_\nu|\ll 1\,, \qquad (2)$$

where

$$\lambda_\nu^2=(A_\nu^2-1)(M_\nu^2-1)/(M_\nu^2+A_\nu^2-1)>0\,.$$

Eq. (1) then becomes

$$\delta_1=F_1\varepsilon_1+G_1\varepsilon_1^2+O(\varepsilon_1^3) \qquad (3)$$

where F_1 and G_1 are functions of A_1^2 and M_1^2 given in (6). On the other hand, A_2, M_2 can be expressed in terms of A_1, M_1, p_1 and δ_1:[2]

$$\begin{aligned}&A_2^2=A_1^2-a_1\delta_1\,,\\&M_2^2=M_1^2-a_1A_1^2\{(\gamma-1)M_1^2+2\}\delta_1\,, \qquad (4)\\&p_2=p_1(1+\gamma a_1A_1^{-2}\delta_1)\,,\end{aligned}$$

where $a_1=A_1^2-1$. Then from Eqs. (1), (2) and (4), λ_2^2 and δ_2 can be expressed as

$$\begin{aligned}\lambda_2^2&=\lambda_1^2(1-R\delta_1)+O(\varepsilon^2)\,,\\ \delta_2&=(F_1+F_2\delta_1)\varepsilon_2+G_1\varepsilon_2^2+O(\varepsilon^3)\,,\end{aligned}\tag{5}$$

where R and F_2 are functions of A_1^2 and M_1^2:

$$\begin{aligned}R&=\frac{M_1^4+\{(\gamma-1)a_1-1\}M_1^2+2a_1}{(M_1^2-1)(M_1^2+a_1)}\,,\\ F_1&=\frac{2(M_1^2-1)(M_1^2+a_1)}{M_1^2\{3(M_1^2-1)+(\gamma+1)a_1\}}\,,\\ F_2&=\frac{2a_1 f}{A_1^2M_1^4\{3(M_1^2-1)+(\gamma+1)a_1\}^2}\,,\\ G_1&=\frac{2(M_1^2-1)^2(M_1^2+a_1)g}{A_1^2M_1^4\{3(M_1^2-1)+(\gamma+1)a_1\}^3}\,,\\ f&=-(2-\gamma)\{(2-\gamma)a_1+1\}M_1^6\\ &\quad+\{3(5-3\gamma)a_1+(5-\gamma)\}M_1^4\\ &\quad-\{(\gamma^2-1)a_1^2+3(6-\gamma)a_1+3\}M_1^2\\ &\quad-2a_1\{(\gamma+1)a_1-3\}\,,\\ g&=-\{(2-\gamma)a_1+1\}M_1^4\\ &\quad+\{(\gamma-1)(\gamma-2)a_1^2+(7-4\gamma)a_1+1\}M_1^2\\ &\quad-2a_1\{(2-\gamma)a_1+4\}\,.\end{aligned}\tag{6}$$

Using Eqs. (2) to (5), the condition for the regular reflection, i.e. $\tan\theta_1=\tan\theta_2$, yields

$$G'\varepsilon_2^2+(F_1+R'\varepsilon_1)\varepsilon_2-(F_1\varepsilon_1+G'\varepsilon_1^2)=0 \tag{7}$$

where

$$G'=G_1+(\cos^2\alpha_1-\tfrac{1}{2})F_1+\sin^2\alpha_1 F_1^2$$

and

$$R'=F_1F_2+(\cos^2\alpha_1-\tfrac{1}{2})RF_1^2\,,$$

and terms of $O(\varepsilon^3)$ have been neglected. Thus, the regular reflection is possible in the range of ε_1 satisfying $D\equiv(F_1+R'\varepsilon_1)^2+4G'(F_1\varepsilon_1+G'\varepsilon_1^2)\geqq 0$, and hence the value of ε_1 corresponding to $D=0$ (say ε_{1e}) gives the limiting shock angle α_e by use of Eq. (2). The values of ε_{1e} as a function of A_1^2, M_1^2 are shown in Fig. 2. The effect of the magnetic field on the limiting curve for the occurrence of regular reflection is shown in Fig. 3. For $M_1>1$ and $1\gg A_1-1>0$ only regular reflection can take place, since the possible value of α_1, such that $90°\geqq\alpha_1\geqq\cot^{-1}\lambda_1$, is contained in the vicinity of $\cot^{-1}\lambda_1$, where it has been found that regular reflection occurs; in fact $\alpha_e\doteqdot 90°$ in this case.

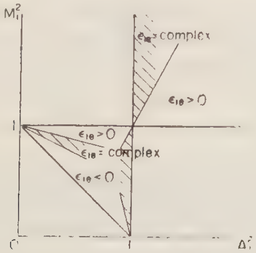

Fig. 2. Values of ε_{1e} as function of A_1^2, M_1^2.

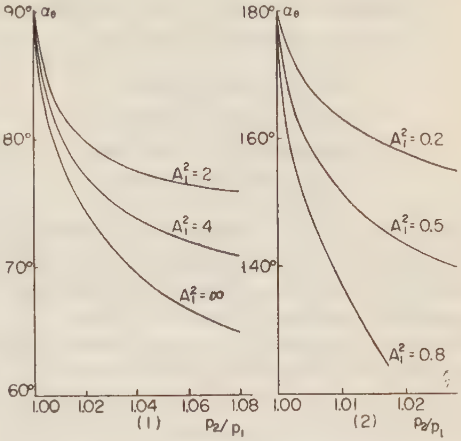

Fig. 3. Effect of magnetic field on limiting curve, above which regular reflection is theoretically impossible. (1) for A_1, $M_1>1$, (2) for A_1, $M_1<1$ and $M_1^2+A_1^2+1>0$.

In general, the presence of the magnetic field tends to enlarge the range of the shock angle in which regular reflection can occur.

References

1) W. Bleakney and A. H. Taub: Rev. Mod. Phys. **21** (1949) 584.
2) S. Morioka: J. Phys. Soc. Japan **15** (1960) 1516.

J. PHYS. SOC. JAPAN **16** (1961) 1796~1797

Some Extra Lines in Paramagnetic Resonance Spectrum of Heavily Cr^{3+} Doped $K_3Co(CN)_6$

By Takeshi MITSUMA
Electrotechnical Laboratory,
Nagatacho, Tokyo, Japan

(Received June 8, 1961)

Baker, et al[1] have observed the magnetic resonance spectrum of undiluted $K_3Cr(CN)_6$ and suggested the existence of rather strong isotropic exchange interaction between Cr^{3+} ions.

We have observed the paramagnetic resonance spectrum of Cr^{3+}-doped $K_3Co(CN)_6$ with Cr^{3+} concentration of 10% and 15% by weight with an aim of studying nature of exchange interaction in strong covalent bonding crystal.

Measurements have been made at 4.2°K and room temperature using 9.4 Gc/s frequency. The samples are rotated in the *bc*-plane.

In addition to three normal Cr^{3+} lines a number of extra lines are observed. A major part of typical resonance spectrum of $K_3(Cr_{0.10}Co_{0.90})(CN)_6$ is shown in Fig. 1. This curve is obtained at 4.2 °K and in the direction of static magnetic field H_0 forming an angle of 20° with the *c*-axis. Angular variation of the resonance fields of stronger lines are shown in Fig. 2. Lines 'a', 'b' and 'c' are allowed lines and 'd', 'e' and 'f' are forbidden lines of Cr^{3+} ions respectively. This assignment is proceeded using the following spin-Hamiltonian in *bc*-plane,

$$\mathscr{H}=g\beta H_0S_z+(1/2)(3E\cos2\varphi-D)(S_z^2-5/4)$$
$$+(D+E\cos2\varphi)(S_+^2+S_-^2)+i(1/4)E\sin2\varphi$$
$$\times[(S_zS_++S_+S_z)-(S_zS_-+S_-S_z)]\,, \quad (1)$$

where φ is the angle between *b*-axis and H_0.

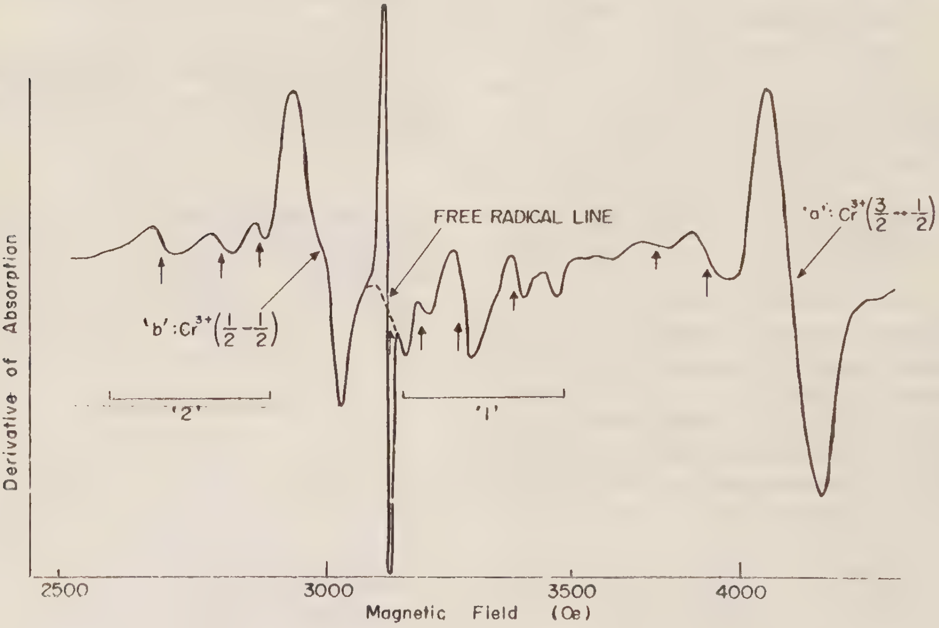

Fig. 1

On the other hand, the group '1', '2' and '3', '4' are the extra lines. Besides these, there are some lines in the neighborhood of lines 'a' and 'c'. The angular dependence of these lines is not so clear.

At room temperature, some of these extra lines are obscure.

The origin of these extra lines is not clear at the moment. But the following experimental evidences are interesting. These lines are not observed in the more diluted salt, $K_3(Cr_{0.01}Co_{0.99})(CN)_6$. Since their angular variation is rather similar and spectrochemical analysis does not show the presence of any other ions in this salts, it seems reasonable to assume that the observed extra lines are produced by Cr^{3+} ions themselves. Considering these facts, our experimental result may be interpreted by the effect of polytypism reported by J. O. Artman, et al[2]. The presence of line '4' may, however, indicate the presence of some other origins, for example, exchange interaction of Cr ions like the case of Cr^{3+} ions in Ruby[3).]** In our case, more careful investigation of the temperature variation of individual lines will be required in order to identify the origin of the extra lines as caused by exchange interaction of Cr ions.

---

* Present address: Sony Corporation Research Laboratory, Hodogaya, Yokohama.

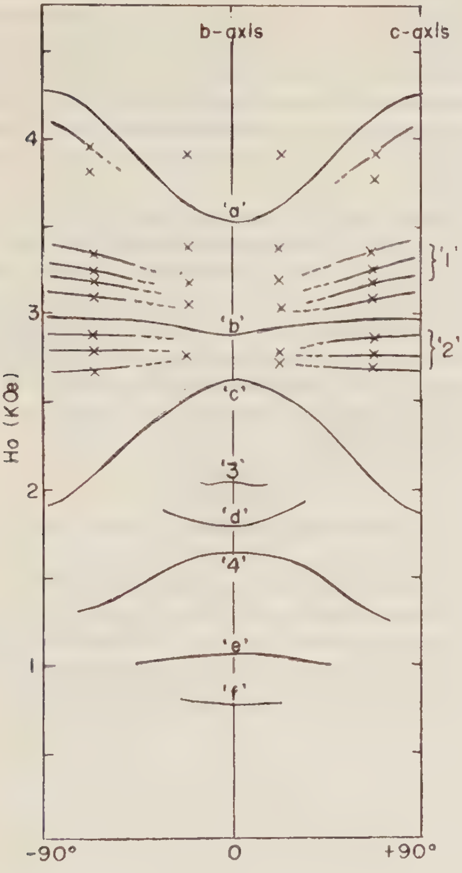

Fig. 2.

References

1) J. M. Baker, B. Bleaney and K. D. Bowers: Proc. Phys. Soc. (London) **B 69** (1956) 1205.
2) J. O. Artman, J. C. Murphy, J. A. Kohn and W. D. Townes: Phys. Rev. Letters **4** (1960) 607.
3) L. Rimai, H. Statz, M. J. Weber, G. A. deMars and G. F. Koster: Phys. Rev. Detters **4** (1960) 125.

** Similar example is also presented in the case of heavily Fe^{3+} doped $K_3Co(CN)_6$. The anisotropic exchange interaction among Fe^{3+} ions is introduced there for explanation of observed fine structure. (T. Ohtsuka: J. Phys. Soc. Japan **15** (1960) 939.)

J. Phys. Soc. Japan **16** (1961) 1797~1798

Electrical Properties of TlSe

By Ryuichi Mori* and Kimio Hashimoto

Department of Physics, Faculty of Science
Kyusyu University, Hukuoka

(Received May 25, 1961)

The electrical resistivity ρ and the Hall coefficient R of TlSe single crystals were measured in the temperature range between about 100° and 450°K. The temperature dependences of ρ and R are shown in Figs. 1 and 2, respectively. These values were

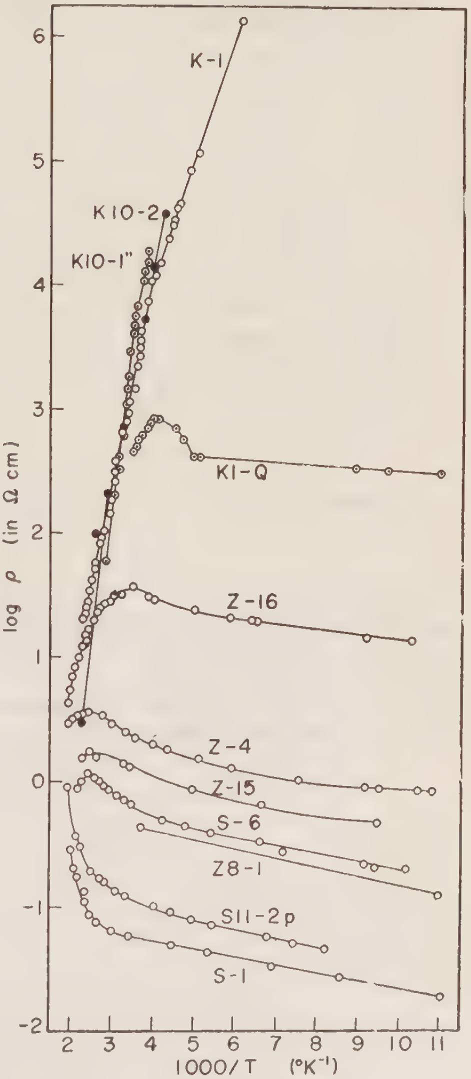

Fig. 1. Resistivity of TlSe as a function of temperature. The symbols denote the samples growing with normal freezing (S), zone-melting (Z) and pulling (K) techniques. The sample K1-Q is the specimen quenched after the measurement of the sample K-1.

---

* Now at Oki Electric Industry Co., Ltd., Tokyo.

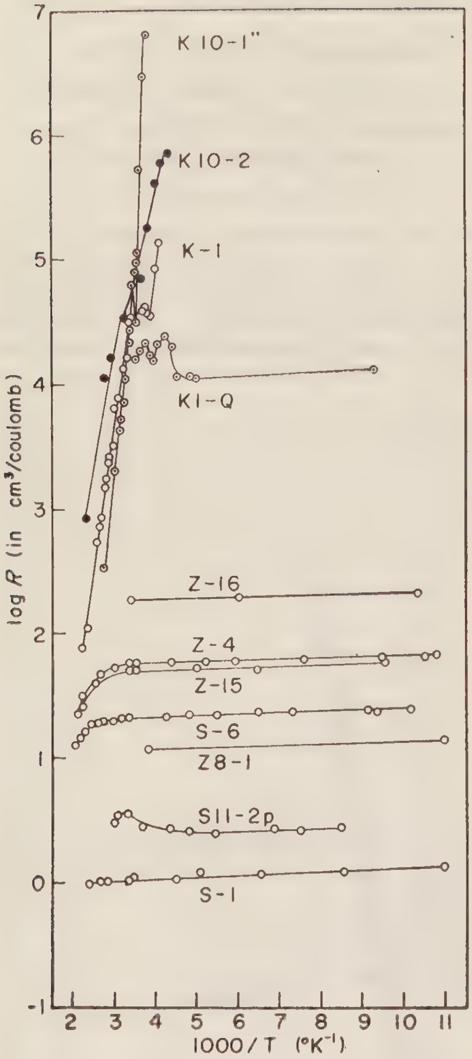

Fig. 2. Hall coefficient of TlSe as a function of temperature.

obtained from the d.c. measurements on the parallelepiped specimens; two of the long side surfaces were the cleavage surfaces.

The Hall coefficients of all the specimens investigated are positive. Although the temperature variations of ρ and R show the characteristics of typical semiconductors, the anomalous humps of R are observed on the some specimens at about 250°K. These humps seem to become marked by heat treatment as the anomalous Hall coefficient on SnSe[1].

Mooser *et al*[2] reported that the intrinsic activation energy of TlSe was 0.57 eV and also Akhundov *et al*[3] reported that it was 0.56 eV. These values were obtained from the temperature dependence of the resistivity. From the present investigations, however, at least two activation energies of about 0.6 and 1.3 eV are obtained. The values of the activation enegies reported earlier might be those of acceptor levels.

References

1) S. Asanabe and A. Okazaki: Proc. Phys. Soc. **73** (1959) 824.
2) E. Mooser, P. Fielding and G. Fisher: J. Phys. Chem. Solids **8** (1959) 434.
3) G. A. Akhundov, G. B. Abdullaef and G. D. Guseinov: Soviet Physics, Solid State **2** (1961) 1378 (Fiz. tver. tera **2** (1960) 1518).

PROGRESS OF THEORETICAL PHYSICS

CONTENTS

Progress of Theoretical Physics Vol. 25, No. 6, June 1961

The Single Pion Production Process in π^--p Collision at 1 Bev and the Sakata Model........................S. SAWADA, T. UEDA and M. YONEZAWA.. 873

The Effect of Exchange and Correlation on Binding Energy of Compressed Atoms..M. P. KAWATRA.. 888

The Composite Model of Mesons as a Limit of Meson Theory...Yasusi ATAKA.. 895

Internal Degrees of Freedom and Elementary Particles. I...Takehiko TAKABAYASI.. 901

General Theory of Superexchange Interaction...............Mitsuru FUKUCHI.. 939

General Theory of Superexchange Interaction. II...........Mitsuru FUKUCHI.. 956

An Expansion Theorem for the Electric Conductivity of Metals. I—*Electric Conductivity for Longitudinal Electric Field*—........Takeo IZUYAMA.. 964

Dispersion Relations and High Energy Limits in Quantum Field Theory. III —*Necessary Condition for Existence of Solutions in Dispersion Relations*—..Seiya ARAMAKI.. 981

On the Structure of Generalized Fokker-Planck Equation of a High Temperature Plasma.......................Y. H. ICHIKAWA and Y. SASAKURA.. 989

Interactions in Nucleon Core..................................Shigeo MINAMI..1006

Dispersion Relations for Virtual Pion-Nucleon Scattering...J. IIZUKA and A. KLEIN..1017

The Σ-Λ Relative Parity and the $\bar{K}$-N Reaction. II.........Yukihisa NOGAMI..1028

Note on the Pairing Correlation in Nuclear Matter.......................... .. T. MARUMORI, T. MUROTA, S. TAKAGI, H. TANAKA and M. YASUNO..1035

Letters to the Editor:

On the Green Function of the Spin System. I.....................................K. KAWASAKI and H. MORI..1043

On the Green Function of the Spin System. II.....................................K. KAWASAKI and H. MORI..1045

Remarks on the Mass Formula in the Sakata Model ....K. MATUMOTO..1047

Expansion of the Linear Boltzmann Operator...............A. SIEGEL..1049

Vibration of Spherical Nuclei...........T. TAMURA and T. UDAGAWA..1051

Evolution of a Star with Intermediate Mass after Hydrogen Burning ....C. HAYASHI, M. NISHIDA and D. SUGIMOTO..1053

Note on the Integral Representation of Absorptive Part of Vertex Function...K. YAMAMOTO..1056

Contents and Author Index to Vol. 25 ....i-xi

Contents of Journal of Phys. Soc. of Japan, Vol. 16, No. 5

Progress of Theoretical Physics Vol. 26, No. 1, July 1961

Observables in the Extreme Relativistic Representation of the Dirac Equation ....P. M. MATHEWS and A. SANKARANARAYANAN.. 1

On the Quantization of Physical Space-Time Operators. II......Ichie WATANABE.. 7

Nuclear Interactions in the $p_{1/2}$-$g_{9/2}$ Configurations ....V. K. THANKAPPNN, Y. R. WAGHMARE and S. P. PANDYA.. 22

Self-Trapping of an Electron by the Acoustical Mode of Lattice Vibration. I ....Yutaka TOYOZAWA.. 29

The Pair Correlation Function of an Imperfect Electron Gas in High Densities ....Seizo UEDA.. 45

Space-Time Correlation Function in the Theory of Electrical Conductivity ... . Isao MANNARI.. 51
Particle-Hole Bound States in the Many Fermion System ....Tetsuo GOTÔ.. 84
Some Converging Examples of the Perturbation Series in the Quantum Field Theory ....Yusuke KATO.. 99
Magnetohydrostatic Equilibrium for Fluid Enclosed in an Axisymmetric Toroidal Surface ....Yusuke KATO..123
On a Convergent Model of Quantum Field Theory with Indefinite Metric .... Kai-ichi YOKOYAMA..131

Letters to the Editor:

Operator Equations in Two Field Theory Models......P. G. FEDERBUSH..148
A New Model for the High Energy Nuclear Interaction ...S. HASEGAWA..150
Hard Core and Shape Parameter in the Effective Range Expansion .. .. T. HAMADA and I. D. JOHNSTON..153

Errata:

Dynamical Theory of Ultrasonic Attenuation in Metals (Vol. 25, p. 327) ....N. TAKIMOTO..155
Contents of Journal of the Phys. Soc. of Japan, Vol. 16, No. 6

Price	\$ 1.25 per copy
	\$ 15.00 per year (postage inclusive)
Annual dues for foreign members (individual subscribers)	
	\$ 12.00 (postage inclusive)
〃 for foreign members of the Physical Society of Japan	
	\$ 10.00 (postage inclusive)

Application for membership, subscriptions and orders for back numbers should be sent, directly or through book-dealers, to

The Publication Office
in
Yukawa Hall, Kyoto University, Kyoto, Japan

. . . .

ANNOUNCEMENT

REVISED Price List of Back Numbers (for subscribers abroad)

*Vols. 1–4	\$ 6.40 each
*Vols. 5 & 6	\$ 13.00 each (single copy: \$ 2.50)
*Vols. 7 and succeeding ones	\$ 8.00 each (single copy: \$ 1.50)

Bach number prices are effective for volumes other than last four (4) volumes (the current volume inclusive).

Thus, volemes 1 through 16 will be regarded as back numbers while volume 20 is being published.

The revised prices will be effective on and after August 1, 1958.

. . . .

JOURNAL OF THE PHYSICAL SOCIETY OF JAPAN, Vol. 16, No. 10, OCTOBER, 1961

Angular Distributions of Photo-protons from Li, Al, S, Ni, and Cu

By Masayoshi MASUDA

Department of Physics, Faculty of Science, University of Osaka

(Received June 26, 1961)

Thin foils of lithium, sulfur, aluminum, nickel and copper have been irradiated with the X-ray beam from a betatron at Osaka University, and angular distribution of photo-protons were obtained by means of a ZnS scintillation detector.

The angular distribution of photo-protons thus obtained can be classified into two broad types, one isotropic and the other forward asymmetric. Aluminum and nickel (21 MeV) belong to the former type; while lithium, sulfur, nickel (18 MeV) and copper fall under the latter type, which is represented by the theoretical form, $a+b\sin^2\theta(1+c\cos\theta)^2$.

As an exceptional case, copper has shown an abnormal angular distribution having a maximum in the forward direction and also a rise up in the backward direction. The functional form which fits best to this distribution has been calculated by a Bendix computor and compared with the recent theory of photo-nuclear reactions.

§ 1. Introduction

It is well known that the process of photo-proton emission is divided into two categories, one is the evaporation process which exhibits an isotropic angular distribution of photo-protons, and the other is the direct process which gives the 90° symmetric and forward asymmetric angular distribution explained by Courant[1] as well as by Levinger[2].

A number of experiments of measuring the angular distribution of (γ, p) have been carried out to study the direct process, and the validity of this model has been confirmed in the energy region of 50–200 MeV.

On the other hand, in the energy region of 20–25 MeV, measurements have shown various types of angular distribution depending on the nuclei. An attempt[3],[4] to ascertain the direct process, which is generally mixed in various processes in this energy region, has been performed with heavier elements as target nuclei, in view of the possibility that the high Coulomb barrier will greatly reduce the number of evaporated protons and the direct process may account for almost all of the emitted protons. But even among these elements, Ce has shown an isotropic distribution.

The aim of this work is to collect as much experimental information as possible about the angular distribution of photo-protons with the special target assembly treated in this paper.

This work has come to a success due to the use of a technique[5] developed recently with regard to the decay properties of the scintillator. By using the decay properties, the discrimination of photo-protons from the strong γ-ray background has been achieved.

§ 2. Experimental Procedure

The experimental arrangement is shown in Fig. 1. The X-ray beam from the betatron was doubly collimated with lead walls. The first collimator has a precise taper angle to the X-ray beam.

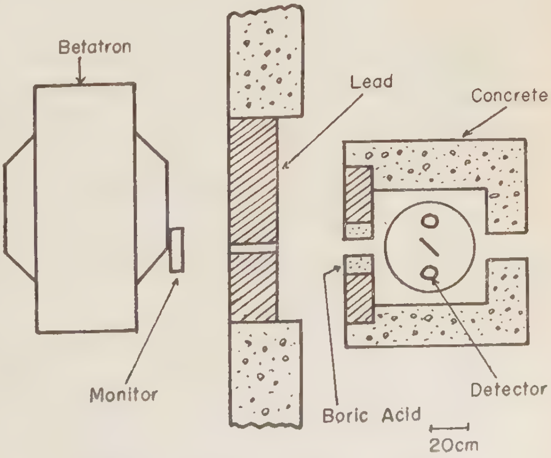

Fig. 1. Experimental arrangement.

As a misalignment of this collimator is one of the most definitive factors which influence the experimental results, the setting has been performed carefully. The optical and the photographic means assuring the coincidence of the center of X-rays with that of the target have been carried out. The detector consists of a Du-Mont 6292 photomultiplier tube and a ZnS scintillator backed by a semi-spherical light reflector. The scintillator has been made by depositing ZnS powder on a glass plate, 1 cm×2 cm in size. The detector and a target foil have been set on a rotating disk, which rotates as a unit about the inciden, X-ray beam.

Angles are set with an accuracy of better than 1 degree.

Measurements have been made simultaneously with two identical counters fixed at 180 degrees with respect to each other, the overall covering region being 30 to 330 degrees. It has been impossible to obtain the intervals from 150 to 210 degrees and from 330 to 30 degrees, because in these regions the X-ray beam strikes the detector assembly.

The typical discrimination curve of photo-protons from a nickel target is shown in Fig. 2. The steeply rising portion of this curve shows the effect of the pile-up of electrons or photons scattered strongly into forward direction due to the Compton effect. The relatively flat portion of this curve is due to the protons from the reaction of Ni (γ, p).

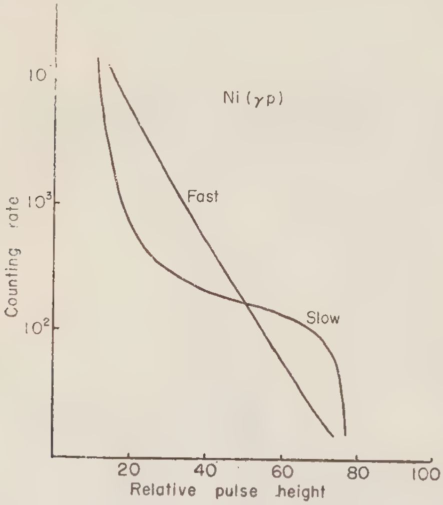

Fig. 2. Amplitude discrimination of proton from Ni(γ, p).

The powdered ZnS phosphors are opaque to own radiation in the thickness which corresponds roughly to the range of one MeV proton. For protons with energies from 1 to 10 MeV, which are mainly studied in this experiment, the light yield from ZnS is approximately independent of the energy. Fig. 2 does not give the energy distribution of photo-protons from Ni, but shows the discrimination curve of protons against the pile-up photons. The thickness of ZnS layer is 10–20 mg/cm². This has been selected for the finest discrimination of protons against the pile-up photons. The targets are foils of natural isotopic composition and their thicknesses are shown in Table I.

The most important thing in the measurement of the angular distribution of photo-protons is to know the energy of the detected protons. Even on the surface of the target the energy distribution of the photo-protons should be strongly deformed from its original form, because the target is sufficiently thick (5–10 MeV range) for the proton energy. Hence only the protons having higher energies are capable of escaping from the inside to the surface of the target. In addition, the air and the aluminum foil which is used as the window of the detector correspond to an energy loss of about 2 MeV when protons pass through these materials. A rough calculation has been carried out on Cu(γ, p) reaction. The result from Byerly and Stephens[6] has been used for the original energy distribution of photo-protons from copper. The target thickness and the proton transmission in various materials must deform this distribution. This is shown in Fig. 3 as "to be detected". This means that the photo-protons which are to be detected by the ZnS scintillator after transmission must have this energy

Table I. Thicknesses of target nuclei.

Target nucleus	Lithium	Aluminum	Sulfur	Nickel	Copper
Thickness in mg/cm²	133	135	160	178	178

distribution. The result of comparison of this experimental energy distribution with the theoretical one for the direct process, which has been calculated from Courant's formula, is shown in Fig. 3 as "direct process". The formula used is:

$$y(e) \approx (Z^2/4A^{4/3})aF(e)\int(N_\gamma(E)/E^3)\,dE \qquad (1)$$

where $y(e)$ is the number of protons of energy e per mole per roentgen ejected by a beam of photons with energy distribution $N(E)$, with maximum energy $E_{\max}$ and $E_{\min}=B_p+e$ (B_p is the proton binding energy); a is Avogadro's number and $F(e)$ is the Coulomb barrier penetration cross section. The photon energy distribution has been taken from the table calculated by using Schiff's formula[7].

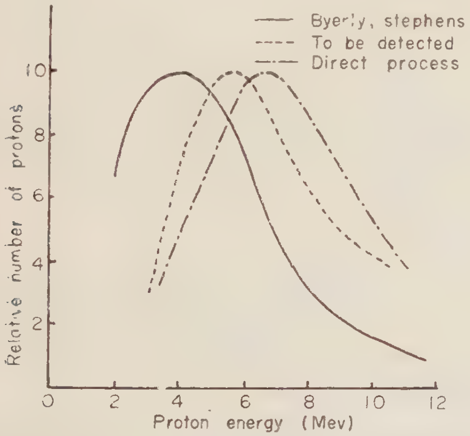

Fig. 3. Proton energy distribution from Cu(γ, p) reaction. The solid line is the result reported by Byerly and Stephens[6]. The dotted line is the energy distribution of detected protons under the present experimental condition. The broken line shows the calculated direct process.

The Coulomb barrier penetrability has been taken from Weisskopf's table[8] using $r_0=1.5\times10^{-13}$ cm. The value of B_p has been taken from the data of Byerly and Stephens ($B_p=6.1$ MeV). The copper foils of natural isotopic composition have been used for the target, but the yield of photo-protons from Cu^{63} and Cu^{65} is 1.07×10^6 p/mole/r and 0.37×10^6 p/mole/r respectively. Besides, the binding energy for Cu^{65} is 7.4 MeV, which is heigher than that for Cu^{63}. Therefore the calculation has been carried out only for Cu^{63}. The result shown in Fig. 3 as "to be detected" agrees roughly with the theoretical prediction for the direct process.

§ 3. Results and Discussion

The angular distributions from the various elements are shown in Figs. 4, 5, 6, 7 and 8.

When the nucleon absorbs the incident photon by electric dipole, the angular distribution has the form, $a+b\sin^2\theta$. The ratio of b/a is given by Courant's formula:

for the $l\to l+1$ transition:

$$b/a=(l+2)/2l \qquad (2)$$

for the $l\to l-1$ transition:

$$b/a=(l-1)/2(l+1)\,, \qquad (3)$$

where l is the orbital angular momentum of the ejected proton before photon absorption. If the electric quadrupole absorption is mixed in the electric dipole, the interference between the two modes gives an angular distribution of the form,

$$a+b\sin^2\theta(1+c\cos\theta)^2\,. \qquad (4)$$

To fit the present experimental data to this equation, the least square fit has been made and the constants have been determined except for the particular case of copper, which will be discussed in detail later. The determined constants are summarized in Table II.

Lithium

The rolled metallic lithium foil, sealed from the air in a polyethylene sack with a nitrogen gas to avoid oxidation of the surface, has been irradiated in a scattering chamber shown in Fig. 1. Even with this treatment the metallic lithium has been oxidized in about

Table II. Results of angular distribution of photo-protons.

Element	Angular distribution	b/a
Lithium	$1+0.25\sin^2\theta(1+0.90\cos\theta)^2$	0.25 ± 0.08
Aluminum	isotropic	
Sulfur	$1+0.57\sin^2\theta(1+0.23\cos\theta)^2$	0.57 ± 0.01
Nickel (21 MeV)	isotropic	
Nickel (18 MeV)	$1+6.0\sin^2\theta(1+0.87\cos\theta)^2$	6.0 ± 0.5

two days, during which period the measurement has been finished.

Some excitation curves of photo-proton reactions with lithium have been reported previously. One can find some curious facts in these results. Different detecting systems have given different results for the excitation function of the photo-proton reaction. For instance, there exists a sharp peak in the cross section curve reported by Titterton and Brinkley[9] but not in that reported by Tucker[10]. In the case reported by Rubin and Walker[11] two sharp peaks exist in the cross section curve, one at 15 MeV and the other at 20 MeV. This arouses interest in studying the angular distribution of photo-protons from lithium in the energy region from 15 to 22 MeV.

Bremsstrahlung of 21 MeV max. energy has been used for excitation of lithium in the present work. The measured angular distribution of photo-protons has a large forward asymmetry as shown in Fig. 4.

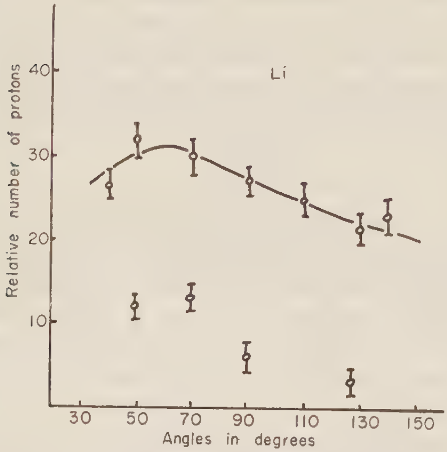

Fig. 4. Angular distribution of photo-protons from lithium for maximum excitation energy of 21 MeV. The smooth curve drawn by the least square has the form,

$$1+0.25\sin^2\theta(1+0.90\cos\theta)^2 .$$

The white dots quoted from the result of Whitehead[12], for excitation with 96 MeV are shown for comparison.

Further interest lies in the angular distribution when lithium is excited by lower energy, 15-18 MeV, where another peak exists in a cross section curve. Unfortunately, the counting rate of protons has been too small to measure the angular distribution of photo-protons with 18 MeV excitation.

There is a report[12] on the angular distribution of photo-protons with bremsstrahlung of 96 MeV, the result of which is similar to that of the present work. Thus it may be concluded that for both excitation energies the same mechanism of photon absorption, that is the direct process, is responsible.

Aluminum

A thin foil of metalic aluminum having a thickness listed in Table I has been irradiated for 100-200 minutes for each measured angle with bremsstrahlung of 21 MeV max., the resultant angular distribution being shown in Fig. 5. This is interpreted to be isotropic.

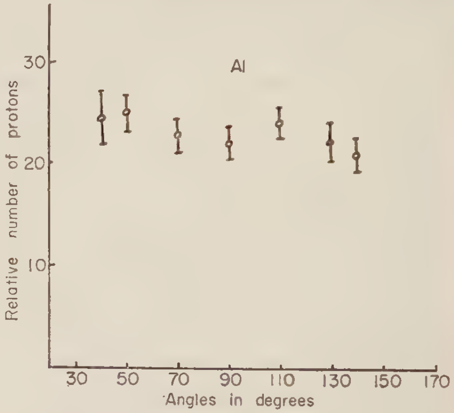

Fig. 5. Angular distribution of photo-protons from aluminum.

According to Ferrero[13], the excitation function for photo-protons of aluminum indicates that the evaporation process is predominant in the energy region of 12-20 MeV, but the direct process begins to contribute above 18 MeV excitation. Thus the excitation by 21 MeV bremsstrahlung will result mainly in the isotropic angular distribution.

Sulfur

Powdered sulfur has been melted so as to form a thin foil between two plane glass plates and has been cooled down in the room temperature, and the foil has been irradiated just after this treatment to avoid curling. The thickness of the foil is shown in Table I.

The angular distribution of photo-protons from sulfur is shown in Fig. 6. A symmetry almost at 90° has been obtained, except for a minor part of forward asymmetry. The expression obtained from the least square fit for this measurement is

$$1+0.57\sin^2\theta(1+0.23\cos\theta)^2\,.$$

The part with 90° symmetry can be interpreted by the direct process proposed by Courant. The value obtained of b/a is 0.57 in the present measurement.

Nickel

As the yield of photo-protons from nickel has been very large, measurement has also been carried out with bremsstrahlung of 18 MeV besides 21 MeV. The results are shown in Fig. 7. The counting rate of photo-protons with 18 MeV excitation has been found to be about 1–2 counts per minute, which is one tenth of the counting rate with 21 MeV excitation. The total count corresponding to one point in the figure is 100–200. The different behaviors of the two curves may be understood as follows. The detecting efficiency of high energy protons relative to that of low energy ones will be higher for 18 MeV excitation than for 21 MeV excitation, because of the effect of energy loss both in the target and in the air of emerging protons and also of the effect of Coulomb barrier supression. This will result in an enhanced forward asymmetry for the case of lower excitation. The larger isotropic part obtaided with a slightly higher excitation, however, can not be considered to be of much value from this point of view. This isotropic distribution agrees nearly with the result reported by Mann and Halpern[14], who used the same instrumental arrangement as that in the present experiment.

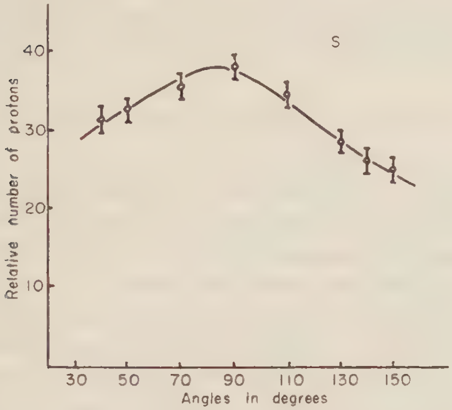

Fig. 6. Angular distribution of photo-protons from sulfur. The experimenta dots fit the expression, $1+0.57\sin^2\theta(1+0.23\cos\theta)^2$.

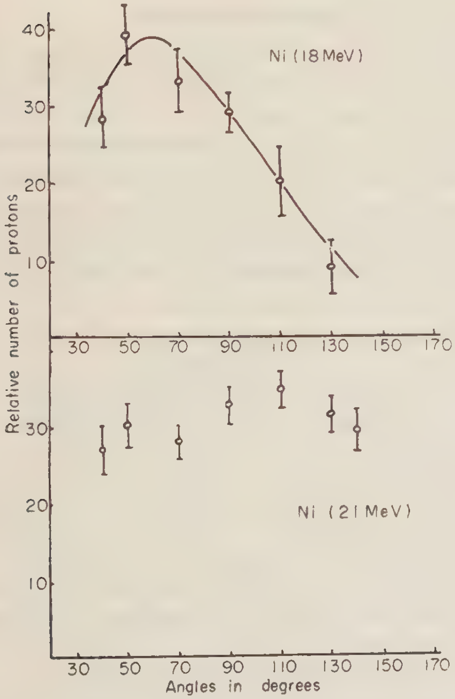

Fig. 7. Angular distribution of photo-protons from nickel. The results of the least square to fit the experimental plots with 18 MeV bremsstrahlung are described with the form,

$$1+6.0\sin^2\theta(1+0.87\cos\theta)^2\,.$$

Copper

A thin foil having a natural isotopic composition has been irradiated with 21 MeV bremsstrahlung, and the irradiation has been repeated 140 times for each angle for a total of 600 minutes in order to eliminate un-

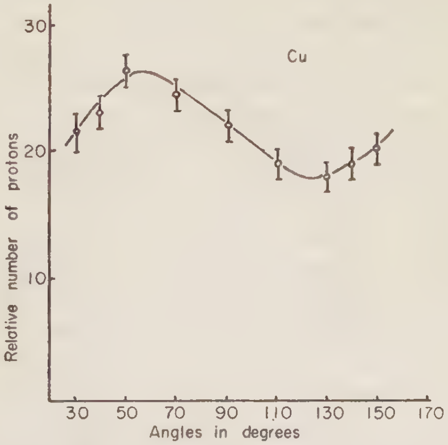

Fig. 8. Angular distribution of photo-protons from copper. The coefficients obtained by the least square fit are listed in Table III, assuming that the form is $\sum_{l=0}^{4} C_l P_l(\cos\theta)$.

certainty of the measurement in the backward direction, which offers a theoretical interest as will be discussed later.

The result is shown in Fig. 8, which indicates an abnormal result. There is a maximum at 50 degrees and a minimum at 130 degrees. The former effect has been found out not only in the present work but also in many references and has been well explained by theory; but the latter effect has never been reported definitely in the case of photonuclear reaction. A similar result has been reported by Spicer[16] for the angular distribution of photo-protons from argon 40. In this reference, higher energy protons showed an angular distribution having a minimum at 130 degrees, which is very similar to the present result. But the author of this reference has stated that this minimum should not be taken seriously since the statistics of the measurement at angles greater than 120 degrees were very poor. In the present measurement, an obvious minimum exists at 130 degrees.

This result has been analyzed by making the least square fit assuming that the form of the angular distribution is:

$$d\sigma/d\Omega=\sum C_l P_l(\cos\theta) \qquad (5)$$

and

$$d\sigma/d\Omega=\sum a_i \cos^i\theta \qquad (6)$$

where θ is the angle between the X-ray beam and the proton detector, $P_l(\cos\theta)$ the Legendre polynomials, and a_i and C_l the coefficients of the two functions.

Table III. Angular distribution coefficients for copper.

Legendre polynomials		Power series	
C_0	21.0494	a_0	21.112
C_1	3.0044	a_1	5.8524
C_2	−1.6930	a_2	8.2572
C_3	−6.0504	a_3	28.449
C_4	−1.0342	a_4	−16.445
		a_5	−55.612

The coefficients have been calculated with the Bendix G-15-D computor and listed in Table III. A good fit is shown in Fig. 8.

The result has been compared with the new theory which is based on the "two-stage mechanism" developed by Sawicki[17]. This mechanism is essentially a two-stage process: the γ-ray interacts with the surface oscillations of the nucleons; a proton bound to the rest of the nucleus interacts with the oscillating core and is emitted.

The copper nucleus has the last proton in a p-state, and according to the theory photoprotons form such a nucleus have an angular distribution showing a minimum in the backward direction, the form of which is given by

$$a+b\sin^2\theta+A\cos\theta(C_1+C_2\cos^2\theta-3C_3\sin^2\theta) \qquad (7)$$

where the term $a+b\sin^2\theta$ refers to the Courant theory and the rest are the interaction terms. Our experimental result is qualitatively in agreement with this theory.

The present result may be compared with those of other works: a forward asymmetry was reported by Mann, Halpern and Rothmann[14] with 25 MeV bremsstrahlung, and for excitation with higher energies, the isotropic angular distribution was reported by Dawson[15] who used 70 MeV bremsstrahlung.

Acknowledgement

The author is indebted to Professor T. Asada for the encouragement given to him throughout the course of the present work. Gratitude is also due to Messrs. M. Okumura, J. Okuma and K. Sasaki for their assistance in the operation of the betatron. Finally, the author wishes to thank Dr. K. Okamoto for his helpful discussion on the result of this work.

References

1) E. D. Courant: Phys. Rev. **82** (1951) 703.
2) J. S. Levinger: Phys. Rev. **84** (1951) 43.
3) M. E. Toms and W. E. Stephens: Phys. Rev. **92** (1953) 362.
4) M. E. Toms and W. E. Stephens: Phys. Rev. **98** (1955) 626.
5) T. Asada, M. Masuda, M. Okumura and J. Okuma: J. Phys. Soc. Japan **14** (1959) 1766.
6) P. R. Byerly and W. E. Stephens: Phys. Rev. **83** (1951) 54.
7) L. I. Schiff: Phys. Rev. **70** (1946) 87.
8) J. M. Blatt and V. F. Weisskopf: Theor. Nucl. Phys.
9) E. W. Titterton and T. A. Brinkley: Proc. Phys. Soc. **A**, **66** (1953) 194.
10) B. L. Tucker and E. C. Gregg: Phys. Rev. **91** (1953) 1579.

11) R. Rubin and M. Walker: Helv. Phys. Acta. **27** (1954) 163.
12) C. Whitehead: Phys. Rev. **110** (1958) 941.
13) Ferrero: Nucl. Phys. **9** (1958) 32.
14) Mann, Halpern and Rothmann: Rhys. Rev. **87** (1952) 146.
15) W. K. Dawson: Can. J. Phys. **34** (1956) 1480.
16) B. M. Spicer: Phys. Rev. **100** (1955) 791.
17) J. Sawicki: Nucl. Phys. **6** (1958) 525.

JOURNAL OF THE PHYSICAL SOCIETY OF JAPAN Vol. 16, No. 10, OCTOBER, 1961

Photoprotons from Silicon and Phosphorus

By Katsufusa SHODA, Shoichi SHIINA*, Keisuke KOBAYASHI**, Ken ABE and Motoharu KIMURA

Department of Physics, Tohoku University, Sendai, Japan

(Received March 31, 1961)

Photoprotons from Si and P produced by a 24-MeV betatron have been observed in nuclear emulsions. Fine structures are observed in the energy spectrum of Si, showing a fairly similar shape to the excitation curve of Al (p, γ) reaction. The appearance of these structures is expected by resonating group model and probably by the channel coupling theory as well. The distances of the proton peaks in the spectrum are nearly equal to those expected by these theories. The type of spectrum of Si is different from that of P, and such difference seems to appear between even and odd Z neighbouring nuclei.

The angular distributions for P have large maxima around 90°, but those for Si have not so large maxima and minima. This suggests that the shell structure may have some effects on the photonuclear reactions.

§ 1. Introduction

In the energy region of the giant resonance of photonuclear reactions, the nucleus is highly excited and a large number of levels of the compound nucleus contributes to the transition. In the earliest stage of study of photonuclear reactions, however, the giant resonance was regarded as a broad resonance of the electric dipole interaction of photons with the nucleus[1),2)]. Katz et al.[3)] found first the fine structures of (γ, n) cross sections in their measurement of C^{12}, and O^{16}. Many fine structures have been observed in light nuclei afterward.

Wilkinson[4)] put forward the theory of single particle excitation in photonuclear reactions. According to his theory, fine structures will appear corresponding to single particle transitions. His theory seems to agree with several experiments.

Recently some fluctuations of cross sections or gross structures were also observed in (p, p'), (p, α), (n, n') and some other reactions in the intermediate energy region (10～30 MeV). These fluctuations do not seem to be explained so well by the usual model, and the fine structures of photonuclear reactions mentioned above may have some relations to these fluctuations. Shaw[5)] and Izumo et al.[6)] have calculated the effect of local heating of the nucleus using a resonating group model. On the other hand, Tamura et al.[7)] are trying to explain this phenomenon using the idea of channel coupling. These calculations expect some structures in the cross section curves and also in the energy spectrum of emitted particles for all reactions in the intermediate energy region.

The earlier experiments for the proton energy distributions of (γ, p) reactions of almost all elements in the giant resonance region were plotted with about 1 MeV interval which might be too large to find the fine structure. These roughly plotted proton spectra are in agreement with the predictions of the statistical theory for light and middle weight nuclei. The angular distribution shows a large difference from nucleus to nucleus. The photoproton spectra in several nuclei such as C^{12}, N^{15}, and O^{16} etc. show some fine structures, and the angular distributions have different shapes for different proton energies. De Sabbata[8] has reviewed these experiments and summarized the results.

---

* Now at Department of Physics, College of Science and Engineering, Nihon University, Tokyo, Japan.

** Now at Department of Nuclear Engineering, Kyoto University, Kyoto, Japan.

We have investigated the energy and angular distributions of the photoprotons from Si^{28} and P^{31} with good statistics. Si^{28} and P^{31} are neighboring nuclei for the proton number, and the last shell has six $1d_{5/2}$ protons and one $2s_{1/2}$ proton, respectively. The results for Si^{28} and P^{31} (γ, p), therefore, may help us to understand the effect of shell structure to the reaction mechanism.

Si^{28} (γ, p) was investigated by Emma et al.[9], but the data were given only for the angular distributions. Čujec-Dobovišek[10] have also investigated the Si^{28} (γ, p), P^{31} (γ, p) and S^{32} (γ, p) by 32 MeV bremsstrahlung. According to her results a peak is found at about 8 MeV in the energy spectra for Si and S. This peak corresponds to $1d_{5/2} \rightarrow 1f_{7/2}$ transition at $E_\gamma \sim 20$ MeV through the mechanism stated by Wilkinson. The relatively high fractional yield of high energy protons is in good agreement with the theory. The angular distributions of her results involve a rather significant forward asymmetry, being interpreted to show an intereference between $E1$ and $E2$ absorption.

Our experiment has been done by 24 MeV bremsstrahlung. The reactions will be regarded as simpler at this energy than at 32 MeV.

§ 2. Experimental Procedure and Apparatus

Photoprotons emitted from Si and P irradiated by 24 MeV bremsstrahlung from Tohoku University betatron were detected by Ilford G-special emulsions, which were 600 μ thick and $\frac{1}{2}'' \times 2\frac{1}{2}''$ in size. Two plates and sample were placed on the holder mounted in a evacuated chamber which was combined with the collimator defining the beam area to 0.5 cm × 1.0 cm at the target. (Fig. 1).

The distance between the plates and the targets was about 2 cm and the maximum glancing angle of the plate was about 30°. Such a large glancing angle increases photoproton detection efficiency and reduces the ratio of the neutron-recoil protons to the photoprotons in the emulsion. The background was evaluated by the tracks entering the emulsions from wrong directions, and was lower than 2 percent. The background by the (n, p) reaction at the targets was estimated by the stray neutron number. It was proved to be negligible. In spite of the large glancing angle, the proton energy resolution is determined only by the uncertainty of proton energy absorption arised from target thickness.

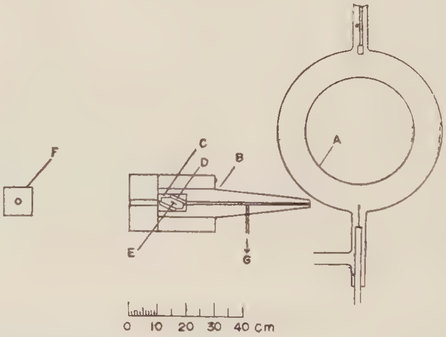

Fig. 1. Experimental arrangement showing A-betatron doughnut, B-lead stacked collimator and reaction chamber, C-plate and target holder, D-nuclear plates, E-target, F-monitor, G-vacuum pump.

The targets were the red phosphorus (19.4 mg/cm²) deposited on the Au-foil, and the natural silicon powder (9.38 mg/cm²) bound on the Au-foil by the cellulose acetate (0.2 mg/cm²). The size of its grain was about several micron in diameter. The thickness of Au foils was 0.19 mg/cm² for both targets. The background from the Au foil and the binder was estimated to be negligible.

The energy of the bremsstrahlung from the betatron was calibrated by the threshould energies of the Cu^{63} (γ, n) (10.8 MeV), Fe^{54} (γ, n) (13.8 MeV) and C^{12} (γ, n) (18.7 MeV) reactions and the drift of the energy was about ±0.05 per cent. The intensity was measured by a Victoreen thimble embedded at the center of a 10 cm cube of Lucite behined the plate chamber and was calibrated to the intensity without the collimator. The uncertainty of the dose values was about 20 per cent.

The plates were processed by dry temperature development with amidol developer. The best condition for hot stage was ninety minutes at 18.5°C for reducing fogs and increasing transparency of the emulsion. The photo-proton tracks were scanned with TIYODA binocular microscopes at a magnification of 600×. The scanned area was 2 mm×40 mm for Si and 3 mm×40 mm for P, and a longer side was parallel to the targets. For each measured proton track, the range, the angle to the beam direction and the corretion for the energy loss due to the target thickness were calculated. Barka's Table[11] was used for the proton range-energy relation. For the energy loss correction, the energy loss due to the effective half target thickness was added to each measured proton energy. The solid angle subtended by the scanned area for each proton direction was calculated geometrically at each point on the target and averaged on the beam area within the range of 10° around the several standard directions. The angular distributions were obtained using this solid angle.

The Table I indicates the exposure data.

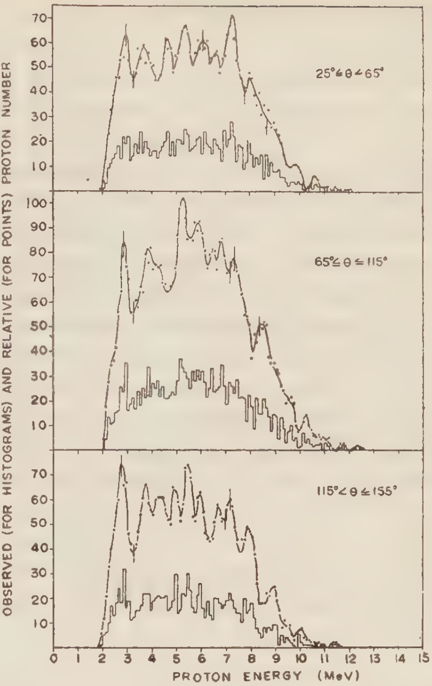

Fig. 2. Energy distributions of protons from Si^{28} for three directional groups. The smoothed results are shown by the points.

Table I. Exposure Data

Element	Si	P
(γ, p) threshold (MeV)	11.59	7.30
(γ, np) threshold (MeV)	24.65	17.91
Betatron energy (MeV)	24	24
Target thickness (mg/cm^2)	9.38	19.4
Roentgens at sample	5000	
Emulsion type	Ilford G-special 600 μ	
Area scanned (cm^2)	1.6	2.4
Total proton number $25° \leq \theta \leq 155°$	4366	3833

Resolution for energy loss by half target thickness

$E_p \sim 3$ MeV	θ	70°, 110°	28%	56%
		30°, 150°	34	68
$E_p \sim 6$ MeV	θ	70°, 110°	9	18
		30°, 150°	12	24
$E_p \sim 10$ MeV	θ	70°, 110°	5.8	7.6
		30°, 150°	5.0	10

§ 3. Experimental Results

Silicon

The measured energy distributions are shown in Fig. 2 for the three directional ranges, and in Fig. 3 for the total protons. The energy distributions were plotted with 0.1 MeV interval which was much smaller than the resolution, hence, they were smoothed out by the method of Ferreira and Valoshek[12] and the smoothed results are shown in the same figures. These spectra exibit many peaks.

The theoretical energy distributions were calculated using the statistical theory of nuclear reactions. One would not expect the statistical theory to be applicable to such light nuclei as Si^{29} and P^{31}. However, the proton spectra for Mg^{25} (γ, p)[13], Al^{27} (γ, p)[14),15),16], P^{31} (γ, p)[10], A^{40} (γ, p)[17] and other reactions indicated that the statistical theory could reproduce the general features of the observed spectra. Hence we compared the experimental spectra with those of the statistical theory. Both spectra were normalized to fit to experimental points as shown in Fig. 3.

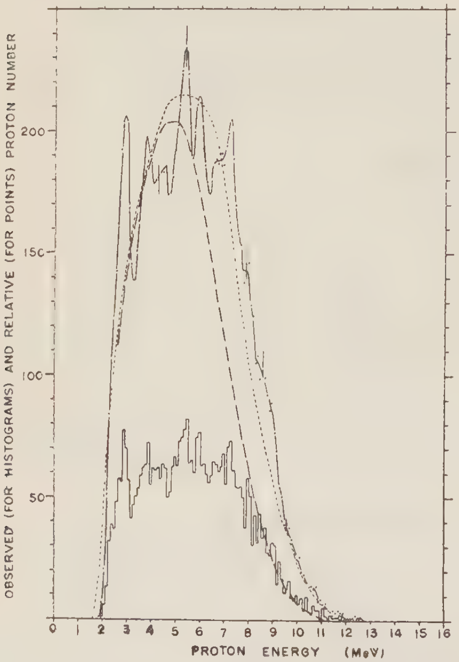

Fig. 3. Energy distribution of total observed protons and calculated distributions by the statistical theory from Si^{28}.

Full line: Observed spectrum smoothed out by the method of Ferreira and Valoshek.

Broken line: Calculated spectrum using $\omega = C \exp[2\sqrt{0.45\,E}]$ MeV^{-1}

Dotted line: Calculated spectrum using $\omega = C \exp[E/2.8]$ MeV^{-1}

Each curve is normalized to best fit to experimental points.

The proton energy distribution based on the statistical theory is given by

$$I(\varepsilon_p) = \varepsilon_p \cdot \sigma_c(\varepsilon_p) \int_{B_p+\varepsilon_p}^{E_{\gamma\,\max}} \times \frac{\sigma_{\gamma n}(E_\gamma) N(E_\gamma, E_{\gamma\,\max}) \omega(E_\gamma - B_p - \varepsilon_p)}{\int_0^{\varepsilon_\gamma - B_n} \varepsilon_n \sigma_c(\varepsilon_n) \omega(E_\gamma - B_n - \varepsilon_n) d\varepsilon_n} dE_\gamma \tag{1}$$

where ε_p and ε_n are the proton and the neutron energy, $\sigma_c(\varepsilon_p)$ and $\sigma_c(\varepsilon_n)$ are the capture cross sections by the residual nuclei for protons of energy ε_p and for neutrons of energy ε_n, which were used by Blatt-Weisskopf's calculations[18]. $\omega(E_\gamma - B_p - \varepsilon_p)$ and $\omega(E_\gamma - B_n - \varepsilon_n)$ are the level densities of residual nuclei after protons and neutrons were emitted, B_p, B_n being the binding energy. The experimental result of Katz et al.[19] was used for $\sigma_{\gamma n}(E_\gamma)$. $N(E_\gamma, E_{\gamma\,\max})$ is the photon spectrum, for which the Schiff spectrum[20] was used. The level density may be represented by using the Blatt-Weisskopf's table[18],

$$\omega = C \exp[2\sqrt{0.45\,E}] \text{ MeV}^{-1}. \tag{2}$$

On the other hand, according to Endt et al.,[21]

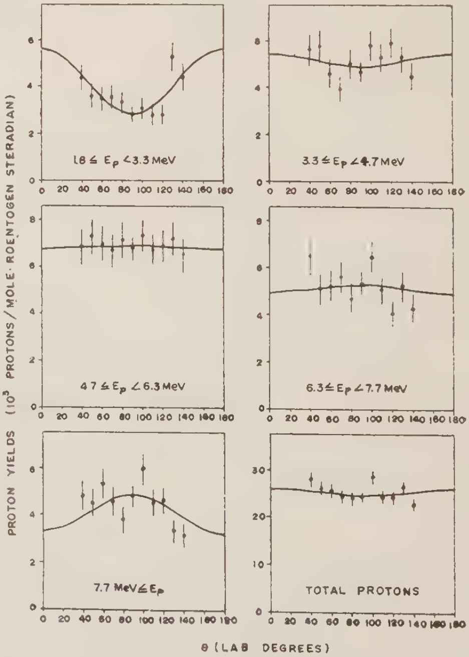

Fig. 4. Angular distributions of protons from Si^{28}. Full lines are obtained by least squares.

the following is deduced from the known levels of Al^{27}:

$$\omega = C \exp[E/2.8] \text{ MeV}^{-1}. \qquad (3)$$

The latter is in good agreement with that obtained from $Al^{27}(p, p')$ reaction which is shown as follows[22]:

$$\omega \propto \exp[E/2.7].$$

The energy spectra were compared for these two level densities.

Table II. Angular distributions calculated by least squares for $a+b \sin^2 \theta$.

Element	Proton energy (MeV)	Augular distributions
Si^{28}	1.8–3.3	$1-(0.50\pm0.39)\sin^2\theta$
	3.3–4.7	$1-(0.09\pm0.44)\sin^2\theta$
	4.7–6.3	$1+(0.01\pm0.40)\sin^2\theta$
	6.3–7.7	$1+(0.06\pm0.49)\sin^2\theta$
	larger than 7.7	$1+(0.48\pm0.73)\sin^2\theta$
	Total	$1-(0.05\pm0.20)\sin^2\theta$
P^{31}	2.7–4.5	$1+(0.85\pm0.42)\sin^2\theta$
	4.5–6.0	$1+(0.35\pm0.34)\sin^2\theta$
	6.0–8.5	$1+(1.31\pm0.59)\sin^2\theta$
	larger than 8.5	$(-0.08\pm0.18)-\sin^2\theta$
	Total	$1+(1.10\pm0.27)\sin^2\theta$

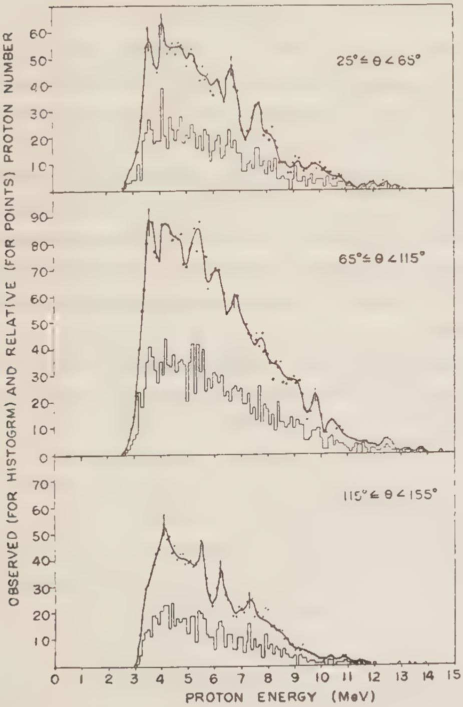

Fig. 5. Energy distributions of protons from P^{31} (γ, p) for three directional groups. The smoothed results are shown by the points.

The angular distributions corrected for the solid angle and devided into several proton energy regions are shown in Fig. 4. In all cases, the observed distributions were fitted with curves of the form $a+b\sin^2\theta$ assuming the symmetric angular distribution. a and b were determined by the least square fit and the calculated distributions are also shown in Fig. 4 and in Table II.

The yield of photoprotons corrected for the angular distribution was 2.9×10^5 protons per roentgen.

Phosphorus

The measured energy distributions are

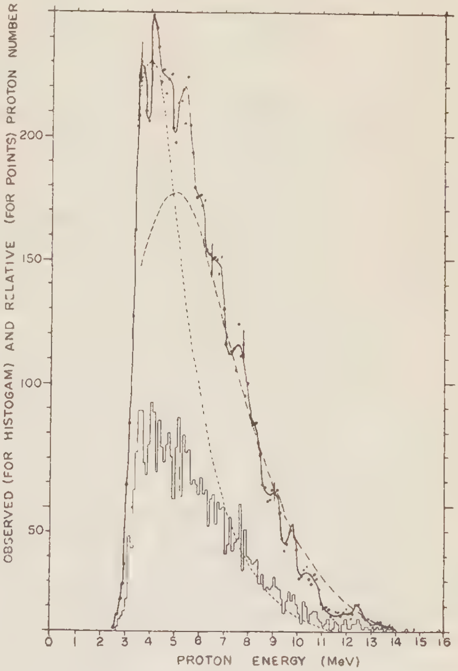

Fig. 6. Energy distribution of total observed protons and calculated distributions by the statistical theory from P^{31}.

Full line: Observed spectrum smoothed out by the method of Ferreira and Valoshek.

Broken line: Calculated spectrum using

$$\omega = C \exp[2\sqrt{0.52\,E}] \text{ MeV}^{-1}$$

Dotted line: Calculated spectrum using

$$\omega = C \exp[2\sqrt{2.42\,E}] \text{ MeV}^{-1}.$$

Each curve is normalized to best fit to experimental points.

shown in Fig. 5 and Fig. 6 in the same treatment as for Si. The proton energy resolution is worse than that for Si, but the spectra seem to exhibit some peaks. Photoprotons from the (γ, np) reactions are not included in Si^{28} results, but in the case of P^{31} they may affect the spectra and angular distributions for the proton energy region lower than 6 MeV.

The theoretical curves based on the statistical theory as in Si are also shown in Fig. 6. Two types of the level density of the residual nucleus were assumed as follows:

$$\omega = C \exp\,[2\sqrt{0.52\,E}]\ \mathrm{MeV}^{-1} \qquad (4)$$

$$\omega = C \exp\,[2\sqrt{2.42\,E}]\ \mathrm{MeV}^{-1} \qquad (5)$$

In Eq. (4) the parameter 0.52 corresponds to Blatt-Weisskopf's table for $A=30$[18]. Montalbetti et al.'s data[23] were used for $\sigma_{\gamma n}(E_\gamma)$ which appear in Eq. (1).

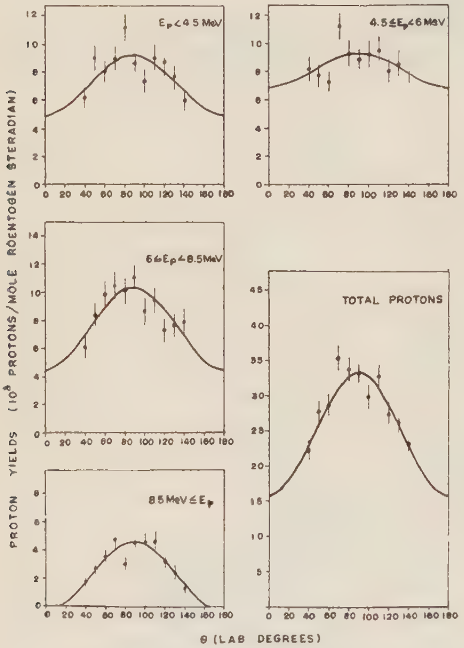

Fig. 7. Angular distributions of protons from P^{31}. Full lines are obtained by least squares.

The angular distributions are shown in Fig. 7. They are all nearly 90° symmetric. The best fitted curves of the form $a + b \sin^2\theta$ were obtained by the least square fit and are also shown in Fig. 7 and in Table II.

The yield of photoprotons corrected for the angular distributions was 3.2×10^5 protons per mole per roentgen according to the result using other plate.

§ 4. Discussion

The yields are compared with the statistical theory. Both calculated and observed values are shown in Table III. The experimental yield for Si^{28} is smaller than the theoretical calculations. In the case of P^{31}, the residual nucleus for (γ, p) is even-even and that for (γ, n) is odd-odd. In general the level density of the former is smaller than the latter. We calculated the yields for two values of the ratio of level density parameter C of even-even nuclei to that of odd-odd nuclei. The ratio is denoted as α. If we assume the following relation[24]

$$4C\,(\text{even-even}) = 2C\,(\text{even-odd}) = C(\text{odd-odd}),$$

α is equal to 1/4 for P^{31} target. The calculated yields using $\alpha = 1/4$ and level density (5) are in good agreement with observed values.

It is difficult to discuss exactly about the energy spectra and the angular distributions for the photoprotons, because bremsstrahlung has a continuous photon energy spectrum. Proton distributions do not uniquely correspond to specific transitions among the nuclear states.

According to the statistical theory, the photoproton spectra calculated by using con-

Table III. Photoproton yields

Element	Observed yield (protons/mol/r)	Calculated yield		α
		Level density	Yield (protons/mol/r)	
Si^{28}	2.9×10^5	Eq. 3	8.5×10^5	1
P^{31}	3.2×10^5	Eq. 4	8.0×10^5	1
			2.0×10^5	$\frac{1}{4}$
		Eq. 5	12.7×10^5	1
			3.2×10^5	$\frac{1}{4}$

Table IV. Collection of data. The shapes of proton energy distributions are denoted by *A* and *B* for the nearly same type of proton spectra smoothed out from Si^{28} and P^{31} results respectively.

Element	Z	E_{max} (MeV)	Highest excitation (MeV)	Type of proton energy distribution	Best fitted level density	Yield (protons/mol/r)	ref.
Mg^{25}	12	24	11.93	A	deduced from known $N_a{}^{24}$ levels	1.74×10^5	13
Al^{27}	13	20.8	12.55	$\sim B$	only $\omega=$const. was calculated		14
		25	16.75	B	$C\exp[2\sqrt{0.50\,E}]$	about 0.3 times of Cu^{63} (γ, n)	15
		31	22.75	B			16
Si^{28}	14	32	20.41	$\sim A$		3.7×10^5	10
		24	12.41	A	$C\exp[E/2.8]$	2.9×10^5	present data
P^{31}	15	32	24.70	B	$C\exp]2\sqrt{0.53\,E}]$	4.3×10^5	10
		24	16.70	B	$C\exp[2\sqrt{0.52\,E}]$	3.2×10^5	present data
S^{32}	16	32	23.14	$\sim A$		4.8×10^5	10
A^{40}	18	22.5	10.47	$(\sim B)$	$\exp(E)$	6.6×10^5	17

tinuous cross sections for Si^{28} (γ, n) and for P^{31} (γ, n) are in fairly good agreement with the observed ones except fine structures (Fig. 3 and Fig. 6). The best fit level densities are the following: $\omega\propto\exp[E/2.8]$ for Al^{27} and Si^{27} in the case of Si^{28} target, and $\omega\propto\exp[2\sqrt{0.52\,E}]$ for Si^{30} and P^{30} in the case of P^{31} target.

The observed energy spectrum for A^{40} (γ, p)[17] is in good agreement with the calculated spectrum using the level density $\omega(E)\propto\exp(E)$ and the Coulomb barrier height of 2.5 MeV which is lower than other calculations and expected to arise from a fuzzy nuclear surface. Such lowering of the Coulomb barrier height may be expected to make better agreement for the case of Si^{28} and P^{31}. The large neutron excess would be effective for a fuzzy surface, which may dominate for A^{40} than for P^{31} and Si^{28}.

Table IV contains the photoproton energy distributions for neighbouring nuclei. The proton energy spectra of odd Z and of even Z nuclei seem to have their own definite shapes different from each other. The intensity of photoprotons has broad maximum ranging over several MeV for even Z nuclei as seen in Si^{28}, the type of which we denoted as "*A*" in Table IV. On the other hand, the photoprotons emitted from odd Z nuclei have rather sharp maximum as seen in P^{31}, the type of which we denoted as "*B*" in the Table. It may be expected that the level densities of residual nuclei are different between (γ, p) reactions of odd Z and even Z nuclei. The threshold energies of (γ, p) for the odd Z nuclei are a few MeV lower than those for the even Z nuclei. Now we consider that some amount of energy concentrate on a proton in the nucleus to be emitted after absorption of photon, and that the excitations by the gamma rays of the same energy are equal in both the even Z and the odd Z nuclei. Then, the excitation of residual nuclei after proton emission with the same energy is a few MeV higher for the even Z nuclei than for the odd Z nuclei, and this difference may cause the different proton energy spectra. The spin and parity are different between the ground states of the even and the odd nuclei, then the condition of these compound nuclei and their residual nuclei are also different in the reaction. Under these condition, the different excitation of particles in the nucleus may cause the different particle emission modes or different selection rules of transitions. It is desirable to compare the proton spectra from various elements at the same excitation energy above the threshold.

It is interesting that we have another experiments showing similar features to that described above for difference between proton energy spectra. Allan[25,26] observed two types of proton energy spectrum in (n, p) reaction. For example, the proton energy distributions for Fe^{54} and Fe^{56} are very different. Although this difference is independent of Z, it is similar to that between $Si^{28}(\gamma, p)$ and $P^{31}(\gamma, p)$. As the proton energy distributions of (n, p) reaction are not known so much, we shall not discuss further this points.

For such light nuclei as O^{16}, which have large level spacings, fine structures in the cross section and the energy spectrum have been observed in both (γ, p) and (γ, n) reactions. Now, in the present experiment, several peaks are found in the energy distributions of photoprotons from both Si^{28} and P^{31}, although the one of the latter might be somewhat obscured because of its poor resolutions. Čujec-Dobovišek[10] calculated the energies of protons emitted through the direct process according to the Wilkinson model[4]. She obtained the strongest $1d_{5/2} \to 2p_{3/2}$ direct transition at $E_p = 8.5$ MeV in the case of $Si^{28}(\gamma, p)$. Although one finds some trace of a peak at $E_p = 8.5$ MeV in the present result, it is not definite. Further, in smaller energy region, there exist many peaks which do not always agree with the Wilkinson theory. It should be pointed out here, however, that the energies of transitions assumed in the Wilkinson model are strongly criticized[27] and new theories[28)-30] are proposed to explain this problem. Therefore the agreement of the proton energy may be expected, but it is not definite.

The cross section measurement of $Al^{27}(p, \gamma)$ reaction[31),32),33] in which the transition to the first excited state of Si^{28} is stronger than that to the ground state shows many fluctuations by proton bombarding energies. Let us assume now that all protons from $Si^{28}(\gamma, p)$ come from the transitions to the ground state of Al^{27} (hereafter abbreviated to ground state protons), and that the cross section of $Al^{27}(p, \gamma_0)$ (gamma transition to the ground state of Si^{28}) is negligible compared with that of $Al^{27}(p, \gamma_1)$ (gamma transition to the first excited state (1.78 MeV) of Si^{28}). We can then calculate the cross sections of $Si^{28}(\gamma, p)$ from the photoproton energy spectrum by dividing with the photon number and correcting the energy scale for the recoil of the residual nucleus. On the other hand, we can also calculate the same cross section from the $Al^{27}(p, \gamma)$ data using the detailed balance theorem, assuming that the excitation energy of the compound nucleus Si^{28} is given by $E_{ex} = \frac{27}{28}E_p + 9.81$ MeV, (9.81 MeV is the Q value of γ_1).

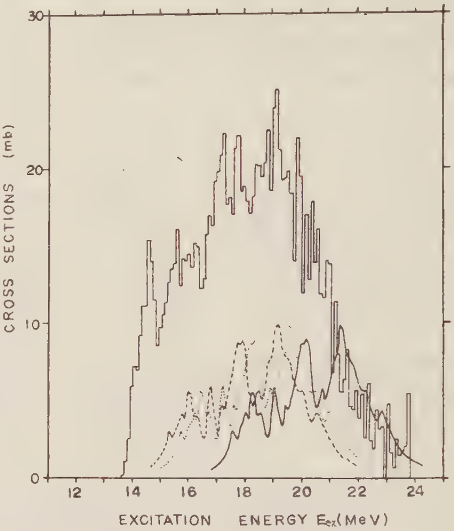

Fig. 8. Comparison of experiments for $Si^{28}(\gamma, p)$ Al^{27} and for $Al^{27}(p, \gamma)$ Si^{28}. The histogram shows $Si^{28}(\gamma, p)$ Al^{27} cross section assuming all proton transitions are to Al^{27} ground state. Heavy curve is $Si^{28}(\gamma, p)$ Al^{27} cross section calculated by detailed balancing from $Al^{27}(p, \gamma)$ Si^{28} cross section using the same Q value as that of γ_0. Dotted curve is the cross section using the Q value of γ_1. Broaken curve is obtained by shifting the dotted curve 0.5 MeV lower to best fit the histogram.

Fig. 8 shows the comparison of these two cross sections. We may find some parallelism between the two cross sections. We see, however, the energy discrepancy of about 0.5 MeV. If the Q value in the cross section from $Al^{27}(p, \gamma)$ is given by that value corresponding to γ_0, this cross section is further shifted to the higher energy side.

Of course there are many points which should be examined more carefully. These two experiments, $Si^{28}(\gamma, p)$ and $Al^{27}(p, \gamma)$, are not the exact inverse processes, because a fairly large number of the photoprotons are not the ground state protons, and also because the shape of the cross section of $Al^{27}(p, \gamma_0)$ may be different from that of (p, γ_1) that we plotted in Fig. 8. In fact the experiment at Chalk River finds the difference between both reactions (p, γ_0) and (p, γ_1)[31]. However if we infer the shape of Al (p, γ_0) from the sentence of ref 31, still the discrepancy in energy between Si^{28} (γ, p) and Al^{27} (p, γ_0) seems to exist. Therefore, although the experimental accuracy and also the assumptions used in deducing the cross sections must be checked more carefully, the existence of this discrepancy will not be excluded. If this is true, it may be an interesting problem from theoretical viewpoint.

According to Izumo's calculation[6], some resonating groups with about seven nucleons in the nucleus play a role in the intermediate energy nuclear reactions, and the gross levels may be found with larger distances than natural nuclear level distances in the same excitation. The distance of peaks in the photo-proton spectra from Si^{28} are about 600 KeV, which is in good agreement with our result. It should be noted, however, that these gross structures can be explained also by the channel coupling theory[7].

The angular distributions corresponding to each proton energy group show nearly the

Table V. Computed angular distributions for photoprotons, assuming the compound process.

$$A+\gamma \rightarrow A^* \longrightarrow B+p$$
$$J_A+l_\gamma \rightarrow J_C \longrightarrow J_B+l_p$$

J_B is the final channel spin.

(a): Si^{28} (γ, p) $J_A=0^+$

Transition	J_c	l_p	J_B	J of residual state	Angular distribution
$E1$	1^-	1	0	$1/2^+$	$\sin^2\theta$
		0	1	$1/2^-$, $3/2^-$	constant
		2	1	$1/2^-$, $3/2^-$	$2+3/2\sin^2\theta$
		1	1	$1/2^+$, $3/2^+$	$1-1/2\sin^2\theta$
		1	2	$3/2^+$, $5/2^+$	$1+1/6\sin^2\theta$
		2	2	$3/2^-$, $5/2^-$	$1-1/2\sin^2\theta$
		3	2	$3/2^+$, $5/2^+$	$1+\sin^2\theta$
		2	3	$5/2^-$, $7/2^-$	$1+1/4\sin^2\theta$
$M1$	1^+	1	0	$1/2^-$	$\sin^2\theta$
		1	1	$1/2^-$	$1-1/2\sin^2\theta$
$E2$	2^+	1	1	$1/2^-$	$1-1/2\sin^2\theta$
		3	1	$1/2^-$	$1+2\sin^2\theta-5/2\sin^4\theta$

(b): P^{31} (γ, p) $J_A=1/2^+$

Transition	J_c	l_p	J_B	J of residual state	Angular distribution
$E1$	$1/2^-$	1	1/2	0^+	constant
	$3/2^-$	1	1/2	0^+	$1+3/2\sin^2\theta$
$M1$	$1/2^+$	0	1/2	0^+	constant
	$3/2^+$	2	1/2	0^+	$1+3/2\sin^2\theta$
$E2$	$3/2^+$	2	1/2	0^+	$1-1/2\sin^2\theta$
	$5/2^+$	2	1/2	0^+	$1+2\sin^2\theta-5/2\sin^4\theta$

same distributions in each nucleus. The angular distributions expected from the transitions between single levels and a compound nucleus of definite J_c formed in the reaction are shown in Table V. Some of the cases are in good agreement with each experimental angular distribution.

Other angular distributions are expected by the $l \rightarrow l \pm 1$ transitions of the direct photoelectric effect models led by Courant[34] and Wilkinson[4].

According to Courant's calculation, the distributions of the photoprotons are

$$N(\theta)=l+\frac{1}{2}(l+2)\sin^2\theta$$

for the $l \rightarrow l+1$ transition,

$$N(\theta)=l+\frac{1}{2}(l-1)\sin^2\theta$$

for the $l \rightarrow l-1$ transition.

l is the orbital angular momentum carried by the emitted proton while it was within the nucleus. The Wilkinson model predicts that only the $l \rightarrow l+1$ transitions are important. The experimental angular distributions for Si^{28} are almost isotropic within the experimental error except for $E_p \gtrsim 7.7$ MeV. The angular distribution of photoprotons greater than 7.7 MeV can be attributed to the d state transition, but the isotropic parts cannot be predicted in this model. One of the angular distributions observed for P^{31} (γ, p) agrees with that from s state transition of the direct model and others agree with p or d state transitions.

Si^{28} and P^{31} are neighbouring nuclei, but the angular distributions are different from each other. This suggests that the shell structure may have some effects on these photoreactions.

§ 5. Acknowledgements

The authors gratefully acknowledge helpful discussions with Dr. K. Okamoto. They also wish to thank Dr. Izumo for kind advices and suggestions. They are also indebted to Mr. T. Ishizuka for useful help in numerical works.

References

1) A. Migdal: J. Phys. USSR **8** (1944) 331.
2) M. Goldharber and E. Teller: Phys. Rev. **74** (1948) 1046.
3) L. Katz, R. N. H. Haslam, R. J. Horsley, A. G.W. Cameron and R. Montalbetti: Phys. Rev. **95** (1954) 464.
4) D. H. Wilkinson: Physica, **22** (1956) 1039.
5) G. L. Shaw: Annals of Phys. **8** (1959) 509.
6) S. Igarasi, K. Izumo and T. Udagawa: Prog. Theor. Phys. **21** (1959) 468.
7) T. Tamura: Private communication.
8) V. De Sabbata: Nuovo Cimento, **11** supp. 2 (1959) 225.
9) V. Emma, C. Milone and A. Rubbino: Nuovo Cimento, **9** (1958) 343.
10) B. Čujec-Dobovišek: *Comptes Rendus du Congres International de Physique Nucleaire,* Dunod, Paris, (1958) 634.
11) M. M. Shapira: *Handbuch der Physik,* S. Flügge, ed., Vol. 45, (Springer Verlag, Berlin, 1958) p. 366.
12) E. P. Ferreira and P. Ya Valoshek: *Proceedings of the International Conference in Geneva* (August, 1955), 2 (1958), p. 147.
13) M. E. Toms and W. E. Stephens: Phys. Rev. **82** (1951) 709.
14) B. C. Diven and G. M. Almy: Phys. Rev. **80** (1950) 407.
15) M. M. Hoffmann and A.G.W. Cameron: Phys. Rev. **92** (1953) 1184.
16) C. Milone, R. Ricamo and A. Rubbino: Nuovo Cimento, **5** (1957) 528.
17) B. M. Spicer: Phys. Rev. **100** (1955) 791.
18) J. M. Blatt and V. F. Weisskopf: *Theoretical Nuclear Physics,* (John Wiley and Sons, 1954) p. 311.
19) L. Katz, R. N. H. Haslam, J. Goldenberg and J. G. V. Taylor: Can. J. Phys. **32** (1954) 580. **32** (1954) 580.
20) L. I. Schiff: Phys. Rev. **83** (1951) 252.
21) P. M. Endt and J. C. Kluyver: Rev. Mod. Phys. **26** (1954) 95.
22) P. C. Gugelot: Phys. Rev. **93** (1954) 425.
23) R. Montalbetti, L. Katz and J. Goldemberg: Phys. Rev. **91** (1953) 659.
24) V. F. Weisskopf and D. H. Ewing: Phys. Rev. **57** (1940) 472.
25) D. L. Allan: Proc. Phys. Soc. Lond. A **68** (1955) 925.
26) D. L. Allan: Nuclear Physics, **6** (1958) 464.
27) B. L. Cohen. J. B. Mead, R. E. Price, K. S. Quisenberry, and C. Martz: Phys. Rev. **118** (1960) 499.
B. L. Cohen and R. E. Price: Nuc. Phys. **17** (1960) 129.
28) G. E. Brown and M. Bolsterli: Phys. Rev. Letters **3** (1959) 472.
29) K. A. Brueckner and R. Thieberger: Phys. Rev. Letters **4** (1960) 466.
30) J. H. Carver and D. C. Peaslee: Phys. Rev. **120** (1960) 2155.

31) H. E. Gove, A. E. Litherland and R. Batchelor: Phys. Rev. Letter, **3** (1959) 177.
32) D. S. Gemell, A. H. Morton and W.I.B. Smith: Nuc. Phys. **10** (1959) 45.
33) M. Kimura, K. Shoda, N. Mutsuro, T. Tohei, K. Sato, K. Kuroda, K. Kuriyama and T. Akiba: J. Phys. Soc. Japan **15** (1960) 1128 and Nuc. Phys. **23** (1961) 338.
34) E. D. Courant: Phys. Rev. **82** (1951) 703.

JOURNAL OF THE PHYSICAL SOCIETY OF JAPAN, Vol. 16, No. 10, OCTOBER, 1961

A Linear Electron Accelerator as the Injector of 1 BeV Synchrotron

By Tetsuji NISHIKAWA*, Jiro TANAKA, Akira MIYAHARA
and Hiroo KUMAGAI

Institute for Nuclear Study, University of Tokyo, Tokyo, Japan

(Received April 8, 1961)

The design study and the general aspect of a linear electron accelerator is described. Since this linear accelerator is used for the injector of the strong focusing synchrotron under construction, the spread of the output energy is desired to be as small as possible. For this purpose the cause of the energy spread has been reexamined and divided into two kinds; one is the different phase motions of the electrons injected at the various phase angles and the other is the variations of the microwave power, frequency, and other parameters. By the careful design, especially on the buncher, and by the use of the prebuncher and the stable power system, the output energy spread of about three percents has been obtained at the energy of 6.5 MeV.

§ 1. Introduction

This is the first paper of the series on the linear electron accelerator which has been constructed as the injector for 1 BeV electron synchrotron in the Institute for Nuclear Study. This work began in the spring of 1956. The design study was performed in 1957[1]. Then, we started to the experimental tests for the pumped klystron amplifier, pulse transformer, test cavities, electroforming of the accelerator tube, etc. These preliminary studies were finished in 1959[2], and we spent about one year or more for the overall construction of the accelerator. The accelerator began to operate successfully in the beginning of this year.

Usually, a pulse transformer or a d. c. generator type accelerator such as Van de Graaff generator is used as the injector for an electron synchrotron. While, if we use a linear accelerator, we shall get more intense beam than the previous ones. The peak current of a linear accelerator will reach up to some hundred milliamperes. In general, however, the energy spread of the output beam of a linear accelerator is unfavourably large. Especially, if the output energy is low, the energy spread of ready-made linear accelerators are larger than 10 percent. On the other hand, the tolerable energy spread of the electron beam which can be trapped into synchrotron orbit is less than 3%, so that the use of a linear accelerator becomes inefficient[3]. We reexamined the cause of the energy spread of the linear accelerator and carefully designed and constructed the accelerator as the injector for the synchrotron so as to have a good energy spectrum and stability. The spread of a few percent is aimed at the energy of 6 MeV and the beam current of 100–200 mA. Although the synchrotron has not yet been completed, the linear accelerator is operating very well and the performance is close to the designed values.

---

* Present Adress: Department of Physics, Faculty of Science, University of Tokyo, Tokyo, Japan.

§ 2. General Performance

The general performance of the linear accelerator is shown in Table I. The output energy of 6 MeV is sufficiently high in order to use the fixed frequency RF acceleration for the synchrotron, since the velocity of the electron reaches to 0.997c at this energy. For higher energy, we had a little difficulty to get the microwave power tube available in Japan, especially to keep its maintenance cost cheap. Also this energy is the most favourable to the injection problem from the linac to the synchrotron.

Table I.

Beam energy	6 MeV
Beam current	100 mA (peak)
Pulse repetition rate	21.5 pps
Beam pulse width	2μ second
Beam energy spread	$<5\%$
Beam diameter	<10 mm
Beam divergence	$\sim 10^{-3}$ radian
Total length on the machine	<5 m.

The repetition cycle of 21.5 c/s is that of the synchrotron magnet power supply. The pulse width of more than 1 μsec is enough to the injection time which is required from the synchrotron operation. The microwave frequency, 2759 Mc, was chosen arbitrarily, though some lower frequencies seemed to be more favourable. The block diagram is shown in Fig. 1. We shall discuss details of this diagram in the later section. The type of the accelerator is the $\pi/2$-mode travelling wave type such as that of the Mark III accelerator of Stanford[4], while the shunt impedance is somewhat lower. The microwave power is obtained from a pumped klystron amplifier with a maximum peak power of 5 MW. The total length of the accelerator is about 3 m.

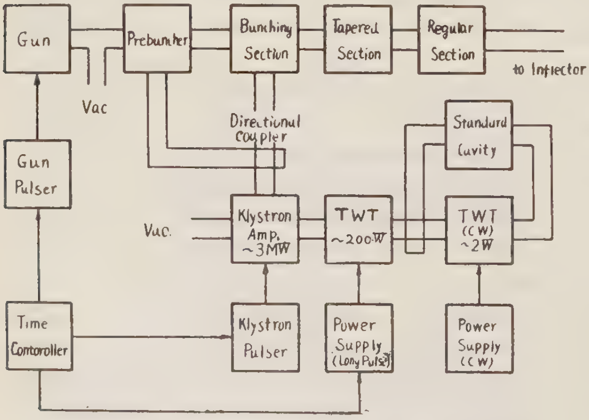

Fig. 1. Block diagram of the linear accelerator.

§ 3. Discussions on the Energy Spectrum

Two types of the causes for the energy spread are considered. The first is the fluctuations such as the instabilities of microwave frequencies and powers, or the thermal change of dimensions of the accelerator cavities. The second is the phase oscillation of electron beam which gives different average electric field during the transit through the accelerator for each electron injected in different phases. The second cause is more serious if we want to bunch the electron beam within a small phase angle in the earlier part of the accelerator so called the bunching section.

The energy spread of the output of the bunching section of Stanford Mark III accelerator was reported to be 2 MeV at the center value of about 5 MeV. For the low energy linac, the second effect becomes more important than the first one. So we shall discuss the second type of energy spread, at first.

a. *Energy spread due to different phase motions*

The electron on the phase angle, $\Delta(z)$, with respect to the point on the travelling wave $\pi/2$ ahead of the point of maximum acceleration, has the output energy, V, which is given by

$$V=\int_0^{z_0} eE(z)\sin\Delta(z)dz\,, \qquad (1)$$

where $E(z)$ is the maximum field strength, and z is the length along the accelerator axis. As is shown in Fig. 1, we shall divide the accelerator tube into three sections, that is, the regular section, the tapered section, and the bunching section. In the regular section we can use an accelerator tube, in which the phase velocity of the wave is matched with the light velocity, since the electron energy is sufficiently high in this section. The dimensions of each cavity in this section are same for all. Before being injected into this section, the electron beam is bunched so as to have a small phase spread, $\pm\delta\Delta$. Thus, if we write the center value of the phase angle of the electron bunch as Δ, we can assume that Δ is constant and $\delta\Delta$ is small enough in this section. The energy spread, δV, caused by the phase spread in this section will be written as,

$$\frac{\delta V_r}{V_r} \approx \frac{\sin\Delta_r - \sin(\Delta_r \pm \delta\Delta_r)}{\sin\Delta_r}, \qquad (2)$$

where the suffix r means the value of regular section. V_r is the energy gained by the electron in this section. Equation (2) has a minimum value when $\Delta_r = \pm(\pi/2)$: $\Delta_r = -(\pi/2)$ corresponds to the maximum acceleration. Near this position, we have

$$\frac{\delta V_r}{V_r} \approx (\delta\Delta_r)^2 . \qquad (3)$$

As is shown later, V_r is about 2 MeV, and we must take $\delta\Delta_r \approx 10°(\approx 1/6\,\mathrm{rad})$ in order to get the spread of total output energy less than 1%. This condition on the phase shift seems to be very serious, but is found to be necessary if we consider the accumulating effects discussed later.

Then, we shall consider the effects of the energy and phase spread in the input of the regular section to the output energy spread. To study these effects, we shall use the Hamiltonian which is given by Slater[5] for the description of the electron motion in a linear accelerator. The Hamiltonian function expressed by the axes moving with the velocity v_w of the travelling wave is given by

$$H/m_0c^2 = \frac{1-\beta_e\beta_w}{\sqrt{1-\beta_e^2}} - \frac{\alpha\beta_w}{2\pi}\cos\Delta , \qquad (4)$$

where the non-dimensional parameters, β_e, β_w and α are v_e/c, v_w/c and $eE\lambda_0/m_0c^2$, respectively.

Since this Hamiltonian function does not involve the time explicitly, it remains constant during the motion of an electron. If we write the value of the input and the output using the suffix 1 and 2, respectively, we have a relation

$$\sqrt{\frac{1-\beta_{e,r2}}{1+\beta_{e,r2}}} - \frac{\alpha_{r2}}{2\pi}\cos\Delta_{r2} = \sqrt{\frac{1-\beta_{e,r1}}{1+\beta_{e,r1}}} - \frac{\alpha_{r1}}{2\pi}\cos\Delta_{r1} , \qquad (5)$$

in the regular section, for which $\beta_w = 1$.

We can also safely assume that $\beta_{e,r1} \approx \beta_{e,r2} \approx 1$, in the regular section and that $\delta\Delta_{r1}$, $\delta\Delta_{r2} \ll 1$ where $\delta\Delta_{r1} = \Delta_{r1} + (\pi/2)$, i.e. $\delta\Delta_{r1}$ is the deviation of phase angle from $-\pi/2$. Then equation (5) becomes

$$\frac{1}{\gamma_{r1}} - \frac{1}{\gamma_{r2}} = \frac{1}{\pi}(\alpha_{r1}\delta\Delta_{r1} - \alpha_{r2}\delta\Delta_{r2}) , \qquad (6)$$

where $\gamma = 1/(\sqrt{1-\beta_e^2})$ is the nondimensional parameter corresponding to the total energy of the electron. Since the velocity of the electron is slightly smaller than the light velocity, $\delta\Delta_{r2}$ is smaller than $\delta\Delta_{r1}$ due to the phase slip.

If we write $\alpha_{r1} = \alpha_{r2} + \delta\alpha_r$ $(\delta\alpha_r > 0)$ taking into account the attenuation of the guide, we have

$$\frac{1}{\gamma_{r1}} - \frac{1}{\gamma_{r2}} = \frac{1}{\pi}[\alpha_{r1}(\delta\Delta_{r1} - \delta\Delta_{r2}) + \delta\alpha_r\delta\Delta_{r2}] , \qquad (6')$$

from equation (6). Using equation (3), the phase slip, $(\delta\Delta_{r1} - \delta\Delta_{r2})$ must be less than $2\delta\Delta_r$ and also $|\delta\Delta_{r2}| \leq \delta\Delta_r (\delta\Delta_{r2} \leq 0)$, so that we can obtain

$$\frac{1}{\gamma_{r1}} - \frac{1}{\gamma_{r2}} \lesssim \frac{1}{\pi}(\alpha_{r1} + \alpha_{r2})\delta\Delta_r . \qquad (7)$$

In our case, $\alpha_{r1} + \alpha_{r2} \approx 1$, $\delta\Delta_r = 1/6\,\mathrm{rad}$, and $\gamma_{r2} = 13$. Thus we have $\gamma_{r1} \gtrsim 8$, i.e. the injection energy into the regular section must be higher than 3.5 MeV to obtain a good energy spectrum. We had set it as 4 MeV.

In order to be bunched within a small phase spread, the electron injected in various phases must oscillate in several complete cycles in the low energy side of the accelerator. Ponce de Leon[6] discussed the bunching action in detail in the design study for the Stanford Mark IV accelerator. We also used the similar formula for the parameters α_b, Δ_b in the bunching section, like as

$$\alpha_b = 0.4 + 0.3\sin\frac{\pi}{2}\left(\frac{\xi - 4}{4}\right), \qquad (8a)$$

$$\Delta_b = -\frac{\pi}{6}\left[1 + \sin\frac{\pi}{2}\left(\frac{\xi - 4}{4}\right)\right], \qquad (8b)$$

where ξ is the distance from the input of the accelerator measured by the free space wave length, λ_0. Since electrons experience the considerably large defocusing force from the electro-magnetic wave in the bunching section and also the defocusing force is different for phase angles, it is somewhat difficult to focus the electron beam by a proper longitudinal magnetic field. This gives the upper limit for the length of bunching section, so that we take $0 \leq \xi \leq 8$. At the output of the bunching section, the energy of electrons will reach to about 1 MeV, and the phase to the microwave will be bunched within ±1/6 rad. After this section, electrons enter into the tapered section where $\alpha_t=0.7$ (const.) and $\varDelta_t=-\pi/3$ (const.). The dimensions of cavities in this section are tapered so as to match the wave velocity with the electron velocity. These values of α_t and $\varDelta_t$ can also be matched with the values of the regular section by a little phase shift at the output of the tapered section. The so-called buncher of our accelerator includes these two sections, the bunching section and the tapered section.

As discussed above, the Hamiltonian of an electron remains constant during the phase motion, unless there were non-adiabatic change in parameters. Thus, the area of a closed orbit in the phase space, which is written by an electron, remains also constant during its phase motion around the phase stable position. If we take the amplitude of phase and energy oscillation of an electron as $\delta\gamma$ and $\delta\varDelta$ as is given above, we have

$$\delta\gamma\delta\varDelta=\text{constant} \tag{9}$$

through the accelerator guide. At the input of the bunching section, we took the phase stable position $\varDelta_{b1}=0$ so as to give the desirable condition for the bunching action as was shown in equation (8b). Then, from equation (4), we can find the formula for $\delta\gamma_{b1}$ to be

$$\delta\gamma_{b1}\approx\frac{2\beta_{w,b1}}{\sqrt{1-\beta_{w,b1}^2}}\left[\frac{\alpha_{b1}\beta_{w,b1}}{\pi\sqrt{1-\beta_{w,b1}^2}}(1-\cos\delta\varDelta_{b1})\right]^{1/2}, \tag{10}$$

on the assumption that the electrons injected into the accelerator have the phase spread $\delta\varDelta_{b1}$ and just the energy matched with the wave velocity. $\delta\gamma_{b1}$ corresponds to the amplitude of the energy oscillation when the injected electron at $\delta\varDelta_{b1}$ started the phase oscillation. Taking $\alpha_{b1}=0.1$ corresponding to equation (8a) and $\beta_{w,b1}=\frac{1}{2}$ corresponding to the injection energy of 80 kV, $\delta\gamma_{b1}$ is given by

$$\delta\gamma_{b1}\approx0.15[1-\cos\delta\varDelta_{b1}]^{1/2}\,. \tag{10$'$}$$

Since there is no appreciable phase bunching action both in the tapered and regular sections, $\delta\gamma\cdot\delta\varDelta$ is less than $0.2\times(1/6)\approx0.03$, corresponding to the output energy spread of 100 keV. Thus, at the input of the bunching section the electrons only injected within the phase angle of $\pm\pi/6$ will satisfy the conditions for the output energy spread.

This is serious and is the reason that we use a prebuncher before the injection of the bunching section.

In the prebuncher, which is an ordinary velocity modulator of an electron beam, the electron beam suffers a non-adiabatic change of parameters, and can be bunched into a small angle without considerable changes in energy. A design study on the prebuncher was made[1], and it was found that about 2/3 of electrons injected having the uniform distributions for the phase angle can be bunched into the phase spread within $\pm\pi/6$. The energy change due to the phase prebunching is small enough, and found to be less than ±15 kV, so that the area is constant at the

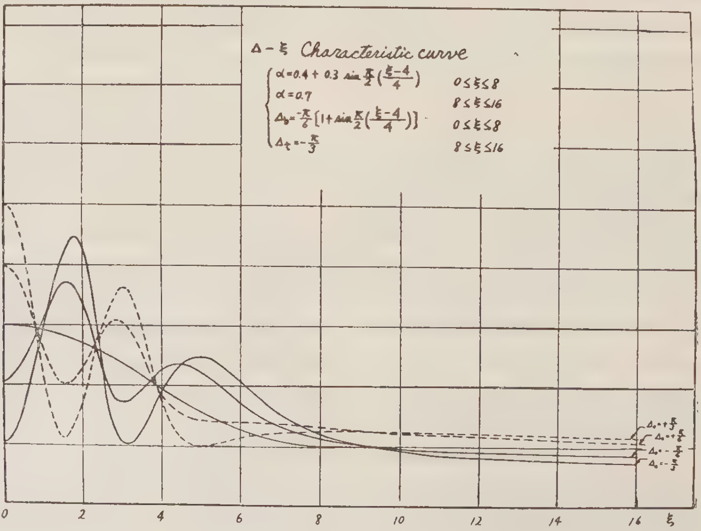

Fig. 2. $\varDelta-\xi$ characteristic curve for the buncher.

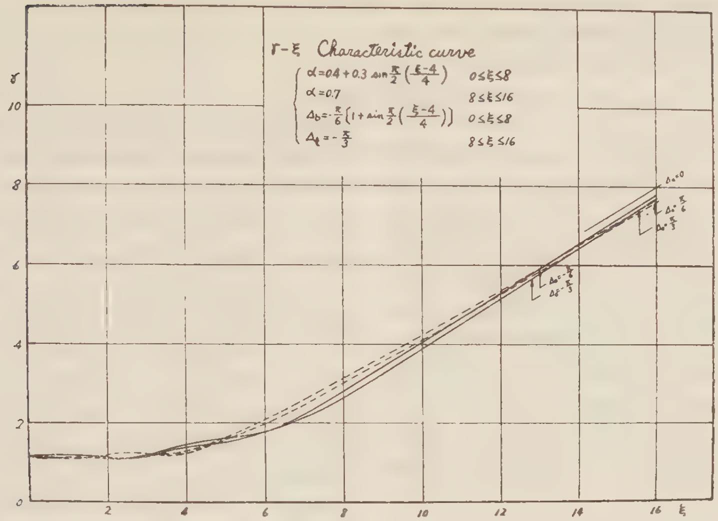

Fig. 3. $\gamma-\xi$ characteristic curve for the buncher.

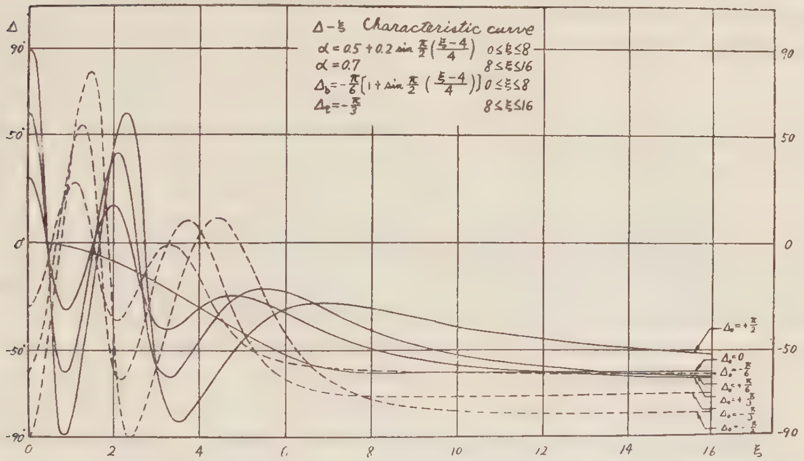

Fig. 4. $\Delta-\xi$ curve when the parameters were changed from the designed values.

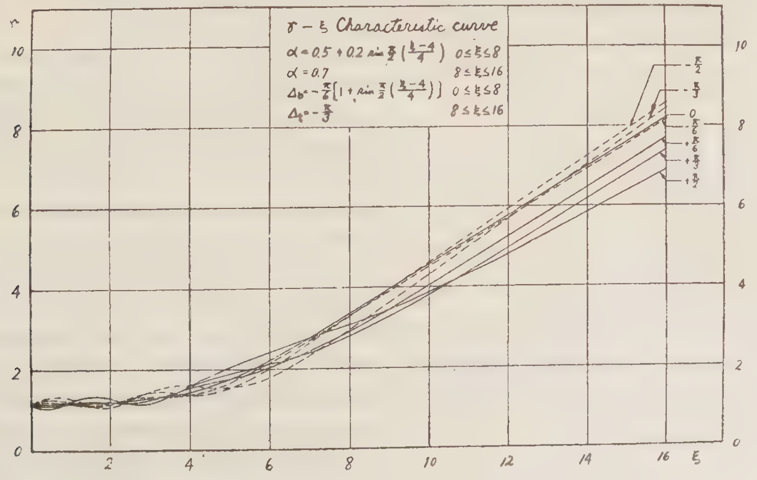

Fig. 5. $\gamma-\xi$ curve when the parameters were changed from the designed values.

output of the phase prebuncher, $\delta\gamma_{p2}\cdot\delta\Delta_{p2}$, is less than 0.03. The required power to the prebuncher is only 5–10 kW, which is fed from a directional coupler attached to the main waveguide.

We had checked the above considerations in the buncher including the tapered section using a digital computor of Yurin-Calculation Service Center, and the results are shown in Fig. 2 and Fig. 3. The calculated results show good characteristics of the bunching and tapered sections. This graph shows that, actually, the electrons having the phase spread of about 120°, which is twice the value discussed by the adiabatic theorem, may be used. Some modifications on parameters would destroy such good characteristics as shown in Figs 4 and 5.

b. *Energy spread due to variation of the microwave power and frequency*

The phase angle Δ, when $v_e \approx c$, can be written as

$$\Delta=\omega\left(t-\frac{z}{v_p}\right)\approx 2\pi\frac{z}{\lambda_0}\left(\frac{1}{\beta_e}-\frac{1}{\beta_w}\right)$$
$$=2\pi z\left(\frac{1}{\lambda_0\beta_e}-\frac{1}{\lambda_g}\right), \tag{11}$$

where λ_g is the wavelength in the accelerator guide. Thus the phase shift, $\delta\Delta_f$, due to the variation of wavelength, $\delta\lambda_0$, is given to be

$$\delta\Delta_f=2\pi z\left(\frac{\delta\lambda_g}{\lambda_g{}^2}-\frac{1}{\beta_w}\frac{\delta\lambda_0}{\lambda_0{}^2}\right)$$
$$=\frac{2\pi z}{\lambda_0}\left(\frac{c}{v_g}-\frac{1}{\beta_w}\right)\frac{\delta\lambda_0}{\lambda_0}. \tag{12}$$

In this expression, v_g is the group velocity along the accelerator guide and is equal to $d(1/\lambda_0)/d(1/\lambda_g)$. In our case, c/v_g is order of 10^2, whereas β_w is 0.5–1, so that $\delta\Delta_f$ can be approximated as,

$$\delta\Delta_f\approx\frac{2\pi z}{\lambda_0}\frac{c}{v_g}\frac{\delta\lambda_0}{\lambda_0}. \tag{13}$$

This equation becomes

$$\delta\Delta_f=Uz\frac{\delta f}{f}, \tag{14}$$

if the variation of $\delta\lambda_0/\lambda_0$ is replaced by the frequency variation $\delta f/f$, and $c/v_g\cdot 2\pi/\lambda_0$ by U. Using this formula we can calculate the energy spread in the regular and the tapered section; the results are

$$\left(\frac{\delta V_r}{V_r}\right)\approx\frac{1}{6}L_r{}^2U^2\left(\frac{\delta f}{f}\right)^2, \tag{14a}$$

and

$$\left(\frac{\delta V_t}{V_t}\right)\approx\frac{L_t}{2\sqrt{3}}U\left(\frac{\delta f}{f}\right), \tag{14b}$$

where L_r and L_t are the length of the regular section and the tapered section, respectively. In the above calculation, we assumed that the group velocity is constant through the guide and that the attenuation of the power is sufficeintly small. Taking $L_r=L_t=1$ m, $V_t=3$ MeV, δV_r, $\delta V_t=100$ keV and $V_g=0.017\,c$, we find that the frequency instability must be less than 1.5×10^{-4} in the regular section and 3×10^{-5} in the tapered section. In the bunching section. In the bunching section, the instability will not give any serious effect on the energy variation because of the phase stability. Thus the frequency allowance is the most serious in the tapered section and the fluctuation should be within ±50 kc.

Such frequency stability is achieved by the power system shown in Fig. 1. The main oscillator is the TWT feed back oscillator having the standard cavity made from invar. About two watts continuous output power is obtained from this oscillator, and amplified up to about two hundred watts by a pulsed travelling wave tube amplifier. Then the TWT amplifier is used as the driver of the pumped klystron amplifier, the peak power of which is about 3 MW.

This klystron amplifier is designed with an improvement on the vacuum pump and will be discussed in the second paper[7].

The change in the microwave power also affects the output energy of the electron beam. Since the field strength is proportional to the root of the power flow, it is necessary that the power level should be kept within the instabilities of 4% to keep the energy instabilities less than 2%. Since the klystron amplifier is used at nearly saturated driving power, the output power change is mainly caused by voltage variation of the pulsed power supply. The linear droop of beam voltage during the pulse is responsible to the energy spread as discussed by Stanford Mark III linac group[4]. The energy spread is given by $(5x/4)(t_p-t_F)$ percent from this effect, taking the linear droop x percent per μsec, the filling time t_F, and the duration of electron pulse t_p. Corresponding to the parameters $t_p=2$ μsec and $t_F=0.6$ μsec, the droop must be held $x=1$ percent/μsec in order to limit the spread to 2 percents or less. Also if we wish to keep the value of the maximum energy within the instability of 3 percents, variation in beam voltage between pulses must be less than 2.5 percents. We have established such stable pulsed power supply by some technical refinements on the usual line type pulser and the pulse transformer as discussed in the second article[7].

c. *Other effects*

The temperature variation will cause the change of resonant frequencies of the accelerator cavities which corresponds to the phase shift of electrons to the wave. This effect can be treated as well as the effect due to the frequency variations. By a reasonable estimation, we can find that the change of temperature by about 1°C will cause the output energy shift of about 2%. This effect, however, will not so much affect the energy spread, unless there were some short time fluctuations. Our accelerator has a temperature control system, which controls the temperature change in the accelerator guide within ±1°C, though we do not use it at the present stage.

Dimensional errors in accelerator cavities also cause the phase shift, and will destroy the designed characteristics of the accelerator guide. The phase shift due to dimensional errors, $\delta\Delta_m$, in an accelerator cavity is given by

$$\delta\Delta_m = \frac{\pi}{2}\beta_w \frac{c}{v_g}\left(\frac{\delta f_0}{f_0}\right), \tag{15}$$

where δf_0 is the error in the resonant frequency, f_0, of that cavity. If we take random dimensional errors in cavities, the overall phase shift of electrons will be given by $\sqrt{N}\delta\Delta_m$ after the transit through N cavities. It is desirable that the shift is less than 1/6 rad which is the value discussed in Sec. 3a. Since the total number of cavities is about 100, $\delta\Delta_m$ must be less than 1.5×10^{-2} rad. From equation (15), we can obtain the tolerance of the resonant frequency, $\delta f_0 \leq 200$ kc, for $v_g/c \approx 0.017$. In practice, the cavities were made so accurate that the corresponding errors in their resonant frequencies are less than ±100 kc as shown in the third paper[8].

Finally, the transverse beam spread may cause the spread in the output energy of electrons. Since the diameter of beam can be held as small as 1 cm by a longitudinal magnetic field, and since the wave-length is sufficiently large as 10 cm, this effect, which depends on the value of

$$J_0\left(j\frac{\sqrt{1-\beta_w^2}}{\beta_w}\frac{r}{\lambda_0}\right),$$

is negligibly small, except near the entrance of the bunching section.

§ 4. Determination of Cavity Dimensions

The principle to determine cavity dimensions in a travelling wave linear accelerator is as follows:

1) First, we settle the frequency of microwave which will be used.

2) Then, the distribution of the phase velocity of the wave along the accelerator guide is assumed.

3) Dimensions of cavities can be determined from the frequency and the phase velocity, if the wave mode of the guide is decided.

4) We can also estimate the attenuation constant along the guide, which determines the microwave power loss.

5) If the available microwave power and the desired beam intensity are fixed, we can calculate the field strength along the guide.

6) Immediately, the velocity change of electrons is determined from the field strength.

7) The velocity of electrons must be in accord with the phase velocity of the wave everywhere in the accelerator.

Actually, the calculations are made by means of successive approximations. In our design study, several methods published previously by the Stanford and A.E.R.E. groups[9] have been used to determine the field distribution and the phase velocity along the guide. The effect of beam loading is treated as well

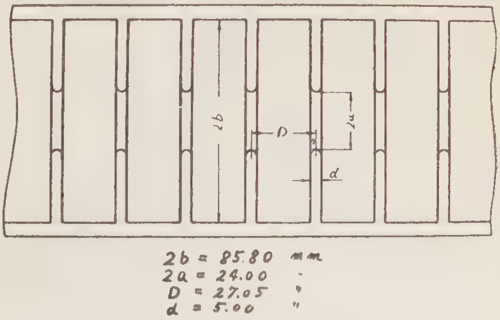

Fig. 6. Dimensions of the regular section.

as the methods worked by Saxon and by Neal[10]), with a little modification to the tapered section. The cavity dimensions in the regular section are shown in Fig. 6. Some curves which give the calculated values of the dimensions of cavities of the buncher varying with the normalized length, ξ, are shown in Fig. 7.

In order to calculate cavity dimensions, we used a modified method of Slater's four-terminal network theory[11]) on the periodically loaded waveguide. Our formula used is for $\pi/2$-mode,

$$\frac{\chi}{2}=\cot k(D-d)\,, \tag{16}$$

where

$$\frac{\chi}{2}=\frac{3}{2}\,\frac{\pi b^4}{a^3}\,k\left\{\frac{J_1(2.405)}{2.405}\right\}=0.1098\,\frac{b^4}{a^3}k\,, \tag{17a}$$

and

$$k^2=\frac{\omega^2}{c^2}-\left(\frac{2.405}{b}\right)^2. \tag{17b}$$

χ is the normalized susceptance of the disk loading in the cylindrical waveguide, and cal-

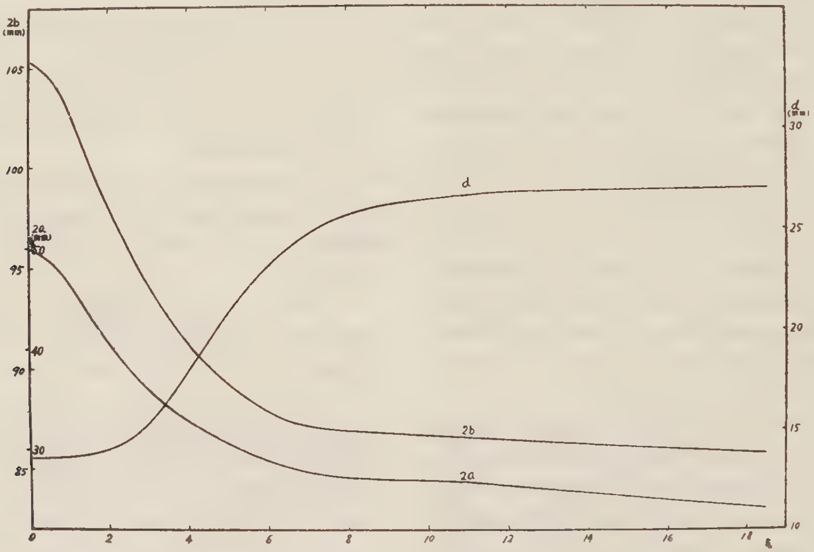

Fig. 7. Dimensions of the buncher.

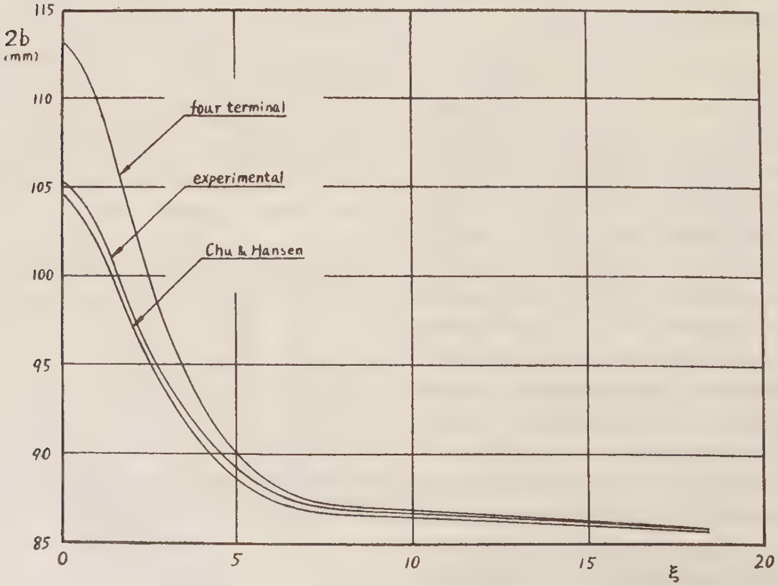

Fig. 8. Comparison between the calculated and experimental values of $2b$.

culated by a quasi-static field method. This formula is simpler than the others and has good accuracy which is enough to give the values of dimensions of the test cavities, by which the accurate dimensions are determined experimentally. The comparison between the calculated values and the experimental ones of $2b$ for the given values of $2a$, D, d and β_w, are shown in Fig. 8. This is obtained from a careful experiment of test cavities reported in a separate article[12]. The error in resonant frequency is less than one megacycle in the regular and tapered sections, while it becomes considerably large as several ten megacycles in the first cavity of the bunching section, in which the disk hole is too large and the disk spacing is too small for the approximation used. Actually, the resonant frequency considerably depends on the shape of the cross section of the disk, and was corrected to that of the standard one using a perturbing theorem.

It is the distinctive feature of this method that the equation (16) is convenient to estimate the changes of resonant frequency, δf_0, due to some dimensional changes. Such esti-

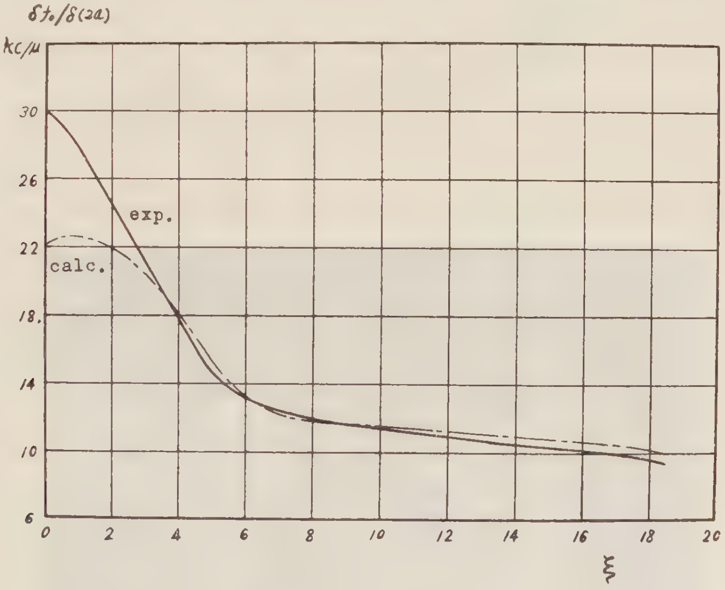

Fig. 9. Comparison between the calculated and experimental values of $\delta f_0/\delta(2a)$.

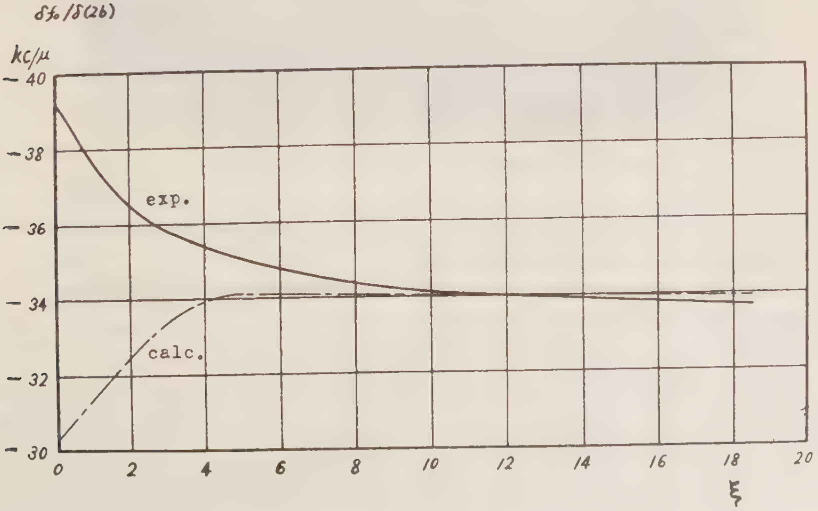

Fig. 10. Comparison between the calculated and experimental values of $\delta f_0/\delta(2b)$.

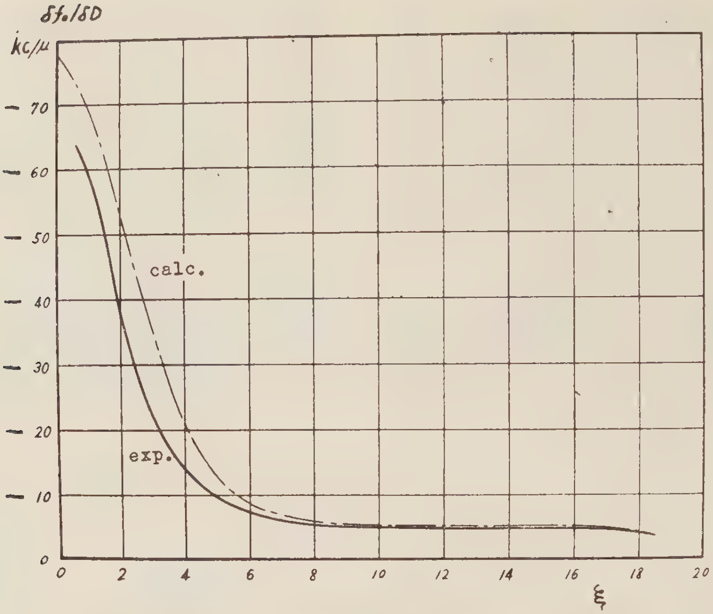

Fig. 11. Comparison between the calculated and experimental values of $\delta f_0/\delta D$.

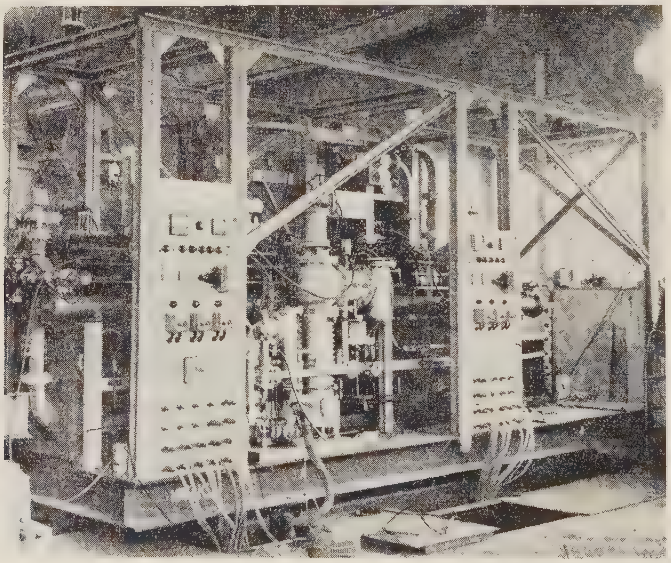

Fig. 12. Photograph of the linear accelerator.

mations are useful for the determination of the accurate dimensions by the experiment of test cavities, and also for the discussion on the effect of the phase shift due to the temperature variations and machining errors, discussed in Sec. 3c. Figs. 9, 10 and 11 give the comparison between the calculated values (dotted lines) and the experimental ones (real lines). The agreement is fairly good, although the calculated curve of $\delta f_0/\delta(2b)$ differs from the experimental results in the neighbourhood of the entrance of the buncher.

§ 5. Results and Discussions

The picture of the linear accelerator is given in Fig. 12.

The accelerator was constructed carefully so as to accord with the designed features, and found to operate meeting with the expectation. The energy spectrum was obtained by a spectrometer using an analyzing magnet. An observed spectrum is shown in Fig. 13, which shows the total spread of about three percents at 6.5 MeV. When we did not use the prebuncher, the spread increased to about 5 percents. It was found that the shape of the spectrum depends on the microwave power and the beam loading, the cause of which seemed to be due to the improper field distributions to match the electron velocity with the wave velocity. This effect would probably become important in the tapered section. The detailed characteristics are now being studied.

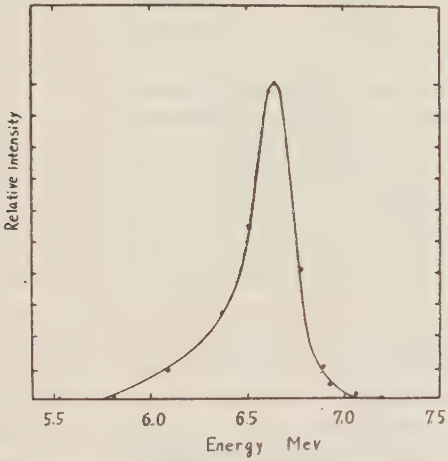

Fig. 13. An observed energy spectrum.

The details of the practical construction will be reported in the following articles.

Acknowledgement

The authors wish to express their hearty thanks to the synchrotron group of the Institute for Nuclear Study of the University of Tokyo for their useful discussions. The contribution of Dr. Y. Kobayashi and Mr. R. Yamada in measuring the characteristic performance of the accelerator is also appreciated.

References

1) T. Nishikawa, A. Miyahara and J. Tanaka: INS-TH-28 (1957) (Japanese).
2) T. Nishikawa, A. Miyahara and J. Tanaka: INS-J-18 (1959).
3) Y. Kobayashi: Private Communication.
4) M. Chodorow et al.: Rev. Sci. Inst. **26** (1955) 134.
5) J. C. Slater: Rev. Mod. Phys. **20** (1948) 473.
6) J. M. Ponce de Leon: Rep. No. 265, Microwave Lab., Stanford Univ. (1955).
7) A. Miyahara: J. Phys. Soc. Japan. (to be published)
T. Nishikawa, H. Kumagai, A. Miyahara, J. Tanaka, K. Ishii and I. Ito: INS-R-28 (1961).
8) J. Tanaka: J. Phy. Soc. Japan. (to be published)
9) E. L. Chu and W. W. Hansen: J. App. Phys. **18** (1947) 996, **20** (1949) 280; W. Walkinshaw: Proc. Phys. Soc. **61** (1948) 246.
10) G. Saxon: Proc. Phys. Soc. B **67** (1954) 705.
11) J. C. Slater: "Microwave Electronics" McGraw-Hill (1950).
12) J. Tanaka, T. Nishikawa, A. Miyahara and K. Kobayashi: INS-TH-38 (Japanese).

JOURNAL OF THE PHYSICAL SOCIETY OF JAPAN Vol. 16, No. 10, OCTOBER, 1961

" Gamma Rays from the Proton Bombardment of Sulphur and the O$^+$ Second Excited State of ^{32}S "

By Yasuo HIRAO

Department of Physics and the Laboratory of Nuclear Studies,
Faculty of Science, Osaka University, Osaka

(Received April 19, 1961)

The analysis of gamma rays from natural sulphur, separated sulphur-32 and sulphur-34 bombarded by protons up to 5.7 MeV was carried out.

Excitation function of the 2.24 MeV gamma ray due to the transition (1st-ground state of ^{32}S) was measured. Resonances were found at Ep=4.77, 5.10, 5.35 and 5.60 MeV, which correspond to the excitation energies of 6.93, 7.24, 7.48 and 7.71 MeV of ^{33}Cl, respectively.

Gamma rays were observed with a single and three crystal spectrometers. In addition, using gamma-gamma cascade coincidence and sum coincidence methods, energies and decay scheme were determined as follows:

^{32}S: 0.92 MeV (5th-2nd), 1.20 (6th-2nd), 1.54 (2nd-1st), 2.23 (3rd-1st), 2.24 (1st-ground) and ~4.3 (3rd or 4th-ground).

^{34}S: 0.97 (7td-3rd), 1.17 (2nd-1st), 2.13 (1st-ground), 3.30 (2nd-ground), 3.91 (3rd-ground) and 4.11 (5th-ground).

The 3.78 MeV gamma ray due to the transition (2nd-ground of ^{32}S) was not found.

The angular correlation between the cascade gamma rays of 1.54 and 2.24 MeV shows good agreement with the transition of O$^+$(E2)2$^+$(E2)$^+$. Then the 2nd state of ^{32}S at 3.78 MeV has a spin of O$^+$. This assignment agrees with the calculation of the j-j coupling shell model.

With a three crystal spectrometer, nuclear pair from the 2nd state of ^{32}S at 3.78 MeV was searched. The intensity of the nuclear pair was about 2% or less of the 1.54 MeV gamma ray.

The configurations of this O$^+$ second state and the ground state of ^{31}P are also discussed.

§ 1. Introduction

The analyses of gamma ray spectra from excited states of various nuclei have brought valuable informations on the properties of nuclei. So far detailed investigations have been carried out for the gamma ray transitions from various nuclear excited states following the decays of radioactive nuclides and from excited states formed by proton or neutron capture. As compared with the amount of these investigations, gamma rays from the excited states formed by inelastic scattering have been studied only for a few elements in spite of many advantages such as; that the method can be applied to most of the nuclei, that the cross section is relatively large, and that it is especially suitable for studying low-lying states. For the last four years we have investigated the gamma rays due to inelastic scattering of protons up to 5.7 MeV[1] and of 10 and 14 MeV[2] for several elements. In this paper also, the analysis of gamma rays from natural sulphur, separated sulphur-32 and sulphur-34 bombarded by protons up to 5.7 MeV will be reported.

^{32}S:

Natural abundances of sulphur isotopes are 95.018, 0.750, and 4.215% for ^{32}S, ^{33}S, and ^{34}S, respectively. Several investigators have reported the measurements on the excitation energies of the low-lying states of ^{32}S. By a magnetic analysis of ^{35}Cl$(p, \alpha)^{32}$S reaction[3], levels were found at 2.237±0.008, 3.780±0.008, and 4.287±0.008 MeV, 4.465±0.10, and 4.698±0.10 MeV.

From the measurement of neutron angular distributions in ^{31}P$(d, n)^{32}$S reaction[4], 1_p's were assigned as 0 for the transitions to the ground and the 2nd states, and as 1 for the transition to the 1st state. Since the ground state of ^{31}P have been known to have a spin of 1/2 and even parity, the value of $1_p=0$ for the transition to the ground state of ^{32}S indicates that it has even parity and a spin of 0 or 1. This is in agreement with the fact that the spin of all even-even nuclei is 0.

In the case of the transition to the 1st state, the value of $l_p=2$ indicates that it has even parity and spin 1, 2, or 3. Considering the results of the reaction ^{32}S(e, e')[5] and the reaction ^{31}P$(p, \gamma)^{32}$S[6], the spin and parity of this state has been assigned to be 2^+. It is consistent with the general tendency for light even-even nuclei that the 1st state possesses the spin and parity of 2^+.

The value of $l_p=0$ for the transition to the 2nd state at 3.78 MeV indicates that this state has even parity and spin 0 or 1. On the other hand, there are several reports that the 3.8 MeV gamma rays were observed in the reactions ^{31}P$(p, \gamma)^{32}$S[7] and ^{32}Cl$(\beta^+)^{32}$S$^*(\gamma)$[8],[9]. The authors of these papers concluded that these gamma rays were due to the direct transition from the second state to the ground state. It follows that the assignment of spin 0 to this state is excluded. Considering these results, it has been hitherto assigned to be 1^+. It is worthy of attention that the 2nd state has a spin of 1 and even parity. Several authors[10],[11] have discussed the configurations of these states and the ground state of ^{31}P on the basis of the shell model. They pointed out the difficulty of any interpretation for the 1^+ state at such low energy as will be discussed in §4. It seems that experimentally these is no doubt that $l_p=0$ is the correct assignment. We suspect, however, that the gamma ray of 3.8 MeV is not due to the transition from the 2nd state, but due to the transition between higher states of ^{32}S. From these reasons it is of interest to find out the branching ratio of the gamma rays from this state to the ground and the 1st states, using the reaction ^{32}S$(p, p'\gamma)$, which leads to only several low-lying excited states. In addition it is also of interest to measure the cascade gamma-gamma angular correlation if these gamma rays could be found.

^{34}S:

By a magnetic analysis of the ^{37}Cl$(p, \alpha)^{34}$S at $E_p=7.0$ MeV, levels were found at 2.127, 3.302, 3.915, 4.073, 4.114, 4.621, 4.685 and 4.876 MeV, all ±0.008 MeV[3].

The spin and parity of the 1st state at 2.127 MeV is found to be 2^+ from the allowed characters of β^- decay of ^{34}P$(J=1^+)$ to the ground and the 1st states of ^{34}S[12] and of β^+ decay of ^{34}Cl$^m(J=3^+)$ to the 1st state of ^{34}S[13].

The spin and parity of the 2nd state of ^{34}S is also found to be 2^+ from gamma-gamma angular correlation[14]. This assignment is consistent with the β^+ decay of ^{34}Cl^m[13].

From the decays of ^{34}P and ^{34}Cl^m, about 4 MeV gamma rays were also observed[15],[16]. If these gamma ray energies are accurately equal, this gamma emitting state of ^{34}S should also have 2^+ for the same reason as in the 1st state of ^{34}S.

§ 2. Experimental Methods

Molecular ion beam of hydrogen accelerated by Osaka University 44 inch cyclotron was used. The energy of the proton was estimated to be 5.7 MeV ±0.1 MeV, and it was degraded at 100 keV intervals by aluminum absorbers in order to measure the excitation curve. The beam defining slit was made of a gold plate with a circular hole one mm in diameter The proton beam current was about one mμa for the gamma-gamma coincidence experiments, and was about ten mμa for the other experiments. The targets were prepared by painting BaSO$_4$ powder onto thick gold plates. Most of the measurements were made with a natural sulphur target, but a few were made

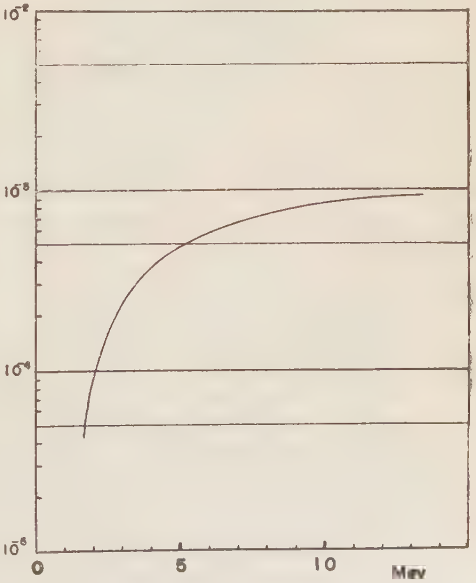

Fig. 1. The energy-efficiency curve of the three crystal pair spectrometer, as shown in Fig. 2, for gamma rays incident to the front surface of the centre crystal.

with separated ^{32}S and ^{34}S. The target of ^{34}S was a thin Pb_2S layer spattered on a thick gold backing.

We used a NaI(Tl) scintillator, 3-inch diameter by 3-inch long, for the measurements of gamma ray spectra and the excitation curve. We also used a three crystal scintillation spectrometer[17]. The energy-efficiency curve of this spectrometer was calculated and is shown in Fig. 1. This spectrometer have a NaI(Tl) scintillator 1½ inch diameter by 4-inch long as a center crystal and two NaI(Tl) scintillators, 3-inch diameter by 3-inch long, as side crystals. For the measurements of gamma-gamma coincidence spectra, sum coincidence spectra, and gamma-gamma angular correlations, two NaI(Tl) scintillators, 3-inch diameter by 3-inch long were used, and sometimes a scintillator, 5-inch diameter by 4-inch long, was used. For the nuclear pair detection, we used another spectrometer, which was a sort of three crystal pair spectrometer, having a well-type plastic scintillator, 1½-inch diameter by 2-inch long, as the centre detecter. All the spectra were analyzed by a 20 channel and a 30 channel pulse height analyzer, having a dead time of about 2.5 μsec. The coincidence method is a so-called "fast-slow" method. The resolving the of fast coincidence is about 5×10^{-8} sec using a diode bridge coincidence circuit[18]. This resolving time was chosen according to the frequency of the cyclotron. The block diagram of the coincidence experiments is shown in Fig. 3.

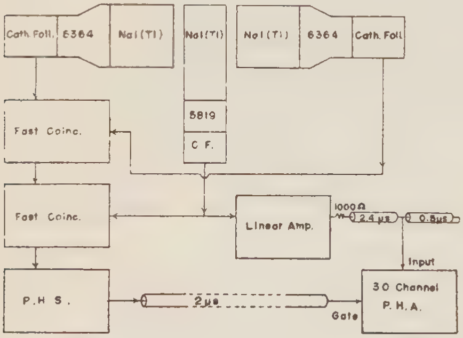

Fig. 2. Block diagram of the three crystal pair spectrometer.

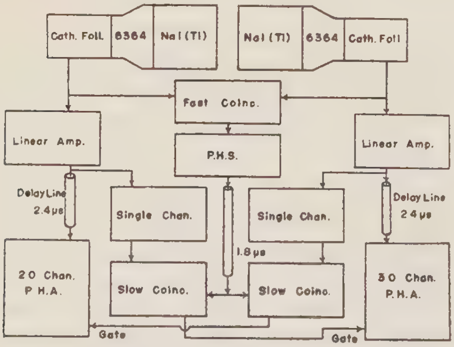

Fig. 3. Blook diagram of the coincidence experiment.

§ 3. Experimental Results

Excitation Function of 2.24 MeV Gamma Ray:

The intensity of the most intense gamma ray of 2.24 MeV, which is almost due to the transition from the 1st to the ground state of ^{32}S, was measured as the function of incident proton energy, using a NaI(Tl) scintillator, 3-inch diameter by 3-inch long. The result is shown in Fig. 4. The Q-value of $^{32}S+p$ reaction is 2.285 MeV. So far several resonances have been found at $E_p=0.59$, 1.90, 2.30, 2.81, 2.90, 2.92, 3.09, 3.19, 3.38 and 3.72 MeV[19]. In the present experiment, resonances have been found at $E_p=4.77$ and 5.10 MeV. These correspond to the excitation energies of 6.93 and 7.24 MeV of ^{33}Cl, respectively. At $E_p=5.35$ and 5.60 MeV also, broad resonances were found, which corresponded to 7.48 and 7.71 MeV of ^{33}Cl, respectively. The result is

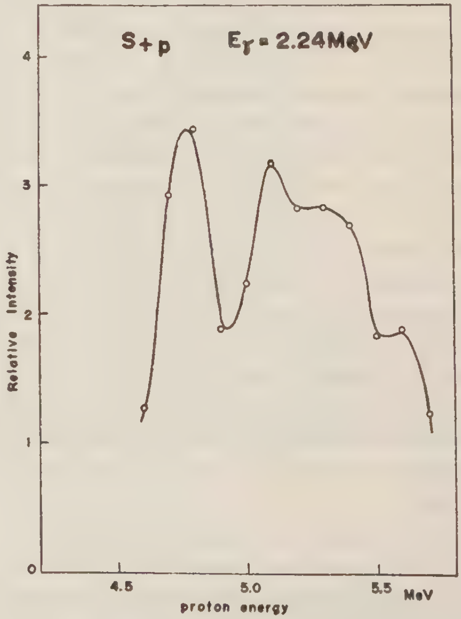

Fig. 4. Excitation function of 2.24 MeV gamma ray, observed with a NaI(Tl) scintillator, 3-inch diameter by 3-inch long, at right angles to the incident proton beam direction.

Table I. Resonances in the excitation function of the 2.24 MeV gamma ray and the corresponding level energies in ^{33}Cl.

Proton energies at resonances	Corresponding level energies in ^{33}Cl
4.77 MeV	6.93 MeV
5.10 〃	7.24 〃
~5.35 〃	~7.48 〃
~5.60 〃	~7.71 〃

tabulated in Table I.

Table II. Gamma ray energies, possible origins and relative intensities of the three crystal pair spectrum at 5.7 MeV of incident proton energy, at 90° to the proton beam direction. Relative intensities were corrected using the energy-efficiency curve in Fig. 1.

γ ray energies	Possible origins	Relative intensities
1.17 MeV	2nd-1st of ^{34}S 6th-2nd of ^{32}S	$\gtrsim 40$
1.54 〃	2nd-1st of ^{32}S (7th-2nd of ^{34}S)	10^2
2.24 〃	1st-ground of ^{32}S 4th-1st of ^{32}S 1st-ground of ^{34}S	10^3
3.30 〃	2nd-ground of ^{34}S	7
(3.85 〃)	(2nd-ground of ^{32}S) (3rd-ground of ^{34}S)	$\lesssim 2$
4.4 〃	3rd-ground of ^{32}S 4th-ground of ^{32}S	~ 7

Gamma Ray Spectra:

Fig. 5 and Fig. 6 show the gamma ray pulse height distributions from the single NaI(Tl) scintillation spectrometer, 3-inch diameter by 3-inch long, and the three crystal scintillation pair spectrometer, respectively, at right angles to the incident proton direction. Natural sulphur compound was used as a target. These spectra were measured at the incident proton energy of 5.7 MeV. Arrows in Fig. 5 and Fig. 6 indicate the positions of the gamma ray energies expected from the well established level energies. These show good agreements with the peak positions of the spectra. The possible origins and the relative intensities of the gamma rays in Fig. 5 are tabulated in Table II. These values have been corrected by the energy-efficiency curve of Fig. 1. The efficiency at about 1.2 MeV is too low to

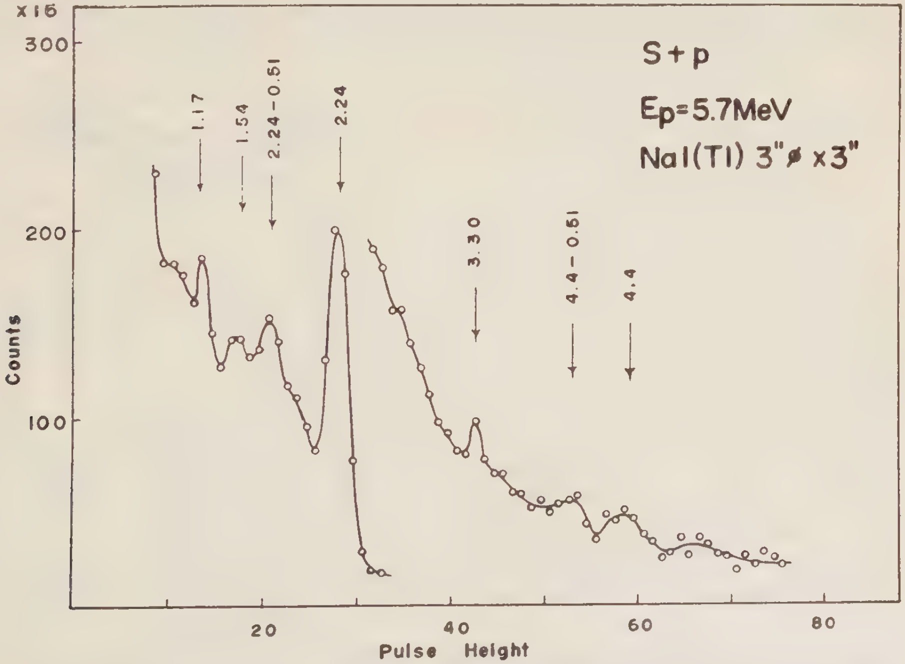

Fig. 5. Gamma ray pulse height distribution from the single NaI(Tl) scintillation spectrometer, 3-inch diameter by 3-inch long, at right angles to the proton beam direction. Target was made with natural sulphur compound, $BaSO_4$, and incident proton energy was 5.7 MeV. Arrows in Figs. 5, 6, etc. indicate the positions of the gamma ray energies expected from the well established level energies.

estimate the relative intensity of the 1.2 MeV gamma ray. As tabulated in Table 2, previously reported gamma rays, 1.17 (2nd-1st of ^{34}S), 2.24 (1st-ground of ^{32}S) and 3.30 MeV (2nd-ground of ^{34}S), were found and 2.13 MeV gamma ray (1st-ground of ^{34}S) was comprised in the peak of the intense 2.24 MeV gamma ray (1st-ground of ^{32}S). The intensity ratio

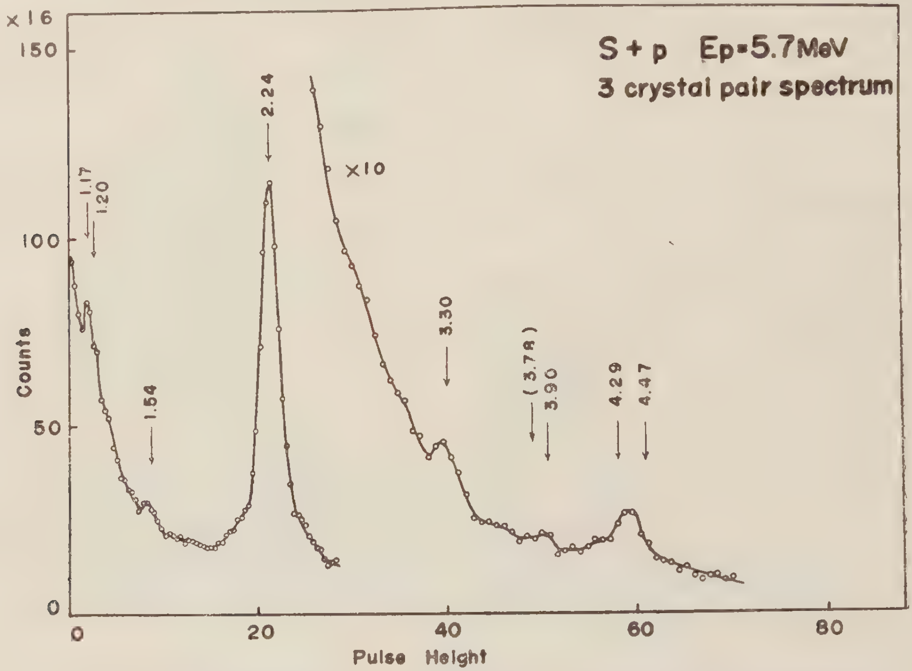

Fig. 6. Three crystal pair spectrum at proton energy of 5.7 MeV and right angles to the proton beam direction. Natural sulphur compound, BaSO$_4$, was used as a target.

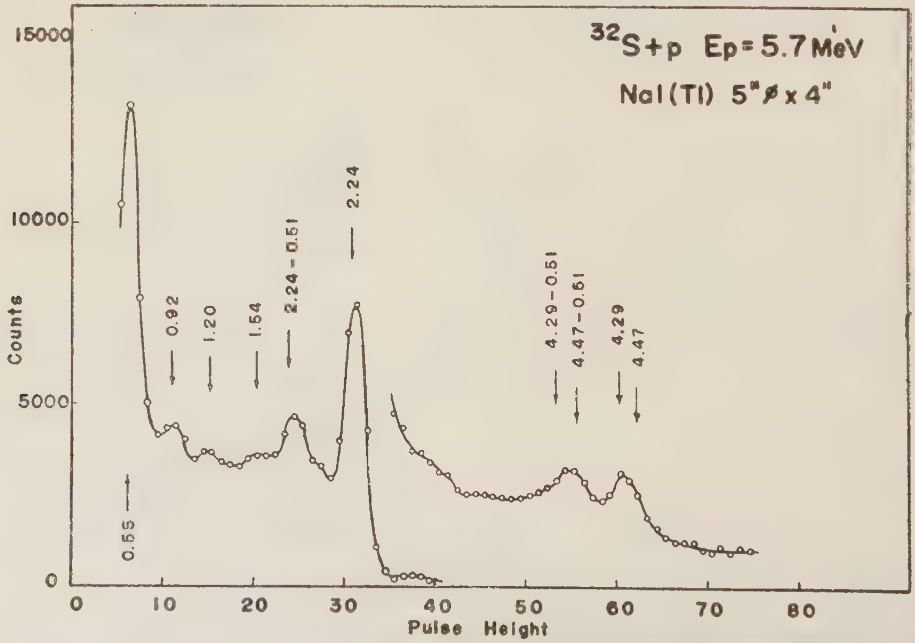

Fig. 7. Gamma ray spectrum from proton bombardment of the target of separated sulphur-32 compound, BaSO$_4$, at incident proton energy of 5.7 MeV, using a NaI(Tl) scintillation spectrometer, 5-inch diameter by 4-inch long.

of the 1.17 Mev to the 3.30 MeV gamma rays was found to be $\gtrsim 40/7$, while the ratio previously reported is 73/27[14]. This discrepancy indicates that the peak at 1.17 MeV may comprise 1.20 MeV gamma ray (6th-2nd of ^{32}S). The gamma ray of 1.54 MeV was newly found and may be due to the transition (2nd-1st of ^{32}S) while the gamma ray of 3.78 MeV (2nd-ground of ^{32}S) was not found, which was reported by other authors[7],[8],[9] as was mentioned in § 1. This fact brings forward once more the problem whether the spin of the 2nd state is 1 or 0. Very weak gamma ray at about 3.9 MeV may be due to the transition (3rd-ground of ^{34}S), although it is scarcely noticeable. The peak at about 4.3 MeV is, perhaps, of the gamma ray transition (3rd-ground of ^{32}S) and (4th-ground of ^{32}S) in part.

Next the gamma ray spectrum from proton bombardment of separated ^{32}S target, at $E_p = 5.7$ MeV, was observed. The result is shown in Fig. 7 and Table III. Observed peaks are well explained with the energies expected from ^{32}S. However, as the abundance of ^{34}S in this separated target as an impurity is not accurately known, the spectrum may comprise the gamma rays from the excited states of ^{34}S in part. An intense peak at 0.55 MeV is due to coulomb excitation of Au target backing. 0.92 MeV gamma ray may be due to the transition (5th-2nd of ^{32}S). The other higher energy peaks are of the same gamma rays as of Figs. 5 and 6. 3.3 MeV gamma ray (2nd-ground of ^{34}S) vanishes, while 1.2 MeV gamma ray still remained. This result supports the above consideration that this gamma ray is due to the transition (6th-2nd of ^{32}S).

Table III. Gamma ray energies, possible origins and relative intensities of the single spectrum from separated sulphur-32 target using a NaI(Tl) scintillator, 5-inch diameter by 4-inch long, at 5.7 MeV of incident proton energy, at right angles to the incident proton direction. Relative intensities were corrected for the efficiencies of the spectrometer.

γ ray energies	Possible origins	Relative intensities
0.55 MeV	Au	—
0.92 〃	5th-2nd of ^{32}S	10
1.20 〃	6th-2nd 〃	40
1.54 〃	2nd-1st 〃	10^2
2.24 〃	1s-ground 〃 4th-1st 〃	10^3
4.29 〃 (4.47)	3rd-ground 〃 (4th-ground 〃)	~20

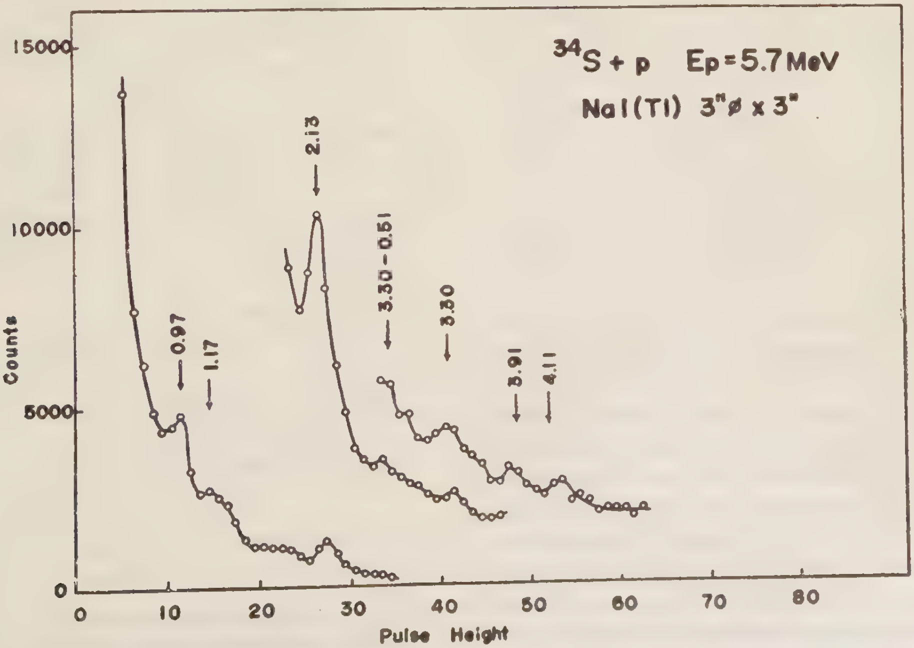

Fig. 8. Gamma ray spectrum from proton bombardment of the target of separated sulphur-34 compound, Pb_2S, at incident proton energy of 5.7 MeV, using a NaI(Tl) scintillation spectrometer, 3-inch diameter by 3-inch long.

Next the gamma ray spectrum from proton bombardment of separated ^{34}S target, at E_p= 5.7 MeV, was observed. The result is shown in Fig. 8 and Table IV. Observed peaks can also be explained with the energies expected from the well established levels of ^{34}S. The peak at about 1 MeV may be due to the transition (7th-3rd of ^{34}S). The peaks at 1.17, 2.13 and 3.30 MeV correspond to the previously reported gamma ray transition (2nd-1st of ^{34}S), (1st-ground of ^{34}S) and (2nd-ground of ^{34}S) respectively. The peaks at 3.9 MeV and at 4.1 MeV are due to the transitions (3rd-ground of ^{34}S) and (5th-ground of ^{34}S), respectively. These gamma rays may be the same as previouly observed in the decays of ^{34}Cl^m(β^+) ^{34}S*(γ) and ^{34}P(β) ^{34}S*(γ). One cannot find gamma ray at about 1.5 MeV, and this fact indicates that the 1.54 MeV gamma ray, described above, is not of ^{34}S, but of ^{32}S.

Table IV. Gamma ray energies, possible origins and relative intensities of the single spectrum from separated sulphur-34 target, using a NaI(Tl) scintillator, 3-inch diameter by 3-inch long, at 5.7 MeV of incident proton energy, at right angles to the incident proton direction. Relative intensities were corrected for the efficiency of the spectrometer.

γ ray energies	Possible origins	Relative intensities
0.97 MeV	7th-3rd of ^{34}S	≲10
1.17 〃	2nd-1st 〃	≲15
2.13 〃	1st-ground 〃	40
(2.75) 〃	(7th-1st 〃)	—
3.30 〃	2nd-ground 〃	7
3.91 〃	3rd-ground 〃	5
4.11 〃	5th-ground 〃	10

Coincidence Spectra:

Next, we observed the coincidence spectra gated by the 2.24 MeV gamma ray at several bombarding energies, using natural sulphur target as shown in Fig. 9. The energies and the relative intensities of these gamma ray at 5.7 MeV incident proton energy were tabulated in Table V. The incident beam current was chosen to be small so that the accidental coincidence counts would be negligible. In order to establish the decay scheme of these gamma rays, the incident proton energy was degraded with aluminum absorbers wtih 100 keV intervals. As shown in Fig. 8, the intensities of each coincidence gamma rays became smaller with the degradations of proton energy, while the excitation curve of 2.24 MeV gamma ray observed with the single NaI(Tl) scintillator had a peak at 5.1 MeV and then the intensity of the 2.24 MeV gamma ray was rather higher at lower incident proton energies as was shown in Fig. 4. From these facts it is concluded that the 2.2 MeV gamma

Table V. Coincidence gamma rays gated between 2.00–2.35 MeV were listed at proton energy of 5.7 MeV. Natural sulphur target and two NaI(Tl) scintillators, 3-inch diameter by 3-inch long, were used. Relative intensities were corrected for the efficiency of the spectrometer.

γ ray energies	Possible origins	Relative intensities
0.96 MeV	(5th-2nd of ^{32}S) (7th-3rd of ^{34}S)	5
1.19 〃	2nd-1st of ^{34}S (6th-2nd of ^{32}S)	22
1.54 〃	2nd-1st of ^{32}S (7th-2nd of ^{34}S)	60
2.23 〃	4th-1st of ^{32}S	23

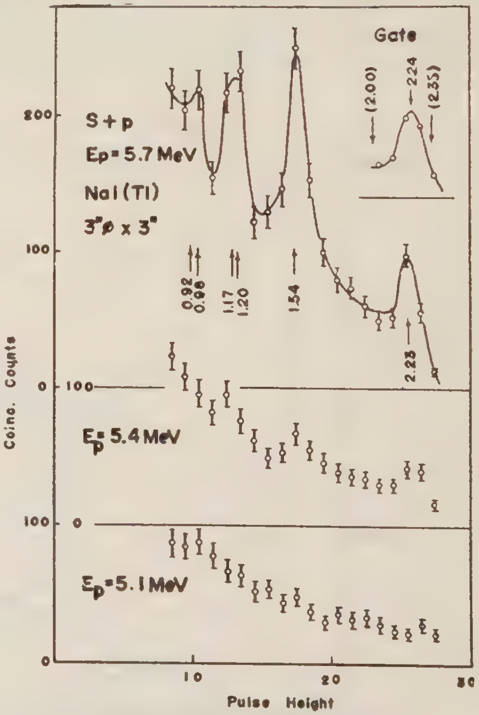

Fig. 9. Coincidence spectra gated by the gamma rays of 2.00–2.35 MeV, using two NaI(Tl) scintillators, 3-inch diameter by 3-inch long, at proton energies of 5.7, 5.4 and 5.1 MeV. Target was a natural sulphur compound, BaSO$_4$.

ray coincident with 2.24 MeV gamma ray is hardly due to accidental coincidence but the true cascade gamma ray of the transition (4th-1st of ^{32}S). These results confirm at the same time that the 1.54 MeV gamma ray is due to the cascade transition (2nd-1st of ^{32}S) and accidental counts are negligible. The gamma ray of about 1.2 MeV is almost due to the transition (2nd-1st of ^{34}S), but a part of it may be due to the transition (6th-2nd of ^{32}S), in comparison with the coincidence spectra of separated ^{32}S target, as will be described later. The gamma ray of about 0.9 MeV energy is perhaps due to the transition (5th-2nd of ^{32}S). All of these coincidence gamma rays are consistent with the single spectra and three crystal pair spectrum as were described already.

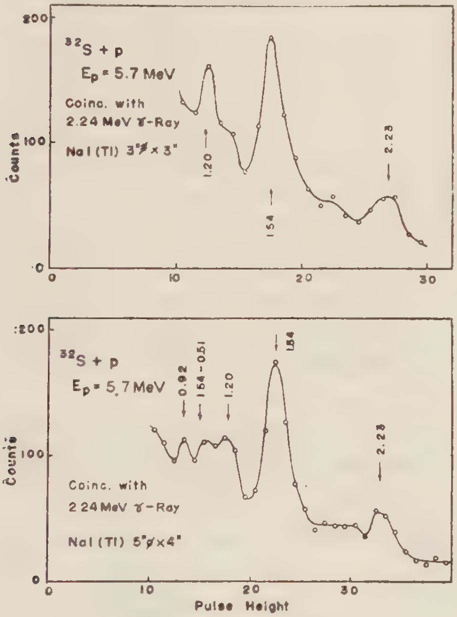

Fig. 10. Coincidence spectra gated by the gamma rays of 2.00-2.35 MeV, using two NaI(Tl) scintillators, 3-inch diameter by 3-inch long and 5-inch diameter by 4-inch long, at proton energy of 5.7 MeV. Target was a separated sulphur-32 compound, $BaSO_4$.

Table VI. Coincidence gamma rays gated between 2.00-2.35 MeV were listed at proton energy of 5.7 MeV. Separated sulphur-32 target and two NaI(Tl) scintillators, 3-inch diameter by 3-inch long and 5-inch diameter by 4-inch long, were used. Relative intensities were corrected for the efficiency of the spectrometer.

γ ray energies	Possible origins	Relative intensities
0.92 MeV	5th-2nd of ^{32}S	4
1.20 〃	6th-2nd 〃	18
1.54 〃	2nd-1st 〃	60
2.23 〃	4th-1st 〃	20

Cascade coincidence spectra were also observed using separated ^{32}S target. Results are shown in Fig. 10, and are tabulated in Table VI. These results also show that these coincidence gamma rays are almost due to the cascade transitions of ^{32}S.

Sum Coincidence Spectra:

Next we observed a sum coincidence spectrum(20) of the 2.24 MeV and 1.54 MeV gamma rays, in order to confirm the decay of the second state at 3.78 MeV of ^{32}S. The gate of the sum coincidence was set at 3.78 MeV. Geometrical and circuit arrangement for this experiment are the same as in the cascade coincidence experiment with the exception of interposition of a summing network of two output pulses from two detectors just before the gating single-channel pulse-height analyzer. The result is shown in Fig. 11. This spectrum shows a typical shape of simple cascade decay. In this case, also, the accidental coindence counts were negligible, considering the single counting rate of the 2.24 MeV gamma ray from each detector. In a sum coincidence measurement, one most take care to avoid a false peak caused by any inadequate gate setting, in which case the spectrum is not symmetric about the mean energy of two cascade gamma rays. The result of sum coincidence measurement, as shown in Fig. 11, supports the result of cascade coincidence that the 1.54 MeV gamma ray and the 2.24 MeV gamma ray are emitted in cascade and the former may be due to the transition from the 2nd state at 3.78 MeV to the 1st state at 2.24 MeV of ^{32}S. From the consideration of the detection efficiencies of these experiments, it is concluded that the 2nd state decays in cascade and branching ratio of the direct transition to the cascade transition is less than 5%. The 1^+ assignment for the 2nd state becomes, therefore, not exclusive. Then, in order to determine the spin of this state, we have measured the gamma-gamma angular correlations of the cascade gamma rays from this state. If this state has spin 0, the direct gamma ray transition to the ground state is forbidden.

Gamma-Gamma Angular Correlations:

Gamma-gamma angular correlation measurements can be separated into three parts. First, we measured the angular distributions of the 1.54 MeV gamma ray in coincidence with the 2.24 MeV gamma ray, rotating two detectors with fixed angles to each other around

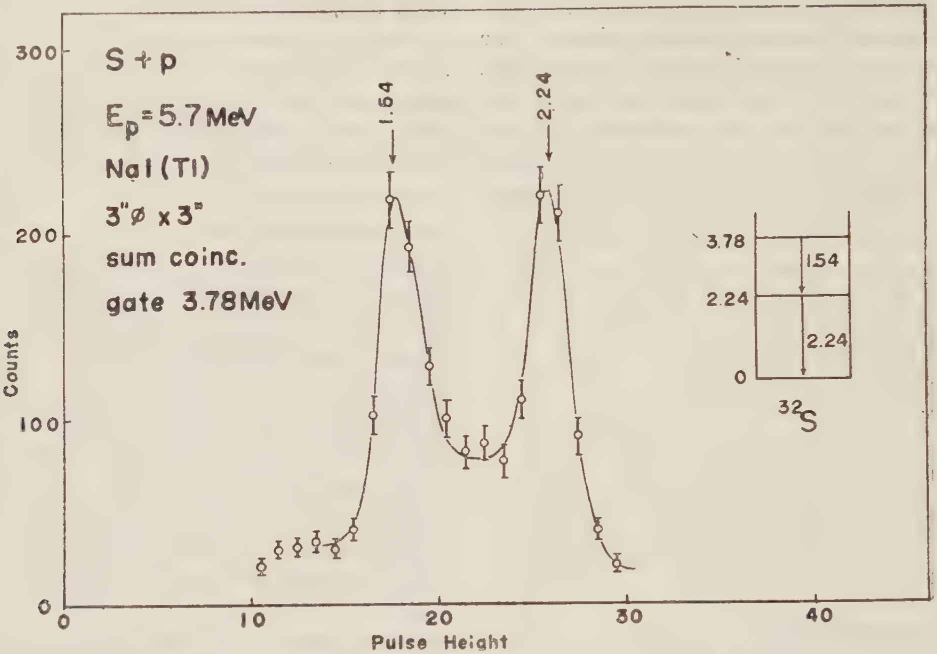

Fig. 11. Sum coincidence spectrum gated at 3.78 MeV, using two NaI(Tl) scintillators, 3-inch diameter by 3-inch long, at proton energy of 5.7 MeV, using natural sulphur compound, $BaSO_4$, as a target.

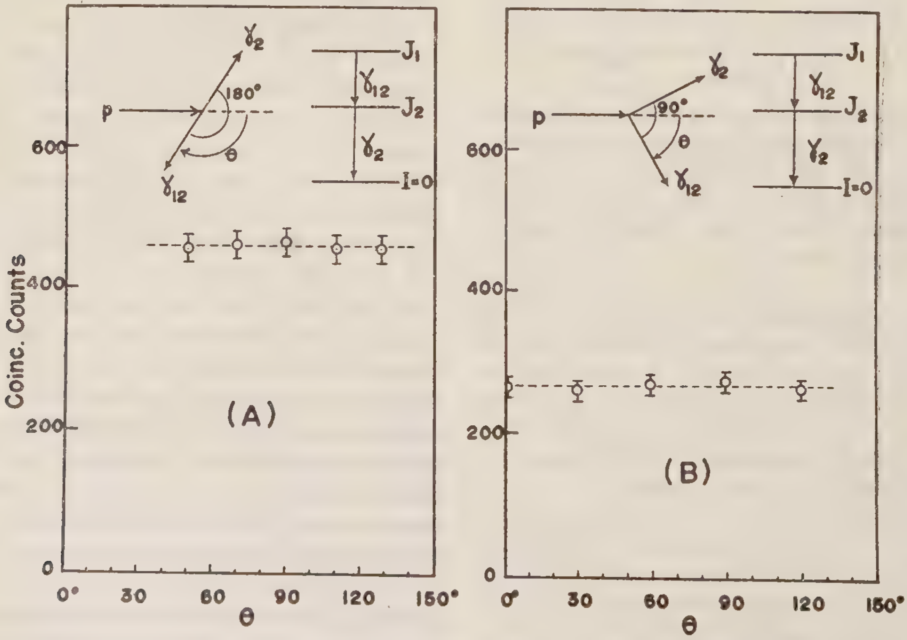

Fig. 12. Angular distribution of the 1.54 MeV gamma ray in coincidence with the 2.24 MeV gamma ray, rotating two detectors, 3-inch diameter by 3-inch long, with fixed angle to each other, about the axis as shown in figure.

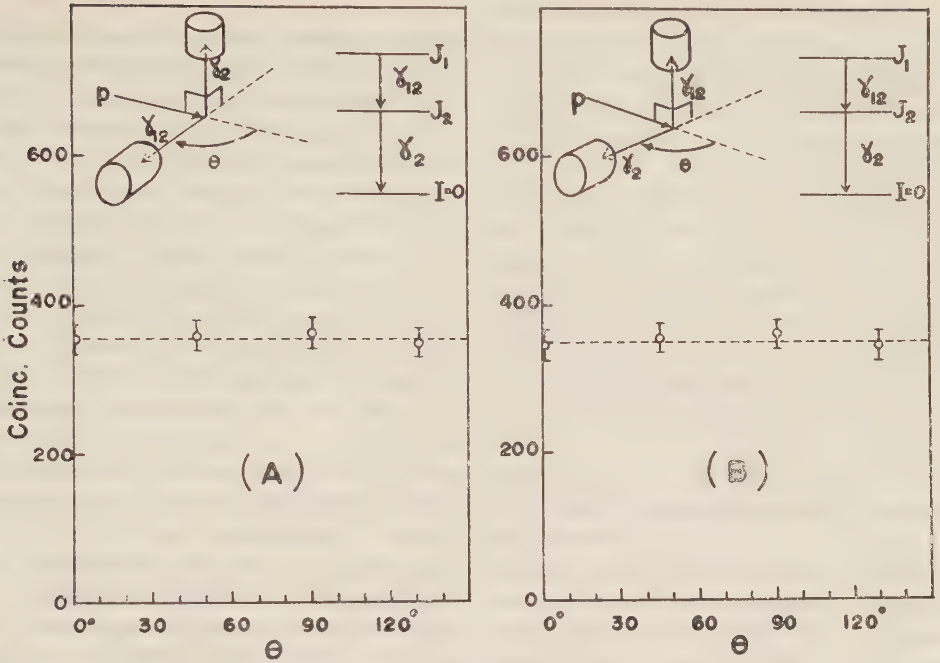

Fig. 13. Angular distributions of the 1.54 MeV and 2.24 MeV gamma rays in coincidence with the 2.24 MeV and 1.54 MeV gamma rays, respectively, using two detectors, 3-inch diameter by 3-inch long, one of which was fixed on the rotating axis and the other was rotated in the plane which includes the proton beam direction, as shown in the figure.

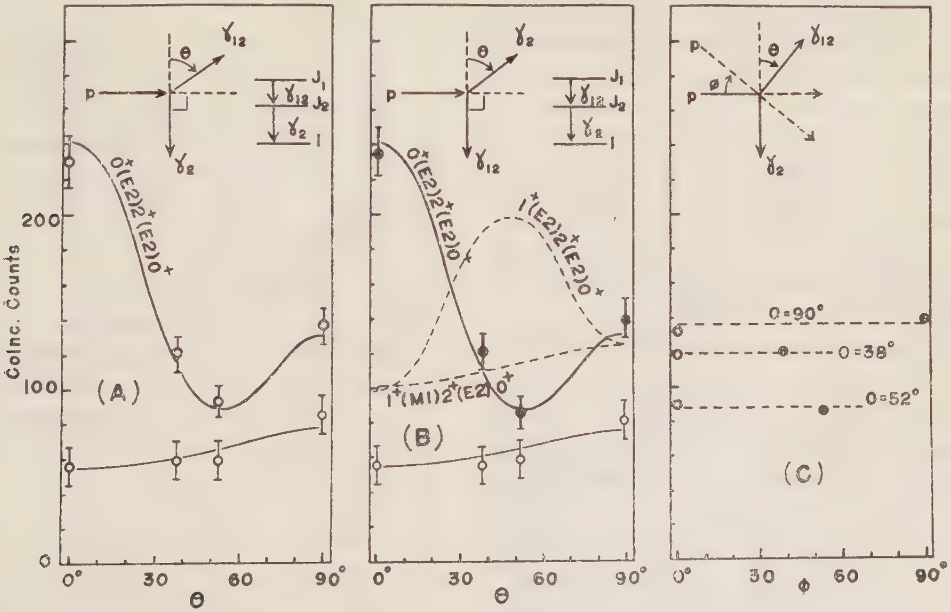

Fig. 14. Angular correlations of the 1.54 MeV and 2.24 MeV gamma rays using two detectors, 3-inch diameter by 3-inch long, one of which was fixed at right angles to the beam direction and the other was rotated about the axis at right angles both to the beam direction and to the direction of the fixed detector, as shown in the figure. Solid and dashed curves represent the calculated angular correlation curves, corrected by the finite solid angles of the detectors. In (A) the 2.24 MeV gamma ray (γ_2) was fixed and in (B) the 1.54 MeV gamma ray (γ_{12}) was fixed. The lower curves show the angular correlations of the 2.23 and 2.24 MeV gamma rays observed in the same way. In (C) the identity of two correlation curves is shown.

the axis through the target position and perpendicular to the plane which includes both the detectors and the incident proton direction. The measured results are shown in Fig. 12. The distributions were found to be isotropic within statistical errors.

Next, one detector was placed on the rotating axis and the other was rotated around the same axis. In this case also, the distribution was found to be isotropic as shown in Fig. 13. These results indicate that the nuclei followed by the gamma emission are not aligned and, therefore, cascade gamma-gamma angular correlation can be treated in the same way as for a radioactive nuclide.

The gamma-gamma angular correlation was measured in the same arrangement as the first case but one detector was fixed at right angles to the incident proton direction and another was rotated around the same axis. In this experiment also, two multichannel pulse height analyzers and two single-channel pulsd height analyzers were used as shown in Fig. 3, in order to gate one another by the 2.24 MeV gamma ray. The results are shown in Fig. 14. These results agree with the theoretical calculation for the transitions $0^+(E2)2^+(E2)0^+$ as shown in Figs. 14(A), (B). The theoretical angular correlation for this transition is as follows:

$$W(\theta)=1+0.357P_2+1.07P_4 .$$

The theoretical curves in Fig. 14 have been corrected for the effect of finite solid angles of the detectors. On the other hand, the theoretical angular correlation for the cascade, $1^+(M1, E2)2^+(E2)0^+$, is as follows:

$$W(\theta)=(1-0.250P_2)+\delta^2(1+0.679P_2-0.762P_4)$$
$$+2\delta(1+0559P_2) ,$$

where δ represents a mixing ratio. The first and the second terms are the correlation functions for the pure cascades $1^+(M1)2^+(E2)0^+$ and $1^+(E2)2^+(E2)0^+$, respectively. The third term is the contribution due to the interference between M1 and E2 transitions. One can not fit the experimental results with $1^+(M1, E2)2^+(E2)0^+$ even if any large mixing ratio is assumed.

It is interesting that two kinds of tripple angular correlations, one of which are gated by γ_2 at fixed detector and the other gated by γ_2 at rotating detector as shown in Figs. 14(A) and (B) respectively, become identical for the case that $I=0$ and $L_{12}=L_2=J_2$, where these symboles are also shown in Figs. 14. This fact makes the analysis of tripple angular correlation simple. For an even-even nucleus, it is the case that γ_{12} is pure E2 transition. In the present case J_1 have been restricted to be 1^+ or 0^+ from the result of the reaction $^{31}P(d, n)^{32}S$ as was previously described. Therefore, as the further analysis, mere consideration of pure E2 transition from 1^+ state for γ_{12} will do, considering the identity of angular distributions in Fig. 14(A) and Fig. 14(B), even if there be not the evidence of isotropic distribution for γ_{12} or there be any accidently cancellation of angular distribution, although the fact is that there are evidences of isotropic distributions, as shown in Fig. 12 and Fig. 13. In such tripple correlation, also, it is found that one can not fit the experimental angular correlations to calculated curve of $1^+(E2)2^+(E2)0^+$. It is, therefore, concluded that the spin and parity of the 2nd state at 3.78 MeV are 0 and even. At the same time, it is confirmed that the 1st state at 2.24 MeV has the spin of 2 and even parity, which has been assigned tentatively.

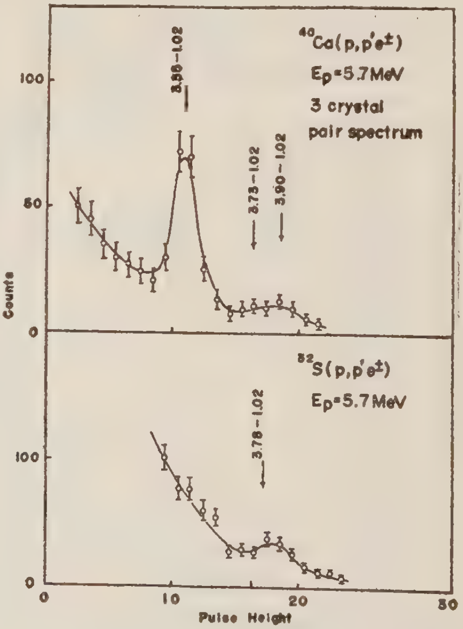

Fig. 15. The spectrum of the nuclear pairs from the 1st state of ^{40}Ca, using three crystal pair spectrometer with a well type plastic scintillator as a centre detector. The lower curve shows the pair spectrum from the proton bombardment of natural sulphur compound, BaSO$_4$, as a target.

Nuclear Pair Detection:

We searched the nuclear pair from the 2nd state to the ground state using a three crystal pair spectrometer as shown in Fig. 2. For a test of the detector, we observed the nuclear pairs from the 1st state of ^{40}Ca using the reaction ^{40}Ca$(p, p'e^{\pm})^{40}$Ca. The result was shown in Fig. 15. Using the same arrangement, we searched the nuclear pairs from the 2nd state of ^{32}S, but no distinct pair peak was found. Considering the detection efficiencies of the spectrometers and the proton beam currents, it was deduced that the intensity of nuclear pairs is about 2% or less of that of the 1.54 MeV gamma ray.

On the other hand, the 1st 0^+ state of ^{40}Ca at 3.35 MeV has a half-life of 1.4×10^{-9} sec, while the estimated half-life using the single particle model is 4.9×10^{-12} sec for E2 transition of 1.54 MeV gamma ray. From these fact it is estimated that the intensity of the nuclear pair from the 2nd 0^+ state of ^{32}S may be about 0.4% of that of 1.54 MeV gamma ray. We think that the efficiency and resolution of the spectrometer is too low to detect such low intensity pairs.

§ 4. **Discussions**

0^+ Second Excited State of ^{32}S:

As mentioned already in § 1, several authors[10),11)] pointed out the difficulty of any theoretical explanation for the 2nd state of ^{32}S that possesses the spin of 1 and even parity. R. Huby and H. C. Newns discussed as follows[10)]. They assumed for this state to be double, one component having 0^+ and the other some reasonable spin and parity, say 2^+ or 4^+, and to lie in energy closer than 20 KeV, which is the accuracy of the energy determination. With these assumptions the stripping reaction ^{31}P$(d,n)^{32}$S could excite both these levels but the transition to the component having 0^+ masked the other. In addition the gamma ray transition to the ground state now no longer makes 0^+ impossible since it can arise from the component having non-zero spin. On the other hand, A. Arima calculated the energy levels, spins and parities of ^{32}S, on the basis of the j-j coupling shell model[11)]. From the results of his calculations the first $T=1$ state appears at 7.18 MeV, the first $J=1$ states appears at 8.00 MeV, and the 0^+ excited state appears at 4.12 MeV. According to his discussions, if it is experimentally sure that there is no low-lying 0^+ state in ^{32}S, the theoretical low-lying 0^+ state in this nuclei shows the inadequacy of the values of the parameters in the calculation.

The assignment of 0^+ for the 2nd state, however, can remove these theoretical difficulties. The configuration of the theoretically calculated state at about 4 MeV may be $(s_{1/2})_0^2(d_{3/2})_0^2(T=0, J=0)$, while the ground state is $(s_{1/2})_0^4$. If these two state are formed by s-wave protons from the ground state of ^{31}P as found in the reaction ^{31}P$(d, n)^{32}$S, it is deduced that the configuration of the ground state of ^{31}P may be mixed with $(s_{1/2})^1_{1/2}(d_{3/2})_0^2$ and $(s_{1/2})^3_{1/2}$. This configuration gives reasonable agreement with the theoretically calculated magnetic moment on the basis of the j-j coupling shell model. If this configuration is pure $(s_{1/2})^3_{1/2}$, the calculated magnetic moment can not explain the experimental valve. This configuration mixing of the ground state of ^{31}P are supported by the angular distribution measurement of protons in the reaction ^{31}P$(d, p)^{32}$P[22)].

Recently, B. D. Kern carried out the search of the 3.8 MeV gamma ray in the reaction ^{32}S$(n, n'\gamma)$ when $^2D(d, n)^3$He neutrons of energies greater than 3.8 MeV but less than 4.32 MeV were used to bombard a sulphur sample[23)]. No 3.8 MeV gamma ray was found with two different geometrical arrangements. This fact confirms our experimental result.

If the 2nd state of ^{32}S has a spin of 0^+, we meet another question why the higher excited states decay scarcely to the 0^+ ground state but to the 0^+ 2nd state. According to the single particle estimations, the intensities of the direct transitions of the states at about 5 MeV to the ground state are not less than 10^2 times of those of the cascade transitions through the 2nd state, even if these are E1 or M1 transitions. Experimentally the intensities of the direct transitions are not more than about a half of those of the cascade transitions. It is considered that some unknown selection rules may exist or these cascade gamma rays may be due to the transitions between higher excited states of ^{32}S than 3.78 MeV.

The 3rd and 4th States of ^{32}S:

The cascade transition from the 3rd state to the 1st state of ^{32}S could not be observed.

If the observed gamma ray of about 4.3 MeV is attributed to the direct transition from the 3rd state to the ground state, the 3rd state may have a spin of 1^- or 2^+.

On the other hand, the 4th state decays through the 1st state by the emissions of the cascade gamma rays of 2.23 and 2.24 MeV. The angular distribution data between these cascade gamma rays, as is shown in Fig. 14, can be tentatively explained with the transition $1^-(E1)2^+(E2)0^+$, although the data are too poor to assign definitely the spin of the 4th state. If the spin of this state is 1, the direct transition to the ground state may also exist comprised in the peak at about 4.3 MeV. Moreover, it is possible that the 3rd state has a larger spin and is scarcely excited by the inelastic scattering process and the gamma ray at about 4.3 MeV is almost due to the transition from the 4th state, although there is a little ambignity of the energy determination. For the spin assignments of these states it is necessary to measure the more accurate energies and intensities for the gamma rays of about 4.3 MeV.

The Excited States of ^{34}S:

The 3.91 and 4.11 MeV gamma rays were found. Considering the results of $^{34}\mathrm{Cl}^m(\beta^+)\,^{34}\mathrm{S}^*(\gamma)$[16], it is deduced that the 3.91 MeV state has a spin of 3^+ and the 4.11 MeV state has a spin of 2^+. The 4.88 MeV state decays with the cascade gamma ray of 0.97 MeV to the 3.91 MeV state. Then the spin of the 4.88 MeV state may be 2 or 3.

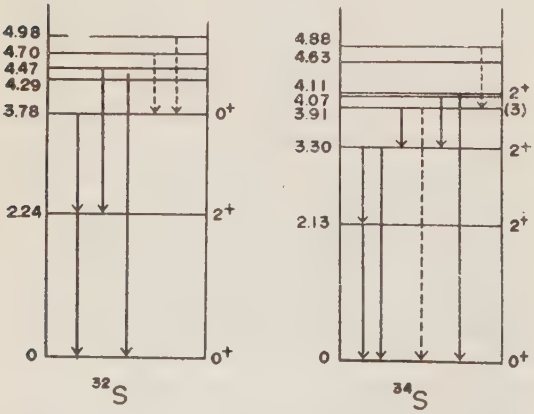

Fig. 16. The level schemes of ^{32}S and ^{34}S. Arrows indicate the gamma ray transitions observed in the present experiment. Only the 0.62 and 0.77 MeV gamma rays were observed not in the present experiment but in the decay of $^{34}\mathrm{Cl}^m$.[16]

Acknowledgments

The author wishes to thank Mr. K. Kaneko and his collaborators for the separation of sulphur isotopes at the Institute for Nuclear Study, University of Tokyo. The author is very grateful to Prof. T. Wakatsuki for his continual guidance, encouragement and discussion throughout the progress of this work. He is also indebted to Mr. I. Miura for many valuable collaborations and discussions.

References

1) Y. Hirao, E. Okada, I. Miura and T. Wakatsuki: J. Phys. Soc. Japan **13** (1958) 233. E. Okada, I. Miura, T. Wakatsuki and Y. Hirao: J. Phys. Soc. Japan **13** (1958) 541. I. Miura, T. Wakatsuki, Y. Hirao and E. Okada: J. Phys. Soc. Japan **14** (1959) 239.
2) T. Wakatsuki, Y. Hirao, E. Okada, I. Miura, K. Sugimoto and and A. Mizobuchi: J. Phys. Soc. Japan **15** (1960) 1141.
3) P. M. Endt, C. H. Paris, A. Sperduto and W. W. Buechner: Phys. Rev. **103** (1956) 961.
4) F. A. El, Bedewi and M. A. El, Wahab: Proc: Phys. Soc. **68A** (1955) 754.
5) R. H. Helen: Phys. Rev. **104** (1956) 1466.
6) H. Paul, H. E. Gove, A. E. Litherland and G. A. Bartholomew: Phys. Rev. **99** (1955) 1339.
7) B. D. Kern and I. W. Cockran: Phys. Rev. **104** (1956) 711.
8) Breckon, Henrikson, Martin and Fostor: Can. J. Phys. **32** (1954) 223.
9) N. W. Glass and J. R. Richardson: Phys. Rev. **98** (1955) 1251.
10) R. Huby and H. C. Newns: Proc. Phys. Soc. **68A** (1955) 758.
11) A. Arima: Prog. Theor. Phys. **19** (1958) 421.
12) E. Bleuler and W. Zuenti: Helv. Phys. Acta **19** (1946) 137.
13) D. Green and J. R. Richardson: Phys. Rev. **101** (1956) 1368. A. R. Quinton and W. T. Doyle: Phys. Rev. **101** (1956) 669.
14) H. E. Handler and J. R. Richardson: Phys. Rev. **102** (1956) 833.
15) H. Morinaga and E. Bleuler: Phys. Rev. **103** (1956) 1423.
16) T. Tōhei: J. Phys. Soc. Japan **15** (1960) 372.
17) I. Miura, Y. Hirao, E. Okada and T. Wakatsuki: Genshikaku Kenkyu in Japan **3** (1957) 76.
18) E. F. Shrader: Rev. Sci. Instr. **21** (1950) 883.
19) Lewis, Olness and Haeberls: Bull. Am. Phys. Soc. Ser. II, I, (1956) 213.
20) A. M. Hoogenbom: Nuclear Instruments **3** (1958) 57.
21) M. Umezawa: Prog. Theor. Phys. **8** (1952) 509.
22) A. W. Dalton, S. Hinds and G. Parry: Proc. Phys. Soc. **A 70** (1957) 586.
23) B. D. Kern: Private communication.

Journal of the Physical Society of Japan, Vol. 16, No. 10, October, 1961

Reaction $O^{16}(\gamma, p)N^{15}$ by 20.5 MeV Polarized Bremsstrahlung

By Katsufusa Shoda

*Department of Physics, Tohoku University,
Sendai, Japan*

(Received May 6, 1961)

D_2O soaked, H_2O soaked and unsoaked emulsions were irradiated simultaneously at the characteristic angle by the 20.5 MeV polarized bremsstrahlung from a thin Al target in a betatron. The linear polarization of the gamma rays from 4 MeV to 6 MeV was estimated to be 31.7±5.0% by observing the azimuthal angular distribution of photoprotons from deuterons. The H_2O soaked emulsion and unsoaked one were used to study $O^{16}(\gamma, p)$ reaction. The proton energy spectrum shows a structure which agrees with the earlier results except a peak at 1.1 MeV of proton energy. This peak which has never been found corresponds to the well-known resonance in $N^{15}(p, \gamma)O^{16}$ at 1.05 MeV of proton energy. The azimuthal angular distributions of photoprotons caused by several photon energy regions were observed. From these angular distributions it is shown that a resonance at a photon energy of 17.3 MeV is $E1$ transition, and the corresponding level of O^{16} is considered to have $J=1^-$, $T=1$, which is in good agreement with the theoretical calculation in the intermediate coupling.

§1. Introduction

The photoproton emission from O^{16} has been studied recently[1-9], and many proton peaks in the energy spectrum have been observed. In principle these structures of the spectra should not be compared directly with those of the cross section, because the transitions to the excited states of the residual nucleus plays an important role in the case of the proton spectra. In practice, however, Johansson et al.[7] and Milone et al.[9] studied the cross section and the branching ratios to the levels of N^{15} using nuclear emulsions and oxigen gass targets, and found that almost all proton emissions in the region before the giant resonance ($E_\gamma<20$ MeV) accompany mainly ground state transitions. Then the cross section can be obtained from the proton energy spectrum in this low energy region.

Spicer[1] found a large photoproton resonance at $E_\gamma=14.7$ MeV and concluded, by observing the proton angular distribution, that this transition must be $M1$ or $E2$ absorption. Johansson and Forkman[3),7] examined the proton energy spectra and angular distributions using 20.5 MeV and other higher energy bremsstrahlung. They found the several peaks in the cross section. They estimated the types of main transitions using the angular distributions and ratios between photoproton and photoneutron yields. According to their estimation there exists $E1$ or $M1$ absorption at $E_\gamma\approx17$ MeV, $M1$ or $E2$ absorption at $E_\gamma\approx19$ MeV and $E1$ absorptions around 21 MeV and 23.5 MeV.

The reaction $N^{15}(p, \gamma_0)O^{16}$ is considered to be the inverse process of $O^{16}(\gamma, p)N^{15}$ at smaller photon energy than about 20 MeV (suffix 0 denotes the transition to the ground state), because almost all photoproton transitions are the ground state transitions in these energy regions. Schardt et al.[10] observed a large resonance at $E_p=1.05$ MeV which corresponded to the level of O^{16} at 13.09 MeV ($J=1^-$, $T=1$). Wilkinson et al.[11] examined the (p, γ_0) resonance up to $E_p=4$ MeV. Excepting the 1.05 MeV resonance, they found no pronounced resonance. This result is inconsistent with the existence of a large resonance at $E_\gamma=$ 14.7 MeV in Spicer's data. Tanner et al.[12] observed the cross section of (p, γ_0) in the proton energy region between about 4 MeV and 8 MeV. They found the peaks of cross section at 5.6 MeV and 7.4 MeV which were in good agreement with the photoproton results[3),7),9)]. In the giant resonance region Cohen et al.[13] observed the cross section of (p, γ_0) and found that this cross section agreed with the cross section of ground state transition of photoprotons[2),4),7),9)].

Elliott and Flowers[14)] calculated the properties of the odd parity states of O^{16} which might be considered to arise from the configurations $p^{-1}d$ and $p^{-1}2s$. The calculation was performed in the intermediate coupling scheme including the spin-orbit splittings of the p and d shells. According to their calculations five levels of $J=1^-$, $T=1$ appear at 13.1, 17.3, 20.4, 22.6 and 25.2 MeV having the electric dipole widths 0.06, 0.14, 0.02, 12 and 5.8 keV respectively. Some of these energy levels are in fairly good agreement with the photoproton experimental data. The 22.6 and 25.2 MeV levels correspond to the giant resonance.

A large peak of the observed (γ, p) cross section below the giant resonance corresponds to the 17.3 MeV level. According to the results of Johansson et al. the absorption for $M1$. The experimental angular distribution this level is $E1$ or corresponds to the d wave emission or s wave emission of photoproton for $E1$ or $M1$ absorption respectively. Elliott and Flowers' calculation shows that the 17.3 MeV level corresponds to the $p^{-1}d$ state and agrees with the experimental angular distribution if the absorption is $E1$. However, according to the comparison made by Johansson et al. between the cross sections of (γ, n) and (γ, p), the assumption of d wave emission does not seem to be reasonable. On the other hand, Weisskopf[15)] suggests that the photon absorption below the giant resonance may be $M1$ absorption. We see from these discussions that the property of the 17.3 MeV level is not clear. The 13.1 MeV level predicted by Elliott and Flowers' calculation was not found in photodisintegration, but this level has been observed in $N^{15}(p, \gamma_0)O^{16}$ reaction[10),11)].

In general, the multipole order in photodisintegration can be estimated by the polar angular distribution of emitted particles, but the parity of multipole can not be estimated by this distribution only. Agodi[16)] calculated the effect of photon polarization on nuclear photoeffect. The polar angular distribution of the emitted particles in the photoreaction induced by unpolarized photon and the azimuthal angular distribution in a plane orthogonal to the incident polarized photon beam may be expressed as follows respectively,

$$I(\theta)=N_p(a_0+a_2\cos^2\theta) \qquad (1)$$

$$F(\phi)=N_A(1+P\alpha_0\cos 2\phi) \qquad (2)$$

where P is the ratio of the intensity of polarized photons to the total photons and ϕ denotes the emission angle from the direction of the electric vector of photons on the plane orthogonal to the beam. According to his calculation, if a single multipole is responsible for the transition, the relations between Eq. (1) and Eq. (2) are as follows,

$$\alpha_0=(-1)^\sigma\frac{a_2}{a_0} \quad \text{for dipole transition} \qquad (3)$$

$$\alpha_0=(-1)^\sigma\frac{a_2}{5a_0} \quad \text{for quadrupole transition} \qquad (4)$$

where σ is defined as zero for magnetic and 1 for electric multipoles. Owing to these results, the absolute value of the ratio of α_0 to a_2/a_0 exibits a large difference for dipole and quadrupole transitions and the sign of α_0 relative to a_2/a_0 distinguishes the electric multipole transition from the magnetic one when the multipole order is known. The maxima and minima in the azimuthal angular distribution are interchanged in each case.

The linear polarization effect of bremsstrahlung produced by electrons in MeV region has been studied recently[17)-25)]. According to the theoretical calculation the largest polarization appears at the characteristic emission angle, $\Theta=mc^2/E_0$, where m is the electron rest mass and E_0 is the electron total energy. The degree of polarization of the 17 MeV photons in the 20.5 MeV bremsstrahlung is theoretically estimated to be about 10%.

The azimuthal angular distribution of 17 MeV photoproton groups from O^{16} caused by the polarized 20.5 MeV bremsstrahlung may give the more detailed properties of this level if it is combined with the polar angular distribution of the experiment of Johansson et al.[7)]

§ 2. Experimental Procedure and Apparatus

The degree of polarization of bremsstrahlung is strongly dependent on the photon emission angle. The multiple scattering of electrons in the target, the oscillation and the beam cross section of circulating electrons in the betatron doughnut affect the photon emission angle and will reduce the degree of polarization. In order to reduce these effects, a thin Al target (2.5 mg/cm²) of 1 mm×5 mm was used and the beam stopper (Pt 1.5 mm thick) was placed at 15 mm from the stable orbit near the opposite to the target. The expander current was chosen as small as possible, and the cross section and the oscillation amplitude of the electron orbit were measured by autoradiography of induced activity on a thin Cu target. The best position of the target was determined for the same condition as shown in ref. 25.

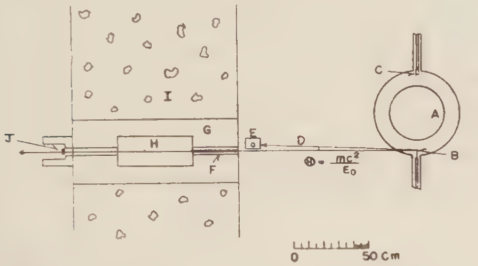

Fig. 1. Experimental arrangement showing **A**-betatron doughnut, **B**-bremsstrahlung target (Al 2.5 mg/cm² thick), **C**-electron gun and beam stopper, **D**-direction of the center of bremsstrahlung, **E**-monitor, **F**-lead collimator, **G**-lead shield, **H**-sweep magnet, **I**-concrete wall, **J**-nuclear plates.

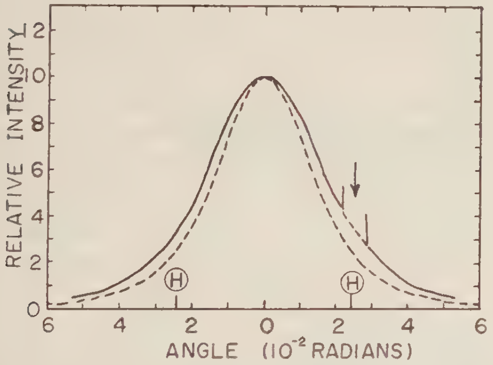

Fig. 2. The angular distribution of the bremsstrahlung. Full line: experimental result. Broaken line: theoretical curve. The direction of the irradiation beam is shown by an arrow.

After these preliminaly experiments, D_2O soaked, H_2O soaked and unsoaked plates mounted on thin watertight bakelite holders were irradiated simultaneously by the 20.5 MeV bremsstrahlung at the characteristic angle as shown in Fig. 1. Each plate was 1″×1″ in size cut from a 1″×3″ Ilford C2 200 μ thick nuclear plate.

The effects of multiple scattering of electrons in the target, the oscillation and the cross section of the incident electron beam were examined by the angular distribution of the bremsstrahlung with Fuji Type 80 X-ray film. The results of photometric observation of the angular distribution of bremsstrahlung and the determination of the angle between the direction of the beam center and that irradiating the plates are shown in Fig. 2. The theoretical curve for a very thin target was calculated by the simple formula[26]

$$F(\theta)=1/[1+(E_0\theta/mc^2)^2]^2 .$$

This was also shown in the same figure. The deviation of the experimental result from the theoretical curve is not so large.

The irradiation dose was measured by a Victoreen chamber embedded in a small cube of Lucite which was calibrated by the chamber at the center of a 10 cm cube of Lucite. The experimental dose value may have large error owing to large back ground. The plates were developed by an amidole developer, pH. of which was adjusted with HCl in order to minimize fogging. Tiyoda binocular microscope was used for the scanning at a multiplication of 60×1.5×10.

The range of protons was determined by measuring the projected length of the tracks on the plane of the emulsion and their depth corrected for the schrinkage factor. The latter was determined by measuring the thick-

Table I. Exposure data.

Betatron energy (MeV)	20.5
Roentgens at plates (r)	3.6
Emulsion type	Ilford C-2 200 μ

	D_2O soaked plate	H_2O soaked plate	Non-soaked plate
Impregnation in unit volume of emulsion (g/cm³)	1.84	2.17	——
Aria scanned (cm²)	0.656	1.49	1.60
Observed proton number	1407	1197	379

ness of emulsion after soaking with a micrometer and measuring the thickness after development by the microscope. For the range-energy relations of D_2O and H_2O soaked emulsions, the table calculated by Krohn and Schrader[27] was used.

The data of exposure are given in Table I.

§ 3. Experimental Results and Discussions

a) *Polarization of 20.5 MeV bremsstrahlung*

The relation between the energy of the photoproton from deuteron (E_p) and the incident photon energy (k) are given by

$$E_p=\frac{k-\varepsilon}{2}+\sqrt{\frac{k-\varepsilon}{4Mc^2}}\,k\cos\theta\,, \qquad (5)$$

where ε is the threshold energy of deuteron photodisintegration, θ is the emission angle of photoprotons, and M is the proton mass. The proton spectra expressed by the photon energy using Eq. (5) and the azimuthal angular distributions for several energy groups are shown in Figs. 3 and 4 for D_2O and H_2O soaked plates. In these figures the number of protons in the H_2O soaked plate is normalized to the same number of oxigen atoms as in the D_2O soaked plate. H_2O soaked plate is used for the back ground subtraction for the deuteron photodisintegration. The glancing angle of the observed protons is between ±45°. Under such condition of observation, the difference

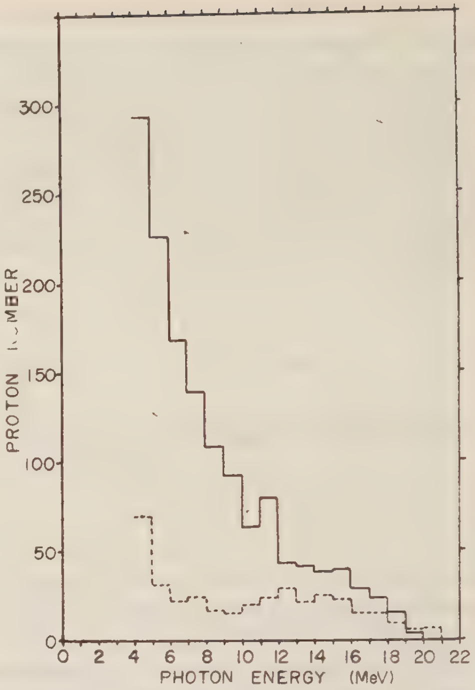

Fig. 3. Energy spectra of photoprotons from D_2O and H_2O soaked plates. The abscissa is calculated photon energy using Eq. (1) assuming that all the photoprotons come from deuteron photodisintegration. The proton number from the H_2O plate is normalized to the same number of oxigen atoms as in the D_2O soaked plate. The full line and the broaken one are the results of D_2O and H_2O soaked plates respectively.

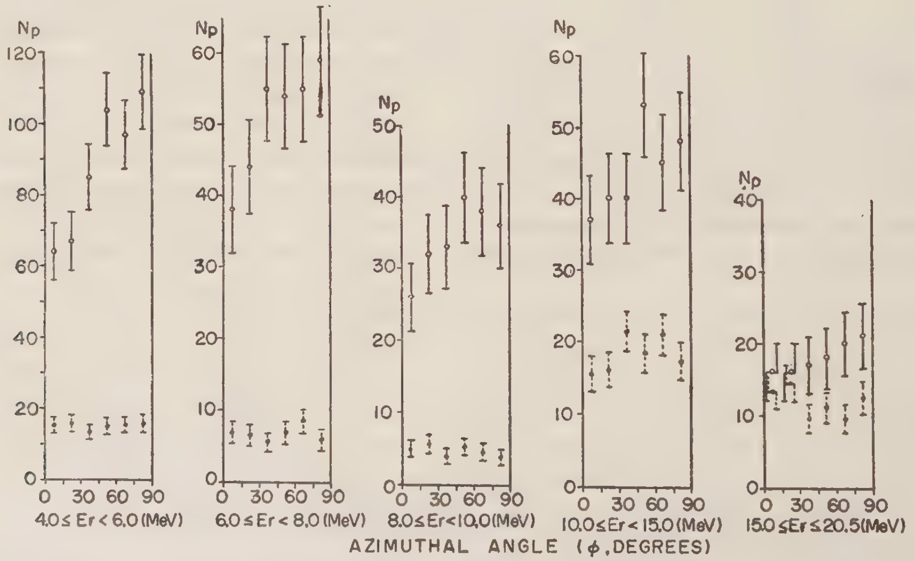

Fig. 4. Azimuthal angular distributions in D_2O and H_2O soaked plates. The proton number from the H_2O plate is normalized to the same number of oxigen atoms as in the D_2O soaked plate. Open and closed circles are the results by D_2O and H_2O soaked plates respectively.

of the thickness of the emulsions affects the effective volume of observation. However, the thickness is not so different between the two emulsions, that the effective volume can be assumed to be equal for the two plates. The best fitted angular distributions of the form $a+b\sin^2\phi$ for the H_2O soaked plate are calculated by the least squares and are subtracted from the observed angular distributions by the D_2O soaked plate. Using the subtracted angular distribution, the best fitted angular distributions of photoprotons from deuteron are calculated as in H_2O soaked plate.

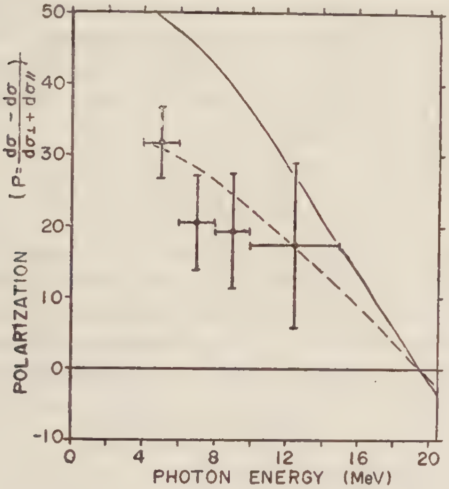

Fig. 5. Energy dependence of polarization % of 20.5 MeV bremsstrahlung. The solid curve is a calculated one using the Gluckstern and Hull's equation. The broaken curve shows a normalized one with the experimental point.

The polarization of the bremsstrahlung is calculated by these angular distributions assuming the $E1$ transition for the deuteron photodisintegration. In Fig. 5, the photon energy dependence of polarization of 20.5 MeV bremsstrahlung is given from the results shown in Fig. 4. The calculated curve by Gluckstern and Hull[18] and also the normalized curve best fitting the experimental points are shown in the figure.

b) *Photoprotons from* O^{16}

The observed photoproton energy spectra for the H_2O soaked and unsoaked plates are shown in Fig. 6. The glancing angle of the observed protons is between ±60° or ±45°.

The photoprotons in the H_2O soaked emulsion involve the back ground protons emitted from nuclei other than O^{16}. In order to obtain the spectrum of photoproton emitted from O^{16}, the back ground protons must be subtracted from the proton spectrum of the H_2O soaked plate.

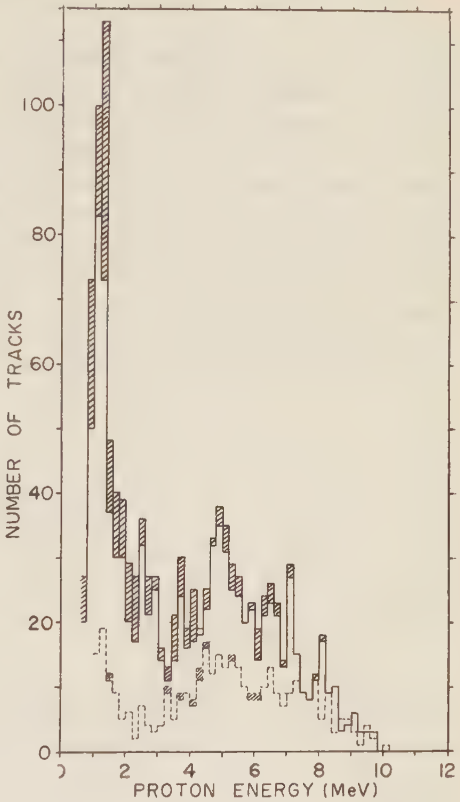

Fig. 6. Observed photoproton energy spectra for the H_2O soaked and unsoaked plates. Full line: for the H_2O soaked plates. Broaken line: for the unsoaked plates. The shaded parts show the protons with the glancing angle between 45° and 60° in plus and minus.

If we denote by N the total proton tracks in the unit area of emulsion for all directions, and denote by n those in ±45° of glancing angle, N is proportional to n

$$N=fn\ .$$

f will be a function related to the thickness of emulsion at exposure, proton energy and polar angular distribution. If the last is denoted by $A(1+B\cos^2\theta)$, f is given by

$$f=\frac{4\left(1+\frac{B}{3}\right)}{\sqrt{2}\left(2+\frac{B}{3}\right)-\frac{R}{D}\left(1+\frac{B}{4}\right)}$$

$$\text{when}\quad \frac{D}{R}\geq\cos 45^\circ\ .$$

$$=\frac{2\left(1+\frac{B}{3}\right)}{\frac{D}{R}\left[1+\frac{B}{6}\left(\frac{D}{R}\right)^2\right]}\,.$$

$$\text{when}\quad \frac{D}{R}\leq\cos 45°\,,$$

where D and R are the thickness of the emulsion and proton range respectively. n and n' are assumed to be decomposed as $n=n_0+n_b$ and $n'=n_0'+n_b'$ for H_2O soaked and unsoaked plates respectively, where oxigen and back ground are denoted by the suffixes 0 and b. Denoting the f function for n_0, n_b, n_0', n_b' by f_0, f_b, f_0', f_b', the following relations are obtained for each plate,

$$f_0N=f_0(n_0+n_b)=f_0n_0+\frac{f_0}{f_b}f_bn_b$$

$$f_0'N'=f_0'(n_0'+n_b')=f_0'n_0'+\frac{f_0'}{f_b'}f_b'n_b'\,.$$

The number of atoms which emitt the back ground protons is equal in the same area of the two emulsions because these two plates are cut out from the one plate, and therefore the total number of back ground protons in each plate is the same i.e. $f_bn_b=f_b'n_b'=N_b$. According to Johansson et al.'s result[7] of angular distributions, B is assumed to be $-7/9$, 0.6 for the region of proton energy 4.4–5.0 MeV, 6.2–7.3 MeV respectively, and 0 for other regions. These of B values are continued smoothly. We assume $B=0$ for the back ground protons. Using these values, f_0/f_b and f_0'/f_b' are calculated. These ratios are nearly equal and can be equated to the mean value F in each proton energy within the error of 1.5%. Considering the relations mentioned above, a method of subtraction is obtained as follows

$$f_0N-FN_b=f_0n_0$$

$$f_0'N'-FN_b=f_0'n_0'\,,$$

where f_0n_0 and $f_0'n_0'$ show the total proton number from oxigen in the two plates. Actually, the observed two proton spectra Fig. 6 were normalized to the same area, multiplied by f_0 and f_0' and subtracted the same

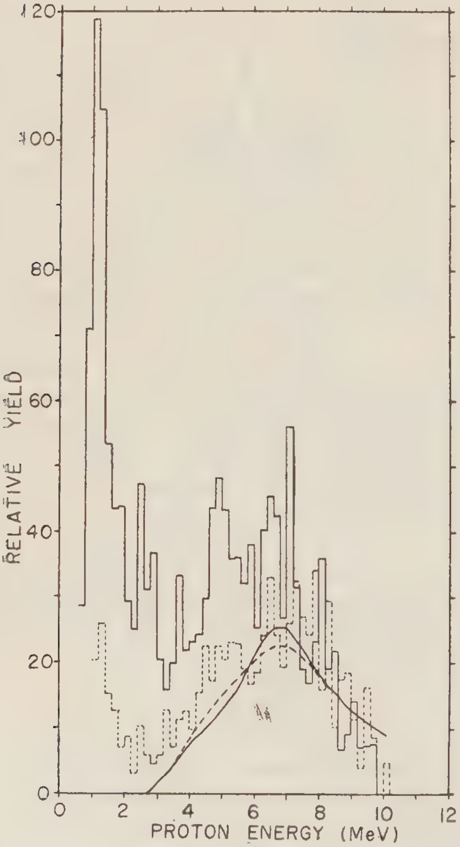

Fig. 7. The proton energy spectra corrected for the emulsion thickness and the back ground spectrum to be subtracted. Full line hystogram: for the H_2O soaked plate; broaken line hystogram: for the unsoaked plate; full curve: spectra of back ground to be subtracted (FN_b); broaken curve: spectra of back ground (N_b).

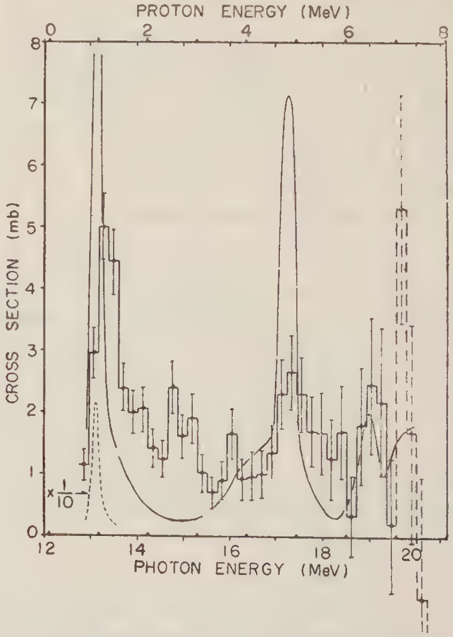

Fig. 8. Cross section of $O^{16}(\gamma, p)N^{15}$ assuming that all proton transitions are those to the ground state of N^{15}. The hystogram is the present result and the curves are the calculated cross sections from the experimental (p, γ_0) cross section using the detailed balance theorem.

spectra (FN_b) to give the same shape of subtracted results. In Fig. 7, f_0N, $f_0'N'$, FN_b, and N_b are shown. After subtraction, f_0n_0 is considered to be the photoproton spectrum from O^{16}.

The cross section of $O^{16}(\gamma, p)$ was then obtained and the results are shown in Fig. 8. The energy on the abscissa is given by $E_\gamma = 12.11 + (17/16)E_p$. The proton spectrum and the cross section are in fairly good agreement with the results of Johansson et al. except the region lower than 14 MeV of photon energy. In this energy region, almost all transitions are those to the ground state of N^{15}, and the (γ, p) cross section can be calculated by the experimental (p, γ_0) cross section using the detailed balance theorem. The cross section obtained by such a calculation is also shown in Fig. 8. The agreement in the shape between the two cross sections is good. The absolute values of the present experimental cross section are smaller than the calculated one. In the present experiment, however, the energy resolution is lower than the others and the error in the value of dose is probably large.

The peak at 14.8 MeV of photon energy has never been observed in $N^{15}(p, \gamma_0)O^{16}$. Spicer[1] found a strong peak at 14.7 MeV in (γ, p) reaction. In the results of Johansson et al.[7] a small peak was found corresponding to this energy in the photoproton spectrum caused by 20.5 MeV bremsstrahlung. In both of the present case and that of Johansson et al. a peak may be expected by the transition from resonances at about 20 MeV to the excited level at 5.3 MeV in N^{15}. This may be included in the peak at 14.8 MeV. The examination using the lower energy bremsstrahlung would be desirable for more complete study.

The azimuthal angular distributions of protons with the glancing angle smaller than 60° are shown in Fig. 9 for both H_2O soaked and unsoaked plates. The errors in the figure are only the statistical ones. The angular distributions after subtraction of the back ground fit the form $A + B\sin^2\phi$ using the least squares. The results are shown in Table II together with other values.

The theoretical azimuthal angular distri-

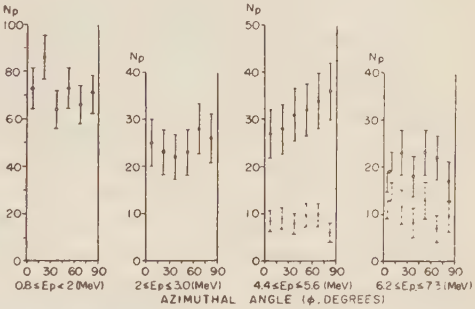

Fig. 9. Azimuthal angular distributions of protons in several energy regions. Open circles show the results in H_2O soaked plate. Closed circles are for the back ground plate.

Table II. Results of the azimuthal angular distributions of photoprotons from O^{16}.

E_p (MeV)			0.8–2.0	2.0–3.0	4.4–5.6	6.2–7.3
Calculation data	$\alpha_0 = a_2/a_0$*		0	−0.091	−0.78	0.6
	$E\gamma$ (MeV)		~13.3	~14.8	~17.3	~19.1
	P (%)†		16	12	6	1
	$P\alpha_0 \times 10^2$	$E1$	0	1.1	4.7	−0.6
		$M1$	0	−1.1	−4.7	0.6
		$E2$	0	0.2	0.9	0.02
		$M2$	0	−0.2	−0.9	−0.02
Experimental results	$P\alpha_0 \times 10^2$		−6.4±6.0	6.5±9.0	21±11	14±23

* Obtained by ref. 7.

† Present data of polarization.

The polar and azimuthal angular distributions are represented as follows:

$$I(\theta) = N_p(a_0 + a_2\cos^2\theta)\,, \qquad F(\phi) = N_A(1 + P\alpha_0\cos 2\phi)\,.$$

butions were calculated using Eqs. (1)-(4). In these calculations the results of the polar angular distributions obtained by Johansson et al.[7] and the polarization degrees obtained in the present experiment were used. For the proton group of $0.8 \leq E_p < 2$ MeV, the polar angular distribution has not been observed in $O^{16}(\gamma, p)N^{15}$, but it was estimated by the angular distribution of radiation in $N^{15}(p, \gamma_0)O^{16}$ reaction[10],[11],[28] which was measured to be isotropic within about 10%. This (p, γ_0) result was used in the present calculation. The angular distributions are nearly isotropic and are of no use to determine the parity of multipolarity except for the region of $4.4 \leq E_p \leq 5.6$ MeV. For the proton group $4.4 \leq E_p \leq 5.6$ MeV which corresponded to the transition induced by photon around 17.5 MeV, the asymmetry of the azimuthal angular distribution was observed though the experimental error was large. The sign of the assymetry shows that the transition is $E1$ as shown in Table II when $E1$ or $M1$ transition is possible[7].

According to Elliott and Flowers' calculation, the levels having $J=1^-$, $T=1$ below 20.5 MeV which correspond to the peaks of $E1$ transition are expected at 13.1 and 17.3 MeV. These energies are in good agreement with the present result. For the 13.1 MeV level the present result can not determine the multipolarity of transition, but the experimental result of angular distribution of gamma rays in $N^{15}(p, \gamma_0)O^{16}$ [10],[11],[28] shows that it is a strong $E1$ transition[10],[11],[28],[29]. Wilkinson et al.[11] suggested that this state of O^{16} was well described as $p^{-1}2s$ and probably contained less than 3% in intensity of $p^{-1}d$. These facts are in good agreement with Elliott and Flowers' result. For the 17.3 MeV level, the present result suggests it is caused by $E1$ transition, and therefore the polar angular distribution of the results of Johansson et al. shows that the proton emission from the 17.3 MeV level of O^{16} is d-wave[7], so that the configuration of this level is mainly $p^{-1}d$ which is in good agreement with Elliott and Flowers' result. Thus Elliott and Flowers' calculation gives a good interpretation of the $E1$ transition in photodisintegration of O^{16}.

The author would like to thank Prof. M. Kimura for his interest and encouragement in the course of the present work, and also Dr. K. Okamoto for his discussions. He is indebted to Mr. R. Togei for his useful help in the earlier stage of the experiment. Thanks are also due to Miss Y. Nagahama for scanning many plates.

References

1) B. M. Spicer: Phys. Rev. **99** (1955) 33.
2) W. E. Stephens, A. K. Mann, B. J. Patton and E. J. Winhold: Phys. Rev. **96** (1955) 839.
3) S. A. E. Johansson and B. Forkmann: Phys. Rev. **99** (1955) 1031.
4) L. Cohen, A. K. Mann, B. J. Patton, K. Reibel, W. E. Stephens and E. J. Winhold: Phys. Rev. **104** (1956) 108.
5) W. E. Stephens: Physica **22** (1956) 1143 A.
6) S. L. Livesey: Can. J. Phys. **34** (1956) 1022.
7) S. A. E. Johansson and B. Forkman: Ark. f. Fys. **12** (1957) 359.
8) C. Milone and R. Ricamo: Nuovo Cimento **5** (1957) 1338.
9) C. Milone, S. Milone-Tamburino, R. Rinzivillo, A. Rubbino and C. Tribuno: Nuovo Cimento **7** (1958) 729.
10) A. Schardt, W. A. Fowler and C. C. Lauritsen: Phys. Rev. **108** (1957) 735.
11) D. H. Wilkinson and S. D. Bloom: Phys. Rev. **105** (1957) 683.
12) N. W. Tanner, G. C. Thomas and W. E. Meyerhof: Nuovo Cimento **14** (1959) 257.
13) S. G. Cohen, P. S. Fisher and E. K. Warburton. Phys. Rev. **121** (1961) 858.
14) J. P. Elliott and B. H. Flowers: Proc. Roy. Soc. **A**, **242** (1957) 57.
15) J. M. Blatt and V. F. Weisskopf: *Theoretical Nuclear Physics*, (John Wiley and Sons, 1954) p. 651.
16) A. Agodi: Nuovo Cimento **5** (1957) 21.
17) M. M. May: Phys. Rev. **84** (1951) 265.
18) R. L. Gluckstern and M. H. Hull, Jr.: Phys. Rev. **90** (1953) 1030.
19) K. Phillips: Phil. Mag. **44** (1953) 169.
20) C. Tzara: Compt. rend. **239** (1954) 44.
21) E. G. Muirhead and K. B. Mather: Australian J. Phys. **7** (1954) 527.
22) J. M. Dudley, F. W. Inman and R. W. Kenney: Phys. Rev. **102** (1956) 925.
23) J. W. Motz: Phys. Rev. **104** (1956) 557.
24) D. Jamnik and P. Axel: Phys. Rev. **117** (1960) 194.
25) K. Shoda: J. Phys. Soc. Japan **16** (1961) 1271.
26) L. H. Lanzl and A. O. Hanson: Phys. Rev. **83** (1951) 959.
27) V. E. Krohn, Jr. and E. F. Shrader: Phys Rev. **86** (1952) 391.
28) A. A. Kraus, Jr.: Phys. Rev. **94** (1954) 975.
29) D. H. Wilkinson: Phys. Rev. **90** (1953) 721.

JOURNAL OF THE PHYSICAL SOCIETY OF JAPAN Vol. 16, No. 10, OCTOBER, 1961

Angular Distribution for the $N^{14}(d, p)N^{15}$ Ground State Reaction

By Susumu MORITA, Toshiyuki ISHIMATSU and Tetsuji CHÔ
Department of Physics, Kyusyu University, Hukuoka
Yutaka NAKAJIMA,
Department of Physics, University of Tokyo, Tokyo
Nawoyuki KAWAI and Tôru MURATA
Nippon Atomic Industry Group Co. Ltd., Chiyoda-ku, Tokyo
Yûki HACHIYA
Nippon Electric Co. Ltd., Minato-ku, Tokyo

(Received May 8, 1961)

Angular distributions for the $N^{14}(d, p)N^{15}$ ground state reaction were studied at the deuteron energies of 15.2 and 13.8 MeV, and were compared with the angular distributions for the $C^{12}(\alpha, p)N^{15}$ ground state reaction at such alpha-particle energies that the compound nucleus 0^{16} would be produced at the same excitation energies as would be produced by the bombardment of N^{14} with deuteron of the above energies. Similar comparisons between the two reactions were made by using the available experimental results including our previous results. It is seen that the $N^{14}(d, p)N^{15}$ ground state reaction proceeds mainly via the stripping process at deuteron energies above 8 MeV showing no appreciable change of the angular distribution with deuteron energy, though the angular distribution for the $C^{12}(\alpha, p)N^{15}$ ground state reaction shows critical energy dependence in the corresponding energy range.

§ 1. Introduction

Previously, some of the authors[1)] reported the angular distributions for the $N^{14}(d, p)N^{15}$ ground state reaction at the deuteron energies of 16.2 and 16.7 MeV. The results are compared with the deuteron stripping theory and it is also pointed out that these angular distributions are quite similar to those for the $C^{12}(\alpha, p)N^{15}$ ground state reaction[2)] at such bombarding alpha-particle energies that the compound nucleus 0^{16} will be produced at the same excitation energies as will be produced by the bombardment of N^{14} with deuteron of the above energies. In order to see whether the correspondence between the two reactions with regard to the compound nucleus 0^{16} is accidental, the $N^{14}(d, p)N^{15}$ ground state reaction was studied at lower deuteron energies corresponding to the alpha-particle energies where the critical energy dependence of the angular distribution for the $C^{12}(\alpha, p)^{15}$ ground state reaction is reported[2)].

The deuteron beam was accelerated with the cyclotron of the Institute for Nuclear Study at University of Tokyo. The experimental arrangements of the slit system, scattering chamber and particle detectors were the same as those used in the previous experiment. As the target, melamine ($C_3H_6N_6$) of 1.63 mg/cm² in thickness evaporated onto the silver foil was used, instead of nitrogen gas filled in the gas cell which had been used in the previous experiment. Two sets of scintillation counter, composed of $C_sI(Tl)$ crystal of 2 mm in thickness, were mounted at 180° to each other on the turn table in the scattering chamber, and the measurements were done simultaneously at two opposite directions to the deuteron beam. The values of the differential cross sections at 90° in the laboratory system obtained with the two counters at each deuteron energy agreed reasonably each other showing that the error due to the geometrical arrangement was sufficiently small. A monitor counter of similar construction was set at 55° to the beam direction.

The angular distributions for the $N^{14}(d, p)N^{15}$ ground state reaction in the center-of-mass system at different deuteron energies are shown in Fig. 1. In this figure, the angular distributions at the deuteron energies of 16.7, 16.2, 15.2 and 13.8 MeV are the results obtained in our experiments and those at the deuteron energies of 11.4 and 7.9 MeV are the results obtained by M. Takeda[3] and W. M. Gibson and E. E. Thomas[4], respectively, and those at 3.2 and 2.5 MeV are the results by one of the authors, N. Kawai[5]. In Fig. 1, the angular distributions for the $C^{12}(\alpha, p)N^{15}$ ground state reaction, obtained by I. Nonaka *et al.*[2] and M. Takeda[6], are also shown by dotted curves. The angular distributions for the two reactions shown together refer to the bombarding deuteron and alpha-particle energies which correspond to nearly the same excitation energy of the compound nucleus 0^{16}.

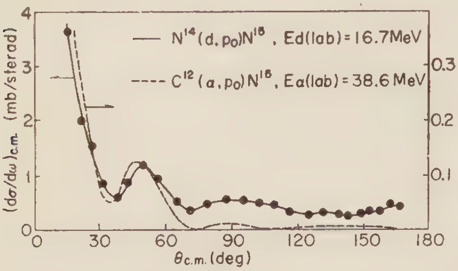

(a)

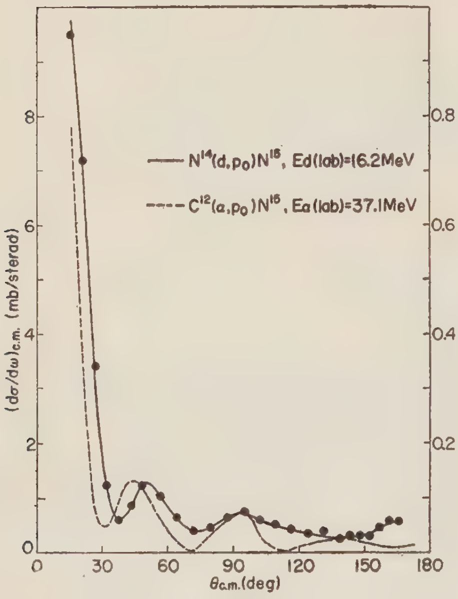

(b)

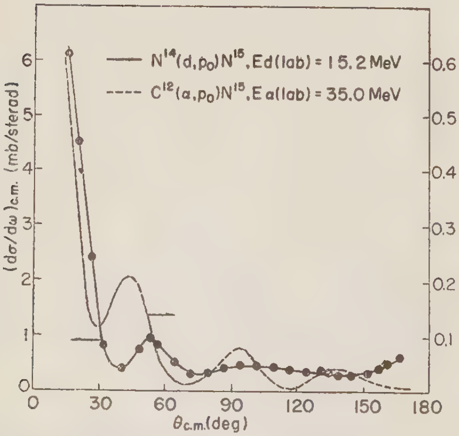

(c)

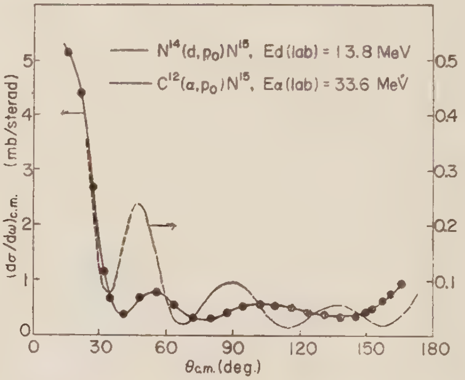

(d)

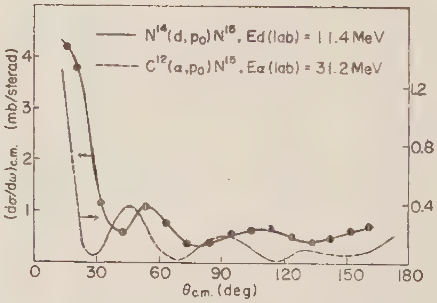

(e)

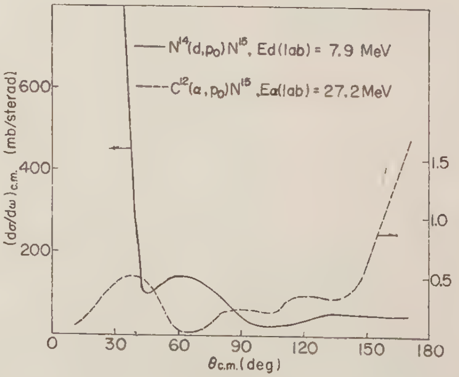

(f)

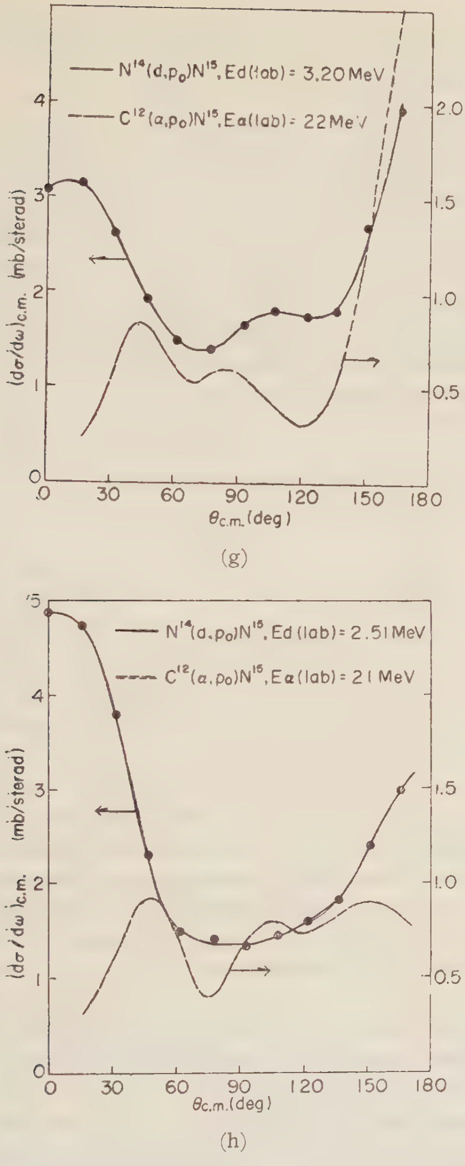

(g)

(h)

Fig. 1. The angular distributions for the $N^{14}(d, p)N^{15}$ ground state reaction at different energies, including the experimental results obtained by other authors. Dotted curves are the angular distributions for the $C^{12}(\alpha, p)N^{15}$ ground state reaction obtained by Nonaka *et al.*[2)] and Takeda[6)]. The solid and dotted curves shown together correspond to nearly the same excitation energy of the compound nucleus 0^{16}.

Contrary to the expectation described in the previous paper[1)], the angular distributions for these two reactions become quite different as the bombarding energies get lower, particularly in the extremely forward and backward directions. It is evident that the $N^{14}(d, p)N^{15}$ ground state reaction proceed mainly via the stripping process in the energy range of deuteron above 8 MeV. Since the compound nucleus process is expected generally to have somewhat larger contribution to the (α, p) reaction than to the (d, p) reaction, the compound nucleus process might have some contribution to the critical energy dependence of the angular distribution for the $C^{12}(\alpha, p)N^{15}$ ground state reaction. It seems reasonable, however, that this energy dependence of the angular distribution is due to an interference effect of some direct processes in view of the high alpha-particle energy and high excitation energy of the compound nucleus involved. In order to understand the remarkable energy dependence of the angular distribution for the $C^{12}(\alpha, p)N^{15}$ ground state reaction, it will be significant to see whether some correspondence between this reaction and the deuteron induced reactions on N^{14} other than the (d, p) reaction with regard to the compound nucleus 0^{16} exists, in the wide range of deuteron energy, as we did about the $N^{14}(\alpha, p)N^{15}$ reaction in the present work.

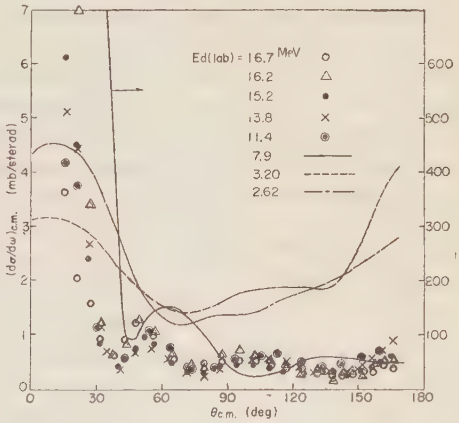

Fig. 2. The angular distributions for the $N^{15}(d, p)N^{15}$ ground state reaction at different deuteron energies.

In Fig. 2, the angular distributions for the $N^{14}(d, p)N^{15}$ ground state reaction, shown in Fig. 1, are replotted together in order to facilitate the comparison. The angular distribution at the deuteron energy of 2.6 MeV shown in this figure is also the result obtained by Kawai. The scale on the ordinate at the right side, which refers to the differential cross section at the deuteron energy of 7.9 MeV obtained by Gibson and Thomas[4)], gives a value larger by two orders of magnitude than the scale on the ordinate at the left side, which refers to the differential cross sections at the other deuteron energies, does. The differential cross section at 7.9 MeV may be erroneous in its estimation.

Fig. 3 shows the same angular distributions plotted against, instead of the angle θ, the momentum transfer k defined by

$$k=k_d^2+k_p^2-2k_dk_p\cos\theta\ ,$$

where k_d and k_p are the amplitudes of the wave number vectors of the incoming deuteron and the outgoing proton respectively. The plane wave approximation of the stripping theory predicts the angular distributions which are represented by the square of the spherical Bessel function, $\{j_1(kr)\}^2$, multiplied by a factor which decreases monotonically with the increasing angle and does not depend critically on the bombarding deuteron energy. Therefore, it is expected that the maxima and minima in the angular distributions for a certain reaction at different deuteron energies occur at the same values of k, if the reaction concerned can be well explained by the plane wave approximation of the stripping theory using the interaction radius, r, approximately independent of the bombarding energy. It is noted that the positions of the maxima and minima of the angular distributions shown in Fig. 3 are more convergent to each other than those shown in Fig. 2 are.

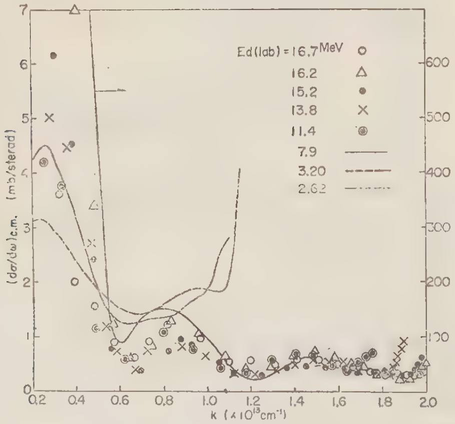

Fig. 3. The angular distributions for the $N^{15}(d, p)N^{15}$ ground state reaction, plotted against the momentum transfer k instead of the reaction angle.

This behavior of the angular distribution is consistent with the results found in the reactions $C^{12}(d, p)C^{13}$ and $0^{16}(d, p)0^{17}$ by E. W. Hamburger[7].

The values of the interaction radius, which were determined by fitting the simple deuteron stripping theory to the experimental angular distributions at different deuteron energies, are plotted against the deuteron energy and are shown in Fig. 4. The interaction radius is approximately independent of deuteron energy and tends to get larger as deuteron energy decreases.

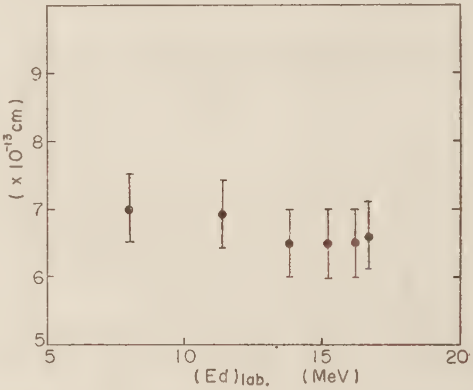

Fig. 4. The values of the interaction radius for the $N^{14}(d, p)N^{15}$ ground state reaction at different deuteron energies, estimated from the experimental angular distributions using the simple deuteron stripping theory.

The authors are very grateful to the cyclotron crew of the Institute for Nuclear Study of University of Tokyo for operation of the cyclotron. They are also much indebted to Prof. E. W. Hamburger and Dr. M. Takeda for sending their results prior to publication.

References

1) S. Morita, N. Kawai, N. Takano, Y. Gotô, R. Hanada, Y. Nakajima, S. Takemoto and Y. Yaegashi: J. Phys. Soc. Japan **15** (1960) 361.
2) I. Nonaka, H. Yamaguchi, T. Mikumo, I. Umeda, T. Tabata and S. Hitaka: J. Phys. Soc. Japan **14** (1959) 1260.
3) M. Takeda: Private communication.
4) W. M. Gibson and E. E. Thomas: Proc. Roy. Soc. London **A**, **210** (1951) 543.
5) N. Kawai: J. Phys. Soc. Japan **16** (1951) 157.
6) M. Takeda: Private communication.
7) E. W. Hamburger: Private communication.

JOURNAL OF THE PHYSICAL SOCIETY OF JAPAN Vol. 16, No. 10, OCTOBER, 1961

(α, p) Reactions near $Z=26$

By Itaru NONAKA, Hisashi YAMAGUCHI, Takashi MIKUMO,
Iwao UMEDA*, Tatsuro TABATA** and Saburo HITAKA***

Institute for Nuclear Study, University of Tokyo,
Tanashi-machi, Kitatama-gun, Tokyo, Japan

(Received May 11 1961)

Spectra of protons from the (α, p) reactions on Ti, Cr, Fe, Ni, Cu and Zn were measured at the energy of alpha particles near 28 MeV. For Ti and Fe the shapes of the spectra and the distributions of the observed levels of residual nuclei resemble each other. This is also true for Cr and Ni, and for Cu and Zn.

Angular distributions of the first, the second and the third proton groups for Ni, and of the first and the second proton groups for Zn were all known to show the direct process type forward peaking. The integrated total cross sections of these proton groups are 0.5_4(first), 0.4_9(second) and 0.7_2(third) mb for Ni and 0.2_4(first) and 0.2_4(second) mb for Zn respectively.

§ 1. Introduction

A variety of experiments have been performed by many investigators to implement the understanding of the mechanisms of medium energy nuclear reactions. On the (α, p) reactions most of the experiments are studies of angular distributions of protons from the reactions. However, sufficient experimental informations concerning emission spectra will be important for the understanding of reaction mechanisms.

Concerning the (α, p) reactions, emission spectra have been measured by R. M. Eisberg and others[1] at alpha particle energy of 40 MeV on heavy elements, by W. Swenson and N. Cindro[2] at 30.5 MeV on medium weight elements, and by N. O. Lassen and V. A. Sidrov[3] at 19.3 to 11.9 MeV on medium weight elements. Main purpose of these investigations, however, seems to be in studies of level density distributions in the residual nuclei.

In the (α, p) reactions of medium energy it is certain from the studies of angular distributions of protons that there are considerable contributions from the direct process type reaction mechanisms. We tried to measure the emission spectra of protons from the (α, p) reactions on medium weight nuclei in the forward directions where the direct process type reaction will predominate. It is considered that by the above method we can obtain some informations on the levels of residual nuclei which are strongly excited by the (α, p) reactions.

§ 2. Experimental Procedures

The experimental arrangements and procedures are the same as those in our previous experiments[4),5)]. The external alpha particle beam of 28.4 MeV from the I.N.S. variable energy cyclotron was brought into the 100 cm scattering chamber and the emitted protons were detected by a thin NaI(Tl) scintillation counter located in the scattering chamber. The energy scales of the detected protons were determined by making use of the known energy values of the recoil protons which were originated from the moisture contamination on the surfaces of target foils.

The targets used were foils of natural elements of Ti, Cr, Fe, Ni, Cu and Zn which were 1.21, 3.5, 2.06, 2.31, 3.45 and 4.58 mg/cm² thick respectively. They were set to make an angle of 45° to the beam direction. The energy values of alpha particles in the centres of the targets were between 28.0 and 28.3 MeV according as the thickness of each target foil.

The spectra were measured at angles of 11° and 30° for Ti, Cr, Fe and Cu. For Ni and Zn, measurements were performed at several angles and the angular distributions of the first, the second and the third proton groups were obtained.

---

* Kyoto University. Now at Technical Research Laboratory, Japan Steel and Tube Corporation, Kawasaki, Kanagawa-ken

** Kyoto University.

*** Kyushu University. Now at Central Laboratory, Hitachi Ltd., Kokubunji-machi, Tokyo.

§ 3. Results and Discussions

In Fig. 1, the proton spectra at 30° (lab.) expressed as $(d^2\sigma/d\omega.\,dQ)_{\text{cm}}$ v.s. Q-value are shown. Reaction particles other than protons are considered to be not contained in the spectra because the aluminium absorber of 269 mg/cm² in thickness inserted in front of the scintillation counter can stop the elastically scattered alpha particles and also the deuterons from the (d, α) reactions which have high negative Q-values. The (α, np) and $(\alpha, 2p)$ reactions have also high negative Q-values and have little contributions in the observed proton spectra.

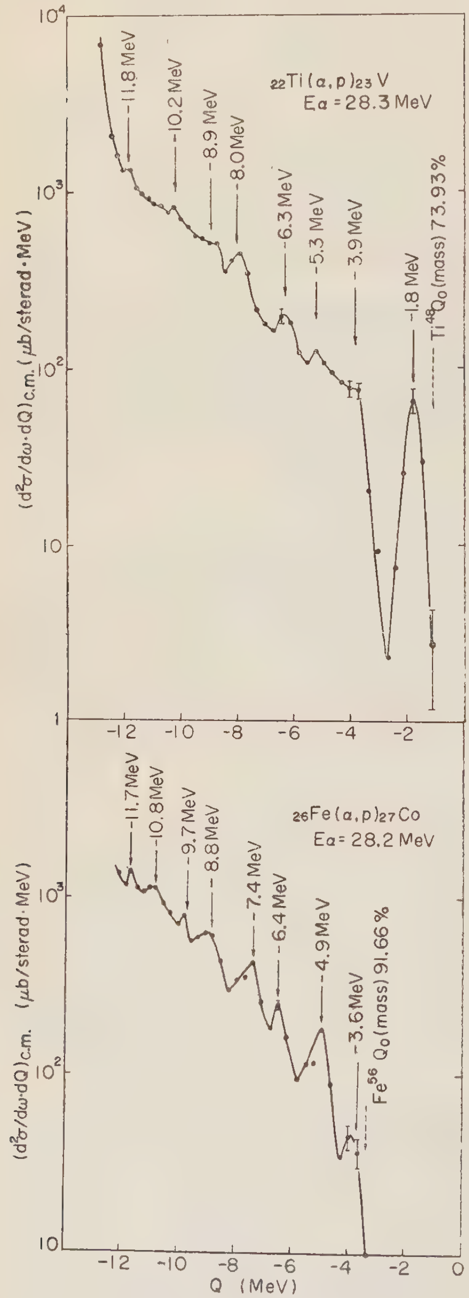

Fig. 1 (a). Spectra of protons at 30°(lab.) from $_{22}$Ti$(\alpha, p)_{23}$V and $_{26}$Fe$(\alpha, p)_{27}$Co.

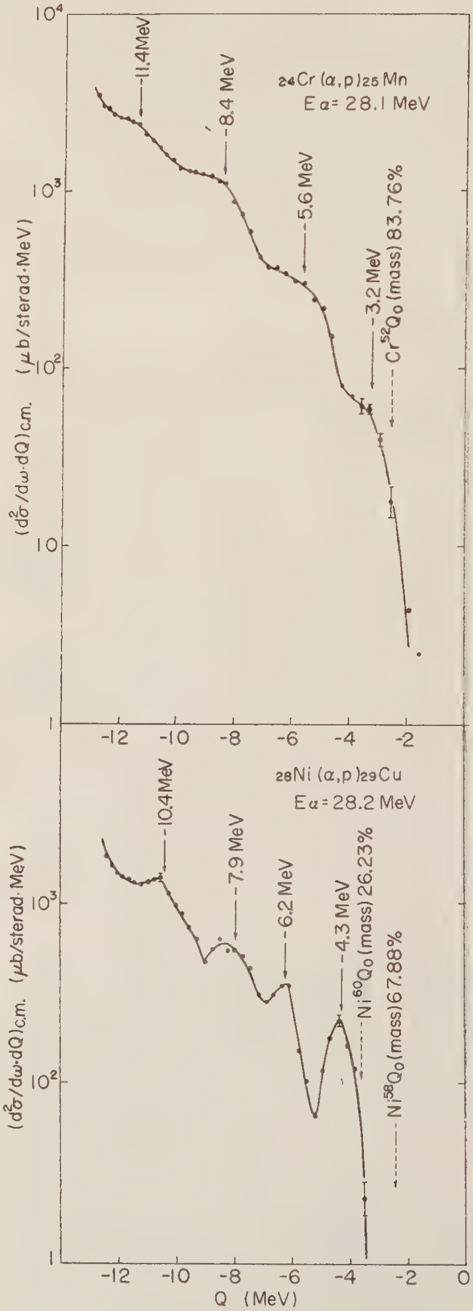

Fig. 1 (b). Spectra of protons at 30°(lab.) from $_{24}$Cr$(\alpha, p)_{25}$Mn and $_{28}$Ni$(\alpha, p)_{29}$Cu.

For $_{22}$Ti and $_{26}$Fe the shapes of spectra resemble each other. This is also true for, $_{24}$Cr and $_{28}$Ni, and for $_{29}$Cu and $_{30}$Zn. Positions of the excited levels of residual nuclei measured from the lowest ones which are excited by the (α, p) reactions are shown in Fig. 2. The distributions of the observed levels have good correspondence between the above mentioned pairs of reactions, $_{22}$Ti$(\alpha,p)_{23}$V and $_{26}$Fe$(\alpha, p)_{27}$Co, $_{24}$Cr$(\alpha, p)_{25}$Mn and $_{28}$Ni$(\alpha, p)_{29}$Cu, $_{29}$Cu$(\alpha, p)_{30}$Zn and $_{30}$Zn$(\alpha, p)_{31}$Ga.

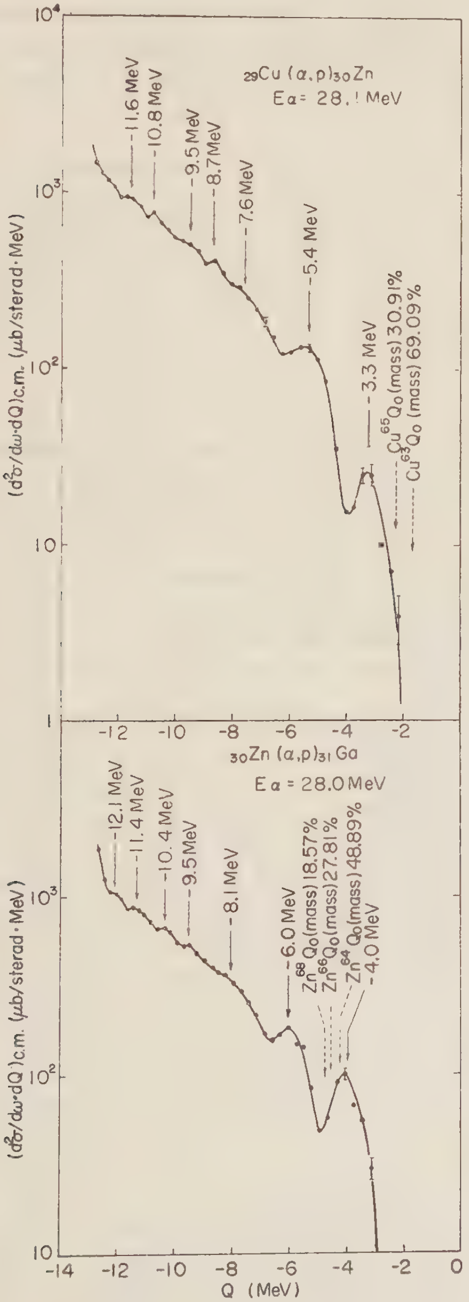

Fig. 1(c). Spectra of protons at 30°(lab.) from $_{29}$Cu$(\alpha, p)_{30}$Zn and $_{30}$Zn$(\alpha, p)_{31}$Ga.

The targets were of natural elements. but in the cases of Ti, Cr and Fe the reactions might be considered to be produced by the single isotopes $_{22}$Ti^{48}, $_{24}$Cr^{52} and $_{26}$Fe^{56} respectively, because other isotopes have abundances smaller than 10 per cent. In the cases of Ni, Cu and Zn, however, the reactions might not be considered to be produced by single isotopes.

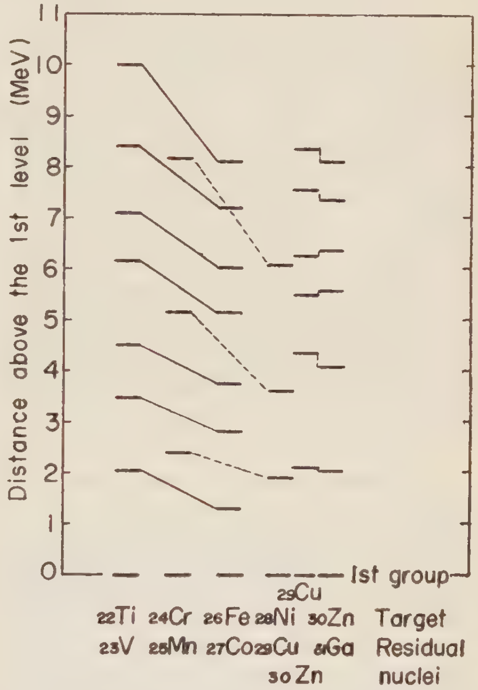

Fig. 2. Positions of levels excited by the (α, p) reactions measured from the first proton groups.

In some cases, Q-value of the lowest observed level does not coincide with that of the ground state of the residual nucleus calculated from known mass values[6] which is indicated as Q_0 in Fig. 1. Especially, in the cases of Ni and Cu targets these discrepancies are considered to be greater than the experimental errors (~0.3 MeV), so we must conclude that the ground states are difficult to be produced by the (α, p) reactions in these cases. N. O. Lassen and V. A. Sidrov[3] also found that the ground state of $_{30}$Zn^{66} was not produced by the $_{20}$Cu$^{63}(\alpha, p)_{30}$Zn^{66} reaction in the region of alpha particle energies between 11.9 and 19.3 MeV.

If we consider the (α, p) reaction to proceed through stripping of the incident alpha particle into a proton and a triton as J. L. Yntema[11] does in the case of the (α, t) reaction, then the states of residual nucleus which are strongly excited by the (α, p) reaction will be those which are nearly expressed by a system of the target nucleus plus a triton. The level structures shown in Fig. 2 are considered to show the distributions of such states in the residual nuclei. The reason why the distributions of these levels should have the characters shown in Fig. 2 is not known in the present states of theoretical consideration.

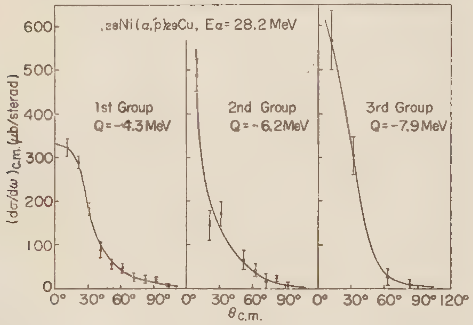

Fig. 3 (a). Angular distributions of the proton groups from Ni target.

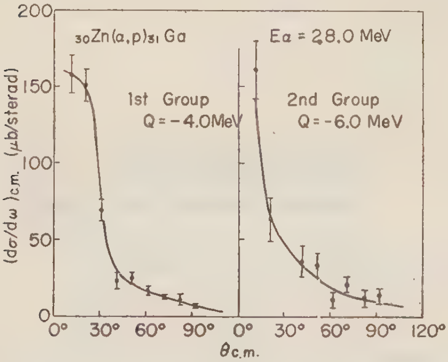

Fig. 3 (b). Angular distributions of the proton groups from Zn target.

The angular distributions of the first, the second and the third proton groups for Ni, and of the first and the second proton groups for Zn were all known to show the direct process type forward peaking which has negligibly small differential cross sections at angles greater than 90° as shown in Fig. 3.

Total cross sections of these proton groups were obtained by integrating the angular distributions and the results are shown in Table I.

Table I. Integrated total cross section.

Target	E_α (MeV)	Total cross section (mb)		
		First group	Second group	Third group
$_{28}$Ni	28.2	0.5_4	0.4_9	0.7_2
$_{30}$Zn	28.0	0.2_4	0.2_4	

The authors express their cordial thanks to the cyclotron technical staffs of the Institute for Nuclear Study.

References

1) R. M. Eisberg, G. Igo and H. E. Wegner: Phys. Rev. **100** (1955) 1309.
3) W. Swenson and N. Cindro: Private communication.
3) N. O. Lassen and V. A. Sidrov: Private communication.
4) I. Nonaka et al.: J. Phys. Soc. Japan **14** (1959) 1260.
5) H. Yamaguchi: J. Phys. Soc. Japan **16** (1961) 583.
6) A. H. Wapstra: Handbuch der Physik (S. Flüge) **38/1** (1958) 1.
7) J. L. Yntema: Phys. Rev. Letters **4** (1960) 297.

JOURNAL OF THE PHYSICAL SOCIETY OF JAPAN, Vol. 16, No. 10, OCTOBER, 1961

Resonant Scattering of Photons in Mg and Si

By Masumi SUGAWARA

Department of Physics, Faculty of Science,
Tohoku University, Sendai, Japan

(Received May 21, 1961)

An NaI(Tl) scintillation spectrometer was used to study the resonant scattering of photons generated by the bremsstrahlung x-rays. The resonant levels were found at 10.2 and 9.3 MeV in Mg and at 11.3 MeV in Si. Their level widths were obtained by the self absoption method. They are 3.8 eV and 0.9 eV in Mg, and 8.3 eV in Si, respectively. The spins and parities of these levels were assigned to be 1^+ by considering the isotopic spin multiplets.

§1. Introduction

The resonant scattering of photons has been studied in the energy region below the particle thresholds using bremsstrahlung or gamma rays from nuclear reactions. Very few reports are available concerning the reaction of this kind using bremsstrahlung x-rays, because the cross sections averaged over the energy are rather small as compared with the electronic cross sections and the continuous spectrum of bremsstrahlung makes very troublesome background. Although the measurement is difficult, it is interesting to investigate the properties of the nuclei when irradiated by the photons. Such a kind of experiment may give information on the energies, widths, spins and parities of the levels. On the other hand, the experiment at the energies around the particle thresholds may give the relation between the phenomena of gamma-ray scattering by the discrete levels and by the continuous region.

Broad peaks in the elastic scattering cross section around the particle threshold energies were found and have been explained as those corresponding to the lower part of the giant resonance.[1)2)] These broad resonances in light nuclei are composed of several isolated levels and have a magnetic dipole character, but in heavier nuclei it is not clear whether they are divided into isolated levels, nor is it known what type of the electromagnetic interaction they have.

The experiments of this kind have been done for some light nuclei using the bremsstrahlung x-rays.[3)–7)] They are 3.56 MeV level in Li^6, 4.46 MeV and 5.03 MeV in B^{11}, 15.1 MeV in C^{12}, 10.15 MeV in Mg and 11.4 MeV in Si. γ-rays from $F^{19}(p, \alpha\gamma)O^{16}$ were also used to take a survey of the averaged character of resonant elastic scattering on several tens of elements at the energies of about 6 or 7 MeV.[8)]

The purpose of the present report is to clarify some of the problems mentioned above. Recently Tobin reported the resonant scattering by Mg and Si.[7)] The present results do not agree very well with his results and we shall discuss the discrepancies between his results and ours and also the problems which he did not mention.

§2. Experimental arrangement

The experiment was performed using the bremsstrahlung x-rays from the platinum target in a 25 MeV betatron whose repetition rate is 50 cycles per second. Produced x-rays were defined by iron and lead collimators and electrons in the beam were swept away by a sweep magnet set in a tunnel in the shielding wall which consisted of heavy concrete and water saturated with boric acid. Blocks made of lead, iron or paraffin were used to avoid the neutron and x-ray background. Then the x-ray beam brought into the next room hit the scatterer which was located in front of the detector. The distance between the platinum target and the scatterer was about 4 meters. The x-ray beam had a diameter of 4.0 cm at the scatterer and was hardened by a graphite absorber of 5.65 g/cm² in thickness which was directly attached to the front of the collimator.

The beam intensities were monitored by the thin walled transmission ionization chamber with electrodes composed of seven aluminum foils 30 μ in thickness and 10 cm in diameter. The current fed by the ionization chamber was measured by a vibrating reed electrometer and was recorded.

A scattered photon detector was an 8″×8″ NaI(Tl) crystal viewed by three photomultipliers (Du Mont 6363). The crystal, the photomultipliers and a cathode follower were all located in the lead shield with walls 15 cm thick in the side of the betatron room and 10 cm thick in other sides, surrounded with blocks made of paraffin and a mixture of boric acid and paraffin.

The detector was placed at 120 degrees from the incident beam direction and subtended the solid angle of 0.108 ster. through a hole 15 cm long tapered toward the center of the scatterer in a lead collimater which was located in front of the detector. The hole was filled with alluminum plug 5 cm thick and covered with a 4 cm thick paraffin plate in order to filter out soft x-rays and electrons. The front surface of the NaI detector was 40 cm distant from the scatterer.

The width of the primary x-rays was broadened to about 20 μ sec. to diminish the pile up effect. The pulses from the cathode follower were amplified by a somewhat fast dipole amplifier and were analysed by a 30 channel pluse height analyser. The amplifier was biased to discriminate small pulses caused by low energy photons and other processes. The pulse height analyser was operated for about 40 μ sec. in each betatron cycle simultaneously with betatron pulses to reduce the cosmic ray background.

Stability of the electronic detecting circuits was monitored at every three hours by 1.28 MeV monochromatic γ-rays of Na^{22}. The scatterer and the absorber of Mg were metal plates. The thickness was 1.74 cm and 1.54 cm respectively, and the diameter was 9.0 cm in both cases. In the case of Si, metal powder contained in thin walled cans made of aluminum, 10 cm in diameter and 2 cm thick as a scatterer and 8.0 cm in diameter and 2 cm thick as an absorber, were used.

Each scatterer was situated so that the direction normal to the surface of the scatterer might divide equally the angle between the direction of the incident beam and that of the axis of the NaI(Tl) crystal. Each absorber was placed in the incident beam at 50 cm forward the scatterer. The position of the absober will be called "the absorber position" in the following sections. The experimental arrangement is shown in Fig. 1. The place marked by a broken line is "the absorber position".

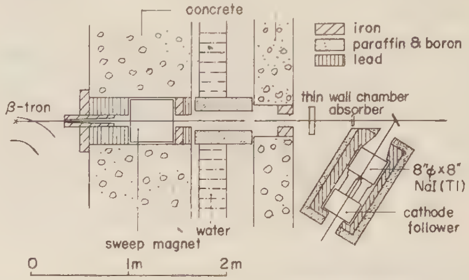

Fig. 1. The arrangement of the apparatus. The place marked by the broken line is "the absorber position" used in the self absorption measurements.

§ 3. Experimental procedure

The thickness of Mg and Si scatterers used was 3.03 g/cm^2 and 2.20 g/cm^2 respectively, as shown in Table I.

The spectra of photons scattered from the targets were measured when these are bombarded with the bremsstrahlung x-rays. The betatron energy was set to be 16.0 MeV, since the bremsstrahlung of this maximum energy has photons enough to excite nuclei to about 10 MeV without giving much background x-rays to the detector. The measured spectra are shown in Figs. 2 and 3 by the solid lines.

Table I. Thickness of the scatterer and the absorber.

Element	Thickness of scatterer used	Thickness of absorber used
Mg	3.03 g/cm^2	2.84 g/cm^2
Si	2.20 g/cm^2	2.26 g/cm^2

In the spectrum of Mg, a large broad peak was found at about 10 MeV and two small peaks at about 8 and 6 MeV. The peak at 10 MeV was divided into two photon groups which corresponded to 10.2 MeV and 9.3 MeV levels, and the existence of this splitting was verified by the excitation yield curve as shown later. It was not determined exactly whether the peak at 8 MeV was due to another resonant level or occured from other processes.

The last one around 6 MeV was identified to be the photons of neutron capture process in lead, because it was found even in the measurement in which the gating pulses were delayed to exclude the photons induced by the scattering process.

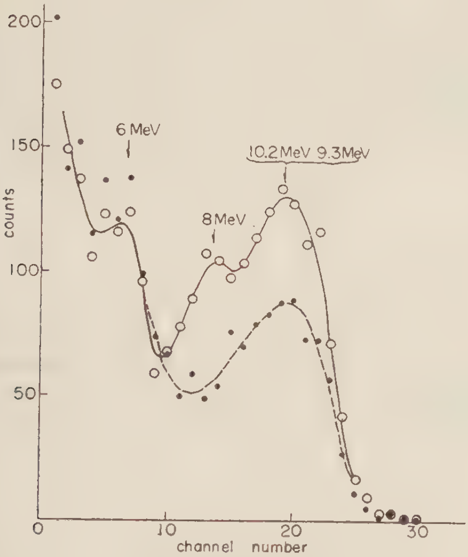

Fig. 2. The spectra of the scattered photons from the Mg scatterer. The solid line is the spectra measured without the Mg absorber and the broken line with the absorber. They are all normalized to the unit charge of the ionization chamber.

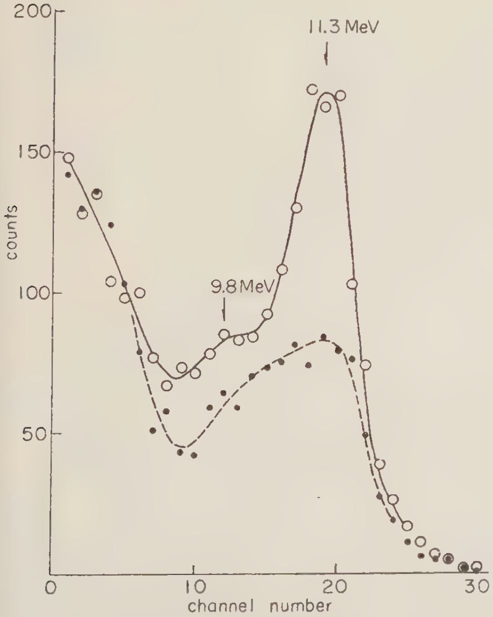

Fig. 3. The same as Fig. 2 with Si scatterer and absorber.

In the spectrum of Si, a large peak was found at about 11 MeV and a small one at about 10 MeV.

Setting the absorber between the scatterer and the monitor, the scattered photon spectra were measured by the same procedure and at the same maximum energy of the bremsstrahlung as that without the absorber. The thickness of the absorbers was 2.84 g/cm^2 in Mg and 2.26 g/cm^2 in Si. The spectra were shown by broken lines in Figs. 2 and 3. It was clear that the photons corresponding to the main peaks were considerably reduced by the absorber in both elements, since the photons to be scattered were seriously absorbed into the same level of the absorber.

Excitation curves were studied to determine more definitely the energies of the levels. Fig. 4 shows the excitation curve of Mg measured by changing the maximum energy of the bremsstrahlung at intervals of 0.33 MeV and 0.50 MeV. At each energy the counts from 6th to 27th channel were summed to get the yields and normalized to the unit charge fed by the ionization chamber. These channels can involve photons of 7 MeV to 14 MeV.

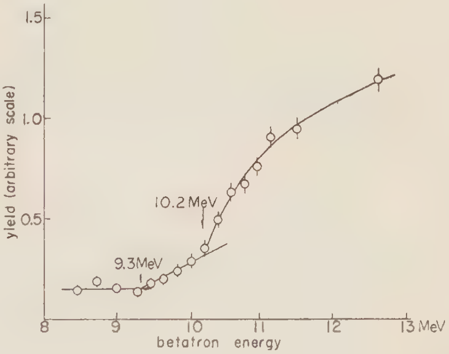

Fig. 4. The yield curve for Mg. The count at each bombarding energy of the incident bremsstrahlung was normalized to the unit charge from the monitor. The vertical lines show the statistical errors.

The caliblation of the maximum energy of the bremsstrahlung x-rays was made by measuring the resonant scattering of photons by 15.1 MeV level in C^{12} and the threshold energy of Cu$^{63}(\gamma, n)$ reaction, 10.8 MeV. Activities of Cu^{62} were detected by a G–M counter. There were two clear breaks at 9.3 MeV and 10.2 MeV. Comparing with the scattered photon spectra shown in Fig. 2, it was found that both breaks correspond to the broad peak at about 10 MeV. The break corresponding to 8 MeV peak was not obtained in the yield curve measurement, because of relatively high background at these lower energies. However, the spectrum shows clearly that there is a photon group of about 8 MeV. The yield curve was used to estimate the ratio of the 9.3 MeV photon group to that of 10.2 MeV group to be 0.35±0.08, both groups being normalized to a unit number of incident photons. This value was used to get the ratio of the two level widths, as shown in the next sections.

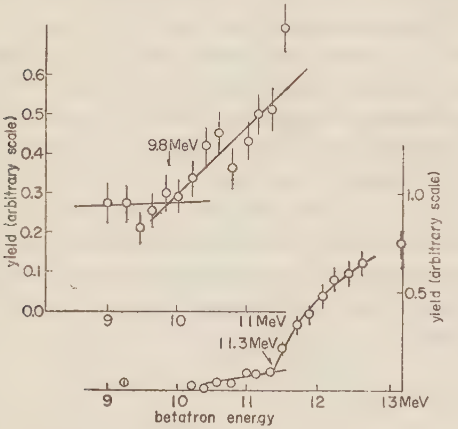

Fig. 5. The excitation curve of Si. The upper curve was obtained by the counts of 1st to 14th channel and the lower curve by the counts of 16th to 24th.

Fig. 5 shows the excitation curves of Si. The lower curve was obtained by the sum of counts from 16th to 24th channel normalized to the unit charge of the monitor and it had a clear break at 11.3 MeV. In the upper curve, the summed counts from 1st to 14th channel were plotted to get another break at 9.8 MeV. Two channel groups can contain photons of 6.0 MeV to 10.0 MeV and 10.5 MeV to 13,0 MeV, respectively. The energies corresponding to these breaks were in agreement with those corresponding to the peaks in the spectra shown in Fig. 3.

To obtain the level widths by the self absorption measurement, the ratio of the photon yields without the absorber to the yields with the absorber in the absorber position must be estimated from the spectra shown in Fig. 2 and Fig. 3.

In the case of Mg the ratio $A(\varDelta)/A(0)$ was given by

$$\left(\frac{A(\varDelta)}{A(0)}\right)_{(10.2+9.3)}=0.67\ ,$$

where $A(\varDelta)$ and $A(0)$ were yields with and without the absorber and the suffix implies the levels involved, i.e. 10.2 MeV and 9.3 MeV levels. The yield could not be separated into each level.

The ratio for the case of Si was estimated as

$$\left(\frac{A(\varDelta)}{A(0)}\right)_{(11.3)}=0.60$$

for 11.3 MeV level.

§ 4. Calculation

When the scatterer was set in front of the detecter and the absorber in the absorber position, the yield of photons by a single resonant level is given by

$$A(\varDelta)=g\int_0^\infty \varPhi(E)\frac{\sigma_s}{\sigma_n+2\sigma_e}e^{-(\sigma_n+\sigma_e)\varDelta N}\\ \times[1-e^{-(\sigma_n+2\sigma_e)NT/\cos\beta}]dE\ , \qquad (1)$$

where $\varDelta$; absorber thickness in cm, T; scatterer thickness in cm, N; number of the atoms per unit volume of the target and the absorber, β; the angle between the incident beam and the normal to the front face of the scatterer, $\varPhi(E)$; bremsstrahlung spectrum, σ_s; elastic scattering cross section of photon, σ_n; nuclear absorption cross section, σ_e; electronic absorption cross section, and g; other factors which do not depend on energy, for example, geometrical factor.

Assuming that $\varPhi(E)$ and σ_e are constant in the energy interval where σ_s and σ_n are not zero but have the finite values, we get a more convenient form as

$$A(\varDelta)=g\varPhi(E)e^{-\sigma_e\varDelta N}\int\frac{\sigma_s}{\sigma_n+2\sigma_e}e^{-\sigma_n\varDelta N}\\ \times[1-e^{-(\sigma_n+2\sigma_e)NT/\cos\beta}]dE\ . \qquad (2)$$

Though the level widths are broadened to several tens of eV by the Doppler effect caused by the lattice oscillation in the target metal, this effect is not so serious as to invalidate the approximation of taking $\varPhi(E)e^{-\sigma_e\varDelta N}$ out of the integrand in (1). If the measurement with and without the absorber is performed by the bremsstrahlung of the same maximum energy, the yield ratio of the former case to the latter is given by

$$\frac{A(\varDelta)}{A(0)}$$
$$=e^{-\sigma_e \varDelta N}\frac{\int \frac{\sigma_s}{\sigma_n+2\sigma_e} e^{-\sigma_n \varDelta N}[1-e^{-(\sigma_n+2\sigma_e)NT/\cos\beta}]dE}{\int \frac{\sigma_s}{\sigma_n+2\sigma_e}[1-e^{-(\sigma_n+2\sigma_e)NT/\cos\beta}]dE} \tag{3}$$

since $\varPhi(E)$, σ_e and g have the same values in both cases. Provided that σ_s has the same shape as σ_n, but differs only in magnitude, the ratio is rewritten as

$$\frac{A(\varDelta)}{A(0)} e^{+\sigma_e \varDelta N}=\frac{I(\varDelta)}{I(0)}, \tag{4}$$

where

$$I(\varDelta)\equiv\int \frac{\sigma_n}{\sigma_n+2\sigma_e} e^{-\sigma_n \varDelta N}[1-e^{-(\sigma_n+2\sigma_e)NT/\cos\beta}]dE$$

and $I(0)$ is the value without the absorber. An absorption cross section is expressed using the Doppler width, δ, and the total level width at half maximum, $\varGamma$, as

$$\sigma_n=\sigma_n{}^0 \frac{1}{2\sqrt{\pi t}} \int_{-\infty}^{\infty} \frac{e^{-(x-y)^2/4t}}{1+y^2} dy, \tag{5}$$

where $\sigma_n{}^0$ is the peak value of the total absorption cross section, $t=(\delta/\varGamma)^2$, and $x=2(E-E_0)/\varGamma$.[9] δ is given by $\delta=E_0(2kT/Mc^2)^{1/2}$ where E_0 is the resonant energy, M the mass of the target nucleus, k the Boltzman constant, c the velocity of light and T the effective temperature in the sample.

When the values, $A(\varDelta)$ and $A(0)$, are measured separately at each resonant level and $\sigma_n{}^0$ is known, the level width, $\varGamma$, can be determined by comparing the experimental value of $\{A(\varDelta)/A(0)\}\exp(\sigma_e \varDelta N)$ with $I(\varDelta)/I(0)$ given by the numerical calculation in (4). It is not easy to obtain the level widths when $A(0)$ and $A(\varDelta)$ are not separated into each level in experiments, as it appeared in the case of Mg. When two levels of widths, $\varGamma_1$ and $\varGamma_2$, contribute, the yields are given by $A(\varDelta)=A_1(\varDelta)+A_2(\varDelta)$ and $A(0)=A_1(0)+A_2(0)$. If $\sigma_e(E_{01})$ nearly equals to $\sigma_e(E_{02})$,

$$\frac{A(\varDelta)}{A(0)} e^{\sigma_e \varDelta N}=\frac{I_1(\varDelta)+I_2(\varDelta)\varPhi(E_{02})/\varPhi(E_{01})}{I_1(0)+I_2(0)\varPhi(E_{02})/\varPhi(E_{01})}, \tag{6}$$

where $\varPhi(E_{01})$ and $\varPhi(E_{02})$ are the photon fluxes in the unit energy interval at the resonant levels. The level widths $\varGamma_1$ and $\varGamma_2$ can be obtained by calculating the right hand side of (6) with adequate pairs of $\varGamma_1$ and $\varGamma_2$ which are allowed by the ratios estimated from the excitation curves, and by comparing with the experimental values in the left hand side.

In calculation it was assumed that all of the absorption processes of x-rays are dipole, i.e. $\sigma_n{}^0=6\pi\lambda\!\!\!^{-2}$ and that the resonant levels decay only to the ground state and the isotopes which contribute to these resonances are Mg^{24} and Si^{28}. The discussion on these assumptions will be given later.

In the case of Mg there are three levels as mentioned in the last section, i.e. at 10.2 MeV, 9.3 MeV and at about 8 MeV. Since $A(0)$'s corresponding to 10.2 MeV and 9.3 MeV were not separated because of the poor resolution of the detector, the yield ratio of two photon groups, $A_{9.3}(0)/A_{10.2}(0)$ was determined using the excitation curve in Fig. 4. From this ratio the relation between $\varGamma_{9.3}$ and $\varGamma_{10.2}$ were calculated by

$$\frac{A_{9.3}(0)}{A_{10.2}(0)} \cdot \frac{\varPhi(10.2)}{\varPhi(9.3)}=\frac{I_{9.3}(0)}{I_{10.2}(0)}, \tag{7}$$

where suffixes 9.3 and 10.2 in $A(0)$ denote the energies of the levels. The resultant relation between $t_{9.3}^{1/2}=\delta/\varGamma_{9.3}$ and $t_{10.2}^{1/2}=\delta/\varGamma_{10.2}$ is shown in Fig. 6, in which the solid line is the ratio and the broken lines are the limits of the statistical errors.

Finally $\varGamma_{9.3}$ and $\varGamma_{10.2}$ were given by substituting $I(0)$ and $I(\varDelta)$ calculated for the allowed pairs of $\varGamma_{9.3}$ and $\varGamma_{10.2}$ into the right hand side of (6) and by comparing with the

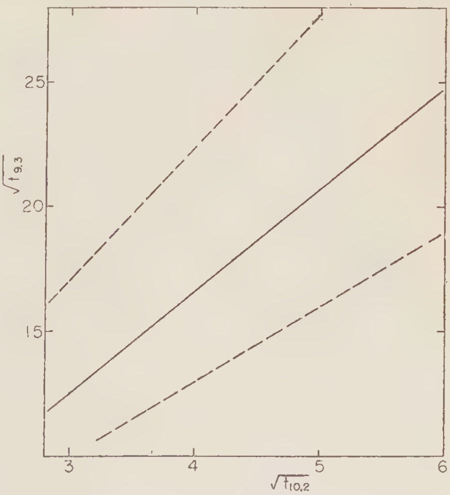

Fig. 6. Relation between $t_{10.2}^{1/2}=\frac{\delta}{\varGamma_{10.2}}$ and $t_{9.3}^{1/2}=\frac{\delta}{\varGamma_{9.3}}$. The broken lines are the limits of the statistical errors.

experimental values (in the left hand side). This procedure is shown in Fig. 7. In the figure the curve is the calculated value of $\frac{I_{10.2}(\Delta)+I_{9.3}(\Delta)\Phi(9.3)/\Phi(10.2)}{I_{10.2}(0)+I_{9.3}(0)\Phi(9.3)/\Phi(10.2)}$ by making use of the $\Gamma_{9.3}$ and $\Gamma_{10.2}$ given by Fig. 6 and the horizontal bar crossing the curve shows the experimental value of

$$\left(\frac{A(\Delta)}{A(0)}\right)_{(10.2+9.3)} e^{\sigma_e \Delta N}=0.71\,.$$

The level widths, $\Gamma_{10.2}$ and $\Gamma_{9.3}$, were determined to be $3.8^{+1.2}_{-0.6}$ eV and 0.9 eV respectively. The width for 8 MeV level was approximately estimated to be 0.9 eV from the spectra in Fig. 2 by

$$\Gamma_8=\Gamma_{10.2}\cdot\frac{A_8(0)}{A_{10.2}(0)}\cdot\frac{6\pi\bar{\lambda}^2_{10.2}}{6\pi\bar{\lambda}^2_8} \qquad (8)$$

where $\bar{\lambda}_{10.2}$ and $\bar{\lambda}_8$ are the wavelength of 10.2 MeV and 8 MeV photons. The errors were estimated only for the statistical fluctuations.

In the case of Si, the width for 11.3 MeV state was easily calculated by (4), to be 8.3 ± 2.5 eV, since the spectra in Fig. 3 were separated into two photon groups which belong to 11.3 MeV and 9.8 MeV levels. The width of 9.8 MeV level was found by using the ratio of this level to 11.3 MeV photon

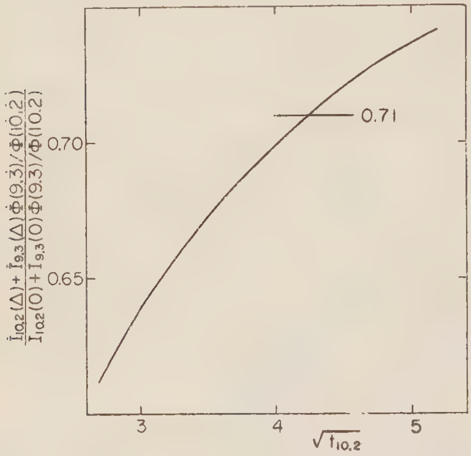

Fig. 7. The curve is $\frac{I_{10.2}(\Delta)+I_{9.3}(\Delta)\Phi(9.3)/\Phi(10.2)}{I_{10.2}(0)+I_{9.3}(0)\Phi(9.3)/\Phi(10.2)}$ calculated by using the values of $t^{1/2}_{10.2}=\delta/\Gamma_{10.2}$ and $t^{1/2}_{9.3}=\delta/\Gamma_{9.3}$ given in Fig. 6. The horizontal bar is the experimental value, $\left\{\frac{A(\Delta)}{A(0)}\right\}_{(10.2+9.3)} e^{\sigma_e \Delta N}=0.71$.

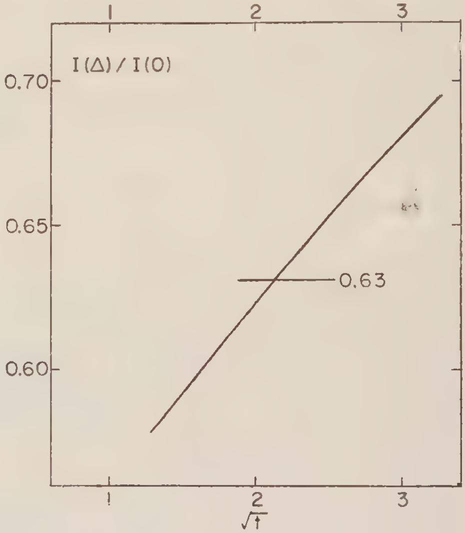

Fig. 8. The curve is $I(\Delta)/I(0)$ vs. $\sqrt{t}$. The horizontal bar shows the experimental value, $\left\{\frac{A(\Delta)}{A(0)}\right\}_{(11.3)} e^{\sigma_e \Delta N}=0.63$.

Table II. The energies of levels found in the present experiment, the Doppler widths and the peak absorption cross sections used to calculate the level widths, and the resultant level widths. The level widths shown in blacket in the last column are Tobin's data[7].

Element	Level energy (MeV)	Doppler width (eV)	Peak absorption cross section (b)	$t^{1/2}$	Level width (eV)
Mg	10.2	16.0	71.7	$4.26^{+1.3}_{-0.7}$	$3.8^{+1.2}_{-0.6}$ $(4.80^{+1.6}_{-1.4})$
	9.3	14.5	86.2	18.	0.9
	8.		117.		0.5
Si	11.3	17.5	58.4	2.12 ± 0.65	8.3 ± 2.5 $(2.89^{+1.0}_{-0.8})$
	9.8		77.7		0.9

group in the sameway as in Mg. These results are listed in the 6th column in Table II.

§ 5. Discussion

The isotope abundance and the particle threshold energies were considered in order to determine which isotope made the dominant contribution to the resonant scattering in the present experiment. A single level of higher energy than the particle threshold hardly scatters photons, since the particle emission predominates over photon scattering. Thus, the isotopes which have the particle threshold energies lower than the photon energies of interest need not be considered. Isotopes of little abundance are also excluded in this experiment.

In the calculation of the level widths the type of the photon absorption was assumed to be dipole, and the excited states were assigned to decay only to the ground states by electromagnetic transition. In the measurements the cascade gamma rays have chances to occur through the first excited state of Mg^{24} or Si^{28}, since these states are of 2^+ in both elements. If the cascade takes place, the energy of such photons should be about 8 MeV for Mg^{24} and 10 MeV for Si^{28}. In the case of Si, the gamma-rays of about 9.8 MeV were detected in the scattered photon spectra, but they were identified as the photons decaying from a 9.8 MeV resonant level to the ground state by analysing the spectra and the excitation curves. The circumstances are somewhat complicated in the case of the 8 MeV gamma-rays of Mg^{24}. We can not exclude the possibility of cascade decay since the excitation curve was not measured at the energies around 8 MeV. However, the existence of the 8 MeV level was assigned considering the fact that most of the states of various elements excited by photon absorption hardly decay in cascade.

Another assumption was that the excited states do not emit alpha particles. If these levels were assigned to $T=1$ as shown later, this assumption is acceptable since $T=1$ states do not decompose into two $T=0$ particles. The forbiddenness of the alpha particle emission was found in the excited state of 15.1 MeV in C^{12}. The same circumstances seem to occur in Mg and Si.

Table III. The isotope abundance and the particle threshold energies.

Element	Abundance (%)	Particle threshold (γ, p)	Particle threshold (γ, n)
Mg^{24}	78.60	11.69 MeV	16.56 MeV
Mg^{25}	10.11	12.06	7.33
Mg^{26}	11.29	14.03	11.11
Si^{28}	92.18	11.59	17.20
Si^{29}	4.71	12.34	8.47
Si^{30}	3.12	13.79	10.61

The angular momenta of the photons which excited the nuclei to these weak levels were not determined in the present experiment, and so there is no clear evidence for the dipole transition. Therefore, the levels of 8 MeV in Mg^{24} and 9.8 MeV in Si^{28} may be of 1^+, 1^- or 2^+. Tobin recently reported that breaks in his excitation curves corresponding to the present ones at 9.3 MeV in Mg and 9.8 MeV in Si were made by neutron emission from $Mg^{25}(\gamma, n)Mg^{24}$ and $Si^{29}(\gamma, n)Si^{28}$ reactions respectively, but the present experiment found that his arguments were not true, by measuring the capture photon spectra caused by the neutrons in the targets and the enviroments of the detector.

The level width of the present experiment agrees with Tobin's in Mg^{24}. In Si^{28} there is a large discrepancy between his value and the present one, i.e. the latter is about three times as large as the former.

The parities of the highly excited states, 11.3 MeV in Si^{28} and 10.2 and 9.3 MeV states in Mg^{24}, were not determined experimentally. However, there are important evidences that these levels are 1^+ and the transitions between these levels and the ground state are caused by magnetic dipole. If the isotopic spin multiplet theory is applicable to these levels and the 9.3 MeV level in Si^{28} is the lowest $T=1$ level, a 1^+ level corresponding to the 1.37 MeV 1^+ level in Al^{28} 10) must appear at the excitation energy of about 11 MeV in Si^{28}. In the same reason two 1^+ levels may occur around 10 MeV in Mg^{24} corresponding to 0.47 and 1.34 MeV 1^+ levels in Na^{24}. The interval of the two levels is 0.9 MeV in both Mg^{24} and Na^{24}. The 8 MeV level of Mg^{24} can not be explained along the same line at present.

The level schemes which help to understand these discussions are shown in Fig. 9 and

Fig. 10. According to a discussion about the magnetic dipole transition in a self conjugate nucleus,[11] these identifications of the transitions have more solid foundation, since the isotopic spin selection rule reduces the M1 transition strengths between levels with the same *T*.

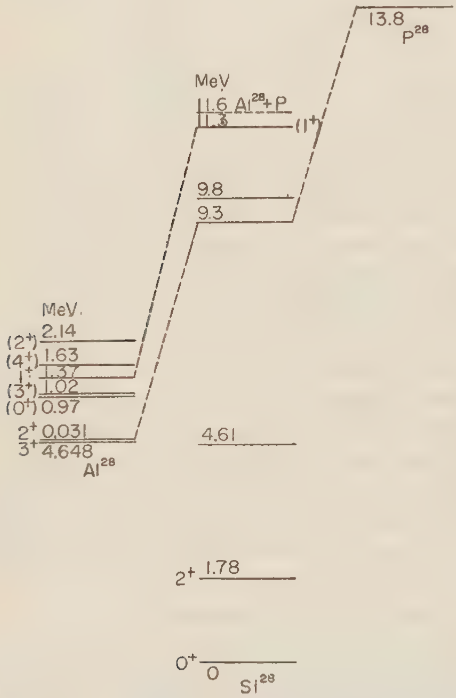

Fig. 9. Correspondence between the levels in Si^{28} and Al^{28}.

It seems interesting that the strong resonant absorptions just below particle thresholds are made by magnetic dipole in most of elements studied by measurements similar to the present one. The 15.1 MeV state of C^{12}, 3.56 MeV state of Li^6 and 4.46 MeV state of B^{11} are also excited by M1. Regarding the isotopic spins, all transitions were induced between $T=1$ excited states and $T=0$ ground states in even-even nuclei.

The excitation energies of the lowest $T=1$, $J^{\pi}=1^+$ levels seem to decrease with mass number systematically in light elements composed of alpha particles, such as Be^8, C^{12}, O^{16}, Ne^{20}, Mg^{24}, Si^{28} and S^{32}. Such a level has not been found for O^{16} so far. It is difficult to observe the level of O^{16} by the photon scattering, since the excitation energy is higher than the particle threshold. In the case of Ne^{20} the level whose energy is about 11 MeV and is lower than the particle threshold has not been found, but it will be measured by this scattering method if the target is available.

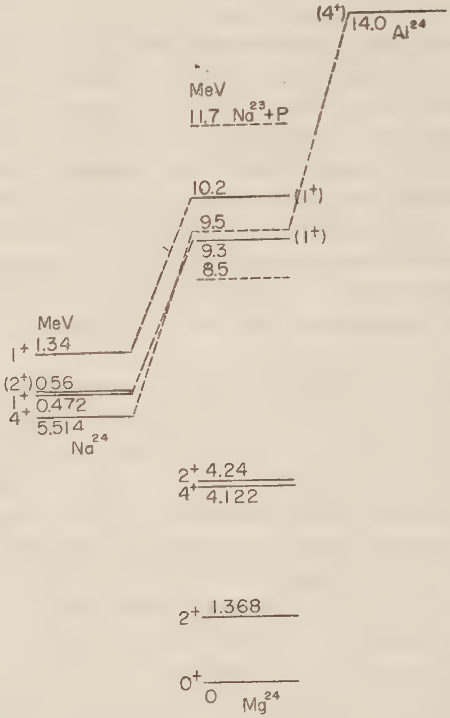

Fig. 10. Correspondence between the levels in Mg^{24} and Na^{24}.

The elastic scattering cross sections of photons were measured at the energies 5 to 14 MeV in many elements.[2] The cross sections have a broad peak around 8 to 10 MeV with a few exceptions. Those peaks are probably composed of several sharp resonance levels in lighter elements, and also in heavier elements they will have the same structure, although the actual measurement could not resolve the fine structure. It may be possible to suggest that these broad resonance peaks just below the particle threshold consist of an assembly of levels induced by magnetic dipole processes. It was also noted by Weisskopf that the electric dipole absorption is depressed by correlation of nucleons at the lower energies and M1 becomes important.

The author would like to express his sincere gratitude to Professor M. KIMURA for helpful discussions and continual interests throughout this work. Thanks are also due to Dr. T.

Tohei for his encouragement in the earlier stage and to Mr. S. Mori for discussions in detail and operation of the machine.

References

1) E. G. Fuller and E. Hayward: Phys. Rev. **101** (1956) 692.
2) T. Tohei, M. Sugawara, S. Mori and M. Kimura: unpublished.
3) L. Cohen and R. A. Tobin: Nucl. Phys. **14** (1959) 243.
4) L. Cohen, R. A. Tobin and McEclhinney: Phys. Rev. **114** (1959) 593.
5) E. Hayward and E. G. Fuller: Phys. Rev. **106** (1957) 991.
6) E. L. Garwin: Phys. Rev. **114** (1959) 143.
7) R. A. Tobin: Private communication.
8) K. Reibel and A. K. Mann: Phys. Rev. **118** (1960) 701.
9) W. E. Lamb: Phys. Rev. **55** (1939) 190.
10) P. M. Endt and C. M. Braams: Rev. Mod. Phys. **29** (1957) 706.
11) G. Morpurgo: Phys. Rev. **110** (1958) 721.

JOURNAL OF THE PHYSICAL SOCIETY OF JAPAN, Vol. 16, No. 10, OCTOBER, 1961

Effect of Impurity-Core on Carrier Mobility in Heavily Doped Germanium

By P. CSAVINSZKY

Research Division, General Dynamics/Electronics, Rochester, New York

(Received May 25, 1961)

The effect of the impurity core on the mobility of charge carriers in heavily doped Ge is investigated by analyzing the role the core plays in the process of ionized impurity scattering. It is concluded, in agreement with experiments, that at the same doping level the electron mobility in an Sb-doped Ge crystal should be larger than in an As-doped Ge crystal. The dependence of the mobility ratio on the electron concentration is also investigated and found to be due to changes in the screening of the impurity ions.

§ 1. Introduction

Recent measurements[1] on the electron mobility in heavily doped n-type Ge show an interesting effect. It has been found that at a given electron concentration and compensation the electron mobility in the degenerate semiconductor depends on the specific nature of the dopant. The findings[1] can be summarized in two points.

1. At $T=293$°K and at electron concentrations of $n=$several times 10^{18}/cc the $\mu(\mathrm{Sb})/\mu(\mathrm{As})$ mobility ratio, as inferred from the published figure[1] is between about 1.2 and 1.4.

2. In the above concentration range the $\mu(\mathrm{Sb})/\mu(\mathrm{As})$ ratio is a monotonic function of electron concentration and increases a few percent with increasing n. An extrapolation of the measured mobility values towards lower electron concentrations shows that the mobility ratio asymptotically decreases to unity at $n \approx 10^{18}$/cc.

§ 2. Theory

For these findings the following explanation is proposed.

1. The mobility difference at a given electron concentration is due to the difference in the total cross section of ionized impurity scattering which, in the present case, is assumed to be the dominant scattering process. The difference in the total scattering cross section is attributed to the difference in the potential of the Sb^+ and As^+ impurity cores.

2. The concentration dependence of the mobility ratio is due to the fact that as the electron concentration in a degenerate Ge crystal increases the screening of the impurity ions by the free electrons becomes more

effective. This means a decrease in the "range" of the ion potential, which, inturn, means that the short range core potential, becomes more important.

In what follows we shall show that the above assumptions can lead to an explanation of findings 1 and 2.

1. *Mobility Difference at a given Electron Concentration.*

In a degenerate Ge sample the electron mobility is given by

$$\mu = \frac{e}{m^*}\tau_F \,, \qquad (1)$$

where e is the electronic charge, m^* is the effective mass of the electron, assumed to be isotropic for the present purposes, and τ_F is the relaxation time taken simply at the Fermi surface as indicated by the suffix F. In the the case of ionized impurity scattering the relaxation time can be expressed[2] as

$$\tau_F = \frac{1}{N_i v_F Q_F} \,, \qquad (2)$$

where N_i is the number of scattering ions/cc, v_F is the velocity of an electron at the Fermi surface and Q_F is the total scattering cross section of an electron of velocity v_F. It follows from Eqs. (1) and (2) that

$$\frac{\mu(\mathrm{Sb})}{\mu(\mathrm{As})} = \frac{Q_F(\mathrm{As}^+)}{Q_F(\mathrm{Sb}^+)} \,. \qquad (3)$$

Let us assume now that the potential of an Sb^+ ion in the Ge crystal differs from that of an As^+ ion only in the core region[3] while far from the nuclei both potentials approach the same screened Coulomb type potential[4]. This is shown schematically in Fig. 1, where the potential energy of an electron is plotted as a function of the distance from the nucleus of an Sb^+ and an As^+ ion. It is assumed that the core potentials are such that the potential energies of the electron satisfy the relation

$$\eta(r) = V_{\mathrm{As}^+}(r) - V_{\mathrm{Sb}^+}(r) \leq 0 \,.$$

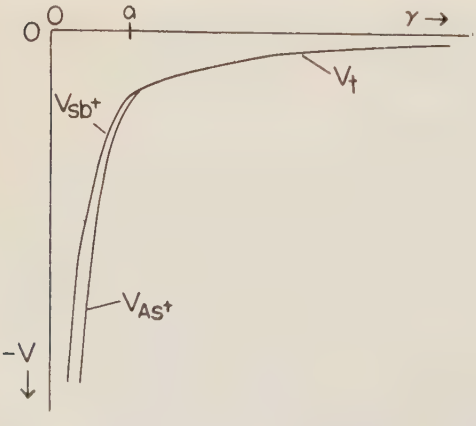

Fig. 1. Schematic representation of the potential energy of an electron as a function of the distance from the nucleus of an Sb^+ and an As^+ ion in a Ge crystal. In the $0<r<a$ core region the ion potentials are different and in the $r>a$ region both approach the same screened Coulomb potential, V_t.

The basis for this assumption is the fact that in Ge semiconductor the ionization energy of an As donor is roughly 30% larger than that of an Sb donor[5]. In this case if $V_{\mathrm{Sb}^+}(r)$ is associated with the ground level E_{Sb}, described by a wave function ψ, then, using first order perturbation theory, $V_{\mathrm{As}^+}(r)$ leads to an energy level $E_{\mathrm{As}} = E_{\mathrm{Sb}} + \varepsilon$, where

$$\varepsilon = \int |\psi|^2 \eta \, dv \,.$$

Since ε is known to be a negative quantity it follows that η is also negative.

Using the Born approximation[6] the scattering amplitude for scattering of an electron by an Sb^+ ion is given by

$$f_{\mathrm{Sb}^+}(\vartheta) = -\frac{8\pi^2 m^*}{h^2}\int_0^\infty \frac{\sin Kr}{Kr} V_{\mathrm{Sb}^+}(r) r^2 dr \,, \qquad (4)$$

where

$$K = 2k_F \sin(\tfrac{1}{2}\vartheta) \,. \qquad (5)$$

In Eq. (5) k_F stands for the wave number of an electron at the Fermi surface and can be determined from

$$E_F = \frac{h^2}{8m^*}\left(\frac{3n}{\pi}\right)^{2/3} = \frac{h^2 k_F^2}{8\pi^2 m^*} \,.$$

To determine the sign of $f_{\mathrm{Sb}^+}(\vartheta)$ in Eq. (4) use is made of the fact that at large distances from the impurity nucleus the potential is a screened Coulomb potential with screening length[4] R. The screening factor[4] depends on R as $\exp(-r/R)$ and, for this reason, in the integrand of Eq. (4), $V_{\mathrm{Sb}^+}(r)$ becomes very small if $r>R$. In this case the upper limit of integration in Eq. (4) can be replaced by R with a good approximation. If Kr is smaller than π, then $(\sin Kr)/Kr$ is positive from $r=0$ to $r=R$. For an n-type Ge crystal with an electron concentration of several times 10^{18}/cc it can be shown that $Kr = 2k_F r \cdot \sin(\tfrac{1}{2}\vartheta) < \pi$ for all values of ϑ. It is seen, now, that $f_{\mathrm{Sb}^+}(\vartheta)$ is positive since $V_{\mathrm{Sb}^+}(r)$ is everywhere negative.

Knowing the scattering amplitude the total scattering cross section is calculated[6] from

$$Q_F(\mathrm{Sb}^+)=2\pi\int_0^\pi [f_{\mathrm{Sb}^+}(\vartheta)]^2 \sin\vartheta d\vartheta\ . \qquad (6)$$

For an As^+ ion, using the $V_{\mathrm{As}^+}(r)=V_{\mathrm{Sb}^+}(r)+\eta(r)$ relation one obtains

$$f_{\mathrm{As}^+}(\vartheta)=f_{\mathrm{Sb}^+}(\vartheta)+\varphi(\vartheta)\ , \qquad (7)$$

where

$$\varphi(\vartheta)=-\frac{8\pi^2m^*}{h^2}\int_0^\infty \frac{\sin Kr}{Kr}\eta(r)r^2dr\ . \qquad (8)$$

One may again replace the upper limit of integration by R in Eq. (8) and show by the same arguments as those used in connection with Eq. (4) that $\varphi(\vartheta)$ is a positive quantity since $\eta(r)$ is everywhere negative.

The total scattering cross section for scattering of an electron by an As^+ ion can now be written as

$$Q_F(\mathrm{As}^+)=Q_F(\mathrm{Sb}^+)+q_1+q_2\ , \qquad (9)$$

where

$$q_1=2\pi\int_0^\pi 2f_{\mathrm{Sb}^+}(\vartheta)\varphi(\vartheta)\sin\vartheta d\vartheta\ , \qquad (10)$$

and

$$q_2=2\pi\int_0^\pi [\varphi(\vartheta)]^2 \sin\vartheta d\vartheta\ ,$$

are positive quantities. Substituting Eq. (9) into Eq. (3) one obtains that

$$\frac{\mu(\mathrm{Sb})}{\mu(\mathrm{As})}=1+\frac{q_1+q_2}{Q_F(\mathrm{Sb}^+)}\ . \qquad (11)$$

Since both the q's and Q_F are positive quantities, the right hand side of Eq. (11) is larger than unity. This explains finding No. 1.

2. *Dependence of the Mobility Ratio on Electron Concentration.*

To show why for two different electron concentrations n_1 and n_2, where $n_2>n_1$, the relation[1]

$$\left[\frac{\mu(\mathrm{Sb})}{\mu(\mathrm{As})}\right]_{n_2}>\left[\frac{\mu(\mathrm{Sb})}{\mu(\mathrm{As})}\right]_{n_1}\ , \qquad (12)$$

exists we rewrite Eq. (12) with the aid of Eq. (11) as

$$\frac{Q_F(\mathrm{Sb}^+,n_1)}{Q_F(\mathrm{Sb}^+,n_2)}>\frac{q_1(n_1)+q_2}{q_1(n_2)+q_2}\ . \qquad (13)$$

Neglecting the term q_2 in the above expression, since it is quadratic in the correction term φ, and making use of Eq. (6) and (10) one can rewrite Eq. (13) as

$$\frac{\left[\int_0^\pi [f_{\mathrm{Sb}^+}(\vartheta)]^2 \sin\vartheta d\vartheta\right]_{n_1}}{\left[\int_9^\pi [f_{\mathrm{Sb}^+}(\vartheta)]^2 \sin\vartheta d\vartheta\right]_{n_2}}>\frac{\left[\int_0^\pi f_{\mathrm{Sb}^+}(\vartheta)\varphi(\vartheta)\sin\vartheta d\vartheta\right]_{n_1}}{\left[\int_0^\pi f_{\mathrm{Sb}^+}(\vartheta)\varphi(\vartheta)\sin\vartheta d\vartheta\right]_{n_2}}\ . \qquad (14)$$

Let us consider for the moment only small angle scattering, when $\vartheta\to0$. In this case, using the expansion $\sin(\frac{1}{2}\vartheta)\approx\frac{1}{2}\vartheta$, Eq. (5) becomes

$$K\approx k_F\vartheta\ .$$

Similarly, applying the expansion on $\sin Kr$

$$\frac{\sin Kr}{Kr}\approx1\ .$$

It follows now from Eqs. (4) and (8) that f_{Sb^+} and φ do not depend on ϑ and, for this reason, they can be taken out from under the integral sign in Eq. (14). As a result, one obtains

$$\frac{[f_{\mathrm{Sb}^+}(\vartheta\to0)]_{n_1}}{[f_{\mathrm{Sb}^+}(\vartheta\to0)]_{n_2}}=\frac{\left[\int_0^\infty V_{\mathrm{Sb}^+}(r)r^2dr\right]_{n_1}}{\left[\int_0^\infty V_{\mathrm{Sb}^+}(r)r^2dr\right]_{n_2}}>1\ . \qquad (15)$$

If one assumes that $V_{\mathrm{Sb}^+}(r)=V^c_{\mathrm{Sb}^+}(r)+V_t(r)$, where c and t refer to the core and the screened Coulomb tail respectively, then one has to focus attention only on the concentration dependent term involving $V_t(r)$*.

In a degenerate semiconductor the screening length, R, appearing in the screening

---

* Here we wish to make a few remarks about the validity of the Born approximation. It follows from the previous discussion that in the interval $a<r<R$, $V_{\mathrm{Sb}+}(r)\approx V_t(r)$. One can show that for $n=$several times 10^{18}/cc

$$k_Fr\ll1 \qquad (A)$$

in the above range of r. In this case the criterion for the validity of the Born approximation becomes[7]

$$\frac{8\pi^2m^*e^2r}{\kappa h^2}\ll1\ , \qquad (B)$$

which can also be shown to hold.

In the range of $r>a$ no conclusion can be drawn concerning the validity of the Born approximation since the potential is not known in that region.

In the range of $r>R$ both Eqs. (A) and (B) break down and the Born approximation gradually ceases to be valid. This region, however, as discussed earlier, is of no importance for the present considerations.

factor, $\exp(-r/R)$, is given by[4]

$$R=\frac{h\kappa^{1/2}}{3^{1/6}4\pi^{5/6}em^{*1/2}}n^{-1/6}\,, \qquad (16)$$

where κ is the dielectric constant of Ge. It is seen from Eq. (16) that $R(n_1)$ is larger than $R(n_2)$. This makes

$$\exp[-r/R(n_1)]>\exp[-r/R(n_2)]\,.$$

Consequently, $V_{\mathrm{Sb}^+}(r)$ in Eq. (15) is larger at n_1 than at n_2 which makes the ratio of the integrals larger than unity. This explains finding No. 2 for the case of small angle scattering. For large angle scattering no proof could be worked out.

§ 3. Discussion

The present work has been based on the assumption that at a donor concentration of $N_D \sim 10^{18}$/cc the donor ions scatter individually. This assumption needs some justification since one would expect that at high donor concentrations the scattering of an electron by a donor ion is influenced by the neighboring donors. Unfortunately, there is no theory available at the present time from which one could infer to what degree the picture of individual scattering is valid at a particular electron concentration. One can only give a plausibility argument, for a regular and a random donor distribution, which shows that at electron concentrations of $\sim 18^{18}$/cc the assumption of individual scattering is still a reasonable one.

Let us assume at first that the donor ions are distributed regularly in the Ge crystal. In this case, denoting the distance between two donor ions by $2R_s$, one obtains R_s from

$$(4\pi/3)R_s^3=N_D^{-1}\,.$$

If $N_D=10^{18}$/cc, then $R_s=62$Å. At the same concentration the screening length, calculated from Eq. (16) (assuming $m^*=0.25m_0$) is $R=29$Å. Since $R_s>R$, the conclusion is drawn that in the act of scattering the electron "feels" only the scatterer's potential and is practically undisturbed by donor ions surrounding the scatterer.

The assumption of a regular donor distribution in the host crystal is probably too idealized, however. If the distribution is random then one expects that a fraction of the scattering acts will be influenced to various degrees by more than one donor ion at a time. The question is how large is this fraction for which the picture of individual scattering is violated? Since in the act of a single scattering the dominant contribution to the total scattering cross section comes from a sphere of radius R, drawn around the scatterer, it is reasonable to assume that the scattering becomes significantly disturbed only when there is another donor ion nearer than $2R$. Sonder and Schweinler[7] have shown, assuming a Poisson distribution, that the probability of no neighbors closer than a distance r from a given donor is

$$P=\exp[-(r/R_s)^3]\,.$$

In the present case one finds, upon substitution of $r=2R$, that $P=\exp(-0.83)=0.44$. From this it is concluded that for about 44% of the scattering acts the assumption of individual scattering is "strongly" valid, while for the remaining 56% it is violated to a smaller or larger degree. The Poisson distribution may or may not correspond to the actual donor distribution. Any deviations from it might subject the probability P to changes. As Sonder and Schweinler remark such a deviation may occur because there is an electrostatic interaction energy among the donor ions. This interaction energy rises sharply for small donor-donor separation distances and, for this reason, one may assume that the distribution is not completely random. A favored distribution might be one in which the donors tend to be separated as far as possible. If this is the case, then P is increased which, in turn, means that the picture of individual scattering is better than concluded from a Poisson type distribution.

Finally, it should be mentioned that as the donor concentration in a Ge crystal increases one expects an increasing perturbation on the band structure of Ge. This, in other words, means that the effective electronic mass, m^*, should be dependent on electron concentration. The arguments in Section II-1 are not affected by such an effect since they refer to a particular electron concentration, n, and do not depend on the actual value of m^*. In Section II-2 strictly speaking, different electron masses should have been used for concentrations n_1 and n_2. This, however, has not been done because one can always assume that n_2 is only slightly larger than n_1 in which case the use of the same electron mass is justified.

The question of how large can be the concentration range over which the use of a constant electron mass is justified cannot be answered at the present time since there is no theory available for the concentration dependence of the effective mass.

§4. Concluding Remarks

To arrive at numerical results some specific model must be chosen. It can only be done if the potentials of the Sb^+ and As^+ ions in Ge are known with some reliability at all values of r. The construction of such potentials is a very complex problem which has not been attempted in the present paper. Finally, we wish to note that the above considerations, with appropriate rephrasing, should also be valid for the scattering of holes on acceptor ions in a heavily doped degenerate p-type Ge crystal.

References

1) Y. Furukawa: J. Phys. Soc. Japan **15** (1960) 730.
2) C. Erginsoy: Phys. Rev. **79** (1950) 1013.
3) Cf. "Corrections to the Effective Mass Formalism" in W. Kohn, Solid State Physics, edited by F. Seitz and D. Turnbull. (Academic Press, Inc., New York, 1957) Vol. 5.
4) R. B. Dingle: Phil. Mag. **46** (1955) 831.
5) H. Y. Fan and P. Fisher: J. Phys. Chem. Solids **8** (1959) 270.
6) L. I. Schiff: Quantum Mechanics (McGraw-Hill Book Co., Inc., New York, 1855) 2nd Ed. p. 161 ff.
7) E. Sonder and H. C. Schweinler: Phys. Rev. **117** (1960) 1216.

JOURNAL OF THE PHYSICAL SOCIETY OF JAPAN, Vol. 16, No. 10, OCTOBER, 1961

Sample Sandwiched Plastic Scintillators for Activation Measurements by Use of Fast Neutrons

By Masakatsu SAKISAKA, Bunzaburō SAEKI, Michio TOMITA

Department of Physics, Kōnan University, Kōbe

and Fumio FUKUZAWA

Department of Physics, Hyōgo University of Agriculture
Sasayama, Hyōgo-ken

(Received June 2, 1961)

Plastic scintillator plates sandwiched between thin radioactive samples were viewed with two photomultipliers and the coincident outputs were measured.

For β^--rays, the pulse-height distributions showed approximately triangular shapes and the pulse-height endpoints were proportional to their maximum energies. Similar characteristics were also found in the case of γ-rays. The counting efficiencies were empirically determined as functions of radiation energies in both cases.

The sandwich scintillators having aluminium, copper or silver foils as samples were exposed to 14 Mev neutrons and the induced activities of the samples only were counted effectively. Thus the $Al^{27}(n, p)$, $Cu^{63}\cdot(n, 2n)$ and $Ag^{107}(n, 2n)$ reaction cross sections were obtained with small standard deviations.

Other applications are suggested.

§1. Introduction

It is often necessary to know absolutely the intensities of very weak activities. An example is seen in the measurements of neutron induced reaction cross sections by activation method. Since the fast neutron flux is generally small, one cannot obtain an appreciable amount of hot atoms in the irradiated sample. If the specific activity of the sample is very weak, as much quantity of the sample as possible and hence a large detector are required for having a good counting statistics. However, for absolute counting, this necessitates large corrections for the scattering and absorption of radiations as well as for the geometrical efficiency. On the other hand, it is desirable that the background counts of detector are as small as possible, which means that the sensitive volume of the detector must be small. These requirements are inconsistent with each other, and the detectors of ordinary types are frequently inapplicable to the absolute measurements of weak activities. When the activities decay in a short time, the samples and detectors applicable will be much more restricted.

The activation researches with fast neutrons have been reported by many workers[1)-9)]. In all of their experiments ordinary samples, detectors and arrangements of them have been adopted, and so difficulties have been often experienced from complicated corrections, poor net counts, large background counts or inferior geometrical efficiencies.

Table I. Neutron induced reactions of carbon.

Reaction	Half life of the reaction product	Q (Mev)
$C^{12}(n, p)B^{12}$	0.02 s	−12.6
$C^{12}(n, 2n)C^{11}$	20.4 m	−18.7
$C^{12}(n, d)B^{11}$	stable	−13.7
$C^{12}(n, \alpha)Be^{9}$	stable	− 5.7
$C^{12}(n, n')3\alpha$		− 7.3
$C^{13}(n, p)B^{13}$	0.035 s	−11
$C^{13}(n, 2n)C^{12}$	stable	− 5.0
$C^{13}(n, d)B^{12}$	0.02 s	−15.3
$C^{13}(n, \alpha)Be^{10}$	2.5×10^{6} y	− 3.8

Plastic scintillators are, for the most part, composed of carbon and hydrogen atoms.* As will be seen in Table I, the nuclear reactions of carbon by fast neutrons** are out of question so far as one considers the reaction products having half lives ranging from few seconds to several days. Therefore, if thin samples and plastic scintillator plates are piled up alternately so as to form one block and if such a block is irradiated by fast neutrons,** only the induced activities of the samples would produce scintillations in the plastic scintillators after the irradiation. They could be counted by conventional electronic circuits.

In the present paper are described the properties of such sample sandwiched plastic scintillators and their application to neutron research.

§ 2. Properties of Sandwich Scintillator

Plastic scintillator plates of 7.5 mm×28mm in area and 1 mm in thickness and thin samples of the same area were piled up alternately so as to form a sandwich block, and they were bound tightly with a strip of "celotape" as shown at the upper left in Fig. 1. The block thus formed was about 30 mm in height.

The pulses in the sandwich scintillator were detected from the two sides facing to each other with two photomultipliers RCA 6342, and they were fed to two separate circuits composed of amplifiers and pulse-height discriminators, as shown in Fig. 1. Each cir-

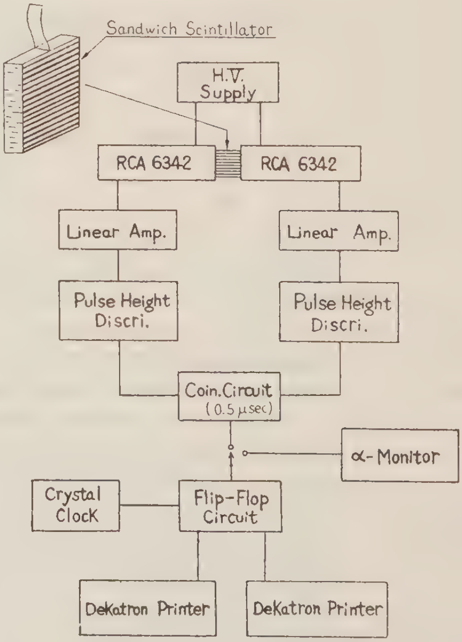

Fig. 1. Sandwich scintillator and block diagram of the circuits.

---

* The scintillator used is styrene + 1% P-terphenyl + 0.03% POPOP+0.002% zinc stearate. This was manufactured by the Polymer Research Section of Matsushita Electric Works.

** The neutron energies must be below the threshold energy of the $C^{12}(n, 2n)C^{11}$ reaction.

cuit was so adjusted as to have the same characteristic. Their outputs were counted or analysed through a coincidence circuit, its resolving time having been chosen as 0.5 μ·sec. A clock using a quartz crystal, count printers for automatic recording of the decaying activities and an α-monitor of the T(d, n)α reaction are also shown in the figure.

(1) *Pulse-height Distributions*

At first, papers of 5.1 mg/cm² in thickness, weakly activated with Pm^{147}, Tl^{204} or $Sr^{90}+Y^{90}$ by immersing in an active solution, were used as samples. The properties of these radioisotopes originally given by Strominger *et al*[10] are tabulated in Table II. The typical pulse-height distribution in the case of $Sr^{90}+Y^{90}$ is shown in Fig. 2, A. It is a superposition of two spectra of approximately triangular shapes, which correspond to Sr^{90} and Y^{90} β^--rays.

Table II. Properties of radioisotopes.

Nuclide	Half life	Energy of radiation (Mev)
Pm^{147}	2.64 y	β^-: 0.223 (~100%) γ: very weak
Tl^{204}	3.56 y	β^-: 0.764 (98%) EC: (2%)
Sr^{90}	27.7 y	β^-: 0.545 (100%)
↓ Y^{90}	64.2 h	β^-: 2.26 (>99%) 0.53 (~0.02%) γ: (~0.02%)
In^{116m}	54 m	β^-*: 1.00 (51%) 0.87 (28%) 0.60 (21%) γ: present

* The mean energy is 0.88 Mev.

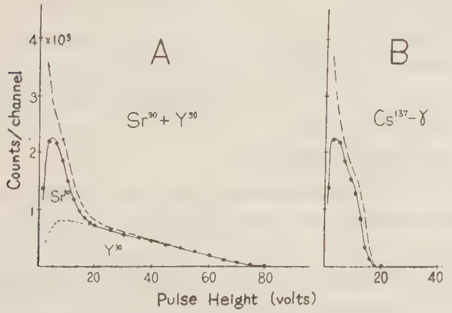

Fig. 2. Pulse-height distributions for $Sr^{90}+Y^{90}$ β^--rays and Cs^{137} γ-rays. The solid circles were obtained by analysing the output pluses from one amplifier which was gated by the outputs above 1 volt from the other amplifier. The broken lines show the non-coincident spectra.

The scintillator having non-radioactive white papers as samples (blanck scintillator) was exposed to Cs^{137} γ-rays. The pulse-height distribution is as shown in Fig. 2, B, which is also of a nearly triangular shape. However, a slight shoulder corresponding to the Compton edge is seen in this case, while a long tail exists on the higher energy side in the case of β^--rays. This is attributed to the essential difference of the energy spectra between Compton electrons and β^--rays.

The tail-end voltages of the pulse-height distributions were plotted for Pm^{147}, Tl^{204}, Sr^{90} and Y^{90} β^--rays as well as for Cs^{137} and Na^{22} γ-rays, taking their maximum energies as abscissas. The relation is linear as seen in Fig. 3. This shows that the mixing of radiations of different energies would be fairly well known by this detector.

(2) *Counting Efficiencies*

The β^--rays emitted from various number of piled sheets of Pm^{147}, Tl^{204} or $Sr^{90}+Y^{90}$-

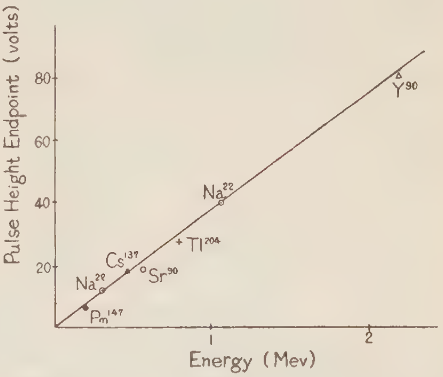

Fig. 3. Linearity. The maximum energy of the Compton electrons is introduced for γ-radiation.

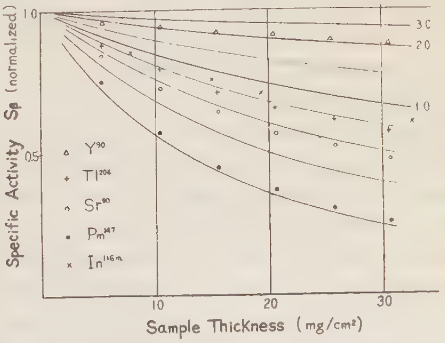

Fig. 4. Dependence of the apparent specific activity on the thickness of sample and the β^--energy.

active paper were counted by a 4π flow counter.* In Fig. 4, the apparent specific activities (normalized) are plotted as a function of the thickness of sample for each radionuclide. Referring to the maximum energies of these β-rays, the apparent specific activity *vs* sample thickness curves could be drawn by taking maximum β^--ray energy as a parameter. They are shown by solid lines in the same figure. The applicability of this graph to indium foils was examined using the $In^{115}(n, \gamma)\cdot In^{116m}$ reaction by thermal neutrons. The experimental values were found to be in agreement with the one predicted from Table II within the error of 1%.

Since the total number of electrons emitted from each radioactive paper was thus known, the counting efficiency of sandwich scintillator was easily obtained for given β^--rays. The efficiency is given by the ratio of the scintillation counts to the counts of a 4π counter obtained with the same sample. The results are shown in Fig. 5. The efficiencies for Sr^{90} and Y^{90} β^--rays were estimated by measuring the corresponding areas in Fig. 2, A.

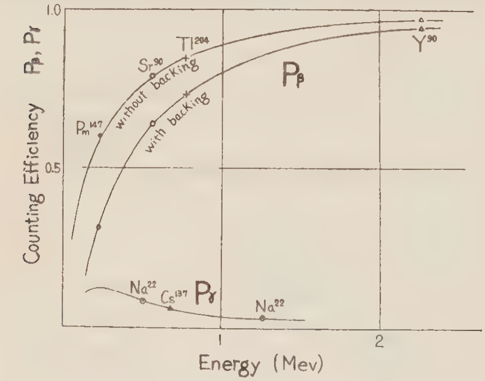

Fig. 5. Counting efficiencies for β^-- and γ-rays. The measurements were done by setting both discriminator voltages at 1 volt.

In some cases it is more convenient to use samples in powder form than foil. Powder samples are conveniently sandwiched by thin backing papers and fixed with ethyl acetate solution of plastic, although there may be some loss of counting probability because of the absorption of β^--rays by backing papers. In order to examine the effect, experiments were done by adding the backing papers of 2.6 mg/cm^2 in thickness to the radioactive papers in the sandwich scintillator, and the resultant efficiency curve is shown in Fig. 5.

Finally the blanck scintillator was irradiated by Cs^{137} and Na^{22} γ-rays of known intensities. The counting probabilities for 0.51**, 0.67 and 1.27 Mev γ-rays thus obtained are also shown in Fig. 5.

As is well known, the counting efficiencies are dependent on the amplifier gains and the discriminator voltages. Therefore the stabilities and characteristics of all circuits were carefully tested before each experiment.

(3) *Absolute Counting*

The decay scheme and the radiation energies of the activity must be previously known for absolute counting by the sandwich scintillator method.

The number of true counts of the sample, N_0, is expressed by $N_0 = N_c/F$ where N_c is that of the coincident net counts. F is a correction factor depending on the decay scheme, radiation energies and sample thickness.

For a simple β^--decay, $F = S_\beta P_\beta$, where S_β is the specific activity for the given sample thickness and maximum β^--ray energy which can be read from Fig. 4. P_β is the counting efficiency referring to Fig. 5. For $\beta^- \to \gamma$ transition having shorter γ-life than the resolving time of counting circuit, $F = 1-(1-S_\beta P_\beta)(1-P_\gamma)$ where P_γ is the counting probability for the given γ-ray energy.

In the case of β^+-decay, a positron is accompanied by a pair of 0.51 Mev γ-rays emitted within or in the neighborhood of the scintillator. Therefore, the correction factor is given by $F = 1-(1-S_\beta P_\beta)(1-P_\gamma)^2$, where S_β and P_β are the same quantities as those for β^--decay. But P_γ is the counting efficiency for 0.51 Mev radiation.

The correction factor for any complicated decay would be likewise derived easily.

§ 3. Activation Cross Section Measurements

The sandwich detectors which had aluminium, copper or silver foils as samples were irradiated by 14.1 Mev neutrons. The neutrons were produced by the 400 KV Cockcroft-

---

* The commercially called "Q-gas" was applied as counting gas.

** 0.51 Mev γ-radiations are produced by the annihilation of positron from Na^{22}.

Walton type accelerator of the Konan University using $T(d, n)\alpha$ reaction. The deuteron beam energy was chosen as 170 Kev and the sandwich scintillators were arranged 10 cm apart from the tritium target on the plane perpendicular to the beam, facing the $28 \times 30\ mm^2$ side of the scintillator to the target. A cadmium cover of 1 mm in thickness was used for each scintillator in order to filter the probable thermal neutrons. Since the sandwich detector is small, the loss or the slowing down effect of the incident neutrons can be neglected.

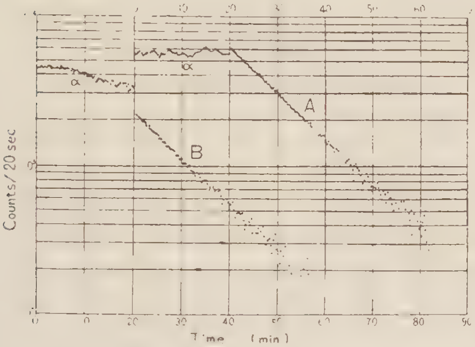

Fig. 6. Alpha and activity counts in the $Cu^{63}(n, 2n)$ and $Al^{27}(n, p)$ reaction experiments.
A: $Cu^{63}(n, 2n)Cu^{62}$ experiment
B: $Al^{27}(n, p)Mg^{27}$ experiment

The neutrons produced were monitored by counting the associated α-particles with a CsI crystal mounted on a photomultiplier DuMont 6292. The number of α-counts in every given time-interval was recorded automatically by two count printers operated alternately. The time-signals were taken from a precision quartz clock. Therefore the fluctuations of neutron intensities were easily known.

After the irradiation, the sandwich scintillator was arranged as shown in Fig. 1 and the coincident outputs were counted and recorded similarly as for the α-counts. A and B of Fig. 6 are the data of $Cu^{63}(n, 2n)Cu^{62}$ and $Al^{27}(n, p)Mg^{27}$ reaction experiments respectively. The both decay curves of the reaction products, Cu^{62} and Mg^{27}, are linear on the semi-logarithmic graph. From these curves their half lives were obtained as 9.90 ±0.04 min. and 10.00±0.03 min. respectively. The blanck scintillator showed no induced activities even after exposed to the neutrons, as is expected from Table I.

Table III. Reaction cross sections by 14 Mev neutrons.

Reaction	Half life of the reaction product (min)	Cross section (mb)			
		Forbes	Paul and Clarke	Yasumi	Present
$Al^{27}(n, p)Mg^{27}$	10.00±0.03	79± 6	52.4±9.4	87.2±7.0	85.0±2.8
$Cu^{63}(n, 2n)Cu^{62}$	9.90±0.04	510±36	482±72	556±28	458±10
$Ag^{107}(n, 2n)Ag^{106}$	24.5*	560±56	519**±260	458±51	537±15
Neutron energy (Mev)		14.1	14.5	14.1	14.1 (±0.2)

* This value was not obtained in the present experiment because Ag^{108} ($T_{1/2}=2.3$ min) of the $Ag^{109}(n, 2n)Ag^{108}$ reaction contributed to the decay of Ag^{106}.

** Lower limit since only one isomer was observed.

Some of the present author's results on the activation cross section are shown in Table III together with the data of Forbes,[3] Paul and Clarke[4] and Yasumi.[6] The present 85.0±2.8 mb for $Al^{27}(n, p)Mg^{27}$ reaction is in good accordance with 87.2±7.2 mb obtained by Yasumi, but other cross sections agree better with those of Forbes or Paul and Clarke than with Yasumi's. Especially, the authors' 458±10 mb for $Cu^{63}(n, 2n)Cu^{62}$ reaction is quite consistent with the data of Ferguson and Thompson,[8] 378±34 mb at 13.77±0.20 Mev and 507±45 mb at 14.74±0.27 Mev. But 889±66 mb at 14.4±0.3 Mev recently obtained by Rayburn[9] for $Ag^{107}(n, 2n)Ag^{106}$ reaction differs greatly from the present 537±15 mb.

§ 4. Discussions

The standard deviations of the present results in the activation experiments were very small. This is due to the facts that a comparatively large amount of sample—1∼2 gr—was applied to the detector of so small volume as several cm^3 and that the solid angle subtended by the sample at the detector was nearly equal to 4π. Therefore the sandwich scintillator may be said to be one of the improved detectors for measuring weak activities. Most of the difficulties met in ordinary detectors are easily surmounted by the sandwich scintillator.

There is another usefulness of this detector. Since the plastic scintillator is mainly sensitive to β-rays, the $\beta-\gamma$ coincidence technique would be available if an NaI(Tl) crystal is brought closely to the sandwich detector. Of course each of the two detectors should be viewed with a photomultiplier independently.

The cross sections of photonuclear reactions would be also measurable with this detector. As the (γ, p), (γ, n) or (γ, α) reaction products of carbon nuclei would not disturb the observations* just as in the 14 Mev neutron activation studies, the activation experiments by γ-rays could be done more precisely. Furthermore, its application to the measurements of thermal neutron flux in reactor materials would be practised. These suggest interesting developments in the activation analysis field.

Acknowledgements

The authors wish to express their sincere thanks to Profs. B. Arakatsu, S. Kawata, S. Tokunaga and K. Yuasa for their continuous encouragements. Their indebtedness to Mr. Arimura, a senior student of the Kōnan University, for his assistance in operating the accelerator must be gratefully appreciated.

This work was supported by the 1960 Scientific Research Expenditure of the Ministry of Education and its Subsidy for Private University.

References

1) J. L. Fowler and J. M. Slye, Jr.: Phys. Rev. **77** (1950) 787.
2) H. C. Martin and B. C. Diven: Phys. Rev. **86** (1952) 565.
3) S. G. Forbes: Phys. Rev. **88** (1952) 1309.
4) E. B. Paul and R. L. Clarke: Can. J. Phys. **31** (1953) 267.
5) A. V. Cohen and P. H. White: Nuc. Phys. **1** (1956) 73.
6) S. Yasumi: J. Phys. Soc. Japan **12** (1957) 443.
7) C. S. Khurana and H. S. Hans: Nuc. Phys. **13** (1959) 88.
8) J. M. Ferguson and W. E. Thompson: Phys. Rev. **118** (1960) 228.
9) L. A. Rayburn: Phys. Rev. **122** (1961) 168.
10) D. Strominger, J. M. Hollander and G. T. Seaborg: Rev. Mod. Phys. **30** (1958) 585.

---

* Again the energies of incident γ-rays must be below the threshold energy of the $C^{12}(\gamma, n)C^{11}$ reaction.

JOURNAL OF THE PHYSICAL SOCIETY OF JAPAN, Vol. 16, No. 10, OCTOBER, 1961

On the New Magnetic Phase in Manganese-Aluminium-Copper System

By Ichiro TSUBOYA

Electrical Communication Laboratory,
Nippon Telegraph and Telephone Public Corporation,
Musashino-shi, Tokyo, Japan

(Received February 9, 1961)

It was found that there exists a new ferromagnetic phase in Cu poor Mn–Al–Cu alloy in the composition range of 25 to 45 at % Mn, 37.5 to 50 at % Al and 12.5 to 25 at % Cu. The crystal structure is CsCl type and the lattice parameter is 2.984 Å. This structure is the same as the κ phase in Mn–Al–Fe system. The magnetic properties may be interpreted in terms of the ferromagnetic structure composed of the Mn atoms which occupy two different sublattices.

§ 1. Introduction

In Mn–Al–Cu system, it has been known that there is a ferromagnetic phase corresponding to the composition of Cu_2MnAl which is well known as the Heusler alloy[1]. But the other ferromagnetic phase has not yet been observed in this system.

It was already reported by Tsuboya et al. that there is a ferromagnetic phase in Fe poor Mn–Al-Fe alloy[2]. Recently, the similar ferromagnetic phase was also found for Mn–Al–Cu[3], –Ni[4] and –Co[5] ternary alloys.

In this paper, the author reports the magnetic and crystallographic natures of the ferromagnetic phase that exists in Cu poor Mn–Al–Cu alloy. Their magnetic natures are able to be explained by the ferrimagnetism originating from an antiferromagnetic interaction between the body center and the cube corner Mn atoms in b.c.c. lattice.

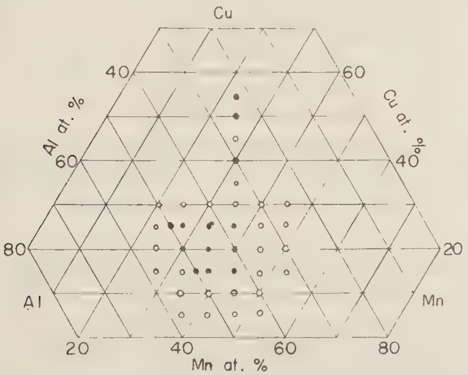

Fig. 1. The composition range of the specimens and results of magnetic testing.
●: ferromagnetic specimens.
○: non magnetic specimens.

§ 2. Preparation of Specimens

The composition range of the specimens used in this experiment is indicated in Fig. 1. For the preparation of the specimens, the electrolytic manganese (99.9%), the electrolytic copper (99.9%) and aluminium (99.99%) were mixed in a suitable proportion and melted in an alumina crucible with the Tammann furnace in the atmosphere of air. Then they were cast into rods of the size 10 mm in diameter. The weight of the ingot is about 80 to 100 gr corresponding to 2 mols for each composition. The cast rods were annealed for one hour at 900°C in vacuum to remove the segregations, then cooled to room temperature at the rate of 150°C/hr.

It was confirmed by the chemical analysis that the deviation of composition of 20 at % Cu, 40 at % Mn and 40 at % Al turned out to be the final composition of 21.1 at % Cu, 38.8 at % Mn and 40.1 at % Al. The densities of the specimens are about 5.0 to 5.6 gr/cc. All specimens are very hard and brittle, and can be pulverized easily with a stampmill.

It was found by the magnetic testing that the specimens indicated by the solid circles in Fig. 1 were found to be ferromagnetic, and open circles do not show ferromagnetism.

§ 3. Crystal Structure

The crystal structures were determined by means of powder method with X-ray diffractometer. The specimens were crushed with the stampmill and were sieved under 100 mesh for X-ray analysis.

The results of X-ray analysis are shown in Fig. 2. The structure of two specimens containing above 50 at% Cu is f.c.c. ordered structure known as the Heusler alloy, and their lattice parameters are both 5.96 Å. This value is almost consistent with the data previously reported.

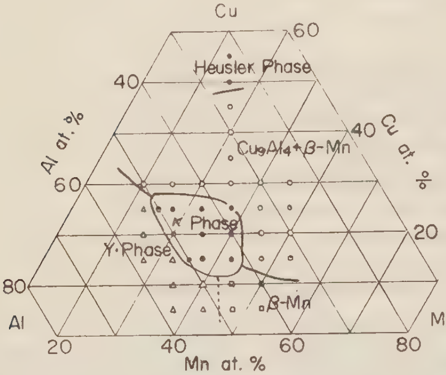

Fig. 2. The results of X-ray analysis.

●: Heusler phase in Cu rich region and the κ phase in Cu region.

○: The mixed structure of β-Mn and Cu_9Al_4 phase.

□: The β-Mn phase

△: Orthorhombic *Y*-phase.

The Heusler and κ phases are ferromagnetic and others are non magnetic.

All specimens showing ferromagnetism in the Cu poor regions have a single cubic phase, similarly to the κ phase in Mn-Al-Fe system[1]. The crystal structure of this phase will be discussed in detail later. The specimens having the composition between the κ phase and the Heusler alloy phase, show the mixed structure of the β-Mn and Cu_9Al_4 phases. The Cu_9Al_4 phase is pseudo-cubic and nearly γ-brass like structure[7]. This mixed phase seems to be extended to Mn rich side of the κ phase. The lattice parameter of this Cu_9Al_4 phase is 8.69 Å. The β-Mn phase exists in the Cu poor region, and the orthorhombic *Y*-phase[8] exists above 50 at% Al region. This *Y*-phase seems to be the same structure as the ζ phase[9] or the η phase[10] for Mn-Al system.

The composition range of the κ phase is 25 to 45 at% Mn, 37.5 to 50 at% Al and 12.5 to 25 at% Cu, and agrees with that determined from magnetic measurement. The κ phase has the body centered cubic superstructure of CsCl type (B2 type). Its lattice parameter is 2.984±0.005 A and does not show appreciable dependence on the composition.

The intensity of the (100) superlattice line is changed with a change of Al content, and it becomes maximum for 50 at% Al specimens and decreases with a decrease of Al. Considering the similarity of the X-ray scattering factors between Mn and Cu atoms, it can be understood that these superstructure lines are observed as a result of the ordered arrangement of Al, and Mn or Cu.

It can be qualitatively understood that for 50 at% Al specimens, Al atoms nearly perfectly occupy the one sort of lattice sites (e. g. A site), and Mn and Cu atoms the other sort of sites (B site). In the case of less than 50 at% Al, the excess Cu or Mn atoms are considered to enter into the A sites together with the Al atoms.

The observed X-ray density is nearly equal to the value of usually measured density. A little discrepancy between these values should be expected on account of the existence of small holes or cracks in the specimens.

§ 4. Magnetic Measurements

Temperature dependence of saturation magnetization, Curie temperature and temperature dependence of magnetic susceptibility above the Curie temperature were measured. The saturation magnetization σ and its temperature dependence above liquid-nitrogen

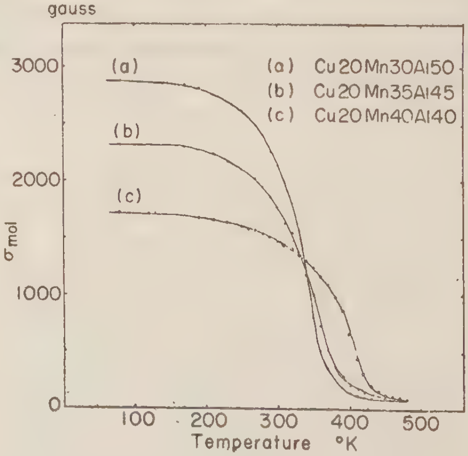

Fig. 3. $\sigma_{mol}-T$ curves for the specimens with the composition of
(a) 20 at% Cu, 30 at% Mn and 50 at% Al;
(b) 20 at% Cu, 35 at% Mn and 45 at% Al;
(c) 20 at% Cu, 40 at% Mn and 40 at% Al, respectively. (Hex=13 KOe)

temperature were measured by means of the ballistic galvanometer and magnetic balance.

Fig. 3 shows the $\sigma_{\text{mol}}-T$ curves for the specimens with the composition of 20 at % Cu, 30, 35 or 40 at % Mn, which are measured in the magnetic field of 13 kOe. It is seen in this graph that the saturation magnetization decreases with an increase in Mn content. The extraporated saturation magnetization (per mol) at 0°K is 2900 gauss for 30 at % Mn, and 1700 gauss for 40 at % Mn (Fig. 4).

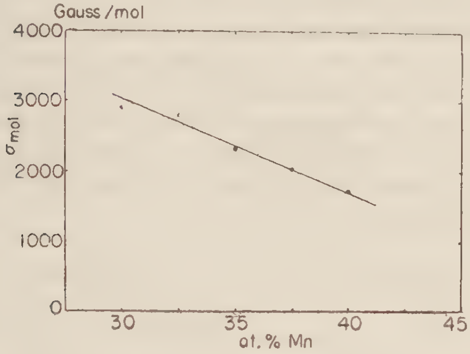

Fig. 4. Composition dependence of saturation magnetization σ_{mol} measured for 20 at % Cu specimens.

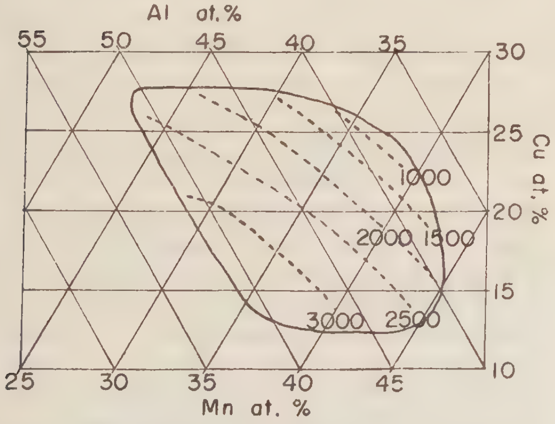

Fig. 5. Saturation magnetizations σ_{mol} (broken line) and phase boundary (solid line) of the phase in Mn-Al-Cu ternary system.

The composition dependence of magnetization, together with the phase boundary of the κ phase is shown in ternary diagram in Fig. 5. The maximum of saturation magnetization is 3300 gauss for 15 at % Cu, 35 at % Mn and 50 at % Al, and its minimum is found to be 500 gauss for 25 at % Cu, 37.5 at % Mn, and 37.5 at % Al. From these results, it can be concluded that the saturation magnetization is large for Al rich and Cu poor region and small for Mn rich and Cu rich region.

The Curie temperature was also measured by means of a magnetic balance with a very weak field. In general, the Curie temperature of κ phase is slightly higher than the room temperature, and shows an appreciable composition dependence. It is obvious in Fig. 3 that the Curie temperature for Cu 20 at % specimens are low in Mn poor region and high in Mn rich. The composition dependence is shown in Fig. 6 for 20 at % Cu and in Fig. 7 for all ternary system.

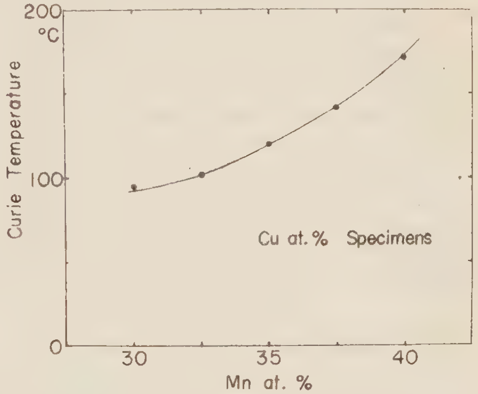

Fig. 6. The composition dependence of Curie temperature for 20 at % Cu specimens.

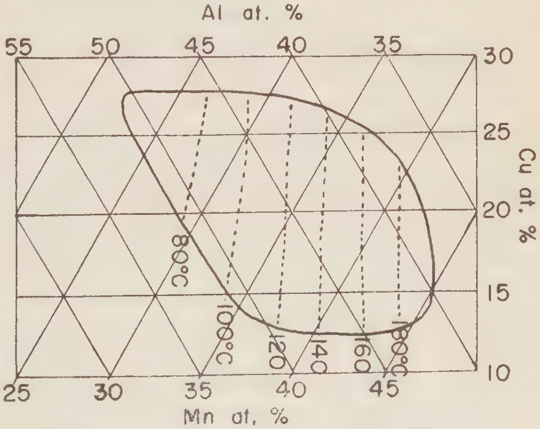

Fig. 7. The Curie temperature of κ phase in Mn-Al-Cu ternary system.

According to the above results, the rise in Curie temperature is not necessarily accompanied with the increase of saturation magnetization. For example, for 20 at % Cu specimens, the Curie temperature rises with

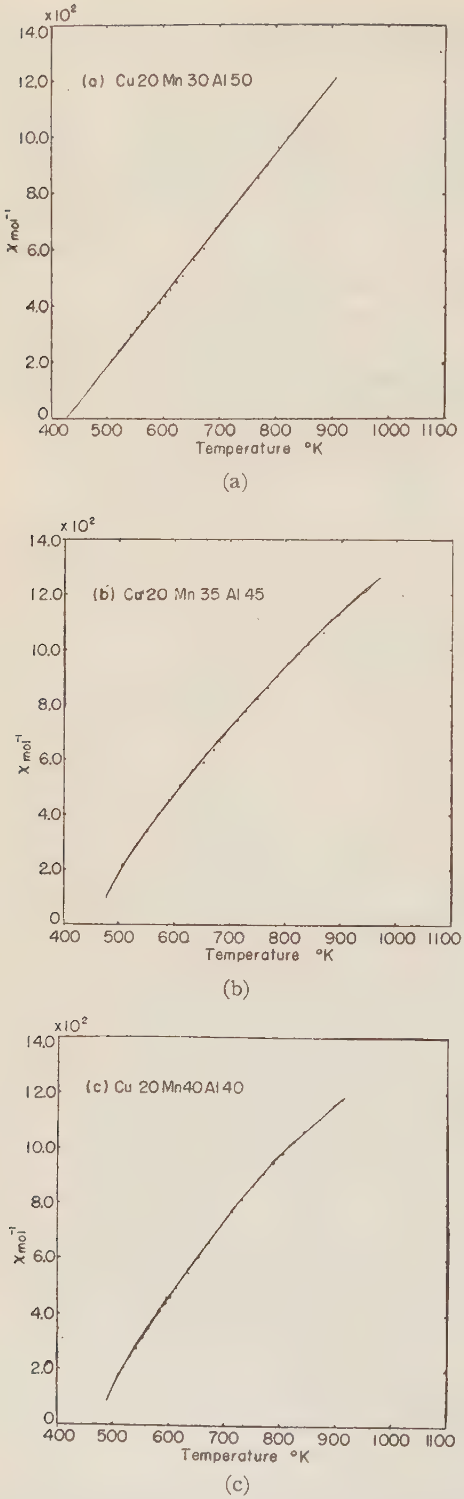

(a)

(b)

(c)

Fig. 8. The temperature dependence of inverse-susceptibility ($\chi_{mol}^{-1}-T$) for three 20 at % Cu specimens. There is a linear relation for 50 at % Al specimen (a) and nonlinear relations for 45 at % Al (b) and 40 at % Al (c).

an increase of Mn content, while the saturation magnetization decreases. As for the specimens equally containing Mn and Al, the saturation magnetization increases with a decrease of Cu content, but the Curie temperature remains constant.

The temperature dependence of inverse susceptibility above Curie temperature ($\chi_{mol}^{-1}-T$) was measured by a magnetic balance up to 800°C. The typical results are shown in Fig. 8 for three specimens containing 20 at % Cu and different Mn contents. It is easily seen in Fig. 8, the curve form for 50 at % Al specimen is linear, while it is not for 45 and 40 at % Al. This rule is also valid for any Cu content specimens.

These results suggest us that the interaction is ferromagnetic for 50 at % Al specimens, while it is rather ferrimagnetic for other specimens.

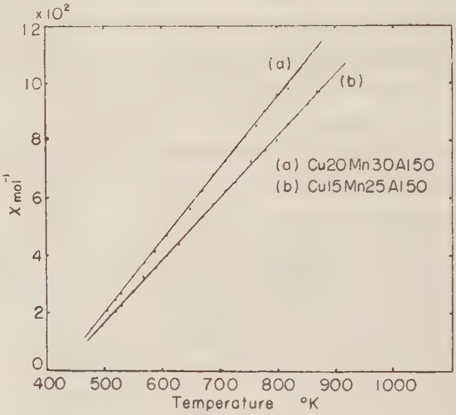

Fig. 9. $\chi_{mo}^{-1}-T$ curve for 50 at % Al, 30 at % Mn, 20 at % Cu (a) and 50 at % Al, 35 at % Mn, 15 at % Cu (b) specimens respectively. The slopes (7.05/6.0) is almost inversely proportional to the Mn content (7/6).

Fig. 9 shows the $\chi_{mol}^{-1}-T$ relations for 50 at % Al, 30 at % Mn, 20 at % Cu specimen and 50 at % Al, 35 at % Mn, 15 at % Cu specimen. Both curves are linear and their slopes are almost inversely proportional to the Mn contents.

§ 5. Discussion

The experimental results described above suggest that the magnetic natures of κ phase are due to the ferrimagnetism originated in the antiferromagnetic interaction between Mn atoms. Generally, the magnetic interaction between Mn atoms is considered to be antiferromagnetic if the distance between nearest-neighbour Mn atoms is shorter than about 2.8 Å, and be ferromagnetic if the distance is larger than about 2.9 Å.[11] The atomic distance between the nearest Mn atoms is about 2.54Å for these alloy, it can be assumed that the interaction between them is antiferromagnetic.

As for the atomic arrangement, it is considered that, for the specimens containing 50 at% Al in which the most intense superstructure line is observed, one sublattice is perfectly occupied by Al atoms and the other sublattice is occupied by Cu and Mn atoms, whereas for the specimens containing Al less than 50 at% in which the superstructure line is less intense, it is supposed that some of the Mn atoms occupy one sublattice together with the Al atoms, while Cu and the remaining Mn atoms occupy the other.

According to the above considerations, the following assumptions are proposed to explain the experimental results:

(1) All Al atoms and a part of Mn atoms occupy the body center site (A site): i.e. $N_{\mathrm{Al}}+N_{\mathrm{Mn}}^{\mathrm{A}}=50$, where N_{Al} is the content of Al atoms and $N_{\mathrm{Mn}}^{\mathrm{A}}$ that of Mn atoms in the A sites.

(2) All Cu atoms and residual Mn atoms occupy the cube corner site (B site): i.e. $N_{\mathrm{Cu}}+N_{\mathrm{Mn}}^{\mathrm{B}}=50$, where N_{Cu} is the content of Cu atoms and $N_{\mathrm{Mn}}^{\mathrm{B}}$ the content of Mn atoms in the B sites ($N_{\mathrm{Mn}}^{\mathrm{A}}+N_{\mathrm{Mn}}^{\mathrm{B}}=N_{\mathrm{Mn}}$).

(3) The sign of the exchange interaction between Mn atoms in different sites is negative. Then, the magnetic moments of Mn atoms in different sites point antiparallel to each other. As the distance between nearest-neighbour A and B site is 2.54 Å, this assumption will be reasonable.

(4) The sign of the exchange interaction between Mn atoms in the same sites is positive. Then. the magnetic moments of Mn atoms in the same site point parallel. As the distance between each A site is 2.98 Å, this assumption will be also reasonable.

(5) The Curie temperature is mainly determined by the number of nearest-neighbour Mn pairs between A and B sites (A–B interaction) and that between B sites (B–B interaction). The effect of Mn pairs in A sites is neglected, because the concentration of Mn atoms in A sites is relatively small.

From these assumptions, following three conclusions can be deduced.

(a) The saturation magnetization is proportional to the difference in the number of Mn atoms between A and B sites:

$$\sigma_{\mathrm{mol}}\simeq|N_{\mathrm{Mn}}^{\mathrm{B}}-N_{\mathrm{Mn}}^{\mathrm{A}}|=|N_{\mathrm{Al}}-N_{\mathrm{Cu}}|$$

(b) The temperature dependence of inverse susceptibility is linear for the specimens containing 50 at% Al, while is not linear for other specimens. This result is interpreted as follows. For the specimens containing 50 at% Al, all A sites are occupied by Al atoms, or $N_{\mathrm{Mn}}^{\mathrm{A}}=0$. Consequently, there is no antiferromagnetic interaction between Mn atoms. In other specimens, however, a part of Mn atoms always occupy A site. Then there must be some antiferromagnetic interaction between Mn atoms in A and B sites, so that $\chi^{-1}-T$ curves deviates from linear relations.

(c) The composition dependence of Curie temperature must be as follows:

i) For the specimens containing constant Cu content, the Curie temperature should rise with an increase of Mn.

ii) For the specimens containing constant Al content, the Curie temperature should fall with an increase of Cu.

iii) For the specimens containing constant Mn content, the Curie temperature should fall with an increase of Al.

In the first case, since $N_{\mathrm{Mn}}^{\mathrm{B}}$ must have the constant value, the Mn atoms exceeding this value replace the Al atoms in A site, then the number of A–B interaction bonds between Mn atoms increases so that the Curie temperature should be increased by this process. In the second case, however, Mn atoms in B sites are replaced by the increased Cu atoms, then B–B and A–B interactions between Mn atoms should be decreased and the Curie temperature is expected to fall. In third case, with an increase of Al, Mn atoms in A site are transferred to B site, then the number of A–B interaction bonds between Mn atoms decreases, but that of B–B interaction increases. The contributions of these interactions to the Curie temperature are opposite to each other. But assuming that the A–B interaction is more effective than B–B interaction, the Curie temperature is expected to fall with an increase of Al content.

These conclusions of (a) to (c) satisfactorily agree with the experimental results. Fig. 10 shows the observed saturation magnetization (per mol) as a function of $(N_{\mathrm{Al}}-N_{\mathrm{Cu}})$. The curve in this figure seems to be almost linear, supporting the conclusion (a).

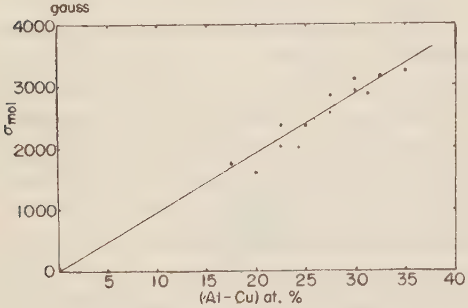

Fig. 10. The relation between saturation magnetization (per mol) σ_{mol} and $(N_{\mathrm{Al}}-N_{\mathrm{Cu}})$ (at %).

The conclusion (b) agrees with the experimental results on the temperature dependence of inverse susceptibility. The composition dependence of the Curie temperature that is mentioned in the conclusion (c) also agrees with the experimental results in Fig. 5.

The magnetic moment per Mn atom which is calculated along the line in the above consideration from the slope of Fig. 10 is 1.7 μ_B. It is, however, observed that this value shows slight dependence on the composition, detailed discussion of which is difficult at the present stage.

§ 6. Summary

It has been believed that there is only a ferromagnetic phase, the so-called Heusler alloy with composition of Cu_2MnAl in Cu-Mn-Al alloy. Besides the Heusler alloy, however, there is a new ferromagnetic phase, the κ phase, in the composition range of 25 to 45 at % Mn, 37.5 to 50 at % Al and 12.5 to 25 at % Cu. The crystal structure of this phase is CsCl type and its lattice parameter is 2.984 Å. Its magnetic natures are interpreted in terms of the ferrimagnetism originating from the uncompensated magnetic moment in the antiferromagnetic interaction between body center and cube corner Mn atoms. Further studies for κ phase in Mn-Al-Ni or Mn-Al-Co systems will be reported later.

Acknowledgement

The author wishes to express his great gratitude to Dr. M. Sugihara for his kind advice and encouragement througout the present experiment. The author also wishes to express his hearty thanks to Prof. S. Chikazumi, the Institute for Solid State Physics, University of Tokyo for his kind discussion of the results. Furthermore, the author is deeply indebted to Drs. Y. Shichijo and K. Aoyagi for valuable discussion and encouragement, and to Mr. K. Kado for sample preparation.

References

1) O. Heusler: Ann. Phys. [5] **19** (1934) 155.
2) I. Tsuboya and M. Sugihara: J. Phys. Soc. Japan **15** (1960) 1534.
3) I. Tsuboya and M. Sugihara: J. Phys. Soc. Japan **16** (1961) 571.
4) I. Tsuboya and M. Sugihara: J. Phys. Soc. Japan **16** (1961) 1257.
5) I. Tsuboya and M. Sugihara: Umpublished.
6) A. J. Bradley and J. W. Rodgers: Proc. Roy. Soc. **A**, **144** (1934) 340.
7) W. B. Pearson: *A Hand Book of Lattice Spacings and Structures of Metals and Alloys* (Pergamon Press, London, 1958) p. 330.
8) W. B. Pearson: Op. Cit. p. 339.
9) H. Kono: J. Phys. Soc. Japan **13** (1958) 1444.
10) A. J. J. Koch, et al.: J. Appl. Phys. **81** (1960) 75 S.
11) C. Guillaud: Rev. Mod. Phys. **25** (1952) 605.

JOURNAL OF THE PHYSICAL SOCIETY OF JAPAN Vol. 16, No. 10, OCTOBER, 1961

Magnetic and Electric Properties of Chalcopyrite

By Teruo TERANISHI

Technical Research Laboratories, Japan Broadcasting Corporation, Tokyo, Japan

(Received February 25, 1961)

The torque of a natural single crystal of chalcopyrite in a uniform magnetic field is measured. At room temperature and liquid nitrogen temperature the torque of a disc parallel to (110)-plane shows two-fold symmetry and the easy direction is $[1\bar{1}0]$.

The temperature dependence of the torque is also measured. The torque vanishes at 550°C. Two principal susceptibilities parallel and perpendicular to c-axis, $\chi_{//}$ and $\chi_{\perp}$, are calculated from the torque and the powder susceptibility.

The conductivity, the Hall coefficient and their temperature dependences and the thermoelectric power are also measured. Their behaviours are those of typical semiconductors. Hall mobility and thermoelectric power are rather large, although chalcopyrite contains transition element, Fe, in its chemical foumula. The crystal structure, the electronic states of constituent elements, magnetic and electric properties are considered together, and it is concluded that the 3d-shell in this material is independent of the valence bond which consists of sp^3 bond.

§1. Introduction

Chalcopyrite which has a chemical formula, $CuFeS_2$, has been known as a semiconductor with its rectifying property.

As typical valence semiconductors Ge and Si and some metallic compounds are investigated in detail but for semiconducting compounds, especially three components compounds, there is few investigations. However, chalcopyrite is a very interesting semiconductor, since it contains typical magnetic ion, $Fe^{(+)}$, as a component.

Crystal structure and the atomic distribution in the crystal have been examined by many investigators1),2),3). Two ways of atomic arrangement had been presented. However, Donnay *et al.*3) recently determined atomic arrangement by neutron diffraction which was just the same as that determined by Pauling and Brockhouse2). According to their investigation each metal is surrounded by sulphur and each sulphur by metal tetrahedrally. It has been reported by Hiller and Probsthain4) that there is a transition at about 550°C, below which the crystal structure is an ordered arrangement of Cu and Fe, and above which the calcium fluoride structure is realized. The latter is considered to be disordered chalcopyrite structure. Pauling and Brockhouse suggested the ionic valency state of cations in this crystal. They considered that chalcopyrite was a mixture with two ionic states, $Cu^{+}\ Fe^{+++}\ S_2$ and $Cu^{++}\ Fe^{++}\ S_2$, from the consideration of lattice constants and ionic radii of cations. By an experiment of X-ray K-absorption spectrum in chalcopyrite, at least two valency states, monovalent and divalent, of copper were supposed by Kurylenko5). But there has not been clarified the relation between this ionic state and physical properties, especially electric and magnetic properties. Many compounds, which have the same crystal structure with chalcopyrite are known6). These have the general formula, ABX_2 where A represents monovalent ion Ag^+ or Cu^+ and B is trivalent ion Al^{3+}, Ga^{3+}, In^{3+} or Tl^{3+} and X is S^{2-}, Se^{2-} or in some cases Te^{2-}.

Their optical and electric properties were examined by some investigators7)–10). Considering together these experimental results with the electronegativities of the constituent elements and crystal structure, Goodman9) proposed that these compounds with chalcopyrite structure are typical semiconductors. It will not be able to decide easily whether the same consideration is allowed to chalcopyrite itself because it contains transition element, Fe. Austin *et al.*8) observed also the infrared absorption and the Hall effect of a natural crystal of chalcopyrite and obtained 0.5 eV as the energy gap and 30 cm²/volt-sec as the mobility of positive holes. As far as they observed the optical and electrical properties there was not remarkable difference between chalcopyrite and the other compounds with chalcopyrite type structure which do not contain transition element. Boltaks and Tarnovskii[10] measured the temperature dependence of electric conductivity and thermoelectric power above room temperature on both natural and synthetic specimens of chalcopyrite. Above about 300°C the conductivity increased with the increase of temperature and the activation energy 0.2~0.6 eV was obtained. They also examined the rectifying property and found that it was much improved under a certain condition of surface etching. The thermoelectric power was very large and 200~300μV/deg. was obtained at room temperature.

About the magnetic properties, Donnay *et al.*[3] carried out a neutron diffraction experiment. Their interest was mainly confined to the symmetry consideration on magnetic structure and chalcopyrite was taken up as an example in order to examine whether their symmetry consideration was applicable. Nevertheless, it was clarified that chalcopyrite was antiferromagnetic at least at room temperature and the direction of antiferromagnetism was parallel to c-axis. The magnetic moment of iron and copper were 3.85μ_B and 0±0.2μ_B, respectively.

The present study reports the temperature dependence of the magnetic torque and the susceptibility of a single crystal, giving the Néel temperature and the direction of antiferromagnetism. Experimental results of electric properties, that is, the conductivity, the Hall effect and the thermoelectric power, which show behaviours of typical semiconductor are also given.

§ 2. Specimen and specimen preparation

A large natural single crystal which was found at Arakawa Mine, Japan, was used for magnetic and electric measurements. According to chemical analysis this crystal contains 33.54 weight % of copper, 31.7% iron, 33.9% sulphur and 0.90 weight % of insoluble matter. The analysis for detection of other impurity elements was not carried out. The chemical formula obtained from the above contents of constituent elements is $Cu_{1.00}Fe_{1.03}S_{2.01}$. Therefore, more metal atoms than the ratio of stoichiometry are contained in the crystal.

The synthetic specimen was obtained by a direct reaction of constituent elements in a evacuated silica tube. As starting materials sulphur redistilled in vacuum and electrolytic copper and iron were used. The tube was kept at 450°C for 7 days and then heated at 900°C for two days and then slowly cooled at the rate 25°C/hr. Though, as the melting point of chalcopyrite, temperatures of 950°C[11] and 875±10°C[10] were reported, it seems that 875±10°C is more reliable since at 900°C chalcopyrite already melts in vacuum in our study. For electrical measurement melted and non porous specimen was used.

An effort to form a single crystal by very slow cooling of a melted specimen was made but was unsuccessful. Austin *et al.*[8] also made an attempt to form a single crystal of other chalcopyrite type compounds and reported that their attempts were not successful because of an anisotropic thermal expansion of the crystal. Despite an advantage of rather low melting point the reason of the failure for chalcopyrite will be same to what reported by Austin *et al.*

According to X-ray diffraction all specimens include no other phase than chalcopyrite type structure.

§ 3. Experimental procedure

For the magnetic torque measurement a disc parallel to (110)-plane was cut out from a single crystal. The diameter of disc is 12.2 mm and the thickness 4.1 mm. The torque was measured by a torque magnetometer in a uniform magnetic field of 10200 œ from the liquid nitrogen temperature to about 600°C. Powder susceptibility was measured by a Sucksmith's type spring magnetometer.

Electric measurements have been performed on both natural single crystal and synthetic crystal. Two slabs which have [001] and [$1\bar{1}0$] directions as the longest axes were used. The electric conductivity was measured by four point method, and the Hall effect was measured by five electrodes. Electrodes are thin platinum wires and attached to the specimen by the method of current discharge. The contact of electrodes to the specimen is good even at high temperatures but the current will not be sufficiently uniform in the specimen.

All measurements were performed in the evacuated tube both at high and low temperatures.

§ 4. Experimental Results of Magnetic Measurements

Fig. 1 shows the torque curves in a uniform magnetic field of 10200 œ measured at −172°C and 20°C. At both temperatures they shows two-fold symmetry and the easy direction is [1$\bar{1}$0].

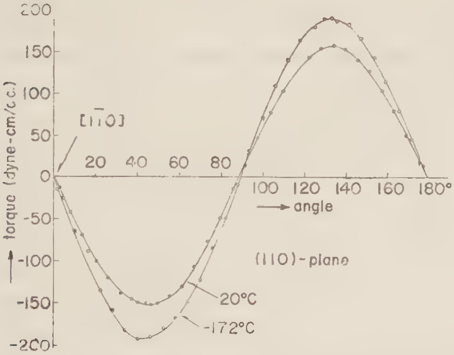

Fig. 1. Torque curve of (110)-plane at liquid nitrogen temperature and room temperature.

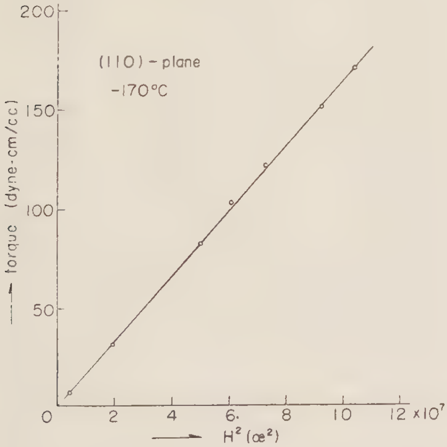

Fig. 2. The curve of maximum torque versus square of the magnetic field strength.

The variation of maximum torque with the square of magnetic field strength at −172°C is found to be linear as shown in Fig. 2. Accordingly, the torque T is given by the formula

$$T = \frac{m}{2M} H^2(\chi_\perp - \chi_{//}) \sin 2\theta \,, \qquad (1)$$

where m is the mass, H the magnetic field strength, M the molecular weight, $\chi_\perp$ and $\chi_{//}$ the two molal susceptibilities perpendicular and parallel to c-axis, respectively, and θ the angle of rotation. Up to the field strength of 10200 œ the higher term is not found.

The temperature dependence of maximum torque at the field strength of 10200 œ is illustrated in Fig. 3. It decreases with the rising of temperature and vanishes at about 550°C, where two principal susceptibilities, $\chi_\perp$ and $\chi_{//}$, are equal and this temperature may be the Néel temperature of antiferromagnetism. As the easy direction of the torque is [1$\bar{1}$0], the direction of antiferromagnetism is [001].

Powder susceptibility of the specimen (obtained by grinding the single crystal used for the torque measurement) has been measured. Its temperature variation is illustrated in Fig. 4 as χ_p, which is corrected by diamagnetism

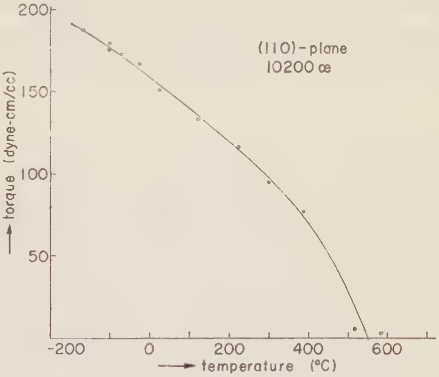

Fig. 3. Temperature dependence of the maximum of torque.

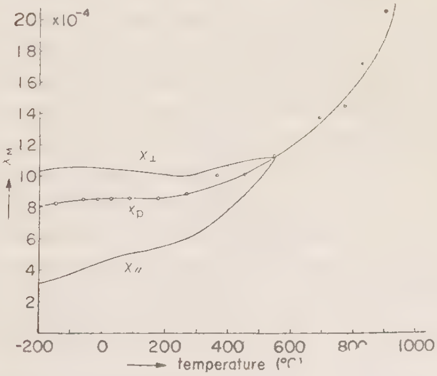

Fig. 4. Temperature variations of susceptibilities.

of constituent ions. χ_p increases with temperature from liquid nitrogen temperature to 550°C and continues to increase above 550°C. Therefore, unfortunately it is not able to calculate the effective Bohr magneton numbers of magnetic atomes from $1/\chi - T$ curve. This continuous increasing is probably due to the decomposition of the specimen into other substances one of which (for example, FeS) has high magnetic susceptibility. When chalcopyrite in the evacuated silica tube is quenched from 900°C, a considerable amount of sulphur is observed adhering on the wall of the silica tube. But we could not detect other substances than chalcopyrite by X-ray diffraction method.

In order to prevent the decomposition of the specimen two capsules, one of which was fulfilled with argon gas of 1 atmosphere besides the specimen and the other is with sulphur were prepared, and the magnetic measurement were made. In both cases the susceptibility of chalcopyrite increased with temperature above the Néel temperature and the Bohr magneton number was not obtained.

Below the Néel temperature the powder susceptibility is expressed by the formula,

$$\chi_p=\frac{2}{3}\chi_\perp+\frac{1}{3}\chi_{//}\,. \qquad (2)$$

Therefore, we can obtain two principal susceptibilities, $\chi_\perp$ and $\chi_{//}$, from the torque (1) and the powder susceptibility (2). The results are plotted in Fig. 4. $\chi_\perp$ is nearly constant with the temperature and $\chi_{//}$ goes down to zero as the temperature comes near to absolute zero, just as the theory of antiferromagnetism suggests.

§ 5. Experimental Results of Electric Measurements

The temperature dependence of two conductivities $\sigma_\perp$ and $\sigma_{//}$, perpendicular and parallel to c-axis, are illustrated in Fig. 5. Both conductivities increase with the rising of temperature from liquid nitrogen temperature to about −50°C and then decrease. Beyond about 300°C they increase again sharply. These behaviours resemble to that of a typical semiconductor. It seems that an intrinsic conduction occurs in the temperature range beyond 300°C and impurity conduction in the range below −50°C.

The results of the temperature dependence of conductivity by Boltaks and Tarnovskii are illustrated by dotted curves in Fig. 5. Though in their synthetic specimens there is a second decreasse of conductivity with the rising temperature at 500°C, we could not find such a second decrease.

While at high temperatures above about 450°C two conductivities, $\sigma_\perp$ and $\sigma_{//}$, are almost equal, there is a discrepancy between them at low temperatures. This anisotropy at room temperature is compared with those of natural single crystals measured by Wintenberger[12] in Table I. The conductivities of synthetic melted polycrystals which have the formulae $CuFeS_2$ and $CuFeS_{1.9}$ are also illustrated in Fig. 5. They are much larger than that of natural crystal, although it is expected that synthetic $CuFeS_2$ has less impurities and more stoichiometric composi-

Table I.

Specimen	$\rho_{//}$(Ω-cm)	$\rho_\perp$(Ω-cm)	$\rho_\perp/\rho_{//}$
ours	0.05	0.13	2.6
1	0.09	0.145	1.30
2	0.12	0.165	1.36
3	0.14	0.21	1.5

The numbers in the first column refer to the sample number of Wintenberger's specimens.

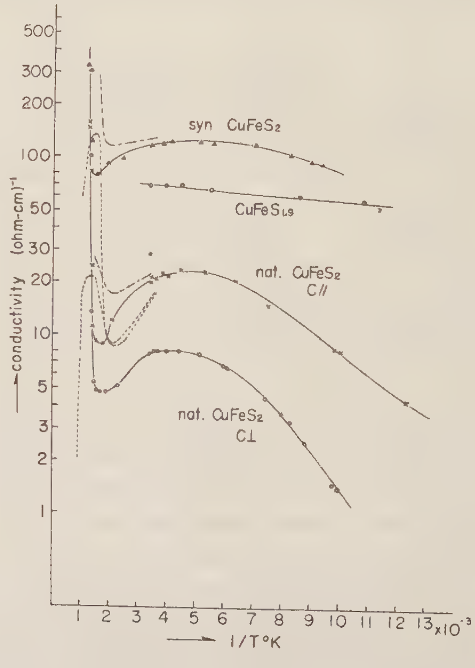

Fig. 5. Temperature variations of electric conductivities.

tion than the natural crystal. But beyond about 450°C the conductivity of synthetic $CuFeS_2$ coincides with that of natural crystal where the conduction seems to be in the intrinsic range.

The result of conductivity measurement is not completely reproducible after the measurement at high temperatures. The conductivity parallel to c-axis measured at room temperature after the heating at 560°C is plotted by a black circle in Fig. 5. This value is larger by 26% than that before the heating. However, the reproducibility is not so bad as to destroy the general behaviour of the temperature dependence of conductivity completely.

Hall effects of natural single crystal and synthetic $CuFeS_{1.9}$ are observed from liquid nitrogen temperature to about 150°C. Temperature dependence of Hall coefficients and number of conducting carriers are illustrated in Fig. 6. Beyond 150°C the reproducibility is so poor that we could not obtain precise values. The results of $CuFeS_{1.9}$ are very diverse. For both specimens the signs of Hall coefficients are negative and so the conductions are of N-type. The mobilities obtained from Hall coefficients and conductivities are illustrated in Fig. 7. The mobility of natural single crystal reaches to 35 cm²/volt-sec at liquid nitrogen temperature.

The thermoelectric power of the natural single crystal to copper is measured at room temperature. A large value, 480μV/deg., is obtained and the sign is negative which agrees with that obtained from the Hall effect measurement.

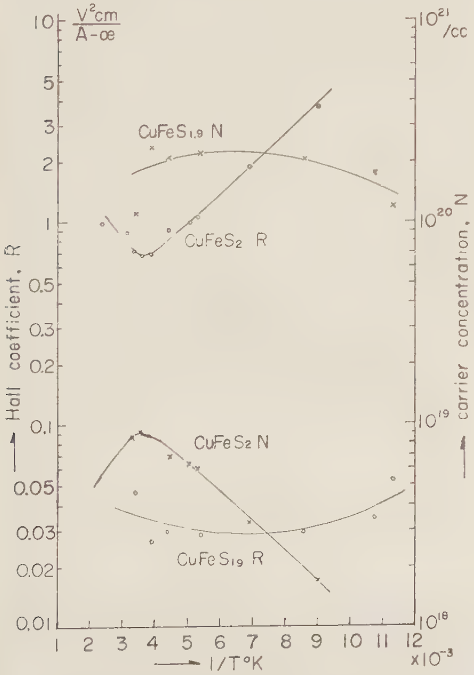

Fig. 6. Temperature variations of Hall coefficient and numbers of conduction carriers.

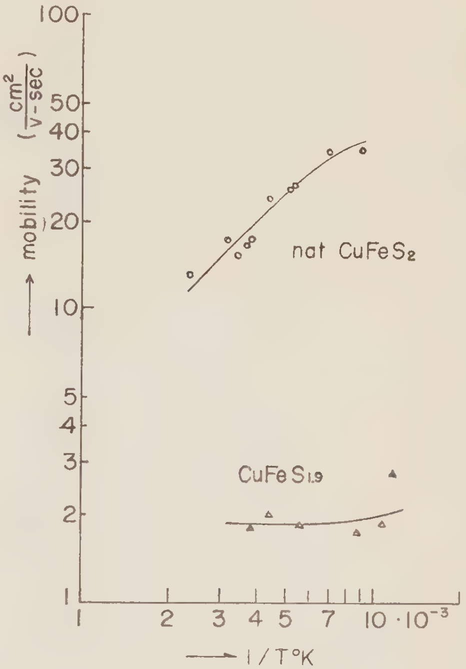

Fig. 7. Temperature variations of Hall mobilities.

§ 6. Discussion

From the results of experiments on magnetic properties it is concluded that chalcopyrite is an antiferromagnetic substance with the Néel temperature at about 550°C. The direction of antiferromagnetism is [001] direction, being in accord with the result of neutron diffraction[3]. As has been mentioned at about 550°C there is a crystal structure transition from chalcopyrite structure to calcium fluoride structure[4]. But taking into consideration the gradual decrease of the magnetic torque with the rising of temperature from liquid nitrogen temperature to 550°C (Fig. 3), it will be probable that the temperature 550°C is the antiferromagnetic Néel temperature, even though chalcopyrite begins to decompose from this temperature range.

Using the Néel temperature and the susceptibility perpendicular to the c-axis we can estimate the spin quantum number of the magnetic ion. The Néel temperature T_N is expressed as

$$T_N=\frac{2JzS(S+1)}{3k}\,, \tag{3}$$

while $\chi_\perp$ is expressed as

$$\chi_\perp=\frac{Ng^2\mu_B{}^2}{4Jz}\,, \tag{4}$$

where J is the exchange integral and z the number of nearest neighbors of magnetic atoms. Inserting the experimental values of T_N and $\chi_\perp$, we get $S=3/2$ as the most appropriate value. The effective Bohr magneton number of iron obtained from the neutron diffraction is $3.85\mu_B$, that is, $S=3/2$. It is noticed this good agreement does not hold if we take the next nearest neighbour interaction between magnetic ions into account.

Pauling and Brockway[2)] and Kurylenko[5)] suggested that chalcopyrite was a mixture of two ionic states, that is, $Cu^+Fe^{3+}S_2{}^{2-}$ and $Cu^{2+}Fe^{2+}S_2{}^{2-}$. However, our results of electric measurements will suggest that chalcopyrite is a typical semiconductor and we are strongly inclined to conclude that the bonding should be dominantly covalent, especially considering its large thermoelectric power of 480μV/deg.

The idea of a mixture of two ionic states and the rather large conductivity comparable with that of magnetite suggests a possibility that the conduction is made by hopping motion of electrons[13)]. But the electron mobility of 30 cm^2/volt-sec at room temperature is rather large and the carrier concentration of 8×10^{18}/cm^3 seems to be too small for this hopping motion mechanism.

The crystal structure of chalcopyrite is a substitutional analogue of that of diamond[9)]. Therefore all atoms, both metal and sulphur, are tetrahedrally sited in the lattice. In a diamond type structure each atom has four valency electrons and forms the tetrahedrally directed sp^3 bonds. In chalcopyrite all atoms will also form covalent sp^3 bonds when copper atom contributes one electron and iron atom 3 electrons to the covalent bond. Frueh[18)] suggests that if the above numbers of electrons are contributed to the valence bonds of metal atoms a Brillouin zone is filled with electrons.

Standing on a model of semiconductor, it seems from the data of Fig. 5 that beyond 350°C the conduction is in the intrinsic range and below −50°C in the extrinsic range. Activation energies in each range are 1.3 eV and 0.03 eV, respectively. Austin *et al.*[8)] reported from their experiment of infrared absorption that the energy band gap was more than 0.5 eV. This value, as compared with our value of 2.6 eV in the intrinsic range, seems too small. Frueh[14)] did not determine the energy band gap from his conductivity measurement because he thought that the decomposition would take place before the intrinsic range was reached. The above fact is also explained by his assumption. However, according to Austin *et al.* the energy band gaps of chalcopyrite structure $CuInS_2$, $CuInSe_2$ and $CuInTe_2$ are 1.2 eV, 0.92 eV and 0.95 eV, respectively. Therefore there is a possibility that the energy band gap of chalcopyrite is fairly large, far beyond the value of 0.5 eV.

There are some scattering of data as to the types of carrier in this compound. For instance, some investigators[10),15)] observed large negative thermoelectric power, while the sign of Hall coefficient observed by Austin *et al.*[8)] for a natural crystal was positive. Our measurements of the thermoelectric power and the Hall effect indicate that the conduction is of N-type. Although we have not enough knowledge about the impurities contained in our specimen, we assume now that the N-type conduction will be an intrinsic property of chalcopyrite. According to the phase diagram of Cu-Fe-S system[11),16)] chalcopyrite phase region extends to metal-rich side, while in the sulphur-rich region, pyrite, FeS_2 precipitates easily (Fig. 8). In order to check this point, compounds with the compositions $CuFeS_{1.9}$ and $CuFeS_{2.1}$ are synthesized by firing the mixture of copper, iron and sulphur in the appropriate proportion in an

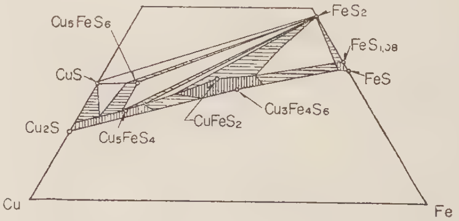

Fig. 8. Phase diagram of the Cu-Fe-S system after Merwin and Lombard.[16)]

evacuated tube. It was found by X-ray diffraction that there are extra lines for $CuFeS_{2.1}$ while for $CuFeS_{1.9}$ no extra lines appear. Therefore the variation of stoichiometry in chalcopyrite will favourably be on the sulphur deficient side. This is consistent with the N-type conduction of the compound, since it is well known that some compounds, for example, lead sulphide and zinc sulphide, have an N-type conduction(17) when these compounds contain excess metal atoms.

It is noticed that we cannot yet obtain the accurate knowledge of the valence state of the transition metal in chalcopyrite. But from the considerations about the crystal structure and the result of measurements of thermoelectric power and electric properties it is understood that chalcopyrite is an intrinsic semiconductor and probably when it becomes non-stoichiomentric it shows an N-type conduction. This means the d-shell of the transition metal seems to be independent of the valence bond.

According to our most simple model the five unpaired electrons should remain in the d-shell of each iron, but this is not confirmed by the magnetic measurement. However, it is probable that the cubic close packed structure of sulphur atoms will prevents the formation of *d-d* bonding(19).

There is the same kind of discussion in the compounds with NiAs-type structure(19),(20). In these cases it should be kept in mind that the splitting of half-filled d-level due to antiferromagnetism(21), might be playing some role.

The author express his hearty thanks to Prof. Miyahara for his valuable discussions and encouragement and to Prof. Harada who kindly delivered him the single crystal of chalcopyrite. He is also much indebted to Dr. Akio Kobayashi and Dr. Yamadaya.

A most part of this work was carried out at Department of Physics, Hokkaido University and a part of expenses was payed by the Fund of the Ministry of Education in Aid of Scientific Research.

References

1) C. L. Burdick and J. H. Ellis: Proc. Natl. Acad. Sci. U. S. **3** (1917) 644, J. Am. Chem. Soc. **39** (1917) 2518.
2) L. Pauling and L. O. Brockway: Z. Krist. **82** (1932) 188.
3) G. Donnay, L. M. Corliss, J. D. H. Donnay, N. Elliott and J. M. Hastings: Phys. Rev. **112** (1958) 1917.
4) J. E. Hiller und K. Probsthain: Z. Krist. **108** (1950) 108.
5) C. Kurylenko: Bull. soc. franç. minéral. **65** (1942) 59.
6) H. Hahn, G. Frank, W. Klinger, A. D. Meyer und G. Störger: Z. anorg. u. allg. Chem. **271** (1953) 153.
7) C. H. L. Goodman and R. W. Douglas: Physica **20** (1954) 1107.
8) I. G. Austin, C. H. L. Goodman and A. E. Pengelly: J. Electrochem. Soc. **103** (1956) 609.
9) C. H. L. Goodman: J. Phys. Chem. Solids **6** (1958) 305.
10) Б. И. Болтакс и. Н. Н. Талновскии: Жур. Техн. Физ. **25** (1955) 402.
11) H. Schlegel und A. Schüller: Z. Metallkunde **43** (1952) 421.
12) M. Wintenberger: Compt. rend. **244** (1957) 1801.
13) E. J. W. Verwey and J. H. de Boer: Rec. Trav. Chim. Pays-Bas, **55** (1936) 531.
14) A. J. Frueh: Amer. Min. **44** (1959) 1010.
15) M. Telkes: Amer. Min. **35** (1950) 536.
16) H. E. Merwin and H. P. Lombard: Econ. Geol. **32** (1937) 203.
17) *cf. Semiconductors* ed. by N. B. Hannay: Reinhold Pub. Co., New York, 1959.
18) A. J. Frueh: Geochim. et Cosmochim. Act. **6** (1954) 79.
19) F. Hulliger: Helv. Phys. Act. **32** (1959) 615.
20) W. B. Pearson: Canad. J. Phys. **35** (1957) 886.
21) J. C. Slater: Phys. Rev. **84** (1951) 179.

JOURNAL OF THE PHYSICAL SOCIETY OF JAPAN, Vol. 16, No 10, OCTOBER, 1961.

Effect of the Substructure upon Magnetic Properties of Iron-Silicon Single Crystals

By Yoji NAKAMURA

Faculty of Science, Kyoto University

(Received March 6, 1961)

The substructure was observed by means of the X-ray diffraction microscopy and the magnetic properties were measured at room temperature on single crystals of 4% Si-Fe alloys as produced from the melt at various growth rates. Single crystals produced at slow cooling rate consist of large subgrains with a small orientation difference and have small coercive force and large remanent magnetization, as compared with those produced at fast cooling rate. Such a dependence of magnetic properties upon the substructure is discussed in terms of the nature of sub-boundaries.

§ 1. Introduction

It is well known that single crystals grown from the melt are not crystallographically perfect, but they consist of a large number of fairly perfect regions called subgrains. The configuration and origin of the substructure have been studied extensively in detail[1]. In general, there is a slight difference in orientation between adjacent subgrains and also a difference in amount of impurities between the subgrain boundaries and the interior of the subgrains. In other words, the sub-boundary can be considered as a network of dislocations and also as a region with higher concentration of impurities. The effect of dislocations upon the motion of ferromagnetic domain boundaries was discussed theoretically by Vicena in detail[2], and the effect of the impurity segregation or of the so-called " inclusion " was also discussed mainly by Néel[3]. Thus, the substructure in crystal may have an influence upon the bulk magnetic properties of ferromagnetic materials owing to its hindrance effect against the domain boundary movement. So far as I know, however, any experimental study concerning the effect of substructure upon the magnetic properties has not yet been performed.

The configuration of substructure depends mainly upon the following four factors, namely, the concentration of impurities, orientation and rate of crystal growth, and temperature gradient at the melting point. It is convenient to investigate the effect upon the magnetic properties of the substructure produced at various growth rates under a constant temperature gradient. To observe the effect of the growth rate, the test sample is desired to have the following characteristics. First, the specimen must have no phase transition below the melting point. Secondly, the orientations of single crystals coincide with the direction of easy crystal growth, since such single crystals are actually likely to be prepared at various growth rates. Lastly, the direction of easy crystal growth coincides with the direction of easy magnetization, because this is the most structure-sensitive direction. After Takaki *et al.*[4], in iron-silicon alloys, the direction of easy crystal growth is the [100] direction along which the magnetization is easiest. So, we have studied the configuration of substructure and its effect upon the magnetic properties of iron-silicon alloy containing 4% Si.

§ 2. Preparation of Single Crystal Specimens

The material used is a commercial iron-silicon alloy which contains 4.03% Si, 0.08% C, 0.07% Mn, 0.02% P, 0.026% Cr, 0.31% Cu, 0.007% S and 0.31% Ni. We successfully used a vacuum Tammann furnace to produce single crystals by the Bridgman method[4]. The temperature gradient of the furnace is about 80°C per cm near the point where the solidification occurs. Using a single crystal rod with the rod axis along [100] direction as the " seed " crystal, several single crystal rods were produced by changing the growth rate from 0.4 to 11 mm per min. Thus obtained single crystals rods, 3 mm in diameter and 20∼25 cm in length, have the [100] orientation within 1°, which was checked by the back-reflection Laue method.

§ 3. Substructure

The existence of subgrains in single crystals was detected by the split-up of Laue reflection spots in the course of the determination of their orientations.

To observe the substructure, the (100) surfaces of the specimens were polished mechanically and electropolished in a mixed solution of chromic acid and phosphoric acid. Then the specimens were annealed in vacuum at 1000°C for 2 hours.

For the optical observation of sub-boundaries, the electrolytical etching was effectively made in 1 N potassium dichromate solution (Ruder's solution) at about 50°C for 2 or 4 hours, using the current density of 0.02~0.05 Amp per cm^2. The observations under a low-power microscope revealed irregular patterns of sub-boundaries such as shown in Photo. 1.

This optical examination, however, gives no information about the misorientation between neighbouring subgrains. Consequently, the method of the X-ray diffraction microscopy called the Berg-Barett technique was applied to the (100) surfaces prepared as mentioned above. The reflection plane employed here is the (220) plane. X-ray emmitted from a vertical line source 3.5 mm × 1 mm was used, employing an iron target; the radiation consisted predominantly of the Fe$_{\alpha1\alpha2}$ doublet. The specimen crystal was held on a goniometer 45.5 cm distant from the source.

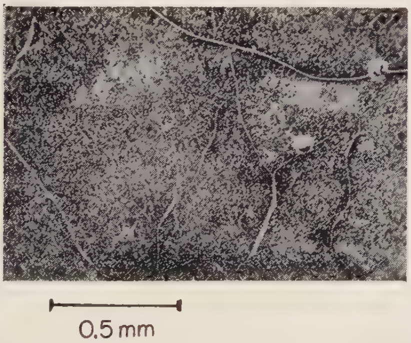

Photo. 1. Optical micrograph of the (100) surface of a 4% Si-Fe single crystal grown at 5 mm/min.

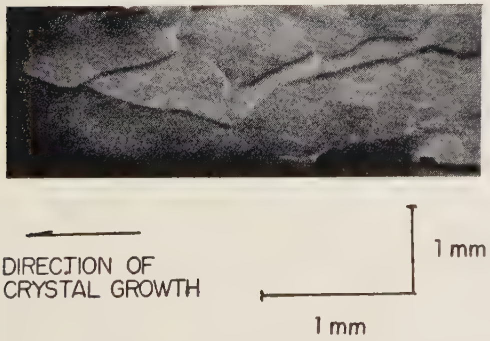

Photo. 2. Berg-Barett photograph of a 4% Si-Fe single crystal grown at 0.4 mm/min. Fe K_α, specimen face: 100, reflection plane: (220), voltage: $30K_V$, current density: 10 mA, exposure: 10 min.

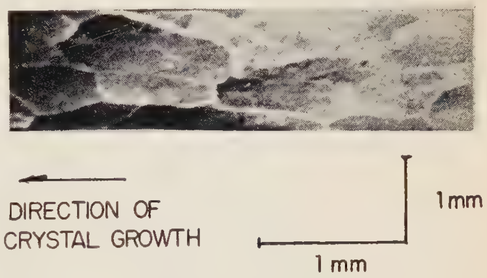

Photo. 3. Berg-Barett photograph of a 4% Si-Fe single crystal grown at 5 mm/min take under the same condition as in Photo. 2.

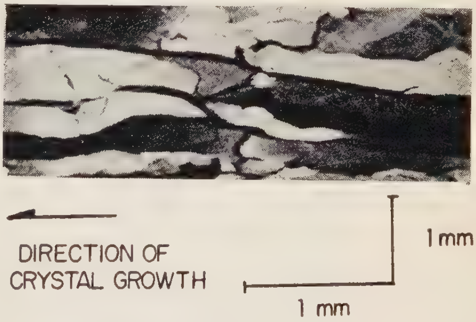

Photo. 4. Berg-Barett photograph of a 4% Si-Fe single crystal grown at 11 mm/min taken under the same condition as in Photo. 2.

Several X-ray microphotographs thus obtained are shown in Photos. 2, 3 and 4. In these photographs the direction of the incident X-ray beam is parallel to the direction of the rod axis, namely that of crystallization. The interpretation of Berg-Barett photographs of the sub-boundaries has been given in detail by Hume[6], and, hence, no further statements may be necessary here. From these photographs, we can see that the shape of subboundaries is rather irregular as compared with that in pure metal crystals where subgrains usually appear as elongated rods of approximately hexagonal or square cross-section[1]. In general, the size of subgrains increases as the rate of the growth decreases. The mean linear dimensions of subgrains as estimated by counting the number of subgrains in the same area of each photograph decreases from 1 mm for the lowest rate to 0.4 mm for the highest growth rate. Next, a very rough estimation of the mean difference in orientation was made by observing the width of overlapping or failing of images of neighbouring subgrains. The mean orientation difference thus obtained increases with increasing growth rate, being in the range from 10′ for the lowest growth rate to 30′ for the highest rate.

§ 4. Magnetic Properties

Before measuring the magnetic properties, the specimens were annealed in vacuum at 1000°C for 2 hours and slowly cooled in the furnace. Magnetization curves were measured by the conventional ballistic method at room temperature. Typical magnetization curves obtained are shown in Fig. 1, which indicates that the specimen becomes magnetically softer with decreasing growth rate.

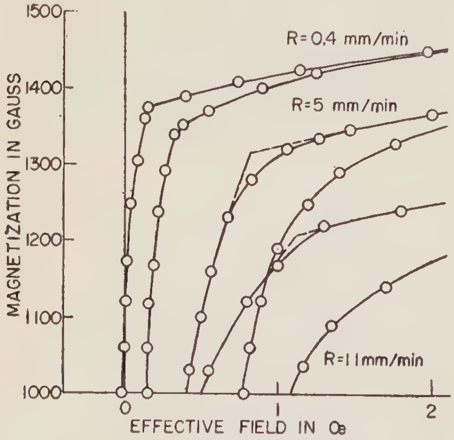

Fig. 1. Magnetization curves of 4% Si-Fe single crystals produced at various growth rates, *R*.

One can see more clearly the effect of growth rate upon magnetic properties when the coercive force and remanent magnetization are taken as measures of magnetic softness. The dependence of coercive force on the growth rate is represented in Fig. 2.

As seen from Fig. 1 the descending hysteresis curve of the single crystal specimen produced at slower growth rate shows the sharper break near the point where the effective magnetic field is approximately equal to zero. The intensity of magnetization at the break, therefore, may be considered as the remanent magnetization. The hysteresis curve of the single crystal specimen produced at fast growth rate, however, has no such a sharp break but shows a gradual bend in the corresponding region, so that it is difficult to define accurately the remanent magnetization. Therefore, for such single crystal specimens the intensity of magnetization at the intersection of the two tangents of the comparatively straight portions of the curve on both sides of the bend, as shown by dotted line in Fig. 1, was taken, for convenience, as the remanence. The relation between the remanent magnetization and the growth rate is shown in Fig. 3, which indicates a decrease in remanent magnetization with increasing growth rate.

The domain patterns of the specimens were examined by means of the powder pattern

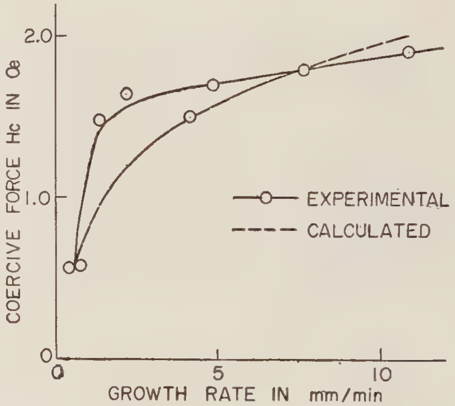

Fig. 2. Coercive force as a function of the growth rate, in 4% Si-Fe single crystals.

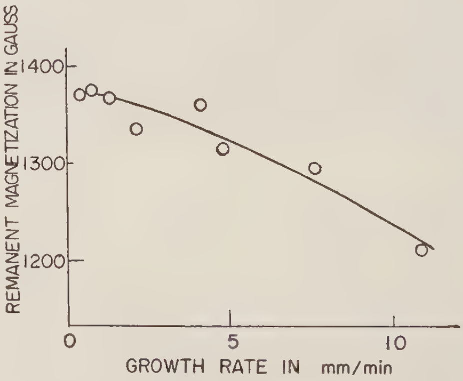

Fig. 3. Remanent magnetization as a function of growth rate, in 4% Si-Fe single crystals.

technique[7]. The observed patterns on the (100) plane show that the domain boundaries are continuous across the sub-boundaries. The domain structure is mainly constructed by the 180° walls which are parallel to the rod axis and separate the neighbouring domains by about 10^{-2} cm. The mean distance between 180° walls decreases with increasing growth rate, ranging from 1 mm for the lowest growth rate to 0.4 mm for the highest rate.

§ 5. Discussions

Although no observation was made about the difference of the impurity concentration in the sub-boundaries and in the interior of the subgrains, the observed substructure seems to be the so-called impurity substructure[1], because the concentration of impurities in the specimen is high as stated above (§ 2). Thus the origin of the formation of this substructure may be the constitutional supercooling[1]. If the rate of diffusion of impurities in the liquid was balanced with the rate of cooling, the long-rod-shaped subgrains could appear as in the case of pure metals. The balance, however, is difficult to be maintained steadily during cooling in this case because of a high concentration of impurities. As the result crystal nuclei may be formed randomly in the liquid phase before the subgrain in question develops and elongates, and the before-mentioned substructure containing irregularly shaped subgrains is formed. No further consideration is made on the origin of the configuration of the substructure, since it is the chief aim of this paper to show the effect of the substructure upon the magnetic properties.

As previously mentioned, sub-boundaries can also be considered as dislocation networks regardless of the impurity concentration in the material. The motion of the domain wall in a ferromagnetic crystal is affected by the dislocation. The interation between the domain wall and dislocation was theoretically investigated in detail by Vicena[2]. He calculated the effect of the stress field of the dislocation upon the motion of the 180° domain wall across the dislocation and showed that the magnetoelastic energy of the domain wall changes when the wall moves over the dislocation. This interaction is more effective for the motion of the domain wall than any other magnetic energy. Based on a simplified assumption, he expressed the coercive force as a function of the dislocation density, which has been verified experimentally[8]. Further, the influence of dislocations arranged along the boundary separating the mosaic blocks was also discussed by him. If the mosaic blocks are cubic whose faces coincide with the {100} faces of cubic crystal, and 180° domain walls are parallel to those faces, the coercive force is given by

$$H_c=\frac{\sqrt{d\cdot l}}{\sqrt{2}\,I\cdot L}\,\frac{\tan\theta}{a}\left(ln\frac{L}{d}\right)^{1/2}\frac{\Delta E}{d}, \qquad (1)$$

where d is the domain wall thickness, I the saturation magnetization, L the separation of 180° wall, l the linear dimension of mosaic block, θ the orientation difference between neighbouring mosaic blocks, a the lattice constant, and ΔE the maximum energy change (magnetoelastic) of the domain wall per unit length.

The substructure observed here consists of subgrains with irregular shape whose dimension and misorientation are larger than those considered by him. However, when l and θ are replaced by the linear dimension and misorientation of subgrains, respectively, of which the values were given in § 3, his calculation can also be applied to the present author's experiments, because it is seen from his paper that the orders of magnitude of l and θ may not affect essentially the result of the calculation. By using Eq. (1) one can easily obtain the value of coercive force for each growth rate by taking $\Delta E=0.35\times10^{-5}$ erg/cm[2]; $d=10^{-8}$ cm; $I=1500$ e.m.u. and the values for l, L and θ as already given in the preceeding section. The obtained results as shown by a dashed line in Fig. 2 show that the calculated values agree qualitatively well with the observed ones. Thus, it can be said that the coercive force is related to the sub-boundaries constructed by dislocations.

Finally, an interpretation is required to account for the dependence of the shape of hysteresis curve, especially of the remanence upon the substructure. When the externally applied field is reduced from the value required to magnetize the specimen to saturation, the nucleous of reverse magnetization may be created at some regions of imperfection and the magnetization decreases as the nucleous grows. The nucleation and growth of reverse domain in the case of iron-silicon single crystals were studied by Bates and Martin[9]. They showed that the surface pits or nonmagnetic inclusions could be the nucleation centers and that nucleation of reverse magnetization and its growth which reduced the remanent magnetization could take place before the magnetic field was reduced to zero.

In our single crystal specimens sub-boundaries may be considered as the nucleation centers of reverse domains, because they contain therein the higher concentration of impurities as compared with the interior of the subgrains. The observed round shoulder in the descending hysteresis curve and low remanent magnetization shown in Fig. 1 and Fig. 3 may be explained by a probable appearance of many reverse domains at sub-boundaries. Further, under high applied magnetic field the magnetostatic energy associated with magnetic poles distributed at sub-boundaries due to the misorientation between nighbouring subgrains must be taken into account, although its contribution to the total magnetic energy is small, and the magnetostatic energy can be reduced when reverse domains appear at boundaries[10]. This energy reduction makes easy the appearance of reverse domains.

In conclusion the author wishes to express his hearty thank to Professor H. Takaki for his kind guidance and encouragement throughout the work. He is also greatly indebted to Dr. M. Koyama who helped the measurement and gave valuable discussions in the study of substructures.

References

1) C. Elbaum: Progr. Metal Phys. **8** (1959) 203.
2) F. Vicena: Czechosl. J. Phys. **5** (1955) 480.
3) L. Néel: Cah. Phys. **25** (1944) 21, Ann. Univ. Grenoble **22** (1946) 299.
4) H. Takaki et al.: J. Phys. Soc. Japan **9** (1954) 204.
5) W. Berg: Naturwiss. **19** (1931) 391. C. S. Barrett: Trans. AIME, Metals Div. **161** (1945) 15.
6) K. F. Hulme: Act. Met. **2** (1954) 810.
7) H. J. Williams, R. M. Bozorth and W. Shockelly: Phys. Rev. **75** (1949) 155.
8) Z. Malek: Z. Angew. Phys. **9** (1957) 279.
9) L. F. Bates and D. H. Martin: Proc. Phys. Soc. **B69** (1956) 145.
10) J. B. Goodenough: Phys. Rev. **95** (1954) 917.

JOURNAL OF THE PHYSICAL SOCIETY OF JAPAN, Vol. 16, No. 10, OCTOBER, 1961

Dislocation Images in Pure Iron Observed by Transmission Electron Microscopy

By Hiroshi FUJITA and Zenji NISHIYAMA

Institute of Scientific and Industrial Research,
Osaka University

(Received March 7, 1961)

The dislocation image has a line or dotted feature, which depends essentially upon the reflecting condition. This dependency has been clarified by the dark field image method and also by the method of small variation of the incident angle of electron beam, as follows:—

Line images of dislocations: 1) Generally the contrast of dislocation image near an extinction contour is mainly due to the reflection of the same index as that of the contour. 2) The dislocation image usually appears as a single line, sometimes as a double image, when it is due to one reflection. 3) On the contrary, sometimes the image looks like a single line even when it is due to multiple reflections. 4) The image having black contrast is generally accompanied by white side-lines, and when the latter predominates, the image is observed as a white dislocation image. 5) Near the intersection of dislocations of two families, there are found some variations in the image features, which may be not only due to the interaction between strain fields of the intersecting dislocations, but also due to the systematic interaction of the reflections.

Dotted images of dislocations: 1) Each dot in the dotted images is frequently composed of the white and the black regions lying side by side and distributed alternately along the dislocation line. 2) The zig-zag image is considered as a special feature of the dotted image, which is occasionally produced by two reflections. 3) Complex features of the dotted images, for instance, the image interposed between two black lines, are due to multiple reflections.

Finally, it is shown that the foil is bent by the dislocation for relief of the dislocation stress, and that some of the image features may be affected by this phenomenon because of variation of the reflecting condition.

§ 1. Introduction

An interpretation of the contrast of dislocation images observed by transmission electron microscopy has recently been given by Hirsch *et al.*[1], and it has been shown that the contrast of the images depends essentially upon the condition of the Bragg reflection. They applied the kinematical theory to interpret the experimental results of f.c.c. metals such as aluminium, and explainned a number of basic features of the observed images. The theory does not, however, explain more complex characteristics of the images. To study the characteristics of the dislocation, unambiguous interpretation for the image is needed, for which more definite data showing the relation between dislocation images and reflecting conditions must be supplied. The present work has been carried out to obtain such data in the case of pure iron.

§ 2. Specimens

Specimens were taken from a 99.9% purity iron plate rolled at room temperature to 0.2 mm in thickness, and they were subjected to annealing for 30 min. at 1000°C followed by furnace-cooling. They were then beaten at about −70°C. To make foils for the electron micrograph, electro-polishing was performed using an electrolyte (phosphoric acid 100 cc and chromic acid 100 g) kept at 80°C.

The electron microscope used was of Hitachi HU-11 type operated at 100 kV.

§ 3. Experimental Results

1. Line images of dislocations

A. *The change of image with the distance from an extinction contour*

It is general that the contrast of dislocation images observed by transmission electron microscopy tends to become faint with increasing the distance from the region where an extinction contour exists. Since the contrast of the extinction contour results from bending of the specimen in this case, the distance from the extinction contour is roughly considered to represent the deviation angle from the Bragg condition if it is not so large. Therefore, the relation between dislocation images and the deviation angle from a Bragg condition will be presumed from detailed observation of images of the dislocations belonging to the same family, around the extinction contour. Fig. 1 was taken for this

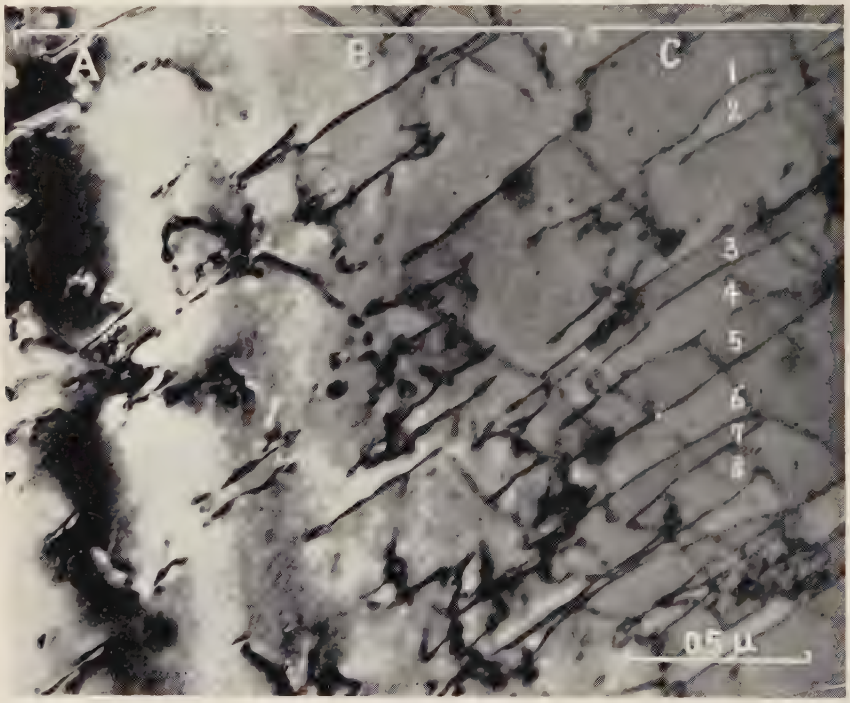

Fig. 1. Variation of the dislocation image with distance from an extinction contour.

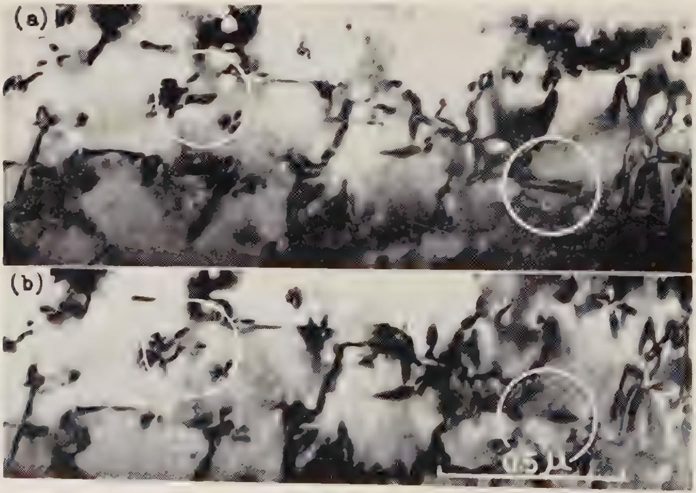

Fig. 2. Variation of the image features, from double to single, by small change of the incident angle.

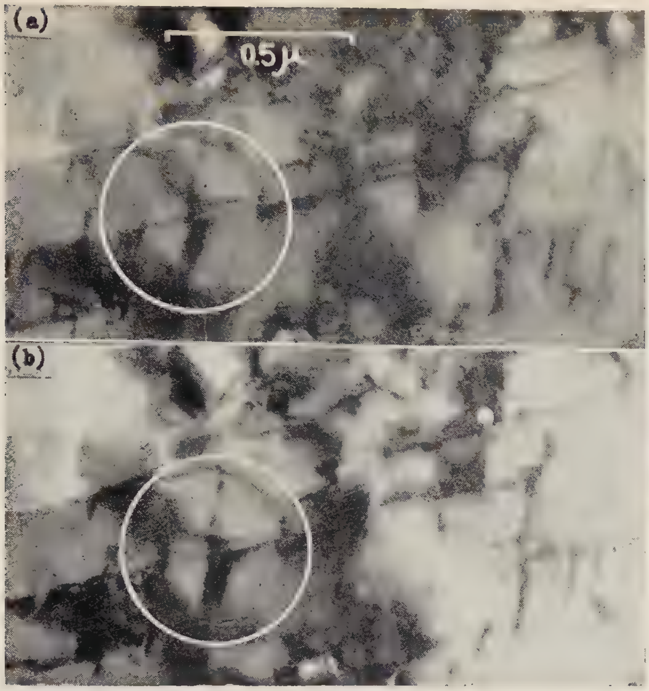

Fig. 3. Triple image appearing at the intersect on of dislocations.

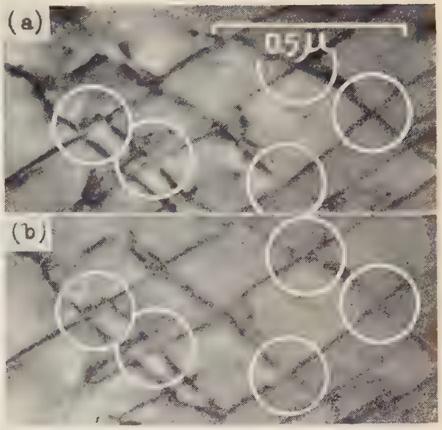

Fig. 5. Dislocation images running from upper left to lower right are lost in contrast at the intersection, but those intersecting these images are not.

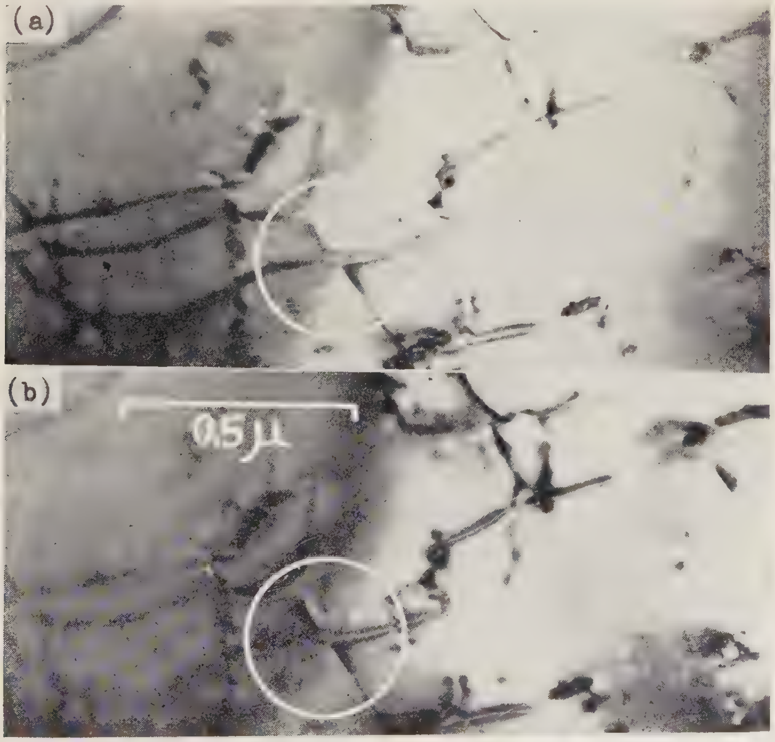

Fig. 4. Double image intersecting another dislocation.

purpose. In this figure dislocation lines running from lower left to upper right are thought to belong to the same family from their arrangement. As for their behaviors, it is found that the feature of dislocations varies considerably with the distance from an

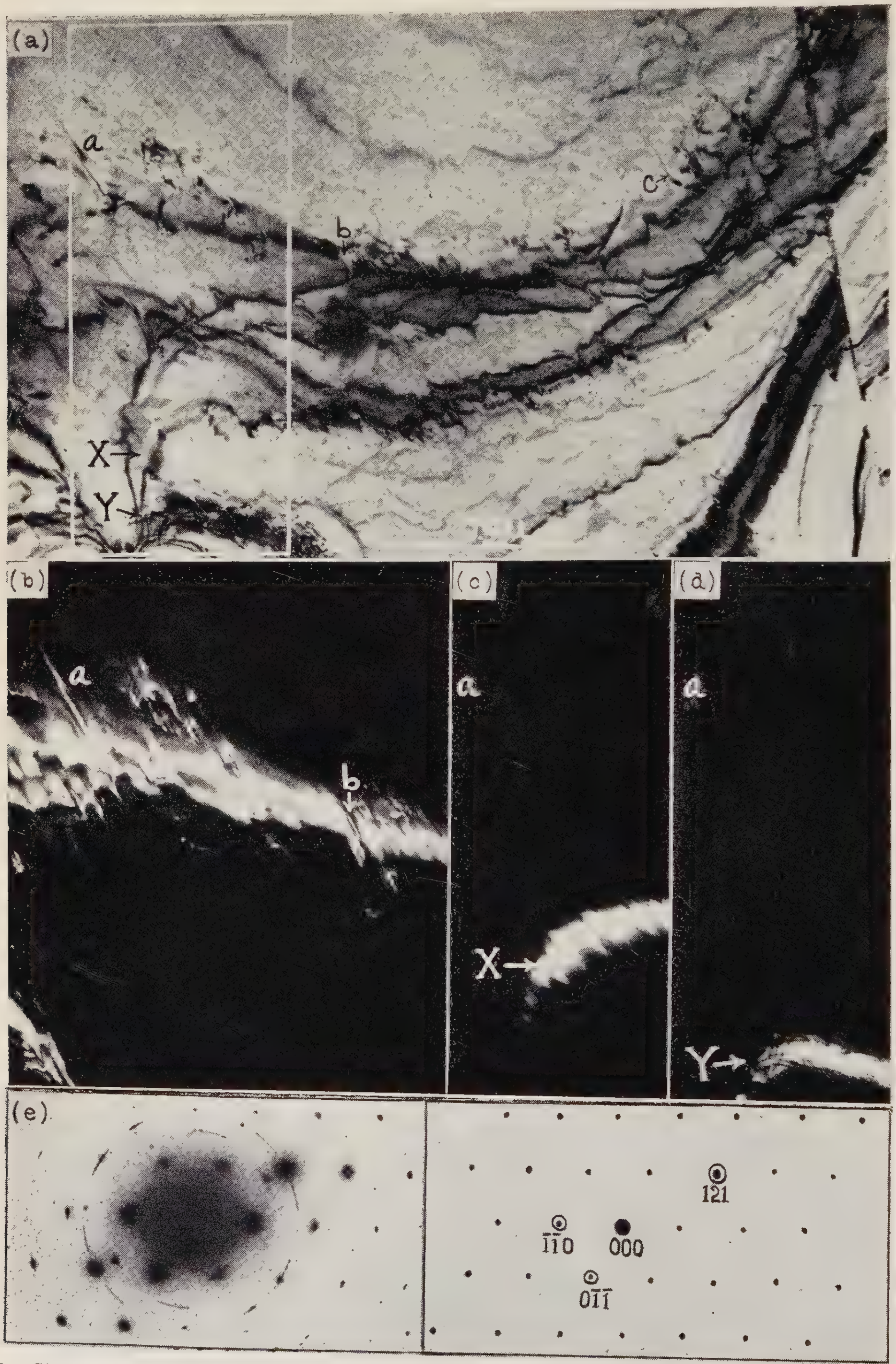

Fig. 6. Single image of dislocation accompanied by white side-lines. (b) is a dark field image of 121 reflection. In (c) and (d) which are dark field images of $0\bar{1}\bar{1}$ and $\bar{1}10$ reflections respectively, of white-framed region in (a), there is no image *a*. (e) is the selected-area electron diffraction pattern of (a).

extinction contour situated at the left side: i.e. in region A dislocation image has the shape of a black line accompanied with white lines, in region B it is often of a double lines, and in region C it is of a black single line. It should also be noted in Fig. 1 that dislocation images are apt to take a dotted shape with approaching the left side, which will be discussed later. The dynamical effect may play an important role in the contrast and the shape of the image, because there is a difference in thickness, i.e. the foil is thicker to the right.

B. *The change of image due to variation of the incident angle*

From the results mentioned above, it is evident that the dislocation image depends upon the distance from the extinction contour. This dependency can also be confirmed with the micrographs taken at slightly varied incident angles by changing the condensor lens current. Figs. 2, 3 and 4 are examples taken in this way, in which considerable changes between (a) and (b) are observable at encircled regions; in Fig. 2 some double images are changed to single ones, and in the triple image in Fig. 3 the distance between the outer two images and the central one is varied with changing the incident angle. Such a triple image is occasionally found near the intersection of dislocation of two families, as seen in this figure.

In encircled regions in Fig. 4 there is seen a typical double image of dislocation, which shows the effect of the intersection with another dislocation lying on the same or neighbouring plane. The right part of the horizontal dislocation shows a double image, while the left part shows a single image which is continued approximately to the white mid portion of the right double image. On the other hand, as for the intersecting dislocation, the position of black contrast is interchanged from one side to the other at the intersection.

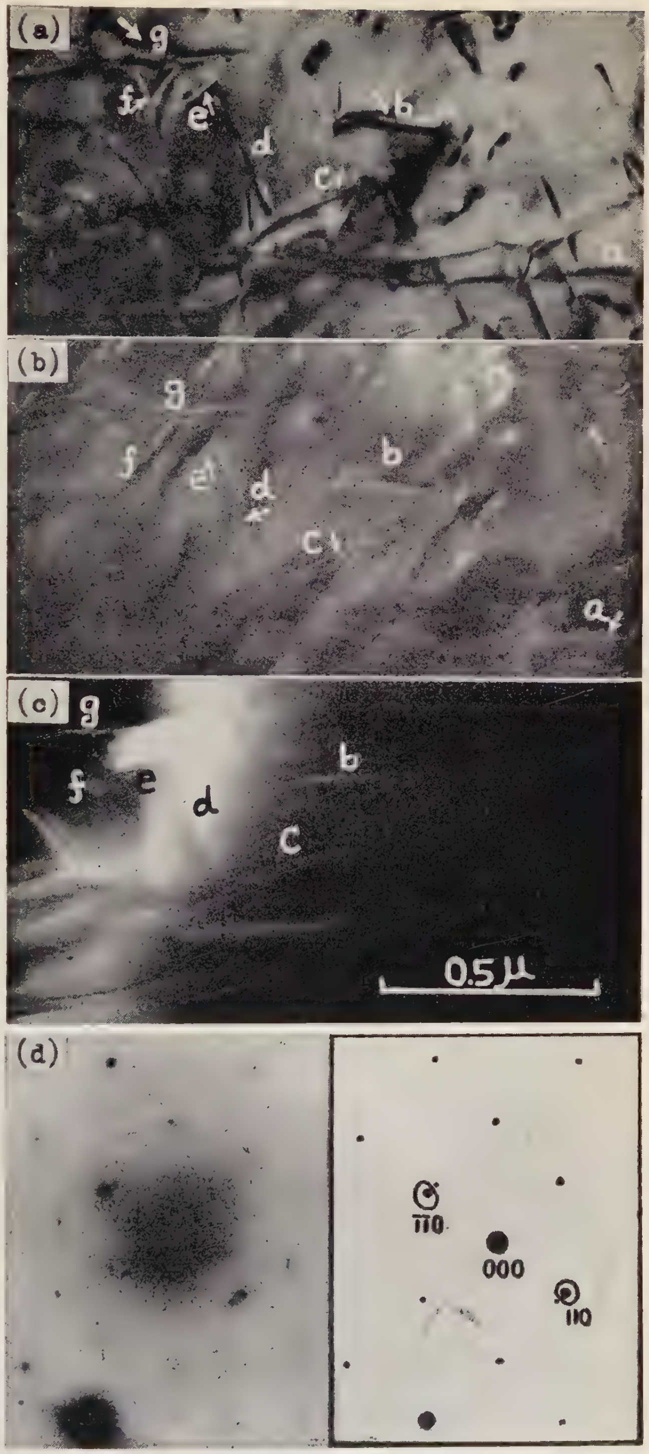

Fig. 7. Double image and white dislocations (e and f). (b) and (c) are dark field images of 110 and $\bar{1}10$ reflections, respectively. (d) is the selected-area electron diffraction pattern of (a).

Intersecting dislocation images are also observed in Fig. 5, in which dislocations of two families may be situated different depth from the surface. The image of one family is lost in contrast at the intersection, while the image of the other is not. These features may be not only due to the interaction between strain fields of the intersecting dislocations, but also due to the systematic interaction of the reflections.

C. *The relation of image to the index of reflection*

In order to find the relation between the image and the Bragg condition more definitely, it is necessary to know the index of reflection of the dislocation image. For that purpose, the dark field image method is convenient and effective. In the present work, it was used under the same condition as in the bright field image, and the non-variation of

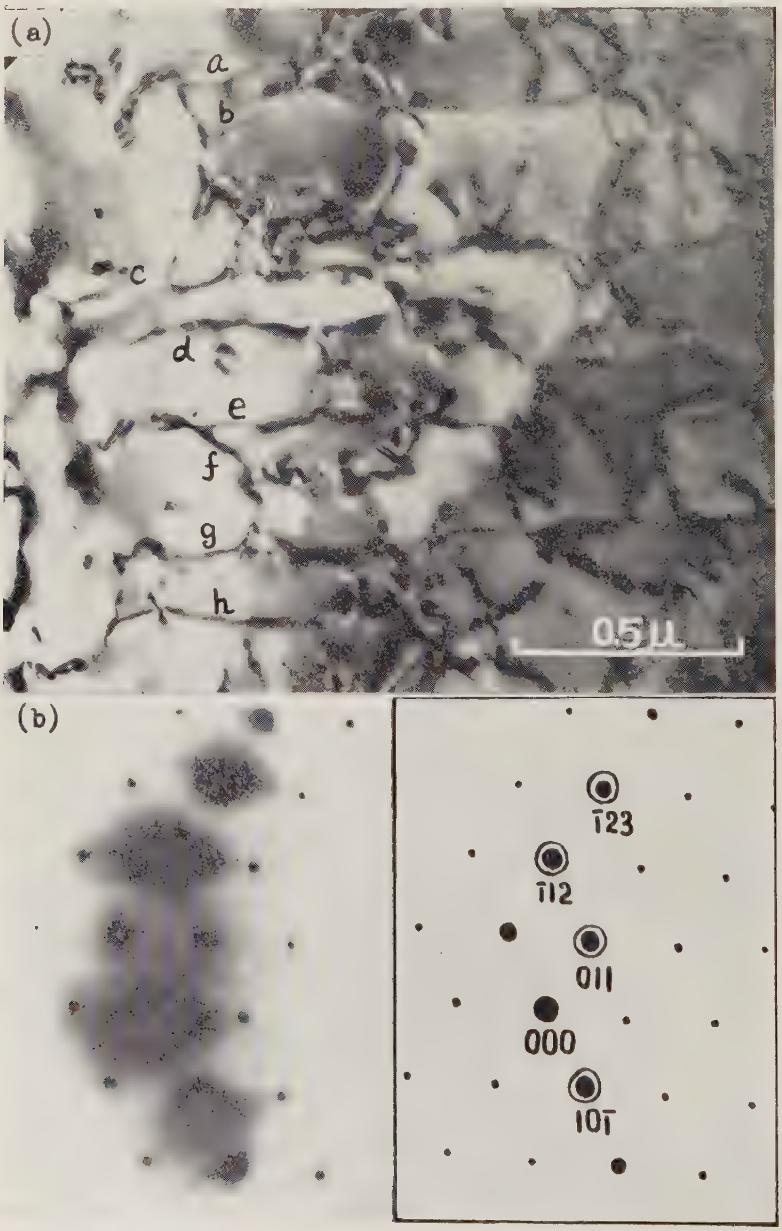

Fig. 8 (a) and (b). Single images produced by multiple reflections. (b) is the selected-area electron diffraction pattern of (a).

the reflecting condition during this operation was checked by comparing two bright field images taken before and after this operation.

From the results of the dark field image method, the following relations between the dislocation images and the conditions of the

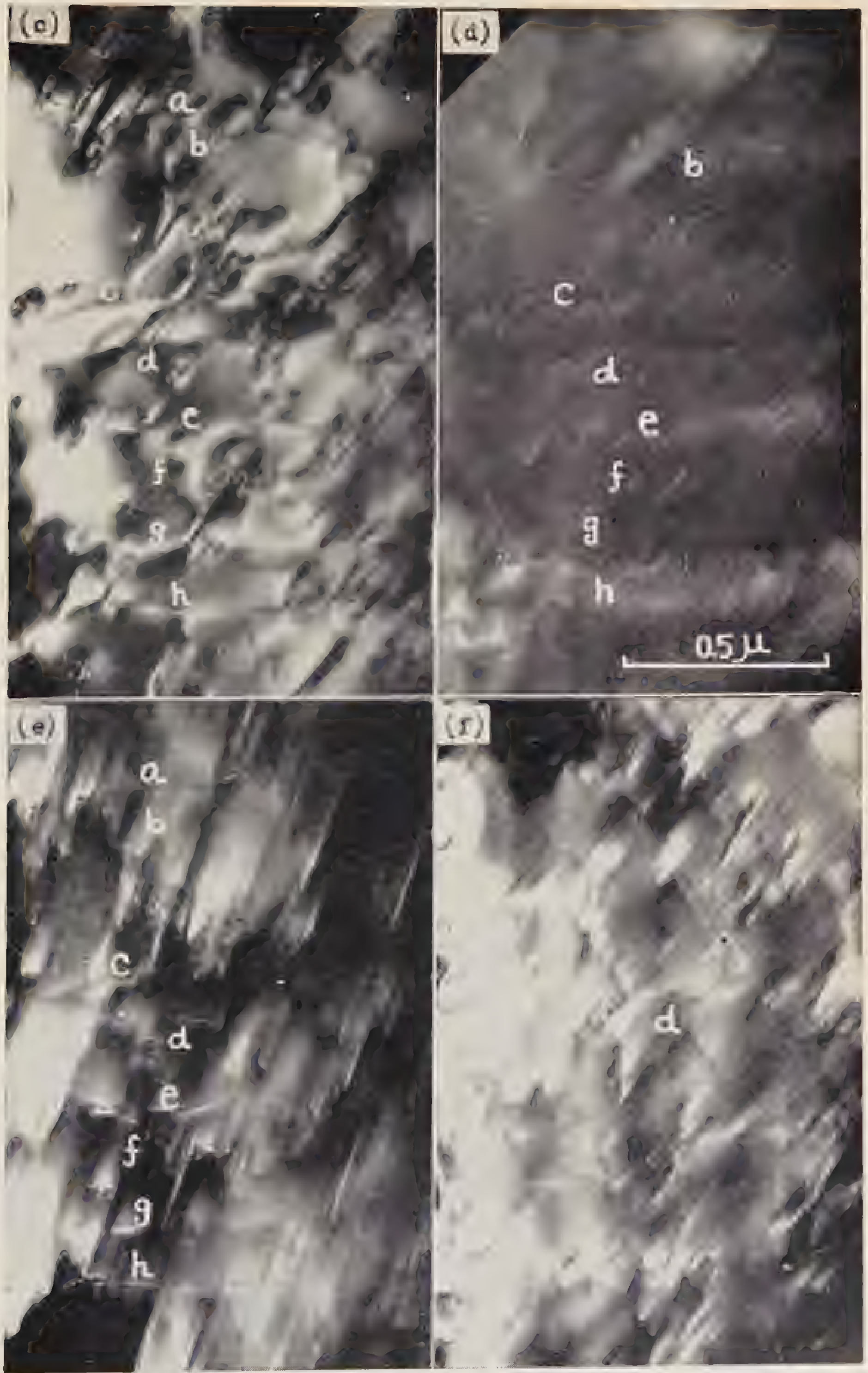

Fig. 8(c)–(f). (c), (d), (e) and (f) are dark field images of $\bar{1}12$, $10\bar{1}$, $\bar{1}23$ and 011 reflections, respectively.

Bragg reflections were clarified:—

(i) Dislocation contrast revealed by a single reflection

When an extinction countour appears separately and sharp, the contrast of dislocations nearby is generally due to the reflection of the same index as that of the extinction contour. Fig. 6 will show such a case. Comparing bright field image (a) with dark field images, 121 reflection (b), $0\bar{1}\bar{1}$ (c) and $\bar{1}\bar{1}0$ (d), it is found concerning (a) that the black contrast of the image a^* is due to (121) reflection from a region extremely near the dislocation and that on both sides of the image there are white lines which mean strong transmission of the electron beam. Images *b* and *c* also have the same character.

However, it can not always be said that the dislocation image appears as a single line when one reflection occurs. For example,

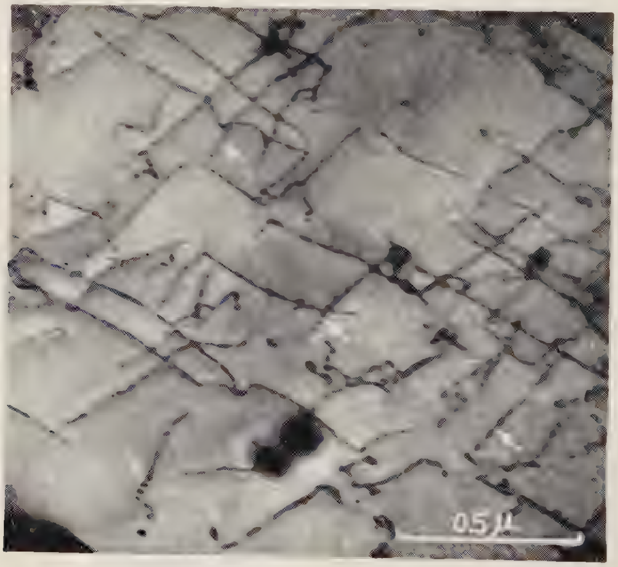

Fig. 9. Dotted appearance (↑) near the specimen surface.

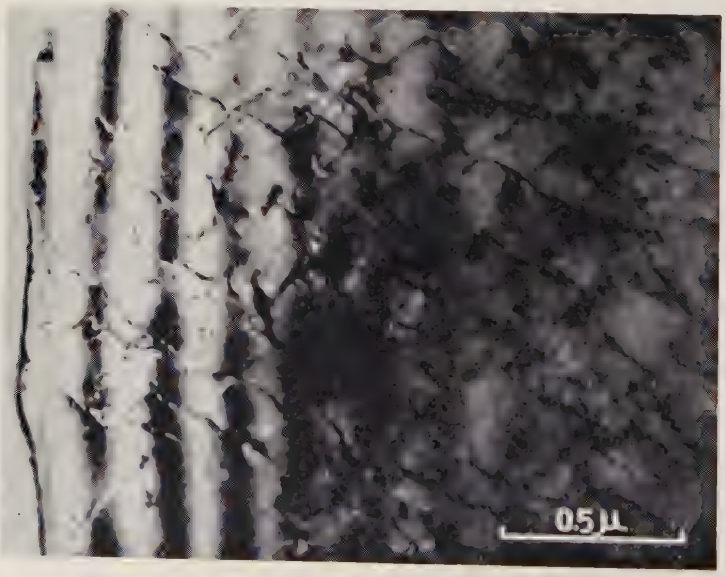

Fig. 10. The dotted image and the equal-thickness fringes appearing in the wedge-shaped region (left).

---

[*] This kind of image sometimes appears as a triple image, whis is accompanied by broad side lines.

Fig. 7 is a case of the double image produced by one reflection: i.e. the double image *a* is composed of two lines of which one has a strong contrast but the other faint in the bright field image. From its dark field image of 110 reflection, Fig. 7 (b), one of the image lines may be considered to be main, and the other a subsidiary line. This interpretation, however, has a difficulty, because the index of the reflection is low[1]. In Fig. 7 (a) the dislocation images *e* and *f* are observed as white lines, but in the dark field images, (b) and (c), those portions have black contrast accompanied by side lines of white contrast. It is therefore reasonable to conclude that the white dislocation image[1] is an extreme case of the dislocation image accompanied by the white side-line; i.e. in this case the contrast of the white side-line is strong as compared with that of the black dislocation image.

It is also noted in Fig. 6 that with increasing the distance from the extinction contour the contrast and the width of the single reflection image becomes weaker and narrower.

(ii) Dislocation contrast revealed by two or more reflections

Dislocation images *b* and *c* in Fig. 7 (a) have similar features as those in Fig. 4 and Fig. 3, respectively. These images are also observed in dark field image (b) of 110 reflection as well as in (c) of $\bar{1}\bar{1}0$ reflection. This confirms that these images are formed with two reflections, as expected from the feature composed of two or three lines. However, sometimes the image looks like a single line even when it is due to multiple reflections. Fig. 8 is a typical example of such a case, in which each dislocation image is rather broad. Comparing Fig. 8 (a) with its dark field images, (c) $\bar{1}12$, (d) $10\bar{1}$, (e) $\bar{1}23$ and (f) 011, the following facts are found: Image *a* is due to the overlapping of $\bar{1}12$ and $\bar{1}23$ reflections, images *b*, *c*, *e*, *f*, *g* and *h* are all due to three reflections $\bar{1}12$, $10\bar{1}$ and $\bar{1}23$, and image *d* is indeed due to four reflections $\bar{1}12$, $10\bar{1}$, $\bar{1}23$ and 011.

Furthermore, it is especially interesting that

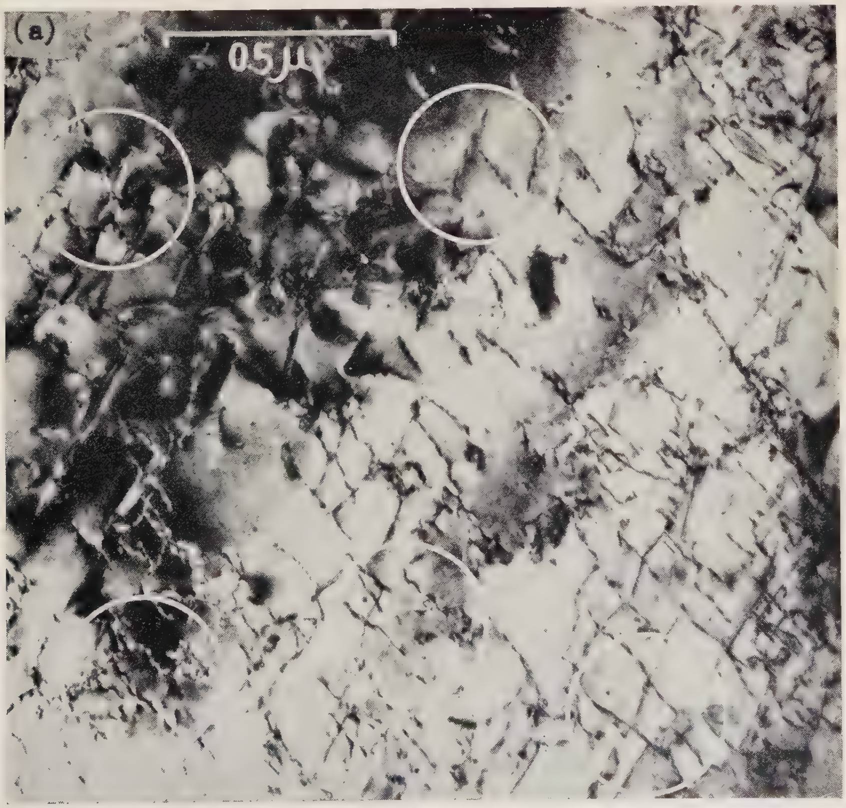

Fig. 11 (a). Relation between the dotted images and an extinction contour.

in Fig. 8 (c) of $\bar{1}12$ reflection each dislocation appears as a double image separated with a narrow and sharp black line which is observed as white in other reflections. And the both lines in the double image in $\bar{1}12$ reflection seem to have comparable intensities. Therefore, it will be improbable that one of the double lines is a subsidiary reflection of the other.

II. Dotted images of dislocations

Besides the line feature, the dislocation image occasionally takes a dotted feature, which has recently been considered as an effect of Pendellösung occurring when the dislocation is inclined to the plane of foil.

The dislocation image is apt to take a dotted shape with approaching the specimen

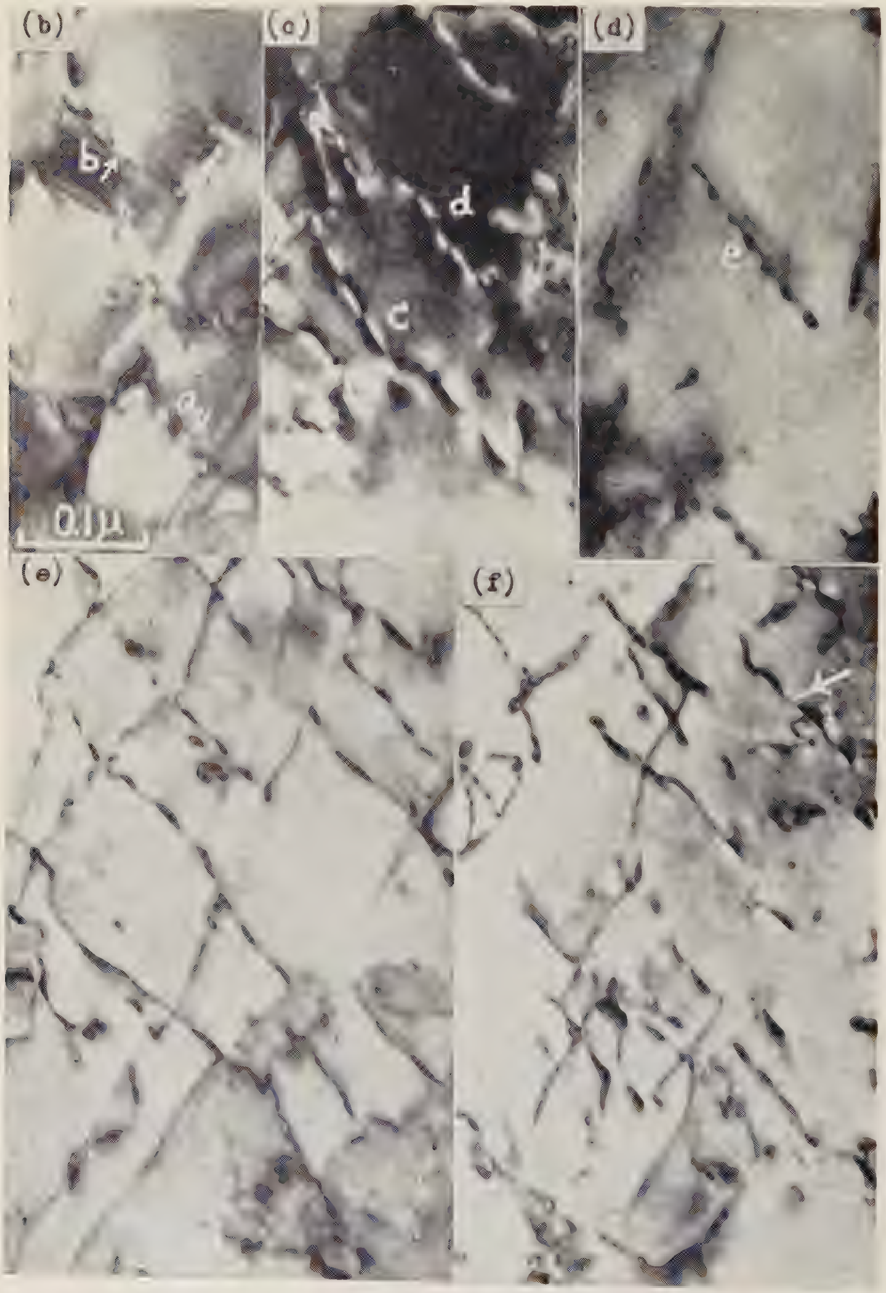

Fig. 11 (b)~(f). Enlargements of parts of Fig. 11 (a).

surface or with decreasing the specimen thickness, as seen in Fig. 1. Dislocation images in Fig. 9 have a dotted appearance (↑) on their segments near the specimen surface. In Fig. 10, a wedge-shaped edge of the specimen is seen at the left. The dislocation images running from upper left to lower right have the dotted appearance which is clear in the thin region. The number of the dots in some images, is about the same as that of the equal-thickness fringes appearing in the left region from the image.

The dislocation line near the foil surface has a tendency to become normal to the surface, and therefore the effect mentioned above on the image may be interpreted by the nature of the dislocation.

Fig. 11 (a) is a typical example showing various kinds of the dotted images, which suggests that the dotted image also has an important relationship with the condition of the Bragg reflection. Fig. 11 (b)-(f) are enlargements of parts of Fig. 11 (a), which reveal many interesting characters of the dotted images as follows: In (b), image *a* shows a dotted image interposed between two black side-lines, and image *b* has a feature similar to but a little different from the image *a*. In (c), each dot in image *c* is composed of the white and the black regions lying side by side and in a row distributed alternately. In this type of the image the boundary between the two side regions is considerably sharp and is on a line throughout the dislocation concerned, and thus the white regions are observed as dots in a zig-zag row as seen at image *d*. It should be also noted at the lower right of the image *c* that the black contrast of one side of the dotted image becomes so faint with the distance from the dark matrix in the photograph that only a part of the boundary is visible. Image *e* in Fig. 11 (d) consists of a row of small dots whose size is about half that of the image *c*, notwithstanding the dislocations of both images seem to belong to the same family. The dotted images in Fig. 11 (e) are considered to result from that the contrast of one side of the image is decreased due to further deviation from its Bragg condition, as mentioned about Fig. 11 (c). Figs. 11 (f) and 12 have a remarkable zig-zag appearance (↑) which is a special feature of the dotted image. Comparing these images, it is noted that the zig-zag image changes to the dotted one (A) with the distance from the dark region of the matrix. This means that this kind of image also depends on the reflecting condition.

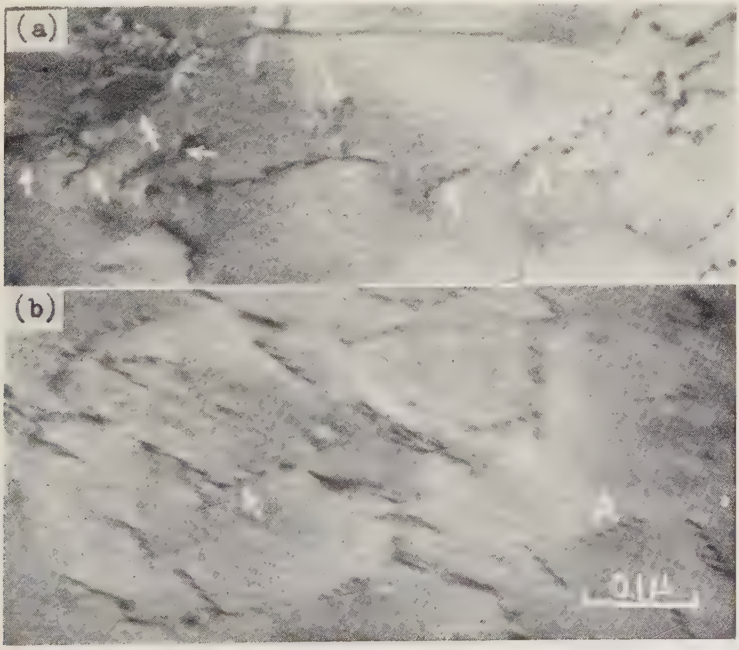

Fig. 12. Zig-zag images of dislocations. See the variation of the image from zig-zag (↑) to dotted (A) with the distance from the left region of the matrix.

From the results of the dark field image method, many of the complex images as mentioned above will be interpreted as follows:—In Fig. 13, (a) is the bright field image and (c) and (d) are the dark field images of 110 and 220 reflections, respectively. The dislocation images *a* and *b* in Fig. 13 (a) are similar to those described in Fig. 11 (b), which have two black side-lines. Comparing (c) with (d), it is found that those dislocation images are produced by two reflections, 110 and 220. Images *v*, *w*, *x*, *y* and *z* in (a) have some feature like the zig-zag image seen in Fig. 12. These images, especially image *x*, are also due to two reflections; i.e. two parts of the image *x* having different curvatures from each other are observed on different reflections 110 and 220, respectively. Therefore, it is expected that one side of the zig-zag image of dislocation becomes faint and finally disappears when

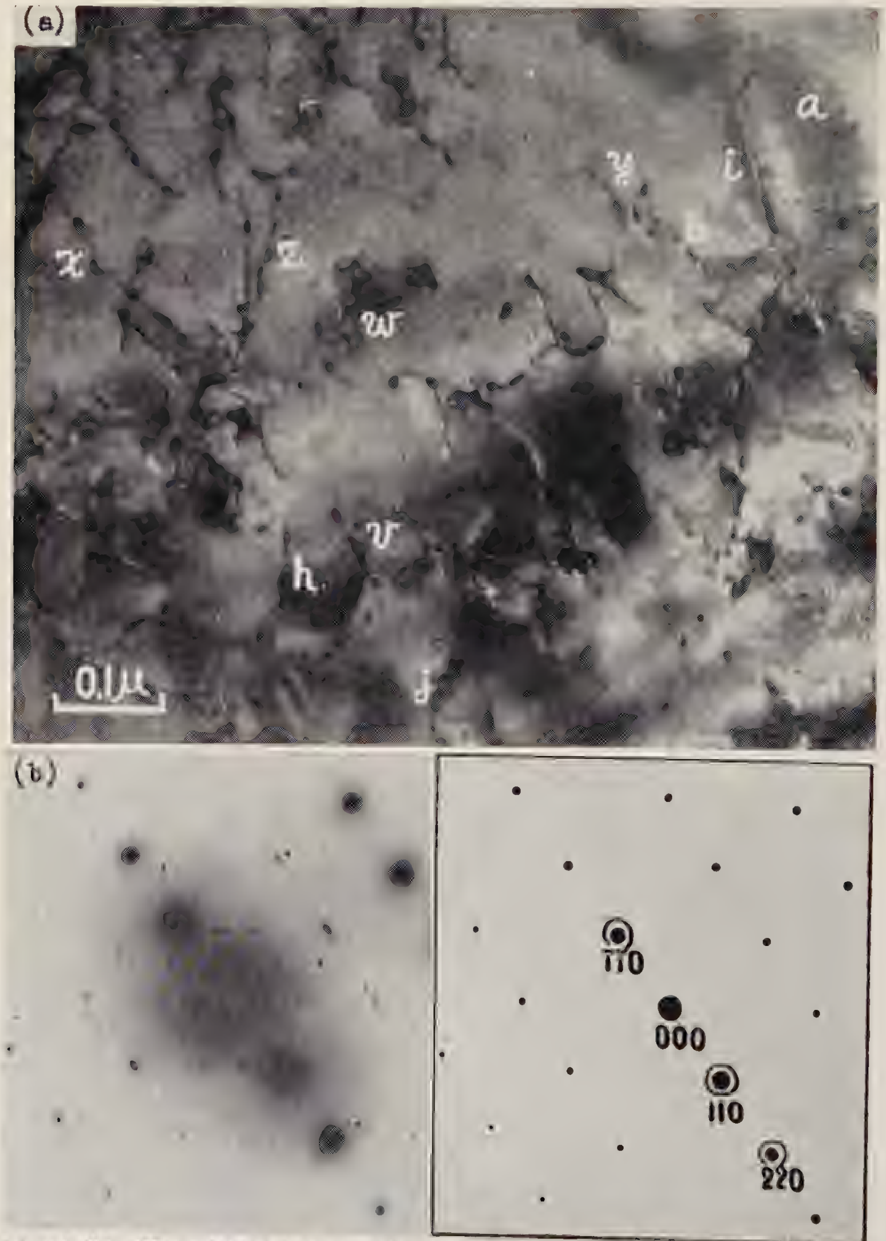

Fig. 13 (a) and (b). The relations between the dotted images and the reflecting conditions. (b) is the selected-area electron diffraction pattern of (a).

one of the two reflections becomes weaker with deviation from its Bragg condition. The example is seen at the image *c* in Fig. 11 (c). The dislocation image *i* in Fig. 13 (a), which looks like a single line, is also due to two reflections; i.e. one is 110 reflection

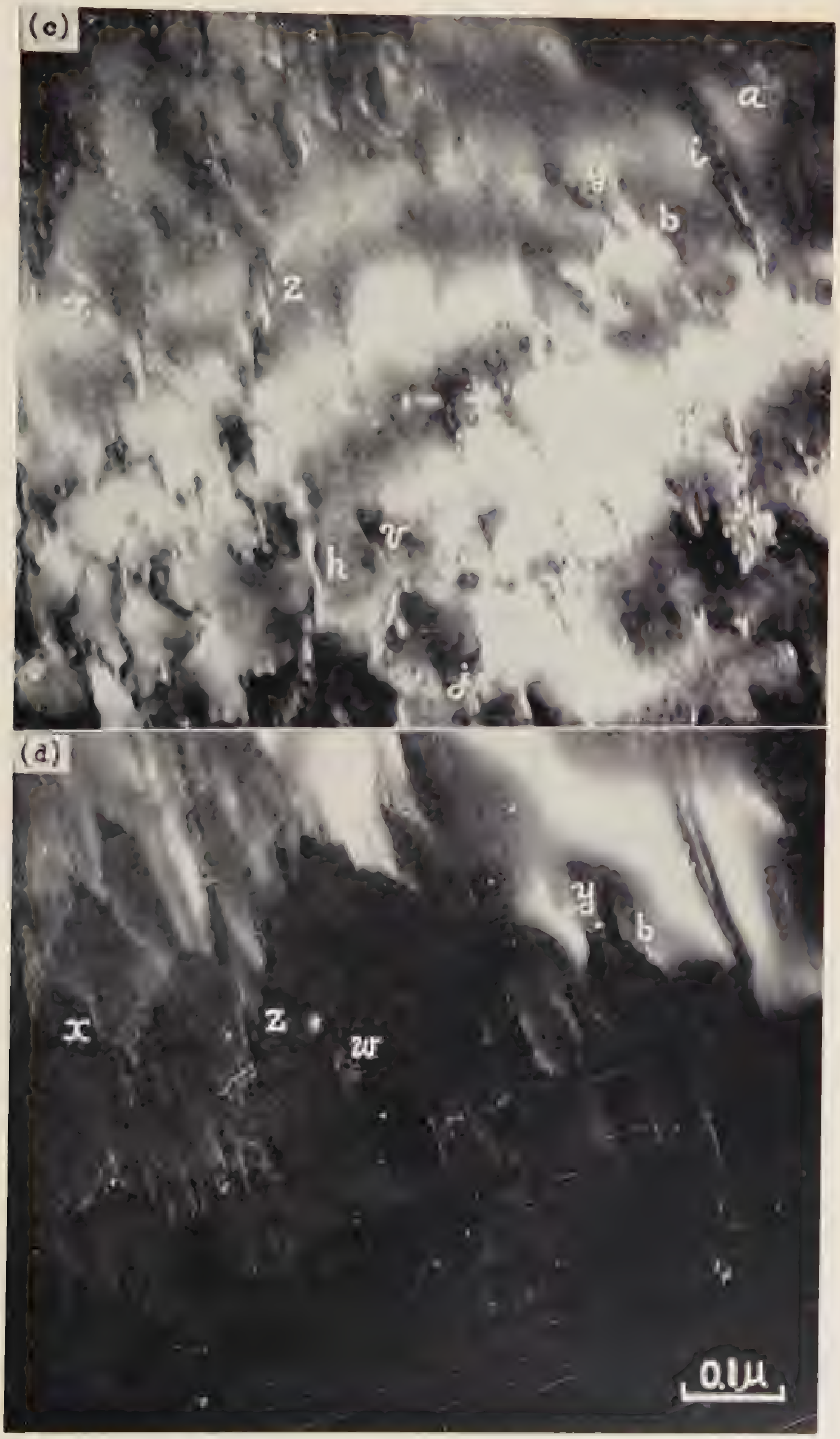

Fig. 13 (c) and (d). Dark field images of 100 and 200 reflections, respectively.

producing the dotted image of a long pitch and the other is 220 reflection producing the line image. The image *d* observed in Fig. 7 is also due to such reflections, though the appearance is slightly different. Besides, there are in Fig. 13, many examples showing the image contrast formed by various reflections; for instance, in image *h* the position of reflection is changed from one side to the other of the dislocation, and in image *j* 110 reflection is considered to be concerned.

Finally, it is concluded that the complex features of the dotted image are due to multiple reflections as in the case of the line images.

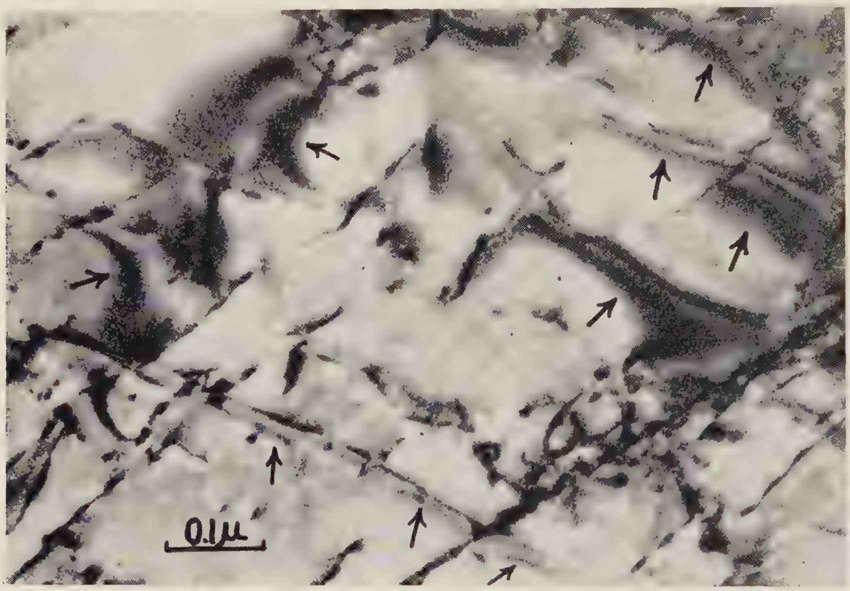

Fig. 14. Extinction contour due to the local bending which is considered as a result of relief of the dislocation stress.

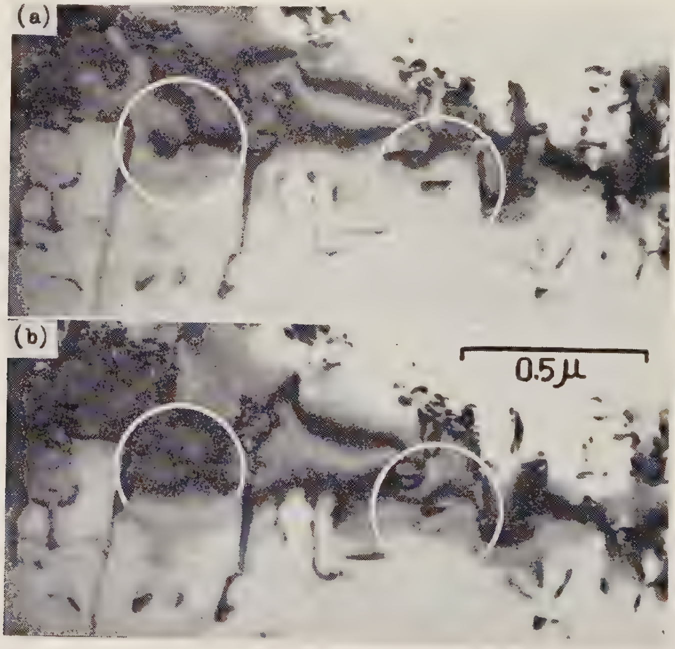

Fig. 15. Local bending due to dislocation stress.

3. Bending of the Specimen owing to the Dislocation

From the dislocation theory[2], it is expected that the thin specimen is bent by a dislocation for relief of the dislocation stress. Since the thickness of the specimen used for the electron micrograph is very small, about 1000–2000Å, the role of such bending in the image should be taken into consideration because the bending changes the reflecting condition. It is frequent that some difference is observed in the contrast of the matrix across the dislocation image due to such bending, as seen at region 1–8 in Fig. 1. Fig. 14 is also another good example, in which some of the dislocation images are accompanied by broad black bands (↑) along them. These images are likely to be considered as the extinction contours formed by rather macroscopic bending, because in the bands there is no special curvature at small crooks of the dislocation images. At the left side of Fig. 14, curved extinction contours are observed in a region subdivided with two dislocation images, which are probably due to the local bending of the specimen for relief of the stress of the dislocations. In encircled regions of Fig. 15, the concentric contours are observed around the ends of the dislocation, their positions being varied by small change of the incident angle.

§ 4. Discussion

The present work has revealed several images of dislocation that are difficult to interpret with the kinematical theory proposed by Hirsch *et al.*[1]. In the preceding section, it was shown that the foil specimen was locally bent by the dislocation for relief of the dislocation stress. This suggests a considerable possibility that some of the images observed result from such bending because it changes the reflecting condition. First of all, the difference in the contrast of the matrix across the dislocation image, as seen in Fig. 1, can be interpreted as follows: When an edge dislocation having a Burgers vector parallel to the foil surface is present within the foil surface, the specimen is bent by the dislocation as shown in Fig. 16 (a). In this case, the phase angle of the electron beam is advanced on one side of the specimen and delayed on the other as well as in the case of usual extinction contour[1]. Hence a contrast is possible to appear between these two sides. From the dislocation theory[2] it is expected that such bending becomes prominent under the limited condition that the dislocation is of the edge type, the dislocation line and its Burgers vector being nearly parallel to the foil surface, and moreover its arrangement simple. When unlike dislocations are situated closely and in parallel with each other, as in Fig. 16 (b), the dislocation stress will be relieved so easily that the surface of the region between them becomes nearly flat. Regions 3–7 in Fig. 1 are considered to be the case.

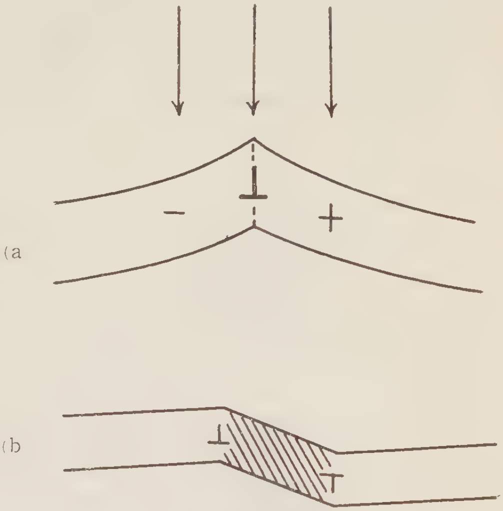

Fig. 16.

In Fig. 4, the position of black contrast in the image* of the intersecting dislocation is interchanged from one side to the other at the intersection. This interchange of the image contrast is considered to be a result from the phase difference as indicated by signs in Fig. 16 (a).

As mentioned above, the condition of the crystal around a dislocation line is quite similar to the case of the extinction contour due to the usual bending. The Bragg angle of 110–220 reflections is about 30′–1° (in 100 kV), which may be an attainable value as the inclination of a crystal plane around the dislocation if the specimen thickness is about 500–1000Å and an edge dislocation exists in the middle. Therefore, there is a possibility** to form a line image on either side of the dislocation line, as shown at *a* and *b* in Fig. 17 (a). The separation of the two images is determined by the index of reflection and the curvatute of the crystal which is inversely proportional to the foil thickness. The rough estimation of the separation is a few hundred Å. So is the width of the images. When the index of reflection is as low as (110), the image will take a simple feature as considered so far[1]. Since the dislocation line and its Burgers vector are not always parallel to the foil surface, either one of the two images will be observed in general, and its width will be rather broad because of small curvature. Broad lines (↑) accompaning the dislocation images, for instance, images *b* and *g* in Fig. 7 and images observed at the lower side of Fig. 14, are considered as this kind of image.

---

* The index of reflection of the intersecting dislocation image is different from that of the dark matrix.

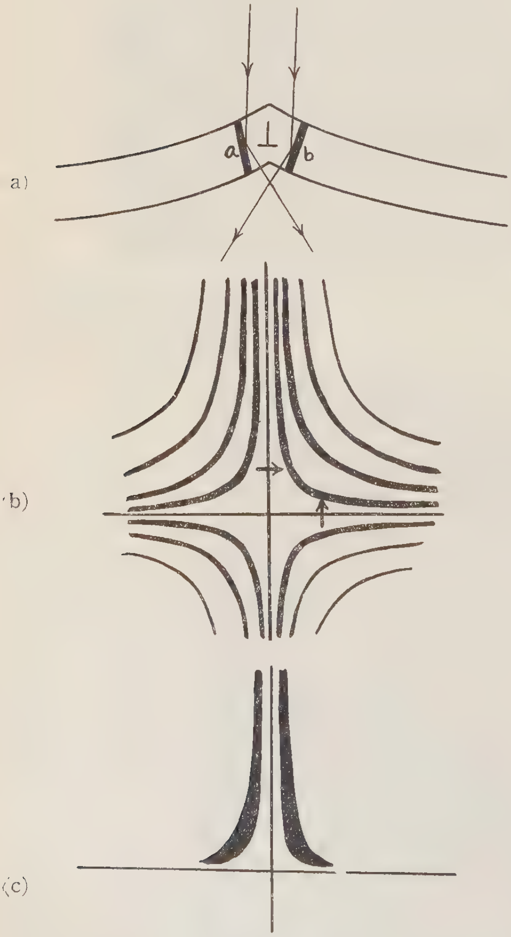

Fig. 17.

When two dislocations of different families intersect each other, the local bending by dislocation becomes more complex. Fig. 17 (b) illustrates the case, in which cross-lines, arrows and contour lines indicate two intersecting dislocations, their Burgers vectors and positions of equi-inclination planes owing to the dislocation stresses, respectively. When a reflection occurs on a net plane parallel to the vertical line, the image due to local bending produced by this reflection is expected to appear as a double image, as shown in Fig. 17 (c), whose shape is decided by the relationship between Burgers vectors of the two dislocations. The double image in Fig. 4 is considered to have been produced under such a condition. This interpretation will also be applied to the side-lines of a triple image, in which the central image is produced by another reflection, as seen at image *c* in Fig. 7. Since both side-regions of the vertical dislocation line are also affected by the local bending, the images, right and left, are not necessarily produced under the same reflecting condition. This idea will interpret the reduction of contrast at the central image of the right part of a horizontal dislocation in the encircled regions in Figs. 3 and 4. It is also understood that the separation of the lines in a image which is due to the local bending is sensitive to the incident angle and that their widths are broad, as seen in Figs. 3 and 4, because of the small curvature as compared with that of a region extremely near the dislocation.

The idea mentioned above does not yet elucidate the double image produced by a single reflection, as seen at image *a* in Fig. 7. More detailed results about these images will be desirable in addition to the full decision of the foil shape due to the local bending.

One may be thrown into confusion by the fact that the additional images are formed by the local bending because of the thin specimen. On the other hand, however, the local bending by dislocation is noticeable in the case of the edge dislocation, and therefore such additional images will enable us to distinguish the edge from the screw dislocation.

In the present work, a number of interesting features of dislocation and the relations

---

** This possibility is increased by the divergency of the incident beam ($\simeq 10^{-3}$ rad.)

between its images and the condition of the Bragg reflection could be clarified. In order to analyze these results by the diffraction theory, photographs must be taken under more definite conditions, i.e. with smaller divergence of the electron beam and under no local bending of the specimen.

It is expected that in very near future the complex images observed under certain conditions will be elucidated by some advanced diffraction theory. But, in case only the position of the dislocation is studied, it is desirable to take its image in a simple shape.

If the simple line image is produced by one reflection, by means of some technique such as gradual change of the incident angle with a precision goniometer, definite informations about the characters of the dislocation can be derived without so much theoretical difficulty. Therefore, the operation suitable for this purpose will be the best way we have to do at present, although of course the theoretical treatment such as the dynamical theory will be necessary for more profound interpretation of the stress field.

The authors wish to thank Mr. A. Kore-eda for helping to take electron micrographs.

References

1) P. B. Hirsch, A. Howie and M. J. Whelan: Phil. Trans. Roy. Soc. **A 252** (1960) 499.
2) For example, A. H. Cottrell: *Dislocations and Plastic Flow in Crystals*, Clarendon Press, (1953).

Journal of the Physical Society of Japan Vol. 16, No. 10, October, 1961

The Thermoelectric Power of the Gamma-Brasses

By Seiichiro Noguchi

Department of Physics, Tokyo Metropolitan University, Tokyo

(Received March 29, 1961)

The thermoelectric power of the gamma-phase alloys in the copper-zinc system has been measured at room temperature relative to pure copper. The thermoelectric power is found to be a smooth function of composition except in the range between 64.4 and 65.4 at.% Zn where there is a discontinuous change.

Analysis based on a band-approximation suggests that such a discontinuity can be attributed to the extinction of a band of electron holes or the initiation of a band of overlap electrons. However, there is a practical difficulty in distinguishing between the two processes, since the discontinuity occurs in the same and negative direction in either case. This difficulty was overcome with recourse to extra information concerning the Brillouin zone of the gamma-phase, and the discontinuity was interpreted in terms of the electron overlap across the {411} plane.

§1. Introduction

The electronic structure of pure indium and indium-lead alloys have recently been studied by Tomasch and Reitz[1] by means of measurements of the thermoelectric power. Their theory indicates that a discontinuity of the thermoelectric power can be explained in terms of band extinction or initiation. For the application of their theory to the experimental results, the thermoelectric power of the indium-thallium alloys must be subtracted from that of the indium-lead alloys.

The subtraction was made to remove the major effects of impurity scattering and to leave only the pure electronic concentration effect. Such a treatment, however, is not always correct because the anomalies in the electronic structure, such as the extinction and the initiation of bands, may occur even in an alloy which consists of two elements of the same valence[2].

In this paper, the author will propose a more simple treatment which is based on a band approximation and analyze the band structure of gamma-phase alloys in copper-zinc system. The analysis indicates that the gamma-brasses have no electron overlaps in the relatively low concentration-ranges of zinc but they have an overlap across the {411} planes in the higher concentration-ranges.

§ 2. Experimental Procedure and Results

All samples studied were prepared from copper of 99.99% and zinc of 99.9% pure. These alloys were melted in almina crucibles, and were sucked up into thin quartz tubes of about 2 mm in diameters. They were sealed in quartz tube with argon gas and annealed at 650°C for two weeks in order to be homogenized, then quenched into cold water. Although an appreciably long wire are desirable as the specimen for ordinary thermoelectric measurements, the brittleness of the gamma-brasses prevents us to obtain such a long wire of these alloys. The samples measured in this investigation are not longer than 10 cm. Hence, a differential method has been employed for the present measurement instead of the ordinary one. The alloy-rod and a constantan wire are placed parallel to each other and copper leads are welded to both of them in a way which is presented in Fig. 1. When one end of the sample is heated to produce the temperature

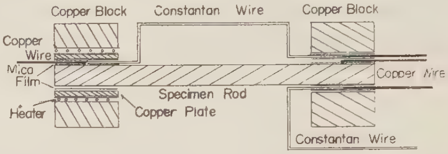

Fig. 1. Schematic diagram of the arrangement used on the thermoelectric measurement.

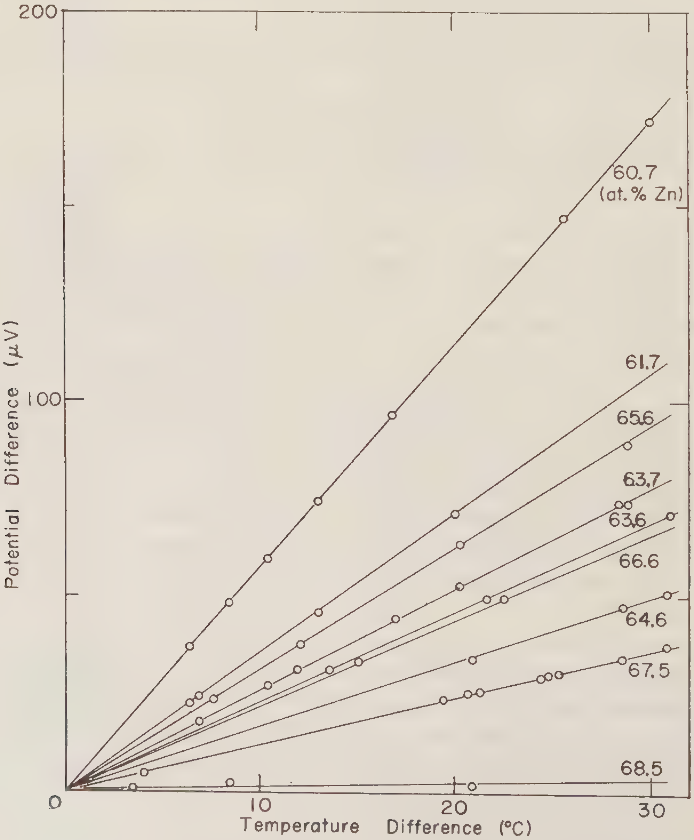

Fig. 2. The thermoelectric voltage of the gamma-brasses against copper as a function of temperature-difference.

difference, the potential difference between the two ends of the sample can be measured. The temperature differences up to about 30°C are measured from the potential difference of the constantan-copper thermo-couple. The thermoelectric power of nine gamma-phase alloys against pure copper are thus measured at room temperature (see Fig. 2).

The absolute thermoelectric power of the samples are then obtained by adding the absolute thermoelectric power of pure copper, 0.83 μV/deg, obtained by Cusack and Kendall[4]. The results are presented in Fig. 3 as a function of composition of the alloy.

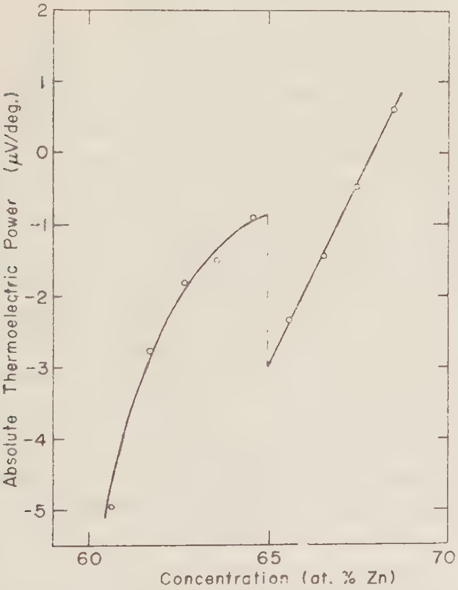

Fig. 3. The absolute thermoelectric power of the gamma-brasses as a function of composition.

§ 3. Discussion

A. *Band-model approximation*

As long as the initiation or extinction of bands are concerned, the following assumptions may be justified: (1) Each band referred to has relatively small number of electrons. (2) The band has the standard form.

If the electrons of an alloy are distributed over a number of bands each of which has the standard form, we can write the thermoelectric power in the form

$$S=\frac{\sum_i \sigma_i S_i}{\sum_i \sigma_i}, \tag{1}$$

where σ_i and S_i are conductivity and thermoelectric power, respectively, when only one band is present[5].

The relaxation time of the electrons can be expressed from the separate relaxation times associated with the various electronic scattering processes. It is assumed that impurity or solute scattering and thermal scattering are primarily responsible for coupling between the carriers and the lattice. For impurity scattering, the energy dependence of the relaxation time is proportional to $E^{-1/2}$, where E is the energy of carriers. On the other hand, the energy dependence of the relaxation time for thermal scattering is usually expressed to be $\tau_T \propto E^{3/2}$, but if the band occupation is less than one quarter carrier per atom, then we have $\tau_T \propto E^{-1/2}$. Hence, the total relaxation time is proportional to $E^{-1/2}$ for a band which is occupied by a small number of carriers. For such a band, it can be derived that $\sigma_i S_i$ is independent of the energy of electrons. When the overlap of a band j has just been initiated, the thermoelectric power can be expressed as

$$S=\lim_{E_j\to 0}\frac{\sum_i \sigma_i S_i}{\sum_i \sigma_i}=\frac{-e\pi^2k^2T\,C_j/3m_j^*+\sum_{i\neq j}\sigma_i S_i}{\sum_{i\neq j}\sigma_i}, \tag{2}$$

where C_j is a parameter independent of the energy. For the difference of the thermoelectric power just before and after initiation of a band j, we have

$$\varDelta S=\frac{-e\pi^2k^2TC_j}{3m_j^*\sum_{i\neq j}\sigma_i}. \tag{3}$$

This indicates that the initiation of an electron overlap gives rise to the discontinuous change of the thermoelectric power.

In the case of the extinction of a band, for instance, k, we can discuss in a similar way. The difference of the thermoelectric power just after and before extinction of a hole is obtained as follows;

$$\varDelta S=\frac{-e\pi^2k^2TC_k}{3m_k^*\sum_{i\neq k}\sigma_i}. \tag{4}$$

The extinction of a hole causes the discontinuity of the thermoelectric power which is in the same direction as in the case of the initiation of an overlap.

B. *The application to the gamma-phase alloys*

The gamma-phase alloys behave like semimetals, namely they are hard, brittle and highly diamagnetic[6]. It should therefore be expected that a Brillouin zone of the gamma-alloys is only just capable of accommodating the valency electrons, so that their Fermi level is everywhere near the zone boundary. The Brillouin zone polyhedron, shown in Fig. 4, has thirty-six sides at a distance $3\sqrt{2}\,\pi/a$ from the origin, and is nearly a sphere. This polyhedron can contain exactly ninety electrons per unit cell, while the inscribed sphere can contain eighty. The typical composition of the gamma-brass is $Cu_{20}Zn_{32}$, which has eighty-four electrons per unit cell. Therefore the Fermi surface must be very close to the zone boundary.

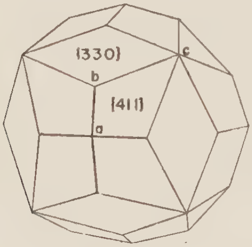

Fig. 4. The first Brillouin zone of the gamma-brass. a, b and c represent the three kinds of the corners.

The electron near the corners of the polyhedron may behave as electron holes which are classified into three kinds by their position in the Brillouin zone. When the electron number of these alloys is increased, the extinction of the holes of these three kinds may take place at electron concentrations which are not so different from each other, since the distance from the origin of the zone to the corners are nearly the same.

The results of the present measurement show a discontinuous change of the thermoelectric power at the composition between 64.4 and 65.4 at.% Zn. The alloy of this composition has about 85.8 electrons per unit cell which are considerably less than ninety. The discontinuity should therefore be attributed to the initiation of an electron overlap into the second zone in this composition.

The polyhedron has the faces of two different types, i.e. {411} and {330}. As the both types of the faces have the same distance from the origin of the polyhedron, the overlap occurs into the second zone across the face in which the energy gap is less than that in another. According to the X-ray data⁷⁾, it has been shown that the energy gap for {411} plane is appreciably less than that for {330} plane. Then the discontinuity may be interpreted as the initiation of the overlap across the {411} plane.

§ 4. Conclusion

It is the purpose of this article to point out that the initiation and the extinction of a band always give rise to a discontinuous change of the thermoelectric power by making the only assumption that all the bands referred to are of standard form and are occupied by relatively small number of carriers. The interpretation is substantiated by the results of the thermoelectric measurement of the gamma-phase alloys in which some electron overlap into second zone is expected.

Acknowledgements

The author is indebted to Prof. T. Sato for his support and valuable discussions.

References

1) W. J. Tomasch and J. R. Reitz: Phys. Rev. **111** (1958) 757.
2) W. Hume-Rothery and G. V. Raynor: Proc. Roy. Soc. **A**, **174** (1940) 471.
3) N. Cusack and P. Kendall: Proc. Phys. Soc. **72** (1958) 898.
4) A. H. Wilson: *Theory of Metals* (Cambridge University Press, New York, 1954).
5) H. Endo: Sci. Rep. Tohoku Imp. Univ. **14** (1925) 479.
6) A. J. Bradley and J. Thewlis: Proc. Roy. Soc. **A**, **112** (1926) 678.

JOURNAL OF THE PHYSICAL SOCIETY OF JAPAN, Vol. 16, No. 10, OCTOBER, 1961

Magnetic Anisotropy of Evaporated Films.
I. Iron Films Formed in Magnetic Field

By Minoru TAKAHASHI, Denjiro WATANABE, Tetsuzo SASAGAWA,*
Tatsuo KONO and Shiro OGAWA

The Research Institute for Iron, Steel and Other Metals,
Tohoku University, Sendai, Japan

(Received May 1, 1961)

The induced magnetic anisotropy of iron films formed on silica substrates by evaporation in a magnetic field was measured by torque magnetometer. The results obtained are as follows: (1) The axis of easy magnetization does not coincide with the direction of magnetic field, H_d, applied during evaporation and the direction of this axis is considerably changed from specimen to specimen. (2) The uniaxial anisotropy constant, K_u, does not depend on H_d. (3) It is difficult to get K_u as a function of the film thickness. (4) K_u decreases with increasing substrate temperature and begins to increase again at about 300°C. (5) K_u tends to vanish after a prolonged magnetic annealing. (6) Estimated values of the rotational hysteresis integral range between 1.3 and 2.4 for all films examined.

In order to investigate the origin of the uniaxial anisotropy, several factors are discussed. The directional ordering of imperfections may be probable. It may be necessary, however, to consider the minute structure of evaporated films for discussing the origin in question.

§ 1. Introduction

For the last several years many papers have been published on ferromagnetic thin films. Most of them concern fundamental studies. For example, electrodeposited or evaporated films of Iron, nickel or cobalt were investigated experimentally by Reimer[1)], Andrä, *et al*[2)] and Knorr and Hoffman[3)], and magnetic domain pattern as well as the magnetic anisotropy was studied by Willams and Sherwood[4)]. Evaporated films of iron-80% nickel, i.e., of permalloy, were, on the other hand, made an object of investigation of the dynamic magnetic behaviour in U.S.A.[5)], and the effect of preparation condition on this behaviour was mainly studied[6)]. The studies on permalloy films are closely related to memory cores of the computer and are considered to be very important and useful from a viewpoint of application of thin films, though a successful application seems not yet to be done[7)]. It will be reasonable under the above circumstances that the studies on thin ferromagnetic films are now being started in many of laboratories in our country.

It seems, however, that very few systematic studies have been done on the relation between magnetic properties and various preparation conditions of thin films and that the direct measurement of the magnetic anisotropy of films has very rarely been done except the study by Andrä *et al.*[2)] Thus, an investigation was undertaken in our laboratory, in order to inquire systematically into the origin of the magnetic anisotropy of evaporated films formed in a magnetic field. The present paper concerns evaporated iron films only and describes chiefly experimental results obtained by the torque measurements under various conditions of film preparation. The thorough investigation on the origin of the magnetic anisotropy will be done in the future.

§ 2. Experimental

An evaporation chamber as shown in Fig. 1 was used. The temperature of the substrate onto which metallic iron is evaporated is able to be raised by an electric furnace directly wound on a silica tube. This furnace consists of nichrom wire which is non-magnetically wound. It was confirmed by a fluxme-

---

[*] Now at The Central Research Laboratory, Fuji Iron and Steel Co.

ter that no appreciable magnetic field was induced at the substrate position by the furnace. The magnetic field required was generated by an electromagnet which was removable from the position illustrated in Fig. 1 whenever desired. The maximum field attainable was 2,500 Oe. A disc of fused silica 13 mm in diameter with a handle 150 mm long was almost always used as the substrate. A mark is bored in the disc, so that the direction of the magnetic field applied during the evaporation was easily known.

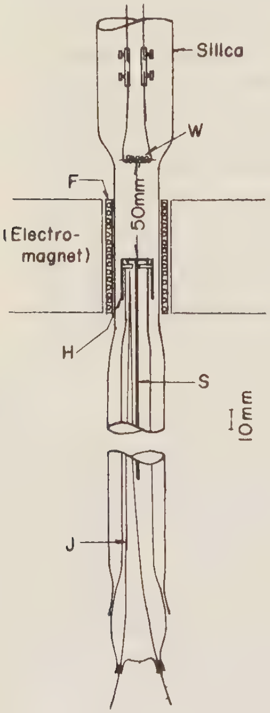

Fig. 1. Evaporation chamber.

W: tungsten filament,
F: furnance,
H: substrate holder made of quartz,
S: substrate,
J: Pt-Pt·Rh thermocouple.

The surface of the disc was finely finished so as to be optically flat, and it was sufficiently cleaned with acid and baked at 500°C in vacuum before the evaporation. The evaporation chamber was outgassed overnight and the degree of vacuum was maintained at 1×10^{-4} mm Hg during the evaporation. Iron was evaporated from a wire 0.07 mm in diameter laid in a small tungsten filament. The duration of evaporation ranged from several ten seconds to two minutes. The thickness of films was estimated from evaporated quantity of the metal.

A torque magnetometer used is an shown in Fig. 2. The measurements were carried out by the usual method but in vacuum of about 10^{-4} to 10^{-5} mm Hg. The torque value was obtained from difference between the value for the substrate with an iron film and that for the substrate alone the film on which was dissolved away by *aqua regia*. The available maximum field was 414 Oe, a Helmholtz coil being used as a field source. The mean of torque values obtained from

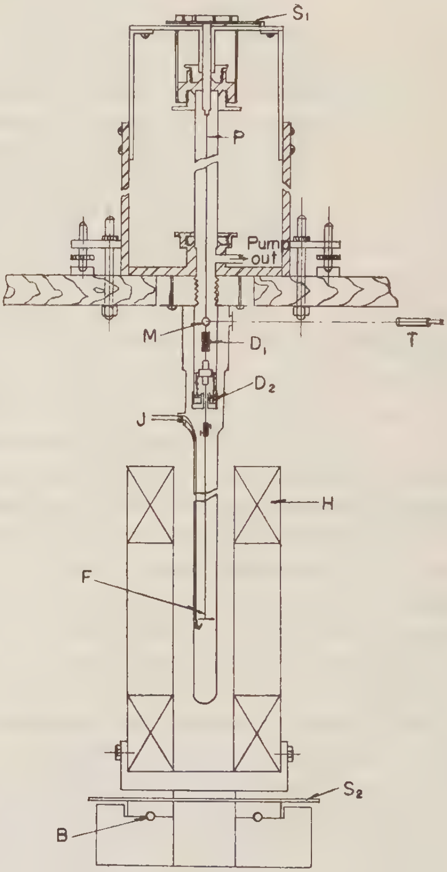

Fig. 2. Torque magnetometer.

S_1, S_2: circular scale,
P: phosphor bronze wire,
M: mirror,
T: telescope,
D_1: copper block,
D_2: oil damper,
J: thermocouple,
H: Helmholtz coil,
F: substrate with an evaporated film,
B: ball bearing.

the clockwise (cw) and the counter-clockwise (ccw) rotation of the specimen was used as a torque value under various measuring fields. (See Fig. 12 (a)). The substrate was joined with a phosphor bronze wire 0.06 mm in diameter and 29.2 cm in length. The torsion angle was measured by mirror and telescope, the distance between which was 130 cm. The sensitivity was 5×10^{-4} dyne·cm/mm.

The accelerating voltage of electron diffraction was 50 KV and the camera length was 309 mm.

§ 3. **Results**

1. *Measurements of the uniaxial anisotropy energy*

As is well known, ferromagnetic films formed in magnetic field show the uniaxial anisotropy[2),4),5)]. In the present study, the anisotropy energy was obtained through the torque measurements as a function of the magnetic field applied during deposition, H_a, the thickness of films, D, the temperature of the substrate during deposition, t_s, and the material of the substrate. The torque measurements were always done two or three hours after deposition of films. The background of torque curves sometimes influences seriously the accuracy of torque measurements, but there seemed to be only low background in most of measured curves in the present experiment. Fig. 3 is one of a few examples, in which the considerably high background was found.

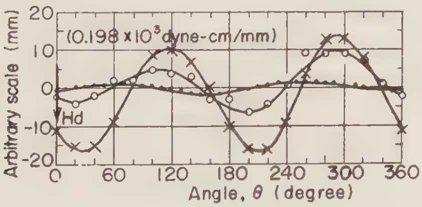

Fig. 3. Torque curves measured under the field of 414 Oe.

○, ×: film thickness=200Å.

●: substrate only.

i) *Relation between the torque and H_a*

Keeping the substrate temperature at 20°C and the film thickness at 600 Å, the torque was measured, changing H_a from 0 to 2510 Oe. The result is shown in Fig. 4. It should be noted that a marked anisotropy with two-fold symmetry is observed even when H_a is zero. The curves show that the H_a direction lies not along the axis of easy magnetization but rather near the axis of difficult magnetization. After the torque has reached the minimum value at $H_a=250$ Oe, it again increases with increasing H_a. As the measuring field, H_m, was so low that the torque

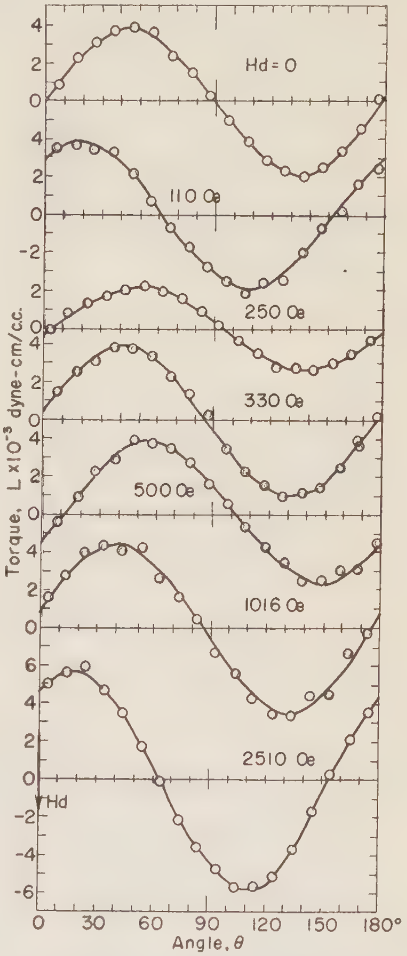

Fig. 4. The torque curves of films 600Å in thickness, formed under various field strength. The measuring field strength was 414 Oe.

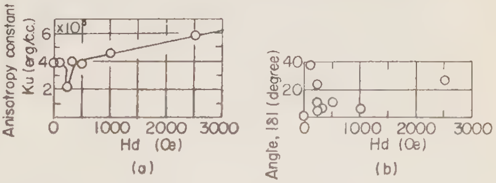

Fig. 5 (a) Induced anisotropy constant plotted against H_a.

(b) Angle $|\delta|$ between the H_a direction and the axis of difficult magnetization, plotted against H_a.

curves were not represented by $\sin\theta$, the curves were analyzed by Fourier method and the coefficient of $\sin 2\theta$ was plotted as a function of $1/H_m$ and extrapolated into $H_m\to\infty$. This extrapolated value, K_u, is plotted against H_a in Fig. 5 (a), and the angle, $|\delta|$, between the H_a direction and the axis of difficult magnetization is plotted against H_a in Fig. 5 (b). As seen from this figure, the values of $|\delta|$ are scattered with varying H_a.

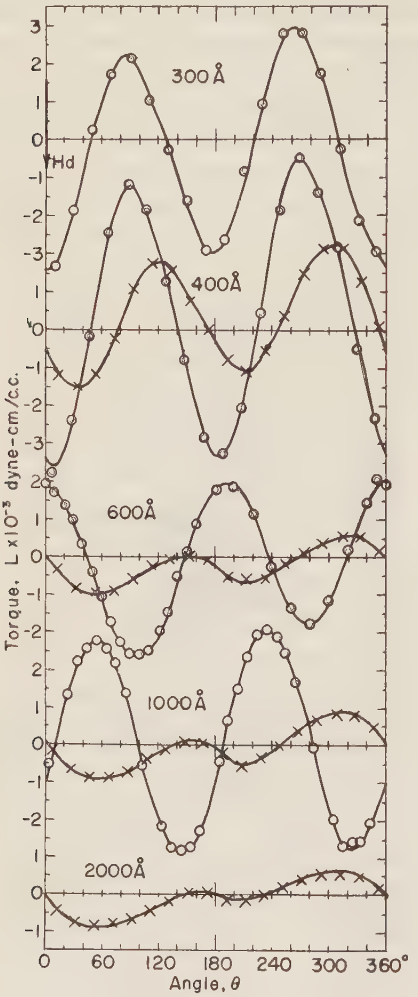

Fig. 6. Variation of torque curves with film thickness.

○: substrate temperature was held at $t_s=20°C$, $H_a=250$ Oe.

×: substrate temperature was held at $t_s=300°C$, $H_a=250$ Oe.

ii) *Relation between the torque and the film thickness*

Fig. 6 gives the variation of the torque with the film thickness at $t_s=20°C$ and $t_s=300°C$ and at $H_a=250$ Oe. The H_a direction is in the neighbourhood of the axis of difficult magnetization in the case of $t_s=20°C$, while it nearly coincides with the axis of easy magnetization in the case of $t_s=300°C$. From these torque curves the anisotropy energy was calculated. The coefficient of $\sin\theta$, K_1, was obtained by extrapolating to $H_m\to\infty$ in the same way as in K_u. The values of K_u and K_1 are summarized in Table I and plotted in Figs. 7 (a) and (b). It is remarkable that measured torque values are considerably scattered in the thickness

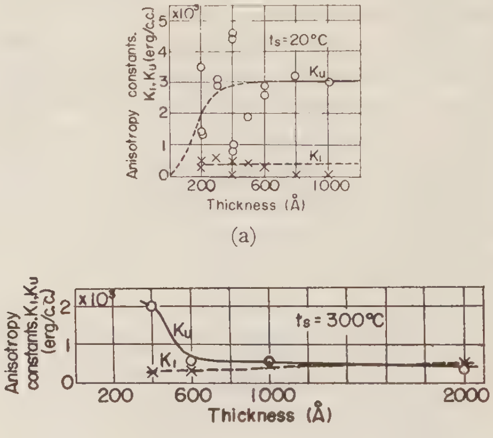

(a)

(b)

Figs. 7 (a) and (b). Anisotropy constant plotted against film thickness.

Table I. Relation between the anisotropy constant and the film thickness at $t_s=20°C$.

Thickness (Å) Anisotropy constant	200	300	400	500	600	800	1000	2000
$K_1\times10^{-3}$ erg/c.c.	0.3	0.7	~0(0.3*)	0.4	0.3(0.3*)	~0	~0(0.5*)	(0.5*)
$K_u\times10^{-3}$ erg/c.c.	1.4~3.4	2.9~3.2	0.6~4.4 (2.0)*	1.9	2.6(0.5*)	3.2	3.0(0.7*)	(0.4*)

* $t_s=300°C$.

range below 500 Å, especially, at t_s=20°C. It is very difficult, therefore, to get K_u as a function of the film thickness.

iii) *Relation between the torque and the substrate temperature*

The torque was measured for the films evaporated under various substrate temperatures. In this case, the film thickness and H_d were fixed at 600 Å and 250 Oe, respectively. H_d was continuously applied until the substrate was cooled down to room temperature after the evaporation. As soon as the evaporation was finished, the furnace current was switched off. The temperature fell down from 300°C to room temperature in about 45 minutes. Fig. 8 shows the change of the torque with the substrate temperature, t_s. The H_d direction lies between the axis of easy magnetization and that of difficult magnetization but approaches the former axis with increasing t_s. The curve shows a good two-fold symmetry at t_s=20°C. It is deformed and lowered in its amplitude with increasing t_s but again recovers its amplitude at t_s =400°C. The anisotropy energy obtained from Fig. 8 is plotted against t_s in Fig. 9.

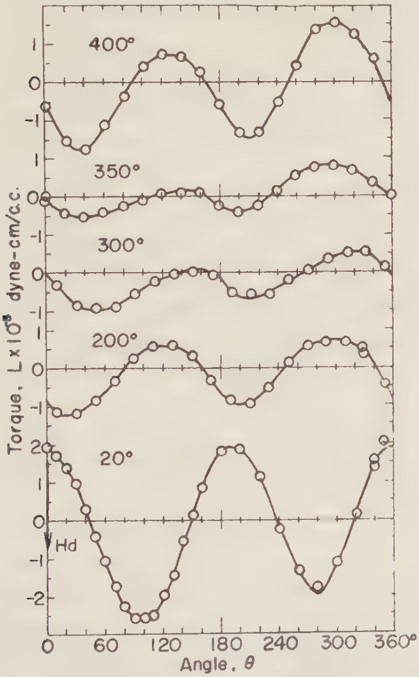

Fig. 8. Change of the torque curve with the substrate temperature, t_s. The thickness of films was 600 Å and H_d was 250 Oe.

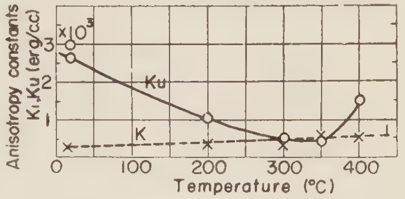

Fig. 9. Relation of the anisotropy to substrate temperature.

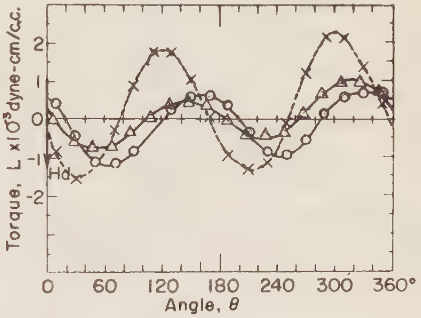

Fig. 10. Torque curves obtained after annealing in a magnetic field for various durations at 200°C. Film thickness was 600 Å, t_s 200°C, H_d 250 Oe and annealing magnetic field, H , 250 Oe.

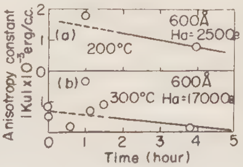

Figs. 11 (a) and (b). Magnetic anisotropy plotted against the magnetic annealing time.

Table II. Relation between the anisotropy constant and the substrate temperature (D=600Å).

t_s (°C) / Anisotropy constant	20	200	300	350	400
$K_1\times10^{-3}$ erg/c.c.	0.3	0.4	0.3	0.6	0.5
$K_u\times10^{-3}$ erg/c.c.	2.6∼2.9	1.1	0.5	0.4	1.4

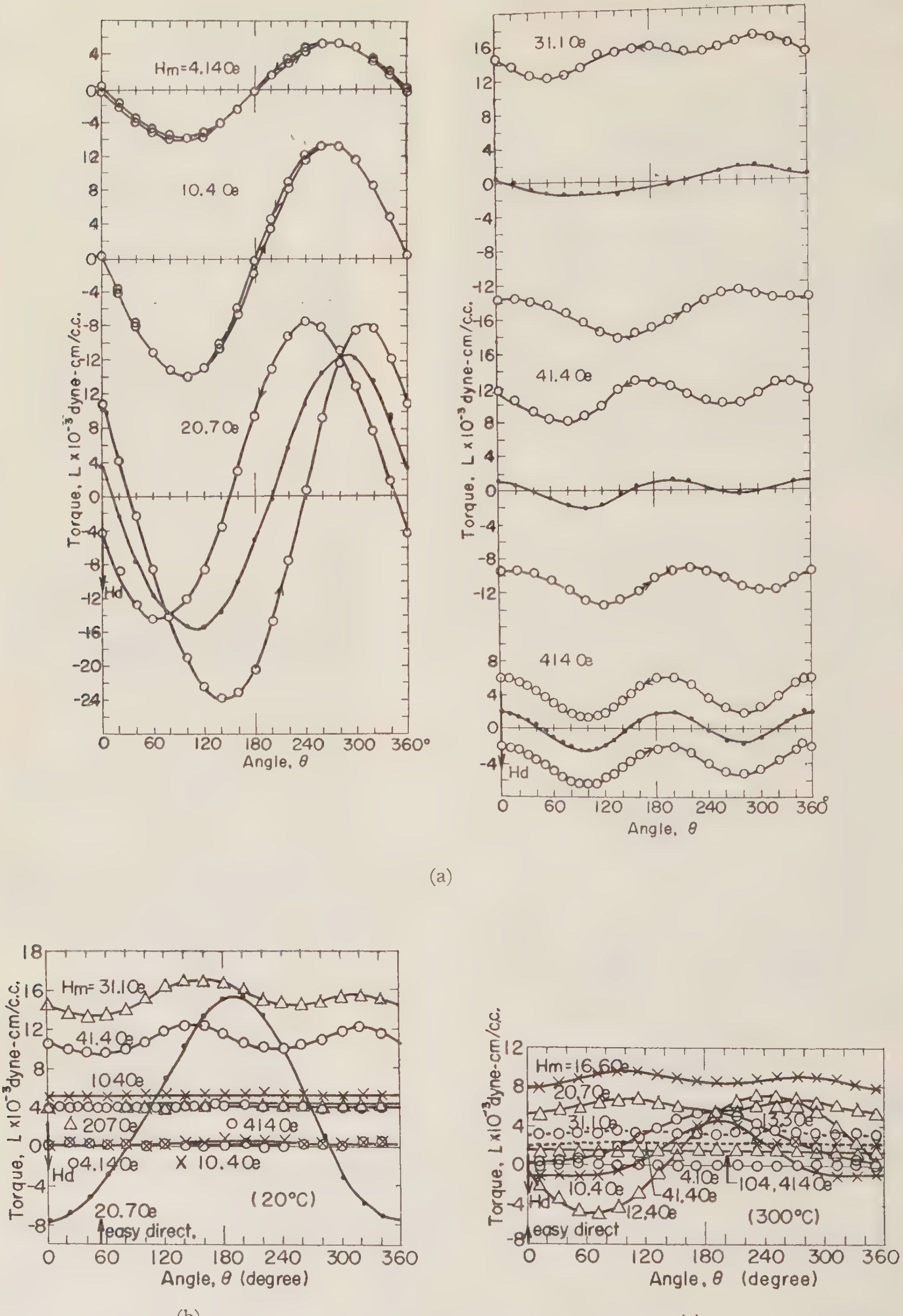

(a)

(b)

(c)

Fig. 12 (a). Torque curves under various measuring fields. Marks, ○ and ●, represent torque values measured in clockwise and counterclockwise directions and the mean torque values, respectively. Film thickness = 600 Å, $H_d = 250$ Oe, $t_s = 20°C$.
(b) and (c). The half of the torque difference plotted against θ. $t_s = 20°C$ in (b) and $t_s = 300°C$ in (c)..

A temperature at which K_u attains the minimum value seems to be a little above 300°C, while K_1 is nearly constant, independent of t_s. Numerical values of the anisotropy energy at various substrate temperatures are summarized in Table II.

iv) *Annealing of films in magnetic field*

Films 600 Å thick were formed under the field H_d=250 Oe at t_s=200 or 300°C. They were annealed for several hours without intermission of the applied field and the heating. An example of the results obtained is shown in Fig. 10. The anisotropy energy, K_u, was calculated from this figure and is shown in Figs. 11 (a) and (b). The magnetic field applied during annealing, H_A, is 250 Oe in Fig. 11 (a) and 1700 Oe in Fig. 11 (b). In these cases, the H_d direction does not coincide accurately with the axis of easy magnetization at the early period of annealing but approaches this axis as the annealing proceeds, and then the anisotropy tends to vanish after a long duration of annealing.

v) *Influence of the substrate material upon the uniaxial anisotropy*

The exchange of the substrate from silica to glass gave some change to the anisotropy constant. For example, with a glass substrate K_u was 0.7×10^3 erg/c.c. at $t_s=20$°C and 0.6×10^3 erg/c.c. at 300°C when the thickness was kept at 600 Å and H_d at 250 Oe, while K_u was 2.6×10^3 erg/c.c. with a silica substrate at t_s=20°C.

2. *Rotational hysteresis loss*

The torque was measured in clockwise and counterclockwise directions at the film thick ness of 600 Å and at H_d=250 Oe, H_m being changed from 4.14 to 414 Oe. The mean value of clockwise and counterclockwise measurements was adopted. Fig. 12 (a) shows the results obtained, t_s being kept at 20°C. The half of the torque difference between the clockwise and counterclockwise values which were denoted $\vec{L}$ and $\overleftarrow{L}$, was plotted against the angle at various H_m values. This relation is represented in Figs. 12(b) and (c), where the influence of t_s is clearly seen. It is easily seen from these figures that the torque curves are expressed by $\sin\theta$ term in low measuring fields but by $\sin 2\theta$ term in high measuring fields. Furthermore the torque difference is constant independent of θ in the lowest and the highest measuring fields. A similar behavior was found in powder magnets by Jacobs and Luborsky[8]. In Figs. 12(b) and (c) the area surrounded by the curve and the abscissa between 0° and 360° is denoted W_r. This is called the rotational hysteresis loss. This corresponds to $\int_0^{2\pi} T d\theta$, where T is $\frac{1}{2}(\vec{L}-\overleftarrow{L})$. W_r is related to H_m in Fig. 13. It is negligibly small at small H_m but abruptly increases with increasing H_m and attains the peak value. The field strength giving this peak is called the anisotropy field, H_p. The

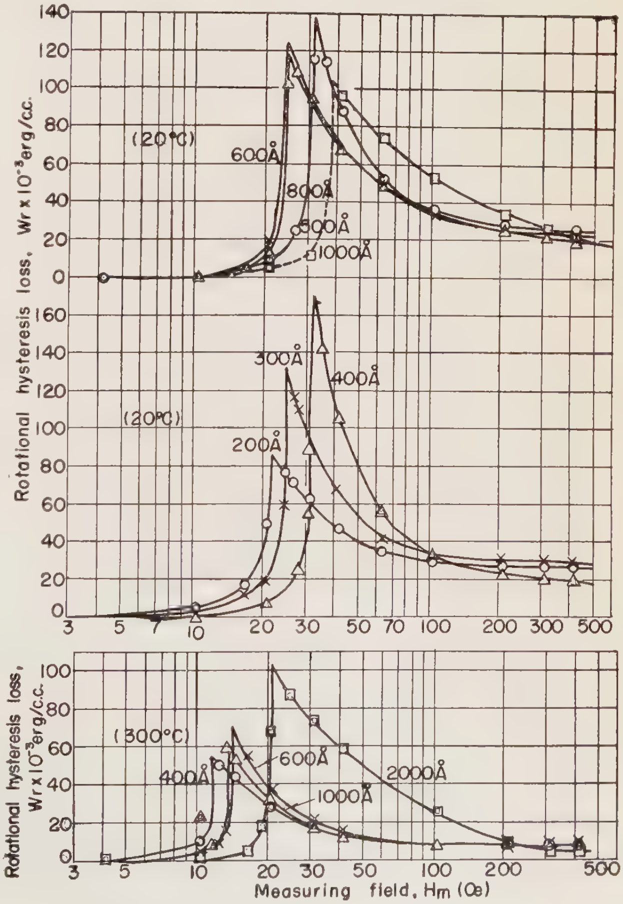

Fig. 13. Rotational hysteresis loss observed as a function of measuring fields for films with various values of thickness, evaporated at t_s=20°C and 300°C in H_d=250 Oe.

values of rotational hysteresis integral, $\int_0^\infty (W_r/I_s)d(1/H)$, are obtained from Fig. 13 and shown in Table III for films prepared under various conditions. I_s in the integral means the saturation magnetization and was assumed to be 1710 gauss which was the same value as for bulk material. W_r slowly decreases after passing the peak but does not vanish even at the maximum field, 414 Oe, attainable in the present experiment. It is thus clear that this maximum field is insufficient, though it was expected at the beginning of the present study that this field would be sufficient. The relation between H_p and the film thickness is shown in Fig. 14 and Table IV. Fig. 15 shows the influence of t_s upon the W_r-H_m curves. From this figure the relation between H_p and t_s is obtained and shown in Table V. It is plotted in Fig. 16 which much resembles Fig. 9. Thus the H_p-t_s relation is likely to correspond to the K_u-t_s relation.

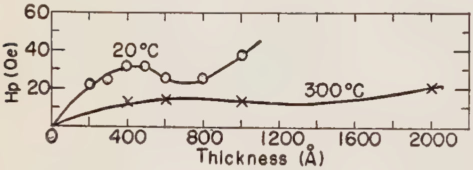

Fig. 14. H_p obtained from Fig. 13 as a function of the film thickness.

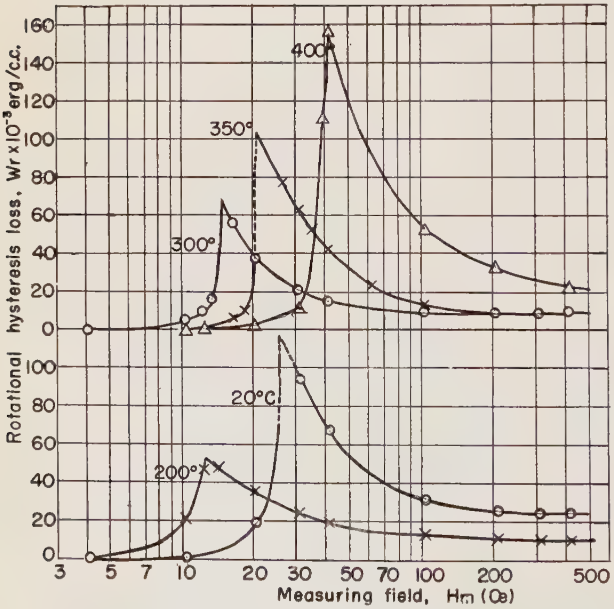

Fig. 15. Rotational hysteresis loss observed as a function of measuring field for films formed at various temperatures. The film thickness was 600 Å and H_a=250 Oe.

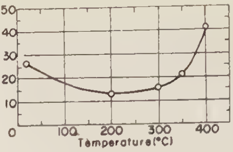

Fig. 16. H_p obtained from Fig. 15 as a function of the substrate temperature.

3. *Structure examination by electron diffraction*

The structure of evaporated films was examined by the reflection method of electron diffraction. The two directions of the incident beam were used, i.e., one is parallel with the H_a direction and the other is perpendicular to this. In all cases the diffraction pattern was not different between these two directions. This fact means any fibrous structure not to be detected in the films examined.

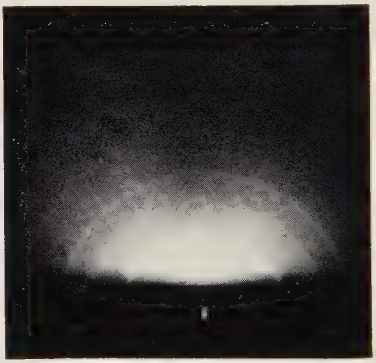

Photo. 1. Electron diffraction pattern of iron film formed in magnetic field. D=200 Å, t_s=20°C.

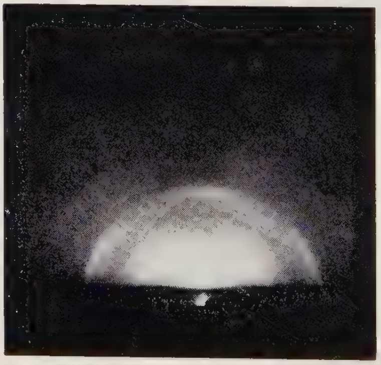

Photo. 2. Electron diffraction pattern of iron film annealed at 300°C for 1 hr D=2000 Å, t_s=20°C

Table III. The values of the rotational hysteresis integral at various values of thickness, substrate temperature and annealing time at 200°C.

D (Å)		200	300	400	500	600	800	1000	2000
$\int \frac{W_r}{I_s} d\left(\frac{1}{H}\right)$	$t_s=20$°C	2.03	1.71	1.41	1.53	1.50	1.76	1.21	-
	$t_s=300$°C	—	—	1.49	—	1.30	—	1.29	1.66
t_s (°C) (D=600Å)		20	200	300	350	400			
$\int \frac{W_r}{I_s} d\left(\frac{1}{H}\right)$		1.50	2.06	1.30	1.27	1.48			
Annealing time at 200°C (D=600Å, t_s=200°C)		~0	1 hour	2 hour					
$\int \frac{W_r}{I_s} d\left(\frac{1}{H}\right)$		2.06	1.67	2.38					

Table IV. Relation between the anisotropy field, H_p, and the film thickness.

Thickness (Å)		200	300	400	500	600	800	1000	2000
H_p (Oe)	$t_s=20$°C	22	25	32	32	25	25	38	
	$t_s=300$°C			13		14		13	21

Table V. Relation between the anisotropy field, H_p, and the substrate temperature, t_s. ($D=600$Å)

t_s (°C)	20	200	300	350	400
H_p (Oe)	25	13	15	21	41

The pattern yielded body-centred cubic rings characteristic of the low temperature phase of iron, when t_s was 20°C, as shown in Photo 1, but faint diffuse rings were found besides iron rings, when t_s was 300°C. Diffuse rings also appeared when films formed at t_s =20°C were annealed at 300°C, as shown in Photo. 2. These faint rings seem to have been caused by FeO rather than by Fe_3O_4.

§ 4. Discussion

For the origin of the magnetic annealing effect of alloys, the atoms pair orientation theory has been proposed by Néel[9] and independently by Taniguchi[10] and Chikazumi[11]. Although the origin of the induced magnetic anisotropy in thin films of pure metals and alloys evaporated in a magnetic field is not yet thoroughly made clear, the following three factors may be considered to be more or less related to the origin: (1) Formation of crystalline texture, (2) anisotropic planar stress caused by the difference in the expansion coefficient between film and substrate material, and (3) directional formation of lattice imperfections such as impurity atoms, vacancies, dislocations and stacking faults, etc. Some discussions will be done on these possibilities in the following.

(1) According to Knorr and Hoffman[3], the formation of the fibrous structure in evaporated thin films is responsible for the induced magnetic anisotropy. They formed iron films, evaporating with a relatively large incidence angle, and obtained a very large anisotropy energy (4×10^4 erg/c.c.). In the present study, however, the formation of the fibrous texture was not expected, because the evaporation was carried out under the normal incidence. Actually, this texture was not detected by electron diffraction, as already described in § 3, and the magnitude of the measured anisotropy energy was much smaller than that obtained by Knorr and Hoffman. It is sure that the fibrous texture caused by the oblique incidence of metallic vapor contributed considerably to the increase of the induced an-

isotropy. It is obvious, however, that the anisotropy in the present experiment may have to be explained in another way.

(2) As the second possibility, an anisotropic planar stress caused by the magnetoelastic coupling constants and the difference in thermal expansion coefficients between metal film and substrate may be considered, as reported by Macdonald[12]. The magnitude of the anisotropy caused by this effect, if it exists, must depend on the substrate material and decrease with increasing film thickness. In order to see the effect of the difference in thermal expansion, discs of silica and of glass were used as the substrates in the present study, because glass has almost the same linear expansion coefficient, about $1.2 \times 10^{-5}\,\mathrm{deg}^{-1}$, as metals, while silica has a very small coefficient, i.e. about $0.06 \times 10^{-5}\,\mathrm{deg}^{-1}$. A little dependence of the magnetic anisotropy upon the substrate material was found when the substrate temperature was 20°C. When this temperature was raised to 300°C, on the other hand, no effect was observed. The dependence of the anisotropy on the film thickness was not definitely observed. At any rate, the anisotropic planar stress connot be thought to be a powerful possibility.

(3) The directional ordering of lattice imperfections seems to be related to the magnetic anisotropy, too. This mechanism has already been proposed by Williams and Sherwood[4] and by Andrä *et al*[2] in terms of the spontaneous magnetic anisotropy. In general evaporated films contain a large number of lattice imperfections in an as-deposited state. When thin films are formed in magnetic field, the anisotropic alignment of lattice imperfections may occur as a result of existence of magnetostriction and give rise to the uniaxial magnetic anisotropy. Hoffman, Daniels and Crittenden[13] measured the intrinsic stress in thin evaporated metal films as a function of temperature during evaporation and of subsequent annealing and concluded that the number of lattice imperfections decreases with increasing temperature below about 300°C but increases above this temperature. Based on their conclusion, the following two results of the present study may qualitatively be explained; (i) change of the magnetic anisotropy with the subtrate temperature (Fig. 9) and (ii) disappearance of the anisotropy after the prolonged magnetic annealing (Fig. 11). The magnetic anisotropy is thus strongly related to the lattice imperfections.

After all, the last one of the above three possibilities may be probable, but a definite conclusion will be unable to be drawn before more detailed experimental investigations will be done. It may also be necessary to consider a minute structure of evaporated films for discussing the origin of the uniaxial anisotropy. If individual crystallites, several ten Å in size, constituting the film structure, are coated with non-magnetic thin layer, e.g. with oxide, and separated from one another, the film may be considered as a powder magnet. Using the saturation magnetization (I_s) of 1710 gauss for bulk iron, the rotational hysteresis integral, $\int (W_r/I_s)d(1/H)$, was estimated for the present experiment. The estimated values of this integral, ranging from 1.3 to 2.4, coincide very well with those which Jacobs and Luborsky calculated for powder magnet using the fanning model with chains of spherical particles. This coincidence seems to support the assumption that a film is composed of individual crystallites coated with oxide.

The authors are indebted to Mr. Y. Sugai for preparation of the specimens and for helping the torque measurements.

The present investigation has partly been supported by the fund of the Ministry of Education in Aid of Scientific Researches.

References

1) L. Reimer: Z. Naturforsch. **11**a (1956) 649; **12**a (1957) 1014.
2) W. Andrä, Z. Malek, W. Schüppel and O. Stemme: J. Appl. Phys. **31** (1960) 442.
3) T. G. Knorr and R. W. Hoffman: Phys. Rev. **113** (1959) 1039.
4) H. J. Williams and R. C. Sherwood: J. Appl. Phys. **28** (1957) 548.
5) M. S. Blois, Jr: J. Appl. Phys. **26** (1955) 975. C. D. Olson and A. V. Pohm: J. Appl. Phys. **29** (1958) 274; D. O. Smith: J. Appl. Phys., **29** (1958) 264.
6) Proceedings of the 4th Conference on Magnetism and Magnetic Materials, Supplement of J. Appl. Phys. **30** (1959) 254S–276S.
7) D. O. Smith: Supplement to J. Appl. Phys. **30** (1959) 264S.

8) I. S. Jacobs and F. E. Luborsky: Proc. Conf. on Magnetism and Materials, Boston (1956) 145; J. Appl. Phys. **28** (1957) 467.
9) L. Néel: Compt. Rend. **237** (1953) 1468; J. Phys. et Radium **15** (1954) 225.
10) S. Taniguchi: Sci. Rep. Res. Inst. Tohoku Univ., A**7** (1955) 269.
11) S. Chikazumi and T. Oomura: J. Phys. Soc. Japan **10** (1955) 842; S. Chikazumi: J. Phys. Soc. Japan **11** (1956) 551.
12) J. Ross Macdonald: Phys. Rev., **106** (1957) 890.
13) R. W. Hoffman, R. D. Daniels and E. C. Crittenden: Proc. Phys. Soc. B**67** (1954) 497.

JOURNAL OF THE PHYSICAL SOCIETY OF JAPAN Vol. 16, No. 10, OCTOBER, 1961

The Effect of Heat Treatment on the Minority Carrier Lifetime in Silicon

By Toshihumi ASAKAWA

The Electrical Communication Laboratory, Nippon Telegraph and Telephone Public Corporation, Kichijoji, Musashino, Tokyo, Japan

(Received May 11, 1961)

Heat treatment centers introduced in silicon were observed by measuring a minority carrier lifetime. Immediately after quenching, a donor-like level at 0.34 eV from the valence band was observed. This level was transformed into several kinds of recombination levels during the annealing process at room temperature, one of which was located at a distance larger than 0.45 ± 0.05 eV from the band edges. Other transformed centers having a small activation energy could not be explained by Shockley-Read formula. These observed properties have a good correspondence with those of iron, so that, it is reasonable to consider that thermally introduced center is iron, and that iron acts as a recombination center even when it is inactive to electrical conductivity. This result is consistent with previously reported properties of heat treated silicon.

§ 1. Introduction

Diffused *p-n* junctions are usually produced in silicon by heat treatment in a quartz tubes at temperatures above 1100°C. Such a treatment lowers the carrier lifetime extremely even when diffusant impurities are absent. It is said that changes in lifetime are due to diffusion of impurities from the sample surface having a large diffusion constant of about 10^{-5} cm^2 sec^{-1} (1).

In a heat treated silicon crystal, an iron donor level was found from the temperature dependence of Hall coefficient[2,3], but a level close to a copper donor level was observed from the temperature dependence of the minority carrier lifetime. The recombination level in a heat treated *p*-type crystal reported by Ross and Madigan[4] is located between 0.063 eV from the valence band, and the levels obtained by Galkin[1] and by Carlson[5] are located at a distance of about 0.13 eV from the valence band. Even in "as-grown" crystals, these levels were observed by Bittman and Bemski[6]. They suggested from these energy levels that among the impurities which are responsible for the lifetime, copper is the most prominent. However, according to the Hall coefficient measurements the density of the thermally introduced copper donor is less than 5×10^{12} cm^{-3} [10].

Recently, Blakemore[7] showed that the activation energy of about 0.18 eV obtained from the lifetime measurements might be due to a resultant of two separated levels which were located at 0.34 eV from the valence band and at 0.54 eV from the conduction band and suggested that the 0.34 eV level was a gold donor level and that the 0.54 eV level was an iron donor level or an unknown transition metal donor level. His result is most probable because these levels correspond to actual impurity levels.

If the resultant of several deep levels is regarded as one recombination level, the resultant activation energy will be smaller than each activation energy. In quenched silicon crystals, such a circumstance would be expected. The recombination level in a quenched crystal giving low activation energy may be a resultant of several deep levels.

In order to clear these situations, the measurements of the minority carrier lifetime were carried out with grown junctions which were heated at 1100°C in oxygen for 30∼60 minutes and quenched by dropping into ethylene glycol. It was found that the level of the thermally introduced recombination center was apparently an iron donor level rather than a copper donor level.

§ 2. Experimental

The grown junctions made from duPont grade I silicon by doping boron and phosphorus during growth of crystals were used. Resistivities of the sample are lying in the range of 0.05 to 47 Ω-cm. Usually, as the resistivity of the one side of the junction is very much lower than that of the other side, the forward current is carried by one kind of minority carrier, whose lifetime is to be measured. Resistivities of each side of junctions ane minority carrier lifetimes of the samples before heat treatment are shown in Table I.

Table I. Resistivities and Lifetimes of the Samples before Heat Treatments.

Sample No.	Resistivity		Lifetime in high resistivity side
	p-type side	*n*-type side	
I	14.0 Ω-cm	0.05 Ω-cm	50 μsec
II	5.5 〃	0.07 〃	38 〃
III	0.04 〃	5.9 〃	45 〃
IV	0.07 〃	47.0 〃	30 〃

Carrier lifetimes near *p*-*n* junctions were measured using Kingston's[8] method, based on dependence of the junction recovery time on carrier lifetime. This method does not depend on the analysis of the shape of the observed curve. If a junction is biased in the forward direction and suddenly changed into the reverse direction, the junction is sustained in a short circuit state immediately after reversed. The short circuit current is limited by external circuit. The time sustained in a short circuit state t is determined by the forward bias current I_f, the reverse short circuit current I_r, and the minority carrier lifetime τ. The relation among those quantities was given by Kingston[8] as follows;

$$\mathrm{erf}\left(\sqrt{\frac{t}{\tau}}\right)=\frac{1}{1+I_r/I_f}\,. \tag{1}$$

Hence, if I_r/I_f is constant, τ equals to t multiplied by some constant.

The dependence of minority carrier lifetime on excess carrier density δn is determined by the forward bias current I_f as follows;

$$\delta n=I_f\sqrt{\tau}/\sqrt{D}\,Sq\,, \tag{2}$$

where D is the diffusion constant of minority carrier, S is the junction area, and q is the electronic charge.

In order that the measurements can be carried out precisely, I_f must be carried by one kind of minority carrier only, and the saturation backward current I_{s0} must be negligible compared with I_r. In several samples, it was confirmed that the emitting efficiency which was calculated from the relation between the forward current I_f and the forward voltage V_f of the diode was greater than 0.99 and that I_{s0} was much smaller than I_r.

Kingston's method is not satisfactory to measure the dependence of τ on δn, since Eq. (1) is not valid, when τ varies with δn. τ can not be expressed in a simple form when τ depends upon δn. However, when τ does not depend too much upon δn, Eq. (1) and Eq. (2) can be used approximately. Particulary, in the case where t is much smaller than τ, dependence of τ on δn can be determined more precisely. As the lower limit of t was restricted by the rise time of the apparatus, the measurement was carried out under the condition where $I_r=I_f$, or $\tau\simeq 4t$.

On the other hand, as it was more convenient to measure the dependence of the lifetime on excess carrier density using Kalashnikov and Penin's[9] method at low injection level, this method was also used to compare with the result obtained by Kingston's method. At low injection level, both methods showed good agreement.

The dependence of the lifetime on temperature was measured using the cryostat shown in Fig. 1. An electronic temperature controller was used to maintain the sample box at a constant temperature within the accuracy of 0.5°C during the measurement. These apparatus can change the temperature of a sample from 200°K to 400°K in 20 minutes. If the temperature of a sample could not be changed rapidly, the permanent changes of the lifetime would be caused during the measurement. Usually, the measurement was carried out in 30 minutes or 40 minutes, and it was assured that the lifetimes at room temperature were kept unchanged before and after the measurement.

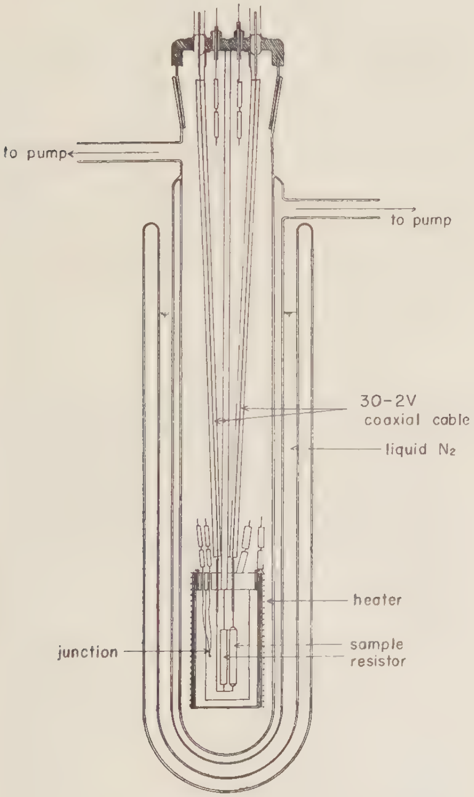

Fig. 1. Cutaway view of the cryostat.

As lead wires to the sample, 3C-2V coaxial cables were used to avoid the ringing current of the circuit. Maximum value of the ringing current due to diode capacity and lead wire inductance was suppressed below 30% of the reverse short circuit current, and its duration was suppressed within about 0.05 μsec.

To measure the lifetime, Tektronix plug-in unit R and Tektronix 545 oscilloscope were used as pulse generator and oscilloscope. Rise time of the pulse was about 0.03 μsec and rise time of the oscilloscope was 0.012 μsec. This circuit diagram is shown in Fig. 2.

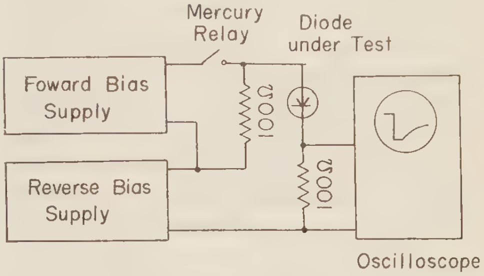

Fig. 2. Circuit diagram measuring the minority carrier lifetime.

Accuracies of measured lifetimes were about ±0.012 μsec at temperatures below 300°K and about ±0.025 μsec at temperature above 300°K.

The relation between the resistivity changes and the lifetime changes was measured by the four-point method and by the photoconductivity decay method having an accuracy of 0.5 μsec. The photoconductivity decay method was also used to measure the dependence of the lifetime on heating temparature.

§ 3. Result

(a) *The relation between the resistivity changes and the lifetime changes.*

The changes in resistivity of silicon by heat treatment are known to be due to the deep lying donor levels, and there is a marked relation between the lifetime changes and the resistivity changes. In order to observe this relation, a p-type crystal with an initial resistivity of 33 Ω-cm and an initial lifetime of 25 μsec was quenched after 1 hour heating at 1100°C in oxygen, and both profiles of resistivity and lifetime were measured. The decreases in carrier density obtained from the resistivity measurements and the increases in inverse lifetime were plotted against the distance from the sample surface. These are shown in Fig. 3. These curves have a similar shape, and are well fitted by Fick's law curve. So that, it is reasonable to consider that a donor impurity which diffuses into the crystal from the surface acts as recombination centers. Such an impurity has a large diffusion constant of 10^{-5} cm^2 sec^{-1} at 1100°C as calculated from

Fig. 3. Near the surface of the sample, a curve showing the lifetime changes deviates from Fick's law curve. It is probably due to both the accuracy of the measurements and the resistivity changes.

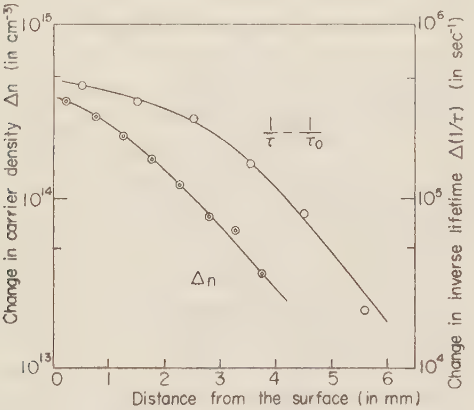

Fig. 3. Comparison of the changes in carrier density with the changes in inverse lifetime.

(b) *The dependence of the lifetime on heating time and heating temperature.*

The lifetime shows a monotonous decrease with increasing time of heating, although resistivity shows a complicated change. The changes in lifetime by heat treatment are larger in a p-type crystal than in an n-type crystal in the same way as the changes in resistivity. The temperatured pendence of the lifetime becomes different when the sample is exposed to successive heat treatments and when the cooling rate during heat treatment is changed. Rapid quenching produces simple recombination behaviors, but slow cooling caused complicated behaviors due to the introduction of several kinds of centers. It is reasonable to consider that the centers introduced during heat treatments are partly transformed into electrically inactive forms by annealing[2),3),10)], and that even when they are electrically inactive, they affect the recombination process.

Fig. 4 shows the temperature dependence of the low level lifetime τ_0, in an n-type crystal which was exposed to successive heat treatments in oxygen at 1100°C for 15 minutes. The initial activation energy obtained from Fig. 4 was 0.25 eV. When heat treatments were repeated, temperature dependence of τ_0 at room temperature began to decrease, and the activation energy could not be obtained on assuming that one kind of recombination center was active.

Fig. 5 shows the same behavior in a p-type crystal whose initial activation energy was about 0.22 eV. After the first heat treatment, τ_0 was decreased to about 1/50 of its initial value, whose activation energy could not be determined. After several heat treatments, its low level life time τ_0 became less than 0.1 μsec, so that these life times are not shown

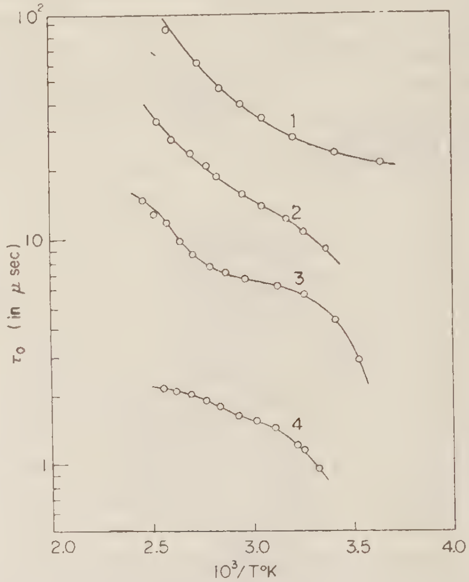

Fig. 4. Temperature dependences of low level lifetime in an n-type crystal (samle IV) which was exposed to successive heat treatments at 1100°C for 15 minutes. (1) obtained in "as-grown" state; (2), (3) and (4) obtained after 1st, 2nd and 3rd heat treatment respectively.

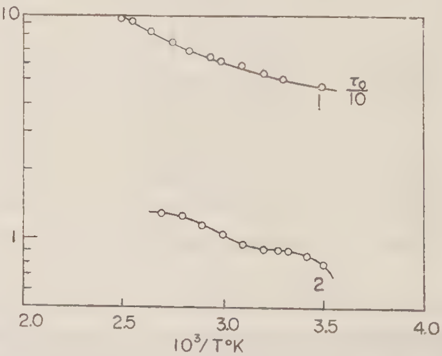

Fig. 5. Temperature dependences of low level lifetime in a p-type crystal (sample I) which was exposed to successive heat treatments at 1100°C for 15 minutes. (1) obtained in "as-grown" state; (2) obtained after 15 minutes heating.

in Fig. 5, because the precies measurements were impossible.

On the other hand, the changes in resistivity in a p-type crystal reached to a maximum value after the first heat treatment, and decreased gradually when heat treatments were repeated.

Fig. 6 shows the dependences of the lifetime on heating temperature in p-type crystals. Curve A is obtained on a pulled p-type crystal with a resistivity of 33 Ω-cm and a lifetime of 20 μsec which was heated at each temperature shown by circles on the curve in Fig. 6 for 30 minutes in oxygen and quenched. Curve B is obtained on the same crystal as curve A which was cleaned by ion bombardment prior to heat treatments and quenched by radiation after 30 minutes joule-heating in high vacuum. Curve C is obtained on a Merck's p-type crystal with a resistivity of 250 Ω-cm and a lifetime of 1500 μsec which was treated in the same way as the sample shown by curve B. Curve B and curve C show a filament lifetime and not a bulk lifetime.

The decreases in lifetime shown on the curve A may be concluded to be due to the introduction of surface impurities, because these changes were not reproducible during heating and annealing cycles. Decreases of curve B at high temperatures are less than that of curve A and probably due to evaporation of impurities precipitated on the dislocation lines, because the changes shown by curve B were reproducible by heating and annealing cycles. But it is not clear what impurity has been contained. Curve C did not exhibit any change and the measured lifetime were probably determined by surface recombination only.

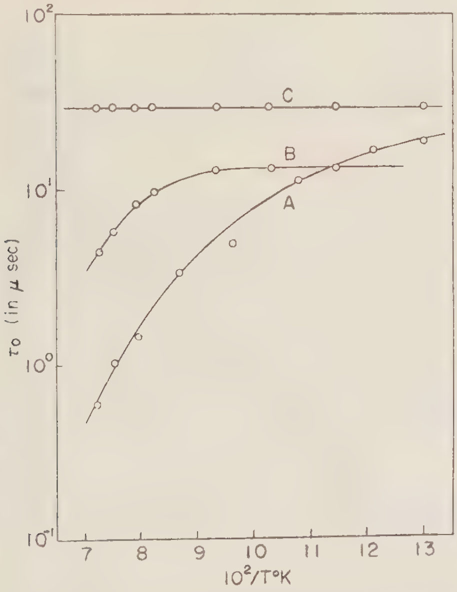

Fig. 6. Lifetime as a function of heat treatment temperature. (A) obtained on a pulled 33 Ω-cm p-type crystal heated in oxygen. (B) obtained on a pulled 33 Ω-cm p-type crystal joule-heated in high vacuum. (C) obtained on a floating zone 250 Ω-cm p-type crystal joule-heated in high vacuum.

These curves show without the impurities introduced from the surface, any appreciable changes would not be caused by heat treatment and that lattice defects also would not affect the lifetime considerably.

As pointed out in the previous paper[10], these results differ from those obtained by Law[11], who found the trapping centers by heat treatment. His centers are considered to be a different kind of center which might be originated from the strain during the heating.

(c) *The energy level of the recombination center introduced by heat treatment.*

In order to determine the energy level of the recombination centers introduced, the dependences of the lifetime on temperature and on excess carrier density were measured. The samples which were heated in oxygen at 1100°C for 30∼60 minutes and quenched by dropping into ethylene glycol, gave different result from those obtained with samples which were heated in the same way and cooled slowly. The former was quite unstable even at room temperature and its electrical characteristic was changed into another one on heating at temperatures above 100°C for several hours. So that, the measurement must be carried out in 1 hour after quenching and the temperature of the sample must be kept below 100°C during the measurement. In order to avoid such an annealing effect, when lead wires were soldered to the sample, junction region was dipped in water lest the temperature of the junction should rise above 100°C.

In p-type crystals, the densities of introduced centers are lying in the range of $5\times10^{13}\,\mathrm{cm}^{-3}$ to $10^{14}\,\mathrm{cm}^{-3}$ immediately after quenching according to the resistivity measurement, so that these are negligible compared with initial majority carrier density of $10^{15}\,\mathrm{cm}^{-3}$. In n-type crystals, the densities of introduced centers would be expected to be the same as in

p-type crystals, although these could not be measured directly.

The lifetime measured by Kingston's method is a steady state lifetime which was given by Shockley and Read[12] in a p-type crystal in the case of single recombination centers as follows;

$$\tau=\frac{\tau_{p0}[n_0+n_1+\delta n]+\tau_{n0}[p_0+p_1+N_t p_1(p_0+p_1)^{-1}+\delta p]}{n_0+n_1+N_t p_0 p_1(p_0+p_1)^{-1}+(p_0\delta n+p_1\delta p(p_0+p_1)^{-1}}, \tag{3}$$

where

$n_1=N_c \exp[-(E_c-E_t)/kT]$,
$p_1=N_v \exp[-(E_t-E_v)/kT]$,
δn=density of excess electrons,
δp=density of excess holes,
n_0=density of electrons,
p_0=density of holes,
N_v=density of recombination centers,
E_t=energy level of recombination centers,
E_v=energy level of the valence band edge,
E_c=energy level of the conduction band edge,
N_v=density of states in the valence band,
N_c=density of states in the conduction band,
τ_{n0}=lifetime in a strongly p-type crystal,
τ_{P0}=lifetime in a strongly n-type crystal.

In an n-type crystal, lifetimes are obtained by exchanging n and p.

Usually δn does not equal to δp, but if N_t is small compared with other quantities and no trapping occurs at the recombination centers, δn equals to δp, so that Eq. (3) is reduced to Eq. (4).

$$\tau=\frac{\tau_{p0}(n_0+n_1+\tau_{n0}(p_0+p_1)+\delta n(\tau_{p0}+\tau_{n0})}{n_0+p_0+\delta n} \tag{4}$$

In our experiment, N_t is about 10% of majority carrier density, so that Eq. (4) may be valid.

Furthermore, if the recombination level is lying in the lower half of the energy gap, the the lifetime has the form

$$\tau=\frac{\tau_{n0}(1+p_1/p_0)+(\tau_{p0}+\tau_{n0})\delta n/p_0}{1+\delta n/p_0} \tag{5}$$

because n_0 and n_1 can be neglected compared with p_1, p_0 and δn. Eq. (5) gives a linear relationship between $\tau(1+\delta n/p_0)$ and $\delta n/p_0$ for a p-type crystal.

Fig. 7 shows such linear relationships observed on a p-type crystal which was heat treated as described above. These curves give the low level lifetime $\tau_0=\tau(1+\delta n/p_0)$ and the

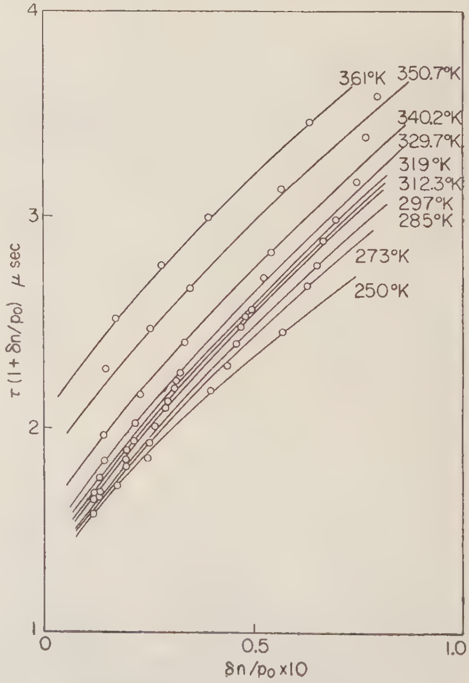

Fig. 7. Dependences of $\tau(1+\delta n/p_0)$ on $\delta n/p_0$ at various temperatures immediately after quenching, for sample I (p-type 15 Ω-cm).

lifetime at infinite injection level $\tau_\infty=\tau_{p0}+\tau_{n0}$ and their temperature dependences. These curves deviate from the linear relationship slightly at high and low temperatures. This means that the recombination takes place through several kinds of centers. However, these deviations are small, so that a single kind of centers will be predominant and Eq. (5) is applicable.

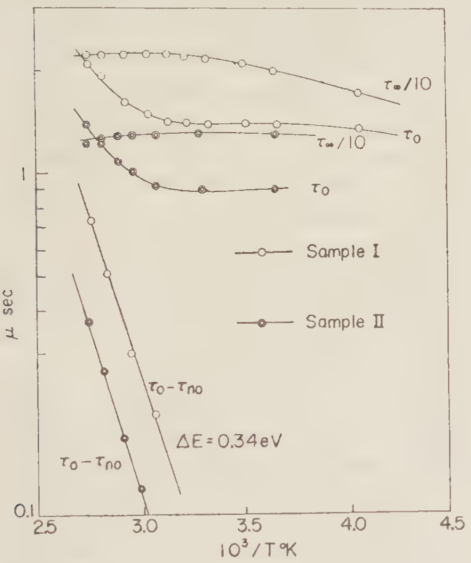

Fig. 8. Temperature dependences of τ_0 and $\tau_\infty/10$ immediately after quenching, for sample I. (p-type 14 Ω-cm), and sample II (p-type 5.5 Ω-cm). Activation energy is obtained from the slope of $(\tau-\tau_{n0})$.

Fig. 8 shows the temperature dependence of τ_0 and τ_∞ for several quenched p-type crystals. If the temperature dependence of τ_0 is fitted by

$$\tau_0=\tau_{n0}\left[1+\frac{N_v}{p_0}\,\mathrm{exy}\left(-\frac{E_t-E_v}{kT}\right)\right], \qquad (6)$$

following values are obtained for sample I, assuming that τ_{n0} is independent of temperature,

$$\tau_0=1.41\left[1+1.25\frac{N_v}{p_0}\exp\left(-\frac{0.34}{kT}\right)\right]\mu\text{sec}\,, \qquad (7)$$

where N_v is calculated assuming that $m^*/m=0.39$[18]. For sample II, the same activation is obtained, but τ_∞ is almost independent of temperature. Capture cross section ratio at 300°K is 0.062 for sample I, and is 0.077 for sample II. These quantities show that a donor-like level lies at a distance of 0.34 eV from the valence band, and that this level is introduced by heat treatment.

This level lies close to a gold donor level, but the capture cross section ratio differs from that of gold[14], and also a gold acceptor level was not observed in a heat treated n-type crystal, so that this seems to differ from a gold donor level.

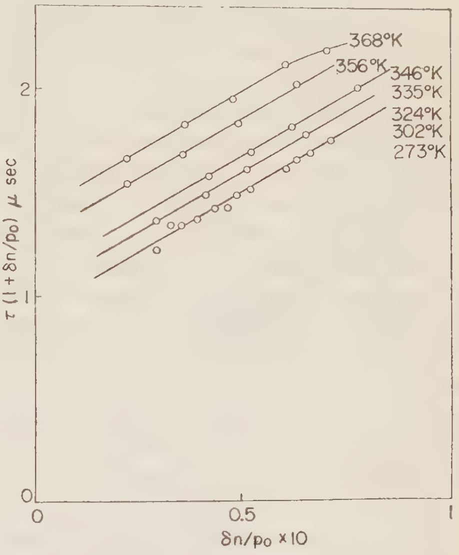

Fig. 9. Dependences of $\tau(1+\delta n/p_0)$ on $\delta n/p_0$ at various temperatures immediately after quenching, for sample II. (p-type 5.5 Ω-cm).

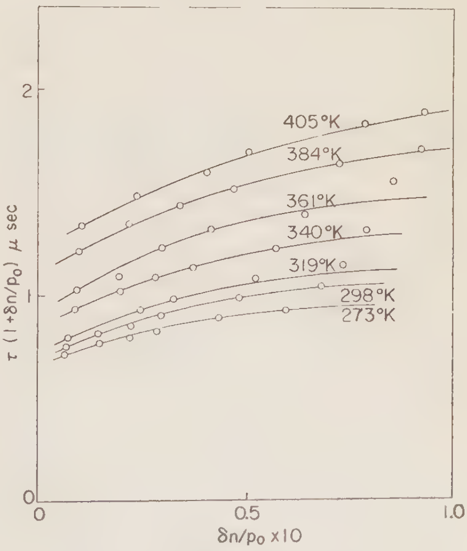

Fig. 10. Dependences of $\tau(1+\delta n/p_0)$ on $\delta n/p_0$ at various temperatures after subsequent annealing at room temperature, for sample II (p-type 5.5 Ω-cm).

The level like this was also observed by Blakemore[7] in "as-grown" *p*-type crystals and his numerical values are in good agreement with ours, but he also found another donor-like level with this level, which is located at a distance of 0.54 eV from the conduction band. In our experiment, the latter level was scarcely observed immediately after quenching.

The lifetimes of such a sample were not constant with time even at room temperature, and this 0.34 eV level was transformed slowly into other levels.

Fig. 9 shows the dependence of lifetime on excess carrier density for sample II, immediately after quenching. Fig. 10 shows the same one after subsequent 72 hour annealing at room temperature, and Fig. 11 shows the same one after re-heating at 300°C for 15 minutes following the annealing. Curve in Fig. 10 does not show the linear relationship, so that several centers were formed in 72 hours after quenching. Curves in Fig. 11 show that by re-heating at 300°C for 15 minutes, the low level lifetimes were increased and almost independent of temperature between 300°K and 340°K, and that τ_∞ were decreased moreover.

These behaviors show that the annealing after quenching caused the transformation of an introduced center into several types of new centers, one of which has a small value of τ_∞ and that by re-heating at 300°C, initial center appeared again to some extent and transformed new centers disappeared except one having a small value of τ_∞. As the lifetimes in a heat-treated *p*-type crystal measured by several authors are usually shown in such diagrams as Fig. 10 and Fig. 11, the activation energies are fairly small, say 0.13 eV[1] or 0.14 eV[5].

Fig. 12 shows the dependence of lifetime on excess carrier density for a quenched *n*-type crystal of sample III and Fig. 13 shows the temperature dependence of τ_0 and τ_∞ obtained

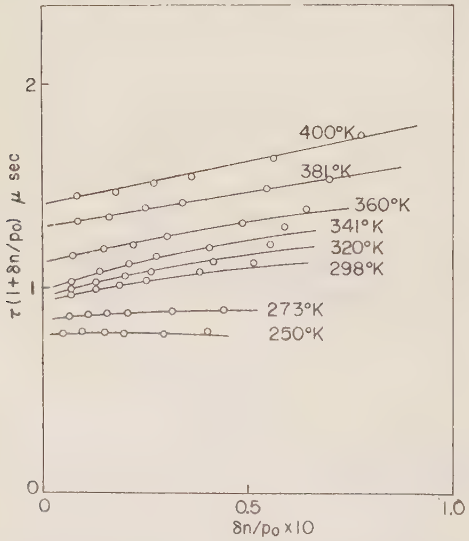

Fig. 11. Dependences of $\tau(1+\delta n/p_0)$ on $\delta n/p_0$ at various temperatures after re-heating at 300°C for 15 minutes following the annealing, for sample II (*p*-type 5.5 Ω-cm).

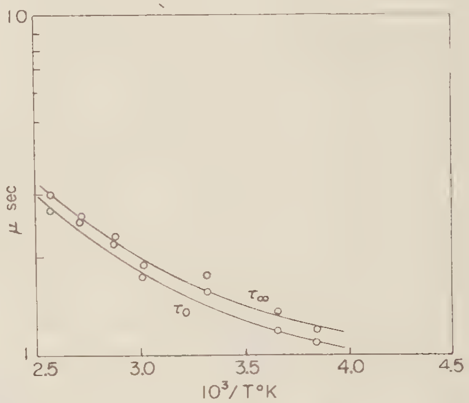

Fig. 13. Temperature dependences of τ_0 and τ_∞ immediately after quenching. for sample III (*n*-type 5.9 Ω-cm).

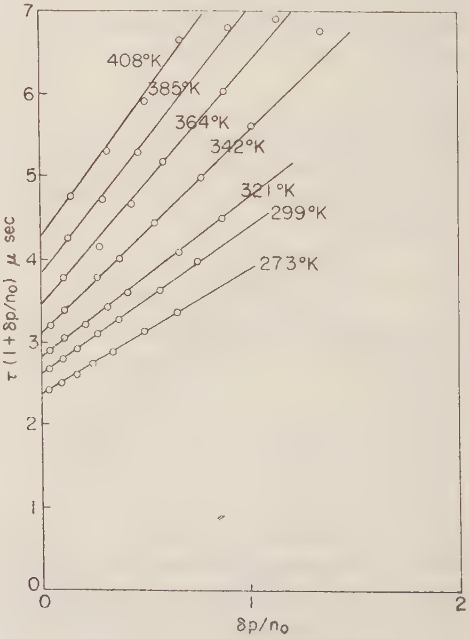

Fig. 12. Dependences of $\tau(1+\delta p/n_0)$ on $\delta p/n_0$ at various temperatures immediately after quenching, for sample III (*n*-type 5.9 Ω-cm).

from Fig. 12. In this sample, τ_0 does not differ from τ_∞ appreciably, and their temperature dependences show the same behavior. This implies that temperature dependence of τ_0 is probably due to temperature dependence of capture cross section and not due to carrier distribution in recombination centers. If it is assumed that temperature dependence of τ_0 should arise from carrier distribution in recombination centers, the activation energy will become very small, say 0.05 eV, and these centers will be acceptor-like. This result is inconsistent with the fact that the changes in resistivity of an *n*-type crystal by heat treatment were not observed at temperatures between 77°K and 400°K. Furthermore, thermally introduced recombination centers in both *n*- and *p*-type crystals are unstable at room temperature, and on heating above 100°C, these centers are transformed into other centers, so that they seem to be the same in both types of crystals. This assumption is supported by the fact that capture cross section ratio $\gamma=\tau_{n0}/\tau_{p0}$ in sample I at room temperature obtained from Fig. 8 is approximately equal to that obtained from Fig. 12 assuming that τ_0 of sample III depends upon the capture cross section only.

However, this assumption that the same center is active in both types of crystals after rapid quenching is inconsistent with following facts. First, the temperature dependence of τ_∞ in a *p*-type crystal is not the same as that in an *n*-type crystal. Secondly, the temperature dependence of τ_{p0} does not obey the prediction of Lax. In first point, the temperature dependence of τ_∞ is different even among *p*-type crystals, and annealing at room temperature causes the decrease of τ_∞ and its temperature dependence, so that, without the annealing effect, the temperature dependence of τ_∞ would be the same in both types of crystals. In second point, according to the prediction of Lax[15)], the temperature dependence of τ_{p0} for neutral centers must vary as $T^{-1/2}$, but in our samples, τ_{p0} is almost independent of temperature or increases with increasing temperature. This means that the capturing process is such a complicated one as the reverse ionization process[16)]. So that, it is desirable to investigate a mechanism of the recombination in full detail.

In an *n*-type crystal, the annealing effect was also observed. Fig. 14 and Fig. 15 show the 48 hours and 72 hours annealing effects of sample III, respectively. The annealing

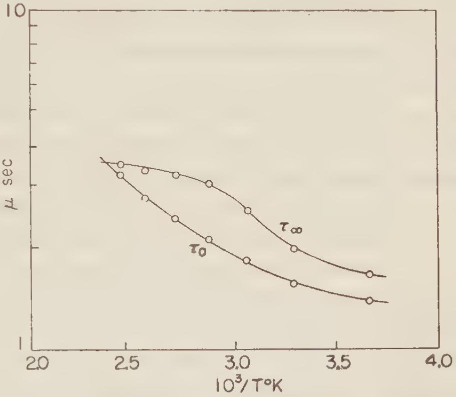

Fig. 14. Temperature dependences of τ_0 and τ_∞ after subsequent 48 hours annealing at room temperature, for sample III (*n*-type 5.9 Ω-cm).

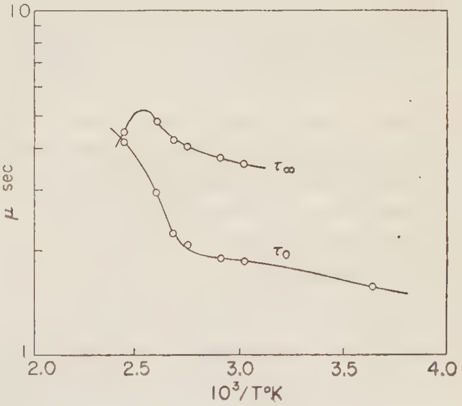

Fig. 15. Temperature dependences of τ_0 and τ_∞ after subsequent annealing at room temperature, for III (*n*-type 5.9 Ω-cm).

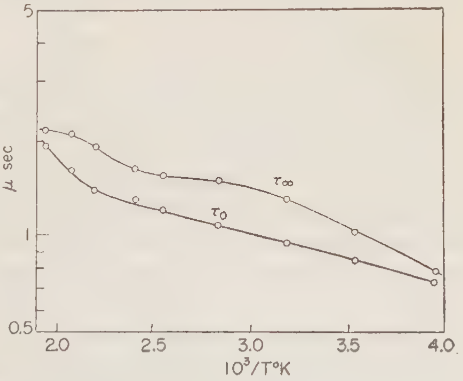

Fig. 16. Temperature dependences of τ_0 and τ_∞ after subsequent re-heating at 300°C for 15 minutes, for sample III (*n*-tyse 5.9 Ω-cm).

effects caused the increase of τ_∞ and its temperature dependence to be small at room temperature, but linear relationship almost remained unchanged.

One of the transformed centers in sample III has a large activation energy of 0.45±0.05 eV as shown in Fig. 16. Of course, this value does not give the energy level of the transformed center, because several transformed centers might be formed in subsequent 72 hours annealing.

Such transformed levels disappeared by reheating at 300°C for 15 minutes and the temperature dependences of lifetime were recovered to initial states to some extent. Fig. 16 shows such a recovered feature after reheating at 300°C for 15 minutes. Curve of τ_0 is the almost same as the initial curve but the curve of τ_∞ is slightly different from the initial curve.

In all samples measured, these behaviors of of the changes in lifetime by heat treatment were the same except little differences of measured values.

In both n- and p-type crystals, the annealing and the reheating at low temperatures did not cause appreciable changes in low level lifetime but caused large changes in lifetime at an infinite injection level.

In annealed samples, the correlation between n and p-type crystals was not observed. This must be because, in an n-type crystal the prodominant recombination center seemed to be an acceptor-like or neutral center, but in a p-type crystal the predominant recombination center seemed to be a donor-like center according to Shockley-Read formula of a singly charged recombination center.

§ 4. Discussion

Immediately after quenching, the lifetimes in both n- and p-tpye crystal were decreased considerably. As shown in Fig. 3, Fig. 4, Fig. 5 and Fig. 6, it is obvious that the surface impurities diffused in and reduced the lifetime, and these phenomena have been observed by several authors[17]. What impurities diffuse in, depends upon the heat treatment conditions.

In our experiment, the heat treatment was carried out in oxygen, so that the oxide films formed on the sample surface during the heat treatment would impede the particular impurities diffusing in. Under these conditions, copper and gold would not react with the oxide films easily, but iron which became ferric oxide would be easily transformed into various iron silicate[18]. So that, iron would easily penetrate through the silicate film into the interior of silicon. Such iron was observed by Hall coefficient measurement[2),3] and by spin resonance experiment[10].

If it is assumed that thermally introduced impurity is iron, the changes in resistivity and in lifetime can be explained consistently. In iron doped silicon, the changes take place which cause a conversion[19] in activation energy and an annihilation of active centers[20]. After rapid quenching, a donor level 0.4 eV from the valence band is observed in iron doped silicon and the conversion to a level at 0.55 eV from the conduction band occurs in a week at room temperature. Furthermore, the annihilation of active centers occurs in weeks or months at room temperature and speeds up at higher temperatures. So that, the changes in resistivity disappear in weeks or months at room temperature.

In heat treated p-type silicon, the 0.4 eV level was observed after rapid quenching, and the conversion in activation energy was reporated[3),10] and also the annihilation of active centers was detected from the resistivity changes[10]. But the lifetime changes was almost constant in spite of the annihilation of active centers. These behaviors are similar to those of iron doped silicon.

However, it is very difficult to confirm that the thermally introduced recombination center is iron, because of the annealing effects. Various results were obtained by several authors for lifetime measurement[1),4),5]. They gave the low activation energy of the recombination, so that the recombination centers introduced during heat treatment did not seem to be iron. However, immediately after rapid quenching, a fairly large value of the activation energy was observed for a p-type crystal. This value is close to those of gold and the lattice defects, but the capture cross section ratio differs from those of gold and the lattice defects. If this level is not due to gold or lattice defects, among the impurity levels reported up to the present, the 0.4 eV level of iron is the most probable one. However, the observed activation energy is smaller than that of iron. This discrepancy is probably due to following reasons.

It was assumed that τ_{n0} was independent of temperature in obtaining Eq. (7), although if τ_{n0} varies as $T^n(n=1\sim4)$[15], larger activation energy will be obtained. Also, the transformed centers cause the decrease in activation energy in p-type crystals. By these corrections, the observed activation energy will be increased to 0.4 eV.

During the annealing process, the level with an activation energy larger than 0.45 ± 0.05 eV was observed in an n-type crystal. In the annealing stage of a p-type crystal as shown in Fig. 10, if it is assumed that the curves in Fig. 10 are resultants of two kinds of centers, both of which show linear dependence on $\delta n/p_0$, the level which has a very small capture cross section ratio and scarcely depends upon temperature, is found. These may probably correspond to the 0.55 eV level of iron.

Other transformed levels which had a smaller τ_∞ in a p-tpye crystal and a larger τ_∞ in an n-type crystal and a small activation energy, were observed. If it is valid that introduced impurity is iron, these centers also must be due to iron, but there is no correlation with the levels of iron. These centers are probably due to aggregated or precipitated iron atoms, and can not be fitted by Shockley-Read formula, because the low level lifetime does not saturated with decreasing temperature and can not be expressed as Eq. (6).

As discussed above, iron introduced by heat treatment has three different states and combinations of these tree states would give rise to any activation energies ranging from 0.05 eV to 0.55 eV.

Also, iron which has been initially contained may affect, because Sandiford[16] and Blakemore[7] found the deep lying recombination levels in "as-grown" crystals. But the density of such iron may be less than $5\times10^{12}\,\text{cm}^{-3}$ from the resistivity changes of the cleaned surface crystal which was joule-heated in high vacuum[10]. So that, it is negligible compared with that of introduced one.

In early stage, changes in resistivity due to heat treatments were observed in an n-tpye crystal, but recently used crystal does not exhibit such changes. This means that the densities of copper and gold contained in raw materials became less than before.

Origin of such iron is considered to be the ambient gas and the furnace wall heated at high temperatures, because when the sample was heated in a quartz tube in gas ambient, the changes in lifetime and in resistivity were larger than those by other treatments. However, a treatment in a floating zone refining apparatus or joule-heating in high vacuum produced scarcely any change. So that, without an ambient gas and a quartz tube heated at high temperatures, iron would not be introduced.

Acknowledgement

Our thanks are here expressed to Dr. T. Niimi and Mr. H. Izumi for their encouragement and to N. Ogawa and K. Ikegami for preperation of samples.

References

1) G. N. Galkin: Fiz Tverd. Tela. **2** (1960) 8.
2) T. Asakawa and M. Kondo: Annual Meeting of Phys. Soc. of Japan April, 1960.
3) Y. Matsukura: J. Phys. Soc. Japan **16** (1961) 192.
4) B. Ross and J. R. Madigan: Phys. Rev. **108** (1957) 1428.
5) R. O. Carlson: Phys. Rev. **108** (1957) 1390.
6) C. A. Bittman and G. Bemski: J. App. Phys. **28** (1957) 1390. G. Bemski: Phys. Rev. **100** (1955) 523.
7) J. S. Blakemore: Phys. Rev. **110** (1958) 1301.
8) R. H. Kingston: Proc. I.R.E. **42** (1954) 829.
9) S. G. Kalashnikov and N. A. Penin: Zhur. Tekh. Fiz. **25** (1955) 1111.
10) T. Asakawa and T. Igo; to be published.
11) J. T. Law: J. Phys. Chem. Sold. **14** (1960) 9.
12) W. Shockley and W. T. Read, Jr.: Phys. Rev. **87** (1952) 835.
13) Dresselhause, Kip and Kittel: Phys. Rev. **98** (1954) 368.
14) G. Bemski: Phys. Rev. **114** (1959) 1515. W. D. Davis: Phys. Rev. **114** (1959) 1006.
15) M. Lax: Second Symposium of Semiconductors Washington, October, 1956.
16) D. J. Sandiford: Proc. Phys. Soc. London **71** (1958) 1002.
17) M. Waldner and L. Sivo: J. Electrochem. Soc. **107** (1960) 298. S. T. Silverman and J. B. Singleton: J. Electrochem. Soc. **105** (1958) 591.
18) J. W. Mellor: *Inorganic and theoretical chemistry, Longmans Green and Co.* **6** (1957) 905.
19) C. B. Collins and R. O. Carlson: Phys. Rev. **108** (1957) 1409.
20) H. H. Woodbury and G. W. Ludwig: Phys. Rev. **117** (1960) 102.

JOURNAL OF THE PHYSICAL SOCIETY OF JAPAN Vol. 16, No. 10, OCTOBER, 1961

Magnetic Anisotropy of $KCoF_3$ and $KNiF_3$

By Kazuyoshi HIRAKAWA, Takasu HASHIMOTO and Kinshiro HIRAKAWA

Department of Physics, Faculty of Science, Kyushu University, Fukuoka

(Received May 22, 1961)

Magnetic anisotropy of single crystals $KCoF_3$ and $KNiF_3$ was investigated by the torque magneto-meter in the temperature range from 78° to 300°K. In the antiferromagnetic region, torque curves of these crystals when suspended along one of the cube edges can be expressed by the formula

$$T=C_1H^2\sin 2\theta-C_2H^4\sin 4\theta\ ,$$

where H is the magnetic field intensity, θ the angle of rotation of H relative to one of the cubic axes, and C's are constants. In the case of $KCoF_3$ the 4θ-term was not observed, while in $KNiF_3$ the 4θ-term was rather dominant in all specimens when no external stress was applied. The amplitude of the 2θ-term is sensitive to the stress in both cases. The experimental results on $KCoF_3$ and $KNiF_3$ are well interpreted by taking the antiferromagnetic spin axis to be parallel to the c-axis below their Néel temperatures. The origin of the 4θ-term which was observed in $KNiF_3$ is discussed, and it is concluded that this term arises from reversible movements of the antiferromagnetic domain walls existing in this compound.

§ 1. Introduction

In the previous paper, we have reported evidence of antiferromagnetism occurring in perovskite type KMF_3 (M: Mn, Fe, Co, Ni and Cu)[1]. Recently neutron diffraction experiments on KMF_3 were carried out by Scutturin *et al.*[2], who found that both $KCoF_3$ and $KNiF_3$ have the G-type antiferromagnetic super-structure below their Néel temperatures. Then it may be interesting to investigate the magnetic anisotropy of these compounds, because from considerations of the symmetry of these crystals and the G-type antiferromagnetic structure, there should not exist any magnetic anisotropy which is caused by classical dipole-dipole interactions.

In the present paper we shall describe the results of anisotropy measurements on $KCoF_3$ and $KNiF_3$. In some cases, however, the determination of these anisotropies is not so simple, because these cubic crystals so often come to have a slight deformation from the cubic symmetry and consequently have a domain (twinned-) structure below their Néel temperatures. It is already known that $KCoF_3$ becomes tetragonal below its Néel temperature ($T_N=114$°K) with $(c-a)/a\cong-0.002$, whereas no deformation has been observed on $KNiF_3$ ($T_N=275$°K) by X-ray examination even at 78°K[3]*. Our purpose of this paper is to find out the orientation of the spin axis in the crystal by means of torque measurements. Another purpose of this paper is to make clear the origin of the 4-fold symmetry which appears in the torque curves of $KNiF_3$. Similar phenomenon has already been observed on several compounds**, especially on MnO investigated by Uchida *et al.*, and a theoretical interpretation for this has been given by Nagamiya[4]. At first he proposed two possible mechanisms[5], one of which was originated from an intrinsic nature of the crystal, and the other from reversible movements of the antiferromagnetic domain walls when magnetic field was applied. In the recent paper[4], however, he has pointed out that the latter mechanism is much more favorable than the former. It will be shown that our experimental results are well interpreted by the latter mechanism.

---

* We tried to observe any symmetry change in $KNiF_3$ through the polarized microscope at about 150°K but we could not observe any transformation from the cubic symmetry. We believe, however, that there exists some kind of deformation (perhaps due to magneto-strictions) and consequently domain structure below its Néel temperature.

** Coexistence of both 2θ- and 4θ-terms in the (111) torque in NiO crystal has been observed by Roth and Slack[6]. Coexistence of both 2θ- and 6θ-terms in the torque in the easy plane (0001) of MnTe crystal has been observed by Hirakawa[7].

§ 2. Experimental Procedures

Single crystals were prepared by the flux method in the platinum crucible (200 cc) under the mixed atmosphere of argon and hydrogen fluoride. Large crystals prepared by this method were usually rectangular form of about 10×10×3 m/m in size. They were examined under the polarized microscope and the optically isotropic parts were cut out, so that rather small crystals (1×1×2 m/m) were used for measurements.

Torque was measured by the torsion balance of usual type. The specimen was cemented carefully to the bottom of the qualtz rod with collodion cement. Phosphor-bronze wire (0.1 mm dia.) was used for suspension. In order to study the effect of external stress, a clamper which was made of phosphor-bronze was attached at the bottom of the qualtz rod. The strength of the maximum stress applied by this clamper was roughly estimated as ~100 kg/cm². Generally the torque due to impurities contained in the clamper was fairly smaller than that of the crystals. This stray torque obtained by the preliminary measurement was subtracted from the observed one. Intensities of magnetic field were measured by direct insertion of the probe of proton resonance.

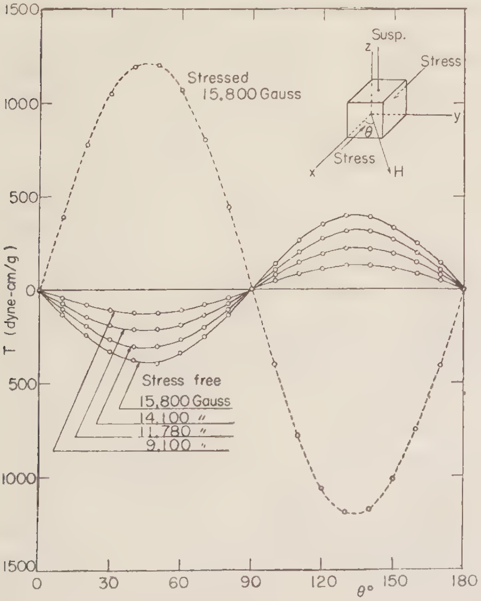

Fig. 1. Torque curves around the [001] axis of $KCoF_3$ measured at 78°K: The curves shown by the full lines are for the free crystal under the various field intensities and the dotted line is for the clamped crystal.

§ 3. Experimental Results

$KCoF_3$:

The torque curves for $KCoF_3$ measured at 78°K under the various field intensities are shown in Fig. 1. The torque curves for the crystal before applying the external stress are shown by the full lines and a curve for the stressed crystal is shown by a dotted line. All of the torque curves can be expressed by the formula

$$T=C_1H^2\sin(2\theta+\varepsilon_1)\,, \qquad (1)$$

where θ is the angle of rotation of magnetic field H relative to one of the cubic axes, C_1 a constant and ε_1 the phase constant. ε_1 is practically equal to zero within the experimental errors. Fig. 2 shows the field dependence of the torque amplitudes which are proportional to H^2.

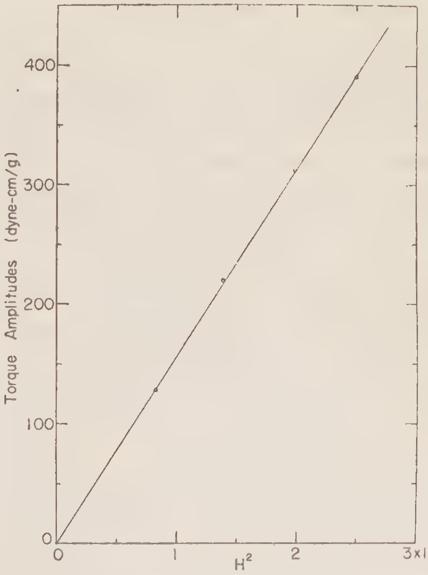

Fig. 2. Field dependence of the torque amplitudes of $KCoF_3$ plotted against H^2.

Fig. 3 shows the temperature dependence of torque amplitudes of $KCoF_3$. The observed Néel temperature of 119°K is in agreement with the result reported in the previous paper within the experimental errors of ±5° near 120°K.

$KNiF_3$:

The torque curves for the free crystal of $KNiF_3$ which was measured at 78°K under the various field intensities are shown in Fig. 4. These torque curves can be divided into two Fourier components, one of which has the period of 180° whose amplitude being proportional to H^2 and another has the period of 90° whose amplitude being proportional to H^4. Fig. 5 shows such field dependences of both amplitudes on H^2 and H^4 respectively. Thus the torque curves can be expressed by the formula

$$T=C_1H^2\sin(2\theta+\varepsilon_1)-C_2H^4\sin(4\theta+\varepsilon_2)\,, \quad (2)$$

where θ is the angle of rotation of the applied

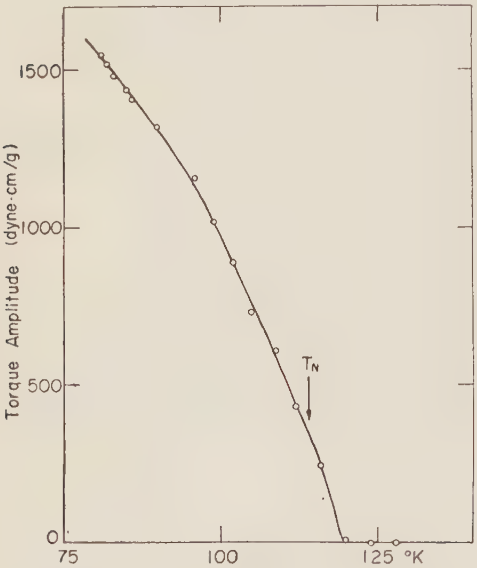

Fig. 3. Temperature dependence of the torque amplitudes of $KCoF_3$. T_N, shown by the arrow in the figure, represents the Néel temperature obtained in the previous work.

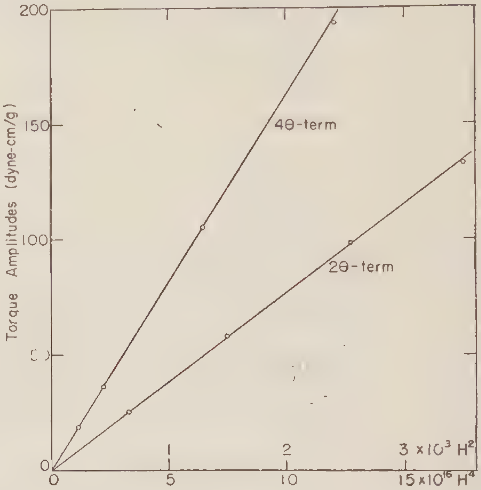

Fig. 5. Field dependence of the amplitudes of both 2θ- and 4θ-terms which are the Fourier components of the observed torque measured at 78°K.

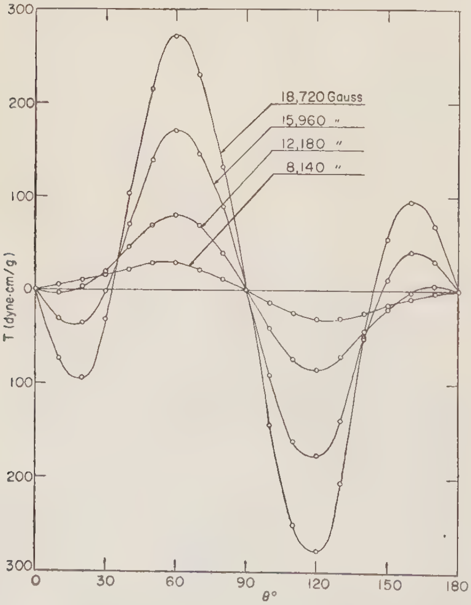

Fig. 4. Torque curves around the [001] axis measured on the free crystal of $KNiF_3$ at 78°K

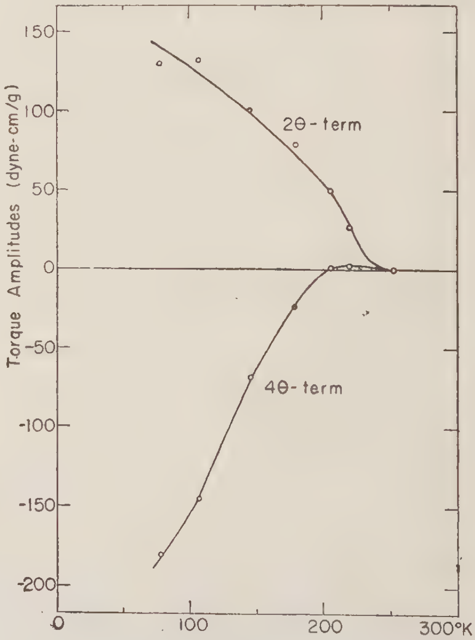

Fig. 6. Temperature dependenue of the torque amplitudes of both 2θ- and 4θ-terms in $KNiF_3$ measured at a constant field intensity of 18,720 Gauss.

field H relative to one of the cubic axes, C's are the amplitude constants and ε's the phase constants. From the fact that ε_1 and ε_2 are always equal to zero, it is concluded that the antiferromagnetic spin axis in $KNiF_3$ is parallel to one of the cubic axes.

Fig. 6 shows the temperature dependence of the amplitudes of 2θ- and 4θ-terms respectively. As shown in this figure, the curve of the amplitudes of the 2θ-term which is proportional to that of the powder susceptibility falls down to zero near the Néel temperature of 253°K, which was found from specific heat measurements[1]. On the other hand, the amplitudes of the 4θ-term decrease much more rapidly with increasing temperatures, falling down to zero at about 200°K, taking small values of opposite sign and then approach to zero at the Néel temperature.

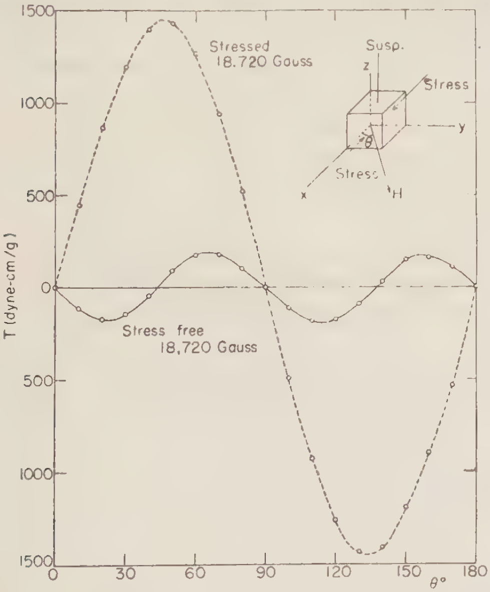

Fig. 7. Change of the torque curve before (the full line) and after (the dotted line) applying the unidirectional stress along one of the cubic axes.

Fig. 7 shows the effect of the applied external stress on the torque curve in $KNiF_3$. When no external stress is applied, the amplitude of the 2θ-term of this specimen is quite small compared with that of the 4θ-term, but as the stress is increased it grows up so large and the 4θ-term diminishes perfectly as shown in this figure. This suggests that the specimen becomes nearly the single domain crystal by applying the stress. From the observed 2θ-term and $(\chi_{\perp}-\chi_{//})$, we can estimate the parameter p_1 which will appear in the next section to be 0.87.

§ 4. Discussions

$KCoF_3$:

Below the Néel temperature (114°K), $KCoF_3$ has a tetragonal structure with $(c-a)/a \simeq -0.002$, consequently if a unidirectional stress is applied along one of the edges of the twinned crystal, it may become a single domain with its c-axis being parallel to the direction of the stress. The direction of the spin axis can be determined immediately from the torque measurements on such a crystal. The change of the observed torque curve before (full line) and after (dotted line) the stress treatment is shown in Fig. 1. From the equilibrium position of the torque curve it can immediately be known that the susceptibility along the direction of stress is smaller than that for normal to it, consequently the direction of the spin axis should be parallel to the c-axis.

$KNiF_3$:

As already described, the observed torque curves for $KNiF_3$ can be expressed by the Eq. (2) with ε_1 and ε_2 being practically equal to zero. This means that the spin direction in $KNiF_3$ is parallel to one of the cubic axes as well as in the case of $KCoF_3$. The origin of the 4θ-term, which do not appear in the case of $KCoF_3$, may be treated by the same idea proposed by Nagamiya for MnO. He has proposed two possible mechanisms, one of which is originated to an intrinsic nature of the crystal and another to reversible movements of antiferromagnetic domain walls. Now we shall discuss the observed torque curves on $KNiF_3$ in this point of view.

i) *The case of the intrinsic nature*

The anisotropy energy per unit volume of the cubic crystal consisted of single domain can be expressed by the formula

$$E=K_1(\alpha_1^2\alpha_2^2+\alpha_2^2\alpha_3^2+\alpha_3^2\alpha_1^2)$$
$$+K_2(\alpha_1^2\alpha_2^2\alpha_3^2)+\cdots, \qquad (3)$$

where K's are the anisotropy constants and α's the direction cosines of the spin axis relative to the three cubic axes. Neglecting all higher order terms other than the lst and confining ourselves to the case in which the crystal is suspended along [001] axis, the energy expression (3) is reduced to

$$E=\frac{1}{4}K_1\sin^2(2\theta^*)\,, \tag{4}$$

where θ^* is the angle of small deflection of the spin axis from the equilibrium position of x-axis (See Fig. 8). Then the free energy per unit volume when magnetic field H is applied in the direction θ with respect to the x-axis is

$$F=-\frac{1}{2}\chi_\perp H^2\sin^2(\theta+\theta^*) -\frac{1}{2}\chi_{//}H^2\cos^2(\theta+\theta^*)+\frac{1}{4}K_1\sin^2(2\theta^*)\,, \tag{5}$$

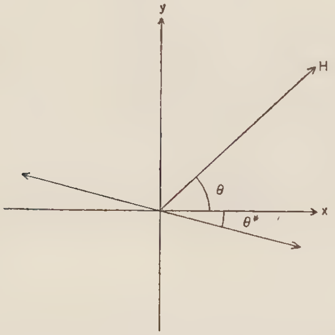

Fig. 8. A diagram illustrating the deflection of the spin axis with respect to the crystal axis in the xy-plane by the application of magnetic field.

where $\chi_\perp$ and $\chi_{//}$ are the susceptibilities per unit volume normal and parallel to the spin axis respectively. Using the condition that θ^* is very small and $(\partial F/\partial\theta^*)_\theta=0$, we have

$$\theta^*=\frac{(\chi_\perp-\chi_{//})}{4K_1}H^2\sin 2\theta\,. \tag{6}$$

Then, the torque equation can be expressed by the formula

$$T=\frac{1}{2}(\chi_\perp-\chi_{//})H^2\sin 2\theta +\frac{1}{8K_1}(\chi_\perp-\chi_{//})^2H^4\sin 4\theta\,. \tag{7}$$

In order to compare this formula with the torques of actual crystals, it should be rewritten in the following form

$$T=\frac{1}{2}p_1(\chi_\perp-\chi_{//})H^2\sin 2\theta +\frac{1}{8K_1}p_2(\chi_\perp-\chi_{//})^2H^4\sin 4\theta\,, \tag{8}$$

where p_1 and p_2 are the parameters related to the volumes of the three kinds of domains in each of which the spin axis directed along each x-, y- and z-axis. For the crystal having equal volumes of such domains, we have immediately $p_1=0$ and $p_2=2/3$. By comparing both equations (2) and (8), we can find the sign of the 4θ-term is opposite to each other. This means that the origin of the 4θ-term is not expected by such an intrinsic mechanism.

ii) *The case of movements of domain walls*

$KNiF_3$ should more or less be deformed tetragonally, though no evidence could been obtained by X-ray examination, because as stated before no deformations due to exchange interaction can't be considered but only the magneto-striction may cause a deformation. Then the existence of domain (twinned-) structure may naturally be considered. Let us consider that the crystal consists of two kinds of domains in each of which the direction cosines of the spin axis relative to the cubic axes are 0,1,0 and 1,0,0 respectively, as shown in Fig. 9. The torque equation around the [001]-axis of such a crystal, when movements of domain walls are taken into account, can immediately obtained by substituting these numerical values of the direction cosines into the equation led by Nagamiya[4],

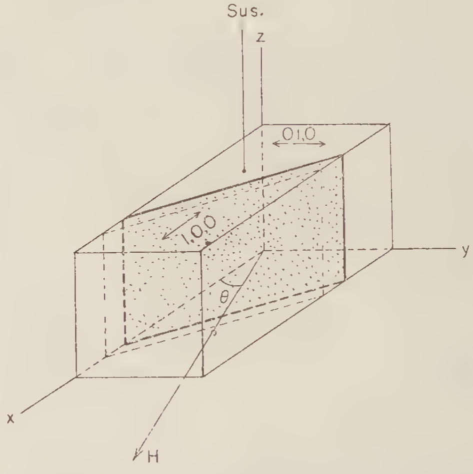

Fig. 9. A diagram illustrating the spin directions in the different two kinds of domains. The dotted line shows the displacement of an antiferromagnetic domain wall by the application of magnetic field. The 1,0,0 and 0,1,0 represent the direction cosines of the antiferromagnetic spin axes in each domain respectively.

$$T=-\frac{1}{4c}(\chi_\perp-\chi_{//})^2H^4\sin 4\theta\,, \tag{9}$$

where c is the force constant of restoring domain walls and θ the angle of rotation of H from the x-axis. This equation holds for the case of unit area of the domain wall, in order to compare it with the actual case, a constant A of plus sign which is related to the total area of such walls should be multiplied. Thus we may rewrite (9) in the form

$$T=-\frac{A}{4c}(\chi_{\perp}-\chi_{//})^2H^4\sin 4\theta\ . \tag{10}$$

This equation for the 4θ-term is consistent qualitatively with the observed torque in sign ($T<200°\mathrm{K}$).

In order to make confirmation of this mechanism, we examined the temperature dependence of the amplitudes of the 4θ-term near the Néel temperature. As in the case of MnO, the amplitudes of the 4θ-term in $KNiF_3$ decrease very rapidly with increasing temperatures. This supports, as predicted by Nagamiya, that the origin of the 4θ-term is due to reversible movements of domain walls rather than the intrinsic mechanism. Our case in $KNiF_3$ is, however, somewhat peculiar. The amplitudes fall down to zero at about 200°K and then take small positive values up to the Néel temperature. We may tentatively give an interpretation that in this region the intrinsic mechanism exceeds to that of domain wall displacements.

Furthermore, we examined the effect of the external stress on the torque curves. One of our results is shown in Fig. 7. As shown in that figure, the 2θ-term grows up very large but the 4θ-term diminishes perfectly within the experimental errors by applying the stress. This change is considered such that the total area of domain walls in the crystal are greatly reduced by the application of the stress and the amplitude of the Eq. (10) approaches to zero. The antiferromagnetic domain walls in $KNiF_3$ correspond, in a sence, to the S wall in NiO proposed by Roth[8], which moves very easily by the application of mechanical stress or magnetic field.

It is to be noticed that the calculation of anisotropy constant in cubic crystals from the field dependence of the susceptibilities can't be achieved without serious precautions.

The authors wish their hearty thanks to Prof. T. Nagamiya for his kind advices and encouragements. We are also grateful to the Kowa Shindo K.·K. for supplying us the various sorts of phosphor-bronze wire. This work was supported by the Expenditure of the Ministry of Education.

References

1) K. Hirakawa, K. Hirakawa and T. Hashimoto: J. Phys. Soc. Japan **15** (1960) 2063.
2) V. Scutturin, L. Corliss, N. Elliot and J. M. Hastings: to be published.
3) A. Okazaki and Y. Suemune: J. Phys. Soc. Japan **16** (1961) 671.
4) E. Uchida, H. Kondoh, Y. Nakazumi and T. Nagamiya: J. Phys. Soc. Japan **15** (1960) 466.
5) T. Nagamiya: State of Atoms in Magnetic Crystals, read at the Second Welch Foundation Conference (Texas, Houston, Dec. 1958).
6) W. L. Roth and G. A. Slack: J. Appl. Phys. **31** (1960) 352S.
7) K. Hirakawa: read at the Annual Meeting of the Physical Society of Japan (1957).
8) W. L. Roth: J. Appl. Phys. **31** (1960) 2000.

Journal of the Physical Society of Japan Vol. 16, No. 10, October, 1961

Electron Paramagnetic Resonance for Metals with Two Conduction Bands

By Tsuyoshi Murao*

Department of Physics, Tôhoku University, Sendai

(Received May 29, 1961)

Theoretical expressions of electron paramagnetic resonance absorption are given for metals with two conduction bands by assuming that the Bloch type equations involving interband "cross" terms and diffusion terms are applicable. Some typical examples of the absorption curve are shown to illustrate the interband "cross" effect and the diffusion effect. A possibility to determine the diffusion constants of the 3*d*-electrons in transition metals is discussed.

§ 1. Introduction

Dyson[1] has give a theory of electron paramagnetic resonance (EPR) for metals with a single conduction band, and the experiment of EPR for sodium metal carried out by Feher and Kip[2] has been analyzed in their paper by using Dyson's theory to give interesting informations on the diffusion constant of conduction electrons.

It may be interesting to apply Dyson's idea to determine the diffusion constants of the 3*d*-electrons in transition metals. These metals, however, have in general two conduction bands, say *s*- and *d*-bands. It is, therefore, desirable to give a theoretical expression of EPR absorption for metals with two conduction bands. Such an expression will be also applicable to analyzing the experimental data of EPR on some other metals with two conduction bands (alkaline earth metals, for instance).

§ 2. Differential Equations for Magnetizations

It has been proved by Kaplan[3] that Dyson's Green function formalism is equivalent to adding simply the term

$$D\nabla^2 \boldsymbol{M}(\boldsymbol{r}, t) \qquad \text{(for all components of } \boldsymbol{M}) \tag{1}$$

to the Bloch equations and imposing

$$\boldsymbol{n}\cdot\nabla \boldsymbol{M}(\boldsymbol{r}, t)=0 \quad \text{(for all components of } \boldsymbol{M}) \tag{2}$$

as the boundary conditions on the surface. The constant D in (1) is the diffusion constant which is connected with the Fermi velocity v_F and the mean free path l of conduction electrons through $D=v_F l/3$, and $\boldsymbol{n}$ in (2) is the normal vector on the metal surface. The mean free path l is determined by impurity scattering and electron-photon interaction in a single-band case.

The time variation of the magnetizations of two bands may be given by the following differential equations;

$$\dot{M}_{1x}=\gamma_1{}^0(\boldsymbol{M}_1\times\boldsymbol{H})_x-\nu_1 M_{1x} -\mu_1 M_{2x}+D_1\nabla^2 M_{1x}\,, \tag{3}$$

and

$$\dot{M}_{2x}=\gamma_2{}^0(\boldsymbol{M}_2\times\boldsymbol{H})_x-\nu_2 M_{2x} -\mu_2 M_{1x}+D_2\nabla^2 M_{2x}\,, \tag{4}$$

where suffices 1 and 2 indicate the numbers of the bands, $\gamma_i{}^0$ are the gyromagnetic ratios, $\nu_i{}^{-1}$ the transverse relaxation times, and μ_i the relaxation rates that are responsible for a "cross" effect of the two bands. Similar equations such as (3) and (4) are also valid for the y-component and those for the z-component are not necessary unless the saturation effect is considered. The interband "cross" effect can arise not only from a usual exchange type interaction as in discussed by Solomon[4] but also from Mott's *s*-*d* scattering by phonons[5] which is accompanied by the real interband transition of electrons. This Mott's process obscures the meaning to mention that a particular electron belongs to a *s*-band or a *d*-band. Therefore, in order that the diffusion constant of each band can be defined in (3) and (4), the condition

$$\tau_C\equiv l/v_F\ll\tau_S \qquad \text{(for both bands)}\,, \tag{5}$$

must be fulfilled, where τ_S is a mean time between two successive (Mott's) *s*-*d* scattering of a conduction electron and l is the mean free path of the electrons which appears in the electrical conductivity. The magnitude of l is determined through several mechanism; impurity scattering, Mott's s-d scattering Kasuya's s-d scattering$^{6),7)}$, and the usual interband scattering by phonons.

---

* Present address: Research Institute of Electrical Communication, Tohoku University, Sendai.

The magnetic field $\boldsymbol{H}$ in (3) and (4) is given through the Maxwell equations;

$$\nabla\times\boldsymbol{E}=-c^{-1}\{\dot{\boldsymbol{H}}+4\pi(\dot{\boldsymbol{M}}_1+\dot{\boldsymbol{M}}_2)\}\ , \qquad (6)$$

$$\nabla\times\boldsymbol{H}=4\pi c^{-1}\sigma\boldsymbol{E}\ , \qquad (7)$$

where σ $(=\sigma_1+\sigma_2)$ is the conductivity of the metal.

The term due to the displacement current is neglected in (7).

§ 3. Calculation of Surface Impedance

We assume that the metal sample under consideration extends from $z=0$ to $z=\infty$ in the z-direction and the static magnetic field $\boldsymbol{H}_0$ and the incident direction of the microwave are in the z-direction. The present argument is restricted within a temperature region of normal skin effect, so that $\boldsymbol{E}$, $\boldsymbol{H}$, $\boldsymbol{M}_1$, $\boldsymbol{M}_2$ vary as $\exp[i\omega t-\kappa z]$ with time and space, where ω is the frequency of the microwave and κ a complex number which is to be determined below.

Let us now introduce the variables

$$\begin{aligned}\mathfrak{M}_i&=M_{iX}-iM_{iY}\ ,\\ \mathscr{H}&=H_X-iH_Y\ ,\\ \mathfrak{E}&=E_X-iE_Y\ ,\end{aligned}\qquad (8)$$

and use (3), (4), (6) and (7), then the condition that $\mathfrak{M}_1$, $\mathfrak{M}_2$ and $\mathscr{H}$ have non-zero solutions is written as*

$$\begin{vmatrix}\kappa^2D_1-\nu_1-i(\omega-\omega_{10}) & -\mu_1 & -i\omega_{10}\chi_{10}\\ -\mu_2 & \kappa^2D_2-\nu_2-i(\omega-\varpi_{20}) & -i\omega_{20}\chi_{20}\\ -i4\pi & -i4\pi & (\delta^2\kappa^2/2)-i\end{vmatrix}=0\ , \qquad (9)$$

where $\omega_{i0}=\gamma_i{}^0H_0$, $\delta^2=c^2/2\pi\sigma\omega$, and χ_{i0} are the static susceptibilities of conduction electrons. The value of κ is determined by solving (9). If three independent solutions of (9) are denoted by κ_1, κ_2, and κ_3, all of which satisfy the condition

$$\mathscr{R}_e\,\kappa_n>0\ , \qquad (10)$$

where $\mathscr{R}_e$ means to take the real part, then other solutions of (9), $-\kappa_n$, are unphysical so that we should leave out these solutions. Let $\mathscr{H}_n$ be $\mathscr{H}$ corresponding to κ_n. The continuity condition of $\mathscr{H}$ and $\mathfrak{E}$ at the metal surface are then written, respectively, as

$$\mathscr{H}_1+\mathscr{H}_2+\mathscr{H}_3=\mathscr{H}_0\ , \qquad (11)$$

$$u_1\mathscr{H}_1+u_2\mathscr{H}_2+u_3\mathscr{H}_3=\mathfrak{E}_0\equiv\mathscr{H}_0X_0\ , \qquad (12)$$

where

$$u_n=ic\kappa_n/4\pi\sigma\ , \qquad (13)$$

$$X_0=\mathfrak{E}_0/\mathscr{H}_0\equiv(c/4\pi)Z\ , \qquad (14)$$

$$Z=\text{surface impedance}\ , \qquad (15)$$

and $\mathscr{H}_0$ and $\mathfrak{E}_0$ are respectively the values of $\mathscr{H}$ and $\mathfrak{E}$ immediately outside the surface. Due to the present condition that the mean diffusion constant of conduction electrons in each band can be defined (cf. (5)), we assume that Dyson's boundary condition can now be written as

$$\boldsymbol{n}\cdot\nabla\mathfrak{M}_1=0\ , \qquad (16)$$

$$\boldsymbol{n}\cdot\nabla\mathfrak{M}_2=0\ , \qquad (17)$$

which mean that the normal components of the diffusion velocity of the conduction electrons in each band are zero on the metal surface. From (11), (12), (16) and (17), we obtained

$$\begin{vmatrix}1 & 1 & 1 & 1\\ u_1 & u_2 & u_3 & X_0\\ v_{11}\kappa_1 & v_{12}\kappa_2 & v_{13}\kappa_3 & 0\\ v_{21}\kappa_1 & v_{22}\kappa_2 & v_{23}\kappa_3 & 0\end{vmatrix}=0 \qquad (18)$$

in order that $\mathscr{H}_n$ and $\mathscr{H}_0$ are non-zero, where

$$v_{in}=\frac{i}{4\pi}\,\frac{4\pi\beta_i-\gamma_i(2^{-1}\delta^2\kappa_n{}^2-i)}{L_i{}^2\kappa_n{}^2-1-i\alpha_i+\gamma_i}\ , \qquad (19)$$

$$\beta_i=\omega_{i0}\chi_{i0}/\nu_i\ , \qquad (20)$$

$$\gamma_i=\mu_i/\nu_i\ , \qquad (21)$$

$$\alpha_i=(\omega-\omega_{i0})/\nu_i\ , \qquad (22)$$

$$L_i{}^2=D_i/\nu_i\ . \qquad (23)$$

The surface impedance Z (or X_0) can be obtained from (18). The real absorption rate is given by

$$P=(c/4\pi)(\mathscr{R}_e\,Z)|\mathscr{H}_0|^2\ .$$

The surface impedance obtained from (18) contains κ_n in its expression, while our purpose is to express Z only in terms of the physical quantities involved in (3) and (4).

---

* The following calculation to obtain the surface impedance is an extention of Ament and Rado's method$^{8)}$.

Let us now rewrite (9) in the form

$$
\begin{aligned}
0&=\kappa^6-C_1\kappa^4+C_2\kappa^2-C_3\\
&\equiv(\kappa^3-C_1'\kappa^2+C_2'\kappa-C_3')\\
&\quad\times(\kappa^3+C_1'\kappa^2+C_2'\kappa+C_3')\ ,
\end{aligned}
\tag{24}
$$

where

$$
\begin{aligned}
C_1&=\kappa_1{}^2+\kappa_2{}^2+\kappa_3{}^2\ ,\\
C_2&=(\kappa_1\kappa_2)^2+(\kappa_2\kappa_3)^2+(\kappa_1\kappa_3)^2\ ,\\
C_3&=(\kappa_1\kappa_2\kappa_3)^2\ ,
\end{aligned}
\tag{25}
$$

and

$$
\begin{aligned}
C_1'&=\kappa_1+\kappa_2+\kappa_3\ ,\\
C_2'&=\kappa_1\kappa_2+\kappa_2\kappa_3+\kappa_1\kappa_3\ ,\\
C_3'&=\kappa_1\kappa_2\kappa_3\ .
\end{aligned}
\tag{26}
$$

The κ_n have functional relations with the physical quantities in (3) and (4) only through the combinations of κ_n given in (25) (i.e. C_p), while the actual factorization of κ_n involved in the surface impedance Z can not be carried out unless C_p' are also used. The factorization is a tedious but straightforward calculation so that its detail is not shown here. The C_p' are connected with C_p through the relations

$$
\begin{aligned}
C_1'&=+(C_1+2C_2')^{1/2}\ ,^*\\
C_2'&=\pm(C_2+2C_1'C_3')^{1/2}\ ,\\
C_3'&=\pm C_3{}^{1/2}\ .
\end{aligned}
\tag{27}
$$

Equations (27) can be solved successively for C_p' only in the following cases:

(i) $\varepsilon_i{}^2\equiv 2D_i/\delta^2\nu_i\equiv T_2{}^{(i)}/T_D{}^{(i)}\ll 1$ (for both bands),

(ii) $\varepsilon_i{}^2\gg 1$ (for both bands),

where $T_2{}^{(i)}=\nu_i{}^{-1}$ and $T_D{}^{(i)}=\delta^2/2D_i$ which is introduced by Dyson[1)] as a mean diffusion time of conduction electrons across the skin depth δ. We consider the two cases separately in what follows.

Case (i). In this case it is convenient to introduce the following quantities;

$$
\begin{aligned}
\varepsilon^2\kappa^2&=K^2\ ,\\
\varepsilon^2\kappa_n{}^2&=K_n{}^2\ ,
\end{aligned}
\tag{28}
$$

where $\varepsilon=\varepsilon_1\varepsilon_2$. The corresponding C_p are rewritten as

$$C_1=\xi+\xi^{-1}+i(\varepsilon^2+\xi\alpha_1+\xi^{-1}\alpha_2)\ , \tag{29}$$

$$C_2=1-\gamma_1\gamma_2+4\pi\varepsilon^2(\xi\beta_1+\xi^{-1}\beta_2)-\varepsilon^2(\xi\alpha_1+\xi^{-1}\alpha_2)-\alpha_1\alpha_2+i[\varepsilon^2(\xi+\xi^{-1})+\alpha_1+\alpha_2]\ , \tag{30}$$

$$C_3=\varepsilon^2\{4\pi(\beta_1+\beta_2-\gamma_1\beta_2-\gamma_2\beta_1)-(\alpha_1+\alpha_2)+i[1-\gamma_1\gamma_2+4\pi(\alpha_1\beta_2+\alpha_2\beta_1)-\alpha_1\alpha_2]\}\ , \tag{31}$$

where

$$\xi=\varepsilon_2/\varepsilon_1\ , \tag{32}$$

In most experiments of EPR for transition metals, the condition

$$\beta_i\ll 1 \tag{33}$$

may be fulfilled on account of the fairly large line width, so that, from (29), (31),

$$|C_3|\sim\varepsilon^2|C_1 \text{ or } C_2| \tag{34}$$

if

$$4\pi(\gamma_1\beta_2+\gamma_2\beta_1)\ll 1\ . \tag{35}$$

In such a case (27) can be solved in the form of power series in ε. The signs of C_2' and C_3' (cf. (27)) are always taken to be positive so that our final result reduced to a single band case coincides with Dyson's result. By expanding in powers of β_i, the final result for the real part of the surface impedance is given by

---

* Due to (10), the negative sign should be abandoned for C_1'.

$$\mathscr{Re}\, Z=(\sigma\delta)^{-1}[F_0+4\pi\beta_1F_1+4\pi\beta_1\varepsilon_1^2F_2+\cdots]\,, \tag{36}$$

where

$$F_0=1\,, \tag{37}$$

$$\begin{aligned}F_1=&(u_+^2+u_-^2)^{-1}\{(\alpha_1\beta+\alpha_2)[2^{-1}(u_++u_-)+\alpha_1+\alpha_2]\\&+(1+\beta-\gamma_1\beta-\gamma_2)[2^{-1}(u_++u_-)-(\alpha_1+\alpha_2)]\}\,,\end{aligned} \tag{39}$$

$$\begin{aligned}F_2=&4(u_+^2+u_-^2)^{-2}\{u_+u_-[(1+\xi^2+t_+)(\alpha_1\beta+\alpha_2)-(1+\beta-\gamma_1\beta-\gamma_2)(1+\xi^2-t_+)\\&-(\xi^2+\beta)u_-]+(\alpha_1+\alpha_2)(u_++u_-)[1+\xi^2-t_+)(\alpha_1\beta+\alpha_2)\\&-(1+\beta-\gamma_1\beta-\gamma_2)(1+\xi^2+t_+)-(\xi^2+\beta)u_+]\}\\&+2(u_+^2+u_-^2)^{-1}(v^2+w^2)^{-1}(\xi^2\gamma_1+\gamma_2)\{(\alpha_1\beta+\alpha_2)(vu_-+wu_+)\\&-(1+\beta-\gamma_1\beta-\gamma_2)(vu_+-wu_-)\}\\&+(\gamma_1\gamma_2)^{-1}[(\xi^2(\gamma_1-1)-(\gamma_2-1))^2+t_-^2]^{-1}[v^2+w^2]^{-1}\{[\xi^2(\gamma_1-1)-(\gamma_2-1)]w-t_-v\}\\&\times\{\xi^2[\gamma_2-\gamma_1\beta][w-v]+[\xi^2\gamma_1+\gamma_2][\gamma_2(\gamma_2-1-\alpha_2)-\xi^2\gamma_1\beta(\gamma_1-1-\alpha_1)]\}\\&+2(\gamma_1\gamma_2)^{-1}[(\xi^2(\gamma_1-1)-(\gamma_2-1))^2+t_-^2]^{-1}[u_+^2+u_-^2]^{-1}\{\{\xi^2[\gamma_2-\gamma_1\beta]w\\&+[\xi^2+1][\gamma_2\alpha_2-\xi^2\gamma_1\beta\alpha_1]-[\gamma_2(\gamma_2-1)-\xi^2\gamma_1(\gamma_1-1)\beta]t_+\}\\&\times\{[\gamma_2-1)-\xi^2(\gamma_1-1)]u_-+t_-u_+\}\\&-\{\xi^2[\gamma_2-\gamma_1\beta]v+[\xi^2+1][\gamma_2(\gamma_2-1)-\xi^2\gamma_1(\gamma_1-1)\beta]+[\gamma_2\alpha_2-\xi^2\gamma_1\beta\alpha_1]t_+\}\\&\times\{[\xi^2(\gamma_1-1)-(\gamma_2-1)]u_++t_-u_-\}\}\,.\end{aligned} \tag{39}$$

In (37) (39), the following abbreviations were used:

$$\begin{aligned}t_\pm&=\alpha_2\pm\xi^2\alpha_1\,,\\u_\pm&=1-\gamma_1\gamma_2-\alpha_1\alpha_2\pm(\alpha_1+\alpha_2)\,,\\v&=(\gamma_1-1)(\gamma_2-1)-\alpha_1\alpha_2\,,\\w&=(\gamma_1-1)\alpha_1+(\gamma_2-1)\alpha_1\,,\\\beta&=\beta_2/\beta_1\,.\end{aligned} \tag{40}$$

In deriving the term F_2 in (36), the condition

$$\gamma_1\gamma_2>\beta_i \tag{41}$$

has been used in order to allow a power series expansion in β_i.

In (36) the diffusion effect is contained in F_2 term and the subsequent ones through ε_1 and ξ.

Case (ii). Instead of (28), introduce the following K and K_n;

$$\begin{aligned}2^{-1/2}\delta\kappa&=K\,,\\2^{-1/2}\delta\kappa_n&=K_n\,.\end{aligned} \tag{42}$$

Then, C_p are rewritten as

$$C_1=\epsilon_1^2+\epsilon_2^2+i(1+\epsilon_1^2\alpha_1+\epsilon_2^2\alpha_2)\,, \tag{43}$$

$$\begin{aligned}C_2=&\epsilon_1^2\epsilon_2^2(1-\gamma_1\gamma_2)+4\pi(\epsilon_1^2\beta_1+\epsilon_2^2\beta_2)-\epsilon_1^2\epsilon_2^2\alpha_1\alpha_2\\&+\epsilon_1^2\alpha_1(-1+i\epsilon_2^2)+\epsilon_2^2\alpha_2(-1+i\epsilon_1^2)+i(\epsilon_1^2+\epsilon_2^2)\,,\end{aligned} \tag{44}$$

$$\begin{aligned}C_3=&\epsilon_1^2\epsilon_2^2[4\pi(\beta_1+\beta_2-\gamma_1\beta_2-\gamma_2\beta_1)+\alpha_1(-1+i4\pi\beta_2)\\&+\alpha_2(-1+i4\pi\beta_1)+i(1-\gamma_1\gamma_2-\alpha_1\alpha_2)]\,,\end{aligned} \tag{45}$$

where $\epsilon_i=\varepsilon_i^{-1}$. As can be seen from (43), (45),

$$|C_1|\sim1\,,\qquad|C_2|\sim\epsilon^2\,,\qquad|C_3|\sim\epsilon^4\,, \tag{46}$$

so that, in order that (26) are to be consistent among their equations, it is demanded that

$$|C_1'|\sim 1\,,\qquad |C_2'|\sim\epsilon\,,\qquad |C_3'|\sim\epsilon^2\,. \tag{47}$$

This allows to solve (27) in the form of power series in ϵ to give the surface impedance. By using the same notations as (40) and the following abbreviations

$$\begin{aligned}
&s_{\pm}=\alpha_1\pm\xi^2\alpha_2\,,\\
&\eta^{+}=\{[(\alpha_1+\alpha_2)^2+4^{-1}(u_{+}+u_{-})^2]^{1/2}+\alpha_1+\alpha_2\}^{1/2}\\
&\eta_{-}=(\text{sign of } u_{+}+u_{-})\{[(\alpha_1+\alpha_2)^2+4^{-1}(u_{+}+u_{-})^2]^{1/2}-(\alpha_1+\alpha_2)\}^{1/2}\,,\\
&\xi=\epsilon_2/\epsilon_1\,,
\end{aligned} \tag{48}$$

the real part of the surface impedance is given, up to $O(\epsilon)$, by

$$\mathscr{R}_e Z=(\sigma\delta)^{-1}|I|^{-2}(G_0+4\pi\beta_1\epsilon_1G_1+\cdots)\,, \tag{49}$$

where

$$I=I_1+iI_2\,, \tag{50}$$

$$\begin{aligned}
I_1=\,&2^{-1}\gamma_1\gamma_2\{[\xi^2(\gamma_2-1)-(\gamma_1-1)]\eta_{-}-s_{-}\eta_{+}\}\{[(\sqrt{2}\,\xi(\eta_{-}-\eta_{+})-s_{+})^2\\
&\quad+(1+\xi^2+\sqrt{2}\,\xi(\eta_{+}+\eta_{-}))^2]^{1/2}+\sqrt{2}\,\xi(\eta_{-}-\eta_{+})-s_{+}\}^{1/2}\\
&+2^{-1}\gamma_1\gamma_2\{[\xi^2(\gamma_2-1)-(\gamma_1-1)]\eta_{+}+s_{-}\eta_{-}\}\{[(\sqrt{2}\,\xi(\eta_{-}-\eta_{+})-s_{+})^2\\
&\quad+(1+\xi^2+\sqrt{2}\,\xi(\eta^{+}+\eta_{-}))^2]^{1/2}-(\sqrt{2}\,\xi(\eta_{-}-\eta_{+})-s_{+})\}^{1/2}\,,
\end{aligned} \tag{51}$$

$$\begin{aligned}
I_2=\,&2^{-1}\gamma_1\gamma_2\{[\xi^2(\gamma_2-1)-(\gamma_1-1)]\eta_{-}-s_{-}\eta_{+}\}\{[(\sqrt{2}\,\xi(\eta_{-}-\eta_{+})-s_{+})^2\\
&\quad+(1+\xi^2+\sqrt{2}\,\xi(\eta_{+}+\eta_{-}))^2]^{1/2}-(\sqrt{2}\,\xi(\eta_{-}-\eta_{+})-s_{+})\}^{1/2}\\
&+2^{-1}\gamma_1\gamma_2\{[\xi^2(\gamma_2-1)-(\gamma_1-1)]\eta_{+}+s_{-}\eta_{-}\}\{[(\sqrt{2}\,\xi(\eta_{-}-\eta_{+})-s_{+})^2\\
&\quad+(1+\xi^2+\sqrt{2}\,\xi(\eta_{+}+\eta_{-}))^2]^{1/2}+\sqrt{2}\,\xi(\eta_{-}-\eta_{+})-s_{+}\}^{1/2}\,,
\end{aligned} \tag{52}$$

$$G_0=1\,, \tag{53}$$

$$\begin{aligned}
G_1=\,&\xi I_1\{[\gamma_2(\gamma_1+\xi^2)-\gamma_1(1+\xi^2\gamma_2)\beta]v+[\gamma_2\xi^2\alpha_2-\gamma_1\beta\alpha_1]w\\
&\quad-[\gamma_1(\gamma_1-\xi^2)\beta-\gamma_2(\xi^2\gamma_2-1)]u+[\xi^2\gamma_1\alpha_2-\gamma_2\alpha_1](\alpha_1+\alpha_2)\}\\
&+\xi I_2\{-[\gamma_2(\gamma_2+\xi^2)-\gamma_1(1+\xi^2\gamma_2)\beta]w+[\gamma_2\xi^2\alpha_2-\gamma_1\beta\alpha_1]v\\
&\quad-[\gamma_1(\gamma_1-\xi^2)\beta-\gamma_2(\xi^2\gamma_2-1)](\alpha_1+\alpha_2)+[\xi^2\gamma_1\beta\alpha_2-\gamma_2\alpha_1]u\}\\
&-2^{-1}I_1\{-\eta_{+}+\eta_{-}\}\{[\gamma_2(\gamma_1-1)-\xi^2\gamma_1(\gamma_2-1)\beta]s_{+}+\xi^2(\gamma_2-\gamma_1\beta)[\alpha_1+\alpha_2+w]\\
&\quad+[(\gamma_1+1)+\xi^2(\gamma_2+1)][\xi^2\gamma_1\beta\alpha_2-\gamma_2\alpha_1]\}\\
&-2^{-1}I_1\{\eta_{+}+\eta_{-}\}\{-[\xi^2\gamma_1\beta\alpha_2-\gamma_2\alpha_1]s_{+}+\xi^2(\gamma_2-\gamma_1\beta)[u-v]\\
&\quad+[(\gamma_1+1)+\xi^2(\gamma_2+1)][\gamma_2(\gamma_1-1)-\xi^2\gamma_1(\gamma_2-1)\beta]\}\\
&-2^{-1}I_2\{\eta_{+}+\eta_{-}\}\{[\gamma_2(\gamma_1-1)-\xi^2\gamma_1(\gamma_2-1)\beta]s_{+}+\xi^2(\gamma_2-\gamma_1\beta)[\alpha_1+\alpha_2+w]\\
&\quad+[(\gamma_1+1)+\xi^2(\gamma_2+1)][\xi^2\gamma_1\beta\alpha_2-\gamma_2\alpha_1]\}\\
&+2^{-1}I_2\{-\eta_{+}+\eta_{-}\}\{[\xi^2\gamma_1\beta\alpha_2-\gamma_2\alpha_1]s_{+}+\xi^2(\gamma_2-\gamma_1\beta)[u-v]\\
&\quad+[(\gamma_1+1)+\xi^2(\gamma_2+1)][\gamma_2(\gamma_1-1)-\xi^2\gamma_1(\gamma_2-1)\beta]\}\,.
\end{aligned} \tag{54}$$

The necessary conditions to derive the above results are

$$\begin{aligned}
&\epsilon_1^2\alpha_1 \quad\text{and}\quad \epsilon_2^2\alpha_2\ll 1\,,\\
&\epsilon_1^2\epsilon_2^2\gamma_1\gamma_2\ll 1\,,\\
&\beta_1 \quad\text{and}\quad \beta_2\ll(\gamma_1\gamma_2)\,,\\
&\epsilon_1^2\epsilon_2^2(\gamma_1\beta_2+\gamma_2\beta_1)\ll 1\,.
\end{aligned} \tag{55}$$

In this case, the diffusion effect resides in all terms but the first in (49). This reason has been already explained by Dyson[1].

§ 4. Discussion

It may be interesting to determine experimentally the physical quantities involved in

(3) and (4), particularly the diffusion constants D_1 and D_2. In a temperature region where the case (ii) is applicable, there are five parameters which determine the shape of the absorption curve of the term G_1 in (49), i.e.,

$$g_2/g_1\,,\quad \chi_{20}/\chi_{10}\,,\quad \gamma_1\,,\quad \gamma_2\,,\quad \xi\,, \tag{56}$$

and the diffusion effect appears through ξ. It is expected that the magnitudes of these parameters, particularly the last four ones, change with temperature.

In a temperature region where the case (i) is valid, the diffusion effect comes from the third term F_2 in (36). The parameters which determine the shape of the absorption curve due to F_1 are then reduced to the first four ones in (56), so that it seems more favorable to make an experiment firstly in this temperature region to determine the magnitude and the temperature dependence of the four parameters.*

It can be easily shown that the term F_1 is reduced to the well-known formula of a single band case[1),9)], i.e.,

$$F_1 \to 2\pi\beta_1 \frac{1-\alpha_1}{1+\alpha_1^2} \propto (\chi'(\omega)+\chi''(\omega))\,, \tag{57}$$

by putting**

$$\nu_2=\mu_2=\chi_{20}=\gamma_2^0=D_2=0\,. \tag{59}$$

As the sign of F_1 depends on the choice of the signs in (27), the validity of what was mentioned below (35) is thus confirmed.

We can find the following characteristic features for the absorption curves of F_1 from several numerical examples given in Appendix:

(1) Exchange broadening occurs through the μ_i-term of (3) and (4).

(2) Shift of the peak arises from the interference between the absorptions of the 1st and the 2nd bands.

(3) When $\gamma_1<1$, the apparent width of the absorption curve of the 2nd band is nearly proportional to ν_2, while it is not proportional when $\gamma_1>1$.

(4) There can be a case where negative absorption (dispersion) is strongly enhanced.

Several numerical examples of the absorption curves due to F_2 are also given in Appendix, which indicate that general trend of the diffusion effect is to enhance the mixing of the dispersion into the real absorption but the effect is much more complicated than in the single band case.

It should be noticed that in practical experiments the short range ordering of spins may contribute to the line width[10)] if the Curie or Néel points present near to the experimental temperature, the effect of which is not considered in the present paper. For this reason, the experimental data on Ni metal given by Bloembergen[11)] is beyond the scope of the present theory.

It may be also interesting to extend the present formalism to the case of semiconductors in which impurity band exists. If a semiconductor sample has a resistivity smaller than $10^{-2}\,\Omega$cm, then the displacement current can be neglected in (7) for $\omega\sim10^{10}$ c.p.s. and the dispersion is mixed into the real absorption.

Acknowledgements

The author wishes to express his gratitude to Prof. A. Morita and the members of his Laboratory for helpful discussions, and to Drs. N. Takimoto and T. Ohtsuka for stimulating conversations in the early stage of this work.

Appendix

The following typical relation and values

Table I.

Case	γ_1	γ_2	ν_2/ν_1
[A] (1)	0.2	0.55	0.44
(2)		1.1	0.22
(3)		2.2	0.11
[B] (1)	0.5	0.55	1.1
(2)		1.1	0.55
(3)		2.2	0.275
[C] (1)	1	0.55	2.2
(2)		1.1	1.1
(3)		2.2	0.55
[D] (1)	2	0.55	4.4
(2)		1.1	2.2
(3)		2.2	1.1

---

* It may be expected in a practical problem that the values of g_1 and g_2 are nearly constant with temperature, then temperature-dependent parameters are reduced to three.

** Since (38) has been derived via the conditions (33) and (35), one must put (58) by the following ordered process:

(1) $\gamma_2\to0$,
(2) χ_{20} and $\omega_{20}\to0$,
(3) $\nu_2\to0$.

are assigned for several parameters;

$$\mu_2=(\gamma_2{}^0/\gamma_1{}^0)\mu_1\ ,^{4)}\qquad\text{(A1)}$$

$$g_2/g_1=1.1\ ,^{11)}\quad \chi_{20}/\chi_{10}=10\ ,\quad \omega_{10}/\nu_1=10\ .\qquad\text{(A2)}$$

The function F_1 is calculated for twelve cases shown in Table I by choosing $(\gamma_1{}^0/\nu_1)(H-H_0)$ as the variable, and the results are illustrated in Fig. 1. For the values given in (A2), the peaks of the absorption curves of the 1st and 2nd bands should appear at $(\gamma_1{}^0/\nu_1)(H-H_0)=0$ and -0.90909, respectively, if the interference between the both absorption and the mixing

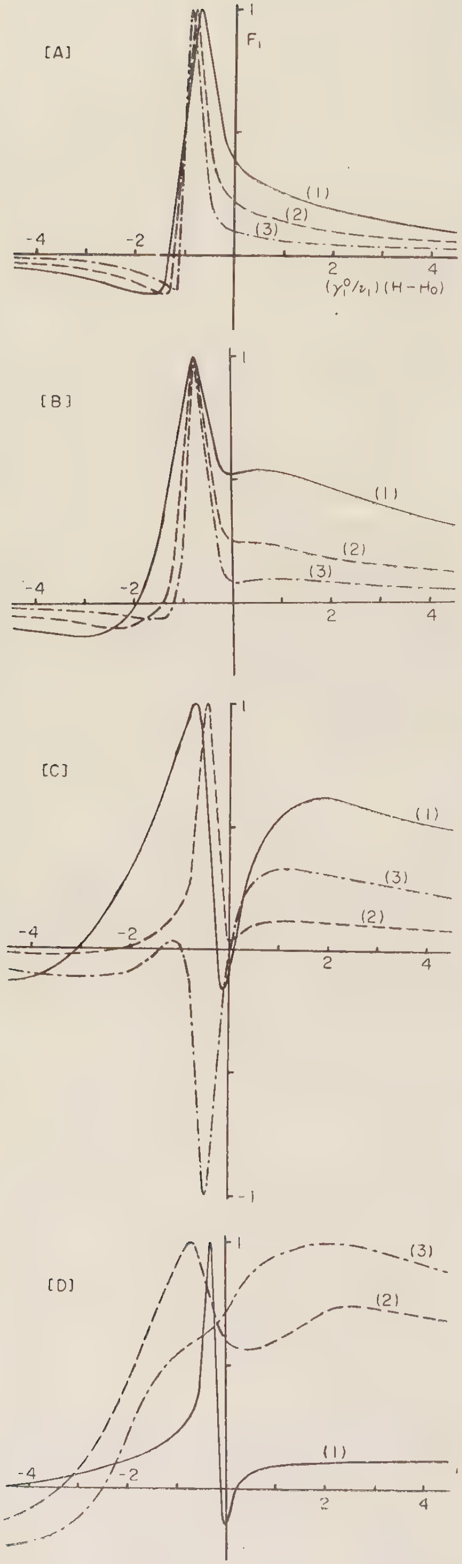

Fig. 1. Calculated curves of F_1 for the cases shown in Table I. Maximum (or minimum) values are normalized to 1 (or -1).

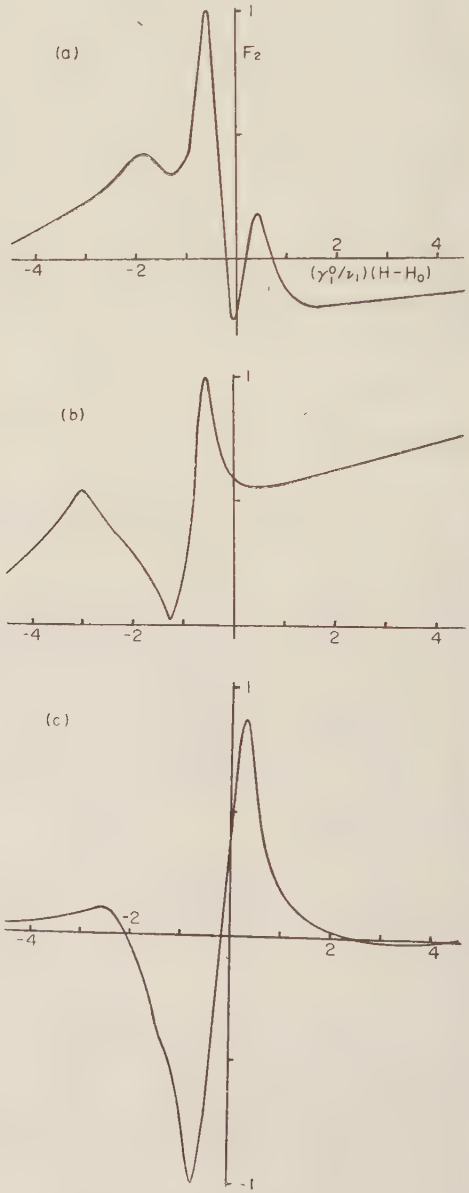

Fig. 2. Calculated curves of F_2 for the case [B] (1) with the following values; (a) $\xi=0.1$, (b) $\xi=1$, (c) $\xi=10$.

of the dispersion are not present. The function F_2 is calculated for three values of ξ in the case [B] (1) and is shown in Fig. 2.

References

1) F. J. Dyson: Phys. Rev. **98** (1955) 349.
2) G. Feher and A. F. Kip: Phys. Rev. **98** (1955) 337.
3) J. I. Kaplan: Phys. Rev. **115** (1959) 575.
4) I. Solomon: Phys. Rev. **99** (1955) 559.
5) N. F. Mott: Proc. Roy. Soc. **A**, **153** (1935) 699.
6) T. Kasuya: Prog. Theor. Phys. **16** (1956) 58.
7) N. F. Mott and K. W. H. Stevens: Phil. Mag. **2** (1957) 1364.
8) W. S. Ament and G. T. Rado: Phys. Rev. **97** (1955) 1558.
9) N. Bloembergen: J. Appl. Phys. **23** (1952) 1383.
10) Y. Osaka: Prog. Theor. Phys. **25** (1961) 510.
T. Matsubara: private communication.
11) N. Bloembergen: Phys. Rev. **78** (1950) 572.

JOURNAL OF THE PHYSICAL SOCIETY OF JAPAN, Vol. 16, No. 10, OCTOBER, 1961

Theory of Cyclotron Resonance in Anisotropic Metals

By Hideo SUZUKI, Masumi HATTORI and Kanetaka ARIYAMA
Physical Institute, Nagoya University

(Received May 31, 1961)

The semi-classical Boltzmann theory of Rodriguez for an isotropic metal is extended to the simplest model of a uniaxial anisotropic metal, in which the surfaces of constant energy take the form of ellipsoids of revolution about the principal axis of the crystal. The surface impedance, in the extreme anomalous skin effect region and in the presence of a constant magnetic field parallel to the metal surface, is calculated assuming the specular reflection boundary condition and including the interaction between the individual circular motion of the conduction electrons and the electric field produced by a polarization of the charge distribution in the metal. This model, although somewhat artificial, makes it possible to carry out the calculation exactly and we can see the main features of the phenomenon of cyclotron resonance in anisotropic metals.

§ 1. Introduction

In a series of theoretical papers, Azbel' and Kaner[1] have proposed a new kind of cyclotron resonance in metals, which is possible in the extreme anomalous skin effect region when the constant magnetic field is parallel to the metal surface. This resonance in metals differs essentially from the well-known diamagnetic resonance in semiconductors in three respects:

(1) A resonance is in general expected when the oscillating electric field, which is also parallel to the surface, is parallel to the magnetic field as well as when they are perpendicular to one another, even if, the Fermi surface is spherical.

(2) Cyclotron resonance occurs not only when the imposed frequency ω is equal to the cyclotron frequency of the conduction electrons ω_c, but also at the low integral multiple of ω_c, whether the Fermi surface is spherical or not.

(3) Cyclotron resonance in metals is possible, only when the constant magnetic field is strictly parallel to the metal surface, or more exactly, if the angle between the surface and the field satisfies the condition $\delta_{\mathrm{eff}}/r_c \geq \phi$, where δ_{eff} is the effective depth of penetration of the oscillating electric field and r_c is the cyclotron radius of conduction electrons.

On the contrary, cyclotron resonance in semiconductors, which we call the diamagnetic resonance after Azbel' and Kaner, is possible only when the imposed frequency is equal to ω_c, and its longitudinal resonance in which the electric field is parallel to the magnetic field is observed only if the Fermi surface is asymmetric and the fields are not along a symmetry axis[2]. Moreover, it is not essential for the magnetic field to be parallel to the surface in semiconductors.

These differences between metals and semiconductors are caused by the fact that in metals the effective skin depth of the microwave electric field is small compared with the cyclotron radius of the conduction electrons r_c whereas the opposite is true in semiconductors. According to the theory of normal skin effect, the ratio of the skin depth δ to r_c in the resonance condition with $\omega \approx \omega_c \gg \tau^{-1}$, where τ is the time of relaxation of the conduction electrons, is given by

$$\frac{\delta}{r_c} = \frac{H}{\sqrt{8\pi n E}}\,, \tag{1.1}$$

where n is the density of the conduction electrons, E their energy and H the magnetic field. In semiconductors, E is approximately equal to κT, where κ is the Boltzmann constant, and T the absolute temperature, while in metals it is nearly equal to the Fermi energy at low temperatures. Therefore, if one assumes $m \sim 10^{-28}$ g, $\tau \sim 10^{-10}$ sec, $T \sim 4°$K, $n \sim 10^{14}$ cm^{-3} for semiconductors, and $n \sim 10^{22}$ cm^{-3} for metals, one finds that

$$\frac{\delta}{r_c}_{\text{semi}} \ll \frac{mc}{|e|}\frac{1}{\sqrt{n\kappa T}} \sim 0(10^2)\,, \tag{1.2}$$

$$\frac{\delta_{\text{eff}}}{r_c}_{\text{metal}} \sim \frac{\sqrt{m}}{h} n^{-5/6} H \sim 0(10^{-6}H)\,, \tag{1.3}$$

where c is the speed of light, h the Planck constant, m the electron mass, and e the electronic charge.

Following the original theory of Azbel' and Kaner, various authors have studied cyclotron resonance in metals both experimentally and theoretically. The phenomenon predicted by Azbel' and Kaner was first observed by Fawcett[3] in tin and copper, later in tin by Kip *et al.*[4] and also by Bezuglyi and Galkin[5], in lead by Bezuglyi and Galkin[5], in bismuth by Aubery and Chambers[6], in zinc by Galt *et al.*[7], in aluminium by Langenberg and Moore[8] and also by Fawcett[9], and in copper by Langenberg and Moore[10]. As regards the theory, Kaner and Azbel'[11] have extended their original theory to arbitrary field-strengths and studied the magnetic field and the temperature dependence of the surface impedance tensor, and Kaner[12] has discussed the possibility of cyclotron resonance in a metal with the magnetic field inclined to the surface. The derivation of the Azbel' and Kaner result in terms of Pippard's "ineffectiveness" concept has been given by Heine[13], and also Mattis and Dresselhaus[14] have derived a slightly different result from that obtained by Azbel' and Kaner and discussed the de Haas-van Alphen type of variation of the surface impedance by quantum-mechanical treatment of anomalous skin effect. An extension of the semi-classical theory of Mattis and Dresselhaus for a spherical Fermi surface has been made by Rodriguez[15], to take account of the interaction between the individual circular motion of the conduction electrons and the electric field produced by a polarization of the charge distribution in the metal.

The combined effect of the space charges and the anisotropy of the Fermi surface has however not previously been studied. In the ordinary theory of the skin effect, the increase of the space charge is opposed by two forces. The first is equivalent to a harmonic restoring force and its force constant is ω_p^2, where ω_p is the plasma frequency of the electron gas. The second force is of a viscous nature and is inversely proportional to the time of relaxation of the conduction electrons. However, the viscous nature in the anomalous skin effect is essentially different from that in the normal skin effect, in the sense that we can obtain a finite surface impedance, even if, under the extreme anomalous limit. This difference in the viscous nature is brought by the fact that in the anomalous skin effect region, the current density at any point in the metal is not determined by the electric field at the same point alone but also by its value within a sphere centered at the point under consideration and of a radius comparable to the mean free path of the condition electrons. In such a case, the combined effect above mentioned must be carefully examined.

Therefore, in this paper, the semi-classical Boltzmann theory of Rodriguez is extended to the simplest model of a uniaxial anisotropic metal, in which the surfaces of constant energy take the form of ellipsoids of revolution about the principal axis of the crystal. This model, although somewhat artificial, makes it possible to carry out the calculation exactly, and we can see the main features of the combined effect of the space charges and the anisotropy of the Fermi surface. As a result, it should seem that cyclotron resonance in metals is affected by a polarization of the space charges when the anisotropy of the Fermi surface is complicated and the magnetic field is not along a symmetry axis.

The method of our calculation consists in the solution of the Boltzmann transport equation in conjunction with Maxwell's equations for the electric field. In Sec. 2, the concept of the tube integrals which was originally introduced by Shockley[16)] for the warped energy surface is briefly explained and is applied to the spheroidal energy surface. It is useful to employ the concept of the tube integrals, in order to set up and solve the Boltzmann equation for the distribution function of the conduction electrons.

The general expression for the current density is derived in Sec. 3, subject to the following assumptions which seem to be reasonable under anomalous skin effect conditions in a magnetic field of magnitude between 10^3 and 10^4 oersteds:

(i) We set up the Boltzmann equation in which the collision integral is replaced by a phenomenological expression such as

$$\left(\frac{\partial f}{\partial t}\right)_{\text{scatt.}}=-\frac{1}{\tau(\boldsymbol{k})}(f-f_0)\,, \tag{1.4}$$

where $\boldsymbol{k}$ is the wave vector related to the crystal momentum, and f_0 is the Fermi distribution function. For the phenomenological description of cyclotron resonance in metals, it seems to be of only minor importance.

(ii) We accept the Lorentz law of force. There seems no obvious need of modification until the radius of the cyclotron orbit of electrons is as small as the wavelength of an electron at the Fermi surface.

(iii) We neglect as usual the product of the oscillating electric field with the perturbed distribution function, and the effect of the oscillating magnetic field which is always accompanied by the oscillating electric field, as we can make the amplitude of the electric field sufficiently small.

(iv) The effective depth of penetration of the oscillating electric field is assumed to be small compared with the linear dimensions of the specimen, so that it is permissible to regard the surface of metal as plane and infinite in extent. This condition is always satisfied in practice for specimens of ordinary dimensions at the temperatures and frequencies at which the anomalous skin effect appears.

(v) We assume that the electrons arriving at the surface are scattered specularly. This is not the only possible assumption, but since it was found by Reuter and Sondheimer[17)] that the surface impedance obtained by the specular reflection boundary condition differes from that of the diffuse reflection case only by a factor of 8/9 under the extreme anomalous limit, it will be assumed to be of only minor importance. On the other hand, the gain in mathematical simplicity for specular reflection is considerable.

(vi) Finally, we assume a highly degenerate electron gas.

In Sec. 4, we first consider the case of semiconductors in order to clarify the validity of our theory. The effect of the space charges of cyclotron resonance in semiconductors is well-known as the plasma resonance, which was first studied by Dresselhaus *et al.*[18)] on InSb both experimentally and theoretically.

In Sec. 5, the most interesting case of extreme anomalous limit in the metal, where the conditions $l \gg r_c \gg \delta_{\text{eff}}$ are satisfied, is discussed in detail for spheroidal energy surfaces.

Finally, the theoretical results thus obtained are discussed in Sec. 6. The evaluation of the integrals which will appear in the calculation of the current density is made in the Appendix.

§ 2. Tube Integrals for Spheroidal Energy Surfaces

The fluted or warped quality of the energy surfaces, such as that near the valence band edge in germanium and silicon, have a complicated effect on the cyclotron resonance frequency, because there is no longer a single cyclotron frequency for a given orientation of the constant magnetic field, but a distribution of resonance frequencies. In such a case, it is very useful to employ the concept of the tube integrals. As will be seen later in this section, the tube mass for the spheroidal energy surface does not depend on the specific tube, but it is still useful to simplify and solve the Boltzmann transport equation.

Now let us suppose, for simplicity, that $E=E(\boldsymbol{k})$ is a unique continuous function of the wave vector $\boldsymbol{k}$, inside a zone, giving the energy of a single band, without overlap. Then a general effective mass Hamiltonian in a electromagnetic field is given as

$$H=E(\boldsymbol{k})+eV(\boldsymbol{r})\,,\quad \hbar\boldsymbol{k}=\boldsymbol{p}-\frac{e}{c}\boldsymbol{A}(\boldsymbol{r})\,,\qquad (2.1)$$

where $\hbar\boldsymbol{k}$ is the crystal momentum, $\boldsymbol{p}$ the canonical momentum, $\boldsymbol{r}$ the lattice vector, and $\boldsymbol{A}(\boldsymbol{r})$ and $V(\boldsymbol{r})$ are the vector and scalar potential of the field, respectively. Thus

$$\hbar\boldsymbol{v}=\frac{\partial E(\boldsymbol{k})}{\partial\boldsymbol{k}}\,,\qquad \hbar\frac{d\boldsymbol{k}}{dt}=e\boldsymbol{E}+\frac{e}{c}\Big[\boldsymbol{v}\times\boldsymbol{H}\Big]\,,\qquad (2.2)$$

where $\boldsymbol{v}$ is the group velocity of the electron, and $\boldsymbol{E}$ the electric field.

When there is no electric field, the constant magnetic field does not change the energy of the electron moving on the energy surface, nor does it change the projection k_H of the $\boldsymbol{k}$-vector along the magnetic field direction. Therefore, the representative point of the electron in $\boldsymbol{k}$-space traces out the path of intersection of the surfaces

$$E(\boldsymbol{k})=\text{constant}, \qquad k_H=\text{constant}. \qquad (2.3)$$

Around this orbit the motion is governed by the Lorentz equation

$$\frac{dk}{dt}=\frac{eH}{c\hbar}v_{\perp}\,, \qquad (2.4)$$

where dk is an element of the path in the $\boldsymbol{k}$-space and $v_{\perp}$ is the component of the velocity vector of the electron perpendicular to the magnetic field. That is, in the presence of oscillating electric fields of small amplitude, the motion of the electron in $\boldsymbol{k}$-space is confined to the region in dk_H at k_H and with energy in dE at E, which has been called a tube by Shockley[16]. For spherical energy surfaces, the tube is a torus with a parallelogram cross section. For more complex surfaces and for energies, for which the surfaces reach the boundary of the Brillouin zone and we need in general the repeated zone scheme, the tube may possibly take a helical path and eventually fill most of the space between E and $E+dE$. We shall here discuss only simple closed tubes for which the period of an oscillation can be defined.

According to (2.4), this is just

$$T=\frac{c\hbar}{eH}\oint\frac{dk}{v_{\perp}}\,, \qquad (2.5)$$

where the integral is taken round the orbit. Thinking of the cyclotron frequency for free electrons, we may use (2.5) to define a mass parameter m_H^* such that $T=(2\pi m_H^*c)/(eH)$. Then

$$m_H^*=\frac{\hbar}{2\pi}\frac{\partial}{\partial E}A(k_H)\,, \qquad (2.6)$$

where $A(k_H)$ is the area of the plane $k_H=$ constant lying within the contour of intersection with $E(\boldsymbol{k})=$constant. This quantity has been called the tube mass by Shockley and is, in principle, quite different from any effective mass which we have usually used. Moreover, Shockley mapped out the electron distribution in terms of a new set of coordinates in $\boldsymbol{k}$-space, that is E, k_H, and a new phase angle ψ, called the tube angle, which measures the position of the representative point in its motion round the orbit (2.4). That is,

$$\psi=\frac{\hbar}{m_H^*}\int\frac{dk}{v_{\perp}}\,, \qquad (2.7)$$

where the integral is taken from some arbitrary origin. The essential property of this variable is that it obeys the simple equation of motion

$$\frac{d\psi}{dt}=\frac{eH}{m_H^*c}\equiv\omega_H\,, \qquad (2.8)$$

as may be easily proved from (2.4) and (2.7).

Now let us consider the tube integrals for the spheroidal energy surfaces. First we suppose that the energy surfaces are described by the equation

$$E(\boldsymbol{k})=\frac{\hbar}{2}\left(\frac{k_1^2+k_2^2}{m_1}+\frac{k_3^2}{m_3}\right)\,, \qquad (2.9)$$

choosing as special local axes in $\boldsymbol{k}$-space the principal axes of these spheroids, and the relation between these coordinates and the original coordinates system fixed in $\boldsymbol{k}$-space is given by

$$\begin{array}{c|ccc} & k_x & k_y & k_z \\ \hline k_1 & 0\,, & \sin\varphi\,, & -\cos\varphi\,, \\ k_2 & -\sin\theta\,, & \cos\theta\cos\varphi\,, & \cos\theta\sin\varphi\,, \\ k_3 & \cos\theta\,, & \sin\theta\cos\varphi\,, & \sin\theta\sin\varphi\,. \end{array} \qquad (2.10)$$

The relative positions of the two coordinates system is indicated in Fig. 1. The plane of the paper denotes the xy-plane with the positive z-axis pointing upwards. The first rotation specified by an angle φ brings this plane into the position k_2Ox and the second rotation specified by an angle θ is in the negative sence about the Ok_1-axis. The expression of the energy surface in the system of (k_x, k_y, k_z) is then

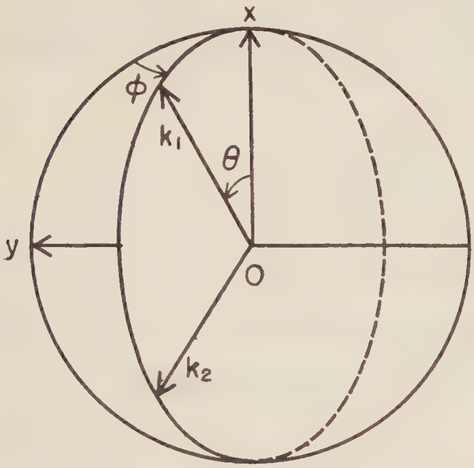

Fig. 1. Coordinate system. The xy-plane is the surface of the metal which occupies the space $z>0$.

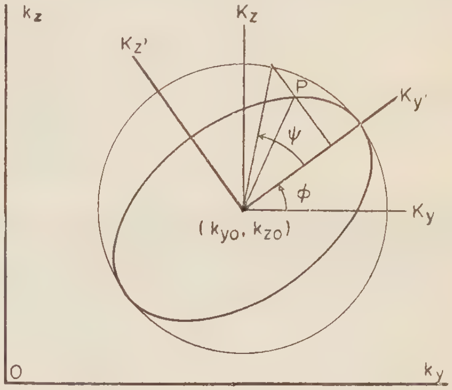

Fig. 2. The geometrical meaning of the tube angle.

$$E=\frac{\hbar}{2}(\Delta_1 k_x^2+\Delta_2 k_y^2+\Delta_3 k_z^2+2\Delta_4 k_x k_y+2\Delta_5 k_x k_z+2\Delta_6 k_y k_z)\ , \tag{2.11}$$

where

$$\begin{array}{lll} \Delta_1=\dfrac{\hbar}{m_1}(1+L^2\Delta)\ , & \Delta_4=\dfrac{\hbar}{m_1}LM\Delta\ , & \\ \Delta_2=\dfrac{\hbar}{m_1}(1+M^2\Delta)\ , & \Delta_5=\dfrac{\hbar}{m_1}LN\Delta\ , & \Delta\equiv\left(\dfrac{m_1-m_3}{m_3}\right)\ , \\ \Delta_3=\dfrac{\hbar}{m_1}(1+N^2\Delta)\ , & \Delta_6=\dfrac{\hbar}{m_1}MN\Delta\ , & \end{array} \tag{2.12}$$

and

$$L=\cos\theta\ ,\qquad M=\sin\theta\cos\varphi\ ,\qquad N=\sin\theta\sin\varphi\ . \tag{2.13}$$

Next we assume that the xy-plane is in the surface of the metal which occupies the space $z>0$, and the magnetic field is along the x-axis. Then the coordinates of the centre of the conic section with k_x=constant are obtained from (2.11) as

$$k_{y_0}=\frac{\hbar k_x}{m_1}\frac{\Delta_4}{\Delta_6^2-\Delta_2\Delta_3}\ ,\qquad k_{z_0}=\frac{\hbar k_x}{m_1}\frac{\Delta_5}{\Delta_6^2-\Delta_2\Delta_3}\ . \tag{2.14}$$

Let (K_y, K_z) be the new coordinates of a point P under consideration referred to the system of rectangular axes which are obtained by the transferring the origin 0 to (k_{y_0}, k_{z_0}), and let the new axes be rotated through the angle φ, rewritten as

$$\tan 2\varphi=(2\Delta_6)/(\Delta_2-\Delta_3)\ . \tag{2.15}$$

Then the standard form of the conic section is obtained as

$$E=\frac{\hbar^2 k_x^2}{2m_1}\frac{1+\Delta}{1+\Delta(1-L^2)}+\frac{\hbar}{2}(aK_{y'}^2+bK_{z'}^2)\ , \tag{2.16}$$

where $(K_{y'}, K_{z'})$, being the coordinates of the point P referred to the final system, are given by

$$K_{y'}=K_y\cos\varphi+K_z\sin\varphi\ ,\qquad K_{z'}=-K_y\sin\varphi+K_z\cos\varphi\ , \tag{2.17}$$

and a and b are determined by the equations

$$a+b=\Delta_2+\Delta_3\ ,\qquad ab=\Delta_2\Delta_3-\Delta_6^2\ . \tag{2.18}$$

That is, if $\pi/2\geqslant\varphi>0$, they must satisfy the conditions $a>b$, for $\Delta_6>0$, and $a<b$, for $\Delta_6<0$.
Now, from (2.16) and (2.18), $A(k_x)$ is obtained as

$$A(k_x)=\frac{2\pi}{\hbar^2}\frac{m_1}{\sqrt{1+\Delta(1-L^2)}}\left(E-\frac{\hbar^2k_x^2}{2m_1}\frac{1+\Delta}{1+\Delta(1-L^2)}\right). \tag{2.19}$$

Thus

$$m_H{}^*=\frac{m_1}{\sqrt{1+\Delta(1-L^2)}}\ . \tag{2.20}$$

Thus, the tube mass for a spheroidal energy surface does not depend on k_x, and is equal to the ordinary effective mass, m^*.

Combining (2.7) with (2.16), (2.18), and (2.20), we have the following relations:

$$K_{y'}=\sqrt{\frac{2E'}{\hbar a}}\cos\psi\ ,\qquad K_{z'}=\sqrt{\frac{2E'}{\hbar b}}\sin\psi\ , \tag{2.21}$$

where E' is given by

$$E'=E-\frac{\hbar^2k_x^2}{2m_1}\frac{1+\Delta}{1+\Delta(1-L^2)}\ . \tag{2.22}$$

We can see the geometrical meaning of the tube angle ψ immediately from Fig. 2. Thus, from (2.2), (2.17), and (2.14), we obtain the group velocity of the electron as follows:

$$\left.\begin{aligned}v_x&=A_1k_1+B_1K_{y'}+C_1K_{z'}\ ,\\ v_y&=\qquad\quad\ +B_2K_{y'}+C_2K_{z'}\ ,\\ v_z&=\qquad\quad\ +B_3K_{y'}+C_3K_{z'}\ ,\end{aligned}\right\} \tag{2.23}$$

where

$$A_1=\frac{\hbar}{m_1}\frac{1+\Delta}{1+\Delta(1-L^2)}\ , \tag{2.24}$$

and

$$\left.\begin{aligned}B_1&=\Delta_4\cos\varphi+\Delta_5\sin\varphi\ ,& C_1&=-\Delta_4\sin\varphi+\Delta_5\cos\varphi\ ,\\ B_2&=\Delta_2\cos\varphi+\Delta_6\sin\varphi\ ,& C_2&=-\Delta_2\sin\varphi+\Delta_6\cos\varphi\ ,\\ B_3&=\Delta_6\cos\varphi+\Delta_3\sin\varphi\ ,& C_3&=-\Delta_6\sin\varphi+\Delta_3\cos\varphi\ ,\end{aligned}\right\} \tag{2.25}$$

Using the relations thus obtained, we can evaluate the current density explicitly.

§ 3. The Fundamental Equation

The Boltzmann equation for the distribution function of the conduction electrons is assumed from (1.4) and (2.2) to be

$$\frac{\partial f}{\partial t}+\boldsymbol{v}\cdot\frac{\partial f}{\partial \boldsymbol{r}}+\frac{e}{\hbar}\left(\boldsymbol{E}+\frac{\boldsymbol{V}\times\boldsymbol{H}_0}{c}\right)\cdot\frac{\partial f}{\partial \boldsymbol{k}}+\frac{f-f_0}{\tau(\boldsymbol{k})}=0\ , \tag{3.1}$$

where H_0 is the constant magnetic field. From the assumption already mentioned in Sec. 1. f is written in the form

$$f=f_0+f_1(\boldsymbol{v},z)\exp(i\omega t) \tag{3.2}$$

and then, using the tube angle, the linearized equation for f_1 found to satisfy the equation

$$f_1+\tau^* v_z\frac{\partial}{\partial z}f_1+\omega_c\tau^*\frac{\partial}{\partial\psi}f_1=-e\tau^*(\boldsymbol{v}\cdot\boldsymbol{E})\frac{\partial}{\partial E}f_0\ , \tag{3.3}$$

where $\tau^*=\tau/(1+i\omega\tau)$, and $\omega_c=(eH)/(m^*c)$. Equation (3.3) is a linear partial differential equation with the independent variables z and ψ. Therefore, its formal solution can most easily be found by introducing the Fourier transform of the function f_1 and the field $\boldsymbol{E}(z)$, which are defined by the following equations for the specular reflection case:

$$f_1(q)=\frac{1}{\sqrt{2\pi}}\int_{-\infty}^{\infty}f_1(z)\exp(-iqz)dz\ , \tag{3.4}$$

$$\boldsymbol{E}(q)=\frac{1}{\sqrt{2\pi}}\int_{-\infty}^{\infty}\boldsymbol{E}(z)\exp(-iqz)dz\ . \tag{3.5}$$

The equation for $f_1(q)$, which is equivalent to (3.3), is then

$$\left[\frac{\partial}{\partial\psi}+\gamma(1+iq\tau^* v_z)\right]f_1(q)=-\frac{e}{\omega_c}\boldsymbol{v}\cdot\boldsymbol{E}(q)\frac{\partial f_0}{\partial E}\ , \tag{3.6}$$

where $\gamma=1/(\omega_c\tau^*)$. The solution of (3.6), satisfying the periodic conditions $f_1(q,\psi+2\pi)=f_1(q,\psi)$ and $\boldsymbol{v}(\psi+2\pi)=\boldsymbol{v}(\psi)$, is given by

$$f_1(q)=\frac{\delta(E-E_f)(e/\omega_c)}{[\exp(2\pi\gamma)-1]}\int_{\psi}^{\psi+2\pi}d\psi'(\boldsymbol{v}(\psi')\cdot\boldsymbol{E}(q))\exp(S(\psi')-S(\psi))\ , \tag{3.7}$$

where $\delta(E-E_f)$ is the Dirac function, E_f the Fermi energy, and

$$S(\psi)=\gamma[\psi-iq\tau^*(\hbar/m_H^*)k_y(\psi)]\ . \tag{3.8}$$

Here we have used the facts that

$$\int^{\psi}z_z(\psi')d\psi'=-(\hbar/m_H^*)k_y(\psi)\ , \tag{3.9}$$

and

$$-\frac{\partial f_0}{\partial E}=(E-E_f)\ , \tag{3.10}$$

which holds for a highly degenerate electron gas.

The Fourier transform of the current density can now be calculated by means of the formula

$$\boldsymbol{I}(q)=\frac{1}{4\pi^3}\int e\boldsymbol{v}f_1(q)d\boldsymbol{k} \tag{3.11}$$

which is equivalent to

$$\boldsymbol{I}(z)=\frac{1}{4\pi^3}\int e\boldsymbol{v}f_1(z)d\boldsymbol{k}\ , \tag{3.12}$$

where $d\boldsymbol{k}$, in term of k_H, ψ, and E, is in general given by

$$d\boldsymbol{k}=(m_H^*/\hbar^2)dE\,dk_H\,d\psi\ . \tag{3.13}$$

From (3.7), (3.11), (3.13), and (2.19), we obtain

$$\begin{aligned}\boldsymbol{I}(q)&=(1/4\pi^3)(e^2m^*/\omega_c\hbar^2)(\exp(2\pi\gamma)-1)^{-1}\\&\quad\times\int_{-k_m}^{k_m}dk_x\int_0^{2\pi}d\psi\int_{\psi}^{\psi+2\pi}d\psi'\,\boldsymbol{v}(\psi)(\boldsymbol{v}(\psi')\cdot\boldsymbol{E}(q))\exp(S(\psi')-S(\psi))\ ,\end{aligned} \tag{3.14}$$

where k_m, obtainable from (2.19), is

$$k_m=(2m_1E_f/\hbar^2)[(1+\Delta(1-L^2))/(1+\Delta)]^{1/2} \tag{3.15}$$

and $S(\psi')-S(\psi)$ is rewritten from (2.17), (2.18), and (2.28) as

$$S(\psi')-S(\psi)=\gamma(\psi'-\psi)+\frac{iq\hbar}{m^*\omega_c}\left[\frac{8E_f'}{\hbar}\left(\frac{\cos^2\varphi}{a}+\frac{\sin^2\varphi}{b}\right)\right]^{1/2}\sin\left(\frac{\psi'-\psi}{2}\right)\sin\left(\frac{\psi'+\psi}{2}+\Theta\right), \tag{3.16}$$

where E_f' denotes that the value of E' at the Fermi surface is to be used, and the angle Θ is defined by

$$\tan\Theta=\sqrt{a/b}\tan\varphi\ . \tag{3.17}$$

Equation (3.14) defines a conductivity tensor in the q-space. We can write,

$$I_i(q)=\Sigma_k\sigma_{ik}(q)E_k(q)\ . \qquad (i,\ k=x,\ y,\ z) \tag{3.18}$$

The expression of the components of the tensor have been given in the Appendix.

Using the current density thus obtained, we must next solve the Maxwell's equation for the electric field components. In the q-space, the equations in which the boundary conditions are already contained are given by

$$(-q^2+\omega^2/c^2)E_k(q)=(4\pi i\omega/c^2)I_k(q)+\sqrt{\frac{2}{\pi}}E_k'(0)\ , \tag{3.19}$$

$$E_z(q)=(4\pi i/\omega)I_z(q)\ , \tag{3.20}$$

where $E_k'(0)$ denotes that the derivative of $E_k(z)$ with respect to z is to be evaluated at $z=0$, and the index k denotes the components $(x,\ y)$ of the electric field. These equations are equivalent to

$$\left(\Delta-\text{grad. div}-\frac{1}{c^2}\frac{\partial^2}{\partial t^2}\right)\boldsymbol{E}(z,\ t)=(4\pi/c^2)\frac{\partial}{\partial t}\boldsymbol{I}(z,\ t)\ . \tag{3.21}$$

Using (3.20), we can rewrite (3.18) as follows:

$$I_i(q)=\Sigma_k\sigma_{ik}'(q)E_k(q)\ , \qquad (i,\ k=x,\ y) \tag{3.22}$$

$$\sigma_{ik}'=\sigma_{ik}-(\sigma_{iz}\sigma_{zk})/(\sigma_{zz}+i\omega/4\pi)\ . \tag{3.23}$$

The surface impedance Z is defined as the ratio of the electric field at the surface of the total current per unit surface area, that is,

$$Z_x=(4\pi/c)(E_x(0)/H_y(0))\ , \qquad Z_y=-(4\pi/c)(E_y(0)/H_x(0))\ , \tag{3.24}$$

for the two cases of longitudinal and transverse cyclotron resonance respectively. Therefore, from (3.19), (3.23) and (3.24), we obtain the following formulae:

$$Z_k=(8i\omega/c^2)\int_0^\infty dq\left[q^2+(4\pi i\omega/c^2)\sigma_{kk}'-\frac{\omega^2}{c^2}\right]^{-1}. \qquad (k=x,\ y) \tag{3.25}$$

§ 4. Plasma Resonance in Semiconductors

In order to test the validity of our theory, it is most reasonable to consider the case of semiconductors, because the effect of the space charges of cyclotron resonance in semiconductors is well-known as the plasma resonance of the experimental and theoretical studies of Dresslhaus *et al.*[18] on In Sb.

As already mentioned in Sec. 1, the condition $O(r_c/\delta)\ll 1$ holds in semiconductors at the microwave resonance, so that it is sufficient to consider only up to the second order terms of Σ-functions which are defined by the equation (A. 5), expanding these functions in the ascending powers of s defined by (A. 6). The power-series representation of Σ-functions are given in the Appendix (Equations (A. 7) to (A.11)). The first terms of these correspond to those investigated by Dresselhaus *et al.*, and the difference between the Boltzmann and the Drude-Lorentz theory begins to appear only only from the second terms. Here we confine ourselves, for simplicity, only to the case of isotropic energy surfaces.

In the case of longitudinal cyclotron resonance, the σ_{xz}-component vanishes and the σ_{xx}-component is given by

$$\sigma_{xx}=\sigma\left[1-\frac{1}{5}\,\frac{(v_f\tau q)^2}{(1+i\omega\tau)^2+(\omega_c\tau)^2}\right], \tag{4.1}$$

where v_f is the group velocity of the electron at the Fermi surface, and $\sigma=(ne^2\tau^*/m)$. Therefore the surface impedance is not affected by the space charges. From (3.19), we can now obtain the condition for excitation of plasma oscillations. For instance, in the case when $\omega_c=0$ and $\omega\tau\gg1$, we obtain the well-known formula

$$\omega^2=\omega_p{}^2+(3/5)q^2v_f{}^2\ , \tag{4.2}$$

where $\omega_p{}^2=(4\pi ne^2/m\varepsilon)$, and ε is the dielectric constant of the crystal.

Next, in the case of transverse cyclotron resonance, where the microwave electric field is perpendicular to the magnetic field, the σ_{yy}'-component is expressed as

$$\sigma_{yy}'=\frac{\sigma\gamma^2}{1+\gamma^2}\left[1-\frac{(4\pi i\sigma/\varepsilon)}{(1+\gamma^2)\omega-\gamma^2(4\pi i\sigma/\varepsilon)}\right]+\alpha q^2\ , \tag{4.3}$$

where

$$\alpha=\frac{\sigma}{5}\,\frac{v_f{}^2}{\omega_c{}^2}\,\frac{(8-\gamma^2)}{(1+\gamma^2)(4+\gamma^2)}\left[1+\frac{48\pi i\sigma}{\varepsilon\omega}\,\frac{\gamma^2(1+\gamma^2-(3\pi i\sigma/\varepsilon\omega))}{(1+\gamma^2-\gamma^2(4\pi i\sigma/\varepsilon\omega))^2}\right]. \tag{4.4}$$

Here the first term corresponds to that investigated by Dresselhaus *et al.* and the second results from the fact that the kinetic theory takes into account the non-local effect of the electric field within a cyclotron radius, and the second terms in parentheses of (4.3) and (4.4) express the contribution from the space charges. As will be discussed below, the first term in (4.3) agrees completely with that obtained by Dresselhaus *et al.*.

Writting D as the depolarization factor, $\boldsymbol{P}$ as the dielectric polarization, and χ as the dielectric susceptibility, we obtain the equation of motion for conduction electrons in semiconductors as

$$m(\boldsymbol{v}+\tau^{-1}\boldsymbol{v})=e\boldsymbol{E}_L+(e/c)(\boldsymbol{v}\times\boldsymbol{H})\ , \tag{4.5}$$

where $\boldsymbol{E}_L$ is determined by the equations

$$\boldsymbol{E}_L=\boldsymbol{E}-D\boldsymbol{P}=\boldsymbol{E}-D(ne\boldsymbol{r}+\chi\boldsymbol{E}_L)\ . \tag{4.6}$$

When the medium is semi-infinite in extent, we can suppose

$$D_{xx}=0\ ,\qquad D_{yy}=0\ ,\qquad D_{zz}=4\pi\ , \tag{4.7}$$

and

$$\varepsilon=1+4\pi\chi\ . \tag{4.8}$$

Therefore, taking the external fields as

$$\boldsymbol{E}=(0,E,0)\ ,\qquad \boldsymbol{H}_0=(H_0,0,0)\ , \tag{4.9}$$

we can obtain

$$\sigma_{yy}=\frac{ne^2\tau}{m}\,\frac{(1+i\omega'\tau)}{[(1+i\omega'\tau)(1+i\omega\tau)+(\omega_c\tau)^2]}\ , \tag{4.10}$$

where $\omega'=\omega-\omega_p{}^2\omega^{-1}$. This is the same as the first term of (4.3). The drift-velocity treatment of Dresselhaus *et al.* is valid, when the effect of $o((r_c/\delta)^2)$ can be neglected.

Finally, from (3.25), we can obtain the surface impedance in semiconductors which can be expressed by the skin depth as

$$Z_k=(4\pi i\omega/c^2)\delta_k\ , \qquad (k=x,\ y) \tag{4.11}$$

for the two cases of longitudinal and transverse resonance, where the skin depth δ_k are given as follows:

$$\delta_x=\left[\left(\frac{4\pi i\omega\sigma}{c^2}-\frac{\varepsilon\omega^2}{c^2}\right)\left(1-\frac{(4\pi i\omega\sigma/5c^2)(v_f\tau)^2}{(1+i\omega\tau)^2+(\omega_c\tau)^2}\right)\right]^{-1/2}, \tag{4.12}$$

$$\delta_y=\left[\left(\frac{4\pi i\omega\sigma_{yy}}{c^2}-\frac{\varepsilon\omega^2}{c^2}\right)(1+(4\pi i\omega/c^2)\alpha)\right]^{-1/2}, \tag{4.13}$$

§ 5. The Surface Impedance in the Extreme Anomalous Limit

We shall consider the cyclotron resonance in metals in the absence of inclination of the magnetic field to the metal surface; a short discussion on the inclination effect of the magnetic field will be given in the following section.

As before mentioned, the condition $s\gg 1$ holds for metals, so it is necessary to obtain the asymptotic form of the Σ-functions. These are given in the Appendix (Equations (A. 30) to (A. 34)). We first consider a spherical Fermi surface; in this case, we obtain

$$I_x(q)=3\sigma K_2E_x(q)\ , \qquad I_z(q)=3\sigma K_2E_z(q)\ , \tag{5.1}$$

for the longitudinal resonance, where

$$K_1\sim\frac{i\pi\gamma}{4s}\coth(\pi\gamma)\ , \qquad K_2\sim-\frac{\gamma^2}{s^2}\ , \tag{5.1}$$

and

$$s=(iqv_f)/\omega_c\ . \tag{5.3}$$

These equations show that just as in semiconductors the effect of the space charges have no influence upon the surface impedance at microwave frequencies. However, the combination of $I_z(q)$ with (3.20) showes that the excitation of the plasma oscillations will occur at the much higher frequency

$$\omega=12\pi i\sigma K_2\ . \tag{5.4}$$

In the transverse resonance, the non-vanishing components of the conductivity tensor are

$$\sigma_{yy}=3\sigma K_1\ , \qquad -\sigma_{yz}=\sigma_{zy}=3\sigma K_3\ , \qquad \sigma_{zz}=3\sigma K_2\ , \tag{5.5}$$

where

$$K_3\sim\frac{i+1}{2}\sqrt{\frac{\pi}{2}}\frac{\gamma^2}{s^{5/2}}\frac{\cos((2qv_f/\omega_c)-(\pi/4))}{\sin(\pi i\gamma)}-\frac{i\pi\gamma^2}{4s^3}\coth(\pi\gamma)\ . \tag{5.6}$$

Thus, from (3.23), we have

$$\sigma_{yy}'=3\sigma K_1-(12\pi i\sigma K_3{}^2)/(\omega-12\pi i\sigma K_2) \tag{5.7}$$

which satisfies the conditions $E_y(-q)=E_y(q)$, and $I_y(-q,\ -\omega_c)=I_y(q,\ \omega_c)$. In the region of microwave frequency, the condition $|12\pi i\sigma K_2|\gg\omega$ holds in metals, so the second term in (5.7) has the asymptotic form $(K_s)^2/K_2$ which can be expressed as

$$K_3{}^2/K_2\sim(i\pi\gamma^2/4s^3)\cos^2(-2is-(\pi/4))/\sin^2(i\pi\gamma)\ . \tag{5.8}$$

That is, the effect of the space charges occurs at the order of s^{-3}.

For the case when the microwave electric field is not parallel to the magnetic field, the conductivity for the current parallel to the electric field, say $\sigma_{\mathrm{para.}}$, is given by

$$\sigma_{\mathrm{para.}}(q)=3\sigma K_1-\sin^2 \Lambda(i\pi\gamma/8s^3)\coth(\pi\gamma)\,, \tag{5.9}$$

neglecting the effect of the space charges, where Λ is the angle between the magnetic field and the electric field. The part of angular change makes also a small contribution of the order of s^{-3}.

Next we consider the spheroidal Fermi surface, assuming, for simplicity, that $(\pi/2)\geqslant\varphi>0$, and $\Delta>0$. In this case, a and b must be given from (2.18) as

$$a=(\hbar/m_1)[1+\Delta(1-L^2)]\,,\qquad b=(\hbar/m_1)\,. \tag{5.10}$$

Then, combining (5.10) with (3.17), (A. 3), (A. 4), and (2.25), we can obtain the following relations:

$$\cos 2\Theta S_3^- -\sin 2\Theta P_3+S_3^+=0\,, \tag{5.11}$$

$$\cos 2\Theta S_5^- -\sin 2\Theta P_5+S_5^+=0\,, \tag{5.12}$$

$$\cos 2\Theta S_6^- -\sin 2\Theta P_6+S_6^+=0\,, \tag{5.13}$$

$$S_3^+=\Delta_5\,,\qquad S_5^+=\Delta_6\,,\qquad S_6^+=\Delta_3\,, \tag{5.14}$$

$$\cos 2\Theta S_1^- -\sin 2\Theta P_1+S_1^+ +\hbar A_1^2(k_m^2/E_f)=\frac{2\hbar}{m_1}\,\frac{1+\Delta(1-M^2)}{1+\Delta N^2}\,, \tag{5.15}$$

$$\cos 2\Theta S_4^- -\sin 2\Theta P_4+S_4^+ =\frac{2\hbar}{m_1}\,\frac{1+\Delta(1-L^2)}{1+\Delta N^2}\,. \tag{5.16}$$

Then, neglecting terms whose order is higher than s^{-2} (the terms of $O(s^{-3/2})$ being also of a small contribution, because they oscillate rapidly in the extreme anomalous limit), we can obtain the σ_{xx}-, and the σ_{yy}- component of conductivity tensor as follows:

$$\sigma_{kk}=q^{-1}(e^2m_1E_f/2\pi\hbar^3)G_{kk}(L,\,M,\,N)\coth(\pi\gamma)\,,\qquad (k=x,\,y) \tag{5.17}$$

where

$$G_{xx}=(1+\Delta(1-M^2))/(1+\Delta)^{1/2}(1+\Delta N^2)^{3/2}\,, \tag{5.18}$$

$$G_{yy}=(1+\Delta(1-L^2))/(1+\Delta)^{1/2}(1+\Delta N^2)^{3/2}\,. \tag{5.19}$$

Therefore, if the displacement current is neglected, the surface impedance is given by

$$Z_k=\frac{8}{3\sqrt{3}}(1+i\sqrt{3})\left(\frac{\pi^3\omega^2\hbar^3}{2c^4e^2m_1E_fG_{kk}}\right)^{1/3}\tanh^{1/3}(\pi\gamma)\,, \tag{5.20}$$

for the two cases of longitudinal and transverse resonance, respectively.

Finally, we consider the effect of the space charges on the conductivity tensor in the q-space. Using the relations already obtained (Equations (5.11) to (5.14)), we have the components of the conductivity tensor required for the present purpose as follows:

$$\sigma_{xz}=\sigma_{zx}=-(2e^2m^*E_fk_m\gamma/\pi^2\omega_c\hbar^3)\Delta_5 s^{-2}\,, \tag{5.21}$$

$$\sigma_{yz}=\sigma_{zy}=-(2e^2m^*E_fk_m\gamma/\pi^2\omega_c\hbar^3)\Delta_6 s^{-2}\,, \tag{5.22}$$

$$\sigma_{zz}=-(2e^2m^*E_fk_m\gamma/\pi^2\omega_c\hbar^3)\Delta_3 s^{-2}\,. \tag{5.23}$$

Here the contribution from the terms of $o(s^{-1})$ and $o(s^{-3/2})$ have vanished, as may be seen immediately from (5.11), (5.12) and (5.13), and we have considered only up to the second order terms of s^{-1}. The correction term of $\sigma_{ik}(q)$ due to the effect of the space charges, say $\Delta\sigma_{ik}(q)$, has an asymptotic form like $-(\sigma_{iz}\sigma_{zk})\sigma_{zz}$ at microwave frequencies, so that

$$\Delta\sigma_{xx}=(2e^2m^*E_fk_m\gamma/\pi^2\omega_c\hbar^3)(\Delta_5^2/\Delta_3)s^{-2}\,, \tag{5.24}$$

$$\Delta\sigma_{yy}=(2e^2m^*E_fk_m\gamma/\pi^2\omega_c\hbar^3)(\Delta_6^2/\Delta_3)s^{-2}\,, \tag{5.25}$$

From these equations, we can see that the effect of the space charges occurs through the anisotropy of the Fermi surface, although it is only of the second order of s^{-1} for the present case and the orientation of the fields relative to the principal axis of the crystal has complicated influence on $\Delta\sigma_{kk}$. From the facts that $\Delta\sigma_{yy}$ is of the third order of s^{-1} for an isotropic Fermi surface,, and then it becomes of the second order for the spheroidal one, we imagine that the effect of the space charges will occur at the principal order s^{-1} for more complicated Fermi surface. We shall discuss this problem in the following section.

§ 6. Concluding Remarks

The semi-classical Boltzmann theory of Rodriguez for an isotropic metal was extended to the simplest model of a uniaxial anisotropic Fermi surface, using the concept of the tube angle which had been originally introduced by Shockley[16]. The method of our calculation consisted in the solution of the Boltzmann equation for the distribution function of the conduction electrons in conjunction with the Maxwell's equations for the electric field. The general expression for the current density was derived, subject to some assumptions which seem to be reasonable under the anomalous skin effect conditions in a magnetic field of the order of 10^4 oersteds. The quantum effect of the electron field was not considered in the present paper, becuase de Broglie wavelength of an electron at Fermi surface is very small compared with δ_{eff} at the temperatures and frequencies at which the anomalous skin effect appears. Therefore, it is reasonable to consider that the motion of electrons is nearly classical. Another quantum effect of the photon field was not also considered, which may be appear in the optical and near infrared frequency region. But, as already discussed by Holstein[19], and later by Gurzhi[20], we obtain from this discussion merely a information about the physical meaning of the effective relaxation time of the conduction electrons, so it is not essential for our phenomenological description.

On the other hand, according to the theory of a Fermi liquid proposed by Landau[21], it is considered that the conduction electrons in metals are rather different from the model of quasi-free electrons. For this reason, the theoretical work by Silin[22] on anomalous skin effect from the point of view of the Landau theory is worth nothing.

Ignoring the problem of these different starting points, the correctness of our formulation should first be examined. Therefore, in Sec. 3, we first considered the well-known plasma resonance in semiconductors which was originally investigated by Dresselhaus *et al.* on InSb both experimentally and theoretically. In fact, it was shown that the drift-velocity treatment of Dresselhaus *et al.* is valid when the effect of $o(s^{-2})$ can be neglected.

In contrast with the quantum effects above mentioned, and the temperature dependence of the surface impedance discussed by Kaner and Azbel'[11] which seems to be small for the degenerate electrons, the inclination effect of the magnetic field to the surface is essential for the cyclotron resonance in metals. At present, δ/r_c is regarded as the measure of the critical angle, as is easily seen: The electron having the velocity components $v_{\parallel}$ and $v_{\perp}$, parallel and perpendicular to the magnetic field respectively, will contribute

$$(\delta/2\pi r_c(v_{\perp})\phi')\times(v_{\perp}/v_{\parallel})$$

times to the resonance, where ϕ' is the inclination angle of the magnetic field. Hence, if we take ϕ' as $\delta/2\pi r_c$ (r_c being the cyclotron radius of the electron having $v_{\perp}=v_{\parallel}$), it is easily seen that electrons contribution at least more than once to the resonance are only those satisfying $v_{\perp}\geqslant v_{\parallel}$. But, when $v_{\perp}$ becomes large, $r_c(v_{\perp})$ too becomes large, and accordingly, the contribution does not necessarily increase. Since, moreover, the lower limit of $v_{\parallel}$ is limited by the relaxation time to be of the order of $v_f\times(r_c/l)$, the contribution from the neighbourhood of $v_{\parallel}=0$ is of the order of $(\omega_c\tau/2\pi)\times(r_c/l)$. Thus, when the inclination amounts to about δ/r_c, the contribution to the resonance is lowered by about one power of s.

Finally, we will discuss the effect of the space charges on the surface impedance in metals. This effect was first considered by Heine[13] qualitatively and later by Rodriguez[15] for spherical energy surfaces, and it has been concluded that the effect of the space charges is in general small. But, as mentioned in Sec. 1, the combined effect of the space coarges and the anisotropy of the Fermi surface must be carefully examined in the anomalous skin effect region: According to the Drude-Lorentz theory of normal skin effect, the increase of the space charges is opposed by two forces, as may be seen immediately from (4.5) and (4.6). The first is a harmonic restoring force of which force constant is ω_p^2. The second force is of a viscous nature and is inversely proportional to the relaxation time of the conduction electrons. On the other hand, another viscous nature appears in the anomalous skin effect region. In order to clarify this fact, it is convenient to consider the imaginary part of the dielectric constant in the q-space. This is given by

$$\varepsilon_2 = -(\omega_p^2/\omega)\tau \,, \qquad (\omega\tau \ll 1)$$

$$\varepsilon_2 = -(\omega_p^2/\omega)(1/v_f q) \,, \qquad ((\omega/v_f q) \ll 1)$$

for the two cases of the normal and the extreme anomalous skin effect respectively. Thus, $(v_f q)^{-1}$ in the latter plays a role of the relaxation time in the former, and so we can obtain a finite surface impedance, even if, under the extreme anomalous limit. Therefore, it is possible, in principle, to consider that the effect of the space charges in metals occurs at the principal order s^{-1} when the anisotropy of the Fermi surface is complicated, and the magnetic field is not along a symmetry axis. In fact, as pointed out in the preceding section, the order of the contribution of this effect to the conductivity is lowered by one power of s^{-1} for the spheroidal energy surface whereas it is the third order of s^{-1} for an isotropic metal.

The authors wish to express their hearty thanks to Dr. D. Shoenberg who has kindly read and criticized the manuscript, and to Professor H. Nakano and Mr. K. Yamada of Nagoya University for their helpful discussions.

Appendix

Using the fact that the integrals for k_x in (3.14) vanish except for the even term of k_x in the products $v_i(\phi)v_j(\phi')$, we can obtain the formal solution of the conductivity tensor in the q-space. For the present purpose, it is convenient to write both the nine components of the conductivity tensor and the five functions Σ_i as the components of row vectors,

$$\boldsymbol{\sigma} = \frac{1}{4\pi^3} \cdot \frac{e^2 m^*}{\omega_c \hbar^3} \boldsymbol{\Sigma}(\boldsymbol{M}) \,, \qquad (\text{A. } 1)$$

where

$$\boldsymbol{\sigma} = (\sigma_{xx}, \sigma_{xy}, \sigma_{xz}, \sigma_{yx}, \sigma_{yy}, \sigma_{yz}, \sigma_{zx}, \sigma_{zy}, \sigma_{zz}) \,,$$
$$\boldsymbol{\Sigma} = (\Sigma_1, \Sigma_2, \Sigma_3, \Sigma_4, \Sigma_5) \,.$$

Here the transpose matrix of $(\boldsymbol{M})$, $(\boldsymbol{M})^T$, has been defined by

$$\left|\begin{matrix}
\hbar A_1^2 \,, & S_1^- \,, & P_1 \,, & S_1^+ \,, & 0 \\
0 \,, & S_2^- \,, & P_2 \,, & S_2^+ \,, & -(m^*/m_1)\Delta_5 \\
0 \,, & S_3^- \,, & P_3 \,, & S_3^+ \,, & (m^*/m_1)\Delta_4 \\
0 \,, & S_2^- \,, & P_2 \,, & S_2^+ \,, & (m^*/m_1)\Delta_5 \\
0 \,, & S_4^- \,, & P_4 \,, & S_4^+ \,, & 0 \\
0 \,, & S_5^- \,, & P_5 \,, & S_5^+ \,, & (\hbar/m^*) \\
0 \,, & S_3^- \,, & P_3 \,, & S_3^+ \,, & (m^*/m_1)\Delta_4 \\
0 \,, & S_5^- \,, & P_5 \,, & S_5^+ \,, & -(\hbar/m^*) \\
0 \,, & S_6^- \,, & P_6 \,, & S_6^+ \,, & 0
\end{matrix}\right| \qquad (\text{A. } 2)$$

where

$$\left.\begin{matrix}
S_1^\pm = a^{-1}B_1^2 \pm b^{-1}C_1^2 \,, & S_2^\pm = a^{-1}B_1B_2 \pm b^{-1}C_1C_2 \,, \\
S_3^\pm = a^{-1}B_1B_3 \pm b^{-1}C_1C_3 \,, & S_4^\pm = a^{-1}B_2^2 \pm b^{-1}C_2^2 \,, \\
S_5^\pm = a^{-1}B_2B_3 \pm b^{-1}C_2C_3 \,, & S_6^\pm = a^{-1}B_3^3 \pm b^{-1}C_3^2 \,,
\end{matrix}\right\} \qquad (\text{A. } 3)$$

$$\left.\begin{matrix}
P_1 = \dfrac{m^*}{\hbar}(2B_1C_1) \,, & P_2 = \dfrac{m^*}{\hbar}(B_1C_2 + B_2C_1) \,, \\
P_3 = \dfrac{m^*}{\hbar}(B_1C_3 + B_3C_1) \,, & P_4 = \dfrac{m^*}{\hbar}(2B_2C_2) \,, \\
P_5 = \dfrac{m^*}{\hbar}(B_2C_3 + B_3C_2) \,, & P_6 = \dfrac{m^*}{\hbar}(2B_3C_3) \,,
\end{matrix}\right\} \qquad (\text{A. } 4)$$

and the column vector of the Σ-functions, $\boldsymbol{\Sigma}^T$, as follows:

$$\boldsymbol{\Sigma}^T=[\exp(2\pi\gamma)-1]^{-1}\int_{-k_m}^{k_m} dk_x \int_0^{2\pi} d\psi \int_{\psi}^{\psi+2\pi} d\psi' \left|\begin{matrix} k_x{}^2\,, \\ E'\cos(\psi'+\psi)\,, \\ E'\sin(\psi'+\psi)\,, \\ E'\cos(\psi'-\psi)\,, \\ E'\sin(\psi'-\psi)\,, \end{matrix}\right| \exp[S(\psi')-S(\psi)]\,. \tag{A. 5}$$

The change of variables $2\xi=(\psi'+\psi)$ and $2\eta=(\psi'-\psi)$, that is,

$$\int_0^{2\pi} d\psi \int_{\psi}^{\psi+2\pi} d\psi' = 2\int_0^{\pi} d\eta \int_{\eta}^{\eta+2\pi} d\xi$$

enables one to calculate (A. 5) in the ascending powers of s, which is defined by

$$s=\frac{i\hbar q}{m^*\omega_c}\left[\frac{2E_f}{\hbar}\left(\frac{\cos^2\varphi}{a}+\frac{\sin^2\varphi}{b}\right)\right]^{1/2}, \tag{A. 6}$$

as follows:

$$\Sigma_1=\frac{4\pi}{\gamma}\,k_m{}^3\sum_{m=0}^{\infty}\frac{1}{(2m+3)(2m+1)}s^{2m}\Pi(m)\,, \tag{A. 7}$$

$$\Sigma_2=-\frac{4\pi}{\gamma}\cos 2\Theta E_f k_m\sum_{m=0}^{\infty}\frac{2m}{(2m+3)(2m+1)}s^{2m}\Pi(m)\,, \tag{A. 8}$$

$$\Sigma_3=-\tan 2\Theta\Sigma_2\,, \tag{A. 9}$$

$$\Sigma_4=\frac{4\pi}{\gamma}\,E_f k_m\sum_{m=0}^{\infty}\frac{2(m+1)}{(2m+3)(2m+1)}s^{2m}[\Pi(m)-(m+1)(2m+1)\Pi(m+1)]\,, \tag{A. 10}$$

$$\Sigma_5=-4\pi E_f k_m\sum_{m=0}^{\infty}\frac{2(m+1)}{2m+3}s^{2m}\Pi(m+1)\,, \tag{A. 11}$$

where

$$\Pi(m)=1/\prod_{\mu=1}^{m}(\gamma^2+\mu^2)\,,\qquad \Pi(0)=1\,. \tag{A. 12}$$

The magnitude of s is of the order of r_c/δ_{eff}, which is very large compared with unity for the metal in the anomalous skin effect conditions in a magnetic field of magnitude between 10^3 and 10^4 oersteds. Therefore, it is necessary to obtain the asymptotic expansion of Σ-functions.

Using the Anger-function[23], which is defined by

$$J_\nu(Z)=\frac{1}{\pi}\int_0^{\pi}\cos(\nu\theta-Z\sin\theta)d\theta\,, \tag{A. 13}$$

we can obtain the following relations:

$$\sum_{m=0}^{\infty}\frac{1}{(2m+3)(2m+1)}s^{2m}\Pi(m)=Z^{-3}\int_0^Z dZ(Z\Gamma(Z))\,, \tag{A. 14}$$

$$\sum_{m=0}^{\infty}\frac{2m}{(2m+3)(2m+1)}s^{2m}\Pi(m)=\left(Z\frac{\partial}{\partial Z}\right)\left(Z^{-1}\int_0^Z dZ\,Z\Gamma(Z)\right), \tag{A. 15}$$

$$\sum_{m=0}^{\infty}\frac{2(m+1)}{(2m+3)(2m+1)}s^{2m}\Pi(m)=\left(Z^{-1}\frac{\partial}{\partial Z}\right)\left(Z^{-1}\int_0^Z dZ\,Z\Gamma(Z)\right), \tag{A. 16}$$

$$\sum_{m=1}^{\infty}\frac{2m}{2m+1}s^{2m}\Pi(m)=\left(Z\frac{\partial}{\partial Z}\right)(Z^{-1}\Gamma(Z))\,, \tag{A. 17}$$

$$\sum_{m=1}^{\infty}\frac{(2m)^2}{2m+1}s^{2m}\Pi(m)=\left(Z\frac{\partial}{\partial Z}\right)^2(Z^{-1}\Gamma(Z))\,, \tag{A. 18}$$

where

$$\Gamma(Z)\equiv\frac{\nu\pi}{2\sin\nu\pi}\int_0^Z dZ(J_\nu(Z)+J_{-\nu}(Z))\,. \tag{A. 19}$$

and

$$\nu\equiv 2i\gamma\,,\qquad Z\equiv -2is\,. \tag{A. 20}$$

Here we have used the fact that

$$\sum_{m=0}^{\infty}s^{2m}\Pi(m)=\frac{\nu\pi}{2\sin\nu\pi}(J_\nu(Z)+J_{-\nu}(Z))\,. \tag{A. 21}$$

As the asymptotic expansion of $(J_\nu(Z)+J_{-\nu}(Z))$ is given by

$$J_\nu(Z)+J_{-\nu}(Z)\sim\left(2\sqrt{\frac{2}{\pi}}\cos\frac{\nu\pi}{2}\right)\frac{\cos(Z-\pi/4)}{\sqrt{Z}}-\left(\frac{2\nu\sin\nu\pi}{\pi}\right)\frac{1}{Z^2}\,, \tag{A. 22}$$

we obtain

$$\begin{aligned}\Gamma(Z)&=\frac{\nu\pi}{2\sin\nu\pi}\left[\int_0^\infty dZ(J_\nu(Z)+J_{-\nu}(Z))+\int_\infty^Z dZ(J_\nu(Z)+J_{-\nu}(Z))\right]\\&\sim\frac{\nu\pi}{2}\cot\frac{\nu\pi}{2}+\left(\frac{\nu\pi}{\sqrt{2\pi}\sin\nu\pi/2}\right)\frac{\sin(Z-\pi/4)}{\sqrt{Z}}+\frac{\nu^2}{Z}\,.\end{aligned} \tag{A. 23}$$

Similarly,

$$\begin{aligned}\int_0^Z Z\Gamma(Z)dZ&\sim Z^2\left(\frac{\nu\pi}{4}\cot\frac{\nu\pi}{2}\right)+Z\nu^2\\&\quad-\sqrt{Z}\cos\left(Z-\frac{\pi}{4}\right)\nu\pi\left(\sqrt{2\pi}\sin\frac{\nu\pi}{2}\right)^{-1}+\frac{\sqrt{2}}{4}\nu\pi\left(\sin\frac{\nu\pi}{2}\right)^{-1}.\end{aligned} \tag{A. 24}$$

Therefore, we can obtain the following asymptotic form:

$$(\text{A. }14)\sim\frac{1}{Z}\left(\frac{\nu\pi}{4}\cot\frac{\nu\pi}{2}\right)+\frac{1}{Z^2}(\nu^2)-\frac{\cos(Z-\pi/4)}{Z^{5/2}}\left(\frac{\nu\pi}{\sqrt{2\pi}\sin(\nu\pi/2)}\right), \tag{A. 25}$$

$$(\text{A. }15)\sim-\frac{1}{Z}\left(\frac{\nu\pi}{4}\cot\frac{\nu\pi}{2}\right)+\frac{\sin(Z-\pi/4)}{Z^{3/2}}\left(\frac{\nu\pi}{\sqrt{2\pi}\sin(\nu\pi/2)}\right)-\frac{1}{Z^2}(2\nu^2)\,, \tag{A. 26}$$

$$(\text{A. }16)\sim\frac{1}{Z}\left(\frac{\nu\pi}{4}\cot\frac{\nu\pi}{2}\right)+\frac{\sin(Z-\pi/4)}{Z^{3/2}}\left(\frac{\nu\pi}{\sqrt{2\pi}\sin(\nu\pi/2)}\right), \tag{A. 27}$$

$$(\text{A. }18)\sim\frac{1}{Z}\left(\frac{\nu\pi}{2}\cot\frac{\nu\pi}{2}\right)-\sqrt{Z}\sin\left(Z-\frac{\pi}{4}\right)\left(\frac{\nu\pi}{\sqrt{2\pi}\sin(\nu\pi/2)}\right)+\frac{1}{Z^2}(4\nu^2)\,, \tag{A. 28}$$

$$(\text{A. }17)\sim-\frac{1}{Z}\left(\frac{\nu\pi}{2}\cot\frac{\nu\pi}{2}\right)+\frac{\cos(Z-\pi/4)}{\sqrt{Z}}\left(\frac{\nu\pi}{\sqrt{2\pi}\sin(\nu\pi/2)}\right)-\frac{1}{Z^2}(2\nu^2)\,. \tag{A. 29}$$

If we confine ourselves only up to the second order term of $(1/s)$, the asymptotic form of the Σ-functions are then given by

$$\Sigma_1\sim\frac{4\pi}{\gamma}k_m^3\left[\frac{1}{Z}\left(\frac{\nu\pi}{4}\cot\frac{\nu\pi}{2}\right)+\frac{1}{Z^2}(\nu^2)\right]+O(Z^{-5/2})\,, \tag{A. 30}$$

$$\Sigma_2 \sim \frac{4\pi}{\gamma} \cos 2\Theta E_f k_m \left[\frac{1}{Z}\left(\frac{\nu\pi}{4} \cot \frac{\nu\pi}{2}\right) - \frac{\sin (Z-\pi/4)}{Z^{3/2}} \left(\frac{\nu\pi}{\sqrt{2\pi} \sin (\nu\pi/2)} \right) + \frac{1}{Z^2}(2\nu^2) \right], \tag{A. 31}$$

$$\Sigma_3 = -\tan 2\Theta \Sigma_2 , \tag{A. 32}$$

$$\Sigma_4 \sim \frac{4\pi}{\gamma} E_f k_m - \left[\frac{1}{Z}\left(\frac{\nu\pi}{4} \cot \frac{\nu\pi}{2}\right) - \frac{\sin (Z-\pi/4)}{Z^{3/2}} \left(\frac{\nu\pi}{\sqrt{2\pi} \sin (\nu\pi/2)} \right) \right], \tag{A. 33}$$

$$\Sigma_5 \sim O(Z^{-5/2}) . \tag{A. 34}$$

From these equations, we can obtain the conductivity in the extreme anomalous limit.

References

1) M. Ia. Azbel' and E. A. Kaner: J. Exptl. Theoret. Phys. (U.S.S.R) **30** (1956) 811; **32** (1957) 896.
2) W. Shockley: Phys. Rev. **90** (1953) 491.
3) E. Fawcett: Phys. Rev. **103** (1956) 1582.
4) A. F. Kip *et al.*: Phys. Rev. **108** (1957) 494.
5) P. A. Bezuglyi and A. A. Galkin: J. Exptl. Theoret. Phys. (U.S.S.R.) **33** (1957) 1076; **34** (1958) 236.
6) J. E. Aubrey and R. G. Chambers: J. Chem. Phys. Solid **3** (1957) 128.
7) J. K. Galt *et al.*: Phys. Rev. Letters **2** (1959) 292.
8) D. N. Langenberg and T. M. Moore: Phys. Rev. Letters **3** (1959) 137.
9) E. Fawcett: Phys. Rev. Letters **3** (1959) 139.
10) D. N. Langenberg and T. M. Moore: Phys. Rev. Letters **3** (1959) 328.
11) E. A. Kaner and M. Ia. Azbel': J. Exptl. Theoret. Phys. (U.S.S.R.) **33** (1957) 1461.
12) E. A. Kaner: J. Exptl. Theoret. Phys. (U.S.S.R.) **33** (1957) 1472.
13) V. Heine: Phys. Rev. **107** (1957) 431.
14) D. C. Mattis and G. Dresselhaus: Phys. Rev. **111** (1958) 403.
15) S. Rodriguez: Phys. Rev. **112** (1958) 1616.
16) W. Shockley: Phys. Rev. **39** (1950) 191.
17) G. E. H. Reuter and E. H. Sondheimer: Proc. Roy. Soc. **A**, **195** (1948) 336.
18) Dresselhaus, Kip and Kittel: Phys. Rev. **98** (1955) 368; **100** (1955) 618.
19) T. Holstein: Phys. Rev. **96** (1954) 535.
20) R. N. Gurzhi: J. Exptl. Theoret. Phys. (U.S.S.R.) **33** (1957) 660.
21) L. D. Landau: J. Exptl. Theoret. Phys. (U.S.S.R.) **30** (1956) 1058.
22) V. P. Silin: J. Exptl. Theoret. Phys. (U.S.S.R.) **33** (1957) 1282.
23) G. N. Watson: *Theory of Bessel Functions* (Cambridge, 1922).

JOURNAL OF THE PHYSICAL SOCIETY OF JAPAN, Vol. 16, No. 10, OCTOBER, 1961

The Shielding of a Fixed Charge in a Metal

By Shozo SHINOHARA

Department of Physics, Faculty of Science, Hokkaido University, Sapporo, Japan

(Received June 3, 1961)

The shielding of a fixed charge of an impurity atom in a metal has been calculated self-consistently by means of the first order perturbation theory without use of Poisson's equation. It has turned out that the displaced charge density of conduction electrons is finite at the center of the fixed charge, and that the dependence of the exchange potential upon the wave vector results in an uniformly displaced charge density in the crystal. The theory has been extended to the case of the degenerate electron gas including two static charges.

§ 1. Introduction

If a few impurities are put in a monovalent metal and are ionized, the new conduction electron density of the metal is determined by the static charges of the ionized impurities and the mutual Coulomb interaction of the electrons. As a result the charges of impurities are shielded by these displaced electrons. Mott and others[1)–7)] have studied this problem with various approximate methods. For example, Friedel attempted to attack this problem with a self-consistent method which was a physically reasonable approximation, and Langer and Vosko solved it by the quantum-mechanical many-body theory and made it clear how far the displaced charge density depends upon the correlation of electrons due to their mutual Coulomb interaction. Most of these calculations, however, dealt with only the Coulomb interaction but not the exchange one.

The present author and Toya treated this problem with the linear approximation of the perturbation theory taking the two interactions into account. To assure the self-consistency of the Coulomb and the exchange potential, however, they had to use a rough approximation. Their displaced charge density turned out to be of the Thomas-Fermi type, of which the shielding constant was larger than in the case that only the Coulomb potential existed, and therefore, to diverge at the center of the impurity ion.

In the present paper we shall treat a monovalent metal, into which a fixed charge, $(Z+1)e$, of impurity ion is inserted. To determine the distributions of conduction electrons in this metal, we shall consider the Coulomb potential of the impurity charge and the mutual Coulomb and the exchange interaction of electrons. Using self-consistent method, we shall estimate the charge density of these displaced electrons with the first order perturbation theory, but with out using the Poisson's equation. It will be shown that the displaced charge density is finite at the center of the impurity ion and has a longer tail than in the case of the Coulomb potential alone, and that an uniformly displaced charge density appears in the crystal owing to the denpendence of the exchange potential upon the wave vector of the electron, though it does not appear in the case of the Coulomb potential alone.

§ 2. Effective Potential

We write the Hamiltonian of one electron approximation of Hartree-Fock for the system as follows;

$$H=H_0+H' . \tag{1}$$

Here, the perturbation term H' consists of three terms, that is the Coulomb interaction energy, V_1, and the exchange energy, A, of a conduction electron with the other electrons, and the Coulomb interaction energy, V_2, with the ionized impurity;

$$H'=V_1+V_2+A . \tag{2}$$

The eigenfunctions and the eigenvalues of the Hamiltonian H_0 of the unperturbed system are assumed to be those of the free electrons,

$$H_0\Psi_k=E_k\Psi_k \tag{3}$$

$$\Psi_k=\frac{1}{\sqrt{\Omega}}e^{i\boldsymbol{k}\cdot\boldsymbol{r}}\chi_s , \tag{4}$$

and

$$E_k=\frac{\hbar^2}{2m}k^2 . \tag{5}$$

In (4) χ_s is the spin function, and Ω is the volume of the crystal.

The perturbed states of the Hamiltonian H can be written in the first order approximation of H' as follows;

$$\varphi_k=\Psi_k+\sum_{k'\neq k}\frac{H'_{kk'}}{E_k-E_{k'}}\Psi_{k'}+\cdots\ , \tag{6}$$

where we assume that φ_k have the unmixed spin states. Each of V_1, V_2 and A in (2) is expanded in the Fourier series,

$$V_1=\frac{1}{N}\sum_{q}V_1(\boldsymbol{q})e^{i\boldsymbol{q}\cdot\boldsymbol{r}}\ , \tag{7}$$

$$V_2=\frac{1}{N}\sum_{q}V_2(\boldsymbol{q})e^{i\boldsymbol{q}\cdot\boldsymbol{r}}\ , \tag{8}$$

and

$$A=\frac{1}{N}\sum_{q}A(\boldsymbol{q})e^{i\boldsymbol{q}\cdot\boldsymbol{r}}\ , \tag{9}$$

where N is the number of the lattice points. For these Fourier coefficients

$$V_1(\boldsymbol{q})=\frac{N}{\Omega}\int V_1e^{-i\boldsymbol{q}\cdot\boldsymbol{r}}d\boldsymbol{r}\ , \tag{10}$$

$$V_2(\boldsymbol{q})=\frac{N}{\Omega}\int V_2e^{-i\boldsymbol{q}\cdot\boldsymbol{r}}d\boldsymbol{r} \tag{11}$$

and

$$A(\boldsymbol{q})=\frac{N}{\Omega}\int Ae^{-i\boldsymbol{q}\cdot\boldsymbol{r}}d\boldsymbol{r}\ . \tag{12}$$

The relations (7), (8) and (9) give being substituted into (6),

$$\varphi_k=\left(\frac{1}{\Omega}\right)^{\frac{1}{2}}e^{i\boldsymbol{k}\cdot\boldsymbol{r}}\ \chi_s\left[1+\frac{1}{N}\sum_{q\neq0}\frac{V_1(\boldsymbol{q})+V_2(\boldsymbol{q})+A(\boldsymbol{q})}{E_k-E_{k+q}}e^{i\boldsymbol{q}\cdot\boldsymbol{r}}\right]. \tag{13}$$

Since V_1 is the Coulomb interaction operator between conduction electrons, and A the exchange interaction operator, V_1 and A are defined as follows[8)],

$$V_1\Psi_{\boldsymbol{K}}(\boldsymbol{r}_1)=\sum_{s_2}\sum_{k}\int\varphi_k^*(\boldsymbol{r}_2)\varphi_k(\boldsymbol{r}_2)U(r_{12})d\boldsymbol{r}_2\Psi_{\boldsymbol{K}}(\boldsymbol{r}_1)\ , \tag{14}$$

and

$$A\Psi_{\boldsymbol{K}}(\boldsymbol{r}_1)=-\sum_{k}\int\varphi_k^*(\boldsymbol{r}_2)\Psi_{\boldsymbol{K}}(\boldsymbol{r}_2)U(r_{12})d\boldsymbol{r}_2\varphi_k(\boldsymbol{r}_1)\ . \tag{15}$$

Here, the set of functions $\varphi_k(\boldsymbol{r})$ are the occupied one-particle states of the electron gas, $U(r_{12})$ is the electron-electron interaction, $\Psi_{\boldsymbol{K}}(\boldsymbol{r}_1)$ is any one-electron wave function, and $\sum_{s_2}$ represents the summation with respect to spin states.

Then we rewrite eq (10) as:

$$V_1(\boldsymbol{q})=\frac{N}{\Omega}\int e^{-i(\boldsymbol{K}+\boldsymbol{q})\cdot\boldsymbol{r}_1}\alpha_1V_1e^{i\boldsymbol{K}\cdot\boldsymbol{r}_1}\alpha_1d\boldsymbol{r}_1\ , \tag{16}$$

where α_1 is the spin-up function. When the relation (14), in which $\Psi_{\boldsymbol{K}}(\boldsymbol{r}_1)$ is replaced by $\{\exp(i\boldsymbol{K}\cdot\boldsymbol{r}_1)\}\alpha_1$, is substituted into (16),

$$V_1(\boldsymbol{q})=\frac{N}{\Omega}\int e^{-i(\boldsymbol{K}+\boldsymbol{q})\cdot\boldsymbol{r}_1}\alpha_1\sum_{2}\sum_{k}\int\varphi_k^*(\boldsymbol{r}_2)\varphi_k(\boldsymbol{r}_2)U(r_{12})d\boldsymbol{r}_2e^{i\boldsymbol{K}\cdot\boldsymbol{r}_1}\alpha_1d\boldsymbol{r}_1\ . \tag{17}$$

Similarly, from (12) and (15)

$$A(\boldsymbol{q})=-\frac{N}{\Omega}\int e^{-i(\boldsymbol{K}+\boldsymbol{q})\cdot\boldsymbol{r}_1}\alpha_1\sum_{k}\int\varphi^*(\boldsymbol{r}_2)e^{i\boldsymbol{K}\cdot\boldsymbol{r}_2}\alpha_2U(r_{12})d\boldsymbol{r}_2\varphi_k(\boldsymbol{r}_1)d\boldsymbol{r}_1\ , \tag{18}$$

where spin states have the same direction.

If we use eq. (13) for φ_k in (17) and (18), we obtain the following relations of $V_1(\boldsymbol{q})$ and $A(\boldsymbol{q})$ in the first order approximation;

$$\begin{aligned}V_1(\boldsymbol{q})=2\sum_{k}\Bigg\{&\frac{(2\pi)^3}{\Omega}J(\boldsymbol{q})\delta(\boldsymbol{q})+\frac{1}{N}J(\boldsymbol{q})\frac{V_1(\boldsymbol{q})+V_2(\boldsymbol{q})+A(\boldsymbol{q})}{E_k-E_{k+q}}\\&+\frac{1}{N}J(\boldsymbol{q})\frac{V_1^*(-\boldsymbol{q})+V_2^*(-\boldsymbol{q})+A^*(-\boldsymbol{q})}{E_k-E_{k-q}}\Bigg\}\ ,\end{aligned} \tag{19}$$

and

$$A(\boldsymbol{q})=-\sum_{\boldsymbol{k}}\left\{\frac{(2\pi)^3}{\Omega}J(\boldsymbol{K}-\boldsymbol{k})\delta(\boldsymbol{q})+\frac{1}{N}J(\boldsymbol{K}-\boldsymbol{k})\frac{V_1(\boldsymbol{q})+V_2(\boldsymbol{q})+A(\boldsymbol{q})}{E_{\boldsymbol{k}}-E_{\boldsymbol{k}+\boldsymbol{q}}}\right.$$
$$\left.+\frac{1}{N}J(\boldsymbol{K}-\boldsymbol{k}+\boldsymbol{q})\frac{V_1^*(-\boldsymbol{q})+V_2^*(-\boldsymbol{q})+A^*(-\boldsymbol{q})}{E_{\boldsymbol{k}}-E_{\boldsymbol{k}-\boldsymbol{q}}}\right\}, \tag{20}$$

where $J(\boldsymbol{q})$ is the Fourier coefficient of $U(r)$;

$$J(\boldsymbol{q})=\frac{N}{\Omega}\int U(r)e^{i\boldsymbol{q}\cdot\boldsymbol{r}}\,d\boldsymbol{r}\,. \tag{21}$$

Since $U(r)$ is the Coulomb interaction between electrons,

$$J(\boldsymbol{q})=\frac{N}{\Omega}\frac{4\pi e^2}{q^2}\,, \qquad q\neq 0\,. \tag{22}$$

Using (5) and (22), and replacing the summation over $\boldsymbol{k}$ in (19) by the integration, $V_1(\boldsymbol{q})$ with $\boldsymbol{q}\neq 0$ becomes as follows;

$$V_1(\boldsymbol{q})=-\frac{2e^2mk_0}{\pi\hbar^2q^2}f(q)(V_1(\boldsymbol{q})+V_2(\boldsymbol{q})+A(\boldsymbol{q}))\,, \qquad q\neq 0\,, \tag{23}$$

where

$$f(q)=1+\frac{4k_0^2-q^2}{4k_0q}\log\left|\frac{2k_0+q}{2k_0-q}\right|, \tag{24}$$

and k_0 is the magnitude of the wave vector of the Fermi-surface.

In the similar way, from eq. (20), $A(\boldsymbol{q})$ with $\boldsymbol{q}\neq 0$ is equal to

$$A(\boldsymbol{q})=-\frac{\Omega}{(2\pi)^3N}(V_1(\boldsymbol{q})+V_2(\boldsymbol{q})+A(\boldsymbol{q}))\int d\boldsymbol{k}\frac{J(\boldsymbol{K}-\boldsymbol{k})+J(\boldsymbol{K}+\boldsymbol{k}+\boldsymbol{q})}{E_{\boldsymbol{k}}-E_{\boldsymbol{k}+\boldsymbol{q}}}\,, \qquad q\neq 0\,. \tag{25}$$

It is very difficult to integrate (25) over $\boldsymbol{k}$ analytically for any $\boldsymbol{K}$. However, when $\boldsymbol{K}$ has the same direction with $\boldsymbol{q}$ the integration of (25) can be done, and $A(\boldsymbol{q})$ becomes

$$A(\boldsymbol{q})=\frac{2e^2m}{\hbar^2\pi q}F(q;K)(V_1(\boldsymbol{q})+V_2(\boldsymbol{q})+A(\boldsymbol{q}))\,, \qquad q\neq 0\,, \tag{26}$$

where

$$F(q;K)=\int_0^{k_0}dk\frac{k}{k^2+K^2+Kq}\left\{\log\left|\frac{2k+q}{2k-q}\right|+\log\left|\frac{K+k}{K-k}\right|-\log\left|\frac{K+q+k}{K+q-k}\right|\right\}. \tag{27}$$

It seems that eq. (26) represents approximately the dependency of the exchange potential on the magnitude of wave vector $\boldsymbol{K}$, though it is not the equation for any direction of $\boldsymbol{K}$, and we assume that the exchange potential does not depend on the direction of $\boldsymbol{K}$.

For convenience we shall measure q, k and K in units of k_0. Putting q, k and K to be equal to k_0x, k_0y and k_0z respectively, $f(q)$ and $F(q;\ K)$ become as follows;

$$f(x)=1+\frac{4-x^2}{4x}\log\left|\frac{2+x}{2-x}\right|, \tag{28}$$

$$F(x;\ z)=\int_0^1 dy\frac{y}{y^2+z^2+xz}\left\{\log\left|\frac{2y+x}{2y-x}\right|+\log\left|\frac{z+y}{z-y}\right|-\log\left|\frac{z+x+y}{z+x-y}\right|\right\} \tag{29}$$

Fig. 1 shows the curves of $f(x)$ and $F(x;\ z)$ vs. x, in which z has the value zero or 1.

The exchange potential of the free electrons decreases with the magnitude of the wave $\boldsymbol{K}$, vector and its value of the electron which has $\boldsymbol{K}=0$ (or $z=0$) is about three times as large as that of the Fermi wave vector ($z=1$).

From eqs. (23) and (26) the ratio of $A(\boldsymbol{q})$ and $V_1(\boldsymbol{q})$ becomes

$$\frac{A(x)}{V_1(x)}=-\frac{xF(x;\,z)}{f(x)}\,, \tag{30}$$

and therefore, the correction by the exchange interaction depends on the function $xF(x;\,z)$. The curves of $xF(x;\,z)$ vs. x are represented in Fig. 2 in two cases of $z=0$ and 1.

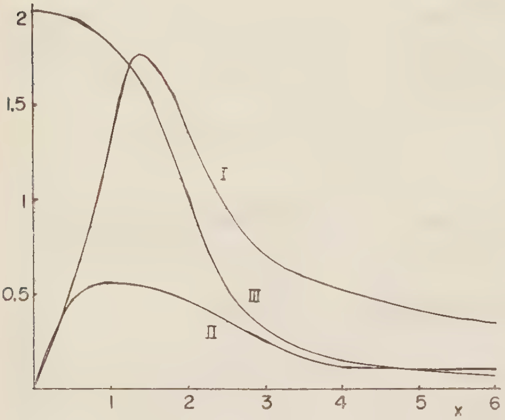

Fig. 1. The behaviors of $F(x;\,z)$ and $f(x)$ vs. x. The curve I is $F(x;\,0)$, the curve II $F(x;\,1)$ and the curve III $f(x)$.

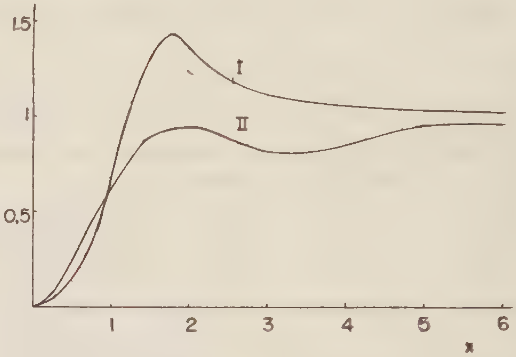

Fig. 2. The behaviors of $xF(x;\,z)$ vs. x, of which the curve I is $xF(x;\,0)$ and the curve 2 $xF(x;\,1)$.

The Fourier coefficients of the Coulomb and the exchange potential are obtained by solving simultaneously eqs. (24) and (26);

$$V_1(\boldsymbol{q})=-V_2(\boldsymbol{q})\frac{(2k_0/\pi a_H)\,f(q)}{q^2+(2k_0/\pi a_H)\,f(q)-(2q/\pi a_H)\,F(q;\,K)}\,,\qquad q\neq 0 \tag{31}$$

and

$$A(\boldsymbol{q})=V_2(\boldsymbol{q})\frac{(2q/\pi a_H)F(q;K)}{q^2+(2k_0/\pi a_H)\,f(q)-(2q/\pi a_H)\,F(q;\,K)}\,,\qquad q\neq 0\,, \tag{32}$$

where a_H is the Bohr radius $\hbar^2/me^2$.

In the next place, when we do not consider the exchange interaction between conduction electrons, we obtain the following $V_1(\boldsymbol{q})$ from eq. (23) in which A equals to zero;

$$V_1^{(B)}(\boldsymbol{q})=-V_2(\boldsymbol{q})\frac{(2k_0/\pi a_H)\,f(q)}{q^2+(2k_0/\pi a_H)f(q)}\,,\qquad q\neq 0\,. \tag{33}$$

The formula (33) is equivalent to the result without use of (14), but with use of Poisson's equation.

§ 3. The Displaced Electron Density

The charge density due to the displaced electrons is

$$\begin{aligned}\Delta n(r)&=\sum_s\Bigl(\sum_{\boldsymbol{k}}^{k_0}\varphi_{\boldsymbol{k}}^*\varphi_{\boldsymbol{k}}-\sum_{\boldsymbol{k}}^{k_F}\Psi_{\boldsymbol{k}}^*\Psi_{\boldsymbol{k}}\Bigr)\\&=\frac{1}{3\pi^2}(k_0^3-k_F^3)+\frac{4}{\Omega N}\sum_{\boldsymbol{k}}\sum_{\boldsymbol{q}\neq 0}\frac{V_1(\boldsymbol{q};\,\boldsymbol{k})+V_2(\boldsymbol{q})+A(\boldsymbol{q};\,\boldsymbol{k})}{E_{\boldsymbol{k}}-E_{\boldsymbol{k}+\boldsymbol{q}}}\,e^{i\boldsymbol{q}\cdot\boldsymbol{r}}\,,\end{aligned} \tag{34}$$

where k_F refers to the magnitude of the Fermi wave vector in the unperturbed system, and

(k_0-k_f) is very small as compared with k_F. The Fourier coefficients $A(\boldsymbol{q})$ depend on the wave vector $\boldsymbol{k}$ from (26), and therefore it is difficult to carry out the summation over $\boldsymbol{k}$ in eq. (34).

Here, we neglect the dependency of $A(\boldsymbol{q})$ and $V_1(\boldsymbol{q})$ on $\boldsymbol{k}$, and put the second term in the right hand side of eq. (34) to be equal to the term

$$\frac{4}{\Omega N}\sum_{\boldsymbol{q}\neq 0}(V_1(\boldsymbol{q};K)+V_2(q;K)+A(q;K))\sum_{\boldsymbol{k}}\frac{1}{E_{\boldsymbol{k}}-E_{\boldsymbol{k}+\boldsymbol{q}}}e^{i\boldsymbol{q}\cdot\boldsymbol{r}},$$

by introducing the appropriate value K of $\boldsymbol{k}$ in $A(\boldsymbol{q})$ and $V_1(\boldsymbol{q})$;

$$\Delta n(r)=\frac{k^2{}_F}{\pi^2}(k_0-k_F)-\frac{mk_0}{2N\pi^2\hbar^2}\sum_{\boldsymbol{q}\neq 0}(V_1)q;K)+V_2(q(+A(q;K))e^{i\boldsymbol{q}\cdot\boldsymbol{r}}f(q)\,. \tag{35}$$

If $V_1(\boldsymbol{q})$ and $A(\boldsymbol{q})$ do not depend on $\boldsymbol{k}$ at all, for example in the case neglecting the exchange potential, the first term in the right hand side of eq. (34) is equal to the second term for $\boldsymbol{q}=0$ by the Friedel's condition, that the Fermi energy does not vary by the perturbation[9]. Therefore, the summation over $\boldsymbol{q}$ can be taken by including $\boldsymbol{q}=0$, and the uniformly displaced charge density disappears.

When $V_1(\boldsymbol{q})$ and $A(\boldsymbol{q})$ depend on $\boldsymbol{k}$, the first term of (35) is not always equal to the second term of $\boldsymbol{q}=0$, and the uniformly displaced charge density appears in the metal including the impurity atom.

Since

$$V_2=-(Ze^2/r)\,, \tag{36}$$

we have

$$V_2(\boldsymbol{q})=-\frac{N}{\Omega}\frac{4\pi Ze^2}{q^2}\,,\quad q\neq 0\,, \tag{37}$$

where Z is the difference of valency between a matrix atom and the impurity.

If Eqs. (31), (32) and (37) are substituted into (35), and the summation over q is replaced by the integration, the displaced charge density is obtained;

$$\Delta n(r)=\frac{k_F{}^2}{\pi^2}(k_0-k_F)+\frac{Zk_F}{\pi^3a_H}\int_0^\infty dq\frac{q\sin qr}{r}\frac{f(q)}{q^2+(2k_F/\pi a_H)f(q)-(2q/\pi a_H)F(q;K)}\,, \tag{38}$$

where the integrand in the second term of the right hand side is zero in the point $q=0$.

The Fermi wave vector k_0 of the perturbed system is determined by the normalization of $\Delta n(\boldsymbol{r})$;

$$4\pi\int_0^\infty \Delta n(r)r^2dr=Z\,. \tag{39}$$

In the case of no exchange interaction, the displaced charge density becomes exactly

$$\Delta n^{(B)}(r)=\frac{Zk_F}{\pi^3a_H}\int_0^\infty dq\frac{q\sin qr}{r}\frac{f(q)}{q^2+(2k_F/\pi a_H)f(q)}\,, \tag{40}$$

by using (32) instead of (31) and (33), and it coincides with the result obtained by Langer and Vosko, who consider only the bubble diagrams of Gell-Mann and Brueckner.

We measure k in units k_F, r in $1/k_F$, and $\Delta n(r)$ in $(k_F)^3$. Then introducting the density via

$$n_0=1\Big/\left(\frac{4\pi}{3}r_s{}^3a_H{}^3\right)\,, \tag{41}$$

and putting r_s and Z to be 3 and 1 respectively, we rewrite the second term of (38) as follows;

$$5.041\times 10^{-2}\int_0^\infty dx\frac{x\sin xr}{r}\frac{f(x)}{x^2+0.9951f(x)-0.9951xF(x;\bar{z})}\,. \tag{42}$$

Fig. 3 shows three curves of (42), of which the parameter $\bar{z}$ is equal to zero and 1 and $F(x;\,\bar{z})$ is zero respectively, in comparison with the Thomas-Fermi charge density.

The curve I is the charge density in which the exchange potential is overestimated, and the curve II is the case of its too small estimation. The curve III is $\Delta n^{H}(r)$ of Langer and Vosko, which is eq. (40).

Table I. The formulae (42) and (40), and the Thomas-Fermi charge density for $r_s=3.0$

r	Formula (42)		Formula (40)*	Thomas-Fermi charge density*
	$\bar{z}=0$	$\bar{z}=1$		
0	0.231	0.147	0.1276	
0.4	0.173	0.105	0.08847	0.2242
1.0	0.105	0.0548	0.04441	0.03847
1.6	0.0429	0.0224	0.01767	0.01031
2.2	0.00275	0.00497	0.004651	0.003217
2.5	−0.00625	0.00101	0.001680	0.001854
3.1	−0.0101	−0.00137	−0.0002945	
3.7	−0.00477	−0.000886	−0.00006459	

* According to the reference (6).

In the case of only the Coulomb part as the perturbation potential, the number of electrons in the region from the origin of the curve III to its first node is equal to about 1, and the positive charge of the impurity is nearly shielded. The curve I or II shows that more electrons than 1 crowd in the equivalent region by the attractive force of the exchange interaction, and then the next region connected by it is positively charged. Accordingly, the displaced charge density of the curve I or II has a more far-reaching tail than the curve III.

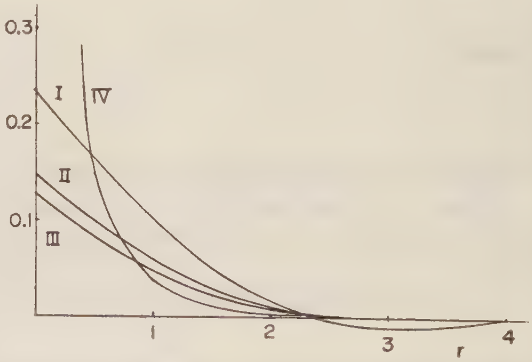

Fig. 3. The displaced charge densities for $r_s=3.0$ vs. r. The curve I corresponds to the formula (42) for $\bar{z}=0$, the curve II to that for $\bar{z}=1$, the curve III to that for $F(x;\,\bar{z})=0$ and the curve VI represente the Thomas-Fermi charge density.

§ 4. The Case Including Two Static Charges

The Hamiltonian of the electron gas system, in which there are two ionized impurities separated by $\boldsymbol{R}$ with each other, can be written to be

$$H=H_0+V_1+V_2(|\boldsymbol{r}|)+V_3(|\boldsymbol{r}-\boldsymbol{R}|)+A\,. \tag{43}$$

The Fourier coefficients $V_1(\boldsymbol{q})$ and $A(\boldsymbol{q})$ for $\boldsymbol{q}\neq 0$ must satisfy the following self-consistent equations in a similar approximation as in eqs. (23) and (26):

$$V_1(\boldsymbol{q})=-\frac{2e^2mk_0}{\pi\hbar^2q^2}f(q)(V_1(\boldsymbol{q})+A(\boldsymbol{q})+V_2(\boldsymbol{q})+\tfrac{1}{2}V_3(\boldsymbol{q})e^{-i\boldsymbol{q}\cdot\boldsymbol{R}}+\tfrac{1}{2}V_3(\boldsymbol{q})e^{i\boldsymbol{q}\cdot\boldsymbol{R}}) \tag{44}$$

and

$$A(\boldsymbol{q})=\frac{2e^2m}{\pi\hbar^2q}\{F(q;\,K)(V_1(\boldsymbol{q})+A(\boldsymbol{q})+V_2(\boldsymbol{q})+F_1(q;\,K)V_3(\boldsymbol{q})e^{-i\boldsymbol{q}\cdot\boldsymbol{R}}+F_2(q;K)V_3(\boldsymbol{q})e^{i\boldsymbol{q}\cdot\boldsymbol{R}}\}\,, \tag{45}$$

where

$$F_1(q;\,K)=\int_0^{k_0}dk\frac{k}{qK+K^2+k^2}\left\{\tfrac{1}{2}\log\left|\frac{q+2k}{q-2k}\right|+\log\left|\frac{K+k}{K-k}\right|\right\}, \tag{46}$$

$$F_2(q;\,K)=\int_0^{k_0} dk \frac{k}{qK+K^2+k^2}\left\{\tfrac{1}{2}\log\left|\frac{q+2k}{q-2k}\right|-\log\left|\frac{K+q+k}{K+q-k}\right|\right\}, \tag{47}$$

and

$$F(q;\,K)=F_1(q;\,K)+F_2(q;\,K)\,. \tag{48}$$

The displaced charge density of this case becoms as follows;

$$\begin{aligned}\Delta n_2(r)&=\frac{k_F{}^2}{\pi^2}(k_0-k_F)-\frac{mk_0}{2N\pi^2\hbar^2}\sum_{\boldsymbol{q}\neq 0}(V_1(q;\,K)+V_3(\boldsymbol{q})e^{-i\boldsymbol{q}\cdot\boldsymbol{R}}+A(q;\,K))e^{i\boldsymbol{q}\cdot\boldsymbol{r}}f(q)\\&=\frac{k_F{}^2}{\pi^2}(k_0-k_F)+\Delta n(r)+\Delta n(|\boldsymbol{r}-\boldsymbol{R}|)\\&\quad+\frac{Zk_F}{\pi^3 a_H}\int_0^\infty \frac{dq}{q}\left(\frac{\mathrm{sid}\,q|\boldsymbol{r}-\boldsymbol{R}|}{|\boldsymbol{r}-\boldsymbol{R}|}-\frac{\sin q|\boldsymbol{r}+\boldsymbol{R}|}{|\boldsymbol{r}+\boldsymbol{R}|}\right)\frac{f(q)(\frac{1}{2}f(q)-F_2(q;\,K))}{q^2+(2k_0/\pi a_n)f(q)-(2q/\pi a_H)F(q;\,K)},\end{aligned} \tag{49}$$

where the Fermi wave vector k_0 of the perturbed system is determined by the normalization of $\Delta n_2(r)$;

$$4\pi\int \Delta n_2(r)r^2 dr=2Z\,. \tag{50}$$

In conclusion, the magnitude of the correction by the exchange interaction of free electrons is about 30 percents of the displaced charge density caused by only the Coulomb interaction, and there appears some uniformly displaced charge density when the perturbation potential depends on the wave vector $\boldsymbol{k}$.

References

1) N. F. Mott and H. Jones: *Properties of Metals and Alloys* (1936).
2) S. Shinohara: J. Faculty of Science, Hokkaido Univ. II, Vol. IV 377 (1955).
3) J. Friedel: Adv. Phys. **3** (1954) 446.
4) W. Kohn and S. H. Vosko: Phys. Rev. **119** (1960) 912.
5) N. Takimoto: J. Phys. Soc. Japan **14** (1959) 1142.
6) J. S. Langer and S. H. Vosko: J. Phys. Chem. Solids **12** (1960) 196.
7) B. D. Silverman and P. R. Weiss: Phys. Rev. **114** (1959) 989.
8) A. W. Overhauser: J. Phys. Chem. Solids **13** (1960) 71.
9) K. Yosida: Phys. Rev. **106** (1957) 893.

Journal of the Physical Society of Japan Vol. 16, No. 10, October, 1961

Galvanomagnetic Effects in Bismuth Selenide Bi_2Se_3

By Kimio Hashimoto

Department of Physics, Faculty of Science,
Kyusyu University, Hukuoka

(Received June 5, 1961)

The galvanomagnetic effects have been investigated in single crystal specimens of *n*-type Bi_2Se_3 at 90°K. The experimental results are shown to be reasonably consistent with the six-valley model of the band structure in which the energy minima are situated on the reflection planes. The constant energy surfaces associated with the valley are ellipsoidal and the ratios of the principal effective masses are $m_2/m_1=0.33$ and $m_3/m_1=4.2$. The ellipsoids are stretched in a direction nearly parallel to the three-fold axis of the crystal. The measured values of the Hall coefficient and thermo-electric power are nearly isotropic.

§1. Introduction

Bi_2Se_3 as well as Bi_2Te_3 and their solid solutions has been the subject of a number of investigations[1)–6)] in recent years mainly because of the interest in their thermo-electric applications.

Some information on the structure of the energy band in Bi_2Te_3 has been obtained by several authors[7)–11)]. Drabble and his coworkers[8),9)] investigated the galvanomagnetic effects, and they attempted the determination of the band structure of Bi_2Te_3 by the six-valley model. However, there are only few investigations on Bi_2Se_3, because probably of the difficulty in the preparation of its single crystals, but the researches of the galvanomagnetic effect in this materials may be of fundamental interest. It is highly desirable to carry out the study on Bi_2Se_3.

The crystal of Bi_2Se_3 belongs to the Laue symmetry D_{3d} which has one three-fold axis perpendicular to a cleavage surface, three two-fold axes of rotation in the cleavage surface, and three reflection planes including the three-fold axis; this structure is of the same crystal symmetry as that of Bi_2Te_3.

The investigations of the resistivity, Hall coefficient, thermal conductivity and thermo-electric power on the polycrystal or single crystal specimens of Bi_2Se_3 have been published by some authors[1)–5)]. According to their works Bi_2Se_3 is a semiconductor which has the energy gap of 0.2∼0.3 ev. No investigation of *p*-type Bi_2Se_3 has yet been carried out, because the conduction type of Bi_2Se_3 is unable to be changed from *n*- to *p*-type even by the deviation of compound compositions or by doping a number of impurity elements.

This paper reports the experimental measurements of the resistivity, Hall coefficient and thermo-electric power in the temperature region from about 90°K up to room temperature, and the galvanomagnetic effects at about 90°K in single crystals of *n*-type Bi_2Se_3.

The phenomenological analysis on the galvanomagnetic effects of the crystals having Lauesymmetry D_{3d} has been carried out by Juretschke[12)], and Okada[13)]. Drabble and his coworkers[8),9)] have reported the analysis of galvanomagnetic effects for *n*- and *p*-type Bi_2Te_3 using the results of Drabble and Wolfe[7)], and discussed the galvanomagnetic coefficients on the basis of the many-valley model applying Juretschke's phenomenological theory to the crystal of the crystal class 3 m. The present analysis for Bi_2Se_3 has been treated by mean of the almost same way as in the study[7)–9)] on Bi_2Te_3.

§2. Theory

2.1 *Phenomenological theory*

The general expression for the current $\boldsymbol{I}$ in terms of the electric field $\boldsymbol{E}$, the magnetic field $\boldsymbol{H}$ and the temperature gradient grad T is[14)]

$$I_i=\sigma_{ij}E_j+\sigma_{ijk}E_jH_k+\sigma_{ijkl}E_jH_kH_l+\theta_{ij}\frac{\partial T}{\partial x_j}\,, \tag{1}$$

where the usual summation convention applies, and the terms of higher order are neglected. This equation defines the conductivity, Hall conductivity, magneto-conductivity and thermo-electric conductivity tensors. The resistivity, Hall coefficient, magnetoresistance and thermo-electric coefficient tensors are defined by the inverse relation,

$$E_i=\rho_{ij}I_j+R_{ijk}I_jH_k+\rho_{ijkl}I_jH_kH_l+Q_{ij}\frac{\partial T}{\partial x_j}\,. \tag{2}$$

The number of independent components of these tensors and the relations among all of the non-zero components are determined by using the results of phenomenological analysis[13] to the crystal having Laue symmetry D_{3d}. Referred to an orthogonal set of axes in which x_3-axis is parallel to the three-fold axis of the crystal and x_1-axis is one of the two-fold axis, and x_2-axis is lying in one of the reflection planes, there are twelve independent components of the isothermal resistivity tensors ρ_{ij}, R_{ijk} and ρ_{ijkl}, and are two of the thermoelectric coefficient tensors Q_{ij}. These components and their relation to the independent components of the conductivity tensors σ_{ij}, σ_{ijk}, σ_{ijkl} and θ_{ij} are

$$\left.\begin{aligned}
&\rho_{11}=\frac{1}{\sigma_{11}}\,, && R_{213}=\frac{\sigma_{123}}{\sigma_{11}{}^2}\,,\\
&\rho_{33}=\frac{1}{\sigma_{33}}\,, && R_{132}=\frac{\sigma_{312}}{\sigma_{11}\sigma_{33}}\,,\\
&\rho_{1111}=-\frac{\sigma_{1111}}{\sigma_{11}{}^2}\,, && \rho_{3311}=-\frac{\sigma_{3311}}{\sigma_{33}{}^2}-\frac{\sigma_{312}{}^2}{\sigma_{11}\sigma_{33}{}^2}\,,\\
&\rho_{1122}=-\frac{\sigma_{1122}}{\sigma_{11}{}^2}-\frac{\sigma_{312}{}^2}{\sigma_{11}{}^2\sigma_{33}}\,, && \rho_{3333}=-\frac{\sigma_{3333}}{\sigma_{33}{}^2}\,,\\
&\rho_{1133}=-\frac{\sigma_{1133}}{\sigma_{11}{}^2}-\frac{\sigma_{123}{}^2}{\sigma_{11}{}^3}\,, && \rho_{2311}=-\frac{\sigma_{2311}}{\sigma_{11}\sigma_{33}}\,,\\
&\rho_{1123}=-\frac{\sigma_{1123}}{\sigma_{11}{}^2}\,, && \rho_{2323}=-\frac{\sigma_{2323}}{\sigma_{11}\sigma_{33}}+\frac{1}{2}\frac{\sigma_{123}\sigma_{312}}{\sigma_{11}{}^2\sigma_{33}}\,,
\end{aligned}\right\} \tag{3}$$

$$Q_{11}=-\frac{\theta_{11}}{\sigma_{11}}\quad\text{and}\quad Q_{33}=-\frac{\theta_{33}}{\sigma_{33}}\,. \tag{4}$$

2.2 *Expressions of the conductivity tensors for a single valley*

The contribution to the conductivity tensors of Eq. (1) from the ith valley are given by the following expressions[7),14)]:

$$\left.\begin{aligned}
\sigma_{pq}{}^{(i)}&=-\frac{e^2}{\hbar^2}\int\frac{\partial\varepsilon}{\partial k_p}\tau\frac{\partial\varepsilon}{\partial k_q}\frac{\partial f_0}{\partial\varepsilon}\,d\boldsymbol{k}\,,\\
\sigma_{pqr}{}^{(i)}&=-\frac{e^3}{\hbar^4}\int\frac{\partial\varepsilon}{\partial k_p}\tau\frac{\partial\varepsilon}{\partial k_l}\frac{\partial}{\partial k_m}\left(\tau\frac{\partial\varepsilon}{\partial k_q}\right)\varepsilon_{rlm}\frac{\partial f_0}{\partial\varepsilon}\,d\boldsymbol{k}\,,\\
\sigma_{pqrs}{}^{(i)}&=-\frac{e^4}{\hbar^6}\int\frac{\partial\varepsilon}{\partial k_p}\tau\frac{\partial\varepsilon}{\partial k_n}\frac{\partial}{\partial k_0}\left\{\tau\frac{\partial\varepsilon}{\partial k_l}\frac{\partial}{\partial k_m}\left(\tau\frac{\partial\varepsilon}{\partial k_q}\right)\right\}\\
&\qquad\qquad\times\left\{\frac{1}{2}(\varepsilon_{slm}\varepsilon_{rn0}+\varepsilon_{rlm}\varepsilon_{sn0})\right\}\frac{\partial f_0}{\partial\varepsilon}\,d\boldsymbol{k}\,,\\
\theta_{pq}{}^{(i)}&=-\frac{\epsilon^2}{\hbar^2}\Phi\int\frac{\partial\varepsilon}{\partial k_p}\tau\frac{\partial\varepsilon}{\partial k_q}\frac{\partial f_0}{\partial\varepsilon}\,d\boldsymbol{k}-\frac{e}{\hbar^2}\frac{1}{T}\int\varepsilon\frac{\partial\varepsilon}{\partial k_p}\tau\frac{\partial\varepsilon}{\partial k_q}\frac{\partial f_0}{\partial\varepsilon}\,d\boldsymbol{k}\,,
\end{aligned}\right\} \tag{5}$$

where, $-e$ is the charge of the electron, $\hbar$ is the Planck's constant h devided by 2π, τ is the relaxation time, $f_0=2f/(2\pi)^3$, f is the Fermi distribution function, $\boldsymbol{k}$ is the wave number vector, ε is the kinetic energy of carriers, and ε_{pqr} is the permutation symbol.* Also

$$\Phi=T\frac{\partial}{\partial T}\left(\frac{\zeta}{eT}\right)+\frac{1}{e}\frac{\partial E_0}{\partial T}\,, \tag{6}$$

---

* $\varepsilon_{pqr}=0$ unless p, q, r all different,
$\varepsilon_{pqr}=+1$ if $pqr=123$, 231 or 312 and
$\varepsilon_{pqr}=-1$ if $pqr=213$, 321 or 132.

where ζ is the partial Fermi level, E_0 is the energy at the band edge, and T is the absolute temperature.

For the evaluation of the integrals in Eq. (5), we assume that[7]:

1. Only one type of current carrier is present. (For Bi_2Se_3 these carriers are assumed to be electrons at low temperatures.)
2. The ith constant energy surface in $\boldsymbol{k}$-space is ellipsoidal in the vicinity of $\boldsymbol{k}_0^{(i)}$, and the energy may be written in the form

$$\varepsilon=\frac{\hbar^2}{2}\left[\frac{(k_1^{(i)}-k_{10}^{(i)})^2}{m_1}+\frac{(k_2^{(i)}-k_{20}^{(i)})^2}{m_2}+\frac{(k_3^{(i)}-k_{30}^{(i)})^2}{m_3}\right], \tag{7}$$

where, m_1, m_2 and m_3 are the principal effective masses. Similar ellipsoids are centred about the several equivalent points related by the symmetry operations of the crystal.

3. The relaxation time τ exists and is isotropic and a function of energy only.

Hence, the conductivity tensors are lead to the following expressions for the ith valley;

$$\left.\begin{aligned}
\sigma_{pq}^{(i)}&=\frac{A}{m_p}\delta_{pq}\,,\\
\sigma_{pqr}^{(i)}&=\frac{B}{m_pm_q}\varepsilon_{pqr}\,,\\
\sigma_{pqrs}^{(i)}&=\frac{C}{m_pm_qm_l}\left\{\frac{1}{2}(\varepsilon_{psl}\varepsilon_{rql}+\varepsilon_{prl}\varepsilon_{sql})\right\},\\
&\text{and}\\
\theta_{pq}^{(i)}&=\Phi\frac{A}{m_p}\delta_{pq}+\frac{1}{eT}\frac{D}{m_p}\delta_{pq}\,,
\end{aligned}\right\} \tag{8}$$

where the superscript (i) is used to denote tensor components relative to the principal axes of the ith valley, and δ_{pq} is the Kronecker's delta. The parameters A, B, C and D depend on the forms of f_0 and τ, and they are given by the following expressions:

$$\left.\begin{aligned}
A&=-\frac{4\pi}{3\hbar^3}e^2(2m^*)^{3/2}\int\tau\varepsilon^{3/2}\frac{\partial f_0}{\partial\varepsilon}d\varepsilon\,,\\
B&=\frac{4\pi}{3\hbar^3}e^3(2m^*)^{3/2}\int\tau^2\varepsilon^{3/2}\frac{\partial f_0}{\partial\varepsilon}d\varepsilon\,,\\
C&=-\frac{4\pi}{3\hbar^3}e^4(2m^*)^{3/2}\int\tau^3\varepsilon^{3/2}\frac{\partial f_0}{\partial\varepsilon}d\varepsilon\,,\\
&\text{and}\\
D&=-\frac{4\pi}{3\hbar^3}e^2(2m^*)^{3/2}\int\tau\varepsilon^{5/2}\frac{\partial f_0}{\partial\varepsilon}d\varepsilon\,,
\end{aligned}\right\} \tag{9}$$

where $m^*=(m_1m_2m_3)^{1/3}$.

2.3 *Expressions of the conductivity tensors for the six-valley model*

For Bi_2Se_3 crystal, the possible valley configuration in $\boldsymbol{k}$-space might be one of the following five alternatives[8];

1. one spheroidal valley centred at the origin,
2. two spheroidal valleys centred on the three-fold axis,
3. six ellipsoidal valleys centred on the two-fold axes,
4. six ellipsoidal valleys centred on the reflection planes, the x-axis of the ith valley centred at $(0, k_y, k_z)$ is in the direction of the x_1-axis of the crystal,
5. twelve ellipsoidal valleys centred in an arbitrary position and having arbitrary orientation.

The models 1, 2 and 3 are too simple to represent the anisotropic magnetoresistance of Bi_2Se_3. The six-valley model of the case 4 seems reasonably consistent with the experimental results of the magnetoresistance coefficients. The analysis for the model 5 has not been attempted, since the comparison with experiment is very difficult.

For the model of the case 4, the independent components of the isothermal conductivity tensors are obtained as following expressions[7),18)];

$$\left.\begin{aligned}
\sigma_{11}&=3A\left(\frac{1}{m_1}+\frac{c^2}{m_2}+\frac{s^2}{m_3}\right),\\
\sigma_{33}&=6A\left(\frac{s^2}{m_2}+\frac{c^2}{m_3}\right),\\
\sigma_{123}&=\frac{6B}{m_1m_2m_3}(s^2m_2+c^2m_3),\\
\sigma_{312}&=\frac{3B}{m_1m_2m_3}(m_1+c^2m_2+s^2m_3),\\
\sigma_{1111}&=-\frac{3}{4}\frac{C}{m_1m_2m_3}\left\{s^2\left(\frac{m_3}{m_1}+\frac{m_1}{m_3}-2\right)+c^2\left(\frac{m_2}{m_1}+\frac{m_1}{m_2}-2\right)+3c^2s^2\left(\frac{m_3}{m_2}+\frac{m_2}{m_3}-2\right)\right\},\\
\sigma_{1122}&=-\frac{3}{4}\frac{C}{m_1m_2m_3}\left\{3s^2\left(\frac{m_3}{m_1}+\frac{m_1}{m_3}-2\right)+3c^2\left(\frac{m_2}{m_1}+\frac{m_1}{m_2}-2\right)+c^2s^2\left(\frac{m_3}{m_2}+\frac{m_2}{m_3}-2\right)+8\right\},\\
\sigma_{1133}&=-\frac{3C}{m_1m_2m_3}\left(c^4\frac{m_3}{m_2}+s^4\frac{m_2}{m_3}+c^2\frac{m_3}{m_1}+s^2\frac{m_2}{m_1}+2c^2s^2\right),\\
\sigma_{1123}&=-\frac{3}{2}\frac{C}{m_1m_2m_3}cs\left(c^2\frac{m_3}{m_2}-s^2\frac{m_2}{m_3}+\frac{m_2}{m_1}-\frac{m_3}{m_1}+s^2-c^2\right),\\
\sigma_{3311}&=-\frac{3C}{m_1m_2m_3}\left(c^4\frac{m_2}{m_3}+s^4\frac{m_3}{m_2}+c^2\frac{m_1}{m_3}+s^2\frac{m_1}{m_2}+2c^2s^2\right),\\
\sigma_{3333}&=-\frac{6C}{m_1m_2m_3}c^2s^2\left(\frac{m_3}{m_2}+\frac{m_2}{m_3}-2\right),\\
\sigma_{2311}&=-\frac{3}{2}\frac{C}{m_1m_2m_3}cs\left(c^2\frac{m_2}{m_3}-s^2\frac{m_3}{m_2}+\frac{m_1}{m_2}-\frac{m_1}{m_3}+s^2-c^2\right),\\
\sigma_{2323}&=\frac{3C}{m_1m_2m_3}\left\{c^2s^2\left(\frac{m_3}{m_2}+\frac{m_2}{m_3}-2\right)+1\right\},
\end{aligned}\right\}\quad(10)$$

in which $c=\cos\theta$, $s=\sin\theta$, and θ is the angle of rotation about the x-axis which makes the principal axis of the ith valley coincide with the crystal axes. The thermo-electric coefficient tensor components are found that,

$$Q_{11}=Q_{33}=-\Phi-\frac{1}{eT}\frac{D}{A}. \qquad (11)$$

Thus the thermo-electric coefficient should be isotropic.

The thermo-electric power Q relative to a metal, such as copper or platinum, are given by

$$Q=\frac{k}{e}\left(\eta-\frac{1}{kT}\frac{D}{A}\right), \qquad (12)$$

where k is Boltzmann's constant, η is the reduced Fermi level and the absolute thermo-electric power of the metal is neglected, and this condition is practically fulfilled in our experiment.

§ 3. Experiment

3.1 *Preparation of specimens*

The component materials of Bi_2Se_3 used came from Johnson-Matthey's bismuth (99.99% pure) and from Shin Dengen Kogyo's selenium (99.999%). A mixture of Bi and Se was sealed in an evacuated silica tube, where the weighed selenium was about 0.2% (wt) excess from the stoichiometric composition[5)], and the melt of the mixtures was kept for about 20 hrs in an electrical furnace of about 800°C. The single crystal was grown by a slow cooling.

The parallelepiped specimens were cut out by a small saw from the disks of the cleaved specimens held between a small vice. The specimens obtained by this procedure were free from visible cracks.

A rectangular parallelepiped specimen which have an elongated side surface along the cleavage surface (Specimen 1) was of shape of about 2 mm × 2 mm × 10 mm. (Figs. 1a and

1b. The orthogonal set of axes for Specimen 1 are those in which the x- and y-axes are on the cleavage surface. The z-axis, therefore, is parallel to the x_3-axis of crystal. The x-axis of the specimen and x_1-axis of the crystal make an angle ϕ.)

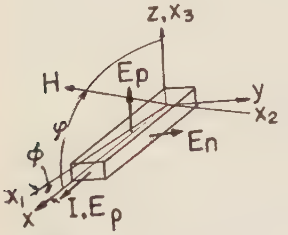

(a) Arrangement 1 Specimen 1

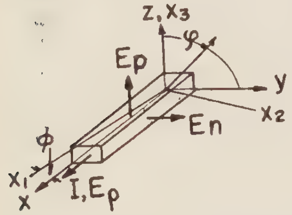

(b) Arrangement 2 Specimen 1

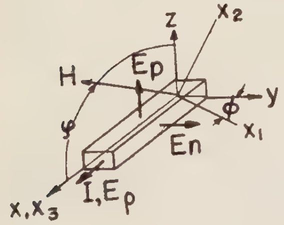

(c) Arrangement 3 Specimen 2

Figs. 1a, 1b and 1c. Experimental arrangements.

A rectangular parallelpiped specimen elongated in the perpendicular direction to the cleavage surface (Specimen 2) was of shape of about 3 mm×3 mm×7 mm. (Fig. 1c. The orthogonal set of axes for Specimen 2 are the x-axis along the perpendicular direction to the cleavage surface, and the y- and z-axes lying in a cleavage surface. The x-axis is parallel to the x_3-axis, and y-axis and x_1-axis make an angle ϕ.)

Specimens 1 and 2 of each sample were obtained from the same cleaved disk which prepared from an ingot.

3.2 *Experimental arrangement*

For the determination of the twelve independent components of the isothermal resistivity tensor, the three different experimental arrangements are prepared using the two different specimens, Specimens 1 and 2.

A current of density I is flowed in the direction of the x-axis of the specimens. The electric fields, which must be measured, are E_ρ the component parallel to the current, E_n along the y-axis, and E_p along the z-axis.

Arrangement 1. (Fig. 1a.) By using Specimen 1, the magnetic field H is applied in the x–z plane. The following expressions are obtained for the isothermal condition:

$$\left.\begin{aligned}\frac{E_\rho}{I}&=\rho_{11}+H^2\{\rho_{1111}\cos^2\varphi+\rho_{1133}\sin^2\varphi+\rho_{1123}\sin 2\varphi\sin 3\phi\}\,,\\ \frac{E_n}{I}&=HR_{213}\sin\varphi+H^2\rho_{1123}\sin 2\varphi\cos 3\phi\,,\\ \frac{E_p}{I}&=H^2\{\rho_{2311}\cos^2\varphi\sin 3\phi+\rho_{2323}\sin 2\varphi\}\,,\end{aligned}\right\}\tag{13}$$

where φ is the angle between the x-axis of the specimen and the magnetic field.

Arrangement 2. (Fig. 1b.) By using Specimen 1, the magnetic field is applied in the y–z plane. Then

$$\left.\begin{aligned}\frac{E_\rho}{I}&=\rho_{11}+H^2\{\rho_{1122}\sin^2\varphi+\rho_{1133}\cos^2\varphi+\rho_{1123}\sin 2\varphi\cos 3\phi\}\,,\\ \frac{E_n}{I}&=HR_{213}\cos\varphi-H^2\rho_{1123}\sin 2\varphi\sin 3\phi\,,\\ \frac{E_p}{I}&=-HR_{132}\sin\varphi-H^2\rho_{2311}\sin^2\varphi\sin 3\phi\,,\end{aligned}\right\}\tag{14}$$

where φ is the angle between the z-axis and the magnetic field.

Arrangement 3. (Fig. 1c.) By using Specimen 2, the magnetic field are applied in the x–z plane. Then

$$\left.\begin{aligned}\frac{E_\rho}{I}&=\rho_{33}+H^2\{\rho_{3311}\sin^2\varphi+\rho_{3333}\cos^2\varphi\}\,,\\ \frac{E_n}{I}&=HR_{132}\sin\varphi-H^2\rho_{2311}\sin^2\varphi\sin 3\phi\,,\\ \frac{E_p}{I}&=-H^2\{\rho_{2311}\sin^2\varphi\cos 3\phi-\rho_{2323}\sin 2\varphi\}\,,\end{aligned}\right\}\tag{15}$$

where φ is the angle between the x-axis and the magnetic field.

The angles ϕ are determined by mean of the Laue pattern of X-rays and also the analysis of the measured values by Eqs. (13), (14) or (15). Both values of ϕ obtained by X-rays and by electrical methods are in agreement within ±5°.

3.3 *Measurement of the isothermal coefficients*

The d.c. measurements of the resistivity and Hall coefficient were carried out in following way: The voltage between resistance probes and Hall voltage were measured by a chopper type d.c. micro-volt meter. The out-puts of the micro-volt meter were recorded on the ordinate on an X–Y recording chart and the

Table I. Experimental and calculated values of the galvanomagnetic coefficients of Bi_2Se_3 single crystals.

Sample	15		153		17		20		173	
Temp. (°K)	90		92		90		90		93	
	Obs.	Calc.	Obs.	Calc.	Obs.	Calc.	Obs.	Calc.	Obs.	Calc.
	$\times 10^2$		$\times 10^2$		$\times 10^2$		$\times 10^3$		$\times 10^3$	
σ_{11}	+2.10	2.10*	2.11	2.11*	9.17	9.17*	1.91	1.91*	2.99	2.99*
σ_{33}	+0.45	0.40	0.372	0.40	1.18	1.71	0.373	0.36	0.775	0.56
									$(ohm)^{-1}(cm)^{-1}$	
	$\times 10^6$		$\times 10^5$		$\times 10^6$		$\times 10^6$		$\times 10^6$	
σ_{312}	− 0.26	0.24	1.64	1.62	0.347	0.52	0.20	0.19	0.65	0.48
σ_{123}	− 1.28	1.28*	8.69	8.69*	2.78	2.78*	1.01	1.01*	2.55	2.55*
									$(ohm)^{-2}(cm)(coul)^{-1}$	
	$\times 10^9$		$\times 10^8$		$\times 10^9$		$\times 10^8$		$\times 10^9$	
σ_{1111}	− 0.12	0.44	0.53	1.74	0·071	0.40	0.33	0.53	—	0.12
σ_{1122}	− 1.7	2.0	9.1	7.9	1.4	1.8	3.0	2.4	—	0.51
σ_{1133}	−10	10 *	39	39 *	9.0	9.0*	12	12 *	2.5	2.5*
σ_{1123}	− 0.20	0.49	1.8	1.9	0.51	0.44	1.7	0.58	1.5	0.12
σ_{3311}	− 0.47	0.35	2.1	1.4	0.48	0.31	0.8	0.42	0.38	0.09
σ_{3333}	− 0.6	0.59	2.0	2.3	0.45	0.53	1.6	0.71	0.6	0.15
σ_{2311}	− 0.12	0.091	3.1	0.36	0.8	0.082	2.8	0.11	0.5	0.023
σ_{2323}	+ 1.7	0.93	5.1	3.6	2.7	0.84	0.78	1.1	—	0.23
									$(ohm)^{-3}(cm)^3(coul)^{-2}$	
B^2/AC	1.02		1.19		1.22		0.58		1.14	
σ_{11}/σ_{33}	+ 4.7	5.36	5.5		7.8		5.1		3.9	
$\sigma_{123}/\sigma_{312}$	+ 4.9	5.36	5.3		8.0		5.1		3.9	
$\sigma_{1111}/\sigma_{1133}$	+ 0.012	0.045	0.014		0.008		0.027		—	
$\sigma_{1122}/\sigma_{1133}$	+ 0.17	0.202	0.23		0.16		0.25		—	
$\sigma_{1123}/\sigma_{1133}$	+ 0.020	0.0486	0.046		0.057		0.14		0.60	
$\sigma_{3311}/\sigma_{1133}$	+ 0.047	0.0344	0.054		0.053		0.067		0.15	
$\sigma_{3333}/\sigma_{1133}$	+ 0.06	0.0590	0.051		0.050		0.13		0.24	
$\sigma_{2311}/\sigma_{1133}$	+ 0.012	0.0091	0.079		0.089		0.23		0.18	
$\sigma_{2323}/\sigma_{1133}$	− 0.17	0.0930	0.13		0.30		0.065		—	

* Adjusted to the experimental values.

rotational angle of the magnetic field from 0 to about 200° were recorded on the abscissa. This record was obtained by a potentiometer which was set on a rotational axis of the electromagnet. Since the magnet could not be rotated automatically, the slow rotation of the magnet in order to eliminate the inductive voltage was difficult. When the magnet was continuously rotated by hand, the recorded trace was complicated by the appearance of additional voltage. The trace, which was obtained from the record during the rotation of the magnet, included the true voltage and an additional voltage due to the magnetic induction. For the elimination of these additional voltages, the magnet was rotated by about 3° and stopped for a few times at each step. Then the true trace of the voltage as a function of the rotational angle of the magnetic field was given by the curve which connected the recorded points at the rest position of the magnet as shown in Fig. 5.

Also, the voltages were measured by a potentiometer at several cases in order to check their results on the X–Y records, and the values obtained from the record were in good agreement with the values measured by the potentiometer.

As no appreciable dependence of the coefficients on the current and magnetic field strength was found for currents up to 1 Amp. and for magnetic fields up to 10,000 oersteds, most of the measurement were carried out by using a magnetic field strength of 9,000 oersteds and current of 50∼500 mA.

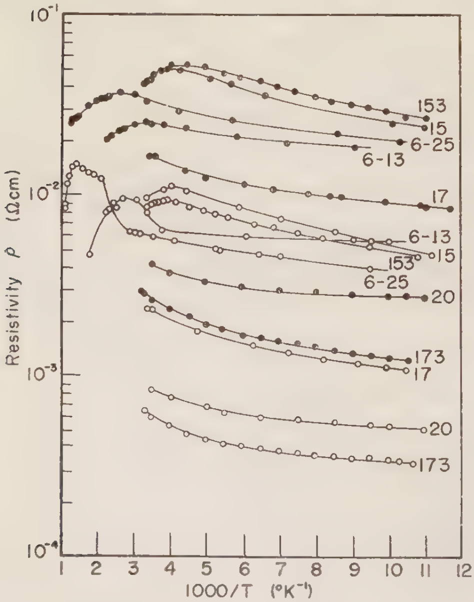

Fig. 2. The electrical resistivity of Bi_2Se_3 single crystals. The symbols ○ and ● for each sample refer to ρ_{11} and ρ_{33}, respectively.

3.4 *Measurement of the thermo-electric power*

The thermo-electric powers were observed on Specimens 1 and 2. The temperature gradient was applied in the direction of the x-axis of each specimen. The copper-constantan thermo-couples were used to measure the temperature. The given temperature difference between the thermo-couples was less 5°C, and the thermo-electric powers were estimated from the linear relationship between the temperature differences and the thermo-electric voltages.

§ 4. Results

The measurements were carried out on the five samples given in Table I. Among those samples Nos. 15 and 153 were obtained from the same ingot. The resistivities and the Hall coefficients for each sample were meas-

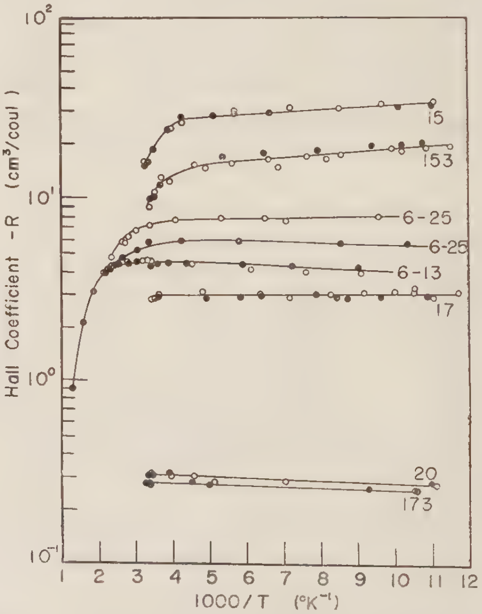

Fig. 3. The Hall coefficient of Bi_2Se_3 single crystals. The symbols ○ and ● for each sample refer to R_{213} and R_{132}, respectively. The Hall coefficients of the samples Nos. 6–13 and 6–25 shown in the figure have been corrected for the sample geometry. The illustrated values of these samples in the previous report[5] are uncorrected values for the sample geometry.

ured over the temperature range from 90°K to room temperature. The temperature dependences of the resistivity and the Hall coefficient are shown in Figs. 2 and 3, and in these figures the results on the single crystal samples in our previous reports⁵⁾ are also plotted together with the present results. The Hall coefficients are almost constant in the range from 90° to 200°K as shown in Fig. 3, and are proved to be isotropic. The slight temperature dependences, which are found for the samples Nos. 15 and 153, may be related to the activation energy to the donor level⁵⁾. The ratios of the resistivity components are found to be nearly constant in this temperature region as shown in Fig. 2.

The temperature dependences of the thermo-electric powers are plotted in Fig. 4. The thermo-electric powers are found to be practically isotropic, and supporting the assumption of the isotropic relaxation time.

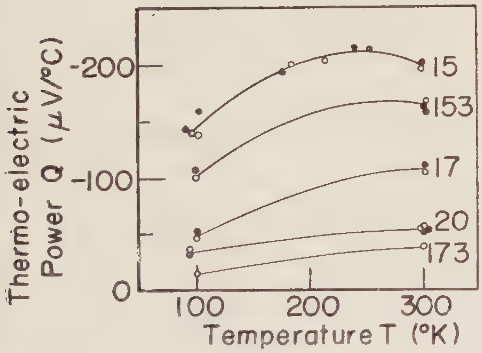

Fig. 4. Thermo-electric power. The symbols ○ and ● for each sample refer to the thermo-electric powers of Specimens 1 and 2, respectively.

The experimental values of the components of the conductivity tensors at about 90°K are summarized in Table I. The examples of the measured voltage against the rotational angle φ of the magnetic field are illustrated in Fig. 5. The observed variation of the voltages with φ are in good agreement with the theoretical prediction.

The parameters m_2/m_1, m_3/m_1 and $\sin^2\theta$ appearing in Eq. (10) are determined by using values of σ_{ij}, σ_{ijk} and σ_{ijkl} obtained by the experiments. In particular, the conductivities, the Hall conductivities and σ_{1133} and σ_{3333}, which are more accurate in our experiment than other magneto-conductivity coefficients, were used to obtain those parameters. In performing this analysis, the results on Samples Nos. 15, 153 and 17 have been used since these are probably the accurate ones. From the results of this analysis, it was concluded most probably that the shape and orientation of the valleys are defined by the following values;

$$\left.\begin{aligned} &\frac{m_2}{m_1}=0.33\,, \quad \frac{m_3}{m_1}=4.2 \\ \text{and} \quad &\sin^2\theta=0.045\,, \end{aligned}\right\} \tag{16}$$

because most of the observed galvanomagnetic tensor components of these samples are quite

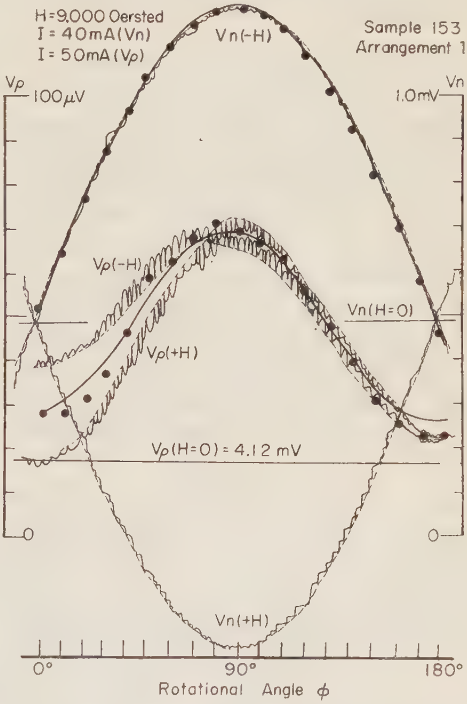

Fig. 5. The voltages between conductivity probes V_ρ and between Hall probes V_n against the rotational angle φ of magnetic field of sample arrangement 1 on sample No. 153 at 92°K. $+H$ and $-H$ denote plus and minus direction of the magnetic field, respectively. The straight traces denoted by $V_\rho(H=0)$ and $V_n(H=0)$ are the positions of the voltage in zero magnetic field. The dotted curves are the one estimated as the true trace of the voltage, which connects the recorded points at the rest position of the magnet. The disagreement between the traces of $V_\rho(+H)$ and $V_\rho(-H)$ seems due to an additional Hall voltage by miss setting of the potential probes. The symbols ● denote the values measured by the potentiometer. The solid curves show the angular dependences expected from Eq. (13).

well described by these values.

Hence the ellipsoidal surfaces of constant energy are compressed in a direction to the x_2-axis and are stretched in a direction nearly parallel to the three-fold axis of the crystal.

By using the above values, Eq. (16), the galvanomagnetic tensor components and the ratio B^2/AC can be calculated, and are given in Table I, where A/m_1, Bm_1/m^{*3} and C/m^{*3} are adjusted to represents the experimental values of σ_{11}, σ_{123} and σ_{1133}.

The ratio B^2/AC is found by taking into account a degeneracy of samples and by making choice of scattering mechanisms. In particular, if the relaxation time τ is given by the relation

$$\tau = b\varepsilon^{-\lambda}, \tag{17}$$

where λ and b depend on the scattering mechanism, and b is a function of temperature, the ratio B^2/AC for the complete degenerate samples should be the unity for any value of λ. For the samples used in the present analysis, this relation is shown to be nearly satisfied, and also it may be estimated from measurements of thermo-electric power that these samples are highly degenerate.

Using the anisotropic factor, 0.763, determined by the parameters in Eq. (10), the Hall coefficient $R = R_{213} = R_{132}$ can be obtained;

$$R = -0.763\frac{1}{en}, \tag{18}$$

where n is the density of carriers. Assuming the relation of Eq. (18), then, it is possible to obtain the values of a conductivity mobility of electrons defined by following relations:

$$\left.\begin{aligned} \sigma_{11} &= en\mu_{11}, \\ \sigma_{33} &= en\mu_{33}, \end{aligned}\right\} \tag{19}$$

The variations of the conductivity mobility with temperature are shown in Fig. 6, and they have straight form on log-log scale. For Samples Nos. 15 and 153, the mobilities are given by the form

$$\mu \propto T^{-1.3} \tag{20}$$

over the range from 90°K to room temperature. This behaviors of the mobilities seem to obey $T^{-3/2}$ relationship.

If λ is assumed to be 1/2 (covalent lattice scattering) the effective mass m^* of electrons is estimated to be about 0.1 m_0, where m_0 is free electron mass, from the observed thermo-electric powers of the Samples Nos. 15 and 153 at 100°K. This value can be compared with the effective mass, $m^*/m_0 = 0.18$, previously obtained[5]. However, it may be only an accidental agreement, since the large spread of the temperature dependences of conductivity mobility or Hall mobility between the various samples suggests that carriers are scattered in more complicated way than that assumed in Eq. (17). A further study is necessary to improve this situation.

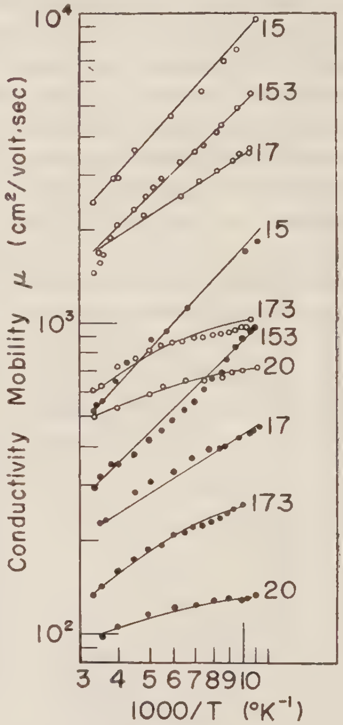

Fig. 6. The conductivity mobility. The symbols ○ and ● for each sample refer to μ_{11} and μ_{33}, respectively.

§ 5. Conclusion

By the six-valley model of the energy band structure, the interpretations of the anisotropic galvanomagnetic effects of n-type Bi_2Se_3 at 90°K have been attempted.

The experimental values of σ_{1111} deviates from the calculated values. The discrepancy may probably be due to the inaccuracy of ρ_{1111}, since ρ_{1111} is too small compared with the other terms in Eq. (13). The disagreements between the observed and calculated values of σ_{1123} and σ_{2311} may be due to the inaccuracy of ϕ. So that the experimental results seem consistent with the present theory.

It may be resonable to conclude that each ellipsoidal surface centred in a reflection plane has the following shape and orientation;

$m_2/m_1=0.33$, $m_3/m_1=4.2$ and $\sin^2\theta=0.045$.

Further, it is of interest that the Hall coefficient and the thermo-electric power are shown to be isotropic.

Acknowledgement

The author wishes to express his hearty thanks to late Prof. A. Okazaki for his kind guidance. He is also indebted to Prof. T. Okada for his interest and discussions throughout this work. A part of this work was supported by the Scientific Research Expenditure of the Ministry of Education.

References

1) V. A. Davidenko: J. Phys. (USSR) **4** (1941) 170.
2) E. Mooser and W. B. Pearson: Phys. Rev. **101** (1956) 492.
3) J. Black, E. M. Conwell, L. Seigle and C. W. Spencer: J. Phys. Chem. Solids **2** (1957) 240.
4) P. P. Konorov: Zh. tekh. Fiz. **26** (1956) 394.
5) K. Hashimoto: Mem. Fac. Sci. Kyusyu Univ. **B2** (1958) 141, 187.
6) N. Fuschillo, J. N. Bierly and F. J. Donahoe: J. Phys. Chem. Solids **8** (1959) 430.
7) J. R. Drabble and R. Wolfe: Proc. Phys. Soc. **B69** (1956) 1101.
8) J. R. Drabble, R. D. Groves and R. Wolfe: Proc. Phys. Soc. **71** (1958) 430.
9) J. R. Drabble: Proc. Phys. Soc. **72** (1958) 380.
10) A. E. Bowley, R. Delves and H. J. Goldsmid: Proc. Phys. Soc. **72** (1958) 401.
11) J. R. Drabble: J. Phys. Chem. Solids **8** (1959) 428.
12) H. J. Juretschke: Acta Cryst. **8** (1955) 716.
13) T. Okada: Mem. Fac. Sci. Kyusyu Univ. **B1** (1955) 157.
14) O. Madelung: *Handbuch der Physik*, (Springer-Verlag, Berlin, 1957) Vol. **20**, p. 95.

JOURNAL OF THE PHYSICAL SOCIETY OF JAPAN, Vol 16, No. 10, OCTOBER, 1961

Hall Effect in *N*- and *P*-type Germanium at 24 Gc

By Naozo WATANABE

Electrical Communication Laboratory,
Musashinoshi, Tokyo

(Received June 21, 1961)

A method to measure Hall mobility at microwave frequencies using a double mode cavity is presented. Hall mobility measured by this method corresponds to $\mu_H=(1/B)\cdot|\sigma_1|/\mathrm{Re}(\sigma_0)$, where σ_0 and σ_1 are a diagonal and an off-diagonal components of conductivity matrix, and it is expected to be frequency independent if a constant relaxation time is assumed. Frequency dependence is expected when the energy dependent relaxation time is assumed. For *n*-type germanium, Hall mobility measured by this method at 24 Gc is in excellent agreement with that predicted from the theory using d.c. value and assuming acoustical mode scattering, between room temperature and 100°K. For *p*-type germanium, the same consideration explains the essential part of the difference between experimental values at 24 Gc and d.c., though there remains some discrepancies to be clarified

§1. Introduction

Hall effect of several metals at microwave frequencies was first observed by Cooke[1], using a double mode cavity. The same method was applied to germanium by Nishina and Spry[2]. However, they obtained their results using a too much simplified formula, though some refinement was done recently. Portis and Teaney[3] devised a method to obtain an impedance tensor with unbalanced double mode cavity. Their method has many advantages for the observation of magnetic resonance, but it is not so accurate method for our purpose, because of the presence of ambiguous quantities such as filling factors. Yamagata4) derived formulae for the measurement of Hall mobility making use of equivalent circuit method, but Hall mobility measured at room temperature and at 9 Gc was 3 to 4 times smaller than expected for *p*-type germanium.

Hambleton and Gärtner5) obtained Hall mobility of *n*- and *p*-type germanium and silicon at 20 Gc using crossed wave guide method. Their results were extended from room temperature to 80°K. They insisted that they observed high frequency effects for *p*-type germanium at temperatures lower than 150°K. However, they applied their formulae at too strong magnetic field where their formulae breaked down.

Another interesting method to study similar effect is the observation of Faraday rotation at microwave frequencies, and valuable informations were obtained by several authors6) with this method.

Previously a theory concerning properties of cylindrical double mode cavity was formed by the author7). In the theory the effects of cavity walls and coupling irises and a sample were all considered. A method to measure Hall mobility at microwave frequencies was discussed as a special case of the theory. In this paper, electrical conduction in a finite sample at high frequencies is first discussed in terms of Boltzmann Equation on the same assumption as was employed by Dresselhaus *et al.*8) for the discussion of magneto-plasma resonance experiment. Then, the method of measurement of Hall mobility is reviewed briefly, and the results of measurements at 24 Gc between room temperature and 100°K are presented and discussed.

§ 2. Conductivity Matrix in a Finite Semiconductor Sample

Electrical conduction in a finite sample at high frequency is complicated because of the presence of a boundary surface. We first review a method to include such effects in the calculation of conductivity matrix. In the case, where carrier densities are so small that the plasma wave length is far longer than the sample dimension, effects of a boundary can be treated by the same method as Dresselhaus *et al.*8) and Date9) employed for the investigation of magneto-plasma resonance in semiconductors. In this section Boltzmann Equation is solved under simplifying assumptions to see such effects on electrical conduction in a spheroidal sample.

Before solving Boltzmann Equation, the effective electric field acting in a sample will be considered. The effective field in the sample is

$$\boldsymbol{E}_{\mathrm{eff}}=\boldsymbol{E}-L\boldsymbol{P} \tag{1}$$

where L is the depolarizing coefficient and

$$\boldsymbol{P}=(\varepsilon-\varepsilon_0)\boldsymbol{E}_{\mathrm{eff}}+\int\boldsymbol{J}\,dt \tag{2}$$

where the first term is due to the polarization of bound charges and the second is the polarization of free charges, and $\boldsymbol{J}$ is the current density. Putting Eq. (2) into Eq. (1) $\boldsymbol{E}_{\mathrm{eff}}$ is solved as follows:

$$\boldsymbol{E}_{\mathrm{eff}}=\boldsymbol{E}_i-\frac{L_i}{j\omega}\boldsymbol{J} \tag{3}$$

where

$$\boldsymbol{E}_i=\frac{\boldsymbol{E}}{1+L(\varepsilon-\varepsilon_0)}\,,$$

$$L_i=\frac{L}{1+L(\varepsilon-\varepsilon_0)}$$

and the sinusoidal change with time is assumed. The effects of polarization of bound charges are included in $\boldsymbol{E}_i$ and L_i.

Boltzmann Equation for oscillating electric field with the assumption of energy dependent relaxation time can be expressed as follows:

$$e[\boldsymbol{E}+\boldsymbol{v}\times\boldsymbol{B}]\cdot\frac{1}{\hbar}\nabla_k f(\boldsymbol{k},\boldsymbol{r})+\boldsymbol{v}\cdot\nabla_r f(\boldsymbol{k},\boldsymbol{r})$$

$$=-\left(j\omega+\frac{1}{\tau}\right)(f-f_0)\,. \tag{4}$$

In this equation, $\boldsymbol{E}$ in the first term in the left hand side should be replaced by Eq. (3) in our case. The last term in the left hand side will be neglected, because it is appreciable only at the boundary and a negligible part of charge carriers are accumulated at the boundary at moderate electric field. Therefore, the effect of polarization was taken into account in the second term of Eq. (3). With static magnetic field applied in the z-direction and oscillating electric field in (x, y) plane, Boltzmann Equation (4) can be solved putting10)

$$f=f_0-\boldsymbol{v}\cdot\boldsymbol{\phi}\frac{\partial f_0}{\partial\varepsilon}\,. \tag{5}$$

The solutions are as follows:

$$\phi_x=\frac{\tau' e[E_{\mathrm{eff},x}+(\omega_c\tau')E_{\mathrm{eff},y}]}{1+(\omega_c\tau')^2}\,, \tag{6}$$

$$\phi_y=\frac{\tau' e[-(\omega_c\tau')E_{\mathrm{eff},x}+E_{\mathrm{eff},y}]}{1+(\omega_c\tau')^2}\,, \tag{7}$$

$$\phi_z=0 \tag{8}$$

where

$$\omega_c=\frac{eB}{m^*}\,, \tag{9}$$

$$\tau'=\frac{\tau}{j\omega\tau+1}\,. \tag{10}$$

The current density is obtained by

$$\boldsymbol{J}=\frac{e}{4\pi^3}\int \boldsymbol{v}f\,d\boldsymbol{k}=-\frac{e}{4\pi^3}\int \boldsymbol{v}(\boldsymbol{v}\cdot\boldsymbol{\phi})\frac{\partial f_0}{\partial\varepsilon}\,d\boldsymbol{k} \tag{11}$$

and

$$J_x=e^2\cdot K_1'E_{ix}+e^2K_1''E_{iy}+j\lambda\cdot K_1'J_x+j\lambda K_1''J_y\,, \tag{12}$$

$$J_y=-e^2K_1''E_{ix}+e^2K_1'E_{iy}-j\lambda K_1''\cdot J_x+j\lambda\cdot K_1''J_y \tag{13}$$

where

$$\begin{aligned}K_1'&=-\frac{1}{4\pi^3}\int\frac{v_x^2\tau'}{[1+(\omega_c\tau')^2]}\frac{\partial f_0}{\partial\varepsilon}\cdot dk\\&=\sum_k\frac{n_k}{m_k^*}\left\langle\frac{\tau'}{1+(\omega_c\tau')^2}\right\rangle_k=\sum_k\frac{n_k}{m_k^*}\left\langle\frac{(j\omega\tau+1)\tau}{(j\omega\tau+1)^2+(\omega_c\tau)^2}\right\rangle_k\,,\end{aligned} \tag{14}$$

$$\begin{aligned}K_1''&=-\frac{1}{4\pi^3}\int\frac{v_x\cdot\omega_c\tau'^2}{[1+(\omega_c\tau')^2]}\frac{\partial f_0}{\partial\varepsilon}\,dk\\&=\sum_k\frac{n_k}{m_k^*}\left\langle\frac{\tau'^2}{1+(\omega_c\tau')^2}\right\rangle_k\omega_{ck}=\sum_k\frac{n_k}{m_k^*}\left\langle\frac{\tau^2}{(j\omega\tau+1)^2+(\omega_c\tau)^2}\right\rangle_k\omega_{ck}\,,\end{aligned} \tag{15}$$

$$\lambda=\frac{eL_i}{\omega}\,, \tag{16}$$

$$\langle g\rangle=\frac{4}{3\sqrt{\pi}}\int_0^\infty g x^{3/2}e^{-x}\,dx\,,$$

where integrals in K_1' and K_1'' extend over all bands (or valleys), taking part in electrical conduction. m_k^* and n_k are respectively the effective masses and the densities of carriers of the k-the bands (or valleys). Boltzmann statistics are assumed in the derivation.

From Eqs. (12), (13), conductivity matrix is obtained

$$\begin{pmatrix}J_x\\J_y\end{pmatrix}=\begin{pmatrix}\sigma_0&\sigma_1\\-\sigma_1&\sigma_0\end{pmatrix}\begin{pmatrix}E_{ix}\\E_{iy}\end{pmatrix}, \tag{17}$$

$$\sigma_0=\frac{je^2}{\lambda}\left(1-\frac{P}{P^2-Q^2}\right),$$

$$\sigma_1=\frac{e^2}{\lambda}\frac{Q}{P^2-Q^2}\,,$$

where

$$P=1-j\lambda K_1'\,,$$

$$Q=\lambda K_1''\,.$$

These results are identical with Date's[9] if constant relaxation times are assumed.

In the following section it will be shown that our method of measurement of Hall effect gives Hall mobility defined by

$$\mu_H=(1/B)\cdot|\sigma_1|/\mathrm{Re}(\sigma_0)\,.$$

This quantity is obviously identical with the ordinary Hall mobility when the frequency of applied electric field is set equal to zero. We will here investigate this quantity in the low field approximation, neglecting terms higher than second order in B. To this approximation K_1' and K_1'' are

$$K_1'=\sum_k\frac{n_k}{m_k^*}\left\langle\frac{\tau}{j\omega\tau+1}\right\rangle_k\,, \tag{18}$$

$$K_1''=\sum_k\frac{n_k}{m_k^*}\left\langle\frac{\tau^2}{(j\omega\tau+1)^2}\right\rangle\omega_{ck}\,, \tag{19}$$

and σ_0 and σ_1 are expressed as follows:

$$\sigma_0=\frac{e^2\sum\frac{n_k}{m_k^*}\left\langle\frac{\tau}{j\omega\tau+1}\right\rangle_k}{1-j\lambda\sum\frac{n_k}{m_k^*}\left\langle\frac{\tau}{j\omega\tau+1}\right\rangle_k}\,, \tag{20}$$

$$\sigma_1=\frac{e^3B\sum\frac{n_k}{m_k^{*2}}\left\langle\frac{\tau^2}{(j\omega\tau+1)^2}\right\rangle_k}{\left(1-j\lambda\sum\frac{n_k}{m_k^*}\left\langle\frac{\tau}{j\omega\tau+1}\right\rangle_k\right)^2}\,. \tag{21}$$

From Eqs. (20), (21) Hall mobility defined above can be shown to be simplified to

$$\mu_H=\frac{\left|e\sum\frac{n_k}{m_k^{*2}}\left\langle\frac{\tau^2}{(j\omega\tau+1)^2}\right\rangle_k\right|}{\mathrm{Re}\left(\sum\frac{n_k}{m_k^*}\left\langle\frac{\tau}{j\omega\tau+1}\right\rangle_k\right)}\,. \tag{22}$$

The effects of depolarization of free charge carriers do not enter into this expression. Eq. (22) can be simplified further if the relaxation times are assumed to be the same for all bands (or valleys).

$$\mu_H=\frac{e\sum\frac{n_k}{m_k^{*2}}}{\sum\frac{n_k}{m_k^*}}\cdot\frac{\left|\left\langle\frac{\tau^2}{(j\omega\tau+1)^2}\right\rangle\right|}{\mathrm{Re}\left\langle\frac{\tau}{j\omega\tau+1}\right\rangle}\,. \tag{23}$$

To apply this final result to the case of germanium, it must be remembered that conduction band consists of 4 or 8 ellipsoids and valence band consists of two warped spheres. Therefore, the above results are directly applicable to holes, if the warping of the bands are neglected. For electrons $\sum n_k/m_k^*$ and $\sum n_k/m_k^{*2}$ must be replaced by $(n/3)\cdot(2/m_\perp+1/m_\parallel)$ and $(n/3)\cdot(2/m_\perp m_\parallel+1/m_\perp^2)$ respectively[12], where n is the total number of electrons and $m_\perp$ and $m_\parallel$ are transverse and longitudinal masses respectively. If the relaxation time is assumed to be independent of energy, $\tau=\tau_0$, μ_H is independent of frequency of the applied electric field· That is:

$$\mu_H=\frac{e\sum\frac{n_k}{m_k^{*2}}}{\sum\frac{n_k}{m_k^*}}\cdot\tau_0\,. \tag{24}$$

Therefore, if any discrepancy exists between Hall mobility measured at d.c. and at microwaves, it must be due to the combined effect of $\omega\tau_0\gtrsim 1$ and the energy dependence of τ. The frequency dependence of μ_H can be calculated, if τ is given as a function of energy of free charge carriers.

If we assume $\tau=\tau_0(\varepsilon/kT)^{-1/2}$, as is usually done for the acoustical mode scattering[11], the dependence of μ_H on $\omega\tau_0$ is as shown in Fig. 1. To illustrate the effect of energy dependence of τ on the frequency dependence of μ_H, the dependence of μ_H on $\omega\tau_0$ is also plotted, when $\tau=\tau_0(\varepsilon/kT)^{-1}$.

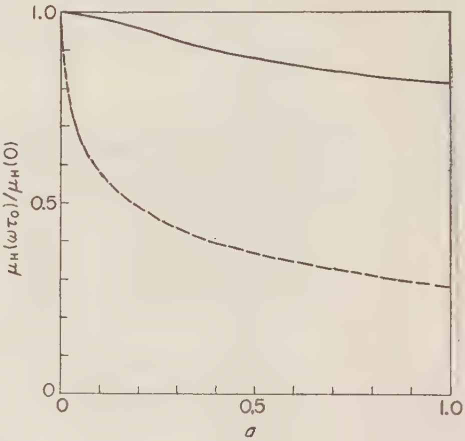

Fig. 1. Frequency dependence of Hall mobility: $a=\omega\tau_0$, solid curve—Hall mobility expected on the assumption $\tau=\tau_0(\varepsilon/kT)^{-1/2}$, dashed curve—Hall mobility expected on the assumption $\tau=\tau_0(\varepsilon/kT)^{-1}$.

§ 3. Method of Measurement of Hall Mobility at Microwaves

Measurement was carried out with the use of double mode cavity, the same one as was used by Nishina and Spry[2], except the latter used a rectangular cavity instead of our cylindrical one. According to our previous work[7], the S-matrix of the double mode cavity shown in Fig. 2 is as follows:

$$\begin{pmatrix}I_1^-\\ I_2^-\end{pmatrix}=\begin{pmatrix}a_{11} & a_{12}\\ a_{21} & a_{32}\end{pmatrix}\begin{pmatrix}I_1^+\\ I_2^+\end{pmatrix}$$
$$=\begin{pmatrix}\dfrac{(M_{Q_1}-M_0)(M_{Q_2}+M_0)-M_1^2}{(M_{Q_1}+M_0)(M_{Q_2}+M_0)+M_1^2}\,, & \dfrac{-2M_1\sqrt{M_{Q_1}M_{Q_2}}}{(M_{Q_1}+M_0)(M_{Q_2}+M_0)+M_1^2}\\ \dfrac{2M_1\sqrt{M_{Q_1}M_{Q_2}}}{(M_{Q_1}+M_0)(M_{Q_2}+M_0)+M_1^2}\,, & \dfrac{(M_{Q_1}+M_0)(M_{Q_2}-M_0)-M_1^2}{(M_{Q_1}+M_0)(M_{Q_2}+M_0)+M_1^2}\end{pmatrix}\begin{pmatrix}I_1^+\\ \\ I_2^+\end{pmatrix} \tag{25}$$

where

I_1^-, I_2^-: Outgoing components of microwaves from input 1 and input 2 respectively,

I_1^+, I_2^+: Incoming components of microwaves to input 1 and input 2 respectively,

$$M_0 = j\frac{2\Delta\omega}{\omega_0} + \frac{1}{Q_S} + \frac{1}{Q_W},$$

$$M_1 = \frac{\sigma_1}{\mathrm{Re}\,(\sigma_0)} \cdot \frac{1}{Q_S},$$

$$M_{Q_1} = \frac{1}{Q_{\mathrm{ex}\,1}} = \frac{v_{\Delta 1}^{2}}{\varepsilon_0\omega_0 Z_{10}},$$

$$M_{Q_2} = \frac{1}{Q_{\mathrm{ex}\,2}} = \frac{v_{\Delta' 2}^{2}}{\varepsilon_0\omega_0 Z_{20}},$$

$$\Delta\omega = \omega - \omega_0 + \frac{\omega_0}{2}\left\{(\kappa-1)|E_0\cdot E_0'|\cdot v_s + \int\frac{\delta}{2}|H\ |^2\,da + \frac{\mathrm{Im}\,(\sigma_0)}{\varepsilon_0\omega_0}|E_0'|^2\cdot v_s\right\}.$$

$$\frac{1}{Q_S} = \frac{\mathrm{Re}\,(\sigma_0)}{\varepsilon_0\omega_0}\cdot|E_0'|^2\cdot v_s,$$

$$\frac{1}{Q_W} = \int\frac{\delta}{2}|H_{.}|^2\,da,$$

$\dfrac{1}{Q_S}$, $\dfrac{1}{Q_W}$: Quality factors arrising from the losses due to a sample and a wall,

$\dfrac{1}{Q_{\mathrm{ex}\,1}}$, $\dfrac{1}{Q_{\mathrm{ex}\,2}}$: Quality factors concerning the coupling between cavity modes and input 1 and input 2,

v_s: Volume of a sample,

κ : $\varepsilon/\varepsilon_0$.

To obtain this formula, impedance matrix of the cavity was first derived following Slater's method[13)], and it was transformed into S-matrix[14)]. The impedance matrix was derived in two steps: First, a small spheroidal sample with a dielectric constant ε is placed on the symmetry axis of the cylindrical cavity with its axis of rotation in the direction of the symmetry axis of the cavity. The sample modifies the TE_{11} mode of the cavity in two ways: The resonance frequency is shifted as represented by the third term in the formula of $\Delta\omega$, and the $\boldsymbol{E}$ vector of the TE_{11} mode is modified to

$$\boldsymbol{E}_0' = 1/\{1+L(\varepsilon-\varepsilon_0)\}\cdot\boldsymbol{E}_0$$

in the sample[15]. Second, the effects of the cavity wall, the coupling irises and the sample conductivity are introduced as the perturbation to this modified TE_{11} mode. From these considerations and the formulations presented in the preceding section, the conductivity matrix derived in the preceding section is obviously applicable in the formulation of this section.

From Eq. (25), a_{11} for vanishing magnetic field and a_{21} for finite magnetic field can be obtained as follows:

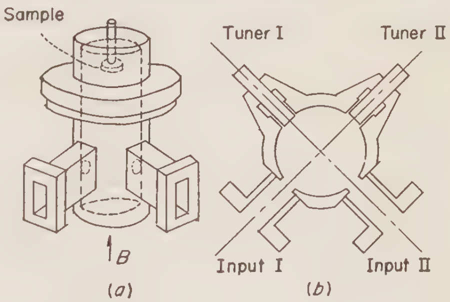

Fig. 2. Double mode cavity: (*a*) external appearance, (*b*) a cross section.

$$a_{11}(B=0) = \frac{\dfrac{1}{Q_{\mathrm{ex}}} - \left(\dfrac{1}{Q_S}+\dfrac{1}{Q_W}\right)}{\dfrac{1}{Q_{\mathrm{ex}}}+\dfrac{1}{Q_S}+\dfrac{1}{Q_W}}, \tag{26}$$

$$a_{21}(B) = \frac{2\cdot\dfrac{\sigma_1}{\mathrm{Re}\,(\sigma_0)}\cdot\dfrac{1}{Q_{\mathrm{ex}}}\cdot\dfrac{1}{Q_S}}{\left(\dfrac{1}{Q_{\mathrm{ex}}}+\dfrac{1}{Q_S}+\dfrac{1}{Q_W}\right)^2+\left(\dfrac{\sigma_1}{\mathrm{Re}\,(\sigma_0)}\right)\dfrac{1}{Q_{S2}}}. \tag{27}$$

These quantities correspond respectively to the reflection coefficient and the transmission coefficient of the cavity, at the resonance frequency. In these equations the couplings to both inputs are assumed to be equal, $1/Q_{\mathrm{ex}\,1}=1/Q_{\mathrm{ex}\,2}=1/Q_{\mathrm{ex}}$. With the use of formulae (26), (27), a method to measure Hall mobility defined in the preceding section can be formulated as follows:

1. The ratio of $1/Q_{\mathrm{ex}}$ to $1/Q_W$ can be obtained by the measurement of the reflection coefficient of the cavity before inserting a sample.

2. The ratio of $1/Q_{\mathrm{ex}}$ to $(1Q_S+1/Q_W)$ can be obtained by the measurement of the reflection coefficient of the cavity after the sample being inserted.

From 1. and 2. the ratio, $1/Q_{\mathrm{ex}}$: $1/Q_W$: $1/Q_S$, can be obtained.

3. $\mu_H=(1/B)\cdot|\sigma_1|/\mathrm{Re}\,(\sigma_0)$ is obtained from the measurement of the transmission coefficient when magnetic field is applied, using formula (27) and the above obtained ratio, $1/Q_{\mathrm{ex}}$: $1/Q_W$: $1/Q_S$. The last term in the denominator of a_{21} is neglected, because it is second order in B.

If the couplings are not equal, $1/Q_{\mathrm{ex}\,1}\neq 1/Q_{\mathrm{ex}\,2}$, the processes 1. and 2. must be carried out for both inputs and the factor, which should be multiplied to the transmission coefficient to obtain μ_H, is given by the geometric mean of the factors relative to each input obtained by the above processes, 1. and 2. It is seen from the original formula (25).

Hall mobility under strong magnetic field may also be obtained from these formulae, but the procedure is much more complicated, because there are many factors causing the quadratic decrease of the transmission coefficient. The greatest factor is the last term in the denominator of a_{21}, which comes from the coupling between the two modes of the cavity. Another factor is the magneto-resistance effect in $1/Q_S$, which varies with $\mathrm{Re}\,(\sigma_0)$. Moreover, even if these factors are properly taken account of, the resultant quantity μ_H thus obtained includes the magneto-resistance effect.

§ 4. Experimental Details

The circuit diagram used to measure Hall mobility is shown in Fig. 3. A klystron Raytheon 2K33 was used as a source of microwaves at 24 Gc. A standing wave detector, employing a 1N26 crystal for microwave power detection, was used to measure the reflection coefficients of the cavity. Switch I was used to feed microwave power to the sample circuit and to the reference circuit alternatively. Switch II was used when the detection systems I and II were adjusted so as to have the same sensitivity. In this case microwave power through the reference circuit was switched to Det I and Det II alternatively with Switch I and the gains of AFAmp I and AFAmp II were adjusted so that the amplitudes of the traces in the oscilloscope had the same height. After this, Switch II was set so that Det I and Det II should detect microwave power from the sample circuit and the reference circuit respectively.

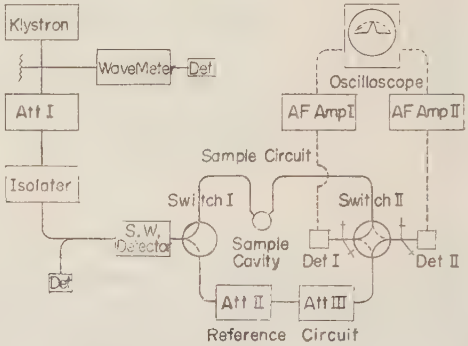

Fig. 3. Block diagram of experimental arrangement: solid lines for microwave circuit, dashed lines for audio frequency circuit.

The sample cavity was as shown in Fig. 2. Tuner I and Tuner II were used to adjust the resonance frequencies of the two modes of the cavity seen from two inputs. Samples were circular discs about 0.5 mm thick and 2 mm in diameter, which were placed on the symmetry axis of the cavity about 1~4 mm apart from the bottom of it with a teflon rod of 1 mm in diameter.

Measurement was carried out as follows: First, microwave power was switched to the sample circuit with Switch I and the standing wave ratio was measured before inserting a sample. Second, switch setting was the same as before, and the standing wave ratio was measured after inserting the sample into the cavity. Third, the transmission coefficient was measured as a function of magnetic field. This procedure was accomplished as follows; microwave power was fed to the reference circuit and AFAmp I and AFAmp II were adjusted so as to have the same sensitivity using Switch II. Then, microwave power was switched to the sample circuit with Switch I under the application of magnetic field. Input power to the sample circuit was controlled with Att I so that the transmitted power through the cavity should have the same level as that in the previous stage of adjustment of detecting systems. Microwave power was again switched to the reference circuit and the transmitted power was adjusted with Att II and Att III to the same level as that in the previous stage, and the readings of Att II and Att III gave the transmission coefficients of the cavity. These processes were necessary, because the difference in the characteristics of crystal detectors may influence the obtained results. The input power to the cavity was always kept below 10 mW, with Att I, because too much power caused temperature rise in the sample and Hall output decreased gradually after the application of microwave power.

The reflection coefficients were measured under continuous microwaves and detected by microammeter. The transmission coefficients were measured by modulating the repeller voltage of the klystron by saw-tooth waves at 200 c/s and detecting with oscilloscope.

Throughout the measurement the greatest error was expected to arise from the measurement of the standing wave ratios, because the square law characteristics were assumed for the crystal detector and the bended wave guide was intervening between the standing wave detector and the sample cavity. These situations would cause the maximum error of about 10% in the final result. In fact, the fluctuation of measured Hall mobility did not exceed 5%, when the measurement was repeated changing the sample positions in the cavity, consequently changing Q_S of the sample.

For the measurement at low temperatures the cavity was covered with a copper can and dipped into liquid air or dry ice. The space in the can was kept at 1 atmospheric pressure, but the circulation of air from the outside was kept away to avoid freezing of water in the cavity. The temperature was measured at the outer surface of the cavity near the sample with a copper-constantan thermocouple. A slight change in temperature between 100°K and 130°K was achieved by changing a contact of the can with liquid air.

§ 5. Experimental Results and Discussions

Hall mobility was measured for 0.33 ohm-m (33 ohm-cm) *n*-type and 0.55 ohm-m (55 ohm-cm) *p*-type germanium at several points between room temperature and 100°K. Samples for d.c. measurement were cut from the same wafer in a "bridge" shape. An example of measurements of the quantity $(P_{\mathrm{out}}/P_{\mathrm{in}})^{1/2}$ is shown versus applied magnetic field in Fig. 4, where P_{out} and P_{in} are microwave power output from and input to the cavity respectively. As seen from the figure, there is some zero-field output power because of the lack of symmetry of the structure. The Hall outputs are obtained by taking the mean values of $(P_{\mathrm{out}}/P_{\mathrm{in}})^{1/2}$ when the magnetic field was applied in plus and minus directions. In Fig. 5 the measured Hall mobility $\mu_H{}^*$ is plotted versurs applied magnetic field, where $\mu_H{}^*$ is obtained by

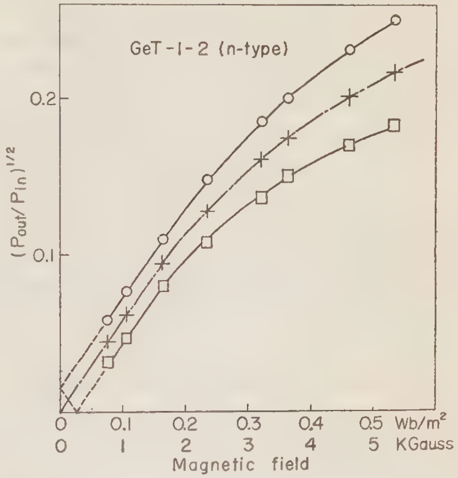

Fig. 4. Plot of transmission coefficient of the cavity *vs.* applied magnetic field for *n*-type germanium at 102°K: ⊙—magnetic field in plus direction, ⊡—magnetic field in minus direction, +—mean values.

$$\mu_H{}^* = \frac{1}{B}\cdot\frac{\left(\dfrac{1}{Q_W}+\dfrac{1}{Q_S}+\dfrac{1}{Q_{\mathrm{ex}}}\right)^2}{2\dfrac{1}{Q_S}\cdot\dfrac{1}{Q_{\mathrm{ex}}}}\left(\frac{P_{\mathrm{out}}}{P_{\mathrm{in}}}\right)^{1/2}. \tag{28}$$

In the case of *n*-type germanium $\mu_H{}^*$ decreases quadratically with B, as was pointed out in the preceding section. In the *p*-type case, the field dependence of $\mu_H{}^*$ resembles that of Hall coefficient at d.c. measurement, though the quadratic decrease as seen in the

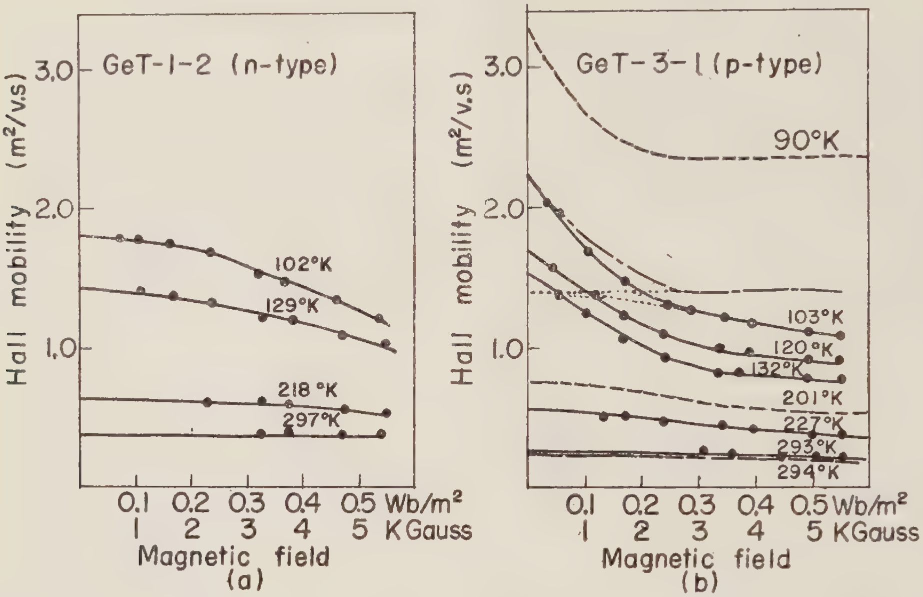

Fig. 5. Hall mobility *vs.* magnetic field: solid curves —$\mu_H{}^*$ measured at 24 Gc, dashed curves in (b)—Hall mobility at d.c. defined by $R\sigma_0$, a dot dashed curve—approximate behaviour of μ_H obtained from 103°K data after the correction of quadratic decreases, as shown by a dotted curve.

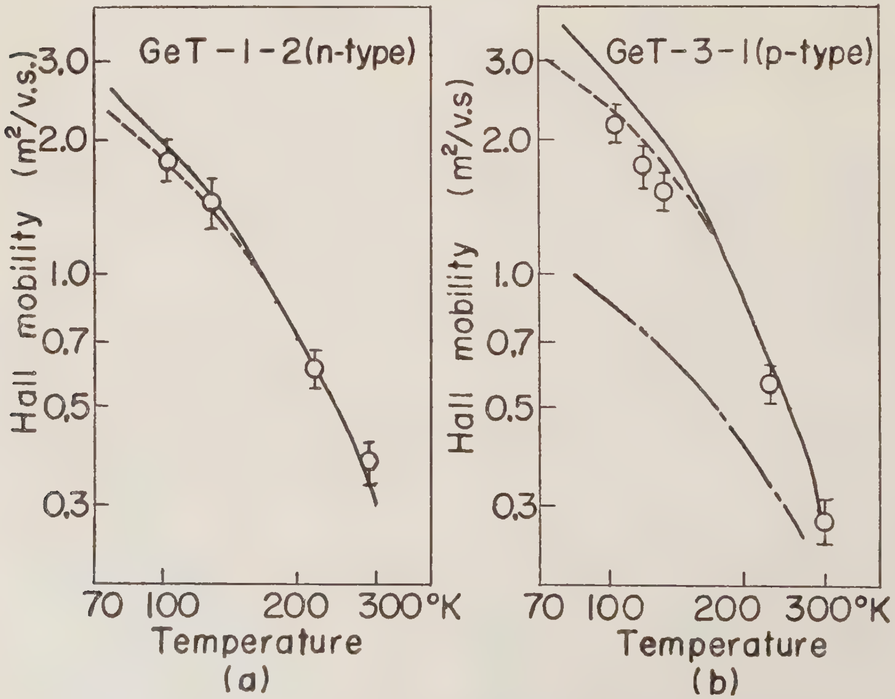

Fig. 6. Plot of Hall mobility extrapolated to vanishing magnetic field *vs.* temperature: solid curves —d.c. measurement, circles—24 Gc measurement, dashed curves—values expected on the assumption $\tau=\tau_0(\varepsilon/kT)^{-1/2}$, a dot dashed curve—values expected on the asumption $\tau=\tau_0(\varepsilon/kT)^{-1}$.

n-type case is also superposed on it. As was pointed out already, these quadratic behaviour is not easy to treat strictly, and only the zero-field mobility is compared with that in the d.c. case. In the limit of vanishing field, $\mu_H{}^*$ is obviously identical with μ_H. In Fig. 6 $\mu_H{}^*$ $(B=0)$ is plotted versus temperature. On the same figure, Hall mobility measured at d.c. for vanishing magnetic field $\mu_0=R_0/\rho_0$ is also plotted.

As was already pointed out in the preceding section, the deviation of the microwave Hall mobility from the d.c. value can be obtained theoretically from Fig. 1, if the dependence of the relaxation time is assumed (for example, $\tau=\tau_0(\varepsilon/kT)^{-1/2}$) and τ_0 is known (therefore, $\omega\tau_0$ is known). In the n-type case, d.c. Hall mobility was used to determine τ_0 from the relation:

$$\mu_0=R_0\sigma_0=\frac{\frac{1}{3}\left(\frac{2}{m_\perp m_\parallel}+\frac{1}{m_\perp{}^2}\right)}{\frac{1}{3}\left(\frac{2}{m_\perp}+\frac{1}{m_\parallel}\right)}\cdot\frac{e\langle\tau^2\rangle}{\langle\tau\rangle} \tag{29}$$

where R_0 and σ_0 are low field Hall coefficient and conductivity respectively, and $m_\perp$ and $m_\parallel$ are taken to be $0.082m_0$ and $1.58m_0$ as determined by cyclotron resonance experiment17). In the p-type case, τ_0 was determined from d.c. Hall mobility at large magnetic field and the following formula:

$$\mu_\infty=R_\infty\sigma_0=\frac{\left(\frac{n_h}{m_h}+\frac{n_l}{m_l}\right)}{n_h+n_l}e\langle\tau\rangle \tag{30}$$

where R_∞ is the high field Hall mobility and m_h and m_l are heavy and light hole masses respectively. Cyclotron masses17), $0.34m_0$ and $0.042m_0$, were used for m_h and m_l, and the relation, n_l: $n_l=m_h{}^{3/2}$: $m_l{}^{3/2}$, was assumed. Hall coefficient obtained at 90°K and 0.3 Wb/m² (3,000 Gauss) was regarded as R_∞, where R had already reached the flat region of Hall coefficient versus magnetic field curve.

The results thus obtained assuming $\tau=\tau_0(\varepsilon/kT)^{-1/2}$ are plotted in Fig. 6 by dashed curves. In Fig. 6(b) the behaviour of μ_H expected on the assumption $\tau=\tau_0(\varepsilon/kT)^{-1}$ is also plotted to illustrate the effect of energy dependence of the relaxation time on the microwave Hall mobility. Generally speaking, if changes of the relaxation time among possible states in $\boldsymbol{k}$-space are greater, μ_H would decrease more rapidly with frequency.

The results theoretically deduced from d.c. Hall mobility assuming acoustical mode scattering are in agreement with experimental results at 24 Gc. Especially in n-type case, the agreement is very good, but, in p-type case, the experimental results at 24 Gc are somewhat smaller than expected theoretically. This fact suggests the energy dependence of of the relaxation time somewhat steeper than $\varepsilon^{-1/2}$ for p-type germanium, if the above mentioned assumptions concerning valence bands are justified.

The acoustical mode scattering and the optical mode absorption and emission processes predict $\tau\sim1/\sqrt{\varepsilon}$, $1/\sqrt{\varepsilon+h\nu}$, $1/\sqrt{\varepsilon-h\nu}$ respectively. Though the optical mode emission process is more sharply dependent on energy it does not play a significant role in these temperature region. The addition of ionized impurity scattering makes the situation worse. It may be possible that the energy dependence of τ is different for heavy and light holes16), for example, owing to impurity scattering, and the low field Hall mobility suffers high frequency effect more severely. However, it is not the case as seen from Fig. 5. As shown by a dot dash curve in Fig. 5(b), μ_H would be obtained approximately from $\mu_H{}^*$ correcting the quadratic decrease for increasing magnetic field. The approximate behaviour of μ_H shows that μ_0/μ_∞ in the microwave case is not smaller than in the d.c. case. Another possibility is the warping of the energy bands, which is not considered, because our sample is not oriented.

Hall mobility measurements at microwave frequencies by the "power transmission" method were reported by several authors2),4),). Especially Hambleton and Gärtner5) measured Hall mobility at 20 Gc between room temperature and 80°K by a "crossed wave guide" method, and reported that Hall mobility in n-type germanium deviated very irregularly from d.c. values at low temperatures, and in p-type germanium went below d.c. values for temperatures lower than 150°K and showed saturation with the lowering of temperature below 100°K. According to them, Hall mobility measured using the formula $\mu_H=(1/B)\cdot(P_{\text{out}}/P_{\text{in}})^{1/2}$ corresponds to $\mu_H=1/m^*(j\omega+(1/\tau))$, and they insisted that they observed high frequency effect in p-type germanium. However, it would be shown by a simple consideration that power absorbed by the sample ($P_{\rm in}$) and available power from the sample due to Hall effect ($P_{\rm out}$) were proportional to $\mathrm{Re}(\sigma_0)$ and $(1/4)\cdot|\sigma_1|^2/\mathrm{Re}(\sigma_0)$ at low magnetic field, and $\mu_H=(2/B)\cdot(P_{\rm out}/P_{\rm in})^{1/2}=(1/B)\cdot|\sigma_1|/\mathrm{Re}(\sigma_0)$ would be independent of frequency on the simple constant τ model, as was discussed previously. (This formula may be obtained from Eq. (27) putting $1/Q_{\rm ex}=1/Q_S\gg 1/Q_W$) Secondly, they used formula $\mu_H\sim(1/B)(P_{\rm out}/P_{\rm in})^{1/2}$ at 0.5 Wb/m² (5,000 Gauss), but it would fail at temperatures near 100°K, where $\mu\sim 2\ \mathrm{m^2/v\cdot s}$ (20,000 cm²/v·s) and μB approached unity. For this reason, the deviation of Hall mobility from d.c. values observed by them would include considerable factors other than the effect of high frequencies.

§ 6. Conclusions

A method to measure Hall mobility at microwave frequencies using a double mode cavity was presented. Hall mobility measured by this method was expected to deviate from the d.c. value, when the microwave frequency approached the mean relaxation frequency and the relaxation time varied from state to to state. Both these conditions were shown to be necessary theoretically.

Hall mobility was measured at 24 Gc for high resistivity *n*- and *p*-type germanium at several points between room temperature and 100°K. The acoustical mode scattering explains the essential features of Hall mobility at 24 Gc. However, there remains some discrepancies to be clarified in *p*-type germanium.

The author would like to express his sincere thanks to Dr. T. Niimi for his continual encouragement, and to Mr. Y. Kanai and Mr. R. Nii for many valuable discussions throughout this work. The author also wishes to thank to Mr. K. Miya-uchi and Mr. I. Nakagawa for the discussion about the microwave circuit elements, and to Mr. N. Kakuta for preparing germanium samples.

References

1) S. P. Cooke: Phys. Rev. **74** (1948) 701.
2) Y. Nishina and W. J. Spry: J. Appl. Phys. **29** (1958) 230. Y. Nishina: Private Communication.
3) A. M. Portis and D. Teaney: J. Appl. Phys. **29** (1958) 1692. A. M. Portis: J. Phys. Chem. Solids **8** (1959) 326.
4) K. Yamagata: Sci. Rep. Tohoku Univ. **A, 12** (1960) 235. K. Yamagata and T. Fukuroi: Sci. Rep. Tohoku Univ. **A, 12** (1960) 248.
5) G. E. Hambleton and W. W. Gärtner: J. Phys. Chem. Solids **8** (1959) 329.
6) H. Suhl and G. L. Pearson: Phys. Rev. **A, 92** (1953) 858. R. R. Rau and M. E. Caspari: Phys. Rev. **100** (1955) 632. J. K. Furdyna and S. Broersma: Phys. Rev. **120** (1960) 1995.
7) N. Watanabe: Rev. of Electrical Communication Laboratory **8** (1960) 256.
8) G. Dresselhaus, A. F. Kip and C. Kittel: Phys. Rev. **100** (1955) 618.
9) M. Date: J. Phys. Soc. Japan **15** (1960) 1488.
10) F. J. Blatt: Solid State Physics, edited by Seitz and Turnbull Vol. **4** (1957) 214.
11) B. Donovan and N. March: Proc. Phys. Soc. (London) **B, 69** (1956) 528.
12) F. J. Blatt: Solid State Physics Vol. **4** (1957) 271.
13) J. C. Slater: *Microwave Electronics*, D van Nostrand Co. Inc., (New York, 1950).
14) S. Tomonaga, T. Miyazima and K. Shimoda: *Theory of Microwaves*, (in Japanese) Risunaa Co., (Tokyo, 1950).
15) T. Fukuroi and K. Yamagata: Sci. Rep. Tohoku Univ. **A, 11** (1959) 285.
16) A. C. Beer and R. K. Willardson: Phys. Rev. **110** (1958) 1286.
17) C. Dresselhaus, A. F. Kip and C. Kittel: Phys. Rev. **98** (1955) 368.

JOURNAL OF THE PHYSICAL SOCIETY OF JAPAN Vol. 16, No. 10, OCTOBER, 1961

Structure of Thin Layers of Some F. C. C. Metals Deposited on Oriented Ag, Pd and Ni Films

By Shunji SHIRAI, Yoshiichi FUKUDA and Masayoshi NOMURA*
College of Arts and Sciences, Tohoku University, Kawauchi, Japan

(Received May 29, 1961)

Some f. c. c. meas—Ni, Cu, Pd, Al, Au, Ag and Pb—were evaporated *in vacuo* on to oriented Ag, Pd and Ni films and the structure of the films was studied by the transmission method of electron diffraction. Some films were composed of intermetallic compounds of deposit and substrate metals. But some films were composed of two layers of deposit and substrate metals. In the latter case, the deposit metals grew in the (001) or (111) oriented over growth on a substrate metal at a temperature higher than an epitaxial temperature. The occurrence of these two kinds of oriented overgrowth depended mainly on the percentage misfits.

§ 1. Introduction

So far cleavage surfaces of some minerals or salts[1] have frequently been used as the substrates on which oriented overgrowths of some materials from the vapour phase were formed. But there are only a few investigations[2] of the oriented overgrowth of metal deposited on the surface of metallic single crystal. In order to obtain more informations concerning the mechanism of epitaxy, it seems to be very desirable to make further systematic studies on metal layers deposited on single crystal metal surfaces. In the present paper, an investigation will be described in which some f.c.c. metals—Ni, Cu, Pd, Al, Au, Ag and Pb—were deposited from the vapour phase on oriented Ag, Pd and Ni films and the structure of the films was examined by the transmission method of electron diffraction. Some films were composed of intermetallic compounds of deposit and substrate metals. But some films were composed of two lager of deposit and substrate metals. In the latter case, the deposit metals grew in an oriented overgrowth on a substrate at a temperature higher than an epitaxial temperature. Two kinds of oriented overgrowth were observed and their occurrence depended mainly on the percentage misfit.

§ 2. Experimental Method

Oriented metal films about 40 mμ in thickness were deposited *in vacuo* on a cleavage surface of NaCl crystal heated to about 200°C (for Ag) or about 400°C (for Pd and Ni). After the dissolution of NaCl crystal in water, the oriented metal film was caught on a hole 0.1 mm in diameter perforated in a thin Ni plate. After it was ascertained by the method of electron diffraction that the metal film was a quasi-single crystal film having the (001) plane parallel to the film surface and the (111) twinning was comparatively less marked, it used as a substrate.

Ni, Cu, Pd, Al, Au, Ag and Pb metals were deposited *in vacuo*, generally about 30 mμ in thickness, on an oriented Ag, Pd or Ni film. When an oriented Ag or Pd film was used as a substrate, it was maintained at -196°C or temperatures ranging at an interval of 100°C between -100°C and 400°C during the evaporation of sample. When an oriented Ni film was used as a substrate, it was maintained at temperatures ranging at an interval of 100°C between 0°C and 400°C. A definite quantity of sample put in a small coil furnace made of tungsten wire 0.2 mm in diameter was evaporated by supplying a heating current 4.5 A for 5 sec. The distance between the tungsten coil furnace and substrate was about 3.5 cm. A copper plate with a slit 4 mm in diameter was placed at a distance 1 cm from the copper block supporting the substrate to prevent this as much as possible from the rise of temperature due to the radiation from the coil furnace.

When the substrate in the evacuated evaporation tube was cooled externally, it did not reach -100°C even after 7 hours or more. In this case the evaporation tube was beforehand filled with hydrogen gas about 10 mmHg in pressure from which condensable gases were removed by cooling with liquid nitrogen. Then the substrate in the evaporation tube could be cooled externally to −100°C or −196°C in less than about 15 min. When the substrate reached a desired temperature, hydrogen gas was evacuated from the evaporation tube and then the sample was evaporated.

---

* The present address is Central Research Laboratory, Hitachi Ltd., Kokubunji, Tokyo.

In general the pressure of residual gas was $5\times10^{-5}\sim5\times10^{-6}$ mmHg before the sample was evaporated, and it became $5\times\times10^{-4}$ mmHg or more after the evaporation was completed. The structure of bimetal films about 70 mμ in thickness prepared in this way was examined by the transmission method of electrons of an accelerating potential about 40 kv.

§ 3. Experimental Results

The films are classified in the following two groups from the view point of their structure: (I) The films are composed of intermetallic compounds of deposit and substrate metals. (II) The films are composed of two layers of deposit and substrate metals.

(I) Al on Ag; Cu on Pd (the substrate temperature was 400°C in this case); Al on Pd; Pb on Pd and Al on Ni. The pairs of deposit and substrate metals belonging to this group are able to be alloyed in intermetallic compounds[3]. The componets of film as a function of the substrate temperature (t_b) and the crystal structures of intermetallic compounds are summarized in Table I.

The orientations of component crystallites are as follows.

Table I. The components of film as a function of the substrate temperature t_b and the crystal structures of intermetallic compounds[3].

t_b°C	−196	−100	0	100	200	300	400
Al on Ag	Al	Ag_2Al	Ag_2Al	Ag_2Al	Ag_2Al	Ag_2Al Ag_3Al	Ag_2Al
Cu an Pd							CuPd
Al on Pd	Al	Al	Al	Al Pd_2Al_3	Al Pd_2Al_3	Pd_2Al_3	Pd_2Al_3
Pb on Pd	Pb_2Pd	Pb_2Pd	Pb_2Pd_3	Pb_2Pd_3 $PbPd_3$	Pb_2Pd_3 $PbPd_3$	$PbPd_3$	
Al on Ni			Al	Al	Al	AlNi Al_3Ni_2	AlNi Al_3Ni_2

Ag_2Al: h.c.p. type, $a=2.817$Å, $c=4.662$Å, $c/a=1.624$ at 27 at. % Al−$a=2.885$Å, $c=4.582$Å, $c/a=1.588$ at the Al-rich saturation limit. In the present experiment the values of a, c and c/a were respectively 2.86Å, 4.64Å and 1.62.

Ag_3Al: β-Mn type, $a=6.92-6.93$Å.

CuPd: CsCl type, $a=2.96$Å.

Pd_2Al_3: Ni_2Al_3 type, $a=4.22$Å, $c=5.19$Å, $c/a=1.22$.

Pb_2Pd: $CuAl_2$ type, $a=6.835$Å, $c=5.812$Å, $c/a=0.852$.

Pb_2Pd_3: NiAs type partially filled-in, $a=4.465$Å, $c=5.704$Å, $c/a=1.275$ at the Pd-rich side.

$PbPd_3$: Cu_3Au type, $a=4.0135$Å.

AlNi: CsCl type, $a=2.8814$Å.

Al_3Ni_2: Ni_2Al_3 type, $a=4.0282$Å, $a=4.8906$Å, $c/a=1.2141$.

Al on Ag.

Al: A part of Al crystallites in the deposit layer was randomly oriented and the remaining part had the fibre structure with the $[111]_{Al}$ axis perpendicular to the film surface.

Ag_2Al[4]: When t_b's were −100°C, 0°C, 100°C and 200°C, Ag_2Al crystallites had random orientation. When t_b's were 300°C and 400°C, a smaller part of Ag_2Al crystallites was radomly oriented and the remaining greater part had the orientation $(0001)_{Ag_2Al}\|\{111\}_{Ag}$ and $\langle 11\bar{2}0\rangle_{Ag_2Al}\|\langle 110\rangle_{Ag}$, Ag_2Al crystallites being rotated in a range of small angle (Fig. 1).

Ag_3Al: Ag_3Al crystallites had the orienta-

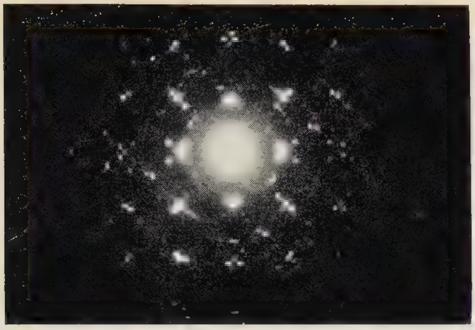

Fig. 1. Al on Ag, sub. temp. 400°C.

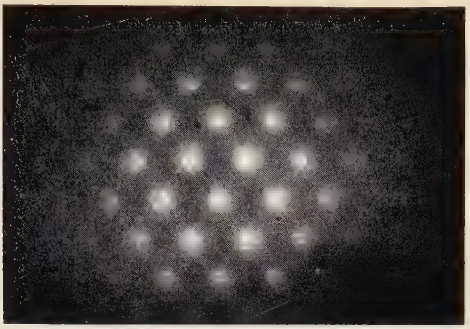

Fig. 4b. The same sample as in Fig. 4a rotated rotated 45° about $[010]_{Ag}$.

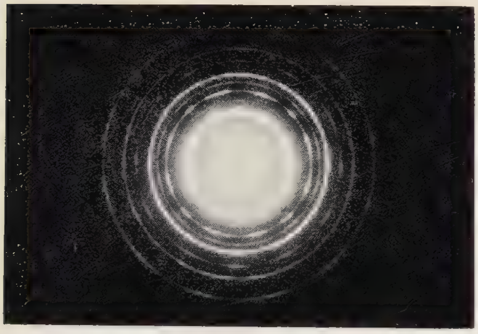

Fig. 2. Cu on Pd, sub. temp. 400°C.

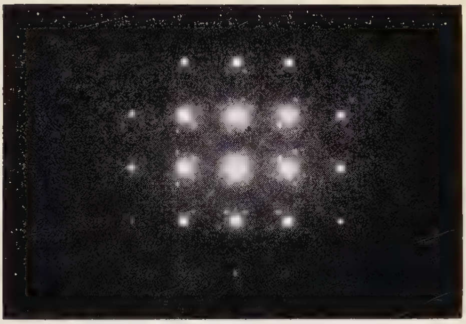

Fig. 5. Pb on Ag, sub. temp. 200°C.

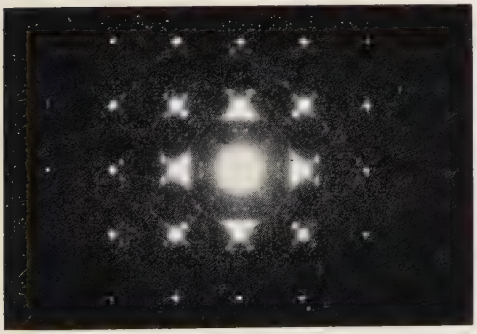

Fig. 3. Al on Ni, sub. temp. 400°C.

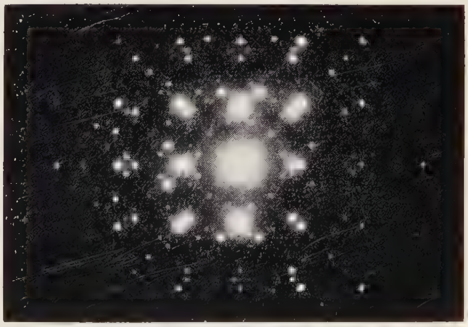

Fig. 6. Ag on Ni, sub. temp. 400°C.

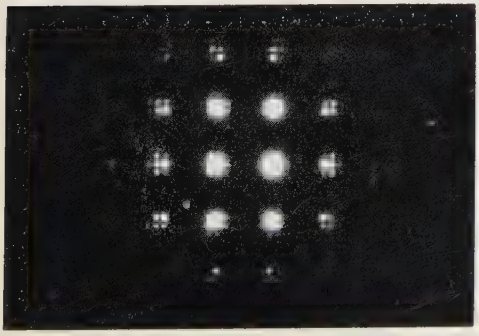

Fig. 4a. Ni on Ag, sub. temp. 400°C.

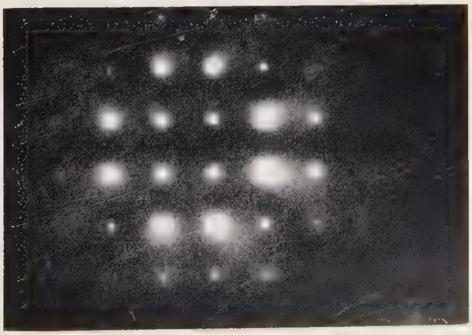

Fig. 7. Au on Ag, sub. temp. 100°C.

tion $(001)_{Ag_3Al} || (001)_{Ag}$ without further limitations.

Cu on Pd.

CuPd: When t_b was 400°C, the film was composed of CuPd crystallites crystallizing in the ordered state with random orientation. On the plate only the diffraction pattern due to CuPd appeared, but no pattern due to the substrate Pd (Fig. 2).

Al on Pd.

Al: Al crystallites in the deposit layer had random orientation.

Pd_2Al_3: When t_b was 200°C, Pd_2Al_3 had the orientation $(1\bar{1}0\bar{1})_{Pd_2Al_3} || (001)_{Pd}$ and $[11\bar{2}0]_{Pd_2Al_3} || [100]_{Pd}$ or $[010]_{Pd}$. When t_b's were 300°C and 400°C, Pd_2Al_3 crystallites gave a weak pattern of arcs due to the above orientation superimposed on strong D. S. rings.

Pb on Pd.

Pb_2Pd: Pb_2Pd crystallites were randomly oriented.

Pb_2Pd_3: Pb_2Pd_3 crystallites had the orientation $(01\bar{1}0)_{Pb_2Pd_3} || (001)_{Pd}$ and $[10\bar{1}0]_{Pb_2Pd_3} || [110]_{Pd}$ or $[1\bar{1}0]_{Pd}$.

$PbPd_3$: When t_b's were 0°C, 100°C and had 200°C, a greater part of $PbPd_3$ crystallites had random orientation and the remaining smaller part had the orientation $(001)_{PbPd_3} || (001)_{Pd}$ and $[100]_{PbPd_3} || [110]_{Pd}$. When t_b was 300°C, $PbPd_3$ caystallites were randomly oriented crystallizing in the ordered state.

Al on Ni.

Al: Al crystallites in the deposit layer were randomly oriented.

AlNi: AlNi crystallites had the orientation $(001)_{AlNi} || (001)_{Ni}$ and $[100]_{AlNi} || [110]_{Ni}$.

Al_3Ni_2: Al_3Ni_2 crystallites had the orientation $(10\bar{1}0)_{Al_3Ni_2} || (001)_{Ni}$ and $[01\bar{1}0]_{Al_3Ni_2} || [110]_{Ni}$ or $[1\bar{1}0]_{Ni}$ (Fig. 3).

(II) Ni on Ag, Cu on Ag, Pd on Ag, Au on Ag, Ag on Ag, Ni on Pd, Cu on Pd (t_b was lower than 300°C in this case), Pd on Pd, Au on Pd, Ag on Pd, Ni on Ni, Cu on Ni, Pd on Ni, Au on Ni and Ag on Ni. The pairs of deposit and substrate combinations belonging to this group are able to form solid solutions over limited ranges or a continuous series of solid solutions[3]. The results in the case (II) are summarized in Table II. The epitaxial temperature for each combination is shown

Table II.

b	Ag				Pd				Ni			
a	*m* %	*m'* %	t_{ep} °C	Or	*m* %	*m'* %	t_{ep} °C	Or	*m* %	*m'* %	t_{ep} °C	Or
Ni	−13.8	−25.4	100	□	−9.4	−21.5	100	□	0	−13.4	300	□
Cu	−11.5	−23.4	0	□	−7.1	−19.5	−100	□*	2.6	−11.1	200	□**
Pd	−4.8	−17.6	<−196	□	0	−13.4	100	□	10.4	−4.4	300	□
Al	−0.9	−14.2			4.1	−9.8			14.9	−0.5		
Au	−0.02	−13.4	−100	□	4.9	−9.2	−100	□	15.7	0.2	300	⊠
Ag	0	−13.4	<−196	□	5.0	−9.1	−100	□	16.0	0.5	300	⊠
Pb	21.1	4.9	−100	△	27.3	10.2			40.5	21.7		

a: deposit metal.

b: substrate metal.

m%: percentage misfit for parallel overgrowth.

m'%: a percentage multiple misfit for (111) oriented overgrowth on (001) surface of substrate.

t_{ep} °C: epitaxial temperature.

Or: orientation.

□: $(001) || (001)_b$ and $[100] || [100]_b$.

△: $(111) || 001)_b$ and $[\bar{1}10] || [110]_b$ or $[\bar{1}10]_b$.

⊠: □ and △ occur simultaneously.

*: random orientation of CuPd in the ordered state at $t_b = 400$°C.

**: Weak D. S. rings due to deposit also always appeared at a substrate temperature higher than t_{ep} °C.

in the 4th, 8th and 12th columns. The structure of deposit layer obtained at a substrate temperature higher than the epitaxial temperature is shown in the 5th, 9th and 13th columns.

Two kinds of oriented overgrowth were observed. One kind was such that the orientation of crystallites in a deposit layer was $(001)_a \| (001)_b$ and $[100]_a \| [100]_b$. This parallel overgrowth is quoted hereafter as the (001) orientation. As an example in this case a diffraction pattern due to a Ni-Ag bimetal film is shown in Figs. 4a and 4b. In addition to the spots due to Ni and Ag crystallites, the secondary diffraction spots due to Ni crystallites of diffracted beams due to Ag crystallites are also seen in Figs. 4a and 4b. The other kind of oriented overgrowth was such that the orientation of crystallites in a deposit layer was $(111)_a \| (001)_b$ and $[\bar{1}10]_a \| [110]_b$ or $[\bar{1}10]_b$. This oriented overgrowth is quoted hereafter as the (111) orientation. As an example in this case a diffraction pattern due to a Pb-Ag bimetal film is shown in Fig. 5. Besides the spots due to Pb and Ag the secondary diffraction spots due to Pb crystallites of diffracted beams due to Ag crystallites are also seen in Fig. 5. In the cases of Ag on Ni and Au on Ni both the (001) and (111) orientations occurred simultaneously in the deposit layer (Fig. 6). In general the orientation of crystallites in a deposit layer was random, when the substrate temperature was lower than an epitaxial temperature. The case of Ni on Ni was an exception, where Ni crystallites in a deposit layer gave, superimposed on D.S. rings, an arc pattern due to the following orientation: $(111)_a \| (001)_b$ and $[\bar{1}10]_a \| [110]_b$ or $[\bar{1}10]_b$. In the patterns due to Au-Ag bimetal films there always appeared diffuse bands (Fig. 7).

In the present experiment it could not be ascertained whether the deposit atoms interdiffused with the substrate atoms or not in the case of each combination belonging to the (II) group. In the case of Pb on Ni no diffraction pattern was obtained which was so perfect as to be analysed.

§ 4. The (001) and (111) Orientations and the Percentage Misfit

The single crystal film of f.c.c. metal evaporated on to a cleavage surface of NaCl crystal has generally an atomically rough surface. It has been reported5) that, if copper is deposited on to gold the copper deposit, at the initial stage, diffuses into the gold substrate as shown by the electron reflection method. Though the transmission method of electron diffraction failed to detect alloying of deposit with substrate in the cases of all deposite and substrate combinations belonging to the (II) group, it may not be concluded that deposit and substrate atoms do not diffuse into each other.

In the following, it is assumed that the

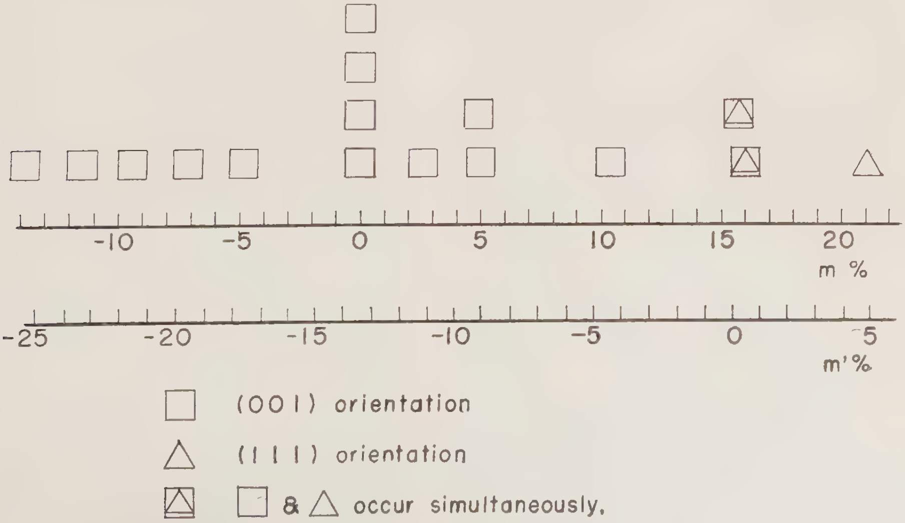

Fig. 8.

surface of substrate is the (001) plane, and the kind of oriented overgrowth *versus* percentage misfits is plotted in Fig. 8. One of two percentage misfits in two orthogonal directions for the (111) oriented overgrowth on the (001) surface of substrate is equal to the percentage misfit $m\%$ for parallel overgrowth on the (001) surface of substrate. The other misfit $m'\%$ (a multiple misfit) is equal to $(0.866\,m-13.4)\%$. $m\%$ is tabulated in the 2nd, 6th and 10th columns in Table II. $m'\%$ is tabulated in the 3rd, 7th and 11th columns in Table II. It will be seen from Fig. 8 that the (001) orientation occurs when $m\%$ is smaller than about 16%, and the (111) orientation occurs for low values of $m'\%$. It will be noteworthy that there is a correlation between the kind of oriented overgrowth and the percentage misfits in spite of using an atomically rough surface as a substrate.

This work has been supported partly by the fund of the Ministry of Education in Aid of Scientific Researches.

References

1) J. H. van der Merwe: Disc. Faraday Soc. No. 5 (1949) 201.
Z. G. Pinsker: *Electron Diffraction* (1953) (Butterworth, London, 1953).
H. Mayer: *Physik Dünner Schichten*, Teil II (Wissenschaftliche Verlag., Stuttgart, 1955).
D. W. Pashley: Adv. in Phys. **5** (1956) 173.

2) L. Brück: Ann. Physik **26** (1936) 233.
O. Haase: Z. Naturforsch. **11a** (1956) 862. Ibid. **16a** (1961) 202. Ibid. **16a** (1961) 206.
R. C. Newman and D. W. Pashley: Phil. Mag. **46** (1955) 927.
R. B. Kehoe, R. C. Newman and D. W. Pashley: Phil. May. **1** (1956) 783.
R. C. Newman: Phil. Mag. **2** (1957) 750.
E. Grünbaum: Proc. Phys. Soc. **72** (1958) 459.
E. Grünbaum, R. C. Newman and D. W. Pashley: Phil. Mag. **3** (1958) 1337.

3) M. Hansen: *Constitution of Binary Alloys* (McGraw-Hill, New York, 1958).
W. B. Pearson: *A Handbook of Lattice Spacings and Structures of Metals and Alloys* (Pergamon, London, 1958).

4) H. Göttsche: Z. Phys. **134** (1953) 504.
D. Watanabe: J. Phys. Soc. Japan **11** (1956) 1072.

5) C. A. Bassett, J. W. Menter and D. W. Pashley: *Structures and Properties of Thin Films* ed. by C. A. Neugebauer et al. (John Wiley & Sons, New York, 1959) 11p.

JOURNAL OF THE PHYSICAL SOCIETY OF JAPAN, Vol. 16, No. 10, OCTOBER, 1961

X-ray and Magnetic Studies of the Manganese-Germanium System

By Tetuo OHOYAMA

Department of Physics, Faculty of Science,
Tokyo Metropolitan University

(Received June 3, 1961)

The constitution of Mn-Ge system within the range of composition 21.8～35.7 at.% Ge was examined by X-ray powder diffraction, and magnetic properties of each phase were studied. The existence of four phases——high- and low-temperature phases at about 22～23.5 at.% Ge (ε, ε_1), a high temperature phase around 28 at.% Ge (ζ), and a low-temperature phase at 28.6 at.% Ge (κ)——was established. The κ phase is ferrimagnetic below the Curie point 710°K, and the spontaneous magnetization is reversed at 395°K (N type). The other phases exhibit quite anomalous magnetism. The Debye diagram for ζ phase could be indexed assuming a hexagonal structure with lattice parameters $a=7.18_6$ Å and $c=13.0_8$ Å.

§1. Introduction

The phase diagram of the binary alloy system of manganese-germanium was investigated in detail by Zwicker et al.[1], and was partly corrected in the later work by Zwicker[2]. According to them, there exist four intermetallic compounds in this system: $Mn_{3.25}Ge$, Mn_5Ge_2, Mn_5Ge_3, and Mn_3Ge_2. The compound $Mn_{3.25}Ge$ (23.5 at.% Ge) is formed peritectically at 900°C from γ-Mn solid solution and the melt. The compound Mn_5Ge_2 (28.6 at.% Ge) is formed at 920°C and undergoes a phase transition at 630°C. The compound Mn_5Ge_3 is formed at 932°C for the composition of 37.5 at.% Ge, and has the appreciable range of solid solution toward the manganese-rich side, which is reduced with lowering of temperature. The compound Mn_3Ge_2 is formed at 745°C by a peritectic reaction between Mn_5Ge_3 and the melt with 50.5 at.% Ge.

As for the crystal structures of these compounds, Zwicker et al.[1] reported that $Mn_{3.25}Ge$ had a hexagonal close-packed structure in which a superstructure of $D0_{19}$ (Ni_3Sn) type formed after annealing the specimen for two days at 750°C. They also reported that the Debye diagram for the high-temperature phase of Mn_5Ge_2 suggested a structure being closely related to B8 (NiAs and Ni_2In) type, but there were superstructure lines which could not be indexed. The only work carried out later to determine the crystal structure of the compound in the system is due to Castelliz[3], who showed that the Debye diagram for Mn_5Ge_3 can be satisfactorily explained by assuming a $D8_8$ (Mn_5Si_3) type of structure.

The existence of a ferromagnetic phase in this system was noted first by Hames and Eppelsheimer[4]. Zwicker et al.[1] reported that Mn_5Ge_3 was strongly ferromagnetic and the high-temperature phase of Mn_5Ge_2 was weakly ferromagnetic. But no quantitative measurements had been made until Castelliz[5] determined the ferromagnetic moment per manganese atom and the Curie temperature of Mn_5Ge_3. Quigg et al.[6], in the course of their researches for new permanent magnet materials, measured the values of saturation magnetization, remanence, and coercive force at the room temperature for their unhomogenized specimens of Mn_5Ge_3 and Mn_5Ge_2. Recently, Fakidov et al.[7],[8] found an anomalous magnetic behavior in the specimen containing 70 at.% Ge.

Systematic investigations to survey the magnetic properties of the intermetallic compounds of iron group transition metals with IVb group elements in the periodic table had been undertaken by Yasukōchi, Kanematsu and Ohoyama, who discovered several new ferro-, ferri-, and antiferromagnetic materials in these systems[9)-14)]. In the manganese-germanium system, the anomalous magnetic behavior of Mn_3Ge_2 and the ferromagnetism of Mn_5Ge_3 were studied in details[15], and, as for the other two compounds, the antiferromagnetic behavior of $Mn_{3.25}Ge$ which was quenched from 750°C[9], the phase transition for the same compound[12], and the ferrimagnetism of the low-temperature phase of

Mn_5Ge_2[10] were reported. Further examinations on these two compounds, however, revealed that the effects of heat treatments on the magnetic behaviors were very complicated and could never be understood on the basis of the existing phase diagram due to Zwicker et al. Thus it became essential to make a closer inspection of the phase diagram in order to discuss the magnetism of these intermetallic compounds. In this paper are reported the results of some X-ray and magnetic studies which have been carried out on the alloys of the system containing from 21.8 to 35.7 at.% Ge.

§ 2. Preparation of Specimens and Experimental Methods

The specimens used for this study were prepared as follows: Powders of electrolytic manganese (99.9%) and germanium (seven-nine purity) were mixed in the desired proportions, and each mixture charged in an alumina crucible was sealed in an evacuated quartz tube, and melted at 1150°C in an electric furnace. After homogenized at 800°C for two days, they were quenched into cold water. Pieces of the alloys thus obtained were sealed again in evacuated quartz tubes separately, and held at various temperatures in electric furnaces, for two days at 700°C, for example, and for more than ten days at 450°C. Finally they were quenched into water. The crystal structures were examined by X-ray diffraction with Cu$K\alpha$ and Fe$K\alpha$ radiations. The Debye diagrams were obtained by means of a recording X-ray diffractometer as well as a Debye-Scherrer camera of 90 mm in diameter. A pulse height analyzer was set between the scintilation counter and the ratemeter of the diffractometer. The temperature dependences of the magnetization of the specimens were measured under the field of 9 kilo-oersteds from the liquid nitrogen temperature up to about 600°C, by means of a magnetic torsion balance. The magnetization was determined from the force exerted on the specimens placed in an inhomogeneous field. Temperatures were measured by means of thermocouples, Pt–Pt 13% Rh for the high-temperature, and copper-constantan for the low-temperature regions.

§ 3. Results of X-ray Studies

More than ten alloys were prepared within the composition range between 21.8 and 35.7 at.% Ge. In particular, relatively many alloys were prepared for the compositions near $Mn_{3.25}Ge$ and Mn_5Ge_2. They were examined by X-ray diffraction after heat treatments, in order to identify the phases and to detect changes in the crystal structure or formations of superstructures, if any.

ε and ε_1 phases

From the Debye diagram for the specimens quenched from 800°C, it was concluded that the composition range of the most manganese-rich compound, which has usually been referred to as $Mn_{3.25}Ge$ after Zwicker et al., is less narrow—about 22 to 23.5 at.% Ge—than their estimation, and 22.7 at.% Ge ($Mn_{3.4}Ge$) was chosen as the representative composition of the phase. Moreover it has been found that it undergoes a phase transformation as has been mentioned. In the following we shall refer to the high-temperature and the low-temperature phases as ε and ε_1 respectively.

a) *ε phase*

The crystal structure of the high-temperature phase is of A3 (h.c.p.) type and the lattice parameters were determined for the specimens quenched from 800°C to be $a=2.67_2$Å, $c=4.31_0$Å, and $c/a=1.61_3$ at the germanium-rich side and $a=2.66_7$Å, $c=4.31_8$Å, and $c/a=1.61_9$ at the manganese-rich side. These values are in substantial agreement with those given by Zwicker et al. In contrast to their result, however, no superstructure lines were observed even for the specimen annealed at 650°C for a week. But the existence of some degree of ordering may not be denied, for the difference in the atomic scattering factors for the two kinds of atom is not large enough.

At the composition of 22.7 at.% Ge, the lattice parameters $a=2.66_8$Å, $c=4.30_9$Å and $c/a=1.61_5$, and the picnometric density 7.45 g/cm^3 gave 0.46 formula weights of $Mn_{3.4}Ge$ or, in total, 2.0 atoms per unit cell.

b) *ε_1 phase*

The low-temperature ε_1 phase was realized by annealing the specimens of ε phase at a temperature below 500°C. It has a tetragonal A6 (f.c.t.) type of structure with the lattice parameters $a=3.80_3$Å, $c=3.61_8$Å, and $c/a=$

0.951 at 22.7 at.% Ge as reported previously by Ohoyama, Yasukōchi and Kanematsu[12]. The picnometric density 7.46 g/cm^3 gives 0.88 formula weights of $Mn_{3.4}Ge$ or 3.9≈4 atoms per unit cell. The transformation is presumably performed by the rearrangement of hexagonal (0001) planes to form tetragonal (111) planes. Thus, if a superstructure of $D0_{19}$ (Ni_3Sn) type was established in ε phase, it would be transformed into a tetragonal, $L6_0$ (Ti_3Cu) type of structure. But no superstructure lines were observed either.

The high-temperature ε phase was supercooled down to the room temperature, by the furnace-cooling at a rate of about 200°C/hr. The transformation took place so slowly that a long-time annealing was needed for its completion, but it was promoted to a considerable extent by a quenching from 800°C followed by a tempering at 450°C.* Thus the transformation will never be detected by means of the thermal analysis at the usual cooling rate. The transformation temperature was estimated to be about 500°C, which was also supported by the magnetic measurements.

Table I. Debye diagram of ζ-$Mn_{2.65}Ge$.

d^{-2}(Å^{-2}) obs.	*I*	*hk.l*	d^{-2}(Å^{-2}) calc.
.0831	w	11.1	.0833
.0936	w	00.4	.0936
.1004	s	11.2	.1009
.1201	vvw	10.4	.1194
.1269	vvw	20.2	.1267
.1717	vw	11.4	.1710
.1877	w	21.1	.1866
.1964	m	20.4	.1968
.2239	vs	11.5	.2236
.2321	vs	30.0	.2324
.2751	m	21.4	.2743
.2887	m	11.6	.2880
.3143	w	20.6 22.1	.3138 .3157
.3257	w	30.4	.3260
.4560	s	22.5	.4560
.5211	w	22.6	.5204
.5456	vw	31.6	.5462
.5656	vw	41.2	.5657
.5841	m	32.4 00.10	.5842 .5847
.6871	s	20.10 41.5	.6880 .6884
.6955	s	33.0	.6972
.7664	m	21.10	.7655
.7921	m	50.5	.7917
.8081	vvw	51.1	.8063
.8187	s	42.4	.8166
.9321	s	60.0	.9296

η phase

The crystal structure of the compound Mn_5Ge_3, to which we shall refer as η in the following, was identified to be of $D8_8$ (Mn_5Si_3) type by Castelliz[3]. In the present study, the lattice parameters for the alloys of manganese-rich side were determined to be $a=7.18_8$ Å, $c=5.03_7$Å, and $c/a=0.701$ at the room temperature.

ζ phase

The specimen with 27.4 at.% Ge ($Mn_{2.65}Ge$) annealed at 800°C was found to have a hexagonal structure with the lattice parameters $a=7.18_6$Å, $c=13.0_8$Å, and $c/a=1.82_0$. In the following we shall refer to this phase as ζ.

The strong diffractions can be indexed with $a'=a/\sqrt{3}=4.15$ Å, $c'=c/2.5=5.23$ Å and $c'/a'=1.26$. These parameters and the relative intensities of these diffraction lines suggest that the structure is closely related to that of $B8_2$ (Ni_2In) type, as was stated by Zwicker et al.[1] for their high-temperature phase of Mn_5Ge_2 (28.6 at.% Ge). In the Debye diagram of our specimen with 28.6 at.% Ge, however, a trace of the diffraction line from the more germanium-rich η phase was recognized. Thus it is likely that ζ phase exists at the composition with more manganese than Mn_5Ge_2. The specimen containing 27.4 at.% Ge quenched from 800°C was chosen as the representative of this phase in the magnetic

Table II. Debye diagram of κ-Mn_5Ge_2.

d^{-2}(Å^{-2})	*I*	d^{-2}(Å^{-2})	*I*
.0902	s	.5561	vs
.1066	w	.5646	vw
.1152	m	.5802	w
.1263	w	.5970	m
.1349	w	.6694	vw
.1394	m	.6757	s
.1677	w	.7035	s
.1729	s	.7241	w
.2068	s	.7467	m
.2213	vvs	.7586	w
.2451	vvs	.7735	vs
.2542	vvs	.7978	m
.3028	s	.8059	s
.3200	s	.8190	m
.3469	vw	.8398	s
.3591	w	.8561	vw
.3671	w	.8815	s
.3847	vw	.9179	m
.3979	vw	.9561	w
.4240	s	.9637	w
.4426	w	.9771	vs
.4608	s	.9916	s
.5033	w	1.0019	w
.5326	m	1.0140	vs

---

* A similar phenomenon was also seen in 'Mn_5Ge_2'.

study, since the diffractions from other phases were absent in the Debye diagram. The picnometric density of our specimen was 7.12 g/cm^3, which gives 11.7 formula weights of $Mn_{2.65}Ge$ or 42 atoms (30.5 Mn+11.5 Ge) per unit cell. Further determination of the crystal structure will be carried out in future.

Though the phase decomposed after a long time annealing at 500°C or lower, it was supercooled to the room temperature and the crystals of this phase which is easily cleaved along its (0001) plane was obtained by a furnace-cooling of the specimen from the melt. A quenching from 750°C followed by a tempering at 650°C promoted again the metallurgical reaction, and the precipitation of a greater amount of η phase in the specimen with 28.6 at.% Ge (Mn_5Ge_2) after such a treatment was detected by the X-ray examination.

κ phase

The specimen containing 27.4 at.% Ge ($Mn_{2.65}Ge$) decomposed into two phases when annealed at a temperature below 500°C: A small amount of ε_1 phase described above and a large amount of another phase which will be referred to as κ. The specimen containing 28.6 at.% Ge (Mn_5Ge_2), when annealed at the same temperature range, became to give only the diffractions from κ phase, which are shown in Table II. In the course of the transformation, the single crystal of ζ phase was changed into an aggregate of microscopic crystallites of κ phase which gave *continuous* Debye rings, so that the single crystal technique was not available for the analysis of the crystal structure. Although the powder pattern has not been successfully indexed, the structure seems not to be of a very low symmetry.

This phase might correspond to the 'low-temperature modification of Mn_5Ge_2' of Zwicker et al., but the Debye diagram is far from being related to that for the 'high-temperature modification', contrary to their statement. It may be possible that duration of their heat treatment was too short for the specimen to undergo the phase transformation to a considerable extent, and that their X-ray photograph was taken for the mixture of the high- and low-temperature modifications.

Two phase regions

Diffractions from κ phase were found as well in the two-phase specimens annealed at a temperature below 500°C ($\varepsilon_1+\kappa$ or $\kappa+\eta$). κ phase continued to exist after these specimens were annealed at 600°C, while ε_1 phase was replaced by ε phase. After these were heated up to above about 630°C, which was reported by Zwicker et al. to be the transition temperature of 'Mn_5Ge_2', κ phase disappeared and ζ phase appeared instead.

The diffractions from ε phase were recognized in the Debye diagram of the specimen with 27.5 at.% Ge annealed at 700°C, which disappeared after it was annealed at 800°C.

The phase diagram

The result of the X-ray studies may be summarized as follows.

(1) The composition $Mn_{3.4}Ge$ may be considered to be in the middle of the homogeneity range of the most manganese-rich compound (ε and ε_1 phases).

(2) The hexagonal ε phase transforms into the tetragonal ε_1 phase when annealed at a temperature below about 500°C.

(3) The range of solid solution of the complex hexagonal ζ phase, which corresponds to the high-temperature phase of Mn_5Ge_2 of Zwicker et al., is about from 27 to 28.5 at.% Ge at 800°C, and diminishes as the temperature is lowered. It is also probable that the maximum point of the liquidus curve lies in a little more manganese-rich side than Mn_5Ge_2.

(4) Corresponding to the low-temperature phase of Mn_5Ge_2 of Zwicker et al., a phase exists at the composition of Mn_5Ge_2 with a very narrow range of solid solution (κ phase).

(5) The alloy with the composition of Mn_5Ge_2 (28.6 at.% Ge) consists of two phases $\zeta+\eta$ between 650° and 850°C.

(6) The two-phase alloys $\kappa+\eta$ change into $\zeta+\eta$ when heated at a temperature above about 630°C.

These experimental results clearly show that the phase diagram due to Zwicker et al., shown in Fig. 1(a), should be revised. Since it seems difficult, if not impossible, to imagine that the alloy with 28.6 at.% Ge is of single ζ phase at temperatures just above 630°C, the experimental evidences (4) and (5) have led the author to assume the existence of two reactions, as shown in Fig. 1(b), instead of a transformation $\zeta \rightleftarrows \kappa$. The other possibility that the two reactions are $\zeta \rightleftarrows \varepsilon+\eta$ at, say, about 650°C and $\varepsilon+\eta \rightleftarrows \kappa$ at about 630°C was denied because diffractions from η phase were not found in any specimens containing less germanium than 27.8 at.%. If it were the case, the appearance of the ferromagnetic η phase would have been easily detected through the magnetic measurements described below.

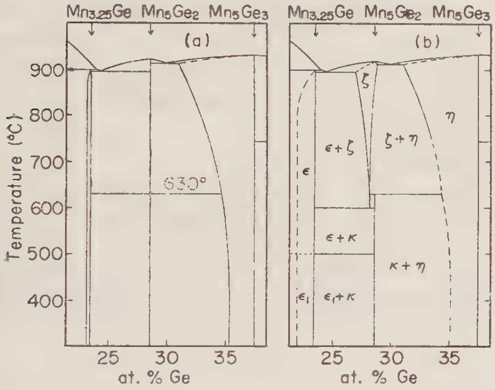

Fig. 1. Partial phase diagrams of Mn-Ge system, the one after Zwicker et al.[1] (a), and the alternative proposed (b).

§ 4. Magnetic Properties of the Intermetallic Compounds

The results of the studies on the magnetic properties of the intermetallic compounds, which were carried out standing on the basis of the findings given in the last section, will be presented below.

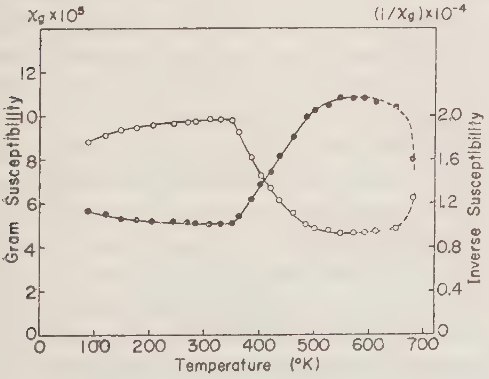

Fig. 2. Temperature dependences of magnetic susceptibility (○) and its reciprocal (●) of ε-$Mn_{3.4}Ge$.

ε phase

In Fig. 2 is plotted against temperature the magnetic susceptibility of a specimen containing 22.7 at.% Ge ($Mn_{3.4}Ge$) quenched from 850°C (ε phase). Its reciprocal is also shown in the same figure. The susceptibility χ_g stays nearly constant at 1.0×10^{-4} from the liquid nitrogen temperature up to 350°K, where it begins to fall. The hump in the susceptibility as seen in the isotypic compound $Mn_{11}Sn_3$[14] was not found. The $1/\chi_g$-T curve rises straight between 350° and 480 °K, and thereafter the effect of the transition of the metastable ε phase into the stable ε_1 phase is seen, which is promoted remarkably when the specimen is heated up to about 400°C (670°K). The Debye photograph taken for the specimen used in this magnetic measurement after cooled to the room temperature showed the diffractions from ε_1 phase besides those from ε phase. The asymptotic Curie point and the paramagnetic moment per manganese atom for ε phase were roughly estimated from the straight part of the curve as 210°K and 2.89 μ_B respectively.

It might be somewhat questionable to specify the magnetism of ε-$Mn_{3.4}Ge$ as antiferromagnetism, because the sharp maximum of the susceptibility is absent. But there still remains a possibility that the absence might be due to a feeble ferromagnetism parasitic on the antiferromagnetism.

Now a few words should be added here to take back the previous report[9] that the magnetism of this phase was typical of antiferromagnetism. The repeated examinations were carried out thereafter to reveal that the magnetism was such that described in the present paper. The anomaly in the susceptibility which was observed in the previous specimen $Mn_{3.25}Ge$ may be due to a small amount of ζ phase unexpectedly contained in it. The susceptibility of ζ phase forms an anomalously large peak, as shall be shown below, near the superficial Néel point of '$Mn_{3.25}Ge$', while that of ε phase stays nearly constant at a relatively small value. Thus the χ-T curve of the specimen may be readily affected by the presence of ζ phase. It may be considered rather probable now that the composition $Mn_{3.25}Ge$, which was found to be at the phase boundary in the present work, as well as the peritectic nature of the reaction concerned, had allowed the specimen to contain that phase, though its diffraction was not observed in the Debye chart.

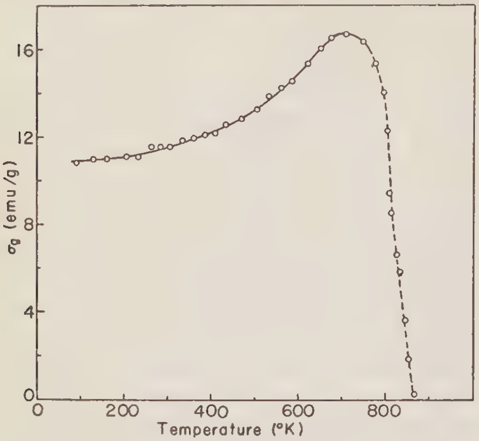

Fig. 3. Temperature dependence of saturation magnetization of ε_1-$Mn_{3.4}Ge$[12].

ε_1 phase

In Fig. 3[12] is shown the saturation magnetization of the same specimen ($Mn_{3.4}Ge$ or 22.7 at.% Ge) after annealed at 430°C for 9 days (ε_1 phase). The low-temperature phase is much more strongly magnetic than the high-temperature phase. The saturation magnetization is nearly constant at low temperatures and may be extrapolated to be 11 cgs emu/g at 0°K. On heating above the room temperature, it increases toward its maximum 17 cgs emu/g, and then falls off quite rapidly owing to the phase transformation into the high-temperature phase (ε) which is paramagnetic at these temperatures. The smallness of the value of the magnetic moment 0.15 μ_B per Mn and the anomalous form of the σ-T curve suggests a kind of ferrimagnetism. It is true that the ferrimagnetic structure is difficult to understand because all the atomic sites are crystallographically equivalent to each other in the disordered structure as concluded above, but it might be still possible that some degree of order is present associated with the stoichiometric excess of manganese, which were not detected by means of the X-ray diffraction. It may be probable that the superexchange interaction between manganese atoms through the intervening germanium atom, which was found to be effective in understanding the magnetism of the intermetallic compounds of manganese-tin[14] and iron-germanium[13] systems, plays an important role again in this compound of manganese with germanium.

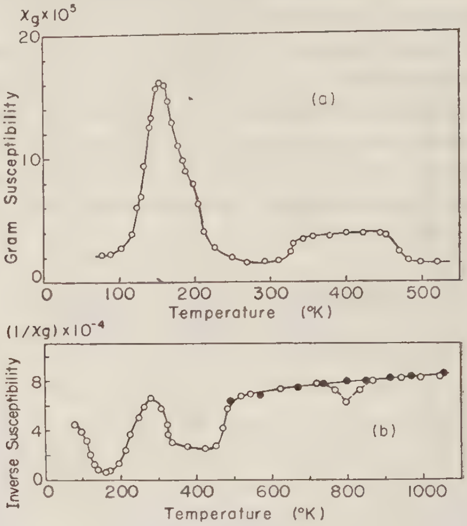

Fig. 4. Temperature dependences of magnetic susceptibility (a) and its reciprocal (b—○: heating; ●: colling) of ζ-$Mn_{2.65}Ge$.

ζ phase

In Fig. 4(a) is shown the dependence of the susceptibility of the specimen with 27.4 at.% Ge quenched from 800°C (ζ phase). The reciprocals of the susceptibility up to higher temperature are shown in Fig. 4(b). The drop at about 800°K of the inverse susceptibility in the heating curve is ascribed to the the precipitation of κ phase. The metallurgical reaction from the metastable to the stable states ($\zeta \rightarrow \varepsilon + \kappa$) was promoted by the heat treatment imposed on the specimen, quenching from 800°C followed by heating up to 500°C, as has been mentioned. The successive heating turned the specimen back into the homogeneous ζ phase, which was left unchanged on cooling.

Apart from this drop, the magnetic behavior is quite anomalous, but it might be considered that this would be associated with a kind of antiferromagnetism. Although the crystal structure has not been fully analyzed, it must be closely related to that of $B8_2$ type. Thus we shall now consider the magnetism of this phase from the standpoint of the simple rule with respect to the spin values of iron group elements in the compounds with $B8_2$ or related types of structure[14),16].

In the $B8_2$ type of structure, the whole lattice may be divided into two sublattices: sublattice A consisting of 2(a) sites and sublattice B consisting of 2(c) and 2(d) sites. According to the rule[16], the spin values are given as follows:

$S=3/2$ for Mn in A sublattice,
$S=1$ for Mn in B sublattice.

The unit cell of ζ phase, which is 7.5 times as large as that of the associated $B8_2$ lattice, contains 42 atoms as has been mentioned. Though the distribution of the atoms among the lattice sites remains unknown until the analysis of the intensity of the X-ray diffractions is carried out, it may be not unreasonable to assume that the 5.6 atoms (4.07 Mn + 1.53 Ge) per unit cell of the associated $B8_2$ lattice are distributed as in the following, because Mn_5Ge_3 crystallizes in a $D8_8$ type of structure which may be regarded as of the deformed $B8_2$ type, with one-third of the manganese atoms in A sublattice replaced by atomic holes.

1.60 Mn + 0.40 holes in A sublattice,
2.47 Mn + 1.53 Ge in B sublattice.

Then it is seen that the resultant magnetization is nearly canceled out, if we further assume that the interaction between the two sublattices is negative (antiparallel coupling). Antiferromagnetism might come from such an situation in this phase, though it can not explain the whole shape of the χ-T curve.

κ phase

In Fig. 5[10] the saturation magnetization of the specimen containing 28.6 at.% Ge (Mn_5Ge_2) annealed at 500°C (κ phase) is shown as a function of temperature. On elevating the temperature from 90°K, the magnetization under a field of 7.5 kilo-oersteds first decreases monotonically and become vanishingly small at 395°K. Then it grows again toward its maximum at 630°K and finally falls off at 710°K. The reciprocal of the susceptibility at higher temperatures are also shown in the same figure. The reversal of the magnetization at 395°K was ascertained from the simple demonstration which had been made by Gorter et al.[17] for their LiFeCr spinels, as well as from the deflections of a galvanometer induced by pulling a coil off the specimen rod, which was heated in the absence of field after magnetized at the room temperature. Thus the first example of Néel's N type ferrimagnetism among the group of the intermetallic compound was established.

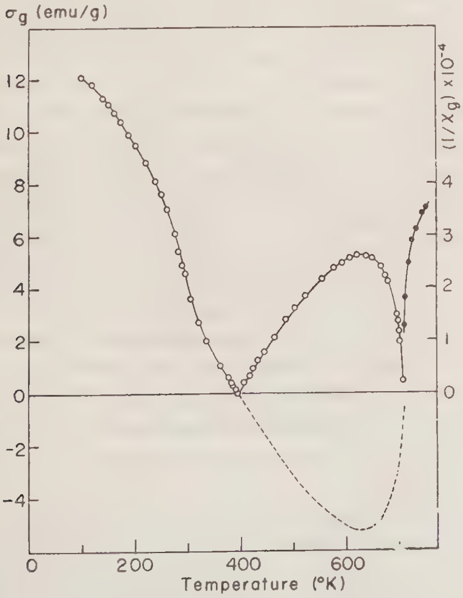

Fig. 5. Temperature dependences of saturation magnetization (○) and reciprocal susceptibility (●) of κ-Mn_5Ge_2,[10] dotted curve showing the reversal of spontaneous magnetization.

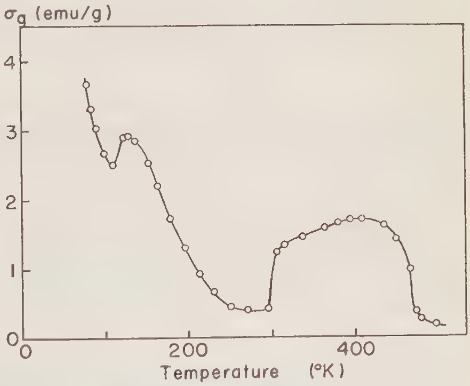

Fig. 6. Dependence of magnetization of Mn–28.6 at.% Ge quenched from 850°C ($\zeta+\eta$).

In Fig. 6 is shown the magnetization of a specimen containing 28.6 at.% Ge (Mn_5Ge_2) quenched from 850°C as a function of temperature. At first this curve was considered to be purely due to the 'weak ferromagnetism of the 'high-temperature phase of Mn_5Ge_2', but the careful X-ray study has clarified that the specimen contained a trace of η phase, so that the σ–T curve may be regarded as a mere superposition of the ferromagnetism of η phase and the anomalous magnetism of ζ phase. The anomalies at 140° and about 400°K may be ascribed to those of ζ phase (Fig. 4).

§ 5. Summary

The binary alloy system of manganese with germanium of the concentration ranging from 21.8 to 35.7 at.% was studied by means of X-ray powder diffraction, and the magnetic property of each phase was surveyed. The conclusions obtained are as follows.

(1) It was found that the phase diagram due to Zwicker et al. should be revised in the composition range concerned and an alternative partial diagram was presented.

(2) ζ phase, which corresponds to the high-temperature phase of Mn_5Ge_2 of Zwicker et al., has a range of solid solution which diminishes as the temperature is lowered.

(3) The Debye diagram for ζ phase can be indexed by assuming a hexagonal structure. The unit cell contains 42 atoms.

(4) ε-$Mn_{3.4}Ge$ (high-temperature phase) exhibits an anomalous magnetic behavior which may be considered to be based upon antiferromagnetism.

(5) Magnetism of ε_1-$Mn_{3.4}Ge$ (low-temperature phase) may be classified under ferrimagnetism.

(6) ζ-$Mn_{2.65}Ge$ (high-temperature phase) has a quite anomalous magnetism which also may be considered to be based upon antiferromagnetism.

(7) κ-Mn_5Ge_2 (low-temperature phase) provides the first example of N type ferrimagnetism among the group of intermetallic compounds.

The results obtained encourages the author to execute further studies to throw light upon the origin of the anomalous magnetic behavior of each phase. The anomaly must have a close connection with the complexity of its crystal structure. The X-ray researches to analyze the structure of ζ and κ phases, as well as to find out any evidences of the formation of the superlattice in ε and ε_1 phases, are now in progress.

This work forms a part of the surveying research on the magnetic properties of the intermetallic compounds of iron group with IVb group elements in which the author has kept his co-operation with Prof. K. Yasukōchi and Dr. K. Kanematsu of Nihon University, to whom indebtedness is acknowledged for their help and discussions.

The author wishes to express his hearty thanks to Prof. R. Kimura for his constant encouragement and valuable suggestions and to Profs. E. Fukushima and T. Sato for the facilities of their laboratories. Thanks are also due to Mr. K. Endo for his assistance. He is especially grateful to Prof. H. Takaki of University of Kyoto for his interest in this work and for reading the manuscript critically.

References

1) U. Zwicker, E. Jahn and K. Schubert: Z. Metallkde. **40** (1949) 433. See also J. H. Downing and D. Cubicciotti: J. Amer. Chem. Soc. **73** (1951) 4025.
2) U. Zwicker: Z. Metallkde. **42** (1951) 327.
3) L. Castelliz: Monatsh. Chem. **84** (1953) 765.
4) F. A. Hames and D. S. Eppelsheimer: Nature **162** (1948) 968.
5) L. Castelliz: Z. Metallkde. **46** (1955) 198.
6) R. J. Quigg, G. P. Conard and J. F. Libsch: J. Metals **7** (1955) 359.
7) S. D. Margalin and I. G. Fakidov: ΦMM. **6** (1958) 157.
8) I. G. Fakidov and Yu. N. Tsiovkin: ΦMM. **7** (1959) 685.
9) K. Yasukōchi, T. Ohoyama and K. Kanematsu: J. Phys. Soc. Japan **14** (1959) 1820.
10) K. Yasukōchi, K. Kanematsu and T. Ohoyama: J. Phys. Soc. Japan **15** (1960) 932.
11) K. Kanematsu, K. Yasukōchi and T. Ohoyama: J. Phys. Soc. Japan **15** (1960) 2358.
12) T. Ohoyama, K. Yasukōchi and K. Kanematsu: J. Phys. Soc. Japan **16** (1961) 352.
13) K. Yasukōchi, K. Kanematsu and T. Ohoyama: J. Phys. Soc. Japan **16** (1961) 429.
14) K. Yasukōchi, K. Kanematsu and T. Ohoyama: J. Phys. Soc. Japan **16** (1961) 1123.
15) K. Yasukōchi and K. Kanematsu: to be published.
16) K. Yasukōchi, K. Kanematsu and T. Ohoyama: Presented at the annual meeting of the Physical Society of Japan, April 1961. To be published in Proceedings of the International Conference on Magnetism and Crystallography, 1961. K. Kanematsu: to be published.
17) E. W. Gorter and J. A. Schulkes: Phys. Rev. **90** (1953) 487.

JOURNAL OF THE PHYSICAL SOCIETY OF JAPAN, Vol. 16, No. 10, OCTOBER, 1961

Friction and Deformation of Polymers

By Kyuichiro TANAKA

Faculty of Engineering, Kanazawa University, Kanazawa, Japan

(Received June 6, 1961)

The deformation caused to the surface of polymers by hard hemispheres of different radii was observed and the friction between the hemisphere and the plate was measured. The deformation produced was deduced from Newton's rings and grooved track. Hertz's equation was found to give the size of the contact circle. Wave-like deformation was observed near the contact region. When a tangential force is applied, the deformation increased on one side of the contact region and decreased on the other side. Two types of sliding contact were observed. One was attributed to the retarded elasticity and the other to the frictional heating. From the former, the retardation time was obtained. The production of grooved tracks was attributed to the non-recoverable deformation. The deformation was discussed in connection with the friction and the wave-like deformation of polymer surface was suggested as the source of frictional resistance.

§ 1. Introduction

The adhesion theory of friction[1], developed for metals, has been used to interpret the friction of polymers[2)–7)]. With metals, it was observed that the pressure at the region in true contact is sufficient to produce plastic flow and strong adhesion. With polymers, as Lincoln pointed out[4], the contact is very often elastic. According to the adhesion theory, it is deduced that the frictional force is directly proportional to the area of contact. This was verified in polymers as well as metals[1,2,4,6]. However, the direct evidence indicating that adhesion really occurs in the elastic contact of polymers has not yet been obtained. It is quite doubtful that adhesion occurs when there is no plastic flow. It is therefore desirable to carry out further investigations concern the mechanism of polymer friction.

Although several studies have been made on the contact of polymers[2,4,6], they were limitted to measurement of area of contact and no observations were made of the deformation of polymer surface in the neighbourhood of the contact region. In addition, the area of contact is usually measured from the observation of the indentation or grooved track produced on the polymer surface. This technique, however, is insufficient to show the deformation of polymer by elastic contact. Lincoln determined the area of contact by optical interference (Newton's rings) in the contact region, but his observation was limitted to the static contact. However, Newton's rings no doubt must be capable of revealing the deformation by sliding contact as well. In this work, the deformation and friction in the static and sliding contact between a flat plate of various polymers and two hard hemispheres have been studied. One of the hemispheres is of glass and the other is of steel. The deformation of polymers produced by the glass hemisphere is

Table I.

Polymer sample	Young's modulus E (Kg/cm^2)
Polyvinyl chloride (PVC)	2.88×10^4
–30 parts plasticized-(PVC-30)	8.83×10^2
–50 parts plasticized-(PVC-50)	9.38×10
Polystyrene	2.05×10^4
Polymethyl methacrylate (PMMA)	2.75×10^4
Nylon 6	1.03×10^4
Polyethylene-high density (Hizex 7000)*	8.94×10^3
Polyethylene-low density (Sumikathene G-20)*	1.37×10^3
Polytrifluorochloroethylene (PTFCE)	1.55×10^4
Polytetrafluoroethylene (PTFE)	1.21×10^4
Phenol resin	4.03×10^4

* Commercial name.

examined by means of Newton's rings. The steel hemisphere is of smaller radius than the glass hemisphere. The deformation produced by the steel hemisphere is examined by means of the frictional track. The purposes of this work are, firstly, to clarify the deformation of polymers at the contact region and its neighbourhood, secondly, to find out if there is a new source of frictional resistance.

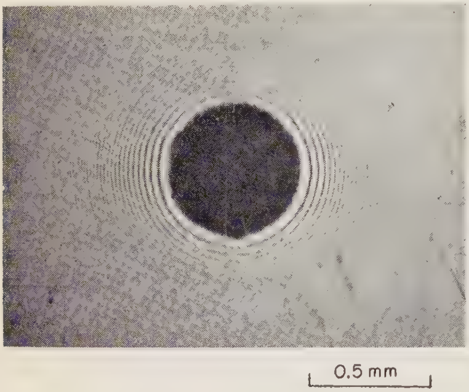

Fig. 1. An example of Newton's rings observed in the contact region. Polystyrene: Load 350 g.

§ 2. Experimental Procedures

2.1 Samples

The samples of polymers used in this experiment are listed in Table I with the values of Young's moduli obtained in the present experiment. The glass hemispheres are all approximately 4 cm in radius. The steel hemispheres are 0.24 cm in radius. The surface of both kinds of hemisphere is very smooth and free from scratches. On the other hand, the surface of the polymers is not so smooth as the hemispheres being scratched a little, but Newton's rings as are illustrated in Fig. 1 were observed near the contact between the glass hemisphere and the plate of polymer. The polymers and hemispheres were made as clean as possible by rubbing with cloth under alcohol before mounting them in the apparatus.

2.2 Apparatus and procedures

Fig. 2 shows the experimental apparatus with the glass hemisphere (H) in place. The glass hemisphere at the end of arm (A) can be easily replaced with the steel hemisphere. The pair of spring plates (S) forms the parallel spring system and the polymer sample (P) is mounted on the ends of the springs. The other ends of springs are fixed to the carriage (C) which is driven by an electric motor. The force of contact between the hemisphere and the polymer is determined by the dead load (W) placed on the arm. The recording parts of this apparatus is essentially similar to the apparatus used by Eldredge and Tabor[8]. When the hemisphere is pressed on the polymer and the carriage driven, the resistance to the slip produces a small deflexion in the springs, and this is amplified by the V-shaped piece of spring wire (I) which also functions as a stylus for recording. In this way, the stylus traces a fric-

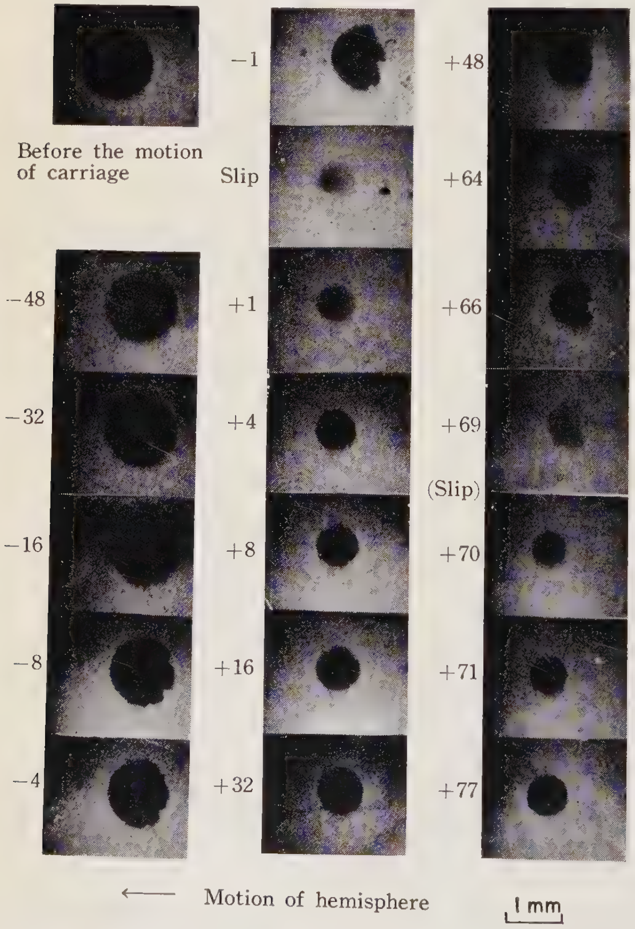

Fig. 7. Picture of the contact region of PVC-30. Load 56 g.

tional record on a layer of soot deposited on a microscopic slide (R). The carriage is driven at the speed of 0.04 cm/sec and at this speed the applied tangential force increases at the rate of approximately 55 g/sec provided no slip occurs. The carriage was set in motion in many of the measurements after the hemisphere had been loaded for 1 minute. The light source for observing the Newton's rings, was a sodium lamp but the xenon discharge flash bulb was also used in some of the experiments. When the glass hemisphere is pressed on the polymer, the deformation of the hemisphere is negligibly small and accordingly the shape of the polymer surface can be determined by measuring the distance *r* from the centre of contact to each dark ring. The contact region is given by the central dark part which is usually circular when the contact is static and is called the contact circle. The height *h* from the position of contact circle to the polymer surface is a measure of the deformation of the surface. The experiments were mainly carried out at a practicable range of loads between 56 g and 760 g, and at room temperatures of about 20°C.

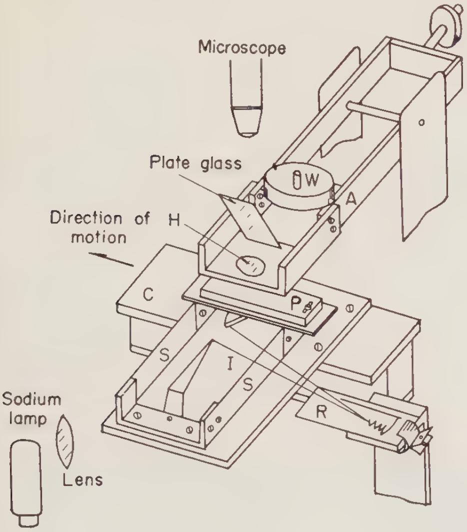

Fig. 2. Experimental apparatus

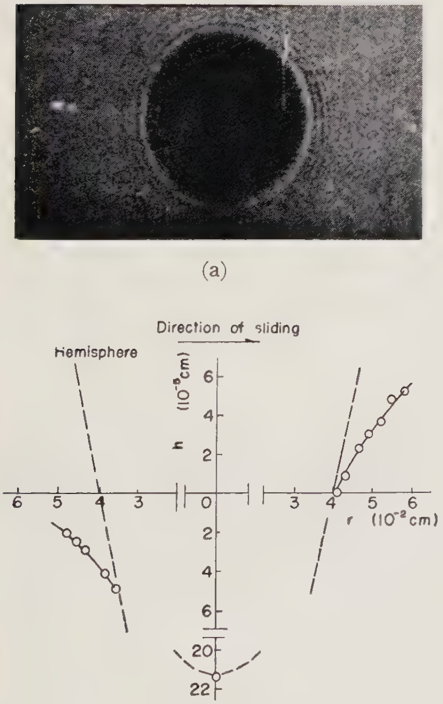

(a)

(b)

Fig. 8. Deformation produced when the glass hemisphere is sliding on Hizex at the speed of 0.04 cm/sec. Load 350 g, Frictional force 133 g.
(a) Newton's rings.
(b) Deformation obtained by Newton's rings (a).

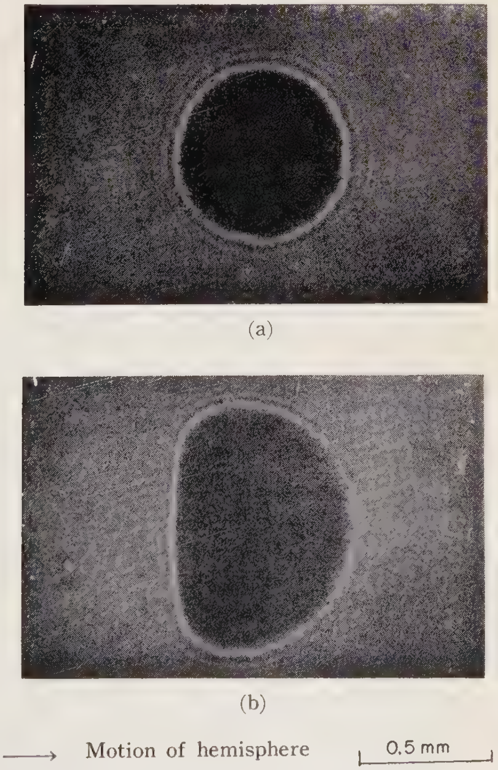

(a)

(b)

Fig. 11. Instantaneous photograph of the contact region of sliding during the abrupt slip.
(a) Polystyrene. Load 350 g.
(b) Sumikathene. Load 113 g.

§ 3. Experimental Results

3.1 Deformation by static contact

a) *Diameter of contact circle*

When a hard hemisphere is pressed on a flat surface of polymer, Hertz's equation for elastic contact is written as[9]

$$D^3=6(1-\sigma^2)\frac{RW}{E}\,. \qquad (1)$$

Where D is the diameter of contact circle, W the contact load, R the radius of curvature, E and σ is Young's modulus and Poisson's ratio of the polymer, respectively. It must be noticed that E and σ are generally dependent upon the loading time. With polymers, Poisson's ratio has a value of about 1/3 in the glassy state and of about 1/2 in the rubbery state[10]. Hence, the change of Poisson's ratio does not affect much the diameter of contact circle. In the present paper a value of 0.4 is adopted as a rough approximation of Poisson's ratio of all polymer samples. The measurements of the diameter of contact circle at a loading time of 1 minute were made on various polymer as a function of load. The results indicated that the cube of diameter of contact circle is directly proportional to the load. By using four different glass hemispheres: 2.53, 4.24, 7.80 and 15.1 cm in radius, when the load is of 760 g, the measurements of the diameter of contact circle at a loading time of 1 minute were made on PMMA and Hizex as a function of the radius. These results indicate that the cube of the diameter of contact circle is again directly proportional to the load. Next, the measurements of the diameter of contact circle at two different loads were made on PMMA and Hizex by varying the loading time and by using Hertz's equation (1) the time dependence of $1/E$ was obtained. These results are shown in Fig. 3. It is seen that

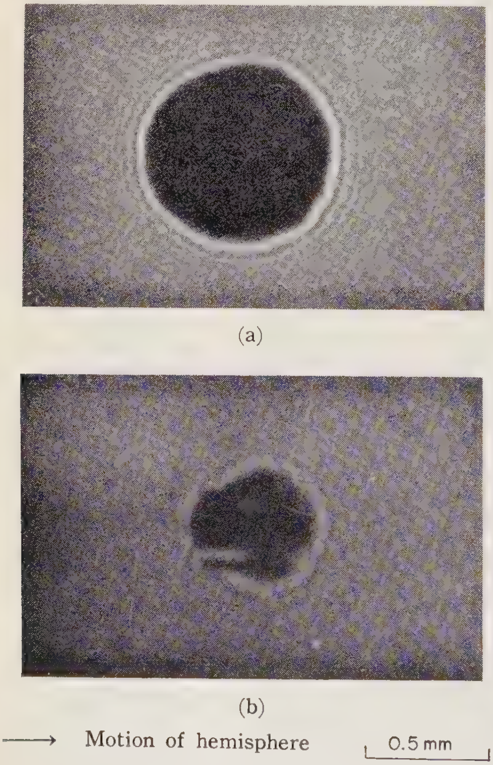

Fig. 12. Effect of the thermal softening during the abrupt slip.
(a) Polystyrene. Load 522 g.
(b) PMMA. Load 350 g.

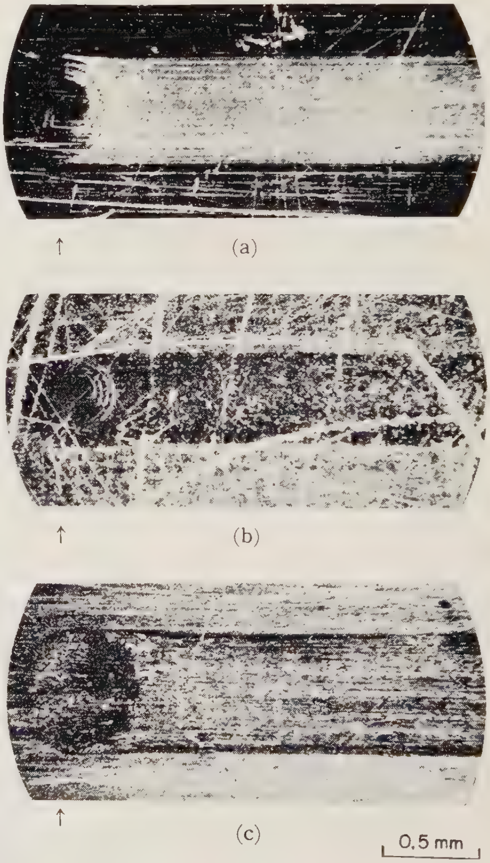

Fig. 16. Photomicrographs of the track produced when the steel hemisphere slid on the polymers. The arrow shows the place where the hemisphere initially pressed on the polymers.
(a) Hizex. Load 522 g.
(b) Nylon. Load 522 g.
(c) PTFE. Load 350 g.

for Hizex the time dependence obtained at two different loads is represented by a single curve over the range of loading time used. But for PMMA the time dependence is affected by the load when the time of loading is too long and here the deformation is of a non-linear type. From the above measurements, it is to be concluded that Hertz's equation is applicable to the elastic contact of polymers, although when the loading time is very long Young's modulus in the equation is also dependent upon the load as well as the loading time. Young's moduli of polymers, which were obtained by the application of Hertz's equation to the relations between the cube of the diameter of contact circle at a loading time of 1 minute and the load, were already summarized in Table I.

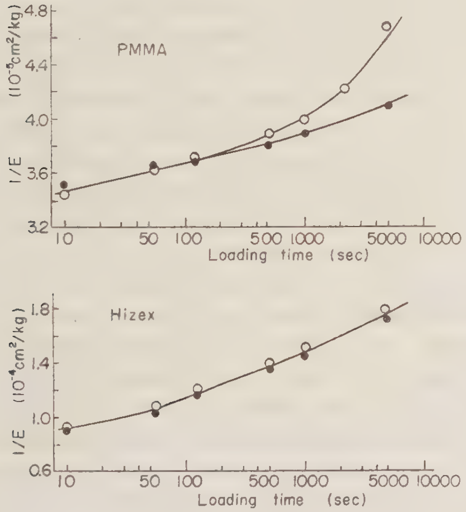

Fig. 3. Time dependendence of $1/E$. ○ and ● are obtained at the load of 56 g and of 760 g, respectively.

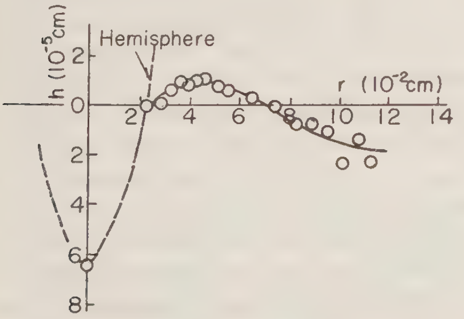

Fig. 4. Deformation of PMMA surface in the neighbourhood of the contact region. Load 113 g.

b) *Deformation of polymer surface*

From the examination of Newton's rings appearing when the glass hemispheres were pressed on the polymers, it was found that the polymer surface neighbouring the contact region is deformed as illustrated in Fig. 4. It was impossible to cover all the deformed region of the surface, because the observation of Newton's rings was restricted to a comparatively small area near the contact region. However, it is evident that the wave-like deformation of polymer surfaces occurs in the neighbourhood of the contact region. From the deformation observed at various loads, measurement was made of the magnitude of deformation. The results are shown in Fig. 5, in which the abscissa is the contact depth instead of the load. It seems that the size of deformation of polymer surface is proportional to the contact depth.

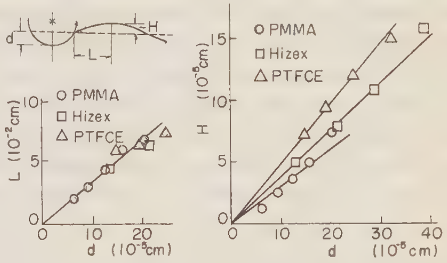

Fig. 5. Relation between the size of deformation (H, L) and the contact depth d.

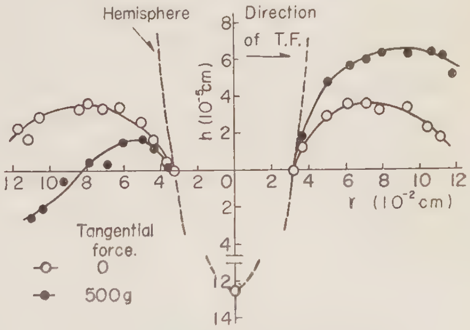

Fig. 6. Effect of the tangential force on the deformation of PMMA surface. Load 350 g.

In order to find the effect of tangential force on the deformation of polymer surface, examination of Newton's rings were again made on various polymers after displacing the carriage by a given amount. In this experiment, a load of 350 g was used and applied tangential force was of about 85 percent of the maximum static frictional force. An example of the results is shown in Fig. 6. It is seen that when the tangential force is applied the deformation of surface increases on the front side of contact region, where the glass hemisphere compresses the polymer surface in tangential direction, and decreases on the other side (back side). It is also seen that on the front side the height from the position of the contact circle to the deformed surface of polymer exceeds one-half of the amount of contact depth and the deformation extends to a very wide region of surface. From the above-mentioned behaviour of polymer surface, it may be concluded that in applying the tangential force the contact region is slightly displaced on the polymer surface and the resistance to slipping of the glass hemisphere is derived from the deformation of the polymer surface. When slipping does not occur, a constant tangential force can be applied to the contact region by a given displacement of the carriage. When the slow slip occurs after carriage is displaced by a given amount, the applied tangential force decreases gradually. This was observed with Hizex, Sumikathene, PVC-30 and PVC-50. The sliding speed in slow slipping was of the order of 10^{-4} cm/sec for Hizex. When the applied tangential force was gradually increased by moving the carriage, abrupt slip occured with all polymers used in the experiment when the tangential force became too large, and hence the maximum static frictional force could be determined (see **3.3**). On the other hand, slow slip occurred when a force slightly smaller than the maximum static frictional force was applied. Therefore, the slow slip seems to be due to the flow property of the polymer. If the flow takes place easily on the polymer surface, it is impossible to determine the static friction. Although the slow slip was detected only with comparatively soft polymers, still slower slip may be occurring in hard polymers such as PMMA.

3.2 Deformation during frictional process

a) *Cinematographic observation*

Moving picture of Newton's rings during the movement of the carriage were taken on several polymers on 8 mm films at a speed of 16 frames per second. In the experiment, the carriage was set in motion after pressing the glass hemisphere for 4 minutes, because it took time to adjust the position of the centre of Newton's rings on the picture frame. By cinematography usually only a few fringes of Newton's rings were observable and with softer polymers such as PVC-30 only the central dark region. As the frictional force, i.e. tangential force, produces a slight deflexion in the arm supporting the glass hemisphere, the centre of Newton's rings is displaced in the frame in proportion to the frictional force, and hence by using this displacement the frictional force corresponding to each frame can be determined. In order to express the results obtained from the picture positive and negative serial numbers were assigned to a series of frames, the negative numbers being given to the frames exposed before the slipping occurred and the positive numbers to those exposed thereafter. The picture for PVC-30 is illustrated in Fig. 7. In this illustration, the friction process is of stick-slip type and after the initial abrupt slip the sticking occurs until the second abrupt slip occurs at the frame numbered +69. It is seen that the shape and area of the contact region change with the increasing tangential force and the rear part of contact becomes very small immediately before the abrupt slip. With PVC-50, more marked changes of contact were observed. However, with other polymers, no changes of contact appeared during the stick. The examination of Newton's rings on the frame, −1 showed that the deformation at the maximum static friction was similar to the deformation observed in applying the smaller tangential force (see **3.1**). With Hizex and PTFE, smooth sliding in which the sliding speed was same as the speed of carriage and the recorded sliding friction was approximately constant took place after the abrupt slip. While the smooth sliding was in progress the periphery of contact was circular in the front but not in the rear. An example of the frame in the cinematography of the smooth friction on Hizex is shown in Fig. 8 (a). The deformation of surface obtained from Newton's rings in this frame is shown in Fig. 8 (b). It is seen that the deformation of surface is very large on the front side of the contact region and comparatively small on the back side. The shape of the rear part of contact is to be attributed to the retarded elasticity of polymers and will be discussed later.

The relation between the frictional force and the frame number is illustrated in Fig. 9, in which the straight portions of each graph correspond to the sticks. The graph of PVC-30 in Fig. 9 is obtained from the cinematography shown in Fig. 7. In the graph of PVC-30, the portion near the second abrupt slip is not straight and hence it shows the occurrence of surface flow. The relation between the contact depth and the frame number is illustrated in Fig. 10, in which each graph corresponds to that in Fig. 9. After the initial abrupt slip has occurred, the glass hemisphere sticks at a new place on the polymer surface and during the stick the contact depth increases with time of contact but the rate of increase of contact depth becomes smaller. On the other hand, during the stick the carriage is moving and as the results of this the applied tangential force increases in proportion to the contact time. In such condition, when the abrupt slip occurs again during the stick, the friction is of the stick-slip type. Therefore, it is evident that the rates of increase of the contact depth and tangential force play an important part in the polymer friction. In examining the maximum static friction at the sticks, it was deduced that the frictional force is nearly proportional to the contact depth.

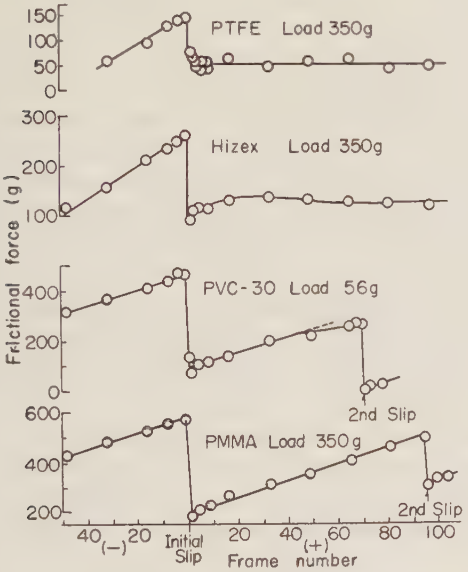

Fig. 9. Relation between the frictional force and the frame number. The graph for PVC-30 is obtained from Fig. 7.

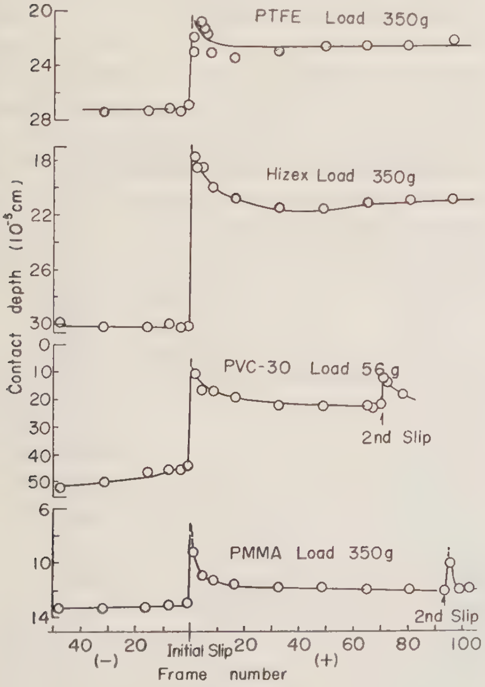

Fig. 10. Relation between the contact depth and the frame number. Each graph corresponds to the graphs in Fig. 9.

b) *Deformation during abrupt slip*

By using the xenon discharge flash bulb as the light source, the instantaneous photograph of Newton's rings during the abrupt slip was taken on several polymers. The sliding speed was estimated at an order of a few centimeters per second. Two types of the shape of contact were obtained in the photograph. One was similar to the shape of contact observed in the smooth friction, i.e. the front half part of contact is semicircular and the rear part is smaller than the front part. Thus, this type of shape in the abrupt slip is attributed to the retarded elasticity of polymers. Two examples of this type are shown in Fig. 11. The other type was of the shape in which the rear part was elongated to the back side of the contact region. Two examples of this type are shown in Fig. 12. This type did not appeared in either of the cases of low load and low sliding speed. In addition, with phenol resin which is not softened by heat, this type did not appear even at heavy loads. Therefore, it seems that the shape is originated from the softening of polymers due to the frictional heat generated during the abrupt slip. From the instantaneous photograph of Newton's rings produced in the contact between a glass hemisphere of known radius and an optical flat, the effective wave-length of the flash light was determined corresponding to each ring. By using this wave-length, the deformation of polymer surface was obtained from Newton's rings in the instantaneous photograph of the abrupt slip. The results showed that the deformation during the abrupt slip was similar to the deformation observed in smooth friction. With Sumikathene, the shape of contact during the abrupt slip was far from circular, but the shapes at different loads were nearly similar to one another and the area A followed the relation $A \propto W^{2/3}$, where W is the load. The same relation was also obtained for other polymers provided the shape of contact was due to the retarded elasticity of polymers.

3.3 Coefficient of friction

With the glass and steel hemispheres on various polymers, measurement was made of the coefficient of friction as a function of the load. The friction between a polymer and a harder material is considered to be independent of the nature of the harder material[2]. Thus, when different frictional behaviours are observed with the two kinds of hemispheres, these are essentially due to the difference in radius of the hemispheres.

a) *Glass hemisphere on polymers*

The plots of the coefficient of static friction μ_s against the load W are illustrated in Fig. 13, in which both coordinates are in the logarithmic scale. In the figure, the solid lines represent a relation $\mu_s \propto W^{-1/3}$ and are drawn through the plots obtained when the contact region seems to be of single contact circle. It is seen that the observed value of the coefficient of static friction becomes smaller with the decrease of the load, in comparison with the value which is predicted by solid line. This is due to the effect of multiple point contact which has been reported by Archard[11]. As minute irregularities exist on the polymer surface, the contact is made at more points in the contact circle with the decrease of the load. In such way, the frictional behaviour is affected by the smoothness of the polymer surface. Therefore, it may be deduced that the relation between the coefficient of static friction and the load is still represented in the lower range of load by the solid line, provided the polymer surface is very smooth. This result also shows that the frictional force is proportional to $W^{2/3}$. On the other hand, the area of static contact is also proportional to $W^{2/3}$, because Hertz's equation is obeyed. It is, therefore, concluded that the frictional force is proportional to the area of contact. However, it is remarkable that the load dependence of the coefficient of friction is same for PVC-30 and PVC-50 as for the other polymers, although

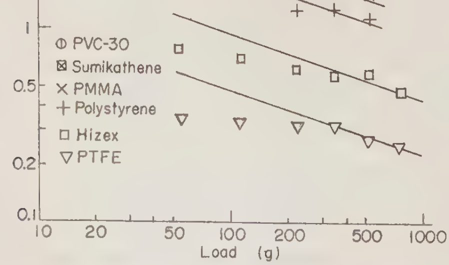

Fig. 13. Load dependence of the coefficient of static friction μ_s observed between the glass hemisphere, 4 cm in radius and the plate of polymers.

Table II. Coefficient of friction (μ_s, μ_k)*.

Polymer	$\mu_s W^{1/3}$	$\mu_k W^{1/3}$
PVC	8.9	(stick-slip)
PVC-30	30	(stick-slip)
PVC-50	62	(stick-slip)
Polystyrene	8.3	(stick-slip)
PMMA	12	(stick-slip)
Nylon	11	10
Hizex	4.4	2.2
Sumikathene	14	(stick-slip)
PTFCE	11	(stick-slip)
PTFE	2.2	1.0
Phenol resin	7.8	(stick-slip)

* W is the load (in g.).

marked changes of area and of the shape of contact appeared with the increase of applied tangential force. The coefficient of sliding friction μ_k observed in the smooth sliding were also represented by the relation $\mu_k \propto W^{-1/3}$. The values of $\mu_s W^{1/3}$ and $\mu_k W^{1/3}$ for various polymers are summarized in Table II. From the value of $\mu_s W^{1/3}$, the static frictional force per unit area of contact f was obtained. The plots of f against Young's modulus E of polymer are shown in Fig. 14. It is seen that f is closely connected with E, usually increasing as E increases. With Hizex, the effect of the loading time on the static friction was also examined at a load of 350 g. In this experiment, the frictional force increased by 21 percent over a time range from 1 to 15 minutes, on the other hand the area of contact again increased by the same amount. Therefore, this result also indicates that the frictional force is proportional to the area of contact.

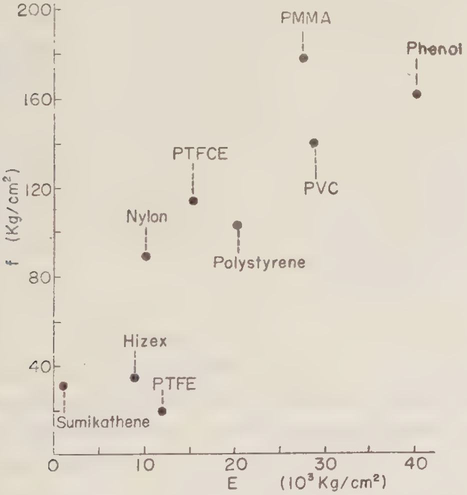

Fig- 14. Relation between the static frictional force per unit area of contact f and Young's modulus E.

b) *Steel hemisphere on polymer*

The load dependence of the coefficient of friction with steel hemispheres was found markedly different from that with the glass hemisphere. The relation between the coefficient of static friction μ_s and the load W is illustrated in Fig. 15, in which both coordinates are in the logarithmic scale. It is seen that over the observed range of load μ_s follows the relation $\mu_s \propto W^{-n}$, where the index n is dependent upon the kind of polymer. The load dependence of the coefficient of sliding friction μ_k was also same as that of μ_s. As described later, Hertz's equation is also obeyed for the contact between the steel hemisphere and the polymers. In addition, the effect of multiple point contact is expected to be less on the friction with the steel hemisphere, because the contact pressure is higher. Therefore, it is noticed that with the steel hemisphere the frictional force is not proportional to the area of contact.

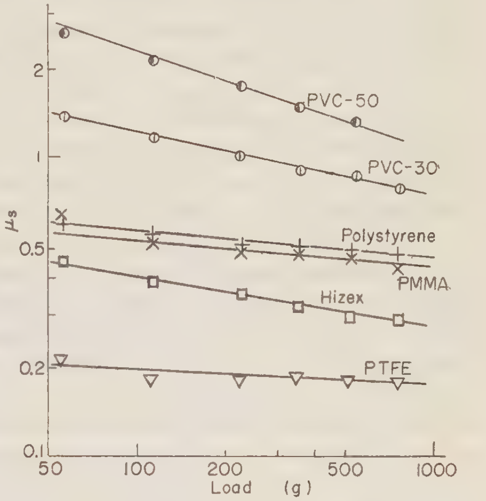

Fig. 15. Load dependence of the coefficient of static friction μ_s observed between the steel hemisphere, 0.24 cm in radius and the plate of polymers.

3.4 **Observation of frictional track**

In examining the frictional track produced on the polymer surfaces, the polymers were coated with a layer of alminium after the measurements of the coefficient of friction. Without such coating examination of the frictional track under the microscope was almost impossible. When the steel hemisphere slides on the polymers, grooved tracks were produced on the surface of many polymers. On the other hand, with the glass hemisphere, the frictional track is so slight that it was usually invisible under the microscope even with the alminium coating. The grooved tracks produced when the steel hemisphere slides smoothly on the polymers without stick-slip are illustrated in Fig. 16. From the examination of the scratches traversing the track, it is deduced that the track originated mainly in the non-recoverable part of the deformation produced when the steel hemisphere compressed the polymer underneath it, and the displacement of polymers from the front of the steel hemisphere (ploughing out) has very little to do with the production of track. It is further seen that the indentation produced at the place where the steel hemisphere is initially pressed on the polymers is circular in shape. This means that the steel hemisphere does not plough out the polymers in the front of the hemisphere at the start of sliding but compresses the polymers underneath itself and makes a slight climbing in its foreward motion.

With a few polymers, the circular indentations were clearly observed and then their diameters were measured at various loads. When the cube of the diameter of indentation was proportional to the load, Young's moduli for the polymers were calculated by Hertz's equation and the values obtained were nearly equal to those obtained with the glass hemishpere (see Table I). It is, therefore, deduced that the contact between the steel hemisphere and the polymers are of the elastic nature just as in the case of the glass hemisphere.

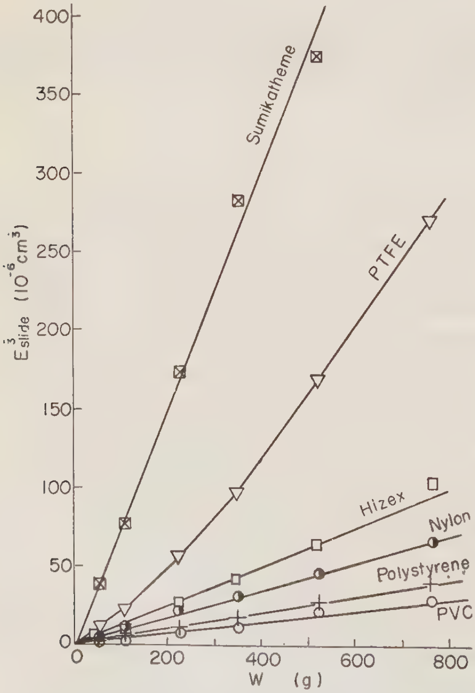

Fig. 17. Relation between the cube of track width D^3_{slide} and the load W

However, with PTFE, the cube of the diameter of indentation was not proportional to the load but the square of the diameter was proportional to the load at higher ranges of the load. Hence, with PTFE, the contact is rather of the plastic nature. On the other hand, the width of the grooved tracks produced when the steel hemisphere slid smoothly was observable with various polymers. Fig. 17 shows the relation between the cube of the track width and the load. It is seen that for all the polymers, except PTFE, the cube of track width is also proportional to the load. With the steel hemisphere, the shape of sliding contact is supposed to be nearly semicircular, because the rear part makes very little contact with the polymer surface on account of the non-recoverable deformation produced by the front part of contact. In addition, it is also assumed that no appreciable frictional heat is generated on smooth friction in which the sliding speed does not exceed 0.04 cm/sec and accordingly the shapes at different loads are similar to one another. Therefore, from the result showing that the cube of track width is proportional to the load, it may be assumed that Hertz's equation is to be modified for the sliding contact as

$$D^3_{\text{slide}} = 6(1-\sigma^2)\frac{RW}{E_{\text{slide}}}, \qquad (2)$$

where D_{slide} is the track width, E_{slide} corresponds to Young's modulus and depends upon the sliding speed. The value of E_{slide} obtained from the graphs in Fig. 17 are shown in Table III. In this table, in order to compare E_{slide} with Young's modulus E shown in Table I, the ratios of E_{slide}/E are also shown. This result shows that E_{slide} is slightly larger than E and hence a reasonable one, because E_{slide} is expected to corresponds to Young's modulus observed at a short time of static contact. Therefore, the relation (2)

Table III.

Polymer	E_{slide} (Kg/cm^2)	E_{slide}/E
PVC	3.2×10^4	1.1
Polystyrene	2.4×10^4	1.2
Nylon	1.4×10^4	1.4
Hizex	1.0×10^4	1.1
Sumikathene	1.6×10^3	1.2

may be applicable to the sliding contact. From the above examination of the grooved tracks it is concluded that the deformation produced by the steel hemisphere is elastic in all the polymers except PTFE in spite of the generation of a marked non-recoverable deformation.

§ 4. Discussions

4.1 The effect of retarded elasticity of polymers on the sliding contact

It is evident that the shape and area of sliding contact are closely connected with the retarded elastic behaviours of polymers. However, the load dependence of the area of sliding contact is usually same as that of the area of static contact. Since Hertz's equation is applicable to the elastic contact of polymers, in a limitted range of time of loading the area of static contact is proportional to $W^{2/3}$, where W is the load. On the other hand, the diameter of the semicircular front part where the hemisphere makes contact with the polymer surface in the sliding contact is proportional to $W^{1/3}$ as shown in the relation (2). Therefore, the area of sliding contact is also proportional to $W^{2/3}$ although the shape of contact is not a complete circle, provided the shapes of sliding contact at different loads are similar to one another. This was directly verified in the examination of the contact during the abrupt slip. It was also seen that the area of sliding contact is not proportional to $W^{2/3}$ provided the frictional heating occurs during the abrupt slip.

The shape of sliding contact is always semicircular in the front part of contact but not in the rear part. The shape of the rear part of contact have relation to the retarded elasticity of polymers. Bueche and Flom[12] predicted by their theoretical treatment of rolling friction the retardation time of polymers would be determined from the shape of contact. From the shape of the sliding contact, it would be also possible to obtain the retardation time. To examine this, the following simple analysis was made on the sliding contact. Consider a hard hemisphere with radius R, sliding at the speed v, on the material of which the mechanical properties are represented by the retarded elastic model shown in Fig. 18 (a). In this case, the spring, having a modulus constant, E and the dashpot, having viscosity, η, both resist deformation in the Z-direction. For simplicity, let us consider the contact in the vertical plane involving the centre of hemisphere and the sliding direction (Fig. 18 (b)) and assume that the surface is flat on the front side of contact. In Fig. 18 (b), the surface of material is represented by the solid line, FACBE, and the hemisphere makes contact with the material in the portion, ACB, where r_1 and r_2 represent the sizes of contact in the front part and the rear part, respectively. On the portion, ACB, making contact, the following relation holds.

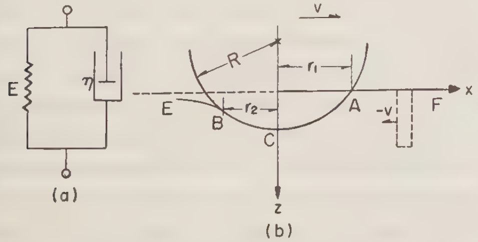

Fig. 18. Diagram for calculating the retardation time.

$$z = \frac{1}{2R}(r_1^2 - x^2) \,. \tag{3}$$

We will now consider that the increasing compressive deformation in the Z-direction is suffered by the material during the passage through the portion AC and recovery sets in after the point C is passed over. Then, the rate of deformation in the Z-direction is given by

$$\frac{dz}{dt} = -\frac{x}{R}\frac{dx}{dt} = -\frac{v}{R}x \,. \tag{4}$$

The pressure p in the Z-direction is given by

$$p = Ez + \eta\frac{dz}{dt} \,. \tag{5}$$

When (3) and (4) are substituted in (5), we obtain

$$p = \frac{E}{2R}(r_1^2 - x^2) - \frac{\eta v}{R}x \,. \tag{6}$$

In the place where the hemisphere loses contact with the material, the pressure must be zero. Hence, the size of the rear part of sliding contact, r_2, is given by the value of x, when the right hand side of (6) becomes zero. The result is written as follows,

$$\tau v = \frac{r_1^2 - r_2^2}{2r_2} \,, \tag{7}$$

where η/E is replaced by the retardation time τ. The relation (7) shows that the retardation time is obtainable from the sliding contact. From the data obtained by the cinematograph and the instantaneous photograph, the sizes of sliding contact (r_1, r_2) were measured and by using the relation (7) the retardation time of polymers was calculated. The results are shown in Table IV with the ratio r_2/r_1. It is evident that the mechanical properties of polymers is not represented by the simple model as used in analysis. In addition, the deformation of polymer surface neighbouring the contact region was left out of consideration in the above analysis. However, it seems that the values of τ are reasonable order of magnitude for the retardation time of polymers. At least, this means that the sliding friction is closely connected to the deformation of polymer surface. When more exact analysis is carried out, it is to be expected that more detailed mechanical properties of polymer surface will be determined from the sliding contact. In such case, the use of Newton's rings is very helpful.

Table IV.

Polymer	r_2/r_1	τ (sec)	Method	
			Photo*	Load
Polystyrene	0.94	9.8×10^{-4}	I	350 g
Hizex	0.88	1.3×10^{-1}	C	350 g
Sumikathene	0.44	3.0×10^{-2}	I	113 g
PTFCE	0.97	2.0×10^{-4}	I	350 g
PTFE	0.87	1.5×10^{-1}	C	350 g
Phenol resin	0.96	3.7×10^{-4}	I	522 g

* I : Instantaneous photograph (abrupt slip).
C : Cinematograph (smooth sliding).

4.2 Mechanism of polymer friction

The adhesion theory seems to be applicable to the friction between the glass hemisphere and the polymers, because the frictional force is proportional to the area of contact. On the other hand, other experimental results seem to indicate that the friction of polymers is due to the deformation of polymer surface. When the hemisphere is pressed on the polymer, the surface neighbouring the contact region is deformed as shown in Fig. 19 (a). The wave-like deformation extends to a considerable distance from the contact region as compared with the radius of contact circle. Application of a tangential force increases the size of surface deformation on the front side of contact region and decreases on the back side as shown in Fig. 19 (b). A similar deformation also occurs on sliding. The experimental results also show that the polymer surface on the front of contact region is compressed downward as well as in the tangential direction, when the hemisphere starts to slip and is sliding on the polymer.

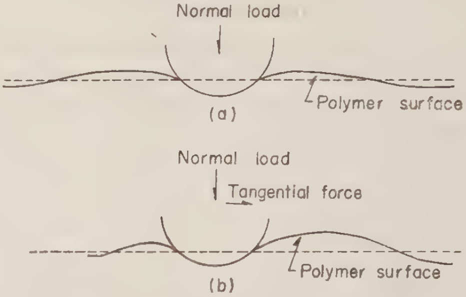

Fig. 19. Deformation of surface of polymer neighbouring the contact region.

Therefore, it is expected that the polymer surface neighbouring the contact region plays an important part in the resistance against the slip of hemisphere. When the deformation of surface resists the slip, it is not suprising that the hemisphere starts to slide very slowly without the abrupt slip when a tangential force smaller than the maximum static frictional force is applied. If we assume adhesion occurs and strong junctions are formed at the contact region, it will be difficult to explain this slow sliding. When the applied tangential force is increased, the polymer surface at the back side becomes depressed. When the depression is very large, the hemisphere loses contact with the polymer surface at the rear and then the area of contact decreases. In this case, the large elevation of surface at the front side resists the slip although the area of contact is small. This explains the changes of the shape of static contact observed in the cinematograph shown in Fig. 7. The result that the frictional force per unit area of contact f is closely connected with Young's modulus of polymers may also indicate that the friction is due to the deformation of surface. On the other hand, it is very doubtful that adhesion occurs in elastic contact. For example, on the basis of the adhesion theory, the area of true contact must be about 40 percent of the area of apparent contact circle in order to account for the frictional resistance between the glass hemisphere and PMMA. This implies that adhesion occurs at the true contact region under the contact pressure of about 1/20 of the bulk yield strength when the load is of 100 g. However. It is difficult to suppose adhesion occurs at such a low pressure as compared with the bulk yield strength. It was observed that the frictional force obtained with the steel hemisphere was not proportional to the area of contact. This must be attributed to the production of a grooved track. Since the contact depth of the steel hemisphere is larger than that of the glass hemisphere, the elevation of the surface will be also large. Therefore, it may be considered that when the polymer is compressed underneath the steel hemisphere the deformation is non-recoverable, and results in the grooved track. In fact, examination indicates that the grooved track is produced with a little displacement from the front of the hemisphere. Assuming that the polymer is ploughed out from all the front of the steel hemisphere and this contributes to the friction in such a way as dealt by Bowden[13], the coefficient of friction μ_p produced by the ploughing is given by

$$\mu_p=\frac{1-\sigma^2}{2}\frac{S}{E}, \qquad (8)$$

where S is the pressure required to displace the polymer and is of the same order as the bulk yield strength, E and σ is Young's modulus and Poisson's ratio of the polymer respectively. Since the value of S/E is estimated to be of the order of 10^{-2},[14] the estimated value of μ_p is considerably smaller than the coefficient of friction measured in the experiment. This points out that the friction with the steel hemisphere can not be explained by the adhesion theory. From the above considerations, it is natural to conclude that the friction of a polymer is due to the tangential resistance produced by the deformation of its surface neighbouring the contact region rather than by the shearing of the junctions formed at the contact region.

§ 5. Conclusion

From the observation of the deformation and friction in the static and sliding contact between a flat plate of various polymers and two hard hemispheres of different radii, the following conclusions are drawn.

1) Hertz's equation for elastic contact is applicable to polymers. In a wide range of time of loading, Young's modulus in the equation is also dependent upon the load as well as the loading time. The diameter of the semicircular front part in which the hemisphere makes sliding contact with the polymers is also expressed by Hertz's equation, although Young's modulus loses the usual meaning.

2) The shape of sliding contact region is divided into two types. One is attributed to the retarded elasticity of polymers and the other to the frictional heating. From the theoretical treatment of the former case, the retardation time is obtainable for polymer.

3) The frictional force is proportional to the area of contact provided no grooved track is produced. When the grooved track is produced, this experimental relation does not hold. However, the production of a track is mainly caused by the non-recoverable deformation and hence the polymer is a little ploughed out from the entire front of the hemisphere.

4) The friction of a polymer may be due to the tangential resistance produced by the deformation of polymer surface neighbouring the contact region. Wave-like deformation takes place on the polymer surface neighbouring the contact region. During the frictional process, the deformation increases on one side of the contact region and decreases on the other side and in this way the polymer surface produces the tangential resistance.

5) In applying the tangential force smaller than the maximum static frictional force a very slow slip occurs instead of the abrupt slip.

Acknowledgement

The author is greatly indebted to Prof. U. Nakaya of Hokkaido University for his continual guidance and encouragement throughout this study. He also wishes to express his sincere thanks to Dr. S. Iwayanagi and Dr. T. Hidesima of the Institute of Physical and Chemical Research and Mr. Z. Otaki of Tokyo University for their helpful suggestions, and

Prof. H. Wakasima of Kanazawa University for kindness in coating the polymer samples. His particular thanks are due to the Sumitomo Bakelite Co. for furnishing many polymer samples.

References

1) F. P. Bowden and D. Tabor: *The Friction and Lubrication of Solids* (Oxford Univ. Press, London, 1954).
2) K. V. Shooter and D. Tabor: Proc. Phys. Soc. London. **B65** (1952) 661.
3) N. Gralén: Proc. Roy. Soc. **A212** (1952) 491.
4) B. Lincoln: Brit. J. Appl. Phys. **3** (1952) 260.
5) R. F. King and D. Tabor: Proc. Phys. Soc. London. **B66** (1953) 728.
6) M. W. Pascoe and D. Tabor: Proc. Roy. Soc. **A235** (1956) 210.
7) F. P. Bowden: Endeavour. **16** (1957) 5.
8) K. R. Eldredge and D. Tabor: Proc. Roy. Soc. **A229** (1955) 181.
9) See for instance, D. Tabor: *The Hardness of Metals* (Oxford Univ. Press, London, 1951) 44p.
10) F. Schwarzl: Kollid-Z. **148** (1956) 47.
11) J. F. Archard: Proc. Roy. Soc. **A243** (1957) 190.
12) A. M. Bueche and D. G. Flom: Wear. **2** (1958) 168.
13) See the reference 1), 91 p.
14) R. Buchdahl: J. Polymer Sci. **28** (1958) 239.

JOURNAL OF THE PHYSICAL SOCIETY OF JAPAN, Vol. 16, No. 10, OCTOBER, 1961

Self-Absorption of Spectral Line

By Toshiharu TAKO

National Research Laboratory of Metrology, Tokyo

(Received June 3, 1961)

The line shape, line width and other properties of self-absorbed line are discussed by introducing several models on the spatial distributions of the emitting and absorbing atoms. The simple models in which the emitting atoms decrease linearly from the center to the outside proves to be sufficient to explain the general views on the self-absorption. The shapes of the visible triplet lines emitted by Hg^{198} and Cd^{114} lamps are observed without being disturbed by hyperfine structure of isotopes using a direct recording Fabry-Perot interferometer. From these observations, the effect of self-absorption of these lines is made clear and is shown to agree well with the results theoretically obtained. Moreover it is found that Hg^{198} and Cd^{114} lamps can be approximately represented by the model in which the emitting atoms decrease linearly from the maximum at the center to zero at the wall. The values of absorption parameter evaluated are able to be explained consistently, taking the population and decay time of the triplet states and their quenching due to collisions with carrier gas and electrons into consideration.

§ 1. Introduction

The broadening of spectral line has been studied by many authors such as Michelson, Lorentz, Holtsmark, Margenau and others from both of the classical and the quantum-mechanical standpoints, and the causes of the broadening have been classified into the Doppler width, natural width, resonance width, pressure broadening, Stark broadening, and so on. In addition to these primary causes, however, the secondary effect due to the self-absorption is also thought not to be small, especially for the lines which have the metastable or the ground state as the lower level.

Among a number of papers which deal with the intensity of spectral lines and their absorption, there are several papers which deal theoretically with the self-absorption problem. However, their treatments are limited only to two special cases; a homogeneous light source (Burger and van Cittert[1)]) and the light source with the emitting center only along its central axis (Cowan and Dieke[2)]). In this paper, several problems of the self-absorption effect in the more general case are discussed by introducing several reasonable models.

In the previous reports[3)-5)] on the spectral lines of Hg^{198} and Cd^{114} which were a part of the study of the unit of length, the present author reported that the visible triplet lines emitted by Hg^{198} and Cd^{114} electrodeless lamps were easily subjected to the self-absorption. The further development of these observations will be described in detail in § 3 to verify the reliability of the present treatments of the self-absorption.

The error resulting from the self-absorption is serious, when the concentration of a particular element is estimated by the relative line intensity, or when the high temperature of plasma must be estimated from the line shape and its half-width. However, the line affected by self-absorption gives a possibility of revealing the spatial distribution and density of atoms (or molecules), which emit or absorb the radiation in the source, and the mean life of atoms in the lower state.

§ 2. The shape of self-absorbed spectral lines

2.1. *The radial distribution of emitting and absorbing atoms*

At first, let us assume that atoms are excited symmetrically to the axis of a cylindrical tube of radius R and that the radiation is emitted only to the direction perpendicular to the tube axis. To discuss the shape of self-absorbed line, the information on the radial distributions of emitting and absorbing atoms: $n_e(r)$ and $n_a(r)$ is indispensable. Hitherto, the following two simple special cases have been discussed by several authors;

a) The uniformly excited source in which the excitation is homogeneous. The typical examples are a flame source and a discharge tube of suitable design.

b) The source having emitting and absorbing atoms spatially separated: all the emitting atoms are concentrated in the center (or around the central axis) while all the absorbing atoms are distributed outside this region, for example, an arc.

In actual sources an intermediate state between a) and b) will be the case. For this reason, Cowan and Dieke[2)] introduced a parameter n to indicate the states of excitation-decrease from the center of the source to its outside; $n=1$ corresponds to the preceding special case a) and $n=\infty$, to the case b). The authors derived a formula expressed in an infinite series for the shape of self-absorbed lines in general. However, not only their assumption has poor ground for actual sources but also the numerical evaluation of their formula is complicated and troublesome, although a possible approximate expression of their formula was discussed by Preobrazhenski[6)] et al.

Before a possible and practical assumption on $n_e(r)$ and $n_a(r)$, especially for a discharge tube, is given, the radial distribution of electrons $n_{el}(r)$ is to be discussed. On this point, Schottky[7)] discussed the electrical field in the homogeneous positive column of a low pressure discharge (about 0.1–10 mmHg), and showed theoretically that $n_{el}(r)$ can be given by the following relation:

$$n_{el}(r)=N_0 J_0(2.4\ r/R)\ , \tag{2.1}$$

if $\lambda_e \ll R$, where λ_e is the mean free path length of electron and J_0 represents Bessell function of order zero. In order to calculate the radial force approximately, Townsend[8)] assumed that the number of electrons at the wall of the tube was half of the number at the axis, that is,

$$n_{el}(r)=N_0 J_0(1.52\ r/R)\ . \tag{2.2}$$

Emeleus and Burns[9)] showed that the concentration of electrons fell off parabolically from the maximum value at the axis to zero at the wall, that is,

$$n_{el}(r)=\frac{2i(8mkT/\pi)^{1/2}}{\pi R^2 e^2 \lambda_e E}(1-r^2/R^2)\ , \tag{2.3}$$

where i represents the current through the tube and E, the longitudinal electric field in the tube.

On the other hand, Yarnold and Holmes[10)] showed experimentally that $n_{el}(r)$ is given by the following expression, which is approximately close to Schottky's formula,

$$n_{el}(r)=N_0J_0(2.2\ r/R)$$

for a low pressure discharge (about 0.5–1 mmHg), and that the electrons are apt to be centralized as the gas pressure increases. It is noticeable that $n_{el}(r)$ coincides with $n_e(r)$, which was obtained from their experiment.

On the bases of these theories and experiments, the nine models of light source, of which $n_{el}(r)$'s are taken to have similar form to $n_e(r)$'s as shown in Fig. 1, are chosen and used for all following discussions.

The curves 1 and 2 show the above mentioned two special cases a) and b) respectively; the curves 4 and 7 (Eq. (2.2)) illustrate the cases in which the number of emitting atoms at the wall of the tube become half of the number at the axis; and the curves 3, 6 (Eq. (2.1)) and 9 (Eq. (2.3)), the cases in which the number of emitting atoms becomes just zero at the wall of the tube. The curves 5 and 8 illustrate the cases in which the positive column of discharge is restricted within $R/2$ as may be seen in a high pressure discharge.

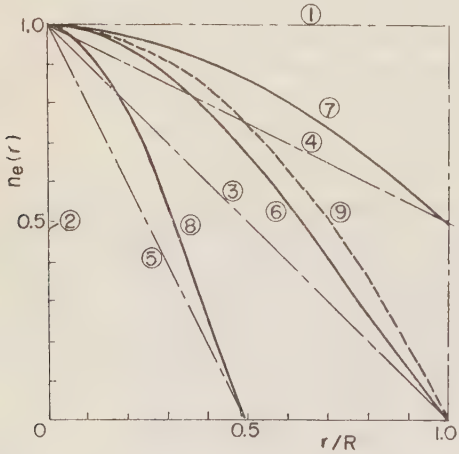

Fig. 1. The radial distribution of emitting atoms for the nine models discussed in this paper.

On the other hand, the curves 6, 7 and 8 illustrate the models in which the decrease of the number of emitting atoms from the center to the outside are expressed by zero order Bessell functions; the curves 3, 4 and 5, by linear functions (as a first approximation); and the curve 9, by parabolic function, respectively.

The radial distribution of absorbing atoms $n_a(r)$ is not always independent to that of emitting atoms. In most lines easily subject to the self-absorption, however, the mean life of absorbing atoms in metastable (or ground) state is far longer than that of emitting atoms in a upper excited state, so that the absorbing atoms may be diffused uniformly in the tube. In the following sections the shapes of self-absorbed lines are discussed by assuming that $n_a(r)$ is constant, and in § 2.5 some considerations will be given for the case in which $n_a(r)$ is not constant.

2.2. *The shape of self-absorbed line*

In this section, only the radiation passing through the center of the tube is considered. The radiation energy in an interval dr is proportional to the density of the emitting atoms existing in this interval and depends on the spectral distribution of the emission line $f_e(u)$. Thus the energy can be given by the expression: $Ef_e(u)n_e(r)dr$, where u is $\nu-\nu_0$, and ν_0 is the central frequency of the line. The absorption of the radiation passing through the tube depends on the total number of absorbing atoms between r and R, and on the spectral distribution of absorption line $f_a(u)$. For the sake of simplicity, $f_e(u)$ and $f_a(u)$ are assumed to be unity and independent to r, if $u=0$, *ie.* $f_e(0)=f_a(0)=1$. Since the intensity of radiation emitted in an interval dr and leaving the wall of the tude is proportional to

$$Ef_e(u)n_e(r)dr\cdot\exp\left(-Af_a(u)\int_r^R n_a(r)\,dr\right),$$

the total intensity distribution is given by

$$I(u)=\int_{-R}^{R}Ef_e(u)n_e(r)\exp\left\{-Af_a(u)\int_r^R n_a(r)dr\right\}dr\,. \tag{2.4}$$

Under the restriction that $n_a(r)$ is constant in the tube, Eq. (2.4) is reduced to

$$I(u)=\frac{I_0f_e(u)}{2}\int_{-1}^{1}\frac{n_e(x)}{n_e(0)}\exp\{-pf_a(u)(1-x)\}dx \tag{2.5}$$

$$x=r/R\,,\qquad I_0=En_e(0)\cdot 2R\,,\qquad p=An_a(r)R\,,\tag{2.6}$$

where p is identical with the quantity introduced by Cowan and Dieke. It may be seen that the intensity of the radiation of ν_0 is reduced to e^{-1} for $p=1$ and hereafter, the degree of self-absorption is indicated by p.

i) The two special cases.

Case 1. (Fig. 1. Curve 1.): If $n_e(r)$ is constant, Eq. (2.5) is reduced to

$$I_1(u)=\frac{I_0}{2p}\frac{f_e(u)}{f_a(u)}\{1-\exp(-2pf_a(u))\}\,.\tag{2.7}$$

As Cowan and Dieke pointed out, it is important for Eq. (2.7) that $n_e(r)$ and $n_a(r)$ are not necessarily constant, but the ratio $n_e(r)/n_a(r)$ must be constant.

Case 2. (Fig. 1. Curve 2.): If $n_e(r)$ is not zero only at $r=0$, Eq. (2.5) is reduced to

$$I_2(u)=I_0 f_e(u)\exp(-pf_a(u))\,.\tag{2.8}$$

It is noticeable here that Eq. (2.8) is independent of $n_a(r)$, and also applicable to the case in which the tube for absorbing atoms is separated from the one for emitting atoms.

ii) The linear distribution. For the sake of mathematical simplicity, the density of the emitting atoms is assumed to decrease linearly from the center to the wall of the tube, as illustrated by curves 3, 4 and 5 in Fig. 1.

Case 3. (Fig. 1. Curve 3.): If $n_e(r)=n_0(1-|x|)$, Eq. (2.5) is reduced to

$$I_3(u)=\frac{I_0}{2p^2}\frac{f_e(u)}{f_a(u)^2}\{1-\exp(-pf_a(u))\}^2.\tag{2.9}$$

Case 4. (Fig. 1. Curve 4.): If $n_e(r)=n_0(1-|x|/2)$, Eq. (2.5) is reduced to

$$\begin{aligned}I_4(u)&=\frac{I_0}{4p^2}\frac{f_e(u)}{f_a(u)^2}\{1-\exp(-pf_a(u))\}^2+\frac{I_0}{4p}\frac{f_e(u)}{f_a(u)}\{1-\exp(-2pf_a(u))\}\\&=\frac{1}{2}(I_3(u)+I_1(u))\,.\end{aligned}\tag{2.10}$$

Case 5. Fig. 1. (Curve 5.): If $n_e(r)=n_0(1-2|x|)$, Eq. (2.5) is reduced to

$$I_5(u)=\frac{I_0 f_e(u)}{p^2 f_a(u)^2}\left\{1-\exp\left(-\frac{p}{2}f_a(u)\right)\right\}^2\exp\left\{-\frac{p}{2}f_a(u)\right\}.\tag{2.11}$$

iii) J_0 distribution and parabolic distribution.

Case 6, 7, 8. (Fig. 1. Curves 6, 7, 8.): If $n_e(r)$ is expressed by J_0 functions as shown by the curves 6, 7, and 8 in Fig. 1, $I(u)$ is given by the following equation;

$$I_{6,7,8}(u)=\frac{I_0 f_e(u)}{2}\int_{-1}^{1}J_0(cx)\exp\{-p(1-x)f_a(x)\}dx\,,\tag{2.12}$$

where $c=2.4$, 1.2 and 4.8, respectively.

Case 9. (Fig. 1. Curve 9.): If $n_e(r)=n_0(1-x^2)$, Eq. (2.5) is reduced to

$$I_9(u)=\frac{I_0 f_e(u)}{p^3 f_a(u)^3}\Big[\Big(\exp(-2pf_a(u))+1\Big)(pf_a(u)+1)-2\Big]\,.\tag{2.13}$$

To compare the effects of self-absorption in these nine cases, several numerical evaluations of Eqs. (2.7)~(2.13) were carried out. These line shapes, when $p=2$, are shown in Fig. 2, assuming that $f_e(u)$ is identical with $f_a(u)$, which is the valid assumption practically, and that both $f_e(u)$ and $f_a(u)$ are Doppler distribution or Lorentz distribution. Both these distributions are typical ones in spectral lines. Doppler distribution is predominant in a source of low pressure and high temperature, and is expressed by

$$f_e(u)=f_a(u)=\exp\left(-\frac{4\ln 2}{\delta_D{}^2}u^2\right), \quad (2.14)$$

where δ_D is half-width. On the other hand, Lorentz distribution represents the shape of line affected by such causes as natural width, resonance width, and pressure broadening, and is expressed by

$$f_e(u)=f_a(u)=1\Big/1+\left(\frac{2u}{\delta_L}\right)^2, \quad (2.15)$$

where δ_L is half-width. Some numerical calculations of Eq. (2.12) were carried out by means of an electronic computer.

Moreover, the line shapes in the Case 3 for several p's are shown in Fig. 3. The comparison of the curves in Figs. 2 and 3 discloses the followings.

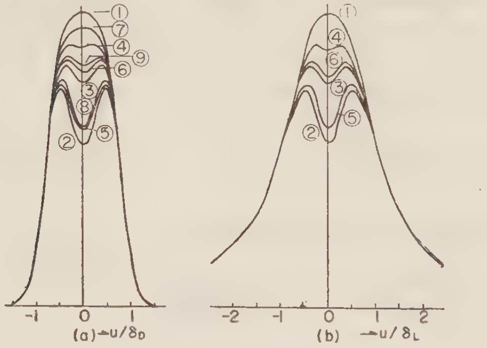

Fig. 2. Line shapes for Doppler distribution (a) and Lorentz distribution (b) when $p=2$. Curve numbers are coincide with that of Fig. 1.

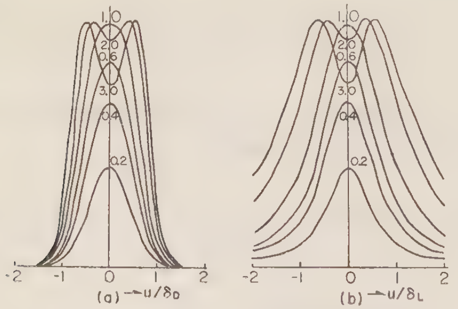

Fig. 3. Line shapes with various p for Doppler distribution (a) and Lorentz distribution (b) in the Case 3.

1) The shapes of self-absorbed lines are distinguished from others in the neighbourhood of the central frequency, but coincide at the tail.

2) The degrees of the intensity reduction and the self-reversal increase with the centralization of the emitting atoms.

3) When the line reverses, the maximum value of $I(u)$ is independent of p in every case.

4) For the spectral line with Doppler distribution the line broadening with p is not so large, while for the line with Lorentz distribution, the broadening is considerably large, especially at the both wings of the line.

Some of these conclusions are identical with the results derived by Cowan and Dieke.

2.3. *The increase of half-width for unreversed line*

For p smaller than 0.6, the shape of line with self-absorption can hardly be distinguished from the one with no self-absorption without a detailed observation. In order to determine p for unreversed line, the relation between the increase of half-width and p is useful. Fig. 4 shows the curves representing the increase of half-width with p for each of $n_e(r)$ of the three cases. The curves for all other cases lie between the corresponding curves. It is noticed in Fig. 4 that the increase of half-width for Doppler distribution is slower than that of Lorentz distribution for all cases, and that the increase is faster for the states that have larger centralization of emitting atoms for each of these two distributions.

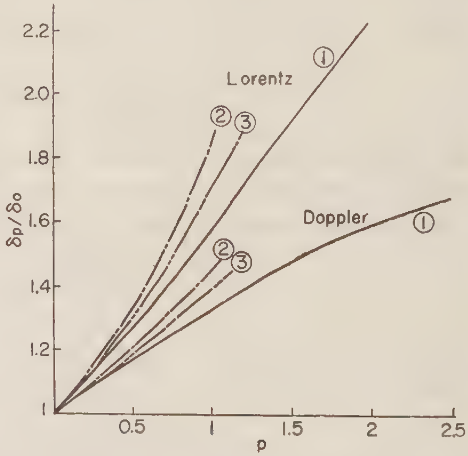

Fig. 4. The increase of half-width with p for typical cases of $n_e(r)$.

2.4. *The evaluation of the degree of self-reversal*

Except the Case 1 (the uniformly excited source), the spectral lines always reverse, when p exceeds 1, as shown in Fig. 3. The degree of self-reversal is evaluated by the two following factors,

1) the wave number (or wave length) separation corresponding to two side maxima: $\Delta_{\max}$,

2) the ratio of the central minimum to the side maximum: $I(0)/I_{\max}$. In the Case 2 (Eq. 2.8.), $\Delta_{\max}$ for Doppler and Lorentz distributions are given by the following equations, respectively,

$$\left.\begin{aligned}\Delta_{\max}&=\delta_D\sqrt{\ln p}/\sqrt{\ln 2}\,, \\ \text{and}\quad \Delta_{\max}&=\delta_L\sqrt{p-1}\,.\end{aligned}\right\}\tag{2.16}$$

For typical cases of $n_e(r)$ the variation of $\Delta_{\max}$ versus p is given in Fig 5.

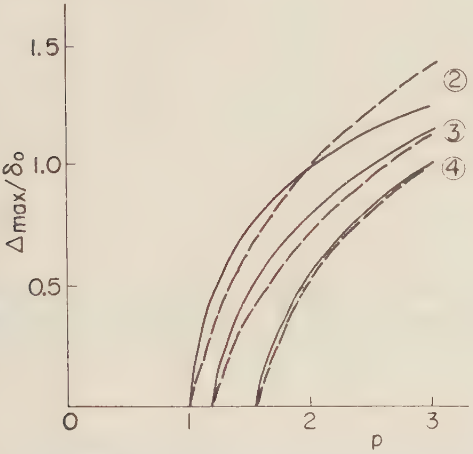

Fig. 5. The relation between $\Delta_{\max}$ and p for typical cases of $n_e(r)$ for Doppler distribution (solid line) and Lorentz distribution (dotted line).

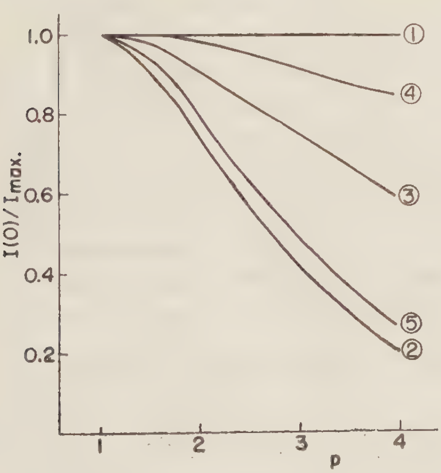

Fig. 6. The relation between $I(0)/I_{\max}$ and p for typical cases of $n_e(r)$.

Because $I(0)/I_{\max}$ is independent of the spectral distribution $f(u)$, this ratio is more useful than $\Delta_{\max}$, for the evaluation of the degree of self-reversal. The curves of $I(0)/I_{\max}$ are plotted against p in Fig. 6 for typical cases of $n_e(r)$. All asymptotic lines of these curves are focused nearly on a point. This fact indicates that the effects of self-absorption in the Case 3, Case 4, $\cdots$ Case 9 should be nearly identical with the one in the Case 2, if the values of p's of the former cases are replaced by ap, where a is an appropriate number less than unity (above 0.6 for Case 3), and these curves seems to make clear the meaning of the Cowan and Dieke's conclusions which were given with somewhat ambiguous expression only for some special cases.

2.4. *The self-absorpton in off-centered light*

Hither-to the discussions were devoted only to the light passing through the center (A in Fig. 7.). In this section, the off-centered light (B in Fig. 7) is considered.

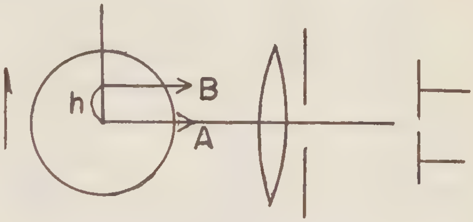

Fig. 7.

At first, in Fig. 7 the ratio of the intensity of the light B to that of the light A: I_h/I_0 is formulated for the line with no self-absorption. This ratio is useful to obtain the distribution of emitting atoms $n_e(r)$ from observed curves, when $n_e(r)$ is expected to be the same for all lines. In general, I_h/I_0 is given by the relation:

$$\frac{I_h}{I_0}=\int_0^{\sqrt{1-h^2}} n_e(\sqrt{h^2+x^2})\,dx\Big/\int_0^1 n_e(x)dx\,. \tag{2.17}$$

Eq. (2.17) is reduced to the following equations according to the various cases of $n_e(r)$, for Case 1, $$\frac{I_{h1}}{I_0}=\sqrt{1-h^2}\;; \tag{2.18}$$

for Case 3, $$\frac{I_{h3}}{I_0}=\sqrt{1-h^2}+h^2\log\frac{h}{1+\sqrt{1-h^2}}\;; \tag{2.19}$$

for Case 4, $$\frac{I_{h4}}{I_0}=\sqrt{1-h^2}+\frac{h^2}{3}\log\frac{h}{1+\sqrt{1-h^2}}\;; \tag{2.20}$$

for Case 5, $$\begin{aligned}\frac{I_{h5}}{I_0}&=\sqrt{1-4h^2}+4h^2\log\frac{2h}{1+\sqrt{1-4h^2}} &&\text{for}\quad 0<h<\frac{1}{2}\,,\\ &=0 &&\text{for}\quad h\geqslant\frac{1}{2}\;;\end{aligned} \tag{2.21}$$

for Cases 6, 7, 8, $$\frac{I_{h6,7,8}}{I_0}=\int_0^{\sqrt{1-h^2}}J_0(c\sqrt{h^2+x^2})dx\Big/\int_0^1 J_0(cx)dx\,,\quad\text{where}\quad c=2.4,\ 1.2,\ 4.8\;; \tag{2.22}$$

and

for Case 9, $$\frac{I_{h9}}{I_0}=(1-h^2)^{3/2}\;; \tag{2.23}$$

where h is expressed taking R as unit. These relations are shown in Fig. 8. It is seen that the differences between the curves 3 and 6; 4 and 7; 5 and 8; and 6 and 9 are almost indistinguishably small.

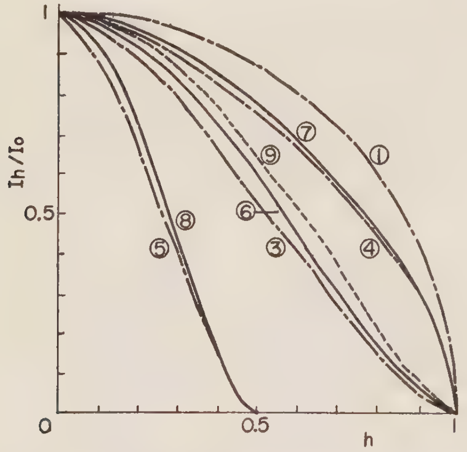

Fig. 8. Radial intensity distributions for various cases of $n_e(r)$ without self-absorption.

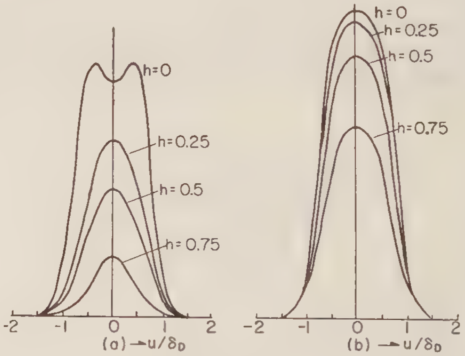

Fig. 9. Line shapes of off-centered light in the Case 3 (a) and Case 1 (b) for Doppler distribution ($p=2$).

Now, the line shape of the self-absorbed line in the off-centered light is given by

$$I_h(u)=\frac{I_h f_e(u)}{2}\int_{-\sqrt{1-h^2}}^{\sqrt{1-h^2}}\frac{n_e(\sqrt{h^2+x^2})}{n_e(0)}\exp\{-pf_a(u)(\sqrt{1-h^2}-x)\}dx\,, \tag{2.24}$$

instead of Eq. (2.5) for the centered light. Eq. (2.24) is reduced to the following equations according to the various cases of $n_e(r)$.

Case 1, $$I_{h1}(u)=\frac{I_{h1}f_e(u)}{2pf_a(u)}\left\{1-\exp(-2pf_a(u)\sqrt{1-h^2})\right\}. \tag{2.25}$$

$I_{h1}(u)$ is identical in the form to $I_1(u)$ if p is replaced by $p\sqrt{1-h^2}$ (see Eq. (2.7)).

Case 3,
$$I_{h3}(u)=\frac{I_{h3}\,f_e(u)}{2}\left[\frac{1-\exp\left(-2pf_a(u)\sqrt{1-h^2}\right)}{pf_a(u)}\right.$$
$$\left.-\exp\left(-pf_a(u)\sqrt{1-h^2}\right)\int_{-\sqrt{1-h^2}}^{\sqrt{1-h^2}}\sqrt{h^2+x^2}\exp\left(pf_a(u)x\right)dx\right], \tag{2.26}$$

where the first term is identical with Eq. (2.25) in Case 1. Some numerical evaluations of the second term were carried out by means of an electronic computer. The shapes of $I_{h1}(u)$ and $I_{h3}(u)$ at $h=0$, 0.25, 0.5 and 0.75 when $p=2$ are shown in Fig. 9.

For Case 4, $I_{h4}(u)$ is the same as Eq. (2.25) except that the second term is multiplyed by 0.5.

Case 5,
$$\begin{aligned}I_{h5}(u)&=\frac{I_{h5}\,f_e(u)}{2}\left[\frac{1-\exp\left(-2pf_a(u)\sqrt{1/4-h^2}\right)}{pf_a(u)}-\exp\left(-pf_a(u)\sqrt{\frac{1}{4}-h^2}\right)\right.\\&\quad\left.\times\int_{-\sqrt{1/4-h^2}}^{\sqrt{1/4-h^2}}2\sqrt{h^2+x^2}\exp\left(pf_a(u)x\right)dx\right]\exp\left\{-pf_a(u)\left(\sqrt{1-h^2}-\sqrt{\frac{1}{4}-h^2}\right)\right\}\\&\qquad\qquad\text{for}\quad 0<h<\frac{1}{2},\\&=0\qquad\qquad\text{for}\quad h\geqslant\frac{1}{2},\end{aligned} \tag{2.27}$$

Case 9,
$$I_{h9}(u)=\frac{I_{h9}\,f_e(u)}{p^3 f_a(u)^3}\left[\left(pf_a(u)\sqrt{1-h^2}+1\right)\left\{\exp\left(-2pf_a(u)\sqrt{1-h^2}\right)+1\right\}-2\right]. \tag{2.28}$$

The formulas for the Cases 6, 7, and 8 were omitted because of the difficulty of their analytical calculation, but general tendencies of these cases will not differ much from the Cases 3, 4 and 5, respectively.

2.5. *Several remarks*

Through these discussions, it is shown that the simple models, in which the emitting atoms decrease linearly from the center to its outside in the light source while the absorbing atoms are constant in number, are sufficient to explain the general views on the properties of self-absorbed lines above mentioned.

In actual cases the absorbing atoms are not always uniformly distributed. In the extreme case, however, in which the distribution of absorbing atoms coincides with that of emitting atoms, the line shapes are identical to that of the Case 1 (Eq. (2.7)) as is remarked there. Thus now, the problems remain unsolved for the models in which the absorbing atoms are distributed more widely than the emitting atoms, but not completely uniformly. However, the effect of self-absorption for these models may be deduced from the preceding discussions. For example, the line shape for the model in which the emitting and absorbing atoms are distributed as the curves 3 and 4 in Fig. 1 may be approximately given by Eq. (2.10) in the Case 4 in which the emitting and absorbing atoms are distributed as the curves 4 and 1 in Fig. 1.

§ 3. Measurements of the spectral line shape and its half-width

3.1. *Direct recording Fabry-Perot interferometer*

The direct tracing of spectral line shapes on a linear scale was carried out by the pressure scanning type Fabry-Perot interferometer of which characteristics were reported by the present author in Japanese.[4] The line to be measured is separated from other lines by a monochromator and is let to pass through a Fabry-Perot etalon in an air tight vessel and the image of exit slit of the monochromator is focussed on the screen with a pin-hole so as to build a concentric ring interference pattern. The light from the center of the interference pattern passes through the pin-hole and strikes the photocathode of a highly sensitive photomultiplier (EMI 6256B). The output of the photomultiplier is amplified and supplied to a pen recorder. By changing the pressure of air in the etalon vessel, the refractive index of the air between the interferometer plates can be changed and therefore, the wavelength of the light at the center of the interference pattern can also be varied with time. Since the change of the refractive index is linearly proportional to the pressure of air and the rate of leakage of air is almost constant at low pressure, the intensity distribution of the interference fringe of consecutive orders will be recorded in an equal distance as shown in Fig. 10. Therefore its apparent half-width δ is obtained readily by comparing it with the interference fringe separation $\varDelta\nu$. Since the 50 mm etalon was used in Fig. 10, $\varDelta\nu$ is 0.100 cm^{-1} and then δ is determined to 0.0224 cm^{-1}.

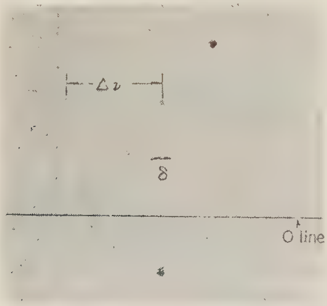

Fig. 10. An example of recorded shape of λ5461 emitted by Hg^{198} lamp at 0°C. Spectral range $\varDelta\nu$: 0.100 cm^{-1}, half-width δ: 0.0224 cm^{-1}.

Since the apparatus half-width of the Fabry-Perot interferometer decreases rapidly with the increase of the reflectance of the interference plates, the dielectric reflecting films having a reflectance of more than 90% for a range covering over 1000Å were used on the plates. Three reflecting films of suitable coating suffice to cover the visible region, but an appropriate choice of them is necessary in accordance with the wavelength of line to be measured. The etalons have spacers of 62.5, 50 and 40 mm. Under these conditions the apparatus half-width is estimated to be about 0.002 cm^{-1} (less than 1/10 of the measured line width), and this was checked by preliminary observations[4] using the various spacers. The true half-widths are computed using a similar method[11] to Burger and van Cittert's[12]. Moreover, careful considerations should be given to the scanning width due to the aperature size of the pin-hole disk, the imperfection of parallelism of the interference plates, the error in centering of the interference fringe pattern in the pin-hole disk, the asymmetry of the observed line shape due to the scanning speed, the intensity fluctuations of the light source, and the non-linearity of response of the photomultiplier.

3.2. *Measurements on the triplet line of Hg^{198}*

The spectrum of Hg^{198} obtained from neutron-irradiated gold was first observed by Wiens and Alvarez and the electrodeless Hg^{198} lamp, so called "Meggers lamp", was developed by Meggers and others (1950)[13]. In the preliminary reports[3],[4], the present author showed that the Hg^{198} lines, especially the visible triplet lines, are affected markedly by self-absorption. As the observations of the shapes of these lines can be made without being disturbed by hyperfine structure of Hg isotopes, these lines are convenient for

Table I. Half-width of the λ 5461 line of Hg^{198}.

Lamp	Amount of Hg^{198} isotope (mg)	Carrier gas (mmHg)	Observed half-width ($\times 10^{-3}$ cm^{-1})		Degree of self-absorption evaluated at 20°C
			0°C	20°C	
GEC	(>3)	argon 0.25	17.5	26.0	1.3
No. 7	0.35	argon 3	19.3	23.4	0.53
NBS	(3)	argon 3*	20.3	22.0	0.22
No. 2	0.2	argon 4.8	19.8	23.6	0.47
Baird	0.2	(argon 10)	21.8	22.5	0.08
No. 4	0.2	argon 8.9	21.0	22.0	0.13
No. 3	0.3	neon 4.8	17.7	25.5	1.1

* NBS lamp has been used extensively for several years and the observation of half-widths of this lamp show that its pressure of the carrier gas at present may be higher than 3 mmHg.

the study of self-absorption, taking the theory given in § 2 into consideration. For this purpose the following lamps and lines were used.

i) Tested lamps: In this measurement the three foreign lamps and several lamps* made in this laboratory[14] were used. One of the former was presented from National Bureau of Standards of U.S.A. and the other two were made in Baird Co. and General Electric Co. The amounts of isotope and the pressure of carrier gas in these lamps are shown in Table I. But for the foreign-made lamps, both of these two quantities are unknown and their estimated values are bracketed. All these lamps are electrodeless type, about 10–15 cm in length and about 5–6 mm in inner diameter, and they are excited by a high frequency oscillator (60 MHz, 100 W) in a water jacket. The temperature of cooling water was maintained at about 0°C or 20°C.

ii) λ5461 line: The lower level of the green line of Hg, λ5461 ($6^3P_2-7^3S_1$) is a metastable state and the large effects of self-absorption are expected. An example of observed line shape of λ5461 at 0°C is shown in Fig. 10. The observed half-widths at 0°C and 20°C for several lamps are given in Table I and their curves plotted against pressure of carrier gas in the lamps are shown in Fig. 11.

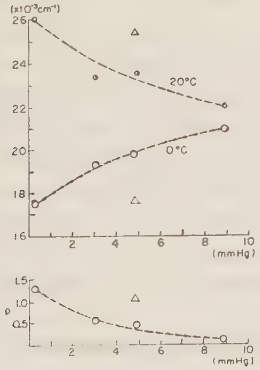

Fig. 11. The variations of the half-width (δ) and evaluated value of p with the pressure of argon (○) and neon (△) in Hg^{198} lamps for λ5461.

The curves in Fig. 11 show that as the pressure of argon in the lamp increases, the line width of λ5461 increases at 0°C, but decreases at 20°C. Though the detail of the analysis of these behaviours of the line width will be published later, the conclusions will be summarized as follows. 1) The observed minimum value of the line width at 0°C for the GEC lamp with argon of pressure less than 1 mmHg is found to be 0.0173 cm^{-1} which is proved to be the sum[15] of the Doppler width: 0.0153 cm^{-1} and the Lorentz type width: 0.0035 cm^{-1}. The increase of the line width at 0°C with that of the pressure of argon is thought to be purely due to the pressure effect broadening, because the increase of the former is proportional to the pressure. This is confirmed from the measurements of the shift of the wave-length accompanied with the pressure effect broadening. 2) The difference in width between at 0°C and 20°C for each lamp is attributed to self-absorption discussed in previous sections. 3) The fact that the No. 3 lamp with neon of 5 mmHg has the same tendency as the GEC lamp with argon of less than 1 mmHg proves the weaker pressure effect of neon. The degree of self-absorption p of the λ5461 line for these lamps are obtained referring to the theoretical curve (the Case 3) in Fig. 4, and given in the last column of Table I and in Fig. 11.

iii) λ4358 and λ4047 lines: The line shapes and their half-widths of the rest of visible triplet of Hg, λ4358 ($6^3P_1-7^3S_1$) and λ4047 ($6^3P_0-7^3S_1$) were also measured. For these lines, the differences in the half-width between at 0°C and 20°C are not so large as for λ5461. Even for the GEC lamp which was most seriously affected by self-absorption, the evaluated values of p's of λ4358 and of λ4047 are about 1/5 and 1/3 of the value of λ5461 respectively as shown in Table II.

Table II. Observed half-widths (δ) and degree of self-absorption (p) at 20°C for the visible triplet lines of Hg^{198} (GEC lamp).

λ (Å)	δ (×10^{-3} cm^{-1})		p
	0°C	20°C	
5461	17.5	26.0	1.3
4358	24.4	26.9	0.26
4047	29.1	33.2	0.36

---

* These lamps are numbered. Its isotope Hg^{198} is prepared by the Atomic Energy of Canada Limitted and its composition measured by mass-analysis is reported to be Hg^{198} of 98.74%, Hg^{199} of 1.49%, Hg^{200} of 0.07% and the sum of rests of less than 0.01%.

iv) End-on view: When the lamp is observed by end-on view, the path of light in the tube is more than 10 times as long as that of side-on view, so the degree of self-absorption increases markedly. The output intensity of the λ5461 line is weakened considerably and the λ4358 line is about to self-reverse. The evaluated values of p's are

for λ5461	$p>5$
for λ4358	$p=1.0\sim1.2$
for λ4047	$p=1.8\sim2.5$

respectively, and the ratio of these p's is nearly equal to the one in Table II.

3.3. *Measurements on the triplet lines of* Cd^{114},

In the visible region of Cd spectrum, there are four intense lines, namely, the red line λ6438 which is well known as the primary standard of wave length in spectroscopy, and the triplet lines λ5086 ($5^3P_2-6^3S_1$), λ4800 ($5^3P_1-6^3S_1$) and λ4678 ($5^3P_0-6^3S_1$). The visible triplet lines of Cd^{114} are affected markedly by self-absorption and are suitable for the investigation of self-absorption on the same reason as those of Hg^{198}.

i) Tested Cd^{114} lamps: Several electrodeless lamps with Cd^{114} isotope were prepared in this laboratory[16]. The isotope was obtained by reducing the Oak Ridge's Cd^{114} 0 with hydrogen, its isotopic purity being published to be 98.2%. These lamps are heated to 250 ∼360°C by a small heater and excited by a 60 MHz high frequency oscillator. As the dependence of self-absorption on pressure and nature of carrier gas for Cd^{114} lamp is similar to the one for Hg^{198} lamp, the detailed observations were made for a lamp which was similar to the above mentioned Hg^{198} lamp and contained the Cd^{114} isotpe of about 7 mg and neon of 3 mmHg.

ii) Temperature dependence of self-absorption: As the temperature of Cd lamp can be varied more easily than that of Hg lamp, the temperature dependence of self-absorption of Cd^{114} lamp can be observed in detail. The shapes of the λ5086, 4800 and 4678 lines were observed at several temperatures between 250 and 360°C under the same experimental condition except the lamp temperature, and a typical example of recorded shape of λ5086 is shown in Fig. 12. It is seen that the temperature dependences of the line intensity and the line shape differ from each other. The λ5086 line has a nearly constant intensity for this temperature range, and this fact agrees well with the theoretical consideration in § 2 (see Fig. 3). The degree of self-absorption of the λ5086 line is the largest while that of the λ4678 line is the smallest among these three lines. On the other hand, the temperature dependence of the intensity of the λ4800 line is the largest and its maximum intensity is observed at about 300°C and it is several times as intense as the ones at 250 or 350°C.

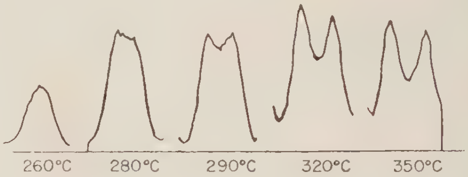

Fig. 12. Recorded shapes of λ5086 line for Cd^{114} lamp at several temperatures.

Every reversed line in Fig. 12 shows some asymmetry in shape and the maximum height of longer wave-length side is higher than the order side. If it is assumed that the shift of the absorption line is slightly less than the shift (about $0.002\sim3\ \mathrm{cm}^{-1}$) of the emission line which increases with the temperature or vapour pressure of Cd, this asymmetry can be explained.

In Table III, the theoretical Doppler width

Table III. The theoretical Doppler- and the observed half-widths for the visible triplet lines of Cd^{114}.

λ (Å)	Theoretical Doppler width ($\times10^{-3}$ cm^{-1})			Observed width ($\times10^{-3}$ cm^{-1})		
	250°C	300°C	350°C	250°C	300°C	350°C
5086	30.1	31.4	32.8	36	reverse	reverse
4800	31.8	33.3	34.8	34	67	reverse
4678	32.7	34.2	35.8	34	64	reverse

and the observed widths at 250, 300 and 350°C for the visible triplet lines of Cd^{114} are shown. The former values were obtained under the assumption that the inner temperature of the lamp was identical with the surrounding temperature. The agreement of the theoretical Doppler- and the observed widths at about 250°C, which is the lowest temperature for the emission of Cd line, suggests that only Doppler effect are significant for the line broadening at this temperature. However, the increase of the observed half-widths with the lamp temperature are more than 10 times as large as that of the Doppler width, so this is considered to be due to the self-absorption like that of Hg^{198}. Then, the temperature dependence of p for each line is obtained from the ratio of the central minimum (or the average of both maxima if the shape is asymmetry) using the curve 3 in Fig. 6, because the $n_e(r)$ in the tested Cd^{114} lamp is very close to that of the curve 3 corresponding to the Case 3 as is shown in the next section, and in shown in Fig. 13.

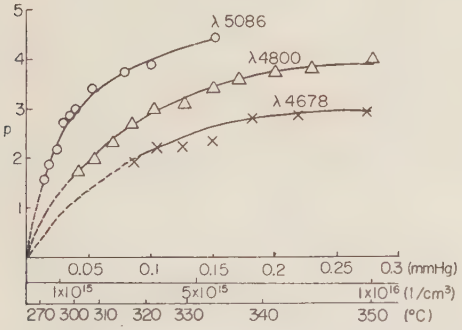

Fig. 13. Relation between the evaluated values of p for Cd^{114} triplet lines and vapor pressure in the lamp.

3.4. *Experiments on the self-absorption in off-centered light*

If the line intensity and the line shape are measured with the lamp shifted to the side way as shown in Fig. 7, the radial dependences of them can be determined. In this experiment an enlarged image of the source was produced on the monochromator slit (about 0.1 mm width) by the use of a condenser lens having an aperture stop and subtending an angle not too large at the source (less than 10 degree), so that the only light which passes almost parallel to the optical axis of the monochromator was used. Though the correction for the lens action of the lamp wall was estimated and applied to the results, the accuracy of intensity measurement in neighbour of the wall was lower than that of the center.

At first, from the measurements of the radial dependence of the intensity for such lines which are hardly subjected to self-absorption as λ5791 and 5770 of Hg, and λ6438 of Cd, the radial distributions of emitting atoms in these lamps were determined using the curves in Fig. 8. The curves a) and b) in Fig. 14 show the radial dependence of intensity of Hg^{198} (λ5791) and Cd^{114} (λ6438) lamps

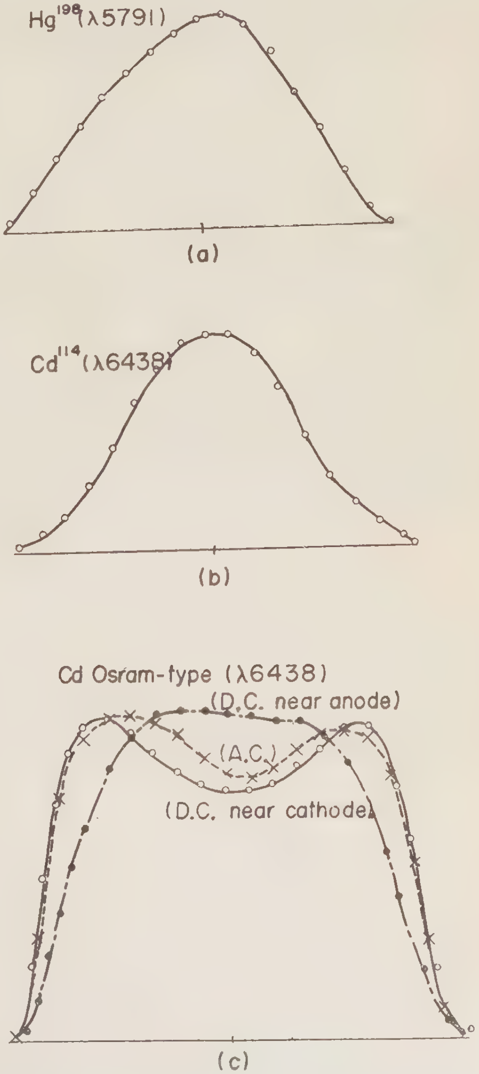

(a)

(b)

(c)

Fig. 14. The radial variations of intensity for three lamps.

respectively, and it is seen that the former is close to the curve 3 corresponding to the Case 3 of $n_e(r)$, while the later, is close to the curve 6 or 3 corresponding to the Case 6 or 3. In contrast with these lamps a commercial Cd lamp has a distribution as shown in Fig. 14. c). This lamp is a small Osram type lamp having a discharge tube of about 25 mm long with an inner diameter of about 10 mm and excited by D.C. or A.C. of about 1.2 A. The appearance of the radial intensity distribution of the $\lambda 6438$ line varies when the excitation is changed from D.C. to A.C. In the D.C. case, the curve is approximately close to the curve 1 in Fig. 8 at a part near the anode, while in the A.C. case, the corresponding curve has a minimum in the center of the tube. The latter shows that the lamp is excited strongly in a ring form in the tube and this is an interesting fact in the study on gaseous discharge, but the discussions for the Cd Osram type lamp in this paper are restricted within the treatment of the former as an example of the uniformly excited source.

The observed radial variations of the line shape and the width of self-absorbed line are as follows.

i) Hg^{198} lamp: Fig. 15 shows the radial variation of the shape of the $\lambda 5461$ line emitted by the GEC lamp which was the most seriously affected by self-absorption at 20°C. Its half-width decreases from 0.0256 cm^{-1} to 0.0187 cm^{-1} as the observing point goes from the center of the tube to the wall. On the other hand, for the lamp No. 7 (see Table I) which contains argon of high pressure and was hardly affected by self-absorption, the half-width has a constant value of about 0.020 cm^{-1}.

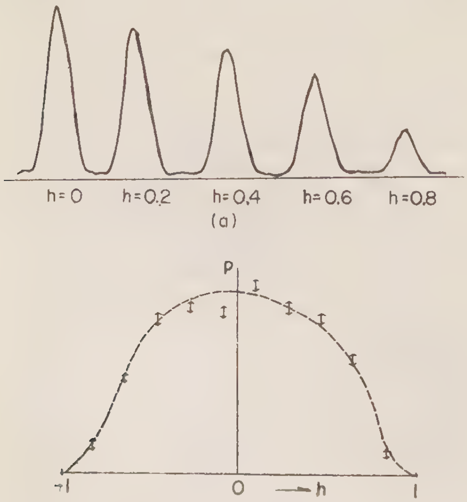

Fig. 15. The radial variations of observed shapes (a) and evaluated values of p for $\lambda 5461$ line emitted by GEC lamp.

ii) Cd^{114} lamp: Fig. 16 shows the radial variations of the shapes of the $\lambda 5086$ line emitted by the Cd^{114} lamp at 304°C. The dotted lines show the theoretical curves calculated using Eq. (2.26) for $p=3$ and a Doppler

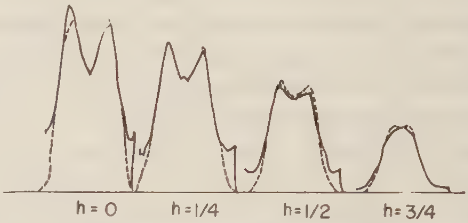

Fig. 16. The radial variations of recorded shapes of $\lambda 5086$ line for Cd^{114} lamp. The dotted lines show the theoretical curves of Eq. (2.26) for $p=3$.

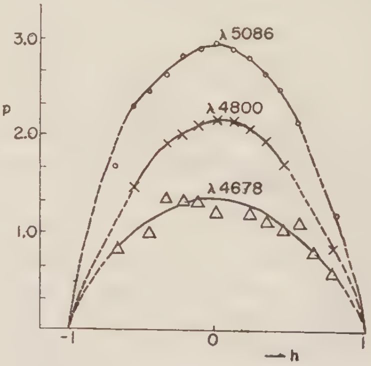

Fig. 17. The radial dependences of evaluated values of p for Cd^{114} triplet lines.

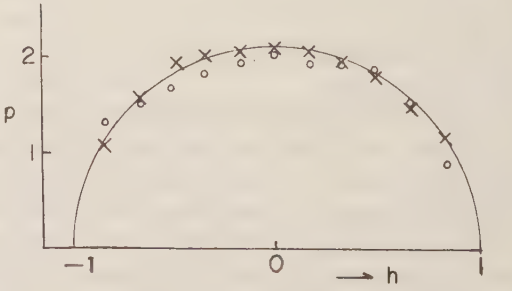

Fig. 18. The radial dependences of observed intensity (×) and the evaluated values of p (○) for $\lambda 4678$ line emitted from the part near the anode of Osram type Cd lamp when it is exicited by D.C.

distribution (Eq. (2.14)) for both $f_e(u)$ and $f_a(u)$, and agree well with the observed curves, except that their tails do not fall down sufficiently owing to the overlapping of the next order fringe. The radial dependence of p obtained from the observed shapes for each line is shown in Fig. 17.

iii) Osram type Cd lamp: The radial dependence for the λ4678 line emitted from the part near the anode of the Osram type Cd lamp excited by D.C. is shown in Fig. 18, and the curve thus obtained agrees well with the theoretical curve (solid line) for the uniformly excited source.

§ 4. Discussion and Summary

4.1. *Energy diagram*

Both Hg and Cd have two valence electrons and show similar spectra, which differ only in separation of energy levels. The visible triplet lines of Hg: λ5461, 4358 and 4047 correspond to those of Cd: λ5086, 4800 and 4678 respectively.

It is accepted in general that the mean life of atoms in the resonance state 6^3P_1 of Hg is shorter than the ones in the metastable states 6^3P_2 and 6^3P_0, and therefore, the λ4358 line is less affected by self-absorption than the λ5461 and 4047 lines, and the case is the same for Cd. However, the rates of the transition to these triplet states have also to be taken into consideration. Since all triplet states are closely related together through collisions with electrons or atoms of carrier gas as pointed out by Gaviola[17)], Kenty[18)] and others, the more detailed discussions are required to explain the mechanism of self-absorption of Hg and Cd.

4.2. *The Hg^{198} lines*

Table IV. Summarized data of the triplet lines of Hg.

V_e; excitation potential for lower states, g; statistical weight ($=2j+1$),
n_B; Boltzmann population for $T_e=1.16\times10^4$°K ($kT_e=1$ eV),
τ_e; decay time for $6\ ^3P_{2,1,0}$ states (Panevkin[21)]),
p; degree of self-absorption at 20°C evaluated in § 3,
k; absorption coefficient at 42°C (Kenty[18)]),

λ (Å)	V_e (eV)	g	relative value of $g\nu^3$	n_B (cm^{-3}) (20°C)	τ_e (s)	relative value of		
						$n_B\tau_e$	p	k
5461	5.43	5	100	9.2×10^{11}	4×10^{-5}	100	100	100
4358	4.86	3	117	9.8	1	27	20	25
4047	4.66	1	49	4.0	6	65	28	46

The data necessary to discuss this problem are summarized in Table IV. The λ5461, 4358 and 4047 lines are radiated from 7^3S_1 state with the ratio of $g\nu^3$. However, only a part of the $6^3P_{2,1,0}$ states is supplied by these transitions and the rest part is supplied by collision of electrons and the ratio of these two parts was estimated to be less than 1/10 by Kenty. If the 6^3P states and the electrons are in thermal equilibrium at the temperature T_e, the Boltzmann populations would be given by the well known equation:

$$n_B = n_a \frac{g}{g_a} \exp\left(-eV_e/kT_e\right)\,, \tag{4.1}$$

where n_a is the concentration of normal atoms (for example, 4.2×10^{13} cm^{-3} at 20°C), g_a and g are the statistical weights of atoms in the normal state and 6^3P state in question and V_e is its excitation potential. The electron temperature T_e in dischage tube depends on the discharge current, the pressure and nature of carrier gas and the temperature of lamp, but its dependences to these factors are not very large. For Hg lamps, T_e were found to be 1.11×10^4°K by Easley[19)], basing upon a probe measurement in the fluorescent lamp with 3 mmHg argon at 42°C, and $1.1\sim1.5\times10^4$°K by Verweij[20)], basing upon the measurement of its variation against the discharge current, the pressure of argon and the temperature of lamp. Since the condition of the present author's discharge tube is much the same to Verweij's, of which T_e and kT_e were $1.1\sim1.3\times10^4$°K and $0.95\sim1.1$ eV respectively, the Boltzmann population n_B was calculated as shown in Table IV assuming that $kT_e = 1\,\text{eV}$.

The values of the decay time for these triplet states $6^3P_{2,1,0}$ of 4×10^{-5}, 1×10^{-5}, and 6×10^{-5} s, were given by Panevkin[21]. The value of 1×10^{-5} s for 6^3P_1 state is much larger than the life time of 1.08×10^{-7} s given by Mitchell and Zemansky[22] who collected in a table the values of the life time for this state given by many authors. As was discussed by Holstein[23], the energy of the radiation λ2537 (so called "imprisoned radiation") will be able to transfer from atom to atom by the repetition of absorption and re-emission before escape from the tube wall. Therefore, the effective life of the order of 1×10^{-5} s concerned with the self-absorption seems to be reasonable. The same conclusion was reached by Kenty who found this value to be 0.76×10^{-5} s. Also the preceding Panevkin's value are thought to justify the models introduced in § 2 for the theoretical investigation of self-absorption. Namely, as Hg atoms have a mean velocity of about 1.75×10^4 cm/s at room temperature, the absorbing atoms in the triplet states $6^3P_{2,1,0}$ will have the mean free path lengths of about 0.7, 0.2 and 1.0 cm for 4, 1 and 6×10^{-5} s respectively, while the emitting atoms in the upper excited state 7^3S_1, the path length is less than 2×10^{-4} cm for the life time of less than 1×10^{-8} s. The former accounts for that the absorbing atoms may be distributed uniformly in the observed tube of radius of about 0.2∼0.3 cm and the latter, that the distribution of the emitting atoms coincide with those of electrons.

Using theses values of the Boltzmann population n_B and the decay time, or effective life time τ_e of Panevkin, the products of n_B and τ_e turns out nearly proportional to the evaluated values of p's in § 3 and then to the number of atoms contributing to self-absorption.

The evaluated values of p's also well agree with the relative absorption coefficient determined by Kenty from the absorption measurements of these lines in a D.C. discharge tube with argon of 3 mmHg.

Next, the variation of p with the argon pressure for the λ5461 line is anticipated to be caused only by the quenching of metastable states due to collisions of argon atoms. But this conflicts with the work of Kenty, who described that quenching of metastables by argon was negligible in comparison with quenching by electrons, however, it is probably difficult to explain the variation of p by the latter. To account for the observed p's of 1.3, 0.53 and 0.13 for the GEC, No. 7, and No. 4 lamps, respectively (see Table II), under the assumption that the quenching of metastable states by electrons is negligible*, the values of τ_e of 6^3P states for these lamps are estimated to be 1×10^{-4}, 4×10^{-5} and 1×10^{-5} s in reference to the value 4×10^{-5} s for the lamp with argon of 3 mmHg. Moreover, the mean intervals T_c between successive collisions of atoms of each mercury metastable atoms with argon atoms are estimated to be about 4×10^{-7}, 3.3×10^{-8} and 1×10^{-8} s respectively, in reference to the value 1×10^{-7} s for the lamp with argon of 1 mmHg. Consequently, the ratios τ_e/T_c giving the efficiency of the quenching by argon are estimated to be 2.5×10^2, 1.2×10^3 and 1×10^3 for the GEC, No. 7 and No. 4 lamps respectively. Then the good agreement of these values for No. 7 and No. 4 lamps would justify the preceding assumption at least for the lamp with argon more than 3 mmHg. The small value of the ratio for the GEC lamp with argon of 0.25 mmHg seems to show that the quenching by electrons is comparable to the one by argon atoms and the ratio of the former to the latter about 3:1. Moreover the fact that the value of p for the No. 3 lamp with neon is twice that of the No. 4 lamp with argon of the same pressure (see Table I) seems to be attributed to the difference in the cross-section of collisions, namely the ratio of atomic radii of neon and argon is about 1:1.4 and then the ratio of cross-sections, 1:2.

4.3. *The Cd^{114} lines*

As shown in Fig. 13, the observed values of p's for the λ5086, 4800, 4678 lines depend on the lamp temperature and their ratio is 10 : 7.5 : 5.5 at 300°C and 10 : 8 : 6 at the temperature where p's are saturated. As is expected, the observed p of λ4800 is smaller than that of λ5086, but larger than that of λ4678.

Unfortunately, no detailed information exists of the electron temperature in Cd lamp

---

* The quenching by mercury atoms is always negligible because of the low vapour pressure at room temperature (about 2 μHg).

Table V. Data of the triplet lines of Cd.

V_e; excitation potential for lower states, g; statistical weight,
n_B; Boltzmann population with $kT_e=1$ eV,
p; degree of self-absorption evaluated in § 3.

λ (Å)	V_e (eV)	g	relative value of $g\nu^3$	n_B (cm^{-3}) 250°C	n_B (cm^{-3}) 300°C	relative value of p
5086	3.92	5	100	16.5×10^{12}	15.1×10^{13}	100
4800	3.78	3	71	11.4	10.4	75∼80
4678	3.71	1	26	4.1	3.7	55∼60

and the values of the decay time of the triplet states of Cd. However, there are at least the following fundamental differences between the triplet states of Hg and Cd: i) The mean life of the 5^3P_1 state of Cd is 2.5×10^{-6} s and about 20 times longer than that of Hg. ii) The difference in energy between the 5^3P_1 and 5^3P_0 states of Cd is only 0.07 eV, comparable value to the relative kinetic energy of the gas molecules at the temperature of 300°C. Then the atoms in 5^3P_0 state may be easily brought to the 5^3P_1 state by collision. Therefore it is expected that the values of the effective life of the triplet states of Cd may be larger than that of Hg, and that the difference in effective life between the 5^3P_1 and 5^3P_0 states may be smaller than that of Hg.

Assuming that kT_e was 1 eV to make the comparison easy to the case of Hg lamp, the Boltzmann populations of these states were calculated and shown in Table V. Provided that the degree of self-absorption is nearly proportional to the product of n_B and τ_e in the same manner as the Hg lamp, the self-absorption of λ4678 is likely to be smaller than that of λ4800. If it is true, a similar fact should be expected for the triplet lines of Zn which also has two valence electrons and the energy separations smaller than that of Cd. Indeed, a measurement of self-absorption of Zn shows that the self-absorption of λ4680 is the smallest among the triplet lines: λ4810 ($4^3P_2-5^3S_1$), λ4722 ($4^3P_1-5^3S_1$), and λ4680 ($4^3P_0-5^3S_1$), which are emitted by a similar electrodeless lamp of Zn at 500°C, and thus the above mentioned fact is confirmed experimentally.

4.4. *Summary*

The investigation of the self-absorption which was made clear in the present paper as the important secondary effect to cause the broadening of spectral line can be summarized as follows.

1) The line shape of self-absorbed line was formulated assuming that the distribution of the emitting atoms in the light source from the center to the outside is by various functions; linear, zero order Bessell's and parabolic functions, and that the distribution of the absorbing atoms was thoroughly uniform. For comparison, the same treatment was given for the two special models which had already been presented by several authors. Appling these results to the quantitative treatment of line of the Doppler or Lorentz distribution, the relation between the variation of the line shape and the degree of self-absorption indicated by p was made clear. The increase of line width δ_p/δ_0 for the unreversed line and the ratio of the central minimum to the side maximum $I(0)/I_{\max}$ for the reversed line were obtained and plotted in curves against p. Moreover, the line shape and intensity for the off-centered light were also obtained. Through these discussions, it was proved that the simple models in which the emitting atoms decrease linearly from the center to the outside were satisfactory to explain the general views of self-absorbed line.

2) Using a direct recording Fabry-Perot interferometer, the shapes of the visible triplet lines emitted by Hg^{198} and Cd^{114} electrodeless lamp were observed without being disturbed by the hyperfine structure of isotopes. From these observations the effect of self-absorption of these lines was made clear, and was shown to agree well with the results theoretically obtained. From the measurements of the radial variation of the line intensity and the line shape, the following

results were obtained: Hg^{198} and Cd^{114} lamps can be approximately represented by the model in which the density of emitting atoms decrease linearly from the maximum at the center to zero at the wall, and the Osram type Cd lamp excited by D.C., by the model of uniform excitation at a part near the anode. Then the values of the parameter p's were evaluated by the use of the relations of p to δ and $I(0)/I_{\max}$ for these lines for various conditions of the lamp temperature, the nature and pressure of carrier gas. These values can be explained consistently, taking the population and decay time of the triplet states and the quenching due to collisions of them with carrier gas and electrons into consideration.

Acknowledgement

The author wishes to express his sincere thanks to Professors M. Kiuti, Z. Koana, M. Hirata, H. Hasunuma, K. Ishiguro and G. Kuwabara of University of Tokyo, and R. Yoneda of Kogakuin University for their continual encouragements and valuable discussions. Sincere thanks are also due to Mrs. M. Ohi of our laboratory for her helpful cooperation.

References

1) H. C. Burger und P. H. van Cittert: Z. Phys. **51** (1928) 638.
2) R. D. Cowan and G. H. Dieke: Rev. Mod. Phys. **20** (1948) 418.
3) T. Tako, I. Miyasato and I. Kono: Rep. C.I. I.W.M. **6** (1957) 489, (in Japanese).
4) T. Tako and I. Kono: Rep. C.I.I.W.M. **7** (1958) 10.
5) T. Tako: to be published.
6) N. G. Preobrazhenski: Opt. Spectr. **6** (1959) 74.
7) W. Schottky: Phys. Zeit. **25** (1924) 342, **25** (1924) 635.
8) J. S. Townsend: Phil. Mag. **11** (1931) 1112.
9) K. G. Emeleus and J. A. Burns: Brit. J. App. Phys. **5** (1954) 277.
10) G. D. Yarnold and S. Holmes: Phil. Mag. **22** (1936) 988.
11) T. Tako: Rep. C.I.I.W.M. **10** (1961) 14.
12) H. C. Burger und P. H. van Cittert: Z. Phys. **44** (1927) 58.
13) W. F. Meggers and T. O. Westfall: J. Rev. N.B.S. **44** (1950) 447; W. F. Meggers and K. G. Kessler: J. Opt. Soc. Amer. **40** (1950) 737.
14) T. Tako: J. App. Phys. Jap. **28** (1959) 527, (in Japanese).
15) T. Tako: Rep. C.I.I.W.M. **10** (1961) 20.
16) T. Tako: Rep. C.I.I.W.M. **8**-4 (1960) 44.
17) E. Gaviola: Phil. Mag. **6** (1928) 1154, **6** (1928) 1167.
18) C. Kenty: J. App. Phys. **21** (1950) 1309.
19) M. A. Easley: see Ref. 18.
20) W. Verweij: Physica **25** (1959) 980.
21) K. Panevkin: Papers of Acad. of Sci. USSR **59** (1948) 683. see Ref. 18.
22) A. C. G. Mitchell and M. W. Zemansky: *Resonance Radiation and excited Atoms* (Cambridge 1934) 147.
23) T. Holstein: Phys. Rev. **72** (1947) 1212.

JOURNAL OF THE PHYSICAL SOCIETY OF JAPAN, Vol. 16, No. 10, OCTOBER, 1961

Structure and Properties of A-Centers in KCl

By Kazuko KOJIMA, Noriko NISHIMAKI
Department of Physics, Osaka Women's University, Tezukayama, Osaka
and Tadanobu KOJIMA
Research Institute for Atomic Energy, Osaka City University
Minami-Ogimachi, Osaka

(Received June 15, 1961)

In additively colored KCl crystals containing sodium, irradiation in the *F*-band causes its complete conversion in two absorption bands which are termed A_1 and A_2. By investigating their thermal, photochemical, and dichroic properties, these two bands are found to arise from a common species of centers called *A*-centers, and are identified with Petroff's *A*- and *B*-bands which have been found in nominally pure specimens. From the analysis of dichroic spectra, peak energy and half-width are determined for each band at several temperatures. The observed oscillator strength is 0.90 for the A_1-band and 0.81 for the A_2-band. The *A*-centers are destroyed thermally with an activation energy 0.43 eV. A model is proposed for the *A*-center that it consists of an *F*-center having a sodium ion as a nearest neighbor to the vacancy. A calculation of energy levels by the method of molecular orbitals is presented.

§ 1. Introduction

The *A*- and *B*-bands, which were first discovered by Petroff[1], appear in the vicinity of the *F*-band when an additively colored KCl crystal is irradiated with *F*-light at near room temperature. Since his discovery, these bands have not been studied seriously for a long time, and attention has been directed rather to the other absorption bands such as *M* or *R*, which appear subsequently during irradiation in the *F*-band. Only recently, study of the *A*-band has been revived by Lüty[2], Ohkura and his collaborators[3),4], Hirai[5], and Tomiki[6]. Especially, Lüty found that *A*-centers which are responsible for the *A*-band have ⟨100⟩-type symmetry, and proposed a model that the *A*-center may be an associated vacancy-pair of opposite sign which has captured an electron. On the basis of this model, it is hardly expected that an *A*-center could capture another electron, or could be stable at temperatures higher than room temperature, because its ionization energy is estimated by the method of Pincherle[7] to be of the order of 0.1 eV. Experimentally, however, as described in the preceding papers[8),9], the *A*-center appears to be able to capture another electron to become an *A′*-center and, moreover, the *A*-band does not disappear in the dark with an appreciable rate unless it is heated to temperatures above 60°C. These facts suggest that Lüty's model is not appropriate and so an alternative model must be sought.

In reference 9), it was concluded from experiments that both the *A*- and *B*-bands arise from a common absorption center, and are associated with Na^+ ions which happened to occur in specimens employed for the experiments. In view of these findings, a new model for the *A*-center has been proposed that it consists of an *F*-center which has a Na^+ ion as a nearest neighbor of the constituent vacancy, as illustrated in Fig. 1. It would therefore be more appropriate to call alternatively the *A*-band as the A_1-band and the *B*-band as the A_2-band; this terminology will be followed throughout this paper.

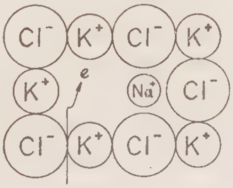

Fig. 1. Model of an *A*-center. The ionic radii are drawn approximately to scale, but the distortion of the ions around the vacancy is not included.

In the present paper, experiments on thermal and optical properties of A-centers which were previously reported only briefly are described in more detail, and a calculation of energy levels is also presented.

§ 2. Experimental Procedure

Experiments were made on nominally pure crystals as well as on crystals doped with sodium. Single crystals of nominally pure KCl were grown from reagent grade KCl by the Kyropoulos method using an unglazed crucible. Single crystals doped with sodium were made by adding 1 molar percent of reagent grade NaCl to the KCl melt. Both kinds of crystals were colored by heating in potassium vapor at about 550°C for approximately 2 hours. Subsequently, they were reheated to 500°C for several seconds and quenched rapidly on a copper plate. This last procedure was necessary in order to remove a small amount of M-centers which had been introduced during the additive coloration. All crystals which had been received the above treatments showed about the same absorption spectrum and still exhibited a trace of the A_1-band besides the ordinary F-band. The initial concentration of F-centers was about $1.5\times10^{17}\,\mathrm{cm}^{-3}$ in every specimen, with the exception of one which is referred to in § 3 (5).

Absorption measurements were carried out with a Hitachi EPU-2 spectrophotometer. Monochromatic light needed for bleaching experiment was obtained also by the use of the spectrophotometer, and the spectral bandwidth of the light was kept to about 10 mμ throughout this work. Crystal temperatures were measured with a copper-constantan thermocouple which was soldered to a copper plate holding the specimen in a Dewar flask.

§ 3. Optical and Thermal Properties

1) *Growth of the A_1-band*

The A_1-band develops fairly rapidly when an additively colored KCl is irradiated with F-light at appropriate temperatures. Within the range between −30°C and 25°C, the initial growth-rate is nearly independent of temperature, as has been shown in Fig. 1 in reference 8). The most favorable temperature to produce A-centers was found to be about −30°C, where the A_1-band grows with irradiation and eventually reaches a saturation value. At higher temperatures, the A_1-band once emerged decays again and simultaneously the M-band appears with continued irradiation. At lower temperatures such as −70°C, the appearance of the A_1-band can not be clearly seen owing to the rapid growth of the F'-band, but it is almost certain that A-centers are created at least as an intermediate product since the the A'-band develops with prolonged irradiation with F-light as described later.

2) *Photochemical reactions*

A sample, in which A-centers had been produced to their saturated concentration at −30°C, was irradiated again with 530 mμ-light at room temperature. The result was that absorption intensity near the peak of the F-band increased along with the M-band and absorption in the outside spectral regions decreased, as shown by curves (b) and (c) in Fig. 2. Subsequent irradiation in the M-band, after it had been fully developed by F-light, caused not only a bleaching of it as usual, but also a continued decrease of the A_1-band [Fig. 2(d)]. However, the M-band as well as the A_1-band did not completely disappear by this procedure.

The crystal which had been subjected to the above treatments was again irradiated

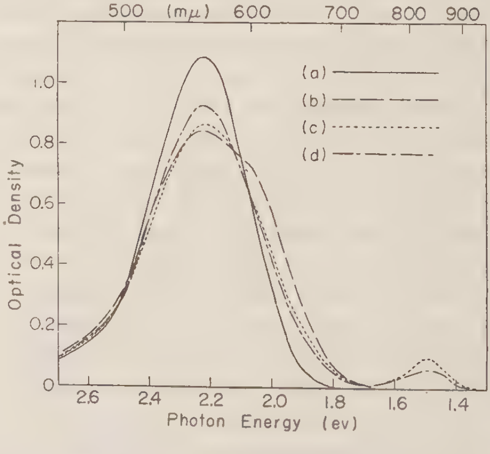

Fig. 2. A sequence of absorption spectra showing the F-band and the A_1-band in their various equilibrium conditions (absorption measured at +20C). (a) initial, (b) after 40 min. irradiation with λ=520 mμ at −30°, (c) after additional 5 min. irradiation with λ=530 mμ at +20°C, (d) after additional 30 min. irradiation with λ=830 mμ at +20°C.

with 530 mμ-light at −30°C. The A_1-band was then found to increase with the same growth-rate as in a virgin specimen; Fig. 3 illustrates a typical example of this recovery. Also with a specimen corresponding to Fig. 2(*c*) or a specimen in which *A*-centers had been destroyed by heating to a high temperature, the A_1-band developed again with the same growth-rate as before by reirradiation with 530 mμ-light at −30C. These facts imply that constituent units of *A*-centers may be distributed in a crystal in the same fashion before and after they have been subjected to the above-mentioned photochemical or thermochemical processes.

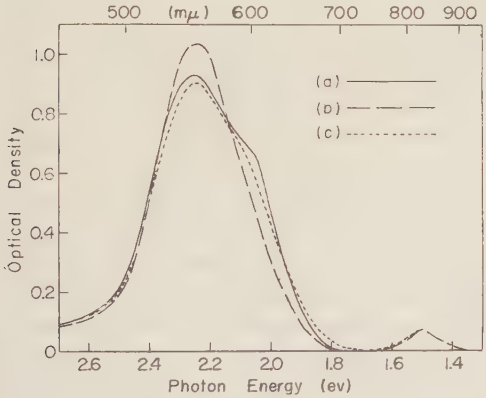

Fig. 3. Absorption spectra showing temperature dependence of the A_1-band in its saturated intensity (absorption measured at −70°C). (*a*) initial [the same as Fig. 2(*b*)], (*b*) after 5 min. irradiation with $\lambda=530$ mμ and subsequent 30 min. irradiation with $\lambda=830$ mμ at +20°C [the same as Fig. 2(*d*)], (*c*) after additional 20 min. irradiation with $\lambda=520$ mμ at −30°C.

3) *Thermal stability*

A-centers are thermally much less stable than *M*-centers; most of them are converted into *F*-centers in a period of about 1 hour by heating to 50°C in the dark. The thermal bleaching of the A_1-band was studied as a function of time at several temperatures. In this experiment, *A*-centers were produced at −30°C as before, the absorption intensity at 640 mμ was measured and the contribution of the *F*-band was estimated and subtracted. Some results are shown in Fig. 4. It is noticed that the bleaching of the A_1-band obeys the exponential decay law, and hence the density of *A*-centers may be written as

$$N=N_0\exp(-t/\tau)\,, \qquad (1)$$

τ being the mean lifetime for the destruction of *A*-centers. We shall assume the from as usual

$$\frac{1}{\tau}=\frac{1}{\tau_\infty}\exp(-E/kT)\,, \qquad (2)$$

where *E* is the activation energy for the destruction. By use of Eq. (1) and the bleach-

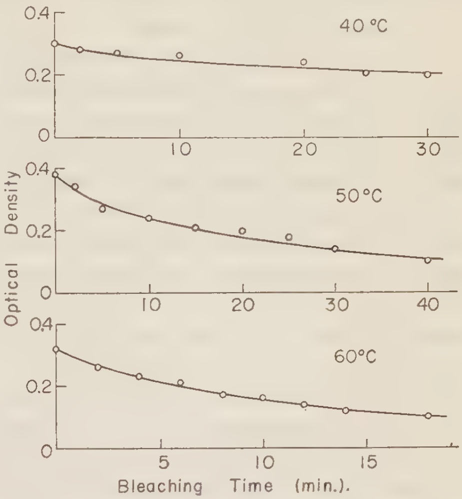

Fig. 4. Thermal bleaching of the A_1-band with time in the dark at various temperatures. The vertical scale expresses optical density at the peak wavelength of the A_1-band, corrected by subtracting the contribution of the overlapping *F*-band.

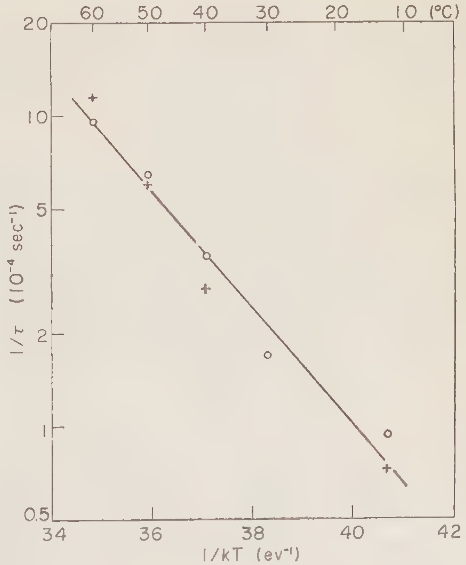

Fig. 5. Temperature variation of lifetime for the thermal bleaching of the A_1-band. +—obtained from Fig. 4 and other similar data; ○—obtained from the decay of dichroism (see § 3 (6)).

ing curves as given in Fig. 4, we obtain the reciprocal lifetime $1/\tau$ as a function of $1/kT$. This is shown in Fig. 5, which gives us by Eq. (2) an approximate value

$$E=0.43 \text{ eV} .$$

In Fig. 5, the reciprocal lifetime for the decay of dichroism, that will be explained in § 3(6), is also plotted together.

4) *Formation of the A′-band*

At the early stage of irradiation with F-light at −70°C the F'-band appears at the expense of the F-band. However, prolonged irradiation gives rise to another broad band, which has been called the A'-band[8], to the longer wavelength side of the F-band. The emergence of the new band may be discerned with changes in the absorption spectrum, particularly with a drop of the absorption beyond 800 mμ as illustrated by Fig. 2 in reference 8).

It was found that the A'-band possesses the following properties: (1) With a specimen containing A-centers in large quantities, irradiation with A_1-light at any temperature between −50°C and −130°C causes a rapid growth of the A'-band and a simultaneous decrease of the A_1-band as shown in Fig. 6.

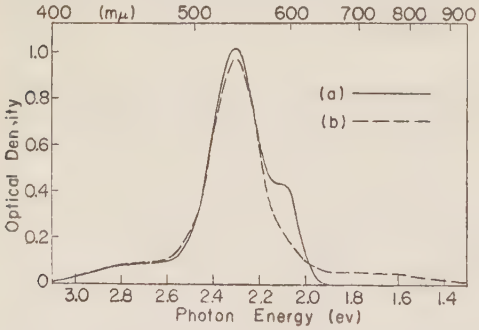

Fig. 6. Formation of the A'-band by irradiating with 620 mμ-light (absorption measured at −180°C). (*a*) before irradiation (F- and A-centers alone), (*b*) after 10 min. irradiation at −90°C (F- and A'-centers produced).

(2) The A'-band is slightly narrower than the F'-band; it does not absorb light of wavelength beyond 950 mμ, whereas the F'-band extends further into the infrared. This can be seen most distinctly on a doped specimen where substantially no F-centers and hence no F'-centers are involved [Fig. 7(*c*)]. (3) During warming up to room temperature, the A'-band disappears accompanying recovery of the A_1-band, most rapidly in the neighborhood of −40°C. (4) At −50°C the half lifetime of A'-centers is approximately 500 seconds, so that it is about 10 times longer than that of F'-centers. In view of these observations, it appears quite plausible to assume that an A'-center consists of an A-center which has captured another electron.

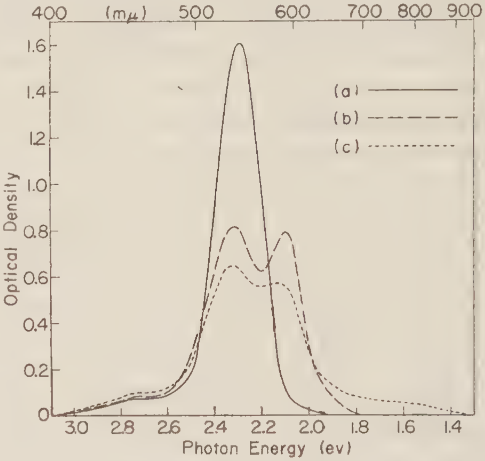

Fig. 7. Photochemical convesion in a doped crystal (absorption measured at −180°C). (*a*) initial, (*b*) after 40 min. irradiation with 520 mμ-light at −30°C (F-centers changed completely into A-centers), (*c*) after additional 10 min. irradiation with 620 mμ-light at −125°C (A'-centers were produced).

It is to be noted here that the lowest temperature at which the A'-band can be developed by A_1-light to an extent of observable intensity is about −135°C, which is somewhat higher than −150°C, the corresponding temperature for the F'-band.

5) *Properties of doped crystals*

In the case of specimens doped with sodium, the absorption spectrum changed by irradiating with 520 mμ-light at −30°C, as shown in Fig. 7. This new spectrum was identified with the A-bands, because it exhibited all the properties characteristic of the A-bands, such as thermal stability, dichroic properties, and optical conversion into the A'-band below −40°C [Fig. 7(*c*)]. The spectrum after the conversion may be resolved into constituent bands as shown by broken lines in Fig. 8a, using the shape of the A_1- and A_2-bands which is determined in § 3 (6). Fig. 8b represents the corresponding spectra for an undoped specimen. It is noticed that virtually all *F*-centers were transformed into *A*-centers in the doped specimen, while a part of *F*-centers remained unchanged in the undoped specimen. In the case of undoped crystals, however, complete conversion was also observed in a lightly colored specimen containing only about 2×10^{16} *F*-centers/cm^3.

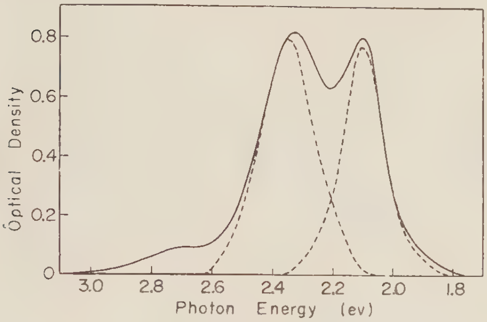

a. Doped crystal

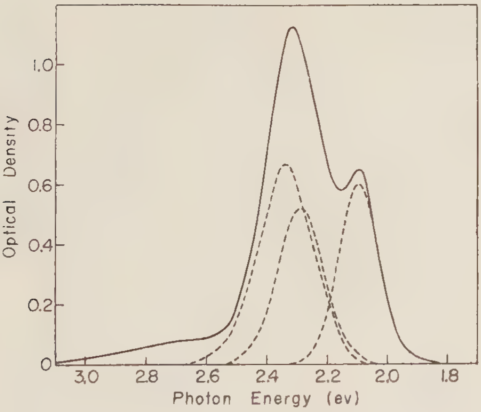

b. Undoped crystal

Fig. 8. Resolution of absorption curves (absorption measured at −180°C). *A*-centers were produced by irradiating with 520 mμ-light for 40 min. at −30°C.

Table I. Ratio of the changes in absorption intensity for the *A*-bands and the *F*-band due to the optical transformation.

Crystal	Treatment	Temperature	$\Delta A/\Delta F$
1	Na-doped	− 70°C	1.026
2	Na-doped	+ 10°C	1.013
3	Na-doped	−180°C	0.953
4	Undoped	−180°C	0.959
5	Undoped	− 70°C	1.012
	Mean		0.993

Changes of the area under the absorption curves due to the formation of *A*-centers were measured on five samples including two undoped specimens. The results are listed in Table I, where ΔA denotes the increase in the area of the *A*-bands and ΔF the decrease in that of the *F*-band. The mean value for $\Delta A/\Delta F$ is 0.993, so that the area under absorption curves may be considered as practically conserved during the transformation.

6) *Dichroic properties*

a) Preliminary considerations

Before describing experimental results on the dichroism, it will be more expedient to consider some theoretical aspects of the problem. We assume that the A_1-band is caused by an electric dipole transition with its optical dipole moment parallel to the symmetry axis of each *A*-center, and the A_2-band is caused by a similar transition with its optical dipole perpendicular to the symmetry axis of each center. Let the number of *A*-centers per unit volume be *N*, and suppose that among these centers *xN*, *yN*, and *zN* are oriented parallel to the [100], [010], and [001] directions respectively. Then, writing the intensity of the A_1- and A_2-bands as I_1 and I_2, and taking [001] as the direction of observation, we can easily show that

$$\begin{aligned} I_1 &= (x+y)Cf_1N\,, \\ I_2 &= (x+y+2z)Cf_2N\,, \end{aligned} \tag{3}$$

where f_1 and f_2 represent the oscillator strengths and, according to Smakula's formula, *C* is a constant given by

$$C = \frac{(n^2+2)^2}{n}\frac{\pi e^2 h}{9mc}\,, \tag{4}$$

with the refractive index *n*. Likewise, expressing the absorption intensity measured with [100]- or [010]-polarized light by attaching the suffix *x* or *y* to I_1 and I_2, we get

$$\begin{aligned} I_{1x} &= xCf_1N\,, \\ I_{2x} &= (y+z)Cf_2N\,, \end{aligned} \tag{5}$$

and

$$\begin{aligned} I_{1y} &= yCf_1N\,, \\ I_{2y} &= (x+z)Cf_2N\,. \end{aligned} \tag{6}$$

Although f_1 may be a little different from f_2, we assume for the present that they are both equal to a common value *f* for the sake of simplicity.

Let us now consider the case where a crystal containing only *A*-centers has been

Table II. Distribution of A-centers and intensity of A-bands after exposed to various types of light. Absorption intensities are given in units of CfN.

Irradiation	Final distribution of centers			Absorption intensity measured with					
				Unpolarized light		[100]-light		[010]-light	
	x	y	z	I_2	I_1	I_2	I_1	I_2	I_1
Unpolarized A_1	0	0	1	0	0	1	0	1	0
Unpolarized A_2	0.4	0.4	0.2	0.6	0.4	0.6	0.4	0.6	0.4
[100]-A_1	0	0.6	0.4	0.7	0.3	1	0	0.4	0.6
[100]-A_2	1	0	0	0.5	0.5	0	1	1	0

irradiated with unpolarized light absorbed in the A_2-band but not in the A_1-band. In this case, assuming that an A-center excited with A_2-light can change its orientation in any of the three directions with an equal probability, we can easily show that the distribution of A-centers will eventually reach a ratio $x:y:z=2:2:1$, and hence, by Eq. (3), the ratio of the intensity for the two bands will become $I_1:I_2=2:3$. Table II summarizes final distributions and the corresponding absorption strengths to be expected when measured with polarized or unpolarized light after being irradiated with light as indicated in the first column. In the case of irradiation with A_1-light polarized along [100], the final distribution expected depends on the initial one; numerical values for [100]-A_1 in Table II are referred to the initial distribution $x:y:z=2:2:1$.

When an absorption band whose optical dipole is oriented along the ⟨100⟩ directions has been irradiated with [110]-polarized light, the absorption spectrum will exhibit no dichroism, but when it has been irradiated with [100]-polarized light, dichroism will be observed so long as measuring light contains some component of electric vector along the [100] direction. This situation is displayed in Table III along with the cases of ⟨110⟩- and ⟨111⟩-type symmetry. In this Table, the plus

Table III. Dichroism to be produced by bleaching with polarized light. $+$means that dichroism occurs and $-$means that dichroism does not occur.

Direction of optical dipole	Dichroism measured with [100]- and [100]-light after bleached with light polarized along		Dichroism measured with [110]- and [110]-light after bleached with light polarized along	
	[100]	[110]	[100]	[110]
⟨100⟩	+	−	−	−
⟨110⟩	+	−	−	+
⟨111⟩	−	−	−	+

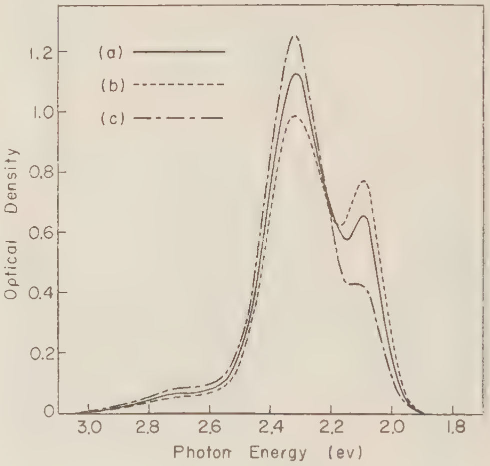

a. Undoped crystal

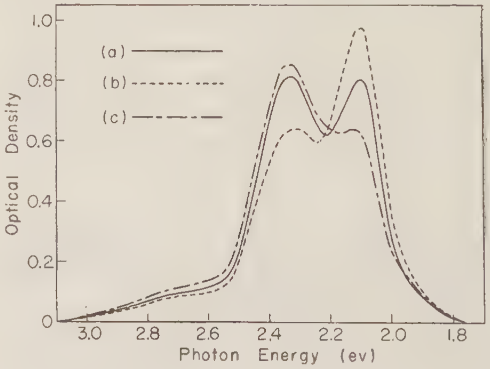

b. Doped crystal

Fig. 9. Dichroism produced by irradiating with 520 mμ-light polarized along [100] at −30°C (absorption measured at −180°C). (a) before irradiation, (b) measured with [010]-polarized light after irradiation, (c) measured with [100]-polarized light after irradiation.

sign denotes that dichroism is expected to occur and the minus sign denotes otherwise, when measured with light polarized along the direction as indicated and with light polarized perpendicular to it.

b) Experimental results

Fig. 9 shows absorption spectra measured at −180°C with unpolarized light and with polarized light. In Fig. 9a, curve (*a*) was obtained immediately after the conversion of *F*-centers to *A*-centers by irradiating with unpolarized 520 mμ-light at −30°C. Curve (*b*) and curve (*c*) were measured with polarized light along [010] and along [100] respectively, after irradiated with 520 mμ-light polarized along [100] at −30°C. No dichroism was found to occur when measured with [110]- and [1$\bar{1}$0]-polarized light. In order to confirm the ⟨100⟩-type symmetry found by Lüty, irradiation was made with A_2-light polarized along [110]. The result was that dichroism appears neither in the [110] direction nor in the [100] direction. Therefore, as Table III shows, this demonstrates that the *A*-center possesses ⟨100⟩-type symmetry.

Fig. 9b presents the result for a crystal containing substantially no *F*-centers. Dichroism was produced by irradiating with 520 mμ-light polarized along [100] at −30°C and measurement was made at −180°C. The area under curve (*a*) in Fig. 9b can be divided into the A_1- and A_2-bands with a ratio of about 2 to 3. According to Table II, this corresponds to the distribution $x=y=0.4$ and $z=0.2$, so that the ideal situation mentioned there appears to be approximately realized. On the other hand, the distribution associated with curves (*b*) and (*c*) is estimated by the use of Eqs. (5) and (6) to be $x=0.5$, $y=0.33$, and $z=0.17$, which means that 17 percent of the *A*-centers have changed their orientation as a result of irradiation with [100]-light. At temperatures near −180°C, irradiation with the polarized A_2-light yielded a dichroism analogous to that shown in Fig. 9a, however, with a much slower rate of appearance.

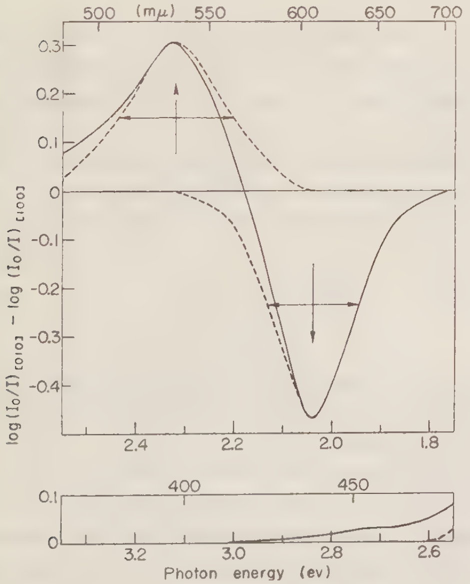

Fig. 10. Dichroic difference spectrum for *A*-centers at −70°C. Broken lines represent separate contributions from the A_1-band and the A_2-band.

Fig. 10 gives a dichroic difference spectrum which is obtained by taking the difference between two absorption curves measured with [100]- and [010]-polarized light. Broken lines represent separate contributions from the A_1- and A_2-bands, each of which has been assumed to have a symmetrical band shape. The small area remaining at the shorter wavelength tail may be attributed to transitions to higher excited states. It is clearly seen that the two regions bordered by the abscissa and the dichroic difference curve have approximately equal area. Furthermore, the shape of the curve was always the same at a given temperature in all specimens on which measurements were made. These two facts may be considered as the most strongest evidence that the A_1- and A_2-bands arise from common absorption centers. The peak location and half-width of these bands measured at three temperatures are listed in Table IV, along with those for the *F*-band obtained by Konitzer and Markham[10].

The data given in Fig. 10, as combined with other data, enable us to estimate the oscillator strengths of the A_1- and A_2-bands. As men-

Table IV. Peak positions and half-widths of the A_1- and A_2-bands measured at various temperatures (in eV).

Temperature	A_1-band		A_2-band		*F*-band	
	Peak	Width	Peak	Width	Peak	Width
+ 10°C	2.01	0.23	2.30	0.30	2.23	0.34
− 70°C	2.04	0.18	2.32	0.24	2.21	0.28
−180°C	2.09	0.15	2.35	0.20	2.30	0.20

tioned before, the integrated absorption intensity of the *F*-band is very nearly equal to that of the *A*-bands in case of the complete optical transformation. Since the integrated absorption of the *F*-band is given by $Cf_F N$, we are led to, according to Eq. (3),

$$\tfrac{1}{2}[(x+y)f_1+(x+y+2z)f_2]/f_F \doteq 1 . \qquad (7)$$

On the other hand, comparing the two areas bordered by broken curves in Fig. 10, we get approximately

$$f_1 : f_2 = 1 : 0.9 . \qquad (8)$$

Putting then $x=y=0.4$, and $z=0.2$ in Eq. (7), and assuming that $f_F=0.85$[11], we finally obtain

$$f_1=0.90 \quad \text{and} \quad f_2=0.81 .$$

Although Hirai[5], and later Ohkura and Awane[3] have obtained values of 0.73 and 0.50, respectively, for the oscillator strength of the A_1-band, their procedures are unsatisfactory because they did not take any account of effects of the symmetry and hence of the orientational distribution of *A*-centers, and moreover, at those times they were unaware of the possibility that both the A_1- and A_2-bands arise from a common absorption center.

The dichroism was found to decay exponentially with time. The lifetime of the dichroism measured at several temperatures has been plotted in Fig. 5. It is noticed that the lifetime of the dichroism agrees with that of the thermal bleaching within experimental errors.

§ 4. Theory of Energy Levels

Although accurate calculation of energy levels of an *A*-center based on the model proposed here would be considerably difficult, the following simple argument will serve for understanding the manner in which the energy levels and hence absorption peaks shift from those of an *F*-center.

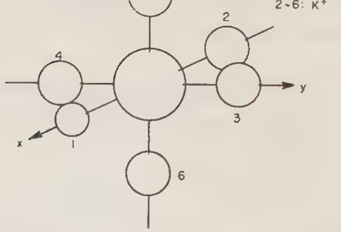

Fig. 11. A diagram showing coordinates for the *A*-center. The anion vacancy is represented by a large circle, and its neighboring cations by numbered small circles. The *z*-axis is taken along the direction of irradiation.

We shall label the six cations surrounding a negative ion vacancy comprising the *A*-center as illustrated in Fig. 11, and take a set of coordinate axes as indicated therein. For the present we shall confine ourselves to the case of an *F*-center, which may be obtained by replacing the sodium ion labeled as 1 with a potassium ion. Then the Hamiltonian H_0 for a trapped electron of the *F*-center may be written as

$$H_0=T+\sum_k U_k , \qquad T=-\frac{\hbar^2}{2m}\nabla^2 , \qquad (9)$$

where U_k stands for the Coulomb potential arising from the ion *k*, and may be understood to include the exchange interaction with the trapped electron. The sum should be taken over all ions comprising the crystal. Let us now approximate the ground state wave function Φ_s of the trapped electron by a linear combination of atomic orbitals φ_i, each localized on the six labeled cations:

$$\Phi_s=\sum_{i=1}^{6} \varphi_i/(6+24S)^{1/2} . \qquad (10)$$

Here, φ_i may be represented by a mixture of the 4*s* and the 4*p* functions for a free potassium atom:

$$\varphi_i=as_i+(1-a^2)^{1/2}p_i , \qquad (11)$$

where the direction of p_i is so chosen that its positive lobe points the origin of the coordinate axes. In Eq. (10), *S* is the overlap integrals over neighboring φ_i's, and other smaller overlap integrals are neglected. The wave functions for the triply degenerate excited states may be likewise approximated by

$$\Phi_x=(\varphi_1-\varphi_2)/2^{1/2} , \qquad (12)$$

$$\Phi_y=(\varphi_3-\varphi_4)/2^{1/2} , \qquad (13)$$

$$\Phi_z=(\varphi_5-\varphi_6)/2^{1/2} , \qquad (14)$$

where φ_i is assumed to have the same form as Eq. (11). Actually, it would be better to use a somewhat different value of *a* for the excited states, but we shall neglect this difference here for the purpose of simplicity.

In the case of the *A*-center, the Hamiltonian should be replaced by

$$H=T+V_1+\sum_k{}' U_k , \qquad (15)$$

where V_1 is the potential due to the sodium ion located at the site 1, and the prime attached to the summation means that the sum is taken over all ions except the ion 1. The ground state wave function corresponding to Eq. (10) may be approximately taken as

$$\Psi_s=(\phi_1+\sum_{i=2}^{6}\varphi_i)/(6+24S)^{1/2} \qquad \subset\Sigma\,. \tag{16}$$

Here ϕ_1 is a function consisting of the $3s$ and $3p$ functions for a free sodium atom combined in the form of Eq. (11) with the same coefficient a, and the overlap integral S is also assumed to be unaltered by replacing φ_1 with ϕ_1. For the excited states, the wave function corresponding to Eq. (12) may be written as

$$\Psi_x=(\phi_1-\varphi_2)/2^{1/2} \qquad \subset\Sigma^*\,, \tag{17}$$

and the other two functions remain unchanged in the present approximation:

$$\Psi_y=\Phi_y \qquad \subset\Pi\,, \tag{18}$$

$$\Psi_z=\Phi_z \qquad \subset\Pi\,. \tag{19}$$

The increase in the ground state energy resulting from replacement with a sodium ion at the site 1 will then be given by

$$\Delta E_s=\langle\Psi_s|H|\Psi_s\rangle-\langle\Phi_s|H_0|\Phi_s\rangle\,. \tag{20}$$

By substituting Eqs. (15) and (16), the first term of the right hand side in Eq. (20) is rewritten as

$$\begin{aligned}\langle\Psi_s|H|\Psi_s\rangle=[&\langle\phi_1|T+V_1|\phi_1\rangle+\langle\phi_1|\Sigma'U_k|\phi_1\rangle\\ &+\sum_i{}'\langle\phi_1|H_0|\varphi_i\rangle+\sum_i{}'\langle\varphi_i|H_0|\phi_1\rangle\\ &+2\sum_i{}'\langle\phi_1|V_1-U_1|\varphi_i\rangle+\sum_{ij}{}'\langle\varphi_i|H_0|\varphi_j\rangle\\ &+\sum_{ij}{}'\langle\varphi_i|V_1-U_1|\varphi_j\rangle]/(6+24S)\,.\end{aligned} \tag{21}$$

The first term in the bracket is equal to the negative of the ionization energy I for the orbital ϕ_1:

$$\langle\phi_1|T+V_1|\phi_1\rangle=-I\,. \tag{22}$$

The next three terms may be replaced approximately as

$$\langle\phi_1|\Sigma'U_k|\phi_1\rangle\approx\langle\varphi_1|\Sigma'U_k|\varphi_1\rangle\,, \tag{23}$$

$$\langle\phi_1|H_0|\varphi_i\rangle\approx\langle\varphi_1|H_0|\varphi_i\rangle\,, \qquad (i\neq1)\,, \tag{24}$$

$$\langle\varphi_i|H_0|\phi_1\rangle\approx\langle\varphi_i|H_0|\varphi_1\rangle\,, \qquad (i\neq1)\,. \tag{25}$$

As V_1-U_1 becomes a large value only in the neighborhood of the sodium nucleus, we have

$$\langle\phi_1|V_1-U_1|\varphi_i\rangle\approx0\,, \tag{26}$$

$$\langle\varphi_i|V_1-U_1|\varphi_j\rangle\approx0\,. \tag{27}$$

The second term in Eq. (20) is rewritten by virtue of Eqs. (9) and 10,

$$\begin{aligned}\langle\Phi_s|H_0|\Phi_s\rangle=[&\langle\varphi_1|T+U_1|\varphi_1\rangle+\langle\varphi_1|\Sigma'U_k|\varphi_1\rangle\\ &+\sum_{ij}{}'\langle\varphi_i|H_0|\varphi_j\rangle]/(6+24S)\,.\end{aligned} \tag{28}$$

Writing the ionization energy for the orbital φ_1 as I_0, we get

$$\langle\varphi_1|T+U_1|\varphi_1\rangle=-I_0\,. \tag{29}$$

Using these expressions, we arrive finally at a simple expression:

$$\Delta E_s=(I_0-I)/(6+24S)\,. \tag{30}$$

The increase in the excited state energies due to the replacement with a sodium ion:

$$\Delta E_x=\langle\Psi_x|H|\Psi_x\rangle-\langle\Phi_x|H_0|\Phi_x\rangle\,, \tag{31}$$

$$\Delta E_y=\langle\Psi_y|H|\Psi_y\rangle-\langle\Phi_y|H_0|\Phi_y\rangle\,, \tag{32}$$

$$\Delta E_z=\langle\Psi_z|H|\Psi_z\rangle-\langle\Phi_z|H_0|\Phi_z\rangle \tag{33}$$

can also be calculated in a similar fashion. We shall give here only final expressions:

$$\Delta E_x=(I_0-I)/2\,, \tag{34}$$

$$\Delta E_y=\Delta E_z=0\,. \tag{35}$$

Since S is obviously positive, and the ionization energy is larger for sodium than for potassium, *i.e.* $I_0-I<0$, Eq. (30) tells us that the ground state, Σ, of the *A*-center is lower than that of the *F*-center. Eqs. (34) and (35) mean that the excited states of the *F*-center split into a doubly degenerate level Π and a nondegenerate level Σ^*, and that the Σ^* level is lower than the corresponding level of the *F*-center whereas the Π level remains unchanged, by replacing with a sodium ion at the site 1. By taking the difference between Eqs. (30) and (31), we find that the absorption band associated with the transition $\Sigma\rightarrow\Sigma^*$ appears to the longer wavelength side by the amount of

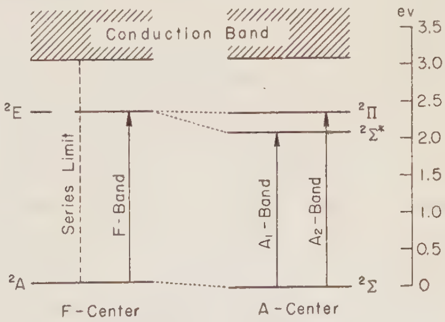

Fig. 12. Level scheme for the *A*-center, as compared with that for the *F*-center. Levels are drawn so that the level differences indicated by arrows coincide with the corresponding observed absorption peaks at −180°C. Series limit for the *F*-center is estimated at 3.0 eV [see reference 12)]. Level shift between the *F*-center and the *A*-center is tentatively fixed by taking account of the calculation in the text.

$$\Delta\varepsilon_1=|I_0-I|\left(\frac{1}{2}-\frac{1}{6+24S}\right). \tag{36}$$

Likewise, the absorption band associated with the transition $\Sigma\to\Pi$ is predicted to appear to the shorter wavelengths by the amount of

$$\Delta\varepsilon_2=|I_0-I|/(6+24S) . \tag{37}$$

Therefore, we may identify the transition $\Sigma\to\Pi^*$ with the A_1-band and the transition $\Sigma\to\Pi$ with the A_2-band [Fig. 12]. By taking the ratio of Eqs. (36) and (37), we obtain

$$\Delta\varepsilon_1/\Delta\varepsilon_2=2+12S , \tag{38}$$

which indicates that the shift of the absorption peaks from the F-band is larger for the A_1-band than for the A_2-band, in agreement with observation.

In order to find the magnitudes of $\Delta\varepsilon_1$ and $\Delta\varepsilon_2$, it is required to estimate the values of S and I_0-I. The value of S may be obtained in the following way. According to Eqs. (10) and (11), the probability density of an F-center electron at a potassium nucleus adjacent to the vacancy is given by

$$\Phi_s{}^2(0)=a^2s_1{}^2(0)/(6+24S) . \tag{39}$$

The corresponding experimental value obtained from electron spin resonance data is equal to 0.70 A^{-3} [12]. The value of $s_1{}^2(0)$ is evaluated to be 7.5 A^{-3} with the use of hfs data on free potassium atoms. On the other hand, the remaining unknown constant a^2 is difficult to estimate; we shall assume as an extreme case $a^2=1$ which corresponds to pure s-character, and as a more reasonable value $a^2=3/4$ which means 25 percent mixing of p-character.

Table V. Values of parameters specifying location of absorption bands.

	S	I_0-I	$\Delta\varepsilon_1/\Delta\varepsilon_2$	$\Delta\varepsilon_1$
$a^2=1$	0.20	−0.80 eV	4.4	0.32 eV
$a^2=3/4$	0.08_5	−0.68 eV	3.0	0.25 eV
Exp			3.1	0.22 eV

Then we get the corresponding values of S and hence of $\Delta\varepsilon_1/\Delta\varepsilon_2$ as displayed in Table V. The value of I_0-I may be obtained from the experimental values of ionization energy for free potassium and sodium atoms. The ionization energies are 4.32 eV (4s electron of normal K atom), 2.71 eV (4p electron of excited K atom), 5.12 eV (3s electron of normal Na atom), and 3.02 eV (3p electron of excited Na atom). Hence I_0 and I are given by

$$I_0=4.32a^2+2.71(1-a^2) , \tag{40}$$

$$I=5.12a^2+3.02(1-a^2) , \tag{41}$$

in the units of eV. By the use of these expressions, we get the values for I_0-I and $\Delta\varepsilon_1$ as shown in Table V. In this Table, experimental values of $\Delta\varepsilon_1/\Delta\varepsilon_2$ and $\Delta\varepsilon_1$ are also included. The agreement between theory and experiment may be considered as satisfactory, especially for the case of $a^2=0.75$. However, such good agreement must not be taken too seriously because we have many simplifying approximations.

§ 5. Discussion

1) The thermal destruction of A-centers may be understood in the following way. Since the ground state of an A-center cannot presumably be higher than that of an F-center, as mentioned in § 4, the probability for the thermal ionization of an A-center will be negligibly small at temperatures in the vicinity of 50°C. Accordingly, the destruction of the A-center at such moderate temperatures must be considered as caused by a motion of the constituent vacancy. The activation energy 0.43 eV for the thermal destruction may then be interpreted as representing an energy required to dissociate the A-center into an F-center and an isolated Na^+ impurity. Although this value is much smaller than the activation energy for migration of a negative ion vacancy, 2.6 eV[14], it would be of some interest that it is very close to the activation energy for colloidal formation due to the aggregation of F-centers, 0.46 eV, obtained by Theisen and Scott[15]. That the activation energy for the disappearance of the dichroism agress with that for the thermal destruction indicates that the disappearance of the dichroism is merely a consequence of the thermal destruction of A-centers. This is contrasted to the case of M-centers where the thermal destruction occurs at much higher temperatures than the thermal disorientation which results in the disappearance of the dichroism.

2) Ohkura and Uchida[4] observed that at −180°C irradiation with 600 mμ-light in a crystal, in which the A- and B-bands have been developed by bleaching the F-band, causes transformation of a part of the A-band into the B-band, and conversely, the resulting B-band goes back again into the A-band by irradiating with 510 mμ-light. Assuming that

there are two different species of centers, called A and B, they have interpreted this phenomenon as a mutual conversion induced by light between the A- and B-centers. On the basis of our model, however, this should be interpreted rather as a consequence of reorientations caused by the irradiation, since virtually no photoelectrons can be produced at such a low temperature, as may be inferred from the fact that the A'-band does not appear under such circumstances. As mentioned in § 3 (6), if we assume that an A-center when raised in excited states has a tendency to change its orientation towards any possible direction, irradiation with A_1-light will cause reorientation of some centers from [100] and [010] to the [001] direction and hence a decrease of the A_1-band and simultaneously an increase of the A_2-band. The reverse process may also be explained in an analogous manner. It is to be noted here that Ohkura and Uchida divided their absorption curves erroneously into constituent bands as the exact location and shape of the A-bands were not known at that time. Table II tells us that the intensity ratio of the A_1-band to the A_2-band does not exceed a value of about 2/3, and Table IV that the ratio of the band-widths is approximately equal to 3/2. As a consequence, we may expect that the absorption coefficient of the A_1-band can never be larger than that of the A_2-band at their peak wavelengths in contrast with Ohkura and Uchida's analysis.

3) Hirai[5] measured the growth-rate of the A_1-band for several samples containing different concentrations of F-centers. With specimens having about the same optical density, he found that the saturated optical density of the A_1-band is nearly a constant value for specimens containing less than 1.3×10^{17} F-centers per cm^3, and is roughly proportional to the F-center concentration for specimens containing higher amounts of F-centers [see, Fig. 4–C and Table I in his paper]. This means that the saturated concentration of A-centers was roughly independent of the initial F-center concentrations in the case of the heavily colored crystals, and both quantities were approximately proportional to each other in the case of the lightly colored crystals. This result may easily be understood if we assume that sodium ions were present as an impurity in a form available to generate A-centers by an amount of approximately 1.3×10^{17} cm^{-3} in his specimens.

4) At present it is difficult to imagine the exact processes which would occur in crystals during irrradiation in the F-band. In the first place, it is not obvious whether sodium ions incorporated in crystals are dispersed at random or they are located preferentially along dislocations. It appears possible that they have a tendency to segregate along dislocations which have at least a component of edge character, forming Cottrell atmospheres, as their ionic radius is smaller than that of potassium ions. Secondly, the fate of Schottky vacancies which have been present at high temperatures is not very clear. During the quenching of specimens, most of the excess vacancies would disappear by being absorbed in existing dislocations or forming new dislocation rings. It might also be possible that some of the negative ion vacancies are trapped by sodium ions and become immobile, since then elastic energy associated with the vacancies will be somewhat reduced. Each of such units, if exists, would immediately become an A-center by capturing an electron moving in the conduction band.

We shall now suggest a possible mechanism for the formation of A-centers. Photoelectrons produced by F-band irradiation at moderate temperatures, say at −30°C, will arrive at dislocations and become trapped after wandering about in the lattice. Then a sort of rearrangement of ions will occur around each electron trapped at dislocations as a result of unbalancing of electrical charge distributions and a number of positive and negative ion vacancies may be created. A negative ion vacancy thus created will move in the vicinity of a sodium ion possibly in the form of a paired vacancy combined with a positive ion vacancy. A unit consisting of a sodium ion and a pair of vacancies of opposite sign will then be temporarily formed. This unit will be able to capture another photoelectron and the positive ion vacancy will soon be expelled from it remaining behind an A-center. The mechanism described above is of course highly speculative and so further investigation will be required in order to settle this problem.

5) The authors would like to make a remark concerning the dichroism of Z_2-centers

found by Ishiguro *et al*[16]. They observed a dichroism to occur in an additively colored crystal containing Z_2-centers when measured with [100]- and [010]-polarized light, after irradiating with 605 mμ-light or 508 mμ-light both polarized along the [100] direction. They attributed this dichroism to Z_2-centers. However, it appears more plausible to assume that the dichroism was caused by A-centers which might happen to occur in their specimen, since their dichroic difference spectra agree quite well with that characteristic of A-centers described in the present paper. If our viewpoint is correct, the dichroism should disappear by warming a similar specimen to temperatures in excess of 60°C. It should be mentioned here that Chiarotti *et al*[17] observed that dichroism does not occur when measured with [100]- and [010]-polarized light in a similarly colored crystal, which has been subjected to partial bleaching with [100]-polarized light absorbed in the Z_2-band. Only difference in experimental conditions between the two works is that Italian workers made the bleaching at −95°C, while the Japanese workers made the irradiation at room temperature. Therefore, it seems likely that in the Italian specimens either there was not an appreciable amount of sodium impurity, or A-centers were not produced owing to the low temperature even if a fairly large amount of sodium was involved.

References

1) St. Petroff: Z. Phys. **127** (1950) 443.
2) F. Lüty: a paper presented at the International Symposium on Color Centers in Alkali Halides, Corvallis, Oregon, September, 1959 (unpublished).
3) H. Ohkura and K. Awane: J. Phys. Soc. Japan **15** (1960) 1349.
4) H. Ohkura and T. Uchida: J. Phys. Soc. Japan **15** (1960) 2114.
5) M. Hirai: J. Phys. Soc. Japan **14** (1959) 1400.
6) T. Tomiki: J. Phys. Soc. Japan **15** (1960) 488.
7) L. Pincherle: Proc. Phys. Soc. **A64** (1951) 648; see also V. L. Vinetskii: J. Exptl. Theoret. Phys. (U.S.S.R.) **33** (1957) 780 [Sov. Phys. JETP **6** (1958) 601].
8) K. Kojima and N. Nishimaki: J. Phys. Soc. Japan **16** (1961) 121.
9) N. Nishimaki, K. Kojima, and T. Kojima: J. Phys. Soc. Japan **16** (1961) 576.
10) J. D. Konitzer and J. J. Markham: J. Chem. Phys. **32** (1960) 843.
11) R. H. Silsbee: Phys. Rev. **103** (1956) 1675; W. T. Doyle: Phys. Rev. **111** (1958) 1072.
12) R. L. Wild and F. C. Brown: Phys. Rev. **121** (1961) 1296.
13) A. F. Kip, C. Kittel, R. A. Levy, and A. M. Portis: Phys. Rev. **91** (1953) 1066; G. Feher: Phys. Rev. **105** (1957) 1122.
14) L. W. Barr, I. M. Hoodless, J. A. Morrison, and R. Rudham: Trans. Faraday Soc. **56** (1960) 697.
15) F. E. Theisen and A. B. Scott: J. Chem. Phys. **20** (1952) 529.
16) M. Ishiguro, E. Sugioka, and N. Takeuchi: J. Phys. Soc. Japan **15** (1960) 1302.
17) G. Chiarotti, F. G. Fumi, and L. Giulotto: "*Defects in Crystalline Solids*" (The Physical Society, London, 1955) 317p.

JOURNAL OF THE PHYSICAL SOCIETY OF JAPAN, Vol. 16, No. 10, OCTOBER, 1961

Microscope Observations of Crystals Appearing in the Process of Cooling Aqueous Solutions of Alcohols

By Kenji YAMAJI

Institute of Low Temperature Science, Hokkaido University, Hokkaido, Japan

(Received April 17, 1960)

The crystals growing from aqueous solutions of alcohols (methanol, ethanol, iso-propanol, *n*-propanol, ethylene glycol, propylene glycol, and glycerol) were photographed with ordinary and movie (16 mm) cameras through a microscope.

The sample was cooled by the use of liquid oxygen (or nitrogen). The temperatures measured by thermocouples were recorded automatically.

Crystal forms were classified into two main groups, *i.e.*, hexagonal crystal and cubic crystal. To the former belong hexagonal fernlike crystals, "soft" hexagonal plates, and "soft" spherical crystals, and to the latter cubic crystals that appear only in ethanol, *n*-propanol, and iso-propanol solutions.

Among the cubic crystals, only the one appearing in iso-propanol solution was found to show double refraction at temperatures below −51°～−52°C. Phase transition does occur in the crystal. The crystal systems below and above the transition temperature are most probably tetragonal and cubic, respectively, as inferred from the analogy of similar phase transition in metals and other substances.

The results of centrifugal precipitation and the similarity in crystal form to snow indicate that the constituent of hexagonal crystals may well be assumed as ice.

What the cubic crystal consists of remains as yet unknown, though the fact that various concentrations and cooling speeds always lead to phase transition at the same temperature gives a positive proof of the definite proportion of constituents (alcohol and water). The growing speed of cubic crystals is much faster than that of hexagonal crystals, which also seems to suggest that the constituents of cubic crystal are the associated molecules of water and alcohol.

§ 1. Introduction

There have been only few reports on soft hexagonal crystals in aqueous solutions of alcohols. Barendrecht[1], as far back as in 1896, found the hexagonal crystal in ethanol solution, though he could not confirm if it was ice or not. Recently B. Luyet[2] conducted studies on the patterns of ice formation in some aqueous solutions in connection with biological liquids, the results of which are in some respects similar to those obtained in the present experiment.

As for the cubic crystals in aqueous solutions of ethanol, *n*-propanol, iso-propanol, allyl alcohol and aldehyde, several papers have been published, but the fact that phase transition takes place in cubic crystals in iso-propanol solution has never been reported.

Apart from aqueous solutions, the subject of cubic ice has recently been dealt with in some papers[3),4),5)]. This problem has very little to do with our present investigation, though Rau's[6] observation of cubic ice below −72°C and Cwilong[7] and Brewer-Palmer's objection stating that the cubic crystals as observed by Rau could not be reproduced without the contamination of alcohols, ether, or acetone are of great interest. Our results support the objection against Rau's work.

The main objects in conducting the present investigation were to observe the crystals developed in aqueous solutions of various kinds of alcohols at various concentrations, to examine the dependence of their forms on cooling speed, to inquire into their structure and composition, to measure the growth velocity, and to study the phase transition of cubic crystal which happened to be found in iso-propanol solution.

§ 2. Experimental Procedures

The alcohols used were: methanol CH_3OH, ethanol C_2H_5OH, iso-propanol $(CH_3)_2CHOH$, *n*-propanol $CH_3CH_2CH_2CH$, ethylene glycol $CH_2(OH)CH_2(OH)$, propylene glycol CH_3CHOH-CH_2OH, and glycerol $C_3H_5(OH)_3$, which are all completely soluble in water. The purified water used whose specific resistance amounted to more than $5\times10^6\Omega$ cm was prepared by the use of ion-exchange resins.

The apparatus devised for the observation is shown diagrammatically in Fig. 1. The sample sealed in the vessel is cooled by liquid oxygen (or nitrogen) through the intervening medium of aqueous solution of ethylene glycol, so as not to produce too great a temperature gradient within the sample.

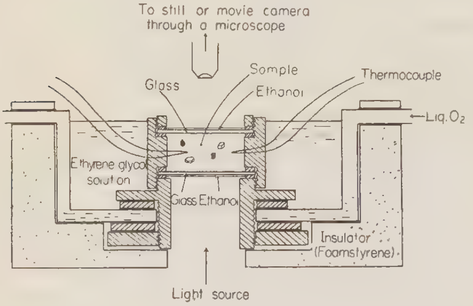

Fig. 1. Experimental apparatus.

The temperatures, measured by means of two 0.08 mm Cu-constantan thermocouples, fixed at two points 0.6 cm and 1.2 cm from the wall of the vessel, were recorded automatically. Temperatures at various distances from the wall can be obtained through extrapolation or interpolation, by assuming concentric distribution and linear gradient of temperature. Cooling speed can easily be determined from the tangent of the recorded temperature curve.

The crystals appearing in the sample were observed under a microscope with polarized or ordinary light and photographed by using 16 mm "Arriflex" movie camera as well as an ordinary camera (Leicasize "Canon").

In order to prevent frosting, the vessel glass was occasionally coated with pure ethanol. When this precedure was intentionally put off for some long time, condensing water diluted the ethanol, which on account of freezing point elevation caused ice crystals to appear on the ethanol solution film. These crystals manifested by themselves some interesting features, as will be discribed later.

§ 3. Results and Discussions

As the result of a series of observations, it was found that crystal forms depend upon the concentration and cooling speed (though in the case of varying cooling speed the dependency comes out not simple, as will be discussed later).

When the concentration of alcohol is relatively low (less than about 35%), crystals appearing on the inside wall of the vessel grow very rapidly towards the center of the vessel and no isolated crystal is segregated in the solution. In this case the growing edge takes fernlike form when the cooling is very slow (1°C/min) (as shown in Photo. 8 (a)), but as the cooling speed increases (5°C/min～10°C/min) fernlike structure becomes less and less evident (Photo. 8 (b)) until the edge reduces to a sharp outline (Photo. 8 (c)) as observed under a low power microscope. When the concentration is increased (up to more than 35% or so), isolated crystals begin to appear not only on the wall but also here and there within the solution. If the cooling speed exceeds 15°C/min, the solution turns out so vitreous (supercooled) that no appreciable crystallization takes place; only, when this vitreous state is maintained for a sufficiently long time a considerable number of crystal germs make their appearence so that

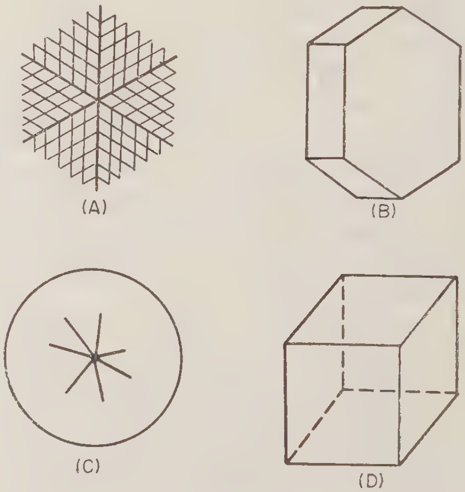

Fig. 2.

the solution becomes cloudy, or, when the temperature is raised again there appear crystals somewhat spherical or hexagonal (Photo. 6). The cooling speed of 10°～15°C/min causes the segregation of spherical crystals which grow radially from the centers (See Fig. 2 (C) and Photo. 7). In the case of slow cooling speed, 5°C/min or so, there grow

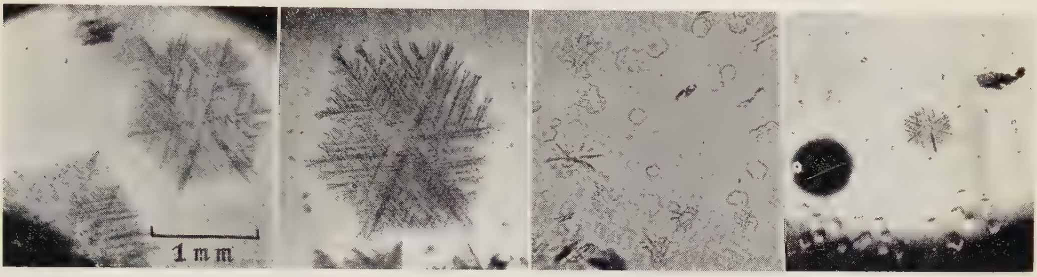

(a) ethylene glycol 50% (b) *n*-propanol 90% −24°C (c) *n*-propanol 90% −22°C (d) iso-propanol 80% −52°C

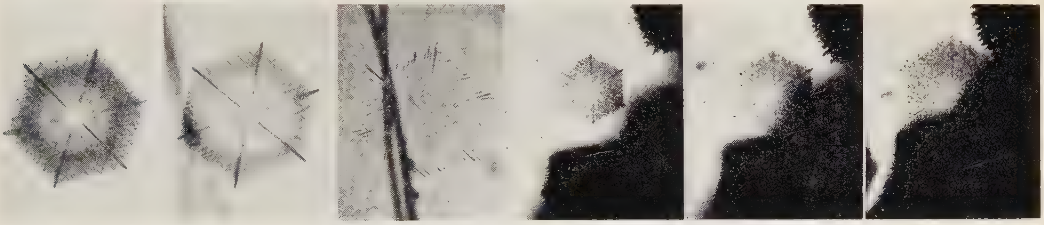

(e) (f) (g) methanol 55% (h) −52°C (i) −51°C (j) −49°C propylene glycol 52%

Photo. 1. Fernlike crystals.

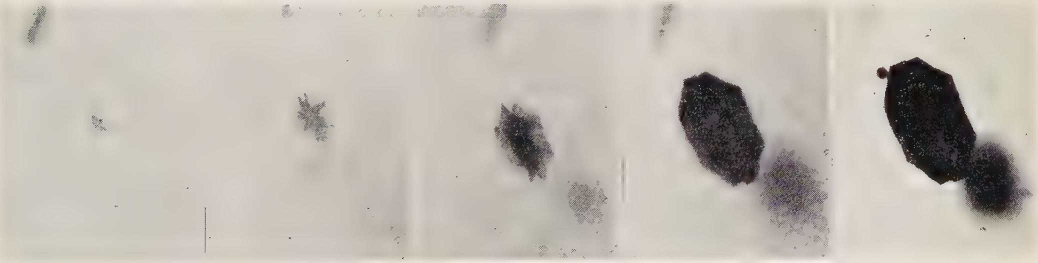

(a) propylene glycol 52% −47°C (b) −50°C (c) −52°C (d) −70°C (e) −88°C

Photo. 2. Fernlike crystal growing to hexagonal plate.

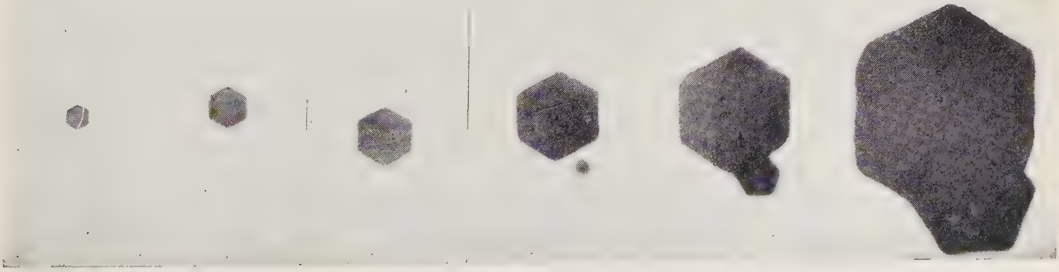

(a) (b) (c) (d) (e) (f)

ethylene glycol 55% −65°C

Photo. 3. Growth of hexagonal plates.

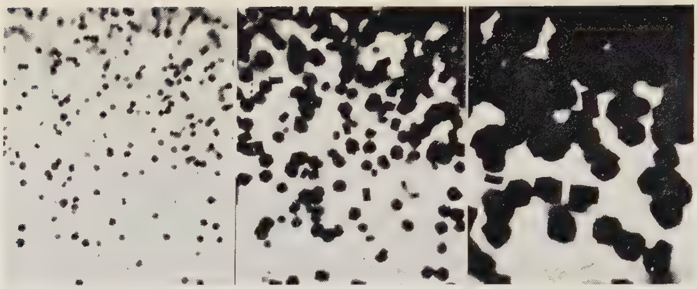

(a) propylene glycol 52% −60°C (b) (c)

Photo. 4. Hexagonal plates for fast cooling speed.

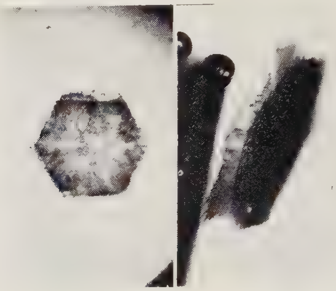

(a) ethanol 55% (b) ethylene glycol 50%

Photo. 5. Several fernlike crystals piled up.

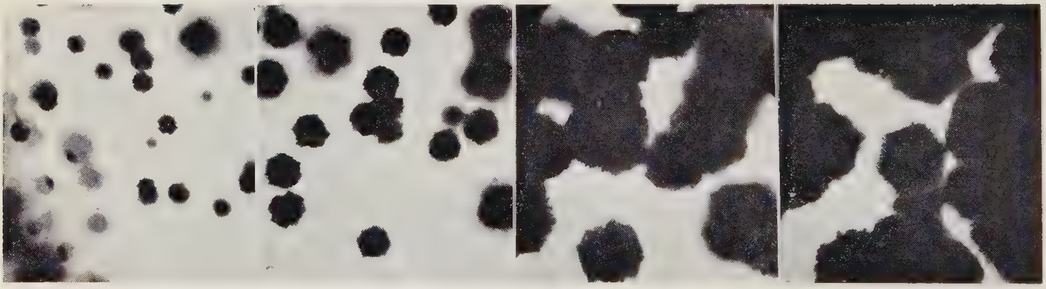

(a) ethylene glycol 55% −75°C (b) −68°C (c) −62°C (d) −60°C

Photo. 6. Crystals appearing in the course of warming up the solutions in vitreous state.

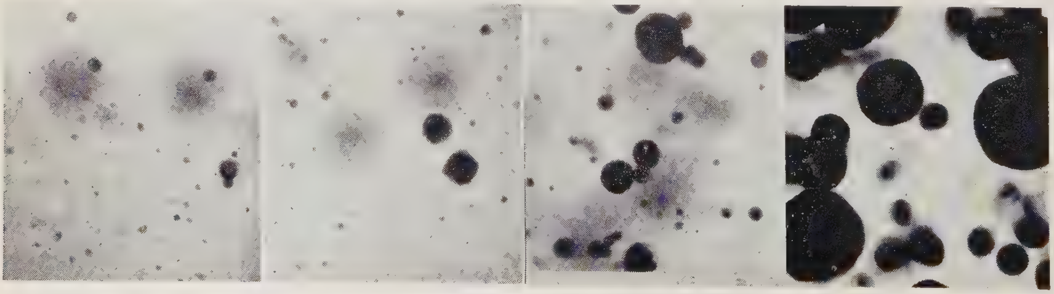

(a) (b) (c) (d)

etylene glycol 50% −90°C

Photo. 7. Spherical crystals.

hexagonal plates (Fig. 2 (B), Photo. 3). Sometimes hexagonal plates grow thin at the center and thick at the outer edges. When the cooling speed is very low, 1°C/min or less, there grow hexagonal fernlike crystals (Fig. 2 (A), Photo. 1) similar to snow crystals.

It is to be noticed that in any of the above-mentioned cases the segregated crystals are mechanically soft, something like ice cream, with delicate fine structures.

The aqueous solutions of ethanol, n-propanal, and iso-propanol have a remarkable feature that cubic crystals appear along with hexagonal crystals (Fig. 2 (D), Photo. 10). The

(a) ethylene glycol 35% cooling speed 3°C/min (b) 6°C/min (c) 12°C/min

Photo. 8. Edges of crystals for various cooling speeds.

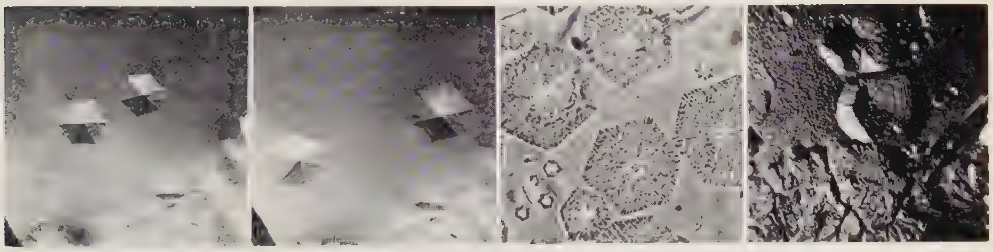

(a) (b) (c) (d)

Photo. 9. Hexagonal crystals appearing on the ethanol film for frost prevention.

(a) ethanol 55% (b) n-propanol 90% −75°C (c) iso-propanol 55% −50°C

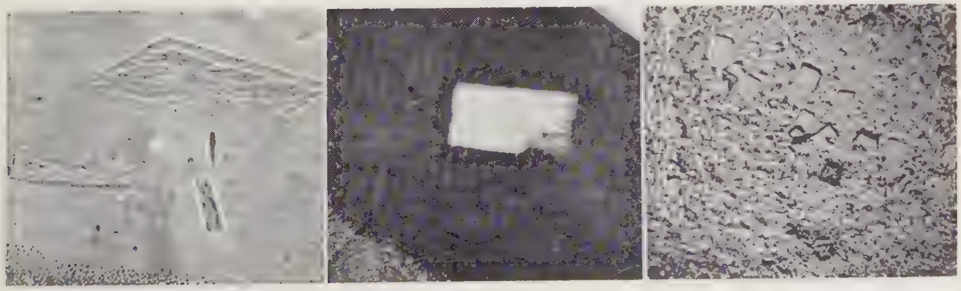

(d) iso-propanol 90% −60°C (e) iso-propanol 90% −60°C (f) iso-propanol −80°C (surface)

Photo. 10. Cubic and tetragonal crystals.

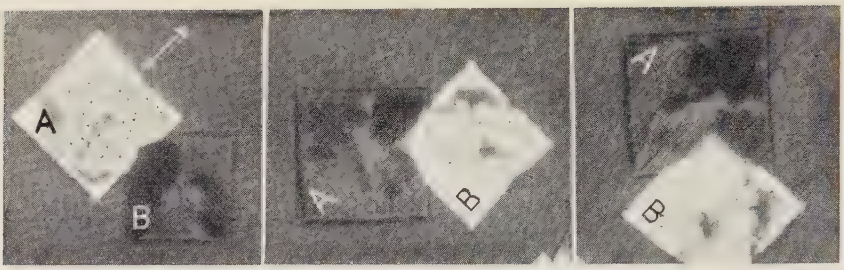

(a) (b) (c)

iso-propanol 55% −60°C

Photo. 11. Tetragonal crystals showing double refraction in iso-propanol solution.

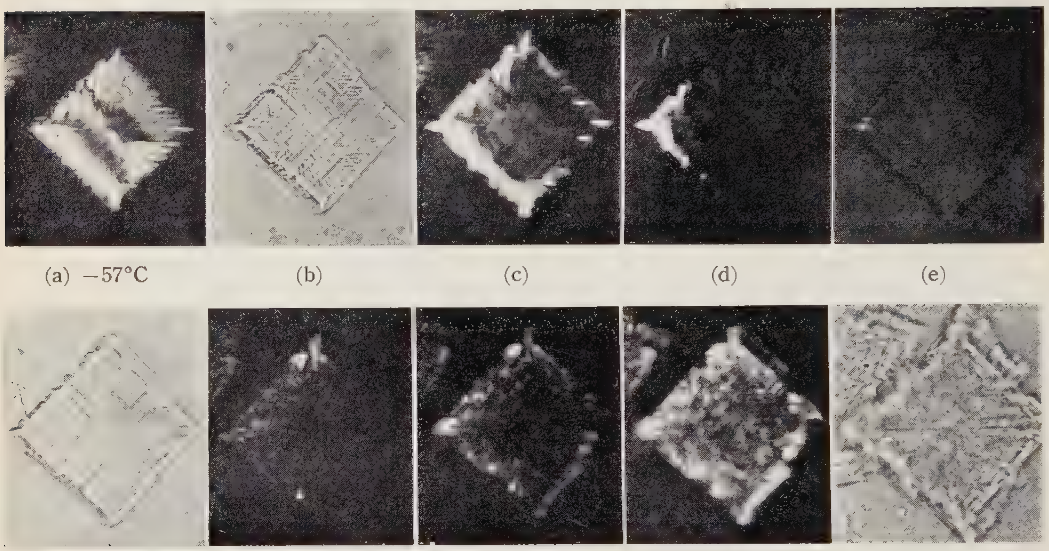

(a) −57°C (b) (c) (d) (e)

(f) −48°C (g) (h) (i) −60°C (j)

Photo. 12. Phase transition of the cubic crystal in 55% iso-propanol solution.

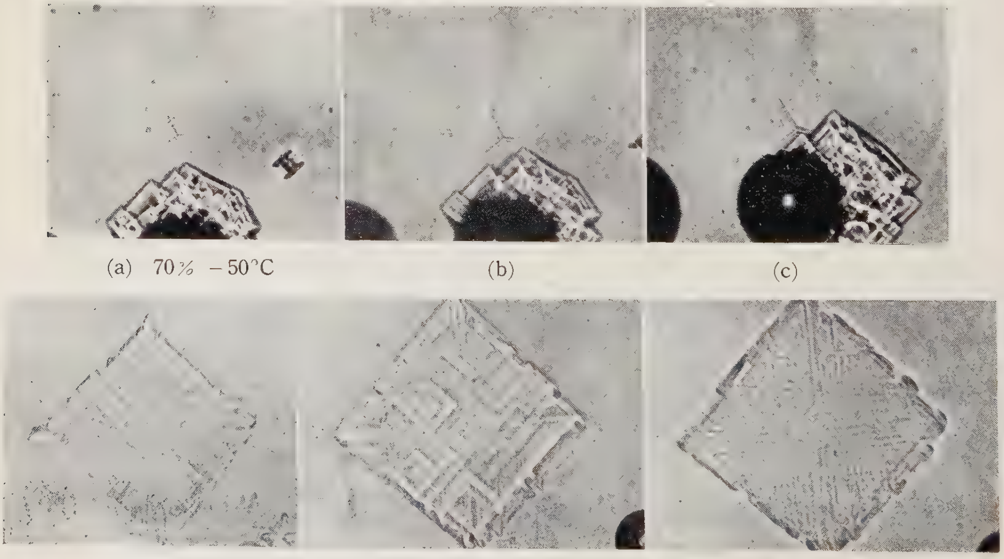

(a) 70% −50°C (b) (c)

(d) 55% −50°C (e) (f)

Photo. 13. Spiral growth of cubic crystal in iso-propanol solution.

cubic crystals in iso-propanol solution is further characterized by the fact that they exhibit a phase transition at a definite temperature.

Details of crystal forms, fine structures, and their behavior will be described in the following, by making reference to Photos. 1～13.

(a) *Fernlike Crystals*

Fernlike crystals are shown in Photo. 1 (a)～(j). It seems that these crystals have three axes, intersecting each other at angles of 60°, and many thin branches starting from each axis grow parallel to the neighboring axes. Subbranches, parallel to the axis, also grow from these branches. If the growth had occurred within one and the same plane, the branches starting from one axis would have interrupted the growth of those intersecting branches which had started from other axes. Actually, however, these branches grow without interruption as far as the periphery of a perfect hexagon, so to say, in concert with one another. The crystal has a textile structure, which is really an unartificial work of art. A fernlike crystals, which happened to be observed in the course of elevation of temperature, are illustrated in (e), (f) and (g). As can be seen from these pictures, the main branches that remain after the subbranches have disappeared mainfest the above-mentioned textile structures. For the sake of contrast, the fernlike crystals in the developing stage are shown in Photos. (h), (i) and (j). These were obtained likewise as the temperature was being elevated. One may ask why the crystals can grow during temperature elevation. The reason* is this: Before the temperature was raised, the solution had been cooled rapidly down to a temperature somewhat below the freezing point, so that the excess water began to form ice crystals which kept on growing until temperature reached the freezing point, that is, until the remaining solution attained the equilibrium concentration. The mode of crystal growth is very similar to the case where the solution is cooled down sufficiently slowly (see Photo. 1 (a), (b)).

A fernlike crystal growing into hexagonal plate is shown in Photo. 2. Propylene glycol solution was first cooled very slowly, when a small fernlike crystal appeared (a). While the cooling was continued, the crystal grew bigger and bigger ((b) and (c)). At this point more liquid oxygen was added to increase the cooling speed, then the fernlike crystal developed into a hexagonal plate ((d) and (e)). (Notice: These crystals are viewed from a direction oblique to the crystal plane.)

(b) *Hexagonal Plates*

In the case of moderate cooling speed (5°～10°C/min), hexagonal plates are formed. Within this range of cooling speed, relatively slower speeds yield big crystals, but small in number (Photo. 3), while faster ones produce a number of small hexagonsl plates (Photo. 4 (a), (b) and (c)).

Hexagonal plates are constructed of several fernlike crystals piled up together. This state of affairs can be seen most clearly in Photo. 5 (a) and (b). (a) is an example of a few fernlike crystals piled up together, whose lateral positions are a bit displaced from one another.

(c) *Spherical Crystals and the Freezing Front*

If the solution is subjected to very fast cooling speed (more than 15°C/min), and cooled down to the temperature far below the melting point, vitreous state is achieved. In this state no crystallization takes place unless it is brought to higher temperatures or is kept at that temperature for a very long time. Phote. 6 illustrates the crystal growth in (55%) ethylene glycol solution first brought to vitreous state and then warmed up. Photo. 7 shows the spherical crystals appearing in ethylene glycol solution, which grew at the cooling speed of 12°C/min.

Photo. 8 shows the front of crystals which grew from the wall of the vessel towards the center of the vessel. The differences in form are due to the variation in cooling speed. Cooling speeds corresponding to (a), (b) and (c) are 3°C/min, 6°C/min and 12°C/min, respectively, which, if isolated crystals had appeared, would have yielded fernlike crystal, hexagonal plate, and spherical crystal, respectively. Here, however, no isolated crystal was segregated owing to low concentration of alcohol.

(d) *Hexagonal Crystals on Ethanol Surface*

In order to prevent frosting on the upper and lower glasses of the vessel, pure ethanol was coated on the glass occasionally. Coating has to be repeated at proper intervals, or else condensation of water vapor lowers the ethanol concentration. When the concentration is lowered, the freezing point is elevated and crystallization takes place on the coated film (Photo. 9 (a) and (b)). These crystals are floating on the film and can change their positions, as can be seen in the photographs. Their size and number increase very rapidly until finally all the surface is covered by ice crystals ((c) and (d)). In (d) very remarkable steps of growing are noticed.

---

* Full discussion will be given later.

(e) *Cubic Crystals and Phase Transition*

In ethanol, *n*-propanol and iso-propanol solutions, cubic crystals grow together with hexagonal crystals.

They are shown in Photo. 10 (a), (b) and (c). The crystals in *n*- and iso-propanol solutions show textile structure with ice "threads" running parallel to the diagonals or edges, while no fine structure can be observed in the case of crystals appearing in ethanol solution. In iso-propanol solution there also appear cubic crystals in plate form, as shown in (d) and (f), the latter being those appearing on the surface of frost-preventing iso-propanol film coated on the glass. The crystals in iso-propanol solution have a further characteristics that at the temperatures above −51°∼−52°C they remain cubic, so that no double refraction can be detected, but below −51°∼−52°C they exhibit double refraction. This phase transition involves the transformation of cubic into (most probably) tetragonal*.

Photo. 10 (e) shows the double refraction observed with crossed polaroids. In Photo. 11 are shown two tetragonal crystals intersecting at 45° interposed between crossed polaroids. In (a) the crystals are located such that crystal A appears with maximum brightness, while crystal B appears dark. The direction of vibration of the incident linearly polarized light is indicated in Photo. (a) by an arrow. If we rotate the crystal by 45° either clockwise or counterclockwise, the crystal A becomes dark while B becomes bright (Photos. (b) and (c)). The brightness alternates between A and B at each 45° rotation. The crystal axes lie obviously in the diagonal directions.

Successive stages of phase transition are illustrated in Photo. 12 (a)∼(j). (a) is the crystal exhibiting the double refraction at −57°C; (b) is the same crystal photographed by ordinary light. When the temperature is gradually elevated, the temperature gradient being positive toward the right, the crystal begins to lose its brightness successively from right to left, as soon as the temperature exceeds −51°∼−52C° ((c), (d) and (e)), until the whole crystal turns out dark. This final stage, as seen with ordinary light, is reproduced in (f), which is similar to (b) and shows that the crystal has undergone no appreciable change in external appearance during phase transition. The process of phase transition is completely reversible, as is evidenced by (g), (h) and (i). (j) is again the same crystal as seen with ordinary light.

Phase transition of cubic crystals occurring at −51°∼−52°C was invariably observed for various concentrations of iso-propanol and for different cooling speeds, which fact leads to the conclusion that the cubic crystal consists of definite proportions of constituents (alcohol and water). For precise determination of constituents and structure, more extensive studies, such as X-ray analysis, the measurement of specific heat, latent heat, dielectric constant, and so forth, will have to be carried out.

(f) *Spiral Growth*

In case the cooling speed is very slow, figures of spiral growth are observed on each of the six planes of the cubic crystal appearing in iso-propanol solution (Photo. 13). So long as the cube is very small, there is only one spiral figure on each plane ((a), (b) and (c)). As it grows bigger, however, spiral figures increase in number on each plane ((d) and (e)). Photos. (e) and (f) show the same growing crystal viewed from the same side; only, in the former the microscope is focused upon the outer surface of the crystal, while in the latter upon the interior surface. Thus we see that the spiral growth takes place at the surface, while the internal texture runs parallel to diagonals or edges. What kind of role such textural structure plays is still open to question.

---

* By the optical method alone, it is impossible to determine the crystal system to which the crystal below the transition temperature belongs. However from the analogous phase transitions frequently observed in metals and other substances, it may well be inferred that the system in question is tetragonal.

When the growing speed is high, layer-by-layer growth was observed visually as well as by means of movie camera.

(g) *Centrifugal Precipitation*

With a view to separating crystals from the solution, use was made of a centrifuge.

Ethylene glycol solution was poured into a glass vessel, in which an inner container whose bottom was made of fine brass-wire net was inserted (Fig. 3 (A)). This then was cooled in a cold box down to the temperature more than 70°C below zero. The frozen sample together with the inner container was removed into a metal vessel (Fig. 3 (B)), set in a centrifuge, and was made to revolve with centrifugal acceleration amounting to 1500*g* for about 5 to 12 minutes. The solution passed through the net and was collected in the metal vessel, while in the inner container there remained solid crystals. Had we put the sample to revolution for too long a time, the whole sample would have melted, since the centrifuge was operated at room temperature. Table I gives the concentration of ethylene glycol of the initial solution and those after centrifugation in the inner container (A) and in the metal vessel (B). It is evident from this table that a large proportion of water has been separated from the solution to the crystal. The less the concentration of the initial solution, the more marked increase in water percentage in the inner container results. Since with increasing concentration the freezing point lowers and hence the solution becomes more and more viscous, longer time is required for the separation of solution, so that the limitation of the separating time by the above-mentioned reason causes the incomplete separation for higher concentrations.

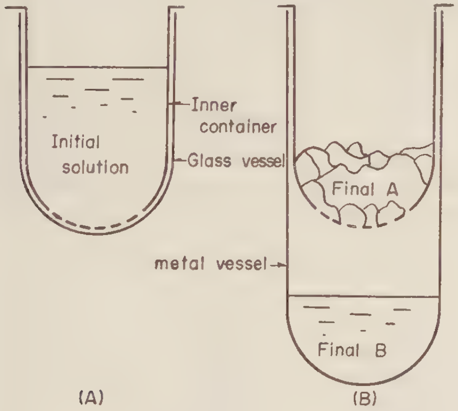

Fig. 3.

Table I. Concentrations of ethylene glycol before and after centrifugal separation.

Initial	Final	
	A	B
50%	39.0%	56.5%
40%	25.0%	51.5%
30%	4.5%	41.5%
20%	3.5%	35.5%

There is now no room for doubt that the hexagonal crystal consists of ice, which can also be inferred from the similarity in crystal form to snow. As for the cubic crystals, no satisfactory separation could be achieved, since they are so brittle that they could not withstand the filtration.

(h) *Growing Speed*

The growing speed of a crystal from a solution depends on the degree of supercooling, diffusion velocity of the molecules, heat conductivity of the medium through which the heat liberated on crystallization flows away, and other factors.

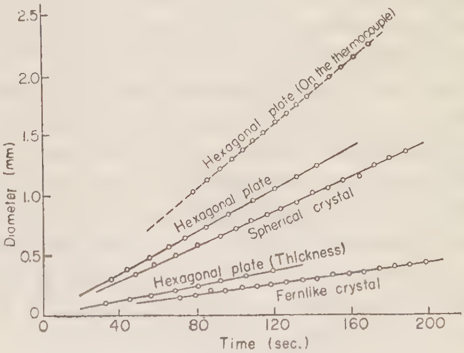

Fig. 4. Rate of growth.

The size of crystals in 50% ethylene glycol solution is plotted against time in Fig. 4. One sees that crystal size increases linearly with time. The growing speed of hexagonal plates is the greatest, next come spherical crystals, and fernlike crystals grow most slowly. Growth in thickness of hexagonal plates has nearly the same speed as fernlike crystals. The crystal forms arranged in the order of decreasing amount of supersaturated water molecules are: spherical, hexagonal, and fern like. The highest growing speed is therefore to be expected for spherical crystal, so long as the degree of supersaturation is concerned. The fact is however contradictory to this expectation. In order to explain this discrepancy, diffusion velocity has to be taken into account. As mentioned before, spherical crystals are produced in the case of high cooling speed. Since, then, the temperature descends so low that the solution becomes highly viscous, slow diffusion of water molecules will result and consequently overcompensate the degree of supersaturation.

In Fig. 4 the broken line represents the growth of a hexagonal plate, which happened to be formed on the tip of the thermocouple. The large growing speed in this case can well be accounted for by assuming that the removal of heat liberated on crystallization was favored by the conduction through the thermocouple wires. Similar effects were observed for crystals growing in the solutions of other alcohols.

The growing speed of cubic crystals proved several times faster than that of hexagonal crystals. This may be interpreted as due to small latent heat of fusion. In view of the theoretical expectation that the cubic crystal transformed from tetragonal system is in a disordered state, *i.e.*, similar in character to the liquid state, smallness of heat of fusion is not an arbitrary assumption. The conclusion mentioned before that the constituent of cubic crystal must be the associated molecule of alcohol and water is also consistent with the rapid growth of cubic crystals, since the segregation of pure ice or alcohol crystal from the solution involves the process of extraction so that only limited supply of crystallizing elements is expected.

(i) *Factors Governing the Crystal Forms*

The freezing curve for aqueous solution of alcohol is, in general, of the form as shown in Fig. 5.

If the solution, whose initial state is represented by P, is cooled, it goes down the path PA, parallel to the temperature axis without changing its concentration, and when the temperature reaches T_A freezing will begin to take place. In most cases, however, crystallization actually occurs somewhat (sometimes far) below the freezing temperature on account of supercooling. Point B in Fig. 5 indicates the supercooled state where the segregation of crystal commences. The freezing path there after can no longer be parallel to the temperature axis but follows various directions depending on the velocity of cooling. If the temperature is kept constant at T_B, the concentration of the solution varies along the path BD until the equilibrium state is achieved at point D where the growth of the crystal ceases. In the case of extremely large cooling speed, the solution reaches the vitrified state following the path BG, without segregating any crystal. For intermediate cooling speeds paths such as BF or BE will be realized.

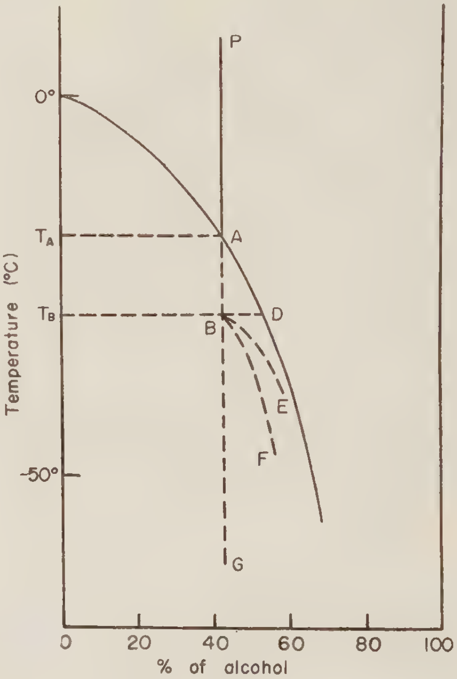

Fig. 5. Freezing curve of aqueous solution of alcohol.

Horizontal distance from a point on the path to the freezing curve is a measure for the amount of supersaturated or supercooled water molecules, which play a role similar to supersaturated water vapor in the growth of snow crystals. In fact, the phenomena which present a close resemblance to the growth of snow crystals were observed. For instance, the crystal shown in Photo. 1 (b) grew under the following conditions. The solution was cooled to −25°C and then the temperature was kept constant. At the earlier stage of growing, there must be sufficient number of supercooled water molecules in the solution for the crystal to grow into a fernlike form. But as the growth of crystal proceeds, the quantity of supercooled water becomes smaller and smaller until the temperature reaches the equilibrium point, at which no supercooled water remains. The crystal form then undergoes a change, namely, a hexagonal plate manifests itself at the extreme edge of each branch. This state of affairs has a striking resemblance to the case of snow crystals which grow to fernlike crystals under high vapor pressure while to hexagonal plates under low vapor pressure.

Thus, the growth of ice crystals from solution may be treated in a way analogous to the growth of snow crystals.

At the beginning of this section it was noticed that in the case of varying cooling speed, crystal forms are not uniquely determined by the concentration and cooling speed only. This situation is now clear, since the degree of supersaturation of water is to be regarded as a predominating factor in determining the crystal form.

Acknowledgement

The author wishes to express his great appreciation to Professor Takeo Hori for continual guidance and suggestions.

References

1) H. P. Barendrecht: Z. Phys. Chem. **20** (1896) 234.
2) B. Luyet and G. Rapatz: Biodynamica **8** (1958) 156.
3) M. Blackman and N. D. Lisgarten: Proc. Roy. Soc. **A, 239** (1957) 93.
4) H. Koenig: Nachr. Akad. Wiss. in Goettingen, Math.-Phys. Kl. **1** (1942) 1.
5) H. Koenig: Z. Kristallogr. **A, 105** (1943) 279.
6) W. Rau: Schrift. deut. Akad. Luft. **8** (1944) 65.
7) B. M. Cwilong: J. Glaciology **1** (1947) 53.
8) A. W. Brewer and H. P. Palmer: Proc. Phys. Soc. **B, 64** (1951) 765.

JOURNAL OF THE PHYSICAL SOCIETY OF JAPAN, Vol. 16, No. 10, OCTOBER, 1961

High Temperature Determination by a New Gas Thermometer with Constant Bulb Temperature.

I. Measuring Methods

By Jiro OISHI

Physics Department, Tokyo Institute of Technology
Oh-Okayama, Meguro-ku, Tokyo

(Received April 19, 1961)

A gas thermometer with constant bulb temperature has been devised to renew determination of Kelvin temperature of the gold point. For the thermometer gas to be of a definite volume, the gas is isolated from the manometer by mercury seal in a capillary U-tube with which device the gas pressure is obtained indirectly by applying due correction to the pressure read on the manometer when the isolation is deleted by lowering the sealing mercury to the bottom of the capillary U-tube. Description of the apparatus and measuring principle are given. This method of determining the gas pressure is applicable to gas thermometer of any other type.

§ 1. Introduction

For the revision of the International Practical Temperature Scale of 1948, temperature determination of defined fixed points, the gold and silver points in particular, is of major importance. The values given to the gold and silver points are based on the historical experiments by A. L. Day et al. about fifty years ago. Urged by the Comité consultatif de thermométrie, C.I.P.M., a few laboratories are now revising the determination on the gold and silver points by gas thermometer. The results on the gold point so far obtained at the Tokyo Institute of Technology in 1956[1] and 1958[2] and at the Physikalisch-Technische Bundesanstalt[3] in 1957 are not consistent with each other; there is a discrepancy of about 1 deg though the accuracy of all these determinations was asserted to be 0.1 deg. To clear the matter, the determination was renewed by using this time a newly installed gas thermometer with constant bulb temperature developed at the Physikalisch-Technische Bundesanstalt.[4] Recently, the Mendeleev Institute of Metrology[5] published results on the gold point, the value of which is close to that of the P.T.B.

In constant volume gas thermometry for high temperature, there are two major sources of error, one is due to gas desorption on the walls of gas thermometer bulb when its temperature is raised to a high temperature to be measured and the other to dead space in the mercury manometer. The former will be greatly reduced by introducing the constant bulb temperature method and the latter by isolating the thermometer gas from the manometer by using a mercury seal in a capillary U-tube as H. Moser[4] devised.

It seems that H. Moser et al.[3] achieved the measurements with the constant bulb temperature gas thermometer, reducing the pressure measurement to volume determination and using their original differential manometer. The content of 21 cm^3 of their thermometer bulb seems however too small, and, for larger bulb, their method of pressure-volume reduction is not easily applicable. Thin diaphragm of beryllium copper or phosphor bronze for example is of use to isolate the thermometer gas from the manometer, but the exact volume of the space necessary for the construction of the diaphragm will be difficult to measure with sufficient accuracy.

With the newly devised gas thermometer, the pressure of the thermometer gas is measured indirectly.

§ 2. Measuring Principle

In the constant bulb temperature method, the thermometer bulb is kept always at the temperature that is to be measured, and the auxiliary bulb, the content of which is made variable, at a reference temperature, the temperature value of which is to be known on the thermodynamic temperature scale.

Schematic diagram of the gas thermometer is shown in Fig. 1. V is a double-walled thermometer bulb, inner volume of which is V_t at temperature t which is to be measured, and v_1 is an auxiliary bulb connected to the thermometer inner bulb, its volume v_1 is made variable with mercury. Volume v_2 of another auxiliary bulb connected to the thermometer outer bulb is made likewise. Capillary U-tube m of very fine bore filled with mercury isolates the gas in inner bulb from that in outer bulb when the head of the mercury is raised the U-tube serving as a differential manometer for rough indication of gas pressures in inner and outer bulbs. The parts v_1, v_2, m and connecting capillaries are kept at a constant reference temperature t_r in a water thermostat W. A mercury manometer M with a standard scale S, is connected to the right hand side of m by a capillary.

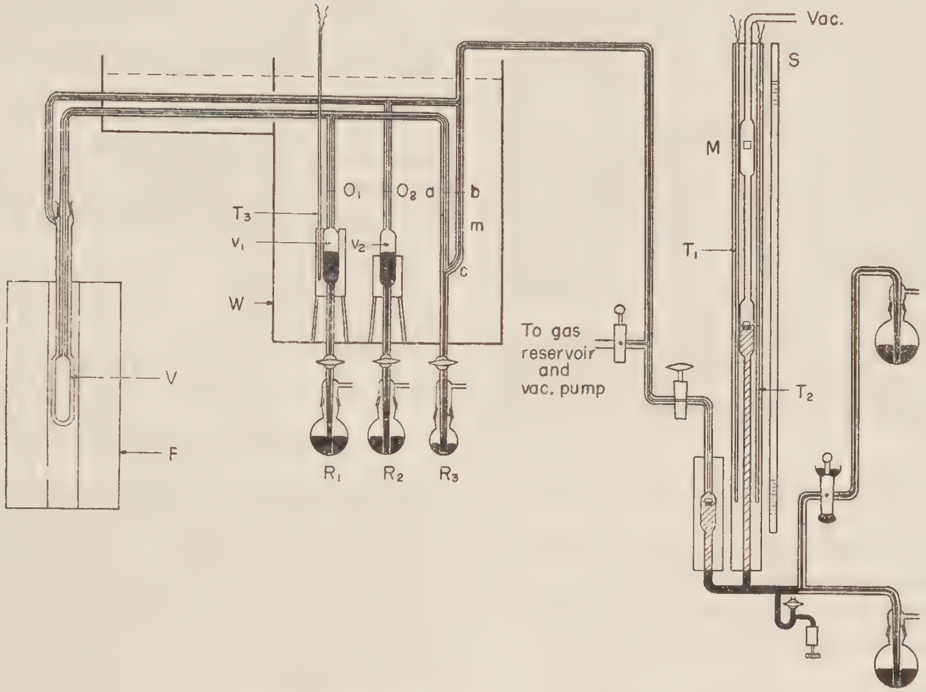

Fig. 1. Schematic diagram of the gas thermometer.

The thermometer gas is introduced into the setting to the pressure of about 1 atm with the heads of mercury at zero levels O_1 and O_2 in bulbs v_1 and v_2 respectively and in U-tube m at level c just under the bend. In this state, called State I-1, $v_1 = v_2 = 0$, and the whole gas in the thermometer is at the same pressure p which is read on the manometer M. The mercury is then raised in m to mark a isolating the gas in the thermometer inner bulb. In this state, called State I-2, the pressure P_1 of the gas in the inner bulb is obtained with a correction on p due to the volume of the capillary between a and c, that is v_{ac}, as

$$P_1 = p\left[1 + \frac{v_{ac}}{V_t}\frac{T}{T_r}\left\{1 - \frac{T}{V_t}\left(\frac{v_r}{T_r} + \sum_n \left(\frac{v_s}{T_s}\right)_n\right)\right\}\right], \tag{1}$$

where T and T_r are Kelvin temperatures of t and t_r respectively, v_s is the volume at temperature t_s of the s-th part of the capillary of the thermometer bulb from the top level of the electric furnance to the side box wall of the water thermostat, and v_r is the rest of the volume of the capillary to the marks O_1 and a in the water thermostat at temperature t_r. With the present setting, this correction will be less than 0.1 %.

Next, the mercury in the bulb v_1 is drawn out into the reservoir R_1 till the pressure of the gas is reduced to about one half of that in State I. The mercury in the bulb v_2 is also drawn out into the reservoir R_2 to bring the mercury heads in m back to their original level a–b. In this state, called State II–1, the volumes v_1 and v_2 at temperature t_r are determined by the increase in weights of respective reservoirs. The pressure p' of the gas in the thermometer outer bulb is then read on the manometer M. The pressure P_2 of the gas in the thermometer inner bulb now becomes close to p'.

The two mercury heads in m are then lowered from a–b to c whereby the gas pressures in inner and outer bulbs become equalized. In this state, called State II–2, the pressure p'' is read on the manometer, and the accurate value of P_2 is now obtained by calculation with due correction.

If we take the unit of volume as $pv=1$ for $p=1$ atm and $T=T_0=273.15$°K, the ice point, the mass conservation equation for real gases is

$$\Sigma\left[\frac{pv}{T}\left(1-B_t\frac{T_0}{T}p\right)\right]=\text{const.}[4]\,, \qquad (2)$$

where B_t is the second virial coefficient of the gas at temperature t.

In State II–1, the gas is in two parts; for the one at pressure P_2 we put

$$\begin{aligned} U\equiv&\frac{V_t}{T}\left(1-B_t\frac{T_0}{T}P_2\right)\\ &+\left(\frac{v_1}{T_r}+\frac{v_r}{T_r}\right)\left(1-B_r\frac{T_0}{T_r}P_2\right)\\ &+\sum_n\left(\frac{v_s}{T_s}\left(1-B_s\frac{T_0}{T_s}P_2\right)\right)_n \end{aligned} \qquad (3)$$

and for the other at pressure p'

$$\begin{aligned} U'\equiv&\frac{V'}{T}\left(1-B_t\frac{T_0}{T}p'\right)\\ &+\left(\frac{v_2}{T_r}+\frac{v_r'}{T_r}\right)\left(1-B_r\frac{T_0}{T_r}p'\right)\\ &+\sum_n\left(\frac{v_s'}{T_s'}\left(1-B_s'\frac{T_0}{T_s'}p'\right)\right)_n\\ &+\frac{v_M}{T_M}\left(1-B_M\frac{T_0}{T_M}p'\right), \end{aligned} \qquad (4)$$

where V' is the volume of the space between the walls of the gas bulb at temperature t, v_s' is the volume of the s-th part of the connecting composite tube to the outer bulb from the top level of the furnace to the side box wall of the water thermostat, v_r' is the total volume of the capillaries in the water thermostat to the marks O_2 and b, and v_M is the volume occupied by the gas outside the water thermostat to the manometer at temperature t_M. Then we have for the whole gas in State II–1 or State II–2

$$P_2U+p'U'=p''\left(U+U'+\frac{v_{a,cb}}{T_r}+\Delta\right), \qquad (5)$$

from which we have the value of P_2 as

$$P_2=p''-(p'-p'')\frac{U'}{U}+p''\frac{v_{acb}/T_r}{U}+p''\frac{\Delta}{U}, \qquad (6)$$

where $v_{a,cb}$ is the volume of the capillary U-tube between the levels a–b and c which is determinable with sufficient accuracy, and Δ is a small quantity which is

$$\begin{aligned} \Delta=&\left(\frac{V_t}{T}\frac{B_t}{T}+\cdots\right)T_0(P_2-p'')\\ &+\left(\frac{V'}{T}\frac{B_t}{T}+\cdots\right)T_0(p'-p'')\\ &-\frac{v_{a,cb}}{T_r}B_r\frac{T_0}{T_r}p''\,. \end{aligned} \qquad (7)$$

Δ is negligibly small for the pressure difference between P_2 and p' or p'', the difference being smaller than 10 mmHg. p'' is about 380mmHg and $p'-p''$ remains within 3 mmHg at the most if the mercury heads at a and b are kept level. The pressure can be determined with an accuracy of 0.01 mmHg by the manometer M. Hence, for obtaining the exact value of P_2 it is sufficient to have the value U' with an accuracy not lower than 1/300, the value of which is not easy to be measured with high accuracy. Strictly speaking, U' is not the same in State II–1 and State II–2, or in rasing and lowering the mercury in the U-capillary, for there may be some difference in shapes of the meniscus of mercury in the lower manometer level, but this uncertainty in U' is less than the said amount of 1/300, even if there were a difference of 0.3 mm in the heights of the meniscus of mercury which is not likely to happen in the present measuring method with the manometer tube of 20 mm in diameter. Hence, the value of the pressure P_2 of the thermometer gas is determined with sufficient accuracy.

For the thermometer gas, the mass of which remains the same in State I–2 and State II–1, we have the relation

$$P_1U_1=P_2U_2\,, \qquad (8)$$

where U_1 is U of Equation (3) in which v_1 and P_2 are replaced with v_{11} and P_1 respectively and U_2 is that in which v_1 is replaced with v_{12}. For practical measurement, it is not essential to keep the mercury head exactly at the level O_1 in the bulb v_1 in State I. Hence, v_{11} and v_{12} are the volumes measured from O_1 in State I and State II respectively.

Neglecting correction terms of the second order in Equation (8), we obtain Kelvin temperature T from the following relation:

$$T=T_r\left(\frac{P_1}{P_2}-1\right)\frac{V_t}{v_{12}+v_r}\frac{A}{B}\,, \tag{9}$$

where

$$A=1-B_t\frac{T_0}{T}(P_1+P_2) \tag{10}$$

and

$$B=1-\frac{P_1}{P_2}\frac{v_{11}+v_r}{v_{12}+v_r}-\left(\frac{P_1}{P_2}-1\right)\frac{T_r}{v_{12}+v_r}$$
$$\times\sum_n\left(\frac{v_s}{T_s}\right)_n-B_r\frac{T_0}{T_r}P_2\,. \tag{11}$$

V_t is determined from the relation

$$V_t=V_0(1+\lambda t)\,, \tag{12}$$

where V_0 is the volume at 0°C and λ is the mean expansion coefficient between 0° and t°, the latter being determined from the mean linear expansion coefficient of a piece of rod of the same material the bulb is made of.

The measuring method described here is also applicable to gas thermometer of any other type.

§ 3. Description of the Apparatus

The double-walled thermometer bulb V is made of silica glass. The inner bulb, 28 mm in inner diameter, 168 mm in length and about 100 cm^3 in volume, is joined to a silica capillary of 0.5 mm bore. The outer bulb, 49 mm in outer diameter and 185 mm in length, has a silica neck tube of 10 mm in diameter and 430 mm in length, encasing the capillary of the inner bulb. The top of this neck tube and the capillary are made into a conical joint by thickening the wall of the capillary. A silica capillary of 1 mm bore is joined to the side of the neck tube at its top. Each of the above two capillaries is fused on to a pyrex capillary of the same bore inside the side box of the water thermostat W extending to the capillary U-tube m of 0.5 mm bore. These two capillaries have each a branch capillary through which the inner and outer bulbs are connected to the auxiliary bulbs v_1 and v_2 of pyrex glass with cylindrical copper casing. All the three parts, v_1, v_2 and m, are placed in the water thermostat W and are provided with mercury reservoirs R_1, R_2 and R_3 respectively.

The mercury manometer M is of U-tube type of 20 mm bore; its available range is 20 mmHg at 1 and 0.5 atm pressures. The whole of the manometer column which is of pyrex glass is encased in a nickel-plated copper cylinder of 45 mm in diameter. The mean temperature of the mercury column is measured with two platinum resistance thermometers T_1 and T_2; their platinum wires are stretched alongside the column from the lower mercury level to the heights of 760 mm for T_1 and 380 mm for T_2. Each thermometer comprises two parallel straight platinum wires fused together at their ends, the thickness of the wires being so chosen that the total resistance becomes about 25 Ω. The platinum wires and their lead wires are sandwitched between two thin and long copper pieces of semi-circular cross section with mica insulation and inserted into the manometer casing through 4 mm hole in its top cover. Construction of other parts of the manometer is similar to that described in a previous paper.[1)]

The electric furnance F, in which the thermometer bulb is heated and kept at temperature t, is the same as used previously by the author,[1)] except for a subsidiary heater which is added around the bulb neck tube at the top end of the furnace to prevent from any temperature gradient along the silica capillary in the furnace being produced.

The water thermostat W is of 50 lit capacity, the temperature of which is kept constant and uniform by pump circulation and with a temperature regulator. The temperature is determined with a standard platinum resistance thermometer T_3 placed inside the casing of v_1.

The gold point determination carried out at the Physikalisch-Technische Bundesanstalt[3)4)] in Germany and at the Mendeleev Institute of Metrology[5)] in U.S.S.R. will be discussed in a succeeding paper.

The author wishes to express his hearty thanks to Dr. H. F. Stimson of the National Bureau of Standards in Washington, Professors H. Moser and J. Otto and Dr. W.

Thomas of the Physikalisch-Technische Bundesanstalt at Braunschweig for their kind discussion on gas thermometry after which he completed the device of the present gas thermometer.

References

1) J. Oishi, M. Awano and T. Mochizuki: J. Phys. Soc. Japan **11** (1956) 311.
2) J. Oishi et M. Awano: Procès-verbaux des séances du comité international des poids et mesures **26-A** (1958) T 75.
3) H. Moser, J. Otto und W. Thomas: Z. Phys. **147** (1957) 76.
4) H. Moser: Temperature, Its Measurement and Control in Science and Industry. Vol. 2, ed. by H. C. Wolfe (Reinhold Pub. Corp., 1955) 103. H. Moser, J. Otto und W. Thomas: Z. Phys. **147** (1957) 59.
5) A. S. Arjanov, A. N. Gordov and U. V. Diikov: Bull. Inst. Metrology **49** (1960) 5 (in Russian). N. V. Arefieva, U. V. Diikov, K. S. Izrailov, I. I. Kirenkov and N. V. Shemetillo: ibid. **49** (1960) 13 (in Russian).

Short Notes

This section is intended to secure prompt publication of important discoveries in physics. The reports should not exceed 800 words in length. A figure of size 7 cm×7 cm will be counted as 150 words.

J. PHYS. SOC. JAPAN **16** (1961) 2061

The Specific Heat of $Ni(NH_3)_6Cl_2$ and $Ni(NH_3)_6Br_2$ at Low Temperatures

By Kazutoshi UKEI and Eizo KANDA

The Research Institute for Iron, Steel and Other Metals, Tohoku University, Sendai, Japan

(Received August 9, 1961)

The anomaly at low temperature in the proton resonance of some nickel salts including $Ni(NH_3)_6Cl_2$ and $NiCl_2 \cdot 6H_2O$ has been observed by Kim and Sugawara[1]. In the case of $NiCl_2 \cdot 6H_2O$, it has been shown that the anomaly is due to the antiferromagnetic ordering[2]. The magnetic susceptibility of $Ni(NH_3)_6Cl_2$ powder becomes nearly constant in the temperature range between 1.2°K and 1.6°K[3),4]. These phenomena may be explained by the spin ordering, though there may be another explanation by the splitting of the lowest spin levels.

The crystal structure of $Ni(NH_3)_6Cl_2$ and $Ni(NH_3)_6Br_2$ is K_2PtCl_6 type[5], and nickel ions each of which is surrounded octahedrally by six NH_3 molecules form a face-centered cubic lattice. The ordering above 1°K in such a spin system, if occurred, is unusual, and the ordering of the face-centered spin system may be interesting theoretically. These facts lent an impetus to our specific heat measurements of these salts between 1.1°K and 4.0°K.

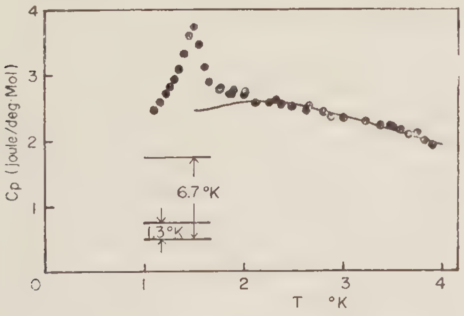

Fig. 1. The molal heat capacity of $Ni(NH_3)_6Cl_2$.

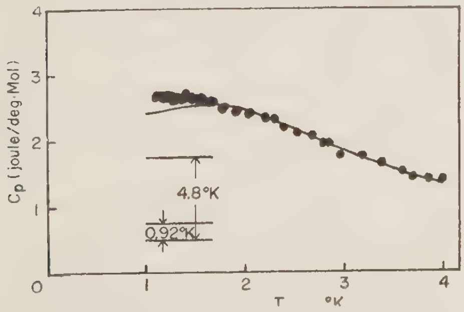

Fig. 2. The molal heat capacity of $Ni(NH_3)_6Br_2$.

The results of measurements are shown in Fig. 1 and Fig. 2. The solid line shows the calculated Schottky specific heat assuming the Stark splitting of the ground state shown in the figure. It has been observed by the electron spin resonance experiments of $Ni(NH_3)_6Cl_2$ at liquid nitrogen temperature that the symmetry of the crystalline field changes at 74°K from the cubic to the lower one as temperature is lowered[6]. This fact together with the color changes of these salts at liquid nitrogen temperature is thought to be the results of the phase change at these temperatures and to be consistent with the deviation of the level scheme from the cubic symmetry as shown in Fig. 1 and Fig. 2. The discrepancy of the values of the level splitting between ours and that given by Watanabe[3] is thought to be due to his little consideration of the spin ordering.

In $Ni(NH_3)_6Cl_2$, the specific heat curve has λ-type anomaly at 1.5°K probably due to the cooperative phenomenon of the spin system. This result is consistent with the recent observation by Poulis that the proton resonance absorption line of a $Ni(NH_3)_6Cl_2$ single crystal splits below 1.5°K[7]. The discrepancy between the observed value and the calculated curve of $Ni(NH_3)_6Br_2$ may be attributable to the short range order of the cooperative phenomenon. The specific heat measurements below 1°K are necessary to ascertain it. The results in detail will be reported in a forthcoming paper.

References

1) P. H. Kim and T. Sugawara: J. Phys. Soc. Japan **13** (1958) 968.
2) T. Haseda, H. Kobayashi and M. Date: J. Phys. Soc. Japan **14** (1959) 1724.
W. K. Robinson and S. A. Friedberg: Phys. Rev. **117** (1960) 402.
3) T. Watanabe: J. Phys. Soc. Japan **16** (1961) 1131.
4) H. Kobayashi and T. Haseda: Private communication.
5) R. W. G. Wyckoff: *Crystal Structure*, vol. 2 (Interscience Pub., N. Y., 1951) chap. 10, p. 34.
6) M. Date: J. Phys. Soc. Japan. to be published.
7) Informed by T. Haseda now in Leiden on leave from Sendai.

J. PHYS. SOC. JAPAN **16** (1961) 2062

The Relaxation Phenomena in Polyelectrolytes Solutions

By Noboru NISHIDA

Premedical Course, Sapporo Medical College

(Received July 27, 1961)

The stability of a lyophylic sol in water is determined by two factors, that is, layer of water molecules and its electric charge. Small amount of the electrolytes have no coagulating effect on a lyophilic sol (c. f. agar sol)1). It is evident that other factor, in addition to the charge, may play a role in determining the stability of the sol. The fact that a lyophylic sol becomes sensitive to electrolytes as well as to alcohol supports the above conception. Alcohol may remove the stabilized layer of water from a lyophylic sol. Polyelectrolyte aqueous solutions also show the same phenomenon.

In order to obtain an information concerning these mechanisms, the dynamic relaxation phenomenon in aqueous solutions of sodium carboxy-methyl cellulose (Na-CMC, the degree of etherification c.a. 0.7) is studied. The 1% Na-CMC aqueous solution is used as an original solution. Ethanol is used as the dehydrating agent and sodium chloride, magnesium chloride as neutralizer of electric charge. Dynamic viscoelasticity of these samples is measured at the frequency of 500 c.p.s., over the temperature range of 0°C–50°C using the electromagnetic transducer method2) with plate vibrator and the alternating current bridge. The results are shown in Figs. 1, 2. Because of both ionization groups and hydroxyl groups of Na-CMC, in the concentrated solution, the ionic interactions between the polyions3) and the solvation effect on the polymer become stronger and may play an important role in the viscoelastic1),4) properties. The characteristic shapes of the relaxation curves for the original solution, in Figs. 1, 2, seem to be expected from the above conception. When ethanol is added to the original solution, one relaxation mechanism, appearing at lower temperature, is not affected essentially, but the other, appearing at higher temperature, seems to disappear gradually with the increase in ethanol amount. This phenomenon seems to be explained as follows; the ethanol affects on the hydration, and decreases the interaction between solute molecules and solvent molecules. The former is affected by NaCl and $MgCl_2$, but the latter is not affected essentially by them. The absorption curves observed in the same time also support the above consideration. The dependency of the magnitude of dynamic modulus on the amount of the NaCl or $MgCl_2$ seems to indicate that this phenomenon depends on the charge of ion. The relaxation mechanism, appearing at lower temperature, seems to be due to mainly the ionic interactions between the ions. From the view-point of the mobility of polymer molecules it does seem rather reasonable to consider that the relaxation mechanisms due to hydration appears at higher temperature, and the phenomenon associated with ionic interactions may appear at lower temperature.

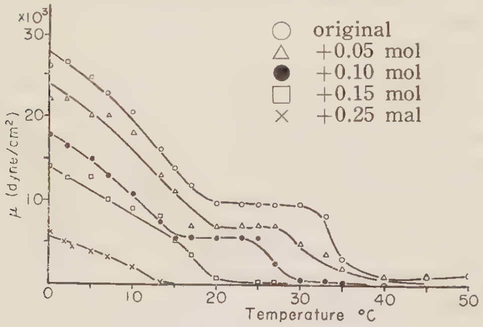

Fig. 1. Dynamic modulus vs. temperature for Na-CMC aqueous solutions of various ethanol additions.

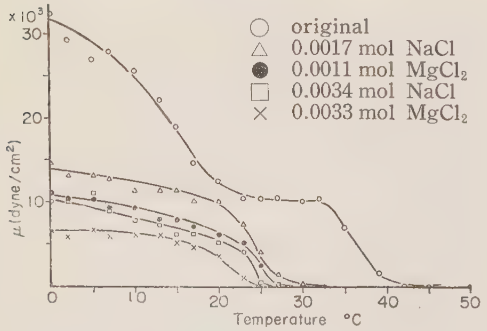

Fig. 2. Dynamic modulus vs. temperature for Na-CMC aqueous solutions of various salts additions.

The auther wishes to express his hearty thanks to Profs. J. Furuichi, M. Kaneko, S. Sugai, Y. Terayama for their continuous advice and encouragement.

References

1) H. R. Kruyt: Kolloid. Z. **30** (1922) 338.
2) E. R. Fitzgerald and J. D. Ferry: J. Colloid Sci. **8** (1953) 1.
3) R. M. Fuoss and R. Signer: J. Amer. Chem. Soc. **73** (1951) 1901.
4) M. Eigen and E. Wicke: J. Phys. Chem. **58** (1954) 702.

J. PHYS. SOC. JAPAN **16** (1961) 2063

Observation of Optical Maser Oscillation in Ruby

By Kanji KUBOTA and Kazuo HAYASHI

Fundamental Research Laboratory, Nippon Electric Company, Kawasaki

(Received July 31, 1961)

Recently, stimulated emission and relaxation oscillations were observed for the fluorescence from the ruby rod whose ends were silvered[1),2)].

This note reports the observation of these phenomena for ruby by using multiple dielectric layers tuned in the wavelength of the fluorescence (6943 Å) as mirrors of the maser cavity.

The samples of Linde Al_2O_3 containing 0.05% Cr_2O_3 were prepared in the form of rods, cut 60° with the *C* axis. The ends were polished flat and parallel, and were deposited with optical thin films. Details of them are given in Table I.

Table I. Figures of the samples.

	sample 1	sample 2
size	4 mm dia. ×40 mm	5.5 mm dia. ×40 mm
parallelism of ends	20 seconds	25 seconds
thin films,		
one end	Ag (5% transmission)	(CeO_2+MgF_2) multiple layers
other end	Ag (no transmission)	$(ZnS+MgF_2)$ multiple layers

At room temperature, the sample was set in the middle of a spiral xenon flash tube made by us, which was surrounded by a cylindrical aluminium-foil as a reflector. One end of the ruby was supported in a cone which allowed emergence only of the fluorescence. The decay of this light was detected through a filter or a grating spectrometer with the photomultiplier on a oscilloscope.

Under low excitation conditions the trace showed an ordinary fluorescence decay of the exponential type (Fig. 1(a)). When the energy discharged through the lamp exceeded a certain value, the trace became of a character entirely different from that observed below the threshold.

These values of input energies were 850 joules (sample 1) and 1020 joules (sample 2). Trace (b) shows the shape for sample 1 at about 900 joules. Break in trace is the maser-output.

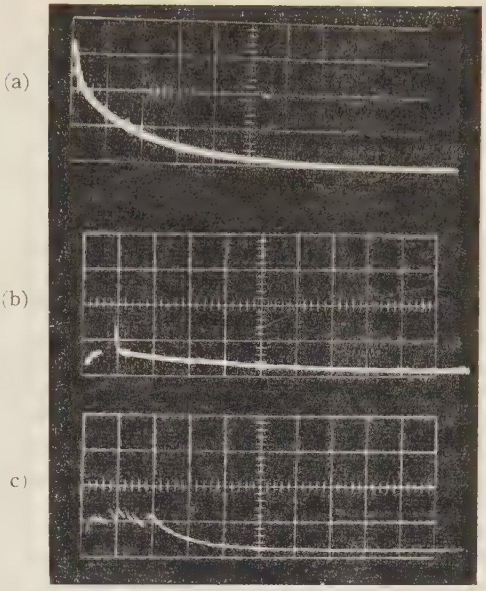

Fig. 1. Fluorescence decay curves at different pump-power levels.
(a) Decay of fluorescence for low excitation level (sample 2)
(time scale 2 milliseconds/div)
(b) Patterns at high excitation level (sample 1)
(time scale 500 microseconds/div)
(c) Stimulated emission region (sample 2)
(time scale 50 microseconds/div)

At this time, a red and intense light beam at 6943 Å suddenly emerged from the end of ruby. This excess signal in the fluorescence consists of a series of short spikes in the emission, called a relaxation-oscillation. Trace (c) shows that of sample 2 at 1090 joules.

After the pulsed light powerfully excited the samples several times, the degeneration of the thin films around the center were observed. As the reflection coefficients decreased, the threshold energies increased to 1200 joules (sample 1) and 1600 joules (sample 2). However, only the (CeO_2+MgF_2) multiple layers were safe. The heat from the lamp or the cavity losses of the maser might cause this damage.

According to the experimental conditions, the threshold energy may be much improved[3)].

Preparing a sample in which the *C* axis lies in the direction of rod and cooling the sample or the lamp will change the efficiency, which are our next plans.

The authors wish to express their thanks to Dr. Y. Ishikawa for his encouragement.

References

1) T. H. Maiman: Nature **187** (1960) 493.
2) R. J. Collins et al.: Phys. Rev. Letters **5** (1960) 303.
3) H. Statz et al.: I. R. E. **49** (1961) 960.

J. PHYS. SOC. JAPAN **16** (1961) 2064

Frequency Dependence of Ferromagnetic Crystalline Anisotropy of $Ni_xFe_{3-x}O_4$

By Seiji USAMI, Nahonori MIYATA and
Zenya FUNATOGAWA

Department of Physics, Yokohama National University, Yokohama

(Received August 3, 1961)

Bozorth *et al*[1] reported previously that the ferromagnetic crystalline anisotropy constant of $Ni_{0.8}Fe_{2.2}O_4$ at low temperature depended on the method of the experiment. They obtained $K_1 = -4.2 \times 10^4$ erg/cc from the torque method and $K_1 = -7.4 \times 10^4$ erg/cc from the ferromagnetic resonance method at 77°K and attributed the difference to the relaxation phenomenon of electrons in the B-site of the spinel lattice.

The interesting character of the ferromagnetic crystalline anisotropy of $Ni_xFe_{3-x}O_4$ system, where $x=0.20$, 0.35, 0.52 and 0.75, was obtained recently by one of the authors[2] from the torque method.

Experiments on the ferromagnetic resonance absorption of microwave, 9300 Mc/sec, have been carried out to obtain the ferromagnetic anisotropy, K_1 and K_2, and g-value with specimens cut from the same crystals used for torque measurements. The comparison between them is presented here.

The anisotropy observed by the resonance method shows the similar temperature dependence to that obtained from the torque method: it increases with decreasing temperature. But at low temperature its value, $K_1\,(\text{resonance}) = (K_1/M)M$, is much smaller than that of the latter, K_1 (torque), as shown in Fig. 1. The saturation magnetization M is measured for the same specimens. The difference, $\Delta K_1 = K_1\,(\text{resonance}) - K_1\,(\text{torque})$, at 90°K is given in Fig. 2. As seen from the figure, ΔK_1 at 90°K is nearly linearly proportional to $(1-x)$ and seems to become zero for pure Ni-ferrite. The quantitative disagreement to the results obtained by Bozorth *et al*[1] may be attributable to the difference in the density of Fe^{2+}-ions caused by the different method of the preparation of specimens. In Fig. 3 $\Delta g = g(77°K) - (290°K)$ is plotted as a function of x and shows the similar tendency to ΔK_1.

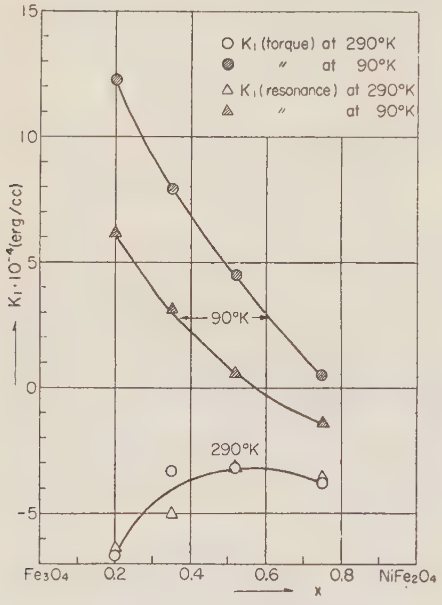

Fig. 1. K_1 (torque) and K_1 (resonance) *vs.* composition at 90°K and 290°K.

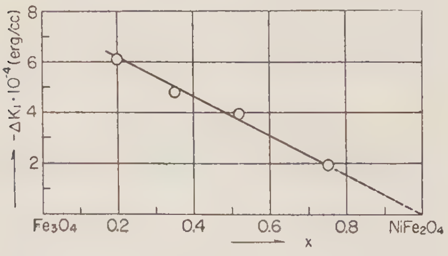

Fig. 2. ΔK_1 *vs.* composition at 90°K [$\Delta K_1 = K_1\,(\text{resonance}) - K_1\,(\text{torque})$].

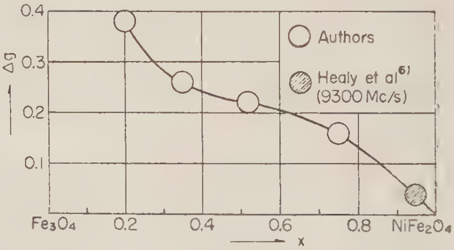

Fig. 3. Δg *vs.* composition [$\Delta g = g\,(77°K) - g\,(290°K)$].

Frequency dependence of K_1 in $Ni_x\,Fe_{3-x}O_4$ mentioned here is in marked contrast to that in $Mn_xFe_{3-x}O_4$ system[2-4] in which K_1 does not depend on the frequency for, almost all specimens in the temperature range between 90°K and 290°K.

Details of experimental procedures and discussions will be published in the other paper[5].

References

1) R. M. Bozorth *et al*: Phys. Rev. **99** (1955) 1898.
2) N. Miyata: J. Phys. Soc. Japan **16** (1961) 1291.
3) Z. Funatogawa *et al*: J. Phys. Soc. Japan **14** (1959) 1583.
4) J. C. Slonczewski: J. Appl. Phys. **32** (1961) 253S.
5) S. Usami *et al*: Sci. Rep. Yokohama Nat'l Univ. Sec. 1, **8** (1961).
6) D. W. Healy *et al*: Phys. Rev. **104** (1956) 634.

J. Phys. Soc. Japan **16** (1961) 2065~2066

Nuclear Magnetic Resonance of Fe^{57} in Fine Powdered Iron

By Shizuko OGAWA and Setsu MORIMOTO
Physics Department, Ochanomizu University, Tokyo, Japan

(Received May 11, 1961)

The observation of NMR of Fe^{57} in natural iron has been made with a frequency modulated marginal oscillator and a recording system which reproduces the second derivertive of the resonance line. Particles having diameters less than 1 μ exhibited a weak signal intensity. In those cases a superregenerative oscillator was used with a quench frequency of 180 kc/sec which resolves side band resonances. Particle sizes of commercially obtained powdered pure iron (1) and the further grounded one (2) were measured by photomicroscope. Much smaller particles of iron were obtained by electrodeposition on a mercury cathode¹⁾. By this method (3), (4) and (5) were obtained in varying the current of electrodeposition. These particle sizes were measured with an electronmicroscope. They scattered about 20% around the mean value and their shape was spherical. The particle size and the internal strain were estimated from the broadening of Debye-Sherrer lines with a *Co Kα* radiation observed with a X-ray microphotometer²⁾. The degree of oxidation and impurity content were also examined. It is suggested from the Table that the line width is sensitive to internal strain and particle size. To remove the internal strain, samples were annealed at 700°C in vaccum system. X-ray investigation of annealed sample showed no observable broadening other than caused from the geometrical arrangement.

The line width of NMR for inhomogeneous broadening contributing some fraction to total width was expressed by Suhl³⁾. The fractional spread is $\delta\nu/\nu \sim (E_a/kT)^{1/2}\delta M/M$, where $\delta M/M$ is thermal deviation in spontaneous magnetization and E_a is anisotropy energy. The average thermal deviation of the electronic spin density causing the hyperfine field at the nuclei is shown to vary through the wall. If the crystal anisotropy energy of 4×10^5 erg/cc for iron is substituted for E_a, a line width of 13 kc/sec is calculated. The experimental value of annealed iron (1) was 11 kc/sec which seems to agree reasonably with the calculated one.

Table

Fe	Size (A)	Mean strain e ($\times10^{-3}$)	Line width (kc/sec.)
(1)	10^6	0.18	50.9±7
$(1)_a$	10^6	0	11.0±1
(2)	10^4	0.26	74.5±7
$(2)_a$	10^4	0	15.4±2
(3)	800	0.02	35.4±5
$(3)_a$	800	0	18.4±2
(4)	600	0	26.1±3
(5)	250	0	41.4±3

$(\ )_a$ is the annealed sample.

The effect of internal strain to line width is shown in Fig. 1. From the figure a linear relation between the line width and the internal strain is observed. The magnetoelastic energy associated with the internal stress does not account for the amount of the observed broadening and is far less than the value. A hydrostatic pressure of 10^4 kg/cm² shifts the iron resonance frequency to lower side about 74 kc/sec⁴⁾. This hydrostatic pressure will produce a volume change of 0.6%. The volume change in the present experiment is calculated from the observed internal strain assuming isotropic strain, and the width expected from this volume change is shown by a solid curve in Fig. 1.

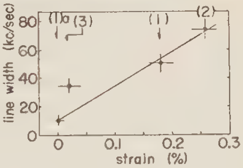

Fig. 1.

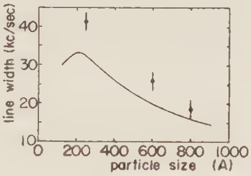

Fig. 2.

The line width of the annealed particle having diameter less than 1 μ became larger as shown in Fig. 2. In fine powder the coercive force shows similar variation, though it depends variously upon particle size, surface coating, packing factor and preperation method etc. In iron particle of various size coercive force was measured by Meiklejohn⁵⁾. The solid line in Fig. 2 is a calculated curve with the value of the anisotropy energy estimated by assuming the proportionality to the observed coercive force. The deviation of this curve from the observed result shows the necessity of taking into account the increase of thermal fluctuation in smaller particles.

Authors are indebted to Dr. Y. Abe of Tokyo University of Education for operation the electronmicroscope and to Mr. Y. Kashiwase of Tokyo Institute of Technology for taking the photograph of Debye-Sherrer lines.

References

1) W. H. Meiklejohn and C. P. Bean: Phys. Rev. **105** (1957) 904.
2) M. Kuriyama: J. Phys. Soc. Japan **15** (1960) 1426.
3) H. Suhl: Bull. Am. Phys. Soc. Ser. 11, **5** (1960) 175.
4) G. B. Benedeck and J. Armstrong: J. Appl. Phys. **32** (1961) 106s.
5) W. H. Meiklejohn: Rev. Mod. Phys. **25** (1953) 302.

J. PHYS. SOC. JAPAN **16** (1961) 2066

Stress Annealing Effect in Cobalt

By Takashi SAMBONGI and Tadayasu MITUI

Department of Physics, Faculty of Science, Hokkaido University, Sapporo

(Received May 27, 1961)

In the foregoing study on the magnetic annealing effect[1),2),3)] in pure Co it was made clear that when the specimen is transformed in a magnetic field the crystal orientation is so restricted that the (00.1) plane of h.c.p. phase makes as small angle with the direction of magnetic field as possible.

This is a preliminary report of our experiment to see if a similar effect can be induced also by a mechanical stress.

A Co ingot of purity 99.3% melted and cast in vacuo, which was kindly prepared by Dr. Y. Nakagawa of Gakushuin University, was machined into a rod of 9.1 mm in diameter and 50 mm in length, and then annealed at 1000°C for a week. The specimen was placed in a testing machine and heated with an electric furnace. Argon gas was passed through the furnace from the lower end to prevent the specimen from oxidation. A Pt-PtRh thermocouple was attached to the top of the specimen to measure the temperature.

After maintained at 600°C for 2 hours, the specimen was cooled slowly and compression of weight ca. 200 kg (ca. 4 kg/mm²) was applied from above the transformation temperature to 350°C. Four discs were cut from the specimen; two from the the plane parallel (A) and the other two from the plane perpendicular (B) to the axis of compression. Torque was measured at room temperature with these discs by an air-bearing torque magnetometer. The results with discs (A) and (B) are shown in Fig. 1.

The direction of easy magnetization was found to be parallel to the direction of compression in (A), while it is random in (B). The observed torque curves in (B) are irregular in their shape and the maximum amplitude do not exceed one quarter of that in (A). The anisotropy must be an accidental one and perhaps comes during disc preparation, because any direction in the disc plane makes equal angle to the axis of the stress. No further attention was paid to discs (B).

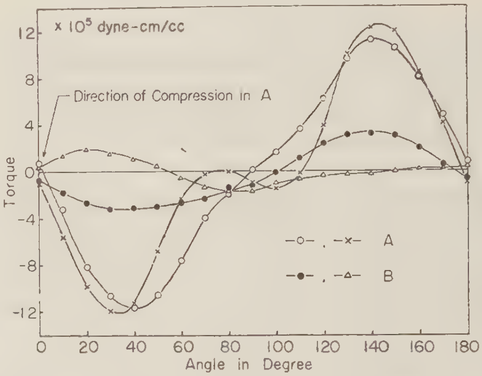

Fig. 1. Torque curves with discs parallel (A) and perpendicular (B) to the axis of compression.

The origin of the induced anisotropy energy observed in (A) is probably similar to that of the case of the magnetic annealing. In the allotropic transformation of Co, the h.c.p. (00.1) plane should be parallel to one of the 4 sets of the f.c.c. (111) plane. But under a mechanical stress the orientation of the (111) plane to be transformed into (00.1) plane will be restricted by the stress and some of the magnetocrystalline anisotropy energy will be observed.

Stress dependence of the induced anisotropy energy K_1 was also measured. The magnitude of K_1 increases with increasing stress and saturates near at 10 kg/mm².

The detailed report will be published later.

References

1) M. Takahashi and T. Kono: J. Phys. Soc. Japan **15** (1960) 936.
2) C. D. Graham Jr.: J. Phys. Soc. Japan **16** (1961) 1481.
3) T. Sambongi and T. Mitui: J. Phys. Soc. Japan **16** (1961) 1478.

J. PHYS. SOC. JAPAN **16** (1961) 2067~2068

Heavily Deffused Si pn-Junction

By Masakatsu TOKUNAGA and Katsufusa SHONO*
Research Institutes, Yuasa Battery Company,
Takatsuki, Osaka

(Received July 12, 1961)

It is of considerable interest to make a detailed study of the behavior of the heavily diffused Si pn-junctions[1] which do not remain the intermediate π or ν-region, as a result of the compensation of the donor and the acceptor impurities. The heavily diffused junction, which has the different gradient of the compensated impurity density near the center of the Si-slices, was adjusted by changing the thickness of Si-slices as the duration time of diffusion was kept constant at 100 hours. Si raw meterials of resistivity ranging between 3 and 5 ohm crn are used. The first step in preparation is to lap the Si-slices into a thickness of 100 to 400 microns. The simultaneous double diffusion technique is used to process the Si-slices. Here, one of the two faces is painted with a solution of phospherous pentoxide in methyl cellosolve; the other face is painted with a solution of boron oxide in methyl cellosolve. After it dries at temperature somewhat higher than the room temperature, they are closely stacked on edge in an alundum container with like painted faces together. Next, they are kept at a temperature of 1300°C in an open end furnance.

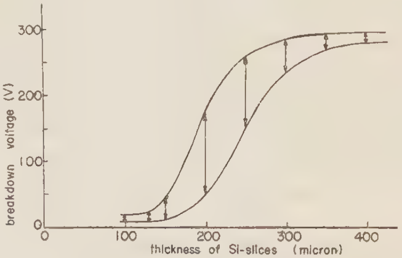

Fig. 1. Breakdown voltage as a function of the thickness of Si-slices.

Fig. 1 indicates the breakdown voltages V_B as a function of the thickness l of Si-slices. As indicated by the arrows in the figure, the fluctuations in the value of V_B is rather large for the thickness l ranging between 200 and 300 microns. This may be due to the irregular variation in thickness of Si-slices and the non-uniform condition of diffusion process. But the abrupt change of V_B between 200 and 300 microns can be explained by considering that, as a result of impurity compensation, the effective impurity gradient may vary strongly according to the thickness of Si-alices. In case of $l \leq 130$ microns, it seems that V_B nearly saturates and it is easily verified that this tendency does not depend on the resistivity of the raw Si-slices in the range tested. That V_B begins to saturate at the thickness $l=130$ microns, corresponds to the fact that the gradient of the compensated impurity density near the center of the junction has its maximum value at $l=\sqrt{8Dt} \simeq 130$ microns, where D is the diffusion coefficient and t is the duration time of diffusion process. On the other hand, in case of $l \simeq 350$ microns, V_B also seems to saturate. This tendency depends on the resistivity of the raw Si-slices. For higher resistivity samples, V_B becomes higher and the shape of pn-junction changes to the pπn- or pνn-junction.

Samples	l (micron)	V_B (volt)	C_o (farad)	V_i (volt)	N (meter^{-3})	C_B (farad)	E_B (volt/meter)
No. 1	300	230	530×10^{-12}	0.53	2.6×10^{20}	27×10^{-12}	4.1×10^{6}
No. 2	200	90	695×10^{-12}	0.57	4.9×10^{20}	55×10^{-12}	3.5×10^{6}
No. 3	150	30	2460×10^{-12}	0.71	76×10^{20}	370×10^{-12}	8.0×10^{6}
No. 4	100	10	7160×10^{-12}	0.80	720×10^{20}	1970×10^{-12}	13.8×10^{6}

The heavily diffused Si junctions in this work might be the step junctions where the depletion layer extends beyond the transition region. Assuming that the diffusion constant and the surface impurity density of the diffusants are kept constant, the relation between the applied voltage V and the junction capacitance C for the step junction could be given as,

$$\frac{1}{C^2}=\frac{4(V+V_i)}{q\varepsilon_0\varepsilon_r NS^2},$$

where V_i is the internal or "built in" barrier voltage, q is the magnitude of electronic change, ε_0 is the dielectric constant in vacuum, ε_r is the specific constant of Si, N is the donor or acceptor impurity density and S is the junction area ($=10\ \mathrm{mm}^2$). In Fig. 2, the plots V vs. $1/C^2$ are given for four samples. From the gradient of straight lines and extraporating them to $1/C^2$-axis, the impurity concentration N and the "built in" barrier voltage V_i are obtained, respectively. It is to be noted that the "built in" barrier voltage V_i varies according to the thickness of Si-slices.

---

* Now at Reseaach Laboratory, Sony Corporation, Hodogaya, Yokohama.

Using these values for N and V_i, and substituting V_B for V, we can get the capacitance C_B at the breakdown voltage V_B. Thus the breakdown field intensity E_B is obtained from the next relation,

$$E_B=\frac{V_B C_B}{\varepsilon_r \varepsilon_0 S}\,.$$

These values above mentioned are described in the table. The values of E_B needed for Zener breakdown[2)] are expected to be over $10^9\ V/m$. For the lowest breakdown voltage obtained here, the maximum breakdown field intensity becomes at most $1.4\times10^7\ V/m$, lower by roughly a factor of 100 compared with Zener one. Hence it might be concluded that it is impossible to get the Zener diodes, but we can get only the usual avalanche diodes, using such simultaneous double-diffusion technique.

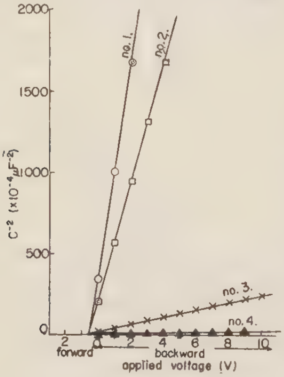

Fig. 2. Applied voltage vs C^{-2} for the heavily diffused Si pn-junctions-

References

1) Tokunaga and Shono: J. Phys. Soc. Japan **16** (1961) 1029-1030.
2) C. Zener: Proc. Roy. Soc. **145** (1934) 523-529.

J. Phys. Soc. Japan **16** (1961) 2068

Phonon Spectrum of Germanium-Silicon Alloys

By R. Braunstein, A. R. Moore and F. Herman

Radio Corporation of America,
RCA Laboratories,
Princeton, N.J.

(Received July 18, 1961)

The problem of determining theoretically the lattice vibrational spectrum of real (three-dimensional) disordered crystals is one that has not yet been solved successfully. Therefore, all experimental information bearing on this problem is of considerable value, since it should serve both as a spur to and as a check of subsequent theoretical work. The Ge-Si alloy system is of considerable interest in this connection, since the lattice spectra of the pure constituents are now known in considerable detail. By taking advantage of this knowledge, it is possible to identify particular phonon energies in the intermediate composition range. Ando[1)] has recently done this for the phonons which assist indirect electronic transitions in the range 0 to 9.1 atomic per cent Ge by using the current-voltage characteristics of Esaki (tunnel) diodes at liquid helium temperatures.

The composition dependence of some of these phonons had already been studied by the present authors nsiug optical absorption measurements near the band edge[2)]. The composition dependence of the infra-red lattice absorption spectrum has also been measured and interpreted over the full composition range by Braunstein[3)]. The results of these three independent sets of measurements are in substantial agreement with each other.

However, Ando states that his experimental findings for the composition dependence of certain phonon energies are not in accord with theoretical predictions given in the earlier paper[2)]. While this is true in itself, Ando gives the impression that we were not aware of this fact. Actually, we presented the results of a theoretical calculation based on the virtual crystal model specifically to demonstrate that this model did not account for our own experimental findings, which are more extensive than those of Ando. It would have perhaps been more to the point for Ando to say that his experiments demonstrate once again that the virtual crystal model is incapable of representing the composition dependence of short wave phonons in disordered crystals.

References

1) K. Ando: J. Phys. Soc. Japan **15** (1960) 2360.
2) R. Braunstein, A. R. Moore and F. Herman: Phys. Rev. **109** (1958) 695.
3) R. Braunstein: "Infra-Red Lattice Absorption of Ge-Si Alloys", Abstracts of the International Conference on Semiconductor Physics, Prague, 1960, p. 60. A detailed account will be published shortly.

J. Phys. Soc. Japan **16** (1961) 2069~2070

Helium Discharge Chamber

By Shūji Fukui, Satio Hayakawa,
Ryoichi Kajikawa and Ken Kikuchi
Physical Institute, Nagoya University,
Nagoya, Japan

(Received July 27, 1961)

After the short note on the "discharge chamber"[1), a new particle detector named as the "spark chamber" has been employed in experiments with high energy machines[2) and of cosmic-rays[3). The gas filled in these chambers was a mixture of neon and argon, as we originally used. However, other kinds of gases can be used in principle. We then constructed the discharge chamber filled with helium gas at atmospheric pressure, for the purposes of studying the proton-α scattering and the polarization of protons. Preliminary tests have been made with the proton beams from cyclotrons. The procedures of the construction and the operation of the chamber are the same as described in the previous report[1).

Figs. 1 and 2 are two examples of tracks of 5 Mev protons. The inner size of the chamber is 20 cm × 28 cm × 1.2 cm. One of the sides of the chamber has a mylar window with the thickness of 1.4 mg/cm^2. A collimated proton beam passed through an Al foil of 16μ stuck on the hole of 3 mm diameter and traversed the air of about 2 cm and then entered the chamber. The chamber was stationarily hit by the proton beam. A clearing field of 500 volt was constantly applied by dry-cells. The high voltage pulses, whose time constant and peak voltage were fixed to 10^{-7} sec and 16 kV respectively, were applied to the chamber at a rate of one pulse per two seconds. The discharges exhibiting the tracks were photographed through the conductive glass (Nesa) used as the electrode. The intensity of protons hitting the chamber was estimated to be about 0.15 mμA ($\sim 9\times10^8$ protons/sec). From the sensitive time of the chamber the number of protons expected during one high voltage pulse may be $\sim$10 protons. The average width of a track was estimated to be 1 mm.

Fig. 3 shows one of examples of tracks which were due to protons scattered from Sn bombarded by a 55 Mev proton beam. Each size of the chamber is 8.5 cm × 13 cm × 1 cm. In this case the high voltage pulse was triggered by the proton beam through the gate-circuit which was closed at a rate

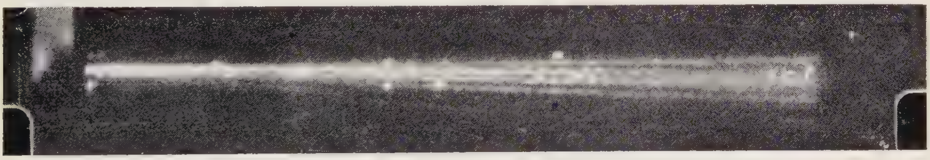

Fig. 1. Tracks of 5 Mev protons.
This photograph exhibits coulomb multiple scattering of 5 Mev protons in Mylar and in He. The length of tracks was 27 cm and the mean width of a track was estimated to be 1 mm. Peak value of high voltage pulse of CR=10^{-7} sec was 16 kV/1.2 cm. Clearing field of 500 volt was constantly applied to the chamber.

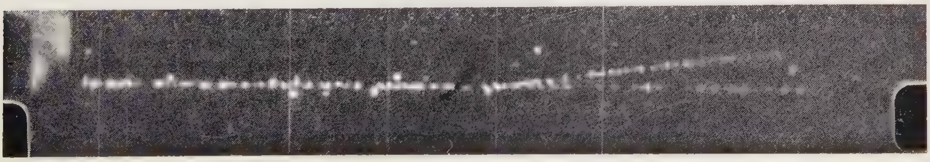

Fig. 2. One example of scattering 5 Mev proton.
The operational condition was the same as in Fig. 1.

Fig. 3. A track of scattered proton from Sn bombarded by 55 Mev proton beam.
Peak value of high voltage pulse of CR=10^{-7} sec was 12 kV/1 cm. The length of track in each chamber was 9 cm.

of one per two seconds. The clearing field was not applied.

In these cases the film used was Fuji SSS and developed with "Promicrol". The f-stop of the lens was 1/1.4.

From the photographs it can be expected that the chamber filled with helium will be employed in the same way as that with the neon-argon mixture, with some advantages in using this particular kind of gas.

The authors express their sincere thanks to Professors T. Wakatsuki and S. Yamabe and other members of Osaka cyclotron for their generous arrangement which made it possible to perform this experiment.

References

1) S. Fukui and S. Miyamoto: Nuovo Cimento, **11** (1959) 113.
2) Proc. of the International Conference on the Instrumentation for the High Energy Physics at Berkeley (1960). The Spark Chamber Symposium: Rev. Sci. Instr. **32** (1961) No. 5.
3) K. Kamata: Sci. Papers, I.P.C.R. **55** (1961) No. 2.

J. Phys. Soc. Japan **16** (1961) 2070

Electron Microscopic Observation of the Aggregates of Vacancies in Germanium

By Kenzo Tanaka, Michihiko Mannami, Kunihide Izumi and Hiroko Niwa

Department of Physics, Kyoto University, Kyoto

(Received July 29, 1961)

No direct evidence of the aggregate of vacancies in germanium has been obtained so far. In this paper, based upon the electron microscopic observation, we present an evidence indicating that the vacancies aggregate into clustering spongy regions in germanium quenched from temperatures higher than 750°C.

The crystals used had resistivities of more than 5 Ωcm. After heating them contained in an evacuated quartz tube from 750° to 800°C, the crystals were quenched by dropping the tube into water. Thin foils were prepared by polishing the crystals chemically in the C-P4 solution. The polishing conditions used were those given by Igaki and Ohashi¹⁾. These thin foils were then examined by transmission method in the electron microscope. Annealing treatment to precipitate the quenched-in vacancies was not carried out, because the foils were heated in the course of chemical polishing and in the electron microscope by the irradiation of electrons.

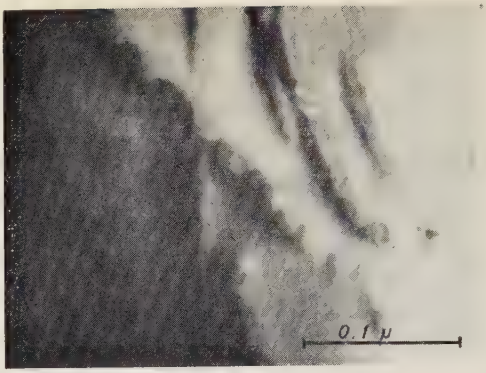

Fig. 1. Electron micrograph of germanium quenched from 780°C.

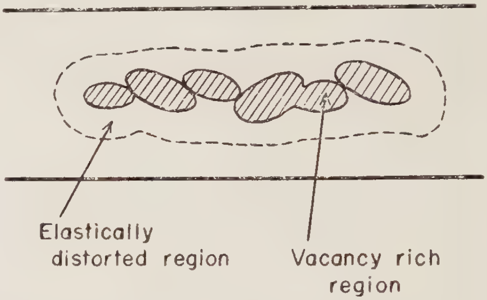

Fig. 2. Model of the aggregate of vacancies.

An electron micrograph of germanium quenched from 780°C is shown in Fig. 1, in which the aggregates of excess vacancies can be seen. The aggregate appears as a chain with dark region on one side. As the direction of the incident electron to the foil changes, the contrast either appears on both sides of the chain or disappears leaving behind a vague chain. This indicates that the elastic lattice distortion is dominant in the region of widths of about 200Å on both sides of the chain (see Fig. 2) and that the chain is due to some irregularity in the lattice. From the fact that the contrast is not so sharp as that of dislocation, the aggregate is not seen as a chain composed of small dislocation loops or clustering voids.

It is supposed that the structure of the aggregate is a cluster of spongy regions with elastically distorted regions around them as shown in Fig. 2. We cannot find the crystallographic orientation of of the aggregate to the lattice of germanium.

We wish to thank Prof. J. Takamura for his discussion.

Reference

1) K. Igaki and N. Ohashi: Read before the annual meeting of the Metallurgical Society of Japan, 1959.

J. Phys. Soc. Japan **16** (1961) 2071~2072

Theory of Non-Linear Responses of Many Variable Systems

By Koji Okano
The Institute of Physical and Chemical Research, Bunkyo-ku, Tokyo
and Osamu Nakada
Hitachi Central Research Laboratory, Kokubunji, Tokyo

(Received July 28, 1961)

In a previous publication[1] one of the present authors (O.N.) has established a phenomenological equation which describes a non-linear response of a physical system to a single time dependent stimulus or excitation. The equation is given in a form of a series of multiple convolution integrals containing the excitation and after effect functions of various orders. The assumptions upon which the equation is based are of quite general nature, namely: (1) the convergence of the series, (2) the principle of causality, (3) the stationary property of the response relation. And hence it has a wide range of applicability as far as the non-linear response relation between a pair of variables as excitation and response is concerned.

The present note is a short summary of the results of our investigations in which the previous theory is extended to the case of many variable (non-linear) response system—that is, to the case in which several excitations are applied to a system simultaneously.

1. *Fundamental non-linear response relations of many variables*

Let us take a stationary system. Let $X_i(t)$ $i=1, 2, \cdots$ be the variables expressing the excitations applied to the system and $x_\alpha(t)$ $\alpha=1, 2, \cdots$ be the response of the system to the excitations. Then, assuming the convergence of the series, we have* as an extension of the previous result,

$$x_\alpha(t)=\sum_i\int_{-\infty}^{+\infty}J_i{}^\alpha(t-\tau)X_i(\tau)d\tau+\sum_{ij}\int_{-\infty}^{+\infty}\int_{-\infty}^{+\infty}J_{ij}{}^\alpha(t-\tau_1,\ t-\tau_2)X_i(\tau_1)X_j(\tau_2)d\tau_1 d\tau_2+\cdots\,, \tag{1.1}$$

in which $J_i{}^\alpha(t)$, $J_{ij}{}^\alpha(t_1, t_2)\cdots$ are the characteristic after effect functions of various orders. The principle of causality requires that

$$\text{if } t_s<0 \text{ for any } s\ (s=1, 2, \cdots)\,, \qquad J^\alpha_{ijk\cdots}(t_1, t_2, \cdots)=0\,. \tag{1.2}$$

2. *The frequency response functions of higher orders and the Kramers-Kronig relations*

The Fourier representation of the fundamental equation (1.1) is

$$\bar{x}_\alpha(\omega)=\sum_i \bar{J}_i{}^\alpha(\omega)\bar{X}_i(\omega)+\sum_{ij}\int_{-\infty}^{+\infty}\int_{-\infty}^{+\infty}\delta(\omega-\omega_1-\omega_2)\bar{J}_{ij}{}^\alpha(\omega_1, \omega_2)\bar{X}_i(\omega_1)\bar{X}_j(\omega_2)d\omega_1 d\omega_2+\cdots\,, \tag{2.1}$$

in which

$$\left.\begin{array}{ll}\bar{x}_i(\omega)=\dfrac{1}{2\pi}\displaystyle\int_{-\infty}^{+\infty}x_i(t)e^{-i\omega t}dt\,, & \bar{X}_i(\omega)=\dfrac{1}{2\pi}\displaystyle\int_{-\infty}^{+\infty}X_i(t)e^{-i\omega t}dt\,, \\ \bar{J}_i{}^\alpha(\omega)=\displaystyle\int_{-\infty}^{+\infty}J_i{}^\alpha(t)e^{-i\omega t}dt\,, & J_{ij}{}^\alpha(\omega_1, \omega_2)=\displaystyle\int_{-\infty}^{+\infty}\int_{-\infty}^{+\infty}J_{ij}{}^\alpha(t_1, t_2)e^{-i\omega_1 t_1-i\omega_2 t_2}dt_1 dt_2\,, \\ \cdots\cdots\cdots & \end{array}\right\} \tag{2.2}$$

By making use of the condition (1.2), which is the mathematical expression of the principle of causality, and using the function theoretical method[3], the following relations between real and imaginary parts of the higher order frequency response functions are obtained as extensions of the well-known Kramers-Kronig relation[4] for a linear system to a non-linear many variable system:

$$\mathrm{Re}\,\bar{J}^\alpha_{ijk\cdots}(\omega_1, \omega_2, \cdots, \omega_l, \cdots)=-\frac{1}{\pi}P\int_{-\infty}^{+\infty}\mathrm{Im}\,\bar{J}^\alpha_{ijk\cdots}(\omega_1, \omega_2, \cdots\omega_l{}', \cdots)\frac{1}{\omega_l{}'-\omega_l}d\omega_l{}'\,, \tag{2.3}$$

$$\mathrm{Im}\,\bar{J}^\alpha_{ijk\cdots}(\omega_1, \omega_2, \cdots, \omega_l, \cdots)=\frac{1}{\pi}P\int_{-\infty}^{+\infty}\mathrm{Re}\,\bar{J}^\alpha_{ijk\cdots}(\omega_1, \omega_2, \cdots, \omega_l{}', \cdots)\frac{1}{\omega_l{}'-\omega_l}d\omega_l{}'\,. \tag{2.2}$$

3. *Discussion about the reciprocal relations*

Let us take a stationary thermodynamic system—a system in equilibrium in the absence of the excitations. Let $x_i(t)$ be a thermodynamic extensive variable and $X_i(t)$ be the intensive one conjugate to $x_i(t)$. A statistical mechanical consideration based upon the theory of Bernard and Callen[5] leads to

---

* This equation has also been obtained by Yamamoto and Ohki[2] independently of us.

$$\left.\begin{aligned}
&\int_t^\infty J_i{}^\alpha(\eta)d\eta=\beta\langle x_i(0)x_\alpha(t)\rangle^{(0)} , \\
&\int_t^\infty\int_t^\infty J_{ij}{}^\alpha(\eta_1, \eta_2)d\eta_1 d\eta_2=\frac{1}{2!}\beta^2\langle x_i(0)x_j(0)x_\alpha(t)\rangle^{(0)} , \\
&\int_t^\infty\int_t^\infty\int_t^\infty J^{\alpha}_{ijk}(\eta_1, \eta_2, \eta_3)d\eta_1 d\eta_2 d\eta_3 \\
&\qquad\qquad=\frac{1}{3!}\beta^3[\langle x_i(0)x_j(0)x_k(0)x_\alpha(t)\rangle^{(0)}-\langle x_i(0)x_j(0)\rangle^{(0)}\langle x_k(0)x_\alpha(t)\rangle^{(0)} \\
&\qquad\qquad-\langle x_j(0)x_k(0)\rangle^{(0)}\langle x_i(0)x_\alpha(t)\rangle^{(0)}-\langle x_k(0)x_i(0)\rangle^{(0)}\langle x_j(0)x_\alpha(t)\rangle^{(0)}] , \\
&\cdot\ \cdot\ \cdot\ \cdot\ \cdot\ \cdot\ \cdot\ \cdot\ \cdot\ \cdot ,
\end{aligned}\right\}\tag{3.1}$$

in which $\langle\ \rangle^{(0)}$ means the phase average over the equilibrium ensemble free from external perturbations, the excitations, and $\beta=1/kT$. In deriving eqs. (3.1) it has been assumed that $\langle x_i\rangle^{(0)}=0$. The eqs. (3.1) connect the causal response of a thermodynamic system to the action of external perturbations—the left hand side—to the statistical correlation in spontaneous fluctuations in the absence of excitations—the right hand sides. The principle of microscopic reversibility and the stationary property of the equilibrium state lead to

$$\left.\begin{aligned}
&\langle x_i(0)x_\alpha(t)\rangle^{(0)}=\langle x_i(t)x_\alpha(0)\rangle^{(0)} , \\
&\langle x_i(0)x_j(0)x_\alpha(t)\rangle^{(0)}=\langle x_i(t)x_j(t)x_\alpha(0)\rangle^{(0)} , \\
&\langle x_i(0)x_j(0)x_k(0)x_\alpha(t)\rangle^{(0)}=\langle x_i(t)x_j(t)x_k(t)x_\alpha(0)\rangle^{(0)} , \\
&\cdot\ \cdot\ \cdot\ \cdot\ \cdot\ \cdot\ \cdot\ \cdot\ \cdot ,
\end{aligned}\right\}\tag{3.2}$$

provided that x_i's are even variables. Hence we have

$$J_i{}^\alpha(t)=J_\alpha{}^i(t) , \tag{3.3}$$

as has already been proved[6], whereas for higher order response functions we have in general

$$\left.\begin{aligned}
&J_{ij}{}^\alpha(t_1, t_2)\neq J_{\alpha j}{}^i(t_1, t_2)\neq J_{i\alpha}{}^j(t_1, t_2) , &&(t_1, t_2)\neq(0, 0) , \\
&J^{\alpha}_{ijk}(t_1, t_2, t_3)\neq J^{i}_{\alpha jk}(t_1, t_2, t_3)\neq\cdots , &&(t_1, t_2, t_3)\neq(0, 0, 0) , \\
&\cdot\ \cdot\ \cdot\ \cdot\ \cdot\ \cdot\ \cdot\ \cdot\ \cdot
\end{aligned}\right\}\tag{3.4}$$

Thus the principle of microscopic reversibility leads to reciprocal relations in the first order response functions (linear terms), but not in higher order response functions (non-linear terms).

References

1) O. Nakada: J. Phys. Soc. Japan **15** (1960) 2280.
2) M. Yamamoto and S. Ohki: Paper presented before the spring meeting of the physical society of Japan, Ueda (1961).
3) For example, L. D. Landau and E. M. Lifshitz: Statistical Physics, Pergamon Press, 1958, p. 391.
4) H. A. Kramers: Atti Congr. intern. fis. Como., **2** (1926) 545. R. de Kronig: J. Opt. Soc. Am., **12** (1926), 547.
5) W. Bernard and H. B. Callen: Revs. Modern Phys., **31** (1959) 1017.
6) R. Kubo: J. Phys. Soc. Japan **12** (1957) 570.

J. PHYS. SOC. JAPAN **16** (1961) 2072～2073

Several Experiments on the Memory Effect in αFe_2O_3

By Masako IWATA, Takao IWATA
and Mikio YAMAMOTO

The Research Institute for Iron, Steel and Other Metals, Tôhoku University, Sendai

(Received July 7, 1961)

It has recently been discovered that αFe_2O_3 memorizes the remanent magnetization after subjected to a thermal cycle through the magnetic transition at −15°C[1]. We made several experiments on this curious phenomenon with specimens prepared by sintering pure αFe_2O_3 powder (produced by heating from $Fe(NO_3)_3\cdot 9H_2O$) at 1100°C in an oxygen gas stream and obtained some interesting results.

The hysteresis loop measurements in a magnetic field range of ±12.6 kOe, made by means of a pendulum magnetometer using strain gauges as a transducer, show that, while the remanent magnetization and coercive force at room temperature are

0.204 emu/g and 3.37 kOe, respectively, the hysteresis loop at −192°C of the virgin specimen is a perfectly straight line passing through the origin ((a) in Fig. 1), there being apparently no sign of ferromagnetism. The hysteresis loop at −192°C of the specimen, which acquired the remanent magnetization by an application of the magnetic field of 12.6 kOe at room temperature, is again a straight line with the same slope as that of the virgin specimen. However, this straight line is displaced slightly (by 0.013 emu/g) upwards or downwards from that of the virgin specimen, according as the remanent magnetization acquired at room temperature is directed towards the plus or minus direction ((b) and (c) in Fig. 1). This indicates that αFe_2O_3 really has a weak ferromagnetism at low temperatures and that the magnetization of this ferromagnetism is dependent on the remanent state produced at room temperature.

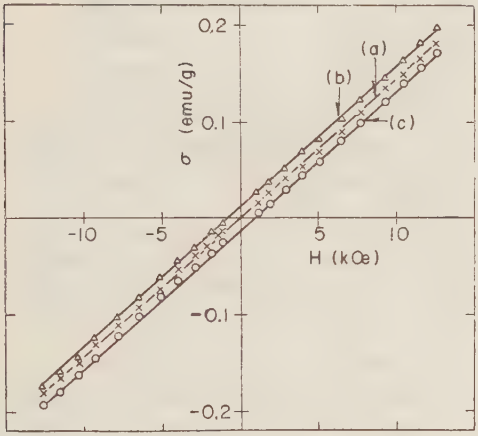

Fig. 1. Hysteresis loops of αFe_2O_3 at −192°C.

Next, the remanent magnetization, σ_R, acquired by the specimen after it was magnetized by various magnetic fields, H_R, at room temperature and the magnetization, σ_M, memorized by the same specimen after it (in the remanent state) was cooled to liquid air temperature and then brought back to room temperature were measured using a torsion magnetometer somewhat simillar to that designed by Penoyer. It has been found that both σ_M and σ_R are constant and their ratio is 0.52 in the measured range of H_R from 10 to 100 kOe. The effects of the application and subsequent removal of the magnetic field, H_L, up to 145 kOe at liquid air temperature on the way of the just-mentioned experiments are as shown in Fig. 2. The memorized magnetization, σ_M, after H_L was applied along the same direction as that of σ_R is not at all changed for H_L up to 110 kOe ((a) in Fig. 2). After H_L was applied along the direction inverse to that of σ_R, σ_M is again not changed for H_L up to 50 kOe, but, as H_L becomes higher than 50 kOe, σ_M is decreased gradually and vanishes for $H_L \approx 90$ kOe. As H_L further increases, σ_M appears in the inverse direction, namely, in the direction of H_L, and seems to reverse completely for $H_L \approx 160$ kOe ((b) in Fig. 2). Further, after a virgin specimen was subjected to a strong field, H_L, at liquid air temperature and then it was brought to room temperature without the field, the residual magnetization was detected for H_L higher than 50 kOe and it increased gradually with increasing H_L.

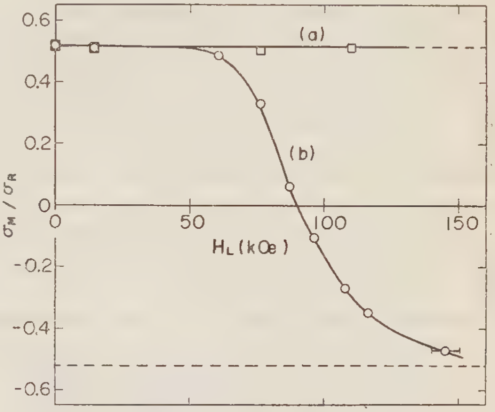

Fig. 2. The ratio of the memorized magnetization, σ_M, to the original remanent magnetization, σ_R, as dependent on the field, H_L, once applied at −192°C on the way of a thermal cycle through the low-temperature magnetic transition in αFe_2O_3.

It may be concluded, from these experiments, that the very weak ferromagnetism observed at low temperatures plays an essential rôle in the memory effect in αFe_2O_3.

References

1 G. Haigh: Phil. Mag. **2** (1957) 877. S. T. Lin: J. Appl. Phys. **31** (1960) 273S. K. Siratori, A. Tasaki and S. Iida: J. Phys. Soc. Japan **15** (1960) 2357.

J. PHYS. SOC. JAPAN **16** (1961) 2074～2075

Photoconduction of γ-ray Irradiated KCl Single Crystals at Higher Electric Field

By Yoshio INUISHI and Yung-Kwun SUNG

College of Engineering, Osaka University, Osaka, Japan

(Received August 3, 1961)

In our previous paper, the effects of γ-ray coloration on dielectric strength of KCl were reported[1,2]. The mechanism of these effects has been investigated by us in connection with pulse photoconduction at prebreakdown range, and some of the preliminary results are presented here.

Pulled KCl single crystals after three re-crystalization cycles were well annealed and cleaved to form the specimen ($20\times15\times0.3$ mm^3) furnished with conducting glass cathode and evaporated golden anode with guard ring. After introduction of proper amount (N_F) of F-center with γ-ray irradiation from Co^{60} at room temperature, pulse photoconduction of the specimen was observed by a synchroscope with excitation of F-band light ($\lambda=550$ mμ) of 500 μs duration through conducting glass cathode.

The peak photocurrents I_P are shown in Fig. 1(a), (b), (c) as the function of applied field E for various temperature and N_F.

These saturation curves can be expressed by the well known "Schubweg" formula[3] for uniform release of F electron,

$$I_P=e\eta N_0\frac{W}{l}\left[1-\frac{W}{l}\left(1-\exp\left(\frac{l}{W}\right)\right)\right]=e\eta N_0\frac{W}{l}2\phi(W), \qquad (1)$$

where e, N_0, l are electronic charge, incident photon number per unit time, and sample thickness (0.3 mm) respectively. η is the quantum yield for the liberation of electron from F-center, $W=\mu E\tau$ is the Schubweg; μ, τ being electron mobility and life time respectively.

By comparing[4] the experimental saturation curves (Fig. 1) with equation (1) we can estimate $W_0=\mu\tau$ and $eN_0\eta$ or the quantity proportional to η at a definite illumination.

Mobility life time ($\mu\tau$) and quantum yield η (in arbitrary unit) thus obtained are shown in Fig. 2 with comparison to $\eta\mu\tau$ measured by Pohl at low field photocurrent[3] (dotted line).

From these data we can conclude the following items;

(1) $\mu\tau$ increases with decreasing temperature due to the increase of mobility and the saturation fields decrease also with decreasing temperature.

(2) At prebreakdown field, charge multiplication occurs possibly due to the impact ionization of F-centers.

(3) The decrease of $\eta\mu\tau$ below -150°C at higher field (present data) is not so remarkable as that obtained by Pohl in low field. This may be due to the Zener-type release of electrons from the excited state of F-centers at higher field as was proposed by Lüty[5].

(4) Apparently, η increases remarkably above -60°C.

Although detailed mechanism is not clear, this fact may be related to the efficiency of F electron

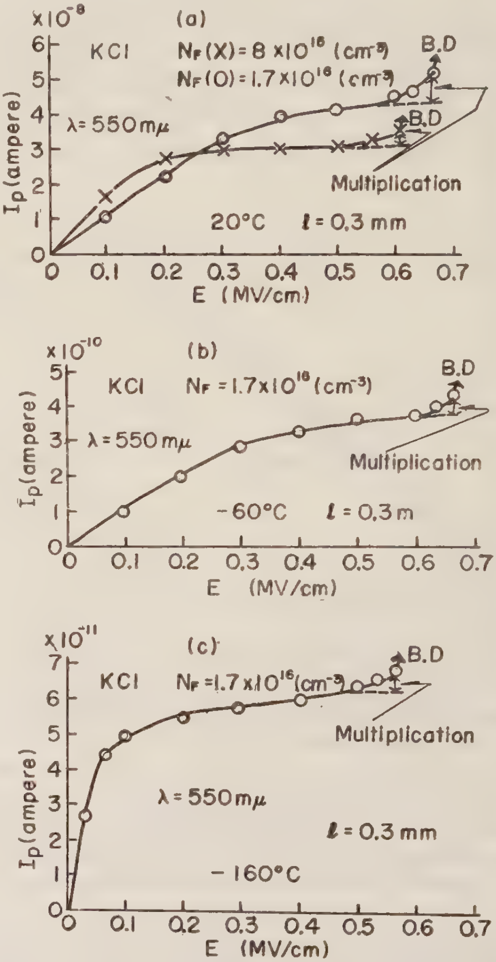

Fig. 1.

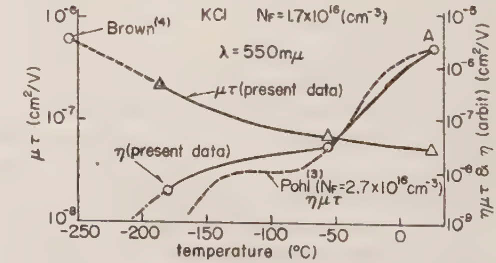

Fig. 2. (η and $\eta\mu\tau$ curve are made to cross at point A.

liberation at coagulated F-centers created around dislocation by γ-ray irradiation. A full paper will be published soon.

References

1) Y. Inuishi and T. Suita: Phys. Rev. **109** (1958) 1507.
2) Y. Inuishi and Y. Sung: Tech. Rept. Osaka Univ. **7** (1957) 257.
3) N. F. Mott and R. W. Gurney: *Electronic Processes in Ionic Crystals*, pp. 117–137.
4) R. L. Wild and F. C. Brown: Phys. Rev. **121** (1961) 1296.
5) F. Luty: Zeit. f. Physik: **153** (1958) 247.

J. PHYS. SOC. JAPAN **16** (1961) 2075

On the Coupling between Optical Lattice Vibrations and Carrier Plasma Oscillations in Polar Semiconductors

By Isaaki YOKOTA

Department of Physics, Faculty of Science,
Niigata University

(Received July 22, 1961)

When carrier concentration in a polar semiconductor amounts to $10^{17}\sim10^{18}\,\mathrm{cm}^{-3}$, the frequency of carrier plasma oscillations becomes of the same order of magnitude as that of the lattice vibrations of the optical modes and notable coupling between them is to be expected. Taking, e.g., carrier effective mass, $m^*=0.3m$, optical dielectric constant, $\varepsilon_\infty=10$ and carrier concentration, $n_0=10^{17}\,\mathrm{cm}^{-3}$, we find as the plasma oscillation frequency which is given by

$$\omega_p=\left(\frac{4\pi n_0 e^2}{\varepsilon_\infty m^*}\right)^{1/2},$$

$\omega_p=10^{13}\,\mathrm{sec}^{-1}$, which is of the order of magnitude of *Reststrahlungsfrequenz* of typical ionic crystals.

In this note, we will give an elementary theory of the coupling between lattice vibrations of the optical modes and carrier plasma oscillations both of long wave lengths in polar semiconductors.

The lattice vibrations of the optical modes of long wave lengths in ionic crystals can be described by the following pair of equations¹⁾:

$$\frac{\partial^2 \boldsymbol{w}}{\partial t^2}=-\omega_t^2\boldsymbol{w}+b_{12}\boldsymbol{E}\,, \tag{1}$$

$$\boldsymbol{P}=b_{21}\boldsymbol{w}+\frac{\varepsilon_\infty-1}{4\pi}\boldsymbol{E}, \tag{2}$$

where $\boldsymbol{w}$ is the displacement of the positive ion relative to the negative, $\boldsymbol{u}_+-\boldsymbol{u}_-$, multiplied by the square root of the reduced mass, $M=M_+M_-/(M_++M_-)$,per unit volume:

$$\boldsymbol{w}=\sqrt{\frac{\bar{M}}{\Omega_0}}(\boldsymbol{u}_+-\boldsymbol{u}_-)\,,$$

Ω_0 being the volume of the unit cell, $\boldsymbol{P}$ is the dielectric polarization and $\boldsymbol{E}$ is the electric field, ω_t is the frequency of the transverse waves and

$$b_{12}=b_{21}=\omega_t\left(\frac{\varepsilon_0-\varepsilon_\infty}{4\pi}\right)^{1/2},$$

ε_0 being the static dielectric constant.

On the other hand, the plasma oscillations of carriers of long wave lengths are described by the hydrodynamic equation of motion and the equation of continuity, which are simplified in linear approximation respectively to

$$m^*\frac{\partial \boldsymbol{v}}{\partial t}=e\boldsymbol{E} \tag{3}$$

and

$$\frac{\partial n_1}{\partial t}+n_0(\nabla\cdot\boldsymbol{v})=0\,, \tag{4}$$

where $\boldsymbol{v}$ is the hydrodynamic carrier velocity and n_1 is the deviation of carrier concentration from its average value, n_0.

These twy oscillating systems are coupled through the Poisson equation

$$(\nabla\cdot\boldsymbol{D})=4\pi e n_1\,, \tag{5}$$

where $\boldsymbol{D}$ is the electric displacement

$$\boldsymbol{D}=\boldsymbol{E}+4\pi\boldsymbol{P}\,. \tag{6}$$

Eliminating $\boldsymbol{D}$, $\boldsymbol{E}$, $\boldsymbol{P}$, and $\boldsymbol{v}$ from Eqs. (1) to (6) we get the following simultaneous equations for n_1 and $(\nabla\cdot\boldsymbol{w})$:

$$\frac{\partial^2 n_1}{\partial t^2}=-\omega_p^2 n_1-\frac{4\pi n_0 e b_{21}}{\varepsilon_\infty m^*}(\nabla\cdot\boldsymbol{w})\,,$$

$$\frac{\partial^2(\nabla\cdot\boldsymbol{w})}{\partial t^2}=-\omega_l^2(\nabla\cdot\boldsymbol{w})-\frac{4\pi e b_{12}}{\varepsilon_\infty}n_1\,,$$

where $\omega_l=(\varepsilon_0/\varepsilon_\infty)^{1/2}\omega_t$ is the frequency of the longitudinal waves. We see that only longitudinal modes of optical lattice vibrations can be coupled with carrier plasma oscillations and find as the eigen frequencies of the coupled oscillations

$$\omega^2=\frac{1}{2}\{\omega_p^2+\omega_l^2\pm[(\omega_p^2+\omega_l^2)^2-4\omega_p^2\omega_t^2]^{1/2}\}\,.$$

Reference

1) M. Born and K. Huang: *Dynamical Theory of Crystal Lattices*, (Oxford, 1954), 82 p.

J. Phys. Soc. Japan **16** (1961) 2076~2077

Electron Spin Resonance of the *M* center in Potassium Chloride

By Hiroshi Ohkura and Kazuo Murase

Department of Applied Physics,
Osaka City University,
Osaka, Japan

(Received August 3, 1961)

The two kinds of atomic model of the *M* center have been proposed; the one is a one-electron center suggested by Seitz[1] and Knox[2], and the other is a two-electron center suggested by van Doorn, Haven[3] and Pick[4]. For assignment of these models, it would be highly important to determine whether the *M* center is a paramagnetic center or a diamagnetic one. Kawamura and Ishiwatari reported the narrowed absorption curve of the electron spin resonance (**ESR**) of an optically bleached KCl, which they interpreted as arising from the *M* center resonance[5].

We measured the **ESR** traces of additively colored KCl crystals by using the X-band microwave with high frequency modulation of 455 Kc/sec, under static magnetic field of about 3,500 gauss. A rectangular resonant cavity operating in a TE_{101} mode was slotted horizontally at the lower portion of one of the narrow sides to permit the entry of the *F*-band light, and the cavity had a series of slots parallel to the narrow face of waveguide to permit penetration of magnetic modulation field.

Furthermore, the optical density of the specimen was measured immediately after the **ESR** trace was obtained at each stage of *F*-band bleaching. The result can be discussed with reference to a typical example shown in Fig. 1. Curves (a) in Fig. 1 show both the **ESR** trace and the optical absorption of a freshly colored crystal, respectively. Curves (b) show the results after the specimen was irradiated with *F*-band light at room temperature. The *M*-band is increased at the expense of the *F*-band. The reduction of about 40% of the intensity in the **ESR** trace is followed by the reduction of more than 30% in the *F*-band peak. This discrepancy may be interpreted in terms of the overlap of absorption band due to the higher excited states of the *M*-band with the *F*-band. The change of the curve shape in the **ESR** trace was not observed with reference to the trace in the curves (a). Curves (c) show the results for the heavily bleached specimen by successive irradiation. The intensity in the **ESR** trace is decreased to 40%, while the *F*-band peak is decreased to 60%. More than 10% narrowing in the **ESR** absorption curve is observed. If this heavily bleached specimen is subjected to a pulse annealing, both **ESR** intensity and optical density are fully recovered. In every case, the appreciable shift of g-value is not observed.

Two characteristics drawn from above results, namely, the correspondence between intensities of **ESR** traces and optical densities in the *F*-band, and the invariance in the curve shape of **ESR** for the specimen containing *F* and *M* centers, lead one to conclude that the **ESR** trace arises only from *F* centers. So long as one stands on the one-electron model of the *M* center, the absence of **ESR** absorption due to the *M* centers could be explained tentatively by assuming a homogeneously broadened line with a considerably long relaxation time, but, this assumption would not be plausible in viewpoint of optical studies. Then, it seems reasonable to conclude the *M* center is a diamagnetic center.

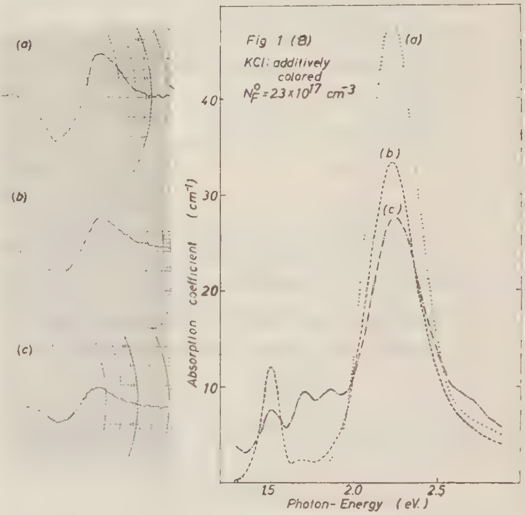

(A) (B)

Fig. 1. (A), **ESR** traces of additively colored KCl obtained by using the **ESR** apparatus having the equal sensitivity. (a), before irradiation, (b), after irradiation with *F*-band light, (c), after heavily irradiation.
(B), Absorption spectra for specimen whose **ESR** traces are shown in Fig. (A).
Measurements are all made at room temperature.

We would like to express our thanks to Professers Kawamura and Tomura for their kind discussion and Mr. H. Sugimoto and S. Nagata for technical assistance.

Just after we finished this work, Dr. Wolf kindly informed us his work[6]. He arrived the same conclusion as ours, by using the low frequency modulation.

References

1) F. Seitz: Rev. Mod. Phys. **18** (1946) 384.
2) R. S. Knox: Phys. Rev. (L) **2** (1959) 87.

3) C. Z. van Doorn and Y. Haven: Philips Res. Rep. **12** (1957) 309.
4) H. Pick: Z. Physik **159** (1960) 69.
5) H. Kawamura and K. Ishiwatari: J. Phys. Soc. Japan **13** (1958) 33.
6) H. Gross and H. C. Wolf: Naturwiss **48** (1961) 299.

J. PHYS. SOC. JAPAN **16** (1961) 2077~2078

Ultrasonic Attenuation in Al and Al-Cu Alloys at Low Temperature

By Kazuo KAMIGAKI and Tokutaro HIRONE

The Research Institute for Iron, Steel and Other Metals, Tohoku University, Sendai

(Received August 4, 1961)

The low temperature internal friction peak in metals or Bordoni peak[1] has been considered to be due to the relaxed motion of dislocation. According to Seeger's theory[2], in which the dislocation line moves between adjacent potential troughs by generating kink pairs, the Bordoni peaks in Cu[3] were analyzed successfully. On the other hand, in aluminum, an internal friction peak was observed for the farquencies 10^4c/s, 10^6c/s[4], and 10^7c/s[5], respectively. At the latter two frequencies the results were inconsistent with each other, the reason for which was suggested to be due to the impurities contained in the specimen. But the effects of interaction between the dislocation line and the impurity atoms on the behavior of the Bordoni peak were not considered in detail. The authors planned to measure the longitudinal ultrasonic attenuation between 100° and 300°K in polycrystalline specimens of 99.99% aluminum and Al −3.7 wt% Cu alloy at frequencies of 5 and 15 Mc/s.

In Fig. 1 the attenuation coefficient of Al at 5 Mc/s was plotted against temperature. A broad peak was observed at about 152°K and the height of the peak was increased by a plastic deformation of the specimen but reduced by subsequent annealings. On the specimen annealed just below the melting point for 5 hours, the peak was hardly observed. At 15 Mc/s similar features of attenuation were observed and the peak was shifted to 165°K. Assuming a relaxation process with a single relaxation time, the activation energy obtained was 4400 cal/mole. This value was larger than that of 99.8% Al[5], and the temperature of the 5 Mc/s peak was close to 99.94% Al[4].

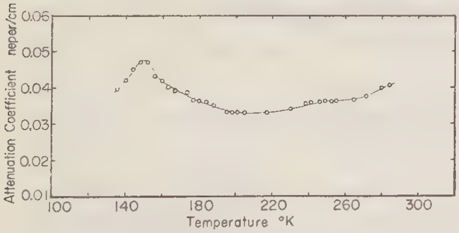

Fig. 1. Ultrasonic attenuation coefficient in a 99.99% Al polycrystal at 5 Mc/s.

The attenuation coefficient at 5 Mc/s in the Al-Cu alloy, quenched from 500°C, was plotted in Fig. 2. In the attenuation curve a broader peak than in pure Al was observed at about 150°K. The height of the peak was reduced by half by annealing at 100°C for 30 minutes. Another peak was observed at about 260°K in the quenched state but the height was reduced by annealing. At 15 Mc/s, the attenuation was three times as high as that at 5 Mc/s.

In the Al-Cu alloy, a broadening of the width and a lowering of height of the low temperature peak with annealing would be due to the locking of dislocation lines by solute atoms. Moreover, in Fig. 2, the low temperature side of the peak became broad and the apparent peak point was shifted to low temperature. Hence the inconsistent results obtained in the previous measurements of Al[4,5] would be due to the impurity effect as shown in the present experiment.

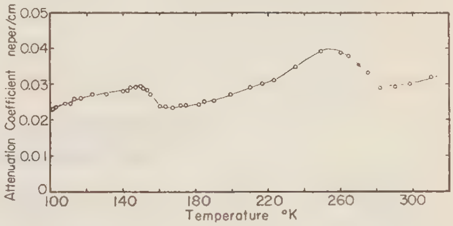

Fig. 2. Ultrasonic attenuation coefficient in a Al-3.7 wt% Cu polycrystal, quenched from 500°C, at 5 Mc/s.

For the high temperature peak in the Al-Cu alloy, the activation energy determined from the shift of the center of the peak with changing frequency was 7700 cal/mole. Because of the close value of activation energy to that of the vacancy annealing in Al, the high temperature peak should be originated from the relaxed motion of quenched-in vacancies, composed of several kinds of complexes in respect to the broad spectrum. Cu atoms are dissolved in the matrix by rapid cooling from high tempereratures but are squeezed out by annealing. Annealed-out Cu atoms form small clusters and then grow into the G-P zone. During annealing, the motion of dislocation lines or vacancies would be reduced by a locking of solute atoms and peak heights were reduced. By subsequent annealing, the peak height was reduced monotonously and the solute atoms grew into precipitates. For this reason, the elementary processes of precipitation are classified into two parts, one acts as a locking of dislocation lines and the other is a coupling of vacancies with solute atoms.

References

1) P. G. Bordoni: J. Appl. Phys. **26** (1954) 495.
2) A. Seeger: Phil. Mag. **1** (1956) 651.
3) D. H. Niblett and J. Wilks: Phil. Mag. **1** (1956) 415.
4) T. S. Hutchison and A. J. Filmer: Canad. J. Phys. **34** (1956) 159.
5) N. G. Einspruch and R. Truell: Phys. Rev. **109** (1958) 652.

Errata

Magnetic Properties of Iron Phosphide Fe_2P

By Shū CHIBA

J. Phys. Soc. Japan **15** (1960) 581

Page		Wrong	Corrected
583	Fig. 4	$T^2\times10^4$	$T^2\times10^{-4}$
	Fig. 5	$H^{-2}\times10^{-9}$	$H^{-2}\times10^9$
584	Fig. 9	$\rho\times10^{-4}$	$\rho\times10^4$

Local Description of the Flow behind a Steady, Two-Dimensional, Curved Shock Wave

By Zirō HASIMOTO and Shigeki MORIOKA

J. Phys. Soc. Japan **16** (1961) 1616

p. 1617, Eq. (4). The equation of continuity should be written in the form

$$\rho_{,\alpha}u_\alpha+\rho u_{\sigma,\sigma}=0$$

p. 1622, Fig. 6. The scales 2, 3, 4 on the axis of abscissa should be read 1.5, 2, 2.5, respectively.

p. 1622, Fig. 7. M should be read M_1

Measurement of Anomalous Absorption Coefficients of Electrons for MgO Crystals

By Kazutake KOHRA and Hiroshi WATANABE

J. Phys. Soc. Japan **16** (1961) 580

Page	Column	Line		should be read
580	right	7	$\dfrac{\cos(\sqrt{1+w})\|v_h\|\lambda t/2\pi)}{\sqrt{1+w^2}}$	$\dfrac{\cos(\sqrt{1+w^2}\|v_h\|\lambda t/2\pi)}{1+w^2}$
580	right	11	$\dfrac{v_{0i}\lambda}{2\pi\sqrt{1+w^2}}$	$\dfrac{v_{0i}\lambda}{2\pi}$
580	right	12	$\dfrac{\|v_{hi}\|\lambda}{2\pi\sqrt{1+w^2}}$	$v_{hi}\dfrac{v_h}{\|v_h\|}\dfrac{\lambda}{2\pi\sqrt{1+w^2}}$

Proceedings of

INTERNATIONAL CONFERENCE ON COSMIC RAYS AND THE EARTH STORM

HELD IN KYOTO, JAPAN, SEPTEMBER 4～15, 1961

To be published early in 1962
Supplement to Volume 17 of Journal of the Physical Society of Japan

About 440 papers presented at the Conference, together with discussions, are contained.

Sectional headings are as follows:

Part I. Earth Storm

- Morphology of Magnetic Storms
- Disturbances in Polar Regions
- Theory of Magnetic Storms and Aurorae
- Aurora and Airglow including Auroral X-Rays
- Ionospheric Disturbances
- Summary of the Disturbances in the Ionospheric Regions.

Approx. 370 pages

Part II. Joint Sessions of Part I and Part III

- Hydromagnetics
- Geomagnetic Rapid Variation
- Whistlar and VLF Emission
- Radiation Belts
- Solar Radiation (Electromagnetic Wave, Particles)
- Modulation (World-Wide and Secular Variation, Geomagnetic Effect, Diurnal Variation and Continuous Observation)
- Interplanetary Plasma
- Synthetic Theory of the Earth Storms.

Approx. 650 pages

Part III. Cosmic Rays

- Composition
- Primaries
- Origin
- EAS
- μ-Mesons
- Jet
- High Energy Theory
- Future Prospect
- Astrophysics
- Accelerator Physics

Approx. 550 pages

The prices (Postage included) are listed below:

	Members	Non Members
Part I Earth Storm	\$ 3.00	\$ 4.50
Part II Joint Sessions	\$ 6.00	\$ 9.00
Part III Cosmic Rays	\$ 4.50	\$ 7.00
One Set of Three Parts	\$ 12.00	\$ 18.00

Orders should be sent to the PHYSICAL SOCIETY OF JAPAN, No. 342, Physics Building, Faculty of Science, University of Tokyo, Bunkyo-ku, Tokyo, Japan.

Proceedings of

INTERNATIONAL CONFERENCE ON MAGNETISM AND CRYSTALLOGRAPHY

HELD IN KYOTO, JAPAN, SEPTEMBER 25～30, 1961

To be published early in 1962
Supplement to Volume 17 of Journal of the Physical Society of Japan

About 320 papers presented at the Conference, together with discussions, are contained.

Sectional headings are as follows:

Part I. Magnetism

Domain Structure Nuclear Magnetic Resonance in Metals Anisotropy and Relaxation in Ferrites Metals and Alloys Mössbauer Effect Magnetic Thin Films Theory Anisotropy and Relaxation in Metals Paramagnetic Resonance and Relaxation Oxides and Other Compounds Magnetism at Low Temperature Y.I.G. and Ferromagnetic Resonance Ferromagnetic and Antiferromagnetic Resonance Technical Magnetization Physical Problems of Rock Magnetism.

Approx. 710 pages:

Part II. Electron and Neutron Diffraction

Gas Electron Diffraction Scattering Phenomena in Electron Diffraction Diffraction Effects in Electronmicroscopic Images General Problems of Neutron Diffraction Inelastic Scattering in Neutron Diffraction Structure Studies by Neutron Diffration Technique and Application of Electron Diffraction Structure Study by Electron Diffration.

Approx. 400 pages:

Part III. Joint Sessions of Part I and Part II.

Neutron Diffraction Study of Magnetic Materials I, II.

Approx. 90 pages:

The prices (postage included) are listed below:

	Members	Non Members
Part I Megnetism	$ 6.00	$ 9.00
Part II Electron and Neutron Diffraction	$ 4.00	$ 6.00
Part III Joint Sessions	$ 1.00	$ 1.50
One Set of Three Parts	$ 10.00	$ 15.00

Orders should be sent to the PHYSICAL SOCIETY OF JAPAN, No. 342, Physics Building, Faculty of Science, University of Tokyo, Bunkyo-ku, Tokyo, Japan.

JOURNAL OF THE PHYSICAL SOCIETY OF JAPAN, Vol. 16, No. 11, NOVEMBER, 1961

The Construction and Test Operation of INS-Linear Electron Accelerator

By Jirō TANAKA

Institute For Nuclear Study, University of Tokyo
Tanashi-machi, Kitatama-gun, Tokyo

(Received April 8, 1961)

This is the third article in the series on the 6 MeV linear accelerator to be used for the injector of 1 BeV electron synchrotron, and describes the construction and early tests of the accelerator including the fabrication and the assembly of the components (accelerator guide, waveguide system, electron gun and vacuum system etc.) The accelerator guide has been carefully fabricated so as to match the designed structure reported in the preceding paper. An rf driven prebuncher has been provided in order to obtain a narrow energy spread and high trapping efficiency. The results obtained by the preliminary tests were the energy spread of about 3 percent at 6.6 MeV, whereas the spread increased up to 5-6 percent without the prebuncher.

§ 1. Introduction

A number of linear electron accelerators have been previously constructed, but the ordinary linear accelerator has a rather broad energy spread (10–15% at several MeV).

For the injector of the synchrotron, it is

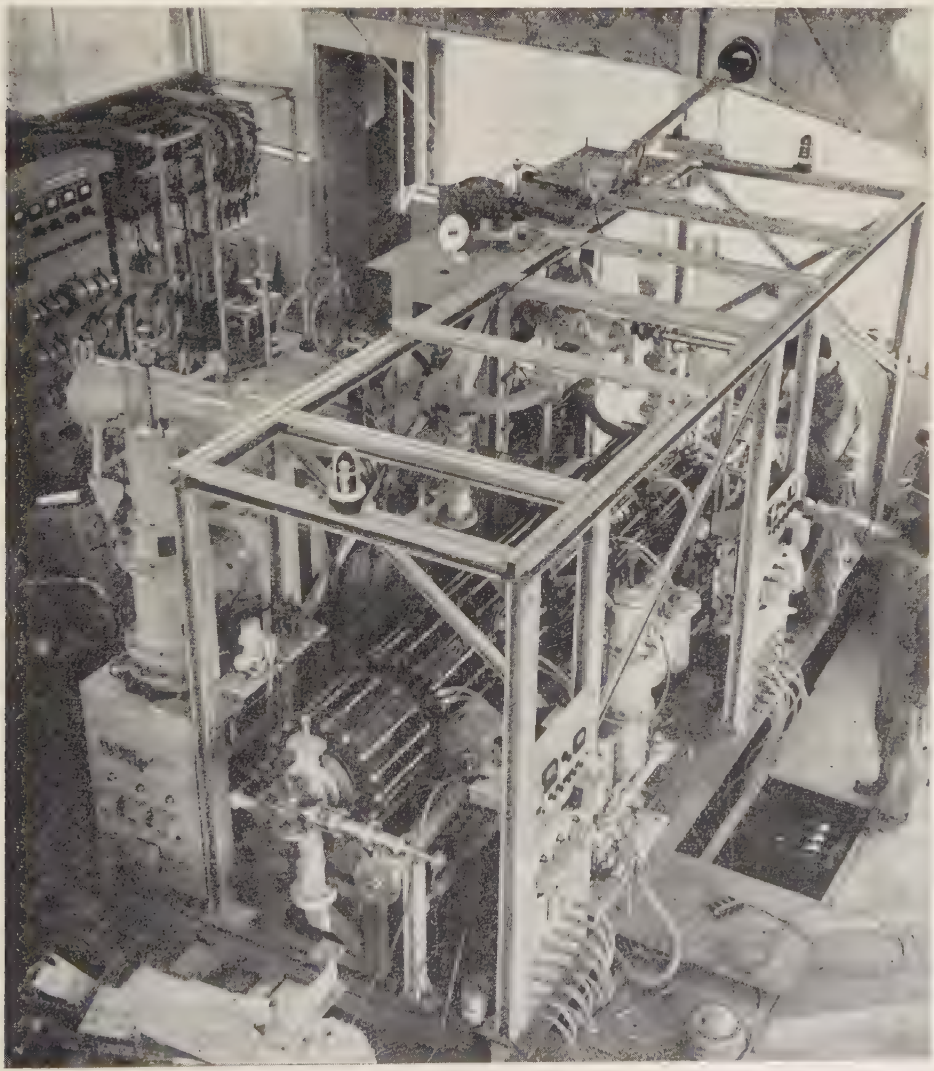

Fig. 1. View of the 6 MeV linear accelerator, mounted on the movable steel base.

required to have a narrow energy spread ($\lesssim 5\%$ at 6 MeV)[1]. Consequently, the design and the fabrication of the linear accelerator used for the injector, must be carefully performed. In particular, the energy spread depends largely on the design and the accuracy of the accelerator guide.

To obtain such an accelerator guide, the calculated dimensions were corrected by the low power rf measurements of the test-cavities, and the actual fabrication was accomplished using the available highest techniques.

In this paper, the processes of the construction used in achieving such a narrow energy spread and the performance of the early test operations are described.

§ 2. Construction of the Linear Accelerator

The accelerator and major electronics are placed on a movable steel base in size of 2m×4.5 m. A 3 MW pumped klystron[2] including 8″+3″ vacuum pumps, and two cabinets containing klystron pulser and 200 W *TWT* are placed on a half side of the base. On the other half the accelerator guide, electron gun, waveguide system and associated vacuum systems are placed.

The accelerator guide is mounted on the steel framework bolted to the base at four points, in order to avoid bending of the accelerator guide due to loading on the base, so that the whole assembly can be moved without destroying the accelerator alignment.

§ 3. Main Components of the Accelerator

Fig. 2 is a block diagram of the accelerator. The microwave power produced by the klystron is fed through a waveguide to a 20 db directional coupler where the rf power is divided into two parts; the main part is fed into the bunching section of the accelerator guide through a "door knob" coupler. Another part which is about a hundredth of the main power, is fed to the prebuncher cavity through a phase shifter and an attenuator.

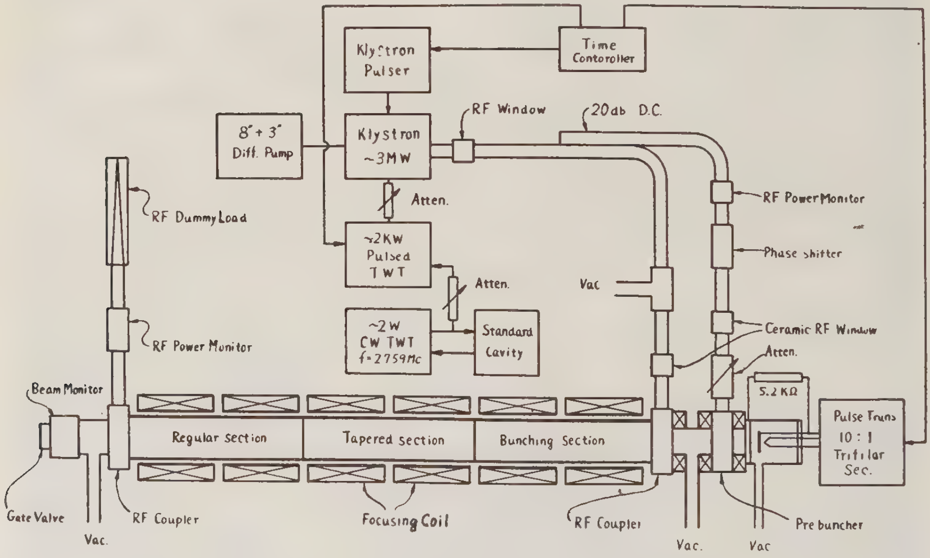

Fig. 2. Block diagram of the accelerator.

The residual rf power reaching the end of the regular section is brought via the output coupler to an rf dummy load where it is absorbed. Two rf power monitors are installed at the input and output sides of the waveguide system.

The electron gun is pulsed by the modulator which is essentially similar to that of the klystron. It differs, however, in that the secondary of the pulse transformer has trifilar windings in order to be used for the bombarded cathode.

The defocusing forces acting on the electron beam, especially at the bunching section, must be neutralized by the use of the focusing coil, which is divided into six sections corresponding to the units of the accelerator guide.

The accelerator guide, waveguide system

and electron gun are evacuated by a 6″+3″ oil diffusion pump system. Although the pump system has a nitrogen cold trap, it is not used.

§ 4. Accelerator Guide

The accelerator guide has a total length of 3 m, and is divided into six units, each length of which is about 50 cm. The first two units are the bunching section, the next two are the tapered section and the last two are the regular section. Each unit is fabricated by means of an electroforming procedure.

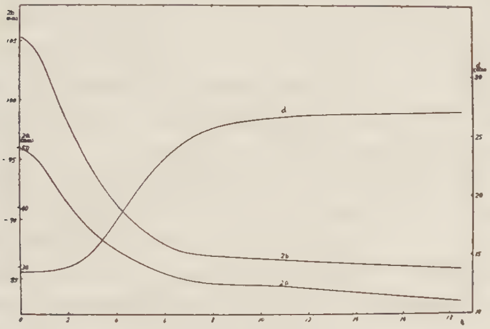

Fig. 3. Dimensions of the accelerator guide vs. distance. ξ is the distance measured by the free space wave-lengths.

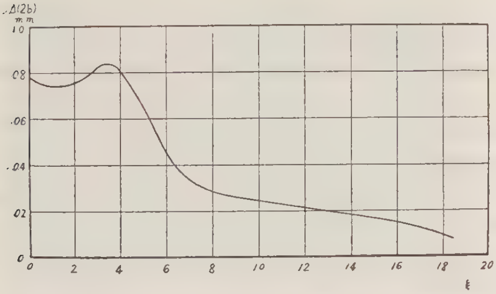

Fig. 4. Correction curve of the inner diameter 2b. $\varDelta(2b)=2b$ (experimental)-$2b$ (calculated).

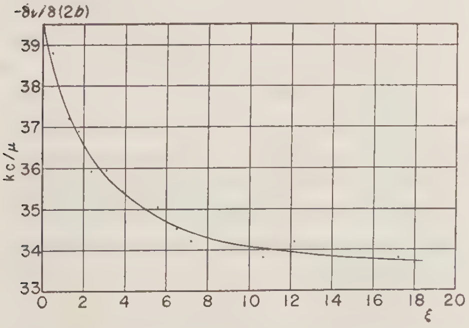

Fig. 5 (a). Frequency changes due to variation of the dimensions. $\delta\nu/\delta(2b)$.

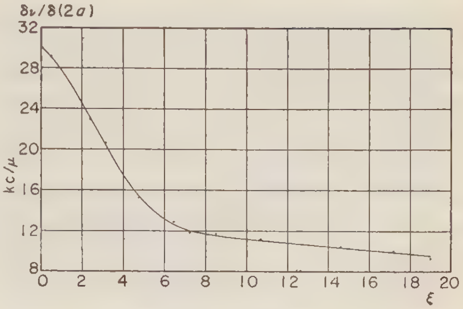

Fig. 5 (b). $\delta\nu/\delta(2a)$.

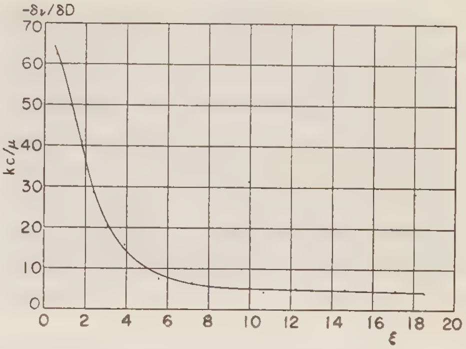

Fig. 5 (c). $\delta\nu/\delta D$.

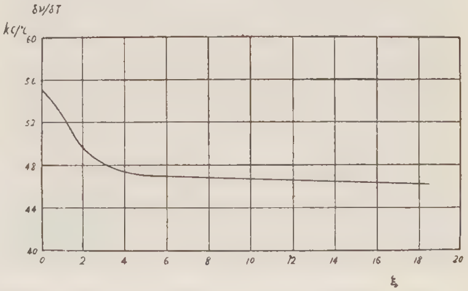

Fig. 5 (d). $\delta\nu/\delta T$.

The dimensions of the accelerator guide are calculated from the design study[3]. The dimensions $2a$, $2b$ D and d are shown in Fig. 3. In order to obtain the good energy spread, the dimensions must be corrected by the measurements of the test cavities[4]. The buncher including the tapered section is 2 m in length, and contains 92 disks. Seventeen points were chosen along the buncher in appropriate distances for the test. At each point, three or four two-disk cavities which have the same $2a$ and D but different $2b$'s, were made. For given $2a$'s and D's, the inner diameter $2b$'s which have a resonance of $\pi/2$ mode at 2759.0 Mc in vacuum at 30°C, were determined. The correction curve to the calculated value of $2b$ along the buncher is plotted in Fig. 4. Not only the corrected $2b$, but also the frequency changes due to the variations of $2a$, $2b$ and D, and due to the variation of the temperature were obtained. (Fig. 5)

These results are important to the fabrication of the accelerator guide, and the machining tolerances of the dimensions are determined to be,

$$\Delta 2a = \pm 3\mu$$
$$\Delta 2b = \pm 5\mu$$
$$\Delta D = \pm 5\mu$$
$$\Delta d = \pm 3\mu$$

Fabrication of the accelerator guide

The accelerator guide was fabricated by means of the improved electroforming[5]. This procedure provides one-body structure of each unit and therefore has the advantages of electrical contact and vacuum tightness. Especially in the fabrication of the bunching section in which the dimensions vary with the length, this is a facile methode compared to the others.

This procedure consists of (1) machining of the copper disks and Al-alloy 24-s spacers, (2) copper plating on the spacers, (3) assembling of the disks and spacers on a jig placed in water, (4) electroforming of the assembly, (5) etching of the spacers, and (6) final machining. The disks are made of oxygen free copper plate of 6 mm thickness. The copper is soft and gives worse machinability compared to other metals. The use of diamond tools and a high speed lathe gives the high precision maching of copper[6]. The facing operation determines the final thickness of the disk and the accuracy of the contour shape of the disk hole, as well as the surface roughness of the disks. Consequently it must be carefully performed. To achieve a smooth finish a crossfeed of 4μ/turn has been found desirable.

The cutting diamond tools must be carefully selected. Although constant linear cutting was not used, the surface roughness of 0.3 S was obtained. It was checked by the multiple beam interferometer, to avoid scraches. From the test cavity experiments, it was found that the resonant frequency of the accelerator sections largely depends on the contour shape of the hole. Although the measuring and consequently the machining of $2a$, $2b$, D and d are relatively easy, those of the contour shape are difficult. Moreover the variation of the area of 1 mm² at the section of the contor causes the frequency change of 4.8 Mc. In other words, the frequency of $\pi/2$ mode resonance can be varied by only the change of the contour shape keeping other dimensions constant. The contour shaping is performed by a shaping jig and two dial gauges which are used for setting the jig at a correct position.

This gives the precision hole contour. The reproducibility of the hole contour is very important in the fabrication of the accelerator guide, consequently the disks are checked by a profile projector and an rf test, without destruction of the disks. The obtained accuracy of the disk holes is within $\pm 2\mu$, and the deviation of resonant frequencies from the standard disk is within ±50 kc.

The spacers are made of Al-alloy 24-s. The form of the spacers is shown in Fig. 8. The spacers in the buncher have a step on the middle of the periphery of the spacers. After machining the spacers are zincated and copper plated, and then the both ends are machined to size. The tolerance of the diameter is $\pm 5\mu$ and that of the height is $\pm 5\mu$.

The disks and spacers are assembled on an assembly jig placed in water. The disks are properly spaced by means of the spacers, which are placed alternately with the disks on the jig, and the SUS-7 mandrel is stuck through the assembly. The assembly is deposited by a thick copper wall (about 1 cm). After electroforming, the spacers are etched out in a caustic soda solution, final cleaning is carried out, and the outer wall is machined[5].

rf Tests of accelerator units

The electroformed units are checked by low power rf measurements[4]. Each unit is built with an even number of disks. This means that if both ends are capped off, the units will resonate in the $\pi/2$ mode. The measurements are carried out in vacuum, since the shift of the resonant frequency occurs due to both air and humidity. The temperature of the units is measured by the thermo junction, and the resonant frequencies are corrected to the value at 30°C. In the units having an even number of disks, the only alternate cavities including end half cavities are sensitive to the resonant frequency of the $\pi/2$

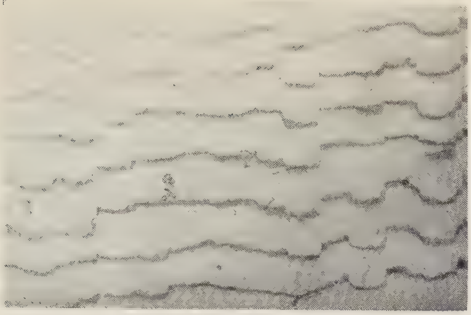

Fig. 6. Multiple-beam fringes of the disk surface, showing surface roughness of $<0.3\mu$. (Distance between the adjacent fringes is 0.3μ).

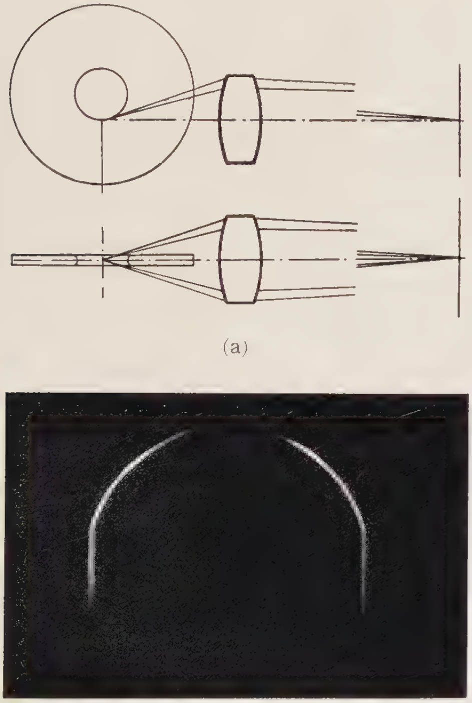

(a)

(b)

Fig. 7. (a) Schematic diagram of the profile projector. (b) Projected sections of the disk hole contour.

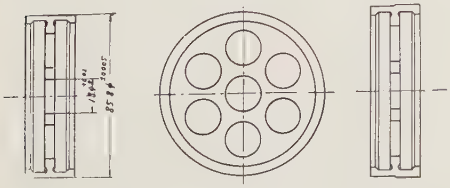

(a) (b)

Fig. 8. (a) 24-s spacer for the regular section. (b) 24-s spacer for the buncher.

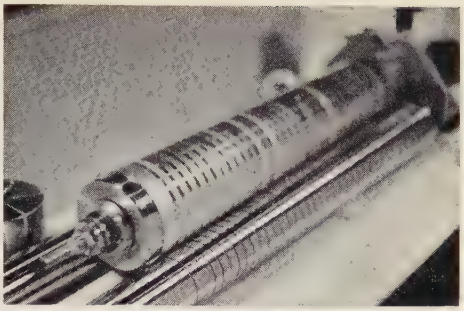

Fig. 9 (a). Disk-spacers assembly on the jig.

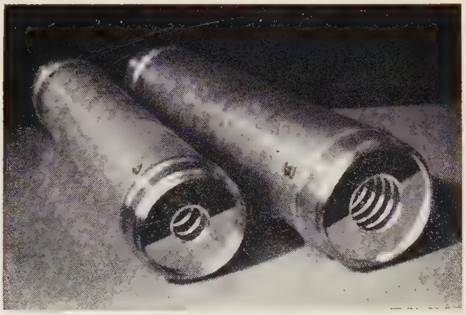

Fig. 9 (b). Completed acccelerator units.

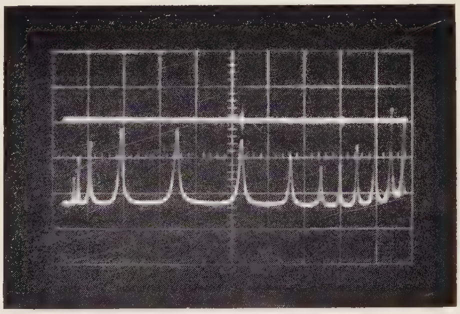

Fig. 10. Resonances of the accelerator unit. The center is the $\pi/2$ mode resonance.

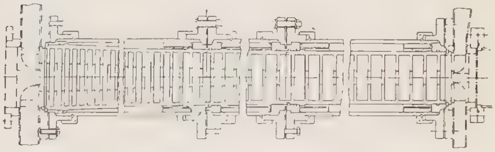

Fig. 11. Structure of the accelerator guide including the water jackets and the "door knob" couples.

mode[7]. However, when the accuracy of the fabrication is sufficiently high, this method gives accurate results.

The $\pi/2$ mode resonant frequencies of the six units are as follows:

Bunching section No. 1, 2760.20 Mc at 30°C in vac.

〃 No. 2, 2759.07

Tapered section	No. 1,	2759.09
〃	No. 2,	2759.06
Regular section	No. 1,	2759.03
〃	No. 2,	2759.08

In the regular sections, unloaded Q's of more than 10,000 were obtained, while in the bunching section No. 1, Q of 7,000 was obtained. The disk spacings are narrow in the No. 1 unit compared to other sections and the wall loss is large compared with the others. Also, its resonant frequency deviates from the operating frequency 2759.0 Mc. The reason is considered that $\delta\nu/\delta(2b)$, $\delta\nu/\delta(2a)$, $\delta\nu/\delta D$ are large at the input side of this unit. (see Fig. 5)

The phase shift $\delta\Delta_m$ due to the fabrication error is given by

$$\delta\Delta_m = \frac{\pi}{2}\beta_w\frac{c}{v_g}\frac{(\delta\nu_0)}{\nu_0}\,.$$

According to the above results, $\delta\nu_0$'s of each cavity of accelerator sections are less than 0.1 Mc. Therefore, for the regular section

$$\delta\Delta_m \lesssim 3.4\times10^{-3}\ \text{rad}\,.$$

This is sufficiently small compared to the design value.

The completed accelerator units are installed on the water jackets which have the flanges at both ends. The flanges are used to assemble the accelerator sections. The structure of the completed accelerator guide is shown in Fig. 11.

§ 5. Waveguide System

The whole waveguide system is shown in Fig. 2. As the waveguide system is evacuated to eliminate the danger of sparking in the guide, all the waveguide components (bends, tee tuners, directional couplers, rf windows, etc.) are connected together using vacuum tight choke flanges. The voltage standing wave ratio of the components is not greater than 1.05.

Directional couples

Two directional couplers are used, one of them is the 12 hole 20 db directional coupler, which is used for feeding the rf power to the prebuncher cavity. Another is the two hole 40 db directional coupler connected to the rf power monitor, and the holes are sealed by ceramic windows, in order to allow the atmospheric pressure at the low power side.

R. F. Windows

The rf windows are provided for isolating the waveguide system from the accelerator guide and for evacuating them independently. The geometry and structure are determined by the low power and high power rf tests. The ceramic plate which has 56 mm diameter and 3 mm thickness, is soldered at an inclined angle to the axis of the waveguide in order to avoid sparking. The V. S. W. R. of the windows is 1.02 at 2759 Mc.

Phase shifter

The phase shifter used in this system consists of a high alumina ceramic wedge placed in the rectangular waveguide parallel to its narrow face[8]. The wedge is carried by two ceramic shafts and can be displaced perpendicularly to the narrow face of the guide. The shafts are vacuum sealed by O rings, and moved by a synchronous motor from the remote control room. The phase of the rf wave can be changed by 290 degrees by this phase shifter. The V. S. W. R. is less than 1.05.

Dummy Load

The rf dummy load is a tapered ridged waveguide and is made of 13-Cr steel[9] (SUS-2). The length is 1.4 m and the inside is polished to prevent sparking at a high power operation. The load has no need of cooling. The V. S. W. R. is less than 1.10.

Waveguide-to-accelerator couplers

Two waveguide-to-accelerator couplers are used, one of them is placed at the input side of the bunching section where β is 0.5, in order to feed the rf power to the accelerator guide, and the other is placed at the output side of the regular section where β is $\sim$1.0. The type of the coupler is "door knob"[10], and the form and dimensions are experimentally determined. The final optimum matching is obtained by the adjustment of the short plunger.

§ 6. Assembly of the Accelerator Guide and Waveguide System

The accelerator guide units are mounted on the individual supporter which is made of cast brass. The radial displacement and inclination of the axis are carried out by screws. On the supporter, the focusing coil is also mounted coaxially to the accelerator section.

The supporters mounting the accelerator units and coils are slided on the rails welded on the frame work, placed at the positions and bolted together. (Fig. 12) The alignment of the accelerator guide is performed by means of a microalignment telescope and glass targets which can be mounted at both ends of the units. Next, the " door knob " couplers are installed at both ends of the accelerator guide, and the other waveguide components are assembled.

The whole waveguide system is checked and adjusted by the low power rf test.

First, the input coupler is adjusted to give a minimum V. S. W. R. For this purpose, the low power rf dummy load made of wooden tapered bar is inserted from the output side of the accelerator guide to the bunching section, and the short plunger of the coupler is adjusted to give the minimum V. S. W. R. at the frequency of 2759.0 Mc. The same procedure is performed at the output coupler. Then the rf dummy load is connected to the output couplers and the accelerator guide is checked on the joints of the accelerator sections. A frequency modulated klystron oscillator is used for the rf test, and, if the imperfection exists at the joints, the reflection is observed on a scope. (Fig. 13 (a))

The position of the imperfections is detected by the insertion of the wooden dummy load since the resonance curve disappears as the dummy load arrives at the position. (Fig. 13 (b)). Finally, the accelerator guide and waveguide system are evacuated and the whole system is adjusted to give minimum V. S. W. R. at 2759 Mc (Fig. 14). The measured V. S. W. R. is less than 1.10 and the attenuation of the accelerator guide including the waveguide system is 3 db in good agreement with the design value.

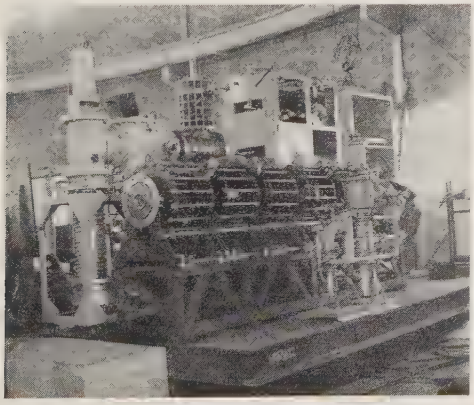
Fig. 12. The accelerator units and the focusing coil sections mounted on the supporters.

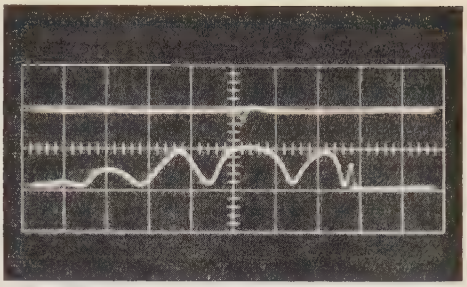
(a)

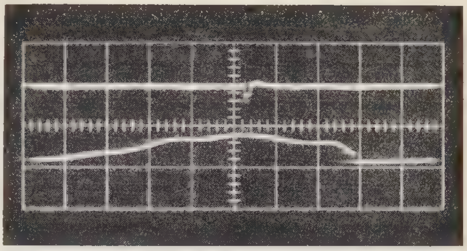
(b)

Fig. 13. (a) Reflection from the imperfection at the joint. (b) Dummy load is inserted to the imperfect joint (reflection disappears).

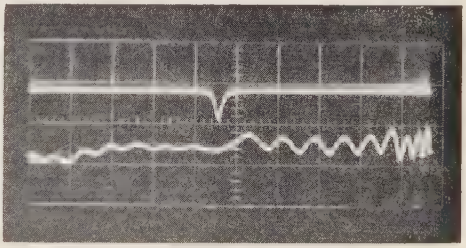
Fig. 14. Reflection of the whole wave guide system viewing from the input side. (in the region around 2759 MC, reflection disappears).

§ 7. Prebuncher

The electron beam is injected continuously from the gun during the pulse duration, and therefore the electrons are uniformly spread in the rf cycle.

However, the electrons trapped by buncher are limited to the ones riding on the proper parts of the rf phase angles. Consequently, if the electrons are bunched in the appropriate phase angles prior to the injection to the buncher, the acceptance of the buncher is improved and the energy spread of the beam is reduced. For this purpose, the prebuncher cavity which has the same function as that of the cavity of a klystron, is placed between the accelerator guide and the electron gun[1]. The cavity is a reentrant type and the resonant frequency is adjusted by the short plunger. The measured Q of the cavity is about 1,500. The drift space of 30 cm length between the cavity and the buncher permits the density bunching of the velocity modulated electrons. Theoretically, about 66% of the direct current per rf cycle is bunched in ±30 degrees, at the bunching parameter of 1.84. The electron bunches must be properly phased with respect to the rf wave in the buncher for acceptance. This is accomplished by the use of the rf phase shifter which provides about 300-deg. phase shifts. The power fed to the cavity is 30 kW maximum and is variable by the attenuator.

Around the drift space, the focusing solenoids are provided to control the beam diameter and the angular dispersion.

§ 8. Focusing Coil

The defocusing forces act on the electrons such that $-\pi/2 < \Delta < \pi/2$ where the electrons are stable longitudinally, and the forces must be neutralized by the axial magnetic field.

The minimum required field to focus the electron beam is given by[3]

$$B = \frac{2\sqrt{\pi}\, m_0}{e} \nu \sqrt{\alpha \frac{(1-\beta^2)^{1/2}}{\beta} \cos \Delta} ,$$

where, ν is the frequency of the rf wave and Δ is the phase angle of the electron with respect to the rf wave.

The magnetic field B in the case of $\Delta=0$ is plotted in Fig. 15. This magnetic field is approximated with the coils divided into several sections. The actual focusing coils are divided into six sections corresponding to the accelerator units; each of two coils around the bunching section is divided into five subsections and each subsection is supplied by dc current individually. The maximum field of 1,000 gauss can be produced. The coils around the tapered section are composed of three subsections, respectively, and their maximum field is 500 gauss, and the coils of the regular section are single and the maximum field is 200 gauss, so that the optimum field is obtained by changing the current independently in each subsection coil. The coils are mounted in coaxial with respect to the accelerator sections, and their axes are adjusted by means of eccentric rings.

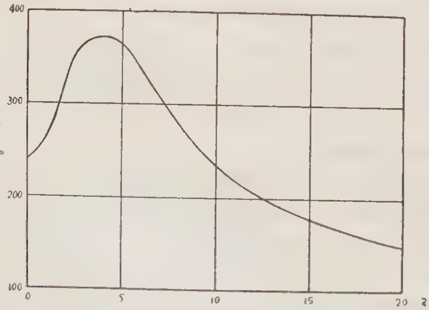

Fig. 15. Minimum required magnetic field in the buncher,

§ 9. Vacuum System and Cooling System

The vacuum system is composed of a 500 l/min. mechanical pump, a 6″+3″ oil diffusion pump system[11] and the associated vacuum manifold including an automatic gate valve, L valves, etc. The mechanical pump is placed on the outside of the radiation shield and connected to the diffusion pump system which is mounted on the movable steel base, through the tubing and the rubber hose.

The vacuum manifold with five connections to the accelerator guide, the waveguide system and the electron gun, is placed along the accelerator guide and made of SUS-7 tubing 10 cm o. d. and 4 m length. The accelerator guide is evacuated from the both sides, the waveguide system is evacuated through the slits 20 cm length 4 mm width, and the electron gun is evacuated from both the side-tubing and the anode side where a thin gate valve is installed, so that the gun can be isolated from the other system, in the case of replacement of the cathode or filament.

At the output of the accelerator, a pneumatic gate valve is mounted, which is closed automatically in case of the vacuum failure of the synchrotron. The pump system consists of the 6″ and 3″ oil diffusion pumps which are connected in series. Although a nitrogen cold trap is provided, it is not used without any trouble to date. A normal ionization gauge mounted on the pump head and two bared ionization gauges mounted at both ends of the manifold are used for monitoring of the vacuum. A philips gauge is used for the interlock of the system.

The pressure of the vacuum system measured by a normal gauge is 1–2×10^{-6} mm Hg and that by a bared gauge is 1–1.5×10^{-5} mm Hg at an operating condition.

The accelerator guide is cooled by pure water cooling system, and maintained at 30°±1°C. The focusing coil and the electron gun are maintained at 30°±10°C by another cooling system.

In order to prevent the dew-drops in the wet season, the cooling temperature of 30°C is used.

§ 10. Electron Gun

The electron beam from the gun is injected to the accelerator guide at 80 kV ($\beta_e=0.5\,c$) and the pulse duration of 2 μsec. The cathode of the gun is used at the temperature limited region. The cathodes tried to date are the tungsten spiral filament, the tantalum bombarded cathode, and the oxide coated cathode. The spiral filament is a simple cathode, while, the deformation of the filament due to the high temperature causes the reduction of the transmission current and defocusing of the electron beam. The tantalum cathode is heated by 2 kV electron bombardment from a tungsten filament. Although the bombarded cathode is a suitable one for the pumped system, the emission current is sensitive to the bombarder current and the operation is not simple. In spite of various difficulties as described in the other paper7), the oxide coated cathode was also tested. However all guns used thus far must be regarded as tentative ones.

The cathode and the filament are pulsed to 80 kV negative through a 10:1 step up pulse transformer, which is biased by a dc current12). The pulse transformer has trifilar secondary windings in order to be used for the bombarded cathode, and the 5.2 KΩ dummy load is connected to the secondary. The 5C-22 hydrogen thyratron is used as a switching tube and a 52 Ω cable of 200 m in length is used as the pulse forming line which gives the pulse duration of 2μ sec.

The trigger to the pulser is delayed by 0–2μsec. with respect to the klystron pulser trigger, because of the filling time of the accelerator guide.

The electron beam injected from the gun is lost due to the angular misalignment or to the defocusing forces, and the steering coils and the focusing coils are placed in the space between the gun and the accelerator guide.

§ 11. Preliminary Test and Performance

The testing of the accelerator primarily involves the measurements of the electron beam current and the energy spectrum. The beam current is measured by both the Faraday cup and the ferrite core induction probe, and the energy spectrum is measured by an analyzer magnet.* An induction probe is used as the beam current monitor. The energy spectrum and the beam current are measured at the same time.

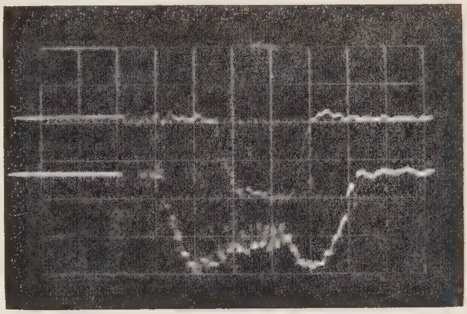

Fig. 16. The upper pulse shows the beam current of 80 mA, 2μs. The lower pulse shows the residual rf power affected by the beam loading input rf power; 1.9 MW, pulse length; 4μs).

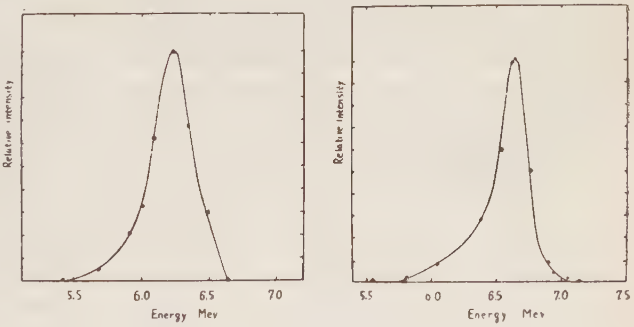

(a) (b)

Fig. 17. The energy spectrum. (a) without prebuncher, (b) with prebuncher.

---

* We are indebted to Dr. Y. Kobayashi and Mr. R. Yamada for making the analyzer magnet and the induction probe.

The misalignment of the beam is corrected by the steering coils placed in front of the gun. The magnetic fields in the drift space and in the bunching section are critical, but those over tapered section have only little effect on the beam current. The maximum beam current obtained thus far is 220 mA with a 2μ sec. pulse length; for the input rf power of 1.7 MW, the energy at the maximum beam intensity is 4.3 MeV.

The effect of the beam loading is observed on the scope by the rf power monitor at the output as shown in Fig. 16. The rf pulse shortening is observed at the start of the operation in the case of the low rf power and the heavy beam loading, but it disappears gradually.

The energy spread was found to have a half width of 5.4% at 6.2 MeV without the prebuncher (input rf power: 2 MW, total beam current: 40 mA), and a half width of about 3% at 6.6 MeV with the prebuncher (input rf power 2 MW, total beam current 30 mA). (Fig. 17)

It is found that the use of the prebuncher improves the acceptance of the buncher as well as the energy spread.

Acknowledgements

The construction of the accelerator was due to the Linear accelerator group of INS-High energy division. The author expresses his hearty thanks to Prof. H. Kumagai and Prof. T. Nishikawa for their encouragement, support and valuable advice, and to Mr. Miyahara. Mr. G. Horikoshi. Mr. H. Baba, Mr. K. Ishii, Mr. K. Kobayashi and M. I. Itō for their valuable cooperation and assistance. The author also thanks to the other staff of the INS-High energy division for ther discussion and support, and to the members of Mitsubishi Heavy Industries Reorganized Ltd., Tokyo Seimitsu Sokuki Co. and Shimada Physical and Chemical Co. for their aid in bringing the accelerator to its present status.

References

1) T. Nishikawa, A. Miyahara and J. Tanaka: INS-TH-28. 1957.
2) A. Miyahara:、 J. Phys. Soc. Japan. To be published.
3) T. Nishikawa, J. Tanaka, A. Miyahara and H. Kumagai: J. Phys Soc. Japan **16** (1961), J. M. Ponce de Leon: M. L. Report No. 265. 1955.
4) J. Tanaka, T. Nishikawa, and A. Miyahara: INS-TH-30 1957. J. Tanaka, T. Nishikawa, A. Miyahara and T. Kobayashi INS-TH-38. 1961.
5) J. Tanaka, T. Nishikawa, A. Miyahara, and etal: INS-Report-26. 1961. J. A. Pope Plating. (1959) 1291.
6) T. Nishikawa, J. Tanaka, T. Amano, I. Ikawa: Machinery. **22** (1959) 1385.
7) M. Chodorow, E. L. Ginzton and etal: Rev. Sci. Instr. **26** (1955) 134.
8) C. W. Miller: Proc. I. E. E. **101** (1954) 207.
9) M. Chodorow. E. L. Ginzton, I. R. Neilsen and S. Sonkin: Pro. I. R. E. **41** (1953) 1584.
10) L. B. Mullett, B. G. Loach: Proc. Phys. Soc. **61** (1948) 271.
11) G. Horikoshi, H. Kumagai, S. Yamaguchi and T. Kakuyama: INSJ-27. 1960. (TH-36).
12) T. Nishikawa, H. Kumagai, A. Miyahara, J. Tanaka, K. Ishii, I. Itò: INS-Report-28. 1961-3.

JOURNAL OF THE PHYSICAL SOCIETY OF JAPAN, Vol. 16, No. 11, NOVEMBER, 1961

Angular Distributions of High Energy Gamma Rays from the $F^{19}(p, \gamma)Ne^{20}$ Reaction

By Kiichi ETOH*, Kazuo HISATAKE**, Takatoshi KOBAYASHI***,
Kinuko HORIE****, Haruko OHMURA and Yozo NOGAMI

Department of Physics, Faculty of Science, University of Tokyo,
Bunkyo-ku, Tokyo, Japan

(Received June 30, 1961)

The reaction $F^{19}(p, \gamma)Ne^{20}$ was studied for proton energies from 550 to 1500 keV. The 1322 keV resonance reported previously was not observed. The angular distributions of the gamma rays from Ne^{20} compound states corresponding to the $E_p=669$ and 1425 keV resonances to the first excited state were found to the isotropic within 2% in both cases. The angular distribution of the gamma ray to the first excited state of Ne^{20} at $E_p=1090$ keV was found to be $W(\theta)=(1\pm0.028)+(0.363\pm0.051)P_2(\cos\theta)-(0.019\pm0.069)P_4(\cos\theta)$. From this result the spin and parity of the 13.91 MeV state of Ne^{20} was determined to be 2^-.

§1. Introduction

The investigation of $F^{19}(p, \gamma)Ne^{20}$ reaction is important as a means to study the structure of Ne^{20} nuclei. Experimental results on this reaction, however, are not as numerous as those on the competing reaction $F^{19}(p, \alpha\gamma)O^{16}$ because of the following reason: The cross-section of the reaction $F^{19}(p, \gamma)Ne^{20}$, is, in general, less than 1% of the cross-section for the reaction $F^{19}(p, \alpha\gamma)O^{16}$ and the resonance energies for both reactions coincide in most cases[4]. Therefore the former reaction is liable to be obscured by the latter in spite of the difference in energies of prominent gamma rays, i.e. 6∼7 MeV for the reaction $F^{19}(p, \alpha\gamma)O^{16}$ and more than 10 MeV for the reaction $F^{19}(p, \gamma)Ne^{20}$ [4)–6)]. A tedious procedure has to be followed to separate the yield of high energy gamma rays from that of the pile-up of low energy gamma rays.

For the 669 keV resonance in the $F^{19}(p, \gamma)Ne^{20}$ reaction the energy of the most intense high energy gamma ray was found to be 11.88 MeV which indicated that the transition occurs between the 13.511 and 1.632 MeV excited state of Ne^{20}. Clegg et al.[6], also found that the 11.88 MeV gamma ray was in coincidence with the 1.63 MeV gamma ray. Farney et al.[4] found that the angular distribution of

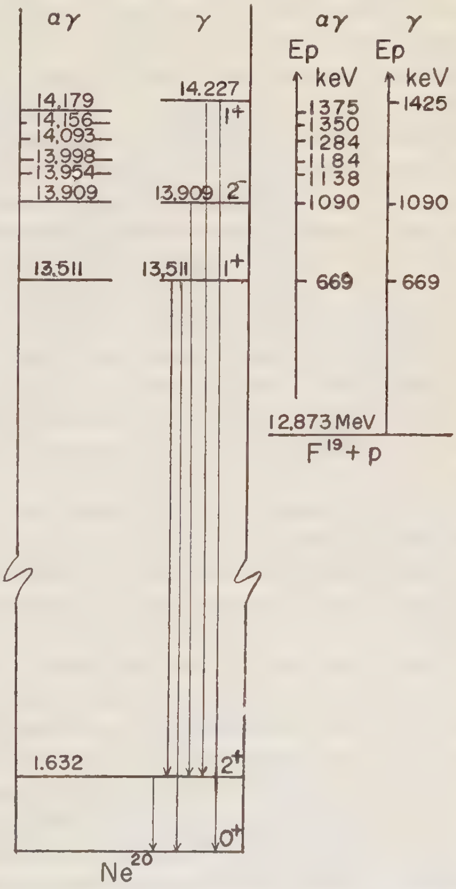

Fig. 1. Shows the pertinent levels of the Ne^{20} nuclide.

---

* Nippon Atomic Industry Group Co., Ltd., Hibiya Mitsui Bldg., Chiyoda-ku, Tokyo.

** Department of Physics, Tokyo Institute of Technology, Meguro-ku, Tokyo.

*** Mitsubishi Atomic Industries Incorporated. Ohtemachi Bldg., Chiyoda-ku, Tokyo.

**** Radio Isotopes Laboratory, University of Tokyo, Bunkyo-ku, Tokyo.

the high energy gamma ray was isotropic within 2%, which was compatible with $J=1^+$ assignment for the compound state corresponding to the 669 keV resonance.

In the present paper the gamma rays for the resonances at $E_p=669$, 1090, and 1425 keV are studied. The angular distributions of the gamma rays which go to the 1.63 MeV excited state are also investigated at those resonances. From the observed angular distribution functions the spins and parities of the compound states are discussed.

§ 2. Experimental Arrangement and Procedure

The bombarding protons for the present experiment were provided by the electrostatic accelerator at the University of Tokyo. The proton energy was held constant within 0.1 % during each run by means of a 45° magnetic analyzer and a feed-back system. The beam current of 2.0 to 3.5 μA was generally used and its fluctuation was kept as small as possible.

A target chamber used for the present experiment was made with one millimeter thick brass cylinder of 5 cm in diameter and 7 cm in height. The chamber was electrically insulated from the beam duct to measure the beam current by a current integrator. Two kinds of targets were prepared by evaporating CaF_2 on 0.15 millimeter thick tantalum backings. The one which was used for excitation curve measurement was about 4.7 keV thick for 874 keV protons and the other for the angular distribution measurements was about 16.3 keV thick for protons of 874 keV.

Two scintillation counters were used for the measurement of gamma-ray spectra. One of them was a 3″×3″ NaI(Tl) crystal and was used for high energy gamma rays ($E\gamma>10$ MeV). It was mounted on a rotating arm for the purpose of angular distribution measurements. The output pulses were fed into a twenty-channel pulse height analyzer. The other counter was a 2″×2″ NaI(Tl) crystal and was used for low energy gamma rays ($E\gamma>4$ MeV). The output pulses of this counter were fed into a single-channel pulse height analyzer. This counter was used for counting 6~7 MeV gamma rays in measuring the excitation curve, and was also used as a monitor counter in angular distribution measurements.

For the study of the excitation curves of the $F^{19}(p, \gamma)Ne^{20}$ and $F^{19}(p, \alpha\gamma)O^{16}$ reactions the high energy detector and the low energy detector were set at 50° and 140° to the beam, and at 9.0 cm and 8.7 cm from the target, respectively. In order to detect only the gamma rays between the compound states of Ne^{20} and the 1.63 MeV first excited state, the bias of the twenty-channel pulse height analyzer was set to an appropriate value which cuts off 6~7 MeV gamma rays completely and was changed with the energy of bombarding protons. The energy scale of the gamma ray detector was frequently checked by measuring the intense gamma ray of 6.14 MeV from the $F^{19}(p, \alpha\gamma)O^{16}$ reaction. The integral bias of the single-channel pulse height analyzer was set to record gamma rays above 4 MeV in order to detect the gamma rays from the $F^{19}(p, \alpha\gamma)O^{16}$ reaction mostly.

§ 3. Pile-up Correction

Because of the presence of the strong resonances for the low energy gamma rays induced by the $F^{19}(p, \alpha\gamma)O^{16}$ reaction, the effect of pile-up in the gamma rays spectrum appeared very strongly even at about 12 MeV, so that the correction for this effect was necessary. The following two methods of correction were applied in the measurements of the excitation curves and the angular distributions respectively.

In the case of the excitation curve measurements the method of Farney et al.[4] was used. The Total number of counts N_{tot} which appear in the high energy region is composed of the true high energy gamma ray counts N_{tru}, background counts N_b, and pile-up counts N_p or

$$N_{tot}=N_{tru}+N_b+N_p=N_{tru}+N_b+\alpha N^2/T$$

where N is 6~7 MeV gamma ray counts during the time of observation T. N_p is linear in N^2/T and coefficient α contains all unknown factors which can be determined experimentally.

In this experiment the value of α was determined by bombarding a fluorine target by 874 keV protons. It was assumed that there were only 6~7 MeV gamma rays in the 874 keV resonance, which were induced by the

$F^{19}(p, \alpha\gamma)O^{16}$ reaction and that all the counts in the high energy region came from either the pile-up or the background. N_{tot} and N_b were counted for several values of constant beam current. The resultant counts in the high energy region after subtracting the background counts were plotted as a function of N^2/T, as is shown in Fig. 2. From the figure the coefficient of the slope, α, is determined to be 1.5×10^{-7} sec/counts. In the study of the excitation curve, the pile-up counts were corrected by using this value.

It would be desirable if the pile-up counts and the background counts could be eliminated automatically by subtraction. In the study of angular distribution, the excitation curve was measured near the interested resonance using the target of 16.3 keV thickness. In Fig. 3 the excitation curves near the 1090 keV resonance of $F^{19}(p, \alpha\gamma)$ and $F^{19}(p, \gamma)$ are shown. In this figure closed circles and open circles show the yields of the high energy gamma rays and low energy gamma rays, respectively. An arrow B indicates the proton energy where the yield of low energy gamma rays is the same as at the resonance energy indicated by an arrow A. The position indicated by arrow A is at the exact resonance of the reaction $F^{19}(p, \gamma)Ne^{20}$ but the position of arrow B is assumed off-resonance. The high energy gamma ray angular distribution at the 1090 keV and 1425 keV resonances in the reaction $F^{19}(p, \gamma)Ne^{20}$ were obtained by making the following subtraction method. The high energy gamma ray counts at arrow A are generally composed of the true high energy gamma ray counts, pile-up counts and background counts. On the other hand the high energy gamma ray counts at arrow B are assumed to consist only of pile-up counts and background counts. Thus the true high energy counts were obtained by subtration the high energy gamma ray counts at arrow B from the high energy gamma ray counts at arrow A.

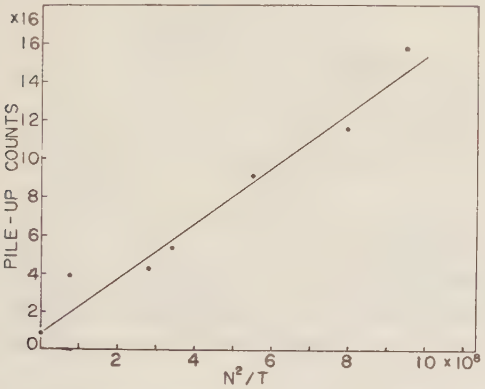

Fig. 2. Pile-up counts vs N^2/T for proton bombardment of fluorine at $E_p=874$ keV. N is total yield and T is counting time.

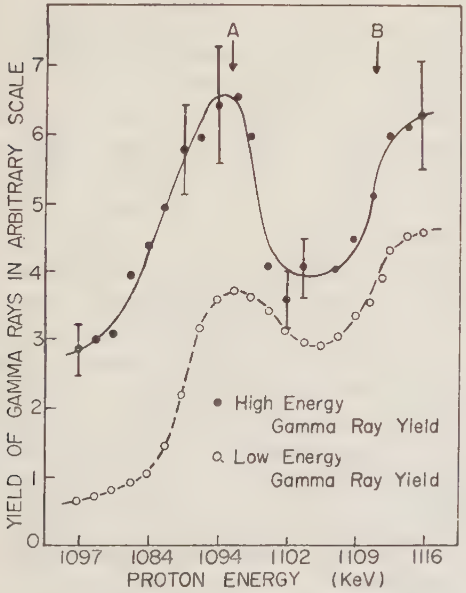

Fig. 3. Excitation curve obtained near the $E_p=1090$ keV resonance using the target of 16.4 keV thickness.

§ 4. The Experimental Results

(a) Two excitation curves were obtained by measuring the gamma rays associated with the transition from Ne^{20} compound states to the first excited state and the gamma rays of $F^{19}(p, \alpha\gamma)O^{16}$. The target thickness was 4.7 keV. In this measurement the proton energy was changed in 1 keV step near resonance energies and in 4 keV step elsewhere. These results are shown in Fig. 4, where curve A is yield of gamma ray with energies above 4 MeV, curve B is the yield of the gamma rays resulting from the transition from Ne^{20} compound states to the first excited state of Ne^{20} correted only for background counts, and curve C is the excitation curve corrected for the pile-up. Proton energy was calibrated by referring to the 990.8 ± 0.2 keV resonance in the reaction $Al^{27}(p, \gamma)\cdot Si^{28}$. The errors in proton energies were estimated to be less than 3 keV. In curve A of Fig. 4,

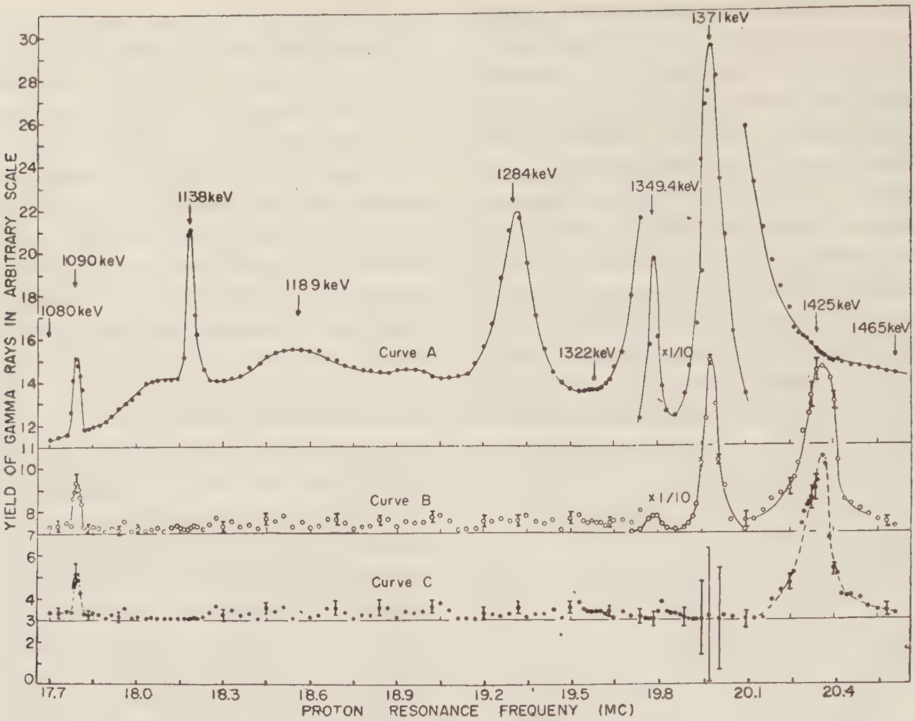

Fig. 4. Gamma ray yield from proton bombardment of 4.7 keV thick calcium floride target. Curve A shows the yield of gamma ray with energies higher than 4 MeV, curve B shows the yield of gamma rays with energies higher than 10 MeV and curve C shows the 12 MeV gamma ray yield corrected for pile up.

peaks are found at $E_p=1090$, 1138, 1184, 1284, 1350 and 1375 keV, which are to be considered as the previously reported resonances of the $F^{19}(p, \alpha\gamma)O^{16}$ reaction[7)-11)]. In curve B peaks are found 1090, 1350 and 1425 keV. In the corrected excitation curve (curve C), only two peaks are found at 1090 and 1425 keV. These two peaks are considered to be the resonances of $F^{19}(p, \gamma)Ne^{20}$ reaction[4),5)]. The peak at 1350 keV in curve B disappears after the pile-up correction.

The resonance at $E_p=1322$ keV, which was reported by Sinclair[5)] and Farney et al.[4)] was not observed. The cross-section at the peak of this resonance was estimated to be less than 20% of the peak cross-section of the 1090 keV resonance, which was measured to be less than 0.05 mb by Sinclair[5)]. The widths of the 1090 and 1425 keV resonance were found to be about 1 keV and 15 keV, respectively.

(b) Fig. 5 shows the gamma ray spectra taken at $E_p=669$, 1090, and 1425 keV. The resonance energies are indicated on each curve. In each curve of Fig. 5, arrows a, a′ and a″ show the expected position of the full energy peaks of the gamma rays resulting from the transition from the compound state of Ne^{20} to the ground state, and arrows b, b′ and b″ show the expected positions of the full energy peaks of the transition to the first excited state. The energies at arrows b, b′ and b″ are 11.88, 12.29 and 12.59 MeV, respectively. Arrows c, c′ and c″, and d, d′ and d″ show the expected position of the one quantum escape and two quanta escape peaks of the gamma rays corresponding to arrows b, b′ and b″, respectively. Arrows e, e′ and e″ show the expected position of the full energy peaks of the 6.14 MeV gamma ray of the $F^{19}(p, \alpha\gamma)O^{16}$ reaction. The ratio of the gamma ray yield (the area under arrow a″) corresponding to the ground state transition to that of the transition to the first excited state (the area under the arrow b″ for the 1425 keV resonance) was measured to be less than 4%.

(c) In the measurements of the angular distributions at the resonances 669, 1090 and 1425 keV, the high energy gamma rays (11.88, 12.28 and 12.59 MeV) were detected at $\theta_{lab}=0°$, $22.5°$, $45°$, $67.5°$, $90°$ and $107.5°$ with respect to the proton beam. The high energy gamma ray yield was obtained by adding all counts that appeared in channel 65 to channel 75.

The angular distribution of the 11.88 MeV gamma ray at $E_p=669$ keV was found to be almost isotropic. This result is consistent with the previously reported assignment[4),12)] of $J=1^+$ for the 13.511 MeV compound level of Ne^{20}.

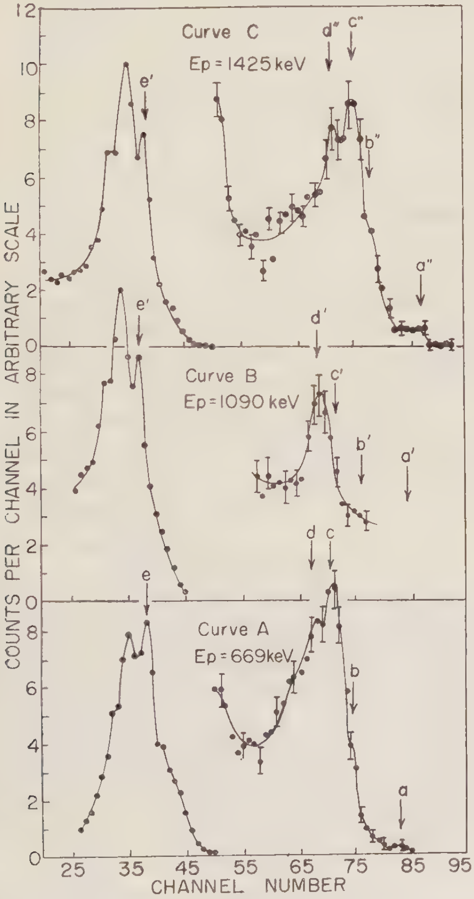

Fig. 5. Spectra of the gamma rays from $F^{19}(p,\gamma)Ne^{20}$ at $E_p=669$, 1090 and 1425 keV. Arrows a and b show the expected position of the full energy peaks of gamma ray resulting from the transition from Ne^{20} compound state to the ground state and to be first excited state, respectively. Arrows c and d show the expected positions of the one quantum escape and two quanta escape peaks of the gamma ray corresponding to the one arrow b, respectively. The arrow e shows the full energy peaks of the 6.14 MeV gamma ray of the $F^{19}(p, \alpha\gamma)O^{16}$ reaction.

The angular distribution of the 12.28 MeV gamma ray at $E_p=1090$ keV was taken at on-resonance and off-resonance. These measurements were repeated three times and the energy scale of the spectrometer was adjusted before and after the counts were taken. The least square fit[13)] to the measured angular distribution of the 12.28 MeV gamma ray at $E_p=1090$ keV was

$$W(\theta)=(1\pm0.028)+(0.363\pm0.051)P_2(\cos\theta)$$
$$-(0.019\pm0.069)P_4(\cos\theta)\ .$$

The curve of the least square fit is shown in Fig. 6 together with the measured points.

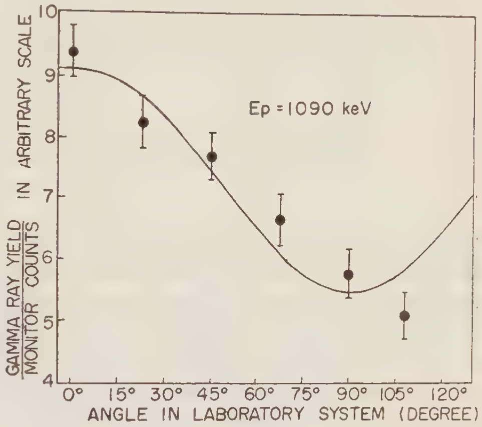

Fig. 6. Angular distribution at $E_p=1090$ keV. The solid line represents the least square fit.

The angular distribution at $E_p=1425$ keV was measured in a similar procedure. The least square fit to this angular distribution was

$$W(\theta)=(1\pm0.012)-(0.01\pm0.01)P_2(\cos\theta)$$
$$-(0.01\pm0.02)P_4(\cos\theta)\ .$$

These results were not corrected for the finite solid angle of the detectors, since the correction factor for the coefficient of $P_2(\cos\theta)$ was estimated to be less than 1%[13)].

§ 5. Discussion

The theoretical coefficients of the angular distribution of (p, γ) reaction for several values of spins and parities of compound states are shown in Table I. According to this table and the experimental distribution of the 12.28 MeV gamma ray at $E_p=1090$ keV which was obtained in the last section, $J=2^-$ assignment for the 13.909 MeV compound level of Ne^{20} is most plausible. In this re-

Table I. The theoretical angular distribution coefficients of (p, γ) reactions[15]. l is the orbital angular momentum of incident protons, S is the channel spins and J^{π} is the spins and parities of the compound state. The angular distribution function is represented by $W(\theta)=1+a_2P_2(\cos\theta)+a_4P_4(\cos\theta)$.

l	S	J^{π}	Mode	a_2	a_4
1	0^+	1^-	E1	−0.1	0
1	0^+	1^-	M2	−0.5	0
1	1^+	1^-	E1	+0.05	0
1	1^+	1^-	M2	+0.25	0
1	1^+	2^-	E1	+0.35	0
1	1^+	2^-	M2	+0.11	0
2	0^+	2^+	E2	−0.15	−0.49
2	0^+	2^+	M1	+0.50	0
2	1^+	1^+	M1	−0.05	0
2	1^+	1^+	E2	−0.25	0
2	1^+	2^+	M1	+0.25	0
2	1^+	2^+	E2	−0.08	+0.33
2	1^+	3^+	M1	−0.34	0
2	1^+	3^+	E2	+0.12	+0.45

sonance the gamma ray induced by the $F^{19}(p, \alpha\gamma)O^{16}$ reaction was also observed. The assignment of $J=2^-$ is consistent with the fact that the compound level of Ne^{20} which decays to the 2nd, 3rd and 4th levels of O^{16} by emission of alpha particles have even J—odd parity or odd J—even parity so far as observed[1].

The ground state transition at $E_p=1090$ keV resonance is negligible small compared with the transition to the first excited state. No information was obtained for the cascade transition to the 4.97 MeV level which was reported by Kane et al.[2]. It is known for $E_p=669$ keV resonance that the transition to the first excited state is predominant in comparison with the transition to the ground state[2),4]. The present experiment confirms this fact. The theoretical explanation of this fact was given by Kane, Pixley and Wilkinson[2].

The angular distribution of the gamma rays for the $E_p=669$ keV resonance which corresponded to the transition between the 13.511 MeV compound state of Ne^{20} and the first excited state was found to be isotropic within 2%. This result is consistent with $J=1^+$ assignment for the compound state which was reported previously[4].

The result of the angular distribution of the 12.6 MeV gamma ray for the $E_p=1425$ keV resonance was found to the also isotropic within 2%. It is compatible with the assignment of $J=1^+$ for the 14.227 MeV compound level of Ne^{20} which was obtained by the result of $F^{19}(p, p)F^{19}$ experiment[12]. It should be noted that the $F^{19}(p, \alpha\gamma)O^{16}$ reaction was not observed in this resonance in contrast to the resonance of $E_p=669$ keV.

Acknowledgements

The authors would like to thank Mr. K. Katori, Mr. S. Matsumoto, Mr. M. Koike, Mr. A. Ohuchi and the members of the Van de Graaff Group, University of Tokyo, for their assistance in the experiment. They are also indebted to Dr. Y. Hashimoto and Mr. Y. Nakajima for their helpful discussions in the interpretation of the result.

References

1) F. Ajzenberg-Selove and T. Lauritsen: Nuclear Phys. **11** (1959) 1.
2) J. V. Kane, R. E. Pixley and D. H. Wilkinson: Phys. Rev. **120** (1960) 952.
3) H. J. Lipkin: *Proceedings of the Rehovoth Conference on Nuclear Structure*, (North Holland Publishing Company, Amsterdam 1958) 1759.
4) G. K. Farney, H. H. Givin, B. D. Kern and T. H. Hahn: Phys. Rev. **97** (1955) 720.
5) R. M. Sinclair: Phys. Rev. **93** (1954) 1082.
6) A. B. Clegg, G. A. Jones and D. H. Wilkinson: Proc. Phys. Soc. (London) **A68** (1955) 538.

7) S. E. Hunt and K. Firth: Phys. Rev. **99** (1955) 786.
8) J. D. Kington, J. K. Bair, H. O. Cohn and H. B. Willard: Phys. Rev. **99** (1955) 1393.
9) C. Y. Chao, A. V. Tollestrup, W. A. Fowler and C. C. Lauritsen: Phys. Rev. **79** (1950) 108.
10) T. W. Bonner, J. E. Evans: Phys. Rev. **73** (1948) 666.
11) J. W. Butler and C. R. Gossett: Phys. Rev. **108** (1957) 1473.
12) E. U. Baranger: Phys. Rev. **99** (1955) 145.
13) M. R. Rose: Phys. Rev. **91** (1953) 610.
14) W. T. Sharp, J. M. Kenedy, B. J. Sears and M. G. Hoyle: CRT-556, (1953), *Table of Coefficients for Angular Distribution Analysis.*

JOURNAL OF THE PHYSICAL SOCIETY OF JAPAN, Vol. 16, No. 11, NOVEMBER, 1961

Breakup of Deuterons by the Reactions $H(d, p)pn$ with $E_d=18$ MeV and $D(p, p)pn$ with $E_p=9$ MeV

By Keigo NISIMURA

Institute for Nuclear Study, University of Tokyo, Tanashi-machi, Kitatama-gun, Tokyo, Japan

(Received July 27, 1961)

The energy spectra of protons from the reactions $H(d, p)pn$ with $E_d=18$ MeV and $D(p, p)pn$ with $E_p=9$ MeV have been measured as a function of angle. After conversion to the c.m. system, the shapes of the spectra have been examined in connection with pair interaction between nucleons in the final state. The differential cross section of protons emitted by the reaction $p+d\rightarrow p+p+n$ has a minimum at about 120° similar to the cross section of $p+d$ elastic scattering.

§ 1. Introduction

The breakup of deuterons by nucleon bombardment is the simplest nuclear three-body reaction. Especially at low energies where the transit time of the bombarding nucleon across the interaction region is of the order of that of the internal motion of the deuteron, it is expected that the bombarding nucleon interacts with both particles of the deuteron and the study of this reaction is of importance to study the mechanism of the nuclear three-body interaction.

Recently the energy spectra of neutrons from the reaction $p+d\rightarrow p+p+n$ at an approximate total reaction energy (the total kinetic energy in the c.m. system of the three particles after deuteron breakup) of 4 MeV were investigated at 0° and 180° by N. A. Vlasov and his co-workers[1]. These spectra show interesting structure which can be satisfactorily explained by pair interaction between the nucleons in the final state[2]. But in spite of its importance, the amount of information on the angular dependence of the energy spectrum of emitted nucleons is scanty. (There is an attempt to obtain the spectra of breakup protons by the reaction $H(d, p)pn$, which are at backward angles in the case of an incident nucleon[3].)

Previously we reported the measurement of the spectra of breakup protons at several angles at $E_p=14$ MeV[4]. In this paper, the energy spectra of the protons from the reaction $p+d\rightarrow p+p+n$ at various c.m. angles between 20° and 150° at a total reaction energy of 3.8 MeV are investigated. The conversion to c.m. angles was made using the measurements of the spectrum of breakup protons at various laboratory angles for the reactions $H(d, p)pn$ with 18 MeV deuterons and $D(p, p)pn$ with 9 MeV protons.

§ 2. Experimental Arrangements and Procedures

This work was carried out on the INSJ-160 cm variable energy cyclotron. The experimental arrangements were almost the same as those used in the previously-reported study on $D(p,p)pn$ at $E_p=14$ MeV. The external proton and deuteron beams of the cyclotron (whose energies were adjusted by the conditions of cyclotron operation and were determined by measurement of the range in Al foil) were collimated and focussed at the center of the 100 cm diameter scattering chamber. At the center of the scattering chamber, a 15 cm diameter gas target chamber with a 25 micron-thick mylar window extending to 290° of arc was located. On the turntable a detector slit system and a particle-selecting counter telescope composed of an improved five-layer proportional counter and an NaI scintillation counter were placed to detect the breakup protons.

At some angles, a part of the breakup proton spectrum in the pulse height distribution of NaI counter output pulses was masked by elastically-scattered or recoil deuteron pulses. For these portions, the five-layer proportional counter was used to separate the proton and the deuteron signals and to remove the deuteron pulses from the NaI counter output pulses by means of the smallest-pulse-selecting circuit and a coincidence-anticoincidence circuit. For the other parts of the spectra, the telescope counter was used only as a telescope to reject background counting in the NaI counter output due to γ-rays and neutrons. The block diagram of the counting electronics is shown in Fig. 1. The five-layer proportional counter used in the previous 14 MeV $p+d$ experiment was changed to a wide-window type in order to reduce the particle loss due to multiple scattering, and its calculated particle loss was less than 1% for 3 MeV protons.

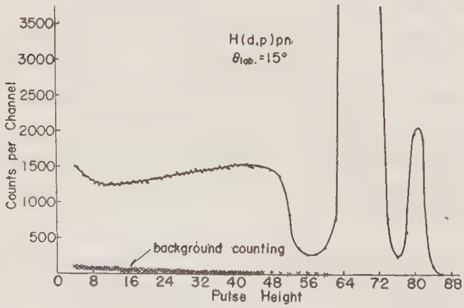

Fig. 2. Pulse height distribution in the NaI counter in coincidence with the five-layer proportional counter pulses.

Fig. 2 is an example of the spectrum of NaI counter output pulses in coincidence with the five-layer proportional counter pulses. When coincidence with the five layer proportional counter was used, the background became negligible at all angles larger than 10° both in the case of incident protons and of incident deuterons, and the background correction was small even at 10°. At 10° the background spectrum obtained with the gas-evacuated target was subtracted from the spectrum of the gas-filled target.

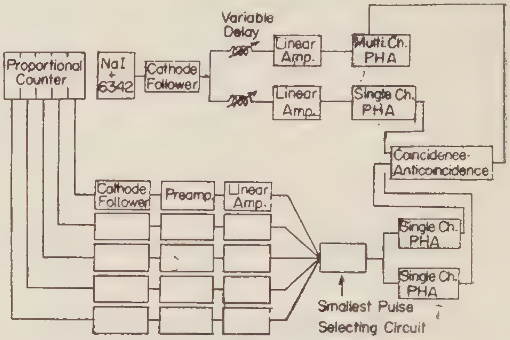

Fig. 1. Block diagram of the counting electronics.

Breakup proton spectra were obtained at laboratory angles between 10° and 50° for the case of incident protons and between 10° and 45° for the case of incident deuterons.

§ 3. Results

After subtracting the background and the elastically-scattered and recoil particle tails, which were discussed in the previous paper⁵⁾, the observed pulse height distribution at each angle was converted to an energy spectrum using the pulse height-energy conversion curve obtained by means of the pulse heights of elastically-scattered and recoil protons at various scattering angles and their kinematic relationships. In our detector system, the cut-off energy for protons was 2.6 MeV.

Then the energy spectra were converted into the center of mass system. However, the conversion of continuous spectra to the center of mass system is very complicated, because each point on the spectrum at one laboratory angle corresponds to a point on the spectrum at a different center of mass angle respectively, and because the spectrum at one center of mass angle is composed of points on the spectra of a range of laboratory angles. In order to obtain the spectrum at each center of mass angle, we had to do as follows:

At first, the angle and the energy of each point of the proton spectrum at each laboratory angle were converted to the respective angle and energy in the center of mass system, and the cross section of each point in the center of mass system was obtained by correcting for the difference of its solid angle and dE in the laboratory system and in the center of mass system. Then the data were replotted as an angular distribution of the cross section at each center of mass energy. Interpolating these graphs, we obtained the energy spectrum at each center of mass angle. The energy spectra thus obtained are shown in Fig. 3. The values of cross section indicated in these figure correspond to one half of the proton yield and indicate the reaction cross section for deuteron breakup, because in any one event two protons are emitted. The results have an accuracy of at least ±5 percent.

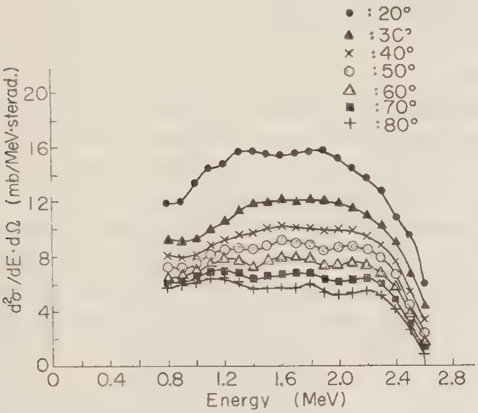

Fig. 3 a. Energy spectra of protons emitted by the reaction $p+d\rightarrow p+p+n$ at center of mass angles between 20° and 80°.

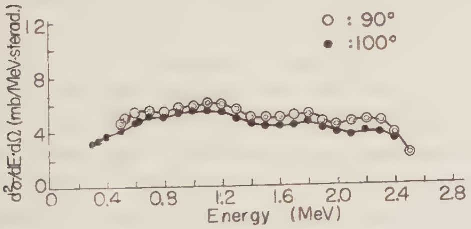

Fig. 3 b. Energy spectra of protons emitted by the reaction $p+d\rightarrow p+p+n$ at center of mass angles 90° and 100°.

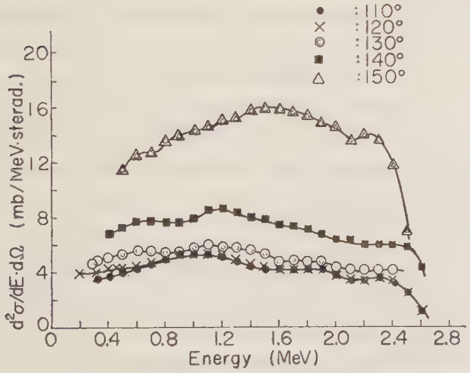

Fig. 3 c. Energy spectra of protons emitted by the reaction $p+d\rightarrow p+p+n$ at center of mass angles between 110° and 150°.

The spectra we obtained have not shown any remarkable structures such as the spectra of neutrons at 0° and 180° measured by Vlasov and his co-workers. But there are some characteristic features:

1) At forward angles (20°, 30° and 40°), the cross section smoothly decreases with higher energy. But at angles larger than 60°, the distributions near their upper bounds are rather flat, and at 150° the spectrum shows a small peak at its upper bound.

2) At backward angles, where we could observe the lower energy parts of spectra, especially at 130° and 140°, the spectrum shows a broad swelling in the neighborhood of 0.6 MeV. At forward angles, at the lower end of the spectrum (0.8–0.9 MeV), the curves have a flat or rather upward tendency towards the low energy side and this tendency may suggest the existence of a peak or a swelling in the neighborhood of 0.6 MeV, although we do not have any data to be discussed in

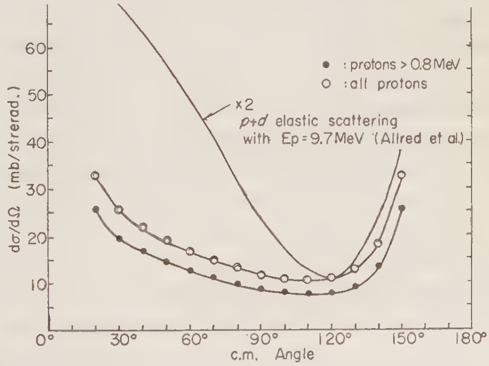

Fig. 4. Angular distributions of the differential cross section of protons emitted by the reaction $p+d\rightarrow p+p+n$.

this energy region at the forward angles.

3) In the middle energy region there is some structure.

The angular distribution of the differential cross section of protons emitted by the reaction $p+d \to p+p+n$ with energies greater than 0.8 MeV, and the angular distribution of the differential cross section of emitted protons of any energy, which was obtained by some assumptions about the form of the spectra down to zero energy, are shown in Fig. 4. These distribution are compared with the angular distribution of the differential cross section of $p+d$ elastic scattering with $E_p=9.7$ MeV. These curves have a minimum at about 120° similar to the cross section of elastic scattering.

§4. Discussion

The effect of pair interaction in the final state on the slow nucleon spectrum was considered by Migdal[6]. According to his calculation, the distribution in relative energy E between two nucleons near $E=0$ for a proton and neutron pair has the from

$$d\omega = \text{const.} \frac{\sqrt{E}}{E+\varepsilon} dE \ ,$$

where $\varepsilon=0.07$ MeV for the singlet state and 2.23 MeV for the triplet state. The distribution has a maximum at an energy of the order of ε. For two protons, the relation is more complicated due to Coulomb repulsion.

In our case, it seems that the interaction of a proton and a neutron in the final singlet state affects the shape of the spectrum near its upper bound due to another proton and also affects the shape at its lower energy side in the neighborhood of 0.6 MeV due to the proton interacting with the neutron. The interaction of two protons may affect the shape of the spectrum at its middle and low energy region, because in this case the relative energy of the two protons is not necessarily small in the region of the maximum of $d\omega$ and the distribution of the relative energy of the two protons is considerably broadened due to Coulomb repulsion.

If the peak at the upper bound of the spectrum is due to the final state interaction of a proton and a neutron in the singlet state, it may correspond to the lower energy side peak of the neutron spectrum at 0° c.m. obtained by Vlasov and his co-workers. Its appearence at backward angles may signify a large probability of neutron pickup in the forward direction by the incoming proton, and the angular variation of the swelling at the upper bound may correspond to the angular variation of the probability of neutron pickup.

In the middle energy region, the interference due to two proton interaction and to proton-neutron interaction may be effective in explaining the shape of the spectrum, and in the region between the middle and low energy region two proton interaction and proton-neutron interaction may be effective. However, in order to discuss these effects, a more detailed calculation is required.

If we integrate the cross section over angles between 20° and 150°, and over energies larger than 0.8 MeV, we obtain a partial reaction cross section of 94 mb. Futhermore, if we make some assumptions about the form of the spectra down to zero energy and extrapolate to 0° and 180°, we obtain a rough estimate of the total reaction cross section of 200 mb. This value is not inconsistent with other experimental knowledge about $p+d$ or $n+d$ reactions and with Frank and Gammel's estimation of the total reaction cross section of $p+d$ breakup reaction.

Acknowledgements

The author wishes to express his thanks to Professor J. Sanada for his continuous encouragement and discussion. His thanks are also expressed to Drs. S. Suwa, I. Hayashi, K. Fukunaga, N. Ryu, H. Hasai, R. Chiba and S. Hiradate for their active participation in obtaining the data, and to Prof. D. C. Worth for comments to the manuscript. Gratitude is due to the operating crew of the cyclotron, particularly Messrs. T. Karasawa and H. Ogawa.

References

1) N. A. Vlasov, S. P. Kalinin, B. V. Rybakov and V. A. Sidorov: JETP (USSR) **38** (1960) 1733 Similar results were obtained by M.P. Nakada et al.
2) V. V. Komarov and A. M. Popova: JETP (USSR) **38** (1960) 1559.
3) K. W. Brockman: private communication.
4) S. Kikuchi, J. Sanada, S. Suwa, I. Hayashi, K. Nisimura and K. Fukunaga: J. Phys. Soc. Japan. **15** (1960) 748.
5) S. Kikuchi, J. Sanada, S. Suwa, I. Hayashi, K. Nisimura and K. Fukunaga: J. Phys. Soc. Japan **15** (1960) 9.
6) A. B. Migdal: JETP (USSR) **28** (1955) 3.

JOURNAL OF THE PHYSICAL SOCIETY OF JAPAN, Vol. 16, No. 11, NOVEMBER, 1961

Inelastic Scattering of Protons from Several Light Odd-Even Nuclei in the Energy Range from 6.0 MeV to 7.5 MeV

By Jun KOKAME

Institute for Chemical Research, Kyoto University, Kyoto

(Received July 31, 1961)

Protons accelerated by the 105 cm cyclotron of Kyoto University were used to investigate the energy dependence of the angular distributions and the reaction mechanism of the inelastically scattered protons from the odd-even nuclei, B^{11}, F^{19}, Al^{27} and P^{31} at 6.0~7.5 MeV using conventional electronic techniques. It was found that (a) the energy dependence of the angular distribution has close relation to the excitation energy of the compound system, namely above the excitation energy of about 13 MeV in the compound system, many patterns of the angular distributions including that of the light even-even nuclei were relatively energy-independent: (b) Total cross sections were considerably smaller than that of the neighbouring even-even nuclei and less energy-dependent: (c) In the case of F^{19} the shapes of the angular distributions suggested the existence of a direct interaction: (d) The relative yields from the various levels of Al^{27} might have some relation to its nuclear structure in the Nilsson model.

§1. Introduction

Both experimental[1−17)] and theoretical[18−24)] investigations for the inelastic scattering of protons from various nuclei in the energy range from several MeV to a few tens of MeV have been performed by many authors.

From these results, it seems to be fairly well established that in medium weight and light-medium weight nuclei, such as Ti, Cr, Fe, Ni and Zn,[2,8,9,13)] the experimental results show generally a forward peak in the angular distributions at the proton energies greater than 6~7 MeV. These peaks in differential cross sections are almost independent of proton energy in considerably wide range[16)] so that the evidence of the direct interaction can be confirmed at these incident energies. In fact, satisfactory agreements between experimental results and theoretical descriptions in the angular distribution were obtained in many cases.[2,8,16)]

In these nuclei the forward peak becomes less prominent according as the incident energy decreases, while the backward cross sections increase almost uniformly.[8,13)] At the incident energy less than several MeV, these angular distributions become fairly isotropic.[9)] This tendency does not conflict with the concept of the compound nucleus process with the continuum and statistical assumptions which show an isotropic or 90° symmetric angular distribution[25,26)] for such medium weight nuclei in that energy range. Thus, in the nuclei of medium weight, it could be concluded generally that the reaction takes place mostly through the compound nucleus process at the relatively low energies, and the direct interactions come to play an important role beyond several MeV of incident energy.

On the other hand, in the light nuclei such as C^{12}, Ne^{20}, Mg^{24}, Si^{28} and S^{32}, the matters are not so clear as in the case of medium weight nuclei. There are many experimental evidences[3,10,16)] to show the violent change in the pattern of the angular distributions with a little change in incident energy, especially in the energy range from several MeV to about 10 MeV or more. It has been understood by many authors[4,6,13)] that these change in the pattern of the differential cross sections with energy is mainly attributed to the interference effect in the compound nucleus[26)], because inadequate number of levels for satisfying the statistical assumption are excited in such a light nuclei at these low energies. (In some cases the interference between the compound nucleus and direct interaction mechanism was also suggested.[10)]) But these circumstances are difficult to be confirmed by the reasonable agreement between experimental results and theoretical calculations. There is not yet any decisive evidence to exclude the direct process in the light nuclei at relatively low energies where the the pattern may be energy-dependent.[27)]

The most investigations performed up to date about the (p, p') reaction at various incident energies are restricted to the scattering from the even-even nuclei except rather a few cases (Li^7 [6)] and Be^9 [5,49)]). Little study was made about the energy dependence of the angular distributions of the (p, p') scattering of the odd-A nuclei, to the best of the author's knowledge. It seems to be worthwhile to investigate the (p, p') reaction using the odd-A nuclei for obtaining further knowledges about the reaction mechanism.

The inelastic scattering of protons from the odd-A nuclei has some characteristics in comparison with those of the even-even nuclei. (a) The excitation of the compound nucleus, which may be formed by the target nucleus plus an incident proton, is considerably higher than that of the neighbouring even-even nuclei for the same incident proton energy. (b) The thresholds of the (p, n) reaction of the odd-A nuclei are considerably lower than that of the even-even nuclei. (c) The spins and parities of both the ground level and the excited levels have much variety, whereas that of the even-even nuclei is restricted to $0+$, $2+$, $4+\cdots$. Thus the momentum transfers are not necessarily limited to an even value, which is mostly 2 in the even-even nuclei already investigated. (d) Relatively many levels of different spins of the residual nucleus could be expected to be excited, so that it is possible to compare the angular distributions and the cross sections with their energy dependence between the proton groups leaving the residual nucleus in the different excited states. (e) The (p, p') scattering of the light odd nuclei are the mirror reactions of the (p, n) reactions of the same target. Since the residual mirror nucleus can be expected to have the same spin-parity in the corresponding level, the comparison of these two reactions in the angular distribution and in the cross section at the same incident energy is very intersting to understand the reaction mechanism.

In the present paper B^{11}, F^{19}, Al^{27} and P^{31} are investigated at several proton energies ranging from about 6.0 MeV to 7.5 MeV.

§ 2. Experimental Procedure

A beam of protons accelerated by the 105 cm cyclotron of Kyoto University[29)] is deflected out and focused by a couple of quadrupole magnets[30)] on a tantalum slit of the collimator just before a scattering chamber so that a circular spot, 5 mm in diameter, is produced at the target. The scattering chamber[31)], 52 cm in inner diameter, has a turn table on which a set of scintillation counter described below is set up in such a way that the axis of the slit system of the counter cross the centre line of the turn table. A monitor counter which is the same as the detector on the turn table is connected to the outside wall of the chamber across a view window at a laboratory angle of 90° to the direction of the incident beam.

A Faraday cup is placed behind the chamber in order to measure the beam current. At the bottom of it a narrow hole is provided which has a graphite shutter with a piece of small magnet behind it. Usually the shutter is closed by the force of an electromagnet outside the vacuum, the field of which also prevents the escape of secondary electrons from the Faraday cup. When the current of the electromagnet is cut off, the shutter is opened so that the beam can be brought out from the vacuum through an aluminum foil, 40 μ in thickness, to an energy measurement device. This device and the method of measuring the energy are the same as that of the INS*, University of Tokyo[8,14)].

From the Bragg curve thus measured, the energy of the proton beam was determined after the manner of Mather and Segrè[32)], and the range energy relation published by Bichsel *et al.*[33)] The maximum energy of 7.45 MeV and the maximum current of about 0.1 μA at the Faraday cup were obtained. The incident energy was changed by the stacked aluminum foils placed in front of the collimator.

The energy spread of the beam after passing through the collimator is considered to be less than 50 keV. The change of the incident energy during the measurements was kept to be less than one percent.

The main detector on the turn table in the scattering chamber is shown in Fig. 1. A thin CsI (Tl) or NaI (Tl) scintillation crystal, about 25 mm in diameter, 0.6 mm and 1.5 mm

---

* Institute for Nuclear Study.

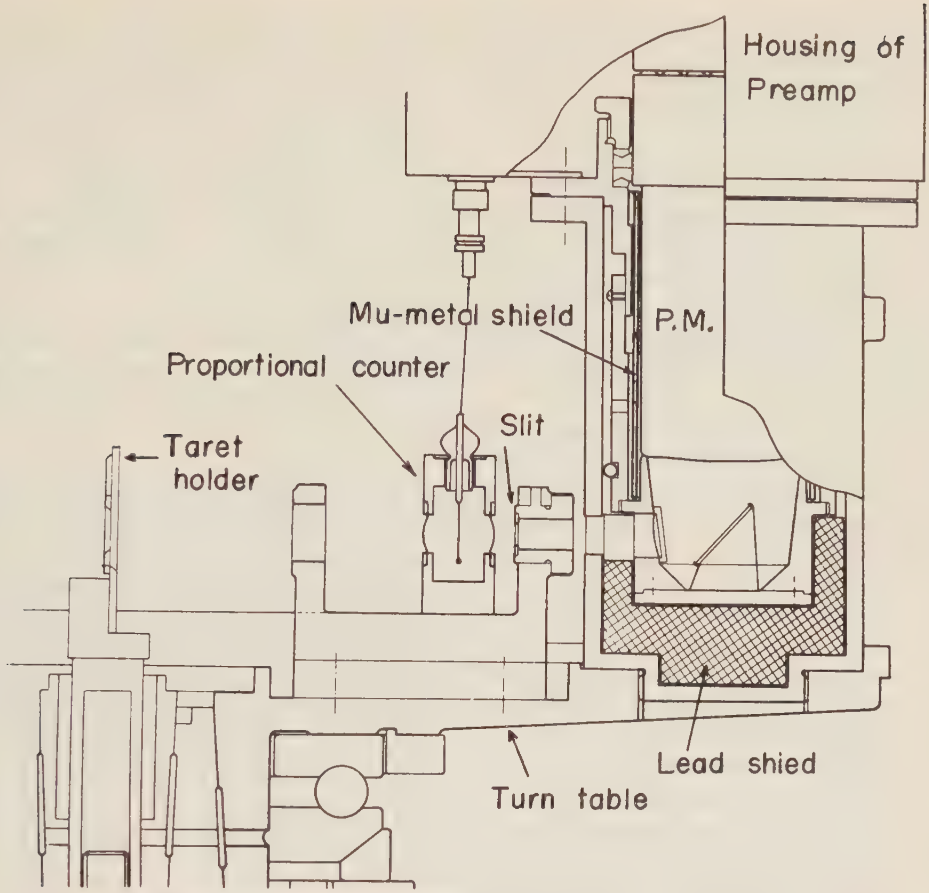

Fig. 1. The assembly of the detector on the turn table in the scattering chamber.

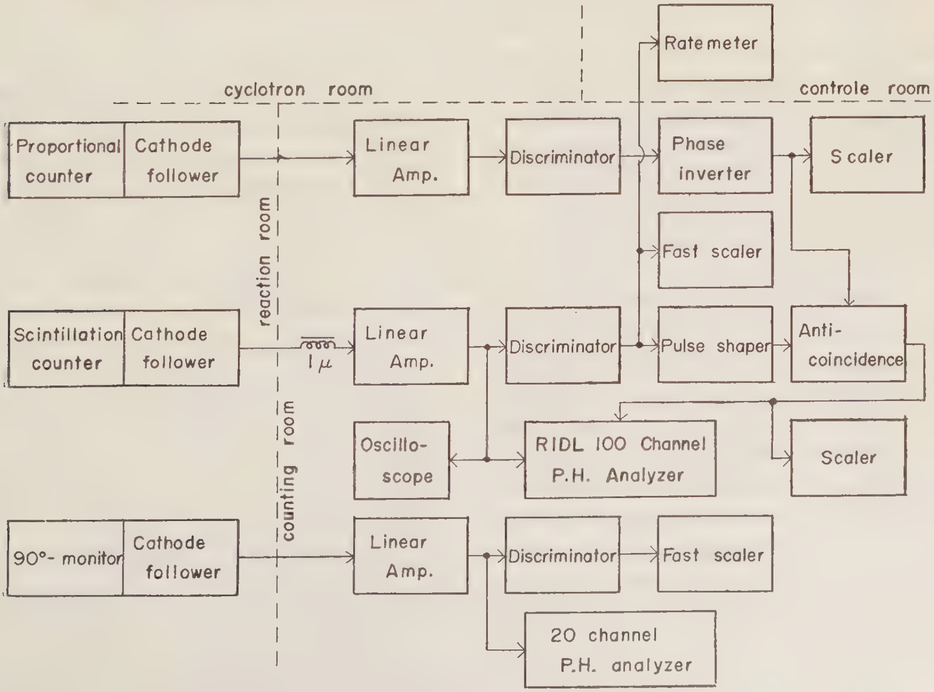

Fig. 2. The block diagram of the electronics.

in thickness respectively, was supported by fine wires[8)] in the reflection room painted with titanium oxide paint at an angle of elevation of about 30° to the direction of scattered particles. They plunge into the room for light reflection through 6 μ aluminum foil for light shield. A photomultiplier, RCA 6342A or 5819, with annealed mu-metal shield was mounted on the reflection room as shown in the figure. The inside of the housing of the detector was evacuated through a light-shielded hole together with the scattering chamber by an oil diffusion pump.

When the NaI(Tl) crystal was used, the whole detector was desiccated for several days in a dry box in which the humidity was kept below 10%. No change was discerned on the crystal surfaces before and after the experimental runs continued for several days.

A proportional counter**, of which gas pressure is about 40 cm Hg of argon with a few percent of CO_2, was used to discriminate the pulses of the alpha-particles produced by the competing (p, α) reaction from that of the scattered protons. Sometimes the counter was also used to eliminate the γ-ray background by usual coincidence techniques.

The signal pulses from these counters were brought to the counting room through the cathode followers connected closely to the counters in the scattering chamber and through the coaxial cables, 30 m long. They were amplified, dicriminated, and displayed on the multichannel pulse-height analyzer in an usual manner. The block diagram of the experimental set-up in electronics is shown in Fig. 2.

Amoung the four kinds of target materials, B, F, Al and P, B^{11} enriched to 96.7% was obtained from ORNL Isotope Division in the form of fine metallic powder. Targets of B^{11} and P^{31} were made by allowing the suspension of boron or red phosphorus in alcohol to settle onto an about 0.2 mg/cm² thick gold foil backing with a thin copper frame, and allowing alcohol to evaporate at room temperature. A cylindrical wall of teflon was used to fill alcohol on the gold backing which is placed on a thin teflon sheet. The sedimented B^{11} powders were found to cohere themselves fairly well, but to adhere rather poorly to the gold backing. However no binder was used for the reason that the most binders contain carbon in them so that elastically scattered protons from boron could not be distinguished from those of carbon. The boron targets 0.5~4.0 mg/cm², estimated by weighing, were prepared by this method. As for the uniformity, it was considered to be satisfactorily good for the targets heavier than about 0.5 mg/cm².

In the case of phosphorus, it was found to adhere well to the gold backing without any binder. The thickness of about 1 mg/cm² was used.

For the target of F^{19}, poly-tetra-fluorethylene (teflon) foils, about 2–2.5 mg/cm² in thickness, were used. The method of preparation will be reported elsewhere. The teflon target was found to suffer progressive damage by the bombardment of the beam so that the target was raised step by step before suffering from the serious damage. Absolute cross sections were measured at one angle using a fresh and sufficiently uniform foil of known weight with the low intensity beam.

For the target of Al^{27}, the commercially available aluminum foils of 0.67 mg/cm² were used.

§ 3. Experimental Measurements and Results

Boron 11.

The typical pulse-height spectrum of protons scattered from the target is shown in Fig. 3. The charged particles from the competing reactions in this energy range are only the alpha-particles from the reaction $B^{11}(p, \alpha)Be^8$ and those from break-up of residual nucleus Be^8. From the preliminarily calculated kinematics, some alphas were expected to overlap with the peak of inelastically scattered protons in the pulse-height spectrum. The proportional counter was used to discriminate the protons from the alpha particles. Fig. 4 shows an example of the dE/dx spectrum obtained from the counter. For reference, the pulse-height spectrum of these alphas from the scintillation counter displayed on the multichannel analyzer is shown in Fig. 5, which was obtained by the coincidence technique. In the (p, p') measurement, protons were distinguished from these alpha-particles by the anticoincidence technique, so that only the pulses of protons are

---

** The author is indebted to Dr. K. Fukunaga for the design and preparation of the counter.

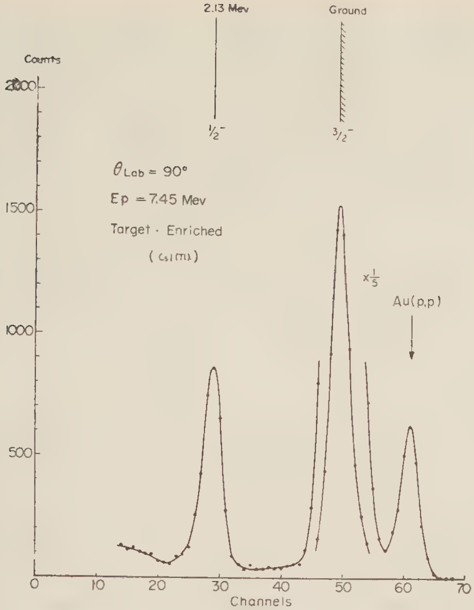

Fig. 3. The pulse-height spectrum of the scattered protons from the boron target. The energy levels corresponding to the peaks are also shown in the upper part of the figure.

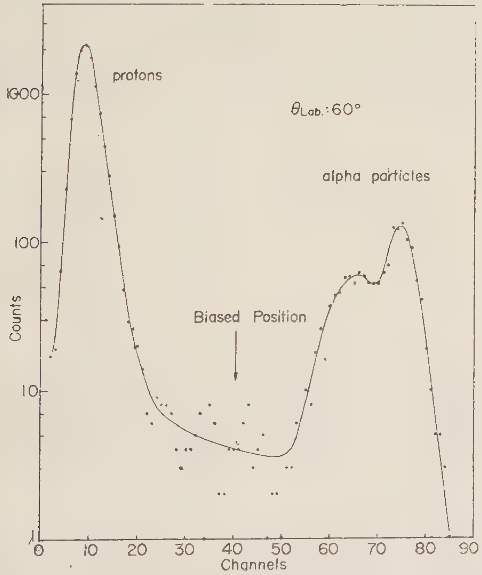

Fig. 4. The dE/dx spectrum from the proportional counter in the case of relatively thick boron target.

displayed on the multichannel analyzer.

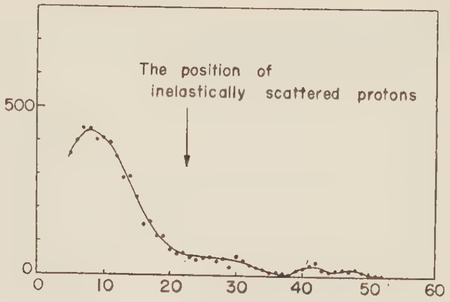

Fig. 5. The spectrum of the alpha particles from the reaction $B^{11}(p, \alpha)Be^8$ from the relatively thick boron target.

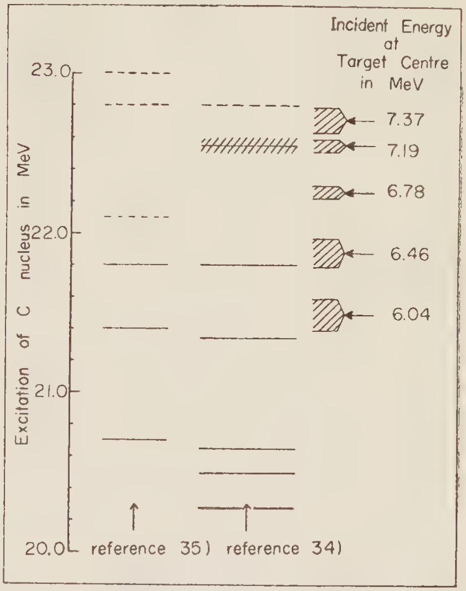

Fig. 6. Level schemes of C^{12} from the references 34) and 35), together with the positions of the excitation corresponding to the incident energy to the incident energy of the present experiment. The energy spread caused by the target thickness are also indicated.

Several targets were prepared because of the brittleness. However, the same target was safely used throughout the measurement of the angular distribution at least at a fixed incident energy. Corresponding to the five incident energies, three targets of different thicknesses were used, i.e. 2.37 mg/cm² for E_p=7.45 MeV, 0.95 mg/cm² for 7.22 MeV and 6.81 MeV, and 2.35 mg/cm² for 6.55 MeV and 6.14 MeV respectively. In every case, the proton group scattered from the contaminated hydrogens which may be attributed to very small amounts of H_2O in the target was observed at the angles less than 90° lab. This peak masked the inelastic peak at about 30° lab in each incident energy so that the differential cross section of the angle was missed.

The boron nucleus and a proton form the

compound nucleus C^{12} of which excitation is 15.9 MeV$+E_p$ (in C.M.), that is about 22 MeV in the present experiments. The incident energies were chosen in such a way that either the known levels[34,35] in the compound nucleus are just excited or the excitation would be located between the known levels. In Fig. 6 levels of the compound nucleus C^{12} and the positions excited by the incident beam are shown with the energy spread caused by the target.

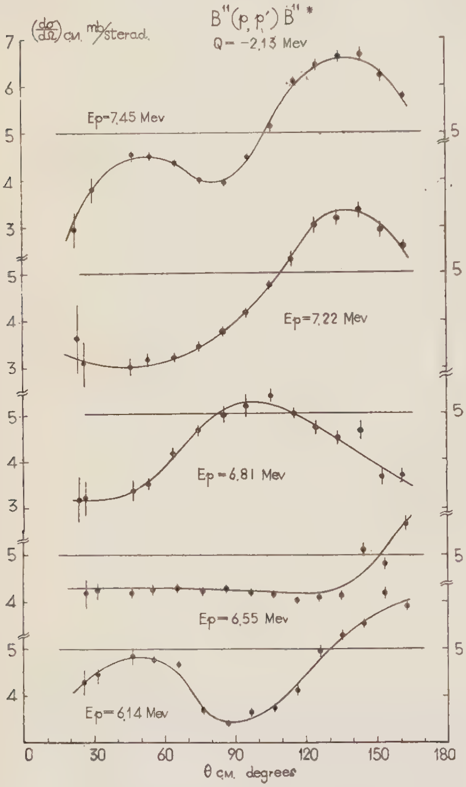

Fig. 7. Angular distributions of the protons from the $B^{11}(p, p')B^{11*}$ reactions leaving B^{11} in the first excited state. The incident energies (in laboratory system) are denoted in the figure.

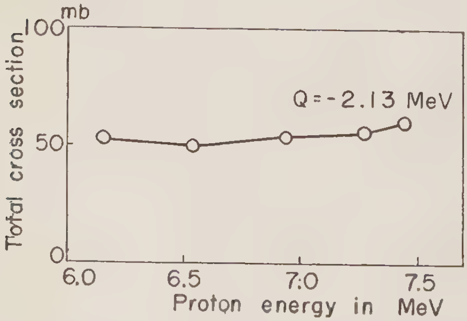

Fig. 8. Total cross sections of the $B^{11}(p, p')B^{11*}$ reactions leaving B^{11} in the first excited state.

The energy-dependence of the angular distribution is shown in Fig. 7. It was also observed that the angular distributions obtained by the relatively thick target (4.2 mg/cm^2) for $E_p \simeq 7.3$ MeV and $E_p \simeq 6.9$ MeV (not illustrated in the figure) show nearly the same pattern as that of the respective energy in Fig. 7.

The total cross sections calculated graphically from the observed angular distributions are shown in Fig. 8.

Fluorine 19.

Lowlying levels consist of several relatively well separated groups which contain two or three neighbouring levels respectively were excited as shown in Fig. 9. The correspondence between the excited level of the residual nucleus and the observed peak is also shown.

The reaction $F^{19}(p, \alpha)O^{16}$ can compete with (p, p') scattering and α-particles are located in nearly the same position of the second inelastic group. However, these amounts observed were so small[36] compared with those of protons that it could be subtracted in a the smooth background subtraction. It was confirmed by the check experiment in which the α-pulses were eliminated using the pro-

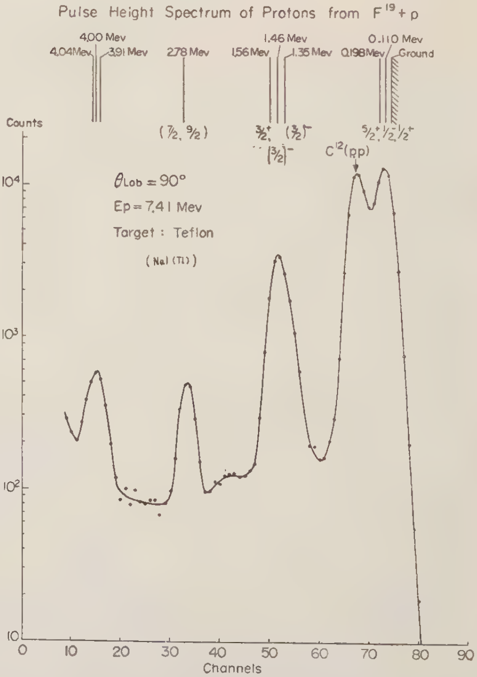

Fig. 9. The pulse-height spectrum of the scattered protons from the teflon target.

portional counter, throughout the angles studied.

Fig. 10 shows the resultant angular distribution and its energy-dependence of the inelastically scattered protons from three levels, 1.35 MeV, 1.46 MeV and 1.56 MeV. Those of protons scattered from 2.78 MeV level are shown in Fig. 11. In these cases, energy losses in the targets are estimated as about 150 KeV. The energy-dependence of the total cross sections is shown in Fig. 12.

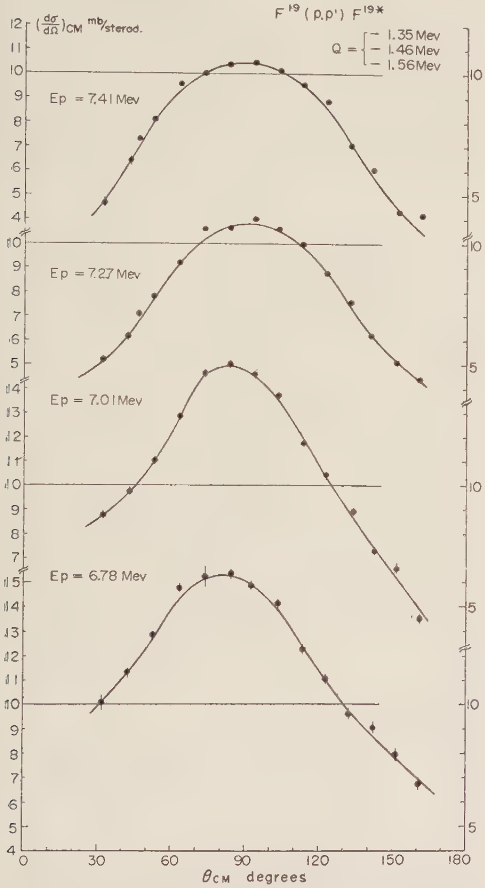

Fig. 10. Angular distributions of the protons from the $F^{19}(p, p')F^{19*}$ reactions leaving F^{19} in the third, fourth and fifth excited levels. Incident energies are denoted in laboratory system.

There is few report about the angular distributions of the $F^{19}(p, p')F^{19*}$ scattering, except the experiment performed by Gibson *et al.*[12] at the proton energy of 9.5 MeV. It is interesting that the angular distribution of p_6' (this notation means the inelastically scattered protons leaving the residual nuclei at the excitation of the sixth level) at E_p =9.5 MeV has the same shape as the present results at lower energy, whereas that of $p_3'+p_4'+p_5'$ is markedly different.

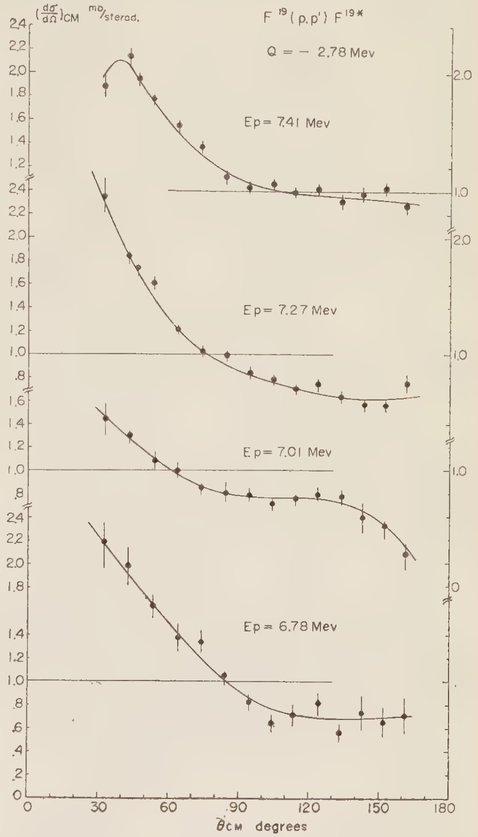

Fig. 11. Angular distributions of the protons from the $F^{19}(p, p')F^{19*}$ reactions leaving F^{19} in the sixth excited state.

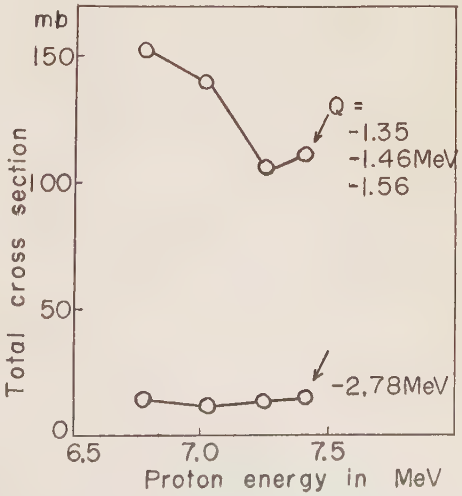

Fig. 12. Total cross sections of the $F^{19}(p, p')F^{19*}$ reactions. Two groups are denoted in the figure.

Aluminum 27.

The pulse-height spectrum of the scattered protons from Al^{27} target is shown in Fig. 13. Although the (p, α) reaction could occur energetically, the energies of these α-particles are relatively low on account of the low Q value so that the proportional counter was of use merely as an absorber for α-particles to shift their peacks sufficiently apart from the proton peaks. Some proton peaks from the higher excited levels seriously suffered from the effect of γ-ray background at backward angles in lower bombarding energies. Therefore, the proportional counter was used to eliminate the γ-ray background in these cases.

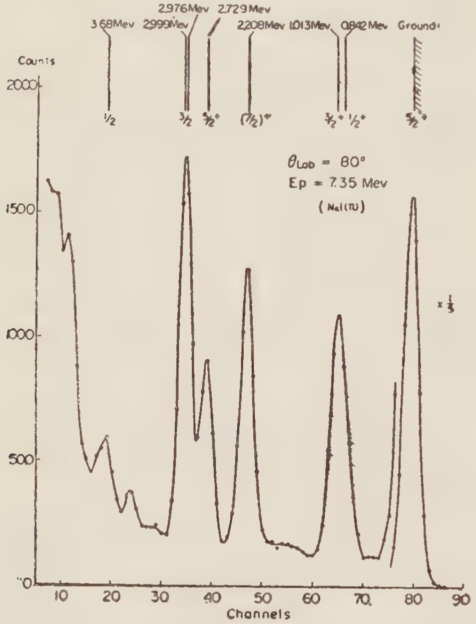

Fig. 13. The pulse-height spectrum of the scattered protons from the aluminum target.

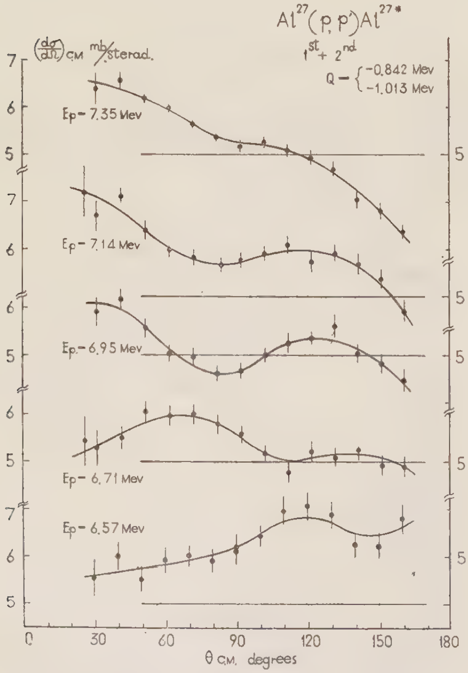

Fig. 14. Angular distributions of the protons from the $Al^{27}(p, p')Al^{27*}$ reactions leaving Al^{27} in the first and second excited levels. Incident energies are denoted in laboratory system.

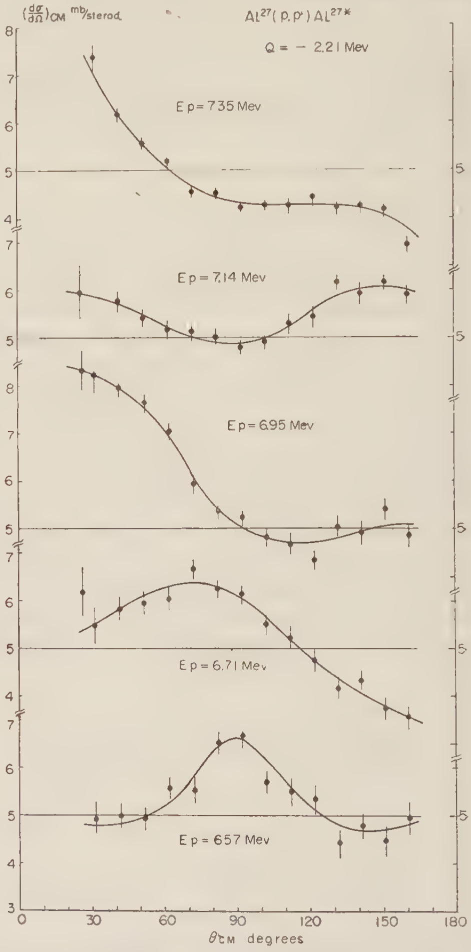

Fig. 15. Angular distributions of the protons from the $Al^{27}(p, p')Al^{27*}$ reactions leaving Al^{27} in the third excited state.

Four proton groups inelastically scattered were resolved as shown in Fig. 13. The angular distributions of these groups, i.e. $p_1' + p_2'$, p_3', p_4' and $p_5' + p_6'$, at several incident energies are shown in Figs. 14, 15, 16 and 17 respectively. The total cross sections of these groups are shown in Fig. 18.

The inelastic scattering of protons from

Al^{27} has been studied by Seward[9)] at the energies of 7.00 MeV and 7.12 MeV. These results are reproduced together with the present data in Fig. 19. The absolute cross sections of the latter are normalized to Seward's results at 90°. It is necessary to multiply the present value by the factor of about 1.5. This disagreement may be caused by the manner of the normalization used by Seward, who assumed the elastic scattering at 23° is pure coulomb scattering. However, the shapes of the angular distribution of both results show excellent agreement especially in case of 7.0 MeV.

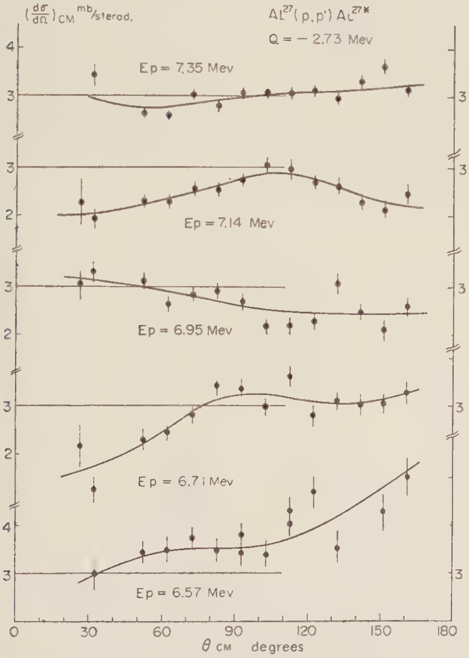

Fig. 16. Angular distributions of the protons from the $Al^{27}(p, p')Al^{27*}$ reactions leaving Al^{27} in the fourth excited states.

Barros, Forsyth, Jaffe and Taylor[38)] have studied the $Al^{27}(p, p')Al^{27*}$ with a broad range spectrograph at $E_p = 5$ MeV. They have obtained the angular distributions peaking backward for p_2', p_3' and p_4'. The tendency of peaking backward appears in the present data of $p_1' + p_2'$ and p_4' at 6.5 MeV.

Phosphorus 31.

The typical pulse-height distribution is shown in Fig. 20. In this case some trouble was experienced. The progressive increase of carbon contamination was observed, which was probably caused by the vapour of diffu-

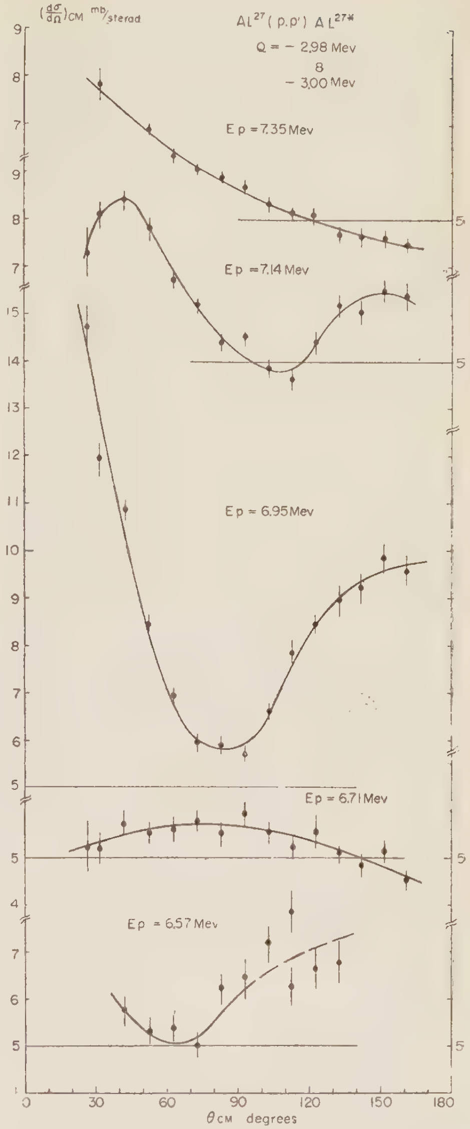

Fig. 17. Angular distributions of the protons from the $Al^{27}(p, p')Al^{27*}$ reactions leaving Al^{27} in the fifth and sixth excited states.

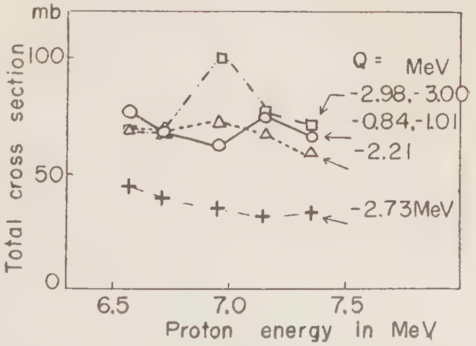

Fig. 18. Total cross sections of the $Al^{27}(p, p')Al^{27*}$ reactions. Four groups are denoted in figure.

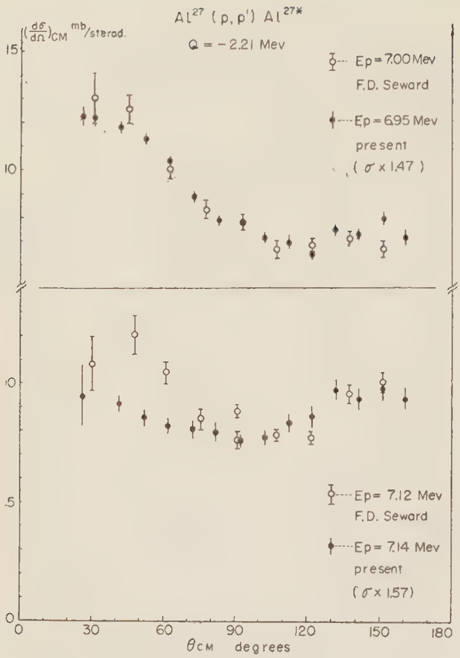

Fig. 19. Comparison of the data obtained by Seward with the present results. Note that values of differential cross sections of the former are larger than the latter about 50% in both cases.

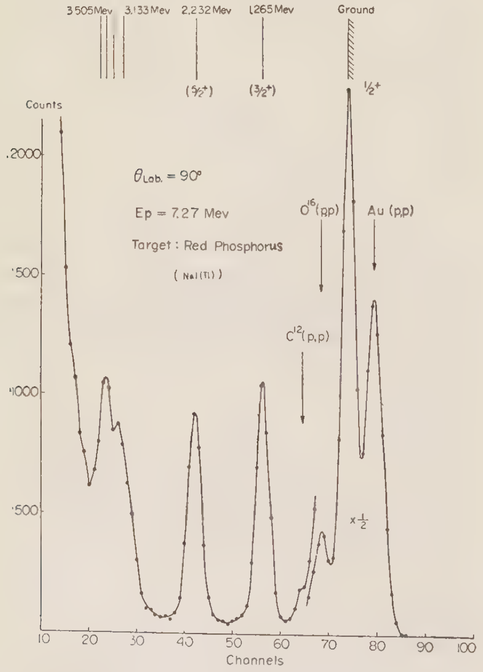

Fig. 20. The pulse-height spectrum of the scattered protons from the phosphorus target.

sion pump oil. The peak of the elastically scattered protons by carbons unfortunately overlaps on the peak of p_1' from P^{31} at the angles greater than about 130°. It became of comparable order or more with the latter in some cases so that the same target could not be used for long measurement. However, it was found that the fresh target can be used without appreciable increase of the contamination for several hours. Thus each measurement was started initially from an angle, say 120°, at which the carbon peak can be resolved clearly, and then the angles between 160° and 120° were scanned. Negligibly small changes in contamination were thus confirmed by checking the carbon peak at the reference angle (120°) occasionally. At several angles between 90° and 130°, the carbon peak was well isolated from the neighbouring peaks of protons, so that its anglar distributions were

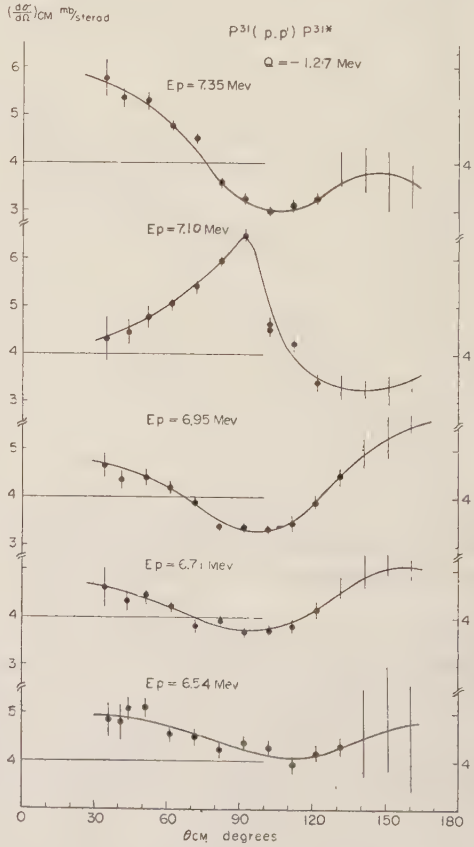

Fig. 21. Angular distributions of the protons from $P^{31}(p, p')P^{31*}$ reactions leaving P^{31} in the first excited state. Incident energies are denoted in laboratory system. Rather large errors at backward angles are caused by carbon contaminations in the target (see text).

extrapolated to the angular region in which the peaks overlap using the data reported by Nagahara[15)] and Schneider[37)]. Thus the relatively large errors at backward angles were introduced. Figs. 21 and 22 show the angular distributions of p_1' and p_2' respectively. The same target was used in the early runs, i.e. 1.2 mg/cm² at E_p=7.35, 6.95 and 6.54 MeV and fresh targets of 1.0 and 1.1 mg/cm² were used in each run at E_p=7.10 MeV and 6.71 MeV respectively. The energy losses of the incident beam in these targets are estimated as about 80 KeV.

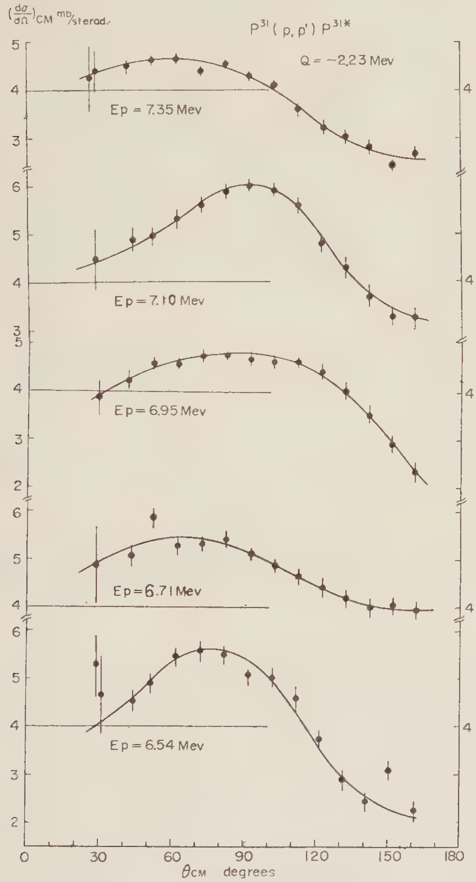

Fig. 22. Angular distributions of the protons from $P^{31}(p, p')P^{31*}$ reactions leaving P^{31} in the second excited state.

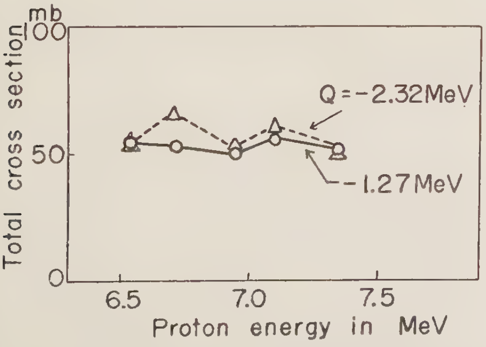

Fig. 23. Total cross sections of the $P^{31}(p, p')P^{31*}$ reactions. Two groups are denoted in the figure.

From Fig. 21, it can be seen that there is a very distinct anomaly in the angular distribution of p_1' at E_p=7.10 MeV. This anomaly was re-examined twice by different targets. Similar results were obtained with almost the same incident energy.

The total cross sections are shown in Fig. 23.

§ 4. Discussion

It can be seen from the survey of the present experimental results that the angular distributions for F^{19} and P^{31} show little change in their shapes with incident proton energy, whereas those of B^{11} and Al^{27} are considerably energy-dependent, with a little exception in Al^{27}. Therefore, the cases of F^{19} and P^{31} will be taken up at first in the following discussions.

Fluorine:

The stability of the pattern of the angular distributions with energy is fairly good for both inelastic groups. This is a striking contrast to the inelastic scattering of protons from the neighbouring even-even nucleus Ne^{20}. Ne^{20} as well as C^{12} and Mg^{24} have been studied elaborately in the wide range of incident energy and by a small step of energy changes by the INS-Tokyo group.[7a, 7b, 15, 16)] Very interesting characteristics became clear about these nuclei, one of which is described as follows: The energy region studied (7∼16 MeV) could be divided into two parts, in one of which the patterns of angular distributions of both elastic and inelastic scattering strongly change with incident energy, and in the other part higher than the former the pattern is stabilized except some fluctuations. The boundary of these two parts is fairly distinct in all cases studied and it locates at about 12 MeV of the incident energy. On the contrary, in the case of F^{19} now studied, there is little energy-dependence even in the range 6.5∼7.5 MeV.

This fact seems to suggest that it is reasonable to consider as follows: The excitation energies in the compound nucleus formed by $F^{19}+p$ are between 20 MeV and 19 MeV in the present experiment, while the excitation of the compound nucleus of $Ne^{20}+p$ is only about 10 MeV at the incident energy of 7.5 MeV (cf. Table I). In the case of Ne^{20}, the pattern is stabilized with energy beyond the boundary energy of 12 MeV as mentioned above, at which the excitation of the compound nucleus is about 14 MeV. Thus the boundary may not be intrinsic primarily for the incident energy, but it depends on the height of the excitation of the compound state.

It can be concluded in both cases of F^{19} and Ne^{20} that at the excitation energy of more than about fourteen MeV in the compound state, relatively sufficient number of overlapping levels may be concerned with the reaction so that the angular distribution contributed from the compound process approaches 90° symmetric or isotropic distribution. Any marked deviation from these simplicities could be primarily considered as the contribution of the direct interactions, if such a pattern is independent of energy.

The angular distributions of protons from the sixth excited level at 2.78 MeV of F^{19} suggest strongly the existence of the direct interactions in their shapes. The same figure was obtained at the incident energy of 9.5 MeV by Gibson *et al.*[12] However, since the spin-parity of the ground state is 1/2+ and that of the sixth level is assigned probably to be 7/2 or 9/2[34], it is impossible to locate the peak in such a forward angle with reasonable value of the nuclear radius by the simple direct interaction theories[18], whichever even or odd parity the level has.

On the other hand, the inelastic group leaving the residual nuclei at the excitation of about 1.5 MeV is considered to consist of protons from three levels, 1.35, 1.46 and 1.56 MeV, of which spins and parities are $(3/2)^-$, $(3/2)^-$ and 3/2+ respectively.[34b] The allowed momentum transfers to these residual nuclei are 1, 1 and 2 respectively according to the selection rules of the usual direct processes[20]. The direct interaction model of the single particle excitation developed by Butler[20] was used to fit the experimental values. In Fig. 24 the dashed curves show, in arbitrary unit, the square of the spherical Bessel functions, $j_1^2(Qr)$ and $j_2^2(Qr)$, corresponding to the momentum transfers 1 and 2 respectively, where $Q=|\boldsymbol{k}_f-\boldsymbol{k}_i|$, $\boldsymbol{k}_f$ and $\boldsymbol{k}_i$ are the wave vectors of the scattered and incident protons respectively and r is the nuclear radius. The solid curve shows the resultant value of these spherical Bessel functions with an arbitrary mixing ratio. The nuclear radius r was chosen to be 3.84×10^{-13} cm. Though the fit seems to show some agreement between the experiment and the theory, no decisive conclusion could be drawn owing to the arbitrariness in mixing the rate of contributions from these three levels. It must be also pointed out that this inelastic scattering group shows markedly different shape in the angular distribution at 9.5 MeV observed by Gibson *et al.*[12], contrary to the case of the sixth level. The possibility of relatively large contributions from the compound process may not be excluded in the present stage until we can confirm whether that is an anomaly only at 9.5 MeV or not.

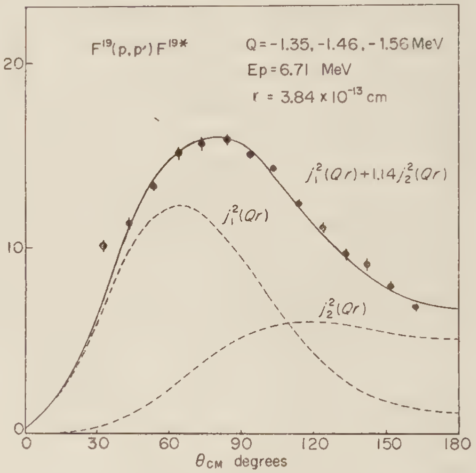

Fig. 24. A theoretical fit with the observed angular distribution of $p_3'+p_4'+p_5'$ of the $F^{19}(p, p')F^{19*}$ reactions.

It should be necessary for profound analyses to use the direct interaction theories based upon the distorted Born approximation as developed by Levinson and Banerjee[39], Glendenning[40], Rost and Austern[41] and others. They seem to be one of the most promising approach because of their success[42] even in the cases where simple direct theories have failed. These calculations have not been tried for the present result.

Phosphorus:

In the case of P^{31}, the patterns of angular distributions for p_1' and p_2' do not change remarkably with energy, except the strong anomaly at 7.1 MeV for p_1'. Though the shapes of angular distributions of the p_1'- and p_2'-groups are different from each other, the ratio of the total cross sections of the p_2'-group to that of p_1'-group is almost unity, i.e. 1.1∼1.3 in the energy range studied, including the anomaly.

The excitation of the compound nucleus is above 15 MeV in the studied range. On the other hand, the excitation of the compound nucleus formed by the neighbouring nucleus $S^{32}+p$ is about 14 MeV with the incident energy 11 MeV (cf. Table I), above which the shape of the angular distributions no more changes violently with energy as reported by the INS group.[7b)] Thus the similar discussion about the relation between the energy-dependence of the angular distributions and the compound excitation stated in the case of F^{19} and Ne^{20} may be applicable to the target nuclei of $A\simeq 30$.

If we assume that the reaction may proceed through a direct process such as the theory treated by Glendenning, the predicted angular distributions of p_1' and p_2' may be of similar shape to each other, according to the examples shown in Figs. 5 and 6 in the reference 40. Because, in both cases the momentum transfer must be of the same value, 2, and the wave functions of the scattered protons corresponding to the first and the second residual excitations may take some similar values.

Table I.

Target nucleus	E_x MeV	E_c MeV	$Q_{p,n}$ MeV	σ total/level mb	Literature
Be^9	6.59	<12	−1.85	120 at about 6 MeV	5), 49)
B^{11}	15.95	>23	−2.76	50 〃 7 〃	present
C^{12}	1.94	13	−18.30	400 〃 11 〃	15)
N^{14}	7.29	(17)	−5.92	250 〃 8 〃	7b)
O^{16}	0.60	>15		80 & 120 〃 13 〃	14)
F^{19}	12.87	<19	−4.02	13 & 45 〃 7 〃	present
Ne^{20}	2.45	13		250 〃 11 〃	7b), 16)
Mg^{24}	2.27	14	−14.84	320 〃 8 〃	7b), 16)
Al^{27}	11.59	>19	−5.58	35 & 65 〃 7 〃	present
Si^{28}	2.72	>16	−14.59	240 〃 8 〃	7b)
P^{31}	8.86	<15	−6.21	60 〃 7 〃	present
S^{32}	2.29	14	−13.95	120 〃 8 〃	7a), 7b)
A^{40}	7.80	13	−2.29	30 〃 8 〃	7b)

E_x: Binding energy of a proton of the compound nucleus, obtained from the reference 28).

E_c: Excitation of the compound nucleus where the pattern of the angular distribution changes its energy-dependent character. See text for more complete explanations.

$Q_{p,n}$: The Q-values of the (p, n) reaction, obtained from the reference 28).

Thus, at the present stage, it seems to be natural to consider that the contribution of the compound nuclear process is prominent in the energy range studied for the inelastic scatterings from P^{31}. It should also be noticed that the nearly 90° symmetric patterns can be seen frequently in the angular distributions of p_1' and p_2' as shown in Figs. 21 and 22.

The very distinct irregularity at 7.1 MeV in p_1' may be caused by the anomaly in the compound nucleus at that excitation. But no such irregular behavior can be observed in the excitation function and both in p_2' and in the elastic scattering of P^{31}.[31)]

It should be emphasized that the results show little energy-dependence in the angular distributions of both elastic and inelastic scatterings, the total cross sections and in the ratio of the cross sections of p_2' and p_1'.

Boron:

Total cross section calculated graphically is almost independent of incident energy, as shown in Fig. 8. Although present data are not sufficient for examining the detailed excitation function, yet it seems that there is no appreciable resonance phenomena near the known levels of the compound nucleus C^{12}. On the contrary, the relatively marked energy-dependence of the angular distributions is observed in this energy range.

The excitation of the compound nucleus is fairly high even in the incident energy of 7 MeV, but the number of levels concerning the reaction should be relatively small because of the light weight of the nucleus and of the structure of the compound nucleus, C^{12} (doubly closed subshells). Therefore, the effect of the intereference between the compound levels of different parities should appear in the angular distributions. The change of the pattern with proton energy is primarily understood in this case as the suggestion of the compound process associated with the strong interference effect.

It should be worthwhile to point out that the irregular behaviours of the patterns of angular distributions with energy in the $C^{12}(p, p')C^{12*}$ scattering were recently successfully understood on the basis of the direct interactions by Okai and Tamura[43], who developed the so-called channel coupling theory[44]. Thus the violent energy-dependence of the pattern alone could not be the reliable evidence of the interference phenomena. In that model both elastic and inelastic scatterings relate to each other so closely that it would be expected that the irregularity appears at the same time on the patterns of both scatterings as in the case of C^{12}. However, the patterns of the elastic scattering from B^{11} are less energy-dependent than that of inelastic scattering in the present energy regions as mentioned elsewhere[31]. It would not conflict with this theory to conclude the existence of interference effects in the present $B^{11}(p, p')B^{11*}$ reactions.

It is interesting to compare the present results with that obtained by Ajzenberg-Selove *et al.*[50] about the $B^{11}(p, n)C^{11}$ reaction at $E_p=7.0$ MeV. In the latter, which is the mirror reaction of $B^{11}(p, p')B^{11*}$ reaction, the obtained differential cross sections to the first level of C^{11} at the angle of 20° seem to suggest the magnitude of 1∼4 mb/sterad, while that of the (p, p') scattering at the angle of 23° is very close to the value of the (p, n) cross section, namely about 3 mb/sterad at $E_p=7.2$ and 6.8 MeV. Further detailed investigations of the (p, n) reactions are desired for the comparison with the (p, p') reactions.

Aluminum:

The angular distributions of the four groups of inelastically scattered protons, $p_1'+p_2'$, p_3', p_4' and $p_5'+p_6'$ are energy-dependent. Amoung them the patterns of $p_1'+p_2'$ and p_4' show relatively smooth variation with energy whereas those of p_3' and $p_5'+p_6'$ change violently in their shapes. The excitation of the compound nucleus formed by Al^{27} with a proton is above 18 MeV in the present study, which is considerably higher than the case of P^{31} above mentioned. Nevertheless the patterns are more energy-dependent than that of P^{31}. This discrepancy may be solved by the following consideration. The compound nucleus of $Al^{27}+p$ is Si^{28} in which the sub-shells are just closed in both protons and neutrons so that the less dense level density should be supposed compared with the neighbouring nuclei. Thus the possibility remains that the interference between the relatively small number of excited levels in the compound nucleus affects the angular distribution considerably.

It is pointed out also that the energy losses in the target is about 40 KeV so that relatively less average of the differental cross sections over the incident energy was made compared with the case of P^{31} in which the energy losses are about 80 KeV.

In this case, as well as in the case of B^{11}, the elastic scattering at the same energy show little energy dependence[31]. It seems there is no obstacle in concluding that the reaction proceeds mainly through the compound process.

However, it is pointed out that the total cross sections of each inelastic scattering, p_1', p_2' and p_4' are all about 35 mb, assuming the equal contributions from p_1' and p_2'. Only the total cross section of the third excited state takes relatively large value of about 65 mb in the energy range studied. This fact might have some relations to the structure of Al^{27}.

According to the Nilsson model,[55,46] the third level (probably 7/2+ not 3/2+ as listed for a long time)[47,51] is the second member of the ground state band, $K=5/2+$ (K is the component of the angular momentum to the axis of the deformation), and the first, second and fourth levels are the member of the first excited state $K=1/2+$. The cross sections of the inelastically scattered protons leaving the residual nuclei in these three excited states are nearly equal and the energy dependence of the angular distributions are relatively smooth compared with that of the third excited state.

This third level of Al^{27} should have equivalent characters with the third level of Mg^{25} on the basis of the Nilsson model. Mg^{25} and Al^{27} belong to the same group of the nuclei with the odd particle number 13. It was reported recently[47)] that the reduced quadrupole transition probability $B(E2)$ of the third level of Mg^{25} is very large compared with that of the lower two excited states. This also may have some relation to the relatively large cross section of the third level of Al^{27} compared with the neighbouring levels in the present experiment.

These facts seem to support the direct process. Thus, further exact data, especially the correct amounts of contribution to the cross section from p_1' and p_2' respectively, are necessary to confirm the reaction mechanism.

The energy dependence of the total cross sections of all inelastically scattered proton groups is relatively little, except one case of $p_5'+p_6'$ at the incident energy of 6.95 MeV.

Generalization:

(a) The height of the excitation of the compound nucleus and the energy dependence of the pattern of the angular distribution seem to have close relation to each other, as discussed over again in this section. To confirm yet this fact, the results obtained by many authors for the various target nuclei are summarised in Table I together with the present data from this point of view. E_x in the table denotes the excitation energy of the compound nucleus formed by the target nucleus listed in the first column plus a zero energy proton, namely the binding energy of a proton in the compound nucleus. E_0 is the compound excitation beyond which the pattern of the angular distribution becomes relatively energy-independent. At energies less than E_0 the pattern shows experimentally the obvious energy dependence. Some values of E_0 are calculated from the incident energy which confirmed in the original paper as the boundary energy in the sense above mentioned. Some values with the notation $<$ mean that above the energy cited the pattern is relatively stabilized with energy and the lower limit of this is not yet confirmed experimentally. The notation $>$ means that up to the cited energy the experimental result still shows energy dependent pattern and the upper limit of E_0 would be higher than the value cited. The values with parentheses are somewhat uncertain.

It can be seen readily that the many values of E_0 are distributed around 13 MeV$\sim$14 MeV, whichever the target is even or odd in mass number, and are independent of E_x. Some exceptions are B^{11}, O^{16}, Al^{27} and Si^{28}, which are the nuclei near the doubly closed shells or closed subshells.

The meaning of these values of E_0 seems to be clarified in the relation with the level densities at that excitation of the compound system. However, the level densities of the individual light nuclei at such excitation are not known precisely. Generally speaking, level densities of these light nuclei at the excitation of about 13 MeV could not be considered to be sufficient for the *thorough cancellation* of the interference effect of the compound levels according to the theory of Hauser and Feshback[25)]. Using some theoretical formula, for example deduced by Newton[48)], the level densities are calculated for some of these nuclei. They give at most 40–100 levels per MeV without $(2J+1)$ factor.

(b) In the fifth column of the Table I, the total cross sections of the inelastically scattered protons from one level of the residual nucleus are listed with the incident energy. These values only show their magnitude so that one must refer the original reports for the exact value.

It is apparent that the total cross sections of the even-even nuclei are considerably larger than that of the odd-A nuclei. This can be understood by the following reasons: In the latter the threshold of the competing (p, n) reaction is always low compared with that of the even-even nuclei as listed in the fourth column in the table. Therefore the considerable part of the reaction can proceed in the (p, n) channel in the case of the odd-A nuclei, whereas these channels are closed up to the higher excitation for the even-even nuclei. (The same situation occurs even among the even-A nuclei as already pointed out by Oda *et al.*[7b)]) Furthermore, the odd-A nuclei have relatively many levels which could be excited by inelastically scattered protons than the even-even nuclei so that the cross section per channel decreases still more. These facts show that in the inelastic scattering of protons from odd-A nuclei, the compound process is the leading reaction mechanism at the proton energy of 6∼7 MeV.

§ 5. Conclusion

In the case of B^{11} and P^{31}, the reaction mechanism seems to be mainly the compound process.

In the case of F^{19}, the angular distributions suggest the existence of the direct process in addition to the compound process. But simple direct interaction theories cannot fit the data. The relative amounts of the both processes are not clear.

In the case of Al^{27}, there is no conflict in concluding that the reaction proceeds mainly through the compound process, but some fact which needs further experimental check seems to suggest the relation between the nuclear structure of Al^{27} in the Nilsson model and the (p, p') scattering. Thus further experiments are necessary to confirm the reaction mechanism.

The energy dependence of the pattern of angular distributions not primarily depends on the incident proton energy but on the height of the excitation of the compound nucleus.

In the most light nuclei $A \lesssim 40$, whichever, even or odd in mass number, the pattern of angular distributions changes little in the shape except some fluctuations above the incident energy leading the compound excitation to about roughly 13 MeV. Some exceptions are the nuclei near the doubly closed shells or closed subshells.

Above this energy in the compound system, the interference between the levels of different parities concerning the reaction seems to affect little to the energy dependence of the pattern of angular distributions.

Observed total cross sections per level of odd-A nuclei are considerably smaller than that of the even-even nuclei. This depends largely on the low Q-values of the (p, n) reactions of these nuclei. This suggest that the compound process would be the leading mechanism in these odd-A nuclei.

The energy dependence of the total cross sections is relatively little throughout the present data.

Acknowledgements

The author wishes to thank Professor K. Kimura and Dr. Y. Uemura for their advice and encouragement throughout the course of this experiment. He also wishes to thank Dr. R. Ishiwari, Dr. K. Fukunaga, Dr. J. Muto, Dr. I. Kumabe, Dr. H. Ogata, Mr. T. Ohama and Mr. Y. Ohmori for their cooperations and many valuable discussions. The author is indebted to Dr. T. Yanabu for the target preparation of teflon, Professor S. Shimizu and Dr. T. Hyōdō for lending RIDL multichannel analyzer and its accessory equipments and Dr. K. Matsuda (INS, University of Tokyo), for the method of measuring the beam energy and the copy of the foil changer. Thanks are also due to many other members of the Laboratory for their helps and hospitalities.

Finally, the author wants to express gratefulness to Dr. M. Kawai (Tokyo Institute of Technology) and Dr. K. Izumo (INS, University of Tokyo), for their helpful discussions and comments.

References

1) H. E. Gove and H. F. Stoddart: Phys. Rev. **86** (1952) 572.
G. E. Fisher: Phys. Rev. **96** (1954) 704.
C. P. Browne and J. R. Lamarsh: Phys. Rev. **104** (1956) 1099.
R. W. Peelle: Phys. Rev. **105** (1957) 1311.
2) G. Schrank, P. C. Gugelot and I. E. Dayton: Phys. Rev. **96** (1956) 1156.
3) P. C. Gugelot and P. R. Phillips: Phys. Rev. **101** (1956) 1614.
4) R. M. Eisberg and N. M. Hintz: Phys. Rev. **103** (1956) 645.
5) S. W. Rasmussen: Phys. Rev. **103** (1956) 186.
J. Benveniste, R. G. Finke and E. A. Martinelli: Phys. Rev. **101** (1956) 655.
R. G. Summers-Gill: Phys. Rev. **109** (1958) 1591.
6) H. E. Conzett: Phys. Rev. **105** (1957) 1324.
7a) S. Yamabe: J. Phys. Soc. Japan **13** (1958) 237.
M. Kondo and T. Yamazaki: J. Phys. Soc.

Japan **13** (1958) 771.
S. Yamabe, M. Kondo, T. Yamazaki and A. Toi: J. Phys. Soc. Japan **13** (1958) 777.
Y. Oda, M. Takeda, C. Hu and S. Kato: J. Phys. Soc. Japan **14** (1959) 396, 1255.
7b) Y. Oda, M. Takeda, N. Takano, T. Yamazaki, C. Hu, K. Kikuchi, S. Kobayashi, K. Matsuda, and Y. Nagahara: J. Phys. Soc. Japan **15** (1960) 760.
8) K. Kikuchi, S. Kobayashi and K. Matsuda: J. Phys. Soc. Japan **14** (1959) 121.
C. Hu, K. Kikuchi, S. Kobayashi, K. Matsuda, Y. Nagahara, Y. Oda, N. Takano, M. Takeda and T. Yamazaki: J. Phys. Soc. Japan **14** (1959) 861.
S. Kobayashi, K. Matsuda, Y. Nagahara, Y. Oda and N. Yamamuro: J. Phys. Soc. Japan **15** (1960) 1151.
9) F. D. Seward: Phys. Rev. **114** (1959) 514.
10) G. W. Greenlees and A. E. South: Proc. Phys. Soc. London **A 69** (1956) 686.
G. W. Greenlees, B. C. Haywood, L. G. Kuo and M. Petravic: Proc. Phys. Soc. London **A 70** (1957) 331.
G. W. Greenlees, L. G. Kuo, J. Lowe and M. Petravic: Proc. Phys. Soc. London **A 71** (1958) 347.
11) G. W. Greenlees, L. G. Kuo and M.P etravic: Proc. Roy. Soc. **A 243** (1957) 206.
12) W. M. Gibson, D. J. Prowse and J. Rotblat: Proc. Roy. Soc. **A 243** (1957–8) 237.
13) G. W. Greenlees and P. M. Rolph: Proc. Phys. Soc. London **A 75** (1960) 201.
14) S. Kobayashi: J. Phys. Soc. Japan **15** (1960) 1164.
15) Y. Nagahara: *Kingston Conference on Nuclear Structure* (1960) 234; J. Phys. Soc. Japan **16** (1961) 133.
16) K. Matsuda: *Kingston Conference on Nuclear Structure* (1960) 225, 228.
17) T. A. Belote, E. Kashy and J. R. Risser: Phys. Rev. **122** (1961) 920.
18) N. Austern, S. T. Butler and H. McManus: Phys. Rev. **92** (1953) 350.
S. Hayakawa and S. Yoshida: Proc. Phys. Soc. London **A 68** (1955) 656; Progr. Theor. Phys. **14** (1955) 1.
D. M. Brink: Proc. Phys. Soc. London **A 68** (1955) 994.
19) J. R. Lamarsh and H. Feschbach: Phys. Rev. **104** (1956) 1633.
20) S. T. Butler: Phys. Rev. **106** (1957) 272.
21) H. Ui: Progr. Theor. Phys. **18** (1957) 163.
22) M. Sano, S. Yoshida and T. Terasawa: Nucl. Phys. **6** (1958) 20.
23) S. T. Butler, N. Austern and C. Pearson: Phys. Rev. **112** (1958) 1227.
24) J. Blair: Phys. Rev. **115** (1959) 928.
25) W. Hauser and H. Feshbach: Phys. Rev. **87** (1952) 366.
26) H. Feshbach: *Nuclear Spectroscopy*, Part B (1960) 625.
27) H. A. Lackner, G. F. Dell and H. T. Hausman: Phys. Rev. **114** (1959) 560.
28) V. J. Ashby and H. C. Catron: UCRL-5419.
29) K. Kimura *et al*: To be published.
30) T. Yanabu and A. Katase: To be published.
31) K. Kimura, Y. Uemura, R. Ishiwari, J. Kokame, K. Fukunaga, J. Muto, I. Kumabe, H. Ogata, T. Ohama, Y. Ohmori and A. Katase: To be published in this Journal.
32) R. Mather and E. Segrè: Phys. Rev. **84** (1951) 191.
33) H. Bichsel, R. F. Mozley and W. A. Aron: Phys. Rev. **105** (1957) 1788.
34a) F. Ajzenberg-Selove and T. Lauritsen: Nucl. Phys. **11** (1959) 1.
34b) F. Ajzenberg-Selove and T. Lauritsen: Ann. Rev. of Nucl. Sci. **10** (1960) 409.
35) M. Furukawa, Y. Ishizaki, Y. Nakano, T. Nozaki, Y. Saji and S. Tanaka: J. Phys. Soc. Japan **15** (1960) 2167.
36) S. Yamashita: To be published.
37) H. Schneider: Helv. Phys. Acta **29** (1956) 55.
38) F. de S. Barros, P. D. Forsyth, A. A. Jaffe and I. J. Taylor: Proc. Phys. Soc. London **A 73** (1958) 793.
39) C. A. Levinson and M. K. Banerjee: Ann. of Phys. **2** (1957) 471, 449; **3** (1958) 67.
40) N. K. Glendenning: Phys. Rev. **114** (1959) 1297.
41) E. Rost and N. Austern: Phys. Rev. **120** (1960) 1375.
42) F. G. J. Perey: *Kingston Conference on Nuclear Structure* (1960) 387.
43) S. Okai and T. Tamura: INS Repord 34 (1961).
44) S. Yoshida: Progr. Theor. Phys. **19** (1958) 169.
45) S. G. Nilsson: Danske Videnskab. Selskab, Mat. Medd. **29** (1955) No. 16.
46) A. E. Litherland, E. B. Paul, G. A. Bartholomew and H. E. Gove: Phys. Rev. **102** (1956) 208.
47) H. E. Gove: *Kingston Conference on Nuclear Structure* (1960) 438.
48) T. D. Newton: Can. J. Phys. **34** (1956) 804.
49) R. Ishiwari: To be published.
50) F. Ajzenberg-Selove, G. D. Johnson, A. Rubin and M. Mazari: Phys. Rev. **103** (1956) 356.
51) P. M. Endt and C. M. Braams: Rev. Mod. Phys. **29** (1957) 683.

JOURNAL OF THE PHYSICAL SOCIETY OF JAPAN, Vol. 16, No. 11, NOVEMBER, 1961

(d, α) Reactions on O^{16}, N^{14} and C^{12} by 14.7 MeV Deuterons

By Takuji YANABU

Institute for Chemical Research, Kyoto University, Kyoto

(Received July 31, 1961)

Angular distributions of α particles resulting from $O^{16}(d, \alpha_0)N^{14}$ (ground state), $N^{14}(d, \alpha_0)C^{12}$ (ground state), $N^{14}(d, \alpha_1)C^{12}$ (first excited state), $C^{12}(d, \alpha_0)B^{10}$ (ground state) and $C^{12}(d, \alpha_1)B^{10}$ (first excited state) reactions were studied. α particles from the $O^{16}(d, \alpha_0)N^{14}$, $C^{12}(d, \alpha_0)B^{10}$ and $C^{12}(d, \alpha_1)B^{10}$ reactions exhibited forward peaks and backward peaks simultaneously, while α particles from $N^{14}(d, \alpha_0)C^{12}$ reaction showed forward peaks and oscillatory behavior.

α particles leaving N^{14} and C^{12} nuclei in their $T=1$ state were also observed in the forward angle, and the isotopic spin conservation rule seemed to be violated.

The reaction mechanism is then discussed on the basis of the surface direct reaction, the compound nucleus formation and α particle clustering in the target nucleus. It is concluded that α clustering may play an important role in the (d, α) reaction.

§ 1. Introduction

The (d, α) reaction is one of the well-known nuclear reactions. At the early stage of the research on this reaction, the levels of residual nuclei were studied only by the measurements of the energy spectra of α particles, since the accurate experimental determination of α particle energy was easier than that of γ ray energy. Further, these studies were concerned mostly with light nuclei and some of intermediate heavy ones up to Ca^{40} [1].

But, experimental and theoretical studies have recently been developed, having been stimulated by some successful aspects of the theories on deuteron stripping reactions, which might disclose the mechanism of (d, α) reactions. Many experimental results have so far been published by some workers. Especially, Freemantle[2], Fischer[3], Dalton[4], Browne[5] and Hu[6] studied on $O^{16}(d, \alpha)N^{14}$ reaction for various deuteron energies, Gibson[7], Fischer[3] and Hu[6] on $N^{14}(\alpha, \alpha)C^{12}$ reaction, and El Bedewi[8] and Green[9] pursued experiments on $C^{12}(d, \alpha)B^{10}$ reaction.

Up to now, most experiments on (d, α) reactions are discussed with an idea of the surface direct reaction; Hu[6] discussed his experimental results comparing with Butler's deuteron stripping theory[10] as well as with El Nadi's[11] and Newns'[12] two particles stripping theories, while Fischer[3] discussed his results on the basis of the pick-up theory[10] and so on.

When a nucleus is bombarded by intermediate energy deuterons, many types of reactions such as (d, p), (d, n), (d, t), (d, α) can occur, and the characteristic behavior of the deuteron-induced reactions comes from the fact that a deuteron breaks up easily. This fact promoted the deuteron stripping theory. This idea, however, seems to be contradictory to an idea that a deuteron would pick up one or two nucleons at the nuclear surface, by which experimental results of some of (d, t) reactions can be explained satisfactorily.

On the other hand, since deuteron and α particle are both isotopic spin 0 particles, the (d, α) reaction can afford an experimental evidence for the conservation of isotopic spin quantum number[13]. Experiments so far done in this respect were on O^{16}, Ne^{20}, Mg^{24}, Si^{28}, and S^{32} bombarded by deuterons with energy less than 10 MeV[14]. The results obtained showed that the isotopic spin is not always the good quantum number and the mixing of levels with different isotopic spins may occur by the Coulomb interaction. This fact means that in the (d, α) reaction at intermediate energy, the compound nucleus effects cannot be ignored.

In the recent experiment on (d, α) reactions of heavy nuclei, reported by Mead and Cohen[15], high energy parts in the spectrum of the emitted α particles increased with mass number. They pointed out that the phenomenon could not be explained by the simple pick-up process.

Reflecting on the history of studies on the (*d*, *α*) reactions, the present work has been carried out with the purpose to clarify some ambiguities concerned with the very interesting and important problems of the reaction mechanism and isotopic spin conservation.

§ 2. Experimental Procedure

2-1 *Layout of the apparatus*

The deuteron beam from the Kyoto University 105 cm Cyclotron was focused by a pair of the quadrupole magnet and collimated by two tantalum plates with 2 mm diameter holes and 36.0 cm apart. The collimated beam was then brought to the scattering chamber of 52 cm in diameter. Details of this apparatus will be published elsewhere. A beam spot at the target was nearly 3 mm in diameter. The *α* particle detector was mounted on the periphery of the rotating disc, and maximum angle between the direction of the beam and the axis of detector is 165°. Angular distribution measurements were made from 20° to 160° by 10° steps. The angular position of the detector was read with an accuracy less than 0.05° and target setting was accurate within 0.001 mm with respect to the rotating axis of the disc, and the inclination of the target foil was accurate within the limit of 0.2°.

The beam after passing through the target was caught by the Faraday cup and the beam current was measured by a 100% feedback type current integrator. Most experiments were pursued by about 0.1 μA beam intensity, but the smaller beam intensity was needed to diminish unnecessary backgrounds when forward-angular distribution was detected.

The scattering chamber was equipped with four holes at the side wall of the chamber, and monitoring of the beam and target was possible at angle 35°, 90° and 135° to the beam direction respectively. In the present experiments, a thin CsI crystal (about 0.7 mm thick) coupled with a photomultiplier (usually 5819 or 6342) was used as a monitor countor.

The deuteron energy was determined by measuring the range of the deuteron in aluminum and by using the range-energy relation given by Bichsel[16]. The estimated value of the beam energy was 14.7 MeV, but small differences ranging from 14.7 MeV to 14.8 MeV were experienced. The detailed description of this method will be given elsewhere.

Overall characteristics of the system were tested by observing the elastic scattering of deuterons from gold, and the result is shown in Fig. 1. The experimental values obtained agreed very well with those estimated by the pure Rutherford scattering formula.

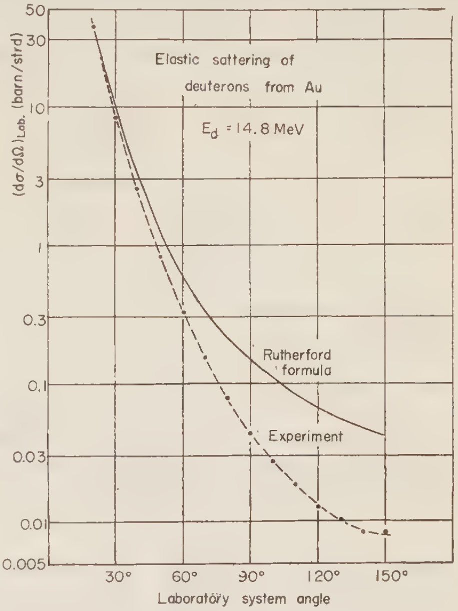

Fig. 1. Elastic scattering of deuterons from gold. E_d=14.8 MeV. Solid line; Rutherford scattering formula. Dotted line; experimental value.

2-2. *The target preparation and detection method*

The experimental procedure of the $O^{16}(d, \alpha)N^{14}$ reaction is divided into four stages. In the first stage, a mylar ($C_8H_4O_2$) film was used as an O^{16} target, and *α* particles were detected by a thin CsI(Tl) crystal. The target thickness was about 0.8 mg/cm². Its non-uniformity was less than 4%. The thickness of the CsI crystal was chosen to be 0.16 mm by the condition that energetic deuterons or protons could easily pass through it while the *α* particles stopped in it. A suitable aluminum absorber was placed in front of the crystal in the forward angle detection. This system failed to detect *α* particles emitted in the backward angle. In the second stage, a mylar film was also used as an O^{16} target, and *α* particles passing through the small proportional counter were detected by the CsI(Tl) crystal. The proportional counter in the detection system gave pulses proportional to the energy loss of a particle in the counter, and the CsI crystal gave information about the total energy of that particle. By the coincidence countings of both pulses, effects of other particles than alphas could be eliminated. The geometrical arrangement of the detector system is shown in Fig. 2 and its block diagram is also given in Fig. 3. The pulse-height spectra by this coincidence method is shown in Fig. 4. In the third stage, natural oxygen gas was used as an O^{16} target and particles emitted from O^{16} were detected by the method similar to that mentioned above. The gas target was a cylindrical chamber with a narrow window covered by a mylar foil of 35 mil thickness. The gas pressure of the chamber was about 400 mmHg. In the fourth stage, a mylar film was again used as a target, and particles were detected only by a single proportional counter of which construction will be explained in the following section for the $C^{12}(d, \alpha)B^{10}$ reaction.

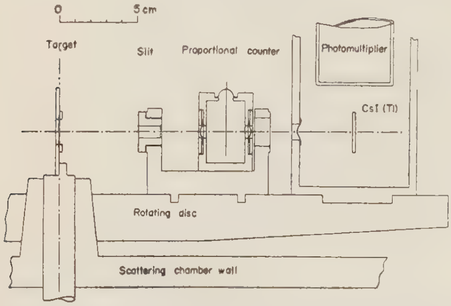

Fig. 2. Schematic view of counter telescope. Proportional counter works as ΔE counter and crystal counter works as E counter.

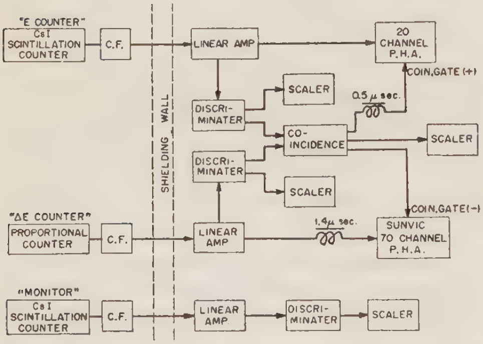

Fig. 3. Electronic diagram of counter telescope system for alpha detection. C.F. means cathode follower.

The $N^{14}(d, \alpha)C^{12}$ experiment is divided into two stages. In the first stage, melamine varnish* was used as an N^{14} target, and alphas were detected by the CsI(Tl) crystal. Melamine varnish is essentially melamine-formaldehyde and condenses to a solid film when kept at 120° for 20 minutes or so. The film was made by pouring this melamine varnish on a flat glass and then heating in the oven. But stripping off of this film from a glass plate was so difficult that a thinner film with thickness less than 66 micron was not produced. Since this film had various chemical compositions according to the condition of condensation polymerization, it was unsuitable for absolute determination of the reaction cross section. The CsI(Tl) crystal used was of 0.3 mm thick in the case of the forward angle experiment, and of 0.16 mm thick in the backward angle experiment. An aluminum absorber was also used in the latter case.

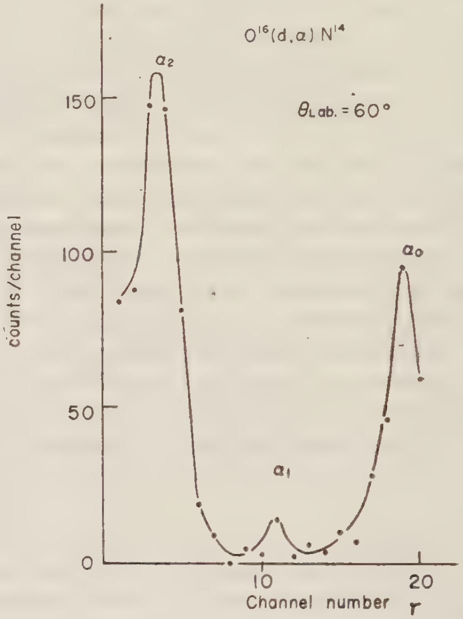

Fig. 4. Coincidence gated spectrum of alpha particles from $O^{16}(d, \alpha)N^{14}$ reaction. Target is Mylar. $E_d = 14.7$ MeV.

In the second stage, the natural nitrogen gas was used as an N^{14} target, and α particles were counted by the counter telescope system similar to that used in the O^{16} experiment.

---

* We are indebted to the Kansai Paint Co. for the supply of this sample.

The pulse height spectra are shown in Fig. 5. The effective solid angle subtended by the gas target at the counter system was calculated by the formula proposed by Johnston and Swenson[17].

In the $C^{12}(d, \alpha)B^{10}$ experiment, a polystyrene film of 0.2 mg/cm² thickness was used as a C^{12} target, non-uniformity of which was less than 5%. The films were made by the usual method, i.e. by pouring the dilute solution of polystyrene in benzene onto a deck glass and stripping it off from the glass in water. The α particle detector used was a single proportional counter. This was mounted in the scattering chamber, connected to the outside manometer and gas storage vessel by a capillary tube. By this device the pressure of the proportional counter gas was controlled easily according to the kinematics of the reaction so as to make the α particle range in counter to be nearly the geometrical depth of the counter. The construction of the proportional counter is shown in Fig. 6, and the pulse-height spectra obtained by this counter are

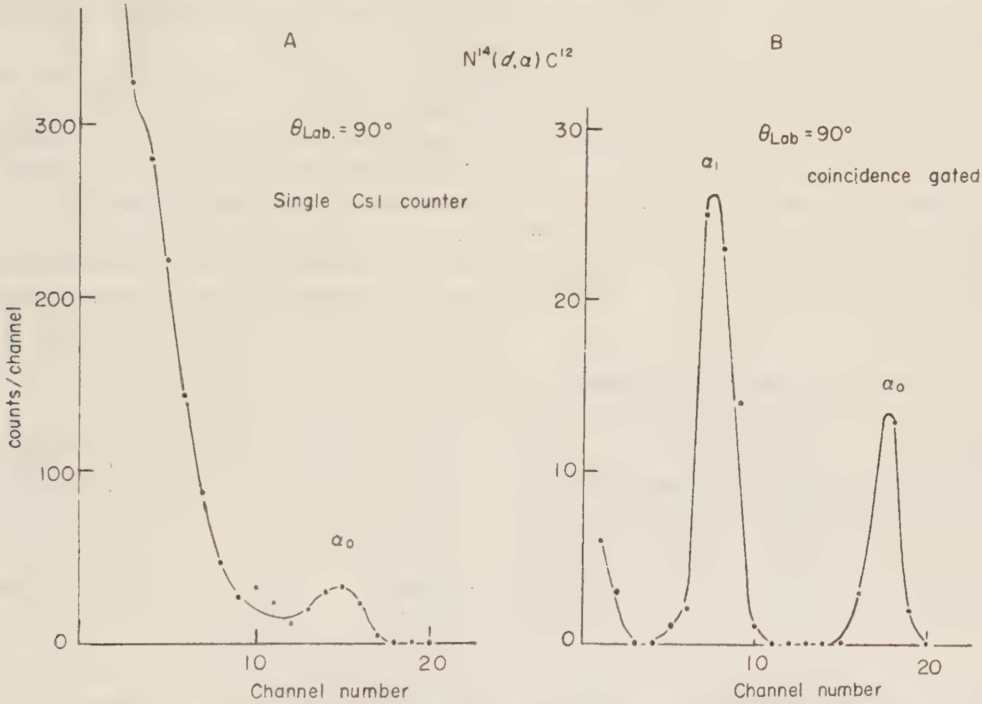

Fig. 5. Pulse-height spectrum of alpha particles from $N^{14}(d, \alpha)C^{12}$ reaction.
A: simple spectrum of E counter.
B: coincidence gated spectrum of E counter. Angle of detection is the same as in A.
Target used is natural nitrogen gas.

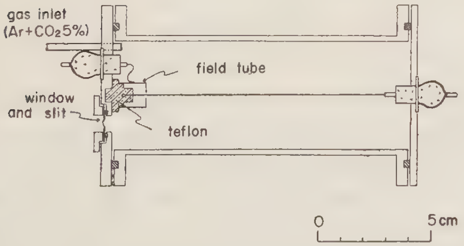

Fig. 6. View of the proportional counter used in $C^{12}(d, \alpha)B^{10}$ reaction. Counter gas is $A_r + CO_2$ (5%). Gas pressure is variable from outside the scattering chamber.

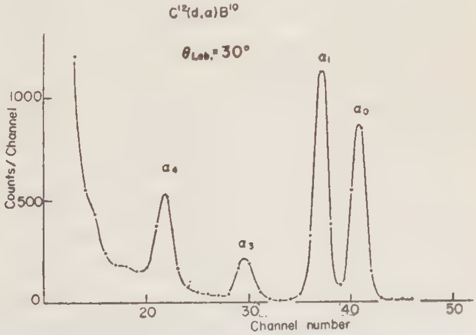

Fig. 7. Pulse-height spectrum of alpha particles from $C^{12}(d, \alpha)B^{10}$ reaction. $\theta_{lab} = 30°$.

given in Figs. 7 and 8.

§3. Results and Discussion

3-1. *General*

Errors in these experiments come from the following various causes:

1) Irregularity in the target thickness;
2) The leakage of the beam integrator and time resolution of the total charge counting;
3) The angle resolution of counting system;
4) The divergence of the beam spot and beam energy;
5) The energy loss of the deuteron beam in target materials;
6) The energy loss of emitted particles in target material and window foils of the detector;
7) The finite energy resolution of the detector system;
8) The background subtraction and the spectrum analysis;
9) The statistical fluctuation of the radiation counting;
10) The linearity fluctuation of the electronic circuits.

These errors vary from one experiment to another, and some of them were difficult to be estimated. But most of them are of the order of a few percent, and the overall error comes essentially from the background subtraction, counting statistics, and fluctuation of the ratio of the monitor counting to the total beam current integration. After all, the relative value of the angular distribution contains an error less than 10%, and the absolute cross section is accurate within 20%.

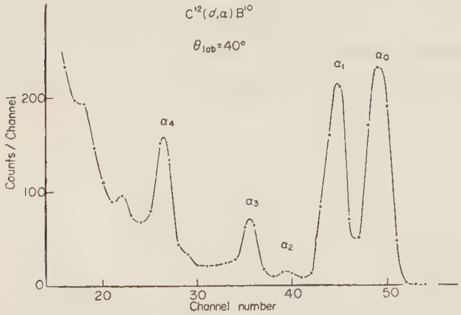

Fig. 8. Pulse-height spectrum of alpha particles from $C^{12}(d,\alpha)B^{10}$ reaction at $\theta_{lab}=40°$. Alpha particles leaving B^{10} in $T=1$ level (α_2) is observed. α_2 was observed from $\theta_{lab}=40°$ to $\theta_{lab}=90°$.

Table I. Coefficients of Legendre polynomial expansion. $W(\theta)=\sum_{i=0}^{6} a_i P_i(\cos\theta)$.

Reaction	a_0	a_1	a_2	a_3	a_4	a_5	a_6
$O^{16}(d,\alpha_0)N^{14}$	0.774	−0.028	1.044	−0.150	−0.089	−0.130	−0.253
$N^{14}(d,\alpha_0)C^{12}$	0.235	−0.200	0.210	0.195	0.374	0.219	0.253
$N^{14}(d,\alpha_1)C^{12}$	0.720	0.246	0.428	0.093	0.220	−0.095	0.084
$C^{12}(d,\alpha_0)B^{10}$	2.780	0.770	2.236	−0.586	−0.692	−1.489	−0.133
$C^{12}(d,\alpha_1)B^{10}$	3.261	−0.155	2.295	0.669	0.012	−3.363	−1.873

The error bars shown in the figures are calculated ones due to background subtraction errors plus counting statistics errors only. The results obtained are grouped into three categories. First, the angular distributions are expanded by the Legendre polynomials up to the sixth order by the method of least squares. Coefficients of these expansions are shown in Table I. The comparison of these polynomial expansions with experimental results are shown in Figs. 9, 10, 11, 12 and 13.

Second, differential cross sections are represented as a function of momentum transfer to the nucleus. Here, the quantity of momentum transfer can be defined by three ways as follows:

$$Q_{\text{knock-out}}=\left[\left(\frac{A-4}{A}\right)k_d-\left(\frac{B-2}{B}\right)k_\alpha\right] \qquad (1)$$

$$Q_{\text{pick-up}}=\left[\left(\frac{A-2}{A}\right)k_d-k_\alpha\right] \qquad (2)$$

$$Q_{\text{heavy particle stripping}}=k_d+\frac{2}{B}k_\alpha \qquad (3)$$

where A is the mass of the target nucleus, B the mass of the residual nucleus, k_d the wave number vector of a deuteron in the center of mass frame, and k_α the wave number vector of an α particle in the center of mass frame.

Results are shown in Figs. 14, 15 and 16. Here, abscissae show momentum transfer in the case of the knock-out process. Dotted lines are the smoothed curves for experimental values.

Finally, the smoothed curves for experimental values are trially represented by the suitable $j_l(QR)$ functions. Here $j_l(X)$ is a spherical Bessel function of order l, and l is the angular momentum change in the reaction.

When the direct reaction is assumed, the value of l is determined by the spin and parity conservation principle. Allowed l values for each reaction are listed in Table II.

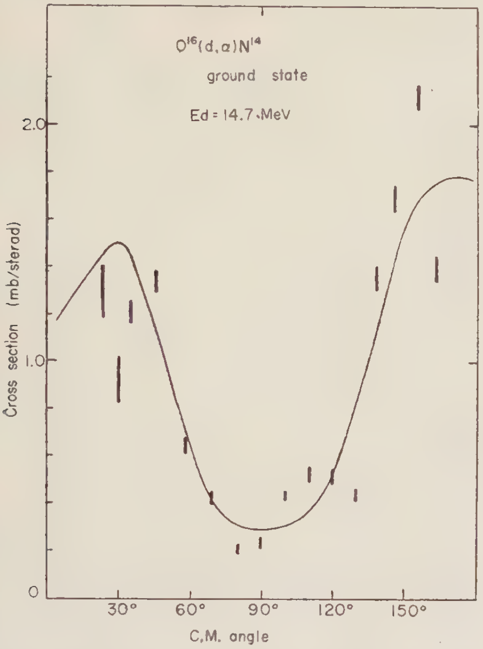

Fig. 9. Angular distribution of alpha particles from $O^{16}(d, \alpha)N^{14}$ reaction leaving N^{14} in its ground state. Solid line is the Legendre polynomial fit.

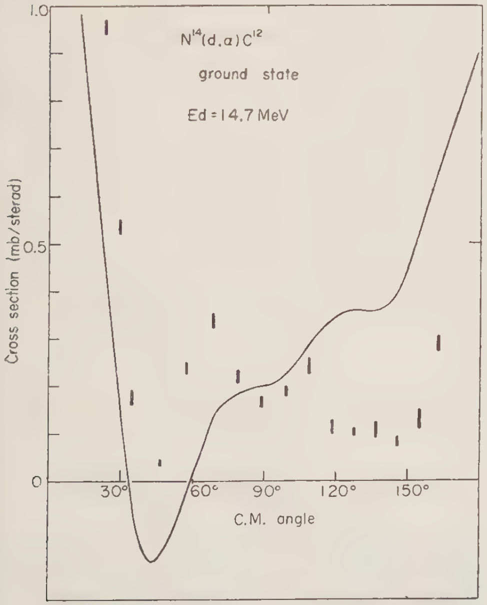

Fig. 10. Angular distribution of alpha particles from $N^{14}(d, \alpha)C^{12}$ reaction leaving C^{12} in it ground state. Solid line is the Legendre polynomial fit.

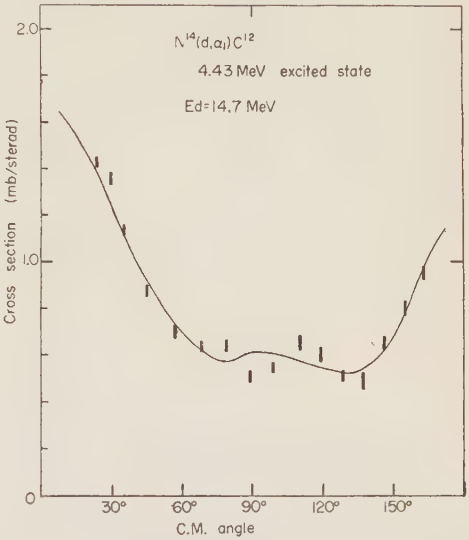

Fig. 11. Angular distribution of alpha particles from $N^{14}(d, \alpha)C^{12}$ reaction leaving C^{12} in its first excited state. Solid line is the Legendre polynomial fit.

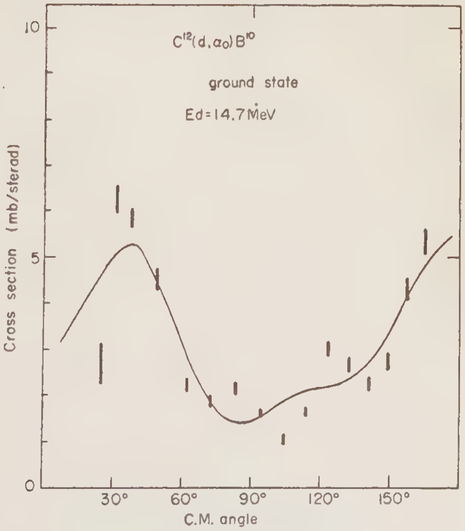

Fig. 12. Angular distribution of alpha particles from $C^{12}(d, \alpha)B^{10}$ reaction leaving B^{10} in its ground state. Solid line is the Legendre polynomial fit.

3-2. *Characteristics in each reaction*

3-2-1. *The* $O^{16}(d, \alpha)N^{14}$ *reaction*

As shown in Fig. 9 and in Table I, the Legendre polynomial fit is rather poor, but crudely speaking, P_0 and P_2 are dominant compared with other terms. This fact suggests that the α emission leaving N^{14} nucleus in its ground state is caused mainly by *s*-wave and *p*-wave deuterons. If the nuclear

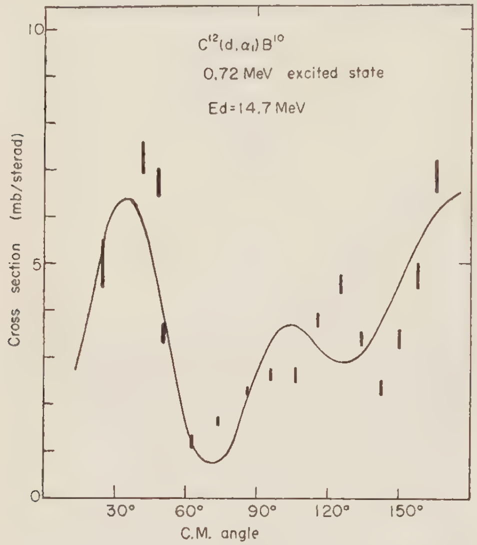

Fig. 13. Angular distribution of alpha particles from $C^{12}(d, \alpha)B^{10}$ reaction leaving B^{10} in its first excited state. Solid line is the Legendre polynomial fit.

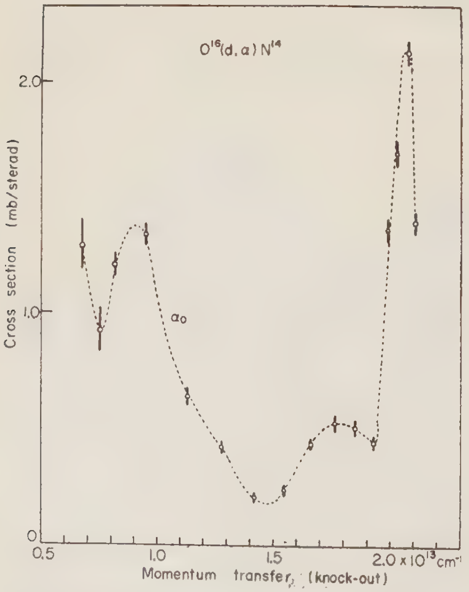

Fig. 14. Differential cross sections as a function of momentum transfer. Reaction; $O^{16}(d, \alpha_0)N^{14}$ (ground state). Momentum transfer is calculated as knock-out process.

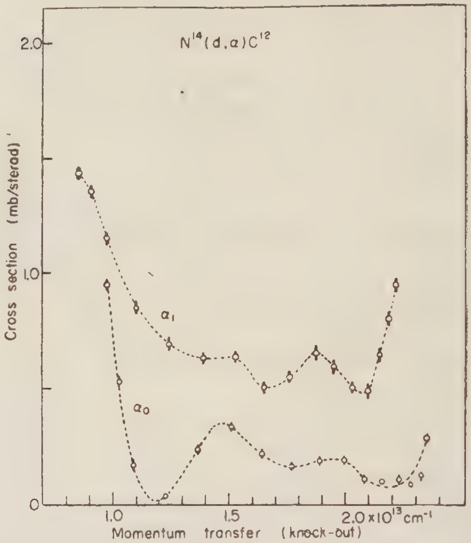

Fig. 15. Differential cross sections as a function of momentum transfer. Reaction; $N^{14}(d, \alpha)C^{12}$. Upper curve refers to α_1 leaving C^{12} in its first excited state, while lower curve refers to α_0 leaving C^{12} in its ground state. Momentum transfer is calculated as knock-out process.

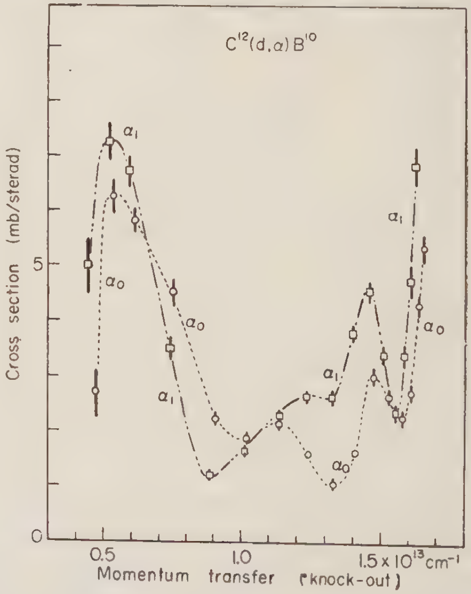

Fig. 16. Differential cross sections as a function of momentum transfer in $C^{12}(d, \alpha)B^{10}$ reaction. Dotted line is a smoothed curve of experimental results referring to alpha particles leaving B^{10} in its ground state. Dot and solid line refers to α_1, leaving B^{10} in its first excited state.

Table II. Spin and parity selection rule.

Reaction	Initial nucleus	Final nucleus		Δl Spin change	Δl Parity change	Δl Allowed
	J^π. T.	J^π. T.	Exc. energy			
$O^{16}(d, \alpha_0)N^{14}$	0^+, 0	1^+, 0	ground	0, 1, 2	even	0, 2
(d, α_1)		0^+, 1	2.31 MeV	1	even	forbidden
(d, α_2)		1^+, 0	3.95 MeV	0, 1, 2	even	0, 2
$N^{14}(d, \alpha_0)C^{12}$	1^+, 0	0^+, 0	ground	0, 1, 2	even	0, 2
(d, α_1)		2^+, 0	4.43 MeV	0, 1, 2, 3, 4	even	0, 2, 4
(d, α_2)		0^+, 0	7.66 MeV	0, 1, 2	even	0, 2
$C^{12}(d, \alpha_0)B^{10}$	0^+, 0	3^+, 0	ground	2, 3, 4	even	2, 4
(d, α_1)		1^+, 0	0.72 MeV	0, 1, 2	even	0, 2
(d, α_2)		0^+, 1	1.74 MeV	1	even	forbidden
(d, α_3)		1^+, 0	2.15 MeV	0, 1, 2	even	0, 2
(d, α_4)		2^+, 0	3.58 MeV	1, 2, 3	even	2

radius is assumed to be $(1.7+1.22\,A^{1/3})\times10^{-13}$ cm, and the deuteron radius is taken to be 2.18×10^{-13} cm, the maximum angular momentum k_dR is of the order of 7 when the 14.7 MeV deuteron hits the O^{16} nucleus. Here, k_d is the wave number of incident deuteron and R is the interaction radius. The $O^{16}(d, \alpha)N^{14}$ reaction here considered, therefore, may be caused rather by deuterons with small impact parameter than by those hitting near nuclear surface. As shown in Fig. 14, the curve for the angular distribution of α particles *versus* momentum transfer has sharp peaks in forward (small momentum transfer) region as well as in backward (large momentum transfer) region, and its up-and-down is quite different from a periodic function of momentum transfer. It may be said that several modes of angular distribution are mixed in this reaction. From the standpoint of the surface direct reaction, the forward peak is considered as a result of the pick-up or knock-out process, and the backward peak is understood as the heavy particle stripping. But the backward peak is not favoured to the heavy particle stripping representation unless very large nuclear radius is assumed.

The forward and backward peaks also appeared in the experiments with 7.03 MeV deuteron[5] and 19 MeV deuteron[2]. According to the direction of momentum in the center of mass system, the forward peak may be caused by incident deuteron, and the backward one must be due to the incident nucleus. But it seems very difficult to reproduce overall angle distribution by the present surface direct reaction theory. Therefore, the simplest way to compare experimental result with $j_l(QR)$ is adopted. It is shown in Fig. 17. The allowed l-values are 0 and 2 in this case, and the mixing of $l=0$ and 2 seemed

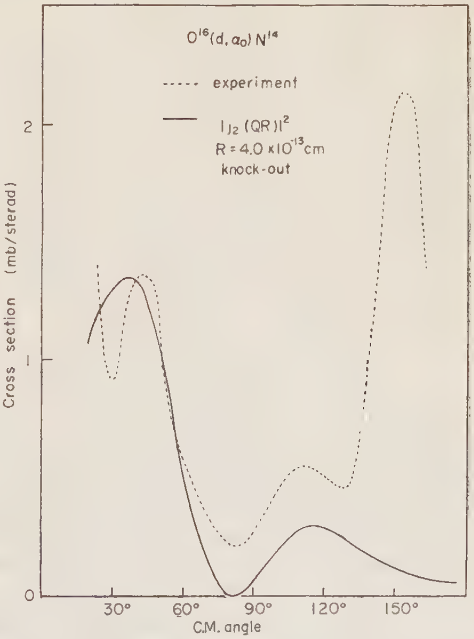

Fig. 17. Trial representation by $j_2(QR)$ in $O^{16}(d, \alpha_0)N^{14}$ reaction. Dotted line is a smoothed curve of experimental results. Solid line is $|j_2(QR)|^2$ normalized at $\theta_{C.M.}=40°$. Q is momentum transfer calculated as knock-out process. $R=4.0\times10^{-13}$ cm.

to be good, but it was difficult to find suitable parameters to reproduce first dip and first peak simultaneously by mixing j_0 and j_2.

3-2-2. *The* $N^{14}(d, \alpha)C^{12}$ *reaction*

The α particles leaving C^{12} nucleus in its ground state and first excited state show very different angular distribution. As shown in Fig. 10 and Table I, the Legendre expansion does not agree with the experimental data in the case of α_0, and seven terms from P_0 to P_6 each term are approximately of the same order of magnitude. Therefore, it may be concluded that the α_0 emission is caused purely by the surface direct reaction of some kind with the high angular momentum deuteron wave passing near the surface of the N^{14} nucleus. The $j_0(QR)$ fit gives also the reasonable agreement in this case (Fig. 18). On the other hand, the $N^{14}(d, \alpha^1)C^{12}$ (first excited state) reaction seems to be caused by the different mechanism compared to the $N^{14}(d, \alpha_0)C^{12}$ reaction. This conclusion comes from the facts that, in the $N^{14}(d, \alpha_1)C^{12}$ reaction, the angular distribution of α particles is fitted well by the Legendre polynomial expansion, and that lower order terms (namely P_0 and P_2) are dominant among seven terms of polynomials. These facts indicate that, the $N^{14}(d, \alpha_1)C^{12}$ reaction is not of surface direct nature, and may be caused by the small angular momentum deuteron wave. This situation is strengthened by the fact that the $j_0(QR)$ fit disagrees the experimental result. (Fig. 19).

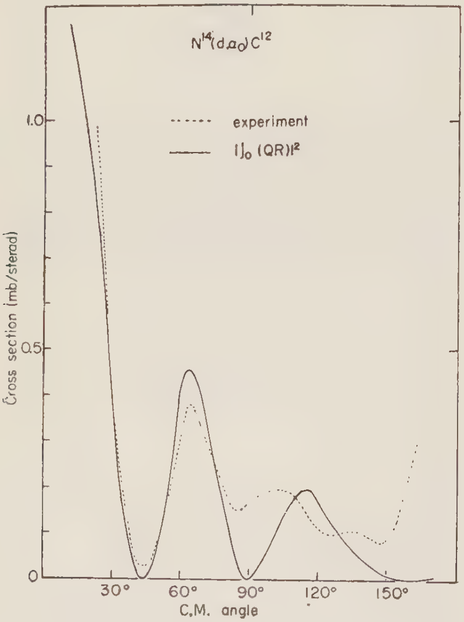

Fig. 18. Trial representation by $j_0(QR)$ in $N^{14}(d, \alpha_0)C^{12}$ reaction. Dotted line is a smoothed curve of experimental results. Solid line is $|j_0(QR)|^2$ normalized at $\theta_{C.M.}=30°$. Q is momentum transfer calculated as pick-up process. $R=4.4 \times 10^{-13}$ cm.

3-2-3. *The* $C^{12}(d, \alpha)B^{10}$ *reaction*

The α particles leaving B^{10} nucleus in its ground state and first excited state were observed over all angles, and alphas leaving residual nucleus in the second, third and fourth excited states were observed in forward angles. The $C^{12}(d, \alpha_0)B^{10}$ and $C^{12}(d, \alpha_1)B^{10}$ reactions show very similar behaviours. That is, the angular distribution shows peaks and dips at nearly the same momentum transfer, yields of α particles are nearly equal over all angles observed, (Fig. 16), and from Table I, P_0, P_2 and P_5 are dominant compared with other terms in both cases.

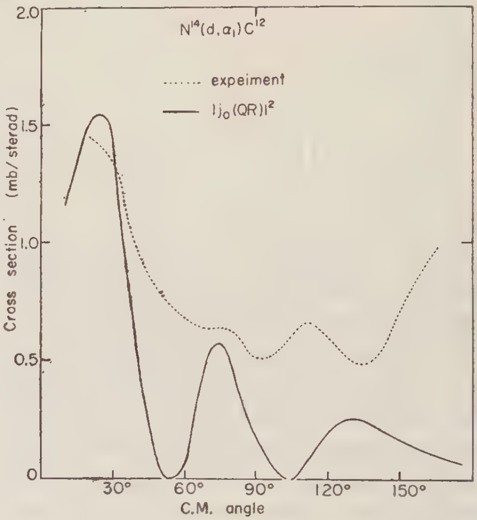

Fig. 19. Trial representation by $j_0(QR)$ in $N^{14}(d, \alpha_1)C^{12}$ reaction. Dotted line is a smoothed curve of experimental results. Solid line is $|j_0(QR)|^2$ normalized at $\theta_{C.M.}=30°$. Q is momentum transfer calculated as pick-up process. $R=4.4 \times 10^{-13}$ cm, equal to the value in α_0 distribution.

If the direct reaction process is assumed, allowed l-values are 2 and 4 in α_0 emission, and 0 and 2 in α_1 emission. Since both figures show similar nature, it may be concluded that $l=2$ is reasonable because this value is common in both cases. The trial representations by $j_2(QR)$ are shown in Figs. 20 and 21, in which are also shown the trial representations by taking the heavy particle stripping process into account. It was found to be difficult to reproduce the backward increase of the angular distribution by a spherical Bessel function with an argument Q_2R_2, unless an interaction radius was assumed to be enormously large.

The angular distributions of α_3 and α_4 are shown in Figs. 22 and 23. For the angular distribution there seems to be a tendency of being 90° symmetrical or isotropic.

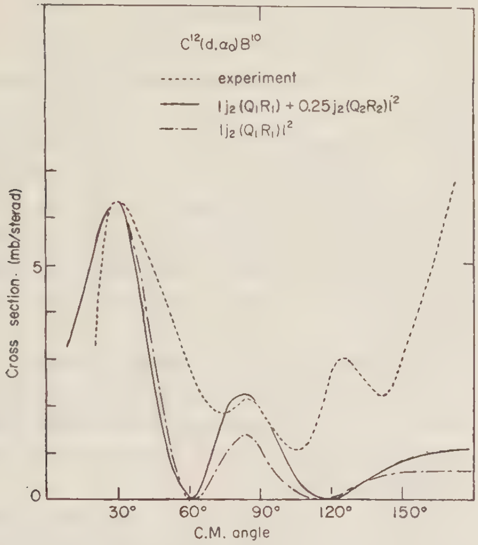

Fig. 20. Trial representation by $j_2(QR)$ in $C^{12}(d, \alpha_0)B^{10}$ reaction. Dotted line is smoothed curve of experimental result. Solid line is $|j_2(Q_1R_1)+0.25j_2(Q_2R_2)|^2$ normalized at $\theta_{C.M.}=30°$. Q_1 is momentum transfer calculated as knock-out process. Q_2 is momentum transfer as heavy particle stripping. $R_1=6.46\times10^{-13}$ cm, $R_2=6.8\times10^{-13}$ cm. Dot and solid line is $|j_2(Q_1R_1)|^2$, normalized at $\theta_{C.M.}=30°$. Q_1 or R_1 is the same to the one mentioned above.

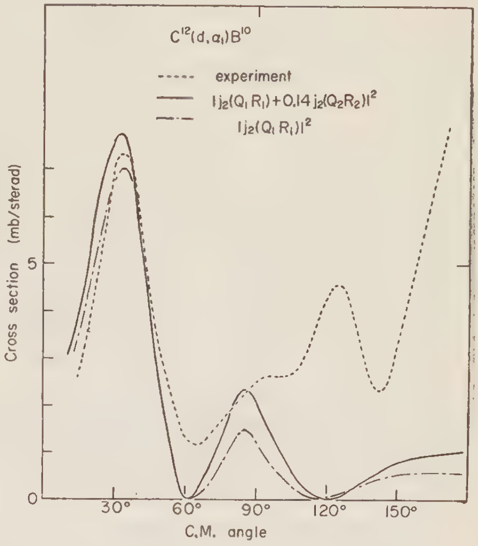

Fig. 21. Trial representation by $j_2(QR)$ in $C^{12}(d, \alpha_1)B^{10}$ reaction. Dotted line is smoothed curve of experimental result. Solid line is $|j_2(Q_1R_1)+0.14j_2(Q_2R_2)|^2$ normalized at $\theta_{C.M.}=40°$. Q_1 is momentum transfer calculated as knock-out process. Q_2 is momentum transfer as heavy particle stripping process. $R_1=6.45\times10^{-13}$ cm, $R_2=6.85\times10^{-13}$ cm. Dot and solid line is $|j_2(Q_1R_1)|^2$ only.

3-2-4. *The forbidden alpha group*

The $O^{16}(d, \alpha)N^{14}$ and $C^{12}(d, \alpha)B^{10}$ reactions offer another problem. Since both deuteron and α particle have isotopic spin 0, as Adair13) pointed out, if the isotopic spin is a good quantum number, the target nucleus and residual nucleus must have the same isotopic spin quantum number. By this reason, the $O^{16}(d, \alpha)N^{14}$ reaction leaving N^{14} nucleus in its first excited state is forbidden, as easily known from Table II. The same is true in the case of the $C^{12}(d, \alpha)^{10}$ reaction when the B^{10} nucleus is left in its second excited state. But, early in 1956 Browne5) observed a forbidden group of alphas emitted from the $O^{16}(d, \alpha)N^{14}$ reaction by 5~7 MeV incident deuterons, and he explained this apparent violation of isotopic spin conservation by noticing that the Coulomb interaction might admix a different T-spin state in the intermediate compound system. Further theoretical investigations given by Lane and Thomas14) reveal that, if

$$\langle H_c\rangle \ll D^J \qquad \text{(L.T. 5-2)},$$

or

$$\langle H_c\rangle \ll \langle \Gamma^J\rangle \qquad \text{(L.T. 5-3)},$$

the isotopic spin quantum number is a good quantum number and strictly conserves in the nuclear reaction process. Here $\langle H_c\rangle$ is the coulomb interaction matrix element, D^J is the level spacing between levels with the same spin J and parity, and $\langle \Gamma^J\rangle$ is the mean total width of those levels. Later, Morinaga18) discussed this violence of isotopic spin conservation in the case of the $Mg^{25}(\gamma, p)$ and $Mg^{26}(\gamma, p)$ reactions, and he gave

$$a(t) \simeq H_c t/\hbar$$

as an amplitude of different T-state mixing, where H_c is the Coulomb interaction energy and t is the life-time of the compound intermediate system.

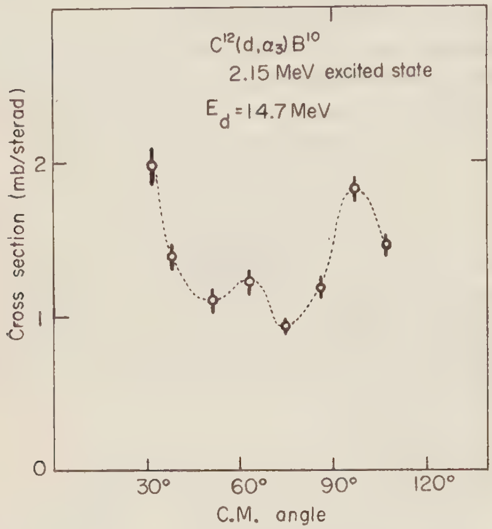

Fig. 22. Angular distribution of alpha particles from $C^{12}(d, \alpha)B^{10}$ reaction leaving B^{10} in its third excited state. Dotted line is a smoothed curve connecting experimental points.

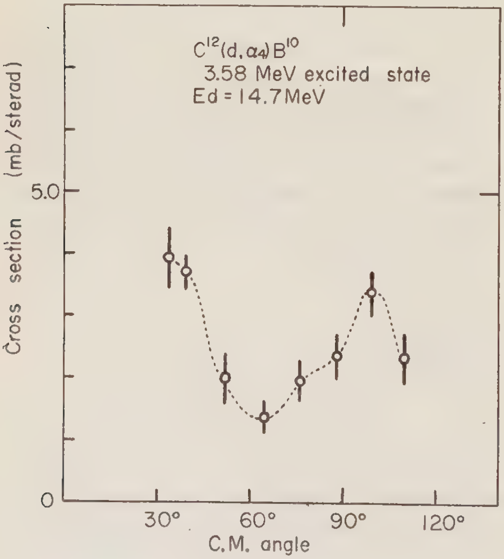

Fig. 23. Angular distribution of alpha particles from $C^{12}(d, \alpha)B^{10}$ reaction leaving B^{10} in its fourth excited state. Dotted line is a smoothed curve connecting experimental points.

By these considerations it has become clear that if a reaction is the purely direct process, i.e. when the reaction finishes in a time-interval comparable with the time necessary for the incident nucleon to pass through the target nucleus, the conservation of isotopic spin quantum number holds strictly.

In recent experiments by Dalton *et al.*[4] and Hu[6] on the $O^{16}(d, \alpha)N^{14}$ reaction, forbidden groups were also observed in the range of incident deuteron energies from 6.8 MeV to 11 MeV. They discussed these α particle emissions as the proof of violation of the isotopic spin conservation.

From the standpoint of spin-parity conservation, however, if the direct reaction is assumed, these reactions are forbidden simultaneously. From Table II, if both target nucleus and residual nucleus have 0^+ spin-parity, this transition is impossible through (d, α) reaction. Therefore, the $O^{16}(d, \alpha_1)N^{14}$ (first excited state) and $C^{12}(d, \alpha_2)B^{10}$ (second excited state) are doubly forbidden by both the spin-parity conservation and T-spin conservation.

In the present work, α_1 group from $O^{16}+d$ and α_2 group from $C^{12}+d$ were also observed in the forward region. These facts may suggest that the (d, α) reaction cannot be a purely direct process.

As Harvey and Cerny[19] discussed about the $C^{12}(\alpha, d)N^{14}$ reaction, and as Hashimoto and Alford[20] explained their experimental data for the $Ca^{40}(d, \alpha)K^{38}$ reaction, if the compound nucleus formation is assumed, the intensity of the forbidden group would be of the order of one-severalth of the allowed transition, when the spin and parity conservation only is considered. As discussed above, this α emission is further forbidden by the T-spin conservation rule in our case. Consequently, a few percent emission of allowed transition may be understood if the compound nucleus formation is assumed.

§ 4. Concluding Remarks

Total solid angle cross sections are given in Table III. From this table it may be seen that comparing the same channel spin reaction, O^{16} and C^{12} targets yield larger number of α particles than N^{14} target. Preliminary experiments* on the (d, α) reaction in our laboratory teach us that C^{12}, O^{16}, Ne^{20}, Mg^{24} and S^{32} targets yield more α particles than N^{14}, F^{19}, Al^{27} and P^{31}. These facts suggest

---

* To be published in a near future.

Table III. Total solid angle cross sections.

Reaction	$(J)^\pi$		σ (total angle)
	Target nucleus	Residual nucleus	
$O^{16}(d, \alpha_0)N^{14}$	0^+	1^+	9.9 mb
(d, α_1)	0^+	0^+	1~3% of α_0 from $20°_{lab}$ to $80°_{lab}$
$N^{14}(d, \alpha_0)C^{12}$	1^+	0^+	3.2 mb
(d, α_1)	1^+	2^+	9.1 mb
$C^{12}(d, \alpha_0)B^{10}$	0^+	3^+	34 mb
(d, α_1)	0^+	1^+	42 mb
(d, α_2)	0^+	0^+	2~3% of α_0 from $40°_{lab}$ to $90°_{lab}$
(d, α_3)	0^+	1^+	18 mb Isotropic distribution is assumed
(d, α_4)	0^+	2^+	31 mb ditto

that if target nucleus (not compound nucleus!) is of the type of the integral multiple of α particles, there occurs the (d, α) reaction easier than in other cases. From this fact one hypothesis may be well assumed that in the (d, α) reaction, α cluster formation in the intermediate system plays an important role.

The following phenomena may perhaps be the evidences for this cluster formation.

1) The forward and backward peaks in the $O^{16}(d, \alpha)N^{14}$ and $C^{12}(d, \alpha)B^{10}$ reactions are likely to be due to the nucleon exchange or charge exchange effect.

2) The doubly forbidden transition in the $O^{16}(d, \alpha)N^{14}$ and $C^{12}(d, \alpha)B^{10}$ reactions can occur in intermediate energy. This fact suggests that according to Morinaga's criterion the reaction time in the (d, α) reaction is much longer than that in the direct process. If H_c is assumed to be $\simeq 1$ MeV, the reaction time is of the order of 10^{-21} sec. This lifetime is in accord with the width of the broad resonance found by Dalton *et al.*[4] and also by Hu[6] on the $O^{16}(d, \alpha)N^{14}$ reaction. This phenomenon is related to the charge exchange in intermediate state, and then to the angular distribution of allowed α groups.

3) In the cases of $O^{16}+d$, $N^{14}+d$ and $C^{12}+d$, the excitation energies of the target nucleus plus the incident deuteron energies are about 21, 34 and 23 MeV, respectively. A neutron or proton of the deuteron moves with a half of this energy. If the Fermi energy is assumed to be 28 MeV, the energy of neutron or proton in the intermediate state nuclei will be 38 MeV, 45 MeV and 40 MeV, respectively. Now, according to the theoretical discussion given by Hayakawa *et al.*[21] a mean free-path of the nucleon in a nucleus changes greatly at around the energy of 40 MeV (see Fig. 24). Therefore, when N^{14} is bombarded by a 14.7 MeV deuteron, a mean free-path of the incident deuteron in the nucleus is small and the direct process is essential. On the other hand, when O^{16} or C^{12} is bombarded by a deuteron with the same energy, the deuteron can live during very longer time interval than in the former case. This fact is in accord with the T-spin admixture problem and the difference between

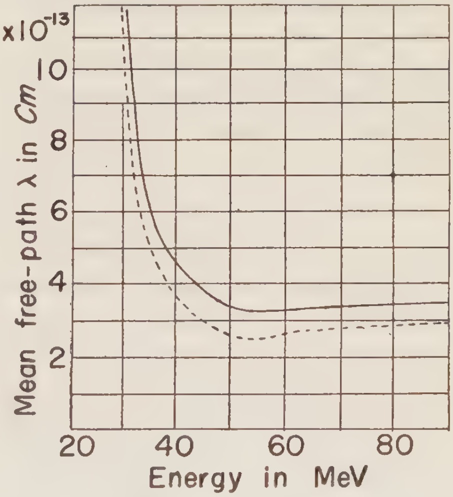

Fig. 24. Mean free path λ *versus* nucleon energy in the nucleus. Solid curve and dashed curve refer to results calculated on the assumption of the inverse energy and the energy-independent cross sections respectively. After S. Hayakawa, M. Kawai and K. Kikuchi: Reference 21).

α particle angular distributions for $O^{16}(d, \alpha)$, $N^{14}(d, \alpha)$ and $C^{12}(d, \alpha)$ reactions.

Acknowledgements

The author would like to thank Professors K. Kimura, Y. Uemura and S. Shimizu for their continuous encouragements during the work. He is indebted to his collaborators, S. Yamashita, T. Nakamura, K. Takamatsu, A. Masaike, S. Kakigi and Dai Ca Nguyen for their helpful co-operation and stimulating discussions. He also appreciates the hospitality of members of the Cyclotron Laboratory of Kyoto University, on whom the maintenance and feasibility of the experimental apparatus mainly depend.

References

1) D. M. Van Patler and W. Whaling: Rev. Mod. Phys. **29** (1957) 757.
2) R. G. Freemantle, W. M. Gibson, D. J. Prowse and J. Rotblat: Phys. Rev. **92** (1953) 1268.
3) G. E. Fischer and V. K. Fischer: Phys. Rev. **114** (1959) 533.
4) A. W. Dalton, S. Hinds and G. Parry: Proc. Phys. Soc. **A, 71** (1958) 252.
5) C. P. Browne: Phys. Rev. **104** (1956) 1598.
6) C. Hu: J. Phys. Soc. Japan **15** (1960) 1741.
7) W. M. Gibson and E. E. Thomas: Proc. Roy. Soc. **A, 210** (1952) 543.
8) F. A. El Bedewi and I. Hussein: Proc. Phys. Soc. **A, 70** (1957) 238.
9) T. S. Green and R. Middleton: Proc. Phys. Soc. **A, 69** (1956) 28.
10) S. T. Butler: Phys. Rev. **106** (1957) 272.
11) M. El Nadi: Phys. Rev. **119** (1960) 242.
12) Quoted by C. Hu.
13) R. K. Adair: Phys. Rev. **87** (1952) 1041.
14) A. M. Lane and R. G. Thomas: Rev. Mod. Phys. **30** (1958) 345.
15) J. B. Mead and B. L. Cohen: Phys. Rev. Let. **5** (1960) No. 3. 105.
16) H. Bichsel: Phys. Rev. **112** (1958) 1089.
17) L. H. Johnston and D. A. Swenson: Phys. Rev. **111** (1958) 212.
18) H. Morinaga: Phys. Rev. **97** (1955) 444.
19) B. G. Harvey and J. Cerny: Phys. Rev. **120** (1960) 2162.
20) Y. Hashimoto and W. P. Alford: Phys. Rev. **116** (1959) 981.
21) S. Hayakawa, M. Kawai and K. Kikuchi: Prog. Theor. Phys. **13** (1955) 415.

JOURNAL OF THE PHYSICAL SOCIETY OF JAPAN, Vol. 16, No. 11, NOVEMBER, 1961

Nuclear Interactions Produced by Heavy Nuclei of Primary Cosmic Radiation in Nuclear Emulsions

Yoshihiro TSUZUKI
Department of Physics, Kobe University, Kobe, Japan

(Received July 27, 1961)

Fifty-two nuclear interactions produced by the nuclei of cosmic radiation with charge $Z=6$, 7 and 8, and with energies around 4×10^{10} eV/nucleon were studied in nuclear emulsions. The ratio of the number of interactions with heavy nuclei (Ag and Br) to that with light nuclei (H, C, N and O) was found to be 1.03, which is in good agreement with the value calculated by assuming the geometrical cross sections of the colliding nuclei. The features of interactions in which the colliding volume of an incident nucleus was equal to that of an alpha-particle were similar to those of a free alpha-particle. The average number of heavily ionizing tracks, N_h, indicated the exponential increase as the impact parameter decreased. The distribution of the total charge of the fragments showed rather regular bumps at even charge. Almost all shower particles ejected with the smallest angles to the primary direction (shower axis) were the nucleons which came from primary nuclei. The angular distribution of mesonic shower particles was nearly isotropic in C. M. system at these energies.

§ 1. Introduction

A large number of works have been made on high energy nuclear interactions utilizing cosmic radiation by means of nuclear emulsions. Most of these were, however, the investigations concerning the characteristics of nuclear interactions induced by single nucleons or alpha-particles.

So far, studies on the heavy nucleus-nucleus collisions were almost confined to the following two problems, the one concerning the fragmentation probabilities which is necessary to find the composition of heavy primary cosmic-ray particles and their flux at the top of the atmosphere, and the other concerning the rare nuclear events at ultra high energies, because the events resulting from such nucleus-nucleus collisions generally appear as too complicated phenomena to be analysed unambiguously. However, the knowledge about general features of such interactions should be of great importance for understanding of the structure of nucleus, the multiple meson production in nuclear collisions at high energies, the contribution of heavy primaries to the extensive air showers and the behaviour of those particles in the cosmic space.

An emulsion stack equiped with an orientation control instrument was exposed at high altitude in order to obtain the east-west effect for heavy primary cosmic-ray particles in 1957. The general characteristics on nucleus-nucleus collisions based on 52 nuclear interactions induced by carbon, nitrogen and oxygen nuclei in this stack, are described in this note. This selection of events may more or less simplify the interpretation of the intricate phenomena. The other data published by Fowler et al.,[1] Cester et al.,[2] Hopper et al.[3] and Rajopadhye et al[4] were also considered together with ours to improve the statistics in some of the following sections. We shall, hereafter, refer to those data as [F], [C], [H] and [R]. About 700 heavy primaries with $Z\geq6$ were found in this stack. These results will be reported in elsewhere in the near future.

§ 2. Experimental Procedure

A stack of Ilford G5 emulsion consisting of 66 pellicles, 15 cm×10 cm large and 600μ thick was used in this work. It was exposed with the 15 cm side in the vertical direction for 6 hours, over the Central Districts in Japan ($\lambda_{\text{mag}}=24°$N) at the atmospheric depth of about 10 g/cm^2 in September, 1957.

The scanning was carried out along lines parallel to and 1 cm inside the top and both side edges, and on the half upper parts of both sides. All heavy nuclei which cross the scanning volume and have more than 10 δ-rays per 1 mm were accepted and followed through until they left the stack or interacted.

In all cases of the interactions where the primary heavy nucleus did not undergo a destructive collision, the remaining heavy fragments were followed further in the same way.

Due to the circumstance that the stack was flown at very high altitude and at the area of the magnetic cut off of 5.5 BeV/nucleon, all entering heavy nuclei had relativistic velocities and ionization loss in the air above the stack and in the stack itself was negligibly small and the primary charge were determined by measuring the δ-ray density in the relativistic region.

By scanning the half upper parts of both sides, we obtained more than 150 nuclear interactions caused by heavy nuclei ($Z \geq 6$) out of which 52 events induced by the collisions of carbon, nitrogen or oxygen nuclei with those in the emulsion were selected for this analysis. Those interactions were classified with respect to F_z—the charge of heavy fragments ($z \geq 3$), N_α—the number of helium nuclei, N_s—the number of charged shower particles (ionization ≤ 1.4 minimum ionization), and N_h—the number of heavily ionizing tracks (grey and balck tracks).

In Table I the details of the observed interactions are given.

§ 3. Prong Distribution of Target Nuclei in Interactions

The distribution of heavily ionizing tracks (grey and black) associated with the interactions is given in Fig. 1. The distribution given in the figure includs the data of [F], [C], [H] and [R] together with ours.

It is noted that there is a change of distribution which shows a sudden decrease at the line of demarcation between $N_h=6$ and $N_h=7$, and the nearly uniform distribution continues hereafter up to $N_h \simeq 20$. This change can possibly be attributed to the existence of two kinds of target nuclei in the emulsion, the light nuclei (H, C, N aud O) and the heavy nuclei (Ag and Br). Most of the events with $N_h \leq 6$ should naturally be attributed to the interactions with light nuclei and the remainder ($N_h \geq 7$) to the interactions with heavy nuclei.

If we assume that the interactions with $N_h \leq 6$ produced on heavy target nuclei have the same prong distribution as that of the events with $6 < N_h < 20$, then we can estimate the contribution of heavy target nuclei in the region of $N_h \leq 6$. The dotted line in Fig. 1 shows the average number of events with $7 \leq N_h \leq 18$. From the above assumption, it was very reasonably estimated that 22.4% of the interactions with $N_h \leq 6$ was induced on heavy target nuclei in the emulsion. This estimate leads to a result that 50.7±5.7% of all events was the interactions with heavy nuclei. Hence, the interactions with light nuclei was 49.3±5.8%. Assuming that the geometrical cross sections of nuclei are valid for the interactions considered here and taking the content of the nuclear emulsion into account, the calculation gives the values of 56% and 44% for the fractions of heavy and light nucleus interactions, respectively. These are in good agreement with the result obtained from our experiment.

The interactions were divided into 4 groups in terms of P_i, the number of charged nucleons in the splitting, i.e., the charge of incident nucleus (Z_p) minus total charge of heavy fragments (F_z+2N_α). In other wards, P_i means the number of fast charged nucleons among the shower particles. Figs. 2 (a), (b), (c), and (d) give the prong distributions for the case of $P_i \leq 2$, $P_i=3$ to 4, $P_i=5$ to 6 and $P_i=7$ to 8, respectively

In the case of $P_i \leq 2$, the colliding volume of nucleus is considered to be the same as that of alpha-particle events. The dotted line in Fig. 2 (a) shows the data of the interactions produced by alpha-particles given by Daniel et al.[5] and are normalized at $N_h=0$. One can see good agreement between both distributions in the region of $N_h < 10$.

There is, however, a discrepancy between these two distributions for the higher values of N_h (>10). If it is assumed that the heavy fragments are the residual nuclei resulted from the removal of nucleons in the overlapped volume of the incident and target nuclei in the collision, and the excitation energy of the residual nucleus comes from the friction energy and the change in the surface energy[6],[7], then this result may be understood by taking account of an impact parameter: that is, a central collision is pos-

Table I. Summary of events recorded in the emulsions.

Number of event	Charge of primary nucleus	N_α	N_h	N_s	F_z	P_i	n_s	γ_c
8	6	3	0	0		0	0	
38′	6	0	0	10		6	4	
45	6	0	4	21		6	15	
46	6	0	19	141		6	135	3.4
49	6	0	4	8	4	2	6	
50	6	3	0	3		0	3	
52	6	0	17	30		6	24	2.8
60	6	0	2	18		6	12	
71	6	0	0	23		6	17	
93	6	0	5	14		6	8	
94	6	1	5	3	3	1	2	
100	6	0	19	48		6	42	2.1
102	6	1	4	23		4	19	6.2
218	6	1	16	30		4	26	1.6
216	6	0	3	10		6	4	
219	6	1	4	40		4	36	4.4
222	6	2	2	5		2	3	
226	6	3	5	8		0	8	
233	6	3	2	2		0	2	
237	6	1	11	21		4	17	4.7
30	7	2	0	3		3	0	
59	7	0	3	13		7	6	
65	7	1	18	27		5	22	2.2
67	7	1	15	26		5	21	1.9
103	7	0	0	2	5	2	0	
117	7	1	13	27		5	22	3.2
201	7	0	15	101		7	94	4.6
202	7	0	0	14	4	3	11	
204	7	2	26	51		3	48	5.6
205	7	0	5	1	6	1	0	
206	7	1	18	34		5	29	3.1
215	7	1	5	14		5	9	
217	7	0	5	38	5	2	36	10.6
1	8	0	8	43		8	35	4.8
3	8	0	23	54		8	46	2.7
35	8	0	22	70		8	62	5.2
38	8	1	1	1	6	0	1	
44	8	1	7	20		6	14	
47	8	0	12	5	5	3	2	
48	8	0	9	19		8	11	
56	8	0	10	42		8	34	3.8
58	3	2	21	33		4	29	3.5
72	8	0	1	6	3	5	1	
76	8	0	21	129		8	121	4.8
78	8	0	3	13	6	2	11	6.4
98	8	2	3	12		4	8	
107	8	1	5	18		6	12	
116	8	2	2	4		4	0	
203	8	0	8	6	7	1	5	
212	8	2	2	13		4	9	
221	8	2	5	31		4	27	7.0
224	8	1	2	4	6	0	4	

sible for a free alpha-particles, but in the case of a heavy nucleus, there must be a lower limit of the impact parameter in those collisions.

In the interactions with larger impact parameter, the nucleus can not be too excited to give more than 10 prongs, as shown by the full line in Fig. 2(a). The interactions having the smaller impact parameter than this lower limit should belong to the other categories ($P_i \geq 3$).

From Figs. 2(b), (c) and (d), it appears that the maxima of the prong distributions for heavy target nuclei shift to the higher values of N_h when P_i is increased, as expected.

The correlation between the average

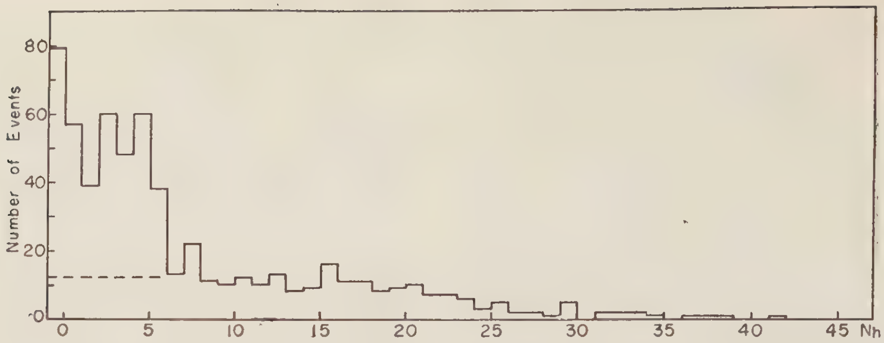

Fig. 1. The distribution of heavily ionizing tracks, N_h, for all events.

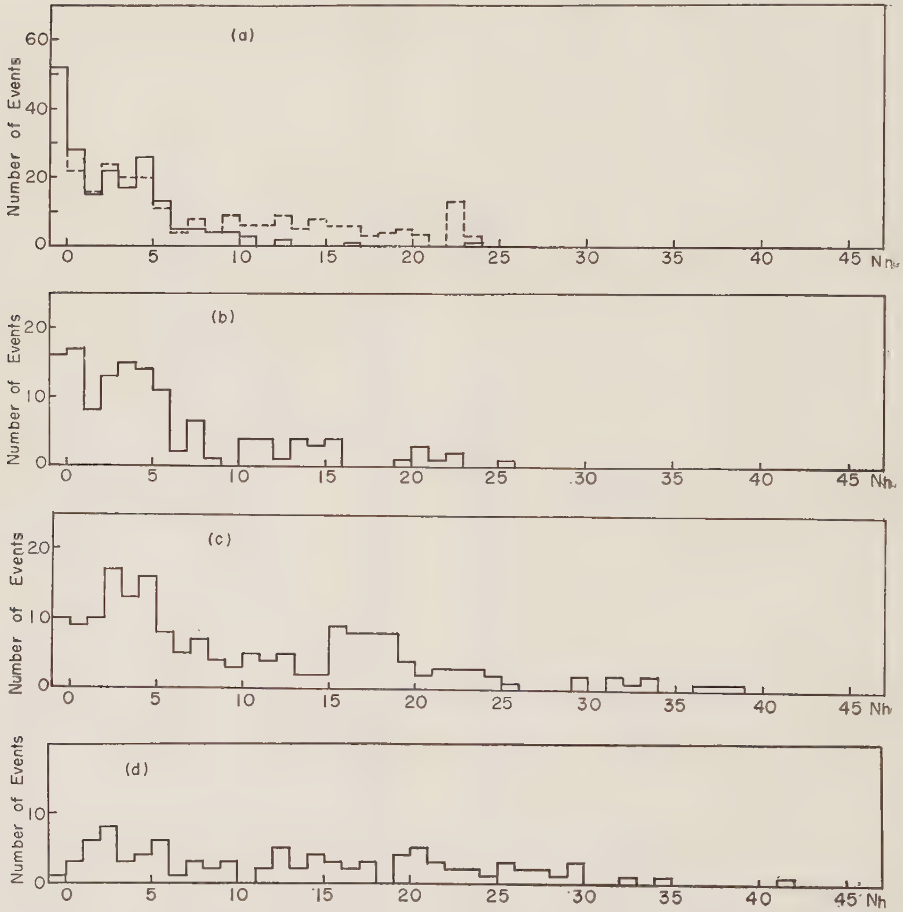

Fig. 2. The distribution of N_h. (a) for $P_i \leq 2$, (b) for $P_i=3$ to 4, (c) for $P_i=5$ to 6, (d) for $P_i=7$ to 8. The dotted line is the events of alpha-particles by Daniel et al.

number of N_h and P_i was plotted in Fig. 3. An increasing function of the average N_h on P_i is expressed approximately by an exponential form.

§ 4. Fragments of Incident Nuclei

The fragments produced by the interaction of heavy nucleus have been discribed as the results of the evaporation process in the rest system of the incident nucleus.

In an effort to see the nature of these fragments, the frequency of the interactions in which the fragments (alphas and heavy nuclei with $Z \geq 3$) with the total charge of

$Z_p - P_i$ were produced, was plotted in Fig. 4 for three kinds of the primary nuclei. It is reasonably understood that the frequency of the events with $Z_p - P_i = 1$ must be zero, because we can not recognize a nucleon evaporated from the primary nucleus as a fragment.

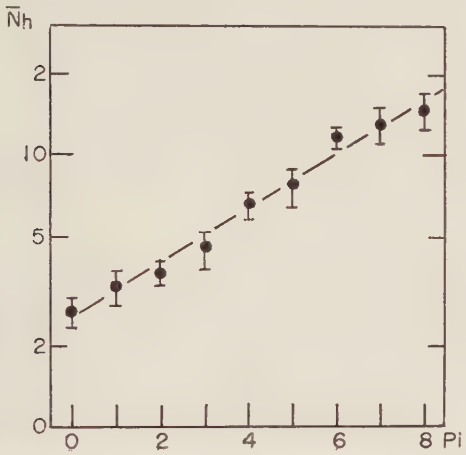

Fig. 3. Average number of N_h as a function of P_i.

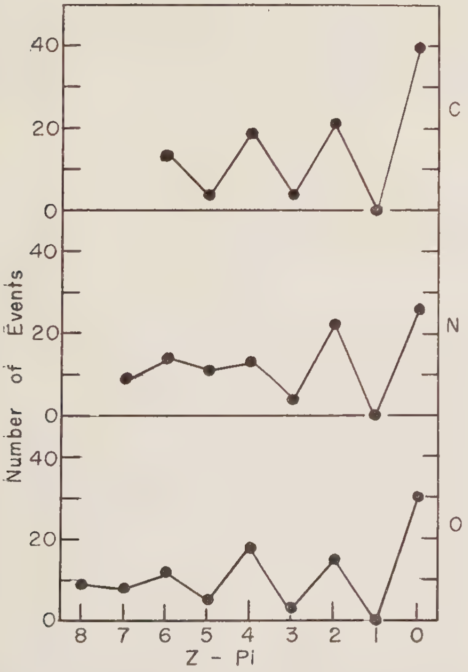

Fig. 4. The frequency of the total charge of fragments, alphas and heavy nuclei with $Z \geq 3$.

Accordingly, we should consider that these events are included in the events with $Z_p - P_i = 0$.

As seen in Fig. 4, it is definitely recognized that the distribution of the total charge of fragments shows the regular bumps at the abscissa of the even charge. As we do not have any information about the nucleons evaporated from the residual nucleus of the incident particle, we do not know the exact charge of the nucleus which was left at the excited state immediately after the collision. In the case that the total charge of the fragments were even, the fragments with even charge were always observed, but the fragments with odd charge were never observed, as expected from the nuclear stability consideration. When the total charge was odd, single fragments with odd charge were frequently observed.

Table II. The classification of the fragments.

Total charge of remained nucleus	Fragments	Number of fragments	%
2	α	122	
3	L_i	20	
4	Be	14	13.3
	2α	91	86.7
5	B	23	60.6
	$\alpha + L_i$	15	39.4
6	C	26	33.3
	$\alpha + B_e$	11	14.1
	3α	41	52.6
	$L_i + L_i$	0	0
7	N	18	66.7
	$\alpha + B$	9	33.3
	$2\alpha + L_i$	0	0
	$L_i + B_e$	0	0
8	O	3	25.0
	$\alpha + C$	6	50.0
	$2\alpha + B_e$	1	8.3
	4α	2	16.7
	$2B_e$	0	0
	$L_i + B$	0	0
$\alpha = 478$	$\left.\begin{matrix} L_i = 35 \\ B_e = 26 \\ B = 32 \end{matrix}\right\} 93$	$\left.\begin{matrix} C = 26 \\ N = 18 \\ O = 3 \end{matrix}\right\} 47$	

Because of the complexity of the phenomena and the ambiguity of the evaporated nucleons, it would be difficult to deduce too definite conclusion about the excited nucleus after the nuclear interaction from the results stated above, but we feel that we could obtain more information about it by improving the statistics.

§ 5. Angular Distribution of Secondary Shower Particles

(*a*) *Angular Distribusion of Laboratory System*

As already described in § 1, we found 52 interactions produced by carbon, nitrogen and oxygen nuclei of primary cosmic radiation. The space angles between the directions of shower particles and the incident primary nucleus were carefully measured by a Koristka microscope for all events.

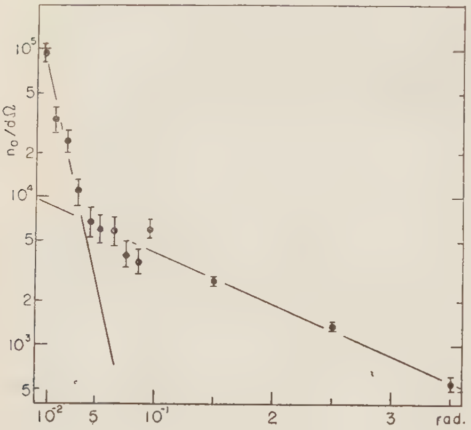

Fig. 5 (a). Angular distribution of shower particles in L-system for all events.

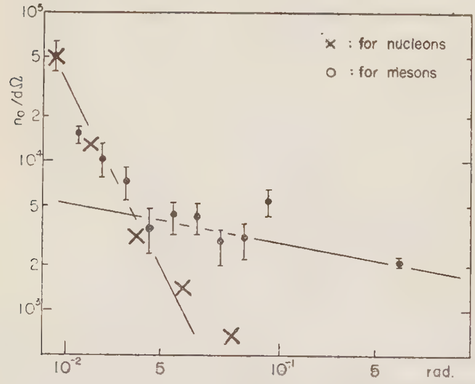

Fig. 5 (b). Angular distribution of shower particles in L-system.

Fig. 5 (a) shows the angular distribution of shower particles emitted in the unit solid angle. The distribution might be approximated by two straight lines. From the consideration of the nature of the heavy nucleus interactions, it is presumed that the steep line indicates the distribution of nucleons of the primary nucleus and the other line corresponds to the mesons created by the collisions.

In order to get the clearer evidence for such interpretations, the events with high and low multiplicities of mesons were selected from the events described above. In Fig. 5 (b), the circles indicate the distribution for the events with high multiplicity of mesons in whith P_i is less than 20% of N_s, and the crosses are for low multiplicity, n_s being less than P_i, where N_s is the total number of charged shower particles and n_s is equal to N_s-P_i. Thus almost all particles in the latter showers consist of the fast nucleons and the larger fraction of particles in the former group is thought to be the mesons produced in the collisions.

As can be seen from this figure, it is evident that most of the shower particles ejected with the angle less than 3×10^{-2} rad. are attributed to the nucleons which come from the primary nucleus.

(*b*) *Angular Distribution of Mesons in C. M. System*

If a nucleus-nucleus collision can be considered as the superposition of the individual nucleon-nucleon collisions, then the Lorentz factor γ_c of the center of momentum system (C. M. system) is determined from Castagnoli's method[8] as follows,

$$\ln \gamma_c=\frac{1}{n_s}\sum_{i=1}^{n_s}\ln\cot\theta_i\ .$$

An angle of the shower particle in C. M. system, $\theta_i{}^*$, is related to γ_c as

$$\theta_i{}^*=2\tan^{-1}(\gamma_c\tan\theta_i)\ .$$

22 events with high multiplicity were satisfied with the criteria that P_i was less than 20% of N_s and N_s was greater than 10. They were accepted for the investigation of the angular distribution of mesons, because we thought that the nucleons included in those showers did not have too large influence in calculating the angular distribution of the ejected mesons.

The angular distribution in Fig. 6 shows the results obained by using Castagnoli's method by taking all shower particles into account. The average value of γ_c' thus calculated is 4.5 in this case. This makes the distribution nearly symmetrical with respect to forward and backward directions but strongly anisotropic.

If it is, however, desirable to know the angular distribution of mesons created by the primary collisions, we have to take account of the influence of nucleons from the primary nucleus at the small angles as mentioned already and of the mesons produced by the "secondary process" at the large angles.

The events were separated into two groups according to the multiplicities of the shower particles. One group, consisting of the events with the multiplicity less thae 7 P_t, gives the distribution of the full line in Fig. 7, and the other one drawn by the dotted line shows that of higher multiplicity. There is a noticeable peak at a small angle in the distribution of low multiplicity which should correspond to the nucleons from the primary nucleus. But the distribution for high multiplicity is similar to the one of all events as given in Fig. 6. The concentrations of shower particles in forward and backward directions are to be attributed to the lower estimation of γ_c and to the presence of the shower particles created by the secondary process.

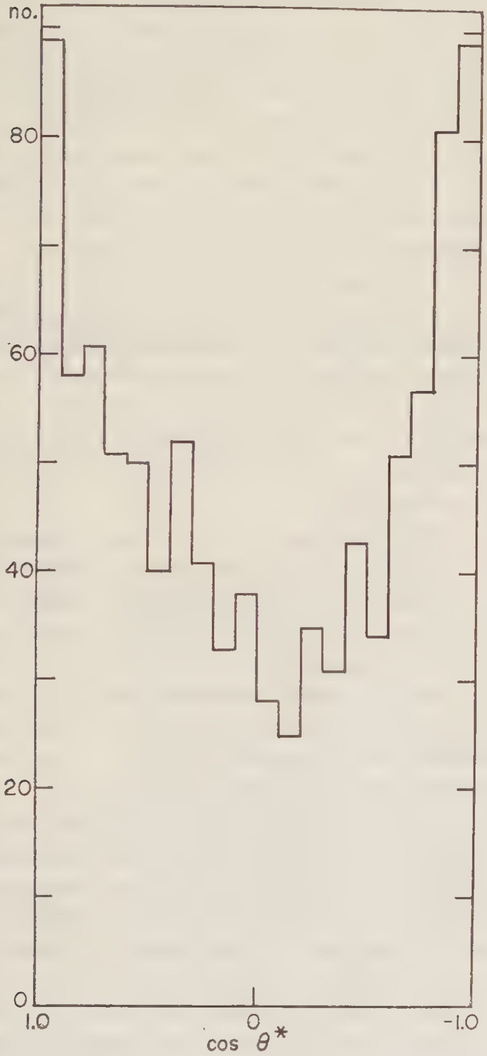

Fig. 6. Angular distribution of all shower particles in C. M. system.

In order to take the primary nucleons and the mesons arising from the secondary process out of the shower particles, we assumed that P_t shower particles emitted with the smallest angles within 3×10^{-2} rad. were the primary nucleons and also that the particles with the angles greater than a certain value in each event derived in the previous paper[10] were produced by the secondary processes. At this angle the smooth continuity of the distribution in the F-plot[9] of all shower particles of an event was broken and its slope changed. We could practically find this angle in the F-plot on all of each event with the high multiplicity.

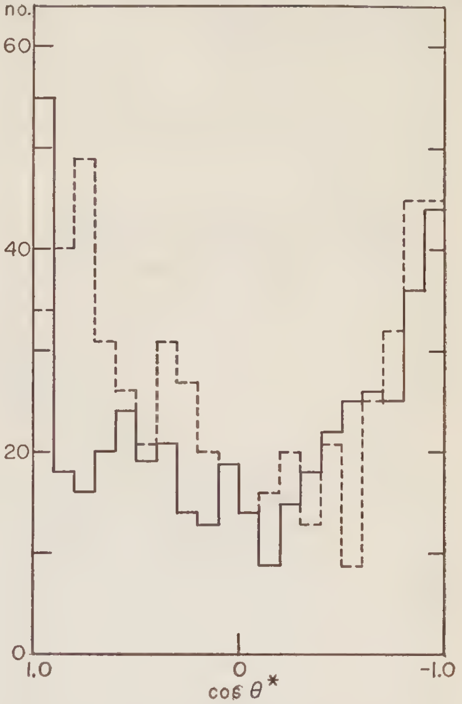

Fig. 7. Angular distribution of shower particles separated by the multiplicities. Full line: for the low multiplicity. Dotted line: for the high multiplicity.

We have, again, calculated γ_c from the angular distribution of the selected shower particles obtained by removing those at the small and the large angles. The γ_c thus obtained refers only to the angular distribution of shower particles produced by the primary collision in the nucleus. Fig. 8 gives the angular distribution in C. M. system of the accepted shower partieles. In this case, the average value of γ_c is 4.3. The full and the dotted lines in Fig. 8 indicate the angular distributions of shower particles associated with the low and the high multiplicity events, respectively. Within the statistics available here, they are not inconsistent with each other and are not appreciably different from the isotropic distribution.

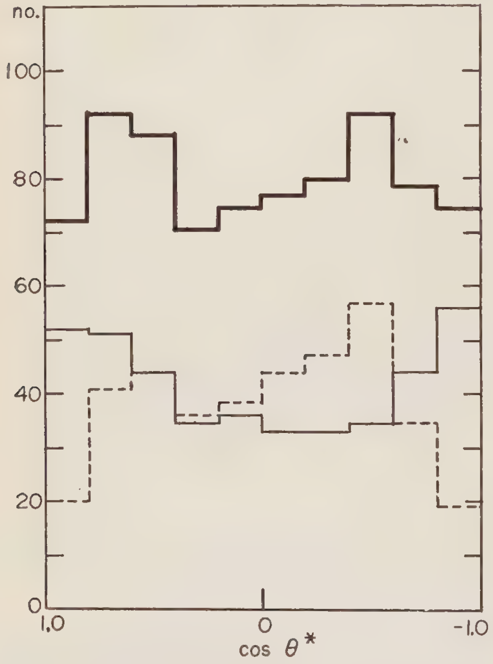

Fig. 8. Angular distribution of meson shower particles in C. M. system. Full line: for the low multiplicity ($n_s<7P_i$). Dotted line: for the high multiplicity ($n_s>7P_i$). Heavy line: the sum of the above two distributions.

The angular distribution shown by the heavy line in Fig. 8, the sum of the two distributions described above, is rather in good agreement with the isotropic angular distribution. This agrees with the results obtained by the measurements of nucleon-nucleon collisions at the same energy range[11]. Thus the features of the nucleus-nucleus collisions at the energies less than 10^{11} eV/nucleon can be interpreted in terms of the successive collisions[12].

§ 6. Conclusions

The experimental results concerning the interactions produced by carbon, nitrogen and oxygen nuclei can be summarized as follows;

(1) In nucleus-nucleus collisions at energies around 4×10^{10} eV/nucleon, it was estimated that 22.4% of the nuclear events with $N_h\leq6$ was attributed to the interactions with heavy nuclei in the emulsion (Ag and Br). From this result, we could obtain the ratio of the number of interactions with heavy nuclei to that with light nuclei (H, C, N and O), 50.7/49.3=1.03, which is in good agreement with the value derived by the calculation using the assumption of the geometrical cross sections of the nuclei.

(2) It seemed that the characteristics of the collisions of the nuclei with $P_i\leq2$ (the colliding volume of the incident nucleus was the same as that of a free alpha-particle) were similar to those of free alpha-particles.

(3) The average number of heavily ionizing tracks, N_h, increased exponentially with the increase of P_i.

(4) The distribution of the total charge of the fragments showed the regular bumps at the abscissa of the even charge, which probably came from the stability of the nucleus in the excited state after the collision.

(5) In Laboratory system, most of the shower particles within angles 3×10^{-2} rad. are the nucleons of the primary nuclei. It is possible to reject almost all nucleons of the incident nucleus and the mesons produced in the secondary process among all the shower particles. After those corrections were made, the angular distribution in C. M. system of mesons produced in the primary collision is nearly isotropic, which is in agreement with the other results in the same energy range of interactions. Those facts could suggest the successive collisions in the same nucleus.

The author wishes to express his gratitudes to Professors O. Minakawa, I. Kita and G. Fujioka for their valuable comments and discussions during the course of this work. His sincere appreciation and thanks are also due to Mr. M. Miyagaki and Mrs. Y. Maeda for their cooperative efforts, and to the staff of Emulsion Research Group in Japan for making the balloon flight possible.

References

1) P. H. Fowler, R. R. Hillier and C. J. Waddington: Phil. Mag. **2** (1957) 292.
2) R. Cester, A. Debenedetti, C. M. Garelli, B. Quassiati, L. Tallone and M. Vigone: Nuovo Cim. **7** (1958) 371.
3) V. D. Hopper, J. E. Laby and Y. K. Lim: Nuovo Cim. **7** (1958) 552.
4) V. Y. Rajopadhye and C. J. Waddington: Phil. Mag. **3** (1958) 19.
5) M. V. K. Appa Rao, R. R. Daniel and K. A. Neelakantan: Proc. Indian Acad. Sci., **A43** (1956) 181.
6) Y. Eisenberg: Phys. Rev. **96** (1954) 1378.
7) W. Heitler and Ch. Terreaux: Proc. Phys. Soc. (London) **A63** (1950) 259.
8) C. Castagnoli, G. Cortini, C. Franzinetti, A. Manfredini and D. Moreno: Nuovo Cim. **10** (1953) 1539.
9) N. M. Duller and W. D. Walker: Phys. Rev. **93** (1954) 215.
10) P. *K*. Malhotra and Y. Tsuzuki: Nuovo Cim. **18** (1960) 982.
11) G. Fujioka: J. Phys. Soc. Japan, **16** (1961) 1107.
12) I. Kita: J. Phys. Soc. Japan, **16** (1961) 1099.

JOURNAL OF THE PHYSICAL SOCIETY OF JAPAN, Vol. 16, No. 11, NOVEMBER, 1961

On the Magnetism of Mn- and Co-Ammonium Tutton Salts at Very Low Temperatures

By Norikiyo URYÛ

Department of Physics, Faculty of Science,
Kyushu University, Hukuoka

(Received May 19, 1960, Revised July 5, 1961)

The parasitic ferromagnetism found in the ammonium tutton salt of Mn and Co ions is discussed. By assuming the two sublattice model, we look for the lowest energy state of spin direction, where the exchange and dipole interactions are taken into account. It can be shown that the origin of parasitic ferromagnetism in MnNH$_4$-tutton salt is the crystalline field and in CoNH$_4$-tutton salt the anisotropic dipolar and exchange interactions. The estimate of the angle with which the spins incline to the K_1K_2-plane are found to be 21°42′ and 10°42′ for Mn- and Co-NH$_4$-tutton salts respectively, agreeing well with the experimental results. It appears theoretically that the spin direction for the lowest energy state lie within a plane which inclines to the K_1K_3-plane with angle $-15°2'$ and $-9°53'$ for Mn- and Co-tutton salts respectively. The Néel temperature and the susceptibilities are also calculated in rather good agreement with the measured values. It is noted that the directions corresponding to the maximum and minimum values of susceptibility within K_1K_2-plane deviate considerably from K_1- and K_2-axes.

§1. Introduction

The paramagnetic crystals of the iron group ions have hitherto been studied extensively, both experimentally and theoretically, and in particular the tutton salts and alums, as typical substances for adiabatic demagnetization, have been studied fully with the use of microwave resonance techniques. For the Co-tutton salt, there are susceptibility measurements by Jackson[1], X-ray crystal structure analysis by Hofmann[2], measurements of the g-factor by Benzie and Cooke[3], susceptibility measurements at liquid helium temperatures by Garrett[4], and studies of the spin-lattice relaxation time by Gorter *et al.*[5] and Haseda[6]. Abragam and Pryce[7] have discussed the splitting of the energy levels of Co^{++} ion due to the crystalline field and have explained the large anisotropy of the g-factor observed by Bleaney *et al.*[8]. In a previous paper, Nakamura and Uryû[9] have calculated the magnetic contribution to the specific heat, and further, by using the wave functions obtained by Abragam and Pryce, the writer[10] has calculated the high temperature susceptibilities and found their anisotropies to agree well with Jackson's results. There is also a recent report[11] on the evaluation of the spin-spin relaxation time. For other tutton salts, there are also many studies, *e.g.* the calculation of the spin-lattice relaxation time in Cu-tutton salt[12] and the theory of the paramagnetic relaxation in Ni-tutton salt[13].

As stated above, Garrett measured the susceptibilities of Co-tutton salt at liquid helium temperatures. He used the paramagnetic relaxation method and the results are reproduced in Fig. 1. This salt has a rather low Néel temperature of $T_N=0.084$°K, and below this temperature there seems to be a typical antiferromagnetic ordering. The crystal has a monoclinic structure in which each Co^{++} ion is surrounded tetragonally by six water molecules. The unit cell contains two Co^{++} ions whose tetragonal axes incline to each other. As described in reference 9 (hereafter referred to as (I)), the lattice constants, the directions of the macroscopic principal axes and the microscopic tetragonal axes are as follows (see also Figs. 2 and 3):

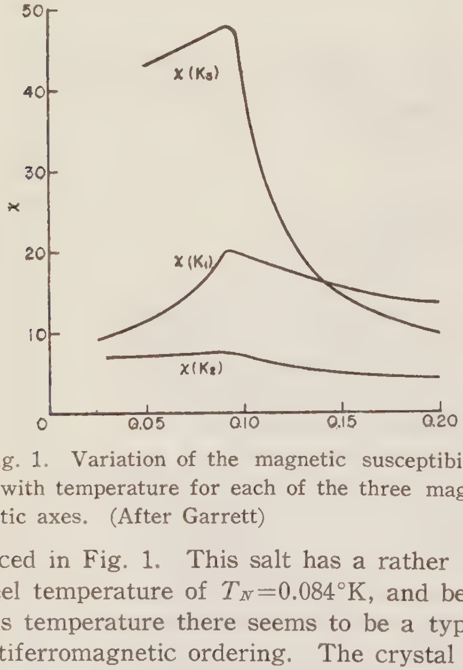

Fig. 1. Variation of the magnetic susceptibility with temperature for each of the three magnetic axes. (After Garrett)

$$a_0 = 9.205\ (\text{Å}) \qquad \beta = 105°^*$$

$$b_0 = 12.475 \qquad \psi = 137°^*$$

$$c_0 = 6.225 \qquad \alpha = 34°.$$

Ions with tetragonal axes T_1 and T_2 will be denoted as I and II, respectively. The ions I are situated on the lattice points of the monoclinic lattice and the ions II on the face centre points of the *ab*-plane; one is derived from the other by a translation $(\frac{1}{2}, \frac{1}{2}, 0)$ followed by a reflection by the *ac*-plane.

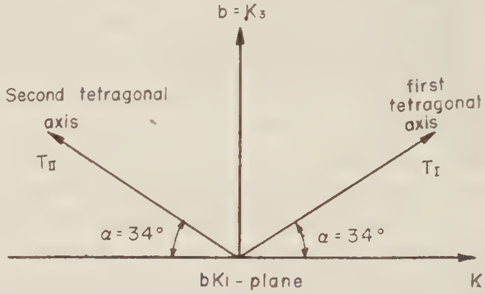

Fig. 2. Tetragonal axes of ions I and II in the K_1K_3-plane (normal to the *ac*-plane).

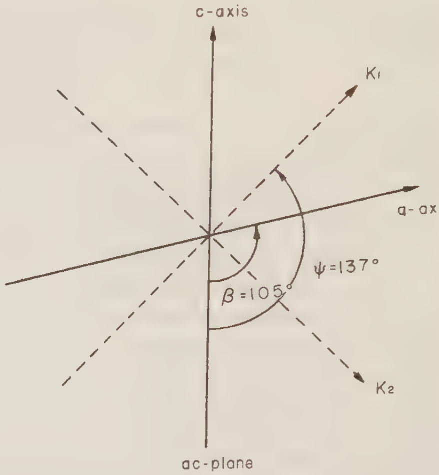

Fig. 3. Crystallographic (*a*, *b*, *c*) and magnetic (K_1, K_2, K_3) axes.

Miedema, Van den Broek, Postma and Huiskamp[14] have studied the magnetic behaviours of Mn- and Co-tutton salts at very low temperatures. They have measured the paramagnetic absorption and dispersion at several values of entropy below the Néel point (0.084°K for $CoNH_4$-tutton salt and 0.14°K for $MnNH_4$-tutton salt), and have shown that $CoNH_4$- and $MnNH_4$-tutton salts are very similar to each other near their Néel temperatures but above 1°K the manganese salt behaves nearly isotropically in contradistinction to the cobalt salt. The characteristic feature of their measurements as compared with Garrett's is that the susceptibilities in the K_1- and K_3-directions as functions of longitudinal field have been determined. The samples investigated were of the shape in which they had grown, not an ellipsoidal form, but the susceptibilities were corrected to their values for a spherical sample. The susceptibility curves in the K_1-direction (Fig. 4 a) show an antiferromagnetic character, the transition from the antiferromagnetic into the paramagnetic state occurring at fields of a few hundred oersted. The χ_3 versus H curves are shown in Fig. 4 b; the susceptibility remains nearly constant at small fields but decreases sharply at a field whose value is the largest for the lowest entropy. At fields greater than 150 Oe, χ_3 becomes again nearly constant and has a value of $\chi_3=8.32$. This field dependence indicates a ferromagnetic character, and in fact there is a parasitic ferromagnetism as will be mentioned below. Miedema *et al.* give the following qualitative interpretation.

---

* These values are after reference 14). In (I), we adopted the data of $(NH_4)_2Zn$-tutton salt for Co-tutton salt, data on the latter being unavailable.

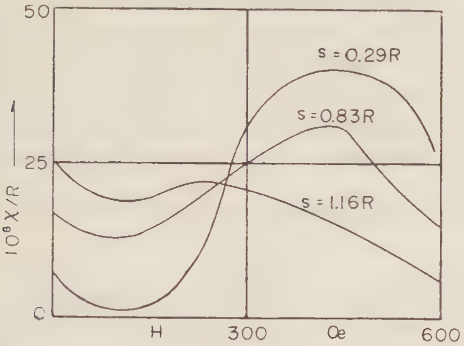

Fig. 4 a. The susceptibility in the K_1-direction as a function of longitudinal field. R denotes the gas constant. ($MnNH_4$-tutton salt)

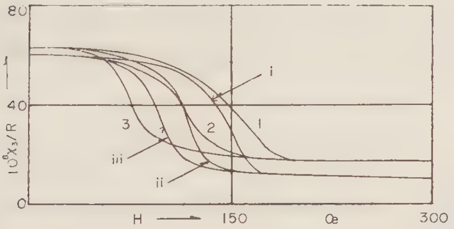

Fig. 4 b. The susceptibility in the K_3-direction as a function of longitudinal field.

$MnNH_4$-tutton salt:
1 ($S=0.29R$), 2 ($S=0.83R$), 3 ($S=1.07R$)
$CoNH_4$-tutton salt:
i ($S=0.050R$), ii ($S=0.262$R), iii ($S=0.365R$)

At temperatures lower than T_N, the sublattice magnetizations are not antiparallel to each other but they deviate from their respective tetragonal axes in the way shown in Fig. 5 either a or b. The resultant magnetization has no component in the K_1-direction but it has a non-vanishing component in the K_3-direction. Two equally possible arrangements, a and b, are supposed to form domains in the crystal. In small field applied in the K_3-direction, domains with magnetization opposite to the field will be transformed into domains with the right direction of magnetization. The high value of χ_3 in small field is explained in this way, but saturation will occur at higher fields. At high enough external fields, only domains of one type will be left and the whole crystal will have one large domain. In $CoNH_4$-tutton salt, the ferromagnetic magnetization at temperatures much lower than T_N is given by $N\langle\mu\rangle \sin\cdot(34°-\theta_M)$ with $\langle\mu\rangle=3.1\,\mu_0$, the measured ferromagnetic saturation magnetization being $M_f=7.07\times10^3$ *emu/mol*, where μ_0 is the Bohr magneton. In $MnNH_4$-tutton salt, the ferromagnetic magnetization is given by $Ng\frac{5}{2}\mu_0\cdot\sin(32°-\theta_M)$, the measured value of M_f being 7.82×10^3 *emu/mol*. From these data, the estimate of θ_M is found by Miedema *et al.* to be 16° and 10° for Mn- and Co-salts respectively. In the present paper, we study the origin of such spin arrangements in the two salts and calculate the angle of inclination which the spin moments make with the K_1-axis in the ordered state. The origin of the weak ferromagnetism should be different for the two salts. In $MnNH_4$-tutton salt, the Mn^{++} ions are almost in the S-state, so that the exchange interaction should be isotropic and it cannot make the two sublattice magnetizations incline to each other. Even when magnetic dipole interaction is taken into account, one has still a completely antiparallel arrangement of spins which lie in the K_1K_2-plane. The weak ferromagnetism of $MnNH_4$-tutton salt has to be caused by the anisotropy energy of the one ion type, DS_z^2, which would make the spins I and II seek to align along their respective microscopic tetragonal axes and thus give rise to the arrangement shown in Fig. 5. However, it will be shown that in the ordered state the spins are in a plane which intersects with the K_1K_3-plane along the K_3-axis.

In CoNH$_4$-tutton salt, the lowest state of the magnetic ions Co^{++} is a Kramers doublet, so that the anisotropy energy of the one ion type disappears. However, the g-factor of these ions is strongly anisotropic, namely its principal value along the microscopic tetragonal axis is about twice as large as the other two principal values. As a result, both the exchange and magnetic dipole interactions are modified in such a way that they are strongly anisotropic in the lowest Kramers doublet. These modified interactions will turn the spins I and II toward the K_3-axis.

In § 2, the ordered state in MnNH$_4$-tutton salt will be discussed. As unfortunately we do not have sufficient information about the exchange integrals, including their signs, we shall estimate them from the measured Weiss constant, with reference to the results obtained in (I) concerning the signs and the ratio of the magnitudes of the two exchange integrals between the first and second nearest neighbours. The Néel temperature of this salt will be estimated in this section, too. A similar treatment for CoNH$_4$-tutton salt will be given in § 3. Reasonable results are obtained with the use of the dipole sums and exchange integrals estimated in (I). In § 4, we shall calculate the antiferromagnetic susceptibilities for the two salts by using the Weiss approximation.

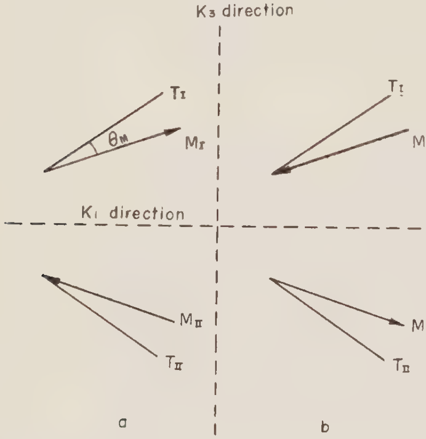

Fig. 5. Two possible structures, a and b, in CoNH$_4$-tutton salt in ordered state. M_I, M_{II} represent the directions of the sublattice magnetizations and T_I, T_{II} the tetragonal field axes.

§ 2. The case of MnNH$_4$-tutton salt (the ordered state)

The lowest state of Mn^{++} is ^6S. Abragam and Pryce[15] have pointed out that this sixfold degenerate state splits into three Kramers doublets owing to an ellipsoidal deformation of the electronic density in the tetragonal crystalline field. However, this splitting is not very large compared with kT_N ($T_N=0.14$°K) (the total separation being 0.17 cm^{-1})[16]. Furthermore, according to Bleaney and Ingram[16], the g-factor is nearly isotropic and is the same as that of the free ion ($g=2$). Therefore, we have to consider the following three energies. First, the dipole interaction:

$$\mathscr{H}_{\rm dip}=\sum_{i>k} r_{ik}^{-3}[\boldsymbol{\mu}_i\cdot\boldsymbol{\mu}_k-3(\boldsymbol{\mu}_i\cdot\boldsymbol{t}_{ik})(\boldsymbol{\mu}_k\cdot\boldsymbol{t}_{ik})]\ , \tag{2.1}$$

where $\boldsymbol{t}_{ik}$ is the unit vector connecting the ions i and k and $\mu_i=g\mu_0 S_i$ ($S=5/2$) the magnetic moment. Second, the exchange interaction:

$$\mathscr{H}_{\rm ex}=-2\sum_{i>k} J_{ik}\boldsymbol{S}_i\cdot\boldsymbol{S}_k\ , \tag{2.2}$$

which is isotropic. Third, the energy which comes from the tetragonal crystalline potential:

$$D\left\{S_{\zeta'}^2-\frac{1}{3}S(S+1)\right\}\ , \tag{2.3}$$

where ζ' denotes the direction of the tetragonal axis.

For the time being, we consider only the dipolar and exchange interactions between Mn^{++} spins. We shall use suffixes λ, μ, ν, etc. to represent coordinates x, y and z, whose axes are taken respectively along the K_1, K_2 K_3-directions, and we shall specify with i, k the ions I and with α, β the ions II. Then the Hamiltonian of the l-th spin can be written as

$$\mathscr{H}=\mathscr{H}_{\rm dip}+\mathscr{H}_{\rm ex}=\sum_{m\mu\nu} C_{\mu\nu}^{(lm)}S_{l\mu}S_{m\nu}\ . \tag{2.4}$$

In the following, we shall assume the two-sublattice model and treat the spins as classical vectors. Each sublattice consists of ions of the type I or II and composes a pseudo-cubic structure (see Fig. 6). Due to the crystalline symmetry, $\sum C_{xz}^{(lm)}$ and $\sum C_{yz}^{(lm)}$ will vanish, and the non-zero coefficients are given by

$$\begin{aligned}
&\sum_k C^{ik}_{\lambda\lambda}=\sum_\beta C^{\alpha\beta}_{\lambda\lambda}=\mu_0{}^2g^2G_{1\lambda}-4J_1\ ,\\
&\sum_\alpha C^{i\alpha}_{\lambda\lambda}=\mu_0{}^2g^2G_{2\lambda}-8J_2\ ,\\
&\sum_k C^{ik}_{xy}=\mu_0{}^2g^2G^{(1)}_{xy}\ ,\\
&\sum_\alpha C^{i\alpha}_{xy}=\mu_0{}^2g^2G^{(2)}_{xy}\ .
\end{aligned}\tag{2.5}$$

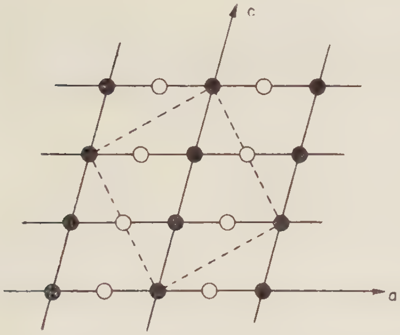

ac-plane

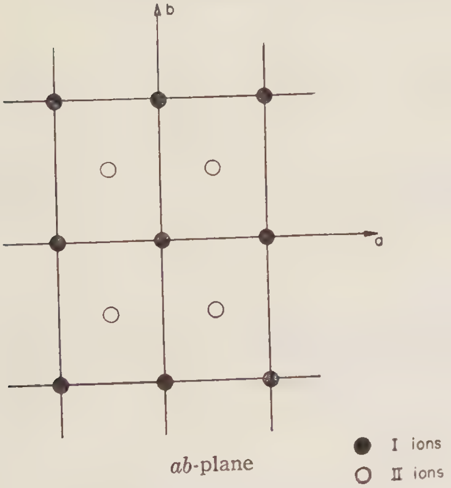

ab-plane

Fig. 6. The pseudo-cubic structure of magnetic ions.

Here J_1 is the exchange integral between ions of the same kind lying along the *c*-axis (nearest neighbours) and J_2 that between ions of the different kinds in the *ab*-plane (second nearest neighbours), and

$$\begin{aligned}
&\sum_k (1-3(t^\lambda_{ik})^2)/r^3_{ik}=G_{1\lambda}\ ,\\
&\sum_\alpha (1-3(t^\lambda_{i\alpha})^2)/r^3_{i\alpha}=G_{2\lambda}\ ,\\
&-3\sum_k t^\lambda_{ik}t^\mu_{ik}/r^3_{ik}=G^{(1)}_{\lambda\mu}\ ,\\
&-3\sum_\alpha t^\lambda_{i\alpha}t^\mu_{i\alpha}/r^3_{i\alpha}=G^{(2)}_{\lambda\mu}\ .
\end{aligned}\qquad(\lambda\neq\mu)\tag{2.6}$$

These $G_{1\lambda}$ and $G_{2\lambda}$ can be considered to have the same numerical values with those already given in (I) (errors due to a difference in assumed lattice constants being negligible). The numerical values of (2.6) are given in table I.

When we consider the total energy, l and m run over both kinds of ions I and II in the summation of (2.4), and we write $4/N$ (N is the total number of molecules) times the total energy as

$$E=\sum A_{ij}\xi_i\xi_j\ ,\qquad (A_{ij}=A_{ji})\tag{2.7}$$

where i and j represent 1, 2, $\cdots$, 6 and (ξ_1, ξ_2, ξ_5) and (ξ_3, ξ_4, ξ_6) denote the components of classical spin vectors I and II, respectively, namely,

$$\begin{aligned}
(\xi_1,\ \xi_2,\ \xi_5)&=(S_{xi},\ S_{zi},\ S_{yi})\ ,\\
(\xi_3,\ \xi_4,\ \xi_6)&=(S_{x\alpha},\ S_{z\alpha},\ S_{y\alpha})\ ,
\end{aligned}\tag{2.8}$$

If we neglect (2.3), the matrix A_{ij} can be reduced to a form consisting of a 4×4 submatrix whose non-zero elements are

Table I. Numerical values of $G_{r\lambda}$ and $G^{(r)}_{\lambda\mu}$. (in cm^{-3})

λ	$G_{1\lambda}\times10^{-22}$	$G_{2\lambda}\times10^{-22}$	$\lambda\mu$	$G^{(1)}_{\lambda\mu}\times10^{-22}$	$G^{(2)}_{\lambda\mu}\times10^{-22}$
x	−0.4097	0.3670	xy	+0.8585	+0.1571
y	−0.7398	0.4982	yz	0	0
z	1.1629	−0.8670	zx	0	0

$$\begin{aligned}
&A_{11}=A_{33}=\sum_k C^{ik}_{xx}\ , && A_{13}=\sum_\alpha C^{i\alpha}_{xx}\ ,\\
&A_{15}=A_{36}=\sum_k C^{ik}_{xy}\ , && A_{16}=A_{35}=\sum_\alpha C^{i\alpha}_{xy}\ ,\\
&A_{55}=A_{66}=\sum_k C^{ik}_{yy}\ , && A_{56}=\sum_\alpha C^{i\alpha}_{yy}\ ,
\end{aligned}\tag{2.9a}$$

and a 2×2 submatrix consisting of

$$A_{22}=A_{44}=\sum_k C_{zz}^{ik}\,,\qquad A_{24}=\sum_\alpha C_{zz}^{i\alpha}\,. \tag{2.9b}$$

The problem of finding the minimum value of (2.7) under a weak condition

$$\xi_1^2+\xi_2^2+\cdots+\xi_6^2=\text{const.}$$

can be reduced to the diagonalization of these 4×4 and 2×2 matrices. If the eigenvector belonging to the lowest energy value obtained corresponds to a physically realistic solution, everything should be right. The diagonalization can be achieved by the transformation with the following matrix:

$$U=1/\sqrt{2}\begin{bmatrix} \cos\theta_1 & 0 & \cos\theta_1 & 0 & \sin\theta_1 & \sin\theta_1 \\ 0 & \sqrt{2}\cos\varphi & 0 & \sqrt{2}\sin\varphi & 0 & 0 \\ -\sin\theta_1 & 0 & -\sin\theta_1 & 0 & \cos\theta_1 & \cos\theta_1 \\ 0 & -\sqrt{2}\sin\varphi & 0 & \sqrt{2}\cos\varphi & 0 & 0 \\ \cos\theta_2 & 0 & -\cos\theta_2 & 0 & \sin\theta_2 & -\sin\theta_2 \\ -\sin\theta_2 & 0 & \sin\theta_2 & 0 & \cos\theta_2 & -\cos\theta_2 \end{bmatrix} \tag{2.10}$$

where θ_1, θ_2 and φ are given by

$$\tan 2\theta_1=\frac{2(A_{15}+A_{16})}{A_{11}+A_{13}-A_{55}-A_{56}}\,,\quad \tan 2\theta_2=\frac{2(A_{15}-A_{16})}{A_{11}-A_{13}-A_{55}+A_{56}}\,,\quad \tan 2\varphi=\frac{2A_{24}}{A_{22}-A_{44}}\,. \tag{2.11}$$

Unless we can estimate the exchange integrals, we cannot find the lowest eigenvalue and the corresponding eigenvector. But if we use the values of J_1 and J_2 to be estimated in Section 2.1, it can be shown that the eigenvector corresponding to the lowest eigenvalue is given by

$$\frac{1}{\sqrt{2}}(\cos\theta_2,\ 0,\ -\cos\theta_2,\ 0,\ \sin\theta_2,\ -\sin\theta_2) \tag{2.12}$$

whence the orientations of spins I and II are found to be respectively

$$\frac{1}{\sqrt{2}}(\cos\theta_2,\ 0,\ \sin\theta_2)\,,$$

$$-\frac{1}{\sqrt{2}}(\cos\theta_2,\ 0,\ \sin\theta_2)\,.$$

This solution corresponds to a realistic solution, and accordingly it gives the lowest energy state. The spins I and II are then completely antiparallel in the K_1K_2-plane.

Let us now see how the situation will be modified by taking into account the anisotropy energy of the one ion type. Introducing (2.3) into (2.7), we have another non-vanishing matrix elements A_{12} and A_{34}. If we denote by Θ_0 the angle between the spin direction and the microscopic tetragonal axis, (2.3) can be written classically as

$$D\{S^2\cos^2\Theta_0-35/12\}=D\{S_x^2\cos^2\alpha+S_z^2\sin^2\alpha+S_x\cdot S_z\sin 2\alpha-35/12\}\,. \tag{2.13}$$

Abbreviating the matrix A_{ij} as

$$\begin{bmatrix} a & b & d & 0 & t & u \\ b & c & 0 & f & 0 & 0 \\ d & 0 & a & -b & u & t \\ 0 & f & -b & c & 0 & 0 \\ t & 0 & u & 0 & v & w \\ u & 0 & t & 0 & w & v \end{bmatrix}, \tag{2.14}$$

we have now following expressions for the matrix elements:

$$\begin{aligned} a&=\mu_0{}^2g^2G_{1x}-4J_1+2D\cos^2\alpha\,, & t&=\mu_0{}^2g^2G_{xy}^{(1)}\,, \\ b&=2D\sin\alpha\cos\alpha\,, & u&=\mu_0{}^2g^2G_{xy}^{(2)}\,, \\ c&=\mu_0{}^2g^2G_{1z}-4J_1+2D\sin^2\alpha\,, & v&=\mu_0{}^2g^2G_{1y}-4J_1\,, \\ d&=\mu_0{}^2g^2G_{2x}-8J_2\,, & w&=\mu_0{}^2g^2G_{2y}-8J_2\,. \\ f&=\mu_0{}^2g^2G_{2z}-8J_2\,, \end{aligned} \tag{2.15}$$

To diagonalize the matrix (2.14), we transform it with the following orthogonal matrix:

$$V=1/\sqrt{2}\begin{bmatrix} 1 & 0 & 1 & 0 & 0 & 0 \\ 0 & 1 & 0 & -1 & 0 & 0 \\ 0 & 0 & 0 & 0 & 1 & 1 \\ 1 & 0 & -1 & 0 & 0 & 0 \\ 0 & 1 & 0 & 1 & 0 & 0 \\ 0 & 0 & 0 & 0 & 1 & -1 \end{bmatrix}. \tag{2.16}$$

Then (2.14) is reduced, with regard to the new coordinate $\boldsymbol{\xi}'=V\boldsymbol{\xi}$, to following two 3×3 submatrices:

$$\begin{bmatrix} a+d & b & t+u \\ b & c-f & 0 \\ t+u & 0 & v+w \end{bmatrix}, \tag{2.17a}$$

$$\begin{bmatrix} a-d & b & t-u \\ b & c+f & 0 \\ t-u & 0 & v-w \end{bmatrix}. \tag{2.17b}$$

The eigenvalues of the matrices (2.17a) and (2.17b) can be obtained numerically. But the matrix elements involve the exchange integrals, and the form of the eigenvector corresponding to the lowest eigenvalue depends largely on them. In the below we shall examine this situation by estimating the exchange integrals.

2.1. The estimation of J_1 and J_2.

It is now necessary to estimate J_1 and J_2 separately. This estimation has been made in the case of Co-salt[9], where we used three different values of measured Weiss constants for the paramagnetic state. In Mn-salt, the paramagnetic susceptibility should also be of anisotropic character below about 0.1°K, as will be discussed in § 4.3. However, the anisotropic Weiss constants derivable from the magnetic susceptibility of Mn-salt are not available.

Erickson and Roberts[17] reported the Weiss constant Θ for MnNH$_4$-salt to be -0.003°K, where it is assumed that $\chi=C/(T-\Theta)$ and $C=N\mu_0{}^2g^2\ S(S+1)/3k=4.385$ $(S=5/2)$. From this Θ-value for powder sample at rather high temperatures, we can estimate J_1+2J_2 by comparing with it the average value of the theoretical Weiss constant. The average Weiss constant is obtained from (4.29) as

$$\Theta=2\frac{S(S+1)}{3k}(2J_1+4J_2)\,. \tag{2.18}$$

In this expression, contributions from the dipolar interaction and crystalline field effect average out to zero, because we have, for example,

$$G_{1x}+G_{1y}+G_{1z}=0\ .$$

In this way, we obtain J_1+2J_2 as

$$-2(J_1+2J_2)=0.071\times10^{-18}\ . \tag{2.19}$$

To determine J_1 and J_2 separately, we must have another relation. Considering the case of Co-salt treated in (I), we may expect that J_1 and J_2 are of comparable order to each other and $J_1>0$, $J_2<0$. We assume these signs of J_1 and J_2 for Mn-salt and furthermore assume the same ratio $|J_1|/|J_2|=1.29$ (see also § 3) as that for Co-salt. Then we have from (2.19)

$$2J_1=+0.129\times10^{-18}\ , \qquad -2J_2=0.100\times10^{-18}\ .$$

Computation of (2.15) with the use of these values and also of numerical values given in table I leads to the result in table II. According to Bleaney and Ingram, D in dilute salt is $+2.77\times10^{-2}\,\mathrm{cm}^{-1}$ at 20°K, but it is more likely that D is negative, since the Kramers doublet with $S_z=\pm5/2$ is the lowest, as pointed out by Miedema *et al.*. So we assumed the magnitude of D to be that in dilute salt but with negative sign, -5.4846×10^{-18} ergs.

Table II. Numerical values of (2.15)*. (in ergs)

$a=-9.5556\times10^{-18}$	$d=\ 1.6618\times10^{-18}$	$u=+0.5401\times10^{-18}$
$b=-4.9298$ 〃	$f=-2.5809$ 〃	$v=-2.8016$ 〃
$c=\ 0.6601$ 〃	$t=+2.9517$ 〃	$w=\ 2.1129$ 〃

* According to Bleaney et al.[16] the value of $\alpha=32°$ is used for MnNH$_4$-tutton salt.

2.2. The ordered state.

With the use of the numerical values given in table II, the eigenvalues of the submatrices (2.17a) and (2.17b) are obtained respectively from the following cubic equations (in units of 10^{-18}):

$$\varepsilon^3+5.342\varepsilon^2-58.875\varepsilon+5.160=0\ , \tag{2.20a}$$

$$\varepsilon^3+18.053\varepsilon^2+55.995\varepsilon-24.718=0\ . \tag{2.20b}$$

The lowest eigenvalue is obtained from (2.20b) as $\varepsilon_{\min}=-13.89$. The corresponding eigenvector is given by

$$\frac{1}{\sqrt{2}}(p,\ q,\ -p,\ q,\ r,\ -r), \tag{2.21}$$

whence the orientations of spins I and II are found to be respectively

$$\frac{1}{\sqrt{2}}(p,\ \ q,\ \ r)\ ,$$

$$-\frac{1}{\sqrt{2}}(p,\ -q,\ r)\ ,$$

where p, q, and r are determined by the conditions

$$p^2+q^2+r^2=1\ ,$$

$$\frac{p}{(c+f-\varepsilon)(v-w-\varepsilon)}=\frac{q}{b(v-w-\varepsilon)}=\frac{r}{(t-u)(c+f-\varepsilon)}\ . \tag{2.22}$$

They are numerically as follows:

$$p=0.8973, \qquad q=0.3696, \qquad r=-0.2411 .$$

Considering the form of the eigenvector, we can conclude that the spins I and II lie in a plane which is perpendicular to the K_1K_2-plane and makes a certain angle φ with the K_1K_3-plane. In this plane, the x and y components of tee spins I and II are both antiparallel, whereas the z-components are parallel. The angle θ with which the spins incline to the K_1K_2-plane and the angle φ are evaluated from the relations $\sin\theta=q$, $\cos\theta\sin\varphi=r$, as

$$\theta=21°42' , \qquad \varphi=-15°2' . \tag{2.23}$$

The experimental value of θ is 16°. Thus the agreement is reasonably good.

2.3. The Néel point.

We shall estimate the Néel point in the Weiss approximation. If we at first neglect the exchange interaction, the next lowest spin level is separated from the lowest level by $4D$, which is about $1.1\times10^{-1}\,\mathrm{cm}^{-1}$. This so-called initial splitting is rather large compared with the exchange energy. Due to this situation, we have first to calculate the paramagnetic susceptibilities in the representation which diagonalizes the anisotropy energy of the one-ion type.

Let $(H_x^+\ H_y^+\ H_z^+)$ and $(H_x^-\ H_y^-\ H_z^-)$ be the magnetic fields applied to the sublattices I and II. The induced magnetic moments of the two sublattices, $(M_x^+\ M_y^+\ M_z^+)$ and $(M_x^-\ M_y^-\ M_z^-)$, are then written in the following form:

$$\begin{aligned}
M_x^\pm &= \frac{C}{2T}\{(f_\xi\sin^2\alpha+f_\zeta\cos^2\alpha)H_x^\pm\pm\sin\alpha\cos\alpha(f_\zeta-f_\xi)H_z^\pm\} ,\\
M_y^\pm &= \frac{C}{2T}\,f_\eta H_y^\pm ,\\
M_z^\pm &= \frac{C}{2T}\{\pm\sin\alpha\cos\alpha(f_\zeta-f_\xi)H_x^\pm+(f_\xi\cos^2\alpha+f_\zeta\sin^2\alpha)H_z^\pm\} .
\end{aligned} \tag{2.24}$$

Here C denotes the Curie constant, $N(g\mu_0)^2S(S+1)/3k$, and

$$\begin{aligned}
f_\xi &= -\frac{3kT}{S(S+1)(2S+1)}\sum_{MM'}\frac{e^{-E_M/kT}-e^{-E_{M'}/kT}}{E_M-E_{M'}}|(M|S_\xi|M')|^2 ,\\
f_\eta &= -\frac{3kT}{S(S+1)(2S+1)}\sum_{MM'}\frac{e^{-E_M/kT}-e^{-E_{M'}/kT}}{E_M-E_{M'}}|(M|S_\eta|M')|^2 ,\\
f_\zeta &= \frac{3}{S(S+1)(2S+1)}\sum_{M}e^{-E_M/kT}|(M|S_\zeta|M)|^2 .
\end{aligned} \tag{2.25}$$

where M denotes the eigenvalues of S_ζ and $E_M=D(M^2-S(S+1)/3)$. Due to the tetragonal symmetry in the present case, we have $f_\xi=f_\eta$. f_ξ, f_η and f_ζ tend to unity at high temperatures, as can be seen in Fig. 7.

The molecular field $(H_x^\pm\ H_y^\pm\ H_z^\pm)$ are given by

$$\begin{aligned}
H_x^\pm &= -q_1M_x^\mp-q_2M_x^\pm-q_3M_y^\mp-q_4M_y^\pm ,\\
H_y^\pm &= -q_1'M_x^\mp-q_2'M_x^\pm-q_3'M_y^\mp-q_4'M_y^\pm ,\\
H_z^\pm &= -q_1''M_z^\mp-q_2''M_z^\pm ,
\end{aligned} \tag{2.26}$$

where q_1, q_2, q_3, q_4, q_1', q_2', q_3', q_4', q_1'', and q_2'' denote d, $a-2D\cos^2\alpha$, u, t, u, t, w, v, f, and $c-2D\sin^2\alpha$ of (2.15), multiplied by $2/N(g\mu_0)^2$, respectively. Substituting (2.26) into (2.24), we obtain homogeneous equations for $M_x^\pm$, $M_y^\pm$ and $M_z^\pm$. The Néel point can be obtained from the condition that these equations are satisfied by non-vanishing $M_x^\pm$, $M_y^\pm$ and $M_z^\pm$. This brings about a secular equation of the sixth order and the Néel point is obtained as the highest root of it. It can be shown that the highest root is a solution of the following equation:

$$\begin{array}{c}
\begin{array}{ccc} M_x{}^+ - M_x{}^- & M_y{}^+ - M_y{}^- & M_z{}^+ + M_z{}^- \end{array} \\
\left| \begin{array}{ccc}
2T/C+(q_2-q_1)f & (q_4-q_3)f & (q_1{}''+q_2{}'')f' \\
(q_2{}'-q_1{}')f_\eta & 2T/C+(q_4{}'-q_3{}')f_\eta & 0 \\
(q_2-q_1)f' & (q_4-q_3)f' & 2T/C+(q_1{}''+q_2{}'')f''
\end{array} \right| =0\,,
\end{array} \tag{2.27}$$

where

$$\begin{aligned}
f &= f_\xi \sin^2\alpha + f_\zeta \cos^2\alpha\,, \\
f' &= (f_\zeta - f_\xi)\sin\alpha\cos\alpha\,, \\
f'' &= f_\xi \cos^2\alpha + f_\zeta \sin^2\alpha\,.
\end{aligned} \tag{2.28}$$

A calculation using numerical values given in the preceding section, we obtain from (2.27) the Néel point to be $T_N=0.125$°K, which can be compared with the observed value of 0.14°K.

It is interesting to see the temperature dependence of the orientation of spins. At the Néel point, this orientation is obtained from the eigenvector of (2.27) belonging to the root $T=T_N$; we have

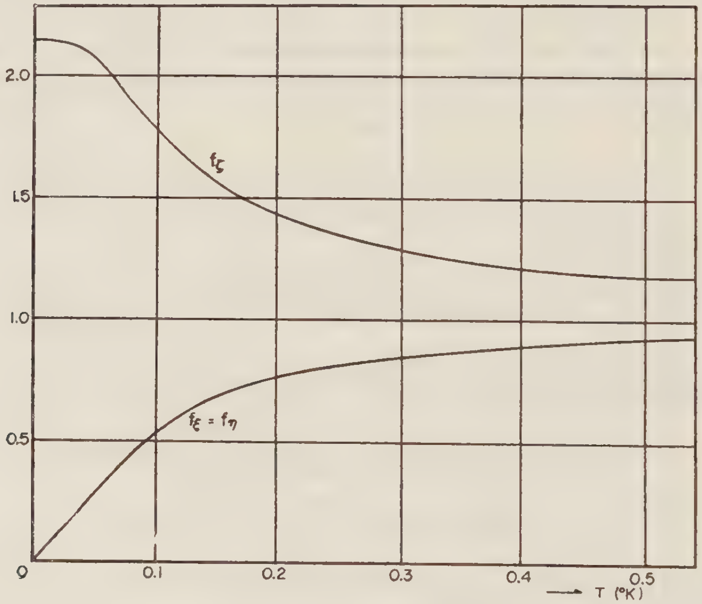

Fig. 7. Temperature dependence of f_ξ and f_ζ.

$$\theta=15°8'\,, \qquad \varphi=-24°48'\,.$$

Thus, comparing these results with (2.23), we see that θ decreases and $|\varphi|$ increases with increasing temperature, though their changes are not very appreciable.

§ 3. The case of CoNH$_4$-tutton salt

Here again we consider dipolar and exchange interactions, but since in this salt the lowest Kramers doublet is separated from the next one by 245 cm^{-1} [7], we can confine ourselves to the lowest Kramers doublet in discussing the ordered state. This Kramers doublet has a highly anisotropic g-factor, whose parallel and perpendicular components to the microscopic tetragonal axis have been determined to be 6.45 and 3.06, respectively. Due to this anisotropy, the dipolar and exchange interactions are anisotropically modified in this doublet. By using the effective spin operator $\boldsymbol{\sigma}$ of magnitude one half (which is not the Pauli spin operator), formula corresponding to (2.1) can be written as follows:

$$\mathscr{H}_{\rm dip}=\mu_0{}^2 \sum_{i>k} r_{ik}^{-3}\Big\{ \sum_{\lambda\mu\nu} g^i_{\lambda\mu} g^k_{\lambda\nu} \sigma_{i\mu}\sigma_{\nu k} - 3\sum_{\lambda\mu}\sum_{\nu\nu'} t^\lambda_{ik} t^\mu_{ik} g^i_{\lambda\nu} g^k_{\mu\nu'} \sigma_{\nu i}\sigma_{\nu' k}\Big\}\,, \tag{3.1}$$

$$(\mathscr{H}_{\mathrm{ex}})_{ik}=\sum_{\lambda\mu} J_{ik}^{\lambda\mu}\sigma_{\lambda i}\sigma_{\mu k}\ , \qquad (\mathscr{H}_{\mathrm{ex}})_{i\alpha}=\sum_{\lambda\mu} J_{i\alpha}^{\lambda\mu}\sigma_{\lambda i}\sigma_{\mu\alpha}\ , \tag{3.2}$$

where $g_{\lambda\mu}$ and $J^{\lambda\mu}$ are the tensorial g-factor and exchange integral which were estimated in (I) (see Table III). Writing the Hamiltonian for the l-th spin in the form (2.4), we have now non-vanishing coefficients of the following form:

Table III. The numerical values of $J_{st}^{\lambda\mu}$ (the common factor $-J_1$ or $-J_2$ is omitted) and $g_{\lambda\mu}$.

$(\lambda,\ \mu)$	$(s,\ t)$	
	$(i,\ k)$	$(i,\ \alpha)$*
(xx)	8.631	7.528
(yy)	3.031	3 031
(zz)	5.579	4.475
(zx)	3.778	0.446
(xz)	3.778	−0.446

$g_{\parallel}$	$g_{\perp}$	g_1	g_3	g_4
6.45	3.05	5.39	4.11	1.58

* We commited a careless mistake in (I). The figures in (I), corresponding to this column, should be corrected. See Appendix about further details.

$$\begin{aligned}
A_{11}&=\sum_k C_{xx}^{ik}=\mu_0^2(g_1^2G_{1x}+g_4^2G_{1z})+z_1J_{ik}^{xx}\ ,\\
A_{12}&=\sum_k C_{xz}^{ik}=\mu_0^2(g_1g_4G_{1x}+g_3g_4G_{1z})+z_1J_{ik}^{xz}\ ,\\
A_{13}&=\sum_\alpha C_{xx}^{i\alpha}=\mu_0^2(g_1^2G_{2x}-g_4^2G_{2z})+z_2J_{i\alpha}^{xx}\ ,\\
A_{14}&=\sum_\alpha C_{xz}^{i\alpha}=\mu_0^2(-g_1g_4G_{2x}+g_3g_4G_{2z})+z_2J_{i\alpha}^{xz}\ ,\\
A_{15}&=A_{36}=\sum_k C_{xy}^{ik}=\mu_0^2g_1g_2G_{xy}^{(1)}\ ,\\
A_{16}&=A_{35}=\sum_\alpha C_{xy}^{i\alpha}=\mu_0^2g_1g_2G_{xy}^{(2)}\ ,\\
A_{22}&=\sum_k C_{zz}^{ik}=\mu_0^2(g_4^2G_{1x}+g_3^2G_{1z})+z_1J_{ik}^{zz}\ ,\\
A_{23}&=\sum_\alpha C_{zx}^{i\alpha}=-\sum_\alpha C_{xz}^{i\alpha}\ ,\\
A_{24}&=\sum_\alpha C_{zz}^{i\alpha}=\mu_0^2(-g_4^2G_{2x}+g_3^2G_{2z})+z_2J_{i\alpha}^{zz}\ ,\\
A_{33}&=\sum_\beta C_{xx}^{\alpha\beta}=\sum_k C_{xx}^{ik}\ ,\\
A_{34}&=\sum_\beta C_{xz}^{\alpha\beta}=-\sum_k C_{xz}^{ik}\ ,\\
A_{44}&=\sum_\beta C_{zz}^{\alpha\beta}=\sum_k C_{zz}^{ik}\ ,\\
A_{55}&=\sum_k C_{yy}^{ik}=\mu_0^2g_2^2G_{1y}+z_1J_{ik}^{yy}\ ,\\
A_{66}&=\sum_\beta C_{yy}^{\alpha\beta}=\sum_k C_{yy}^{ik}\ ,\\
A_{56}&=\sum_\alpha C_{yy}^{i\alpha}=\mu_0^2g_2^2G_{2y}+z_2J_{i\alpha}^{yy}\ .
\end{aligned}\tag{3.3}$$

(The matrix A_{ij} is symmetric.) The total energy E is given in the form (2.7), except that $\sigma_{\lambda i}$ has replaced ξ_i.

3.1. The ordered state.

Now the problem of minimizing E under the condition $\sum_{i=1}^{6} \xi_i^2=\text{const.}$ can be solved by the same procedure as that in § **2**. In the present case, the matrix A can be abbreviated as

$$\begin{bmatrix} a & b & d & e & t & u \\ b & c & -e & f & 0 & 0 \\ d & -e & a & -b & u & t \\ e & f & -b & c & 0 & 0 \\ t & 0 & u & 0 & v & w \\ u & 0 & t & 0 & w & v \end{bmatrix}, \tag{3.4}$$

and with the transformation matrix (2.16), (3.4) can be reduced to the following to 3×3 submatrices:

$$\begin{bmatrix} a+d & b-e & t+u \\ b-e & c-f & 0 \\ t+u & 0 & v+w \end{bmatrix}, \tag{3.5a}$$

$$\begin{bmatrix} a-d & b+e & t-u \\ b+e & c+f & 0 \\ t-u & 0 & v-w \end{bmatrix}. \tag{3.5b}$$

The numerical values of (3.3) or (3.4) are given in table IV. The eigenvalues of (3.5a) and (3.5b) are then obtained respectively from the following cubic equations (in units of 10^{-18})

Table IV. Numerical values of $J_{st}^{\lambda\mu}$, and the matrix elements of (3.4). (in ergs)

$\lambda\mu$	$J_{ik}^{\lambda\mu}\times 10^{18}$	$J_{i\alpha}^{\lambda\mu}\times 10^{18}$		
xx	-14.654	9.871	$a=-37.0428\times 10^{-18}$	$f=10.0786\times 10^{-18}$
xz	-6.413	-0.585	$b=-9.3366$ 〃	$t=+12.1237$ 〃
zx	-6.413	0.585	$c=-2.9063$ 〃	$u=+2.2180$ 〃
zz	-9.471	5.868	$d=50.4874$ 〃	$v=-16.2059$ 〃
yy	-5.145	3.974	$e=-9.8499$ 〃	$w=19.8833$ 〃

$$\varepsilon^3+4.1371\varepsilon^2-378.86\varepsilon-2028.21=0\ , \tag{3.6a}$$

and

$$\varepsilon^3+116.45\varepsilon^2+1806.01\varepsilon-35238.0=0\ . \tag{3.6b}$$

The lowest eigenvalue is involved in (3.6b) and $\varepsilon_{\min}=-92.9$. The corresponding eigenvector is therefore given by the same form as (2.21). The components, p, q, and r are now evaluated as

$$p=0.9681\ , \qquad q=0.1855\ , \qquad r=-0.1687\ .$$

Correspondingly, we obtain the values of θ and φ, defined in § **2**, as

$$\theta=10°42'\ , \qquad \varphi=-9°53'\ . \tag{3.7}$$

This result for θ is somewhat far from the measured value, $\theta=24°$. However, as in the case of Mn-salt, an interesting theoretical prediction is that the plane containing the spins I and II makes an angle φ with the K_1K_3-plane. This is not yet confirmed experimentally.

The numerical values in table IV have been evaluated by using the results obtained in (I) (see also Appendix). In there we estimated the values of J_1 ($=0.0123k$) and J_2 ($=-0.0095k$) from the Weiss constants Θ_i ($i=1, 2, 3$) measured by Garrett, and these constants are included as common factors in $J_{ik}^{\lambda\mu}$, $J_{i\alpha}^{\lambda\mu}$. Values of $G_{r\lambda}$ and $G_{\lambda\mu}^{(r)}$ ($r=1, 2$) in table I, which are also included in the matrix elements of (3.4), were calculated by the direct sum method taking the lattice points in a spherical region. Although we have confidence in our estimates of J_1 and J_2, U. Kh. Kopvillem, in his calculation of the spin-spin relaxation time of the Co-tutton salt, has recently reported that he obtained the values $J_1/k=0.017$, $J_2/k=-0.0104$ after correcting for an arithmetical error in (I). The point of his correction may be in our careless mistake which is corrected in Appendix. When his results are used, the eigenvector for the lowest eigenvalue is again given by (2.21), but (3.7) becomes

$$\theta=12°26' , \qquad \varphi=-8°10' ,$$

and rather high value of $T_N=0.201°\mathrm{K}$ is obtained (c.f. the result of the next paragraph).

3.2. The anisotropic molecular field and the Néel point.

In this subsection we shall evaluate the Néel point of CoNH$_4$-tutton salt. The anisotropic interaction of the l-th spin of the + sublattice with the surroundings can be written

$$\sum_m \sum_{\mu\nu} C_{\mu\nu}^{(lm)} \overset{+}{\sigma}_{l\mu}\sigma_{m\nu} . \tag{3.8}$$

Replacing $\sigma_{m\nu}$ by their thermal average values, this becomes

$$\sum_{\mu\nu} a_{\mu\nu}\, \overset{+}{\sigma}_{l\mu}\langle\sigma^+\rangle_\nu + \sum_{\mu\nu} c_{\mu\nu}\, \overset{+}{\sigma}_{l\mu}\langle\sigma^-\rangle_\nu , \tag{3.9}$$

where $a_{\mu\nu}$ and $c_{\mu\nu}$ are

$$a_{\mu\nu}=\sum_m{}^+ C_{\mu\nu}^{(lm)} , \qquad c_{\mu\nu}=\sum_m{}^- C_{\mu\nu}^{(lm)} , \tag{3.10}$$

the summations being taken over the + and − sublattices, respectively.

The Néel point can be determined in a similar way to that in the case of Mn-salt. Expanding the Boltzmann factor

$$\exp\left[-\frac{1}{kT}\left\{\sum_\nu a_{\mu\nu}\, \overset{+}{\sigma}_{l\mu}\langle\sigma_\nu{}^+\rangle_{Av} + \sum_\nu c_{\mu\nu}\, \overset{+}{\sigma}_{l\mu}\langle\sigma_\nu{}^-\rangle_{Av}\right\}\right]$$

in powers of $1/kT$ and taking the linear term, we have

$$\langle\sigma_\mu{}^+\rangle_{Av}=-\frac{S'(S'+1)}{3kT}\sum_\nu \{a_{\mu\nu}\langle\sigma_\nu{}^+\rangle_{Av}+c_{\mu\nu}\langle\sigma_\nu{}^-\rangle_{Av}\} \qquad \mu=x,\ y \text{ and } z \tag{3.11}$$

where S' is the spin quantum number of the fictitious spin ($S'=1/2$). In the same way, we have

$$\langle\sigma_\mu{}^-\rangle_{Av}=-\frac{S'(S'+1)}{3kT}\sum_\nu \{c_{\mu\nu}\langle\sigma_\nu{}^+\rangle_{Av}+a_{\mu\nu}\langle\sigma_\nu{}^-\rangle_{Av}\} \qquad \mu=x,\ y \text{ and } z. \tag{3.12}$$

Equations (3.11) and (3.12) are homogeneous with respect to $\langle\sigma_x{}^\pm\rangle$, $\langle\sigma_y{}^\pm\rangle$ and $\langle\sigma_z{}^\pm\rangle$, and the non-zero solution appears at a temperature where the determinant composed of the coefficients vanishes. As is easily seen, the roots of the secular equation thus obtained, $3kT/S'\cdot(S'+1)$, are equal to the eigenvalues of (3.4) reversed in sign. The Néel point, T_N, can then be determined from the lowest eigenvalue of (3.4), as

$$\frac{3kT_N}{S'(S'+1)}=-\varepsilon_{\min} . \tag{3.13}$$

So we obtain $T_N=0.168$°K, which can be compared with the experimental value of $T_N=0.084$°K. It may be noted that the 'eigenvector' belonging to this lowest root is the same as that which belongs to the lowest eigenvalue of (3.4) and, accordingly, the orientation of the sublattice spins is independent of temperature up to the Néel point. This situation is different from that which we observed in Mn-salt, where the anisotropy energy of the one-ion type is effective in determining the spin orientation and thus theoretically the spin orientation has to depend on temperature.

§ 4. The susceptibility

As shown by the experiments of Garrett and Miedema *et al.*, $CoNH_4$- and $MnNH_4$-tutton salts have antiferromagnetic susceptibility along the K_1-axis below the Néel point (0.084°K and 0.14°K, respectively). Along the K_3-axis they have the largest susceptibility in weak field, caused possibly by transformation of domains, but above about 150 Oe they show a ferromagnetic saturation magnetization and at the same time a perpendicular susceptibility. In this section, we shall discuss quantitatively these susceptibilities.

As before, we shall use the Weiss molecular field approximation, but our treatment will be confined to 0°K and T_N.

4.1. Susceptibilities at 0°K.

We shall calculate the susceptibilities at 0°K in the classical way. Let us denote the direction cosines of the spins belonging to sublattice I by (ξ_0, η_0, ζ_0) in the absence of magnetic field. The direction cosines of the spins belonging to sublattice II can be denoted by $(-\xi_0, -\eta_0, \zeta_0)$. In the presence of a magnetic field, however, the direction cosines of these sublattice spins will be denoted as (ξ, η, ζ) and (ξ', η', ζ'), respectively. If the polar and azimuthal angles corresponding to (ξ_0, η_0, ζ_0) and (ξ, η, ζ) are $\pi/2-\theta_0$ and $\pi/2-(\theta_0+\theta)$ and $\varphi_0+\varphi$, respectively, we have

$$\begin{aligned}\xi&=\cos(\theta_0+\theta)\cos(\varphi_0+\varphi)\,,\\ \eta&=\cos(\theta_0+\theta)\sin(\varphi_0+\varphi)\,,\\ \zeta&=\sin(\theta_0+\theta)\,,\end{aligned}\tag{4.1a}$$

and

$$\begin{aligned}\xi'&=-\cos(\theta_0+\theta')\cos(\varphi_0+\varphi')\,,\\ \eta'&=-\cos(\theta_0+\theta')\sin(\varphi_0+\varphi')\,,\\ \zeta'&=\sin(\theta_0+\theta')\,.\end{aligned}\tag{4.1b}$$

We expand (4.1a) in powers of θ and φ and have

$$\begin{aligned}\xi&=\xi_0\left\{1-\frac{1}{2}(\theta^2+\varphi^2)\right\}-\frac{\xi_0\zeta_0}{\sqrt{1-\zeta_0^2}}\theta-\eta_0\varphi+\frac{\eta_0\zeta_0}{\sqrt{1-\zeta_0^2}}\theta\varphi\,,\\ \eta&=\eta_0\left\{1-\frac{1}{2}(\theta^2+\varphi^2)\right\}-\frac{\eta_0\zeta_0}{\sqrt{1-\zeta_0^2}}\theta+\xi_0\varphi-\frac{\xi_0\zeta_0}{\sqrt{1-\zeta_0^2}}\theta\varphi\,,\\ \zeta&=\zeta_0\left(1-\frac{1}{2}\theta^2\right)+\sqrt{1-\zeta_0^2}\,\theta\,.\end{aligned}\tag{4.2}$$

Similar expressions for ξ', η' and ζ' are obtained from (4.1b). If we substitute these expressions into the energy expression (2.7), terms linear with respect to θ, φ, θ', and φ' will be seen to vanish, because (ξ_0, η_0, ζ_0) and $(-\xi_0, -\eta_0, \zeta_0)$ represent the stable spin orientations in the absence of magnetic field. Therefore, the energy up to quadratic terms can be written as

$$\begin{aligned}E=\frac{N}{4}\left(\frac{\mu}{\mu_0}\right)^2\{&E_0+A(\theta^2+\theta'^2)+B(\varphi^2+\varphi'^2)\\ &+C(\theta\varphi+\theta'\varphi')+F(\theta\varphi'+\theta'\varphi)+H\theta\theta'+I\varphi\varphi'\}\,,\end{aligned}\tag{4.3}$$

Here μ denotes $\mu_0 S$ and $A, B, \cdots$ etc. are given by

$$\begin{aligned}
A=&A_{11}\left[\frac{\xi_0^2\zeta_0^2}{1-\zeta_0^2}-\xi_0^2\right]-4A_{12}\xi_0\zeta_0+2A_{15}\left[\frac{\xi_0\eta_0\zeta_0^2}{1-\zeta_0^2}-\xi_0\eta_0\right]\\
&+A_{22}(1-2\zeta_0^2)+A_{55}\left[\frac{\eta_0^2\zeta_0^2}{1-\zeta_0^2}-\eta_0^2\right]+A_{13}\xi_0^2-A_{24}\zeta_0^2\\
&+A_{56}\eta_0^2+A_{16}\xi_0\eta_0+A_{35}\xi_0\eta_0-A_{14}\xi_0\zeta_0+A_{23}\xi_0\zeta_0\ ,\\
B=&A_{11}(\eta_0^2-\xi_0^2)-A_{12}\xi_0\zeta_0-4A_{15}\xi_0\eta_0+A_{55}(\xi_0^2-\eta_0^2)\\
&+A_{13}\xi_0^2+A_{56}\eta_0^2+A_{16}\xi_0\eta_0+A_{35}\xi_0\eta_0-A_{14}\xi_0\zeta_0\ ,\\
C=&4\frac{\xi_0\eta_0\zeta_0}{\sqrt{1-\zeta_0^2}}(A_{11}-A_{55})+2A_{12}\left[\frac{\eta_0\zeta_0^2}{\sqrt{1-\zeta_0^2}}-\eta_0\sqrt{1-\zeta_0^2}\right]+4A_{15}\frac{\zeta_0}{\sqrt{1-\zeta_0^2}}(\eta_0^2-\xi_0^2)\\
&+2A_{35}\frac{\xi_0^2\zeta_0}{\sqrt{1-\zeta_0^2}}-2\frac{\eta_0\zeta_0}{\sqrt{1-\zeta_0^2}}\{A_{13}\xi_0-A_{56}\xi_0+A_{16}\eta_0-A_{14}\zeta_0\}\ ,\\
F=&2\frac{\xi_0\eta_0\zeta_0}{\sqrt{1-\zeta_0^2}}(-A_{13}+A_{56})+2\frac{\zeta_0}{\sqrt{1-\zeta_0^2}}(A_{16}\xi_0^2-A_{35}\eta_0^2)\\
&+2A_{23}\eta_0\sqrt{1-\zeta_0^2}\ ,\\
H=&-2\frac{\zeta_0^2}{1-\zeta_0^2}\{A_{13}\xi_0^2+A_{56}\eta_0^2+A_{16}\xi_0\eta_0+A_{35}\xi_0\eta_0\}\\
&+2A_{24}(1-\zeta_0^2)-2(A_{14}-A_{23})\xi_0\zeta_0\ ,\\
I=&-2(A_{13}\eta_0^2+A_{56}\xi_0^2)+2(A_{16}+A_{35})\xi_0\eta_0\ ,
\end{aligned}\tag{4.4}$$

in which A_{ij}'s are defined by (2.9a), (2.9b) or (3.3). The magnetic moment along each coordinate axis can be expressed in the following form:

$$\begin{aligned}
M_x=&\frac{1}{2}N\mu\left\{g_1(\xi+\xi')+g_4(\zeta-\zeta')\right.\\
=&\frac{1}{2}N\mu\left[g_1\left\{\frac{\xi_0\zeta_0}{\sqrt{1-\zeta_0^2}}(\theta'-\theta)+\eta_0(\varphi'-\varphi)\right\}\right.\\
&\left.+g_4\sqrt{1-\zeta_0^2}(\theta-\theta')\right]\ ,
\end{aligned}\tag{4.5a}$$

$$\begin{aligned}
M_y=&\frac{1}{2}N\mu g_2(\eta+\eta')\\
=&\frac{1}{2}N\mu g_2\left\{\frac{\zeta_0\eta_0}{\sqrt{1-\zeta_0^2}}(\theta'-\theta)+\xi_0(\varphi-\varphi')\right\}\ ,
\end{aligned}\tag{4.5b}$$

$$\begin{aligned}
M_z=&\frac{1}{2}N\mu\{g_3(\zeta+\zeta')+g_4(\xi-\xi')\}\\
=&N\mu(g_3\zeta_0+g_4\xi_0)+\frac{1}{2}N\mu\left[g_3\sqrt{1-\zeta_0^2}(\theta+\theta')\right.\\
&\left.-g_4\left\{\frac{\xi_0\zeta_0}{\sqrt{1-\zeta_0^2}}(\theta+\theta')+\eta_0(\varphi+\varphi')\right\}\right]\ ,
\end{aligned}\tag{4.5c}$$

where we neglected higher order terms with respect to θ, θ', φ and φ'. The first term in the right-hand side of (4.5c) gives a ferromagnetic component along the K_3-axis. The lowest spin orientation in the presence of a magnetic field H_0 can be obtained by minimizing $E-\boldsymbol{M}\boldsymbol{H}_0$ with respect to θ, φ, θ' and φ'. Then, we can write the magnetic moment by substituting θ, φ, θ' and φ' with those which correspond to the lowest spin orientation, and so obtain the susceptibility χ_i. Let us discuss separately the case of Mn-salt and that of Co-salt.

Mn-tutton salt.

In this case, $g_1=g_2=g_3\equiv g$ and $g_4=0$. The minimization of $E-M_yH_0$ leads to

$$\theta+\theta'=0\,, \qquad \varphi+\varphi'=0\,, \tag{4.6}$$

and we have

$$\theta=-\theta'=-\frac{1}{2}\alpha gF_1\,, \qquad \varphi=-\varphi'=\frac{1}{2}\alpha gF_2\,, \tag{4.7}$$

where

$$\alpha=\mu H\Big/\frac{1}{4}\left(\frac{\mu}{\mu_0}\right)^2, \tag{4.8}$$

and

$$F_1=\frac{(\zeta_0\eta_0/\sqrt{1-\zeta_0^2})(2B-I)+\xi_0(C-F)}{(2A-H)(2B-I)-(C-F)^2}\,,$$

$$F_2=\frac{\xi_0(2A-H)+(\eta_0\zeta_0/\sqrt{1-\zeta_0^2})(C-F)}{(2A-H)(2B-I)-(C-F)^2}\,. \tag{4.9}$$

The susceptibility along the y-axis, χ_2, can therefore be written as

$$\chi_2=2N(g\mu_0)^2\left[\frac{\zeta_0\eta_0}{\sqrt{1-\zeta_0^2}}F_1+\xi_0F_2\right], \tag{4.10}$$

if we substitute (4.7) into (4.5b).

Let us next calculate χ_1. Since $g_4=0$ in Mn-tutton salt, we have a solution of the type (4.6), with θ and φ given by

$$\theta=-\theta'=-\frac{1}{2}\alpha gF_1'\,, \qquad \varphi=-\varphi'=-\frac{1}{2}\alpha gF_2'\,, \tag{4.11}$$

where

$$F_1'=\frac{(\xi_0\zeta_0/\sqrt{1-\zeta_0^2})(2B-I)-\eta_0(C-F)}{(2A-H)(2B-I)-(C-F)^2}\,,$$

$$F_2'=\frac{\eta_0(2A-H)-(\xi_0\zeta_0/\sqrt{1-\zeta_0^2})(C-F)}{(2A-H)(2B-I)-(C-F)^2}\,. \tag{4.12}$$

So we have

$$\chi_1=2N(g\mu_0)^2\left[\frac{\xi_0\zeta_0}{\sqrt{1-\zeta_0^2}}F_1'+\eta_0F_2'\right]. \tag{4.13}$$

Finally, to find χ_3 in the presence of a magnetic field along the z-axis, we note that there is a solution

$$\theta=\theta'\,, \qquad \varphi=\varphi'\,, \tag{4.14}$$

with

$$\theta=\frac{1}{2}\alpha gF_1''\,, \qquad \varphi=\frac{1}{2}\alpha gF_2''\,, \tag{4.15}$$

where

$$F_1''=\frac{(2B+I)\sqrt{1-\zeta_0^2}}{(2A+H)(2B+I)-(C+F)^2}\,,$$

$$F_2''=-\frac{(C+F)\sqrt{1-\zeta_0^2}}{(2A+H)(2B+I)-(C+F)^2}\,. \tag{4.16}$$

The susceptibility is thus written as

$$\chi_3 = 2N(g\mu_0)^2 F_1''\sqrt{1-\zeta_0^2}\,. \tag{4.17}$$

The numerical values of these susceptibilities for Mn-tutton salt are given in the following list:

	(comp.)	(obs.)
χ_1	2.177	3.33
χ_2	13.804	11.64
χ_3	13.067	14.97

It is seen that the theoretical and experimental values agree reasonably well.

Co-tutton salt

The calculations can be proceeded in parallel with the case of Mn-tutton salt, though there is a difference in that the *g*-factor is anisotropic in the present case. Especially, a complication arises from the appearance in (4.5) of g_4, namely the *xz*-component of the *g*-tensor.

The susceptibility χ_2 is given by the same expression as (4.10), except that g is replaced by g_2.

To find χ_1, we notice that the minimizing conditions of $E-M_xH_0$ lead to

$$\begin{aligned} \theta &= -\theta' = -\frac{1}{2}\alpha\{g_1F_1' - g_4F_1''^*\}\,, \\ \varphi &= -\varphi' = -\frac{1}{2}\alpha\{g_1F_2' - g_4F_2''^*\}\,, \end{aligned} \tag{4.18}$$

where

$$\begin{aligned} F_1''^* &= \frac{(2B-I)\sqrt{1-\zeta_0^2}}{(2A-H)(2B-I)-(C-F)^2}\,, \\ F_2''^* &= -\frac{(C-F)\sqrt{1-\zeta_0^2}}{(2A-H)(2B-I)-(C-F)^2}\,, \end{aligned} \tag{4.19}$$

whence we get

$$\begin{aligned} \chi_1 = 2N\mu_0^2\Big\{ & g_1^2\Big(\frac{\xi_0\zeta_0}{\sqrt{1-\zeta_0^2}}F_1' + \eta_0F_2'\Big) \\ & + g_4^2\sqrt{1-\zeta_0^2}\,F_1''^* - 2g_1g_4\sqrt{1-\zeta_0^2}\,F_1'\Big\}\,. \end{aligned} \tag{4.20}$$

Similarly, the minimizing conditions in the presence of magnetic field along the *z*-axis are written as

$$\begin{aligned} \theta &= \theta' = \frac{1}{2}\alpha\{g_3F_1'' - g_4F_1'^*\}\,, \\ \varphi &= \varphi' = \frac{1}{2}\alpha\{g_3F_2'' - g_4F_2'^*\}\,, \end{aligned} \tag{4.21}$$

where

$$\begin{aligned} F_1'^* &= \frac{(\xi_0\zeta_0/\sqrt{1-\zeta_0^2}\,)(2B+I) - \eta_0(C+F)}{(2A+H)(2B+I)-(C+F)^2}\,, \\ F_2'^* &= \frac{\eta_0(2A+H) - (\xi_0\zeta_0/\sqrt{1-\zeta_0^2}\,)(C+F)}{(2A+H)(2B+I)-(C+F)^2}\,. \end{aligned} \tag{4.22}$$

So we get

$$\begin{aligned} \chi_3 = 2N\mu_0^2\Big\{ & g_3^2\sqrt{1-\zeta_0^2}\,F_1'' + g_4^2\Big(\frac{\xi_0\zeta_0}{\sqrt{1-\zeta_0^2}}F_1'^* + \eta_0F_2'^*\Big) \\ & - 2g_3g_4\sqrt{1-\zeta_0^2}\,F_1'^*\Big\}\,. \end{aligned} \tag{4.23}$$

The estimated numerical values of these χ are listed and compared with the experimental values as follows:

	(comp.)	(obs.)
χ_1	0.6570	6~7 (1.66*)
χ_2	4.593	7~8 (5.82*)
χ_3	7.131	7.48

* These values are due to Miedema's remeasurements18). He finds that χ_1 is much smaller than that given by Garrett.

4.2. The principal axes of the susceptibility tensor at 0°K.

Mn-tutton salt.

It should be noted here that all the K_1, K_2 and K_3-axes are not the principal axes of the susceptibility tensor. Let us inquire into this situation for Mn-salt. In the below, we shall denote χ_1, χ_2 and χ_3 by χ_{xx}, χ_{yy} and χ_{zz}, respectively. In this new notation, χ_{xy}, which is equal to χ_{yx}, is written

$$\chi_{xy}=2N(g\mu_0)^2\left(\frac{\xi_0\zeta_0}{\sqrt{1-\zeta_0^2}}F_1-\eta_0F_2\right), \tag{4.24}$$

when we substitute (4.7) into (4.5a). In Mn-salt, $g_4=0$ and hence the magnetic field along the x- and y-axes can only induce the spin rotation of the type $\theta=-\theta'$ and $\varphi=-\varphi'$, which cannot produce any component of the magnetic moment along the z-axis, as can be seen in (4.5). Accordingly, we have $\chi_{yz}=\chi_{zx}=0$. The susceptibility tensor of Mn-salt is thus obtained as

$$\begin{pmatrix} \chi_{xx} & \chi_{xy} & 0 \\ \chi_{yx} & \chi_{yy} & 0 \\ 0 & 0 & \chi_{zz} \end{pmatrix}. \tag{4.25}$$

The principal values and axes of the χ-tensor are given as

$$\chi_{\rm I}\ (\cos\phi,\ \sin\phi,\ 0), \qquad \chi_{\rm II}\ (-\sin\phi,\ \cos\phi,\ 0), \qquad \chi_{\rm III}\ (0,\ 0,\ 1), \tag{4.26}$$

where

$$\begin{pmatrix}\chi_{\rm I}\\ \chi_{\rm II}\end{pmatrix}=\frac{1}{2}\left[(\chi_{xx}+\chi_{yy})\mp\sqrt{(\chi_{xx}-\chi_{yy})^2+4\chi_{xy}^2}\right],$$
$$\tan 2\phi=\frac{2\chi_{xy}}{\chi_{xx}-\chi_{yy}}, \tag{4.27}$$

and the direction cosines of the axes are referred to the K_1, K_2 and K_3-axes.

With the assumed values of parameters we can estimate χ_{xy} to be $+2.859$, whence we have $\chi_{\rm I}=1.512$, $\chi_{\rm II}=14.469$, $\chi_{\rm III}=13.067$ and $\phi=-13°6'$.

The above principal axes are concerned with the susceptibility tensor of the single domain crystal. In actuality, the zero field susceptibility measures the susceptibility of a multi-domain crystal; the crystal may be composed of two types of domain, one being derived from the other by reversing the spin direction. The χ-tensor should be invariant with respect to this reversal because of the property of the tensor being of the second rank, and hence (4.26) and (4.27) should also give the χ-tensor for multi-domain crystal.

Co-tutton salt.

The χ-tensor for Co-salt may be obtained in a similar way, though the situation is a little more complicated than that for Mn-salt because $g_4\neq0$. However, as can be seen easily by substituting (4.18) and (4.21) into (4.5), χ_{yz} and χ_{zx} vanish also in this case. If we substitute (4.7) into (4.5a) we have

$$\chi_{xy}=2N\mu_0^2g_2\left\{g_1\left(\frac{\xi_0\zeta_0}{\sqrt{1-\zeta_0^2}}F_1-\eta_0F_2\right)-g_4\sqrt{1-\zeta_0^2}\,F_1\right\}. \tag{4.28}$$

The principal values and axes of the χ-tensor are given in the same form as (4.26) and

(4.27). With the assumed numerical values, we can estimate χ_{xy} to be $+1.354$, whence we have $\chi_{\mathrm{I}}=0.237$, $\chi_{\mathrm{II}}=5.014$, $\chi_{\mathrm{III}}=7.131$ and $\phi=-17°16'$.

4.3. Susceptibility at and above the Néel point.

Mn-tutton salt.

The paramagnetic susceptibility of Mn-salt obeys the Curie-Weiss law at rather high temperatures, but this is not the case near the Néel temperature where the $1/T$-expansion of the one-ion type energy breaks down. We shall derive a more accurate expression than before for the paramagnetic susceptibility on the basis of the molecular field approximation. The magnetic moments of the two sublattices are given by (2.24), in which $H_x^{\pm}$, $H_y^{\pm}$ and $H_z^{\pm}$ are given by the same expression as (2.26), except that the external magnetic field, H_x, H_y and H_z, should now be added to the molecular field (2.26). The magnetic moment induced by the external magnetic field can be obtained by solving a set of inhomogeneous equations (2.24). After a somewhat troublesome calculation, we get

$$\frac{1}{\chi_{xx}}=\frac{1}{Cf}\Bigg(T+\frac{1}{2}Cf(q_1+q_2)$$

$$-\frac{C}{2}\,\frac{\begin{array}{r}2Tf'^2(q_1''-q_2'')\{2T+Cf_\eta(q_3'+q_4')\}+C^2ff_\eta(f'^2-ff'')(q_1'+q_2')\\ \cdot(q_1''-q_2'')(q_3+q_4)+2CTf^2f_\eta(q_1'+q_2')(q_3+q_4)\end{array}}{\{2T+Cf_\eta(q_3'+q_4')\}[2fT-C(ff''-f'^2)(q_1''-q_2'')}\Bigg),$$

$$\frac{1}{\chi_{yy}}=\frac{1}{Cf_\eta}\Bigg(T+\frac{1}{2}Cf_\eta(q_3'+q_4')$$

$$-\frac{1}{2}Cf_\eta(q_1'+q_2')(q_3+q_4)\,\frac{(Cf')^2(q_1''-q_2'')+Cf\{2T-Cf''(q_1''-q_2'')}{\begin{array}{r}\{2T-Cf''(q_1''-q_2'')\}\{2T+Cf(q_1+q_2\}\\ +(Cf')^2(q_1+q_2)(q_1''-q_2'')\end{array}}\Bigg),$$

$$\frac{1}{\chi_{zz}}=\frac{1}{Cf''}\Bigg(T+\frac{1}{2}Cf''(q_1''+q_2'')$$

$$-\frac{C}{2}\,\frac{(2Tf')^2(q_1-q_2)+2TCf_\eta f'^2\{(q_1'-q_2')(q_3-q_4)-(q_1-q_2)(q_3'-q_4')\}}{\begin{array}{r}\{2T-Cf_\eta(q_3'-q_4')\}[2f''T-C(ff''-f'^2)(q_1-q_2)]\\ +C^2f_\eta(f'^2-ff'')(q_1'-q_2')(q_3-q_4)\end{array}}\Bigg),$$

$$\chi_{xy}=-\frac{Cf_\eta(q_1'+q_2')}{2T+Cf_\eta(q_3'+q_4')}\chi_{xx}\,,$$

$$\chi_{yz}=\chi_{zx}=0\,. \tag{4.29}$$

The paramagnetic susceptibilities along the K_1, K_2 and K_3-axes have been calculated with the assumed values of J_1 and J_2, and the results are plotted in Fig. 8a. Numerical values of the χ-tensor at the theoretical Néel temperature (0.125°K) are given below with the measured values at the observed Néel temperature.

	(comp.)	(obs.)
χ_{xx} (χ_1)	61.2	20.8
χ_{yy} (χ_2)	32.5	15.0
χ_{zz} (χ_3)	∞	52.4
χ_{xy}	-23.8	

From these results, the principal values and axes of the χ-tensor are found to be

$$\begin{array}{ll}\chi_{\mathrm{I}}\ =74.64\,, & (\ \cos\phi,\ \sin\phi,\ 0)\,,\\ \chi_{\mathrm{II}}\ =19.06\,, & (-\sin\phi,\ \cos\phi,\ 0)\,,\\ \chi_{\mathrm{III}}=\infty\,, & (\quad 0,\qquad 0,\quad 1)\,,\end{array}$$

$$\phi=-29°27'\,. \tag{4.30}$$

Comparing the principal axes of the χ-tensor at the Néel temperature, (4.30), with those at 0°K, (4.26), it is predicted that the principal axes of χ depend on temperature, though detailed numerical values will be more or less different in actual case. To confirm this prediction, measurements of the angular dependence of the zero-field susceptibility may be useful.

At temperatures well above the Néel point, the paramagnetic susceptibility obeys the Curie-Weiss law with anisotropic Curie and Weiss constants. Expanding f_ξ, f_η and f_ζ of (2.25) in powers of $1/T$, we have

$$\begin{aligned} f_\xi=f_\eta&=1+\frac{1}{30}(2S-1)(2S+3)\frac{D}{kT}\ , \\ f_\zeta&=1-\frac{1}{15}(2S-1)(2S+3)\frac{D}{kT}\ . \end{aligned} \tag{4.31}$$

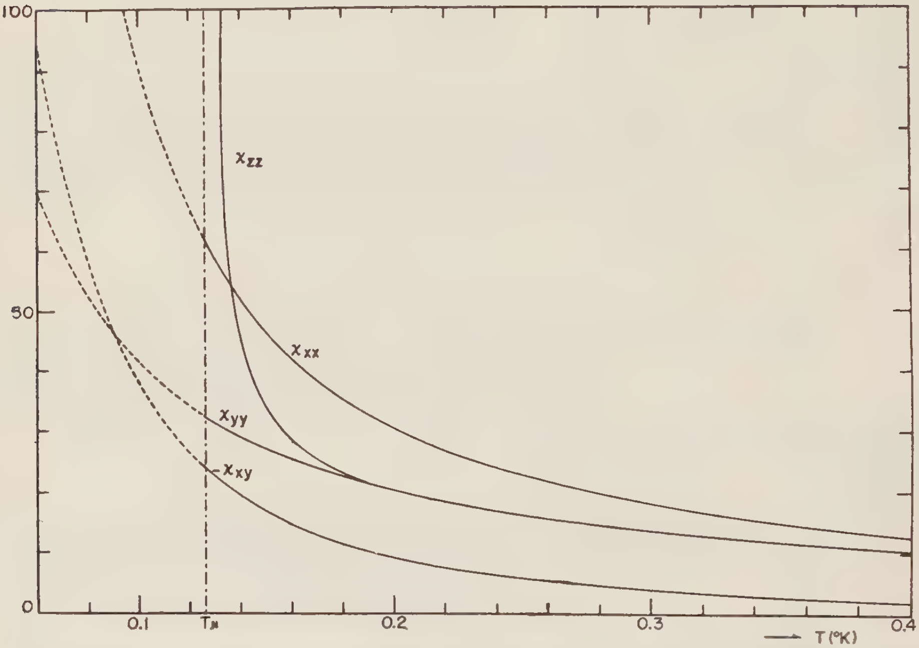

Fig. 8 a. The (isothermal) paramagnetic susceptibilities along K_1, K_2 and K_3-axes. (Mn-tutton salt)

If we substitute these expressions into (4.29) and discard higher order terms with respect to $1/T$, the following Curie-Weiss law can be proved:

$$\begin{aligned} \chi_i&=C/(T-\Theta_i)\ , \\ \Theta_1&=-\frac{S(S+1)}{3k}\{\mu_0^2g^2(G_{1x}+G_{2x})-8J_2-4J_1\} \\ &\quad+\frac{D}{30k}(2S-1)(2S+3)(\sin^2\alpha-2\cos^2\alpha)\ , \\ \Theta_2&=-\frac{S(S+1)}{3k}\{\mu_0^2g^2(G_{1y}+G_{2y})-8J_2-4J_1\} \\ &\quad+\frac{D}{30k}(2S-1)(2S+3)\ , \\ \Theta_3&=-\frac{S(S+1)}{3k}\{\mu_0^2g^2(G_{1z}+G_{2z})-8J_2-4J_1\} \\ &\quad+\frac{D}{30k}(2S-1)(2S+3)(-2\sin^2\alpha+\cos^2\alpha)\ . \end{aligned} \tag{4.32}$$

Here χ_1, χ_2 and χ_3 refer respectively to the K_1, K_2 and K_3-axes which coincide with the principal axes of the χ-tensor in the temperature region considered. Estimates of Θ_1, Θ_2 and Θ_3 are 0.0492, -0.0278 and -0.0312, respectively.

Co-tutton salt.

The paramagnetic susceptibility for Co-salt can be obtained from (3.11) and (3.12), the external magnetic field now being included. Details of the calculation will not be reproduced here, but the result obtained are as follows:

$$\begin{aligned}
\chi_{xx} &= \frac{N\mu_0^2C'}{\Delta}[g_1^2\{T+C'(v+w)\}\{T+C'(c-f)\} \\
&\quad +g_4^2\{T+C'(a+d)\}\{T+C'(v+w)\} \\
&\quad -2g_1g_4C'(b-e)\{T+C'(v+w)\}-(g_4C')^2(t+u)^2]\ , \\
\chi_{yy} &= \frac{N\mu_0^2C'g_2^2}{\Delta}[\{T+C'(c-f)\}\{T+C'(a+d)\}-C'^2(b-e)^2]\ , \\
\chi_{zz} &= \frac{N\mu_0^2C'}{\Delta^*}[g_3^2\{T+C'(a-d)\}\{T+C'(v-w)\} \\
&\quad +g_4^2\{T+C'(v-w)\}\{T+C'(c+f)\} \\
&\quad -2g_3g_4C'(b+e)\{T+C'(v-w)\}-(g_3C')^2(t-u)^2]\ , \\
\chi_{xy} &= \frac{N(\mu_0C')^2}{\Delta}g_2(t+u)[g_1\{T+C'(c-f)\}-g_4C'(b-e)]\ , \\
\chi_{yz} &= \chi_{zx}=0\ ,
\end{aligned}$$

where

$$\begin{aligned}
C' &= S'(S'+1)/3k\ , \\
\Delta &= \{T+C'(a+d)\}\{T+C'(v+w)\}\{T+C'(c-f)\} \\
&\quad -C'^2(t+u)^2\{T+C'(c-f)\}-C'^2(b-e)^2\{T+C'(v+w)\}\ , \\
\Delta^* &= \{T+C'(a-d)\}\{T+C'(v-w)\}\{T+C'(c+f)\} \\
&\quad -C'^2(t-u)^2\{T+C'(c+f)\}-C'^2(b+e)^2\{T+C'(v-w)\}\ .
\end{aligned} \tag{4.33}$$

The results of computation are plotted in Fig. 8b. The calculated numerical values of the χ-tensor at the theoretical Néel temperature (0.168°K) are also given below, together with the measured values at the observed Néel temperature (0.084°K).

	(comp.)	(obs.)
χ_{xx} (χ_1)	16.00	~ 20
χ_{yy} (χ_2)	5.08	~ 7.5
χ_{zz} (χ_3)	∞	~ 48
χ_{xy}	1.25	

The principal values and axes of the χ-tensor at the Néel point follow from these results to be

$$\begin{aligned}
\chi_{\mathrm{I}} &= 16.14,\ (\ \cos\phi,\ \sin\phi,\ 0)\ , \\
\chi_{\mathrm{II}} &= 4.94,\ (-\sin\phi,\ \cos\phi,\ 0)\ , \\
\chi_{\mathrm{III}} &= \infty,\ (\ 0,\ 0,\ 1)\ , \\
&\phi=+6°27'\ ,
\end{aligned} \tag{4.34}$$

which may be compared with the corresponding quantities at 0°K ($\chi_{\mathrm{I}}=0.237$, $\chi_{\mathrm{II}}=5.014$, $\chi_{\mathrm{III}}=7.131$ and $\phi=-17°16'$)

As in the case of Mn-salt, the principal axes of the χ-tensor depend on temperature. At high temperatures where the principal axes of χ-tensor coincide with K_1, K_2 and K_3-axes, the susceptibility obeys the Curie-Weiss law. (See Appendix about the anisotropic Curie-Weiss constants of Co-salt in this temperature region.)

§ 5. Conclusion and Summary

We have made an attempt to explain the experimental results of Miedema *et al.* on MnNH$_4$- and CoNH$_4$-tutton salts at very low temperatures, extending the theory developed in (I) and making some results of it. A satisfactory quantitative explanation was given. In the crystals of these salts, the dipolar interaction acts ferromagnetically along the K_1- and K_2-directions between ions of the same kind and antiferromagnetically between ions of the two different kinds, *i.e.*, those on crystallographically different positions. Along the K_3-direction it acts ferromagnetically between ions of different kinds and antiferromagnetically between ions of the same kind.

In the case of $MnNH_4$-tutton salt, the dipolar and exchange interactions give rise only to an antiferromagnetic arrangement in the K_1K_2-plane. The essential mechanism that yields a parasitic ferromagnetism arises from the one-ion type energy, *i.e.*, the anisotropy energy due to the crystalline field acting on each ion. This energy tilts each spin toward the relevant microscopic tetragonal axis. Since the crystalline fields for ions of the two different kinds are in mirror images with respect to the *ac*- (or K_1K_2-) plane, a ferromagnetic component perpendicular to this plane results.

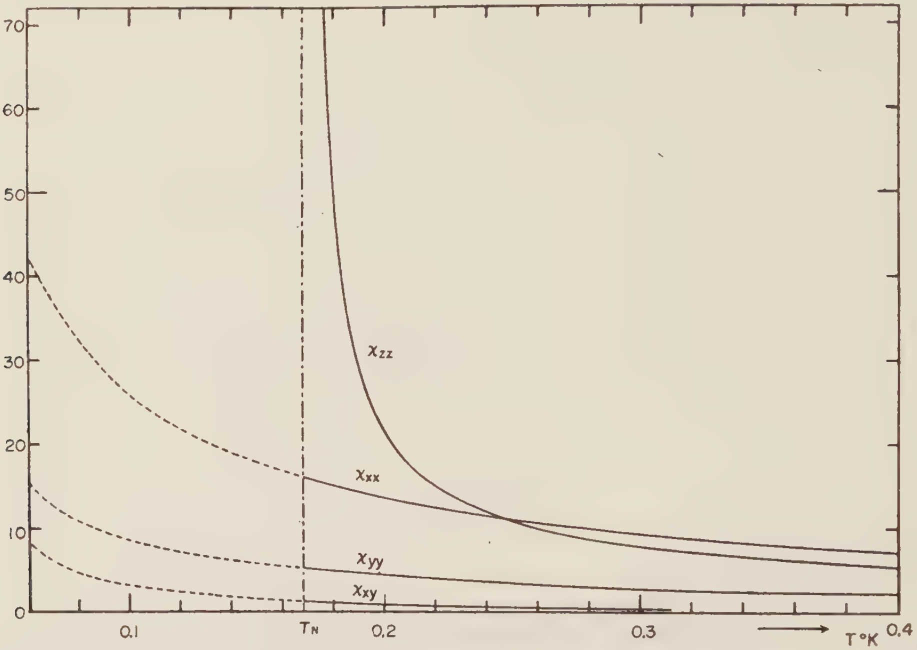

Fig. 8 b. The (isothermal) paramagnetic susceptibilities along K_1, K_2 and K_3-axes. (Co-tutton salt)

In the case of $CoNH_4$-tutton salt, the combined dipolar and exchange interaction acts ferromagnetically along the K_3-direction between ions of both the same kind and different kinds. In this case the lowest Kramers doublet is highly anisotropic, in which the parallel component of the *g*-factor to the microscopic tetragonal axis, 6.45, is about twice as large as the perpendicular component, 3.05. Due to this high anisotropy, both the dipolar and exchange interactions become highly anisotropic and the spins are thus tilted again toward the microscopic tetragonal axes.

Some points of our results will be noted in the following.

1) The spin directions for the lowest energy state lie within a plane which inclines to the K_1K_3-plane with an angle φ. Estimates of φ are $-15°2'$ and $-9°53'$ for Mn- and Co-salt, respectively. This inclination comes from an interplay of dipolar interaction and crystal structure of low symmetry. However, we have so far no experimental evidence revealing this feature.

2) Estimates of θ, the angle with which the spins incline to the K_1K_2-plane, are $21°42'$ and $10°42'$ for Mn- and Co-salt, respectively. The corresponding quantities have

been measured to be 16° and 24°, respectively. It may be noted that the value of $\theta=24°$ for Co- salt cannot be claimed to be accurate. Miedema *et al.* estimated it in such a way that $N\langle\mu\rangle\sin\theta$ is equal to the measured value of the ferromagnetic component assuming $\langle\mu\rangle$, the magnetic component along the microscopic tetragonal axis, to be $3.1\,\mu_0$. However, this way of estimation will be unreliable if the spins deviate far from the tetragonal axes. According to (4.5c) with $\mu=\mu_0 S$, the ferromagnetic component parallel to the K_3-axis is given by

$$M_f=\frac{1}{2}N\mu_0(g_3\sin\theta_0+g_4\cos\theta_0\cos\varphi_0).$$

Hence the correct orientation of spin may be determined from

$$\frac{1}{2}(g_3\sin\theta_0+g_4\cos\theta_0\cos\varphi_0)=3.1\sin 24°\ ,$$

which includes φ_0 as well as θ_0. Our estimate, $\theta=10°42'$ and $\varphi=-9°53'$ gives 1.15 for the left-hand side of the above equation, which may be compared with $3.1\sin 24°=1.26$.

3) Due to the complication of the calculation, the temperature dependence of the ferro- and sublattice magnetizations has not been studied. Only the spin pattern at the Néel point has been studied and compared with that at 0°K. It may be pointed out that the spin orientation in Co-salt remains practically invariable with temperature while that of Mn-salt does not. This difference comes from the fact that the spin orientation in the former salt depends only on the inter-ionic interactions while that in the latter salt it depends on the one-ion type energy. The predicted values of θ and φ for Mn-salt at the Néel point are 15°8′ and −24°48′, respectively, and hence we see that θ decreases and $|\varphi|$ increases with increasing temperature, though their temperature dependence is not appreciable.

4) Estimate of the Néel point is 0.125°K for Mn-salt and 0.168°K for Co-salt, which may be compared with the measured values 0.14°K (Mn-salt) and 0.084°K (Co-salt). The estimate for Co-salt is larger than the measured value by a factor of 2 and that for Mn-salt is a little smaller than the measured value. This disagreement is partly due to an ambiguity in the estimates of the exchange integrals (especially for Mn-salt) and partly due to the molecular field approximation.

5) The magnetic susceptibility at 0°K and at the Néel point have been calculated. The principal axes of the susceptibility tensor do not coincide with the K_1, K_2 and K_3-axes. Further, they depend on temperature. These features could be confirmed by measuring the angular dependence of the susceptibility. Our magnetic susceptibility at the Néel point concerns the isothermal susceptibility but not the adiabatic susceptibility. The difference between these two kinds of susceptibilities disappears at the temperature of 0°K but may be appreciable at the Néel point. The adiabatic susceptibility is of course smaller than the isothermal one, and hence the adiabatic susceptibility along the K_3-axis may be finite at the Néel point, though the isothermal susceptibility along the same axis should be infinite. Any discussion about this point is not given in the present paper.

Acknowledgements

The author wishes to express his sincere gratitude to Professor T. Nagamiya and Dr. T. Nakamura of Osaka University for numerous valuable discussions in carrying out the present work. The author is also indebted to Mr. S. Toshima for kind discussion.

Appendix

In this appendix, we should like to correct erroneous results in (I) due to a careless mistake. In (16) of (I), $\sin\alpha\cos\alpha$ should be read $\sin 2\alpha$, and hence J_b in (18) should be multiplied by a factor 2. The second column in Table I should then be revised as in Table III of this paper. Table IV should be read:

λ	$a_\lambda\times10^2$	b_λ/k	c_λ/k
1	−2.039	5.21	6.82
2	+0.350	1.52	3.03
3	+0.503	4.25	2.64

Due to this situation, the numerical values of J_1 and J_2 to be fitted to the observed Weiss constants should be revised. In place of Table V in (I), we have:

	exp.	theoret.
Θ_1	−0.021°K	−0.0207
Θ_2	−0.007	−0.0067
Θ_3	+0.032	+0.0322
J_1/k		+0.0123
J_2/k		−0.0095

In this table, the experimental Weiss constants are obtained from the slope of curves in Garrett's Fig. 4[4]. The values are different from those given by Garrett, which we had used in (I). We failed to fit J_1 and J_2 to the Garrett's Weiss constants so as to get reasonable magnitude of magnetic specific heat, basing on the anisotropic exchange interaction revised. However, Garrett's data do not seem to be unreasonable for adopting the values given in the above table as experimental Weiss constants. Eq. (47) in (I) should be read

$$(C_vT^2/R)_{\text{dip-ex}}=-10^{-2}k^{-1}(2.16J_1-0.07J_2)\ .$$

Table VIII should now be read:

theoret.	38.3	dip-dip	17.8
		dip-ex	− 2.7
		ex-ex	23.2
exp.	27		

References

1) L. C. Jackson: Trans. Roy. Soc. (London) **A 224** (1924) 1.
2) W. Hofmann: Z. fur Krist. **78** (1931) 279.
3) R. J. Benzie and A. H. Cooke: Nature **164** (1949) 837.
4) C. G. B. Garrett: Proc. Roy. Soc. (London) **A 206** (1951) 242.
5) L. J. Smits, H. E. Derksen, J. C. Verstelle and C. J. Gorter: Physica **XX II** (1956) 773.
6) T. Haseda: Physica **XX IV** (1958) 93.
7) A. Abragam and M. H. L. Pryce: Proc. Roy. Soc. **A 206** (1951) 173.
8) B. Bleaney and D. J. E. Ingram: Proc. Roy. Soc. **A 208** (1951) 143.
9) T. Nakamura and N. Uryû: J. Phys. Soc. Japan **11** (1956) 760.
10) N. Uryû: J. Phys. Soc. Japan **11** (1956) 770.
11) U. Kh. Kopvillem: Soviet Physics. J. E. T. P. **35** (1959) 349.
12) Y. Nagaoka: J. Phys. Soc. Japan **13** (1958) 1328.
13) T. Moriya and Y. Obata: J. Phys. Soc. Japan **13** (1958) 1333.
14) A. R. Miedema, J. Van den Broek, H. Postma and W. J. Huiskamp: Physica **25** (1959) 1177.
15) A. Abragam and M. H. L. Pryce: Proc. Roy. Soc. **A 205** (1951) 135.
16) B. Bleaney and D. J. E. Ingram: Proc. Roy. Soc. **A 205** (1951) 336.
17) R. A. Erickson and L. D. Roberts: Phys. Rev. **93** (1954) 957.
18) A. R. Miedema: private communication.

JOURNAL OF THE PHYSICAL SOCIETY OF JAPAN, Vol. 16, No. 10, NOVEMBER, 1961

On the Magnetic Properties of 12 Percent Aluminium-Iron Alloy

By Makoto SUGIHARA

The Electrical Communication Laboratory, Nippon Telegraph and Telephone Public Corporation, Musashino-shi Tokyo, Japan

(Received December 27, 1960)

A sharp maximum of permeabilities has been found in the narrow concentration range of about 12 percent aluminium in the slow cooled iron-aluminium alloys. It is found, however, that the permeabilities of this alloy are decreased and its coercive force is increased by the reheat-treatment at temperatures between 400° and 650°C, followed by slow cooling. For example, after reheating the alloy to 550°C μ_m was decreased from 23,500 to 4,800, μ_0 from 1,600 to 1,000 and H_c was increased from 0.09 to 0.37 Oe. Since such a reheating effect was not found in the other concentration of iron-aluminium alloys, it is concluded that the phenomenon is due to something characteristic of 12 percent aluminium-iron alloy, that is the growth of a small quantity of precipitation or the short range order, which would result in an increase of internal strain.

§ 1. Introduction

Investigations on magnetic properties of iron-aluminium alloys had been limited into a low concentration of aluminium, until Masumoto and Saitô[1] discovered the existence of the composition range of the alloy showing high permeability. This alloy has a high concentration of aluminium and is named Alperm. Nachman and Buehler[2] found a method of working this alloy into sheets. Stimulated by these results many investigations on the magnetic properties of the alloy have been carried out. At the same time many studies of magnetic properties in connection with the superlattice existing in this alloy have been made. Recently Arrott and Sato[3] found that the alloys between 15.8 percent (28 atomic percent) and 19.2 percent (33 atomic percent) aluminium are ferromagnetic at room temperature but show a transition to antiferromagnetism at low temperature. They found that the antiferromagnetism exists only in the ordered structures.

High permeabilities are observed in the comparatively narrow concentration range between 11.5 and 12.9 percent aluminium only when they are melted in vacuum, hydrogen gas or innert gas. The investigation of magnetic properties of the alloy containing about 12 percent aluminium has been carried out by Nachman and Buehler[4], and the author[5]. This high permeability alloy is named Alfenol 12 in America, Hipermal in Japan. It is known that the magnetocrystalline anisotropy constant K_1 is zero at the concentrations near 12 and 16 percent aluminium for slow cooled alloys[6],[7]. The high permeability of the alloy containing about 12 percent aluminium is obtained only in a very narrow concentration range and the high permeability is not obtained for the alloy quenched in water from high temperatures in contrast to the alloy containing about 16 percent aluminium. These experimental facts suggest that we must attribute the origin of the high permeability to some characteristic of the alloy near the concentration of about 12 percent aluminium.

In order to study the cause for its high permeability the author investigated variation of the magnetic properties of the alloy containing 12 percent aluminium caused by heat treatment.

§ 2. Specimen and Experimental Methods

The specimen is the one that was used in the previous experiment[5] containing 12.12 percent aluminium and of the size: 27 mm in outer diameter, 19 mm in inner diameter, and 0.8 mm in thickness.

The specimen was at first annealed at 1000°C for 1 hour and then furnace cooled in vacuum. Subsequently various heat treatments were carried out in a non-inductive electric furnace after heating at 800°C for 30 minutes. In the case of reheat-treatment the specimen was heated to the desired temperatures at the rate of about 300°C per hour, held for 5 minutes and then cooled. The cooling rate is always about 150°C per hour.

The measurement of magnetization of the specimen was made at room temperature by a recording flux meter after demagnetized with A. C. field.

§ 3. Experimental Results

First the specimen was cooled from 800°C to temperature T and quenched in water. The results of the measurement of the initial permeability μ_0, the maximum permeability μ_m, and the coercive force H_c ($B_m=10{,}000$ G) are shown in Fig. 1 as a function of the quenching temperature T. By quenching from temperatures over 350°C μ_0 and μ_m were decreased, and H_c was increased. Such an abrupt change in magnetic properties has not been observed by the previous investigators[1], who used the specimen which was melted in air, instead of melting in a high vacuum as in the present case.

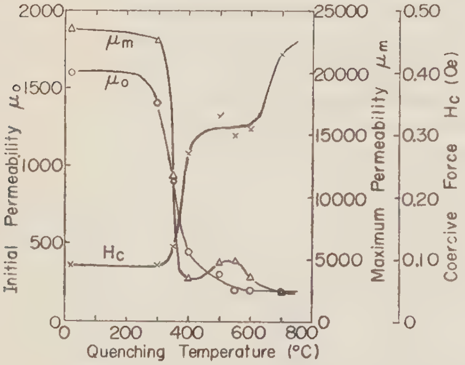

Fig. 1. The initial and maximum permeabilities and coercive force as a function of quenching temperature.

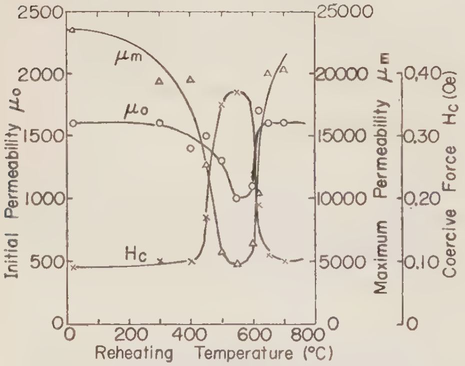

Fig. 2. The initial and maximum permeabilities and coercive force as a function of reheating temperature.

Next the specimen was cooled from 800°C to room temperature, reheated to temperature T below 700°C, held for 5 minutes and cooled to room temperature. The results of the measurement of μ_0, μ_m and H_c are shown in Fig. 2 as a function of the reheating temperature T. There is a striking decrease in μ_0 and μ_m, and an increase in H_c between 400°C and 620°C, the effect of which is maximum at 550°C.

Fig. 3 shows the comparison of, the magnetization curves and the hysteresis loops between the specimens reheated at 450°, 550° or 620°C, and the one without reheating. From the figure it is understood that the curves are most influenced by the reheating to 550°C.

Then the specimen was cooled from 800°C to a temperature T below 550°C and then reheated to 550°C. Fig. 4 shows the results of measurement of μ_0, μ_m and H_c as a function of the temperature T. From the figure it is recognized that μ_m and H_c are mostly influenced by the heat treatment when $T<$ 500°C.

§ 4. Considerations

The reheating effect on μ_0, μ_m and H_c as seen in Fig. 2 is not observed for the alloy containing aluminium 10.20, 11.18, 13.28, 14.09 and 16.05 percent, respectively. Accordingly, it is supposed the reheating effect is characteristic of the alloy containing about 12 percent aluminium.

The changes in physical properties by quenching from high temperatures such as specific resistance[1),8)], lattice constant[9),10),11)], mechanical hardness[5)] and tensile strength[12)] are observed for the alloys containing more than 10 percent aluminium. The amount of change, however, is very small and shows no anomaly at 12 percent aluminium. The change in specific heat of iron-aluminium alloys with temperatures was measured by Saitô[13)], who supposed the small abnormal change observed at high temperatures at the concentration range of 5–13 percent aluminium corresponding to the transformation of superlattice $Fe_{13}Al_3$. The change is not characteristic of the alloy containing about 12 percent aluminium only.

From the measurement of the change in

thermal expansion as a function of temperature, McQueen and Kuzynski[14)] reported that the order-disorder transformation temperature is about 520°C for Fe_3Al (13.9 percent aluminium) and decreases with the decrease of aluminium content, being 470°C at 12 persent aluminium and 360°C at 10.7 percent aluminium. Recently Lihl and Stickler[15)] found by means of a differential thermal analysis that the short range order develops in the concentration range of 4–12 percent aluminium. In both cases, however, any change characteristic of the alloy containing 12 percent aluminium was not found.

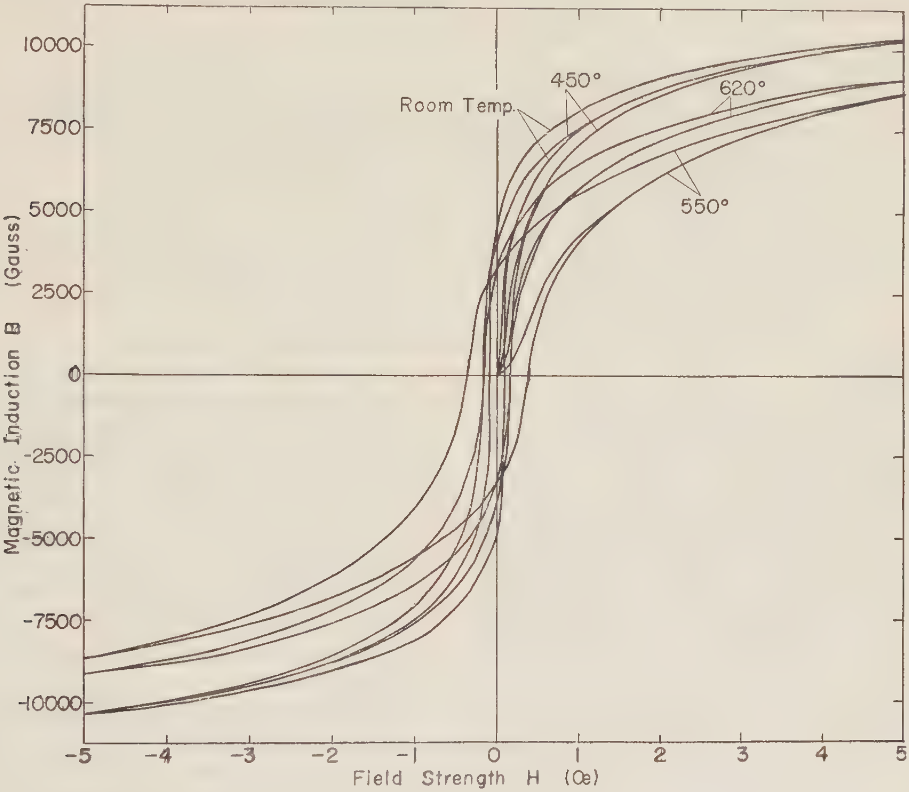

Fig. 3. Magnetization curves and hysteresis loops before and after reheating. The temperatures indicated are the reheating ones.

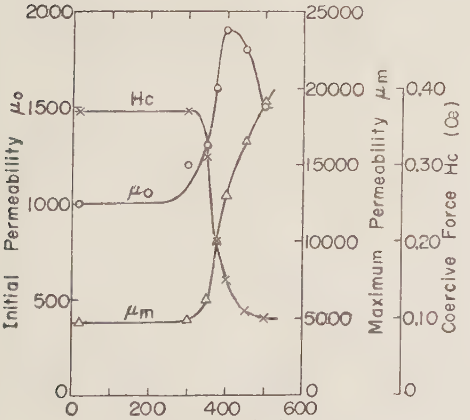

Fig. 4. The initial and maximum permeabilities and the coercive force as a function of the temperature *T*, to which the specimen was cooled from 800°C and then reheated to 550°C.

The powders of the alloy pulverized by filing that were heat treated as previously, were used for X-ray analysis. Any phase change was not detected after reheating.

This result of X-ray analysis indicated that the change of magnetic properties by reheating is not owing to an ordinary phase change. Order-disorder transformation generally occurs reversibly and is not able to cause such a change of magnetic properties by reheating. Besides it is obvious that the reheating effect has no relation to such hysteresis phenomenon as the α–γ transformation of iron-nickel alloy.

Therefore, as a result of the consideration mentioned above, the reheating effect should be interpreted as follows: the growth of a small quantity of precipitation or the short range order, the amount of which is too small to be detected by X-ray analysis etc., results in an increase of internal strain influencing remarkably the magnetic properties.

Previously the author[16] reported that μ_0 and μ_m are decreased and H_c is increased after cooling in a magnetic field from 550°C only for the alloy containing 12.12 percent aluminium of iron-aluminium alloys. It turns out, however, that this result is not due to the effect of magnetic heat treatment, but simply due to the reheat-treatment.

§ 5. Summary

The slow cooled iron-aluminium alloy containing about 12 percent aluminium shows high permeability. It was found, however, that the permeabilities are decreased and the coercive force is increased, remarkably by the reheat-treatment at temperatures between 400° and 650°C, followed by slow cooling. Since this reheating effect has not been found in the other concentration of aluminium, it is concluded that the phenomenon is characteristic of the alloy containing 12 percent aluminium. By X-ray analysis any phase change of the alloy was not detected after the reheat-treatment. Consequently, it is supposed that the remarkable decrease of permeabilities and the striking increase of coercive force are caused by the increase of internal strain that is arisen by the growth of a small quantity of precipitation or the short range order during reheating.

In conclusion the author wishes to express his hearty thanks to Dr. Y. Shichijô, the chief of the magnetic research section of the Electrical Communication Laboratory, for his encouragement throughout the work.

References

1) H. Masumoto and H. Saitô: Sci. Rep. RITU **A3** (1951) 523; **A4** (1952) 321; 338.
2) J. F. Nachman and W. J. Buehler: J. Appl. Phys. **25** (1954) 307.
3) A. Arrott and H. Sato: Phys. Rev. **114** (1959) 1420.
4) J. F. Nachman and W. J. Buehler: NAVORD Report 4130, (1955).
5) M. Sugihara: Reports of the E. C. L. NTT **7** (1959) 333.
6) H. Gengnagel: Naturwiss. **45** (1958) 630.
7) R. C. Hall: Trans. Am. Inst. Met. Engr. **212** (1958) 703; J. Appl. Phys. **30** (1959) 816.
8) C. Sykes and H. Evans: Proc. Roy. Soc. **A145** (1934) 529; J. Iron and Steel Inst. **131** (1935) 229.
9) A. J. Bradley and A. H. Jay: Proc. Roy. Soc. Lond. **A136** (1932) 210.
10) A. Taylor and R. M. Jones: J. Phys. Chem. Solids **6** (1958) 16.
11) F. Lihl and E. Burger: Arch. Eisenhüttenw. **31** (1960) 129.
12) W. Justusson, V. F. Zackay and E. R. Morgan, Trans. Amer. Soc. Metals **49** (1957) 905.
13) H. Saitô: Nippon Kinzoku Gakkai-Shi **B14** (1950) No. 5, 6.
14) H. J. McQueen and G. C. Kuczynski: Trans. Am. Inst. Met. Engr. **215** (1959) 619.
15) F. Lihl and R. Stickler: Arch. Eisenhüttenw. **31** (1960) 47.
16) M. Sugihara: J. Phys. Soc. Japan **15** (1960) 1456.

JOURNAL OF THE PHYSICAL SOCIETY OF JAPAN, Vol. 16, No. 11, NOVEMBER 1961

Effect of Quenched-in Vacancies on the Weak Magnetization of Nickel

By Yoji NAKAMURA

Faculty of Science, Kyoto University

(Received March 6, 1961)

The change in magnetization in weak magnetic field of nickel quenched from high temperatures was measured by means of a sensitive astatic magnetometer, and it was found that the magnetization increased nearly proportionally to the logarithm of the time elapsed after quenching. It is shown that the effect can be analyzed phenomenologically by one of formal theories proposed on the magnetic after effect. On the other hand, the formation energy of the vacancies was estimated roughly to be 1.4 eV, which showed a good agreement with the results of other observations. It is, therefore, quite likely that the observed change in magnetization is entirely due to the annihilation of the frozen-in vacancies.

§ 1. Introduction

The quenching of a crystal from high temperatures can be considered not only as a method by which one can bring the high-temperature phase to low temperatures, but also applied as a tool by which a large number of point defects which are in thermal equilibrium at high temperatures can be frozen. It is well known for close-packed metals that almost all of the frozen point defects from lattice vacancies rather than interstitials owing to the smaller formation energy of the former. Therefore, the quenching is quite effectively used to introduce only one kind of point defects, i.e. vacancies, into a metal.

Physical properties of the metal should undergo fairly large changes under the existance of these quenched-in vacancies. During the past several years the effects of quenched-in vacancies upon the mechanical hardening[1)], electrical resistivity[2)], density[3)], and elastic modulus[4)] have been studied on various metals extensively. However, no study on the effect of vacancies upon the magnetic properties seems to have been performed, although some works concerning the relations between lattice imperfections other than lattice vacancies and the magnetic properties of ferromagnetic materials have been accumulated. The effect of impurity atoms has long been investigated in connection with the magnetic viscosity. The contribution of the impurity segregation or non-magnetic inclusions to the coercive force was studied mainly by Néel[5)]. Vicena[6)] has pointed out that the density of dislocations which prevent the domain wall movements is the main factor controlling the coercive force. Recently Heidenreich and Nesbitt[7)] demonstrated that the stacking faults might play an important role in the field-cooling effect in perminvar. Thus, it is desirable to study directly the effect of vacancies upon the magnetic properties.

In this work, we dealt with the lattice vacancies created and frozen in metal and its contribution to magnetic properties. In general, quenched-in vacanies in a metal are expelled out of the surfaces of the specimen or otherwise absorbed by pre-existing grain boundaries and dislocations. But, there is another case in which the vacancies come together to form the so-called "clustering" when its concentration is high. During the process of the annihilation of the excess vacancies, the intensity of magnetization in the ferromagnetic metal might vary when the specimen is placed in magnetic field. The observation of this change may offer an information to the mechanism of the vacancy annihilation.

§ 2. Specimen and the Experimental Apparatus

To detect the vacancy effect on the magnetic proporties, it is required to choose the specimen having the following characteristics. First, owing to the very small concentration of excess vacancies, the expected magnetic change may be very small. The magnetic properties of the specimen should, therefore, be quitely structure- or defect-sensitive. Secondly, to exclude the effects due to any metallurgical change (for example, the precipitation of a different phase from the matrix) during the annihilation of vacancies, the specimen should not be an alloy. Thus, only the pure metal with high purity and without any phase change is desirable.

We adopted a polycrystalline wire of 99.98% pure nickel as the specimen of the present experiment, since nickel is a very structure-sensitive ferromagnetic metal owing to its large magnetostriction and small crystal anisotropy, and it has no phase change in the temperature range below its melting point. Impurities contained in the specimen are 0.002% Fe, 0.0006% Pb, 0.002% C, 0.002% Cu and the trace of S. To obtain a sufficiently high concentration of vacancies, a fine wire of 2 mm in diameter was used.

The specimen was annealed in vacuum at 1000°C for two hours to take off internal stress and then held for about 10 minutes at a specified temperature from which it was quenched. The number of the vacancies thus produced can be considered to correspond to the concentration in the thermal equilibrium at that temperature. The quenching was done by letting the specimen drop into a low temperature bath containing iced-brine water or ethylene glycol whose temperature was about −10°C. Even immediately after quenching, the complete thermal demagnetization was not performed but the specimen was slightly magnetized to about 1 gauss because of earth's magnetic field.

To observe the change of the magnetization occuring during a prolonged time after quenching, it is necessary to produce over the specified period a steady magnetic field, whose strength corresponds to the initial permeability range of the specimen since in this range the magnetic property is most structure-sensitive. The production of such a field was rather difficult, so that we used earth's magnetic field of which the intensity is 0.310 Oe at Kyoto district where our laboratory is located and whose fluctuation during one day is less than 3×10^{-4} Oe except when some strong earth magnetic storms occur.

A sensitive satatic magnetometer was employed to measure the change in magnetization of the specimen by mounting a quenched wire (the specimen) and a well-annealed wire as shown in Fig. 1. In such orientations the couple between the latter wire and the upper magnet of the astatic magnetometer may be balanced by the couple between the former wire and the lower magnet. The only couple that changes with time is that between the specimen and the lower magnet, and the deflection of the astatic magnetometer can be attributed to the change in magnetization of the specimen. The sensitivity of the astatic magnetometer is very high, being in general higher than 10^{-8} Oe per mm scale. The precise adjusting technique has been fully described in Kumagai and Kawai's paper[8].

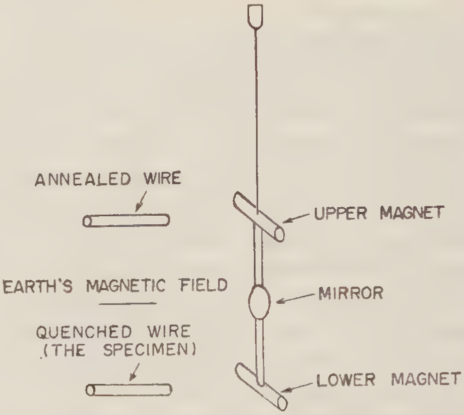

Fig. 1. Schemaic diagram showing the mounting of the specimen on the astatic magnetometer.

After quenching from high temperature, the specimen was mounted rapidly on the astatic magnetometer and then the measurement was done for about ten days or more at room temperature.

§ 3. Results and Discussions

Observations with the astatic magnetometer on specimens quenched from various temperatures showed that the intensity of magnetization increased with time in a quasi-logalithmic way as shown in Figs. 2 and 3.

The following facts seem to be sufficient in order to attribute these time changes of the magnetization to the effect of the gradual annihilation of the frozen vacancies. First, the time variation of magnetization could not be observed at all on a well annealed specimen of the same material. Secondly, the impurities involved in the specimens are so rare, as already stated, that neither the after effect due to the impurity migration nor the effect due to any precipitation could take place at room temperature. Thirdly, the quenched specimen shrink with time, which can be easily recongnized from the reduction of its volume[3]. This reduction of volume can be explained resonably on the basis of the annihilation of excess vacancies.

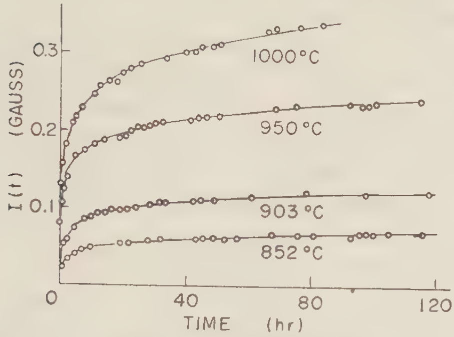

Fig. 2. Increase in magnetization, $I(t)$, at room temperature as a function of the time lapsed after quenching from various temperatures.

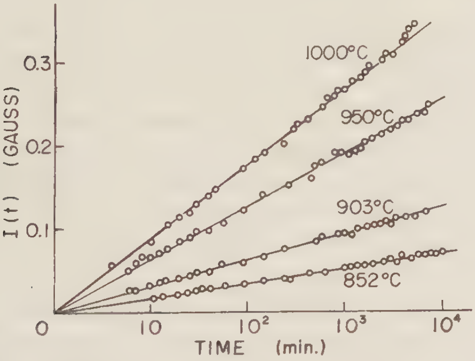

Fig. 3. $I(t)$ as a function of $\log t$ after qunching from various temperatures.

Now, the spontaneous magnetization around vacancies might have smaller intensity as compared with that without the defect, owing to the distortion of surrounding lattice points. The concentration of excess vacancies, however, is so small that the observed fairly large change of the magnetization can not be ascribed to the change in spontaneous magnetization. It may presumably be associated with the domain boundary displacements. Thus, the phenomena may be a kind of the magnetic aging or after-effect. The analysis of this effect has already been treated by several authors. Assuming that distribution of the relaxation times of domain walls is constant over a wide region, the change of the magnetization I, with time, t, can be expressed as follows[9] :—

$$I(t)=AI_0t\,, \quad \text{for very small } t, \qquad (1)$$

$$I(t)=BI_0(\log t+C)\,, \quad \text{for medium } t, \qquad (2)$$

$$I(t)=I_0\left\{1-D\frac{\exp(-t/E)}{t}\right\}\,, \quad \text{for very large } t, \qquad (3)$$

where I_0 is the total change of magnetization, namely, the difference between the magnetization as determined immediately after quenching and that as obtained when the concentration of vacancies attains the thermodynamically equilibrium value at room temperature, and A, B, C, D, and E are constants which contain quantities relevant to the upper and lower limits of relaxation times. It may be reasonable to assume that the total change of magnetization, I_0, is in proportional to the concentration of frozen-in vacancies and expressed as

$$I_0=A_0\exp(-E_f/kT_Q)\,, \qquad (4)$$

where the constant A_0 is the product of the entropy factor and the proportional factor showing the concentration of vacancies, E_f the formation energy of a vacancy, k the Boltzmann constant, and T_Q the quenching temperature.

Since, after quenching, it takes several minutes to set the specimen on the magnetometer, no observation applicable to Eq. (1) was made. Next, by putting $t=\infty$ in Eq. (3), we obtain

$$I(\infty)=A_0\exp(-E_f/kT_Q)\,.$$

This expression corresponds to Eq. (4). Actual observations we made are applicable to Eq. (2), where t is of the order of 10^6 sec. The time dependence of the change in magnetization, therefore, is expected to be nearly linear with $\log t$ regardress the quenching temperature, T_Q, which differs from one to the other as shown in Fig. 3. It is also expected that the slope of the $I(t)$ curve becomes steeper as the quenching temperature rises, as indicated by Eqs. (2) and (4).

Logarithmic plot against $1/T_Q$ of the values of the changes of magnetization, I, obtained for the same t for all quenching temperatures yields a reasonably straight line as shown in Fig. 4. From the slope of this straight line, we can roughly estimate the value of E_f as about 1.4 eV, which is in good agreement with the result obtained from the data on the volume contraction after quenching[3]. Moreover, the obtained E_f value shows a fairly good correspondence with the activation energy for self-diffusion, which is 2.7 eV according to Burgess and Smoluchowsky[10], since it is well known that the formation energy of vacancy in close-packed metals is about one half of that required in self-diffusion. It can be concluded, therefore, that the observed change of magnetization is caused by the disappearance of excess vacancies doped in the specimen.

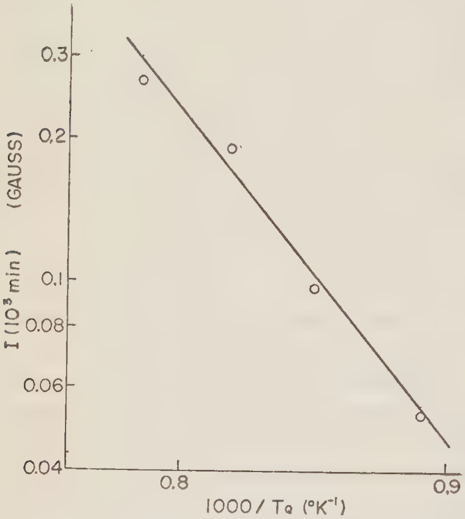

Fig. 4. Semilogarithmic plot of the increase of magnetization for $t=10^3$ min as a function of reciprocal of the quenching temperature.

The above-mentioned analysis is entirely phenomenological; no physical interpretation as to the domain wall displacements associated with the annihilation of excess vacancies has not yet given. Vacancies absorbed into grain boundaries have no contribution to the magnetic change because the domain boundaries are already fixed at grain boundaries. The clustering of vacancies would not occur in the present case bacause of the low concentration of excess vacancies. The only origin of the change may be due to the domain wall displacements associated with the dislocation movements generated by the absorption of vacancies.

When quenched-in vacancies would migrate in the specimen and encounter edge dislocations in which they are absorbed, we can expect the climbing of the edge dislocations perpendicular to their slip planes, if a sufficient number of jogs exist in the dislocations. The climbing of the dislocation without thermal jogs is to occur through jogs which were created previously in the dislocations through their crossing with screw dislocations. Such a climbing, however, needs so large activation energy that it would hardly occur. However, according to Seeger[11], the activation energy for jog formation in nickel may be far smaller than that required in self-diffusion, suggesting that there always exist a sufficient number of jogs which facilitate the climbing of the dislocations. Accordingly, the climbing of the edge dislocation may be plausible even at room temperature where the present experiments were made.

It is, then, supposed that, at some stage during the annihilation process of the vacancies, a certain number of domains have their boundaries located and stabilized where edge dislocations exist, in other words, the domain walls being anchored by the dislocations[6]. When the climbing of the dislocations occurs in these domain boundaries, the former is followed by the latter. Consequently, the cause of the observed increase in magnetization may be domain boundary displacements accompanied by the climbing of the edge dislocations by which the domains with magnetization parallel to applied magnetic field expand.

Finally, if the change in magnetization is interpreted as stated above, the estimated order must agree with that observed. The crude order estimation of the probable value of I_0 will be available, though the following assumptions are required for the sake of simplicity. First, the domain walls responsible for the phenomena mentioned above are merely the 180° walls separated from each other by the distance of about 10^{-3} cm[12] and the total volume of a grain is divided only by the plane 180° wall which is always held flat even in its motion. Secondly, the edge dislocations have the density of 10^8 lines per cm^2[13]. Thirdly, the orientations of grains in the specimen, whose size is in the order of 10^{-2} cm, are at rondom. Lastly, one tenth of the excess vacancies whose concentration was estimated from the volume contraction are absorbed into the edge dislocations. Under these assumptions we can roughly estimate the change of magnetization to be in the range of the order of 10^{-1} gauss which agrees with the observed one.

Acknowledgement

The author wishes to express his hearty thank to Professor H. Takaki for his interest and encouragement during the course of the work. He is also greatly indebted to Professor J. Takamura, who suggested the problem and helped the measurements in the preliminary stage of this work. His acknowledgement is also given to Dr. N. Kawai who kindly constructed the astatic magnetometer and gave valuable discussions.

References

1) R. Maddin and A. H. Cottrell: Phil. Mag. **46** (1955) 735.
2) J. E. Bauerle and J. S. Koehler: Phys. Rev. **107** (1957) 1493.
3) J. Takamura: Metal Physics Japan **2** (1956) 112. (in Japanese)
4) R. C. Folweiler and F. R. Brotzen: Act. Met. **7** (1959) 716.
5) L. Néel: Cah. Phys. **25** (1944) 21, Ann. Univ. Grenoble **22** (1946) 299.
6) F. Vicena: Czechosl. J. Phys. **5** (1955) 480.
7) R. D. Heidenreich and E. A. Nesbitt: J. App. Phys. **30** (1959) 995.
8) N. Kumagai and N. Kawai: Mem. College Sci. Univ. of Kyoto **B 20** (1953) 305.
9) R. Becker and W. Döring: *Ferromagnetismus* (Springer, Berlin, 1939) 242 p.
10) H. Burgess and R. Smoluchowsky: J. App. Phys. **26** (1955) 401.
11) A. Seeger: *Defects in Crystalline Solids* (Rep. Bristol Conference, 1955) 391 p.
12) D. H. Martin: Proc. Phys. Soc. **70** (1957) 77.
13) P. B. Hirsch: Progress in Metal Phys. **6** (1957) 236.

JOURNAL OF THE PHYSICAL SOCIETY OF JAPAN, Vol. 16, No. 11, NOVEMBER, 1961

Study of the Phase Transition in $NaNO_2$ by Polarized Infrared Radiation

By Yoshiki SATO, Kazuo GESI and Yutaka TAKAGI

Division of Physics, Japan Atomic Energy Research Institute, Tokai-mura, Naka-gun, Ibaraki-ken, Japan

(Received June 26, 1961)

The absorption spectra of the fundamental ν_2 of the nitrite ions in $NaNO_2$ crystals were investigated over the temperature range between 25°C and 190°C with infrared radiation plane-polarized at various angles with respect to the crystallographic axes. Marked changes were observed around the transition point of 163°C. The contours of the absorption band tell us that the amplitude of the torsional oscillation of the nitrite ions around the a axis is fairly large as compared with the amplitude around the c axis. The amplitude around the a axis grows larger with increasing temperature, whereas that around the c axis remains very limited over the whole range of temperatures of experiments. The contours of the absorption band observed with polarized radiation parallel to the c axis show no trace of inversion doubling even in the high temperature phase. Hence the possibility of the tunneling of the N atoms through the potential hill was ruled out.

§ 1. Introduction

The phase transition of $NaNO_2$ was first observed by Strijk and MacGillavry[1),2)] and later Sawada and Nomura[3)] found that this substance showed ferroelectricity below the transition point of 163°C, the spontaneous polarization being parallel to the b axis. The crystal structure has been investigated by many workers.[1),2),4)–8)] The space groups of the two phases are C_{2v}^{20} and V_h^{25}, respectively. The NO_2^- ion is a symmetric non-linear group and lies parallel to the bc plane. The bisectrix of the angle ONO is aligned to, say, $+b$ axis below the transition point, whereas parallel to either $+$ or $-b$ axis with equal probability above the critical point. This is a kind of order-disorder transition, and the change of the long range order with temperature has recently been determined by Shibuya.[9)] The reorientation of the group in the transition may be carried out through either a single or composite process of (1) the rotation of the NO_2^- ions around the a axis, (2) the rotation of the NO_2^- ions around the c axis, and/or (3) the tunneling of the N atoms through the potential barrier between the two equilibrium configurations.

Betsuyaku and Itoh[10)] supported the process (2), based upon their NMR observation of Na^{23} in this substance.

If the process (2) is the actual one, the amplitude of the torsional vibration of the nitrite ions around the c axis should grow larger with increasing temperature until the ions can assume with equal probability the opposite orientations above the transition point. If on the other hand the process (1) is the actual one then it should be the amplitude around the a axis that grows with increasing temperature. We can study the details if we use the polarized radiation, because the transition moment of the bending vibration of a nitrite ion, which is usually denoted by ν_2, is parallel to the bisectrix of the angle ONO. It is well established by many workers that the nitrite ions almost retain normal modes of vibration of the isolated ions, and that the three fundamental vibrations ν_1, ν_2, and ν_3 turn out to be almost independent of the partner cations. Among them the ν_2 band is most favourable to the present purpose because it is sharp enough and suffers little overlapping with the other bands.

If, on the other hand, the N atom tunnels through a potential hill between the two oxygen atoms in the same group, each degenerate energy level associated with two potential wells on both sides of the hill splits into two levels by a tunnel effect. The ν_2 band must split into two peaks, or even in the case of insufficient separations, it must become broader at least.

We have measured the contour of this band at various temperatures and at various setting of single crystal specimens with respect to the plane of polarization of the infrared radiation.

§ 2. Experimentals

Single crystals of $NaNO_2$ were grown by means of Kyropoulos method from molten salt of reagent grade, rated as more than 98% pure, in a platinum crucible under an atmosphere of dry air, and were cooled very slowly to room temperature at a rate of about 1°C/hour. They were clear, transparent and slightly yellow. After determination of the crystallographic axes through the use of cleavage planes (101), the specimens were cut out and carefully etched with an alcohol-water solution. Their areas ranged from 2×5 mm² to 10×10 mm² and average thickness from 150 to 250 μ.

The absorption spectra of the ν_2 mode of the nitrite ion were recorded on a double beam infrared spectrometer, the Koken Model #401G, which is equipped with a Boush & Lomb replica grating and a potassium bromide fore prism (covering 3955～560 cm⁻¹ frequency range) in combination with a silver chloride polarizer as described by Makas and Shurcliff.[11] The crystal was set successively at various angles with respect to the plane of polarization. Measurements were undertaken by the conventional method or with a micro-illuminator, both equipped with a high temperature cell, so that the specimens could be maintained at appropriate temperatures between 25°C and 190°C. The temperature of the heating block was measured by a copper-constantan thermocouple of very fine wire whose junction was embedded between the cell and the specimen. Wave length was calibrated against the 10.5 μ vibration-rotation spectrum of ammonia. The calibration was checked periodically.

§ 3. Results and Discussions

The absorption bands observed with specimens cut perpendicularly to the *a* and *c* axes, respectively, are shown in Figs. 1 and 2. Each curve was obtained with radiation polarized along the specified direction, the angle of which was measured from the *b* axis.

The vibration spectra of crystals of $NaNO_2$ have been studied by Newman[12], Bailey and Thompson[13], Weston and Brodasky[14], and Greenberg and Hallgren[15]. They identified the bands at 831 cm⁻¹, 834 cm⁻¹, 828.4 cm⁻¹, and 826 cm⁻¹, respectively, as the ν_2 band associated with the bending vibration. Sidman[16),17)]

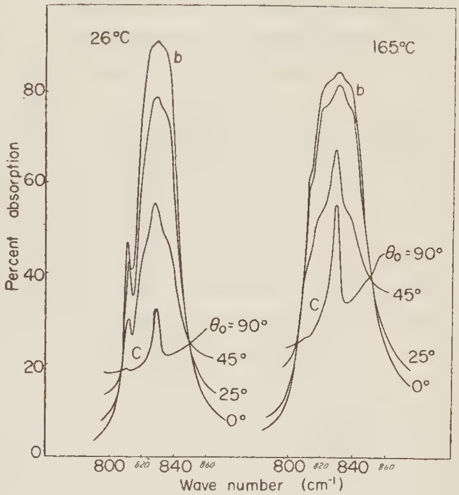

Fig. 1. Contours of the ν_2 band of the NO_2^- ions in $NaNO_2$ single crystal plates cut perpendicularly to the *a* axis. θ_0 denotes the angle of plane of polarization measured from the crystallographic *b* axis.

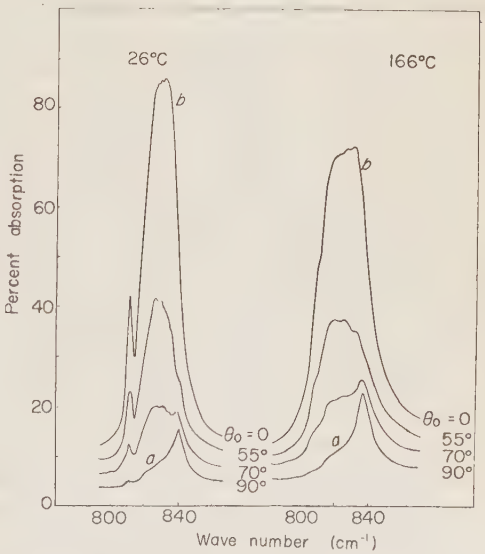

Fig. 2. Contours of the ν_2 band of the NO_2^- ions in $NaNO_2$ single crystal plates cut perpendicularly to the *c* axis. θ_0 denotes the angle of plane of polarization measured from the crystallographic *b* axis.

and Tomotsu *et al.*[18] obtained respectively $829 \pm 2\,\mathrm{cm}^{-1}$ and $830\,\mathrm{cm}^{-1}$ from a fine structure of the fluorescence spectra ($\pi^* \rightarrow n$ transition). The discordance in their wave numbers may be due to the difference in temperatures at which their measurements were carried out. In the present experiment, an extremely sharp peak as shown in the c spectrum in Fig. 1 should no doubt be assigned to the ν_2 band. Our result is $826\,\mathrm{cm}^{-1}$ at room temperature. As seen clearly in Fig. 1, considerable absorption is observed even for the radiation polarized along the c axis, whereas no definite amount of absorption can be detected if the radiation is polarized along the a axis. The reason for the appearance of the ν_2 band in the c polarization should be sought for neither in incompleteness of the polarization nor in an inaccuracy of crystal cutting, because both failures, if any, must be negligible, since the temperature dependence of the peak intensities observed with the b polarization is entirely different from that obtained from the c polarization (see Fig. 3). The intensity in the c polarization can, therefore, be interpreted only in terms of torsional oscillation of the nitrite ion around the a axis. The rotation around the c axis seems to be highly restricted.

In addition, there is no trace of inversion doubling. The half-width of the c spectrum of the vibration ν_2 remains unchanged over the whole range of the temperatures of experiments. The contour can be well approximated with a Lorentzian curve with a half-width of $6\,\mathrm{cm}^{-1}$. It is known that the height of potential hill for inversion of ammonia is 0.25[19] ev and the force constant for the corresponding bending mode is 0.5 md/A[19]. If the proportionality holds, we can estimate that the height of the potential hill for inversion of nitrite ion may be about 1 ev, for the force constant for the bending mode turns out to be 1.7 md/A. This barrier seems too high for an inversion to occur.

The low-frequency peak at $808\,\mathrm{cm}^{-1}$ probably originates from isotopic molecule containing N^{15} instead of N^{14}. The separation from the main peak, $19\,\mathrm{cm}^{-1}$, is in good agreement with the calculated value, $22\,\mathrm{cm}^{-1}$, based upon the Urey-Bradley type potential function. However, the ratio of integrated intensities, 1/120, obtained from a well separated curve, is nearly three times as large as that expected from the known isotopic abundance ratio, 1/350.

A weak band located at $840\,\mathrm{cm}^{-1}$ in the a spectra may be assigned to the ν_2 band of NO_3^- ions contained as impurities. This band is weak in a sample just after the preparation, but becomes more appreciable after a few weeks. In addition, other bands of the nitrate ions, a band at $720\,\mathrm{cm}^{-1}$ and those in the region 2,000 to $2{,}500\,\mathrm{cm}^{-1}$, are also perceptible. However, the fundamental band in the region $1{,}000\,\mathrm{cm}^{-1}$ are so badly disturbed by very strong bands ν_1 and ν_3 of the nitrite ions that they can hardly be identified. From the dichroism shown by these bands, we can conclude that the nitrate ions lie in the bc plane and one of the three N-O bonds is on the b axis. The temperature dependence of the peak intensity of this band is shown in Fig. 4. This band becomes stronger with increasing temperature. The fact tells us that the ν_2 mode of the nitrate ions couples more strongly with lattice mode with increasing temperature.

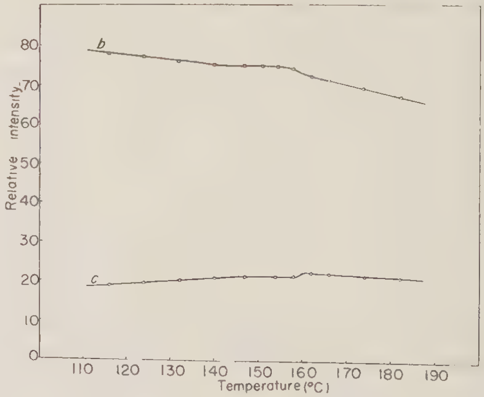

Fig. 3. Dependence on temperature of the intensities of the b and c spectra.

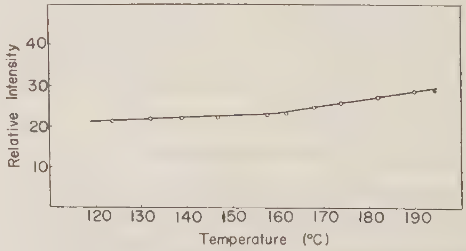

Fig. 4. Temperature effect on the intensity of the ν_2 band of NO_3^- contained as impurity in single crystals of $NaNO_2$.

Two shoulders are seen in the *b* spectra in Figs. 1 and 2. They have approximately equal intensity and are symmetrically disposed with respect to the center of the ν_2 band of the nitrite ion. They can be interpreted as a summation and a difference band combined with a certain lattice vibration, whose transition moment is parallel to the *b* axis. They disappear in the *c* spectrum.

Fig. 5 shows the dichroism and temperature dependence of another band observed at 972 cm^{-1}. This band can be assigned to a summation band specifically combined with the ν_2 band, because a band which might correspond to a difference band can also be observed at 730 cm^{-1} and because the intensity of the 972 cm^{-1} band decreases with increasing temperature. As seen from the dichroism, the transition moment of this band lies parallel to the *c* axis. This may be assigned to the torsional oscillation of the nitrite ion as a whole around the *a* axis, for the frequencies associated with the translational motions must be far lower. Hence we obtain the value 145 cm^{-1} for the frequency of the torsional vibration of the nitrite ion around the *a* axis.

Tanisaki[20] has recently found that "a micro domain structure", something like the antiphase domain in AuCu alloys, persists somewhile above the transition point. Hoshino and Shibuya[21] have carefully measured thermal expansion of the lattice and found that there is another transition point at 178°C. We[22] also observed that dielectric constant of this substance shows an anomaly at the same point. But so far as the infrared absorption was concerned no trace of anomaly could be detected around this temperature.

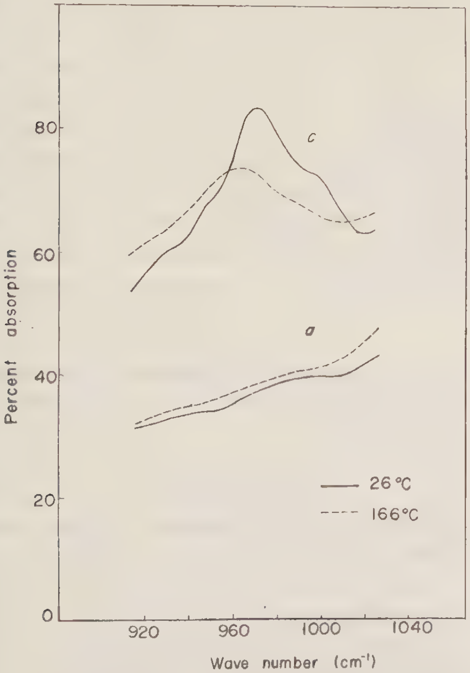

Fig. 5. Temperature dependence and dichroism of the band centered at 927 cm^{-1} measured in the *ac* plane of $NaNO_2$.

§ 4. Distribution Function of the Orientation of NO_2^- Ions

If the probability of finding the bisectrix of a NO_2^- ion at a direction θ is represented by $p(\theta)d\theta$, in which the angle θ is measured from the *b* axis in the crystallographic *bc* plane, $p(\theta)$ is written as follows:

$$p(\theta)=\sum_v|\Psi_v(\theta)|^2\exp(-E_v/kT)/\sum_v\exp(-E_v/kT)$$

where $\Psi_v(\theta)$ is the eigenfunction describing the state of the rotator which carries out an oscillation in a potential well determined by its environments, E_v is the eigenvalue, and the suffix v is the quantum number. If the plane of polarization of infrared radiation is set so as to make an angle θ_0 with the *b* axis, the observed band intensity should be in proportion to the quantity

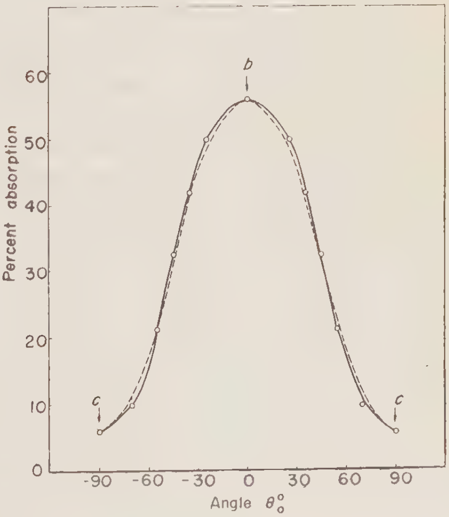

Fig. 6. Observed (solid curve) and calculated calculated (broken curve) intensity of the ν_2 band in the *bc* plane as a function of polarizer angle measured from the *b* axis.

$$\int p(\theta)\cos^2(\theta-\theta_0)\,d\theta=\frac{1}{2}(1+a\cos 2\theta_0),$$

$$a=\int p(\theta)\cos 2\theta d\theta.$$

The variation of the intensity of the band in the *bc* plane is shown in Fig. 6 as a function of θ_0 We see that the solid curve (observed intensity) can be well approximated by the broken curve (calculated by the above formula). I_c, the absorption intensity for the radiation with the polarization perpendicular to the *b* axis, has a non-zero value unless the bisectrix of the nitrite ions are strictly confined on the *b* axis. The larger is the amplitude of the torsional oscillation, the greater is the intensity observed at right angle to the *b* axis.

As seen in Fig. 3, I_c increases with increasing temperature in the low temperature phase, changes discontinuously at the transition point, and then decreases very slowly above this point. On the other hand, I_b decreases with increasing temperature in the low temperature phase, showing more or less abnormal behaviors around the transition point. The rate of decrease in the ferroelectric phase is smaller than that in the paraelectric phase.

The temperature dependence of the intensities of the absorption band may surely be a result caused by many complicated origins. But we may be justified in regarding the ratio I_c/I_b as determined mainly by the change of the potential curve, for all causes other than that may influence both I_c and I_b in very similar manners. This ratio is shown in Fig. 7 (b). We can see that the potential well becomes shallower with increasing temperature. If, for the sake of simplicity, we assume the form $p(\theta)=\exp(-\mu E\cos\theta/kT)$ where μ denotes the dipole moment of the nitrite ion and E the effective field acting upon it, we can easily obtain the values of $\mu E/k$ by comparing the calculated values with the observed intensity ratios. The result is shown in Fig. 7 (a). It first decreases rather rapidly and then slowly as temperature approaches the transition point, changes discontinuously at this point, and afterwards maintains a constant value in the high temperature phase.

If the intensities I_b and I_c are extrapolated to higher temperatures, they will intersect at around 690°K, we can thus estimate the depth of the potential well at about 480 cm^{-1}. Seeing that the change of I_c/I_b is rather slight (Fig. 7 (b)), we may suppose this gives a rough estimate of the potential well over the whole range of temperatures covered by the present investigation. The potential well in the *ac* plane must be very deep, because the intensity of the *a* spectrum is always very weak and remains so even above the transition temperature. This conclusion is supported by another experiment; no appreciable change was detected in the *a* spectrum near the transition point even when an *ac* field of about 8,000 v/cm was applied externally parallel to the *a* axis during the absorption measurement.

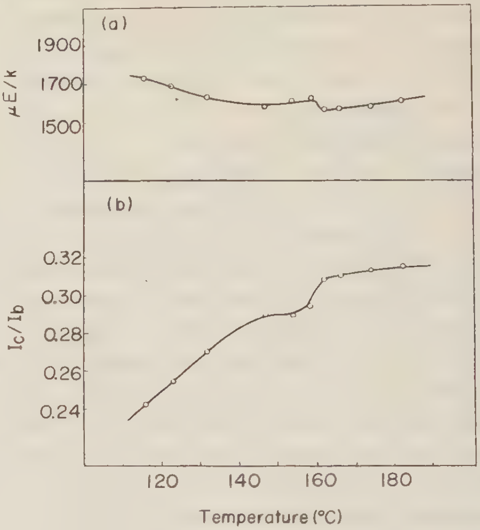

Fig. 7. (a) Variation of the $\mu E/k$ in °K with temperature.
(b) Variation of the intensity ratio I_c/I_b with temperature.

Acknowledgement

The authors wish to express their hearty thanks to Mr. H. Betsuyaku for his helpful discussions.

References

1) B. Strijk and C. H. MacGillavry: Rec. trav. chim. **62** (1943) 705.
2) B. Strijk and C. H. MacGillavry: Rec. trav. chim. **65** (1946) 127.
3) S. Sawada, S. Nomura, S. Fujii and I. Yoshida: Phys. Rev. Letters **1** (1958) 320.
4) G. E. Ziegler: Phys. Rev. **38** (1931) 1040.
5) G. B. Carpenter: Acta Cryst. **5** (1952) 132.
6) M. R. Truter: Acta Cryst. **7** (1954) 73.

7) B. C. Frazer, R. Ueda and M. I. Kay: Presented at the Meeting of the Physical Society of Japan, held at Sapporo, Sept. 26–28, 1960.
8) M. I. Kay and B. C. Frazer: Acta Cryst. **14** (1961) 56.
9) I. Shibura: J. Phys. Soc. Japan **16** (1961) 490.
10) H. Betsuyaku and J. Itoh: to be published.
11) A. S. Makas and W. A. Shurcliff: J. Opt. Soc. Amer. **45** (1955) 998.
12) R. Newman: J. Chem. Phys. **20** (1952) 444.
13) C. R. Bailey and J. W. Thompson: Nature **135** (1935) 913.
14) R. E. Weston and T. F. Broadsky: J. Chem. Phys. **27** (1957) 683.
15) J. Greenberg and L. J. Hallgren: J. Chem. Phys. **33** (1960) 900.
16) J. W. Sidman: J. Amer. Chem. Soc. **78** (1956) 2911.
17) J. W. Sidman: J. Amer. Chem. Soc. **79** (1957) 2669, 2675.
18) T. Tomotsu, M. Hirata, S. Makishima and S. Shionoya: Presented at the Meeting of the Physical Society of Japan, held at Sapporo, Sept. 26–28, 1960.
19) G. Herzberg: "*Infrared and Raman Spectra of Polyatomic Molecules*" (D. Van Nostrand Company, Inc., New York, 1945), pp. 177, 224.
20) S. Tanisaki: J. Phys. Soc. Japan **16** (1961) 579.
21) S. Hoshino and I. Shibuya: J. Phys. Soc. Japan **16** (1961) 1254.
22) Y. Takagi and K. Gesi: to be published.

JOURNAL OF THE PHYSICAL SOCIETY OF JAPAN, Vol. 16, No. 11, NOVEMBER, 1961

Current–Voltage Characteristics of Plastically Deformed Germanium *P*-N Junctions

By Osamu RYUZAN

Semiconductor Dep., Kobe Kogyo Corp., Kobe

(Received June 29, 1961)

The influence of dislocations which were introduced into germanium crystal by plastic deformation on the current-voltage characteristics of the *p-n* junction was investigated experimentally using grown junction diode bars. It was revealed that the theory of carrier generation and recombination in a *p-n* junction was applicable to explain the junction characteristics. When the width of the transition layer in a *p-n* junction was as great as about 200 micron, the anomalous characteristics were observed after plastic deformation by twisting. Some considerations were made about the *p-n-p-n* structure which was produced in the original *p-n* junction region by plastic deformation.

§ 1. Introduction

General characteristics of a *p-n* junction are affected by dislocations and defects in the crystal in a greater or less degree. The current-Voltage characteristics of a *p-n* junction containning many dislocations will deviate from the ideal rectification characteristics. Average dislocation densities are $10^2 \sim 10^3\,\mathrm{cm}^{-2}$ in ordinary germanium single crystals and they are rather too small to give appreciable variation in junction characteristics. It is possible to introduce many dislocations into a crystal up to the order of $10^6 \sim 10^8\,\mathrm{cm}^{-2}$ by plastic deformation. Dislocations in the deformed crystal are distributed over the *p*-type, *n*-type and the transition region, however, it is the last case that give significant effects on the junction characteristics.

Crystallographical structures of the edge-type dislocations in germanium and their influence on electrical properties of the crystal have been studied fairly well by many peoples.[1] It is known that dislocations act as acceptors in germanium and in *n*-type crystals the acceptor sites along the dislocation are partially filled and the dislocation line is negatively charged. The charge is neutralized by a cylindrical space charge of fixed donors around the dislocation. Dislocations in a crystal, therefore, have significant effects on the energy band structure[2] and the mobility of carriers[3]. On the other hand, it has been confirmed that dislocations produce the recombination centers and the minority carrier lifetime is drastically decreased by plastic deformation[4].

It is expected that the current-voltage characteristics of a *p-n* junction which was deformed plastically deviate from the ideal case of the diffusion model. These were confirmed experimentally and some quantitative explanations were given. Furthermore anomalies in the forward characteristics which have been observed in the special *p-n* junction are described and discussed.

§ 2. Experimental Procedures

The samples used in these experiments were obtained from a grown junction crystal pulled in the ⟨111⟩ or ⟨100⟩ direction. In the *p*-type region of the crystal indium was doped and excess antimony was added in the *n*-type region. Resistivities in both regions were nearly equal and about 0.2 ohm-cm at room temperature. Diode bars shown in Fig. 1, were cut from the crystal whose dimensions were about 2 mm × 3 mm × 20 mm with the long axis of the bars along the ⟨111⟩ or ⟨100⟩ direction. The *p-n* juction plane is located near the center of the bar and laid on the (111) or (100) plane. The samples were cleaned by etch and covered with films consisting of vacuum-evaporation of gold in order to minimize effect of contamination on the samples at elevated temperature. The bar was placed in stainless steel jaws as shonw in Fig. 2 and heated in argon atomosphere to 600°C in a furnace for a plastic deformation. The samples were plastically deformed by twisting about their long axes or by bending about an arbitraly axis parallel to the junction plane. The temperature of the sample was indicated by a thermocouple attached near it and recorded in a recorder during this process. The rate of cooling to 300°C was about 300°C/min. and all processes were performed within five minutes. All samples were plastically deformed under the same conditions. Deformations were mainly performed by twisting for the following reasons; (1) it is convenient to introduce many dislocations and to control. (2) very little has been known about the experiments by twisting.

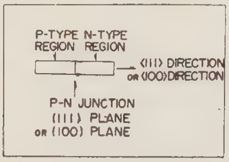
P-TYPE REGION
N-TYPE REGION
⟨111⟩ DIRECTION OR ⟨100⟩ DIRECTION
P-N JUNCTION (111) PLANE OR (100) PLANE

Fig. 1. A germanium grown junction diode bar.

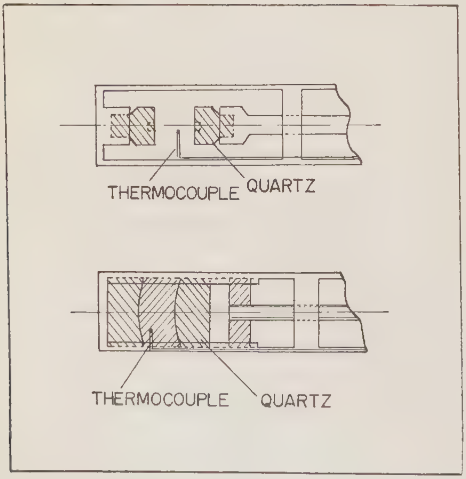

Fig. 2. Tools used for plastic deformation of germanium. The upper is a twisting tool and the lower is a bending one.

After measurements of the twist angle or the bending radius, the samples were ground to remove gold-alloy layer on their surfaces. The bar was then etched in a mixture of 5 parts nitric acid, 5 parts hydrofluoric acid, and 7 parts acetic acid to reveal the *p-n* junction. Platinum leads were fastened near the junction by soldering for voltage terminals and at two ends of the bar for current terminals. The sample was then cleaned by etch in the above mixture for one minute followed by a rinse in deionized water for ten minutes and dried in a desiccator for 12 hours.

The current-voltage characteristics of the junction and other characteristics were measured on the sample soaked in silicone-resin (DC-200). It may be well understood that gold films themselves have no effect on the properties of germanium crystal and the junction characteristics under the conditions of the heat-treatment in which plastic deformations were performed. For the sake of abbreviation, the plastic twisting about the ⟨111⟩ axis as twist axis (where the function is parallel to (111) planes) is called ⟨111⟩ twist, and the twisting about the ⟨100⟩ axis as twist axis (where the junction is parallel to (100) planes) is called ⟨100⟩ twist throughout this paper.

§ 3. Experimental Results

(1) Current-voltage Characteristics of a plastically Deformed *P-N* junction

The current-voltage characteristics of a plastically deformed *p-n* junction are appreciably different in both forward and reverse directions from the characteristics before plastic deformation.

(a) very small applied bias ($|V|<kT/q$)

When the applied bias is less than kT/q, the current is proportional to the voltage and follows essentially the ohmic law as in the normal diode characteristics. The conductance at zero bias of twisted samples increases as the twist angle θ_t (degree/centimeter) increases. The forward characteristics are shown in Fig. 3 for the samples with various twist angles and for a few bent samples.

(b) small forward bias ($kT/q<V<\phi$)

As forward-bias increases to the built-in voltage ϕ, the current varies according to $\exp(qV/nkT)$, where n is between 1 and 2. The forward characteristics of the deformed samples are presented in Fig. 4 for ⟨111⟩ twist and in Fig. 5 for ⟨100⟩ twist. The characteristics of the bent samples are not very different from the characteristics of the twisted samples as shown in Fig. 6.

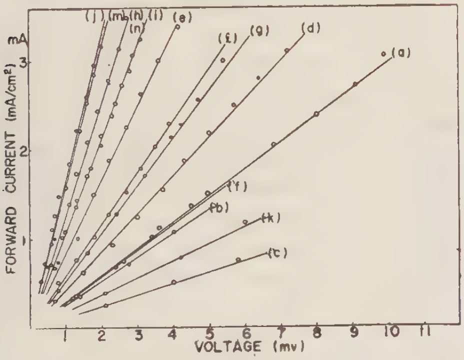

Fig. 3. Forward currents of plastically deformed diode bars under very small bias ($V<kT/q$) at room temperature.

(a)	G-707	(2)	⟨111⟩	9.3°/cm	Twisting
(b)	G-708	(2)	⟨111⟩	8.6	
(c)	G-711	(2)	⟨111⟩	4.8	
(d)	G-712	(2)	⟨111⟩	17.4	
(e)	G-722	(2)	⟨100⟩	14.2	
(f)	G-723	(2)	⟨100⟩	6.6	
(g)	G-724	(2)	⟨100⟩	10.8	
(h)	G-727	(2)	⟨100⟩	16.5	
(i)	G-728	(2)	⟨100⟩	15.4	
(j)	G-729	(2)	⟨100⟩	25.2	
(k)	G-730	(2)	⟨100⟩	8.7	
(l)	G-709	(2)	⟨111⟩	10 cm	Bending
(m)	G-714	(2)	⟨111⟩	7	
(n)	G-726	(2)	⟨100⟩	9	

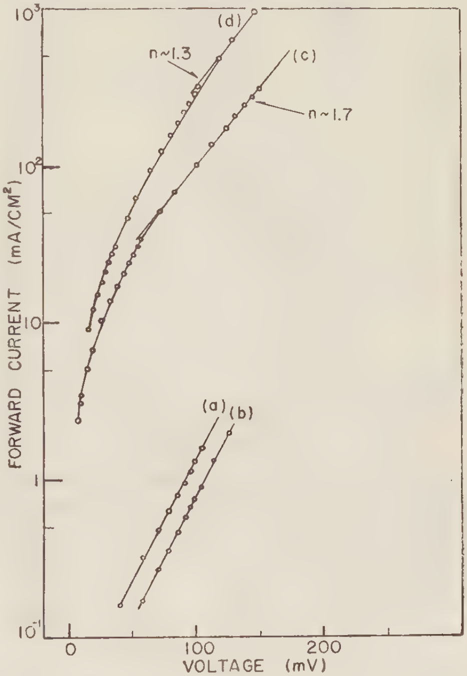

Fig. 4. Forward current-voltage characteristics of the ⟨111⟩ twisted samples at room temperature.

Curve	Sample	Twist	Angle
(a)	G-707 Before twist		——
(b)	G-712 Before twist		——
(c)	G-707 After twist	⟨111⟩	9.3°/cm
(d)	G-712 After twist	⟨111⟩	17.3°/cm

(c) Reverse bias ($|V|>kT/q$)

The reverse current increases linearly in the ohmic region followed by a region where the current increases slightly as the bias voltage increases and then increases according to about $V^{1/m}$ ($m=2\sim3$) as far as the soft breakdown region. The current voltage characteristics in the reverse direction are presented in Fig. 7 for ⟨111⟩ twisted samples, in Fig. 8 for ⟨100⟩ twisted samples and Fig. 9 for bent samples. The reverse current generally increased by plastic deformation, sometimes becoming about one hundred times as large as the original saturation current, and increased as the twist angle increased.

(2) Temperature Dependence of Reverse Current

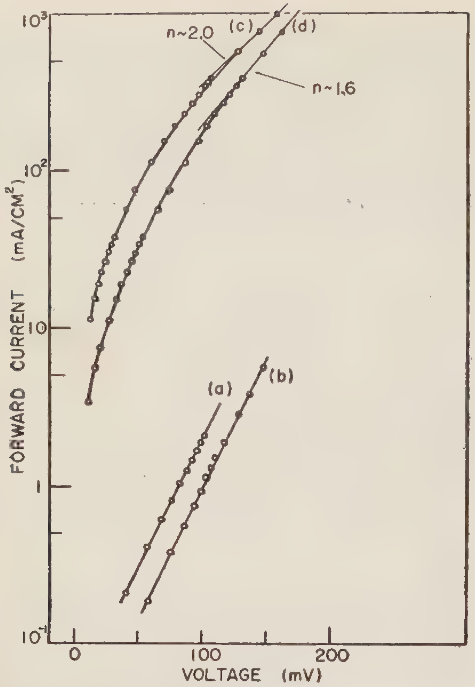

Fig. 5. Forward current-voltage characteristic of the <100> twisted samples at room temperature.

Curve	Sample	Twist	Angle
(a)	G-722 Before twist		——
(b)	G-723 Before twist		——
(c)	G-722 After twist	<100>	14.2°/cm
(d)	G-723 After twist	<100>	6.6°/cm

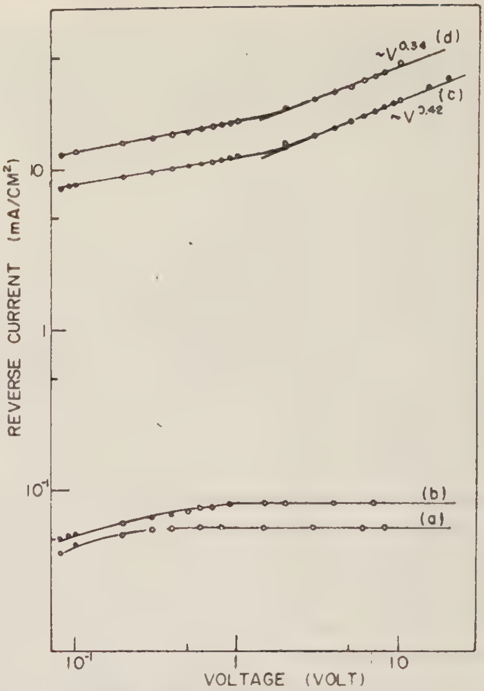

Fig. 7. Reverse characteristics of the <111> twisted samples at room temperature.

Curve	Sample	Twist	
(a)	G-712 Before twist	——	
(b)	G-708 Before twist	——	
(c)	G-708 After twist	<111>	8.6°/cm
(d)	G-712 After twist	<111>	17.4°/cm

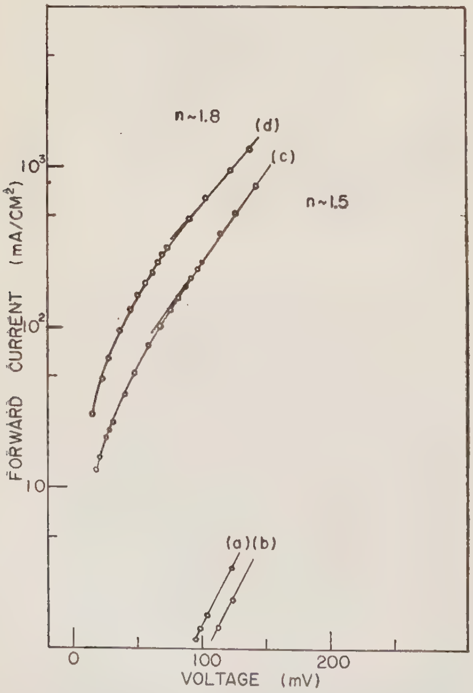

Fig. 6. Forward current-voltage characteristics of the bent samples at room temperature.

Curve	Sample	Radius
(a)	G-709 Before bend.	——
(b)	G-714 Before bend.	——
(c)	G-709 After bend.	10 cm
(d)	G-714 After bend.	7 cm

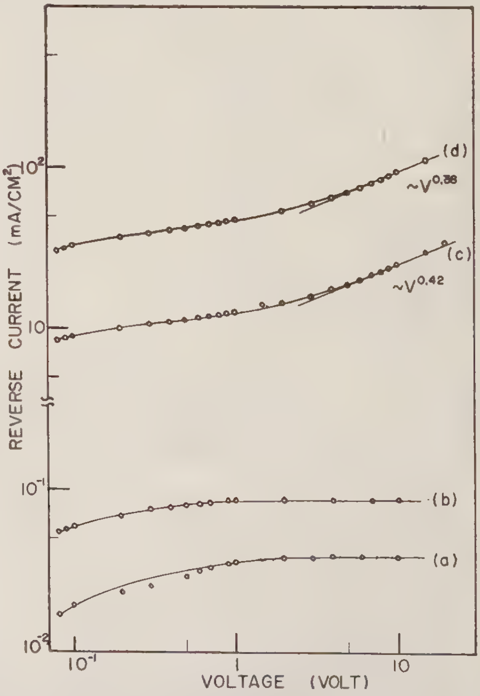

Fig. 8. Reverse characteristics of the <100> twisted samples at room temperature.

Curve	Sample	Twist	
(a)	G-723 Before twist	——	
(b)	G-722 Before twist	——	
(c)	G-723 After twist	<100>	6.6°/cm
(d)	G-722 After twist	<100>	14.2°/cm

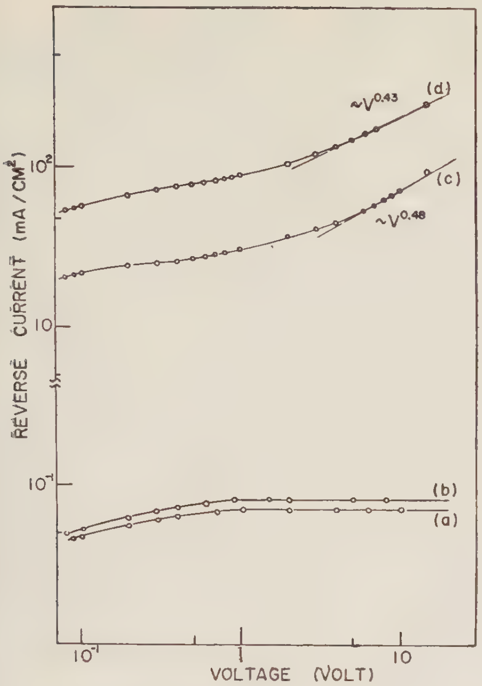

Fig. 9. Reverse characteristics of the bent samples at room temperature.

Curve	Sample	Radius
(a)	G-713 Before bending	——
(b)	G-714 Before bending	——
(c)	G-713 After bending	13 cm
(d)	G-714 After bending	7 cm

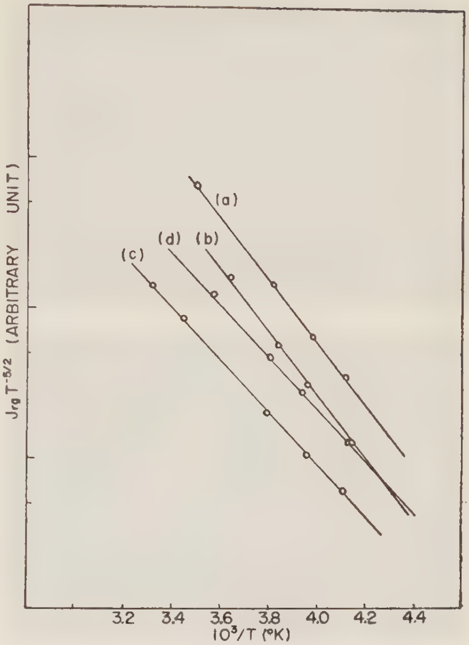

Fig. 10. Variation of reverse current at 2 Volt bias with temperature. $J_{rg}T^{-5/2}$ is plotted against T^{-1} for the ⟨111⟩ twisted and the ⟨100⟩ twisted samples.

Curve	Sample	Twist axis	θ_t (°/cm)	Slope (eV)
(a)	G-707 (2)	⟨111⟩	9.3	0.43
(b)	G-708 (2)	⟨111⟩	8.6	0.43
(c)	G-722 (2)	⟨100⟩	14.2	0.35
(d)	G-723 (2)	⟨100⟩	6.6	0.35

The variation of the reverse current in the deformed samples with temperature are shown in Fig. 10 for ⟨111⟩ and ⟨100⟩ twist. From the slope of these curves the energy difference between the trap level and the intrinsic Fermi-level can be determined as stated in later section. It should be noticed that the slope for ⟨111⟩ twist is some what different from the one for ⟨100⟩ twist

(3) Anomalies in Forward Characteristics

The results described in the section (1) and (2) were obtained about the deformed samples in which the width of the transition layer in the original *p-n* junction was about in the range 20 to 80 microns. For the samples deformed by ⟨111⟩ twisting in which the width of the transition region in the original junction was about 200 microns, a negative resistance was observed in the for ward current-voltage characteristic, that is, a small forward current similar to a saturation current in the reverse direction flowed until a critical voltage was reached where a sudden transition occured into a low-resistance branch resembling a forward diode characteristics before twist. On reducing the current below a certain minimum value, the characteristics changed back to the high-resistance branch. Some typical examples of the forward characteristics with a negative resistance are presented in Fig. 11. The breakdown voltage in forward direction and the forward current in the pre-break-down high-resistance part of the characteristics increases as the twist angle increases. The current-voltage characteristics were plotted in Fig. 12 with the twist angle as parameter. For the samples in which the width of the transition region in the original *p-n* junction was about or greater than 400 microns, no sharp breakdown was seen in forward direction before the beginning thermal breakdown. Moreover, these anomalies in forward characteristics were never seen for the samples which were merely heat-treated or twisted very slightly.

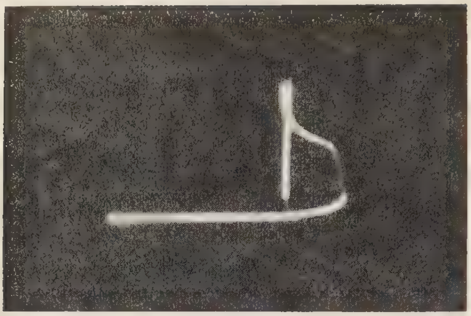

Fig. 11 (a).

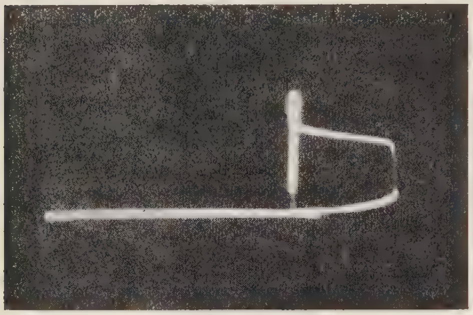

Fig. 11 (b).

Fig. 11. Oscilloscope display of the current-voltage characteristics with a negative resistance in forward direction.

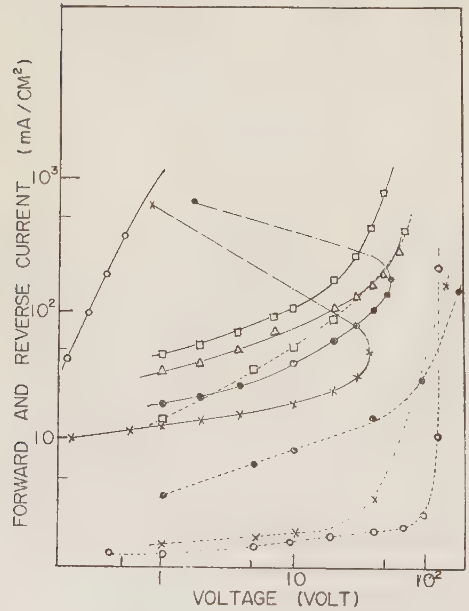

Fig. 12. Current-voltage characteristics of the <111> twisted sample with twist angle as parameter. Variation of the conductance at low level with twist angle seems to be different from the case seen in Fig. 3.

Sample G-106
○ 2°/cm —— Forward
× 9 ---- Reverse
● 18
△ 27
□ 40

§ 4. Discussions

When a germanium crystal was plastically deformed by twisting or bending, the minority carrier lifetime could be drastically reduced owing to the recombination centers which were introduced into the crystal. Sah, Noyce, Shockley[5] studied carrier generation and recombination in p-n junctions, and they predicted theoretically that for semiconductors with short lifetime, the current generated in the space charge region may be greater than the diffusion current under reverse bias and the recombination current is important at forward bias smaller than the built-in voltage. Assuming that these considerations may be applied for the current-voltage characteristics in the p-n junction which was plastically deformed, the experimental results obtained in § 3 (1), (2) are examined on the basis of the theory of carrier generation and recombination.

The ohmic current under very small bias ($|V|<kT/q$) is given by

$$J_{rg} \cong \frac{\pi}{2}\cdot\frac{q n_i W}{\phi\sqrt{\tau_{p0}\tau_{n0}}}\cdot V \qquad (1)$$

where the definition of symbols are as follows:

J_{rg}: recombination-generation current density in the space charge layer
q: magnitude of electronic charge
n_i: density of electrons or holes in an intrinsic specimen

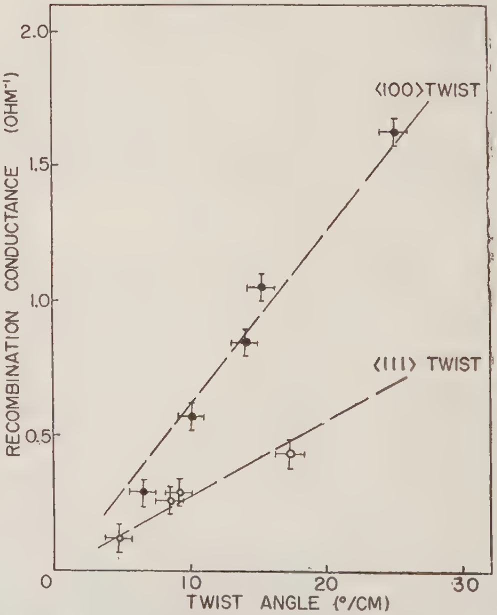

Fig. 13. Recombination conductance Vs twist angle.

W: width of the space charge layer
ϕ: built-in voltage
τ_{p0}: lifetime for holes injected into highly n-type specimen
τ_{n0}: lifetime for electron injected into highly p-type specimen

The recombination conductance is represented by the factor $(\pi/2)\cdot qn_i W/(\tau_{p0}\tau_{n0})^{1/2}\phi$. The values of this conductance obtained from Fig. 3 are plotted against the twist angle in Fig. 13. It is seen that the recombination conductance increases linearly with increasing twist angle in this range. When it is assumed that W and ϕ are hardly changed by the plastic deformation, and $\tau_{p0}=\tau_{n0}=\tau_0$, the trap density is increased linearly with the twist angle, as τ_0 is inversely proportional to the trap density. In Fig. 13 it should be noticed that the proportionality constant is larger for ⟨100⟩ twist than for ⟨111⟩ twist. Moreover dislocation density increases linearly with the twist angle, provided that the trap density is proportional to the dislocation density. This agrees with the experimental results obtained about the fraction of volume occupied by space charge tubes around dislocations by using Hall effect in n-type germanium which was plastically deformed by twisting. Assuming that W is 20 micron, and ϕ is 0.3 volt, then τ_0 becomes 0.1 microsecond when θ_t is about 9.3 degree per centimeter. For the bent samples, the recombination conductance is rather great in general as seen in Fig. 3.

At a forward bias greater than kT/q and less than ϕ, the recombination-generation current can be written as

$$J_{rg} \cong \frac{qn_i W}{\sqrt{\tau_{p0}\tau_{n0}}} \frac{2\sinh(qV/2kT)}{(\phi-V)q/kT}\cdot f(b) \qquad (2)$$

where

$$f(b)=\int_{z_1}^{z_2}\frac{dz}{z^2+2bz+1} \qquad (3)$$

$$b\cong\exp(-qV/2kT)\cosh\left[\frac{E_t-E_i}{kT}+\frac{1}{2}\ln\frac{\tau_{p0}}{\tau_{n0}}\right] \qquad (4)$$

$$z_{1,2}=(\tau_{p0}/\tau_{n0})^{1/2}\exp[\mp(\phi-V)q/2kT]\,. \qquad (5)$$

Here E_t is the energy level of the traps and E_i is the intrinsic Fermi level.

When the traps are located near the intrinsic Fermi level, that is, $E_t\cong E_i$, then

$$f(b)\cong\pi/2-b$$
$$b\cong\exp(-qV/2kT)\,.$$

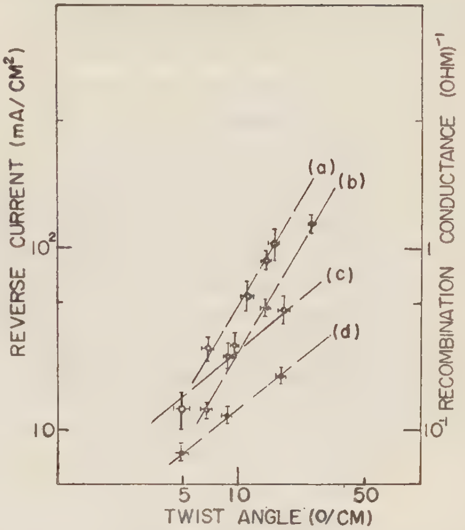

Fig. 14. Reverse current at 1 Volt bias *VS* twice angle. Variation of the recombination conductance is plotted together.
(a) Recombination conductance: ⟨100⟩
(b) Reverse current: ⟨100⟩
(c) Recombination conductance: ⟨111⟩
(d) Reverse current: ⟨111⟩

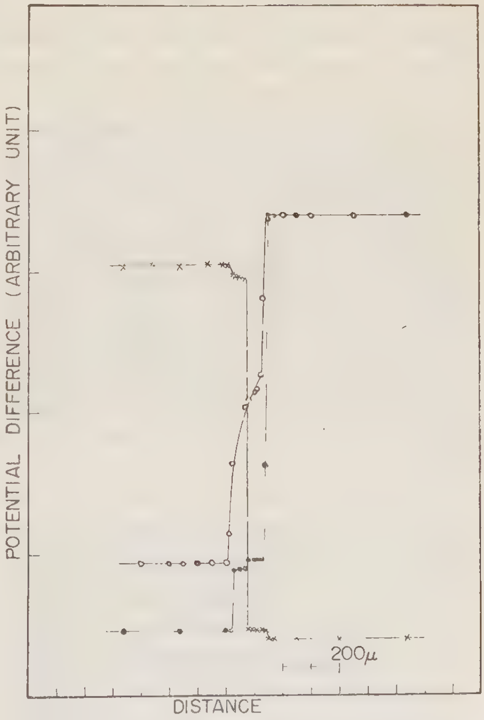

Fig. 15. Potential distribution across the junction under forward and reverse bias.

Sample G-353 (2) 4.7°/cm
—○——○— Reverse before twist
—●——●— Reverse after twist
—×——×— Forward after twist

The depletion layer width for an abrupt junction varies with the applied voltage as

$$W \propto (\phi - V)^{1/2}$$

so that from (2), J_{rg} varies approximately as

$$J_{rg} \propto \frac{\sinh(qV/2kT)}{(\phi-V)^{1/2}} \cdot \left(\frac{\pi}{2} - b\right) \qquad (6)$$

in this case. Thus the recombination current will vary slightly faster than $\exp(qV/2kT)$ under the bias of this range as can be seen from (6). An apparent $\exp(qV/nkT)$ dependence of the forward current shown in Figs. 4, 5, 6 may be explained by this argument.

At a reverse bias greater than kT/q, the recombination current is given by

$$J_{rg} = \frac{qn_i}{\sqrt{\tau_{p0}\tau_{n0}}} \cdot \frac{2kT}{q} \cdot \frac{W}{\phi - V} \cdot \sinh\left(\frac{qV}{2kT}\right) \cdot \frac{\ln 2b}{b} \,. \qquad (7)$$

Furthermore J_{rg} is written approximately as follows

$$J_{rg} \cong \frac{qn_i}{\sqrt{\tau_{p0}\tau_{n0}}} \cdot \frac{W}{2} \cdot \left[\cosh\left\{\frac{E_t - E_i}{kT} + \frac{1}{2}\ln\frac{\tau_{p0}}{\tau_{n0}}\right\}\right]^{-1} . \qquad (8)$$

Thus the recombination-generation current under the reverse bias in this range shows the same voltage dependence as the width of the space charge layer. The reverse voltage-current characteristics shown in Fig. 7, 8, 9 can be understood for the reason mentioned above.

The reverse current at 1 volt bias is plotted against the twist angle in Fig. 14 together with the recombination conductance shown in Fig. 13. The fact that the rates of increase of these quantities for the twist angle are almost the same indicates that the reasoning based on the theory of carrier generation and recombination is not wrong. In Fig. 14 the difference in the slope of the curves for ⟨111⟩ and ⟨100⟩ twist may be attributed to the difference in the electronic structures of germanium which is plastically deformed by twisting. Since n_i is proportional to $T^{3/2}\exp(-E_{G0}/2kT)$ where E_{G0} is the energy gap at 0°K,

$$\frac{d}{d(1/T)}\{\ln[J_{rg}(kT)^{-5/2}]\} = -\frac{E_{G0}}{2k} - \frac{E_t - E_i}{k} \cdot \tanh\left[\frac{E_t - E_i}{kT} + \frac{1}{2}\ln\frac{\tau_{p0}}{\tau_{n0}}\right]$$

is obtained from (7) approximately.

The activation energy of the traps, therefore, is obtained from the slope of a plot of the logarithm of the reverse current as a function of the reciprocal of temperature at a constant reverse bias. But the value of $E_t - E_i$ cannot be uniquely determined from this experiment since $\cosh[(E_t - E_i)/kT + \frac{1}{2}\ln\cdot(\tau_{p0}/\tau_{n0})]$ makes the sign uncertain. From Fig. 10, $|E_t - E_i|$ is 0.06 eV for ⟨111⟩ twist and 0.03 eV for ⟨100⟩ twist assuming that $E_{G0} = 0.75$ eV.

The anomalies in the forward characteristics described in § 3 (3) are rather special properties of a plastically deformed junction. The observed current-voltage characteristics are very like those of *p-n-p-n* switching diode. It is confirmed from the results of the following experiments that there exists actually a *p-n-p-n* structure in the *p-n* junction region which is plastically deformed by twisting.

(a) A measurement of the potential distribution

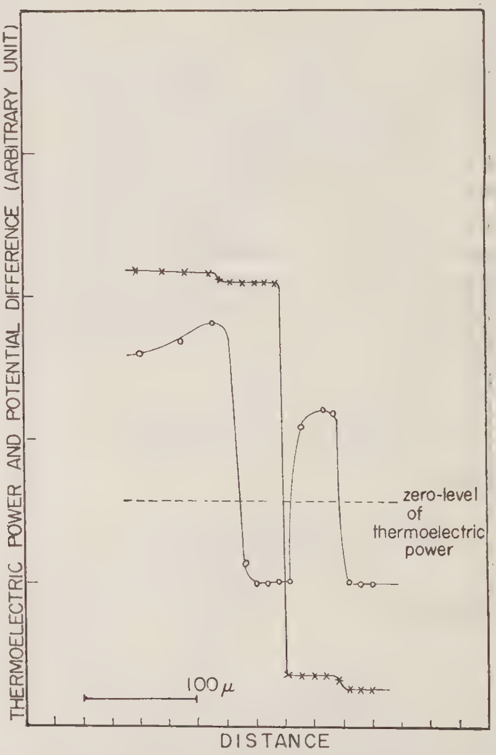

Fig. 16. Plot of the thermoelectric power together with potential distribution for reference.

Sample G-167 (2) 2.3°/cm
—○——○— Thermoelectric power
—×——×— Potential difference under forward bias

The potential difference between the two tungsten needleprobes which were pressure-contacted on each side of the *p-n* junction, was measured by a potentiometer. In Fig. 15 the potential difference between two probes was plotted, with one probe moved across the junction by a micro-manipulater.

(b) A measurement of the thermoelectric power

Thermoelectric power was measured in the same way as described above except that one of the probes was used as a hot probe. The relative variation of the thermoelectric power was shown in Fig. 16 together with the potential distribution.

(c) A measurement of the photo-response

The photo-reponse was measured illuminating the junction by a chopped light beam whose width was about 50 micron. The linear spot of light was adjusted to be parallel to the *p-n* junction and moved across it. The results of measurement was plotted in Fig. 17.

The newly produced -*n-p*-regions by twisting are in the transition region of the original *p-n* junction as seen in Fig. 15.

By a heat treatment of the sample, the anomalous characteristics in forward direction are changed as follows. About the samples which were heat-treated at 400°C for 1.5 hours and at 550°C for 66 hours in a vacuum of 1×10^{-5} mm Hg, no appreciable change of the anomalous characteristics was observed, but when the samples were heat-treated at 800°C for 3 hours, the anomalous characteristics disappeared and the normal diode characteristics before twist were almost recovered.

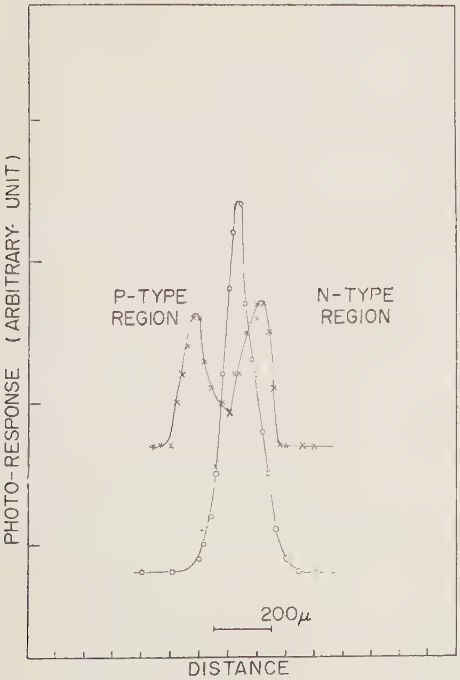

Fig. 17. Plot of the photo-response under forward and reverse bias.

Sample G-506 (2) 3.9°/cm
—○——○— Forward biased
—×——×— Reverse biased

It follows from the experimental results mentioned above that the anomalous current-voltage characteristics of the plastically deformed junction may be due to the dislocations or defects introduced into the crystal by the plastic deformation.

A metallographic examination of chemical etch was performed about the samples which were deformed by ⟨111⟩ twisting. They were etched in a solution of one part hydrofluoric acid and one part nitric acid at 80°C. The photomicrograph presented in Fig. 18 (a) illustrates the appearance of slip bands parallel to the intersections of (111) planes with the surfaces of the sample. Among them, slip bands perpendicular to the twist axis are most

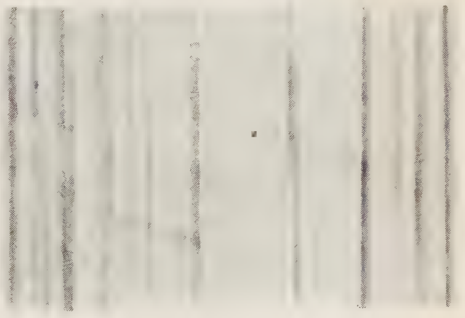

Fig. 18 (a). Photomicrograph of the (111) slip bands pattern revealed by chemical etch.

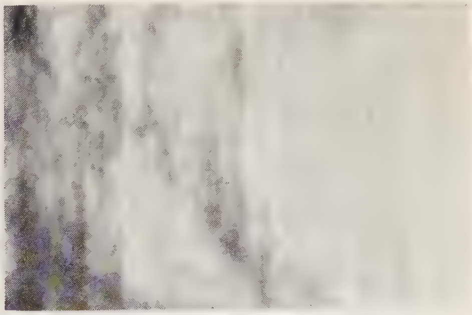

Fig. 18 (b). Photomicrograph of the specimen after heat-treatment at 800°C for 3 hours.

clear as shown in Fig. 18 (a). The average distance of the two closely-spaced slip bands is decreased as the twist angle is increased and changed in the range 120 microns to 60 micron or less. When the sample was heat-treated at 550°C the same slip band pattern was reproduced by the etch but after a heat treatment at 800°C for 3 hours, slip bands were hardly distinguished as shown in Fig. 18 (b).

A special case is considered where one slip band was produced in *n*-type region of the transition layer in a graded junction. If a slip plane is a plane with acceptors as a tilt boundary, the energy band structures in the junction can be represented as in Fig. 19. This corresponds to the cases shown in Figs. 15, 16, 17. Since the parallel slip bands are produced with a certain distance, the situation as shown in Fig. 19 can hardly be realized when the width of the transition layer is less than the mean separation of slip bands. When the width of the transition layer is much greater than the mean separation of slip bands, on the contrary, a structure similar to multiple-junctions may be produced in the transition region. This is the case illustrated in Fig. 20. It may be concluded from the considerations described above that the anomalies in forward characteristics of the *p-n* junction which was plastically deformed by twisting are associated with lattice misfits by slip on a (111) plane.

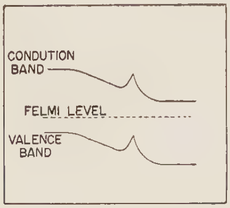

Fig. 19. A probable energy band structure of the twisted samples which have the anomalous characteristics in forward direction. The variations in local energy band are smoothed out.

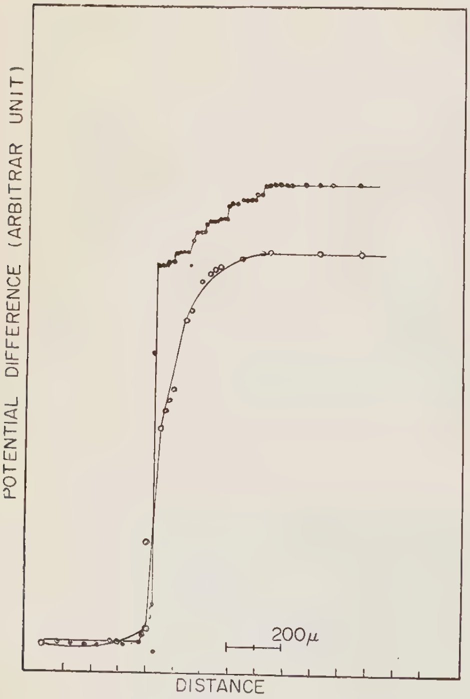

Fig. 20. Potential plotting of a twisted diode bar whose original width of the transition layer was about 400 micron.

Sample G-329 (2) 3.3°/cm
—○——○— Reverse before twist
—●——●— Reverse after twist

§ 5. Conclusions

Many dislocations or defects were introduced into germanium crystal with a *p-n* junction by plastic deformation and these effects on the current-voltage characteristics of the *p-n* junction were studied experimentally and discussed. Bernard[6] reported the results of measurements about soft breakdown of the plastically bent *p-n* junction which were not included in this paper.

The width of the transition layer of a *p-n* junction was found to be of importance with regard to the influence of dislocations on the current-voltage characteristics of a *p-n* junction. In ordinary grown junctions, dislocations introduced by plastic deformation of the crystal seem to have no explicit effects on the current-voltage characteristics of the *p-n* junction, but affect implicitly as recombination centers. When the width of the transition layer in a *p-n* junction is sufficiently large, the effects of the dislocations themselves on the current-voltage characteristics appear explicitly as in the case described in § 3 (3). The mechanism of an apparent -*n*-*p*-“ hook ” generation in the transition region of the junction is not known well. However, one of the probable models is presented in this paper. Recently Ota[7] has demonstrated a possibility of appearance of the anomalous characteristics in a forward current due to a dislocation with some simplifing assumptions.

It was found in the present experiments that electrical properties of the ⟨100⟩ twisted crystal are somewhat different from those of the ⟨111⟩ twisted crystal. Electrical properties of the plastically deformed germanium crystals which were twisted about the twist axes in different orientations are expected to be not the same.

Acknowledgement

The auther wishes to express his thanks to S. Maekawa for his helpful discussions and constant encouragements during this work and to T. Ota for his continued interest in this subject. He would like also to thank T. Maeda for the assistance in the measurements.

References

1) C. J. Gallagher: Phys. Rev. **88** (1952) 721, ibid. **92** (1953) 846. F. L. Vogel: J. Metals **8** (1956) 946. W. T. Read: *Dislocations in Crystals*(McGraw-Hill Book Company, Inc., New York, 1953). H. G. Van Bueren: *Imperfections in Crystals* (North-Holland Publishing Company-Amsterdam, 1960). S. Amelinckx and W. Dekeyser: The Structure and Properties of Grain Boundaries, in *Solid State Physics*, ed. by E. Seitz and D. Turnbull (Academic Press, Inc., New York 1959), Vol. 8, P327. W. Bardsley: The Electrical Effects of Dislocations in Semiconductors, in *Progress in Semiconductors*, ed. by A. F. Gibson et al. (Heywood & Company Ltd., 1960), Vol. 4, P. 155. A. G. Tweet: Phys. Rev. **99** (1955) 1245. G. L. Pearson, W. T. Read and F. J. Morin: Phys. Rev. **93** (1954) 666.
2) W. T. Read: Phil. Mag. **45** (1954) 775, ibid. **45** (1954) 1119. S. R. Morrison: Phys. Rev. **104** (1956) 619.
3) W. T. Read: Phil. Mag. **46** (1955) 111. R. A. Legon, G. L. Pearson and D. A. Kleinman: J. Appl. Phys. **30** (1959) 855.
4) G. K. Wertheim and G. L. Pearson: Phys. Rev. **107** (1957) 694.
5) C. T. Sah, R. N. Noyce and W. Shockley: Proc. Inst. Radio Eng. **45** (1957) 1228.
6) M. Bernard and B. Leduc: J. Phys. Chem. Solids **13** (1960) 168.
7) T. Ota: (private communication). T. Ota: Bussei **1** (1960) 125. (Japan)

JOURNAL OF THE PHYSICAL SOCIETY OF JAPAN, Vol. 16, No. 11, NOVEMBER, 1961

Magnetic Anisotropy Energy in Nickel Arsenide Type Crystals

By Kengo ADACHI

The Research Institute for Iron, Steel and Other Metals,
Tohoku University, Sendai, Japan

(Received June 30, 1961)

The theoretical consideration of the magnetic anisotropy energies of magnetic compounds with a nickel arsenide type crystal structure was made. The anisotropy energy due to the magnetic dipolar interaction for an appropriate spin structure in this crystal structure, and the one originating from the spin orbit interaction and the interaction related to this were studied by assuming the ionic constitution of transition metal elements, from the stand point of one ion approximation. Some experimental data are explained by the present theoretical results.

§1. Introduction

Many compounds with a nickel arsenide structure or slightly deformed structure have been found to show a ferro- or antiferromagnetic behavior. Also the magneto-crystalline natures of these substances have recently been revealed by magnetic torque measurements as well as the neutron diffraction technique. Since the magnetism of these compounds is considered to come from the magnetic moment of metallic atoms or ions in the crystal lattice, the magneto-crystalline anisotropy is closely related to the electronic state of metallic atoms or ions in the crystal.

The present author undertook to discuss the nature of magneto-crystalline anisotropy energies of these substances by calculating the dipolar interaction for a given magnetic structure and by considering the spin orbit and the intra spin-spin interaction originated from the usual one ion approximation[1),2)] for the transition metal element with an ionic constitution in the nickel arsenide type crystal lattice.

§ 2. Magnetic Structures in a Crystal Lattice of the NiAs Type

The binding nature of the compounds with a NiAs structure can not be considered as completely ionic but is regarded as the intermediate between ionic and metallic, or between ionic and covalent bindings, since their electrical conductivities are more or less better than in the case in which they are regarded as an ionic compounds. However, Table I shows that the number of effective magnetons due to the measurements of paramagnetic susceptibility is well reproduced by

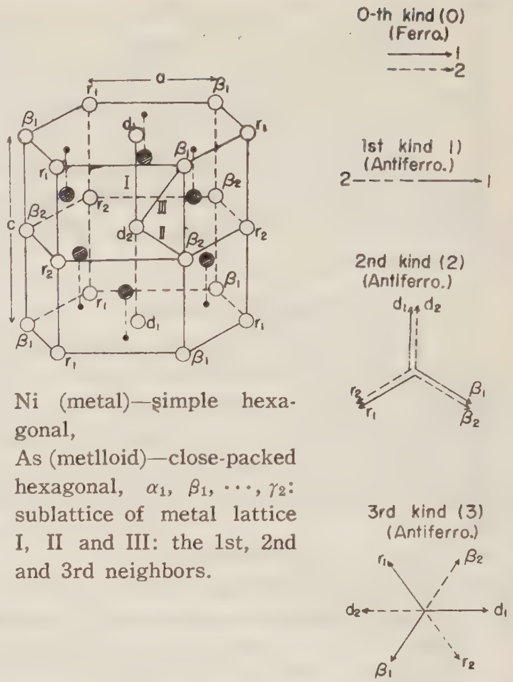

○ Ni (metal)—simple hexagonal,

▨ As (metlloid)—close-packed hexagonal, α_1, β_1, $\cdots$, γ_2: sublattice of metal lattice I, II and III: the 1st, 2nd and 3rd neighbors.

Fig. 1. NiAs type crystal structure and its sublattices: The stable magnetic ordering in NiAs structure.

Table I. The magnetic data on the compounds with NiAs structure (containing modified NiAs structure).

Substance	a (Å)	c/a	T_c or T_N (°K)	θ_p (°K)	P_A (μ_B)	P_{eff} (μ_B)	Easy direction of magnetic moment (°K)
NiS	3.439	1.555	(A) 150	−3000		2.35	←
CoS	3.374	1.537	(A) 358	− 632		1.69	
FeS*	3.456(d)	1.70†	(A) 593	− 917		5.22	↑ ··· (411) ···←
Fe_7S_8*	3.433(d)	1.655	(Fr) 578	−2000	0.25	5.93	↖ ···←
Cr_5S_6*	3.454(d)	1.675	(Fr) 303	− 150	0.35	4.8	←(R. T.)
VS	3.367	1.730	(A) 1040	−3000		3.67	
TiS	3.30	1.96	(WCP)	——			
NiSe	3.66	1.46					
CoSe	3.614	1.460					
Fe_7Se_8*	3.617(d)	1.625	(Fr) 425	−2600	0.20	4.9	{↖ ··· (150) ↑ ··· (200)} ···←
Fe_3Se_4*	3.537(d)	1.579	(Fr) 320		0.23		←
CrSe	3.684	1.638	(A) 279	− 320		4.9	↖ (N.D.)
VSe	3.587	1.670	(A) 163	−2570		4.2	
TiSe	3.566	1.748	(WCP)	——			
NiTe	3.957	1.353	(A)	−1110		0.99	
$Co_{0.8}Te$	3.894	1.381	(A)	−1400		2.70	
$Fe_{0.7}Te$	3.816	1.482	(A)	− 800		3.00	
MnTe	4.412	1.618	(A) 310	− 650		5.10	←
CrTe	3.95	1.55	(F) 333	333	2.4	4.08	↑
VTe	3.813	1.609				1.7	
TiTe	3.834	1.67	(WCP)	——			

Table I. (Continued).

Substance	a (Å)	c/a	T_c or T_N (°K)	θ_p (°K)	P_A (μ_B)	P_{eff} (μ_B)	Easy direction of magnetic moment (°K)
CoP♯	3.274(d)	1.547					
FeP♯	3.089(d)	1.676	(A)	−50		3.42	
MnP♯	3.167(d)	1.657	(F) 298		1.2		
VP	3.18	1.96					
TiP*	3.487	1.67					
NiAs	3.602	1.391					
CoAs♯	3.51(d)	1.47					
FeAs♯	3.366(d)	1.613					
MnAs(♯)	3.710	1.534†	(F) 312 (A) 400	283	3.40	4.95	←
CrAs♯	3.479(d)	1.647	(A) 823				
TiAs*	3.642	1.656					
NiSb	3.94	1.31	(D)				
CoSb	3.866	1.342	(A) 40	−320		1.36	
$Fe_{1.22}Sb$	4.06	1.26	(Fr) 4.2	−150		2.7	
MnSb	4.128	1.402	(F) 587	608	3.53(N.D.)	4.10	↑
CrSb	4.108	1.324†	(A) 718	−550	2.7 (N.D.)	4.92	↑
TiSb	4.07	1.55	(WCP)				
MnBi(*)	4.286	1.427†	(F) 633 (Fe) 483	440	3.95		←···(80)···↑

*	with super structure
♯	MnP type structure
(d)	with lattice distortion
a, c.	lattice parameters of origenal NiAs structure at room temperature
(WCP)	weak, constant paramagnetism
†	with considerable temperature dependence on axial ratio
(A)	antiferromagnetic
(F)	ferromagnetic
(Fr)	ferrimagnetic
(D)	diamagnetic

In this Table, the crystallographic and magnetic data are mainly quoted from M. Hansen, "*Constitution of Binary Alloys*" (McGraw-Hill Book Company Press, U.S.A., 1958) and T. Hirone "*LANDOLT BÖRNSTEIN*, **6** *Anflage*, II *Band*; *Magnetische Eigenschaften*" (Springer Verlag. Press, Göttingen, 1962) and some of them are due to the unpublished works in Professor Hirone's Laboratory.

T_c, T_N	Curie, Néel temperature
θ_p	paramagnetic (asymptotic) Curie temperature
P_A	magnetic moment per atom
P_{eff}	effective magnetic moment
(N.D.)	neutron diffraction study
↑···(°K)···←	easy axis of magnetic moment: parallel to c-axis at low temperature and perpendicular to c-axis at high temperature and its transition occurs at (°K).

assuming that the transition metal elements have ionic constitution concerning $3d$-electrons taking account of some contribution about the orbital magnetic moment, and that the partners of metallic elements, the VI-th group and the V-th group elements, are divalent and trivalent anions respectively.

In a NiAs type crystal structure as shown in Fig. 1, the magnetic ions form a simple hexagonal structure and the non-magnetic ions a close packed hexagonal structure. If we consider the exchange interactions of the direct and super types among the metallic ions on the simple hexagonal lattice site, it is necessary to consider even the interaction of the third neighbour. Then, to express the energy of the system, the simple hexagonal lattice should be divided into at least six sublattices as shown in Fig. 1. In this case three equivalent sublattices were chosen for every two triangular lattices on adjacent planes in the hexagonal layer, and then taking the three exchange interactions as above into account, the following four types of magnetic superstructures[3] can be stabilized*, which are also shown in Fig. 1, that is, three types of antiferromagnetic (first, second and third kind ordering) and a ferromagnetic structures. The first kind ordering is an antiferromagnetic structure with an antiparallel spin arrangement between adjacent hexagonal layers and parallel within the layer, the second kind ordering is a triangular antiferromagnetic structure, where spins on the three equivalent sublattices of all the hexagonal layers make an angle of 120° to each other and the third kind is also a triangular structure, but the spins on adjacent layers orient antiparallel directions to each other.

According to the molecular field approximation, Curie and Néel points for the arrangements mentioned above are given as follows;

$$\left.\begin{array}{ll} T_c=(C/6)(-A_1-A_2-A_3)\ , & \text{for ferromagnetic structure,} \\ T_{N1}=(C/6)(A_1-A_2+A_3)\ , & \text{for 1st kind of antiferro. structure,} \\ T_{N2}=(C/6)\{-A_1+(A_2/2)+(A_3/2)\}\ , & \text{for 2nd kind of antiferro. structure,} \\ T_{N3}=(C/6)\{A_1+(A_2/2)-(A_3/2)\}\ , & \text{for 3rd kind of antiferro. structure,} \end{array}\right\} \quad (1)$$

where $C=Ng^2\mu_B{}^2S(S+1)/3k$ is the Curie Weiss constant and $A_n=(6/N)2z_nJ_n/g^2\mu_B{}^2$, $(n=1, 2$ or 3), is the molecular field coefficient due to the exchange interaction between the first, second or third neighbouring atome respectively. J_n takes the positive sign for an antiferromagnetic interaction. Also the paramagnetic Curie point θ_i for each magnetic structure is given by $\theta_i=(C/6)(-A_1-A_2-A_3)$, $(i=f, 1, 2, 3)$; and θ_i/T_i takes the value of -1 to $+5$.

In the triangular antiferromagnetic structures with second and third kind ordering, it should be noted here that the anisotropic character of antiferromagnetic susceptibility is different from that of the 1st kind antiferromagnetic structure mentioned above in which parallel and perpendicular susceptibility, $\chi_{/\!/}$ and $\chi_\perp$, is expected to be $\chi_{/\!/}(0)=0$ and $\chi_\perp(T)=2(A_1+A_3)^{-1}=a$ constant below T_N. For the two types of triangular antiferromagnetic structure, defining $\chi_{/\!/}$ and $\chi_\perp$ the susceptibility parallel and perpendicular to the plane in which the triangular spins are lying, the following temperature dependence of susceptibilities is easily obtained:

For the 2nd kind of ordering;

$$\chi_{/\!/}(T)=\chi_\perp(T)=6\{(3A_2/2)+(2A_3/2)\}^{-1}=\text{a constant below } T_{N2}\ , \quad (2)$$

for the 3rd kind of ordering;

$$\chi_{/\!/}(0)=6\{4A_1+(3A_2/2)-(A_3/2)\}^{-1}\ , \qquad \chi_{/\!/}(T_{N3})=\chi_\perp(T_{N3})\ , \quad (3)$$

and

$$\chi_\perp(T)=6\{2A_1+(3A_2/2)+(A_3/2)\}^{-1}=\text{a constant below } T_{N3}\ , \quad (4)$$

where, $\chi_{/\!/}(0)/\chi_\perp(0)$ takes the value from zero to one in the stable range of the third kind of ordering. A_1, A_2 and A_3 can not be determined from the observed values of T_N, θ_i and $\chi(T_N)$, because the expressions for these quantities described above are not independent to each other.

§ 3. Magnetic Anisotropy Energy due to the Dipole-Dipole Interaction

A part of the anisotropy energy comes from the magnetic dipolar interaction of metallic ions in the crystal lattice, which is calculable from the dipolar sum about the lattice for each type of magnetic superstructure as mentioned in the previous section. In this case the anisotropy energy is expressed by $K_D\cos^2\vartheta$. In the case of the ordering of ferromagnetic and antiferromagnetic 1st kind, ϑ stands for an angle between c-axis (trigonal axis) of this crystal and the direction of magnetic moment, whereas in the cases of antiferromagnetic 2nd and 3rd kinds, it means an angle between the c-axis and the plane in which the triangular antiferromagnetic ordering is formed. Within the plane formed by the triangular spins, anisotropy energy can not be produced from the magnetic dipolar

---

* In NiAs structure, if we take the interactions of more than the third neighbouring lattice point, there is a possibility of stabilizing other types of ordering including the screw arrangement.

Table II. The dipolar anisotropy energies for each kind of ordering and crystal field coefficients as a function of axial ratio.

	Dipolar anisotropy energies (cm^{-1}/ion)								Crystal field coefficients		
	D_i				D_i'						
$\frac{c}{a}$	ferro.	1st kind	2nd kind	3rd kind	ferro.	1st kind	2nd kind	3rd kind	$\mathscr{A}_2^0$ $\times 10^{-5}$ cm^{-1}	$\mathscr{A}_4^0$ $\times 10^{-5}$ cm^{-1}	$\mathscr{A}_4^3$ $\times 10^{-5}$ cm^{-1}
1.2	−6.96	9.70	−11.3	7.67	−31.9	44.5	−51.8	35.2	5.67	−3.90	79.5
1.3	−4.77	8.51	− 8.55	5.47	−21.9	39.1	−39.2	25.1	4.07	−2.65	74.5
1.4	−3.36	7.52	− 6.87	4.17	−15.4	34.5	−31.5	19.1	2.77	−1.87	67.5
1.5	−2.20	6.87	− 5.58	2.98	−10.1	31.5	−25.6	13.7	1.81	−1.45	60.5
1.6	−1.36	6.28	− 4.63	2.12	− 6.24	28.8	−21.3	9.73	1.01	−1.04	53.8
1.65	−1.06	6.10	− 4.25	1.78	− 4.87	28.0	−19.5	8.16	0.668	−0.916	50.5
1.7	−0.811	5.99	− 3.91	1.47	− 3.72	27.5	−17.9	6.73	0.320	−0.820	47.5
1.8	−0.389	5.80	− 3.32	0.899	− 1.79	26.6	−15.2	4.12	−0.284	−0.677	41.4

The dipolar anisotropy energy for given ordering, K_{D_i} or K'_{D_i}, is calculated from $D_i(c/a)$ or $D_i(c/a)$ as follows:

$$K_{D_i}=D_i\times\frac{(gS)^2}{a^3}\ \text{cm}^{-1}\ \text{per ion}\quad\text{or}\quad K'_{D_i}=D_i'\frac{(gS)^2}{a^6}\ \text{erg per cm}^3\,,$$

where a (lattice parameter) is taken in Å-unit.

The crystal field coefficient, A_l^m, can be obtained from $A_l^m(c/a)$ as;

$$A_2^0=\mathscr{A}_2^0\times\frac{\nu}{a^3}\ \text{cm}^{-1}\,(\text{Å})^{-2}\quad\text{and}\quad A_4^{0,3}=\mathscr{A}_4^{0,3}\times\frac{\nu}{a^5}\ \text{cm}^{-1}\,(\text{Å})^{-4}\,,$$

where ν means ionic valency for given substance and a is taken in Å-unit.

Table III. Dipolar anisotropy energies of NiAs type compounds.

Substance	gS	Magnetic ordering	D_i (cm^{-1}/ion)	D_i' (erg/cm^3)
NiS	2 (χ)	1st kind*	0.65	7.5×10^6
CoS	1 (χ)	1st kind*	0.17	2.1×10^6
FeS	4.26 (χ)	1st kind*	2.6	2.8×10^7
VS	3 (χ)	1st kind*	1.4	1.7×10^7
CrSe	4 (χ)	3rd kind*	0.67	5.7×10^6
	4 (χ)	1st kind*	2.0	1.8×10^7
VSe	3 (χ)	1st kind*	1.2	1.2×10^7
MnTe	5 (g)	1st kind*	2.2	1.5×10^7
CrTe	2.4 (m_s)	ferro	0.15	1.1×10^6
MnAs	3.4 (m_s)	ferro	0.44	3.9×10^6
MnSb	3.53 (m_s)	ferro	0.55	3.5×10^6
MnBi	3.95 (m_s)	ferro	0.61	3.5×10^6
CrSb	4 (χ)	1st kind	1.9	1.3×10^7
	2.7 (N.D.)	1st kind	0.86	5.7×10^6

gS' were determined from the data of the paramagnetic susceptibility (χ), the saturation magnetization (m_s), g-value (g) and the neutron diffraction analysis (N.D.).

* in the column of magnetic ordering is one of the structure assumed.

interaction itself.

The values of dipolar anisotropy energy for the above four kinds of magnetic ordering can be obtained as a function of the parameter c/a by use of the direct sum method for the magnetic moments contained in the sphere of radius $4a$ with a small percentage error.

The anisotropy energies, at the absolute zero of the temperature $K_{Di}(0)$, are obtained by using the followihg formula:

$$K_{Di}(0)=D_i(gs)^2/a^3\ \text{cm}^{-1}/\text{ion}\,, \qquad (5)$$

$$D_{Di}'(0)=D_i(gs)^2/a^6\times 10^8\ \text{erg/cm}^3\ . \qquad (5')$$

In these expressions, the Å-unit is taken for the lattice parameter, a, and the factors D_i and D_i' $(i=f, 1, 2, 3)$ are shown as a function of c/a in Table II.

Within the range of axial ratio, $c/a=1.2\sim 1.8$, the obtained results show that the easy direction of magnetic moments is along the c-axis for the ferromagnetic order, $(K_{Df}<0)$, and in the c-plane for the antiferromagnetic 1st kind, $(K_{D1}>0)$; and the easy plane of triangular spins is parallel to the c-axis for the 2nd kind*, $(K_{D2}<0)$, and perpendicular to the c-axis for the 3rd kind $(K_{D3}>0)$. In Table III, the values of $K_{Di}(0)$ for several magnetic substances with a NiAs structure are estimated, based on the observed and assumed magnetic structures. At finite temperature, the dipolar anisotropy energy is proportional to the square of the average sublattice magnetization, $\langle S\rangle^2$, then its temperature dependence is given by $K_D(T)=K_D(0)\langle S\rangle^2/S^2$.

§ 4. Magnetic Anisotropy Energy due to the Spin-Orbit Interaction

Based on knowledge about the energy levels for each kind of magnetic ion with $3d^n$ $(n=1, 2, \cdots, 9)$ electron configuration in the crystal field of NiAs type, the magnetic anisotropy energies concerning with the spin orbit interaction for each system are obtained from the stand point of one ion approximation.

(A) *Energy levels and matrix elements of* $(\boldsymbol{L}\cdot\boldsymbol{S})$

(1) Energy levels for each state with $3d^n$ electrons

In a NiAs crystal structure, the crystal fields acting on $3d$ electrons of a cation consist of the second and the fourth order fields from the surrounding simple hexagonal cation lattice and close packed hexagonal anion lattice, which can be expressed as follows,

$$V(r)=A_2^0(3z^2-r^2)+A_4^0(35z^4-30z^2r^2+3r^4)+A_4^3z(x^3-3xy^2)\ , \qquad (6)$$

where A_l^m's are the coefficients of the crystal field. In Table II the values of A_l^m are shown for $c/a=1.2\sim 1.8$, which are obtained by the direct sum method within a sphere of radius $4a$. The result shows that the uniaxial part of the crystal field coefficient, A_2^0, in NiAs structure changes its sign at about $c/a=1.7$, while this change occurs at $c/a=1.63$ when a cubic crystal receives certain trigonal distortion.

Now the lowest multiplet of free magnetic ion with $3d^n$ electron configuration is denoted as follows,

$$\left.\begin{matrix} 3d^1\ {}^2D,\ 3d^6\ {}^5D \\ 3d^4\ {}^5D,\ 3d^9\ {}^2D \end{matrix}\right\}\ \text{for the } D\text{-state}\ , \qquad \left.\begin{matrix} 3d^2\ {}^3F,\ 3d^7\ {}^4F \\ 3d^3\ {}^4F,\ 3d^8\ {}^3F \end{matrix}\right\}\ \text{for the } F\text{-state}$$

and $3d^5\ {}^6S$, respectively. For the basal wave function φ_{Lm}, (L, m) is taken as $(L=2, m=\pm 2, \pm 1, 0)$ for the D-state and $(L=3, m=\pm 3, \pm 2, \pm 1, 0)$ for the F-state. The S-state $(L=0)$ is not affected by the crystal field, since its wave functions have the nature of spherical symmetry.

Based upon the above set of wave functions, the matrix of crystal field V can be derived by $V_{mm'}=\int\varphi_m{}^*V(r)\varphi_{m'}\,dr$, then the eigenvalues and eigenvectors of the system can be obtained as $\boldsymbol{E}=\boldsymbol{C}\boldsymbol{V}\boldsymbol{C}^{-1}$ and $\psi=\boldsymbol{C}\varphi$ respectively by finding the transformation matrix $\boldsymbol{C}$. Matrices, $\boldsymbol{V}$ and $\boldsymbol{C}$ for each D- and F-state are shown in Appendix I. The following term splittings will occur under the influence of the crystal field shown above.

For the D-state it is given as follows;

$$\left\{\begin{array}{ll} E_0=2A+6B & \text{(singlet)}\ , \\ E_1=(A-4B)\sin^2\theta+(-2A+B)\cos^2\theta-2C\sin\theta\cos\theta & \text{(doublet)}\ , \\ E_2=(A-4B)\cos^2\theta+(-2A+B)\sin^2\theta+2C\sin\theta\cos\theta & \text{(doublet)}\ , \end{array}\right. \qquad (7)$$

with

---

* In the second kind ordering, weak ferromagnetism occurs parallel to the c-axis due to the unbalance of triangular spins.

$$\tan 2\theta = 2C/(3A-5B) \qquad (0 \leq \theta \leq \pi)\,, \tag{8}$$

where

$$\begin{cases} A = \pm(2/7)A_2{}^0\langle r^2\rangle\,, \\ B = \pm(8/21)A_4{}^0\langle r^4\rangle\,, \\ C = +(2/21)A_4{}^0\langle r^4\rangle\,, \end{cases} \tag{9}$$

the double sign corresponds to the state of ($3d^1$, $3d^6$) and ($3d^4$, $3d^9$) respectively, and $\langle r^2\rangle$ and $\langle r^4\rangle$ are the average values for r^2 and r^4 concerning the $3d$-wave function in the crystal.

For the F-state it is given as follows;

$$\begin{cases} E_0 = 5A' + 3B' & \text{(singlet)}\,, \\ E_1 = (-4A'+6B')\sin^2\theta_1 + (5A'+3B')\cos^2\theta_1 - 6\sqrt{10}\,C'\sin\theta_1\cos\theta_1 & \text{(singlet)}\,, \\ E_2 = (-4A'+6B')\cos^2\theta_1 + (5A'+3B')\sin^2\theta_1 + 6\sqrt{10}\,C'\sin\theta_1\cos\theta_1 & \text{(singlet)}\,, \\ E_3 = (-3A'+B')\cos^2\theta_2 - 7B'\sin^2\theta_2 + 2\sqrt{10}\,C'\sin\theta_2\cos\theta_2 & \text{(doublet)}\,, \\ E_4 = (-3A'+B')\sin^2\theta_2 - 7B'\cos^2\theta_2 - 2\sqrt{10}\,C'\sin\theta_2\cos\theta_2 & \text{(doublet)}\,, \end{cases} \tag{10}$$

with

$$\begin{cases} \tan 2\theta_1 = 2\sqrt{10}\,C'/(-3A'+B') & (0 \leq \theta_1 \leq \pi)\,, \\ \tan 2\theta_2 = 2\sqrt{10}\,C'/(-3A'+8B') & (0 \leq \theta_2 \leq \pi)\,, \end{cases} \tag{11}$$

where

$$\begin{cases} A' = \mp(2/35)A_2{}^0\langle r^2\rangle\,, \\ B' = \mp(8/21)A_4{}^0\langle r^4\rangle\,, \\ C' = \mp(2/105)A_4{}^3\langle r^4\rangle\,, \end{cases} \tag{12}$$

and the double sign means the states for ($3d^2$, $3d^7$) and ($3d^3$, $3d^8$) respectively. Sometimes the admixing of the P-state[4),5)] is important for F-state such as the influence of the ${}^4P$-state on the ${}^4F$-state, but for brevity the P-state is not considered here.

In Fig. 2 an example of energy levels for each D-state ($3d^1$, $3d^6$) and the F-state ($3d^2$, $3d^7$) is shown as a function of the c/a-value, where relevent values, of $\langle r^2\rangle = 1\,\text{Å}^2$, $\langle r^4\rangle = 1.5\,\text{Å}^4$ and $a = 3.5\,\text{Å}$, are taken. Also the inversed energy scheme holds for the case of the D-state ($3d^4$, $3d^9$) and the F-state ($3d^3$, $3d^8$).

As seen from the Figs. 2_D and 2_F, the lowest state for the electrons configurations $3d^1$ and $3d^6$ is the orbital singlet (E_0) or the doublet (E_2) depending upon whether the

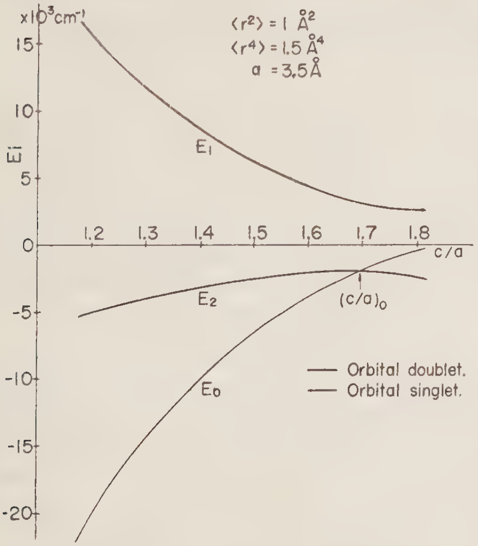

Fig. 2_D. The energy levels for D-state in the NiAs type crystal fields.

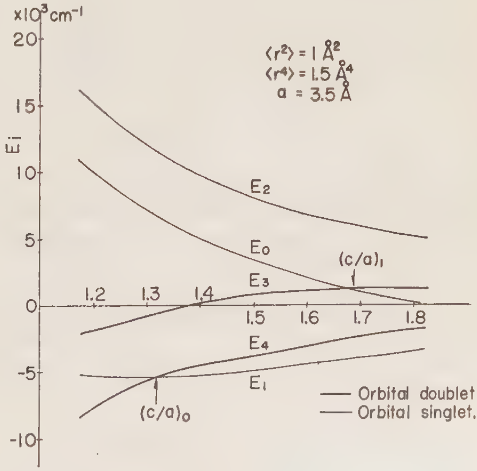

Fig. 2_F. The energy levels for F-state in the NiAs type crystal fields.

c/a-value is smaller or larger than a certain c/a-value, $(c/a)_0$, which depends on the value $\langle r^2\rangle$ and $\langle r^4\rangle$ and takes the value 1.73∼1.67 for the range $\langle r^4\rangle/\langle r^2\rangle=0.5\sim2.0$ in Å-units. For the $3d^4$ and the $3d^9$, the lowest state is always present at doublet level E_1. For $3d^2$ and $3d^7$, the lowest state is singlet E_1 for $c/a\gtrsim1.33$ and doublet E_4 for $c/a\lesssim1.33$ in the range of $\langle r^4\rangle/\langle r^2\rangle=0.5\sim1.5$ in Å-units. For $3d^3$ and $3d^8$ the singlet state E_2 is always lowest, and the next lowest level is the singlet E_0 or the doublet E_3 and the c/a-value where two levels cross each other takes 1.73∼1.69 for the range of $\langle r^4\rangle/\langle r^2\rangle=0.5\sim1.5$. This relative position of the next lowest two levels plays an important role for the anisotropy energy of this configuration as will be mentioned in later pages.

(2) Matrix elements of $\lambda(\boldsymbol{L}\cdot\boldsymbol{S})$

The matrix elements of $\lambda(\boldsymbol{L}\cdot\boldsymbol{S})$ among energy levels of the D- and the F-state mentioned above are obtained by the transformation of the matrix element of $(\boldsymbol{L}\cdot\boldsymbol{S})$ in the free magnetic ion with $\boldsymbol{C}$ and the results are given as follows;

$\boldsymbol{C}_D(\boldsymbol{L}\cdot\boldsymbol{S})_D\boldsymbol{C}_D^{-1}=$

$$\begin{array}{c|c|c|c|c|c|}
0 & & -\sqrt{3/2}\cos\theta S^- & \sqrt{3/2}\sin\theta S^- & -\sqrt{3/2}\cos\theta S^+ & -\sqrt{3/4}\sin\theta S^+ \\
1 & -\sqrt{3/2}\cos\theta S^+ & (1-3\sin^2\theta)S_z & -3\cos\theta\sin\theta S_z & & -S^- \\
2 & \sqrt{3/2}\sin\theta S^+ & -3\cos\theta\sin\theta S_z & (1-3\cos^2\theta)S_z & -S^- & \\
1 & -\sqrt{3/2}\cos\theta S^- & & -S^+ & (3\sin^2\theta-1)S_z & -3\cos\theta\sin\theta S_z \\
2 & -\sqrt{3/2}\sin\theta S^- & -S^+ & & -3\cos\theta\sin\theta S_z & (3\cos^2\theta-1)S_z
\end{array} \tag{13}$$

for the D-state, and

$\boldsymbol{C}_F(\boldsymbol{L}\cdot\boldsymbol{S})_F\boldsymbol{C}_F^{-1}=$

$$\begin{array}{c|c|c|c|c|c|c|c|}
0 & & 3\cos\theta_1S_z & 3\sin\theta_1S_z & -\sqrt{3/4}\sin\theta_2S^- & -\sqrt{3/4}\cos\theta_2S^- & \sqrt{3/4}\sin\theta_2S^+ & -\sqrt{3/4}\cos\theta_2S^+ \\
1 & 3\cos\theta_1S_z & & & \sqrt{3}\,a(\theta_1,\theta_2)S^- & \sqrt{3}\,b(\theta_1,\theta_2)S^- & \sqrt{3}\,a(\theta_1,\theta_2)S^+ & -\sqrt{3}\,b(\theta_1,\theta_2)S^+ \\
2 & 3\sin\theta_1S_z & & & \sqrt{3}\,c(\theta_1,\theta_2)S^- & \sqrt{3}\,d(\theta_1,\theta_2)S^- & \sqrt{3}\,c(\theta_1,\theta_2)S^+ & -\sqrt{3}\,d(\theta_1,\theta_2)S^+ \\
3 & -\sqrt{3/4}\sin\theta_2S^+ & \sqrt{3}\,a(\theta_1,\theta_2)S^+ & \sqrt{3}\,c(\theta_1,\theta_2)S^+ & (1-3\sin^2\theta_2)S_z & -3\cos\theta_2\sin\theta_2S_z & & -\sqrt{5/2}\,S^- \\
4 & -\sqrt{3/4}\cos\theta_2S^+ & \sqrt{3}\,b(\theta_1,\theta_2)S^+ & \sqrt{3}\,d(\theta_1,\theta_2)S^+ & -3\cos\theta_2\sin\theta_2S_z & (1-3\cos^2\theta_2)S_z & -\sqrt{5/2}\,S^- & \\
3 & -\sqrt{3/4}\sin\theta_2S^- & \sqrt{3}\,a(\theta_1,\theta_2)S^- & \sqrt{3}\,c(\theta_1,\theta_2)S^- & & -\sqrt{5/2}\,S^+ & (3\sin^2\theta_2-1)S_z & -3\cos\theta_2\sin\theta_2S_z \\
4 & -\sqrt{3/4}\cos\theta_2S^- & -\sqrt{3}\,b(\theta_1,\theta_2)S^- & -\sqrt{3}\,d(\theta_1,\theta_2)S^- & -\sqrt{5/2}\,S^+ & & -3\cos\theta_2\sin\theta_2S_z & (3\cos^2\theta_2-1)S_z
\end{array} \tag{14}$$

for the *F*-state, with

$$\left.\begin{aligned} a(\theta_1,\theta_2)&=-\sin\theta_1\cos\theta_2+2^{-1}\cos\theta_1\sin\theta_2\ ,\\ b(\theta_1,\theta_2)&=\sin\theta_1\sin\theta_2+2^{-1}\cos\theta_1\cos\theta_2\ ,\\ c(\theta_1,\theta_2)&=\cos\theta_1\cos\theta_2+2^{-1}\sin\theta_1\sin\theta_2\ ,\\ d(\theta_1,\theta_2)&=-\cos\theta_1\sin\theta_2-2^{-1}\sin\theta_1\cos\theta_2\ . \end{aligned}\right\} \tag{15}$$

The above results show that the singlet term in the *D*-state, E_0, has no orbital angular momentum with the exception of those which occur through perturbations among higher energy levels, however the doublets, E_1 and E_2, have the orbital angular momentum which is given as, $l_z(E_1)=\pm(1-3\sin^2\theta)$ and $l_z(E_2)=\pm(1-3\cos^2\theta)$, respectively. $l_z(E_1)$ and $l_z(E_2)$ take the value ±1 to ∓2 for the change of c/a. On the other hand, for the *F*-state the non-degenerate levels, E_0, E_1 and E_2, have no angular momentum and the degenerate levels, E_3 and E_4, have the angular momentum given by $l_z(E_4)=\pm(1-3\sin^2\theta_2)$ and $l_z(E_3)=\pm(1-3\cos^2\theta_2)$, respectively, and each value takes ±1 to ∓2 for the change of c/a. The values of $l_z(E_i)$ for the degenerate *D*- and *F*-states in the NiAs type of crystal field and also the one in the cubic crystal with the trigonal distortion are shown in Fig. 3 as a function of c/a and $\langle r^4\rangle/\langle r^2\rangle$.

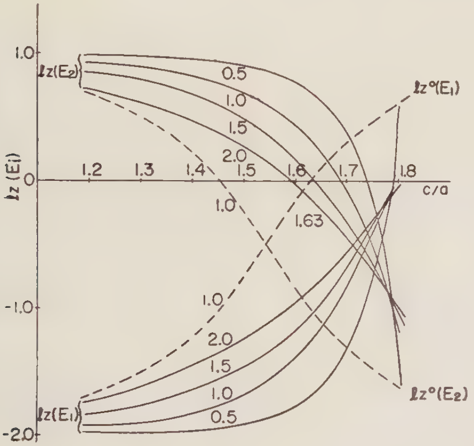

Fig. 3_D. The orbital angular momentum, $l_z(E_i)$, for *D*-state as a function of c/a and $\langle r^4\rangle/\langle r^2\rangle$.

--- $l_z(E_i)$ for cubic crystal with trigonl distortion.

—— $l_z(E_i)$ for NiAs type crystal.

The figures beside the curves mean $\langle r^4\rangle/\langle r^2\rangle$ (in Å-units).

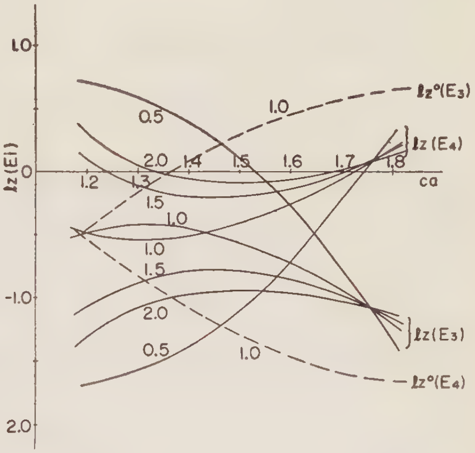

Fig. 3_F. The orbital angular momentum, $l_z(E_i)$, for *F*-state as a function of c/a and $\langle r^4\rangle/\langle r^2\rangle$.

--- $l_z^0(E_i)$ for a cubic crystal with trigonal distortion.

—— $l_z(E_i)$ for NiAs type crystal.

The figures besides the curves mean $\langle r^4\rangle/\langle r^2\rangle$ (in Å-unit).

(B) *Uniaxial magnetic anisotropy energy*

Based on the results of the matrix element of $\lambda(\boldsymbol{L}\cdot\boldsymbol{S})$ obtained above, the anisotropy energy can be obtained by means of the perturbational calculation or by considering the spin levels with an adequate approximation for each lowest energy state of given electron configuration.

(1) Case of non-degenerate ground state

In this case, the uniaxial anisotropy energy can be obtained from the usual second order perturbation method[6),1)], and the results are given as follows.

For each of *D*- and *F*-states, the anisotropy energy at absolute zero, $K(0)$, is given as follows:

$3d^6\ {}^5D$

$$\left.\begin{aligned} &E_{gs}=E_0 \quad \text{for} \quad c/a<(c/a)_0\ ,\\ &K(0)=3\lambda^2\{(\cos^2\theta/\Delta E_1)+(\sin^2\theta/\Delta E_2)\}S(S-(1/2))\ . \end{aligned}\right\} \tag{16}$$

In this case $K(0)$ always takes a positive value, hence the easy axis of spin lies in the c-plane.

$3d^1$ ^2D

In the case, $S=1/2$, no anisotropy occurs from the above perturbation.

$3d^8$ ^3F and $3d^3$ ^4F

$$\left.\begin{aligned}&E_{gs}=E_2\\&K(0)=3\lambda^2\{(2/\Delta E_3)(\cos\theta_1\cos\theta_2+2^{-1}\sin\theta_1\sin\theta_2)^2\\&\qquad+(2/\Delta E_4)(-\cos\theta_1\sin\theta_2+2^{-1}\sin\theta_1\cos\theta_2)^2-(3/\Delta E_0)\sin^2\theta_1\}S(S-(1/2))\,.\end{aligned}\right\}\tag{17}$$

The first and the second terms give positive contributions, whereas the third term a negative contribution to the anisotropy coefficient. The sign of $K(0)$ and its magnitude depends upon the axial ratio of the crystal as shown in Table II and the average value of $\langle r^2\rangle$ and $\langle r^4\rangle$. The $(c/a)_1$-value where K changes its sign depends on the relative position of the energy states, E_0 and E_3, and takes a larger value than 1.63 within the range of values $\langle r^4\rangle/\langle r^2\rangle=0.5\sim3.0$ (in Å-units). Then the results are as follows; if $c/a<(c/a)_1$, the easy axis coincides with the c-axis ($K<0$), and if $c/a>(c/a)_1$, it lies in the c-plane.

$3d^7$ ^4F and $3d^2$ ^3F

$$\left.\begin{aligned}&E_{gs}=E_1\,,\quad\text{for}\quad c/a>(c/a)_0\,,\\&K(0)=3\lambda^2\{(2/\Delta E_3)(-\sin\theta_1\cos\theta_2+2^{-1}\cos\theta_1\sin\theta_2)^2\\&\qquad+(2/\Delta E_4)(\sin\theta_1\sin\theta_2+2^{-1}\cos\theta_1\cos\theta_2)^2-(3/\Delta E_0)\cos^2\theta_1\}S(S-(1/2))\,.\end{aligned}\right\}\tag{18}$$

Here, each term of this expression has the same meaning as the above case of $3d^8$ ^3F and $3d^3$ ^4F. In the present case, however, E_4 is smaller than E_0 and E_3, hence as a whole the anisotropy coefficient $K(0)$ takes a positive value.

It can be considered that the influence of some mixing of the P-state does not change the qualitative characteristics of the anisotropy energy. For the case, $\Delta E_n\sim\lambda$, the above perturbation method can not be allowed.

The temperature dependence of uniaxial anisotropy energy is given by putting $\langle S_z^2\rangle^{(*)}$ in place of $S(S-(1/2))$ in (16), (17) or (18). Also the directional dependence of this type anisotropy energy obtained from the second order perturbation method has the form $K\cos^2\vartheta$.

(2) The case of degenerate ground state

When the ground state has orbital degeneracy with the non-quenched orbital angular momentum, spin and orbital momenta are coupled directly by spin-orbit interaction. In this case the c-axis in the crystal becomes the easy direction of magnetization, since the angular momentum contained in the ground state has only the z-component, l_z, the values of which are shown in the previous paragraph.

By way of the first approximation, as was shown by Slonczewski(7), taking into account the $(2S+1)$ spin levels in the degenerated lowest orbital state, which is split by the exchange interaction and spin-orbit interaction of the system, the energies of this spin level are given as follows,

$$E_{l_z,m_s}(\vartheta)=-\sqrt{(2zJ\langle S\rangle)^2+(\lambda l_z)^2-2(2zJ\langle S\rangle)(\lambda l_z)\cos\vartheta}\;m_s\,,\tag{19}$$

with $m_s=S, S-1, \cdots, -S$,

where ϑ means an angle between the trigonal axis and the direction of quantization axis of

---

(*) $\langle S_z^2\rangle=\frac{1}{2}\{3m_z^2-S(S+1)\}$, with $m_z^2=\dfrac{\sum_{m_s=-s}^{s} m_s^2\exp\left(\frac{2zJ\langle S\rangle}{kT}m_s\right)}{\sum_{-s}^{s}\exp\left(-\frac{2zJ\langle S\rangle}{kT}m_s\right)}$

$\langle S_z^2\rangle$ approaches $\langle S\rangle^2$ at $T\sim T_c$ and vanishes at $T=T_c$.

spin. Based on the energy levels shown in (19), the expression of free energy of the system (per ion) at finite temperature is given as,

$$F(\vartheta, \langle S\rangle)=(1/2)2zJ\langle S\rangle^2-kT\ln\left[\sum_{m_s,l_z}\exp\{-E_{m_sl_z}(\vartheta, \langle S\rangle)/kT\}\right]. \tag{20}$$

If $\langle S\rangle$ is determined as a function of angle ϑ and temperatures from the equation, $\partial F/\partial\langle S\rangle=0$, the above expression of free energy $F(\vartheta, T)$ gives the anisotropy energy as a function of ϑ and T. For the case of $2zJ\langle S\rangle\gg|\lambda l_z|$, $E_{m_sl_z}(\vartheta)=-(2zJ\langle S\rangle+\lambda l_z\cos\vartheta)m_s$, therefore, $\langle S\rangle$ can be approximated with the Brillouin function, and also the anisotropy energy for each state can be approximated as follows, except when T is near T_c, or T_N.

$$F(\vartheta, T)=-kT\ln\{\cosh(\lambda l_z S\cos\vartheta/kT)\}\,. \tag{21}$$

At absolute zero, this expression gives the anisotropy energy $-|\lambda l_z S\cos\vartheta|$. On the other hand, at the temperature near the Curie or Néel point, ($|\lambda l_z|\gg 2zJ\langle S\rangle$), the above expression of anisotropy energy takes the following form;

$$F(\vartheta, T)=-\alpha(2zJ\langle S\rangle)^2\cos^2\vartheta/kT\ , \tag{22}$$

where α takes the value 1/8, 1/3, 5/8 and 1 for each state of $S=1/2$, 1, 3/2 and 2 respectively.

In this case the anisotropy energy can not in general be expressed by the form $K\cos^2\vartheta$. The anisotropy energy of this type changes with $|\cos\vartheta|$ at low temperature ($kT<|\lambda l_z|$), the amplitude being proportional to $|\lambda l_z S|$. At intermediate temperature ($|\lambda l_z|<kT<kT_{c.N}$), the amplitude is proportional to $(\lambda l_z)^2/kT$, then it vanishes at the transformation temperature with the form given by (22). For the case of $2zJ\langle S\rangle\sim|\lambda l_z|$ the qualitative behavior of the anisotropy energy does not change. In some cases, also the anisotropy energies produced by the perturbation from higher energy states, such as given in the preceding part, exist. However, the discussion about this term is omitted here.

It is to be noted that the saturation magnetic moment in this case has an angular dependence, which is given at absolute zero of temperature by $\mu_B(2S\pm l_z|\cos\vartheta|)$, where sign $\pm$ corresponds to $\lambda\lessgtr 0$.

(3) Other origins of magnetic anisotropy energy

For one of the origins of magnetic anisotropy energy, one due to intra spin-spin interaction is to be taken into account, which is written as the following expression[8)],

$$-\rho\{(\boldsymbol{L}\cdot\boldsymbol{S})^2+(\boldsymbol{L}\cdot\boldsymbol{S})/2-L(L+1)S(S+1)/3\}\,, \tag{23}$$

where ρ means the coupling constant. The uniaxial anisotropy energy, K_ρ, originating from the first term is obtained from $(\boldsymbol{L}\cdot\boldsymbol{S})^2$ as a first order perturbation. Though the value of ρ is much smaller than that of λ (Table IV), the contribution due to the intra spin-spin term in some cases can not be neglected, since the anisotropy energy is produced by the lower order perturbation treatment. The anisotropy energy K_ρ is given by use of the transformation matrix C as

$$K_\rho(0)=-\rho[C(\boldsymbol{L}\cdot\boldsymbol{S})^2C^{-1}]_{\text{ground state}}\,. \tag{24}$$

For each D- and F-state, the coefficient of anisotropy K_ρ at absolute zero and the direction of easy spin axis are given as follows:

D-state

E_0 ground state

$$K_\rho(0)=3\rho S(S-(1/2))\,,\qquad \text{in the } c\text{-plane}\,; \tag{25}$$

E_1 ground state

$$K_\rho(0)=-(3/2)\rho(1-3\sin^2\theta)S(S-(1/2))\,,\qquad \begin{aligned}&\text{along the } c\text{-axis if } \sin^2\theta<1/3\,,\\ &\text{in the } c\text{-plane if } \sin^2\theta>1/3\,;\end{aligned} \tag{26}$$

E_2 ground state

$$K_\rho(0)=-(3/2)\rho(1-3\cos^2\theta)S(S-(1/2))\,,\qquad \begin{aligned}&\text{along the } c\text{-axis if } \cos^2\theta<1/3\,,\\ &\text{in the } c\text{-plane if } \cos^2\theta>1/3\,;\end{aligned} \tag{27}$$

F-state

E_1 ground state

$$K_\rho(0)=6\rho(1-(9/4)\cos^2\theta_1)S(S-(1/2))\,,\qquad \begin{aligned}&\text{along the } c\text{-axis if } \cos^2\theta_1>4/9\,,\\ &\text{in the } c\text{-plane if } \cos^2\theta<4/9\,;\end{aligned} \tag{28}$$

E_2 ground state

$$K_\rho(0)=6\rho(1-(9/4)\sin^2\theta_1)S(S-(1/2))\,,\qquad \begin{aligned}&\text{along the } c\text{-axis if } \sin^2\theta_1>4/9\,,\\ &\text{in the } c\text{-plane if } \sin^2\theta_1<4/9\,;\end{aligned} \tag{29}$$

E_4 ground state

$$K_\rho(0)=(9/2)\rho\sin^2\theta_2 S(S-(1/2))\,,\qquad \text{in the } c\text{-plane}\,. \tag{30}$$

The temperature dependence and the angular dependence of this kind of anisotropy energy, $K_\rho(T,\vartheta)$, are the same as in the case of one caused by the spin orbit interaction for the non-degenerated state.

On the other hand, in a system with the state $S=1/2$ ($3d^1$, $3d^9$), the anisotropy energy due to the anisotropic exchange interaction is important[1]. However, we will not discuss

Table IV. The easy directions of magnetic moment due to the spin orbit interaction and the intra spin spin interaction with trigonal distortions for $3d^n$ electron configuration.

	Spin orbit interaction			Intra spin spin interaction		
	λ (cm^{-1}) free ion	$c/a<(c/a)_{0.1}$	$c/a>(c/a)_{0.1}$	ρ (cm^{-1}) free ion	$c/a<(c/a)_{0.1}$	$c/a>(c/a)_{0.1}$
$3d^1$	154 (Ti^{3+})	⇠ or ⇡	⬆			
$3d^2$	104 (V^{3+})	⬆	←	0.24 (Ti^{2+}) 0.24 (V^{3+})	←	$\left(\sin^2\theta_1>\frac{4}{9}\right)$ ↑
$3d^3$	55 (V^{2+}) 87 (Cr^{3+})	↑	←	0.4 (V^{2+}) 0.44 (Cr^{3+})	$\left(\cos^2\theta_1>\frac{4}{9}\right)$ ↑	$\left(\cos^2\theta_1<\frac{4}{9}\right)$ ←
$3d^4$	57 (Cr^{2+}) 85 (Mn^{3+})	⬆	⬆	0.42 (Cr^{2+}) 0.8 (Mn^{2+})	$\left(\sin^2\theta>\frac{1}{3}\right)$ ←	$\left(\sin^2\theta<\frac{1}{3}\right)$ ↑
$3d^6$	−100 (Fe^{2+})	←	⬆	0.95 (Fe^{2+})	←	$\left(\cos^2\theta>\frac{1}{3}\right)$ ←
$3d^7$	−180 (Co^{2+})	⬆	←	1.50 (Co^{2+})	←	$\left(\sin^2\theta_1>\frac{4}{9}\right)$ ↑
$3d^8$	−335 (Ni^{2+})	↑	←	5.31 (Ni^{2+})	$\left(\cos^2\theta_1>\frac{4}{9}\right)$ ↑	$\left(\cos^2\theta_1<\frac{4}{9}\right)$ ←
$3d^9$	−852 (Cu^{2+})	⬆	⬆			

↑ and ←: The easy axis of magnetic moment is parallel and perpendicular to the trigonal axis as for the lowest non-degenerated orbitals.

⬆: The easy axis of magnetic moment is parallel to the trigonal axis as for the lowest degenerated orbitals.

⇠ and ⇡: The easy direction of magnetic moment due to the anisotropic exchange interaction for the cases $J/2>\lambda l_z$ and $J/2<\lambda l_z$ respectively.

this case here, because such a substance does not appear in NiAs type compounds.

In Table IV, the easy direction of spin in a NiAs crystal structure is shown in conclusion for the various electron configurations and the axial ratios in conformity with the results as discussed above.

(C) *The anisotropic characters of g-factors*

According to the results of Pryce[6)], *g*-factors $g_{xx}=g_{yy}=g_a$, $g_{zz}=g_c$ and $g_{xy}=g_{yz}=g_{zx}=0$ in the ground state with non-degenerated orbital are expressed as follows:

(1) *D*-state ($3d^1$, $3d^6$) with $E_{gs}=E_0$ for $c/a<(c/a)_0$;

$$g_a=2-6\lambda\{(\cos^2\theta/\Delta E_1)+(\sin^2\theta/\Delta E_2)\}\ , \qquad g_c=2\ . \tag{31}$$

(2) *F*-state ($3d^8$, $3d^3$) with $E_{gs}=E_2$;

$$\begin{aligned}&g_a=2-12\lambda\{(\cos\theta_1\cos\theta_2+2^{-1}\sin\theta_1\sin\theta_2)^2/\Delta E_3+(-\cos\theta_1\sin\theta_2+2^{-1}\sin\theta_1\cos\theta_2)^2/\Delta E_4\}\ ,\\&g_c=2-18\lambda(\sin^2\theta_1/E_0)\ ,\end{aligned} \tag{32}$$

(3) *F*-state ($3d^7$, $3d^2$) with $E_{gs}=E_1$ for $c/a>(c/a)_0$;

$$\begin{aligned}&g_a=2-12\lambda\{(-\sin\theta_1\cos\theta_2+2^{-1}\cos\theta_1\sin\theta_2)^2/\Delta E_3+(\sin\theta_1\sin\theta_2+2^{-1}\cos\theta_1\cos\theta_2)^2/\Delta E_4\}\ ,\\&g_c=2-18\lambda(\cos^2\theta_1/\Delta E_0)\ .\end{aligned} \tag{33}$$

When the ground state of the system has an orbital degeneracy, the above formula for the *g*-factors does not hold, since the thermal average of angular momentum of the system has a temperature dependence on account of $\lambda l_z \sim kT$ at ordinary temperatures. Hence it can be shown that the inverse susceptibility in this case does not obey the Curie-Weiss law but has a concave curve for the temperature axis in the case of $\lambda>0$ and a convex one in $\lambda<0$.

(D) *Anisotropic susceptibility above the transformation point*

The anisotropic character of magnetic susceptibility above the Curie or Néel point is given by high temperature expansion of the effective spin Hamiltonian[1)]. For the non-degenerate ground state, including the term due to the dipolar interaction, it is expressed af follows,

$$\chi_c-\chi_a=(D_d\chi_c\chi_a/2Ng^2\mu_B^2)-(C_c-C_a)(T+\theta)^{-1}-D\chi_p\{4S(S+1)-3\}/10kT\ , \tag{34}$$

where χ_p, g and C_c-C_a are given as $\chi_p=(\chi_c+2\chi_a)/3$, $g=(g_c+2g_a)/3$ and $C_c-C_a=(N\mu_B^2/3k)S(S+1)(g_c^2-g_a^2)$ respectively. In the above expression, the first term originates from dipolar interaction, the second from the spin-orbit interaction and the last from both spin-orbit and intra spin-spin interaction. Usually the second and the third terms are larger than the first for the *D*- and *F*-state, while the first term is important for *S*-state. If the contribution of each term in the above expression is separately estimated from the experimental data of paramagnetic susceptibilities above the transformation point and the knowledge on the anisotropy energies as discussed above, it is possible to determine in principle the values, g_a, g_c and D empirically. In the case with a degenerated orbital state, $\chi_c-\chi_a$ can not be expressed by the above simple form.

§ 5. Explanation of the Experimental Results

Recently, the various magnetic properties including the magnetic anisotropy energies and the magnetic susceptibilities in several compounds with an NiAs structure were made clear. These experimental results will be illustrated, based on the theories developed in the preceding paragraph.

(A) *Nickel sulfide*

According to Tsubokawa[10)], NiS with the NiAs structure was found to be antiferromagnetic with the Néel point at 150°K. Its ionic constitution of the metal ion can be regarded as Ni^{2+} ion as shown in Table I. Since χ_c is found to be larger than χ_a, the easy axis of antiferromagnetic spin lies in the *c*-plane below the Néel point.

Above the Néel point, using the magnetic data obtained by Tsubokawa, $\chi_c-\chi_a$ is given by Eq. (34) as follows,

$$\chi_c-\chi_a=-2.83\chi_p{}^2+(g_c{}^2-g_a{}^2)(T+3000)^{-1}$$
$$\times 2.75\times 10^{-3}+0.5D\chi_p/kT \text{ per gram .} \quad (35)$$

According to his experimental data, the first term in the above expression can be neglected as compared with the other two terms. Also the temperature dependence of $\chi_c-\chi_a$ in the measured result by Tsubokawa can well be reproduced by putting $g_c{}^2-g_a{}^2=0.005$ and $D=0.59\,\mathrm{cm}^{-1}$ per ion. In this case D is considered to consist of the terms of the spin-orbit interaction and intra spin-spin interaction, and the fact, $\chi_c>\chi_a$ above T_N, means that the anisotropy energies due to those origins have the easy axis parallel to the c-axis, then we have a value of anisotropy energy due to the above two origins at absolute zero as, $K(0)=-DS(S-(1/2))=-0.3\,\mathrm{cm}^{-1}$ per ion.

Now, if we assume the first kind antiferromagnetic ordering for this compound, the anisotropy energy due to the magnetic dipolar interaction takes the value, $K_D=0.65\,\mathrm{cm}^{-1}$ per ion with an easy axis in the c-plane as shown in Table II. On the other hand, the anisotropy energy due to the spin orbit interaction and the intra spin-spin interaction can be calculated from Eq. (17) and Eq. (29) respectively. If we apply the relevant crystal field to this substance, which is obtained from Table II with the value $c/a=1.56$ and takes the order of magnitude $1\,\text{Å}^2$ and $1\,\text{Å}^4$ for the value $\langle r^2\rangle$ and $\langle r^4\rangle$ respectively, the anisotropy energies due to both origins have a negative sign as directing the spin along the c-axis. In our calculation, however, it is necessary to take a smaller value for λ and ρ as low as a few tenth in the free ion state to give the order of the observed anisotropy energy obtained above.

Consequently, from the above estimation of values, K and K_D, it can be understood that the anisotropy energy due to dipolar interaction is preferential, and hence below T_N spins lie in the c-plane.

It is to be noted here that the easy axis of spin in VS and VSe[11] is possible to predict from the above consideration, though their anisotropy energies have not yet been measured. Since the orbital state for both $\mathrm{Ni}^{2+}(3d^8\,{}^3F)$ and $\mathrm{V}^{2+}(3d^3\,{}^4F)$ ions in a given crystal field has the same energy level scheme, it can be expected that the spins in these substance lie in the c-plane according to the same reason as described above.

(B) *Iron sulfide and selenide*; $\mathrm{Fe_7S_8}$ *and* $\mathrm{Fe_7Se_8}$.

It was found that the easy axis of magnetic moment for the ferrimagnetic compound $\mathrm{Fe_7S_8}$[12] as well as $\mathrm{Fe_7Se_8}$[13] changes from the direction near the c-axis to one in the c-plane with rising temperature (shown in Fig. 4). Such change is considered to be due to the spin-orbit interaction of Fe^{2+} ion under the peculiar crystalline field of these substances.

$\mathrm{Fe_7S_8}$ and $\mathrm{Fe_7Se_8}$ have a pseudo NiAs type crystal structure. In the case of $\mathrm{Fe_7S_8}$ lattice[14], every second (001) net plane composed of the iron atoms has vacancies, the distribution of which has the period $C=4c$, $B=2\sqrt{3}\,a$ along [001] as well as [110] direction, and the crystal lattice is accompanied by a small monoclinic distortion. In $\mathrm{Fe_7Se_8}$, there are two types of superlattice[15], one like that of $\mathrm{Fe_7S_8}$ with small triclinic distortion and the other like that of the lattice constant $C=3c$ without distortion.

Fe^{2+} ions on the sites of each sublattice are affected by certain different crystal fields due to the difference of the relative positions of surrounding holes and Fe^{3+} ions. Thus some Fe^{2+} ions are set in the field corresponding to the case, $c/a>(c/a)_0$ in a NiAs crystal field and some ones in the case $c/a<(c/a)_0$, namely it can be considered that the Fe^{2+} ion with the hole at the site above it corresponds to the former and one with the hole at the side site corresponds to the latter, and at the same time they are affected by certain orthorhombic fields due to surrounding holes and the Fe^{3+} ions.

As was shown in the preceding paragraph, in the case $c/a>(c/a)_0$ and $c/a<(c/a)_0$ Fe^{2+} ion (D-state) in a NiAs crystal field has different types of anisotropy energy in connection with their temperature dependence as well as angular one. Then the total anisotropic free energy for ϑ can be written by the following form with the approximation, $2zJ\langle S\rangle\gg\lambda$, in Eq. (21).

$$F_{an}(\vartheta)=-c_1kT\,1_n[\cosh\{2(\lambda l_z\cos\vartheta+R)/kT\}]$$
$$+c_2K\cos^2\vartheta\,, \quad (36)$$

where the first term means the anisotropy energy coming from the degenerated orbital state with the preferred c-axis, which is split by the somewhat smaller orthorhombic field and its width takes $2R$, and the second one is the anisotropy energy with the easy axis in the c-plane which comes from the perturbation in the non-degenerate orbital state and the magnetic dipolar interaction. c_1 and c_2 are the numerical factors for each term.

The easy direction of magnetic moment is determined from $\partial F/\partial\vartheta=0$, which give the following relation,

$$(c_2K(T)/c_1\lambda l_z)\cos\vartheta =\tanh\{2(\lambda l_z\cos\vartheta+R)/kT\} . \qquad (37)$$

As will be shown below, it can be considered for Fe_7Se_8 that the energy due to the orthorhombic field, R, is very small as compared with λl_z. Then if we take $R=0$ in the above equation, the easy direction at absolute zero, denoted by $\vartheta(0)$, is given as

$$\cos\vartheta(0)=c_1\lambda l_z/c_2K(0) . \qquad (38)$$

For the case, $c_1\lambda l_z/c_2K(0)\geqq 1$, in the above equation, $\vartheta(0)=0$ is given and in this case the departure temperature T_0 of the magnetization from the c-axis is given by the following formula,

$$c_2K(T_0)/c_1\lambda l_z=\tanh(2\lambda l_z/kT_0) . \qquad (39)$$

Next, the temperature, $T_{\pi/2}$, where the magnetic moment reaches the c-plane ($\vartheta=\pi/2$) is shown as follows,

$$kT_{\pi/2}=2c_1(\lambda l_z)^2/c_2K(T_{\pi/2}) . \qquad (40)$$

Then we have the following relations for λl_z by elimination of c_1/c_2 from equations (38), (39) and (40);

$$\lambda l_z=K(T_{\pi/2})kT_{\pi/2}/\{2K(0)\cos\vartheta(0)\} \quad \text{for} \quad c_1\lambda l_z/c_2K(0)<1 , \qquad (41)$$

and

$$\lambda l_z=(kT_{\pi/2}K(T_{\pi/2})/2K(T_0))\tanh(2\lambda l_z/kT_0) \quad \text{for} \quad c_1\lambda l_z/c_2K(0)>1 . \qquad (42)$$

Now $K(T)$ consists of two parts; one due to the spin orbit-coupling, which is proportional to $\langle S_z^2\rangle$, and the other due to dipolar energy, proportional to $\langle S\rangle^2$. However, the former has the main contribution for K, since ΔE is not very large as compared with λ according to our knowledge of the energy level schemes in this system. Therefore, we adopt, $K(T)\propto\langle S_z^2\rangle$, for the following estimations described below.

Since $\vartheta(0)=20°$ in Fe_7Se_8 ($C=4c$)[18] the case for $c_1\lambda l_z/c_2K(0)<1$ holds, while in Fe_7Se_8 ($C=3c$) the one for $c_1\lambda l_z/c_2K(0)>1$ holds, because $\vartheta=0$ for $0<T<T_0$. The valve λl_z for either substance can be estimated from experimental data as follows:

$$\lambda l_z=60.5\ \text{cm}^{-1} \quad \text{for} \quad Fe_7Se_8\ (C=4c) ,$$

where $T_{\pi/2}=220°\text{K}$, $T_{\pi/2}/T_c=0.5$ and $K(T_{\pi/2})/K(0)=0.743$ are used;

$$\lambda l_z=40\ \text{cm}^{-1} \quad \text{for} \quad Fe_7Se_8\ (C=3c) ,$$

where $T_{\pi/2}=150°\text{K}$, $T_0=100°\text{K}$ and $K(T_0)/K(0)=0.92$ are used. The theoretical results of $\vartheta-T$ relation for either case are shown in Fig. 4 and are in good agreement with the experimental results.

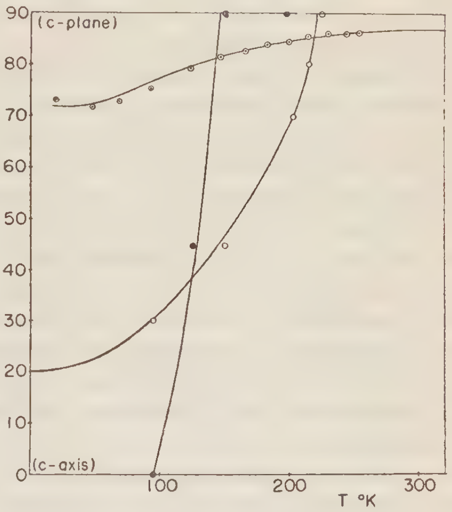

Fig. 4. The relation between the easy direction and temperature for Fe_7Se_8 ($C=4c$), Fe_7Se_8 ($C=3c$) and Fe_7S_8 ($C=4c$).

——— Theoretical curves.

○, ●, ⊙ Experimental values of Fe_7Se_8 ($4c$), Fe_7Se ($3c$), Fe_7S_8 respectively.

In the case of Fe_7S_8, $\vartheta(T)$[*] has the value of about 70° at absolute zero and decreases continuously, reaching 87° at room temperature. So far as the rotation of easy direction in Fe_7S_8 is concerned, the effect of orthorhombic field, R, can not be disregarded to explain the behavior of $\vartheta(T)$.

---

[*] $\vartheta(T)$ can be obtained approximately from Pauthenet's data of thermomagnetic curves, $\sigma_c(H, T)$ and $\sigma_a(H, T)$, by the following extraporation for H: $\tan\vartheta(T)=\sigma_{0a}(T)/\sigma_{0c}(T)$ with $\sigma_c(H, T)=\sigma_{0c}(T)+\chi_cH$ and $\sigma_a(H, T)=\sigma_{0a}(T)-bH^{-1}$. $\vartheta(T)$ thus obtained is plotted in Fig. 3 together with those in Fe_7Se_8.

Now we return to Eq. (37). Its solution at high temperature can be obtained easily from λ/kT expansion, which is shown as,

$$(\cos\vartheta)^{-1}=(c_2K/2c_1\lambda l_zR)kT-(\lambda l_z/R)\ . \qquad (43)$$

Hence ϑ has a temperature dependence with smooth changes which is different from the cases in Fe_7Se_8. Thus, the following values of λl_z and R in Fe_7S_8 are estimated.

λl_z 66.3 cm^{-1} and $R=15.3\ cm^{-1}$

for Fe_7S_8 $(C=4c)$,

where $T_{\pi/2}=100$°K, $\vartheta(0)=72°$ and $\lambda l_z/R=4.33$. The theoretical curves are shown in Fig. 4 in good agreement with the experimental plots.*

(C) *Manganese telluride*

MnTe shows an antiferromagnetic property and Mn-ion in this substance is regarded as having the electron configuration of $Mn^{2+}(3d^5)$, from the data of g-factor $(g=2.00)$[16], though the number of effective Bohr magneton in this substance is given by the value $5.10\,\mu_B$[17]. Then the main origin of its anisotropy energy is considered to be one due to the magnetic dipolar interaction, since Mn^{2+} ion with the lowest ^6S-state is not subject to the influence of crystal field except one originated from certain small perturbation between considerably higher states.

According to the data of magnetic susceptibilities in the single crystal measured by Hirakawa[18], χ_c below the Néel point is independent of temperature and χ_a depends on temperature and takes about half the value of χ_c at low temperatures, so that it can be considered that the easy axis of spins lies in the c-plane. From these results the spin arrangement of the first kind or the third kind mentioned in § 2 is available. The relation $\chi_a(0)=\chi_c(0)/2$ in the first kind ordering can be explained by considering the crystallographic domains, such as twins with common c-axis, in which spin is fixed along certain directions within the c-plane by means of a six-fold anisotropy energy in the c-plane, though the origin of anisotropy energy of this type is not clear at present. Further work done by Hirakawa[18] on the behavior of torque curves in the c-plane in a stress-annealed sample shows that there is a possibility of the first kind ordering rather than the third one.

Then if we assume the first kind ordering for MnTe, the value of anisotropy energy due to the dipolar interaction is given as, $K_D=2.20\ cm^{-1}/ion$ or $K_{D1}'=1.46\times10^7\ erg/cm^3$, from the Table III in § 3. On the other side, the anisotropy energy of this type can be determined from the value $\chi_c-\chi_a$ above the Néel point by using the first term in Eq. (34) in § 4, but no experimental data for it have yet been obtained.

(D) *Chromium selenide*

In the antiferromagnetic substance, CrSe, it is considered that a Cr^{2+}-ion is responsible for their magnetic properties from the data of magnetic susceptibility[19]. On the other hand, in conformity with the analysis of neutron diffraction patterns Corliss suggested[20] a possibility of new type of antiferromagnetic ordering at low temperature. This type has an intermediate magnetic structure between the third and the first kind orderings, and each spin on the three sublattices in the same layer has the inclination from the c-axis with an angle of about 45° (" umbrella structure " according to Corliss).

As was given in § 4, the lowest state of the Cr^{2+}-ion in the crystal field of NiAs type is the orbital doublet with the orbital angular momentum, $l_z=1-3\cos^2\theta$, which introduces an anisotropy energy with the easy direction along the c-axis, its order of magnitude being $-\lambda l_zS$. On the other hand, the system has the anisotropy energy due to the magnetic dipolar interaction which is given by $K_D(\vartheta_0)$ as a function of angle, ϑ_0, between the spin and c-axis. Then, in order that the intermediate structure between the third and the first kind orderings as obtained by neutron diffraction experiment may be realized, it is necessary that the following relation between the anisotropy energies and the exchange energies holds for the second and third neighbours at absolute zero,

$$\cos\vartheta_0=\lambda l_zS\{2^{-1}(2z_2J_2-2z_3J_3)S^2+K_D(\vartheta_0)\}\ . \qquad (44)$$

Now, T_N and θ_p in this substance are given by 280°K and −320°K respectively $(\theta_p/T_N=1.14)$. Then A_1 can be regarded as being larger than A_2 and A_3 in the expressions for

---

* Recently the rotation of magnetic easy axis in Fe_7S_8 has been reported by T. Hihara [J. Sci. Hiroshima Univ. Ser. **A**, **24** (1960) 31] and his result seems to correspond to the one obtained by Pauthenet.

T_N and θ_p of the third kind ordering in §2, and also $K(\vartheta_0)$ will be given by a small value of the order of 1 cm⁻¹ from Table II. Hence, if l_z is taken less than one in this substance, and λl_z and $2z_2J_2-2z_3J_3$ have values of the same order of magnitude, it will be reasonable that ϑ_0 takes the same angle as obtained from the neutron diffraction experiment.

(E) *Chromium telluride*

As was shown in Table I, CrTe is a ferromagnetic substance with the Curie point at 330°K[21]. The moment 2.4 μ_B[21] per Cr is obtained from the saturation value of magnetization, while the effective magneton number estimated from the paramagnetic susceptibility above the Curie point takes a value of 4.08 μ_B[22]. According to the results of measurements by Hirone and Chiba[23], the value of anisotropy coefficient K is -5×10^6 erg/cm³ or -1 cm⁻¹ per Cr atom at low temperature.

Now if the present ionic model is suitable for this case, the magnetic moment of Cr^{2+} ion is given as $(2S-l_z)\mu_B$ $(\lambda>0)$, and if we put $(2S-l_z)\mu_B=2.4\ \mu_B$, it turns out that the Cr^{2+} ion in this crystal reserves the orbital angular momentum, $l_z=1.6$, in its lowest state. Consequently, the effective magneton number determined from the experiment can be taken apparently as a smaller value than 4.90 μ_B for $S=2$, so far as the width of energy levels due to the spin-orbit coupling is not much less than kT_c. Thus the anisotropy energy due to both the spin-orbit interaction and the magnetic dipolar interaction in this ferromagnet has the easy direction parallel to the c-axis as mentioned in preceding paragraphs.

The value of uniaxial anisotropy energy obtained by Hirone and Chiba takes about -1 cm⁻¹ per ion at low temperature, and shows the normal temperature dependence expressed roughly by the square of the magnetization. On the other hand, the value of dipolar anisotropy energy is calculated as -0.2 cm⁻¹ per ion, where the observed magnetic moment 2.44 μ_B per ion and the expression K_{Df}, shown in Table II, are used. Therefore, it can be interpreted that the remaining part of anisotropy energy consists of one due to the spin-orbit interaction.

As was shown in the preceding paragraph, however, the uniaxial anisotropy energy originated from the degenerated orbitals has to take the value of order of magnitude, λl_z, at low temperature and show the particular temperature dependence as described above. This result seems to contradict the fact that the anisotropy energy obtained from the experiment shows rather a small value at low temperature with the normal temperature dependence as compared with the one expected theoretically.

(F) *Chromium antimonide*

CrSb is an antiferromagnetic substance with a Néel point of 710°K and the number of effective magnetons is given as 4.92 μ_B[24]. Also according to the results of neutron diffraction analysis observed by Snow[25], its magnetic structure is the first kind ordering with the easy direction parallel to the c-axis and the magnetic moment 2.7 μ_B. The value of uniaxial anisotropy energy at room temperature measured by Tsubokawa[26] is given as about -7×10^5 erg/cm³ or -0.1 cm⁻¹/ion, which is obtained from the relation for susceptibilities with field dependence between powdered and single crystals of CrSb.

From these data, it is considered that the presence of Cr^{2+} ion in CrSb is probable. Thus, as the case in CrTe discussed above, it can be regarded that the retained orbital angular momentum, l_z, in lowest state takes a value of 1.3 resulting in the total magnetic moment at low temperature having the value, $(2S-l_z)\mu_B=2.7\ \mu_B$. Then the magnetic moment should orient along the c-axis with a considerably strong anisotropy energy. On the other side, in the first kind antiferromagnetic structure the dipolar anisotropy energy prefers to keep its spin within the c-plane. Hence, as compared with the experimental results it can be concluded that the term due to the spin-orbit interaction predominates over the dipolar term.

Based on such a consideration, the observed anisotropy energy, K_{obs}, can be written as follows,

$$K_{obs}=K_{LS}+K_D=-0.1\ \text{cm}^{-1}\,, \tag{45}$$

where K_D can be estimated from Table II and III and for K_{LS} the approximation $\lambda l_z<kT<kT_N$, in the Eq. (21) is used. From this equation, λ can be estimated as about 13 cm⁻¹ by taking $S=2$, $l_z=1.3$ and $T=300$°K, which is rather a small value as compared with one of the free ions, 57 cm⁻¹. This can be confirmed by the fact that the effective

magneton number at high temperature takes nearly a free spin value, 4.90 μ_B ($S=2$).

§ 6. Discussions

As was shown in the above paragraphs, we could elucidate the experimental results about uniaxial anisotropy energies for the several compounds with a NiAs structure from our theory based on the assumption for the ionic constitution of transition metal element in conformity with their magnetic data. However, further studies should be made on the above problems.

First, we assumed somewhat boldly the ionic constitution of $3d$ electrons in the transition metal element with the realization of the Hund rule. There are still some unanswered questions for this assumption, especially, for several substances whose magnetic data can not be explained satisfactorily by the ionic constitution, as was shown in Table I. According to our empirical stand point for the compounds in sulfides and selenides of transition elements with NiAs structure except those of titanium, the ionic constitution is considerably satisfactory. On the other hand, for the compounds with heavy metalloid elements and those which form a MnP type crystal structure, however, the ionic character is not always satisfied. In the latter compounds, it can be regarded that considerable parts of metallic binding and covalent binding must be important for their binding nature. Then in order to obtain the expression of anisotropy energy in these substances, it will be necessary to know their detailed electronic structure, taking their ionic and metallic or ionic and covalent characters into account.

Next, the crystal fields calculated only from the point charge model are not very correct for a substance with a NiAs structure. It can be regarded that there exists the considerable overlap of charge clouds between neighbouring ions, from the disagreement between their ionic radii and lattice parameters, and so in some cases its correction will be important.

Also the crystal fields acting on the cation are subject to an effect of the electric field caused by the multipole moment of the anions due to certain deformation of their charge clouds in a given crystal field. In NiAs type crystals the electric quadrupole fields would be important, whereas in such a crystal with vacant lattice sites as Fe_7S_8, metallic ions suffer the effect of electric dipole field. Moreover, under certain circumstances the crystal fields would be affected by the covalent bonding or the screening effects due to the conduction electrons in the crystal in some substance which has somewhat high electric conductivity. Therefore, it can be considered that the valves of $\langle r^2 \rangle$ and $\langle r^4 \rangle$ for each substance are controlled by these factors, and also the coupling constant of spin orbit interaction in the crystal takes a different smaller value than the one in the free ion, as was estimated in some substances mentioned above.

In conclusion, it can be confirmed by the present study of anisotropy energy that the ionic constitution of transition metal elements is realized in the comprehensive compounds with NiAs structures. In order to explain the detailed magnetic properties as for the magnetic anisotropy energy in a NiAs structure, a more refined theory should be expected, and it is also desirable to obtain the experimental data for the spin structure, the magnetic anisotropy energy and other properties in still more NiAs type compounds.

The author wishes to express his sincere gratitude to Professor T. Hirone for his valuable discussions and cordial encouragement during the course of this study, and to thank members of Professor Hirone's research laboratory for communicating their many interesting experimental results, and also to sincerely thank Dr. K. Hirakawa and Dr. L. M. Corliss for communicating unpublished experimental results. The present investigation was partly supported by Scientific Research Funds from the Ministry of Education.

Appendix I.

The energy matrix of crystal fields, V, and the transformation matrix, C, for D- and F-state appearing in § 4 are given as follows:

$$V_D=\begin{array}{c|ccccc} m & & & & & \\ 0 & 2A+6B & & & & \\ 1 & & A-4B & C & & \\ -2 & & C & -2A+B & & \\ -1 & & & & A-4B & -C \\ 2 & & & & -C & -2A+B \end{array},$$

$$C_D=\begin{array}{c|ccccc} 0 & 1 & & & & \\ 1 & & \cos\theta & \sin\theta & & \\ -2 & & -\sin\theta & \cos\theta & & \\ -1 & & & & \cos\theta & -\sin\theta \\ 2 & & & & \sin\theta & \cos\theta \end{array},$$

for D-state, and

$$V_F=\begin{array}{c|ccccccc} m & & & & & & & \\ 0 & -4A'+6B' & -3\sqrt{5}C' & 3\sqrt{5}C' & & & & \\ 3 & -3\sqrt{5}C' & 5A'+3B' & & & & & \\ -3 & 3\sqrt{5}C' & & 5A'+3B' & & & & \\ 1 & & & & -3A'+B' & \sqrt{10}C' & & \\ -2 & & & & \sqrt{10}C' & -7B' & & \\ -1 & & & & & & -3A'+B' & -\sqrt{10}C' \\ 2 & & & & & & -\sqrt{10}C' & -7B' \end{array},$$

$$C_F=\begin{array}{c|ccccccc} 0 & & 1/\sqrt{2} & 1/\sqrt{2} & & & & \\ 3 & \sin\theta_1 & \cos\theta_1/\sqrt{2} & -\cos\theta_1/\sqrt{2} & & & & \\ -3 & -\cos\theta_1 & \sin\theta_1/\sqrt{2} & -\sin\theta_1/\sqrt{2} & & & & \\ 1 & & & & \cos\theta_2 & \sin\theta_2 & & \\ -2 & & & & -\sin\theta_2 & \cos\theta_2 & & \\ -1 & & & & & & \cos\theta_2 & -\sin\theta_2 \\ 2 & & & & & & \sin\theta_2 & \cos\theta_2 \end{array},$$

for F-state.

References

1) T. Nagamiya, K. Yosida and R. Kubo: Advances in Phys. **4** (1955) 1.
2) K. Yoshida and M. Tachiki: Progr. Theor. Phys. **17** (1957) 331.
3) T. Hirone and K. Adachi: J. Phys. Soc. Japan **12** (1957) 156.
4) A. Abragam and M. H. L. Pryce: Proc. Roy. Soc. A, **206** (1951) 173.
5) J. Kanamori: Progr. Theor. Phys. **17** (1957) 177.
6) M. H. L. Pryce: Proc. Phys. Soc. London **63** (1950) 25.
7) J. C. Slonczewski: Phys. Rev. **110** (1958) 1341.
8) M. H. L. Pryce: Phys. Rev. **80** (1950) 1107.
9) I. E. Dzialoshinskii: Sov. Phys. JETP **5** (1957) 1295.
10) I. Tsubokawa: J. Phys. Soc. Japan **13** (1958) 1432.
11) I. Tsubokawa: J. Phys. Soc. Japan **14** (1959) 196.
12) R. Pauthenet: Compt. rend. **234** (1952) 2261.
13) K. Hirakawa: J. Phys. Soc. Japan **11** (1956) 930.
14) F. Bertaut: J. Phys. radium **13** (1952) 372.
15) A. Okazaki and K. Hirakawa: J. Phys. Soc. Japan **11** (1956) 930; **14** (1958) 112; and A. Okazaki: J. Phys. Soc. Japan **16** (1961) 1162.
16) L. R. Maxwell and T. R. McGuire: Rev. Mod. Phys. **25** (1953) 279.
17) E. Uchida and H. Kondoh: J. Phys. Soc. Japan **11** (1956) 27.
18) K. Hirakawa: private communication.
19) I. Tsubokawa: J. Phys. Soc. Japan **15** (1960) 2243.
20) L. M. Corliss, N. Elliott, J. M. Hasting and R. L. Sass: Phys. Rev. **122** (1961) 1402.
21) C. Guillaud and S. Barbezat: Compt. rend. **222** (1946) 386.
22) I. Tsubokawa: J. Phys. Soc. Japan **11** (1956) 662.
23) T. Hirone and S. Chiba: J. Phys. Soc. Japan **15** (1960) 1991.
24) T. Hirone, S. Maeda, I. Tsubokawa and N. Tsuya: J. Phys. Soc. Japan **11** (1956) 1083.
25) A. I. Snow: Phys. Rev. **85** (1952) 227.
26) I. Tsubokawa: J. Phys. Soc. Japan **16** (1961) 277.

JOURNAL OF THE PHYSICAL SOCIETY OF JAPAN, Vol. 16, No. 11, NOVEMBER, 1961

Dielectric Properties of Ferroelectric $NaNO_2$

Shozo SAWADA, Shoichiro NOMURA and Yohko ASAO

Department of Physics, Tokyo Institute of Technology

(Received July 7, 1961)

In $NaNO_2$ crystals, prepared by both of the fusion method and the aqueous solution method, the *D-E* hysteresis loops were observed by the 50 c/s *ac* field and the dielectric constant along the ferroelectric *b* axis, ε_b, was measured by the 100 kc/s *ac* voltage. The pyroelectric current was measured by the usual galvanometer method. The values of the spontaneous polarization determined by two methods agreed well with each other. ε_b showed a distinct anomaly around the Curie temperature and obeyed the Curie-Weiss law below and above the Curie temperature. The ratio of two Curie constants was found to be 9.6:1. Some discussions, taking account of the crystal structure, were made.

§ 1. Introduction

$NaNO_2$ has a transition at about 163°C and above this temperature its crystal structure is nonpolar and belongs to the orthorhombic system, its space group being D_{2h}^{25}-*Immm*[1,2]. Below the transition temperature, the crystal structure is still orthorhombic but is polar along the *b* axis, its space group being C_{2v}^{20}-*Imm*[3,4,5]. The low-temperature phase is known to be piezoelectric and further has been found to be ferroelectric by the authors and their co-workers[6]. The details of the domain structure of $NaNO_2$ arising from its ferroelectricity have also been reported[7]. Sonin *et al* have very recently reported the dielectric properties of $NaNO_2$ crystals[8]. Our result of measurement of the dielectric properties of $NaNO_2$ will now be described in detail. The methods of preparation of crystals and of treatment of them have been mentioned in the previous paper[7].

§ 2. Results of Experiments

1. *D-E Hysteresis Loop*

Photo. 1 shows the *D-E* hysteresis loops of a crystal prepared by the fusion method observed by the usual Sawyer-Tower method at various temperatures on cooling, using the 50 c/s *ac* electric field ($E_{\max}=8.86$ kV/cm). The *D-E* relation was a straight line above 166°C and the loop began to open out from about 165°C, became a ferroelectric one at about 159.5°C and changed again to a straight line at about 100°C owing to the extremely high value of the coercive field below this temperature. Photo. 2 shows the amplitude dependence of the hysteresis loop observed at 138°C on heating, where the absolute values of *E* and *D* are shown and they are also applicable to Photo 1. The temperature dependence of the spontaneous polarization and the coercive field obtained from Photo. 1 are shown in

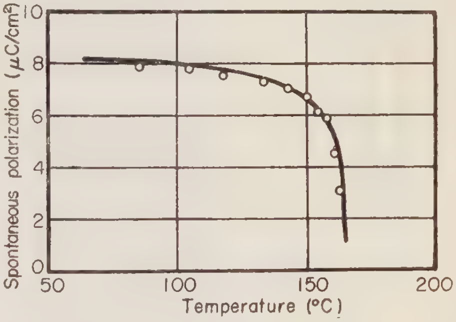

Fig. 1. Temperature dependence of the spontaneous polarization determined by the hysteresis loop.

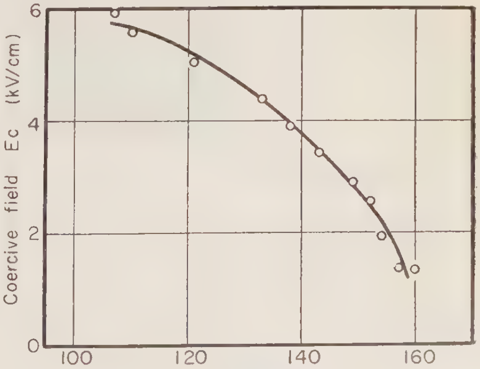

Fig. 2. Temperature dependence of the coercive field ($E_{\max}=8.86$ kV/cm).

Figs. 1 and 2, respectively. The amplitude dependence of the residual polarization reduced by its saturated value and that of the coercive field obtained from Photo. 2 are shown in Figs. 3 and 4, respectively. The spontaneous polarization and the coercive field at 150°C were found to be about 7μC/cm^2 and 3 kV/cm, respectively. The double hysteresis loop was observed in a temperature range of several degrees above 160°C as seen in Photo. 1, a typical example being further shown in Photo. 3. Although the hysteresis loop of crystals prepared by the aqueous solution method showed a little incomplete saturation, their spontaneous polarization and coercive field were nearly the same as shown in Figs. 1, 2, 3 and 4.

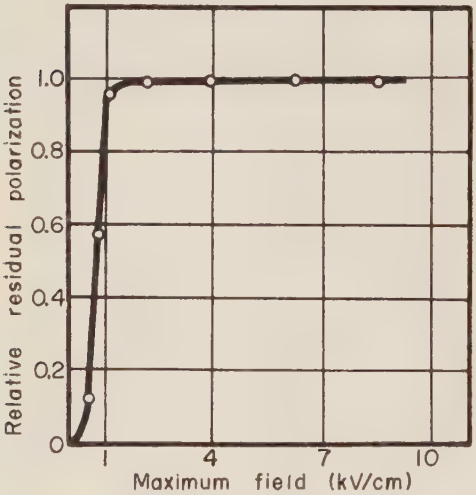

Fig. 3. Amplitude dependence of the relative residual polarization (138°C).

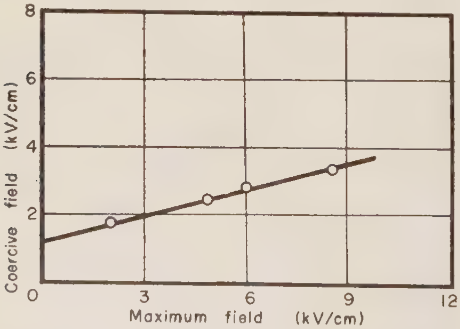

Fig. 4. Amplitude dependence of the coercive field (138°C).

2. *Pyroelectric current*

Fig. 5 shows the temperature dependence of the pyroelectric current of a crystal prepared by the fusion method measured by the usual galvanometer method on heating in the rate of 0.63°C/min, after a treatment by the *dc* field of 10 kV/cm on cooling from 130°C to

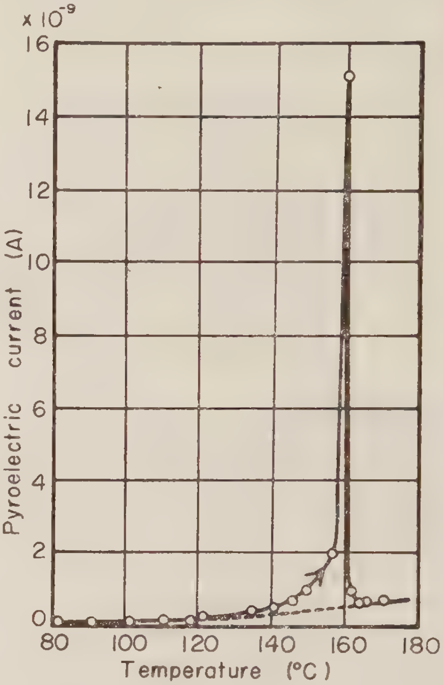

Fig. 5. Temperature dependence of the pyroelectric current.

Poling: 10 kV/cm, on cooling from 130°C to room temperature during 0.5 hr.

Heating rate: 0.63°C/min. Electrodes area: 0.35 cm².

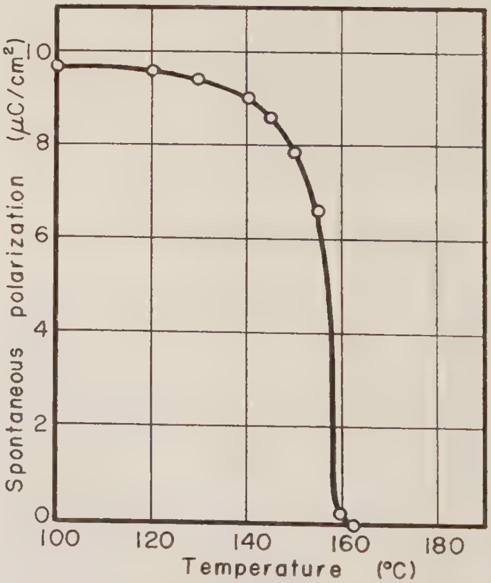

Fig. 6. Temperature dependence of the spontaneous polarization determined by the pyroelectric current.

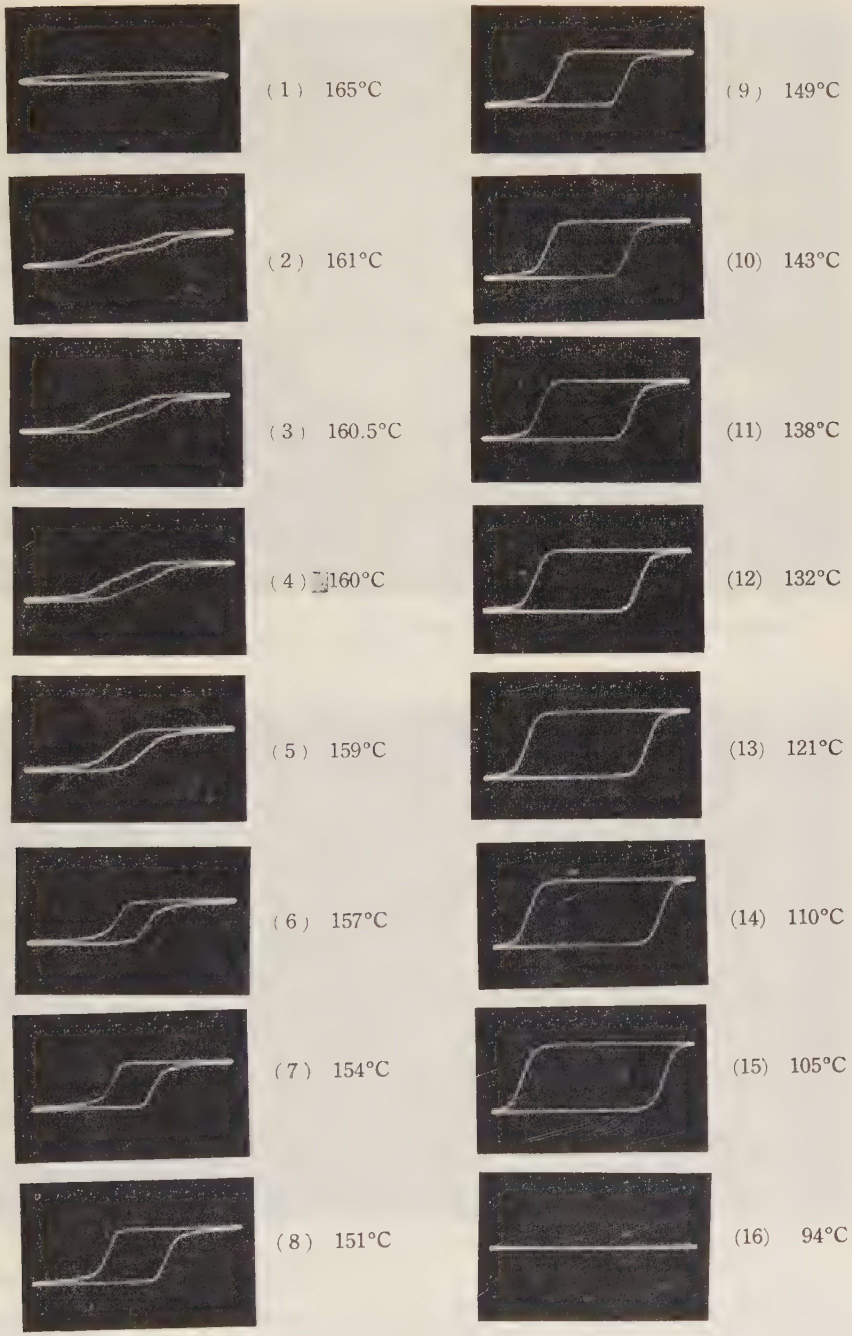

(1) 165°C
(2) 161°C
(3) 160.5°C
(4) 160°C
(5) 159°C
(6) 157°C
(7) 154°C
(8) 151°C
(9) 149°C
(10) 143°C
(11) 138°C
(12) 132°C
(13) 121°C
(14) 110°C
(15) 105°C
(16) 94°C

Photo. 1. D-E hysteresis loops observed at various temperatures on cooling (50 c/s, $E_{\max}=8.86$ kV/cm).

room temperature during 0.5 hr. When the field treatment was made in the reverse polarity, the pyroelectric current was completely reversed. The spontaneous polarization obtained from these measurements of the pyroelectric current is shown in Fig. 6, which agrees well with the one shown in Fig. 1, determined by the observation of the hysteresis loop.

3. *Dielectric constant*

The dielectric constants along the a- and c- axes are small throughout the temperature range from room temperature to 180°C and show only a slight anomaly at the Curie

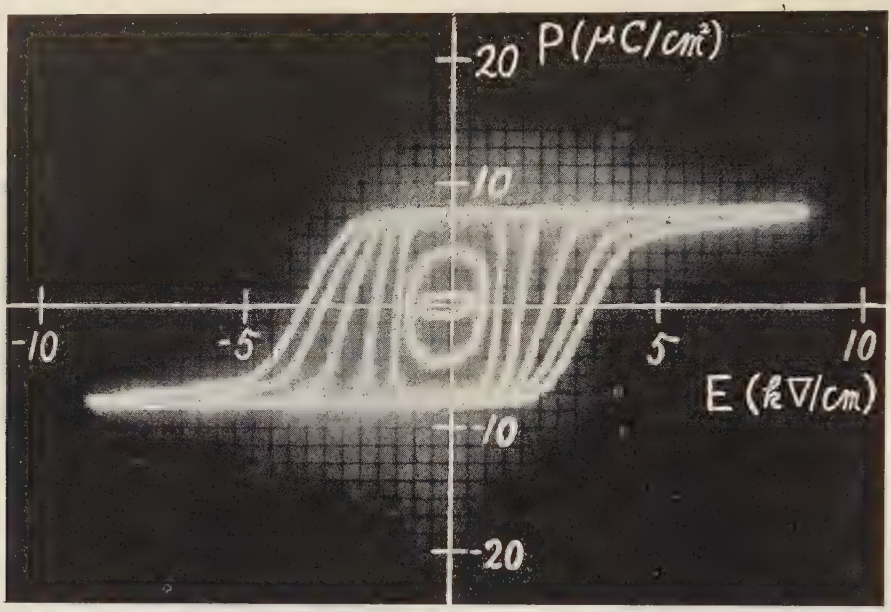

Photo. 2. Amplitude dependence of the hysteresis loop observed at 138°C on heating (50 c/s).

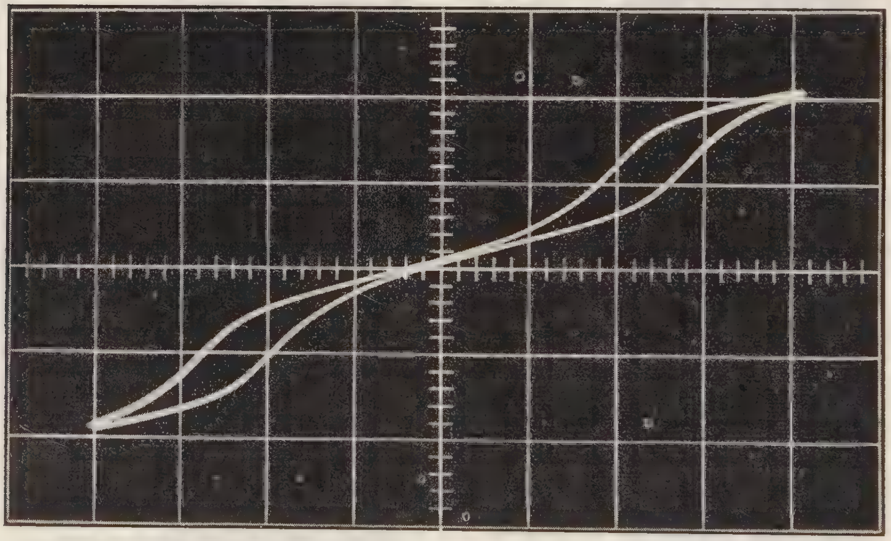

Photo. 3. Double hysteresis loop just above the Curie point (50 c/s, 165°C).

point. Fig. 7 shows the dielectric constant along the b axis, ε_b, of a crystal prepared by the aqueous solution method measured by a C-meter using the 100 kc/s *ac* voltage, where a distinct anomaly is seen around the Curie temperature. Fig. 8 shows that ε_b obeys the Curie-Weiss law above and below the Curie temperature. In the paraelectric phase, the Curie constant and the Curie-Weiss temperature were found as $C=4.7\times10^3$°K and $T_0=162$°C, respectively. The ratio of the Curie constants below and above the Curie temperature was found as 9.6:1.

4. *Low-temperature Measurements*

In order to clarify whether any other transition point exists or not below 163°C, the observation of the hysteresis loop and the measurement of the dielectric constant along three crystal axes were performed from room temperature down to the liquid nitrogen temperature, but any distinct anomaly was not discerned.

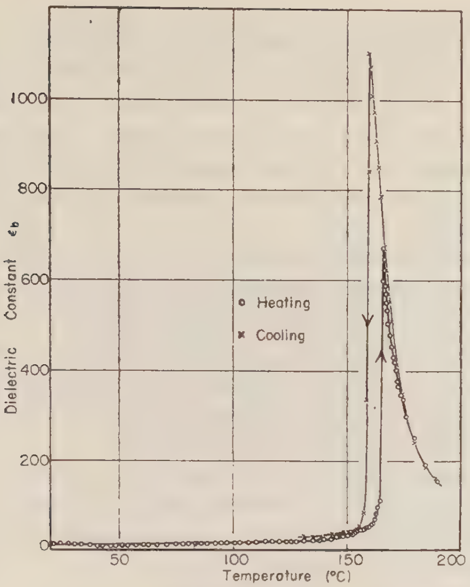

Fig. 7. Dielectric constant along the *b* axis (a crystal prepared by the aqueous solution method, 100 kc/s).

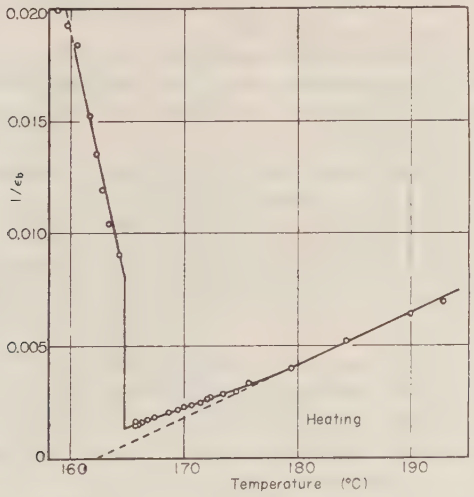

Fig. 8. Curie-Weiss law of ε_b.

§ 3. Discussion

It is clear from the results of the analysis of crystal structure[3),4),5)] that the spontaneous polarization of $NaNO_2$ along the *b* axis below 163°C comes from the fact that in this temperature range the NO_2 groups are aligned in one, *e. g.*, (+) sense of the *b* axis and accordingly the Na ions are displaced in this direction. Further, it is nearly certain that the ferroelectricity of $NaNO_2$ in the low-temperature phase arises from the reversal of NO_2 groups and the transfer of Na ions from the original positions to the other ones quite symmetric to the original ones, by the external electric field. Nothing can be said, however, only by the result of dielectric measurements mentioned above, concerning what process the direction of the NO_2 groups is reversed in. The translational motion of the N atom on the line which is perpendicular to the O-O bond and equally divides it and the rotation of the NO_2 group, as a whole about its O-O bond along the *c* axis, have the effect of reversal of the permanent dipole on the NO_2 group, but such motions are unlikely to occur only by themselves. It seems more reasonable to suppose that such translational or rotational motions would be realized accompanied with oscillations or rotations about the *a*- or *b*-axes. The data of the nuclear magnetic resonance[9)] and the infrared absorption[10)] would be useful in clarifying the mechanism of reversal of the NO_2 groups. Anyhow, $NaNO_2$ may be said to have, in some degree, a character of " molecular-rotational ferroelectrics ", judged from the fact that the polarization reversal in $NaNO_2$ is supposed to be fairly related with the rotational motions of the NO_2 groups.

There is scarcely doubt to say that $NaNO_2$ belongs to the order-disorder type ferroelectrics, that is, even in the low-temperature phase, not all of the NO_2 groups are aligned in one, *e.g.*, (+) direction of the *b* axis, but only a portion of them, in a definite degree at each temperature, is considered to be aligned in this direction and the remainder in the reverse one. Fig. 1 shows not only the temperature dependence of the spontaneous polarization but also that of the degree of order, as far as the dipole moments on the NO_2 groups and those due to the displacement of the Na ions are assumed to be independent of the temperature. The temperature dependence of the degree of order has been recently studied by the measurement of the temperature dependence of the Bragg reflections of X-ray[11)], nearly the same result as shown in Fig. 1 having been obtained.

Although the positions of each atom have precisely been determined in the low-temperature phase[3),4),5)], the value of spontaneous polarization calculated from the values of the atomic positions, assuming the valencies of Na, N and O atoms as +1, +3 and −2, respectively, is about 70μC/cm^2 and is about ten times as large as the observed value. Such a discrepancy is surely due to the covalent character of the N-O bond, but the calculated valencies of N and O such as -0.36 and -0.32, taking the valence of Na as $+1$ and adopting the observed value of the spontaneous polarization[5], might be not so reliable, at least quantitatively. However, it is not doubtful that the NO_2 group in $NaNO_2$ lattice has the dippole moment not so different in magnitude from that of the free NO_2 molecule (0.4 D.U.) and accordingly the contribution of the NO_2 groups to the spontaneous polarization is not larger than 15% of the total.

The experimental results that the spontaneous polarization is not discontinuous at the Curie point and that the paraelectric Curie point nearly coincides with the ferroelectric one support the opinion that the transition is of the second order. On the other hand, those that a temperature hysteresis of about 3°C is seen between heating and cooling processes, that the dielectric constant is slightly discontinuous at the Curie point, that the ratio of the Curie constants below and above the Curie point is near not 2:1 but 8:1 and that the double hysteresis loop is observed just above the Curie point support the contrary opinion, *i.e.*, that the transition is of the first kind. Considering the low accuracy in determining the temperature dependence of the spontaneous polarization around the Curie point, it would be adequate to say that the transition is the first kind one which is very near the second kind one.

The vanishing of the spontaneous polarization above 163°C is surely due to the equal distribution of the NO_2 groups and the Na ions along the positive and negative directions of the *b* axis, but the detailed atomic positions in the high-temperature phase reported by several authors[1],[2] do not necessarily agree with each other. Tanisaki[12] reported that the NO_2 groups are aligned on a line running along the *b* axis up to enough high temperatures, such chains exist in an antiparallel manner, seen along the *a* axis, with a period of about four cells just above the Curie point and that such a regularity along the *a* axis gradually vanishes with the increase of temperature. Hoshino and Shibuya[13] reported a new phase, supposed to be antiferroelectric, in the temperature range from 163°C to 178°C.* Such regular arrangement of the NO_2 groups above the Curie temperature may be supposed to be transferred to the domain structure in the ferroelectric phase, in which the domain boundaries are almost always the *a* planes, passing through the stage of "microdomain" closely around the Curie temperature. Anyhow, the dielectric and other measurements in the paraelectric phase would be valuable to clear up the mechanism of the polarization reversal in the ferroelectric phase.

The authors wish to express their sincere thanks to Dr. I. Yoshida, Mr. E. Ichinoe and Mr. H. Sugie for their cooperations in experiments.

References

1) B. Strijk and C. H. Mac Gillavry: Rec. trav. chim. **62** (1943) 705; **65** (1946) 127.
2) B. C. Frazer, R. Ueda and M. I. Kay: Acta Cryst. **13** (1960) 1089.
3) M. R. Truter: Acta Cryst. **7** (1954) 73.
4) G. B. Carpenter: Acta Cryst. **8** (1955) 852.
5) M. I. Kay and B. C. Frazer: Acta Cryst. **14** (1961) 56.
6) S. Sawada, S. Nomura, S. Fujii and I. Yoshida: Phys. Rev. Letters **1** (1958) 320.
7) S. Nomura, Y. Asao and S. Sawada: J. Phys. Soc. Japan **16** (1961) 917.
8) A. S. Sonin, I. S. Zheludev and G. F. Dobrzhanski: Izv. Akad. Nauk Ser. Fiz. **24** (1960) 1209.
9) H. Betsuyaku and J. Itoh: Preprint of the Annual Meeting of the Phys. Soc. Japan No. 3, p. 189 (1960).
10) Y. Sato and Y. Takagi: J. Phys. Soc. Japan to be published.
11) I. Shib uya: J. Phys. Soc. Japan **16** (1961) 490.
12) S. Tanisaki: J. Phys. Soc. Japan **16** (1961) 579.
13) S. Hoshino and I. Shibuya: J. Phys. Soc. Japan **16** (1961) 1254.

---

* A rather gradual bend is seen around 176°C in Fig. 8, which may correspond to this transition. However, such a slight deviation from the linear relation of $1/\varepsilon$ -T curve would be caused by various reasons.

JOURNAL OF THE PHYSICAL SOCIETY OF JAPAN, Vol. 16, No. 11, NOVEMBER, 1961

On the Theory of Mixed Conduction with Special Reference to the Conduction in Silver Sulfide Group Semiconductors

By Isaaki YOKOTA

Department of Physics, Faculty of Science, University of Niigata

(Received July 12, 1961)

A macroscopic theory of mixed conduction——partly electronic and partly ionic conduction——is developed with special reference to the conduction in silver sulfide group semiconductors. Current equations combined with continuity equation give an equation which can be reduced to a diffusion equation under simplifying assumptions. It can be integrated with ease under boundary conditions which are prescribed by the nature of electrodes employed.

General expressions for potential distributions are derived. Two kinds of potentials are distinguished. One is the potential as measured by the use of probes consisting of electronic conductor, and the other as measured by the use of probes consisting of ionic conductor such as silver iodide for silver sulfide. The former reveals the relative electrochemical potential of electrons and the latter that of ions.

Calculated time variations of potential distributions for formation and decay processes of stationary polarizations are compared with experiments for $Ag_{1.93}Te$ at 161°C showing satisfactory agreements.

§ 1. Introduction

By the terminology silver sulfide group semiconductors we mean sulfides, selenides, and tellurides of silver and monovalent copper and their alloys. The conduction properties of these substances have been investigated by Reinhold[1)-4)], Wagner[5)-7)], and particularly in details by Miyatani[8)-17)]. They are characterized by the fact that they exhibit mixed conduction, i. e., partly electronic and partly ionic conduction[18)].

From stoichiometric point of view, they belong to non-stoichiometric or Bertholide compounds[19)]. The M/X ratio (M stands for Ag or Cu and X for S, Se, or Te) can deviate from the stoichiometric value to a certain extent without bringing about any discontinuous change in their physical properties. Moreover, the M/X ratio can be controlled by means of the galvanic cell $Ag|AgI|Ag_{2+x}X|Pt$ or $Cu|CuBr|Cu_{2+x}X|Pt$. And this circumstance enables us to control also the electronic carrier concentrations continuously and reversibly.

These characteristics of silver sulfide group semiconductors can be interpreted in terms of the peculiar imperfection in their crystal structure[20)], the so-called average structure. In their high temperature forms (α-forms), negative ions are arranged on body-centered or face-centered cubic lattices, and positive ions are more or less statistically distributed on the interstitial sites and are able comparatively with ease to pass from one site to an unoccupied neighbouring one.

Several years ago the present author published a paper on a macroscopic theory of mixed conduction for the conduction in cuprous sulfide[21)]. The present work is intented to be the revision and the generalization of the previous work so as to cover all the silver sulfide group semiconductors. The general scheme of the theory developed in this work, however, will be applicable to any mixed conductors.

§ 2. Fundamental Equation and Electrode Conditions

After Wagner's theory[22),23)], one may express the electronic and ionic current densities in a mixed conductor respectively as

$$j_e = \sigma_e \frac{\partial(\tilde{\mu}_e/e)}{\partial x} = \sigma_e \frac{\partial(\mu/e)}{\partial x} - \sigma_e \frac{\partial(\tilde{\mu}_i/e)}{\partial x} , \qquad (1)$$

and

$$j_i = -\sigma_i \frac{\partial(\tilde{\mu}_i/e)}{\partial x} , \qquad (2)$$

where σ_e and σ_i are the electronic and ionic conductivities, $\tilde{\mu}_e$ and $\tilde{\mu}_i$ are the electrochemical potentials of electrons and of silver (copper) ions, and

$$\mu=\tilde{\mu}_i+\tilde{\mu}_e \tag{3}$$

is the chemical potential of neutral silver (copper) atoms. The total current density j is then equal to the sum of the above two:

$$\begin{aligned} j&=j_e+j_i \\ &=\sigma_e\frac{\partial(\mu/e)}{\partial x}-\sigma\frac{\partial(\tilde{\mu}_i/e)}{\partial x}, \end{aligned} \tag{4}$$

where

$$\sigma=\sigma_e+\sigma_i \tag{5}$$

is the total electric conductivity. Eliminating $\tilde{\mu}_i$ from Eqs. (1) and (2) by the use of Eq. (4), we have

$$j_e=\frac{\sigma_e}{\sigma}j+\frac{\sigma_e\sigma_i}{\sigma}\frac{\partial(\mu/e)}{\partial x}, \tag{6}$$

and

$$j_i=\frac{\sigma_i}{\sigma}j-\frac{\sigma_e\sigma_i}{\sigma}\frac{\partial(\mu/e)}{\partial x}. \tag{7}$$

It will be reasonable to assume that all silver (copper) atoms in silver sulfide group semiconductors exist in the form of Ag^+ (Cu^+) ions. Denoting the concentration of stoichiometric excess of silver (copper) atoms by N, that of conduction electrons by n, and that of electron holes by p, we should have

$$N=n-p \tag{8}$$

as far as the charge neutrality is established.

Then the equation of continuity for electronic or ionic current, combined with Eqs. (6) or (7), yields

$$\frac{\partial N}{\partial t}=\frac{1}{e}\frac{\partial}{\partial x}\left\{\frac{\sigma_e}{\sigma}j+\frac{\sigma_e\sigma_i}{\sigma}\frac{d(\mu/e)}{dN}\frac{\partial N}{\partial x}\right\}, \tag{9}$$

where we have utilized the fact that the chemical potential of silver (copper) atoms, μ, is a function of N only.

In connection with the boundary conditions for Eq. (9), two kinds of electrodes must be distinguished. If one employs platinum or any other inert electronic conductor as electrodes, the ionic component of the current is perfectly checked at the electrodes and only the electronic component is allowed to pass across. Such electrodes may be called to be electronic, for which the boundary conditions become

$$j_i=0, \quad \text{at} \quad x=0, L, \tag{10}$$

(L being the specimen length) or from Eq. (7)

$$\frac{\partial N}{\partial x}=\frac{ej}{\sigma_e(d\mu/dN)}, \quad \text{at} \quad x=0, L, \tag{11}$$

as far as the current intensity is not enough to precipitace metallic silver (copper) at the negative electrode.

One may also employ Ag|AgI system (or Cu|CuBr system*) as electrode in such an arrangement as $Ag|AgI|Ag_{2+x}X|AgI|Ag$ (or $Cu|CuBr|Cu_{2+x}X|CuBr|Cu$), where the current in AgI (or CuBr) is exclusively carried by Ag^+ (or Cu^+) ions and hence no electronic current in the specimen is able to pass across the boundaries. Such electrodes may be called to be ionic, for which the boundary conditions become

$$j_e=0, \quad \text{at} \quad x=0, L, \tag{12}$$

or, from Eq. (6)

$$\frac{\partial N}{\partial x}=-\frac{ej}{\sigma_i(d\mu/dN)}, \quad \text{at} \quad x=0, L. \tag{13}$$

§ 3. Potential Distribution

In connection with the two kinds of electrode conditions aforementioned one may distinguish the two kinds of potentials. If one measures the potential between two platinum probes, the measured quantity is the difference of the electrochemical potential of electrons divided by electronic charge:

$$V_e=-\left[\frac{\tilde{\mu}_e}{e}\right], \tag{14}$$

which is equal to

$$V_e=-\int\frac{j}{\sigma}dx-\int\frac{\sigma_i}{\sigma}\frac{\partial(\mu/e)}{\partial x}dx \tag{15}$$

according to Eqs. (1) and (6). In the latter expression the first term is of ohmic nature while the second is the polarization potential.**

On the other hand, if we measure the potential by the use of Ag-AgI (Cu-CuBr) probes, the measured quantity is the difference of the electrochemical potential of silver (copper) ions divided by e:

$$V_i=\left[\frac{\tilde{\mu}_i}{e}\right], \tag{16}$$

which is equal to

---

* CuBr is essentially a mixed conductor. Hence Cu|CuBr system is available as ionic electrode (see below) only above 350°C where ionic conduction is far predominant.

** In this paper the terminology polarization is used for the concentration polarization, i. e., the non-uniform distribution of silver (copper) ions and hence of electronic charge carriers.

$$V_i = V_e + \left[\frac{\mu}{e}\right] \tag{17}$$

according to Eqs. (3) and (14), or to

$$V_i = -\int \frac{j}{\sigma} dx + \int \frac{\sigma_e}{\sigma} \frac{\partial(\mu/e)}{\partial x} dx \tag{17'}$$

according to Eqs. (2) and (7).

Since μ, σ_i, and σ_e are functions of N only, Eq. (9) can in principle be solved with the boundary conditions, Eqs. (11) or (13), and with appropriate initial condition. Then one may calculate the potential distribution according to Eqs. (15) or (17).

§ 4. Formation and Decay Processes of Polarization

In the followings we confine ourselves to the case where the current density is so small that the linear approximation is valid, i. e., it is sufficient to take into account the variation of the concentration of stoichiometric excess of silver (copper) atoms only up to the first order. In this approximation one may consider $d\mu/dN$, σ_e, and σ_i in Eqs. (9), (11), and (13) to be independent on coordinate, and equal to those in the unpolarized state. The latters we signify by the suffices 0. Then Eq. (9) is reduced to a simple diffusion equation:

$$\frac{\partial N}{\partial t} = D \frac{\partial^2 N}{\partial x^2} \tag{18}$$

with

$$D = \frac{\sigma_{i0}\sigma_{e0}}{\sigma_0 e^2}\left(\frac{d\mu}{dN}\right)_0 , \tag{19}$$

and the boundary conditions (Eqs. (11) and (13)) become

$$\frac{\partial N}{\partial x} = \frac{1}{\sigma_{e0}} \frac{ej}{(d\mu/dN)_0} , \quad \text{at} \quad x=0, L , \tag{20}$$

for the electronic electrodes, and

$$\frac{\partial N}{\partial x} = -\frac{1}{\sigma_{i0}} \frac{ej}{(d\mu/dN)_0} , \quad \text{at} \quad x=0, L , \tag{21}$$

for the ionic electrodes.

These boundary value problems can easily be solved. Taking the instant of switching on as the time zero, we have

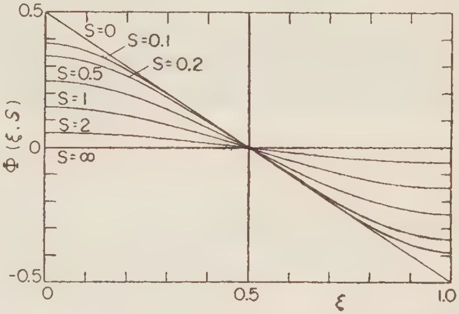

Fig. 1. $\Phi(\xi, s)$ defined by Eq. (24) is plotted against ξ for several values of s.

$$N = N_0 + \frac{ejL}{\sigma_{e0}(d\mu/dN)_0}\left\{\frac{x}{L} - \frac{1}{2} + \Phi\left(\frac{x}{L}, \frac{t}{\tau}\right)\right\} \tag{22}$$

for the electronic electrodes, and

$$N = N_0 - \frac{ejL}{\sigma_{i0}(d\mu/dN)_0}\left\{\frac{x}{L} - \frac{1}{2} + \Phi\left(\frac{x}{L}, \frac{t}{\tau}\right)\right\} \tag{23}$$

for the ionic electrodes, where

$$\Phi(\xi, s) = \frac{4}{\pi^2} \sum_{m=0}^{\infty} \frac{1}{(2m+1)^2} \exp\left[-(2m+1)^2 s\right] \cos\left[(2m+1)\pi\xi\right] , \tag{24}$$

and τ is defined by

$$\frac{1}{\tau} = D\frac{\pi^2}{L^2} = \frac{\pi^2}{L^2} \frac{\sigma_{i0}\sigma_{e0}}{\sigma_0 e^2}\left(\frac{d\mu}{dN}\right)_0 \tag{25}$$

and may by called as the time of diffusion. $1/\tau$ is a measure of the time rate at which the stationary polarization is attained.

In Fig. 1 $\Phi(\xi, s)$ is plotted against ξ for several values of s. For $s=0$, we have

$$\Phi(\xi, 0) = -\xi + \tfrac{1}{2} ;$$

and for $s>0$, all Fourier terms beyond the second decay out very rapidly compared with the first as s increases; $\Phi(\xi, s)$ may be approximated by the first term $(4/\pi^2)\exp(-s)\cos\pi\xi$ within an error of one percent already at $s=0.3$.

For the stationary state (for $t=\infty$), we have

$$N=N_0+\frac{ej}{\sigma_{e0}(d\mu/dN)_0}\left(x-\frac{L}{2}\right) \tag{26}$$

for the electronic electrodes, and

$$N=N_0-\frac{ej}{\sigma_{i0}(d\mu/dN)_0}\left(x-\frac{L}{2}\right) \tag{27}$$

for the ionic electrodes. It should be noted that in stationary polarization N is a linear function of the coordinate and its spacial gradients are opposite in sign for electronic and ionic electrodes.

In the absence of the current the boundary conditions, Eqs. (11) and (13), are reduced to

$$\frac{\partial N}{\partial x}=0\,, \qquad \text{at} \qquad x=0, L\,. \tag{28}$$

If the current is switched off after the stationary polarization is attained, the decay process of the polarization may be described by the solution of the diffusion equation Eq. (18) under the boundary conditions Eq. (28), and the initial condition Eqs. (26) or (27). We have

$$N=N_0-\frac{ejL}{\sigma_{e0}(d\mu/dN)_0}\,\Phi\left(\frac{x}{L},\frac{t}{\tau}\right) \tag{29}$$

for the electronic electrodes, and

$$N=N_0+\frac{ejL}{\sigma_{i0}(d\mu/dN)_0}\,\Phi\left(\frac{x}{L},\frac{t}{\tau}\right) \tag{30}$$

for the ionic electrodes.

In calculating the potential distributions according to Eq. (15), it will be sufficient in our approximation to take the variation of the conductivity, σ, to the first order of $N-N_0$ or of $\mu-\mu_0$. In the silver sulfide group semiconductors the ionic conductivity, σ_i, is insensitive to small deviations of the M/X ratio from the stoichiometric value and hence may be considered to be independent of the coordinate. In this approximation, we have for the formation process of the polarization

$$V_e=-j\int_{L/2}^{x}\frac{dx}{\sigma_0+(d\sigma/dN)_0(N-N_0)}-\frac{\sigma_{i0}}{e(d\sigma/d\mu)_0}\log\left[1+\left(\frac{d\log\sigma}{d\mu}\right)_0\left(\frac{d\mu}{dN}\right)_0(N-N_0)\right], \tag{31}$$

into which Eqs. (22) or (23) should be inserted for $N-N_0$. The potential zero is taken at the midpoint of the specimen, $x=L/2$.

Especially for sufficiently weak current*, we have

$$V_e^{(e)}=-\frac{j}{\sigma_{e0}}\left(x-\frac{L}{2}\right)-\frac{\sigma_{i0}}{\sigma_0}\,\frac{jL}{\sigma_{e0}}\,\Phi\left(\frac{x}{L},\frac{t}{\tau}\right) \tag{32A}$$

for the electronic electrodes, and

$$V_e^{(i)}=\frac{jL}{\sigma_0}\,\Phi\left(\frac{x}{L},\frac{t}{\tau}\right) \tag{32B}$$

---

* $\frac{1}{\sigma_{e0}}\left(\frac{d\log\sigma}{d\mu}\right)_0 ejL\ll1$, for the electronic electrodes, and $\frac{1}{\sigma_{i0}}\left(\frac{d\log\sigma}{d\mu}\right)_0 ejL\ll1$, for the ionic electrodes. The former condition means that the initial voltage applied to the specimen is far smaller than kT/e (see § 5.).

for the ionic electrodes. For $t=0$ these are both reduced to $-(j/\sigma_0)(x-L/2)$ as they should be so.

For stationary polarization, inserting Eqs. (26) or (27) into Eq. (31), we have

$$V_e{}^{(e)}=-\frac{1}{e(d\log\sigma/d\mu)_0}\log\left[1+\frac{ej}{\sigma_{e0}}\left(\frac{d\log\sigma}{d\mu}\right)_0\left(x-\frac{L}{2}\right)\right] \tag{33A}$$

for the electronic electrodes, and

$$V_e{}^{(i)}=0 \tag{33B}$$

for the ionic electrodes. In the latter case the first and the second term in Eq. (31) cancel out each other. For sufficiently weak current Eq. (33A) is reduced to

$$V_e{}^{(e)}=-\frac{j}{\sigma_{e0}}\left(x-\frac{L}{2}\right) \tag{33A$'$}$$

This equation can be obtained of course also from Eq. (32A) putting $t=\infty$.

It should be noted that for stationary polarization with purely ionic electrodes, the electrochemical potential of electrons is constant throughout the specimen as exhibited by Eq. (33B); electrons are in thermal equilibrium in spite of the existence of stationary ionic current, with no electronic current not only at the boundaries but also everywhere throughout the specimen (see also Eq. (1)). The voltage- current characteristic for electronic electrodes can be easily obtained from Eq. (33A). We find

$$j=\frac{\sigma_{e0}}{L}\,\frac{\tanh\left[(e/2)(d\log\sigma/d\mu)_0V\right]}{(e/2)(d\log\sigma/d\mu)_0}, \tag{34}$$

where V is the applied voltage. Eq. (34) is reduced for sufficiently weak current to

$$j=\frac{\sigma_{e0}}{L}V \tag{35}$$

as it should be so.

For the decay process of polarization, the potential distribution is given by Eq. (31) with $j=0$:

$$V_e=-\frac{\sigma_{i0}}{e(d\sigma/d\mu)_0}\log\left[1+\left(\frac{d\log\sigma}{d\mu}\right)_0\left(\frac{d\mu}{dN}\right)_0(N-N_0)\right], \tag{36}$$

where for $N-N_0$ Eqs. (29) or (30) should be inserted if the current is switched off after stationary polarization is attained. At the instant of switching off, we have

$$V_e{}^{(e)}=-\frac{\sigma_{i0}}{e(d\sigma/d\mu)_0}\log\left[1+\frac{ej}{\sigma_{e0}}\left(\frac{d\log\sigma}{d\mu}\right)_0\left(x-\frac{L}{2}\right)\right] \tag{37A}$$

for the electronic electrodes, and

$$V_e{}^{(i)}=-\frac{\sigma_{i0}}{e(d\sigma/d\mu)_0}\log\left[1-\frac{ej}{\sigma_{i0}}\left(\frac{d\log\sigma}{d\mu}\right)_0\left(x-\frac{L}{2}\right)\right] \tag{37B}$$

for the ionic electrodes. Comparing Eq. (37A) with Eq. (33A) we remark that for the electronic electrodes the potential measured by the use of electronic probes drops to the fraction σ_{i0}/σ_0 of the stationary value at the instant of switching off.

For sufficiently weak current, we see that the potential decays as

$$V_e{}^{(e)}=\frac{\sigma_{i0}}{\sigma_0}\,\frac{jL}{\sigma_{e0}}\,\Phi\left(\frac{x}{L},\frac{t}{\tau}\right) \tag{38A}$$

for the electronic electrodes, and

$$V_e^{(i)} = -\frac{jL}{\sigma_0}\,\Phi\left(\frac{x}{L},\frac{t}{\tau}\right) \tag{38B}$$

for the ionic electrodes. These are reduced for $t=0$ to

$$V_e^{(e)} = -\frac{\sigma_{i0}}{\sigma_0}\,\frac{j}{\sigma_{e0}}\left(x-\frac{L}{2}\right) \tag{37A$'$}$$

and

$$V_e^{(i)} = \frac{j}{\sigma_0}\left(x-\frac{L}{2}\right), \tag{37B$'$}$$

which of course agree with Eqs. (37A) and (37B) for sufficiently weak current, respectively. It should be noted that Eq. (38B) differs from Eq. (32B) only in its sign.

As for Eq. (17) which gives the potential as measured by the use of ionic probes, the variation of μ may be approximated by

$$\mu-\mu_0 = \left(\frac{d\mu}{dN}\right)_0 (N-N_0)\,. \tag{39}$$

For formation process of stationary polarization, inserting Eqs. (22) or (23) into Eq. (39) and adding Eqs. (32A) or (32B) to it, we have

$$V_i^{(e)} = \frac{jL}{\sigma_0}\,\Phi\left(\frac{x}{L},\frac{t}{\tau}\right) \tag{32C}$$

for the electronic electrodes, and

$$V_i^{(i)} = -\frac{j}{\sigma_{i0}}\left(x-\frac{L}{2}\right) - \frac{\sigma_{e0}}{\sigma_0}\,\frac{jL}{\sigma_{i0}}\,\Phi\left(\frac{x}{L},\frac{t}{\tau}\right) \tag{32D}$$

for the ionic electrodes. These are both reduced to $-(j/\sigma_0)(x-L/2)$ for $t=0$, as they should be so.

For stationary polarization we have, putting $t=\infty$ in Eqs. (32C) or (32D)

$$V_i^{(e)} = 0 \tag{33C}$$

for the electronic electrodes, and

$$V_i^{(i)} = -\frac{j}{\sigma_{i0}}\left(x-\frac{L}{2}\right) \tag{33D}$$

for the ionic electrodes.

It should be noted that for stationary polarization with the electronic electrodes the electrochemical potential of silver (copper) ions are constant throughout the specimen as exhibited by Eq. (33C); silver (copper) ions are in thermal equilibrium in spite of the existence of stationary electronic current, with no ionic current not only at the boundaries but also everywhere throughout the specimen.

For the decay process of stationary polarization, we have

$$V_i^{(e)} = -\frac{jL}{\sigma_0}\,\Phi\left(\frac{x}{L},\frac{t}{\tau}\right) \tag{38C}$$

for the electronic electrodes, and

$$V_i^{(i)} = \frac{\sigma_{e0}}{\sigma_0}\,\frac{jL}{\sigma_i}\,\Phi\left(\frac{x}{L},\frac{t}{\tau}\right) \tag{38D}$$

for the ionic electrodes. These are reduced for $t=0$ to

$$V_i^{(e)}=\frac{j}{\sigma_0}\left(x-\frac{L}{2}\right), \tag{37C}$$

and

$$V_i^{(i)}=-\frac{\sigma_{e0}}{\sigma_0}\,\frac{j}{\sigma_{i0}}\left(x-\frac{L}{2}\right). \tag{37D}$$

Comparing Eq. (37D) with Eq. (33D) we remark that for the ionic electrodes the potential as measured by the use of ionic probes drops to the fraction σ_{e0}/σ_0 of the stationary value at the instant of switching off.

§ 5. Dependences of N and σ on μ

It is very likely that the chemical potential of silver (copper) ions, μ_i, in silver sulfide group semiconductors in their high temperature forms (α-forms) is practically insensitive to the small variation of M/X ratio from its stoichimetric value, i. e., μ_i is independent of N [16),23),24)]. Accordingly we are allowed to identify the Fermi level of electrons, μ_e, with the chemical potential of neutral silver (copper) atoms, μ, as far as the variation of N is concerned, since μ is simply the sum of μ_i and μ_e

$$\mu=\mu_e+\mu_i \tag{41}$$

and we are interested only in the relative value of μ. Then we see from Eq. (8) that N is related to μ according to the equation

$$N=n-p=N_c\frac{2}{\sqrt{\pi}}F_{1/2}\left(\frac{\mu}{kT}\right)-N_v\frac{2}{\sqrt{\pi}}F_{1/2}\left(-\frac{\mu+\varepsilon_g}{kT}\right), \tag{42}$$

where N_c and N_v are effective state densities of conduction and valence bands, respectively,

$$N_c=2\frac{(2\pi m_n kT)^{3/2}}{h^3}, \qquad N_v=2\frac{(2\pi m_p kT)^{3/2}}{h^3}, \tag{43}$$

$F_\nu(\eta)$ is the Fermi-Dirac function of order ν

$$F_\nu(\eta)=\int_0^\infty \frac{x^\nu}{e^{x-\eta}+1}dx, \tag{44}$$

the Fermi level μ is measured from the bottom of the conduction band, and ε_g is the energy gap. The standard form of energy lattice momentum relation has been assumed for both conduction and valence bands, m_n and m_p are effective masses of conduction electrons and electron holes.

Differentiating Eq. (42) with respect to μ, we find the following expression for $dN/d\mu$ in Eqs. (22), (23) et al.:

$$\frac{dN}{d\mu}=\frac{1}{kT}\left\{N_c\frac{2}{\sqrt{\pi}}F'_{1/2}\left(\frac{\mu}{kT}\right)+N_v\frac{2}{\sqrt{\pi}}F'_{1/2}\left(-\frac{\mu+\varepsilon_g}{kT}\right)\right\}. \tag{45}$$

When the electronic charge carriers are not degenerate, Eq. (45) can be simplified to

$$\frac{dN}{d\mu}=\frac{1}{kT}(n+p) \tag{46}$$

In the silver sulfide group semiconductors in their α-forms the ionic conductivity is also insensitive to the variation of N in contrast to the N-dependence of the electronic conductivity. The latter can be represented also in terms of Fermi-Dirac functions if we assume that the free path length of carriers l is proportional to some power of carrier energy ε.

Assuming $l=l_0(\varepsilon/kT)^r$, we have[15]

$$\begin{aligned}\sigma_e&=\sigma_n+\sigma_p\\&=ev_nN_c\frac{1}{\Gamma(r+1)}F_r\left(\frac{\mu}{kT}\right)+ev_pN_v\frac{1}{\Gamma(r+1)}F_r\left(-\frac{\mu+\varepsilon_g}{kT}\right),\end{aligned}\tag{47}$$

where σ_n and σ_p are electron and hole conductivities, v_n and v_p are the mobilities of electrons and holes and expressible as

$$v_n=\frac{4\Gamma(r+2)}{3}\frac{el_{0n}}{\sqrt{2\pi m_nkT}},\quad\text{and similar for } v_p.\tag{48}$$

Hence, we have for $d\sigma/d\mu$ in Eqs. (31), (33A), et al.

$$\frac{d\sigma}{d\mu}=\frac{e}{kT}\frac{1}{\Gamma(r)}\left\{v_nN_cF_{r-1}\left(\frac{\mu}{kT}\right)-v_pN_vF_{r-1}\left(-\frac{\mu+\varepsilon_g}{kT}\right)\right\},\tag{49}$$

where we have tacitly assumed that carrier mobilities are independent on N and hence on μ. In the limit of classical statistics Eq. (49) is reduced to

$$\frac{d\sigma}{d\mu}=\frac{1}{kT}(\sigma_n-\sigma_p)\tag{50}$$

with

$$\sigma_n=ev_nn\,,\qquad\sigma_p=ev_pp\,.\tag{51}$$

Experimentally, the dependences of N and σ on μ in $Ag_{2+x}X$ ($Cu_{2+x}X$) can be found by utilizing the galvanic cell $Ag|AgI|Ag_{2+x}X|Pt$ ($Cu|CuBr|Cu_{2+x}X|Pt$). We note that the chemical potential μ of silver (copper) atoms in the $Ag_{2+x}X$ (Cu_{2+x}) specimen of the cell is related to the e. m. f., E, of the cell by the equation

$$\mu-\mu^0=-eE\tag{52}$$

where μ^0 is the chemical potential of silver (copper) atoms in metallic silver (copper)[5,6]. E is zero if the specimen is saturated with metallic silver (copper); and E increases according as silver atoms are extracted from the specimen through AgI (CuBr) by making a current pass through the cell in the direction from the platinum electrode to the silver one.

§ 6. Comparison with Experiments

In § 3 and 4 we have distinguished the four cases in connection with the two kinds of probes and the two kinds of electrodes. These are recapitulated in the following table:

Case	Probes	Electrodes	Notation for potential
A	electronic	electronic	$V_e^{(e)}$
B	electronic	ionic	$V_e^{(i)}$
C	ionic	electronic	$V_i^{(e)}$
D	ionic	ionic	$V_i^{(i)}$

Table I.

	σ_e ohm^{-1} cm^{-1}	σ_i ohm^{-1} cm^{-1}	σ ohm^{-1} cm^{-1}	τ sec	τ (calc.) sec
(a)	5.7*	1.1	6.8	72	
(b)	—	—	7.3	76	
(c)	—	—	7.8	75	
(d)	5.7	1.3*	7.0	76	
				(mean) 75*	84

In Fig. 2 are shown the time variations of potentials between two probes set on a $Ag_{1.93}Te$ specimen at the formation and decay processes of stationary polarizations at 161°C. $Ag_{1.93}Te$ is preferred because of its relatively large ionic conductivity[14]. The experimental situations are schematically shown in the figure. The probes are set symmetrically with respect to the midpoint of the specimen so as to cancel out the effect of the variation of electronic conductivity due to polarization to the first order. (a), (b), (c), and (d) correspond to the cases A, B, C, and D, respectively. The dots are observed values. The corresponding theoretical expressions, Eqs. (32A, B, C, D) and (38A, B, C, D) are compared with the observations. The unknown parameters are estimated so as to yield the best fit with observations for each case, and tabulated in Table 1. The error involved may amount to ten percent for σ's. The estimated values are seen to be consistent within experimental error. τ is also calculated by the use of Eq. (25), in which $d(eN)/d(\mu/e)$ is estimated to be 2.5×10^2 coulomb cm^{-3} volt^{-1} from the experimental titration curve[6),7)], and is given in Table 1 as τ (calc.). The deviations from the observed values are within experimental error.

The value σ_e for case (a) and the value σ_i for case (d) are most reliable, since they are estimated from the stationary potential values which should be equal to jl/σ_e and jl/σ_i respectively after Eqs. (33A′) and (33D), l being the probe separation. With these and with the mean value of τ, the time variations of the potential differences between the probes are calculated by the use of Eqs. (32A, B, C, D) and (38A, B, C, D) and plotted in the figure in full curves. The agreements between calculated and observed time variations are

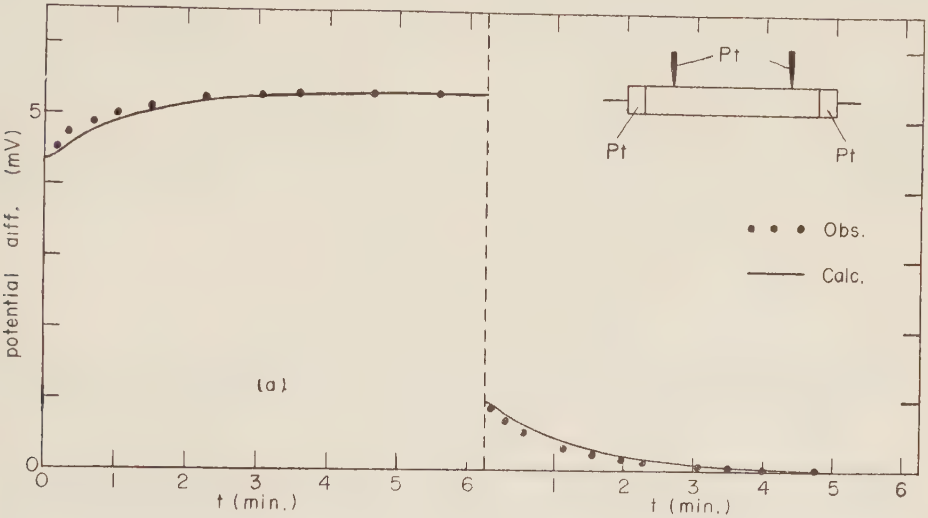

Fig. 2(a).

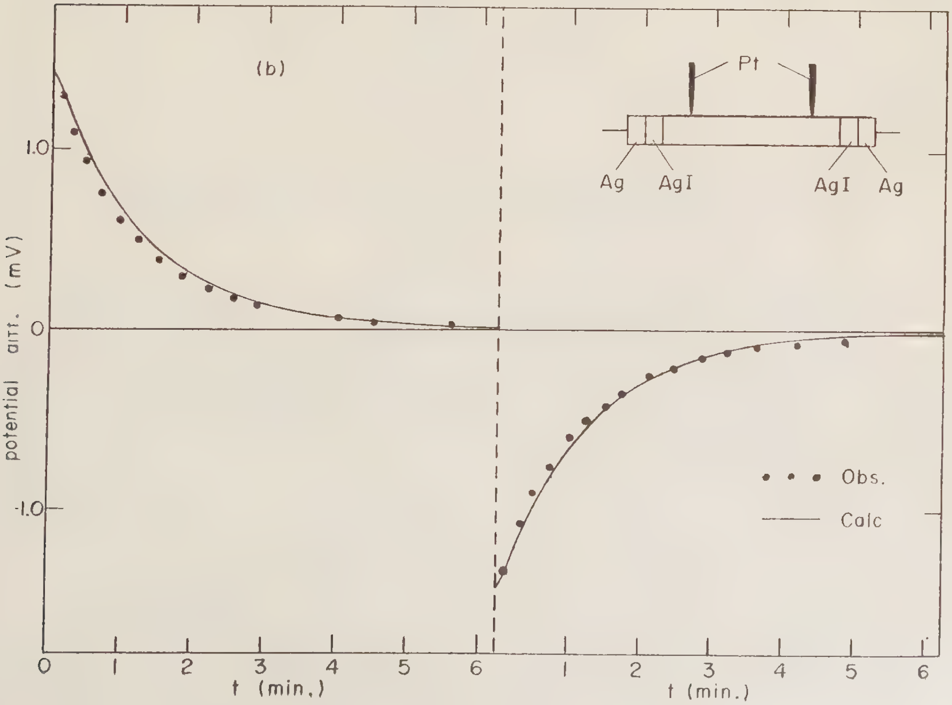

Fig. 2(b).

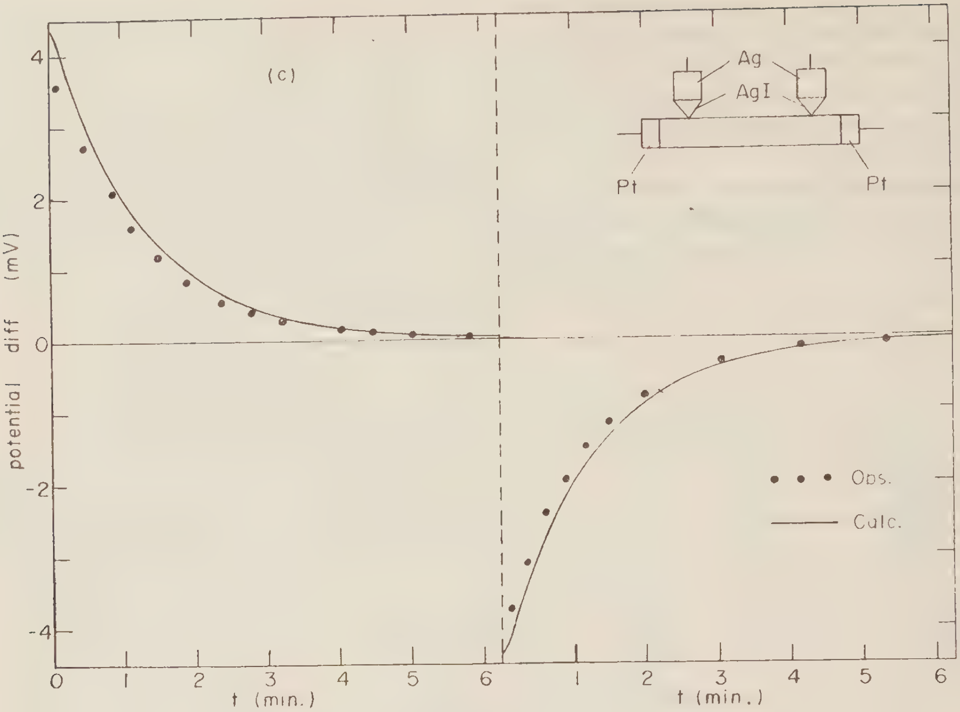

Fig. 2(c).

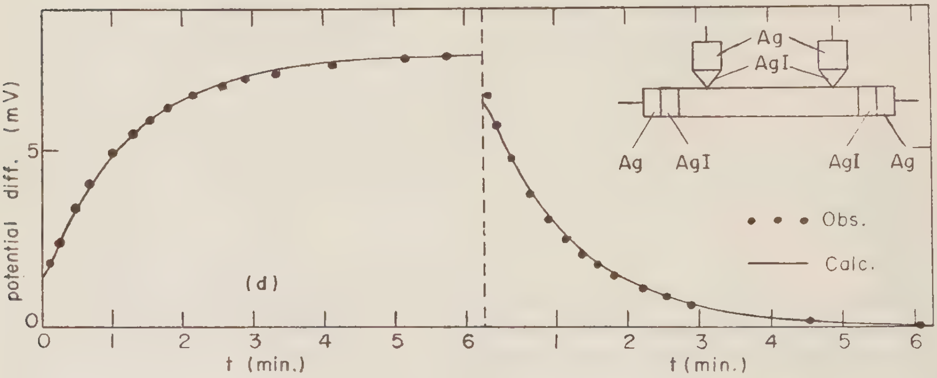

Fig. 2(d).

Fig. 2. Comparisons of observed and calculated time variations of potentials as measured between two probes set on a Ag$_{1.93}$Te specimen at the formation (left halves) and decay (right halves) processes of stationary polarizations at 161°C. (a), (b), (c), and (d) correspond to the cases A, B, C, and D in the text, respectively. The experimental conditions are as follows. Specimen length (L): 1.88 cm, probe separation (l): 1.33 cm, current density (j): 22.8 mA cm^{-2} for (a) and (c), and 7.46 mA cm^{-2} for (b) and (d). The numerical values with asterisk in Table 1 are used in computations of the full curves.

satisfactory.

In conclusion the author wishes to express his cordial thanks to Dr. S. Miyatani for his kindness to take the trouble to make experiments for the sake of the present work and for his many valuable suggestions.

The present work was financially supported by the Science Research Fund of the Ministry of Education.

References

1) H. Reinhold und H. Möhring: Z. phys. Chem. **B38** (1937) 221.
2) H. Reinhold und H. Seidel: Z. phys. Chem. **B38** (1937) 245.

3) H. Reinhold und H. Bräuninger: Z. phys. Chem. **B41** (1939) 397.
4) H. Reinhold und K. Schmitt: Z. phys. Chem. **B44** (1939) 75.
5) C. Wagner: J. Chem. Phys. **21** (1953) 1819.
6) J. Bruce Wagner and C. Wagner: J. Chem. Phys. **26** (1957) 1602.
7) C. Lorenz and C. Wagner: J. Chem. Phys. **26** (1957) 1607.
8) S. Miyatani: J. Phys. Soc. Japan **8** (1953) 680.
9) S. Miyatani and Y. Suzuki: J. Fac. Sci. Niigata Univ. Ser. 1, **1** (1953) 1.
10) S. Miyatani: J. Fac. Sci. Niigata Univ. Ser. 1, **1** (1953) 11.
11) S. Miyatani: J. Phys. Soc. Japan **10** (1955) 786.
12) S. Miyatani: J. Phys. Soc. Japan **11** (1956) 1059.
13) S. Miyatani: J. Phys. Soc. Japan **13** (1958) 317.
14) S. Miyatani: J. Phys. Soc. Japan **13** (1958) 341.
15) S. Miyatani and I. Yokota: J. Phys. Soc. Japan **14** (1959) 750.
16) S. Miyatani: J. Phys. Soc. Japan **14** (1959) 996.
17) S. Miyatani: J. Phys. Soc. Japan **15** (1960) 1586.
18) F. Seitz: *Modern Theory of Solids* (1940) 67p.
19) A. F. Wells: *Structural Inorganic Chemistry*, 2nd ed. (1950) 143p.
20) P. Rahlfs: Z. phys. Chem. **B31** (1936) 157.
21) I. Yokota: J. Phys. Soc. Japan **8** (1953) 595.
22) C. Wagner: Z. phys. Chem. **B21** (1933) 25.
23) M. H. Hebb: J. Chem. Phys. **20** (1951) 185.
24) C. Wagner: Z. Elektrochem. **60** (1956) 4.

JOURNAL OF THE PHYSICAL SOCIETY OF JAPAN, Vol. 16, No. 11, NOVEMBER, 1961

Electrical Resistivity and Defect Energy Levels in Reduced Titanium Dioxide at Low Temperatures

By Ryukiti R. HASIGUTI
Department of Metallurgy, University of Tokyo, Tokyo
Kazuko MINAMI
National Research Institute for Metals, Tokyo
and
Hirō YONEMITSU
Low Temperature Laboratory, Toshiba Electric Company, Kawasaki

(Received May 22, 1961)

The resistivity of reduced rutile was measured from 80°K down to about 2°K. Activation energies derived from the slopes of resistivity curve are $0.01\sim0.02$ eV above about 20°K and $0{\cdot}0005\sim0.005$ eV below about 20°K. It is proposed that the electronic conduction in this substance below about 20°K is due to the "defect level conduction". Conduction mechanisms at higher temperatures are also discussed.

§ 1. Introduction

It is well known that reduced rutile shows n-type semiconductivity, and it is believed that oxygen vacancies are responsible for giving rise to donor centers.[1] However, the detailed mechanism of electronic conduction in this substance is not yet established.

If the concentration of donor centers in reduced rutile is increased to such an extent that the wave functions of donor centers nearly overlap with each other, a defect level conduction is expected. If this is the case, this kind of conduction may occur at very low temperatures. A preliminary experiment was carried out to sound this unexplored field.

We have made electrical measurements at low temperatures down to about 2°K, and we think we are now in a situation that we can propose a new mechanism of electronic conduction in reduced rutile.[1]

§ 2. Experimental Results

Single crystals of rutile (99.99% pure) were used either as grown crystal* or as reduced** in hydrogen atmosphere. The temperature range of measurements is from 1.7°K to about 80°K. The results of resistivity measurements are reproduced in Fig. 1. The resistivities of reduced crystal as a function of temperatures (curve 1) may be conveniently divided into two temperature ranges, namely ranges 3 and 4. This nomenclature will be explained in the following section. It is found that the range 3 extends from about 20°K to about 200°K, if we extend the measurements to higher temperatures[2]. Our measurements at higher temperatures agree well with those by Breckenridge and Hosler.[1]

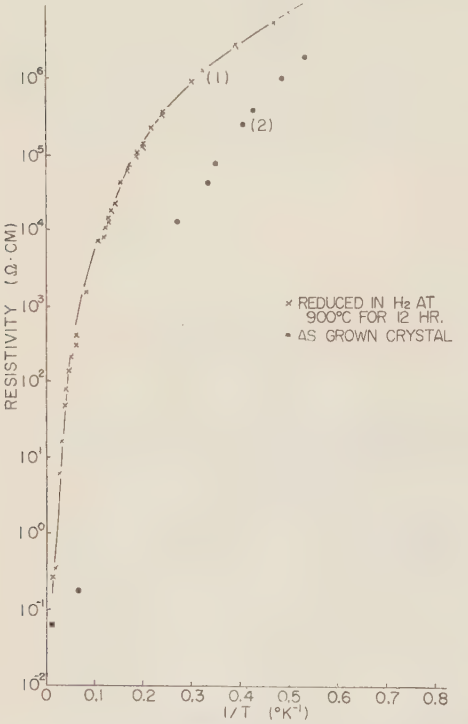

Fig. 1.

§ 3. Discussions

If we take into consideration high temperature results[1),2),3)] together with our low temperature measurements, four temperature ranges can be distinguished as are shown in Table 1. Range 1 is considered to be the intrinsic range[1),3)], which we do not discuss here. Our new proposition concerns the ranges 2, 3 and 4.

Table 1. Four temperature ranges of electrical conductivity

Range	Temperature range in K°	Activation energy in eV
1	1700~800	3.1 and 3.7
2	800~200	0.1~0.2
3	200~20	0.01~0.02
4	20~1.7	0.0005~0.005

Breckenridge and Hosler[1] considered that the range 2 and 3 are due to conductions in impurity or defect bands formed by the overlapping of wave functions of donor centers. We consider that this is not the case, but that the ranges 2 and 3 are due to the conduction in 3d band of titanium, carriers being produced by the first (range 3) and second (range 2) ionizations of donors. The reasons will be shown later.

The range 4 is a newly-discovered range. We propose that this is due to the defect level conduction. If the wave functions of donors overlap sufficiently, a defect band will be formed, giving rise to a defect band conduction. If the overlapping is insufficeint, it will result in a defect level permutation conduction with appropriate compensation by acceptors. The proposed energy level diagram is illustrated in Fig. 2.

Now our model of donor center will be shown in Fig. 3. An oxygen vacancy has an effective charge of +2, and it traps two electrons, one in a deep level and the other in a shallow level. The orbital of shallow trapped electron is shematically represented in Fig. 3. The deep trapped electron should have a much smaller radius of orbital. It is represented as $V_0^{+}=V_0^{++}+e$ in the figure, where V_0 is an oxygen vacancy. It is considered that the first and second ionization energies correspond to $\varepsilon_3=0.01\sim0.02$ eV and $\varepsilon_2=0.1\sim0.2$

---

* The Crystal grown by Verneuil method contains a large number of lattice defects, which are considered to be vacancies.

** The grown crystal was annealed to eliminate inherent lattice defects, and then it was reduced in hydrogen atmosphere.

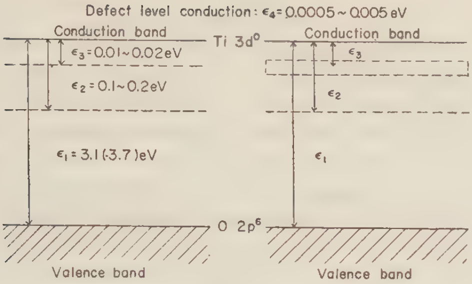

Fig. 2.

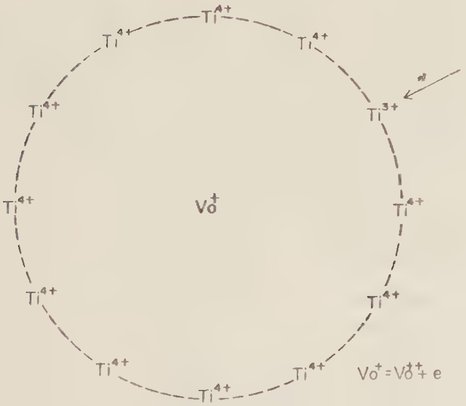

Fig. 3.

eV, respectively (Fig. 2 and Table 1).

The reason why we propose such a conduction mechanism is as follows.

(1) The mobility of electrons increases as the temperature is lowered in the ranges 2 and 3[1),2)].

This shows that the conduction is not due to a hopping process of trapped electrons, but due to the electrons moving in a conduction band.

(2) The mobility at room temperature is 0.1~1 cm²/volt. sec., which is a typical value for the electrons in 3d band. Thus the conduction in the ranges 2 and 3 must be achieved by the electrons in 3d conduction band. ε_3 and ε_2 should be considered, therefore, to be the first and second ionization energies of donors.

(3) The first ionization energy is calculated by the equation

$$\varepsilon_3 = \frac{13.6}{\kappa^2} \cdot \frac{m^*}{m}, \qquad (2)$$

if a model of hydrogen-like centers embedded in a medium of dielectric constant κ is considered. Here m^* is the effective mass of electron, and m is the mass of free electron. If $\kappa=25$, which is adopted according to Kubo's criterion[4)], $\varepsilon_3=0.022$ eV is obtained with $m^*=m$. The radius of orbital r is calculated by the equation

$$r = 0.53 \frac{m}{m^*} \kappa, \qquad (2)$$

as $r=13$ Å. The excellent agreement between calculated and experimental ionization energies indicates the correctness of our model.

Now we may, from the following reasons, certainly conclude that the range 4 is due to a defect level conduction, which is similar to an impurity level conduction in semi-conductors.

(1) The general feature of resistivity curves in Fig. 1 and the magnitudes of activation energies in the range 4 (Table 1) are quite typical for a defect (or impurity) level conduction.

(2) A conclusive evidence at present was rather obtained from electron spin resonance experiments[5)]. Resonance spectra were observed below about 20°K, especially sharply around liquid helium temperature, which shows that electrons concerned are neither in a conduction band nor in a helium-like paired state in this temperature range. Date and Nakazumi[5)] conclude from g-values and motional narrowing of spectra that electrons reside at Ti^{4+} ions resulting in Ti^{3+} ions, and that electrons move very quickly with frequencies higher than Zeemann frequency from ion to ion. If the concentration of donor centers is sufficiently high, it is considered that electrons move from center to center resulting in a defect level permutation conduction.

Now the concentration of donors in our reduced crystal is estimated from carrier concentration derived from Hall coefficient measurements[2)] in the range 3 to be $5\sim10\times10^{18}$/cc. This gives $r_s\approx33$Å, where r_s is a radius of atomic sphere surrounding each donor, which has a volume corresponding to the reciprocal of donor concentration.

The radius r of orbital of our donor was calculated, as mentioned above, to be about 13 Å. Thus we can obtain the ratio

$$r_s/r \approx 2.5$$

in our reduced crystal. It is interesting to note that this ratio is 2~3 in n-type germanium in its intermediate donor concentration range, which is a range of transition from weakly to strongly interacting donors.[6)]

Acknowledgements

The authors wish to express their appreciation to Prof. M. Date and Dr. Y. Nakazumi for valuable discussions and for supplying them with their electron spin resonance data before publication. They also wish to thank Profs. T. Muto and Y. Toyozawa for stimulating discussions.

References

1) R. G. Breckenridge and W. R. Hosler: Phys. Rev. **91** (1953) 793.
2) R. R. Hasiguti and K. Minami: Preprint of Annual Meeting of Phys. Soc. Japan (in Japanese), Part 3, P. 211 (1960).
3) D. C. Cronemeyer: Phys. Rev. **87** (1952) 876.
4) R. Kubo: J. Phys. Soc. Japan **3** (1943) 254.
5) M. Date and Y. Nakazumi: To be published.
6) H. Fritzsche: J. Phys. Chem. Solids, **6** (1958) 69.

JOURNAL OF THE PHYSICAL SOCIETY OF JAPAN Vol. 16, No. 11, NOVEMBER, 1961

Relativistic Dynamical Theory of Electron Diffraction

By Kunio FUJIWARA

The Institute for Solid State Physics,
Tokyo University, Tokyo, Japan

(Received May 4, 1961)

Multiple elastic scattering of electrons by crystals is considered based on the Dirac's wave equation with the perturbation method. The result shows that besides the usual relativistic correction for wave-length, a new correction factor appears in the intensity formula of reflection, corresponding to the mass correction of electron. The new correction factor plays an important role in the dynamical theory of electron diffraction, and, for instance, it brings about an essential modification in the nonrelativistic result concerning the dependence of the reflection intensity on wave-length. It follows that the dynamical effect does not vanish at the limit $\lambda\to 0$.

§ 1. Introduction

In some recent experiments of electron diffraction, the incident electron beams accelerated by fairly high voltages, sometimes as high as 500 KV, have been utilized. For electrons with such high energy, however, the relativistic effect is expected to be far from negligible. In current theories of electron diffraction based on Schrödinger's non relativistic wave equation, the relativistic correction has been applied by replacing nonrelativistic values of wave-length of electrons in the scattering formula with relativistic values.

By adopting the first Born approximation, Laue[1)] treated the scattering of electrons by an electrostatic potential of arbitrary distribution on the basis of Dirac's wave equation, and gave a generalized justification for the usual relativistic correction of the wavelength. The scattering formula derived by him, however, contained a new factor representing another relativistic correction. The magnitude of this factor depends on the electron energy and increases from unity to appreciable values at high energy of electrons, but the importance of this factor in both experiment and theory, in particular in the dynamical theory of diffraction, seems to have so far been not properly recognized. The relativistic reformulation of the dynamical theory is in this respect highly desirable, although it seems to be tedious to pursue along the conventional line of Bethe's dynamical theory[2)].

Recently, Cowley and Moodie[3)] developed a new diffraction theory based on the physical optics, and gave a convenient approach to the dynamical theory from the kinematical theory. The present author has developed in a previous paper[4] a non-relativistic theory of the scattering of electrons by crystals by a perturbation method and confirmed Cowley and Moodie's result on the basis of wave mechanics. In the present paper, it is shown that a development of the relativistic dynamical theory is similarly feasible by applying the perturbation method to Dirac's wave equation. As the result, it is revealed that the correction factor introduced into the scattering formula by Laue plays an important role in the dynamical theory and affects some of conclusions of this theory. It is shown, for instance, that some reservation is required of the theoretical works of Miyake[5], Fujimoto[6] and Fujiwara[4] and the experimental work of Honjo and Kitamura[7] concerning the dependence of the scattering intensity on the wave-length.

In Appendix, the magnetic scattering of electrons by crystals is discussed briefly, as no theoretical consideration seems to have previously been done on it, although the corresponding scattering cross section is expected to be very small.

§ 2. Perturbation Theory in Interaction Representation and Dirac's Equation

(a) *Perturbation theory in interaction representation*[8].

The wave equation in the Schrödinger representation

$$i\hbar\frac{\partial\Psi'}{\partial t}=H\Psi' , \qquad H=H_0+H' , \tag{2.1}$$

can be transformed to that in the interaction representation

$$i\hbar\frac{\partial\Psi}{\partial t}=\overline{H}(t)\Psi , \qquad \overline{H}(t)=\exp\left(\frac{i}{\hbar}H_0t\right)\cdot H'\cdot\exp\left(-\frac{i}{\hbar}H_0t\right) \tag{2.2}$$

by the unitary transformation

$$\Psi'(t)=\exp\left(-\frac{i}{\hbar}H_0t\right)\Psi(t) .$$

The perturbation H' is assumed to be independent of t in what follows. The transformation function $U(t, t_0)$ which transforms $\Psi(t_0)$ to $\Psi(t)$ as

$$\Psi(t)=U(t, t_0)\Psi(t_0) \tag{2.3}$$

is given from (2.2) in the form

$$U(t, t_0)=1+\sum_{n=1}^{\infty}\left(\frac{1}{i\hbar}\right)^n\int_{t_0}^{t}dt_1\int_{t_0}^{t_1}dt_2\cdots\int_{t_0}^{t_{n-1}}dt_n\,\overline{H}(t_1)\,\overline{H}(t_2)\;\cdots\;\overline{H}(t_n) . \tag{2.4}$$

The operator $U(+\infty, -\infty)$ is the so-called S matrix and is related to the scattering matrix R as

$$U(+\infty, -\infty)=S\equiv1+R . \tag{2.5}$$

If the system is in an eigen state a of H_0 at $t=-\infty$, the probability W_{ba} that the system is found in another eigen state b at $t=+\infty$ is given by

$$W_{ba}=|\langle b|R|a\rangle|^2 . \tag{2.6}$$

In order to calculate R from (2.4) and (2.5) we modify $\overline{H}(t)$ in (2.2) as

$$\overline{H}(t)=\exp\left(\frac{i}{\hbar}H_0t\right)H'\exp\left(-\frac{i}{\hbar}H_0t\right)\exp(-\varepsilon|t|) , \tag{2.7}$$

where ε is an infinitesimal positive number. This modification is called adiabatic process. Since the energy is conserved before and after the transition, R takes the form

$$\langle b|R|a\rangle = -2\pi i\delta(E_b - E_a)\langle b|\boldsymbol{R}|a\rangle\ . \tag{2.8}$$

From (2.4) and (2.7) the transition matrix $\boldsymbol{R}$ is given as

$$\langle b|\boldsymbol{R}|a\rangle = \sum_{n=1}^{\infty} \langle b|\boldsymbol{R}^{(n)}|a\rangle\ , \tag{2.9}$$

$$\langle b|\boldsymbol{R}^{(1)}|a\rangle = \langle b|H'|a\rangle\ , \tag{2.10}$$

$$\langle b|\boldsymbol{R}^{(n)}|a\rangle = \sum_{c_1}\sum_{c_2}\cdots\sum_{c_{n-1}} \frac{\langle b|H'|c_{n-1}\rangle\langle c_{n-1}|H'|c_{n-2}\rangle\cdots\langle c_1|H'|a\rangle}{(E_a - E_{c_{n-1}} + i\varepsilon)\cdots(E_a - E_{c_1} + i\varepsilon)}\ , \tag{2.11}$$

where $c_1, c_2, \cdots, c_{n-2}$ and c_{n-1} specify the virtual intermediate states.

(b) *Dirac's equation*[9]

Dirac's equation for an electron interacting with an electromagnetic field ($\boldsymbol{A}$, V) is given by

$$i\hbar\frac{\partial\psi}{\partial t} = H\psi = \{\boldsymbol{\alpha}(c\boldsymbol{p} + e\boldsymbol{A}) + \beta m_0c^2 - eV\}\psi\ , \tag{2.12}$$

where c is the light velocity, m_0 the rest mass of electron, $-e$ the charge of electron, and $\boldsymbol{\alpha}$ and β are the 4-row, 4-column matrices which anticommute each other and are expressed as

$$\alpha_x = \begin{pmatrix} 0&0&0&1\\ 0&0&1&0\\ 0&1&0&0\\ 1&0&0&0 \end{pmatrix},\quad \alpha_y = \begin{pmatrix} 0&0&0&-i\\ 0&0&i&0\\ 0&-i&0&0\\ i&0&0&0 \end{pmatrix},\quad \alpha_z = \begin{pmatrix} 0&0&1&0\\ 0&0&0&-1\\ 1&0&0&0\\ 0&-1&0&0 \end{pmatrix},\quad \beta = \begin{pmatrix} 1&0&0&0\\ 0&1&0&0\\ 0&0&-1&0\\ 0&0&0&-1 \end{pmatrix}. \tag{2.13}$$

For a free electron, (2.12) is reduced to

$$i\hbar\frac{\partial\psi}{\partial t} = (-ic\hbar\boldsymbol{\alpha}\cdot\nabla + \beta m_0c^2)\psi\ , \tag{2.14}$$

where $\boldsymbol{p}$ is substituted by $-i\hbar\nabla$. The solution of (2.14) is given by a plane wave form

$$\psi = (2\pi)^{-3/2}u\exp\left[i\left(\boldsymbol{K}\boldsymbol{r} - \frac{E}{\hbar}t\right)\right]. \tag{2.15}$$

The wave number vector $\boldsymbol{K}$ and the energy E satisfy the relation

$$E = \pm\sqrt{c^2\hbar^2\boldsymbol{K}^2 + m_0{}^2c^4}\ . \tag{2.16}$$

The amplitude u is a four component quantity. If $\boldsymbol{K}$ is given, we have four eigen-solutions $u_{\boldsymbol{K}s}$ ($s=1, 2, 3, 4$), of which $u_{\boldsymbol{K}1}$ and $u_{\boldsymbol{K}2}$ are the solutions for $E>0$ with $+$, $-$ spin, respectively, and $u_{\boldsymbol{K}3}$ and $u_{\boldsymbol{K}4}$ the solutions for $E<0$ with $+$, $-$ spin, respectively.

If Q's are operators composed of α's and β, we have the relations

$$\sum_{s'=1}^{4} (u^*_{\boldsymbol{K}s}Q_1u_{\boldsymbol{K}'s'})(u^*_{\boldsymbol{K}'s'}Q_2u_{\boldsymbol{K}''s''}) = (u^*_{\boldsymbol{K}s}Q_1Q_2u_{\boldsymbol{K}''s''})\ , \tag{2.17}$$

$$\sum_{s'=1}^{2} (u^*_{\boldsymbol{K}s}Q_1u_{\boldsymbol{K}'s'})(u^*_{\boldsymbol{K}'s'}Q_2u_{\boldsymbol{K}''s''}) = \left(u^*_{\boldsymbol{K}s}Q_1\frac{H_{\boldsymbol{K}'} + |E_{\boldsymbol{K}'}|}{2|E_{\boldsymbol{K}'}|}Q_2u_{\boldsymbol{K}''s''}\right)\ , \tag{2.18}$$

$$\sum_{s=1}^{2} (u^*_{\boldsymbol{K}s}Qu_{\boldsymbol{K}s}) = \mathrm{Spur}\left(Q\frac{H_{\boldsymbol{K}} + |E_{\boldsymbol{K}}|}{2|E_{\boldsymbol{K}}|}\right)\ , \tag{2.19}$$

where

$$H_{\boldsymbol{K}} = c\hbar\boldsymbol{\alpha}\cdot\boldsymbol{K} + \beta m_0c^2\ . \tag{2.20}$$

If P's are products of α's and β, and $\boldsymbol{a}$ and $\boldsymbol{b}$ are fixed vectors, we have the relations

$$\mathrm{Spur}\ P_1P_2P_3=\mathrm{Spur}\ P_2P_3P_1=\mathrm{Spur}\ P_3P_1P_2\ , \tag{2.21}$$

$$\mathrm{Spur}\ P=0\ , \quad \text{if the numbers of factors } \beta \text{ and } \alpha \text{ are not both even,} \tag{2.22}$$

$$\mathrm{Spur}\ \alpha_j{}^2=\mathrm{Spur}\ \beta^2=4 \qquad (j=x,\ y,\ z)\ , \tag{2.23}$$

$$\mathrm{Spur}\ (\boldsymbol{\alpha a})(\boldsymbol{\alpha b})=4(\boldsymbol{ab})\ . \tag{2.24}$$

The formulas from (2.17) to (2.24) are useful in calculations in the present paper.

§ 3. The First Approximation of Scattering Matrix in Electron Diffraction

We apply the perturbation theory in § 2 to the problem of electron diffraction by a crystal. The shape of the crystal is assumed to be an infinite plate with thickness D, and the z-axis is chosen in the direction normal to the surface as shown in Fig. 1. If the periodic field in the crystal is derived from a scalar potential

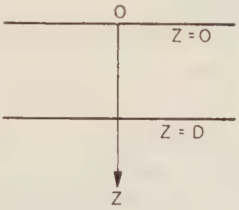

Fig. 1.

$$V(\boldsymbol{r})=\sum_{\boldsymbol{h}} v_{\boldsymbol{h}} \exp(2\pi i\boldsymbol{hr})\ , \qquad \text{for } 0\le z\le D\ , \tag{3.1}$$

the Hamiltonians H_0 and H' are given respectively by

$$H_0=-ic\hbar\boldsymbol{\alpha}\cdot\nabla+\beta m_0c^2 \tag{3.2}$$

and

$$H'=-eV(\boldsymbol{r})\ . \tag{3.3}$$

The wave function of the electron which is incident on the surface of the crystal $z=0$ with the wave vector $\boldsymbol{K}_0$ is put

$$\Psi(-\infty)=(2\pi)^{-3/2}u_{\boldsymbol{K}_0s_0}\exp(i\boldsymbol{K}_0\boldsymbol{r})\ , \tag{3.4}$$

where s_0 takes 1 or 2 according as the electronic spin is parallel or anti-parallel to the z-axis, respectively. Similarly, a diffracted wave with wave vector $\boldsymbol{K}$ is put

$$\langle \boldsymbol{r}|\boldsymbol{K}s\rangle=(2\pi)^{-3/2}u_{\boldsymbol{K}s}\exp(i\boldsymbol{Kr}) \tag{3.5}$$

with $s=1$ or 2.

From (2.10) and (3.3), the element of the transition matrix in the first approximation is calculated by

$$\langle \boldsymbol{K}s|\boldsymbol{R}^{(1)}|\boldsymbol{K}_0s_0\rangle=-e\langle \boldsymbol{K}s|V|\boldsymbol{K}_0s_0\rangle\ .$$

Using (3.1), we have

$$\begin{aligned}\langle \boldsymbol{K}s|\boldsymbol{R}^{(1)}|\boldsymbol{K}_0s_0\rangle &= -\frac{e}{2\pi i}\sum_{\boldsymbol{h}}\delta(K_{0x}+2\pi h_x-K_x)\\ &\times\delta(K_{0y}+2\pi h_y-K_y)\\ &\times\frac{\exp\{i(K_{0z}+2\pi h_z-K_z)D\}-1}{K_{0z}+2\pi h_z-K_z}v_{\boldsymbol{h}}(u^*_{\boldsymbol{K}s}u_{\boldsymbol{K}_0s_0})\ .\end{aligned} \tag{3.6}$$

With the use of

$$E_{\boldsymbol{K}_0s_0}=+\sqrt{\hbar^2c^2K_0{}^2+m_0{}^2c^4} \tag{3.7}$$

$$E_{\boldsymbol{K}s}=+\sqrt{\hbar^2c^2K^2+m_0{}^2c^4}\ , \tag{3.8}$$

the element of the scattering matrix is written according to (2.8) as

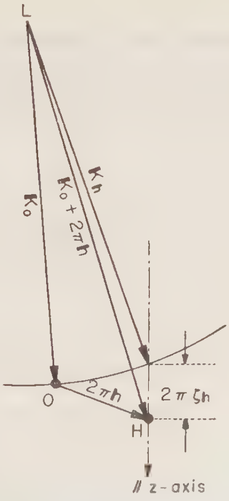

Fig. 2.

$$\langle \boldsymbol{K}s|R^{(1)}|\boldsymbol{K}_0s_0\rangle = -2\pi i\delta\left(\sqrt{\hbar^2c^2K^2+m_0{}^2c^4}-\sqrt{\hbar^2c^2K_0{}^2+m_0{}^2c^4}\right)\langle \boldsymbol{K}s|\boldsymbol{R}^{(1)}|\boldsymbol{K}_0s_0\rangle \tag{3.9}$$

Now we introduce a wave vector $\boldsymbol{K}_{\boldsymbol{h}}=(K_{hx}, K_{hy}, K_{hz})$ which is related to a reciprocal lattice vector $\boldsymbol{h}=(h_x, h_y, h_z)$ and the incident wave vector $\boldsymbol{K}_0=(K_{0x}, K_{0y}, K_{0z})$ in a way as shown in Fig. 2. Here, $\boldsymbol{K}_0{}^2=\boldsymbol{K}_h{}^2$ and $K_{hz}>0$. Taking account of

$$\begin{aligned}
&\delta\left(\sqrt{\hbar^2c^2K^2+m_0{}^2c^4}-\sqrt{\hbar^2c^2K_0{}^2+m_0{}^2c^4}\right)\delta(K_{0x}+2\pi h_x-K_x)\delta(K_{0y}+2\pi h_y-K_y)\\
&\quad=\delta\left(\frac{\hbar^2c^2(K_x{}^2+K_y{}^2+K_z{}^2-K_{hx}^2-K_{hy}^2-K_{hz}^2)}{2\sqrt{\hbar^2c^2K_0{}^2+m_0{}^2c^4}}\right)\delta(K_{0x}+2\pi h_x-K_x)\delta(K_{0y}+2\pi h_y-K_y)\\
&\quad=\delta\left(\frac{\hbar^2c^2(K_z{}^2-K_{hz}^2)}{2E_{\boldsymbol{K}_0}}\right)\\
&\quad=\frac{E_{\boldsymbol{K}_0}}{\hbar^2c^2K_{hz}}\left[\delta(K_z-K_{hz})+\delta(K_z+K_{hz})\right] ,
\end{aligned} \tag{3.10}$$

we obtain

$$\begin{aligned}
\langle \boldsymbol{K}s|R^{(1)}|\boldsymbol{K}_0s_0\rangle = \frac{eE_{\boldsymbol{K}_0}}{\hbar^2c^2}\sum_{\boldsymbol{h}}\left[\delta(K_z-K_{hz})+\delta(K_z+K_{hz})\right]\\
\times\frac{\exp\{i(K_{0z}+2\pi h_z-K_z)D\}-1}{K_{hz}(K_{0z}+2\pi h_z-K_z)}\cdot v_{\boldsymbol{h}}(u^*_{\boldsymbol{K}s}u_{\boldsymbol{K}_0s_0}) ,
\end{aligned} \tag{3.11}$$

where we abbreviated $E_{\boldsymbol{K}_0s_0}$ as $E_{\boldsymbol{K}_0}$. $\delta(K_z-K_{hz})$ in the first square bracket corresponds to a scattered wave with a positive z-component of wave vector K_{hz}, and $\delta(K_z+K_{hz})$ corresponds to another one with a negative component of wave vector $-K_{hz}$. The latter wave can be interpreted as the reflection of the former at the surfaces of the crystal.* Since, as already discussed in the previous paper[4], this wave is negligible so long as $\boldsymbol{K}_0$ is not nearly parallel to the surface of crystal, only the scattered waves with the wave vectors having positive z-components (*i.e.* transmitted waves) are taken into account in the following computations. Then, by integrating (3.11) over a small region of Ewald sphere around $\boldsymbol{K}_h$, the element of scattering matrix corresponding to the transition from $(\boldsymbol{K}_0, s_0)$ to $(\boldsymbol{K}_h, s)$ is given by

$$\langle \boldsymbol{K}_{\boldsymbol{h}}s|R^{(1)}|\boldsymbol{K}_0s_0\rangle = \frac{eE_{\boldsymbol{K}_0}}{\hbar^2c^2K_{hz}}\cdot\frac{\exp(-2\pi i\zeta_{\boldsymbol{h}}D)-1}{-2\pi\zeta_{\boldsymbol{h}}}\cdot v_{\boldsymbol{h}}(u^*_{\boldsymbol{K}_{\boldsymbol{h}}s}u_{\boldsymbol{K}_0s_0}) , \tag{3.12}$$

where $\zeta_{\boldsymbol{h}}$ represents the excitation error defined by

$$-2\pi\zeta_{\boldsymbol{h}}\equiv K_{0z}+2\pi h_z-K_{hz} . \tag{3.13}$$

as shown in Fig. 2.

§ 4. The Second Order Term of Scattering Matrix

In this paragraph, we take account of the indirect transition through intermediate states $(\boldsymbol{k}, s')$. In this process, $E_{\boldsymbol{K}_0s_0}$ or $E_{\boldsymbol{K}s}$ is not required to be equal to the energy of the virtual state $(\boldsymbol{k}, s')$

$$E_{ks'}=\pm\sqrt{c^2\hbar^2k^2+m_0{}^2c^4} . \tag{4.1}$$

By the requirement of closure property of eigen-solutions, all possible $\boldsymbol{k}$ and all of the four states for a given $\boldsymbol{k}$ including the negative energy states must be considered as the virtual states.

According to (2.11), the second term in the series expansion of the transition matrix is given by

$$\langle \boldsymbol{K}s|\boldsymbol{R}^{(2)}|\boldsymbol{K}_0s_0\rangle = \sum_{s'=1}^{4}\int d\boldsymbol{k}\,\frac{\langle \boldsymbol{K}s|H'|\boldsymbol{k}s'\rangle\langle \boldsymbol{k}s'|H'|\boldsymbol{K}_0s_0\rangle}{E_{\boldsymbol{K}_0}-E_{ks'}+i\varepsilon} . \tag{4.2}$$

---

* The present author owes this interpretation to Dr. H. Fengler's thesis (Berlin University, 1960) and the discussion with Dr. K. Kambe.

Taking account of (3.3), (3.1), (3.4), (3.5) and

$$\langle \boldsymbol{r}|\boldsymbol{k}s'\rangle=(2\pi)^{-3/2}u_{\boldsymbol{k}s'}\exp(i\boldsymbol{k}\boldsymbol{r})\ , \tag{4.3}$$

we obtain

$$\begin{aligned}\langle \boldsymbol{K}s|\boldsymbol{R}^{(2)}|\boldsymbol{K}_0s_0\rangle=&\frac{e^2}{(2\pi)^6}\sum_{\boldsymbol{g}_2}\sum_{\boldsymbol{g}_1}\sum_{s'=1}^{4}\int\frac{d\boldsymbol{k}}{E_{\boldsymbol{K}_0}-E_{\boldsymbol{k}s'}+i\varepsilon}\\ &\times\int_{\text{crystal}}d\boldsymbol{r}_2\exp\{i(\boldsymbol{k}+2\pi\boldsymbol{g}_2-\boldsymbol{K})\boldsymbol{r}_2\}\cdot\int_{\text{crystal}}d\boldsymbol{r}_1\exp\{i(\boldsymbol{K}_0+2\pi\boldsymbol{g}_1-\boldsymbol{k})\boldsymbol{r}_1\}\\ &\times v_{\boldsymbol{g}_2}v_{\boldsymbol{g}_1}(u^*_{\boldsymbol{K}s}u_{\boldsymbol{k}s'})(u^*_{\boldsymbol{K}s'}u_{\boldsymbol{K}_0s_0})\ .\end{aligned}\tag{4.4}$$

We can make a replacement

$$\frac{1}{E_{\boldsymbol{K}_0}-E_{\boldsymbol{k}s'}+i\varepsilon}\rightarrow\frac{E_{\boldsymbol{K}_0}+E_{\boldsymbol{k}s'}}{c^2\hbar^2(\boldsymbol{K}_0{}^2-\boldsymbol{k}^2+i\varepsilon)}\ , \tag{4.5}$$

considering that ε is a small positive quantity, and allowing for the relations

$$\frac{1}{E_{\boldsymbol{K}_0}-E_{\boldsymbol{k}s'}+i\varepsilon}=\frac{E_{\boldsymbol{K}_0}+E_{\boldsymbol{k}s'}+i\varepsilon}{E^2_{\boldsymbol{K}0}-|E_{\boldsymbol{k}s'}|^2+2i\varepsilon E_{\boldsymbol{K}_0}-\varepsilon^2}\ ,$$

and

$$E^2_{\boldsymbol{K}_0}-|E_{\boldsymbol{k}s'}|^2=c^2\hbar^2(\boldsymbol{K}_0{}^2-\boldsymbol{k}^2)\ .$$

The summation over s' can then be performed by using the formula (2.17) and the relations

$$E_{\boldsymbol{k}s'}u_{\boldsymbol{k}s'}=H_{\boldsymbol{k}}u_{\boldsymbol{k}s'}\ , \tag{4.6}$$

$$H_{\boldsymbol{k}}=c\hbar\boldsymbol{\alpha}\boldsymbol{k}+\beta m_0c^2\ , \tag{4.7}$$

and we obtain

$$\begin{aligned}\langle \boldsymbol{K}s|\boldsymbol{R}^{(2)}|\boldsymbol{K}_0s_0\rangle=&\frac{e^2}{(2\pi)^6c^2\hbar^2}\sum_{\boldsymbol{g}_2}\sum_{\boldsymbol{g}_1}\iiint_{-\infty}^{\infty}\frac{dk_xdk_ydk_z}{\boldsymbol{K}_0{}^2-\boldsymbol{k}^2+i\varepsilon}\\ &\times\int_{\text{crystal}}d\boldsymbol{r}_2\exp\{i(\boldsymbol{k}+2\pi\boldsymbol{g}_2-\boldsymbol{K})\boldsymbol{r}_2\}\cdot\int_{\text{crystal}}d\boldsymbol{r}_1\exp\{i(\boldsymbol{K}_0+2\pi\boldsymbol{g}_1-\boldsymbol{k})\boldsymbol{r}_1\}\\ &\times v_{\boldsymbol{g}_2}v_{\boldsymbol{g}_1}(u^*_{\boldsymbol{K}s}(E_{K_0}+H_{\boldsymbol{k}})u_{\boldsymbol{K}_0s_0})\ .\end{aligned}\tag{4.8}$$

The integrals in Eq. (4.8) with respect to $\boldsymbol{r}_1$ and $\boldsymbol{r}_2$ become

$$\begin{aligned}&\int_{\text{crystal}}d\boldsymbol{r}_2\exp\{i(\boldsymbol{k}+2\pi\boldsymbol{g}_2-\boldsymbol{K})\boldsymbol{r}_2\}\cdot\int_{\text{crystal}}d\boldsymbol{r}_1\exp\{i(\boldsymbol{K}_0+2\pi\boldsymbol{g}_1-\boldsymbol{k})\boldsymbol{r}_1\}\\ &\quad=(2\pi)^4\delta(k_x+2\pi g_{2x}-K_x)\delta(k_y+2\pi g_{2y}-K_y)\delta(K_{0x}+2\pi g_{1x}-k_x)\delta(K_{0y}+2\pi g_{1y}-k_y)\\ &\quad\times\int_0^D dz_2\exp\{i(k_z+2\pi g_{2z}-K_z)z_2\}\cdot\int_0^D dz_1\exp\{i(K_{0z}+2\pi g_{1z}-k_z)z_1\}\ .\end{aligned}\tag{4.9}$$

We may put approximately

$$\int_0^D dz_2\int_0^D dz_1\ (integrand)\simeq\int_0^D dz_2\int_0^{z_2}dz_1\ (integrand)\ . \tag{4.10}$$

The contribution from $\int_{z_2}^{D}dz_1$ is negligibly small, since it corresponds to the contribution of the intermediate states with negative z-components of wave vectors. The approximation in (4.10) is nothing but that previously adopted by Cowley and Moodie[3] and by the present author[4]. With this approximation and the relations

$$
\begin{aligned}
&K_{0x}+2\pi g_{1x}=K_{\mathbf{g}'x}\ ,\\
&K_{0y}+2\pi g_{1y}=K_{\mathbf{g}_1 y}\ ,\\
&K^2_{0x}+K^2_{0y}+K^2_{0z}=K^2_{\mathbf{g}_1 x}+K^2_{\mathbf{g}_1 y}+K^2_{\mathbf{g}_1 z}\ ,
\end{aligned}
$$

and by carrying out the integrations over k_x and k_y in (4.8), we obtain

$$
\begin{aligned}
\langle \boldsymbol{K}s|\boldsymbol{R}^{(2)}|\boldsymbol{K}_0 s_0\rangle=&\frac{1}{(2\pi i)^2}\left(\frac{e^2}{c^2\hbar^2}\right)\sum_{\mathbf{g}_2}\sum_{\mathbf{g}_1}\delta(K_{0x}+2\pi(\boldsymbol{g}_1+\boldsymbol{g}_2)_x-K_x)\\
&\times\delta(K_{0y}+2\pi(\boldsymbol{g}_1+\boldsymbol{g}_2)_y-K_y)\int_{-\infty}^{\infty}\frac{dk_z}{K^2_{\mathbf{g}_1 z}-k_z^2+i\varepsilon}\\
&\times\frac{1}{K_{0z}+2\pi g_{1z}-k_z}\left[\frac{\exp\left[i\{K_{0z}+2\pi(\boldsymbol{g}_1+\boldsymbol{g}_2)_z-K_z\}D\right]-1}{K_{0z}+2\pi(\boldsymbol{g}_1+\boldsymbol{g}_2)_z-K_z}\right.\\
&\left.\qquad-\frac{\exp\left(i(k_z+2\pi g_{2z}-K_z)D\right\}-1}{k_z+2\pi g_{2z}-K_z}\right]\\
&\times v_{\mathbf{g}_2}v_{\mathbf{g}_1}(u^*_{\mathbf{K}s}(E_{\mathbf{K}_0}+H_{(k_z)})u_{\mathbf{K}_0 s_0})\ ,
\end{aligned}
\tag{4.11}
$$

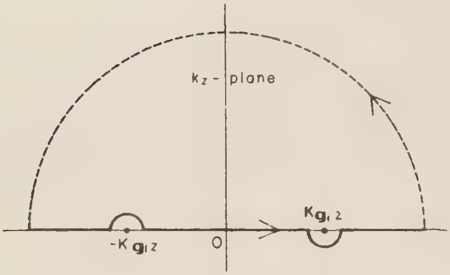

Fig. 3.

where

$$
H_{(k_z)}\equiv c\hbar(\alpha_x K_{\mathbf{g}_1 x}+\alpha_y K_{\mathbf{g}_1 y}+\alpha_z k_z)+\beta m_0 c^2\ . \tag{4.12}
$$

The integrand of the integral over k_z in (4.11) has simple poles at

$$
k_z=\pm\left(K_{\mathbf{g}_1 z}+\frac{i\varepsilon}{2K_{\mathbf{g}_1 z}}\right).
$$

The existence of the infinitesimal positive number ε suggests that path of integral should be taken as shown in Fig. 3. Using the theorem of residues, we obtain

$$
\begin{aligned}
\langle \boldsymbol{K}s|\boldsymbol{R}^{(2)}|\boldsymbol{K}_0 s_0\rangle=&-\frac{1}{2\pi i}\left(\frac{e^2}{c^2\hbar^2}\right)\sum\sum_{\mathbf{g}_1}\frac{1}{2K_{\mathbf{g}_1 z}}\delta(K_{0x}+2\pi h_x-K_x)\delta(K_{0y}+2\pi h_y-K_y)\\
&\times\frac{1}{K_{0z}+2\pi g_{1z}-K_{\mathbf{g}_1 z}}\left[\frac{\exp\{i(K_{0z}+2\pi h_z-K_z)D\}-1}{K_{0z}+2\pi h_z-K_z}-\frac{\exp\{i(K_{\mathbf{g}_1 z}+2\pi g_{2z}-K_z)D\}-1}{K_{\mathbf{g}_1 z}+2\pi g_{2z}-K_z}\right]\\
&\times v_{\mathbf{g}_2}v_{\mathbf{g}_1}(u^*_{\mathbf{K}s}(E_{\mathbf{K}_0}+H(K_{\mathbf{g}_1}))u_{\mathbf{K}_0 s_0})\ ,
\end{aligned}
\tag{4.13}
$$

where we put $\boldsymbol{h}=\boldsymbol{g}_1+\boldsymbol{g}_2$ and

$$
H(K_{\mathbf{g}_1})=c\hbar\boldsymbol{\alpha}\boldsymbol{K}_{\mathbf{g}_1}+\beta m_0 c^2\ . \tag{4.14}
$$

Taking account of (2.8), (3.10), (3.13) and (4.13), and introducing the excitation error of reciprocal lattice point $\boldsymbol{g}_1$ as

$$
-2\pi\zeta_{\mathbf{g}_1}\equiv K_{0z}+2\pi g_{1z}-K_{\mathbf{g}_1 z}\ , \tag{4.15}
$$

we finally obtain

$$
\begin{aligned}
\langle K_{\boldsymbol{h}}s|R^{(2)}|K_0 s_0\rangle=&\left(\frac{e}{c^2\hbar^2}\right)^2 E_{\mathbf{K}_0}\cdot\sum_{\mathbf{g}_1}\frac{1}{K_{\boldsymbol{h}z}K_{\mathbf{g}_1 z}}\\
&\times\frac{1}{2\pi\zeta_{\mathbf{g}_1}}\left[\frac{\exp(-2\pi i\zeta_{\boldsymbol{h}}D)-1}{2\pi\zeta_{\boldsymbol{h}}}+\frac{\exp\{2\pi i(\zeta_{\mathbf{g}_1}-\zeta_{\boldsymbol{h}})D\}-1}{2\pi(\zeta_{\mathbf{g}_1}-\zeta_{\boldsymbol{h}})}\right]\\
&\times\frac{1}{2}v_{\mathbf{g}_2}v_{\mathbf{g}_1}(u^*_{\mathbf{K}_{\boldsymbol{h}}s}(E_{\mathbf{K}_0}+H(K_{\mathbf{g}_1}))u_{\mathbf{K}_0 s_0})\ .
\end{aligned}
$$

§ 5. General Terms in Series Expansion of Scattering Matrix

The n-th order term of transition matrix can be evaluated by starting from

$$\langle \boldsymbol{K}s|\boldsymbol{R}^{(n)}|\boldsymbol{K}_0 s_0\rangle = \sum_{s'=1}^{4}\sum_{s''=1}^{4}\cdots\sum_{s^{(n-1)}=1}^{4}\iint\cdots\int d\boldsymbol{k}'d\boldsymbol{k}''\cdots d\boldsymbol{k}^{(n-1)} \times \frac{\langle \boldsymbol{K}s|H'|\boldsymbol{k}^{(n-1)}s^{(n-1)}\rangle\cdots\langle \boldsymbol{k}''s''|H'|\boldsymbol{k}'s'\rangle\langle \boldsymbol{k}'s'|H'|\boldsymbol{K}_0 s_0\rangle}{(E_{\boldsymbol{K}_0}-E_{\boldsymbol{k}^{(n-1)}s^{(n-1)}}+i\varepsilon)\cdots(E_{\boldsymbol{K}_0}-E_{\boldsymbol{k}''s''}+i\varepsilon)(E_{\boldsymbol{K}_0}-E_{\boldsymbol{k}'s'}+i\varepsilon)}, \tag{5.1}$$

where $(\boldsymbol{k}', s')$, $(\boldsymbol{k}'', s'')$, $\cdots$ and $(\boldsymbol{k}^{(n-1)}, s^{(n-1)})$ represent $n-1$ intermediate states. The computations can be carried out similarly as those in § 4 by adopting the approximation replacing the integral

$$\int_0^D dz_n \int_0^D dz_{n-1}\cdots\int_0^D dz_2\int_0^D dz_1\ (integrand)\,,$$

by

$$\int_0^D dz_n \int_0^{z_n} dz_{n-1}\cdots\int_0^{z_3} dz_2\int_0^{z_2} dz_1\ (integrand)\,.$$

Then, the matrix element is given by

$$\begin{aligned}&\langle \boldsymbol{K}_h s|R^{(n)}|\boldsymbol{K}_0 s_0\rangle\\ &\quad=\left(\frac{e}{c^2\hbar^2}\right)^n\cdot E_{\boldsymbol{K}_0}\cdot\sum_{g_{n-1}}\cdots\sum_{g_2}\sum_{g_1}\frac{v_{h-(g_1+\cdots+g_{n-1})}v_{g_{n-1}}\cdots v_{g_2}v_{g_1}}{K_{hz}K_{g_1+\cdots+g_{n-1},z}\cdots K_{g_1+g_2,z}K_{g_1z}}\\ &\quad\times Z_n(\zeta_1,\ \zeta_2,\ \cdots,\ \zeta_{n-1},\ \zeta_h;\ D)\\ &\times\frac{1}{2^{n-1}}(u^*_{\boldsymbol{K}_h s}(E_{\boldsymbol{K}_0}+H(\boldsymbol{K}_{g_1+\cdots+g_{n-1}}))\cdots(E_{\boldsymbol{K}_0}+H(\boldsymbol{K}_{g_1+g_2}))(E_{\boldsymbol{K}_0}+H(\boldsymbol{K}_{g_1}))u_{\boldsymbol{K}_0 s_0})\,,\end{aligned} \tag{5.2}$$

where

$$\begin{aligned}&Z_n(\zeta_1,\ \zeta_2,\ \cdots,\ \zeta_{n-1},\ \zeta_h;\ D)\\ &\quad=\frac{1}{(2\pi)^n}\left[\sum_{m=1}^{n-1}\frac{\exp\{2\pi i(\zeta_m-\zeta_h)D\}-1}{\zeta_m(\zeta_m-\zeta_h)\prod\limits_{\substack{k=1\\k\neq m}}^{n-1}(\zeta_m-\zeta_k)}+(-1)^n\frac{\exp(-2\pi i\zeta_h D)-1}{\zeta_h\prod\limits_{k=1}^{n-1}\zeta_k}\right]\end{aligned} \tag{5.3}$$

and

$$H(\boldsymbol{K}_{g_1+\cdots+g_m})=c\hbar\boldsymbol{\alpha}\cdot\boldsymbol{K}_{g_1+\cdots+g_m}+\beta m_0c^2\,. \tag{5.4}$$

Reference may be made to the previous paper[4] concerning the definitions of the excitation errors ζ_m and the wave vector $\boldsymbol{K}_{g_1+\cdots+g_m}$.

§ 6. Transition Probabilities

If the incident beam is unpolarized, the probability of the transition from the incident wave $\boldsymbol{K}_0$ to the diffracted wave $\boldsymbol{K}_h$ is given as*

$$I_{h0}=\frac{1}{2}\sum_{s_0=1}^{2}\sum_{s=1}^{2}|\langle \boldsymbol{K}_h s|R|\boldsymbol{K}_0 s_0\rangle|^2\,. \tag{6.1}$$

Then, (6.1) may be computed using the formulas (2.18)～(2.24) in the following ways.

a) *The first approximation*

From (3.12) and (5.3) we may write the first approximation of (6.1) as

$$I^{(2)}_{h0}=\frac{1}{2}\sum_{s=1}^{2}\sum_{s_0=1}^{2}|\langle \boldsymbol{K}_h s|R^{(1)}|\boldsymbol{K}_0 s_0\rangle|^2$$

---

* So far as the scattering by electrostatic field is concerned, (6.1) can be used regardless of the spin state of the incident electron.

$$=\frac{e^2E^2_{\boldsymbol{K}_0}}{\hbar^4c^4K^2_{hz}}\cdot|Z_1(\zeta_h;\ D)|^2\cdot v_h{}^*v_h$$

$$\times\frac{1}{2}\sum_{s=1}^{2}\sum_{s_0=1}^{2}(u^*_{\boldsymbol{K}_0s_0}u_{\boldsymbol{K}_hs})(u^*_{\boldsymbol{K}_hs}u_{\boldsymbol{K}_0s_0})\ , \tag{6.2}$$

where $\boldsymbol{\alpha}^*=\boldsymbol{\alpha}$ has been taken into account. Applying (2.18) and (2.19) to $\sum\limits_{s=1}^{2}$ and to $\sum\limits_{s_0=1}^{2}$, respectively, and allowing for $E_{\boldsymbol{K}_h}=E_{\boldsymbol{K}_0}$, we obtain

$$\frac{1}{2}\sum_{s=1}^{2}\sum_{s_0=1}^{2}(u^*_{\boldsymbol{K}_0s_0}u_{\boldsymbol{K}_hs})(u^*_{\boldsymbol{K}_hs}u_{\boldsymbol{K}_0s_0})$$

$$=\frac{1}{8E^2_{\boldsymbol{K}_0}}\ \mathrm{Spur}\ (H_{\boldsymbol{K}_h}+E_{\boldsymbol{K}_0})(H_{\boldsymbol{K}_0}+E_{\boldsymbol{K}_0})$$

$$=\frac{1}{8E^2_{\boldsymbol{K}_0}}\ \mathrm{Spur}\ [c^2\hbar^2(\boldsymbol{\alpha K}_h)(\boldsymbol{\alpha K}_0)+c\hbar\boldsymbol{\alpha K}_h(\beta m_0c^2+E_{\boldsymbol{K}_0})$$

$$+\beta m_0c^2(c\hbar\boldsymbol{\alpha K}_0+E_{\boldsymbol{K}_0})+\beta^2m_0{}^2c^4$$

$$+E_{\boldsymbol{K}_0}(c\hbar\boldsymbol{\alpha K}_0+\beta m_0c^2)+E^2_{\boldsymbol{K}_0}]\ , \tag{6.3}$$

where the subtitution has been made of

$$H_{\boldsymbol{K}_h}=c\hbar\boldsymbol{\alpha K}_h+\beta m_0c^2\ , \tag{6.4}$$

$$H_{\boldsymbol{K}_0}=c\hbar\boldsymbol{\alpha K}_0+\beta m_0c^2\ . \tag{6.5}$$

Noticing that the second, the third and the fifth terms vanish according to (2.22) and using (2.23) and (3.7), we get

$$\frac{1}{2}\sum_{s=1}^{2}\sum_{s_0=1}^{2}(u^*_{\boldsymbol{K}_0s_0}u_{\boldsymbol{K}_hs})(u^*_{\boldsymbol{K}_hs}u_{\boldsymbol{K}_0s_0})$$

$$=\frac{1}{8E^2_{\boldsymbol{K}_0}}\ \mathrm{Spur}\ [c^2\hbar^2(\boldsymbol{\alpha K}_h)(\boldsymbol{\alpha K}_0)+m_0{}^2c^4+E^2_{\boldsymbol{K}_0}]$$

$$=\frac{1}{E^2_{\boldsymbol{K}_0}}\left[m_0{}^2c^4+c^2\hbar^2K_0{}^2\left(\frac{1+\cos\theta_{0h}}{2}\right)\right], \tag{6.6}$$

where θ_{0h} is the angle between $\boldsymbol{K}_0$ and $\boldsymbol{K}_h$.

Substituting (6.6) into (6.2), we finally obtain

$$I^{(2)}_{h0}=\left(\frac{m_0e}{\hbar^2}\right)^2\cdot\frac{|v_h|^2}{K^2_{hz}}\cdot\frac{\sin^2(\pi\zeta_hD)}{(\pi\zeta_h)^2}\cdot\left[1+\frac{\hbar^2K_0{}^2}{m_0{}^2c^2}\left(\frac{1+\cos\theta_{0h}}{2}\right)\right]. \tag{6.7}$$

b) *Higher approximations*

The next order term of the probability of transition from $\boldsymbol{K}_0$ to $\boldsymbol{K}_h$ may be written as

$$I^{(3)}_{h0}=\frac{1}{2}\sum_{s=1}^{2}\sum_{s_0=1}^{2}[\langle\boldsymbol{K}_0s_0|R^{(1)*}|\boldsymbol{K}_hs\rangle\langle\boldsymbol{K}_hs|R^{(2)}|\boldsymbol{K}_0s_0\rangle$$

$$+\langle\boldsymbol{K}_0s_0|R^{(2)*}|\boldsymbol{K}_hs\rangle\langle\boldsymbol{K}_hs|R^{(1)}|\boldsymbol{K}_0s_0\rangle]$$

$$=\left(\frac{m_0e}{\hbar^2}\right)^3\sum_{g_1}\frac{1}{K^2_{hz}K_{g_1z}}[v_h{}^*v_{h-g_1}v_{g_1}Z_1{}^*(\zeta_h;\ D)Z_2(\zeta_{g_1},\ \zeta_h;\ D)$$

$$+v_hv^*_{h-g_1}v^*_{g_1}Z_1(\zeta_h;\ D)Z_2{}^*(\zeta_{g_1},\ \zeta_h;\ D)]$$

$$\times\left(1+\frac{\hbar^2K_0{}^2}{m_0{}^2c^2}\right)^{1/2}\cdot\left\{1+\left(\frac{\hbar^2K_0{}^2}{m_0{}^2c^2}\right)\left(\frac{1+\cos\theta_{0h}+\cos\theta_{hg_1}+\cos\theta_{0g_1}}{4}\right)\right\}, \tag{6.8}$$

where Z_1 and Z_2 is the functions defined by (5.3) and θ_{hg_1} and θ_{0g_1} are the angles between

$\boldsymbol{K}_h$ and $\boldsymbol{K}_{g_1}$ and $\boldsymbol{K}_0$ and $\boldsymbol{K}_{g_1}$, respectively. Since, in usual experimental conditions, $\boldsymbol{K}_h$ and $\boldsymbol{K}_{g_1}$ are nearly parallel to $\boldsymbol{K}_0$, we may put

$$\cos\theta_{0h}\simeq 1\,,\qquad \cos\theta_{hg_1}\simeq 1\,,\qquad \cos\theta_{0g_1}\simeq 1\,.$$

Then, the product of the last two factors in (6.8) reduces to

$$\left(1+\frac{\hbar^2 K_0{}^2}{m_0{}^2c^2}\right)^{3/2}. \tag{6.9}$$

If we notice that only the waves with small scattering angle are appreciable in electron diffraction, the general term $I_{0h}^{(N)}$ may be easily found to be as follows. Since all $\boldsymbol{K}$'s are nearly parallel, we may put

$$H_{\boldsymbol{K}_h}\simeq H_{\boldsymbol{K}_0},\ H(\boldsymbol{K}_{g_1})\simeq H_{\boldsymbol{K}_0},\ \cdots,\ H(\boldsymbol{K}_{g_1+\cdots+g_{n-1}})\simeq H_{\boldsymbol{K}_0})\,.$$

Then, Eq. (5.2) may be written approximately as

$$\begin{aligned}\langle \boldsymbol{K}_h s|R^{(n)}|\boldsymbol{K}_0 s_0\rangle \simeq \left(\frac{e}{c^2\hbar^2}\right)^n\cdot E_{\boldsymbol{K}_0}^n\cdot\sum_{g_{n-1}}\cdots\sum_{g_1}\frac{v_{h-(g_1+\cdots+g_{n-1})}\cdots v_{g_1}}{K_{hz}\cdots K_{g_1z}}\\ \times Z_n(\zeta_1,\ \zeta_2,\ \cdots,\ \zeta_h;\ D)\cdot(u_{\boldsymbol{K}_h s}^* u_{\boldsymbol{K}_0 s_0})\,,\end{aligned} \tag{6.10}$$

where the relation

$$(u_{\boldsymbol{K}_h s}^*(E_{\boldsymbol{K}_0}+H_{\boldsymbol{K}_0})^{n-1}u_{\boldsymbol{K}_0 s_0})=2^{n-1}\cdot E_{\boldsymbol{K}_0}^{n-1}\cdot(u_{\boldsymbol{K}_h s}^* u_{\boldsymbol{K}_0 s_0})$$

has been taken into account. Using (6.10) allowing for

$$\frac{1}{2}\sum_{s_0=1}^{2}\sum_{s=1}^{2}(u_{\boldsymbol{K}_0 s_0}^* u_{\boldsymbol{K}_h s})(u_{\boldsymbol{K}_h s}^* u_{\boldsymbol{K}_0 s_0})\simeq\frac{m_0{}^2c^4}{E_{\boldsymbol{K}_0}^2}\left(1+\frac{\hbar^2K_0{}^2}{m_0{}^2c^2}\right)$$

and

$$E_{\boldsymbol{K}_0}=m_0c^2\left(1+\frac{\hbar^2K_0{}^2}{m_0{}^2c^2}\right)^{1/2},$$

we obtain the N-th order term of the transition probability in the form

$$\begin{aligned}I_{h0}^{(N)}=\left(\frac{m_0e}{\hbar^2}\right)^N\cdot\left(1+\frac{\hbar^2K_0{}^2}{m_0{}^2c^2}\right)^{N/2}\sum_{n=1}^{N-1}\Bigg[\sum_{g_{n-1}}\cdots\sum_{g_1}\cdot\sum_{g'_{N-n-1}}\cdots\sum_{g_1'}\\ \times\frac{(v_{h-(g_1+\cdots+g_{n-1})}^*\cdots v_{g_1}^*)\cdot(v_{h-(g_1'+\cdots+g'_{N-n-1})}\cdots v_{g_1'})}{(K_{hz}\cdots K_{g_1z})\cdot(K_{hz}\cdots K_{g_1'z})}Z_n{}^*Z_{N-n}\Bigg].\end{aligned} \tag{6.11}$$

Eq. (6.11) may be compared with the corresponding nonrelativistic formula which was deduced in the previous paper[4]:

$$\begin{aligned}I_{h0}^{(N)}(N.R.)=\left(\frac{m_0e}{\hbar^2}\right)^N\cdot\sum_{n=1}^{N-1}\Bigg[\sum_{g_{n-1}}\cdots\sum_{g_1}\cdot\sum_{g'_{N-n-1}}\cdots\sum_{g_1'}\\ \times\frac{(v_{h-(g_1+\cdots+g_{n-1})}^*\cdots v_{g_1}^*)(v_{h-(g_1'+\cdots+g'_{N-n-1})}\cdots v_{g_1'})}{(k_{hz}\cdots k_{g_1z})\cdot(k_{hz}\cdots k_{g_1'z})}Z_n{}^*Z_{N-n}\Bigg],\end{aligned} \tag{6.12}$$

where k_z's denote the wave vectors in the nonrelativistic theory and Z's are to be understood to contain nonrelativistic ζ's.

§ 7. Discussion on the Relativistic Effect

The relativistic correction usually applied to the nonrelativistic scattering formula consists only of the replacement of the nonrelativistic value of wave-length

$$\lambda' = 2\pi/k = h/\sqrt{2em_0 U} \tag{7.1}$$

with the relativistic one

$$\lambda = 2\pi/K = (h/\sqrt{2em_0 U})\cdot[1+(eU/2m_0c^2)]^{-1/2}\,, \tag{7.2}$$

where U is the accelerating voltage of electron.

The kinematical formula for the transition probability (6.7) contains a factor

$$1+\frac{\hbar^2 K_0^2}{m_0^2 c^2}\left(\frac{1+\cos\theta_{0h}}{2}\right). \tag{7.3}$$

This factor has been given by Laue[1] in the treatment of Born approximation. It is, further, easily shown by comparing (6.11) with (6.12) that the corresponding factor in the N-th order term of transition probability is approximately given by

$$\left(1+\frac{\hbar^2 K_0^2}{m_0^2 c^2}\right)^{N/2}. \tag{7.4}$$

The factor (7.3) or (7.4) arises from the relativistic correction for mass itself, since it is proved that

$$\sqrt{1+(\hbar^2 K_0^2/m_0^2 c^2)} = 1\Big/\sqrt{1-\left(\frac{u}{c}\right)^2}\,, \tag{7.5}$$

where u is the velocity of electron.

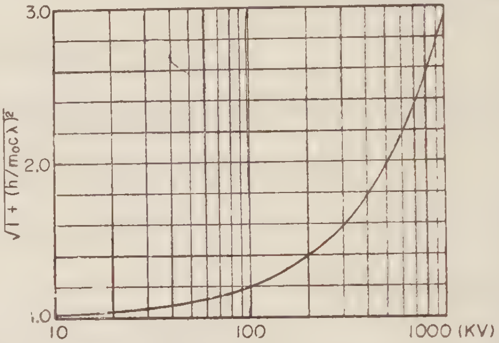

Fig. 4. The relativistic correction factor for mass $\sqrt{1+(h/m_0c\lambda)^2}$ *versus* the accelerating voltage of electron.

As pointed out by Laue and shown in Fig. 4, this correction factor becomes large at the high energy of electron. For the evaluation of (7.5), the expression

$$\begin{aligned}\sqrt{1+(\hbar^2K^2/m_0^2c^2)} &= \sqrt{1+(2eU/m_0c^2)[1+(eU/2m_0c^2)]}\\ &= 1+1.96(eU)_{\mathrm{MeV}}\,,\end{aligned} \tag{7.6}$$

may be convenient. In the derivation of the right hand side of (7.6), $m_0c^2=0.51$ MeV has been taken into account. Here, $(eU)_{\mathrm{MeV}}$ means the kinetic energy of electron measured in the unit of MeV.

Almost all phenomena of electron diffraction take place at small scattering angles, and under this condition the new correction factor assumes a comparatively simple form as shown by (7.4). This implies that the relativistic revision of the theory of electron diffraction based on nonrelativistic Schrödinger wave equation may be obtained by the replacements

$$\lambda' \to \lambda$$

and

$$m_0 \to m_0\sqrt{1+(\hbar^2K^2/m_0^2c^2)}\,.$$

The experimental aspects of the relativistic effects in the dynamical theory will be dealt with in near future[10)]. In order to see one of the influence of the factor (7.4) on the dynamical theory, however, we consider now the dependence of the intensity of reflection on wave-length. If only the correction for wave-length is adopted as usual, the transition probability may be expanded as is seen from (6.12) into power series of λ as

$$I_{h0} = \sum_{n=2}^{\infty} C_n(v_h,\,\cdots;\,\zeta_h,\,\cdots;\,D)\cdot(m_0\lambda)^n\,, \tag{7.7}$$

where the dependence of ζ on λ is neglected since it is not essential for the present argument. On the basis of (7.7), Miyake[5)], Fujimoto[6)] and the present author[4)] previously concluded that the intensity approaches the kinematical value (*i.e.* $I_{h0}^{(2)}$) when $\lambda\to 0$. If this were correct, it would be advantageous for the structure analysis to raise the energy of incident electrons. The existence of the factor (7.4), however, place a grave limitation on this conclusion. Instead of (7.7), we should have a power series

$$I_{h0}=\sum_{n=2}^{\infty} C_n \cdot (m_0 \sqrt{1+(h^2/m_0{}^2c^2\lambda^2)} \cdot \lambda)^n \,. \tag{7.8}$$

As shown in Fig. 5, the quantity

$$\lambda\sqrt{1+(h^2/m_0{}^2c^2\lambda^2)}$$

approaches not zero but a finite value as $\lambda\to 0$. The limiting value $h/m_0c=0.0242$ Å is the Compton wave-length of electron and is equivalent to the wave-length of about 215 KeV-electron. It follows, then, that the terms of higher order ($n>2$) in (7.8) do not vanish at the limit $\lambda\to 0$. In other words, the so-called dynamical effect cannot be eliminated by raising the energy of electrons. The kinematical intensity, on the other hand, may be attained by reducing the crystal size, since

$$C_n=O(D^n)\,.$$

In conclusion the author wishes to express his sincere thanks to Prof. Shizuo Miyake for his kind guidance and encouragement throughout the present work.

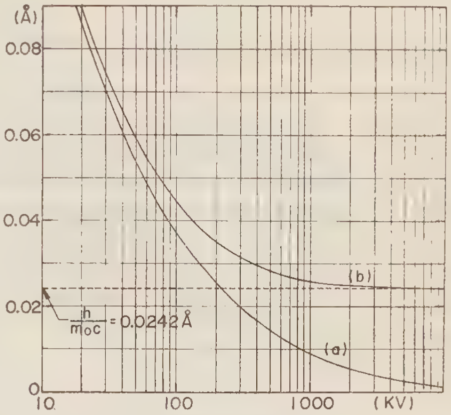

Fig. 5. a) The wave-length *versus* the accelerating voltage of electron.

b) The quantity $\lambda\sqrt{1+(h^2/m_0{}^2c^2\lambda^2)}$ *versus* the accelerating voltage. The limit is the Compton wave-length of electron $h/m_0c=0.0242$ Å.

Appendix

Magnetic Scattering of Electron by Crystal

There exist two kinds of interactions in magnetic scattering of electron by crystal, namely the dipole-dipole interaction and the exchange interaction between two electrons. In the following, we shall discuss the former interaction, since this can be dealt with by the similar calculation developed in the present paper.

We shall restrict ourselves to the scattering by an antiferromagnetic crystal. In this case, the field caused by the magnetic moments of electrons in crystal is considered to be derived from a periodic vector potential

$$\boldsymbol{A}(\boldsymbol{r})=\sum_{h} \boldsymbol{A}_k \exp(2\pi i\boldsymbol{hr})\,.$$

The Fourier component $\boldsymbol{A}_h$ has been calculated by Miyake[11], and takes the form

$$\boldsymbol{A}_h = i2\mu_B\rho_h{}^m[\boldsymbol{h},\ \boldsymbol{M}]/|\boldsymbol{h}|^2\,, \tag{A.1}$$

where μ_B is Bohr magneton, $\boldsymbol{M}$ the unit vector in the direction of magnetization, and $\rho_h{}^m$ is the Fourier component of the electron contributing to magnetism. Adopting

$$H'=-e\sum_{h} (v_h-\boldsymbol{\alpha}\cdot\boldsymbol{A}_h)\exp(2\pi i\boldsymbol{hr})$$

as perturbation and calculating the element of scattering matrix as before, we can easily obtain the kinematical formula for the transition probability:

$$I_{h0}=\left(\frac{m_0e}{\hbar^2}\right)^2 \frac{1}{K_{hz}^2} \frac{\sin^2(\pi\zeta_h D)}{(\pi\zeta_h)^2}\Bigg[|v_h|^2\cdot\left(1+\frac{\hbar^2K_0{}^2}{m_0{}^2c^2}\cdot\frac{1+\cos\theta_{0h}}{2}\right)$$
$$-\frac{\hbar}{2m_0{}^2c^3}\cdot E_{K_0}\cdot(v_h{}^*\boldsymbol{A}_h+v_h\boldsymbol{A}_h{}^*)\cdot(\boldsymbol{K}_h+\boldsymbol{K}_0)$$

$$+\frac{\hbar^2}{2m_0^2c^2}\{(\boldsymbol{K}_0\cdot\boldsymbol{K}_0-\boldsymbol{K}_h)(\boldsymbol{A}_h{}^*\boldsymbol{A}_h)+(\boldsymbol{A}_h{}^*\boldsymbol{K}_h)(\boldsymbol{A}_h\boldsymbol{K}_0)+(\boldsymbol{A}_h\boldsymbol{K}_h)(\boldsymbol{A}_h{}^*\boldsymbol{K}_0)\}\Big]\,. \qquad (\mathrm{A}.2)$$

As is apparent from (A.2), the ratio of the intensity of magnetic scattering (*i.e.* the third term in the square bracket in (A.2)) to the electrostatic one (*i.e.* the first term) increases with the energy of incident electron, and approaches to a constant value

$$|\boldsymbol{A}_h|^2/|v_h|^2\,.$$

By using (A.1) and assuming $1/|\boldsymbol{h}|\sim 0.5$ Å, we obtain

$$|\boldsymbol{A}_h|^2/|v_h|^2\simeq 10^{-4}\cdot|F_h{}^m/F_h|^2\,, \qquad (\mathrm{A}.3)$$

where F_h is the structure amplitude in the ordinary sense and $F_h{}^m$ is that of magnetic electrons. From (8.4), it may be concluded theoretically that the magnetic scattering of electron by the first mechanism is hard to observe.

As to the exange interaction, it is conceived that its magnitude decreases rapidly as the energy of the incident electron increases, since the exchange energy involves overlapping integral of wave function of atomic electron and incident plane wave which oscillates rapidly if it has large wave number. The exchange interaction, however, may be important in the diffraction of slow electron.

References

1) M. v. Laue: Materiewellen und ihre interferenzen (Akademische Verlagsgesellschaft Geest & Portig K. G., Leipzig, 1948).
2) H. A. Bethe: Ann. Physik **87** (1928) 55.
3) J. M. Cowley and A. F. Moodie: Acta Cryst. **10** (1957) 609.
4) K. Fujiwara: J. Phys. Soc. Japan **14** (1959) 1513.
5) S. Miyake: J. Phys. Soc. Japan **14** (1959) 1347.
6) F. Fujimoto: J. Phys. Soc. Japan **14** (1959) 1558.
7) G. Honjo and N. Kitamura: Acta Cryst. **10** (1957) 533.
8) For example, M. Gell-Mann and M. L. Goldberger: Phys. Rev. **91** (1953) 398. S. Tomonaga, N. Fukuda and H. Fukuda: Ba no Ryoshi-Ron (A monograph in the Gendai-Butsuri Series, Iwanami, Japan, 1955) (in Japanese) 94.
9) W. Heitler: The Quantum Theory of Radiation (Oxford at the Clarendon Press, 1954).
10) S. Miyake, K. Fujiwara and K. Suzuki: to be published.
11) S. Miyake: private communication.

JOURNAL OF THE PHYSICAL SOCIETY OF JAPAN, Vol. 16, No. 11, NOVEMBER, 1961

Studies on the Radial Distribution Analysis in Diffraction Methods
III. Extrapolation of Intensity Data to Small Scattering Angle* **

By Tadashi INO

Faculty of Science, Osaka City University, Osaka, Japan

(Received June 30, 1961)

The extrapolation was performed by the approximation in the series of Legendre polynomials and the error in the radial distribution function caused by a failure of the extrapolation was discussed. As the result, the method is inferred to be successfully applied to the experimental data so that the extrapolation can be obtained straightforwardly without any assumption of the structure in advance. Furthermore, the criterion for judging the uniqueness and correctness of the extrapolation is proved to be the absence of the ripple beyond non-zero range in the radial distribution curve.

§ 1. Introduction

In order to directly derive the structural information from the diffraction data of gaseous, liquid, and amorphous materials we calculate the radial distribution function $D(r)$, i.e., the Fourier transformation of a certain function $I(s)$ which is regarded as sensitive to the structure:

$$rD(r)=(1/2\pi^2)\int_0^\infty sI(s)\sin sr\,ds\,, \qquad (1)$$

where the variable s is $(4\pi/\lambda)\cdot\sin(\theta/2)$, θ the scattering angle, and λ the wavelength. In electron diffraction study of gaseus molecule, the following function is usually treated to obtain the nuclear distribution[1),2)]

$$I(s)=\frac{\text{total intensity}}{\text{background intensity}}-1\,. \qquad (2)$$

Practically, $I(s)$ cannot be obtained in the whole range of s for the following reasons. The wavelength limits the observable range of s, and even in the limited range the diffraction intensity for large s is usually too weak to detect. Furthermore, the intensity near the diffraction center is extremely difficult to measure, and in the case of a substance consisting of different kinds of atoms the intensity $I(s)$ in Eq. (2) at small scattering angle is not available, since there the unitary atomic scattering factors do not well satisfy the equaliy requirement in the treatment of Eq. (2)[3),4)]. Consequently, the integration in Eq. (1) cannot be extended over the whole range of s but over the limited range (s_0, s_1).

The integral over the range (s_0, s_1) is mathematically expressed as the convolution[5)] of $(\sin s_1r-\sin s_0r)/r$ and $rD(r)$ in Eq. (1), and it has quite different features from $rD(r)$ and has extraneous maxima and minima. The spurious features due to the absence of the data for $s>s_1$ can be greatly diminished by multiplying the integrand by a suitable convergence factor, and so-called artificial temperature factor[6)], $\exp(-as^2)$, has been often applied for this purpose. The problem caused by the lack of the data for $s<s_0$ has been treated, in the case of small gas molecules, by the use of the intensity calculated from an approximate model of the structure as the extrapolation function[3),7)]. Since the intensity in this range is insensitive to the small change in the model, this is a useful procedure of convenience; still the intensity has a large contribution to the radial distribution as low frequency components. In the case of large gas molecules and liquid, and amorphous substances, however, the proper extrapolation can be hardly obtained by the above treatment, since it is difficult to estimate the appropriate intensity because of the vast number of the structure parameters and the con-

---

* Read at the Meeting of the Physical Society of Japan, in Tokyo, April, 1955, and at the Fourth International Congress of I.U.Cr., July, 1957, in Montreal (Acta Cryst. **10** (1957) 862).

** The first and the second papers in the series were presented in this Journal by T. Ino and by K. Katada respectively. See the references 9 and 4.

ceivably possible models. If we fail to judge the correctness of the extrapolation to $s=0$, an incorrect result may be derived by the deceptively false radial distribution.

In the present paper, the uniqueness of the extrapolation to $s=0$ will be discussed, and a procedure to extrapolate the available data for (s_0, s_1) to $s=0$ without any assumption of a model will be described.

§ 2. Properties of the Error

Suppose that an empirical function is available as the proper structure sensitive function, $I(s)$, for $s \geq s_0$, but not available for $s<s_0$. Let $I^*(s)$ be a function extrapolated to $s=0$. Then the radial distribution function $D^*(r)$ obtained from the extrapolated function is expressed as follows:

$$2\pi^2 r D^*(r)=\int_0^{s_0} sI^*(s)\sin sr\,ds+\int_{s_0}^{\infty} sI(s)\sin sr\,ds\ .$$

From Eq. (1), it follows that

$$r\Delta D(r)=r(D(r)-D^*(r))=(1/2\pi^2)\int_0^{s_0} s\Delta I(s)\sin sr\,ds\ , \tag{3}$$

where $\Delta I(s)=I(s)-I^*(s)$. By repeated partial integration, since $\Delta I(s_0)=0$, $r\Delta D(r)$ can be asymptotically expanded:

$$r\Delta D(r)\sim(1/2\pi^2)\{(s\Delta I(s)'_{s=s_0}\sin(s_0r)/r^2+(s\Delta I(s))''_{s=s_0}\cos(s_0r)/r^3$$
$$-(s\Delta I(s))'''_{s=s_0}\sin(s_0r)/r^4\cdots\}\ . \tag{4}$$

The error in the distribution function calculated from the extrapolation has such an asymptotic ripple as defined by the discreteness of the derivatives between $I(s)$ and $I^*(s)$ at $s=s_0$ according to Eq. (4). Then, if there does not exist such a ripple, $I^*(s)$ should be the analytically connected function of $I(s)$ so that all the derivatives of $s\Delta I(s)$ at $s=s_0$ be zero; thus $I^*(s)$ is proper extrapolation function.

The radial distribution must be vanish, when r exceeds a certain value R_0, so-called non-zero range[9]. Consequently, if $D^*(r)$ has no ripple for $r>R_0$, $I^*(s)$ is the correct extrapolation function, and the converse of the proposition holds true. Therefore, it must be a necessary and sufficient criterion for judging the extrapolation to $s=0$ that $D^*(r)$ should have no ripple beyond R_0.

Since Legendre polynomials form a complete set of orthogonal functions, $s\Delta I(s)$ can be expanded as

$$s\Delta I(s)=s(I(s)-I^*(s))=\begin{cases}(\pi/2)^{1/2}\sum_{k=0}^{\infty}(-1)^k a_k P_{2k+1}(s/s_0) & |s|<s_0\\ 0 & |s|>s_0\ ,\end{cases} \tag{5}$$

where $P_{2k+1}(t)$ is the Legendre polynomial of (odd) order $2k+1$. Using the Fourier inversion relations[10),11)] between Legendre polynomials and spherical Bessel functions* such that

$$\int_0^1 P_{2k+1}(t)\sin xt\,dt=(-1)^k j_{2k+1}(x)\ ,$$

$$\int_0^{\infty} j_{2k+1}(x)\sin xt\,dx=\begin{cases}(\pi/2)(-1)^k P_{2k+1}(t) & |t|<1\\ 0 & |t|>1\ ,\end{cases}$$

$r\Delta D(r)$ in Eq. (3) can be transformed:

$$r\Delta D(r)=s_0(2\pi)^{-3/2}\sum_{k=0}^{\infty}a_k j_{2k+1}(s_0r)\ . \tag{6}$$

---

*) Spherical Bessel function is defined stch that

$$j_n(x)=(\pi/2x)^{1/2}J_{n+1/2}(x)\ ,$$

Where $J_{n+1/2}(x)$ is an ordinary Bessel function.

Consequently, the error of the radial distribution function due to that of the extrapolated function is composed of spherical Bessel functions of odd order, and since $j_{2k+1}(x)$ forms a set of orthogonal functions, it never vanishes unless all a_k's are zero.

Next, let us derive the relations useful for the determination of a_k's so as to obtain the correct extrapolated function.

Relation (i).

From Eq. (5) it follows that[12)]

$$(2/\pi)^{1/2}(s\varDelta I(s))_{s=s_0}=\sum_{k=0}^{\infty}(-1)^k a_k P_{2k+1}(1)=\sum_{k=0}^{\infty}(1)^k a_k\ , \tag{7}$$

$$(2/\pi)^{1/2}\frac{d^n}{ds^n}(s\varDelta I(s))_{s=s_0}=\sum_{k=0}^{\infty}(-1)^k a_k P_{2k+1}^{(n)}(1)=\sum_{k=1}^{\infty}(-1)^k a_k\frac{(2k+n+1)!}{2^n n!(2k-n+1)!}\ .$$

Since $sI(s)$ is known at $s=s_0$ and its derivatives can be derived from the data for $s>s_0$ by the numerical differentiation, the above relations can be adopted as the equations in terms of a_k's.

Relation (ii).

Eq. (5) leads another relation:

$$(2/\pi)^{1/2}\frac{d}{ds}(s\varDelta I(s))_{s=0}=\sum_{k=0}^{\infty}(-1)^k a_k P'_{2k+1}(0)=\sum_{k=0}^{\infty}\frac{(2k+2)!a_k}{2^{2k+1}k!(k+1)!}\ . \tag{8}$$

On the other hand, following relation can be derived from Eq. (1).

$$\frac{d}{ds}(sI(s))_{s=0}=4\pi\int_0^{\infty}r^2D(r)\,dr\ .$$

This integral is a constant characteristic of the matter studied and can be determined independently of the accuracy of the diffraction data. In the case of gas molecules, it is regarded proportional to $(\sum_i Z_i)^2-\sum_i Z_i^2$, where Z_i is the atomic number of the constituent atoms and the summation extends over all the atoms in a molecule. In the case of liquid and amorphous substances, it is zero, because $I(s)$ is usually treated so as to correspond to $\{D(r)-D_0\}$ instead of $D(r)$, where D_0 is the volume average of $D(r)$[13)]. Hence, Eq. (8) is very restrictive condition for the determination of a_k's.

Relation (iii).

By the differentiation of $r\varDelta D(r)$ in Eq. (3) we can derive the equations as follows:

$$2\pi^2\frac{d^{2n+1}}{dr^{2n+1}}(r\varDelta D(r))_{r=0}=(-1)^n\int_0^{s_0}s^{2n+2}\varDelta I(s)\,ds-(-1)^n(\pi/2)^{1/2}\sum_{k=0}^{\infty}(-1)^k a_k\int_0^{s_0}s^{2n+1}P_{2k+1}(s/s_0)ds\ ,$$

and then

$$\left.\begin{aligned}(2\pi)^{3/2}\frac{d}{dr}(r\varDelta D(r))_{r=0}&\quad s_0^2a_0/3\ ,\\ -(2\pi)^{3/2}\frac{d^3}{dr^3}(r\varDelta D(r))_{r=0}&=s_0^4(a_0/5-2a_1/35)\ ,\\ (2\pi)^{3/2}\frac{d^5}{dr^5}(r\varDelta D(r))_{r=0}&=s_0^6(a_0/7-4a_1/63+8a_2/693)\ ,\\ \cdots\cdots&\cdots\cdots\cdots\cdots\ ,\end{aligned}\right\} \tag{9}$$

where the relations[12)]

$$\int_0^1 t^{2n+1}P_{2k+1}(t)\,dt=\begin{cases}0 & n<k\\[4pt] \dfrac{(2n+1)!2^{2k+1}(n+k+1)!}{(2k+2n+3)!(n-k)!} & n\geq k\ .\end{cases}$$

are used. Therefore, the first equation in Eq. (9) will determine directly a_0 and the successive equations will determine the successive coefficients of the polynomials in Eq. (5). These features are advantageous for the determination of a_k's. The derivatives of $rD(r)$ at $r=0$ can be estimated in advance; in case of gas molecules the derivatives of the first few orders may be regarded as zero, and in the case of liquid and amorphous substances they may be regarded as zero, except the first derivative which may be regarded as $-D_0$ according to the usual treatment mentioned in *Relation* (ii). Hence, the first few members of the equations in Eq. (9) can be adopted as the equations in terms of a_k's.

Relation (iv).

The criterion mentioned before claims the following equation:

$$r\Delta D(r)=s_0(2\pi)^{-3/2}\sum_{k=0}^{\infty} a_k j_{2k+1}(s_0 r)=0 \qquad r>R_0\,, \tag{10}$$

where R_0 is the non-zero range. Since the numerical table of $j_{2k+1}(x)$ is available, Eq. (10) yields a number of equations in terms of a_k's.

As the result, the correction of the extrapolated function can be performed by solving the simultaneous equations consisting of Eq. (7) to Eq. (10) for a_k's.

§ 3. Extrapolation Prodedure

Provided that $I^*(s)=0$ for $0<s<s_0$, Eqs. (3), (5), and (6) lead

$$s\Delta I(s)=sI(s)=(\pi/2)^{1/2}\sum_{k=0}^{\infty}(-1)^k a_k P_{2k+1}(s/s_0) \qquad |s|<s_0\,, \tag{11}$$

$$\left.\begin{aligned} &2\pi^2 rD^*(r)=\int_{s_0}^{\infty} sI(s)\sin sr\,ds\,, \\ \text{and}\quad & \\ &r\Delta D(r)=rD(r)-rD^*(r)=s_0(2\pi)^{-3/2}\sum_{k=0}^{\infty} a_k j_{2k+1}(s_0 r)\,. \end{aligned}\right\} \tag{12}$$

Hence, without any assumption about the intensity $s<s_0$, the proper extrapolation can be directly obtained through Eq. (11) by determining a_k's so as to satisfy the same relations as mentioned in § 2.

Although ordinary functions should be expanded by an infinite series of Legendre polynomials, we are actually forced to approximate it by a finite series, since we cannot handle equations containing the infinite number of coefficients. With the help of the orthogonal relation of spherical Bessel function[10] such that

$$\int_0^{\infty} j_n(x)j_m(x)dx=\begin{cases}0\,, & m\neq n \\ \pi/(4n+2)\,, & m=n\,,\end{cases}$$

we can derive the relation from Eq. (11)

$$(\pi/2)^{1/2}a_k=4\pi(4k+3)\int_0^{\infty}\rho D(\rho)j_{2k+1}(s_0\rho)d\rho\,. \tag{13}$$

For simplicity, the substance is assumed to have such a radial distribution[5] as follows:

$$rD(r)=\sum_{ij}{}' c_{ij}[\delta(r-r_{ij})-\delta(r+r_{ij})]_1 r_{ij}\,,$$

where $\delta(x)$ is Dirac delta function and r_{ij} is the atomic distance of atom pair (ij) and the sum extends all over pairs. Then, a_k can be easily obtained:

$$(\pi/2)^{1/2}a_k=4\pi(4k+3)\sum_{ij}{}'\frac{c_{ij}}{r_{ij}}j_{2k+1}(s_0 r_{ij})\,.$$

Therefore, the contribution to a_k of an (ij) pair can be estimated from the value of $j_{2k+1}(x)$ at $x=s_0 r_{ij}$. According to the above discussion, we can roughly predict the magnitude of a_k's and the number of terms to be taken for good approximation. All the coefficients of higher terms than the $(2k+1)$th term may be neglected, if $j_{2k+1}(x)$ is small enough in the range $(0, s_0R_0)$, where R_0 is the non-zero range of the substance, because the first term in power expansion of $j_{2k+1}(x)$ is $x^{2k+1}/\{(4k+3)(4k+1)....5.3\}$[11]. As long as the substance has a finite non-zero range, in consequence, the adequate extrapolation can be achieved by a finite series of the expansion. The more terms should be taken, in case the substance has the longer non-zero range and the larger value of s_0 is to be employed.

§ 4. Example

In order to study the applicability of this method to a actual structure analysis, the author has taken up an instance where the structure sensitive function, $I(s)$, is given by $100 \sin(1.54s)/s$ in the range $(2\pi, 8\pi)$ and unknown elsewhere. First, $rD^*(r)$ in Eq. (12) was computed by punched-card method, where the integral was approximated by the sum over evenly spaced s-values (spacing $\Delta s=\pi/5$) and a damping factor $\exp(-s^2/10\pi^2)$ was used. It has spurious maxima and minima outside the peak at $r=1.54$Å as illustrated in Fig. 2. Using the values of $sI(s)$, its 1st and 2nd derivatives at $s=2\pi$ and the values of the 1st, 3rd, and 5th derivatives of $rD^*(r)$ at $r=0$, the author succeeded in determining a_0, a_1, and a_2 according to *Relations* (iii) and a_3, a_4, a_5, and a_6 according to *Relation* (i) and (ii): $a_0=20.17$, $a_1=-36.85$, $a_2=-21.75$, $a_3=162.18$, $a_4=-174.15$, $a_5=79.31$, and $a_6=-15.47$.

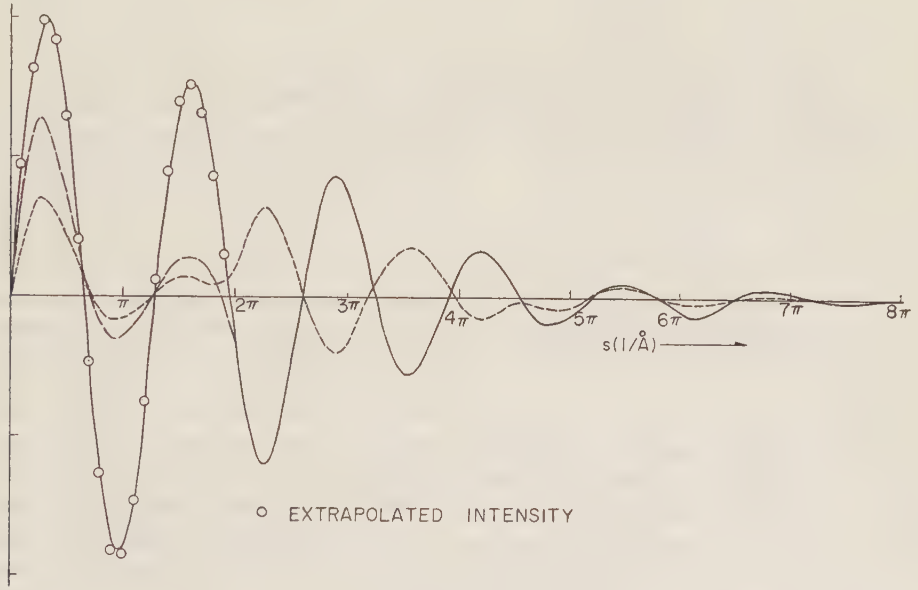

Fig. 1. The solid line shows the function $100\exp(-s^2/10\pi^2)\sin(1.54s)$. The small circles represent the function obtained by the extrapolation produre. The dotted line indicates the Fourier inversion of the negative parts of $rD^*(r)$. The dashed line is the curve obtained by non-negativity criterion after the 3rd correction.

Thus, the extrapolation function was determined by these according to Eq. (11) and was found to be almost the same as $100\exp(-s^2/10\pi^2)\sin(1.54s)$, as shown in Fig. 1. The radial distribution function was computed from the extrapolated intensity. As shown in Fig. 2, it has almost no ripples outside of the peak $r=1.54$Å and no appreciable difference from the intensity in the range of $(0, 8\pi)$. Thus, the extrapolation function was found to be very satisfactory.

An attempt was made to extrapolate only according to the non-negativity criterion proposed by Karle and Karle[8], stating that the radial distribution should be everywhere positive. In case the information of $sI(s)$ for $s<s_0$ is not available, the extrapolation should be made so as to remove at least the negative parts of $rD^*(r)$. Then the extrapolation function should be made of the Fourier inversion of the negative parts of $rD^*(r)$. The inversion has generally large value outside of $(0, s_0)$, as illustrated in Fig. 1, so that the extrapolation thus obtained may not entirely remove the negative parts. This process should be repeated untill the negative parts would vanished. In this example, it was repeated three times. But the resultant extrapolation and radial distribution functions were far from satisfactory, as shown in Figs. 1 and 2.

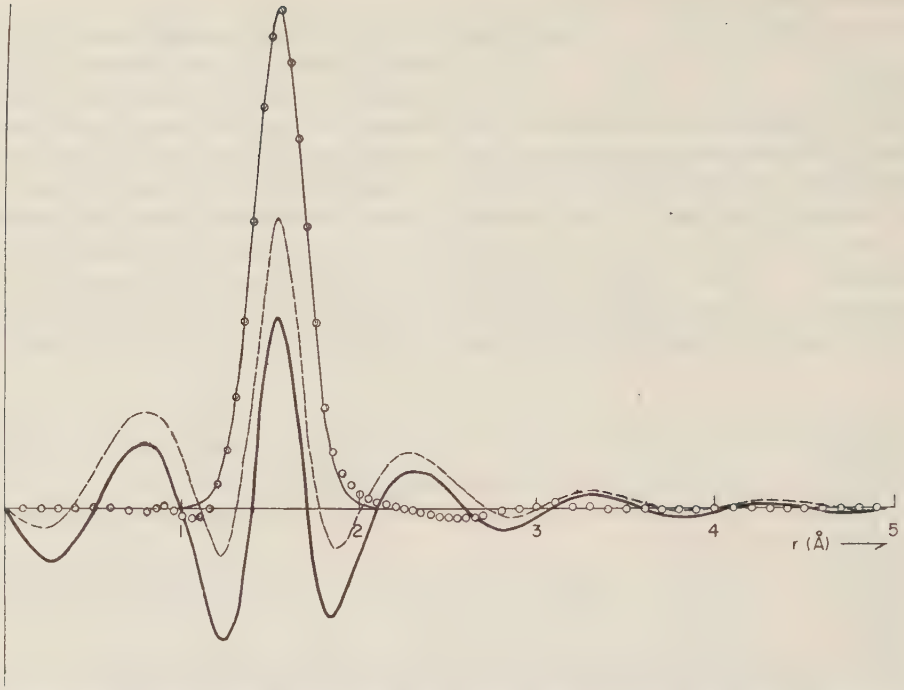

Fig. 2. The thin and heavy lines show $rD(r)$ and $rD^*(r)$, respectively. The small circles represent the radial distribution function obtained from the extrapolated intensity. The dashed line is the radial distribution curve obtained by non-negativity criterion after the 3rd correction.

§ 5. Dsicussion

Since $I(s)$ is considered analytic, its exact knowledge for even an arbitrarily small range of s will define uniquely $I(s)$ for all the rest of s by the principle of analytic continuation. The function to be extrapolated to $s=0$ must be analytically connected at $s=s_0$ with the known function $I(s)$ for $s>s_0$. As experimental data always contain some degree of error and the derivatives at $s=s_0$ cannot be obtained exactly, the process of analytic continuation is not available for the extrapolation of the empirical function.

As mentioned in § 2, the error of the radial distribtion due to that of the intensity for $s<s_0$ has asymptotic ripple caused by wrong continuation at $s=s_0$ of the extrapolation, and furthermore it is composed of the series of spherical Bessel functions. From the mathematical behavior of the error, the necessary and sufficient criterion for the extrapolation is derived to be the absence of ripple beyond non-zero range R_0 in the radial distribution curve calculated from the extrapolation. This may be called non-ripple criterion. The non-negativity one has been conveniently used in the case of small gas molecules but it is not sufficient but necessary criterion. As shown in § 4, it may not be powerful unless the assumed intensity is good enough, but the non-ripple one is quite useful in any case.

The extrapolation procedure consists in the approximation by the Legendre polynomials. From Eq. (13) it follows that the proper approximation can be made by a finite series, as long as the non-zero range of the material is limited. Furthermore, in the case of liquid and amorphous substances, it is necessary, from a standpoint of the approximation, that the intensity should be treated so as to correspond to the deviation of $rD(r)$ from its average D_0 instead of $rD(r)$, because the former has much shorter non-zero range than the latter. Proper extrapolation function can be determined through Eq. (11), where a_k's should satisfy the Relations (i) to (iv). *Relations* (i), (ii), and (iii) contain the differential derivatives of the experimental data, and the number of the avaliable equations derived from them is practically limited, since the derivatives of high order cannot be exact. The calculation in § 4 was made taking account of these facts, and such a satisfactory intensity function was derived that the correction was not tried. The correction can be also made, if desired, by using more coefficients a_k's and solving more simultaneous equations in Eq. (11) claimed by non-ripple criterion by means of least squares. As the result, the method proposed in this paper is inferred to be successfully applied to the experimental data so that the extrapolation can be obtained straightforwardly without any assumption of the structure in advance.

Acknowledgement

The author wishes to express his sincere thanks to Dr. K. Katada for his kind and constant help and Prof. J. Kakinoki and Prof. R. Uyeda for their valuable discussion. The author also expresses his thanks to the Osaka Municipal Office for making available to him a set of electrical accounting machines of I.B.M. Corporation. The author is indebted to the Ministry of Education for the research grant.

References

1) P. Debye: J. Chem. Phys. **9** (1941) 55.
2) I. L. Karle and J. Karle: J. Chem. Phys. **17** (1949) 1052.
3) L. S. Bartell, L. O. Brockway and R. H. Schwendeman: J. Chem. Phys. **23** (1955) 1854.
4) K. Katada: J. Phys. Soc. Japan **13** (1958) 51.
5) J. Waser and V. Schomaker: Rev. Mod. Phys. **25** (1953) 671.
6) W. L. Bragg and J. West: Phil. Mag. **10** (1930) 823.
7) P. A. Shaffer, Jr., V. Schomaker and L. Pauling: J. Chem. Phys. **14** (1946) 659.
8) J. Karle and I. L. Karle: J. Chem. Phys. **18** (1950) 957.
9) T. Ino: J. Phys. Soc. Japan **12** (1957) 495.
10) G. H. Watson: *Theory of Bessel Functions* (Cambridge University Press, Cambridge, 1944).
11) P. M. Morse and H. Feshbach: *Methods of Theoretical Physics* (McGraw-Hill Book Company, INC, New York, 1953).
12) E. T. Whittaker and G. N. Watson: *A Course of Modern Analysis* (Cambridge University Press, London, 1935).
13) P. Debye and H. Menke: Ergebn. Tech. Röntgenk, **2** (1931) 1.

JOURNAL OF THE PHYSICAL SOCIETY OF JAPAN, Vol. 16, No. 11, NOVEMBER, 1961

Observations on the Polygonization of Bent LiF Crystals by the Berg-Barrent Method

By Mitsuru YOSHIMATSU

Rigaku Denki Co. Ltd., Haijima, Akijima, Tokyo

(Received June 29, 1961)

Weakly bent LiF crystals are successively annealed at various temperatures from 400°C to 800°C and the polygonization process is observed. Slip lines disappear at about 450°C and appear again at about 500°C. At higher temperatures than 500°C, edge dislocations move to form polygon walls. The complete polygon walls are produced at 660°C, and coarsening of polygon domains occurs above this temperature. The coarsening proceeds through either of two processes: coalescence of two branches of the Y-shaped polygon walls and absorption of a polygon wall by another parallel polygon wall. The L-shaped polygon domains are formed when two glide systems, perpendicular to each other, are acting, which are predominant on either side of the neutral plane, respectively.

§ 1. Introduction

In these several years, studies on polygonization have been especially done by the optical method using decoration or etch pit techniques[1]. Recently X-ray diffraction has been successfully used for observing lattice defects such as dislocations. In the X-ray studies, although the resolving power is generally not so high as in the optical studies, the specimen does not suffer from the change of its state which could not be more or less avoided on etching or decoration. Among various techniques of X-ray diffraction, the refined Berg-Barrett method developed by Newkirk[2] is suitable for studing the surface of crystals. Using this method, Newkirk observed cleavage surfaces of LiF crystals plastically deformed by compression or cleaving, and later Yoshimatsu and Kohra[3] studied also the state of cleavage surface of LiF crystals in detail. In the present paper, the polygonization process in weakly bent LiF crystals was studied at various annealing temperatures.

§ 2. Experimental

Several specimens about 2×2×10 mm^3. in dimension were prepared by cleaving from a large block of LiF crystal*. At the room temperature specimens were bent by pressing between two matched metal pieces with cylindrical surface of 10 cm. in radius. Weak bending was made in the present study, because the resolving power of the present method is limited. Specimens were bent around the [100] axis perpendicular to the cleavage face (100), as shown in Fig. 1. They were then annealed at various temperatures up to about 800°C for three hours at each annealing. Aiming to know qualitatively various stages of polygonization, X-ray photographs were successively taken from the (100) surface at the room temperature. Cr radiation was used. {220} reflections mostly, and (200) reflections, sometimes, were used. The technical details of the refined Berg-Barrett method were described in the previous paper.

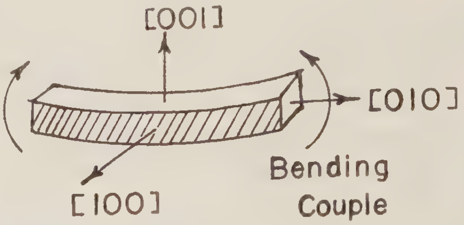

Fig. 1. The orientation relationship of bent crystals. Crystals were bent around the [100] axis. The hatched surface was photographed with (202) and (2$\bar{2}$0) reflections.

§ 3. Observations at Various Stage of Annealing

Typitical photographs at two stages of a specimen are given in Fig. 2. The upper was taken immediately after bending and the lower after annealing at 700°C. The same part of the photographs taken at various stages of annealing was enlarged and shown in Fig. 3.

---

* The crystals which were classified as monochromator quality were purchased from the Harshow Chemical Co..

First, let us see the photograph of Fig. 2 (a). Along the horizontal, central line in the photograph a white line is seen, which corresponds to the neutral plane of bending. Two kinds of slip lines parallel to the [0$\bar{1}$1] and [011] directions can be seen except the neutral region, or at least less in that region. The [011] glide system is predominant in the upper region, while the [0$\bar{1}$1] glide system is predominant in the lower region, on the contray to the expectation that two glide systems would appear with equal probability over the whole area. The tendency that one of both directions is predominant in one region was observed in other specimens. On the other hand, crossed slip lines are always found near the upper and lower surfaces of crystals.

It is also observed that short slip lines are arranged side by side in the direction vertical to themselves, forming diffuse bands in appearance. This implies that the specimen is bent more heavily in the diffuse bands than in other regions.

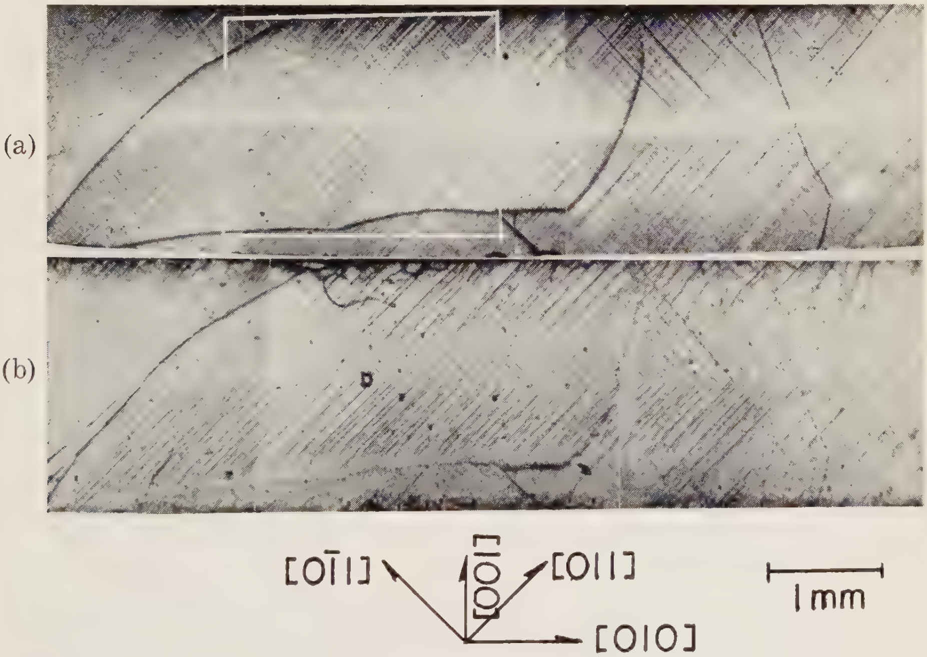

Fig. 2. General views of slip lines, (a) and polygon walls, (b). A region surrounded by white lines were enlarged and shown in Fig. 3.

Next, the specimens were annealed at various temperatures. To examine changing process with time at a certain temperature, a specimen was annealed at 600°C for one hour to 30 hours. It was found that no appreciable change appeared with annealing after one hour, although a change was clearly seen with further annealing at an elevated temperature. Accordingly, annealing time was fixed for three hours in order to study the qualitative nature of the change in state with temperature.

Let us describe general features after each annealing.

(i) With the annealing up to 400°C, no change from the initial state was observed.

(ii) After annealing at 450°C, it is seen that most of slip lines and the neutral line became unclear except some slip lines showing the strong intensity contrast near the circumference, as shown in Fig. 3 (b). This fact is observed in the whole region of the present crystal. It seems to correspond to the one reported by us that dislocations near the surface produced by cleaving disappear easily

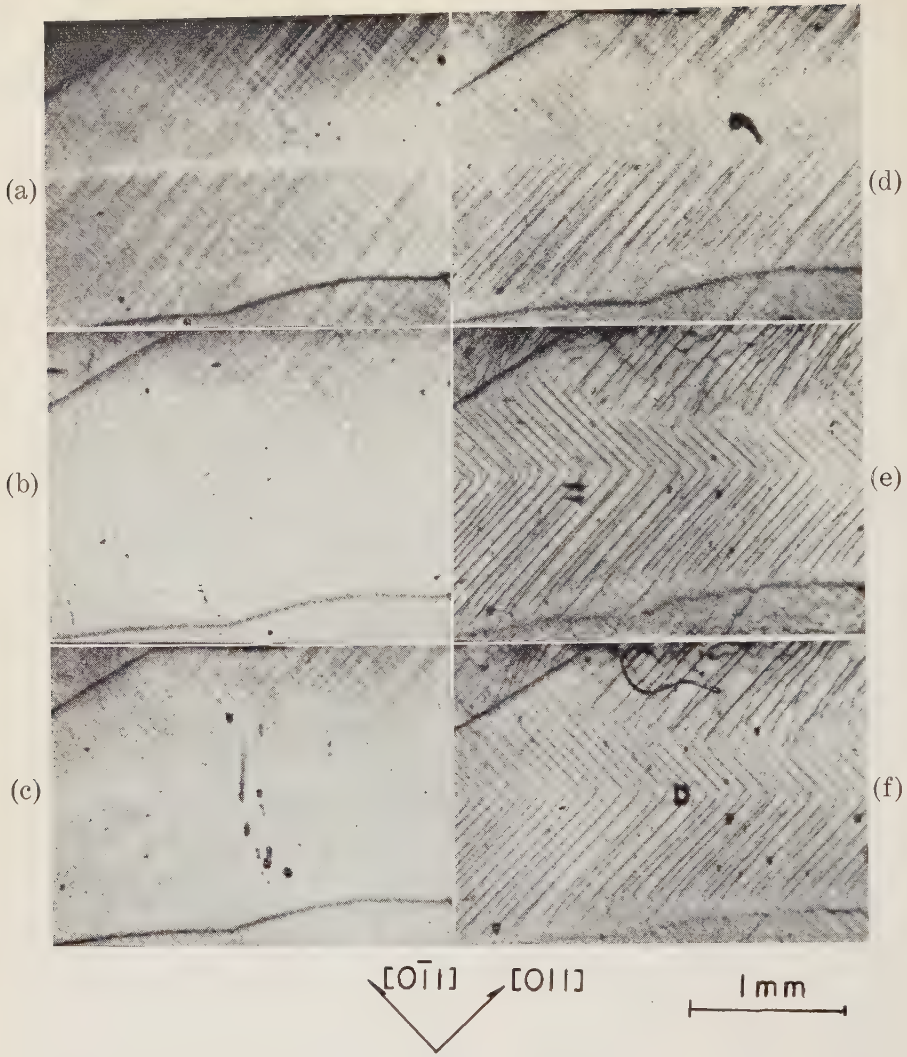

Fig. 3. Successive change in state in the various stages of annealing. (a), after bending. (b), (c), (d), (e) and (f), after annealing at 450°, 510°, 600°, 660° and 700°C, respectively. These photographs were obtained from the same region surrounded by white lines in Fig. 2.

by heating the crystal. In order to study this fact more in detail, another bent crystal annealed at 450°C, in which slip lines disappeared in the same way as above, was cleaved into halves. The new surface, which corresponds to the interior, was different in appearance from the old surface, and similar to the one before the heat-treatment, that is, slip lines appeared again in the similar way to the surface before the heat-treatment. From this fact, it can be said that the disappearance of slip lines with the heat-treatment at 450°C is limited to the region near the surface, while the state of the interior does not change at this temperature. Although it is difficult to give a decisive explanation for this phenomenon, it can be said that the dislocation loops near the surface more easily disappear at the surface.

With further annealing at a higher temperature, 510°C, new short streaks of the same direction as the initial slip lines and the neutral line which is narrower than the initial one appeared again as seen in Fig. 3(c). These new streaks can be more clearly seen in Fig. 4(a) which was photographed on another specimen. In the similar way to the initial state before heat-treatment, these short streaks are closely arranged side by side in the direction perpendicular to themselves.

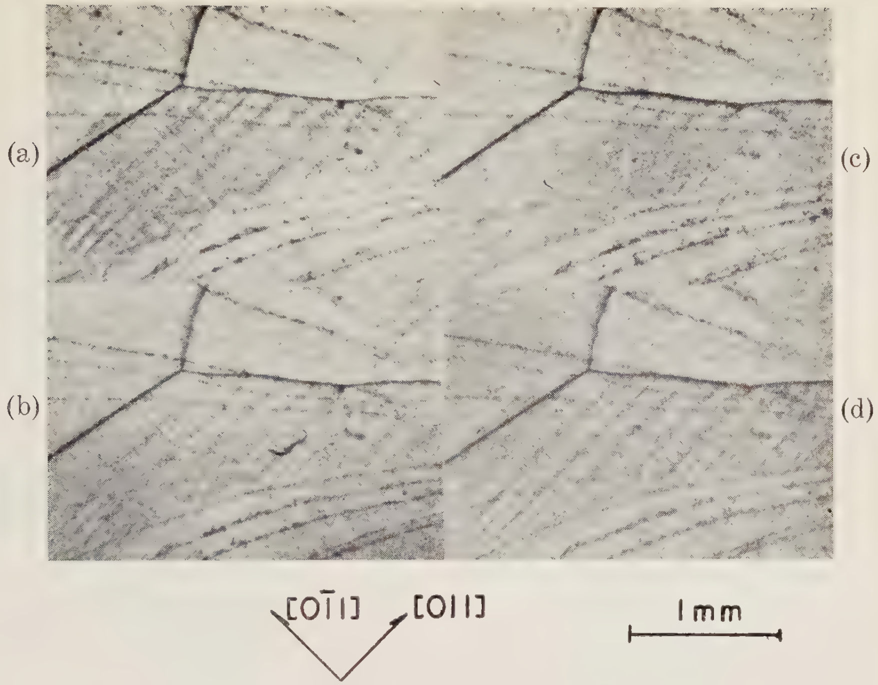

Fig. 4. Photographs showing the process from the stage of the thermally induced glide to that of the beginning of polygonization. (a), (b), (c) and (d) were obtained after annealing at 500°, 530°, 560°, and 580°C, respectively.

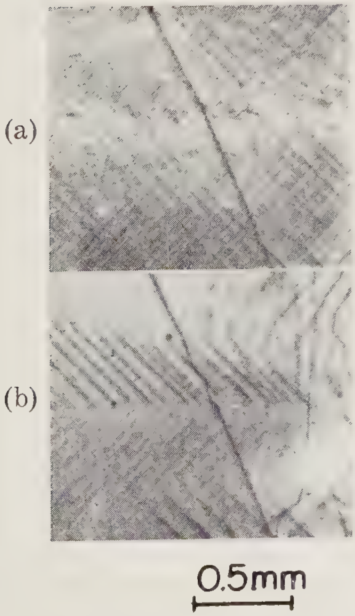

Fig. 5. Interaction between a subgrain boundary and a polygon wall. (a) is the initial state and (b) is after annealing at 700°C.

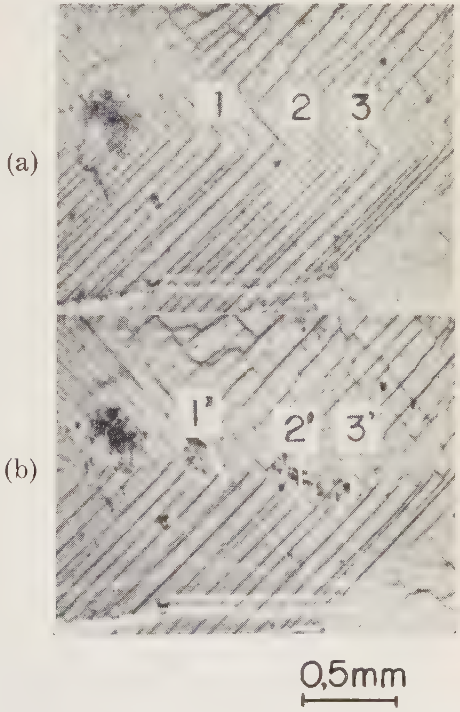

Fig. 6. Growth of polygon domains bounded by the nearly parallel polygon walls. (a), after annealing at 700°C, (b), after annealing at 730°C.

Hibbard and Dunn[4] found a similar phenomenon in the region near the neutral line for bent Fe-Si single crystals with etch pit technique, and considered these slip lines to be caused by the residual stress. They named this phenomenon the thermally induced glide.

(iii) The details of change with successive annealing from 500°C to 580°C for another specimen are shown in Fig. 4. The thermally induced slip lines became again gradually indistinct as shown in Figs. 4 (b) and (c), and then straight bands appeared in the direction perpendicular to the initial slip lines, that is, in the [011] direction as seen in Fig.

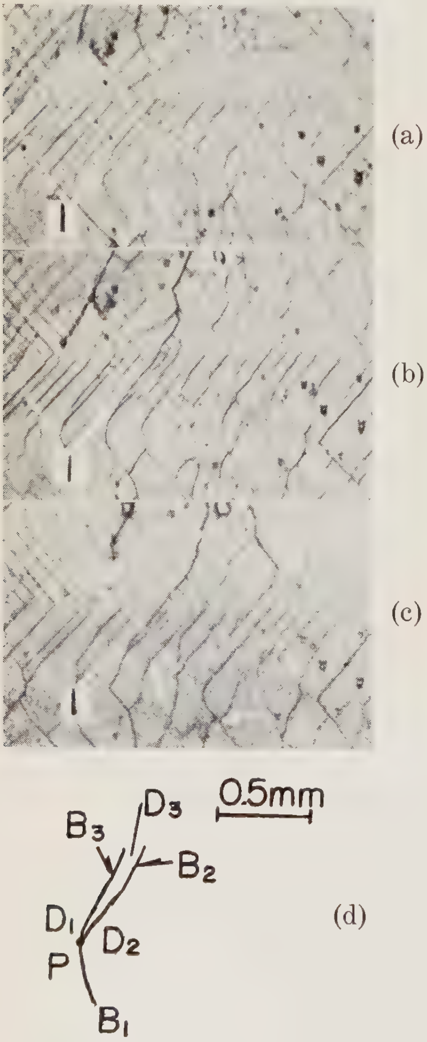

Fig. 7. Growth of polygon domains with Y-shaped polygon walls. (a), (b) and (c), after annealing at 700°, 730° and 790°C, respectively. (d) is a schematic drawing of a Y-shaped wall indicated by the arrow 1.

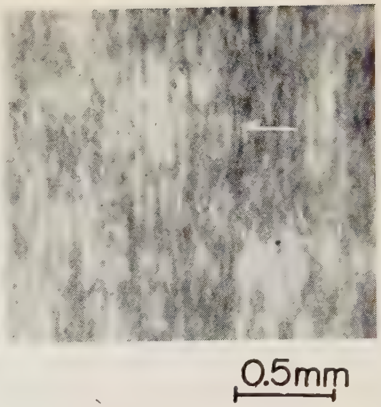

Fig. 8. The transmission Berg-Barrett photograph obtained with the (020) reflection, showing overlapped images due to dislocation lines in polygon walls. The arrow indicates a image due to a single dislocation line.

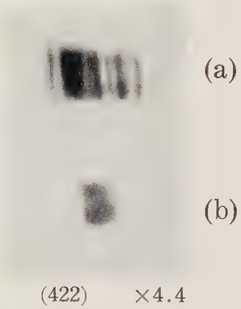

Fig. 9. Two kinds of the Laue subspots obtained from crystals immediately after bending.

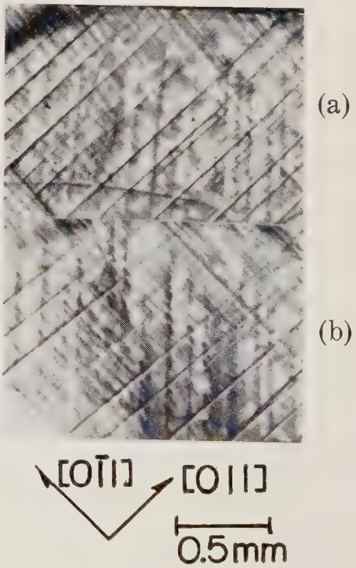

Fig. 10. The Berg-Barrett photographs obtained from the same crystal shown in Fig. 9(a). (a) is the (202) reflection and (b) is the (2$\bar{2}$0) reflection.

4 (d). These bands also seem to consist of piling up of very short lines and to correspond to the beginning state of polygon walls as seen later.

In Fig. 3 (d), taken after annealing at 600°C, the diffuse bands consisting of short lines became narrower and more distinct. With further annealing at 660°C, as seen in Fig. 3 (e), the diffuse bands become sharp. These are no more than polygon walls. These straight polygon walls are mainly found in the inner part or in the region where only one direction of slip lines is predominant.

It is, also, to be noted in Fig. 3 (e) that the polygon walls of irregular directions exist near the circumference, especially near the upper part, besides those of parallel directions. It seems that such irregular polygon walls are found in the region where the crystal was heavily distorted or two different slip directions were active.

(iv) With further annealing at a higher temperature, say 700°C, the coarsening of polygon domains is observed (Fig. 3 (f)), although it can be said that the generation of polygon walls has finished for the heat-treatment at 660°C. The photograph from the whole region for this stage is given in Fig. 2 (b). The details of the coarsening will be discussed in the next paragraph.

In the case where a polygon wall intersects a small-angle subgrain boundary, an interaction was observed between them as shown in Fig. 5. Dislocation lines constituting the subgrain boundary are absorbed into the polygon wall, and the direction of the subgrain boundary is changed near the intersecting point in such a way that the dislocation lines tend to be connected with shorter distance to the polygon wall. It was observed that the interaction become strong with decrease of the intersecting angle between the polygon wall and the subgrain boundary.

§ 4. Coarsening of Polygon Domains

After formation of polygon walls, polygon domains continue to grow gradually with annealing at higher temperatures. As the process through which the growth of polygon domains proceeds, the following two characteristic features were observed.

(i) The growing process of polygon domains bounded by nearly parallel, straight polygon walls is shown in Figs. 6 (a) and (b), which were taken after annealing at 700°C and 730°C, respectively. The intensity contrast of the polygon wall indicated by **2** in Fig. 6 (a), which are located at a equal distance to the adjacent walls, become reduced in Fig. 6 (b), but it's relative position to the adjacent walls remains to the same as before. On the other hand, the wall **1** and **3** are shifted toward the neighbouring walls, respectively, and their intensity contrast is generally reduced, although it changes along the length. It is considered that the reduction of intensity contrast is due to the decrease of the dislocation density in the wall and the missing dislocations are absorbed individually or in the form of a short array into the adjacent walls. Especially, the dislocations in the wall 2 are considered to be absorbed with nearly equal extent into the walls of both sides. It is to be noted that an attraction force exists between parallel dislocation arrays with a distance as long as 40μ. The polygon wall, which seems to be in the process of disappearing, has been observed optically by Hibbard and Dunn[5] by means of the etch pit technique. Amelinckx and Dekyser[1] proposed a probable mechanism of coarsening for such polygon domains. According to them, if a semi-finite wall is situated between two infinite walls, the dislocation at the top of the semi-finite wall is absorbed successively into the adjacent infinite wall. However, as mentioned above, the dislocations in the infinite wall (not at the top) are also probable to be absorbed into the adjacent infinite wall.

(ii) Another process of coarsening are observed in the Y-shaped boundary, where three polygon walls meet together at a point, forming the boundary of irregular shape. A series of photographs, which were obtained from another specimen, are shown in Fig. 7. The points where three polygon walls meet are indicated by the arrows. The boundary indicated by the arrow **1** in Fig. 7 (b) is given schematically in Fig. 7 (d). With elevation of the annealing temperature, polygon walls B_2 and B_3 recede, and the point P proceeds upperwards. As a result, the domain D_3 is reduced, while the domains D_1 and D_2 grow at the neighbourhood of the point P. As a general tendency, the irregular boundary seems to be rearranged so as to be parallel to the diagonal directions [0$\bar{1}$1] or [011]. The polygon domains of irregular shape grown through the process above mentioned are generally larger than those of parallel shape grown through the process mentioned in (i). The similar coarsening process of Y-shaped polygon domains has been already reported by Gilman6), and Hibbard and Dunn4),5), who found it in the polygonization of bent Zn crystals and Fe-Si crystals, respectively, with etch pit technique.

§ 5. Shape of Polygon Domains

In Figs. 3 (e) and (f) or 2 (b), it is seen that most of polygon walls are parallel to [011] in the lower side than the neutral line, while in the upper side they are parallel to [0$\bar{1}$1] near the neutral line and further to [011] near the circumference. These directions of polygon walls correspond respectively to the direction perpendicular to the predominant direction of slip lines before the heat-treatment. Thus, L-shaped polygon walls are formed.*

Since X-ray penetration depth into the crystal is in order of 10μ, the observations mentioned above are practically restricted to the thin layer near the crystal surface. In order to see the difference in state between the surface and the interior of specimen, two bent crystals of about 2 mm. thick, which were annealed at 660°C and 710°C, respectively, were cleaved into halves. The both photographs from old and new surfaces were found to be essentially the same in appearance in the both cases. Accordingly, it can be said that the observations on the side surface of bent crystals are usually valid for the interior of crystal.

Furthermore, in order to know whether the polygon walls lie vertically to the side surface or not, the transmission Berg-Barrett photograph8) of a thin specimen (0.35 mm. thick) was taken, which was bent with the same radius of curvature of 100 mm. as before and annealed at 700°C for three hours. In Fig. 8, the photograph is given, which was obtained with the (020) reflection. It can be seen that most lines run parallel to the bending axis, some lines are diffuse, being considered to be due to overlapped dislocation lines, while some lines are sharp, probably corresponding to individual lines. In any case, it can be said that the dislocation lines are generally parallel to the bending axis, that is, perpendicular to the side surface. Further, it can be said that the polygon walls are vertical to the side surface of bent and annealed crystals. In this way, L (or double L)-shaped slabs lie perpendicularly to the side surface.

§ 6. Comparison with the Ordinary Laue Method

It has been often reported that the diffraction spots obtained by the Laue method split into subspots, although not well defined, for bent crystals before the heat-treatment. From this fact, some investigators have considered that the polygonization occurred immediately after bending at the room temperature. On the other hand, Gilman6) took a stand againgt this opinion and remarked that the observation by the X-ray diffraction alone does not constitute satisfactory evidence of polygonization.

We have also tried to take diffraction photographs by the ordinary Laue method immediately after bending. The photographs are given in Fig. 9. Fig. 9 (a) was obtained from a crystal bent by three point loading, where more heavy bending is given than the case of cylindrical bending above mentioned. The spot splits into subspots, in each of which the intensity enhancement is seen at both ends along the length. This pattern is similar to the ones which were obtained by some previous workers and was explained to be due to polygonization. But this explanation will be proved to be wrong, if the Berg-Barrett photograph obtained from the same crystal is observed. The Berg-Barrett photographs of (202) and (2$\bar{2}$0) diffractions obtained from the same region as Fig. 9 (a) are shown in Figs. 10 (a) and (b), respectively. It is seen that sharp, narrow lines exist parallel to the [011] direction with spacing of about 0.2 mm. and they are closely accompanied by a white line, the relative position of which changes with both diffractions. Since white lines imply that the diffraction did not take place, these lines are not a simple boundary constituted by dislocations, but a boundary with local lattice rotation. The number of domains bounded by these lines are approximately equal to that of the Laue subspots. With subsequent annealing, moreover, the polygonization was found to take plane in the domains by the Berg-Barrett method, but not recognized by the Laue method. Accordingly, these boundaries are considered to correspond not to polygonization walls but to the regions where the lattice was heavily rotated.

---

* The existence of L-shaped crystallites was also concluded by Hosoya *et al*7), in the study on the polygonization of bent NaCl crystals by the etch pit technique and the ordinary Laue method.

In Fig. 9 (b), the Laue spot from the specimen is given, which was weakly bent in the same way as done hitherto in the present paper. The intensity is enhanced at upper and lower ends, but splitting in the lateral direction is not seen. It is considered that the two broad subspots resulted from diffraction at the both sides of the neutral plane of bending. It is clear that the polygonization does not take place in the present stage, the diffuse spots result from the intensity enhancement due to the dense dislocations at the both sides of the neutral plane.

§ 7. Discussions and Conclusions

The Berg-Barrett method is generally difficult, although not impossible, to obtain the image of good contrast due to individual dislocations outcropping on the surface as reported in the previous paper³⁾. However, since the intensity contrast is greatly increased when dislocations are congregated into an array, the present method provided us an useful means for observing the phenomena such as the present polygonization process. As mentioned in § 1, the present method was able to present us the information of the phenomena successively caused by the heat-treatment. For instance, two processes of coarsening of polygon domains, which have been only inferred from the fragmental observations by the etch pit technique, were actually observed by the present method.

In the present method, also the phenomena limited in the very thin surface layer are not overlooked as mentioned in § 3 (ii). This is a great advantage of the Berg-Barrett method.

By the use of these characteristics, polygonization process was observed. The process are roughly divided into three succeeding processes, (i) the disappearance of some dislocations in the slip lines through the crystal surface and regeneration of slip lines, (ii) the formation of polygon walls and (iii) the growth of polygon domains.

In this study, it was a purpose to show an availability of the Berg-Barrett method for the study on the lattice defects as an X-ray method. The work was confined to be quite qualitative. However, the kinetics of polygonization would be possible to be studied by following the change of the state with time.

Acknowledgements

The author wishes to express his hearty thankfulness to Prof. K. Kohra, University of Tokyo, for his guidance and to Dr. Y. Shimura, President of Rigaku Denki Co. Ltd., for his encouragement during the course of this study, and also to Profs. E. Fukushima, Tokyo Metropolitan University, and A. Ookawa, Gakushuin University, for their valuable discussions, and to Mr. Y. Sugiyama for his technical assistance.

References

1) As a general survey, S. A. Amelinckx and W. Dekyser: *Solid State Physics, Volume 8* (1959), Academic press, New York and London.
2) J. B. Newkirk: J. Appl. Phys. **29** (1958) 995; Trans. AIME **215** (1959) 483.
3) M. Yoshimatsu and K. Kohra: J. Phys. Soc. Japan **15** (1960) 1760.
4) W. R. Hibbard and C. G. Dunn: *Creep and Recovery* (1957) ASM, Cleveland.
5) W. R. Hibbard and C. G. Dunn: Acta Met. **3** (1955) 409; **4** (1956) 306.
6) J. J. Gilman: Acta Met. **3** (1955) 277.
7) S. Hosoya, S. Satake and S. Takagi: J. Phys. Soc. Japan **11** (1956) 1228.
8) M. Yoshimatsu and K. Kohra: J. Phys. Soc. Japan **15** (1960) 2367.

JOURNAL OF THE PHYSICAL SOCIETY OF JAPAN, Vol. 16, No. 11, NOVEMBER, 1961

Variation of Electron Diffraction Intensity with Wavelength of Electrons

by Norihisa KITAMURA

Physics Department, Tokyo Institute of Technology,
Oh-okayama, Meguro-ku, Tokyo, Japan

(Received July 31, 1961)

Intensity of electron diffraction Debye-Scherrer rings of evaporated films of alminium, nickel, gold and sodium fluoride was measured for electrons in a range of wavelength λ from 0.1 to 0.025 Å (accelerating voltage from 15 to 200 kV).

Logarithm of observed intensity varies linearly with λ^2 for not too large λ in accordance with the dynamical theory of two-wave approximation. The value extrapolated to $\lambda=0$ coincides with the kinematical value within experimental errors 5~15%. The gradient of the linear relation, too, coincides with the value calculated from the theory. No complication was found which requires explicitly the many-wave theory. The deviation from the linearity for large λ was reasonably explained as a result of absorption.

§ 1. Introduction

Crystal structure analysis based on intensity data of electron diffraction has been developed recently by many workers[1),2),3)] in view of the following advantages: (1) A very small amount of substance produces sufficiently intense reflections, making it possible to work with single crystal patterns even for substances of very poor crystallization. (2) In potential distribution maps given by this method, light atoms produce higher peaks than in electron density maps given by X-ray method. (3) Shifts of bonding electrons have a larger effect on electron diffraction than on X-ray diffraction.

To take advantage of the method fully, especially in respect to (2) and (3), however, a number of difficulties must be overcome. Difficulties in specimen preparation and control and those arising from poor angular resolution of the diffraction patterns are considerable. A more serious and essential difficulty, however, consists in the fact that the dynamical effect is significant in electron diffraction.

Analysing earlier intensity data of powder patterns, Blackman[4)] pointed out that the primary extinction effect is hardly negligible even for small crystals composing evaporated films. From intensity data of powder patterns due to Yamzin[5)], Pinsker drew the conclusion that the effect is not so important in practical samples[1)]. Lennander[6)] and Kuwabara[7)], however, concluded the contrary based on their experiments similar to Yamzin's experiment.

These workers studied the variation of Debye-Scherrer ring intensity which occurred when the particle size of specimens was varied. It is difficult to control and determine accurately the particle size. And too much reduction of the particle size impairs the accuracy of intensity measurement as a result of increased overlapping of intensity profiles of rings. Therefore, examinations of the dynamical effect by particle size variation were limited in accuracy. On the other hand, the wavelength of electrons, which is another important parameter of the effect, can be varied finely and determined accurately. Moreover, the effect of the change can be examined sample by sample. In a previous paper[8)], a preliminary result of such an examination was reported, showing that the observed intensity for an evaporated film of aluminium tends to the kinematical value when the wavelength tends to zero. This result was in accordance with the theory of primary extinction formulated for the case of electron diffraction by Blackman[4)] using the two-wave approximation of the dynamical theory[9)]

In the meanwhile, Hoerni[10)] pointed out that the systematic interaction of various reflections from the same reflecting plane is significant in electron diffraction in addition to the interaction between the primary wave and the reflected wave. In connection with this, Miyake[11] revealed a paradox of Bethe's second approximation, namely that it leads not to the kinematical potential but to the dynamical potential, including many wave interaction, at the limit when the product of wavelength and thickness of crystal tends to zero. And he pointed out the importance of many-wave theory. Concerning the problem, the pseudokinematical theory[12] and Cowley and Moudie's theory[13] based on the principle of physical optics have been developed. Fujimoto[14] and Fujiwara[15] have succeeded in solving the dynamical equations containing many-wave interaction. They showed that the intensity should tend to the kinematical value at the limit, although the approach is more complex than that predicted by the two-wave approximation.

Recently, Fujiwara[16] has noticed the practical importance of the relativistic correction in intensity of electron diffraction which had been introduced previously by von Laue.[17] This correction is due to the relativistic correction of electron mass. In this connection, Miyake et al.[18] gave a revision of the method to get the kinematical intensity by wavelength change.[8]

In view of these situations, it is of interest to re-examine electron diffraction intensity due to powder samples by a refined technique.

§ 2. A review of theories

According to the dynamical theory of two-wave approximation applied to a plane parallel plate crystal of thickness D, the integrated intensity of electron diffraction is given by

$$I_h = I_0 \frac{\lambda^3}{2\theta}\left(\frac{2\pi m_0 e}{h^2}\right)^2 \frac{|v_h|^2}{V_0^2} f(A_h)\cdot V\ , \quad (1)$$

where I_0 is the incident intensity, v_h the Fourier potential of crystal concerned, θ the Bragg angle, V_0 the unit cell volume and V the irradiated volume of crystal. The function $f(A_h)$ is the primary extinction factor defined by[4]

$$f(A_h) = \frac{1}{A_h}\int_0^{A_h} J_0(2x)\,dx\ , \quad (2)$$

where

$$A_h = \lambda\cdot\left(\frac{2\pi m_0 e}{h^2}\right)\frac{|v_h|}{V_0}\cdot D\ , \quad (3)$$

and $J_0(x)$ is the zero-th order Bessel function.

An approximation

$$f(A_h) = \exp\left(-\frac{1}{3}A_h^2\right) \quad (4)$$

holds for $A \leq 2$ within an error less than 1% (Fig. 11).

Then, for $A \leq 2$,

$$\ln I_h = \ln \frac{I_0 \lambda^3 V}{2\theta V_0^2}\left(\frac{2\pi m_0 e}{h^2}\right)^2 |v_h|^2 - \frac{1}{3}\left(\frac{2\pi m_0 e}{h^2}\right)^2 \lambda^2 \frac{|v_h|^2}{V_0^2} D^2\ . \quad (5)$$

The logarithm of relative intensity, which is measured practically, is

$$\ln\frac{I_h}{I_r} = \ln \frac{\theta_r}{\theta_h}\cdot\frac{|v_h|^2}{|v_r|^2} - \frac{1}{3}\frac{1}{V_0^2}\left(\frac{2\pi m_0 e}{h^2}\right)^2 (|v_h|^2 - |v_r|^2)\lambda^2 D^2\ , \quad (6)$$

where r is the index of the standard reflection. Eq. (6) shows that there is a linear relation between $\ln(I_h/I_r)$ and λ^2 so far as two-wave interaction is concerned. The kinematical value of intensity can be obtained by a linear extrapolating method.

When many wave interaction is taken into account, the situation is not so simple, although the observed intensity tends eventually to the kinematical value at $\lambda = 0$. By taking account of the systematic interactions, Fujimoto has given power series expressions for the intensity in terms of $(\lambda\cdot D)$.[19] But their convergence does not seem to be sufficiently good to give a certain prospect of λ-dendence of intensity for practical cases.

According to the relativistic theory of electron diffraction due to Fujiwara[16], the Fourier potential v_h should be replaced by an effective Fourier potential[18]

$$v_h\cdot(1+h^2/m_0^2c^2)^{1/2}\ .$$

When the correction is introduced in eq. (6),

$$\varLambda \equiv \lambda\cdot(1+h^2/m_0^2c^2)^{1/2} \quad (7)$$

takes the place of λ in the non-relativistic form. This implies that the kinematical value of intensity is reached at $\varLambda = 0$ instead of $\lambda = 0$.

§ 3. Experiment

The intensity of transmission electron diffraction patterns from polycrystalline films of aluminium, nickel, gold and sodium fluoride was measured by a photographic method for electrons of accelerating voltage ranging from 15 to 200 kV.

(1) *Apparatus*

A new high tension electron diffraction camera was constructed for this experiment, in which electrons are accelerated in two stages by potential in a 2:1 ratio fed from a Shimadzu cascade-type generator composed of two 100 kV transformers. The higher potential to the gun is led through a shock-proof cable and only the lower potential to the first anode is exposed to the atmosphere. In this way, accelerating voltage for electrons can be applied up to 200 kV without any trouble even in very humid atmosphere. The camera can be operated as routine as conventional ones of lower accelerating voltage.

Hillier type high resolution optical system[20] produces small primary spots of diameter about 15 and 30 μ for specimen-plate distances 50 and 100 cm, respectively. A s^1-sector consisting of two circular disk[21] can be placed in front of the photographic plate. One dozen of 8 cm×10.5 cm plates can be loaded at one time.

The movable specimen chamber provides the specimen with the translational motions in a plane perpendicular to the electron beam. The specimen holder, attached to a wall of the chamber, provides the specimen with rotational motions. A specimen grid is put on a circular disk, which can be rotated around the axis perpendicular to the disk. This disk can be tilted, around the axis of the holder perpendicular to the electron beam, in a range ±70° without masking the transmission pattern of specimen film.

(2) *Specimen*

Specifications of specimens are listed in Table I. They were prepared by vacuum evaporation. Metallic specimens were self-supporting, deposited on glass plates coated with collodion and detached from the substrates by solving away collodion in acetone. Sodium fluoride specimens were supported on collodion films of thickness about 100 Å on which they were directly deposited. The thickness T of specimen film was estimated from the quantity evaporated. The mean crystal size $\bar{H}$ of specimen was determined from the observed line breadth B using an approximate Scherrer type formula

$$\bar{H}=\lambda/(B-B_0)\ , \qquad (8)$$

where B_0 is the instrumental breadth and was estimated from the line breadth of Debye-Scherrer rings from highly crystallized thallium chloride films.

(3) *Intensity measurement*

a) *Photographic plates and processing.*

Fuji process hard photographic plates were used and developed by dilute solution 1:1 of D-72 developer at 20°±1°C for 3 minutes. The plates developed under these conditions have been proved to have an exellent character.[22] A Nalumi optically balanced type microphotometer was used.

The same diffraction pattern from a specimen for an accelerating voltage was recorded five times on one plate with different exposures. Photometer traces of optical density were transformed to intensity curves by Karle and Karle's method.[23]

b) *Examination of the Schwarzschild-Villiger (S. V.) effect.*[24]

Karle and Karle's method has been established in the field of gas diffraction and applied also to the case of crystalline diffraction patterns. Intensity distribution in crystalline patterns, however, changes much more steeply than in patterns from gas. It should be noticed that the S. V. effect might be serious in such a case. Readings of optical density

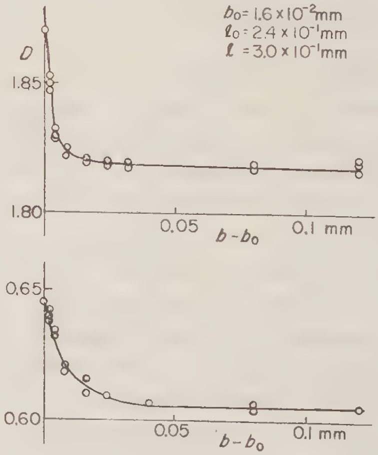

Fig. 1. a) Variation of optical density readings for two Debye-Scherrer rings of a half-width 0.18 mm, when the slit width is changed. Slits S_0 and S, which limit the light flux before and behind the plate examined, were focused on the testing plate. b_0, b and l_0, l represent the width and length of the images of the slits. b_0, l_0 and l were kept constant at values in the figure and b was varied.

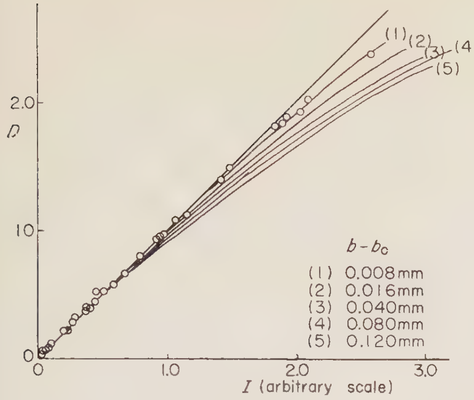

Fig. 1. b) D. I. curves for various slit width b.

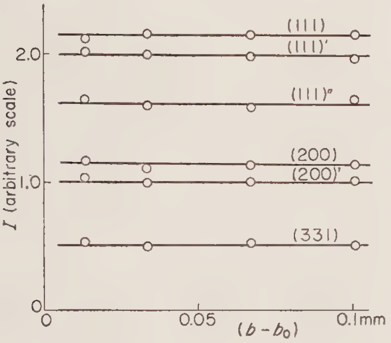

Fig. 1. c) Relative intensity data determined by various slit width b for Debye-Scherrer rings of aluminium film with a half-width 0.18 mm.

of peak of Debye-Scherrer rings were found to vary when the relative width of two slits before and after the plate in the optical path of microphotometer was changed (Fig. 1. a). Thus, the S. V. effect did occur. For our purpose, however, it is not the absolute optical density but the relative intensity which is required. The relative intensity of Debye-Scherrer rings determined using the appropriate density-intensity (D. I) curves, which vary with the width of slits (Fig. 1. b), gives a definite value within a certain range of the slit width (Fig. 1. c). In effect, although the S. V. effect does occur in photometry of crystalline diffraction patterns, it can be eliminated through Karle and Karle's method.

c) *Effect of preferred orientation*

Preferred orientation in specimen films was examined by observing intensity variation along Debye-Scherrer rings produced from the films tilted up to ±70°. For sodium fluoride, some films of almost perfectly random orientation could be prepared (Fig. 2. a). The intensity for all Debye-Scherrer rings of this substance was measured relatively to that for the (422) rings. The Fourier potential of this reflection is small, but it gives comparatively high peak on account of a large multiplicity. This is a favourable condition for the reference peak in the present study.

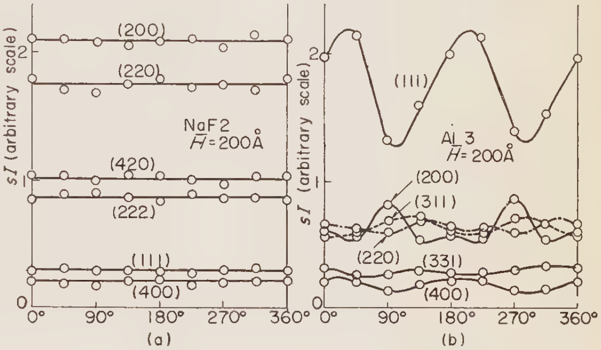

Fig. 2. Intensity variation along Debye-Scherrer rings due to (a) sodium fluoride and (b) aluminium films, both tilted 70° to incident electrons of 100 kV.

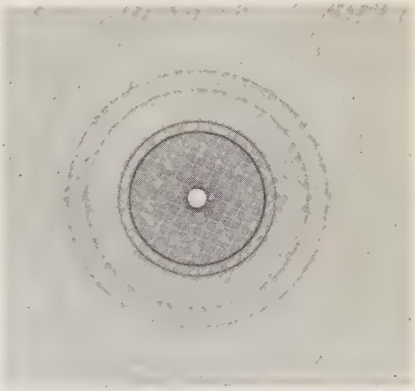

Fig. 3. Debye-Scherrer pattern from which the intensity variation of Fig. 2. b) was obtained.

All metallic films prepared had more or less preferred orientation. Some times this was revealed by photometry of patterns taken with large tilting angle, even when no arcing was recognized by visual examination on the fluorescent screen (Fig. 2. and Fig. 3). Therefore, for metallic specimens, the relative intensity was concerned only with (111) and (222) reflections. For the relative intensities of reflections from different lattice planes, the data fluctuated more than 20% with a slight change of specimen setting.*

d) *Accuracy*

Some examples of photometer traces are reproduced in Fig. 4. and Fig. 5. Noise ripples have been smoothed out for the traces other than Fig. 5. a). Since all these traces were taken in almost linear ranges of D.I. curves, they approximate to intensity curves.

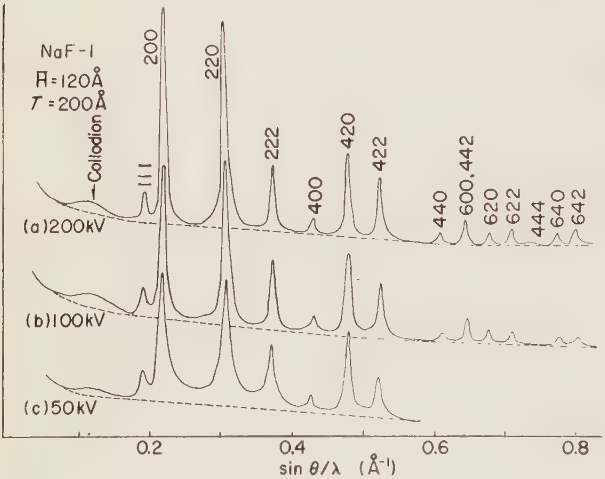

Fig. 4. Microphotometer traces of Debye-Scherrer patterns from the specimen NaF-2 (Table I) for accelerating voltages a) 200 kV, b) 100 kV and c) 50 kV. s^1-sector was used.

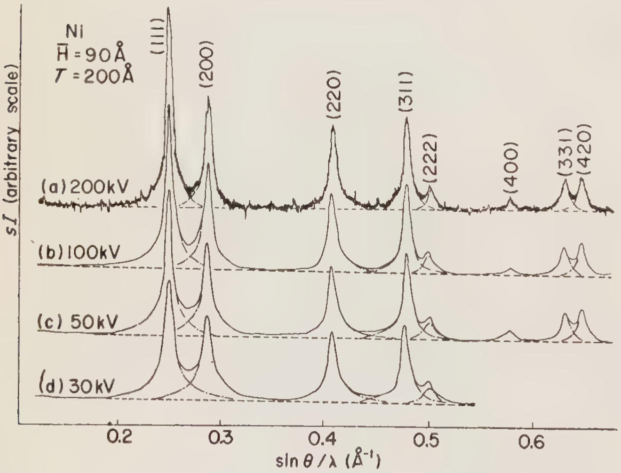

Fig. 5. Microphotometer traces of Debye-Scherrer patterns from the specimen Ni-2 (Table 1) for accelerating voltage a) 200 kV, b) 100 kV and c) 50 kV and d) 30 kV. s^1-sector was used.

The intensity data were obtained from the peak heights of Debye-Scherrer rings. The peak shape was determined of reflections well separated from the other peaks at least on one side. Peaks of (220) and (422) reflections were used for the determination. Assuming a similar shape for the other reflections, a smooth background was drawn and peak height above it was measured. The first peak due to collodion substrate for sodium fluoride can be found in Fig. 4. The height of the other peaks due to collodion should be less than one fifth of that of the first peak. Therefore, the collodion substrates have no effect for intensity measurement of Debye-Scherrer rings from sodium fluoride.

Generally one of the most important sources of errors in intensity measurement is the ambiguity in subtraction of background from intensity curve. To minimize the ambiguity, the background were flatted by making use of the s^1-sector and specimens of comparatively large crystal size were used in the present experiment.

Sodium fluoride gives rise to well separated Debye-Scherrer rings, all higher odd order reflections being vanishingly weak. For the substance, the error of intensity measurement due to the ambiguity mentioned above was less than 5% for strong reflections and not more than 15% for most of the observed reflections. In the measurement of the relative intensity I_{111}/I_{222} for metallic substances, a serious difficulty arises from the separation of overlapping (311) peak from (222) peak. Error due to the separation may be in the neighbourhood of 10%.

The standard deviations of experimental values were determined from the measurements on the series of photographs taken with different exposures. They are shown in Table I and II and represented by vertical lines in Figs. 7, 8, 9 and 10.

---

* From peak values of arc patterns due to oblique textures, relative intensity free from geometrical factors may be known.[2] But an accurate measurement of the values should take into account the shifts of peaks due to the slight but not negligible curvature of Ewald sphere. It was not undertaken in the present work.

Table I.

Specification				$\ln(\lvert v_h\rvert^2/\lvert v_r\rvert^2)$			Gradient of linear part.		Mean crystal size
Substance and No.	Thickness Å	Mean crystal size $\overline{H}$ (Å)	Reflexions concerned	extrapolated to $\Lambda=0$	extrapolated to $\lambda=0$	cal	exp. (Å^{-2})	cal. (Å^{-2})	$\overline{D}$ (Å)
Al-1	200	100±20	(111) / (222)	2.19±0.04	2.16±0.04	2.14	59±5	51	120±5
Al-2	200	120±30	(111) / (222)	2.24±0.07	2.20±0.06		120±10	74	133±5
Al-3	200	200±50	(111) / (222)	2.22±0.07	2.15±0.06		160±20	206	178±5
Al-4	200	120±30	(111) / (222)	2.11±0.04	2.08±0.04		75±7	74	121±5
Al-5	400	120±30	(111) / (222)	2.09±0.09	2.05±0.08		83±10	74	127±5
Ni-1	200	70±15	(111) / (222)	1.80±0.04	1.75±0.04	1.73	120±10	127	68±5
Ni-2	200	90±20	(111) / (222)	1.87±0.10	1.77±0.08		190±20	211	90±5
Ni-3	200	120±30	(111) / (222)	1.87±0.15	1.73±0.12		320±50	375	119±8
Au-1	200	100±20	(111) / (222)	—	—	1.47	480±100	457	105±15
Au-2	200	120±30	(111) / (222)	—	—		—	540	—
NaF-1	200	120±30	(111) / (422)	+0.37±0.02	+0.37±0.02	−0.35	0±3	− 5	—
			(200) / (422)	2.58±0.03	2.46±0.03	2.45	75±5	62	131±3
			(220) / (422)	1.88±0.02	1.86±0.02	1.91	41±3	32	—
			(222) / (422)	0.62±0.02	0.62±0.02	0.63	15±3	20	—
NaF-2	200	200±50	(111) / (422)	+0.32±0.02	+0.32±0.02	−0.35	0±3	− 5	—
			(200) / (422)	2.64±0.03	2.52±0.03	2.45	240±10	174	235±5
			(220) / (422)	1.97±0.02	1.90±0.02	1.91	124±6	89	—
			(222) / (422)	0.66±0.02	0.64±0.02	0.63	40±3	56	—

§ 4. Results and Discussions

Weak reflections of sodium fluoride showed no appreciable change of intensity with wavelength change. This suggests that there occurred no appreciable dynamical effect in these reflections. The average observed values $(I_h/I_{422})_{\text{obs.}}$ for these reflections are listed without bracket in the third column of Table II. To examine the reliability of present experiment, these intensity data were compared with the kinematical values calculated theoretically. $(I_h/I_{422})_{\text{obs.}}$ were corrected to $(I_h/I_{422})^0_{\text{obs.}}$ by a temperature factor $\exp(-1.15\sin^2\theta/\lambda^2)$ determined by Bradley and Lu's method[25]. The Fourier potentials $v_{\text{obs.}}$, obtained from $(I_h/I_{422})^0_{\text{obs.}}$, are put on the absolute scale by the statistical method[26] and are listed in the fourth column of Table II and plotted in Fig. 6 by open circles. They show a good agreement with the calculated values.

The logarithms of observed intensities for strong reflections of sodium fluoride and (111) reflections of metallic specimens are plotted against λ^2 in Figs. 7, 8, 9 and 10. It can be seen that almost all of the plots, except those for large λ, fall on straight lines drawn in each figures within experimental errors. When these straight lines are extrapolated to $\Lambda^2=0$ and $\lambda^2=0$ according to eqs. (6) and (7), they give the experimental values of $\ln(\lvert v_h\rvert^2/\lvert v_r\rvert^2)$ listed in Table I.

The differences between the extrapolated values at $\Lambda=0$ and at $\lambda=0$ for metallic specimens were within experimental errors. The values $(I_h/I_{422})_{\text{obs.}}$ in Table II for strong reflections of sodium fluoride were obtained from the extrapolated values in Table I and are shown with brackets. For the (200) reflection, the relativistic effect seems to be beyond the experimental errors. $v_{\text{obs.}}$ from the extrapolated values are shown in Fig. 6 by black circles and crosses for relativistic and non-relativistic values, respectively. The difference between them is of the order of that of $v_{\text{neut.}}$ and $v_{\text{ion.}}$ Within the accuracy of the experiment and calculation of Fourier potentials, the extrapolated values can be said to be in agreement with the kinematical values.

Incidentally, $v_{\text{obs.}}$ for (111) and (400) reflections deviate considerably, and those for (200)

Table II. Intensity data for sodium fluoride

hkl	$\sin\theta/\lambda$	$(I_{hkl}/I_{422})_{\text{obs.}}$	$v_{\text{obs.}}$ (volts)	$v_{\text{neut.}}$ (volts)	$v_{\text{ion.}}$ (volts)
111	0.187	$[1.36\pm0.08]_{\Lambda=0}$ $[1.36\pm0.08]_{\lambda=0}$	$1.2_5\pm0.1$ —	0.28	0.92
200	0.217	$[13.6\pm0.5]_{\Lambda=0}$ $[12.0\pm0.5]_{\lambda-0}$	$6.0_6\pm0.2$ $5.6_9\pm0.2$	5.66	5.36
220	0.306	$[6.88\pm0.25]_{\Lambda=0}$ $[6.55\pm0.25]_{\lambda=0}$	$4.4_7\pm0.2$ $4.2_4\pm0.2$	4.18	4.16
311	0.375	—	—	0.00	0.16
222	0.395	$[1.93\pm0.15]_{\Lambda=0}$ $[1.89\pm0.15]_{\lambda=0}$	$3.4_9\pm0.1$ $3.4_8\pm0.1$	3.44	3.41
400	0.433	0.27 ± 0.03	$2.2_7\pm0.15$	2.88	2.93
331	0.472	—	—	0.05	0.12
420	0.484	1.48 ± 0.10	$2.5_5\pm0.15$	2.51	2.58
422	0.530	1.00 ± 0.10	$2.3_4\pm0.15$	2.23	2.30
511, 333	0.562	—	—	0.10	0.12
440	0.612	0.13 ± 0.03	$1.9_0\pm0.3$	1.84	1.86
531	0.640	—	—	0.14	0.12
600, 442	0.649	0.32 ± 0.04	$1.6_0\pm0.2$	1.70	1.64
620	0.685	0.21 ± 0.04	$1.5_5\pm0.2$	1.52	1.54
533	0.710	—	—	0.12	0.12
622	0.718	0.13 ± 0.01	$1.5_0\pm0.15$	1.37	1.40
444	0.750	$0.03_0\pm0.01$	$1.3_0\pm0.3$	1.27	1.29
711, 551	0.773	—	—	0.10	0.12
640	0.790	$0.08_0\pm0.01$	$1.2_0\pm0.15$	1.19	1.20
642	0.810	$0.13_5\pm0.01$	$1.0_5\pm0.1$	1.15	1.13
731, 533	0.831	—	—	0.10	0.11
800	0.866	0.007 ± 0.01	$0.8_7\pm0.4$	1.02	1.01
733	0.886	—	—	0.10	0.10
820, 644	0.892	$0.05_0\pm0.01$	$0.9_2\pm0.1$	0.98	0.96
822, 660	0.918	0.034 ± 0.005	$0.8_2\pm0.1$	0.92	0.91
751, 555	0.937	—	—	0.09	0.09
662	0.944	0.024 ± 0.005	$0.8_7\pm0.1$	0.87	0.89
840	0.968	0.018 ± 0.005	$0.7_8\pm0.1$	0.83	0.83
911, 753	0.986	—	—	0.08	0.08
842	0.992	0.024 ± 0.005	$0.7_8\pm0.1$	0.79	0.79

$v_{\text{neut.}}$: Fourier potential calculated by atomic scattering factors[27] for neutral atoms based on Hartree-Fock's atomic wave functions.

$v_{\text{ion.}}$: Fourier potential calculated by atomic scattering factors for ions.[2]

and (220) reflections slightly from $v_{\text{neut.}}$. Such deviations may arise from ionization and distortion of electron cloud in crystal, but seem to require further detaited study.

According to eq. (6), the gradient of linear part of $\ln(I_h/I_r)\sim\lambda^2$ plot is given by $-\frac{1}{3}(2\pi m_0 e/h^2)^2(|v_h|^2-|v_r|^2)\bar{D}^2/V_0^2$. The values of $\bar{D}$, which were determined from the observed values of gradient using calculated values for v_h, are listed in the last column of Table I. The observed values $\bar{D}$ showed a good agreement with $\bar{H}$ obtained from eq. (8).

The logarithms of observed values $(I_h/I_r)_{\text{obs.}}$ divided by the kinematical values $(I_h/I_r)_{\text{kin.}}$ are plotted in Fig. 11. a) and b) against $A_h^2=(2\pi m_0 e/h^2)^2\cdot\lambda^2\bar{D}^2|v_h|^2/V_0^2$, using the theoretical values for $|v_h|$. Since $|v|$ is small for the standard reflections, (422) for sodium fluoride and (222) for metallic substances, the variation of I_r with λ is expected to be small. Thus,

$$\ln[(I_h/I_r)_{\text{obs.}}/(I_h/I_r)_{\text{kin.}}] \doteqdot \ln[(I_h)_{\text{obs.}}/(I_h)_{\text{kin.}}]$$

and this should coincide with $\ln f(A)$, if eq. (2) holds. It may be seen in Fig. 11 that most observed values coincide with the chain line for $\ln f(A)$.

It is noticed that the observed relation between $\ln I$ and A^2 deviates from the straight line at values of A smaller than those expected from the limit of the approximation of eq. (4). This can be explained by taking account of absorption. Let a specimen be composed of crystallites of various thickness given by a Gaussian distribution

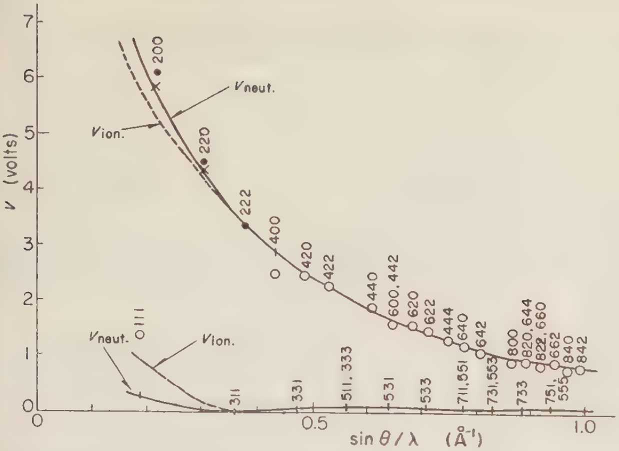

Fig. 6. Fourier potentials of sodium fluoride

○: The observed value for weak reflection obtained without extrapolation.

●: The observed value determined through extrapolation to $\Lambda=0$.

×: The same value to $\lambda=0$.

Full and brocken lines represent $v_{\rm neut.}$ and $v_{\rm ion.}$ respectively.

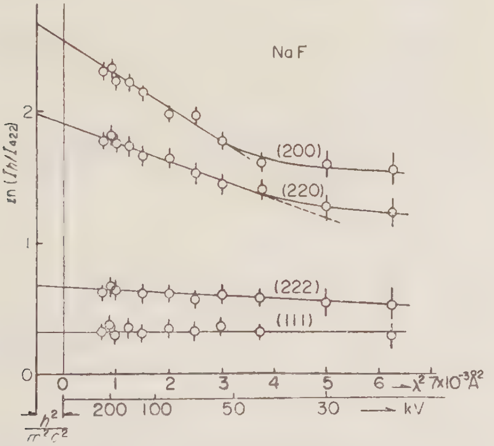

Fig. 7. Variation of relative intensities (I_h/I_{422}) of the specimen NaF-2 with wavelength.

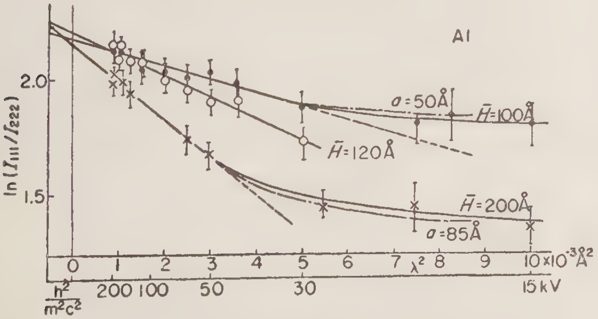

Fig. 8. Variation of relative intensity (I_{111}/I_{222}) of aluminium films with wavelength.

●: for the specimen Al-1, $\bar{H}=100$ Å.

○: for the specimen Al-2, $\bar{H}=200$ Å.

×: for the specimen Al-3, $\bar{H}=200$ Å.

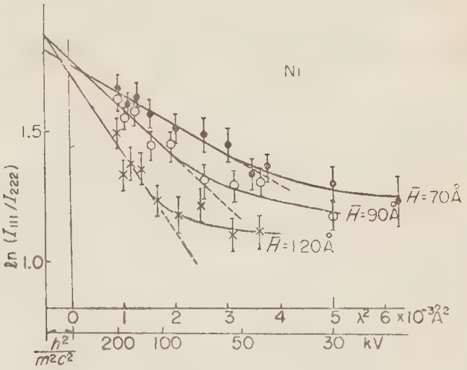

Fig. 9. Variation of relative intensity (I_{111}/I_{222}) of nickel films with wavelength.

●: for the specimen Ni-1, $\bar{H}=70$ Å.

○: for the specimen Ni-2, $\bar{H}=90$ Å.

×: for the specimen Ni-3, $\bar{H}=120$ Å.

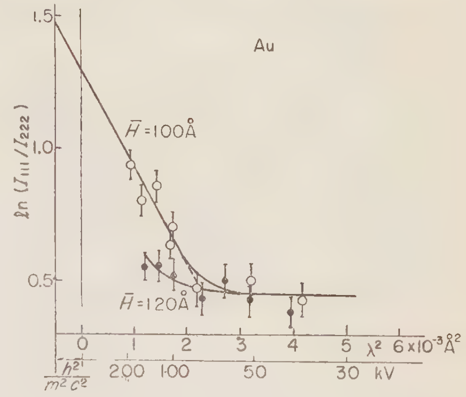

Fig. 10. Variation of relative intensity (I_{111}/I_{222}) of gold films with wavelength.

○: for the specimen Au-1, $\bar{H}=100$ Å.

●: for the specimen Au-2, $\bar{H}=120$ Å.

$$W(H)=C\exp[-(H-H_0)^2/a^2]. \quad (9)$$

Then, the mean crystal size $\bar{H}$ of the specimen as determined by eq. (8) is given by

$$\bar{H}=\frac{\int_0^\infty HW(H)\,dH}{\int_0^\infty W(H)\,dH}=H_0+\frac{a}{\sqrt{\pi}}, \quad (10)$$

if the specimen is not absorptive. In fact, real specimens are more or less absorptive and the absorption coefficient μ increases with increasing λ. Then, the mean crystal size $\bar{H}_{\rm eff.}$ effective for line broadening should be

$$\bar{H}_{\text{eff.}} = \frac{\int_0^\infty HW(H)\exp(-\mu H)\,dH}{\int_0^\infty W(H)\exp(-\mu H)\,dH} = \bar{H} - \frac{a^2\mu}{2} \tag{11}$$

and must decrease with increasing λ.

Similarly, the mean crystal thickness $\bar{D}_{\text{eff.}}$ effective for the dynamical diffraction effect must decrease with increasing λ. Strictly speaking, the dependence of $\bar{D}_{\text{eff.}}$ on λ must be different from that of $\bar{H}_{\text{eff.}}$. But here it may be roughly assumed that they are identical. For aluminium, Terrill[28] has given an experimental formula for change of μ with accelerating potential Φ (in volts) of electrons,

$$\mu = \frac{8\times10^{11}}{\Phi}\rho\,(\text{cm}^{-1}) = 144\,\lambda^4\,(\text{Å}^{-1}),$$

where ρ is the density. Then, from eqs. (10) and (11),

$$\Delta D = \bar{D} - \bar{D}_{\text{eff.}} = \frac{a^2\mu}{2} = 72\,a^2\lambda^4,$$

where a and λ in Å. ΔD are plotted in Fig. 12.

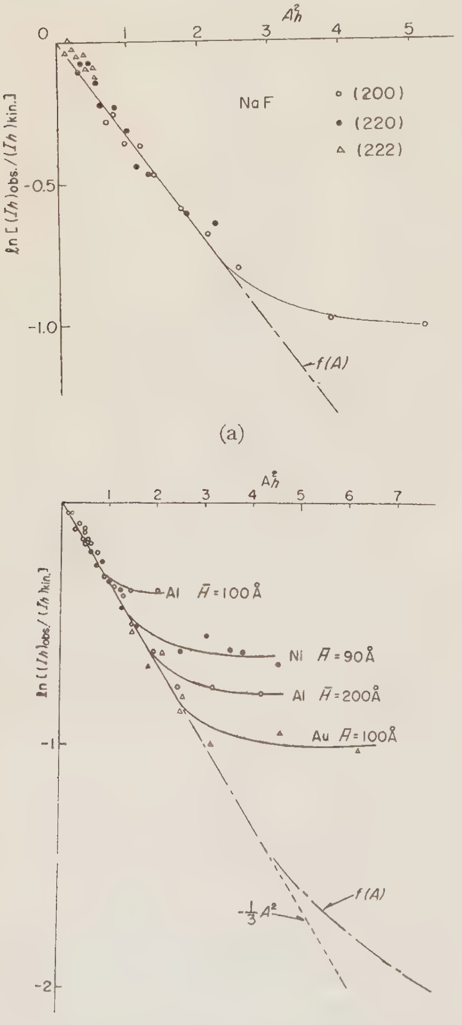

(a)

(b)

Fig. 11. ln $[(I_h)_{\text{obs.}}/(I_h)_{\text{kin}}]$ against A_h^2.

Using this relation, ln $I\sim\lambda^2$ relations were calculated for $\bar{H}=\bar{D}=120$ Å and 178 Å with reasonable values of $a \doteqdot \bar{D}/2$, corresponding to the specimens Al-1 and Al-3, respectively, and they are shown by chain lines in Fig. 8. Thus the observation can be explained reasonably by taking account of absorption.

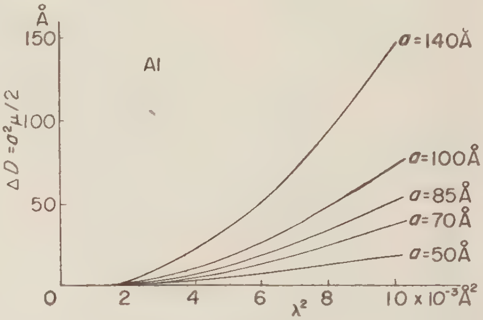

Fig. 12. Change of effective mean crystal size of aluminium with wavelength.

§ 5. Conclusion

Summarising the above results, it can be said that the dynamical theory of two-wave approximation holds in a wide range of wavelength and for the various substances studied in the present experiment. It gives not only the right kinematical values of intensity at the limit of wavelength zero, but also it explains closely the trend of the intensity variation with λ. In a range of large wavelength, a deviation from the two-wave theory was found. There, very complicated interaction must be taking place. But they could be taken adequately into account by an experimental absorption coefficient. Thus, within the reach of present experiment, no complication was found which requires explicitly the many-wave theory.

The conclusion does not imply that many-wave interaction is not important. The many-wave interaction does occur in electron diffraction as proved by the appearence of forbidden reflection (222) from germanium[10),30)] and the anomalously strong intensity of the reflection (222) from cuprous chloride[29),31)].

The intensities of these reflections have been found to decrease with $\lambda \cdot D$[30),31)]. This effect may give rise to a diviation of the gradient of $\ln I \sim \lambda^2$ plot from that expected by two-wave approximation. But, in the strong reflections as observed in the present experiment, the deviation may not be so serious and can hardly be detected on account of insufficient accuracy in determing crystal thickness.

The method of eliminating primary extinction by wavelength variation gives the Fourier potentials as the limiting values with experimental accuracies of the order 5~10%, provided specimens are favourable.

The extrapolated values of low order reflections show sometimes discrepancies with calculated values beyond the experimental accuracy. The Fourier potentials of low order reflections are very sensitive to the actual state of atoms in crystal. Therefore, the final validity of the experimental values obtained by the extrapolation can not be established unless the actual state of atoms is known. The most reliable reference for such comparison may be accurate experimental values of the structure factors for X-rays. Unfortunately, for sodium fluoride, for which our experimental results are most reliable, such X-ray data have not been given yet. While, for sodium chloride, calcium fluoride and lithium fluoride, accurate X-ray data have been given,[32)] but preparation of specimen without preferred orientation was found to be difficult for these substances. It is desirable to develop a technique of accurate intensity measurement of fibrous or single oriented patterns for study of these substances.

The author wishes to thank Prof. Goro Honjo for his guidance and helpful discussions throughout this work. He also wishes to thank Prof. Shizuo Miyake for his guidance and advices. This work was supported by a research grant of the Ministry of Education.

References

1) Z. G. Pinsker: Diffractiya Electronv (1949) A. N. SSSR, Moscow. (Engl. ed. 1953 Butterworth Sci. Pub. London)
2) B. Vainshtein: Structurnaya Electronographiya (1956) A. N. SSSR, Moscow.
3) M. J. Cowley: Acta Cryst. **6** (1953) 516, 522.
S. Nagakura: J. Phys. Soc. Japan **13** (1958) 1005.
S. Kuwabara: J. Phys. Soc. Japan **14** (1959) 1205.
K. Shimaoka: J. Phys. Soc. Japan **15** (1960) 106.
4) M. Blackman: Proc. Roy. Soc. **A173** (1939) 68.
5) I. I. Yamzin: Trudy Inst. Krist. Akad. Nauks (1949) 69.
6) S. Lennander: Arkiv. f. Fys. **8** (1954) 551.
7) S. Kuwabara: J. Phys. Soc. Japan **10** (1955) 416, **12** (1957) 638.
8) G. Honjo and N. Kitamura: Acta Cryst. **10** (1957) 533.
9) H. A. Bethe: Ann. d. Phys. **87** (1928) 55.
10) J. A. Hoerni: Phys. Rev. **102** (1956) 1534.
11) S. Miyake: J. Phys. Soc. Japan **14** (1959) 1347.
12) J. A. Hoerni: Phys. Rev. **102** (1956) 1530.
M. Hayashi: J. Phys. Soc. Japan **15** (1960) 2054.
13) M. J. Cowley and A. F. Moudie: Acta Cryst. **10** (1957) 609.
14) F. Fujimoto: J. Phys. Soc. Japan **14** (1959) 1588.
15) K. Fujiwara: J. Phys. Soc. Japan **14** (1959) 1513.
16) K. Fujiwara: J. Phys. Soc. Japan **16** (1961) 2226.
17) M. von Laue: Materiewellen und Ihre Interferenzen (1948), Akadem. Verlag. Leipzig.
18) S. Miyake, K. Fujiwara, G. Honjo and N. Kitamura; J. Phys. Soc. Japan **16** (1961) 2336.
19) F. Fujimoto: J. Phys. Soc. Japan **15** (1960) 859.
20) J. Hillier and R. F. Baker: J. Appl. Phys. **17** (1946) 12.
21) M. Takagi: Acta Cryst. **10** (1957) 708.
22) M. Takagi, N. Kitamura and S. Morimoto: J. Phys. Soc. Japan **16** (1961) 792.
23) J. Karle and I. I. Karle: J. Chem. Phys. **18** (1950) 957.
24) K. Schwarzschild and M. Villiger: Astrophys. Journ. **23** (1906) 284.
25) A. J. Bradley and S. S. Lu: Z. Krist. **96** (1937) 20.
26) A. J. C. Wilson: Nature **150** (1942) 152.
27) J. A. Ibers: Acta Cryst. **11** (1958) 178.
28) H. M. Terrill: Phys. Rev. **24** (1924) 616.
29) L. H. Germer: Phys. Rev. **56** (1936) 58, **61** (1942) 309.
30) M. Takagi and S. Morimoto: to be published.
31) F. Fujimoto: J. Phys. Soc. Japan **16** (1961) 936.
32) H. Witte und E. Wölfel: Z. physik. Chem. **3** (1955) 296.
J. Klug, H. Witte und E. Wölfel: *ibid.* **4** (1955) 36.
A. Weiss, H. Witte und E. Wölfel: *ibid.* **10** (1957) 98.

JOURNAL OF THE PHYSICAL SOCIETY OF JAPAN, Vol. 16, No 11, NOVEMBER, 1961.

Fluctuations in a Plasma I: Ion-Electron Temperature Relaxation

By Osamu AONO

Department of Physics, Faculty of Science,
University of Tokyo

(Received June 30, 1961)

Fluctuations of the electric field in a plasma are treated on the basis of the fluctuation-dissipation theorem. The treatment is applied to the relaxation between ion and electron temperatures. The interaction between ion and electron which causes the relaxation is reduced to the interaction between the ion and the fluctuating electric field caused by the surrounding electrons. The short range encounters between electrons are neglected but the long range encounters are included through the dielectric permeability which is obtained by use of the fluctuation-dissipation theorem. The rate of relaxation agrees with the result obtained by Kihara et al. who considered that the ion interacts with the individual electrons.

§ 1. Introduction

In a plasma there exist various fluctuations, e.g. density and electric field fluctuations. A fluctuation is related to a transport phenomenon by the fluctuation-dissipation theorem[1]. Our purpose is to calculate the transport coefficients on the basis of the fluctuation theory. We first investigate the ion-electron temperature relaxation in a magnetic field which has been treated by Kihara et al.[2],[3] in the particle aspect.

We consider a plasma which is composed of one type of ion and electrons. The plasma is regarded as a continuous dielectric medium, that has been suggested by Kihara[4]. Both the plasma and the applied static magnetic field are assumed to be uniform in space. The mass, charge and number density of the ion are denoted by m_1, Ze and n_1, respectively; those of the electron are expressed by m_2, $-e$ and n_2. Charge neutrality, $Zn_1=n_2$, is assumed.

Since the mass ratio of an ion and an electron is far from unity, the energy transfer between ion and electron is much smaller than that between ions or electrons. Hence the ion temperature T_1 and the electron temperature T_2 can often be different even when the velocity distributions are both Maxwellian. Here we consider the case where $Z^2 \ll m_1/m_2$ and the mean ion velocity is much smaller than the mean electron velocity:

$$(T_1/m_1)^{1/2} \ll (T_2/m_2)^{1/2} . \tag{1.1}$$

The rate R of the temperature relaxation is defined by

$$\frac{d}{dt}(T_2-T_1)=-(T_2-T_1)R . \tag{1.2}$$

where t denotes the time.

The short-range interaction between electrons is neglected but the long-range interaction is included through the dielectric permeability.

§ 2. Formulation in Terms of the Force Correlation

We follow Kihara et al.[2],[3] in this section.

The particle velocities of the ion and the electron are denoted by $\boldsymbol{v}_1$ and $\boldsymbol{v}_2$, respectively, with $|\boldsymbol{v}_1|=v_1$ and $|\boldsymbol{v}_2|=v_2$. The average value of $m_1v_1^2/3$ is T_1 which is the temperature in energy unit; the time rate of change of T_1 is given by the average value of the time rate of change of $m_1v_1^2/3$:

$$\left.\begin{aligned}\frac{d}{dt}T_1&=\frac{1}{\Delta t}\frac{m_1}{3}\langle|\boldsymbol{v}_1+\Delta\boldsymbol{v}_1|^2-v_1^2\rangle_{av}\\&=\frac{1}{\Delta t}\frac{m_1}{3}\langle 2\boldsymbol{v}_1\cdot\Delta\boldsymbol{v}_1+|\Delta\boldsymbol{v}_1|^2\rangle_{av} .\end{aligned}\right\} \tag{2.1}$$

Here $\Delta\boldsymbol{v}_1$ indicates the increment in the ion velocity due to interaction with the surrounding electrons in a time interval Δt; Δt is taken to be much larger than the time characteristic of the fluctuation of the interaction, yet it must be much smaller than both the relaxation time R^{-1} and the ion gyration period; and $\langle\ \rangle_{av}$ denotes the average with respect to the ion velocity and the interaction with surronding electrons.

When the ion temperature T_1 is much smaller than the electron temperature T_2, the average value of $\boldsymbol{v}_1\cdot\Delta\boldsymbol{v}_1$ can be neglected in comparison with the average value of $|\Delta\boldsymbol{v}_1|^2$; hence

$$\frac{d}{dt}T_1=\frac{1}{\Delta t}\frac{m_1}{3}\langle|\Delta\boldsymbol{v}_1|^2\rangle_{av} \quad \text{for} \quad T_1\ll T_2\,. \tag{2.2}$$

This relation can be generalized into the form

$$\frac{d}{dt}T_1=\frac{1}{\Delta t}\frac{m_1}{3}\langle|\Delta\boldsymbol{v}_1|^2\rangle_{av}\frac{T_2-T_1}{T_2}\,, \tag{2.3}$$

which holds for T_1 satisfying (1.1). The proof given by Kihara[2)] is the following. We are considering the case where (1.1) is satisfied; the quantity $|\Delta\boldsymbol{v}_1|^2$ averaged with respect to the interaction with surrounding electrons is independent of $\boldsymbol{v}_1$; but the average value of $\Delta\boldsymbol{v}_1$ depends linearly upon $\boldsymbol{v}_1$. For fixed T_2, therefore, $\langle|\Delta\boldsymbol{v}_1|^2\rangle_{av}$ is independent of T_1, and $\langle\boldsymbol{v}_1\cdot\Delta\boldsymbol{v}_1\rangle_{av}$ is proportional to T_1. On taking account of the fact that $\langle 2\boldsymbol{v}_1\cdot\Delta\boldsymbol{v}_1+|\Delta\boldsymbol{v}_1|^2\rangle_{av}$ vanishes for $T_1=T_2$, we obtain

$$2\langle\boldsymbol{v}_1\cdot\Delta\boldsymbol{v}_1\rangle_{av}=-\frac{T_1}{T_2}\langle|\Delta\boldsymbol{v}_1|^2\rangle_{av}\,.$$

Then (2.3) follows from (2.1).

By use of the relationship

$$\frac{d}{dt}(n_1T_1+n_2T_2)=0\,,$$

the rate of relaxation R defined by (1.2) is calculated to

$$R=\frac{1}{3}(n_1+n_2)\frac{m_1}{T_2n_2}\frac{1}{\Delta t}\langle|\Delta\boldsymbol{v}_1|^2\rangle_{av}\,. \tag{2.4}$$

The increment in the ion velocity during Δt is given by

$$\Delta\boldsymbol{v}_1=\frac{Ze}{m_1}\int_0^{\Delta t}\boldsymbol{E}(\tau)d\tau\,,$$

where $\boldsymbol{E}(\tau)$ is the fluctuating electric field caused by surrounding electrons and $Ze\boldsymbol{E}(\tau)$ is the force acting on the ion at a time τ. Hence

$$|\Delta\boldsymbol{v}_1|^2=\frac{(Ze)^2}{m_1^{\,2}}\int_0^{\Delta t}\int_0^{\Delta t}\boldsymbol{E}(\tau)\cdot\boldsymbol{E}(\tau')d\tau d\tau'$$

$$\frac{(Ze)^2}{m_1^{\,2}}\int_0^{\Delta t}\int_{-\tau}^{\Delta t-\tau}\boldsymbol{E}(\tau)\cdot\boldsymbol{E}(\tau+t)dtd\tau\,.$$

Since Δt is much larger than the continuance of the force correlation, we have

$$\frac{1}{\Delta t}\langle|\Delta\boldsymbol{v}_1|^2\rangle_{av}=\frac{(Ze)^2}{m_1^{\,2}}\int_{-\infty}^{\infty}\langle\boldsymbol{E}(0)\cdot\boldsymbol{E}(t)\rangle_{av}dt\,. \tag{2.5}$$

As we need only to consider the case $T_1\ll T_2$, ions can be regarded to be at rest, and the average with respect to the ion velocity is not necessary. Hereafter we omit the suffix "*av*" which means average.

§ 3. The Fluctuation of the Electric Field

By use of the formula

$$(2\pi)^{-3}\int e^{-i\boldsymbol{k}\cdot\boldsymbol{s}}d\boldsymbol{k}=\delta(\boldsymbol{s})\,,$$

we have

$$\int_{-\infty}^{\infty}\langle\boldsymbol{E}(0)\cdot\boldsymbol{E}(t)\rangle dt=(2\pi)^{-3}\iiint\langle\boldsymbol{E}(\boldsymbol{r},\tau)\cdot\boldsymbol{E}(\boldsymbol{r}+\boldsymbol{s},\tau+t)\rangle e^{-i\boldsymbol{k}\cdot\boldsymbol{s}}d\boldsymbol{s}dtd\boldsymbol{k} \tag{3.1}$$

The right side is the force correlation expanded in the wave vector $\boldsymbol{k}$; it will be used later.

We consider the Fourier expansion for the electric field $\boldsymbol{E}$ at a position $\boldsymbol{r}$ and a time τ; or inversely

$$\boldsymbol{E}(\boldsymbol{k},\omega)=(2\pi)^{-4}\iint\boldsymbol{E}(\boldsymbol{r},\tau)e^{-i\boldsymbol{k}\cdot\boldsymbol{r}+i\omega\tau}d\boldsymbol{r}d\tau\,.$$

Taking account of the fact that $\langle\boldsymbol{E}(\boldsymbol{r},\tau)\cdot\boldsymbol{E}(\boldsymbol{r}+\boldsymbol{s},\tau+t)\rangle$ depends neither on $\boldsymbol{r}$ nor on τ, we obtain

$$\langle\boldsymbol{E}(\boldsymbol{k},\omega)\cdot\boldsymbol{E}(\boldsymbol{k}',\omega')\rangle=(E^2)_{\boldsymbol{k}\omega}\delta(\boldsymbol{k}+\boldsymbol{k}')\delta(\omega+\omega')\,, \tag{3.2}$$

where

$$(E^2)_{\boldsymbol{k}\omega}=(2\pi)^{-4}\iint\langle\boldsymbol{E}(\boldsymbol{r},\tau)\cdot\boldsymbol{E}(\boldsymbol{r}+\boldsymbol{s},\tau+t)\rangle e^{-i\boldsymbol{k}\cdot\boldsymbol{s}+i\omega t}d\boldsymbol{s}dt\,. \tag{3.3}$$

In particular

$$(E^2)_{\boldsymbol{k}0}=(2\pi)^{-4}\iint\langle\boldsymbol{E}(\boldsymbol{r},\tau)\cdot\boldsymbol{E}(\boldsymbol{r}+\boldsymbol{s},\tau+t)\rangle e^{-i\boldsymbol{k}\cdot\boldsymbol{s}}d\boldsymbol{s}dt\,. \tag{3.4}$$

The relation (3.1) can be expressed in terms of $(E^2)_{k0}$ by

$$\int_{-\infty}^{\infty} \langle \boldsymbol{E}(\tau)\cdot\boldsymbol{E}(\tau+t)\rangle dt=2\pi\int (E^2)_{k0}d\boldsymbol{k}\ . \tag{3.5}$$

The Eq. (3.5) shows that we need only to know the fluctuation of electric fields for $\omega=0$. Then, rot $\boldsymbol{E}=0$ or $\boldsymbol{k}\times\boldsymbol{E}(\boldsymbol{k},0)=0$; from div $\boldsymbol{\varepsilon}\cdot\boldsymbol{E}=4\pi\rho$ follows

$$\boldsymbol{E}(\boldsymbol{k},0)=-i\frac{4\pi\rho(\boldsymbol{k},0)}{\boldsymbol{k}\cdot\boldsymbol{\varepsilon}(\boldsymbol{k},0)\cdot\boldsymbol{k}}\boldsymbol{k}\ , \tag{3.6}$$

where ρ is the charge density, $\boldsymbol{\varepsilon}$ is the dielectric permeability tensor of the plasma. Furthermore we have the relation

$$\boldsymbol{k}\cdot\boldsymbol{\varepsilon}(\boldsymbol{k},0)\cdot\boldsymbol{k}=k^2+k_d{}^2\ , \qquad k_d{}^2=\frac{4\pi n_2e^2}{T_2}\ , \tag{3.7}$$

a proof being given in the next section.

By use of (3.2), (3.6) and (3.7), the electric field fluctuation is related to the density fluctuation:

$$(E^2)_{k0}=\frac{(4\pi k)^2}{(k^2+k_d{}^2)^2}(\rho^2)_{k0}\ , \tag{3.8}$$

where $(\rho^2)_{k0}$ is defined similarly to (3.2).

The charge density of electrons is given by

$$\rho(\boldsymbol{r},\tau)=-\sum_{i=1}^{N} e\delta(\boldsymbol{r}-\boldsymbol{r}_i(\tau))\ ,$$

where $\boldsymbol{r}_i(\tau)$ is the position of i'th electron at a time τ, and N denotes the number of the electrons which gives the number density, n_2, when divided by the plasma volume. The Fourier components are

$$\rho(\boldsymbol{k},\omega)=\frac{-e}{(2\pi)^4}\int\sum_i \exp\{-\boldsymbol{k}\cdot\boldsymbol{r}_i(\tau)+i\omega\tau\}d\tau\ .$$

The correlation is

$$\begin{aligned}\langle\rho(\boldsymbol{k},\omega)\rho(\boldsymbol{k}',\omega')\rangle&=\frac{e^2}{(2\pi)^8}\sum_{i,j}\iint d\tau d\tau'\,\langle\exp\{-i\boldsymbol{k}\cdot\boldsymbol{r}_i(\tau')-i\boldsymbol{k}'\cdot\boldsymbol{r}_j(\tau)+i\omega\tau'+i\omega'\tau\}\rangle\\&=\frac{e^2}{(2\pi)^8}\sum_{i}\iint d\tau dt\,\langle\exp\{-i(\boldsymbol{k}+\boldsymbol{k}')\cdot\boldsymbol{r}_i(\tau)+i(\omega+\omega')\tau-i\boldsymbol{k}\cdot\boldsymbol{s}_i(t)+i\omega t\}\rangle\ ,\end{aligned}$$

where $t=\tau'-\tau$, $\boldsymbol{s}_i(t)=\boldsymbol{r}_i(\tau')-\boldsymbol{r}_i(\tau)$; the terms including two different electrons vanish unless $\boldsymbol{k}=\boldsymbol{k}'=0$, $\omega=\omega'=0$, but in this case the electron density is canceled by the charge neutrality. As all electrons are equivalent, we can omit the suffix "i", and multiply N in place of the summation. Considering the fact that $\boldsymbol{r}(\tau)$ is arbitrally and that $\langle\exp\{-i\boldsymbol{k}\cdot\boldsymbol{s}(t)\}\rangle$ is independent of τ, we obtain

$$\langle\rho(\boldsymbol{k},\omega)\rho(\boldsymbol{k}',\omega')\rangle=\frac{n_2e^2}{(2\pi)^4}\delta(\boldsymbol{k}+\boldsymbol{k}')\delta(\omega+\omega')\int\langle e^{i\omega t-i\boldsymbol{k}\cdot\boldsymbol{s}(t)}\rangle\,dt\ . \tag{3.9}$$

Therefore

$$(\rho^2)_{k0}=\frac{n_2e^2}{(2\pi)^4}\int\langle e^{-i\boldsymbol{k}\cdot\boldsymbol{s}(t)}\rangle\,dt\ . \tag{3.10}$$

Finally we obtain from (2.4), (2.5), (3.5), (3.8) and (3.10)

$$R=(n_1+n_2)\frac{2Z^2e^4}{3\pi m_1 T_2}\iint\frac{k^2}{(k^2+k_d^2)^2}\langle e^{-i\boldsymbol{k}\cdot\boldsymbol{s}(t)}\rangle\,dt\,d\boldsymbol{k}\,. \tag{3.11}$$

§ 4. The Dielectric Permeability

In a number of cases it proves possible to connect the fluctuations with effects on the system of certain external influences. For a physical quantity in this category there exists an external influence which is described by the perturbation,

$$-x_a f_a\,, \tag{4.1}$$

in the Hamiltonian, (a summation is implied over repeated suffixes), and for which the time rate of change in energy is expressed by

$$-x_a\dot{f}_a\,. \tag{4.2}$$

Here f_a are the perturbing forces, which are given functions of the time; x_a are the corresponding physical quantities; and $\dot{f}_a=df_a/dt$. If all quantities are expressed in complex forms by means of a Fourier transformation, whose time dependence is given by the factor $e^{-i\omega t}$, the relation between f_a and x_a takes the form

$$f_a(\omega)=\alpha_{ab}(\omega)x_b(\omega)\,. \tag{4.3}$$

The connection between f_a and α_{ab} is expressed1) as

$$\langle f_a(\omega)f_b(\omega')\rangle=\frac{i\hbar}{4\pi}(\alpha_{ab}-\alpha_{ba}^*)\coth\frac{\hbar\omega}{2T}\delta(\omega+\omega')\,, \tag{4.4}$$

where $2\pi\hbar$ is Planck's constant, T is the temperature of the system. In the classical limit ($\hbar\omega\ll T$), (4.4) takes the form

$$\langle f_a(\omega)f_b(\omega')\rangle=\frac{T}{2\pi\omega}i(\alpha_{ab}-\alpha_{ba}^*)\delta(\omega+\omega')\,. \tag{4.5}$$

In order to use the general formula (4.5) we must establish the relations between the electromagnetic quantities and the quantities f_a and x_a. This is done as follows.

As a result of fluctuations in the position and motions of the electrons in a plasma, a spontaneous local current occurs; let the value of this current per unit area be $\boldsymbol{j}(\boldsymbol{r},t)$. We suppose that $\boldsymbol{j}(\boldsymbol{r},t)$ is not a spontaneously arising quantity but a result of external action, and calculate the consequent change in energy in the plasma. The time rate of this change is given by

$$-\int\boldsymbol{E}(\boldsymbol{r},t)\cdot\boldsymbol{j}(\boldsymbol{r},t)d\boldsymbol{r}=-(2\pi)^3\int\boldsymbol{E}(-\boldsymbol{k},t)\cdot\boldsymbol{j}(\boldsymbol{k},t)d\boldsymbol{k}\,, \tag{4.6}$$

where

$$\boldsymbol{j}(\boldsymbol{k},t)=\frac{1}{(2\pi)^3}\int\boldsymbol{j}(\boldsymbol{r},t)e^{-i\boldsymbol{k}\cdot\boldsymbol{r}}d\boldsymbol{r}\,,\qquad\text{etc.}$$

Comparing (4.6) with (4.2) we see that, if x_a are taken to be $(2\pi)^3E_\alpha(-\boldsymbol{k},t)d\boldsymbol{k}$, then the corresponding $\dot{f}_a$ will be $j_\alpha(\boldsymbol{k},t)$. In (4.2) the suffix "$a$" numerates both the space component "α" and the Fourier component "$\boldsymbol{k}$":

$$\begin{cases} x_a\to(2\pi)^3E_\alpha(-\boldsymbol{k},t)d\boldsymbol{k} \\ \dot{f}_a\to j_\alpha(\boldsymbol{k},t)\,. \end{cases} \tag{4.7}$$

The Maxwell equations for Fourier components are given by

$$\left\{\begin{aligned} &i\boldsymbol{k}\times\boldsymbol{E}(\boldsymbol{k},\omega)=\frac{i\omega}{c}\boldsymbol{H}(\boldsymbol{k},\omega) \\ &i\boldsymbol{k}\times\boldsymbol{H}(\boldsymbol{k},\omega)=-\frac{i\omega}{c}\boldsymbol{\varepsilon}(\boldsymbol{k},\omega)\cdot\boldsymbol{E}(\boldsymbol{k},\omega)+\frac{4\pi}{c}\boldsymbol{j}(\boldsymbol{k},\omega)\ , \end{aligned}\right. \tag{4.8}$$

where $\boldsymbol{\varepsilon}(\boldsymbol{k},\omega)$ is the dielectric permeability tensor, and

$$\boldsymbol{E}(\boldsymbol{k},\omega)=(2\pi)^{-4}\iint\boldsymbol{E}(r,t)e^{-i\boldsymbol{k}\cdot\boldsymbol{r}+i\omega t}drdt\ , \qquad \text{ètc.}$$

On eliminating $\boldsymbol{H}(\boldsymbol{k},\omega)$, we have

$$\boldsymbol{j}(\boldsymbol{k},\omega)=\frac{i\omega}{4\pi}\left[\varepsilon(\boldsymbol{k},\omega)+\frac{c^2}{\omega^2}(\boldsymbol{kk}-k^2)\right]\cdot\boldsymbol{E}(\boldsymbol{k},\omega)\ . \tag{4.9}$$

This expression corresponds to (4.3), if we rewrite (4.9) as

$$\frac{ij_\alpha(\boldsymbol{k},\omega)}{\omega}=-\frac{1}{4\pi}\int\left[\varepsilon_{\alpha\beta}(\boldsymbol{k},\omega)+\frac{c^2}{\omega^2}(k_\alpha k_\beta-k^2)\right]\frac{\delta(\boldsymbol{k}+\boldsymbol{k}')}{(2\pi)^3}(2\pi)^3E_\beta(-\boldsymbol{k}',\omega)d\boldsymbol{k}'\ , \tag{4.10}$$

and take $\alpha_{ab}(\omega)$ and $f_a(\omega)$ to be

$$\left\{\begin{aligned} &\alpha_{ab}\rightarrow\frac{-1}{4\pi}\left[\varepsilon_{\alpha\beta}(\boldsymbol{k},\omega)+\frac{c^2}{\omega^2}(k_\alpha k_\beta-k^2)\right]\frac{\delta(\boldsymbol{k}+\boldsymbol{k}')}{(2\pi)^3} \\ &f_a\rightarrow\frac{ij_\alpha(\boldsymbol{k},\omega)}{\omega}\ . \end{aligned}\right. \tag{4.11}$$

Finally we obtain from (4.5)

$$\langle j_\alpha(\boldsymbol{k},\omega)j_\beta(\boldsymbol{k}',\omega')\rangle=\frac{T_2\omega}{(2\pi)^5}\frac{i}{2}[\varepsilon_{\beta\alpha}{}^*(-\boldsymbol{k},\omega)-\varepsilon_{\alpha\beta}(\boldsymbol{k},\omega)]\delta(\boldsymbol{k}+\boldsymbol{k}')\delta(\omega+\omega')\ , \tag{4.12}$$

where the temperature must be the electron temperature.

From the charge conservation law, we have

$$\boldsymbol{k}\cdot\boldsymbol{j}(\boldsymbol{k},\omega)=\omega\rho(\boldsymbol{k},\omega)\ .$$

Then (4.12) is reduced to

$$\langle\rho(\boldsymbol{k},\omega)\rho(\boldsymbol{k}',\omega')\rangle=\frac{i}{2}\boldsymbol{k}\cdot[\boldsymbol{\varepsilon}^*(-\boldsymbol{k},\omega)-\boldsymbol{\varepsilon}(\boldsymbol{k},\omega)]\cdot\boldsymbol{k}\frac{T_2}{\omega(2\pi)^5}\delta(\boldsymbol{k}+\boldsymbol{k}')\delta(\omega+\omega')\ . \tag{4.13}$$

Using (3.9), (4.11), (4.13) and Kramers-Kronig's relation for α_{ab},

$$\alpha_{ba}{}^*(\omega)+\alpha_{ab}(\omega)=\frac{i}{\pi}\int\frac{\alpha_{ba}{}^*(\omega')-\alpha_{ab}(\omega')}{(\omega'-\omega)}d\omega'\ ,$$

where the integral takes the principal value, we have

$$\begin{aligned} \boldsymbol{k}\cdot[\boldsymbol{\varepsilon}^*(-\boldsymbol{k},0)+\boldsymbol{\varepsilon}(\boldsymbol{k},0)]\cdot\boldsymbol{k}-2k^2&=\frac{(2\pi)^5}{T_2}\frac{2}{\pi}\int(\rho^2)_{\boldsymbol{k}\omega'}d\omega' \\ &=\frac{4\pi n_2e^2}{T_2}\frac{1}{\pi}\iint e^{i\omega't}\langle e^{-i\boldsymbol{k}\cdot\boldsymbol{s}(t)}\rangle dtd\omega' \\ &=8\pi n_2e^2/T_2 \\ &=2k_a{}^2\ , \end{aligned} \tag{4.14}$$

where k_a is the Debye shielding constant, and on the left side the value of $\boldsymbol{\varepsilon}$ for $\omega\rightarrow\infty$ is subtracted. From (4.13) and (4.14) we have

$$\boldsymbol{k}\cdot\boldsymbol{\varepsilon}(\boldsymbol{k},0)\cdot\boldsymbol{k}=k^2+k_d^2\,. \tag{3.7}$$

The relation (3.7) has thus been proved.

The relation (3.7) is apparent from the fact that the static electric potential arround a charge is of the Debye type with the Debye shielding constant[1], k_d, whether the plasma is in a magnetic field or not.

Effects of ions on the Debye shielding constant can be excluded because we are considering the interaction between one ion and its surrounding electrons.

§ 5. The Rate of Relaxation

In (3.11), $s(t)$ corresponds to the spiral orbit of the electron along the magnetic field,

$$|s(t)|=v_2|t|[1-Y^2\sin^2\theta]^{1/2}\,,$$

where θ denotes the angle between the magnetic field and the velocity of the electron, and

$$Y^2=1-\frac{2(1-\cos y)}{y^2}\,,\qquad y=\omega_2 t\,,$$

with the gyration frequency of the electron, ω_2. The integral in (3.11) is expressed as

$$\iint\frac{k^2}{(k^2+k_d^2)^2}\langle e^{-i\boldsymbol{k}\cdot\boldsymbol{s}(t)}\rangle\,dt\,dk=\iiint\frac{k^2}{(k^2+k_d^2)^2}\left(\frac{m_2}{2\pi T_2}\right)^{3/2}\exp\left\{-i\boldsymbol{k}\cdot\boldsymbol{s}(t)-\frac{m_2v_2^2}{2T_2}\right\}dv_2dtdk$$

$$=\int dt\iint\frac{k^4}{(k^2+k_d^2)^2}\exp\left\{-\frac{k^2T_2t^2}{2m_2}[1-Y^2\sin^2\theta]\right\}2\pi\sin\theta d\theta dk\,, \tag{5.1}$$

where use has been made of the formula

$$\int_0^\infty\sin(ax)\exp(-x^2)xdx=\frac{\sqrt{\pi}\,a}{4}\exp(-a^2/4)\,.$$

(I) *The case of no magnetic fields*

In this case, $\omega_2=0$, $Y^2=0$. Integrating (5.1) with respect to the angle and the time, we obtain

$$4\pi\left(\frac{2\pi m_2}{T_2}\right)^{1/2}\int_0^{k_M}\frac{k^3dk}{(k^2+k_d^2)^2}\,,$$

the range of large wave numbers must be cut off at the k_M, which correspond to the impact parameter smaller than the radius of the sphere of strong interaction, Ze^2/T_2, i.e., $k_M=T_2/Ze^2$. In the range of small wave numbers the integral converges, because we have considered the long-range many-body interaction between electrons through the dielectric permeability.

The rate of relaxation defined by (1.2) is given by

$$R=R_0\ln\frac{T_2}{Ze^2k_d}\,,\qquad R_0=\frac{8}{3}(n_1+n_2)\frac{m_2}{m_1}\left(\frac{Ze^2}{T_2}\right)^2\left(\frac{2\pi T_2}{m_2}\right)^{1/2}. \tag{5.2}$$

(II) *The case in which a magnetic field is present*

In this case, it is sufficient to consider the range

$$k_M^{-2}\ll l^2=\frac{T_2t^2}{2m_2}[1-Y^2\sin^2\theta]\ll k_d^{-2}\,, \tag{5.3}$$

because the contribution of the part with large values of l to the integral (5.1) is small. The range of small l, ($l<k_M^{-1}$), and the range of small $\cos\theta$ must be cut off, because real interaction between the ion and the electron is much smaller than the interaction between the ion and the electron moving spirally. The range (5.3) is expressed as

$$t_s\ll|t|\ll t_p\,,$$

where $t_p=(m_2/T_2)^{1/2}k_d^{-1}$, the period of plasma oscillation, and $t_s=(m_2/T_2)^{1/2}k_M^{-1}$, the mean time of passage through a sphere of strong interaction.

Hence (5.1) becomes

$$2\pi\left(\frac{2\pi m_2}{T_2}\right)^{1/2}\int_{t_s}^{t_p} dt\,\frac{1}{tY}\ln\frac{1+Y}{1-Y}\,.$$

The rate of relaxation is given by

$$R=R_0\int_{t_s}^{t_p}\frac{dt}{2tY}\ln\frac{1+Y}{1-Y}\,, \qquad (5.4)$$

which agrees with the result of Kihara et al.[3] The expression (5.4) is essentially equivalent to

$$R/R_0=\begin{cases}\ln t_p/t_s & \text{for } \omega_2<t_p^{-1}\\ \ln t_p/t_s+\frac{1}{2}(\ln\omega_2 t_p)^2 & \text{for } \omega_2>t_p^{-1}\,.\end{cases} \qquad (5.5)$$

The form for weak magnetic fields and the form of (5.2) are the same. The expression (5.2) and (5.5) are exact as weak interaction asymptotes for $t_p/t_s\gg 1$.

Acknowledgement

The author wishes to express his sincere thanks to Prof. Kihara for his continual guidance and valuable suggestions.

References

1) L. D. Landau and E. M. Lifshitz: *Statistical Physics* (Pergamon Press, 1958), chap. XII, p. 404. See also, *Electrodynamics of Continuous Media* (1960), chap. XIII.
2) T. Kihara: J. Phys. Soc. Japan **14** (1959) 1751.
3) T. Kihara, Y. Midzuno, K. Sakuma and T. Shizume: J. Phys. Soc. Japan **15** (1960) 684.
4) T. Kihara: J. Phys. Soc. Japan **14** (1959) 402.

JOURNAL OF THE PHYSICAL SOCIETY OF JAPAN, Vol. 16, No. 11, NOVEMBER, 1961

Magnetic Perturbation of an Ammonia Maser on the 3, 2 Line

By Koichi SHIMODA

Department of Physics, Faculty of Science, University of Tokyo, Tokyo

(Received July 31, 1961)

Effects of external magnetic field on the amplitude and frequency of ammonia maser oscillator employing the $J=3$, $K=2$ line were measured and compared with theory. The variation of the traveling-wave effect by the external field is calculated and theoretical curves of the frequency shift as a function of the external field are given. Definitions of line center by magnetic perturbation method are discussed. It is concluded that the resettability with an accuracy of a few parts in 10^{11} can be obtained, when the variation of maser frequency of about 0.5 cps. caused by a magnetic perturbation of 2 to 3 oersteds can be detected and corrected.

§ 1. Introduction

The frequency of oscillation of an ammonia beam maser is primarily determined by the energy levels of the molecule, but it is subject to small shifts due to several reasons[1]. In order to get rid of the complicated behavior caused by the quadrupole hyperfine structure[2),3)], ammonia masers on the $J=3$, $K=2$ line of $N^{14}H_3$ have been constructed and tested. Design, construction, and operating characteristics were reported in the previous paper[4]. Particularly the variation of the frequency pulling by the cavity was measured against focuser voltage and was explained theoretically. Frequency shifts due to traveling wave component in the cavity, due to background pressure and the fringing electric field were also reported.

Because the maximum amount of frequency pulling by the cavity is as large as 2 to 3 kc, cavity tuning for maximum output cannot determine the line center with an accuracy of better than $\pm 1\times 10^{-9}$. It was proposed before[1] to employ a magnetic perturbation method for tuning the cavity. If the resonant frequency of the cavity is different from the frequency of the line, the frequency of oscillation of the maser changes with the applied magnetic field, because the magnitude of frequency shift increases with the broadening of the line. Only when the cavity is tuned on the frequency of the line, the frequency of oscillation is expected to be unchanged with application of magnetic field. Magnetic perturbation methods of tuning were tried in several laboratories, but they were not successful on the $J=3$, $K=3$ line because of the existence of quadrupole hyperfine structure.

Experimental and theoretical studies of the magnetic perturbation method on the $J=3$, $K=2$ line of $N^{14}H_3$ are described in this paper. The method may well apply to a maser using $N^{15}H_3$.

§ 2. Zeeman Effect of the 3, 2 Line of Ammonia

Spectroscopic investigations on the magnetic hyperfine structure and the Zeeman effect of the 3, 2 line have been carried on in this laboratory. Details of the experimental results and their theoretical analysis will be reported later and only the weak field Zeeman pattern which is necessary for the analysis of magnetic perturbation is briefly described below.

The observed hyperfine structure of the 3, 2 line of ammonia consists of a strong main line at the center and two pairs of magnetic hyperfine satellites. A picture displayed on a cathode-ray oscilloscope is shown in Fig. 1. The inner satellites are separated from the main line by 24.35±0.15 kc, and the outer by 62.59±0.30 kc[5].

The spectrum was observed with a one-klystron system which is similar to that described before[6]. The maser employed was the same one as described in the previous paper[4]. Helmholtz coils of 20 cm radius were used for spectroscopy, while those of 13 cm radius were used for magnetic perturbation

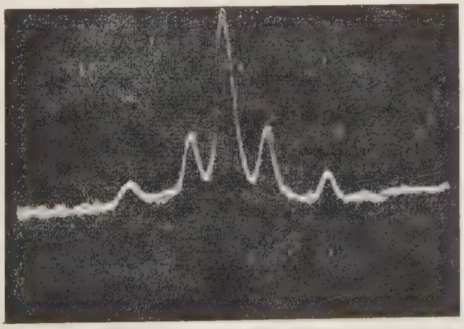

Fig. 1. The magnetic hyperfine structure of the 3, 2 line. The main line is strongly staturated.

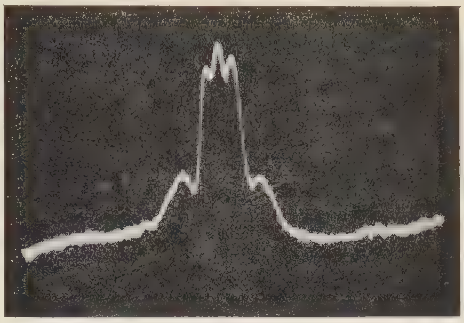

(a) $H=8.3$ oe.

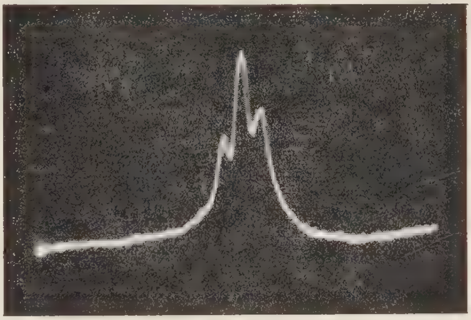

(b) $H=13.5$ oe.

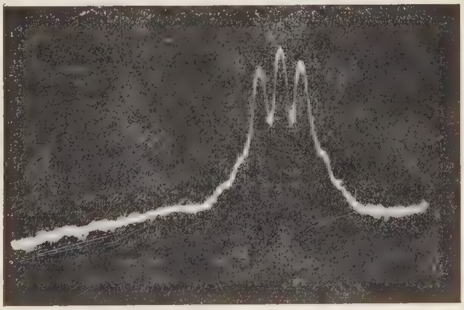

(c) $H=17.4$ oe.

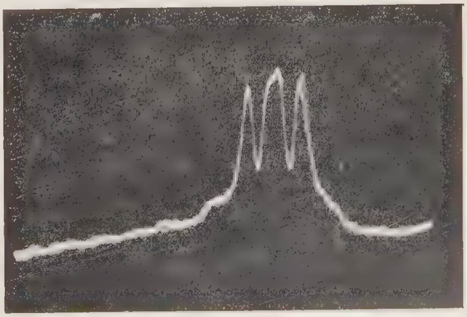

(d) $H=26.0$ oe.

Fig. 2. C. R. O. pictures of weak field Zeeman pattern.

of the maser oscillator which will be described in the following sections.

When the dc magnetic field is parallel to the axis of the TM_{010} cavity, very little change in the intensity and width of the line was observed with the maximum available field intensity of more than 100 oersteds. Weak field Zeeman patterns in the magnetic field perpendicular to the cavity axis observed by the maser spectrometer are shown in Fig. 2. The main line split into three groups of components at a field below 20 oersteds. In a field beyond 20 oersteds the central component further splits into two groups as shown in Fig. 2 (d).

Preliminary results of the frequencies of resolved Zeeman components are plotted in Fig. 3. The outer satellites split into many components and becomes very weak in a field which is stronger than several oersteds. Only the strong components are shown in Fig. 3. The inner satellites do not merge in the Zeeman components of the main line in a weak field. Therefore, only the Zeeman components of the main line seem to be required in describing the characteristics of the maser oscillator on the 3, 2 line. Further discussions will be found in the following paper.

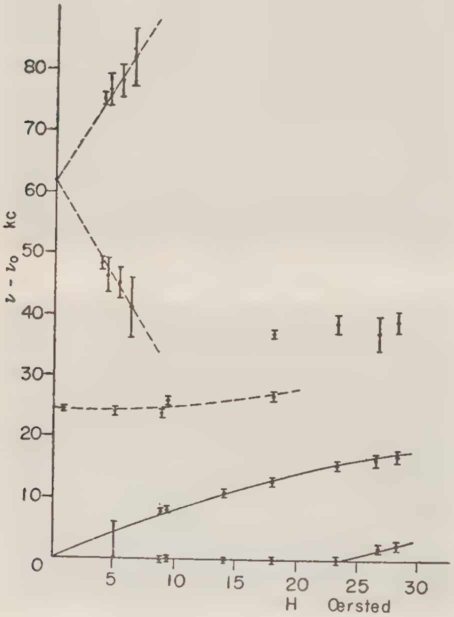

Fig. 3. Zeeman splitting vs. dc magnetic field which is perpendicular to the axis of the cavity.

§ 3. Amplitude of Oscillation in Magnetic Field

The relative intensities of the three groups of Zeeman components are described as $(1-C)/2:C:(1-C)/2$, and the splitting as $\Delta\nu_H$. The theoretical value is calculated to be $C=0.389$. It is difficult to calculate the exact line-shape because of the velocity distribution of molecules and of the effect of unresolved components. The Lorentzian line-shape is assumed for simplicity of calculation.

When the rf amplitude is so low that the saturation may be neglected, the imaginary part of the resultant susceptibility $\chi=\chi'+i\chi''$ of molecules under weak magnetic field is written as

$$\chi''=\left(C+\frac{1-C}{1+u^2}\right)\chi_0=\frac{1+Cu^2}{1+u^2}\chi_0\,, \qquad (1)$$

where u is the frequency shift of the side component devided by the half-width, $\Delta\nu$, that is

$$u=\frac{\Delta\nu_H}{\Delta\nu}$$

and χ_0 is the imaginary part of susceptibility of the molecular beam without magnetic field.

The amplitude of oscillation is given by Eq. (9) in the previous paper[4] as

$$\frac{n_{\text{eff}}}{n_{\text{th}}}=\frac{\theta^2}{\sin^2\theta}\,, \qquad (2)$$

where θ represents the amplitude of rf electric field E in the cavity of length L,

$$\theta=\frac{xL}{2\langle v\rangle}=\frac{\bar{\mu}E}{\hbar}\,\frac{L}{2\langle v\rangle}\,,$$

and n_{eff} is the effective beam intensity at zero dc magnetic field. The susceptibility of the molecular beam is of course proportional to the beam intensity so that

$$\frac{\theta^2}{\sin^2\theta}=\frac{1+Cu^2}{1+u^2}\rho^2\,, \qquad (3)$$

where $n_{\text{eff}}/n_{\text{th}}=\rho^2$ may be called the normalized beam intensity in the absence of magnetic field.

The variation of θ with the magnetic field is calculated from Eq. (3) and shown in Fig. 4. The observed amplitude of oscillation is the relative value of x or E. In order to compare it with the theoretical result, the observed amplitude A was divided by the critical radial velocity v_c which was shown in Fig. 2 in the previous paper[4], because v_c is approximately

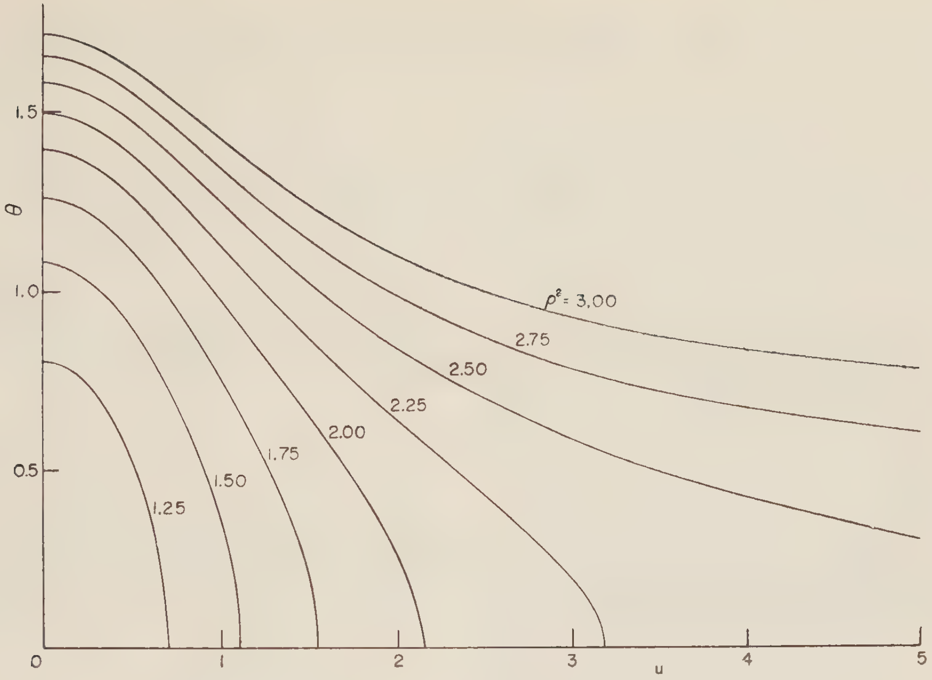

Fig. 4. Theoretical values of θ vs. magnetic field, where parameters are $n_{\mathrm{eff}}/n_{\mathrm{th}}=\rho^2$.

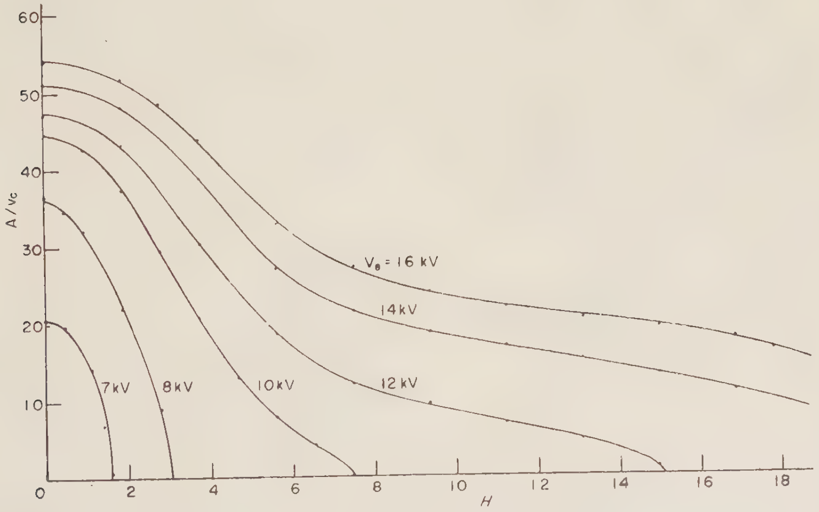

Fig. 5. Experimental values of A/v_c vs. magnetic field, where parameters are the focuser voltage.

proportional to $\langle v\rangle$. Fig. 5 shows the experimental values of the amplitude of oscillation plotted against applied dc field.

When Fig. 5 is compared with Fig. 4, somewhat larger decrease of the observed amplitude of oscillation is found in a higher magnetic field. This is undoubtedly due to the incipient splitting of the central component which was observed as two lines in the magnetic field of more than 20 oersteds.

§ 4. Frequency Pulling by the Cavity and the Line-Width

The frequency of oscillation can be calculated from the real part of susceptibility of the molecular beam. The real part of susceptibility of Lorentzian lines at frequencies, $\nu_0\pm\Delta\nu_H$, with a half width $\Delta\nu$ is expressed by

$$\frac{(\nu-\nu_0\mp\Delta\nu_H)\Delta\nu}{(\nu-\nu_0\mp\Delta\nu_H)^2+(\Delta\nu)^2}\chi_0\ .$$

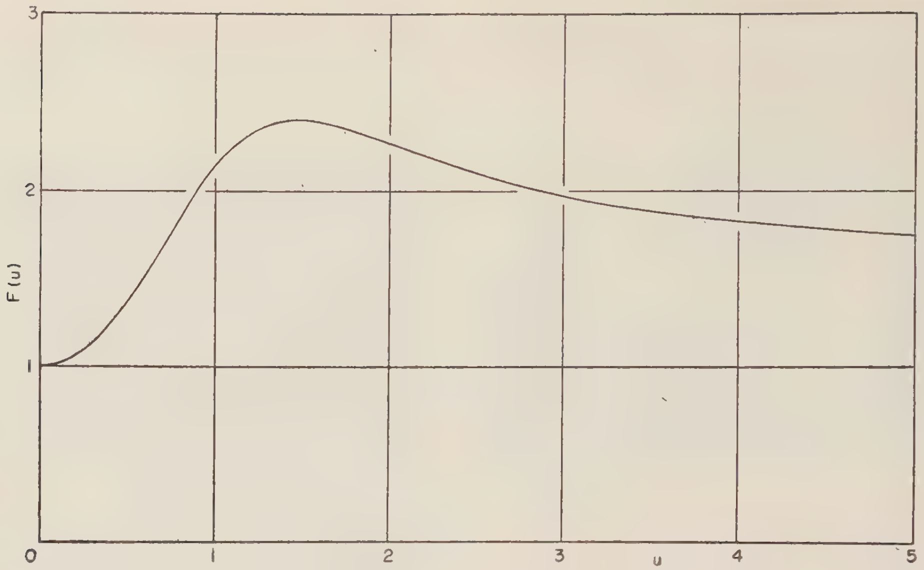

Fig. 6. Theoretical variation of cavity pulling vs. magnetic field is shown by $F(u)=(1+u^2)^{3/2} \times(1+Cu^2)^{1/2}[1+(3C-1)u^2+Cu^4]^{-1}$.

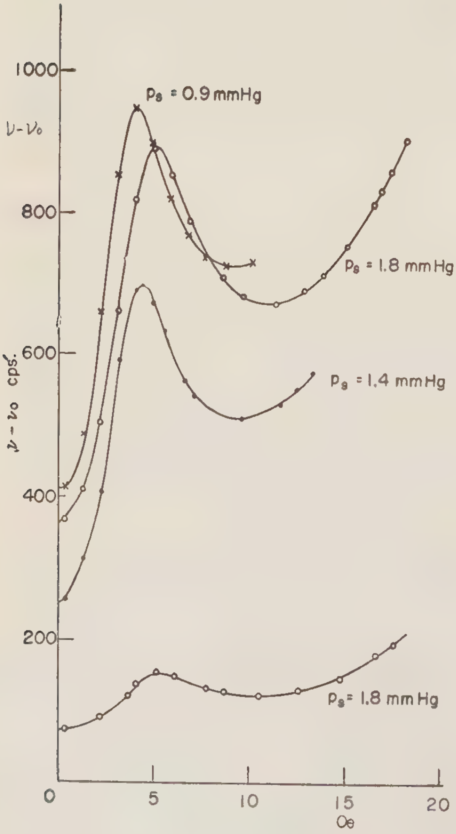

Fig. 7. Observed frequency shift vs. magnetic field, when $\omega_c > \omega_0$. The source pressure p_s is shown in mmHg.

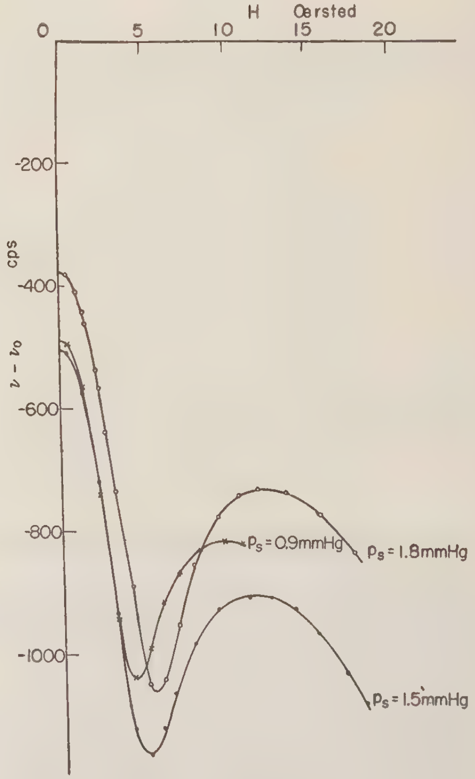

Fig. 8. Observed frequency shift vs. magnetic field, when $\omega_c < \omega_0$. The source pressure p_s is shown in mmHg.

Then the resultant susceptibility of the three groups of Zeeman components at frequencies of ν_0 and $\nu_0 \pm \Delta\nu_H$ is given by

$$\chi' = \chi_0 \left[C + (1-C)\frac{1-u^2}{(1+u^2)^2} \right] \frac{\nu-\nu_0}{\Delta\nu}$$

$$= \chi_0 \frac{1+(3C-1)u^2+Cu^4}{(1+u^2)^2} \cdot \frac{\omega-\omega_0}{2\pi\Delta\nu} . \qquad (4)$$

Now the frequency of maser oscillation ω is obtained from Eq. (40) in the paper by Shimoda, Wang and Townes[1]. The condition for self-sustained oscillation can be expressed by

$$\frac{1}{Q} + 2i\frac{\omega-\omega_c}{\omega_c} = -4\pi i(\chi' + i\chi'') , \qquad (5)$$

where ω_c is the resonant frequency of the cavity resonator with a quality factor Q.

The effect of saturation was calculated for a uniform velocity of the beam as having a factor[1]

$$\frac{1}{3} f_2(\theta) = \frac{1}{3} \cdot \frac{1-\cos 2\theta}{1-(\sin 2\theta)/2\theta} . \qquad (6)$$

Calculation of the saturation effect of the beam with velocity distribution and with Zeeman splitting of the line has not been carried out, but it may be expressed by the factor of Eq. (6), where θ is given by Eq. (3). Then the frequency of oscillation may by given from Eqs. (5) and (6) by

$$\frac{\omega-\omega_c}{\omega_c} = -\frac{3}{2Q} \cdot \frac{1-(\sin 2\theta)/2\theta}{1-\cos 2\theta} \cdot \frac{\chi'}{\chi''} , \qquad (7)$$

where $\chi' + i\chi''$ represents the small signal susceptibility of the beam.

The numerical value of $(1/3) f_2(\theta)$ agrees to $(\sin\theta)/\theta$ within 3 percent, when $0 \leqq \theta \leqq 2.4$. This approximation allows an explicit expression of the frequency of oscillation as follows. From Eq. (3) one obtains

$$\frac{1}{3} f_2(\theta) \approx \frac{\sin\theta}{\theta} = \frac{1}{\rho}\sqrt{\frac{1+u^2}{1+Cu^2}} , \qquad (8)$$

where ρ can be expressed by the value of θ without magnetic field, θ_0, as

$$\rho = \frac{\theta_0}{\sin\theta_0} = \sqrt{\frac{n_{\mathrm{eff}}}{n_{\mathrm{th}}}} .$$

Then the frequency of oscillation is calculated from Eqs. (1), (4) and (7) as

$$\frac{\omega-\omega_0}{\omega_0} = \frac{Q}{Q_l} \frac{\omega_c-\omega_0}{\omega_0 \rho} \cdot \frac{(1+u^2)^{3/2}(1+Cu^2)^{1/2}}{1+(3C-1)u^2+Cu^4} , \qquad (9)$$

where $Q_l = \nu_0/2\Delta\nu$. Thus the change in oscillation frequency with the applied magnetic field has been expressed by the last factor in Eq. (9), which is shown graphically in Fig. 6 for $C=0.389$.

Experimental values of the frequency change with magnetic field were obtained by beating one maser with another one which is oscillating outside the magnetic field. Observed results for the cases when the cavity is tuned considerably off-resonant are shown in Fig. 7 and Fig. 8.

The variation of oscillation frequency in the magnetic field of weaker than about 10 oersteds agrees fairly well with the theoretical result. The amount of frequency pulling increases to nearly twice the initial value at a magnetic field of 5 oersteds. The increase of frequency pulling observed in a field stronger than 10 oersteds, contrary to the simplified theoretical computation, is undoubtedly due to the incipient splitting of the central component which was resolved into two lines in a field of larger than 20 oersteds. A systematic change with the source pressure can be seen in Figs. 7 and 8. The field intensity of a corresponding point is found to increase with the increase of source pressure or source flux.

The width of the line, when the maser is oscillating, can be determined from Figs. 7 and 8 as shown in Table I. The observed increase of line-width with the source flux can be explained by saturation broadening of the line due to the increase of the amplitude of oscillation.

Table I. Observed line-width of the maser oscillator.

source pressure p_s	half line-width
0.9 mmHg	2.10±0.1 kc
1.4	2.25
1.5	2.35
1.8	2.60

An approximate expression of the saturation broadening is obtained as[7]

$$\Delta\nu = \sqrt{(\Delta\nu_0)^2 + \left(\frac{x}{2\pi}\right)^2} , \qquad (10)$$

where $\Delta\nu_0$ is the half width of the line under small rf amplitude. Since the Lorentzian line-shape has been assumed, it is reasonable to obtain the above equation by using the distribution of the time of flight τ of molecules in the cavity as $\exp(-\tau/T)$.

The small signal line-width observed by a TM_{010} cavity with the beam of uniform velocity is

$$2\Delta\nu_0 \doteqdot 0.9\frac{v}{L},$$

where L is the length of the cavity. When the velocity distribution is taken into account, the average of the time of flight cannot be given by $L/\langle v\rangle$, since divergent molecules cannot travel the whole length of the cavity.

Because the transition probability is proportional to τ^2, the amplitude of oscillation varies as $\langle\tau^2\rangle^{1/2}$ and the line-width is given by $\langle\tau^2\rangle^{-1/2}$ as shown by Venkates and Strandberg[8]. The time of flight for molecules which collide with the cavity wall is $\tau \doteqdot R/v_r$, while for molecules which pass through the cavity it is $\tau \doteqdot L/v_z$, where v_r and v_z are respectively the radial and the axial components of the molecular velocity. Then by using

$$\xi=\frac{v_z}{\alpha}, \qquad \eta=\frac{L}{R}\frac{v_r}{\alpha},$$

$$a=\frac{L}{R}\frac{v_c}{\alpha}, \qquad b=\frac{2}{\pi}\frac{l}{R'}\frac{v_c}{\alpha},$$

average of τ^2 can be calculated according to the velocity distribution theory[2]. Since the flux of molecules with the velocity components v_r, v_z is given by

$$\frac{4NA_t}{\alpha^2\sqrt{\pi}}v_r v_z e^{-v^2/\alpha^2}dv_r dv_z,$$

one obtains

$$\langle\tau^2\rangle=\frac{\int_0^a\int_\eta^b \frac{\eta}{\xi}e^{-\xi^2}d\xi d\eta+\int_0^a\int_0^\eta \frac{\xi}{\eta}e^{-\xi^2}d\xi d\eta}{\int_0^a\int_0^b \xi\eta e^{-\xi^2}d\xi d\eta}$$

$$=\frac{L^2}{\alpha^2}\frac{y(a,b)}{a^2(1-e^{-b^2})}, \qquad (11)$$

where $y(a,b)$ is the function given by Eq. (6) in the previous paper[4]. The width of the line with a TM_{010} cavity may be expressed as

$$2\Delta\nu_0=0.9\langle\tau^2\rangle^{-1/2}=0.9\frac{\alpha}{L}\sqrt{\frac{a^2(1-e^{-b^2})}{y(a,b)}}. \qquad (12)$$

Numerical values for the experimental conditions mentioned above are $v_c=2.24\times10^3$ cm/s for focuser voltage of 15 kV, $\alpha=5.33\times10^4$ cm/s, $L=12$ cm, $l=40$ cm, $R'=0.53$ cm. Then the factor in Eq. (12) becomes

$$a\sqrt{\frac{1-e^{-b^2}}{y(a,b)}}=0.78$$

and the line-width is calculated as

$$2\Delta\nu_0=3.1\ \text{kc}.$$

From this value the saturation broadened line-width while the maser is oscillating is calculated by Eq. (10) and shown graphically in Fig. 9 as a function of the source flux.

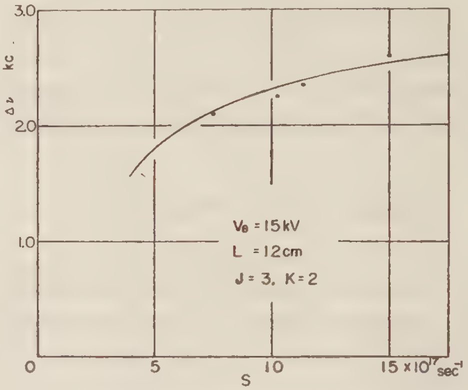

Fig. 9. Saturation broadened line-width vs. source flux. The starting flux for oscillation is 3.9×10^{17} molecules per second with a non-directional source.

The source pressure of 0.9 mmHg corresponds to a source flux of about 7.5×10^{17} molecules per second. Then the observed values in Table I are also plotted in Fig. 9 by assuming that the source flux S is proportional to the source pressure. The agreement between theoretical curve and experimental results seems good.

§ 5. Traveling-Wave Effect under Magnetic Perturbation

On comparing Fig. 7 with Fig. 8, a slight asymmetry of the pulling characteristics between lower and higher frequency sides is found. From a simplified theory one may expect that the frequency of oscillation does not change by magnetic perturbation, if the cavity is exactly tuned on the frequency of the line.

However, careful measurements have shown small variations of the oscillation frequency with magnetic field even when the cavity is tuned on the center of the line. Some of the experimental results near the center of the line are shown in Fig. 10, where the zero of the frequency shift may not be the exact line center and hence only the variation of frequency is important.

Now the frequency shift due to the traveling-wave component is considered for the maser under magnetic perturbation. Decrease of the amplitude of oscillation as shown in Figs. 4 and 5 will change the Doppler effect due to the traveling-wave component in the cavity. By combining Eq. (3) in this paper with Eq. (18) in the previous paper[4)], the shift due to traveling-wave effect can be calculated as a function of applied field intensity.

The value of frequency shift depends on the relative beam intensity and on the average position Z of power dissipation in the cavity which is expressed by a parameter $d=(L-Z)/L$. If the rf electric field is uniform along the length of the cavity, the effective value of Z is given by

$$Z=\frac{Q}{Q_0}\frac{L}{2}+\frac{Q}{Q_1}L_1\,, \qquad (13)$$

where L_1 shows the position of the output coupling measured from the inlet hole of the cavity, Q_1 the Q of the coupling, and Q_0 the unloaded Q of the cavity. Then the parameter d is written by

$$d=\left(1-\frac{Q}{2Q_0}\right)-\left(1-\frac{Q}{Q_0}\right)\frac{L_1}{L}\,, \qquad (14)$$

and is shown in Fig. 11.

The effective value of d for an actual cavity depends on the distribution of electric field caused by the slight change in diameter along the length and by the inlet and outlet holes for the beam. Besides, the effect of beam divergence must be taken into consideration. Therefore, theoretical calculation of the accurate value of d is difficult.

Now using a semi-empirical value of d, the traveling-wave effect given by Eq. (18) in the previous paper[4)] is

$$\frac{\omega'-\omega_0}{\omega_0}=\frac{\pi}{2Q}\frac{v}{c}\frac{L}{\lambda}[4-f_2(\theta)]\left[\frac{1}{f_2(\theta)}-d\right]. \qquad (15)$$

Variations of the amplitude of oscillation near the center of the line due to slight detuning of the cavity are negligible. Then the amplitude of oscillation in a magnetic field is given by Eq. (3). On substituting the approximation of Eq. (8), the traveling-wave effect is written as

$$\nu'-\nu_0=A\left(4-\frac{3}{\rho}\sqrt{\frac{1+u^2}{1+Cu^2}}\right)\times\left(\frac{\rho}{3}\sqrt{\frac{1+Cu^2}{1+u^2}}-d\right), \qquad (16)$$

where A is a constant given by

$$A=\frac{\pi}{2Q}\frac{vL}{\lambda^2}\,.$$

Because the additional frequency shift $\nu-\nu'$ due to cavity pulling is expressed by Eq. (9), the resultant frequency shift can be written as

$$\nu-\nu_0=A\left(4-\frac{3}{\rho}\sqrt{\frac{1+u^2}{1+Cu^2}}\right)\left(\frac{\rho}{3}\sqrt{\frac{1+Cu^2}{1+u^2}}-d\right)+\frac{B}{\rho}\sqrt{\frac{1+Cu^2}{1+u^2}}\cdot\frac{(1+u^2)^2}{1+(3C-1)u^2+Cu^4}\,, \qquad (17)$$

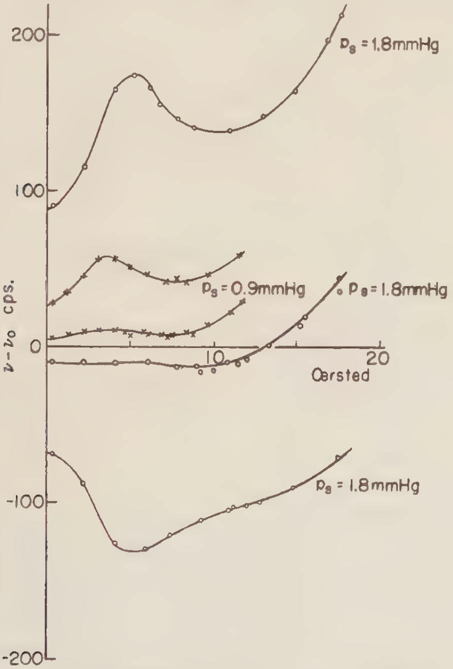

Fig. 10. Oscillation frequency vs. magnetic field near the center of the line.

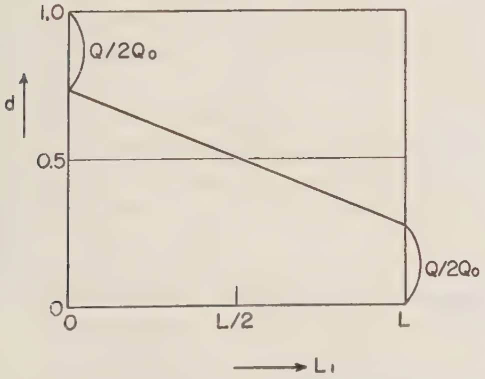

Fig. 11. Traveling-wave parameter $d=(L-Z)/L$ as a function of the position of the output waveguide L_1.

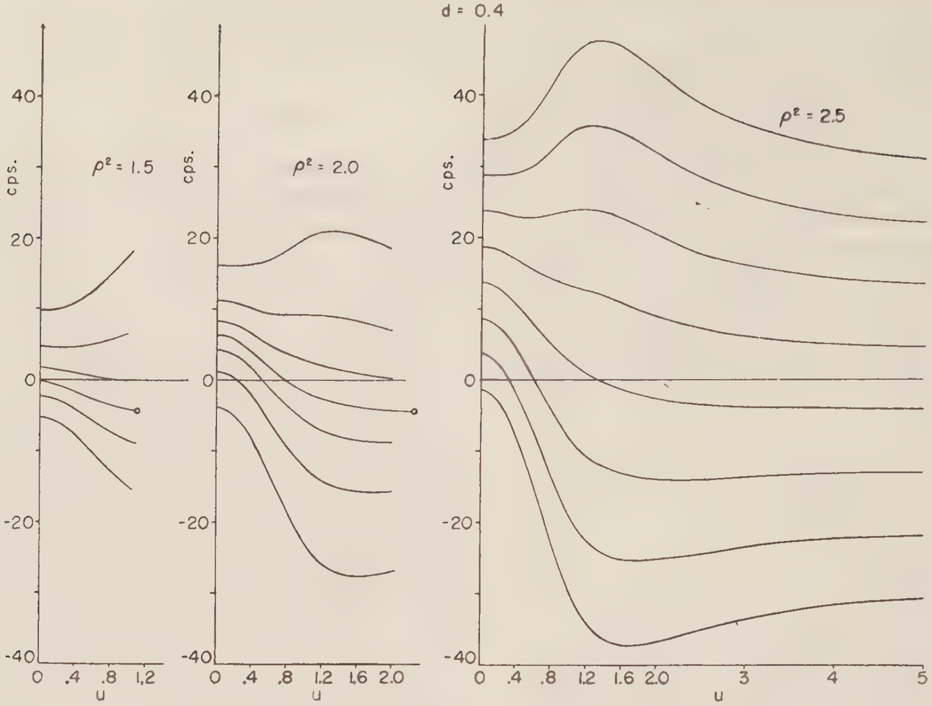

Fig. 12. Frequency shift for $d=0.4$ vs. magnetic field.

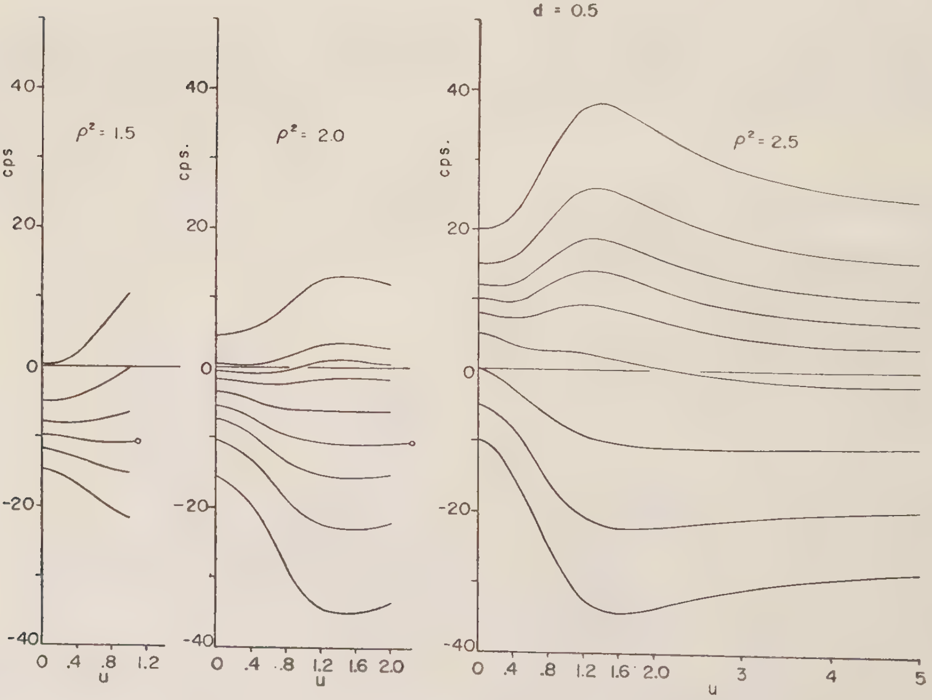

Fig. 13. Frequency shift for $d=0.5$ vs. magnetic field.

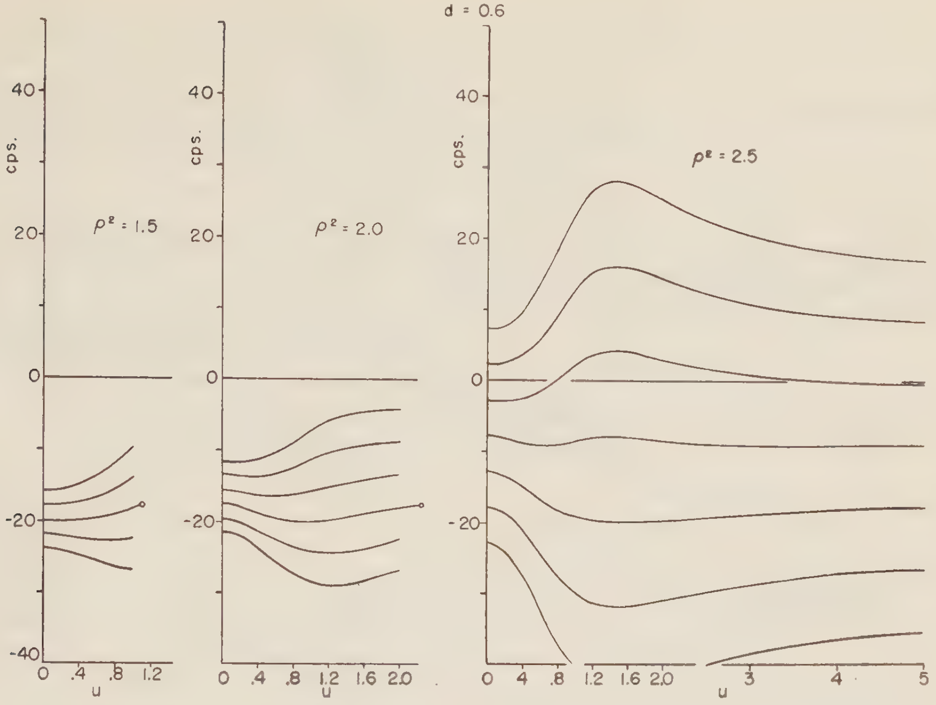

Fig. 14. Frequency shift for $d=0.6$ vs. magnetic field.

where B is a parameter which is proportional to the detuning of the cavity.

$$B=\frac{Q}{Q_l}(\nu_c-\nu_0)=2Q\Delta\nu\frac{\nu_c-\nu_0}{\nu_0}$$

From the values of experimental apparatus, $Q=8000$, $L=12\,\text{cm}$, $\lambda=1.3\,\text{cm}$, and $v=\alpha\sqrt{\pi}/2 =4.73\times10^4\,\text{cm/s}$ which is the average of v_z in the beam, the constant becomes $A=66\,\text{cps}$. Computed values of the frequency shift from Eq. (17) are shown against the applied magnetic field in Figs. 12, 13 and 14 for $d=0.4$, 0.5, and 0.6 respectively. These results show that the agreement with experimental results of Figs. 7, 8, and 10 is good in a weaker field for which u is smaller than about 3. A more detailed comparison near the center of the line is shown in Fig. 1 of the following paper, where discrepancies between theoretical and experimental curves in a higher field will be discussed.

§ 6. Definitions of Line Center by Magnetic Perturbation

As shown above, the frequency of the 3, 2 line maser oscillation varies in a complicated way with the applied magnetic field, when the beam intensity is large. Therefore, it is not easy to determine an exact and unique center of the line, especially when the beam is intense. Three kinds of definitions of line center by magnetic perturbation methods are described and compared in the following.

(1) *Infinitesimal magnetic perturbation*

The theoretically simplest and unanimous definition of the line center is given by the frequency at zero magnetic field when $\partial\nu/\partial H^2=0$. This may be called the line center by infinitesimal perturbation. After differenciation of Eq. (17) with respect to u^2, the condition of cavity tuning to give the line center is expressed by

$$B=\frac{A}{15}(4\rho^2-9d). \qquad (18)$$

Then the line center (at $u=0$) is obtained as

$$\nu-\nu_0=A\left(\frac{8}{5}\rho+\frac{12d}{5\rho}-1-4d\right). \qquad (19)$$

Calculated values of the frequency of the line center for $A=66\,\text{cps}$ are shown in Fig. 15. Although the infinitesimal perturbation is simple for a theoretical treatment, the practical magnitude of magnetic perturbation must be finite.

(2) *Maximum perturbation*

If the beam intensity is not very large,

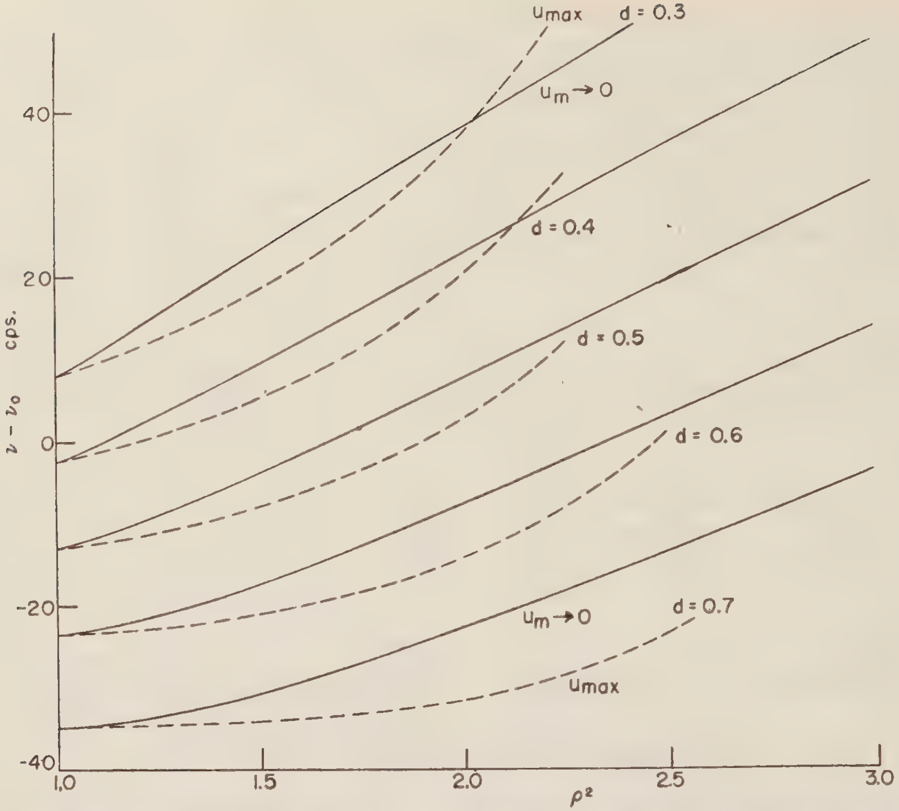

Fig. 15. The line center by magnetic perturbation plotted against the effective beam intensity ρ^2. Solid lines for infinitesimal perturbation and broken lines for maximum perturbation.

the oscillation of the maser is quenched at a magnetic field which is given by taking $\theta=0$ in Eq. (3).

$$\frac{1+Cu_{\max}^2}{1+u_{\max}^2}=\frac{1}{\rho^2} \tag{20}$$

The condition that the frequency of oscillation just before it is quenched is equal to the zero-field frequency, determines a line center by maximum perturbation.

The maximum perturbing field is obtained from (20) by

$$u_{\max}^2=\frac{\rho^2-1}{1-C\rho^2},$$

where $C=0.389$ for the 3, 2 line of $N^{14}H_3$. The frequencies of oscillation given by Eq. (17) for $u=0$ and for $u=u_{\max}$ become equal, when the cavity is so tuned that

$$\frac{3B}{A}=\frac{(4\rho-9d)\{2-(3C+1)\rho^2+2C\rho^4\}}{2+2\rho-(3C-1)\rho^2-2C\rho^3}. \tag{21}$$

Then the frequency of the line center by maximum perturbation is obtained by putting Eq. (21) and $u=0$ into Eq. (17) as

$$\nu-\nu_0=\frac{A}{3}\left\{\frac{(1-C)\rho^2(4\rho-9d)}{2+2\rho-(3C-1)\rho^2-2C\rho^3}+1-3d\right\}. \tag{22}$$

Calculated values for $A=66$ cps, $C=0.389$ are shown in Fig.15 by broken lines. These calculations cannot be applied when ρ^2 is large, because the observed frequency shift differs considerably from the theoretical values when the magnetic field is strong.

(3) *Perturbation of constant amplitude*

The most practical method of perturbation is to intermittently apply a magnetic field of a constant intensity. The relative Zeeman splitting changes from $u=0$ to $u=u_m$. When the cavity is tuned so that the frequency of oscillation does not change between $u=0$ and $u=u_m$, the condition for line center may be expressed by

$$\frac{A}{3}\left(4\rho^2-\frac{9d}{k}\right)(1-k)=B\left\{\frac{k(1+u_m{}^2)^2}{1+(3C+1)u_m{}^2+Cu_m{}^4}-1\right\}, \tag{23}$$

where

$$k=\sqrt{\frac{1+Cu_m^2}{1+u_m^2}} \qquad \text{or} \qquad u_m^2=\frac{1-k^2}{k^2-C}\,. \tag{24}$$

Then the frequency of oscillation determined by the square-wave magnetic perturbation between $u=0$ and u_m, is written after some manipulations as

$$\nu-\nu_0=A\left[\frac{1+k}{2+3k+ku_m^2}\left\{\frac{4}{3}k\rho(3+u_m^2)+\frac{6d}{k\rho}\right\}-1-4d\right]. \tag{25}$$

Typical examples for $u_m^2=1$ and 0.5 are shown in Fig. 16. The modulation amplitude for $u_m=1$ is 2.8 oersteds when $\Delta\nu=2.1$ kc at a source pressure of 0.9 mmHg which is the typical operating condition. It may by noted that when $u\to 0$ and $k\to 1+\frac{1}{2}(C-1)u^2$, Eq. (25) gives the line center by infinitesimal perturbation.

The sensitivity of magnetic perturbation can be expressed by

$$S=\frac{\delta(\nu_m-\nu_0)}{\delta(\nu-\nu_0)}=\frac{(1+u_m^2)^{3/2}(1+Cu_m^2)^{1/2}}{1+(3C-1)u_m^2+Cu_m^4}-1\,,$$

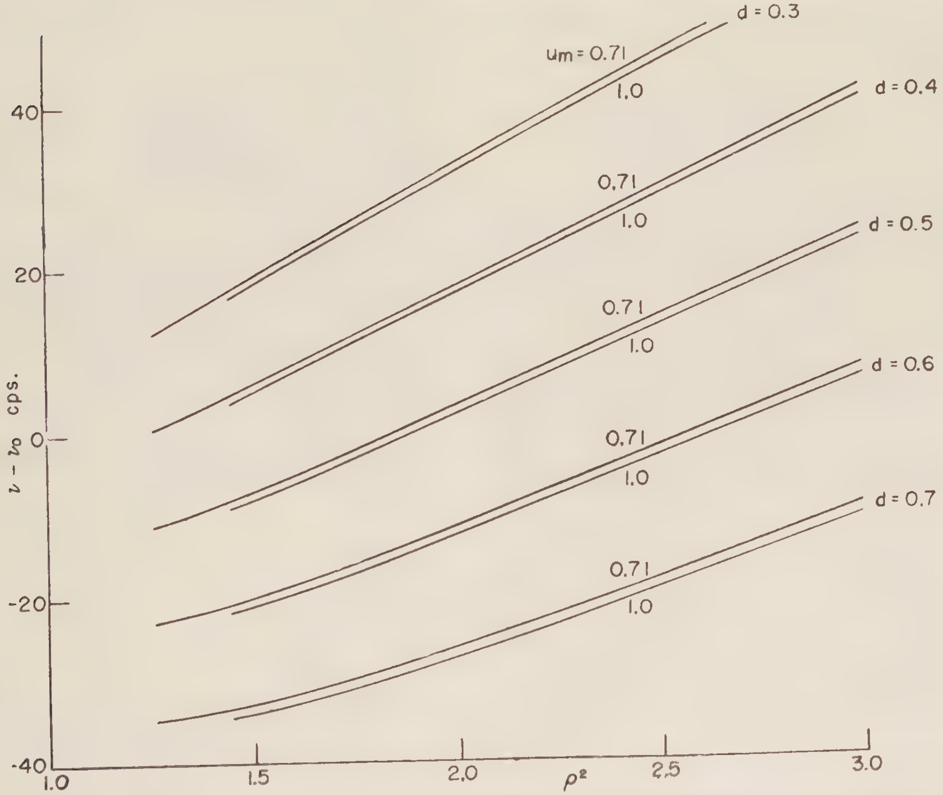

Fig. 16. The line center by square-wave magnetic perturbation between $u=0$ and u_m, poltted against the effective beam intensity.

where ν and ν_m are the frequencies of oscillation without and with a magnetic field respectively. The function $S+1$ was graphically shown in Fig. 6. For $u_m=1$ and 0.707 the sensitivity is 1.14 and 0.69 respectively.

§ 7. Conclusion

When the frequency change of about 0.5 cps due to the perturbing magnetic field of 2.8 oersteds is detected so that the cavity can be tuned in, the frequency of oscillation becomes accurate to within $\pm 2\times 10^{-11}$. Decrease of the perturbing field from 2.8 to 2.0 oersteds produces a frequency shift of only 1 cps, hence the fluctuation of the amplitude of magnetic field by 10 percent gives an error of less than $\pm 1\times 10^{-11}$.

Variation of the magnetic perturbation line

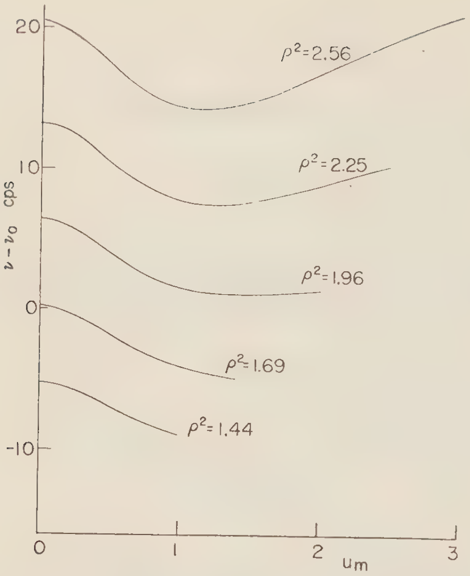

Fig. 17. Variation of the line center against the amplitude of perturbing field when $d=0.5$.

center with the amplitude of perturbing field is shown in Fig. 17 for the case of $d=0.5$. This curve indicates that a larger amplitude of per turbing field (about 4 oersteds) gives better performance. But it requires stronger beam intensity which accompanies some unfavorable factors such as larger frequency dependence on the focuser voltage[4] and the deterioration of vacuum. Thus the recommended magnitude of perturbing field is 2.0∼2.8 oersteds for the 3, 2 line maser with a cavity of 12 cm length.

The pressure of ammonia due to scattered molecules in the cavity increases the frequency of oscillation. Although this type of frequency shift will be discussed in the paper which will describe the details and performances of an ammonia frequency standard, one may here conclude that, if the maser is operated in a good vacuum, an accuracy of a few parts in 10^{11} can be achieved by the magnetic perturbation on the 3, 2 line maser oscillator.

Acknowledgment

The author expresses his sincere thanks to Mr. N. Kohno for his assistance in the experiments.

References

1) K. Shimoda, T. C. Wang and C. H. Townes: Phys. Rev. **102** (1956) 1308.
2) K. Shimoda: J. Phys. Soc. Japan **12** (1957) 1006.
3) K. Shimoda: ibid. **13** (1958) 939.
4) K. Shimoda: ibid. **16** (1961) 1728.
5) K. Shimoda and K. Kondo: ibid. **15** (1960) 1125.
6) H. Takuma, T. Shimizu and K. Shimoda: ibid. **14** (1959) 1595.
7) K. Shimoda, H. Takuma and T. Shimizu: ibid. **15** (1960) 2036.
8) H. G. Venkates and M. W. P. Strandberg: J. Appl. Phys. **31** (1960) 396.

JOURNAL OF THE PHYSICAL SOCIETY OF JAPAN Vol. 16, No. 11, NOVEMBER, 1961

Dependence of Magnetic Coupling Constant of Ammonia on the Inversion State

By Koichi SHIMODA

Department of Physics, Faculty of Science, University of Tokyo, Tokyo.

Observed increase of the frequency of an ammonia maser with magnetic field on the $J=3$, $K=2$ line which was determined by a magnetic perturbation method is explained by assuming a small difference between magnetic coupling constants of upper and lower inversion states. Theoretical analysis developed by neglecting the magnetic moment of nitrogen nucleus is given. The magnetic coupling constant in the upper inversion state is found to be smaller by 0.5±0.2 percent. This seems to be a reasonable magnitude, when the dependences of interatomic distances and of the rotational magnetic moment on the inversion state are considered.

§ 1. Introduction

The frequency of an ammonia beam maser on the $J=3$, $K=2$ line can be determined within 1 cps at the oscillation frequency of 22834.185 Mc. The frequency of oscillation varies with the dc magnetic field which is applied in a perpendicular direction to the rf electric field along the cavity axis. The observed variation of frequencies in a weaker field agrees with the theoretical result which has been described in the preceding paper.$^{1)}$ However, in the magnetic field of stronger than 8 oersteds somewhat large increase of the oscillation frequency with magnetic field was found. Theoretical and experimental frequency shifts near the center of the line are compared in Fig. 1.

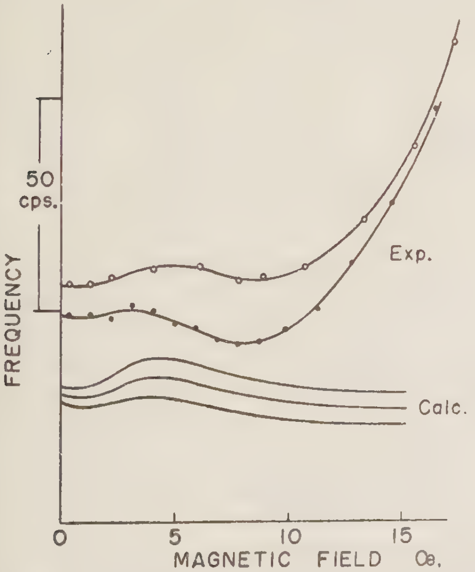

Fig. 1. Observed frequency shifts vs. magnetic field, when the cavity is tuned to near the center of the line. Lower curves are the calculated shifts due to traveling wave and pulling effects.

The increase of frequency in a stronger field may be due to the second order Zeeman effect. The usual diamagnetic second order Zeeman effect is expressed by$^{2)}$

$$\Delta W_2 \approx \frac{H^2e^2}{8mc^2}\sum\overline{x^2+y^2}\,.$$

This gives a much smaller shift of about 1 cps at a magnetic field of 20 oersteds and hence negligible.

The observed hyperfine structure of the 3, 2 line of ammonia has a strong main line at the center and two pairs of magnetic hyperfine satellites.$^{3)}$ Since Zeeman components of the inner satellites do not merge in the Zeeman components of the main line in a weaker field, only the main line and the outer satellites will be taken into consideration in discussing the frequency of the maser oscillator.

§ 2. Description of Energy Levels for the $J=3$, $K=2$ State

Because of lack of quadrupole coupling for the $J=3$, $K=2$ state, the conventional coupling scheme which is described by $\boldsymbol{F}_1=\boldsymbol{J}+\boldsymbol{I}_N$ and $\boldsymbol{F}=\boldsymbol{F}_1+\boldsymbol{I}_H$ is not appropriate in this case. Since the magnetic moment of a proton is much larger than that of the nitrogen nucleus, the strongest magnetic coupling is the one between the rotational magnetic moment of the molecule and the nuclear magnetic moment of three protons. Therefore, a better coupling scheme is made up by

$$F_2=J+I_H\ , \quad \text{and} \quad F=F_2+I_N\ ,$$

where I_H is the resultant spin of three protons and I_N the spin of nitrogen nucleus. When this coupling scheme is used, contributions of off-diagonal matrix elements become very small in calculating the energy levels of the magnetic hyperfine structure. Thus the angular momentum F_2 is considered to be a pretty good quantum number and the energy levels are given by diagonal elements of the Hamitonian to a good approximation. The levels are shown in Fig. 2, and agree within ±1 kc with the exact calculation by Hadley.[4]

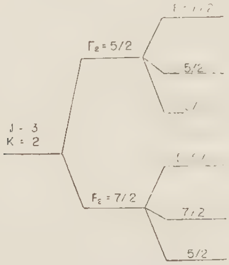

Fig. 2. Hyperfine levels of the $J=3$, $K=2$ state of $N^{14}H_3$.

The outer satellites of the hyperfine structure of the 3, 2 line correspond to the $\Delta F_2=\pm 1$ transitions, while the main line corresponds to the $\Delta F_2=0$ and $\Delta F=0$ transition. Three components in each outer satellite corresponding to three different values of F have not been resolved. The inner satellites correspond to the $\Delta F_2=0$ and $\Delta F=\pm 1$ transitions, and the Zeeman shifts of these lines are small. Therefore, one may neglect the contribution of I_N in discussing the magnetic perturbation of the main line.

Now two pairs of inversion levels, $F_2=5/2$ and $F_2=7/2$ are considered. The magnetic hyperfine energy is given by the expression

$$W(F_2)=\left(A+\frac{CK^2}{J(J+1)}\right)(\boldsymbol{I}\cdot\boldsymbol{J}) \qquad (1)$$

where I_H is abbreviated as I, and

$$(\boldsymbol{I}\cdot\boldsymbol{J})=\{F_2(F_2+1)-I(I+1)-J(J+1)\}/2 \qquad (2)$$

Since $I=1/2$ for $J=3$ and $K=2$, the above expression gives $(\boldsymbol{I}\cdot\boldsymbol{J})=1.5$ for $F_2=7/2$ and -2.0 for $F_2=5/2$.

By using the coupling constants obtained by Gordon,[5] one obtains $W_{5/2}=36$ kc and $W_{7/2}=-27$ kc, the accuracy being about ±1 kc. The separation of $\Delta W=W_{5/2}-W_{7/2}=63$ kc agrees with the observed separation of the outer satellites. The simplified energy levels and the corresponding spectrum is shown in Fig. 3.

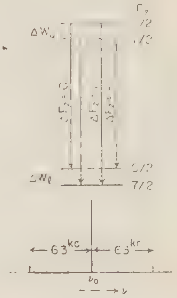

Fig. 3. The simplified energy levels ($I_N=0$) and the corresponding spectrum.

Energies of hyperfine levels $F_2=5/2$ and $7/2$ of the 3, 2 state of ammonia in a magnetic field H can be calculated by the Breit-Rabi formula for atomic hyperfine structure.[6] After a slight modification of notations, it can be written as

$$W=\frac{\Delta W}{2(2J+1)}-g_J\mu_N MH$$
$$\pm\frac{\Delta W}{2}\sqrt{1+\frac{4Mx}{2J+1}+x^2} \qquad (3)$$

where μ_N is the nuclear magneton, M the component of F_2 along the magnetic field, and

$$x=\frac{g_I-g_J}{\Delta W}\mu_N H\ . \qquad (4)$$

From the values for the $J=3$, $K=2$ state of $N^{14}H_3$:

$g_J=-0.535$, $g_I=5.585$, $\Delta W=63$ kc, and

$x=0.0611\,H$,

the energy levels are calculated as shown in Fig. 4. Because the value of the second term is comparable to that of the third term, variation of the energy levels shown in Fig. 3 is somewhat different from that of atoms for which the second term is almost negligible.

§ 3. Spectrum of the 3, 2 Line of $N^{14}H_3$ in a Magnetic Field

The inversion spectrum of the 3, 2 line of $N^{14}H_3$ in a perpendicular magnetic field is made of $\Delta F_2=0$, ±1 and $\Delta M=\pm 1$ transitions. Then the Zeeman components of the main line correspond to the $\Delta F_2=0$ and $\Delta M=\pm 1$ transitions.

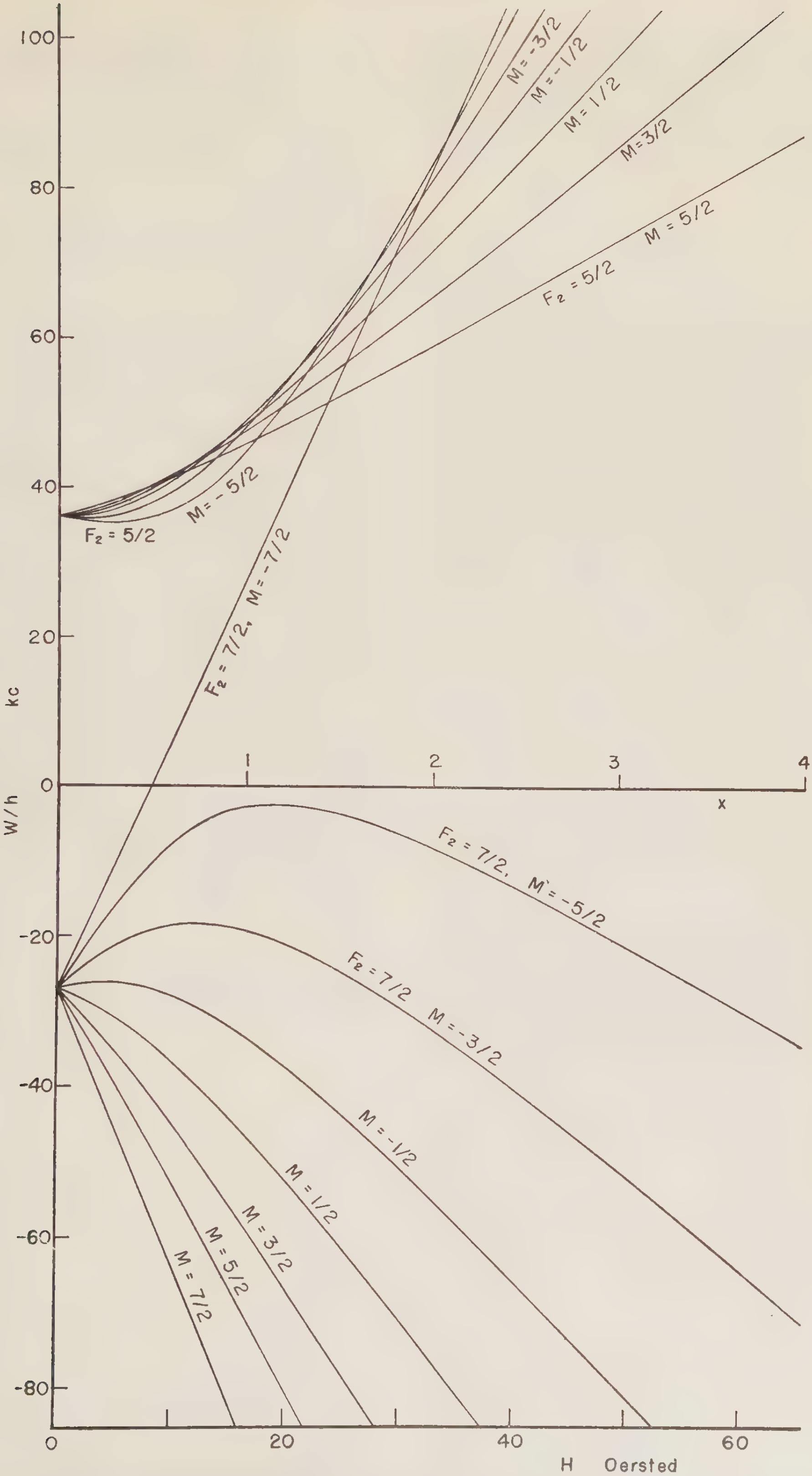

Fig. 4. The magnetic field dependence of the magnetic hyperfine levels of each inversion state of ammonia. $J=3$, $K=2$, and $I_H=1/2$, $I_N=1$.

Since the energy levels for $F_2=5/2$ are closely spaced when $x<1$ or $H<16$ oersteds, Zeeman shifts of $F_2=5/2\rightarrow 5/2$ lines are small. They are observed as a single unshifted line. The transitions $F_2=7/2\rightarrow 7/2$ and $\varDelta M=\pm 1$ are shifted by

$$\varDelta\nu_{\mathrm{H}}=\pm\left\{g_J+\frac{g_I-g_J}{2J+1}\right\}\mu_{\mathrm{N}}H=\pm 0.95\times 10^3 H \quad \text{(cps)}$$

when $x\ll 1$. The splitting in a higher field becomes smaller than that given by the above equation except for a pair of components corresponding to the $M=7/2\rightleftarrows 5/2$ transitions. Thus the Zeeman components of the main line are divided into three groups: the central group is the $F_2=5/2\rightarrow 5/2$ and $M\rightarrow M\pm 1$ transitions; the group in the higher frequency is the $F_2=7/2\rightarrow 7/2$ and $M\rightarrow M+1$ (emission) transition; and the group in the lower frequency is the $F_2=7/2\rightarrow 7/2$ and $M\rightarrow M-1$ transition. Observed Zeeman patterns have been shown in the preceding paper.[1)]

If the magnetic coupling constant and the g-values are equal in the upper and lower inversion states, the Zeeman pattern is exactly symmetric with respect to the center of the line which does not move. However, if their values in the upper and in the lower inversion states are different, the frequency of the central line varies slightly with the magnetic field. The magnetic coupling constant and hence the splitting $\varDelta W$ are considered to be proportional to $\mu_{\mathrm{mol}}\mu_{\mathrm{H}}\langle 1/r^3\rangle$, where r is the distance of a charge from the proton and $\mu_{\mathrm{H}}=\frac{1}{2}g_I\mu_{\mathrm{N}}$ is the proton magnetic moment. Variations of the average distance may be considered by the inter-nuclear distance d_{NH}, because the distance between an electron and the proton varies approximately in proportion to d_{NH}. The inter-nuclear distance will be larger in the upper state, and the splitting should be smaller for the vibrationally excited state. The molecular g-factor given by $\vec{\mu}_{\mathrm{mol}}=g_J\mu_{\mathrm{N}}\boldsymbol{J}$ does not vary so much with the vibrational state.

For simplicity of discussion, g_J may be assumed to be equal in the upper and lower states, while the splitting is $\varDelta W_u$ in the upper state and $\varDelta W_l$ in the lower state. Then the average frequency of $F_2=5/2$ and $\varDelta M=\pm 1$ transitions in a weak field is obtained from Eq. (3) in the form

$$\nu-\nu_0=(\varDelta W_l-\varDelta W_u)\left(\frac{1}{4}-\frac{\langle M^2\rangle}{49}\right)\frac{x^2}{h}$$
$$=0.22(\varDelta W_l-\varDelta W_u)x^2 \qquad (5)$$

where $\langle M^2\rangle$ is an average of M^2 with weight of the relative intensities of the corresponding transitions.

When the dependence of g_J on the inversion state is taken into calculation, Eq. (5) is replaced by

$$\nu-\nu_0=-\left(\frac{\delta\varDelta W}{\varDelta W}+\frac{\delta g_J}{g_I-g_J}\right)\left(\frac{1}{4}-\frac{\langle M^2\rangle}{49}\right)\frac{\varDelta W}{h}x^2$$
$$\doteqdot-\left(\frac{\delta\varDelta W}{\varDelta W}+0.106\frac{\delta g_J}{g_J}\right)\times 52H^2 \qquad (6)$$

where H is in oersted and $\nu-\nu_0$ in cycles per second. When $\delta\varDelta W=\varDelta W_u-\varDelta W_l$ is negative, Eq. (6) gives the frequency increase of the central group of the Zeeman component, while the average frequency shift of two groups corresponding to the $F_2=7/2$ and $\varDelta M=\pm 1$ transitions is negative and its absolute value is equal to Eq. (6).

These three components overlap in a weaker field. The frequency of the maser is given by the susceptibility of the molecule as $\chi'=0$, if the traveling wave effect and the cavity pulling are missing. On the assumption of Lorentzian line-shapes for the three groups of Zeeman components one obtains from Eq. (4) of the preceding paper[1)]

$$\frac{\chi'}{\chi_0}=C\frac{\nu-\nu_0-KH^2}{\varDelta\nu}$$
$$+\frac{1-u^2}{\varDelta\nu(1+u^2)^2}\left\{(1-C)(\nu-\nu_0)+CKH^2\right\}, \qquad (7)$$

where KH^2 represents the shift given by Eq.

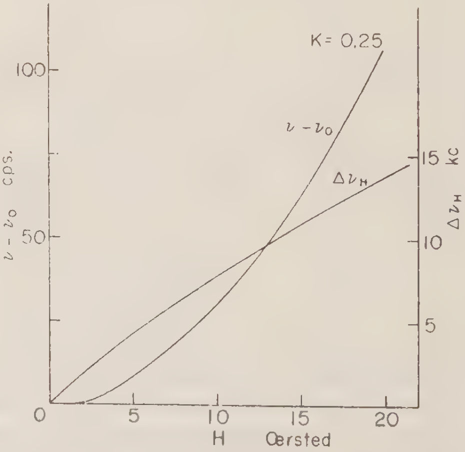

Fig. 5. Calculated frequency shift $\nu-\nu_0$ and the observed Zeeman splitting $\varDelta\nu_H$.

(6), $\Delta\nu_H = u\Delta\nu$ is the splitting of groups, and C the relative intensity of the central group. Then the frequency of oscillation ν to make $\chi' = 0$ is calculated from Eq. (7) as

$$\nu - \nu_0 = KH^2 \frac{Cu^2(3+u^2)}{1+(3C-1)u^2+Cu^4} . \qquad (8)$$

Computed values of $\nu - \nu_0$ for $C = 0.389$, $\Delta\nu =$ 2.5 kc, and $K = 0.25$ is shown in Fig. 5, where the observed variation of $\Delta\nu_H$ with the magnetic field is also shown.

§ 4. Comparison with Experimental Results

Observed variation of the oscillation frequency of the 3, 2 line maser in a weak field is complicated because of superposition of the traveling wave effect and the pulling effect of the cavity. In a somewhat stronger field of near 20 oersteds the central line is broadened and weakened by the spread of unresolved Zeeman components. Therefore, exact comparison between the theory and experiment is not easy, but the observed increase of the frequency of the maser in a higher field as shown in Fig. 1 can be explained by the dependence of the magnetic coupling constant on the inversion state.

By comparing frequency shifts in Fig. 1 with those in Fig. 5 in the region between about 8 and 16 oersteds an estimate is obtained as $K = 0.25 \pm 0.08$. This gives that

$$\frac{\delta \Delta W}{\Delta W} + 0.106 \frac{\delta g_J}{g_J} = -(0.48 \pm 0.15) \times 10^{-2} . \qquad (9)$$

Dependence of g_J on the inversion state is considered to be smaller than that of ΔW so that one may take

$$0.106 \frac{\delta g_J}{g_J} \ll \frac{\delta \Delta W}{\Delta W} .$$

Then the difference of the splitting or $A + CK^2/J(J+1)$ in the upper and lower inversion states is

$$\frac{\delta \Delta W}{\Delta W} = -(0.5 \pm 0.2) \times 10^{-2} . \qquad (10)$$

This decrease of the magnetic coupling constant by 0.5% in the upper state seems to be a reasonable magnitude because it corresponds to the increase of molecular size by 0.1% in the upper inversion state, or the increase of NH distance by 0.001Å.

Eq. (10) leads to $\delta\{A + CK^2/J(J+1)\} = \delta(A + C/3) = 90 \pm 35$ cps. If I_N is taken into consideration, the magnetic hyperfine structure must be slightly asymmetric with respect to the main line which is composed of closely spaced doublets. However, these effects are too small to be observed by the present spectrometer.

Acknowledgment

The author is grateful for helpful discussions with Mr. K. Kondo.

References

1) K. Shimoda: J. Phys. Soc. Japan, **16** (1961).
2) J. H. Van Vleck: "The Theory of Electric and Magnetic Susceptibilities" (1932) p. 178.
3) K. Shimoda and K. Kondo: J. Phys. Soc. Japan, **15** (1960) 1125.
4) G. F. Hadley: Phys. Rev. **108** (1958) 291.
5) J. P. Gordon: Phys. Rev. **99** (1955) 1253.
6) G. Breit and I. I. Rabi: Phys. Rev. **38** (1931) 2082; S. Millman, I. I. Rabi and J. R. Zacharias: Phys. Rev. **53** (1938) 384.

JOURNAL OF THE PHYSICAL SOCIETY OF JAPAN, Vol. 16, No. 11, NOVEMBER, 1961

Single and Double Ionization of Na, K and Mg by Electron Impact

By Yozaburo KANEKO

Department of Physics, Faculty of Science, Tokyo Metropolitan University, Setagaya, Tokyo

(Received August 1, 1961)

The ionization efficiency curves for Na^+, Na^{++}, K^+, K^{++}, Mg^+ and Mg^{++} are studied with essentially monoenergetic electrons.

It is proved that Na^+, K^+ and Mg^+ follow the linear law up to 1.5 eV, 0.8 eV and 2 eV above the thresholds, respectively, and that Na^{++} and K^{++} follow the square law up to about 20 eV and 15 eV above the thresholds, respectively. These results agree with the theoretical prediction that n-fold multiple ionization would be proportional to a n-th power of excess electron energy.

Two remarkable humps are found in the I. E. curve for Mg^+, which are attributed to autoionization processes. These processes occur at 2.3 ± 0.1 eV and 5.0 ± 0.2 eV above the ionizotion potential, the first one may correspond to the excited states of Mg atom, $^1F^\circ$ and $^3D^\circ$, but any excited states to be correlated to the second one is not known.

Contrary to expectation, the I. E. curve for Mg^{++} is not a square curve of excess energy but has a complex shape. In order to explain the shape, possibility of autoionization due to excitation of inner shell electron is suggested.

§ 1. Introduction

Some experimental studies on the probability of ionization by electron impact near threshold for atoms or molecules have been made recently.

Hickam, Fox, and Kjeldaas[1] found that the formation of He^+ is proportional to the first power of the excess energy of impact electron. The result did not agree with Wannier's theory[2] in which he predicted that the probability of single ionization would be proportional to 1.127 power of excess electron energy, but agreed with Geltman's theory[3] in which he predicted a linear law for single ionization.

Further, Fox[4] found that the formation of He^{++} is proportional to the second power of excess energy. This agreed with Wannier's[5] and Geltman's[3] theories. They derived independently the relation between the probability of n-fold multiple ionization and excess energy as

$$P(X^{n+})=K(E-Ec)^n \, . \qquad (1)$$

Here, $n=1, 2, \cdots$, E is electron energy, Ec is ionization potential of X, and K is a constant.

In his measurement on multiple ionization of Xe, from Xe^+ to Xe^{7+}, however, Fox found that the multiple ionizations of the atom do not follow the power law mentioned above, but are linear to the excess energy, for all ions[4]. He explained the fact that the multiple ionizations of Xe do not follow the power law by the occurrence of Auger transition due to ionization of an inner shell electron. On the other hand, Morrison et al[6],[7] and Krauss, Reese and Dibeler[8], through the experiment on rare gases, obtained the results which do not agree with Fox's results but follow the power law. The conclusion for this problem has never been obtained[9],[10]. Dibeler and Reese[11] reported that the power law is applicable to Na^+, Na^{++} and Na^{+++}. Blais and Mann[12] reported that Au^{++} is linear to electron energy.

It is very powerful for this kind of studies to use monoenergetic electrons. The author reported previously the study on ionization efficiency curves for A^+, Kr^+, N_2^+ and CO^+ by the use of monoenergitic electrons[13]. It is concluded from the study that the ionization efficiency curves (I. E. curves) for single ionization is linear to excess energy, and that occurrence of ionization to an excited level of ionic state appears as a " break " of the I. E. cvrve, and occurrence of autoionization appears as a "hump" in the I. E. curve.

The study on Na^+, Na^{++}, K^+, K^{++}, Mg^+ and Mg^{++} by the use of monoenergetic electrons is reported in this paper. These ions seem to be adequate for study on threshold law, because energy separation between ground state and excited level is so large for these ions that the ionization to the excited level is not necessary to be considered.

There are studies on Na by Tate and Smith[14], and Dibeler and Reese[11], and on K by Tate and Smith[14]. These experiments, however, were made not by monoenergetic electrons but by electrons with wide energy width. The experiments on metal atoms by the use of monoenergetic electrons have been made for Hg[15], and Cd, Zn and Hg[16], and Cu, Ag, and Au[12]. All of the I. E. curves of these metal atoms have complex shapes which cannot be found in I. E. curves of rare gas atoms. Therefore, it can be expected to find unknowns tructures in the I. E. curves of Na, K, and Mg by the use of monoenergetic electrons.

§ 2. Apparatus and Experimental Procedure

The mass spectrometer used in this study is of 60° type and its radius is 20 cm. The R. P. D. method (Retarding Potential Difference method) was used for ion source as in the previous study[13], therefore, ionization could be effected by essentially monoenergetic electron beam. A secondary electron multiplier was used for the ion current detector.

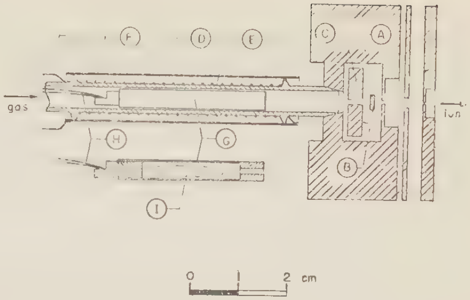

Fig. 1. Details of ion source and furnace.

A: ionization chamber.
B: cross section of electron beam.
C: ion repelling electrodes.
D: stainless steel radiation shield.
E: qualtz tube.
F: tungsten heater—0.2 mmϕ, 2 mm pitch.
G: stainless steel crucible.
H: alumel-chromel junction.
I: sample.

In order to vaporize metalic samples a furnace was mounted near the entrance of the ionization chamber. The details of the furnace are shown in Fig. 1. The furnace consists of a qualtz tube wound with tungsten wire and a stainless steel radiation shield. A stainless steel crucible is set into the qualtz tube at a fixed position, the size of the crucible being so close to the qualtz tube that the atomic beam may be always effused into the center of the ionization chamber. An alumel-chromel junction is spot welded to the top of the crucible. Temperature of the crucible can be raised to any desired points up to 1,000°C in twenty minutes after it is begun to heat. Though temperature of the junction seemed to be a little lower than that of the center of the crucible, fluctuation of the temperature of the junction was less than ±2°C/hr at 560°C. For example, in case of Mg, fluctuation of peak height (i.e. ion current) was ±2%/hr. The temperature of the crucible was kept at 248°C for Na and K, and at 560°C for Mg. For example, 90 mgs of Mg metal is sufficient for 70 hours of operation. Peak height does not decrease with decrease of the amount of the sample through the measurement. The peak height is changed only by temperature of the crucible, and begins to decrease suddenly when the sample is consumed completely. In order to test the characteristics of the mass spectrometer, gas samples can be introduced simultaneously. As the existence of the crucible hinders the gas flow, however, the sensitivity for gas samples decreases relatively. Metal atoms effused from the crucible condense upon the wall of the ion source, especially upon the ion repelling electrodes. Once the source is exposed to a low vacuum, it becomes a serious obstruction by oxidation of surface, though it is not so troublesome in high vacuum. Therefore, when the sample is changed, the ion source must be dismantled and refreshed.

It is important to keep the "effective" number of ionizing electrons constant when electron accelerating voltage is varied. As ions detected at the collector of mass spectrometer seem to be made at a very small part in the ionization chamber, electrons only which pass through this part could be "effective". As previously reported[13),17)], it is very difficult to examine experimentally the "effective" number of electrons being kept constant. Therefore, the I. E. curve obtained over a wide energy range may have possibility including some errors. Even for the experiment in a short energy range, it is necessary to measure the I. E. curve of the sample gas and referring gas simultaneously, for more precise study. The first ionization potentials of metal atoms, however, are so low that adequate referring gas samples cannot be found.

In this study mixed sample of Na and K metals was used and measured alternately in order to compare the I. E. curve of each metal. Though, for Mg^{++} ion, Ne^+ ion was used as a referring ion, Mg^+ had to be measured independently.

The metal samples used in this experiment are purest in commercial grade, and were not refined especially.

§ 3. Experimental Results

The I. E. curves measured for Na^+, Na^{++}, K^+, K^{++}, Mg^+ and Mg^{++} are shown in Fig. 2-4. Dotted curves in Fig. 2 and 3 are the I. E. curves obtained by Tate and Smith[14)]. As described in section 2, these I. E. curves measured over a wide energy range may include some errors. In this experiment, however, as the mixed sample of Na and K is used, and the I. E. curves are measured alternately, the relative difference between them could be believed. The results obtained in this experiment agree qualitatively with

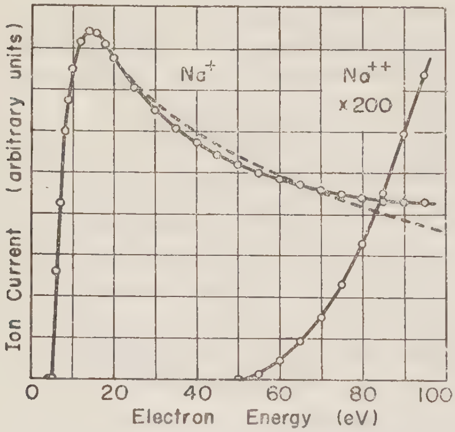

Fig. 2. I. E. curves for Na^+ and Na^{++}. Dotted line is Na^+ curve measured by Tate and Smith.

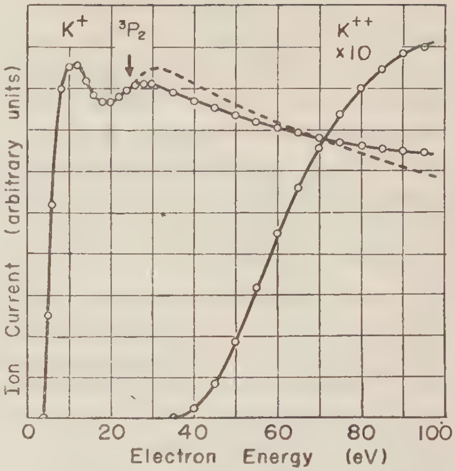

Fig. 3. I. E. curves for K^+ and K^{++}. Dotted line is K^+ curve measured by Tate and Smith.

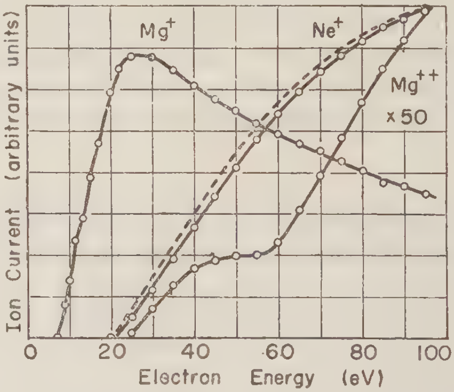

Fig. 4. I. E. curves for Mg^+, Mg^{++} and Ne^+. Dotted line is Ne^+ curve measured by Bleakney.

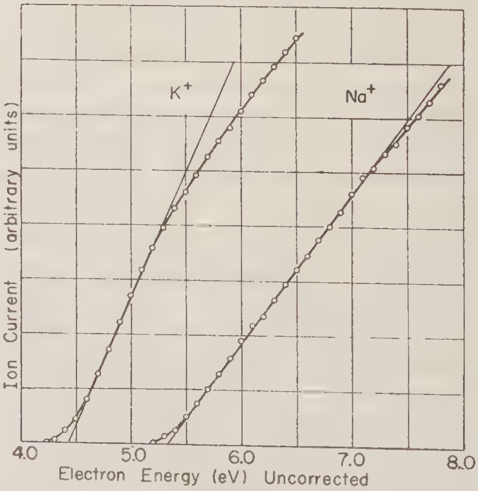

Fig. 5. I. E. curves for Na^+ and K^+ near the thresholds.

that of Tate and Smith as seen in Figs. 2 and 3. I. E. curve for Ne^+, measured as referring ion for Mg^{++}, is shown in Fig. 4. Dotted curve is Ne^+ curve obtained by Bleakney[18] and the curves agree well with each other. The I. E. curve for Mg^{++} obviously differs from that for Ne^+.

The sensitivity factors for double ionization in Figs. 2–4 are not corrected with ion-electron conversion efficiency of the secondary electron multiplier. The pulsing method and retarding method only were used in these measurements, instead of the R. P. D. method, because electron energy width did not affect the I. E. curves so much for wide energy range. The I. E. curves for each ion near the thresholds are shown in Figs. 5–8. These curves were measured by the R. P. D. method with ΔV_R (i.e. energy width of ionizing electron) being 0.2 V.

§ 4. Discussion

Na^+ and K^+

The first excited state of Na^+, $^3P^\circ_2$, lies 32.85 eV* above the ground state of the ion, $^1S_0$, and there are no levels between these states. The I. E. curve for Na^+ is linear over a range of 1.5 eV, and deviates from the straight line above the range. Therefore, the result obtained indicates that the ionization follows the linear law for Na^+ up to 1.5 eV above the threshold.

The first excited state of K^+, $^3P^\circ_2$, lies 20.15 eV above the ground state of the ion, $^1S_0$, and there are no levels between these states.

The I. E. curve for K^+ is linear over a range of 0.8 eV, and deviates from the straight line above the range. Therefore, the result obtained indicates that the ionization follows the linear law for K^+ up to 0.8 eV above the threshold.

The position of $^3P^\circ$ state is indicated by an arrow in Fig. 3, but it is difficult to explain the occurrence of the second maximum only by the existence of this state. The energy difference between the initial onsets of Na^+ and K^+ is measured as 0.75±0.05 eV which agree with spectroscopic value of 0.799 eV.

Na^{++} and K^{++}

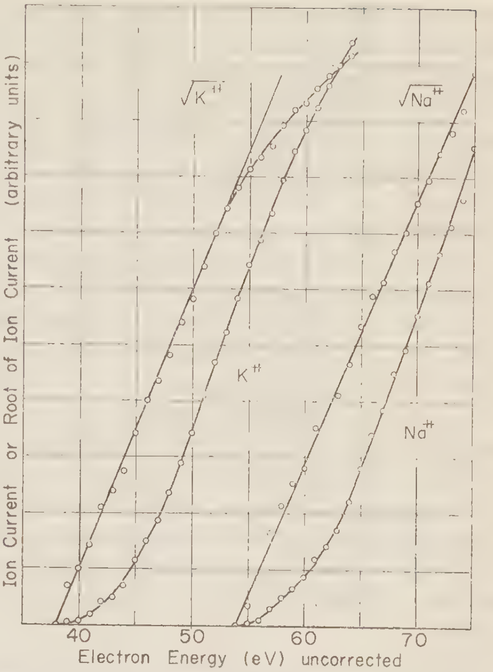

Fig. 6. I. E. curves and their square root plots for Na^{++} and K^{++}.

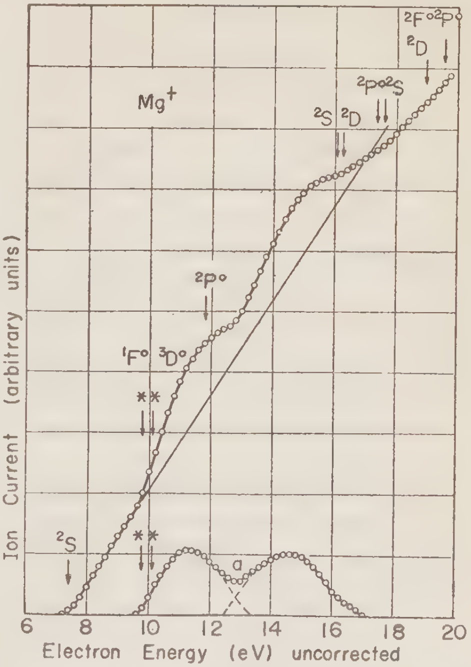

Fig. 7. I. E. curve for Mg^+ near the thresholb Curve **a** is the residual obtained by subtracting the linear part from the I. E. curve.

The first excited state of Na^{++} is $^2S_{1/2}$ which lies 32.83 eV above the ground state $^2P^\circ_{3/2}$, and no levels are known between them. The I. E. curves for Na^{++} bend upward near the threshold. When the square roots of the ion currents of Na^{++} are plotted, the points plotted lie on a straight line as seen in Fig. 6, and the line intersects the energy axis nearly at the initial onset of the I. E. curve. Therefore, it can be said that the square law is applicable to Na^{++} up to about 20 eV above the threshold.

---

* The values of energy states in this paper were cited from "Atomic Energy Levels", National Bureau of Standard, Circ. 467, No. 1.

The circumstance is quite the same of K^{++}. The first excited state $^2S_{1/2}$ lies 16.19 eV above the ground state $^2P^\circ_{3/2}$. The square root plots again fit a straight line, and the line intersects the energy axis nearly at the initial onset of the I. E. curves. Hence, it can be said that the square law is also applicable to K^{++} up to about 15 eV above the threshold.

The energy difference between two intersections is 15.5±1 eV, which agrees with difference of the second ionization potential between Na and K.

Mg$^+$

The I. E. cvrve for Mg$^+$ is quite different from Na$^+$ and K$^+$ as seen in Fig. 7. The characteristic shape of the curve did not change in several measurements changing the operating conditions of the ion source. The measurement was made for ^{24}Mg, and background of the mass spectra were not found at $M/e=24$. The curve is linear up to 9 eV and has two humps, at about 11 eV and 14 eV, and again becomes linear. The extension of the first linear part agrees with or lies a little above the upper linear part. The residual part of the I. E. curve by subtracting the lower linear part is shown in Fig. 7**a**.

Such a shape of I. E. curve as in Mg$^+$ have been observed in Zn$^+$, Cd$^+$ and Hg$^+$ by Hickam[16] and Cu$^+$, Ag$^+$, and Au$^+$ by Blais et al[12]. Those curves had one hump or two in them, which are explained by autoionization.* Though Blais et al correlated the humps to groups of excited levels, Hickam could not correlate the humps to known excited levels completely, because knowledge for excited state, especially optically forbidden state, were insufficient.

The ionization potential for Mg$^+$ is 7.644 eV, and the ground states is $1s^2\ 2s^2\ 2p^6\ 3s\ ^2S_{1/2}$. The excited states, $3p\ ^3P^\circ$, $4s\ ^2S$, $3d\ ^2D$, $\cdots$ are shown by arrows in Fig. 7. In addition, excited states of neutral atom, $3p\ 3d\ ^1F^\circ$ and $3p\ 3d\ ^3D^\circ$ lie 2.36 eV and 2.71 eV above the ionization limit, respectively. These states are shown by stars in Fig. 7. Such humps as in Fig. 7 seem not to be caused by direct ionization, but by autoionization. The curve in Fig. 7**a** can be devided into two parts which rise at 2.3±0.1 eV and 5.0±0.2 eV above the initial onset. The first hump may correspond to $^1F^\circ$ and $^3D^\circ$ states, though any excited states to be correlated to the second hump is not known.

Autoionization processes are also observed in the previous study on N$_2^+$ and CO$^+$[13], but the processes in Mg are much prominent. So prominent are they that the breaks which would be observed in the I. E. curve corresponding to the ionic excitation are masked. The rising part of curve in Fig. 7**a** is approximately proportional to the square root of electron energy, as in N$_2^+$ and CO$^+$, but the curve descends steeply after reaching the maximum. In order to explain the I. E. curve for Mg$^+$ completely, the knowledge for presence of excited states and for excitation probability is necessary. It is proved, however, that the linear law is applicable to Mg$^+$ up to 2 eV above the threshold.

Mg^{++}

The I. E. curve for Mg^{++} rises steeply from the threshold and tends to saturate and then

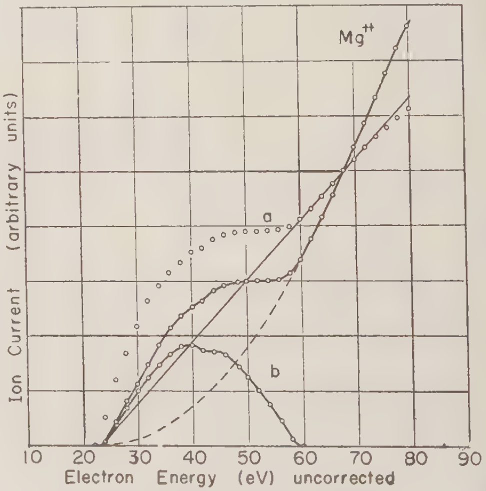

Fig. 8. I. E. curve for Mg^{++}. Curve **a** is the square root plot. Dotted line is a parabola connecting threshold and upper part of the I. E. curve. Curve **b** is the residual obtained by subtracting the parabola from the I. E. curve.

---

* Autoionization is the ionization caused by radiationless transition to an ionic state from an excited state of atom which lies above ionization limit.

rises again steeply. Background of mass spectra at $M/e=12$ where Mg^{++} ion appears was too small to be considered. The energy difference between the initial onset of Mg^{++} and Ne^{++} measured as referring ion is 1.8 ± 0.2 eV, which is a little higher than spectroscopic value of 1.11 eV. The difference between the I. E. curves for Mg^{++} and Ne^{+}, however, is quite remarkable as seen in Fig. 4. Hence, the shape of Mg^{++} is not instrumental but substantial.

The ionization potential for Mg^{++} is 22.67 eV, and the ground state of the ion is $1s^2 2s^2 2p^6\ {}^1S_0$. The first excited state $2p^5 3s\ {}^2P^\circ_{3/2}$ lies 52.8 eV above the ground state and there are no levels between them. Such a shape of I. E. curve cannot be observed in direct ionization process. A possible speculation is that autoionization caused by excitation of inner shell electrons may occur near the threshold, and the probability of the autoionization exceeds that of direct ionization. The square root of ion current of Mg^{++} is plotted in Fig. 8. The extension of upper linear part intersects the energy axis just at or a little above the initial onset of the I. E. curves. If the initial onset and upper part of the I. E. curve are connected by a parabola, which is subtracted from the I. E. curve, then the residual curve becomes as shown in Fig. 8**b**, which resembles the curve in Fig. 7**a**. Therefore, the speculation described above may not be so groundless.

§ 5. Conclusion

In the study on Na, K and Mg by the use of monoenergetic electron, the following conclusions are derived.

Na^{+} and K^{+} follow the linear law up to 1.5 eV and 0.8 eV above the thresholds, respectively. Though Mg^{+} follows the linear law up to 2 eV above the threshold, it has two humps beyond the region. The humps are attributed to autoionization, and the probabilities are relatively large compared with that of direct ionization. Na^{++} and K^{++} follow the square law up to about 20 eV and 15 eV above the threshold. Mg^{++}, however, contrary to expectation, is not so simple.

It was A^{+} only that does not follow the linear law in the seven ions which have been measured by the author. Also there are few exceptions in the studies by the other investigators. Consequently, it can be said that the linear law is applicabe to almost single ionization. On the contrary, though the square law was proved to be applicable to He^{++} by Hickam et al[1] and to Na^{++} and K^{++} in this study, there are some exceptions for double ionization.

Fox pointed out the possibility of Auger transition due to ionization of an inner shell electron. It is also suggested in this study that the autoionization due to excitation of the inner shell electron may occur in Mg^{++}.

Acknowledgement

The author would like to express cordial appreciation to Professor Kiyoshi Kido for his interest in this research. The author also feels grateful to Professor Ichiro Kanomata for his kind encouragement and helpful discussion throughout the work, and to Messrs. Takeo Oguri, Tsutomu Maeda, Arimichi Minō and Toshiyuki Nakazawa for their cooperations rendered to assemble the apparatus.

References

1) W. M. Hickam, R. E. Fox, and T. Kjeldass, Jr.: Phys. Rev. **96** (1954) 63.
2) G. H. Wannier: Phys. Rev. **90** (1953) 817.
3) S. Geltman: Phys. Rev. **102** (1956) 171.
4) R. E. Fox: Advance in Mass Spectrometry, edited by J. D. Waldron (Pergamon Press, London, 1959) 397p.
5) G. H. Wannier: Phys. Rev. **100** (1955) 1180.
6) J. D. Morrison and A. J. C. Nicholson: J. Chem. Phys. **31** (1959) 1320.
7) F. H. Dorman, J. D. Morrison and A. J. C. Nicholson: J. Chem. Phys. **31** (1959) 1335.
8) M. Kraus, R. M. Reese and V. H. Dibeler: J. Res. Nat. Bur. Stand. **63A** (1959) 201.
9) R. E. Fox: J. Chem. Phys. **33** (1960) 200.
10) F. H. Dorman and J. D. Morrison: J. Chem. Phys. **34** (1961) 1407.
11) V. H. Dibeler and R. M. Reese: J. Chem. Phys. **31** (1959) 282.
12) N. C. Blais and J. B. Mann: J. Chem. Phys. **33** (1960) 100.
13) Y. Kaneko: J. Phys. Soc. Japan: **16** (1961) 1587.
14) J. T. Tate and P. T. Smith: Phys. Rev. **46** (1934) 773.
15) W. B. Nottingham: Phys. Rev. **55** (1939) 203.
16) W. M. Hickam: Phys. Rev. **95** (1954) 703.
17) I. Kanomata, Y. Kaneko and T. Oguri: J. Appl. Phys. Japan: **30** (1961) 502.
18) W. Bleakney: Phys. Rev. **36** (1930) 1303.

JOURNAL OF THE PHYSICAL SOCIETY OF JAPAN, Vol. 16, No. 11, NOVEMBER 1961

Radiation Effects in LiF Crystals

By Kazuko KUBO

Japan Atomic Energy Research Institute
Tokai-mura, Ibaraki-ken, Japan

(Received June 23, 1961)

Recovery behaviors of lattice expansion and optical absorption of neutron-irradiated LiF crystals have been measured as a function of annealing temperature. Remarkable correspondence between the two properties leads an interpretation of steps or humps and reduction in recovery curves of lattice constant respectively by formation of colloidal centers which are probably coagulations of vacancies and recombination of vacancies and interstitials.

Optical microscopic observations reveal the fact that the square cavities, considered to be coagulations of vacancies remaining after displacement of atoms by neutron irradiation, preferentially formed on dislocation lines, along which F_2 gas escapes from the crystals.

It is suggested that the colloidal centers are formed by clustering of point defects and some of them, which probably consist of vacancies, grow to square cavities during heat treatment.

Introduction

Differing from typical alkali halides, LiF is known as a marked material because of its particular properties which may be due partly to the small ionic radius of Li. Not only does this situation remain the same when LiF is taken up for the study of radiation damage but also in this case a complexity which follows the (n, α) reaction of Li^6 comes into consideration and as the result, various interesting phenomena can be seen in irradiated LiF. These circumstances show that the phenomena seen in irradiated LiF can not always be generalized to similarly irradiated other ionic crystals. This is a rather undesirable circumstance. From another point of view, however, by generating tremendous lattice defects, the (n, α) reaction economizes neutrons to be incident upon the crystal to produce damaging effects, which makes LiF to be convenient for the study of radiation effects when the particularity is properly taken into account. In fact several papers have dealt with this subject. Among them studies on the expansion[1)-4)] and post-annealing cavity formation of neutron-irradiated LiF crystals[5)-8)] and optical absorption induced by the ionizing radiations[9)-17)] are remarkable and a general feature of neutron-irradiation effects on LiF including mechanical property change has been well shown by Gilman and Johnston[8)].

The present paper includes the changes of the lattice constant and optical absorption of neutron-irradiated LiF crystals during annealing, which have been preliminarily reported[18)], and the steps in the recovery curves of lattice constant have been interpreted as being caused by the coagulations of vacancies or interstitials which are accompanied by the colloidal bands. In addition, preferential formation of square cavities along the dislocation lines during high temperature annealing observed in the neutron-irradiated LiF crystal is also reported.

Part 1.

1.1 *Radiation induced optical absorption of LiF crystals*

The optical absorption bands of LiF induced by the ionizing radiations have been thoroughly investigated[9)-17)]. But the absorption centers are still unknown at present except the *F*-center and the identification of the absorption bands of LiF is not established. This circumstance may be due to the particular nature of LiF, that is, the absorption bands arise in the shorter wave-length region with more stablility at room temperature than other ionic crystals. In spite of the above difficulty Penneman and Powers[19)] have proposed the following classification:

Peak wavelength (in mμ)	222	250	313	340	380	450	518	620
	—	*F*	R_1	—	R_2	*M*	—	*F′*

Although these do not form a complete whole, the proposals are very useful. In the following, this classification is applied with the additional bands: 518 $m\mu$- and 540 $m\mu$-bands corresponding to N_1 and N_2 respectively, and a few absorption bands in the near infra-red region which have been observed by the present author when the irradiation was sufficient to make the visible region completely opaque.

Irradiations of LiF specimens, which were cleaved from a single crystal obtained from the Harshaw Chemical Co., have been made in JRR-1 (water boiler type reactor) in some instances and in the 10 kc Co^{60} γ-irradiation facility in other instances. The temperature of the specimen during irradiation is assumed not to exceed the ambient temperature on the average (<50°C).

Table I. The radiation induced optical absorption in LiF crystals.

Radiation source	Radiation dose	Absorption bands					
Co^{60}	3×15^5 r	F					
	1×10^6 r	F	M				
	6×10^6 r	F	M	N_2			
	1×10^8 r	F	M	R_1	R_2	N_2	
Reactor	5×10^{13} nvt	F	M				
	1×10^{14} nvt	F	M	R_1	R_2	(N_2)	
	3×10^{15} nvt	F	M	R_1	R_2	N_2	
	1.5×10^{16} nvt	795 $m\mu$			Absorption limit		$=560$ $m\mu$
	5×10^{16} nvt	795 $m\mu$					$=570$ $m\mu$
	1×10^{17} nvt	795 $m\mu$	960 $m\mu$				$=620$ $m\mu$
	2×10^{17} nvt	795 $m\mu$					$=650$ $m\mu$
	3.5×10^{17} nvt	1400 $m\mu$					$=700$ $m\mu$

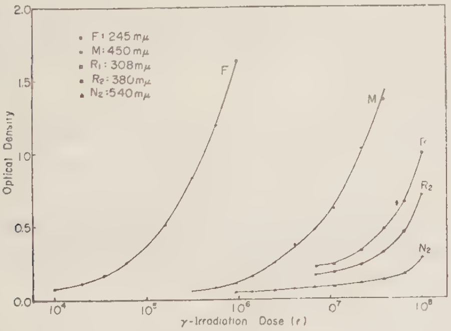

Fig. 1. Variation of the optical absorption bands of LiF crystal with the successive γ-irradiation.

The absorption bands induced by irradiations are shown in Table I and the growth of each absorption band during successive γ-irradiation is seen in Fig. 1.

As seen in Fig. 1, the optical density of the each absorption band increases monotonously with successive irradiation until it exceeds the measurable range of the instrument. When the dose is sufficiently high the absorption bands superpose each other and as the result the continuous spectrum from ultra-violet to red appears to be almost absorbed and makes an opaque region. Letting the longest wavelength of the continuous absorption spectrum with optical densities above 2.0 be called the absorption limit, the absorption limit varies to longer wavelengths with increasing neutron-irradiation, as is shown in Table I.

1.2 *Changes in optical absorption of irradiated LiF crystal by heat treatment*

As the knowledge of the structure of the absorption bands in the opaque region was required, the irradiated specimens were heated and the changes of the optical absorption have been measured in the present experiment. Although this method does not directly make the process of the radiation damage clear but rather gives the knowledge of the defect coagulation by heat treatment, the wide knowledge of this kind over various radiation doses will at least qualitatively give information on the mechanism of radiation damage together with its recovery behavior.

The heat treatment has been carried out mainly by means of a constant pulst annealing at the successively higher temperatures

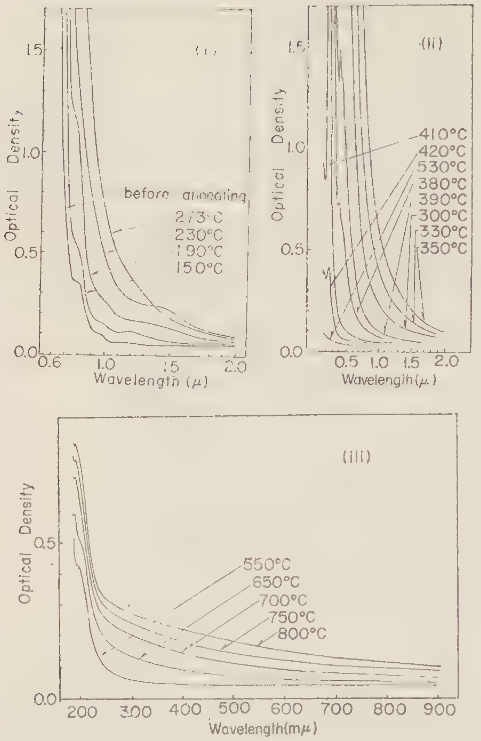

Fig. 2. Change in the optical absorption of LiF specimen, the cleaved wafer of 0.5 mm in thickness irradiated up to 2×17^{17} nvt, with successive annealing at the temperatures from 150°C to to 800°C. (i) from room temperature up to 280°C, (ii) from 300°C up to 530°C, (iii) from 550°C up to 800°C.

Table II. Variation of reversal temperature with radiation dose.

Condition of successive annealing	Radiation dose (nvt)	Reversal temperature (°C)
10°C interval 10 min. pulse	3.5×10^{17}	260
	2×10^{17}	273
	1×10^{17}	280
20°C interval 5 min. pulse	2.5×10^{17}	290
	1.5×10^{17}	330

from 150°C up to 800°C. The change in the absorption of 2×10^{17} nvt irradiated specimens, a cleaved wafer of 0.5 mm thickness, is illustrated in Fig. 2. There are three temperature ranges characterized by the recovery behavior as shown by (i), (ii) and (iii). In the range (i) the absorption limit moves toward longer wavelengths and in the range (ii) the absorption limit comes back toward shorter wavelengths as is expected from the common knowledge of recovery process. The M-band and a colloidal band near F-band are confirmed during the thermal bleaching. After the absorptions have bleached out another broad absorption spectrum grows in the range (iii).

The radiation dose dependence of the above described general feature of the change in absorption is not so clearly seen so far as the dose is sufficiently high to make the opaque region. But the reversal temperature, at which the absorption limit reverses and the common recovery begins as described, becomes low with increasing radiation dose under the same annealing condition, as shown in Table II.

As to the annealing condition, the shorter the succession interval in temperature and the longer the pulse period, the reversal occurs at the lower temperatures.

It is considered that the reversal occurs when the increase of the absorption centers,

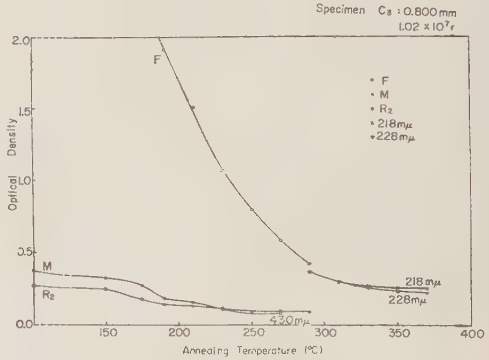

Fig. 3. Variation of optical absorption bands with successive annealing in the specimen irradiated by γ-rays up to 1.02×10^{7} r.

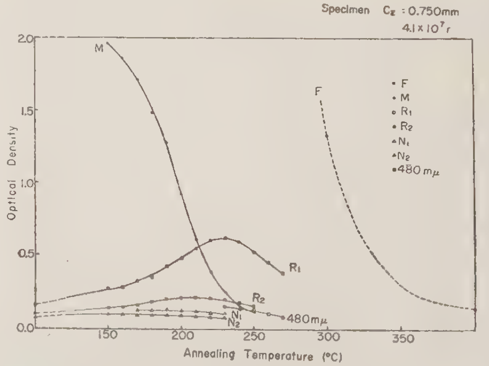

Fig. 4. Variation of optical absorption bands with successive annealing in the specimen irradiated by γ-rays up to 4.1×10^{7} r.

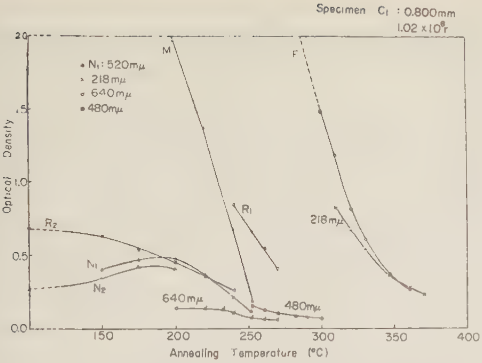

Fig. 5. Variation of optical absorption bands with successive annealing in the specimen irradiated by γ-rays up to 1.02×10^8 r.

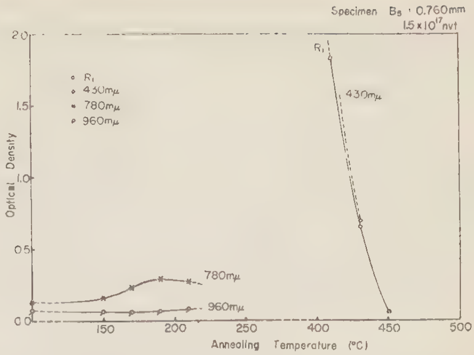

Fig. 8. Variation of optical absorption bands with successive annealing in the specimen irradiated by neutrons up to 1.5×10^{17} nvt.

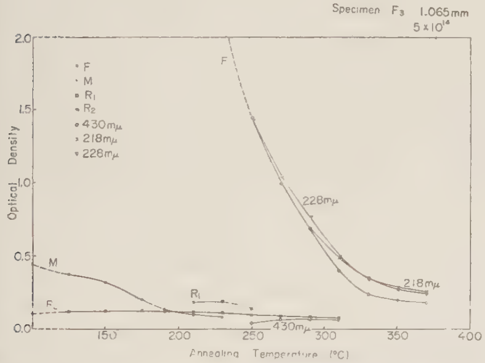

Fig. 6. Variation of optical absorption bands with succesive annealing in the specimen irradiated by neutrons up to 5×10^{14} nvt.

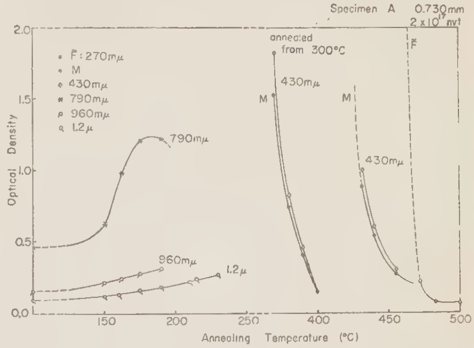

Fig. 9. Variation of optical absorption bands with successive annealing in the specimen irradiated by neutrons up to 2×10^{17} nvt.

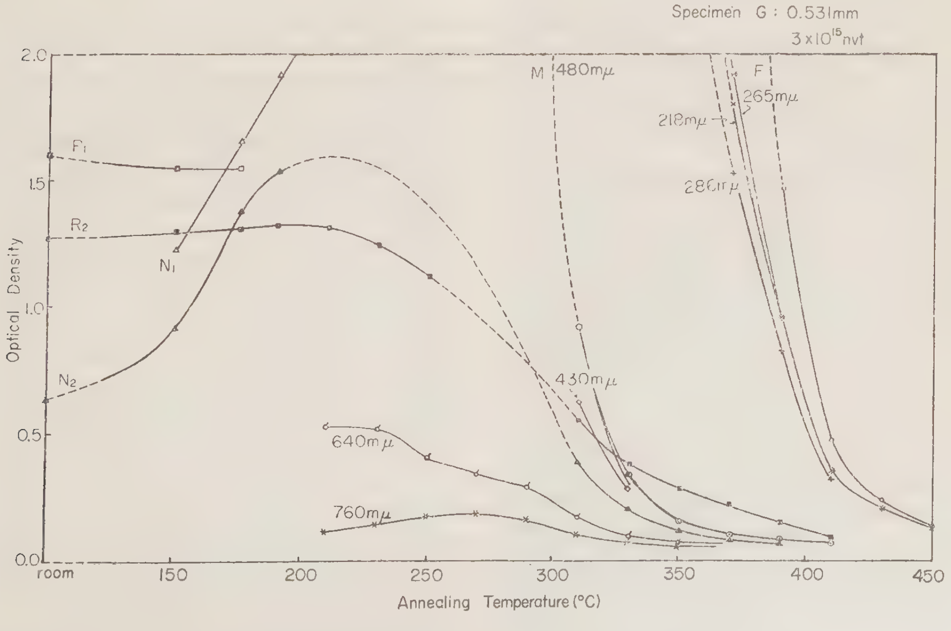

Fig. 7. Variation of optical absorption bands with successive annealing in the specimen irradiated by neutrons up to 3×10^{15} nvt.

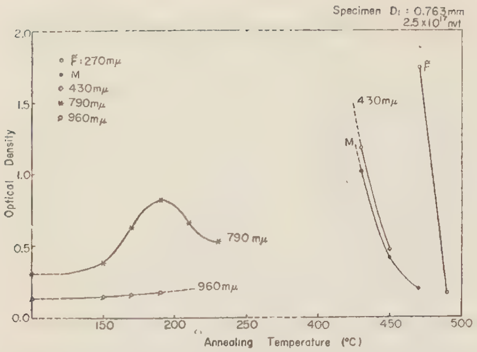

Fig. 10. Variation of optical absorption bands with successive annealing in the specimen irradiated by neutrons up to 2.5×10^{17} nvt.

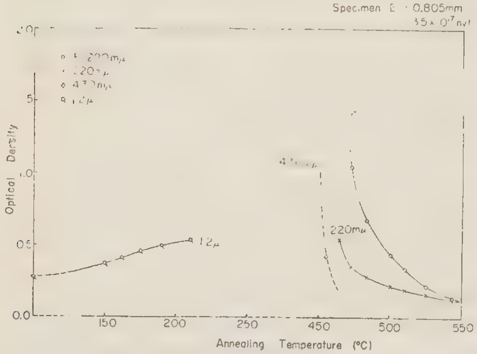

Fig. 11. Variation of optical absorption bands with successive annealing in the specimen irradiated y neutrons up to 3.5×10^{17} nvt.

which may be some coagulation of the defects in the crystal lattice, and the thermic transformation of the centers are in a state of equilibrium. Then the reversal must closely relate with some absorption band which is thermally produced.

Some of the thermally produced absorption bands are seen in the range (ii). When the *M*-band appears on the heat treatment at about 380°C it accompanies another absorption band at 430 $m\mu$. The other absorption maximum is found at about 270 $m\mu$. This band is known as a colloidal band which has been suggested to have some connection with the F-band.

Since the formation of the colloidal band appears to depend on the concentrations of the defects the measurements have been made for several specimens of various radiation doses under the same heating conditions. The results are shown in Figs. 3 to 11 which illustrate the behaviors of all the optical absorption bands existing in the temperature range. In these results, four more bands, which have been paid little attention, are newly found in the wavelengths at 223, 480, 520 (N_1) and 640 $m\mu$, together with a doublet structure existing in 270 and 223 $m\mu$-bands, the 270 $m\mu$-bands, is composed of 260 and 280 $m\mu$-bands and the 223 $m\mu$-band is composed of 218 and 228 $m\mu$-bands, which is confirmed by isothermal annealings. The important absorption bands will be discussed later.

1.3 *Change in lattice constant of irradiated LiF crystals by heat treatment*

The lattice constants of the same specimens were measured by X-ray diffraction after each optical absorption measurement, and the recovery curves have been obtained for lattice expansion induced by neutron irradiations. The Figs. 12 and 13 illustrate the data for the specimens irradiated to 1×10^{17} nvt and 2×10^{17} nvt respectively. A few steps or humps, positively exceeding the experimental error, can be seen in these curves. The

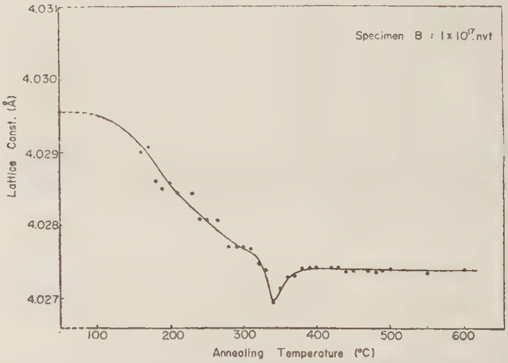

Fig. 12. Variation of lattice constant of LiF crystal irradiated by neutrons up to 1×10^{17} nvt with successive annealing.

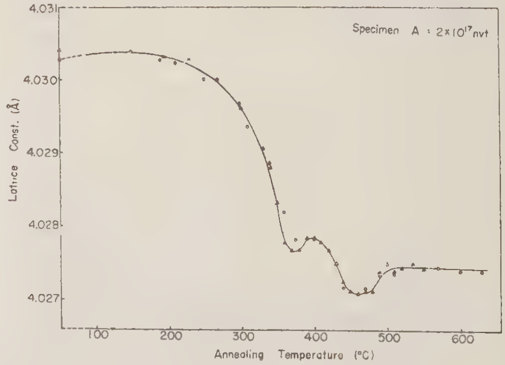

Fig. 13. Variation of lattice constant of LiF crystal irradiated by neutrons up to 2×10^{17} nvt with successive annealing.

values at room temperature and 150°C indicate that there may be an additional small increase below 150°C. The increments depend on the specimen. As for the specimen 2×10^{17} nvt irradiated, the lattice constant decreases from 150°C, and the decrease is interrupted at about 190°C, 300°C and 380°C before the smallest value of lattice constant is reached at about 440°C. The smooth steps, which sometimes grow to humps, begin at the temperatures. After keeping the smallest value for somewhile, the lattice constant again increases at about 500°C.

It is noted that the steps, with the exception of the last increase, scarcely exceed the experimental error when the specimens are irradiated to 1×10^{17} nvt as seen in Fig. 12, in which the total extent of recovery is much smaller than what is illustrated in Fig. 13.

The 10^8 r γ-irradiated specimen, which has been subjected to the same treatment, shows no recovery, namely, the variation of the measured values of the lattice constant was completely within the experimental error throughout the temperature range of annealing. But this result is not important since 10^8 r γ-irradiation is equivalent to 3×10^{15} nvt reactor irradiation for optical absorption production according to Table I, and this radiation dose is considered to be too low to cause a detectable lattice expansion, apart from the intrinsic difference between the radiations.

1.4 *Discussion on the experimental results*

It is interesting to compare the results obtained from the optical and X-ray measurements. One can find the following correspondence between these recovery behaviors: The first step on the curve of lattice constant vs. annealing temperature begins at about 190°C and ends at 270°C where the reversal of optical absorption limit occurs, that is to say, the region (i) is over and (ii) begins. The second step ceases at about 360°C where the 430 mμ-band is to have a maximum density. The third step at about 380°C similarly corresponds to the production of the 270 mμ-band. The last step rises where the region (ii) is over and (iii) begins. The absorption in the region (iii) shows that the crystals get turbid gradually still after the lattice constant reached the final value, and this state is related to cavity formation as will be seen later. The rise of 760 mμ-band, which transfered from 795 mμ with elevating annealing temperature and becomes maximum at about 185°C as can be seen from Figs. 8 to 10, corresponds to the preceding small increase below 150°C. In conclusion all the steps on the recovery curve of lattice constant correspond to the formation of colloidal bands with the exception that the step at 190°C corresponds to the reversal of the absorption limit, which has been named for convenience and the true character is now demanded to be revealed.

Fig. 7, with the aid of Fig. 5, introduced the behavior of *N*-bands in range between 150°C and 300°C. This behavior indicates that the reversal occurs at the point where density of the *N*-band becomes a maximum. Since no other absorption bands are found to behave as the *N*-bands, the absorption limit probably represents the longer wavelength part of the N_2-band until 430 mμ- and *M*-bands become dominant.

Now after the reversal has been identified with the *N*-bands, the above conclusion has no more exception and all the steps can be associated with the colloidal bands. This means that the decrease in the optical density of the colloidal bands during heat treatment is mainly due to the transformation of the colloidal centers because there should not be a volume change, which is seen in the recovery curves of lattice constant, if it is due to the thermal release of trapped electrons or holes. It is almost certain that the colloidal centers consist of clustered vacancies or interstitials and act to expand the crystal lattice, whereas the recombination of vacancies and interstitials reduces the lattice constant, although the structure and mode of the transformation of each colloidal center are unknown and whether recombination takes place between single vacancy and single interstitial or between clustered ones is also an open question.

It is worthwhile here to mention each absorption band since it may give a key to the problem of the absorption centers.

When a colored LiF crystal is exposed to UV light containing *F*-light at room temperature, the *F*-band bleaches and the *M*-band rises a little. The R_1- and R_2-bands decrease also, keeping a nearly constant ratio, and the N_2-band slowly reduces. In the case the specimen has the 270 mμ-band, this band decreases after an initial small increase with a shift to longer wavelengths. This phenomenon can be understood to be optical bleaching of 260 mμ-band since the 270 mμ-band is composed of 260 and 280 mμ-bands, to be consistent with the result of Pringsheim[12] who reported that 280 and 222 mμ-bands were found in a specimen having the 270 mμ-band after exposure to UV-light. These facts mean that at least the 260 mμ-band is not due to Mie's scattering of light by colloidal Li particles because the UV-radiation can not alter the size, shape and concentration of the particles which determine Mie's scattering and colloid band. The 260 mμ-band, which appears to follow some clustered defects, may be vacancies, and the 280 mμ-band must be attributed to a more complex center since the heavier the irradiation, the closer to 280 mμ the so-called 270 mμ-band is and the 280 mμ-band survives to higher temperatures than the 260 mμ-band during thermal annealing. A similar circumstance to the latter is seen in the 223 mμ-band which is composed of 218 and 228 mμ-bands (see Fig. 14). There is little knowledge of these bands except the F-center concentration dependence, namely these are produced in a rather *F*-center poor specimen while the 270 mμ-band is easily produced in an *F*-center rich specimen.

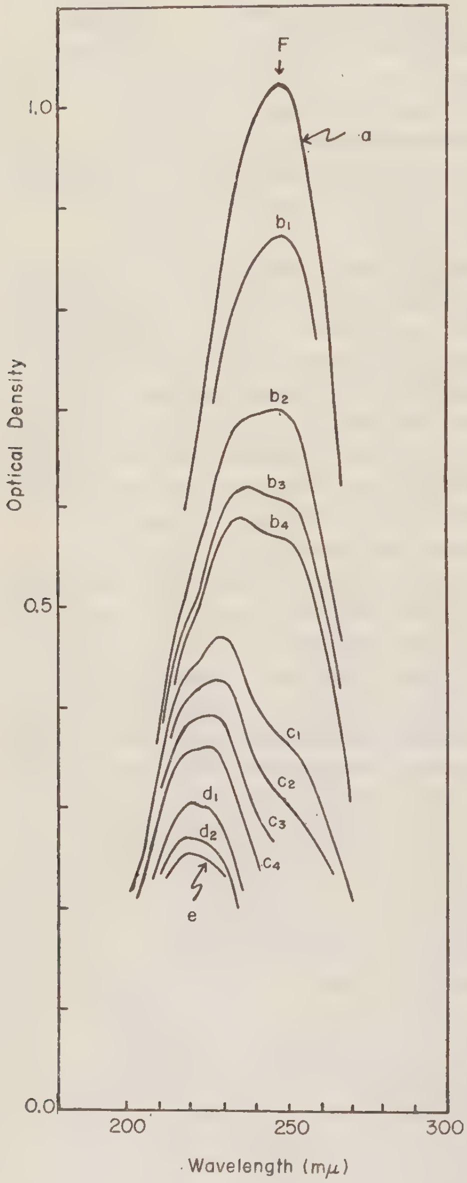

Fig. 14. Transformation of the F-band of LiF to 218 and 228 mμ-bands by the isothermal annealings. (a) after annealing at 210°C for 40 min. (b_1) after further annealing at 240°C for 6 min. (b_2) ditto for 12 min. (b_3) ditto for 20 min. (b_4) ditto for 28 min. (c_1) after further annealing at 270°C for 6 min. (c_2) ditto for 12 min. (c_3) ditto for 20 min. (c_4) ditto for 35 min. (d_1) after further annealing at 300°C for 7 min. (d_2) ditto for 20 min. (e) after further annealing at 330°C for 6 min.

The experiment of isothermal annealing from 170 to 220°C shows that the annealing kinetics of the *F*-band is of the first order with the activation energy of 0.48 ev in this temperature range. The experiment of successive isothermal annealing above 270°C, however, shows that the process here is of the second order and the activation energies of annealing are 0.80 ev from 270 to 350°C and 1.21 ev from 310 to 360°C. These results do not at all contradict each other because there are at least two considerable annealing mechanisms of *F*-center, namely one is thermal release of a trapped electron from *F*-center and the other is recombination of an interstitial and a vacancy, a constituent of *F*-center, through diffusion process. The former takes place from low temperature but the latter occurs at rather high temperatures. The activation energy of annealing of *F*-band as a function of the temperature will reveal the transition between these processes. This experiment is in progress.

The isothermal annealing of the 270 mμ-band was also carried out but the result showed that this annealing process was complicated with an activation energy of a few ev. Further precise experiments are demanded to understand the colloidal centers.

Attention must be given to *M*- and 430 mμ-band. The *M*-band is not bleached by exposure to *M*-light at room temperature. On the successive pulse annealing the *M*-band bleaches at about 450–470°C and small 480 mμ-band follows this final stage. The 430 mμ-band appears to be formed at about 250°C and survives to 460°C. The 430 mμ-band becomes dominant with increasing radiation dose.

Since all the absorption centers, except F-center, of LiF are unknown and the present knowledge of colloidal bands are far from satisfaction, LiF may provide good knowledge of colloidal centers.

Part 2.

2.1 *Formation of square cavities*

Square cavities, parallelepipeds with the faces parallel to (100), have been known to be produced in a neutron-irradiated LiF

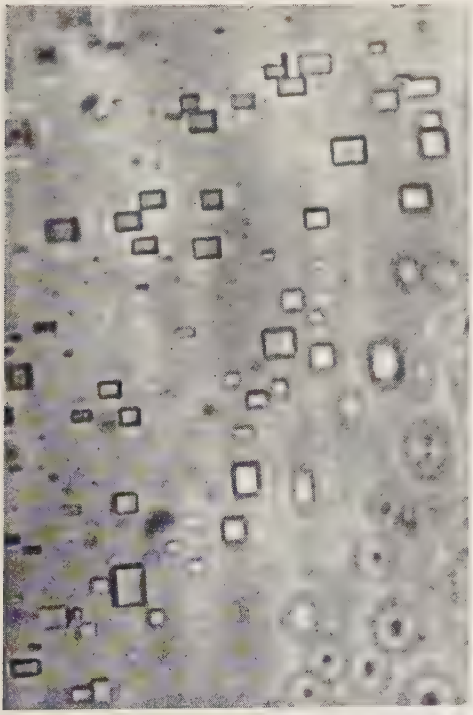

Photo. 1. Rectangular cavities produced in neutron-irradiated LiF crystals after annealing. A few complexes, showing a way of growing of cavities, are found.

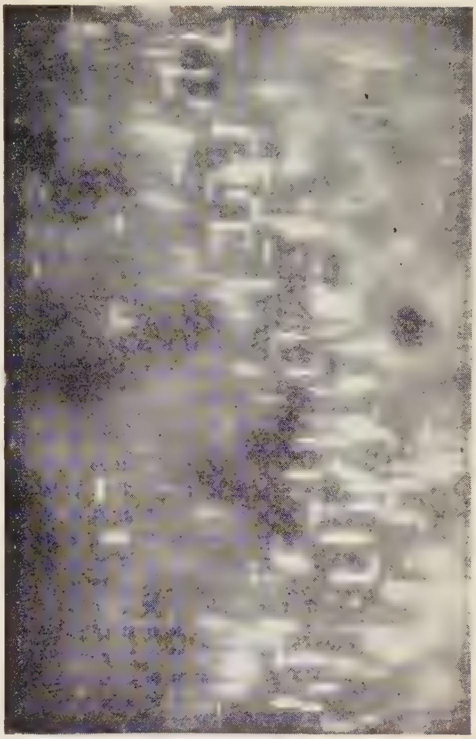

Photo. 2. Thin cavities growing in (110) cut and ground specimen. Focal plane is parallel to (110).

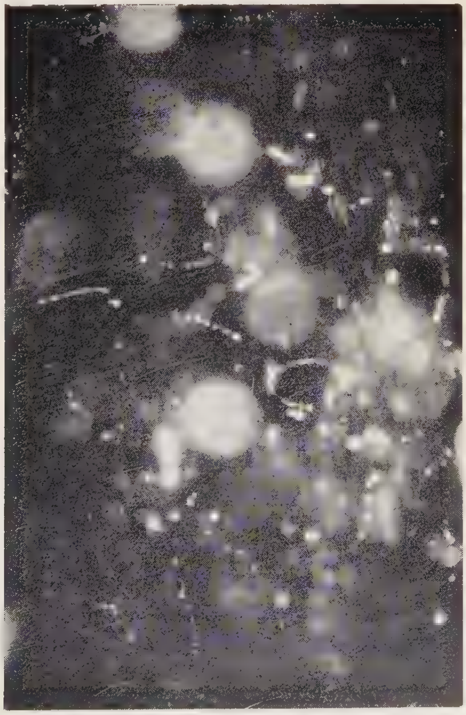

Photo. 3. Isolated cavities in sub-grain, making series on 3-dimensional lines.

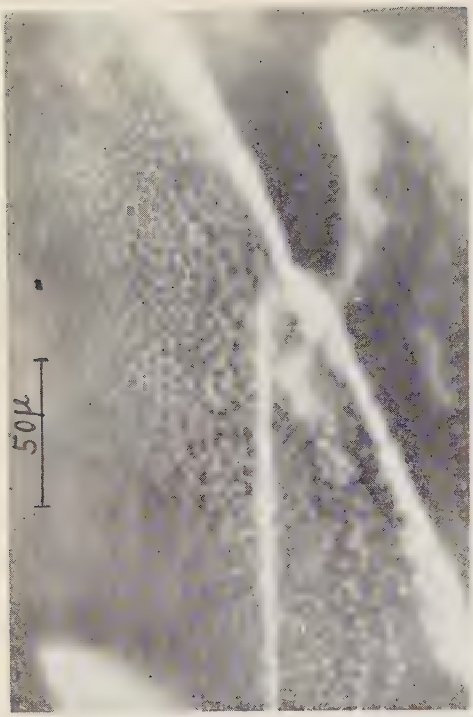

Photo. 4. Polygonal dislocation network decorated with cavities. The network gets untied at the end.

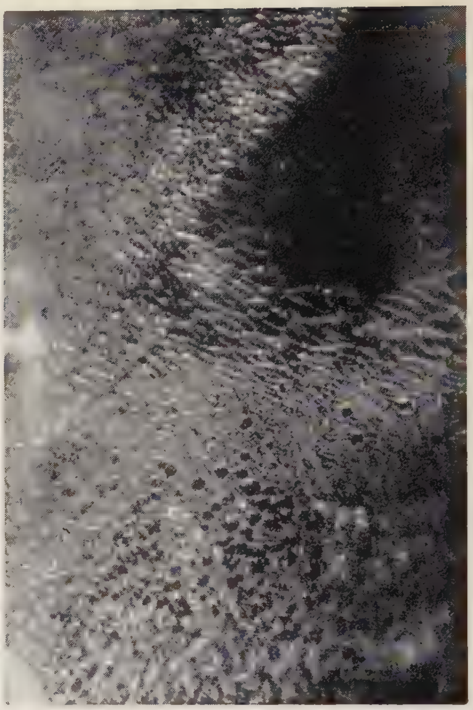

Photo. 6. Dislocation network containing the part on which cavity decoration is uncompleted.

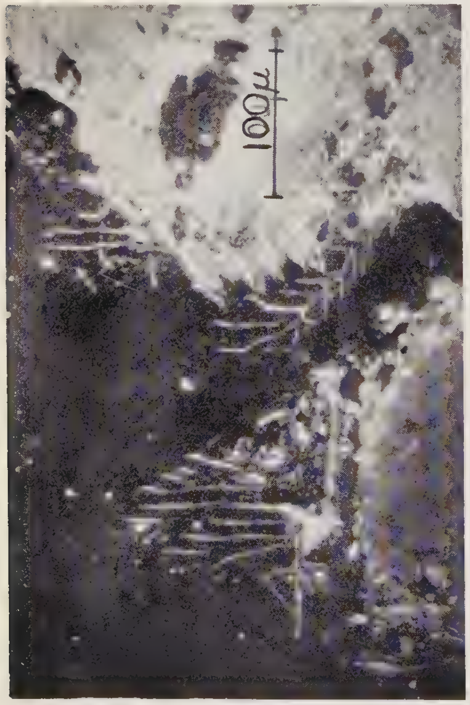

Photo. 5. Dislocation network existing near cracks on an outer surface, constituent dislocation lines are nearly parallel to [100] and [110].

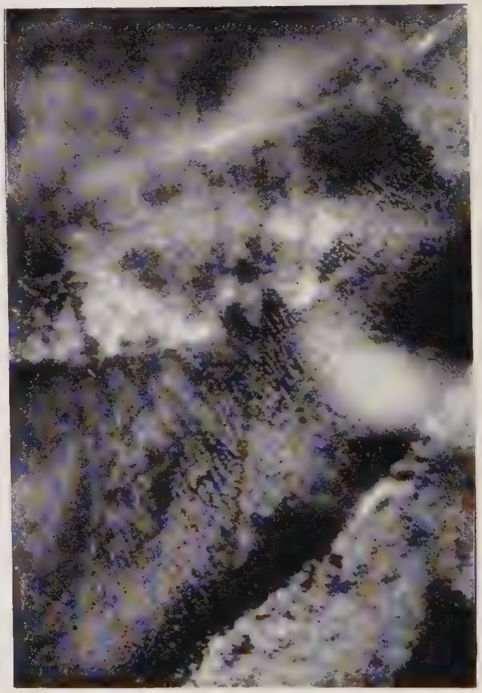

Photo. 7. Parallel dislocation network existing in crack-front.

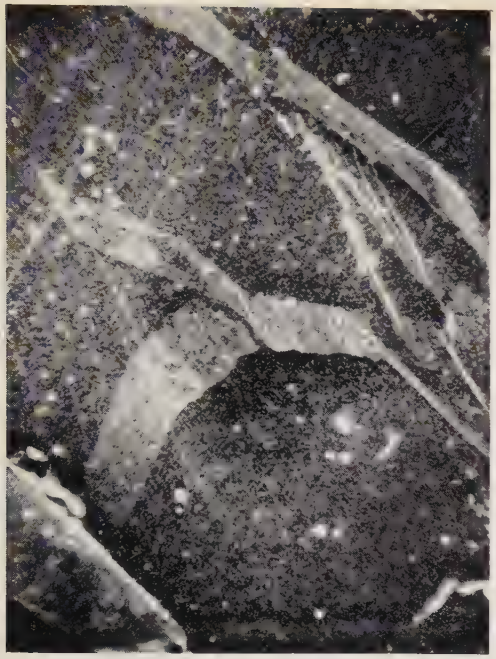

Photo. 8. Sub-grains in a single crystal of LiF revealed by cavities. Bright parts of the picture are sub-boundaries in which cavities scatter light in dark field of microscope and make the parts bright.

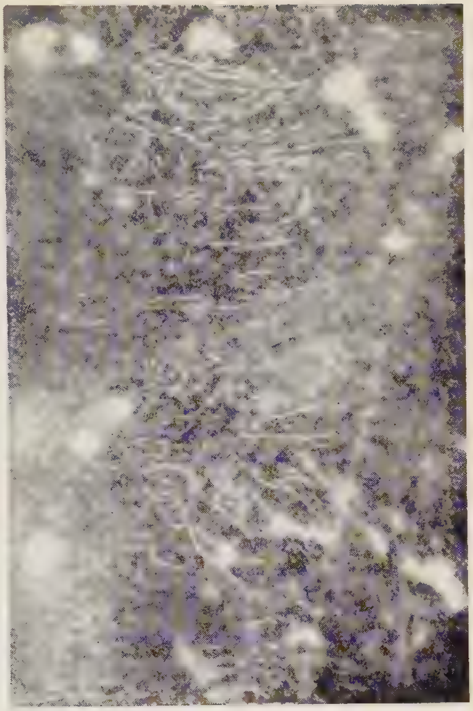

Photo. 10. Various dislocation lines on a sub-boundary laying parallel to close cleaved surface.

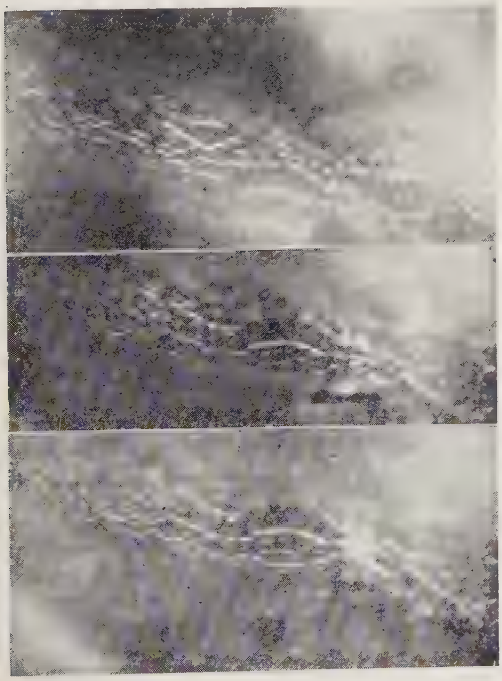

Photo. 9. Dense arrangements of dislocation lines on a sub-boundary. Focal plane was changed for about 30 mμ.

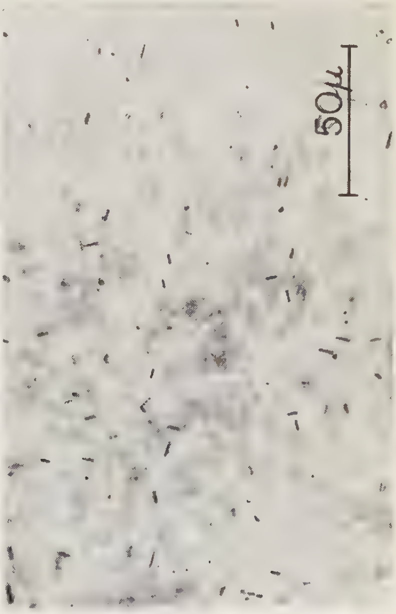

Photo. 11. The short dislocation lines including small loops, produced by irradiation, several microns in length and orienting in random direction.

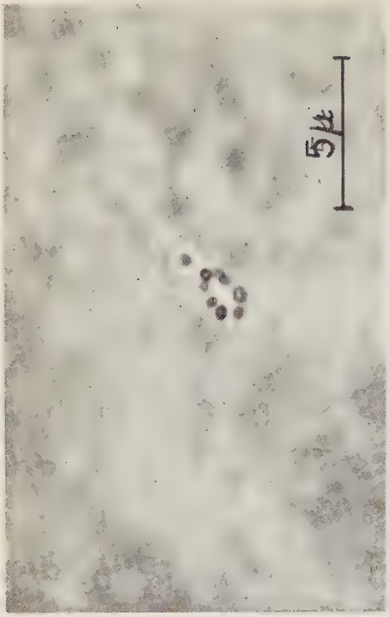

Photo. 12. Small loop decorated by cavities which are connected by faint lines one another.

crystal by high temperature annealing. Senio[5] has observed that the size of the cavities is a function of temperature and period of annealing, and Gilman and Johnston[8)] have reported that the cavities were densely produced near cracks and subboundaries.

In the present experiment, optical microscopic observations were carried out after each annealing with Leitz' Panphoto with phase-contrast condenser. The observed specimens had a pair of planes cut parallel to (110) in some instances and (100) cleaved planes in other instances and were so placed as these planes were perpendicular to the optical axis of microscope. The transmission method permits one to observe throughout the specimen when the magnification of the objective lens is not large. Nothing has been observed after annealing below 450°C, but some scatterers of light are found in the dark field after 450°C annealing. These scatterers increase in number and are clearly observed after 500°C annealing. The rectangular shapes of cross section of the cavity, framed with diffraction color, can be recognized after 550°C annealing, and after that the cavities increase both in number and in size. This fact agrees with Senio's results. The framing diffraction color varies according to the thickness of the cavity, and disappears when the cavity becomes sufficiently large, say an order of ten microns. The cross sections of the cavities are, in general, rectangles or complexes of rectangles, which means the cavities are parallelepipeds or the complexes surrounded by three pairs of planes parallel to basic lattice planes. The appearance of complexes reveals the way of cavity growing (Photo. 1). Extreme shapes of the cavities are found as thin rods parallel to [100] and thin platelets.

The distribution of the cavities of various shapes appears to be ruled by something. For example, the cavities found at a place close to outer surface of the specimen are often thin rods. Many cavities in the forms of thin rods and platelets are also observed in an specimen with (110) cut planes which were ground and polished before irradiation (Photo. 2). These examples suggest that the formation of the cavities is influenced by some stresses and has some connection with dislocations. In addition, assemblies of similar long rectangular cross sections oriented in the same direction are seen near the subboundary. They are so crowded that the sub-grain is surrounded by walls which consist of the cavities. In sub-grains, on the other hand, cavities exist isolatedly and some of them make a series along some lines which are concluded to be dislocation lines (Photo. 3). Thus nearly all the observed results show that the cavity formation is related with dislocation lines, especially the series of cavities along dislocation lines suggest that the cavities are formed preferentially on dislocation lines. This suggestion has been confirmed by the proper annealing experiment, which is shown in the following.

2.2 *Observation of dislocation lines*

Annealing of a rather short period at about 700°C provides observability of dislocation lines in neutron-irradiated LiF crystals. The cavities are small and lie closely with one another on dislocation lines. In other words, cavities decorate dislocation lines. Thus various dislocation lines have been observed[20)] inculding dislocation networks (Photo. 4). It is easily seen that the above described isolated cavities in a sub-grain correspond to dislocation lines which are sparsely located in the sub-grain. Similarly the dense arrangement of cavities near a crack are understood to be a formation of cavities on a dislocation network which exists near the crack as Photo. 5 to 7 (also Photo. 6 in the previous short note[5]) shows. As to crowded cavities near sub-boundaries, proper annealing has exposed the topography of sub-grains in the crystal (Photo. 8) and further each dislocation line in the dense arrangement on sub-boundaries (Photo. 9 and 10). Thus one can see a resemblance between assemblies of thin roddy cavities of the same orientation and groups of parallel dislocation lines, especially those parallel to [100], on sub-boundary.

It is concluded that the cavities are preferentially formed on dislocation lines, and this gives a rule in cavity formation. At present, however, there is little reliable knowledge of the dislocation lines on which cavities are formed. Many possibilities of the introduction of these dislocation lines in addition to the pre-existing ones can be considered, namely, some external stress, internal stress caused by irradiation or by quenching between successive annealing, etc. It is generally difficult to infer the course of the dislocation lines from only the observation in this way. But there are specific dislocation lines which are probably produced by irradiation. These are short lines of 3-dimensional random orientation and small loops observed in crystals irradiated to more than 2×10^{17} nvt (Photo. 11). The radiation dose dependence of this kind of dislocation clearly shows the dislocations are caused by irradiation. The cavities on the small loops are found to be connected with very faint lines one another (Photo. 12), the average loop diameter being a few microns and the average length of the dislocation lines in the random direction being nearly equal to the range of α-particles with 2.1 Mev in LiF crystal which is 6.1 microns. It may go too far to say but it seems very likely that small dislocation lines of this kind represent tracks of α-particles and the following knocked-on atoms and each cavity has grown smaller dislocation loops produced by displacement spikes or collapse of vacancy clusters which were formed during irradiation.

2.3 *Mechanism of the cavity formation*

It has been well known that cavities are produced in neutron-irradiated LiF crystals by heat treatment. Whapham and Makin[6] have shown similar square cavities on the surface of a LiF crystal irradiated with 1 MeV electrons along [110]. In contrast with those cases no square cavity was found in the γ-irradiated LiF crystal after any annealing. These facts assert that the cavity formation is related with displacement of atoms caused by particle irradiation. It is natural here to consider the cavities to be condensation of vacancies produced by the displacement of atoms. Although the determination of the material which fills the cavities is an open question, high saturation of colors emerged by interference of light reflected from two parallel planes of the cavities shows that refractive index of the material is about 1, and uniformity of the color over the area of rectangular cross section of cavities which are generated in the inner part of the crystal and the non-existence of strains around the cavities show the low pressure of the material in the cavities. Probable answers of this question are given by vacuum, dilute fluorine or helium gas. As to fluorine gas, Guinier[22] has confirmed F_2 gas of rather high pressure after neutron-irradiation in a container which was evacuated and sealed prior to the irradiation, and Ring et al.[23] have ascertained F_2 gas, by nuclear magnetic resonances, together with the existence of colloidal Li matal. Then one can see the diffusion of displaced F-atom and the resulting F_2 gas in the crystal and the escape from the crystal, during irradiation and annealing. It is possible that F_2 gas fills the cavities which have been formed by condensation of vacansies remaining after displacement of atoms. The same is possible for the He gas which is produced by (n, α) reaction of Li^6 though there is no confirmation of the gas.

In addition to the rectangular cavities in crystals, large rectangular cavities with round corners are found near the outer surface of the crystal after annealing at high temperature near melting point and bubbles of irregular shape are observed on the outer surface. The arrangements are quite similar to those of the cavities described previously, that is, the dense distribution at a place where many dislocation lines possibly exist. On the basis of the etch pits produced during heat treatment on the scar lines of grinding, these bubbles are suggested to consist of escaping F_2 gas probably along dislocation lines.

In conclusion, dislocation lines must play an important role in cavity formation or F_2 gas escape, giving locations of condensation or ways of diffusion respectively. The confirmation of these matters appears to be beyond optical microscopic research.

Summary

Lattice parameter recovery of neutron-irradiated LiF crystals during thermal annealing has been made to correspond to the optical absorption change under the same conditions. As the result, steps or humps in in the recovery curves are interpreted as an equibrium of the formation and the reduction, which is effected by recombination of vacancies and interstitials, of colloidal centers.

Several colloidal bands are observed to be produced during irradiation and during an nealing. The production of these bands which depends on the radiation dose must be an attribute of some coagulation of several vacancies which are produced by irradiation.

On the other hand, cavities microscopically observed in neutron-irradiated LiF crystals after annealing at high temperature are found to have been formed preferentially on dislocation lines. Then various dislocation lines can be observed by cavity decoration. The cavities are considered to be coagulated vacancies which remain after displaced atoms.

Thus both the colloidal center and the cavity appear to have the constitution of vacancies. However, it might be unreasonble here to consider the two from the same viewpoint since there is a great gap in size between the two. The investigation of the coagulation of vacancies of intermediate size is beyond the limit of optical research. One of the promising methods for this purpose is an X-ray small angle scattering by which Guinier and Lambert[7] have made studies of neutron-irradiated LiF crystals. They have determined the size and number of X-ray scatterers growing during annealing after irradiation. One can see that the formation and recovery of colloidal centers and cavities described in the present paper qualitatively agree with their data. This means that X-ray scatterers coincide with colloidal centers and cavities in the cases of annealing at rather low and high temperatures respectively. It is suggested then that X-ray scatterers originate as colloidal centers which are known to have close relation with dislocations and grow to cavities.

Further investigations are required before conclusive confirmation can be offered on the mechanism of radiation effect and its recovery.

Acknowledgement

The author wishes to express her gratitude to Prof. Y. Takagi, Dr. H. Suzuki and Dr. F. E. Fujita for their helpful advice and valuable discussions. Her hearty thanks are also due to Mr. H. Motohashi for X-ray measurements and to Mr. Y. Katano for assistance in microscopic observations and preparing micrographs.

References

1) D. Binder and W. J. Sturm: Phys. Rev. **96** (1954) 1519, **99** (1955) 603, **107** (1957) 106.
2) D. T. Keating: Phys. Rev. **97** (1955) 823.
3) Mayer, Pirio, Gigon and Tournarie: P/362 (1955).
4) P. Senio and C. W. Tucker, Jr.: KAPL-M-POS-1 (1956).
5) P. Senio: Science **126** (1957) 208.
6) R. E. Smallman and B. T. M. Willis: Phil. Mag. **2** (1957) 1018.
7) M. Lambert and A. Guinier: Comptes rend. **244** (1957) 2791, **245** (1957) 526.
8) J. J. Gilman and W. G. Johnston: J. Appl Phys. **29** (1958) 877, **30** (1959) 129.
9) P. Pringsheim and P. H. Yuster: Phys. Rev. **78** (1950) 293.
10) C. J. Delbecq and P. Pringsheim: J. Chem. Phys. **21** (1953) 794.
11) C. J. Delbecq, P. Pringsheim and P. H. Yuster: Z. Phys. **138** (1954) 266.
12) P. Pringsheim: Z. Phys. **136** (1954) 573.
13) W. Primak, C. J. Delbecq and P. H. Yuster: Phys. Rev. **98** (1955) 1708.
14) W. Primak: Phys. Rev. **112** (1958) 1075.
15) J. A. Ghormley and H. A. Levy: J. Phys. Chem. **56** (1952) 548.
16) I. L. Mador, R. F. Wallis, M. C. Williams and R. C. Herman: Phys. Rev. **96** (1954) 617.
17) D. A. Wiegand and R. Smoluchowski: Phys. Rev. **116** (1959) 1069.
18) K. Kubo, H. Motohashi and Y. Katano: Research report of JAERI 1014 (1960).
19) R. A. Penneman: AECD-1859 (1945).
J. A. Powers: Dissertation, University of Notre Dame (1950).
20) K. Kubo and Y. Katano: J. Phys. Soc. Japan **16** (1961) 347.
21) A. D. Whapham and M. J. Makin: Phil. Mag **5** (1960) 237.
22) A. Guinier: Lecture held at JAERI (1959).
23) P. J. Ring, J. G. O'Keefe and P. J. Bray: Phys. Rev. L. **1** (1958) 453.

JOURNAL OF THE PHYSICAL SOCIETY OF JAPAN, Vol. 16, No. 12, NOVEMBER, 1961

Numerical Solution of the Navier-Stokes Equations for the Flow in a Two-Dimensional Cavity

By Mitutosi KAWAGUTI

Railway Technical Research Institute, Tokyo

(Received June 12, 1961)

The flow of viscous fluid in a two-dimensional rectangular cavity has been studied. It is assumed that the cavity is bounded by three rigid plane walls, on which the fluid velocity is zero, and by a flat plate moving in its own plane. For the ratio of the lengths of sides of rectangular cross section, three cases have been chosen: 2:1, 1:1, 1:2. The Reynolds number of the flow is varied as 0, 1, 2, 4, 8, 16, 32, 64, 128. For these cases, the Navier-Stokes equations have been numerically integrated with the aid of high-speed electronic digital computers. Streamlines, equi-vorticity lines, and isobaric lines for some typical cases are shown in figures. Velocity distributions along the centre line and pressure distributions over the both side walls are also shown.

§ 1. Introduction

It is well known that the flow of viscous fluid can be treated successfully with the Navier-Stokes equations. However, owing to the mathematical difficulty inherent in the nonlinear character of the equations, only a few exact solutions, either analytical or numerical, have been obtained. Recently, the labour of numerical integration of partial differential equations has been greatly reduced due to the remarkable progress of high-speed electronic computers. Now it becomes possible to work out numerically the exact solutions of the Navier-Stokes equations for significant cases, which will be useful to elucidate the general feature of these equations.

In this paper, the flow of viscous fluid in a two-dimensional rectangular cavity has been studied. It is assumed that the cavity is bounded by three rigid plane walls, on which the fluid velocity is zero, and by a flat plate moving in its own plane. For the ratio of the lengths of sides of rectangular cross section, three cases have been chosen: 2:1, 1:1, 1:2. The Reynolds number of the flow is varied as 0 (Stokes' solution), 1, 2, 4, 8, 16, 32, 64, 128. For these cases, the Navier-Stokes equations have been numerically integrated with the aid of high-speed electronic digital computers.

§ 2. Problem

We study the steady flow of a viscous fluid in a two-dimensional cavity of which cross section is ABCD (cf. Fig. 1. a) and the lengths of AD and AB are a and b, respectively. We consider that AB, BC, and CD are rigid walls on which the velocity of the fluid vanishes, while the velocity along AD is prescribed arbitrarily parallel to itself. In the present paper, however, the latter velocity is assumed to be constant ($=-U$) for the sake of simplicity. The cases where the velocity along AD is not uniform could be treated with an analogous method to that described in the following. The Reynolds number for our problem may be defined as Ua/ν, ν being the kinematic viscosity.

When the Reynolds number is rather low, similar problems to ours have been investigated by several authors: K. Hidaka[1] has studied much the same problem as ours except that shearing stress instead of velocity is given on AD, by integrating numerically the Stokes equations, and then calculated the correction term due to inertia terms. A. Thom and C. J. Apelt[2] have dealt with the flow past a two-dimensional static hole in the wall of a channel by expanding the solution in power series in the Reynolds number, and obtained the first three terms by numerical integration. Thom and Apelt's case may be regarded as the limiting case of ours when the ratio b/a tends to infinity.

§ 3. Equations of Motion and Boundary Conditions

Let us take the x-axis along the side $\overrightarrow{BC}$, and the y-axis along the side $\overrightarrow{BA}$. For simplicity, all the quantities are expressed non-dimensionally, the reference length and velocity being the length of the side BC and the fluid velocity along the side DA, respectively. Then the length of the sides AB and CD is expressed by $\beta=b/a$ (cf. Fig. 1. b).

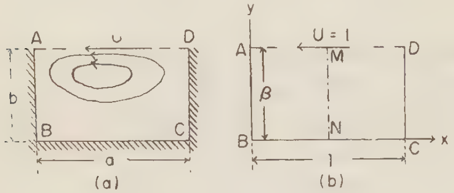

Fig. 1.

In terms of the stream function ψ and the vorticity ω, the equations of motion for two-dimensional flow can be written as follows:

$$\frac{\partial(\psi,\omega)}{\partial(x,y)}+\frac{1}{R}\Delta\omega=0, \tag{3.1}$$

and

$$\omega=-\Delta\psi\ , \tag{3.2}$$

where

$$\Delta=\frac{\partial^2}{\partial x^2}+\frac{\partial^2}{\partial y^2}\ . \tag{3.3}$$

The boundary conditions are then expressed as

$$\psi=0,\ \partial\psi/\partial x=0 \quad \text{on AB}, \tag{3.4}$$
$$\psi=0,\ \partial\psi/\partial y=0 \quad \text{on BC}, \tag{3.5}$$
$$\psi=0,\ \partial\psi/\partial x=0 \quad \text{on CD}, \tag{3.6}$$
$$\psi=0,\ \partial\psi/\partial y=-1 \quad \text{on DA}. \tag{3.7}$$

§ 4. Reduction to Finite Difference Equations

For the numerical integration of equations (3.1) and (3.2), we must divide the whole region into meshes, and find the relations among the values of ψ and ω at one mesh point and its neighbouring points from the equations of motion and the boundary conditions.

First we group all the mesh points into three classes: (i) ordinary (inner) points, (ii) points on the sides AB, BC, and CD, and (iii) points on the side DA.

(i) *Ordinary (inner) points.*

Neglecting the terms of order O (h^4), we obtain the relation:

$$f_0=f_M-(h^2/4)\Delta f\ , \tag{4.1}$$

where f is any function of the point, h is the mesh constant, and the suffixes 0 and M indicate the value at the point 0, and the average value for the four neighbouring points, respectively.

For f, we take ψ and ω, and for $\Delta\psi$ and $\Delta\omega$, we use the expressions obtained from (3.1) and (3.2), and finally we replace the differentials by the differences. Thus the following two relations are obtained which take the place of the differential equations (3.1) and (3.2):

$$v_0=v_M+\frac{R}{16}\{(u_1-u_3)(v_2-v_4)-(u_2-u_4)(v_1-v_3)\}\ , \tag{4.2}$$

$$u_0=u_M-\frac{1}{4}v_0\ , \tag{4.3}$$

where

$$u=\psi\ , \qquad v=-h^2\omega\ , \tag{4.4}$$

and suffixes 1, 2, 3, 4 indicate that the values for the points 1, 2, 3, 4 in Fig. 2.a should be taken, respectively.

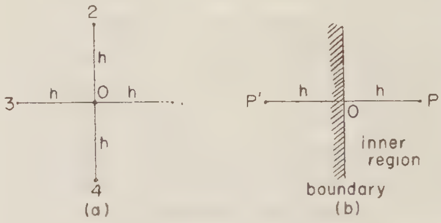

Fig. 2.

(ii) *The points on the sides* AB, BC, *and* CD.

At these points, ψ must be zero, from the first conditions of (3.4)-(3.6). Thus

$$u_0=0. \tag{4.5}$$

On the other hand, we may find v_0 from (4.3), considering that the value of u is zero on the boundary points, and replacing the normal differentials by the corresponding differences. Thus we have

$$v_0=u_p+u_{p'}$$
$$=2u_p\ , \tag{4.6}$$

because of the relation

$$u_p-u_{p'}=0\ , \tag{4.7}$$

which follows from the second conditions of (3.4)-(3.6). Suffixes p and p' indicate that the values for the points on either side of the boundaries should be taken (cf. Fig. 2. b).

(iii) *The points on the side* AD.

In this case, we must take

$$u_p-u_{p'}=2h\ , \tag{4.8}$$

in place of (4.7), from the second condition of (3.7). Thus we have

$$u_0=0\,, \tag{4.9}$$

$$v_0=2u_p-2h\,. \tag{4.10}$$

§ 5. Procedure of Computation

We take the following mesh constants:

1/14 for the cases $\beta=b/a=0.5$,
1/10 for the cases $\beta=1$,
1/7 for the cases $\beta=2$,

hence we have 121 mesh points (81 inner points) for the cases $\beta=1$, and 120 mesh points (78 inner points) for the cases $\beta=0.5$ and 2, respectively.

Numerical integration of (3.1) and (3.2) is carried out by iterative procedures according to the following steps:

(i) Approximate values of u and v are assumed at all the mesh points. These values may be chosen for each case by relevant method.

(ii) Then the values of v for the boundary points are corrected using the equation (4.6) or (4.10).

(iii) Thirdly, values of u and v for the inner points are corrected from point to point making use of the relations (4.2) and (4.3).

The procedures (ii) and (iii) make one cycle of the iterative calculation.

The numerical calculations have been carried out on the electronic digital computer PC-1 at the Department of Physics, Faculty of Science, University of Tokyo.

§ 6. Results

We have performed the numerical integration for the cases:

$\beta=0.5$, $R=0$, 8, 32, 64,
$\beta=1.0$, $R=0$, 1, 2, 4, 8, 16, 32, 64, 128,
$\beta=2.0$, $R=0$, 8, 32, 64.

In all cases except one ($R=128$, $\beta=1.0$), the iterated values converged within five digits in fixed decimal point method, when we took the starting values as 0 for simplicity and the iterating procedures (ii) and (iii) were carried out for about one hundred cycles.

The calculation took about twenty minutes for each case including the printing time once for each fifty interative cycles.

For $R=128$ ($\beta=1.0$), the iterative process on PC-1 did not converge. Then, we reexmined the same case on another electronic digital computer Bendix G-15D at the Railway

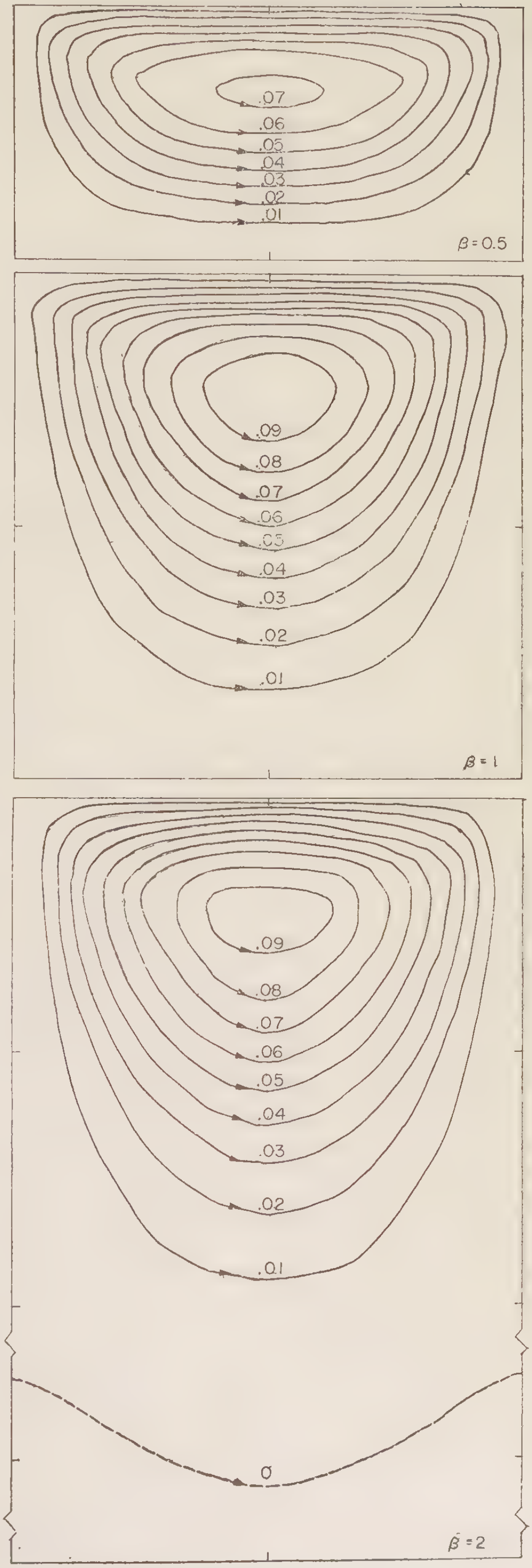

Fig. 3. Streamlines ($R=8$).

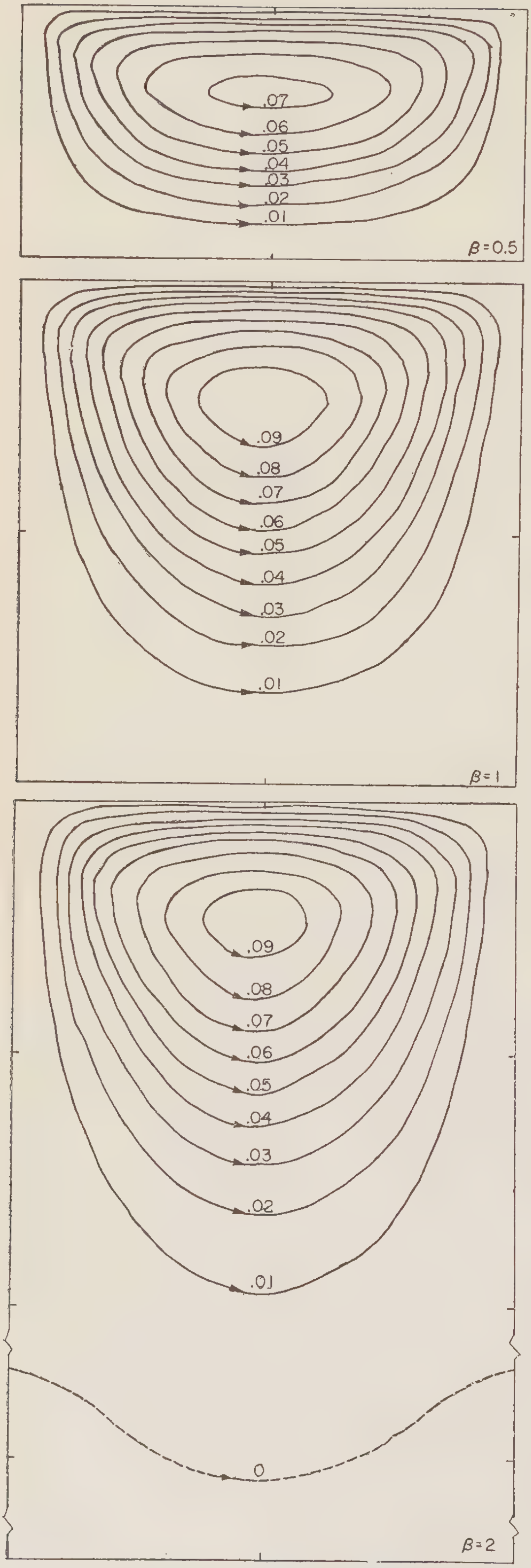

Fig. 4. Streamlines ($R=0$).

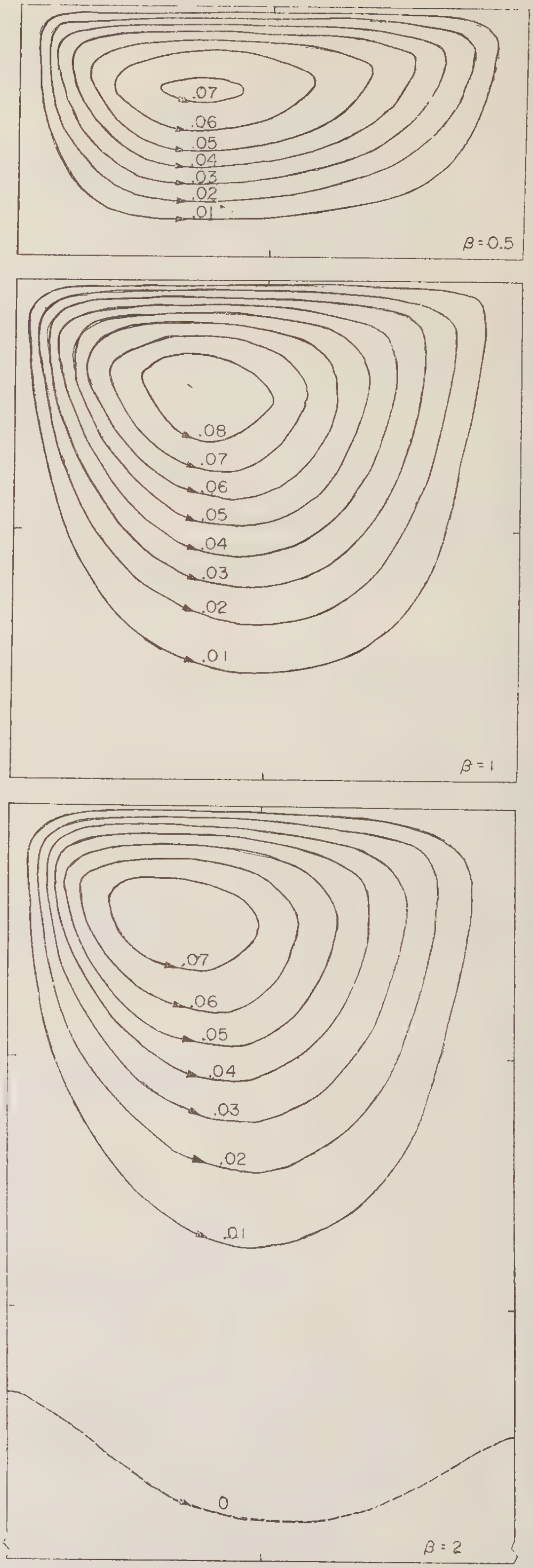

Fig. 5. Streamlines ($R=64$).

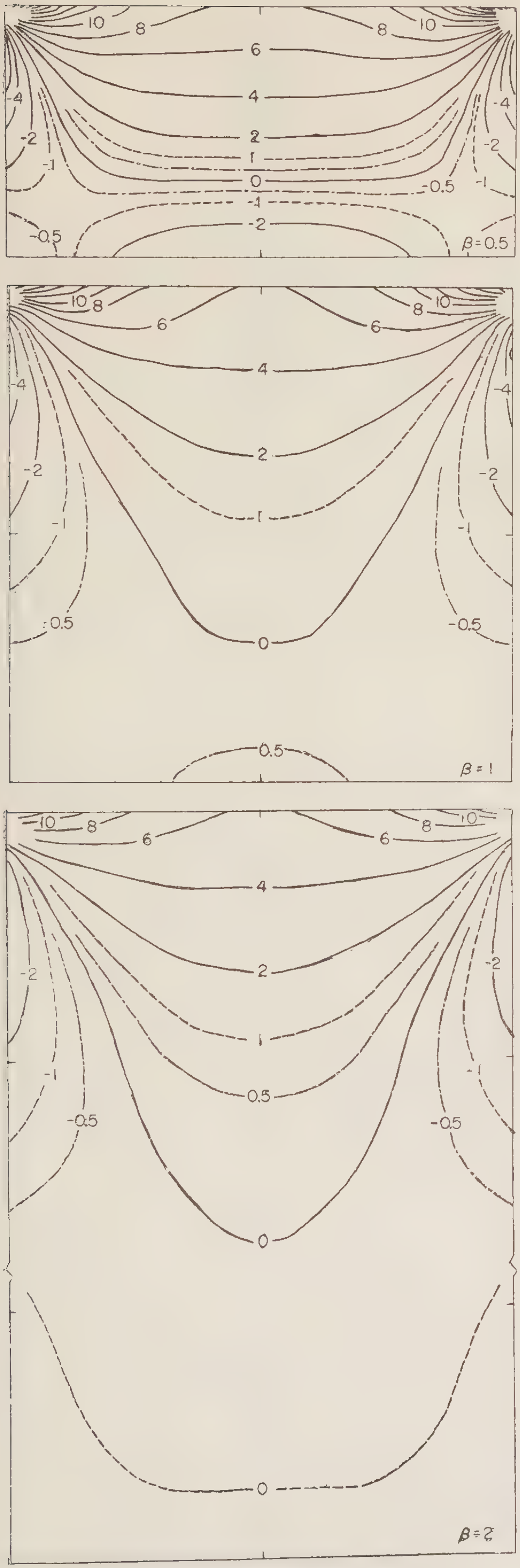

Fig. 6. Vorticity (*R*=8).

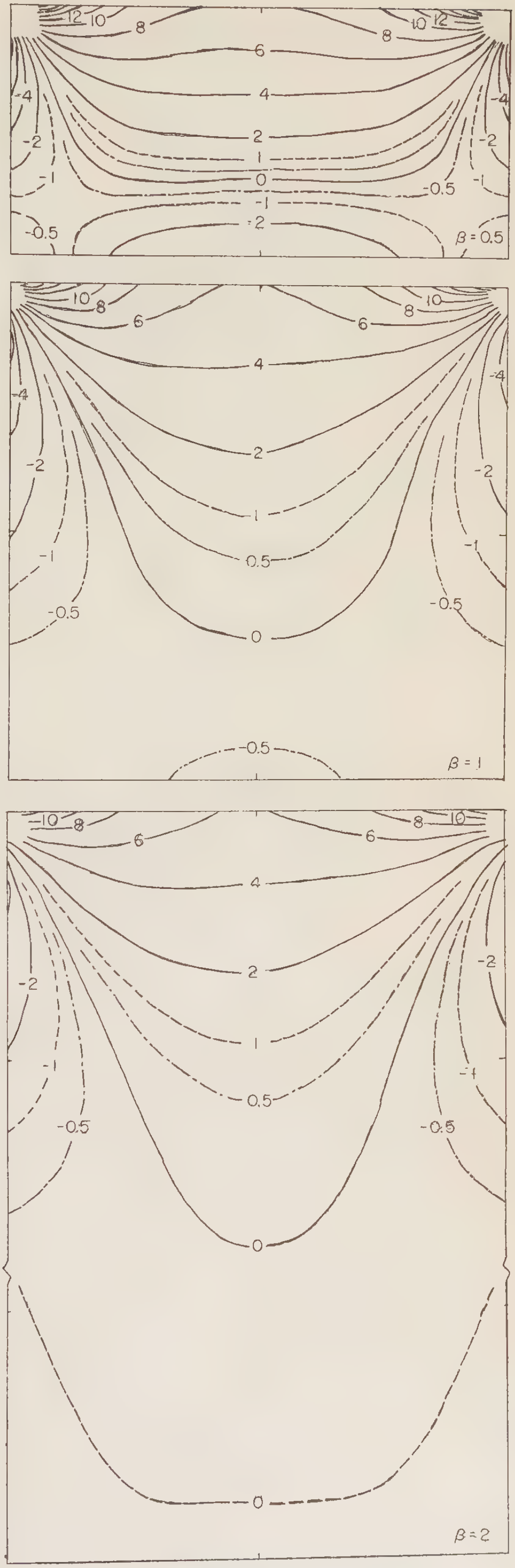

Fig. 7. Vorticity (*R*=0).

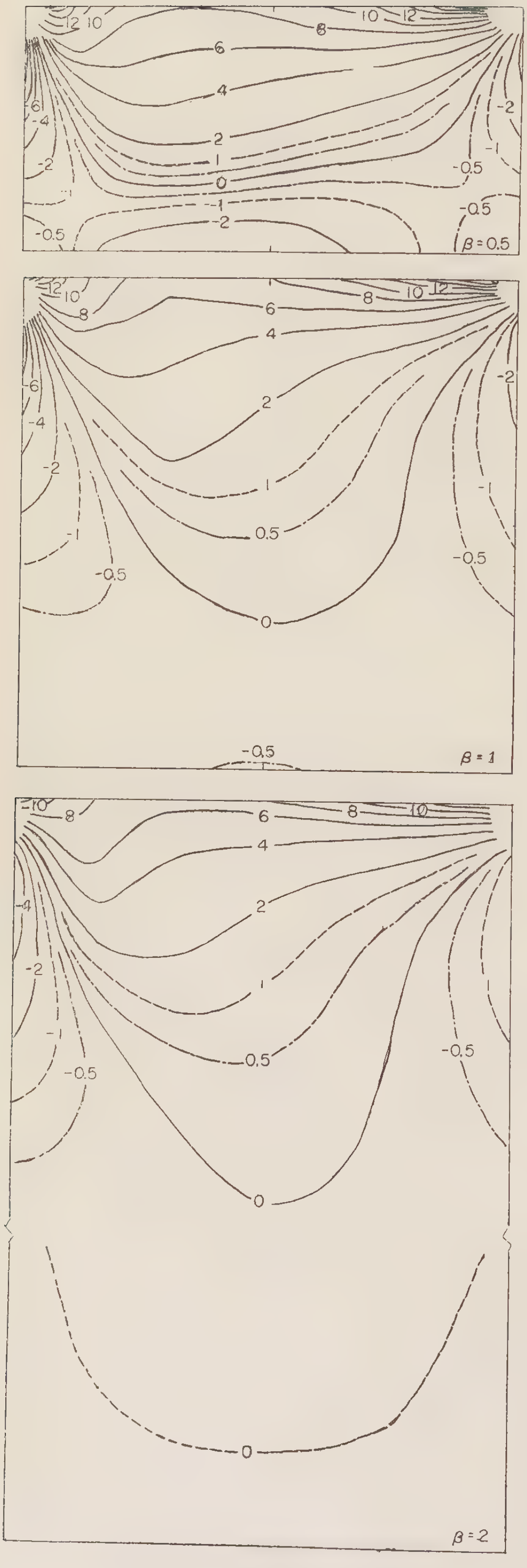

Fig. 8. Vorticity ($R=64$).

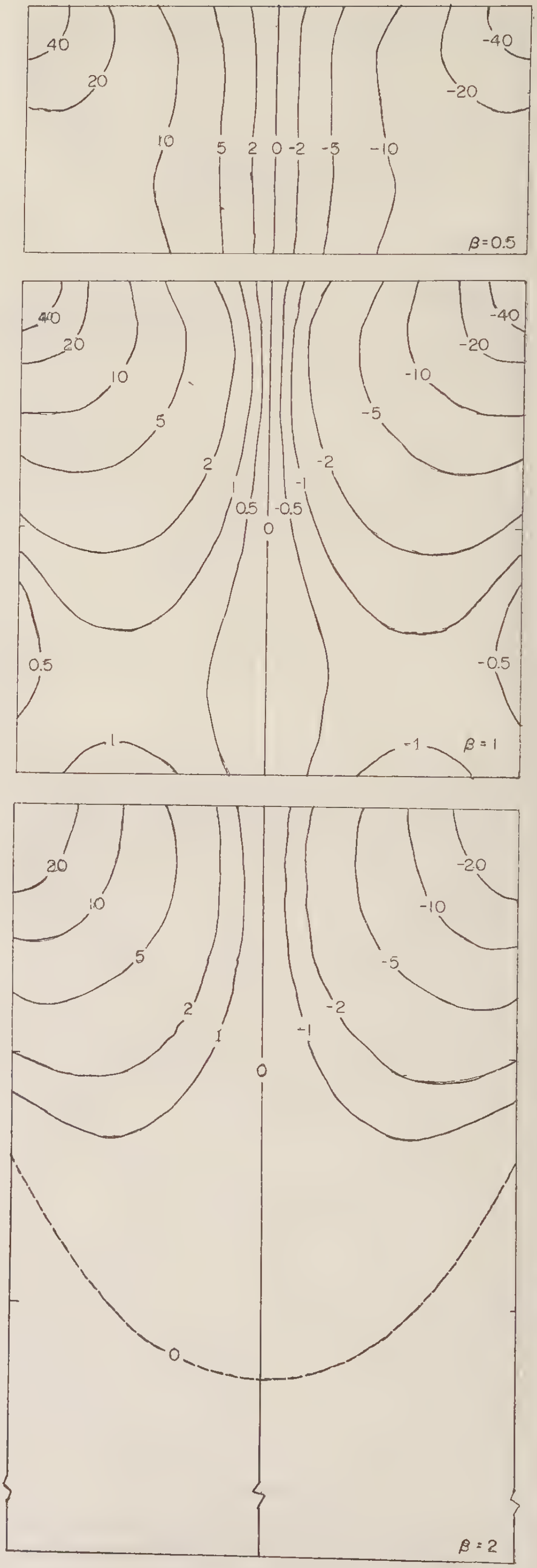

Fig. 9. Pressure: C_pR ($R=0$).

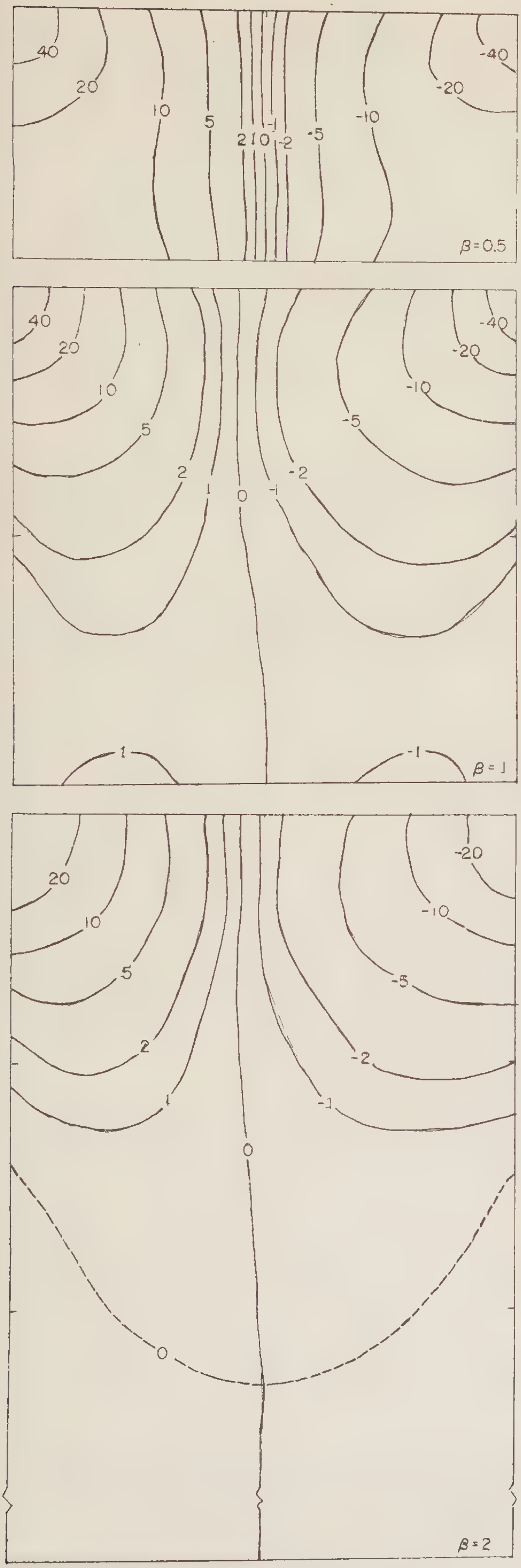

Fig. 10. Pressure: C_pR ($R=8$).

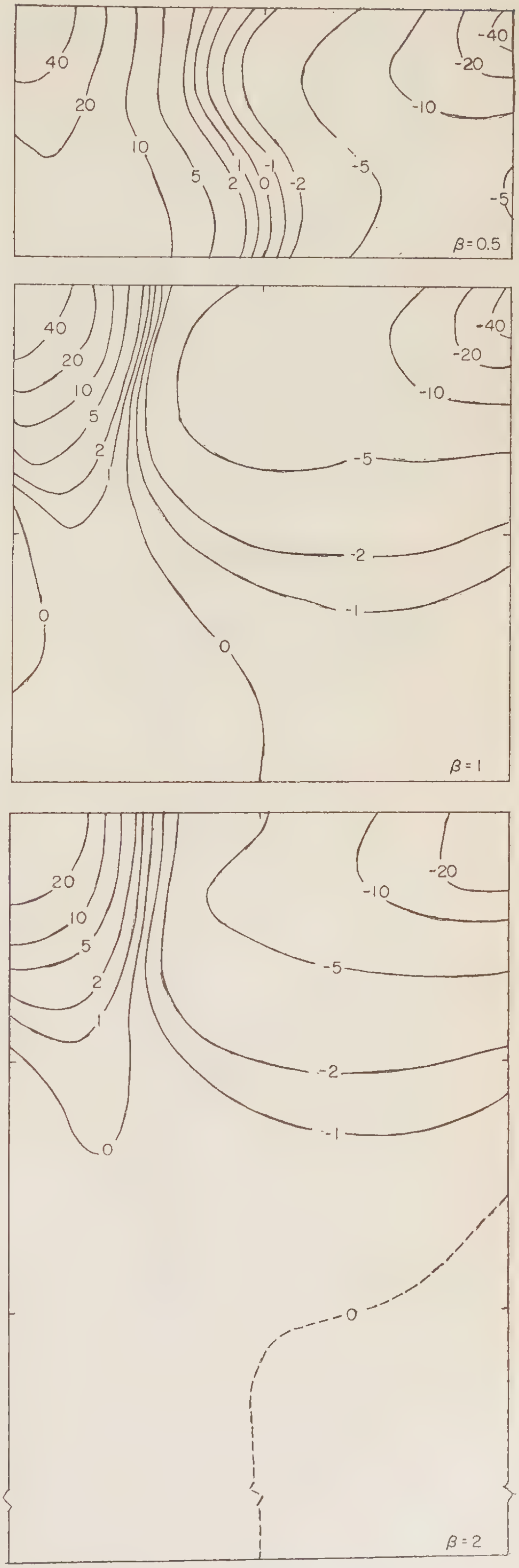

Fig. 11. Pressure: C_pR ($R=64$).

Technical Research Institute, Tokyo, by use of which we could calculate in five digits in floating decimal point method, putting the results for $R=64$ ($\beta=1.0$) as initial values, and printing the results after every two iteration cycles. Although no extraordinary phenomena were observed in first few iteration cycles, some of the values became larger and larger in absolute magnitude as the number of iteration cycles increased, and at last in the 18th process they caused overflow, which showed that one of them at least exceeded 10^{38} in magnitude. This divergence may be caused by the nature of the Navier-Stokes equations, or by the nature of the difference method, or by the use of rather coarse meshes. At present, we cannot decide which is the case.

In Figs. 3–11, distributions of ψ, vorticity ω, pressure p are shown for some typical cases: $R=0$, 8, 64; $\beta=0.5$, 1.0, 2.0. For convenience, we have used C_pR instead of p itself where $C_p=(p-p_0)/(\frac{1}{2}\rho U^2)$ and R is the Reynolds number. The pressure at the middle point of BC has been taken as the reference pressure p_0. In Fig. 12, the distribution of the x-component velocity along the centre line MN of the cavity is given. The pressure distributions over the both sides AB and CD and the bottom wall BC are shown in Fig. 13.

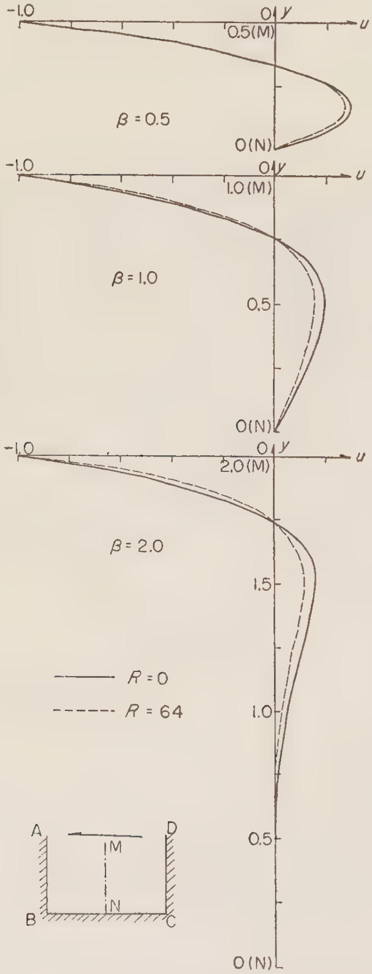

Fig. 12. Velocity distribution along the centre line MN.

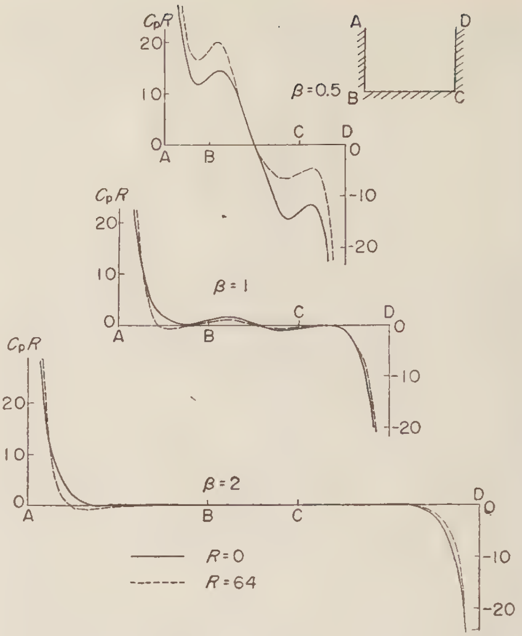

Fig. 13. Pressure distribution over the sides AB, BC, and CD.

§ 7. Conclusions

From the numerical results described in § 6 and shown in Figs. 3–13, following qualitative conclusions concerning the flow in the cavity may be drawn:

(i) In every case, there exists a circulating flow extending the whole length of the cavity. The pressure on the wall AB (downstream) is higher and that on the wall CD (upstream) is lower compnred with the pressure at the middle point N on the bottom wall.

(ii) The general feature of the flow in the upper region remains almost unchanged as the depth of the cavity increases ($\beta=0.5\sim2.0$, cf. Fig. 12).

In the deep cavity ($\beta=2.0$), there appears quite a large region near the bottom where the fluid velocity is very small and exist weak secondary flows even when $R=0$. On the other hand, no secondary flow seems to occur in the shallow cavities ($\beta=0.5$, 1.0) at least for the Reynolds number less than 64. However the accuracy of our calculations is not so good that we cannot determine exactly the flow patterns in these regions.

(iii) The flow patterns for the cases of small Reynolds numbers are quite similar to that of Stokes flow ($R=0$). The deviations of ψ and ω at each point from those in the latter flow are proportional to the Reynolds number when $R<10$.

(iv) As the Reynolds number is increased, the centre of the vortex moves downstream, and the pressure gradient in the region downstream becomes steeper, while that in the region upstream less steep.

(v) In shallow cavities (e.g. $\beta=0.5$), the flow in the middle portion can be well approximated by the parabolic flow, i.e.

$$V_x \propto y^2, \quad V_y \sim 0,$$

where V_x and V_y are the x- and y-components of the flow velocity.

(vi) When the Reynolds number is less than 64, the iterative procedure does converge for our problem. However, it diverges for the case $R=128$ ($\beta=1$). At present, we cannot determine the origin of the divergency. In relation to this problem, further studies, both analytical and numerical, seem to be desirable.

In conclusion, I wish to express my sincere gratitude to Professor Isao Imai for his discussion and kind inspection of the manuscript, to Dr. Hideo Takami for his discussion and aid in programming and operation of PC-1, and to Mr. Kôtarô Mano for his aid in programming and operation of Bendix G-15D.

References

1) Hidaka, K.: Mem. of Imperial Marine Obs., Kobe, **7** (1939) 21.
2) Thom, A. and Apelt, C. J.: Brit. Aero. Res. Council R. and M., No. 3090 (1958).

JOURNAL OF THE PHYSICAL SOCIETY OF JAPAN, Vol. 16, No. 11, NOVEMBER, 1961

On Similar Solutions of the Unsteady Quasi-Two-Dimensional Incompressible Laminar Boundary-Layer Equations

By Nisiki HAYASI*

National Aeronautical Laboratory, Mitaka, Tokyo

(Received July 28, 1961)

Unsteady three-dimensional boundary-layer equations can be reduced to two-dimensional type, if one component of the velocity and the pressure gradient in that direction are negligible throughout the boundary layer. Conditions for the existence of similar solutions for such *quasi-two-dimensional* boundary layer are obtained. In particular it is found that the velocity at the outer edge of the boundary layer must be proportional to $Y_1 \exp(at/Y)$, $Y_1(bt+Y)^{a/b}$ or $(x+Y_1)/(bt+Y)$, where a and b are constants, Y and Y_1 are arbitrary functions of y. Here x, y, z are geodesic normal plane coordinates (the x-axis being the geodesic of the body surface $z=0$). New similar solutions are found, and velocity distributions for various cases are calculated. All the known similar solutions, being two-dimensional, are only special cases of our results. Axisymmetric similar solutions are also among our results.

§ 1. Introduction

Since the concept of the boundary layer was introduced, many exact solutions of the unsteady incompressible laminar boundary-layer equations have been obtained. Some of them are *similar* or affine solutions, for which a component of the velocity has such a property that two velocity profiles at different coordinates differ only by a scale factor. In general, it is assumed that the radius of curvature of the wall is far greater than the thickness of the boundary layer and that the streamlines of the external flow outside the boundary layer are stationary and coincide with geodesics of the surface. Thus Blasius[1] obtained similar solutions for the parallel flow due to the impulsively or uniformly accelerated motion of an infinite plane wall. Watson[2] found similar solutions when the velocity of a flat plate moving in its own plane is proportional to t^a or e^{bt} and the velocity normal to the plate vanishes, where t is the time, and a, b are constants. Their solutions are closely correlated to the so-called Rayleigh's problem, in which the assumption of parallel flow is used instead of the boundary-layer assumption. Schuh[3] showed that similar solutions may be obtained when the velocity at the outer edge of the boundary layer U is proportional to t^a, e^{bt} or x/t, where x is the distance along the flow. Recently Yang[4),8)] obtained similar velocity profiles for the stagnation flow, in which U is proportional to $x/(a-bt)$. All the similar solutions so far obtained are those for the *two-dimensional* flow.

Now we consider the *three-dimensional* boundary-layer flow. We choose the x-axis along one of the streamlines of the external flow outside the boundary layer and the y-axis along one of their orthogonal trajectories. For such coordinate axes, we have shown[5] that the component of the velocity in the y-direction vanishes throughout the boundary layer, if the component of the velocity of the wall (if it is moving) in that direction vanishes. In these cases, the boundary-layer flow is essentially two-dimensional. We call such a flow 'quasi-two-dimensional'. In a previous paper[6] all the exact solutions of the steady incompressible quasi-two-dimensional boundary-layer equations have been obtained. In this paper, we search for all similar solutions for *unsteady* incompressible quasi-two-dimensional flow.

§ 2. Conditions for the Existence of Similar Solutions

The equations for the quasi-two-dimensional laminar boundary layer were obtained in our previous paper[5]. Using the curvilinear planar coordinates (x, y, z), in which the x-axis is the geodesic of the wall and the scale factors are 1, $r(x, y)$, 1, the equations for incompressible fluid can be written as

---

* A part of this work was done when the author was in Transportation Technical Research Institute, Mitaka, Tokyo.

$$\partial(ru)/\partial x+\partial(rw)/\partial z=0\ , \tag{2.1}$$

$$\frac{\partial u}{\partial t}+u\frac{\partial u}{\partial x}+w\frac{\partial u}{\partial z}=-\frac{1}{\rho}\frac{\partial p}{\partial x}+\nu\frac{\partial^2 u}{\partial z^2}\ , \tag{2.2}$$

where u and w are components of the velocity in the directions of x and z respectively, t the time, ρ the density, ν the kinematic viscosity, and p is the pressure. The boundary conditions for u and w are

$$\left.\begin{array}{lll} u=w=0 & \text{at} & z=0\ , \\ u=U(x, y, t) & \text{for} & z\to\infty\ . \end{array}\right\} \tag{2.3}$$

From Bernoulli's theorem, we have

$$-\frac{1}{\rho}\frac{\partial p}{\partial x}=\frac{\partial U}{\partial t}+U\frac{\partial U}{\partial x}\ . \tag{2.4}$$

Let us consider the conditions under which the boundary-layer flow is similar. For this purpose, we assume

$$u=U(x, y, t)f'(\zeta)\ , \tag{2.5}$$

where $\zeta=z/\{\nu^{1/2}g(x, y, t)\}$ and dash denotes differentiation. Naturally g is considered to be proportional to the thickness of the boundary layer. The boundary conditions for f are

$$f(0)=f'(0)=0\ ;\qquad f'(\infty)=1\ . \tag{2.6}$$

Integrating (2.1) with respect to z and using (2.5) and (2.6), we have

$$\frac{w}{U}=-\frac{\nu^{1/2}gf}{rU}\frac{\partial(rU)}{\partial x}+\nu^{1/2}(f'\zeta-f)\frac{\partial g}{\partial x}\ . \tag{2.7}$$

Substituting (2.4), (2.5) and (2.7) into (2.2), we obtain

$$\begin{aligned} \frac{f'''}{g^2}&+\left(\frac{U}{r}\frac{\partial r}{\partial x}+\frac{\partial U}{\partial x}+\frac{U}{g}\frac{\partial g}{\partial x}\right)ff'' \\ &+\frac{\partial U}{\partial x}(1-f'^2)+\frac{1}{g}\frac{\partial g}{\partial t}f''\zeta \\ &+\frac{1}{U}\frac{\partial U}{\partial t}(1-f')=0\ . \end{aligned} \tag{2.8}$$

Hence we must have

$$\frac{1}{U}\frac{\partial U}{\partial t}=\frac{a}{g^2}\ , \tag{2.9a}$$

$$\frac{1}{g}\frac{\partial g}{\partial t}=\frac{b}{2g^2}\ , \tag{2.9b}$$

$$\partial U/\partial x=d/g^2\ , \tag{2.9c}$$

$$\frac{U}{g}\frac{\partial g}{\partial x}+\frac{U}{r}\frac{\partial r}{\partial x}=\frac{e}{g^2}\ , \tag{2.9d}$$

a, b, d and e being certain non-dimensional constants. Then Eq. (2.8) is reduced to

$$\begin{aligned} f'''&+(d+e)ff''+d(1-f'^2) \\ &+\frac{b}{2}\zeta f''+a(1-f')=0\ . \end{aligned} \tag{2.10}$$

When $a=b=0$, the flow is steady. Such a case has already been studied in our previous paper⁶⁾, so that in this paper we assume that $a^2+b^2\neq 0$.

Differentiating (2.9a) with respect to x and using (2.9b) and (2.9c), we have, after some transformations,

$$(a+b)d=aU\partial(g^2)/\partial x\ . \tag{2.11}$$

Similarly we have from (2.9b)

$$2(a+b)e=bU\partial(g^2)/\partial x\ . \tag{2.12}$$

Differentiating (2.11) with respect to t and employing (2.9a) and (2.9b), we have

$$a=0\quad \text{or}\quad g=g(y, t)\ , \tag{2.13}$$

and always

$$(a+b)d=0\ . \tag{2.14}$$

Similarly we have from (2.12)

$$a=0\quad\text{or}\quad b=0\quad\text{or}\quad g=g(y, t)\ ; \tag{2.15}$$

in the latter two cases

$$(a+b)e=0\ . \tag{2.16}$$

From these relations we can conclude, after some simple considerations, that there are only the following possibilities:

(*1*) The case $a=0$,

$$\left.\begin{array}{l} b\neq 0\ ,\quad d=0\ ,\quad U=U(y)\ ,\quad r=r(y)\ , \\ g^2=(2ex/U)+bt+Y(y)\ , \end{array}\right\} \tag{2.17}$$

where Y is an arbitrary function of y. Therefore the form of the wall allowing such similar solutions must be a cylinder.

(*2*) The case $a\neq 0$,

$$g^2=bt+Y(y)\ ,\quad (a+b)d=(a+b)e=0\ . \tag{2.18}$$

(*2.1*) The case $a+b=0$,

$$\left.\begin{array}{l} b=-a\neq 0\ , \\ U=\{dx+Y_1(y)\}/\{bt+Y(y)\}\ , \end{array}\right\} \tag{2.19}$$

where Y_1 is an arbitrary function of y.

(*2.11*) The case $d=0$,

$$r=Y_2(y)\exp\{ex/Y_1(y)\}\ , \tag{2.20}$$

where Y_2 is an arbitrary function of y.

(*2.12*) The case $d\neq 0$,

$$r=Y_2(y)\{dx+Y_1(y)\}^{e/d}\ . \tag{2.21}$$

(*2.2*) The case $a+b\neq 0$,

$$d=e=0\ ,\quad r=r(y)\ ,\quad w=0\ . \tag{2.22}$$

(*2.21*) The case $b=0$,

$$U=Y_1(y)\exp[at/\{g(y)\}^2]\ . \qquad (2.23)$$

(*2.22*) The case $b\neq 0$,

$$U=Y_1(y)\{bt+Y(y)\}^{a/b}\ . \qquad (2.24)$$

It should be remarked here that, when $g=g(y,t)$, we have

$$\partial^2 u/\partial x^2=f'\partial^2 U/\partial x^2=0\ ,$$

so that Eq. (2.10) is the same as what should be reduced from Navier-Stokes' equation.

§ 3. Asymptotic Behaviour of the Similar Solutions

If we put $f=\zeta+C+G$, where C is a constant, Eq. (2.10) becomes

$$G'''+\left\{\left(\frac{b}{2}+d+e\right)\zeta+(d+e)(C+G)\right\}G''$$
$$-\{(a+2d)+dG'\}G'=0\ . \qquad (3.1)$$

From boundary conditions (2.6), we know that G, G' and G'' are small when ζ is large. Here we consider the asymptotic behaviour of G' for large values of ζ.

(*1*) If

$$b+2d+2e\neq 0 \quad \text{and} \quad a+2d\neq 0\ ,$$

we can neglect each of the second terms in the bracketed expressions of (3.1), obtaining

$$G'''+\left(\frac{b}{2}+d+e\right)\zeta G''-(a+2d)G'=0\ . \qquad (3.2)$$

In terms of the new variables

$$x=-(b+2d+2e)\zeta^2/4\ , \qquad y=G'/\zeta\ , \qquad (3.3)$$

the above equation becomes

$$xy''+\left(\frac{3}{2}-x\right)y'-Dy=0\ , \qquad (3.4)$$

where

$$D=(-2a+b-2d+2e)/2(b+2d+2e)\ .$$

Two independent solutions of this equation are given by

$$\left.\begin{aligned} &y_1=F\left(D,\frac{3}{2};x\right) \\ \text{and}& \\ &y_2=x^{-1/2}F\left(D-\frac{1}{2},\ \frac{1}{2};\ x\right)\ , \end{aligned}\right\} \qquad (3.5)$$

respectively, where $F(\alpha,\gamma;x)$ is the confluent hypergeometric function defined as

$$F(\alpha,\gamma;x)=1+\frac{\alpha}{\gamma}\frac{x}{1!}+\frac{\alpha(\alpha+1)}{\gamma(\gamma+1)}\frac{x^2}{2!}+\cdots\ . \qquad (3.6)$$

(*1.1*) If $b+2d+2e>0$, these two solutions can be transformed into

$$\left.\begin{aligned} &y_1=F\left(\frac{3}{2}-D,\ \frac{3}{2};\ |x|\right)e^{-|x|} \\ \text{and}& \\ &y_2=i|x|^{-1/2}F\left(1-D,\ \frac{1}{2};\ |x|\right)e^{-|x|}\ , \end{aligned}\right\} \qquad (3.7)$$

respectively. Now we have the asymptotic expansion

$$F(\alpha,\gamma;x)\sim\frac{\Gamma(\gamma)}{\Gamma(\alpha)}e^x x^{\alpha-\gamma}\left\{1+\sum_{m=1}^{N}(-1)^m\frac{(\gamma-\alpha)_m(1-\alpha)_m}{m!}x^{-m}+O(x^{-N})\right\}$$
$$+\frac{\Gamma(\gamma)}{\Gamma(\gamma-\alpha)}e^{i\pi\alpha}x^{-\alpha}\left\{1+\sum_{m=1}^{N}(-1)^m\frac{\alpha_m(\alpha-\gamma+1)_m}{m!}x^{-m}+O(x^{-N})\right\} \qquad (3.8)$$

for large positive values of x[7], where $\beta_m=\beta(\beta+1)\cdots(\beta+m-1)$. Hence if we form the linear combination

$$y=-2\pi^{-1/2}\Gamma(D)(\sin\pi D)y_1+i(\pi|x|)^{-1/2}\Gamma\left(D-\frac{1}{2}\right)(\cos\pi D)\,y_2\ , \qquad (3.9)$$

we have

$$y\sim e^{-|x|}|x|^{D-3/2}\left\{1+\sum_{m=1}^{N}(-1)^m\frac{(1-D)_m(\frac{3}{2}-D)_m}{m!}|x|^{-m}+O(|x|^{-N})\right\}\ .$$

Thus one solution $G'=y|x|^{1/2}$ tends to zero as $\exp(-\zeta^2)$ when $\zeta\to\infty$*. Let us call such a solution a 'strong solution'.

(*1.11*) If $D>1/2$, both $y_1|x|^{1/2}$ and $y_2|x|^{1/2}$ tend to zero in the order of negative powers of ζ as $\zeta\to\infty$, as can be seen from (3.7) and (3.8).* Such solutions may be called 'weak solutions'. However, in this case, we may have a strong solution as given by the linear combination (3.9). Thus the boundary conditions (2.6) are expected to be unable to determine uniquely a solution of (2.10).

(*1.12*) If $D\leq 1/2$, neither $y_1|x|^{1/2}$ nor $y_2|x|^{1/2}$ tend to zero as $\zeta\to\infty$. Hence, in this case, there is only one strong solution (3.9). Thus it may be possible to determine a unique solution of (2.10) satisfying the boundary conditions (2.6).

(*1.2*) If $b+2d+2e<0$, it can be seen from (3.5) and (3.8) that both $y_1 x^{1/2}$ and $y_2 x^{1/2}$ tend to infinity as $\zeta\to\infty$*. Let us take the linear combination:

$$y=\frac{-2\pi^{1/2}}{\Gamma(D-\frac{1}{2})}F\left(D,\ \frac{3}{2};\ x\right)+\frac{(\pi/x)^{1/2}}{\Gamma(D)}F\left(D-\frac{1}{2},\ \frac{1}{2};\ x\right). \qquad (3.10)$$

By use of (3.8), we have

$$y\sim x^{-D}\left\{1+\sum_{m=1}^{N}(-1)^m\frac{D_m(D-\frac{1}{2})_m}{m!}x^{-m}+\mathrm{O}(x^{-N})\right\}. \qquad (3.11)$$

Thus we have the following conclusions.

(*1.21*) If $D\leq 1/2$, we have no solution.

(*1.22*) If $D>1/2$, we may have one weak solution.

(*2*) If

$$b+2e\neq 0 \quad \text{and} \quad a=0\,,$$

we have $d=0$ from (2.17), so that we can neglect the second term in the first brackets of (3.1). Thus we obtain

$$G'''+\left(\frac{b}{2}+e\right)\zeta G''=0\,,$$

whose general solution is given by

$$G'=A\int\exp\{-(b+2e)\zeta^2/4\}\,d\zeta+B\,,$$

where A and B are integration constants. Therefore, we have no solution if $b+2e<0$. If $b+2e>0$, there is a possibility for the existence of a strong solution or solutions.

(*3*) If

$$a\neq 0 \quad \text{and} \quad b=0\,,$$

we have $d=e=0$ from (2.22), so that the second term in the second brackets of (3.1) vanishes. Thus we obtain

$$G'''-aG'=0\,.$$

Therefore, we have no solution if $a<0$. If $a>0$, we may have a solution

$$G'=A\exp(-a^{1/2}\zeta)\,.$$

Let us call such a solution a 'medium solution', in view of the asymptotic behaviour for $\zeta\to\infty$.

The treatment in this section does not cover all the possible cases of the solution. It has been clarified, however, that there are three kinds of solutions, i.e., *strong*, *medium* and *weak*.

§4. Similar Solutions for Case (*1*) in §2

In this section we consider the case (*1*) in §2, where $a=0$ and $b\neq 0$. U, r and g are given by (2.17). Eq. (2.10) is now reduced to

$$f'''+eff''+\frac{b}{2}\zeta f''=0\,. \qquad (4.1)$$

When $e=0$, the strong solution of (4.1) has been given by Blasius[1] as

$$f'=u/U=\mathrm{erf}\,(b^{1/2}\zeta/2)\,, \qquad (4.2)$$

where $\mathrm{erf}\,x=2\pi^{-1/2}\int_0^x\exp(-x^2)dx$. From (2.7) and (2.17), we have

$$w=0\,. \qquad (4.3)$$

When $e\neq 0$, after the transformations $F=(|b|/2)^{1/2}f$ and $x=(|b|/2)^{1/2}\zeta$, Eq. (4.1) is reduced to

$$\pm F'''+2\varepsilon FF''+xF''=0\,, \qquad (4.4)$$

where $\varepsilon=e/b$ and the upper sign is for $b>0$ and the lower sign is for $b<0$. The boundary conditions for F are

$$F(0)=F'(0)=0 \quad \text{and} \quad F'(\infty)=1\,.$$

From (2.7) and (2.17), we have

$$w=\frac{\pm\varepsilon(2\nu)^{1/2}(F'x-F)}{(|2\varepsilon xU^{-1}+t+b^{-1}Y|)^{1/2}}\,. \qquad (4.5)$$

From (2.17), it is clear that the point where g=const moves with the speed $-bU/2e$, when $e\neq 0$.

From the arguments in the previous section, we know that we may have strong solutions when $b(1+2\varepsilon)>0$. Numerical solutions of Eq. (4.4) have been obtained by the electronic digital computers Bendix G-15D and Burroughs Datatron 205. Calculations by the former employed single or double precision arithmetic, that is, five or twelve significant figures, and calculations by the latter were of eight significant figures. The integration was done by using the Runge-Kutta method with fourth-order accuracy. The velocity distributions for the cases where $b>0$ and $2\varepsilon=1$ (strong), 0 (Blasius, strong) and -1 (medium) are shown together in Fig. 1(a). When $b<0$, there are three cases; when $2\varepsilon>-3.824$, we have no solution; when $2\varepsilon=-3.824$, we have a strong unique solution; when $2\varepsilon<-3.824$, we have two strong solutions. The velocity distributions for the cases where $b<0$ and $2\varepsilon=-3.824$, -4 and -5 are shown together in Fig. 1(b).

---

* When α is either zero or negative integer, $F(\alpha, \gamma; x)$ reduces to a polynomial. Hence the same results can be derived in a simpler manner.

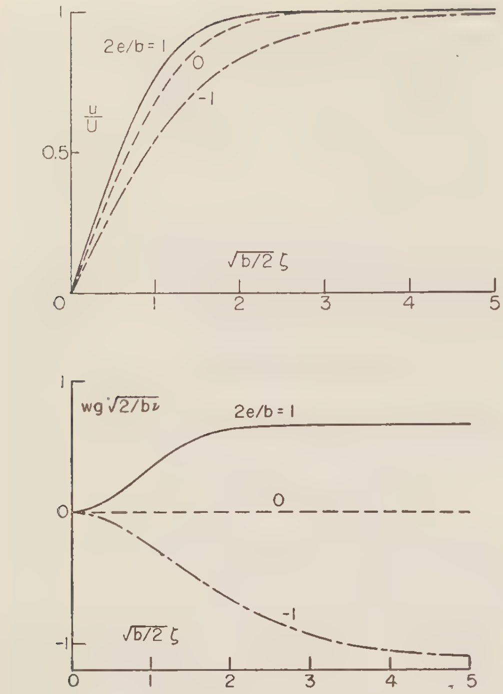

Fig. 1(a). Similar velocity profiles when $a=d=0$, $b>0$. ($e=0$ is given by Blasius.)

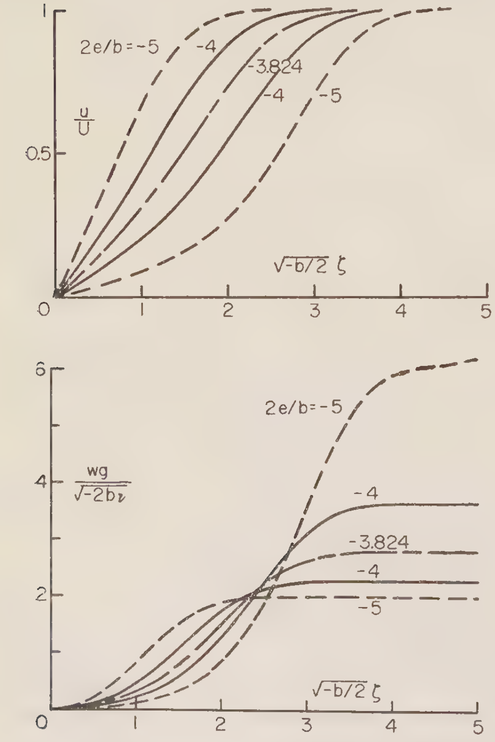

Fig. 1(b). Similar velocity profiles when $a=d=0$, $b<0$.

§ 5. Similar Solutions for Case (*2.11*) in § 2

In this section we consider the case (*2.11*) in § 2, where $a=-b\neq 0$ and $d=0$. From (2.19), we have

$$U=Y_1(y)/\{bt+Y(y)\}\ . \tag{5.1}$$

g and r are given by (2.18) and (2.20), respectively. After the transformations $\zeta=|b|^{-1/2}\xi$ and $f=\pm|b|^{1/2}\{F-(\xi/2)\}/e$ (assuming $e\neq 0$), Eq. (2.10) is reduced to

$$\pm F'''+FF''+F'=m\ , \tag{5.2}$$

where $m=(1/2)+\varepsilon$, and the upper sign is for $b>0$, while the lower sign is for $b<0$. Boundary conditions are:

$$F(0)=0\ ,\quad F'(0)=1/2\quad \text{and}\quad F'(\infty)=m\ .$$

The velocity distributions are given by

$$u/U=(2F'-1)/(2m-1)\ .$$

From (2.7), (2.18), (2.20) and (5.1), we have

$$w=-[\nu/\{bt+Y(y)\}]^{1/2}ef\ . \tag{5.3}$$

From the arguments in § 3, it is clear that there may exist a strong solution when $b<0$ and $m<0$; a strong and weak solutions when $b>0$ and $m>0$; and a weak solution when $b<0$ and $m>0$. If $b>0$ and $m<0$, Eq. (5.2) has no solution. For example, when $e=0$ ($m=1/2$), we have

$$f'=u/U=2Z(\mathrm{Di}\,Z)\exp(-Z^2)+AZ\exp(-Z^2) \tag{5.4}$$

for $b>0$, and

$$f'=\pi^{1/2}Z(1-\mathrm{erf}\,Z)\exp Z^2 \tag{5.5}$$

for $b<0$, where $Z=|b|^{1/2}\zeta/2$, A is an integration constant, and $\mathrm{Di}\,Z$ is the integral defined by

$$\mathrm{Di}\,Z=\int_0^Z \exp x^2\,dx\ .$$

The first term of (5.4) is weak, and the second strong. The constant A cannot be determined from the boundary conditions. The various solutions corresponding to different values of A would represent flows corresponding to various initial conditions. Anyhow both solutions (5.4) and (5.5) are weak and tend to unity as Z^{-2}. The velocity distributions calculated by (5.5) or by the electronic digital computers are plotted in Figs. 2(a) and 2(b)*. (*Solid*, *chain* and *broken* lines correspond to *strong*, *medium* and *weak* solutions, respectively.) When $b>0$ and $m=0$, we have medium solutions. Only the solution that approaches most rapidly to unity is shown in the figure.

Here we consider the boundary layer on the axisymmetric body surface, which is formed by rotating a plane curve L on the Xr-plane about the X-axis. Now we assume that the ordinate r of this curve is given by (2.20). Since the surface is axisymmetric,

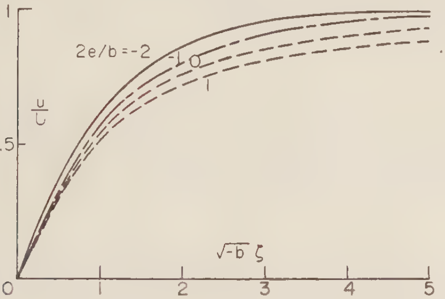

Fig. 2(a). Similar velocity profiles when $d=0$ and $a=-b>0$.

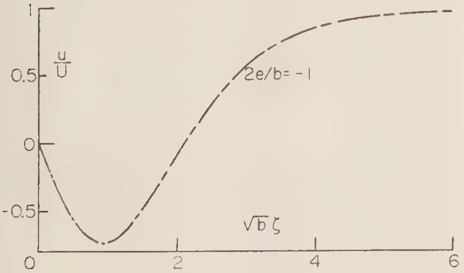

Fig. 2(b). Similar velocity profile when $d=0$, $e/b=-0.5$ and $a=-b<0$.

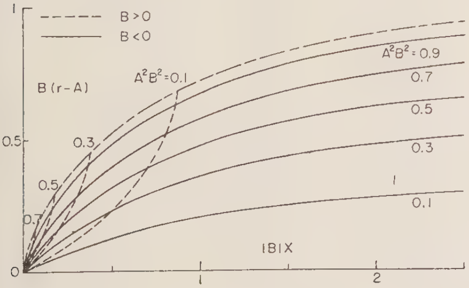

Fig. 3. The forms of the wall allowing similar velocity profiles when $a=-b\neq0$ and $d=0$.

$Y_2(y)=\text{const}=A$, $e/Y_1(y)=\text{const}=B$, so that we have $r=Ae^{Bx}$. Clearly we have

$$dx=(dX^2+dr^2)^{1/2} \quad \text{or} \quad dX=(dx^2-dr^2)^{1/2} . \tag{5.6}$$

Hence, integrating, we have

$$BX=\frac{1}{2}\int_{A^2B^2}^{t} t^{-1}(1-t)^{1/2}\,dt$$

$$=(1-t)^{1/2}-\tanh^{-1}(1-t)^{1/2}+C ,$$

where $t=B^2r^2$ and

$$C=-(1-A^2B^2)^{1/2}+\tanh^{-1}(1-A^2B^2)^{1/2} .$$

The curve L is shown in Fig. 3, for the cases $A^2B^2=0.1$, 0.3, 0.5, 0.7 and 0.9.

It is evident that the above arguments can be readily extended to the general quasi-two-dimensional boundary layer.

§ 6. Similar Solutions for Case (*2.12*) in § 2

In this section we consider the case (*2.12*) in § 2, where $a=-b\neq0$ and $d\neq0$. U, g and r are given by (2.19), (2.18) and (2.21), respectively. Now Eq. (2.10) is reduced to

$$f'''+(d+e)ff''-df'^2+\frac{b}{2}\zeta f''$$
$$+bf'+(d-b)=0 . \tag{6.1}$$

After the transformations $f=|d|^{-1/2}F$ and $\zeta=|d|^{-1/2}\xi$, Eq. (6.1) reduces to

$$\pm F'''+(1+\gamma)FF''-F'^2+1$$
$$=\beta\left(\frac{\xi}{2}F''+F'-1\right) , \tag{6.2}$$

where $\beta=-b/d\neq0$ and $\gamma=e/d$, the upper and lower signs corresponding to $d>0$ and $d<0$, respectively. The boundary conditions for F are

$$F(0)=F'(0)=0 \quad \text{and} \quad F'(\infty)=1 .$$

From (2.7), (2.18), (2.19) and (2.21), we have

$$w=-[\nu/\{bt+Y(y)\}]^{1/2}(\gamma+1)\,df . \tag{6.3}$$

From the arguments in § 3, we know that we may have a strong solution together with weak solutions when $d(2-\beta+2\gamma)>0$ and $d(2+\beta)<0$, a strong solution when $d(2-\beta+2\gamma)>0$ and $d(2+\beta)>0$, and a weak solution when $d(2-\beta+2\gamma)<0$ and $d(2+\beta)>0$. When $d(2-\beta+2\gamma)<0$ and $d(2+\beta)<0$, we have no solution. In this connection it may be noted that Yang[4),8)] has obtained the numerical solutions of (6.2) for the case $d>0$, $\gamma=0$ and $-3\leq\beta\leq1.6$. His solutions are applicable to the quasi-two-dimensional boundary layer along a cylindrical surface.

The case where $\gamma=1$ and $d>0$ is practically important, as shown later. (Cf. Eq. (6.12).) For this case we have obtained the numerical solutions for various values of β. When $\beta<-2$, the preceding paragraph shows that we may have strong and weak solutions. However numerical calculation shows that a unique strong solution only exists in this case. The velocity distributions for $\gamma=1$ are presented in Table I. The value of $d^2F/d\xi^2$ at the wall ($\xi=0$) is $(\nu|d|)^{-1/2}g\tau/\rho U$, where τ is the skin friction. This is also given in Table I.

---

* The solution (5.4) is plotted in Fig. 6(c) for comparison.

In the case where $\gamma=-2$, on integrating twice with respect to ξ and using the boundary conditions, Eq. (6.2) is reduced to a generalized Riccati equation

$$\pm\phi'-\beta\eta\phi-\phi^2+(1+\beta)\eta^2=\pm n\eta\ , \qquad (6.4)$$

where $\phi=2^{-1/2}F$, $\eta=2^{-1/2}\xi$ and $n=\phi''(0)=(2/|d|)^{1/2}f''(0)$. The boundary condition for ϕ is $\phi(0)=0$. The constant n is to be determined from the condition $\phi'(\infty)=1$.

Case 1. $d>0$.

It can be readily shown that we have a strong (or medium) solution when $\beta\leq-2$. Indeed, putting $n=-(\beta+2)$, we have the general solution of (6.4) in the form:

$$\phi=\eta+1-\frac{\exp\{-(n/2)\eta^2+2\eta\}}{A+\int_0^\eta \exp\{-(n/2)\eta^2+2\eta\}\,d\eta}$$

Here the integration constant A is determined as 1, from the boundary condition. Thus we have a medium solution

$$\phi'=u/U=\tanh^2\eta \qquad (6.5)$$

Table I. Velocity distributions u/U and skin friction τ for the case $U=\{dx+Y_1(y)\}/\{bt+Y(y)\}$, $a=-b\neq0$, $d>0$ and $\gamma=e/d=1$. $\tau=\rho\{dx+Y_1(y)\}(\nu d)^{1/2}\{bt+Y(y)\}^{-3/2}F''(0)$.

ξ \ β	−3.7171	−3	−2	−1	(0)	1	2	3
0	0	0	0	0	0	0	0	0
0.1	0.0135	0.0432	0.0763	0.1033	0.1262	0.1461	0.1636	0.1792
0.2	.0530	.1044	.1602	.2050	.2424	.2743	.3019	.3261
0.3	.1157	.1802	.2492	.3037	.3486	.3865−	.4188	.4468
0.4	.1970	.2668	.3404	.3980	.4450	.4843	.5176	.5461
0.5	.2914	.3599	.4311	.4865	.5316	.5692	.6009	.6280
0.6	.3928	.4549	.5188	.5683	.6087	.6425−	.6710	.6954
0.7	.4952	.5476	.6011	.6426	.6766	.7054	.7299	.7509
0.8	.5930	.6345	.6763	.7087	.7358	.7590	.7792	.7966
0.9	.6822	.7127	.7429	.7665	.7867	.8044	.8202	.8342
1.0	.7598	.7806	.8005−	.8161	.8299	.8426	.8543	.8651
1.2	.8759	.8828	.8880	.8920	.8960	.9006	.9057	.9112
1.4	.9442	.9445	.9431	.9412	.9398	.9395−	.9403	.9420
1.6	.9782	.9769	.9739	.9705−	.9672	.9645	.9630	.9625
1.8	.9927	.9915	.9892	.9864	.9832	.9801	.9776	.9760
2.0	.9979	.9973	.9960	.9942	.9919	.9893	.9867	.9847
2.2	.9995−	.9992	.9987	.9978	.9963	.9945−	.9924	.9904
2.4	.9999	.9998	.9996	.9992	.9985−	.9973	.9957	.9940
2.6	1.0000	1.0000	.9999	.9997	.9994	.9987	.9976	.9963
2.8			1.0000	.9999	.9998	.9994	.9987	.9978
3.0				1.0000	.9999	.9998	.9994	.9987
3.2					1.0000	.9999	.9997	.9992
3.4						1.0000	.9998	.9995
3.6							.9999	.9997
3.8							1.0000	.9998
4.0								.9999
4.2								.9999
4.4								1.0000
$F''(0)$	0	.3358	.7166	1.0354	1.3119	1.5570	1.7775	1.9782

for $\beta=-2$, and a strong solution

$$\psi'=u/U=1+(2n)^{1/2}sG^{-1}+G^{-2}\,, \tag{6.6}$$

where $s=(n/2)^{1/2}(\eta-2/n)$ and

$$G=[(\pi/2n)^{1/2}\{\operatorname{erf} s+\operatorname{erf}(2/n)^{1/2}\}+e^{-2/n}]\exp s^2$$

for $\beta<-2$. It should be noted here that the medium solution tends to unity as $e^{-2\eta}$, and the strong solution tends to unity as $\eta\exp(-n\eta^2/2)$.

When $\beta<-2$, weak solutions also exist beside strong solutions. For example, when $\beta=-3$ and $n=0$, we have

$$\psi=\eta-\left\{\eta+\left(\frac{2}{\pi}\right)^{1/2}\frac{\exp(-\eta^2/2)}{\operatorname{erf}(2^{-1/2}\eta)}\right\}^{-1}\,,$$

and

$$\begin{aligned}\psi'&=u/U\\&=1-\{1+(\pi/2)^{1/2}\eta\exp(\eta^2/2)\operatorname{erf}(2^{-1/2}\eta)\}^{-1}\\&\quad+\{\eta+(2/\pi)^{1/2}\exp(-\eta^2/2)/\operatorname{erf}(2^{-1/2}\eta)\}^{-2}\,,\end{aligned} \tag{6.7}$$

which tends to 1 as η^{-2}.

The results (6.6) and (6.7) are in agreement with the above statement that we may have strong and weak solutions when $d(2-\beta+2\gamma)>0$ and $d(2+\beta)<0$. ($\gamma=-2$ in this case.)

Case 2. $d<0$.

When $\beta>-1$, we can show that there exists a weak solution. In fact, putting $n=(\beta+2)(\beta+1)^{1/2}$ and making the substitutions

$$(\beta+2)^{1/2}\Psi=\psi-\eta-(\beta+1)^{1/2}\,,$$

$$s=(\beta+2)^{1/2}\eta+2^{1/2}N\,,$$

$$N=\{2(\beta+1)/(\beta+2)\}^{1/2}\,,$$

we can reduce (6.4) to

$$\Psi'+s\Psi+\Psi^2+1=0\,.$$

The solution is given by $\Psi=-s+G$, where

$$G=\frac{2^{-1/2}\exp(s^2/2)}{\operatorname{Di}(2^{-1/2}s)+N^{-1}\exp N^2-\operatorname{Di}N}\,.$$

Hence, we have

$$\psi'=u/U=1+(\beta+2)(-1+sG-G^2)\,. \tag{6.8}$$

When $d<0$, $\beta=-1$, we have again a weak solution such that $n=1$. Thus

$$\psi=-1+H\,,$$

with

$$H=\frac{2^{-1/2}}{Z}\left\{1+\frac{\exp Z^2}{2Z(\operatorname{Di}Z-\operatorname{Di}2^{1/2})-\exp Z^2+2^{1/2}Ze^2}\right\}\,,$$

where $Z=2^{1/2}+2^{-1/2}\eta$, so that we have

$$\psi'=u/U=-1+2^{1/2}ZH-H^2\,. \tag{6.9}$$

The results (6.8) and (6.9) do not contradict with the statement that we may have a strong solution together with weak solutions when $d(2-\beta+2\gamma)>0$ and $d(2+\beta)<0$.

When $\beta=-4$, it can be readily seen that we have a weak solution such that $n=2$. Thus

$$\psi=\eta-1+(\eta+1)^{-1}\,,$$

so that

$$\psi'=u/U=1-(\eta+1)^{-2}\,. \tag{6.10}$$

This agrees with the statement that we may have a weak solution when $d(2-\beta+2\gamma)<0$ and $d(2+\beta)>0$. ($\gamma=-2$ and $\beta=-4$ in this case.)

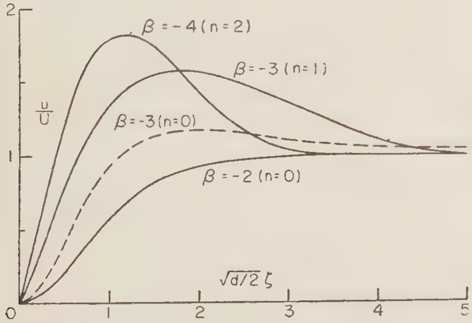

Fig. 4(a). Similar velocity profiles when $d>0$ and $\gamma=e/d=-2$.

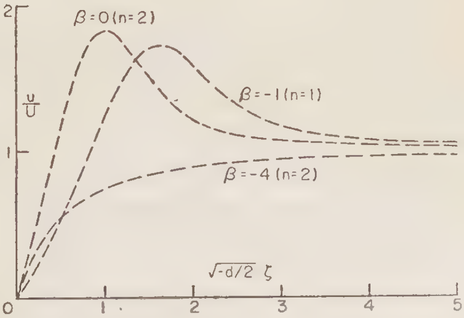

Fig. 4(b). Similar velocity profiles when $d<0$ and $\gamma=e/d=-2$.

These solutions for the cases *(1)* and *(2)* are plotted in Figs. 4(a) and 4(b), respectively. It may be interesting to remark that u/U given by (6.6) to (6.9) exceed unity for some finite values of ζ.

Next we shall consider the boundary layer on the axisymmetric body surface, as is done in the previous section. In this case, we have

$$r=A(x+B)^{\gamma}\ , \tag{6.11}$$

where $A=Y_2$, $B=Y_1$, respectively and $\gamma\neq 0$. From (5.6) and (6.11), we have

$$dX/dr=\pm\{(r^{q}/\gamma^{2}A^{2+q})-1\}^{1/2}\ ,$$

where $q=2(1-\gamma)/\gamma$ and the upper sign is for $\gamma>0$ and the lower sign is for $\gamma<0$. When $\gamma=1$, we have $q=0$, and hence

$$X=(A^{-2}-1)^{1/2}(r-AB)\ . \tag{6.12}$$

This corresponds to the practically important case of a circular cone.

When $\gamma\neq 1$ and so $q\neq 0$, we have

$$I(j)\pm EX=I(\hat{\rho})\ , \tag{6.13}$$

where

$$I(\hat{\rho})=\int(\hat{\rho}^{q}-1)^{1/2}\,d\hat{\rho}$$

and $E=\gamma^{-2/q}A^{-1-2/q}$, $\hat{\rho}=Er$, $j=EAB^{\gamma}$. For example,

$$\begin{aligned} I(\hat{\rho})&=\tfrac{1}{2}[\hat{\rho}(\hat{\rho}^{2}-1)^{1/2}-\ln\{\hat{\rho}+(\hat{\rho}^{2}-1)^{1/2}\}] && (\gamma=1/2)\\ &=\tfrac{2}{3}(\hat{\rho}-1)^{3/2} && (\gamma=2/3)\\ &=\hat{\rho}(-1+\hat{\rho}^{-1})^{1/2}-\tan^{-1}(-1+\hat{\rho}^{-1})^{1/2} && (\gamma=2)\\ &=(1-\hat{\rho}^{2})^{1/2}-\ln\{1+(1-\hat{\rho}^{2})^{1/2}/\hat{\rho}\}\ . && (\gamma=\infty) \end{aligned}$$

These are plotted in Figs. 5(a) and 5(b), where the cases $\gamma=-1$ and -2 are also included.

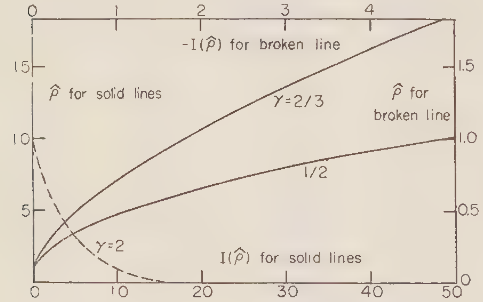

Fig. 5(a). The forms of the wall allowing similar velocity profiles when $a=-b\neq 0$, $d\neq 0$ and $\gamma=e/d>0$.

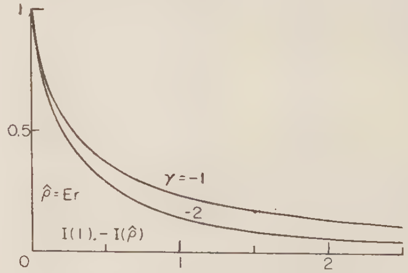

Fig. 5(b). The forms of the wall allowing similar velocity profiles when $a=-b\neq 0$, $d\neq 0$ and $\gamma=e/d<0$.

§ 7. Similar Solution for Case *(2.21)* in § 2

In this section we consider the case *(2.21)* in § 2, where $a\neq 0$ and $b=0$. U, w, g and r are given by Eqs. (2.23), (2.22) and (2.18). Now Eq. (2.10) is reduced to

$$\phi''-a\phi=-a\ ,$$

where $\phi=f'=u/U$. The boundary-layer type 'medium' solution of this equation has been given by Schuh[3] as

$$\phi=u/U=1-\exp(-a^{1/2}\zeta)\,. \tag{7.1}$$

We must have $a>0$, so that $|U|$ increases with t.

§ 8. Similar Solutions for Case (*2.22*) in § 2

In this section we consider the case (*2.22*) in § 2, where $a+b\neq 0$, $a\neq 0$ and $b\neq 0$. We have $d=e=0$. U, w, g and r are given by (2.24), (2.22) and (2.18). Eq. (2.10) is reduced to

$$\phi''+\frac{b}{2}\zeta\phi'-a\phi=-a\,, \tag{8.1}$$

where $\phi=f'=u/U$. The boundary conditions for ϕ are

$$\phi(0)=0 \qquad \text{and} \qquad \phi(\infty)=1\,. \tag{8.2}$$

Blasius[1] has given the analytical solution of (8.1) for $\alpha=a/b=1$. Görtler[9] integrated this equation numerically for $\alpha=2$, 3 and 4. Watson[2] obtained the solution in terms of parabolic cylinder functions. He also calculated the numerical values of u/U for $\alpha=-0.5(0.5)3$ and $b>0$. From the arguments given in § 3, it is clear that we may have a strong solution when $b>0$ and $\alpha>0$, a strong solution as well as weak solutions when $b>0$ and $\alpha<0$, and a weak solution when $b<0$ and $\alpha<0$; and that if $b<0$ and $\alpha>0$, then Eq. (8.1) has no solution. These conclusions agree with the result obtained by Watson*. Now we show the typical expressions for $\phi=u/U$.

(*1*) Strong solutions for $b>0$ and $\alpha>0$:

$$\phi=1+\pi^{1/2}Z(1-\text{erf}\,Z)-\exp(-Z^2)\,, \qquad (\alpha=1/2)$$

$$\phi=1-(1+2Z^2)(1-\text{erf}\,Z)+2\pi^{-1/2}Z\exp(-Z^2)\,; \qquad (\alpha=1)$$

$$\phi=1+\pi^{1/2}Z\left(\frac{3}{2}+Z^2\right)(1-\text{erf}\,Z)-(1+Z^2)\exp(-Z^2)\,, \qquad (\alpha=3/2)$$

$$\phi=1-\left(1+4Z^2+\frac{4}{3}Z^4\right)(1-\text{erf}\,Z)+\frac{2}{3}\pi^{-1/2}(5Z+2Z^3)\exp(-Z^2)\,, \qquad (\alpha=2)$$

(*2*) Strong and weak solutions for $b>0$ and $\alpha<0$:

$$\phi=1-\frac{(2Z)^{1/2}}{\Gamma(1/4)}\exp\left(-\frac{Z^2}{2}\right)\left\{K_{1/4}\left(\frac{Z^2}{2}\right)+AI_{1/4}\left(\frac{Z^2}{2}\right)\right\}, \qquad (\alpha=-1/4)$$

$$\phi=1-(1+A\,\text{Di}\,Z)\exp(-Z^2)\,, \qquad (\alpha=-1/2)$$

$$\phi=1-(1-2Z^2)\exp(-Z^2)+A\{Z+(1-2Z^2)\exp(-Z^2)\,\text{Di}\,Z\}\,, \qquad (\alpha=-3/2)$$

$$\phi=Z^2+(3Z-2Z^3)(A+\text{Di}\,Z)\exp(-Z^2)\,, \qquad (\alpha=-2)$$

$$\phi=1-\left(1-4Z^2+\frac{4}{3}Z^4\right)\exp(-Z^2)+A\{5Z-2Z^3+(3-12Z^2+4Z^4)\exp(-Z^2)\,\text{Di}\,Z\}\,,$$
$$(\alpha=-5/2)$$

(*3*) Weak† solutions for $b<0$ and $\alpha<0$:

$$\phi=1-\frac{(2Z)^{1/2}}{\Gamma(1/4)}K_{1/4}\left(\frac{Z^2}{2}\right)\exp\left(\frac{Z^2}{2}\right), \qquad (\alpha=-1/4)$$

---

* It should be noted here that Watson's notation is different from ours: a, b, α and Z in the present paper correspond to a/ν, $-2b/\nu$, $-b\alpha/|b|$ and η in Watson's paper, respectively.

† Weak solutions in (*2*) and (*3*) tend to unity as $Z^{2\alpha}$.

$$\phi=1-(1-\mathrm{erf}\,Z)\exp Z^2\,, \qquad (\alpha=-1/2)$$

$$\phi=1+2\pi^{-1/2}Z-(1+2Z^2)(1-\mathrm{erf}\,Z)\exp Z^2\,, \qquad (\alpha=-3/2)$$

$$\phi=-Z^2+\pi^{1/2}\left(\frac{3}{2}Z+Z^3\right)(1-\mathrm{erf}\,Z)\exp Z^2\,, \qquad (\alpha=-2)$$

$$\phi=1+\frac{2}{3}\pi^{-1/2}(5Z+2Z^3)-\left(1+4Z^2+\frac{4}{3}Z^4\right)(1-\mathrm{erf}\,Z)\exp Z^2\,, \qquad (\alpha=-5/2)$$

Table II. Skin friction τ for the case $U=Y_1(y)\{bt+Y(y)\}^\alpha$.
$\tau=\rho\nu^{1/2}Y_1(y)\{bt+Y(y)\}^{\alpha-1/2}\phi'(0)$.

Case of $b<0$ Values of α	$\phi'(0)$	Case of $b>0$ Values of α
$\alpha\geq 0$	no solution	
-0.25	$2^{3/2}\pi\{\Gamma(1/4)\}^{-2}=0.6760$	
-0.5	$2\pi^{-1/2}=1.128$	(0)
-1	$\pi^{1/2}=1.772$	0.5
-1.5	$4\pi^{-1/2}=2.257$	1
-2	$(3/2)\pi^{1/2}=2.659$	1.5
-2.5	$(16/3)\pi^{-1/2}=3.009$	2
	not uniquely determined	$\alpha<0$

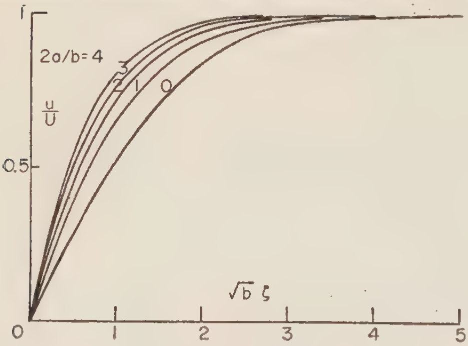

Fig. 6(a). Similar velocity profiles when $d=e=0$, $a>0$ and $b>0$. (Strong solution $a=0$ is given by Blasius and is shown for comparison.)

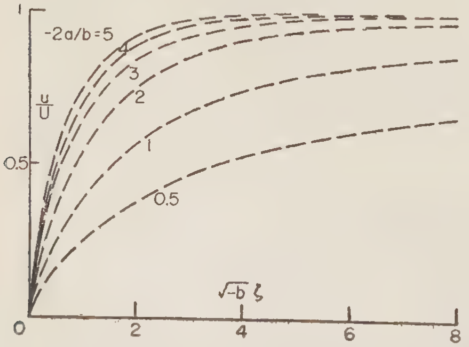

Fig. 6(b). Similar velosity profiles when $d=e=0$, $a>0$ and $b<0$.

where $Z=|b|^{1/2}\zeta/2$, and I and K are the modified Bessel functions. When $b>0$ and $\alpha<0$, the integration constant A cannot be determined from the boundary conditions. (When α is not a negative integer, $A=0$ gives the strong solution.) The value of $d\phi/dZ$ at the

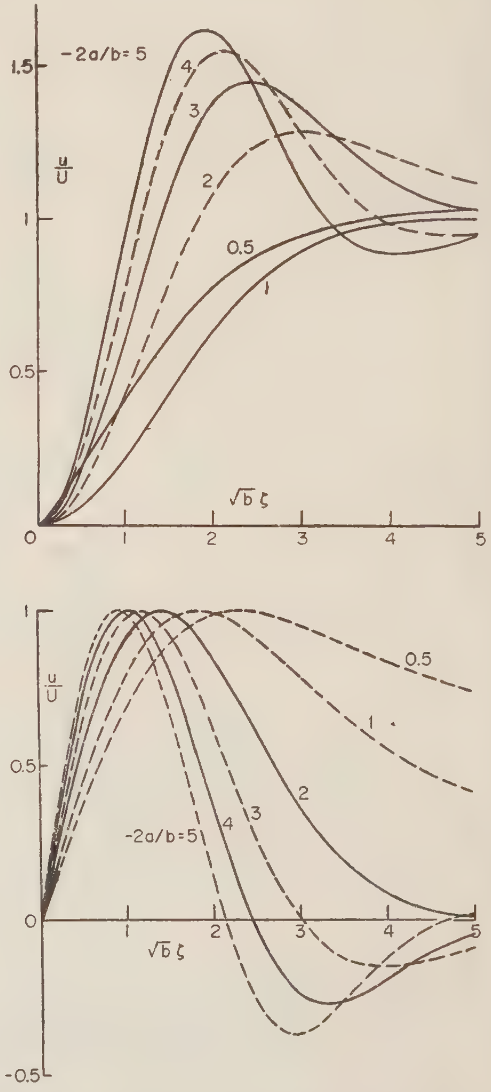

Fig. 6(c). Similar velocity profiles when $d=e=0$, $a<0$ and $b>0$. (Superpositions of solid and broken lines give the velocity distributions.)

Table III.

If we assume	We have	Asymptotic behaviour			From numerical calculation (or analysis)			Case of §2	Solutions
$a=0$ $b\neq 0$	$d=0$ $U=U(y)$ $g^2=\frac{2ex}{U}+bt+Y(y)$ $r=r(y)$	$b(1+2\varepsilon)>0$		S	$b>0,\ \varepsilon>-1/2$		1 S	*(1)*	§4. Figs. 1(a) & 1(b)
					$b<0$	$\varepsilon<-1.912$	2 S		
						$\varepsilon>-1.912$	none		
		$\varepsilon=-1/2$			$b>0$		M		
					$b<0$		none		
		$b(1+2\varepsilon)<0$		none					
$a\neq 0$ $a+b=0$ $d=0$	$b\neq 0$ $U=Y_1(y)/\{bt+Y(y)\}$ $g^2=bt+Y(y)$ $r=Y_2(y)\exp\{ex/Y_1(y)\}$	$b<0$	$\varepsilon<-1/2$	1 S	1 S			*(2.11)*	§5. Figs. 2(a), 2(b) & 6(c)
			$\varepsilon>-1/2$	1 W	1 W				
		$b>0$	$\varepsilon>-1/2$	W & 1 S					
			$\varepsilon<-1/2$	none					
$ad\neq 0$ $a+b=0$	$b\neq 0$ $U=\{dx+Y_1(y)\}/\{bt+Y(y)\}$ $g^2=bt+Y(y)$ $r=Y_2(y)\{dx+Y_1(y)\}^{e/d}$	$d(2+\beta)>0$	$d(2-\beta+2\gamma)>0$	1 S				*(2.12)*	§6. Table I, Figs. 4(a) & 4(b)
			$d(2-\beta+2\gamma)<0$	1 W					
		$d(2+\beta)<0$	$d(2-\beta+2\gamma)>0$	W & 1 S					
			$d(2-\beta+2\gamma)<0$	none					
$a\neq 0$	$d=e=w=0,\ g=g(y),\ r=r(y)$	$a>0$		1 M	(1 M)			*(2.21)*	§7. Eq. (7.1)
$b=0$	$U=Y_1(y)\exp[at/\{g(y)\}^2]$	$a<0$		none	(none)				
$ab\neq 0$ $a+b\neq 0$	$d=e=0$ $U=Y_1(y)\{bt+Y(y)\}^{a/b}$ $g^2=bt+Y(y)$ $r=r(y)$	$a>0$	$b>0$	1 S	(1 S)			*(2.22)*	Fig. 6(a)
			$b<0$	1 W	(1 W)				§8. Fig. 6(b)
		$a<0$	$b>0$	W & 1 S	(α is negative integer W; otherwise W & 1 S)				Fig. 6(c)
			$b<0$	none					

(S=strong, M=medium, W=weak)

wall ($Z=0$) is $\nu^{-1/2}g\tau/\rho U$. This is given in Table II. The velocity distributions for these cases are shown in Figs. 6(a), 6(b) and 6(c).

§ 9. Summary

Conditions for the existence of similar solutions for the quasi-two-dimensional incompressible laminar boundary layer have been obtained. Since the steady cases have been already investigated in our previous paper[6)], the present paper is concerned with the unsteady cases. All the possible cases are investigated in detail, which are characterized by the condition that the velocity at the outer edge of the boundary layer U must be proportional to

$$Y_1(y)\exp\{at/Y(y)\}\ ,$$

$$Y_1(y)\{bt+Y(y)\}^{a/b}\ ,$$

or

$$\{x-Y_1(y)\}/\{bt+Y(y)\}\ .$$

Asymptotic behaviours of the similar solutions are also investigated. It has been shown that three different kinds of solutions (*strong*, *medium* and *weak*) can exist, such that the velocity distributions tend to the free-stream velocity as $\exp(-z^2)$, e^{-z} or z^{-n}, respectively. Numerical solutions have been obtained by means of electronic digital computers. The results are summarized in Table III.

Acknowledgements

In conclusion, the author wishes to express his sincere gratitude to Prof. Isao Imai and Prof. Saburô Asaka for their valuable discussions on this work. His cordial thanks are also due to Mr. Hirotaro Mano and Mr. Yoshio Itagaki for their kind advice concerning the computation technique.

References

1) H. Blasius: Z. Math. Phys. **56** (1908) 1.
2) E. J. Watson: Proc. Roy. Soc. **A**, **231** (1955) 104.
3) H. Schuh: *50 Jahre Grenzschichtforschung*, ed. by H. Görtler and W. Tollmien. (Friedr. Vieweg Sohn, Braunschweig, 1955) 147 p.
4) K.-T. Yang: J. Appl. Mech. **25** (1958) 421.
5) N. Hayasi: J. Phys. Soc. Japan **15** (1960) 208.
6) N. Hayasi: J. Phys. Soc. Japan **15** (1960) 522.
7) E. W. Barnes: Trans. Cambr. Phil. Soc. **20** (1908) 258.
8) K.-T. Yang: J. Appl. Mech. **26** (1959) 171.
9) H. Görtler: Ing.-Arch. **14** (1944) 286.

Errata

On the Quasi-two-dimensional Laminar Boundary Layer

By Nisiki HAYASI

J. Phys. Soc. Japan **15** (1960) 208

Page

208 Received date should be read as November 5, 1959.

208 Eqs. (1) and (10) should be read as follows:

$$ABC\frac{\partial\rho}{\partial t}+\frac{\partial}{\partial x}(\rho BCu)+\frac{\partial}{\partial y}(\rho CAv)+\frac{\partial}{\partial z}(\rho ABw)=0\ , \qquad (1)$$

$$B\frac{\partial\rho}{\partial t}+\frac{1}{A}\frac{\partial}{\partial x}(\rho Bu)+\frac{\partial}{\partial z}(\rho Bw)=0\ . \qquad (10)$$

	Column	Line		Should be read
208	right	25	Then	For the steady flow,
208	right	35	$\frac{\partial u^*}{\partial t}+u^*\frac{\partial u^*}{\partial\xi}$	$u^*\frac{\partial u^*}{\partial\xi}$
208	right	37	$\frac{\partial I}{\partial t}+u^*\frac{\partial I}{\partial\xi}$	$u^*\frac{\partial I}{\partial\xi}$
208	right	37	$-\frac{\partial p}{\partial t}-u^*\frac{\partial p}{\partial\xi}$	$-u^*\frac{\partial p}{\partial\xi}$

Errata

On Similar Solutions of the Steady Quasi-two-dimensional Incompressible Laminar Boundary-layer Equations

By Nisiki HAYASI

J. Phys. Soc. Japan **15** (1960) 522

Page	Column	Line		Should be read
522	Synopsis	10	$G(\alpha, \gamma)$	$G(\alpha, \beta)$
522	Synopsis	12	geometry	geometry.
523	left	Eq. (4)	$\frac{\partial A}{\delta \gamma}$	$\frac{\partial A}{\partial \gamma}$
523	right	5	**Similaritly**	**Similar**

JOURNAL OF THE PHYSICAL SOCIETY OF JAPAN, Vol. 16, No. 11, NOVEMBER, 1961

Two-Dimensional Viscous Flow part a Rotationally-Oscillating Circular Cylinder

By Tosio MIYAGI

Junior College of Engineering, University of Osaka Prefecture, Neyagawa, Osaka

(Received July 27, 1961)

Two-dimensional flow of a viscous incompressible fluid past a rotationally-oscillating circular cylinder is investigated on the basis of Oseen's equations of motion. The cylinder is assumed to oscillate about its axis periodically. It is found that the solution is composed of a steady part and a periodic part, the latter of which is due to the periodic motion of the cylinder. The forces acting on the cylinder are calculated by two different methods; in one method the law of momentum conservation is applied to the flow region surrounded by a large control surface, while in the other the viscous stresses on the surface of the cylinder are integrated. The results by these two methods do not agree with each other, however, and there appears to exist something like Garstang's paradox. The flow field is calculated numerically at several instants of time in one period, and the flow patterns are shown graphically.

§ 1. Introduction

The two-dimensional steady flow of a viscous fluid past a circular cylinder was investigated by many authors (Goldstein[1]), Faxén[2]), Tomotika and Aoi[3]), Tomotika and Miyagi[4])) on the basis of Oseen's equations of motion. The steady flow pattern around the cylinder can be drawn using the numerical results by these authors (the flow pattern at Reynolds number 4.0 is given in Reference 4).

Recently, Lin[5]) discussed the periodically-oscillating wake of a cylinder using Oseen's linearized equations of motion. He investigated the asymptotic behaviour of the solution which is periodic with respect to time. His discussions are quite general, and, as suggested by von Kármán, they can be applied to the wake behind an oscillating aerofoil. It will be very interesting if one can find the relationship between the above oscillatory wake and the periodic motion of the aerofoil.

As a first step towards this problem, we here consider the flow field past a circular cylinder oscillating periodically about its axis. For simplicity, however, we shall confine our considerations to the flow at small Reynolds numbers and deal with Oseen's linearized equations of motion. It is found that the solution is composed of a steady part and a periodic part, the latter of which is caused by the oscillatory motion of the cylinder.

The forces acting on the cylinder at any instant of time may be calculated by two different methods; in one method the law of momentum conservation is applied to the flow region surrounded by a large control surface, while in the other the viscous stresses over the surface of the cylinder are integrated. It is found that the drag is constant irrespectively of the time and is the same as that in the case of steady flow; in other words, the drag is not affected by the oscillation of the cylinder. On the other hand, the lift varies periodically with time. It takes different numerical values depending on the method of calculation and this situation seems to be similar to Garstang's paradox[6] in the case of flow past a rotating circular cylinder.

Details of the flow field at an arbitrary instant of time can be obtained by numerical calculation of the present solution and we here give the flow patterns at four different phases of the periodic oscillation of the cylinder. These flow patterns show clearly how vortices are shed in one period from the frictional layer on the surface of the cylinder.

§ 2. Oseen's Equations of Motion and Boundary Conditions

Let us consider the two-dimensional unsteady flow of a viscous incompressible fluid past a circular cylinder oscillating periodically about its axis. We take the two-dimensional Cartesian coordinate system (x, y) in the plane of fluid motion in such a way that the origin coincides with the centre of the circular cylinder and the x-axis is along the direction of the uniform stream. Then, Oseen's equations of motion and the equation of continuity can be written as:

$$\left.\begin{aligned} &\frac{\partial u}{\partial t}+U\frac{\partial u}{\partial x}=-\frac{1}{\rho}\frac{\partial p}{\partial x}+\nu\Delta u\,,\\ &\frac{\partial v}{\partial t}+U\frac{\partial v}{\partial x}=-\frac{1}{\rho}\frac{\partial p}{\partial y}+\nu\Delta v\,,\\ &\frac{\partial u}{\partial x}+\frac{\partial v}{\partial y}=0\,, \end{aligned}\right\} \tag{1}$$

where U is the velocity of the uniform stream at infinity, u and v are the x- and y-components of the fluid velocity, ρ is the density, ν the coefficient of kinematic viscosity, p the pressure, t the time and Δ stands for $\partial^2/\partial x^2+\partial^2/\partial y^2$. The last equation is satisfied by the stream function ψ such that

$$u=\frac{\partial\psi}{\partial y}\,,\qquad v=-\frac{\partial\psi}{\partial x}\,. \tag{2}$$

Thus, eliminating p from the above equations, we obtain the equation of motion in terms of ψ as follows:

$$\Delta\left(\Delta-2k\frac{\partial}{\partial x}-\frac{1}{\nu}\frac{\partial}{\partial t}\right)\psi=0\,, \tag{3}$$

where $k=U/2\nu$.

In the present problem, the boundary conditions at infinity and on the surface of the cylinder with the radius a are given, respectively, as follows:

$$\left.\begin{aligned} &u\to U\,, \qquad v\to 0 &&\text{for}\quad r\to\infty\,,\\ &u_r=0\,, \qquad u_\theta=\Theta\,\mathrm{Re}\,(e^{i\omega t}) &&\text{at}\quad r=a\,, \end{aligned}\right\} \tag{4}$$

where (r, θ) is the polar coordinates, u_r and u_θ are the r- and θ-components of the velocity, and Θ and ω the velocity amplitude and the angular frequency of the oscillatory motion of the cylinder respectively.

§ 3. Method of Solution

In order to obtain the solution of the above boundary value problem, we decompose the stream function in the following form:

$$\psi=\psi_s+\psi_u\ , \tag{5}$$

where and hereafter subscripts s and u denote the steady and unsteady parts of the motion respectively. The stream functions ψ_s and ψ_u must satisfy Eq. (3) separately, and the boundary conditions (4) are split up into the following two parts for the steady and unsteady parts of the motion:

$$\left.\begin{array}{lll} u_s \to U\ , & v_s \to 0 & \text{for} \quad r\to\infty\ , \\ (u_s)_r=0\ , & (u_s)_\theta=0 & \text{at} \quad r=a\ , \end{array}\right\} \tag{6}$$

$$\left.\begin{array}{lll} u_u \to 0\ , & v_u \to 0 & \text{for} \quad r\to\infty\ , \\ (u_u)_r=0\ , & (u_u)_\theta=\Theta\,\mathrm{Re}\,(e^{i\omega t}) & \text{at} \quad r=a\ . \end{array}\right\} \tag{7}$$

The steady solution of Eq. (3) subject to the boundary conditions (6) has already been obtained by Tomotika and Miyagi (see Reference 4) in the following form:

$$\begin{aligned} \psi_s = {} & Ur\sin\theta - b_0\theta + \sum_{n=1}^{\infty} B_n\left(\frac{r}{a}\right)^{-n}\sin n\theta \\ & + b_0\int_0^\theta kr[K_1(kr)+K_0(kr)\cos\theta]e^{kr\cos\theta}\,d\theta \\ & + e^{kr\cos\theta}\sum_{n=0}^{\infty} b_n K_n(kr)\sin n\theta\ , \end{aligned} \tag{8}$$

where K_n is the modified Bessel function of order n, and the b_n's and the B_n's are the constants which satisfy the following set of algebraic equations:

$$\left.\begin{array}{ll} C_{s-1}+\sum\limits_{n=0}^{\infty} c_n I_{n+s}(ka)K_n(ka)=0\ , & s=1,\,2,\,3\cdots, \\ \sum\limits_{n=0}^{\infty} c_n I_{n-s}(ka)K_n(ka)=\begin{cases}-U\ , \\ 0\ , \end{cases} & \begin{array}{l} s=0\ , \\ s=1,\,2,\,3\cdots, \end{array} \\ C_0=B_0\ , \qquad C_n=nB_n\ , & n=1,\,2,\,3\cdots, \\ c_0=k\left(b_0-\dfrac{b_1}{2}\right), \qquad c_n=\dfrac{k}{2}(b_n-b_{n+1})\ , & n\ \ 1,\,2,\,3\cdots. \end{array}\right\} \tag{9}$$

Now we proceed to find the unsteady part of the solution ψ_u. It is obvious from the symmetry of Eq. (3) with respect to y that the symmetric and antisymmetric stream functions can be the solutions of Eq. (3) respectively. Then the symmetry of the boundary conditions (7) with respect to θ, or y $(=r\sin\theta)$, shows clearly that the antisymmetric part of ψ_u must be zero identically. Thus, the unsteady solution ψ_u which is a symmetric function of θ may be written as:

$$\left.\begin{array}{l} \psi_u=\mathrm{Re}\left[\left\{\sum\limits_{n=1}^{\infty}\alpha_n\left(\dfrac{r}{a}\right)^{-n}\cos n\theta+e^{kr\cos\theta}\sum\limits_{n=-\infty}^{\infty}\beta_n K_n(\lambda r)\cos n\theta\right\}e^{i\omega t}\right] \\ \text{with} \\ \lambda^2=k^2+\dfrac{i\omega}{\nu}\ , \end{array}\right\} \tag{10}$$

where the α_n's and the β_n's are imaginary constants to be determined by the boundary conditions on the surface of the cylinder. In the above solution, the term representing the circulation, namely:

$$\psi_{u,0}=\mathrm{Re}\left[\left(\alpha_0 \ln \frac{r}{a}\right)e^{i\omega t}\right]$$

has been omitted because of the one-valuedness of the pressure.

Applying the boundary conditions (7) to the solution (10) and making use of the formulae:

$$\left.\begin{aligned} e^{kr\cos\theta}&=I_0(kr)+2\sum_{p=1}^{\infty} I_p(kr)\cos p\theta\ , \\ e^{kr\cos\theta}\cos n\theta&=I_n(kr)+\sum_{p=1}^{\infty}[I_{n-p}(kr)+I_{n+p}(kr)]\cos p\theta\ , \\ e^{kr\cos\theta}\sin n\theta&=\sum_{p=1}^{\infty}[I_{n-p}(kr)-I_{n+p}(kr)]\sin p\theta\ , \end{aligned}\right\} \tag{11}$$

we have the following infinite set of algebraic equations for determining the α_n's and the β_n's:

$$\left.\begin{aligned} &\sum_{n=-\infty}^{\infty}\beta_n\left[\frac{\partial}{\partial r}\{I_n(kr)K_n(\lambda r)\}\right]_{r=a}=-\Theta\ , \\ &\sum_{n=-\infty}^{\infty}\beta_n\left[r\frac{\partial}{\partial r}\{I_{n+s}(kr)K_n(\lambda r)\}+sI_{n+s}(kr)K_n(\lambda r)\right]_{r=a}=0\ , \quad s=1,2,3\cdots, \\ &\alpha_s=-2\sum_{n=-\infty}^{\infty}\beta_n[I_{n+s}(kr)K_n(\lambda r)]_{r=a}\ , \qquad s=1,2,3\cdots. \end{aligned}\right\} \tag{12}$$

§ 4. Forces experienced by the Cylinder

There are two different methods for calculating the forces acting on the cylinder. First, we may apply the law of the conservation of momentum to the two-dimensional flow region W surrounded by a large control circle Σ. Integrating the Navier-Stokes equations over the region W, we have the following expressions for the drag X and the lift Y exerted on a unit length of the cylinder:

$$\left.\begin{aligned} -X&=\rho\iint_W\frac{\partial u}{\partial t}dS+\rho\int_\Sigma\left[(U+u)\{l(U+u)+mv\}+\frac{lp}{\rho}+m\nu\zeta\right]d\Sigma\ , \\ -Y&=\rho\iint_W\frac{\partial v}{\partial t}dS+\rho\int_\Sigma\left[v\{l(U+u)+mv\}+\frac{mp}{\rho}-l\nu\zeta\right]d\Sigma\ , \end{aligned}\right\} \tag{13}$$

where $\zeta=\partial v/\partial x-\partial u/\partial y$ is the velocity, and $(l,\ m)$ denote the direction cosines of the outward normal to the curve Σ. The above formulae can be linearized using the Oseen's approximation, and we have

$$\left.\begin{aligned} -X'&=\rho\iint_W\frac{\partial u}{\partial t}dS+\rho U\int_\Sigma lud\Sigma+\rho\int_\Sigma\left(\frac{lp}{\rho}+m\nu\zeta\right)d\Sigma\ , \\ -Y'&=\rho\iint_W\frac{\partial v}{\partial t}dS+\rho U\int_\Sigma lvd\Sigma+\rho\int_\Sigma\left(\frac{mp}{\rho}-l\nu\zeta\right)d\Sigma\ , \end{aligned}\right\} \tag{14}$$

where X' and Y' denote the drag and lift calculated by the linearized formulae. Here we have used the relations; $\int_\Sigma U^2 l d\Sigma=0$, and $\int_\Sigma U(lu+mv)d\Sigma=0$.

Another method of calculating the forces is to integrate the viscous stresses on the surface of the cylinder, and this method gives (see Reference 3)

$$\left.\begin{aligned}-X_C&=\rho\int_C\left(\frac{l_C p}{\rho}+m_C\nu\zeta\right)dC\,,\\ -Y_C&=\rho\int_C\left(\frac{m_C p}{\rho}-l_C\nu\zeta\right)dC\,,\end{aligned}\right\}\tag{15}$$

where (l_C, m_C) is the direction cosines of the outward normal to the circumference C of the cylinder, and the suffix C to the integral implies the contour integration along the circumference C. The pressure in the formulae (14) and (15) can be given as follows by integrating Oseen's equations of motion:

$$\frac{p}{\rho}=\frac{\partial}{\partial t}\int_0^\theta r\frac{\partial\phi_h}{\partial r}d\theta-U\frac{\partial\phi_h}{\partial y}\,,\tag{16}$$

where subscript h means the harmonic part of the solutions (8) and (10).

Substituting the solutions (8) and (10) and the expression (16) into the formulae (14) and (15), we obtain the forces acting on a unit length of the cylinder as follows:

$$\left.\begin{aligned}X'&=2\pi a\rho UB_0\,, & Y'&=2\pi a\rho\,\mathrm{Re}\,(i\alpha_1\omega e^{i\omega t})\,,\\ X_C&=2\pi a\rho UB_0\,, & Y_C&=Y'+\pi a\rho U\Theta\,\mathrm{Re}\,(e^{i\omega t})\,.\end{aligned}\right\}\tag{17}$$

From the above results it will readily be seen that the drag is the same as that in the steady case (see Reference 3). It is rather strange, however, that the two methods give different values to the lift. This situation seems to be quite similar to that of the so-called Garstang's paradox in the case of flow past a rotating circular cylinder, and it may be ascribed to the fact that Oseen's approximate equations do not satisfy the law of the momentum conservation. Since the difference between the two values of the lift is comparable with the coincident terms, this part of the result may not be taken as reliable.

§ 5. Change of Flow Pattern in One Period

The instantaneous flow fields are obtained through numerical calculations of the solutions (8) and (10). It is generally recognized that in the steady cases Oseen's approximation gives fairly good results for Reynolds numbers up to the order of unity. In the present calculation we have taken the value of Reynolds number as $R=4ka=4$. Further, the Strouhal number S and the angular amplitude of oscillation θ_0 have been chosen as:

$$S=\frac{1}{2\pi}\frac{1}{ka}\frac{a^2\omega}{\nu}=\frac{(2.6)^2}{2\pi}\,,\qquad \theta_0=\frac{\Theta}{U}\frac{1}{\pi S}\doteqdot 34°\,,\tag{18}$$

where in the latter expression the value of Θ/U has been taken as 2. The calculations of the flow pattern have been carried out at several instants in one period of oscillation. The solution (10) has been calculated up to the third term and the solution (8) up to the fifth term. The numerical calculation of the flow pattern has been carried out at four different phases as shown in Fig. 1. Fig. 2 shows the flow pattern at the phase corresponding to the maximum angular displacement of the cylinder. In this figure,

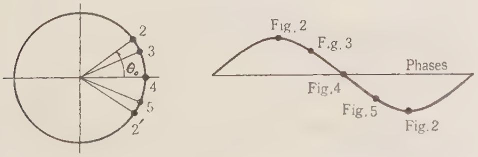

Fig. 1. Illustration of phases corresponding to Figs. 2~5.

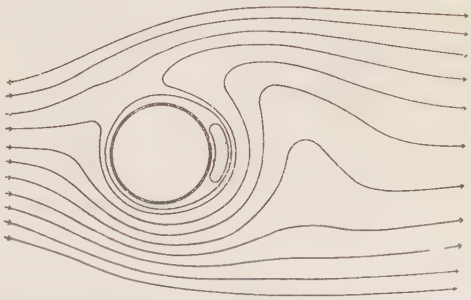

Fig. 2. Calculated streamlines past a rotationally-oscillating circular cylinder.

there is a closed streamline around the cylinder, and the fluid inside oscillates together with the cylinder. Within this closed streamline there exists a vortex on the downstream side of the cylinder, and at this instant of time this vortex whirls in the counter-clockwise sense. Figs. 3, 4 and 5 show successively the flow patterns at three instants when 1/8, 1/4 and 3/8 of one period have elapsed respectively since the instant corresponding to Fig. 2. It is obvious that the flow patterns at various instants in the subsequent half-period can be obtained by the reflection of Figs. 2∼5 with respect to the x-axis, and the vortices shed in this half-period are of the clockwise sense. We can observe from these results how vortices are generated inside the frictional layer on the surface of the cylinder and are shed into the outer flow region.

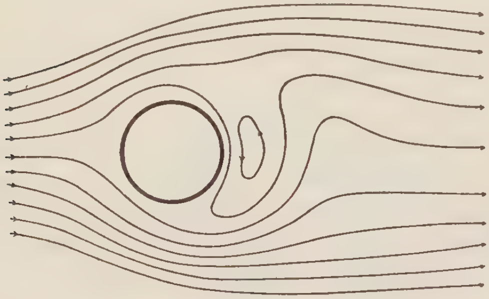

Fig. 3. Calculated streamlines past a rotationally-oscillating circular cylinder.

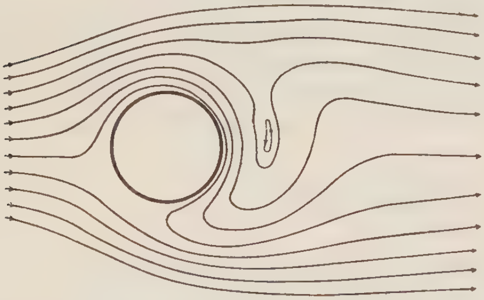

Fig. 4. Calculated streamlines past a rotationally-oscillating circular cylinder.

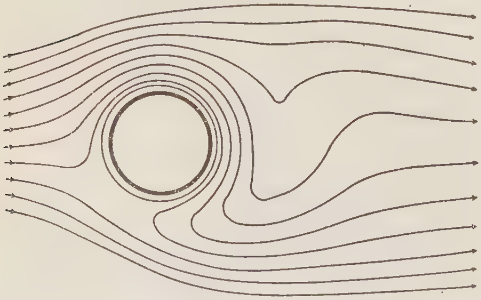

Fig. 5. Calculated streamlines past a rotationally-oscillating circular cylinder.

In Figs. 2, 3, 4 and 5 the centre of the vortex is located at 1.17a, 1.53a, 1.94a and 2.38a respectively downstream from the centre of the cylinder, so that the average velocity V of the vortex during this 3/8 period is given by

$$V=\frac{2.38a-1.17a}{2\pi/\omega\times 3/8}=\frac{1.21}{2\pi}\cdot\frac{8}{3}\,\frac{a^2\omega}{\nu}\,\frac{U/2}{ka}\doteqdot 1.74U\,. \tag{19}$$

The flow pattern at an instant by a half-period later that corresponding to Fig. 2 is obtained by reflecting Fig. 2 with respect to the x-axis, and we observe in this figure that the vortex has already vanished.

Thus it seems impossible to obtain, at this small value of Reynolds number, a clear double-row structure of the velocity field which corresponds to the Kármán vortex street in an inviscid fluid. In order to derive theoretically the double-row vortices in the wake of a cylinder, we have to calculate the flow pattern at much higher Reynolds numbers. The important problem of finding the relationship between the linear dimension of the vortex street and the size of the cylinder as well as the relationship between the phase velocity of the vortices and the velocity of the uniform stream might be solved if the detailed structure of the velocity field at larger Reynolds numbers would be found by numerical calculations.

Acknowledgements

The writer wishes to express his cordial thanks to Professor S. Tomotika for his interest and encouragement throughout this work. The writer's thanks are also due to Professor K. Tamada who suggested this problem and to Dr. H. Yosinobu for their valuable discussions.

References

1) S. Goldstein: Proc. Roy. Soc. **A, 123** (1929) 225.
2) H. Faxén: Nova Acta Regiae Societatis Scientiarum Upsaliensis, Volumen extra ordinem (1927) 1.
3) S. Tomotika and T. Aoi: Quart. J. Mech. Appl. Math. **3** (1950) 140.

4) S. Tomotika and T. Miyagi: Memoirs Coll. Sci. Univ. of Kyoto **30** No. 1 (1962) 1.
5) C. C. Lin: *Studies in Mathematics and Mechanics presented to Richard von Mises*, ed. by G. Birkhoff, G. Kuerti and G. Szegö (Academic Press, New York, 1954) 170.
6) T. E. Garstang: Proc. Roy. Soc. **A**, **142** (1933) 491.

Errata

Structure and Properties of A-Centers in KCl

By Kazuko KOJIMA, Noriko NISHIMAKI
and Tadanobu KOJIMA

J. Phys. Soc. Japan **16** (1961) 2033

Page	Line		should be read
2034	Fig. 2	+20C).	+20°C).
2034	Fig. 2	−30°,	−30°C,
2035	left column line 10	−30C.	−30°C.
2035	right column line 2	from	form
2036	Fig. 6	(*F*- and *A*′-centers	(*F*′- and *A*′-centers
2038	Table II	Unpolarized light	unpolarized light
		I_2 I_1	I_2 I_2
		0 0	1 0
2039	Table IV	2.21 0.28	2.26 0.28
		2.30 0.2_0	2.30 0.20
2042	left column line 7	$\Sigma \rightarrow \Pi^*$	$\Sigma \rightarrow \Sigma^*$
2042	left column line 25	0.70 A^{-3} 12).	0.70 A^{-3} 13).
2042	right column line 11	have many	have made many

Errata

Gamma Rays from Neutron Inelastic Scattering of Magnesium. Aluminum, Iron and Bismuth

By Masano HOSOE and Shoji SUZUKI

J. Phys. Soc. Japan **14** (1959) 699

P. 706 The value of 2.436 in Eq. (9) should be changed to 1.684.

Eq. (10) is incorrect (Private communication, D. M. Van Patter, May 25, 1961). Such errors might not be so remarkable that the final result should be changed.

Short Notes

This section is intended to secure prompt publication of important discoveries in physics. The reports should not exceed 800 words in length. A figure of size 7 cm×7 cm will be counted as 150 words.

J. PHYS. SOC. JAPAN **16** (1961) 2336

Relativistic Correction to the Method of Eliminating the Primary Extinction in Electron Diffraction

By Shizuo MIYAKE, Kunio FUJIWARA,

The Institute for Solid State Physics, University of Tokyo, Shinryudo-cho, Minato-ku, Tokyo, Japan.

Goro HONJO and Norihisa KITAMURA

Physics Department, Tokyo Institute of Technology, Oh-okayama, Meguro-ku, Tokyo, Japan.

(Received July 29, 1961)

Two of the present authors (G. H and N. K.) proposed previously a method of obtaining the kinematical values of reflexions in electron diffraction by extrapolation of the observed intensities at various wave-lengths λ to the limit $\lambda=0$[1]. Their method was based on the theory of primary extinction, according to which the observed intensity I_h is approximately given by

$$I_h=K\cdot\exp\left(-\frac{1}{3}A^2\right)\cdot|v_h|^2\,,\quad A=\frac{2\pi m_0 e}{h^2}\lambda\cdot|v_h|\cdot D\,, \tag{1}$$

so long as A is small, where D is the effective crystal thickness, v_h the Fourier potential and K a constant of the reflexion concerned.

Recently, another of the authors (K. F.) has emphasized the practical importance of the relativistic correction factor in scattering formulae of electron diffraction[2], which had beed introduced previously by Laue[3] and is due to the relativistic correction of electron mass. Since, however, the electron mass appears in scattering formulae of electrons always combined with v_h, the relativistic revision of current kinematical and dynamical theories of electron diffraction can be obtained merely by the replacement of Fourier potential as follows:

$$v_h\to v_h\cdot\left(1+\frac{h^2}{m_0{}^2c^2\lambda^2}\right)^{1/2}. \tag{2}$$

Then, the logarithm of a relative intensity is expressed, when corrected for the relativistic effect, as

$$\ln\frac{I_h}{I_{h'}}=2\ln\frac{|v_h|}{|v_{h'}|}-\frac{1}{3}\left(\frac{2\pi m_0 e}{h^2}\right)^2 \times\left(\lambda^2+\frac{h^2}{m_0{}^2c^2}\right)\cdot(|v_h|^2-|v_{h'}|^2)\cdot D^2+C\,. \tag{3}$$

Since the term C is a geometrical quantity, the relative value of $|v_h|/|v_{h'}|$ is obtained at the virtual limit $\Lambda^2\equiv(\lambda^2+h^2/m_0{}^2c^2)=0$, but not at the limit $\lambda^2=0$ as was proposed previously. The quantity h/m_0C corresponds to Compton wave-length 0.0243 Å.

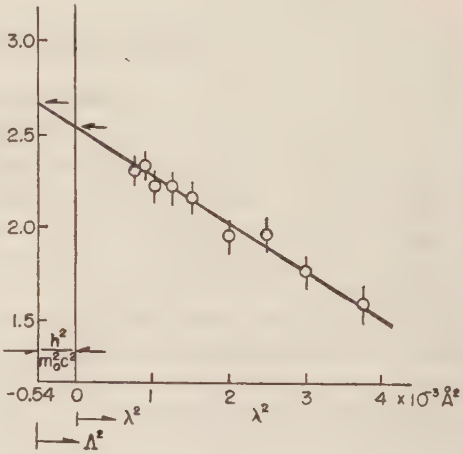

Fig. 1.

Fig. 1 shows the variation with wave-length of the observed intensity ratio I_{200}/I_{422} in powder patterns from an evaporated sodium fluoride film of mean crystal size about 200 Å. The limiting values of $|v_{200}|/|v_{422}|$ are 3.74 ± 0.07 and 3.42 ± 0.07 at $\Lambda=0$ and $\lambda=0$, respectively. The difference between these values is about five percent and is of the order of that between the values of Fourier potentials calculated on various models, say, neutral and ionic states, of atoms. If Fourier potential and mean crystal size are larger than those in the persent case, the difference may be more serious.

References

1) G. Honjo and N. Kitamura: Acta Cryst. **10** (1957) 533.
2) K. Fujiwara: J. Phys. Soc. Japan **16** (1961) 2226.
3) M. von Laue: Materiewellen und Ihre Interferenzen, (1948) Akadem. Verlag. Leipzig.

J. PHYS. SOC. JAPAN **16** (1961) 2337

Electron Spin Resonance of Diluted $(NH_4)Fe(SO_4)_2 12H_2O$

By Shigeru MAEKAWA

Electrotechnical Laboratory, Nagatacho,
Tokyo, Japan

(Received July 15, 1961)

ESR studies have been made on NH_4-Fe alum, $(NH_4)Fe(SO_4)_2 12H_2O$, diluted with non-magnetic isomorphous NH_4-Al alum, $(NH_4)Al(SO_4)_2 12H_2O$. Earlier experiments[1] on this complex salt could only split the fine structure incompletely. Bleaney and Trenam[2] attributed this incomplete splitting mainly to the inhomogeneity in the crystalline fields in different parts of the crystal. This note reports the angular dependence of more resolved lines in this salt.

Single crystal of the atomic ratio Fe : Al as 1 : 100 was carefully grown from a saturated aqueous solution lowering temperature at the rate of 1.0°C/day within the accuracy of ±(1/50)°C. The ESR measurements were made using a 3-cm wave length apparatus of the reflection type.

As is shown in Fig. 1, fine structure lines are well resolved and their variations with angle in the (001) plane at room temperature are shown in Fig. 2. In Fig. 2, the displacements of the main and subsidiary maxima from 0° and 45° respectively, reveal that the cubic axes of the crystalline fields incline from those of the crystal. The rotation angle, ϕ, of the cubic axes of the crystalline fields about the [111] axis of the crystal is estimated to be 10°. It is therefore concluded that this alum has the α-type structure[3] at room temperature. The cubic field parameter, $|a|$, is about 0.012 cm^{-1}. The trigonal field parameter, $|D|$, is much smaller than $|a|$, and is estimated to be 0.005 cm^{-1}. On the other hand, Ubbink et al. gave $|D|=0.016\ \text{cm}^{-1}$ at 4.2°K[1]. To investigate the origin for the difference between these two results, measurements of the temperature dependence of the spectrum are in progress.

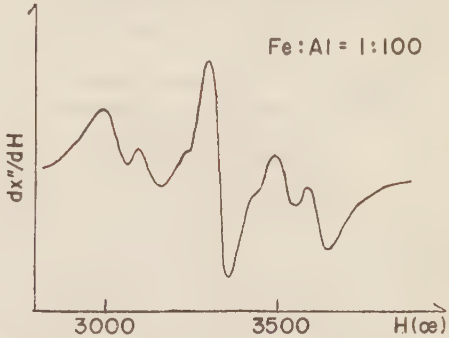

Fig. 1 A typical trace of the resonance line in the (001) plane at room temperature.

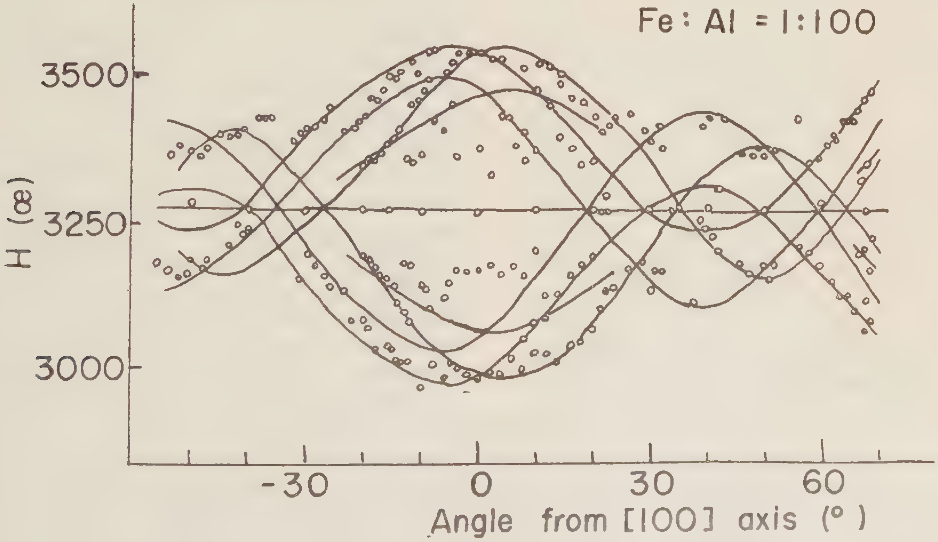

Fig. 2 Variation of the spectrum in the (001) plane at room temperature.

References

1) R. T. Weidner, P. R. Weiss, C. A. Whitmer and D. R. Blosser: Phys. Rev. **76** (1949 1727.
J. Ubbink, J.A. Poulis and C.J. Gorter: Physica **17** (1951) 213.
P. H. E. Meijer: Physica **17** (1951) 899.
2) B. Bleaney and R. S. Trenam: Proc. Roy. Soc. **A223** (1954) 1.
3) K. D. Bower and J. Owen: Repts. Progr. Phys. **18** (1955) 304.

J. PHYS. SOC. JAPAN **16** (1961) 3838~2339

Electron Spin Resonance in Irradiated Polytetrafluoroethylene: Temperature Dependence of the Spectra

By Naoyuki TAMURA

Tokyo Laboratories, Japanese Association for Radiation Research on Polymers,
Komagome-Kamifujimae,
Bunkyo-ku, Tokyo

(Received August 21, 1961)

We have shown in the previous paper that the ESR spectrum of polytetrafluoroethylene irradiated in vacuum at room temperature is composed of at least three kinds of curves, i. e. double quintet, triplet, and smeared out broad line[1]. The double quintet spectrum with doublet splitting of 87 gauss and quintet splittings of 32 gauss is due to the radical $\sim CF_2-CF-CF_2\sim$, α-fluorine giving the doublet and four β-fluorines quintet.

In the present paper the temperature dependences of the spectral shape will be examined and some discussions will be given in the relation between the spectral changes and the properties and structures of the polymers.

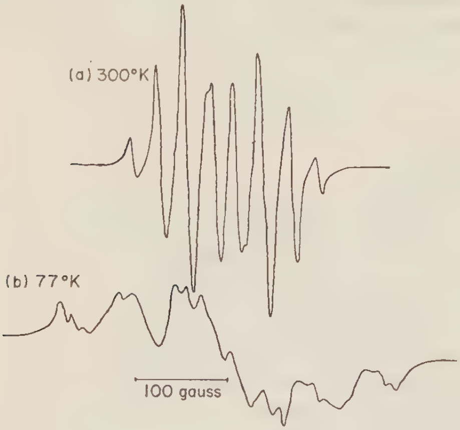

Fig. 1. ESR spectra of irradiated polytetrafluoroethylene taken at 300°K (a) and at 77°K (b).

Fig. 1 (a) shows a derivative tracing of the double quintet spectrum obtained at 300°K for the sample (Polyflon) irradiated with electrons from a Van de Graaff accelerator with dose of up to 10^9 rad. Other components except double quintet were eliminated by warming up the sample as previously reported[1]. This spectrum was found to vary its shape with temperature. The widths of the component lines become broader with decreasing temperature in the region of crystalline phase transition, where the rotational motion of molecular chains is reported to cease according to the nuclear magnetic resonance studies. For 10^9 rad irradiated sample this transition in the line width was observed to shift to lower temperature compared with the samples irradiated with lower dosage, probably because the high dosage produces a larger number of defects and chain scissions in the crystalline regions, increasing the molecular mobilities.

Broadening of the line width in ESR with decreasing temperature here may be ascribed to the variation of anisotropic hyperfine splitting arising from the dipole-dipole interaction between the unpaired electron and fluorine nuclei. This broadening of line width was compared for the irradiated sample of low dosage with that of broad component line in NMR. For $5\times10^7 r$ irradiated sample with ^{60}Co γ rays the transition temperature T was found to be 300°K for ESR and 287°K for NMR. The correlation frequencies ν_c of molecular motions at these temperatures were calculated from the values of line widths according to the method of Gutowsky[2]. The values of ν_c calculated for ESR and NMR are 2.1×10^7 c/s and 4.0×10^4 c/s respectively. The dependence of ν_c on temperature may be written as

$$\nu_c=\nu_0\exp(-E/RT)\,. \qquad (1)$$

Using the above values of ν_c and T for ESR and NMR and assuming a straight line for log ν_c vs T plot an apparent activation energy E of 79 kcal/mole was obtained. This value agrees fairly well with the activation energy of 70 kcal/mole determined by Wada[3] for this transition from the transition map of mechanical dispersion. These results indicate that the above transition of the ESR lines is ascribed to the similar mechanism to the transitions found in the NMR and the dynamic mechanical properties.

With decreasing temperature in the temperature region succeeding the region where the line width broadens the variation of the isotropic hyperfine splitting was observed. Fig. 1 (b) shows the transformed spectrum observed at 77°K, which can be interpreted as consisting of double quintet, the splitting of doublet being 87 gauss, but those of quintet 61 gauss, with fine structures on each line. The change of the quintet splitting from 32 gauss to 61 gauss indicates that some change has occurred in the interaction of the unpaired electron with four β-fluorines. This result may tentatively be interpreted by considering that at low temperature when the molecular chains are in the rigid state, the quintet splittings will be determined by the positions of β-fluorines relative to the p orbital of the radical carbon atom, whereas at high temperature when they are in motional or rotational states, the splittings from four β-fluorines will average to small values of 32 gauss.

The author is deeply indebted to Dr. K. Shinohara for his encouragement and interest.

References

1) N. Tamura: J. Phys. Soc. Japan **15** (1960) 943.
2) H. S. Gutowsky and L. H. Meyer: J. Chem. Phys. **21** (1953) 2122.
3) Y. Wada: J. Phys. Soc. Japan **16** (1961) 1226.

J. PHYS. SOC. JAPAN **16** (1961) 2339~2340

Activation Energy of Acceptors Introduced into Germanium by Plastic Twisting

by Osamu RYUZAN

Semiconductor Dep., Kobe Kogyo Corp., Kobe

(Received May 29, 1961)

It has been known that dislocation acceptors can be introduced into germanium crystal by plastic bending at temperature above 500°C. Pearson, Read, Morin[1], and Tweet[2] found that the acceptor levels lie 0.2 eV bellow the conduction band and 0.15 eV above the valence band. Acceptors can be introduced in the same way by plastic twisting. One of these acceptor levels was determined in this note from the measurements of temperature variation of Hall coefficient and resistivity.

The samples were obtained from an antimony-doped zone leveled crystal grown in the <111> direction. The room temperature resistivity was 30~40 ohm-cm n-type. Bars were cut from the crystal whose dimensions were about 2 mm × 3 mm × 20 mm, with the long axis of the bars along the <111> direction. In order to minimize the effect of contamination on a specimen at elevated temperature, samples were covered with films made by vacuum-evaporation of gold which were sandblasted and etched after twisting.

Specimens were heated to 600°C in argon atmosphere and held at that temperature for approximately 40 seconds during deformation by twisting about <111> direction and then cooled rapidly. These treatments were performed within 5 minutes. These specimens were converted to p-type, where twist angles were usually larger than a few degrees per centimeter. A bar of dimensions about 1 mm × 2 mm × 18 mm was cut from the twisted bar, with the long axis parallel to the twist axis and magnetic field was applied at right angle to that axis in which the direction of current was parallel to the same axis. The results of measurements of Hall coefficient and resistivity are presented in Fig. 1.

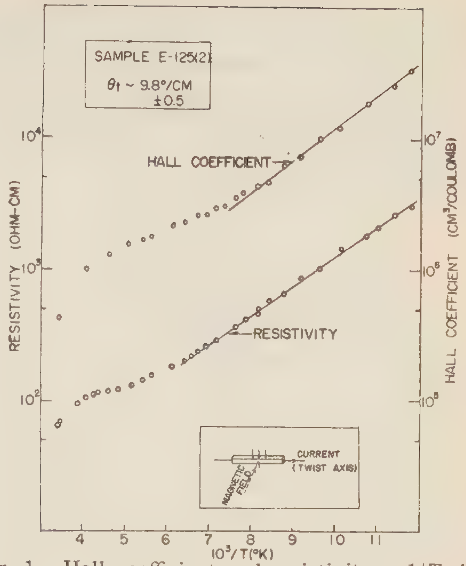

Fig. 1. Hall coefficient and resistivity *vs* $1/T$ plots for a sample plastically deformed by twisting, where the angle of twist is 9.8°/cm. This sample is slightly p-type converted from n-type by the deformation. The straight line portion of these curves indicates an acceptor level thus introduced into germanium.

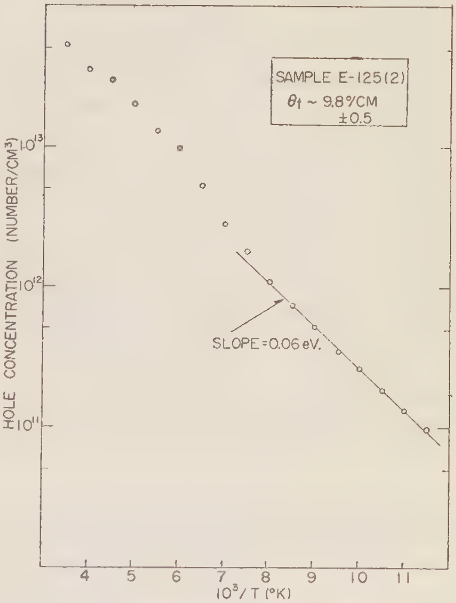

Fig. 2. Hole concentration *vs* $1/T$ plot for the same sameple as in Fig. 1. The points are computed from the data obtained in Fig. 1. and Fig. 3.

On the other hand, it was confirmed that no appreciable change of the resistivity beyond experimental error was caused in the specimen by the heat treatment under the same conditions as for the deformed specimens and that such an acceptor level as found in the twisted sample was not observed before twisting. This suggests that the acceptor level which appeared in the twisted specimen is not introduced thermally but is associated with dislocations or other lattice defects produced by the plastic twisting.

Values of the electron and the hole mobility in the deformed crystal which were used to calculate the hole density were determined experimentally from data of the extrinsic samples shown in Fig. 3., neglecting small differences of twist angles. The hole density is plotted against $1/T$ (°K)$^{-1}$ in Fig. 2. indicating activation energy of 0.06 eV,

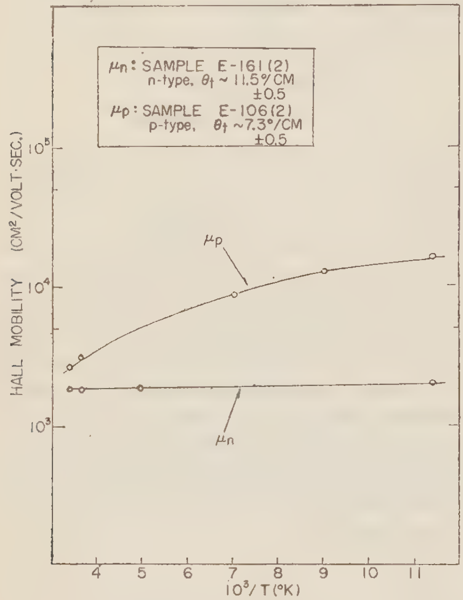

Fig. 3. Hall mobility of electron and hole *vs* $1/T$ plots for the sample plastically deformed by twisting.

The electron mobility at room temperature decreases as the twist angle increases, but the hole mobility remains nearly constant. The mobility of electron and hole in the twisted samples have a characteristic temperature dependence, that is, the electron mobility is approximately constant in the range 300°K to 90°K, but the hole mobility is increased according to about $T^{-1.5}$ in this range as shwon in Fig. 3.

These results suggest that electrical properties of a twisted crystal are somewhat different from those of a bent crystal[3].

References

1) G.L. Pearson, W.T. Read, J.R. and F. J. Morin : Phys. Rev. **93** (1954) 666.
2) A.G. Tweet : Phys. Rev. **99** (1955) 1245.
3) R. L. Logan, G. L. Pearson and D. A. Kleinman : J. Appl. Phys. **30** (1959) 885.

J. Phys. Soc. Japan **16** (1961) 2340~2341

Magnetic Properties of Chromium Oxide Modified by Vanadium Oxide

By Buichi Kubota, Tomozo Nishikawa
and Akira Yanase

Research Department, Wireless Division,
Matsushita Electric Industrial Co., Ltd.
Kadoma-cho, Kitakawachi-gun, Osaka-fu, Japan.

(Received July 7, 1961)

The magnetic properties of chromium dioxide modified by vanadinm oxide were studied.

Specimens were prepared essentially in the same way as that described in early papers[1, 2]. A mixture of chromic acid anhydride and ammonium metavanadate were prepared by concentrating and drying the aqueous solution of chromic acid and ammonium meta-vanadate on a water bath. The specimens were prepared by heating the mixture under an oxygen pressure of 700 atmospheres at 410°C for 14 hours.

The results of X-ray analysis and magnetic measurements of these specimens are shown in Table 1. It was found that the X-ray diffraction patterns of specimens incorporated with vanadium oxide exhibit broadening peaks. Magnetic measurements were done by a magnetic balance. In Fig. 1 the temperature dependence of the magnetization at low

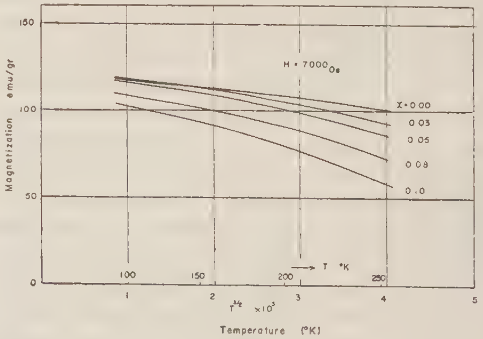

Fig. 1.

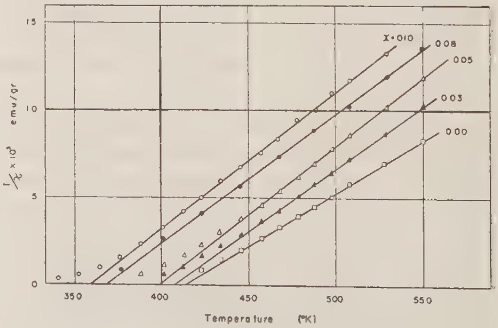

Fig. 2.

Table 1. X-ray analysis and magnetic properties of $Cr_{1-x}V_xO_2$

contents of vanadium X	Curie temperature T_c(°K)	paramagnetic Curie temperature θ_p(°K)	Curie constant C(emu/gr)×10^3	lattice constant a_0(Å)	c_0(Å)	X-ray analysis
0.00	389.5	414	16.4	4.421	2.916	CrO_2 single phase
0.01	389.5	411	14.3	4.425	2.916	〃
0.02	385.5	411	12.8	4.427	2.915	〃
0.03	384.5	408	13.9	4.427	2.916	〃
0.05	381.5	399	12.7	4.429	2.914	〃
0.06	363.5	380	13.9	4.432	2.911	〃
0.08	344	368	13.5	4.438	2.908	〃
0.10		359	12.8	4.441	2.906	〃

temperatures is expressed as a function of $T^{3/2}$ (T, the absolute temperature). In this study the value of magnetic moment was measured at a magnetic field of 7000 Oe where the specimens would be saturated sufficiently. Fig. 1 shows that the variation in saturation magnetization of CrO_2 with temperature is governed by the $T^{3/2}$ law of Bloch. Hence, the saturation magnetization at 0°K can be obtained by extraporation. The saturation magnetization was found to be 125.2 emu/gr, that is 1.89 μ_B/ion. This value is smaller than the value, 2.04 μ_B/ion obtained by S. Siratori et al[3] and the value, 2.01 μ_B/ion obtained early by the authors. This result, however, is thought to be more reliable than the previous one because the accuracy of the measurements has been improved. From theoretical considerations, it seems reasonable to conclude that the magnetic moment per ion is smaller than 2.00 μ_B/ion.

The variation in magnetization as a function of temperature of CrO_2 incorporated with vanadium ion is not governed by the law of Bloch. Accordingly, saturation moments at 0°K obtained by extraporation do not seem to be reliable. It should be noted that chromium ions of different valencies may occur when vanadium ions are dissolved in CrO_2. In view of the results of both saturation magnetization and paramagnetic susceptibility measurements (as shown in Fig. 2) it seems reasonable to conclude that the magnesic moments of the vanadium ions and chrome ions other than Cr^{4+} couple ferromagnetically with the moment of Cr^{4+}.

References

1) B. Kubota: J. Phys. Soc. Japan **15** (1960) 1706.
2) B. Kubota: J. Am. Ceram. Soc **44** (1961) 239.
3) K. Siratori and S. Iida: J. Phys. Soc. Japan **15** (1960) 210.

J. Phys. Soc. Japan **16** (1961) 2341~2342

Luminescence Accompanied by Electrolysis in CdS Single Crystals

By Eiichi Maruyama

Hitachi Central Research Laboratory, Kokubunji, Tokyo

(Received September 1, 1961)

A conducting CdS crystal, doped with chlorine, makes a rectifying contact to electrolyte solution. Williams[1] has reported that by the use of a crystal around 10 Ωcm in resistivity at room temperature a saturation reverse current (that is: the crystal is positively biased to the solution) of the order of 10^{-10} A is achieved in the dark and that voltages of 120 V may be applied without catastrophic breakdown of the crystal.

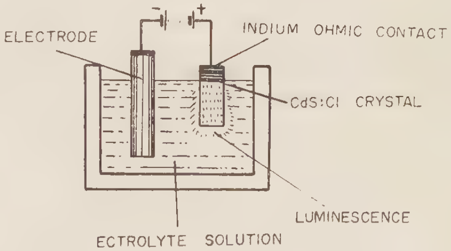

Fig. 1. Schematic drawing of apparatus for observing the luminescence at CdS-electrolyte contact surface.

The case of a crystal about 10^{-1} Ωcm in resistivity, however, is quite different. The reverse dark current rises at first proportionally to the applied voltage. This proportionality breaks above 2-3 V. At 20-25 V a negative-resistance region appears, and then the current begins to rise more rapidly. This breakdown is rather soft and accompanied by orange luminescence in the CdS-electrolyte contact surface (Fig. 1). I–V characteristic of the cell with 1M KCl solution and with a calomel counter-electrode is given in Fig. 2. For the observation of the phenomenon NaH_2PO_4 solution is more satisfactory.

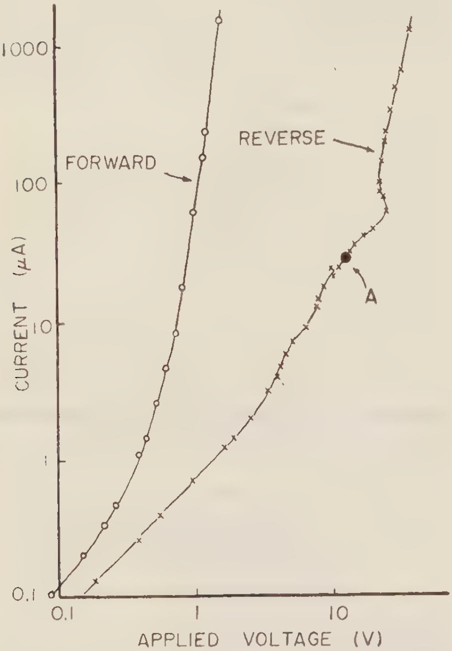

Fig. 2. Log-log plot of current-voltage characteristic of the cell. Luminescence has been detected above point A.

Together with the luminescence, electrolysis of the solution and electrical decomposition of the crystal are also observed. If the reaction is kept on for a period of several tens of second, a yellow layer of sulfur forms on the face of the crystal, and when the crystal is fully decomposed, no luminescence can be seen anymore.

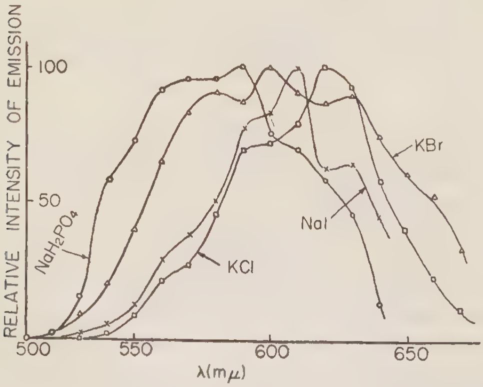

Fig. 3. Spectral distribution of the luminescent emission. These curves were obtained from one same crystal and several different electrolytes.

By means of spectroscopic observation, it has been found that the luminescence has a broad band around 600 mμ and that its spectral distribution is dependent on the kind of negative ions in the electrolyte solution. Sometimes "fine structures" composed of two or three peaks are observed (Fig. 3).

Proportionality between the emission intensity and the current has been verified in the large-current region, though the emission occurs rather abruptly near point A in Fig. 2, around where any proportionality between the intensity and either the current or the decomposition rate of the crystal does not hold. The emission intensity is rather voltage- than current-dependent in the negative-resistance region. It is concluded, therefore, that this luminescence is not caused by chemical reaction of the crystal, but is a sort of electroluminescence in CdS single crystals.

Interesting features of the phenomenon are as follows:

1) This is clearly a surface-luminescence, so that "fine structures" of the spectral distribution may provide with some information concerning the surface of the crystal.

2) Minority carrier injection mechanism does not fit here since the crystals used are n-type and the luminescence is observed only at the negative electrode of the crystal. Either field-emission mechanism or avalanche mechanism must be quoted.

3) The negative-ion dependence of the emission spectra suggests that the luminescence is caused by immediate recombination of injected electrons and trapped holes (perhaps at cation vacancies), while the formers are still retaining their original energy, but quantitative examination of this mechanism has not been fully successful yet.

Reference

1) R. Williams: J. Chem. Phys. **32** (1960) 1505.

J. Phys. Soc. Japan **16** (1961) 2342~2343

The formation of superstructure of Fe_3Ni in fine particles.

By Yoshichika Bandō

Department of Chemistry, Faculty of Science
Kyoto University, Kyoto

(Received June 21, 1961)

The presence of the superstructure of Fe_3Ni has been proposed by Chino[1], Hoselitz, Sucksmith[2], and Kussmann[3], but the experimental evidence is still lacking. This may be partly attributed to the following experimental difficulties.

(1) In addition to difficulty of X-ray technique caused by similar scattering factors of iron and nickel[4], the rate of interdiffusion of iron and nickel and therefore the rate of approach to the ordered state is very slow in iron-nickel alloys.

(2) Iron-nickel alloys with less than 30 atomic per-cent nickel (Fe_3Ni), perform martensitic transformation, before they are cooled to room temperature.

A possible means of accelerating the formation of the superlattice, as proposed by Weil[5], is to make use of the fine particles of alloys in which interdiffusion is fairly rapid. In this connection, we prepared the fine particles of iron-nickel alloy of about $0.2\,\mu$ in mean particle size by reducing a solid solution of oxalate containing required amounts of iron and nickel, in the atmosphere of hydrogen at 600°C for 4 hrs and cooling to room temperature. The alloys, thus obtained, containing more nickel than 25 atomic per-cent, consist of only γ-phase (f. c. c.) because no martensitic transformation takes place in such a fine particle[6].

We have examined the existence of the superstructure by specific heat measurement of this specimens. Fig. 1 shows specific heat temperature curves of the specimens containig 29, 32, 50 and 75 atomic per-cent nickel. The peak at 600°C in Fig. 1 (a), which appears with 75 atomic per-cent nickel, shows the abnormal specific heat which accompanies the magnetic transformation.

In this case, the sample is not in an ordered state of $FeNi_3$ because the reduction temperature, was higher than the critical temperature, 500°C. With 50 atomic per-cent nickel alloy, a small peak, which accompanies the magnetic transformation, is observed. With both 32 and 29 atomic per-cent nickel alloys, the small first peak and the large second peak are observed at about 600°C and about 800°C, respectively. The second peak at about 800°C is not observed with 75 and 50 atomic per-cent nickel samples. Consequently, it is clear that this is not due to the abnormal specific heat caused by the sintering or the recrystallization of fine powders. The investigation on the phase transformation during heating by the use of a high temperature X-ray camera indicated that γ-phase (f. c. c.) is slightly transformed to α (b. c. c.) at about 400°C and that this α-phase disappears again at about 600°C by leaving γ-phase unchanged. So the first peak may correspond to this phase change. But the second peak at 800°C cannot be attributed to any of the sintering, the recrystallization, the magnetic transformation, and the α-γ phase transformation. The peak must be the abnormal specific heat which accompanies the order-disorder transformation. The heat of transformation is about 400 cal/mol. During heating process, there occur sintering and shrinkage in the powdered specimen. Accordingly, the experimental errors, caused by the poor heat conductivity through the free space between the heating vessel and the shrinked specimen, are necessary brought about. Therefore, these abnormal specific heat peaks are not exactly λ-shaped.

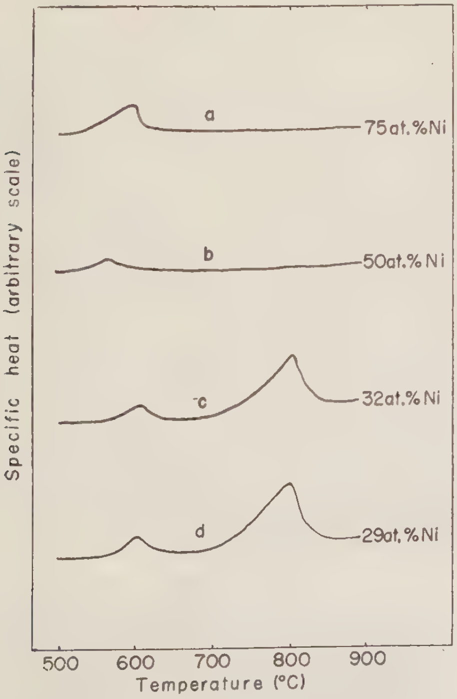

Fig. 1. The specific heat-temperature curves of iron-nickel alloys.

The ordered state of iron-nickel (50 : 50) alloy was not found in this experiment, as seen in Fig. 1 (b).

The author thanks professor S. Kachi, Faculty of Science, Kyoto University, for his invaluable discussions.

References

1) O. Chino : Reported at the Annual Meeting of the Physical Society of Japan. April, 1956.
2) K. Hoselitz and W. Sucksmith : Proc. Roy. Soc. A. **181** (1943) 303.
3) A. Kussmann und K. Jessen : Arch. Eisenhütt. **29** (1958) 585.
4) C. Sykes and P. Leech : Phil. Mag. **27** (1939) 742.
5) L. Weil : Report of A Conference of Strength of Solids. (1948) 138.
6) S. Kachi, Y. Bandō and M. Higuchi : to be published.

J. Phys. Soc. Japan **16** (1961) 2344~2345

Young's Moduli in Ordered and in Disordered States of Fe_3Al Single Crystals.

By Ken'ichi Numakura

The Research Institute for Iron, Steel and Other Metals.
Tohoku University, Sendai

(Received July 4, 1961)

It is very significant to measure the single crystal elastic constants of pure ferromagnetic metals and alloys. Many studies have already been performed on iron[1], cobalt[2] and nickel[3], but there are very few about alloys. It has been known that, by ordering, Young's modulus of Fe-Al polycrystal is decreased[4], while Young's moduli of other common superlattice alloys are increased[5]. Before any conclusion, therefore, the study on single crystals should be done. In the present note the variation of Young's moduli with order of Fe_3Al single crystals along ⟨100⟩, ⟨110⟩ and ⟨111⟩ directions will be described.

A cylindrical single crystal, 10 mm in diameter, which was prepared by the Bridgman method of slow solidification using a vacuum induction furnace and the crucible-lowering rate of 10 mm/hr, was supplied to the present author from Mr. Wakiyama. Its aluminium content was analysed chemically to be 13.13 wt-%, and its orientation was determined by light-figure method[6]. Three small sheet crystal specimens extended along the three principal directions were mechanically cut out of it, using Yamamoto's crystal-cutting machine. Their strained surface layers were removed by etching with saturated $FeCl_3$ solution or with HNO_3 solution, and then their surfaces were made flat by polishing very softly. The width and thickness of specimens thus prepared are given in Table 1. Young's moduli of the crystal specimens in the state annealed at 1000°C for three hours in a vacuum and in the state quenched into water from 850°C higher than the critical temperature of Fe_3Al superlattice formation (about 500°C) were determined in the following manner: The specimen laid on two knife edges, 0.901 cm apart, was bent by loading at its center, and the dip of the loaded point was measured by a microscope using the magnification of 1200 times[3].

Table 1. Orientations, dimensions, and Young's moduli, in annealed and in quenched states of Fe_3Al single crystals.

Orientation	Width cm	Thickness cm	Young's modulus (10^{12} dyne/cm²)	
			in the annealed state	in the quenched state
⟨100⟩	0.1200	0.0684	0.92	1.07
⟨110⟩	0.1287	0.0826	1.31	1.46
⟨111⟩	0.1172	0.0719	1.54	1.70

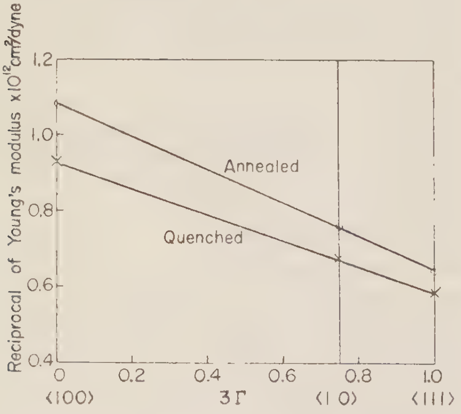

Fig. 1. Relation between the reciprocal of Young's modulus and orientation function for Fe_3Al single crystals.

The measured data are given in Table 1, which indicate that Young's modulus for any direction is higher in ordered state than in disordered state. Fig. 1 shows that the reciprocal of Young's modulus as a function of the orientation function $3\Gamma=3(\gamma^2{}_1\gamma^2{}_2+\gamma^2{}_2\gamma^2{}_3+\gamma^2{}_3\gamma^2{}_1)$, where γ_1, γ_2, γ_3 are direction cosines referred to the crystal axes of the direction along which Young's modulus is measured, is linear, irrespective of the ordered or disordered state, as expected theoretically.

The author wishes to express his hearty thanks to Professor Y. Shirakawa for his kind advice and encouragement, and to Mr. Wakiyama of the Research Institute for Solid State Physics, Tokyo University, for his kind donation of the single crystal from which the crystal specimens used in this work were prepared.

References

1) M. Yamamoto: Nippon Kinzoku Gakkai-shi, **7** (1943) 346.
2) K. Honda and Y. Shirakawa: Sci. Rep. RITU, **A1** (1949) 9.
3) R.M. Bozorth, W.P. Mason and H.J. McSkimin:

Bell System Techn. J. **30** (1951) 970.
4) M. Yamamoto and S. Taniguchi : Sci. Rep. RITU **A8** (1956) 193.
5) S. Siegel : Phys. Rev. **57** (1940) 537.
6) M. Yamamoto, R. Miyasawa and J. Watanabe : Nippon Kinzoku Gakkai-shi, **16** (1952) 475.

J. PHYS. SOC. JAPAN **16** (1961) 2345

Spontaneous Magnetization in Thin Films of Nickel

By Yasuo GONDŌ, Hiroshi KONNO and
Zenya FUNATOGAWA

Department of Physics, Yokohama National University, Yokohama

(Received August 4, 1961)

There are two inconsistent observations on thickness dependence of the spontaneous magnetization in thin films. One concludes that the magnetization decreases with film thickness[1],[2] and the other does that it is quite similar to the one of bulk specimens at room temperature.[3] One reason of this disagreement is suspected to be due to the difference between the conditions of film preparation used by them. That is, Crittenden and Hoffman[1] used a vacuum of the order of 10^{-5} mm Hg, while Neugebauer[3] used an ultra high vacuum of the order of 10^{-9} mm Hg. But the difference between their methods of magnetization measurement also should be considered as another cause of the disagreement. The former used a magnetic field of less than 400 Oe, which was too weak to saturate the specimens, while the latter used one of up to 10,000 Oe, which was enough to saturate them.

In order to make clear the problem, nickel films were prepared by evaporation from a tungsten filament onto glass substrates held at temperature of 100 to 200°C in a vacuum of the order of 10^{-5} mm Hg during evaporation. This condition was similar to the Crittenden's. Immediately after the deposition, the specimens were coated with SiO to avoid oxidation. The film thickness was estimated from the mass of evaporated nickel. The measurement was performed on the films without heat treatment.

A modified torsion pendulum magnetometer has been used in this study, which will be reported in detail elsewhere.[4] In this method the field up to 10,000 Oe is applied to the specimens within the film plane, so all of them can be saturated. The error of the measured value of magnetic moment is less than a few per cent. The experimental error for the magnetization is 10% or less, which entirely depends upon the error of measurement of film thickness.

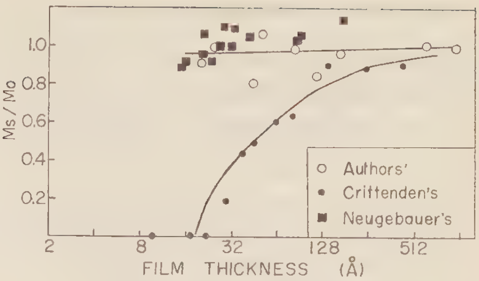

Fig. 1. Thickness dependence of the relative spontaneous magnetization M_s/M_0 in nickel films.

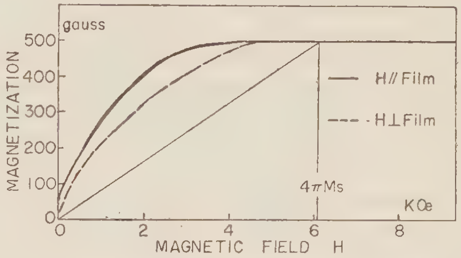

Fig. 2. Magnetization curves parallel and perpendicular to the film plane in a nickel film 605Å thick.

The relative spontaneous magnetization of these films in the 800 to 20 Å range is almost the same at room temperature as that of bulk nickel, as shown in Fig. 1. Most of the nickel films are hardly saturated in the field of less than 3000 Oe, applied within the film plane. Measuring the magnetization perpendicular to the film plane, we found that there is a large anisotropy with an easy axis parallel to the normal to the plane. This anisotropy is supposed to be magnetoelastic one caused from the tensile stress within the film plane, which is calculated to be about 1.3×10^{10} dyne/cm^2 in this example. A pair of these magnetization curves obtained in a film 605 Å thick are plotted in Fig. 2.

We now conclude from the study that thickness dependence of the spontaneous magnetization at room temperature was not noticed at least down to 20 Å thick, like the experiment of Neugebauer's, in spite of the difference of vacuum condition during the film preparation. In very thin films less than 20 Å thick, the temperature dependence of magnetization curve has superparamagnetic character. These investigations are now in progress.

References

1) E. C. Crittenden, Jr. and R. W. Hoffman : Rev. Mod. Phys. **25** (1953) 310.
2) H. Jensen and A. Nielsen : Trans. Dan. Acad. Tech. Sci. No. 2 (1953).
3) C. A. Neugebauer : Phys. Rev. **116** (1959) 1441.
4) Y. Gondō and H. Konno : Sci. Rep. Yokohama Nat. Univ. Sec. I No. 8 (1961) to be published.

J. Phys. Soc. Japan **16** (1961) 2346~2347

On the Shock Configuration in a Perfectly Conducting Gas in the Presence of a Uniform Magnetic Field

By Shigeki Morioka

Department of Physics and Mathematics, Faculty of Science and Engineering, Ritumeikan University, Kyoto

(Recived September 8, 1961)

If a two-dimensional body is placed in a steady, uniform flow of a perfectly conducting gas in the presence of a uniform magnetic field parallel to the flow, an attached or detached shock configuration must occur for certain values of the Mach number M_1 and the Alfvén number A_1 at infinity upstream. The shock wave can be transformed into the curve in the hodograph plane, i.e. the shock polar, which is fixed for given values of M_1 and A_1. Such shock polars have been calculated for various values of M_1 and A_1 by M. N. Kogan[1]. They can be expressed as follows: on the v-θ plane,

$$\frac{v}{v_1}=\frac{1+(A_1{}^2-1)x}{A_1{}^2}\sqrt{\frac{1+\delta^2x^2}{(1+\delta^2)x^2}},\quad \theta=\tan^{-1}\frac{(1-x)\delta}{1+\delta^2x} \tag{1}$$

where v and θ denote the magnitude and the direction of the velocity; $\delta=\tan\alpha$, α is the shock angle; and x the roots of the following equation derived from the shock relations:[2]

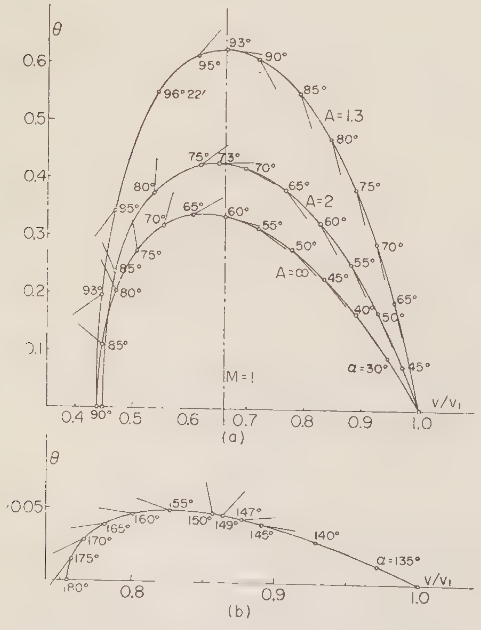

Fig. 1. Shock polar and shock spine (a) for $M_1=2$, $A_1=\infty$, 2, 1.3 and (b) for $M_1=A_1=\sqrt{0.6}$.

$$\begin{aligned}&(\gamma+1)(A_1{}^2-1)^2M_1{}^2x^3+(A_1{}^2-1)\\&\quad\times\{(\gamma+1)M_1{}^2-2A_1{}^2-(\gamma-1)M_1{}^2A_1{}^2\\&\quad-(\gamma M_1{}^2+2A_1{}^2)\delta^{-2}\}x^2\\&\quad-\{(\gamma-1)+(2-\gamma)A_1{}^2\}M_1{}^2\delta^{-2}x-M_1{}^2\delta^{-2}=0\end{aligned} \tag{2}$$

where γ is the ratio of the specific heats, which is taken to be equal to 5/3 for the numerical calculation. Let σ denote the arc-length along the shock line and η the arc-length along the streamline behind the shock. Then, the following relations can be derived from the equations which govern the flow field:

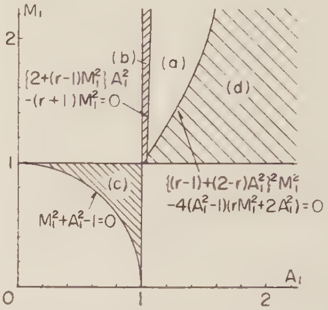

Fig. 2. M_1–A_1 plane.

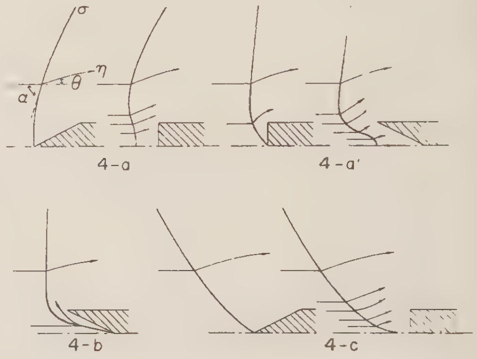

Fig. 3. New types of shock configuration; a, b, c belong to the corresponding regions in Fig. 2.

$$\frac{\partial\theta}{\partial\eta}=\frac{a\mu\delta x\dfrac{\partial\theta}{\partial\alpha}+\lambda\delta^2x^2\left(\dfrac{\mu}{H}\dfrac{\partial H}{\partial\alpha}+\dfrac{\nu}{p}\dfrac{\partial p}{\partial\alpha}\right)}{a\mu\sin\alpha(1-\lambda\delta^2x^2)}\frac{\partial\alpha}{\partial\sigma} \tag{3}$$

$$=-\frac{A^2}{\nu}\frac{a\mu\dfrac{\partial\theta}{\partial\alpha}+\lambda\delta x^2\left(\dfrac{\mu}{H}\dfrac{\partial H}{\partial\alpha}+\dfrac{\nu}{p}\dfrac{\partial p}{\partial\alpha}\right)}{a\mu\delta x\dfrac{\partial\theta}{\partial\alpha}+\left(\dfrac{\mu}{H}\dfrac{\partial H}{\partial\alpha}+\dfrac{\nu}{p}\dfrac{\partial p}{\partial\alpha}\right)}\frac{1}{v}\frac{\partial v}{\partial\eta} \tag{4}$$

where $\partial\theta/\partial\alpha$, $1/H\cdot\partial H/\partial\alpha$, $1/p\cdot\partial p/\partial\alpha$ are the functions of M_1, A_1, α obtained by differentiating the shock relations with respect to α:

$$\left.\begin{aligned}
&\frac{\partial\theta}{\partial\alpha}=1-\frac{\partial\beta}{\partial\alpha}\,,\quad \frac{1}{H}\frac{\partial H}{\partial\alpha}=\frac{1}{\delta}\left(1-\frac{1}{x}\frac{\partial\beta}{\partial\alpha}\right)\\
&\frac{\partial\beta}{\partial\alpha}=\frac{(1+\mu-\lambda\delta^2)\delta^2x^3-2\mu\delta^2x^2+(1+\tau\delta^2)}{(1+\delta^2x^2)(1-\lambda\delta^2x^2)}\\
&\frac{1}{p}\frac{\partial p}{\partial\alpha}=\frac{(a\tau+\nu)\delta^3x^4-2a\tau^3\delta^3x^3+(a\tau-\nu)\delta^3x^2-(\tau-2\nu)\delta x^2-2(\tau-\nu)\delta x+\tau\delta}{-(\nu/\mu)(1+\delta^2x^2)(1-\lambda\delta^2x^2)}
\end{aligned}\right\}\tag{5}$$

where

$$\left.\begin{aligned}
&\lambda=(M^2-1)ab\,,\qquad \mu=\gamma M^2ab\,,\qquad \nu=A^2ab\,,\qquad \tau=\mu-\lambda\\
&a=A^2-1\,,\qquad b=(M^2+A^2-1)^{-1}\,,\qquad A^2=1+(A_1^2-1)x\,,\qquad M^2=\frac{M_1^2\dfrac{v^2}{v_1^2}}{1+\dfrac{\gamma-1}{2}M_1^2\left(1-\dfrac{v^2}{v_1^2}\right)}
\end{aligned}\right\}\tag{6}$$

and H, p, M, A denote the magnetic field intensity, the pressure, the Mach number, the Alfvén number immediately behind the shock, respectively. Eq. (3) expresses the relation between the curvature of the shock line and that of the streamline immediately behind the shock. The coefficient on the right-hand side of Eq. (4) gives the direction of the shock spine. Examples of the shock polar and the shock spines are shown in Figs. 1–a and b for the cases $M_1=2$, $A_1=\infty$, 2, 1.3 and the case $M_1=A_1=\sqrt{0.6}$, respectively. Using the relations (1) to (4), we can determine what kind of shock configuration is possible. As an example, for symmetric wedge profiles of various tip angle, new types of shock configuration such as shown in Figs. 3–a to c may be expected in the regions (a) to (c) of Fig. 3, respectively. Configurations similar to those in the ordinary gasdynamics are possible in the region (d).

References

1) M. N. Kogan: J. Appl. Math. Mech. **23** (1959) 784.

2) S. Morioka: J. Phys. Soc. Japan **15** (1960) 1516.

J. Phys. Soc. Japan **16** (1961) 2347~2348

On Chambers' Solution of the Boltzmann Transport Equation

By Hideo SUZUKI

Physical Institute, Nagoya University

(Received August 16, 1961)

Chambers[1)] suggested a general solution of the Boltzmann transport equation in which the motion of a charged particle is governed by the Lorentz law of force, and the collison integral is replaced by a phenomenological expression such as $-\tau(\boldsymbol{k})^{-1}\times(f-f_0)$, where $\tau(\boldsymbol{k})$ is the relaxation time, $\boldsymbol{k}$ the wave vector related to the crystal momentum, and f_0 the equilibrium distribution function. His formulation is widely used in current researches. For examples, the derivation of Azbel' and Kaner's result on the cyclotron resonance in metals, in terms of Pippard's "ineffectiveness" concept, has been given by Heine[2)]. More recently Cohen, Harrison, and Harrison[3)] have studied the magnetic-field dependence of the ultrasonic attenuration in metals by a method due to Chambers. It is our present purpose to disclose the generality of his "kinetic" argument from the first principle, and to show that it is an exact solution of the Boltzmann equation

$$\frac{\partial f}{\partial t}+\boldsymbol{v}\cdot\frac{\partial f}{\partial \boldsymbol{r}}+\frac{e}{\hbar}\left[\boldsymbol{E}+\frac{1}{c}\boldsymbol{v}\times\boldsymbol{H}\right]\cdot\frac{\partial f}{\partial \boldsymbol{k}}+\frac{1}{\tau}(f-f_0)=0\tag{1}$$

to the linear approximation, which will be described in the following.

First, we neglect as usual the product of the non-uniform electromagnetic fields and the perturbation of distribution function $f_1(\boldsymbol{r},\boldsymbol{v},t)$ which is equal to $f(\boldsymbol{r},\boldsymbol{v},t)-f_0(E)$. Then the linearized equation for f_1 is found to satisfy the following equation

$$\frac{\partial f_1}{\partial t}+\boldsymbol{v}\cdot\frac{\partial f_1}{\partial \boldsymbol{r}}+\frac{e}{c\hbar}[\boldsymbol{v}\times\boldsymbol{H}_0]\cdot\frac{\partial f_1}{\partial \boldsymbol{k}}+\frac{f_1}{\tau}=-e\boldsymbol{v}\cdot\boldsymbol{E}\frac{\partial f_0}{\partial E}\,,\tag{2}$$

where $\boldsymbol{H}_0$ is the constant magnetic field. Here we have used the fact that $\hbar\boldsymbol{v}=\partial E/\partial\boldsymbol{k}$, and that the operator $(\boldsymbol{v}\times\boldsymbol{H})\cdot\partial/\partial\boldsymbol{k}$ applied to a function of energy E alone gives zero. Next we introduce a new set of coordinates in $\boldsymbol{k}$-space, which was first introduced by Shockley[4)], that is E, the projection k_H of $\boldsymbol{k}$ along $\boldsymbol{H}_0$, and the tube angle ϕ defined by

$$\phi(k_H)=(\hbar/m_H)\int v_\perp^{-1}dk\,,\tag{3}$$

where dk is an element of the path in $\boldsymbol{k}$-space, $v_\perp$ the component of $\boldsymbol{v}$ perpendicular to $\boldsymbol{H}_0$, and the tube mass m_H is given by

$$m_H(k_H)=(\hbar/2\pi)\oint v_\perp^{-1}dk\,. \tag{4}$$

The essential property of ψ is that it obeys the simple equation of motion

$$\dot{\psi}(k_H)=eH_0/m_H(k_H)c\equiv\omega_H(k)\,. \tag{5}$$

Then Eq. (2) is rewritten as follows:

$$\frac{\partial f_1}{\partial t}+\boldsymbol{v}\cdot\frac{\partial f_1}{\partial \boldsymbol{r}}+\omega_H\frac{\partial f_1}{\partial\psi}+\frac{f_1}{\tau}=-e\boldsymbol{v}\cdot\boldsymbol{E}\frac{\partial f_0}{\partial E}\,. \tag{6}$$

A solution of this equation can most easily be found by expressing $f_1(\boldsymbol{r},\ \boldsymbol{v},\ t)$ and $\boldsymbol{E}(\boldsymbol{r},\ t)$ as the Fourier integrals:

$$f_1(\boldsymbol{r},\ \boldsymbol{v},\ t)=\int_R f_1(\boldsymbol{q},\ \boldsymbol{v},\ \omega)\exp(i\omega t-i\boldsymbol{q}\cdot\boldsymbol{r})d\boldsymbol{q}d\omega\,, \tag{7}$$

$$\boldsymbol{E}(\boldsymbol{r},\ t)=\int_R \boldsymbol{E}(\boldsymbol{q},\ \omega)\exp(i\omega t-i\boldsymbol{q}\cdot\boldsymbol{r})d\boldsymbol{q}d\omega\,. \tag{8}$$

where the domain of integration is to be determined by the boundary conditions under consideration. The equation for $f_1(\boldsymbol{q},\ \boldsymbol{v},\ \omega)$ is then given by

$$\left[\frac{\partial}{\partial\psi}+\frac{1}{\omega_H\tau}(1+i\omega\tau-i\boldsymbol{v}\cdot\boldsymbol{q}\tau)\right]f_1=-\frac{1}{\omega_H}\left[e\boldsymbol{v}\cdot\boldsymbol{E}(\boldsymbol{q},\ \omega)\frac{\partial f_0}{\partial E}+F(\boldsymbol{q},\boldsymbol{v},\omega)\right], \tag{9}$$

where $F(\boldsymbol{q},\ \boldsymbol{v},\ \omega)$ is defined by

$$\int_R F(\boldsymbol{q},\ \boldsymbol{v},\ \omega)\exp(i\omega t-i\boldsymbol{q}\cdot\boldsymbol{r})d\boldsymbol{q}d\omega\equiv F(\boldsymbol{r},\ \boldsymbol{v},\ t)=0\,. \tag{10}$$

Therefore, the solution of (9) which satisfies the periodicity condition $\boldsymbol{v}(\psi+2\pi)=\boldsymbol{v}(\psi)$ is given as

$$\begin{aligned}f_1(\boldsymbol{q},\ \boldsymbol{v},\ \omega)=&-\int_{\psi_0}^{\psi}[(e\boldsymbol{v}'\cdot\boldsymbol{E}(\boldsymbol{q},\ \omega))\partial f_0/\partial E+F(\boldsymbol{q},\ \boldsymbol{v}',\ \omega)](\omega_H)^{-1}d\psi'\\&\times\exp\left[-\int_{\psi'}^{\psi}(1+i\omega\tau''-i\boldsymbol{q}\cdot\boldsymbol{v}''\tau'')(\omega_H\tau'')^{-1}d\psi''\right].\end{aligned} \tag{11}$$

Here we have assumed that $f_1=0$ at $\psi=\psi_0$. Then, from (7) and (8), we obtain

$$\begin{aligned}f_1(\boldsymbol{r},\ \boldsymbol{v},\ t)=&-\int_{\psi_0}^{\psi}[(e\boldsymbol{v}'\cdot\boldsymbol{E}(\boldsymbol{R}',\ T'))\partial f_0/\partial E+F(\boldsymbol{R}',\ \boldsymbol{v},\ T')](\omega_H)^{-1}d\psi'\\&\times\exp\left[-\int_{\psi'}^{\psi}(\omega_H\tau'')^{-1}d\psi''\right],\end{aligned} \tag{12}$$

where

$$\boldsymbol{R}'=\boldsymbol{r}-\int_{\psi'}^{\psi}\boldsymbol{v}\frac{d\psi''}{\omega_H}\,,\qquad T'=t-\int_{\psi'}^{\psi}\frac{d\psi''}{\omega_H}\,. \tag{13}$$

Now, let us measure the tube angle in terms of the time. Then, from (5), we can easily find that $\boldsymbol{R}'=\boldsymbol{r}(t')$, and $T'=t'$. Thus, from (10), we obtain the final result as follows:

$$f_1(\boldsymbol{r},\ \boldsymbol{v},\ t)=-\frac{\partial f_0}{\partial E}\int_{t_0}^{t}[e\boldsymbol{v}(t')\cdot\boldsymbol{E}(\boldsymbol{r}(t'),\ t')]\exp\left[-\int_{t'}^{t}\frac{dt''}{\tau(t'')}\right]dt'\,. \tag{14}$$

where the integrations with respect to t' and t'' are carried out along the trajectory of a charged particle. This is the same expression that derived qualitatively by Chambers, on the basis of his "kinetic" argument. For a particle scattered specularly at the surface of the specimen, the limit of integration t_0 is $-\infty$, but for a particle scattered diffusely, t_0 is the latest time prior to t that the trajectory cuts the surface.

The author wishes to express his hearty thanks to Professor H. Nakano and Mr. K. Yamada of Nagoya University for their helpful discussions.

References

1) R. G. Chambers: Proc. Phys. Soc. **65 A**, 458 (1952).
2) V. Heine: Phys. Rev. **107**, 431 (1957).
3) Cohen, Harrison, and Harrison, Phys. Rev. **117**, 937 (1960).
4) W. Shockley: Phys. Rev. **79**, 191 (1950).

J. PHYS. SOC. JAPAN **16** (1961) 2349

Concentration Dependence of Electrical Properties of Bismuth-Antimony Alloys

By Seiichi TANUMA

The Research Institute for Iron, Steel and Other Metals
Tohoku University, Sendai

(Received August 28, 1961)

Bismuth and antimony are known to be semimetals whose overlapping energies of electrons and holes are about 0.02 and 0.15 eV respectively, and these two metals make solid solutions in the whole range of concentration. The author[1)] and Jain[2)] found independently that Bi-Sb alloys become semiconductive in the concentration range from 4 to about 50 atomic per cent antimony, while the energy gap is as small as 0.016 eV at its maximum value for the alloys of 15 to 20 per cent antimony. The resistivity ρ, the Hall coefficient R, and the magnetoresistance $\Delta\rho/\rho$ of the alloy are investigated. The specimens are polycrystals prepared from zone-refined component metals by vacuum melting. The effective amount of impurities is estimated to be less than 10^{-16}/cc. The quantities ρ, R and $\Delta\rho/\rho$ at 80°K are plotted against the concentration of antimony in alloys in Fig. 1, where R and $\Delta\rho/\rho$ are the values measured in a rather weak magnetic field of 250 Oe. The sign of Hall coefficient is reversed at 73 per cent from negative at the bismuth side to positive at the antimony side.

The three quantities, namely, the concentration of electrons or holes n*, the mobility of electrons μ_e and that of holes μ_h are calculated from the measured quantities by the approximate relations:

$$1/\rho = ne\cdot(\mu_e+\mu_h),$$

$$R = -(nec)^{-1}\cdot(\mu_e-\mu_h)\cdot(\mu_e+\mu_g)^{-1}$$

and

$$\Delta\rho/\rho = H^2\cdot c^{-2}\cdot \mu_e\mu_h\ ,$$

where H is the magnetic field strength and c is the light velocity. Thus obtained n, μ_e and μ_h are shown as functions of antimony concentration in Fig. 2. The carrier concentration makes a minimum around 15 per cent in the semiconductor range of concentration. This minimum becomes more remarkable with decreasing temperature. The mobilities are large at both ends of composition and decrease towards the intermediate range by virtue of the scattering of carriers by random distributions of both atoms. In the medium composition range, the mobility is expected to have a minimum, but actually, a broad hump occurs. A possible explanation of the fact is as follows: Smearings of the band edges due to an aperiodicity of lattice potential give small state densities which in turn result in small effective masses of carriers.[3)] If the influence of diminution of effective masses due to the disordered alloying exceeds the scattering effect, the mobilities should increase rather than decrease.

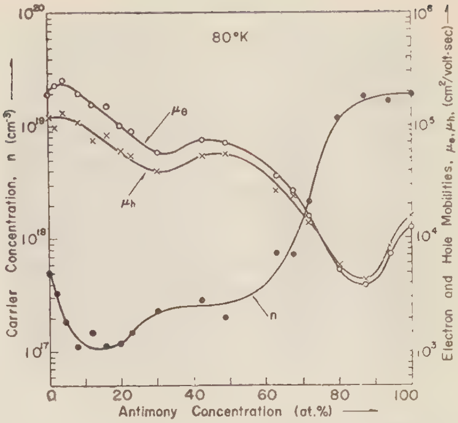

Fig. 2· Concentration of electrons and holes n, electron mobility μ_e and hole mobility μ_h are plotted against antimony concentration.

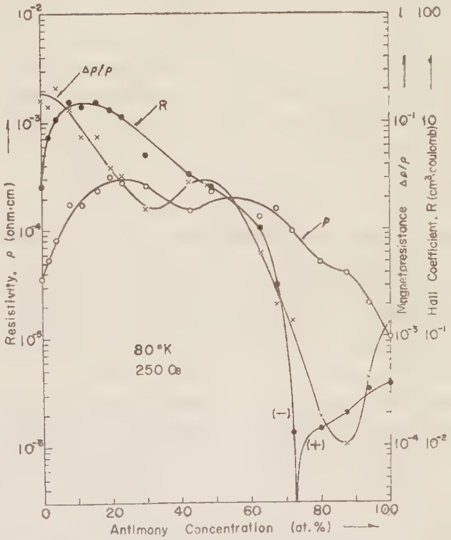

Fig. 1. Resistivity ρ, Hall coefficient R and magneto-resistance $\Delta\rho/\rho$ are plotted against concentration of antimony.

The author wishes to express his hearty thanks to Professor T. Fukuroi for his encouragements and Mr. K. Tanaka and Mr. T. Fukase who kindly helped in carrying out this work.

References

1) S. Tanuma: J. Phy. Soc. Japan **14** (1959) 1246.
2) A. L. Jain: Phys. Rev. **114** (1959) 1518.
3) F. Herman, M. Glicksman and R. H. Parmenter: Progress in Semiconductors **2** (1957), Heywood Co., London, 3.

---

* The difference of concentrations of electrons and holes is as small as the effective amount of impurities.

J. Phys. Soc. Japan **16** (1961) 2350

"New Level Scheme of Pt^{196}".

By Hidetsugu Ikegami, Toshimitsu Yamazaki,
Mitsuo Sakai
Institute for Nuclear Study, University of Tokyo
and Kazusuke Sugiyama
Department of Physics, Tohoku University, Sendai, Japan

(Received August 31, 1961)

In connection with the study of the E0 transitions between the first and the second 2+ states of Pt^{194} and Pt^{196}, radiations from the 5.6 day Au^{196} have been investigated*.

5.6-day Au^{196} was produced by bombarding spectroscopically pure platinum metal with 14 MeV protons in the INS cyclotron. Since the 17 hour Au^{193} and the 38 hour Au^{194} are simultaneously produced, measurements started four weeks after the bombardment. After repeated chemical separation, Au^{196} sources were prepared in a carrier free state.

Very weak new gamma rays of 450, 640, 770, 1095 and 510 keV (annihilation radiations) were detected using scintillation gamma-ray spectrometer. These new gamma rays were all coincident with the 356 keV gamma ray. Therefore the decay energy of the electron capture should be considerably higher than the value reported previously[1].

The internal conversion electron spectrum was carefully measured using two kinds of double focusing magnetic spectrometers. Besides the new gamma rays mentioned above, 518- and 580 keV transitions were also found. No Crossover transition of 689 keV was found. This fact seems to indicate that the 689 Kev state shows a pure harmonic oscillation character which is also free from coupling with particle excitation. It is not consistent with the fact that the energy gap of particle excitation of Pt^{196} is estimated to be about 900 keV from the analysis of even-odd mass difference data.

The 1095 keVγ-356 keVγ directional correlation coefficients gives a spin sequence 3(D)3(Q)0 or 1(D)2(Q)0. Considering no 1450 keV crossover transition and an experimental value of the conversion coefficient of the 1095 keV transition, the 1450 keV state was assigned as 3−, as suggested by Morinaga[2]. Theoretically two 3− states are expected; one is a member of octupole vibration states and the other is a particle state with the $(h_{11/2}, g_{7/2})_p$ configuration. As the energy of this particle state is considered about 4000 keV or more, the 1450 keV state is expected as a member of octupole vibration states. If the 3− state is assumed to be of core excitation, it may be understandable that the log *ft* value for the transition to the 1450 keV state is 7.5, which is rather high for the allowed transition[3].

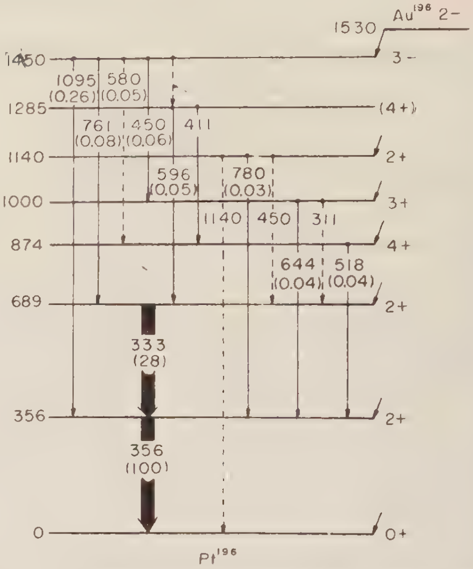

Fig. 1. The tentative decay scheme of the 5.6 day Au^{196}. Relative intensities are given in parentheses.

From the experimental result of the 760-keVγ-350keVγ directional correlation, one is forced to conclude that the correlation function seems to be the mixture of 2+(D+Q)2(Q)0+ with 3−(D)2 +(Q) 2+ and 3−(D)2+(Q)2+(Q)0 sequence. The new 2+ state was therefore assigned at 1140 keV.

The tentative new decay scheme of Au^{196} is shown in the Fig. 1. The level scheme of Pt^{196} is quite analogous to that of Pt^{192} which is also recently investigated by the authors[4]. Further study is now in progress and the more complete decay scheme of Au^{196} will be presented in the near future.

We are indebted to Drs. E. Takekoshi and Z. Matsumoto for the use of a beta ray spectrometer.

References

1) R. K. Gupta: Proc. Phys. Soc. (London) **71** (1958) 330.
2) H. Morinaga: Tokyo Meeting of Phys. Soc. Japan, April (1960).
The 1450 keV level was also discovered by Wapstra.
A. H. Wapstra: Private Communication to Morinaga.
3) H. Ikegami and T. Udagawa: To be published.
4) H. Ikegami, T. Yamazaki, M. Sakai and K. Sugiyama: To be published.

---

* H. Ikegami, K. Sugiyama, T. Yamazaki, M. Sakai and S. Hayashibe, Fukuoka Meeting of Phys. Soc. Japan, October (1960).

J. PHYS. SOC. JAPAN **16** (1961) 2351

Back-Reflection X-Ray Micrography

By Shozo SAITO and Yasumitsu SHIMOMURA
Department of Physics, University of Osaka Prefecture

(Received August 31, 1961)

The thorough interpretation of x-ray reflection micrograph would be very difficult when there is an ambiguity in indexing the individual reflections producing the micrograph. This is not the case for most crystals but is just the case for a twinned crystal of NiO with rhombohedral structure, whose deviation from the cubic can be detected only by back-reflections[1]. A Berg-Barrett photograph of a cleavage face of this crystal is shown in Fig. 1 (a). In producing this pattern, use is made of NiK_α-radiations reflected by {*311*} family* of planes referring to the face-centered lattice distorted slightly from the cubic. The Bragg angles (θ) for these reflections are not so high (ca. 41.2°) as to be able to discriminate different sorts of planes belonging to the {*311*} family, and further twinning nature of this oxide causes a plane in one twin component to be always almost parallel to that in the other which belongs still to the same family[2]. Thus it is very hard to give specific indices to the individual reflections in this micrograph.

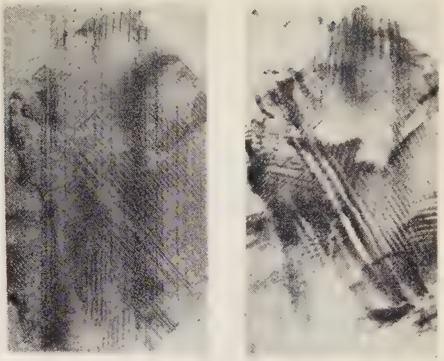
(a) (b)

Fig. 1. X-ray reflection micrographs of a cleavage face of NiO (×6) (a) Berg-Barrett pattern (NiK_α, {*311*}), (b) Back-reflection micrograph (Ni$K_{\alpha 1}$, (*422*)).

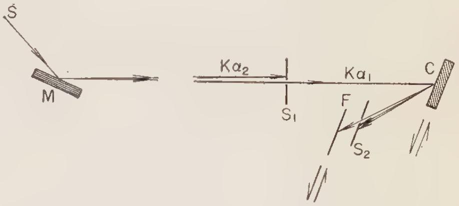

Fig. 2. X-ray optics in back-reflection micrography. S: X-ray source; M: Crystal monochromators; C: Specimen; S_1 and S_2: Slits; F: X-ray film; ⇄: To move C and F together in both directions.

Such an ambiguity for indexing the individual reflections in X-ray micrograph could be removed by making a good use of back-reflections, which can tell one plane from the other among those of the same family. An optimum condition is attained as follows (Fig. 2). The cleavage face is set so that {*422*}-reflections are produced for the incidence of Ni$K_{\alpha 1}$-radiation obtained by a standard method of getting a purely monochromatic parallel beam with a crystal monochromator and a slit (S_1). Among the three kinds of {*422*}-reflections ($\theta \doteqdot 76.5^\circ$) only a single one, (*422*)-reflection for instance, is selected by another slit (S_2) and is used to record the twin structure on a photographic film set parallel and fairly close to the surface. To obtain an image for a wide range, the specimen surface is scanned with the incident beam under the fixed condition of incidence to the surface, by moving the specimen and the film together without any change in their relative positions, as in Lang's technique[3].

A pattern thus obtained with the same surface as that for Fig. 1 (a) is reproduced in (b). Comparing these two patterns, the latter is lacking in sharpness. This is due mainly to the following two reasons: (1) In order not only to avoid an interruption of the incident beam by the photographic film but also to insert the slit (S_2) between the film and the specimen, the film is not allowed to approach too much close to the specimen and further (2) a fairly large dispersion is inevitable for the high-angle reflection in the latter. However, all the individual reflections throughout the latter pattern have the same and known indices.

The technique here mentioned could be applied to many other crystals that obey Mallard's law. The details will be published later.

References

1) H. P. Rooksby: Nature **152** 304 (1943), Y. Shimomura & Z. Nishiyama: Memoirs of the Inst. of Scientific and Indust. Research, Osaka Univ. **6** 30 (1948).

2) Y. Shimomura & S. Saito: Bull. of Univ. of Osaka Prefect. **4A** 111 (1956), C. A. Slack: J. Appl. Physics **31** 1571 (1960), W. L. Roth: J. Appl. Physics **31** 2000 (1960).

3) A. R. Lang: J. Appl. Phys. **30** 1748 (1959).

---

* In the present note, the notation for a '*form*', {*hkl*}, will conveniently be adopted to imply a family of planes of all kinds which would belong to one '*form*' expressed by the same notation if the lattice were not distorted.

J. PHYS. SOC. JAPAN **16** (1961) 2352~2353

Cyclotron Resonance of Hot Electrons in Germanium

Hajimu KAWAMURA, Yoshikazu HAYASHI
and Masakazu FUKAI

Institute for Solid State Physics
University of Tokyo

(Received August 29, 1961)

Present paper is a preliminary report on the cyclotron resonance of hot electrons in germanium. The hot electrons were produced by applying ac voltage of 75 cycle per second with rectangular wave form parallel to the static magnetic field. The cyclotron resonance was measured with 6 mm microwave at 1.6°K. The specimen was slightly n-type ($N_D \sim 7\times10^{12}$ cm^{-3}) germanium of thin slab (10×1.5×0.3 mm).

By means of the irradiation through quartz rod, the photo-generation of the carriers was also possible. Even at the lowest field we measured (11.6 volts/cm), the conduction electrons were multiplied by the ionization of donors by collisions. But in order to get a stable current it was necessary to supply the initial electrons by means of weak illumination.

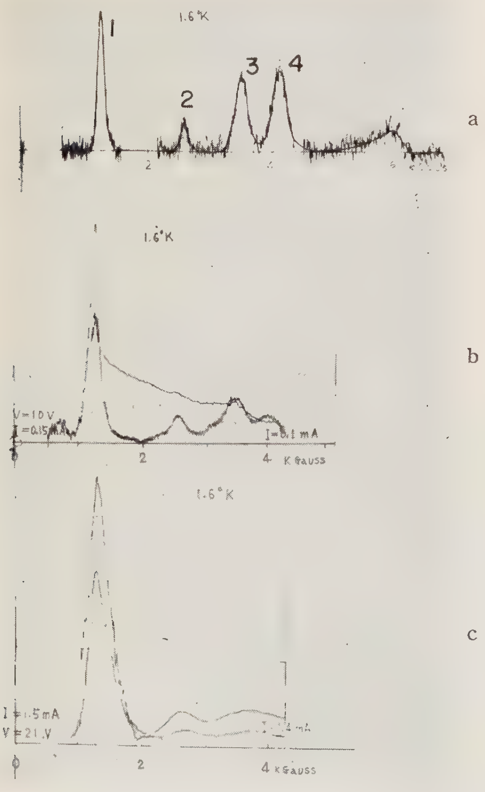

Fig. 1. Absorption signals of cyclotron resonance. a. Carriers are optically generated. b. and c. Electrons are gnerated and multiplied by applying high field. For b. $V=10$ volts and for c. $V=21$ volts.

A few examples of the resonance patterns are shown in Fig. 1. Fig. 1 a. is the resonance signal due to the optically generated carriers. We can observe four peaks due to electrons and one due to heavy holes. From these peak positions it was deduced that the orientation of magnetic field deviate from [111] direction by about 10°. Fig. 1 b. and 1 c are the signals due to the hot electrons obtained by high field applications. The current for Fig. 1 c is ten times as large as for Fig. 1 b. We can see from these figures that the line widths increase with the applied field and the line intensities for valleys of heavier cyclotron mass decrease with the field. Since the ac field was applied along the magnetic field, the effective mass for ac field is smaller for valley with heavier cyclotron mass as shown in the next table. In Fig. 2 the half width of each valley, the ratios of areas under the absorption lines for valley 2 and 3 against for valley 1, and the current density are plotted as the functions of strength of rectangular ac field in semi-log scale. Assuming that hot electrons are scattered only by the spontaneous emission of phonon, one can estimate the effective temperature of hot electrons from these line widths, comparing with the width for electrons in equilibrium with lattice at 4.2°K, where both emission and absorption of phonons are effective. The temperature scale in the figure is obtained by this way. We

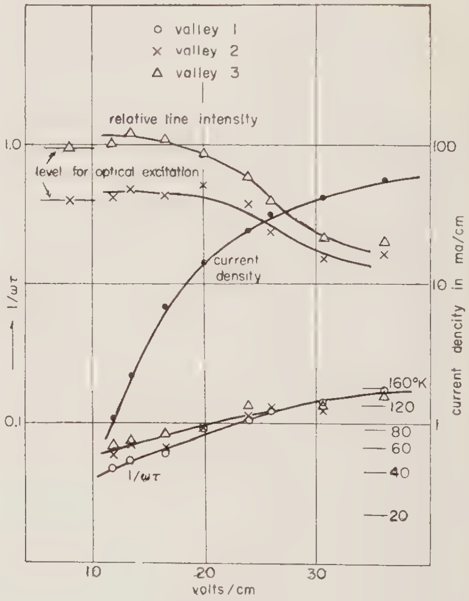

Fig. 2. The half widths, relative line intensities, and current density as the functions of applied field strength.

can see from this figure that the temperature of heavier mass valley is lower than that of lighter mass valley, and both increase with applied field. The electron population of the lighter mass valley,

Valley	1	2	3	4
Cyclotron mass	0.082	0.16	0.22	0.25
Electric field mass	1.5	0.104	0.086	0.085

measured from the relative area of absorption line, decreases as the temperature increases beyond some 100°K. This seems to be quite reasonable, since the hotter electrons in the lighter valley will jump into heavier valley by means of intervalley scattering which requires a rather high energy (~0.03 ev) in order to emit a high energy phonon in the case of pure germanium.[1),2)]

Since the density of carriers is estimated to be less than 10^{11} cm^{-3} even under the highest field, from the field-current density curve and the mobility estimated from line width, the plasma effect can be neglected at these high frequency. The rise of specimen temperature due to Joul's heat is estimated to be less than 4°K, since the specimen is immersed in the superfluid of helium.

References

1) W. Sasaki, M. Shibuya, K. Mizugachi and G. M. Hatoyama: J. Phys. Chem. Solids, **8** (1959) 250.
2) M. Shibuya and W. Sasaki: J. Phys. Soc. Japan, **15** (1960) 207.

J. Phys. Soc. Japan **16** (1961) 2353~2354

Low-lying Excited States in Ba^{136}

By Kazusuke SUGIYAMA, Hiroyoshi SEKIGUCHI and Shogo HAYASHIBE

Department of Physics, Tohoku University, Sendai, Japan

(Received Septembr 1, 1961)

Recently, H. Bernstein and H. H. Forster[1)] have reported that the spin and parity of the 1900 keV level in Ba^{136} was 2+ and the radiation property of the 1065 keV transition between this and the first 2+ level was of *M1* predominant, though the cross-over transition to ground state was extremely weak. Our preliminary results on γ-ray analyses, however, seem to exclude the possibility of their conclusion which might result in some difficulty in the theory of even-even nuclei[2)].

The Cs^{136} (13 days) activity was produced by bombardment of natural barium with 55 MeV protons in the synchro-cyclotron of the I.N.S., University of Tokyo, and was prepared in a chemical form of CsCl in HCl solution. The γ-rays of energies 80, 180, 270, 340, (620), 830, 1065 and 1255 keV (additional weak peaks at 1400, 1660 and 1900 keV which were considered as summing peaks) were observed by a 3″ϕ×3″ NaI(Tl) scintillation spectrometer and were confirmed as belonging to Ba^{136}. In the coincidence spectrum with the gate at 830 keV photopeak shown in Fig. 1, the peak at 830 keV was too high even after a correction of the coincidence contribution from the Compton tails of higher γ-rays which existed in the gate. A 2″ϕ×2″ NaI(Tl) counter was used as a gate side detector. Therefore, it is concluded that the additional γ-ray of about 830 keV exists in the decay of Cs^{136}. γ-γ directional correlation measurements were also made and the results were shown in Figs. 2 and 3 (The experimental arrangement was previously reported[3)].).

On the basis of these results, the spin assignments of the low-lying levels in Ba^{136} were tenta-

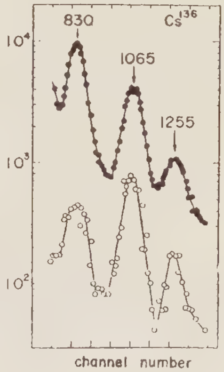

Fig. 1. Single and coincidence γ-ray spectra in Cs^{136}. The upper curve (closed circles) is a single crystal spectrum and the lower curve (open circles) is a coincidence spectrum with the gate at 830 keV photopeak.

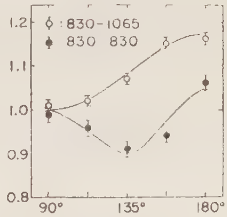

Fig. 2. γ-γ directinal correlation patterns. Open circles show the 830 keV photopeak—1065 keV photopeak correlation and closed circles show the 830 keV photopeak—830 keV photopeak correlation. The solid lines are the least squares fitting curves cor rected for finite angular resolutions of the detectors.

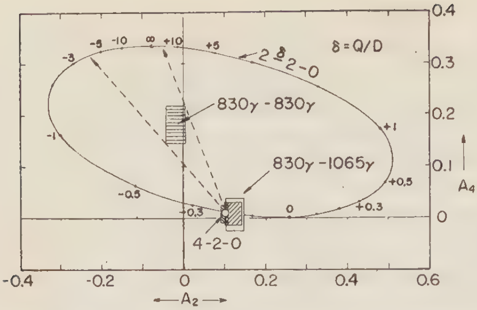

Fig. 3. Parametric curve of quadrupole-dipole mixing ratio δ as a function of coefficients A_2 and A_4 of the spin sequence 2–2–0. The case of 4–2–0 is also shown as an open circle. The part of the ellipse between the ends of the two dashed lines shows a region of the δ of the 830 keV $2' \to 2$ transition. The experimental results by other investigators[1),4)] are also shown.

		Investigator	A_2	A_4
830—1065	▨	Present	0.122 ±0.020	0.008 ±0.022
	▧	Grabowski et al.[4)]	0.100 ±0.008	0.008 ±0.018
	▭	Bernstein and Forster[1)]	0.1253±0.0219	0.0065±0.032
	○	Theoretical 4–2–0	0.102	0.009
830— 830	▤	Present	−0.021 ±0.020	0.182 ±0.038
830— 340		Present	0.110 ±0.010	0.018 ±0.010

tively proposed as follows; 830(2+), 1660(2+), 1900(4+) and 2240 keV (6+). It was considered that those parities were positive. No essential difference from other even-even nuclei has been found, and the transition to the first 2+ level from the second 2+ level had the property of $E2$ predominant and $B(E2{:}2' \to 2)/B(E2{:}2' \to 0) < 100$.

Further study will be made by using the sources produced by the reaction (d, α) since the present sources contain a small amount of the other radioactive nuclides (6 day Cs^{132} and 2 year Cs^{134}).

The authors wish to express their sincere thanks to Professor M. Kimura for his continued guidance and encouragement.

References

1) H. Bernstein and H. H. Forster: Nuclear Phys. **24** (1961) 601.
2) For instance, D. M. Van Patter: Nuclear Phys. **14** (1959/60) 42.
3) K. Sugiyama, A. Fususawa, S. Hayashibe and M. Kimura: J. Phys. Soc. Japan **16** (1961) 1538.
4) Z. Grabowski, S. Gustafsson and I. Marklund: Nuclear Phys. **20** (1960) 159.

J. Phys. Soc. Japan **16** (1961) 2354~2355

Thermoelectric Power of Bismuth-Antimony Alloys

By Seiichi Tanuma

The Research Institute for Iron, Steel and Other Metals
Tohoku University, Sendai

(Received Augnst 28, 1961)

The thermoelectric power of Bi–Sb solid solution is investigated in the temperature range from 15 to 300°K. The specimens are cut from the same ingots as were used in the preceding work.(1) The measured thermoelectric power is plotted against temperature in Fig. 1, and the concentration dependence of thermoelectric power is shown in Fig. 2. The numeral following the ♯ mark on each curve in Fig. 1 denotes the chemically analyzed atomic per cent of antimony in the specimen rounded up to a whole number. The behavior in Fig. 1 is qualitatively explained by the previously mentioned nature[1)] of the alloy system, i.e., a continuous change of electrical property from semimetallic to semiconductive at 4 atomic per cent antimony and again to semimetallic at about 50 per cent antimony. Sample ♯ 100, pure antimony which has the largest Fermi energy, shows the most metallic behavior of linear increase of thermoelectric power with the rise of temperature. The thermoelectric power of ♯ 0, pure bismuth, also shows the increasing behavior in its absolute value, but it tends to saturate with the rise of tempera-

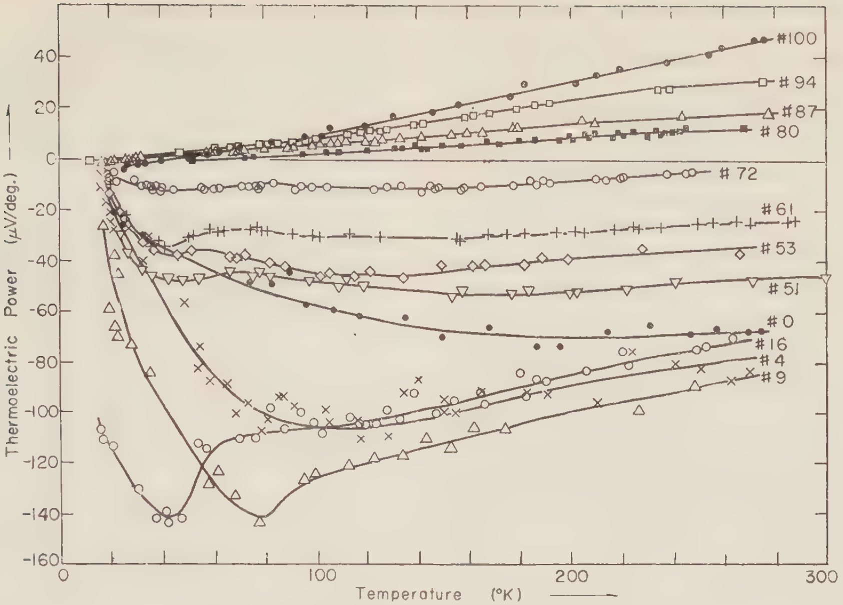

Fig. 1. Thermoelectric power of polycrystalline Bi-Sb alloys plotted against temperature.

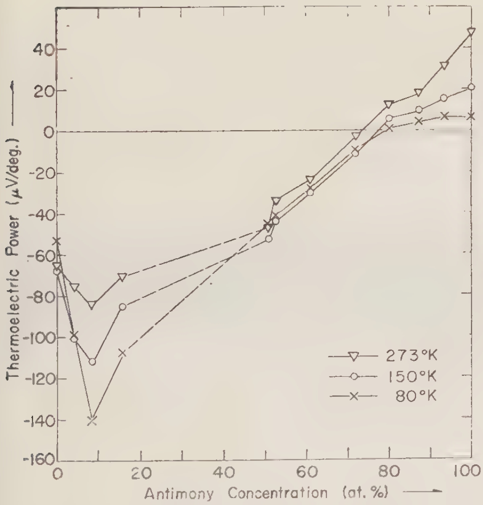

Fig. 2. Thermoelectric power of Bi-Sb alloys plotted against concentration of antimony.

ture. The thermoelectric power of a typical semimetal having zero Fermi energy must be independent of temperature[2]. Bismuth is considered to behave approximately in this way at higher temperatures. The samples #04, #09, #16 etc. show a decrease in the absolute values of thermoelectric power above several tens of degrees Kelvin which corresponds to the property of intrinsic semiconductors. As for the gradients of the curves, the detailed factors such as the temperature coefficients of the energy overlaps or gaps and the effect of the third energy band must be taken into account. At low temperatures, the thermoelectric power tends to decrease rapidly with the temperature decrease. The humps in the absolute values such as the one around 40°K of #16 are not yet definitely explained.

As shown in Fig. 2, the absolute magnitude of the thermoelectric power is large in the semiconductor range of concentration. The sign is reversed at about 70 to 80 per cent antimony from negative to positive with the increase of antimony concentration. This agrees with the sign of Hall effect of the alloys.[1]

The author wishes to express his hearty thanks to Professor T. Fukuroi for his encouragements and to Mr. T. Fukase who kindly helped this experiment.

References

1) S. Tanuma: J. Phys. Soc. Japan **16** (1961) 2349.
2) V. A. Johnson: Progress in Semiconductors **1**, Heywood Co. London (1956) 63.

J. PHYS. SOC. JAPAN **16** (1961) 2356~2357

Effects of Tacticity upon the Temperature Dependence of T_1 of Proton in High Polymers

By Takao KAWAI, Yôko YOSHIMI
Yoshida College
and Akira HIRAI
Department of Physics, Faculty of Science, Kyoto University, Kyoto

(August 22, 1961)

In order to clarify the effects of tacticity upon the temperature dependence of the spin lattice relaxation time (T_1) of proton of high polymers, we have measured the temperature dependence of T_1 of proton of the isotactic and the atactic polypropylene (PP) $(\text{-CH}_2\text{-CHCH}_3\text{-})_n$ by 90°-90° pulse method at 25 Mc/sec. The isotactic PP is the product of Merk Company and the atactic PP is of Hercules Powder Company. The degree of crystallinity of the former is about 60-70%, and the latter is almost amorphous. The experimental apparatus and procedures were already reported1),2).

The results obtained are shown in Fig. 1. The errors in the measurements are about 10% and 30% in the worst case, as previously described in detail2),3). As seen from Fig. 1, the data show the following remarkable features.

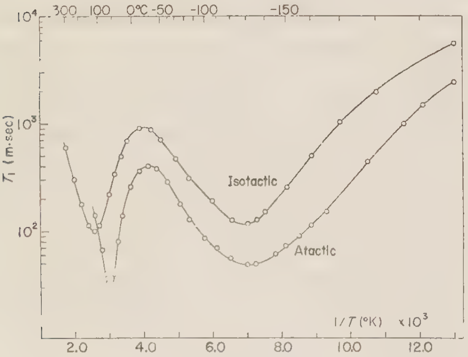

Fig. 1. Temperature dependence of T_1 of proton in PP (Isotactic and Atactic).

(1) The values of T_1 for the isotactic PP were about 3 times larger than those for the atactic PP for nearly over the whole temperature range.

(2) The V-shaped curves in the lower temperature range have their respective minima of T_1 at nearly the same temperature for both samples (−130°C), while in the higher temperature range, they do not, but have at 100°C for the isotactic PP and at 50°C for the atactic PP.

(3) The values of $T_{1\min}$ in the higher temperature range are different between two samples, i.e., 100 msec for the isotactic PP and 28 msec for the atactic PP.

First, we consider the V-shaped parts of the curves in Fig. 1 in the lower temperature region. These parts are considered to be due to the internal motions of methyl groups2). As usual1),2) the data are analyzed by the BPP formula. The results of analyses are;

$$b=2.2\text{Å},\ \tau_0\doteqdot4\times10^{-12}\,\text{sec, and}$$
$$\Delta E=1.9\,\text{Kcal/mol for the isotactic PP,}$$
$$b=1.8\text{Å},\ \tau_0=4\times10^{-12}\,\text{sec, and}$$
$$\Delta E=1.9\,\text{Kcal/mol for the atactic PP.}$$

The difference in the value of T_1 leads to the difference in the interproton distance (b). This difference is to be expected, since the disordered structure of the atactic PP should have a closer effective interproton distance than the isotactic PP4).

The similarity of the two curves in Fig. 1 in the lower temperature region, within the experimental errors, leads to the equal values of the parameters describing the molecular motion, which suggests that the tacticity has little effect upon the local motions of methyl groups.

Next we consider the V-shaped parts in the higher temperature region. These parts are due to the segmental motions.

The difference in the temperature, at which $T_{1\min}$ occurs, suggests that the regular configuration of methyl group in the isotactic PP imposes a greater constraint on the motion of the main chain, perhaps through the effect of crystallinity, than the disordered array in the atactic PP. This result is consistent with the results obtained by the steady state NMR method5),6).

The larger value of T_1 being obtained for the isotactic PP is considered to be due to the largeness of the effective interproton distance at higher temperatures as at lower temperatures and also due to the wider distribution of the correlation time (τ_c) in the isotactic PP than in the atactic, being considered from the fact that the V-shaped part of the curve in Fig. 1 in this temperature region for the isotactic PP is more flat than that for the atactic PP, because in general, the increase in the value of $T_{1\min}$ and the flatness of the V-shaped curve are expected, when we take the distribution of the correlation time into account.

The crystallinity is another important factor which would affect T_1, and this effect is not clear in our present investigation and left for later considerations.

The author would like to express their sincere thanks to Prof. I. Takahashi for his continual interest and discussions. The authors' thanks are also due to Dr. A. Odajima who supplied the samples.

References

1) T. Hashi, A. Hirai, M. Sasaki and T. Kawai: Memoirs Coll. Sci., University of Kyoto, Series A **29** (1959) 205.
2) A. Hirai and T. Kawai: Memoirs Coll. Sci., University of Kyoto, Series A (to be published).
3) T. Kawai: J. Phys. Soc. Japan **16** (1961) 1220.
4) G. Natta: J. Polymer Sci. **16** (1955) 143.
5) J. A. Sauer, R. A. Wall, N. Fushillo and A. E. Woodward: J. Appl. Phys. **29** (1958) 1385.
6) W. P. Slichter and E. R. Mandell: J. Appl. Phys. **29** (1958) 1438.

J. PHYS. SOC. JAPAN **16** (1961) 2357

The Observation of Oscillating Anode Glow by Means of High-Speed Camera

By Kazuyuki OGAWA

Central Research Laboratory, Tokyo Shibaura Electric Co. Kawasaki

(Received August 4, 1961)

The hysteresis of the ionization in the anode sheath—the phenomena such that the ionization is sustained even when the anode drop decreases after the break down of the anode sheath—is necessary to generate the finite length of the negative resistance in the anodic oscillator tube.[1] This proposition has been backed up by the phenomena in which the glow ball appearing on the tip of the anode is maintained over a quarter of the period of the voltage oscillation.[2] But the cause from which the hysteresis comes, and the movement of the glow ball to which the hysteresis corresponds are both still unknown. To find a clue to solve this problem, the glow ball has recently been observed with a high-speed camera. The photograph shows the part in which the frame number per second is closely equal to the oscillation frequency (3 kc/sec) and gradually increases with the passage of time. The time of exposure is about 50 μsec, and the width of observed light pulse is about 100 μsec. It can be confirmed from the photograph that a glow spot appears on the tip of the anode just coincidentally with the break down of the anode sheath, and expands to a sphere. The intensity of the glow ball is slightly varied during the cycle. It is clarified on refering to the results of the observation by means of a photomultiplier tube[2] that the time in which the glow ball grows up to its maximum size corresponds to the build-up time of the light pulse.

Now, the following speculation concerning with the cause of the hysteresis in neon oscillatron[3] may be allowed. That is, the spectral term $2p_9$ (18.5volts) is excited and consequently 6402 Å photon is emitted at the instant of the break down of the anode sheath, because the initial energy of the electron is sufficiently high. If, then, the metastable atoms $1s_5$ (16.6 volts) exist in the space adjacent to the anode tip, the excited atoms $2p_9$ may be replenished by the absorption of 6402 Å photon. The life time of the excited atom $2p_9$ is about 3×10^{-8} sec, while the collision time of the electron is about 10^{-11} sec, therefore the cumulative ionization can take place if the electron energy exceeds 3.0 volts, as the ionization potential is 21.5 volts. Thus the ionization is maintained by the catalytic action of the 6402 Å photon, even if the anode drop is so low that the electron can not directly ionize the atom in the ground state but excite it up to the metastable level. The decrease in the anode drop causes the increase in the electron current concentrating on the anode tip[1], and may give rise to the expansion of the region in which the metastable atoms are created. The expansion of the glow spot may be caused by the expansion of this excitation region.

Fig. 1. The variation of the glow ball in the neon oscillatron the anode sheath breaks at the left in the picture, and the photographic film runs down from left to right with gradually increasing speed.

References

1) K. Ogawa: J. Phys. Soc. Japan **16** No. 12 (to be published)
2) K. Ogawa: J. Phys. Soc. Japan **14** (1959) 1746
3) K. Ogawa: J. Phys. Soc. Japan **14** (1959) 385

J. Phys. Soc. Japan **16** (1961) 2358~2359

Crystal Growth of Zinc-oxide by Chemical Reaction of Zinc-fluoride with Air

By Ikumaro Kubo

Faculty of Liberal Arts and Education, Nagasaki University

(Received August 11, 1961)

Fritsch[1] has obtained zinc-oxide single crystals from its vapour at elevated temperature. Scharowsky[2] has formed crystals by reacting zinc vapour with air, and this method has been improved by Lander.[3] Laudise and Ballman[4] have shown that zinc-oxide crystals could be grown hydrothermally, and recently Nielsen and Dearborn[5] have obtained crystals by precipitation from molten solution.

In the course of producing zinc-fluoride single crystals, it happened that the needlelike zinc-oxide single crystals were easily obtained by chemical reaction of zinc-fluoride with air at elevated temperature.

Zinc-fluoride powder (about 7 g in weight) was charged in a platinum crucible whose size was 35 mm in diameter and 40 mm in depth. The bottom ot the crucible was heated to keep 1050°C by Bunsen burner. The top of the crucible was aircooled and the setposition of the crucible was adjusted to maintain the suitable temperature distribution at the crucible wall. Heating the crucible for several hours, a cluster of hexagonal, yellowish, transparent needlelike crystals was found in radial direction, on the inside wall of the crucible where the temperature was about 950°C (Fig. 1). A typical example of their dimensions is 15 mm in length and 1 mm in cross section. Their appearance is shown in Fig. 2. X-ray diffraction photographs showed that these crystals were of zinc-oxide, and that their growth direction was parallel to the c axis. So the appearance of the crystals obtained by this method resembles with those by Scharowsky's method.

Large crystals could not be formed if the region where the temperature was about 950°C was too close to the bottom of the crucible or to the top, in spite of several hours' heating. Larger crystals were obtained by longer heating. As the amount of the charged zinc-fluoride powder increased, longer time was needed to form large crystals.

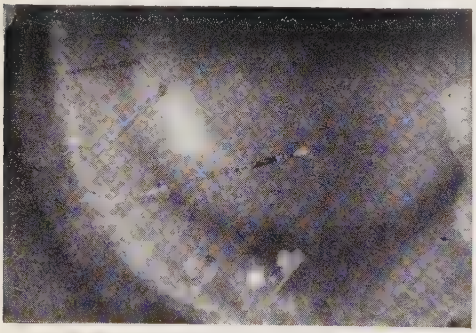

Fig. 1. A cluster of crystal which grew in radical direction on the inside wall of the platinum crucible.

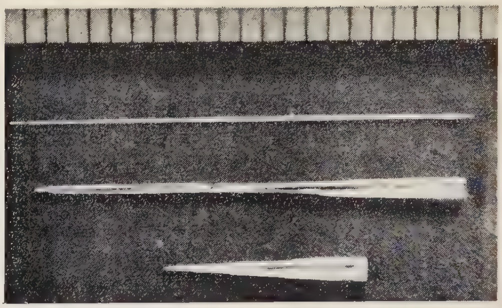

Fig. 2. A typical example of the grown crystals. One division of the scale is 1 mm in length.

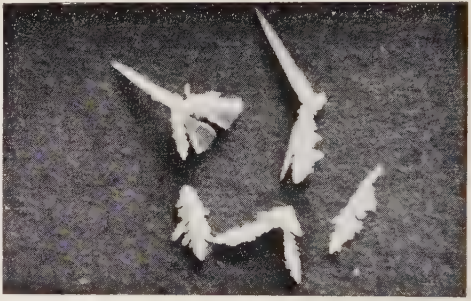

Fig. 3. Dendric crystals.

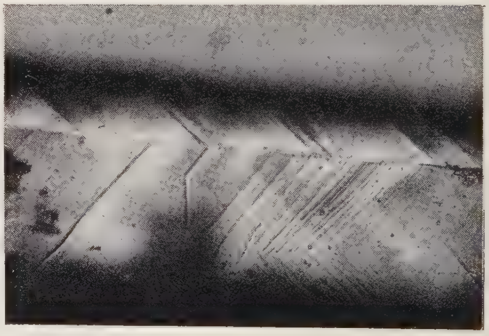

Fig. 4. A steplike figure on the surface of the needlelike crystal observed by micrography. 400 ×. The horizontal line is the edge of the hexagonal crystal.

From these facts, it seems that both oxidation rate of zinc-fluoride and condensation rate of zinc-oxide vapour are the essential factors for this method. Perfectness of the grown crystals was improved by steeper temperature gradient at the crucible wall. For low temperature gradient dendric growth was frequently formed (Fig. 3). On the surface of the grown crystals, a steplike figure was observed by micrography as illustrated in Fig 4. Since the back reflection Laue spots for these crystals were elongated to the direction parallel to the c axis, this figure seems to be mosaic walls due to the lattice rotation about an axis perpendicular to the c axis during the crystal growth.

A further investigation is now being undertaken.

Acknowledgements

The auther wishes to express his cordial thanks to Professor S. Doi for his encouragement throughout this study. His thanks are also due to Professor S. Imai and Assistant Professor N. Shibata for their helpful advices and discussions.

References

1) O. Fritsch: Ann. Physik. **22** (1935) 375.
2) E. Scharowsky: Z. Phys. **135** (1953) 318.
3) J. J. Lander (to be published).
4) R. A. Laudise and Ballman (to be published).
5) J. W. Nielsen and E. F. Dearborn: J. Phys. Chem. **64** (1960) 1762.

J. PHYS. SOC. JAPAN **16** (1961) 2359~2360

Movement of Small Angle Boundary of Ice Crystal

Akira HIGASHI and Naomi SAKAI

Department of Physics, Faculty of Science
Hokkaido University, Sapporo

(Received August 28, 1961)

Through the movement of small angle boundary is believed to be a very powerful tool to study the dislocation mechanism of slip in crystal[1)], it has not been investigated so widely except in the case of zinc. As a part of our extensive studies of slip mechanism in ice crystal, stress induced movement of small angle boundary was investigated. As is the case of zinc, the ice crystal has a basal slip plane that makes this kind of study easy. Due to its transparency, ice crystals have more advantage for observation of the movement than zinc crystals do.

The small angle boundary was made in a rectangular bar (1×1 cm^2 cross section, 10 cm length) of single crystal of ice by the method of central loading. The specimens were cut from large natural single crystals brought from the Mendenhall Glacier, Alaska. The bar has its long axis perpendicular to the crystal *c*-axis and its top and bottom surfaces are parallel to the base plane to make the easy glide. Angle of bending or the angle of misfit at the boundary was controlled by the time duration of bending and also by the weight.

The boundary thus made at the center of bar was used for experiments of the movement. The bar was cramped at one end horizontally and was pulled down by weights at other end making a cantilever bending. The boundary was clearly visible by different transparancy when the bar was examined through crossed polaroids from the side. Measurements of the movement were made by a horizontal microscope with a scale in the eyepiece. An example of the movement is shown in photographs of Fig. 1.

The rate of movement decreases almost linearly with the increasing angle of misfit at the boundary. And it increases linearly with the increase of stress. Temperature dependence of the rate of movement obeys Arrhenins' equation as shown in Fig. 2. Fairly good straight lines can be drawn through ex-

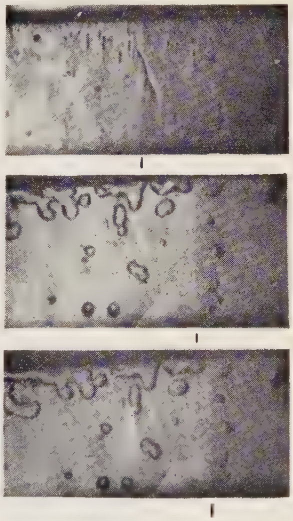

Fig. 1. An example of the movement of boundary, photomicrographs through crossed polaroids.

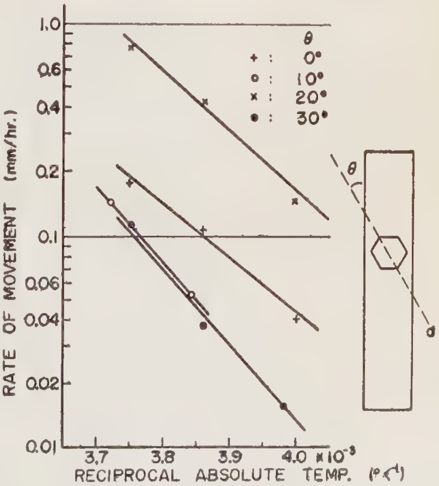

Fig. 2. Temperature dependence of the rate of movement with different horizontal orientations of the ice bar.

perimental points plotted. Error of the estimate of activation energy from the lines is several percent.

A remarkable result obtained is that the activation energy varies with the change of direction of length of specimen with respect to the a-axis. In the following table of the result, θ is the angle between the direction of length of specimen and the crystal a-axis or $\langle 11\bar{2}0\rangle$ direction. The activation energy Q of the rate of movement takes a value of about 12 Kcal/mol and 17 Kcal/mol alternately with every 10° change of the angle θ.

$\theta°$	0	10	20	30
Q Kcal/mol	11.6	16.6	12.9	16.6

It should be noted that the activation evergy for dielectric relaxation[2] and for creep under low stress[3] of ice falls between these two values, though there are some other estimates of the activation energy which are quite different from those values. A dislocation model of the slip mechanism of ice crystal taking account of such an interesting result will be given later. Further experiments on creep, stress-strain relation and self-diffusion are under way.

The detail will be published in the Journal of the Faculty of Science, Hokkaido University in the nearest furture.

References

1) Read, W. T. Jr.: Dislocation in Crystals (1953)
2) Humbel, F et al: Helv. Phys. Acta, **26** (1953), 17.
3) Butkovich, T. R. & J. K. Landauer: SIPRE, Research Report 72 (1960).

J. PHYS. SOC. JAPAN **16** (1961) 2360~2361

The Texture of Vapour Phase Grown ZnS Crystals

By Tomoya OGAWA

The Institute of Physical and Chemical Research
Komagome, Bunkyo-ku, Tokyo, Japan

(Received July 28, 1961)

X-ray studies of the structure in ZnS crystals such as long period structures have been reported by many workers[1]. However, the texture of vapour phase grown ZnS crystals is not well known, although it should play an important part in their electrical properties such as the anomalous large photovoltaic effect[2], the anisotropy of electrical conductivity[2]. In the present note we report some observations on the texture of the crystals which have been made by optical microscopy as well as rotation and Berg-Barrett methods of X-rays.

Photographs obtained from a plate-like crystal are shown in Fig. 1. The photograph (a) taken by a polarized monochromatic light (Hg : 5461 A) exhibits many parallel striations which run normal to the [0001] axis from one end to the other. It is considered that the bright regions are hexagonal-like packing or hexagonal rich regions and dark regions are cubic-like packing or cubic rich regions, since hexagonal form (wurtzite) is uniaxial positive and cubic form (zinc blende) is isotropic. In order to examine these considerations, rotation photographs of X-rays are taken from the both regions, as given in Figs. 1 (c) and (d). The spots of indices $(h-k)=3N\pm1$ are accompanied with clear streaks in the photographs. Accordingly it is considered that the both regions contain stacking faults (refer to Fig. 2). If the crystals were homogeneous, the stacking faults probabilities could be estimated from the analysis of the intensity profiles on the streaks[3),4)]. But such an analysis is actually meaningless, because the crystal is not homogeneous even in the region irradiated by the incident X-ray beam. However there are some differences in spots between the both

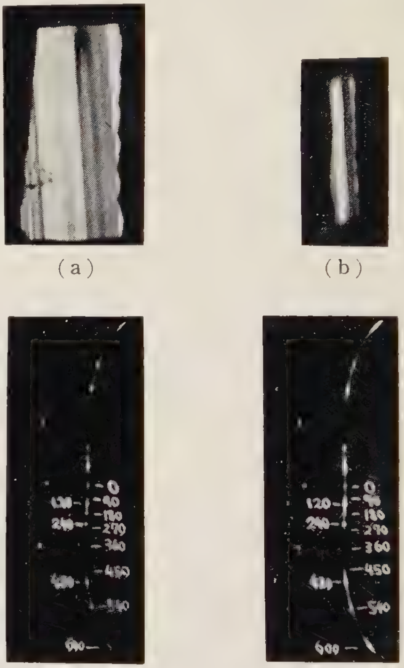

(a) (b)

(c) (d)

Fig. 1 (a): Optical photograph taken by monochromatic polarized light (Hg : 5461 A). (b): X-ray photograph taken by 540° spot or $(1\bar{1}03)$ plane reflection with Cu kα radiation. (c) and (d): X-ray rotation photograghs along [0001] axis from the bright and dark regions, respectively.

photogrphs: for example, 90° and 180° fpots from the bright region are sharp and intense, while those from the dark are diffuse. These facts are in agreement with the expectation from the optical observation. As shown in Fig. 2, the hexagonal stacking order gives strong reflectivity at 540° spot, but cubic stacking order does not show any reflection at 540°, therefore the Berg-Barrett photograph taken by 540° spot is expected to exhibit hexagonal regions of crystal. Moreover, the intensity from a region with stacking faults will be decreased, because the reflectivity of this spot will be decreased by stacking faults as pointed out by Jagodzinski[3] and others[4]. On the other hand, it is expected that the optical birefringence will be also decreased with stacking faults, because the crystalline field anisotropy[5] will be decreased with the increasing cubic stacking sequences. In this way it is explained that the intensity contrast of striation in the Berg-Barrett photograph (Fig. 1 b), corresponds well to the contrast in the optical one (Fig. 1 a). Details of the study will be reported later.

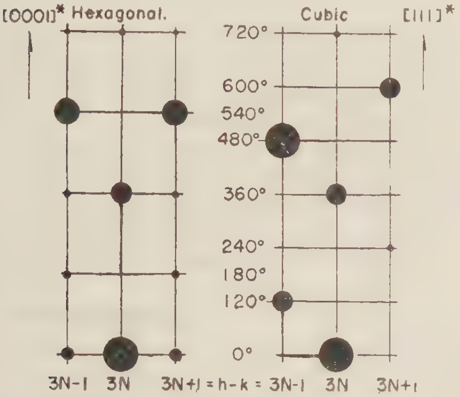

Fig. 2 Reciprocal lattice representation of reflectivities for hexagonal and cubic forms. The size of the circle is proportional to the square of the structure factors and, if there are stacking disorders, the spots of indices $(h-k)=3N\pm1$ are elongated vertically[3][4].

The author wishes to thank Dr. Y. Suge for his guidance and encouragement, and is indebted to Dr. R. Sato of Mitsubishi Metal Mining Co. for his helpful suggestions and discussion.

References

1) For example, F. G. Smith: Am. Mineralogist **40** (1955) 658.
2) For example, A. Lempicki: Phys. Rev. **113** (1959) 1204.
3) Von H. Jagodzinski: Acta Cryst. **2** (1949) 201, 209 and 298.
4) A. J. C. Wilson: Proc. Royal Soc. **A180** (1942) 268; M. S. Paterson: J. Appl. Phys. **23** (1952) 895.
5) F. Keffer et al: J. Chem. Phys. **27** (1957) 675.

J. Phys. Soc. Japan **16** (1961) 2361~2362

Chlorine Nuclear Quadrupole Resonance of $CH_3COCHCl_2$

By Shinhachiro Saito*

Department of chemistry, Tokyo Institute of Technology Meguro-ku, Tokyo

(Received February 8, 1961)

The pure quadrupole resonance spectra of Cl^{25} have been detected with self-quenching super regenerative spectrometer in 1, 1-Dichloro-2-propanone. The absorption signals were recorded on a chart-recorder. Table I gives the resonance frequencies at −77°C with some similar structural molecules.

1, 1-Dichloro-2-propanone was prepared by the action of chlorine on acetone in the presence of a small amount of antimon-pentachloride[1]. The product obtained was thoroughly washed with water[2] and purified by repeated distillation. The final product was checked for purity by the infrared spectra[3],[4] and the specific gravity.

1, 1-Dichloro-2-propanone will not crystallize as temperature is lowered with freezing mixture of dry ice and petroleum ether, but exhibits instead the increase of the viscosity. In case of immediate cooling down with liquid nitrogen, this compound simply solidifies into a transparent glass-like material. Thereupon the sample contained in an ampoule was made to set a small seed (glass-like) at the sharp-pointed bottom with liquid nitrogen, and made to crystallize for about two hours at −77°C.

In immediate cooling of this crystalline sample until −196°C, the resonance lines have not appeared, but frequently continuous weak absorptions which are not due to the nuclear quadrupole interaction have been observed.

If the relations between the nuclear quadrupole resonance frequencies and the ionic character of the C–Cl bonds are considered, one can expect that the resonance frequencies in α, α-dichloroketone are higher about one or more MCPS than in α-mono or α, α'-dichloroketone[5],[6]. The frequencies of this compound are, however, not much different from those of Chloro-2-propanone and 1, 3-Dichloro-2-propanone, as shown in Table I, which have been

---

* Present address: The Research Institute for Iron, Steel and Other Metals, Tōhoku University Sendai.

Table I. Cl^{35} resonance frequencies in some chloropropanones.

Compound	Frequency in MC (at −77°C)
Chloro-2-propanone[a]	34.452
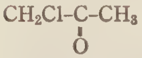 $CH_2Cl\text{-}\underset{\underset{O}{\|}}{C}\text{-}CH_3$	34.461
1, 1-Dichloro-2-propanone	34.504±0.010
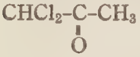 $CHCl_2\text{-}\underset{\underset{O}{\|}}{C}\text{-}CH_3$	34.981±0.005
1, 3-Dichloro-2-propanone[a]	35.441
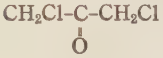 $CH_2Cl\text{-}\underset{\underset{O}{\|}}{C}\text{-}CH_2Cl$	

a) See ref. 6.

observed by H. C. Allen, Jr[6]. Refering to the behavior in the crystalline state of this compound, it would be predicted that there is some of the discontinuity at lower temperature than −77°C.

The author wishes to express his sincere thanks to Professor Kunio Kozima for his kind guidance and encouragement during the course of this work.

References

1) Chem. Zentr. C. 102 (1931) 2056.
2) T. Chiba: Bull. Chem. Soc. Japan, **28** (1955) 19.
3) Nakagawa, Ichisima, Kuratani, Miyagawa, Shimanouchi, and Mizusima: J. Chem. Phys. **20** (1952) 170.
4) L. J. Bellamy and R. L. Williams: J. Chem. Soc. (1957) 4294.
5) K. Kozima and S. Saito: J. Chem. Phys. **31** (1959) 560. H. O. Hooper and P. J. Bray: J. Chem. Phys. **33** (1960) 334.
6) H. C. Allen, Jr.: J. Am. Chem. Soc. **74** (1952) 6074.

JOURNAL OF THE PHYSICAL SOCIETY OF JAPAN, Vol. 16, No. 12, DECEMBER, 1961

Decay of Sr^{83}

By Tokihiro KUROYANAGI

Japan Atomic Energy Research Institute, Tokai Laboratory,
Tokai-mura, Ibaraki-ken

(Received April 24, 1961)

The disintegration of Sr^{83} produced by (γ, n) reaction was studied with the aid of scintillation spectrometer. The gamma-ray spectra showed lines at 40, 385 and 755 keV. And the analysis of the beta-ray spectra defined two groups of beta-ray of the end-point energy of 0.81 and 1.15 MeV. The decay scheme was proposed from the information of the single and coincidence scintillation spectra. In the decay scheme, the 40-, 385- and 755-keV levels were established and the spin and parity assignments of ground and first excited 40-keV levels were confirmed to be 5/2- and 3/2-, respectively.

§1. Introduction

At present, the theoretical interpretation of lower nuclear states in the region of mass number around 80 shows some successes for even-even nuclei. There, the vibrational model seems the fit quite well. However, for odd mass nuclei, such theoretical treatments are not in good shape. Although, systematical information of nuclear levels of many nucleides are very important for the development of such nuclear theories, the information is not quite good with odd mass nuclei. It is, therefore, considered to be worth while accumulating the information on the levels and decay properties of the odd mass nucleides in this region. The decay of Sr^{83} was studied in a hope to help elucidating the situation.

The disintegration of Sr^{83} has not been studied extensively so far. Boyle and Maclure[1] showed that Sr^{83} decayed with a half-life of 35 hours and the beta-ray energy was about 1 MeV. The beta-ray spectrum of the activity has been studied with a double focusing spectrometer by Castner and Templeton,[2] who reported the beta-ray end-point energy of 1.15 MeV and some low energy conversion lines with a half-life of 35 hours. However, the decay properties have not been fixed.

In the present study, an intense source of Sr^{83} was produced by the (γ, n) reaction of Sr^{84} using a strong bremsstrahlung from a linear electron accelerator, in spite of the very low abundance (0.55%) of Sr^{84} in natural strontium.

§2. Experimental procedure

In order to prepare the activity of Sr^{83}, high purity sample of strontium nitrate of 1 gram was irradiated by a 19-MeV bremsstrahlung for 2 hours. The bremsstrahlung was converted from the 19-MeV electron beam of the JAERI linear electron accelerator* using an water cooled gold traget of 0.9 mm in thickness. The photon intensity was estimated to be an order of 10^6 r/min at the sample position. This was monitored with a roentgen rate meter and was checked with activations of Cu, Cs and Pb by using their well known yield curves.[3] At the time of the irradiation the electron beam intensity was measured to be about 40 μA. The energy of the electron beam was found by an use of conventional magnetic analyzer. In order to avoid a heat up or vaporization of the sample by absorption of high beam power, the sample was filled in a cooling box. Fig. 1 shows the target assembly. In the irradiation many isotopes were produced from (γ, n) and (γ, p)

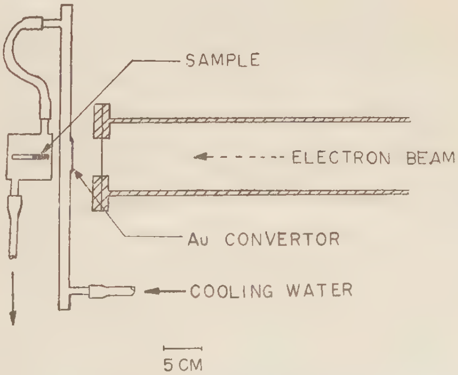

Fig. 1. Target assembly.

---

* The Model D-L-3 linear electron accelerator

reactions. Most of the activities, however, have well known decay characteristics and the interference from these activities was slight and could be corrected for.

The gamma-ray spectrum were measured by means of a conventional scintillation spectrometer which consisted of a NaI(Tl) crystal of 3.8 cm thickness and 3.8 cm in diameter coupled to a Dumont 6292 photomultiplier tube and a 256 channel pulse height analyser. In order to see the low energy part of the spectrum, a 0.2 cm × 2.5 cm NaI(Tl) crystal was used. The spectrometer was calibrated with several well known peaks of the gamma rays from Pb^{203}, Au^{198}, Cs^{137}, Mn^{54} and Na^{22}. In the case of thin crystal, the low energy calibration was made from the KX-rays of In^{114}, Cs^{137} and Pb^{203}. The errors in energy measurements of the gamma rays were within ±5 keV. Photopeak efficiencies of the crystals were taken by means of a coincidence method using the gamma-rays of Pb^{203}, Au^{198} and Co^{60}. The measured spectra were analyzed by the reference spectra of standard sources, and the gamma-ray intensities were calculated from the photopeak efficiency.

The beta-ray spectrometer consists of a plastic scintillator of 2.5 cm in height and 5 cm in diameter shielded for light by 2 mg/cm^2 alminium foil, which was optically coupled with a Dumont 6292 photomultiplier tube. The used electronic circuit and pulse height analyzer was the same as that for the gamma-ray spectrometer. The spectrometer was calibrated with beta-ray end-point energies of the standard sources of In^{114} and Au^{198} and was checked with the positron spectra of Cu^{62} and C^{11} which were obtained from (γ, n) reactions. The resolution of the plastic phospher was determined by the 624-keV internal conversion line of Cs^{137}, which was about 20% at this energy. A check of linearity of the Kurie plot was done, employing a Au^{198} source of 10 mg/cm^2 thick which has been subtructed for contribution of the Compton electrons (Fig. 2). The gamma ray was measured in standard position. The intensity ratio between beta and gamma ray gave a good check of photopeak efficiency.

Strontium sample for beta-ray measurements was prepared as a thin layer obtained from aqueous solution of irradiated $SrNO_3$. The errors in measured end-point energies were within ±50 keV.

In order to determine which of the observed gamma rays is in coincidence with beta rays, beta-gamma coincidence measurements were performed using a conventional coincidence circuit whose resolving time was $2\tau=1$ μsec. Finally, coincidences between gamma rays were investigated with the help of two types of coincidence counting arrangements. The high energy part of the coincidence gamma rays was viewed by a 3.8 cm × 3.8 cm NaI(Tl) crystal, and in the low energy part, a 0.2 cm × 2.5 cm NaI(Tl) crystal was used.

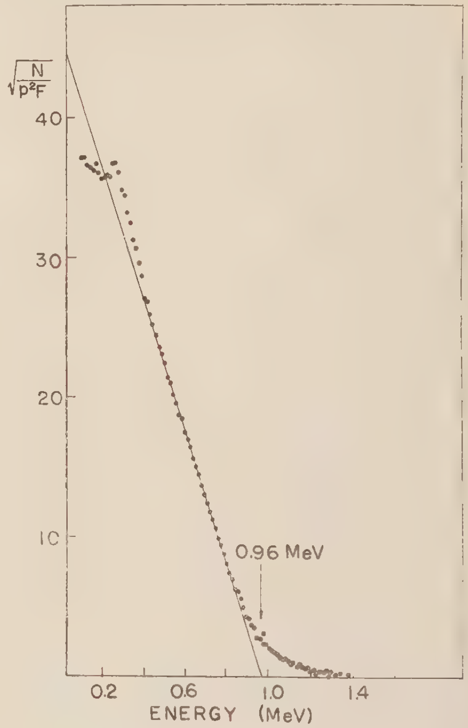

Fig. 2. Kurie plot of Au^{198}.

§ 3. Results and Discussions

3. 1. The Gamma Rays

It was expected that the irradiated strontium sample may have activities of Sr^{87m}, Sr^{85}, Sr^{85m} and Sr^{83} from the (γ, n) reaction, and may have rubidium activities of mass number of 83 and 86 from the (γ, p) reaction. And also, it was suposed, that any confusion may not occur by (γ, α) and (γ, np) products, because the (γ, α) reactions do not give any radioactive nucleides, and the (γ, np) reactions may produce negligible amounts of activities due to the comparatively low bombarding energy.

The measured gamma ray spectra showed

the radiations of the activities mentioned above. In order to assign photopeaks in the spectra, the gamma-ray decay was followed for 20 days. At about 50 hours after the termination of the bombardment, strong disturbances by the short half-lived radiations of Sr^{87m} (2.8 hours) and Sr^{85m} (70 min) diminished. The sharp peaks at the energies of 0.510 and 0.755 MeV were found and there are weak peaks at the energies of 40 and 385 keV. The spectrum at 10 days after showed only 0.515- and 1.07-MeV gamma ray (Fig. 3).

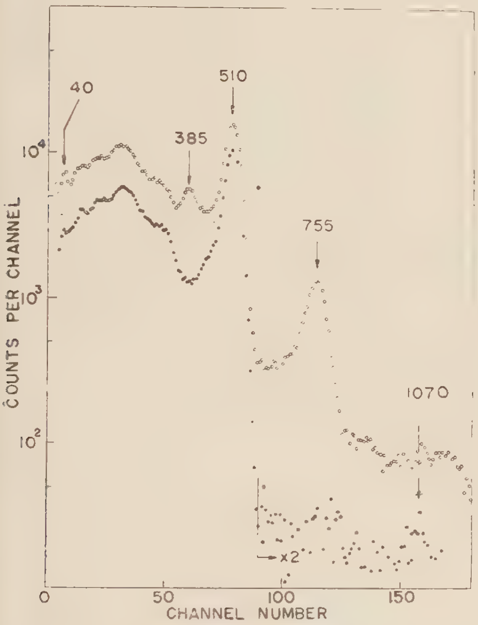

Fig. 3. Gamma-ray spectra of irradiated strontium sample with 19-MeV bremsstrahlung. The circles and dots show the spectra at 50 and 400 hours after the termination of bombardment.

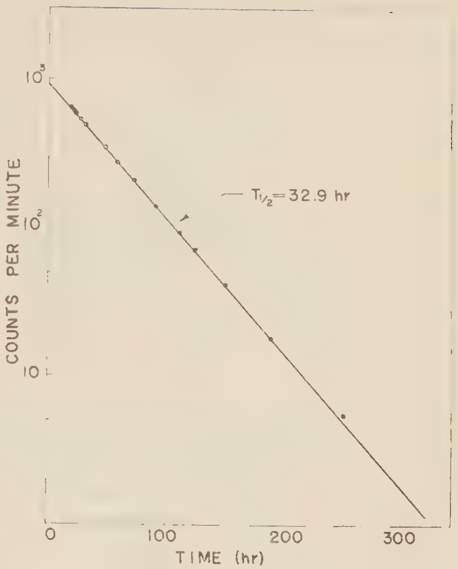

Fig. 4. Decay curve of the gamma ray of 755 keV.

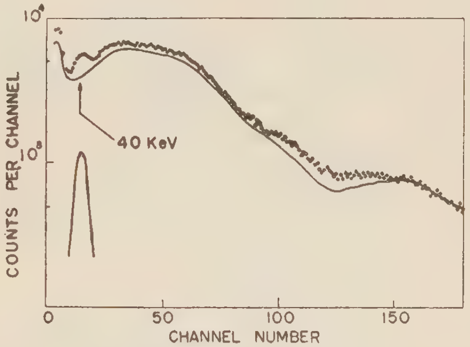

Fig. 5. Gamma-ray spectra of irradiated strontium sample taken by thin crystal scintillation spectrometer. The dots show the spectum at 50 hours after the termination of the bombardment and solid line shows the crystal response for 514 keV gamma ray.

Table I. Relative intensities of the measured gamma rays at the termination of the bombardment

Energy (keV)	Half-life	Nucleide	Relative intensity
40	32.9 h	Sr^{83}	0.18
385	32.9 h	Sr^{83}	0.45
388	2.8 h	Sr^{87m}	145
510	32.9 h	Sr^{83}	1.0
513	65 d	Sr^{85}	0.70
755	32.9 h	Sr^{83}	0.55
1080	19 d	Rb^{86}	2.5×10^{-3}

Following the decays of each peaks, and considering the decay schemes of well known activities, it was found that the gamma ray of 0.515 MeV belongs to Sr^{85}. The spectrum around 1.07 MeV seemed composite, since the decay curve showed that the half-lives were 33 hours and 19 days. Although the spectrum shape was not certain, the 1.07-MeV line in the spectrum at 400 hours after the termination of the bombardment was seen as a gamma ray accompanying the Rb^{86} decay. In addition to the gamma rays, a new gamma-ray group of the energies of 0.040, 0.385, 0.510 and 0.755 was found to have a half-life of 32.9 hours. The half-life was determined from the decay of 0.755-MeV peak without any disturbance from background radiations (Fig. 4). A dead time in the counting was automatically corrected in spectrometer, which was verified by means of a half-life measurement of the well known decay of Sr^{87m} (2.8 hr). Then the low energy part was viewed again with thin scintillation crystal. As shown in Fig. 5, the existence of 40-keV gamma ray with a half-life of 32.9 hours was confirmed. Although the 40-keV line was found in good agreement with the measurement of the internal conversion lines by Castner and Templeton, the other lines of the energies of 74, 101, 151 and 165 keV reported in their article were not observed.

The gamma ray spectra mentioned above were analyzed to each gamma ray using standard crystal response, and the intensities of the gamma rays were calculated from the photopeak areas and the photopeak efficiencies. The results are shown in Table 1.

3. 2. The beta rays

After a sufficiently long time (400 hours), the spectrum was only beta rays accompanying Rb^{86} activity, which was verified from end-point energies of 1.77 and 0.7 MeV of the two groups and the half-life of 19 days. Again, the assignment was checked by a comparison between the beta-ray intensities and the gamma-ray intensity of 19-days component in 1.08-MeV photopeak using the established decay scheme.

The beta-ray decay curve taken below the energy of 1 MeV was found that it consisted of 19 days and 32.9 hours components. The spectrum at 50 hours after the termination of the bombardment was resolved by means of Fermi-Kurie analysis (Fig. 6). In this Kurie plot, contributions of Compton electrons due to the gamma rays have been subtracted. After the subtraction of Rb^{86} beta ray, a known beta-ray group of the energy of 1.15 MeV was found. And from the successive subtraction, a new beta-ray group with a end-point energy of 0.81 MeV was found. The intensity ratio of the 1.15- and 0.81-MeV groups was calculated to be 6 : 4.

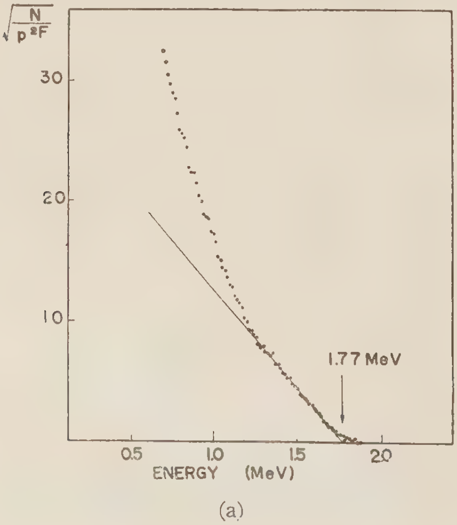

(a)

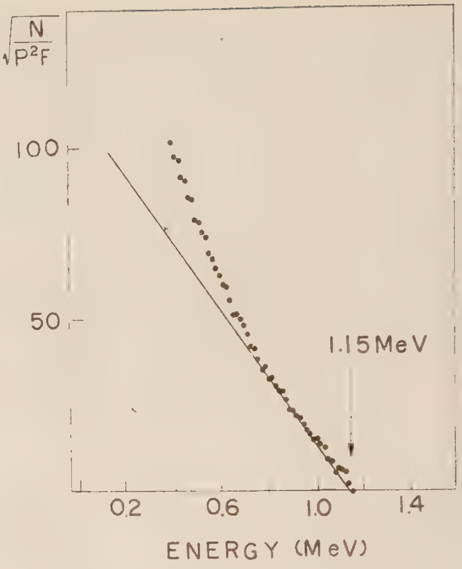

(b)

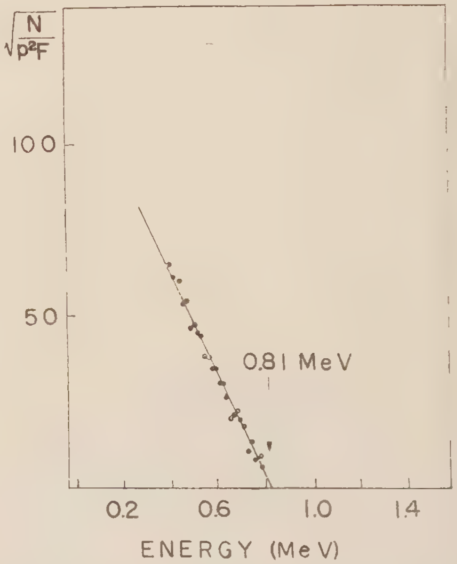

(c)

Fig. 6. (a) is Fermi-Kurie analysis of the beta-ray spectrum of irradiated strontium sample.
(b) and (c) are Fermi-Kurie analysis of Sr^{83} which are obtained from a subtraction of the contribution by Rb^{86}.

3. 3. The Coincidence Measurements

The beta-gamma and gamma-gamma coincidence measurements were very helpful for constructing the decay scheme. The beta-gamma coincidence spectra were taken by setting the single channel windows at 510 and 385 keV. The beta-ray spectrum gated by 510 keV showed the beta groups of Sr^{83} without disturbance by Rb^{86}. The coincidence ratio was obtained to be about 100%. In this calculation, the number of single channel window counts was corrected for the mixing of the 514-keV gamma ray of Sr^{85} using the gamma-ray decay curve.

When the coincidence gate was opened by the photopeak of 385-keV gamma ray, the coincidence beta-ray spectra showed two groups with end-points around 0.81 and 1.15 MeV. The 1.15-MeV beta group was explained to be the coincidence counts with Compton pulses of 0.510-MeV gamma radiation contained in the window. The coincidence ratio between 0.81-MeV beta group and 385-keV gamma ray was 20%. These results suggested that the 510-keV gamma radiations is annihilation quanta of the positron and the 0.81-MeV beta-ray group is in cascade with the 385-keV gamma ray.

The gamma-gamma coincidence gate was set at the photopeak of the 755 keV gamma rays. Weak coincidence spectrum was obtained, which has a photopeak at the energy of 510 keV with the coincidence ratio of 4 percent. The coincidence measurements gated at 510 keV were performed for the relative position of 180° and 90° between two detecting probes. In the case of 180°, an outstanding peak at 510 keV was found, and the coincidence ratio was about 100%, if the 510 keV radiation is actually annihilation quanta. From this results, in addition to previous discribed beta-gamma coincidence measurements, the 510-keV line was confirmed to be the annihilation quanta of the positrons of Sr^{83}. In this window setting, a coincidence peak at 755 keV were found with a coincidence ratio of 2%, which was consistent with the case of 755-keV gate setting.

By the coincidence measurements, at 90° relative position, it was found that the gamma rays of 385 and 755 keV were coincident with annihilation quanta, whose coincidence ratios were 30 and 2%, respectively.

From these coincidence measurements and analyzed single crystal data, it was consistently explained that the gamma-ray of 755 keV is fed by positron decay of 2% and is mainly fed by the electron capture decay, and the 20% of the 385-keV gamma ray is in cascade with the positron decay.

The coincidence spectrum was also observed using the thin NaI(Tl) scintillation crystal. It was found that the 40-keV gamma ray was coincident with only the annihilation radiation, which has a coincidence ratio of 20%. When the coincidence gate was opened by 385- and 755-keV gamma rays, no coincidence gamma ray were found in the low energy region. It was, therefore, concluded that there are three excited levels of the energies of 40, 385 and 755 keV.

§ 4. Decay Scheme and Spin-Parity Assignments

From a straight forward consideration of the experimental data, the decay scheme was tentatively proposed as shown in Fig. 7.

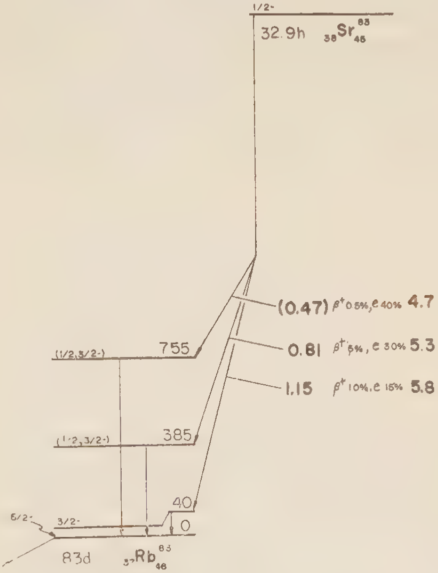

Fig. 7. Decay scheme of Sr^{83}.

In the proposed decay scheme, the computed intensity ratios of beta rays were consistent each other, which had been normalized to the total decay. The log ft values of the positron emission or the electron capture decay were computed using Moszkowski's nomogram.

The high coincidence ratio between annihilation quanta and 40-keV gamma ray suggests that the 40-keV gamma ray has a low multipolarity. Since the half-life for 40-keV gamma-ray emission has been calculated to be the order of 10^{-11}, 10^{-5}, 10^{-10} and 10^{-3} second for E1, E2, M1 and M2 transitions, respectivly, and since the resolving time of the coincidence circuit is 1 μsec, the transition of M2 type cannot be assigned. On the other hand internal conversion coefficients have the theoretical values of 1.4, 24 and 1.8 for E1, E2 and M1 transitions, respectively. Since the E2 transition is highly converted, the E2 transition does not seem to be the case. The experimental conversion coefficients was calculated to be 2 considering the ratio of electron capture and positron decay. Thus the transition of M1 type is suggested.

The ground state of Rb^{83} has been found to be 5/2−.[4] Because of the presence of either the allowed or the first forbidden beta decay to the 40-keV state without any cascade via 40-keV state from higher states, the assignment of 7/2+ (and of course 9/2+) to 32.9 hours Sr^{83} is safely disregarded. The assignment of 1/2−, in the contrary, will make no contradiction. If we assume that the 40-keV level is a 3/2− state, the beta decays from Sr^{83} to the ground and the 40-keV states are explained consistently and the states would be connected by an M1 transition. Moreover any higher states in Rb^{83} attained from Sr^{83} does not necessarily require cascade decay via 40-keV state. Also the appearance of both 3/2− and 5/2− states as the lowest states in Rb^{83} is exactly what is expected from the systematics. As far the higher states observed it seems to be most plausible to assign either 1/2− or 3/2− from the beta decay log ft values. Also from shell model it is difficult to expect any low-spin even-parity states although the log ft values observed do not completely exclude such assignments. Spin and parity assignments of the concerned levels are also shown in Fig. 7.

The author is deeply indebted to Professor H. Morinaga of University of Tokyo and the members of his nuclear spectroscopy group for many discussions in this study. He is also grateful to Mr. T. Tamura for kindly help during the course of the measurements. Finally, he wishes to thank Dr. K. Miyazaki for his interest and encouragement in this work.

References

1) W. S. Boyle and K. Maclure: Proc. Roy. Soc. Canada **45** (1951) 196A.
2) S. V. Castner and D. H. Templeton: Phys. Rev. **88** (1952) 1126.
3) See, for example, R. Montalbetti, L. Katz and J. Goldemberg: Phys. Rev. **91** (1953) 659.
4) See, K. Way et al: Nuclear Data Sheets (1959).

JOURNAL OF THE PHYSICAL SOCIETY OF JAPAN Vol. 16, No. 12, DECEMBER, 1961

Decay of As^{79}

By Tokihiro KUROYANAGI

Japan Atomic Energy Research Institute, Tokai Laboratory,
Tokai-mura, Ibaraki-ken

(Received April 24, 1961)

As^{79} was produced by a strong bremsstrahlung from a linear electron accelerator. It was separated chemically from SeO_2 irradiated by the bremsstrahlung. The decay of As^{79} was studied with the aid of scintillation spectrometers. From the information of the gamma and beta spectra and of the coincidence measurements, the decay scheme of As^{79} was proposed.

§ 1. Introduction

In the previous investigation[1] using a betatron, new gamma rays of 360, 440, 725 and 890 keV were found in the decay of As^{79}. Because the bremsstrahlung from the linear electron accelerator was very intense, the scintillation spectrometry of the radiation from As^{79} was performed with a good statistics, and also with councidence measurements.

Since the lower state of Se^{79} has not been known at all, it was considered worth while trying to construct the decay scheme of As^{79} from such an investigations.

§ 2. Experimental Procedure

The activity of As^{79} was made from the (γ, p) reaction of selenium by bombarding SeO_2 sample for 10 minutes each time. Because of the activation due to the (γ, p) reaction, the accelerator was operated at 24 MeV. When the selenium sample was irradiated by bremsstrahlung, strong disturbances by selenium activities of (γ, n) products occurred. Thus a separation between selenium and arsenic was required. The procedures of chemical treatments are as follows: The irradiated selenium dioxide of 0.5 gram was disolved to hot 10N HCl with arsenic carrier. The arsenic activities could be extracted by CCl_4. Furthermore, in order to measure the beta-ray spectrum, the activities were precipitated on the filter paper as a from of arsenic sulfide. In this case, the arsenic activities in CCl_4 were extracted by dilute NaOH aqueous solution, which were precipitated by using H_2S gas.

The beta and gamma-ray measurements were made with the aid of scintillation methods using conventional scintillation spectrometers. In order to establish the decay scheme, gamma-gamma and beta-gamma coincidence measurements were tried. Details of the spectrometers and the irradiation methods of the sample were same as that described in the previous article[2].

§ 3. Results and Discussion

The gamma-ray spectrum obtained from the chemically treated sample is shown in Fig. 1. This was taken for 2 minutes at 10 minutes after the bombardment. Analyzing the spectra and following the decay, a peak at 540 keV was assigned to belong to As^{79}, besides the previously reported gamma rays. The low energy part below 300 keV except the 96-keV peak seemed to be the bremsstrahlung from

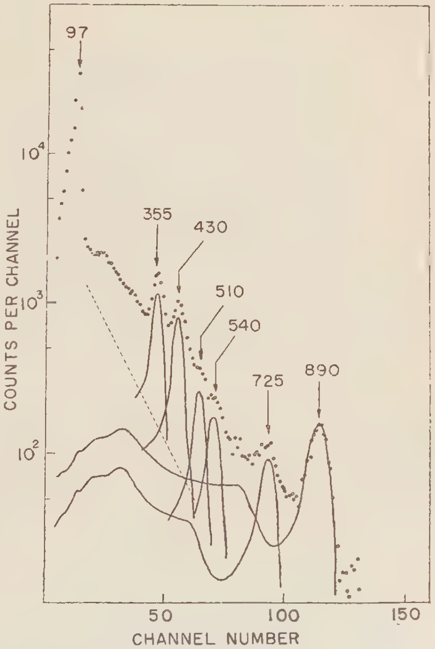

Fig. 1. Gamma-ray spectrum of As^{79}. The dashed line shows the contribution by bremsstrahlung of the beta rays.

Table. I. Relative intensities of the gamma radiations of As^{79}.

Energy (keV)	Percent of total decay
355	2
430	2
540	0.5
725	0.5
890	1

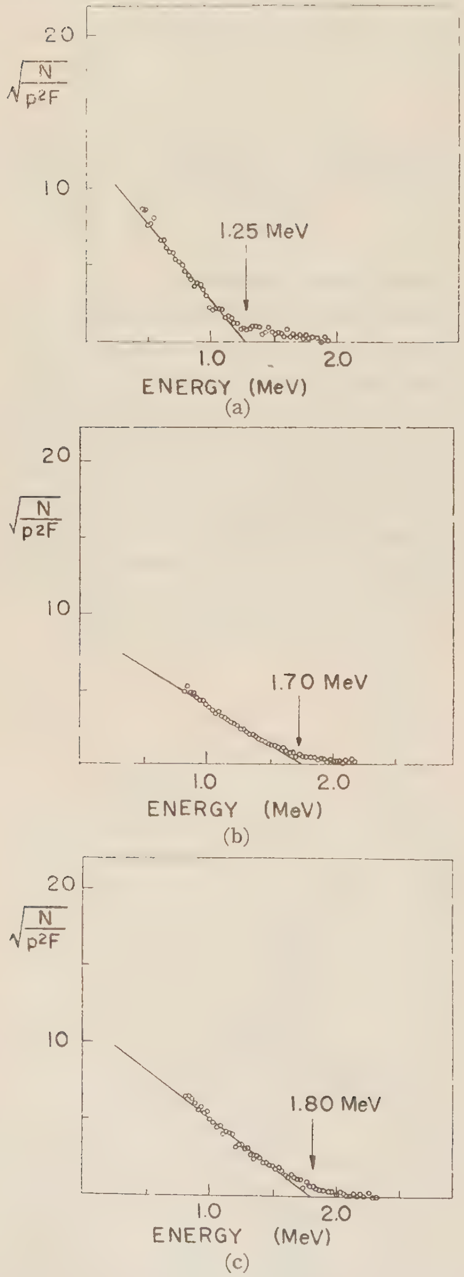

Fig. 2. Kurie plot of coincidence beta-ray spectra. (a), (b) and (c) show the Kurie plots gating by the gamma rays of 890, 430 and 355 keV.

the beta ray of As^{79}, which was checked by using the bremsstrahlung of P^{32} source. From the intensity of 96-keV gamma ray, the number of total disintegration of As^{79} was computed, correcting for the 3.9 min half-life of Se^{79m}. The intensity ratios per total decay were calculated, which is shown in Table I.

Although in the beta-gamma coincidence measurements the linearity of the Kurie plots were not good, the changes of the end-point energy were clearly observed. When the coincidence gates were opened by the gamma rays of 890, 430 and 355 keV, it was found that the end-point energies of the coincidence beta spectra were 1.25, 1.70 and 1.80 MeV as shown in Figs. 2(a), 2(b) and 2(c). In the case

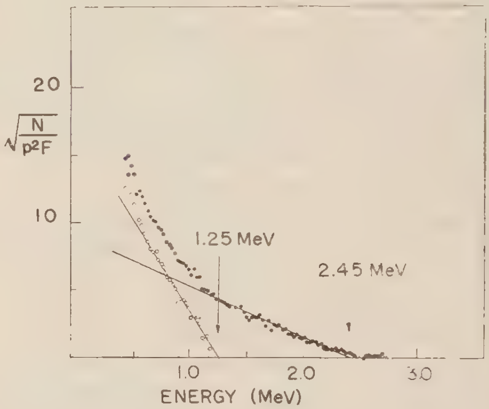

Fig. 3. Fermi-Kurie analysis of beta-ray spectra in coincidence with 540-keV gamma ray.

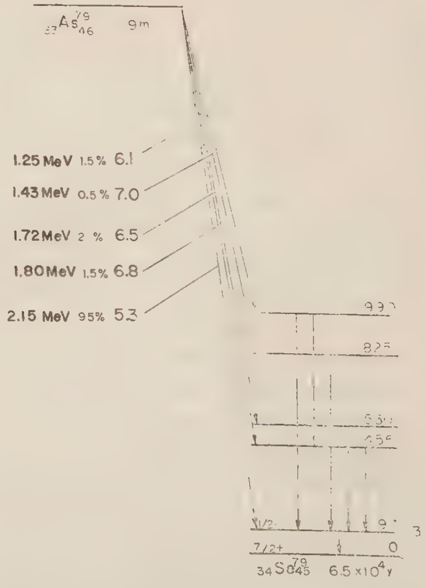

Fig. 4. Decay scheme of As^{79}.

of the gating with the 540-keV gamma ray, the beta-ray spectrum was disturbed by a 2.45 MeV of As^{76} which is in coincidence with a 550-keV gamma ray. However, after subtraction of the 2.45-MeV beta-ray group an end-point energy of 1.25 MeV was obtained. (Fig. 3).

It was, therefore, concluded that there are 455-, 530- and 990-keV states. Because of an absence of any coincidence gamma ray of 725-keV, it was also suggested that a 825-keV states exists. Thus, a tentative decay scheme was proposed as shown in Fig. 4. From the proposed decay scheme and the gamma ray intensity ratios, the log ft values of the associated beta transitions were computed as shown in the same figure. Since the ground state of As^{79} is probably 3/2- from the systematics, the states observed here seem to be mostly 1/2- or 3/2- states.

The author wishes to acknowledge the many discussion with Professor H. Morinaga of University of Tokyô and the members of his nuclear spectroscopy group. He is also grateful to Mr. T. Tamura for kindly help during the course of the measurements. Finally, he wishes to thank Dr. K. Miyazaki for his interest and encouragement in this work.

References

1) T. Kuroyanagi : J. Phys. Soc. Japan **15** (1960) 2179.
2) T. Kuroyanagi : J. Phys. Soc. Japan **16** (1961) No. 12.

JOURNAL OF THE PHYSICAL SOCIETY OF JAPAN Vol. 16, No. 12, DECEMBER 1961

Isomeric Cross Section Ratios for 14 Mev Neutron Reactions

By Fumio FUKUZAWA

Department of Physics, Hyōgo University of Agriculture, Sasayama, Hyōgo-ken

(Received July 26, 1961)

The cross sections for the production of isomeric pairs in the following reactions with 14 Mev neutrons have been measured by the activation method using the sample sandwiched plastic scintillator: $As^{75}(n, p)Ge^{75}$ (25±5 mb), $As^{75}(n, p)Ge^{75m}$ (10±2 mb); $Br^{81}(n, 2n)Br^{80}$ (470±50 mb), $Br^{81}(n, 2n)Br^{80m}$ (510±50 mb); $Ba^{138}(n, \alpha)Xe^{135}$(13±2 mb), $Ba^{138}(n, \alpha)Xe^{135m}$ (13±2mb); $Ho^{165}(n, p)Dy^{165}$ (40±10 mb), $Ho^{165}(n, p)Dy^{165m}$ (<1 mb). Their isomeric cross section ratios are compared with the statistical model calculations based on the method of angular momentum sampling. For $Br^{81}(n, 2n)$ and $Ba^{138}(n, \alpha)$ reactions, these ratios can be reproduced by these calculations with the value of the level density parameter $\sigma=4\pm1$, but not for the other two. The disagreement in $As^{75}(n, p)$ reaction can be explained by the predominance of the direct interaction process.

§ 1. Introduction

The purpose of the present paper is to describe the measurement of some cross sections for the production of isomeric pair by 14 Mev neutrons and to compare their isomeric ratios with the calculations based on the statistical model of nuclear reaction. When the isomeric states are formed through some nuclear reaction, the ratio of the cross sections for the production of each state is called the isomeric cross section ratio or briefly the isomeric ratio[1)]. This ratio seems to be governed mainly by the spins of initial and final states and of these levels which participate in a gamma-ray cascade. Though the cascade process is considerably complicated, there is an experimental evidence indicating that for intermediate and heavy elements the gamma-ray spectrum has an average multiplicity of 3 to 5[2)]. Further, dipole transitions are known to be favored over transitions of high multipolarity in a cascade. Using the above informations and taking appropriately the population of spins of initial state nuclei based on some reaction model, we might have a rough estimation for the isomeric ratio. In such calculations, the spin distribution of the highly excited levels must be considered which is related intimately to the structure of those levels[3]. Then, investigation of the isomeric ratio has a possibility of giving valuable information about the nature of highly excited nucleus. Further, if the reaction proceeds partly through compound nucleus formation and partly through direct interaction process, the isomeric ratio can also be used to give a measure of the relative importance of these processes.

Many experiments on the production of isomeric pairs have been reported[4)-18)]. Meadows *et al*[11]. and Meteosian and Goldhaber[13] have tried to explain their experimental results following the above consideration. Recently Huizenga and Vandenbosch[19] have calculated quantitatively the isomeric ratios for thermal neutron capture reactions and for (γ, n) reactions on the basis of the statistical model. Further, they have measured the isomeric ratios for several reactions which lead to the isomeric pair of Hg^{197} and analysed them successfully by the same kind of method[17].

Such experiments and analyses require further researches on the structure of highly excited nucleus as well as on the reaction mechanism. Generally, the measurement of the cross section for the production of the isomeric state is not always easy, because the radiation from isomeric transition is difficult to be detected. Most of the experiments on the isomeric ratio have been done by the use of thermal neutron or charged particle reactions in which large intensity of incident beam is available. For 14 Mev neutron reactions, as neutron beam intensity is rather small to produce sufficient isomeric state nuclei, there have been only 6 cases examined: $Dy^{164}(n, \gamma)$, $Nd^{142}(n, \alpha)$, $Er^{168}(n, \alpha)$[16], $Hg^{198}(n, 2n)$[17], $Sc^{45}(n, 2n)$ and $Se^{74}(n, 2n)$[18]. Recently, a method of sample sandwiched scintillator, which has an excellent character for the measurement of weak activities, has been developed in Kōnan University. This method being used, the cross sections for the production of each state of isomeric pairs for the reactions shown in Table I have been measured in the present experiment. The resulting isomeric ratios are compared with the calculation similar to that described in reference 17).

Table I. Summary of conditions for measurements. Spins of levels in parentheses are considered tentative.

Reaction	Target material	Competing levels	Spin	Half-life	Detection efficiency
$As^{75}(n, p)Ge^{75}$	As_2O_3	Ge^{75m}	(7/2)	48 s	0.04
		Ge^{75g}	(1/2)	82 m	0.61
$Br^{81}(n, 2n)Br^{80}$	NaBr	Br^{80m}	5	4.4 h	0.01
		Br^{80g}	1	18 m	0.78
$Ba^{138}(n, \alpha)Xe^{135}$	$BaCO_3$	Xe^{135m}	(11/2)	15.6 m	0.12
		Xe^{135g}	(3/2)	9.13 h	0.61
$Ho^{165}(n, p)Dy^{165}$	Ho_2O_3	Dy^{165m}	1/2	1.25 m	0.03
		Dy^{165g}	7/2	139.2 m	0.67

§ 2. Experimental Procedure

2.1 *Sample sandwiched plastic scintillator*

The sample sandwiched scintillator is a block of target foils and plastic scintillator plates which are laminated alternately. After having been irradiated by fast neutrons, this block is viewed from both sides with two photomultipliers to detect the scintillations due to the induced activities. In this way the solid angle subtended by the sample at the detector becomes very large and comparatively large amount of target sample with small thickness is available. These features are especially useful for the detection of weak radiation with small energy. Further, the procedure for setting an irradiated block to the counting device is so simple that the measurement of short-lived activity, such as of the order of several seconds, becomes very easy. The details of this method and the characteristics of the sandwich detector were reported previously[20].

All target materials used were powder forms. In order to make them foil forms, they were ground very finely in an agate mortar and spread uniformly on a thin backing paper. They were fixed with thin ethyl acetate solution of plastic and covered by another backing paper. The thicknesses of the target layers were about 20 mg/cm² in all cases. The uniformity of target thickness thus obtained was rather good and caused almost no error in the final result. The thickness of the backing paper was 2.6 mg/cm².

These target foils of about 20 sheets whose size was 7.5×28 mm in area were piled up alternately with the plastic scintillator plates of 1 mm thick and of the same area, as shown in Fig. 1. They were bound by a strip of "celotape" so as to form a block. The total amount of the target material was about 1 gr in each case.

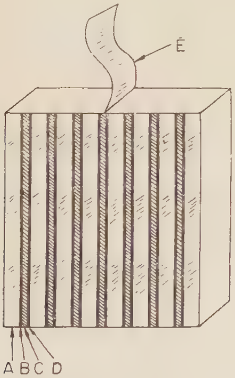

Fig. 1. Schematic illustration of a block of sample sandwiched scintillator. A is a plastic scintillator plate of 1 mm thick and 7.5 mm×28 mm in area. B and D are the backing papers between which a uniform layer of target sample C is firmly held. E is a strip of "celotape". Such layers were piled up about 20 times in actual use.

2.2 *Neutron irradiations and monitoring*

Fast neutrons were obtained by bombarding a tritiated zirconium target with 170 kev deuterons from a Cockcroft-Walton Accelerator. The neutron output from this target was found by counting the associated alpha particles from the $T(d, n)\alpha$ reaction in a known geometry and at an angle of 90° to the beam. Alpha particles were detected with CsI crystal mounted on a photomultiplier Dumont 6292 and its outputs were recorded automatically every specified period of time. Neutron emission from the target varied from 10^7 to 10^8 per second during the course of experiments. A sample sandwiched scintillator for irradiation was centered on the equatorial plane defined by the deuteron beam and the zirconium target and at a radius of 5 cm or 10 cm. Then the energy of neutron at the target was 14.1±0.2 Mev.

2.3 *Activity counting and data analysis*

After neutron irradiation, the activated block was set between two photomultipliers RCA 6342 and their coincident outputs were recorded automatically. The unnecessary activities caused by the neutron irradiation of carbon and oxygen in plastic and backing paper did not complicate the decay curves for our targets. Only the activity of half-life of 7.35 seconds due to the reaction $O^{16}(n, p)N^{16}$ appeared, which did not disturb the analyses of the decay curves.

In calculating the cross sections for the formation of each state of the isomeric pair from the decay curves, it should be taken into account that the nuclei in the metastable state decays via the ground state with some branching ratio. The method of calculation of the cross section for the production of genetically related pair is given in Appendix I. In evaluating the total detection efficiencies η_m and η_g in these formulae, the decay schemes of *Nuclear Data Sheets*[21] were referred to. When the conversion coefficient of any gamma ray was not known, the two extreme cases were compared with each other: in one case this gamma ray had not converted at all, while in the other all gamma rays had converted. Thus it was found that the detection efficiencies were mainly determined by the known data only and the differences of the above two cases were within experimental error. The detection efficiencies for the radiations of each product nucleus are given in Table I. Those for the radiations from the metastable state nuclei are rather small as expected, but their order of magnitude is such that they can be detected.

§ 3. **Results and Discussion**

The measured values of the cross sections

Table II. Cross sections for 14 Mev neutron reactions and their isomeric cross section ratios.

Reaction	Cross section (mb)	$\sigma_{\mathrm{metastable}}/\sigma_{\mathrm{ground}}$ Experimental	Calculated $\sigma=3$ $\nu=3$	$\sigma=3$ $\nu=4$	$\sigma=3$ $\nu=5$	$\sigma=5$ $\nu=4$
As^{75}(n, p)Ge^{75m}	10±2	0.40±0.11	5.3	5.0	4.6	10.0
As^{75}(n, p)Ge^{75g}	25±5					
Br^{81}(n, $2n$)Br^{80m}	510±50	1.09±0.16	1.1	1.0	0.87	2.9
Br^{81}(n, $2n$)Br^{80g}	470±50					
Ba^{138}(n, α)Xe^{135m}	13±2	1.00±0.22	0.92	0.85	0.79	2.7
Ba^{138}(n, α)Xe^{135g}	13±2					
Ho^{165}(n, p)Dy^{165m}	<1	<0.03	0.13	0.14	0.16	0.06
Ho^{165}(n, p)Dy^{165g}	40±10					

are given in Table II. A large percentage of the quoted errors came from counting statistics.

For As^{75}(n, p)Ge^{75g} reaction, Paul and Clarke[22] reported the cross section of 11.8 mb±20% which is about a half of the present value. The total cross section for As^{75}(n, p) reaction, i.e. the sum of two cross sections for the production of each state of Ge^{75}, is 35±6 mb in the present experiment. This agrees very well with the value of 33 mb calculated by Brown and Muirhead[23]. In their calculation the contributions to the cross section of this reaction from the compound nucleus formation and from the direct interaction process were 3 mb and 30 mb respectively. Then, for this reaction the direct interaction process takes a large part in the reaction mechanism. This fact is also inferred from the consideration of the isomeric ratio as will be discussed later.

For Br^{81}(n, $2n$)Br^{80m} reaction, the reported values are 828 mb±20%[22] and 752 mb±9.4%[18], which are considerably large compared with the present value 510±50 mb. While, the total cross section for Br^{81}(n, $2n$) reaction is 980±70 mb in the present experiment, which agrees with the value of 1000 mb calculated on the basis of statistical model[22].

There are no experimental data on Ba^{138}(n, α) and Ho^{165}(n, p) reactions; however, the cross sections for both these reactions are expected to be of the order of 10 mb from the general trend of the measured cross sections for (n, α) and (n, p) reactions by 14 Mev neutron[24]. The present values of total cross sections for Ba^{165}(n, α) and Ho^{165}(n, p) reactions are 26 mb and 40 mb respectively. These are somewhat larger than the expected values.

Let us now consider the isomeric ratio. The experimental and theoretical values for this ratio are given in Table II. The theoretical calculation was done using a method similar to that of Vandenbosch and Huizenga[17], an outline of which is described in Appendix II. The evaluation of the transmission coefficients for the incident and emitted particles are needed in this calculation. For incident particles, the transmission coefficients were calculated from the standard formulae in which use is made of a real potential well having such a depth that zero-energy neutron penetrating into the nucleus has a wave number of 10^{13}/cm^{-1} [25]. Even such approximation of the strong interaction model is sufficient for the calculation of the relative values of the transmission coefficients with various orbital angular momenta. For the emitted particles, for simplicity, they were treated as neutral irrespective of their actual charge. The effect of ignoring the Coulomb barrier is such that the transmission coefficients of the particles with high orbital angular momentum become relatively larger than the actual. But this fact does not seem to affect the final results seriously, because our calculation of isomeric ratios are very rough and only the order of magnitude may be reliable. The energy distribution of the emitted particles is known to be Maxwellian on the statistical model, but all particles were assumed to be emitted with the mean kinetic energy given by evaporation theory. This approximation has been justified in reference 17). The nuclear temperature was assumed to be 2 Mev in consideration of the experimental results of Gugelot[26] and Ashby *et al.*[27] The number of steps in the gamma-ray cascade was taken in actual calculation as 3, 4 and 5 in consideration of the experimental result on the multiplicity of cascade gamma-rays[2]. But, as can be seen from Table II, the variation of this number does not cause serious difference in the calculated values of the isomeric ratios.

For $Br^{81}(n, 2n)$ and $Ba^{138}(n, \alpha)$ reactions, the experimental isomeric ratios can be reproduced by the statistical model calculation with the level density parameter $\sigma=4\pm1$. This value of σ is similar to that deduced for the reactions leading to Hg^{197} pair[17]. Those reactions may then be thought as proceeding mainly via compound nucleus formation. This has also been suggested previously in connection with the total cross section for $Br^{81}(n, 2n)$ reaction.

In $As^{75}(n, p)$ reaction, the calculated isomeric ratio is about 10 times larger than the experimental one. This discrepancy may be attributed to the predominance of the direct interaction process in this reaction. In the direct interaction process the emitted proton may bring out large angular momentum, and consequently the final spin distribution of the residual nuclei may shift considerably toward the part of smaller spins. Then the cross section for the production of the metastable state with larger spin is expected to become smaller than that calculated on the basis of the statistical model. Actually the direction of discrepancy agrees with this consideration.

The experimental isomeric ratio for $Ho^{165}(n, p)$ reaction is somewhat smaller than that of calculation. The direction of discrepancy in this case is opposite to that suggested by the direct interaction process. In order to reproduce the experimental isomeric ratio, it is necessary, for example, to change the value of level density parameter σ. But, as the cross section for the production of the metastable state nuclei in this reaction was too small to determine the isomeric ratio definitely, further careful experiment is needed before considering this problem in more detail.

The method of the angular momentum sampling for the analysis of the isomeric ratio was confirmed to be valuable. But more comparison with other experiments are needed to establish its reliability and further refinement are needed to deduce any useful accounts for the structure of the nucleus and the reaction mechanism.

Acknowledgements

The author would like to express his sincere gratitude to Profs. K. Kimura and M. Kobayasi for their continual encouragements. He is much indebted to Professor M. Sakisaka for his invaluable help and the interest he has shown in this work, and to the members of Cockcroft Walton Accelerator group in Kōnan University, particularly to Mr. M. Tomita for cooperation in measurements. Finally he wishes to thank Profs. K. Ōhira and H. Matsui for providing all convenience to perform this work.

Appendix I
Analysis of decay curve

The cross sections for the production of each state of isomeric pair can be deduced from the decay curve as follows.

Consider the case where the branching ratio between de-excitation and beta-emission for the decay of the metastable state is ε. In the following, suffixes m and g stand for the metastable and ground states respectively. Let x_m and x_g be the numbers of nuclei at the time t after the end of the neutron irradiation, λ_m and λ_g be the decay constants, and η_m and η_g be the detection efficiencies for the radiations from each state. The activity counts per unit time at time t, $n(t)$, is given by

$$\begin{aligned} n(t) &= \eta_m\lambda_m x_m+\eta_g\lambda_g x_g \\ &= \nu_m \exp(-\lambda_m t)+\nu_g \exp(-\lambda_g t)\,, \end{aligned} \tag{1}$$

where

$$\left.\begin{aligned} \nu_m &= \lambda_m x_m^0\left(\eta_m-\varepsilon\eta_g\frac{\lambda_g}{\lambda_m-\lambda_g}\right), \\ \nu_g &= \lambda_g\left(x_g^0\eta_g+\varepsilon x_m^0\eta_g\frac{\lambda_m}{\lambda_m-\lambda_g}\right). \end{aligned}\right\} \tag{2}$$

Here x_m^0 and x_g^0 are the numbers of each nuclei at immediately after the neutron irradiation. Thus, in this case also, the decay curve can be divided in two parts, i.e. $\exp(-\lambda_m t)$ term and $\exp(-\lambda_g t)$ term.

As the beam current fluctuated in time, the total irradiation time was divided in many small time intervals during which beam current could be considered to be constant, and the contributions from every parts were summed to estimate the quantities $x_m{}^0$ and $x_g{}^0$. Now let $Q_m(i)$ and $Q_g(i)$ be the direct production rates within time interval T_i at time t_i before the end of bombardment, then

$$\left.\begin{aligned} x_m{}^0 &= \sum_i \frac{Q_m(i)}{\lambda_m}[1-\exp(-\lambda_m T_i)] \\ &\quad \times\exp(-\lambda_m t_i)\,, \\ x_g{}^0 &= \sum_i \left\{\left[x_{g0}(i)+x_{mg0}(i)\right.\right. \\ &\quad \left.+\frac{\varepsilon\lambda_m}{\lambda_m-\lambda_g}x_{g0}(i)\right]\exp(-\lambda_g t_i) \\ &\quad \left.-\frac{\varepsilon\lambda_m}{\lambda_m-\lambda_g}x_{m0}(i)\exp(-\lambda_m t_i)\right\}, \end{aligned}\right\} \quad (3)$$

where

$$\left.\begin{aligned} x_{m0}(i) &= \frac{Q_m(i)}{\lambda_m}[1-\exp(-\lambda_m T_i)]\,, \\ x_{g0}(i) &= \frac{Q_g(i)}{\lambda_g}[1-\exp(-\lambda_g T_i)]\,, \\ x_{mg0}(i) &= \varepsilon Q_m(i)\left[\frac{1}{\lambda_g}+\frac{1}{\lambda_m-\lambda_g}\exp(-\lambda_m T_i)\right. \\ &\quad \left.+\left(\frac{1}{\lambda_g}+\frac{1}{\lambda_m-\lambda_g}\right)\exp(-\lambda_g T_i)\right]. \end{aligned}\right\} \quad (4)$$

The production rates $Q_m(i)$ and $Q_g(i)$ relate to the relevant reaction cross sections σ_m and σ_g as

$$Q_m(i)=I(i)\sigma_m N\,, \qquad Q_g(i)=I(i)\sigma_g N\,, \quad (5)$$

where $I(i)$ is the flux of the neutrons at the point of target and N is the total number of target nuclei. Combining Eqs. (1)~(5), we have the cross sections

$$\left.\begin{aligned} \sigma_m &= \frac{1}{N}\cdot\frac{\lambda_m-\lambda_g}{(\lambda_m-\lambda_g)\eta_m-\varepsilon\lambda_g\eta_g}\cdot\frac{\nu_m}{S_m}\,, \\ \sigma_g &= \frac{1}{N}\left\{\frac{1}{\eta_g}\cdot\frac{\nu_g}{S_g}\right. \\ &\quad \left.-\frac{\varepsilon\lambda_m}{(\lambda_m-\lambda_g)\eta_m-\varepsilon\lambda_g\eta_g}\cdot\frac{\nu_m}{S_m}\right\}, \end{aligned}\right\} \quad (6)$$

where

$$\left.\begin{aligned} S_m &= \sum_i I(i)[1-\exp(-\lambda_m T_i)\exp(-\lambda_m t_i)\,, \\ S_g &= \sum_i I(i)[1-\exp(-\lambda_g T_i)]\exp(-\lambda_g t_i)\,. \end{aligned}\right\} \quad (7)$$

Appendix II
Statistical model calculation of the isomeric ratio

The isomeric ratios are calculated by spin sampling method similar to that of Vandenbosch and Huizenga[17].

Let the reaction proceed by the compound nucleus formation mechanism. If every particle that penetrates the potential barrier be assumed to be captured, the distribution of the angular momentum, J_c, of the compound nuclei will be given by

$$\sigma(J_c,E)=\pi\lambda\!\!\!^{-2}\sum_{S=|I-s|}^{I+s}\ \sum_{l=|J_c-S|}^{J_c+S}\frac{2J_c+1}{(2s+1)(2I+1)}T_l(E)\,, \quad (1)$$

where $\lambda\!\!\!^{-}$ is the de Broglie wavelength of the incoming projectile, s is the spin of the projectile, I is the spin of the target nucleus and $T_l(E)$ is the barrier transmission coefficient of a particle with orbital angular momentum l and energy E.

This initial distribution of angular momentum values will be modified by the emission of particles and finally gamma-rays.

The relative probability for a compound state with angular momentum J_c to emit a particle with orbital angular momentum l and spin s' leading to an excited residual nucleus with spin J is given by

$$P(J_c,J)\propto\rho(J)\sum_{S=|J-s'|}^{J+s'}\ \sum_{l=|J_c-S|}^{J_c+S}T_l(E)\,, \quad (2)$$

where $T_l(E)$ is the barrier transmission coefficient for an outgoing particle with orbital angular momentum l and energy E. The level density of the residual nucleus with spin J, $\rho(J)$, is predicted theoretically to be of the form[3]

$$\rho(J)\propto\rho(0)(2J+1)\exp[-(J+\tfrac{1}{2})^2/2\sigma^2]\,, \quad (3)$$

where $\rho(0)$ is the density of levels with zero spin, and σ is a parameter characterizing the spin distribution function. The distribution of the spin, J, of the excited residual nuclei is then given by

$$n(J)\propto\sum_{J_c}\sigma(J_c,E)P(J_c,J)\,. \quad (4)$$

If a second particle is to be evaporated, this distribution is modified further. For two particle emission, this becomes

$$n(J)\propto\sum_{J_c,J_m}\sigma(J_c,E)P(J_c,J_m)P(J_m,J)\,, \quad (5)$$

where J_m is the spin of the excited residual nucleus after the emission of the first particle.

The excited residual nucleus decays to the metastable or ground state by the emission of cascade gamma-rays. Instead of considering the actual nucleus with only two states of the isomeric pair, fictitious final nucleus is assumed which can take any value of spin.

After calculating the spin distribution function for this fictitious final nuclei, one deduces the relative populations of each state of isomeric pair from this distribution function by using some appropriate criterion.

For simplicity it has been assumed in our calculation as in reference 17) that all transitions occur through dipole emission and all transition matrix elements are the same. Denoting the probability that the excited residual nucleus with spin J to emit ν dipole gamma-rays leading to a fictitious final nucleus with spin j as $Q_\nu(J, j)$, we have the following distribution of spin, j, of the fictitious final nucleus

$$N_\nu(j) \propto \sum_J n(J) Q_\nu(J, j) . \tag{6}$$

The values of $Q_\nu(J, j)$ can be obtained easily using the rule of the angular momentum coupling. Defining

$$\left.\begin{aligned} \pi_0(j) &= \frac{\rho(j)}{\rho(j-1)+\rho(j)+\rho(j-1)} , \\ \pi_+(j) &= \frac{\rho(j)}{\rho(j)+\rho(j+1)+\rho(j+2)} , \\ \pi_-(j) &= \frac{\rho(j)}{\rho(j-2)+\rho(j-1)+\rho(j)} , \end{aligned}\right\} \tag{7}$$

and

$$\left.\begin{aligned} &\pi_0(0)=0 , \qquad \pi_0(1/2)=\frac{\rho(1/2)}{\rho(1/2)+\rho(3/2)} , \\ &\pi_-(0)=0 , \qquad \pi_-(1)=1 , \qquad \pi_-(1/2)=0 , \\ &\qquad\qquad \pi_-(3/2)=\frac{\rho(3/2)}{\rho(1/2)+\rho(3/2)} , \end{aligned}\right\} \tag{8}$$

we obtain

$$\left.\begin{aligned} Q_1(J, J-1) &= \pi_+(J-1) , \\ Q_1(J, J) &= \pi_0(J) , \\ Q_1(J, J+1) &= \pi_-(J+1) , \end{aligned}\right\} \tag{9}$$

and generally

$$\begin{aligned} Q_{\nu+1}(J, j) &= \pi_+(J-1)Q_\nu(J-1, j)+\pi_0(J)Q_\nu(J, j) \\ &\quad +\pi_-(J+1)Q_\nu(J+1, j) \\ &= Q_\nu(J, j+1)\pi_+(j)+Q_\nu(J, j)\pi_0(j) \\ &\quad +Q_\nu(J, j-1)\pi_-(j) . \end{aligned} \tag{10}$$

In the above calculation it has been assumed that levels of both parity are present in equal number, and then it is not necessary to distinguish the electric and magnetic radiations.

To determine the populations of each state of the isomeric pair from the fictitious final spin distribution thus obtained, the following criterion was taken which differed somewhat from that of Huizenga and Vandenbosch[17,19]. That is, the fictitious final spin distribution is divided into two parts by the middle value of two spins of the isomeric pair, and the number of states in the part containing the spin value of the metastable state is assumed to be the population of the metastable state and that in the other part containing the spin value of the ground state is assumed to be the population of the ground state. Huizenga and Vandenbosch took the spin distribution just before the final cascade gamma-ray instead of the final spin distribution. Since the multiplicity of cascade gamma-rays did not affect so much the final result in our calculation, this difference in criterion was not important for the present. When there is an intermediate level between the metastable and ground states, the division was done with the middle value of the spins of the metastable and intermediate states. This is the case for $Br^{81}(n, 2n)$ reaction.

References

1) E. Segrè and A. C. Helmholz: Rev. Mod. Phys. **21** (1949) 271.
2) C. O. Muehlhause: Phys. Rev. **79** (1950) 277; J. E. Draper and T. E. Springer: Nuclear Physics **16** (1960) 27.
3) H. A. Bethe: Rev. Mod. Phys. **9** (1937) 84; C. Bloch: Phys. Rev. **93** (1954) 1094.
4) L. Seren, H. N. Friedlander and S. H. Turkel Phys. Rev. **72** (1947) 888.
5) P. C. Capron and A. J. Verhoeve-Stokkink. Phys. Rev. **81** (1951) 336.
6) F. Boehm, P. Marmier and P. Preiswerk: Helv. Phys. Acta **25** (1952) 599.
7) A. W. Fairhall and C. D. Coryell: Phys. Rev. **87** (1952) 215.
8) J. Goldemberg and L. Katz: Phys. Rev. **90** (1953) 308.
9) I. Bergström, R. D. Hill and G. de Pasquali: Phys. Rev. **92** (1953) 913.
10) R. E. Wood: Phys. Rev. **95** (1954) 453.
11) J. W. Meadows and R. M. Diamond: Phys. Rev. **102** (1956) 190.
12) P. Axel and J. D. Fox: Phys. Rev. **102** (1956) 400.
13) E. der Mateosian and M. Goldhaber.: Phys. Rev. **108** (1957) 766.
14) M. L. Sehgal, H. S. Hans and P. S. Gill: Nuclear Physics **12** (1959) 261.
15) H. S. Hans, M. L. Sehgal and P. S. Gill: Nuclear Physics **20** (1960) 183.
16) R. G. Willie and R. W. Fink: Phys. Rev. **118** (1960) 242.
17) R. Vandenbosch and J. R. Huizenga: Phys.

Rev. **120** (1960) 1313.
18) L. A. Rayburn: Phys. Rev. **122** (1961) 168.
19) J. R. Huizenga and R. Vandenbosch: Phys. Rev. **120** (1960) 1305.
20) M. Sakisaka, B. Saeki, M. Tomita and F. Fukuzawa: J. Phys. Soc. Japan **16** (1961) 1869.
21) K. Way *et al*: *Nuclear Data Sheets* (National Academy of Sciences, National Research Council).
22) E. B. Paul and R. L. Clarke: Canad. J. Phys. **31** (1953) 267.
23) G. Brown and H. Muirhead: Phil. Mag **2** (1957) 473.
24) R. F. Coleman, B. E. Hawker, L. P. O'connor and J. L. Perkin: Proc. Phys. Soc. London **73** (1959) 215.
25) J. M. Blatt and V. F. Weisskopf: *Theoretical Nuclear Physics* (John Wiley and Sons, Inc., New York, 1952) p. 355 and p. 358 ff.
26) P. C. Gugelot: Phys. Rev. **81** (1951) 51.
27) V. J. Ashby, H. C. Catron, L. L. Newkirk and C. J. Tayler: Phys. Rev. **111** (1958) 616.

JOURNAL OF THE PHYSICAL SOCIETY OF JAPAN, Vol. 16, No. 12, DECEMBER, 1961

Angular Distributions of Alpha-particles from F^{19}, Al^{27} and P^{31} bombarded with Protons

By Sukeaki YAMASHITA

Institute for Chemical Research, Kyoto University, Kyoto

(Received July 31, 1961)

The angular distributions of the alpha-particles were obtained for the reactions $F^{19}(p, \alpha)O^{16}$ leaving the residual nucleus in the ground state, $Al^{27}(p, \alpha)Mg^{24}$ and $P^{31}(p, \alpha)Si^{28}$ leaving the residual nuclei in the ground and first excited states at four bombarding energies between 6.0 MeV and 7.4 MeV. The angular distribution for the reaction $F^{19}(p, \alpha)O^{16}$ shows the backward peak at each energy, but at small angles it depends on the bombarding energy. The angular distributions for the reactions $Al^{27}(p, \alpha)Mg^{24}$ and $P^{31}(p, \alpha)Si^{28}$ are also energy-dependent, but contain a larger isotropic part than those for the reaction $F^{19}(p, \alpha)O^{16}$. The integrated cross sections for the reactions $Al^{27}(p, \alpha)Mg^{24}$ and $P^{31}(p, \alpha)Si^{28}$ leaving the residual nuclei in the first excited states are several times as large as those for the reactions leaving the residual nuclei in the ground states. It appears unlikely that these reactions can be accounted for by the formation of compound nucleus or by simple direct interaction. The possible mechanisms through which these reactions may take place are discussed.

§ 1. Introduction

Many experiments on the (p, α) reaction have been performed so far for light elements. At the energies of incident protons of lower than 4 MeV, the experiments provided some informations about the properties of the levels of compound nuclei and of residual nuclei. At higher energies, however, this reaction cannot be interpreted sufficiently as a process through one or more excited states of compound nucleus, and some forms of direct interaction process must be postulated.

Even at low energies such as 2 or 3 MeV, the (p, α) reaction does not indicate the behaviour of simple resonances of compound nucleus[1], while, at the energies lower than 2 MeV, it may be satisfactorily analysed by using the resonance theory of nuclear reaction[2].

At higher energies, the angular distributions of alpha-particles show that the (p, α) reactions may be given rise by Butler's surface direct interaction process (pick-up or knock-on process)[3, 4, 5] or by quasi free proton-alpha collision process[6]. But, in the energy region between 8 MeV and 12 MeV, the angular distributions of alpha-particles which leave the residual nucleus in the ground state or low lying excited state show that the dependence of these shapes on the incident proton energies is greater than that predicted by the simple direct nuclear reaction theories[5, 7, 8, 9].

At the energies of around 7 MeV of incident protons, therefore, the mechanism of (p, α) reaction is not simple, but may be cleared up by taking account of the nuclear structure, *i.e.*, the nature and the properties of the ground and excited states of nucleus. The investigation of the rearrangement reaction such as (p, α) in this energy region, especially on light elements, is one of the most important steps to make clear the reaction mechanism in connection with the nuclear structure. Since the (p, α) reactions with the protons of around 7 MeV had not yet been studied, the angular distributions for the (p, α) reactions on F^{19}, Al^{27} and P^{31} were measured as a first step. In the reaction $F^{19}(p, \alpha)O^{16}$, the emitted alpha-particles are considered to be little affected by the Coulomb barrier due to the positive large reaction Q-value (8.119 MeV[10]), although the Coulomb effect becomes important for the reactions $Al^{27}(p, \alpha)Mg^{24}$ and $P^{31}(p, \alpha)Si^{28}$, in which the reaction Q-values are 1.595 MeV and 1.920 MeV respectively[11], in this energy region of the incident protons. According to the shell model[12], F^{19} consists of the core (O^{16}) and outer one proton and two neutrons in $2s1/2$ state, Al^{27} has one proton hole in the closed sub-shell of $1d5/2$ (Si^{28}), and P^{31} has the closed sub-shell of $1d5/2$ (Si^{28}) and outer one proton and two neutrons in $2s1/2$ state. The difference of Q-values between the reaction $F^{19}(p, \alpha)O^{16}$ and the reactions $A^{27}(p, \alpha)Mg^{24}$ and $P^{31}(p, \alpha)Si^{28}$ which seems to be due to the difference of hardness of the residual nuclei, is comparable with the incident proton energies. Thus the measurements of the angular distributions of emitted alpha-particles from the reactions of $F^{19}(p, \alpha)O^{16}$, $Al^{27}(p, \alpha)Mg^{24}$ and $P^{31}(p, \alpha)Si^{28}$ at the energies of around 7 MeV are considered to give some informations about the elementary mechanism of the rearrangement reactions. In the present paper, the angular distributions obtained for these reactions are given, and tentative interpretations of the results are attempted.

§ 2. Experimental Procedure

The 7.4 MeV proton beam from 105 cm Kyoto University cyclotron was focused with a pair of the quadrupole magnets in front of the beam collimator which consists of two diaphragms of tantalum plate of 1 mm thick and each with a hole of 2 mm in diameter and 36 cm apart each other. The spread of the beam brought into the scattering chamber was less than 5 mm in diameter on the target. The beam current was collected with a Faraday cup and integrated with the beam integrator similar to that described by Higinbotham *et al.*[13], and its average was about 0.1 μA.

The scattering chamber of 52 cm in diameter has a turn table and a target holder, both of which can be separately rotated about the same axis. The beam centre intersects perpendicularly to the axis. The targets are put on the target holder and can be moved along the axis. One of those can be bombarded at a desired angle with respect to the direction of the beam. The beam energy was determined by measuring the range in aluminium and by using the range-energy relation obtained by Bischal *et al.*[14], and the spread was estimated to be within 100 keV. Lower proton energies are obtained by degrading the beam with aluminium absorbers. The details of the scattering chamber and the method of energy determination will be described elsewhere[15].

The F^{19} target was a teflon $(C_2F_4)_n$ film of 0.6 mg/cm² thick fastened to a copper plate frame. A commercial aluminium foil of 0.18 mg/cm² thick was used as the Al^{27} target, and the target P^{31} consisted of fine powder of red phosphorus deposited on 0.25 mil mylar sheet. The target thickness was 0.3 mg/cm² for P^{31}.

The detector for the reaction $F^{19}(p, \alpha)O^{16}$ was a counter telescope consisting of a proportional counter (dE/dx counter) of effective length of 2.5 cm and of pressure of 40 cmHg ($A+CO_2(5\%)$) and a scintillation counter (E counter) in which the thickness of CsI crystal was 0.16 mm. The defining slit in front of the window of the proportional counter was of 1.4 mm wide and 3.7 mm high, and was placed at a distance of 105 mm from the centre of target. The counter telescope and the associated electronics are schematically shown in Fig. 1. The pulses from the proportional counter were amplified and fed to a discriminator and a 100 channel pulse-height analyser.

It could be confirmed at each run that the level of discriminator was suitable for separating the alpha-particles from the protons. The pulses from the scintillation counter were amplified and fed to a 20 channel pulse-height analyser, of which the gate was opened with the gate pulses from the discriminator mentioned above.

A proportional counter of effective length of 10 cm was used to detect the alpha-particles from the reactions $Al^{27}(p, \alpha)Mg^{24}$ and $P^{31}(p, \alpha)Si^{28}$, because the energies of the emitted alpha-particles are considerably lower than that in the reaction $F^{19}(p, \alpha)O^{16}$. The defining aperture on the counter window was 3.2 mm in diameter. The counter was set on the turn table such a manner that this aperture was at a distance of 87 mm from the centre of the target. The counter gas consisted of A and CO_2 (3%). The pressure of gas could be varied from 10 cmHg to 50 cmHg, so as to fit the maximum range of alpha-particles from the reactions just to the effective length of the counter. Then the pulse-height of the protons could be reduced to a minimum. The pulses from the counter were amplified and fed to a 100 channel pulse-height analyser. A typical example of the pulse-height distribution is shown in Fig. 3.

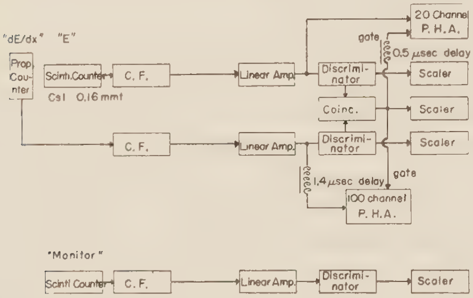

Fig. 1. Detector system used for the alpha-particles from the reaction $F^{19}(p, \alpha)O^{16}$.

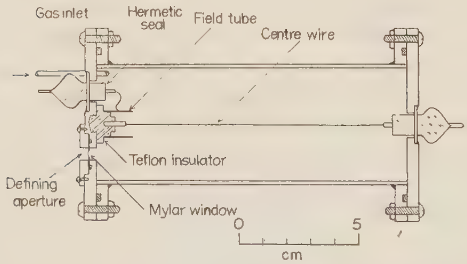

Fig. 2. Proportional counter used for the detection of the alpha-particles from the reactions $Al^{27}(p, \alpha)Mg^{24}$ and $P^{31}(p, \alpha)Si^{28}$.

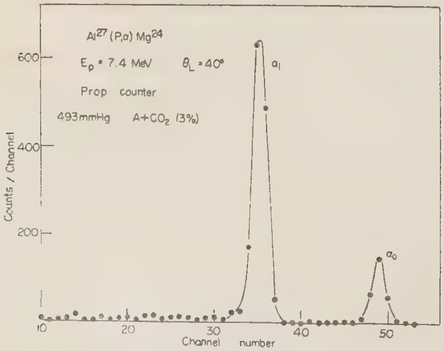

Fig. 3. Typical pulse-height distribution of the alpha-particles from the reaction $Al^{27}(p, \alpha)Mg^{24}$ with 7.4 MeV protons observed at the laboratory angle of 40°.

The monitor counter consisted of a CsI crystal of 0.7 mm thick and a photomultiplier, and was mounted in air to the side-wall window of the scattering chamber at an angle of 35° with respect to the direction of proton beam. The particles scattered by the target passed through an aperture of 2 mm in diameter and an aluminium foil of 13 μ thick, and were stopped in the CsI crystal of 0.7 mm thick. The number of pulses near the elastic peak in the pulse-height distribution was used as a beam monitor.

When the P^{31} target was bombarded, there was an anxiety to dissipate the powder of P^{31} and to vary the ratio of the number of protons scattered by P^{31} to that scattered by the mylar backing. The measurements of the yield of alpha-particles from the reaction $P^{31}(p, \alpha)Si^{28}$ were repeated at the fixed angle after several runs. It was confirmed that there was no dissipation of the powder of P^{31} deposited on the mylar sheet during the measurement of the whole angular distribution of alpha-particles from the reaction $P^{31}(p, \alpha)Si^{28}$.

§ 3. Results and Discussions

Fig. 4 shows the angular distributions of alpha-particles from the reaction $F^{19}(p, \alpha)O^{16}$ leaving O^{16} in the ground state, as obtained at the energies of incident protons of 6.0 MeV, 6.5 MeV, 6.9 MeV and 7.4 MeV, respectively. The error bars represent uncertainties due to counting statistics which are the main part of the overall errors. The errors in the absolute values of differential cross sections were due to uncertainties of beam integration and target

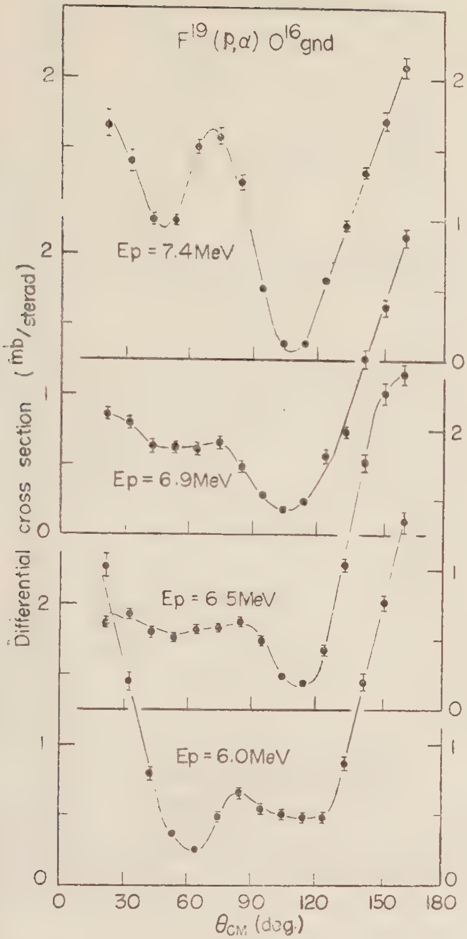

Fig. 4. Angular distributions of the alpha-particles from the reaction $F^{19}(p, \alpha)O^{16}$ leaving O^{16} in the ground state.

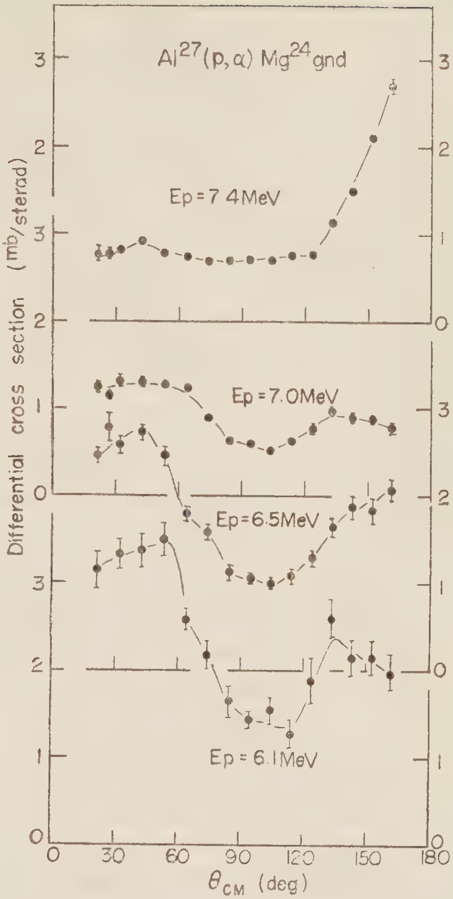

Fig. 5. Angular distributions of the alpha-particles from the reaction $Al^{27}(p, \alpha)Mg^{24}$ leaving Mg^{24} in the ground state.

thickness, and were estimated to be within 20%. The differential cross sections of the angles larger than 100° are quite alike and show backward peaking at each energy. The forward peak appears at the energies of 6.0 MeV and 7.4 MeV, but does not appear at the energies of 6.5 MeV and 6.9 MeV. The angular distribution at the energy of 7.4 MeV is smoothly connected to that obtained by Ogata[4)] with 8.0 MeV protons. The angular distributions at the energies of 6.0 MeV and 6.5 MeV accord in shape with those obtained by Teplov *et al.*[16)] at nearly the same energies but disaccord in the absolute value of cross sections.

The angular distributions for the reaction $Al^{27}(p, \alpha)Mg^{24}$ leaving the residual nucleus in the ground and first excited states at the energies of incident protons of 6.1 MeV, 6.5 MeV, 7.0 MeV and 7.4 MeV are shown in Figs. 5 and 6. The error bars indicate only uncertainties due to the counting statistics, because other sources of error are negligible in comparison with those. The errors in the absolute values of differential cross sections were mainly due to uncertainty of beam integration, and were about 10%.

The shape of the angular distribution varies with the energy of incident protons. The angular dependence of the differential cross sections is weaker than that of the reaction $F^{19}(p, \alpha)O^{16}$.

Figs. 7 and 8 show the angular distributions of the alpha-particles from the reaction $P^{31}(p, \alpha)Si^{28}$ leaving the residual nucleus in the ground and first excited states at the energies of incident protons of 6.1 MeV, 6.5 MeV, 7.0 MeV and 7.4 MeV. The error bars indicate only uncertainties due to the counting statistics for the same reason as in the preceding cases.

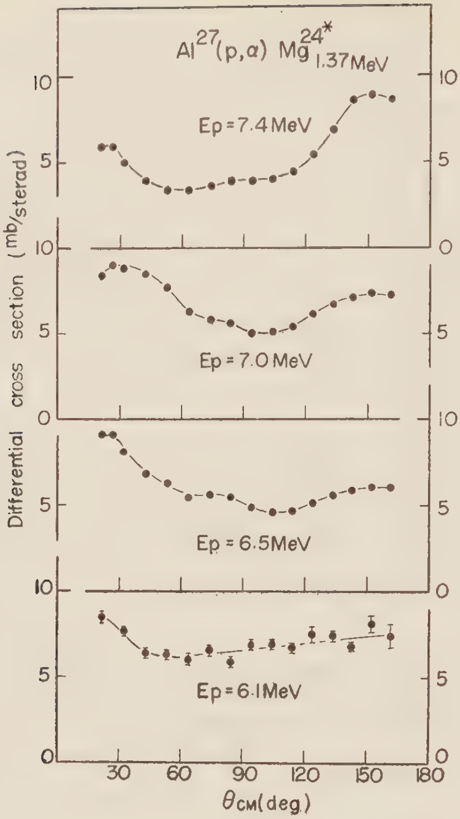

Fig. 6. Angular distributions of the alpha-particles from the reaction Al^{27}(p, α)Mg^{24} leaving Mg^{24} in the first excited state.

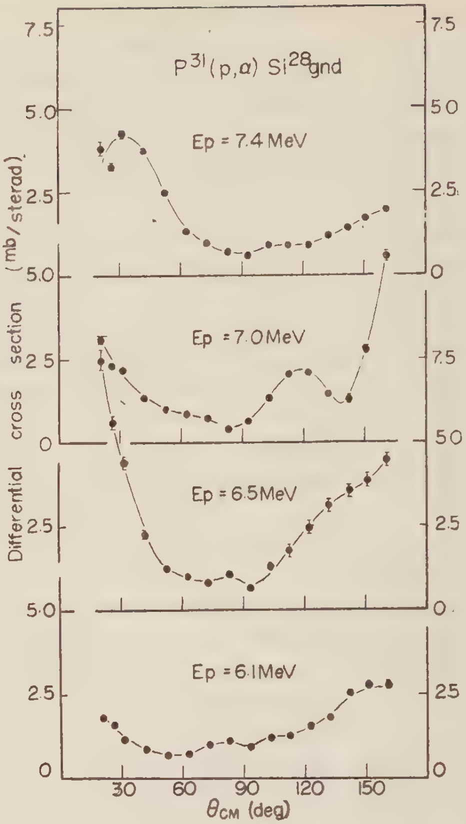

Fig. 7. Angular distributions of the alpha-particles from the reaction P^{31}(p, α)Si^{28} leaving Si^{28} in the ground state.

If the formation of compound nucleus is assumed, the yield of alpha-particles should be more restrained than that of protons. The integrated cross sections for these reactions leaving the residual nuclei in the individual states are comparable with or larger than those for the inelastic scattering of protons from the same elements and in the same energy region[17], and they are larger than those expected from the assumption of the formation of compound nucleus. It appears to be difficult to interpret the experimental results of these reactions on the basis of a compound nucleus model, though the process of the formation of compound nucleus may not be neglected.

The errors in the absolute values of differential cross sections were estimated to be within 30%; the main source of errors was uncertainty in the thickness of the target. The angular distributions depend on the energy of incident protons, and as well as for the reaction Al^{27} (p, α)Mg^{24}, they have larger isotropic components than those for F^{19}(p, α)O^{16}.

The integrated cross sections of the reactions obtained at each energy of incident protons are shown in Fig. 9. The cross sections for the reactions F^{19}(p, α)O^{16}, Al^{27}(p, α)Mg^{24} and P^{31}(p, α)Si^{28} leaving the residual nuclei in the ground states are in the range between 10 and 30 mb, while those leaving Mg^{24} and Si^{28} in the first excited states at 1.37 MeV and 1.78 MeV, respectively, are in the range between 60 and 90 mb. The integrated cross section for each element fluctuates somewhat according to the change in the energy of incident protons, but no sharp resonance appears in this energy region.

If a direct process is postulated for these reactions, the interaction should take place at the nuclear surface, because of the short mean free path of the alpha-particles in nuclei that is known from the experiments on the scattering of alpha-particles[18]. One of the simplest direct interaction models for these reactions is that in which the loosely bound triton in

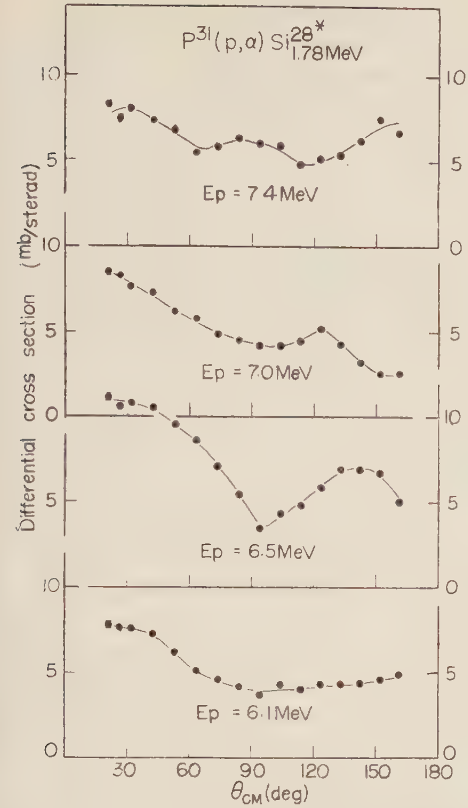

Fig. 8. Angular distributions of the alpha-particles from the reaction $P^{31}(p,\ \alpha)Si^{28}$ leaving Si^{28} in the first excited state.

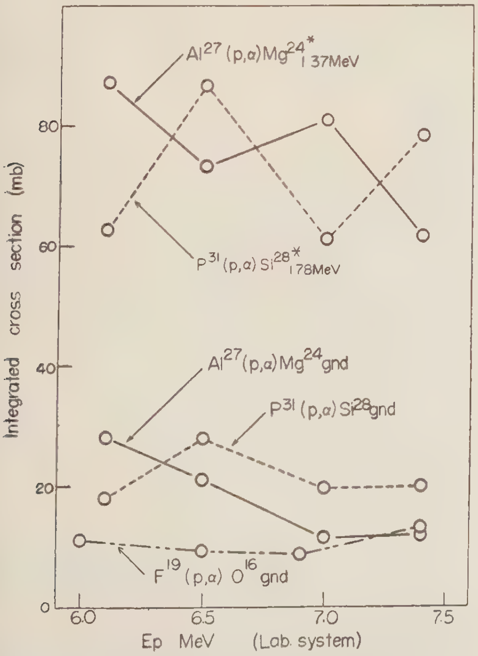

Fig. 9. Integrated cross sections for the reactions $F^{19}(p,\ \alpha)O^{16}$, $Al^{27}(p,\ \alpha)Mg^{24}$ and $P^{31}(p,\ \alpha)Si^{28}$.

the target nucleus is picked up by the incident proton at the surface of nucleus. The theoretical angular distribution is represented approximately by a square of spherical Bessel function $\{j_l(QR_0)\}^2$ which is familiar in the $(d,\ p)$ reactions[19)], though in such an expression the larger value of the interaction radius R_0 must be used than in the expression obtained by Butler[20)]. However, the angular distributions obtained here are quite different from that predicted by the theory of pick-up process, especially because of the energy dependence and the backward peak in the reaction $F^{19}(p,\ \alpha)O^{16}$.

In this type of direct interaction, it is necessary that a triton which consists of one proton and two neutrons outside the core of the target nucleus is captured by the incident proton and transfers the momentum to the core. The energy relations to separate a triton from the target nucleus and to form an alpha-particle with a triton and a proton are as follows :

$$\left.\begin{aligned} F^{19}&=O^{16}+t-11.693\ \text{MeV},\\ Al^{27}&=Mg^{24}+t-18.219\ \text{MeV},\\ P^{31}&=Si^{28}+t-17.889\ \text{MeV},\\ p+t&=\alpha+19.811\ \text{MeV}. \end{aligned}\right\} \qquad (1)$$

On the other hand, the experiments on the $(p,\ \alpha)$ reactions at energies higher than 45 MeV[6)] suggested that there exist alpha-clusters at the surface of nucleus, and also the alpha-particle model succeeded in interpreting the nuclear levels in some light nuclei[21)]. It seems probable that the heavy particle stripping and knock-out process, the so-called exchange process, may take part in these reactions. An alpha-particle outside the core of target nucleus is separated from the core as a result of the interaction between the incident proton and the alpha-particle or between the incident proton and the core, and then the proton is captured by the core. If the two steps are considered separately, the energy relations are as follows :

$$\left.\begin{aligned} F^{19}&=N^{15}+\alpha-3.993\ \text{MeV},\\ &\quad N^{15}+p=O^{16}+12.112\ \text{MeV};\\ Al^{27}&=Na^{23}+\alpha-10.093\ \text{MeV},\\ &\quad Na^{23}+p=Mg^{24}+11.687\ \text{MeV};\\ P^{31}&=Al^{27}+\alpha-9.688\ \text{MeV},\\ &\quad Al^{27}+p=Si^{28}+11.588\ \text{MeV}. \end{aligned}\right\} \qquad (2)$$

If the energy relations (1) and (2) are taken into account, the exchange process is more preferable than the pick-up process, because the latter requires larger momentum transfer than the former. According to the exchange process, it may be interpreted that the angular distributions for the reaction $F^{19}(p, \alpha)O^{16}$ all have the backward peak. The Coulomb effect and the distortion of plane wave may be significant in this energy region, and owing to the smaller Q-value of the reactions the angular distributions for the reactions $Al^{27}(p, \alpha)Mg^{24}$ and $P^{31}(p, \alpha)Si^{28}$ do not show so sharp pattern as in the reaction $F^{19}(p, \alpha)O^{16}$.

The dependence of the angular distributions on the energy of incident protons cannot be interpreted with a simple direct process. Fischer *et al.*[7] and Ogata *et al.*[8] concluded that the variation of the total cross sections and of the shape of angular distributions in the reaction $Al^{27}(p, \alpha)Mg^{24}$ at the energies of incident protons of around 10 MeV might be due to (*a*) a failure of the statistical (or continuum) assumption for the compound nucleus, or to (*b*) the interference between various direct interaction processes or between direct interaction and compound nucleus process, or to (*c*) both the interferences. The variation of the shape of angular distributions with the energy of incident particles for the reactions $B^{11}(d, n)C^{12}$, $C^{13}(He^3, \alpha)C^{12}$ and $Be^9(d, n)B^{10}$ at rather low energies from 2 to 4 MeV was interpreted as a result of the direct interaction involving the heavy particle stripping[22].

The yields of alpha-particle from the reactions $Al^{27}(p, \alpha)Mg^{24}$ and $P^{31}(p, \alpha)Si^{28}$ leaving the residual nuclei in the first excited states are several times as large as that leaving in the ground states. The same fact was found in the reaction $Al^{27}(p, \alpha)Mg^{24}$ at higher energies of the incident protons[8]. It suggests that the overlapping integral, which is a measure of the magnitude of cross sections for the direct interaction, for the reactions leaving the residual nuclei in the first excited states is larger than that for the reactions leaving the residual nuclei in the ground states, because of the deformation of the target nuclei Al^{27} and P^{31} and of the same 2^+ rotational first excited state of both the residual nuclei Mg^{24} and Si^{28} which results from the deformation of the residual nuclei.

The difference between the aspects of the angular distributions for the reaction $F^{19}(p, \alpha)O^{16}$ and the reactions $Al^{27}(p, \alpha)Mg^{24}$ and $P^{31}(p, \alpha)Si^{28}$ may be related to the difference in the Q-values of the reactions. If the energy balances (2) is taken into accout, it appears that the exchange direct process may take place more easily in the reaction $F^{19}(p, \alpha)O^{16}$ than in the reactions $Al^{27}(p, \alpha)O^{16}$ and $P^{31}(p, \alpha)Si^{28}$, and that the time of interaction is shorter for the former than for the latters in the stage of compound system defined by Weisskopf[23]. It may be considered that the alpha-clusters exist at the surface in this time before the formation of compound nucleus on account of the large binding energy of alpha-particles, if the exchange direct process is dominant in these reactions.

Acknowledgements

The author wishes to thank Professors K. Kimura Y. Uemura, S. Shimizu, T. Hyodo and Dr. I. Kumabe for their continuous encouragements. His thanks are also due to Professor T. Yanabu, Dr. T. Nakamura, Messrs. K. Takamatsu, A. Masaike, S. Kakigi and D. C. Nguyen for their co-operation and discussions. He also thanks the members of the cyclotron laboratory for the preparation of the apparatus.

References

1) G. Weber, L. W. Davis and J. B. Marion : Phys. Rev. **104** (1956) 1307 ; W. A. Ranken, T. W. Bonner and J. H. McCrary : Phys. Rev. **109** (1958) 1646 ; S. Bashkin, R. R. Carlson and R. A. Douglas : Phys. Rev. **114** (1959 1543.
2) R. Malm and D. R. Inglis : Phys. Rev. **95** (1954) 993 ; P. H. Stelson : Phys. Rev. **96** (1954) 1584 ; J. W. Cronin : Phys. Rev. **101** (1956) 298 ; R. L. Clarke and E. B. Paul : Can. J. Phys. **35** (1957) 1646 ; A. Isoya, H. Ohmura and T. Momota : Nucl. Phys. **7** (1958) 116 ; A. Isoya : Nucl. Phys. **7** (1958) 126.
3) J. G. Likely and F. P. Brady : Phys. Rev. **104** (1956) 118.
4) H. Ogata : J. Phys. Soc. Japan **14** (1959) 707.
5) I. Kumabe, C. L. Wang, M. Kawashima, M. Yada and H. Ogata : J. Phys. Soc. Japan **14** (1959) 713.
6) P. E. Hodgson : Nucl. Phys. **8** (1958) 1 ; J. W. Meadows : Phys. Rev. **98** (1955) 744 ; H. Muirhead and W. G. V. Rosser : Phil. Mag. **46** (1955) 652.
7) G. E. Fischer, V. K. Fischer, E. A. Remler and M. D. Tatcher : Phys. Rev. **110** (1958) 286(L).
8) H. Ogata, H. Itoh, Y. Masuda, K. Takamatsu,

M. Kawashima, A. Masaike and I. Kumabe: J. Phys. Soc. Japan **15** (1960) 1719.

9) H. Ogata, H. Itoh, Y. Masuda, K. Takamatsu, M. Kawashima, A. Masaike and I. Kumabe: J. Phys. Soc. Japan **15** (1960) 1726.

10) F. Ajzenberg-Selove and T. Lauritsen: Nucl. Phys. **11** (1959) 1.

11) P. M. Endt and C. M. Braams: Rev. Mod. Phys. **29** (1957) 683.

12) M. G. Mayer and J. H. D. Jensen: *Elementary Theory of Nuclear Shell Structure* (John Wiley and Sons, Inc., New York, 1955).

13) W. A. Higinbotham and S. Rankowitz: Rev. Sci. Instr. **22** (1951) 688.

14) H. Bichsel, R. F. Mozley and W. A. Aron: Phys. Rev. **105** (1957) 1788.

15) K. Kimura *et al.*: To be published.

16) I. B. Teplov, O. P. Shevchenko and E. K. Ruuge: Sov. Phys. JETP **12** (1961) 640.

17) J. Kokame: J. Phys. Soc. Japan **16** (1961) 2101.

18) G. Igo and R. M. Thaler: Phys. Rev. **106** (1957) 126; W. B. Cheston and A. E. Glassgold: Phys. Rev. **106** (1957) 1215; R. M. Eisberg and C. E. Porters: Rev. Mod. Phys. **33** (1961) 190.

19) A. B. Bahtia, K. Huang, R. Huby and H. C. Newns: Phil. Mag. **43** (1952) 485.

20) S. T. Butler: Phys. Rev. **106** (1957) 272; S. T. Butler, N. Austern and C. Pearson: Phys. Rev. **112** (1958) 1227; S. T. Butler: *Nuclear Stripping Reactions* (John Wiley and Sons, Inc., New York, 1957).

21) P. D. Kunz: Ann. Phys. **11** (1960) 275.

22) G. E. Owen and L. Madansky: Phys. Rev. **105** (1957) 1766; G. E. Owen, L. Madansky and S. Edward, J.R.: Phys. Rev. **113** (1959) 1575; R. Bardes and G. E. Owen: Phys. Rev. **120** (1960) 1369.

23) V. F. Weisskopf: Rev. Mod. Phys. **29** (1957) 174.

JOURNAL OF THE PHYSICAL SOCIETY OF JAPAN, Vol. 16, No. 12, DECEMBER, 1961

Gamma Rays from the Proton Bombardment of ^{31}P and the Excited States of ^{31}P

By Tetsuo WAKATSUKI, Yasuo HIRAO, Eiji OKADA and Iwao MIURA

Department of Physics and the Laboratory of Nuclear Studies, Faculty of Science, Osaka University, Osaka

(Received August 14, 1961)

Gamma rays from ^{31}P bombarded by protons of up to 5.7 MeV energy were analysed by scintillation spectrometers. Most of the observed gamma rays were attributed to the transitions from the excited states of ^{31}P produced by the inelastic scattering of protons. Gamma ray transition branching ratios from several excited states were determined. The results are in general agreement with the results obtained from the experiments on ^{30}Si$(p, \gamma)^{31}$P reaction, but there are some differences between them which are discussed in detail. In particular, it was noted that the gamma ray of 1.65 MeV energy resulting from the transition from the excited state at 4.784 MeV to 3.133 MeV state is emitted in considerable intensity at the proton bombarding energy of 5.7 MeV. It was suggested that this selective excitation might be the result of the collective nature for the 4.784 MeV excited level. Excitation curve for the gamma ray intensity gave the compound levels of ^{32}S at 13.61, 13.97 and 14.27 MeV.

§1. Introduction

The precise energies of the levels in ^{31}P have been studied by the magnetic analysis of protons scattered from ^{31}P by Endt and Paris[1] up to 5.012 MeV and by Van Patter et al.[2] up to 3.293 MeV.

A detailed study of the levels of ^{31}P and their mode of decay has been carried out by

Broude et al.[3] by the analysis of gamma rays from ^{30}Si(p, γ)^{31}P reaction at several resonances. They could determine the spins and parities of the levels up to the sixth level (at 4.188 MeV) except for the fifth level and compared the results with the predictions of Nilsson model.[4] By taking an oblate distortion to agree with the experimental value of the magnetic moment, it was possible to obtain excellent agreements in energies, spins and parities for those levels.

Hoogenboom[5] also studied the gamma rays from ^{31}P formed in the reaction ^{30}Si(p, γ)^{31}P. He assigned the spins and parities to nine excited states below 5.01 MeV. His results are in general agreement with that of Broude et al. except for some differences in assigning spins to three levels (third, fourth and seventh states).

Litherland et al.[6] studied the second excited state at 2.232 MeV by means of the capture gamma rays from the 1.70 MeV resonance in the reaction ^{30}Si(p, γ)^{31}P. They assigned (5/2 +) to this state in agreement with the assignment by Broude et al. and also by Hoogenboom. They noticed that the cascade gamma rays from the 2.23 MeV state to the first excited state at 1.27 MeV (3/2+) were less than 3% of the transitions to the ground state. This situation is quite similar to the case of ^{29}Si[7] and they suggested that collective model could be applied for both those nuclei. In view of the considerable success for applying Nilsson model to A=25 and 29 nuclei, it seems interesting to look for evidence of collective motion in other nuclei in this region.

To obtain further informations on the mode of decay from the various excited levels of ^{31}P, we have studied the gamma rays in the reaction ^{31}P(p, p' γ) using protons up to 5.7 MeV. The study of gamma rays following inelastic scattering of protons is especially suitable for the study of relatively low lying levels. The intensities of high energy gamma rays from highly excited states formed in capture reactions are low in this case and the spectrum is not complicated as in capture reactions. We did not suffer from the (p, n) reaction as the Q value for ^{31}P(p, n)^{31}S is −5.9 MeV. Gamma rays from the excited states of ^{28}Si are expected as the Q value for ^{31}P(p, α)^{28}Si is 1.911 MeV. We must also consider the gamma rays from ^{31}P(p, γ)^{32}S reaction but its intensity would be smaller than that from the inelastic scattering.

§ 2. Experimental arrangements and procedures

Experimental arrangements were the same as previously described.[8] Proton beam from Osaka University cyclotron was used to bombard lead phosphate target evaporated on gold backing.

Gamma rays were detected by NaI(Tl) scintillation spectrometers. Two crystals, both 3 in. in diameter and length, optically coupled to 6364 photomultipliers, were used as single crystal spectrometers. They were also used as a coincidence spectrometer for the analysis of cascade gamma rays. Accurate values of the energies of the gamma rays were determined by a three crystal scintillation pair spectrometer. In this case, the size of the center crystal was 15. in. in diameter and 4 in. long. Two 3 in. crystals mentioned above were used as side crystals and gamma rays were collimated by a lead collimater with a hole 1 in. in diameter in front of the center crystal. For the single crystal spectrometer, no collimation was used for gamma rays. The crystals were surrounded by three inches of lead to reduce the background.

The output pulses from the spectrometers were analysed by the use of a 20 channel pulse height analyser and a 30 channel pulse height analyser.

§ 3. Results and discussions

Excitation Function:

Fig. 1 shows the excitation curve for the 1.265 MeV radiation from the reaction ^{31}P(p, p' γ)^{31}P, corresponding to the deexcitation of the first excited state in ^{31}P, as a function of the proton bombarding energy.

Resonance peaks were observed at proton energies of 4.90, 5.28 and 5.58 MeV which correspond to the excited levels of ^{32}S at 13.61, 13.97 and 14.27 MeV.

Compound excited levels of ^{32}S were studied by ^{31}P(p, γ)^{32}S reaction up to proton energy of 2 MeV[9], and by ^{31}P(p, α)^{28}Si reaction up to proton energy of 3 MeV.[10]

Van Patter et al.[11] made a survey for the excitation function of ^{31}P(p, p') reaction over a region of 4.53 to 4.71 MeV and found several resonances. Gemmell et al.[12] observed high

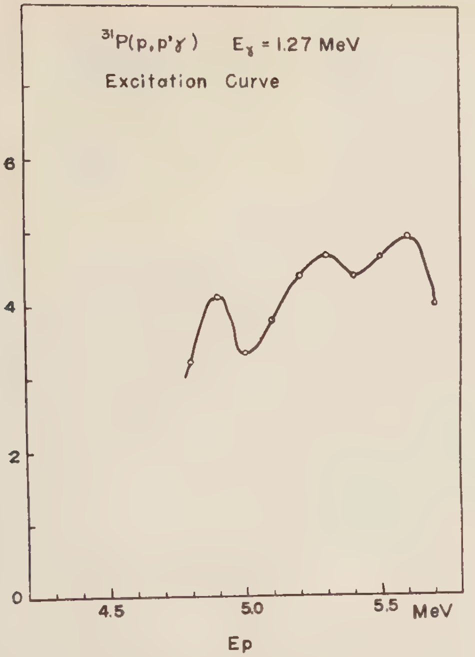

Fig. 1. Excitation curve for the 1.265 MeV gamma ray in the reaction ^{31}P(p, $p'\gamma$).

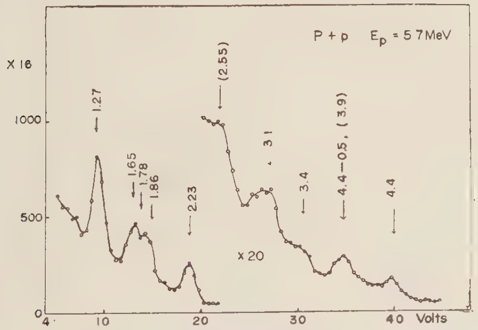

Fig. 2. Single crystal spectrum for gamma rays produced by 5.7 MeV protons on lead phosphate target.

energy gamma rays produced in the reaction ^{31}P(p, γ)^{32}S by the use of 5 to 7.7 MeV protons. They observed pronounced resonances at 6.65, 7.15 and 7.50 MeV and a small peak at 5.6 MeV. Resonance peak at 5.6 MeV agrees with our results.

Gamma Ray Spectra:

Fig. 2 is the single crystal spectrum observed at right angles to the proton beam using 3 in. dia. and 3 in. length NaI crystal. As is evident from Fig. 2, the most intense gamma rays are 1.265 and 2.232 MeV gamma rays from the first and the second excited states of ^{31}P to the ground state. In addition to these, double peaks between them and higher energy gamma rays of 3.1, 3.4 and 4.4 MeV were observed.

To resolve the double peaks at around 1.7 MeV, it is necessary to know the pulse height distribution for monochromatic gamma ray. For this purpose, the pulse height distribution for 2.76 MeV gamme ray from ^{24}Na was measured under the same geometrical conditions. In this way, the contribution at lower energy region in the pulse height distribution of the 2.232 MeV gamma ray was estimated and subtracted. It was found that the double peaks were formed by two gamma rays 1.65 and 1.78 MeV in energy.

Of these two, 1.78 MeV gamma ray is interpreted as the deexcitation gamma ray from the first excited state of ^{28}Si formed in the reaction ^{31}P(p, α)^{28}Si.

To investigate further, the three crystal scintillation pair spectrometer was used and the results are shown in Fig. 3. As is shown in Fig. 3, 1.65, 1.78 and 1.96 MeV gamma rays were found between two gamma rays of 1.27 and 2.28 MeV. From the reaction ^{31}P(p, α)^{28}Si, gamma rays of 2.84 and 3.20 MeV may also be expected which correspond to the deexcitation from the second 4.62 MeV (4$^+$) and the third 4.98 MeV (0$^+$) excited states to the first excited state of ^{28}Si.[13] The 2.9 and 3.1 MeV gamma rays found in Fig. 3 may, in part, be interpreted in this way. Kern and Cockran[9] observed several gamma rays of energy between 2.25 and 10 MeV from the reaction ^{31}P(p, γ)^{32}S using protons of 0.4∼2.0 MeV. They found 3.8 MeV gamma ray in considerable intensity in this reaction. This gamma ray corresponds to 3.9 MeV gamma ray found in Fig. 3. As to the origin of this gamma ray, they suggested this to be due to the transition from the second excited state at 3.78 MeV to the ground state of ^{32}S. But from the analysis of gamma rays produced in the reaction ^{32}S(p, $p'\gamma$)^{32}S,[14] it was confirmed that the second state decays via the first state at 2.24 MeV. By the measurement of angular correlations of 2.24 and 1.56 MeV cascade gamma rays, the second excited state of ^{32}S was assigned 0$^+$. Therefore the 3.8 (or 3.9) MeV gamma ray must be interpreted as due to the transition between higher excited states of ^{32}S.

To investigate the origins of gamma rays,

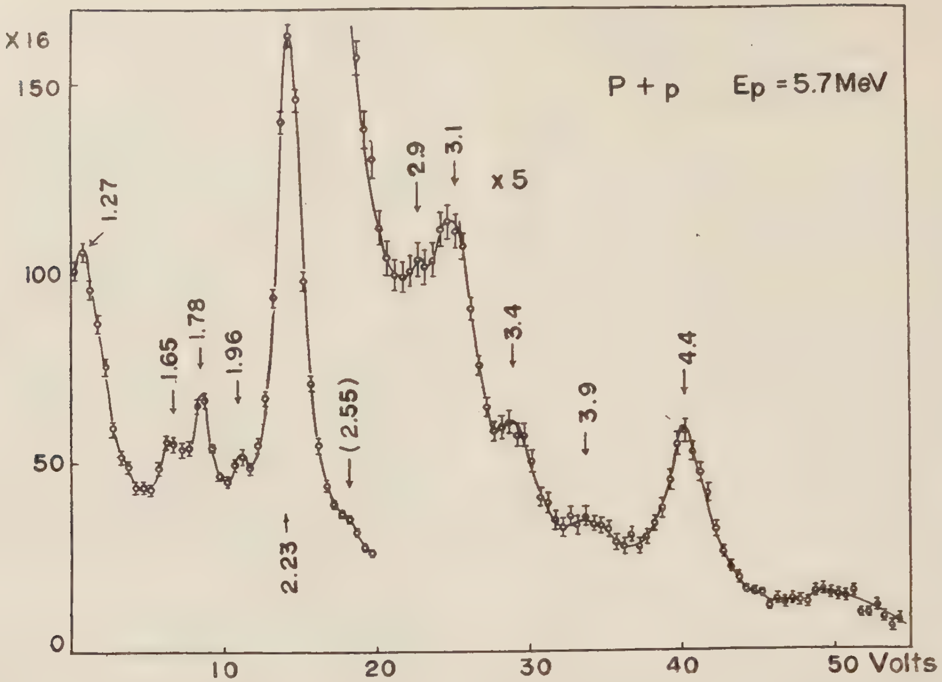

Fig. 3. Three crystal pair spectrum for gamma rays produced by 5.7 MeV protons on lead phosphate target.

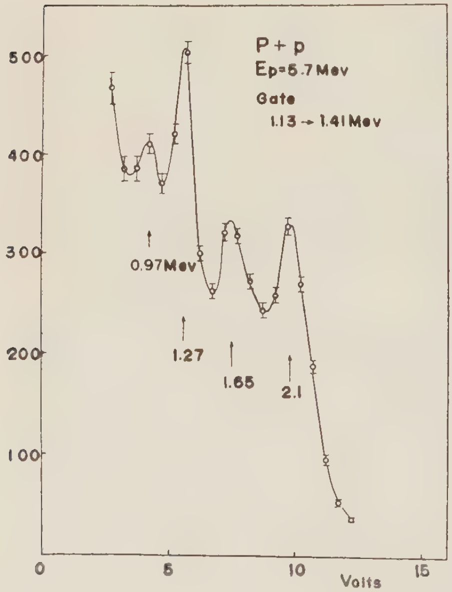

Fig. 4. Coincident spectrum for [the gate pulse height 1.13–1.41 MeV.

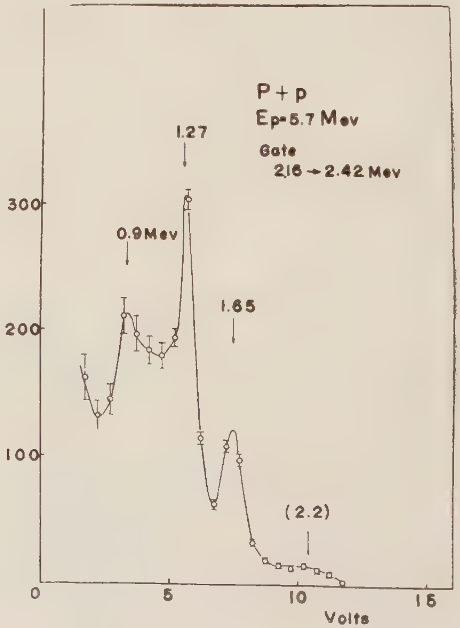

Fig. 5. Coincident spectrum for the gate pulse height 2.16–2.42 MeV.

gamma-gamma coincidence experiments were performed. Two scintillation spectrometers, each 3 in. dia. and length, were placed at 90° to the beam on each side of the target. The pulse height spectrum of one crystal gated by a definite value of pulse height on the other crystal was displayed on the 30 channel pulse height analyser. In this case we must take care for the fact that the peaks due to gamma rays in cascade with gamma rays

Table I

Gamma-ray energy (MeV)	Origin of the gamma-ray	Shown in Fig.	Degree of certainty
	MeV Mev		
0.90	3.133→2.232 (^{31}P)	5, 6, 7	a
0.97	2.232→1.265 (〃)	4	a
1.27	1.265→gnd (〃)	2, 3, 4, 5, 6, 7	a
1.65	4.784→3.133 (〃)	2, 3, 4, 5, 6, 7	a
1.78	1.78 →gnd (^{28}Si)	2, 3	a
1.86	3.133→1.265 (^{31}P)	7	b
1.96	4.188→2.232 (〃)	3	a
2.15	3.414→1.265 (〃)	4	a
2.23	2.232→gnd (〃)	2, 3, 7	a
2.9	4.188→1.265 (〃) (or 4.62 →1.78 (^{28}Si))	3	b
3.1	3.133→gnd (^{31}P) (or 4.98 →1.78 (^{28}Si))	2, 3	a
3.4	3.414→gnd (^{31}P)	2, 3	a
3.9	— (^{32}S)	3	a
4.4	4.430→gnd (^{31}P)	2, 3	a

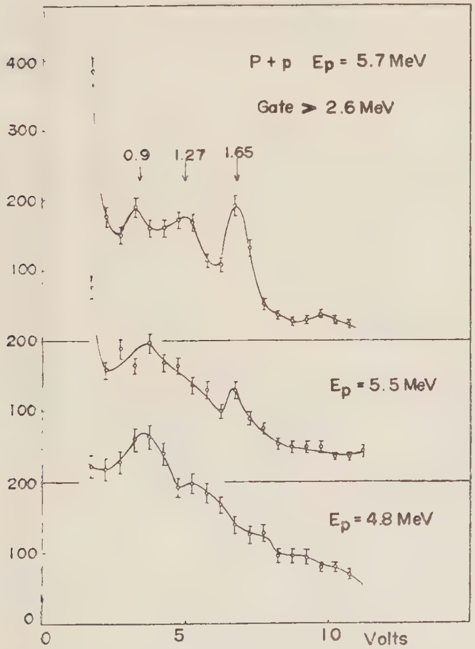

Fig. 6. Variation with bombarding energy of the coincident spectrum for the gate pulse higher than 2.6 MeV.

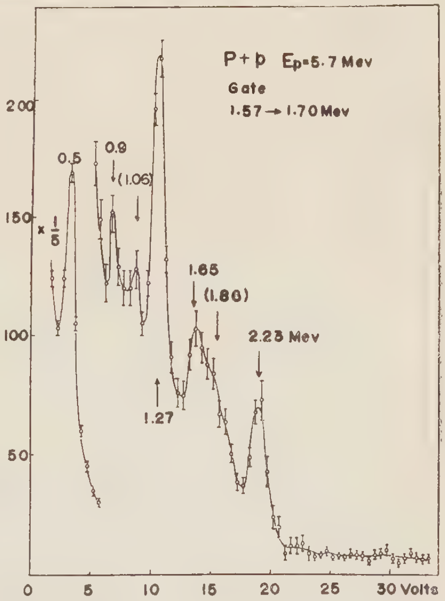

Fig. 7. Coincident spectrum for the gate pulse height 1.57–1.70 MeV.

higher in energy than the gamma rays, for which the gate pulse height was settled, always appear, as the pulse height in a single crystal always extends to lower energy side from its full energy peak. For instance, Fig. 4 is the pulse height spectrum for the gate between 1.13 and 1.41 MeV. It is seen that besides the gamma rays in cascade with 1.265 MeV gamma ray from the first excited state of ^{31}P, 0.97, 1.65 and 2.1 (2.03 and 2.15) MeV, 1.27 MeV gamma ray itself appears as the gate is open by the pulses due to gamma rays higher than 1.13 MeV.

From the analysis of the data shown in Figs. 2–7, the observed gamma rays were classified as tabulated in Table I. The decay scheme from the excited states of ^{31}P is shown in Fig. 8. Our results are in general agreement with that of Broude et al.[3] We have, however, obtained some different results which will be mentioned in the following.

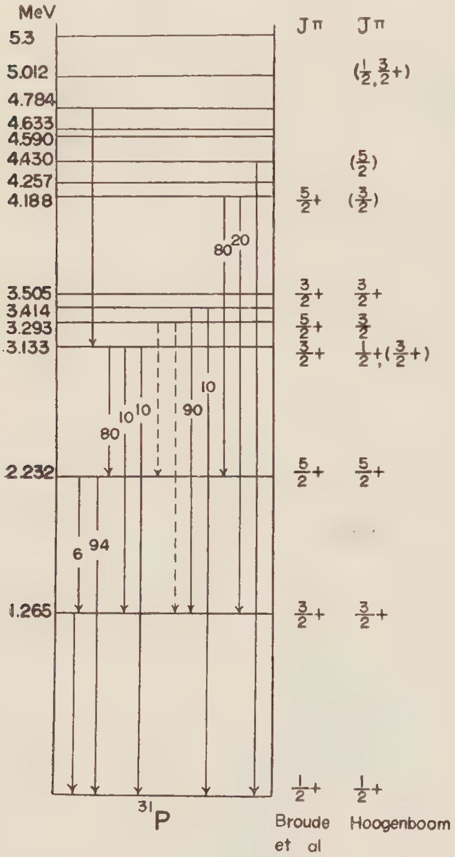

Fig. 8. Gamma decay scheme of levels in ^{31}P.

Decay from the 2.232 MeV State:

Broude et al. observed only the ground state transition from the 2.232 MeV state and estimated the cascade gamma ray to the first state to be less than 5% of the transition to the ground state. Litherland et al.[6] estimated it to be less than 3%. We have observed 0.97 MeV gamma ray from the 2.232 MeV state to the first excited state at 1.265 Mev in coincidence with 1.265 MeV gamma ray as is shown in Fig. 4. Its intensity is estimated to be 6% of the ground state transition.

Decay from the 3.133 MeV State:

Broude et al. observed only the ground state transition from the third excited state at 3.133 MeV. They estimated the intensities of the transitions to the first or second excited states to be less than 5% of the transition to the ground state.

Our results are different from the above. As is evident from Fig. 5 and Fig. 7, we have observed 0.90 MeV gamma ray due to the transition to the second state. In Fig. 7, there is some indication of the presence of 1.86 MeV gamma ray due to the transition to the first state.

Intensity ratio of those gamma rays is about 8 : 1 : 1 for 0.90 : 1.86 : 3.13 MeV gamma ray.

This result indicates that the 3.133 MeV state decays for the most part via the second excited state and is consistent with the interpretation of the 1.65 MeV gamma ray which is discussed later. The presence of the 1.65 MeV gamma ray in considerable intensity, which results from the transition between 4.784 and 3.133 MeV state, leads to the conclusion that the intensity of the 3.133 MeV gamma rays should also be large if the 3.133 MeV state decays entirely by the direct transition to the ground state. The intensity of the 3.133 MeV gamma ray is, however, only about 7% of that of the 1.65 MeV gamma ray.

Decay from the 3.293 MeV State:

Broude et al. observed the gamma rays from the decay of the 3.293 MeV state and the branching ratio obtained was as follows: Hoogenboom's result is that the branching ratio for the first state at 1.265 MeV state is larger than 85%.

In our experiment, the peaks corresponding to the gamma rays shown in Table II do not appear as isolated peaks in Figs. 3, 4 and 5. Therefore no definite conclusions were obtained on the decay of the 3.293 MeV state.

Decay of the 3.414 MeV State:

Table II

Gamma ray energy (MeV)	Decay mode MeV state MeV state	Branching ratio
3.29	3.293 → 0	10
2.03	3.293 → 1.265	45
1.06	3.293 → 2.232	45

For the decay of the 3.414 MeV state, our results are consistent with that of Broude et al. and that of Hoogenboom as shown in Table III.

Decay from the 4.188 MeV State:

Broude et al. concluded that the 4.188 MeV state decays via the second excited state

Table III

Gamma ray energy (MeV)	Decay mode MeV state → MeV state	Branching ratio: Broude et al.	Branching ratio: Hoogenboom	Branching ratio: Present experiment
3.14	3.414 → 0	15		10
2.15	3.414 → 1.265	85	>70	90

(gamma ray energy of 1.96 MeV) and also via the first excited state (gamma ray energy of 2.92 MeV). They estimated the branching ratio to be 35 : 65 for 1.96 : 2.92 MeV gamma rays.

Hoogenboom's estimation is 40 : 60 for the same gamma rays. As is evident in Fig. 3, the intensity of the 1.96 MeV gamma ray is stronger than that of the 2.92 MeV gamma ray. And we estimate this ratio as 80 : 20, contrary to the above authors.

The Origin of the 1.65 MeV Gamma Ray:

Gamma ray of 1.65 MeV energy was found in Figs. 3–7 in sufficient intensity. It can not be attributed to the deexcitation of relatively low excited states ^{31}P or to any other reactions other than inelastic scattering of protons on ^{31}P. To test whether it comes from some impurities in phosphorous, we have bombarded pure P_2O_5 target but obtained the same results.

As is clear from the coincident spectrum shown in Figs. 4, 5 and 6, this gamma ray is emitted by the transition from highly excited states to the excited levels lying between 3.133 and 3.505 MeV.

Precise energy measurement by the three crystal pair spectrometer gave the value 1.65 MeV, which leads to the conclusion that this gamma ray is emitted by the transition between the levels of 4.784 and 3.133 MeV. Fig. 7 shows the coincident spectrum when the gate was 1.65 MeV and is consistent with this interpretation.

As the 1.65 MeV gamma ray is emitted when ^{31}P is excited to the highly situated level at 4.784 MeV, its intensity would decrease rapidly when the incident proton energy is degraded by a small amount from its initial value of 5.7 MeV. To test this point, coincident spectrums were measured at 5.5 and 4.8 MeV bombarding energy and the results are shown in Fig. 6. As shown in Fig. 6, the intensity of the 1.65 MeV gamma ray decreases considerably at 5.5 MeV and disappears completely at 4.8 MeV. It seems very interesting that the excited level of ^{31}P at 4.784 MeV is excited strongly by protons of 5.7 MeV, which is only about 1 MeV higher than the excitation energy, and then decays selectively to 3.133 MeV level.

Interpretation by the Collective Model:

The above mentioned cascade gamma ray of 1.65 MeV energy might be interpreted by assuming that the 4.784 MeV level belongs to the same collective family with the ground state and the 3.133 MeV level. By considering the magnitude of the magnetic moment, ft value in the positron decay of ^{31}S into ^{31}P, and other properties of ^{31}P, Broude et al.[3] concluded that ^{31}P is an oblate shaped nucleus with distortion parameter $\eta=-3$. They calculated the excited levels of ^{31}P taking into account the Kerman coupling and classified the excited levels as follows.

The ground level (1/2+), 2.232 MeV level (5/2+) and 3.133 MeV level (3/2+) form a $K=1/2+$ rotational band (labelled 9 in Nilsson's paper), while the 1.26 MeV (3/2+) and 3.293 MeV (5/2+) levels form another rotational band with $K=3/2+$ (labelled 8 in Nilsson's paper). The 3.414 MeV and 3.505 MeV (3/2+) levels were classified as the members of $K=1/2+$ (labelled 11) rotational band.

In this way, they suggested the spin and parity of the 3.414 MeV level as 1/2+, which was not determined by their experiment.

Moreover, they suggested a 7/2+ level at about 4.7 MeV which belongs to the No. 11 rotational band.

According to their calculations, any other excited levels belonging to No's. 8, 9 and 11 rotational bands lie above 8 MeV.

If we assume that the 4.784 MeV level is just the one predicted by Broude et al. at about 4.7 MeV, we may say that among many excited levels above 4.188 MeV, only the 4.78 MeV level is collectively excited in sufficient intensity, whereas the other levels are relatively difficult to be excited as they are supposed to be due to two particle excitation or core excitation.

Endt and Paris[1), 15)] measured the intensities of the scattered protons at 50°, 90° and 130° at the proton bombarding energy of 7.04 MeV. Their result shows that there are no remarkable differences between the intensities of the scattered protons from the 4.784 MeV level and the other neighbouring levels. Though the integrated cross sections for each levels are not obtained in their experiment, it may be that no selective excitation occurs at the proton energy of 7.04 MeV. This is not contradictory with the above discussions as the protons of enough high energy may excite the levels due to two particle excitation or core excitation as well as the collective levels.

Though the selective excitation can be understood by the presence of the collective level at this energy, the selective transition to the 3.133 MeV level seems difficult to be explained by the classification proposed by Broude et al..

As the 4.784 MeV level is assumed to be a member of the $K=1/2+[200]$ band (No. 11) and the 3.133 MeV level a member of the $K=1/2+[211]$ band (No. 9), the selective transition between the 4.784 and 3.133 MeV levels does not result from the selection rules in terms of the asymptotic quantum numbers.

We must, however, consider the discrepancies between the spins and parities assigned by Broude et al.[3)] and by Hoogenboom[5)], the discrepancies between the values of the branching ratios assigned to the several excited states of ^{31}P by the above authors and by us, before going into detailed discussions.

Those problems should be clarified by further studies.

Acknowledgments

The authors wish to thank Prof. W. W. Buechner and Prof. P. M. Endt for the informations on their experiments.

This work was supported in part by the Grant for Scientific Research of the Ministry of Education.

References

1) P. M. Endt and C. H. Paris: Phys. Rev. **106** (1957) 764.
2) D. M. Van Patter, M. A. Rothman, W. C. Porter and C. E. Mandeville: Phys. Rev. **103** (1956) 656, **107** (1957) 171.
3) C. Broude, L. L. Green and J. C. Willmott: Proc. Phys. Soc. **72** (1958) 1097, 1115, 1122.
4) S. G. Nilsson: Danske Vidensk. Selsk., Math-fys. Medd., **29** (1955) 16.
5) A. M. Hoogenboom: Investigation of the ^{30}Si $(p, \gamma)^{31}$P reaction, Thesis (Utrecht, 1958).
6) A. E. Litherland, E. B. Paul, G. A. Bartholomew and H. E. Gove: Can. Journ. Phys. **37** (1959) 53.
7) D. A. Bromley, H. E. Gove, E. B. Paul, A. E. Litherland and E. Almqvist: Can. Journ. Phys. **35** (1957) 1042.
D. A. Bromley, H. E. Gove and A. E. Litherland: Can. Journ. Phys. **35** (1957) 1057.
8) E. Okada, I. Miura, T. Wakatsuki and Y. Hirao: J. Phys. Soc. Japan **13** (1958) 541.
9) B. D. Kern and L. W. Cochran: Phys. Rev. **104** (1956) 711.
10) R. L. Clarke, E. Almqvist and E. B. Paul: Nucl. Phys. **14** (1960) 472.
D. M. Van Patter, C. P. Swann, W. C. Porter and C. E. Mandeville: Phys. Rev. **103** (1956) 656.
11) D. M. Van Patter, M. A. Rothman, W. C. Porter and C. E. Mandeville: Phys. Rev. **107** (1957) 171.
12) D. S. Gemmell, A. H. Morton and W. I. B. Smith: Nucl. Phys. **10** (1959) 45.
13) C. Broude and H. E. Gove: Proc. Intern. Conf. on Nuclear Structure, Kingston, Canada, 1960, p. 471.
14) T. Wakatsuki, Y. Hirao, E. Okada and I. Miura: Prog. Theor. Phys. **24** (1960) 918.
Y. Hirao: Journ. Phys. Soc. Japan, **16** (1961) 1828.
15) P. M. Endt: Private communication.

JOURNAL OF THE PHYSICAL SOCIETY OF JAPAN, Vol. 16, No. 12, DECEMBER, 1961

New Activities in Rare Earth Region Produced by the (γ, p) Reactions

By Tokihiro KUROYANAGI*, Haruo YUTA**, Kasuke TAKAHASHI***
and Haruhiko MORINAGA***

Department of Physics, Tôhoku University, Sendai, Japan

(Received August 18, 1961)

Several new activities in the rare earth region were identified and also the decay characteristics of some previously reported activities in this region were studied more in detail. They were produced by the (γ, p) reactions and measurement was made with the aid of the scintillation spectrometers.

Results were as follows:

nucleides	half-lives	beta rays	gamma rays
Eu^{159}	19.0±1.0 min	2.2 ±0.1 MeV	(45, 170 keV)
Tm^{173}	7.3±0.5 h	0.90±0.05 MeV	400, 470 keV
Tm^{175}	20 min	2.0 MeV	510 keV
Lu^{178}	30 ±5 min	2.25±0.05 MeV	none
Lu^{178m}	16 min	1.50±0.05 MeV	60, 90, 215, 325, 425 keV
Lu^{179}	7.5±0.5 h	1.35±0.05 MeV	90, 215 keV

Analyses were made with the aid of the unified model.

§1. Introduction

The successful performance of the internal bombarding system[1] of the Tôhoku University betatron made many new investigations on previously unknown activities possible[2]. Such possibilities of studying "holes" in the nuclear chart lie scattered over all mass range and it has been proved that the photo-reaction is sometimes the best way to produce neutron excess odd-Z odd-A isotopes.

In the rare earth region, there are high density of these "holes" in the nuclear chart, and even in the case where the assignment of the activity has been already done, their characteristics are often very poorly known.

This article describes the results of our investigation on these unknown or poorly known activities in the rare earth region. We could obtain many new data from the bombardments of Gd, Yb and Hf. Irradiation of dysprosium was badly disturbed by its high slow-neutron produced activity. For Nd, Sm and Er the data obtained were not quite good enough to analyse.

Since most of the activities we encountered were of short lives, and since the chemical separation of rare earth elements were generally difficult we did not try to perform chemical separation. Neverthless, thanks to the internal bombardment which made it possible to produce enough activity of perform scintillation spectroscopical analysis on samples of approximately 100 mg, we could analyse the radiation characteristics of the produced nucleides fairly well.

The results were analysed in the light of the unified model[3], [4]. All the decay parameters were consistently explained by this model reflecting that the nucleides studied are right in the region where the deformation is stably developed. In Sec. 3, such analyses were made without complete experimental information.

For some assignments it was quite helpful that we could compare the present results with those of another series of investigation, which consist of the studies of activities produced by the fast neutron bombardment of rare earth elements. These latter results are described in the separate article[5].

§2. Experimental Procedure

In the present work, activities were produced from the samples of the pure oxide powder (99.9%) of about 100 mg with the internal target system of a betatron. Since the activites in question are to be produced by the (γ, p) reactions, the betatron was operated at the maximum energy of 25 MeV. The yield of the (γ, n) products, however, still remains about a thousand times larger than that of the (γ, p) products. In some case, measurements were seriously disturbed by the presence of such strong (γ, n) product activities. Irradiations were carried out for a proper time length of the order of an expected half-life of the activity in question ranging from a fraction of minutes to several hours, case by case. Although no specific chemical separation was made in most of the cases, simple chemical treatments were performed occasionally after the irradiations in order to remove the disturbing activities such as O^{15} or Cl^{34}, which was produced from the chlorine impurities in some samples.

---

* Now at Japan Atomic Energy Reseach Institute, Tôkai-Mura, Ibaraki-ken, Japan.

** Now at Department of Physics, University of Pennsylvania, Philadelphia, Pennsylvania, U. S. A.

*** Now at Department of Physics, University of Tôkyô, Bunkyô-ku, Tokyô, Japan.

Half-life measurements were made with a single channel beta ray analyser or an end-window G-M counter, and from the changes of the beta and gamma ray spectra with time recorded by a multichannel spectrometer.

The beta rays from activities were detected with a plastic scintillator of 2.5 cm in thickness and 5.1 cm in diameter, or an anthracene crystal of 0.6 cm in thickness and 2.0 cm in diameter. The scintillator was covered with a 2 mg/cm² aluminum foil and optically coupled to a DuMont type 6292 photomultiplier. Each spectrum was displayed on a conventional 100 channel analyser of the time conversion type. The spectrometer was calibrated with the several well known end-points of the beta rays from Au^{198}, P^{32}, In^{114} and Pa^{234}. The 624-keV internal conversion line of Cs^{137} was also used in some cases to check the linearity of the lower energy side and the resolution of the spectrometer. The resolution of the spectrometer with an anthracene crystal as a detector was about 15 percent for the line. In the case of a plastic scintillator, the resolution was found to be somewhat worse. The Kurie plot analyses of the spectra were performed with the references of the analyses for well known spectra. Fig. 1 shows the typical result of the Kurie plot of In^{114} beta ray obtained with the spectrometer employing the plastic scintillator as a detector. The standard energy calibration curve obtained with the spectrometer is shown in Fig. 2. Since the bombarded samples used here were of the oxide powder, the measured values of the end-points were bound to have some ambiguities of order of 50 keV because of the self-absorption of the sources.

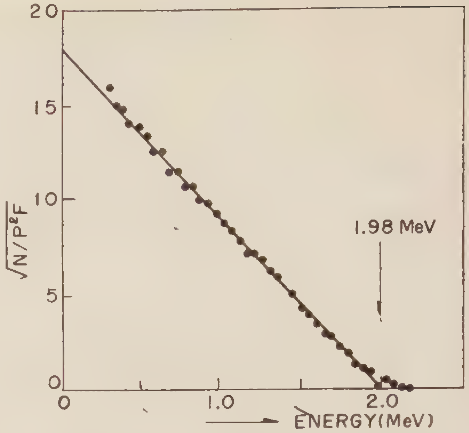

Fig 1. Kurie plot of the beta ray spectrum of In^{114}, obtained with a plastic scintillation spectrometer.

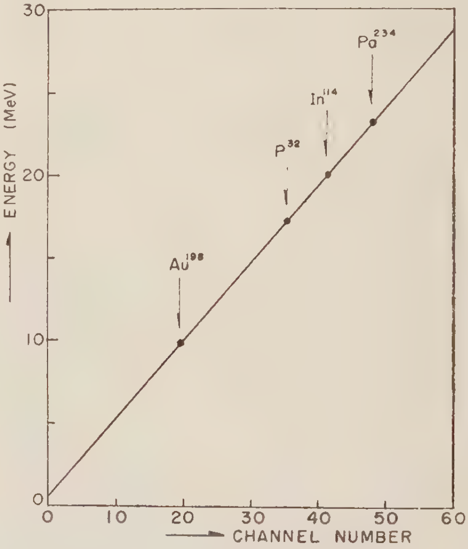

Fig. 2. Typical calibration curve for the beta ray scintillation spectrometer.

Measurements of gamma ray spectrum were carried out with a 100 channel NaI(Tl) scintillation spectrometer. The NaI(Tl) scintillator used was 3.8 cm in thickness and 3.8 cm in diameter and was optically connected to a DuMont type 6292 phototube. Several well known peaks of the gamma rays from In^{114}, Hg^{203}, Au^{198} and Na^{22} were used for the calibration of the spectrometer. Photopeak efficiencies of the spectrometer at various energies were checked by the coincidence method using the sources of Se^{75}, In^{114} and Na^{22}. Counting efficiencies of the beta and gamma rays were interchecked with the source of Au^{198} in the standard counting geometry used. Analyses of the gamma ray spectra were performed by using, as a guide, the spectral shape obtained in the same geometry from the standard sources mentioned above.

§ 3. Results and Discussions

(1) Eu^{159}

There has been no detailed investigation about the nucleide Eu^{159} since Butement first gave its half-life as about 20 min in 1951[6]. We tried to confirm this assignment and also studied its decay characteristics. Since the maximum beta decay energy of Eu^{159} was expected to be about 2.4 MeV from the beta decay energy systematics, a measurement with a G-M counter was performed, using a 0.5 mm aluminum absorber in order to cut off the disturbing lower energy beta rays. Fig. 3 shows typical decay curve thus obtained. After a long time measurement, a long component activity observed in the decay curve shown in Fig. 3 was proved to be due to the 18-h activity from Gd^{159} and the 15.4-h activity from Eu^{157}. Subtracting these long components, we observed an activity of about 19 min. A similar result was obtained from the measurements with a beta ray spectrometer. The value of half-life obtained above was in good agreement with the value previously reported by Butement.

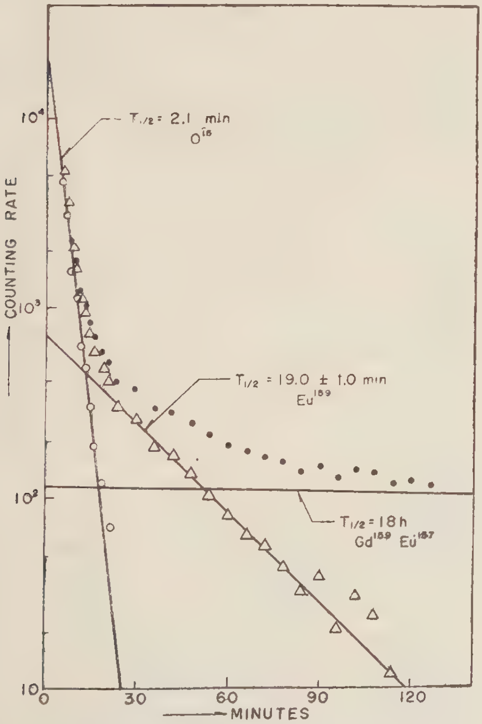

Fig. 3. Decay curve of the beta rays from the irradiated gadolynium sample measured with a G-M counter. A 0.5-mm aluminum absorber was used between the source and the counter in order to cut off lower energy beta rays.

The beta ray spectrum was measured with an anthracene crystal. In order to get rid of disturbing positrons from O^{15}, the spectrum of Eu^{159} was taken at about 20 minutes after the termination of the bombardment. Fig. 4 shows the result of the Kurie plot for the beta ray spectrum thus obtained. The end-point of Eu^{159} was determined to be 2.2 MeV.

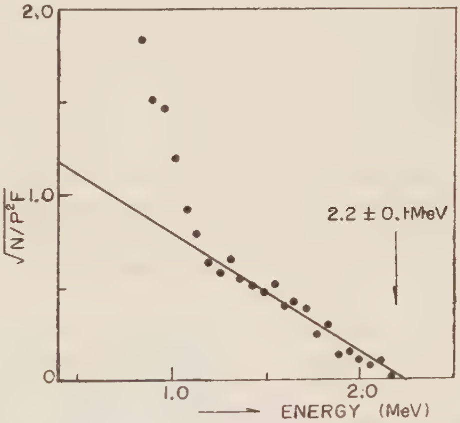

Fig. 4. Kurie plot of the beta ray spectrum of Eu^{159} taken with an anthracene crystal.

From the results of gamma ray measurements, no intense gamma ray was observed at an energy region higher than ~200 keV. Small fractions of peaks at 45 keV and 170 keV showed a decay of approximately 20 min half-life. Consequently, most of the beta rays are considered to feed the ground state or its vicinity. The value of end-point obtained above, therefore, seems to correspond the full decay energy. This confirms the assignment of this 20-min activity to Eu^{159}. The experimental log *ft* value of this beta transition is then calculated to be approximately 6.2.

The ground state of Eu^{159} may probably be the 5/2+[413] state in analogy with the ground states of several known Eu isotopes, or may be the 3/2+[411] orbital which appears as a low-lying excited state in Eu^{153}. From the analysis of the experimental data on the decay of Gd^{159}, Mottelson and Nilsson assign either of two orbitals, 3/2−[521] and 5/2+[642] to the ground state of Gd^{159} with the exclusion of the orbital 5/2−[523]4). The 3/2−[521] orbital, however, may be most favourable because of the conspicuous weakness of the transition to the 7/2+ member of the ground-state rotational band in Tb^{159}. Therefore, one may expect the first forbidden and unhindered (abbreviated as 1u) transition to this state from the 3/2+[411] ground state of Eu^{159}, but, only a first forbidden and hindered transition may be expected from the 5/2+[642] state. Accordingly the observed log *ft* value of about 6.2 seems to favour the assignment 3/2+[411] as the ground state of Eu^{159}. From the systematics of rotational bands in this region, we can expect the 5/2− rotational state of the 3/2−[521] orbit at about 45 keV. To this state, a 1u beta transition is also expected. The weak gamma ray of about 45 keV may be attributed to the M1 transition following the branching. Referring to the intensity ratio of the 45 keV gamma ray, the experimental log *ft* value for this branching is estimated as ∼7.5. This is also a proper value for a 1u transition.

Observation of a weak gamma ray of about 170 keV suggests an existence of a weak branching which may correspond to the beta decay to the orbital 5/2+[642]. The data, however, are not enough for giving anything conclusive about this state.

(2) Tm^{173} and Tm^{175}

As for neutron excess thurium isotopes information has been rather meager. Among those which may be produced by the (γ, p) reactions appreciably only Tm^{172} was known to some extent but of Tm^{173} and Tm^{175} there has been no report. In order to study these isotopes we irradiated ytterbium oxide. Unfortunately, the sample we used was found to contain small amount of chlorine. We, therefore, treated the sample often by hydrochloric acid to remove irradiated chlorine (Cl^{34}) after the bombardment when necessary.

Half-life measurements were done many times often ranging until about a week. Fig. 5 shows the result of one of such measurements. In this case the measurement was

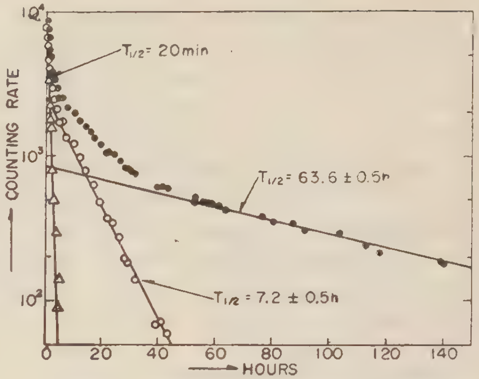

Fig. 5. Decay curve of the electron radiations higher in energy than 0.5 MeV from the irradiated ytterbium sample taken with a plastic scintillator.

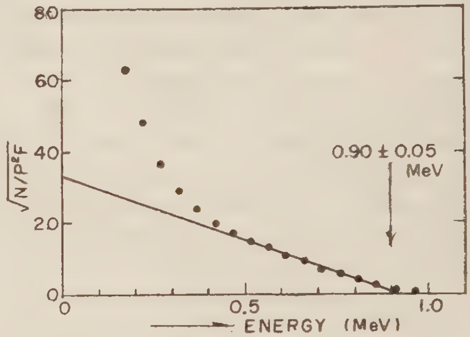

Fig. 6. Kurie plot of the beta ray spectrum of the 7.2-h component after subtracting the known 63.6-h components from Tm^{172}.

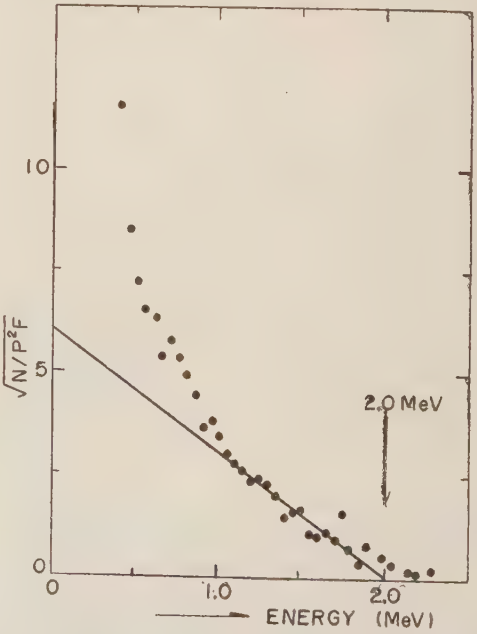

Fig. 7. Kurie plot of the beta ray spectrum of the 20-min component after the subtraction of the two long life components.

performed with a plastic scintillator for beta rays higher than 0.5 MeV. This bias was determined to eliminate the strong activity of $Yb^{175}(T_{1/2}=4.1d, E_{\beta max}=0.47\ MeV)$ produced by the (γ, n) reaction. The 0.96-MeV beta ray of $Au^{198}(T_{1/2}=2.69d)$ was occasionally measured for checking the performance of the spectrometer. After subtracting the 63.6-h activity due to Tm^{172} we identified two components with half-lives of 7.2 hours and 20-minutes.

Recently the beta rays from Tm^{172} have been measured by Orth and Dropesky with a solenoidal beta ray spectrometer7). The "unique" first-forbidden transition of 1.83 MeV and some lower energy branchings of about 0.66 MeV are reported. The 63.7-h beta rays obtained here have shown the similar end-point (about ~2 MeV) and a lower energy branching.

A beta spectrum obtained at about 5 hours after the ending of the bombardment, revealed another component of the beta ray after the subtractions of the known 63.6-h life components from Tm^{172}. The results of the Kurie plot analysis for this component is shown in Fig. 6 and the end-point was determined to be 0.90±0.05 MeV. The decay rate of this 0.90-MeV component was found to be about 7 h. The log *ft* value for this decay is about 6.2 if this is the main branching.

The Kurie plot analysis of the short component beta ray of 20 min was performed after the subtraction of the two long life components. The result of the analysis was not so accurate because of the ambiguities of the subtractions, and is shown in Fig. 7. The end-point of this 20-min component was determined to be 2.0 MeV. No other strong branching of 20 min was observed. Then, the experimental log *ft* value was calculated to be approximetely 5.

Measurements of the gamma ray spectrum were also carried out for rather a long time and the decays of the outstanding peaks at various energies were followed. Fig. 8 shows the typical gamma ray spectra obtained at about three hours (curve (a)) and at about a hundred hours (curve (b)) after the completion of the irradiation. Apparent peaks at different energies of 120 keV, 180 keV, 280 keV, 400 keV, and 470 keV were found and most of these peaks proved to be ascribed to the well known activities of $Yb^{175}(T_{1/2}=4.1d)$ and $Yb^{169}(T_{1/2}=32d)$ from their decay rates. The peak at 400 keV, however, showed the decay rate of about 7 hours in addition to the slow decay rate of about 4 days. The peak at 470 keV, though the intensity was not so large, seems to belong to the 7.2-h activity.

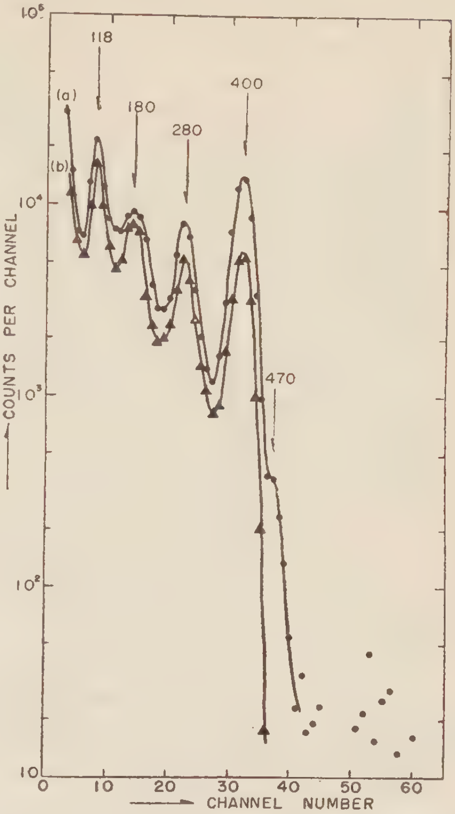

Fig. 8. Gamma ray spectra of the irradiated ytterbium sample taken (a) at about three hours and, (b) at about a hundred hours after the termination of the irradiation.

Fig. 9 shows another gamma ray spectrum obtained at about 20 minutes after the termination of the bombardment. In comparison with the spectra shown in Fig. 8, a new outstanding peak at 510 keV can be seen. The half-life of the peak was measured to be 20±1 min.

The 7.2-h activity is assigned to Tm^{173} from its decay properties and the (γ, p) yield ratios to such well known activity as Tm^{172}. The results of another series of the experiments by fast neutron bombardment of ytterbium also suggested this assignment5). The 0.90-MeV beta ray is considered to populate some excited states of Yb^{173} at about 400 keV because of the existences of the 400-keV and the 470-

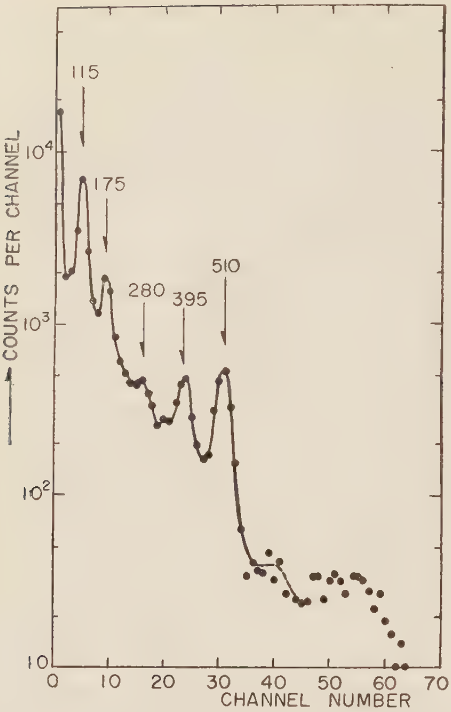

Fig. 9. Gamma ray spectrum of the irradiated ytterbium sample obtained at about 20 minutes after the ending of the irradiation.

keV gamma ray. This argument is also consistent with the maximum available beta decay energy of about 1.5 MeV estimated from the systematics. Since, the log *ft* value of the 0.90-MeV component was calculated to be about 6.2, the transition may be classified as 1u, or as an ah (allowed and hindered) transition in terms of the asymptotic quantum number selection rules. The ground state of Tm^{173} is probably 1/2+[411] as for the other Tm isotopes. Accordingly, one may expect the 1/2−[521] or the 1/2−[510] orbital possible as the excited state of Yb^{173}(N=103) with the reference to the Nilsson diagram. The 1/2−[510] orbital, however, is considered to appear as rather highly excited particle-state of Yb^{173} from the level systematics of such nuclei as Yb^{171}, Hf^{177} and Hf^{179} in this region. On the contrary, the 1/2−[521] orbital which is the ground state of Yb^{171}(N=101) is likely to occur at an excitation energy of about 420 keV. This argument leads to the assignment that the above expected excited state of Yb^{173} which is populated by the 0.90-MeV beta ray should correspond to the intrinsic state of the orbital 1/2−[521]. Taking the proper value of decoupling parameter (a=1.0) of this orbital in Yb^{173}, the 3/2− rotational member of the 1/2−[521] is expected to occur at an excitation energy of about 45 keV higher than the ground 1/2−[521] state at about 400 keV. The ground state of Yb^{173} has been well established to be 5/2−[521]. Furthermore, as is known from the decay analysis of Lu^{173},[44] only the 7/2+[633] intrinsic state is expected to appear at an excitation of 350 keV between the ground state of the 5/2−[512] orbital and the 1/2−[521] intrinsic state, postulated above, at about 400 keV. Therefore, the observed gamma rays of 400 keV and 470 keV may be considered to correspond to the de-excitation gamma rays from these states to the ground state of Yb^{173}. The de-excitation gamma ray of about 45 keV from the 3/2− rotational state to the 1/2−[521] intrinsic state must be observed according to the above argument, but it could not be found clearly because of the presence of the strong KX-ray background from Yb. The beta ray of 0.90 MeV from Tm^{173} is thus consistently interpreted as two component branchings of a 1u transition leading to the 1/2−[521] orbital at about 400 keV and to the 3/2− rotational state at about 450 keV of Yb^{173}, respectively. The separation of these two component, however, was impossible because of the poor resolution of our spectrometer. The lack of the accurate data about the intensity ratio of the de-excitation gamma rays also made the estimation of the branching ratio difficult in spite of a rather simple decay character of Tm^{173}.

From the decay characteristics and the yield of the 20-min activity, it is considered to be assigned to Tm^{175}. The end-point of the beta ray was determined to be about 2.0 MeV, and the log *ft* value obtained for the transition was about 6. This suggests that a 1u transition or an ah transition may occur from Tm^{175}. The ground state of Tm^{175} may also be considered to be 1/2+[411] as in the case of Tm^{173}. The ground state of Yb^{175} is certainly 7/2−[514] as is known from the decay analysis of Yb^{175} to Lu^{175}. Therefore, according to the above-obtained log *ft* value the direct ground state beta transition must be forbidden by the beta decay selection rules in terms of the asymptotic quantum numbers. Since the 2.0-MeV end-point of the beta ray from Tm^{175} differs from the expected value (about 2.5 MeV) predicted from the energy systematics by about 0.5 MeV and since the strong gamma ray of about 510 keV observed, the beta ray is likely considered to lead to some excited state at an excitation energy of about 510 keV or more. The 1/2 −[510] intrinsic state or the 1/2−[521] orbital is the only conceivable state populated by a 1u or an ah beta ray transition from Tm^{175} from the analysis of the Nilsson diagram. An excitation energy of the possible 1/2−[510] intrinsic state is estimated to be about 0.7 MeV from the systematics of surrounding nucleides. On the contrary, the 1/2−[521] state is expected to be more highly excited than 0.7 MeV. The 5/2−[512] intrinsic state which is the ground state of Yb^{173} is expected to appear at about 0.4 MeV. Thus one may very tentatively expect the successive de-excitations from the 1/2−[521] intrinsic state to the ground state of 7/2−[514] via the intermediate state of 5/2 −[512]. The observed 510-keV gamma ray may probably correspond to one of the gamma rays of the cascade transition. The discussions made above, however, are very tentative because of the poor information obtained. It seems necessary to make further studies to complete the decay schemes of the newly found Tm isotopes.

(3) Lu^{178}, Lu^{178m} and Lu^{179}

Butement reports 22-min and 5-h activities in the photoreaction products of hafnium and assigns the former to Lu^{178} and the latter to Lu^{179}.[6] In order to study these activities in detail, we first looked at the half-life of beta ray higher in energy than 1.1 MeV. The bias was set so that we can get rid of the 3.7-hours Lu^{176} activity which has the end-point of 1.1 MeV. The early part of the decay curve is shown in Fig. 10. The long component was found to have a half-life of 7.5 hours, but the shorter one seems to have two components, one having a half-life of about 30 minutes and the other having a half-life of roughly 15 minutes.

From the time change of the beta spectra we separated these three activities and the result is shown in Fig. 11 and Fig. 12. The end-point of the 7.5-h component was found to be approximately 1.35 MeV and shorter components we separated to a 30-min and 2.2-MeV activity and an approximately 15-min activity with an end-point of 1.5 MeV.

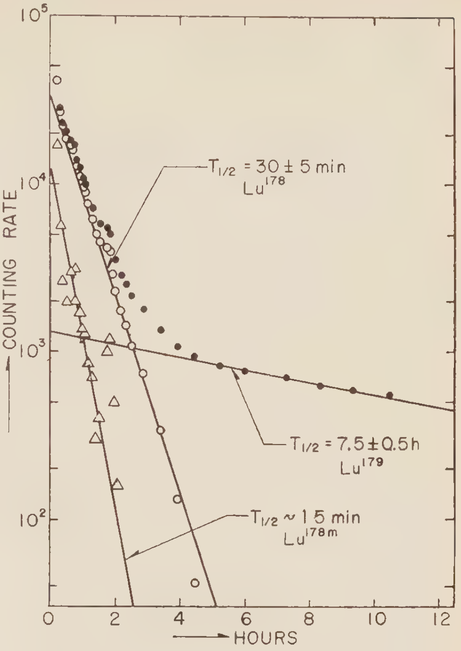

Fig. 10. Decay curve of the beta rays higher than ~1.1 MeV from the irradiated hafnium sample.

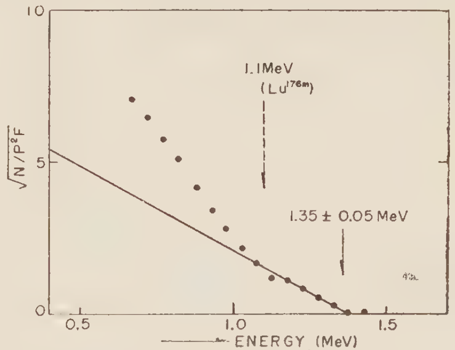

Fig. 11. Kurie plot of the beta ray spectrum of the 7.5-h component from the irradiated hafnium sample.

The gamma spectra indicated, besides peaks due to positrons from O^{15} and the 0.55-MeV radiation of Zr impurity and the long lived Hf^{173} and Hf^{175}, and existence of gamma rays with energies of 60 keV, 90 keV, 125 keV, 325 keV and 425 keV in quite similar intensities which decayed with a half-life of ~16 minutes (see Fig. 13). However no gamma rays decayed with the half-life of 30 minutes. The spectrum taken soon after the irradiation is shown in Fig. 14. Fig. 15 shows the spectrum taken about three hours after the bombardment. We see two gamma rays of 215 keV and 90 keV besides the gamma rays due to Hf^{173} and Hf^{175}. The former radiation was found to decay with a half-life of ~8 h from the time change of the

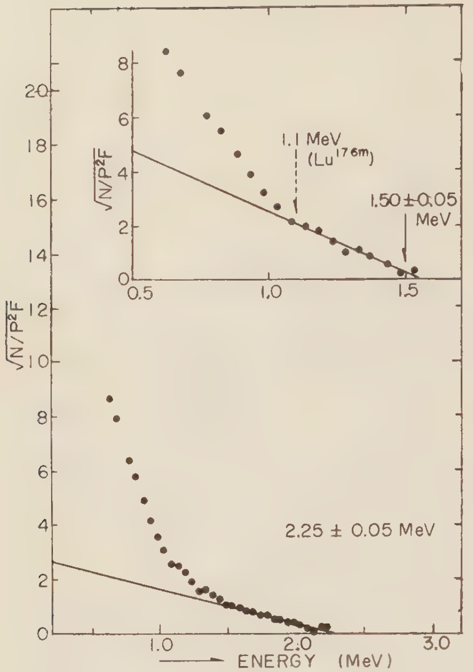

Fig. 12. Kurie plots of the short-lived beta rays from the irradiated hafnium sample after subtracting the 7.5-h component.

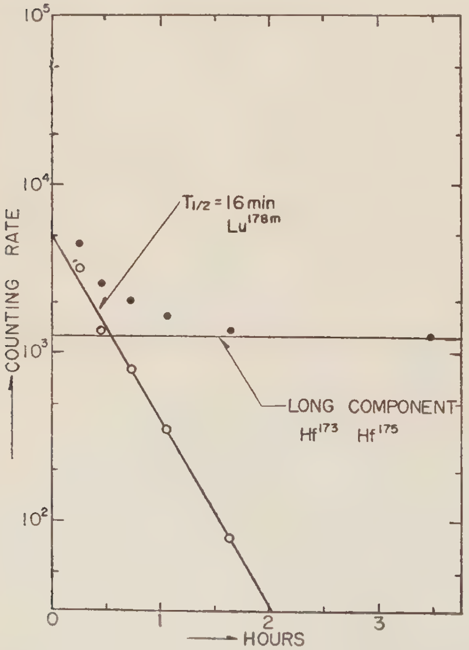

Fig. 13. Decay curve of a gamma ray peak at about 325 keV of the irradiated hafnium sample.

spectrum. The experimental facts stated above are enough to assign these activities to Lu^{178}, Lu^{178m} and Lu^{179}.

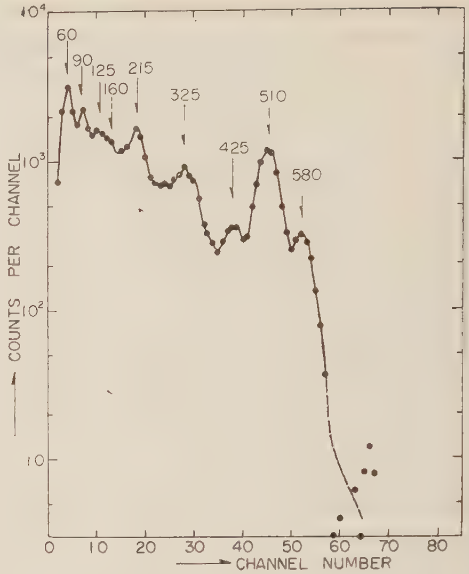

Fig. 14. Typical gamma ray spectrum of the irradiated hafnium sample taken soon after the bombardment.

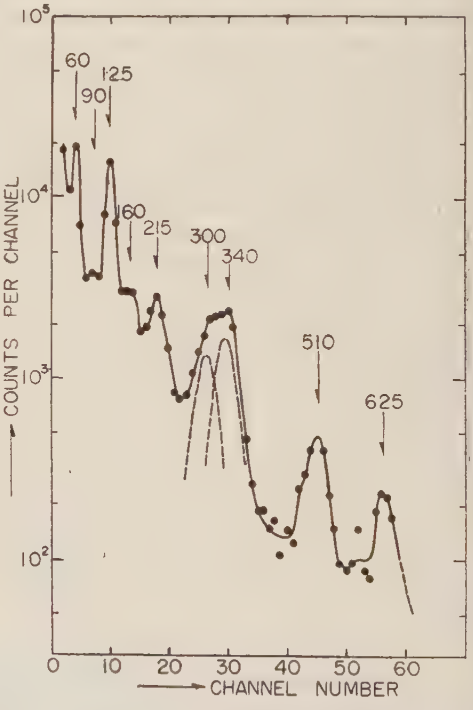

Fig. 15. Gamma ray spectrum of long-lived activities from the irradiated hafnium sample obtained at about three hours after the termination of the irradiation.

First, the 30-min activity is almost pure beta emitter with an end-point energy of 2.2 MeV. This energy is almost equal to the decay energy of Lu^{178} expected from the beta ray systematics (the expected value was approximately 2.1 MeV). Also, the coupling rule of angular momenta in deformed odd-odd nuclei[8] suggests the ground state of Lu^{178} to be 1+ arising from the coupling of 7/2+[404] proton to the 9/2+[624] neutron. The log *ft* value measured as 6.5 is consistent since the transitions to the ground and the first excited state of Hf^{178} are classified as ah.

The 16-min activity has beta end-point of ~1.5 MeV and has several gamma rays. They are considered to be identical to the gamma rays appearing in the decay of the 4.8-sec isomer of Hf^{178}. Therefore, the activity is assigned to Lu^{178m} which probably has a very high spin. Indeed, the coupling rule suggests an existence of a 7+ isomer (the coupling of the 5/2+[402] proton to the 9/2+[624] neutron). If this decays directly to the 4.8-sec isomer which probably is the case because of a very severe requirement of K-selection rule observed in this region the decay energy of isomer becomes 2.65 MeV, which places isomer about ~400 keV higher than the ground state of Lu^{178}. The log *ft* value of the beta decay is about 7 and is consistent with such an assignment made above since the decay is classified as first forbidden. In 1957, Stribel reported the 325-keV and the 445-keV gamma rays in the 18-min activity of Lu^{178}.[9] This must correspond to our Lu^{178m}.

The 7.8-h activity then goes to Hf^{179}. Since the intensity of beta ray was found to be almost equal to that of the 215-keV gamma ray, the decay is probably a simple cascade of a beta and a gamma ray by and large. The 215-keV gamma ray is assigned to the well known transition to the [514]7/2− state to the ground [624]9/2+ state of Hf^{179}. Since the Lu^{179} is expected to have 7/2+[404], a 1u transition is expected in the beta decay. The log *ft* value of 6.8 is in good agreement of this assignment. The low energy gamma rays of 60 keV and 90 keV are assigned to KX-ray of hafnium and probably to the decay of the first rotatinal level of 7/2−[514] level, which is also expected to be populated by beta rays in appreciable amount.

References

1) H. Morinaga and T. Kuroyanagi: Nuclear Instruments and Methods **6** (1960) 66.
2) H. Morinaga, T. Kuroyanagi, H. Mitsui and K. Shoda: J. Phys. Soc. Japan **15** (1960) 213. H. Yuta and H. Morinaga: Nuclear Phys. **16** (1960) 119. K. Kotajima and H. Morinaga: Nuclear Phys. **16** (1960) 231. K. Takahashi and H. Morinaga: Nuclear Phys. **21** (1960) 133.
3) S. G. Nilsson: Mat. Fys. Medd. Dan. Vid. Selsk **29** No. 16 (1955).
4) B. R. Mottelson and S. G. Nilsson: Mat. Fys. Skr. Vid. Selsk **1** No. 8 (1959).
5) K. Takahashi, T. Kuroyanagi, H. Yuta, K. Kotajima, K. Nagatani and H. Morinaga: J. Phys. Soc. Japan **16** (1961) 1664.
6) F. D. S. Butement: Proc. Phys. Soc. (London) **64**A (1951) 395.
7) C. J. Orth and B. J. Dropesky: Phys. Rev. **122** (1961) 1295.
8) C. J. Gallagher and S. A. Moszkowski: Phys. Rev. **111** (1958) 1282.
9) T. Stribel: Z. Naturforsch. **12**a (1957) 519.

Journal of the Physical Society of Japan, Vol. 16, No. 12, December, 1961

Cluster Expansion of Relaxation Function and Its Application to the Theory of Pressure Broadening

Akiko Ohno

Department of Physics, Ochanomizu University, Tokyo

(Received July 11, 1961)

The time relaxation function for pressure broadening is derived in the cumulant expansion form with the number densities of the system as variates. In this derivation the multiple collisions are taken into account and the Boltzmann distribution is assumed. By introducing the Born-Oppenheimer approximation and the statistical approximation, each cumulant can be written as a sum of irreducible integrals. When there is no correlation between perturbers and their effect on the absorber is scalarly additive, all cumulants drop out except the binary collision term. The criterion for the validity of the statistical approximation is that the rate of time change of difference between adiabatic potentials of initial and final states to this difference is much smaller than the frequency deviation from the natural frequency. The reason why the Jablonski's quantum mechanical theory gives the equivalent result with that by the classical method of Kuhn-London is clarified.

§ 1. Introduction

Broadening of absorption and emission lines of atoms and molecules in a gas has been studied by many authors since the end of the nineteenth century, and it has proved to be powerful resources for the insight of interatomic and intermolecular forces.

Theories of the pressure broadening which have appeared up to the present can be divided roughly into two categories. Statistical theory is one, in which perturbing particles (perturbers) are treated statically and considered as statistically distributed around the absorbing particle (absorber) or the emitting particle (emitter). The other is called collision or impact theory which treats a system of an absorber and a perturber dynamically. An unified treatment of these two theories was put forward by Anderson[1] and Anderson and Talman[2], and they showed that the both theories are the limiting cases of a more general formula. For sometime it has been believed that the statistical theory is valid at high density of perturbers and absorbers and the impact theory is good at low density. Both theories and almost all of other methods presented so far assumed that the effects of the perturbers on an absorber could be superposed independently and thus the correlation between perturbers could be neglected. As is shown in the following, we have to consider the higher order collisions to obtain the formula which can be used at the high density in the statistical theory as well as in the impact theory.

It is known that when the density becomes high, shifts or breadths of spectral lines deviate from what the previous theories predict, and that sometimes new satellites appear besides the main bands[3].

At higher densities, interactions between three or more molecules would become effective, and at the same time average collision diameter would become small. The deviation from the theory has been attributed to either multiple collisions or detailed shape of interaction potential between an absorber and a perturber at the close approach. Some works have been attempted to explain high density behavior of the spectral band of alkalis along these lines in qualitative way[4].

In this paper, a general formula which can be used at higher densities as well as at low density is presented and the region of the applicability of the previous theories is investigated. In section 2, we start from the relaxation function of the many-body system which was derived by Kubo[5], and derive a spectral intensity formula. With the use of the cluster expansion method, the relaxation function in grand canonical ensemble is obtained in section 3. The second relaxation function is found. It comes from the correlation between dipole moments of two absorbers and might play some role in a self broadening problem at high density. In section 4, the Born-Oppenheimer approximation is introduced and the particular terms for a special spectral line are selected out from the total relaxation function. For this one-band relaxation function, cumulant form of the expansion is obtained whose first order term gives the same result as the former statistical or impact theories under the suitable approximations. In section 5, by taking a simple case for an example, the general statistical approximation and its validity are discussed. The one-band relaxation function which is free from the Born-Oppenheimer assumption is derived in section 6. The validity of the Jablonski's quantum mechanical theory is also investigated.

§ 2. Spectral Intensity Formula for Pressure Broadening

Let us consider a system consisting of N_1 absorbers (A) and N_2 perturbers (P) per unit volume interacting with each other. We designate the absorbers by α, β, $\cdots$, and perturbers by j, k, $\cdots$. An isolated absorber α is characterised by the Hamiltonian

$$\mathscr{H}_{\rm A}=H_{\rm A}(x_\alpha)+T_{\rm A}\,, \tag{2.1}$$

where $H_{\rm A}$ is the Hamiltonian for internal energy, x_α stands for internal coordinates of the absorber, $T_{\rm A}=p_\alpha^2/2m_{\rm A}$ is the translational kinetic energy, p_α and $m_{\rm A}$ being the memontum and the mass of the absorber. The Hamiltonian of an isolated perturber j is

$$\mathscr{H}_{\rm P}=H_{\rm P}(x_j)+T_{\rm P}\,, \tag{2.2}$$

where $H_{\rm P}$ is the Hamiltonian for internal energy, $T_{\rm P}=p_j^2/2m_{\rm P}$ is the translational kinetic energy, $m_{\rm P}$ the mass of the perturber. We denote the interaction energies between absorbers themselves, perturbers themselves, and an absorber and a perturber by $U_{\rm A}(x_\alpha x_\beta,\, r_\alpha r_\beta)$, $U_{\rm P}(x_j x_k,\, r_j r_k)$ and $U_{\rm AP}(x_\alpha x_j,\, r_\alpha r_j)$ respectively, where r_α is the space coordinate of the center of mass of αth absorber etc.

Then the total Hamiltonian of the system consisting of N_1 absorbers and N_2 perturbers, $\mathscr{H}_{N_1N_2}$, is written as

$$\mathscr{H}_{N_1N_2}=H_{N_1N_2}+T_{N_1N_2}+U_{N_1N_2}\,, \tag{2.3}$$

where

$$H_{N_1N_2}=\sum_{\alpha=1}^{N_1}H_{\rm A}(x_\alpha)+\sum_{j=1}^{N_2}H_{\rm P}(x_j)\,, \tag{2.4}$$

$$T_{N_1N_2}=\sum_{\alpha=1}^{N_1}T_{\rm A}(\alpha)+\sum_{j=1}^{N_2}T_{\rm P}(j)\,, \tag{2.5}$$

$$U_{N_1N_2}=\sum_{N_1\geq\alpha>\beta\geq1}U_{\rm A}(x_\alpha x_\beta,\, r_\alpha r_\beta)+\sum_{N_2\geq j>k\geq1}U_{\rm P}(x_j x_k,\, r_j r_k)+\sum_\alpha\sum_j U_{\rm AP}(x_\alpha x_j,\, r_\alpha r_j)\,. \tag{2.6}$$

When this system is in thermal equilibrium, the response of the system to an external electric field is given by the relaxation function[5]

$$\Phi(\tau)=\int_0^\beta d\lambda\,{\rm Tr}\{\rho\boldsymbol{M}(-i\hbar\lambda)\boldsymbol{M}(\tau)\}-\beta\,{\rm Tr}\{\rho(\boldsymbol{M}^0\boldsymbol{M}^0)\}\,, \tag{2.7}$$

where

$$\rho\equiv\rho_{N_1N_2}=\exp(-\beta\mathscr{H}_{N_1N_2})/Z_{N_1N_2}\,,\qquad \beta=1/kT\,, \tag{2.8}$$

$$Z_{N_1N_2}={\rm Tr}\exp(-\beta\mathscr{H}_{N_1N_2})\,, \tag{2.9}$$

$$\begin{aligned}&\boldsymbol{M}(-i\hbar\lambda)=\exp(\lambda\mathscr{H}_{N_1N_2})\boldsymbol{M}\exp(-\lambda\mathscr{H}_{N_1N_2})\,,\\ &\boldsymbol{M}(\tau)=\exp(i\mathscr{H}_{N_1N_2}\tau/\hbar)\boldsymbol{M}\exp(-i\mathscr{H}_{N_1N_2}\tau/\hbar)\,,\\ &\boldsymbol{M}=\sum\boldsymbol{\mu}_\alpha+\sum\boldsymbol{\mu}_j\,,\end{aligned} \tag{2.10}$$

$\boldsymbol{\mu}_\alpha$ and $\boldsymbol{\mu}_j$ are electric dipole moments of αth absorber and jth perturber, ane $\boldsymbol{M}^0$ is the diagonal part of $\boldsymbol{M}$.

Usually, $\boldsymbol{M}(-i\hbar\lambda)\boldsymbol{M}(\tau)$ is a dyadic, but since we are dealing with the system in a gas phase, off-diagonal parts will drop out when we average over the orientation of $\boldsymbol{M}$, and diagonal part becomes equal to the one third of the scalar product of $\boldsymbol{M}(-i\hbar\lambda)$ and $\boldsymbol{M}(\tau)$ averaged over the orientation of $\boldsymbol{M}$. As we are interested only in the spectrum of absorbers, $\boldsymbol{\mu}_j$ in (2.10) can be neglected. It may be necessary if we consider the spectra of absorber-perturber complexes which might be formed when the density of the system becomes very large. We shall not consider such case, and throughout this paper we put

$$M=\sum_{\alpha-1}^{N_1}\mu_\alpha \tag{2.11}$$

instead of (2.10), and replace dyadics of dipole moments by one-third of their scalar products.

The frequency dependence of the response can be represented by the first term of $\Phi(\tau)$,

$$\varphi(\tau)=\frac{1}{3}\int_0 \mathrm{Tr}\,\{\rho M(-i\hbar\lambda)M(\tau)\}d\lambda\ , \tag{2.12}$$

which is called hereafter the relaxation function, and its Fourier transform

$$I(\omega)=\int_{-\infty}^{\infty}\varphi(\tau)\exp(-i\omega\tau)d\tau \tag{2.13}$$

is called the spectral intensity. It should be noted that the real power absorbed or emitted by the system differs from $I(\omega)$ by the factor proportional to ω^4 [6].

$\varphi(\tau)$ of (2.12) is to be calculated for the system $\mathscr{H}_{N_1N_2}$. Instead of doing that, we deal with the average of $\varphi(\tau)\equiv\varphi_{N_1N_2}(\tau)$ over the grand canonical ensemble,

$$\varphi_G(\tau)=\sum_{N_1=0}^{\infty}\sum_{N_2-0}^{\infty}\varphi_{N_1N_2}(\tau)z_1{}^{N_1}z_2{}^{N_2}Z_{N_1N_2}/Z_GN_1!N_2!\ , \tag{2.14}$$

where Z_G is the grand partition function

$$Z_G=\sum_{N_1=0}^{\infty}\sum_{N_2=0}^{\infty}Z_{N_1N_2}z_1{}^{N_1}z_2{}^{N_2}/N_1!N_2!\ , \tag{2.15}$$

and z_1 and z_2 are the fugacities of the absorber and the perturber.

§ 3. Cluster Expansion of Grand Partition Function and Relaxation Function

3.1. *Grand Partition Function*

The cluster expansion of grand partition function was first introduced by Ursell[7] and Mayer[8] in the classical statistical mechanics and extended to quantum statistical mechanics by Kahn and Uhlenbeck[9]. Recently perturbational treatments of the expansion have been investigated taking into account Bose-Einstein and Fermi-Dirac statistics[10]-[12]. Yokota[13] derived the virial expansion of the grand partition function to the third order taking into account the quantum statistics. Kubo[14] showed the general method to obtain the any order terms of the expansion.

In this paper we deal with only Boltzmann statistics for simplicity and this sets no limitation for practical use. By doing so all the exchange effects are neglected. But we can take into account a part of them by introducing exchange interaction into adiabatic potentials afterwards.

The cluster expansion of the partition function or the grand partition function is a straightforward procedure, and the virial expansion of them can be obtained by the similar way as in the earlier work in classical statistical mechanics. But as we deal with a two-component system taking their internal energy into consideration in addition to their translational motion, it is convenient to define some quantities and to show some relations between them which will be used in the later sections.

The cluster expansion of grand partition function is of the form

$$Z_G=\exp\left(\sum_{l_1+l_2=1}^{\infty}Vb_{l_1l_2}z_1z_2\right)\ , \tag{3.1}$$

where V is the volume of the system.

The relationship between $Z_{N_1N_2}$ and $Vb_{N_1N_2}N!N!$ is the same as that between the cumulants and moments in a distribution. Therefore we can write

$$Z_{N_1N_2}=N_1!N_2!\sum\Pi(Vb_{l_1l_2})^{n_{l_1l_2}}/n_{l_1l_2}!\ , \qquad (\textstyle\sum l_in_{l_1l_2}=N_i,\ i=1,2) \tag{3.2}$$

or

$$b_{N_1N_2}=-\frac{1}{V}\sum(\sum n_{l_1l_2}-1)!\,\Pi(-Z_{l_1l_2}/l_1!l_2!)^{n_{l_1l_2}}/n_{l_1l_2}!\ , \qquad (\textstyle\sum l_in_{l_1l_2}=N_i,\ i=1,2) \tag{3.3}$$

using the result derived by Meeron[15] for the multivariate distribution. In Eqs. (3.2) and (3.3), the summations are carried out over all possible partitions of the set of N_1+N_2 particles into $n_{l_1l_2}$ mutually exclusive subsets, each contains l_1+l_2 particles, under the conditions $\sum l_1n_{l_1l_2}=N_1$ and $\sum l_2n_{l_1l_2}=N_2$.

b_{10} and b_{01} can be written explicitly as follows,

$$b_{10}=\frac{1}{V}\,\mathrm{Tr}\exp(-\beta\mathscr{H}_{10})=\zeta_1/v_1\ , \tag{3.4}$$

$$b_{01}=\frac{1}{V}\,\mathrm{Tr}\exp(-\beta\mathscr{H}_{01})=\zeta_2/v_2\ , \tag{3.5}$$

where

$$\zeta_1=\mathrm{Tr}(i)\exp(-\beta H_{\mathrm{A}})\ , \tag{3.6a}$$

$$\zeta_2=\mathrm{Tr}(i)\exp(-\beta H_{\mathrm{P}})\ , \tag{3.6b}$$

$$v_1^{-1}=\mathrm{Tr}(t)\exp(-\beta T_{\mathrm{A}})=(2\pi\hbar^2\beta/m_{\mathrm{A}})^{3/2}\ , \tag{3.7a}$$

$$v_2^{-1}=\mathrm{Tr}(t)\exp(-\beta T_{\mathrm{P}})=(2\pi\hbar^2\beta/m_{\mathrm{P}})^{3/2}\ , \tag{3.7b}$$

and Tr(i) and Tr(t) mean the traces over internal motion and translational motion respectively.

The number densities of absorber and perturber, ρ_1 and ρ_2, are given by

$$\rho_1=\sum_{N_1=0}^{\infty}\sum_{N_2=0}^{\infty}N_1b_{N_1N_2}z_1^{N_1}z_2^{N_2}\ , \tag{3.8}$$

$$\rho_2=\sum_{N_1=0}^{\infty}\sum_{N_2=0}^{\infty}N_2b_{N_1N_2}z_1^{N_1}z_2^{N_2}\ . \tag{3.9}$$

When $z_1\to0$ and $z_2\to0$, $\rho_i\to(\zeta_i/v_i)z_i$. Then we can obtain the inverse relation of (3.8) and (3.9) in the following form:

$$(\zeta_1/v_1)z_1=\rho_1\exp\left\{-\sum_{k_1=1}^{\infty}\sum_{k_2=0}^{\infty}k_1B_{k_1k_2}\rho_1^{k_1-1}\rho_2^{k_2}\right\}\ , \tag{3.10}$$

$$(\zeta_2/v_2)z_2=\rho_2\exp\left\{-\sum_{k_1=0}^{\infty}\sum_{k_2=0}^{\infty}k_2B_{k_1k_2}\rho_1^{k_1}\rho_2^{k_2-1}\right\}\ , \tag{3.11}$$

$B_{k_1k_2}$ is irreducible integral for two-component system. The relation between $b_{N_1N_2}$ and $B_{k_1k_2}$ or rather $(v_1/\zeta_1)^{N_1}(v_2/\zeta_2)^{N_2}b_{N_1N_2}$ and $B_{k_1k_2}$ has been obtained by Mayer for classical two-component system[16]. The relationship between $b_{N_1N_2}$ and $B_{k_1k_2}$ is a mathematical one and we can use the same formula connecting them also in the case of quantum mechanics if the series in Eqs. (3.8)-(3.11) converge. This convergence is guaranteed because the system is now in gas phase. We write the relation between them in the following.

For $N_1>0$ and $N_2>0$,

$$\left(\frac{v_1}{\zeta_1}\right)^{N_1}\left(\frac{v_2}{\zeta_2}\right)^{N_2}N_1{}^2N_2b_{N_1N_2}=\sum_{n_{1k}n_{2k}}(\sum_k k_2n_{1k})\prod_k(N_1k_1B_k)^{n_{1k}}(N_2k_2B_k)^{n_{2k}}/n_{1k}!n_{2k}!\ , \tag{3.12}$$

where the suffix k stands for a pair of (k_1k_2) and the summation over n_{1k} and n_{2k} is carried out under the conditions

$$N_i=\sum_k(k_i-\delta_{i1})n_{1k}+\sum_k(k_i-\delta_{i2})n_{2k}\ , \qquad i=1,\ 2,\ k_1+k_2\geq 2\ .$$

For $N_1\geq 2$ and $N_2=0$,

$$N_1{}^2(v_1/\zeta_1)^{N_1}b_{N_10}=\sum_{n_k}\prod_k(N_1kB_{k0})^{n_k}/n_k!\ , \tag{3.13}$$

where the summation over n_k is carried out under the conditions

$$\sum(k-1)n_k=N_1-1\ , \qquad N_1\geq k\geq 2\ ,$$

and for $N_1=0$, $N_2\geq 2$,

$$N_2{}^2(v_2/\zeta_2)^{N_2}b_{0N_2}=\sum_{n_k}\prod_k(N_2kB_{0k})^{n_k}/n_k!\ , \tag{3.14}$$

under the conditions

$$\sum(k-1)n_k=N_2-1\ , N_2\geq k\geq 2\ .$$

3.2. *Cluster expansion of Relaxation Function*

Montroll and Ward[17] have given the cluster integral developments of a relaxation function for quantum mechanical systems applying the method which they have used for the expansion of the grand partition function. Their method consists mainly of the application of perturbation methods of the quantum field theory. Yokota[13] showed some formula for the relaxation function in a pressure broadening problem, but the assumptions included in his formula are not explicitly stated.

As the system under consideration includes the internal motion of particles, another approach to the problem is made. The relaxation functions can be divided into two parts:

$$\varphi_{N_1N_2}(\tau)=\varphi^{(1)}_{N_1N_2}(\tau)+\varphi^{(2)}_{N_1N_2}(\tau)\ , \tag{3.15}$$

$$\varphi^{(1)}_{N_1N_2}(\tau)\equiv\frac{N_1}{3}\int_0^\beta \mathrm{Tr}\{\rho\mu_1(-i\hbar\lambda)\mu_1(\tau)\}d\lambda\ , \tag{3.16a}$$

$$\varphi^{(2)}_{N_1N_2}(\tau)\equiv\frac{N_1(N_1-1)}{3}\int_0^\beta \mathrm{Tr}\{\rho\mu_1(-i\hbar\lambda)\mu_2(\tau)\}d\lambda\ , \tag{3.16b}$$

$$\varphi_G(\tau)=\varphi_G{}^{(1)}(\tau)+\varphi_G{}^{(2)}(\tau)\ , \tag{3.17}$$

$$\varphi_G{}^{(1)}(\tau)\equiv\sum_{N_1=1}^{\infty}\sum_{N_2=0}^{\infty}\varphi^{(1)}_{N_1N_2}(\tau)z_1{}^{N_1}z_2{}^{N_2}Z_{N_1N_2}/Z_GN_1!N_2!\ , \tag{3.18a}$$

$$\varphi_G{}^{(2)}(\tau)\equiv\sum_{N_1=2}^{\infty}\sum_{N_2=0}^{\infty}\varphi^{(2)}_{N_1N_2}(\tau)z_1{}^{N_1}z_2{}^{N_2}Z_{N_1N_2}/Z_GN_1!N_2!\ . \tag{3.18b}$$

The first relaxation function $\varphi_G{}^{(1)}$ is the correlation function of the dipole moment of an absorber. $\varphi_G{}^{(2)}$ represents the correlation between the dipole moments of two absorbers. Its contribution to the spectral intensity begins from a term proportional to the square of the absorber fugacity, and it has been neglected in the previous self-broadening theories. It can be dropped also when the interaction between two absorbers has some symmetric properties, spherical, for example. It may not be neglected when the density becomes high and the interaction potential is of low symmetry.

The cluster expansions of the relaxation functions are given by the equation

$$\varphi_G{}^{(p)}(\tau)=z_1{}^p\sum_{m_1=0}^{\infty}\sum_{m_2=0}^{\infty}C_{m_1m_2}^{(p)}(\tau)z_1{}^{m_1}z_2{}^{m_2}\,,\qquad p=1,\,2\,. \tag{3.19}$$

We shall call $C_{m_1m_2}$ the cluster relaxation function. Let us write

$$X_{N_1-p,N_2}^{(p)}(\tau)=\int_0^\beta d\lambda\,\mathrm{Tr}\left\{\exp\left[-\left(\beta+\frac{i}{\hbar}\tau-\lambda\right)\mathscr{H}_{N_1N_2}\right]\mu_1\exp\left[\left(\frac{i}{\hbar}\tau-\lambda\right)\mathscr{H}_{N_1N_2}\right]\mu_p\right\}\,, \tag{3.20}$$

then from the following equation

$$(m_1+p)!\,m_2!\,C_{m_1m_2}^{(p)}(\tau)=\left[\frac{\partial^{m_1+m_2+p}}{\partial z_1{}^{m_1+p}\partial z_2{}^{m_2}}\varphi_G{}^{(p)}(\tau)\right]_{z_1=z_2=0}\,,$$

we get the relation which gives the cluster relaxation function in terms of $X(\tau)$ and $b_{N_1N_2}$,

$$C_{m_1m_2}^{(p)}(\tau)=\frac{1}{3}\sum_{k_1=0}^{m_1}\sum_{k_2=0}^{m_2}X_{k_1k_2}^{(p)}(\tau)/k_1!\,k_2!\sum_{n_l}\Pi(-Vb_{l_1l_2})^{n_{l_1l_2}}/n_{l_1l_2}!\,, \tag{3.21}$$

where the summations over $n_{l_1l_2}$ is carried out under the conditions

$$\sum l_i n_{l_1l_2}=m_i-k_i\,,\qquad i=1,\,2\,.$$

The inverse relations of (3.21) can be obtained from

$$X_{k_1k_2}^{(p)}(\tau)=\left[\frac{\partial^{k_1+k_2+p}}{\partial z_1{}^{k_1+p}\partial z^{k_2}}\varphi_G{}^{(p)}(\tau)Z_G\right]_{z_1=z_2=0}\,.$$

They are

$$X_{k_1k_2}^{(p)}(\tau)=k_1!\,k_2!\sum_{m_1=0}^{k_1}\sum_{m_2=0}^{k_2}C_{m_1m_2}^{(p)}(\tau)\sum_{n_l}\Pi(Vb_{l_1l_2})^{n_{l_1l_2}}/n_{l_1l_2}!\,, \tag{3.22}$$

The summation over $n_{l_1l_2}$ being subject to the conditions

$$\sum l_i n_{l_1l_2}=k_i-m_i\,,\qquad i=1,\,2\,.$$

We note the similarity between Eqs. (3.22) and (3.2). The former is identical with the latter except one special cluster function, $C_{m_1m_2}^{(p)}(\tau)$, which includes in its cluster the first (for $p=1$) or the first and the second (for $p=2$) absorbers. We denote these special absorbers as μ-absorbers, and call other absorbers and perturbers which effect the motion of the μ-absorbers as perturbing particles. In the similar manner like $b_{N_1N_2}$, $C_{m_1m_2}^{(p)}(\tau)$ will be zero unless m_1+m_2 particles belong to the same cluster as μ-absorbers. It means that all the m_1+m_2 particles correlate with μ-absorbers thermally or by collisions during the time interval τ. From the Equation (3.21) we obtain

$$C_{00}^{(1)}(\tau)=\frac{1}{3}\frac{V}{v_1}\sum_{(m,n)}(\exp\{-\beta E_{An}^{0})-\exp(-\beta E_{Am}^{0})\}\exp\{i(E_{Am}^{0}-E_{An}^{0})\tau/\hbar\}(E_{Am}^{0}-E_{An}^{0})^{-1}\,, \tag{3.23}$$

where E_{Am}^{0} is an energy eigenvalue of H_{A}. This term gives the unperturbed absorption or emission spectra which consists of sharp lines at $\omega=(E_{Am}^{0}-E_{An}^{0})/\hbar$.

The second and the third terms,

$$C_{10}^{(1)}(\tau)=\frac{1}{3}[X_{10}^{(1)}(\tau)-X_{00}^{(1)}(\tau)Vb_{10}]\,, \tag{3.24}$$

$$C^{(1)}_{01}(\tau)=\frac{1}{3}[X^{(1)}_{01}(\tau)-X^{(1)}_{00}(\tau)Vb_{01}]\ , \tag{3.25}$$

give the corrections which arise from collisions between μ-absorber and another absorber or a perturber. The higher order terms of $C^{(1)}_{m_1m_2}(\tau)$ give corrections coming from higher order collisions between the absorbing particle and perturbing particles.

The lowest order term of the second relaxation function, $\varphi_G{}^{(2)}$, is

$$C^{(2)}_{00}(\tau)=\frac{1}{3}\int_0^\beta d\lambda\ \mathrm{Tr}\Big\{\exp\Big[-\Big(\beta+\frac{i}{\hbar}\tau-\lambda\Big)\mathscr{H}_{20}\Big]\mu_1\exp\Big[\Big(\frac{i}{\hbar}\tau-\lambda\Big)\mathscr{H}_{20}\Big]\mu_2\Big\}\ . \tag{3.26}$$

If there is no interaction between two absorbers, this term becomes zero after being averaged over the relative orientation of two dipole moments, and in many cases this term may also be averaged out except in some cases where the coupling motion of two absorbers occurs.

We shall hereafter neglect the second relaxation function and drop the superfices because it is less important than the first one on the one hand and because the relations which will be obtained in the following concerning to the first relaxation function can be easily extended to the second one on the other hand.

The Fourier transform of the relaxation function gives the over-all spectrum of the absorber. Usually, however, we are interested only in a certain line or a certain group of lines, either isolated or overlapped, and it is convenient to pick up the terms from $C_{m_1m_2}(\tau)$ which contribute to a particular line or lines under consideration. This procedure has been used by Kubo and Tomita[18] for isolated lines in the case of magnetic resonance absorption. For this purpose, in evaluating $X(\tau)$ or $C(\tau)$, we shall restrict our consideration to a particular sub-space of $\mathscr{H}_{N_1N_2}$. Next step is then to divide the energy space of $\mathscr{H}_{N_1N_2}$, or rather, $\mathscr{H}_{N_1N_2}\times\mathscr{H}_{N_1N_2}$ into suitable sub-space, which will be done in the next section.

§ 4. Adiabatic Approximation for Interaction Potential

If the interacting particles, absorbers and perturbers, are not light particles such as electrons, we can usually make use of the Born-Oppenheimer's adiabatic approximation for the motion of the total system. By this approximation, the eigenfunctions of $\mathscr{H}_{N_1N_2}$ are given as a set of functions $\psi^{(N_1N_2)}_n(x, r)\phi^{(N_1N_2)}_{nv}(r)$ which satisfies

$$[H_{N_1N_2}(x)+U_{N_1N_2}(x, r)]\psi^{(N_1N_2)}_n(x, r)=[E^{(N_1N_2)}_{on}+V^{(N_1N_2)}_n(r)]\psi^{(N_1N_2)}_n(x, r)\ , \tag{4.1a}$$

$$[T_{N_1N_2}+V^{(N_1N_2)}_n(r)]\phi^{(N_1N_2)}_{nv}(r)=\varepsilon^{(N_1N_2)}_{nv}\phi^{(N_1N_2)}_{nv}(r)\ , \tag{4.1b}$$

where $E^{(N_1N_2)}_{on}$ is the nth eigenvalue of $H_{N_1N_2}(x)$ and x stands for a set of internal variables of N_1 absorbers and N_2 perturbers, and r is $3(N_1+N_2)$ dimensional space coordinates of the total system. $V_n{}^{(N_1N_2)}(r)$ is the adiabatic potential of the total system, and v designates the mode of the translational motion.

As the commutator $[T_{N_1N_2}, \psi_n{}^{(N_1N_2)}(x, r)]$ is neglected in this approximation, we obtain

$$\begin{aligned}Z_{N_1N_2}&=\int\cdots\int dxdr\sum_{nv}\psi^{(N_1N_2)*}_n(x, r)\phi^{(N_1N_2)*}_{nv}(r)\exp(-\beta\varepsilon^{(N_1N_2)}_{nv})\psi^{(N_1N_2)}_{nv}(xr)\phi^{(N_1N_2)}_{nv}(r)\\&=\sum_n\exp(-\beta E^{(N_1N_2)}_{on})\mathrm{Tr}(t)\exp[-\beta(T_{N_1N_2}+V_n{}^{(N_1N_2)})]\ .\end{aligned} \tag{4.2}$$

Let us introduce a index w to designate a certain group of spectral lines of absorber. We pick up terms which contribute to the wth group from terms of $C(\tau)$ or $X(\tau)$. The initial and the final states responsible for wth absorption spectrum are designated by a set of indices $(i)=(i_wm_i)$ and $(f)=(f_wm_f)$ where m_i and m_f represent the sub-levels of states i_w and f_w. Then

$$X_{k_1k_2}(\tau)=\sum_w X_{k_1k_2}(\tau;\ w)\ , \tag{4.3}$$

$$X_{k_1-1,k_2}(\tau;\,w)=\sum_{m_i}\sum_{m_f}\int_0^\beta d\lambda\sum_{v_i}\sum_{v_f}\left(iv_i\left|\exp\left[\left(-\beta+\frac{i}{\hbar}\tau-\lambda\right)\mathscr{H}_{k_1k_2}\right]\right|iv_i\right)$$
$$\times(iv_i|\mu_1|fv_f)\left(fv_f\left|\exp\left[\left(\frac{i}{\hbar}\tau-\lambda\right)\mathscr{H}_{k_1k_2}\right]\right|fv_f\right)(fv_f|\mu_1|iv_i)\,. \tag{4.4}$$

This can be transformed into

$$X_{k_1-1,k_2}(\tau;\,w)=\sum_{m_i}\sum_{m_f}\exp(-\beta E_{oi}^{(k_1k_2)})\int_0^\beta d\lambda\exp\{(i\tau-\lambda\hbar)\}\omega_w$$
$$\times\mathrm{Tr}(t)\left\{\exp\left[-\left(\beta+\frac{i}{\hbar}\tau-\lambda\right)(T_{k_1k_2}+V_i^{(k_1k_2)})\right](i|\mu_1(r)|f)\right.$$
$$\left.\times\exp\left[\left(\frac{i}{\hbar}\tau-\lambda\right)(T_{k_1k_2}+V_f^{(k_1k_2)})\right](f|\mu_1(r)|i)\right\}, \tag{4.5}$$

where

$$(i|\mu(r)|f)=\int dx\psi_i^{(k_1k_2)*}(xr)\mu\psi_f^{(k_1k_2)}(xr)\,, \tag{4.6}$$

and

$$\omega_w=E_{of}^{(k_1k_2)}-E_{oi}^{(k_1k_2)}=E_{Af}^{0}-E_{Ai}^{0}\,. \tag{4.7}$$

When the shift or the breadth of the spectral line is much smaller than kT, we can neglect λ in Tr(t) operand of right hand of Eq. (4.5), and $X(\tau;\,w)$ becomes

$$X_{k_1-1,k_2}(\tau;\,w)=\sum_{m_i}\sum_{m_f}\exp(-\beta E_{oi}^{(k_1k_2)})(1-e^{-\beta\hbar\omega_w})e^{i\omega_w\tau}/\hbar\omega_w$$
$$\times\mathrm{Tr}(t)\left\{\exp\left[-\left(\beta+\frac{i}{\hbar}\tau\right)(T_{k_1k_2}+V_i^{(k_1k_2)})\right](i|\mu_1(r)|f)\right.$$
$$\left.\times\exp\left[\frac{i}{\hbar}\tau(T_{k_1k_2}+V_f^{(k_1k_2)})\right](f|\mu_1(r)|i)\right\}. \tag{4.8}$$

The cluster relaxation function for wth spectrum, $C(\tau;\,w)$, is defined by the equation which is obtained from Eq. (3.21) by replacing $X(\tau)$ by $X(\tau;\,w)$. And we define the relaxation function for wth spectrum by

$$\varphi_G(\tau;\,w)=z_1\sum_{m_1=0}^{\infty}\sum_{m_2=0}^{\infty}C_{m_1m_2}(\tau;\,w)z_1^{m_1}z_2^{m_2}\,. \tag{4.9}$$

This form of expansion, however, is not very convenient, nor the lowest term corresponds to the previous theories. If we use perturbation method, we get the power series expansion in τ, and we have to evaluate the shift, breadth or higher moments of the spectral line by the moment method. This method loses its power in the case of a group of overlapping lines. As the results of experiments are described in terms of density rather than fugacity, we seek for a expansion of $\varphi_G(\tau)$ of the form

$$\varphi_G(\tau;\,w)=A_w\exp\phi(\tau;\,w)=A_w\exp\left\{\sum_{\nu_1+\nu_2=1}^{\infty}\gamma_{\nu_1\nu_2}(\tau;\,w)\rho_1^{\nu_1}\rho_2^{\nu_2}\right\}. \tag{4.10}$$

As the first stage to reach (4.10), we expand the double sum in Eq. (4.9) in the following exponential form, or the cumulant expansion form,

$$\sum_{m_1=0}^{\infty}\sum_{m_2=0}^{\infty}C_{m_1m_2}(\tau;\,w)z_1^{m_1}z_2^{m_2}=(A_w/z_1)\exp\left\{\sum_{k_1+k_2\geq1}\Gamma_{k_1k_2}(\tau;\,w)z_1^{k_1}z_2^{k_2}\right\}, \tag{4.11}$$

where the cumulant $\Gamma_{k_1k_2}(\tau;\,w)$ is obtained from the same formula used to get the relation between $Z_{N_1N_2}$ and $b_{N_1N_2}$. We have,

$$\Gamma_{k_1k_2}(\tau;\,w) = -\sum\Big(\sum_m n_m - 1\Big)!\,\Pi\big(-C_{m_1m_2}(\tau;\,w)/C_{00}(\tau;\,w)\big)^{n_m}/n_m!$$

$$\Big(\sum_m m_i n_m = k_i,\ i=1,\,2\Big)\,, \tag{4.12}$$

and

$$A_w = z_1 C_{00}(\tau;\,w)\,. \tag{4.13}$$

In order to make the meaning of the expansion (4.11) clear, we write the essential part of $X_{k_1k_2}$ in interaction representation and make use of a classical picture in which colliding particles follow definite paths in the course of time although the equations are entirely quantum mechanical. It can be written

$$\begin{aligned}
&\mathrm{Tr}(t)\Big\{\exp\Big[-\Big(\beta+\frac{i}{\hbar}\tau\Big)(T_{k_1k_2}+V_i^{(k_1k_2)})\Big](i|\mu_1(r)|f)\\
&\qquad\times\exp\Big[\frac{i}{\hbar}\tau(T_{k_1k_2}+V_f^{(k_1k_2)})\Big](f|\mu_1(r)|i)\Big\}\\
&=\mathrm{Tr}(t)\Big\{\exp[-\beta(T_{k_1k_2}+V_i^{(k_1k_2)})]|(i|\mu_1(r)|f)|^2\\
&\qquad\times\exp_-\Big(-\frac{i}{\hbar}\int^{\tau}V_i'(t)dt\Big)\exp_+\Big(\frac{i}{\hbar}\int_0^{\tau}V_f'(t)dt\Big)\Big\}\,,
\end{aligned} \tag{4.14}$$

where $\exp_-$ and $\exp_+$ are ordered exponentials, and

$$V'(t)=\exp\Big(-\frac{it}{\hbar}T_{k_1k_2}\Big)V\exp\Big(\frac{it}{\hbar}T_{k_1k_2}\Big)\,. \tag{4.15}$$

We have used in Eq. (4.14) the Born-Oppenheimer approximation again, that is, we neglected the commutator of $T_{k_1k_2}$ and $\mu_1(r)$. The first factor in the Tr(t) operand of right hand of Eq. (4.14), $\exp(-\beta(T_{k_1k_2}+V_i^{(k_1k_2)}))$, shows that we take average over the canonical ensemble for the initial state. The ordered exponential functions give the effects of collisions during a time interval τ. According to the initial conditions, there are many possibilities. In some cases, only one perturbing particle may pass near the μ-absorber during the interval τ, and in another cases, a certain number of perturbing particles may affect the motion of the μ-absorber and the rest may not. The latter particles do not appear in ordered exponents, and their possible correlation with the μ-absorber is thermal correlation and indirect collision with other perturbing particles which collide with the μ-absorber directly.

It must be noted that, in $C_{m_1m_2}$, m_1+m_2 perturbing particles are not necessarily close together. Each perturbing particle can collide with the μ-absorber one by one during the time interval τ, having no correlation with each other. Then, if the density of the system is considerably small, perturbing particles can be grouped into some number of sets, any two particles of the different sets have no correlation with each other. To construct $\Gamma_{k_1k_2}$ from $C_{m_1m_2}$'s is equivalent to separate the collisions of groups into mutually independent sets. $\Gamma_{k_1k_2}$ gives correction term due to the correlation between colliding particles. Then, if each collision of perturbing particle with the μ-absorber is independent of other particles, and its effect on the μ-absorber can be considered as additive even though they collide with the μ-absorber at the same time, and if thermally uncorrelated too, $\Gamma_{k_1k_2}=0$ except $k_1+k_2=1$.

This statement can be shown explicitly. Let us start from $\chi_{k_1k_2}$ of Eq. (4.8) of example. Several conditions are necessary in order that we may superpose the effect of each collision independently. The sufficient conditions are:

(1) The adiabatic potential energy of the total system must be additive, that is, it can be expressed as a sum of two-body potentials between the absorber and one of the perturbing particles. There should be no interaction between the latter particles.

(2) The dipole moment of the absorber does not depend on the configuration of the total system, that is, the Condon approximation is valid.

(3) The mass of the absorber can be considered as infinite so that it does not recoil at collisions.

Under these conditions, and assuming w is an isolated line to avoid irrelevancies, we get

$$\begin{aligned} X_{k_1k_2}(\tau;w) &= 3D\sum_q\prod_n \mathrm{Tr}\,(t)\exp\{-\beta(E^{\circ}_{qn}+T_q+V_{iqn})\} \\ &\quad\times\exp_-\left(-\frac{i}{\hbar}\int_0^\tau V'_{iqn}(t)dt\right)\exp_+\left(\frac{i}{\hbar}\int_0^\tau V'_{fqn}(t)dt\right) \\ &\equiv 3D\prod y_q(\tau;w)\ , \end{aligned} \tag{4.16}$$

where

$$3D\equiv\exp(-\beta E^{\circ}_{Ai})(1-e^{-\beta\hbar\omega_w})\,e^{i\tau\omega_w}|(i|\mu|f)|^2V\zeta_1/v_1\hbar\omega_w\ , \tag{4.17}$$

and q runs over the perturbing particles $\alpha=1,2,\cdots,k_1$ and $j=1,2,\cdots,k_2$. T_q is the translational energy of the relative motion between the reference absorber and qth particle, V_{iqn} is the adiabatic potential between them when the absorber is in the initial state and the qth perturber is in the nth state, and E°_{qn} is the nth unperturbed energy of the qth particle.

By means of Eq. (3.21), $C_{m_1m_2}$ becomes

$$\begin{aligned} C_{m_1m_2}(\tau;w) &= \frac{D}{m_1!m_2!}\sum_{k_1=0}^{m_1}\sum_{k_2=0}^{m_2}\binom{m_1}{k_1}\binom{m_2}{k_2}y_1^{k_1}y_2^{k_2}(-Vb_{10})^{m_1-k_1}(-Vb_{01})^{m_2-k_2} \\ &= \frac{D}{m_1!m_2!}(y_1-Vb_{10})^{m_1}(y_2-Vb_{01})^{m_2}\ , \end{aligned} \tag{4.18}$$

for, in this case, $b_{N_1N_2}=0$ except $N_1+N_2=1$. y_1 and y_2 are y_q's for an absorber and a perturber respectively. Now,

$$\sum_{m_1=0}^{\infty}\sum_{m_2=0}^{\infty}C_{m_1m_2}(\tau;w)z_1^{m_1}z_2^{m_2}=D\exp\{(y_1-Vb_{10})z_1+(y_2-Vb_{01})z_2\}\ , \tag{4.19}$$

and comparing Eq. (4.19) with Eq. (4.11), we get

$$\Gamma_{10}=y_1-Vb_{10}\ , \tag{4.20a}$$

$$\Gamma_{01}=y_2-Vb_{01}\ , \tag{4.20b}$$

$$\Gamma_{k_1k_2}=0\ ,\qquad \text{if}\quad k_1+k_2\neq1\ . \tag{4.20c}$$

As the number densities in this case are

$$\rho_l=(\zeta_l/v_l)z_l\ ,$$

we get finally

$$\varphi_G(\tau;w)=z_1D\exp\{\rho_1\gamma_{10}(\tau;w)+\rho_2\gamma_{01}(\tau;w)\}\ , \tag{4.21}$$

where

$$\begin{aligned} \gamma_{10}(\tau;w) &= \frac{v_1}{\zeta_1}\sum_n\exp(-\beta E^{\circ}_{An})\,\mathrm{Tr}\,(t)\Big\{\exp(-\beta(T_A+V_{iAn})) \\ &\quad\times\exp_-\left(-\frac{i}{\hbar}\int_0^\tau V'_{iAn}(t)dt\right)\exp_+\left(\frac{i}{\hbar}\int_0^\tau V'_{fAn}(t)dt\right)-\exp(-\beta T_A)\Big\} \end{aligned} \tag{4.22a}$$

$$\begin{aligned} \gamma_{01}(\tau;w) &= \frac{v_2}{\zeta_2}\sum_n\exp(-\beta E^{\circ}_{Pn})\,\mathrm{Tr}\,(t)\Big\{\exp(-\beta(T_P+V_{fAn})) \\ &\quad\times\exp_-\left(-\frac{i}{\hbar}\int_0^\tau V'_{iPn}(t)dt\right)\exp_+\left(\frac{i}{\hbar}\int_0^\tau V'_{fPn}(t)dt\right)-\exp(-\beta T_P)\Big\}\ . \end{aligned} \tag{4.22b}$$

The first equation represents the effect of the binary collision on the self-broadened spectral line, and the second one gives that on the foreign broadening. If we could assume that $V'(t)$ commuted with $V'(t')$ at all times, the ordered exponentials would be replaced by the ordinary exponential function,

$$\left(\exp_-\left(-\frac{i}{\hbar}\int_0^\tau V_i'(t)dt\right)\exp_+\left(\frac{i}{\hbar}\int_0^\tau V_f'(t)dt\right)=\exp\left(\frac{i}{\hbar}\int_0^\tau (V_f'(t)-V_i'(t))dt\right).$$

This quantity has been evaluated by using various assumptions[3),19)]. For instance, Anderson and Talman evaluated the time integral with the assumption of classical paths for the inverse power potential and calculated the spectral intensity formula[2)].

Returning to the equation (4.11), we note that

$$\phi(\tau;w)=\sum_{\nu_1+\nu_2\geq 1}\gamma_{\nu_1\nu_2}(\tau;w)\rho_1^{\nu_1}\rho_2^{\nu_2}=\sum_{k_1+k_2\geq 1}\Gamma_{k_1k_2}(\tau;w)z_1^{k_1}z_2^{k_2}\,, \tag{4.23}$$

and thus we have

$$\gamma_{\nu_1\nu_2}(\tau;w)=\frac{1}{\nu_1!\nu_2!}\left[\sum_{k_1+k_2\geq 1}\Gamma_{k_1k_2}(\tau;w)\frac{\partial^{\nu_1+\nu_2}z_1^{k_1}z_2^{k_2}}{\partial\rho_1^{\nu_1}\partial\rho^{\nu_2}}\right]_{\rho_1=\rho_2=0}$$

By inserting the Eqs. (3.10) and (3.11), this becomes

$$\gamma_{\nu_1\nu_2}=\sum_{k_1=0}^{\nu_1}\sum_{k_2=0}^{\nu_2}\left(\frac{v_1}{\zeta_1}\right)^{k_1}\left(\frac{v_2}{\zeta_2}\right)^{k_2}\Gamma_{k_1k_2}\sum\prod\frac{(-k_1l_1B_l)^{n_{1l}}}{n_{1l}!}\,\frac{(-k_2l_2B_l)^{n_{2l}}}{n_{2l}!}\,, \tag{4.24}$$

the third summation is to be carried out under the condition

$$\sum(l_j-\delta_{j1})n_{1l}+\sum(l_j-\delta_{j2})n_{2l}=\nu_j-k_j\,,\qquad j=1,2\,.$$

The meaning of the quantity $\gamma_{\nu_1\nu_2}$ is not so clear as $\Gamma_{k_1k_2}$. But it may by remarked that the thermal correlation included in the fugacities are cancelled in $\gamma_{\nu_1\nu_2}$. If there is no thermal correlation, it becomes $\gamma_{k_1k_2}=\Gamma_{k_1k_2}(v_1/\zeta_1)^{k_1}(v_2/\zeta_2)^{k_2}$.

The first few $\gamma_{\nu_1\nu_2}$'s are, by Eqs. (4.12) and (4.24),

$$\gamma_{10}(\tau;w)=(v_1/\zeta_1)(C_{10}(\tau;w)/C_{00}(\tau;w))\,,$$

$$\gamma_{01}(\tau;w)=(v_2/\zeta_2)(C_{01}(\tau;w)/C_{00}(\tau;w))\,,$$

$$\gamma_{20}(\tau;w)=\left(\frac{v_1}{\zeta_1}\right)^2\left\{\frac{C_{20}(\tau;w)}{C_{00}(\tau;w)}-\frac{1}{2}\left(\frac{C_{10}(\tau;w)}{C_{00}(\tau;w)}\right)^2\right\}-2\frac{v_1}{\zeta_1}\frac{C_{10}(\tau;w)}{C_{00}(\tau;w)}B_{20}\,,$$

$$\gamma_{11}(\tau;w)=\frac{v_1}{\zeta_1}\frac{v_2}{\zeta_2}\left\{\frac{C_{11}(\tau;w)}{C_{00}(\tau;w)}-\frac{C_{10}(\tau;w)C_{01}(\tau;w)}{(C_{00}(\tau;w))^2}\right\}$$
$$-\frac{v_1}{\zeta_1}\frac{C_{10}(\tau;w)}{C_{00}(\tau;w)}B_{11}-\frac{v_2}{\zeta_2}\frac{C_{01}(\tau;w)}{C_{00}(\tau;w)}B_{11}\,.$$

§ 5. The Statistical Theory and Diagram Representation of Relaxation Functions

We have obtained the formal formula for the cluster expansion of the relaxation function, and discussed the meaning of the general term of the developments. As we have stated above, if the effect of individual collision on the absorber can be superposed, the binary collision term is sufficient for the relaxation function. This fact is also pointed out by Kolb in the case of the phase shift theory by different argument[20)].

On the contrary, if the interaction between perturbing particles is considerably large, or their interaction is not additive, the higher order terms may increase their relative importance especially at high densities. In this section, we shall investigate the case when the interaction between perturbing particles cannot be neglected. The following assumptions are introduced at this stage:

(1) The translational motion of the particles does not change its feature by the change of electronic states in an absorber, that is, we can put

$$[T_{k_1k_2},\ V_i^{(k_1k_2)}]=0 \tag{5.1}$$

for the system of k_1 absorbers and k_2 perturbers.

By this assumption, we can write

$$\exp_-\left(-\frac{i}{\hbar}\int_0^\tau V_i^{k_1k_2)}(t)dt\right)\exp_+\left(\frac{i}{\hbar}\int_0^\tau V_f^{(k_1k_2)}(t)dt\right)\text{-}\exp\frac{i}{\hbar}\tau\{V_f^{(k_1k_2)}(r)-V_i^{(k_1k_2)}(r)\}\,. \tag{5.2}$$

This implies that the relative translational motion of particles does not contribute to this function, and this leads to the statistical average of the phase shift function (5.2) over the canonical distribution of the particles. We can regard the condition (5.1) as the criterion for the validity of the statistical theory. We shall examine the meaning of this condition later.

(2) All perturbers are in their ground electronic states of energy zero, thus we can put $\zeta_2=1$.

(3) An isolated absorber has only two electronic states $E^o_{\mathrm{A}i}=0$ and $E^o_{\mathrm{A}f}=E=\hbar\omega$, and $E\gg kT$, thus we can put $\zeta_1=1$.

The second and the third assumptions are introduced only in order to strip the problem of irrelevancies, and we can generalize our result obtained below easily without these assumptions.

(4) The Condon approximation is valid, that is, the r-dependence of dipole moment matrix element can be neglected. This assumption may be sound in the case of allowed transition.

(5) The adiabatic potential energy of the total system is additive.

(6) Thermal average can be done classically.

By the first to the fourth assumptions mentioned above, Eq. (4.8) can be written as

$$X_{k_1k_2}(\tau)=3K\,\mathrm{Tr}\,(t)\left\{\exp\left[-\beta(T_{k_1+1,k_2}+V_i^{(k_1+1,k_2)})\exp\left[\frac{i}{\hbar}\tau(V_f^{(k_1+1,k_2)}-V_i^{(k_1+1,k_2)})\right]\right\}\right., \tag{5.3}$$

where

$$3K=\frac{1}{E}\exp(i\omega\tau)|(i|\mu|f)|^2\,.$$

By the fifth assumption, we can write

$$V_i^{(k_1+1,k_2)}=\sum_{k_1\geq\alpha>\beta\geq0}V_{\mathrm{A}i}(\alpha,\beta)+\sum_{\alpha=0}^{k_1}\sum_{j=1}^{k_2}V_{\mathrm{AP}i}(\alpha,j)+\sum_{k_2\geq j>k\geq1}V_{\mathrm{P}}(j,k)\,. \tag{5.4}$$

Then we obtain

$$\begin{aligned}V_f^{(k_1+1,k_2)}-V_i^{(k_1+1,k_2)}&=\sum_{\alpha=1}^{k_1}(V_{\mathrm{A}f}(0,\alpha)-V_{\mathrm{A}i}(0,\alpha))+\sum_{j=1}^{k_2}(V_{\mathrm{AP}f}(0,j)-V_{\mathrm{AP}i}(0,j))\\&\equiv\sum_{\alpha=1}^{k_1}\Delta_\alpha+\sum_{j=1}^{k_2}\Delta V_j\,.\end{aligned} \tag{5.5}$$

We have denoted the absorbing particle as the 0-th absorber. Putting Eq. (5.5) into (5.3), and by the sixth assumption, we get

$$X_{k_1k_2}(\tau)=3K/(v_1^{k_1+1}v_2^{k_2})\int dr\exp\left(-\beta V_i^{(k_1+1,k_2)}+\frac{i}{\hbar}\tau(\sum_\alpha\Delta V_\alpha+\sum_j\Delta V_j)\right). \tag{5.6}$$

If we define following quantities,

$$f_1(\alpha,\beta)=\exp(-\beta V_{\mathrm{A}i}(\alpha,\beta))-1\,, \tag{5.7a}$$

$$f_2(j,k)=\exp(-\beta V_{\mathrm{P}}(j,k))-1\,, \tag{5.7b}$$

$$f_3(\alpha,j)=\exp(-\beta V_{\mathrm{AP}i}(\alpha,j))-1\,, \tag{5.7c}$$

$$g_1(\alpha)\quad=\exp(i\tau\varDelta V_\alpha/\hbar)-1\,, \tag{5.7d}$$

$$g_2(j)\quad=\exp(i\tau\varDelta V_j/\hbar)-1\,, \tag{5.7e}$$

the integrand of Eq. (5.6) is written as a sum of products of f and g, each of which is conveniently represented by a diagram similar to those used in the classical Ursell expansion of partition functions[7),8)].

The graphical representation of one of the products $\Pi f \Pi g$ consists of one reference point 0 and k_1+k_2 numbered points (field points), $\alpha=1,2,\cdots,k_1$ and $j=1,2,\cdots,k_2$, which are connected by a certain number of five kinds of bonds each bond corresponding to one of the factors f or g in the product considered, and g bonds are used only between 0 and other points. One of the products in $X_{k_1k_2}$ of Eq. (5.6) is represented by one or several of connected diagrams. In Eq. (3.21) with $X_{k_1k_2}$ of Eq. (5.6), all of the connected diagrams which do not include the reference point 0, are cancelled out with each other, and the connected diagrams including 0 and m_1+m_2 points contribute to $C_{m_1m_2}$. If we write explicitly,

$$C_{m_1m_2}(\tau)=K/(v_1^{m_1+1}v_2^{m_2}m_1!\,m_2!)\int dr \sum_{\text{(connected diagrams)}}\Pi\ f_s g_t\,, \tag{5.8}$$

where $s=1,2,3$ and $t=1,2$. This is what we expected from the discussion in the preceding section.

If there is such a point in a diagram that we can decompose it into two parts by snipping it at this point, it is called an articulation point, and a diagram which has one or more articulation points is called reducible. An integral corresponding to the reducible diagram can be factorized. If we decompose the diagrams of $C_{m_1m_2}$ first at the reference point, this gives the result

$$C_{m_1m_2}=C_{00}\sum\Pi(\Gamma^*_{k_1k_2}(\tau;w))^{n_k}/n_k!\,,\qquad (\sum_k k_i n_k=m_i\,,\quad i=1,2)\,. \tag{5.9}$$

This is just the inverse relation of (4.12)[15)], and we can put

$$\Gamma^*_{k_1k_2}(\tau)=\Gamma_{k_1k_2}(\tau)=\int dr \sum_{\text{(0 irreducible)}}\Pi\ f_s g_t V v_1^{k_1}v_2^{k_2}k_1!\,k_2!\,, \tag{5.10}$$

by noting that

$$C_{00}=KV/v_1 \tag{5.11}$$

in this case. The summation of (5.10) extends over all the diagrams in which point 0 is not the articulation point. Now it can be shown that $\gamma_{\nu_1\nu_2}$ is the integral of the diagrams which are irreducible and include the point 0, (Cf. Appendix) and,

$$V\gamma_{\nu_1\nu_2}(\tau)=\int dr \sum_{\text{(irreducible)}}\Pi\ f_s g_t/\nu_1!\,\nu_2!\,. \tag{5.12}$$

The graphical simplicity of this expression may be utilized to approximate the total expression of the relaxation function.

Let us examine the criterion for the statistical theory. To obtain (5.2), it is sufficient that the following inequality holds,

$$|[T_{k_1k_2},\,V_f{}^{(k_1k_2)}-V_i{}^{(k_1k_2)}]|\ll(V_f{}^{(k_1k_2)}-V_i{}^{(k_1k_2)})^2\,, \tag{5.13}$$

rather than Eq. (5.1) itself. If the additivity condition (5.5) is assumed, we have, instead of (5.13), a set of equations

$$|[T,\ V(r)]| \ll (\varDelta V(r))^2 \tag{5.14}$$

for each pair of particles. Now, $\exp(-iTt/\hbar)\varDelta V \exp(iTt/\hbar) = \varDelta V(t)$ gives the time variation of the adiabatic potential under the free motion of two particles. Then, the equation

$$(\partial/\partial t)\varDelta V(t) = \exp(-iTt/\hbar)\frac{i}{\hbar}[T,\varDelta V]\exp(iTt/\hbar) \tag{5.15}$$

gives the change of $\varDelta V$ in a unit of time. If the average speed of relative motion is u, $[T,\varDelta V]$ can be put equal to $\hbar u(\delta\varDelta V/\delta r)$, and (5.16) becomes

$$\hbar u|\delta\varDelta V/\delta r| \ll \{\varDelta V(r)\}^2\ , \tag{5.16}$$

for r of the order of average collioion distance. This is satisfied when u or the difference between the slope of the adiabatic potential is sufficiently small. The former condition of small u has been stated by many authors as the validity condition for the statistical theory, and the latter is also mentioned[20)]. But the combined relation (5.16) has not yet stated. We can write Eq. (5.16) in another form:

$$\left|\frac{\partial\varDelta V(t)/\partial t}{V}\right| \ll |\varDelta V/\hbar|\ , \tag{5.17}$$

that is, the rate of time change of difference between adiabatic potentials of initial and final states to this difference is much smaller than the frequency deviation from the natural frequency. It is also noted that the condition (5.16) is independent of the value of τ.

When τ is sufficiently small so that we can neglect the higher powers of τ in the ordered exponentials, and so that we can put

$$\exp_-\left(-\frac{i}{\hbar}\int_0^\tau V_i'(t)dt\right)\exp_+\left(\frac{i}{\hbar}\int_0^\tau V_f'(t)dt\right) \cong \frac{i}{\hbar}(V_f - V_i) \cong \exp\left(\frac{i}{\hbar}\tau(V_f - V_i)\right),$$

we obtain the same expression as the statistical result. This is the so-called wing theorem. The region of τ under which this approximation is possible depends on the form of the interaction.

When temperature is high, f function of (5.7) is proportional to β. As each term of $\gamma_{\nu_1\nu_2}$ has at least $\nu_1+\nu_2-1$ of f factors to connect $\nu_1+\nu_2+1$ particles into one irreducible cluster, $\gamma_{\nu_1\nu_2}$ is proportional to $\beta^{\nu_1+\nu_2-1}$ at high temperatures. If we can introduce a spherical interaction volume b surrounding a particle such that another particle outside this volume does not contribute to f or g functions appreciably, the order of magnitude of $\gamma_{\nu_1+1,\nu_2}/\gamma_{\nu_1\nu_2}$ is $\beta b_1|V_A(r)|$, and the order of magnitude of $\gamma_{\nu_1,\nu_2+1}/\gamma_{\nu_1\nu_2}$ is $\beta bp_2|V_{Ap}(r)|$. Then

$$\beta b\rho_1|V_{\mathrm{A}}(r)| \ll 1\ , \tag{5.18a}$$

$$\beta b\rho_2|V_{\mathrm{AP}}(r)| \ll 1\ , \tag{5.18b}$$

are the criterions that we can neglect higher terms in the expansion of $\phi(\tau)$ in the case of the additive adiabatic potential (5.4). At considerably high temperature we can neglect the higher order terms compared with the binary collision term.

If the adiabatic potential is not additive, the higher order terms may not be neglected at high temperatures as well at low temperatures. The diagram representation can be used in this case too, if new f and g functions for many-body interaction are introduced and included in the many-body irreducible integrals. For example, the following quantity

$$\varDelta\gamma_{20} = \int dr\left\{\exp\left(\frac{i}{\hbar}\tau\varDelta V^{(3)}(012)\right) - \exp\left(\frac{i}{\hbar}\tau\sum_{\alpha=1}^{2}\varDelta V(\alpha)\right)\right\}$$

contributes to the triple collision term γ_{20} at $\beta=0$. For large τ, this term may be averaged out, but for small τ, the order of magnitude of $\varDelta\gamma_{20}$ becomes

$$b^2\langle \Delta V^{(3)}(012)-\Delta V(1)-\Delta V(2)\rangle\tau/\hbar\ .$$

In order that we can neglect this term compared with the binary collision term, we need the inequality

$$b\rho_1|\langle \Delta V^{(3)}(012)-\Delta V(1)-\Delta V(2)\rangle|\ll\langle \Delta V(1)\rangle \tag{5.19}$$

where $\langle V\rangle$ denotes the average value of V.

The binary collision term at $\beta=0$ is

$$\int dr\left\{\exp\left(\frac{i}{\hbar}\tau(V_f-V_i)-1\right)\right\}, \tag{5.20}$$

which was evaluated by Margenau[21] for the inverse power potentials.

§ 6. Cluster Expansion without Born-Oppenheimer Approximation

In this section we shall present the general formula which is free from the adiabatic assumptions.

It is to be noted that in the derivation of Eq. (4.10), the introduction of the Born-Oppenheimer assumption is not essential. It was used just to designate the particular terms in the total relaxation function which is relevant to the spectrum considered. The relations between $X(\tau;w)$, $C(\tau;w)$, $\Gamma(\tau;w)$ and $\gamma(\tau;w)$ do not change by redefinition of $X(\tau;w)$.

Let us assume that the unperturbed initial and the final states have degeneracy whose substates are designated by the quantum numbers m_i and m_f, and that the interaction causes transition only between these degenerate substates. We shall further assume that the breadth of the spectral line is smaller than kT/h. Then we can write

$$\begin{aligned}X_{k_1-1,k_2}(\tau;w)=&\frac{1}{2}(1-\exp(-\beta(E^o_{Af}-E^o_{Ai})))/(E^o_{Af}-E^o_{Ai})\\&\times\mathrm{Tr}\,(t)\sum_{\substack{m_im_f\\m_i'm_f'}}\left(im_i\left|\exp\left[-\left(\beta+\frac{i}{\hbar}\tau\right)\mathscr{H}_{k_1k_2}\right]\right|im_i'\right)(im_i'|\mu|fm_f)\\&\times\left(fm_f\left|\exp\left(\frac{i}{\hbar}\tau\mathscr{H}_{k_1k_2}\right)\right|fm_f'\right)(fm_f'|\mu|im_i)\ ,\end{aligned} \tag{6.1}$$

We introduce a projection operator

$$P_{(i)}(xx')\equiv\sum_{m_i}\psi_{im_i}(x)\psi^*_{im_i}(x')\ , \tag{6.2}$$

and a time developing operator $\exp\left(\frac{i}{\hbar}\int_0^\tau U'(t)dt\right)^\times$ defined by

$$\exp\left(\frac{i}{\hbar}\int_0^\tau U'(t)dt\right)^\times A=\exp_-\left(-\int_0^\tau U'(t)dt\right)A\exp_+\left(\frac{i}{\hbar}\int_0^\tau U'(t)dt\right), \tag{6.3}$$

$$U'(t)=\exp[-it(H_{k_1k_2}+T_{k_1k_2})/\hbar]U\exp[it(H_{k_1k_2}+T_{k_1k_2})/\hbar]\ ,$$

and a notation

$$\mu_{if}\equiv\int P_{(i)}(xx')\mu P_{(f)}(x'x'')dx'\ , \tag{6.4}$$

Then Eq. (6.1) becomes

$$\begin{aligned}X_{k_1-1,k_2}(\tau;w)=&\frac{1}{3}(\exp(-\beta E^o_{Ai})-\exp(-\beta E^o_{Af}))e^{i\omega_w\tau}/(E^o_{Af}-E^o_{Ai})\\&\times\mathrm{Tr}\left\{\exp(-\beta\mathscr{H}_{k_1k_2})\exp\left(\frac{i}{\hbar}\int_0^\tau U'_{k_1k_2}(t)dt\right)^\times\mu_{if}\mu_{fi}\right\}.\end{aligned} \tag{6.5}$$

If we define a g operator;

$$g(pq)\equiv\exp\left(\frac{i}{\hbar}\int_0^\tau U'_{pq}(t)dt\right)^\times-1\,, \tag{6.6}$$

and an f operator

$$f(pq)\equiv\exp_+\int_0^\beta U'_{pq}(-i\hbar\lambda)d\lambda-1\,, \tag{6.7}$$

for each pair of particles, we can expand $X_{k_1k_2}(\tau;w)$ as follows.

$$\begin{aligned}X_{k_1k_2}(\tau,w)=&\frac{1}{3}(\exp(-\beta E^o_{Ai})-\exp(-\beta E^o_{Af}))e^{i\omega_w\tau}/(E^o_{Af}-E^o_{Ai})\\&\times\mathrm{Tr}\Big[\exp(-\beta(H_{k_1+1,k_2}+T_{k_1+1,k_2}))\Big\{1+\sum_{\text{pair}}f(pq)+\sum_{\text{pair}}g(pq)\\&+\sum_{(pq)\neq(p'q')}(f(pq)f(p'q'))_0+(g(pq)g(p'q'))_0\\&+\sum_{(pq)}\sum_{(p'q')}f(pq)g(p'q')+\cdots\Big\}\mu_{if}\mu_{fi}\Big]\,,\end{aligned} \tag{6.8}$$

where $(\ )_0$ means that in each product the order of the $U'(t)$ is to be arranged as determined in the ordered exponentials. For example,

$$\begin{aligned}(g_1g_2)_0A=\hbar^{-2}\Big\{&\int_0^\tau U_1'(t)dt\,A\int_0^\tau U_2'(t)dt+\int_0^\tau U_2'(t)dt\,A\int_0^\tau U_1'(t)dt\\&-\int_0^\tau dt_1\int_0^{t_1}dt_2[U_1'(t_2)U_2'(t_1)+U_2'(t_2)U_1'(t_1)]A\\&-A\int_0^\tau dt_1\int_0^{t_1}dt_2[U_1'(t_1)U_2'(t_2)+U_2'(t_1)U_1'(t_2)]+\cdots\end{aligned} \tag{6.9}$$

Each term of the expansion (6.8) can be represented by a corresponding diagrams as is in the adiabatic potential case. We can readily see that $C(\tau;w)$ corresponds to the connected diagrams, which is the extension of the Montroll-Ward expansion[17] to the case when the internal degrees of freedom are taken into account.

On the other hand, $\Gamma(\tau;w)$ and $\gamma(\tau;w)$ cannot be represented by irreducible diagrams, since in the definition of them, products of trace of operators are included, and in general they are not equal to the trace of the products.

Application of the formulae we have obtained will be shown in the forthcoming paper.

§ 7. Discussions

As the higher order terms of ψ function become important for the long-range interaction between an absorber and a perturber, and also for large interaction between perturbing particles, the cluster expansion method is expected to be useful for the systematic treatment of the Stark broadening problem in the ionic gases. Recently Lewis has evaluated the effect of the high velocity electrons without completed-collision assumption introducing interactions between the perturbers by the pair correlation function[22]. The application of our theory to this problem is being planned.

Here it is mentioned about the relation between the Jablonski theory[23] and the present method. Jablonski has obtained, for the probability distribution of the translational energy change $X=\sum_{i=1}^{N'}(E_i'-E_i)$ of N' perturbers,

$$\int P(X)dX=\int\Big[\delta(X)e^{-\zeta N'}+\sum_{m=1}^{N'}\binom{N'}{m}W^{(m)}(X)\,e^{-\zeta(N'-m)}\Big]dX\,, \tag{7.1}$$

where the first term of the right-hand integral represents the probability for no translational energy change in the system, and the term for $m=1$ gives the probability of a binary collision, and so on, and

$$\zeta=\int W^{(1)}(X)dX\,.$$

(7.1) is essentially the Fourier transform of the expansion of Eq. (3.19) for $\beta=0$. Jablonski did not use the relation, however, and he has restricted his calculation only to the binary collision term $W^{(1)}(X)$. What he has actually done is, putting the spectral intensity as

$$I(\omega)=\sum_{v_i v_f}\left|\int\phi_{iv_i}^{*}(r)\phi_{fv_f}(r)dr\right|^2\delta\left(\frac{i}{\hbar}(\varepsilon_{fv_f}-\varepsilon_{iv_i})+\omega_w-\omega\right), \tag{7.2}$$

where $\phi_{iv_i}(r)$ and $\phi_{fv_f}(r)$ are the solutions of Eq. (4.1b) for two-body interaction, to evaluate the overlapping integral with WKB approximation and with many other simplifications. He has obtained the result which is essentially the same as the Kuhn-London statistical theory[24]. The spectrum shows an infinite relative intensity at the line center and the cause of which has been attributed to the approximations used to avoid the mathematical difficulties. We shall show that it is the definition of $I(\omega)$, Eq. (7.2), which causes the divergence of intensity at the center.

If we evaluate the Fourier transform of the right hand of Eq. (7.2), we obtain, as the relaxation function of the spectrum,

$$\begin{aligned}\varphi(\tau)&=\sum_{v_i v_f}\left|\int\phi_{iv_i}^{*}(r)\phi_{fv_f}(r)dr\right|^2\exp\frac{i}{\hbar}\tau(\varepsilon_{fv_f}-\varepsilon_{iv_i})e^{i\omega_w\tau}\\&=e^{i\omega_w\tau}\,\mathrm{Tr}\,(t)\left\{\exp\left(-\frac{i}{\hbar}\tau(T+V_i)\right)\exp\left(\frac{i}{\hbar}\tau(T+V_f)\right)\right\}.\end{aligned} \tag{7.3}$$

This is proportional to the quantity $X_{01}(\tau)$ if we use the Born-Oppenheimer adiabatic approximation with the Condon approximation. As we can see from the argument in the former sections, $X_{01}(\tau)$ does not represent the proper effect of the binary collisions. $X_{01}(\tau)$ gives the probability distribution of the perturbing energy in two-particle system while in the Kuhn-London theory the same distribution was evaluated by the statistical method. In both cases, there is an infinite probability of two particles being separated out of the force range. No wonder that the both method give the infinite intensity at the line center.

Finally the criteria (5.16) and (5.18) are examined for a inverse power potential. If the adiabatic potential can be written as

$$V_i=C/r^d$$

$$\varDelta V=\varDelta C/r^d$$

the criterion (5.16) for validity of the statistical approximation becomes

$$\hbar ur^{d-1}/|\varDelta C|\ll 1\,. \tag{7.4}$$

This holds for small r if $d>1$, namely, when the density ρ is large, as the average distance between two particles is smaller for larger ρ. However for large ρ, the left hand of Eq. (5.18) becomes large and the importance of higher order collisions increases. If we put

$$\rho\sim r^{-3}\,,$$

Eqs. (7.4) and (5.18) can be written as

$$(\hbar u/|\varDelta C|)^{3/(d-1)}\ll\rho\,, \tag{7.5}$$

$$(\beta b|C|)^{-3/(d+2)}\ll\rho\,. \tag{7.6}$$

In a case for which Eq. (7.5) holds but Eq. (7.6) does not, the statistical approximation is valid but the higher order collisions have to be taken into account.

Acknowledgements

The author would like to express her sincere thanks to Professor R. Kubo for his continuous interest and enlightening discussions. The author is greatful to Professor N. Hashitsume for his encouragement and to Professor Tomita for his discussions.

Appendix

In this appendix, the inverse relation of (4.24) is derived in terms of the irreducible integral $B_{j_1j_2}$.

(1) First we assume that $\Gamma_{k_1k_2}$ has the form of Eq. (5.10), that is, $\Gamma_{k_1k_2}$ is the integral of a sum of products of f and g functions, where the sum goes over all products for which k_1+k_2 particles are connected into one cluster by f's and g's. If a cluster is reducible, the product for this cluster splits into a product of ordinary irreducible integrals $B_{j_1j_2}$'s and a special irreducible integral $\gamma^*_{\nu_1\nu_2}$ which depends on τ. Our first problem is to find how many times a given product of $B_{j_1j_2}$'s and $\gamma^*_{\nu_1\nu_2}$ occurs in the integrand of $\Gamma_{k_1k_2}$. We thus have equations which represent $\Gamma_{k_1k_2}$ of Eq. (5.10) in terms of B and γ.

(2) Next problem is to insert the relations obtained above into the double sum $\sum\limits_{k_1+k_2\geq 1}\Gamma_{k_1k_2}z_1^{k_1}z_2^{k_2}$ and to show that this is equal to $\sum\limits_{\nu_1+\nu_2\geq 1}\gamma^*_{\nu_1\nu_2}\rho_1^{\nu_1}\rho_2^{\nu_2}$. According to the definition of $\gamma_{\nu_1\nu_2}$ of Eq. (4.23), $\gamma^*_{\nu_1\nu_2}$ is equal to $\gamma_{\nu_1\nu_2}$. Thus we can see that: (a) In the statistical theory, $\gamma_{\nu_1\nu_2}$ is a sum of products of f's and g's for irreducible clusters comprising of the 0-th point and $\nu_1+\nu_2$ field points, and (b) the expressions of $\Gamma_{k_1k_2}$ obtained in (1) are the inverse relations of Eq. (4.42) for general $\gamma_{\nu_1\nu_2}$.

For the first problem we do not count the number of a given type of product in $\Gamma_{k_2k_2}$ directly, but we make use of Eqs. (3.12)–(3.14) which give the relation between cluster integral b and irreducible integrals B. If we regard $\gamma^*_{\nu_1\nu_2}$ as one special type of $B_{j_1j_2}$, these equations can be readily used to represent the cluster integral $\Gamma_{k_1k_2}$ in terms of $B_{j_1j_2}$'s and $\gamma^*_{\nu_1\nu_2}$.

Irreducible integrals which appear in Eq. (3.12) are grouped into two classes, one of which is multiplied by a factor Nk with suffix 1, and the other with suffix 2. When ν_1 is positive, we classify $\Gamma_{k_1k_2}$ to the first class, and $\sum j_2n_{1j}$ in Eq. (3.12) (we replace k in Eq. (3.12)–(3.14) by j) becomes $\sum j_2n_{1j}+\nu_2$. We denote the resultant sum for positive ν_1 by $(\Gamma_{k_1k_2})_{\mathrm{I}}$ which is expressed as follows:

$$\begin{aligned}&(v_1/\zeta_1)^{k_1}(v_2/\zeta_2)^{k_2}k_1^2k_2(\Gamma_{k_1k_2})_{\mathrm{I}}\\&\quad=\sum\Big(\sum_j j_2n_{1j}+\nu_2\Big)k_1\nu_1\gamma_{\nu_1\nu_2}\prod(k_1j_1B_j)^{n_{1j}}(k_2j_2B_j)^{n_{2j}}/n_{1j}!\,n_{2j}!\end{aligned}\tag{A. 1}$$

for $k_1>0$ and $k_2>0$. The summation is to be carried out under the condition,

$$\sum_j(j_i-\delta_{i1})n_{1j}+\sum_j(j_i-\delta_{i2})=k_i-\nu_i\,,$$
$$i=1,2\,,\quad \nu_1>0\,,\quad \nu_2\geq 0\,,\quad j_1+j_2\geq 2\,.$$

The rest of $\Gamma_{k_1k_2}$, for which $\nu=0$, is denoted by $(\Gamma_{k_1k_2})_{\mathrm{II}}$. In this case, we classify $\gamma_{0\nu_2}$ to the second class and interchange the first and the second classes. The result is

$$\begin{aligned}&(v_1/\zeta_1)^{k_1}(v_2/\zeta_2)^{k_2}k_1k_2^2(\Gamma_{k_1k_2})_{\mathrm{II}}\\&\quad=\sum\Big(\sum j_1n_{2j}+\nu_1\Big)k_2\nu_2\gamma_{0\nu_2}\prod(k_1j_1B_j)^{n_{1j}}(k_2j_2B_j)^{n_{2j}}/n_{1j}!\,n_{2j}!\end{aligned}\tag{A. 2}$$

and the summation being subject to the condition

$$\sum(j_1-1)n_{1j}+\sum j_1n_{2j}=k_1\,,$$
$$\sum j_2n_{1j}+\sum(j_2-1)n_{2j}=k_2-\nu_2\,,\qquad \nu_2>0\,,\quad j_1+j_2\geq 2\,.$$

For $k_1>0$ and $k_2=0$, we obtain from (3.13),

$$k_1(v_1/\zeta_1)^{k_1}\Gamma_{k_1 0}=\sum \nu_1\gamma_{\nu_1 0}\,\Pi\,(k_1 jB_{j0})^{n_j}/n_j\ , \tag{A. 3}$$

with conditions for summation,

$$\sum (j-1)n_j=k_1-\nu_1\ , \qquad \nu_1>0\ , \quad j\geq 2\ ,$$

and for $k_1=0$ and $k_2>0$, from (3.14),

$$k_2(v_2/\zeta_2)^{k_2}\Gamma_{0k_2}=\sum \nu_2\gamma_{0\nu_2}\,\Pi\,(k_2 jB_{0j})^{n_j}/n_j!\ , \tag{A. 4}$$

with conditions

$$\sum (j-1)n_j=k_2-\nu_2\ , \qquad \nu_2>0\ , \quad j\geq 2\ .$$

(A. 1) to (A. 4) are the answer to the first problem.

For the second problem, we introduce a function

$$G(w, B)=\sum B_j w_1^{j_1} w_2^{j_2}\ , \tag{A. 5}$$

and its derivatives

$$G_i=\partial G(\mathrm{w}, B)/\partial w_i\ , \qquad G_{ij}=\partial^2 G(w, B)/\partial w_1\partial w_2\ . \tag{A. 6}$$

Then we can write $\Gamma_{k_1k_2}$ in integral representation. Noting that

$$\sum j_2 n_{1j}+\nu_2=k_2-\sum (j_2-1)n_{2j}\ ,$$

we obtan

$$\begin{aligned}&(v_1/\zeta_1)^{k_1}(v_2/\zeta_2)^{k_2}k_1(\Gamma_{k1k2})_{\mathrm{I}}\\ &=\sum_{\nu_1-1}^{k_1}\sum_{\nu_2=0}^{k_2}\nu_1\gamma_{\nu_1\nu_2}(2\pi i)^{-2}\oint\oint\frac{(1-w_2G_{22})\exp(k_1G_1)}{w_1^{k_1-\nu_1+1}w_2^{k_2-\nu_2+1}}\exp(k_2G_2)dw_1dw_2\ ,\end{aligned} \tag{A. 7}$$

where the contour of integration is taken within the domain of regularity of the integraned so as to enclose the origin $w_1=w_2=0$.

Let us consider a double infinite series

$$S_1=\sum_{k_1=1}^{\infty}\sum_{k_2=1}^{\infty}k_1(\Gamma_{k_1k_2})_{\mathrm{I}}z_1^{k_1}z_2^{k_2}\ . \tag{A. 8}$$

If z_1 and z_2 are sufficiently small so that the summation converges everywhere on the contour of the integration of (A. 7), we can insert the integral representation of Γ into (A. 8) and interchange the order of summation and integration. It can be transformed into the following form;

$$\begin{aligned}S_1=&\sum_{\nu_1=1}^{\infty}\sum_{\nu_2=0}^{\infty}\nu_1\gamma_{\nu_1\nu_2}\frac{1}{(2\pi i)^2}\oint\oint\frac{(1-w_2G_{22})(\lambda_1\,\mathrm{e}^{G_1})^{\nu_1}(\lambda_2\,\mathrm{e}^{G_2})^{\nu_2}}{(w_1-\lambda_1\,\mathrm{e}^{G_1})(w_2-\lambda_2\,\mathrm{e}^{G_2})}dw_1dw_2\\ &-\sum_{\nu_1=1}^{\infty}\nu_1\gamma_{\nu_1 0}(2\pi i)^{-2}\oint\oint\frac{(1-w_2G_{22})(\lambda_1\,\mathrm{e}^{G_1})^{\nu_1}}{(w_1-\lambda_1\,\mathrm{e}^{G_1})w_2}dw_1dw_2\ ,\end{aligned} \tag{A. 9}$$

where

$$\lambda_1=\zeta_1 z_1/v_1\ , \qquad \lambda_2=\zeta_2 z_2/v_2\ .$$

By a similar procedure, we obtain the following expressions for double infinite series S_2, S_3 and S_4,

$$\begin{aligned}S_2=&\sum_{k_1=1}^{\infty}\sum_{k_2=1}^{\infty}k_2(\Gamma_{k_1k_2})_{\mathrm{II}}z_1^{k_1}z_2^{k_2}\\ =&\sum_{\nu_2=1}^{\infty}\gamma_2\gamma_{0\nu_2}(2\pi i)^{-2}\oint\oint\frac{(1-w_1G_{11})(\lambda_2\,\mathrm{e}^{G_2})^2}{w_2-\lambda_2\,\mathrm{e}^{G_2}}\left(\frac{1}{w_1-\lambda_1\,\mathrm{e}^{G_1}}-\frac{1}{w_1}\right)dw_1dw_2\ ,\end{aligned} \tag{A. 10}$$

$$S_3=\sum_{k_1=1}^{\infty} k_1\Gamma_{k_10}z_1^{k_1}$$

$$=\sum_{\nu_1=1}^{\infty}\nu_1\gamma_{\nu_10}(2\pi i)^{-2}\oint\oint\frac{(\lambda_1\,\mathrm{e}^{G_1})^{\nu_1}}{(w_1-\lambda_1\,\mathrm{e}^{G_1})w_2}dw_1dw_2\ , \qquad (A.\ 11)$$

$$S_4=\sum_{k_2=1}^{\infty} k_2\Gamma_{0k_2}z_2^{k_2}$$

$$=\sum_{\nu_2=1}^{\infty}\nu_2\gamma_{0\nu_2}(2\pi i)^{-2}\oint\oint\frac{(\lambda_2\,\mathrm{e}^{G_2})^{\nu_2}}{w_1(w_2-\lambda_2\,\mathrm{e}^{G_2})}dw_1dw_2\ . \qquad (A.\ 12)$$

By adding (A. 9) and (A. 11),

$$S_1+S_3=\sum_{\nu_1=1}^{\infty}\sum_{\nu_2=0}^{\infty}\nu_1\gamma_{\nu_1\nu_2}(2\pi i)^{-2}\oint\oint(1-w_2G_{22})(\lambda_1\,\mathrm{e}^{G_1})^{\nu_1}(\lambda_2\,\mathrm{e}^{G_2})^{\nu_2}$$

$$\times(w_1-\lambda_1\,\mathrm{e}^{G_1})^{-1}(w_2-\lambda_2\,\mathrm{e}^{G_2})^{-1}dw_1dw_2\ . \qquad (A.\ 13)$$

By Cauchy's integral formula, this integral is a residue at a pole, whose position (w_1, w_2) is determined by

$$w_1=\lambda_1\exp G_1(w, B)\ , \qquad w_2=\lambda_2\exp G_2(w, B)\ .$$

These are the same equations as (3.10) and (3.11) which give the relation between fugacity z and number density ρ, therefore at this pole we can replace w_1 and w_2 by ρ_1 and ρ_2. Then Eq. (A. 13) becomes

$$S_1+S_3=\sum_{\nu_1=1}^{\infty}\sum_{\nu_2=0}^{\infty}\nu_1\gamma_{\nu_1\nu_2}(1-\rho_2G_{22}(\rho, B))\rho_1^{\nu_1}\rho_2^{\nu_2}/D(\rho)\ ,$$

where

$$D(\rho)=(1-\rho_1G_{11}(\rho, B))(1-\rho_2G_{22}(\rho, B))-\rho_1\rho_2(G_{12}(\rho, B))^2\ .$$

In the same way, we obtain

$$S_2+S_4=\sum_{\nu_2=1}^{\infty}\nu_2\gamma_{0\nu_2}(1-\rho_1G_{11}(\rho, B))\rho_2^{\nu_2}/D(\rho)\ . \qquad (A.\ 15)$$

The double sum

$$T_1=\sum_{k_1=1}^{\infty}\sum_{k_2=1}^{\infty}(\Gamma_{k_1k_2})_{\mathrm{I}}z_1^{k_1}z_2^{k_2}+\sum_{k_1=1}^{\infty}\Gamma_{k_10}z_1^{k_1}$$

can be evaluated by integrating (A. 14) over $z_1=0$ to z_1 keeping z_2 equal to a certain constant, that is,

$$T_1=\int_0^{z_1}dz_1(S_1+S_3)/z_1\ , \qquad (z_2=\text{const.})\ . \qquad (A.\ 16)$$

If we put $z_2=$const. in Eqs. (3.10) and (3.11), we get

$$dz_1/z_1=d\rho_1D(\rho)/\rho_1(1-\rho_2G_{22})\ . \qquad (A.\ 17)$$

By inserting (A. 14) and (A. 17) into (A. 16),

$$T_1=\sum_{\nu_1=1}^{\infty}\sum_{\nu_2=0}^{\infty}\gamma_{\nu_1\nu_2}\rho_1^{\nu_1}\rho_2^{\nu_2}\ . \qquad (A.\ 18)$$

In the same way, the second double sum T_2 is defined by

$$T_2=\sum_{k_1=1}^{\infty}\sum_{k_2=1}^{\infty}(\Gamma_{k_1k_2})_{\mathrm{II}}z_1^{k_1}z_2^{k_2}+\sum_{k_2=1}^{\infty}\Gamma_{0k_2}{}^{k_2}\ ,$$

and is written as

$$T_2=\int_0^{z_2} dz_2(S_2+S_4)/z_2\,, \qquad (z_1=\text{const.})$$
$$=\sum_{\nu_2=1}^{\infty}\gamma_{0\nu_2}\rho_2^{\nu_2}\,, \tag{A. 19}$$

where we used the relation

$$dz_2/z_2=d\rho_2 D(\rho)/\rho_2(1-\rho_1 G_{11})\,, \qquad (z_1=\text{const.})\,.$$

Finally we obtain from Eqs. (A. 18) and (A. 19),

$$T_1+T_2=\sum_{k_1+k_2\geq 1}\Gamma_{k_1k_2}z_1^{k_1}z_2^{k_2}$$
$$=\sum_{\nu_1+\nu_2\geq 1}\gamma_{\nu_1\nu_2}\rho_1^{\nu_1}\rho_2^{\nu_2}$$

This is the answer to the second problem.

References

1) P. W. Anderson: Phys. Rev. **86** (1952) 809.
2) P. W. Anderson and J. D. Talman: Bell Telephone Laboratories, Murray Hill, New Jersey (1956).
3) S. Ch'en and M. Takeo: Rev. Mod. Phys. **29** (1957) 20.
4) Robin, Bergeon, Galatry and Vodar: Discussions Faraday Soc. No. 22 (1956) 30. L. Klein and H. Margenau: J. Chem. Phys. **30** (1959) 1956.
5) K. Kubo: J. Phys. Soc. Japan **12** (1957) 570.
6) W. Heitler: *The quantum Theory of Radiation* (Oxford University Press, New York 1944).
7) H. D. Ursell: Proc. Cambridge Phil. Soc. **23** (1927) 685.
8) J. E. and M. G. Mayer: Statistical Mechanics (John Wiley and Sons, Inc., New York 1940).
9) B. Kahn and G. E. Uhlenbeck: Physica **5** (1938) 391.
10) T. D. Lee and C. N. Yang: Phys. Rev. **113** (1959) 1165.
11) E. W. Montroll and J. C. Ward: Phys. Fluids **1** (1958) 55.
12) Shafroth, Butler and Blatt: Helv. Phys. Acta **30** (1957) 93.
13) T. Yokota: J. Phys. Soc. Japan **15** (1960) 779.
14) R. Kubo: (unpublished).
15) E. Meeron: J. Chem. Phys. **27** (1957) 1238.
16) J. E. Mayer: J. Phys. Chem. **43** (1939) 71.
17) E. W. Montroll and J. C. Ward: Physica **25** (1959) 423.
18) R. Kubo and K. Tomita: J. Phys. Soc. Japan **9** (1954) 888.
19) R. G. Breene, Jr.: Rev. Mod. Phys. **29** (1957) 94.
20) A. C. Kolb: Thesis, University of Michigan, 1957. See H. Margenau and M. Lewis: Rev. Mod. Phys. **31** (1959) 569.
21) H. Margenau: Phys. Rev. **82** (1951) 156.
22) M. Lewis: Phys. Rev. **121** (1961) 501.
23) A. Jablonski: Phys. Rev. **68** (1945) 78.
24) H. Kuhn and F. London: Phil. Mag. **18** (1933) 983.

JOURNAL OF THE PHYSICAL SOCIETY OF JAPAN, Vol. 16, No. 12, DECEMBER, 1961

Pressure Effect of Cavitation on Photographic Emulsion*

By Syozo TOTANI

Physical Laboratory, Nagoya City University,
Nagoya, Japan

(Received August 28, 1961)

The nature of the dislocations in photographic emulsion grains is discussed with regard to the tilt boundaries which were generated by the pressure gradient produced by the contraction of cavitation in ultrasonic field. On the mechanism of the latent fog formation by the pressure effect, some remarks are given on the standpoint of the Mitchell theory of development.

§ 1. Introduction

It is known that when the pressure is given on a photographic emulsion grain with complete absence of light, there is found the blackening of the grain by development.[1), 2)] Many experimenters[3), 4)] have reported on the photographic effect produced by high intensity ultrasonic waves in liquids and opinions have been made concerning the origin of the phenomenon. But there is no complete agreement.

From the observation of traces of cavitations moved on the surface of the photographic plate which was dipped in the developer of ultrasonic field, it was speculated that the photographic pressure effect must be concerned with plastic deformation of emulsion grains caused by the pressure gradient generated in the neighbourhood of the cavity.

On the mechanism of latent fog formation by the plastic deformation of the grain, the dislocations of the silver bromide crystals revealed by physical development after exposure, were observed by an electron microscope.

The purpose of this article is to report on the feature of dislocations observed in the micro silver bromide crystals of the practical photographic emulsion grains which received plastic deformation as well as on the mechanism of formation of latent fog specks by pressure.

§ 2. The Blackening by Cavitation

In order to investigate the photographic pressure effect of cavitation, a photographic plate "Process" was dipped vertically in developer (SDP-1) which was contained in cylindrical transducer of barium titanate (508 kc). After the irradiation of ultrasound (1 min), the plate was fixed and then the black spot generated on the plate was observed under an optical microscope. Photo. 1. is the photograph thus obtained. From the photograph the following observations were made.

(a) The black spot has a tail of double consecutive lines which are almost parallel to the resultant direction of the vibration of ultrasound and buoyancy.

(b) The gap between the double lines is 10–20μ and in the domain between them there has never been found any blackening.

(c) The projected length of the double lines to the direction of the propagation of the ultrasonic wave is always shorter than the distance between loop and node of the standing wave.

L. Rayleigh[5)] calculated the pressure developed by the collapse of spherical bubble, neglecting compressibility and viscosity of liquid. From the same consideration, Fig. 1. was obtained as the distribution of pressure around the cavity during its contractions when it is repeating contraction and expansion according to the frequency of vibratian without collapse[6)]. It shows that the pressure gradient is maximum in the distance of 5–10μ from the center of the cavity and the pressure changes in the range 1 atm. to 23 atm..

When the cavity which was generated on the photographic plate moves on the surface of the emulsion grains, the pressure must be given to the emulsion, and the direction of the motion must be the one which is the resultant of buoyancy and the vibration.

The pressure gradient which would be given to the emulsion would always be the same sign of direction on the enevlope of the traces of the motion of the cavity, while the sign of the direction of the pressure gradient would change in the region between the lines of envelope when the cavity passes the region. If the gelatin is already softened in water or in developer, the pressure can develop into the interior of the film. Each emulsion grain in the film which happened to be on the lines of envelope of the trace must always receive the pressure gradient of the same direction when the cavity passes the crystal. So the pressure gradient would give a bending moment, the axis of which would be perpendicular to the surface of the crystal. Moreover, if the sign of the pressure gradient is always the same on a crystal, the periodic change of the pressure would easily give the bending deformation to the crystal.

---

* A part of the following results have been outlined at the International Colloquium of Scientific Photography held at Liège on September 14–19, 1959.

On the other hand, the crystals which were located between the lines of envelope of traces would receive different signs of pressure gradient. So the crystal would be difficult to be deformed because of the change of direction of bending moment as the cavity moves on the crystal.

That is the reason why there is found no blackening between the double lines. If any thermal effect of pressure or effect of light which might be emitted on the cavitation is concerned at all, the blackening between the double lines must be observed.

From the above consideration it is natural to speculate that the double lines of the black spot of Photo. 1. are the traces of cavity on the photographic emulsions and the blackening is the result of the latent fog specks produced by the bending deformation of the emulsion crystals owing to the pressure gradient of the surrounding medium of the cavity.

§ 3. Tilt Boundaries in Silver Bromide Crystal

The silver bromide crystals contained in photographic emulsion are ranged in magnitude of 1–10μ and their shapes are apt to be a tabular triangle or hexagon covered with {111} planes. In a crystal with face-centered cubic lattice, with no permitted stacking faults such as silver bromide, the elementary dislocations have Burgers vector along <110>.[7] As a reason that in rock salt type such as silver bromide the slip direction is not along <100> where the atoms are most closely packed, but along <110>, the greatness of Peierls' force arising from anion closed shell repulsion in ionic crystal is reported.[8],[9]

Owing to the smallness of the ion radius of Ag Br (1.26 Å) compared to that of (1.95 Å), the silver ion is apt to change its position into interstitial when the pressure is given to the crystal. So it is considered that the repelling force between bromine ion cores would be most effective. In this connection it should be mentioned that the slip direction in silver bromide crystal easily tends to <110> along which bromine ions are most packed. The Peierls' force σ of silver bromide is calculated from the formula,[9]

$$\sigma=\frac{2\mu}{1-\nu}\exp\left\{-\frac{2\pi a}{b(1-\nu)}\right\} \qquad (1)$$

in which μ, ν, a, b, denote rigidity modulus (0.073×10^{12} dyn/cm^2), Poisson's ratio (0.37), interval of slip atomic planes and the Burgers vector respectively. If we regard only bromine ions, a must be equal to b, and thus as the critical shear stress to move the dislocation we can estimate about 10 atm..

From Fig. 1. it is found that the pressure

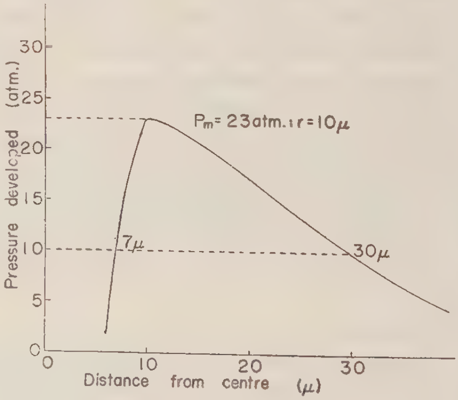

Fig. 1. Pressure p developed in water by contraction of cavity from radius R_0 to R (denoting $z=R^3{}_0/R^3$) is plotted against the distance r from the cntre of cavity by equation $\frac{p-P}{p-Q}=\frac{R}{3r}(z-4)-\frac{R^4}{3r^4}(z-1)$ under the condition that P (the hydrostatic pressure at infinity) is 5 atm., Q (the internal pressure of cavity) is 1 atm. and z is equal to 33. The range of distance r, where the pressure is over 10 atm., is from 7μ to 30μ. The maximum pressure is 23 atm. at the distance $r=10\mu$.

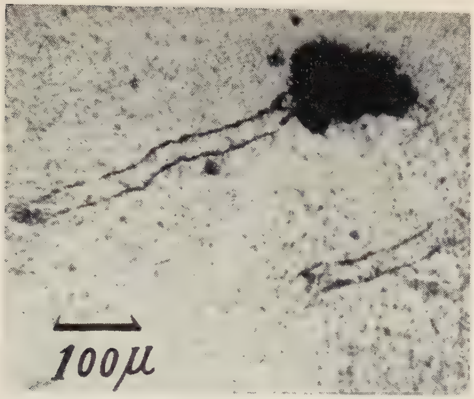

Photo. 1. Photomicrograph of the black spots obtained on the photographic "Process" plate which was irradiated by ultrasonics (508 kc, Cylindrical $BaTiO_3$ Transducer, 1.2 W/cm², 1 min.) in the developer (SDP−1). The consecutive lines represent the traces of cavitation moved on the surface of photographic emulsion of single grain layer.

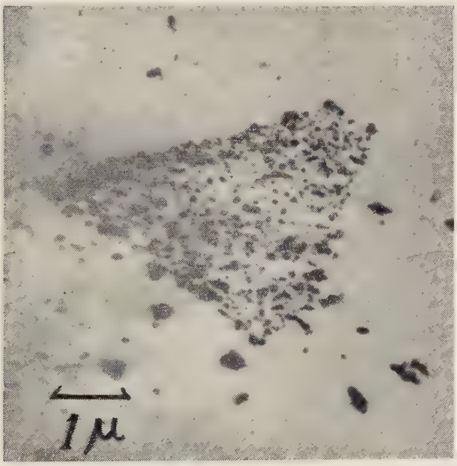

(a)

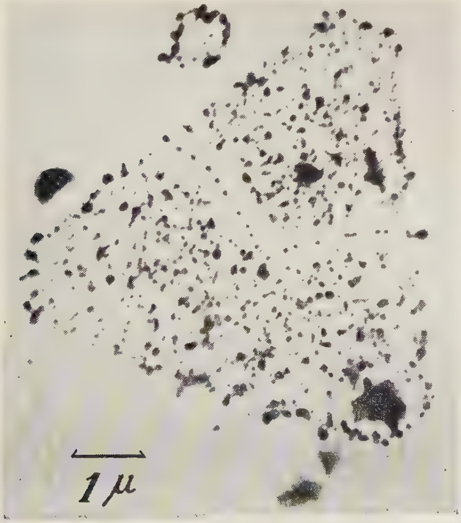

(b)

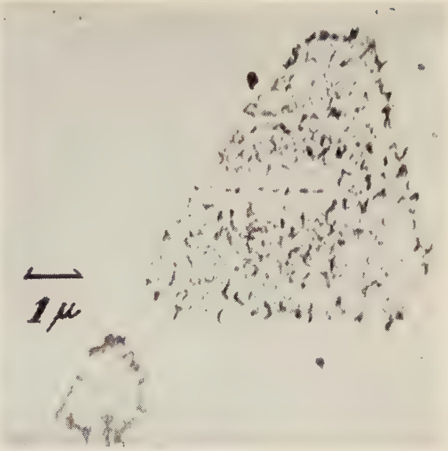

(c)

Photo. 2. Electron micrographs of the tilt boundaries in a silver bromide crystal which was exposed to light after irradiation by the same ultrasonics with Photo. 1., but in water and treated with physical development:
(a) in the directions of ⟨112⟩,
(b) in the directions of ⟨112⟩, but curved owing to the migration,
(c) in the direction of ⟨110⟩.

distribution in the surrounding vicinity of the contracting cavity without collapse is in the order of 10–20 atm.. So it is considered that the plastic deformation of the silver bromide micro crystal of the photographic emulsion is produced when the crystal is located in the region of the above order of pressure which is generated periodically as the cavity contracts. When a torque is exerted by the pressure gradient the plastic deformation will tend to have tilt boundaries.

Frank's equilibrium condition[7] of dislocation net is given by

$$\boldsymbol{d}=\boldsymbol{r}\times\boldsymbol{I}\;2\sin\frac{1}{2}\alpha, \tag{2}$$

where the vector $\boldsymbol{r}$ represents the straight line connecting any two points a sufficient distance apart in the surface which contains the net; $\boldsymbol{d}$ is the sum of the Burgers vectors of all the dislocation lines crossed by any line in that surface which connects the two points; and the difference in orientation of the crystal regions on either side of the net (which are free from strain except in its immediate proximity) corresponds to a rotation by an α about an axis represented by the unit vector

I.

From (2) there could be produced the following two kinds (A), (B) of tilt boundary on the surface of {111} of silver bromide crystal.[7),11),12),13)]

(A) If the dislocation net plane becomes perpendicular to the (111) plane rotating around the axis [112] the dislocation lines which have [110] as direction of Burgers vector, arrange in the plane (110) normal to the surface of the crystal (111), and the ends of edge dislocation lines arrange in a line [112].

(B) When the dislocation net plane becomes perpendicular to the (111) plane rotating around the axis [110], there would be generated a tilt boundary of the dislocation lines which have [112] as Burgers vector. Fig. 2. shows these tilt boundaries appearing on the surface of {111} of silver bromide crystal. In a tilt boundary the elastic strained region along the dislocation wall extends only in the order of interval of dislocations.[14)]

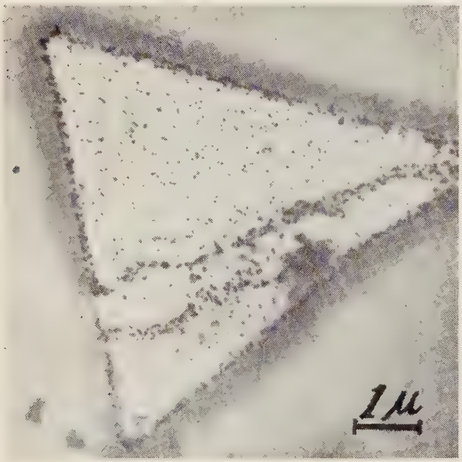

(a)

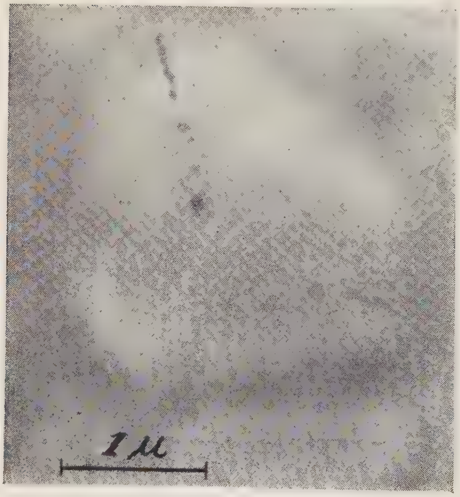

(b)

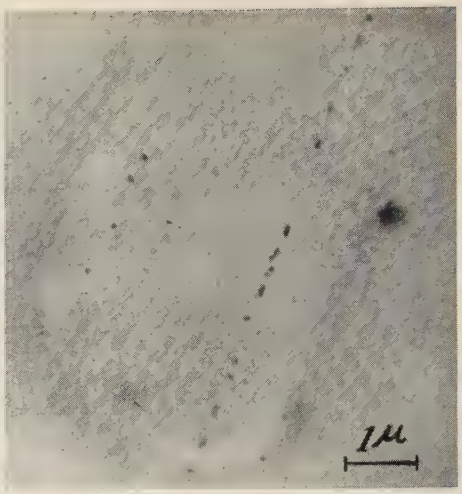

(c)

Photo. 3. Electron micrographs of the tilt boundaries in a silver bromide crystal which was exposed to light after the plastic deformation was given by dropping a steel ball, and treated with physical development:

(a) in the direction of ⟨112⟩, but displaced owing to the migration,

(b) treated internally with physical development, reveals the edge dislocation wall of ⟨112⟩,

(c) treated similarly to (b), reveals the edge dislocation wall of ⟨110⟩.

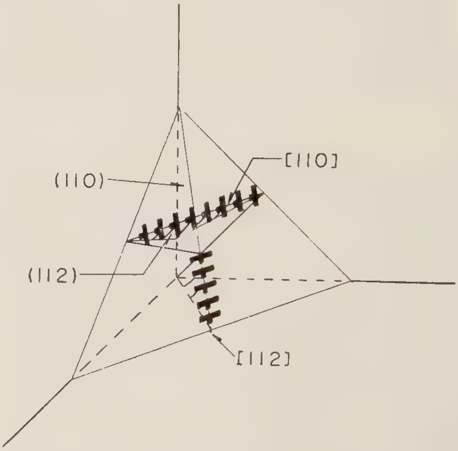

Fig. 2. The tilt boundaries appearing on the surface of {111} of silver bromide crystal.

§ 4. Electron Micrographic Observation

The distributions of latent image in plastically deformed photographic emulsion grains were observed as follows.

The photographic emulsion grains of pure silver bromide with active gelatin were coated in a single grain layer on a triacetate film base. After the treatments described below (I), (II), (III), the base was removed in a solvent, methylene chloride, and the gelatin layer was mounted on the seat mesh and the grain-shaped thin part in the gelatin layer decorated with silver specks was observed under an electron microscope.

(I) The film base covered with the photographic emulsion grains was dipped in water which was contained in cylindrical transducer of barium titanate (508 kc, 1.2 W/cm^2). After the irradiation of ultrasound, the film with grains was exposed to light and physically developed and then fixed.

(II) The impulsive force was given to the film base by dropping a steel ball. Then after exposure to light it was treated with physica developer and fixed.

(III) The impulsive force was given to the film base similarly to (II). But after exposure to light, it was bleached with potassium dichromate before the physical development in order to develop internally.

Photo. 2 (a), (b), (c) are the electron micrographs obtained by the treatment (I). Photo. 3 (a) and (b), (c) are the electron micrographs obtained by the treatment (II) and (III) respectively. Photo. 2 (a), (b) and Photo. 3 (a), (b) indicate tilt boundaries in <112>, while Photo. 2 (c) and Photo. 3 (c) represent these boundaries in <110>. The curvature and displacement of the lines of silver specks in Photo. 2 (b) and Photo. 3 (a) show the migration of the tilt boundaries. In Photo. 2 (a), (b), (c) and Photo. 3 (a) the intervals of silver specks in a row which indicates the ends of edge dislocation lines in a tilt boundary are the order of $1/8\mu$, almost half of the width of the band where no silver particle is found. This shows that the strained region of the boundary extends in the order of interval of dislocations. This fact more confirms that the boundary is a tilt boundary from the feature described in § 3.

If the crystal receives plastic deformation by the bending moment owing to the pressure gradient, the dislocation lines would move to build up a dislocation wall constructing a tilt boundary, and the impurities or interstitial silver ions which are contained in the strained region would segregate to the dislocation wall where the lattice is expanded.

From the equation (2) the tilted angle α between the adjacent parts of the crystal is given by

$$\alpha=2\sin^{-1}(b/2h). \qquad (3)$$

In silver bromide crystals, for slip in {110} the Burgers vector is given by $b=a/\sqrt{2}$ (a=5.77 Å), and assuming that $h=1/8\mu$, we obtain from (3) that the α is 1° approximately. This coincides with the value observed in a large single crystal by Hedges and Mitchell.$^{7)}$ Similarly to the results of J. F. Hamilton et al.$^{15)}$ obtained by etching studies on photographic grains, it was shown that when the grains are subject to a bending deformation, the tilt boundaries are increased.

When the grains contain impurities such as iodide or sulphur atoms as in the case of the grains of commercial photographic emulsions, the substructures must be enhanced$^{16)}$ and the sensitivity depends much upon the nature of the internal surfaces of the boundaries.$^{17)}$ If the grain has a tilt boundary already at the crystal growth, the migration of it will be produced by a bending deformation.$^{18), 19)}$ The migration of a tilt boundary will promote the precipitation of interstitial silver ions.

§ 5. Latent Fog Formation

There are many evidences$^{2), 3), 4), 18)}$ that when dynamic pressure such as produced by ultrasonics or by falling steel ball is given to the photographic emulsion grains, the latent fog specks are formed.

On the mechanism of the latent fog formation by pressure the following experimental results should be summarized.

(1) The blackening by cavitation in developer is obtained always after the gelatin which contains emulsion grains has been softened by the developer. This indicates that the pressure generated by the contraction of cavitation should be given to the grains hydrostatically.

(2) The blackening is observed only on the envelopes of the cavity which moves on the emulsions coated in a single grain layer.

This means that the microcrystals which happen to be situated on the envelopes and receive pressure gradient periodically in the same direction as the cavity moves are blackened.

(3) The pressure generated in the neighbourhood of contracting cavity has the magnitude of the order which is sufficient to produce critical shear stress to move the dislocation in silver bromide crystal.

(4) The electron micrographic observation of photographic emulsion grains which received pressure gradient periodically or impulsively shows that there are often found tilt boundaries.

(5) The photographic emulsion grain which is irradiated with ultrasound in water shows remarkably reduced blackening after development compared to the blackening obtained in developer.

(6) It is known that the pressure effect on a photographic emulsion grain can be revealed by different treatments for development.[2)] The revelation depend upon the fact that when the pressure is applied to the emulsion grains, the pressure track is blackened by normal development and when there is an exposure to light after the pressure, the track becomes of low density by surface development and of high density by internal development. The pressure effect of the ultrasound was comfirmed by the method described above.[19)]

(7) It is also known that the chemically active species (OH, O, H, H_2O_2, etc.) are produced by the cavitation in water.[19),20)]

Considering the above experimental results and investigations one would expect the following phenomena are concerned on the mechanism of latent fog formation.

(A) When the photographic emulsion grain receives a deformation by pressure of cavitation, tilt boundaries are produced. If the grain had the tilt boundaries already at the crystal growth, the migration of them would occur owing to the fact that the necessary shearing stress for the migration is equal order of magnitude to that of the Peierls' force.[21)]

(B) In an ionic crystal of the silver bromide type, the edge dislocation is formed by the insertion of two extra half-planes.[22)] Beyond the edges of these half-planes there is an expansion of the lattice. The stress in that region is relieved by the displacement of interstitial silver ions or vacancies, both of which have a positive volume change associated with them. This leads to a lower activation energy for the segregation of the interstitial silver ions. W.G. Johnston[22)] indicated experimentally that the activation energy for ionic conductivity in the disordered regions of silver bromide is less than 0.198 eV in place of 0.789 eV for that of the intrinsic conductivity. If the tilt boundary migrates or receives the periodic pressure of cavitation, the precipitation of the interstitial silver ions at the edge dislocation wall will be much promoted. It is clear that inspite of the higher mobility for interstitial silver ions in the direction of the dislocation line, the coalescence of the silver ions would be fairly prohibited owing to the positive charge of them.

(C) As to the electronic conductivity, conduction along the dislocation line would also be easier than perpendicular to it owing to the scattering due to the cylindrical space charge which would affect the flow of electrons along the dislocation much less than the normal flow. If there were any reducing substances in adjacent to the ends of the edge dislocation lines at the surface of the crystal, they would transfer electrons along the dislocation lines to the segregated silver ions. By the neutralization of the positive charges of the silver ions the coalescence of them will be accelerated. Then a group of four silver atoms or more will be formed at the end of edge dislocation in the space generated by the escape of the bromine ions.

(D) According to the Mitchell theory of development,[23)] the stable latent image speck of minimum size consists of a four silver atoms. So it is considered that the developable specks of silver atoms would be formed without photoelectron, if there were any substances which can transfer electrons. As to the photographic effects of ultrasonics in water, the generation of active substances by the cavitation has important meanings not only because of the supply of electrons, but also higher concentration of the substances near the cavity which gives the deformation to the crystal. In developer, owing to the great abundance of the reducing molecules, electrons will be easily supplied and still more the ordinary development is continuously followed after the formation of developable specks are attained. That is a reason why the blackening is remarkable in developer, compared to that in water.

(E) Electrostatic neutrality is maintained by the passage of bromine ions into the solution or into the gelatin.

§ 6. Conclusion

The latent fog specks are developable specks formed without photon. On the formation of the latent fog specks, there would be many causes according to the circumstances of the treatment of the photographic emulsion grains. When the pressure effect of cavitation is concerned at all, the tilt boundaries play important roles for the formation. The aggregation of silver atoms to the developable size is attained without photoelectron in the presence of the materials which can transfer electrons to the silver ions for the cancellation of the positive charge. By the escape of the halide ions, the space necessary for the aggregation of silver atoms of developable speck is built as well as the electrostatic neutrality of the grain is maintained.

Acknowledgement

The author wishes to express his cordial thanks to Prof. Y. Uchida of Kyoto University for his encouragement throughout the present work. He is also greatly indebted to Prof. T. Ohta of Defense Academy for his valuable suggestions and to Mr. Y. Nishina of Konishiroku Photo Ind. Co. for his sincere collaboration in this work.

References

1) P. Faelens: Compt. rend., **236** (1953) 1348.
2) Y. Kobayashi and M. Mafune: Konishiroku Rev., **5** (1954) 106.
3) N. Marinesco and J. J. Trillat: Compt. rend., **196** (1933) 858.
4) N. Marinesco: Compt rend., **202** (1936) 757.
5) L. Rayleigh: Phil. Mag., **34** (1917) 94.
6) S. Totani and Y. Nishina: J. Soc. Photo. Japan, **19** (1956) 171 (in Japanese).
7) F. C. Frank: *Defects in Crystallins Solid* (Phys. Soc., London, 1954) 159.
8) T. Suzuki: Report at the annual Meeting of the Phys. Soc. Japan, Kyoto (1958) B-613.
9) H. B. Huntington and J. E. Dickey: Phys. Rev., **100** (1955) 1117.
10) A. H. Cottrell: *Dislocations and Plastic Flow in Crystal* (Oxford Univ. Press, 1953) 64.
11) B. H. Kear: Phil. Mag., **4** (1959) 665.
12) J. T. Bartlett and J. W. Mitchell: Phil. Mag., **5** (1960) 799.
13) J. T. Bartlett and J. W. Mitchell: Phil. Mag., **6** (1961) 271.
14) A. Ohkawa: Metal Physics (Kinzoku Butsuri), **2** (1956) 51 (in Japanese).
15) J. F. Hamilton, L. E. Brady and F. A. Hamm: J. Appl. Phys., **29** (1958) 800.
16) J. F. C. Boardman, R. H. Herz and G. C. Terry: Nature, **182** (1958) 1726.
17) W. Waidelich: Z. Angew. Phys., **10** (1958) 525.
18) S. Totani and Y. Nishina: *Photographic Sensitivity*, **2** (Maruzen, Tokyo, 1958) 155.
19) S. Totani: Bull. Nagoya City Univ., **1** (1955) 45.
20) A. Weissler: J. Acoust. Soc. Am., **25** (1953) 651.
21) S. Amelinckx and W. Dekeyser: *Solid State Physics*, **8** (Academic Press, New York and London, 1959) 325.
22) W. G. Johnston: Phys. Rev., **98** (1955) 1777.
23) J. W. Mitchell: J. Photo. Sci., **6** (1958) 57.

JOURNAL OF THE PHYSICAL SOCIETY OF JAPAN, Vol. 16, No. 12, DECEMBER, 1961

Influences of Heat-treatment upon Cadmium Sulphide Single Crystals

By Saburo KITAMURA

Central Research Laboratory, Matsushita Electric Industrial Co., Ltd., Osaka

(Received January 23, 1961)

Ionization energies and electron trap depths in cadmium sulphide single crystals heat-treated in vacuum or in oxygen were obtained by measuring the dark conductivity as a function of the temperature and the thermally stimulated current, respectively. It was found that, in the case of crystals heat-treated in vacuum, the ionization energies were 0.04 eV, 0.7 eV, 1.0 eV and 1.4 eV, and the major electron trap depth was 0.50 eV below the conduction band, and the dark conductivities and the concentrations of the electron traps were reduced as the crystals were heat-treated in oxygen. And when the crystals were heat-treated in vacuum or in oxygen, it was found that the sensitivity of photocurrent at about 600 mμ was increased.

§ 1. Introduction

The effects of oxygen upon cadmium sulphide (CdS) single crystals have been investigated recently by some workers by observing photoconductivity, dark conductivity and response time of photocurrent. Muscheid[1)] supposed, by the fact that the dark conductivity of CdS single crystal heat-treated in vacuum decreases by exposing to air at room temperature, that the sulphur vacancies in CdS single crystals are apt to be occupied by oxygen atoms. Seraphin[2)] reported that CdS single crystals heat-treated in vacuum have large rise and decay time of photocurrent, while those heat-treated in oxygen have small rise and decay time, and so he supported the consideration proposed by Muscheid. Also Berger *et al*[3)]., and Liebson[4)] reported that the photocurrent of CdS single crystal decreases with increasing pressure of oxygen. No evidence has been reported such that CdS single crystal contains CdO by heat-treatment in oxygen, but as previously reported by the author,[5)] the CdS sintered films heat-treated in oxygen at 400~650°C contain some CdO and their dark conductivities show minima for the heat-treatment at 500~600°C.

In order to investigate the effects of oxygen, we have measured the dark conductivity, the thermally stimulated current as well as the spectral sensitivity of photocurrent for CdS single crystals non-treated and those heat-treated in vacuum of in oxygen. First, the effects of oxygen at high temperatures were studied by measuring the variation of dark conductivity, and next, trap depths were measured at low temperatures. The purpose of the present paper is to study the influences of heat-treatment and the effects of oxygen upon CdS single crystals at the temperature range from room temperature to 600°C. When CdS single crystal was heat-treated in oxygen above 500°C, some CdO was found on the surface. Therefore it was examined whether the photoconductivity of CdS crystal was affected by the presence of CdO on its surface.

§ 2. Preparation of Specimens

CdS single crystals were obtained by sublimation of CdS powder in a flow of argon gas. The purity of CdS powder which was purified chemically, was found by chemical analysis to be 99.99% or more, and by spectroscopic analysis it was found that there were traces of Mg, Si and Zn. CdS powder of amount of 100 g was put in a quartz boat and inserted into a quartz tube in an electric furnace. In the quartz tube argon gas was flowing through pyrogallol, drying agent and liquid nitrogen. CdS powder was sublimated for 8~20 hours at 1050±5°C and CdS single crystals were grown at a part near the edge of the quartz tube (about 950°C). The average size of the crystals produced was 6×3×0.05 mm, the largest ones reaching a size of 12×10×0.1 mm. The dark conductivities of these crystals were $1\times10^{-10}\ \Omega^{-1}\,\mathrm{cm}^{-1}$ or less, and the spectroscopic analysis revealed no impurity of metal in these crystals. Argon gas mixed with 2% of hydrogen gas was also used as carrier gas. Crystals used in the following experiments were mainly obtained by sublimation in a flow of argon gas.

Electrodes of CdS single crystal were formed by evaporation of indium in vacuum. But when the measurements were performed at high temperatures, gold was used as the electrode material, because indium melted at 154°C. Gold electrodes were formed by evaporation on the surface of the crystal bombarded by electron beam accelerated by D. C. 400 volts.[6,7] The property of contact between indium and CdS crystal was ohmic in all range of applied voltage, but the contact between gold and CdS was non-ohmic below 4 volts and ohmic above 4 volts. *I-V* characteristics of CdS crystals having indium or gold electrodes are shown in Fig. 1.

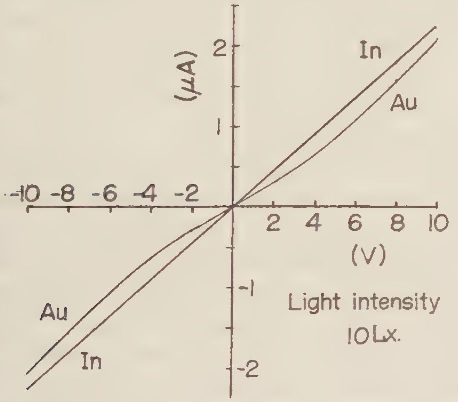

Fig. 1. *I-V* characteristics of CdS crystals with In electrodes or Au electrodes.

§ 3. Experimental Apparatus

The apparatuses used for heat-treatment in vacuum or in oxygen are shown in Fig. 2. The apparatus shown in Fig. 2 (A) was used for heat-treatment of CdS crystals at 400~800°C in vacuum or in oxygen. CdS crystals were heat-treated on a quartz plate placed in a quartz tube on which a platinum wire was wound. The measurement of the dark conductivity of crystals could not be extended to above 300°C because of the influence of visible or infrared radiations from the platinum heater. The apparatus shown in Fig. 2 (B) was used for measuring the dark conductivity of CdS crystals in the range from room temperature to 400°C. A CdS crystal with gold electrodes was placed on the surface of a nickel-electroplated copper block that could be heated by a sheathed heater. Platinum wires were used as the current leads, and the contact between gold electrode and platinum wire was made by silver paste. The apparatus in Fig. 2 (A) can be evacuated to 5×10^{-5} mm Hg at 800°C and the one in Fig. 2 (B) to 1×10^{-5} mm Hg at 400°C.

The dark conductivity as a function of the temperature below room temperature and the thermally stimulated current were measured by an apparatus shown in Fig. 3. A CdS crystal with indium electrodes is set in a copper case which is connected to the bottom of a stainless steel pipe. A 350 watt heater is installed to the bottom of the copper case. This stainless steel pipe is put in a double vacuum flask and the space A of the interior vacuum flask can be evacuated by a vacuum pump. A crystal is radiated with exciting

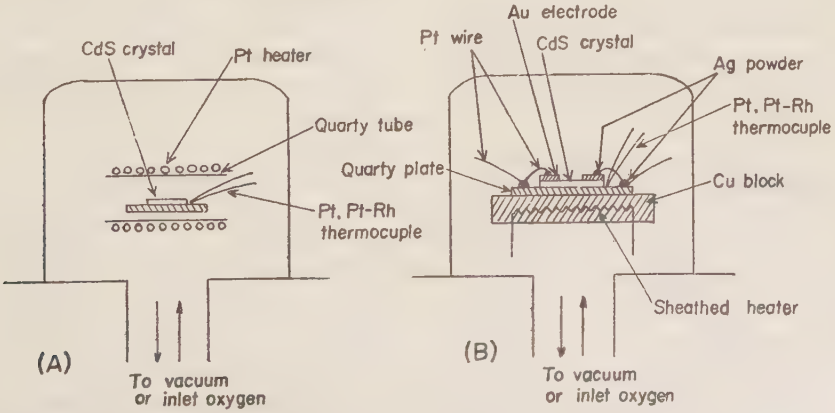

Fig. 2. Schematic diagram of apparatuses used for heat-treatment in vacuum or in oxygen; (A) Used at 400~800°C. (B) Used below 400°C.

light through an optical window at the top of the stainless steel pipe.

In the case of measurement of the dark conductivity as a function of the temperature, the outside vacuum flask is filled with liquid nitrogen, and the CdS crystal is kept at the desired temperature by controlling the pressure in the space A of the interior vacuum flask. In the case of measurement of the thermally stimulated current, the interior vacuum flask is filled with liquid nitrogen and the exterior vacuum flask is emptied. After the stainless steel pipe is pulled out from the vacuum flask, CdS crystal is heated by the heater in the copper case. The dark current and the thermally stimulated current are measured by a vibrating reed electrometer and an X-Y recorder. A block diagram of measuring circuits is shown in Fig. 4.

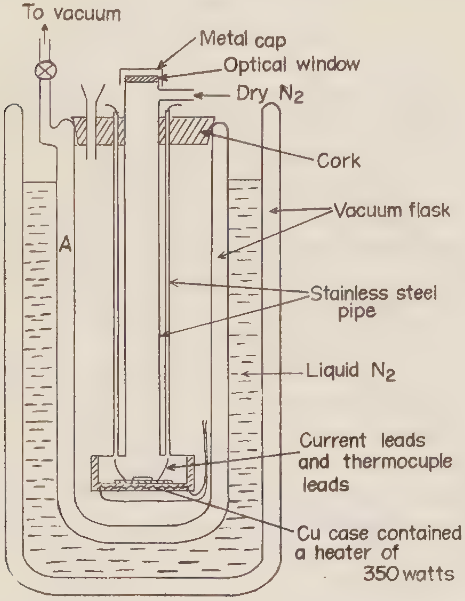

Fig. 3. Schematic diagram of the apparatus for measuring the dark current and the thermally stimulated current in the range of −190~+100°C.

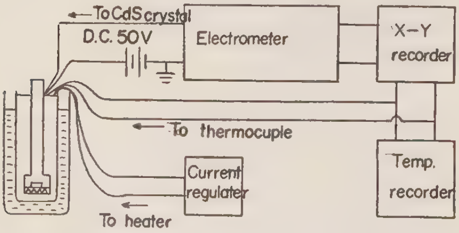

Fig. 4. Block diagram of circuits for measuring the dark current and the thermally stimulated current as a function of temperature.

The spectral sensitivity of photocurrent was measured by a Beckman type spectrophotometer in the range of 400~900 mμ. Light source was a 30 watt incandescent lamp. A specimen was mounted on a fused quartz plate and then this plate was put in a hard glass tube in which nitrogen gas was flowing.

Infrared quenching of photocurrent was measured by using both the bias excitation (from an incandescent lamp passing through a filter: about 540 mμ) and the infrared radiation (from a monochromator) in the range of 700~2000 mμ.

§4. Variations of Dark Conductivity by Heat-treatment

The conductivity of CdS crystal was varied strongly by the influence of air or water vapour.[3] And after having put CdS crystal in darkness, the dacay of photocurrent was kept for several tens of hours. To avoid these effects coming into the results of the measurement, the dark current was measured in the present experiment after the CdS crystal have been heated at 80°C for 30 minutes and kept in darkness for 40 hours in vacuum (7×10^{-6} mm Hg).

4.1 *Heat-treatment in vacuum*

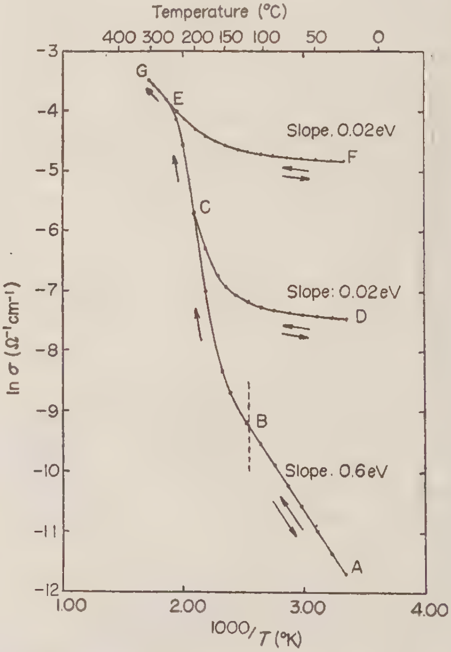

Fig. 5. Variations of the dark conductivity by heat-treatment in vacuum.

The variations of the dark conductivity of CdS crystal with gold electrodes by heat-treatment in vacuum are shown in Fig. 5. The dark conductivity of CdS crystal increases with the rise of temperature as shown in Fig. 5 (A→B→C). The variation of the dark conductivity against the temperature is reversible below 120°C (between A and B), but irreversible above 120°C. When the CdS crystal is heated at 200°C (C) in vacuum and then cooled down to room temperature, the dark conductivity does not return to the initial value but to point D (A→B→C→D in Fig. 5). The dark conductivity of point D is 10^4 times larger than that of point A. When this crystal is heated again in vacuum, the variation of the dark conductivity against the temperature is reversible below 200°C (the range between D and C), and as the temperature is raised to above 200°C the dark conductivity increases along the extraporated initial line A B C. And when the crystal is heated at 250°C (E) in vacuum and then cooled down to room temperature, the dark conductivity varies to point F along the line EF. Further, the dark conductivity is reversible below 250°C (the range between E and F).

4.2 *Heat-treatment in oxygen*

The variations of the dark conductivity of CdS crystal with gold electrodes by heat-treatment in oxygen are shown in Fig. 6; the dark conductivity of a crystal heat-treated in vacuum at 350°C is shown as point A′ at room temperature. When oxygen is introduced into the vacuum chamber at pressure of 200 mm Hg, the dark conductivity of this crystal decreases to point B′. And as the crystal is heated after the chamber is evacuated, the dark conductivity increases to point C′ at 80°C, and then it returns to point A′ at room temperature.

The dark conductivity (A) of the crystal kept at 350°C in vacuum decreases to point C passing through point B as shown in Fig. 6, by introducing oxygen and cooling down to room temperature. And it comes to point D by heating from room temperature to 80°C in vacuum, and it comes to point E by cooling down to room temperature in vacuum. As the crystal is again heated in vacuum, the dark conductivity increases and returns to point A at 350°C.

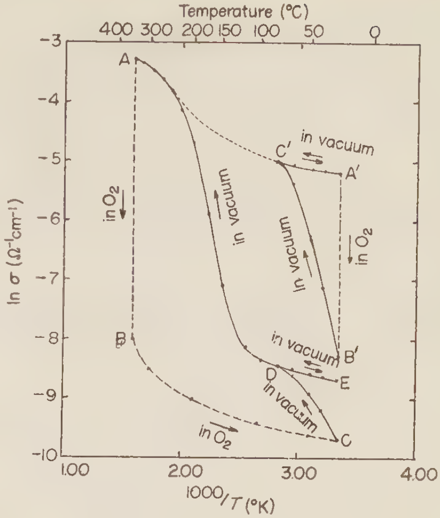

Fig. 6. Variations of the dark conductivity by introduced oxygen at room temperature and at 350°C.

From the fact described above it may be considered that oxygen introduced at room temperature is loosely bound at the surface layer of CdS crystal, and oxygen introduced at 350°C is strongly bound at the surface layer.

§ 5. Dark Conductivity as a Functions of Temperature

Before the measurement of the dark conductivity of CdS crystal, the crystal was set in the apparatus (shown in Fig. 3) and heated at 80°C for 30 minutes in a flow of nitrogen gas. The measurement was also carried out in flowing nitrogen gas.

In Fig. 7 are shown typical examples of the relation between the dark conductivity and $1/T$ (°K) of CdS crystals: curve 1; A-crystal (prepared by sublimation in argon gas), curve 2; AV-crystal (prepared by sublimation in argon gas and then heat-treated in vacuum), curve 3; AVO-crystal (prepared by heat-treating AV-crystal in oxygen), curve 4; H-crystal (prepared by sublimation in argon gas mixed with 2% of hydrogen gas). The dark conductivity values of several crystals prepared by the same method were distributed within a factor of 10. A peak appeared at about 50°C in the curve of the dark conductivity of A-crystal as shown in Fig. 7 (curve 1). On the other hand, when A-crystal was heat-treated in vacuum or in oxygen after heat-treatment in vacuum, there was no peak at about 50°C (curves 2 and 3 in Fig. 7). Also, there was no peak at about 50°C in the case of H-crystal (curve 4 in Fig. 7). The dark conductivities of AV-crystal, AVO-crystal and H-crystal were much larger than that of A-crystal. The slopes of dark conductivity curves of AVO-crystal and H-crystal were approximately equal to those of the AV-crystal.

The high conductivity with the slope of 0.02 eV produced by heat-treatment in vacuum as shown in Figs. 5 and 6 was not observed in this experiment as shown in curves 2 and 3 in Fig. 7. In the experiments described in § **5**, § **6** and § **7**, the crystals were first heat-treated in vacuum or in oxygen and several days later electrodes were formed by evaporating indium and then measurements were carried out. The reasons why the slope of 0.02 eV was not observed in this experiment are not obvious. It may be considered that the donors associated with the slope of 0.02 eV were destroyed by exposing the crystals in air for several days. Although AV- and AVO-crystals have been influenced by exposing in air for a long time, the dark conductivity of these crystals was higher than that of A-crystal and the dark conductivity of AVO-crystal was lower than that of AV-crystal as shown in Fig. 7. Consequently, it may be considered that there remain considerable influences of heat-treatment in vacuum or in oxygen upon AV- and AVO-crystals.

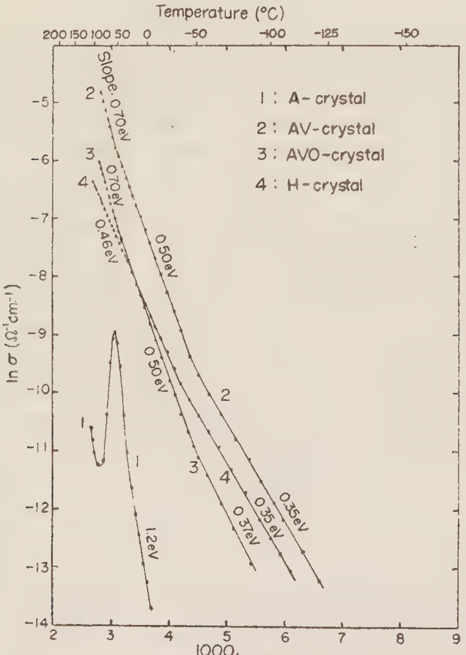

Fig. 7. Dark conductivity as a function of the temperature of the crystal non-treated and heat-treated in vacuum or in oxygen.
Curve 1: A-crystal (prepared by sublimation in argon gas). Curve 2: AV-crystal (prepared by sublimation in argon gas and then heat-treated at 600°C for 20 minutes in vacuum). Curve 3: AVO-crystal (prepared by heat-treating at 500°C for 10 minutes AV-crystal in oxygen). Curve 4: H-crystal (prepared by sublimation in argon gas mixed with 2% of hydrogen gas).

§ 6. Thermally Stimulated Current

Measurements of the thermally stimulated current were made by using the apparatus shown in Figs. 3 and 4 in the following manner: a CdS crystals was cooled down to the liquid nitrogen temperature, and exposed to white light for 5 minutes. Then it was heated in dark at a constant heating-rate with applied voltage of D. C. 50 volts. The difference between the current measured in this way and the normal dark current at the corresponding temperature is the thermally

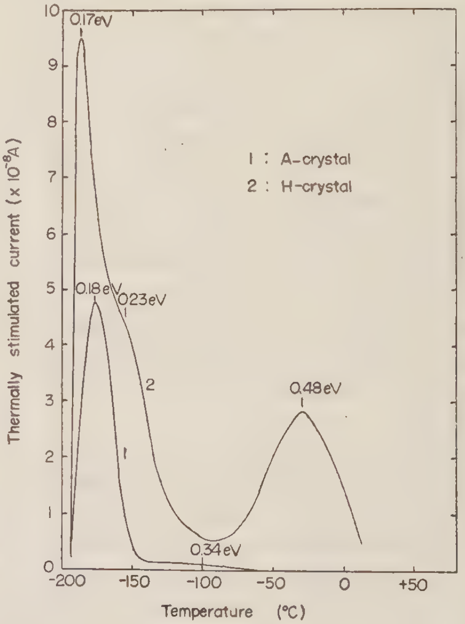

Fig. 8. Thermally stimulated current for A-crystal (prepared by sublimation in argon gas) and H-crystal (prepared by sublimation in argon gas mixed with 2% of hydrogen gas); heating rate: 0.7 deg/sec.

stimulated current. The ratio of the thermally stimulated current and the normal dark current was about 10^7 at -100°C, about 10^2 at 0°C and 10∼1 at room temperature. Therfore, above room temperature, thermally stimulated current could not be measured accurately.

Fig. 8 gives the thermally stimulated current for A-crystal and H-crystal. In the case of A-crystal, there is a single large peak at -177°C, and in the case of H-crystal, there are two large peaks at -187°C and -30°C, and a shoulder at -155°C. These facts were ascertained on several A- and H-crystals.

Typical examples of the thermally stimulated currents of AV-crystal and AVO-crystal are shown in Figs. 9 and 10 respectively. Both curves have three peaks at -189∼-182°C, -100∼-95°C and 0°C. The conductivity at maximum thermally stimulated current of AV-crystal at 0°C is larger than that of AVO-crystal.

The calculations of electron trap depth from thermally stimulated current were carried out by the method used by Randall, Wilkins,[8)] Bube[9,10)] and Kobayashi[11)]. If we neglect the effect of retrapping, trap depth E is given by

$$E=k T_m \ln\left(\frac{\nu k T_m{}^2}{\beta E}\right) . \qquad (1)$$

Where k is the Boltzmann constant, T_m the

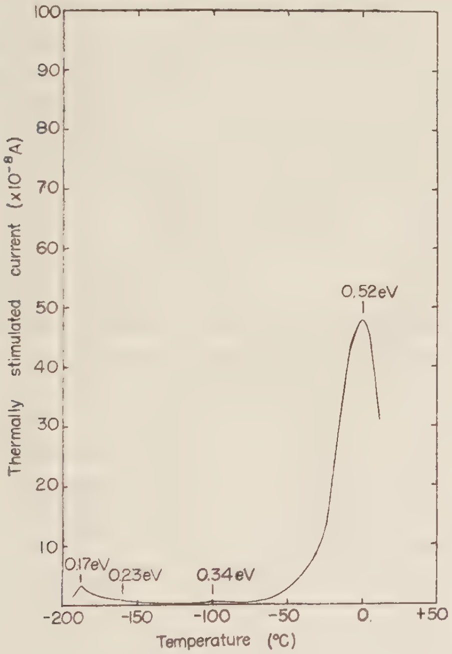

Fig. 9. Thermally stimulated current of AV-crystal (heat-treated at 600°C for 20 minutes A-crystal in vacuum); heating rate: 0.7 deg/sec.

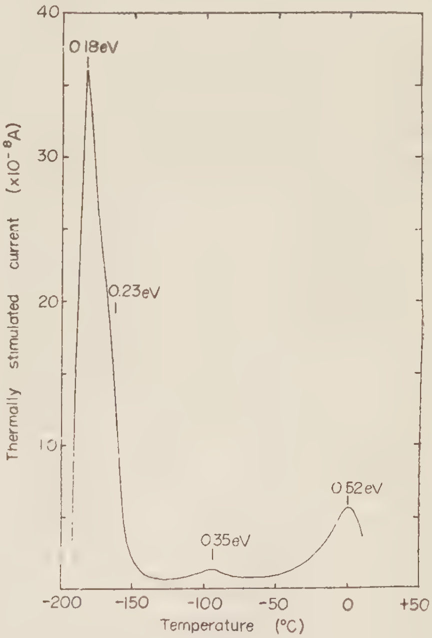

Fig. 10. Thermally stimulated current of AVO-crystal (heat-treated at 500°C for 10 minutes AV-crystal in oxygen); heating rate: 0.7 deg/sec.

Table 1. Major trap depths of CdS crystals obtained by the analysis of curves of the thermally stimulated current.

No.	Preparation of specimen	Trap depths (eV)			
1	A-crystal (Sublimation in argon)	**0.18** (-177°C)	0.34 (-100°C)		
2	H-crystal (sublimation in argon mixed with 2% hydrogen)	**0.17** (-187°C)	0.23 (-155°C)	**0.48** (-30°C)	
3	AV-crystal (heat-treatment in vacuum)	**0.17** (-189°C)	0.23 (-160°C)	0.34 (-100°C)	**0.52** (0°C)
4	AVO-crystal (heat-treatment in oxygen	**0.18** (-182°C)	0.23 (-160°C)	0.35 (-95°C)	**0.52** (0°C)

temperature at maximum of the thermally stimulated current, ν the attempt-to-escape frequency, β the heating rate. Eq. (1) can be transformed as

$$E=kT_m(\ln\nu)(1+\Delta)\,, \qquad (2)$$

where

$$\Delta=\ln(kT_m^2/\beta E)/\ln\nu\,. \qquad (3)$$

In the present calculation, the values of ν and Δ were assumed to be 1×10^9 and 0.1 respectively.[8,9,12] The trap depths thus obtained are shown in Table 1.

§ 7. Spectral Sensitivity of Photocurrent

Before the measurement of spectral sensitivity of photocurrent, the CdS crystal was set in a hard glass tube in which nitrogen gas was flowing, and heated at 80°C for 30 minutes. Measurements were done at room temperature. All crystals had a maximum sensitivity of photocurrent at 514 mμ (corresponding to the absorption edge).

7.1 *In the case of electrodes placed on one surface*

In Fig. 11 are shown typical examples of the spectral sensitivity of photocurrent for A-crystal, AV-crystal and AVO-crystal. The indium electrodes were formed on one surface of a plate-shaped crystal after heat-treatment as shown in the inset in Fig. 11. For several A-crystals there was no peak or no shoulder at longer wavelength side of characteristic photocurrent, but for several AV-crystals or AVO-crystals there was a shoulder at longer wavelength side.

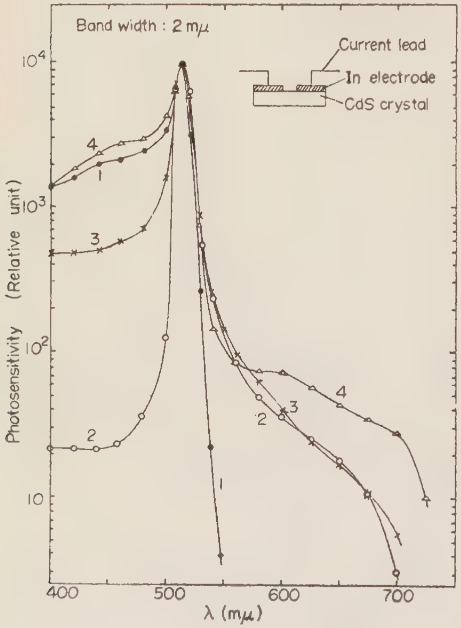

Fig. 11. Spectral sensitivity of the photocurrent of A-crystal AV-crystal, and AVO-crystals.
-●- 1: A-crystal.
-○- 2: AV-crystal.
-×- 3: AVO-crystal (heat-treated in oxygen at 250°C).
-△- 4: AVO-crystal (heat-treated in oxygen at 400°C).

By X-ray diffraction, it was observed that cadmium oxide was produced on the surfaces of CdS crystal by heat-treatment above 500°C in oxygen. The photocurrent and the dark current of crystals heat-treated at 550°C for ten minutes in oxygen were unstable, and therefore the spectral sensitivity of photocurrent could not be measured. The crystals heat-treated at 600°C for the minutes in oxygen had CdO layer on the whole surface between two electrodes, and had no photoconductivity. The conductivities of these crystals were about 1 Ω^{-1} cm.$^{-1}$

7.2 *In the case of electrodes placed on opposite surfaces*

In order to investigate the property of the bulk of CdS crystal with some CdO on the

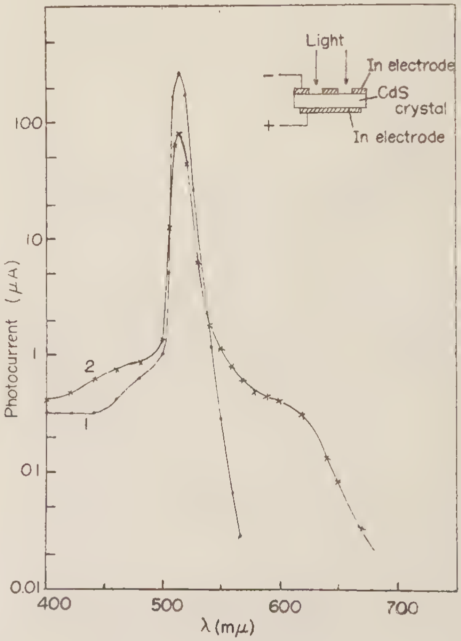

Fig. 12. Spectral sensitivity of the photocurrent of A-crystal, and AVO-crystal with electrodes on opposite surfaces.
-●- Curve 1: A-crystal.
-×- Curve 2: AVO-crystal.

surface, light was irradiated on the surface with the electrode at negative potential as shown in the inset in Fig. 12. There was no shoulder at longer wavelength side in the case of A-crystal, but a shoulder was observed at about 600 mμ in the case of AVO-crystal heat-treated at 500°C for 30 minutes in oxygen.

7.3 *Infrared quenching of the photocurrent*

The infrared quenching curves of photocurrent of A-crystal, AV-crystal and AVO-crystal were obtained by the following method: first, the photocurrent produced by visible rays (540 mμ) was kept constant at above three crystals by controlling the applied voltage, and then infrared rays were irradiated on one surface with two electrodes. There were two quenching valleys at 900 mμ and 1400 mμ with three crystals. The wavelengths of quenching were the same as the values previously reported.[13,14] But the ratio of quenching value at 1400 mμ to that at 900 mμ was 0.70 for A-crystal, 0.87 for AV-crystal and 0.95 for AVO-crystal.

§ 8. Discussions

The experimental results described in the preceding sections are related to each other. Let us consider about the influences of heat-treatment in vacuum or in oxygen.

8.1 *Variation of dark conductivity by heat-treatment in vacuum or in oxygen*

In the case of heat-treatment in vacuum the variation of the dark conductivity against the temperature is reversible below 120°C, and irreversible above 120°C, as shown in Fig. 5. Below 120°C, the dark conductivity may be produced by ionization of donors. It may be considered that above 120°C there are considerable contributions of ionic conduction to the dark conductivity. After CdS crystal is heat-treated above 120°C in vacuum, the slope at point D or F in Fig. 5 is 0.02 eV. The dark conductivity at room temperature after heat-treatment at 200∼250°C in vacuum is 10^4∼10^7 times as large as that before heat-treatment. Consequently it may be concluded that the concentration of the donors formed by heat-treatment in vacuum above 120°C has increased with the rise of temperature of heat-treatment in vacuum.

In the case of CdS crystal with gold electrodes, before the heat-treatment in vacuum the slope of dark conductivity against $1/T$ (°K) is 0.6 eV as shown in Fig. 5 (the slope at point A is 0.6 eV), but in the experiment of the dark conductivity *versus* temperature at low temperature on A-crystal (prepared by sublimation in argon gas) with indium electrodes the slope of 0.6 eV is not observed (curve 1 in Fig. 7). The donors associated with the slope of 0.6 eV may be produced by bombardment of accelerated electron beam before forming gold electrodes.

As shown in Fig. 6, the dark conductivity of the crystal heat-treated at 350°C in vacuum decreases by introducing oxygen at room temperature and when this crystal is heated at 80°C in vacuum and cooled down to room temperature, the dark conductivity returns to the initial value as the oxygen is released from the surface layers of the crystal. When oxygen is introduced on the crystal at 350°C, the dark conductivity also decreases, but the dark conductivity of this crystal does not return to the initial value by heating at 80°C in vacuum and returns to the initial value by heat-treatment at 350°C in vacuum. From the facts shown in Fig. 6, it may be considered that oxygen introduced on CdS crystal at room temperature is absorbed at the surface layers of crystal and oxygen introduced on CdS crystal at 350°C is diffused into the crystal and further oxygen contributes to reducing both the life time of free electron in conduction band and the concentration of donors associated with the slope of 0.02 eV. The slope of 0.02 eV produced by heat-treatment in vacuum is not observed at the experiment of dark conductivity *versus* temperature as shown in curves 2 and 3 in Fig. 7. As described in § **5**, it might be considered that heat-treated crystals used in the experiments described in § **5**, § **6** and § **7** have had some influence of heat-treatment in vacuum or in oxygen.

As shown in Fig. 7, the ionization energy of 2.4 eV derived from the curve on A-crystal (prepared by sublimation in argon gas) below 30°C corresponds to intrinsic conduction, but it cannot be understood why a peak appears at about 50°C in the curve for A-crystal. The ionization energies are 0.70∼0.74 eV, 1.0 eV and 1.4 eV for AV-crystal (heat-treated in vacuum) and AVO-crystal (prepared by heat-treating AV-crystal in oxygen), and the dark conductivity of AVO-crystal is smaller than that of AV-crystal. Although these crystals had been influenced by exposing in air, it might be true that the dark conductivity increased by heat-treatment in vacuum are reduced by heat-treatment in oxygen. Further, H-crystal (prepared by sublimation in argon gas mixed with 2% of hydrogen gas) has donors alike AV-crystal, and accordingly, it may be considered that these donors are associated with sulphur vacancies.[10] At the experiments of the CdS sintered films,[5] it had been revealed that the dark conductivity decreased by the heat-treatment in oxygen.

8.2 *Thermally stimulated current*

The distribution of electron traps obtained by measuring the thermally stimulated current are shown in Table 1. Errors in measurements of trap depth was ±0.03 eV, and therefore, the values of 0.17∼0.18 eV, 0.34∼0.35 eV and 0.48∼0.52 eV may be represented by 0.17 eV, 0.34 eV and 0.50 eV respectively. From Table 1, the following interpretation can be derived: when A-crystals (prepared by sublimation in argon gas) are heat-treated in vacuum, the crystal have electron traps at 0.5 eV below conduction band at 0°C, and the concentration of these traps are reduced by heat-treating the crystals in oxygen. When CdS crystals are prepared by sublimation in reducing atmosphere (H-crystal), the crystals also have electron traps at 0.50 eV at −30°C alike the case of heat-treatment in vacuum. Since the traps at 0.50 eV at −30∼0°C are produced by heat-treatment in vacuum or by growth in reducing atmosphere, these defects are probably associated with sulphur vacancies. The concentration of electron traps at 0.17 eV at about −180°C and at 0.23 eV at about −160°C does not increase remarkably by heat-treatment in vacuum or by growth in reducing atmosphere as shown in Fig. 8 and 9, but it increases by heat-treatment in oxygen as shown in Fig. 10. The traps at 0.17 eV at about −180°C and at 0.23 eV at about −160°C likely are not associated with sulphur vacancies.

Further, on CdS sintered films, a broad peak of the thermally stimulated current was observed near room temperature[5,16] and this peak might be correspond to the peak at about −30∼0°C on CdS single crystal.

8.3 *Spectral sensitivity of photocurrent*

It was found that the spectral sensitivity of photocurrent at longer wavelength side of intrinsic photoconductivity increased by heat-treating the CdS crystal in vacuum or in oxygen. In Figs. 11 and 12, there is a shoulder at about 600 mμ, and this shoulder is produced not only by heat-treatment in oxygen but also by heat-treatment in vacuum. Therefore, the increase of photosensitivity at longer wavelength may not be directly due to the effects of oxygen, but may be due to the defects associated with vacancies.

Berger[8] reported that the photoconductivity at the peak of 520 mμ and in shorter wavelength region decreased by keeping CdS crystals in oxygen atmosphere. In the present experiments, the sensitivity of photocurrent in shorter wavelength region (below 500 mμ), relative to the sensitivity at peak at 514 mμ, decreased by heat-treatment in vacuum, and increased again by heat-treatment in oxygen.

The CdS crystals, when heat-treated in oxygen at 500°C, has some CdO on its surface as described in 7.1, and the spectral sensitivity of photocurrent of there crystals (curve 2 in Fig. 12) was similar to those of the crystals without CdS on its surface (curves 3 and 4 in Fig. 11).

8.4 *Infrared quenching*

Infrared quenching on CdS crystal is proudced by decreasing the concentration of electrons in conduction band by their recombination with free holes by infrared rays.[13,14]

The values of quenching maxima (900 mμ and 1400 mμ), on A-crystals, AV-crystals and

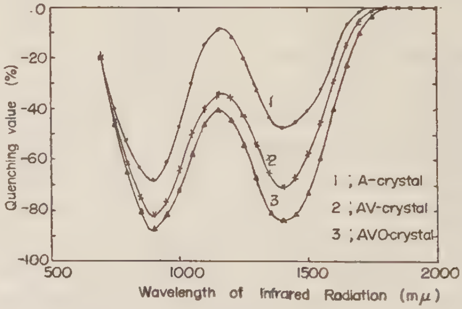

Fig. 13. Infrared quenching of A-crystal, AV-crystal and AVO-crystal Quenching value is indicated as $\{(1-I_{p+s}/I_p+I_s)\}\times 100\,(\%)$, where I_{p+s} is the photocurrent produced by irradiation of infrared rays superposing on visible rays, I_p is the photocurrent by irradiation of visible rays and I_s is the photocurrent produced by irradiation of infrared rays. In this experiment, I_s is nearly zero.

AVO-crystals were nearly equal to those previously reported.[13,14,15] From the experiments of infrared quenching on CdS crystals with and without CdO (Fig. 13), it was found that hole trap levels did not change by heat-treatment in vacuum or in oxygen, but the ratio of the quenching value at 1400 mμ to the one at 900 mμ increased by heat-treatment in vacuum or in oxygen. From these facts, it is considered that by heat-treatment the concentration of the hole traps at 0.89 eV above valence band increases more than that at 1.38 eV.

§ 9. Summary

CdS single crystals used in these experiments had been more or less influenced by the exposing in air, but from the experiments above described following results were obtained.

1) The ionization energies of CdS single crystal, which has been heat-treated in vacuum at high temperature, are 0.04, 0.7, 1.0 and 1.4 eV.

2) The major electron trap depth of CdS single crystal heat-treated in vacuum at high temperature is 0.5 eV.

3) The dark conductivities which are increased by the heat-treatment in vacuum and the concentrations of the electron traps which are produced by the same treatment, are reduced by the heat-treatment in oxygen.

4) When the CdS single crystal is heat-treated in vacuum or in oxygen, the photosensitivity at longer wavelength region increases.

5) The values of quenching maxima (900 mμ and 1400 mμ) of infrared quenching do not change by the heat-treatment in vacuum or in oxygen, but the quenching value at 1400 mμ slightly increase.

6) When the whole surface of the CdS single crystal is covered with CdO by the heat-treatment in oxygen above 600°C, no photoconductivity is detected.

Acknowledgements

The author wishes to express his gratitude to Professor K. Tanaka and Assistant Professor K. Fukuda at Kyoto University for their valuable suggestions rendered during the course of this work. The author is also much indebted to Messrs. T. Kubo and T. Yamashita in his laboratory for their interests and endeavors in measurements and preparations of specimens.

References

1) W. Muscheid: Ann. d. Phys. **13** (1953) 322.
2) B. Seraphin: Ann. d. Phys. **13** (1953) 198.
3) H. Berger, K. W. Böer und E. H. Weber: ZS. f. Phys. **158** (1960) 501. R. H. Bube: Phys. Rev. **101** (1956) 1168.
4) S. H. Liebson: J. Chem. Phys. **23** (1955) 1732.
5) S. Kitamura: Read before the Annual Meeting of the Physical Society of Japan, April (1960); J. Phys. Soc. Japan **15** (1960) 2343.
6) W. M. Buttler und W. Muscheid: Ann. d. Phys. **15** (1954) 82.
7) F. A. Kröger, G. Diemer and H. A. Klasens: Phys. Rev. **103** (1956) 279.
8) J. T. Randall and M. H. F. Wilkins: Proc. Roy. Soc. A **184** (1945) 366.
9) R. H. Bube: J. Chem. Phys. **23** (1955) 18.
10) R. H. Bube: "*Photoconductivity of Solids*" (John Wiley & Sons, Inc., 1960), p. 292.
11) A. Kobayashi: "*Semiconductor*" (Iwanami, Inc., 1960), p. 171 (in Japanese).
12) K. Mitsuhashi and S. Imai: Read before the Annual Meeting of the Physical Society of Japan, Oct. (1959).
13) E. A. Taft and M. H. Hebb: J. Opt. Soc. Amer. **42** (1952) 249.
14) R. H. Bube: Phys. Rev. **99** (1955) 1105.
15) A. E. Hardy: Trans. Amer. Electrochem. Soc. **87** (1945) 355.
R. Frerichs: Phys. Rev. **72** (1947) 594.
16) S. Kitamura: J. Phys. Soc. Japan **15** (1960) 1697.
17) S. Tanaka: J. Appl. Phys. Japan **26** (1957) 280 (in Japanese).

JOURNAL OF THE PHYSICAL SOCIETY OF JAPAN, Vol. 16, No. 12, DECEMBER, 1961

Some Experimental and Theoretical Studies of Ferroelectricity in $NaNO_2$

By Shoichiro NOMURA

Department of Physics, Tokyo Institute of Technology
Oh-okayama, Meguro, Tokyo

(Received July 4, 1961)

The dielectric constant of $NaNO_2$ crystal was measured in a temperature range from r.t. to 200°C and in a frequency range from 60 to 10^6 cycles per second. It shows peak at 164.2°C in heating and at 162.6°C in cooling. Dielectric dispersion, similar to the one observed in other ferroelectrics, exists in all directions of the crystal principal axes in the paraelectric region as well as in the ferroelectric one. The spontaneous polarization was determined by the measurement of the pyroelectric current and the value was estimated to be *ca* 8.6 $\mu C/cm^2$ at r.t.. The ferroelectricity in $NaNO_2$ was discussed in a phenomenological way, where the electrocaloric effect was taken into account. The free energy F was expressed as a function of the polarization P as $F=A(T-T_0)P^2+BP^4+CP^6$, and the coefficients were determined by the dielectric properties as $A=1.22\times10^{-3}{}^{\circ}K^{-1}$, $B=-0.3\times10^{-10}$ esu, $C=1.0\times10^{-19}$ esu and $T_0=436.2°K$. From the dielectric measurements, it is concluded that the transition in $NaNO_2$ is probably of the first kind. It was pointed out by the consideration about the atomic arrangement that the main contribution to the spontaneous polarization comes from the relative displacement between Na^+ and NO^-_2 ions, and further that $NaNO_2$ crystal is a ferroelectric crystal which stands halfway between ionic and molecular crystal.

§ 1. Introduction

Since ferroelectricity was revealed in $NaNO_2$ (sodium nitrite) crystal by the dielectric measurement[1], various properties have been measured by many researchers.* It is considered that the ferroelectricity in $NaNO_2$ has its origin in the arrangement of NO_2^- radicals in the crystal and the transition is accompanied by order-disordering of their senses in the b direction of the orthorhombic structure.[5, 10] And hence $NaNO_2$ has been regarded as a ferroelectric of new type. As the crystal structure of $NaNO_2$[10, 11, 12, 13] is rather simple, we may have a hope that the ferroelectricity will be thoroughly studied as in the case of barium titanate, which also has simple crystal structure, though their natures of chemical bonding and in consequence origins of ferroelectricity are considerably different each other.

The details of domain structure[3] and thermal property[2] of $NaNO_2$ have been already reported by the author and his co-workers. Dielectric properties will be mainly described in this paper. The dielectric constant was measured as a function of frequency as well as of temperature, and the spontaneous polarization was determined by the measurement of the pyroelectric current. Judging from our experimental results on thermal property, it appears that the phase transition in $NaNO_2$ is of the second kind, but the dielectric properties described here are rather favorable to point of view that the transition is of the first kind.

Following the method used by Devonshire,[14] the free energy of $NaNO_2$ crystal is expanded in terms of the polarization, where the coefficients are determined by the use of certain dielectric properties of the crystal, and then prediction of other properties are made. The electrocaloric effect is taken into account, and the dielectric constant calculated is compared with experiments. Results obtained in this way are of course independent of any atomic model. Further we develop several discussion based on atomic pictures, but they are not accurate enough to give definite predictions.

---

* These are thermal property,[2] domain structure,[3] crystal structure,[4, 5, 6, 7] nuclear magnetic resonance,[8] and infrared absorption.[9]

§ 2. Experimentals

§§ 2. 1. Dielectric constant

a) Temperature dependence

The measurements of dielctric constant were made for the samples prepared from the melt, mostly at the frequency of 100 kc/sec by means of C-meter (Type CM 101, Yokogawa Co. Ltd). The sample was put in a silicon oil bath set in the electric furnace, in order to keep an uniform temperature distribution around it. The heating or cooling rate was kept 0.5°C/min in average but was slowed down to a value less than 0.1°C/min in the vicinity of the transition temperature. The temperature was measured with a thermocouple inserted in the bath, beside the sample. Air-drying silver paste was used as the electrode material.

Temperature dependence of the dielectric constants along the crystal principal axes, ε_a, ε_b, and ε_c are shown in Fig. 1, where the dimensions of the samples (the area S of the electrodes and the distance d between them) are

$$\left(\begin{array}{l} S=0.46\ \mathrm{cm}^2 \\ d=0.142\ \mathrm{cm}, \end{array}\right. \qquad \left(\begin{array}{l} S=1.05\ \mathrm{cm}^2 \\ d=0.331\ \mathrm{cm} \end{array}\right.$$

and

$$\left(\begin{array}{l} S=0.88\ \mathrm{cm}^2 \\ d=0.141\ \mathrm{cm}\ \text{respectively.} \end{array}\right.$$

The dielectric constant *vs* temperature curves in heating show peak at 164.2°C in all directions but they are not steep except for the ferroelectric *b* axis, in which the value more than 1000 is observed. It was found that the peak values varies to some extent specimen by specimen and is sensitive to a stress coming from the electrodes or the sample holder. The transi tion is accompanied by a temperature hysteresis and the difference of the transition temperature in heating and cooling is estimated to be *ca* 1.6°C in our measurement. Above the transition temperature, the Curie-Weiss law holds for ε_b as shown in Fig. 2, though a slight deviation is noticed just above the transition temperature It is seen that $1/\varepsilon_b$ varies linearly with temperature below the transition temperature down to about 140°C as well as above the transition temperature. Hence ε_b can be represented as follows,

$$\varepsilon_b=\frac{C_F}{T_1-T}\,(T<T_c)\,, \qquad (1)$$

$$\varepsilon_b=\frac{C_P}{T-T_0}\quad(T>T_c)\,, \qquad (2)$$

where

$$C_F=0.68\times10^3\ {}^\circ\mathrm{K},$$
$$C_P=5.13\times10^3\ {}^\circ\mathrm{K},$$
$$T_0=163.0^\circ\mathrm{C}=436.2^\circ\mathrm{K},$$
$$T_1=166.5^\circ\mathrm{C}=439.7^\circ\mathrm{K},$$
$$T_c=164.2^\circ\mathrm{C}=437.4^\circ\mathrm{K}.$$

We remark here that thevalues of C_F and C_P vary to some extent specimen by specimen. This may be attributed to the effect of electrical conduction, as in the cases of other ferroelectrics, for example, barium titante[15]. A small jump can be clearly discerned on the curve at the transition temperature and the extraporated lines in the two regions above and below the transition temperature intersect

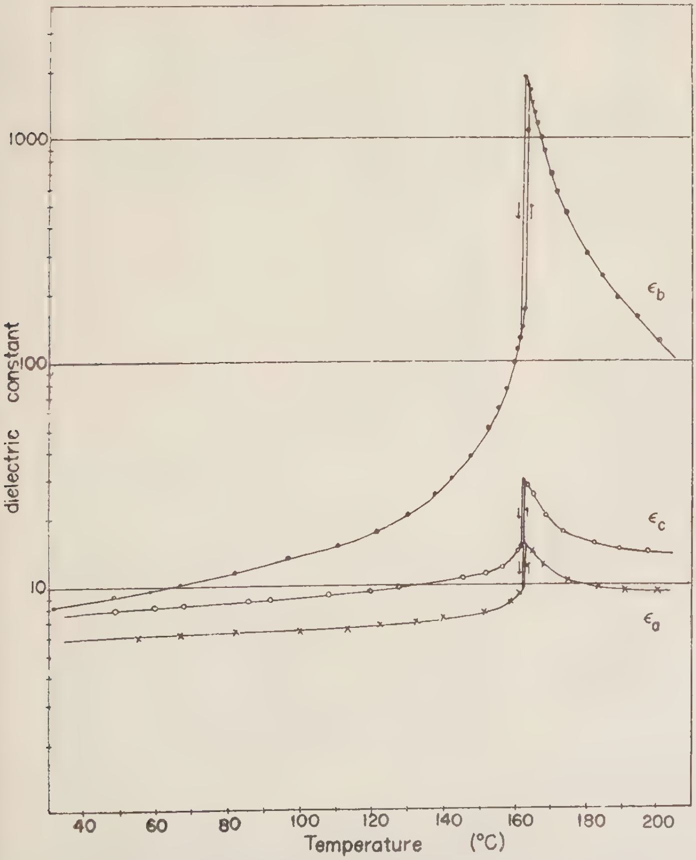

Fig. 1. Temperature dependences of the dielectric constants along the crystal principal axes measured at the frequency of 100 kc/sec.

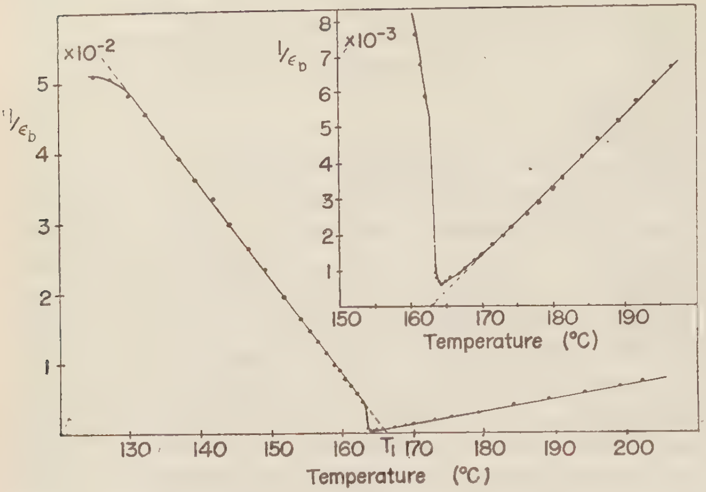

Fig. 2. $1/\varepsilon_b$ *vs* temperature curve near the transition temperature.

the abscissa at different temperatures T_0 and T_1, being apart by *ca* 3.5°C. It is to be noted further that the paraelectric Curie temperature T_0 stands very close to the transition temperature T_c. These characters will be taken into account in the later discussions concerning the kind of transition.

It is plausible to consider that the deviation from the Curie-Weiss law corresponds to the anomaly above the transition temperature observed in the measurement of thermal properties,[2] but it would partly come from the effect due to the stress.

b) Frequency dependence

Frequency dependences of dielectric constant were measured in a frequency range from 60 c/sec to 1 Mc/sec, by a bridge method using a wide band dielectric loss meter (type TR-1B, Ando Electric Co., Ltd). As our measurement mainly aimed at ascertaining the reliability for the experimental data at 100 kc/sec, we shall here not go into details on the dielectric dispersion phenomena, but limit ourselves to touch its outline.

The temperature characteristics of dielectric constant corresponding to various frequencies are shown in Figs. 3 (a), (b) and (c). It is to be noted that some kind of dielectric dispersion exists in all directions of the crystal principal axes in the paraelectric region as well as in the ferroelectric one. In the *a* and *c* directions perpendicular to the polar axis, the values of dielectric constant markedly increase in a side of low frequency. To inquire how the dispersion phenomena take place, the Cole-Cole diagrams were taken, as shown in Figs. 4 (a), (b), and (c), where the experimentally determined values of the real and imaginary parts of complex dielectic constant ε^* corresponding to various frequencies are plotted in Cartesian coordinates. Exclusive of the low frequency side in which departures from the arc are conspicuous, the Cole-Cole law seems to hold in all the cases, that is,

$$\varepsilon^* - \varepsilon_\infty = (\varepsilon_0 - \varepsilon_\infty)\frac{1}{1+(i\omega\tau)^{1-\alpha}} . \tag{3}$$

In this case we may put approximately $\alpha=0$ for the *a* and *c* direction and $\alpha=1/2$ for the *b* direction, and the relaxation time τ may be taken to be of the order of 10^{-5} sec. In the case of $\alpha=0$, the values of ε^* lie on a semicircle having its center on the ε axis, which is identical with those obtained from the simple Debye theory characterized by a single relaxation time. In the case of $\alpha=1/2$, however, the center of the arc is located below the ε axis, indicating a distribution of relax-

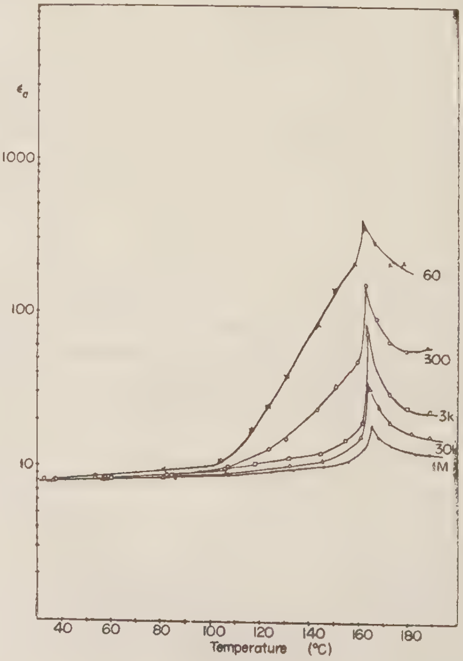

(a)

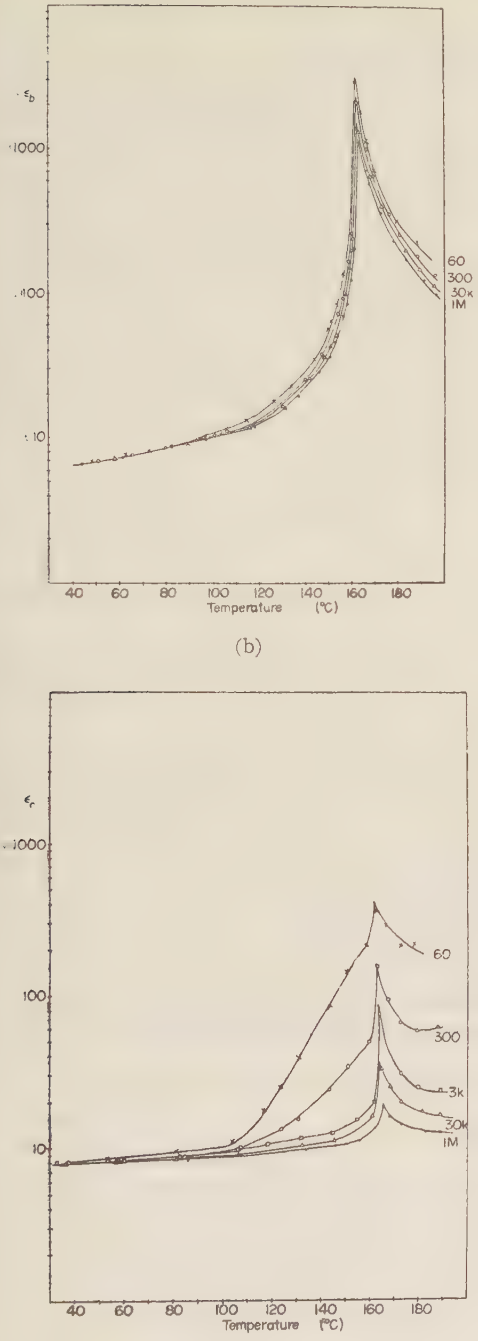

(b)

(c)

Fig. 3. Temperature dependences of the dielectric constants corresponding to various frequencies. (a) a axis, (b) b axis, (c) c axis.

ation times.

The deviations from the arc in the low frequency side must be caused by the effect due to electrical conduction, as has been discussed in the similar experiments for barium titanate[16] and Rochelle salt.[17] As the electrical conductivity of $NaNO_2$ crystal is far larger than that of barium titanate, the effect would be more predominant. Another kind of dispersion should be expected to occur in a range of higher frequency, because the value of ε_∞ estimated from the arc in Fig. 3 (c) keeps yet a large value of 470.

In spite of the remarkable dielectric dispersion, the values of C_F and C_P obtained from $1/\varepsilon_b \sim T$ curves did not change considerably with the frequency, as shown in Fig. 5, though

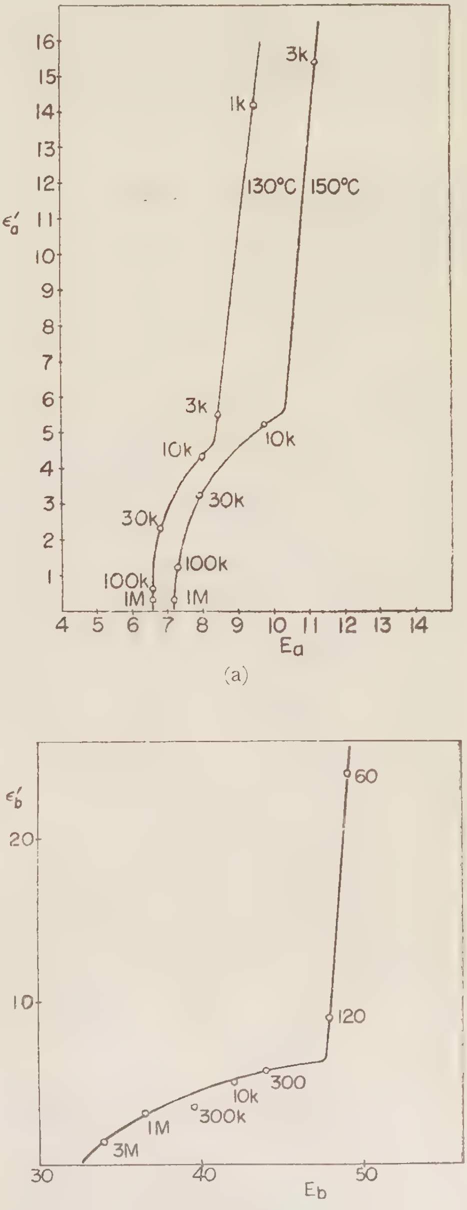

(a)

(b)

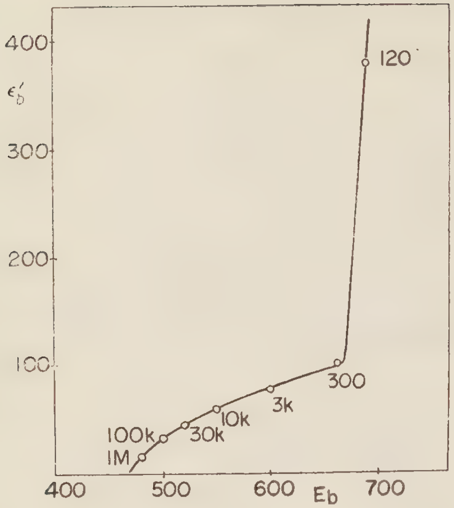

(c)

Fig. 4. Dielectric properties plotted in terms of complex dielectric constant.
(a) *a* axis, at 130°C and 150°C,
(b) *b* axis, at 150°C,
(c) *b* axis, at 170°C.
The similar behavior as seen in (a) was obtained in the *c* direction.

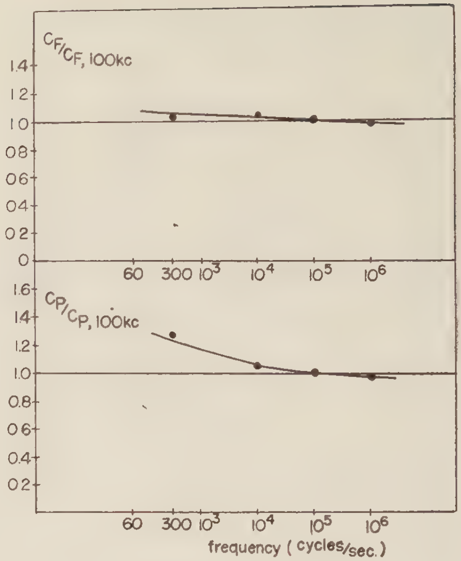

Fig. 5. Values of C_F and C_P at various frequencies.

an increasing tendency of the values is noticed in a low frequency side. The constancy of the values gives us an assurance of using the numerical values of C_F and C_P given in the former section in the phenomenological theory which will be developed in § 4. As the mechanism of the dielectric phenomena represented by the Cole—Cole law is supposed to be complicated and not to have a direct bearing with the ferroelectricity, we shall reserve the interpretation for another occasion.

§§ 2. 2. Pyroelectricity

The spontaneous polarization was obtained from both measurements of the pyroelectric current and the dielectric hysteresis loop displayed at the frequency of 50 c/sec. By the later method, however, the value of the spontaneous polarization was not able to be obtained near the room temperature, because the loop did not open out owing to its large coercive field.[1] We show here the temperature dependence of the pyroelectric current

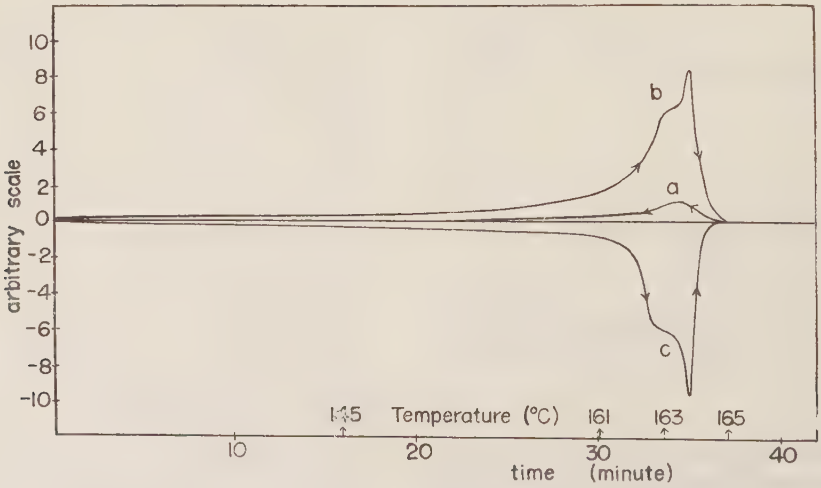

Fig. 6. Pyroelectric current. Curve *a* is the current for the crystal without d.c. field treatment and curves *b* and *c* after the treatment.

and the spontanous polarization obtained from it.

The measurement of pyroelectric current was made by the usual method using a galvanometer (current sensitivity: 2.1×10^{-10} A), in which the rate of temperature variation near the transition temperature was kept *ca* 1°C/min. Since a $NaNO_2$ crystal prepared from the melt was usually composed of antiparallel 180°-domains,[3] only a small fraction of the pyroelectric current could be measured, when any d.c. field had not been applied to the crystal. This case is shown by curve *a* in Fig. 6, which is obtained during a cooling process. When the crystal had been slowly cooled from 170°C to room temperature with applying d.c. field of 1.4 kV/cm, curve *b* or *c* was obtained as the pyroelectric current in heating, according to the sense of the applied electric field. Needless to say, the measurements were made after the charging current had been eliminated by shortcircuitting the electrodes of the crystal. The electric field applied was judged to be sufficient to remove the 180°-domain boundaries, from the observations on the behavior of domains.[3] The current shows a sharp peak near the transition temperature, followed by immediate disappearing. The fact that the pyroelectric current is affected with the applied d.c. field is another tangible evidence for $NaNO_2$ to be ferroelectric.

The temperature dependence of the spontaneous polarization was obtained by integrating the pyroelectric current, as shown in Fig. 7.

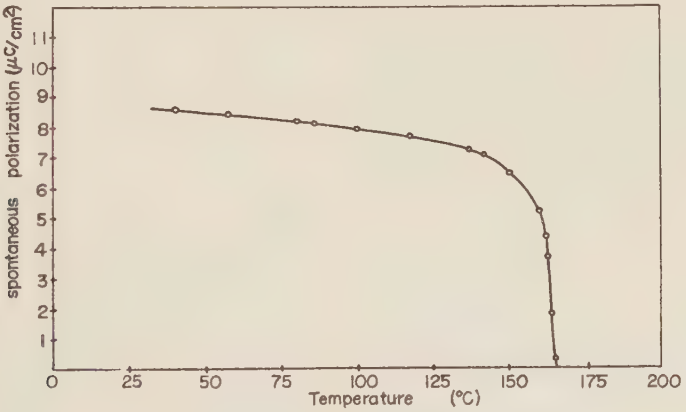

Fig. 7. Temperature dependence of the spontaneous polarization.

§ 3. Phenomenological Theory of the Ferroelectricity

§§ 3. 1. Free energy

We shall begin with expressing the free energy F as a function of polarization and stress, where the stresses are equated to zero. We then have

$$E=A(T-T_0)P^2+BP^4+CP^6 \tag{4}$$

were P is the polarization along the ferroelectric axis and A, B, C are the coefficients of expansion. The zero of the free energy is taken to be that of the unpolarized, unstressed crystal. The terms of the second, fourth and sixth orders are included and we shall find it necessary to take into account all these terms to account for the dielectric behavior of the crystal. The derivative of F with respect to P gives the field E for the free crystal. Hence we have

$$E=\left(\frac{\partial F}{\partial P}\right)_T=2A(T-T_0)P+4BP^3+6CP^5\,. \tag{5}$$

In the absence of an external field the right-hand side of eq. (5) must be zero and we have

$$P\{A(T-T_0)+2BP^2+3CP^4\}=0\,. \tag{6}$$

Further the electric susceptibility, to be exact, the isothermal electric susceptibility χ_t is given by the derivation of E with respect to P as follows,

$$1/\chi_t=\left(\frac{\partial E}{\partial P}\right)_T=2A(T-T_0)+12BP^2+30CP^4\,. \tag{7}$$

In the non-ferroelectric region, eq. (7) becomes

$$1/\chi_t=2A(T-T_0)\,. \tag{8}$$

If A is the constant independent of the temperature, it will be an expression of the

Curie-Weiss law.

The values of the coefficients can be determined by using the experimental data on dielectric properties. Comparing eq. (8) with eq. (2), we have

$$A=2\pi/C_P=1.22\times10^{-3}\ {}^\circ\mathrm{K}^{-1}\,. \tag{9}$$

We shall assume that A is a constant independent of temperature in the whole regions. The coefficients B and C can be so chosen that the value of P calculated from eq. (6) may agree with the observed one at any temperature. It is not necessary for B and C to be quite independent of temperature, but we may assign them nearly constant values

$$B=-0.3\times10^{-10}\ \text{(esu)}$$
$$C=\ 1.0\times10^{-19}\ \text{(esu)}\,,$$

since, for this value of C, the value of B remains almost constant in a wide range of temperature, as seen in Fig. 8, where the values of C for three different values of parameter B, which satisfy eq. (6) are plotted as a function of the temperature.

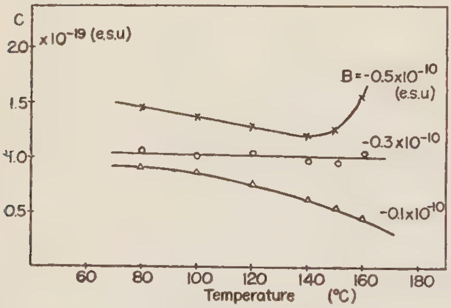

Fig. 8. Relation between the values of B and C which satisfy eq. (6).

It is worth noticing that the magnitudes of the terms BP^4 and CP^6 are of the same order and B is negative while C is positive. This indicates that the transition from ferroelectric to paraelectric phase should be of the first kind. In fact, the situation can be visualized in curves of free energy *vs* polarization. Several curves near the transition temperature are given in Fig. 9, where the figure entered beside each of them means the temperature difference with T_0. The curve denoted by 0 has a minimum at the polarization value of 14.2×10^3 (esu), which represents a stable state to be realized. Therefore the polarization should be the spontaneous polarization expected at T_0. With decreasing temperature, the free energy curve shifts downward and the value of the polarization corresponding to the minimum increases. This means that the ferroelectric state becomes more stable as the temperature decreases. The curves +1 and +2 keep still their minimums for non-vanishing values of P, while those +3 and +5 may keep them only for $P=0$. The extreme values of the polarization are given by eq. (6) as follows,

$$P=0\,,$$

or

$$P^2=\frac{-B+\sqrt{B^2-AC(T-T_0)}}{3C}\,, \tag{10}$$

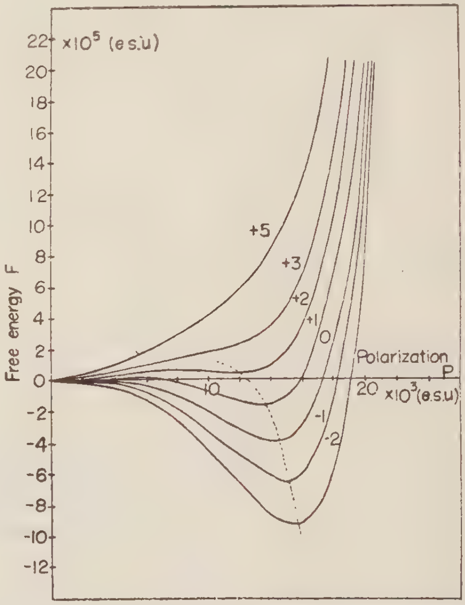

Fig. 9. Free energy *vs* polarization curves in vicinity of the transition temperature.

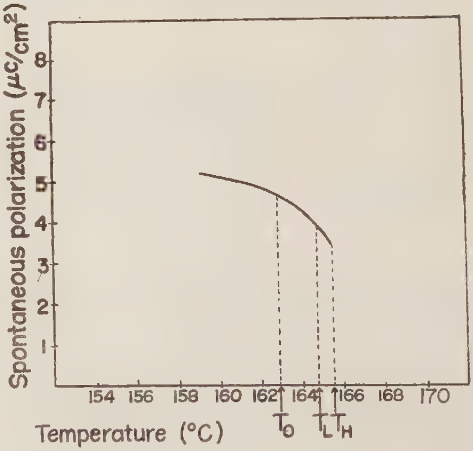

Fig. 10. Calculated values of the spontaneous polarization at the temperatures of T_0, T_L, and T_H.

and their stabitity can be discriminated by the sign of the formula (7). The non-ferroelectric state, in which $P=0$, is always unstable in the temperature region below T_0.

We shall mark two definite temperatures besides T_0 as follows,

T_L: temperature at which the minimum value of the free energy becomes zero with non-vanishing value of P.

T_H: temperature above which the free energy curve has only one minimum corresponding to the state $P=0$.

Then the values of the spontaneous polarization at the temperatures of T_0, T_L, and T_H are given by

$$T_0=163.0^\circ\mathrm{C},\quad P_{T_0}=\sqrt{\frac{-2B}{3C}}=4.71\quad(\mu\mathrm{C/cm^2}), \tag{11}$$

$$T_L=T_0+\frac{B^2}{4AC}=164.8^\circ\mathrm{C},\quad P_{T_L}=\sqrt{\frac{-B}{2C}}=4.08\quad(\mu\mathrm{C/cm^2}), \tag{12}$$

and

$$T_H=T_0+\frac{B^2}{3AC}=165.5^\circ\mathrm{C},\quad P_{T_H}=\sqrt{\frac{-B}{3C}}=3.43\quad(\mu\mathrm{C/cm^2}). \tag{13}$$

Their relation is drawn in Fig. 10. In phenomenological theory in which the effect of thermal vibration is not taken into account, it is natural to consider that the transition occurs at T_H in heating and T_0 in cooling.[19] In the actual crystal, however, it will be doubtful that this is the case. The temperature of the peak in the heating curve of dielectric constant is 164.2°C, which is rather near T_L than T_H. It is likely that the transition occurs at a certain temperature between T_L and T_H in heating, and at a certain temperature between T_0 and T_L in cooling. The temperature hysteresis observed in our dielectric measurement is 1.6°C, which is nearly equal T_L-T_0, 1.8°C.

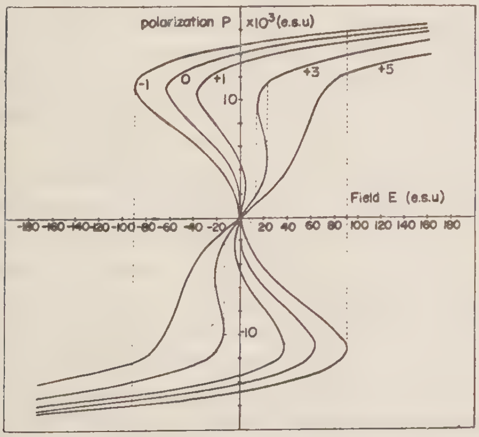

Fig. 11. Polarization *vs* field curves in the vicinity of the transition temperature.

Next we shall discuss about the $P\sim E$ relation near the transition temperature. The curves can be obtained by plotting eq. (5) as shown in Fig. 11. Normal hysteresis loop can be expected for the curves, −1, 0, +1, and double hysteresis loop for +3. The coercive fields estimated from these curves are more than ten times as large as the values obtained from the dielectric hysteresis loops. The circumstances are common in ferroelectric crystals, the coercive fields of actual crystals are governed by the mobility of domain wall, and hence these discrepancies are not serious for our phenomenological theory. Since the double hysteresis loop was actually observed just above the transition temperature,[1] our results obtained seem to be reasonable.

§§ 3. 2. Temperature dependence of the electric susceptibility

In this section, we shall discuss about the temperature dependence of the electric susceptibility below the transition temperature by using the coefficients determined in the former section. In comparing the calculated susceptibility with the measured one, we have to pay attention to the fact that the measurement of the susceptibility was performed under the adiabatic condition, while the formula given by eq. (7) is for the isothermal one. Taking into account of the difference, Wieder[20] tried to interprete the observed value of C_P/C_F in colemanite, which is not 2, as expected from a general phenomenological theory, but 3.2.

The general relation between the adiabatic susceptibility and isothermal one was given by Baumgartner[21] as

$$1/\chi_a - 1/\chi_i+\left(\frac{\partial E}{\partial T}\right)_P^2\frac{T}{\Gamma}, \tag{14}$$

where Γ is the specific heat at constant polarization. Using eq. (5), we have

$$\left(\frac{\partial E}{\partial T}\right)_P=2AP. \tag{15}$$

Substituting eqs. (7) and (15) into eq. (14), we have

$$1/\chi_a=\Sigma_1+\Sigma_2+\Sigma_3, \tag{16}$$

where

$$\Sigma_1=2A(T-T_0)\ , \tag{17}$$

$$\Sigma_2=12BP^2+30CP^4\ , \tag{18}$$

and

$$\Sigma_3=4A^2P^2T/\Gamma\ . \tag{19}$$

In the paraelectric region where the spontaneous polarization vanishes, it has no need of considering the difference between χ_a and χ_i except for the case in which an extremly strong electric field is applied. Fig. 12 shows Σ_1, Σ_2, Σ_3 and $1/\chi_a$ separately as a function of temperature. Σ_1 is a straight line crossing with the abscissa at 163°C and Σ_1 is nearly a straight line in temperature range from 140°C to the transition temperature, and its extrapolated line crosses the abscissa at 164.5°C. Σ_3 is the term responsible for the electrocaloric effect and almost counterbalances the term Σ_1 in its magnitude. In the calculation of Σ_3, the constant value of 0.26 cal/°C gr was adopted as the value of Γ.[2] In the result, $1/\chi_a$ varies almost lineary with the temperature, having the gradient of 18.1×10^{-3} °K^{-1} and its extrapolated line intersects the abscissa at 166.3°C, which is in good agreement with T_1, 166.5°C, Since the gradient in the paraelectric region is given by $2A$, the value of C_P/C_F becomes *ca* 7.4, which coincides fairly good with the observed one, 7.5.

§§ 3. 3. Internal energy

The polarization will be accompanied by a change of internal energy, which will be given by the usual formula[14]

$$U=T\left(\frac{\partial F}{\partial T}\right)_p-F\ , \tag{20}$$

where the suffix p represents that the pressure is kept constant. Now F depends on temperature partly through the polarization, so we can write

$$\left(\frac{\partial F}{\partial T}\right)_p=\left(\frac{\partial F}{\partial T}\right)_{p,\,P}+\left(\frac{\partial F}{\partial P}\right)_{p,\,T}\left(\frac{\partial P}{\partial T}\right)_p$$

$$=\left(\frac{\partial F}{\partial T}\right)_{p,\,P}+E\left(\frac{\partial P}{\partial T}\right)_p\ , \tag{21}$$

and hence for zero field

$$\left(\frac{\partial F}{\partial T}\right)_p=\left(\frac{\partial F}{\partial T}\right)_{p,\,P}. \tag{22}$$

Since we have assumed all the coefficients, A, B, and C to be independent of temperature, eq. (20) becomes

$$V=AT_0P^2-BP^4-CP^6\ . \tag{23}$$

We can now calculate the internal energy as a function of temperature by using the values of the coefficients and the polarization. Substituting the observed value of the polarization in eq. (23), we have 3.74×10^{-8} erg/cm^3 as the value of U at room temperature. On the other hand, the magnitude of the internal energy can be estimated approximately from the transition heat as *ca* 3.37×10^8 erg/cm^3.[2] Considering the experimental accuracy of the measurement of specific heat, it may be said that they show a good coincidence.

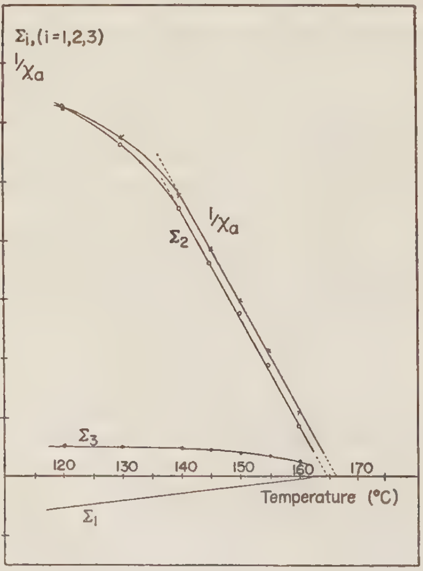

Fig. 12. Temperature dependences of Σ_1, Σ_2, Σ_3, and $1/\chi_a$.

§ 4. Discussions

§§ 4. 1. Carrier of the ferroelectricity

The carrier of the ferroelectricity in $NaNO_2$ is NO^-_2 radical which is non-symmetric in its shape and have a permanent electric dipole moment. It is known that NO_2 molecule is polar, with permanent electric dipole moment of 0.4 Debye unit. In NO_2^-, however, this value will be changed to some extent due to the variation of its electronic configuration. The bond length and angle of NO_2^- in $NaNO_2$ crystal was measured by several crystallographers. The results are given in Table 1, in which Strijk's values are for 205°C, and the others are for room temperature. It is to be noted that the bond length increases and the angle decreases with increasing temperature.

Pauling[22] proposed a picture for NO_2^- radical

Table I. Values of the bond length and angle of NO$_2^-$ radical. Strijk's values are for 205°C and the others are for room temperature.

	Ziegler[11]	Carpenter[12]	Truter[13]	Strijk[10]
N-O bond length (Å)	1.13	1.233±0.04	1.24±0.035	1.31
∠ONO (deg)	132	115.7±3	114.2±4	114

by usual resonance method, where the main contributing structures are

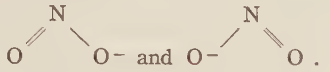

The N$^+$—O distance predicted on this basis was given by

$$R=R_1+(R_1-R_2)\frac{3x}{2x+1}, \tag{24}$$

where R_1 and R_2 are the bond lengths of single and double respectively and x represents the contributing ratio of the double bond. Taking the numerical values as $R_1=1.46$ Å (by Pauling[22]), $R_2=1.15$Å (by Schomaker & Stevenson[23]), Carpenter[12] obtained 1.23 Å as the value of R, which is in good agreement with the x-ray data. Consequently the Pauling's picture seems to be adequate for NaNO$_2$.

Now we shall give a rough estimation for the value of spontaneous polarization by using the x-ray data. In the first step, we shall consider that the spontaneous polarization consists of a term due to the relative ionic displacement between Na$^+$ and NO$_2^-$ ions, in which the minus charge is located in average on the line connecting the two oxygens. The essence of the atomic arrangement contributing to the polarization is visualized schematically in Fig. 13, where two patterns (a) and (b) correspond to the atomic arrangements having the polarization of opposite sense each other. Adopting the value of the relative displacement δ as 0.48 Å from the x-ray data[12] we obtain 2.3 Debye unit as the contribution to the polarization from the ionic term, that leads to *ca* 12 μC/cm^2 as the value of spontaneous polarization obtained from the pyroelectric current.

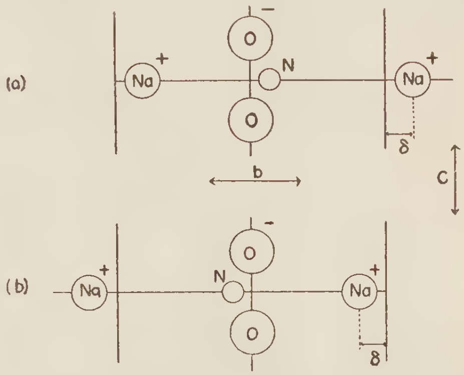

Fig. 13. Relative displacement between Na$^+$ and NO$_2^-$ ions. (a) and (b) correspond to the atomic arrangements having opposite polarization each other.

It is to be noted that the above estimation would be of the upper limit, because the largest value of δ was adopted and the location of the negative charge was taken on the 0–0 line. Effects of thermal vibration will act for the magnitude of δ to diminish somewhat. Provided that some fractions of NO$_2^-$ radicals take the wrong alignment, the circumstances will be more improved. As the ordering parameter s has been estimated as *ca* 0.78 at room temperature,[2] the value of spontaneous polarization ought to be discounted by the factor s and becomes 9.4 μC/cm^2. At any rate, the contribution to the spontaneous polarization from the dipole moment of NO$_2^-$ radical itself will be presumably small owing to its covalent character.

§§ 4. 2. Interatomic distances

NaNO$_2$ crystal has low melting point of 277°C, in comparision with that of a typical ionic crystal such as NaCl. This means that the interatomic interaction is rather weak and so the interatomic distances would be larger than those expected from the corresponding atomic or ionic radii. In fact, the situation is just as supposed, as shown in Table 2, in which the non-bonding interatomic distances resulted from the x-ray data[12] and the sums of the corresponding atomic or ionic radii are compared. The values of the interatomic distances are also entered in Fig. 14. If one NO$_2^-$ radical takes the wrong sense with keeping the others fixed, like ON′O in Fig. 14, we shall have 1.64 Å as the distance of Na$^+$—N, which is far shorter than the sum of the corresponding atomic radii. In that

Table II. Non-bonding interatomic distances and their corresponding sums of atomic (ionic) radii.

	Interatomic distance (Å)	Sum of the atomic radii (Å)
Na^+—O	2.47, 2.52	2.35
Na^+—N	2.61	2.45
N^+—O	3.22	2.90
O—O	3.55	2.80

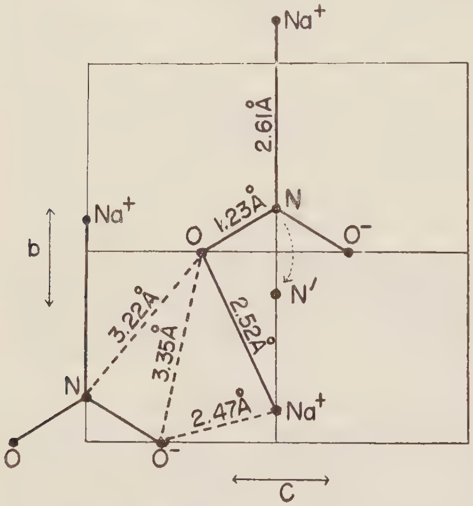

Fig. 14. Interatomic distances. Full and dotted lines represent the interatomic distances between ions located in the same *bc* plane and in the *bc* planes distant by $\frac{1}{2}a$ respectively.

case, the neighboring Na^+ and NO_2^- will be forced to shift along the *b* direction, then it will give the NO_2^- a chance to turn, and finally lead to the reverse turn of the crystal polarization. For the other interatomic distances, the situations are not so serious as for the case of Na^+—N. This circumstance suggests us that the interatomic interaction will be weaker in the direction perpendicular than parallel to the *b* axis. The short range interaction in the *b* direction is cosidered to be the important factor for NO_2^- radical to aligne in one sense in the ferroelectric phase.

When the temperature is raised, $NaNO_2$ crystal expands in the *a* and *b* directions while it contracts in the *c* direction.[2), 7), 10)] That is intimately related to the behavior of the thermal vibration of NO_2^- radical in the lattice. We may judge from the x-ray data on the atomic arrangements above the transition temperature[10)] that the misalignment of NO_2^- radical is responsible for the anomalous thermal expansion in the *b* direction. The expansion in the *a* direction and the contraction in the *c* direction will be understandable qualitatively, if we take into account of rotation or rotational vibration about any axis of the non-spherical NO_2^- radical, which takes its long axis parallel to the *c* direction in the equilibrium.

§§ 4. 3. Kind of transition and comparision with other typical ferroelectrics

We have concluded from the dielectric properties and the phenomenological theory that the transition in $NaNO_2$ is of the first kind. It is to be noted, however, that it stands close to the second kind one, as was seen in the measurement of thermal properties,[2)] in which the anomalies appear far below the transition temperature. Recently, Shibuya has shown by his x-ray study[5)] using Bragg reflections and critical scatterings that the phase transition in $NaNO_2$ can be interpreted by a model of order-disorder type, and noticed that the observed intensity of the critical scattering drops rather abruptly just above the transition temperature. Although the type of the transition is of order-disorder, it does not necessarily follow that it is of second kind. It goes without saying that the same situation exists in the transition of displacive type. Actually Triebwasser has shown in his study[24)] on dielectric property for the system of $KNbO_3$—$KTaO_3$ that the kind of transition changes from the first kind to the second one, according to its constituting ratio. By using a general method of Bethe approximation, Grindlay and Harr[25)] predicted that the transition in KH_2PO_4 can be treated as the first or second kind either, according to the magnitude of coordinating energy of H^+ around PO_4^- radical. He stated that the transition would take place as the first kind when the magnitude of the energy is large and the transition as the second kind when small. The circumstances in $NaNO_2$ are considerably different from that in KH_2PO_4, neverthless, we may imagine that the similar relation will be derived in the case of $NaNO_2$, if the short range interaction between NO_2^- radical, which acts so as to intensify the co-operative character in the transition, becomes strong beyond a certain critical value.

Table III. Comparision of properties between several typical ferroelectrics.
F means to be ferroelectric, and *P* to be paraelectric.

compound	crystal symmetry	transition temperture (°C)	state	spontaneous polarization (μC/cm^2)	Cp (°K)	piezoelectricity in paraelectric region		kind of transition		character of transition	
						yes	no	1st	2nd	displacive	order-dirorder
$BaTiO_3$	rhombohedral orthorhombic tetragonal cubic	−70 5 120	F F F P	26	1.7×10^5		○	○		○	
$NaNO_2$	orthorhombic	164	F P	8.6	5.1×10^3		○	○			○
KH_2PO_4	orthorhombic tetragonal	−150	F P	4.6	3.2×10^3	○			○		○
Colemanite	monoclinic	−7	F P	0.53	5.0×10^2		○		○		○
GASH	rhombohedral	>200	F	0.35	—						
Rochell salt	orthorhombic monoclinic orthorhombic	−18 23	P F P	0.25	1.7×10^3	○			○		?

Tanisaki has found by his x-ray study6) that a micro-domain structure is realized just above the transition temperature. Though its detail is not disclosed, it will be conceivable that the micro-structure is not an evidence for an new phase but a short range ordered arrangement of NO_2^- radicals remaining still in the paraelectric region. However, Hoshino and Shibuya have suggested from their x-ray study7) that another new phase is expected in the temperature range from 163°C to 178°C. and therefore we cannot but say that there ramains some ambiguity about it.

There conceived is another factor which makes the transition the first kind. It is an effect due to the volume change. Kirkwood suggested in his article26) concerning transition phenomena of crystals which contain rotatable dipoles that the first kind transition would occur if the restraining field for the dipoles were affected to a certain degree by the volume change due to the temperature effect. As $NaNO_2$ crystal fairly changes its volume near the transition temperature, the effect may have a direct influence upon the nature of the transition.

The transition in $NaNO_2$ is not accompanied by the change of point group symmetry, though its space group transfers from $C_{2v}^{20}(I_{mm})$ to $D_{2h}^{25}(I_{mmm})$.10) Regarding this point, the situation is the same as in colemanite,20) the crystal symmetry of which is kept monoclinic through the transition. The temperature hysteresis of the transition, however, occurs only in the former case. We add here that the hysteresis of the transition temperature had been already pointed out by Strijk and MacGillavry in their x-ray study.10)

To understand well the situation of $NaNO_2$ crystal, we give Table 3, in which certain properties of several typical ferroelectrics are listed, and the compounds are arranged in order of magnitude of their spontaneous polarization. $NaNO_2$ is ranked in the second, between $BaTiO_3$ of the displacive type and KH_2PO_4 of the order-disorder type. Judging from the discussions in §§ 4.1 and 4.2, it may be said that the transition in $NaNO_2$ stand close the displacive type, even if it is classified in the order-disorder type. $NaNO_2$ crystal is a ferroelectric crystal which stands halfway between ionic and molecular crystal.

§ 5. Additional Remark

It has been cleared by our recent investigation* that the $NaNO_2$ crystal shows a remarkable plasticity in the temperature region above the transition temperature. The plastic nature is regarded as one of the evidence that the rotaional thermal vibration of NO_2^- radical is considerably violent in the paraelectric region.27) It will be necessary to take into account of the plastic effect of $NaNO_2$

---

* S. Nomura: unpublished.

crystal, when we carry out the precise measurement, in particular, above the transition temperature. We may call $NaNO_2$ crystal as a plastic ferroelectric crystal.

Acknowledgements

The author should like to thank Prof. S. Sawada for suggesting this investigation and for guidance throughout the work.

References

1) S. Sawada, S. Nomura, S. Fujii and I. Yoshida: Phys. Rev. Letters **1** (1958) 320.
2) S. Nomura: J. Phys. Soc. Japan **16** (1961) 1352.
3) S. Nomura, Y. Asao and S. Sawada: J. Phys. Soc. Japan **16** (1961) 917.
4) B. C. Frazer, R. Ueda and M. I. Kay: Acta Cryst. **13** (1960) 1089.
5) I. Shibuya: J. Phys. Soc. Japan **16** (1961) 490.
6) S. Tanisaki: J. Phys. Soc. Japan **16** (1961) 579.
7) S. Hoshino and I. Shibuya: J. Phys. Soc. Japan **16** (1961) 1254.
8) H. Betsuyaku and J. Itoh: Preprint of the Annual Meeting of the Phys. Soc. Japan No. **3** (1961) 189.
9) Y. Sato and Y. Takagi: Preprint of the Divisional Meeting of the Phys. Soc. Japan No. **1** (1961) 110.
10) B. Strijk and C. H. MacGillavry: Rec. trav. chim. **62** (1943) 705; **65** (1946) 127.
11) G. E. Ziegler: Phys. Rev. **38** (1931) 1040.
12) G. B. Carpenter: Acta Cryst. **5** (1952) 132.
13) M. R. Truter: Acta Cryst. **7** (1954) 73.
14) A. F. Devonshire: Phil. Mag. **40** (1949) 1040.
15) W. Känzig: Solid State Physics **4** (1957), Ferroelectrics and Antiferroelectrics.
16) F. A. Grant: J. Appl. Phys. **29** (1958) 76.
17) S. Marutake: Bull. Kobayashi Inst. Phys. Res. **6** (1956) 64.
18) C. Kittel: Phys. Rev. **82** (1951) 729.
19) L. P. Kholodenko: Soviet Phys. J. E. T. P. **4** (1957) 847.
20) H. H. Wieder: J. Appl. Phys. **30** (1959) 1010.
21) H. Baumgartner: Helv. Phys. Acta **23** (1950) 651.
22) L. Pauling: Nature of Chemical Bond (1940).
23) V. Schomaker and D. P. Stevenson: J. Am. Chem. Soc. **63** (1941) 37.
24) S. Triebwasser: Phys. Rev. **114** (1959) 63.
25) J. Grindlay and D. ter Haar: Proc. Roy. Soc. **250** (1959) 266.
26) J. G. Kirkwood: J. Chem. Phys. **8** (1940) 205.
27) C. P. Smyth: J. Phys. Chem. Solids **18** (1961) 40.

JOURNAL OF THE PHYSICAL SOCIETY OF JAPAN, Vol. 16, No. 12, DECEMBER, 1961

Hall Effect in the Carbides of Transition Metals

By Takashi TSUCHIDA, Yoji NAKAMURA, Mamoru MEKATA,
Junji SAKURAI and Hideo TAKAKI

Faculty of Science, Kyoto University

(Received July 4, 1961)

Measurements have been made of the electrical resistivity and the Hall constant of the carbides of the fourth and fifth group transition metals at room temperature in order to clarify the electronic structure of these compounds. The Hall coefficients are of the order of -10^{-3} coul^{-1} cm^3 for the fourth group carbides and of -10^{-4} coul^{-1} cm^3 for the fifth ones. Calculating the concentrations of the conduction electron on the basis of the one-band approximation, it was found that the conduction band may be almost empty for the fourth group carbides and may be occupied by about one electron per chemical formula unit for the fifth ones. The results may suggest that all these carbides have similar band structures to each other.

§ 1. Introduction

The carbides of the transition metals of the fourth and the fifth groups of the periodic system are less ductile and less malleable and have a high melting point and an extreme hardness. Nevertheless they possess high electrical and thermal conductivities and metallic luster. These properties seem to be due to the coexistence of metallic nature and directional covalent bond, as have been discussed by several authors.1),2),3)

In order to clarify the electronic structure of these carbides, Hall coefficients and electrical resistivities were measured at room temperature. From these measurements the sign of the predominant carrier can be determined, and the semiquantitative informations of the carrier density and of the mobility can be obtained for each carbide. Furthermore, a comprehensive interpretation can be drawn on the basis of the periodic system for the electronic structure of the carbides of the fourth and the fifth groups, since these compounds form the isomorphic structure of the sodium chloride type.

§ 2. Experimental Procedures

The samples were sintered by hot-press at about 2000°C and 50 kg/cm^2 in a high frequency induction furnace for several hours. The results of chemical analysis of carbides before sintering are given in the first and second colums of Table I. The packing factor of the sintered samples shown in the third colum of Table I was estimated from the apparent density and the lattice constant. The sizes of the specimens used in the measurements were $(3\sim4)\times(0.6\sim0.7)\times(0.02\sim0.1)$ cm^3.

The Hall voltages were measured by means of the three-probes method with primary direct currents up to 4A in the magnetic fields up to 20500 gauss. The electrical resistivities

Table I

	atomic ratio C/Me	impurities	packing factor $(1-P)$
TiC	0.96	free C(<0.5%), Fe(<0.1%), others(<0.06%).	1.00
ZrC	—	—	0.98
HfC	—	—	0.96
V C	0.7	free C(<1%), Fe(<0.25%), Si(<0.1%), Al(<0.16%).	0.94
NbC	0.97	Ta(~2%), C(0.1%), Ti(~0.6%), Fe(~0.1%).	0.71
TaC	1.0	Nb(<1%), C(0.1%), Ti(~0.2%), others(<0.2%).	0.87

were measured by the conventional method.

§ 3. Experimental Results.

As the specimens produced by sintering are porous, the correction of the measured Hall coefficients for the porosities of the specimens should be made on all of these sintered samples. Discussing the relation between the measured Hall coefficient and the porosity of the sample, Juretschke et al.[4] derived the following relation: $R_m=(1-\frac{1}{4}P)R_0/(1-P)$, where R_m is the measured coefficient, R_0 the corrected one and P the porosity. But the difference between this relation and a more simple one $R_m=R_0/(1-P)$, is so slight in the case of small P that we used the latter relation for the correction of porosity. From the corrected Hall coefficients, the carrier concentration were calculated according to the equation of one band model;

$$n=\frac{1}{R_0 e}\frac{M}{Nd_0}=\frac{1}{R_m e}\frac{M}{Nd_m},$$

where e is the electronic charge, M the formular weight, d_0 the density of the single crystal calculated from the lattice constant, d_m the measured one of the sintered specimen, N the Avogadro's number, and n the number of the conduction electrons per chemical formula unit, MeC (a quarter of unit cell).

The temperature dependence of the electrical resistivity and the Hall coefficient of titanium carbide were measured in order to confirm its metallic nature in conduction. The results, given in Fig. 1, show that the Hall coefficient does not noticeably vary and the electrical resistivity increases with increasing temperature. These facts show that titanium carbide is metallic. The same consideration may be extended to other transition metal carbides.

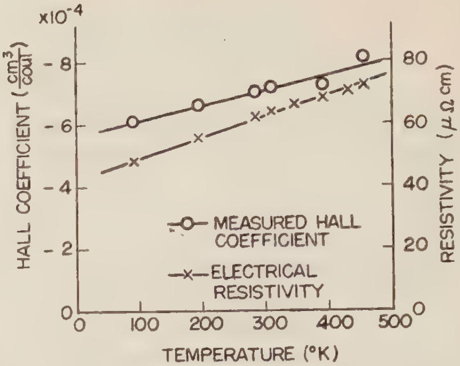

Fig. 1. Hall coefficient and electrical resistivity of TiC.

Table II lists the electrical resistivities, the measured Hall coefficients, the corrected Hall coefficients, the apparent Hall mobilities and carrier concentrations at room temperature.

As easily seen from the table, there are several striking differences between the fourth and the fifth group carbides. They are summarized as follows:

i) The Hall coefficients of the fourth group carbides are of the order of -10^{-3} coul^{-1} cm^3, while those of the fifth ones are of the order of -10^{-4} coul^{-1} cm^3.

ii) The apparent Hall mobilities of the fourth group carbides are larger than those of the fifth ones.

iii) Calculating the concentrations of the conduction electron on the basis of the one-band approximation, the conduction band is found to be almost empty for the fourth group carbides. While the fifth group carbides have nearly one electron per chemical formula unit.

Table II

	electrical resistivity ($\mu\Omega$ cm)	measured Hall coefficient $R_m\left(\frac{\text{cm}^3}{\text{coul}}\right)\times10^4$	corrected Hall coefficient $R_0\left(\frac{\text{cm}^3}{\text{coul}}\right)\times10^4$	apparent Hall mobility $\left(\frac{\text{cm}^2}{\text{volt}\cdot\text{sec}}\right)$	conduction electrons per formula
TiC	63	− 7.04	− 7.04	11	0.18
ZrC	68	−19.4	−19.3	28.6	0.09
HfC	65	−18.8	−18.1	28.9	0.09
V C	98	− 0.97	− 0.91	0.99	1.2
NbC	58	− 1.80	− 1.28	3.2	1.04
TaC	103	− 0.73	− 0.64	0.71	2.2

§ 4. Discussion

As described above, the fourth group monocarbides with eight valence electrons have conduction electrons much less than one per formula; while the fifth group monocarbides with nine electrons have one or more electrons for conduction. These facts suggest that the nonconductive orbitals with the capacity of eight electrons exist in both groups of the carbides. These nonconductive orbitals may consist of the localized orbitals in carbon and of the bonding orbitals binding the metal atoms to the carbon atom. It may be considered that the conductive band and the nonconductive band overlap each other. In this simple model of band structure, a rather small number of electrons (about 0.1/chemical formula) transferred from the bonding band to the conductive one contribute to the electrical conduction in the fourth group carbides. Whereas in the fifth group carbides, the conductive electrons may consist of the uppermost electron (the ninth electron) and of a small number of electrons transferred from the bonding band.

The nature of the bonds of metal to carbon has been discussed by the several authors. In the sodium chloride structure, six carbon atoms octahedrally surround the metal atoms and the latter do the former vice versa. Since a carbon atom has only four valence orbitals, it is unlikely that the bondings with its nearest six metal atoms are to be formed. The concept on the electron-defficient bond was introduced by Rundle⁽¹⁾ in order to explain the above fact. He proposed that the resonance between sp- and p-bonds of the carbon atom led to the octahedral bondings with the metal atoms. On the other hand, for the bond formation of the metal atom with carbon atoms, the d^2sp^3-hybridized orbitals are to be used. Extending his consideration, Bilz⁽³⁾ has suggested a general band scheme of these carbides as shown in Fig. 2. Our experiments show that Bilz's band scheme seems to be valid.

According to Noguchi and Sato⁽⁵⁾, it is possible to understand the thermo-electric power of TiC and VC in terms of the free electron model. Their results may support the validity of the one-band approximation for the electrical conduction in these carbides.

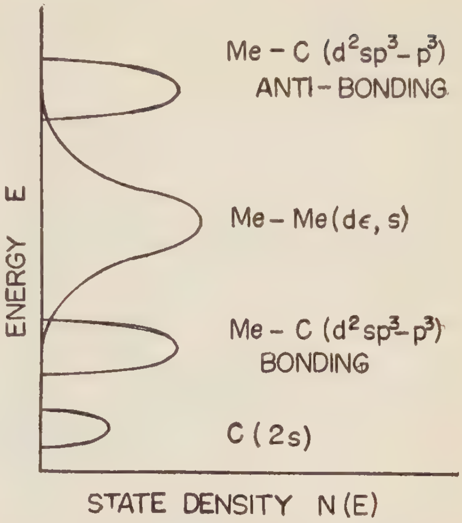

Fig. 2. A proposed band scheme of monocarbide with NaCl structure after Bilz.

But it is hard to understand why the apparent Hall mobilities of the fourth group carbides are larger than those of the fifth group ones. Taking account of the fact that the thermal conductivity of the fourth group carbides is larger than that of the fitth group ones,⁽⁶⁾ we are interested indeed in the fact that the general features of the apparent mobility are analogous to those of the thermal conductivity.

As above mentioned, some electrical properties of the transition metal monocarbides with sodium chloride structure can qualitatively be interpreted on the basis of the band scheme. The samples used in our experiments, however, may not be satisfactory because they were impure, not stoichiometric and further they were porous. Then any more quantitative discussion will be impossible until the measurements will have been carried out on more perfect samples and moreover on single crystals.

The authors are greatly indebted to the members of Toshiba Tungalloy Co., Ltd. and of Nagoya Government Industrial Research Institute for their kindness to prepare the specimens.

References

1) R. E. Rundle: Acta Cryst., **1**, (1948), 180.
2) W. Hume-Rothery: Phil. Mag., **44**, (1953), 1154.
3) H. Bilz: Z. Physik, **153**, (1958), 338.
4) H. J. Juretschke and R. Steinitz: J. Phys. Chem. Solids, **4**, (1958), 118.

5) S. Noguchi and T. Sato: J. Phys. Soc. Japan **15**, (1960), 2359.
6) J. Sakurai et al.: J. Japan Inst. Metals **25**, (1961), 289. (in Japanese)

JOURNAL OF THE PHYSICAL SOCIETY OF JAPAN Vol. 16, No. 12, DECEMBER, 1961

Diffusion of Nickel in Silver*

By Tokutaro HIRONE, Shigeto MIURA and Toshiro SUZUOKA
The Research Institute for Iron, Steel and Other Metals,
Tohoku University, Sendai

(Received July 18, 1961)

The diffusion coefficient of nickel in single-crystal of silver has been measured by the lathe-sectioning technique as a function of temperature throughout the range from 750°C to 950°C using radioactive isotope Ni^{63} as a tracer. The results are expressed as follows:

$$D=(21.9)\exp\left(-\frac{54\ 800}{RT}\right)\ \mathrm{cm^2/sec}\ .$$

The value of activation energy, 54.8 kcal/mole, obtained by the present experiment is in good agreement with the result of the screening theory of impurity diffusion.

§ 1. Introduction

Since Lazarus[1] and other authors[2],[3] put forward the screening theory of impurity diffusion in metals, the diffusion coefficients of various impurity atoms in metals have been measured. The values of activation energies for diffusion in copper of the first transition elements and some neighbouring elements in the periodic table were found to increase in the order of Fe, Co, Ni and decrease from Ni to Zn and increase again at Ga[4)–7)]. The results of these experiments are partly consistent with the screening theory, but many quantitative contradictions have been found. Such a discrepancy might be explained to be attributed to the *s-d* interaction and the variety of the electronic states of the solute atoms which has been hardly taken into account in the theory mentioned above. In the case of impurity diffusion in silver, the experimental results are well reproduced theoretically in the series of diffusing atoms, Cd, In, Sn, Sb as well as Zn, Ge. However, due to the lack of experimental results, the behavior in transition metals has not yet been clear. The purpose of the present research is to study the diffusion of nickel in silver.

§ 2. Experimental Procedure

Single crystals of 99.99% silver were used as specimen. A cylindrical crystal, about 1.5 cm in diameter and 15 cm in length, was grown in high-purity graphite crucibles in a vacuum furnace by means of the Bridgman method. This was set in a resin mould and cut into flat cylinders, 15 mm in length, by a cut-off wheel. To avoid the influence of strains due to the cutting process, the worked surface layer, about 2 mm in thickness, was removed by electropolishing. The surfaces were flattened by polishing with emery paper and again electropolished. The polished crystals were annealed in a vacuum furnace and it was confirmed that no recrystallization occurred on the polished surface. An end surface of the specimen was then electroplated with Ni^{63} isotope containing no carrier. The amount of deposited nickel was calculated from the product of time and current-density

---

* A part of the expense of this investigation was supported by the Grant-in-Aid of the Fundamental Scientific Research of the Ministry of Education.

of electroplating as to be 100 to 500Å.

The electroplated specimen was sealed in a quartz capsule which was filled with pure argon gas and set in a diffusion annealing furnace. The furnace temperatures were maintained constant within ±0.5°C. After the annealing was completed, the specimen was quenched in cold water, then mounted on a precision lathe. To avoid the effect of surface diffusion, a layer about 1 mm in thickness was first removed from the side of the cylindrical specimen. The specimen was then sectioned into many thin slices. Each slice thickness was determined from the slice mass. The thickness was checked by measuring the specimen length with a dial-gauge as well as the specimen weight before and after each sectioning. In order to measure the specimen weight after each sectioning, a specially designed chuck was used. The chuck could be dismounted from the lathe without taking the specimen off and re-mounted on the lathe so that the orientation of the specimen surface was reproducible. The chips were collected in a polystyren chamber surrounding the specimen and sectioning tool. Each collected mass ranged from 98.5% to 99.8% of each slice mass which was estimated from the diminution of the specimen weight due to each sectioning.

Since the short-ranged pure beta rays emitted from Ni^{63} are easily attenuated by the absorption effect, following method for the radioactivity measurement was adopted; each slice was entirely dissolved into 10 N nitric acid, the amount of which was proportional to each slice mass, then a constant volume of the solution was poured in a counting plate of stainless-steel. The solution was dried and measured by using the 2π low back ground counter. Total error for counting decreased to about 1% by these processes.

§ 3. Experimental Results

The penetration curves for the six diffusion runs throughout the temperature range from 950.2°C to 748.5°C are shown in Fig. 1. Each curve strictly linear between logarithm of specific activity and the square of the penetration depth x in the region in which x is greater than $2\sqrt{Dt}$, but shows a deviation from the linearity near the surface. The diffusion coefficient was calculated from the

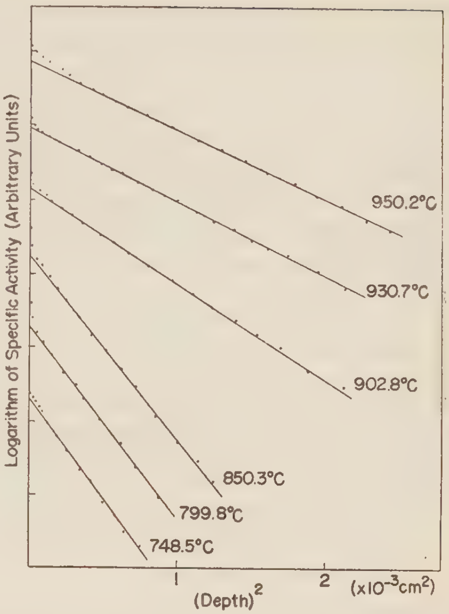

Fig. 1. The penetration curves for the diffusion of Ni^{63} in Ag.

Table I. Diffusion of Ni in Ag.

Curve	Temperature (°C)	Annealing Time (sec)	D (cm²/sec)
1	950.2	3.37×10^4	3.52×10^{-9}
2	930.7	4.32×10^4	2.46×10^{-9}
3	902.8	5.72×10^4	1.49×10^{-9}
4	850.3	9.72×10^4	4.44×10^{-10}
5	799.8	2.60×10^5	1.62×10^{-10}
6	748.5	9.75×10^5	4.07×10^{-11}

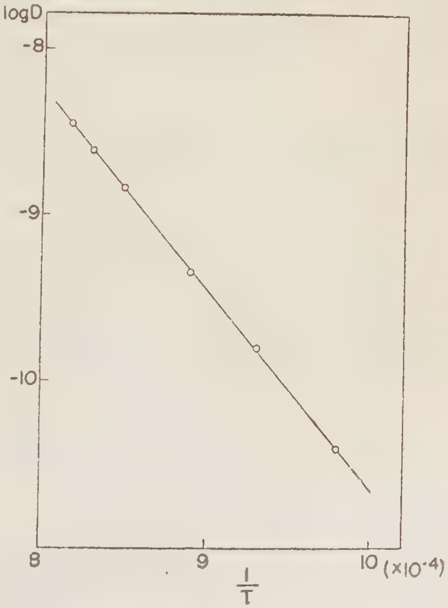

Fig. 2. Diffusion data plotted as log D versus $1/T$.

slope at the region of x greater than $2\sqrt{Dt}$. The error in the D-value was estimated to be 5%. The diffusion coefficient D obtained from these penetration curves, together with annealing time t and temperature are given in Table I. Fig. 2 shows the temperature variation of the diffusion coefficient. As one can see from the curve in Fig. 2, the diffusion coefficient can be perfectly expressed by the Arrhenius relation,

$$D=D_0 \exp\left(-\frac{Q}{RT}\right).$$

Based on the above results, the value of the frequency factor D_0 and the activation energy Q are calculated by the method of least-square as to be

$$Q=(54.77\pm0.50)\times10^3 \text{ cal/mole},$$
$$D_0=21.9\pm4.7 \text{ cm}^2\text{/sec}.$$

§ 4. Discussion of the Results

The activation energy for the diffusion of Ni^{63} in silver obtained by the present experiment is shown by a dotted circle in Fig. 3, which summarizes the activation energies for impurity diffusion in copper and silver as functions of valence difference Z of solute atoms as compared with solvent metals. For obtaining the valence difference, the atomic cores of disolving transition elements in silver or copper are considered to take a closed configuration (d^{10}). As is seen in Fig. 3, the diffusion of Ni^{63} in silver has an activation energy lying between that for self-diffusion of silver and that for Co^{60} in silver[8)-10)]. Fig. 3 also shows that the Q-Z curve is convex to the valence axis at the positive Z side, and by taking into account the result of the present experiment, it can be seen that the Q-Z curve is concave at the negative Z side.

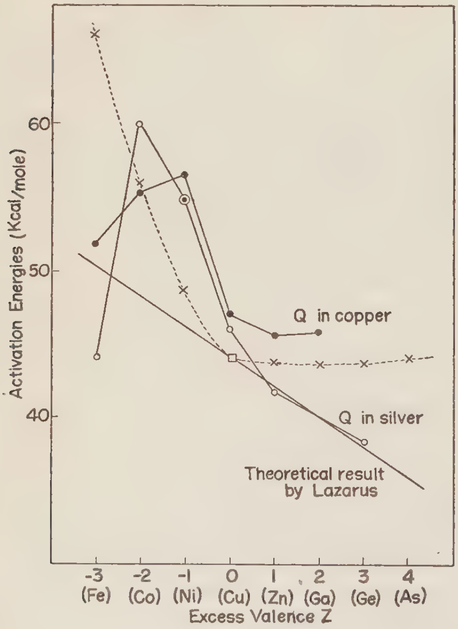

⊙ Results of the authors' present experiment
□ Activation energy for the self-diffution of silver
× Theoretical result by Blatt

Fig. 3. Calculated and experimental activation energies for impurity diffusion in copper and silver plotted as a function of excess valence Z.

For the diffusion of the first transition elements in copper, the curve shows a similar tendency to silver, but this tendency is more pronounced than in silver. From the assumption that the ions of these elements have a constant screening radius in silver, the activation energies linearly increase as Z decreases, as shown by Lazarus. Also it has been proposed by Blatt that if the screening radius increases with decreasing Z, the value of Q increases allowing a convex form to the valence axis as shown in Fig. 3. Although the results of the present experiment and those by other workers are partly consistent with the result by Blatt, the curvature to the valence axis was not consistent and all the calculated values by Blatt are always smaller than experimental values except for Fe in Ag. Such a discrepancy suggests the underestimation of the screening radius in Blatt's theory.

It may be worth noticing that the frequency factor D_0 obtained by the present experiment is large compared with the theoretical expectation. According to Zener's theory[11)], the relation between D_0 and Q is given as follows:

$$D_0=a^2\nu \exp(\lambda\beta Q/RT_m),$$

were a is the lattice constant of the solvent lattice ($a=4.0856$Å), ν Debye frequency ($\nu=4.5\times10^{12}$/sec), λ a numerical constant, 0.55, T_m the melting point of solvent metal ($T_m=1234$°K) and β is defined by

$$\beta=-d(\mu/\mu_0)/d(T/T_m),$$

(μ is the shear modulus, μ_0 the shear modulus at absolute zero of the temperature). β takes a value 0.45 for diffusion of electronegative impurities in silver[12),13)]. Putting these values in the above equation one obtains a value for the frequency factor

$$D_0 = 1.9\ \mathrm{cm^2/sec}\ .$$

This value is about one-tenth as large as the experimental one. Such a discrepancy has been observed also in the diffusion of Ru[12] and Co[9] in silver. Its origin will be discussed in a future paper.

The present authors wish to express their cordial thanks to Mr. H. Yamamoto for his kind advice throughout the work.

References

1) D. Lazarus: Phys. Rev. **93** (1954) 973.
2) F. Blatt: Phys. Rev. **99** (1955) 600.
3) L. C. R. Alfred and N. H. March: Phys. Rev. **103** (1956) 877.
4) C. A. Mackliet: Phys. Rev. **109** (1958) 1964.
5) M. Sakamoto: J. Phys. Soc. Japan, **13** (1958) 847.
6) A. Ikushima: J. Phys. Soc. Japan, **13** (1958) 764.
7) A. Kuper, H. Letaw, J. L. Slifkin, E. Sonder and C. T. Tomizuka: Phys. Rev. **98** (1955) 1870.
8) C. T. Tomizuka: Phys. Rev. **103** (1956) 1182.
9) T. Hirone and H. Yamamoto: J. Phys. Soc. Japan, **16** (1961) 455.
10) J. G. Mullen: Phys. Rev. **121** (1961) 1649.
11) C. Zener: J. Appl. Phys. **22** (1951) 372.
12) C. B. Pierce and D. Lazarus: Phys. Rev. **114** (1959) 686.
13) C. Zener: Imperfection in Nearly Perfect, Crystals (John Wiley and Sons, Inc. New York, 1952) 299.

JOURNAL OF THE PHYSICAL SOCIETY OF JAPAN, Vol. 16, No. 12, DECEMBER, 1961

Diffusion of Thallous Ions into Potassium Bromide Single Crystals

By Tokumichi TAMAI

Research Laboratory, Matsushita Electronics Corporation, Takatsuki, Osaka

(Received July 21, 1961)

The diffusion of thallous ions into potassium bromide single crystals has been measured as a function of temperature. The thallous ions were introduced into the crystal by heating the latter in a vapor of thallium metal. Concentrations of thallous ions were measued by the height of the characteristic absorption band of a thallous ion in a potassium bromide crystal. This height varies linearly with the concentration of thallous ions. Activation energy of the diffusion was 1.98 eV.

§1. Introduction

Several papers have been published on the diffusion of various metal ions into alkali halide single crystals[1]. For the measurements radioactive tracers were mainly used. The author has investigated the diffusion of thallous ions into KBr single crystals by measuring the height of the absorption band at 261 mμ, which is known from KBr-Tl phosphors[2]. A comparative study of the absorption spectra of KBr single crystals with added Tl and KBr-Tl phosphors has shown that these spectra are exactly alike.

The method of evaluating concentrations by measuring the height of the characteristic absorption band was applied in combination with Mizuno's technique of repeatedly polishing off thin layers of the crystal surface in order to measure concentration gradients[3]. In this way the diffusion constants at different temperatures could be calculated. The assumption that the metal concentration is proportional to the height of the absorption band was verified by the polarographic analysis of Tl^+ ions in KBr-Tl phosphors.

§2. Experimental Procedures

KBr single crystals were grown from the melt by the well-known Kyropoulos method. The crystals were heated at various temperatures in a quartz tube in the atmosphere of saturated Tl vapor. After quenching the crystal the absorption spectra were measured at room temperature. Taking the height and width of the absorption band as a measure for the Tl^+ ion concentration, an estimation of the concentration at any distance x from the surface was made in the following way:

1) The absorption coefficient of the 261 mμ band was measured every time after repeatedly taking off a layer of several to 20 microns from the exposed surface by polishing it with red ochre on a silk cloth.

2) The mean absorption coefficient of the 261 mμ band of the removed thin layer was determined by

$$\alpha_m = \frac{C_1 - C_2}{dx} ,$$

where C_1 is the measured absorption coefficient before polishing, C_2 the measured absorption coefficient after polishing, and dx the thickness of the removed layer.

3) The concentration of Tl^+ ions was derived from the absorption coefficient and band width by Smakula's formula[4] assuming the oscillator strength to be 0.073.

This procedure was repeated to a depth of 50 to 500 microns from the exposed surface. Fig. 1 shows a typical example of decreasing absorption with decreasing thickness of the crystal. The absorption measurements were carried out on an automatic recording spectrophotometer at room temperature and the corresponding values of the thickness were read on a micrometer with direct reading to 1 micron. The temperatures of the diffusion of Tl^+ ions were controlled by an automatic regulator with tolerance of 0.5%. The temperature range in the experiments was extended from 520°C to 700°C. Each measured value of the concentration of Tl^+ ions was plotted in the middle of a thin layer. Plots of logarithm of the concentrations of Tl^+ ions *versus* depth are shown in Fig. 2.

The migration of Tl^+ ions into the crystal during the heat process is determined by solving a simple Fick's equation:

$$\frac{\partial n}{\partial t} = D\frac{\partial^2 n}{\partial x^2} , \qquad (1)$$

where D is the diffusion constant.

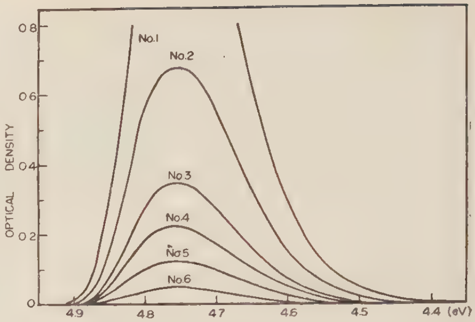

Thickness of polished-off thin layer of the crystal surface

No. 1	0.048 mm	No. 4	0.068 mm
2	0.055	5	0.076
3	0.062	6	0.086

Fig. 1. Characteristic absorption band of Tl^+ ion in a KBr single crystal heated at 595°C, 7H.

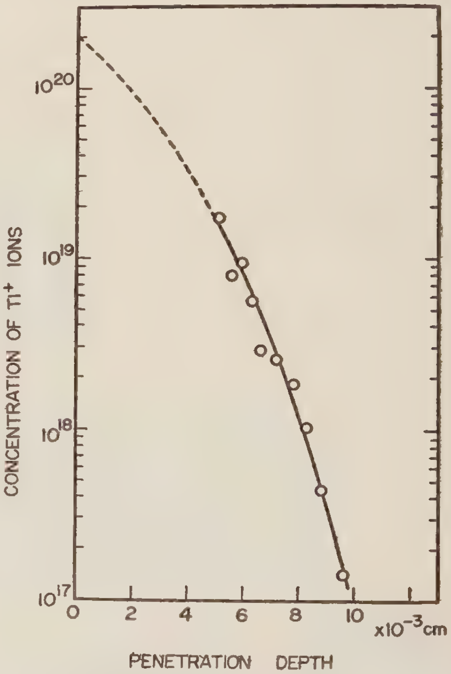

Fig. 2. Logarithm of concentrations of Tl^+ ions *versus* distance from the surface of the crystal. The value near the surface is obtained by extrapolating the data in Fig. 3.

The concentration n_0 of Tl^+ ions in the surface of the crystal is estimated from the density N of the Tl atom in the vapor phase assuming a distribution coefficient κ. That is

$$n_0 = \kappa N . \qquad (2)$$

The solution of Eq. (1) is given by

$$n = n_0 \,\mathrm{erfc}\,[x/2(Dt)^{1/2}] , \qquad (3)$$

which gives

$$\frac{dn}{dx} = -\frac{n_0}{\sqrt{\pi D t}} \exp(-x^2/4Dt) . \qquad (4)$$

The diffusion coefficient D of the thallous ions was obtained from the plot of logarithm of the derivative of the concentration of ions

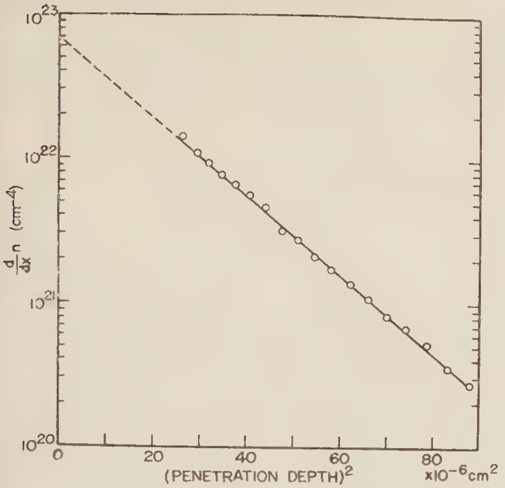

Fig. 3. Logarithm of the derivative of the concentration of Tl^+ ions *versus* square of penetration depth for 595°C, 7H.

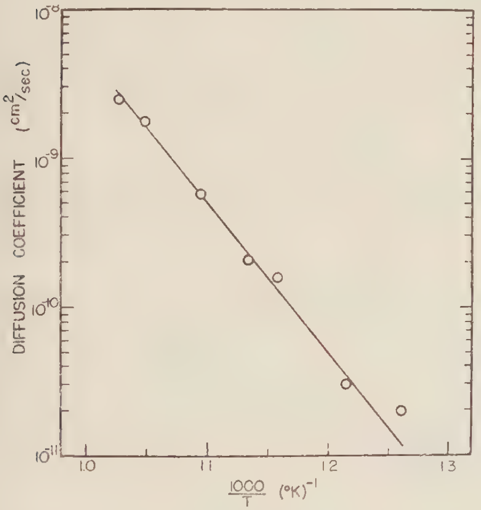

Fig. 4. Plot of the logarithm of diffusion coefficient *versus* the inverse of absolute temperature.

as a function of the square of distance, x^2, of the layer from the surface of the diffusion sample. Such plots yield straight lines as shown in Fig. 3.

The diffusion coefficient of the Tl^+ ions in the crystal at various temperatures is given by

$$D = D_0 \exp(-E/kT)\,, \qquad (5)$$

where E is the activation energy of the diffusion, D_0 is a constant, k is the Boltzmann constant, and T is the absolute temperature.

In Fig. 4 the logarithm of the diffusion constant is plotted as a function of the inverse of the absolute temperature, from which the activation energy of the diffusion is derived as 1.98 eV and $D_0 = 47\ \mathrm{cm^2/sec}$. That is

$$D = 47 \exp(-1.98/kT) \quad (\mathrm{cm^2\,sec^{-1}})\,.$$

§ 3. Oscillator Strength of the 261 mμ Absorption Band

The oscillator strength of the 261 mμ absorption band of KBr-Tl phosphors is 0.073 at room temperature. Single crystals were prepared by dissolving a small quantity of TlBr in the melt of KBr and growing up by the Kyropoulos method. Concentrations of Tl^+ ions were 0.01, and 0.1 mol % in the melt. The crystal was cleaved to a size of 10×10 ×0.5 mm, and the absorption coefficient was measured with the above-mentioned spectrophotometer at room temperature. The shape of the 261 mμ absorption band was clearly asymmetric and Smakula's constant⁴⁾ was equal to the value of double Gaussian shape, which is 1.0645 within experimental error.

The concentrations of Tl^+ ions in the above sample were measured by the polarographic analysis. Fig. 5 shows the relation of the concentration of Tl^+ ions and the absorption coefficients. Yuster *et al.*⁵⁾ have reported the oscillator strength of the corresponding absorption band of KI-Tl as 0.17 at liquid nitrogen temperature. The present value of KBr-Tl is smaller than the one of KI-Tl. The accuracy of the oscillator strength of KBr-Tl was within 10%.

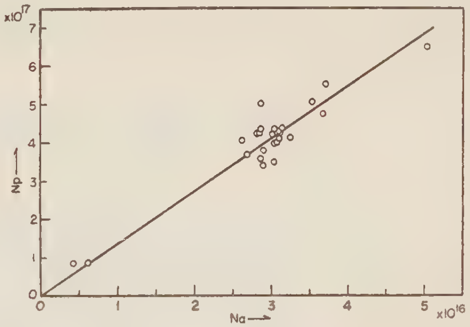

Fig. 5. Ordinate N_p is the concentration of Tl^+ ions as determined by polarographic analysis. Abscissa N_a is the same concentration as derived from the absorption band, assuming the oscillator strength to be unity.

§ 4. Discussion

As shown in Fig. 2, the concentration of Tl^+ ions in the KBr crystal was of the order of 10^{20} cm^{-3} near the surface of the crystal. This means that one Tl^+ ion exists per 100 K^+ ions. In such a case, other thallium activated alkali halide phosphors, for instance KI, NaI[6], show another characteristic absorption band which corresponds to paired thallous ions. But in KBr there was no evidence of such a new absorption band even in the above-mentioned concentration, and the band width was equal in all cases. It is reasonable to conclude that the absorption coefficient varies linearly with the concentration of Tl^+ ions in the region covered by our experiment. Of course this was only verified in the case of rather low concentrations, say, of the order of 10^{18} cm^{-3}.

The thallium diffusion process differs from the process of additive coloring in so far that no absorption band corresponding to an F band is observed. In the outer phase of the crystal there is Tl vapor and inside the crystal there are Tl^+ ions which are apparent from the characteristic absorption band of a Tl^+ ion. However no evidence of other phenomena occurs.

It is reasonable to assume that the thallous ion is introduced according to the following cycle[7].

1) Remove K^+ and Br^- ions from the body of the crystal; the work W_{KBr} is the lattice energy per ion pair of a KBr crystal and is of the value of 6.9 eV.

2) Remove an electron from a thallium atom; the work is I_{Tl}, where I_{Tl} is the ionization potential with the value of 6.106 eV.

3) Add the electron to the K^+ ion; the work is given by $-I_K$, where I_K is the ionization potential with the value of 4.34 eV.

4) Place the Tl^+ and Br^- ions on the surface of the crystal; the necessary work is $-W_{TlBr}$, where W_{TlBr} is the lattice energy per ion pair of TlBr in the KBr crystal.

The sum of all these energies is the energy W required to introduce a Tl^+ ion into the crystal, thus

$$W=W_{KBr}-W_{TlBr}+I_{Tl}-I_K\,, \qquad (6)$$

where only W_{TlBr} is unknown.

The concentration of dissolved Tl^+ ions was about 2×10^{20} per cm^3 near the surface of the crystal at 595°C. At this temperature the density of Tl atoms in the vapor phase is of the order of 10^{15} per cm^3. The Tl atoms in the vapor phase will be in equilibrium with the Tl^+ ions in the crystal at the following rate:

$$\frac{\text{Concentration of the Tl}^+\text{ ions in the crystal}}{\text{Density of the Tl atoms in the vapor phase}}=\kappa=\exp(-W/kT)\,,$$

from which follows $W=-0.94$ eV.

Using Eq. (6) we find

$$W_{TlBr}=9.6\text{ eV}\,.$$

This is the binding energy that the Tl^+ and Br^- ions introduce into the KBr crystal.

The concentrations of various impurities in the KBr single crystal were measured by means of spectroscopic analysis and these were tabulated in Table 1. The concentration of impurities in the crystal was less than the concentration of Tl^+ ions in the scope of the present experiments.

Table 1. Impurity concentration in KBr.

Impurity	Ca	Na	Mg	Si	Al
Concentration (less than)	10^{-5}	10^{-5}	10^{-6}	10^{-6}	10^{-6}

Migration of Tl^+ ions will occur by exchange with positive ion vacancies. That is the same process as in the case of self diffusion of K^+ ions in the KBr crystal.

Let the molar fraction of cation vacancies be y and let w_0 be the probability per unit time that a Tl^+ ion will jump from one position to any other position. If a is the anion-cation separation, then the diffusion coefficient is[8]

$$D=\frac{1}{3}a^2w_0y\,.$$

In general the correlation effect of the diffusion must be taken into account; in an NaCl type lattice this factor is 0.781. Thus, in this case, we have

$$D=0.26a^2w_0y\,.$$

Let W_s be the activation energy of the Schottky defect, then

$$y=B+C\exp(-W_s/2kT)\,, \qquad (7)$$

where B is the molar fraction of cation vacancies induced by the divalent ions, mainly Ca^{++} ions as shown in Table 1, and is of the order of 10^{-6}. C is an entropy factor of the Schottky defect. The value of $W_s/2$ is 0.96 eV. The second term on the right-hand side of Eq. (7) is of the order of 10^{-5} at 595°C, assuming the value of C to be 10. So B can be neglected as compared with

$$C\exp(-W_s/2kT)\ .$$

The diffusion probability w_0 is written as:

$$w_0=\nu\exp(-U/kT)\ ,$$

where ν is the vibrating frequency of the Tl^+ ion and U the energy barrier of the diffusion. Therefore we have

$$D=0.26a^2\nu C\exp\{-(W_s/2+U)/kT\}\ .$$

In the case of a Tl^+ ion the activation energy of the diffusion was 1.98 eV, so the value of U of a Tl^+ ion is 1.02 eV. The corresponding value of a K^+ ion in a KBr single crystal is 0.30 eV. The difference between these two values will depend partly on the difference of ionic radii of these ions. The influence of the divalent ions to the diffusion constant is significant at rather low temperatures, and in the present experiment the discrepancy of the experimental data from the straight line will depend on the above effect as shown in Fig. 4.

Acknowledgments

The author would like to express his gratitude to Prof. Y. Uchida for his guidance and discussions and to Dr. K. Fukuda for helpful discussions throughout this work.

References

1) H. Witt: Z. Phys. **134** (1953) 117. M. Chemla: Ann. Physik **1** (1956) 959. J. F. Laurent and J. Bénard: J. Phys. Chem. Solids **3** (1957) 7.
2) T. Tamai: J. Phys. Soc. Japan **15** (1960) 2116.
3) H. Mizuno and M. Inoue: Phys. Rev. **120** (1960) 1226.
4) A. Smakula: Z. Phys. **59** (1930) 603.
5) P. H. Yuster and C. J. Delbecq: J. Chem. Phys. **21** (1953) 892.
6) Y. Uchida and R. Kato: J. Phys. Soc. Japan **14** (1959) 1408. W. J. van Sciver: Phys. Rev. **120** (1960) 1193.
7) F. Seitz: *The Modern Theory of Solids* (Mc Graw-Hill Book Co. New York, 1940). N. F. Mott and R. W. Gurney: *Electronic Process in Ionic Crystals* (Oxford University Press, New York, 1940).
8) S. Flügge: Handbuch der Physik vol. **XX** (1957).

JOURNAL OF THE PHYSICAL SOCIETY OF JAPAN, Vol. 16, No. 12, DECEMBER, 1961

Diffusion of Color Centers into KBr-Tl Phosphors

By Tokumichi TAMAI
Research Laboratory, Matsushita Electronics Corporation, Takatsuki, Osaka

(Received July 29, 1961)

The diffusion of color centers into a KBr-Tl phosphor has been investigated during a coloring process in potassium vapor. Proceeding from the surface to the interior of the crystal, F-centers, complex centers, and Tl neutral centers were observed successively. The boundary between the crystal region containing these centers and the rest of the crystal containing only Tl^+ ion centers was very distinct. The depth of the front surface of diffusing Tl neutral centers was proportional to the square root of exposure time. Complex centers were composed of a Tl neutral center, a negative ion vacancy and an electron.

§1. Introduction

Additively colored KBr-Tl phosphors have been investigated by several authors. Markham *et al.*[1] reported that the presence of Tl^+ ions did not influence the width of the F-band when the concentration of Tl^+ ions was less than $10^{18}\,cm^{-3}$, whereas in heavily doped KBr-Tl phosphors F-centers could not be formed by additively coloring process. Stasiw[2] assumed an absorption band of thallium neutral centers, even in the case of the above-mentioned high concentration, and he proposed a complex center with an absorption band peaked at 3 eV. Castner and Känzig[3) reported that in a KCl-Tl phosphor irradiated by X-rays, the Tl^+ ions act as electron traps and thus prevent the recombination of electrons and holes produced by X-rays.

The author has investigated the coloring of a KBr-Tl phosphor during a heat process in potassium vapor. After adequate coloration of the KBr-Tl phosphor, three kinds of absorption centers were observed, namely F-centers, Tl neutral centers and complex centers. In the interior of the crystal a region of Tl^+ ions remained. The boundary between the regions of the crystal containing Tl^+ ions at one side and the above-mentioned three centers of the other side was very distinct.

The Tl neutral centers showed an absorption band with a flat part at the higher energy side of 4.15 eV. The complex centers had an absorption band peaked at 3.1 eV. The Tl neutral center was more stable than the other two centers. After heating the crystal these centers disappeared and a new Tl^+ center appeared.

The migration of the boundary is expressed by Fick's equation, from which follows that the penetration depth of the boundary should be proportional to the square root of the time of the heat-treatment.

§ 2. Experimental Procedures

After dissolving a small quantity of TlBr in the melt of KBr, single crystals of KBr-Tl were grown by the well-known Kyropoulos method. Concentrations of Tl^+ ions were respectively 0.8×10^{16}, 1×10^{17} and 4×10^{17} cm^{-3}, determined by a polarographic analysis.

The crystals were heated in a quartz tube in an atmosphere of saturated potassium vapor at various temperatures and for various hours. The temperature was controlled by an automatic regulator with a tolerance of 0.5%. After quenching the crystals, thin layers of about 0.5 mm thickness were successively cleaved off from the surface and the absorption spectra of these thin layers were measured by an automatic recording spectrophotometer at room temperature (Fig. 1). The absorption curve 1 in Fig. 1 is composed of three bands as shown in Fig. 2. Curve 3 was taken near the boundary surface of the crystal and this was an absorption band of Tl neutral centers.

As shown in Figs. 1 and 2, near the surface of the crystal the absorption band of F-centers was observed and more inside the crystal a flat band peaked at 4.15 eV was observed. This flat band corresponds to Tl neutral centers as mentioned by Stasiw. Between these two bands was observed an intermediate band with a maximum at 3.1 eV. Concentration gradients of these three bands are shown in Fig. 3, assuming that for each kind

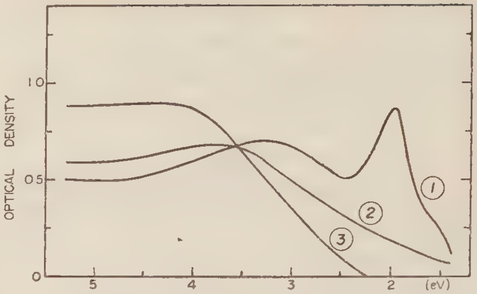

Fig. 1. Absorption spectra of the thin layers of the crystal heated at 540°C for 2 hours. Curves 1, 2 and 3 were taken at 1.2, 3.0 and 7.1 mm depth from the exposed surface, respectively.

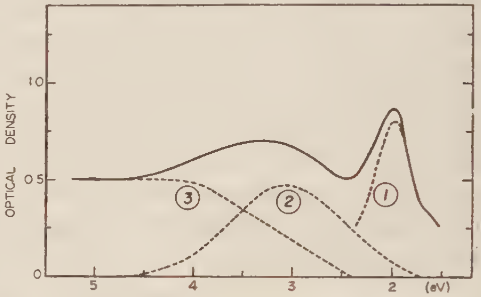

Fig. 2. Curve 1 in Fig. 1 is represented as the combined absorption of 1: F-centers, 2: complex centers, and 3: Tl neutral centers.

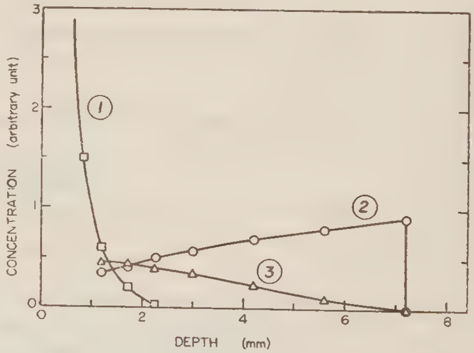

Fig. 3. Concentration gradients of various absorption centers as a function of the distance from the exposed surface of the crystal heated at 540°C for 2 hours. 1: F-centers, 2: Tl neutral centers, and 3: complex centers.

of center the concentration is proportional to the height of the corresponding absorption band. As shown in Fig. 3 a front surface of Tl neutral centers is very distinct. At the inner side of this surface only Tl$^+$ centers are present.

The height of the Tl neutral band near the front surface was proportional to the concentration of Tl$^+$ ions before the heat-treatment. The penetration depth X of the front surface of the Tl neutral centers was plotted as a function of the square root of exposure time, as shown in Fig. 4. It appears that the penetration depth of the boundary is proportional to this square root of exposure time.

When a crystal containing the above-mentioned three centers was heated at 450°C, most of the F-centers and complex centers disappeared after 17 minutes. After 37 minutes the absorption band of Tl$^+$ ions appeared and finally only this absorption band of Tl$^+$ ions was observed (Fig. 5). There was no change in the concentration of Tl$^+$ ions before and after the additively coloring process.

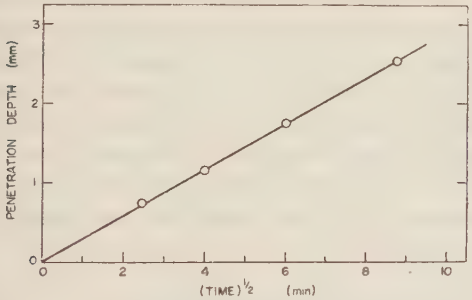

Fig. 4. Penetration depths of the front surface of Tl neutral centers are plotted as a function of the square root of heating time. Temperature: 500°C.

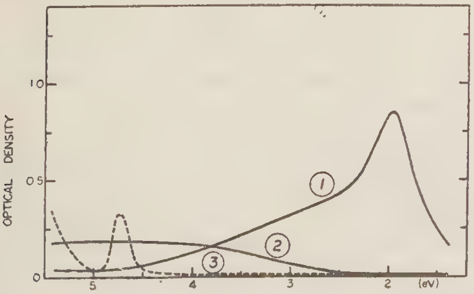

Fig. 5. Thermal effect on the crystal. Thickness of the crystal was 0.42 mm. 1: initial absorption curve, 2: after 17 minutes at 450°C, and 3: after 97 minutes at 450°C.

§ 3. Discussion

Near the surface of the crystal the additively coloring process of a KBr-Tl phosphor will be very similar to the additively coloring of a KBr single crystal. This process is the diffusion of negative ion vacancies into the crystal accompanied by the formation of F-centers which are negative ion vacancies occupied by an electron. Inside the crystal, however, the process will be quite different. From the experimental results, obtained with Tl-doped KBr phosphors, we shall try to explain what happens to the F-centers under the influence of the Tl$^+$ ions.

By measuring the characteristic absorption bands of Tl$^+$ ion centers and Tl neutral centers it was verified that during the heat process each of Tl$^+$ ion centers captured an electron and formed the neutral and complex centers which were mentioned above. It seems reasonable to assume that the electron was released from a potassium vapor atom at the surface of the crystal and trapped by the Tl$^+$ ion. To maintain a charge neutrality of the crystal a negative ion vacancy will be formed and most probably in the environment of the Tl neutral atom. Thus the Tl neutral center will be created.

F-centers and complex centers only appeared in crystal regions where Tl$^+$ ion centers were already transformed into Tl neutral centers. The nature of the complex center may be understood by the concentration characteristics of Fig. 3. If the diffusion of the thallium can be neglected the total concentration of Tl$^+$ ions and Tl neutral centers should be constant over the crystal because before the additive coloring process the concentration of Tl$^+$ ions was constant. As there are no Tl$^+$ ions left in the region near the surface and as the Tl neutral centers increase with the distance from the surface, the decreasing complex centers should be combinations of Tl neutral centers with something else. As there are no F-centers in this region of the crystal where we would expect a normal F-center concentration, it may be assumed that the complex center is composed of a Tl neutral center, a negative ion vacancy and an electron.

An evidence for the assumption that during the heat process the diffusion of Tl neutral centers can be neglected was found in the absorption bands after a second heat-treatment. During such a heat-treatment as mentioned above (Fig. 5) F-centers and complex centers disappeared almost at the same time and finally the transition of the remaining Tl neutral centers into Tl^+ ion centers was observed.

From the present experiment it can be concluded that the diffusion of the electrons occupying negative ion vacancies plays the major role during the heat process, whether they appear as F-centers or as complex centers. It was remarkable that the boundary surface between the crystal regions containing Tl neutral centers at the one side and Tl^+ ion centers at the other side was very distinct. The thickness of this transition layer was less than 0.05 mm. As the electron occupied negative ion vacancies only occur in the region where the Tl^+ ion is neutralized, this boundary surface marks at the same time the penetration depth of these vacancies. An estimation of the penetration depth may be given. Suppose that the diffusion rates of F-centers and complex centers are equal, then the migration of the centers into the crystal during the heat process is determined by Fick's equation[4)]

$$\frac{\partial n}{\partial t}=D\frac{\partial^2 n}{\partial x^2}\,, \tag{1}$$

where n is the concentration of the centers and D is the diffusion constant. Let the density of potassium atoms in the vapor phase be N_0, then it is convenient to write

$$N=\kappa N_0$$

for the concentration of F-centers at the surface of the crystal, where κ is a proportionality factor[5)].

The boundary conditions for solving Eq. (1) are the following;

1) $n=\kappa N_0$ for $x=0$, independent of the time,

2) $n=0$ for $x=X$, independent of the time,

3) $D\dfrac{\partial n}{\partial x}=n_0\dfrac{dX}{dt}$ for $x=X$,

where n_0 is the density of Tl^+ ions in the crystal.

The solution of Eq. (1) under the condition (1) is given by

$$n=\kappa N_0-A\,\mathrm{erf}\left[\frac{x}{2(Dt)^{1/2}}\right], \tag{2}$$

where A is a constant. Condition (2) requires

$$\kappa N_0-A\,\mathrm{erf}\left[\frac{X}{2(Dt)^{1/2}}\right]=0\,, \tag{3}$$

Since Eq. (3) has to be satisfied for all values of the time, X must be proportional to $t^{1/2}$, that is:

$$X=2\lambda(Dt)^{1/2}\,, \tag{4}$$

where λ is a numerical constant to be determined from the remaining condition (3).

Substitution of Eqs. (2) and (4) in Eq. (3) gives

$$\lambda \exp \lambda^2 \,\mathrm{erf}\,\lambda=\frac{\kappa N_0}{\sqrt{\pi}\, n_0}\,. \tag{5}$$

When λ has been calculated from Eq. (5), n can be written down from Eqs. (2), (3) and (4). That is

$$\left.\begin{array}{ll} n=\kappa N_0\left\{1-\dfrac{\mathrm{erf}\,[x/2(Dt)^{1/2}]}{\mathrm{erf}\,\lambda}\right\} & \\ & \text{at}\quad 0<x<X\,, \\ n=0 & \text{at}\quad x>X\,. \end{array}\right\} \tag{6}$$

As n is the concentration of the combinations of a negative ion vacancy and an electron, Fig. 3 will be qualitatively explained by Eq. (6). From Eq. (4) follows that the depth of the front surface of the Tl neutral centers is proportional to the square root of the time of the heat process which is in agreement with the experimental graph of Fig. 4.

Acknowledgments

The author would like to express his gratitude to Prof. Y. Uchida for his guidance and discussions and to Dr. K. Fukuda for helpful discussions throughout this work.

References

1) J. J. Markham and H. N. Hersh: J. Chem. Phys. **32** (1960) 1885.
2) O. Stasiw: Gött. Nachr. (1936) 1.
3) T. G. Castner and W. Känzig: J. Phys. Chem. Solids **3** (1957) 178.
4) H. S. Carslaw and J. C. Jaeger: *Conduction of Heat in Solids*. (Oxford University Press, 1959).
5) R. W. Pohl: Proc. Phys. Soc. **49** (extra part), (1937) 3.

JOURNAL OF THE PHYSICAL SOCIETY OF JAPAN, Vol. 16, No. 12, DECEMBER, 1961

Thermal Conductivity of Sodium Nitrite

By Ikushi YOSHIDA*
The Institute for Solid State Physics, University of Tokyo
and Shozo SAWADA
Department of Physics, Tokyo Institute of Technology, Tokyo

(Received July 31, 1961)

The thermal conductivity of sodium nitrite single crystals has been measured in the temperature range of 70∼190°C along the direction of three crystal axes. Thermal conductivities in the b- and a-directions show a gradual decrease on heating, over a rather wide temperature range of some fifty degrees below the transition temperature. This decrease has been analyzed as an additive thermal resistivity with the help of a measurement at lower temperatures. Any anomalous behavior has not been found in the temperature dependence of thermal conductivity in the c-direction. A tentative model of the order-disorder arrangement of NO_2^- radicals is proposed for the explanation of the origin of the additive thermal resistivity, in which uneven interatomic forces due to the disordered arrangement are considered as scattering centers of phonons. The predicted temperature dependence is in a qualitative accord with the experimental one.

§ 1. Introduction

In insulating crystals, heat is transported by lattice waves and at relatively high temperatures the thermal resistance is due mainly to phonon-phonon scatterings originated from the anharmonicity in the interatomic binding forces. Many other scattering processes of phonon, however, are possible in all real crystals. Any irregularities of the lattice, such as impurities, vacancies, interstitials and dislocations may scatter phonons and hence increase the thermal resistance. The effect of lattice imperfections on the thermal conductivity has been studied to a certain extent by many workers in both dielectrics and metals. The measurement of thermal conductivity appears to supply us with a valuable means of studying the nature of lattice imperfections.

In cases of crystals having complex structures other factors are involved which may influence the thermal conduction, because the complexity in lattice structure leads to an intricate behavior of lattice vibrations and hence to a complex interaction of phonons with each other. Intramolecular radicals may in many cases play a decisive role in the phase transition, and any change in the state of orientation, rotation or vibration of them are observed, in general, as an anomalous specific heat or anomalous coefficient of thermal expansion or others. Anomalies in the thermal conductivity accompanying the phase transition have been observed by several workers[1)–6)].

The present work is concerned with the thermal conductivity of sodium nitrite $NaNO_2$, a substance which has recently been found to be ferroelectric[7)].

The crystal structure of sodium nitrite has been investigated by many workers[8)–11)]. At room temperature it belongs to the space group $C_{2v}^{20}(Im2m)$, and the orthorhombic unit cell contains two molecules of $NaNO_2$, the lattice constants being $a=3.56$Å, $b=5.56$Å and $c=5.38$Å, respectively. The crystal is composed, presumably not in the most closely packed state, of Na^+ ions and NO_2^- radicals. The latters are not linear but of the "V" form, the nitrogen atom being a little deviated from the midpoint of two bonding oxygen atoms. Thus the NO_2^- radical is an asymmetric top elongated parallel to the O-O direction. The apex of the "V", the nitrogen atom, will hereafter be called the head of the radical. The room-temperature phase which is polar and ferroelectric assumes such an arrangement that each radical points its head to the same sense in the b-axis, the O-O direction being parallel to the *c*-axis. Two NO_2^- radicals belonging to one unit cell possess the corner and body-center-positions. On a line parallel to the *b*-axis NO_2^- radicals and Na^+ ions take their positions alternatively. Fig. 1 is a schematic sketch of the molecular stacking in the polar phase.

---

* Now at the Central Research Laboratory, Fuji Iron and Steel Co. Ltd., Nihonbashi-Edobashi, Chuo-ku, Tokyo.

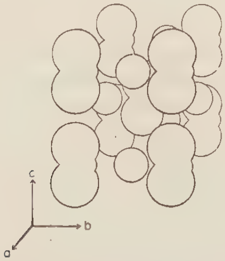

Fig. 1. A schematic bird-eye sketch of the molecular stacking of $NaNO_2$ crystal in the polar phase.

Above the phase transition temperature 163°C the crystal acquires a mirror plane perpendicular to the *b*-direction, the space group changing to $D_{2h}^{25}(Immm)$.

The exact mechanism of the phase transition still remains uncertain, but it is generally believed that the orientation of NO_2^- radicals takes the most important role in the problem. A possibility of some change in the thermal conductivity is therefore expected, arising from the scattering of phonons by irregularities of lattice due to the onset of disorder in the orientation of NO_2^- radicals. The main purpose of the present work was in the investigation of the such radical orientation on the thermal conductivity.

§ 2. Preparation of Specimens and Measurement

Considerably large single crystals of sodium nitrite were obtained by the slow cooling of the melt of raw material. Sodium nitrite of specially pure grade was used as the raw material, after having been dried in 10^{-3} mmHg vacuum at about 120°C for several days. An alumina crucible of 10 cm in diameter filled with the raw material was set in a vertical electric furnace, in which a large temperature gradient existed, and after having been maintained at a temperature a few ten degrees higher than the melting point (271°C) for several hours, it was pulled up slowly (*ca* 6 cm/day) by a low-speed synchronous motor. It did not succeed to crystalize the whole content to a single one. The largest single crystal obtained by cleaving the content was a parallelepiped with the edges of about 3 cm in length.

The crystals were yellowish and transparent, and were cleaved along the (101) plane[12], and the double refraction was conspicuously observed in so cleaved parallelepiped crystals. Sizes and characteristics of specimens are listed in Table I.

Table I. Sizes and characteristics of specimens.

Specimen number	A(cm²)	*l*(cm)	Direction of heat flow	
No. 1	0.405	0.50	[101]	single
	d(cm)			
No. 2	0.369		[010]	single
No. 3	0.288		[100]	single
No. 4	0.300		[001]	single
No. 5	0.2301		[021] not exactly	nearly single

A : cross-sectional area,
l : distance between two points at which the temperature was measured,
d : thickness.

The orientation of crystal was determined by 1) cleavage planes and 2) fine stripes parallel to [001] observed on the (010) plane of crystals etched by water or ammonia water[13].

A measurement at temperatures lower than room temperature was made on the specimen No. 1 using the direct method. Thermal conductivities of other specimens were measured by the comparative method at temperatures higher than room temperature. Apparatuses and details of measurement have been described previously[6]. The printed-heater method adopted for ceramic specimens was made impossible for sodium nitrite by a snapping-off of the heater wire at low temperatures owing perhaps to its rather large coefficient of thermal expansion. Therefore a constantan wire of 0.2 mm in diameter lapped densely on one end of the specimen was used as the heater instead. The heater was varnished in for the improvement of thermal contact with the specimen.

The heat loss by radiation from the surface of the specimen comes out to be a serious obstruction to the direct measurement, especially at temperatures higher than room temperature. The heat leak due to radiation

Q_{rad} reached at 40°C, for example, 18% of the total heat current Q given to the specimen. The thermal conductivity κ was not determined by use of

$$\kappa = \frac{l}{A\cdot\Delta T}Q\,, \tag{1}$$

where A is the cross-sectional area of the specimen and ΔT is the temperature difference at two points separated by l longitudinally in the specimen, but from the gradient of a $\Delta T-Q$ line as shown in Fig. 2. This procedure was effective in the alleviation of the error brought about by the radiation loss, though only at the cost of the accuracy of the measurement of the average temperature of the specimen.

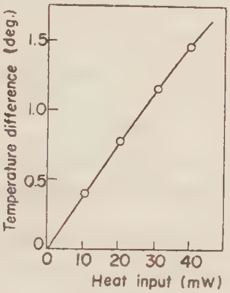

Fig. 2. An example of low-temperature measurement; temperature difference ΔT *vs* heat input Q.

§ 3. Result of Measurements

In Fig. 3 is shown the temperature dependence of thermal conductivity of the specimen No. 1. The thermal conductivity decreases with increasing temperature, nearly obeying $1/T$ law, which can be seen more clearly in Figs. 9 and 10, where the thermal resistivity W *vs* temperature is plotted. Figs. 4, 5 and 6 show respectively the temperature dependences of thermal conductivity along the

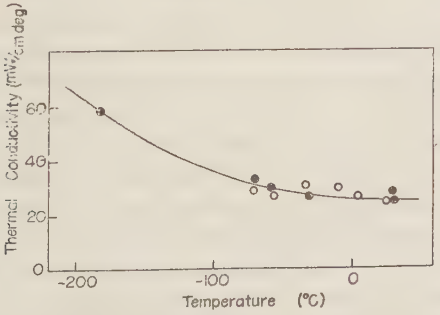

Fig. 3. Thermal conductivity of $NaNO_2$ at low temperatures; speimen No. 1 along [101]. Open circles: first run; solid circles: second run.

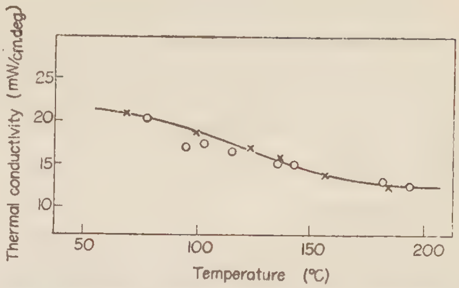

Fig. 4. Thermal conductivity of $NaNO_2$; specimen No. 2; along [010]. Circles: on heating; crosses: on cooling; common to all following Figs.

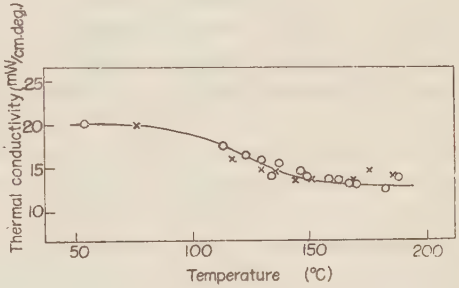

Fig. 5. Thermal conductivity of $NaNO_2$; specimen No. 3; along [100].

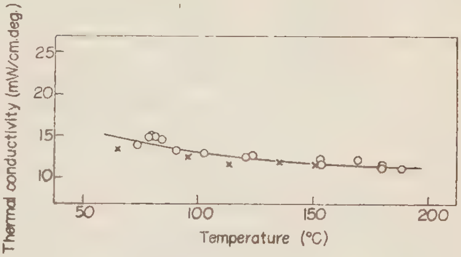

Fig. 6. Thermal conductivity of $NaNO_2$; specimen No. 4; along [001].

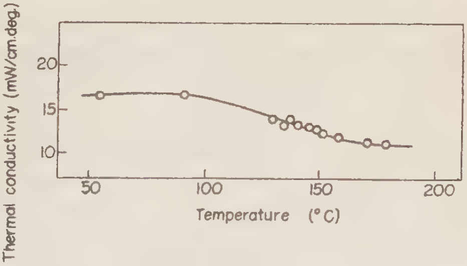

Fig. 7. Thermal conductivity of $NaNO_2$; specimen No. 5; nearly along [021].

b-, a- and c-axes (specimens No. 2, No. 3 and No. 4). A gradual decrease in the thermal conductivity is seen in the b- and a-directions but not in the c-direction. This decrease is also perceived for the specimen No. 5, as is shown in Fig. 7.

§ 4. Discussions

4. 1. *Magnitude of Thermal Conductivity*

From the experimental result that the thermal conductivity of sodium nitrite crystal nearly obeys the Debye $1/T$ law it is inferred that the normal part of the thermal conductivity is due to the flow of phonons which are scattered through the Umklapp-process.

A crystal of $NaNO_2$ containing G molecules, each with 4 atoms, has 12G degrees of freedom. Of these 12G modes, there are 3G degrees of freedom related to the translational motion (accoustical modes) and 3G to the relative motion of Na^+ ions against NO_2^- radicals (optical modes). Of the remaining 6G modes, 3G are associated with the rotational motion of NO_2^- radicals and 3G with the deformational motion of them. Frequencies of the last 3G modes, degenerated G-fold, have been determined by the Raman effect[14] or by the infrared absorption[15] to be 1330 cm^{-1} (asymmetric stretching), 1250 cm^{-1} (symmetric stretching) and 800 cm^{-1} (bending), respectively. Characteristic temperatures corresponding to them are 1910°K, 1790°K and 1150°K, respectively, which fact shows that these modes are scarecely excited thermally in the temperature range which we are now considering, or that NO_2^- radicals can be considered as rigid bodies. Then the crystal resembles an ionic one composed of two interpenetrating body-centered orthorhombic lattices of anions (NO_2^-) and cations (Na^+), in which, of course, the rotational freedom of anions is reserved.

The thermal conductivity of alkali halides, the most representative ionic crystals, has extensively been measured, and it is well established[16] that the thermal conductivity becomes smaller as the mass ratio of cation to anion deviates from the unity. In Fig. 8 is shown the relation between the phonon mean free path l and the mass ratio m/M for alkali halides and also for sodium nitrite at room temperature, l being determined by

$$\kappa=\frac{1}{3}cvl\ , \tag{2}$$

where c and v mean the specific heat per unit volume and the sound velocity, respectively. From Fig. 8 it is readily understood that the phonon mean free path increases with the accessing of mass ratio to the unity and that the phonon mean free path in sodium nitrite is comparable with those in alkali halides. This fact seems to support the above-inferred simple picturing for the crystal structure of sodium nitrite, i. e., that the inner-radical freedom of vibration scarecely contributes to the thermal conduction (or to the thermal resistivity), and that the NO_2^- radical may be treated as the nearly rigid asymmetric top composing the crystal lattice.

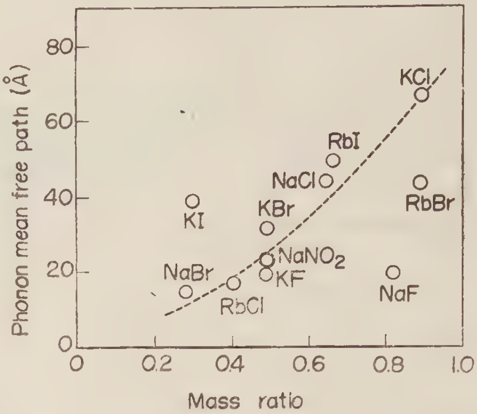

Fig. 8. Phonon mean free path *vs* mass ratio for alkali halides and $NaNO_2$ at room temperature.

4. 2. *Anisotropy in Thermal Conductivity*

The thermal conductivity of sodium nitrite is fairly anisotropic, i. e., it is much smaller along the c-axis than along the b- and a-axes.

Sodium nitrite shows a strong double refraction, that is, refractivities along three crystal axes are[12] as $n_a=1.34$, $n_b=1.425$ and $n_c=1.660$, respectively. The anisotropy in thermal expansion is still more conspicuous. The coefficient of thermal expansion[17] along the c-axis is negative while those along the other axes are positive. It is obvious that the anisotropic nature of sodium nitrite originates from the asymmetric form of the NO_2^- radical. Scarece discussion has been made on the anisotropy of thermal conductivity of crystals, but it seems natural to suppose that there are two factors at least, i. e., the anisotropy in the velocity of sound and that in the probability of scattering of thermal waves. It is not certain which factor more seriously contributes to the anisotropic nature of thermal conductivity in sodium nitrite, but the asymmetric-top form of NO_2^- radicals elongated in the c-direction suggests a possibility that the feature of scattering may be much different for phonons propagating along the c-axis from that for phonons propagating along the b- or a-axis.

4. 3. *Additive Thermal Resistivity*

The thermal resistivities of sodium nitrite are shown as functions of absolute temperature in Figs. 9 and 10, which would be helpful for a better understanding of the nature of the decrease with increase of temperature in the thermal conductivity. These figures correspond to Figs. 4 and 5, respectively. The thin line added to each as the low-temperature part was calculated from Fig. 3, which does not continue to the thick lines above room temperature, for they are measurements not only on different crystals but in different directions. It was difficult to obtain a single crystal long enough in the desired directions to be used as specimens for the low-temperature measurement, and it was necessitated to make such a rather unsatisfactory comparison. The general behavior of temperature dependence, however, is probably similar for every directions, though the absolute value itself is expected to considerably vary from direction to direction.

In $NaNO_2$, anomalies in many physical properties such as spontaneous polarization[18),19)], electrical resistivity[20)], specific heat and thermal expansion[17)] are seen to begin at considerably lower temperature than the transition point, indicating that some change in the structure, presumably of the order-disorder type, takes place preceding the phase transition. An estimation of the additive thermal resistance due to this order-disorder change can be made by subtracting the thermal resistivity in the ordered state from that really measured, the former being estimated by an extrapolation of the gradient at room temperature as are shown by broken lines in Figs. 9 and 10. These additive thermal resistivities are shown in Fig. 11. From the fact that they become noticeable at about 100°C, increase with increasing temperature and tend to saturate above the transition point, it would be inferred that some new mechanism of scattering of phonon occurs with decrease in ordering.

The atomistic discussion of the mechanism

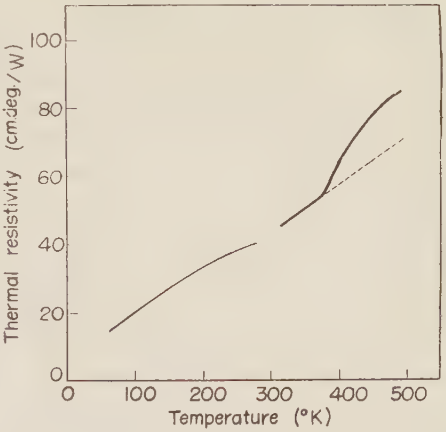

Fig. 9. Thermal resistivity of $NaNO_2$. Thick line: along [010], specimen No. 2; thin line: along [101], specimen No. 1; broken line: estimated resistivity in the ordered state.

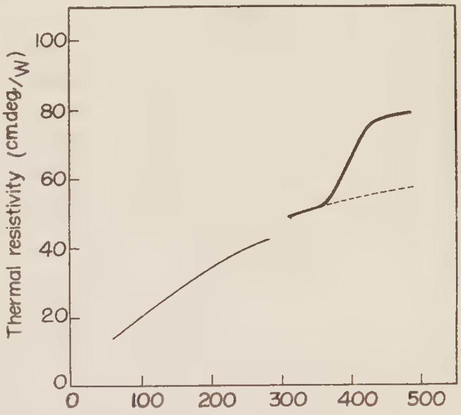

Fig. 10. Thermal resistivity of $NaNO_2$. Thick line: along [100], specimen No. 3; thin line: along [101], specimen No. 1; broken line: estimated resistivity in the ordered state.

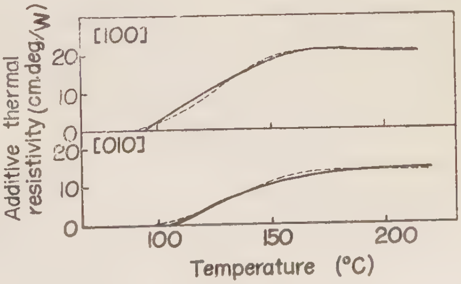

Fig. 11. Additive thermal resistivities of $NaNO_2$ in [100] and [010] directions; full line: observed; broken line: calculated.

of transition from the ferroelectric- to the paraelectric-phase has scarecely been made for sodium nitrite, though it is probably certain that the origin of ferroelectricity exists in the ordered orientation of NO_2^- radicals and the accompanied shift of Na^+ ions in this substance. The paraelectric phase will be realized by the disordering of NO_2^- radicals, which fact is evidenced by the existence of a mirror plane perpendicular to the b-axis in the paraelectric phase. Not a single atomistic picturing is within the range of possibility as for the disordering mechanism of NO_2^- radicals; they may be static but with random orientations in the $+b$- or $-b$-direction, or they may be the change of direction from time to time by the rotation around some axis of inertia either almost freely or hinderedly, or by the oscillation of nitrogen atom on the line bisecting the O-O bond. In either case it is well expected that the disturbance in the periodicity of crystal lattice accompanied by the disordering of the orientation of NO_2^- radicals would become scattering centers of phonons.

Now we consider the thermal resistance which would be produced by the disordering of the orientation of NO_2^- radicals. Analogous to the order-disorder theory of alloys, NO_2^- radicals are assumed to take either the $+b$ orientation or $-b$ orientation with an equal probability. It is also assumed that, on the one hand, the mutual interaction between neighboring radicals favors the ordered or parallel orientation, i. e., each NO_2^- radical has a tendency against the "head to head" arrangement, while, on the other hand, the increase in entropy due to the disordering operates oppositely. The spontaneous polarization P_s will be proportional to the order parameter S, which, on the basis of Bragg-Williams approximation, is equal to the unity at $T \ll T_c$, decreases with increasing temperature, varies approximately as

$$S \propto (T_c - T)^{1/2} , \tag{3}$$

at $T \lesssim T_c$, and vanishes at $T > T_c$.

We consider a crystal containing G molecules and assume the number of neighboring NO_2^- radicals as z*, which interact strongly with a particular NO_2^- radical. The spontaneous polarization P_s is made of two contributions, i. e., from the ordering of permanent dipole moments μ_0 of NO_2^- radicals and from the shift of Na^+ ions. The shift of Na^+ ions is caused by the ordering of NO_2^- radicals, and it will be allowed, in a rough approximation, to include the contribution from the former in the contribution from the latter, or, in other words, we will interpret μ_0 not to be the permanent dipole moment of a NO_2^- radical itself but to contain implicitly the dipole moment induced by the shift of the adjoining Na^+ ion.

The spontaneous polarization per G molecule is given by

$$\begin{aligned} P_s &= \mu_0 (G_+ - G_-) \\ &= P_s^0 (G_+/G - G_-/G) , \end{aligned} \tag{4}$$

where G_+ and G_- are the number of NO_2^- radicals orienting in the $+b$- and $-b$-direction, respectively ($G_+ + G_- = G$), and P_s^0 is the value of P_s when the perfect ordering is achieved, i. e.,

$$P_s^0 = G\mu_0 . \tag{5}$$

The total number of neighboring NO_2^- pairs**, N, is given by

$$N = Gz/2 . \tag{6}$$

Of these N pairs, the number of parallel pairs $N_{\uparrow\uparrow}$ and the number of antiparallel pairs $N_{\uparrow\downarrow}$ are respectively given by, in the Bragg-Williams approximation,

$$N_{\uparrow\uparrow} = z(G_+^2 + G_-^2)/2G , \tag{7}$$

$$N_{\downarrow\downarrow} = z2G_+G_-/2G . \tag{8}$$

Using Eqs. (4) and (6), Eqs. (7) and (8) are rewritten as

$$\begin{aligned} N_{\uparrow\uparrow}/N &= 1 - 2G_+G_-/G^2 \\ &= \{1 + (P_s/P_s^0)^2\}/2 , \end{aligned} \tag{9}$$

$$\begin{aligned} N_{\uparrow\downarrow}/N &= 2G_-G_-/G^2 \\ &= \{1 - (P_s/P_s^0)^2\}/2 , \end{aligned} \tag{10}$$

---

* The number z is considerably ambiguous on account of the irregular form of the NO_2^- radical. Two b-heighbors will presumably interact most strongly. Eight <111>-neighbors are thought to considerably interact also. Two a-neighbors, too, appear not out of the range of consideration. We take z here only as a conventional measure of the number of interacting neighbors, for the present stage of understanding of the mutual interaction between each radical and ion of sodium nitrie is not sufficient to make a strict discussion of z. Such an ambiguous defintion of z, however, would not affect the following discussion explicitly.

** Two b-neighbors are thought to interact most strongly, but they do not form a NO_2^--NO_2^- pair, for there exists Na^+ ion between them. Here the word "pair" is used in a conventional meaning as was pointed out in the former footnote.

respectively. It is likely that the interaction in the antiparallel pair is different from that in the parallel pair, and the deviation from uniformity in the binding forces in the crystal will contribute to the scattering of phonons.

According to Klemens[21], the scattering of phonons due to point imperfections is characterized by a relaxation time τ_D with the frequency dependence given by

$$1/\tau_D = A\omega^4\ , \qquad (11)$$

where A is a temperature-independent constant and is proportional to the density of the point imperfections. At temperatures higher than the Debye temperature θ, the phonon-phonon scattering predominates in the thermal resistivity, and its relaxation time τ_p is given[22] by

$$1/\tau_p = S(T)\omega^2\ . \qquad (12)$$

At $T>\theta$ the inverse relaxation time for phonon-phonon scattering should be proportional to the temperature, i. e.,

$$S(T) = CT\ . \qquad (13)$$

Several works[23]~[25] have recently been made concerning the effect of point imperfections on the thermal resistivity, where Eqs. (11) and (12) are combined. The unanimous conclusion of them tells us that when the effect of point imperfections is rather small it can beexpressed as an additive resistivity ΔW, which is proportional to A in Eq. (11) and is independent of temperature except when the concentration of imperfections are changed. The expression of ΔW is given by

$$\Delta W = 4\pi^3 v\theta A/3h\ . \qquad (14)$$

If the model described above is admitted A is proportional to the product of the concentration of parallel and antiparallel pairs. Then we have

$$\begin{aligned} A &\propto (N_{\uparrow\uparrow}/N)\cdot(N_{\uparrow\downarrow}/N) \\ &= \{1-(P_s/P_s^0)^4\}/4\ . \qquad (15) \end{aligned}$$

Hence, we obtain

$$\Delta W \propto \{1-(P_s/P_s^0)^4\}\ , \qquad (16)$$

i. e., the temperature dependence of additive thermal resistivity is related to that of spontaneous polarization. The additive thermal resistivity calculated from Eq. (16) is shown by broken lines in Fig. 11, where the proportional factor was chosen so as to equate the saturated value of calculated ΔW with that of the observed ΔW, and the temperature dependence of (P_s/P_s^0) was calculated using the Bragg-Williams approximation. The aggreement between the calculated and observed temperature-dependence of ΔW is rather satisfying inspite of the rough approximation used above.

The explanation of the striking anisotropy in the additive resistance appears to be a still more difficult problem. The fact that no additive resistance has been found in the thermal conductivity in the c-direction suggests that the disordering of NO_2^- radicals little affects the c-direction bonding. The model of rotating radicals about the c-axis seems to be more favorable for the explanation of this fact, but there are too much obscurity about the transition mechanism to make a clearer discussion of the nature of additive thermal resistance.

§ 5. Summary and Conclusion

The thermal conduction in sodium nitrite is due to the flow of phonons, the magnitude of which is comparable to that expected in neglect of the internal freedom of the NO_2^- radical. The thermal conductivity is low in the c-direction, and the anisotropy may originate from the anisotropic scattering of phonons by asymmetric NO_2^- radicals.

A decrease in thermal conductivity in the b- and a-directions was distinctly observed in a wide temperature range of some fifty degrees below the transition temperature. The difference between interatomic forces in parallel pairs of NO_2^- radicals was taken as point imperfections. The increase in the number of point imperfections with the disordering of orientation of NO_2^- radicals was considered to be the cause of additive thermal resistivity. The calculated temperature-dependence of the additive thermal resistance is in a qualitative agreement with that observed.

There seem reasonable prospects, after all, of obtaining some knowledge on the mechanism of phase transition by measuring the thermal conductivity, for the latter is considered to be intimately related to the lattice structure and especially to the state of thermal motions of constituting ions or groups of atoms.

The authors would like to express their sincere thanks to Prof. Y. Kakiuchi for his incessant interest and valuable advices.

References

1) A. Eucken and E. Schröder: Ann. Physik **36** (1939) 609.
2) A. N. Gerritsen and P. van der Star: Physica **9** (1942) 609.
3) Cl. v. Simson: Naturwiss **38** (1951) 559.
4) I. Yoshida, S. Nomura and S. Sawada: J. Phys. Soc. Japan **13** (1958) 1550.
5) I. Yoshida and S. Sawada: J. Phys. Soc. Japan **15** (1960) 199.
6) I. Yoshida: J. Phys. Soc. Japan **15** (1960) 2211.
7) S. Sawada, S. Nomura, S. Fujii and I. Yoshida: Phys. Rev. L. **1** (1958) 320.
8) B. Strijk and C. H. MacGillavry: Rec. Trav. Chim. **62** (1943) 705; **65** (1946) 127.
9) G. B. Carpenter: Acta Cryst. **5** (1952) 132; **8** (1955) 352.
10) M. R. Truter: Acta Cryst. **7** (1954) 73.
11) M. I. Kay and B. C. Frazer: Acta Cryst. **14** (1961) 56.
12) M. W. Porter and R. C. Spiller: *The Barker Index of Crystals, vol.* **1** (1951).
13) S. Nomura, Y. Asao and S. Sawada: J. Phys. Soc. Japan **16** (1961) 917.
14) A. Langseth and E. Wells: Z. physik. Chem. **B27** (1934) 209.
15) C. R. Bailey and J. W. Thompson: Nature **135** (1935) 915. D. Williams: J. Am. Chem. Soc. **61** (1939) 2987. F. A. Miller and C. H. Wilkins: Anal. Chem. **24** (1952) 1253.
16) A. Eucken and G. Kuhn: Z. physik. Chem. **134** (1928) 193.
17) S. Nomura: J. Phys. Soc. Japan **16** (1961) 1352.
18) S. Sawada, S. Nomura and Y. Asao: J. Phys. Soc. Japan **16** (1961) 2207.
19) S. Nomura: J. Phys. Soc. Japan **16** (1961) 2440.
20) S. Sawada, R. Ando and Y. Asao: J. Phys. Soc. to be published.
21) P. G. Klemens: Proc. Phys. Soc. London **A68** (1955) 1113.
22) P. G. Klemens: Proc. Roy. Soc. **A208** (1951) 108.
23) V. Ambegaokar: Phys. Rev. **113** (1959) 1046.
24) P. G. Klemens: Phys. Rev. **119** (1960) 507.
25) J. Callaway and H. C. von Baeyer: Phys. Rev. **120** (1960) 1149.

JOURNAL OF THE PHYSICAL SOCIETY OF JAPAN, Vol. 16, No. 12, DECEMBER, 1961

Exchange Integral in Ni and Its Alloy Film from Spin Wave Resonance

By Hiroshi NOSÉ

Department of Physics, Faculty of Science
Tokyo Metropolitan University

(Received August 1, 1961)

The excitation of spin wave resonance is investigated for various Ni films. The observation is possible only in the case of film prepared on the unheated glass substrate. It is sensitive to the inner crystalline structure of film. The exchange coupling constant A in Ni film is estimated to be 0.75×10^{-6} erg/cm and the exchange integral J to be 9.4×10^{-14} erg. Similarly Pd- and Cu-Ni alloy films are prepared. Their concentrations are determined. They are confirmed to have the nearly perfect structure by means of the electron diffraction. With increasing concentration of Pd and Cu, the value of A decreases monotonously to as small as about 2/3 at 35% Pd and 1/5 at 22% Cu respectively. The exchange integrals of these alloys are, however, nearly constant. The temperature variations of A and J are investigated for some Cu-Ni alloy films. The values of J are also invariant up to the Curie point.

§ 1. Introduction

As Kittel[1)] has proposed, the ferromagnetic resonance in thin film can excite the so-called spin wave resonance in some cases. The observation is possible in the case of a static field being perpendicular to the film plane and a uniform rf field in the film plane, provided that a certain condition is satisfied. That is the existence of a certain surface anisotropy, according to Kittel. The confirmation of spin wave resonance has been achieved at first by Seavey and Tannenwald for Permalloy film[2)], next by Nosé for Ni films under various conditions[3)] and for Cu-Ni[4)] and Pd-Ni[5)] alloy films, and recently by Frait[6)] and by Tannenwald and Weber[7)] for cubic Co film.

This resonance is noticeable as a useful method for the determination of the ferromagnetic exchange integral. It may be an epoch-making method because of the possibility *at any temperature*. The method in common use is the one by the measurement of coefficient of the $T^{3/2}$ law in the temperature variation of saturation magnetization, but this is valid only at very low temperatures because of the restriction for the spin wave theory. There is hitherto no information with respect to the exchange integral at higher temperatures either in theory or in experiment.

In the present work, the examination of the condition necessary to the observation of spin wave resonance and the determination of exchange coupling constant and exchange integral are given for various Ni films. Their concentration variations for Pd- and Cu-Ni alloy films are also investigated. At last, the temperature variation for some Cu-Ni alloy films is also studied.

§ 2. Experimental Conditions.

The resonance is measured by using a cavity of transmission type (TE_{10n}) and the method of field modulation (70 C/sec, max. 200 Oe). The static magnetic filed and microwave frequency are determined by the N. M. R in proton and E.S.R. in D.P.P.H., respectively.

Since thin films are known to have a large isotropic and small uniaxial stress in the film plane[8),9)], the usual expression for ferromagnetic resonance condition must be phenomenologically modified. A quantum mechanical modification has been recently achieved by Fraitová[10)]. In the case of a parallel field $H_{/\!/}$ and perpendicular field $H_\perp$ to the film plane, the resonance conditions are written respectively, as follows:

$$(\omega/\gamma)^2=\left(H_{/\!/}+4\pi M+\frac{3\lambda\sigma}{M}+\frac{3\lambda\sigma_u}{M}\cos^2\theta\right)\times\left(H_{/\!/}+\frac{3\lambda\sigma_u}{M}\cos 2\,\theta\right), \quad (1)$$

$$(\omega/\gamma)^2=\left(H_\perp-4\pi M-\frac{3\lambda\sigma}{M}-\frac{3\lambda\sigma_u}{M}+\frac{2A}{M}k^2\right)\times\left(H_\perp-4\pi M-\frac{3\lambda\sigma}{M}+\frac{2A}{M}k^2\right), \quad (2)$$

where M and λ are the saturation magnetization and magnetostriction constant, respectively; σ is a planer stress isotropic in the film plane; σ_u a uniaxial stress lying in the film plane at an angle θ out of the direction of M. Stresses are positive for tension and negative for compression as usual. A uniaxial stress is introduced instead of a uniaxial anisotropy in common use, because the oblique-incidence effect within an angle of about 10° is not taken into account. The term $2Ak^2/M$ expresses the spin wave resonance, where A is the exchange coupling constant; k the magnitude of wave number and $k=p\pi/L$; p the mode number; L the film thickness.

The value of A is determined from the intervals between the subsidiary peaks which correspond to different numbers of p in the case of observation of $H_\perp$, even without knowing of $3\lambda\sigma/M$ and $3\lambda\sigma_u/M$. In the atomic model, A is given by

$$A=nS^2J/a\,, \tag{3}$$

where a is the lattice constant, n the number of lattice points per unit cell ($n=4$ for f.c.c. and $n=2$ for b.c.c.), S the spin quantum number per atom, J the exchange integral. In the same model the value of S is obtained from the relation:

$$M=ngS\mu_B/a^3\,, \tag{4}$$

where g is the spectroscopic splitting factor, μ_B the Bohr magneton. Since the rigorous atomic model has the dilemma of $2S$ thus evaluated being non-integral spin value, S must be considered as the effective value.

The exchange integral is, therefore, estimated from the above two expressions (3) and (4), but it is also the effective value. For the bulk specimen, it is estimated from another method using the $T^{3/2}$ law. The coefficient C of $T^{3/2}$ for the temperature dependence of M is given by the expression in the spin wave theory[11]:

$$C=\frac{0.1174}{n(2S)}\left(\frac{k}{2SJ}\right)^{3/2}. \tag{5}$$

Values of M in usual polycrystalline materials may be determined from resonance measurements. But it is difficult for those special films as submitted to Eqs. (1) and (2) owing to the two effective field $3\lambda\sigma/M$ and $3\lambda\sigma_u/M$. In the present work the values measured by other authors[12] are introduced to most of the value of M in §3 I and II. Values for some films in III are measured by the high sensitive tortion balance[13].

For Ni films magnitudes of σ, σ_u and g are estimated from observations in the case of $H_{/\!/}$ (at intervals of 30°) and $H_\perp$ (at $p=0$) at room temperature, where $f=9300$ MC/sec, $M=490$ and $\lambda=-34\times10^{-6}$. Also for alloy films, the similar procedure is taken especially in order to obtain the g- factors. Half-widths $\Delta H_{/\!/}$ and $\Delta H_\perp$ between maximum slopes on the main peak are also derived respectively in the case of $H_{/\!/}$ and $H_\perp$.

Film thicknesses between 1000 and 3000Å are measured by the multiple beam interferometer with about 5% error.

Ni film are prepared by evaporation under various conditions. Kinds of substrate are the cover glass and cleaved mica. On the cover glass with 0.2 mm in thickness and 7.5 mm in diameter, the film is deposited in a form of circle with 6 mm in diameter. After usual chemical cleaning, the glass substrates are agitated ultrasonicaly in distilled water. The substrate temperature is ranged from room temperature to 320°C. Rate of evaporation is between 50 and 100 Å/sec in vacuum of 4×10^{-5} mmHg. Heat treatments of films are undertaken in vacuum or in air at 200 or 300°C for one hour.

Some Ni films are prepared by electrodeposition on copper plates with current density of about 10 mA/cm². Film thicknesses are estimated to be between 2000 and 5000Å.

The crystalline structures of films are surveyed by means of the reflection method of electron diffraction.

Pd- and Cu-Ni alloy are suitable for the purpose, because they are the simple solid solution and the interesting material from the theoretical standpoint. Since the observation of spin wave resonance in Ni film is possible only in the case of film prepared on unheated glass, these alloy films are similarly prepared on unheated glasses. In order to prevent these films from imperfect alloying, the rate of evaporation is made considerably rapid, such as between 500 and 1000 Å/sec.

§3. Results and Discussions.

I. *Ni films*

According to Kittel, the excitation of spin wave resonance is possible provided that a certain surface anisotropy acts to pin down the surface spins in the film. This surface anisotropy originates from unsymmetry with respect to the interactions leading to magnetocrystalline anisotropy as pointed out by Néel[14]. On the other hand, an antiferromagnetic oxide layer on the surface can also give rise to a surface anisotropy as observed by Meiklejohn and Bean[15] in the magnetization of Co particles. Pincus[16] has used such an exchange surface anisotropy to improve the Kittel theory.

Firstly the surface condition for the excitation of spin wave resonance are experimentally investigated for various Ni films. Among evaporations of several dozens the principal results are summarized in Table I. All observations of those films are done at room temperature.

Since the cleavage surface of mica is fairely clean and smooth, various properties of Ni film on mica are hardly affected by the substrate temperature. Those of film on glass depend strongly upon the surface condition and so upon the temperature of substrate. As the temperature is raised, the film approaches to have a homogeneous structure, such as in the resonance the planer stress σ (tension) and half-width decrease, and in the electron diffraction the fibre structure vanishes and line width becomes narrower.

The observation of spin wave resonance is distinctly possible only in the case of film prepared on unheated glass. An example of the line profile is given in Fig. 1. It is almost impossible in all the other cases of films evaporated on heated glass or on unheated as well as heated mica, and of films electrodeposited on copper plates. The effect of annealing in vacuum acts always so as to vanish the spin wave resonance in any films. Heat treatments in air intensify the NiO line in the electron diffraction, but make indistinct the subsidiary peaks in the spin wave resonance. It seems that only the exchange surface anisotropy is not sufficient for the excitation of spin wave resonance.

Table I. Summary of results in Ni films.
(At room temperature, $f=9300$ MC/sec, $M=490$, $\lambda=-34\times10^{-6}$.)

Substrate	Subs. temp.	L	σ	σ_u	$\Delta H_{\parallel}$	$\Delta H_{\perp}$	g	Spin wave res.	Fibre axis
Mica	18°C	2700Å	4.3[a)]	−0.25[a)]	370Oe	250Oe	2.21	no	no
	100	2000	3.5	−0.15	360	240	2.15	no	weak [111]
	230	3000	6.0	−0.30	410	250	2.16	no	no
	320	3000	5.3	−0.19	300	250	2.20	no	no
Glass	16	2000	15	−0.28	400	180	2.20	clear	[110]
	18	2350	13	−0.64	260	120	2.14	clear	[111]
	18[b)]	2500	13	(−0.9)	(600)	240	2.18	not clear	[110] & [111]
	18[c)]	2000	14	−0.47	260	130	2.17	no	[110]
	18[d)]	1500	11	−0.05	360	300	2.20	no	[110]
	100	2000	6.0	−0.10	290	220	2.15	no	[110]
	245	1000	8.0	−0.23	360	180	2.20	no	no
	320	1500	4.0	−0.05	250	260	2.15	no	no

a): unit of ($\times10^9$ dyne/cm^2). b), c), d): Heat treatment after evaporation is given in vacuum at 100, 200, 320 °C respectively.

These facts show, therefore, that the spin wave resonance in Ni film depends not only on the surface condition as pointed out by Kittel, but also strongly on the inner crystalline structure affected by conditions of substrate and heat treatments.

The presence of a magnetic field about 50 Oe in the course of evaporation or annealing hardly affects the spin wave resonance. The fibre structure with [110] and/or [111] axes normal to the film has no relation with the resonance.

Next, values of exchange coupling constant A and exchange integral J are estimated, as mentioned in § 2. The results are given in Table II. The values for Ni films are $A=0.75\times10^{-6}$ erg/cm and $J=9.4\times10^{-14}$ erg at

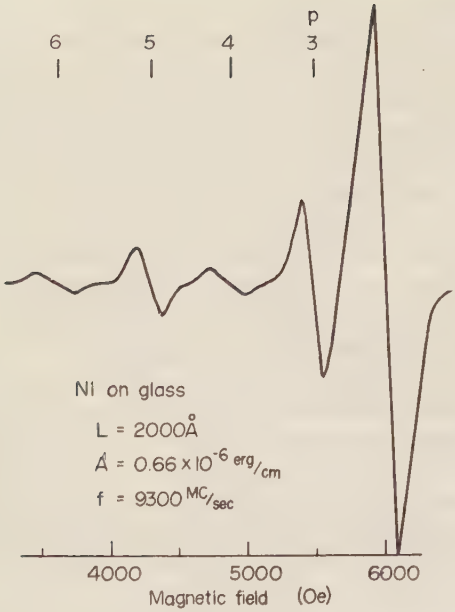

Fig. 1 The line profile of spin wave resonance in Ni film with $L=2000$ Å and $A=0.66\times10^{-6}$ erg/cm.

Table II. Values of A and J in Ni films.

(At room temperature, $f=9300$ Mc/sec, $a=3.52_4$ Å, $g=2.18$, $M=490$ and $2S=0.532$.)

L(Å)	p	$A(\times10^{-6}$ erg/cm)	$J(\times10^{-14}$ erg)
2000	3~6	0.66	8.3
2500	3~5	0.83	10.4
1570	2~4	0.74	9.3
1570	2~4	0.72	9.0
1570	2~4	0.80	10.0
		mean ⟨0.75⟩	mean ⟨ 9.4⟩

room temperature. On the other hand, the value of J for bulk Ni is estimated at very low temperature, making use of Fallot's result[17] $C=8.6\times10^{-6}$ (°K$^{2/3}$). From Eq. (5), $J=8.3\times10^{-14}$ erg.

These two values of J are in good agreement, in spite of the wide difference in the method and the temperature.

II. *Ni alloy films*

In accordance with the procedure on the pure Ni films, Pd- and Cu-Ni alloy as sources are evaporated onto the unheated glass.

The colorimetric analyses of prepared films show that their weight contents of Pd and Cu have increased by a factor of one and two respectively. But the concentration of Cu-Ni film is more precisely determined by measuring the Curie point, as mentioned in § 3 III. By means of the electron diffraction,

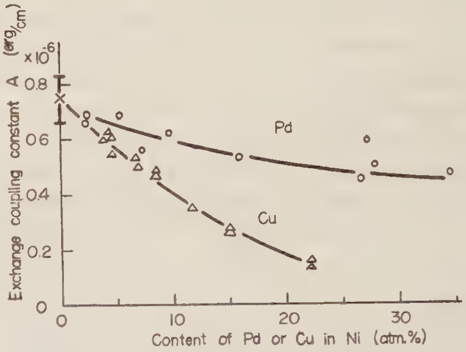

Fig. 2. Concentration variation of exchange coupling constant A for Pd-Ni (○) and Cu-Ni (△) alloy film.

Table III. Values of A and J in Cu-Ni alloy films.

(At room temperature, $f=9300$Mc/sec, $g=2.18$)

at.%Cu	a(Å)	L(Å)	M	$2S$	$A(\times10^{-6}$ erg/cm)	$J(\times10^{-14}$ erg)
0	3.52_4		490	0.53	0.75	9.4
3.8	3.52_7	1450	444	0.48	0.60	9.2
4.3	3.52_8	1200	438	0.47	0.62	9.9
4.5	3.52_8	1200	436	0.47	0.61	9.8
4.5	3.52_8	1280	436	0.47	0.55	8.8
6.6	3.52_9	960	412	0.44	0.54	9.9
6.7	3.52_9	1220	410	0.44	0.50	9.1
8.6	3.52_1	2950	385	0.41	0.49	10.3
8.6	3.53_1	2900	385	0.41	0.49	10.3
11.5	3.53_3	1500	350	0.38	0.35	8.7
15.0	3.53_5	2700	310	0.34	0.28	8.6
15.0	3.53_5	2700	310	0.34	0.28	8.6
22.2	3.54_1	2070	220	0.24	0.15	9.2
22.2	3.54_1	2070	220	0.24	0.13	8.0

Table IV. Values of A and J in Pd-Ni alloy films.
(At room temperature, $f=9300$ Mc)

at.%Pd	a(Å)	M	g	$2S$	L(Å)	$A(\times 10^{-6}$ erg/cm)	$J(\times 10^{-14}$ erg)
2.2	3.53	480	2.18	0.52	800	0.65	8.5
2.4	3.53	480	2.18	0.52	1000	0.69	9.0
5.5	3.55	470	2.21	0.51	940	0.68	9.3
7.3	3.56	464	2.21	0.51	1150	0.56	7.7
9.7	3.57	460	2.18	0.51	1270	0.62	8.5
16.1	3.60	440	2.26	0.49	1380	0.53	8.0
26.8	3.65	410	2.25	0.48	1040	0.45	7.1
27.3	3.65	408	2.33	0.46	1500	0.59	10.2
27.8	3.66	408	2.27	0.47	1600	0.50	8.3
34.6	3.68	494	2.30	0.46	2140	0.47	8.2

it is proved that any film has the f.c.c. structure in single phase and their line widths as narrow as those of pure Ni films. Although the reflection method may be unfavourable for the precise determination of lattice constant, the diffraction pattern shows that lattice constants of present films are nearly consistent with the results by the X-ray diffraction measured on the bulk specimens by other authors[18]. Consequently in present films the nearly perfect structure is confirmed.

The concentration variations of A and J in those alloy films are shown in Fig. 2 and Tables III and IV. It is of interest to see that values of J are nearly constant for any alloy films.

These values of J for Cu-Ni alloy films are also in good agreement with those evaluated by Eq. (5) using the results measured by Kondorskij et al.[19] for bulk Cu-Ni alloy.

III. *Temperature variation for Cu-Ni alloy films*

Recently Tannenwald and Weber[6] have measured the temperature variation of exchange coupling constant and exchange integral in cubic Co film from the spin wave resonance. But their observations have been at fairly low temperatures.

The variation at higher temperatures up to the Curie point is investigated in the present work.*) Some films with the rather low Curie temperature are chosen among the above Cu-Ni alloy films.

The temperature variation of saturation magnetization is measured by the high sensitive torsion balance[13]**), because of the difficulty of determination from resonance measurements as above mentioned. Values of M at each temperature can be determined

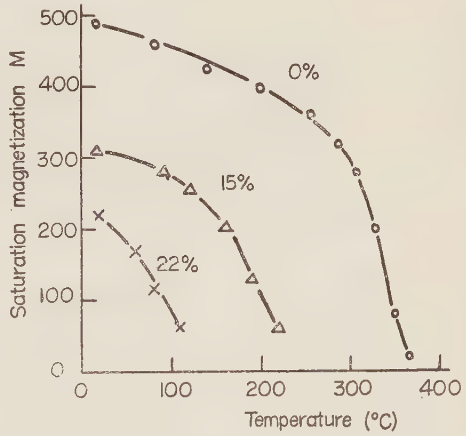

Fig. 3. Temperature dependence of saturation magnetization for Ni ($L=2000$ Å), 15% Cu-Ni ($L=2700$ Å) and 22% Cu-Ni ($L=2070$ Å) films.

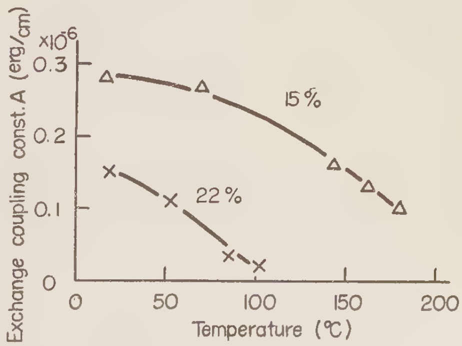

Fig. 4. Temperature variation of exchange coupling constant A for 15% Cu-Ni (△) and 22% Cu-Ni (×) alloy film.

---

*) This measurement has been carried out by Mrs. T. Nosé with the E.S.R. apparatus in the Tokyo Metropolitan Isotope Centre.

**) The detail will be published.

within an error of about 5%, the standard being Ni films, as shown in Fig. 3. This new method can also fix the Curie point within ±10°C in the temperature range between 100 and 400°C. It can correspondingly determine the concentration within ±1% for Cu-Ni alloy films.

As the temperature is raised, values of A for 22% and 15% Cu-Ni decrease and vanish at 100 and 180°C respectively, as show in Fig. 4. It is interesting that the excitation of spin wave resonance is possible even at about 30°C below the Curie point.

Thus the exchange integral J in the atomic model as previously stated is determined. The temperature variations of a and g are negligible. Consequently, it is found that values of J are nearly constant for any film as well as at any high temperature, as given in Table V. A small increase with temperature is perhaps due to variations of a and g.

Table V. Temperature variations of M, A and J.

Film	Temp. (°C)	M	$A(\times 10^{-6}$ erg/cm)	$J(\times 10^{-14}$ erg)
15%Cu-Ni	16	310	0.28	8.6
	69	300	0.27	9.0
	143	230	0.16	9.1
	163	200	0.13	9.7
	179	170	0.10	9.9
22%Cu-Ni	19	220	0.15	9.2
	53	185	0.11	9.6
	86	100	0.032	9.6
	103	80	0.021	9.8

§4. Summary

The excitation of spin wave resonance in Ni film is possible only in the case of film prepared on unheated glass. It is essentially sensitive to the structure of film.

The exchange coupling constants in films of Ni, Pd-Ni alloy, Cu-Ni alloy are investigated. The value in Ni film is $A=0.75\times 10^{-6}$ erg/cm. With increasing concentrations of Pd and Cu, it decreases monotonously to about 2/3 at 35% Pd and 1/5 at 22% Cu respectively. Their exchange integrals are, however, nearly constant and $J=9.4\times 10^{-14}$ erg.

The temperature variations of A and J are studied for some Cu-Ni alloy films. The values of J remain again constant up to the Curie point.

Acknowledgements

The author would like to express his sincere thanks to Professor R. Kimura for his continued encouragement through the present investigation. His thanks are also expressed to Professor M. Shimizu for his helpful discussions, Mr. M. Ichikuni for his kindness in the colorimetric analyses and Mr. T. Watanabe for his allowance to use his torsion balance. His thanks are due to Messrs. T. Yoshikawa, H. Shimazaki, T. Hayashi, S. Shinya, H. Ikeda for the preparations. This work was partly indebted to the Scientific Research Expenditure of the Ministry of Education.

References

1) C. Kittel: Phys. Rev. **110** (1958) 1295.
2) M. H. Seavey and P. E. Tannenwald: Phys. Rev. Letters **1** (1958) 168; J. Appl. Phys. **30** (1959) 227S.
3) H. Nosé: J. Phys. Soc. Japan **15** (1960) 1714.
4) H. Nosé: J. Phys. Soc. Japan **16** (1961) 342.
5) H. Nosé: J. Phys. Soc. Japan **16** (1961) 838.
6) Z. Frait: Czech. J. Phys. **B11** (1961) 360. Z. Frait and M. Ondris: Czech. J. Phys. (to be published).
7) P. E. Tannenwald and R. Weber: Phys. Rev. **121** (1961) 715.
8) J. R. Macdonald: Proc. Phys. Soc. London **A64** (1951) 968; Phys. Rev. **106** (1957) 890.
9) J. D. Finegan and R. W. Hoffman: J. Appl. Phys. **30** (1959) 597.
10) D. Fraitová: Czech. J. Phys. (to be published).
11) For example, C. Herring and C. Kittel; Phys. Rev. **81** (1951) 869.
12) R. M. Bozorth: Ferromagnetism (Van Nostrand, New York, 1951); V. Marian: Ann. physique [11] **7** (1937) 459.
13) T. Watanabe: J. Appl. Phys. Japan **29** (1960) 463.

14) L. Néel: J. phys. radium **15** (1954) 225.
15) W. H. Meiklejohn and C. P. Bean: Phys. Rev. **102** (1956) 143; J. Appl. Phys. **29** (1958) 454.
16) P. Pincus: Phys. Rev. **118** (1960) 658.
17) M. Fallot: Ann. physique **6** (1936) 305.
18) B. R. Coles: J. Inst. Met. **84** (1956) 346. (Cu-Ni alloy). R. Hultgren and C. A. Zapffe: Trans. A. I. M. M. E. **133** (1939) 58. (Pd-Ni alloy).
19) E. I. Kondorskij, V. E. Rode and U. Hoffman: J. phys. radium **20** (1959) 195.

JOURNAL OF THE PHYSICAL SOCIETY OF JAPAN Vol. 16, No. 12, DECEMBER, 1961

Properties of Surface Imperfections Produced on Germanium by Cleaning Treatments

By Akio KOBAYASHI, Koichi SUGIYAMA, Hikaru ARATA
and Zenjiro ODA

Electrical Communication Laboratory, Musashino, Tokyo

(Received August 2, 1961)

Surface conductivity and Hall coefficient of germanium cleaned by ion-bombardment and subsequent annealing have been measured over the temperature range 1.5–300°K. The results indicate that donor levels are produced near the surface by ion-bombardment and are eliminated with subsequent annealing at 500°C in high vacuum making the surface space charge layer p-type. The density of the excess holes near the surface has a magnitude of $8\times10^{11}\,\mathrm{cm}^{-2}$ for an n-type of 8Ω cm and $8.5\times10^{10}\,\mathrm{cm}^{-2}$ for a p-type of 20Ω cm. Ion-bombardment gives rise to a small Hall maximum at low temperatures around 5°K. This maximum shifts to higher temperatures as annealing treatments are repeated and disappears if air is introduced. This maximum is attributed to holes of the order of $10^7\,\mathrm{cm}^{-2}$ in the space charge layer.

§1. Introduction

It has been found that the temperature dependence of Hall coefficient of p-type germanium cleaned by Joule heating in ultra-high vacuum showed a steep maximum at $10°\sim20°\mathrm{K}$[1]. The behaviour is similar to the p-type impurity conduction[2] in bulk crystals. The maximum disappeared if oxygen gas was introduced, thus the phenomenon was ascribable to conduction through surface dangling bonds or a p-type skin doped heavily with foreign impurities. But which model was preferred to could not be decided on.

Law[3] found at that time that boric acid evaporated from a heated glass vessel produced p-type skins on silicon and germanium during heat-treatment in high vacuum, and showed that the skins could be removed by ion-bombardment and subsequent annealing. According to Farnsworth's analysis of germanium surfaces with slow electron diffraction[4], the lattice points of surfaces are distorted by ion-bombardment, and the distortion can be eliminated by subsequent annealing at 600°C in ultra-high vacuum. Forman[5] has found that the field effect mobility drops to zero by ion-bombardment, but restores to several hundred cm²/volt. sec by heating at 650°C.

The purpose of the work presented in this paper is to clear the electrical nature of the germanium surface cleaned by ion-bombardment and its changes with subsequent annealing in high vacuum and with admission of air. In connection with the experimental results obtained, a brief discussion will be made about the relation between surface conduction and grain boundary conduction[6].

§2. Experiments

Fig. 1 (a) shows the electrode arrangement of experimental bulb and Fig. 1 (b) illustrates the geometry of germanium samples. The samples were etched and rinsed in the usual way, and then welded on the leads of thin tantalum ribbons by argon arc as mentioned in the previous paper[1]. They were again etched and rinsed before mounted in the glass bulb. Leads at both ends of the sample shown in Fig. 1 (b) were served as current leads and the other two inside leads as potential probes. Hall voltage could be obtained from change in potentials of one of the inside leads, when magnetic field was reversed.

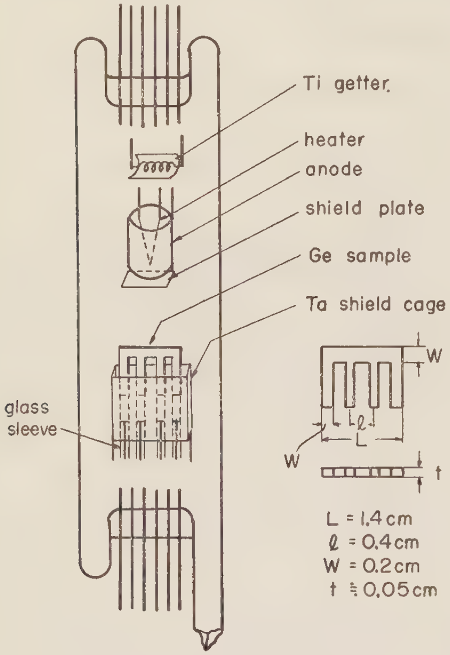

(a) (b)

Fig. 1. (a) Electrode arrangement of the bulb. (b) Geometry of the germanium samples.

Experimental bulbs were evacuated by a mercury diffusion pump for 48 hrs, during which the vacuum system was baked out at 300°C for 30 hrs and the ionization gauge, metal electrodes of the bulb and barium getter were outgassed several times. After the vacuum of 10^{-9} mm Hg was attained, argon was admitted into the bulb through two cold traps and the barium getter bulb until the pressure reached $5\sim7\times10^{-3}$ mm Hg. The pressure used was reduced to such a low pressure that sputtered materials could hardly be returned to the target during discharge. The germanium target was biased -400 volts with reference to a hot tungsten filament, and the cylindrical anode was bisaed about $+60$ volts

It was observed by preliminary experiments that tantalum atoms sputtered from the leads were deposited on the germanium surface and caused an n-type impurity conduction at low temperature. In the present case, therefore, the tantalum leads were completely covered with a tantalum shield cage to which a positive potential of $+50$ volts was applied to avoid sputtering of the leads as shown in Fig. 1 (a). Under these conditions, a target current of about 60μA was obtained. The ion-bombardment was continued for 6 hrs. The amount of net ion charge corresponds to around 1 coulomb per cm^2 of the surface of germanium target. As the sputtering yield of argon ions for germanium is known to be around unity at this ion energy[7], the sputtering can remove 1.4μ from the surface.

After bombardment, the argon was pumped out to 10^{-9} mm Hg and a titanium getter was flashed. Then the bulb was sealed off from the pumping system. Annealing of the surface was made by passing an ac current through the sample in the sealed-off bulb. Temperature dependences of resistivity and Hall coefficient were observed after each treatment. Finally the measurements were carried after air was admitted. The magnetic field used had a magnitude of 4900 gauss.

§ 3. Effects of Ion-Bombardment and annealing on Surface Conductivity at room Temperature

Surface conductivity was preliminarily observed at room temperature with the bulb connected with the pumping system to know the effect of bombardment and annealing. The bulb was ougassed down to 10^{-8} mm Hg after ion-bombardment. Then Hall voltage and resistivity were measured after every following treatment; (1) introduction of air; (2) annealing at 400°∼500°C for an hour after ion-bombardment and evacuation; (3) admission of air after the treatment (2). Surface conductivities were almost unchanged by ion-bombardment in both cases of n- and p-type. It was thus difficult to detect any changes in surface conductivity by subsequent admission of air. But if the samples were annealed in high vacuum after bombardment, the surface conductivity increased by 20∼

100$\mu\mho$ per square and Hall coefficient decreased remarkably. The increased surface conductivity disappeared with admission of air.

It is assumed in this paper according to many investigations[5),9)] that the treatment of the surface exposed to oxygen brings the energy bands very close to the flat band condition. According to this assumption, it is concluded that a p-type space charge layer near the surface is built up only after annealing subsequent to bombardment.

Next, the measurements were carried with the sealed-off bulbs. The results are summarized in Table 1.

In this table, specific resistivities, ρ, and Hall coefficients, R, of n- and p-type crystals vary with treatments mentioned in the first column. First, the data of p-type are to be considered. Both ρ and R increase after ion-bombardment. The results can be explained as follows. Ion-bombardment introduces donors and makes the surface weaker p-type. These donors do not distribute uniformly according to the temperature dependence of ρ and R to be discussed in the next section. R and ρ decrease with the treatment of subsequent annealing in ultra-high vacuum. Thus this treatment makes a p-type accumulation layer near surface.

Table 1. The dependence of resistivities and Hall coefficients of n- and p-type germanium on subsequent surface treatments.

p-type germanium of 0.05 cm in thickness

Treatment	Resistivity Ω cm	Hall coefficient 10^4 cm³/coul	Temperature
p-1. In air	23.01	5.568	16.2°C
p-2. Ion-bombardment	23.31	5.796	〃
p-3. Annealing at 550°C for 1 hr in vacuum	17.34	4.433	〃
p-4. Second annealing at 600°C, 1 hr.	18.28	4.305	〃
p-5. Quenching from 700°C	20.68	5.085	19.9°C
p-6. Admission of air	21.18	5.197	19.9°C

n-type germanium of 0.045 cm in thickness

Treatment	Resistivity Ω cm	Hall coefficient 10^4 cm³/coul	Temperature
n-1. Ion-bombardment	8.328	2.225	21.0°C
n-2. Annealing at 550°C, 1 hr.	8.543	2.250	〃
n-3. Second annealing at 550°C, 1 hr.	8.737	2.257	〃
n-4. Addmission of air	8.989	2.416	〃

In the case of heat-treatment at 700°C referred to p-5 in Table 1, the sample was heated electrically by passing an ac current through it and quenched with radiation cooling. Admission of air after this treatment gives rise to increases in R and ρ as shown in p-6. Assuming that this state satisfies the flat band condition, the conductivity of the accumulation layer near the surface which disappears with exposure to air is obtained as 31.7$\mu\mho$ per square from the difference between the conductivities of p-5 and p-6. Unknown acceptors were introduced into the sample during ion-bombardment and annealing for all efforts. Their concentration is no less than 1.1×10^{12} atoms/cm² given by the difference between the reciprocals of Hall coefficients of p-1 and p-6 in the table. This value is comparable to or more than the concentration of holes in the space charge layer. Therefore one can not compare p-1 with p-6.

Table II. Constants of the space charge layers.

	n-type 8Ω cm	p-type 20Ω cm
Surface conductivity	72.5$\mu\mho$/□	31.7$\mu\mho$/□
Surface potential, $-e\varphi_s$	0.36 eV*	0.128 eV**
Excess holes near the surface Γ_p	8×10^{11}/cm²	8.5×10^{10}/cm²
Excess electrons near the surface, Γ_n	-3×10^{10}/cm²	-1.6×10^{8}/cm
Mobility of surface holes	650 cm²/volt. sec	2480 cm²/volt. sec
Fermi level, E_F	0.268 eV for E_c-E_F	0.272 eV for E_F-E_V
Carrier concentration in bulk	2.5×10^{14}/cm³	1.6×10^{14}/cm³

* assumed $m^*/m=0.3$.

** assumed $\mu_H/\mu=1$, $\mu_n=3940$ cm²/volt. sec.

The p-type surface conductivity of the cleaned n-type sample has a magnitude of $72.5\mu\mho$ per square evaluated from the difference between the conductivities of n-3 and n-4 in Table I.

Table II shows the constants of the p-type space charge layers for p-5 and n-3 calculated from the method of Garrett and Brattain[8]. Electronic energy diagrams obtained are shown in Fig. 2. These results agree with many other investigators[9] at such a qualitative point that there is a strong p-type space charge layer near a cleaned surface. The mobility of surface holes in the n-type sample is reduced to one-third as large as that in bulk, because the width of the space charge potential well is comparable to a mean free path or less[10].

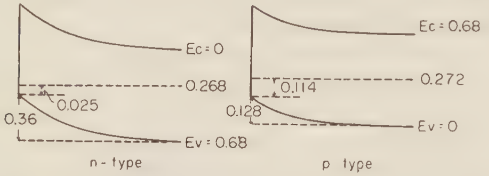

Fig. 2. Electronic energy diagram near the surface of p- and n-type samples. Unit is in eV.

§ 4. Temperature Dependence of Resistivity and Hall coefficient

The temperature dependences of ρ and R vary with different treatments as shown in Fig. 3 for the p-type sample. Fig. 4 shows the same curve from room temperature to 20°K in details. In this figure, Curve 2 for ion-bombardment shows complicate rise and fall. As mentioned in the previous section, ion-bombardment introduces some donor type imperfections which make the surface weaker p-type. The wavy nature of Curve 2 should be ascribed to unevenness in surface distribution of the donors which may be due to embedded argon ions. It is well-known that acceptors are produced in germanium by the bombardment of ions having an energy of 10 KeV or higher[11]. Each ion knocks on germanium atoms in the normal lattice point forming pairs of Frenkel defects. But as the range of the ions used in the present experiment is shorter than 100Å and the sample is warmed up by bombardment, thus most of Frenkel defects may be annealed during ion-bombardment and residual imperfections including embedded argon atoms may affect surface conductivity. Actually, annealing subsequent to ion-bombardment resulted in gas evolution of a magnitude of around 10^{14} molecules which was ten times as large as the gas evolution in the case without bombardment.

As shown in Fig. 4, the rise and fall of Curve 2 is eliminated by subsequent annealing, and finally Hall curve becomes to show a similar broad drop around 40°K to Curve 1, This drop in Hall curve appears as far as the concentration of ionized impurities is so small that light holes can move along the circular orbit of Lorentz force without being scattered by lattice vibrations with decrease in temperature. It can, therefore, be concluded that uniformity and purity of the surface is restored by careful annealing.

Hall maximum at low temperature does not appear before ion-bombardment. It appears at around 5°K after bombardment and shifts toward higher temperature around 7°K after the treatment of quenching down from 700°C. These maxima are not so remarkable as that reported in the previous paper. Surface

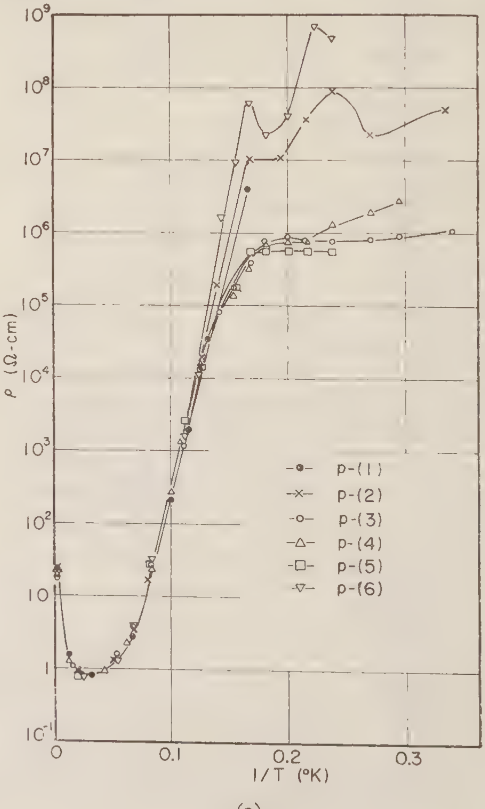

(a)

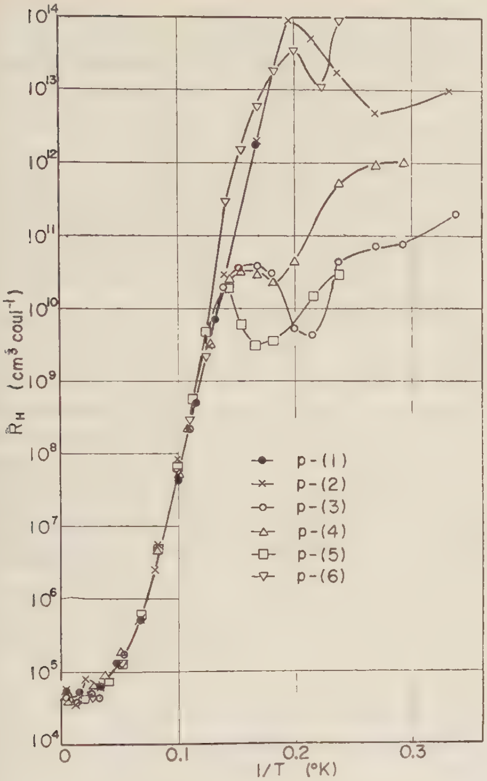

(b)

Fig. 3. Temperature dependence of resistivity (a) and Hall coefficient (b) of a p-type sample.

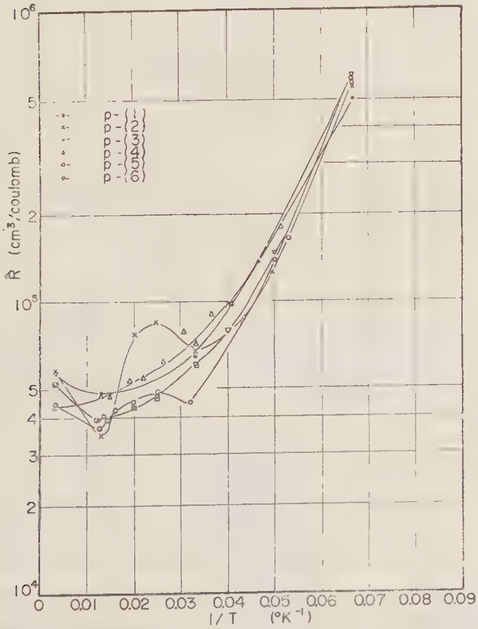

Fig. 4. Detailed curves of Hall coefficient in Fig. 3.

carrier concentration and its Hall mobility are calculated to be 10^7 cm^{-2} and 10^4 cm^2/volt. sec, respectively, from the Hall minimum and the conductivity near 4°K. Since these carriers have a large mobility in spite of their low concentration, this hole conduction should not be attributable to hopping conduction through surface states, but to conduction in the surface space charge layer which is counterbalanced by surface states anti-charged. These surface states are not intrinsic but due to surface lattice defects, because the behaviour of Hall maxima and minima around 4°K is sensitive to the heat-treatments.

Hall maximum at low temperatures could not be observed with n-type samples ion-bombarded and then annealed. The reason is that the resistivity of a p-n junction formed between the bulk and the p-type inversion layer near the surface becomes so large that current can not flow into the inversion layer.

The nature of two-dimensional array of dangling bonds in the surface has been often compared with that of a grain boundary. Anomalous conductivity at low temperature has been found along grain boundaries[6)] and in the surface of germanium cleaned by heat-treatment without bombardment[1)]. However, the present experiment shows that no anomalous conduction can be observed if the surface is cleaned by ion-bombardment and subsequent annealing. Therefore the anomalous conduction mentioned in the previous paper should be attributed to impurities transferred from the glass bulb. This suggests that an anomalous conduction in the grain boundary also might be ascribed to impurities segregated from the matrix.

§ 5. Conclusion

Donors are produced in the surface of germanium by argon ion-bombardment with several hundred volts. They are eliminated with subsequent annealing in ultra high vacuum and finally a strong p-type space charge layer is built up near the surface. The excess density of holes in this layer has a magnitude of 8.5×10^{10} cm^{-2} for a p-type 20Ω cm sample and 8×10^{11} cm^{-2} for an n-type 8Ω cm one at room temperature, but it diminishes 10^7 cm^{-2} for the p-type at 6°K. These holes are counterbalanced by surface states anti-charged. The surface states are not intrinsic but due to surface lattice defects.

The strong p-type conduction at low temperature mentioned in the previous paper can not be observed in the present experiment, so it is concluded that this conduction should not be attributed to surface dangling bonds, but might be caused by impurities, probably boron, transferred from the glass bulb.

Acknowledgements

The authors would like to thank Dr. J. Okada of Toshiba Electric Co. for the kind supply of germanium crystals.

References

1) A. Kobayashi, Z. Oda, S. Kawaji, H. Arata and K. Sugiyama: J. Phys. Chem. Solids, **14** (1960) 37.
2) C. S. Hung and J. R. Gliesman: Phys. Rev. **99** (1955) 406; H. Fritzsche: J. Phys. Chem. Solids **6** (1958) 69.
3) J. T. Law: J. Phys. Chem. Solids **14** (1960) 9.
4) J. A. Dillon and H. E. Farnsworth: J. Appl. Phys. **29** (1958) 1195.
5) R. Forman: Phys. Rev. **117** (1960) 698.
6) B. Reed, D. Weinreich and H. F. Mataré: Phys. Rev. **113** (1959) 454.
7) S. P. Wolsky: Phys. Rev. **108** (1957) 1131; N. Laegreid, G. Wehner and B. Meckel: J. Appl. Phys. **30** (1959) 374.
8) C. G. B. Garrett and W. H. Brattain: Phys. Rev. **99** (1955) 376.
9) P. Handler: J. Phys. Chem. Solids: **14** (1960) 1. D. R. Palmer, S. R. Morrison and C. E. Dauenbaugh: ibid 27, P. Handler and W. M. Portnoy: Phys. Rev. **116** (1959) 516.
10) J. R. Schrieffer: Phys. Rev. **97** (1955) 641.
11) W. D. Cussins: Proc. Phys. Soc. **68** (1955) 213. U. F. Gianola: J. Appl. Phys. **28** (1957) 868.

Journal of the Physical Society of Japan, Vol. 16, No. 12, December, 1961

Dielectric Behavior of KNO_3 in Its Ferroelectric Phase III

Shozo Sawada, Shoichiro Nomura and Yohko Asao

Department of Physics, Tokyo Institute of Technology

(Received August 3, 1961)

The dielectric behavior of KNO_3 crystal was investigated. Mainly in its ferroelectric phase III, which appears in the temperature range of about 125∼115°C on cooling, the *D-E* hysteresis loop along the *c* axis was observed by the usual Sawyer-Tower method using the 50 c/s *ac* electric field, the pyroelectric current in this direction was measured by the usual galvanometer method and the dielectric constants along the three crystal axes were measured by a C-meter using the 100 kc/s *ac* voltage. From the obtained results, the ferroelectricity in the phase III was discussed in relation with the motion of NO_3 groups.

§ 1. Introduction

Potassium nitrate (KNO_3) has the aragonite sructure (orthorhombic, D_{2h}^{16}—*Pnma*) at room temperature[1]. The crystal structure changes from orthorhombic to trigonal at about 130°C on heating, the low- and the high-temperature phases being named the phase II and the phase I, respectively. The phase I is generally believed to have a structure closely related with the calcite structure (trigonal, D_{6d}^{3}—*R3c*)[1,2], but any conclusive determination of its structure has not yet been presented. On cooling, the phase I does not directly change to the phase II, but changes first to an another phase named the phase III at about 125°C and next to the phase II at about 115°C, these transition temperatures fairly depending upon the history of specimens and the cooling rate, *etc.*[3,4]. It is known that by an application of high pressure the phase III is realized also on heating and the temperature range corresponding to the phase III on cooling is broadened[5,4], although the phase III does not appear at all events on heating under atmospheric pressure.

The crystal structures of the phases I and II are nonpolar, but that of the phase III is polar and its space group is C_{3v}^5-R3m[6]. A rhombohedral unit cell in the phase III ($a=4.365$Å, $\alpha=76°56'$ at 120°C), shown in Fig. 1, contains one molecule of KNO_3 and eight K^{+1} ions occupy its corners and one NO_3^{-1} ion nearly its body center. The NO_3 group forms a regular triangle with the N atom at its center. The plane of the NO_3 group is perpendicular to the c axis and it does not exist exactly at the body center of the rhombohedron but in a position slightly deviated from it along the c axis. We have already reported the existence of the ferroelectricity in the phase III of KNO_3, using mainly fused specimens[7] and the result of a measurement of the thermal conductivity of fused specimens, with some discussion of the effect of the rotational motion of NO_3 groups upon the thermal conduction[8]. In the present paper the dielectric behavior of single crystals mainly in the phase III will be described in detail, although the experimental study on single crystals is always somewhat disturbed by the destructibility of the crystal of this substance in passing through the transition points.

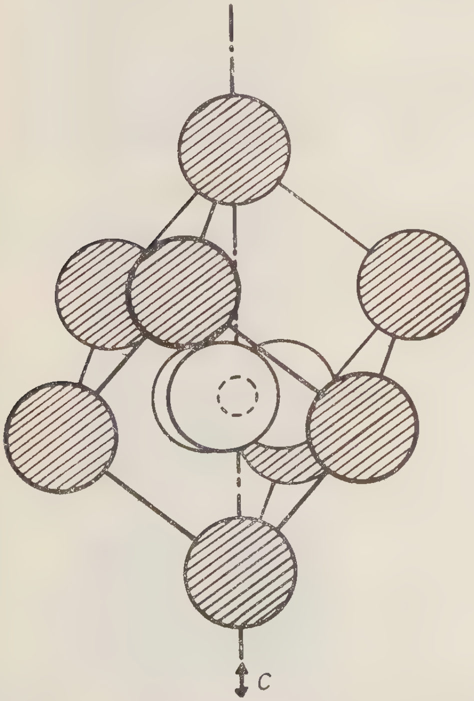

Fig. 1. Rhombohedral unit cell in the phase III of KNO_3. Small, white large and shaded large spheres represent N, O and K, respectively.

§ 2. Preparation and Treatment of Crystals

Although a melt of KNO_3 powder of extra-pure grade, which had beforehand been dried in 10^{-3} mmHg vacuum at about 120°C for several days, solidified into several beautiful crystals at the solidifying point (339°C) on slow cooling, they always broke into a lot of tiny crystallites in passing through the transition points. Thus the fusion method was not useful in preparing single crystals, so the aqueous solution method was adopted.

Good crystals were easily obtained by the slow cooling of an aqueous solution of KNO_3 powder of extra-pure grade. For instance, 500 g KNO_3 solved in 700 cc distilled water was cooled from 43°C down to 38°C during a month. Usually crystals grew most in the c direction and least in the b direction, so they formed hexagonal pillars flattened along the b axis. The dimension of such crystals was about 5 cm × 2 cm × 1 cm at largest. Some crystals formed hexagonal plates in which the c axis lay on and the b axis stood perpendicular to the plane of the plate.

The direction of crystal axes was determined by the X-ray Laue photograph and by the microscopic observation. The cleavage was not discernible in any directions, so specimens oriented in each direction were cut out of crystals using a wet string, then they were polished by emery papers and finally were etched by distilled water for a few seconds. After having been dried for a day in a thermostat kept at about 110°C, they were silver-pasted to form electrodes on their surfaces and were again dried in the thermostat.

§ 3. *D-E* Hysteresis Loop

Photo. 1 shows the hysteresis loop of a c crystal observed on cooling by the usual Sawyer-Tower method, using the 50 c/s *ac* electric field ($E_{max}=9.9$ kV/cm). The D-E loop was nearly a straight line above 127°C, began to open out from about 125°C, showed a typical ferroelectric feature between 123°C and 117°C and finally was again crushed into a straight line at about 115°C. Photo. 2 shows the amplitude dependence of the hysteresis loop observed at 118.5°C, where are denoted the absolute values of E and D which are also applicable to Photo. 1. The temperature dependence of the spontaneous polarization and the coercive field obtained from

Photo. 1 are shown in Figs. 2 and 3, respectively. The spontaneous polarization and the coercive field at 120°C were found to be about 8 μC/cm^2 and 4 kV/cm, respectively. The amplitude dependence of the residual polarization and the coercive field obtained from Photo. 2 are shown in Figs. 4 and 5, respectively. The relative coercive field defined by E_c/E_{max} is also shown in Fig. 5.

It is generally accepted that a crystal of KNO$_3$ is gradually broken into minute crystallites by successive heating and cooling through the transition points and that in such a disarranged state the directions of crystal axes of each crystallite are fairly at random9),10). Although the specimen used in the above observation had initially been a *c* crystal, the directions of its crystal axes may have been irregular in some degree when the above photographs were taken, since it was necessary to first heat the specimen up to about

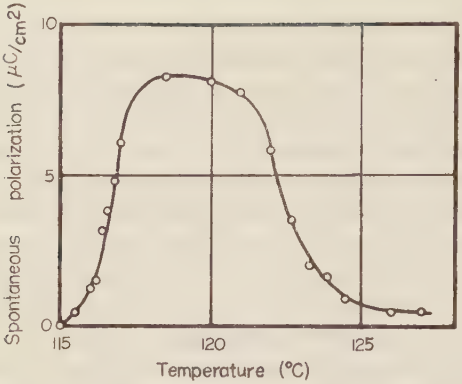

Fig. 2. Temperature dependence of the spontaneous polarization determined by the hysteresis loop (E_{max}=9.9 kV/cm).

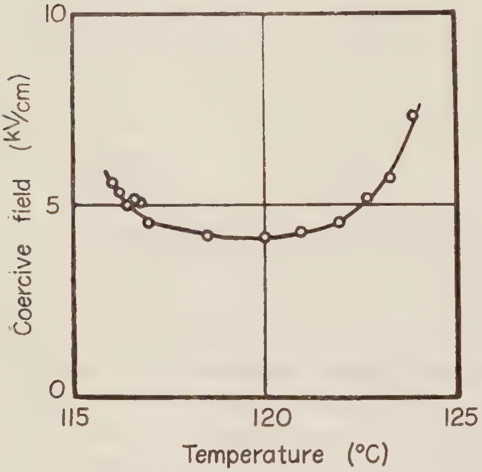

Fig. 3. Temperature dependence of the coercive field (E_{max}=9.9 kV/cm).

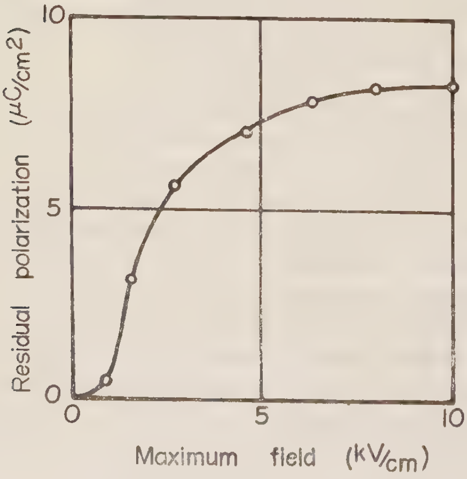

Fig. 4. Amplitude dependence of the residual polarization (118.5°C).

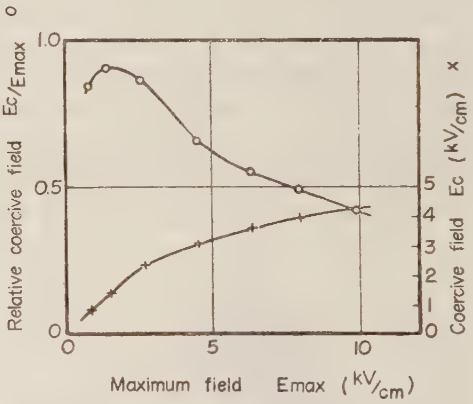

Fig. 5. Amplitude dependence of the coercive field and the relative coercive field (118.5°C).

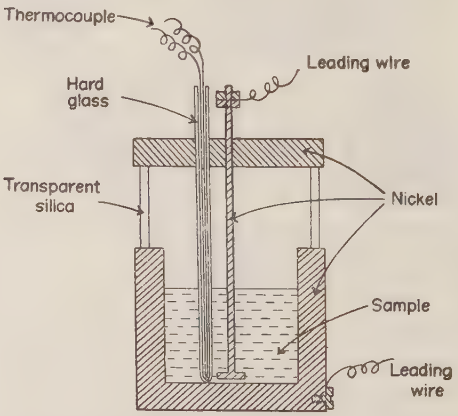

Fig. 6. A nickel crucible to observe the hysteresis loop of a fused specimen.

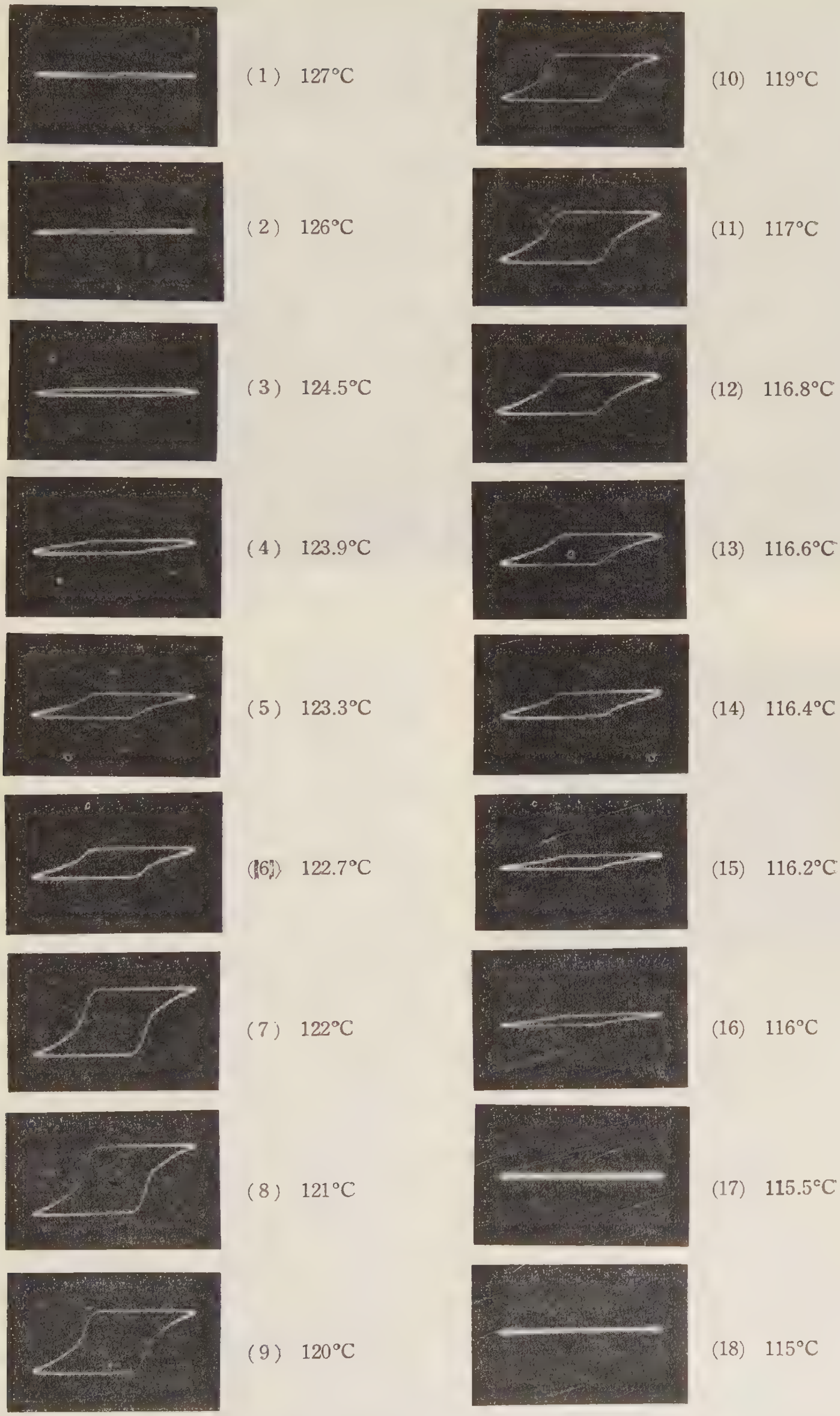

(1) 127°C

(2) 126°C

(3) 124.5°C

(4) 123.9°C

(5) 123.3°C

(6) 122.7°C

(7) 122°C

(8) 121°C

(9) 120°C

(10) 119°C

(11) 117°C

(12) 116.8°C

(13) 116.6°C

(14) 116.4°C

(15) 116.2°C

(16) 116°C

(17) 115.5°C

(18) 115°C

Photo. 1. *D-E* hysteresis loops observed at various temperatures in the phase III on cooling (50 c/s, $E_{max}=9.9$ kV/cm).

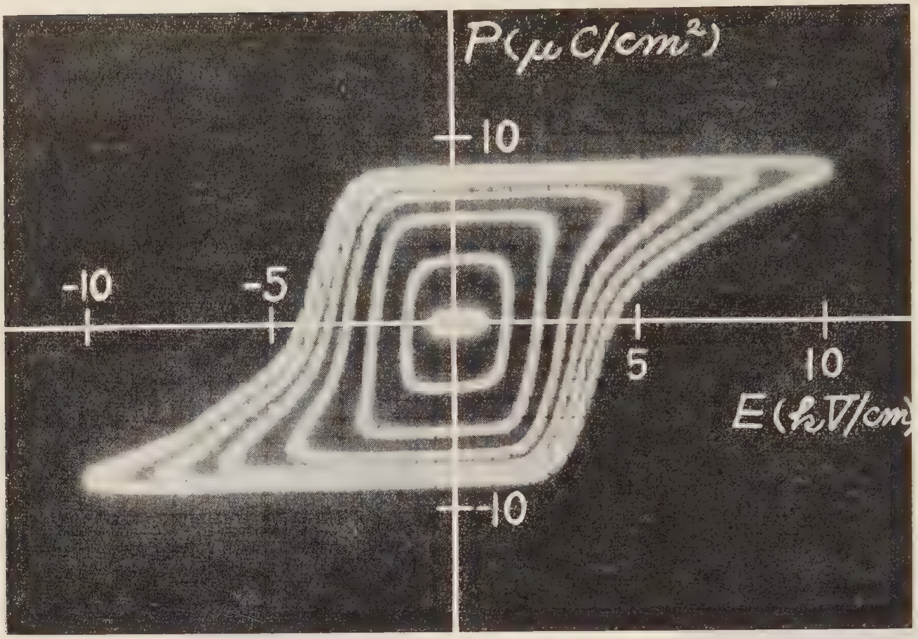

Photo. 2. Amplitude dependence of the hysteresis loop observed at 118.5°C (50 c/s).

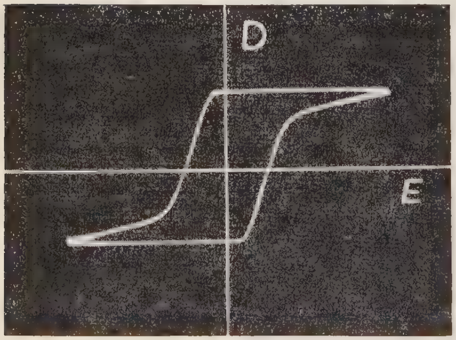

Photo. 3. Hysteresis loop of a fused specimen (50 c/s, 121°C, E_{max}=17 kV/cm).

180°C and next to cool it down, in order to bring it into the phase III, and thus the specimen had once passed through the transition point at 130°C on heating before the above observation was made.

In spite of this situation, the hysteresis loop showed a fairly enough saturation, as seen in Photos. 1 and 2. This fact seems to show that at least the direction of the *c* axis of a crystal is roughly preserved in passing through the transitions, when the *ac* electric field is applied in the original *c* direction of the crystal. Such supposition may be supported by a fact that at room temperature the crystal was found to be still transparent after the observation of the hysteresis loop through the phase III. An application of the *dc* field may be expected to be more effective in keeping the direction of crystal axes unaltered.

When, as shown in Fig. 6, KNO_3 powder was melted in a nickel cylindrical crucible with a nickel disc electrode suspended along its central axis, the crucible itself serving as another electrode and the gap between them being about 0.5 mm, and was slowly cooled down in that condition, a ferroelectric hysteresis loop was also observed for such a fused specimen cooled down from the fused state in the temperature range corresponding to the phase III. An example at 121°C is shown in Photo. 3, where an even more perfect saturation is seen than in the specimen started from the single crystal, although the absolute value of electric polarization could not easily be evaluated, owing to the rather complex arrangement of the electrodes. Such a result may lead us to the supposition that a crystal is only a little cracked in the transition I→III. As the crystal structures of the phases I and III are only slightly different from each other, the transition I→III would not need any serious change of atomic positions. On the contrary, as the crystal structures of the phases I and II are much different from each other, some drastic atomic displacements would be necessary in the transitions II→I and III→II, which seems to be the primary reason of the cracking of crystals in these transitions, and thus the cracking on cooling may be supposed to occur mainly in the transition III→II.

Many authors[4),9),11)] have reported that the moisture, the size of crystal, the cooling rate, *etc.* have some effects to promote or to suppress the appearance of the phase III, but their results are not necessarily in agreement with each other. We have found that the phase III does not appear when a crystal have not been heated up to above about 160°C first, but that the size of crystal and the cooling rate have little influence upon the appearance of the phase III. Sometimes the phase III is said to be a metastable one, but it was ascertained by our observation that the ferroelectric hysteresis loop of a crystal did not change at all even when it was kept at a definite temperature, say 120°C, in the phase III during more than eight hours.

§4. Pyroelectricity

The pyroelectricity in the *c* direction of the crystal was measured by the usual galvanometer method. The crystal was first poled by a *dc* field of 5 kV/cm for about 30 sec at 120°C, where the spontaneous polarization had been found to be maximum by the observation of the hysteresis loop. After the electrodes of the crystal had heen short-circuitted for 2∼15 min at this temperature, the pyroelectric current was measured in each of heating and cooling processes from this temperature. Results of each measurement are shown in Fig. 7 (a) and (b), respectively.*

The spontaneous polarization calculated from Fig. 7 (a) and (b) is shown in Fig. 8 (a) and (b), respectively. The maximum value of the spontaneous polarization turns out to be 10 μC/cm² and 8 μC/cm² in these two cases, respectively, nearly agreeing with the value determined by the hysteresis loop, 8 μC/cm². In addition, the temperature dependence of the spontaneous polarization shown in Fig. 8 is not far from the one shown in Fig. 2, which was obtained by the observation of the hysteresis loop. A tendency that the spontaneous polarization determined by the pyroelectric current is larger than that by the hysteresis loop seems to come from the fact that, when the spontaneous polarization is to be determined by the measurement of the pyroelectric

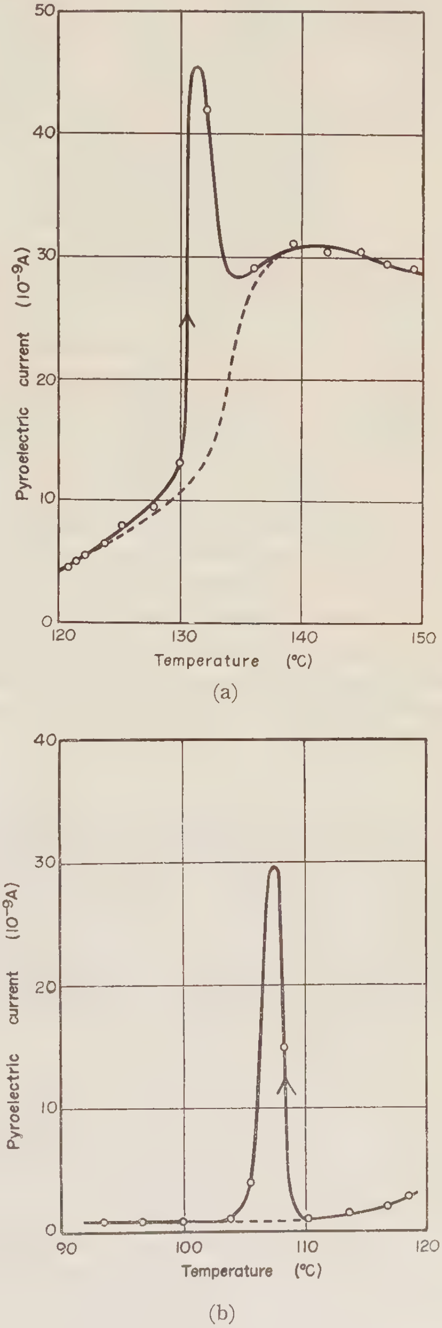

Fig. 7. Temperature dependence of the pyroelectric current. Poling: 5 kV/cm for 30 sec at 120°C.
(a) Heating, electrodes area: 0.20 cm²,
(b) Cooling, electrodes area: 0.23 cm².

---

* In the cases shown in Fig. 7 (a) and (b), specimens were not the same and the absorption currents of 4×10^{-10}A and 3×10^{-10}A were flowing just before the start of measurement, respectively.

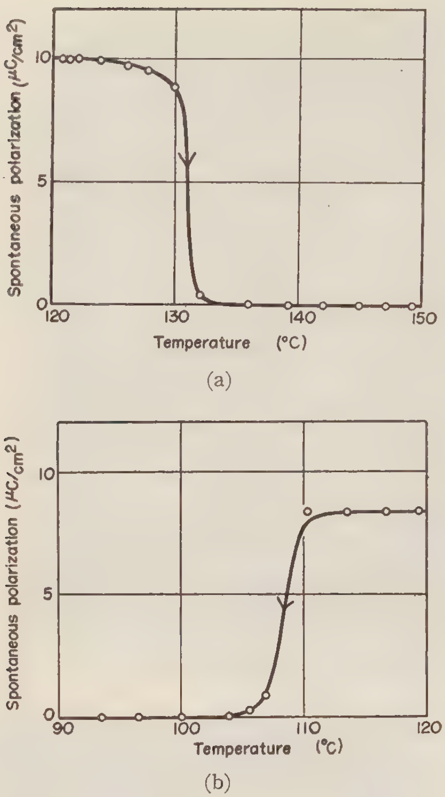

Fig. 8. Temperature dependence of the spontaneous polarization determined by the pyroelectric current
(a) in Fig. 7 (a),
(b) in Fig. 7 (b).

current, an incomplete decay of the absorption current as a result of the field treatment is apt to apparently increase the value of the spontaneous polarization. In the KNO_3 crystal, the absorption current flows for a fairly long time[12], at least one part of which may be due to the above-mentioned crystallites-structure of the crystal.

§ 5. Dielectric Constant

Fig. 9 (a), (b) and (c) show the temperature dependence of the dielectric constants along the *a*, *b* and *c* axes measured by a C-meter using the 100 kc/s *ac* voltage, respectively. Although these results were not quite reproducible owing to the destructibility of the crystal, distinct anomalies were seen at each transition in all of three directions, the one in the *c* direction being the most remarkable. The value of dielectric constant is nearly 5 in any directions at room temperature and it reaches beyond 60 along the *c* axis at the I→III transition point. Above this point, the dielectric constant along the *c* axis obeys the Curie-Weiss law as shown in Fig. 10, where the Curie constant and the paraelectric Curie temperature are found to be $C=5.6\times10^3$°K

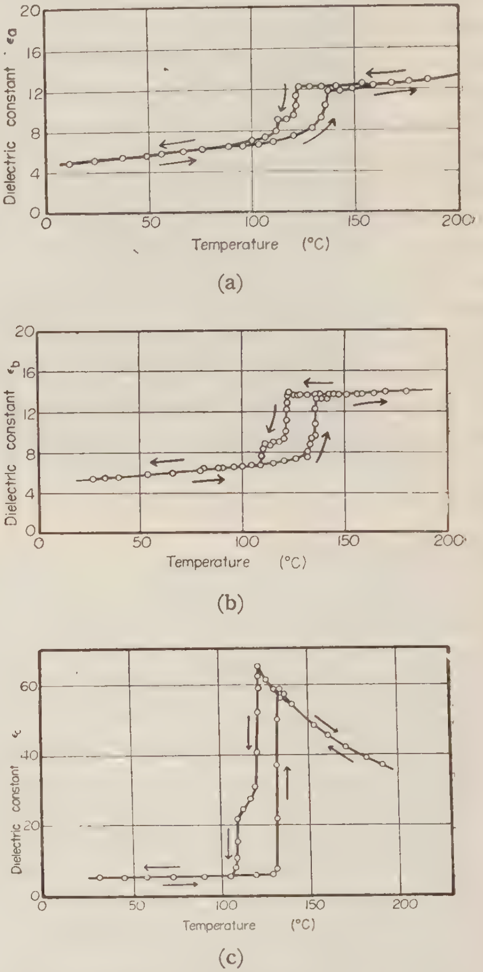

Fig. 9. Temperature dependence of the dielectric constant (100 kc/s).
(a) *a* direction, (b) *b* direction, (c) *c* direction.

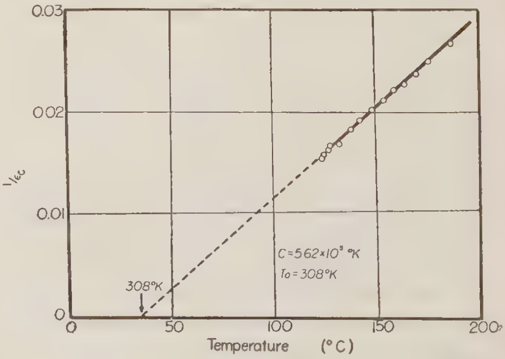

Fig. 10. Curie-Weiss law of ε_c.

and $T_0=308°K$, respectively. This result is just what is expected from the appearance of the ferroelectricity in passing from the phase I to the phase III. The value of C is near that of $NaNO_2$[13),14)], although the difference between the Curie temperature and the paraelectric Curie temperature, T_c-T_0, is rather abnormally large.

Fig. 9 shows that all of the transitions on heating and cooling are of the first order, agreeing with the results of indirect and direct measurements of the specific heat[4),11)] and that of a qualitative measurement on our samples.

§ 6. Discussion

It is nearly certain that the ferroelectricity in the phase III of KNO_3 arises from the fact that the NO_3 group does not exist exactly at the center of the rhombohedral unit cell but in a position slightly shifted from it in one, *e. g.*, positive direction of the *c* axis and that further the NO_3 group can make a jumping motion between two equivalent positions along the *c* axis following the reversal of the external electric field. Assuming the valence of the NO_3 group to be -1, the value of the spontaneous polarization calculated from the amount of shift of the NO_3 group along the *c* axis, 0.55Å, determined by the X-ray analysis at 120°C[6)], turns out to be $11\,\mu C/cm^2$, which is a little larger than the experimental one due to the observation of the hysteresis loop, $8\,\mu C/cm^2$ (Fig. 2) and than the one due to the measurement of the pyroelectric current, 10 or $8\,\mu C/cm^2$ (Fig. 8 (a), (b)). The calculated value may be said to be in good agreement with the experimental ones, considering a tendency that the latter is liable to turn out to be smaller than the former, owing to an incomplete alignment of ferroelectric domains.

It is known that the NO_3 group is able to rotate in crystals under appropriate conditions. For instance, the transition point (275°C) just below the melting point (310°C) of $NaNO_3$ is generally considered to be a temperature at which NO_3 groups begin to rotate almost freely. Hence it would not be unreasonable to imagine that, also in the phase I of KNO_3, NO_3 groups are, more or less, making rotations about the *c* axis and, presumably in accordance with them, oscillations along the *c* axis.[2)] In the phase II, on the other hand, NO_3 groups are considered to be fixed in definite orientations in the *c* plane and accordingly in definite positions along the *c* axis. In the phase III, NO_3 groups are supposed to be in an intermediate state between these two, *i. e.*, they would be able to rotate about the *c* axis, although under a strong hindrance due to the crystal field, and accordingly to oscillate along the *c* axis across a potential barrier at the center.

Such an idea being tentatively accepted, the ferroelectricity in the phase III of KNO_3 can be said to be of the order-disorder type, and further, the above-mentioned speculation that the reversal of the polarization due to the displacement of NO_3 groups seems to be realized accompanied with the rotation of them, *i. e.*, that the former is not likely to occur without the latter, would lead us to consider that KNO_3 has some feature of "molecular-rotational ferroelectrics", as $NaNO_2$[14)], although the rotation of the NO_3 group itself does not contribute to the reversal of the polarization since the regular-triangular NO_3 group has no dipole moment.

The crystal structures of KNO_3 and $NaNO_2$ seem to be considerably related with each other and the rotational behavior of NO_3 groups in KNO_3 may be supposed to be rather simpler than that of NO_2 groups in $NaNO_2$, account being taken of the more symmetric form of the former than the latter. The discussion of the "microdomain" and its linkage to the "macrodomain" may be made fairly parallelly in both of KNO_3 and $NaNO_2$[15),14),16)]. Anyway, the study of the ferroelectricity of any one of these two substances would be useful in understanding of the ferroelectricity of the other.

A little more detailed discussion seems to be possible of the relation between the ferroelectricity and the behavior of NO_3 groups in the phase III of KNO_3, taking account of the crystal structures not only of the phase III but also of the phases I and II, which will soon be described in another paper.

The authors wish to thank Mr. E. Ichinoe for his cooperation in experiments.

References

1) D. A. Edwards: Zeit. Krist. **80** (1931) 154.
2) P. E. Tahvonen: Ann. Acad. Sci. Fennicae, Series A1, 44 (1947).

3) E. Cohen and H. L. Bredée: Zeit. phys. Chem. **A140** (1929) 391.
4) F. C. Kracek: J. Phys. Chem. **34** (1930) 225.
5) P. W. Bridgman: Proc. Amer. Acad. **51** (1916) 579.
6) F. W. Barth: Zeit. phys. Chem. **B43** (1939) 448.
7) S. Sawada, S. Nomura and S. Fujii: J. Phys. Soc. Japan **13** (1958) 1549.
8) I. Yoshida and S. Sawada: J. Phys. Soc. Japan **15** (1960) 199.
9) W. Borchert: Zeit. Krist. **95** (1936) 28.
10) S. W. Kennedy, A. R. Ubbelohde and I. Woodward: Proc. Roy. Soc. **A219** (1953) 303.
11) H. Miekk-Oja: Ann. Acad. Sci. Fennicae, Series A1, 7 (1946).
12) Y. Asao, I. Yoshida, R. Ando and S. Sawada: J. Phys. Soc. Japan (in press).
13) S. Sawada, S. Nomura, S. Fujii and I. Yoshida: Phys. Rev. Letters **1** (1958) 320.
14) S. Sawada, S. Nomura and Y. Asao: J. Phys. Soc. Japan **16** (1961) 2207.
15) S. Tanisaki: J. Phys. Soc. Japan **16** (1961) 579.
16) Y. Shinnaka: Preprint of the Divisional Meeting of the Phys. Soc. Japan No. 6, p. 168 (1960).

JOURNAL OF THE PHYSICAL SOCIETY OF JAPAN, Vol. 16, No. 12, DECEMBER, 1961

Electron Spin Resonance Studies of Irradiated High Polymers: Polyethylene*

By Hisatsugu KASHIWABARA

Japanese Association for Radiation Research on Polymers,
Kamifujimae-cho, Bunkyo-ku, Tokyo
and
Fuji Spinning Company, Chemical Research Laboratory, Nihonbashi, Tokyo

(Received July 28, 1961)

Molecular structures and the behaviours of the free radicals produced in irradiated polyethylene were investigated by means of electron spin resonance. ESR spectra of high polymers are, in general, so complicated that the identifications of h. f. s. of the spectral patterns observed are difficult. Rather reasonable interpretations were, however, made for polyethylene. Variations of spectral shape and spectral intensities at various temperatures were discussed in connection with the identification of the free radicals produced and some of the irradiation effects in polyethylene.

§ 1. Introduction

The importance of the role of free radicals in the chemical changes occurring in irradiated high polymers is well known from a number of investigations. The behaviour of such radicals, therefore, presents an interesting subject of study in radiation chemistry. Of the many methods of investigating free radicals, electron spin resonance method has a rather convenient and advantageous feature¹⁾. By use of this method, informations on some of the primary irradiation acts will be obtained in the solid state without modifying the sample by any post-irradiation treatment.

One of the main purposes of electron spin resonance study in radiation chemistry will be the identification of the molcular structure of free radicals produced. A number of investigations were published in this field recently. In the case of simple organic compound, rather unambiguous interpretations were obtained²⁾. In the case of polymer substances, however, the situations are rather complicated and separations of spectral lines observed or identifications of free radicals produced are very difficult. Causes of the difficulty considered are as follows: a) There exist more than two kinds of free radical species in many irradiated high polymers. b) Line broadening caused by dipolar interaction between electron spin and nuclear spin in neighboring sites makes the h. f. s. of ESR spectra rather diffuse. And c) various physical states in high polymer substances behave differently in trapping free radicals and give the different circumstances for hyperfine interactions, so the resultant spectra become very complicated. Therefore, ESR study of high polymer radicals can be considered not only as a method of identifying the free radicals produced, but also as a tool for investigating the physical properties of substances through the observations of behaviours of free radicals.

---

* The greater part of this paper were reported at meetings of the Physical Society of Japan in 1959 and in 1960.

In the present investigation, ESR spectra of some high polymers, mainly of polyethylene, were observed at various temperatures after the irradiation and the structure of free radicals and the effects of temperature of measurement on the shape of spectra were considered in connection with the physical properties of high polymers in solid state.

It must be noted that in the course of preparation of this paper, a rather extensive investigation on polyethylene by Lawton et. al.[3] was published. Some of the results in this paper are in accord with their results. However, a view somewhat different from that of Lawton et. al. has been obtained on the identification of free radicals corresponding to one of the patterns. This identification seems to be consistent with the consideration on the effect of temperature on the shape of spectral line, which will be discussed in Sec. 3.4.

§ 2. Experimentals

The samples used were pellets and inflated films of high density Marlex 50, pellets of low density Sumikathene*, and other polymers (films of polyvinylfluoride and pellets of polycarbonate). They were sealed in vacuum ampoules, some of which were subjected to heat treatments before irradiation at the temperature range of 100 to 115°C for 7 to 28 hours.

The ampoules including samples were irradiated either by gamma-radiation from Co-60 source of 1000 curies or electrons from 3 Mev Van de Graaff type accelerator of Mitsubishi Electric Company, at various temperatures. Effect of the sort of radiation, gamma-radiation or electrons, did not appear, in general.

Electron spin resonance spectra were observed by use of X-band spectrometer of Nippon Electron Optics Laboratory Co., Ltd., with krystron 2K25, full power of which is 30 mW.

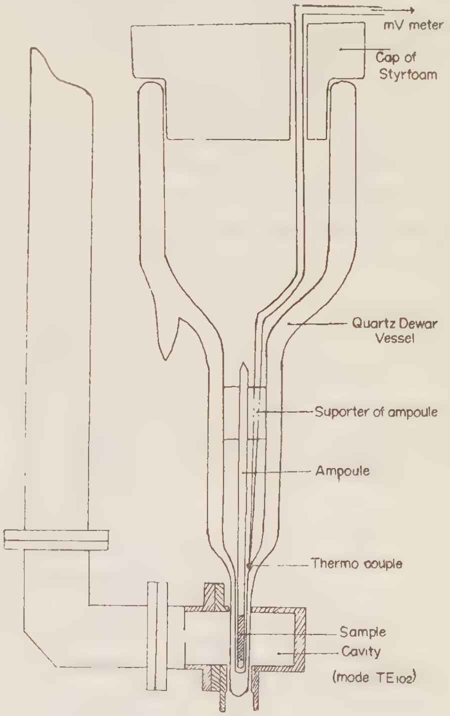

Fig. 1. Dewar vessel used for measurement at lower temperatures.

Dewar vessel as shown in Fig. 1 was used for measurements at low temperatures, in which liquid nitrogen or dry-ice-ligroin mixture was filled for measurements at 77°K and 195°K, respectively. For measurements at the other temperatures, the followieg methods were adopted: For the temperature below the room temperature, ligroin cooled to an appropriate temperature by contacting with liquid nitrogen bath was filled in the dewar vessel. For higher temperatures, heated air was blown into the quartz tube shown in

---

* A product of The Sumitomo Chemical Company.

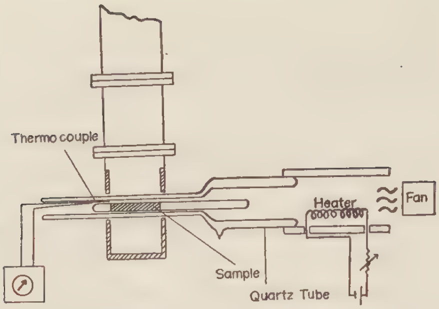

Fig. 2. Quartz tube system used for measurements at higher temperatures.

Fig. 2, in which the sample was supported. The distance of the fan from the cavity and the current of the heater placed in front of the quartz tube determined the temperature of the sample.

§ 3. Results and Discussions

3.1 *General Aspects of ESR Spectra of Irradiated High Polymers*

As mentioned in Sec. 1, ESR spectra of irradiated high polymers are, usually, very complicated, reflecting the coexistence of several sorts of free radicals, and separations of superposed components or the identifications of the structure of free radicals are very difficult. Several examples of the spectra are shown in Fig. 3, which were observed in our laboratory. All spectra in Fig. 3 have almost the same *g*-values as that of DPPH (Diphenyl-pycryl-hydrazyl).

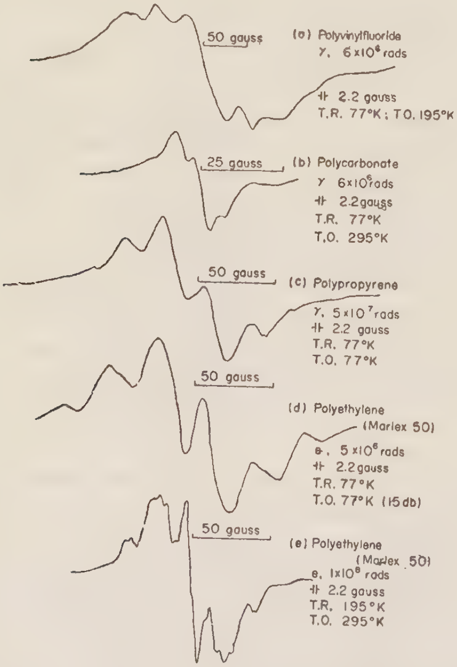

Fig. 3. ESR spectra of some irradiated high polymers. Notations besides the spectra represent the following meanings; e denotes the electron-irradiation, γ denotes the γ-irradiation, -| |- denotes the amplitude of modulation field, and TR and TO represent the temperatures of irradiation and observation, respectively.

All figures in Fig. 3 were obtained with the out-put power of microwave reduced to 10 db. except in special case indicated in the figure. The spin-lattice relaxation time in electron spin resonance of irradiated high polymers seems to be fairly long, and ESR spectra bear the effect of power saturation in the case of full power of our apparatus. An example of power saturation is shown in Fig. 4 for the case of irradiated Marlex 50 observed at 77°K. This shows that the measurement must be made at thoroughly reduced power, especially for a krystron of large power, i. e., X-13, for the purpose of identifications of free radicals in high polymers. In general, the effect of saturation broadening seems to be small in the case of high polymers containing fluorine. It was suggested, recently, by Yoshida[4)] that the saturation broadening in ESR spectra of stable free radicals in polyethylene is inhomogeneous in nature.

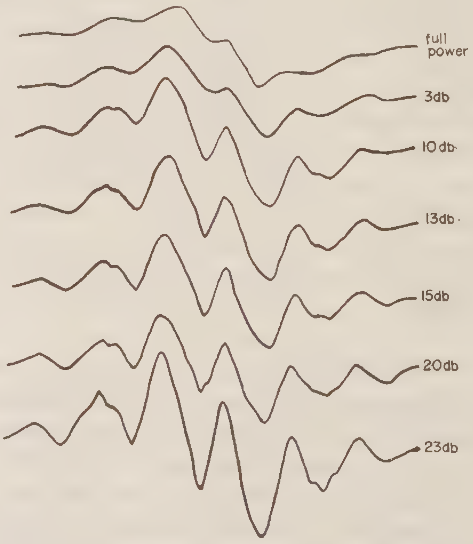

Fig. 4. Variation of spectral line shape at variable power of micro wave. Sample: Heat treated inflation film of Marlex 50 irradiated by electron in does of 3×10^7 rads at 77°K.

The effects of irradiation dose in the order of the dose in this investigation are, in general, negligible.

3.2 *Identifications of Free Radicals Produced in Irradiated Polyethylene and Behaviours of Fast Decaying Component*

In the irradiation of polyethylene, it is customarily assumed that free radicals of alkyl type will be produced which have a large contribution in producing cross-links[5]. When the observation was made at room temperature, however, the structure of the spectra obtained was such that the predominant types of the radical was the one other than that of alkyl type.

When Marlex 50 was subjected to electron irradiation of very high dose rate, 1×10^5 rad/sec, and measured immediately after the irradiation at room temperature, a spectrum of Fig. 5-a was obtained. This spectrum is made up of a superposition of at least two kinds of patterns. It decayed very fast at room temperature and tended to a stable spectrum of Fig. 5-b more than 100 hours after the irradiation. Fig. 7 shows the variation of integrated intensity of spectrum with time. Integrated spectrum of Figs. 5-a and 5-b are shown in Figs. 6-a and 6-b, respectively, which are drawn with the same intensity scales. Subtraction of Fig. 6-b from Fig. 6-a gives the Fig. 6-c, which has h. f. s. of six-line with splitting of approximately 30 gauss and half width of approximately 25 gauss. The intensity ratio of the h. f. s. of Fig. 6-c is 1:5.0:10.8:10.0:4.2:0.8, which is very close to the calculated value expected when magnetic moments of five protons in neighboring sites are equally interacting with the magnetic moment of the unpaired electron. This six-line spectrum would be that of free

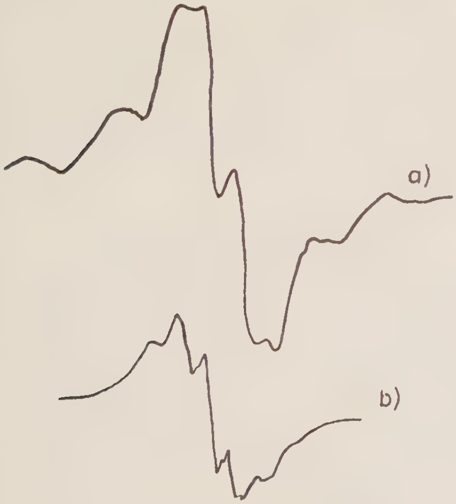

Fig. 5. ESR spectra obtained at 290°K for a pellet of Marlex 50 subjected to electron irradiation in dose of 5×10^6 rads.

a) Spectrum obtained soon after the irradiation.
b) Spectrum obtained after storage for 143 hours at 290°K.

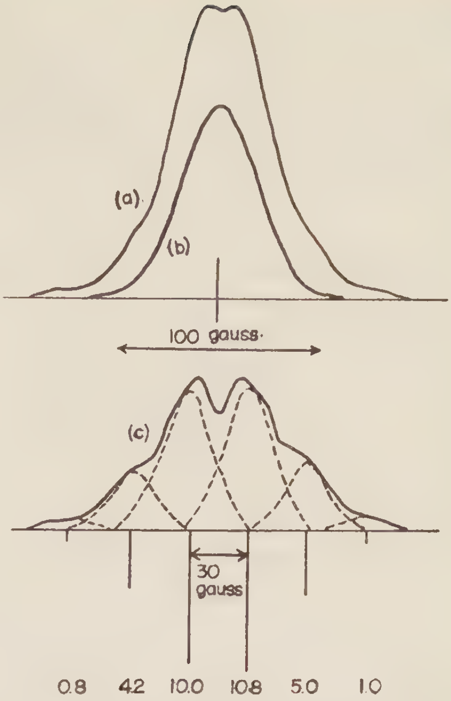

Fig. 6. ESR spectra of electron irradiated Marlex 50: Integral patterns corresponding to those in Fig. 5.

a) Integral pattern corresponding to Fig. 5-a.
b) Integral pattern corresponding to Fig. 5-b.
c) Pattern obtained by subtraction of (b) from (a). This pattern is a fast decaying component and has six h. f. s. components with intensity ratio of 1:5.0:10.8:10.0:4.2:0.8

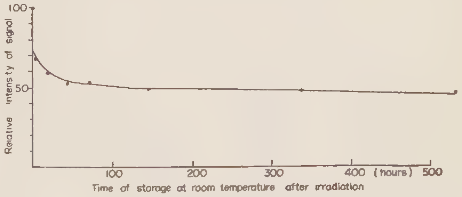

Fig. 7. Integral intensity of ESR spectra of Marlex 50 irradiated by electron at room temperature *vs* time of storage at 290°K after the irradiation.

radicals of alkyl type, $-CH_2\dot{C}HCH_2-$, and existence of such a free radical was suggested in measurements at liquid nitrogen temperature by Smaller and Matheson(2) and Koritsukii(6) et. al. Lawton et. al.(3) also decomposed the same spectrum, recently. A spectrum observed at liquid nitrogen temperature after irradiation at the same temperature, Fig. 3-d, seems to contain the six-line pattern as a dominant part. In the case of low density Sumikathene, the situation was approximately the same, but the rate of the decay of six-line component was very fast.

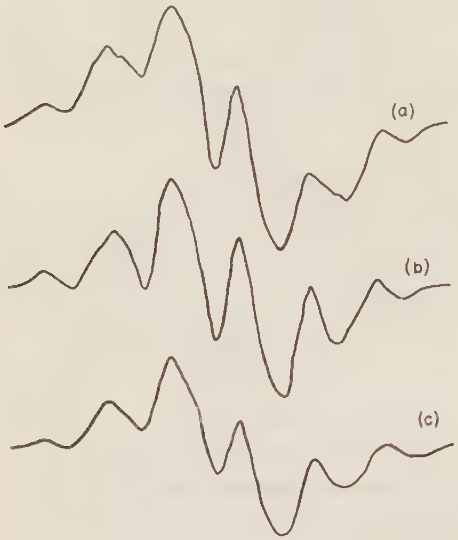

Fig. 8. ESR spectra of Marlex 50 irradiated by electron at 77°K in does of 3×10^7 rads.
a) Observed at 77°K soon after the irradiation.
b) Observed at 195°K.
c) Observed at 77°K after storage for 60 min. at 195°K.

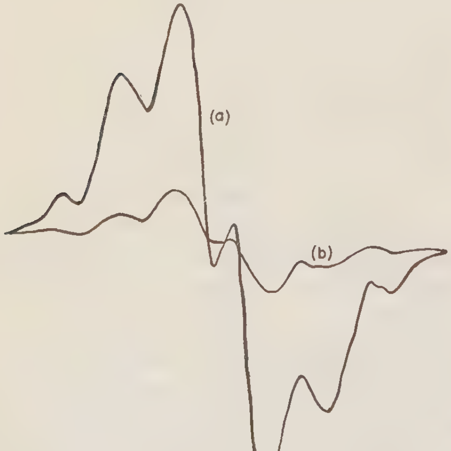

Fig. 9. ESR spectra of Sumikathene irradiated by electron at 77°K in dose of 5×10^7 rads.
a) Observed at 77°K soon after the irradiation.
b) Observed at 77°K after storage for 60 min. at 195°K.

Figs. 8 and 9 show the variation of signal intensities before and after heating to 195°K for 60 min after the irradiation at 77°K. All spectra in the two figures were observed at 77°K except that of Fig. 8-b. Integrated intensities of Figs. 8-c and 9-b are 80% and 15% of respective initial intensities. This means that even at low temperature (195°K) appreciable amounts of free radicals will recombine and this recombination will rapidly occur in branched materials. If the recombination results in cross linking, the difference of the diminished amounts of alkyl type free radicals in branched and linear materials may correspond to the difference of number of cross linkings in both materials at lower temperatures as reported by Lawton et. al.(7)

Sharper spectrum of Fig. 8-b obtained at 195°K seems to reflect the motional effect; if this is the case, the effect of dipolar interaction in the case of electron spin resonance may, also, be related to the physical states of high polymers. When Figs. 8-a, 8-b and 8-c are compared, effect of spin-spin broadening is hardly detectable: The diffuseness of spectrum obtained at low density of unpaired electrons are approximately the same as that of initial stage. The existence of this effect in polyethylene has already suggested by Lawton et. al.(3) Perfect conclusion on this subject seems to be remained in future investigation.

3.3 *Stable Pattern of Polyethylene*

Free radicals corresponding to the spectra obtained at room temperature fairly long time after the irradiation, Fig. 10, are very stable at room temperature. In the case of Marlex 50, the integral intensity of the spectrum observed at room temperature more than four months after the irradiation was 90% of the integral intensity obtained immediately after the irradiation. Decays of the patterns of Figs. 10-a and 10-b are shown in Fig. 11; samples were irradiated by gamma radiation in does of 3×10^7 rads and integral intensities of ESR spectra observed at room temperature were plotted as a function of

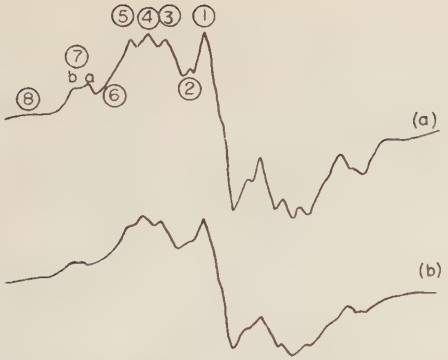

Fig. 10. Characteristic stable patterns of electron irradiated polyethylenes obtained at room temperature.
a) Inflation film of Marlex 50 (1×10^8 rads).
b) Pellet of Sumikathene (5×10^7 rads)

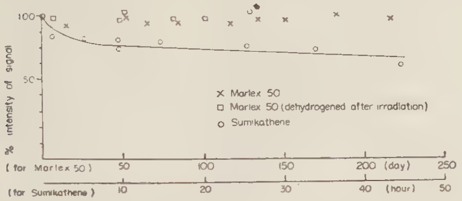

Fig. 11. Decays of stable free radicals of irradiated polyethylene at room temperature. (Temperature range at storage was 285°K～290°K)

the time of storage at the same temperature. Fig. 11 shows the faster decay of the stable pattern produced in low density Sumikathene, which reflects the difference of rigidity of trapped region in each material. If the irradiation does is over 2×10^9 rads, ESR spectrum obtained at room temperature become a diffuse singlet and very stable even at higher temperatures near melting point[8]. However, in the range of the irradiation dose less than the order of 10^8 rads, ESR spectra obtained are ones as shown in Fig. 10.

As to the stable pattern, identification of the corresponding free radicals is not easy. The spectrum of Fig. 10 resembles a seven-line spectrum with splitting of 19 gauss and with additional small structures on main components. Situations are similar for high and low density materials. If the additional small structures are neglected, it can be said that the free radicals corresponding to the seven-line spectrum would be allyl type free radicals, $-\underset{①}{\mathrm{C}}\mathrm{H}{=}\underset{②}{\mathrm{C}}\mathrm{H}-\underset{③}{\dot{\mathrm{C}}}\mathrm{H}-\mathrm{CH_2}-$, as suggested by Koritsukii et. al.[6] If this is the case, reduction of the width of the splitting from 30 gauss to 19 gauss may be due to the sharing of spin density to two carbon atoms, $\underset{①}{\mathrm{C}}$ and $\underset{③}{\mathrm{C}}$, of conjugated double bond with resonance nature and production of negative spin density on carbon atom, $\underset{②}{\mathrm{C}}$. Lawton et. al.[3] suggested that the stable pattern probably corresponds to the free radical of the type of $-\mathrm{CH_2\dot{C}H_2}$, which will be produced by scission of the main chain[5]. As will be mentioned in Sec. 3.5, the stable pattern corresponds to the free radicals trapped in crystalline portion. Molecular fragments produced by scission in crystalline portion will recombine due to the cage effect, and only a few of such fragments will remain and will not be detectable as a free radical of the type of $-\mathrm{CH_2\dot{C}H_2}$. The reduced value of the width of the hyperfine splitting, 19 gauss, may support the discussion which favours the allyl type free radicals. Some considerations about the identifiaction of the free radicals corresponding to the stable pattern will be given in the next subsection in connection with the effect of temperature on the shape of the spectral line.

3.4 *Variation of the Stable Pattern at Various Temperatures*

In a sample of Marlex 50, which was stored at room temperature fairly long after irradiation, there exist very stable free radicals as mentioned before. This sample was cooled to liquid nitrogen temperature and ESR spectrum at the same temperature was observed. As shown in Fig. 12, seven-line pattern changes to nine-line pattern, and when the sample was warmed up to the room temperature again, the ESR spectrum returns back to the original one as before the cooling. It was certified, by several repeated experiments, that the change of the spectral shape was completely reversible and the integral intensity of the spectrum was not changed before and after cooling. At higher temperatures, stable pattern changes to the one as shown in Fig. 13-f, in which small structures diminishes and the line shape approaches the typical seven-line spectrum with gaussian components (Fig. 14). This change at higher temperature range is also completely reversible except the reduction of signal heights caused by the decay of free radicals; dotted line on Fig. 13-f was drawn at the elevated gain of

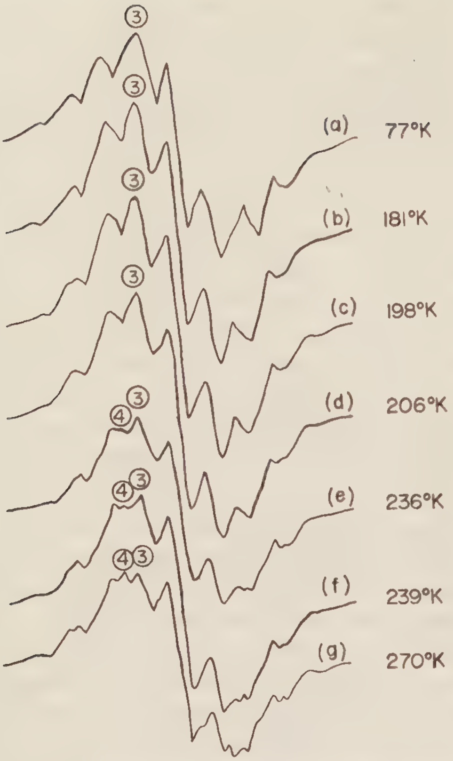

Fig. 12. Variation of spectral line shape at various temperatures. (Lower temperature range) Sample: electron irradiated Marlex 50 (1×10^8 rads)

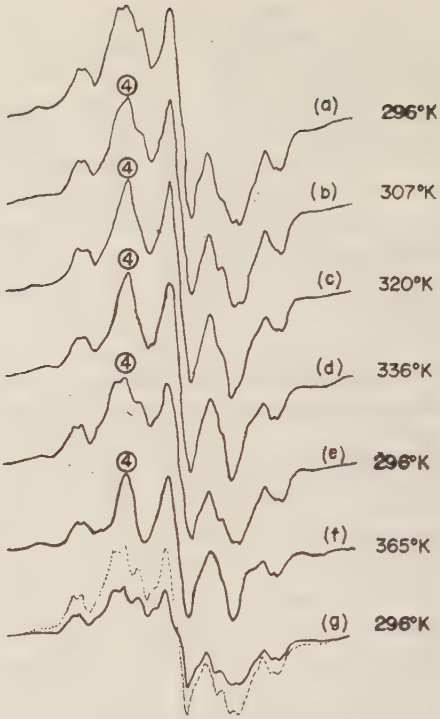

Fig. 13. Variation of spectral line shape at various temperatures. (Higher temperature range)

the recorder.

By observing the ESR spectra obtained at various temperatures, it can be said that the predominant peaks in the derivative curves at the low temperature range are 1, 3, 6, 7 and 8 of Fig. 10 and those at high temperature range are 1, 4, 7 and 8. It was observed that the change of spectral shape in the low temperature range occurred at the temperature near the glass-transition temperature. The peak 4, which is one of the predominant peaks at the higher temperature range, became prominent above 238°K.

From these results it may be considered that variety of steric configuration of protons to the *p*-orbitals of unpaired electron will cause the variable contributions of each proton to hyperfine interaction as suggested by

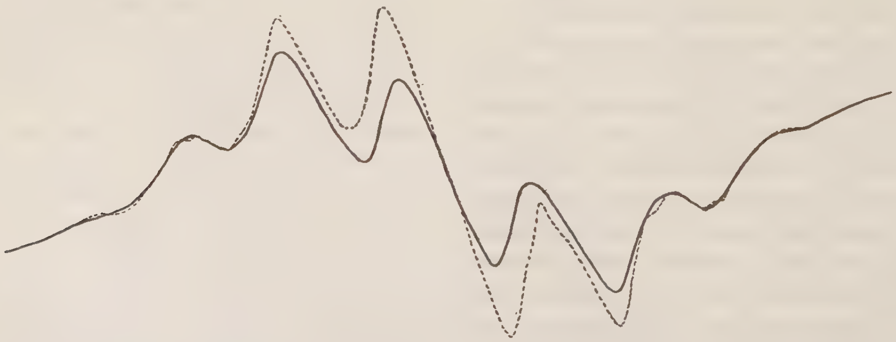

Fig. 14. Comparison of the stable pattern obtained at 365°K, dotted curve, with the calculated pattern, solid curve. Sample is the same as that for Fig. 13. In drawing the solid curve, a ratio of the width of the splitting to the width at maximum slope, $\Delta H_{spl}/\Delta H_{msl}$, was taken as 1.1 and shape of each hfs component was assumed to be gaussian type.

McConnel et. al.[9] in the case of crystalline organic acid, and the ESR spectra obtained have small structures at moderated temperatures. In the higher temperature range, the effects mentioned above will be averaged out and the ESR spectra will tend to the typical seven-line pattern. In Fig. 14, the seven-line pattern observed at higher temperature are compared with the calculated pattern on the assumption that all components are gaussian in shape and a ratio of the width of the splitting to the width at maximum slope is 1.1 Inner peaks of the observed pattern are higher than those of the calculated one. Singlet pattern, which is observed prominently in the case of very large dose, is said to have the width at maximum slope of approximately 17 gauss[8]. The excess heights of the inner peaks of observed pattern will not be of incomprehensive, if the superposition of singlet pattern upon the seven-line pattern is taken into consideration. These considerations suggest the validity of the discussion that the free radicals corresponding to the stable pattern may be the allyl type ones.

3.5 *Post-Irradiation Behaviours of Stable Free Radicals*

High density Marlex 50 and low density Sumikathene were subjected to γ-radiation in dose of 3×10^7 rads at room temperature and the concentrations of free radicals produced were measured after storage for various length of times at various temperatures. Estimations of the concentrations were made by comparing the integral intensities of spectra and that of DPPH solution of known concentration. Fig. 15 shows the variations of radical concentrations with time at various temperatures indicated on each curve. Decay scheme does not agree both with monomolecular and bimolecular reaction schemes. All curves dropped quickly in the initial stage and rather slowly thereafter. As to the production of free radicals in irradiation of polyethylene at room temperature, also, the stationary state between the production and the anihilation was not obtained and the yields of the free radicals increased linearly with the increasing dose of the radiation[10]. Yields of the free radicals at room temperature are proportional to the amounts of crystalline portions of the samples as reported by author previously[10].

Decay of the free radicals in polyethylene can be considered as follows: In storage at various temperatures, concentrations of free radicals will drop suddenly in the initial stage, so that the free radicals will be trapped in crystalline portion existing at the respective temperatures; then, trapped free radicals will decay gradually with fluctuating transition between crystalline and amorphous parts in the state of thermal equilibrium. Such a consideration supports the validity of information about the crystal size distribution in irradiated polyethylene as suggested in the previous paper[10].

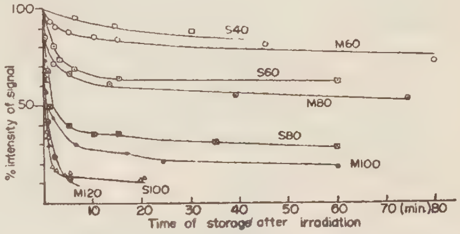

Fig. 15. Relative concentrations of free radicals remaining *vs* time of storage at various temperatures. S and M denote Sumikathene and Marlex 50, respectively. Numerals represent the temperatures of storage.

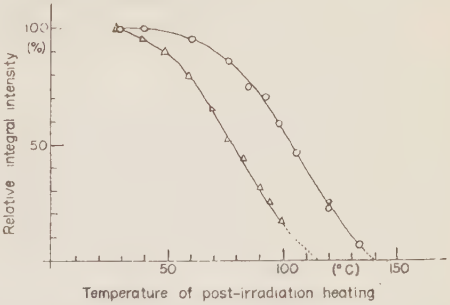

Fig. 16. Relative concentration of free radicals remaining *vs* temperature of post-irradiation heating for 3 min.

Fig. 16 shows the relative number of free radicals remaining *vs* temperature of post-irradiation heating; after the irradiation, samples were stored in a bath of each temperature untill thermal equilibrium was reached, then absorption intensities due to the free radicals remaining were measured. If the polyethylene crystallite is assumed to be composed of *n*-paraffine chains[11], C_nH_{2n+2}, the part of crystalline portions which melts at the given temperature is a portion of *n*-

paraffine chains, melting point of which is below the same temperature. The number of free radicals which vanish at various temperature ranges will be proportional to the portion of *n*-paraffine in the crystallite which are to melt at the same temperature ranges. Therefore, the distribution of crystal size as a function of *n* may be obtained from Fig. 16. Table 1 shows the estimated values of relative densities of *n*-paraffine chains in polyethylene. The values listed in Table 1 are slightly smaller than the values for non-irradiated cases.* The reason is considered as follows: Cross linking junction may be produced in crystalline part also, and neighbours of the cross linking may become non crystalline due to irregular arrangement of molecules caused by intermolecular cross linkings, which, in turn, will be reflected by the reduction of long crystallites. Number of cross linking may be estimated as 1 per 300 carbons in the case of irradiation dose of 3×10^7 rads, provided that the cross linking *G*-value for polyethylene is approximately 3. Then the number of cross linking in a crystallite may be one or less, so the destruction of crystallite shall not be detectable or degree of crystallinity shall not be changed in the case of irradiation dose of order of 3×10^7 rads, which was reported in the several cases[12].

Table 1. Crystal size as *n* in C_nH_{2n+2}.

Range of *n*'s in C_nH_{2n+2}	Percent content in the samples	
	High Density	Low Density
less than 20	0.0%	1%
20~25	1.5	10
25~30	4.5	15
30~35	6.5	16
35~40	6.0	13
40~50	13.0	21
50~60	12	9.5
60~70	10	6
more than 70	47	8

Conclusions

ERS spectra of irradiated high polymers are, in general, very diffuse and the separation of the superposed components are very difficult. In the case of polyethylene, separation of the components are possible by use of difference in rates of decays of respective components. Fast decaying component of six-line pattern is easily identified as corresponding to alkyl type free radicals, which decays faster in low density branched material than in linear material, reflecting the easier production of cross linking in amorphous phase. Stable component of approximately seven-line pattern will be identified as corresponding to allyl type free radicals by considering the number of hyperfine components, splitting width and the effect of temperature on the shape of spectral lines. The effect of temperature on the spectral shape seems to be related closely with the steric configuration atoms in free radicals and observation of ESR spectra in melted state with simultaneous irradiation will be desirable for the purpose of more convenient identification of the structure of free radicals. The variation of the spectral shape at various temperatures of measurements are seen to be interesting subject of future investigations. Effects of pre-irradiation treatments of the sample on the variation of the shapes of ESR spectra will give the more accurate informations about the situations of the hyperfine interactions. These subjects will be discussed in detail in the forthcoming publications.

Acknowledgements

The author wishes to express his sincere thanks to Prof. K. Shinohara for his continuous interests, encouragement and valuable discussions through this investigation and for his kindly reading of the manuscript, to Prof. A. Harasima for his offering valuable discussions, to Drs. Y. Ikeda, S. Ohnishi, N. Tamura and S. Ogawa for their valuable discussions. The author wishes, also, to express his honest acknowledgements to the Directors of the Fuji Spinning Company for their helps during this study.

References

1) For example, see a review article by D. H. Whiffen: Makromolek. Chem. **34** (1959) 170.
2) B. Smaller and M. S. Matheson: J. Chem. Phys. **28** (1958) 1169.
3) E. J. Lawton, J. S. Balwit and R. S. Powell: J. Chem. Phys. **33** (1960) 395 and 405.

---

* For non-irradiated case, more than 50% of the crystallites have the length of more than 100 of *n* in C_nH_{2n+2} [11].

4) H. Yoshida: The paper presented at the Spring Meeting of the Physical Society of Japan (May, 1961).
5) F. A. Bovey: *The Effects of Ionizing Radiation on Natural and Synthetic High Polymers* (Interscience Pub. Inc., New York, 1958) Chap. 5.
6) A. T. Koritsukii et. al.: Vuisokomolek. Soed. Acad. Nauk SSSR **1** (1959) 1182.
7) E. J. Lawton, J. S. Balwit and R. S. Powell: J. Polym. Sci. **32** (1958) 257.
8) S. Ohnishi, Y. Ikeda and I. Nitta: J. Polym. Sci. **47** (1960) 503.
9) H. M. McConnell: J. Chem. Phys. **32** (1960) 1535.
10) A. Kashiwabara and K. Shinohara: J. Phys. Soc. Japan **15** (1960) 1129.
11) A. Charlesby and L. Callaghan: Phys. Chem. Solids **4** (1958) 227.
12) W. P. Slichter and E. R. Mandel: J. Phys. Chem. **62** (1958) 334; H. Kashiwabara: Isotopes and Radiation **2** (1959) 341 (A review article in Japanese)

JOURNAL OF THE PHYSICAL SOCIETY OF JAPAN, Vol. 16, No. 12, DECEMBER, 1961

The Growth of Corona Discharges in Air

By Tikawo TAMURA

Faculty of Technology, Shizuoka University, Hamamatsu

(Received March 20, 1961)

The various stages of growth of corona discharges in a point-to-point gap were photographed in a cloud chamber. The gas investigated was air (40∼400 Torr) and the condensing vapour was water.

On applying an exponentially decaying high voltage pulse, the first cloud track appears on the anode point as a " bead ", and grows to a " boss " and then, the positive streamers shoot out from a circular rim of this " boss ".

When the electric field is adequate a " bead " forms also on the cathode point and, when the electric field at the tip of the negative point becomes appropriately strong by approaching of a positive streamer or of an anode " boss ", a cathode streamer or " spike " dashes out from this " bead " to meet the positive streamer or the anode " boss " at a point one-fourth or one-third of the gap length from the anode. Then a filamentary conducting streamer starts from the anode.

As ion current passes, an air stream is formed near the point electrode causing the shape and position of the pre-onset streamers to be altered. When both air streams collide with each other a track figure of ring shape results.

§ 1. Introduction

The growth of the corona discharges in air has been the subject of a number of investigations[1]. Many features have been revealed by use of suppressed discharges, Kerr cell electro-optical shutters, photomultipliers, oscillographs, Lichtenberg figures, and cloud chamber track pictures. But only the last mentioned shows the ion distribution directly.

In order to see the behaviour of ions in the stages of the burst pulse formation, of the pre-onset streamer formation and of the breakdown discharges, the author photographed cloud track pictures at different stages of development of corona discharges in a point-to-point gap in air at reduced pressures.

§ 2. Experimental Arrangement

The cloud chamber used in this investigation was the same as that used in a previous report[2]. The gas investigated was air and the condensing vapour in the cloud chamber was water. Gas pressures used ranged from 400 mm Hg to 40 mm Hg.

The electrical impulse circuit used is shown shematically in Fig. 1. The condenser C charged to a definite voltage was discharged through a carbon resistance R by means of the drop switch S, whose electrodes were made of silver-tungsten alloy. The exponentially decaying potential drop across this resistance R was applied to the test gap g in Wilson cloud chamber W about 0.2 sec after the expansion of the latter. The electrodes used were sewing needles of 0.8 mm diameter and 0.002∼0.02 mm radius of curvature. The gap length between the electrodes was 10 mm or 15 mm. In order to reduce the mean statistical time lag to the order of 10^{-8} sec, the gap was irradiated with 0.2 mC Strontium 90.

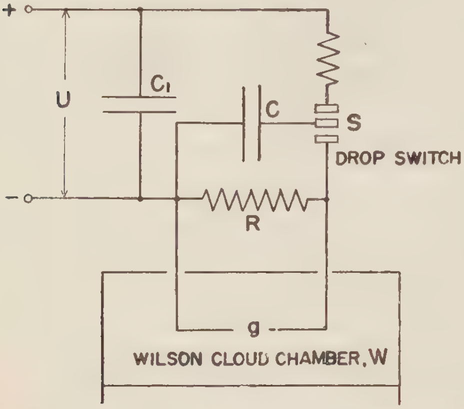

Fig. 1. Schematic diagram of the experimental arrangement.
$C_1=0.1\mu F$, $C=0.00025\mu F$, $R=50\Omega\sim10\,K\Omega$.

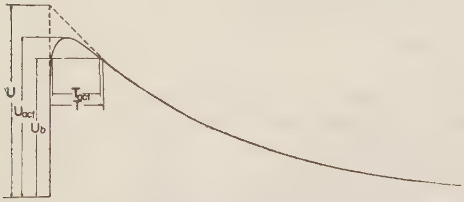

Fig. 2. Exponentially decaying voltage pulse applied to the gap.
(a) --- ideal curve.
(b) —— actual curve.

At 0.1 sec after the application of the voltage pulse to the gap, a xenon discharge lamp was excited to illuminate the cloud tracks which were then photographed.

The pulse time or the time interval T during which the potential drop across the gap would be larger than the starting potential U_b was calculated, assuming that the maximum potential applied to the gap is same as the potential U across C_1, and afterwards the potential decays exponentially as broken curve (a) in Fig. 2. The ratio of U to U_b is denoted in the following as the impulse ratio (I. R.). But actually the wave form of the voltage pulse at the gap differs from the ideal curve (a) but has the finite rise time and would take the form as shown diagrammatically in the solid curve (b).

To make the rise time short the distributed capacity and the inductance of the circuit were made least as possible. The time necessary for the drop switch to make contact depends on the inductance of the circuit and the material of the electrodes. The average value for this time is in the order of 10^{-8} sec[3]. Accordingly the actual pulse time T_{act} may be about 10^{-8} sec shorter than the value of T thus computed. The error due to this cause is negligible in the case of long pulse time but becomes considerable in the case of short pulse time as below 10^{-7} sec.

§ 3. Experimental Results

Many cloud track pictures showing different stages of corona discharges were taken in air at the pressures ranging from 400 mm Hg to 40 mm Hg. Some typical figures obtained in the pressures 400, 300, ···, 50 mm Hg are shown in Fig. 3, 4, ···, 12 for different values of the calculated impulse ratio (*I. R.*) and the pulse time T. The needle on the right side in these photograhs represents the electrode at which the positive voltage pulse was applied.

400 mm Hg Fig. 3 illustrates the step-by-step development of corona discharges in air at 400 mm Hg. The first visual track appears as a tiny glow at the positive point and as a burst pulse glow around the positive needle in a time of the order of 10^{-8} second after application of the impulse voltage. This tiny glow or an "anode bead" is of the same nature as the burst pulse glow around the positive needle and would correspond to the photoelectrically ionized region suggested by Kip.[4] Then a few positive streamers extend out from this anode bead into the gap (Fig. 3(a)-(e)). In a time of about $3\cdot10^{-6}$ second there appears around the negative needle a

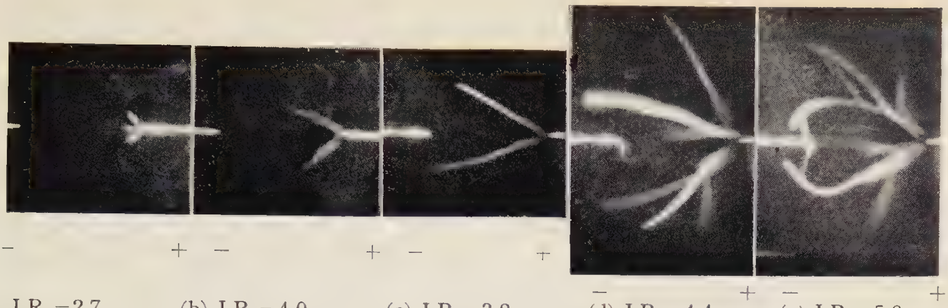

(a) I.R.$=2.7$ $T=3.7\cdot10^{-8}$sec
(b) I.R.$=4.0$ $T=5.1\cdot10^{-8}$sec
(c) I.R.$=3.8$ $T=3.3\cdot10^{-6}$sec
(d) I.R.$=4.4$ $T=3.7\cdot10^{-6}$sec
(e) I.R.$=5.9$ $T=4.5\cdot10^{-6}$sec

Fig. 3. Cloud track pictures at 400 mm Hg.

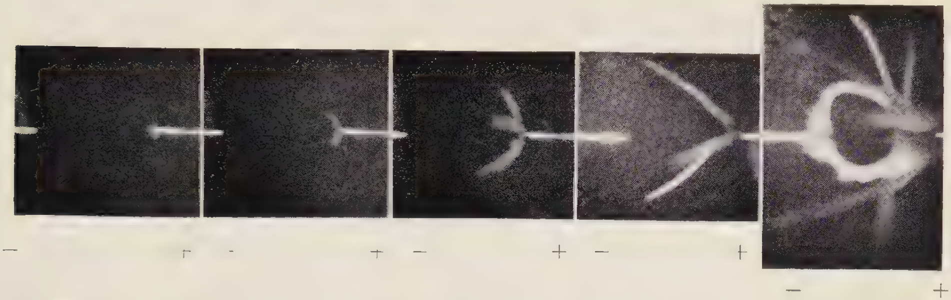

(a) I.R.$=4.8$ $T=2.0\cdot10^{-8}$sec
(b) I.R.$=4.8$ $T=2.0\cdot10^{-8}$sec
(c) I.R.$=4.3$ $T=5.4\cdot10^{-8}$sec
(d) I.R.$=3.4$ $T=3.1\cdot10^{-6}$sec
(e) I.R.$=5.6$ $T=4.3\cdot10^{-6}$sec

Fig. 4. Cloud track pictures at 300 mm Hg.

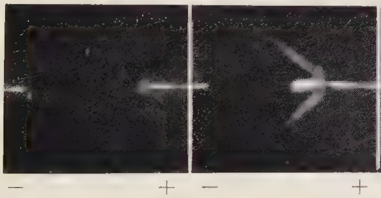

(a) I.R.$=5.1$ $T=2.2\cdot10^{-8}$sec
(b) I.R.$=4.6$ $T=5.6\cdot10^{-8}$sec

Fig. 5. Cloud track pictures at 260 mm Hg.

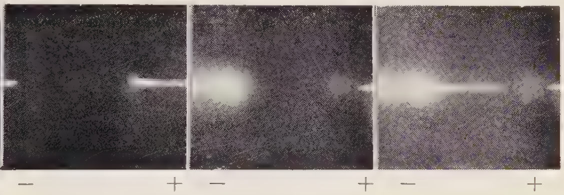

(a) I.R.$=5.2$ $T=2.1\cdot10^{-6}$sec
(b) I.R.$=2.8$ $T=2.5\cdot10^{-8}$sec
(c) I.R.$=2.9$ $T=2.7\cdot10^{-6}$sec

Fig. 6. Cloud track pictures at 240 mm Hg.

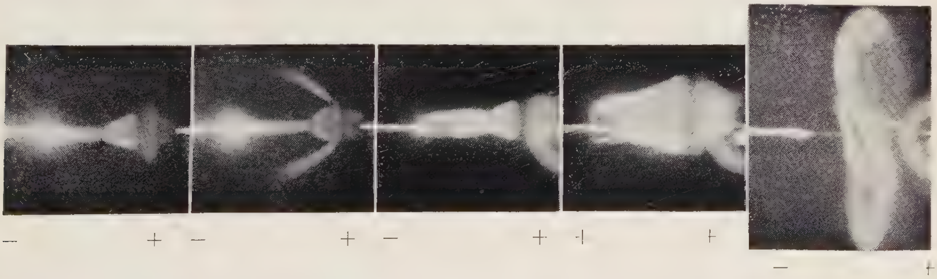

(d) I.R.$=3.6$ $T=3.2\cdot10^{-6}$sec
(e) I.R.$=3.8$ $T=3.3\cdot10^{-6}$sec
(f) I.R.$=4.0$ $T=3.5\cdot10^{-6}$sec
(g) I.R.$=5.0$ $T=4.0\cdot10^{-6}$sec
(h) I.R.$=6.3$ $T=4.6\cdot10^{-6}$sec

Fig. 6. Cloud track pictures at 240 mm Hg.

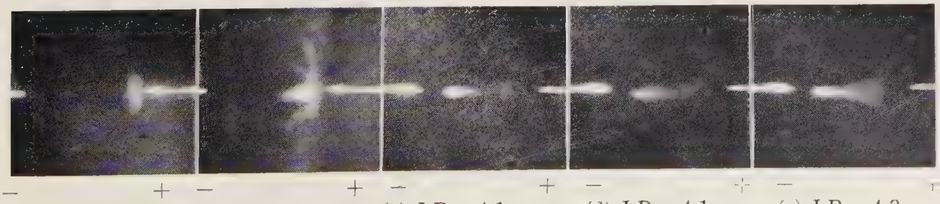

(a) I.R.$=4.0$ $T=5.1\cdot10^{-8}$sec
(b) I.R.$=5.6$ $T=6.4\cdot10^{-8}$sec
(c) I.R.$=4.1$ $T=3.5\cdot10^{-6}$sec
(d) I.R.$=4.1$ $T=3.5\cdot10^{-6}$sec
(e) I.R.$=4.3$ $T=3.6\cdot10^{-6}$sec

Fig. 7. Cloud track pictures at 200 mm Hg.

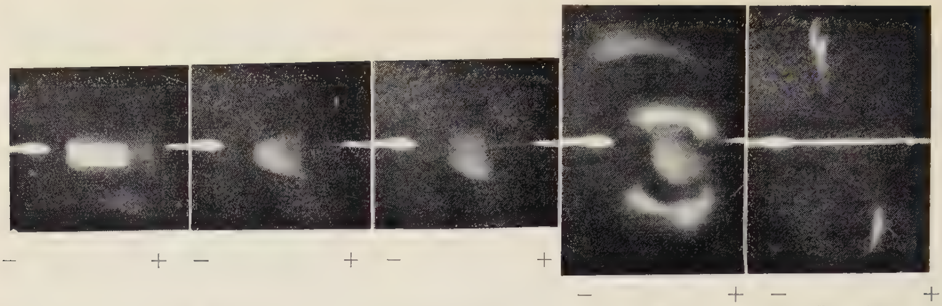

(f) I.R.$=6.7$ $T=4.8\cdot10^{-7}$sec (g) I.R.$=5.1$ $T=8.1\cdot10^{-5}$sec (h) I.R.$=5.3$ $T=8.4\cdot10^{-5}$sec (i) I.R.$=6.7$ $T=9.5\cdot10\ ^{5}$sec (j) I.R.$=6.7$ $T=9.5\cdot10^{-5}$sec

Fig. 7. Cloud track pictures at 200 mm Hg.

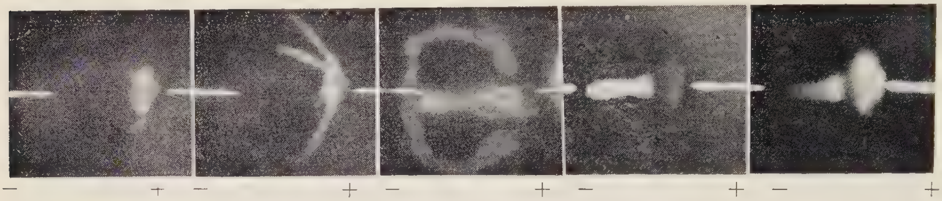

(a) I.R.$=2.4$ $T=2.2\cdot10^{-7}$sec (b) I.R.$=2.6$ $T=2.4\cdot10^{-7}$sec (c) I.R.$=6.5$ $T=4.7\cdot10^{-7}$sec (d) I.R.$=4.1$ $T=3.5\cdot10^{-7}$sec (e) I.R.$=4.5$ $T=1.9\cdot10^{-7}$sec

Fig. 8. Cloud track pictures at 160 mm Hg.

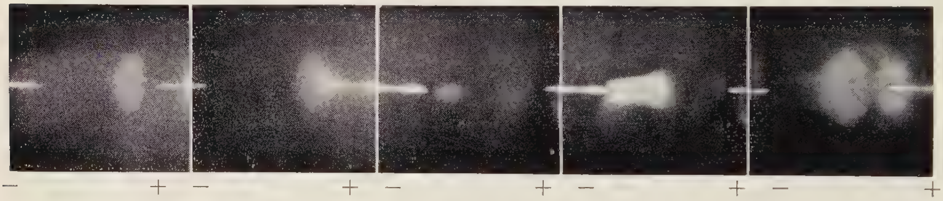

(a) I.R.$=2.5$ $T=2.3\cdot10^{-7}$sec (b) I.R.$=5.2$ $T=6.2\cdot10^{-8}$sec (c) I.R.$=5.6$ $T=6.4\cdot10^{-8}$sec (d) I.R.$=5.9$ $T=6.6\cdot10^{-8}$sec (e) I.R.$=6.7$ $T=7.1\cdot10^{-8}$sec

Fig. 9. Cloud track pictures at 100 mm Hg.

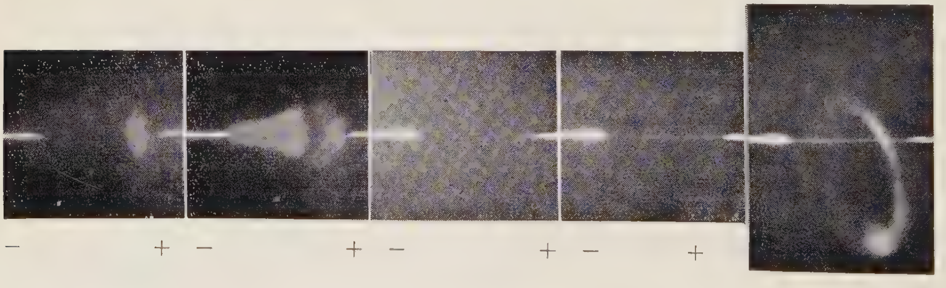

(a) I.R.$=4.1$ $T=1.1\cdot10^{-7}$sec (b) I.R.$=3.0$ $T=2.7\cdot10^{-7}$sec (c) I.R.$=2.8$ $T=5.2\cdot10^{-5}$sec (d) I.R.$=2.8$ $T=5.2\cdot10^{-5}$sec (e) I.R.$=3.2$ $T=5.8\cdot10^{-5}$sec

Fig. 10. Cloud track pictures at 80 mm Hg.

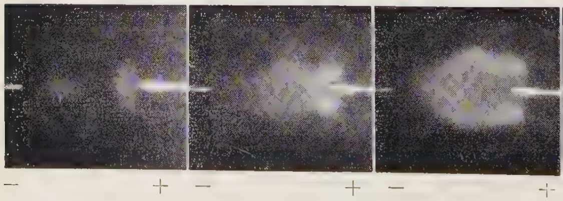

(a) I.R.$=8.1$ $T=2.6\cdot10^{-8}$sec (b) I.R.$=5.8$ $T=6.0\cdot10^{-8}$sec (c)=I.R. 6.2 $T=6.8\cdot10^{-8}$sec

Fig. 11. Cloud track pictures at 60 mm Hg.

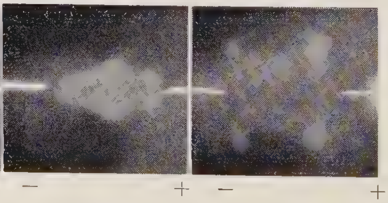

(a) I.R.$=3.5$ $T=3.1\cdot10^{-7}$sec (b) I.R.$=5.9$ $T=4.4\cdot10^{-7}$sec

Fig. 12. Cloud track pictures at 50 mm Hg.

burst-like glow (Fig. 3(c)), and then a tiny glow or a "cathode bead" on the negative point (Fig. 3(d)). When an advancing positive streamer comes to the vicinity of this cathode bead, a negative streamer proceeds from the cathode bead towards the advancing positive streamer to meet it (Fig. 3(e)).

300 mm Hg Fig. 4 shows the similar behaviour as above at 300 mm Hg. Fig. 4(a) shows an anode bead at the positive point and a burst pulse glow around the positive needle. Fig. 4(b)–(d) show the development of positive streamers. In Fig. 4(d) a cathode bead and a faint burst-like glow are seen on the tip and around the negative needle. In Fig. 4(e) two of positive streamers have advanced up to the negative point and were bridged with it. Rarely a negative streamer proceeds from the cathode point at this pressure.

260 mm Hg Fig. 5 illustrates the cloud tracks observed at 260 mm Hg. In Fig. 5(a) (I.R.$=$5.1, $T=2.2\cdot10^{-8}$ sec) an anode bead is seen on the positive point. In Fig. 5(b) (I.R.$=$4.6, $T=5.6\cdot10^{-8}$ sec) an anode bead has grown up to a disc shaped boss. From the circular rim of this boss there appear three positive streamers.

240 mm Hg Fig. 6 represents the different stages of development at 240 mm Hg. Fig. 6(a) (I.R.$=$5.2, $T=2.1\cdot10^{-8}$ sec) shows an anode bead. In Fig. 6(b) (I.R.$=$2.8, $T=2.5\cdot10^{-6}$ sec) –6(c) (I.R.$=$2.9, $T=2.7\cdot10^{-6}$ sec) an anode bead has grown up to an anode boss which has a circular rim around the head. The cathode is also surrounded by the burst-like glow around the needle. In Fig. 6(c) a negative streamer or "spike" is seen extending out from the negative point. In Fig. 6(d) (I.R.$=$3.6, $T=3.2\cdot10^{-6}$ sec) a negative streamer has reached the anode boss. Fig. 6(e) (I.R.$=$3.8, $T=3.3\cdot10^{-6}$ sec) shows the anode streamers extending out from the circular rim around the anode boss. In Fig. 6(f) (I.R.$=$4.0, $T=3.5\cdot10^{-6}$ sec) and in Fig. 6(g) (I.R.$=$5.0, $T=4.0\cdot10^{-6}$ sec) the breadth of the negative streamer broadens, and in Fig. 6(h) (I.R.$=$6.3, $T=4.6\cdot10^{-6}$ sec) both electrodes are bridged by a filamentary streamer and the cloud of the anode boss and the pre-onset negative streamer takes the form of flat rings or a cymbal. The portion of a semi-circular ring, which is seen below the positive point in Fig. 6(f)–(h), is the cut end of a glass cylinder containing Sr^{90} which is used for the purpose of making the statistical time lag short.

200 mm Hg Fig. 7 illustrates the track pictures taken at 200 mm Hg. Fig. 7(a) (I.R.$=$4.0, $T=5.1\cdot10^{-8}$ sec) shows a grown up anode boss. In Fig. 7(b) (I.R.$=$5.6, $T=6.4\cdot10^{-8}$ sec) four positive streamers have extended out from the circular rim around the anode boss. Fig. 7(c) (I.R.$=$4.1, $T=3.5\cdot10^{-6}$ sec)$-$7(h) (I.R.$=$5.3, $T=8.4\cdot10^{-5}$ sec) show the burst-like glow around the negative needle and a pre-onset negative streamer. These tracks of the negative streamers are separated from the cathode. This drift of tracks would be caused by the ion wind which has been built up by the negative ion stream during the pulse time. In Fig. 7(f) the inner portion of intense ionization is surrounded by a less dense layer. In Fig. 7(g)–(i) a filamentary streamer proceeds from the positive point and in Fig. 7(j) it bridges both electrodes.

160 mm Hg Fig. 8 illustrates the behaviour of the growth at 160 mm Hg. In Fig. 8(a) (I.R.$=$2.4, $T=2.2\cdot10^{-7}$ sec) an anode boss is formed and short streamers have just sprung out. Fig. 8(b), (c) show different stages of development of an anode boss and anode streamers. In Fig. 8(d), (e) a negative streamer has proceeded from the negative point to meet the anode boss at about one quarter or one third gap length from the anode.

100 mm Hg Fig. 9 illustrates the track pictures taken at 100 mm Hg. Fig. 9(a), (b) show different stages of growth of an anode boss. In Fig. 9(c)–(e) a cathode streamer is progressing to meet the anode boss.

80 mm Hg Fig. 10 illustrates the different stages of growth of corona discharges at 80 mm Hg. Fig. 10(a) shows an anode boss. Fig. 10(b) shows an anode boss, two short diffuse positive streamers and a broad cathode streamer. In Fig. 10(c) (I.R.$=$2.8, $T=5.2\cdot10^{-5}$ sec) a filamentary streamer is beginning to develop from the positive point. This filamentary streamer proceeds towards the negative point (Fig. 10(d) and bridges the gap (Fig. 10(e)). The cloud ring which encircles the filamentary streamer would be the remain of the cloud track of the pre-onset streamers drawn into a vortex due to the colliding air streams from both electrodes caused by the ion wind during the pluse time as it is explained later. Figs. 11–12 illustrate also the growth of the anode boss, the advancement of the cathode streamer and the formation of the track rings in 60 and 50 mm Hg.

§ 4. Discussion of Results

From the observations described above the following may be said as to the growth of corona discharges in air.

The first visible track of ions is formed at the anode point as a tiny bead in a time less than 10^{-8} sec. This space charge bead of ions corresponds to the photorelectrically ionized region or burst pulse glow observed by Gorrill and Kip[4] and many others[5][6][7]. When the pulse voltage is high the glow also spreads along the needle of the positive electrode.

As the pulse voltage and/or pulse time are increased the anode bead grows to a large ball of a few mm diameter. This would correspond to a burst pulse glow or positive space charge boss observed by Trichel[5] and by Mohr and Weissler[6], and also by Amin[7] at atmospheric pressure. When the pressure p is reduced the final size of the anode boss gets larger approximately as $1/p$ down to 140 mm Hg. Below this pressure it takes nearly the same size of 3.8～4.1 mm diameter and 2.7～2.9 mm height. One of the Lichtenberg figures taken by Przibram[8] and one of the cloud track figures taken by Kroemer[9] may be regarded as displaying this anode boss. It appears that the ion density in this space charge boss is not uniform but shows an internal structure. At the pressure around 260～200 mm Hg it is clearly seen that the boss is crowned by a circular rim around its head, and that the anode positive streamers start from this "circular rim". It has been generally considered tthat pre-onset positive streamers could not start after the space near the positive point has been fouled by the space charge built up by burst pulses. But it now seems probable that the ions or excited atoms or photons produced by the burst pulses might play an important role in the formation of a pre-onset positive streamer.

The breadth of a pre-onset positive streamer is roughly inversely proportional to the pressure down to 160 mm Hg, and becomes 1.25～1.5 mm approximately independent of the pressure below 140 mm Hg. When the electric field at the cathode point becomes adequate there appears a faint track around the point and the needle of the negative electrode. This would correspond to Trichel pulse glow[10][12]. Then it concentrates as a tiny track of ions or a bead on a negative point. This space charge bead would correspond to the bright bluish purple button glow observed by Loeb, Kip, Hudson, and Bennett[11] in negative point corona in air. When the electric field at the cathode bead becomes sufficient because of the overvoltage and prolonged pulse time or by the positive space charge of an approaching anode streamer or of a growing anode boss, a negative streamer starts from this active cathode spot and extends along the lines of force to meet this approaching anode streamer or boss. This pre-onset cathode streamer is observed visualy as a faint bluish glow and would correspond to the "spike" observed by Moore and English[12]. The track of the cathode streamer becomes broad as the pressure gets lower down to 140 mm Hg and takes the shape of a bell or a bottle. In the pressure range 60～240 mm Hg, the cathode streamer meets the anode boss approximately at one quarter or one third gap length from the anode. It may be interesting to note that this proportion of the distances of the meeting place of the cathode streamer and the anode boss from both electrodes is approximately same as that observed by Holzer[13] in atmospheric air and that observed by White[14] with short gap in hydrogen and nitrogen at atmospheric pressure.

Most of the cloud tracks of positive and negativest reamers seem dense at the periphery. This may be due to two causes. Firstly it may be real that the ion density is large at the periphery of these streamers and spikes. And secondly in the process of formation of fog, after building up of fog around the surface layer of an ionic cloud, the fresh vapour is unable to diffuse freely through this surface layer into the ionic cloud, so the depletion of fog density whithin the streamer results.

In the pressures ranging from 100 mm Hg to 250 mm Hg the type of the corona discharge between point-to-point electrodes depends on the chance that from which of the electrodes a pre-onset streamer first begins to start. Sometimes pre-onset positive streamers predominate and sometimes, especially in low pressure range, cathode streamers or spikes predominate. Even when a cathode streamer or spike prevails, an anode boss is always formed and the former joins the latter approximately at one third or one quarter gap length from the anode. This meeting place is defined by the height to which the anode boss has grown.

After joining of a cathode streamer or spike with an anode boss there appears a filamentary breakdown streamer from the positive point and crosses the gap to the negative point. This filamentary streamer is very sharp even at low pressures and has a diameter of approximately 0.1~0.15 mm. The cloud tracks of the anode boss and the positive and negative streamers are blown by the air stream or ion wind caused by the streams of positive and negative ions and change their shape and position.

For instance in Fig. 6 (h) the ratio of electric field strength to gas pressure was 5300 volts/cm. mm Hg at the tip of the needle. If we use the value 2.5 cm^2/volt sec for the mobility of the positive ions[17)] the velocity of the positive ions in the anode boss would be in the neighbourhood of $8.9 \cdot 10^6$ cm/sec at the tip. The momentum of these ions is transformed into the general gas movement or the ion wind. This conversion would be considerably accelerated by the presence of the water vapour which condenses around the ions to form the minute water drops. In the above instance the number of positive ions formed amounted approximetely to $2 \cdot 10^{12}$ and the velocity of the ion wind would have been in the order of 5 cm/sec at the tip of the needle. The blown distance of the ion track would have attained to 5 mm at the time of taking photograph which was about 0.1 second after the formation of the ions. The effect of such an ion wind is clearly seen in the photograph.

Similar change of position is also seen in the cases when the discharge was over in the pre-onset stage before becoming a breakdown. This change of positon is large when the impulse ratio, pulse time, and the duration between the application of impulse voltage and the photographing of the track are large. At the negative point a certain proportion of the electric current in air is carried by negative ions which are formed by dissociative attachment in O_2 in the region of low field to pressure ratio[18)] beyond the tip of the cathode.

For instance in the discharge of Fig. 7 (c) it is estimated from the value of the attachment coefficient given by Harrison and Geballe[18)], that the fraction of the electrons converted to negative ions in the region 1.3 mm from the tip, where E/p is 63.7 volt/cm mm Hg, is 0.266 and the density of the negative ions is $3.3 \cdot 10^{13}$ ions/cm^3. If we take the value 2.8 cm^2/volt. sec for the mobility of negative ions[19)], the drift velocity of the negative ions in this region is around $1.2 \cdot 10^5$ cm/sec and the speed of the ion wind will attain 0.68 cm/sec and the blown distance of the track will amount to 0.68 mm at the time of taking photograph. These values may be considered reasonable at least in order of magnitude as it is seen from the picture.

When the air streams from both electrodes collide with each other a vortex is formed and the track of the pre-onset streamers may take the form of a ring which was shown to be the case.

§ 5. Acknowledgments

The author would like to thank Professor K. Honda and Professor S. Kojima for their interest in the problem and for their valuable discussions. He also wishes to express his appreciation to Miss Kuniko Murakami for assistance in carrying out experiments. This work has been supported by the Grant-in-Aid for Scientific Research from the Ministry of Education.

References

1) For review of recent work see H. Raether, Ergebnisse der Exakten Naturwissenschaften (Springer-Verlag, Berlin) **22** (1949) 73; J. M. Meek and J. D. Craggs, Electrical Breakdown of Gases (Clarendon Press, Oxford) 1953; L. B. Loeb, Basic Process of Gaseous Electronics (University of California Press, Berkley) 1955 ; Handbuch der Physik (edited by S. Flügge, Springer-Verlag, Berlin) 1959 ; F. Llewellyn-Jones, Ionisation and Breakdown in Gases (Metheusen and Company, London) 1957.

2) T. Tamura, Y. Takeyama and B. Nakamura : Kogakubu-Kenkyuhokoku, Shizuoka University,

No. 10 (1959) 1.
3) L. H. Germer: J. Appl. Phys. **22** (1951) 1133, 1138; **23** (1952) 553.
4) A. F. Kip: Phys. Rev. **54** (1938) 139.
5) G. W. Trichel: Phys. Rev. **55** (1939) 382.
6) E. L. Mohr and G. L. Weissler: Phys. Rev. **72** (1947) 294.
7) M. R. Amin: J. Appl. Phys. **25** (1954) 210.
8) K. Przibram: Phys. Zeits. **20** (1919) 299 (Fig. 2).
9) H. Kroemer: Arch. Elektrotechnik **28** (1934) 703 (Bild 18).
10) G. W. Trichel: Phys. Rev. **54** (1938) 1078; A. Kip: Phys. Rev. **55** (1939) 1112. L. B. Loeb: Phys. Rev. **86** (1952) 256.
11) L. B. Loeb, A. F. Kip, G. G. Hudson, and W. H. Bennett: Phys. Rev. **60** (1941) 714; L. B. Loeb: J. Appl. Phys. **19** (1948) 882.
12) D. B. Moore and W. N. English: Phys. Rev. **74** (1948) 1557; J. Appl. Phys. **20** (1949) 370.
13) W. Holzer: Zeits. f. Phys. **77** (1932) 676.
14) H. J. White: Phys. Rev. **46** (1934) 99.
15) L. B. Loeb: Phys. Rev. **93** (1954) 649; **94** (1954) 227.
16) H. Greinacher: Phys. Zeits. **19** (1918) 188.
17) R. N. Varney: Phys. Rev. **89** (1953) 708; E. Huber: Phys. Rev. **97** (1955) 267.
18) R. Geballe and M. A. Harrison: Phys. Rev. **85** (1952) 372; **91** (1953) 1.
19) R. A. Nielsen and N. E. Bradbury: Phys. Rev. **51** (1937) 69; D. S. Burch and R. Geballe: Phys. Rev. **106** (1957) 183.

JOURNAL OF THE PHYSICAL SOCIETY OF JAPAN, Vol. 16, No. 12, DECEMBER, 1961

Anodic Oscillation in Glow Discharge (II) The Gap Properties, Analogous to an Ordinary Electric Oscillator with Linear Circuit Elements

By Kazuyuki OGAWA

Central Research Laboratory, Tokyo Shibaura Electric Co., Kawasaki

(Received July 1, 1961)

The gap of the anodic oscillator tube is described as a special type of dynatron oscillator. The characteristic capacitance C_0 and inductance L_0 of the oscillating gap, being the order of $10^{-3}\mu f$ and $10^{-1}\sim10^{-2}$H respectively, are determined from the frequency change caused by adding externally a variable condenser or inductor. The dynatron-type negative conductance comes principally from the transient ionization in the anode sheath. The behaviors of the quantities characterizing the oscillation such as the amplitude, the frequency, and the wave form can be explained systematically. The brief discussion about the physical meaning of C_0 and L_0 is also given.

§ 1. Introduction

In connection with the impedance measurement of the oscillation-free discharge tube, it was clarified by other investigators[1] that the gap of a glow discharge tube is equivalent to a net work consisting of resistance, capacitance and inductance. On the other hand, it was also proposed long years before[2] that the negative resistance exists in the discharge gap and may cause an oscillation with externally or internally coupled capacitance and inductance. It seems to be quite reasonable to combine the such resonator with the negative resistance for the explanation of the oscillation, but there are no detailed discussions for the actual oscillation.

After the completion of the preliminary investigation[3], the behaviors of the anodic oscillation of the oscillatron have been studied in detail. First of all, the effects of the capacitance or the selfinductance which is connected in parallel with the gap have been found to be most interesting. That is, the change in the frequency caused by adding the capacitance or inductance suggests that the discharge gap is equivalent to an antiresonant circuit consisting of a characteristic capacitance C_0 and selfinductance L_0. This type of resonator, as is well known, should be combined with the dynatron-type negative resistance to sustain the oscillation.

The purpose of this paper is to explain phenomenologically the mechanism of the anodic oscillation with confirming the existance of the negative resistance on the basis of the experimental facts.

§ 2. Experimetal Methods and Results

The basic arrangements of the equipments are the same as that of the former paper, but different on using stabilized D. C. power source. B-type oscillatron with 10 mm gap separation and 50 mmHg of pressure, which consists of a molybdenum disk cathode (20 mm in diameter) and a molybdenum needle anode (1 mm in thick), is principally tested and the gas studied is spectroscopically pure neon. Pure argon and mercury-contaminated argon is also studied besides neon, but substantially different results are not found. The discharge is kept in normal glow. The measurements of the oscillating frequency are made with Tektronix type-545 synchroscope. The frequency or period of the oscillation is defined with that of the fundamental wave, because the wave form observed in many cases is considerably deformed from sinusoidal one. When two or more glow balls appear on the tip of the anode, the distinct wave forms corresponding to each glow ball are observed. In this case, however, to consider the interval of time between the two successive heads of the wave as a period may arouse much discussions, because "period" means the interval of time between the two successive occurence of "identical phenomenon", while two successive heads of the wave may not come from identical phenomenon when two glow balls exist. To be freed from this trouble, the oscillatron having only one glow ball is selected among many samples.

When the precision variable condenser is connected in parallel with the gap, the change in the oscillating frequency with the external capacitance is given empirically by

$$\frac{f}{f_0}=\sqrt{\frac{1}{1+C/C_0}}\,, \tag{1}$$

here, f is the frequency when the capacity of the externally connected condenser is C, and f_0 is the frequency when C tends to zero. The constant C_0 has an important meaning as the characteristic capacitance.

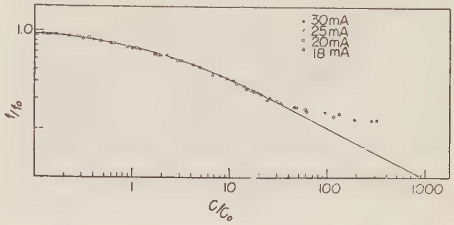

Fig. 1. The relation between C/C_0 and f/f_0.

The curve in the Fig. 1 shows the behavior of the Eq. (1). The points distributed along the curve show the experimental results plotted by using the value of C_0 which is determined at relatively small C. In the region of $C/C_0 < 30$, the rule of the change in the frequency is represented by Eq. (1) to an accuracy of about ±5%. The amplitude behaves as shown in Fig. 2; the dotted curve is such that one plots with the value of C_0 which is lessened by suitably chosen amount from the experimentally determined value at 2 mA of the tube current. The physical meaning of such trial will be discussed in the paragraph which deals with the dependence of the value of C_0 on the tube current. It is interesting that the value of C/C_0 in Fig. 1 at which the discrepancy between Eq. (1) and the experimental results is remarkable almost coincides with the value of C/C_0 in Fig. 2 at which the amplitude falls off.

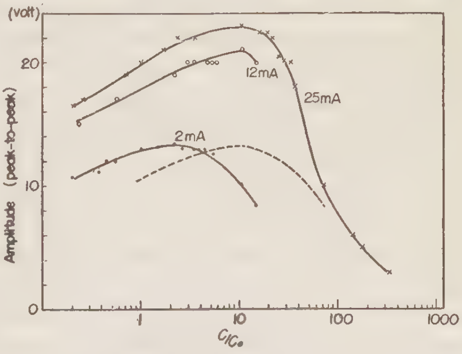

Fig. 2. The relation between C/C_0 and the oscillating amplitude.

At $C/C_0 \approx 15$, the glow ball becomes almost perfect sphere and it goes to a longitudinally-elongated shape with increase in C/C_0. The wave form comes closest to sinusoidal one at $C/C_0 \approx 15$.

Selfinductance L is connected in parallel with the gap through a large (4 μf) blocking condenser. Then the change in the frequency is given by Eq. (2)

$$\frac{f}{f_0}=\sqrt{\frac{1+L/L_0}{L/L_0}}, \qquad (2)$$

where f is the frequency when the externally connected inductance is L, and f_0 is the frequency when L tends to infinity. The constant L_0 is the characteristic inductance. The curve in the Fig. 3 shows the Eq. (2) and the points distributed along this curve show the observed value. When L/L_0 goes to small value (less than 3) the observation become inaccurate because of the outbreak of the relaxation discharge.

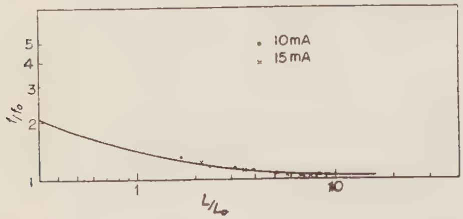

Fig. 3. The relation between L/L_0 and f/f_0.

Finally, the oscillating frequency of the gap without external capacitance or inductance is given by Eq. (3) by using above introduced C_0 and L_0,

$$f_0=\frac{1}{2\pi\sqrt{L_0\ C_0}}. \qquad (3)$$

When the tube current is relatively low, f depends upon the tube current as shown in Fig. 4, and the glow ball grows larger and larger and becomes brighter and brighter with increase in the tube current. In the range from 5 to 14 mA of the tube current, two kinds of wave with the slightly different wave form is frequently observed, and the oscillation is unstable, while only one glow ball appears on the tip of the anode.

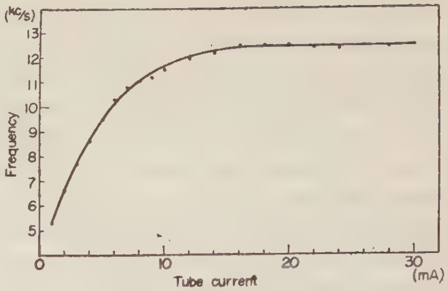

Fig. 4. The relation between the tube current and the frequency.

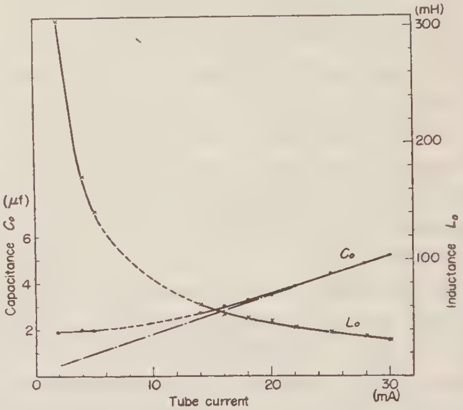

Fig. 5. The dependence of C_0 and L_0 upon the tube current.

This would be probably caused by the fluctuation in the mode of the oscillation. Above 16 mA, the shape of the glow ball becomes steady and the frequency becomes constant, irrespective of the change in the tube current. It is a remarkable fact that Eq. (3) still holds even in the region which the frequency depends upon the tube current. In A-type oscillatron (a tube consisting of a wire anode and concentric cylinder cathode), it is confirmed but in narrow current region that the rule expressed by Eqs. (1), (2), and (3) holds, because the shape or number of the glow ball in this type is so sensitive to the change in the tube current that one can not measure the frequency stably over the wide range of the tube current.

Fig. 5 shows the dependence of C_0 and L_0 upon the tube current. The dotted portion in this figure corresponds to the unstable oscillation region mentioned above in which the frequency measurements can not be made in good accuracy. The measured values of C_0 are on a line passing through the origin in the high current region but apart from the line in the low current region. This change in the behavior of C_0 might not be ascribable to the essential parts of the natures of C_0, but due to the change in the discharge mode. The evidence of this consideration is shown in the relation between the amplitude and C/C_0; that is, if one takes the value $1.9\times10^{-3}\mu$f obtained at 2 mA as a C_0, the relation is shown by solid curve marked "2 mA" in

Fig. 2, on the contrary, if one takes the value $0.5\times10^{-3}\mu f$ which is found by extrapolation of the line obtained at high current region, the curve displayed on the Fig. 2 shifts toward right as shown in dotted curve. Then the value of C/C_0 at which the amplitude falls off agrees with that of the other curves corresponding to the case of high current.

The wave form of the circuit current is greatly affected by the selfinductance ($1\sim10^{-1}$ H) connected in series with the gap, while considerable change in the wave form of the tube drop is not observed. The oscillating amplitude of the tube drop remains almost constant and the oscillating frequency also remains constant during the change in series inductance. The oscillating frequency and amplitude of the tube drop is independent of the series resistance, if the average tube current is kept constant by adjusting the output voltage of the power source. Thus the oscillating frequency and amplitude of the tube drop is independent of the oscillation in the circuit current; in other words, the oscillating gap can be regarded as an A.C. voltage source and generates the alternating current in the circuit.

§ 3. Mechanism of the Oscillation, Analogous to an Ordinary Electric Oscillator with Linear Circuit Elements

Within the limits of $C/C_0<30$, the apparent capacitance and the inductance exists in parallel with the discharge gap, and the oscillating frequency agrees with the resonance frequency in good approximation. The mechanism of the anodic oscillation is proposed on the basis of this experimental facts, and is developed to a certain extent in this section.

3.1 *Separation of the Factors Relating to the Oscillation*

In A-type oscillatron, one can find an interesting fact such that the wave form shown in Fig. 6, similar to the electric wave of the ancient spark oscillator, is occasionally observed at a critical current. Its amplitude decreases exponentially with passing in time as shown in Fig. 7, and each damped oscillation starts with the outbreak of the glow ball. It may be considered from this phenomena that the mechanism which governs the time rate of the voltage change of the oscillating gap has primarily no relation to the mechanism which governs the outbreak of the glow ball.

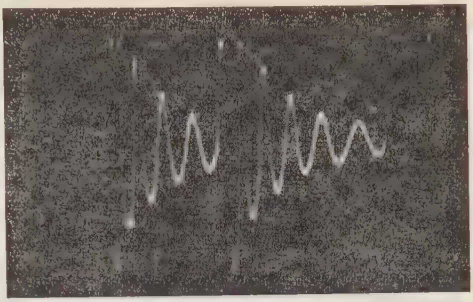

Fig. 6. An example of the damped oscillation appearing in an A-type Oscillatron

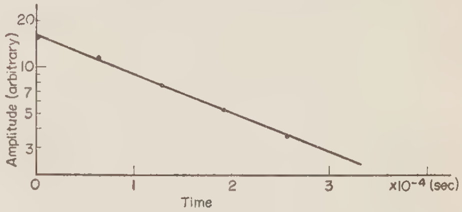

Fig. 7. The logarithmic damping in Fig. 6

3.2 *Growth of the Negative Conductance**

In advance of the introduction of the negative conductance, it is convenient to make a model which shows the oscillation mechanisms. Now, the case in which the average value of the discharge current is constant and sufficiently large compared with the oscillation amplitude of the tube current may be conveniently considered; actually, this assumption is quite conceivable with oscillatron. Fig. 8 shows the potential distribution in such a case.

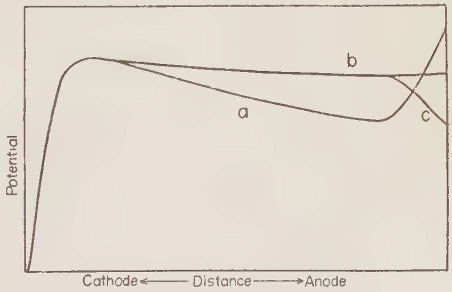

Fig. 8. The potential distribution in the oscillating gap.

---

* Henceforth, the negative conductance is considered in place of the negative resistance for convenience of mathematical expression.

The state with the anode drop is represented by the curve (a); a gentle slope of the potential in the Faraday dark space is checked up experimentally. When E/p in the anode drop gets a certain value, the collision ionization by electron takes place. The ionization may start at the nearest position about the anode, and the positive ions run down along the slope of the anode drop. Then the electron space charge in front of the anode is neutralized. This is the (b) state, in which the ionization ceases now. The electron current supplied from the negative glow to the anode region increases with decrease in the negative gradient of the potential in the Faraday dark space. And consequently, the anode potential further goes down so that the tube current is remain constant. This is the (c) state. The positive ions go back and thus the (a) and (c) states alternately arise. This process is equivalent to the charge-discharge cycle in the ordinary condenser. Whether the oscillation sustains in itself, it depends upon the balance of amount of the positive ion between supply and loss, and also depends upon the manner of the supply of electron.

When i, n, and v are the density of the electron current flowing into the ionizing region at the anode tip, the density of the positive ion created in the ionizing region and its drift velocity along the anode drop respectively, the internal current density j is given by

$$j=nv+i\,. \tag{4}$$

One assumes $n=n(V_a,\ x)$, $v=v(V_a,\ x)$, $i=i(V_f, x)$ though j is independent of x, where V_a is the anode drop, V_f is the voltage drop in the Faraday dark space, and x is the position. If one denotes the cathode drop by V_c, the total tube drop V is given by

$$V=V_c-V_f+V_a\,. \tag{5}$$

The potential drop V_f is not a independent variable, but the function of the anode drop V_a according to the oscillation model. Differentiating the Eq. (4) by V, one obtains the differential conductance

$$\frac{dj}{dV}=\left(n\frac{dv}{dV_a}+v\frac{dn}{dV_a}+\frac{di}{dV_f}\,\frac{dV_f}{dV_a}\right)\frac{dV_a}{dV}\,, \tag{6}$$

here the changes in i, n, v are observed at fixed x. Then

$$v\frac{dn}{dV_a}+\frac{di}{dV_f}\,\frac{dV_f}{dV_a}<0\,, \tag{7a}$$

$$\left|\,v\frac{dn}{dV_a}+\frac{di}{dV_f}\,\frac{dV_f}{dV_a}\right|>n\frac{dv}{dV_a}\,, \tag{7b}$$

have to be fulfiled in order to make $dj/dV<0$, because of the relation $dV_a/dV>0$, $dV_f/dV_a<0$, $di/dV_f>0$, $dv/dV_a>0$. Now, the time rate of the ion production is expressed by

$$\frac{dn}{dt}=F(i)q(V_a)\,. \tag{8}$$

Hence $q(V_a)$ is the effective ionization cross section, and F is the numbers of collision per second. The function $F(i)$ depends upon the process of ionization; if the ionization by single impact is dominant, $F(i)$ is a linear function of i, on the contrary if the cumulative ionization takes place, F contains the cross term of n and i. Eq. (8) leads to

$$\frac{dn}{dV_a}=F(i)q(V_a)\frac{dt}{dV_a}\,. \tag{9}$$

At the beginning of the break down of the anode sheath, dn/dV_a is negative because of $dt/dV_a<0$, and n is very small. Therefore, (7a) and (7b) is simultaneously fulfiled and dj/dV is negative. As time goes on, $q(V_a)$ quickly decreases and finally becomes zero while n increases, $|\,di/dV_f\cdot dV_f/dV_a\,|$ also decreases. When the relation (7b) is broken, dj/dV turns to the positive conductance. So far, the behavior of the differential conductance has been followed with time for convenience' sake, but j is the explicit function of the tube drop V. The relation between j and V is shown in Fig. 9; the ignition voltage is given as V_{ig} and the evolution of the time is shown by the arrow.

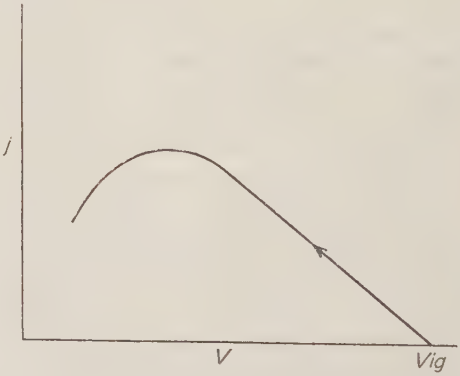

Fig. 9. The dynatron characteristics of the gap.

Chai Yeh and Chaffee[4], in their experiments for the impedance measurements in the low pressure mercury discharge, observed the negative resistance accompanied with the hissing*. In general sense of the geseous discharge, it may be considered that the transient ionization gives rise to the negative conductance (or negative resistance), which has been, however, obtained as a current-controled type. On the contrary, the negative conductance in the oscillatron is voltage-controled or dynatron type. Fig. 10 shows the equivalent circuit of the oscillatron.

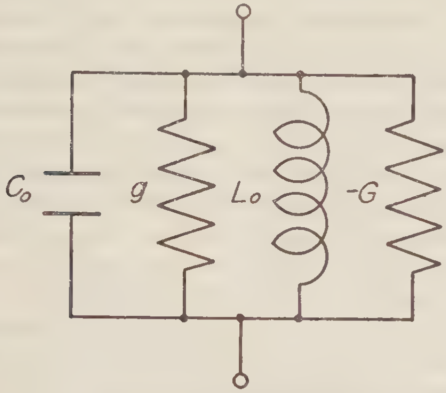

Fig. 10. The equivalent circuit of the oscillatron.

The negative conductance and the loss conductance are represented by $-G$ and g respectively. The analysis of this type of the circuit was made by Van der Pol[5]. According to his theory, the oscillation appears in many kinds of the wave form including even relaxation type with the combination of the dynatron characteristics and the parameters of resonator. The great variety of the wave form in the anodic oscillation may be similarly explained, though it is almost impossible to determine the parameters of the dynatron characteristics in actual case of the oscillatron. The voltage amplitude of the oscillation is determined by the non-linear characteristics of the negative conductance which depends upon the following factors. (i) The process of ionization: the hysteresis of the $q(V_a)$ holds the most important position in the generation of the negative conductance. If there exists no hysteresis, dn/dV_a becomes zero in an instant of the break down of the anode sheath, and consequently the length of the negative slope in the j-V curve will be extremely short. The metastable atom is considered as an important factor which causes the hysteresis. The trace admixture of the hydrogen in rare gas destroys the metastable atoms and therefore the oscillation is weakend or stopped. (ii) The electrostatic energy stored in the gap: $|dj/dV|$ increases as $|di/dV|$ goes up, and $|di/dV|$ increases with the rise of the electrostatic energy of the gap, because the nature of the voltage source is inclined to the constant-voltage character. When the externally added capacitance is too large, the average tube current is no longer kept constant, and therefore the neutralization of the electron space charge in the Faraday dark space is not followed by enhanced lowering of the anode potential. From these, it is understandable that the curve of the voltage amplitude versus the external capacitance shows a peak. The voltage amplitude of the oscillation is also affected by the magnitude of the initial anode drop, though it is not so essential part in contrast to the length of the negative slope of the dynatron characteristics. For example, the oscillation amplitude becomes small when the tube current or gas pressure is low, because the bottom of the potential in the Faraday dark space goes near the anode with decreasing in the tube current or the gas pressure[6] and consequently the E/p comes to the critical value even at comparatively low anode drop.

In conclusion of this section, it should be reminded that the dynatron characteristics does not exist over the whole period of the oscillation. It is presumed from the duration of the glow ball[3] that the negative conductance lasts over a quarter of the period. So the oscillation sustains when the gain of energy during a quarter of the period is equal to the loss of energy during other three quarters of the period.

§ 4. Discussion on the Values of C_0, L_0, and g

The characteristic capacitance of the gap is found at the order of 10^{-3} μf, and independent of the oscillating frequency. First of all, this value is considerably large compared with the value expected from the results of other experiments.[1), 4)] This extraordinary value in the present case may be ascribable to the polarization of the gap.

The magnitude of the characteristic inductance obtained in the oscillatron is $10^{-1}\sim 10^{-2}$H. Benson[1] found the value of the order of 10^{-2}H at 10 kc in 85A1 type voltage regulator tube. Townsand and Depp[7] investigated the change in the impedance with the distance between the anode and the cathode in cold-cathode discharge tube filled neon at 100 mmHg, and found that the inductance increased with the development of the anode drop up to several tens of its initial magnitude 10^{-2}H. In these two author's experiments, the impedance is measured by means of superposing the small amplitude of alternating voltage across the noise-free discharge tube. The inductance coming from the two different methods of experiments agrees with each other, but there are great differences in the dependence on the frequency among the two. The inductance measured by means of superposing the alternating voltage decreases with increase in the frequency. On the contrary, the inductance obtained with the anodic oscillation does not show the dependence on the frequency. Darrow[8] proved that the current density being quadrature with external electric field is proportional to $Y=nme^2\omega/(m^2\omega^2+r^2)$, when an alternating electric field is applied to the ionized gas. Where, m is the mass of the current carrying particle, n is its number density, e is its charge, ω is the angular frequency of the applied field, and r is the coefficient of friction which the charged particle suffers during its motion. If r is very small compared with the $m\omega$ one find $Y=ne^2/m\omega$, and then m/ne^2 is recognized plainly as an inductance which originates from the inertial motion of the charged particle. If one assumes $n=10^9$ cm^{-3} and puts 3.3×10^{-23} gr. for the mass of neon atom, the inductance is about 1H. If one applys Darrow's formula to the case of oscillatron, it is very strange that r must be small compared with $m\omega$ in spite of the fact the collision frequency of the ion is far greater than the oscillating frequency. Probably, r might be seemingly small because of the contribution of the electronic motion induced by the ionic motion to the total current; from the same reason, the value of the inductance calculated from Darrow's formula may be also reduced to the smaller value. Yussuf and Prescott[9] discussed the inductance of the discharge tube and concluded that the inductive character comes from the time lag of the ionization and diffusion of ions. In the present case, however, the time lag of the ionization may be ignored because the build-up time of the light pulse of the glow ball is far fast compared with the voltage change, and the time lag of the diffusion is also ignored at above several kilocycles, as was pointed out by Yussuf.

---

* Hissing accompanied with the electrical oscillation is also observed in the oscillatron.

The positive conductance g comes from the loss of the ions caused by diffusion, running away, and recombination. The frictional force against the ionic motion is to contribute to the positive conductance, but it may not be so effective because of the small r-factor. The glow on the anode is formed into a ball, as the sphere is a shape of making diffusion loss minimum. It should be attributed to the increase in the loss of the ions that the tube wall or other materials close to the anode tip greatly disturb the growth of the oscillation. The magnitude of g can be estimated from the characteristics of the damped oscillation in A-type oscillatron. The amplitude is damped with the factor $exp(-gt/2C_0)$. If one finds the time interval in Fig. 7 for which the amplitude is damped to $1/e$ of its initial magnitude and use $10^{-3}\mu$f for C_0, g comes to 1.14×10^{-5} mho.

§ 5. General Discussion and Conclusions

When C/C_0 is large, the change in the oscillating frequency is not represented by Eq. (1). This may come from the character of C_0 and L_0, which are non-linear elements in themselves. When the additional capacitance C is small, the source impedance at the gap is very high and consequently the fluctuation of the circuit current is very small so that C_0 and L_0 can be regarded as a linear element. When C/C_0 is sufficiently large, the current dependent part in the resultant capacitance becomes very small, while L_0 still remains to be dependent according as shown in Fig. 5. Therefore, the change in the oscillating frequeucy is reduced with increasing C, when C is large and consequently the source impedance is low. The oscillation is to be also non-linear, when the current amplitude is the same order as the magnitude of the average current—this situation arises when the series resistance is very low—but the oscillation of this case was not observed because of the instability.

Above all, it is concluded that the gap of the anodic oscillator tube—oscillatron—can be regarded as a dynatron-type oscillator in which there is a resonator together with a dynatron-type negative conductance. The resonator consists of a characteristic capacitance and a selfinductance. The dynatron-type negative conductance comes from the transient ionization in the anode sheath and the electrostatic energy stored in the gap. The behaviors of the quantities characterizing the oscillation such as the amplitude, the frequency, and the wave form can be explained systematically.

The anthor wishes to express the heartiest thanks to Professor Shoji Kojima of Tokyo University of Education and Mr. Seiichi Takutsu of Electrical Communication Laboratory of Nippon Telegraph and Telephone Public Corporation for the suggestions and fruitful discussions. The author's greatful thanks are also due to Professor Isao Takahashi of University of Kyoto for his interest and encouragement.

References

1) F. A. Benson and G. Mayo: Wireless Eng., **32** (1959) 330, Electronic Eng., **28** (1956) 124.
2) J. J. Thomson: Phil. Mag., **6** (1928) 1254.
3) K. Ogawa: J. Phys. Soc. Japan **14** (1959) 1746.
4) Chai Yeh and E. L. Chaffee: J. App. Phys., **21** (1950) 981.
5) Van der Pol: Phil. Mag., **2** (1926) 978.
6) M. J. Druyvesteyn and F. M. Penning: Rev. Mod. Phys., **12** (1940) 172.
7) M. A. Townsend and W. A. Depp: B. S. T. J., **32** (1953) 1371.
8) K. K. Darrow: B. S. T. J., **11** (1932) 576.
9) S. E. Yussuf and J. C. Prescott: PIEE, 102C (1955) 13.

JOURNAL OF THE PHYSICAL SOCIETY OF JAPAN, Vol. 16, No. 12, DECEMBER, 1961

Confinement of Plasma Particles in a Corrugated Magnetic Field

By Tsuneo AMANO

Department of Nuclear Science Kyoto University, Kyoto

(Received July 18, 1961)

The particle orbits in a corrugated magnetic field having neutral points, at which the magnitude of the field vanishes, are studied. An axially symmetric case is treated in detail and the effect of the curvature is also considered. It is shown that the charged particles do not escape from the neutral points when they are situated several Larmor radii inside the line of force which passes through the neutral points.

The possibility of the confinement of a hot plasma in a general corrugated field including the case studied previously by Kadomtsev is discussed.

§ 1. Introduction

The confinement of a hot plasma in a corrugated magnetic field having the neutral points at which the magnitude of the field becomes zero, as shown in Fig. 1, was studied by several authors[1)–3)]. The Heliotron, a device based on this principle of magnetic confinement, was recently constructed at Kyoto University and is now under experiment. The details of the Heliotron will be reported by K. Uo in another place. Here we investigate the motion of charged particle from the point of view of the orbit theory in order to know the behavior of a plasma in such a magnetic confinement as Heliotron.

In § 2, the characteristics of the corrugated magnetic field are described. In § 3, the motion of a charged particle in the axial symmetric corrugated field is studied. By virtue of the conservations of the energy and the angular momentum of the particle in a static axial symmetric field, we find the allowed region of motion for the charged particles, and thus obtain the condition of their confinement in such a magnetic trap. However, the problems concerning the stability of the confined plasma are out of the scope of this paper.

In § 4, the time averaged angular drift of the guiding center of the particle, $\bar{\dot{\theta}}$, is calculated based on the first order orbit theory and its relation to the interchange instability is discussed. In § 5 we deal with the curved corrugated field. The motion of the particle is the synthesized motion of $\bar{\dot{\theta}}$ drift and the curvature drift. It will be shown that two drifts compensate well each other when $\bar{\dot{\theta}}$ is fairly large. The orbital motion is understood more clearly, if we describe it using the longitudinal adiabatic inveriant, $J=m\oint v_{11}\,dl$ (the particle mass times the integral of the velocity parallel to the field over a complete cycle).

Finally, we compare our results on the confinements of the charged particles with those of Kadomtsev. The latter is found to be valid only for the particles which move near the central axis with small transverse energy. We obtain the more general results applicable to the particles of large transverse energy and near the neutral line (the line of force passing through the neutral points). The angular drifts are found to be strengthened by a factor 3 near the neutral line as compared with the value of Kadomtsev. Thus, the scale of the device is able to be reduced considerably.

§ 2. The Magnetic Field

Let us consider an axially symmetric corrugated magnetic field which is represented, in the cylindrical coordinate r, θ, z, by the vector potential

$$A_\theta=B_0\left\{\frac{1}{2}r-\frac{I_1(kr)}{kI_0(kd)}\cos kz\right\},$$

$$A_r=0,\ A_z=0,\quad (1)$$

which satisfies $\nabla^2 A=0$, where $I_0(kr)$ and $I_1(kr)$ are the 1st kind modified Bessel functions of the zeroth and the first order, respectively, k and d are the parameters to determine the shape of the magnetic field, and B_0 is a constant. The components of the magnetic flux density B_r, B_z are derived from Eq. (1) as

$$B_r=-\frac{\partial A_\theta}{\partial z}=-B_0\frac{I_1(kr)}{I_0(kd)}\sin kz\,,$$

$$B_z=\frac{1}{r}\left\{\frac{\partial}{\partial r}(rA_\theta)\right\}=B_0\left\{1-\frac{I_0(kr)}{I_0(kd)}\cos kz\right\}.\quad (2)$$

The magnitude of the magnetic field becomes zero at the point $r=d$ and $kz=2n\pi$ (n=integer), which will be called neutral points hereafter.

The lines of force is given by

$$rA_\theta=\text{cost.}\,,\quad (3)$$

and their configuration in the r-z plane are shown in Fig. 1. For the lines of force near the axis of symmetry, it is more convenient to use the approximate formula

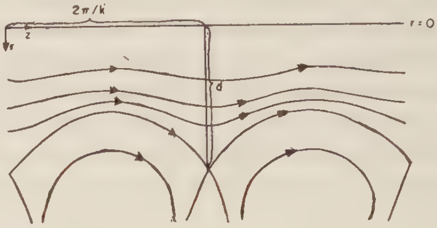

Fig. 1. The line of force with $kd=3$. The point of $kz=2\pi$ and $r=d$ is the neutral point where the magnitude of the field vanishes. The line passing the neutral point is called the neutral line.

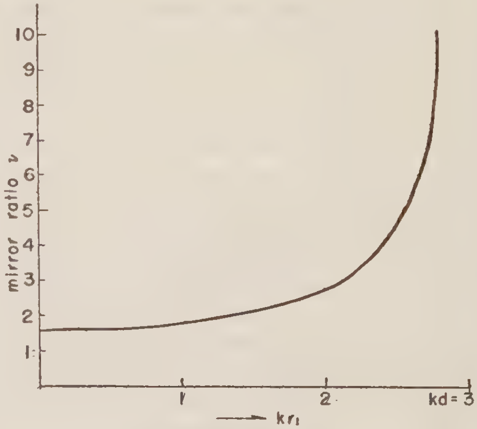

Fig. 2. The mirror ratio of the line of force with $kd=3$ as a function of r_1. (r_1 is the radial coordinate of the line of force at $kz=2\pi$). The mirror ratio becomes infinity for the neutral line.

$$r=r_0+\frac{\varepsilon}{k}I_1(kr_0)\cos kz\,,$$

$$\varepsilon=\frac{1}{I_0(kd)}\,.\quad (3')$$

These have been obtained by expanding the equation

$$\frac{dr}{dz}=-\frac{\varepsilon I_1(kr)\sin kz}{1-\varepsilon I_0(kr)\cos kz},$$

in the powers of $\varepsilon I_0(kr)\cos kz$ and by integrating it under the appropriate boundary condition.

The magnetic field given by Eq. (2) is regarded as a mirror field and we can define the mirror ratio of each line of force:

$$\nu=\frac{B(kz=\pi)}{B(kz=0)}. \tag{4}$$

The value of mirror ratio is shown in Fig. 2 for the line of force of Fig. 1.

Let us consider a particle which has the transverse energy $W_\perp{}^0$ and the total energy W at $r=r_0$ and $z=0$. From Eq. (2), the ratio α of these energies is given by

$$\alpha=\frac{W_\perp{}^0}{W}=\frac{\mu B_0}{W}(1-\varepsilon I_0(kr_0)), \tag{5}$$

where μ is the magnetic moment of the particle. The above particle has the longitudinal energy W_{11}, at z

$$\begin{aligned}W_{11}&=W-\mu B\\&=\mu B_0\varepsilon I_0(kr_0)(\cos kz+\gamma),\end{aligned} \tag{6}$$

where $\gamma=2(1-\alpha)/\alpha(\nu-1)$, and we have used the Eq. (3′) for the line of force which is valid only near the central axis.

§ 3. The Region of Motion for a Charged Particle

The non-relativistic Lagrangian of a charged particle in the field with the vector potential A_θ is in the cylindrical coordinates

$$L=\frac{1}{2}mv^2+\frac{ZeB_0}{c}r\dot{\theta}\left(\frac{1}{2}r-\frac{I_1(kr)}{kI_0(kd)}\cos kz\right), \tag{7}$$

where m, v, and Ze are the mass, velocity and charged of the particle, respectively. It is seen that θ is a cyclic coordinate in Eq. (5), so that the angular momentum $\partial L/\partial\dot{\theta}$ which is the canonical conjugate to θ is the constant of motion. In terms of the momentum of the particle $P=(m\dot{r},\ mr\dot{\theta},\ m\dot{z})$, we obtain

$$\frac{\partial L}{\partial\dot{\theta}}=mr^2\dot{\theta}+\frac{ZeB_0}{c}r\left(\frac{1}{2}r-\frac{I_1(kr)}{kI_0(kd)}\cos kz\right)=rP_\theta+\psi\equiv M, \tag{8}$$

where

$$\psi=\frac{ZeB_0}{c}r\left(\frac{1}{2}r-\frac{I_1(kr)}{kI_0(kd)}\cos kz\right). \tag{9}$$

The Hamiltonian $\mathscr{H}$ is given by

$$\mathscr{H}=\frac{1}{2m}(P_r{}^2+P_z{}^2+P_\theta{}^2)=\frac{1}{2m}(P_r{}^2+P_z{}^2)+\frac{1}{2mr^2}(M-\psi)^2\equiv W, \tag{10}$$

which is also the constant of motion. The charged particle moves in the r-z plane under the influence of a potential $U=1/2\,mr^2\cdot(M-\psi)^2$, so that the region

$$0\leq\frac{U}{W}\leq 1 \tag{11}$$

is accessible to the particle orbit. After a simple calculation Eq. (11) is reduced to

$$-k^2|\rho_0|r+\frac{k^2\rho_0M}{p}\leq\frac{1}{2}(kr)^2-\frac{krI_1(kr)}{I_0(kd)}\cos kz\leq k^2|\rho_0|r+\frac{k^2\rho_0M}{p}, \tag{12}$$

with $\rho_0=cp/ZeB_0$ which will be called the total Larmor radius of the particle (p is the total momentum).

A family of the functions of kr,

$$f(kr,\ kz)=\frac{1}{2}(kr)^2-\frac{krI_1(kr)}{I_0(kd)}\cos kz, \tag{13}$$

is shown in Fig. 3, taking kz as a parameter. In the r-z plane, the particle moves in the region where $f(kr,\ kz)$ takes a value intermediate between the two straight lines

$$y_1=-k^2|\rho_0|r+\frac{k^2\rho_0M}{p},$$

and

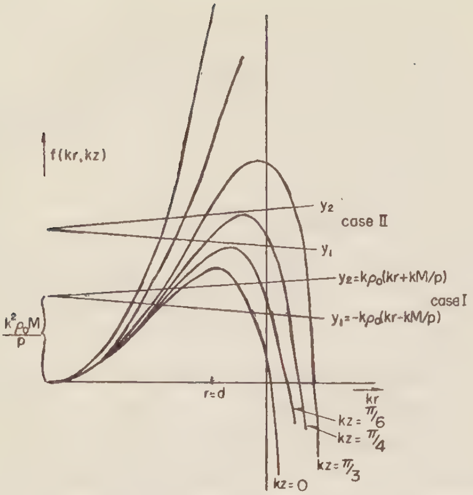

Fig. 3. The region of motion for a charged particle in the $r-z$ plane. The particle moves in the region where the values of $f(kr,\ kz)$ lines between two straight lines y_1 and y_2. In case I, the particle moves in the r direction slightly and the adiabatic approximation is varid. In case II, the adiabatic approximation is violated and the particle can freely move from the interior region of $r=d$ to the exterior.

$$y_2=k^2|\rho_0|r+\frac{k^2\rho_0 M}{p}\ . \tag{14}$$

The constants $k^2\rho_0$ and $k^2\rho_0 M/p$ in the above equation are determined by the initial conditions of the particle;

$$\rho_0=\frac{cp}{ZeB_0}\ ,$$

$$M=r_s p\cos\lambda+\psi(r_s,\ z_s)\ ,$$

and

$$\psi(r_s,\ z_s)=\frac{pr_s}{\rho_0}\left(\frac{r_s}{2}-\frac{I_1(kr_s)}{kI_0(kd)}\cos kz_s\right)\ , \tag{15}$$

where $p\cos\lambda$ is the component of the momentum in the θ direction and r_s, z_s represent the position of the particle at a given time. Among the family of the curves in Fig. 2, the one which lies at the bottom corresponds to the curve of $kz=2n\pi$. It is readily seen that this curve takes its maximum value at the neutral point $r=d$,

$$f(d,\ 0)=\frac{1}{2}(kd)^2-\frac{kdI_1(kd)}{I_0(kd)}\ , \tag{16}$$

Comparing the value $f(d,\ 0)$ with the value y_2 at $r=d$, we find the two alternative cases as shown in the following.

Case (I)

$$k^2|\rho_0|d+\frac{k^2\rho_0 M}{p}<\frac{1}{2}(kd)^2-\frac{kdI_1(kd)}{I_0(kd)}\ . \tag{17}$$

The allowed region of motion is separated into the two parts, $r<d$ and $r>d$, in this case. It is obvious that the particle staying in the inner region, $r<d$, can not move into the outside. It is also seen in Fig. 3 that the particle moves in the r direction only slightly and the adiabatic approximation is valid.

Case (II)

$$k^2|\rho_0|d+\frac{k^2\rho_0 M}{p}>\frac{1}{2}(kd)^2-\frac{kdI_1(kd)}{I_0(kd)}\ . \tag{18}$$

The adiabatic approximation is violated in this case. The particle can freely escape from the interior region, $r<d$. It is also possible that the particle in the outside region, $r>d$, enters the inside again. Thus it follows that the condition of the confinement of the particle inside the neutral field line (the line passing through the neutral points $r=d$, $kz=2n\pi$) is given by

$$|\rho_0|d+\rho_0 r_s\cos\lambda+r_s\left(\frac{r_s}{2}-\frac{I_1(kr_s)}{kI_0(kd)}\cos kz_s\right)<\frac{d^2}{2}-\frac{dI_1(kd)}{kI_0(kd)}\ . \tag{19}$$

The condition given by the Eq. (19) is clearly violated for the particles which just pass through the neutral points.

Now let us consider the particle which lies a little inside the neutral line. The equation of the neutral line is

$$r\left(\frac{1}{2}r-\frac{I_1(kr)}{kI_0(kd)}\cos kz\right)=d\left(\frac{d}{2}-\frac{I_1(kd)}{kI_0(kd)}\right)\equiv\frac{a^2}{2}\ ,$$

where a is the value of r at $kz=\pi/2$. For the particle $kz_s=\pi/2$, $r_s=a-\xi$, the condition (19) becomes

$$\xi^2-2(\rho_0\cos\lambda+a)\xi+2(\rho_0 a\cos\lambda+|\rho_0|d)<0\ . \tag{20}$$

It is obvious from Eq. (20) that the particle is never confined in the magnetic trap unless the particle satisfies the inequality

$$\rho_0^2 \cos^2 \lambda - 2|\rho_0| d + a^2 > 0 \,. \tag{21}$$

By the confinement we mean that the charged particles are trapped inside the neutral line. In the practical case where $\rho_0 \ll a$, the condition (17) becomes simply

$$\xi > |\rho_0| \left(\frac{d}{a} \pm \cos \lambda \right), \tag{22}$$

where ± sings denote ion and electron, respectively. In the case of $\xi > |\rho_0|(d/a+1)$, the particle is thus confined in the inside region of the neutral line regardless of the direction of the velocity vector.

It should be noted that the regions of the confinement are different for the electrons and ions. As far as the energies of the electrons and the ions are not different so much, the Larmor radii of the electrons are much smaller than those of the ions. Therefore the electrons do not escape from the nutral points unless they lie on the line which is very near the neutral line. On the other hand, ions will be lost near the neutral line. Thus it may be expected that the charge separation will arise near the neutral line. This charge separation will be cancelled by the motions of ions, however, since the ions can move freely in the r direction near the neutral line on account of the breaking of the adiabaticity.

§ 4. The Drifts

In the axial symmetric magnetic field the time averaged motion of the guiding center (the center of the Larmor revolution) of a charged particle drifts in the θ direction, and the time average of the $\dot{\theta}$ is estimated by the first-order orbit theory as[4)]

$$\bar{\dot{\theta}} = \frac{c}{e} \left(\oint \frac{W_\perp + 2W_\parallel}{rRB\sqrt{W-\mu B}} dl \right) \Big/ \left(\oint \frac{dl}{\sqrt{W-\mu B}} \right), \tag{23}$$

where R is the curvature radius including the sign and dl the line element of the line of force.

Rosenbluth and Longmire[4)] showed that the stability of the plasma depends upon the sign of the mean value of the $e\bar{\dot{\theta}}$ about the ensemble of the particles. If $\langle e\bar{\dot{\theta}} \rangle$ is positive the plasma is stable against the interchange instability, while the plasma is unstable, if $\langle e\bar{\dot{\theta}} \rangle$ is negative.

In order to perform the integral in Eq. (23) we shall restrict ourselves in this section to the field lines near the axis of symmetry where Eqs. (3′) apply. Now R and dl are given approximately by

$$r = r_0 + \frac{\varepsilon}{k} I_1(kr_0) \cos kz \,,$$

$$dl = \sqrt{1 + \left(\frac{dr}{dr} \right)^2} dz \simeq dz \,,$$

and

$$\frac{1}{R} = -\frac{d^2r/dz^2}{(1+(dr/dz)^2)} \simeq -\varepsilon k I_1(kr_0) \cos kz \,.$$

Substituting these equations and Eq. (6) into Eq. (23) we find

$$\bar{\dot{\theta}} = -C \left[\oint \frac{\cos u du}{\sqrt{\cos u + \gamma}} + \left(\frac{2W}{2W - \mu B_0} \varepsilon I_0(kr_0) - \frac{\varepsilon I_1(kr_0)}{kr_0} \right) \oint \frac{\cos^2 u du}{\sqrt{\cos u + \gamma}} \right] \Big/ \oint \frac{du}{\sqrt{\cos u + \gamma}} \,, \tag{24}$$

where

$$C = \frac{k\varepsilon I_1(kr_0)}{r_0} \frac{C}{eB_0} \,.$$

The integrals in Eq. (24), $\int \frac{\cos u du}{\sqrt{\cos u+\gamma}}$ etc., reduce to the eliptic integrals

$$\int_0^x \frac{dt}{(1-t^2)(1-k^2t^2)} = F(\sin^{-1}x,\ k)\,,\quad \int_0^x \sqrt{\frac{1-k^2t^2}{1-t^2}}\,dt = E(\sin^{-1}x,\ k)\,,$$

by the transformation $\sin u/2=t$.

(I) In the case of $-1<\gamma<1$ when the particle is trapped in the mirror, the range of the integrations in (23) is taken from $u=0$ to $u=\cos^{-1}(-\gamma)$. We find the integrated results:

$$\oint \frac{du}{\sqrt{\cos u+\gamma}} = \sqrt{2}\,F\left(\frac{\pi}{2}\sqrt{\frac{1+\gamma}{2}}\right),$$

$$\oint \frac{\cos u du}{\sqrt{\cos u+\gamma}} = \sqrt{2}\,E\left(\frac{\pi}{2},\ \sqrt{\frac{1+\gamma}{2}}\right) - \sqrt{2}\,F\left(\frac{\pi}{2},\ \sqrt{\frac{1+\gamma}{2}}\right),$$

and

$$\oint \frac{\cos^2 u du}{\sqrt{\cos u+\gamma}} = \frac{\sqrt{2}}{3}(1+2\gamma)F\left(\frac{\pi}{2},\ \sqrt{\frac{1+\gamma}{2}}\right) - \frac{4\sqrt{2}}{3}\gamma E\left(\frac{\pi}{2},\ \sqrt{\frac{1+\gamma}{2}}\right).$$

(II) In the case of $|\gamma|>1$ when the particle passes through the jaws of the mirror, we obtain

$$\int_0^\pi \frac{du}{\sqrt{\cos u+\gamma}} = \frac{2}{\sqrt{1+\gamma}}F\left(\frac{\pi}{2},\ \sqrt{\frac{2}{1+\gamma}}\right),$$

$$\int_0^\pi \frac{\cos u du}{\sqrt{\cos u+\gamma}} = 2\sqrt{1+\gamma}\,E\left(\frac{\pi}{2},\ \sqrt{\frac{2}{1+\gamma}}\right) - \frac{2\gamma}{\sqrt{1+\gamma}}F\left(\frac{\pi}{2},\ \sqrt{\frac{2}{1+\gamma}}\right),$$

and

$$\int_0^\pi \frac{\cos^2 u du}{\sqrt{\cos u+\gamma}} = \frac{2(1+2\gamma^2)}{3\sqrt{1+\gamma}}F\left(\frac{\pi}{2},\ \sqrt{\frac{2}{1+\gamma}}\right) - \frac{4}{3}\gamma\sqrt{1+\gamma}\,E\left(\frac{\pi}{2},\ \sqrt{\frac{2}{1+\gamma}}\right).$$

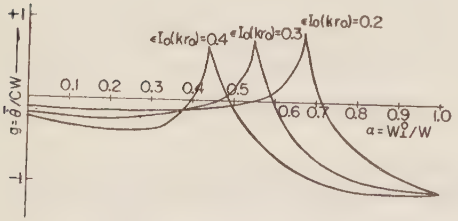

Fig. 4. Angular drift velocities $\bar{\dot{\theta}}$ of the particle in the corrugated magnetic field are plotted for three lines of force. Each curve has its positive maximum value at $\alpha=1/\nu$ (ν is the mirror ratio of the line of force), corresponding to the particle which is just reflected at the jaw of the mirror. The portion $\alpha>1/\nu$ is the region where the particle is trappee in one section of the mirror, while the portion $\alpha<1/\nu$ is the region where the particle passes through the jaw of the mirror. C is a constant defined in Eq. (24).

We plott the values of $\bar{\dot{\theta}}/CW$ in Fig. 4. Each curve has its positive maximum values at $\alpha=1/\nu$ which corresponds to $\gamma=1$. The maximum has the following physical meaning. When the particle has the transverse energy which just satisfies $\gamma=1$, it can reach just the jaw of the mirror, and spends long time in the region where the curvature is negative, giving the largest contribution to the positive $\bar{\dot{\theta}}$ value.

§ 5. The Effect of the Curvature

Thus far, we have considered the motion of the charged particle in the axial symmetric field. The orbit of a charged particle in the corrugated magnetic field including the effect of the curvature of the torus is studied in this section. In the first place, we consider the problem qualitatively in connection with the result of § 4.

Let us consider the time averaged motion of the guiding center projected on a $r-\theta$ plane taking the toroidal coordinate defined as follows. Considering a planar curve with a constant radius of curvature $1/\kappa$, we let $\boldsymbol{e}_r$, $\boldsymbol{e}_\theta$, and $\boldsymbol{e}_z$ be unit vectors in the direction out from the curvature, around the curve with $\theta=0$ measured from a line joining the curve to the center of the curvature, and along the curve, respectively. The time averaged motion of the guiding center on the $r-\theta$ plane is the synthesized motion of the θ revolution argued in §4 and the curvature drift in the direction of $\theta=\pi/2$ or $3\pi/2$. The above argument it valid when the curvature of the torus is sufficiently small to neglect the coupling of the θ drift with the curvature drift. The equation of motion of the particle is given by

$$\frac{d}{dt}(r\cos\theta)=-\omega r\cos\theta\ ,$$

$$\frac{d}{dt}(r\sin\theta)=\omega r\cos\theta+v\quad(\omega=\bar{\dot{\theta}})\ ,$$

where v is the velocity of toroidal drift. Since ω does not depend on r seriously, we assume ω=constant for the qualitative consideration. Then, the equation is readily integrated to give

$$\left(r\cos\theta+\frac{v}{\omega}\right)^2+r^2\sin^2\theta=\text{const.}\ ,$$

which is the equation of the circle with its center on $(-v/\omega,\ 0)$. Thus the curvature drift is well compensated by the angular drifts when v/ω is small, or ω is fairly large. Now,

$$v=\frac{c\kappa}{eB_0}(W_\perp+2W_\parallel)\ ,$$

$$\omega=\bar{\dot{\theta}}=\frac{k\varepsilon I_1(kr_0)}{r_0}\ \frac{cW}{eB_0}g\quad(g=\bar{\dot{\theta}}/CW)\ ,$$

where g is the value plotted in Fig. 4, and r_0 is the value of r coordinate of the field line ot $kz=\pi/2$ on which the particle lies. Hence we have

$$\frac{v}{\omega}=\frac{\kappa r_0}{k\varepsilon I_1(kr_0)}\ \frac{1}{g}\left(2-\frac{\mu B_0}{W}\right). \tag{25}$$

When the machine is not a simple torus but of a race track type with the linear section of the length L and the curved section of radius R, we find for the particle revolving around the race track,

$$\frac{v}{\omega}=\frac{\pi r_0}{L+\pi R}\ \frac{1}{k\varepsilon I_1(kr_0)g}\left(2-\frac{\mu B_0}{W}\right), \tag{25$'$}$$

since particle experiences no curvature drift in the linear section. Eq. (25) can be applied to a particle, which is trapped between the mirrors in the curved section, so far as v/ω is fairly small as compared with d, as confirmed by the numerical results given in table 1, which is calculated for the device of interest. As seen from Fig. 4 the value of $g=\bar{\dot{\theta}}/CW$ is sufficiently large for most of the trapped particles and the particles having $g\approx0$ will soon take large value of g when they drift to the outer line. Therefore it is expected that the curvature drifts are well compensated by the angular drifts for the trapped particles.

Table I. The value of v/ω of the particle which has $\delta=0.8$ and is trapped in one section of the mirror field. The scale of the device are $k=1\ \text{cm}^{-1}$, $d=3$ cm, and $\kappa=0.005\ \text{cm}^{-1}$.

r cm	g	v/ω cm
0	0.5	0.1
1.5	0.9	0.024
1.8	1.1	0.02

In the next place we calculate the orbit of the guiding center of a particle revolving around the torus, making use of the adiabatic invariance of the longitudinal action integral over a complete cycle,

$$J=m\oint v_{11}dl=\text{const.}\ , \tag{26}$$

which is proved by Kadomtsev[2]. He showed that the guiding center drifts from one line of force to another in such a way that the J is conserved. It is difficult to calculate Eq. (26) in general, but for the particle revolving around the torus, the integration can be performed easily by expanding, $v_{11}(=\sqrt{2(W-\mu B)/m})$, in powers of $\varepsilon I_0(kr)$ and κr.

Taking the toroidal coordinate as before, the Eq. (2) which expresses the magnetic flux density is modified by the curvature of the torus

$$\begin{aligned}B_z&\simeq B_0(1-\varepsilon I_0(kr)\cos kz+\kappa r\cos\theta)\ ,\\ B_r&\simeq-B_0\varepsilon I_1(kr)\sin kz\ .\end{aligned} \tag{27}$$

In the following, it is assumed $\varepsilon I_0(kr)\gg\kappa r$, so that the term proportional to $\kappa r\varepsilon I_0(kr)$ will be neglected in comparison with the term $\varepsilon^2I_0(kr)^2$. Some caution is necessary, however, to calculate Eq. (26) near the neutral line where Eq. (3$'$) is not valid. Let η denote the length of the one period of the field line in the case of $\kappa=0$, which passes through the point $kz=\pi/2$ and $r=r_0$, then the integrated result of Eq. (26) can be expressed as

$$\eta=\frac{\varepsilon^2\delta}{8}\left(I_1(kr_0)^2+\frac{\delta}{2(1-\delta)}I_0(kr_0)^2\right)$$
$$-\left(1-\frac{\delta}{2}\right)\kappa r_0\cos\theta=\text{const.}\,, \tag{28}$$

where $\delta=\mu B_0/W$. If we substitute for η the numerically calculated value, we confirm that Eq. (28) is a good approximation even near the neutral line as far as the adiabatic approximation holds.

We show in Fig. 5 the time averaged motions of the guiding centers of the charged particles revolving around the torus projected to a plane $kz=\pi/2$. The quantities of the device are taken the same as before and $\rho_0=0.06$ cm for positive ions. The outer dotted curve shows the neutral line and the inner dotted curve shows the boundary, inside which the adiabatic approximation is valid even for ions. The arrows on the solid curves show the direction of θ revolution of electrons, when the center of the curvature of the torus is in the right hand side and the magnetic field is in the upward direction to the paper. The positive ions revolve the same orbit in the reverse direction, as far as they move in the inside of boundary line. Among the three curves of $\delta=0$ (transverse energy=0), the outermost curve (1) indicates the orbit which just reaches the neutral line when the electron drifts outwards to a maximum extent. The electrons which are located inside this curve draw closed loops in the inner region of this curve as two other curves (2) and (3) with $\delta=0$. The next outer curve (2) of $\delta=0$ indicates the orbit which passes through the adiabatic line for ions at $\theta=0$. The ions located inside of this curve draw closed loops also. We also plott three curves of $\delta=0.7$ (a fairly large transverse energy) which have the same meaning as above.

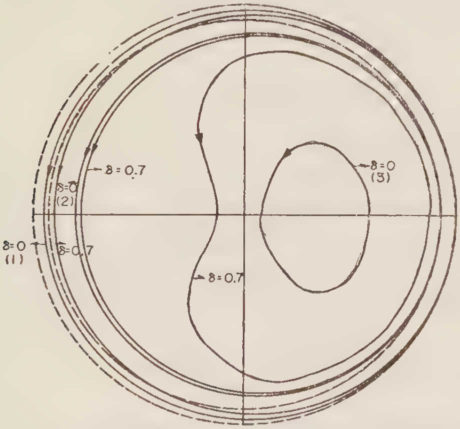

Fig. 5. The particles orbits projected to a $r-\theta$ plane at $kz=\pi/2$. The outer dotted line shows the neutral line and the inner dotted line shows the boundary, inside which adiabatic approximation is valid even for ions. Among the three curves of $\delta=0$ (transverse energy=0), the outermost curve (1) indicates the orbit which just reaches the neutral line when the electron drifts outward to a maximum extent. The electrons which are located inside this curve draw closed loops as illustrated inner two curves (2) and (3). The next outer curve (2) of $\delta=0$ indicates the orbit which passes the adiabatic line for ions at $\theta=0$. The ions located inside of this curve draw closed loops also. Three curves of $\delta=0.7$ are plotted also. They have the same meaning as above.

§6. Discussion

Let us compare our results with those of Kadomtsev. In his treatment the device is a race track type, the linear sections of which have the corrugated field, while the curved sections have the simple toroidal field. The field of a linear section is connected with the field of curved sections and the magnetic field between the two portions is strengthened so as to form a very narrow jaw. Thus, the particles can move from a linear section to a curved section, only if they have a small value of δ enough to pass the strengthened field.

In our treatment, the field is assumed to be a simple toroidal corrugated field, i.e., the corrugated field wounded uniformly around the torus. The result of Kadomtsev concerning the particles orbits is obtained from Eq. (28) by putting $\delta=0$ and multiplying η and $\kappa r\cos\theta$ by the length of linear and curved sections, respectively. Furthermore Kadomtsev calculated the values of η using the equation $r=r_0+\varepsilon/kI_1(kr_0)\cos kz$ for the line of force, which is invalid near the neutral line. On the other hand, we use the values of η which has been calculated numerically, and the θ drifts are found to be strengthened by a factor 3 near the neutral line as compared with the value of Kadomtsev. Therefore, the scale of the device is able to be reduced considerably, even if we take into account of the condition of (19) for the confinement of the particle which is not considered by Kadomtsev.

The problems concerning the stability of the plasma in such a field is not considered in this paper. It will be treated elsewhere.

Acknowledgement

The author wishes to express his thanks to Prof. C. Hayashi for his helpful discussions and encouragement. The author is greatful to Dr. Terashima and Dr. K. Uo for their critical comments. He also whishes to express his great indebtness to Asahi Press for financial support.

References

1) Von R. Lüst und A. Schlüter: Z. Naturforshung. 12 a, (1957) 850.
2) B. B. Radomtsev: Plasma Physics and the Problem of the Controlled Thermonuclear Reactions (Pergamon Press, London, 1959) Vol. 3, p. 340.
3) K. Uo: J. Phys. Soc. Japan **16** (1961) 1380.
4) M. N. Rosenbluth and C. L. Longmire: Annals of Physics **1** (1957) 120.

Optical Properties of LiF in the Extreme Ultraviolet

By Riso Kato

Department of Physics, Faculty of Science, Kyoto University

(Received July 21, 1961)

The reflection spectrum of LiF single crystal was measured in the extreme ultraviolet region at room temperature. The Kramers-Kronig relation was applied to derive the optical constants n and κ from the reflectivity. The maximum absorption coefficient and the peak position of the first fundamental band were determined to be $2.2\pm0.1\times10^6$ cm^{-1} and 12.7 ± 0.1 ev respectively. Variations of the real and imaginary parts of the complex dielectric constant in the given region were analysed by the quantum-mechanical analogue of the Lorentz dispersion formulas and the oscillator strength of the first fundamental band was determined to be 0.4 ± 0.05/molecule. The value supports the excitation model of the exciton discussed by Dexter on NaCl. Experiments and discussions are also described on the effect of hydrolysis of LiF.

§ 1. Introduction

The ultravaiolet absorption[1),2)] of alkali halides has been one of the main subjects of investigation on ionic crystals for many years. The absorption spectra of these materials in the fundamental region have been obtained from transmission measurements on evaporated thin films because of their large absorption coefficients. Difficulties, however, cannot be avoided in the accurate measurements of film-thickness required to the determination of absorption coefficients. Also, the transmission measurements accompany the unknown factors about the degree of lattice perfection of the films, the film stoichiometry, and the amount of surface contamination. For these reasons, it is highly desirable to determine the absorption of the bulk crystal from reflectivity measurements independently[3)].

In the case of LiF, the transmission measurements are more difficult than the other alkali halides for the lack of appropriate substrates. Hence, the investigation by the reflectivity measurements is more important for LiF, though the reflectivity measurements are influenced sensitively by the surface contamination of the specimen.

The purposes of the present paper are (1) to get the optical constants and the absorption coefficient of the bulk crystal of LiF in the extreme ultraviolet from the reflectivity measurements, and (2) to present the oscillator strength of the first fundamental band which is a sensitive test of theoretical studies[4)] on the exciton problem.

Furthermore, the hydrolysis effect of LiF[5] on the absorption spectra is not only of physical interest, but also of interest in the practical use of the crystal as the optical material.

§ 2. Experimental

The vacuum monochromator[6] and the reflectometer used in this experiment are the same as in a previous work[7]. The reflection measurements were carried out with the incident angle of 15° at room temperature. First, a nearly 100 A segment of the hydrogen spectrum of the light source was recorded through the blank window for reference. Then, the sample holder was lowered and rotated through 15° about its vertical axis, and the photomultiplier coated with sodium salicilate was turned through 150° to the front of specimen to catch the reflected light. With these arrangements, the reflected light of the same segment was recorded. The intensity of stray light in each segment was measured through a suitable filter (LiF, quartz, or ultraviolet transmitting glass) for reference and reflected lights respectively. The light source and the detection system were stable to better than two percent during the measurement in any segment.

The mechanical part of the reflectometer was improved in this experiment and the errors arising from its operation were diminished remarkably. Relatively high reflectivities in the previous experiment were due to the defects of the reflectometer. Another cause of errors in the reflectivity was inaccuracy in the evaluation of the contribution from stray lights, particularly in the higher energy region above 13 ev. The intensity of light source became more weak above 13 ev and the background intensity amounted to almost the same order as the signal. Therefore, the error of about 5% in the reflectivity could not be avoided in the region. Below 13 ev, the error remained within 1%. Band widths of lights passing through the exit slit of the monochromator were less than 2 A below 12 ev and about 5 A above 13 ev.

Specimens of LiF crystal were cleaved from the same block as in the previous work which was the purest among those available. (Hereafter, this block is called crystal P.) They were treated carefully to avoid the effect of surface contamination, because the hydrolysis of LiF is accelerated above 40°C in air[5]. Thus, the measurements were made on freshly cleaved specimens below 10°C in winter, in contrast to the previous experiment at about 30°C in summer.

Transmission measurements were made to investigate the hydrolysis effect of LiF (1) on the specimens being kept at about 30°C in air and in water for long days, (2) on the crystal grown up in air, and (3) on the thin films evaporated on celluloid films. The original material of each film was a small fragment of the crystal grown up in air or freshly cleaved one from crystal P.

§ 3. Experimental Results

Fig. 1 shows the reflection and absorption spectra of LiF single crystal P measured at room temperature. Circular Points in the figure represent the intensity ratios of the reflected light to the incident light: $I_{av}^{(r)}/I^{(i)}$. They do not always agree with the reflectivities, R, particularly in the transparent region because of the contribution to the reflected light from the back surface of the specimen. The meaning of $I_{av}^{(r)}$ is interpreted in the following section. The thick line in the figure shows the reflectivity curve derived from $I_{av}^{(r)}/I^{(i)}$ by the method described in the next section. The thin line with square points represents the absorption curve with the correction of the reflection. The maximum reflectivity was found at 12.8±0.1 ev. The observed $I_{av}^{(r)}/I^{(i)}$ shows a depression at nearly 11.8 ev and thence LiF becomes transparent. This is the evidence of the contribution to the reflected light from the back surface of the specimen.

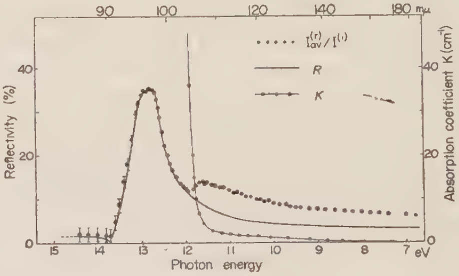

Fig. 1. Reflection and absorption spectra of LiF single crystal measured at room temperature.

Results of measurements on the hydrolysis effects will be shown by Figs. 10–14 in section 6 with some discussions.

§ 4. Analysis of Experimental Results

The observed ratio of the reflected light to the incident light agrees with the reflectivity in the highly absorbing region, but not in the transparent region. According to the theory of multiple reflection[8)], intensities of reflected and transmitted lights from a transparent plate are given by

$$I^{(r)}=\frac{4R\sin^2\delta/2}{(1-R)^2+4R\sin^2\delta/2}\cdot I^{(i)} \tag{1}$$

and

$$I^{(t)}=\frac{(1-R)^2}{(1-R)^2+4R\sin^2\delta/2}\cdot I^{(i)}, \tag{2}$$

where $I^{(i)}$, $I^{(r)}$ and $I^{(t)}$ are the intensities of incident, reflected and transmitted lights respectively, and δ is the phase difference between the neighbouring rays, $\delta=4\pi nd\cos\theta'/\lambda$, as shown in Fig. 2. When $R\ll 1$, *Eq.* (1) may be rewritten approximately as:

$$I^{(r)}\doteqdot\frac{4R}{(1-R)^2}\sin^2\delta/2\cdot I^{(i)}=\frac{2R}{(1-R)^2}(1-\cos\delta)\cdot I^{(i)}. \tag{3}$$

Thus, the reflected light, varies sinusoidally with δ showing interference fringes. In the present case of $d\gg\lambda$, the fringes appear too dense to be detected on account of the rapid change of δ with λ. The variation of $I^{(r)}/I^{(i)}$ *versus* λ is shown schematically by the thin line on the right-hand side in Fig. 2. Therefore, the observed intensities of reflected lights in the transparent region are the average values given by

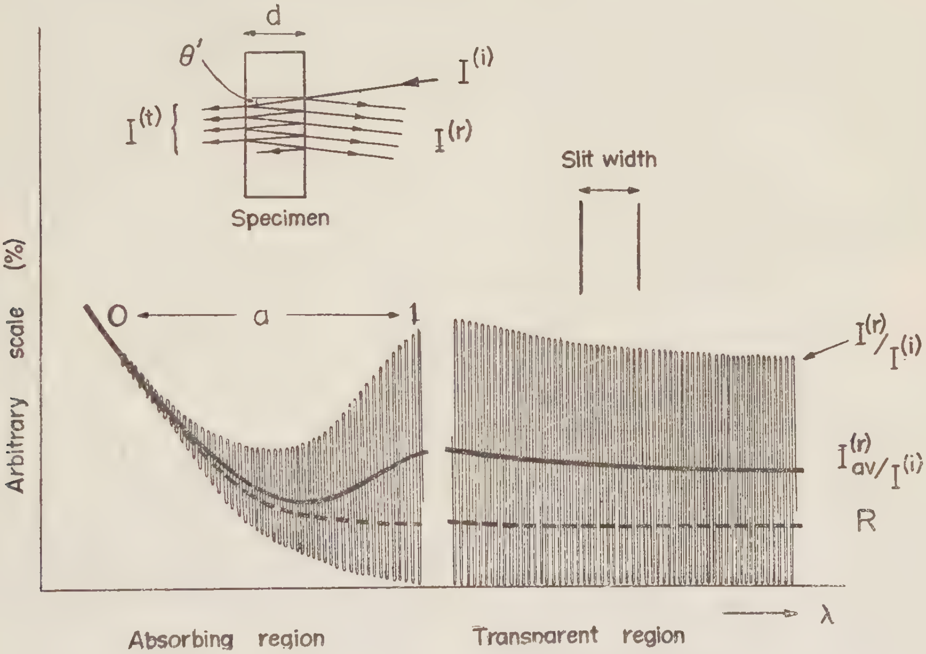

Fig. 2. Schemtic illustration of the multiple reflection.

$$I^{(r)}_{\rm av}=\frac{2R}{(1-R)^2}\cdot I^{(i)}. \tag{4}$$

Circular points in Fig. 1 and the full line in Fig. 2 show $I^{(r)}_{\rm av}/I^{(i)}$. Reflectivities in the transparent region are easily derived from $I^{(r)}_{\rm av}/I^{(i)}$ and they are shown by the dotted line in Fig. 2. The reflectivities below 11 ev in Fig. 1 were derived from the observed value of $I^{(r)}_{\rm av}/I^{(i)}$ using Eq. (4) and they were smoothly connected to those calculated from the known refractive indices of LiF in the near ultraviolet and visible regions.

When a medium becomes absorbing, Eqs. (1) and (2) are modified as follows:

$$I^{(r)}=\frac{\{(1-a^2)^2+4a^2\sin^2\delta/2\}R}{(1-a^2R)^2+4a^2R\sin^2\delta/2}\cdot I^{(i)}, \tag{5}$$

$$I^{(t)}=\frac{a^2(1-R)^2}{(1-a^2R)^2+4a^2R\sin^2\delta/2}\cdot I^{(i)}, \tag{6}$$

where a is the transmission of light for one traversal of the specimen. If the medium is highly absorbing, i.e. $a=0$, Eq. (5) is simplified and gives R directly. This is realized for LiF above 12 ev, as shown in Fig. 1.

The variation of $I^{(r)}/I^{(i)}$ is much complicated for the intermediate value of $a; 0<a<1$. It is shown schematically on the left-hand side in Fig. 2. In this case, the observed intensities are also the average values.

The Fresnel equations for the reflection of light from an absorbing medium involve both real and imaginary parts of complex index of refraction: $N=n-i\kappa$. It is exceedingly troublesome to analyse the reflectivity at non-normal incidence, because the equations are very complicated and the light coming out of the monochromator is partially polarized.

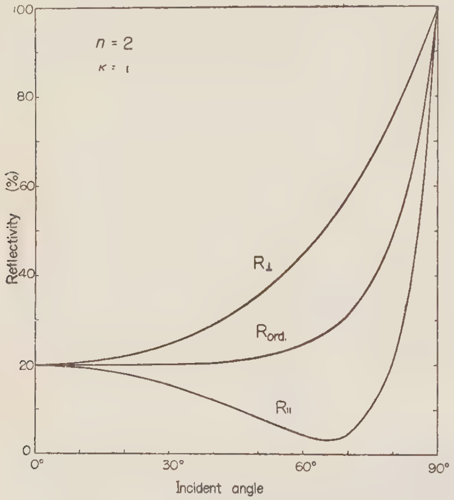

Fig. 3. Variations of reflectivities *versus* incident angle for the medium with $n=2$ and $\kappa=1$.

However, in the case of nearly normal incidence, the reflectivity depends insensibly on the incident angle and the effect arising from the polarization of the incident light is small, as seen in Fig. 3 which shows an example of the variations of reflectivities ($R_{\perp}$, $R_{\parallel}$ and $R_{\mathrm{ord.}}$) *versus* incident angle for $n=2$ and $\kappa=1$. Hence, the reflectivity at the incident angle of 15° may be regarded safely as that at normal incidence within experimental errors and it can be analysed by the much simpler single Fresnel equation.

The Fresnel equation for the complex amplitude of reflection at normal incidence is given by

$$\rho=\frac{n-i\kappa-1}{n-i\kappa+1}=re^{i\theta}, \qquad (7)$$

where $r=\sqrt{R}$. Then, n and κ can be solved in terms of r and θ as follows:

$$n=\frac{1-r^2}{1+r^2-2r\cos\theta}, \qquad (8)$$

$$\kappa=\frac{-2r\sin\theta}{1+r^2-2r\cos\theta}. \qquad (9)$$

Reflectivity measurements determine r^2, hence r. The phase of the complex reflectivity at any frequency can be determined by the inter-relation[9] between the real and imaginary parts of the complex function. From Eq. (7), we have

$$\ln\rho=\ln r+i\theta, \qquad (10)$$

and then θ at any frequency ω_c can be expressed by an intergal taken over the whole range of the frequency:

$$\theta(\omega_c)=\frac{2\omega_c}{\pi}\int_0^{\infty}\frac{\ln r(\omega)-\ln r(\omega_c)}{\omega^2-\omega_c{}^2}d\omega, \qquad (11)$$

which may be rewritten as:

$$\theta(\omega_c)=\frac{1}{\pi}\int_0^{\infty}\frac{d\ln r(\omega)}{d\omega}\ln\left|\frac{\omega+\omega_c}{\omega-\omega_c}\right|d\omega. \qquad (12)$$

This equation shows that the contributions

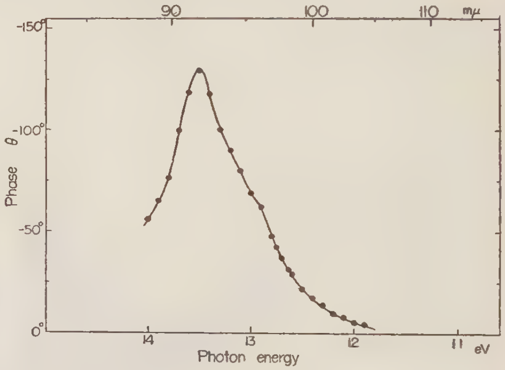

Fig. 4. The phase associated with the complex amplitude of the reflectivity computed by Eq. (12) for the first fundamental band of LiF at room temperature.

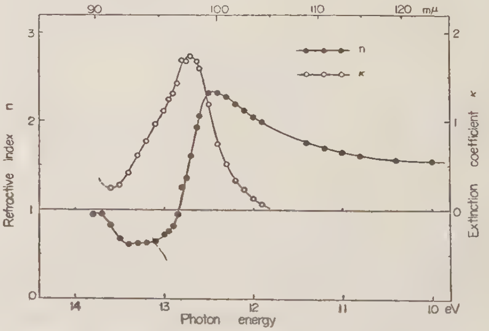

Fig. 5. Optical constants of LiF single crystal at room temperature calculated from the reflectivity.

from the regions remote from the point of interest are small and a constant percentage error in the reflection characteristic does not affect the phase determination.

The phase calculations were carried out with the aid of the table[10] based upon Eq. (12). Reflectivities of LiF above 15 ev and below 2 ev were taken as constants. Because the experimentally determined R above 13 ev contained fairly large error, the reflectivity curve above 13 ev in Fig. 1 was drawn within experimental errors so as to satisfy the requirement that κ is zero in the transparent region. Below 5 ev, the reflectivities calculated from known refractive indices were used in the phase computation, to which the experimental values were smoothly extrapolated. The obtained phase is plotted against the photon energy in Fig. 4. Optical constants calculated from the reflectivity and phase are shown in Fig. 5. The variation of the absorption coefficient, $K=4\pi\kappa/\lambda$, with the photon energy is also given in Fig. 6.

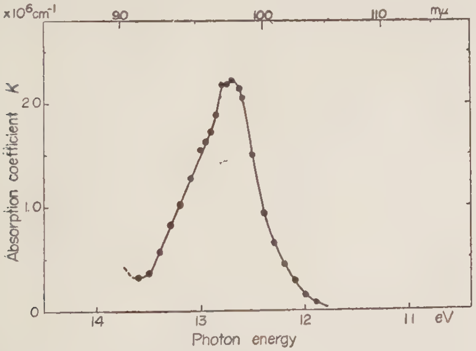

Fig. 6. Absorption coefficient of the first fundamental band of LiF single crystal at room temperature *versus* photon energy as computed from the reflectivity.

§ 5. Discussion of the Results

The peak position and the maximum absorption coefficient of the first fundamental band were determined to be 12.7±0.1 ev and 2.2 ±0.1×10⁶ cm⁻¹ at room temperature respectively. The shape and the position of the band are similar to those[11] of the thin film evaporated on the organic substrate.

In order to get the further knowledges on the absorption, the real and imaginary parts of the complex dielectric constant, $\varepsilon=\varepsilon_1-i\varepsilon_2$, were derived from n and κ by the relations:

$$\varepsilon_1=n^2-\kappa^2, \tag{13}$$

$$\varepsilon_2=2n\kappa, \tag{14}$$

and they were plotted against the photon energy in Fig. 7. The complex dielectric constant is related to the complex polarizability α of the medium by the relation:

$$\varepsilon=1+4\pi\alpha. \tag{15}$$

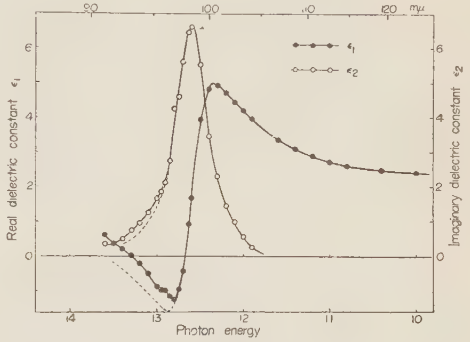

Fig. 7. Real and imaginary parts of complex dielectric constant of LiF at room temperature *versus* photon energy as computed from the reflectivity.

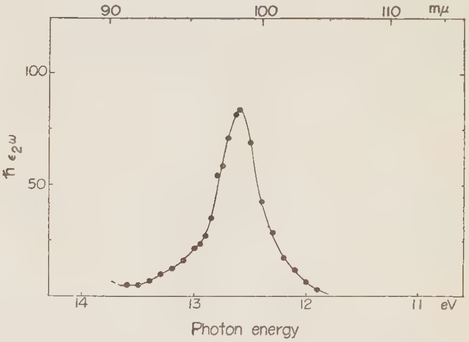

Fig. 8. Variation of $\varepsilon_2\omega$ of LiF single crystal with ω in electron-volt unit.

Hence, the variations of ε_1 and ε_2 with the frequency of the radiation may be expressed by the quantum-mechanical analogue of the Lorentz dispersion formulas:

$$\varepsilon_1=1+\frac{4\pi Ne^2}{m}\sum_j\frac{f_j(\omega'^2_j-\omega^2)}{(\omega'^2_j-\omega^2)^2+\gamma_j^2\omega^2}, \tag{16}$$

$$\varepsilon_2=\frac{4\pi Ne^2}{m}\sum_j\frac{f_j\gamma_j\omega}{(\omega_j'^2-\omega^2)^2+\gamma_j^2\omega^2}, \tag{17}$$

where ω'_j, f_j and γ_j are the resonance frequency, the corresponding oscillator strength and the damping constant respectively. It is clear from Eq. (17) that $\varepsilon_2\omega$ shows its maximum at $\omega=\omega_j'$ with the half-width of γ_j. The variation of $\varepsilon_2\omega$ with ω is plotted in Fig. 8 in electron volt unit. The position and the half-width of the curve are 12.6±0.1 ev and

0.42±0.02 ev respectively. By neglecting the contributions from the tails of higher energy bands, the oscillator strength, defined by Eq. (17), of the first fundamental band was determined by the relation:

$$\frac{4\pi Ne^2}{m}\cdot f=\gamma\cdot(\varepsilon_2\omega)_{\max}\,. \tag{18}$$

The obtained f -value is 0.069±0.005/electron, where N is taken as the total number of the valence electrons per unit volume which contribute to the absorption of the first fundamental band. Since there are six valence electrons per molecule for alkali halides, one may obtain.

$$f=0.42\pm0.03/\text{molecule}.$$

In the above treatment of the problem, the fundamental absorption at 12.7 ev was regarded as a single band though it showed a remarkable asymmetry, and the dispersion formulas were used without the local field correction. If the correction is to be made by using the Lorentz local field, the macroscopic polarizability α is not able to be related to the polarizability α_o of a single oscillator by $N\alpha_o$ but it must be related by the equation:

$$\alpha=\frac{N\alpha_o}{1-\frac{4\pi}{3}N\alpha_o}\,. \tag{19}$$

Since α_o may be expressed, in the region of the absorption considered here, by

$$\alpha_o\simeq\frac{e^2}{m}\frac{f_o}{\omega_o{}^2-\omega^2+i\gamma\omega}\,, \tag{20}$$

α becomes

$$\alpha=\frac{Ne^2}{m}\frac{f_o}{\left(\omega_o{}^2-\frac{4\pi}{3}\frac{Ne^2}{m}f_o\right)-\omega^2+i\gamma\omega}\,. \tag{21}$$

Hence, the effective resonance frequency in the composite system occurs at[12)]

$$\omega_o{}'=\left(\omega_o{}^2-\frac{4\pi}{3}\frac{Ne^2}{m}f_o\right)^{1/2}. \tag{22}$$

The resonance frequency $\omega_j'(j=0)$ in Eqs. (16) and (17) is, therefore, related to ω_o by Eq. (22). The direct determination of ω_o can be made from the experimental values by the relation:

$$\frac{\varepsilon-1}{\varepsilon+2}=\frac{4\pi}{3}N\alpha_o\simeq\frac{4\pi}{3}\frac{Ne^2}{m}\frac{f_o}{\omega_o{}^2-\omega^2+i\gamma\omega}\,, \tag{23}$$

which is derived from Eqs. (15) and (19). The real and imaginary parts of the left-hand side of Eq. (23) were obtained from the experimental values of ε_1 and ε_2, and they are plotted in Fig. 9. The obtained $\hbar\omega_o$ is 13.0±0.1 ev and it is consistent with 13.05 ev determined by Eq. (22) using $\hbar\omega_o{}'=12.6$ ev and $f_o=0.069$/electron. Another determination of f_o is possible from the variations of α_o by the relation

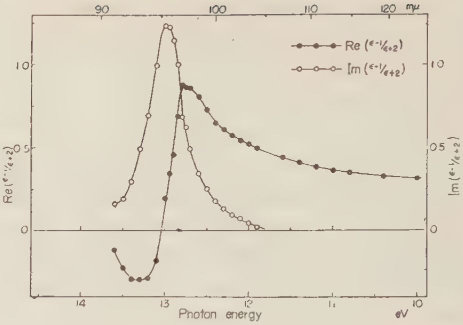

Fig. 9. Real and imaginary parts of $(\varepsilon-1)/(\varepsilon+2)$ of LiF single crystal at room temperature *versus* photon energy.

$$\frac{4\pi}{3}\frac{Ne^2}{m}\cdot f_o=\gamma\cdot\left[\mathrm{Im}\left(\frac{\varepsilon-1}{\varepsilon+2}\right)\cdot\omega\right]_{\max}\,. \tag{24}$$

From this equation we abtained $f_o=0.046$/electron, which shows a fairly large deviation from the value determined by Eq. (18). The deviation is considered to be mainly due to large experimental errors in ε_1 and ε_2 above 13 ev and the contributions to ε_1 and ε_2 near 13 ev from the tails of higher energy bands, because $\mathrm{Im}(\varepsilon-1/\varepsilon+2)$ was more sensitive to ε_1 and ε_2 than ω_o was. Therefore the consistent value of f_o is to be obtained if the calculations are made from the simpler symmetric curves of ε_1 and ε_2. This was done effectively by using the corrected values of ε_1 and ε_2 shown by the dotted curves in Fig. 7. The results are $\hbar\omega_o=13.03$ ev and $f_o=0.061$/electron.

Thus, one may conclude that the oscillator strength of the first fundamental band of LiF is 0.4±0.05/molecule. This f- value is in good agreement with the theoretical one on NaCl calculated by Dexter[13)] on the basis of the excitation model of the exciton.

There is a qualitative resemblance between the reflectivity and absorption spectra. Reflectivity spectra give us approximate knowledges concerning the positions and structures of the absorptions. Strictly speaking, maxima of R, κ, K, $2n\kappa$ etc. occur at different frequencies and their half-widths differ from each other. Table 1 shows their peak posi-

Table 1

		Peak position
Reflectivity	R	12.8±0.1 ev
Extinction coefficient	κ	12.7±0.1
Absorption coefficient	$K=4\pi\kappa/\lambda$	12.7±0.1
Imaginary dielec. const.	$\varepsilon_2=2n\kappa$	12.6±0.1
Energy absorption	$\eta\propto\varepsilon_2\omega$	12.6±0.1
Imaginary part of the polarizability α_0	$Im(\varepsilon-1/\varepsilon+2)$	13.0±0.1

tions on the first fundamental absorption of LiF.

§ 6. Effects of Hydrolysis

It has been found that hydrolysis of LiF is accelerated above 40°C in air and the crystal grown up in air shows an absorption near 2.8μ due to the vibration of O-H bond[5]. Fig. 10 shows the infrared transmission spectra of LiF crystal grown up in air and crystal P in the preceding section.

The hydrolysis effect was also found on the absorption spectrum in the extreme ultraviolet. It gave a broad absorption at the tail of fundamental band. Fig. 11 shows the absorp-

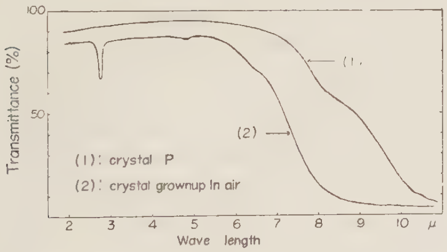

Fig. 10. Transmission spectra of LiF single crystals in the infrared region measured at room temperature.

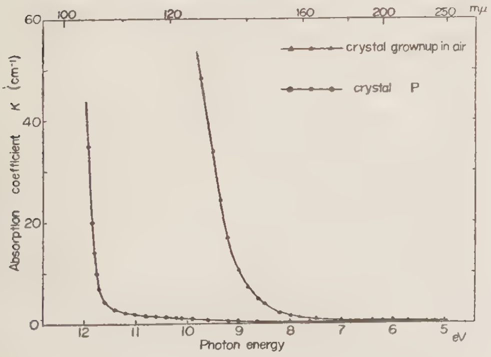

Fig. 11. Absorption spectra of LiF single crystals in the extreme ultraviolet measured at room temperature.

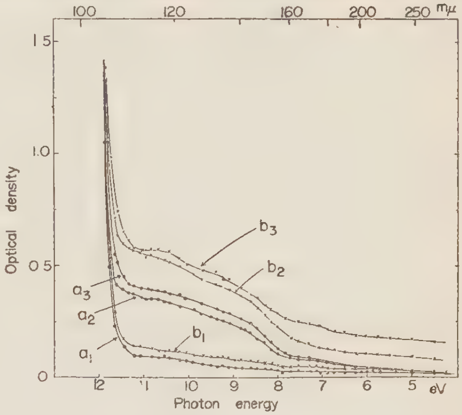

Fig. 12. Growth of the absorption with the progress of surface hydrolysis of LiF crystals.

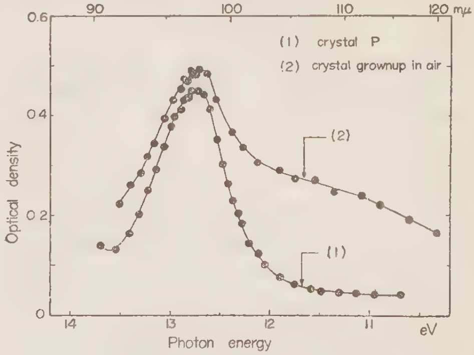

Fig. 13. Absorption spectra of LiF thin films at room temperature evaporated on celluloid films.

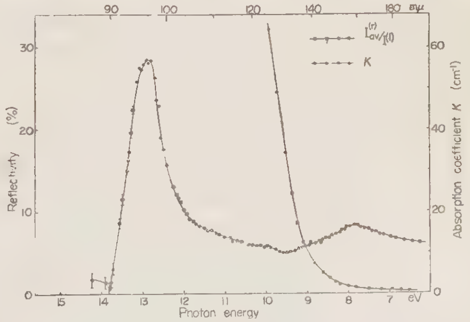

Fig. 14. Reflection and absorption spectra of LiF single crystal grown up in air, measured at room temperature.

tion spectra of LiF crystals in the extreme ultraviolet. The absorption near the tail of fundamental band is more sensitive to hydrolysis than 2.8μ absorption. Fig. 12 shows the growth of the absorptions with the progress of surface hydrolysis of the crystals which were kept in air and in water at about 30°C. The degrees of surface hydrolysis in air and in water do not differ greatly and they are likely to reach the saturating state. It may be said from Figs. 10, 11 and 12 that the surface hydrolysis is limited within a very thin layer of the surface, but the hydrolysis effect is prevalent thoughout the crystal when it is grown up in air. The above difference was also observed in the absorption spectra of thin films evaporated on the organic substrates. The original material of each film was a small fragment of the single crystal grown up in air or freshly cleaved one from crystal P. The absorption spectra of both films are shown in Fig. 13.

The reflection measurement was also made on the crystal grown in air. The results is shown in Fig. 14. No essential differences were detected between the reflection spectra in Fig. 1 and Fig. 14 except rather low reflectivity at the peak in the latter. The decrease in observed $I_{\mathrm{av}}^{(r)}/I^{(i)}$ near 9 ev is due to the absorption arising from the hydrolysis effect.

§ 7. Summary

The optical constants of LiF single crystal have been derived from the reflectivity measurements. The maximum absorption coefficient and its position of the first fundamental absorption were determined: $K_{\max}=2.2\pm0.1\times10^6\ \mathrm{cm}^{-1}$ and $\hbar\omega_{\mathrm{peak}}=12.7\pm0.1$ ev at room temperature. The real and imaginary parts of the complex dielectric constant were obtained from the optical constants and their variations with ω were analysed by the quantum-mechanical analogue of the Lorentz dispersion formulas. Thus, the resonance frequency, the damping constant and the oscillator strength of the first fundamental band were determined: $\hbar\omega_0'=12.6\pm0.1$ ev, $\hbar\gamma=0.42\pm0.02$ ev and $f=0.4\pm0.05$/molecule. The value of the oscillator strength is in good agreement with the theoretical one on NaCl calculated by Dexter on the basis of the excitation model of the exciton. The hydrolysis effect of LiF was found to give a broad absorption at the tail of fundamental band as well as the absorption near 2.8μ.

Acknowledgements

The author wishes to express his sincere thanks to Prof. Y. Uchida for his continual guidance and encouragement throughout this work, and to Dr. K. Fukuda for his kind interest and discussions. His thanks are also due to Messrs. K. Nakamura and A. Matsui for their kind and valuable assistance in this work.

References

1) R. Hilsh and R. W. Pohl: Z. Physik **59** (1930) 812; G. E. Schneider and H. M. O'Bryan: Phys. Rev. **51** (1937) 293. W. Martienssen: J. Phys. Chem. Solids **2** (1957) 257. J. E. Eby, K. J. Teegarden and E. B. Dutton: Phys. Rev. **116** (1959) 1009.

2) P. L. Hartman, J. R. Nelson and J. G. Siegfried: Phys. Rev. **105** (1957) 123. E. A. Taft and H. R. Philipp: J. Phys. Chem. Solids **3** (1957) 1.

3) I. Simon: J. Opt. Soc. Amer. **41** (1951) 336; T. S. Robinson: Proc. Phys. Soc. London **65 B** (1952) 910. T. S. Robinson and W. C. Price: ibid. **66 B** (1953) 969. F. C. Jahoda: Phys. Rev. **107** (1957) 1261. H. R. Philipp and E. A. Taft: Phys. Rev. **113** (1959) 1002, **120** (1960) 37. M. P. Rimmer and D. L. Dexter: J. Appl. Phys. **31** (1960) 775. M. Gottlieb: J. Opt. Soc. Amer. **50** (1960) 343. A. Mitsuishi: J. Phys. Soc. Japan **16** (1961) 533.

4) A. W. Overhauser: Phys. Rev. **101** (1956) 633. D. L. Dexter: Phys. Rev. **83** (1951) 435, **108** (1957) 707. T. Muto and H. Okuno: J. Phys. Soc. Japan **11** (1956) 633. T. Muto, S. Oyama and H. Okuno: Progr. Theor. Phys. **20** (1958) 804. R. S. Knox and N. Inchauspé: Phys. Rev. **116** (1959) 1093. R. A. Pappert: Phys. Rev. **119** (1960) 525.

5) R. Kiyama and S. Minomura: Rev. Phys. Chem. Japan **23** (1953) 10.

6) Y. Uchida *et al.*: J. Appl. Phys. Japan **29** (1960) 492.

7) R. Kato *et al.*: J. Phys. Soc. Japan **15** (1960) 2105.

8) For instance, M. Born and E. Wolf: *Principles of Optics* (Pergamon Press, 1959) P. 322.

9) For instance, H. W. Bode: *Network Analysis and Feedback Amplifier Design* (D. Van Nostrand Company, Inc., New York, 1945) p. 303. P. M. Morse and H. Feshbach: *Methods of Theoretical Physics, I* (McGraw-Hill Book

Co. Inc., 1953) p. 370.
10) D. E. Thomas: Bell Syst. Tech. J. **26** (1947) 870.
11) R. Onaka *et al.*: J. Phys. Soc. Japan **16** (1961) 340.
12) D. L. Dexter: Phys. Rev. **101** (1956) 48; F. Seitz: *The Modern Theory of Solids* (McGraw-Hill Book Co. Inc. 1940) p. 658.
13) D. L. Dexter: Phys. Rev. **108** (1957) 707.

JOURNAL OF THE PHYSICAL SOCIETY OF JAPAN, Vol. 16, No. 12, DECEMBER, 1961

Quadrupole Coupling in the Hyperfine Structure of the Spectrum of La I

By Kiyoshi MURAKAWA

Aeronautical Research Institute, University of Tokyo,
Komaba-machi, Meguro-ku, Tokyo

(Received August 15, 1961)

According to the theory of Sternheimer, it can be written $Q=(1+\Delta)Q'$, in which Q is the true quadrupole moment and Q' is the apparent quadrupole moment obtained by spectroscopic means neglecting the shielding effect; Δ is the so-called shielding correction or core correction. The author obtained in a previous work $\Delta=-0.6$ for $5d^2 6s\,{}^4F_{3/2}$ of La I. In the present work $\Delta=-0.6$ and -0.7 were obtained for $5d^2 6s\,{}^4F_{9/2}$ and ${}^4F_{7/2}$ respectively of La I. They agree with the value for ${}^4F_{3/2}$ within experimental error.

§1. Introduction

The calculation of Sternheimer[1] shows that the presence of nuclear quadrupole moment gives rise to core excitation and this introduces a change of the quadrupole coupling. Thus we have

$$Q=(1+\Delta)Q' ,$$

in which Q is the true quadrupole moment and Q' is the apparent quadrupole moment obtained by spectroscopic means neglecting the above-mentioned effect. There are two types of modes of excitation of the core, namely angular mode ($l'\neq l$) and radial mode ($l'=l$). Corresponding to these two, we have two components of Δ, namely angular part Δ_{ang} and radial part Δ_{rad}. In the case of heavy element, the former gives rise, in general, to shielding effect and the latter to antishielding effect. In the net Δ $(=\Delta_{\text{ang}}+\Delta_{\text{rad}})$, the antishielding effect predominates for heavy elements, but we have called Δ the shielding correction.

According to Sternheimer, calculation of Δ cannot claim high accuracy at present, because Δ is very sensitive to wave functions that are chosen for the calculation. In previous work[2], therefore, we proposed to adopt semi-empirical values of Δ for spectra of heavy element.

The radial part depends on how deeply the electron penetrates the core. In the case of penetrating electron, the antishielding effect is small; if the electron is external to the core, the antishielding effect is large. If $6s$ electron is not present, we assume that Δ does not depend sensibly on the number of equivalent non-s electrons in the case of heavy elements. Under this assumption we deduced $\Delta(6p^n)=-0.1$, $\Delta(5d^n)=-0.3$ and $\Delta(4f^n)=-0.6$.

We may assume that addition of $6s$ to $5d^n$ modifies the radial part of the wave function of $5d^n$, since the $6s$ electron is penetrating and shields the potential. However $\Delta(5d6s)$ was found to be still equal to $\Delta(5d)=-0.3$. If a $5d$-electron is added to $6s5d$, it was found that $\Delta=-0.6$. This was deduced by observation of the quadrupole coupling of the level $5d^2 6s\,{}^4F_{3/2}$ in the spectrum of La I. This large change of Δ in going from $6s5d$ to $6s5d^2$ is somewhat surprising, and it would be desirable to examine the other members, namely $6s5d^2\,{}^4F_{9/2,7/2,5/2}$. The present work is devoted to such an investigation, although it was impossible to measure ${}^4F_{5/2}$ accurately.

The experimental set-up was the same as in the previous work[3]; a liquid-air cooled hollow cathode discharge tube was used as the light source, and a Fabry-Pérot etalon was used in order to resolve the hyperfine structure (hfs).

§ 2. Result of the Experiment

The result of the measurement is shown in Figs. 1 and 2. The level notation is that of Russell and Meggers[4]; the upper level of $\lambda\,5234$ is discussed later.

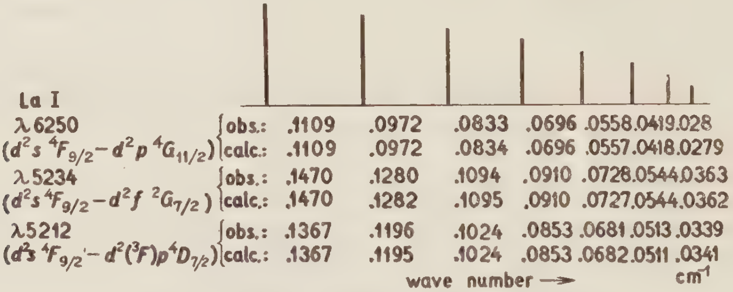

Fig. 1. Hfs. of $\lambda\,6250$, $\lambda\,5234$ and $\lambda\,5212$.

In order to make easy comparison with previous work, the quadrupole coupling constant B' defined by

$$\nu = W_0 + \frac{A}{2}K + B'K(K+1)\,,$$

$$K = F(F+1) - I(I+1) - J(J+1)$$

is used, instead of the constant B defined by

$$\nu = \nu_0 + \frac{A}{2}K + B\left[\frac{\frac{3}{8}K(K+1) - \frac{1}{2}I(I+1)J(J+1)}{I(2I-1)J(2J-1)}\right].$$

In the present work it was not possible to find lines whose hfs allowed us to determine the hfs of the final level directly. In all the lines that were studied, the constants B' of the upper levels were calculated, and then the constant B' of the lower level was determined in combination with the observed hfs.

The level $5d^26s\,{}^4F_{9/2}$ will be treated first; see Fig. 1. The initial level $5d^26p^4G_{11/2}$ of the line $\lambda\,6250$ is the most suited for calculation. The superposition of $5d^24f\,{}^4G_{11/2}$ was assumed to be negligible. Then the constant B' of this level can be calculated by use of the formula given in Table I.

The quadrupole moment Q of La^{139} was determined in previous work[2] to be 0.2_1 barn, in which the shielding correction was taken into account. Putting $\varDelta(5d) = -0.3$, $Z_d^* = 39.7$, $\zeta(5d) = 425$ and $\varDelta(6p) = -0.1$, $Z_p^* = 52$, $\zeta(6p) = 950$ and $I = 7/2$ in the usual formula that connects Q and B', we get the value of $B'(d^2p\,{}^4G_{11/2})$ that is given in Table II.

The hfs of the upper level of $\lambda\,6250$ is negligibly small, so we get from the hfs of $\lambda\,6250$

$$B'(d^2s\,{}^4F_{9/2}) - \frac{91}{66}B'(d^2p\,{}^4G_{11/2}) = -0.00013\cdot10^{-3}\ \mathrm{cm}^{-1}\,,$$

$$B'(d^2s\,{}^4F_{9/2}) = 0.0013\cdot10^{-3}\ \mathrm{cm}^{-1}\,.$$

The upper level of $\lambda\,5234$ is denoted as $1^0_{7/2}$ in ref. 4. Consideration of the energy shows that the main wave function of this level is $5d^24f\,{}^2G_{7/2}$. The level $y^4D^0_{7/2}$ (see Table III) is only 80 cm⁻¹ apart. On the other hand, the configuration $5d^26p$ is, strictly speaking, not of pure LS coupling, so it should contain $d^2({}^3F)p\,{}^4D_{7/2}$, $d^2({}^3P)p\,{}^4D_{7/2}$, $d^2p\,{}^2G_{7/2}$, etc. $5d^24f\,{}^2G_{7/2}$ is, therefore, somewhat perturbed by $y^4D^0_{7/2}$, and this explains the somewhat anomalous g-value of $1^0_{7/2}$ shown in Table III according to ref. 5.

The composition of $1^0_{7/2}$ is, at present, hard to determine, so it was tentatively assumed to consist of pure $5d^24f\,{}^2G_{7/2}$. For the $4f$-part, we assume $\varDelta_f = -0.6$, $Z_f^* = 24$, $\zeta(4f) = 443$. Then we get the value of $B'(d^2f\,{}^2G_{7/2})$ listed in Table II. The hfs of this level is negligibly small. We get, therefore, from the hfs of $\lambda\,5234$

$$B'(d^2s\,{}^4F_{9/2}) - \frac{7}{12}B'(d^2f\,{}^2G_{7/2}) = 0.0011\cdot10^{-3}\ \mathrm{cm}^{-1}\,,$$

Table I.* The matrix element of $\langle(3\cos^2\theta-1)/r^3\rangle$ of some LS-coupling wave functions of La I. $\omega=3\cos^2\theta-1$, $M_J=J$.

(A) The configuration d^2s

$$({}^4F_{9/2}|\omega/r^3|{}^4F_{9/2})=-\frac{2}{175}(42R_2'+7R_2''-24S_2)\langle r_d^{-3}\rangle\,,$$

$$({}^2G_{9/2}|\omega/r^3|{}^2G_{9/2})=-\frac{8}{175}(12R_2'+7R_2''+6S_2)\langle r_d^{-3}\rangle\,,$$

$$({}^4F_{9/2}|\omega/r^3|{}^2G_{9/2})=-\frac{4}{175}(2R_2'+7R_2''-9S_2)\langle r_d^{-3}\rangle\,,$$

$$({}^4F_{7/2}|\omega/r^3|{}^4F_{7/2})=-\frac{4}{525}(51R_2'-14R_2''-12S_2)\langle r_d^{-3}\rangle\,,$$

$$({}^2F_{7/2}|\omega/r^3|{}^2F_{7/2})=-\frac{2}{175}(32R_2'+7R_2''-14S_2)\langle r_d^{-3}\rangle\,,$$

$$({}^2G_{7/2}|\omega/r^3|{}^2G_{7/2})=-\frac{22}{525}(12R_2'+7R_2''+6S_2)\langle r_d^{-3}\rangle\,,$$

$$({}^2G_{7/2}|\omega/r^3|{}^4F_{7/2})=\frac{2}{75}(4R_2'-R_2''-3S_2)\langle r_d^{-3}\rangle\,,$$

$$({}^2F_{7/2}|\omega/r^3|{}^4F_{7/2})=-\frac{1}{1400\sqrt{3}}(302R_2'+189R_2''-304S_2)\langle r_d^{-3}\rangle\,,$$

$$({}^2F_{7/2}|\omega/r^3|{}^2G_{7/2})=-\frac{4}{175\sqrt{3}}(R_2'-14R_2''+13S_2)\langle r_d^{-3}\rangle\,.$$

(B) The configuration d^2p

$$({}^4G_{11/2}|\omega/r^3|{}^4G_{11/2})=-\frac{2}{175}(42R_2'+7R_2''-24S_2)\langle r_d^{-3}\rangle-\frac{2}{5}R'\langle r_p^{-3}\rangle\,,$$

$$(({}^3F)p\,{}^4D_{7/2}|\omega/r^3|({}^3F)p\,{}^4D_{7/2})=-\frac{4}{18375}(1919R_2'+49R_2''-1068S_2)\langle r_d^{-3}\rangle$$
$$-\frac{4}{315}(-11R'+20S)\langle r_p^{-3}\rangle\,,$$

$$(({}^3P)p\,{}^4D_{7/2}|\omega/r^3|({}^3P)p\,{}^4D_{7/2})=\frac{2}{125}(4R_2'+9R_2''+12S_2)\langle r_d^{-3}\rangle-\frac{2}{5}R'\langle r_p^{-3}\rangle\,,$$

$$(({}^3F)p\,{}^4D_{5/2}|\omega/r^3|({}^3F)p\,{}^4D_{5/2})=\frac{8}{385875}(-11689R_2'+3766R_2''+4548S_2)\langle r_d^{-3}\rangle$$
$$+\frac{2}{6615}(277R'-412S)\langle r_p^{-3}\rangle\,.$$

(C) The configuration d^2f

$$({}^2G_{7/2}|\omega/r^3|{}^2G_{7/2})=-\frac{2}{105}\langle r_d^{-3}\rangle-\frac{2}{45}\langle r_f^{-3}\rangle\,.$$

---

* R', S and R_2', R_2'', S_2 are relativity correction factors for $\langle r_p^{-3}\rangle$ and $\langle r_d^{-3}\rangle$ respectively given by Casimir[8]. In the case of La, they are $R'=1.125$, $S=1.21$, and $R_2'=1.03$, $R_2''=1.095$, $S_2=1.03$.

Table II. Quadrupole coupling constants of some levels of La I.

level	B' (10^{-3} cm^{-1})	B (10^{-3} cm^{-1})
$5d6s^2\ {}^2D_{5/2}$	0.0032291*	1.8083*
$5d6s^2\ {}^2D_{3/2}$	0.0088913*	1.4937*
$5d^26s\,{}^4F_{9/2}$	0.0012	2.42
$5d^26s\,{}^4F_{7/2}$	0.0017	2.00
$5d^26s\,{}^4F_{3/2}$	0.0062	1.04
$5d^26p\,{}^4G_{11/2}$	0.00121**	3.73
$5d^2({}^3F)6p\,{}^4D_{7/2}$	0.00137**	1.61**
$5d^2({}^3F)6p\,{}^4D_{5/2}$	0.00138**	0.773**
$5d^24f\,{}^2G_{7/2}$	0.000388**	0.456**

* According to the measurement by Ting[9].
** Calculated.

Table III. Some odd levels of La I.

level	wave number*	g (obs)**	g (LS)
$y^4D^0_{7/2}$	23303.31	1.183	1.429
$1^0_{7/2}$	23221.16	1.078	0.889
$x^4D^0_{7/2}$	25083.42	1.379	1.429
$2^0_{9/2}$	23466.85	1.12	1.111

* According to ref. 4.
** According to ref. 5.

$$B'(d^2s\,{}^4F_{9/2})=0.0013\cdot10^{-3}\ \mathrm{cm}^{-1}\,.$$

If the correction due to the superposition of $d^2({}^3F)p\,{}^4D_{7/2}$ and $d^2({}^3P)p\,{}^4D_{7/2}$ is introduced, this becomes somewhat larger, namely about $0.0014\cdot10^{-3}$ cm^{-1}.

Next we come to the upper level of λ 5212. The main wave function of this level is $5d^2(^3F)6p\,^4D_{7/2}$. The energy of the configuration d^2p is given in the article of Racah[6]. It was found that the energy of the configuration $5d^26p$ of La I can be represented roughly by (using the notation of Racah) the parameter values $A=24702$, $B=346$, $F_2=259$, $G_1=330$, $G_3=20$. The fit is not so satisfactory as we desire, probably due to the neglect of the overlap of the configuration $5d^24f$. The composition thus obtained

$$y\,^4D^0=K_1(^3F)p\,^4D^0+K_2(^3P)p\,^4D^0\ ,$$

$$K_1^2\approx0.9\ ,\qquad K_2^2\approx0.1$$

is probably not so accurate. Under these circumstances $y\,^4D^0_{7/2}$ was assumed to be pure, namely $(^3F)p\,^4D_{7/2}$. By use of the formula given in Table I and the similar procedure for getting $B'(d^2p\,^4G_{11/2})$, we get the value of $B'(y\,^4D^0_{7/2}$ listed in Table II.

The hfs of $y\,^4D^0_{7/2}$ is negligibly small. Thus we get from the hfs of λ 5212

$$B'(d^2s\,^4F_{9/2})-\frac{7}{12}B'(d^2(^3F)p\,^4D_{7/2})$$

$$=0.00018\cdot10^{-3}\,\mathrm{cm}^{-1}\ ,$$

$$B'(d^2s\,^4F_{9/2})=0.00098\cdot10^{-3}\,\mathrm{cm}^{-1}\ .$$

From the hfs of λ 6250, λ 5234 and λ 5212 we have obtained the value of $B'(d^2s\,F_{9/2})$: 0.0013, 0.0013 and 0.00098 respectively in unit of $10^{-3}\,\mathrm{cm}^{-1}$. The weighted mean value is $0.0012\cdot10^{-3}\,\mathrm{cm}^{-1}$.

According to Crawford[7], the wave function of the level $d^2s\,^4F_{9/2}$ is not pure, and he gives

$$^4F_{9/2}{}'=K_1\,^4F_{9/2}+K_2\,^2G_{9/2}\ ,$$

$$K_1=0.9976\ ,\quad K_2=0.0693\ ,$$

$$K_1^2=0.9952\ ,\quad K_2^2=0.0048\ .$$

By use of the formula

$$(^4F_{9/2}{}'|\omega/r^3|^4F_{9/2}{}')=K_1^2(^4F_{9/2}|\omega/r^3|^4F_{9/2})$$

$$+K_2^2(^2G_{9/2}|\omega/r^3|^2G_{9/2})$$

$$+2K_1K_2(^4F_{9/2}|\omega/r^3|^2G_{9/2})$$

and the formula given in Table II, we get from $B'(d^2s\,^4F_{9/2})$ the value of Q':

$$Q'=0.6\ \mathrm{barn}\ .$$

Since the true value of Q is 0.2_1 barn, we get $\Delta=-0.6_5$.

Lastly we treat λ 5177; see Fig. 2. The upper level $5d^2(^3F)6p\,^4D_{5/2}$ can be treated in the same manner as in the case of $^4D_{7/2}$. By use of the formula given in Table I, we get the value of $B'(d^2(^3F)p\,^4D_{5/2})$ listed in Table II.

From the hfs of λ 5177, the hfs of the upper level being negligibly small, we get

$$B'(d^2s\,^4F_{7/2})-\frac{10}{21}B'(d^2(^3F)p\,^4D_{5/2})$$

$$=0.0010\cdot10^{-3}\,\mathrm{cm}^{-1}\ ,$$

$$B'(d^2s\,^4F_{7/2})=0.0017\cdot10^{-3}\,\mathrm{cm}^{-1}\ .$$

The composition of $d^2s\,^4F_{7/2}$ given by Crawford[7] is

$$^4F_{7/2}{}'=K_1\,^4F_{7/2}+K_2\,^2G_{7/2}+K_3\,^2F_{7/2}\ ,$$

$$K_1=0.9966\ ,\quad K_2=-0.0313\ ,\quad K_3=-0.0762\ ,$$

$$K_1^2=0.9932\ ,\quad K_2^2=0.00098\ ,\quad K_3^2=0.0058\ .$$

We thus get from $B'(d^2s\,^4F_{7/2})$

$$Q'=0.7\ \mathrm{barn}\ (\mathrm{from}\ d^2s\,^4F_{7/2})\ .$$

This means that $\Delta=-0.7$.

In summary we have obtained $\Delta=-0.6$ and -0.7 from $5d^26s\,^4F_{9/2}$ and $^4F_{7/2}$ respectively. This is in good agreement within experimental error with $\Delta=-0.6$ obtained from $5d^26s\,^4F_{3/2}$.

Lastly we summarize in Table II the values of B' (and B) of all the levels of La I that have been measured up to the present. It also includes those of the ground $ds^2\,^2D$ term measured by Ting[9]. As remarked at the end of an article of the present author (second of ref. 2), the treatment given by Ting requires a small modification. If this modification is included in the calculation given by Ting, we get $Q(\mathrm{La}^{139})=0.21$ barn from both $ds^2\,^2D_{5/2}$ and $^2D_{3/2}$. This is just the same value as the one that the present author deduced, applying the Sternheimer correction. This shows that although we have to be satisfied with one-digit discussion of the shielding correction at present, the main idea is correct. The fact that the same value of Δ have been obtained for $J=9/2$, 7/2 and 3/2 of $d^2s\,^4F$ of La I[10] makes us convinced of the reality of Δ and makes it worthwhile to study it further. Without the shielding correction, the quadrupole moment obtained from spectroscopic

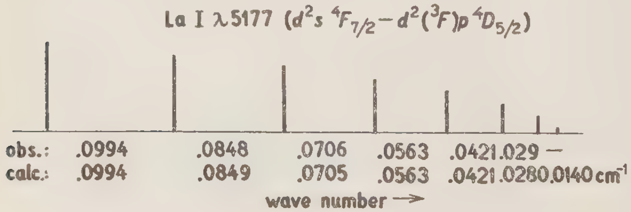

Fig. 2. Hfs. of λ 5177.

data would be physically of poor value.

The exchange of several letters with Dr. Sternheimer was very helpful in clarifying practical problems of the quadrupole shielding correction. His thoughtfulness in this matter is greatly appreciated.

References

1) R. M. Sternheimer: Phys. Rev. **95** (1954) 736; **105** (1957) 158. Sternheimer's $1/(1-R)$ is equal to our $1+\Delta$.
2) K. Murakawa and T. Kamei: Phys. Rev. **105** (1957) 671. K. Murakawa: Phy. Rev. **110** (1958) 393.
3) K. Murakawa and T. Kamei: Phys. Rev. **92** (1953) 325. K. Murakawa: J. Phys. Soc. Japan **9** (1954) 391; **10** (1955) 927; Phys. Rev. **98** (1955) 1285.
4) H. N. Russell and W. F. Meggers: J. Research Natl. Bur. Standards **9** (1932) 625.
5) G. R. Harrison, N. Rosen and J. R. McNally: J. Opt. Soc. Am. **35** (1945) 658.
6) G. Racah: Phys. Rev. **62** (1942) 438. See also J. C. Slater: Quantum Theory of Atomic Structure, Vol. II, p. 296.
7) M. F. Crawford: Phys. Rev. **47** (1935) 768.
8) H. Casimir: Verh. Teylers Tweede Genootschap, Haarlem **11** (1936).
9) Y. Ting: Phys. Rev. **108** (1957) 295.
10) G. Lührs [Z. Physik **141** (1955) 486] obtained $Q'(\mathrm{La}^{139})=0.27$ barn from the hfs of λ6250, giving us the impression as if the shielding correction for $d^2s\,^4F_{9/2}$ were not anomalous. This incorrect result is due to his error of calculation of the matrix element of $(d^2s\,^4F_{9/2}|(3\cos^2\theta-1)/r^3|d^2s\,^4F_{9/2})$.

JOURNAL OF THE PHYSICAL SOCIETY OF JAPAN, Vol. 16, No. 12, DECEMBER, 1961

Eigenvibration for the Membrane between Two Eccentric Circles

By Yûkichi NOMURA and Kasaburô HARUMI

Department of Applied Science, Tohoku University

(Received July 10, 1961)

The solutions of the wave equation for a membrane bounded by fixed two eccentric circles are obtained. By the aid of the addition theorem of the Bessel functions, the boundary condition on two circles is reduced to a set of homogeneous simultaneous linear equations, from which eigenvalues and eigenfunctions are obtained in power series of d (the distance between two centers). Some numerical results are obtained to the order of d^6 or d^4.

§1. Introduction

The solutions of the wave equation for a membrane bounded by two concentric circles are obtained easily, and the numerical values of the eigenvalues for the fixed boundary condition, that is $u=0$ on two circles have been given by several authors.[1].

When the two circles are eccentric, two approximation methods were considered, one of which is the boundary perturbation method, and the other is the method which uses the addition theorem of the Bessel functions in the problem of atomic piles[2].

The boundary perturbation method[3] has been considered by many authors, and has an advantage which enables us to treat different kinds of problems in a similar way, but it has some mathematical difficulties such as in integration, and especially in the degenerate cases.

The other method which is used in the theory of atomic piles assumes that the solution contains only $N_0(kr)$ in the Bessel functions of the second kind; this implies the symmetrical angular dependency in the neighborhood of the inner circle. In this paper, the solutions of the eccentric circles are obtained for the boundary condition $u=0$, without any assumptions such as to be made in the theory of the atomic piles. The solution is assumed to have the Bessel functions $J_n(kr)$ and $N_n(kr')$, where r or r' is the distance from the center of the outer or inner circle to any point.

Using the addition theorem, the Bessel functions of the argument kr are transformed into those of argument kr', and vice versa; then the boundary condition is reduced to solving homogeneous linear equations with infinite unknowns. In solving these equations, the eigenfunctions and the eigenvalues are expanded in powers of eccentric distance d. The eigenvalues are obtained numerically to the order of d^6 or d^4, and the eigenfunctions are also obtained to the order of d^3 or d^2, each corresponding to their eigenvalues.

§ 2. Boundary Condition and Solution

Because any kind of boundary condition may be treated in the same way, we shall treat here the Dirichlet boundary condition which is the vanishing of the wave function on two circles in Fig. 1.

Considering the fact that the Bessel functions $J_n(kr)$ have finite values and the Bessel functions of the second kind $N_n(kr)$ have a singularity at the origin, we may expand the solution by the Bessel functions $J_n(kr)$ and $N_n(kr)$ with the integral order n as

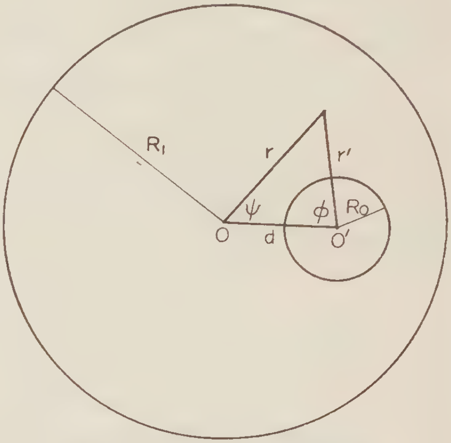

Fig. 1. Eccentric two circles.

$$u=\sum_{n=0}^{\infty}[J_n(kr)\{A_n\cos n\psi+\bar{A}_n\sin n\psi\}+N_n(kr')\{B_n\cos n\varphi+\bar{B}_n\sin n\varphi\}]\,, \tag{1}$$

where r is the distance from the center of the outer circle, and r' is the distance from the center of the inner circle to any point. A_n, $\bar{A}_n$, B_n, $\bar{B}_n$, and k are the functions of distance d between two centers, and when $d=0$, the solution (1) must coinside with that of concentric circles. As is well-known, the eigenfunctions between two concentric circles are expressed as follows

$$\begin{matrix} u_{ml}^{(c)} \\ u_{ml}^{(s)} \end{matrix}=\Big[J_m(k_{ml}r)+c_{ml}N_m(k_{ml}r)\Big]\begin{matrix}\cos\\ \sin\end{matrix}\, m\varphi\,, \tag{2}$$

where l and $m=0, 1, 2, \cdots$, and R_0 or R_1 is the radius of the inner circle or the outer circle, and k_{ml} is the l-th root of the equation

$$D_m^{(0)}=\begin{vmatrix} J_m(k_{ml}R_0) & N_m(k_{ml}R_0) \\ J_m(k_{ml}R_1) & N_m(k_{ml}R_1)\end{vmatrix}=0\,,$$

and (3)

$$c_{ml}=\frac{-J_m(k_{ml}R_0)}{N_m(k_{ml}R_0)}=\frac{-J_m(k_{ml}R_1)}{N_m(k_{ml}R_1)}\,.$$

In obtaining the solution u in Eq. (1), the terms of A_n and B_n with the even angular dependency and the terms of $\bar{A}_n$ and $\bar{B}_n$ with the odd angular dependency separate each other, and these two cases may be treated in a similar way. We treat here the solutions with the even angular dependency of $\cos n\varphi$ and $\cos n\psi$, and exclude the terms with $\bar{A}_n$ and $\bar{B}_n$ in Eq. (1).

Using the addition theorem of the Bessel function[4], it follows from Eq. (1) that

$$\begin{aligned} u &= \sum_{n=0}^{\infty}\Big[A_nJ_n(kr)\cos n\psi+B_n\sum_{m=0}^{\infty}\Big\{\frac{(2)_m}{2}N_m(kr)(J_{m+n}(kd)+(-1)^mJ_{n-m}(kd))\cos m\psi\}] \\ &= \sum_{n=0}^{\infty}\Big[A_n\sum_{m=0}^{\infty}\Big\{\frac{(2)_m}{2}J_m(kr')(J_{m+n}(kd)+(-1)^mJ_{n-m}(kd))\cos m\varphi\Big\}+B_nN_n(kr')\cos n\varphi\Big]\,, \end{aligned} \tag{4}$$

where

$$
\begin{aligned}
(2)_m &= 1 \qquad \text{for} \quad m=0\,, \\
&= 2 \qquad \text{for} \quad \neq 0\,.
\end{aligned}
$$

The Dirichlet boundary condition is

$$u=0\,, \qquad \text{on} \quad r=R_1\,, \quad r'=R_0\,. \tag{5}$$

It follows from Eqs. (4) and (5) that

$$
\begin{aligned}
&A_m J_m(kR_1)+\sum_{n=0}^{\infty}\left[B_n\frac{(2)_m}{2}N_m(kR_1)(J_{n+m}(kd)+(-1)^m J_{n-m}(kd))\right]=0\,, \\
&\sum_{n=0}^{\infty}\left[A_n\frac{(2)_m}{2}J_m(kR_0)(J_{n+m}(kd)+(-1)^m J_{n-m}(kd))\right]+B_m N_m(kR_0)=0\,,
\end{aligned}
\tag{6}
$$

where $m=0, 1, 2, \cdots$.

These equations are a set of homogeneous simultaneous linear equations which have the unknown constants A_m and B_m. In order that they may be solved, the determinant of the coefficient must be zero. That is

$$
\Delta(k,\ d)
=\begin{vmatrix}
J_0(R_1) & N_0(R_1)\times J_0(d) & 0 & N_0(R_1)\times J_1(d) & 0 & N_0(R_1)\times J_2(d)\cdots\cdot \\
J_0(R_0)\times J_0(d) & N_0(R_0) & J_0(R_0)\times J_1(d) & 0 & J_0(R_0)\times J_2(d) & 0\ \cdots\cdot \\
0 & 2N_1(R_1)\times J_1(d) & J_1(R_1) & N_1(R_1)\times (J_2(d)-J_0(d)) & 0 & N_1(R_1)\times (J_3(d)-J_1(d))\cdots\cdot \\
2J_1(R_0)\times J_1(d) & 0 & J_1(R_0)\times (J_2(d)-J_0(d)) & N_1(R_0) & J_1(R_0)\times (J_3(d)-J_1(d)) & 0\ \cdots\cdot \\
0 & 2N_2(R_1)\times J_2(d) & 0 & N_2(R_1)\times (J_3(d)-J_1(d)) & J_2(R_1) & N_2(R_1)\times (J_4(d)+J_0(d))\cdots\cdot \\
2J_2(R_0)\times J_2(d) & 0 & J_2(R_0)\times (J_3(d)-J_1(d)) & 0 & J_2(R_0)\times (J_4(d)+J_0(d)) & N_2(R_0)\cdots\cdot \\
\cdots & \cdots & \cdots & \cdots & \cdots & \cdots \\
\cdots & \cdots & \cdots & \cdots & \cdots & \cdots
\end{vmatrix}=0
\tag{7}
$$

where R_1, R_0, and d means kR_1, kR_0, and kd.

The equation (7) is the condition which determine k as the function of the displacement d for fixed values of R_1 and R_0. When the value k is determined, then we can determine the unknown A_m and B_m corresponding to the value k.

§ 3. Successive Determination of Eigenvalue

The eigenvalue k^2 may be determined from Eq. (7) for any values of d. But we illustrate here the successive approximation method to determine k for small values of d, starting from the l-th root k_{ml} of the concentric circles. In the case of $d=0$, the determinant $\Delta(k,\ d)$ becomes

$$\Delta(k,\ 0)=D_0^{(0)}(k)\cdot D_1^{(0)}(k)\cdot D_2^{(0)}(k)\ \cdots\,, \tag{8}$$

where $D_m^{(0)}(k)$ is the minor determinant with the diagonal elements of $\Delta(k,\ d)$ for $d=0$ and is given in Eq. (3), and the superscript (0) means the zeroth order of d.

The root k_{ml} in Eq. (3) satisfies $D_m^{(0)}(k)=0$, and in consequence satisfies $\Delta(k,\ 0)=0$.

(A) The case of $k_0=k_{0l}$

When $d\neq 0$, k is the function of d, and as is shown in Appendix, k is the even function of d, k may be expanded as

$$k=k_0+k_2d^2+k_4d^4+k_6d^6+\cdots , \tag{9}$$

and we illustrate here that the coefficients k_2, k_4, etc. are obtained successively as the function of k_0, and we take k_{0l}, the l-th root of $D_0^{(0)}(k)$, as k_0.

In order to obtain k_2, k_4, etc., we introduce here a new minor determinant $\Delta_{2m,2m}$ which is the minor determinant with the first $2m$ rows and $2m$ columns in $\Delta(k, d)$, and as $m\to\infty$ $\Delta_{2m,2m}$ becomes $\Delta(k, d)$.

In the determinant $\Delta_{2m,2m}$, each element contains the Bessel functions $J_m(kR_0)$, $N_m(kR_1)$, $J_m(kR_1)$, $N_m(kR_1)$ and $J_m(kd)$, and as k is the function of d and moreover $J_m(kd)$ contains d explicitly, we may expand the Bessel functions in powers of d.

Using these expansions, we expand each element of $\Delta_{2m,2m}$ in powers of d, and in consequence the expansion of $\Delta_{2m,2m}$ in powers of d is obtained as

$$\Delta_{2m,2m}=\Delta^{(0)}_{2m,2m}+\Delta^{(2)}_{2m,2m}d^2+\Delta^{(4)}_{2m,2m}d^4+\cdots , \tag{10}$$

where

$$\Delta^{(0)}_{2m,2m}=D_0^{(0)}(k_0)\cdot D_1^{(0)}(k_0)\cdots D^{(0)}_{m-1}(k_0) ,$$

hence k_{0l} satisfies $\Delta^{(0)}_{2m,2m}=0$ for any values of m.

(a) Determination of k_2

As $\Delta^{(2)}_{44}(k_0, k_2)$ in Eq. (10) is the coefficient of order d^2, $\Delta^{(2)}_{44}(k_0, k_2)$ contains only k_0 and k_2, we may determine k_2 from the equation $\Delta^{(2)}_{44}(k_0, k_2)=0$ as

$$k_2=\frac{k_0^2\bar{D}}{2D} , \tag{11}$$

where

$$\bar{D}=J_0(R_1)N_1(R_1)J_0(R_0)N_1(R_0)+J_1(R_0)N_0(R_0)N_0(R_1)J_1(R_1)$$
$$-\{J_1(R_1)N_1(R_0)+J_1(R_0)N_1(R_1)\}J_0(R_0)N_0(R_1) ,$$

$$D=\{J_1(R_1)N_1(R_0)-N_1(R_1)J_1(R_0)\}$$
$$\times[R_1\{J_0(R_0)N_1(R_1)-N_0(R_0)J_1(R_1)\}+R_0\{N_0(R_1)J_1(R_0)-J_0(R_1)N_1(R_0)\}] ,$$

and $R_0=k_0R_0$, and $R_1=k_0R_1$ in the argument of the Bessel functions.

As is shown in Eq. (7), the elements of Δ_{66} which contain the terms $J_2(d)$ contribute to the same or the higer order of d^4, and the elements which contain $J_3(d)-J_1(d)$ contribute to $\Delta^{(2)}_{66}$ only in the case when these elements are combined to $D_0^{(0)}=\Delta^{(0)}_{22}$, and the elements which contain $J_1(d)$ contribute to $\Delta^{(2)}_{66}$ only when it is combined to $D_2^{(0)}(k)$.

Hence the values k_0 and k_2 which are determined from $D_0^{(0)}$ and $\Delta^{(2)}_{44}=0$ satisfies

$$\Delta^{(2)}_{66}=\Delta^{(2)}_{44}\cdot D_2^{(0)}+D_0^{(0)}\cdot\bar{\Delta}^{(2)}_{66}(k_0, k_2)=0 , \tag{12}$$

where $\bar{\Delta}^{(2)}_{66}(k_0, k_2)$ means the cofactor of $\Delta^{(0)}_{22}$ in the determinant $\Delta^{(2)}_{66}$.

In a similar way $\Delta^{(2)}_{2m,2m}$ vanishes for any $m\geqq 4$, and in consequence $\Delta(k, d)$ vanishes to the order of d^2.

(b) Determination of k_4

The determinants $\Delta^{(0)}_{66}$ and $\Delta^{(2)}_{66}$ in Eq. (10) vanish for the above determined k_0 and k_2 as is proved in (a), whereas $\Delta^{(4)}_{66}$ contain only k_0, k_2, and k_4, because $\Delta^{(4)}_{66}$ is the coefficient of d^4 and the parts of the element which contain k_m for $m\geqq 3$ is a higher order of d^4.

We may determine k_4 as the function of k_0 and k_2 from the equation $\Delta^{(4)}_{66}(k_0, k_2, k_4)=0$, which is the linear equation of k_4. As in the case of (a), k_4 safisfies $\Delta^{(4)}_{2m,2m}=0$ for $m\geqq 4$ and $\Delta(k, d)$ vanishes to the order of d^4.

(c) Determination of k_{2m} for $m\geqq 3$

Because the determinant $\Delta^{(2m)}_{2m+2,2m+2}$ does not contain the coefficients k_{2p} for $p>m$, we may obtain k_{2m} as a function of $k_0, k_2, \cdots,$ and k_{2m-2}, from the equation of $\Delta^{(2m)}_{2m+2,2m+2}=0$, which results in $\Delta^{(2m)}_{2n2n}=0$ for $n>m$ like in the case of $m=1$ and 2.

The expansion of $k=k_0+k_2d^2+k_4d^4\cdots+k_{2m}d^{2m}$ satisfies the equations $\Delta^{(0)}_{2n2n}=\Delta^{(2)}_{2n2n}=\cdots=\Delta^{(2m)}_{2n2n}=0$, for $n\to\infty$ and we may say that the equation $\Delta(k, d)=0$ is satisfied to the order of d^{2m}.

(B) The case of $k_0=k_{ml}$ $(m\neq0)$

We consider next the case when the value of $k=k_0+k_2d^2+\cdots$ is derived from the root $k_0=k_{ml}$ $(m\neq0)$.

Likewise in the case of (A), we start from the value $k_0=k_{ml}$ $(m\neq0)$, and k_2 may be obtained from the principal minor determinant with 6 rows and 6 columns which has two rows attached to each above and below and two columns each on the right and left of the determinant $D_m^{(0)}(k)$ in $\Delta(k, d)$.

Further we may obtain successively $k_4, \cdots,$ and k_{2r}, and the equation $\Delta(k, d)=0$ is satisfied to the order of d^{2r}. When we do not have two rows above and two columns at the left to be attached, the enlarging of the determinant must be continued by attaching two rows below and two columns at the right.

§ 4. Eigenfunction

The eigenfunction u is obtained from the equation (1). In case of the concentric circle, the coefficients A_n and B_n in Eq. (1) are determined by Eq. (3), but in case of the eccentric circle these coefficients become the function of the displacement d, and we may expand these coefficients in powers of d as

$$A_n=d^h(A_n{}^{(h)}+A_n{}^{(h+2)}d^2+A_n{}^{(h+4)}d^4+\cdots)\,, \qquad B_n=d^h(B_n{}^{(h)}+B_n{}^{(h+2)}d^2+B_n{}^{(h+4)}d^4+\cdots)\,. \tag{14}$$

Substituting these coefficients into Eq. (6), and using the expansion of the Bessel functions in powers of d which are given in (A) of § 3, and equating the coefficient of the same order of d as zero, we may determine A_n and B_n.

For simplicity, as the Bessel functions in Eq. (6) are the elements of $\Delta(k, d)$, we may express the element in $\Delta(k, d)$ with the i-th row and j-th column as a_{ij}, and expand a_{ij} in powers of d as

$$a_{2m+1,2j+2}=d^{|m-j|}\sum_{p=0}^{\infty}a^{(|m-j,|+2p)}_{2m+1,2j+2}d^{2p}\,, \qquad a_{2m+2,2j+1}=d^{|m-j|}\sum_{p=0}^{\infty}a^{(|m-j|+2p)}_{2m+2,2j+1}d^{2p}\,. \tag{15}$$

When we start from the root $k_0=k_{il}$ of the i-th equation $D_l{}^{(0)}(k_0)=0$ in Eq. (3), it is easily found that the lowest orders h of A_n and B_n in Eq. (14) are given as $|n-i|$, and reflecting Eq. (15) and the fact that the diagonal elements have the zeroth order of d, we have the following equation of order $d^{2s+|m-i|}$ (s and $m=0, 1, 2\cdots$)

$$\begin{aligned}&\sum_l\,[A_m{}^{(2l+|m-i|)}a^{(2s-2l)}_{2m+1,2m+1}+\sum_j\,(B_j{}^{(2l+|j-i|)}a^{(2s+|m-i|-|j-i|-2l)}_{2m+1,2j+2})]=0\,,\\&\sum_l\,[\sum_j\,(A_j{}^{(2l+|j-i|)}a^{(2s+|m-i|-|j-i|-2l)}_{2m+2,2j+1})+B_m{}^{(2l+|m-i|)}a^{(2s-2l)}_{2m+2,2m+2}]=0\,.\end{aligned}\tag{16}$$

These equations determine successively $A_n{}^{(h+2s)}$ and $B_n{}^{(h+2s)}$ from the lowest order of d, in Eq. (16) l and j are given according to the two cases of $m>i$ and $m<i$

(1) The case of $m>i$

$$\begin{aligned}&s+m\geqq j\geqq i-s \quad \text{or} \quad 0&&\\&\qquad l\leqq s-(j-m) && \text{for}\quad j\geqq m\,,\\&\qquad l=s && \text{for}\quad m\geqq j\geqq i\,,\\&\qquad l\leqq s-(i-j) && \text{for}\quad j\leqq i\,,\end{aligned}\tag{17}$$

(2) The case of $m<i$

$$
\begin{aligned}
&s+i\geqq j\geqq m-s \quad \text{or} \quad 0 \\
&\quad l\leqq s-(j-i) && \text{for} \quad j\geqq i\,, \\
&\quad l\leqq s && \text{for} \quad i\geqq j\geqq m\,, \\
&\quad l\leqq s-(m-j) && \text{for} \quad j\leqq m\,,
\end{aligned}
\tag{18}
$$

§ 5. Numerical Calculation and Conclusion

By the aid of the addition theorem of the Bessel functions, the solution of the wave equation bounded by two eccentric circles has been obtained by the solving of a system of the homogeneous linear equations.

Though it may be possible numerically to obtain the eigenvalues k and the corresponding eigenfunctions for large values of d by the use of the electronic computer, we obtain here the solution explicitely in powers of the distance d of two centers, when d is small.

Numerical solutions are obtained for three cases, one is the case of $k_0=k_{01}$ when $d=0$, and two other cases are for $k_0=k_{11}$ of $u_{11}^{(c)}$* and $u_{11}^{(s)}$*. We illustrate here the computed values only in the case of $k_0=k_{01}$ in Table I, and omitted the values for two other cases, in which k is given to the order of d^4, and omitted the values for three eigenfunctions, in which the eigenfunctions are obtained to the order of d^3 or d^2, each corresponding to their eigenvalue.

Table I. Values of k_0, k_2, k_4, and k_6, in case of $k_0=k_{01}$ of the concentric circle; R_0 or R_1 is the radius of inner or outer circle.

R_1/R_0	k_0	k_2	k_4	k_6
5	0.7635	-0.192	0.528	-1.17
10	0.3312	-8.35×10^{-3}	1.63×10^{-3}	-3.37×10^{-4}
19	0.1612	-6.68×10^{-4}	1.88×10^{-5}	-6.82×10^{-7}
30	0.09903	-1.23×10^{-4}	9.92×10^{-7}	-1.05×10^{-8}
39	0.07473	-4.70×10^{-5}	1.90×10^{-7}	-1.01×10^{-9}

* k_0 and d mean k_0R_0 and d/R_0 in Eq. (9).

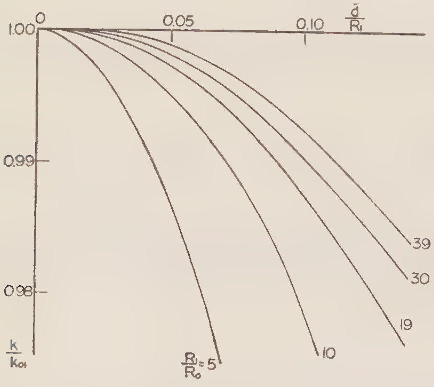

Fig. 2. Shifts of k/k_{01} of $u_{01}^{(c)}$ for d/R_1. Numbers attached to the curves indicate the values of R_1/R_0. Calculated from Table I.

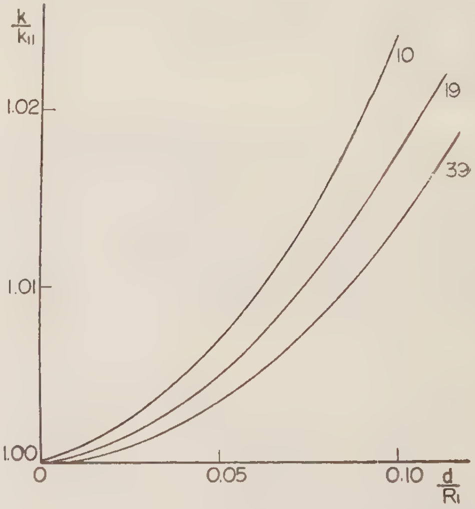

Fig. 3. Shifts of k/k_{11} of $u_{11}^{(c)}$ for d/R_1.

In Figs. 2, 3, and 4 values of k/k_0 for d/R_1 are given for the above three cases, and the eigenfunction with $d/R_0=1$ are shown in Fig. 5, and it is compared to $u_{01}^{(c)}$ of the concentric case with $R_1/R_0=19$.

---

*) $u_{11}^{(c)}$ and $u_{11}^{(s)}$ are the eigenfunctions with $\cos\varphi$ and $\sin\varphi$ in Eq. (2).

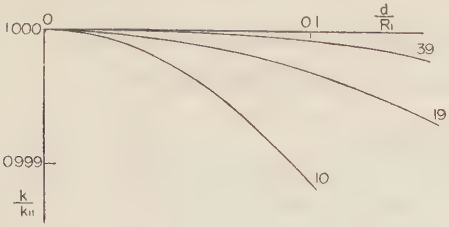

Fig. 4. Shifts of k/k_{11} of $u_{11}^{(s)}$ for d/R_1.

From these figures and Table I, it may be concluded that

(1) In case of concentric circles the eigenvalues for the eigenfunctions with $\cos m\varphi$ and $\sin m\varphi$ are degenerate, but as is shown in Figs. 3 and 4 the degeneracy is removed and the eigenvalues separate, as the inner circle is displaced.

(2) In the case of $u_{11}^{(s)}$ in Fig. 4 when the inner circle is displaced along the nodal line, the shift of k from k_0 is not so large as in the case of $u_{11}^{(c)}$ in Fig. 3, when the inner circle is displaced in a direction perpendicular to the nodal line.

(3) From Table I we see that the approximation to the order of d^2 overestimates the variation of k from k_0.

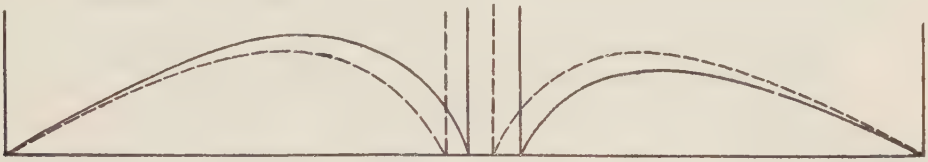

Fig. 5. Amplitudes of the eigenfunctions on the x-axis; dashed curve are of $u_{01}^{(c)}$ for concentric circle, real line are for eccentric circle, each is normalized by $A_0=1$ in Eqs. (1) and (4); $d/R_0=1$, $R_1/R_0=19$.

Appendix

Only the elements $a_{l,4n-l+1}$ ($n=1, 2, \cdots, 4n\leqq l\leqq 1$) in $\varDelta(k, d)$ contains $J_{2m+1}(d)$ of odd order, and $a_{l,4n-l+1}$ change their sign in $\varDelta(k, -d)$ as

$$\begin{vmatrix} a_{11} & a_{12} & 0 & -a_{14} & 0 & a_{16} \cdots\cdot \\ a_{21} & a_{22} & -a_{23} & 0 & a_{25} & 0 \;\; \cdots\cdot \\ 0 & -a_{32} & a_{33} & a_{34} & 0 & -a_{36} \cdots\cdot \\ -a_{41} & 0 & a_{43} & a_{44} & -a_{45} & 0 \;\; \cdots\cdot \\ 0 & a_{52} & 0 & -a_{54} & a_{55} & a_{56} \cdots\cdot \\ a_{61} & 0 & -a_{63} & 0 & a_{65} & a_{66} \cdots\cdot \\ \cdots & \cdots & \cdots & \cdots & \cdots & \cdots \\ \cdots & \cdots & \cdots & \cdots & \cdots & \cdots \end{vmatrix}.$$

The value of $\varDelta(k, -d)$ does not change its sign, when the elements in the both $4n+1$ th and $4n+2$ th rows of $\varDelta(k, -d)$ are multiplied at the same time by -1, or the elements in the both $4n+1$ th and $4n+2$ th columns ($n=0, 1, 2 \cdots$), then we have $\varDelta(k, -d)=\varDelta(k, d)$.

Therefore the function $k(d)$ which is obtained from $\varDelta(k, d)=0$, and the function $k(-d)$ which is obtained from $\varDelta(k, -d)=0$ are exactly the same. Hence k is the even function of d.

References

1) E. Jahnke and F. Emde: *Tables of Functions* (Dover Publications, New York, 1945) 204 p. H. B. Dwight: J. Math. Phys. **27** (1948) 84. S. Chandrasekhar and D. Elbest: Proc. Camb. Phil. Soc. **50** (1954) 266.

2) S. Glasstone and M. C. Edlund: *The Elements of Nuclear Reactor Theory*. (D. Van Nostrand Co., New York, 1952) 284 p. H. L. Garabedian: Control Rod Theory for a Cylindrical Reactor AECD 3666 (United State Atomic Energy Commission, 1950).

3) P. M. Morse and H. Feshbach: *Methods of Theoretical Physics* (Mc-Graw Hill Co., New York, 1953) Vol. 2 1038 p. T. Saito: J. Phys. Soc. Japan, **15** (1960) 2069.

4) G. N. Watson: *Theory of Bessel Functions* (Cambridge University Press, 1958) 360 p.

JOURNAL OF THE PHYSICAL SOCIETY OF JAPAN Vol. 16, No. 12, DECEMBER, 1961

Two-Dimensional Flow of a Weakly Conducting Gas Past a Plane Wall Containing a Magnetic Dipole

By Shigeki MORIOKA

Department of Physics and Mathematics, Faculty of Science and Engineering, Ritumeikan University, Kyoto

(Received July 15, 1961)

In order to find some effects of compressibility on the flow of a conducting gas past a magnetized body, the two-dimensional, steady flow of a weakly conducting gas past a plane wall containing a magnetic dipole, the axis of which is placed parallel to the wall, is considered on the basis of the small perturbation theory. The boundary value problem in terms of perturbation velocity is formulated and solved for subsonic and supersonic flows. In subsonic flow of a comparatively small Mach number, the drag and moment depend only on a parameter N, where $N=R_mS$, R_m is the magnetic Reynolds number and S is the pressure number. In supersonic flow, the velocity distribution on the wall is not monotonus, and becomes more irregular as the Mach number approaches unity.

§ 1. Introduction

The behavior of a conducting fluid past a magnetized body has been investigated for the case of flow past a sphere and a circular cylinder containing a magnetic dipole both for perfect fluid1) and for viscous fluid2). The aim of the present paper is to understand the behavior of a compressible, inviscid, conducting fluid past a plane wall containing a magnetic dipole. The problem is presented as follows: The wall surface is placed along $y=1$ in the Cartesian coordinates; the fluid occupies the region $y>1$ and has a uniform velocity U_∞ parallel to the x-axis at infinity upstream ($x\to-\infty$); the magnetic dipole is placed at the origin with its axis along the x-axis. In the present paper, it is assumed that $R_m \ll N \ll 1$. This means that the interaction between the flow and the magnetic field is weak and that the distortion of the magnetic field due to the flow can be neglected. In Sec. 2, the corresponding boundary value problem in terms of perturbation velocity is formulated and the expressions for the drag and moment are given. The solution of this boundary value problem is obtained in Secs. 3 and 4 for subsonic and supersonic flow, respectively. There are also discussed the velocity distribution on the wall and the drag and moment. The special type of magnetic field assumed in the present paper has been chosen for the sake of physical interest and simplicity of calculation, but it does not mean any essential restriction on our analysis.

§ 2. Fundamental relations

The basic equations to be solved are

$$\left.\begin{aligned} \operatorname{div}(\rho\boldsymbol{v})&=0\\ \rho(\boldsymbol{v}\cdot\operatorname{grad})\boldsymbol{v}&=-\operatorname{grad}p+\boldsymbol{j}\times\mu\boldsymbol{H}\\ \operatorname{div}\boldsymbol{H}&=0\\ \boldsymbol{j}=\operatorname{rot}\boldsymbol{H}&=\sigma(\boldsymbol{E}+\boldsymbol{v}\times\mu\boldsymbol{H})\\ \rho(\boldsymbol{v}\cdot\operatorname{grad})p-\gamma p(\boldsymbol{v}\cdot\operatorname{grad})\rho&=(\gamma-1)\sigma^{-1}\rho\boldsymbol{j}^2 \end{aligned}\right\}\qquad(1)$$

where $\boldsymbol{v}$, $\boldsymbol{H}$, $\boldsymbol{j}$, p and ρ denote the velocity, the magnetic field intensity, the current density, the pressure and the fluid density, respectively; σ, μ, γ denote the electric conductivity, the permeability and the ratio of the specific heats, and all these are assumed to be constant everywhere. For two-dimensional motion, the electric field $\boldsymbol{E}$ is constant throughout the field and may be assumed to be zero. Let us denote the velocity, the pressure and the fluid density at infinity upstream by U_∞, p_∞ and ρ_∞, respectively, and the magnetic field intensity at the point $(0, 1)$ by h_0. Then $\boldsymbol{v}$, $\boldsymbol{H}$, p and ρ may be made non-dimensional as follows,

$$\left.\begin{aligned} \boldsymbol{v}&=U_\infty\boldsymbol{v}'\,, & \boldsymbol{H}&=h_0\boldsymbol{H}'\,,\\ p&=p_\infty p'\,, & \rho&=\rho_\infty\rho'\,, \end{aligned}\right\}\qquad(2)$$

Also the space coordinates will be made non-dimensional by taking the distance L (assumed unity) from the x-axis to the wall surface as the unit of length. Then, Eqs. (1) become

$$\operatorname{div}(\rho'\boldsymbol{v}')=0\qquad(3)$$

$$\rho'(\boldsymbol{v}'\cdot\operatorname{grad})\boldsymbol{v}'$$

$$=-\frac{1}{\gamma M^2}\,\mathrm{grad}\,p'+N(\boldsymbol{v}'\times\boldsymbol{H}')\times\boldsymbol{H}' \tag{4}$$

$$\mathrm{div}\,\boldsymbol{H}'=0 \tag{5}$$

$$\mathrm{rot}\,\boldsymbol{H}'=R_m(\boldsymbol{v}'\times\boldsymbol{H}') \tag{6}$$

$$\rho(\boldsymbol{v}'\cdot\mathrm{grad})p'-\gamma p'(\boldsymbol{v}'\cdot\mathrm{grad})\rho' =\gamma(\gamma-1)M^2N(\boldsymbol{v}'\times\boldsymbol{H}')^2 \tag{7}$$

where $M=(\rho_\infty U_\infty^2/\gamma p_\infty)^{1/2}$, $R_m=\sigma\mu U_\infty L$ and $S=\mu h_0^2/\rho_\infty U_\infty^2$ denote the Mach number, the magnetic Reynolds number and the pressure number, respectively, and $N=R_mS$. Since it is assumed that

$$R_m \ll N \ll 1 \tag{8}$$

the right-hand side of Eq. (6) can be neglected and then $\boldsymbol{H}'$ satisfies Laplace's equation by Eqs. (5) and (6). (Strictly speaking, the distortion of the magnetic field at a great distance cannot be neglected except for the limit $R_m\to 0$. In such a region, however, the field of a magnetic dipole is sufficiently weak and the influence of the distorted magnetic field upon the flow may be neglected.) We can also put

$$\boldsymbol{v}'=(1+u', v'),\quad p'=1+\Delta p,\quad \rho'=1+\Delta\rho \tag{9}$$

where u', v', Δp and $\Delta\rho$ are small quantities of the order of N. Substituting Eqs. (9) into Eqs. (3), (4) and (7) and taking into account that all perturbation quantities vanish at infinity upstream, we obtain the equations in terms of the perturbation velocity:

$$\left.\begin{aligned}(1-M^2)\frac{\partial u'}{\partial x}+\frac{\partial v'}{\partial y}&=\gamma M^2NH_y^2\\ \frac{\partial u'}{\partial x}-\frac{\partial v'}{\partial y}&=N\Big(H_xH_y+\frac{\partial}{\partial y}\int_{-\infty}^{x}H_y^2dx\Big)\end{aligned}\right\} \tag{10}$$

where H_x and H_y denote the components of the undisturbed magnetic field. For the magnetic dipole considered here, we have

$$H_x=\frac{x^2-y^2}{(x^2+y^2)^2},\qquad H_y=\frac{2xy}{(x^2+y^2)^2} \tag{11}$$

It is assumed here that the wall has the some permeability as the fluid. On the other hand, u' and v' have to satisfy the following conditions:

$$\left.\begin{aligned}&v'=0 &&\text{on } y=1\,,\\ &u'=v'=0 &&\text{as } x\to-\infty\,,\\ &u',\ v' &&\text{finite as } x \text{ or } y\to\infty\end{aligned}\right\} \tag{12}$$

Eqs. (10) and (12) represent the boundary value problem in the present paper.

Once u' and v' are found, the pressure distribution on the wall is obtained by the formula:

$$\Delta p=\gamma M^2\Big(-u'+N\int_{-\infty}^{x}H_y^2dx\Big)_{y=1} \tag{13}$$

which can be derived by integrating the modified equation of motion:

$$-\frac{1}{\rho'}\,\mathrm{grad}\,p'=\gamma M^2\Big\{\frac{1}{2}\,\mathrm{grad}\,\boldsymbol{v}'^2-\boldsymbol{v}'\times\mathrm{rot}\,\boldsymbol{v}'-\frac{N}{\rho'}(\boldsymbol{v}'\times\boldsymbol{H}')\times\boldsymbol{H}'\Big\}$$

along the wall surface. The non-dimensional drag on the wall, due to the reaction of the Lorentz force on the fluid, is found by the formula:

$$D=-N\int_1^\infty dy\int_{-\infty}^{\infty}\{(\boldsymbol{v}'\times\boldsymbol{H}')\times\boldsymbol{H}'\}\boldsymbol{i}dx=-N\int_1^\infty dy\int_{-\infty}^{\infty}\{(1+u')H_y-v'H_x\}H_ydx \tag{14}$$

where $\boldsymbol{i}$ denots the unit vector parallel to the x-axis. On the other hand, the non-dimensional moment about the origin is found by the formula:

$$\begin{aligned}\mathfrak{M}&=-N\int_1^\infty dy\int_{-\infty}^{\infty}\boldsymbol{r}\times\{(\boldsymbol{v}'\times\boldsymbol{H}')\times\boldsymbol{H}'\}\boldsymbol{k}dx\\ &=-N\int_1^\infty dy\int_{-\infty}^{\infty}(xH_x+yH_y)\{(1+u')H_y-v'H_x\}dx\end{aligned} \tag{15}$$

where $\boldsymbol{r}$ denotes the position vector and $\boldsymbol{k}$ the unit vector parallel to the z-axis.

§ 3. Solution for subsonic flow

For subsonic flow, $1-M^2=\alpha^2>0$. By the transformations:

$$\xi=x/\alpha,\qquad \eta=y-1,\qquad u=\alpha u',\qquad v=v' \tag{16}$$

Eqs. (10) become

$$\left.\begin{aligned}\frac{\partial u}{\partial \xi}+\frac{\partial v}{\partial \eta}&=\gamma M^2 N H_y^2\\ \frac{\partial v}{\partial \xi}-\frac{\partial u}{\partial \eta}&=\alpha N\Big(H_x H_y+\frac{\partial}{\partial y}\int_{-\infty}^{x} H_y^2\,dx\Big)\end{aligned}\right\}\tag{17}$$

Furthermore, by introducing the complex expressions

$$z=\xi+i\eta,\qquad \bar{z}=\xi-i\eta,\qquad w=u-iv\tag{18}$$

the above equations can be reduced to a single differential equation:

$$\begin{aligned}2i\frac{\partial w}{\partial \bar{z}}&=\left(\frac{\partial v}{\partial \xi}-\frac{\partial u}{\partial \eta}\right)+i\left(\frac{\partial u}{\partial \xi}+\frac{\partial v}{\partial \eta}\right)\\ &=\alpha N\left(H_x H_y+\frac{\partial}{\partial y}\int_{-\infty}^{x} H_y^2\,dx\right)+i\gamma M^2 N H_y^2\equiv N\varphi(z,\bar{z})\end{aligned}\tag{19}$$

Integrating the both sides with respect to $\bar{z}$, and putting

$$\int \varphi(z,\bar{z})d\bar{z}\equiv F(z,\bar{z})\tag{20}$$

we obtain

$$2iw=2v+2ui=N\{F(z,\bar{z})+f(z)\}\tag{21}$$

where $f(z)$ is an arbitrary analytic function of z. Transforming back to the original variables, we obtain the solution in the form

$$\left.\begin{aligned}u'&=\frac{N}{2\alpha}\Im\{F(z,\bar{z})+f(z)\}=u'(x,y)\\ v'&=\frac{N}{2}\Re\{F(z,\bar{z})+f(z)\}=v'(x,y)\end{aligned}\right\}\tag{22}$$

where the function $f(z)$ is regular for $y>1$ and can be determined by the shape of the wall. Conversely, by giving a function of z regular for $y>1$, the corresponding flow field and the shape of the wall may be found. Now, in order to find the function $f(z)$, we take the transformation

$$\zeta=re^{i\theta}=\frac{\alpha z-i}{\alpha z+i}\tag{23}$$

This is clearly the conformal transformation which maps the upper half of the z-plane onto the inside of the unit circle, say K, in the ζ-plane. If Eq. (23) is solved for z, we get

$$z=\xi+i\eta=\frac{-2r\sin\theta}{\alpha(1+r^2+2r\cos\theta)}+i\frac{1-r^2}{\alpha(1+r^2+2r\cos\theta)}\tag{24}$$

On the unit circle K, we therefore obtain

$$z=\bar{z}=-\frac{\sin\theta}{\alpha(1-\cos\theta)}=-\frac{1}{\alpha}\cot\frac{\theta}{2}\tag{25}$$

Hence, the condition on the wall (i. e. $v'=0$ on $\eta=0$) can be written a

$$\Re\{f(\zeta)\}_K=-\Re\{F(z,\bar{z})\}_K\equiv\psi(\theta)\tag{26}$$

Thus the function $f(\zeta)$ can be expressed as

$$f(\zeta)=i\Im\{f(o)\}+\frac{1}{2\pi}\int_0^{2\pi}\psi(\theta)\frac{e^{i\theta}+\zeta}{e^{i\theta}-\zeta}d\theta\tag{27}$$

Transforming back to the original variables by the relation:

$$\zeta=\frac{\alpha z-i}{\alpha z+i}=1-\frac{2(1+\alpha y-\alpha)}{x^2+(1+\alpha y-\alpha)^2}-i\frac{2x}{x^2+(1+\alpha y-\alpha)^2} \tag{28}$$

the final expression for $f(z)$ is obtained.

For the magnetic dipole considered here, $F(z, \bar{z})$ can be obtained as follows:

$$\begin{aligned} F(z, \bar{z})=&-\frac{4\alpha}{(z-\bar{z}+2i)^3}\left(\frac{\pi}{2}+\tan^{-1}\tau\right) \\ &+\frac{1}{2\alpha(z+i)^3}\left(M^2\tan^{-1}\tau+3\tau-\frac{2\tau}{1+\tau^2}\right)-\frac{i}{2\alpha^2(z+i)^3}\left(\tau^2+\frac{1+\alpha^2}{1+\tau^2}\right) \\ &+\frac{\gamma M^4}{2\alpha^3(z+i)^3}\left\{\tan^{-1}\tau-\frac{\tau(1-\tau^2)}{(1+\tau^2)^2}+\frac{8(1+\alpha^2)}{3M^2}\frac{\tau^3}{(1+\tau^2)^3}\right\} \\ &+\frac{4\gamma M^2 i}{3\alpha^2(z+i)^3}\left\{\frac{1}{(1+\tau^2)^2}+\frac{2\tau^2}{(1+\tau^2)^3}\right\} \end{aligned} \tag{29}$$

where

$$\tau=\alpha i\frac{z+\bar{z}}{z-\bar{z}+2i}=\frac{x}{y}$$

Now, remembering that $\alpha=(1-M^2)^{1/2}$, we may expand $F(z, \bar{z})$ with respect to M^2 for subsonic flow. We shall take into account only the first two terms. We thus obtain, by use of Eq. (25),

$$\begin{aligned} \Re\{F(z, \bar{z})\}_K=&-\frac{1}{4}(2+3\cos\theta)(1-\cos\theta)^2 \\ &-\frac{M^2}{16}\Big\{(\pi-\theta)\sin\theta(1-2\cos\theta)(1-\cos\theta) \\ &+(18\cos^2\theta+17\cos\theta+1)(1-\cos\theta)^2+\frac{4\gamma}{3}(1+3\cos\theta)(1-\cos\theta)^3\Big\} \end{aligned} \tag{30}$$

Substituting Eq. (30) into Eq. (27), we have

$$\begin{aligned} f(\zeta)=&\frac{1}{16}(3\zeta^3-8\zeta^2+5\zeta) \\ &-\frac{M^2}{32}\Big\{(\zeta-1)^3\left(1+\frac{1}{\zeta^3}\right)\log(1-\zeta) \\ &+\frac{1}{2}(\zeta-1)\left(9\zeta^3-10\zeta^2-2\zeta-4-\frac{3}{\zeta}+\frac{2}{\zeta^2}\right) \\ &-\frac{\gamma}{3}(\zeta-1)(3\zeta^3-13\zeta^2+23\zeta-25)\Big\} \end{aligned} \tag{31}$$

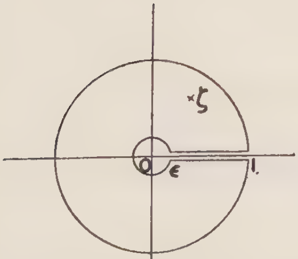

Fig. 1.

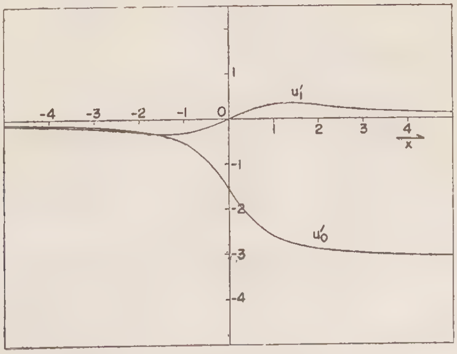

Fig. 2. Curves of u_0' and u_1'

Here, the integration in Eq. (27) can be performed easily by applying the theorem of residues to the contour shown in Fig. 1. Substituting Eqs. (29) and (31) into Eqs. (22) and putting $y=1$, we obtain the velocity distribution on the wall:

$$u'=\frac{N}{4}(u_0'+M^2u_1'+\cdots) \tag{32}$$

where

$$u_0'=-\left(\frac{\pi}{2}+\tan^{-1}x\right)-\frac{x}{2(x^2+1)}\ , \tag{33}$$

$$\begin{aligned} u_1'=&\frac{3x^2-1}{(x^2+1)^3}\tan^{-1}x-\frac{x(x^2-3)}{2(x^2+1)^3}\log\frac{4}{x^2+1} \\ &-\frac{(x^6+7x^4+3x^2+5)x}{4(x^2+1)^4}+\frac{\gamma}{6}\frac{(3x^4+8x^2-3)x}{(x^2+1)^3} \end{aligned} \tag{34}$$

The curves of u_0' and u_1' are shown in Fig. 2. The drag and moment are given, by means of the formulas (14) and (15), as

$$D=\frac{\pi}{8}N\left(1-\frac{\pi}{20}N\right) \tag{35}$$

$$\mathfrak{M}=-\frac{\pi}{4}N\left(1-\frac{\pi}{32}N\right) \tag{36}$$

It should be noted that u' is an odd function of x except for the first constant term and that v' is an even function of x. On the other hand, H_x and H_y are even and odd with respect to x, respectively. Hence only the constant term of u' contributes to the drag and moment, since the integration is symmetric about x. Thus we can conclude that the drag and moment depend only on the parameter N and not on M^2 for compartively small Mach numbers.

§ 4. Solution for supersonic flow

For supersonic flow, $M^2-1=\beta^2>0$. By the transformations:

$$x'=x/\beta\ ,\qquad y'=y\ ,\qquad u=\beta u'\ ,\qquad v=v' \tag{37}$$

Eqs. (10) become

$$\left.\begin{aligned} -\frac{\partial u}{\partial x'}+\frac{\partial v}{\partial y'}&=\gamma M^2NH_y^2 \\ \frac{\partial v}{\partial x'}-\frac{\partial u}{\partial y'}&=\beta N\left(H_xH_y+\frac{\partial}{\partial y}\int_{-\infty}^{x}H_y^2dx\right) \end{aligned}\right\} \tag{38}$$

By further transformations:

$$\xi=x'+y'\ ,\qquad \eta=x'-y'\ ,\qquad U=u+v\ ,\qquad V=u-v \tag{39}$$

the above equations become

$$\left.\begin{aligned} \frac{\partial U}{\partial\eta}&=-\frac{\gamma M^2N}{2}H_y^2+\frac{\beta N}{2}\left(H_xH_y+\frac{\partial}{\partial y}\int_{-\infty}^{x}H_y^2dx\right)\equiv2\frac{\partial}{\partial\eta}G(\xi,\eta) \\ \frac{\partial V}{\partial\xi}&=-\frac{\beta M^2N}{2}H_y^2-\frac{\beta N}{2}\left(H_xH_y+\frac{\partial}{\partial y}\int_{-\infty}^{x}H_y^2dx\right)\equiv2\frac{\partial}{\partial\xi}H(\xi,\eta) \end{aligned}\right\} \tag{40}$$

Thus, these can be integrated in the forms

$$\left.\begin{aligned} U&=2G(\xi,\eta)+2g(\xi) \\ V&=2H(\xi,\eta)+2h(\eta) \end{aligned}\right\} \tag{41}$$

where $g(\xi)$ and $h(\eta)$ are arbitrary functions. Since the disturbance does not propagate upstream, $g(\xi)$ is set equal to zero. On the other hand, $h(\eta)$ can be determined from the condition on the wall. We thus obtain the solution for supersonic flow:

$$\left.\begin{aligned} u' &= \frac{1}{\beta}\{G(\xi,\eta)+H(\xi,\eta)+h(\eta)\} \\ v' &= G(\xi,\eta)-H(\xi,\eta)-h(\eta) \end{aligned}\right\} \tag{42}$$

where $\xi=\beta^{-1}x+y$ and $\eta=\beta^{-1}x-y$.

Applying the foregoing procedure to the case of the magnetic dipole considered here, the following results are obtained:

$$\begin{aligned} u' = \frac{N}{4}\Bigg\{ & -\frac{1}{y^3}\left(\frac{\pi}{2}+\tan^{-1}\frac{x}{y}\right)-\frac{2\gamma}{3}\frac{x}{(x^2+y^2)^2}+\frac{8\gamma}{3}\frac{xy^2}{(x^2+y^2)^3} \\ & +\frac{\gamma M^2}{2\beta(x+\beta y)^2}\left(\frac{M^2}{x+\beta y}\tan^{-1}\frac{x+\beta y}{\beta x-y}-\frac{\beta x-y}{x^2+y^2}\right) \\ & +\frac{\gamma M^2}{2\beta(x-\beta y)^2}\left(\frac{M^2}{x-\beta y}\tan^{-1}\frac{x-\beta y}{\beta x+y}-\frac{\beta x+y}{x^2+y^2}\right) \\ & -\frac{\beta M^2}{2(x+\beta y)^3}\tan^{-1}\frac{x+\beta y}{\beta x-y}-\frac{\beta M^2}{2(x-\beta y)^3}\tan^{-1}\frac{x-\beta y}{\beta x+y} \\ & +\frac{2\beta^2 x}{(x^2-\beta^2y^2)^2}-\frac{x}{(x^2-\beta^2y^2)y^2}+\frac{x}{(x^2-\beta^2y^2)(x^2+y^2)}\Bigg\}+\frac{1}{\beta}h(x-\beta y)\,, \end{aligned} \tag{43}$$

$$\begin{aligned} v' = \frac{N}{4}\Bigg\{ & \frac{(\gamma-1)M^2+1}{2(x+\beta y)^2}\left(\frac{M^2}{x+\beta y}\tan^{-1}\frac{x+\beta y}{\beta x-y}-\frac{\beta x-y}{x^2+y^2}\right) \\ & -\frac{(\gamma-1)M^2+1}{2(x-\beta y)^2}\left(\frac{M^2}{x-\beta y}\tan^{-1}\frac{x-\beta y}{\beta x+y}-\frac{\beta x+y}{x^2+y^2}\right) \\ & -\frac{2\gamma y}{(x^2+y^2)^2}+\frac{8\gamma}{3}\frac{y^2}{(x^2+y^2)^3}\Bigg\}-h(x-\beta y) \end{aligned} \tag{44}$$

where

$$\begin{aligned} h(x) = \frac{N}{4}\Bigg\{ & \frac{(\gamma-1)M^2+1}{2(x+2\beta)^2}\left(\frac{M}{x+2\beta}\tan^{-1}\frac{x+2\beta}{\beta(x+\beta)-1}-\frac{\beta(x+\beta)-1}{(x+\beta)^2+1}\right) \\ & -\frac{(\gamma-1)M^2+1}{2x^2}\left(\frac{M}{x}\tan^{-1}\frac{x}{\beta(x+\beta)+1}-\frac{\beta(x+\beta)+1}{(x+\beta)^2+1}\right) \\ & -\frac{2\gamma}{[(x+\beta)^2+1]^2}+\frac{8\gamma}{3}\frac{1}{[(x+\beta)^2+1]^3}\Bigg\} \end{aligned} \tag{45}$$

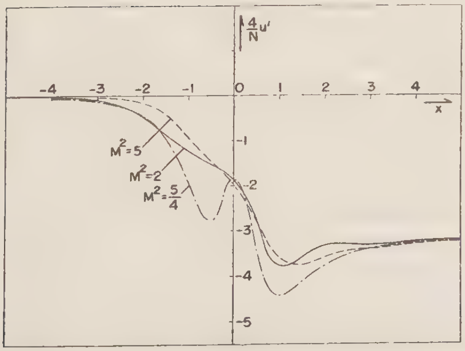

Fig. 3. Velocity distribution on the wall.

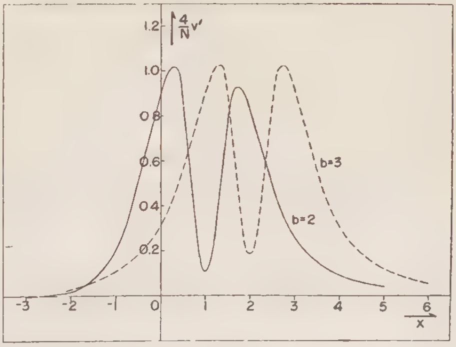

Fig. 4. Vertical component of the velocity along the streamlines for $M^2=2$.

The velocity distributions on the wall are shown in Fig. 3 for the cases of $M^2=5/4$, 2, 5. They are not monotonous curves but contain ups and downs which become larger as the Mach number approaches one.

The streamlines can be approximately expressed in the form

$$y=b+\int_{-\infty}^{x}[v']_{y=b}dx$$

where b is an arbitrary constant larger than unity. The values of $[v']_{y=b}$ are graphically shown in Fig. 4 for $b=2$, 3 and $M^2=2$. From their plots it is seen that each streamline will go up two stairs in the neighborhood of the Mach line through the origin. The drag and moment can be calculated by substituting Eq. (11) and Eqs. (43)-(45) into the formulas (14) and (15). The first terms, due to the interactionbet ween the undisturbed stream and the field of magnetic dipole, are found to be $N\pi/8$ and $-N\pi/4$ as in subsonic flow. The calculation of the second terms, due to the interaction between the perturbation velocity and the field of magnetic dipole, becoms complicated, since $h(x-\beta y)$ in the perturbation velocity is not symmetric about x and the integrations involving it must be carried out. Thus, in this paper, we have not tried to obtain the second approximation.

The writer wishes to express his hearty thanks to Prof. Z. Hasimoto, Dr. T. Sakurai and Mr. Y. Sone for their valuable discussions.

References

1) G. S. S. Ludford and J. D. Murray: J. Fluid Mech. **7** (1960) 516.

2) K. Tamada: 10th. Intern. Congr. Appl. Mech., Stresa, (1960).

JOURNAL OF THE PHYSICAL SOCIETY OF JAPAN, Vol. 16, No. 12, DECEMBER, 1961

Propagation of Elastic Waves in Spherical Symmetric Inhomogeneous Medium

By Koshun TAKAKU

Faculty of Art and Science, Fukushima University

(Received Aug. 21, 1961)

Using the solution of the equations of elastic motion of the spherical symmetric inhomogeneous medium, we have obtained the expressions of the ray and the diffracted waves. They have a simple form and clear physical meanings even if the medium has considerably complicated inhomogeneity.

§ 1. Introduction

Owing to the complexity of the equations of motion[1] of the inhomogeneous elastic medium, the waves have been calculated practically by means of the solutions of the homogeneous medium together with the law of energy conservation. Several years ago we got a solution of the equations by physical intuition.[2]

Using these solutions, we obtained the expressions of the elastic waves in an inhomogeneous medium, where we could not show why they were the solutions of the equations of motion.

Now we will present a consistent theory starting from the original equation of elastic motion, and will obtain a rigorous wave equation, which can be separated into the longitudinal and transverse wave equations approximately. They can be solved easily, and the approximate calculation gives various results, which are simple even if the medium has considerably complicated inhomogeneity, and which have clear physical meanings. The method of calculation in this paper can also be applied to the problems of the non destroying examinations of materials by means of the ultrasonic waves.

§ 2 Wave equations and the Solutions

Generally speaking, the equations of elastic motion in an inhomogeneous medium are too complex to get the wave equations from them. But if the density ρ and the elastic coefficients λ and μ depend only upon the radius r, and further the displacement vector S has no φ-component, we can deduce the wave equation:

$$\nabla\{(\lambda+2\mu)\nabla\cdot\boldsymbol{s}\}-\mu\nabla\times\nabla\times\boldsymbol{s}+\frac{d\mu}{dr}\boldsymbol{A}=\rho\ddot{\boldsymbol{s}}\,, \qquad (1.)$$

where

$$A_r=-2\left\{\frac{2s_r}{r}+\frac{1}{r\sin\theta}\frac{\partial}{\partial\theta}(\sin\theta\, s_\theta)\right\},$$

$$A_\theta=r\frac{\partial}{\partial r}\left(\frac{s_\theta}{r}\right)+\frac{1}{r}\frac{\partial s_r}{\partial\theta},$$

$$A_\varphi=0\,,$$

rigorously from the equations of elastic motion.[1] Putting

$$\boldsymbol{s}=(\nabla\phi+\nabla\times\boldsymbol{a})e^{-i\omega t}\,,$$

both functions ϕ and $\boldsymbol{a}$ will have a plane wave like form in the distant region from the source.

Under the further assumption that all the functions ρ, λ and μ vary with r so slowly that the magnitudes of $\nabla\rho/\rho$, $\nabla\lambda/\lambda$ and $\nabla\mu/\mu$ are of the order of r^{-1}, the last term of the left hand side of (1.1) can be neglected in the region of large r as compared to the other three terms which are all as large as the inverse wave length. Then the equation (1.1) can be separated into;

$$\left.\begin{aligned}&(\lambda+2\mu)\nabla^2\phi+\rho\omega^2\phi=0\,,\\ \text{and}\quad&\\ &\mu\nabla\times\nabla\times\boldsymbol{a}-\rho\omega^2\boldsymbol{a}=0\,.\end{aligned}\right\}\qquad(1.2)$$

If we write

$$\left.\begin{aligned}&\phi=\phi_n(r)P_n(\cos\theta)\,,\\ \text{and}\quad&\\ &\boldsymbol{a}=\nabla\times\boldsymbol{r}\psi_n(r)P_n(\cos\theta)\,,\end{aligned}\right\}\qquad(1.3)$$

the equations in (1.2) are transformed into

$$\left.\begin{aligned}&\phi_n''+\frac{2}{r}\phi_n'+\left(\frac{\rho\omega^2}{\lambda+2\mu}-\frac{n(n+1)}{r^2}\right)\phi_n=0\,,\\ \text{and}\quad&\\ &\psi_n''+\frac{2}{r}\psi_n'+\left(\frac{\rho\omega^2}{\mu}-\frac{n(n+1)}{r^2}\right)\psi_n=0\,.\end{aligned}\right\}\qquad(1.4)$$

We found rigorous particular solutions of the Maxwell's equations in the inhomogeneous medium in the previous paper,[3] but now even the separated equations (1.4) themselves are the approximate ones.

If the function ρ, λ and μ satisfy the relations:

$$\left.\begin{aligned}&\frac{\rho\omega^2}{\lambda+2\mu}=h^2\,r^{2m}\,,\\ \text{and}\quad&\\ &\frac{\rho\omega^2}{\mu}=k^2\,r^{2m}\,,\end{aligned}\right\}\qquad(1.5)$$

the equations (1.4) can be written as:

$$\left.\begin{aligned}&Y''_{nm}(\xi,\,r)+\frac{2}{r}Y'_{nm}(\xi,\,r)\\ &\qquad+\left(\xi^2\,r^{2m}+\frac{n(n+1)}{r^2}\right)Y_{nm}(\xi,\,r)=0\,,\\ &\text{where}\\ &Y^{(1),(2)}_{nm}(\xi,\,r)\equiv\sqrt{\frac{\pi}{2r}}H^{(1),(2)}_{\nu}\left(\frac{\xi r^{m+1}}{m+1}\right),\\ &\nu=\frac{n+1/2}{m+1}\,,\end{aligned}\right\}\qquad(1.6)$$

where $H^{(i)}_\nu$ is the Hankel function, and $\xi=h$ for the longitudinal (P) waves and $\xi=k$ for the transverse (S) waves. We used these functions in the previous paper, and its validity has now been visualised.

§ 3. Boundary Conditions

The reflection and refraction coefficients were already calculated at the free surface and fluid boundary.* We must now calculate the boundary conditions at the continuous boundaries, where ρ, λ and μ are all continuous. Before entering into it, we divide the large spherical symmetric inhomogeneous medium into many laminar concentric layers, among which the layers 1, 2, 3, $\cdots$, c are assumed to be the fluid media and the layers $c+1$, $c+2,\cdots$, N the elastic media. The boundaries $r=r_\sigma(\sigma\neq c,\ N)$ are assumed to be continuous boundaries. If we write λ' and μ' the coefficients of the fluid medium, and write

$$\left.\begin{aligned}&h(\sigma,\,r)=h_\sigma r^{m_\sigma}\,,\\ \text{and}\quad&\\ &k(\sigma,\,r)=k_\sigma r^{m_\sigma}\,,\end{aligned}\right\}\qquad(2.1)$$

where h_σ, k_σ and m_σ are constant in the σ-th layer, then we get the wave functions

$$Y_n{}^{(1),(2)}(\xi_\sigma,\,r),\quad \xi_\sigma=h_\sigma \text{ or } k_\sigma,$$

in the σ-th layer. The ordinary boundary conditions between the elastic media require that

---

* It is the boundary between the elastic and the fluid medium.

(1) $\phi_n' + \dfrac{n(n+1)}{r}\psi_n$

(2) $r^{-1}\{\phi_n + (r\psi_n)'\}$

(3) $-\lambda h^2 r^{2m}\phi_n + 2\mu\left\{\phi_n'' + n(n+1)\left(\dfrac{\psi_n}{r}\right)'\right\}$

(4) $r\{r^{-2}(\phi_n + (r\psi_n)')\}'$

be continuous at the boundary. But now we have additional conditions:

$\xi(\sigma,\ r_\sigma) = \xi(\sigma+1,\ r_\sigma)$, $\xi = h$ and k,
and μ is cotinuous

at the continuous boundaries. The last conditions simplify the calculation very much, and the above four conditions can be transformed into the four conditions that ϕ_n, ϕ_n', ψ_n and ψ_n' be continuous at $r = r_\sigma$, and we get

$$R(r_\sigma) = 0,$$

$$d_{hk}(r_\sigma) = \delta_{hk},\quad \delta\text{: kronecker.}$$

where R denotes various reflection coefficients, and d_{hk} denotes the refraction coefficient for the h wave refracting into the k wave.

§ 4. General Representations of the Waves

We are ready to find the general representations of the waves emitted from the point source $Q(\bar{r},\ 0,\ 0)$ in the medium which varies arbitrarily with r. In general the incident wave produces two kinds of reflected waves and also two kinds of refracted waves at the discontinuous boundaries, while it produces only the same kind of refracted wave at the continuous boundaries. Accordingly there occur 2^Z kind of various waves after Z times reflections and refractions at the discontinuous boundaries. Applying the same method as in the previous paper,[3] we get the following results.

At first the primary waves emitted from the source $Q(\bar{r},\ 0,\ 0)$ are

$$\left.\begin{aligned} O_0(\xi) &= \sum_{n=0}^{\infty} \alpha_n(\xi) D_n^{\xi}(q,\ A-1) Y_n^{(1)}(\xi_A,\ r), \quad A = q,\ q+1, \cdots,\ N, \\ I_0(\xi) &= \sum_{n=0}^{\infty} \beta_n(\xi) C_n^{\xi}(q,\ A) Y_n^{(2)}(\xi_A,\ r), \quad A = q-1,\ q-2, \cdots,\ C+1, \end{aligned}\right\} \tag{4.1}$$

where O and I denote the outgoing and ingoing waves respectively, and

$$\left.\begin{matrix} \alpha_n(\xi) \\ \beta_n(\xi) \end{matrix}\right\} = \frac{i(2n+1)}{(8\pi m_q+1)} P_n(\cos\theta) \left\{\begin{matrix} Y_n^{(2)}(\xi_q,\ \bar{r}) \\ Y_n^{(1)}(\xi_q,\ \bar{r}) \end{matrix}\right., \tag{4.2}$$

and

$$C_n^{\xi}(p,\ q) = \prod_{\sigma=q}^{p} \frac{Y_n^{(2)}(\xi_{\sigma+1},\ r_\sigma)}{Y_n^{(2)}(\xi_\sigma,\ r_\sigma)}, \tag{4.3}$$

$$\left.\begin{aligned} D_n^{\xi}(p,\ q) &= \prod_{\sigma=q}^{p} \frac{Y_n^{(1)}(\xi_\sigma,\ r_\sigma)}{Y_n^{(1)}(\xi_{\sigma+1},\ r_\sigma)}, \\ \xi_\sigma &= h_\sigma \text{ or } k_\sigma\ . \end{aligned}\right\} \tag{4.4}$$

The primary outgoing wave $O_0(h)$ reflects into the ingoing waves $I_1(h,\ h)$ and $I_1(h,\ k)$ at the free surface $r = r_N$, on the other hand the primary ingoing wave $I_0(h)$ produces the secondary waves:

$$\left.\begin{aligned} O_1(h,\ h) &= \sum_{\kappa=0}^{\infty} O_{,}^{(\kappa)}(h_1\ h)\ , \\ &\text{and} \\ O_1(h,\ k) &= \sum_{\kappa=0}^{\infty} O_{,}^{(\kappa)}(h_1\ k)\ . \end{aligned}\right\} \tag{4.5}$$

at the fluid boundary $r = r_c$. The ingoing wave $I_1(h,\ k)$ produces the outgoing waves $O_2(h,\ k,\ h)$ and $O_2(h,\ k,\ k)$ at $r = r_c$, while the outgoing wave $O_1(h,\ k)$ reflects into the ingoing waves $I_2(h,\ k,\ h)$ and $I_2(h,\ k,\ k)$ at $r = r_N$.

They are expressed as follows:

$$I_1(\xi,\ \eta) = \sum_{n=0}^{\infty} \alpha_n(\xi) D_n^{\xi}(q,\ N-1) \frac{Y_n^{(1)}(\xi_N,\ r_N)}{Y_n^{(2)}(\eta_N,\ r_N)} R_n^{\xi\eta}(r_N) C_n^{\eta}(N-1,\ A) Y_n^{(2)}(\eta_A,\ r)\ , \tag{4.6}$$

$$O_1^{(\kappa)}(\xi,\eta)=\sum_{n=0}^{\infty}\beta_n(\xi)\,C_n^{\xi}(q-1,\ c+1)T_n^{(\kappa)}(\xi,\ \eta)D_n^{\eta}(c+1,\ A-1)Y_n^{(1)}(\eta_A,\ r)\ , \tag{4.7}$$

$$\begin{aligned}O_2^{(\kappa)}(\xi,\ \eta,\ \zeta)=&\sum_{n=0}^{\infty}\alpha_n(\xi)D_n^{\xi}(q,\ N-1)\frac{Y_n^{(1)}(\xi_N,\ r_N)}{Y_n^{(2)}(\eta_N,\ r_N)}R_n^{\xi\eta}(r_N)\\&\times C_2^{\eta}(N-1,\ c+1)T_n^{(\kappa)}(\eta,\ \zeta)D_n^{\zeta}(c+1,\ A-1)Y_n^{(1)}(\zeta_A,\ r)\ ,\end{aligned} \tag{4.8}$$

$$\begin{aligned}I_2(\xi,\ \eta,\ \zeta)=&\sum_{n=0}^{\infty}\beta_n(\xi)\,C_n^{\xi}(q-1,\ c+1)\left\{\sum_{\kappa=0}^{\infty}T_n^{(\kappa)}(\xi,\ \eta)\right\}D_n^{\eta}(c+1,\ N-1)\\&\times\frac{Y_n^{(1)}(\eta_N,\ r_N)}{Y_n^{(2)}(\zeta_N,\ r_N)}R_n^{\eta\zeta}(r_N)C_n^{\zeta}(N-1,\ A)Y_n^{(2)}(\zeta_A,\ r)\ ,\end{aligned} \tag{4.9}$$

where

$$T_n^{(0)}(\xi,\ \eta)=\frac{Y_n^{(2)}(\xi_{c+1},\ r_c)}{Y_n^{(1)}(\eta_{c+1},\ r_c)}R_n^{\xi\eta}(r_c)\ , \tag{4.10}$$

$$\begin{aligned}T_n^{(\kappa)}(\xi,\ \eta)=&\frac{Y_n^{(2)}(\xi_{c+1},r_c)}{Y_n^{(2)}(h_c,\ r_c)}c_n^{\xi h}(r_c)\{C_n^{h}(c-1,\ 1)D_n^{h}(1,\ c-1)\}^{\kappa}\\&\times\left\{\frac{Y_n^{(1)}(h_c,\ r_c)}{Y_n^{(2)}(h_c,\ r_c)}R_n'\right\}^{\kappa-1}d_n^{h\eta}(r_c)\,\frac{Y_n^{(1)}(h_c,\ r_c)}{Y_n^{(2)}(\eta_{c+1},\ r_c)}\ ,\end{aligned} \tag{4.11}$$

and R denotes the reflection coefficient, while $c_n^{\xi h}$ and $d_n^{h\eta}$ denote the refraction coefficients at $r=r_c$ for the ingoing and outgoing waves respectively. They are expressed as follows:

$$R_n^{hh}(r_N)=\vartheta(r_N)^{-1}\left\{\frac{n(n+1)}{r_N^2}F^{(2)}E^{(1)}-A^{(1)}B^{(2)}\right\}, \tag{4.12}$$

$$R_n^{hk}(r_N)=\vartheta(r_N)\ ^{1}\{A^{(1)}E^{(2)}-A^{(2)}E^{(1)}\}\ , \tag{4.13}$$

$$R_n^{kk}(r_N)=\vartheta(r_N)^{-1}\left\{\frac{n(n+1)}{r_N^2}F^{(1)}E^{(2)}-B^{(1)}A^{(2)}\right\}, \tag{4.14}$$

$$R_n^{kh}(r_N)=\vartheta(r_N)^{-1}\{B^{(1)}F^{(2)}-B^{(2)}F^{(1)}\}\ , \tag{4.15}$$

$$\vartheta(r_N)=A^{(2)}B^{(2)}-E^{(2)}F^{(2)}\frac{n(n+1)}{r_N^2}\ , \tag{4.16}$$

$$R_n^{hh}(r_c)=\vartheta^{-1}(r_c)\left[-\frac{Y_n^{(2)}(h_c,\ r_c)'}{Y_n^{(2)}(h_c,\ r_c)}\beta^{(21)}-\frac{\lambda'}{2\mu}h(c,\ r_c)^2\alpha^{(21)}\right], \tag{4.17}$$

$$R_n^{hk}(r_c)=-\{r_cB^{(1)}\}^{-1}[E^{(1)}R_n^{hh}(r_c)+E^{(2)}]\ , \tag{4.18}$$

$$c_n^{hh}(r_c)=\vartheta(r_c)^{-1}B^{(1)-1}[\beta^{(11)}\alpha^{(21)}-\alpha^{(11)}\beta^{(21)}]\ , \tag{4.19}$$

$$R_n^{kk}(r_c)=\vartheta(r_c)^{-1}\left[-\frac{Y_n^{(2)}(h_c,\ r_c)'}{Y_n^{(2)}(h_c,\ r_c)}\beta^{(12)}-\frac{\lambda'}{2\mu}h(c,\ r_c)^2\alpha^{(12)}\right], \tag{4.20}$$

$$R_n^{kh}(r_c)=-r_cE^{(1)-1}[B^{(2)}-B^{(1)}R_n^{kk}(r_c)]\ , \tag{4.21}$$

$$c_n^{kh}(r_c)=\vartheta(r_c)^{-1}r_cE^{(1)-1}[\beta^{(11)}\alpha^{(12)}-\alpha^{(11)}\ \beta^{(12)}]\ , \tag{4.22}$$

$$d_n^{hh}(r_c)=\vartheta(r_c)^{-1}B^{(1)}\frac{\lambda'}{2\mu}h(c,\ r_c)^2\left\{\frac{Y_n^{(1)}(h_c,\ r_c)'}{Y_n^{(1)}(h_c,\ r_c)}-\frac{Y_n^{(2)}(h_c,\ r_c)'}{Y_n^{(2)}(h_c,\ r_c)}\right\}. \tag{4.23}$$

$$d_n^{hk}(r_c)=-E^{(1)}\{r_cB^{(1)}\}^{-1}d_n^{hh}(r_c)\ , \tag{4.24}$$

$$R_n'(r_c)=-\vartheta(r_c)^{-1}\left[\beta^{(11)}\frac{Y_n^{(1)}(h_c,\ r_c)'}{Y_n^{(1)}(h_c,\ r_c)}+\frac{\lambda'}{2\mu}h(c,\ r_c)^2\alpha^{(11)}\right], \tag{4.25}$$

$$\vartheta(r_c)=\frac{Y_n^{(2)}(h_c,\ r_c)'}{Y_n^{(2)}(h_c,\ r_c)}\beta^{(11)}+\frac{\lambda'}{2\mu}h(c,\ r_c)^2\alpha^{(11)}\ , \qquad (4.26)$$

where

$$\left.\begin{aligned}
A^{(s)}&=\frac{n(n+1)}{r^2}-\frac{k^2r^{2m}}{2}-\frac{2}{r}\ \frac{Y_n^{(s)}(h,\ r)'}{Y_n^{(s)}(h,\ r)}\ ,\\
B^{(s)}&=\frac{n(n+1)-1}{r^2}-\frac{k^2r^{2m}}{2}-\frac{1}{r}\ \frac{Y_n^{(s)}(k,\ r)'}{Y_n^{(s)}(k,\ r)}\ ,\\
E^{(s)}&=\frac{Y_n^{(s)}(h,\ r)'}{Y_n^{(s)}(h,\ r)}-\frac{1}{r}\ ,\\
F^{(s)}&=\frac{Y_n^{(s)}(k,\ r)}{Y_n^{(s)}(k,\ r)}-\frac{1}{r}\ ,
\end{aligned}\right\} \qquad (4.27)$$

and

$$\left.\begin{aligned}
\alpha^{(st)}&=\frac{Y_n^{(s)}(h_{c+1},\ r_c)'}{Y_n^{(s)}(h_{c+1},\ r_c)}B^{(t)}-\frac{n(n+1)}{r_c^2}E^{(s)}\ ,\\
\beta^{(st)}&=A^{(s)}B^{(t)}-\frac{n(n+1)}{r_c^2}E^{(s)}F^{(t)}\ ,
\end{aligned}\right\} \qquad (4.28)$$

at $r=r_c$,
where the last coefficient R' is that of reflection at the inner side of the fluid boundary $r=r_c$.

§ 5. Ray Expressions of the Waves

The first order approximation by the saddle point method gives the ray expressions. They are good approximations in the region where the geometric-optical ray can reach. Following the method discussed in the previous paper, we get

$$\left.\begin{matrix}0\\ I\end{matrix}\right\}=\frac{1}{4\pi\sqrt{r\bar{r}}}\left[\frac{\tan\tau_Q\ \tan\tau_P}{\sin\theta\displaystyle\int_Q^p\frac{\sin\tau}{\cos^2\tau}ds}\right]^{1/2}F\,exp\left[i\omega\int_Q^p\frac{ds}{v}\right],\quad \frac{\omega}{v_\xi}=\xi(\sigma,\ r)\ , \qquad (5.1)$$

where the contour of the two integrations in the right hand side is the ray determined by the relation:

$$\xi(\sigma,\ r)\ r\sin\tau=\mathrm{con\,st}\ , \qquad (5.2)$$

from the source $Q(\bar{r},\ 0,\ 0)$ to the point $P(r,\ \theta,\ 0)$ and τ is the angle between the ray element ds and the radius. The values of F are given as follows:

$$\begin{array}{ll}
O,\ I & F\\
I_0,\ O_0 & 1\\
I_1(h,\ k) & \left(\dfrac{k_N\cos\tau_N'}{h_N\cos\tau_N}\right)^{1/2}R^{hk}(r_N)\\
I_1(h,\ h) & R_n^{hh}(r_N)\\
O_1^{(1)}(h,\ k) & \left(\dfrac{k_{c+1}\cos\tau_c'}{h_{c+1}\cos\tau_c}\right)^{1/2}R^{hk}(r_c)\\
O_1^{(0)}(h,\ h) & R^{hh}(r_c)\\
O_1^{(\kappa)}(h,\ k) & \left(\dfrac{k_{c+1}\cos\tau_c'}{h_{c+1}\cos\tau_c}\right)^{1/2}c^{hh}R'^{\kappa-1}d^{hk}
\end{array} \qquad (5.3)$$

where τ_i and τ_i' are the angles at $r\quad r_i$ between the radius and the ray of the P and the S waves respectively. The approximate values of the reflection and refraction coefficients are given as follows:

$$R^{hh}(r_N)=D(r_N)^{-1}\left[\sin 2\tau_N \sin 2\tau_N'-\frac{k_N{}^2}{h_N{}^2}\cos^2 2\tau_N'\right], \tag{5.4}$$

$$R^{hk}(r_N)=D(r_N)^{-1}\left[\frac{4i}{h(N,\ r_N)r_N}\cos\tau_N \cos 2\tau_N'\right], \tag{5.5}$$

$$R^{kk}(r_N)=R^{hh}(r_N)\ , \tag{5.6}$$

$$R^{kh}(r_N)=D(r_N)^{-1}\left[\ i\ \frac{k_N{}^2}{h_N{}^2}k(N,\ r_N)r_N \sin\tau_N' \sin 4\tau_N'\right], \tag{5.7}$$

$$D(r_N)=\sin 2\tau_N \sin 2\tau_N'+\frac{k_N{}^2}{h_N{}^2}\cos^2 2\tau_N'\ , \tag{5.8}$$

$$R^{hh}(r_c)=D(r_c)^{-1}\left[\sin 2\tau_c''(\sin 2\tau_c \sin 2\tau_c'-\frac{k^2_{c+1}}{h^2_{c+1}}\cos^2 2\tau_c')+\frac{\lambda'}{\mu}\sin 2\tau_c\right], \tag{5.9}$$

$$R^{hk}(r_c)=D(r_c)^{-1}\left[-\frac{4i}{r_c{}^2h(c+1,\ r_c)}\cos\tau_c \cos 2\tau_c' \sin 2\tau_c''\right], \tag{5.10}$$

$$c^{hh}(r_c)=D(r_c)^{-1}\left[\frac{k(c+1,\ r_c)^2}{h(c,\ r_c)^2}\sin 2\tau_c \cos 2\tau_c'\right], \tag{5.11}$$

$$R^{kk}(r_c)=D(r_c)^{-1}\left[\sin 2\tau_c''(\sin 2\tau_c \sin 2\tau'-\frac{k^2_{c+1}}{h^2_{c+1}}\cos^2 2\tau_c')-\frac{\lambda'}{2\mu}\sin 2\tau_c\right], \tag{5.12}$$

$$R^{kh}(r_c)=D(r_c)^{-1}\left[-2ik(c+1,\ r_c)r_c\frac{k_{c+1}}{h_{c+1}}\sin\tau_c \sin 4\tau_c' \sin 2\tau_c''\right], \tag{5.13}$$

$$c^{kh}(r_c)=D(r_c)^{-1}\left[2ik(c+1,\ r_c)\ r_c\frac{k(c+1,\ r_c)^2}{h(c,\ r_c)^2}\sin 2\tau_c \sin 2\tau_c' \sin\tau_c'\right], \tag{5.14}$$

$$d^{hh}(r_c)=D(r_c)^{-1}\left[\frac{h(c,\ r_c)^2}{h(c+1,\ r_c)^2}\ \frac{\lambda'}{\mu}2\sin\tau_c''\ \cos 2\tau_c'\right], \tag{5.15}$$

$$d^{hk}(r_c)=D(r_c)^{-1}\left[\frac{4i}{k(c+1,\ r_c)r_c}-\frac{h(c,\ r_c)}{k(c+1,\ r_c)}\ \frac{\lambda'}{\mu}\cos\tau_c''\ \sin 2\tau_c\right], \tag{5.16}$$

$$R'(r_c)=D(r_c)^{-1}\left[\sin 2\tau_c''(\sin 2\tau_c \sin 2\tau_c'+\frac{k^2_{c+1}}{h^2_{c+1}}\cos^2 2\tau_c')-\frac{\lambda'}{\mu}\sin 2\tau_c\right], \tag{5.17}$$

$$D(r_c)=\sin 2\tau_c''(\sin 2\tau_c \sin 2\tau_c'+\frac{k^2_{c+1}}{h^2_{c+1}}\cos 2\tau_c')+\frac{\lambda'}{\mu}\sin 2\tau_c\ , \tag{5.18}$$

where τ_c'' is the angle at the inner side of the fluid boundary.

These nine coefficients at $r=r_c$ satisfy the relations:

$$R^{hh}+\frac{c^{hh}\,d^{hh}}{1-R'}=1\ ,\qquad R^{hk}+\frac{c^{hh}\,d^{hk}}{1-R'}=0\ , \tag{5.19}$$

$$R^{kk}+\frac{c^{kh}\,d^{hk}}{1-R'}=-1\ ,\qquad R^{kh}+\frac{c^{kh}\,d^{hh}}{1-R'}-0\ . \tag{5.20}$$

The relations are usefull to calculate the wave whose ray does not touch the fluid core, and its final form is just the same with those of the primary waves.

§ 6. Diffracted Waves

The waves in the shadow region can be calculated by Waston's method. When the above contour of integration in the complex n plane is transformed to pass through the saddle point, it meets with the poles:

$$\frac{\lambda'}{2\mu}h(c,r_c)^2\alpha^{(11)}+\frac{Y_n^{(2)}(h_c,\ r_c)'}{Y_n^{(2)}(h_c,\ r_c)}\beta^{(11)}=0\ , \tag{6.1}$$

of the integrand, where $\alpha^{(11)}$ and $\beta^{(11)}$ were given in (4.28).

Upon putting

$$\left.\begin{aligned}\frac{n_s}{m_{c+1}+1}&=\frac{h(c+1,\ r_c)r_c}{m_{c+1}+1}+\left\{\frac{h(c+1,\ r_c)r_c}{m_{c+1}+1}\right\}^{1/3}x_s^{(1)}\ ,\\ \frac{n_s'}{m_{c+1}+1}&=\frac{k(c+1,\ r_c)r_c}{m_{c+1}+1}+\left(\frac{k(c+1,\ r_c)r_c}{m_{c+1}+1}\right)^{1/3}x_s^{(2)}\ ,\end{aligned}\right\} \tag{6.2}$$

the root n_s of the equation (6.1) can be expanded as:

$$\begin{aligned}x_s^{(i)}=&x_{0s}+\frac{1}{2x_{0s}}y^{(i)}-\frac{1}{8x_{0s}^3}y^{(i)2}+\left(\frac{1}{16x_{0s}^4}+\frac{1}{12x_{0s}^2}\right)y^{(i)3}\\ &-\left(\frac{1}{128}\frac{1}{x_{0s}^7}+\frac{7}{96}\frac{1}{x_{0s}^4}\right)y^{(i)4}+\cdots\ ,\end{aligned} \tag{6.3}$$

or

$$x_s^{(i)}=x_{\infty s}+\frac{1}{y^{(i)}}+\frac{2}{3}x_{\infty s}\frac{1}{y^{(i)3}}-\frac{1}{2}\frac{1}{y^{(i)4}}+\frac{4}{5}\frac{x_{\infty s}^2}{y^{(i)5}}+\cdots\ , \tag{6.4}$$

$$i=1,\ 2,$$

where x_{0s} and $x_{\infty s}$ are the s-th root of the equations

$$J_{2/3}\{\zeta(x)\}-J_{-2/3}\{\zeta(x)\}=0\ , \tag{6.5}$$

and

$$J_{1/3}\{\zeta(x)\}-J_{-1/3}\{\zeta(x)\}=0\ ,\qquad \zeta(x)=\frac{(2xe^{-i\pi})^{3/2}}{3}\ , \tag{6.6}$$

respectively, and

$$y^{(1)}=\frac{i\left(1-\dfrac{k_{c+1}^2}{2h_{c+1}^2}\right)\sqrt{\dfrac{h(c,\ r_c)^2}{h(c+1,\ r_c)^2}-1}\left(\dfrac{h(c+1,\ r_c)r_c}{m_{c+1}+1}\right)^{1/3}}{\dfrac{\lambda'}{4\mu}\dfrac{k_{c+1}^2}{h_{c+1}^2}\dfrac{h(c,\ r_c)^2}{h(c+1,\ r_c)^2}+\sqrt{\dfrac{k_{c+1}^2}{h_{c+1}^2}-1}\sqrt{\dfrac{h(c,\ r_c)^2}{h(c+1,\ r_c)^2}-1}}\ , \tag{6.7}$$

$$y^{(2)}=\left\{\frac{\lambda'h(c+1,\ r_c)}{4\mu k(c+1,\ r_c)\sqrt{\dfrac{k(c+1,\ r_c)^2}{h(c+1,\ r_c)^2}-1}}-\frac{1}{2\sqrt{1-\dfrac{h_{c+1}^2}{k_{c+1}^2}}}\right\}\left(\frac{k(c+1,\ r_c)r_c}{m_{c+1}+1}\right)^{1/3}. \tag{6.8}$$

The primary wave $I_0(\xi)$ produces the secondary waves:

$$O_1(\xi,\ \eta)=\sum_{\kappa=0}^{\infty}O_1^{(\kappa)}(\xi,\ \eta)\ ,$$

where the values of all $O_1^{(\kappa)}$ becomes zero at the poles except for $\kappa=0$. Therefore the only wave $O_1^{(0)}$ contributes to the diffracted waves. After a lengthy calculation using the well known properties of the Hankel functions, we get the following results:

$$\begin{aligned}[O_1(h,\ h)]_1=&\frac{3\sqrt{2}}{\pi\sqrt{\pi}}\sum_s\frac{\left(\dfrac{h(c+1,\ r_c)r_c}{m_{c+1}+1}\right)^{1/3}}{x_s(2x_s+y^{(1)2})\{H_{1/3}^{(1)}(\zeta)\}^2}\left[\frac{\tan\tau_Q\tan\tau_P}{r\bar{r}n_s\sin\theta}\right]^{1/2}\\ &\times\exp\left[i\omega\int_{QA_1A_2P}\frac{ds}{v_h}-\delta n_s\angle A_1OA_2+\frac{5}{12}\pi i\right],\end{aligned} \tag{6.9}$$

$$[O_1(h,\ h)]_2=\frac{1}{2\sqrt{2\pi}}\sum_s\frac{1}{(2x_s+y^{(2)2})\sqrt{1-\dfrac{h_{c+1}^2}{k_{c+1}^2}}}\left[\frac{\tan\tau_Q\tan\tau_P}{r\bar{r}n_s'\sin\theta}\right]^{1/2}$$
$$\times\exp\left[i\omega\int_{QA_1A_2P}\frac{ds}{v_k}-\delta n_s'\angle A_1OA_2+2F(l-1,\ c)+\frac{\pi}{4}i\right],\tag{6.10}$$

$$[O_1(h,\ k)]_1=\frac{i\,12\sqrt{3}\,h_{c+1}}{\pi^2k_{c-1}\,k(c+1,\ r_c)r_c}\frac{\sqrt{\dfrac{k(c+1,\ r_c)}{m_{c+1}+1}}\sqrt{1-\dfrac{h_{c+1}^2}{k_{c+1}^2}}}{\left(\dfrac{h(c+1,\ r_c)r_c}{m_{c+1}+1}\right)^{1/3}\left(\dfrac{h_{c+1}^2}{k_{c+1}^2}-\dfrac{1}{2}\right)}$$
$$\times\sum_s\left[[(2x_s+y^{(1)2})\,x_s\sqrt{2x_se^{-i\pi}}\left\{H_{1/3}^{(1)}(\zeta)\right\}^2H_{1/3}^{(2)}(\zeta)\right]^{-1}$$
$$\times\left[\frac{\tan\tau_Q\tan\tau_P'}{n_sr\bar{r}\sin\theta}\right]\exp\left[i\omega\left\{\int_{QA_1A_2}\frac{ds}{v_k}+\int_{A_2P}\frac{ds}{v_k}\right\}-\delta n_s\angle A_1OA_2\right],\tag{6.11}$$

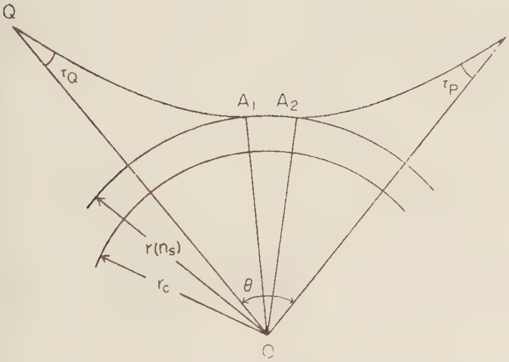

Fig. 1. The contour of integration QA_1A_2P of $[O_1(h, h)]_1$ (6.9) is shown. It touches the surface of the sphere of radius (rn_s) at points A_1 and A_2 The contour goes along the surface of the sphere between A_1 and A_2.

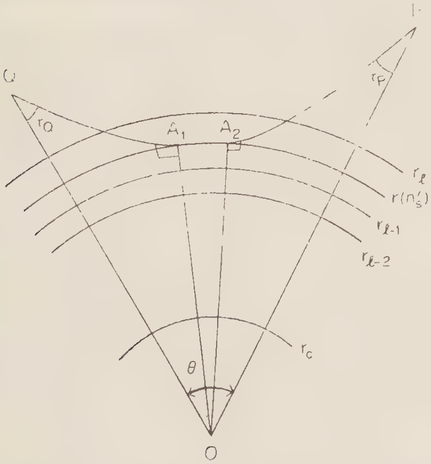

Fig. 2. The contour of integration QA_1A_2P of $[O_1(h, h)]_2$ (6.10). It touches the sphere of radius $r(n_s')$ at A_1 and A_2, where the radius $r(n_s')$ is considerably larger than r_c. It is thus clear that $[O_1(h, h)]_2$ is very small as compared to $[O_1(h, h)]_1$ in the geometric optical shadow region.

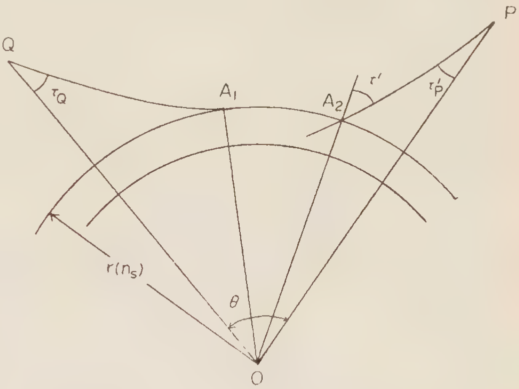

Fig. 3. The contour of integration QA_1A_2P of $[O_1(h, k)]_1$ (6.11). Although the radius $r(n_s)$ is a little larger than the radius r_c, the length A_1A_2 or $\angle A_1OA_2$ is quite large in the geometric optical region, because the angle τ' is smaller than $\pi/2$ and $\sin\tau'=h_{c+1}/k_{c+1}$.

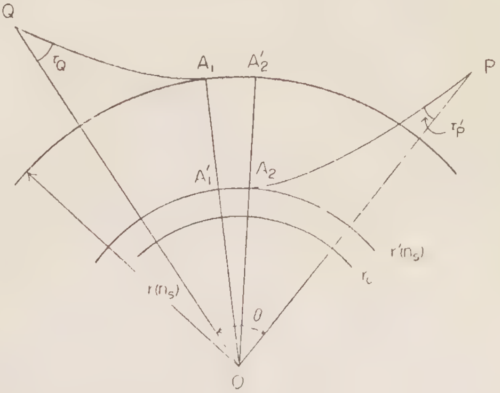

Fig. 4. The contours of integration QA_1A_2' and A_2P or QA_1 and $A_1'A_2P$ of $[O_1(h, k)]_2$ (6.12). The contribution to the wave $[O_1(h, k)]_2$ from these two contours are the same.

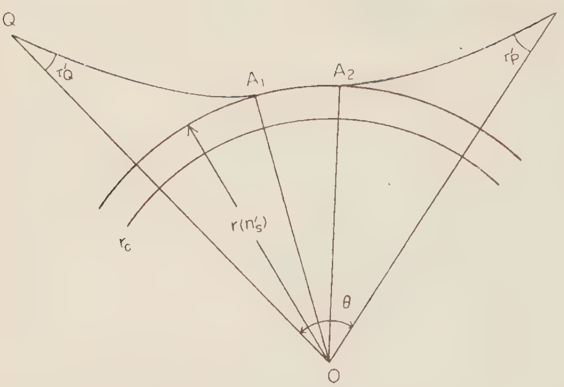

Fig. 5. The contour of integration QA_1A_2P of $[O_1(k,k)]_2$ (6.13).
This wave is one of the two main contributions to the diffraced waves in the geometric optical shadow region. The radius $r(n_s')$ is a little larger than the radius r_c.

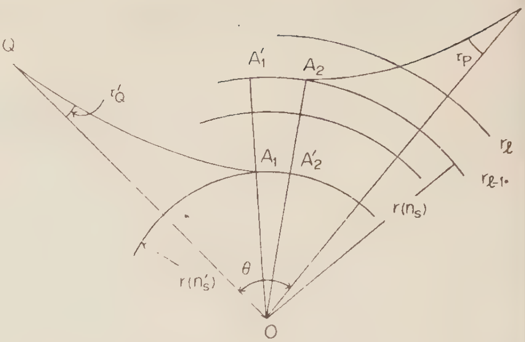

Fig. 7. The contours of integration of $[O_1(k, h)]_2$ (6.15).
The contours are Q_1A_2P. The contribution of these contours are the same.
Toe radius $r(n_s')$ is a little larger than the radius r_c, while the radius $r(n_s)$ is larger than the radius r_c, so that this wave becomes quite small in the shadow region.

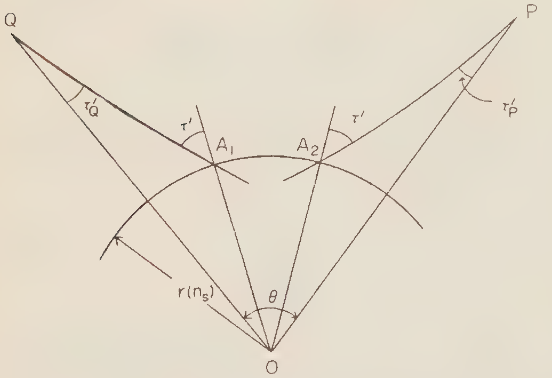

Fig. 6. The contour of integration QA_1A_2P of $[O_1(k, k)]_1$ (6.14). Although the radius $r(n_s)$ is only little larger than the radius r_c, the angle A_1OA_2 is considerably large when P lies in the geometric shadow region because of the small angle of τ', where $\sin\tau'=h_{c+1}/k_{c+1}$.

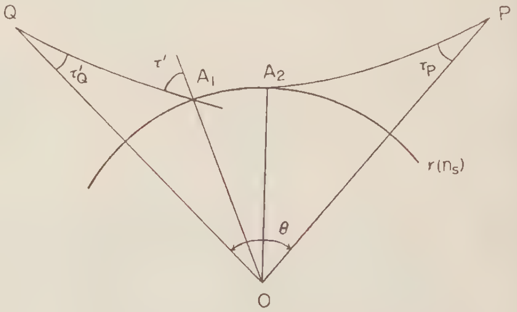

Fig. 8. The contour of integration QA_1A_2P of $[O_1(k, h)]_1$ (6.16).
The radius $r(n_s)$ is a little larger than the radius r_c, but $\tau'<\pi/2$, so that $\angle A_1OA_2$ becomes large in the geometric optical region, and it makes the wave very small.

$$[O_1(h,\ k)]_2=\frac{\sqrt{3}}{\pi\sqrt{(m_{c+1}+1)\,h(c+1,\,r_c)r_c}}$$
$$\times\sum_s\left[(2x_s+y^{(2)2})\sqrt{2x_se^{-i\pi}}\sqrt[4]{\frac{k_{c+1}^2}{h_{c+1}^2}-1}\ H_{1/3}^{(1)}(\zeta)\right]^{-1}\left[\frac{\tan\tau_Q\tan\tau_P}{n_s'r\bar{r}\sin\theta}\right]^{1/2}$$
$$\times\exp\left[i\omega\left\{\int_{QA_1}\frac{ds}{v_h}+\int_{A_1P}\frac{ds}{v_k}\right\}+(\overline{in_s}-\delta n_s)\angle A_1OA_2+F(l-1,c)-\frac{2\pi i}{3}\right],\quad(6.12)$$

$$[O_1(k,\ k)]_2=\frac{3\sqrt{2}}{\pi\sqrt{\pi}}\sum_s\frac{\left(\dfrac{k(c+1,\ r_c)r_c}{m_{c+1}+1}\right)^{1/3}}{x_s(2x_s+y^{(2)2})\left\{H_{1/3}^{(1)}(\zeta)\right]^2}\left[\frac{\tan\tau_Q'\tan\tau_P'}{r\bar{r}n_s'\sin\theta}\right]^{1/2}$$
$$\times\exp\left[i\omega\int_{QA_1A_2P}\frac{ds}{v_k}-\delta n_s'\angle A_1OA_2+\frac{5}{12}\pi i\right],\quad(6.13)$$

$$[O_1(k,\ k)]_1 = -\sqrt{\frac{2}{\pi}}\sum_s \frac{\sqrt{1-\dfrac{h_{c+1}^2}{k_{c+1}^2}\,y^{(1)2}}}{(2x_s+y^{(1)2})\dfrac{k_{c+1}^3}{h_{c+1}^3}\left(\dfrac{h_{c+1}^3}{k_{c+1}^3}-\dfrac{1}{2}\right)^2}\left[\frac{\tan\tau_Q'\tan\tau_P'}{r\bar{r}n_s\sin\theta}\right]^{1/2}$$
$$\times\exp\left[\imath\omega\int_{QA_1}\frac{ds}{v_k}+\int_{A_1P}\frac{ds}{v_k}+i\bar{n_s}\angle A_1OA_2-\delta n_s\angle A_1OA_2+\frac{\pi}{4}\,i\right] \tag{6.14}$$

$$[O_1(k,\ h)]_2 = -\frac{\sqrt{3}}{\pi}\left(\frac{h(c+1,\ r_c)r_c}{(m_{c+1}+1}\right)^{1/3}\frac{k_{c+1}}{h_{c+1}}\,k(c+1,\ r_c)r_c\sqrt[4]{\frac{k_{c+1}^2}{h_{c+1}^2}-1}$$
$$\times\sum_s\left[(2x_s+y^{(2)2})H_{1/3}^{(1)}(\zeta)\sqrt{2x_se^{-\imath\pi}}\right]^{1}\left[\frac{\tan\tau_Q'\tan\tau_P}{r\bar{r}n_s'\sin\theta}\right]^{1/2}$$
$$\times\exp\left[i\omega\left\{\int_{QA_1}\frac{ds}{v_k}+\int_{A_2P}\frac{ds}{v_h}+i\bar{n_s}'\angle A_1OA_2-\delta n_s\angle A_1OA_2+F(l-1,c)+\frac{\pi i}{3}\right]\right.$$
$$\tag{6.15}$$

$$[O_1(k,\ h)]_1 = -\frac{2\sqrt{3}}{\pi}\left(\frac{h(c+1,\ r_c)r_c}{m_{c+1}+1}\right)^{2/3}\sqrt{(m_{c+1}+1)\,k(c+1,\ r_c)}\sqrt[4]{1-\frac{h_{c+1}^2}{k_{c+1}^2}}$$
$$\times\frac{h_{c+1}^2}{k_{c+1}^3}\left(\frac{h_{c+1}^2}{k_{c+1}^2}-\frac{1}{2}\right)^{-1}\sum_s\left[(2x_s+y^{(1)2})H_{1/3}^{(1)}(\zeta)\sqrt{2x_se^{-i\pi}}\right]^{-1}\left[\frac{\tan\tau_Q'\tan\tau_P}{r\bar{r}n_s\sin\theta}\right]^{1/2}$$
$$\times\exp\left[i\omega\left\{\int_{QA_1}\frac{ds}{v_k}+\int_{A_2P}\frac{ds}{v_h}\right\}+i\bar{n_s}\angle A_1OA_2-\delta n_s\angle A_1OA_2-\frac{\pi}{6}\,i\right] \tag{6.16}$$

where $[O_1(\xi,\ \eta)]_1$ and $[O_1(\xi,\ \eta)]_2$ denote the values at the poles near $n=h(c+1,\ r_c)r_c$ and $n=k(c+1,\ r_c)r_c$ respectively, and the meanings of the notations in the right hand side are shown Figs. 1∼8, and

$$F(l-1,\ c)=\omega_{ls}\int_1^{\chi(l,\ l-1)}\frac{\sqrt{1-u^2}}{u}du-\sum_{c+1}^{l-1}\omega_{\sigma s}\int_{\chi(\sigma,\ \sigma-1)}^{\chi(\sigma,\ \sigma)}\frac{\sqrt{1-u^2}}{u}du\ , \tag{6.17}$$

where

$$\chi(\sigma,\ t)=\frac{h(\sigma,\ r_t)r_t}{k(c+1,\ r_c)r_c},\qquad \text{and}\quad h(l,\ r_l)r_l>k(c+1,\ r_c)r_c>h(l,\ r_{l-1})r_{l-1}\ ,$$

$$\omega_{\sigma s}=\frac{n_s}{m_\sigma+1},\qquad \bar{n}_s=n_s+i\delta n_s\ .$$

From the fact that F is always negative and the values of the angle A_1OA_2 in the exponential part of the above waves are considerably different from each other, we can say that only the two waves $[O_1(h,\ h)]_1$ and $[(O_1(k,\ k)]_2$ contribute to the diffracted waves, and the other six waves can be neglected in the shadow region. Thus we may say that there occur only the same kind of the diffracted waves with that of the incident waves.

§ 7 Conclusions

The wave equations of elastic motion of an inhomogeneous medium can be deduced from the equations of motion under several assumptions The wave equation obtained is still rigorous, and we separate it into the longitudinal and transverse parts approximately for the convenience of calculation. The particular solutions thus obtained are the same with those obtained already in the previous paper, where we assumed that they might be the solutions of the wave equations by a physical intuition, and we did not know even the wave equations in an inhomogeneous medium.

Making use of these particular solutions, we discuss the boundary conditions at the continuous boundaries, where the density and the elastic coefficients are all continuous. As the mathematical properties of the wave functions and the various coefficients are similar to those of the electromagnetic waves in an inhomogeneous atmosphere in the previous paper, the same method of calculation can be applied and get the ray waves and the diffracted waves. The behaviour of the ray waves is almost the same with that of the electromagnetic waves, while the diffracted waves have somewhat different properties, because there exist two kinds of waves.

The different kind of the diffracted waves from those of the incident waves are found to be neglisibly small as compared to the same kind of the diffracted waves in the shadow region. If we neglect the former waves, the properties of the diffracted waves are also almost the same with those of the electromagnetic waves.

Acknowledgment

We are indebted to Prof. Y. Nomura for his continuous guidance and encouragement for many years.

References

1) Love, Mathematical Theory of Elasticity, P. 56, P. 79, P. 91.
2) Y. Nomura, K. Takaku: On the Propagation of Elastic Waves in an Inhomogeneous Sphere I. II. Sci. Rep. Tohoku Univ. **4** (1952) 31; Sci. Rep. Tohoku Univ. **5** (1953) 22.
3) Y. Nomura, K. Takaku: On the Propagation of Electromagnetic Waves in an Inhomogeneous Atmosphere I. II. Sci. Rep. Tohoku Univ. **7** (1955) 107; Sci. Rep. Tohoku Univ. **8** (1956) 61; Jour. Phys. Soc. **10** (1955) 700.

JOURNAL OF THE PHYSICAL SOCIETY OF JAPAN, Vol. 16, No. 12, DECEMBER, 1961

Precisionization of Gas Thermometry

By Mitsuru AWANO

Physics Department, Tokyo Institute of Technolog,
Oh-Okayama, Meguro, Tokyo

(Received July 19, 1961)

In order to improve the accuracy of gas thermometry, use of a large bore precision manometer for pressure measurent is contemplated. The loss of accuracy by large dead space inherent to large bore manometer is covered by isolating the manometer with mercury seal in a small U-tube. Between this U-tube and the manometer an auxiliary gas bulb is provided with which the manometer can be set at any desired pressure. Thus, in temperature measurement, the manometer is first set at the pressure calculated for the expected temperature, then the mercury is withdrawn from the U-tube allowing the free passage of gas between the manometer and thermometer bulb. The difference in pressure, if any, before and after the withdrawal of the mercury is read. From this difference, accurate gas pressure is deduced with the least worries about the dead space. An example carried out by this method is shown.

§ 1. Introduction

The determination of thermodynamical absolute temperature of a substance is performed by measuring a physical quantity of which the dependence on the temperature is thermodynamically established. The relations used for the temperature determination are the following: (1) The clausius-Clapeyron equation for the phase transition between liquid and gas. (2) The Planck formula on black body radiation. (3) The Nyquist formula for the mean-square fluctuations in voltage arising from thermal agitation in a passive network[1]. (4) The formula for the sound velocities in gaseous media[2]. (5) The equation of state for gases[3]. At present, temperature measurement by gas thermometers based on the formula (5) gives the highest accuracy in the temperature range from 1°K to 1336°K. However, reduction of dead space is one of deep concerns in gas thermometry: the radius of manometer tube can not be large[4], which, contrariwise, gives rise to large curvature of mercury meniscus[5] limiting the accuracy of pressure reading to 0.01 mm Hg. This has been one of the causes of accuracy of gas thermometry being limited.

On the other hand, perfection of manometer for pressure determination has been a standing problem at leading laboratories[6] of several countries in order to establish the pressure standard and to determine the steam point pressure and sulfur point pressure, and now, pressures less than one atmosphere can be determined with the accuracy of 0.001 mm Hg. In such a manometer, tops of mercury columns must be of large diameter to have the main part of mercury meniscus horizontally flat. But when it is used in gas thermometry, large dead space inherent to large bore of manometer tube lowers the accuracy of temperature determination because of the error involved in the estimation of the dead space.

Such being the case, a layout of a gas thermometer with a precision manometer of large bore was contemplated.

§ 2. Principle of measurement

In gas thermometry, volume and pressure of a gas enclosed in a given bulb are measured in two states of temperature, and the temperature of one state relative to that of the other is determined. The following method of pressure measurement by a precision manometer can be applied to constant pressure gas thermometers and constant bulb temperature gas thermometers[7] as well as to constant volume gas thermometers; here, however, only the constant volume gas thermometers will be dealt with.

2.1. *Layout of the gas thermometer with a small dead space*

The thermometer is shown schematically in Fig. 1. Mercury in small U-tube U of glass capillary separates the gas in bulb V from the gas contained in manometer M in order to eliminate the effect of dead space becoming large by the use of a large bore manometer.

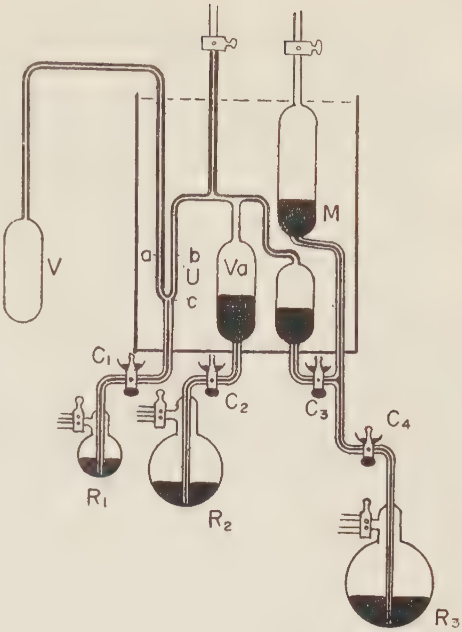

Fig. 1. Gas thermometer with a large bore manometer.
V: Main gas bulb; U: Small U-tube; V: Auxiliary bulb; M: Manometer; C_n: Cock; R_n: Reseroir; **a**, **b**, **c**: Marks.

If the volume of gas bulb V, the thermal expansion coefficient of the bulb material, and the volume and temperature of the gas contained in the capillary from bulb V to mark **a** on the left column of U are known with sufficient accuracy, then, for the constant volume gas thermometer, it is only necessary to measure accurately the gas pressures p_1 and p_2 at two temperatures T_1 and T_2 respectively of the bulb. These two pressures cannot be measured directly by the manometer because of its separation from the bulb by the U-tube mercury. They are determined as follows. The bulb being at temperature T_1, the ice point, the top of the mercury in the U-tube is first set at mark **c** by manipulating the flow of mercury of reservoir R_1, and the pressure p is measured accurately by the manometer. The mercury is then raised to mark **a** and cock C_1 is closed. The mercury in the right column of U comes to mark **b** which is practically level with mark **a** and is marked.

Thd pressure p_1 of the gas enclosed in bulb V in this state, called State I, is calculated from the following equation:

$$p_1\left(\frac{V_1}{T_1v}+\sum_s\frac{v_s}{T_{sv}}\right)=p\left(\frac{V_1}{T_{1v}}+\sum_s\frac{v_s}{T_{sv}}+\frac{v}{T_{mv}}\right), \tag{1}$$

where

V_1=the volume of the gas bulb at temperature T_1,

T_{1v}^*=the temperature of gas occupying V_1.

v_s=the volume of glass capillary between bulb V and mark **a** at temperature T_s,

T_{sv}=the temperature of gas occupying v_s,

v=the volume of capillary between mark **a** and mark **c**,

T_{mv}=the temperature of gas occupying v.

With cock C_3 closed, the bulb temperature is then changed to T_2. The mercury heads in U, which change, are adjusted to original positions **a** and **b** by letting the mercury in reservoir R_2 flow into auxiliary bulb V_a or out of it.

The pressure p_2 of the gas in this state, called State II, is determined as follows. Since we know approximate value of the pressure of gas in the bulb at T_2, the manometer, with cock C_3 still closed, is set at this pressure by manipulating the flow of mercury of reservoir R_3, then cock C_4 is closed. When cock C_3 is opened, there will be some change in the manometer reading. Let this revised pressure be p'. The mercury in U is next lowered to mark **c** and the manometer reading is again taken. Let this pressure be p''.**

The gas pressure p_2 in State II is then obtained by the following equation:

$$p_2=p''+\frac{U'}{U}(p''-p')+\frac{\Delta}{U}p'' , \qquad (2)$$

where

$$U=\frac{V_2}{T_{2v}}+\sum_s\frac{v_s}{T_{sv}} , \qquad (3)$$

$$U'=\frac{V_a}{T_{mv}} . \qquad (4)$$

$$\Delta=\frac{v+v'+w}{T_{mv}} , \qquad (5)$$

and

V_2=the volume of the gas bulb at temperature T_2,

T_{2v}=the temperature of gas occupying V_2,

v'=the volume of the U-tube between marks **b** and **c**,

w=the volume change in the lower column of the manometer caused by lowering of mercury in U to mark **c**,

V_a=the volume of gas occupying the capillaries and V_a between mark **b** and the manometer mercury surface.

Since the pressure difference $p''-p'$ in Eq. (2) can be made sufficiently small, the value of U'/U needs not to be exact; an approximate value of U', and hence, an approximate value of V_a, is all that is required which is calculated from

$$V_a\ p'=(V_a+V_m-V_M)p , \qquad (6)$$

where

V_m=the volume of mercury brought into (or taken out of) auxiliary bulb V_a to effect the pressure change from p to p' (from State I to State II),

V_M=the change in volume in the lower column of the manometer by the change of manometer mercury surface.

V_m is obtained by weighing the mercury of reservoir R_2 in State I and State II, and V_M is obtained from displacement of mercury surface and bore of the tube, which needs not to be exact. But Δ/U, the coefficient of p'' of the last term of Eq. (2), should be accurate for which v, v', and w that appear in Eq. (5) must be measured as accurately as possible despite small quantities. Volumes v and v' are obtained from bore of the capillary and the volume $v+v'$ is obtained from the difference in weights of mercury of reservoir R_1 in two cases when the mercury head is at mark **c** and when it is at marks **a** and **b**. The volume w is obtained from the displacement of the mercury surface and the bore of the tube provided the form of meniscus remains the same.

Now, when the pressures p_1 and p_2 are obtained by Eqs. (1) and (2), the gas temperature T_{2v} is determined by

---

* Temperatures with suffix v mean the temperature on the constant gas thermometer scale.

* State I. Bulb temperature: T_1; Gas pressure: p_1; Mercury heads in U-tube: mark **a** and mark **b**.

State II. Bulb temperature: T_2; Gas pressure: p_2; Mercury heads in U-tube: mark **a** and maar **b**.

p_1: Gas pressure in State I,

p_2: Gas pressure in State II,

p: Manometer reading; mercury top in U-tube at mark **c** before State I,

p': Manometer reading; mercury top in U-tube at marks **a** and **b**, manometer set at pressure expected for gas temperature T_{2v}, then cock C_3 opened,

p'': Manometer reading; mercury top in U-tube lowered to mark **c** after State II.

$$T_{2v}=T_{1v}\frac{p_2}{p_1}\cdot\frac{V_2+T_{2v}\sum_s(v_s'/T_{sv}')}{V_1+T_{1v}\sum_s(v/T_{sv})}\,, \tag{7}$$

and the Kelvin temperature T_2 is given by

$$T_2=T_2v\{1+(\boldsymbol{B}_1-\boldsymbol{B}_2)p_1\}\,, \tag{8}$$

where $\boldsymbol{B}_1$ and $\boldsymbol{B}_2$ are the slopes of $pV-p$ isotherms of the gas at temperatures T_1 and T_2 respectively.

2.2 *Successive approximation method*

In the above-described process of determining the pressure p_2 in State II, the error on w due to the change in form of meniscus becomes large as the bore of tube is large, on which account, use of a large bore manometer lowers rather than improves the accuracy of temperature measurement. To make up for this drawback, successive approximation method for pressure measurement was applied.

In the first step, the mercury is let into or out of the auxiliary bulb so that the reading of the manometer becomes equal to p' given by

$$p'(U+\Delta_1)=p_2{}^*U\,, \tag{9}$$

where

$$\Delta_1=\frac{v+v'}{T_{mv}}\,, \tag{10}$$

$$p_2{}^*=p_1\frac{T_{2v}{}^*}{T_{1v}}\frac{V_1+T_{1v}\sum_s(v_s/T_{sv})}{V_2+T_{2v}\sum_s(v_s'/T_{sv}')}\,, \tag{11}$$

and

$T_{2v}{}^*$ = the gas temperature to be determined. The temperature can be any one of the now established fixed points.

Next, the mercury heads in the U-tube are lowered to mark c and the pressure p'' is measured. If $p_2=p_2{}^*$, it will be $p''=p'$. But in general there is a small difference δp^* $(=p''-p')$ owing to the difference between p_2 and $p_2{}^*$. If δp^* is small, there will be only a small change in height of manometer mercury meniscus and no change in contact area between mercury and manometer walls. This markes the estimation of w a problem, yet there is the following relation

$$w<S\frac{\delta p^*}{2}\,, \tag{12}$$

where S denotes the cross-section of the manometer tube in contact with mercury head. The factor $\frac{1}{2}$ is used on consideration of two mercury meniscuses at the upper and lower column of the manometer.

When the relation $w=(S\delta p^*)/2$ is assumed and used in Eq. (2), an approximate value $p_2{}^{**}$ of the pressure p_2 is obtained as

$$p_2{}^{**}=p_2{}^*+X\delta p^*\,, \tag{13}$$

where

$$X=1+\frac{U'}{U}+\frac{W}{U}\,, \tag{14}$$

$$W=\frac{Sp''}{2T_{mv}}\,. \tag{15}$$

$p_2{}^{**}$ is closer to p_2 than $p_2{}^*$. Substituting this $p_2{}^{**}$ for p_2 in Eq. (7) and denoting the temperature thus obtained by $T_{2v}{}^{**}$, we have

$$T_{2v}{}^{**}=T_{2v}+Y\delta p^*\,, \tag{16}$$

where

$$Y=T_{1v}\frac{V_2X}{p_1V_1}\,. \tag{17}$$

$T_{2v}{}^{**}$ becomes closer to T_{2v} than $T_{2v}{}^*$.

Resetting State I and State II afresh, repeating similar processes, and substituting $T_{2v}{}^{**}$ for $T_{2v}{}^*$ in Eq. (9), we obtain $T_{2v}{}^{***}$ which is still closer to T_{2v} than $T_{2v}{}^{**}$. Such successive approximation can be carried on till δp^* becomes a value which is within experimental error, and eventually the accuracy of measuring the pressure p' determines the accuracy of T_2.

§ 3. Experimental Procedures

As an example in which the preceding method was used, the steam point was determined relative to the ice point by a gas thermometer with a large bore manometer.

3.1. *Apparatus*

Ice point and steam point apparatus used in this work were those used before when we participated in international comparison of fundamental temperature intervals conducted under the auspices of a committee belonging to Bureau International des Poids and Mesures[8]. Reproducibility of these temperatures is within 10^{-3} deg. All glass parts of the gas thermometer are of hard glass. Small U-tube U, auxiliary bulb V_a and manometer M (Fig. 1) are placed in a water thermostat at about 17°C. The U-tube is of 0.4 mm capillary, its bottom T-joint was made with great care for the gas passage to be narrow. Bore of the manometer tube where the pressure is read is 4 cm. The volume of bulb V at 0°C was determined by weighing the mercury that filled the bulb in vacuum. The thermal volume expansion coefficient of the bulb was obtained from the linear expansion coefficient of silica glass in temperature range from 0°C to 100°C which is, according to Beattie et al.,[9] $0.50\times10^{-6}\ \mathrm{deg}^{-1}$, with which the volume of the bulb at temperature t°C was obtained by

$$V=146.980(1+1.86\times10^{-5}t)\ \mathrm{cm}^3 .$$

3.2. *Method of determing the height of manometer mercury surface*

Figs. 2 and 3 explain the method. Glass scale S of 2 mm graduation is set close behind the manometer tube. Scale lines s and their reflected images s′ are viewed through a microscope of 60 times magnification and 50 cm long held nearly horizontal to bring 4 reflected lines into the field of vision. The reflected lines should be neither too many nor too few, lest the discrimination of correspondence between direct and reflected images would become difficult. This means that the portion of the scale about 1 mm above the mercury surface is viewed. An ocular micrometer divides every line interval into 120 equal parts, every part of which is further divided into 5 parts by eye estimation. This gave the error of ±0.0020 mm on the reading of scale S.

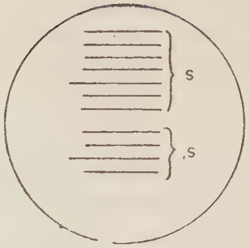

Fig. 3. Image in eye piece.
s: Image of scale; s′: Mirror image of s.

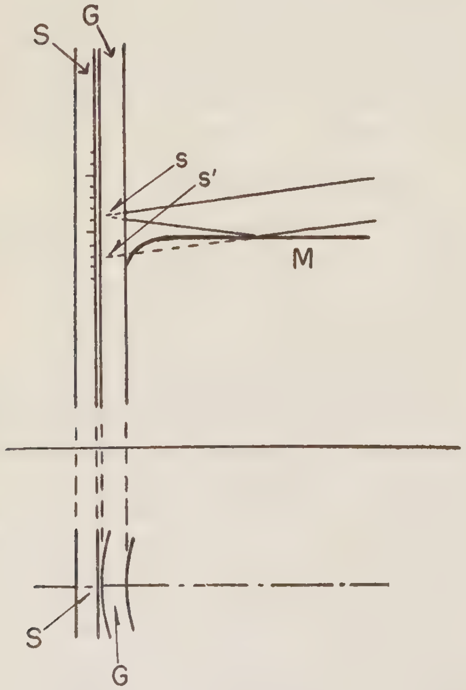

Fig. 2. Method of measuring the height of mercury surface.
S: Glass scale (0.2 mm graduation); s: Image of scale; s′: Mirror image of s; G: Glass wall of manometer; M: Mercury surface.

As the light from the scale is not of parallel rays, graduation intervals of the scale that come into view by direct rays and by reflected rays will be different because of the refraction of manometer wall by different incident angles. However, for the glass cylinder wall of 1.6 mm in thickness and 20 mm in radius of curvature and for the field of vision of less than 1 mm of the scale, the difference in viewed intervals between s and s′ will not exceed 1μ by the law of refraction. In fact, observation made with the ocular microscope gave

$$s/s'=1.004\pm0.006$$

The height of manometer mercury surface was determined by the above means as represented by the center of corresponding pair of direct and reflected scale lines. Error in measuring approximately 100 mm Hg pressure was less than 0.004 mm Hg.

Here it should be noted that, for the estimation of w (Eq. (5)), form of manometer mercury meniscus must always remain the same, for w is the product of cross-sectional area of the tube and displaced level distance of the mercury surface. Therefore, to reproduce the same form of meniscus every time when the manometer reading was taken, the meniscus was made to be in pushed-up condition by varying the amount of mercury in reservoir R_3. However, in a tube of 4 cm bore, volume of gas that fills the space below the horizontal plane tangential to the top of mercury meniscus is estimated at 0.20 cm³.[5] This implies that even a slight difference in the form of meniscus may cause uncertainty of the value of w.

3.3. *Results of measurement*

Nitrogen gas was used as the thermometer gas. The pressure p, p', and p'' were measured in this order by the method of measurement outlined in Section 2, and the values p_1 and p_2 were calculated from Eqs. (1) and (2). The boiling point of water was determined relative to the freezing point $T_0=273.15°\mathrm{K}$ by taking, in one case, the former as State II, the latter as State I, and in another case, the order is reversed. The results obtained are given in the accompanying table: In the calculation the following values were assumed:

$$v=v'=0.004\ \mathrm{cm}^3\,, \qquad \sum_s v_s=0.743\ \mathrm{cm}^3\,,$$

and for the virial coefficients of gas at the ice and steam points

$$B_1=-59.1\times10^{-5}\ \mathrm{m\ Hg}^{-1}\,,$$
$$B_2=38.6\times10^{-5}\ \mathrm{m\ Hg}^{-1}\,.$$

In the table, V_a is the volume which would be the dead space if the manometer were in direct connection with the thermometer bulb; T_{boil} is the temperature of steam of steam point apparatus at the atmospheric pressure measured concurrently; Δ is the difference $T_{\mathrm{obs}}-T_{\mathrm{boil}}$. Standard deviation of Δ was 0.019 deg which is attributed to the errors on manometer reading and w.

Table I. Experimental data.

mm Hg p_1	mm Hg p'	mm Hg p''	cm³ V_a	cm³ w	mm Hg p_2	°K T_{obs}	°K T_{boil}	deg Δ
79.443	109.140	108.631	31.3	—0.326	108.209	373.360	373.357	0.007
80.229	110.418	109.883	34.6	—0.349	109.233	373.171	373.145	0.026
79.994	107.202	108.097	33.7	0.548	108.837	372.957	372.964	—0.007
108.816	80.616	80.161	70.1	—0.299	79.747	373.334	373.353	—0.019
							Standard deviation	0.019

mm Hg p_1	°K T_{biol}	mm Hg p'	mm Hg p''
80.194	373.172	109.177	109.175

The values obtained by the successive approximation method are given in the bottom row of the table. They are free from w. The temperature T_{biol} of steam point boiler was calculated as 373.172°K from the measured value 760.598 mm Hg of the boiling pressure for which the relation between the boiling pressure and temperature given in the Recommendation of 1948 International Practical Temperature Scale (1948 I.P.T.S.) was used. For the verification of this value, pressure of the gas thermometer was set at $p_1=80.194$ mm Hg in State I, and this value and $T_{2v}{}^*=373.201°\mathrm{K}$. which was the value of T_{boil} on the constant volume gas thermometer scale, were used in Eqs. (9) and (11) to obtain p' which was found to be $p'=109.177$ mm Hg. The manometer being set at this pressure, $p''=109.175$ mm Hg, which was then measured, agreed with p' within the experimental error of 0.004 mm Hg. This also proved that the pressure p_2 in State II agreed with $p_2{}^*$ within experimental error.

This verified that the value of T_{boil} determined according to the Recommendation of 1948 I.P.T.S. was correct on the thermodynamic scale. In this case in which the value of the fixed point used was well known on the thermodynamic scale, use of the second step of sccessive approximation was not necessary.

§ 4. Discussion and Conclusion

In the above measurement, the error on manometer reading was 0.04 mm Hg at the pressure of about 100 mm Hg. The accuracy of pressure measurement could not be made higher than this figure and the pressure could not be raised above 120 mm Hg because of the manometer being placed in water thermostat. Therefore, the accuracy of gas thermometry in the present case could not be made higher than that of usual gas thermometry with a manometer capable of measuring pressures up to 760 mm Hg with 0.01 mm Hg accuracy, and the obtained result had error of some magnitude.

When a gas thermometer is used at about 100 mm Hg pressure as in the present experiment, the gas is more alike to the ideal gas than it is at about one atmosphere as in the usual case and $(B_1-B_2)p_1$ in Eq. (8) is small. Thus, the error caused by the difference[10] between the values of virial coefficients B_1 and B_2 obtained by different investigators will not affect the final results. In the case when a gas thermometer with an accurate monometer for low pressures, capable, for instance, of measuring 0.001 mm Hg or less at about 100 mm Hg pressure is to be used, the present method of measurement becomes applicable. It may also be applicable to the case when a wide bore manometer made to measure pressures in the neighbourhood of 760 mm Hg with the accuracy of 0.001 mm Hg is used.

Acknowledgements

The author wishes to express his heartfelt thanks to Prof. J. Oishi for stimulating discussion, and to Dr. M. Kinoshita for reading the manuscript and for his valuable comments.

References

1) J. B. Garison and A .W. Lawson: Rev. Sci. Instr. **20** (1949) 20. H. J. Fink: Can. J. Phys. **37** (1959) 1397.
2) A. D. Brodkii: Bull. of Mendeleev Institute **49** (**109**) (1960) 24.
3) J. Oishi: J. Sci. Research Inst. **43** (1949) 199. J A. Beatlie, M. Benedict and J. Kaye: Proc. Amer. Acad. Arts Sci. **74** (1941) 343.
4) J. Oishi, M. Awano and T. Mochizuki: J. Phys. Soc. Japan **11** (1956) 311.
5) J. E. Sears and J. S. Clark: Proc. Roy. Soc. **A. 139** (1933) 130.
6) H. F. Stimson: Proces.Verbaux CIPM. **23-B** (1952) T 82. R. J. Berry: Can. J. Phys. **36** (1958) 740. K. W. T. Elliott, D. C. Wilson, F. C. P. Mason and P. H. Bigg: J. Sci. Instr. **37** (1960) 162. I. Oyama, K. Koizumi et R. Kaneda: Proces-Verbaux CIPM. **26-A** (1958) T 220.
7) H. Moser, J. Otto und W. Thomas: Z. Phys. **147** (1957) 59 und 76. J. Oishi: J. Phys. Soc. Japan **16** (1961) 2056.
8) C. R. Barber and J. A. Hall: Proces-Verbaux CIPM. **26-A** (1958) T 35.
9) J. A. Beattie, M. Benedict and J. Kaye: Proc. Amer. Acad. Arts Sci. **74** (1941) 343.
10) W. Thomas: Z. Phys. **147** (1957) 92.

JOURNAL OF THE PHYSICAL SOCIETY OF JAPAN, Vol. 16, No. 12, DECEMBER, 1961

A Pumped Klystron Amplifier and RF Power System for the Injector Linac of 1 BeV Electron Synchrotron

By Akira MIYAHARA

Institute for Nuclear Study, University of Tokyo,
Tokyo, Japan.

(Received April 8, 1961)

A power klystron amplifier and its driver system for a 6 MeV linear electron accelerator are described. The klystron is evacuated during its running by specially designed two oil diffusion pumps connected in series. Without using a liquid nitrogen trap the klystron works stable with the peak power output of 2-3 MW. The average life of the oxidecoated cathode was more than 500 hours. In order to keep a good frequency stability a feed back oscillator with an invar cavity and a travelling wave tube is used as a master oscillator. The output of this oscillator is 1-2 W at a frequency of 2759 Mc, with the fluctuation being less than 20 kc. The output signal of the oscillator is amplified by a pulsed travelling wave tube amplifier to drive the power klystron.

§ 1. Introduction

A 6 MeV linear electron accelerator has been constructed for the injector of the 1 BeV electron synchrotron. Because of the acceptance of the synchrotron, this linear electron accelerator is required to have very good energy spectrum such as a few percent at half width.(1) In order to obtain such a narrow energy spread, it is necessary that the microwave frequency has good stability less than ±5 kc in 2759 Mc at the output power of 2-3 MW. Magnetrons are widely used as the rf power source for linear electron accelerators, but they do not have the frequency stability sufficient for our purpose. Then we adopted a klystron amplifier driven by a power from a travelling wave tube which amplifies the output of a travelling wave tube feed back oscillator. The overall block diagram of the rf power system is given in Fig. 1.

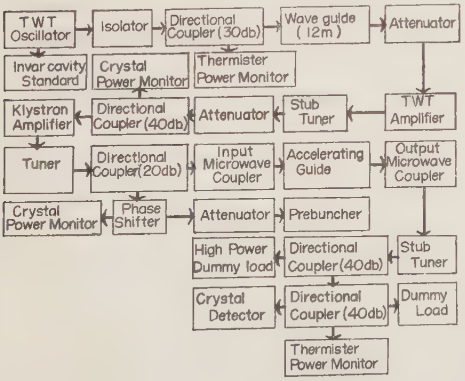

Fig. 1. Block diagram of the rf power system.

Pumped klystrons, which have been used for the linear electron accelerator at Stanford,(2) are pumped by oil diffusion pumps with liquid nitrogen traps. In our case, the klystron is pumped by an improved oil diffusion pump without any refrigerated trap. Moreover, the cathode of the pumped klystron can be replaced by opening a flange of vacuum manifold, and we can get a practically new klystron.

§ 2. The Pumped Klystron

(a) *Vacuum system*

Up to date, pumped klystrons are, as in Stanford, designed to be able to seal off easily when demensions of tubes are determined. Whereas, our klystron is designed as a pumped klystron as a final form. First of all, we take care to keep the cathode in good vacuum. The vacuum manifold around the cathode is 10 inches in diameter, and is connected directly to an 8 inches oil diffusion pump through a 10 inches pipe. To obtain a good ultimate pressure of the pumping system and to reduce the back diffusion of oil, it is necessary to get rid of higher vapour pressure components in the pump oil. For this purpose, we connected two, each 8 inches and 3 inches, well fractionating oil diffusion pumps in series.

We omitted the cooling pipe at the back side pipe of each pump, so that the cooling of the main cylinder is limited to the part where the jet stream strikes the cylinder. As the result, the temperature of the back side pipe is moderately high (50–100°C). Under these conditions, the components of high vapour pressure will pass easily into the backing 3 inches pump and then to the rotary pump. Moreover, to reduce the back diffusion of oil, an attention was paid to the design of the form of the pump jet, especially of the top jet. By setting the thermal shield of the top jet, the back diffusion of the pump system is also reduced largely.[8]

Table I. Indication of the bared and normal ionization gauge for various klystron heater currents.

Heater current (A)	0	20	23
B.G. indication (mmHg)	3.3×10^{-7}	6.6×10^{-7}	7.2×10^{-7}
N.G. indication (mmHg)	2.0×10^{-7}	3.4×10^{-7}	3.6×10^{-7}

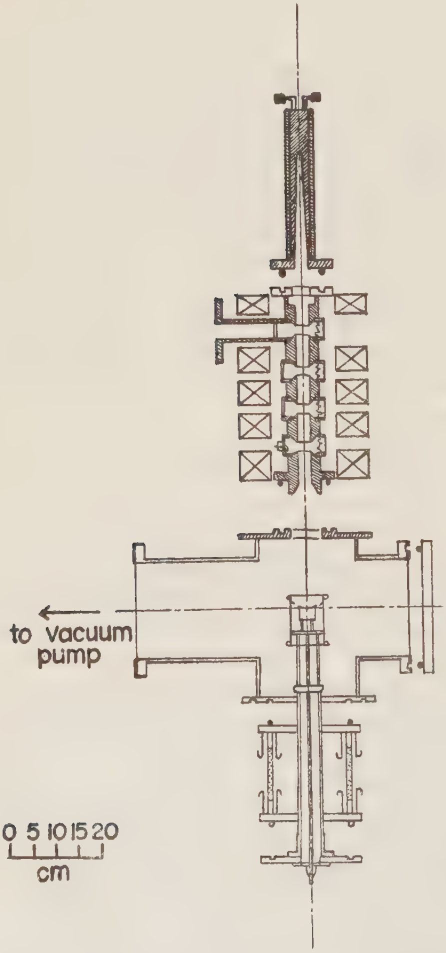

Fig. 2. Construction of the pumped klystron amplifier.

The measurement of the pressure has been done by both vacuum tube type (normal) ionization gauge and bared (so called high speed) ionization gauge. Because of the rapid responce and good sensitivity to the condensable gases, we use the bared gauge mainly, and for the convenience of comparison to other data, we use the normal ionization gauge too.(4) Results of the measurement at room temperature of 20°C are shown in Table 1.

The operation of the vacuum system is almost continuous and it is stopped only from Saturday afternoon till Monday morning. When the pump is stopped, the pressure increases gradually to 1×10^{-3}mmHg in one and a half day by outgassing from walls. But it takes only two hours to reach the pressure below 2×10^{-6}mmHg from the start of the pumping system. A carefully designed control and interlock system defends the klystron and vacuum system against any accidental failures.

(b) *The conversion and performance of the oxide coated cathode*

The behavior of the oxide coated cathode in an continuously evacuated system has been reported by several authors.[5] It is shown that the oxide coated cathode can be used under some considerations. But all their pumping systems have some kinds of the trap such as liquid nitrogen trap, alumina trap(6) or any other refrigerated trap in addition to the oil diffusion pump. If we could get the stable electron emission from the oxide coated cathode without using any cold trap by improving the oil diffusion pump, the treatment of the pumping system would become very simple. We attempted to eliminate the use of any cold trap by use of the pumping system described before.

The cathode of the pumped klystron is 65 mm in diameter. The base metal is made of pure nickel with magnesium as a reducing agent and a fine nickel mesh spot-weldered on it. The cathode is painted with the conventional oxide material ($BaCO_3$, $CaCO_3$, $SrCO_3$‘ ternary compound) suspended by collodion binder. The current density is about 2–3 A/cm^2 at the maximum rating of the klystron.

The design considerations on the cathode heater are as follows: (1) uniform heating of the cathode surface. (2) long life of filament. (operating temperature of the filament is below 2000°C) (3) the filament current less than 25 A since it is desired to use no autotransformer at the high potential terminal of the pulse transformer. The non-uniformity of the cathode is kept within 3–5°C at 900°C, over the cathode surface. The relations between the heater current, heater temperature, and cathode temperature are shown in Fig. 4.

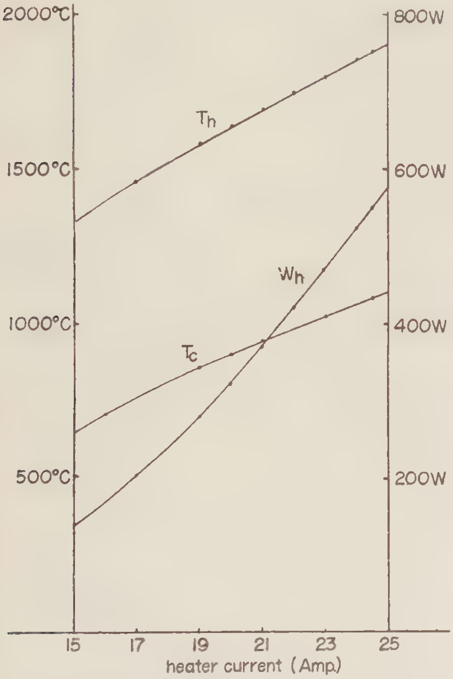

Fig. 4. Heater wattage, heater temperature and cathode temperature vs heater current of the klystron amplifier.

The conversion process of the cathode is not the same as in that of an ordinary seal off vacuum tube. In the earlier stage of our work, many of the cathode had very poor emission in spite of careful processing in good vacuum condition. Such a cathode changed its colour to gray or black, when we took out from the vacuum system. This was caused by the incomplete combustion of the collodion binder. In the ordinary seal off vacuum tube fabrication system, the conductance of the pipe is very small, so the atomosphere of the cathode is full of carbon dioxide gas at the conversion process. The pure carbon, which is produced from the collodion binder by the incomplete combustion, is then oxidized into carbon monoxide and is removed from the cathode. In our case, the conductance of the vacuum manifold around the cathode is very large, so that the pressure of carbon dioxide can be low and the pure carbon can not be oxidized and remains on the surface of the cathode. This hinders the electron emission. In order to avoid this impediment of the incomplete combustion of collodion binder, we must raise the cathode temperature up to the conversion temperature, 850°C, as quick as possible, so as to get high partial pressure of carbon dioxide gas during conversion process. By this process, we can obtain a good converted cathode everytime.

When the conversion of the cathode is finished and the vacuum around the cathode become sufficiently good, about 5×10^{-6}mmHg or lower, we impose the d.c. voltage of 1000 volt as a check of the emission and the perveance. Then we increase the d.c. beam voltage up to 3000 volt and get the beam current of 100–300 mA. By this beam current, the degassing of the klystron cavities and the collector are done. The pressure increases up to 1×10^{-5}mmHg by out gassing of cavity wall and after six to eight hours, the pressure resumes to $2\text{–}3\times10^{-6}$mmHg, then we cease to impose the beam voltage. Thus, the preparations for adding high pulse beam voltage are all over.

Because the activity of the oxide coated cathode in the pumped klystron is rather poor in comparison with the sealed off tube, the cathode must be used at a rather high temperature. The cathode temperatre must be raised higher as the beam voltage increases, in order to operate the cathode in the space charge limited region. If the cathode temperature becomes high, barium and barium oxide evaporate and emission of the oxide cathode becomes poor. The life of the cathode is determined by (1) ion bombardment, (2) flaking of the cathode surfaces by recombination dissociation cycle of barium hydrooxide, and (3) selective evaporation of the most emissive compound barium oxide by raising the cathode temperature. Fortunately, all of these effects are not serious under the vacuum condition of our pumped klystron. The mean life of the cathode is not exactly given, but it is at least more than 500 hours.

(c) *Operation of the pumped klystron*

After the preparations for imposing high pulse beam voltage are all over, we operate the klystron by increasing the pulse beam voltage. When we raise the beam voltage, we must check the discharge occurred in the klystron by the pressure indication near the cathode and by the emission current varaition. We need about 30 minutes to raise the beam voltage up to 150 kV. Then the rf driving power is fed and further outgassing is observed, though this is cleaned up quickly.

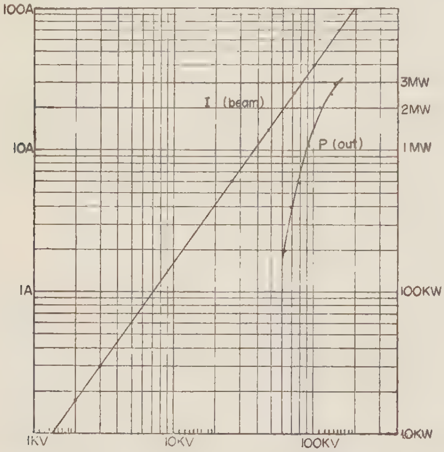

Fig. 5. Klystron peak power output and beam current vs beam voltage.

Measurement of the power has been done by a well calibrated directional coupler and using a thermister bridge power meter. We adjust the resonant cavites and focussing coils so as to get the maximum power output at the given beam voltage. After the abjustment, the klystron operates very stable all day long. Operation characteristics of the klystron are shown in Fig. 5.

§ 3. Pulser and Pulse Transformer

The pulsed high voltage for the klystron is produced by an ordinary line type pulser and a pulse transformer.[7] The hydrogen thyratron 5948 is used as the switching tube and the primary pulse voltage is 12.5 kV. This primary voltage is stepped up to 160 kV by a 13 : 1 pulse transformer. To obtain a good pulse shape, we use a specially designed cable of 400 meters in length as the pulse forming line which has the characteristic impedance of 15 Ω.

Table II. Character of the klystron amplifier

Operating frequency	2760 Mc ± 30 Mc
Operating beam current	150 kV
Operating beam current	60 A
R. F. power output	3 MW
Pulse repetition rate	21.5 cycles
Pulse duration	4 μ sec
R. F. power gain	40 db
Heater power	500 W

Table III. characteristics of the pulse transformer for the klystron amplifier

Primary windings	5 turns
Secondary windings	65 turns
D.C. bias windings	2 turns
Monitor winding	1 turn
Primary impedance	15 Ω
D.C. bias current	10 A
Secondary bifilar current	max. 25 A
Core material	0.1 mm thick grain oriented silicon steel
ΔB	1.5 Wb/m^2
μ_e	3000
A (cross section of the core)	9×9 cm^2
Window size	12×15 cm^2
Peak output voltage	150 kV
Droop	1.5%/μ sec
Rise time	0.3 μ sec

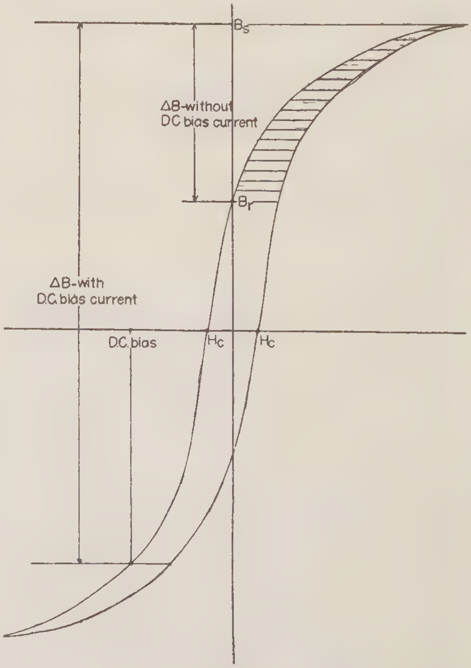

Fig. 6. A hysteresis curve of the core material.

The pulse transformer, with the step up ratio of 13 : 1, uses the d.c. bias method.(8) As the imposed primary pulse voltage is unidirectional, the usable region to the core without the d.c. bias is limited only to the hatched region of Fig. 6.

In other cases, the effective region of the core would be increased by making air gap in the magnetic path or improving the core material so as to have large usable region. This, however, can be achieved at the sacrifice of the high permeability of the core, and as the result the characteristics of the pulse transformer become bad. On the other hand, both large ΔB and high μ can be obtained by d.c. bias method, and we can get a pulse transformer which has such good characteristics as table III.

§4. Driver System of the Klystron Amplifier

(a) *Master oscillator*

As the frequency stability of the rf power system is mainly determined by the frequency stability of the master oscillater, we must take care of the selection of the master oscillator unit. Toshiba model 7851 travelling wave tube is used as an oscillator, by feeding back to the input from the output of the tube through a directional coupler and a standard cavity resonator. The main causes of frequency instability are the drift of the resonant frequency of the cavity by temperature variations and heating up of the helix of the tube.(9) The former can be avoided by using a small expansion coefficent material, invar, as cavity walls. The measured temperature dependance of the resonant frequency of the TE_{111} mode is about 2.7 kc/deg, and it is agreed with the calculated value of 2 kc/deg. The next problem to get the stable operation is to obtain the good electron beam transmission of the tube. The operation of the travelling wave tube becomes unstable due to the heating of the helix if the transmission is poor. To avoid such trouble, we have set

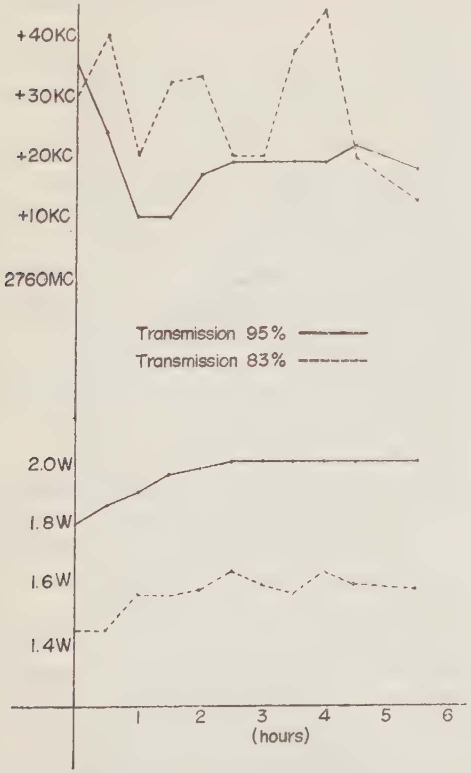

Fig. 7. Frequency stability of the travelling wave oscillator.

Table IV. Characteristics of 7850 travelling wave tube amplifier

Beam voltage	7 kV
Beam current	0.7 A
Pulse duration	5 μ sec
Pulse repetition rate	21.5 cycles
Power gain	25 db

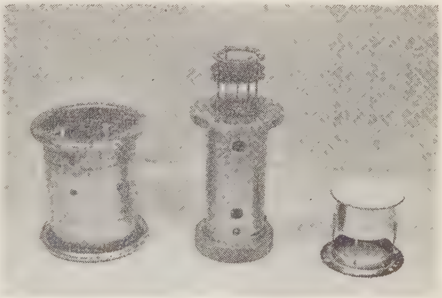

Fig. 3. Cathode and heater mount.

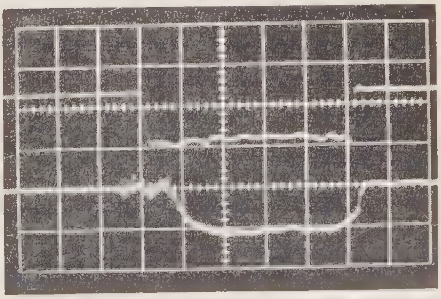

Fig. 8. Microwave pulse rectified by a crystal detector. Upper trace for the travelling wave tube amplifier; lower for the klystron amplifier.

an equalizer in the focussing permant magnet[10] and made the axis of the magnetic field so as to coincide with that of the travelling wave tube. Then we can obtain the transmission of 95%. Although the maximum transmission does not always correspond to the maximum power output, we adjust the apparatus to the maximum transmission in order to get the stable operation.

The microphonic noise, which is mainly caused by the vibrations due to the synchrotron magnet, also brings the bad effect to the stable operation. We set the oscillator in the main control room, about 10 meters apart from the synchrotron room, to reduce this effect. Unidirectional waveguide is used at the output of the oscillator, so as to avoid the long line effect of the waveguide. With such a caution, we get 1–2 watt power output at 2759 Mc with the frequency fluctuation less than 10 kc.

(b) *Buffer amplifier*

To amplify the output power of the oscillator to 200–300 watts, which is sufficient to drive the klystron, we use a pulsed travelling wave tube amplifier. The typical characteristics of this travelling wave tube amplifier are shown in table IV.

The pulser of this amplifier is also an ordinary line type pulser. The hydrogen thyratron 5C22 is used as the switching tube and RG-8U coaxial cable of 500 meters long is used as a pulse forming line. Because the cable has the characteristic impedance of 53 Ω, a dummy load is connected in parallel to the travelling wave tube so as to get good impedance matching. The photograph of the oscilloscope's pattern of the microwave pulse rectified by a crystal detector is given in Fig. 8.

§ 5. Overall Operation of the rf Power System

As previously described, the frequency stability of the rf power system is determined mainly by the frequency stability of the master oscillator. The instability within 20 kc per day can be obtained, satisfying the design requirement of ±50 kc.[1] Power output of the master oscillator is 1–2 watt, and it is sufficiently large to drive the amplifier travelling wave tube. Since the klystron amplifier and the travelling wave tube amplifier are used at the nearly saturated level of the driving power, the power output change of the klystron amplifier is mainly caused by voltage variations of the pulsed power supply. This is influenced by the linear droop of the pulsed beam voltage and variation of the d.c. supply voltage. As was shown in Table III, the linear droop of the pulse wave form is within 1.5%/μsec. As for the primary d.c. voltage, variations of about 5% were observed by the change of line voltage at the time of starting and stopping of the cyclotron in our Institute. Further improvement of the stability of the d.c. voltage will be given by using a vacuum tube type voltage stabilizer in near future.

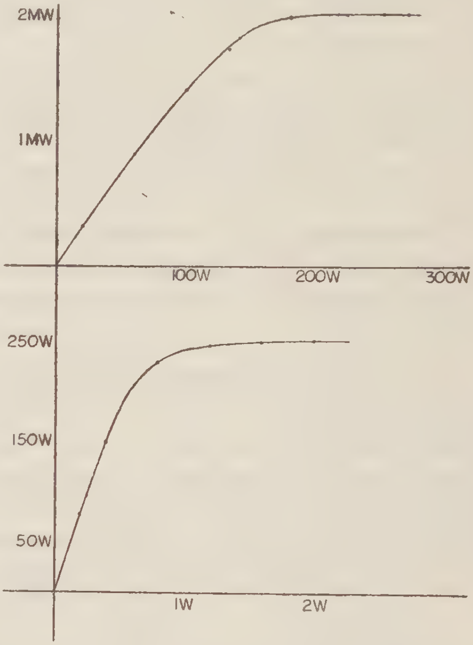

Fig. 9. Input power vs output power of the klystron and travelling wave tube amplifier

The output power of the klystron feeds through the rectangular waveguide and the microwave coupler into the accelerating tube. As the attenuation of the accelerating tube is about 3 db, a half of the input power goes into the end of the accelerating tube. The remaining power goes down into the microwave high power dummy load through a microwave coupler at the end of the accelerating tube. A portion of the microwave power, which is branched by a 20 db directional coupler, is fed into the prebuncher cavity through a phaseshifter and an attenuator. All of the high rf power systems are used in vacuum, the pressure of which is kept below 1×10^{-5}mmHg. The V.S.W.R. of these high power microwave circuits is below 1.1.

The power of the system is monitored by both the thermister bridge average power meter and the oscilloscope's pattern of the microwave pulse rectified by a crystal detector. The check point of the rf power are both at the input and output side of the accelerating tube. Using a well calibrated 40 db directional coupler, we measured average microwave power under duty cycles of 8×10^{-5}. The observation of the microwave pulse wave form is a convenient method for both monitoring the beam loading of the microwave power and the timing relation between the pulses of electron beam and klystron output.

§ 6. Acknowledgements

The author wishes to express his sincere thanks to Professor H. Kumagai for his helpful discussions and continuous encouragement for the present work. He is also grateful to professor T. Nishikawa for his guidances from the experimental aspects, and to Mr. J. Tanaka, Mr. G. Horikoshi, Mr. H. Baba, Mr. K. Ishii, Mr. I. Itō, Mr. K. Kobayashi and all member of the synchrotron group, for their helpful cooperations and discussions.

He further appreciates their kind cooperations of Dr. Y. Aiura and Dr. K. Kakizaki of Tokyo Shibaura Electric Co., Ltd. in the practical design and the construction of the pumped klystron and the travelling wave tubes.

References

1) T. Nishikawa et al.: J. Phys. Soc. Japan **16** (1961) 1817.
2) M. Chodorow et al.: Rev. Sci. Instr. **26** (1955) 134.
3) G. Horikoshi et al.: INSJ-27. March 14, 1960.
4) G. Horikoshi and A. Miyahara: J. Vac. Soc. Japan **3** (1959) 13. No. 1. (Japanese)
5) G. A. Haas and J. T. Jensen Jr.: Rev. Sci. Instr. **28** (1957) 1007.
6) L. A. Harris: Rev. Sci. Instr. **31** (1960) 903.
7) G. N. Glasoe and J. V. Lebacgz: "Pulse Generators" M.I.T. Radiation Laboratory Series, Vol. 5.
8) T. Nishikawa et al.: INS Report 28, 1961.
9) K. Ishii and A. Miyahara: INSJ-39.
10) M. S. Glass: Proc. Inst. Radio Eng. **45** (1957) 1100.

JOURNAL OF THE PHYSICAL SOCIETY OF JAPAN, Vol. 16, No. 12, DECEMBER, 1961

The Discharge Chamber and Its Characteristics

By Shūji FUKUI
Physical Institute, Nagoya University, Nagoya, Japan
and Sigenori MIYAMOTO
Department of Physics, Osaka City University, Osaka, Japan

(Received July 27, 1961)

The discharge chamber is one of the particle detectors which are based on gaseous discharge. The chamber can give a visual indication of the particle tracks. It consists of glass boxes filled with neon and argon gas mixture at atomospheric pressure. The operating conditions and other characteristics are presented and discussed.

§ 1. Introduction

New particle detectors which are based on gaseous discharge have been developed, such as the "hodoscope chamber"[1] and the "triggered spark counter"[2]. After the short report on the "discharge chamber"[3]*, several investigations have been performed on this instrument[4] and the chamber named as "spark chamber" is now widely used as the track detector in experiments of the cosmic-rays[5] and the high energy machine physics[4].

The discharge chamber described here is the same as the one reported in I and consists of glass boxes filled with a mixture of neon and argon gases at atmospheric pressure. Preliminary data on the characteristics of this chamber were presented in I. The discharges showing particles' trajectories are those which developed from electrons ejected by ionizing particles. The discharge chamber has advantages in working dependably for a group of particles and in obtaining the precise traces of particles. The track of the particles can be obtained as the stereoscopical photograph or as the projected one on the plane of electrode. For obtaining good tracks it is essential to decrease the time duration of the applied electric pulse to about 10^{-7} sec.

In this report, firstly, the operating conditions and other characteristics of the chamber are presented in § 3. Next the characteristics of the chamber are discussed in § 4. Some features of pulsed gaseous discharges occured in the chamber are also discussed.

§ 2. Preparation of the chamber and arrangement for the test

The chamber consists of glass boxes filled with a mixture of neon and argon (Ne+0.5% A) at atmospheric pressure. The quantity of argon was confirmed by the mass-spectroscopic analysis. The mixture of neon and argon was used to decrease the required intensity of the pulsed electric field*. The inner size of the box used for the test was 8.5 cm × 13 cm × 1 cm or 2 cm. Ordinary window glass plates (2 mm thick) or borosilicate glass plates (0.5 mm thick) were used for the two large opposite planes (to which the high voltage pulse was applied). The other sides of the box were made of ordinary window glass plates. No significant difference was observed between the characteristics of two boxes using different kind of glass. Before the box was assembled, the glass plates were washed with a chromic and sulphuric acid solution. Then these plates were glued together with Araldite adhesives. A short capillary glass tube was furnished to the box as a filling tube.

On account of the lack of mechanical strength, the box cannot be evacuated directly. The glass boxes were placed in a large metal chamber. After the metal chamber was evacuated, the chamber was filled with a mixture of neon and argon at atmospheric

---

* Hereafter reference 3) is quoted as I.

* The breakdown voltage is minimum in the mixture of Ne+0.2% A because of so-called Penning effect and the value of the breakdown voltage is almost constant even the percentage of argon changes arround the value of 0.2%. But, recently, one of us (S. F.) and his collaborators found that the mixture of Ne+0.2% A give a minimum breakdown voltage only when the d. c. or continious high frequency electric field is applied but the breakdown voltage becomes minimum in the mixture of Ne+~10%A when the pulsed field of very short duration is applied.

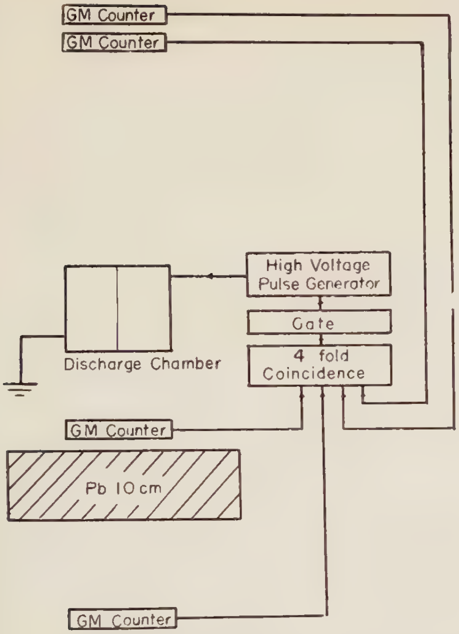

Fig. 1. The experimental arrangement for the test.

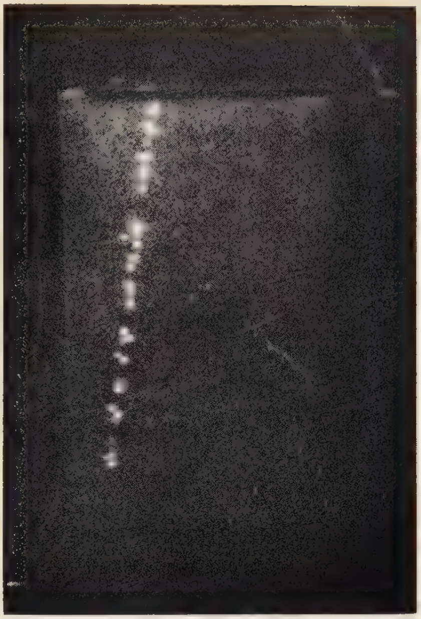

(a)

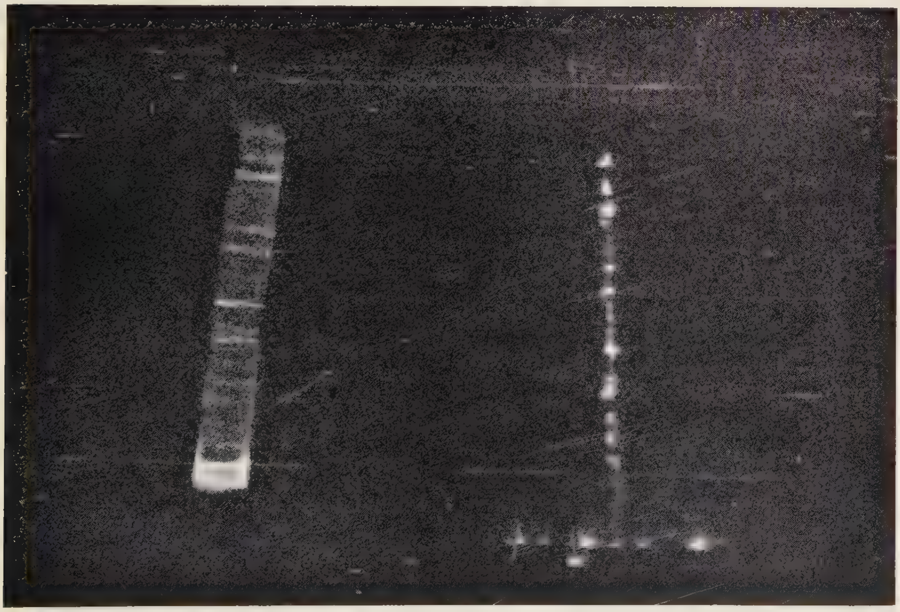

(b)

Fig. 2. Examples of photographs taken with the discharge chamber.
(a) 1 cm depth box. $E_{\text{peak}}=10\,\text{kV}/1\,\text{cm}$. $t_{\text{delay}}=1\,\mu\text{sec}$.
(b) 2 cm depth box. $E_{\text{peak}}=13\,\text{kV}/2\,\text{cm}$. $t_{\text{delay}}=1\,\mu\text{sec}$.
The left side is a view of the discharge columns seen through a side plate. This is the reflected image obtained by a mirror.

pressure. Then the glass boxes were taken out and the capillary glass tubes were sealed off with a torch.

As the electrodes of the discharge chamber, metal plates or conductive glass plates (Nesa) were used and the box was held between these electrodes. We also constructed a box in which one of the two large parallel planes was made of a conductive glass plate whose conductive surface was on the outer side of the box.

The experimental arrangements are schematically shown in Fig. 1. The G-M counter telescope gives a coincidence pulse when an ionizing particle goes through the chamber. This pulse triggers the high voltage pulse generator after passing the gate circuit. The gate circuit was employed to reject coincidence pulses during the recovery time of the whole instrument. The circuit of the high voltage pulse generator is the same as that shown in I. The high voltage pulse has an exponential shape with a time constant defined by C and R.

Two types of arrangements of the chamber are adopted, designated A and B. In A, the discharges are photographed through the conductive glass plates and the tracks thus obtained are those projected on the plane of the electrodes. Examples of photographs are shown in Fig. 2. In B, the discharges are photographed through the side plates, and it is easy to take the stereoscopic photographes. The example is shown in Fig. 3-b of I.

The photographic film was Fuji Neopan SSS and developed using Fuji Pandol for 40~60 minutes. The f stop of the lens was 2.8 and the distance between the camera and the chamber was about 120 cm.

§ 3. Characteristics of the discharge chamber

3.1 *The operating conditions*

The appearance of the discharges showing the trajectories of particles depends essentially on the duration of the pulsed electric field and its peak value. The relation of the features of the discharge to the peak value of the applied electric field is shown in Tables I a and b for the value of $CR=10^{-7}$ sec. From these tables it can be seen that to operate the discharge chamber properly, 13~15 kV/2 cm is required for the chamber of 2 cm depth and 8~10 kV/1 cm for the chamber of 1 cm depth.

When the pulse of $CR=10^{-6}$ sec was applied to the chamber of 2 cm depth, good results

Table I-a. The features of the discharge occurred in the discharge chamber of 2 cm depth with various values of the intensity of pulsed field. ($C=0.001\ \mu f$, $R=100\ \Omega$)

Applied field (peak value)	11 kV/2 cm	12 kV/2 cm	13 kV/2 cm	14 kV/2 cm	15 kV/2 cm
Appearance of the track	None	Tracks are visible but faint.	Tracks are clear.	Clear	Clear
Discharge occurred in other places than the track.	Discharge occurs rarely at the border of the box.	Discharge occurs at the border of the box.	Discharge occurs at the border of the box.	Discharge occurs at the border of the box.	Discharge occurs at the border of the box. Faint glow discharges occur in the whole space of the box.
	No discharge occurs in the boxes through which no cosmic ray particles pass.				

Table I-b. The features of the discharge occurred in the discharge chamber of 1 cm depth with various values of the intensity of pulsed field. ($C=0.001\ \mu f$, $R=100\ \Omega$)

Applied field (peak value)	6 kV/1 cm	7 kV/1 cm	8 kV/1 cm	10 kV/1 cm
Appearance of the track	None	Tracks are visible but faint.	Tracks are clear.	Clear
Discharge occurred in other places than the track.	No additional discharge occurs.	No additional discharge occurs.	Discharge does not occur at the border of the box. Very faint glow discharge occurs in the whole space of the box in which discharge showing the trace of the particles occurs.	In some case, discharges occur at the border of the box. Faint glow discharges occur in the whole space of the box.

can be obtained only with the peak voltage of 8 kV/2 cm. Even in this case, additional glow discharge occurred throughout the box. When the intensity of the field was increased to 9 kV/2 cm, the whole volume of the chamber was dotted with discharge columns and the track could not be recoginized. When the intensity of the field was decreased lower than 8 kV/2 cm the discharge columns showing the particle's path could not be observed.

It is concluded from these results that when the value of $CR=10^{-7}$ sec is adopted the satisfactory results can be obtained with rather wide range of the intensity of the pulsed electric field and that the value of 10^{-6} sec is not suitable for the safe operation of the discharge chamber.

When the 1 cm box was filled with pure argon gas at atmospheric pressure, the row of discharge columns showing the particle's path could be photographed when the peak value of the pulsed field was increased to 38 kV/cm using the time constant of 10^{-7} sec. Since such a high intensity of the electric field is not suitable for practical use, we did not test the argon filled chamber in more detail. Hereafter the time constant CR has been fixed at the value of 10^{-7} sec ($C=0.001\,\mu f$, $R=100\,\Omega$).

3.2 *The lateral displacement of the discharge columns*

The lateral displacement of the discharge columns obtained with the arrangement *A* was examined with various delay times for the application of the pulsed electric field. The results are shown in Table II. The delay time means the time between the instant of the passage of the particles and that of application of the pulsed field. The width is such that within which 80% of the centers of the dischange columns are contained. The width of the discharge columns increases with the delay time.

3.3 *The number of discharge columns and their sizes*

The number of discharge columns along the path of the particle corresponds to the drop density of the cloud chamber tracks. Table III presents the average values measured under the various conditions. The average sizes of the columns are also shown in the table. These values may depend on the photographic conditions, that is, on the transparency of Nesa, the *f* stop of the lens and

Table II. The lateral displacement of discharge columns with various delay times of the application of electric field. The value is the width within which 80% of the centers of discharge columns are contained.

Kind of box	Field Intensity (peak value)	Delay time		
		1 μsec	6 μsec	10.5 μsec
2 cm depth	13 kV/2 cm	1.7±0.2 mm	3.9±0.4 mm	4.6±0.7 mm
1 cm depth	10 kV/1 cm	1.4±0.3 mm	4.0±0.4 mm	

Table III. The number of discharge columns per unit length along the path of the particles and their size.

Kind of box	Field intensity (peak value)	13 kV/2 cm	13 kV/2 cm	13 kV/2 cm	15 kV/2 cm
2 cm depth	Delay time	1 μsec	6 μsec	10.5 μsec	1 μsec
	Number of columns per cm	1.8±0.3	2.2±0.4	2.9±0.7	2.6±0.3
	Diameter of column (mm)	1.3±0.7			2.0±0.4
Kind of box	Field intensity (peak value)	8 kV/1 cm	10 kV/1 cm	10 kV/1 cm	
1 cm depth	Delay time	1 μsec	1 μsec	6 μsec	
	Number of columns per cm	2.4±0.3	2.6±0.4	2.6±0.3	
	Diameter of column (mm)	1.3±0.4	1.4±0.3		

the condition of development of films. The number of discharge columns per unit path length shows a tendency to increase with the delay time. It also increases with increasing intensity of the pulsed electric field. The diameters of discharge columns fluctuate greatly, especially in the 2 cm box. The fluctuation in diameter is somewhat smaller in the 1 cm box.

3.4 *The slanting discharge*

When the path of ionized particle and the direction of electric field form a large angle, a row of many discharge columns occurs along the path of a particle as in case of the arrangement *A*, and in this case the axis of the discharge column is parallel to the direction of the electric field. When the angle is small as in case of the ararngement *B*, only one discharge column occurs along the path of the particle and its axis coincides with the direction of the particle's path as shown in Fig. 3-b of I.

The probability of the occurence of these tracks is shown in Table IV. The chamber used for the test is 2 cm in depth and the intensity of the applied electric field is 14 kV/2 cm. The paths of particles were confirmed by a hodoscope chamber. When the angle is smaller than 15° almost all photographs show only a single discharge column and its axis is on the path of the particle. When the angle is larger than 30° almost all discharge columns have branches or there is more than one column.

Table IV. The probability of the occurrence of the slanting discharge. θ is the angle between the path of the particles and the direction of the applied electric field.

Angle (θ)	$<15°$	$15° \leq \theta < 30°$	$\geq 30°$
Probability of occurrence of slanting discharge	~100%	~70%	~0%

3.5 *The sensitive region*

To investigate the region where the "seeds" produced by an ionizing particle could give rise to discharge columns (the region will be called the sensitive region), the discharge chambers were arranged as shown in Fig. 3. Four boxes were used for the test and two boxes were put above and below to indicate the particle's path. By the aid of the mirror the tracks were photographed from two derections, that is, parallel and normal to the electric field. Comparing the path length of the particle in the box with the region where discharge columns developed, the sensitive region of the chamber was estimated. In case of 2 cm box with 15 kV/2 cm, the sensitive region was estimated to be 70±10% of the depth of the box. Large fluctuations in this value were observed.

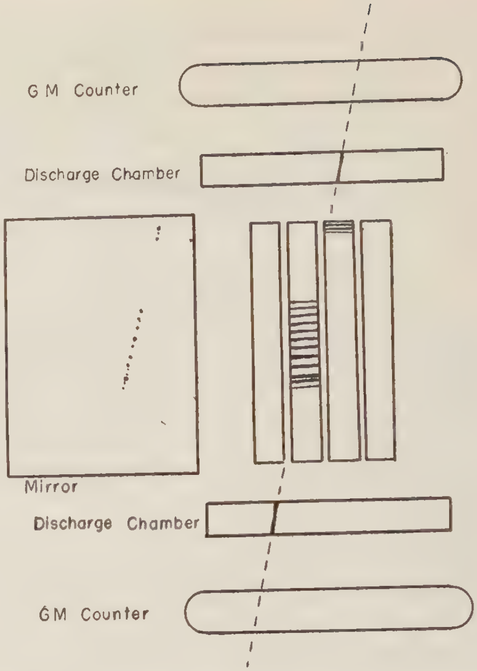

Fig. 3. The arrangement to investigate the sensitive region of the discharge chamber. Two boxes are set above and below the other four boxes to indicate the path of the particles.

The probability of occurrence of the discharge columns seems to be larger in the region near the negative electrode than near the positive one. The sensitive region may vary with the intensity of applied electric field.

3.6 *The sensitive time*

The sensitive time is the interval between the time of the passage of the particle and that at which the delayed application of the high voltage pulse can give the row of the discharge columns recognized as the track. When the chamber was operated in arrangement *A* and applied the pulsed electric field at 10.5 μsec after the passage of a particle, almost all of the photographs did not show longtracks but short diffused ones. Therefore the sensitive time of the chamber is expected to be of the order of 10 μsec.

3.7. *The recovery time*

When a discharge occurs in the chamber, many ions and electrons are produced. If a pulsed electric field is reapplied within some interval of time after the occurrence of the discharge, a spurious discharge takes place. The longest interval of the time within which spurious discharge still occurs will be called the recovery time. For investigating this interval of time, pulsed electric fields were applied periodically while the chamber was being irradiated by γ rays from Co^{60}. If the "seeds" of discharges produced by a former discharge still remain at the instant of the next application of a pulsed field, the number of discharge columns is expected to be increased with time.

When the pulsed field was applied to the 1 cm box at the rate of 4.4 pulses/sec, the number of discharge columns increased if the peak value of the field was greater than 12 kV/1 cm. When the rate was increased to 12 pulses/sec, the critical intensity decreased to 9 kV/1 cm. From these results, it may be concluded that the recovery time depends on the intensity of the pulsed electric field and the order of magnitude is 0.1∼0.2 sec.

The above result was supported by the test using cosmic ray particles. The first application of the pulsed field was triggered by cosmic ray particles passing through the discharge chamber, and the second was applied 0.2 sec after the first pulse. The two discharges were photographed separately and were compared. When the pulses of 10 kV/1 cm for the 1 cm box and 13 kV/2 cm for the 2 cm box were applied, it was verified that there were no discharges produced by the second pulse.

§ 4. Discussions of the characteristics of the discharge chamber

4.1 *On the lateral displacement of discharge columns*

As the cause of the lateral displacement of discharge columns, the diffusion of the "seeds" of discharge columns will be considered. At first the electrons ejected from atoms by the incident particle are assumed as the "seeds" of the discharges and their diffusion from their initial places will be estimated. After a time t, their distribution is given by

$$n(x,t)=\frac{n_0}{\sqrt{4\pi x_0^2}}\exp\left(-\frac{x^2}{4x_0^2}\right), \qquad (1)$$

$$x_0^2=\int_0^t D(t)dt\,, \qquad (2)$$

where n_0 is the number of ejected electrons per unit length along the path of an incident particle at $t=0$; $n(x,t)$ is the density of electrons at x after t sec. D is the diffusion coefficient for the electrons, which depends on the energy of the electrons. At the instant of the ejection the mean energy of the electrons is larger than thermal energy and then the electrons lose their energy through collisions. Therefore the coefficient D is a function of time. From Eq. (1), the width b, within which 80% of electrons are contained, is expressed as

$$\int_{-b/2}^{+b/2} n(x,t)dx=0.8n_0\,, \qquad (3)$$

then

$$b=1.8\sqrt{4\overline{x_0^2}}=3.6\sqrt{\overline{x_0^2}}\,. \qquad (4)$$

The results thus obtained are in good agreement with the experimental values and are shown in Fig. 4. The computed result is almost the same as the value computed using the constant diffusion coefficient for thermal electrons.

As the diffusion width for ions or atoms is two orders of magnitude lower than that for electrons, it may be concluded that the lateral displacement of discharge columns is mainly

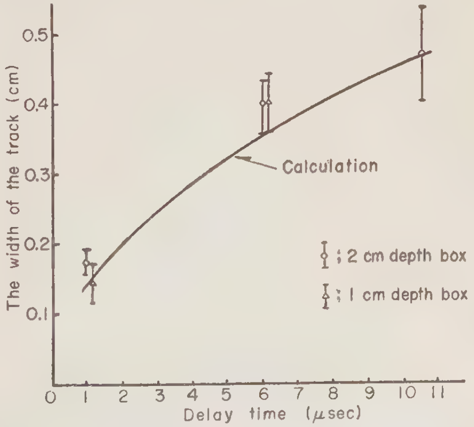

Fig. 4. The comparision between the calculated and observed values of the lateral displacement of discharge columns.

due to the diffusion of electrons. The result also shows that electrons can be the "seeds" of discharge columns. The above fact does not exclude ions from functioning as the "seeds" of discharge columns. But if ions can act as "seeds", in the case of a delay time of 10.5 μsec there must be a row of discharge columns of narrow width at the place where the electrons have been lost by diffusion to the walls. Such a discharge, however, could not be found in any photograph. Thus it is concluded that the "seeds" of discharge columns must be only the electrons ejected from atoms by incident ionizing particles.

When the lateral displacement of discharge columns is measured, the time which elapsed from the instant of passage of the incident particle to the time of application of the pulsed electric field may be estimated with an accuracy of a few μsec.

4.2 *On the number of discharge columns*

The number of discharge columns is one order of magnitude smaller than the number of the ejected electrons expected from the ionization processes of the fast particles. In order to explain the discrepancy between these values, the following reasons may be introduced.

1) The number of free electrons has decreased rapidly owing to recombination or negative ion formation.

2) Discharges can be initiated from the highly ionized region only.

3) The development of the discharge fluctuates and the electron avalanche which has grown in advance of the others disturbs the external field because of its space charge and consequently restricts the development of other avalanches in its neighborhood.

Considering these possibilities, it must be noticed that the observed number of discharge columns per unit track length has a tendency to increase with delay time as shown in Table III. If the number of electrons has rapidly decreased owing to recombination or negative ion formation within the time of about 1 μsec, the number of discharge columns can not be expected to have a tendency to increase with delay time. If the discharge can be initiated from the highly ionized region, these regions must diffuse out with time. Thus it seems that the reasons 1) and 2) can not explain the discrepancy between the number of discharge columns and that of the electrons ejected by the incident particles.

The reason 3) is related to the development of discharge. At the beginning of the discharge, the development of the electron avalanche fluctuates[6], and some advanced avalanches may restrict the development of other neighbouring ones by their space charge field. After the advanced avalanche has grown to a discharge column, the neighbouring ones cannot grow further because of the decrease of the electric field near the discharge column. The tendency for the number of discharge columns to increase with delay time may be understood as being due to the increase of the spread of the electrons, so that fewer electron avalanches are restricted by the advanced one.

Let us estimate this effect over the number of discharge columns. If it is assumed that within a certain distance $2r_s$ from a discharge column, slowly developed electron avalanch can not develop to the discharge column, the number of the discharge columns per unit track length is nearly proportional to $(2r_s+b)/\pi r_s^2$, where b is the region within which seeds of the discharge remain and may be given by Eq. (4). Because in this case the circumstance is similar to the case that cylinders of radius r_s are filled in the space of area $(2r_s+b)\times$unit length. Thus the ratio of the numbers of the discharge columns at different delay times t_a and t_b may be shown as

$$\frac{n(t_a)}{n(t_b)} \simeq \frac{2r_s+b(t_a)}{2r_s+b(t_b)}$$

when the values of $n(t)$ obtained experimentally and the values of $b(t)$ caluculated are inserted in the formula, r_s is obtained as about 0.2~0.3 cm for 2 cm box. For 1 cm box, r_s is obtained as >0.2 cm. These values are consistent with that expected from the number of discharge columns per unit track length. Thus it seems possible that the number of discharge columns is restricted by the space charge field produced by the discharge.

4.3 *On the sensitive time*

The sensitive time of the chamber depends on the life of the electrons ejected by the incident particle. It can be considered that the loss of electrons is due to free diffusion

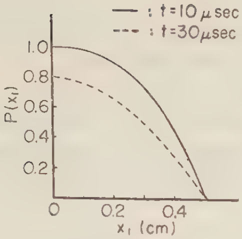

Fig. 5. The probability that an electron remains in the gas of the chamber (1 cm depth box). The initial position of the electron is $x=x_1$.

since the electric field is not applied to the chamber. The probability of the loss due to diffusion can easily be computed. To simplify the computation we deem the diffusion one dimensional. The diffusion equation is given as

$$\frac{\partial n(x,t)}{\partial t}=D\frac{\partial^2 n(x,t)}{\delta x^2}\,, \qquad (5)$$

where $n(x,t)$ is the density of electrons and D is the diffusion coefficient of electrons. It will be assumed that electrons disappear at the wall.

The value of $n(x,t)$ is derived from Eq. (5), (See Appendix A), and the probability that an electron remain in the gas of the chamber is shown in Fig. 5. From the result, it may be concluded that the electron loss due to diffusion determines the sensitive time of the chamber.

4.4 *On the operating conditions*

To develop the discharge only in the region where the particles passed, it was found necessary to apply a pulsed electric field of very short duration ($\lesssim 10^{-7}$ sec). If the duration of the pulsed field is longer, the disharge spreads over the whole space of the box. However, in case of the triggered spark counter, such a short duration of the pulsed field is not required to prevent the discharge from spreading over the counter. The reason may be as follows. In the case of the spark counter, the voltage difference between the plates is decreased rapidly by the first discharge owing to the large spark current, so that secondary discharges can not occur. But in case of the discharge chamber, the electric field does not decrease rapidly at the instant of the first discharge because of the high electrical resistance of the glass plates. Thus when the "seeds" of discharges are produced somewhere in the chamber, new discharges can start from those seeds. The mechanism of the production of the "seeds" may be electron ejection by the photons emitted in the first discharge, so that to prevent the spurious discharge from starting, it is necessary to drop the intensity of the applied field soon after the development of the discharge columns of the track.

Next, the duration t_c within which the electrons give rise to discharge columns will be estimated. According to the streamer theory of the spark mechanism[7], the time required for the dicharge to develop into a spark consists mainly of the time spent by an electoron avalanch in transforming into the streamer. Thus

$$t_c \lesssim 2L/w\,,$$

where $2L$ is the distance between the electrical plates and w is the drift velocity of the electrons. For a 1 cm box with $E=8$ kV/1 cm the value is $t_c \lesssim 10^{-7}$ sec, and for a 2 cm box with $E=13$ kV/2 cm the value is $t_c \lesssim 2\times10^{-7}$ sec. These values are consistent with the observed operating conditions of the discharge chamber. The values are also consistent with the one obtained by Fisher and Zorn[8].

4.5 *On the recovery time*

The experimental result on the recovery time is understood to indicate that the electrons produced by the discharge remain in the chamber for about 0.1~0.2 sec after the pulsed discharge. Let us consider the mechanism of the electron loss. From studying the blackness of the images of the discharge columns on the photographs, the density of electrons and positive ions produced by the discharge is estimated to be at least of the order of 10^{10} to $10^{11}/\text{cm}^3$. If these electrons are lost by the free diffusion to the walls, the elapsed time in this process is estimated to be of the order of 0.005 sec. The time for the ions to diffuse out to the walls is estimated to be of the order of 20 sec. Thus these processes can not explain the recovery time found experimentally.

One possible explanation of this phenomenon is as follows: Due to the electrical forces of the ion cloud, electrons cannot diffuse freely at first but follow ambipolar diffusion. Thus at the beginning electrons are gradually lost by recombination and attachment during the ambipolar diffusion. When the positive charge excess among positive and negative ions decreases so much that the process of electron capture cannot occur any more, electrons may begin to diffuse away freely to the wall of the chamber and are then lost. Following the above process the time until the electrons are lost will be estimated in Appendix B. For the process of the electron attachment the small amount of O_2 contamination is taken into account. The results estimated are shown in Table V.

Table V. The calculated recovery time of the chamber. The values are calculated for 2 cm box. The values for 1 cm box are the same except the value of t_3, and t_3 becomes one fourth of the value of 2 cm box. The unit of t is second.

Pressure of O_2 (mmHg)	$r_0=0.01$ cm				$r_0=0.1$ cm				$r_0=0.2$ cm			
	t_1	t_2	t_3	t	t_1	t_2	t_3	t	t_1	t_2	t_3	t
7.6×10^{-3} (0.001%)	0.005	0	0.003	0.008	0.03	0.08	0.003	0.1	0.03	0.12	0.003	0.2
7.6×10^{-2} (0.01%)	0.005	0	0.003	0.008	0.003	0.01	0.003	0.02	0.003	0.02	0.003	0.03

From these results, it is concluded that if O_2 gas were admixed in the ratio of about 1 to 10^5 in the gas of the chamber, the recovery time would be about 0.1 sec. This amount of O_2 contamination is reasonable when the process of the gas filling into the chamber is taken into consideration. The calculated results suggest that the recovery time may become shorter if more O_2 gas is mixed into the filling gas.

4.6 *On the mechanism of the slanting discharge*

When the angle between the path of the incident particle and the direction of the electric field is small (<30°), a single discharge column develops along the path of the particle. The discharge of this kind was observed also by Charpak using α-rays in argon and propane gas mixture[9]. This phenomenon may be due to the interaction between adjacent electron avalanches in the development of the spark discharge. When two adjacent electron avalanches start simultaneously, one is in front of the other, and if the lateral distance between these two avalances is smaller than a certain value, the succeeding avalanche will be influenced by the foregoing one. If the electrical attraction occurs between each pair of adjacent avalanches, the paths of the avalanches will be not along the electric field but along the row of the electrons ejected from atoms by the incident particles.

Hereinafter, the condition for the occurrence of the slanting discharge will be considered. This condition consists of two parts, one is that the lateral distance between adjacent avalanches must be so small that mutual interaction may occur. The distance may be of the order of the width in which the adjacent avalanches can overlap each other. The other is that the positive ion cloud left behind the electron cloud must be in front of the following electron avalanche in order that the avalanche is attracted to the advanced one. When the mean distance between ejected electrons is denoted by $\bar{d}$, and the angle between the row of electrons and the direction of electric field is θ, the former condition is expressed as

$$\bar{d}\sin\theta \lesssim 2k_1\rho \,. \tag{6}$$

The latter may be expressed by

$$\bar{d}\cos\theta \gtrsim 2k_2\rho \,, \tag{7}$$

where the symbols k_1, k_2 indicate constants of the order of magnitude unity, ρ is the radius of the electron cloud at the head of an electron avalanche. The conditions (6) and (7) can be reduced to

$$\tan\theta \lesssim k_1/k_2 \tag{8}$$

and

$$\bar{d}\sin\theta \lesssim 2k_1\rho_{\max} \,. \tag{9}$$

According to the Meek's theory of spark mechanism[7], the maximum value of ρ is restricted by the fact that an electron avalanche is transformed into a streamer when the radial field produced by the positive ions at the head of the avalanche is of the order of the externally applied field E_{ext}. The criterion is expressed as

$$\frac{4e\alpha e^{\alpha x}}{3\rho} \simeq E_{\text{ext}} \,, \tag{10}$$

where $\rho=\sqrt{2Dt}=\sqrt{2Dx/w}$ is the radius of the electron cloud at the head of an electron avalanche, e is the electronic charge, α is Townsend's ionization coefficient, x is the distance advanced by an avalanche and w is the drift velocity of electrons. If the values of k_1 and k_2 are chosen as unity, the condition (8) is reduced to $\theta \lesssim 45°$.

When equation (10) is applied in the case where an avalanche is developed in Ne+0.5% A gas and the intensity of the externally applied field is 7 kV/cm, the maximum value of ρ is obtained as 0.02 cm. The value of $\bar{d}$ is of the order of 0.02 cm. Thus the condition (9) is satisfied in this case.

Though undetermined parameters k_1 and k_2 are chosen as unity in the above calculation, the result is nearly equal to the value obtained experimentally. Thus the slanting discharge may be explained by the mechanism described in this section.

§ 5. Conclusions

As the characteristics of the discharge chamber, the following may be enumerated.

1) This detector is simple to construct and stable in operation. It is essential for the steady operation of the chamber to keep the duration of the electric pulse to or shorter than 10^{-7} sec.

2) The recovery time is 0.1∼0.2 sec. It would be possible to make this time shorter if a small amount of O_2 gas were mixed into the filling gas.

3) This detector is applicable for detection of multiple particles passing through it simultaneously as shown in Fig. 3-a of I.

4) The diameter of the discharge column is 1 mm∼4 mm and is partly dependent on the intensity of the applied field.

5) The sensitive time is of the order of 10 μsec before the application of the electric field.

6) The "seeds" of the discharge are the electrons ejected by the incident particle. The lateral displacement of the discharge columns is explained as being due to the diffusion of these electrons. When the lateral displacement of discharge columns is measured, the time which elapsed from the instant of passage of the incident particle to the time of application of the pulsed electric field may be estimated with an accuracy of a few μsec.

7) The number of discharge columns is one order of magnitude smaller than that of electrons expected from the ionization process of the incident particles. This may be due to the fluctuation of the development of the discharge and the influence of the space charge field produced by the advanced discharge.

8) The slanting discharge occurs when the angle between the path of the incident particles and the direction of the electric field is small. This seems to be due to the mutual interaction between adjacent electron avalanches.

Acknowledgements

The authors wish to express their gratitude to Professor Y. Watase of Osaka City University for his interest and encouragement. Thanks are also due to Dr. H. Matsuda of Osaka University for the gas analysis using the mass-spectrometer. We wish to thank Drs. M.F. Crouch and S. Ozaki for suggestions in the preparation of the manuscript.

Appendix A.

The estimation of the electron less due to free diffusion

The equation for one dimentional free diffusion of electrons is given by Eq. (5). With the boundary condition that $n(x, t)=0$ at the wall ($x=\pm L$) and the initial condition that at $t=0$ an electron is at $x=x_1$, $n(x, t)$ will be calculated. The result is

$$n(x, t)=\sum_{n=0}^{\infty} C_n \exp(-t/\tau_n) \cos\left\{\frac{(1+2n)\pi}{2L}x\right\}, \tag{A.1}$$

where

$$C_n=\frac{1}{L}\int_{-L}^{+L}\delta(x-x_1)\cos\left\{\frac{(1+2n)\pi}{2L}x\right\}dx$$
$$=\frac{1}{L}\cos\left\{\frac{(1+2n)\pi}{2L}x_1\right\},$$

and

$$\tau_n=\frac{4L^2}{(1+2n)^2\pi^2 D}.$$

Then the probability that an electron which is at $x=x_1$ at $t=0$ remains in the gas of the chamber at time t is

$$P(x_1)=\int_{-L}^{+L} n(x, t)\,dx$$
$$=\sum_{n=0}^{\infty} C_n \exp(-t/\tau_n)\frac{4L}{(1+2n)\pi}\sin\left\{\left(\frac{1}{2}+n\right)\pi\right\}. \tag{A.2}$$

The computed results are shown in Fig. 5.

Appendix B.

The estimation of the rate of electron loss after the discharge

After the external electric field vanishes, electrons in the discharge column continue to excite neutral atoms for short period of a few μsec and the energies of electrons decrease. Then electrons are gradually lost by recombination and attachment being held by the ambipolar diffusion.

The rate of electron losses due to recombination and attachment is given as

$$\frac{dn_e}{dt}=-(\alpha n_+ + h\bar{u}/\lambda_e)n_e \ , \tag{B.1}$$

where n_+ and n_e are the densities of positive ions and electrons, respetively. α is the coefficient of recombination and is $2\times10^{-7}\,\text{cm}^3/\text{ion sec}$ for neon. h is the electron attachment probability per collision and is 2.5×10^{-5}. $\bar{u}$ is the mean velocity of electrons. λ_e is the collsion mean free path for electron in O_2 and expressed as

$$\lambda_e=1/(20\,p_0)\ ,$$

where p_0 is the pressure of O_2 in mm/Hg.

When $\alpha n_+ > h\bar{u}/\lambda_e$, the process of the recombination is predominant and in this stage the electron loss is given as

$$\frac{dn_e}{dt}=-\alpha n_+ n_e\ .$$

If $n_+\simeq n_e\simeq n$ and n_0 is the electron density at $t=0$,

$$n=\frac{n_0}{1+n_0\alpha t} \tag{B.2}$$

The time spent in this stage is

$$t_1\sim\lambda_e/(h\bar{u})\ , \tag{B.3}$$

provided that $n_0\alpha t_1\gg1$.

In the next stage the loss due to the attachment is predominant and the rate of loss is given as

$$\frac{dN}{dt}=-h\frac{\bar{u}}{\lambda_e}N\ ,$$

where N is the total number of electrons. The time t_2, in which the number N_1 decreases to N_2, is estimated as

$$t_2=\frac{\lambda_e}{h\bar{u}}\ln\frac{N_1}{N_2}=\frac{\lambda_e}{h\bar{u}}\ln\frac{n_1V_1}{n_2V_2}\ , \tag{B.4}$$

where N_1 and N_2 are the numbers of electrons at the beginning and the end of this stage, respectively. V_1 and V_2 are the volumes of space occupied by the electrons and ion cloud at the beginning and the end of this stage, respectively.

The ambipolar diffusion will end when the positive electric field of the ion cloud can no longer capture the electrons against their thermal motion. The condition for electron capture by the ion cloud may be given as

$$n_e\simeq n_+ - n_- > \frac{3k}{2\pi e^2}\frac{T}{r^2} \tag{B.5}$$

and

$$\frac{3k}{2\pi e^2}\cdot\frac{T}{r^2}=3\times10^2\frac{T}{r^2}$$

where n_- is the density of negative ions. This formula is based on a plasma of spherical shape. T is the kinetic temperature in degrees of Kelvin and k is the Boltzmann constant; e is the electron charge. The condition based on a spherical shape is used in spite of its actual cylindrical shape because electrons in a spherical plasma escape more easily from a positive ion cloud than from an endless cylindrical plasma, and the condition at the two ends of the cylindrical plasma may be nearly equal to the condition of spherical plasma. If the radius of the ion cloud is changed by diffusion, this critical density varies with time. When the shape of the ion cloud is cylindrical and the change of volume is mainly due to the change of its radius,

$$\frac{n_1V_1}{n_2V_2}\simeq\frac{n_1r_1^2}{n_2r_2^2}$$

where r_1 and r_2 are the radii of the ion cloud at the beginning and the end of this stage respectively. If $n_2=3kT/(2\pi e^2r_2^2)$ is inserted, the value of $n_1V_1/(n_2V_2)$ becomes $2\pi_e{}^2r_1{}^2n_1/(3kT)$. Then the time t_2 is given by

$$t_2\simeq\frac{\lambda_e}{h\bar{u}}\ln\frac{2\pi e^2r_1{}^2n_1}{3kT}\ , \tag{B.4$'$}$$

where n_1 is the final density of the first stage and is given as $h\bar{u}/\alpha\lambda_e$.

Next the time t_3 for the electrons to diffuse out to the wall will be estimated. As shown in Appendix A the first term of equation (A.2) is the predominant one in the density distribution after a long time. Thus the number of electrons which remain longest inside the chamber is

$$N(t)\simeq\int_{-L}^{+L}C_0\exp(-t/\tau_0)\cos\frac{\pi}{2L}x\,dx$$
$$=\frac{4LC_0}{\pi}\exp(-t/\tau_0) \tag{B.6}$$

In this case C_0 is expressed as

$$C_0=\frac{1}{L}\int_{-L}^{+L} n_0' \cos\frac{\pi}{2L} x dx =\frac{4n_0'}{\pi}\,, \qquad \text{(B.7)}$$

where n_0' is given as $\pi r^2 n_e \simeq 3kT/(2e^2)$, which is the number of electrons per unit length along the axis of the discharge column at the time when the condition (B.5) begins to be violated. Then the time t_3 is obtained as

$$t_3 \sim \tau_0 \ln\frac{16Ln_0'}{\pi^2}=\frac{4L^2}{\pi^2 D}\ln\frac{24kT\,L}{\pi^2 e^2} \qquad \text{(B.8)}$$

The time $t\,(=t_1+t_2+t_3)$ was calculated in the case when O_2 gas is mixed in the gas inside the chamber. The results of the calculation are shown in Table V. Where r_0 is the radius of the discharge column at $t=0$. When r_0 is equal to 0.01 cm, the time t_2 is zero. This means that the process of the recombination alone is enough to violate the condition (B.5).

References

1) M. Conversi and A. Gozzini: Nuovo Cimento **2** (1955) 189. M. Conversi, S. Focardi, C. Franzinetti, A. Gozzini and P. Murtas: Suppl. Nuovo Cimento **4** (1956) 234. G. Barsanti, M. Conversi, P. Murtas, C. Rubbia and G. Torelli: Proc. of the Geneva International Conference (1956). M. Gardener, S. Kisdnasamy, E. Rössle and A. W. Wolfendale: Proc. Phys. Soc. **B70** (1957) 687. S. Fukui and S. Miyamoto: INS-TCA **10** (1957) and **11** (1958) (Technical reports at the Institute for Nuclear Study, University of Tokyo). F. Ashton, S. Kisdnasamy and A. W. Wolfendale: Nuovo Cimento **8** (1958) 615. H. Coxell and A. W. Wolfendale: Proc. Phys. Soc. **75** (1960) 378. J. L. Loyd: Proc. Phys. Soc. **75** (1960) 387.

2) T. E. Cranshaw and J. F. DeBeer: Nuovo Cimento **5** (1957) 1107.

3) S. Fukui and S. Miyamoto: Nuovo Cimento **11** (1959) 113.

4) Proc. International Conference on Instrumentation for High-Energy Physics at Berkeley (1960). Spark Chamber Symposium; Rev. Sci. Instr. **32** (1961) No. 5.

5) K. Kamata: Sci. Papers, I. P. C. R. **55** (1961) No. 2.

6) R. A. Wijsman: Phys. Rev. **75** (1949) 833.

7) See, for instance, J. M. Meek and J. D. Craggs: *Electrical Breakdown in Gases* (Oxford University Press, 1953) 517P.

8) J. Fisher and G. T. Zorn: Rev. Sci. Instr. **32** (1961) 499.

9) G. Charpak: Proc. International Conference on Mesons and Recently Discovered Particle, (1957) XVII-II, J. Phys. radium, N. 8-9 (1957) 539 and private communication.

Short Notes

This section is intended to secure prompt publication of important discoveries in physics. The reports should not exceed 800 words in length. A figure of size 7 cm×7 cm will be counted as 150 words.

J. PHYS. SOC. JAPAN **16** (1961) 2586

Absorption Bands in KCl Crystal Containing LiCl

By Shinichi NAKASHIMA

Matsushita Electronics Corporation
Takatsuki, Osaka

(Received September 1, 1961)

It was reported in a previous paper[1] that the position of a colloidal band in KCl crystal containing NaCl shifts to the shorter wavelength side as the doping amount of NaCl increases. The colloidal bands in KCl-NaCl mixed crystals were ascribed to K-Na alloy colloids. Following Doyle's theory[2] the wavelength λ for the absorption maximum in the colloidal band is evaluated from

$$\lambda=(1+2\,n_0^2)^{1/2}\,\lambda_c$$

where n_0 is the refractive index of the host crystal and λ_c is the critical wavelength for ultraviolet transparency of the metal, which is inversely proportional to the square root of the electron density in the metal. Since the electron density of a K-Na alloy is greater than that of the K metal, it is concluded that the colloidal band of a K-Na alloy appears at the shorter wavelength side of the colloidal band of the K-metal. In order to confirm this conclusion, it would be desirable to investigate the absorption band in KCl containing LiCl, because in this case the colloidal band is expected to appear at a much shorter wavelength.

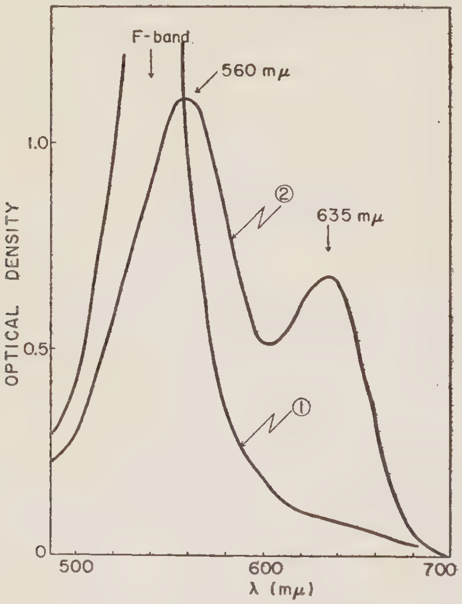

Fig. 1. Absorption curves of additively colored KCl-LiCl
(1); before F-light irradiation,
(2); after F-light irradiation at room temperature; measured at liquid N_2 temperature.

KCl-LiCl crystals were grown from melts containing one mol per cent LiCl. After being additively colored the crystal shows an F-band as in the case of pure KCl. When illuminating this sample with F-light at room temperature the band diminished and two bands with peaks at 5600 Å and 6350 Å appeared at liquid nitrogen temperature (Fig. 1). These absorption bands in KCl-LiCl were first observed by Ishiguro[3]. However, as his measurements were made at room temperature these peaks were not clearly separated.

Upon heating the additively colored KCl-LiCl crystal at 200°C the F-centers were converted to centers with an absorption peak at about 5000 Å (Fig. 2). The position of the band was not altered by cooling the crystal to the temperature of liquid nitrogen. This absorption band may be considered to be the colloidal band of the K-Li alloy. As was expected, its peak position is shifted to the wavelength side shorter than that in the case of a K-Na alloy (i.e., 5900 Å in KCl containing one mol per cent NaCl).

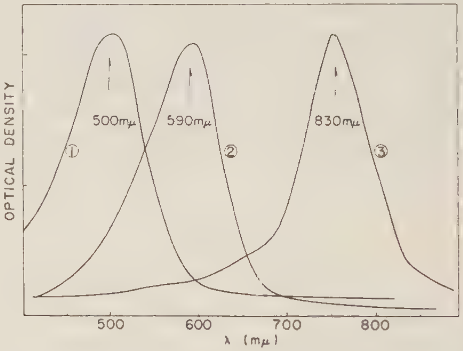

Fig. 2. The absorption curve of the colloidal band in KCl-LiCl (1), is shown in comparison with a colloidal band in KCl-NaCl (2) and that in pure KCl (3).

The author expresses his thanks to Dr. K. Fukuda and Dr. H. Mizuno for their helpful discussions and Prof. Y. Uchida for his encouragement.

References

1) S. Nakashima: J. Phys. Soc. Japan, **16** (1961) 1650
2) W. T. Doyle: Phys. Rev. **111** (1958) 1067
3) M. Ishiguro and E. Sugioka: Phys. Rev. **110** (1958) 1070

J. Phys. Soc. Japan **16** (1961) 2587~2588

Internal Friction of LiF at Low Temperatures

By Akira Ikushima and Taira Suzuki

The Institute for Solid State Physics, University of Tokyo, Tokyo, Japan

(Received October 5, 1961)

In many metals, a well defined internal friction peak, called the Bordoni peak, has been observed at low temperatures in the cold worked state[1]. Seeger[2] has explained quantitatively the peak as due to the oscillatory motion of dislocations over the Peierls hill. According to his theory, it is possible to determine the Peierls stress experimentally, which is one of the most essential quantities for the understanding of the fundamental processes of dislocations in crystals. If so, such an experiment is almost only one available way at present to give the Peierls stress.

It appears, however, that one has not yet confirmed the uniqueness of the proposed model for the Bordoni peak[3]. As a possible way to overcome the present difficulty, it is worth while to study the nature of the peak in other materials such as polar crystals, because theoretical calculations of the Peierls stress to be compared with experimental results could be obtained more likely than in metals. In ionic crystals, however, only a few works have been carried out so far. This note will present a brief account of our recent experiment on LiF.

LiF crystals were obtained from the Harshaw Chemical Company. Specimens of about $1\times1\times1\ \mathrm{cm}^3$ were prepared by cleavage. They were annealed on silica plate in air at about 700°C for 15 hours, and then slowly cooled down to room temperature.

Plastic deformotion of specimens was given in compression with the Instron Testing Machine. Two glide systems always operated, where their Burgers vectors were found to be perpendicular to each other.

Internal friction against longitudinal waves at 15, 25 and 35 Mc/sec was measured by using the pulse-echo method[4]. Typical results are shown in Fig. 1 (a)-(d). In deformed crystals, a well defined main peak and a subsidiary peak at lower temperature are both present. The height of the main peak becomes larger with increasing plastic deformation up to about 4% and the peak-temperature are little affected by the amount of deformation. It appears that these peaks correspond respectively to the Bordoni peak and its subsidiary peak in metals. Whether or no these peaks are due to dislocation motion was checked in a similar way as used in the foregoing works on KCl done by one of the present authors[5]. Curve (b) shows a positive result against the longitudinal wave in the direction normal to both of the Burgers vectors of the operating dislocations.

The rapid rise of attenuation immediately below room temperature is tentatively assumed to be due to a change in the state of bonding material between specimen and quartz transducer. The bonding material used was a stopcock grease "Nonaq".

The present results give the values of the activation energy Q and the attempt frequency ν_0 as

$$Q=0.090\ \mathrm{eV},\quad \nu_0=6\times10^9\ \mathrm{sec}^{-1}$$

for the main peak, and

$$Q=0.02\ \mathrm{eV},\quad \nu_0=1\times10^8\ \mathrm{sec}^{-1}$$

for the subsidiary peak.

The Peierls stress $\tau_p{}^0=3.8\times10^7\ \mathrm{dynes/cm}^2$, where the shear modulus μ is taken to be $6.5\times10^{11}\ \mathrm{dynes/cm}^2$. It follows that $\tau_p{}^0/\mu\simeq5.8\times10^{-5}$. It almost coincides with the value 2×10^{-5} of MgO[6]. It is smaller than that of most metals, however.

Finally, we would like to comment on a similar work on LiF done by Taylor[7], who kindly informed us of his fresh results. His peak temperatures for 40 kc/sec and 6 kc/sec are seemed to lie well on the extrapolation of the present results obtained at higher frequencies, although he has tentatively obtained appreciably different values from ours such as $Q=0.15$ eV and $\nu_0=2\times10^{15}\ \mathrm{sec}^{-1}$.

The full account of the present work will be

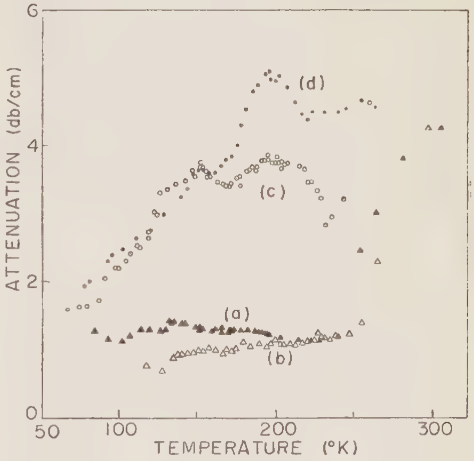

Fig. 1. Ultrasonic attenuation *vs* temperature.

(a) ▲—annealed at 700°C for 15 hours, 15 Mc/sec.

(b) △—cold-worked by 3.1% compression. Longitudinal waves of 35 Mc/sec are directed perpendicular to the Burgers vectors.

(c) ○—cold-worked by 3.1% compression, 35 Mc/sec.

(d) ●—cold-worked by 3.7% compression, 35 Mc/sec.

published in the near future.

References

1) See, for example, D. H. Niblett and J. Wilks: Adv. in Phys. **9** (1960) 1.
2) A. Seeger: Phil. Mag. **1** (1956) 651. A. Seeger, H. Donth and F. Pfaff: Discussions Faraday Society **23** (1957) 19.
3) L. J. Bruner: Phys. Rev. **118** (1960) 399. A. D. Brailsford: Phys. Rev. **122** (1961) 778.
4) R. L. Roderick and R. Truell: J. Appl. Phys. **23** (1952) 267.
5) T. Suzuki, K. Suzuki and K. Kamigaki: J. Phys. Soc. Japan **14** (1959) 731.
6) R. Chang: J. Appl. Phys. **32** (1961) 1127.
7) A. Taylor: Private communication.

J. PHYS. SOC. JAPAN **16** (1961) 2588

Ground State Energies of Donors in Ge and Si

By Koziro NARITA and Tatsuo SHIMIZU

Hitachi Central Research Laboratory,
Kokubunji, Tokyo

(Received August 28, 1961)

The energy levels of shallow impurities in Ge and Si have been treated by the effective mass theory.[1] But the theory can not explain the difference of the energy levels for different impurity atoms.

The ground state of donors in Ge and Si are fourfold and sixfold degenerate respectively in the effective mass approximation. It is known, however, that these states split into singlet and triplet for Ge, and singlet, doublet and triplet for Si as the result of the valley-orbit interaction. In either case, the energy of the singlet state is the lowest. Since the wave functions of all the other states vanish at the center of the impurity atom, their energy levels are expected to be rather well approximated by the effective mass theory. Therefore once the magnitude of the valley-orbit splitting is known, the energy level corresponding to the ground state can be obtained.

It is shown that the valley-orbit splittings are given by 4Δ and 6Δ for Ge and Si,[2)3)] where

$$-\Delta=\int\phi_i^*(r)(H-H_e)\phi_i(r)d\tau\ .$$

Here H and H_e denote respectively the real Hamiltonian $H_0+U(r)$ and the Hamiltonian $H_0-\frac{e^2}{\kappa r}$ used in the effective mass theory, and $\phi_i(r)$ is the donor wave function corresponding to the ith valley.

We assume $U(r)$ to be the following type,

$$U(r)=\begin{cases}-\dfrac{Z_{eff}}{r}e^2+k & r\leqq r_0\\ -\dfrac{e^2}{\kappa r} & r>r_0\ .\end{cases}$$

Here r_0 is the radius of a sphere, inside which the potential due to the impurity deviates from the form of $-e^2/\kappa r$. And k is determined so that the potential is continuous at the surface of the sphere. Then we can write Δ as

$$\Delta=\left(Z_{eff}-\frac{1}{\kappa}\right)I_c\ ,$$

where

$$I_c=\int_{r\leqq r_0}\phi_i^*(r)\left(\frac{e^2}{r}-\frac{e^2}{r_0}\right)\phi_i(r)d\tau\ .$$

The exact form of the wave function, however, is not known. We shall therefore proceed treating I_c as a parameter, and using the following expression for determining Z_{eff}

$$13.6(eV)\times\frac{Z_{eff}^2}{n^2}=I_p$$

where I_p is the ionization potential of the impurity atoms in vaccum[4)], and n is 2, 3, 4, 5 and 6 for Li, P, As, Sb and Bi respectively.

We have performed the calculations, taking the values of parameters to bo $1.02\times10^{-3}eV$ and $2.32\times10^{-4}eV$ for Si and Ge respectively. The results thus obtained are found to be in excellent agreement with the experimental values[1)5)] except for Sb, and are shown in Table 1.

Table 1

	Impurity element	The values of valley-orbit splitting (eV)	Ground state energy	
			calc.(eV)	obs.(eV)
in Si	Li	0.007	0.036	0.033
	P	0.016	0.045	0.044
	As	0.020	0.049	0.049
	Sb	0.024	0.053	0.039
	Bi	0.026	0.055	0.069
in Ge	Li	0.0011	0.0103	0.0100
	P	0.0024	0.0116	0.0120
	As	0.0031	0.0123	0.0127
	Sb	0.0036	0.0128	0.0096

More complete and detailed discussion will be published in the near future.

References

1) W. Kohn: Solid State Physics Vol. 5, 1957.
2) P. J. Price: Phys. Rev. **104** (1956) 1223.
3) T. Shimizu: To be published.
4) C. E. Moore: Atomic Endrgy Levels (National Bureau of Standard).
5) T. S. Moss: Optical Properties of Semi-conductors, 1959.

J. PHYS. SOC. JAPAN **16** (1961) 2589

Origin of Magnetoelectric Effect in Cr_2O_3

By Muneyuki DATE, Junjiro KANAMORI, and
Masashi TACHIKI

Department of Physics, Osaka University,
Nakanoshima, Osaka

(Received September 26, 1961)

Magnetoelectric effect in antiferromagnetic substances has been discussed by several authors[1−5], and detailed experiments of the effect in Cr_2O_3 have been reported recently by Folen, Rado and Stalder[4]. A crystal of Cr_2O_3 is of trigonal symmetry and the spins are oriented along the trigonal axis in antiferromagnetic state. An electric field either parallel or perpendicular to the trigonal axis produces a net magnetization in the direction of the applied field. The case of parallel field will be discussed first. In Cr_2O_3, sites occupied by up spins are equivalent to sites occupied by down spins by an inversion symmetry. Since the presence of an electric field along the trigonal axis destroys this inversion symmetry, such an electric field may produce a difference in absolute magnitude between the magnetizations of up and down spin sublattices. Rado[5] has suggested that the effect arises from the difference of the single ion energy DS_z^2, where the trigonal axis is taken as the z-axis. The derivative of D with respect to the strength of electric field ε, $\partial D/\partial\varepsilon$, of ions of up spin sublattice should have an opposite sign to that of ions of down spin sublattice because of the symmetry relation mentioned above. If this mechanism is responsible for the observed magnetization, $|\partial D/\partial\varepsilon|/g\mu_B$ should be as large as 0.43 oe./kV per cm*. In order to check this point, we have observed paramagntic resonance patterns of Cr^{3+} in a ruby under an electrostatic field applied along the trigonal axis. As will be described below, the result is definitely against Rado's proposal[5]. It is concluded in the present letter that the exchange interaction within the same sublattice is the plausible origin of the effect.

The experiment has been performed by use of 32.35 kMc/sec microwave and a pink ruby sample of $4\times4\times1$ mm size. We have investigated the 1/2 −3/2 transition line in a magnetic field applied along the trigonal axis. The frequency of this line is given by

$$h\nu=g\mu_B H+2(D\pm\varepsilon\partial D/\partial\varepsilon)\ .$$

By use of the field modulation method the resonance line in an electric field has been compared directly on the memoriscope with the line in the absence of electric field. Our experimental accuracy is such that the observable limit of the splitting of the resonance line into two lines is 3 oe. No change of the resonance pattern has been detected in an electric field up to 3 kV per mm. This indicates that $|\partial D/\partial\varepsilon|/g\mu_B$ is less than 0.03 oe./kV per cm, which is one tenth of the value required for the explanation of the magnetoelectric effect.

Denoting an exchange integral by J, we note that $\partial J/\partial\varepsilon$ for one sublattice has an opposite sign to that for the other sublattice if the relevant interaction is the interaction between the spins belonging to the same up or down spin sublattice. Thus an electric field will decrease the absolute magnitude of the molecular field arising form such an exchange interaction for a sublattice and increase it for another sublattice. Since the effect is equivalent to a magnetic field, the induced magnetization is proportional to $(\partial J/\partial\varepsilon)\chi_\parallel\langle S_z\rangle_{av}$. This proportionality of the magnetization to$\chi_\parallel\langle S_z\rangle_{av}$ has been proposed phenomenologically by Rado.[5] Though precise estimation is difficult, we can conclude from perturbation calculations that $|\partial J/\partial\varepsilon|/|J|$ is of the same order of magnitude as $|\partial D/\partial\varepsilon|/|D|$. This indicates that our mechanism is more effective than the mechanism suggested by Rado by two orders of magnitude, since D is 0.19 cm^{-1} and the exchange interaction is probably of the order of 100 cm^{-1}.

When an applied field is perpendicular to the trigonal axis, our mechanism, that is, the change of the exchange integral is ineffective. In this case a change in the direction of the principal axis of the single ion energy[5] or Dzyaloshinsky-Moriya interaction[6] might be responsible for the magnetoelectric effect. Indeed the observed magnitude of the effect is smaller by one order of magnitude than the case of parallel electric field.

Reference

1) L. D. Landau and E. M. Lifshitz: Electrodynamics of Continuous Media (Addison-Wesley Publishing Company, Inc., 1960) p. 119.
2) I. E. Dzyaloshinsky: J. Exptl. Theoret. Phys. (U.S.S.R.) **37** (1959) 881 [translation: Soviet Phys. JETP **10** (1960) 628].
3) D. N. Astrov: J. Exptl. Theoret. Phys. (U.S.S.R.) **38** (1960) 984 [translation: Soviet Phys. JETP **11** (1960) 708].
4) V. J. Folen, G. T. Rado and E. W. Stalder: Phys. Rev. Letters **6** (1961) 607.
5) G. T. Rado; Phys. Rev. Letters **6** (1961) 609.
6) I. E. Dzyaloshinsky: J. Phys. Chem. Solids **4** (1958) 241. T. Moriya: Phys. Rev. **117** (1960) 635.

---

* The value mentioned in the text is about 3.5 times as large as the value cited in Rado's paper. $\chi_\parallel$ assumed in his calculation seems to be too large by the factor 3∼3.5 compared with the experimental $\chi_\parallel$.

J. Phys. Soc. Japan **16** (1961) 2590~2591

Determination of the Impurity Concentration of the P-type Recrystallized Layer by Thermoelectric Power Measurements

By Masakazu Shoji

Hitachi Central Research Laboratory,
Kokubunji, Tokyo

(Received September 18, 1961)

In this report, the acceptor concentration of the *p*-type recrystallized layer has been determined by comparing thermoelectric power of the specimen with that of the standard samples.

Experimental arrangement shown in Fig. 1 is the same as that used by Batifol et al.⁽¹⁾ to determine the diffusion constant of arsenic in germanium.

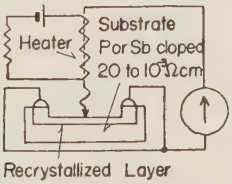

Fig. 1. Experimental arrangement

The specimen was prepared by alloying strips of indium containing 10% tin and various amounts of gallium into *n*-type germanium wafer at 580°C and by cooling rapidly. Indium was removed by amalgamation and ohmic contacts were soldered to the recrystallized *p*-type germanium. Then the bottom part of it was exposed by etching. Standard samples were taken from single crystals doped with gallium and etched on the same condition. Their impurity concentrations were determined by resistivity measurements.

Fig. 2 shows the thermoelectric voltage versus gallium concentration in the alloyed strip $\bar{p}$, together with the result for the standard samples measured on the same condition. Measured thermoelectric voltage decreases almost linearly with logarithm of the acceptor concentration up to 4×10^{19}/cc.

Result of the comparison of thermoelectric power is shown in Fig. 3.

The acceptor concentration of the specimen made by alloying pure indium at 580°C was found to be 1.3×10^{18}/cc which was in good agreement with Lee's⁽²⁾ data.

When $\bar{p}$ was larger than 0.15%, no effect of phosphorous contained in the substrate was observed. Difference in the impurity concentration and conductivity type between the recrystallized layer and its substrate caused no effect on the measured result. This is reasonable because the electronic part of thermal conductivity of germanium is much smaller than the phonon part.

Effect of tin in the alloy metal was also examined. Thermoelectric power of the specimen made by alloying indium containing fixed amount of gallium and various amounts of tin (less than 14%) was not influenced by tin. Further no effect of tin was observed on the thermoelectric power and the Hall mobility of the single crystal specimen containing up to 6.3×10^{19}/cc tin (which was about 45% of the estimated concentration in the regrown region.)

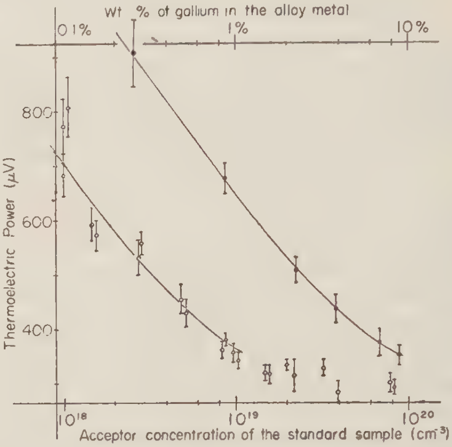

Fig. 2. Thermoelectric power versus impurity concentration. Upper curve is for standard samples (Conc. is given in lower scale.) Lower curve is for regrown samples (Conc. is given in upper scale.)

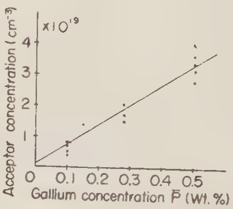

Fig. 3. Acceptor concentration in the recrystallized layer versus $\bar{p}$.

No detectable effect on the measured result was expected from the extrapolation of this data.

This method may give the same result as the infrared transmission method⁽³⁾ if the specimen is prepared on the same condition.

Impurity concentration thus determined is in good agreement with that estimated from the tunnel current data. Details will be reported soon.

The author wishes to express his thanks to Mr. M. Tomono, Mr. M. Tokuyama and Mr. T. Hirai for their kind advices. He is also indebted to Mr. Y. Ito for his assistance in the experiment.

References

1) M. E. Batifol et M. G. Duraffourg: J. de Phys. et Radium **21** (1960) 207A
2) M. A. Lee: Solid State Electronics **1** (1960) 194
3) F. E. Roberts: Solid State Electronics **2** (1961) 8

J. PHYS. SOC. JAPAN **16** (1961) 2591

Epitaxial Vapor Growth of GaAs on Ge Single Crystals

By Takasi OKADA, Takao KANO and Yozo SASAKI

Research Laboratories, Nippon Electric Company Ltd., Tokyo, Japan

(Received October 10, 1961)

Antell and Effer[1] have reported that small crystals of GaAs were deposited on the surface of quartz tube at 1030°C from the vapor which was produced by the reaction between GaAs source and I_2 at 1070°C. It is the purpose of this paper to report that GaAs single crystals are grown epitaxially on substrates of Ge single crystals in a closed quartz tube by the disproportionation reaction between GaAs and I_2.

A quartz tube, which is about 20 mm in diameter and 60 ml in volume, is charged with a germanium seed, 2 g of GaAs polycrystalline source and 120 mg of pure I_2. The Ge seed is roughly rectangular in shape, 150 mm² in area, and has a surface of (111) orientaion. The tube is cooled at a temperature of mixture of dry-ice and alcohol bath and is evacuated to a pressure of 10^{-5} mm Hg. After being sealed off, the quartz tube is placed in an electric furnace. The temperature profile of the furnace is adjusted so that both the source and the seed surfaces may be etched at 780°C and the removed materials may be deposited in a "dump zone" at 700°C (Fig. 1) After 2 hrs' etching, the temperature of the seed region is forced to drop quickly to 700°C. Under these conditions the epitaxial growth of GaAs takes place on the surface of Ge seed at the rate of about 6 μ/hr. The texture of the deposited GaAs is shown in Fig. 2. The (111) crystallographic orientation of the deposited crystal is confirmed by X-ray diffraction method.

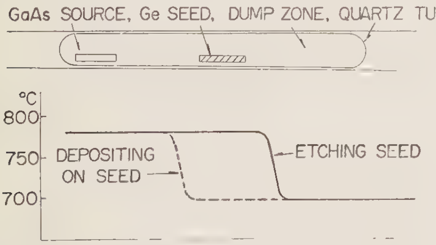

Fig. 1. Diagram of closed-tube method of vapor growth.

Non-doped n-type GaAs having the resistivity of 0.01 Ω cm is used as a source material. It is found that the epitaxially grown layer is also n-type and has almost the same resistivity as that of the source. The resistivity of the layer is estimated from the breakdown voltage measured by point contact method.

Good epitaxial growth is attained when the temperature of the substrate is above 650°C. Below this temperature coarse grey deposit is obtained. (Fig. 3)

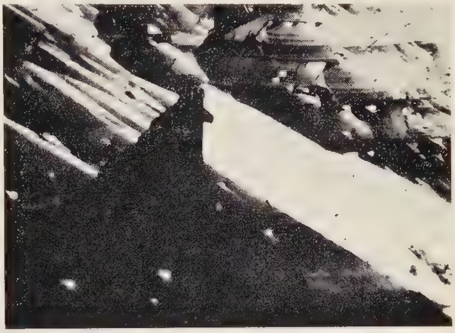

Fig. 2. Typical epitaxial growth of GaAs on the (111) Ge substrate at 700°C. (×150)

Fig. 3. Coarse deposite of GaAs obtained at 600°C. (×150)

The authors would like to express their thanks to Dr. Yoshioki Isikawa for his encouragements. They are also indebted to Mr. Mitsuhiro Maruyama for his supply of GaAs crystals.

References

1) G. R. Antell and D. Effer: J. Electrochem. Soc. **106** (1959) 509.

J. Phys. Soc. Japan **16** (1961) 2592~2593

Transient Phenomena in Ruby Maser

By Fujio Saito

Fundamental Research Laboratory,
Nippon Electric Company, Kawasaki,

(Received July 29, 1961)

Transient phenomena of maser oscillation were observed in an X-band three-level ruby maser and measurements on time lag at oscillation were made. The $-3/2 \leftrightarrow +1/2$ or $+1/2 \leftrightarrow -3/2$ transition was used for pumping and the $+1/2 \leftrightarrow -1/2$ transition was used for signal. The pumping and the signal frequencies were 24 kMc/sec and 9.4 kMc/sec respectively.

A ruby single crystal used in the experiments, containing 0.05% of Cr^{+++}, was about 1 cm^3. Because of large dielectric constant of ruby, most of the electromagnetic energy in the maser cavity was concentrated to the crystal, which might be considered as if it was a resonator itself. The energy concentration to the crystal and consequent decrease of wall loss of the cavity gave the filling factor very close to 100% and the loaded Q of about 10000.

In our experiments, the pumping microwave was chopped by applying square wave voltage to the reflector of the pumping klystron and the corresponding oscillation signal was displayed on a cathode ray tube. A photograph of typical oscillation signal is shown in Fig. 1.

When the pumping microwave was suddenly applied at $t=0$, the oscillation did not build up from $t=0$ but from $t=t_d$ with time lag t_d and reached to steady state with transient amplitude modulation similar to damped oscillation.

Similar phenomena to ours have been reported by Feher et al[1], Chester et al[2] and Kemp[3] for two-level maser and by Kikuchi et al[4] and Statz and de Mars[5] for three-level maser. Theoretical studies on these transient phenomena have been made by Singer et al[6][7], Yariv et al[8] and Kemp[9] for two-level maser and by Statz and de Mars[5] for three-level maser. These theories seem to well describe the principal aspects of the phenomena after building up of oscillation. There have been, however, no experimental and theoretical works on the time lag before building up of oscillation as we mentioned above.

We have measured t_d as a function of the pumping power P (peak value) and the recurrence frequency f of the modulating square wave.

When either P or f decreased, t_d increased, while the shape and duration of the transient amplitude modulation did not change remarkably. The amplitude of the oscillation signal decreased with decrease of P. When the temperature T was lowered from 4.2°K to 2°K, t_d increased slightly but other characteristics did not change. In all cases, the absolute values of t_d were order of few hundreds microseconds.

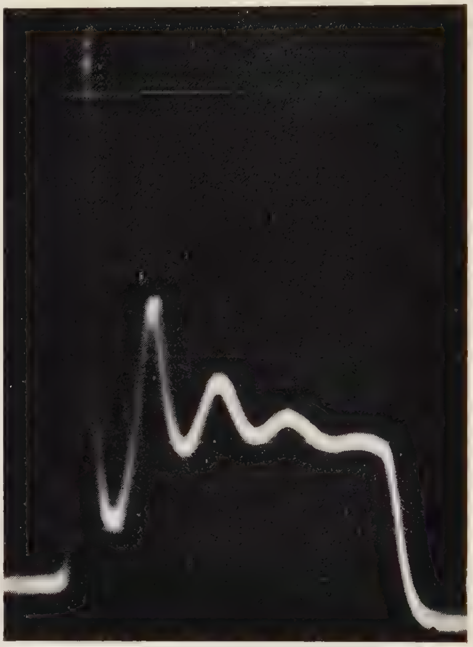

Fig. 1. A photograph of typical oscillation signal.

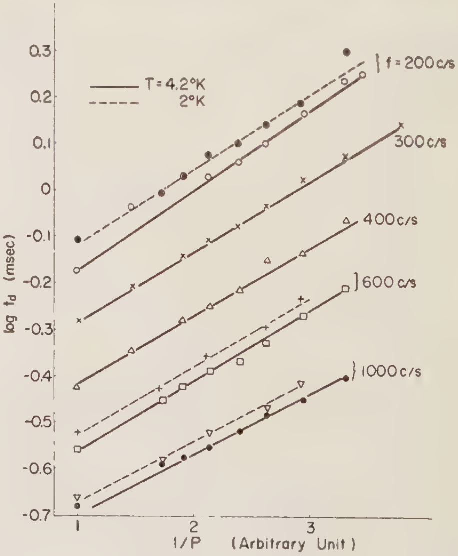

Fig. 2. The plots of $\log t_d$ vs $1/P$ for various values of f at $T=4.2$°K and 2°K.

The results of measurements on t_d are shown in Fig. 2, where $\log t_d$ is plotted as a function of $1/P$ for various values of f at $T=4.2$°K and 2°K.

From the results, it follows that $\log t_d$ is a linear function of $1/P$. From usual rate equations, we obtain the time lag as

$$t_d=-\frac{1}{2W_p}\ln\left(\frac{\Delta n-\Delta n(\infty)^*}{\Delta n(0)-\Delta n(\infty)}\right), \qquad (1)$$

where $\Delta n(t)$ is the population difference between $+1/2$ and $-1/2$ levels before building up of oscillation and Δn^* is the threshold value of $\Delta n(t)$ for oscillation to occur and W_p is the transition probability for the pumping transition.

For sufficiently high pumping power, $\Delta n(0)$, $\Delta n(\infty)$ and Δn^* are independent of P so that t_d is proportional to $1/W_p$ and consequently $1/P$. This result does not agree with the experimental facts and a more detailed consideration is required.

The author wishes to thank Dr. Y. Ishikawa and Dr. K. Hayashi for their kind advice and discussions.

References

1) G. Feher, J. P. Gordon, E. Buehler, E. A. Gere, and C. D. Thurmond; Phys. Rev. **109** (1958) 221.
2) P. F. Chester, P. E. Wagner, and J. G. Gastle, Jr.; Phys. Rev. **110** (1958) 281.
3) J. C. Kemp; Phys. Rev. Letters **7** (1961) 21.
4) C. Kikuchi, J. Lambe, G. Makhov, and R. W. Terhune; J. Appl. Phys. **30** (1959) 1061.
5) H. Statz and G. de Mars; "Quantum Electronics" Columbia University Press, N. Y., (1960) 530.
6) J. R. Singer; "Quantum Electronics" Columbia University Press, N. Y., (1960) 525.
7) J. R. Singer and S. Wang; Phys. Rev. Letters **6** (1961) 351.
8) A. Yariv, J. R. Singer, and J. Kemp; J. Appl. Phys. **30** (1959) 265.
9) J. C. Kemp; J. Appl. Phys. **30** (1959) 1451.

J. PHYS. SOC. JAPAN **16** (1961) 2593~2594

Piezoelectric Properties of Triglycine Sulphate

By Takuro IKEDA, Yoichi TANAKA and Hiroo TOYODA

Electrical Communication Laboratory, Nippon Telegraph and Telephone Public Corporation, Musashino, Tokyo

(Received September 26, 1961)

Some results have been reported on the piezoelectric properties of triglycine sulphate crystal[1)2)]. However, the values of the piezoelectric constants obtained by Konstantinova and others[1)] differ considerably from those after Husimi and Kataoka[2)]. Such discrepancies are supposedly attributed to a lack of prepoling in the former experiment. The purpose of the present study is to measure the temperature dependence of all piezoelectric constants and explain the piezoelectricity by electrostrictive effects of the crystal.

The paraelectric triglycine sulphate crystal belongs to the monoclinic prismatic class $C_{2h}-2/m$, which is centrosymmetric. The transformation into the ferroelectric phase occurs at 47.5°C and the crystal class changes into the monoclinic polar sphenoidal class C_2-2. Nonvanishing piezoelectric constants in the latter phase are d_{21}, d_{22}, d_{23}, d_{25}, d_{14}, d_{16}, d_{34} and d_{35}. The first four constants were obtained for the present.

The constants d_{21}, d_{23} and d_{25} were measured by using y-cut bars. The angles between the long axes of the bars and z-axis (c-axis) are 90°, 0° and ±45°, and the gold electrodes were evaporated on y-faces. Another constant d_{22} was obtained by a y-long bar and the electrodes were attached to end faces. The electromechanical coupling coefficients were determined by the resonance-antiresonance method, with necessary corrections for stray capacities. The specimens were prepoled under the fields of 900 V/cm. During the measurement, *d.c.* biasing field of 90 V/cm was applied, otherwise single domain crystals obtained by prepoling are apt to split up into antiparallel domains when heated and cooled through Curie point, and in the cooling process piezoelectric constants are measured to be reduced.

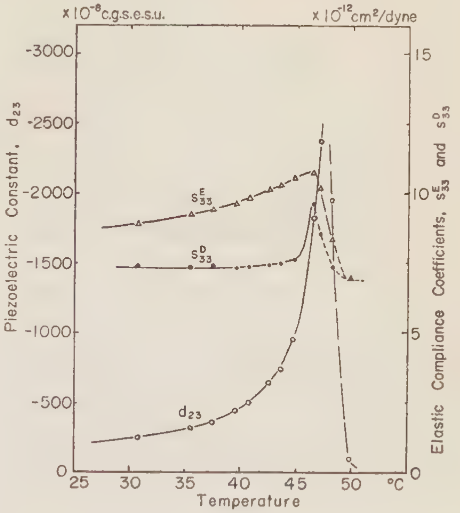

Fig. 1.

The temperature dependence of the piezoelectric constant d_{23} is shown in Fig. 1. This curve is similar to that of the dielectric constant. The temperature dependences of the elastic compliance coefficients $s_{33}{}^E$ and $s_{33}{}^D$ are also shown in the same figure. The value of $s_{33}{}^D$ is nearly independent of temperature except in a narrow range near the Curie point. The results for the other constants are simiar to the above ones. The temperature dependences of the piezoelectric constants d_{21}, d_{22} and d_{25} are shown in Fig. 2.

Barium titanate crystal shows no piezoelectricity above the Curie point, but in the ferroelectric state it is generally accepted that spontaneous polarization gives rise to "induced" piezoelectricity by the effect of the electrostriction[3]. This situation is sharply distinct from the piezoelectricity of rochelle salt, which is "intrinsic" piezoelectric even above the Curie point. The present case, in which no "intrinsic" piezoelectricity exists above the Curic point, is similar rather to the case of barium titanate than rochelle salt, and the observed piezoelectricity appears to be "induced". The electrostrictive strain is represented by $Q\cdot PP$, where P is the polarization and Q the electrostrictive coefficient. In the ferroelectric phase, the piezoelectric constants d_{2i} (i=1, 2, 3 and 5) are given by $2\ Q_{2i}P_s\kappa_{22}^{\Gamma}$, where P_s is the spontaneous polarization parallel to y-axis and κ_{22}^{F} is the dielectric suscptibility. The above obtained values of d_{2i} divided by $2\ P_s\kappa_{22}^{F}$ lead to nearly constant values of Q independent of temperature. From this fact it will be concluded that the piezoelectricity of triglycine sulphate is due to electrostriction, as in the case of barium titanate. The electrostrictive coefficients are thus obtained as follows:

$Q_{21}=1.5$, $Q_{22}=3.0$, $Q_{23}=-4.4$ and $Q_{25}=-0.5$ in 10^{-11} c. g. s. units.

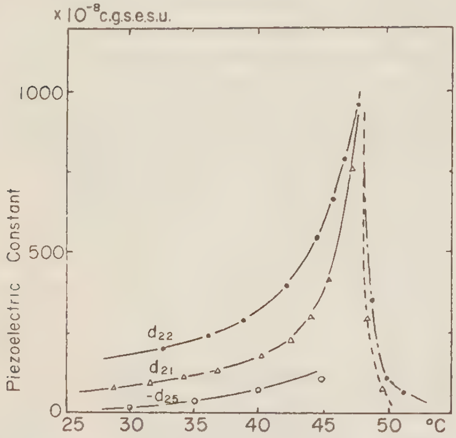

Fig. 2.

The irradiation by x-ray, γ-ray and neutron has been known to give rise to the effect of suppressing the reversals of polarization[4]. The specimens were irradiated by x-ray from a Cu target during poling under the field of 900 V/cm for 0.5, 1.5 and 4.5 hours. Although the measurements were performed without bias, crystals seemed not to split up into domains; that is, when the specimen was kept at about 50°C for half an hour and then cooled through the Curie point, the obtained piezoelectric constants were the same as those before heating. The electromechanical coupling coefficient of the irradiated specimen is greater than that of the virgin crystal by about 15% at room temperature, but the reason for this difference cannot be understood yet.

Full results, including data on the remaining constants, will be published in near future.

Reference

1) V. P. Konstantinova, I. M. Sil'vestrova and K. S. Aleksandrov, Kristallografia **4** (1959) 69.
2) K. Husimi and K. Kataoka, J. Phys. Soc. Japan **14** (1959) 105 (S. N.).
3) A. F. Devonshire, Phil. Mag. **42** (1951) 1065.
4) H. Toyoda and Y. Tanaka, J. Appl. Phys., **29** (1960) 521.

J. PHYS. SOC. JAPAN **16** (1961) 2594~2595

$O^{16}(d, \alpha)N^{14}$ Reaction with Deuterons near 15 MeV.

By Takuji YANABU, Sukeaki YAMASHITA
Institute for Chemical Research, Kyoto University, Kyoto
and
Teruo NAKAMURA, Kunio TAKAMATSU, Akira MASAIKE, Shigeru KAKIGI, Dai Ca NGUYEN, Kiyohiko TAKIMOTO
Department of Physics, Faculty of Science, Kyoto University, Kyoto

(Received September 29, 1961)

One of the authors (T. Y.) has reported the experimental results of the reaction $O^{16}(d, \alpha)N^{14}$ [1]. Soon after this experiment had finished, Pellegrini[2] published the results of the same reaction at the almost same energy. It was remarkable that the results obtained by Pellegrini were somewhat different from those by T.Y., so this reaction was re-investigated in order to answer the question where the difference came from.

The deuteron beam of 14.5 MeV was obtained from a 105 cm cyclotron of Kyoto University. Natural oxygen was used as O^{16} target this time. The angular resolution of the alpha particle detecting system was ±2°. Alpha particle detector was a semiconductor radiation detector of a silicon p–n junction. The energy resolution was less than 1.5%.

The angular distribution of alpha particles leading to the ground state of N^{14} is shown in Fig. 1, together with the results obtained by Pellegrini and by one of the authors. Pellegrini gave a much smaller absolute cross section than the other two.

It must be kept in mind, however, that in calculating the absolute cross section, Pellegrini used $C_{10}(H_2O)_4$ as molecular formula of Mylar, but $C_8H_4O_2$ was used in the paper by T.Y.[1]. The absolute cross section calculated from $C_8H_4O_2$ agreed reasonably with that from O_2 gas target.

From Fig. 1, it might be guessed that the angular distribution is very energy-sensitive, i.e. the angular distributions in forward and backward regions change fairly when the incident deuteron energy changes a little. The absolute value at 90° direction seems to remain unchanged.

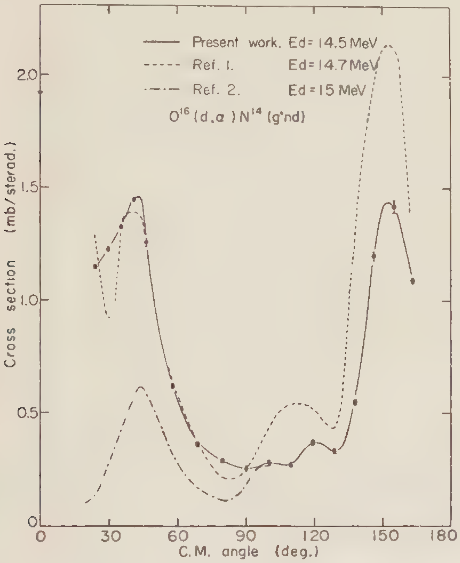

Fig. 1. Angular distributions of alpha particles from $O^{16}(d, \alpha)N^{14}$ (ground state) reaction. Solid line shows the present result. Dotted line shows the former work by one of the authors. Dotted and dashed curve shows the Pittsburg experiment.

Fig. 2 presents the angular distribution of the alpha particles corresponding to the second excited state of N^{14}. A $|j_2(QR)|^2$ fit is also shown in the figure. The momentum transfer was calculated from a knock-out process. It is interesting that: 1) The integrated cross section for the $O^{16}(d, \alpha)N^{14}$ reaction leading to the second excited state of N^{14} is larger than that for the reaction leading to the ground state. Their values are 13 mb and 8 mb respectively. Since the spin-parity of the ground and second excited states of N^{14} are the same, being 1^+, this fact means that there exist some other factors than that of the compound nucleus formation; 2) The location of the first peak coincides in both cases, but the first dip in α_0 corresponds to the second peak in α_2 and so on; 3) The behaviour of the angular distribution of α_2 is very similar to that of the high energy alpha particle groups from the reaction $C^{12}(d, \alpha)B^{10}$ at the almost same energy of incident deuteron[1].

Alpha particles leading to the first $T=1$ level of N^{14} were also observed this time in the forward region. Differential cross sections are 10~30 μb/sterad in the range from 23.6° to 90.5° in C.M. system. The yields were poor and the statistical error amounted to 20% at about 90°, but its angular distribution shows a sligt increase in the forward region (see Fig. 2). This result disaccords with Pittsburg experiment[2]. Furthermore, the recent experiment on $B^{10}(d, \alpha)Be^8$ reaction[3] showed that the principle of isotopic spin conservation is strongly violated in (d, α) reaction, and the excitation energies of the compound nuclei being comparable in these two cases, the violation also prevails in the $O^{16}(d, \alpha)N^{14}$ reaction.

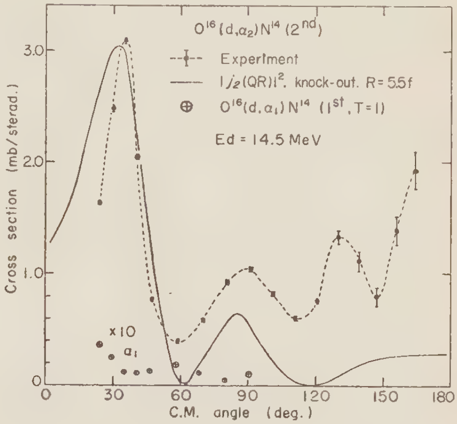

Fig. 2. Angular distribution of alpha particles from the reaction $O^{16}(d, \alpha)N^{14}$ corresponding to the second excited state of N^{14}. The solid line shows the $|j_2(QR)|^2$ fit. Experimental points of α_1 are also shown on magnified scale.

References

1) T. Yanabu: J. Phys. Soc. Japan **16** (1961) 2118.
2) F. Pellegrini: Nucl. Phys. **24** (1961) 372.
3) J. R. Erskine and C. P. Browne: Phys. Rev. **123** (1961) 958.

J. Phys. Soc. Japan **16** (1961) 2596

On the Impurity Concentration of the P-type Recrystallized Layer of Tunnel Diode

By Masakazu Shoji

Hitachi Central Research Laboratory,
Kokubunji, Tokyo

(Received September 26, 1961)

For the detailed analysis of the electrical characteristics of alloyed tunnel diodes it is necessary to know the carrier concentration of the recrystallized region. In this report, method of its determination by analyzing the dependence of tunnel current on the gallium concentration in the alloy metal which was used to form the tunnel junction is described. The values thus determined were compared with that estimated by the measurement of thermoelectric power of the recrystallized region which was reported previously[1].

The analysis was made in the following way. The current-voltage characteristics of the tunnel junction is expressed by the following equation[2].

Tunnel current

$$=\text{const}\cdot Z\cdot\int_{E_C}^{E_V}\rho_C(E)\rho_V(E)\{f_C(E)-f_V(E)\}dE \tag{1}$$

Where Z is the tunneling probability of the electrons and is assumed to be independent of the integral variable. $\rho_C(E)$ and $\rho_V(E)$ are the densities of states of the conduction and valence band respectively and $f_C(E)$ and $f_V(E)$ are the corresponding Fermi functions. E_C and E_V represent the band edge energies. Then assuming the spherical energy surfaces near the band edges and the abrupt tunnel junction one obtaines

$$\sigma_T=\left(\frac{dI}{dV}\right)_0$$

$$=\text{const}\cdot(np)^{1/3}\exp\left[-c\left(\frac{1}{n}+\frac{1}{p}\right)^{1/2}\right]. \tag{2}$$

Where n and p are the carrier concentrations of the n-type and p-type sides of the junction, σ_T is the conductance per unit area of tunnel junction at zero voltage and c is a constant.

Now p is assumed to be proportional to the gallium concentration, $\bar{p}$ (in weight percent), in the alloy metal which was used to form the recrystallized layer.

$$p=p^*\bar{p} \tag{3}$$

Where p^* is a constant. From Eq. (2) and Eq. (3),

$$p^*=\frac{n^2}{\bar{p}^2}\frac{\partial(ln\sigma_T)/\partial n-(1/3n)}{\partial(ln\sigma_T)/\partial\bar{p}-(1/3\bar{p})} \tag{4}$$

All the terms in the right side of Eq. (4) can be determined experimentally.

Tunnel diodes used for this analysis were constructed on the same condition as the samples of the thermoelectric power measurements. The substrate was the n-type germanium doped with phosphorous; indium dot containing 10% tin and various amounts of gallium was alloyed at 580°C. The electrical properties were measured by curve tracer and series resistance of the tunnel junction was corrected by the measurement of reverse characteristics.

Fig. 1 shows the dependence of tunnel current on the donor concentration in the substrate (curve A) and on the gallium concentration in the alloy metal (curve B_1, B_2 and B_3). Tunnel current peak was not observed for $\bar{p}$ lower than 0.1%. The value of p^* was determined from the data shown in Fig. 1 and from Eq. (4). These were determined for three curves B_1, B_2 and B_3. The results are listed in Table I together with the value determined by thermoelectric power measurements.

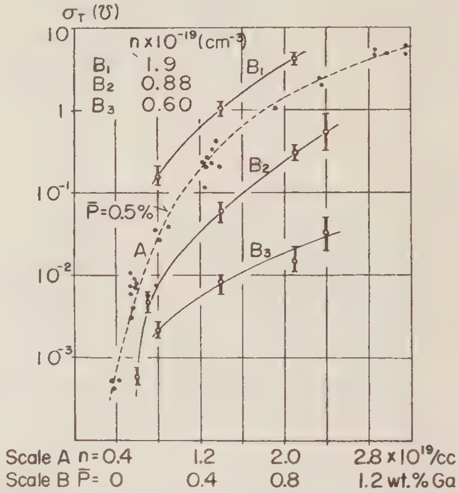

Fig. 1. Dependence of tunnel current on the impurity concentration.

Table I. Comparison of the value of p^*.

p^* (B_1)	7.1×19^{19}/cc·%
p^* (B_2)	3.8×10^{19}
p^* (B_3)	4.4×10^{19}
p^* (thermoelectric)	6.6×10^{19}

The agreement between these is satisfactory considering the crudeness of the analysis. The fundamental assumption made in deriving Eq. (4) is Eq. (3) and this was justified by thermoelectric power measurements[1].

The author wishes to express his thanks to Mr. M. Tomono and Mr. T. Tokuyama for their kind advices. He is also indebted to Mr. Y. Ito for his assistance in the experiment.

Reference

1) M. Shoji: J. Phys. Soc. Japan **16** (1961) 2590.
2) L. Esaki: Phys. Rev. **109** (1958) 603

J. PHYS. SOC. JAPAN **16** (1961) 2597~2598

Experiments on the Possible Existence of a Bound Di-Neutron

By Masakatsu SAKISAKA and Michio TOMITA
Department of Physics, Kōnan University, Kōbe, Japan

(Received August 24, 1961)

So far there has been no decisive evidence for the existence of di-neutrons. However, we have recently found some phenomena which support the possible existence of bound state di-neutrons.

A tritium-titanium target was bombarded by a deuteron beam with energy in the range 160~185 Kev and the target chamber was surrounded by a large paraffin block (36 cm×60 cm×60 cm) or ordinary water in a tank in order to moderate the emitted neutrons. An "aluminium foil sandwiched plastic scintillator"[1] which was covered by cadmium plate of 1 mm in thickness was arranged in the moderator 12.5~27.5 cm apart from the target and exposed to the neutrons. After the irradiation, weak activities of the aluminium (99.99% purity) were counted by coupling the scintillator with two photomultipliers. New phenomena obtained in this way are as follows:

1) The activities were found to have the half lives of 6.6±0.3 min and~18 min. We will temporarily attribute this to the effect of anomalous neutrons.*

2) Some of the cross sections for the anomalous neutrons are shown in the following table. The measurements were done by counting the 6.6 min activity with and without absorber elements or compounds which surrounded the sandwich detector. The results are quite anomalous, because, for instance, the cross sections for CH_2 (paraffin) and H_2O should be nearly equal to each other in the case of ordinary neutrons (E_n>0.5 ev).

Table. Cross section in barns.

Sample	Al	C	P	Fe	Sn	CH_2	H_2O
Cross section	0.5±0.2	9±4	10±4	5±2	10±5	8±3	2±2

3) The anomalous neutron flux was found to decrease more gradually in water in than paraffin, whereas the flux distributions of ordinary neutrons of various energies were nearly equal in both moderators.

4) The anomalous neutrons were not detected in D+d neutrons (E_d=170 Kev). However, when a concave block of lead (1~3 cm in thickness) was placed closely around the tritium target chamber and irradiated by~14 Mev neutrons, an increase of the anomalous neutrons was observed*. Furthermore there was no conclusive evidence that the anomalous neutrons were emitted from the moderator substances.

The present experimental results would be difficult to be attributed to the rare phenomena by ordinary neutrons which might be occasionally observed, but they can be consistently explained as follows, if we assume that the anomalous neutrons are di-neutrons (n^2):

1) The 6.6 min life is due to Al^{29} from $Al^{27}(n^2, \gamma)Al^{29}$ reaction. The~18 min activity** will be ascribed to a new radioisotope or an unknown isomeric state.

2) The difference in the di-neutron flux distributions in paraffin and water can be explained at least qualitatively, if the cross sections of these elements are taken into account.

3) The di-neutron binding energy is estimated as

$$3.01\ \text{Mev} \geq |n^2\ \text{binding energy}| > 2.90\ \text{Mev}^{***}.$$

The lower limit is derived from our observation that the di-nentrons must be produced by T+d reaction at E_d=160 Kev, but the upper limit is based on the hypothesis by Feather[2] that $n^2 \xrightarrow{\beta^-} d$ decay occurs. Then the reaction D(d, n^2)2p should be energetically impossible at E_d=170 Kev, but Pb(n, n^2) reaction is allowable by the incidence of ~14 Mev neutrons.

The yield ratio of the di-neutrons and ordinary neutrons from T+d reaction was estimated to be about 1% in the present experiment. This estimation was done by regarding the cross section for aluminium, 0.5 b, as the activation cross section for the 6.6 min product. Therefore, the detection of recoil He^3 in T(d, n^2)He^3 reaction would be very difficult. This is supported by the fact that the existence of di-neutrons has not been approved by such a recoil particle method[3].

In conformity with Feather's suggestion, we have also used a Bi_2O_3 sandwiched scintillator to detect the di-neutrons, but the Bi_2O_3 showed no appreciable activity under about 10 minute irradiation. In their pile neutron research Fenning and Holt[4] found that no such a reaction as Bi+n^2 occured, but it may be necessary to pursue similar pile neutron experiment by other detecting apparatus in order to confirm whether di-neutrons exist or not.

---

* This word may be inadequate, but it is used provisionally only for convenience of discussion.

* Of course an increase of ordinary neutrons due to Pb(n, 2n) reaction was also observed by another detector.

** A small contribution of Mg^{27} ($T_{1/2}$=10 min) from $Al^{27}(n, p)Mg^{27}$ reaction may be included.

*** The nuclear masses concerned were quoted from Rev. Mod. Phys. **28** (1956) 103.

References

1) M. Sakisaka, B. Saeki, M. Tomita and F. Fukuzawa: J. Phys. Soc. Japan **16** (1961) 1869.
2) N. Feather: Nature **162** (1948) 213.
3) J. E. Brolley, Jr., W. S. Hall, L. Rosen and L. Stewart: Phys. Rev. **109** (1958) 1277.
4) F. W. Fenning and F. R. Holt: Nature **165** (1950) 722.

J. PHYS. SOC. JAPAN **16** (1961) 2598

The Resistance Minimum in a Dilute Cadmium Manganese Alloy

W. B. MUIR*

Physics Dept. University of Ottawa
Ottawa, Ontario, Canada

(Received August 26, 1961)

A minimum followed by a maximum have been observed in the low temperature electrical resistance of dilute alloys of the divalent metal magnesium with manganese[1),2),3)]. Muto, Tawara, Shibuya and Fukuroi[4)] first observed a resistance minimum in a dilute alloy of zinc manganse. Hedgcock and Muir (to be published) have measured the electrical resistance of a series of zinc manganese alloys having compositions extending to near the limit of solid solubility of manganes in zinc. A minimum in electrical resistance was observed in all cases but no evidence of a maximum was found down to temperatures of 1.8°K. The present note reports the observation of a resistance minimum induced by manganese in the divalent solvent cadmium.

The alloy was prepared by melting high purity cadmium (99.999% obtained from the New Jersey Zinc Co.) together with a small quantity of powdered high purity manganese (99.99% obtained from A. D. MacKay Inc.) in a quartz tube under a helium atmosphere. The melt was held at a temperature of 650°C for one hour, and agitated vigorously every 15 minutes. The alloy was quenched in ice water, the ingot cleaned by etching in 50% hydrochloric acid solution and then given an homogenizing anneal in an evacuated pyrex tube at 300°K for 24 hours. The ingot was then quenched in ice water and rolled into a thin strip suitable for resistance measurements. The resistance specimen was etched clean, sealed in an evacuated pyrex tube and given a strain relieving anneal at 300°C for 24 hours. A pure cadmium resistance specimen was prepared in a similar manner except that the strip was rolled directly from a cleaned piece of cadmium cut from the stock. The resistance ratio ($R_{4.2}/R_{273}$) of the pure cadmium solvent was 2.5×10^{-4} while that of the dilute cadmium manganese alloy was 23.2×10^{-4}.

Fig. 1 shows the resistance of the pure cadmium and the cadmium manganese alloy. It can be seen that a shallow minimum occurs in the cadmium manganese alloy at about 4.5°K. Unfortunately little metallurgical information about the cadmium manganese system is available. Attempts to make a cadmium manganese alloy containing a higher concentration of manganese were unsuccessful.

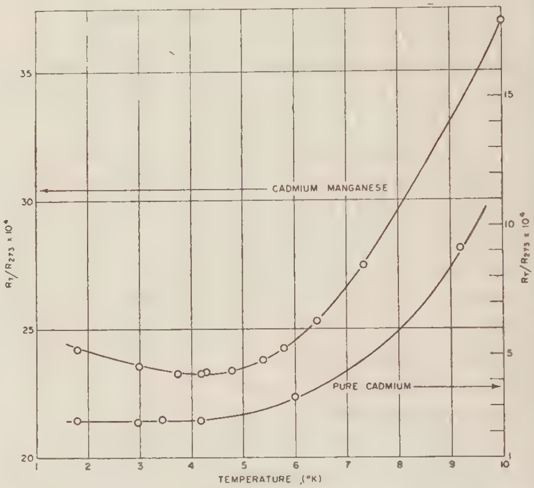

Fig. 1. The relative resistance (R_T/R_{273}) of pure cadmium and a cadmium manganese alloy as a function of temperature.

The author would like to thank Mr. E. E. Wallingford for help in making some of the resistance measurements and the Canadian Defense Research Board for financial support.

References

1) D. A. Sphor and R. T. Webber: Phys. Rev. **105** (1427) 1957.
2) F. T. Hedgcock, W. B. Muir and E. E. Wallingford: Can. J. Phys. **38** (376) 1960.
3) G. Gaudet, F. T. Hedgcock, G. Lamarche and E. E. Wallingford: Can. J. Phys. **38** (1134) 1960.
4) Y. Muto, Y. Tawara, Y. Shibuya and T. Fukuroi: J. Phys. Soc. Japan **14** (380) 1959.

---

* Present address: Franklin Institute Laboratories for Research and Development, Philadelphia, Pa.

J. PHYS. SOC. JAPAN **16** (1961) 2599~2600

Thermoelectric Effects in Mg, Zn and Al Containing Traces of Mn†

F. T. HEDGCOCK* and W. B. MUIR*

Dept. of Physics University of Ottawa
Ottawa, Canada

(Received August 26, 1961)

It has been known for some time that manganese will induce low temperature resistance anomalies in the monovalent metals Cu, Ag and Au. Recent reports have indicated that manganese will induce a low temperature resistive anomaly in the divalent metals Mg[1)], Zn[2)] and Cd[3)] whereas no anomaly is observed in the low temperature resistive behavior of aluminum when a small quantity of manganese is dissolved[1)]. MacDonald and Pearson[4)] have shown experimentally that anomalously large negative thermoelectric powers are associated with the resistance anomalies in copper. Bailyn[5)] in a recent theoretical paper on the electron transport properties of alloys containing magnetic impurities has pointed out that a thermoelectric power anomaly is a necessary but not a sufficient condition for the appearance of a resistive minimum in a dilute alloy. The purpose of the present letter is firstly to show qualitatively that the thermoelectric voltage in divalent metal alloys exhibiting low temperature resistance anomalies is the same as the monovalent metal alloys, and secondly that although the dilute Al-Mn alloys do not show a resistive anomaly they do show a large negative thermoelectric voltage. The thermopower exhibited, however, by the Mg and Zn alloys in the region of the resistance anomaly is much greater than observed in the aluminum alloy in the equivalent temperature interval.

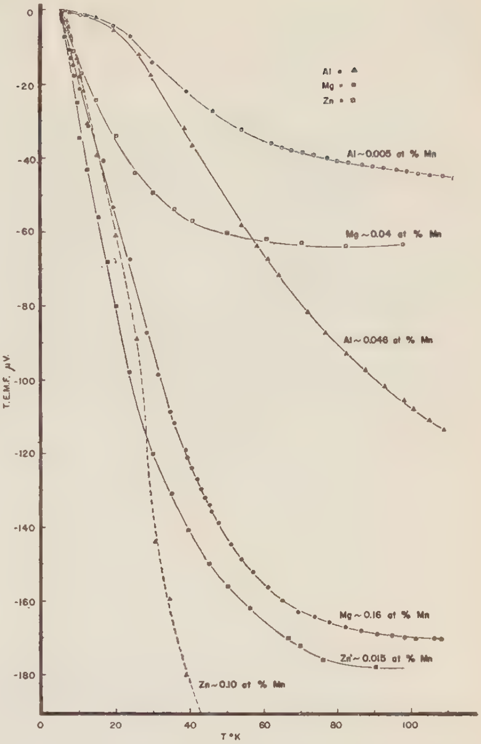

Fig. 1. Thermoelectric voltage of dilute Mg, Zn and Al alloys containing Mn. All of the thermo e.m.f. measurements were made relative to the pure solvent (99.99% pure).

Table 1. Thermoelectric and resistive data of the Mg, Zn and Al alloys.

Metal	At. % Mn	$\frac{R_{4.2}}{R_{273}}$	ρ 273°K/At. % Mn $\mu\Omega$ cm/At. % Mn	μV/°K at 15°K	Thermo e.m.f. at 100°KμV	$\frac{\text{Thermo e.m.f. at 100°K}}{\rho\ 273°\text{K}}$
Mg	0.04 0.16	0.028 0.191	3.5±0.5	−2.47 −3.63	− 65 −170	− 465 − 255
Zn	0.015 0.10	0.040 0.24	1.5±0.2	−5.20 −4.85	−177 −320	−7900 −2130
Al	0.005 0.046	0.014 0.112	5.8±0.5	−0.20 −0.26	− 45 −110	−1550 − 410

The characteristic thermoelectric behavior of the monovalent metal copper with small concentrations of paramagnetic impurity is that that thermo e.m.f. becomes negative and stays negative to relatively high temperature (~100°K). It can be seen in Fig. 1 that the thermoelectric voltage in the divalent metal alloys is also negative in all of the alloys studied. It will also be noticed that the thermo e.m.f. for the Al-Mn alloys, which does not show a resistive anomaly (at least down to temperatures of 1.8°K) is also large and negative. The fact that the magnetic properties of the dilute Al-Mn alloys indicates the formation of a d-band in these dilute

---

† This work was supported by the National Research Council of Canada.

* Present Address: The Franklin Institute, Philadelphia 3, Penna.

alloys[5] is suggestive that the large anomalous thermoelectric power in dilute aluminum alloys is a result of the presence of such an overlapping band.

The data shown in Table 1 illustrates that the thermopower of all of the alloys studied is approximately independent of manganese concentration. This is in agreement with observations of MacDonald and Pearson[4] in the more concentrated copper base alloys. The thermopower of the aluminum manganese alloys is seen to be an order of magnitude smaller at 15°K than for the alloys which show a resistive anomaly. The thermo e.m.f. at higher temperatures, however, is the same order of magnitude for all of the alloys and would appear to increase with the increasing atomic number of the solvent. It is intended to extend the present measurements to include absolute thermoelectric measurements, in particular at temperatures below 4.2°K.

References

1) F. T. Hedgcock, W. B. Muir and E. Wallingford: Can. J. Phys. **38** (1960) 376.
2) Y. Muto, Y. Tawara, Y. Shibuya and T. Fukuroi: J. Phys. Soc. Japan **14** (1959) 380.
3) W. B. Muir: see previous letter.
4) D. K. C. MacConald and W. B. Pearson: Acta Metallurgica **3** (1955) 392; **3** (1955) 403.
5) M. Bailyn: Phys. Rev. (to be published).

Errata

Refractive Index Difference of Dilute Aqueous Solution of Polyvinylpyrolidon

By Yasuhiro MIYAKE and Jiro FURUICHI
J. Phys. Soc. Japan **16** (1961) 1263

"For example" of the footnote should be shifted to the reference, i.e.,

1) For example, D. Streeter and R. Boyer, and so on.

Determination of the Extension of Linear Polymer Molecule in the Solution by the Light Scattering

By Yasuhiro MIYAKE
J. Phys. Soc. Japan **16** (1961) 1703

Page 1705

Table I. Reciprocal reduced intensities $C/I(\theta)$.
Polystyrene F. 1-2 at 30°C in M.E.K.

C	0.15%	0.09%	0.05%
$\sin^2\theta/2$			
0.12	1.47	1.22	
0.20	1.61	1.32	1.08
0.30	1.72	1.47	1.24
0.40	1.82	1.58	1.35
0.50	1.97	1.70	1.47
0.60	2.05	1.79	1.59

Contents

(Vol. 16)

No. 1

Page

Study on Spark Counters of the Rosenblum Type for Counting α Particles and Neutrons .... Suekichi KAWATA 1

On the Theory of the Fracture of Liquids .... Hiromu WAKESHIMA 6

On the Irreversible Behavior of Coupled Oscillators with Application to Time of Flight .... Youzou KOGURE 14

A New Picture of the Vibration of Linear Lattices .... Jun-ichi HORI 23

Crystal Distortion in Copper Ferrite-Chromite Series .... Haruyuki OHNISHI and Teruo TERANISHI 35

Distribution of Interstitials and Vacancies Produced by an Incident Fast Neutron .... Masayuki YOSHIDA 44

On the Electron Emission from Oxide Coated Cathode Subject to Strong Electric Field .... Chokichiro SHIBATA 51

Resistivity Striations in Germanium Single Crystals .... Hiroshi UEDA 61

X-ray Studies on Precipitation of Metastable Centers in Mixed Crystals $NaCl$-$CdCl_2$ .... Kazuo SUZUKI 67

Theory of Ferro- and Antiferromagnetic Resonance Absorption .... Takehiko OGUCHI and Akio HONMA 79

A Method for Measuring High Electron Densities in Plasmas .... Susumu TAKEDA and Michel ROUX 95

Energy Spectrum of Mn^{++} Ion in Calcium Fluorophosphate I .... Koziro NARITA 99

The Wavelength Dependence of Quantum Efficiency and Absorption Coefficient of $ZnSiO_3/Mn$ Powder Phosphor .... Isoo MASUDA 105

Radiation Induced Optical Absorptions in Crystalline Quartz and Fused Silica .... Kazuko KUBO 108

Propagation of Ultrasonics in Triethylamine-water Mixture .... Seiken SHIMAKAWA 113

SHORT NOTES

Paramagnetic Resonance Study in Some Copper Salts .... Hidetaro ABE and Hiroko SHIRAI 118

Magnetic and Crystallographical Properties of Hexagonal Barium Mono-Ferrite, $BaO \cdot Fe_2O_3$ .... Chisato OKAZAKI, Saburo MORI and Fumikazu KANAMARU 119

Electron Linear Accelerator as a Source of Intense Secondary Particle Beams .... Kazuto OKAMOTO 120

A-Centers in Potassium Chloride Crystals .... Kazuko KOJIMA and Noriko NISHIMAKI 121

Vibrational Effect on the Nuclear Quadrupole Coupling in ND_3 .... Yoshifumi KATO 122

Proton Resonance and Spin Quenching Effect in $NiSO_4 \cdot 7H_2O$ .... Hiroshi NAGASAWA and Yuzo TOMONO 123

Electrical Properties of Sb-Doped *n*-Type SnSe .... Jun-ichi UMEDA 124

Change of Surface State of Ge by Electron Bombardment .... Kiichi KOMATSUBARA 125

Antiferromagnetic Magnetostriction in CoO and NiO Single Crystals .... Takuro NAKAMICHI and Mikio YAMAMOTO 126

The Purification of KCl by the Zone Refining Method .... Morio INOUE and Hiroyuki MIZUNO 128

Heat Capacities of Two Manganese Salts .... H. FORSTAT and G. O. TAYLOR 128

Excitation Function for the Reaction $O^{16}(\alpha, pn)F^{18}$ .... Michiaki FURUKAWA and Shigeo TANAKA 129

Mass Spectra of Baryons .... Seitaro NAKAMURA and Ken KAWARABAYASHI 130

Preferential Plastic Deformation in the Surface Region of Al and α-Fe Single Crystals .... Kôji SUMINO and Mikio YAMAMOTO 131

Errata

Study on the Ordered Phases with Long Period in the Gold-Zinc Alloy System .... Hiroshi IWASAKI, Makoto HIRABAYASHI, Kunio FUJIWARA, Denjiro WATANABE and Shiro OGAWA 132

Anisotropic Hall Coefficients in *n*-Type Germanium .... Hisao MIYAZAWA and Hajime MAEDA 132

No. 2

Elastic and Inelastic Scattering of Protons from Carbon Nucleus from 6.5 to 16 Mev .... Yukio NAGAHARA 133
Short-lived Activity of Ag^{106} .... Mitsuo SAKAI, Hidetsugu IKEGAMI and Toshimitsu YAMAZAKI 148
Counting Efficiency of Gamma Rays in Counter Tubes .... Tatsusaburo SUZUKI and Jiro YUHARA 152
On the Protons from the $N^{14}(d, p)N^{15}$ Reaction .... Nawoyuki KAWAI 157
Inelastic Scattering of Neutrons by the Time-of-Flight Method .... Kineo TSUKADA, Shigeya TANAKA and Michio MARUYAMA 166
The Crystal Structure of $KCuF_3$ .... Atsushi OKAZAKI and Yasutaka SUEMUNE 176
Hall Effect on Some of the Magnetic Compounds .... Satoshi FUJIME, Miyuki MURAKAMI and Eiji HIRAHARA 183
Anisotropy of Electrical Conduction in Iron Sulfide Single Crystal .... Miyuki MURAKAMI 187
Heat Treatment Centers in Silicon .... Yasuo MATUKURA 192
On the Energy of the Interstitial Atom in Graphite .... Tadao IWATA, F. Eiichi FUJITA and Hideji SUZUKI 197
Electric Conduction of Ferrites Containing Fe^{2+}-ions .... Nahonori MIYATA 206
Dislocations and Fines Line in Rochelle Salt Crystal .... Terutaro NAKAMURA and Kikuo OHI 209
Observations of Lattice Defects in Graphite by Electron Microscopy, Part I .... F. Eiichi FUJITA and Kazuhiko IZUI 214
A Diffraction Pattern caused by Temperature Diffuse Scattering. I. General Theory .... Yoshiro KAINUMA 228
Inelastic Scattering of Thermal Neutrons by Paramagnetic Ions .... Soitiro TOSIMA 241
Time Decrease of Magnetic Permeability in Some Mixed Ferrites .... Keizo OHTA 250
Oxygen Positional Parameters of Tetragonal Mn_3O_4 .... Ken'iti SATOMI 258
Nuclear Quadrupole Resonance Under High Pressure, I. .... Tokujiro FUKE 266
Magnetic Anisotropy of Chromium Antimonide and its Manganese Substitutes .... Ichiro TSUBOKAWA 277
Extension of High Polymer Molecule and Energy Change by Mixing .... Hiroshi MIZUTANI 282
Proton Magnetic Resonance of Ice Single Crystal .... Kiyoshi KUME and Ryosuke HOSHINO 290
Microwave Attenuation by Cyclotron Resonance in a Slightly Ionized Gas .... Taro DODO 293
Optical Image Formation in Terms of Entropy Transformations .... Edward L. O'NEILL and Toshimitsu ASAKURA 301
Magnetic Hyperfine Structure in the Rotational Spectrum of H_2CO .... Hiroshi TAKUMA 309
Some Remarks on Hydrostatic Pressure and Maxwell Model .... Wataru SEGAWA 317
Rheological Equations of Generalized Maxwell Model and Voigt Model in Three-Dimensional, Non-Linear Deformation .... Wataru SEGAWA 320
The Velocity Distribution at the Interface between Two Liquids .... Setsuo OKUDA 324

SHORT NOTES

Annealing of Radiation Damage on Lifetime in Silicon .... Kenji MATSUURA and Yoshio INUISHI 339
The Fundamental Absorption of Lithium Fluoride and Sodium Fluoride .... Ryumyo ONAKA, Atsuo FUKUDA and Arisato EJIRI 340
The Inverse Solution of the TFD Equation .... Kwai UMEDA, Yasuo TOMISHIMA and Chikao KAWABATA 341
Spin Wave Resonance in Cu-Ni Alloy Films .... Hiroshi NOSÉ 342
Nuclear Magnetic Resonance Study of NaCl Crystal containing Ca Impurities .... Junkichi ITOH, Mitsuo SATOH and Akio HIRAKI 343

Temperature Dependence of the Line Width of Ferrimagnetic Resonance in Polycrystalline Nickel Cadmium Ferrite .... Susumu TAKEMOTO 344
Electrical Resistivity of Ferromagnetic Chromium Dioxide .... Buichi KUBOTA and Eiichi HIROTA 345
Measurements on Collision Frequencies of Electrons in Neon Gas......... Taro DODO 346
Observations of Dislocation Network in Neutron-Irradiated LiF Crystal .... Kazuko KUBO and Yoshio KATANO 347
Spectrum of the Electron Cyclotron Resonance in a Plasma .... Taro DODO 348
On the Inelasticity in High-Energy Nuclear Interactions .... Shigeo MATSUMOTO and Shoji MIKAMO 350
Enhancement of Photoconductivity upon Cadmium Sulphide Single Crystals ...... Saburo KITAMURA, Takao KUBO and Toshio YAMASHITA 351
A New Phase of an Intermetallic Compound Mn$_{3.4}$Ge and its Magnetism .... Tetuo OHOYAMA, Kō YASUKŌCHI and Kazuo KANEMATSU 352

Errata

The Magnetic Investigation of Mn^{++}, Co^{++}, Ni^{++}, Cu^{++} Ammine and Anhydrate Salts................................ Kiyoshi KIDO and Takashi WATANABE 353
On the Superconducting Ground State .... Ziro MIKURA 353

No. 3

Gamma Rays from Inelastic Scattering of Neutrons by Fe, Cu, Zn, Ge and Se .... Kazuaki NISHIMURA 355
Angular Distributions and Excitation Functions of the Be$^9(d, p)$Be^{10} Ground-State Reaction .... Toshiyuki ISHIMATSU, Naoyuki TAKANO, Yûki HACHIYA and Takao NAKASHIMA 367
On the Nuclear Interaction of Mu-Mesons......................... Hiroyuki SHIBATA 372
Quantum Statistics of Surface Effect .... Takuji TSUZUKI 377
Effects of the Special Heat-treatment on Permalloys .... Sadami TOMITA 393
Direct Observation of Subgrain-Growth of Cold-Worked Aluminium by means of Electron Microscopy...................................... Hiroshi FUJITA 397
Cavity Growth by Vacancy Condensation and Transformation to Dislocation Loop in the Graphite Structure .... Takuro TSUZUKU 407
Ferroelectric Properties of X-ray Damaged Rochelle Salt .... Kenkichi OKADA 414
An Effect of Heat Treatment on WO$_3$ Single Crystal, I. Various Patterns........ Tadao HORIE and Tsuruji IWAI 424
Magnetic Properties of Intermetallic Compounds in Iron-Germanium System: Fe$_{1.67}$Ge and FeGe$_2$... Kō YASUKŌCHI, Kazuo KANEMATSU and Tetuo OHOYAMA 429
Magnetic Properties of Perovskites Containing Strontium, II. Lanthanum-Strontium Manganites .... Hiroshi WATANABE 433
Regrowth of Germanium Single Crystal from Indium Melt .... Masami TOMONO 439
An Electron Diffraction Study on Cu-Sn Alloys................. Tomokuni MITSUISHI 453
Diffusion of Cobalt into Silver .... Tokutaro HIRONE and Hisao YAMAMOTO 455
Orientation Dependent Mechanical Breakdown of a Model High Polymer Solid .... C. C. HSIAO, J. E. OSBORN and D. B. ROZENDAL 459
X-Ray Line Broadening in Polyethylene Filaments............... Ken-ichi KATAYAMA 462
Study on the Ordered Alloys of Gold-Manganese System by Electron Diffraction, III. Lattice Modulation in the Ordered Au$_3$Mn .... Denjiro WATANABE 469
The Ferroelectric Phase Transition in (Glycine)$_3$·H$_2$SO$_4$ and Critical X-Ray Scattering .... Iwao SHIBUYA and Toshio MITSUI 479
X-Ray Studies of the Ferroelectric Phase Transition in NaNO$_2$......... Iwao SHIBUYA 490
Ps Function in Electron Diffraction...... Yoshiro KAINUMA and William N. LIPSCOMB 495
Electron Distribution in Cu$_2$O Crystal .... Tadasu SUZUKI 501
A Theory of Electron Impact on Some Polyatomic Molecules.... Tsutomu WATANABE 510
On the Additivity Rule in the Ionization Cross Section of Molecules .... Tsutomu WATANABE 529
The Optical Properties of Cadmium Telluride in the Far Infrared Region .... Akiyoshi MITSUISHI 533

Interaction of Exciton with Electron Trapping Centers in Alkali Halide Crystals
3. Exciton Induced Photoconductivity of *U* center .... Masayasu UETA, Masamitsu HIRAI and Mikihiko IKEZAWA 538
Theoretical Prediction of the Pressure Distribution on a Non-lifting, Thin Symmetrical Aerofoil at Various Transonic Speeds .... Iwao HOSOKAWA 546
Effect of a Magnetic Field upon the Stability of Free Boundary Layers between Two Uniform Streams .... Kanefusa GOTOH 559

SHORT NOTES

On the New Magnetic Phase in Manganese-Aluminium-Copper System .... Ichiro TSUBOYA and Makoto SUGIHARA 571
Optical Absorption and Electrical Conductivity of Reduced $BaTiO_3$ Single Crystal .... Seiji IKEGAMI, Ichiro UEDA and Yukihiko ISE 572
Impedance Changes Induced by Light in ZnS Phosphors .... Ichizo UCHIDA and Kimihiko SATAKE 573
NMR of Co^{59} in Ferromagnetic Cobalt Alloys ....
Yoshitaka KŌI, Akira TSUJIMURA, Tadamiki HIHARA and Toshimoto KUSHIDA 574
Hot Electron Nonequilibrium Carrier Distribution in a Many-Valley Semiconductor .... Louis GOLD 575
Nature of the *A*-Centers in KCl.. .... Noriko NISHIMAKI, Kazuko KOJIMA and Tadanobu KOJIMA 576
Impurity Effect upon Mobility in Heavily Doped Silicon .... Yoshitaka FURUKAWA 577
X-ray Small Angle Scattering from Precipitated Platelets in Al-Ag Alloy .... Yasuharu YONEDA and Kouzou NISHIOKA 578
Microdomain Structure in Paraelectric Phase of $NaNO_2$ .... Sigetosi TANISAKI 579
Measurement of Anomalous Absorption Coefficients of Electrons for MgO Crystals .... Kazutake KOHRA and Hiroshi WATANABE 580

Errata

On the Electron Emission from Oxide Coated Cathode Subject to Strong Electric Field .... Chokichiro SHIBATA 582
Radiation Induced Optical Absorptions in Crystalline Quartz and Fused Silica...... .... Kazuko KUBO 582

Addendum

On the Ferrimagnetic Resonance of Europium Iron Garnet .... W. P. WOLF 582

No. 4

Angular Distributions of Protons from the Alpha Particle Bombardment of B^{10}, N^{14}, O^{16} and Ne^{20} .... Hisashi YAMAGUCHI 583
Resonance Levels in the Reactions $^{28}Si(p, \gamma)^{29}P$, $^{29}Si(p, \gamma)^{30}P$ and $^{30}Si(p, \gamma)^{31}P$ .... Haruko OHMURA, Hiroyasu EJIRI, Yutaka NAKAJIMA, Kinuko HORIE, Kiichi ETOH, Akiji OHUCHI and Yozo NOGAMI 593
The Reaction $Mg^{25}(d, p)Mg^{26}$ in the Energy Range of Deuterons from 1.5 MeV to 3.0 MeV .... Naoyuki TAKANO 598
The Structure of Extensive Air Showers Near the Axes................. Shūji FUKUI 604
On the Transport Equation in Quantum Mechanics..................... Lesser BLUM 616
On the Theory of Adiabatic and Isolated Susceptibilities............. Nobuhiko SAITÔ 621
Convex-Core Model of Molecules in Crystalline State. II............... Saburo KOBA 627
Entropy Production and Variation Principle in the Kinetic Theory of Rigid-Sphere Gas Mixture .... Terutoshi MURAKAMI 633
Temperature Dependence of Magnetic Susceptibilities of $KClO_3$, $KBrO_3$ and KIO_3.. .... Shōtarō TOBISAWA 654
Luminescence of Doped Silver Chloride Crystals.... Sanemi SONOIKE and Kazuo AKIMOTO 658
Internal Friction of Synthetic Quartz.................................... Yosio HIKI 664
The Crystal Structures of $KMnF_3$, $KFeF_3$, $KCoF_3$, $KNiF_3$ and $KCuF_3$ above and below their Néel Temperature ...... Atsushi OKAZAKI and Yasutaka SUEMUNE 671
Anomalous Diffusion at the Interface of Thin Bimetallic Film of Bi and Sb........ .... Ryōji SUGANUMA, Toshio YOSHIDA and Yoshibumi FUJIKI 676

Electrical Properties of Heavily Doped n-Type Germanium...... Yoshitaka FURUKAWA 687
Paramagnetic Resonance of Mn^{++} Associated with Impurities in Alkali Chlorides.. ...... Yasaburo YOKOZAWA and Yukio KAZUMATA 694
Ferromagnetic Resonance Absorption of Single-Crystal Thin Films of Nickel .... Masao KURIYAMA, Hirokage YAMANOUCHI and Sukeaki HOSOYA 701
Specific Heat of Ti_2O_3 ...... Shoichiro NOMURA, Tatsuyuki KAWAKUBO and Taketoshi YANAGI 706
Regrowth of Germanium from Molten Indium or Lead ...... Masami TOMONO 711
Low-Temperature Electrical Breakdown in Germanium...... Jiro YAMASHITA 720
Studies on the Boundary between Etched and Ground Regions of Ge and Si Single Crystal Surface by X-Ray Diffraction Topography...... Zensho ISHII 733
The Switching Circuit Logically or Functionally Equivalent to a System of Biochemical Reactions...... Motoyosi SUGITA 737
Mass Spectrometric Study on the Evaporation of Volatile Components in Polyethylene ...... Kisaku NAKAGAWA 741
Interaction between Polyions and Low Molecular Ions ...... Nobuhisa IMAI 746
Study of the Hydration-Dehydration in Polyelectrolyte Solutions by the Ultrasonic Technique ...... Hiroshi ASAI 761
On the Theory of Cross Relaxation in Maser Materials ...... Motokazu HIRONO 766
"Non-Adiabatic" Behavior in a Low Frequency Beam-Type Maser ...... Tadao SHIMIZU and Koichi SHIMODA 777
Density vs. Exposure Curves of a Photographic Emulsion for 20～200 kV Electrons ...... Mieko TAKAGI, Norihisa KITAMURA and Setsu MORIMOTO 792
On the Steady Motion of an Idealized Elastico-Viscous Liquid Through Channels with Suction and Injection ...... S. K. DATTA 794
Flow of Condensing Vapour with Temporary Supersaturated State due to Heat-Removal Effect ...... Keishiro NIU 798
A Simplified Method Calculating The Laminar Boundary Layer ...... Shin KAWAMATA 805
Refractive Index and Pore Structure of Acid-Leached Surface Layer of Glass...... Koreo KINOSITA 807
Diffraction of Plane Sound Wave by Many Equal Circular Holes Arbitrarily Distributed in an Infinitely Large Rigid Plane Plate ...... Yûkichi NOMURA 819

SHORT NOTES

Effects of Vacancies on Pulse Photoconductions in CdS Single Crystals ...... Junji SHIRAFUJI and Yoshio INUISHI 832
Conductivity of Grain Boundaries in Ge...... Yasuo MATUKURA and Shigezo TANAKA 833
Direct Observation of the Lattice Imperfections in Pearlites by Electron Microscopy ...... Zenji NISHIYAMA, Atsuo KORE'EDA, Isamu EGUCHI and Koshi KATO 834
Proton Magnetic Resonance in Ferroelectric $(CH_3NH_3)\,AlSO_4\cdot 12H_2O$.... Ryosuke HOSHINO 835
Temperature Dependence of ESR Line-Width in $K_2CuCl_4\cdot 2H_2O$ ...... Hidetaro ABE 836
E.S.R. of Irradiated DPPH Protected by Polystyrene... Kohzoh MASUDA and Tokuo SUITA 837
Spin Wave Resonance in Pd-Ni Alloy Films ...... Hiroshi NOSÉ 838
The O-H···O Bond in Orthoboric Acid ...... James A. IBERS and C. H. HOLM 839
Volume Magnetostriction in Nickel-Iron Alloys...... Yoji NAKAMURA, Tetsuo NAKAJIMA and Hideo TAKAMI 840
Decay of Ir^{195} and Ir^{197} ...... Saburo HOMMA, Tokihiro KUROYANAGI and Haruhiko MORINAGA 841
Properties of Grain Boundaries in Silicon...... Yasuo MATSUKURA 842
The O-H···O Bond in Orthoboric Acid ...... Kiyoshi KUME and Yoshinobu KAKIUCHI 843
Linear Potential Barrier Model for Nuclear Surface...... Tutomu INOUE 844

Errata

Rheological Equations of Generalized Maxwell Model and Voigt Model in Three-Dimensional, Non-Linear Deformation ...... Wataru SEGAWA 845
The Velocity Distribution at the Interface between Two Liquids...... Setsuo OKUDA 845
Dislocation Networks and Moiré Patterns of Molybdenite...... Yoshihiro KAMIYA, Kei-ichi ANDO, Minoru NONOYAMA and Ryozi UYEDA 846

Some Remarks on Hydrostatic Pressure and Maxwell Model .... Wataru SEGAWA 846

No. 5

Lateral Density Distribution of Charged Particles in the Central Region of Extensive Air Shower .... Saburo MIYAKE, Kensaku HINOTANI, Itsuo KATSUMATA, Tatsunosuke KANEKO and Nobuo ITO 847
Mu-Meson Component of Air Shower Below the Ground .... Kenji WATANABE 855
A Study on High-Energy Nuclear-Active Particles in Extensive Air Showers .... Yasuo TANAKA 866
Experimental Studies on Electronic Trapping Processes Associated with Dislocation Lines in Alkali Halide Crystals .... Hiroshi OHKURA 881
Interaction of Electrons and Holes with Acoustic Waves in Intrinsic Semiconductors .... Nobuo MIKOSHIBA 895
Growth and Dissolution Processes of GASH Crystal .... Terutaro NAKAMURA, Kikuo OHI and Hiroko KUBOTA 906
Angular Distribution of Electrons Suffering Characteristic Energy Loss in Passage through Metal Films .... Hiroshi WATANABE 912
Domain Structure of $NaNO_2$ .... Shoichiro NOMURA, Yohko ASAO and Shozo SAWADA 917
Perfectness of Macrodomains of $BaTiO_3$ Crystals .... Kêitirô AIZU and Osamu NAKADA 923
Study of the Texture of the Boundary of Etched and Ground Regions of Quartz Plate by X-ray Diffraction .... Einosuke FUKUSHIMA and Hiroshi NIMURA 928
222-Reflection from CuCl in Electron Diffraction .... Fuminori FUJIMOTO 936
The Dipole Moment and End-to-End Length of the Isotactic Vinyl Polymer, III. Convergence of Neumann Series .... Tsugio MORI 944
Mathematical Considerations on Chemical Kinetics of Radiation-Induced Polymerization .... Ayao AMEMIYA and Mitio INOKUTI 949
The Rheological Behavior and Thixotropy of a Fatty Plastic Body .... Toshimaro SONE 961
Scattering of Microwaves from a Cylindrical Plasma in the Born Approximation. I. .... Yukio MIDZUNO 971
Photoconductive Hall Effect in Potassium Bromide .... Masami ONUKI 981
Structures of Photoconductivity Spectra near the Fundamental Absorption Edge of Cadmium Sulfide .... Hiroji MITSUHASHI 989
Smoke Observation on Boundary Layer Transition Caused by a Spherical Roughness Element .... Masako MOCHIZUKI 995
Vibration of a Plate and Sound Radiation Generated by an Impulsive Force .... Yasuo TOKITA 1008
On the Relation between the Change in Modulus of Rigidity in Brass Wires by Cold-Rolling and Rolling Textures .... Jun KUROYANAGI 1019

SHORT NOTES

Dielectric α- and β-dispersions in Polyvinyl Butyral (PVB) .... Yūzō TAKAHASHI 1024
The Double-Grid Ionization Chamber .... Iwao OGAWA and Tadayoshi DOKE 1025
Thermoelectric Behaviours of Rutile .... Kimiko SAKATA 1026
Magnetic Anisotropy of Heusler Single Crystal .... Keizô AOYAGI and Makoto SUGIHARA 1027
Dielectric α-, β- and γ-Dispersions in the Thermosetting Phenolic Resins .... Yūzō TAKAHASHI 1028
Forward Characteristics of Si $p\pi n$-Junctions .... Masakatsu TOKUNAGA and Katsufusa SHONO 1029
Viscous Forces and Brownian Motion .... Naokata TAKEYAMA 1030
Fine Structures of Photoprotons from Si^{28} .... Katsufusa SHODA, Keisuke KOBAYASHI, Shoichi SIINA, Ken ABE and Motoharu KIMURA 1031
Observation of Lattice Defects in Fission Fragment-irradiated Graphite .... Kazuhiko IZUI and F. Eiichi FUJITA 1032
A Note on the Electron Diffusion and the Wall Relaxation in Ferrites .... Hisashi SEKIZAWA 1034
Weak Field Behaviour of the ΔE Effect in Ferromagnetic Cubic Solid Solution Alloys .... Mikio YAMAMOTO and Satoshi TANIGUCHI 1035
Remarks on the Electrical Properties of Alkali Antimonides .... Shunji IMAMURA 1036

The Characteristics of the Discharges in the Crossed Electric and Magnetic Field .... Shigeru HAYAKAWA and Tokuo SUITA 1037
The Electrical Properties of Zinc Telluride .... Hirosi TUBOTA, Hiromichi SUZUKI and Kazuyoshi HIRAKAWA 1038
Internal Magnetic Field in Iron and Iron Alloys Measured by NMR .... Yoshitaka KÔI, Akira TSUJIMURA, Tadamiki HIHARA and Toshimoto KUSHIDA 1040
Slow Decay of Reverse Current and Noise in Field Effect on Ge P^+-N Junction .. Hiroshi EDAGAWA, Yoshinori MORITA, Syun-ichi MAEKAWA and Yoshio INUISHI 1041

Errata

Cavity Growth by Vacancy Condensation and Transformation to Dislocation Loop in the Graphite Structure .... Takuro TSUZUKU 1042
Anomalous Diffusion at the Interface of Thin Bimetallic Film of Bi and Sb .... Ryōji SUGANUMA, Toshiho YOSHIDA and Yoshibumi FUJIKI 1042

No. 6

Elementary Processes Related to the Catalytic Action of μ^- for the p-d Fusion Reaction .... Yukio MIZUNO 1043
Inelastic Scattering of Deuterons from C^{12}, Mg^{24} and Ni^{60} .... Yoshihide ISHIZAKI 1056
Anomalies in the Scattering of Alpha Particles by Carbon .... Takashi MIKUMO 1066
He^3-Alpha Scattering .... Ren CHIBA, Homer E. CONZETT, Haruhiko MORINAGA, Naoshi MUTSURO, Katsufusa SHODA and Motoharu KIMURA 1077
Angular Correlation of the Mo^{95} Gamma-Gamma Cascades .... Atsushi AOKI 1086
Angular Distribution of (α, p) Reactions in Some Light Nuclei .... Michiya KONDO, Takashi YAMAZAKI and Shotaro YAMABE 1091
A Cloud Chamber Study of High Energy Nuclear Interactions of Cosmic Ray Particles (I)—A Possible Evidence of Successive Collisions in Carbon Nuclei .... Isao KITA 1099
A Cloud Chamber Study of High Energy Nuclear Interactions of Cosmic Ray Particles. (II)—Results of Single Nucleon-Nucleon Interactions .. Goro FUJIOKA 1107
Effects of s-d Exchange Interaction and Temperature-Independent Paramagnetism on Susceptibilities of Nickel, Palladium, and Platinum .... Masao SHIMIZU 1114
Magnetic Properties of Intermetallic Compounds in Manganese-Tin System: Mn$_{3.67}$Sn, Mn$_{1.77}$Sn, and MnSn$_2$ .... Kō YASUKŌCHI, Kazuo KANEMATSU and Tetuo OHOYAMA 1123
The Magnetic Investigation of Mn^{++}, Co^{++}, Ni^{++} and Cu^{++} Ammine and Anhydrate Salts at Low Temperature .... Takashi WATANABE 1131
Ultrasonic Attenuation in Tin Single Crystals at Low Temperatures .. Kazuo KAMIGAKI 1141
The Thermoelectric Power of Magnesium-Cadmium Alloys .... Seiichiro NOGUCHI 1145
Resonance Transfer of Ionization Energy in Semiconductors .... Shigeharu KOSHINO and Toshihiko ANDO 1151
Ferroelectricity in (K, NH$_4$), (K, Rb) and (K, Tl) Ferrocyanide Mixed Crystals .... Shigeru WAKU, Kunio MASUNO and Toshisuke TANAKA 1158
The Superstructures of Iron Selenide Fe$_7$Se$_8$ .... Atsushi OKAZAKI 1162
Ultrasonic Attenuation in Magnetite at Low Temperatures .... Kazuo KAMIGAKI 1170
Crystal Structures and Electrical Properties of Alkali Antimonides .... Jun-ichi CHIKAWA, Shunji IMAMURA, Kenzo TANAKA and Makoto SHIOJIRI 1175
Weak Ferromagnetism in β-NaFeO$_2$ .... Hiroshi WATANABE and Masahiro FUKASE 1181
The Crystal Structure of Chloranil and Bromanil .... Ikuhiko UEDA 1185
Study on Precipitation Phenomena in Thin Films of Supersaturated Gold-Nickel Alloy .... Yasushige FUKANO 1195
A Direct Determination of the Crystal Structure of Ethylenediammonium Sulphate .... Kiichi SAKURAI 1205
Study of Metallic Carbides by Electron Diffraction Part IV. Cobalt Carbides .... Sigemaro NAGAKURA 1213
Study on the Internal Motions of Some Acryl- and Methacryl-group High Polymers by Pulsed NMR Method .... Takao KAWAI 1220

Mechanical Dispersions and Transition Phenomena in Semicrystalline Polymers .... Yasaku WADA 1226
Microwave Spectrum of Formaldehyde III. Vibration-Rotation Interaction .... Takeshi OKA and Yonezo MORINO 1235
Double Quantum Transition in Electron Spin Resonance of Diphenyl-Picryl Hydrazyl at Low Magnetic Fields .... Tsuneo HASHI 1243
On the Pendent Drop, I .... Ko TAMADA and Yoshio SHIBAOKA 1249

SHORT NOTES

Observation of Dislocations in Germanium Single Crystal .... Masakazu SHOJI, Shoji TAUCHI, Tomokuni MITSUISHI and Masami TOMONO 1253
Anomalous Temperature Dependence of Lattice Constants of Ferroelectric Sodium Nitrite .... Sadao HOSHINO and Iwao SHIBUYA 1254
Moving Striation in Microwave Discharge Plasma .... Mikio TAKEYAMA, Tanehiro NAKAU, Shōzaburo YAMASAKI and Takeshi ISA 1255
Electron Spin Resonance of Manganese in MgCl$_2$ .... Kuniya FUKUDA, Hiroaki MATSUMOTO, Toru TAKAGI and Yoichi UCHIDA 1256
The New Magnetic Phase in Manganese-Aluminium-Nickel System .... Ichiro TSUBOYA and Makoto SUGIHARA 1257
Effect of Current Injection on Properties of Cadmium Sulfide Crystals .... Hiroji MITSUHASHI 1258
Absorption and Reflection Spectra of Afterglow Plasma .... Shigetoshi TANAKA 1259
The Base Resistance of the Transistor in the Saturated Region .... Osamu NAKAHARA 1260
On the Secondary Tunnelling Phenomena in a *p-n* Junction of Gallium Arsenide .... Akikazu SHIBATA 1261
The Optical Absorption of Localized Exciton in KCl-KI Crystal .... Kaizo NAKAMURA, Kuniya FUKUDA, Riso KATO, Atsuo MATSUI and Yoichi UCHIDA 1262
Refractive Index Difference of Dilute Aqueous Solution of Polyvinylpyrolidon .... Yasuhiro MIYAKE and Jiro FURUICHI 1263
The Electron-Coupled Nuclear Spin Interactions in Ionic Crystals by the Overlap Model .... Tatsuo SHIMIZU 1264
Magnetic Properties of B8 Type Compounds in Manganese-Tin System .... Mitsuru ASANUMA 1265
On the Decomposition of the Ferromagnetic Phase of the Heusler Alloy, Cu$_2$MnAl .... Ren'iti KIMURA, Tetuo OHOYAMA and Keizo ENDO 1266
Microwave Measurement of Fast Time Varying Plasmas .... Susumu TAKEDA 1267
Hot Electron Behavior at High Pressures .... Louis GOLD 1269

Errata

On the Viscosity of Irradiated Polymers. III. Effect of Branching .. Kanji KATSUURA 1270

No. 7

Plane Polarization of 8.5 MeV Bremsstrahlung .... Katsufusa SHODA 1271
Decay of Rh^{102} and Levels in Ru^{102} .... Kazuo HISATAKE 1280
Ferromagnetic Crystalline Anisotropy of MeFe$_2$O$_4$-Fe$_3$O$_4$ Ferrite Solid Solution .... Nahonori MIYATA 1291
Polarization Waves in Solids .... Tatsumi KUROSAWA 1298
Cleavage Fracture in Single Crystals of Silicon Iron .... Ryūkichi HONDA 1309
Some Remarks on the Phenomenological Theory of Ferroelectricity .... Shozo SAWADA and Ikushi YOSHIDA 1322
Fermi Momentum for Free Electron Metals Perturbed by Localized Imperfections .... Akira SUGIYAMA 1327
Antiferromagnetic resonance in CoCl$_2$6H$_2$O .... Muneyuki DATE 1337
Thermal Properties of NaNO$_2$ .... Shoichiro NOMURA 1352
Notes on the Lustre of Moiré Patterns .... Jien NISHIWAKI 1358
Effect of Incoherent Waves on the Electron Microscopic Images of Crystals .... Yoshihiro KAMIYA and Ryozi UYEDA 1361
Flow Birefringence of Polymer Solutions .... Ryuzo KOYAMA 1366

An Expression for Orientation in Cellulose Fibres .... V. D. GUPTA 1377

The Confinement of Plasma by the Heliotron Magnetic Field .... Kōji UO 1380

Microwave Study of Non-ionizing Shock Waves .... Susumu TAKEDA 1395

Scattering of Microwaves from a Cylindrical Plasma in the Born Approximation. II. .... Yukio MIDZUNO 1403

Temperature Dependences of the Fundamental Absorption Tail of KCl and the Absorption due to Bromines in KCl .... Koichi KOBAYASHI and Tetsuhiko TOMIKI 1417

On the Commencement of the Hartmann Flow of Conducting Fluid .... Akira OGAWA and Yoshio SONE 1423

The Hall Effect in the Viscous Flow of Ionized Gas between Parallel Plates under Transverse Magnetic Field. .... Hiroshi SATO 1427

Hydromagnetic Oseen Flow past an Elliptic Cylinder in a Uniform Magnetic Field .... Tosio MIYAGI 1434

Molar Sound Velocity in Inorganic Melts and Solutions .... S. V. SUBRAHMANYAM and J. BHIMASENACHAR 1447

Experimental Studies on Sonoluminescence and Ultrasonic Cavitation.... Katsuo NEGISHI 1450

Experimental Evidence for Frank's Theorem on Dislocations by X-ray Diffraction Micrography .... Mitsuru YOSHIMATSU 1465

SHORT NOTES

Antiferromagnetism of MnHg .... Yasuaki NAKAGAWA and Tomiei HORI 1470

On the Faraday Effect in Many-Valley Semiconductors .... Louis GOLD 1471

Passage Effect in the Electron Spin Resonance of Fe-Doped Silicon .... Takeo IGO 1472

Logarithmic Growth of the Cesium Antimonide Films on Antimony... Kiyoshi MIYAKE 1473

Electron Distribution in KMnF$_3$, KFeF$_3$, KCoF$_3$ and KNiF$_3$ .... Atsushi OKAZAKI and Yasutaka SUEMUNE 1474

A Note on the Magnetoresistance of PbTe at High Magnetic Fields .... Eizaburo YAMADA and Kisaburo SHOGENJI 1475

Optical Constants of LiF in the Extreme Ultraviolet .... Riso KATO 1476

Temporary Bleaching of Color Centers in KCl Crystal .... Masamitsu HIRAI, Mikihiko IKEZAWA and Masayasu UETA 1477

Magnetic Annealing Effect in Cobalt .... Takashi SAMBONGI and Tadayasu MITUI 1478

Mössbauer Effect of the Intermetallic Compound UFe$_2$ .... Shigehiro KOMURA, Nobuhiko KUNITOMI, Poh-Kun TSENG, Naomoto SHIKAZONO and Hidekuni TAKEKOSHI 1479

On Radiations from Plasma in a Static Magnetic Field .... Kenji MITANI and Hiroshi KUBO 1480

Magnetic Annealing of Cobalt .... C. D. GRAHAM, JR. 1481

Drift Mobility of Photo-Injected Electrons in Hexane-Silicone Mixture .... Pyon-un CHONG and Yoshio INUISHI 1482

Magnetic Domain Observation of BaFe$_{12}$O$_{19}$ by Faraday Effect .... Hiroshi KOJIMA and Kimiyoshi GOTO 1483

The Growth of Zinc Sulphide Single Crystals from Flux .... Yo MITA 1484

Effect of Neutron Irradiation on Carrier Lifetime in Si .... Kenji MATSUURA and Yoshio INUISHI 1485

Ferromagnetism of the Intermetallic Compound UFe$_2$ .... Shigehiro KOMURA, Nobuhiko KUNITOMI, Yoshikazu HAMAGUCHI and Masanobu SAKAMOTO 1486

Oscillations in a Plasma in a Weak Magnetic Field .... Shoji KOJIMA, Eiichi KAWASAKI and Kiyoe KATO 1487

ESR Spectra of Irradiated Polyvinylalcohol and Its Related Compounds... Seiji OGAWA 1488

Emission Spectra of Potassium Bromide-Thallium Phosphors .... Tokumichi TAMAI and Eiichi MATSUI 1489

Tetragonal Distortion in Copper Manganite-Chromite System .... Syôhei MIYAHARA, Kiyoshi MURAMORI and Naoki TOKUDA 1490

Errata

A New Method to Determine Hydration Energy of Ion .... Yoshio ISHIDA 1469

No. 8

The Second Excited State of Sn^{120} ....Mitsuhiro KAWAMURA, Atsushi AOKI and Hidetsugu IKEGAMI 1493
Nuclear Ground-State Energies ....Masami YAMADA and Zyun-itiro MATUMOTO 1497
The $N^{14}(d, \alpha)C^{12}$ Ground-State Reaction in the Energy Range of Deuteron from 1.5 to 3.0 MeV ....Toshiyuki ISHIMATSU 1529
Level Structure of Nd^{144} .... Kazusuke SUGIYAMA, Akira FURUSAWA, Shogo HAYASHIBE and Motoharu KIMURA 1538
Magnetic Susceptibilities of Cr and Cr-Fe Alloy ....Masao SHIMIZU and Takeshi TAKAHASHI 1544
Interaction Effects in Potassium Ferricyanide.....................Taiichiro OHTSUKA 1549
Theory of Seebeck Effect in Plastically Deformed Semiconductors ....Tokio OHTA 1561
Measurement of Seebeck Effect in Plastically Bent Germanium....................Tadayoshi YAMASHITA and Tokio OHTA 1565
On the Interference Phenomena of Compton Scattering from Diamond .... Yasuharu YONEDA 1570
The Crystal Structure of Nickel Chloride Hexahydrate, $NiCl_2 \cdot 6H_2O$.......Joji MIZUNO 1574
The Dynamic Bulk and Shear Viscosity of High Polymers, 1 ....Ryusuke KONO 1580
Ionization Efficiency Curves for A^+, Kr^+, N_2^+, and CO^+ by Electron Impact...... .... Yozaburo KANEKO 1587
Three-Level Maser Action in Gas I. Theory of Multiple Quantum Transition and Doppler Effect in Three-Level Gas Maser ....Tatsuo YAJIMA 1594
Some Optical Properties of Lead Activated Potassium Halide Phosphors ....Yozo KAIFU 1605
Local Description of the Flow behind a Steady, Two-Dimensional, Curved Shock Wave ....Zirō HASIMOTO and Shigeki MORIOKA 1616
Two-Dimensional Supersonic Jet of a Conducting Inviscid Gas in the Presence of a Uniform Magnetic Field....................................Shigeki MORIOKA 1625
Steady Temperature in a Composite Elliptic Cylinder................Václav VODIČKA 1630
Ultrasonic Dispersion in Aceton ....C. Raghupathi RAO 1636

SHORT NOTES

Paramagnetic Resonance of Cobalt in Cadmium Chloride and Cadmium Bromide ....Kazuo MORIGAKI 1639
Oscillator Strength of I^--Absorption Band in KCl Crystal ....Takehiko ISHII 1640
Magnetic After Effects in Manganese Zinc Ferrites ....Tsuneo AKASHI and Takeshi OKADA 1641
Some Properties of Complex Oxides $AB_{0.5}B'_{0.5}O_3$ of Perovskite Type ....Shoichiro NOMURA and Tatsuyuki KAWAKUBO 1642
Cross Modulation Line Profiles in Cyclotron Resonance Experiments ......Louis GOLD 1643
Temperature Distribution around the Rest or Moving Solid-Liquid Interface in a Rod ....Mikio YAMAMOTO 1644
Electron Spin Resonance in Neutron-Irradiated LiF................. Kazuo MORIGAKI 1645
Linewidth of Cyclotron Resonance of Pure Germanium....................Hazimu KAWAMURA, Masakazu FUKAI, Yoshikazu HAYASHI and Tamotsu HASHIMURA 1646
Etch Pits on X-Ray Damaged Rochelle Salt ....Kenkichi OKADA 1647
Spin Echoes of Co^{59} in fcc Cobalt Metal ....Kiyoshi SUGIBUCHI, Motohiro MATSUURA and Tsuneo HASHI 1648
Group Velocity of Moving Striations in Hg-A Discharge ....Hiroshi YOSHIMOTO and Yoshihiko YAMASHITA 1649
The Colloidal Band in KCl Containing NaCl.....................Shinichi NAKASHIMA 1650

Errata

A Direct Determination of the Crystal Structure of Ethylenediammonium Sulphate ....Kiichi SAKURAI 1651

No. 9

Nuclear Elastic Scattering of Photons near the Particle Threshold Energy (I) ....Tsutomu TŌHEI, Masumi SUGAWARA, Shigeki MORI and Motoharu KIMURA 1657

Some New Activities Produced by Fast Neutron Bombardments ....Kasuke TAKAHASHI, Tokihiro KUROYANAGI, Haruo YUTA, Kyûya KOTAJIMA, Kunio NAGATANI and Haruhiko MORINAGA 1664
Weak Gamma Rays in the Decay of La^{140}.. ....Hidekuni TAKEKOSHI, Naomoto SHIKAZONO and Poh-Kun TSENG 1674
The Magnetic Investigation of Cu-Butyrate Monohydrate and Cu-Stearate.......... .... Takashi WATANABE 1677
Velocity of Slowly Moving Dislocation ....Tomoyuki TAKEUCHI 1682
A Note on the Theory of Barium Titanate ....Hidetosi TAKAHASI 1685
Internal Magnetic Field in Rare Earth Metals ....Jun KONDO 1690
Quenched-in Vacancy in Solid Solution Alloys.................Yoshikazu HAMAGUCHI 1692
Some Experimental Studies on the Parasitic Ferromagnetism of αFe_2O_3........... ....Akira TASAKI and Shūichi IIDA 1697
Determination of the Extension of Linear Polymer Molecule in the Solution by the Light Scattering...Yasuhiro MIYAKE 1703
Three-Level Maser Action in Gas II. Experimental Study on Formic Acid ....Tatsuo YAJIMA 1709
Plasma Oscillations in External Fields ....Masao SUMI 1718
Characteristics of an Ammonia Beam Maser.........................Koichi SHIMODA 1728
Optical Study of Aniline Hydrobromide Single Crystal..................Tsuruji IWAI 1739
On the *R* Centers in Lithium Fluoride..............................Akizo OKUDA 1746
Impulsive Motion of a Circular Cylinder in a Viscous Fluid at Small Reynolds Numbers...Sinzi KUWABARA 1762
Study of Temperature Variation of Ultrasonic Velocity and Adiabatic Compressibility in Some Liquids Part 1.. .... P. R. K. L. PADMINI and B. Ramachamdra RAO 1770

SHORT NOTES

Scintillation from the Solid Xenon ....Sigeo TAKEMOTO, Takeo HASEGAWA and Saburo HOMMA 1777
Proton Magnetic Resonance and the Polymorphism of Triglycerides ....Haruo NAKAJIMA 1778
Observation of the Tracks of Fission Fragments in Molybdenite ....Kazuhiko IZUI and F. Eiichi FUJITA 1779
On the Extraordinary X-ray Diffraction Intensities of Quenched TiC Powder ....Shiro FUJISHIRO 1780
The Flow of a Viscous Fluid past a Porous Flat Plate...........Mitutosi KAWAGUTI 1781
Observations on the Etch Patterns in Deformed KCl Crystals ...Masayoshi SAKAMOTO 1782
Preparation of Gallium Phosphide Crystals and Their Etch Pattern............... .... Sigeru IIZIMA and Makoto KIKUCHI 1783
Electroluminescence in Gallium Phosphide Single Crystals .... Sigeru IIZIMA and Makoto KIKUCHI 1784
Crystal Distortion of FeO on Cooling past its Néel Temperature ....Yoshiko SUZUKI and Eiichi ASADA 1785
Note on Fe^{3+} ions in Spinel Structure ....Yoshikazu SUGIURA 1786
Surface Field Effect and Noise in Ge Grain Boundary .... Yoshio INUISHI, Ken KOTANI and Ichiro TSURUMI 1787
Semiconducting Properties of $SnSe_2$ and $GeSe_2$ ....Sizuo ASANABE 1789
Temperature Dependence of Nuclear Resonance Absorption Line Width in Dy^{161} .. Poh-Kun TSENG, Naomoto SHIKAZONO, Hidekuni TAKEKOSHI and Tokio SHOJI 1790
Cubic Contribution to EPR of Mn^{++} in $MgCl_2$.................................. Hiroaki MATSUMOTO, Kuniya FUKUDA, Masumi TAKESHIMA and Yoichi UCHIDA 1791
An Evidence for the Existence of a Diffusion Layer in the Melting Process of Semiconductors ....Shoji TAUCHI 1792
The Dynamic Bulk and Shear Viscosities of Polyvinylchloride ....Ryusuke KONO 1793
Reflection of a Weak Shock Wave in a Perfectly Conducting Gas ...Shigeki MORIOKA 1794
Some Extra Lines in Paramagnetic Resonance Spectrum of Heavily Cr^{3+} Doped $K_3Co(CN)_6$ ....Takeshi MITSUMA 1796

Electrical Properties of TlSe .... Ryuichi MORI and Kimio HASHIMOTO 1797

Errata

Cleavage Fracture in Single Crystals of Silicon Iron .... Ryūkichi HONDA 1776

No. 10

Angular Distributions of Photo-protons from Li, Al, S, Ni, and Cu .... Masayoshi MASUDA 1801
Photoprotons from Silicon and Phosphorus .... Katsufusa SHODA, Shoichi SHIINA, Keisuke KOBAYASHI, Ken ABE and Motoharu KIMURA 1807
A Linear Electron Accelerator as the Injector of 1 BeV Synchrotron .... Tetsuji NISHIKAWA, Jiro TANAKA, Akira MIYAHARA and Hiroo KUMAGAI 1817
Gamma Rays from the Proton Bombardment of Sulphur and the O$^+$ Second Excited State of ^{32}S .... Yasuo HIRAO 1828
Reaction O$^{16}(\gamma, p)$N^{15} by 20.5 MeV Polarized Bremsstrahlung .... Katsufusa SHODA 1841
Angular Distribution for the N$^{14}(d, p)$N^{15} Ground State Reaction .... Susumu MORITA, Toshiyuki ISHIMATSU, Tetsuji CHÔ, Yutaka NAKAJIMA, Nawoyuki KAWAI, Tôru MURATA and Yûki HACHIYA 1849
(α, p) Reactions near $Z=26$ .... Itaru NONAKA, Hisashi YAMAGUCHI, Takashi MIKUMO, Iwao UMEDA, Tatsuro TABATA and Saburo HITAKA 1853
Resonant Scattering of Photons in Mg and Si .... Masumi SUGAWARA 1857
Effect of Impurity-Core on Carrier Mobility in Heavily Doped Germanium .... P. CSAVINSZKY 1865
Sample Sandwiched Plastic Scintillators for Activation Measurements by Use of Fast Neutrons .... Masakatsu SAKISAKA, Bunzaburō SAEKI, Michio TOMITA and Fumio FUKUZAWA 1869
On the New Magnetic Phase in Manganese-Aluminium-Copper System .... Ichiro TSUBOYA 1875
Magnetic and Electric Properties of Chalcopyrite .... Teruo TERANISHI 1881
Effect of the Substructure upon Magnetic Properties of Iron-Silicon Single Crystals .... Yoji NAKAMURA 1888
Dislocation Images in Pure Iron Observed by Transmission Electron Microscopy .... Hiroshi FUJITA and Zenji NISHIYAMA 1893
The Thermoelectric Power of the Gamma-Brasses .... Seiichiro NOGUCHI 1909
Magnetic Anisotropy of Evaporated Films. I. Iron Films Formed in Magnetic Field .... Minoru TAKAHASHI, Denjiro WATANABE, Tetsuzo SASAGAWA, Tatsuo KŌNO and Shiro OGAWA 1913
The Effect of Heat Treatment on the Minority Carrier Lifetime in Silicon .... Toshihumi ASAKAWA 1923
Magnetic Anisotropy of KCoF$_3$ and KNiF$_3$ .... Kazuyoshi HIRAKAWA, Takasu HASHIMOTO and Kinshiro HIRAKAWA 1934
Electron Paramagnetic Resonance for Metals with Two Conduction Bands .... Tsuyoshi MURAO 1940
Theory of Cyclotron Resonance in Anisotropic Metals .... Hideo SUZUKI, Masumi HATTORI and Kanetaka ARIYAMA 1947
The Shielding of a Fixed Charge in a Metal .... Shozo SHINOHARA 1963
Galvanomagnetic Effects in Bismuth Selenide Bi$_2$Se$_3$ .... Kimio HASHIMOTO 1970
Hall Effect in N- and P-type Germanium at 24 Gc .... Naozo WATANABE 1979
Structure of Thin Layers of Some F.C.C. Metals Deposited on Oriented Ag, Pd and Ni Films .... Shunji SHIRAI, Yoshiichi FUKUDA and Masayoshi NOMURA 1989
X-ray and Magnetic Studies of the Manganese-Germanium System ... Tetuo OHOYAMA 1995
Friction and Deformation of Polymers .... Kyuichiro TANAKA 2003
Self-Absorption of Spectral Line .... Toshiharu TAKO 2016
Structure and Properties of A-Centers in KCl .... Kazuko KOJIMA, Noriko NISHIMAKI and Tadanobu KOJIMA 2033
Microscope Observations of Crystals Appearing in the Process of Cooling Aqueous Solutions of Alcohols .... Kenji YAMAJI 2045

High Temperature Determination by a New Gas Thermometer with Constant Bulb Temperature. I. Measuring Methods .... Jiro OISHI 2056

SHORT NOTES

The Specific Heat of $Ni(NH_3)_6Cl_2$ and $Ni(NH_3)_6Br_2$ at Low Temperatures .... Kazutoshi UKEI and Eizo KANDA 2061
The Relaxation Phenomena in Polyelectrolytes Solutions .... Noboru NISHIDA 2062
Observation of Optical Maser Oscillation in Ruby.. Kanji KUBOTA and Kazuo HAYASHI 2063
Frequency Dependence of Ferromagnetic Crystalline Anisotropy of $Ni_xFe_{3-x}O_4$ .... Seiji USAMI, Nahonori MIYATA and Zenya FUNATOGAWA 2064
Nuclear Magnetic Resonance of Fe^{57} in Fine Powdered Iron .... Shizuko OGAWA and Setsu MORIMOTO 2065
Stress Annealing Effect in Cobalt .... Takashi SAMBONGI and Tadayasu MITUI 2066
Heavily Deffused Si pn-Junction .... Masakatsu TOKUNAGA and Katsufusa SHONO 2067
Phonon Spectrum of Germanium-Silicon Alloys .... R. BRAUNSTEIN, A. R. MOORE and F. HERMAN 2068
Helium Discharge Chamber .... Shūji FUKUI, Satio HAYAKAWA, Ryoichi KAJIKAWA and Ken KIKUCHI 2069
Electron Microscopic Observation of the Aggregates of Vacancies in Germanium .... Kenzo TANAKA, Michihiko MANNAMI, Kunihide IZUMI and Hiroko NIWA 2070
Theory of Non-Linear Responses of Many Variable Systems .... Koji OKANO and Osamu NAKADA 2071
Several Experiments on the Memory Effect in αFe_2O_3 .... Masako IWATA, Takao IWATA and Mikio YAMAMOTO 2072
Photoconduction of γ-ray Irradiated KCl Single Crystals at Higher Electric Field .... Yoshio INUISHI and Yung-Kwun SUNG 2074
On the Coupling between Optical Lattice Vibrations and Carrier Plasma Oscillations in Polar Semiconductors .... Isaaki YOKOTA 2075
Electron Spin Resonance of the M center in Potassium Chloride .... Hiroshi OHKURA and Kazuo MURASE 2076
Ultrasonic Attenuation in Al and Al-Cu Alloys at Low Temperature .... Kazuo KAMIGAKI and Tokutaro HIRONE 2077

Errata

Magnetic Properties of Iron Phosphide Fe_2P .... Shū CHIBA 2078
Local Description of the Flow behind a Steady, Two-Dimensional, Curved Shock Wave .... Zirō HASIMOTO and Shigeki MORIOKA 2078
Measurement of Anomalous Absorption Coefficients of Electrons for MgO Crystals .... Kazutake KOHRA and Hiroshi WATANABE 2078
Announcement of Proceedings of the International Conference on Cosmic Rays and the Earth Storm 2079
Announcement of Proceedings of the International Conference of Magnetism and Crystallography 2080

No. 11

The Construction and Test Operation of INS-Linear Electron Accelerator .... Jirō TANAKA 2081
Angular Distributions of High Energy Gamma Rays from the $F^{19}(p,\gamma)Ne^{20}$ Reaction .... Kiichi ETOH, Kazuo HISATAKE, Takatoshi KOBAYASHI, Kinuko HORIE, Haruko OHMURA and Yozo NOGAMI 2091
Breakup of Deuterons by the Reactions $H(d,p)pn$ with $E_d=18$ MeV and $D(p,p)pn$ with $E_p=9$ MeV .... Keigo NISIMURA 2097
Inelastic Scattering of Protons from Several Light Odd-Even Nuclei in the Energy Range from 6.0 MeV to 7.5 MeV .... Jun KOKAME 2101
(d,α) Reactions on O^{16}, N^{14} and C^{12} by 14.7 MeV Deuterons .... Takuji YANABU 2118
Nuclear Interactions Produced by Heavy Nuclei of Primary Cosmic Radiation in Nuclear Emulsions .... Yoshihiro TSUZUKI 2131

On the Magnetism of Mn- and Co-Ammonium Tutton Salts at Very Low Temperatures .... Norikiyo URYÛ 2139
On the Magnetic Properties of 12 percent Aluminium-Iron Alloy.... Makoto SUGIHARA 2163
Effect of Quenched-in Vacancies on the Weak Magnetization of Nickel........ Yoji NAKAMURA 2167
Study of the Phase Transition in NaNO$_2$ by Polarized Infrared Radiation .... Yoshiki SATO, Kazuo GESI and Yutaka TAKAGI 2172
Current-Voltage Characteristics of Plastically Deformed Germanium P-N Junctions .... Osamu RYUZAN 2177
Magnetic Anisotropy Energy in Nickel Arsenide Type Crystal .... Kengo ADACHI 2187
Dielectric Properties of Ferroelectric NaNO$_2$ .... Shozo SAWADA, Shoichiro NOMURA and Yohko ASAO 2207
On the Theory of Mixed Conduction with Special Reference to the Conduction in Silver Sulfide Group Semiconductors .... Isaaki YOKOTA 2213
Electrical Resistivity and Defect Energy Levels in Reduced Titanium Dioxide at Low Temperatures .... Ryukiti R. HASIGUTI, Kazuko MINAMI and Hirō YONEMITSU 2223
Relativistic Dynamical Theory of Electron Diffraction........ Kunio FUJIWARA 2226
Studies on the Radial Distribution Analysis in Diffraction Methods. III. Extrapolation of Intensity Data to Small Scattering Angle........ Tadashi INO 2239
Observations on the Polygonization of Bent LiF Crystals by the Berg-Barrett Method .... Mitsuru YOSHIMATSU 2246
Variation of Electron Diffraction Intensity with Wavelength of Electrons........ Norihisa KITAMURA 2254
Fluctuations in a Plasma I: Ion-Electron Temperature Relaxation ...... Osamu AONO 2264
Magnetic Perturbation of an Ammonia Maser on the 3,2 Line .... Koichi SHIMODA 2270
Dependence of Magnetic Coupling Constant of Ammonia on the Inversion State........ Koichi SHIMODA 2283
Single and Double Ionization of Na, K and Mg by Electron Impact .... Yozaburo KANEKO 2288
Radiation Effects in LiF Crystals .... Kazuko KUBO 2294
Numerical Solution of the Navier-Stokes Equations for the Flow in a Two-Dimensional Cavity .... Mitutosi KAWAGUTI 2307
On Similar Solutions of the Unsteady Quasi-Two-Dimensional Incompressible Laminar Boundary-Layer Equations........ Nisiki HAYASI 2316
Two-Dimensional Viscous Flow past a Rotationally-Oscillating Circular Cylinder .... Tosio MIYAGI 2329

SHORT NOTES

Relativistic Correction to the Method of Eliminating the Primary Extinction in Electron Diffraction ...... Shizuo MIYAKE, Kunio FUJIWARA, Goro HONJO and Norihisa KITAMURA 2336
Electron Spin Resonance of Diluted (NH$_4$)Fe(SO$_4$)$_2$12H$_2$O........ Shigeru MAEKAWA 2337
Electron Spin Resonance in Irradiated Polytetrafluoroethylene: Temperature Dependence of the Spectra........ Naoyuki TAMURA 2338
Activation Energy of Acceptors Introduced into Germanium by Plastic Twisting .... Osamu RYUZAN 2339
Magnetic Properties of Chromium Oxide Modified by Vanadium Oxide .... Buichi KUBOTA, Tomozo NISHIKAWA and Akira YANASE 2340
Luminescence Accompanied by Electrolysis in CdS Single Crystals .... Eiichi MARUYAMA 2341
The Formation of Superstructure of Fe$_3$Ni in Fine Particles ...... Yoshichika BANDō 2342
Young's Moduli in Ordered and in Disordered States of Fe$_3$Al Single Crystals .... Ken'ichi NUMAKURA 2344
Spontaneous Magnetization in Thin Films of Nickel .... Yasuo GONDō, Hiroshi KONNO and Zenya FUNATOGAWA 2345
On the Shock Configuration in a Perfectly Conducting Gas in the Presence of a Uniform Magnetic Field........ Shigeki MORIOKA 2346

On Chambers' Solution of the Boltzmann Transport Equation ....Hideo SUZUKI 2347
Concentration Dependence of Electrical Properties of Bismuth-Antimony Alloys .... Seiichi TANUMA 2349
New Level Scheme of Pt^{196} ....Hidetsugu IKEGAMI, Toshimitsu YAMAZAKI, Mitsuo SAKAI and Kazusuke SUGIYAMA 2350
Back-Reflection X-Ray Micrography ....Shozo SAITO and Yasumitsu SHIMOMURA 2351
Cyclotron Resonance of Hot Electrons in Germanium ....Hajimu KAWAMURA, Yoshikazu HAYASHI and Masakazu FUKAI 2352
Low-lying Excited States in Ba^{136} .... Kazusuke SUGIYAMA, Hiroyoshi SEKIGUCHI and Shogo HAYASHIBE 2353
Thermoelectric Power of Bismuth-Antimony Alloys ....Seiichi TANUMA 2354
Effects of Tacticity upon the Temperature Dependence of T_1 of Proton in High Polymers ....Takao KAWAI, Yôko YOSHIMI and Akira HIRAI 2356
The Observation of Oscillating Anode Glow by Means of High-Speed Camera .... Kazuyuki OGAWA 2357
Crystal Growth of Zinc-oxide by Chemical Reaction of Zinc-fluoride with Air..........Ikumaro KUBO 2358
Movement of Small Angle Boundary of Ice Crystal .... Akira HIGASHI and Naomi SASAKI 2359
The Texture of Vapour Phase Grown ZnS Crystals ....Tomoya OGAWA 2360
Chlorine Nuclear Quadrupole Resonance of CH$_3$COCHCl$_2$ ....Shinhachiro SAITO 2361

Errata

Structure and Properties of A-Centers in KCl ....Kazuko KOJIMA, Noriko NISHIMAKI and Tadanobu KOJIMA 2335
Gamma Rays from Neutron Inelastic Scattering of Magnesium, Aluminum, Iron and Bismuth .... Masano HOSOE and Shoji SUZUKI 2335

No. 12

Decay of Sr^{88} ....Tokihiro KUROYANAGI 2363
Decay of As^{79} ....Tokihiro KUROYANAGI 2369
Isomeric Cross Section Ratios for 14 MeV Neutron Reactions ......Fumio FUKUZAWA 2371
Angular Distributions of Alpha-particles from F^{19}, Al^{27} and P^{31} bombarded with Protons .... Sukeaki YAMASHITA 2378
Gamma Rays from the Proton Bombargment of ^{31}P and the Excited States of ^{31}P .... Tetsuo WAKATSUKI, Yasuo HIRAO, Eiji OKADA and Iwao MIURA 2385
New Activities in Rare Earth Region Produced by the (γ, p) Reactions .... Tokihiro KUROYANAGI, Haruo YUTA, Kasuke TAKAHASHI and Haruhiko MORINAGA 2393
Cluster Expansion of Relaxation Function and its Application to the Theory of Paessure Broadening ....Akio OHNO 2402
Pressure Effect of Cavitation on Photographic Emulsion ....Syozo TOTANI 2423
Influences of Heat-treatment upon Cadmium Sulphide Single Crystals.......... Saburo KITAMURA 2430
Some Experimental and Theoretical Studies of Ferroelectricity in NaNO$_2$.......... Shoichiro NOMURA 2440
Hall Effect in the Carbides of Transition Metals ....Takashi TSUCHIDA, Yoji NAKAMURA, Mamosu MEKATA, Junji SAKURAI and Hideo TAKAKI 2453
Diffusion of Nickel in Silver..Tokutaro HIRONE, Shigeto MIURA and Toshiro SUZUOKA 2456
Diffusion of Thallous Ions into Potassium Bromide Single Crystals..Tokumichi TAMAI 2459
Diffusion of Color Centers into KBr-Tl Phosphors ....Tokumichi TAMAI 2463
Thermal Conductivity of Sodium Nitrite ....Ikushi YOSHIDA and Shozo SAWADA 2467
Fxchange Integral in Ni and Its Alloy Film from Spin Wave Resonance .... Hiroshi NOSE 2475
Properties of Surface Imperfections Produced on Germanium by Cleaning Treatments .... Akio KOBAYASHI, Koichi SUGIYAMA, Hikaru ARATA and Zenjiro ODA 2481
Dielectric Behavior of KNO^3 in Its Ferroelectric Phase III .... Shozo SAWADA, Shoichiro NOMURA and Yohko ASAO 2486
Electron Spin Resonance Studies of Irradiated High Polymers: Polyethylene .... Hisatsugu KASHIWABARA 2494

The Growth of Corona Discharges in Air .... Tikawo TAMURA 2503
Anodic Oscillation in Glow Discharge. (II) The Gap Properties, Analogous to an Ordinary Electric Oscillator with Linear Circuit Elements.. Kazuyuki OGAWA 2510
Confinement of Plasma Particles in a Corrugated Magnetic Field ...... Tsuneo AMANO 2517
Optical Properties of LiF in the Extreme Ultraviolet .... Riso KATO 2525
Quadrupole Coupling in the Hyperfine Structure of the Spectrum of La I .... Kiyoshi MURAKAWA 2533
Eigenvibration for the Membràne between Two Eccentric Circles .... Yûkichi NOMURA and Kasaburô HARUMI 2537
Two-Dimensional Flow of a Weakly Conducting Gas Past a Plane Wall Containing a Magnetic Dipole .... Shigeki MORIOKA 2544
Propagation of Elastic Waver in Spherical Symmetric Inhomogeneous Midium .... Koshun TAKAKU 2550
Precisionization of Gas Thermometry .... Mitsuru AWANO 2560
A Pumped Klystron Amplifier and RF Power System for the Injector Linac of 1 BeV Electron Synchroton .... Akira MIYAHARA 2567
The Discharge Chamber and Its Characteristics.. Shūji FUKUI and Sigenori MIYAMOTO 2574

SHORT NOTES

Absorption Bands in KCl Crystal Containing LiCl .... Shinichi NAKASHIMA 2586
Internal Friction of LiF at Low Temperatures .... Akira IKUSHIMA and Taira SUZUKI 2587
Ground State Energies of Donors in Ge and Si .... Koziro NARITA and Tatsuo SHIMIZU 2588
Origin of Magnetoelectric Effect in Cr_2O_3 .... Muneyuki DATE, Junjiro KANAMORI and Masashi TACHIKI 2589
Determination of the Impurity Concentration of the *P*-type Recrystallized Layer by Thermoelectric Power Measurements .... Masakazu SHOJI 2590
Epitaxial Vapor Growth of GaAs on Ge Single Crystal .... Takasi OKADA, Takao KANO and Yozo SASAKI 2591
Transient Phenomena in Ruby Maser .... Fujio SAITO 2592
Piezoelectrie Properties of Triglycine Sulphate .... Takuro IKEDA, Yoichi TANAKA and Hiroo TOYODA 2593
$O^{16}(d, \alpha)N^{14}$ Reaction with Deuterons near 15 MeV .... Takuji YANABU, Sukeaki YAMASHITA, Teruo NAKAMURA, Kunio TAKAMATUS, Akira MASAIKE, Shigeru KAKIGI, Dai Ca NGUYEN and Kiyohiko TAKIMOTO 2594
On the Impurity Concentration of the *P*-type Recrystallized Layer of Tunnel Diode .... Masakazu SHOJI 2596
Experiments on the Possible Existence of a Bound Di-Neutron .... Masakatsu SAKISAKA and Michio TOMITA 2597
The Resistance Minimum in a Dilute Cadmium Manganese Alloy .... W. B. MUIR 2598
Thermoelectric Effect in Mg, Zn and Al Containing Traces of Mn............... F. T. HEDGCOCK and W. B. MUIR 2599

Errata

Refractive Index Difference of Dilute Aqueous Solution of Polyvinylpyrolidon .... Yasuhiro MIYAKE and Jiro FURUICHI 2600
Determination of the Extension of Linear Polymer Molecule in the Solution by the Light Scattering .... Yasuhiro MIYAKE 2600

AUTHOR INDEX TO VOL. 16 NOS. 1~12.

ABE Hidetaro;

– and H. SHIRAI: Paramagnetic Resonance Study in Some Copper Salts.. 118

———: Temperature Dependence of ESR Line-Width in $K_2CuCl_4 \cdot 2H_2O$ (S.N.).. 836

ABE Ken: [cf. SHODA Katsufusa (1031) S.N., (1807)]

ADACHI Kengo: Magnetic Anisotropy Energy in Nickel Arsenide Type Crystal 2187

AIZU Kêitirô;

— and O. NAKADA: Perfectness of Macrodomains of $BaTiO_3$ Crystals.... 923

AKASHI Tsuneo;

——— and T. OKADA: Magnetic After Effects in Manganese Zinc Ferrites (S.N.) 1641

AKIMOTO Kazuo: [cf. SONOIKE Sanemi (658)]

AMANO Tsuneo: Confinement of Plasma Particles in a Corrugated Magnetic Field....2517

AMEMIYA Ayao;

——— and M. INOKUTI: Mathematical Considerations on Chemical Kinetics of Radiation-Induced Polymerization 949

ANDO Kei-ichi: [cf. KAMIYA Yoshihiro (846) Errata]

ANDO Toshihiko: [cf. KOSHINO Shigeharu (1151)]

AOKI Atsushi: [cf. Mitsuhiro KAWAMURA (1493)]

———: Angular Correlation of the Mo^{95} Gamma-Gamma Cascades............1086

AONO Osamu: Fluctuations in a Plasma I: Ion-Electron Temperature Relaxation 2264

AOYAGI Keizô;

——— and M. SUGIHARA: Magnetic Anisotropy of Heusler Single Crystal (S.N.)..1027

ARATA Hikaru: [cf. KOBAYASHI Akio (2481)]

ARIYAMA Kanetaka: [cf. SUZUKI Hideo 1947]

ASADA Eiichi: [cf. SUZUKI Yoshiko (1785) S.N.]

ASAI Hiroshi: Study of the Hydration-Dehydration in Polyelectrolyte Solutions by the Ultrasonic Technique 761

ASAKAWA Toshihumi: The Effect of Heat Treatment on the Minority Carrier Lifetime in Silicon..1923

ASAKURA Toshimitsu: [cf. O'NEILL Edward L. (301)]

ASANABE Sizuo: Semiconducting Properties of $SnSe_2$ and $GeSe_2$ 1789

ASANUMA Mitsuru: Magnetic Properties of B8 Type Compounds in Manganese-Tin System (S.N.)..1265

ASAO Yohko: [cf. NOMURA Shoichiro (917); SAWADA Shozo (2207, 2486)]

AWANO Mitsuru: Precisionization of Gas Thermometry...........................2560

BANDŌ Yoshichika: The Formation of Superstructure of Fe_3Ni in Fine Particles......2342

BHIMASENACHAR J.: [cf. SUBRAHMANYAM S. U. (1447)]

BLUM Lesser: On the Transport Equation in Quantum Mechanics................... 616

BRAUNSTEIN R.;

———: A. R. MOORE and F. HERMAN: Phonon Spectrum of Germanium-Silicon Alloys (S.N.) 2068

CHIBA Ren;

———, H. E. CONZETT, H. MORINAGA, N. MUTSURO, K. SHODA and M. KIMURA: He^3-Alpha Scattering 1077

CHIBA Shū: Magnetic Properties of Iron Phosphide Fe_2P (Errata) 2078

CHIKAWA Jun-ichi;

———, S. IMAMURA, K. TANAKA and M. SHIOJIRI: Crystal Structures and Electrical Properties of Alkali Antimonides 1175

CHŌ Tetsuji: [cf. MORITA Susumu 1849]

CHONG Pyon-un;

——— and Y. INUISHI: Drift Mobility of Photo-Injected Electrons in Hexane-Silicone Mixture (S.N.) 1482

CONZETT H. E.: [cf. CHIBA Ren (1077)]

CSAVINSZKY P.: Effect of Impurity-Core on Carrier Mobility in Heavily Doped Germanium. 1865

DATE Muneyuki: Antiferromagnetic Resonance in $CoCl_26H_2O$ 1337

DATE Muneyuki;
———, J. KANAMORI and M. TACHIKI: Origin of Magnetoelectric Effect in Cr_2O_3 (S.N.) 2589
DATTA S. K.: On the Steady Motion of an Idealized Elastico-Viscous Liquid Through Channels with Suction and Injection.. 794
DODO Taro: Microwave Attenuation by Cyclotron Resonance in a Slightly Ionized Gas.. 293
———: Measurements on Collision Frequencies of Electrons in Neon Gas (S.N.).. 346
———: Spectrum of the Electron Cyclotron Resonance in a Plasma (S.N.).... 348
DOKE Tadayoshi: [cf. OGAWA Iwao (1025) S.N.]
EDAGAWA Hiroshi;
———, Y. MORITA, S. MAEKAWA and Y. INUISHI: Slow Decay of Reverse Current and Noise in Field Effect on Ge P^+-N Junction (S.N.).............1041
EGUCHI Isamu: [cf. NISHIYAMA Zenji (834) S.N.]
EJIRI Arisato: [cf. ONAKA Ryumyo (340) S.N.]
EJIRI Hiroyasu: [cf. OHMURA Haruko (593)]
ENDO Keizo: [cf. KIMURA Ren'iti (1266) S.N.]
ETOH Kiichi: [cf. OHMURA Haruko (593)]
ETOH Kiichi;
———, K. HISATAKE, T. KOBAYASHI, K. HORIE, H. OHMURA and Y. NOGAMI: Angular Distributions of High Energy Gamma Rays from the $F^{19}(p, \gamma)Ne^{20}$ Reaction 2091
FORSTAT H.;
——— and G. O. TAYLOR: Heat Capacities of Two Manganese Salts (S.N.)... 128
FUJIKI Yoshibumi: [cf. SUGANUMA Ryôji (676), (1042) Errata]
FUJIME Satoshi;
———, M. MURAKAMI and E. HIRAHARA: Hall Effect on Some of the Magnetic Compounds 183
FUJIMOTO Fuminori: 222-Reflection from CuCl in Electron Diffraction............... 936
FUJIOKA Goro: A Cloud Chamber Study of High Energy Nuclear Interactions of Cosmic Ray Particles. (II) Results of Single Nucleon-Nucleon Interactions 1107
FUJISHIRO Shiro: On the Extraordinary X-ray Diffraction Intensities of Quenched TiC Powder (S.N.) 1780
FUJITA F. Eiichi: [cf. IWATA Tadao (197); IZUI Kazuhiko (1779, 1032) S.N.]
——— and K. IZUI: Observations of Lattice Defects in Graphite by Electron Microscopy, Part I 214
FUJITA Hiroshi: Direct Observation of Subgrain-Growth of Cold-Worked Aluminium by means of Electron Microscopy 397
——— and Z. NISHIYAMA: Dislocation Images in Pure Iron Observed by Transmission Electron Microscopy 1893
FUJIWARA Kunio: [cf. IWASAKI Hiroshi (132) Errata; MIYAKE Shizuo (2336) S.N.]
———: Relativistic Dynamical Theory of Electron Diffraction................2226
FUKAI Masakazu: [cf. KAWAMURA Hazimu (1646, 2352) S.N.]
FUKANO Yasushige: Study on Precipitation Phenomena in Thin Films of Supersaturated Gold-Nikel Alloy 1195
FUKASE Masahiro: [cf. WATANABE Hiroshi (1181)]
FUKE Tokujiro: Nuclear Quadrupole Resonance under High Pressure, I. 266
FUKUDA Atsuo: [cf. ONAKA Ryumyo (340) S.N.]
FUKUDA Kuniya: [cf. NAKAMURA Kaizo (1262) S.N.; MATSUMOTO Hiroaki (1791) S.N.]
———, H. MATSUMOTO, T. TAKAGI and Y. UCHIDA: Electron Spin Resonance of Manganese in $MgCl_2$ (S.N.)..1256
FUKUDA Yoshiichi: [cf. SHIRAI Shunji (1989)]
FUKUI Shūji: The Structure of Extensive Air Showers Near the Axes 604
———, S. HAYAKAWA, R. KAJIKAWA and K. KIKUCHI: Helium Discharge Chamber (S.N.)..2069
——— and S. MIYAMOTO: The Discharge Chamber and Its Characteristics....2574
FUKUSHIMA Einosuke;
——— and H. NIMURA: Study of the Texture of the Boundary of Etched and Ground Regions of Quartz Plate by X-ray Diffraction 928

FUKUZAWA Fumio: [cf. **SAKISAKA** Masakatsu 1869]
———: Isomeric Cross Section Ratios for 14 MeV Neutron Reactions........2371
FUNATOGAWA Zenya: [cf. **USAMI** Seiji (2064) S.N.; **GONDŌ** Yasuo (2345) S.N.]
FURUICHI Jiro: [cf. **MIYAKE** Yasuhiro (1263) S.N., (2600) Errata]
FURUKAWA Michiaki;
——— and S. **TANAKA**: Excitation Function for the Reaction $O^{16}(\alpha, pn)F^{18}$ (S.N.).. 129
FURUKAWA Yoshitaka: Impurity Effect upon Mobility in Heavily Doped Silicon (S.N.).. 577
———: Electrical Properties of Heavily Doped n-Type Germanium 687
FURUSAWA Akira: [cf. **SUGIYAMA** Kazusuke (1538)]
GESI Kazuo: [cf. **SATO** Yoshiki (2172)]
GOLD Louis: Hot Electron Nonequilibrium Carrier Distribution in a Many-Valley Semiconductor (S.N.) 575
———: Hot Electron Behavior at High Pressures (S.N)......................1269
———: On the Faraday Effect in Many-Valley Semiconductors (S.N.) 1471
———: Cross Modulation Line Profiles in Cyclotron Resonance Experiments (S. N.) 1643
GONDŌ Yasuo;
———, H. **KONNO** and Z. **FUNATOGAWA**: Spontaneous Magnetization in Thin Films of Nickel (S.N.) 2345
GOTO Kimiyoshi: [cf. **KOJIMA** Hiroshi (1483) S.N.]
GOTOH Kanefusa: Effect of a Magnetic Field upon the Stability of Free Boundary Layers between Two Uniform Streams 559
GRAHAM, JR. C.D.: Magnetic Annealing of Cobalt (S.N.) 1481
GUPTA V. D.: An Expression for Orientation in Cellulose Fibres 1377
HACHIYA Yûki: [cf. **ISHIMATSU** Toshiyuki (367); **MORITA** Susumu (1849)]
HAMAGUCHI Yoshikazu: [cf. **KOMURA** Shigehiro (1486) S.N.]
———: Quenched-in Vacancy in Solid Solution Alloys 1692
HARUMI Kosaburo: [cf. **NOMURA** Yukichi (2537)]
HASEGAWA Takeo: [cf. **TAKEMOTO** Sigeo (1777) S.N.]
HASHI Tsuneo: [cf. **SUGIBUCHI** Kiyoshi (1648) S.N.]
———: Double Quantum Transition in Electron Spin Resonance of Diphenyl-Picryl Hydrazyl at Low Magnetic Fields......................................1243
HASHIMOTO Kimio: [cf. **MORI** Ryuichi (1797) S.N.]
———: Galvanomagnetic Effects in Bismuth Selenide Bi_2Se_3 1970
HASHIMOTO Takasu: [cf. **HIRAKAWA** Kazuyoshi 1934]
HASHIMURA Tamotsu: [cf. **KAWAMURA** Hazimu (1646) S.N.]
HASIGUTI R. Ryukiti;
———, K. **MINAMI** and H. **YONEMITSU**: Electrical Resistivity and Defect Energy Levels in Reduced Titanium Dioxide at Low Temperatures 2223
HASIMOTO Zirō;
——— and S. **MORIOKA**: Local Description of the flow behind a Steady, Two-Dimensional, Curved Shock Wave.......................................1616
——— and S. **MORIOKA**: Local Description of the Flow behind a Steady, Two-Dimensional, Curved Shock Wave. (Errata) 2078
HATTORI Masumi: [cf. **SUZUKI** Hideo (1947)]
HAYAKAWA Satio: [cf. **FUKUI** Shūji (2069) S.N.]
HAYAKAWA Shigeru;
——— and T. **SUITA**: The Characteristics of the Discharges in the Crossed Electric and Magnetic Field (S.N.)..1037
HAYASHI Kazuo: [cf. **KUBOTA** Kanji (2063) S.N.]
HAYASHI Yoshikazu: [cf. **KAWAMURA** Hajimu (1646) (2352)]
HAYASHIBE Shogo: [cf. **SUGIYAMA** Kazusuke (1538) (2353)]
HAYASI Nisiki: On Similar Solutions of the Unsteady Quasi-Two-Dimensional Incompressible Laminar Boundary-Layer Equations 2316
HEDGCOCK F. T.;
——— and W. B. **MUIR**: Thermoelectric Effects in Mg, Zn and Al Containing Traces of Mn (S.N.) 2599

HERMAN F.: [cf. BRAUNSTEIN R. (2068) S.N.]
HIGASHI Akira;
——— and N. SASAKI: Movement of Small Angle Boundary of Ice Crystal ..2359
HIHARA Tadamiki: [cf. Kōi Yoshitaka (574, 1040) S.N.]
HIKI Yosio: Internal Friction of Synthetic Quartz.................................. 664
HINOTANI Kensaku: [cf. MIYAKE Saburo (847)]
HIRABYASHI Makoto: [cf. IWASAKI Hiroshi (132) Errata]
HIRAHARA Eiji: [cf. FUJIME Satoshi (183)]
HIRAI Akira: [cf. KAWAI Takao (2356) S.N.]
HIRAI Masamitsu: [cf. UETA Masayasu (538)]
———, M. IKEZAWA and M. UETA: Temporary Bleaching of Color Centers in KCl Crystal (S.N.) 1477
HIRAKAWA Kazuyoshi: [cf. TUBOTA Hiroshi (1038) S.N.]
———, T. HASHIMOTO and K. HIRAKAWA: Magnetic Anisotropy of $KCoF_3$ and $KNiF_3$ 1934
HIRAKAWA Kinshiro: [cf. HIRAKAWA Kazuyoshi 1934]
HIRAKI Akio: [cf. ITOH Junkichi (343) S.N.]
HIRAO Yasuo: [cf. WAKATSUKI Tetsuo (2385)]
———: Gamma Rays from the Proton Bombardment of Sulphur and the O^+ Second Excited State of ^{32}S 1828
HIRONE Tokutaro: [cf. KAMIGAKI Kazuo (2077) S.N.]
——— and H. YAMAMOTO: Diffusion of Cobalt into Silver 455
———, S. MIURA and T. SUZUOKA: Diffusion of Nickel in Silver 2456
HIRONO Motokazu: On the Theory of Cross Relaxation in Maser Materials 766
HIROTA Eiichi: [cf. KUBOTA Buichi (345) S.N.]
HISATAKE Kazuo: Decay of Rh^{102} and Levels in Ru^{102}..............................1280
———: [cf. ETOH Kiichi (2091)]
HITAKA Saburo: [cf. NONAKA Itaru 1853]
HOLM. H.C.: [cf. IBERS. A. James (839) S.N.]
HOMMA Saburo: [cf. TAKEMOTO Sigeo (1777) S.N.]
———, T. KUROYANAGI and H. MORINAGA: Decay of Ir^{195} and Ir^{197} (S.N.).... 841
HONDA Ryūkichi: Cleavage Fracture in Single Crystals of Silicon Iron 1309
———: Cleavage Fracture in Single Crystals of Silicon Iron (Errata) 1776
HONJO Goro: [cf. MIYAKE Shizuo (2336) S.N.]
HONMA Akio: [cf. OGUCHI Takehiko (79)]
HORI Jun-ichi: A New Picture of the Vibration of Linear Lattices 23
HORI Tomiei: [cf. NAKAGAWA Yasuaki (1470) S.N.]
HORIE Kinuko: [cf. OHMURA Haruko (593); ETOH Kiichi (2091)]
HORIE Tadao;
——— and T. IWAI: An Effect of Heat Treatment on WO_3 Single Crystal, I. Various Patterns 424
HOSHINO Ryosuke: [cf. KUME Kiyoshi (290)]
———: Proton Magnetic Resonance in Ferroelectric (CH_3NH_3) $AlSO_4 \cdot 12H_2O$ (S.N.)... 835
HOSHINO Sadao;
——— and I. SHIBUYA: Anomalous Temperature Dependence of Lattice Constants of Ferroelectric Sodium Nitrite (S.N.)...............................1254
HOSOE Masano;
———, and S. SUZUKI: Gamma Rays from Neutron Inelastic Scattering of Magnesium, Aluminum, Iron and Bismuth (Errata).........................2335
HOSOKAWA Iwao: Theoretical Prediction of the Pressure Distribution on a Non-lifting, Thin Symmetrical Aerofoil at Various Transonic Speeds........................ 546
HOSOYA Sukeaki: [cf. KURIYAMA Masao (701)]
HSIAO C. C.;
———, J. E. OSBORN and D. B. ROZENDAL: Orientation Dependent Mechanical Breakdown of a Model High Polymer Solid 459
IBERS A. James;
——— and C. H. HOLM: The O-H....O Bond in Orthoboric Acid (S.N.)...... 839
IGO Takeo: Passage Effect in the Electron Spin Resonance of Fe-Doped Silicon (S.N.)..1472

IIDA Shuichi: [cf. TASAKI Akira (1697)]

IIZIMA Sigeru;

——— and M. KIKUCHI: Preparation of Gallium Phosphide Crystals and Their Etch Pattern (S.N.) 1783

——— and M. KIKUCHI: Electroluminescence in Gallium Phosphide Single Crystals (S.N.) 1784

IKEDA Takuro;

———, Y. TANAKA and H. TOYODA: Piezoelectric Properties of Triglycine Sulphate (S.N.) 2593

IKEGAMI Hidetsugu: [cf. SAKAI Mitsuo (148); KAWAMURA Mitsuhiro (1493)]

———T. YAMAZAKI, M. SAKAI and K. SUGIYAMA: New Level Scheme of Pt^{196}....2350

IKEGAMI Seiji;

——— I. UEDA and Y. ISE: Optical Absorption and Electrical Conductivity of Reduced $BaTiO_3$ Single Crystal (S.N.) 572

IKEZAWA Mikihiko: [cf. UETA Masayasu (538); HIRAI Masamitsu (1477) S.N.]

IKUSHIMA Akira;

———, T. SUZUKI: Internal Friction of LiF at Low Temperatures (S.N.) 2587

IMAI Nobuhisa: Interaction between Polyions and Low Molecular Ions.... 746

IMAMURA Shunji: [cf. CHIKAWA Jun-ichi (1175)]

———: Remarks on the Electrical Properties of Alkali Antimonides (S.N.) ..1036

INO Tadashi: Studies on the Radial Distribution Analysis in Diffraction Methods. III. Extrapolation of Intensity Data to Small Scattering Angle 2239

INOKUTI Mitio: [cf. AMEMIYA Ayao (949)]

INOUE Morio;

——— and H. MIZUNO: The Purification of KCl by the Zone Refining Method (S.N.).... 128

INOUE Tutomu: Linear Potential Barrier Model for Nuclear Surface (S.N.) 844

INUISHI Yoshio: [cf. MATSUURA Kenji (339); SHIRAFUJI Junji (832) S.N.; EDAGAWA Hiroshi (1041) S.N.; CHONG Pyon-un (1482); MATSUURA Kenji (1485) S.N.]

———, K. KOTANI and I. TSURUMI: Surface Field Effect and Noise in Ge Grain Boundary (S.N.) 1787

——— and Yung-Kwun SUNG: Photoconduction of γ-ray Irradiated KCl Single Crystals at Higher Electric Field. (S.N.)....2074

ISA Takeshi: [TAKEYAMA Mikio (1255) S.N.]

ISE Yukihiko: [cf. IKEGAMI Seiji (592) S.N.]

ISHIDA Yoshio: A New Method to Determine Hydration Energy of Ion (Errata) 1469

ISHII Takehiko: Oscillator Strength of I^--Absorption Band in KCl Crystal (S.N.) 1640

ISHII Zensho: Studies on the Boundary between Etched and Ground Regions of Ge and Si Single Crystal Surface by X-Ray Diffraction Topography 733

ISHIMATSU Toshiyuki: [cf. MORITA Susumu 1849]

———, N. TAKANO, Y. HACHIYA and T. NAKASHIMA: Angular Distributions and Excitation Functions of the $Be^9(d, p)Be^{10}$ Ground-State Reaction 367

———: The $N^{14}(d, \alpha)C^{12}$ Ground-State Reaction in the Energy Range of Deuteron from 1.5 to 3.0 MeV....1529

ISHIZAKI Yoshihide: Inelastic Scattering of Deuterons from C^{12}, Mg^{24} and Ni^{60}. 1056

ITO Nobuo: [cf. MIYAKE Saburo (847)]

ITOH Junkichi;

———, M. SATOH and A. HIRAKI: Nuclear Magnetic Resonance Study of NaCl Crystal containing Ca Impurities (S.N.) 343

IWAI Tsuruji: [cf. HORIE Tadao (424)]

———: Optical Study of Aniline Hydrobromide Single Crystal 1739

IWASAKI Hiroshi;

———, M. HIRABAYASHI, K. FUJIWARA, D. WATANABE and S. OGAWA: Study on the Ordered Phases with Long Period in the Gold-Zinc Alloy System (Errata).... 132

IWATA Masako;

—, T. IWATA and M. YAMAMOTO; Several Experiments on the Memory Effect in αFe_2O_3 (S.N.) 2072

IWATA Tadao: [cf. IWATA Masako (2072) S.N.]

———, E. F. FUJITA and H. SUZUKI: On the Energy of the Interstitial Atom in Graphite ... 197

IZUI Kazuhiko: [cf. FUJITA F. Eiichi (214)]

——— and F. E. FUJITA: Observation of Lattice Defects in Fission Fragment-irradiated Graphite (S.N.) ... 1032

——— and F. Eiichi FUJITA, Observation of the Tracks of Fission Fragments in Molybdenite (S.N.) ... 1779

IZUMI Kunihide: [cf. TANAKA Kenzo (2070) S.N.]

KAIFU Yozo: Some Optical Properties of Lead Activated Potassium Halide Phosphors... 1605

KAINUMA Yoshiro: A Diffraction Pattern caused by Temperature Diffuse Scattering. I. General Theory ... 228

——— and William N. LIPSCOMB: P_s Function in Electron Diffraction ... 495

KAJIKAWA Ryoichi: [cf. FUKUI Shūji (2069) S.N.]

KAKIGI Shigeru: [cf. YANABU Takuji (2594) S.N.]

KAKIUCHI Yoshinobu: [cf. KUME Kiyoshi (843) S.N.]

KAMIGAKI Kazuo: Ultrasonic Attenuation in Tin Single Crystals at Low Temperatures ... 1141

———: Ultrasonic Attenuation in Magnetite at Low Temperatures ... 1170

———, and T. HIRONE: Ultrasonic Attenuation in Al and Al-Cu Alloys at Low Temperature (S. N.) ... 2077

KAMIYA Yoshihiro;

———, K. ANDO, M. NONOYAMA and R. UYEDA: Dislocation Networks and Moiré Patterns of Molybdenite (Errata) ... 846

———; and U. Ryozi: Effect of Incoherent Waves on the Electron Microscopic Images of Crystals ... 1361

KANAMARU Fumikazu: [cf. OKAZAKI Chisato (119) S.N.]

KANAMORI Junjiro: [cf. DATE Muneyuki (2589) S.N.]

KANDA Eizo: [cf. UKEI Kazutoshi (2061) S.N.]

KANEKO Tatsunosuke: [cf. MIYAKE Saburo (847)]

KANEKO Yazaburo: Ionization Efficiency Curves for A^+, Kr^+, N_2^+, and CO^+ by Electron Impact ... 1587

———: Single and Double Ionization of Na, K and Mg by Electron Impact .. 2288

KANEMATSU Kazuo: [cf. OHYAMA Tetuo (352) S.N.; YASUKOCHI Kō (429), (1123)]

KANO Takao: [cf. OKADA Takasi (2591) S.N.]

KASHIWABARA Hisatsugu: Electron Spin Resonance Studies of Irradiated High Polymers: Polyethylene ... 2494

KATANO Yoshio: [cf. KUBO Kazuko (347)]

KATAYAMA Ken-ichi: X-Ray Line Broadening in Polyethylene Filaments ... 462

KATO Kiyoe: [cf. KOJIMA Shoji (1487) S.N.]

KATO Koshi: [cf. NISHIYAMA Zenji (834) S.N.]

KATO Riso: [cf. NAKAMURA Kaizo (1262) S.N.]

———: Optical Constants of LiF in the Extreme Ultraviolet (S.N.) ... 1476

———: Optical Properties of LiF in the Extreme Ultraviolet ... 2525

KATO Yoshifumi: Vibrational Effect on the Nuclear Quadrupole Coupling in ND_3 (S.N.) ... 122

KATSUMATA Itsuo: [cf. MIYAKE Saburo (847)]

KATSUURA Kanji: On the Viscosity of Irradiated Polymers. III. Effect of Branching (Errata) ... 1270

KAWABATA Chikao: [cf. UMEDA Kwai (341) S.N.]

KAWAGUTI Mitutosi: The Flow of a Viscous Fluid past a Porous Flat Plate (S.N.) ... 1781

———: Numerical Solution of the Navier-Stokes Equations for the Flow in a Two-Dimensional Cavity ... 2307

KAWAI Nawoyuki: [cf. MORITA Susumu 1849]

———: On the Protons from the $N^{14}(d, p)N^{15}$ Reaction ... 157

KAWAI Takao: Study on the Internal Motions of Some Acryl- and Methacryl- group High Polymers by Pulsed NMR Method ... 1220

———, Y. YOSHIMI and A. HIRAI: Effects of Tacticity upon the Temperature Dependence of T_1 of Proton in High Polymers (S.N.) ... 2356

KAWAKUBO Tatsuyuki: [cf. NOMURA Shoichiro (706), (1642) S.N.]

KAWAMATA Shin: A Simplified Method Calculating the Laminar Boundary Layer.... 805

KAWAMURA Hajimu;

———, M. FUKAI, Y. HAYASHI and T. HASHIMURA: Linewidth of Cyclotron Resonance of Pure Germanium (S.N.) 1646

———; Y. HAYASHI and M. FUKAI, Cyclotron Resonance of Hot Electrons in Germanium (S.N.)........2352

KAWAMURA Mitsuhiro;

———, A. AOKI and H. IKEGAMI: The Second Excited State of Sn^{120} 1493

KAWARABAYASHI Ken: [cf. NAKAMURA Seitaro (130) S.N.]

KAWASAKI Eiichi: [cf. KOJIMA Shoji (1487) S.N.]

KAWATA Suekichi: Study on Spark Counters of the Rosenblum Type for Counting α Particles and Neutrons 1

KAZUMATA Yukio: [cf. YOKOZAWA Yasaburo (694)]

KIDO Kiyoshi;

——— and T. WATANABE: The Magnetic Investigation of Mn^{++}, Co^{++}, Ni^{++}, Cu^{++} Ammine and Anhydrate Salts. (Errata) 353

KIKUCHI Ken: [cf. FUKUI Shūji (2069) S.N.]

KIKUCHI Makoto: [cf. IIZIMA Sigeru (1783, 1784) S.N.]

KIMURA Motoharu: [cf. SHODA Katsufusa (103, 1807) S.N.; CHIBA Ren (1077); SUGIYAMA Kazusuke (1538); TŌHEI Tsutomu (1657)]

KIMURA Norihisa: [cf. TAKAGI Mieko (792)]

KIMURA Ren'iti;

———, T. OHOYAMA and K. ENDO: On the Decomposition of the Ferromagnetic Phase of the Heusler Alloy, Cu$_2$MnAl (S.N.) 1266

KINOSITA Koreo: Refractive Index and Pore Structure of Acid-Leached Surface Layer of Glass 807

KITA Isao: A Cloud Chamber Study of High Energy Nuclear Interactions of Cosmic Ray Particles (I) A Possible Evidence of Successive Collisions in Carbon Nuclei..1099

KITAMURA Norihisa: [cf. MIYAKE Shizuo (2336) S.N.; TAKAGI Mieko (792)]

———: Variation of Electron Diffraction Intensity with Wavelength of Electrons........2254

KITAMURA Saburo;

———, T. KUBO and T. YAMASHITA: Enhancement of Photoconductivity upon Cadmium Sulphide Single Crystals (S.N.) 351

———: Influences of Heat-treatment upon Cadmium Sulphide Single Crystals..2430

KOBA Saburo: Convex-Core Model of Molecules in Crystalline State, II 627

KOBAYASHI Akio;

———, K. SUGIYAMA, H. ARATA and Z. ODA: Properties of Surface Imperfections Produced on Germanium by Clearning Treatments 2481

KOBAYASHI Keisuke: [cf. SHODA Katsufusa (1031) S.N., (1807)]

KOBAYASHI Koichi;

———, and Tetsuhiko TOMIKI: Temperature Dependences of the Fundamental Absorption Tail of KCl and the Absorption due to Bromines in KCl........1417

KOBAYASHI Takatoshi: [cf. ETOH Kiichi (2091)]

KOGURE Youzou: On the Irreversible Behavior of Coupled Oscillators with Application to Time of Flight........ 14

KOHRA Kazutake;

——— and H. WATANABE: Measurement of Anomalous Absorption Coefficients of Electrons for MgO Crystals (S.N.) 580

———, and H. WATANABE: Measurement of Anomalous Absorption Coefficients of Electrons for MgO Crystals (Errata) 2078

KŌI Yoshitaka;

———, A. TSUJIMURA, T. HIHARA and T. KUSHIDA: NMR of Co^{59} in Ferromagnetic Cobalt Alloys (S.N.) 574

———, A. TSUJIMURA, T. HIHARA and T. KUSHIDA: Internal Magnetic Field in Iron and Iron Alloys Measured by NMR (S.N.) 1040

KOJIMA Hiroshi;
  ——— and K. GOTO: Magnetic Domain Observation of $BaFe_{12}O_{19}$ by Faraday Effect 1483
KOJIMA Kazuko: [cf. NISHIMAKI Noriko (576) S.N.]
  ——— and N. NISHIMAKI: *A*-Centers in Potassium Chloride Crystals (S.N.) .. 121
  ———, N. NISHIMAKI and T. KOJIMA: Structure and Properties of *A*-Centers in KCl 2033
  ———, N. NISHIMAKI and T. KOJIMA: Structure and Properties of *A*-Centers in KCl (Errata) 2335
KOJIMA Shoji;
  ———, E. KAWASAKI and K. KATO: Oscillations in a Plasma in a Weak Magnetic Field (S.N.) 1487
KOJIMA Tadanobu: [cf. NISHIMAKI Noriko (576) S.N.; KOJIMA Kazuko (2033), (2335) Errata]
KOKAME Jun: Inelastic Scattering of Protons from Several Light Odd-Even Nuclei in the Energy Range from 6.0 MeV to 7.5 MeV 2101
KOMATSUBARA Kiichi: Change of Surface State of Ge by Electron Bombardment (S.N.) 125
KOMURA Shigehiro;
  ———, N. KUNITOMI, Poh-Kun TSENG, N. SHIKAZONO and H. TAKEKOSHI: Mössbauer Effect of the Intermetallic Compound UFe_2 (S.N.) 1479
  ———, N. KUNITOMI, Y. HAMAGUCHI and M. SAKAMOTO: Ferromagnetism of the Intermetallic Compound UFe_2 (N.S.)....1486
KONDO Michiya;
  ———, T. YAMAZAKI and S. YAMABE: Angular Distribution of (α, p) Reactions in Some Light Nuclei 1091
KONNO Hiroshi: [cf. GONDŌ Yasuo (2345) S.N.]
KŌNO Tatsuo: [cf. TAKAHASHI Minoru (1913)]
KONO Ryusuke: The Dynamic Bulk and Shear Viscosity of High Polymers, 1....1580
  ———: The Dynamic Bulk and Shear Viscosities of Polyvinylchloride (S.N.)..1793
KONDO Jun: Internal Magnetic Field in Rare Earth Metals 1690
KORE'EDA Atsuo: [cf. NISHIYAMA Zenji (834) S.N.]
KOSHINO Shigeharu;
  ——— and T. ANDO: Resonance Transfer of Ionization Energy in Semiconductors 1151
KOTAJIMA Kyûya: [cf. TAKAHASHI Kasuke (1664)]
KOTANI Ken: [cf. INUISHI Yoshio (1787) S.N.]
KOYAMA Ryuzo: Flow Birefringence of Polymer Solutions 1366
KUBO Hiroshi: [cf. MITANI Kenji (1480) S.N.]
KUBO Ikumaro: Crystal Growth of Zinc-oxide by Chemical Reaction of Zinc-fluoride with Air (S.N.)....2358
KUBO Kazuko: Radiation Induced Optical Absorptions in Crystalline Quartz and Fused Silica 108
  ——— and Y. KATANO: Observations of Dislocation Network in Neutron-Irradiated LiF Crystal (S.N.) 347
  ———: Radiation Induced Optical Absorptions in Crystalline Quartz and Fused Silica (Errata) 582
  ———: Radiation Effects in LiF Crystals 2294
KUBO Takao: [cf. KITAMURA Saburo (351) S.N.]
KUBOTA Buichi;
  ——— and E. HIROTA: Electrical Resistivity of Ferromagnetic Chromium Dioxide (S.N.) 345
  ———, T. NISHIKAWA and A. YANASE: Magnetic Properties of Chromium Oxide Modified by Vanadium Oxide 2340
KUBOTA Hiroko: [cf. NAKAMURA Terutaro (906)]
KUBOTA Kanji;
  ——— and K. HAYASHI: Observation of Optical Maser Oscillation in Ruby (S.N.)....2063

KUMAGAI Hiroo [cf. NISHIKAWA Tetsuji (1817)]

KUME Kiyoshi;

——— and R. HOSHINO: Proton Magnetic Resonance of Ice Single Crystal.... 290

——— and Y. KAKIUCHI: The O-H....O Bond in Orthoboric Acid (S.N.) 843

KUNITOMI Nobuhiko: [cf. KOMURA Shigehiro (1479, 1486) S.N.]

KURIYAMA Masao;

———, H. YAMANOUCHI and S. HOSOYA: Ferromagnetic Resonance Absorption of Single-Crystal Thin Films of Nickel.......... 701

KUROSAWA Tatsumi: Polarization Waves in Solids 1298

KUROYANAGI Jun: On the Relation between the Change in Modulus of Rigidity in Brass Wires by Cold-Rolling and Rolling Textures 1019

KUROYANAGI Tokihiro: [cf. HOMMA Saburo (841) S.N.; TAKAHASHI Kasuke (1664)]

———, H. YUTA, K. TAKAHASHI and H. MORINAGA: New Activities in Rare Earth Region Produced by the (α, p) Reactions 2393

———: Decay of Sr 83 2363

———: Decay of As 79 2369

KUSHIDA Toshimoto: [cf. KŌI Yoshitaka (574), (1040) S.N.]

KUWABARA Sinzi: Impulsive Motion of Circular Cylinder in a Viscous Fluid at Small Reynolds Numbers 1762

LIPSCOMB William N: [cf. KAINUMA Yoshiro (495)]

MAEDA Hajime: [cf. MIYAZAWA Hisao (132) Errata]

MAEKAWA Shigeru: Electron Spin Resonance of Diluted $(NH_4)Fe(SO_4)_2 12H_2O$ 2337

MAEKAWA Syun-ichi: [cf. EDAGAWA Hiroshi (1041) S.N.]

MANNAMI Michihiko: [cf. TANAKA Kenzo (2070) S.N.]

MARUYAMA Eiichi: Luminescence Accompanied by Electrolysis in CdS Single Crystals (S.N.) 2341

MARUYAMA Michio: [cf. TSUKADA Kineo (166)]

MASAIKE Akira: [cf. YANABU Takuji (2595) S.N.]

MASUDA Isoo: The Wavelength Dependence of Quantum Efficiency and Absorption Coefficient of $ZnSiO_3$/Mn Powder Phosphor.......... 105

MASUDA Kohzoh;

——— and T. SUITA: E.S.R. of Irradiated DPPH Protected by Polystyrene (S.N.).......... 837

MASUDA Masayoshi: Angular Distributions of Photo-protons from Li, Al, S, Ni, and Cu 1801

MASUNO Kunio: [cf. WAKU Shigeru (1158)]

MATSUI Atsuo: [cf. NAKAMURA Kaizo (1262) S.N.]

MATSUI Eiichi: [cf. TAMAI Tokumichi (1489) S.N.]

MATSUKURA Yasuo: Heat Treatment Centers in Silicon.......... 192

——— and S. TANAKA: Conductivity of Grain Boundaries Ge.......... 833

———: Properties of Grain Boundaries in Silicon.......... 842

MATSUMOTO Hiroaki: [cf. FUKUDA Kuniya (1256) S.N.]

———, K. FUKUDA, M. TAKESHIMA and Y. UCHIDA: Cubic Contribution to EPR of Mn^{++} in $MgCl_2$..........1791

MATSUMOTO Shigeo;

——— and S. MIKAMO: On the Inelasticity in High-Energy Nuclear Interactions (S.N.).......... 350

MATUMOTO Zyun-itiro: [cf. YAMADA Masami (1497)]

MATSUURA Kenji;

——— and Y. INUISHI: Annealing of Radiation Damage on Lifetime in Silicon (S.N.).......... 339

———, and Y. INUISHI: Effect of Neutron Irradiation on Carrier Lifetime in Si (S.N.) 1485

MATSUURA Motohiro: [cf. SUGIBUCHI Kiyoshi (1648) S.N.]

MEKATA Mamoru: [cf. TSUCHIDA Takashi (2453)]

MIDZUNO Yukio: Scattering of Microwaves from a Cylindrical Plasma in the Born Approximation. I. 971

———: Scattering of Microwaves from a Cylindrical Plasma in the Born Approximation. II. 1403

MIKAMO Shoji: [cf. MATSUMOTO Shigeo (350) S.N.]
MIKOSHIBA Nobuo: Interaction of Electrons and Holes with Acoustic Waves in Intrinsic Semiconductors 895
MIKUMO Takashi: [cf. NONAKA Itaru 1853]
———: Anomalies in the Scattering of Alpha Particles by Carbon 1066
MIKURA Ziro: On the Superconducting Ground State (Errata) 353
MINAMI Kazuko: [cf. HASIGUTI R. Ryukiti (2223)]
MITA Yo: The Growth of Zinc Sulphide Single Crystals from Flux (S.N.)..........1484
MITANI Kenji;
——— and H. KUBO: On Radiations from Plasma in a Static Magnetic Field (S.N.) 1480
MITSUHASHI Hiroji: Structures of Photoconductivity Spectra near the Fundamental Absorption Edge of Cadmium Sulfide 989
———: Effect of Current Injection on Properties of Cadmium Sulfide Crystals (S.N.)..........1258
MITSUI Toshio: [cf. SHIBUYA Iwao (479)]
MITSUISHI Akiyoshi: The Optical Properties of Cadmium Telluride in the Far Infrared Region 533
MITSUISHI Tomokuni: [cf. SHOJI Masakazu (1253) S.N.]
———: An Electron Diffraction Study on Cu-Sn Alloys 453
MITSUMA Takeshi: Some Extra Lines in Paramagnetic Resonance Spectrum of Heavily Cr^{3+} Doped $K_3Co(CN)_6$ (S.N.) 1796
MITUI Tadayasu: [cf. SAMBONGI Takashi (1478, 2066) S.N.]
MIURA Iwao: [cf. WAKATSUKI Tetsuo (2385)]
MIURA Shigeto: [cf. HIRONE Tokutaro (2456)]
MIYAGI Tosio: Hydromagnetic Oseen Flow past an Elliptic Cylinder in a Uniform Magnetic Field 1434
———: Two-Dimensional Viscous Flow past a Rotationally-Oscillating Circular Cylinder 2329
MIYAHARA Akira: [cf. NISHIKAWA Tetsuji 1817]
———: A Pumped Klystron Amplifier and RF Power System for the Injector Linac of 1 BeV Electron Synchrotron 2567
MIYAHARA Syôhei;
———, K. MURAMORI and N. TOKUDA: Tetragonal Distortion in Copper Manganite-Chromite System (S.N.)..........1490
MIYAKE Saburo;
———, K. HINOTANI, I. KATSUMATA, T. KANEKO and N. ITO: Lateral Density Distribution of Charged Particles in the Central Region of Extensive Air Shower 847
MIYAKE Kiyoshi: Logarithmic Growth of the Cesium Antimonide Films on Antimony..1473
MIYAKE Shizuo;
———, K. FUJIWARA, G. HONJO and N. KITAMURA: Relativistic Correction to the Method of Eliminating the Primary Extinction in Electron Diffraction ..2336
MIYAKE Yasuhiro;
——— and J. FURUICHI: Refractive Index Difference of Dilute Aqueous Solution of Polyvinylpyrolidon (S.N.) 1263
———: Determination of the Extension of Linear Polymer Molecule in the Solution by the Light Scattering 1703
——— and J. FURUICHI: Refractive Index Difference of Dilute Aqueous Solution of Polyvinylpyroliden (Errata)..........2600
———: Determination of the Extension of Linear Polymer Molecule in the Solution by the Light Scattering (Errata) 2600
MIYAMOTO Sigenori: [cf. FUKUI Shuji (2574)]
MIYATA Nahonori: [cf. USAMI Seiji (S.N.)]
———: Electric Conduction of Ferrites Containing Fe^{2+}-ions 206
———: Ferromagnetic Crystalline Anisotropy of $MeFe_2O_4$–Fe_3O_4 Ferrite Solid Solution 1291

MIYAZAWA Hisao;
  —— and H. MAEDA: Anisotropic Hall Coefficients in n-Type Germanium (Errata) 132
MIZUNO Hiroyuki: [cf. INOUE Morio (128) S.N.]
MIZUNO Joji: The Crystal Structure of Nickel Chloride Hexahydrate, $NiCl_2 \cdot 6H_2O$ 1574
MIZUNO Yukio: Elementary Processes Related to the Catalytic Action μ^- for the p-d Fusion Reaction 1043
MIZUTANI Hiroshi: Extension of High Polymer Molecule and Energy Change by Mixing 282
MOCHIZUKI Masako: Smoke Observation on Boundary Layer Transition Caused by a Spherical Roughness Element 995
MOORE A. R.: [cf. BRAUNSTEIN R. (2068) S.N.]
MORI Ryuichi;
  —— and K. HASHIMOTO: Electrial Properties of TlSe 1797
MORI Saburo: [cf. OKAZAKI Chisato (119) S.N.]
MOKI Shigehi: [cf. TOHEI Tsutomu (1657)]
MORI Tsugio: The Dipole Moment and End-to-End Length of the Isotactic Vinyl Polymer, III. Convergence of Neumann Series 944
MORIGAKI Kazuo: Paramagnetic Resonance of Cobalt in Cadmium Chloride and Cadmium Bromide (S.N.) 1639
  ——: Electron Spin Resonance in Neutron-Irradiated (S.N.) 1645
MORIMOTO Setsu: [cf. TAKAGI Mieko (792); OGAWA Shizuko (2065) S.N.]
MORINAGA Haruhiko: [cf. HOMMA Saburo (841) S.N.; CHIBA Ren (1077); TAKAHASHI Kasuke (1664), KUROYANAGI Tokihiro (2393)]
MORINO Yonezo: [cf. OKA Takeshi (1235)]
MORINO Yoshinori: [cf. EDAGAWA Hiroshi (1041) S.N.]
MORIOKA Shigeki: [cf. HASHIMOTO Ziro (1616), (2078) Errata]
  ——: Two-Dimensional Supersonic Jet of a Conducting Inviscid Gas in the Presence of a Uniform Magnetic Field 1625
  ——: Reflection of a Weak Shock Wave in a Perfectly Conducting Gas (S.N.) 1794
  ——: On the Shock Configuration in a Perfectly Conducting Gas in the Presence of a Uniform Magnetic Field 2346
  ——: Two-Dimensional Flow of a Weakly Conducting Gas Past a Plane Wall Containing a Magnetic Dipole 2544
MORITA Susumu;
  , T. ISHIMATSU, T. CHO, Y. NAKAJIMA, N. KAWAI, T. MURATA and Y. HACHIYA: Angular Distribution for the $N^{14}(d, p)N^{15}$ Ground State Reaction .. 1849
MORITA Yoshinori: [cf. EDAGAWA Hiroshi (1041) S.N.]
MUIR W. B.: [cf. HEDGCOCK F. T. (2599) S.N.]
  ——: The Resistance Minimum in a Dilute Cadmium Manganese Alloy (S.N.) .. 2598
MURAKAMI Miyuki: [cf. FUJIME Satoshi (183)]
  ——: Anisotropy of Electrical Conduction in Iron Sulfide Single Crystal 187
MURAKAMI Terutoshi: Entropy Production and Variation Principle in the Kinetic Theory of Rigid-Sphere Gas Mixture 633
MURAKAWA Kiyoshi: Quadrupole Coupling in the Hyperfine Structure of the Spectrum of La I 2533
MURAMORI Kiyoshi: [cf. MIYAHARA Syohei (1490) S.N.]
MURAO Tsuyoshi: Electron Paramagnetic Resonance for Metals with Two Conduction Bands 1940
MURASE Kazuo: [cf. OHKURA Hiroshi (2076) S.N.]
MURATA Toru: [cf. MORITA Susumu (1849)]
MUTSURO Naoshi: [cf. CHIBA Ren (1077)]
NAGAHARA Yukio: Elastic and Inelastic Scattering of Protons from Carbon Nucleus from 6.5 to 16 Mev 133
NAGAKURA Sigemaro: Study of Metallic Carbides by Electron Diffraction Part IV. Cobalt Carbides 1213
NAGASAWA Hiroshi: [cf. TOMONO Yuzo (123) S.N.]
NAGATANI Kunio: [cf. TAKAHASHI Kasuke (1664)]

NAKADA Osamu: [cf. AIZU Kêitirô (923); OKANO Koji (2071) S.N.]

NAKAGAWA Kisaku: Mass Spectrometric Study on the Evaporation of Volatile Components in Polyethylene 741

NAKAGAWA Yasuaki;

———, and T. HORI: Antiferromagnetism of MnHg (S.N.) 1470

NAKAHARA Osamu: The Base Resistance of the Transistor in the Saturated Region (S.N.) 1260

NAKAJIMA Haruo: Proton Magnetic Resonance and the Polymorphism of Triglycerides (S.N.) 1778

NAKAJIMA Tetsuo: [cf. NAKAMURA Yoji (840) S.N.]

NAKAJIMA Yutaka: [cf. OHMURA Haruko (593); MORITA Susumu (1849)]

NAKAMICHI Takuro;

—— and M. YAMAMOTO: Antiferromagnetic Magnetostriction in CoO and NiO Single Crystals (S.N.) 126

NAKAMURA Kaizo;

———, T. FUKUDA, R. KATO, A. MATSUI and Y. UCHIDA: The Optical Absorption of Localized Exciton in KCl-KI Crystal (S.N.) 1262

NAKAMURA Seitaro;

——— and K. KAWARABAYASHI: Mass Spectra of Baryons (S.N.) 130

NAKAMURA Teruo: [cf. YANABU Takuji (2594) S.N.]

NAKAMURA Terutaro;

——— and K. OHI: Dislocations and Fines Line in Rochelle Salt Crystal 209

———, K. OHI and H. KUBOTA: Growth and Dissolution Processes of GASH Crystal 906

NAKAMURA Yoji: [cf. TSUCHIDA Tashi (2453)]

———, T. NAKAJIMA and H. TAKAMI: Volume Magnetostriction in Nickel-Iron Alloys (S.N.) 840

———: Effect of the Substructure upon Magnetic Properties of Iron-Silicon Single Crystals 1888

———: Effect of Quenched-in Vacancies on the Weak Magnetization of Nickel 2167

NAKASHIMA Shinichi: The Colloidal Band in KCl Containing NaCl (S.N.) 1650

———: The Absorption Bands in KCl Containing LiCl (S.N.) 2586

NAKASHIMA Takao: [cf. ISHIMATSU Toshiyuki (367)]

NAKAU Tanehiro: [cf. TAKEYAMA Mikio (1255) S.N.]

NARITA Koziro: Energy Spectrum of Mn^{++} Ion in Calcium Fluorophosphate I........ 99

——— and T. SHIMIZU: Ground State Energies of Donors in Ge and Si (S.N.)..2588

NEGISHI Katsuo: Experimental Studies on Sonoluminescence and Ultrasonic Cavitation 1450

NGUYEN Dai Ca: [cf. YANABU Takuji (2594) S.N.]

NIMURA Hiroshi: [cf. FUKUSHIMA Einosuke (928)]

NISHIDA Noboru: The Relaxation Phenomena in Polyelectrolytes Solutions 2062

NISHIKAWA Tetsuji;

———, J. TANAKA, A. MIYAHARA and H. KUMAGAI: A Linear Electron Accelerator as the Injector of 1 BeV Synchrotron 1817

NISHIKAWA Tomozo: [cf. KUBOTA Buichi (2340) S.N.]

NISHIMAKI Noriko: [cf. KOJIMA Kazuko (121) S.N., (2033), (2335) Errata]

———, K. KOJIMA and T. KOJIMA: Nature of the *A*-Centers in KCl (S.N.) .. 576

NISHIMURA Kazuaki: Gamma Rays from Inelastic Scattering of Neutrons by Fe, Cu, Zn, Ge and Se 355

NISHIMURA Keigo: Breakup of Deuterons by the Reactions $H(d, p)\,pn$ with $E_d=18$ MeV and $D(p, p)\,pn$ with $E_p=9$ MeV 2097

NISHIOKA Kouzou: [cf. YONEDA Yasuharu (578)]

NISHIWAKI Jien: Notes on the Lustre of Moiré Patterns 1358

NISHIYAMA Zenji: [cf. FUJITA Hiroshi (1893)]

———, A. KORE'EDA, I. EGUCHI and K. KATO: Direct Observation of the Lattice Imperfections in Pearlites by Electron Microscopy (S.N.) 834

NIU Keishiro: Flow of Condensing Vapour with Temporary Supersaturated State due to Heat-Removal Effect 798

NIWA Hiroko: [cf. TANAKA Kenzo (2070) S.N.]

NOGAMI Yozo: [cf. OHMURA Haruko (593): ETOH Kiichi (2091)]

NOGUCHI Seiichiro: The Thermoelectric Power of Magnesium-Cadmium Alloys 1145
———: The Thermoelectric Power of the Gamma-Brasses 1909

NOMURA Masayoshi: [cf. SHIRAI Shunji 1989]

NOMURA Shoichiro: [cf. SAWADA Shozo (2207)]
———, T. KAWAKUBO and T. YANAGI: Specific Heat of Ti_2O_3 706
———, Y. ASAO and S. SAWADA: Domain Structure of $NaNO_2$ 917
———: Thermal Properties of $NaNO_2$ 1352
——— and T. KAWAKUBO: Some Properties of Complex Oxides $AB_{0.5}B'_{0.5}O_3$ of Perovskite Type (S.N.) 1642
———: Some Experimental and Theoretical Studies of Ferroelectricity in $NaNO_2$ 2440

NOMURA Yûkichi: Diffraction of Plane Sound Wave by Many Equal Circular Holes Arbitrarily Distributed in an Infinitely Large Rigid Plane Plate 819
——— and K. HARUMI: Eigenvibration for the Membrane between two Eccentric Circles 2537

NONAKA Itaru;
———, H. YAMAGUCHI, T. MIKUMO, I. UMEDA, T. TABATA and S. HITAKA: (α, p) Reactions near $Z=26$ 1853

NONOYAMA Minoru: [cf. KAMIYA Yoshihiro (846) Errata]

NOSÉ Hiroshi: Spin Wave Resonance in Cu-Ni Alloy Films (S.N.) 342
———: Spin Wave Resonance in Pd-Ni Alloy Films (S.N.) 838
———; Exchange Integral in Ni and Its Alloy Film from Spin Wave Resonance 2475

NUMAKURA Ken'ichi: Young's Moduli in Ordered and in Disordered States of Fe_3Al Single Crystals (S.N.) 2344

ODA Zenjiro: [cf. KOBAYASHI Akio (2481)]

OGAWA Akira;
——— and Y. SONE: On the Commencement of the Hartmann Flow of Conducting Fluid 1423

OGAWA Iwao;
——— and T. DOKE: The Double-Grid Ionization Chamber (S.N.) 1025

OGAWA Kazuyuki: The Observation of Oscillating Anode Glow by Means of High-Speed Camera 2357
———: Anodic Oscillation in Glow Discharge. (II) The Gap Properties, Analogous to an Ordinary Electric Oscillator with Linear Circuit Elements 2510

OGAWA Seiji: ESR Spectra of Irradiated Polyvinylalcohol and Its Related Compounds (S.N.) 1488

OGAWA Shiro: [cf. IWASAKI Hiroshi (132) Errata; TAKAHASHI Minoru (1913)]

OGAWA Shizuko;
——— and S. MORIMOTO: Nuclear Magnetic Resonance of Fe^{57} in Fine Powdered Iron (S.N.) 2065

OGAWA Tomoya: The Texture of Vapour Phase Grown ZnS Crystals 2360

OGUCHI Takehiko;
——— and A. HONMA: Theory of Ferro- and Antiferromagnetic Resonance Absorption 79

OHI Kikuo: [cf. NAKAMURA Terutaro (209, 906)]

OHKURA Hiroshi: Experimental Studies on Electronic Trapping Processes Associated with Dislocation Lines in Alkali Halide Crystals 881
———, and K. MURASE: Electron Spin Resonance of the *M* center in Potassium Chloride (S.N.) 2076

OHMURA Haruko: [cf. ETOH Kiichi (2091)]
———, H. EJIRI, Y. NAKAJIMA, K. HORIE, K. ETOH, A. OHUCHI and Y. NOGAMI: Resonance Levels in the Reactions $^{28}Si(p, \gamma)^{29}P$, $^{29}Si(p, \gamma)^{30}P$ and $^{30}Si(p, \gamma)^{31}P$ .. 593

OHNISHI Haruyuki;
——— and T. TERANISHI: Crystal Distortion in Copper Ferrite-Chromite Series 35

OHNO Akiko: Cluster Expansion of Relaxation Function and its Application to the Theory of Pressure Broadening 2402

OHOYAMA Tetuo: [cf. KIMURA Ren'iti (1266) S.N.; YASUKŌCHI Kō (429, 1123)]

——, K. YASUKŌCHI and K. KANEMATSU: A New Phase of an Intermetallic Compound $Mn_{3.4}Ge$ and its Magnetism (S.N.) 352

———: X-ray and Magnetic Studies of the Manganese-Germanium System .. 1995

OHTA Keizo: Time Decrease of Magnetic Permeability in Some Mixed Ferrites 250

OHTA Tokio: [cf. YAMASHITA Tadayoshi (1565)]

———: Theory of Seebeck Effect in Plastically Deformed Semiconductors.... 1561

OHTSUKA Taiichiro: Interaction Effects in Potassium Ferricyanide........ 1549

OHUCHI Akiji: [cf. OHMURA Haruko (593)]

OISHI Jiro: High Temperature Determination by a New Gas Thermometer with Constant Bulb Temperature. I. Measuring Methods 2056

OKA Takeshi;

———, Y. MORINO: Microwave Spectrum of Formaldehyde III. Vibration-Rotation Interaction........ 1235

OKADA Eiji: [cf. WAKATSUKI Tetsuo (2385)]

OKADA Kenkichi: Ferroelectric Properties of X-ray Damaged Rochelle Salt 414

———: Etch Pits on X-Ray Damaged Rochelle Salt (S.N.) 1647

OKADA Takasi: [cf. AKASHI Tsuneo (1641) S.N.]

———, T. KANO and Y. SASAKI: Epitaxial Vapor Growth of GaAs on Ge Single Crystals (S.N.) 2591

OKAMOTO Kazuto: Electron Linear Accelerator as a Source of Intense Secondary Particle Beams (S.N.) 120

OKANO Koji;

——— and O. NAKADA: Theory of Non-Linear Responses of Many Variable Systems (S.N.) 2071

OKAZAKI Atsushi;

——— and Y. SUEMUNE: The Crystal Structure of $KCuF_3$ 176

——— and Y. SUEMUNE: The Crystal Structures of $KMnF_3$, $KFeF_3$, $KCoF_3$, $KNiF_3$ and $KCuF_3$ above and below their Néel Temperature 671

———: The Superstructure of Iron Selenide Fe_7Se_8........ 1162

———, and Y. SUEMUNE: Electron Distribution in $KMnF_3$, $KFeF_2$, $KCoF_3$ and $KNiF_3$ 1474

OKAZAKI Chisato;

———, S. MORI and F. KANAMARU: Magnetic and Crystallographical Properties of Hexagonal Barium Mono-Ferrite, $BaO \cdot Fe_2O_3$ (S.N.)........ 119

OKUDA Akizo: On the *R* Centers in Lithium Fluoride 1746

OKUDA Setsuo: The Velocity Distribution at the Interface between Two Liquids 324

———: The Velocity Distribution at the Interface between Two Liquids 845

ONAKA Ryumyo;

———, A. FUKUDA and A. EJIRI: The Fundamental Absorption of Lithium Fluoride and Sodium Fluoride (S.N.) 340

O'NEILL Edward L.;

——— and T. ASAKURA: Optical Image Formation in Terms of Entropy Transformations 301

ONUKI Masami: Photoconductive Hall Effect in Potassium Bromide 981

OSBORN J. E.: [cf. HSIAO C. C. (459)]

PADMINI P. R. K. L.;

———, and B. Ramachamdra RAO: Study of Temperature Variation of Ultrasonic Velocity and Adiabatic Compressibility in Some Liquids Part 1 1770

RAO B. Ramachamdra: [cf. PADMINI P. R. K. L. (1770)]

RAO C. Raghupathi: Ultrasonic Dispersion in Aceton 1636

ROUX Michel: [cf. TAKEDA Susumu (95)]

ROZENDAL D. B. [cf. HSIAD C. C. (459)]

RYUZAN Osamu: Current-Voltage Characteristics of Plastically Deformed Germanium P-N Junctions........ 2177

———: Activation Energy of Acceptors Introduced into Germanium by Plastic Twisting 2339

SAEKI Bunzaburō: [cf. SAKISAKU Masakatsu (1869)]
SAITO Fujio: The Transient Phenomena in Ruby Maser (S.N.) 2592
SAITÔ Nobuhiko: On the Theory of Adiabatic and Isolated Susceptibilities 621
SAITO Shinhachiro: Chlorine Nuclear Quadrupole Resonance of $CH_3COCHCl_2$ 2361
SAITO Shozo;
———, and Y. SHIMOMURA: Back-Reflection X-Ray Micrography 2351
SAKAI Mitsuo: [cf. IKEGAMI Hidetsugu (2350) S.N.]
———, H. IKEGAMI and T. YAMAZAKI: Short-lived Activity of Ag^{106} 148
SAKAI Naomi: [cf. HIGASHI Akiro (2359) S.N.]
SAKAMOTO Masanobu: [cf. KOMURA Shigehiro (1486) S.N.]
SAKAMOTO Masayoshi: Observations on the Etch Patterns in Deformed KCl Crystals .. 1782
SAKATA Kimiko: Thermoelectric Behaviours of Rutile (S.N.) 1026
SAKISAKA Masakatsu;
———, B. SAEKI, M. TOMITA and F. FUKUZAWA: Sample Sandwiched Plastic Scintillators for Activation Measurements by Use of Fast Neutrons 1869
——— and M. TOMITA: Experiments on the Possible Existence of a Bound Di-Neutron (S.N.) 2597
SAKURAI Kiichi: A Direct Determination of the Crystal Structure of Ethylenediammonium Sulphate 1205
———: A Direct Determination of the Crystal Structure of Ethylenediammonium Sulphate (Errata) 1651
SAKURAI Junji: [cf. TSUCHIDA Takashi (2453)]
SAMBONGI;
———, and T. MITUI: Magnetic Annealing Effect in Cobalt (S.N.) 1478
———, and T. MITUI: Stress Annealing Effect in Cobalt (S.N.) 2066
SASAGAWA Tetsuzo: [cf. TAKAHASHI Minoru 1913]
SASAKI Yozo: [cf. OKADA Takasi (2591) S.N.]
SATAKE Kimihiko: [cf. UCHIDA Ichizo (573) S.N.]
SATO Hiroshi: The Hall Effect in the Viscous Flow of Ionized Gas between Parallel Plates under Transverse Magnetic Field 1427
SATO Yoshiki:
———, K. GESI and Y. TAKAGI: Study of the Phase Transition in $NaNO_2$ by Polarized Infrared Radiation 2172
SATOH Mitsuo: [ITOH Junkichi (343) S.N.]
SATOMI Ken'iti: Oxygen Positional Parameters of Tetragonal Mn_3O_4 258
SAWADA Shozo: [cf. NOMURA Shoichiro (917); YOSHIDA Ikushi (2467)]
——— and I. YOSHIDA: Some Remarks on the Phenomenological Theory of Ferroelectricity 1322
———, S. NOMURA and Y. ASAO: Dielectric Properties of Ferroelectric $NaNO_2$ 2207
———, S. NOMURA and Y. ASAO: Dielectric Behavior of KNO_3 in Its Ferroelectric Phase III 2486
SEGAWA Wataru: Some Remarks on Hydrostatic Pressure and Maxwell Model 317
———: Rheological Equations of Generalized Maxwell Model and Voigt Model in Three-Dimensional, Non-Linear Deformation 320
———: Rheological Equations of Generalized Maxwell Model and Voigt Model in Three-Dimensional, Non-Linear Deformation (Errata) 845
———: Some Remarks on Hydrostatic Pressure and Maxwell Model (Errata) .. 846
SEKIGUCHI Hiroyoshi: [cf. SUGIYAMA Kazusuke (2353) S.N.]
SEKIZAWA Hisashi: A Note on the Electron Diffusion and the Wall Relaxation in Ferrites (S.N.) 1034
SHIBAOKA Yoshio: [cf. TAMADA Ko (1249)]
SHIBATA Akikazu: On the Secondary Tunnelling Phenomena in a *p-n* Junction of Gallium Arsenide 1261
SHIBATA Chokichiro: On the Electron Emission from Oxide Coated Cathode Subject to Strong Electric Field 51
———: On the Electron Emission from Oxide Coated Cathode Subject to Strong Electric Field (Errata) 582
SHIBATA Hiroyuki: On the Nuclear Interaction of Mu-Mesons 372

SHIBUYA Iwao: [cf. HOSHINO Sadao (1254) S.N.]
——: X-Ray Studies of the Ferroelectric Phase Transition in NaNO$_2$ 490
—— and T. MITSUI: The Ferroelectric Phase Transition in (Glycine)$_3$·H$_2$SO$_4$ and Critical X-Ray Scattering 479
SHIKAZONO Naomoto: [cf. KOMURA Shigehiro (1479) S.N., TAKEKOSHI Hidekuni (1674) TSENG Poh-kun (1790) S.N.]
SHIINA Shoichi: [cf. SHODA Katsufasa (1031) S.N., 1807]
SHIMAKAWA Seiken: Propagation of Ultrasonics in Triethylamine-water Mixture...... 113
SHIMIZU Masao: Effect of s-d Exchange Interactions and Temperature-Independent Paramagnetic on Susceptibilities in Nickel, Palladium, and Platinum 1114
——, and T. TAKAHASHI: Magnetic Susceptibilities of Cr and Cr-Fe Alloy..1544
SHIMIZU Tadao;
—— and K. SHIMODA: "Non-Adiabatic" Behavior in a Low Frequency Beam-Type Maser 777
SHIMIZU Tatsuo: [cf. NARITA Koziro (2588) S.N.]
——: The Electron-Coupled Nuclear Spin Interactions in Ionic Crystals by the Overlap Model (S.N.) 1264
SHIMODA Koichi: [cf. SHIMIZU Tadao (777)]
——: Characteristics of an Ammonia Beam Maser 1728
——: Magnetic Perturbation of an Ammonia Maser on the 3,2 Line 2270
——: Dependence of Magnetic Coupling Constant of Ammonia on the Inversion State 2283
SHIMOMURA Yasumitsu: [cf. SAITO Shozo (2351) S.N.]
SHINOHARA Shozo: The Shielding of a Fixed Charge in a Metal 1963
SHIOJIRI Makoto: [cf. CHIKAWA Jun-ichi (1175)]
SHIRAFUJI Junji;
—— and Y. INUISHI: Effects of Vacancies on Pulse Photoconductions in CdS Single Crystals (S.N.) 832
SHIRAI Hiroko: [cf. ABE Hidetaro (118)]
SHIRAI Shunji;
——, Y. FUKUDA and M. NOMURA: Structure of Thin Layers of Some F.C.C. Metals Deposited on Oriented Ag, Pd and Ni Films 1989
SHODA Katsufusa: [cf. CHIBA Ren (1077)]
——, K. KOBAYASHI, S. SIINA, K. ABE and M. KIMURA: Fine Structures of Photoprotons from Si^{28} (S.N.) 1031
——: Plane Polarization of 8.5 MeV Bremsstrahlung 1271
——, S. SHIINA, K. KOBAYASHI, K. ABE and M. KIMURA: Photoprotons from Silicon and Phosphorus 1807
——: Reaction O^{16} (γ, p) N^{15} by 20.5 MeV Polarized Bremsstrahlung 1841
SHOGENJI Kisaburo: [cf. YAMADA Eizaburo (1475) S.N.]
SHOJI Masakazu;
——, S. TAUCHI, T. MITSUISHI and M. TOMONO: Observation of Dislocation in Germanium Single Crystal (S.N.) 1253
——: Determination of the Impurity Concentration of the p-type Recrystallized Layer by Thermoelectric Power Measurements (S.N.) 2590
——: On the Impurity Concentration of the p-type Recrystallized Layer of Tunnel Diode (S.N.) 2596
SHOJI Tokio: [cf. TSENG Poh-kun (1790) S.N.]
SHONO Katsufusa: [cf. TOKUNAGA Masakatsu (1029), (2067) S.N.]
SONE Toshimaro: The Rheological Behavior and Thixotropy of a Fatty Plastic Body.. 961
SONE Yoshio: [cf. OGAWA Akira (1423)]
SONOIKE Sanemi;
—— and K. AKIMOTO: Luminescence of Doped Silver Chloride Crystals.... 658
SUBRAHMANYAM S. V.;
—— and J. BHIMASENACHAR: Molar Sound Velocity in Inorganic Melts and Solutions 1447
SUEMUNE Yasutaka [cf. OKAZAKI Atsushi (176, 671) (1474) S.N.]

SUGANUMA Ryōji;
——— T. YOSHIDA and Y. FUJIKI: Anomalous Diffusion at the Interface of Thin Bimetallic Film of Bi and Sb 676
——— T. YOSHIDA and Y. FUJIKI: Anomalous Diffusion at the Interface of Thin Bimetallic Film of Bi and Sb (Errata) 1042
SUGAWARA Masumi: [cf. TŌHEI Tsutomu (1657)]
———: Resonant Scattering of Photons in Mg and Si 1857
SUGIBUCHI Kiyoshi;
———, M. MATSUURA and T. HASHI: Spin Echoes of Co^{59} in fcc Cobalt Metal (S.N.) 1648
SUGIHARA Makoto: [cf. TSUBOYA Ichiro (571, 1257) S.N.; AOYAGI Keizô (1027) S.N.]
———: On the Magnetic Properties of 12 percent Aluminium-Iron Alloy 2163
SUGITA Motoyosi: The Switching Circuit Logically or Functionally Equivalent to a System of Biochemical Reactions 737
SUGIURA Yoshikazu: Note on Fe^{3+} ions in Spinel Structure (S.N.) 1786
SUGIYAMA Akira: Fermi Momentum for Free Electron Metals Perturbed by Localized Imperfections 1327
SUGIYAMA Kazusuke: [cf. IKEGAMI Hidetsugu (2350) S.N.]
———, A. FURUSAWA, S. HAYASHIBE and M. KIMURA: Level Structure of Nd^{144} 1538
———, H. SEKIGUCHI and S. HAYASHIBE: Low-lying Excited States in Ba^{136}.... 2353
SUGIYAMA Koichi: [cf. KOBAYASHI Akio (2481)]
SUITA Tokuo: [cf. MASUDA Kohzoh (837) S.N.; HAYAKAWA Shigeru (1037) S.N.]
SUMI Masao: Plasma Oscillations in External Fields 1718
SUMINO Kôji;
———, and M. YAMAMOTO: Preferential Plastic Deformation in the Surface Region of Al and α-Fe Single Crystals (S.N.) 131
SUNG Yung-Kwun: [cf. INUISHI Yoshio (2074) S.N.]
SUZUKI Hideo;
———, M. HATTORI and K. ARIYAMA: Theory of Cyclotron Resonance in Anisotropic Metals 1947
———: On Chambers' Solution of the Boltzmann Transport Equation........ 2347
SUZUKI Hideji: [cf. IWATA Tadao (197)]
SUZUKI Hiromichi: [cf. TUBOTA Hirosi (1038) S.N.]
SUZUKI Kazuo: X-ray Studies on Precipitation of Metastable Centers in Mixed Crystals $NaCl-CdCl_2$ 67
SUZUKI Shoji: [cf. HOSOE Masano (2335) Errata]
SUZUKI Taira: [cf. IKUSHIMA Akira (2587) S.N.]
SUZUKI Tadasu: Electron Distribution in Cu_2O Crystal 501
SUZUKI Tatsusaburo;
——— and J. YUHARA: Counting Efficiency of Gamma Rays in Counter Tubes.. 152
SUZUKI Yoshiko;
——— and E. ASADA: Crystal Distortion of FeO on Cooling past its Néel Temperature (S.N.) 1785
SUZUOKA Toshiro: [cf. HIRONE Tokutaro (2456)]
TABATA Tatsuro: [cf. NONAKA Itaru 1853]
TACHIKI Masashi: [cf. DATE Muneyuki (2589) S.N.]
TAKAGI Mieko;
———, N. KITAMURA and S. MORIMOTO: Density vs. Exposure Curves of a Photographic Emulsion for 20∼200 kV Electrons 792
TAKAGI Toru: [cf. FUKUDA Kuniya (1256) S.N.]
TAKAGI Yutaka: [cf. SATO Yoshiki (2172)]
TAKAHASHI Kasuke: [cf. KUROYANAGI Tokihiro (2393)]
———, T. KUROYANAGI, H. YUTA, K. KOTAJIMA, K. NAGATANI and H. MORINAGA: Some New Activities Produced by Fast Neutron Bombardments 1664
TAKAHASHI Minoru;
———, D. WATANABE, T. SASAGAWA, T. KŌNO and S. OGAWA: Magnetic Anisotropy of Evaporated Films. I. Iron Films Formed in Magnetic Field.. 1913

TAKAHASHI Takeshi: [cf. SHIMIZU Masao (1544)]

TAKAHASHI Yûzō: Dielectric α- and β-dispersions in Polyvinyl Butyral (PVB) (S.N.) .. 1024

——: Dielectric α-, β- and γ-Dispersions in the Thermosetting Phenolic Resins 1028

TAKAHASI Hidetosi: A Note on the Theory of Barium Titanate 1685

TAKAKI Hideo: [cf. TSUCHIDA Takashi (2453)]

TAKAKU Koshun: Propagation of Elastic Waves in Spherical Symmetric Inhomogeneous Medium 2550

TAKAMATSU Kunio: [cf. YANABU Takuji (2594) S.N.]

TAKAMI Hideo: [cf. NAKAMURA Yoji (840) S.N.]

TAKANO Naoyuki: [cf. ISHIMATSU Toshiyuki (367)]

——: The Reaction $Mg^{25}(d, p)Mg^{26}$ in the Energy Range of Deuterons from 1.5 MeV to 3.0 MeV 598

TAKEDA Susumu;

—— and M. ROUX: A Method for Measuring High Electron Densities in Plasmas 95

——: Microwave Measurement of Fast Time Varying Plasmas (S.N.) 1267

——: Microwave Study of Non-ionizing Shock Waves 1395

TAKEKOSHI Hidekuni: [cf. KOMURA Shigehiro (1479) S.N.; TSENG Poh-Kun (1790) S.N.]

——: N. SHIKAZONO and TSENG Poh-Kun: Weak Gamma Rays in the Decay of La^{140} 1674

TAKEMOTO Sigeo;

——, T. HASEGAWA and S. HOMMA: Scintillation from the Solid Xenon (S.N.) 1777

TAKEMOTO Susumu: Temperature Dependence of the Line Width of Ferrimagnetic Resonance in Polycrystalline Nickel Cadmium Ferrite (S.N.) 344

TAKESHIMA Masumi: [cf. MATSUMOTO Hiroaki (1791) S.N.]

TAKEUCHI Tomoyuki: Velocity of Slowly Moving Dislocation 1682

TAKEYAMA Mikio;

——, T. NAKAU and S. YAMAZAKI, T. ISA: Moving Striation in Microwave Discharge Plasma (S.N.) 1255

TAKEYAMA Naokata: Viscous Forces and Brownian Motion (S.N.) 1030

TAKIMOTO Kiyohiko: [cf. YANABU Tokuji (2594) S.N.]

TAKO Toshiharu: Self-Absorption of Spectral Line 2016

TAKUMA Hiroshi: Magnetic Hyperfine Structure in the Rotational Spectrum of H_2CO.. 309

TAMADA Ko;

——, and Y. SHIBAOKA: On the Pendent Drop, I 1249

TAMAI Tokumichi;

—— and E. MATSUI: Emission Spectra of Potassium Bromide-Thallium Phosphors (S.N.) 1489

——: Diffusion of Thallous Ions into Potassium Bromide Single Crystals .. 2459

——: Diffusion of Color Centers into KBr-Tl Phosphors 2463

TAMURA Naoyuki: Electron Spin Resonance in Irradiated Polytetrafluoroethylene: Temperature Dependence of the Spectra 2338

TAMURA Tikawo: The Growth of Corona Discharge in Air 2503

TANAKA Jiro: [cf. NISHIKAWA Tetsuji 1817]

——: The Construction and Test Operation of INS-Linear Electron Accelerator 2081

TANAKA Kenzo: [cf. CHIKAWA Jun-ichi (1175)]

——, M. MANNAMI, K. IZUMI and H. NIWA: Electron Microscopic Observation of the Aggregates of Vacancies in Germanium (S.N.) 2070

TANAKA Kyuichiro: Friction and Deformation of Polymers 2003

TANAKA Shigeo: [cf. FURUKAWA Michiaki (129) S.N.]

TANAKA Shigetoshi: Absorption and Reflection Spectra of Afterglow Plasma (S.N.) .. 1259

TANAKA Shigeya: [cf. TSUKADA Kineo (166)]

TANAKA Shigezo [cf. MATUKURA Yasuo (833) S.N.]

TANAKA Toshisuke: [cf. WAKU Shigeru (1158)]

TANAKA Yoichi: [cf. IKEDA Takuro (2593) S.N.]

TANAKA Yasuo: A Study on High-Energy Nuclear-Active Particles in Extensive Air Showers 866

TANIGUCHI Satoshi: [cf. YAMAMOTO Mikio (1035) S.N.]

TANISAKI Sigetosi: Microdomain Structure in Paraelectric Phase of $NaNO_2$ (S.N.)...... 579

TANUMA Seiichi: Concentration Dependence of Electrical Properties of Bismuth-Antimony Alloys (S.N.) 2349

——— : Thermoelectric Power of Bismuth-Antimony Alloys....................2354

TASAKI Akira;

———, and S. IIDA: Some Experimental Studies on the Parasitic Ferromagnetism of αFe_2O_3 1697

TAUCHI Shoji: [cf. SHOJI Masakazu (1253) S.N.]

——— : An Evidence for the Existence of a Diffusion Layer in the Melting Process of Semiconductors (S.N.) 1792

TAYLOR G.O.: [cf. FORSTAT H. (128) S.N.]

TERANISHI Teruo: [cf. OHNISHI Haruyuki (35)]

——— : Magnetic and Electric Properties of Chalcopyrite....................1881

TOBISAWA Shōtarō: Temperature Dependence of Magnetic Susceptibilities of $KClO_3$, $KBrO_3$ and KIO_3 654

TŌHEI Tsutomu;

———, M. SUGAWARA, S. MORI and M. KIMURA: Nuclear Elastic Scattering of Photons near the Particle Threshold Energy (I) 1657

TOKITA Yasuo: Vibration of a Plate and Sound Radiation Generated by an Impulsive Force....................1008

TOKUDA Naoki: [cf. MIYAHARA Syōhei (1490) S.N.]

TOKUNAGA Masakatsu;

——— and K. SHONO: Forward Characteristics of Si $p\pi n$-Junctions (S.N.)....1029

——— and K. SHONO: Heavily Deffused Si pn-Junction (S.N.)....................2067

TOMIKI Tetsuhiko: [cf. KOBAYASHI Koichi (1417)]

TOMISHIMA Yasuo [cf. UMEDA KWAI (S.N.) (341)]

TOMITA Michio: [cf. SAKISAKA Masakatsu (2597) S.N.]

TOMITA Sadami: Effects of the Special Heat-treatment on Permalloys.................... 393

TOMONO Masami: [cf. SHOJI Masakazu (1253) S.N.]

——— : Regrowth of Germanium Single Crystal from Indium Melt 439

——— : Regrowth of Germanium from Molten Indium or Lead 711

TOMONO Yuzo;

———, and H. NAGASAWA: Proton Resonance and Spin Quenching Effect in $NiSO_4\cdot 7H_2O$ (S.N.) 123

TOSIMA Soitiro: Inelastic Scattering of Thermal Neutrons by Paramagnetic Ions 241

TOTANI Syozo: Pressure Effect of Cavitation on Photographic Emulsion 2423

TOYODA Hiroo: [cf. IKEDE Takuro (2593) S.N.]

TSENG Poh-Kun: [cf. KOMURA Shigehiro (1479) S.N.; TAKEKOSHI Hidekuni (1674)]

———, N. SHIKAZONO, H. TAKEKOSHI and T. SHOJI: Temperature Dependence of Nuclear Resonance Absorption Line Width in Dy^{161} (S.N.)....................1790

TSUBOKAWA Ichiro: Magnetic Anisotropy of Chromium Antimonide and its Manganese Substitutes 277

TSUBOYA Ichiro;

——— and M. SUGIHARA: On the New Magnetic Phase in Manganese-Aluminium-Copper System (S.N.) 571

———, and M. SUGIHARA: The New Magnetic Phase in Manganese-Aluminium-Nickel System (S.N.) 1257

——— : On the New Magnetic Phase in Manganese-Aluminium-Copper System 1875

TSUCHIDA Takashi;

———, Y. NAKAMURA, M. MEKATA, J. SAKURAI and H. TAKAKI: Hall Effect on the Carbides of Transition Metals 2453

TSUJIMURA Akira [cf. KŌI Yoshitaka (574, 1040) S.N.]

TSUKADA Kineo;

———, S. TANAKA and M. MARUYAMA: Inelastic Scattering of Neutrons by the Time-of-Flight Method 166

TSUKUMI Ichiro: [cf. INUISHI Yoshio (1787) S.N.]

TSUZUKI Takuji: Quantum Statistics of Surface Effect 377

TSUZUKI Yoshihiro: Nuclear Interactions Produced by Heavy Nuclei of Primary Cosmic Radiation in Nuclear Emulsions 2131

TSUZUKU Takuro: Cavity Growth by Vacancy Condensation and Transformation to Dislocation Loop in the Graphite Structure 407

——: Cavity Growth by Vacancy Condensation and Transformation to Dislocation Loop in the Graphite Structure (Errata) 1042

TUBOTA Hirosi;

——, H. SUZUKI and K. HIRAKAWA: The Electrical Properties of Zinc Telluride (S.N.) 1038

UCHIDA Ichizo;

—— and K. SATAKE: Impedance Changes Induced by Light in ZnS Phosphors (S.N.) 573

UCHIDA Yoichi: [cf. FUKUDA Kuniya (1256); NAKAMURA Kaizo (1262); MATSUMOTO Hiroshi (1791) S.N.]

UEDA Hiroshi: Resistivity Striations in Germanium Single Crystals 61

UEDA Ichiro: [cf. IKEGAMI Seiji (572)]

UEDA Ikuhiko: The Crystal Structure of Chloranil and Bromanil 1185

UETA Masayasu: [cf. HIRAI Masamitsu (1477) S.N.]

——, M. HIRAI and M. IKEZAWA: Interaction of Exciton with Electron Trapping Centers in Alkali Halide Crystals 3. Exciton Induced Photoconductivity of *U* center 538

UEKI Kazutoshi;

—— and E. KANDA: The Specific Heat of $Ni(NH_3)_6Cl_2$ and $Ni(NH_8)_6Br_2$ at Low Temperatures 2061

UMEDA Iwao: [cf. NONAKA Itaru 1853]

UMEDA Jun-ichi: Electrical Properties of Sb-Doped n-Type SnSe (S.N.) 124

UMEDA Kwai;

——, Y. TOMISHIMA and C. KAWABATA: The Inverse Solution of the TFD Equation (S.N.) 341

UO Koji: The Confinement of Plasma by the Heliotron Magnetic Field 1380

URYÛ Norikiyo: On the Magnetism of Mn- and Co-Ammonium Tutton Salts at Very Low Temperatures 2139

USAMI Seiji;

——, N. MIYATA and Z. FUNATOGAWA: Frequency Dependence of Ferromagnetic Crystalline Anisotropy of $Ni_xFe_{3-x}O_4$ (S.N.) 2064

UYEDA Ryozi: [cf. KAMIYA Yoshihiro (846) Errata, (1361)]

VODIČKA Václav: Steady Temperature in a Composite Elliptic Cylinder 1630

WADA Yasaku: Mechanical Dispersions and Transition Phenomena in Semicrystalline Polymers 1226

WAKATSUKI Tetsuo;

——, Y. HIRAO, E. OKADA and I. MIURA: Gamma Rays from the Proton Bombardment of ^{31}P and the Excited States of ^{31}P 2385

WAKESHIMA Hiromu: On the Theory of the Fracture of Liquids 6

WAKU Shigeru;

——, K. MASUNO and T. TANAKA: Ferroelectricity in (K, NH), (K, Rb) and (K, Tl) Ferrocyanide Mixed Crystals 1158

WATANABE Denjiro: [cf. IWASAKI Hiroshi (132) Errata; TAKAHASHI Minoru (1913)]

——: Study on the Ordered Alloys of Gold-Manganese System by Electron Diffraction, III. Lattice Modulation in the Ordered Au_3Mn 469

WATANABE Hiroshi: [cf. KOHRA Kazutake (580) S.N.; (2078) Errata]

——: Magnetic Properties of Perovskites Containing Strontium, II. Lanthanum-Strontium Manganites 433

——: Angular Distribution of Electrons Suffering Characteristic Energy Loss in Passage through Metal Films 912

——, M. FUKASE: Weak Ferromagnetism in β-$NaFeO_2$ 1181

WATANABE Kenji: *Mu*-Meson Component of Air Shower Below the Ground 855

WATANABE Naozo: Hall Effect in *N*- and *P*-type Germanium at 24 Gc 1979

WATANABE Takashi: [cf. KIDO Kiyoshi (353) Errata]
———: The Magnetic Investigation of Mn^{++}, Co^{++}, Ni^{++} and Cu^{++} Ammine and Anhydrate Salts at Low Temperature 1131
———: The Magnetic Investigation of Cu-Butyrate Monohydrate and Cu-Stearate 1677
WATANABE Tsutomu: A Theory of Electron Impact on Some Polyatomic Molecules.. 510
———: On the Additivity Rule in the Ionization Cross Section of Molecules.. 529
WOLF W. P.: On the Ferrimagnetic Resonance of Europium Iron Garnet (Addendum) 582
YAJIMA Tatsuo: Three-Level Maser Action in Gas I. Theory of Multiple Quantum Transition and Doppler Effect in Three-Level Gas Maser 1594
———: Three-Level Maser Action in Gas II. Experimental Study on Formic Acid 1709
YAMABE Shotaro: [cf. KONDO Michiya (1091)]
YAMADA Eizaburo;
——— and K. SHOGENJI: A Note on the Magnetoresistance of PbTe at High Magnetic Fields (S.N.) 1475
YAMADA Masami;
——— and Z. MATUMOTO: Nuclear Ground-State Energies 1497
YAMAGUCHI Hisashi: [cf. NONAKA Itaru 1853]
———: Angular Distributions of Protons from the Alpha Particle Bombardment of B^{10}, N^{14}, O^{16} and Ne^{20} 583
YAMAJI Kenji: Microscope Observations of Crystals Appearing in the Process of Cooling Aqueous Solutions of Alcohols 2045
YAMAMOTO Hisao: [cf. HIRONE Tokutaro (455)]
YAMAMOTO Mikio: [cf. NAKAMICHI Takuro (126) S.N.; SUMINO Kôji (131) S.N.; IWATA Masako (2072) S.N.]
——— and S. TANIGUCHI: Weak Field Behaviour of the ΔE Effect in Ferromagnetic Cubic Solid Solution Alloys (S.N.) 1035
———: Temperature Distribution around the Rest or Moving Solid-Liquid Interface in a Rod (S.N.) 1644
YAMANOUCHI Hirokage: [cf. KURIYAMA Masao (701)]
YAMASHITA Jiro: Low-Temperature Electrical Breakdown in Germanium 720
YAMAZAKI Syozaburo [cf. TAKEYAMA Mikio (1255) S.N.]
YAMASHITA Sukeaki: [cf. YANABU Takuji (2594) S.N.]
———: Angular Distributions of Alpha-particles from F^{19}, Al^{27} and P^{31} bombarded with Protons 2378
YAMASHITA Tadayoshi;
——— and T. OHTA: Measurement of Seebeck Effect in Plastically Bent Germanium 1565
YAMASHITA Yoshihiko: [cf. YOSHIMOTO Hiroshi (1649) S.N.]
YAMASHITA Toshio: [cf. KITAMURA Saburo (351) S.N.]
YAMAZAKI Takashi [cf. KONDO Michiya (1091)]
YAMAZAKI Toshimitsu [cf. SAKAI Mitsuo (148); IKEGAKI Hidetsugu (2350) S.N.]
YANABU Takuji: (d, α) Reactions on O^{16}, N^{14} and C^{12} by 14.7 MeV Deuterons....2118
———, S. YAMASHITA, T. NAKAMURA, K. TAKAMATSU, A. MASAIKE, S. KAKIGI, D.C. NGUYEN, and K. TAKIMOTO: $O^{16}(d, \alpha)N^{14}$ Reaction with Deuterons near 15 MeV (S.N.) 2594
YANAGI Taketoshi: [cf. NOMURA Shoichiro (706)]
YANASE Akira: [cf. KUBOTA Buichi (2340) S.N.]
YASUKŌCHI Kō: [cf. OHOYAMA Tetuo (352)]
———, K. KANEMATSU and T. OHOYAMA; Magnetic Properties of Intermetallic Compounds in Iron-Germanium System: $Fe_{1.67}Ge$ and $FeGe_2$ 429
———, K. KANEMATSU and T. OHOYAMA: Magnetic Properties of Intermetallic Compounds in Manganese-Tin System: $Mn_{3.67}Sn$, $Mn_{1.77}Sn$ and $MnSn_2$..1123
YOKOTA Isaaki: On the Coupling between Optical Lattice Vibrations and Carries Plasma Oscillations in Polar Semiconductors (S.N.) 2075
———: On the Theory of Mixed Conduction with Special Reference to the Conduction in Silver Sulfide Group Semiconductors 2213

YOKOZAWA Yasaburo;

—— and Y. KAZUMATA: Paramagnetic Resonance of Mn^{++} Associated with Impurities in Alkali Chlorides.......... 694

YONEDA Yasuharu;

—— and K. NISHIOKA: X-ray Small Angle Scattering from Precipitated Platelets in Al-Ag Alloy (S.N.) 578

—— : On the Interference Phenomena of Compton Scattering from Diamond...1570

YONEMITSU Hirō: [cf. HASIGUTI R. Ryukiti (2223)]

YOSHIDA Ikushi: [cf. SAWADA Snozo (1322)]

—— and S. SAWADA: Thermal Conductivity of Sodium Nitrite 2464

YOSHIDA Masayuki: Distribution of Interstitials and Vacancies Produced by an Incident Fast Neutron 44

YOSHIDA Toshio: [cf. SUGANUMA Ryōji (676), (1042) Errata]

YOSHIMATSU Mitsuru: Experimental Evidence for Frank's Theorem on Dislocations by X-ray Diffraction Micrography..........1465

——: Observations on the Polygonization of Bent LiF Crystals by the Berg-Barrett Method..........2246

YOSHIMI Yoko: [cf. KAWAI Takao (2356) S.N.]

YOSHIMOTO Hiroshi;

—— and Y. YAMASHITA: Group Velocity of Moving Striations in Hg-A Discharge (S.N.) 1649

YUHARA Jiro: [cf. SUZUKI Tatsusaburo (152)]

YUTA Haruo: [cf. TAKAHASHI Kasuke (1664); KUROYANAGI Tokihiro (2393)]